Malaysian Journal of Analytical Sciences (MJAS)
Published by Malaysian Analytical Sciences Society

Vol 25 No 1 (2021)

Vol 25 No 2 (2021)

Vol 25 No 3 (2021)

Vol 25 No 4 (2021)

Vol 25 No 5 (2021)

Vol 25 No 6 (2021)

2021

Malaysian Journal of Analytical Sciences Vol 25 No 1 2021

		Page
	Editorial: Celebrating 25 Years of Malaysian Journal of Analytical Sciences *Mohd Basyaruddin Abdul Rahman, Harun Hamzah, Wan Mohd Afiq Wan Mohd Khalik* Malaysian Analytical Sciences Society (ANALIS)	i
1.	ADVANCED ADSORBENTS FOR THE EXTRACTION AND PRECONCENTRATION OF PENICILLIN ANTIBIOTICS: AN UPDATED REVIEW (Penjerap Lanjutan Bagi Pengekstrakan Dan Prapemekatan Antibiotik Penisilin: Satu Tinjauan Terkini) *Wan Ibrahim Thani Abd Halim, Siti Munirah Ishak, Salwani Md Saad, Nadhiratul-Farihin Semail, Ahmad Husaini Mohamed, Mohd Yusmaidie Aziz, Azam Taufik Mohd Din, Nur Nadhirah Mohamad Zain, Nik Nur Syazni Nik Mohamed Kamal, Sazlinda Kamaruzaman, Noorfatimah Yahaya*	1
2.	UNVEILING HOMOGENEOUS CATALYTIC PERFORMANCE OF N,N'-BIS-(3,5-DI-TERT-BUTYLSALICYLIDENE)-2,2-DIMETHYLPROPANE-1,3-DIAMINEPALLADIUM(II) IN THE MIZOROKI-HECK REACTION (Menyingkap Prestasi Pemangkinan Homogen N,N'-bis-(3,5-di-tert-butilsalisilidena)-2,2-dimetilpropana-1,3-diaminapaladium(II) dalam Tindak Balas Mizoroki-Heck) *Siti Kamilah Che Soh, Mohd Sukeri Mohd Yusof, Wan M. Khairul*	16
3.	DUAL-PRODUCTION OF POLYHYDROXYALKANOATE AND RHAMNOLIPID BY *Pseudomonas aeruginosa* UMTKB-5 USING INDUSTRIAL BY PRODUCTS (Dwi-Produksi Polihidroksialkanoat dan Ramnolipid oleh *Pseudomonas aeruginosa* UMTKB 5 dengan Penggunaan Hasil Sampingan Industri) *Noor Fazielawanie Mohd Rashid, Tan Suet May Amelia, Al-Ashraf Abdullah Amirul, Kesaven Bhubalan*	24
4.	STUDIES ON THE PROPERTIES OF NATURAL RUBBER/POLY-3-HYDROXYBUTYRATE BLENDS PREPARED BY SOLVENT CASTING (Kajian Mengenai Sifat Campuran Getah Asli/Poli-3-Hidroksibutirat yang Disediakan Melalui Kaedah Acuan Pelarut) *Asmaa' Zainal Abidin, Noor Hana Hanif Abu Bakar, Mohamad Abu Bakar*	40
5.	DYNAMIC FATTY ACID PROFILES OF ASIAN SEA BASS (*Lates calcarifer*) FROM SETIU WETLANDS, EAST COAST PENINSULAR MALAYSIA Profil Dinamik Asid Lemak Ikan Siakap Asia (*Lates Calcarifer*) Dari Tanah Bencah Setiu, Timur Semenanjung Malaysia *Chan Yu Bin, Loh Saw Hong, Yusof Shuaib Ibrahim, Zainuddin Bachok, Sabiqah Tuan Anuar*	53
6.	THE EXPLOITATION OF UNDERUTILISED *Mangifera indica L*. SEED AS COCOA BUTTER ALTERNATIVE	62

(Exploitasi Biji *Mangifera indica L*. Yang Tidak Di Gunakan Sebagai Alternatif Mentega Koko)
Nur Rahimah Said, Nursabrina Munawar, Quratul Quswa Amir, Siti Norshamshia Abd Hishamuddin

7. MEFENAMIC ACID DETERMINATION IN TABLET FORMULATIONS USING A SELECTIVE AND ACCURATE SPECTROPHOTOMETRIC METHOD BASED ON PRUSSIAN BLUE FORMATION 71
(Penentuan Asid Mefenamik dalam Formulasi Tablet Menggunakan Kaedah Spektrofotometri yang Selektif dan Tepat Berdasarkan Pembentukan Biru Prusian)
Hendri Wasito, Desi Purnamasari, Muhamad Salman Fareza

8. STUDYING THE PERFORMANCE OF DIAPER CHAR PRODUCED VIA PYROLYSIS AS AN EFFICIENT ADSORBENT FOR LEAD REMOVAL 81
(Mengkaji Prestasi Char Lampin yang Dihasilkan Melalui Pirolisis Sebagai Penjerap Berkesan untuk Penyingkiran Plumbum)
Najiyatul Munirah Yasin, Siti Nurul Hidayah Badrul Hisham, Najaa Nur Atiqah Rozulan, Nurul Ashraf Razali

9. NOVEL AND VALIDATED NON-AQUEOUS TITRIMETRIC METHOD FOR DETERMINATION OF PERSPECTIVE POTASSIUM-SPARING DIURETIC DRUG CANDIDATE IN PURE FORM AND PHARMACEUTICAL FORMULATION 95
(Kaedah Titrimetrik Bukan Akues Novel dan Ditentusahkan bagi Penentuan Penahanan Kalium-Dadah Diuretik dalam Formulasi Tulen dan Farmaseutikal)
Alexey Ivanov, Ivan Smirnov, Tatyana Murashko, Marina Trusova, Elena Stepanova

10. COPOLYMERISATION OF METHYL METHACRYLATE AND HYDROXYPROPYL METHYLCELLULOSE VIA EMULSION POLYMERISATION TECHNIQUE 105
(Pengkopolimeran Metil Metakrilat dan Hidroksipropil Metilselulosa Melalui Teknik Pempolimeran Emulsi)
Noor Aniza Harun, Liew Pei Chen, Anis Arina Zainudin, Tan Yea Tzy, Farhanini Yusoff

11. PHYTOCHEMICAL AND ANTIBACTERIAL PROPERTIES ON THREE MEDICINAL PLANTS FOR POTENT ANTI-SOFT ROT AGENTS 119
(Fitokimia dan Sifat Antibakteria Tiga Jenis Pokok Berubat sebagai Agen Anti Reput Buah)
Airiel Daniel Daud, Nur Suhada Azman, Nur Izni Ainina Alias, Norfatihah Syaifudin, Aiza Harun, Noorshilawati Abdul Aziz

12. PREPARATION AND CHEMICAL COMPOSITION OF ALKALINE WATER FROM PLANT COMBUSTION ASH 129
(Penyediaan dan Komposisi Kimia Air Beralkali dari Abu Loji Pembakaran)
Pairin Pongsa and Napa Tangtreamjitmun

13. SYNTHESIS, CHARACTERIZATION AND ELECTROCHEMICAL STUDIES OF TRANSITION METAL COMPLEXES CONTAINING 3,6-BIS(3,5-DIMETHYLPYRAZOLYL) PYRIDAZINE LIGAND 138
(Sintesis, Pencirian dan Kajian Elektrokimia bagi Kompleks Logam Peralihan Mengandungi Ligan 3,6-Bis(3,5-Dimetilpirazolil) Piridazina)
Shankary Selvanathan and Woi Pei Meng

14. A MINI REVIEW ON SENSOR AND BIOSENSOR FOR FOOD FRESHNESS DETECTION 153
(Satu Ulasan Mini Sensor dan Biosensor untuk Pengesanan Kesegaran Makanan)
Wan Elina Faradilla Wan Khalid and Nur Izzatul Afiqah Jais

15. NATURAL RADIOACTIVITY OF ^{210}Pb IN MUSSELS AT THE SEMI-ENCLOSED WATER OF THE JOHOR STRAIT, MALAYSIA THROUGH STATISTICAL APPROACH
(Radioaktiviti Semulajadi ^{210}Pb dalam Kupang di Perairan Separa-Tertutup Selat Johor, Malaysia Melalui Pendekatan Statistik) 166
Noor Affizah Bujang Saili and Che Abd Rahim Mohamed

Malaysian Journal of Analytical Sciences (MJAS)
Published by Malaysian Analytical Sciences Society

Editorial: Celebrating 25 Years of Malaysian Journal of Analytical Sciences

Mohd Basyaruddin Abdul Rahman, Harun Hamzah, Wan Mohd Afiq Wan Mohd Khalik

Malaysian Analytical Sciences Society (ANALIS)

The preface of the first issue in 2021 addresses the recognition of 25 years of history by the Malaysian Journal of Analytical Sciences (abbreviated as *Malay. J. Anal. Sci.* or MJAS), an outstanding moment to focus on its successes and the best time to setup research agenda for the next milestones. Our aim is to publish original research that makes strong contributions to analytical chemistry, electrochemistry, mass spectrometry, environmental analysis, separation techniques, spectroscopy, instrumentation, surface analysis, bioanalysis, structures, chemometrics and data processing in theoretical or experimental contexts.

The scholarly publishing forum in Malaysia worked on a small scale and had marginal impact at the beginning of 1990. The concept of a journal publication for local researchers was introduced thanks to a pioneer community of academia in Malaysian Analytical Science Society (ANALIS). The first MJAS issue was published in 1995, and two issues were published and retained until 2011. Starting the year 2012 till 2014, the issue was increased to 3 times per year. Then, the following year the journal maintained 6 issues per year. Since it was first introduced in 1995, the journal has published more than 1000 research or review articles.

MJAS has been listed in the SCOPUS (since 2010), MyCite (since 2005) and Asean Citation Index (since 2013) because of the tireless efforts of our past or current editors, editorial board, and international advisors. The journal currently ranked 100/119 in CiteScore (Q4 in the subject of analytical chemistry) with 1.0.

In order to improve our system for handling manuscript submission and review, editorial team is mobilizing the efforts to organize an efficient electronic platform for manuscript submission provided by the open journal submission system (*MJAS Open Journal System*). The journal has a rigorous double blind peer review process, setting zero plagiarism and demand for novelty or innovation works to ensure we are publishing the highest quality research papers. The journal has also seen international scientists directly engaged in the peer review process of published manuscripts over the last five years.

Editorial team extends a hearty thanks to all authors, reviewers, and guest editors for their contribution to the scientific quality and achievements for MJAS past 25 years. Editorial team looks forward to working with local and international contributors to support MJAS as the premier, high-quality, and esteemed journal for the rapidly changing in field of analytical sciences. Editors wished to leverage a journal that would meet the needs of an ever-developing and expanding profession between academia and industry.

Editorial team look forward to receiving your critical review, feedback, and possible contributions. We deeply hope that the journal will continue its effort to support study around the world in analytical sciences field. Submission of new manuscript subject to recent trends such as development analytical methodologies for detection of SAR-CoV-2, detection contaminant of emerging concern, artificial intelligence, smart system in instrumentation, big data processing, or etc. are most welcome.

Editorial team wishes you a happy, healthy, and productive 2021!

Best wishes
Mohd Basyaruddin Abdul Rahman (PhD)
Editor in Chief

Harun Hamzah (PhD)
Managing Editor

Wan Mohd Afiq Wan Mohd Khalik (PhD)
Executive Editor

Malaysian Journal of Analytical Sciences (MJAS)
Published by Malaysian Analytical Sciences Society

ADVANCED ADSORBENTS FOR THE EXTRACTION AND PRECONCENTRATION OF PENICILLIN ANTIBIOTICS: AN UPDATED REVIEW

(Penjerap Lanjutan Bagi Pengekstrakan Dan Prapemekatan Antibiotik Penisilin: Satu Tinjauan Terkini)

Wan Ibrahim Thani Abd Halim[1], Siti Munirah Ishak[1], Salwani Md Saad[1], Nadhiratul-Farihin Semail[1], Ahmad Husaini Mohamed[1,2], Mohd Yusmaidie Aziz[1], Azam Taufik Mohd Din[3], Nur Nadhirah Mohamad Zain[1], Nik Nur Syazni Nik Mohamed Kamal[1], Sazlinda Kamaruzaman[4], Noorfatimah Yahaya[1]*

[1]Integrative Medicine Cluster, Advanced Medical and Dental Institute (AMDI), Universiti Sains Malaysia, 13200 Bertam Kepala Batas, Penang, Malaysia
[2]Universiti Teknologi MARA, Cawangan Negeri Sembilan, Kampus Kuala Pilah, Pekan Parit Tinggi, 72000 Kuala Pilah, Negeri Sembilan, Malaysia
[3]School of Chemical Engineering, Engineering Campus, Universiti Sains Malaysia, 14300, Nibong Tebal, Penang, Malaysia
[4]Department of Chemistry, Faculty of Science, Universiti Putra Malaysia, 43400 UPM Serdang, Selangor Darul Ehsan, Malaysia

**Corresponding author: noorfatimah@usm.my*

Received: 13 November 2020; Accepted: 27 December 2020; Published: 20 February 2021

Abstract

Widespread use of penicillins (PENs) has brought about the pollution of wastewater and contamination of food, leading to antibiotic resistance which is detrimental to human life. PEN residues are being constantly identified in different matrices at low concentration. Several studies have been performed to extract these residues from environmental and food matrices. Sample preparation approaches like solid phase extraction (SPE) and liquid phase extraction (LLE) have been developed for their quantitation. SPE, in particular, shows great demand as an essential step to raise both practical efficiency and analytical sensitivity. Conventional SPE methods used for the extraction of antibiotics are relatively expensive, tedious and generally require long analysis time. In this review, recent miniaturized SPE methods and their applications for extraction of PENs from various matrices will be discussed. The methods represent fast, modern and efficient approaches to trace analytes. Selected examples will illustrate the various features of miniaturized SPE methods and their applications in food, biological, and environmental areas. With that, this paper presents a review of previous studies pertaining to miniaturized SPE methods that focused on the analysis of PENs in variety of matrices from the year 2015 to 2020.

Keywords: penicillins, sample preparation, solid phase extraction, advanced solid phase extraction, food security

Abstrak

Penggunaan penisilin (PEN) secara meluas telah menyebabkan pencemaran air kumbahan dan pencemaran makanan, yang berpotensi mewujudkan kerintangan antibiotik yang berbahaya terhadap kehidupan manusia. Sisa PEN kerap kali dikenal pasti dalam matriks berbeza pada kepekatan rendah. Beberapa kajian telah dilakukan untuk mengekstrak sisa ini dari matriks persekitaran dan makanan. Pendekatan penyediaan sampel seperti pengekstrakan fasa pepejal (SPE) dan pengekstrakan fasa cecair (LLE) telah dibangunkan untuk penyukatan secara kuantitatif. SPE, terutamanya, menunjukkan permintaan yang besar sebagai langkah penting untuk meningkatkan kecekapan praktikal dan kepekaan analisis. Kaedah SPE konvensional yang digunakan untuk pengekstrakan antibiotik agak mahal, susah dan biasanya memerlukan masa analisis yang panjang. Dalam tinjauan ini, kaedah SPE yang terkini dan aplikasi mereka untuk pengekstrakan PEN dari pelbagai matriks akan dibincangkan. Kaedah-kaedah ini mewakili pendekatan pantas, moden dan cekap untuk mengesan bahan analit. Contoh-contoh yang terpilih akan memberi gambaran mengenai ciri-ciri SPE lanjutan yang pelbagai dan aplikasi mereka dalam bidang makanan, biologi dan persekitaran. Dengan itu, manuskrip ini memberi tinjauan bagi kajian yang melibatkan kaedah SPE lanjutan yang mengfokuskan kepada analisa PEN di dalam pelbagai matriks dari tahun 2015 sehingga 2020.

Kata kunci: penisilin, penyediaan sampel, pengekstrakan fasa pepejal, pengekstrakan fasa pepejal lanjutan, kawalan makanan

Introduction

Veterinary antibiotics are necessary for efficient production of meat, milk, and eggs in the frame of hygienic management of farms. Antibiotics have multiple uses depending on concentration level. At low levels they act as growth promoters, at intermediate levels they are to prevent diseases, while at high levels they are used as treatment for infected animals [1]. Among the antibiotics, β-lactam antibiotics (BLAs) constitute one of the most widely used drugs in veterinary medicine, especially to treat and prevent bacterial infections of dairy cattle [2]. BLAs can be classified into several subgroups according to their structural characteristics: penicillins (PENs), cephalosporins, and, more recently, carbapenems [3]. The penicillins subgroup is one of the most valuable drugs in primary care [4].

A penicillin's basic structure (as shown in Figure 1) consists of four parts: a thiazolidine ring, a β-lactam ring attached to it which forms 6-aminopenicillanic acid, a side chain R1 in the 6-position, and another side chain R2 which usually holds hydrogen except for the case of esters of some members. R1 determines the stability and the antimicrobial activity of the different derivatives [1]. Several common PENs are shown in Figure 2.

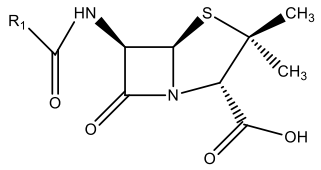


Figure 1. General structure of PENs (R = lateral amino chain)

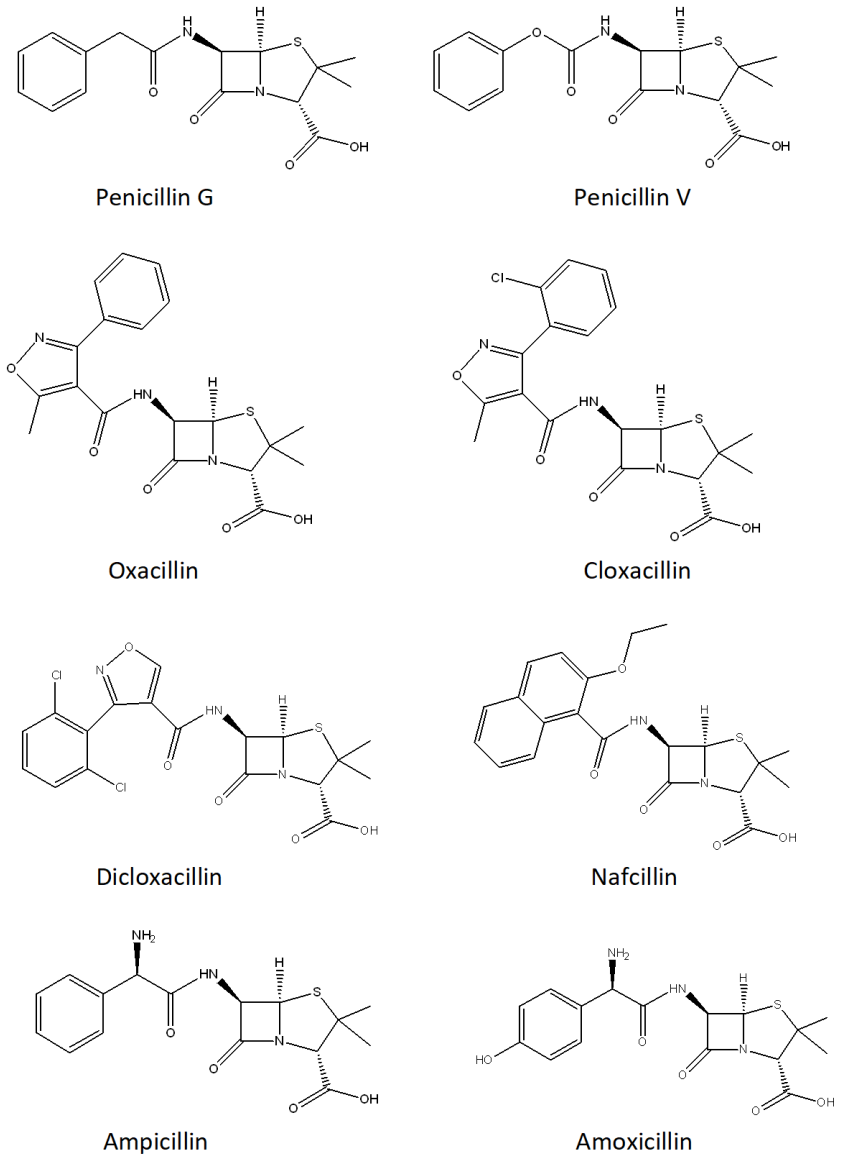


Figure 2. Chemical structure of selected penicillins

PENs are the most frequently used antibiotics in poultry production [5]. In dairy industry, PENs have been used for mastitis treatment [2]. The use of PENs in both treatment and prevention of infection has resulted in antibiotic residues in animal edible tissue [6] and over time, the residues can lead to health problems in human and increase the incidence of microbial resistance against antimicrobial compounds [7]. In the past few years, due to heightened public concern regarding the overuse of antibiotics in food-producing animals and the risk of transmission of antibiotic-resistant bacteria to man, the control of antibiotic residues in edible animal tissues has been made mandatory [8]. To protect consumers from potential health risks, the EU has

defined safe maximum residue limits (MRL) for PENs through Commission Regulation (EU) number 37/2010. The limits implemented in foodstuffs for PENs antibiotics are shown in Table 1.

Excessive use of veterinary antibiotics is one of the major sources of antibiotic residues in environment [9]. Since these compounds are poorly absorbed and metabolized by the animals, approximately 30-90% of them are excreted in the original form while the rest are excreted in the form of metabolites [10]. The use of animal manure as fertilizers on agricultural lands could lead to antibiotic pollution on the environment. Without proper treatment and waste management, antibiotic residues from farms, hospitals, pharmaceuticals and medical wastes would end up contaminating natural environments [11]. The antibiotic residues could enter other environmental media like soil, river and sea or end up in the food chain, further contributing to the appearance and transfer of antibiotic-resistant bacteria to human [8, 11].

To date, high performance liquid chromatography (HPLC) has been the most used technique for analyzing PENs and other BLAs in different matrices, even more so when compared to gas chromatography (GC) method [12]. However, the determination of the antibiotics is a difficult task due to the complexity of matrices like food and biological fluid, caused by the existence of various biochemical compounds such as proteins or fats [13]. Hence, further efficiency requires an improvement in the sample treatment step [14].

Numerous sample treatment methods have been developed to determine veterinary drugs in various samples, which include protein precipitation, liquid-liquid extraction (LLE), and solid phase extraction (SPE) [15]. Among them, SPE is one of the most popular techniques for pre-concentration of analytes in different samples due to its high enrichment factors, low reagent consumption, simplicity, speediness and convenience [16]. For optimization, adsorbent selection plays a key role in SPE procedures [17]. A new method of SPE called solid phase microextraction (SPME) technique has been on the rise since its introduction in the early twentieth century. SPME, which is a sorption-based, is considered to be a miniaturized version of SPE [18]. Following its success, SPME has been widely exploited by optimizing advanced materials which are more selective and have higher adsorption capacity in order to expand the availability of inexpensive, more easily synthesized adsorbents [19]. Other methods such as magnetic solid phase extraction (MSPE), dispersive solid phase extraction (DSPE) and stir bar sorptive extraction (SBSE) also received considerable attention as alternative means to sample preparation. MSPE, which is based on magnetic adsorbent, became an attractive approach in sample preparation due to its excellent adsorption efficiency and facile isolation from the mixture solution without reiterative centrifugation [20, 21].

Meanwhile, in DSPE method, the solid adsorbent is added directly to the sample solution without manipulation processes. Therefore, the extraction process relies only on shaking and centrifugation. The dispersion phenomenon allows the adsorbent to interact with all target rapidly and uniformly [22]. Another novel approach to sample enrichment in aqueous solution is SBSE, where the analyte is extracted by magnetically stirring a stir bar covered with a thick layer of polydimethylsiloxane (PDMS) in the sample solution [23]. In this technique, the phase, similar to GC stationary phases, is coated and bonded onto a magnetic stir bar. The stir bar is then immersed into the liquid sample for extraction [24]. The major advantages of this technique are its ease of use, improved sensitivity, high accuracy of analysis and reduced risk of contamination [25].

Despite its widespread use, conventional SPE extraction processes using the commercially available SPE cartridges are time-consuming and tedious [25]. Design of the column as well as the packed adsorbent are made to restrict flow rates in order to avoid channeling phenomenon, resulting in lengthened extraction process. Another main disadvantage of SPE based on cartridge format is the blockade of frits within passage of dirty samples [26]. On the other hand, in the newly developed miniaturized SPE methods, a number of adsorbent materials including carbon, silica, molecularly imprinted polymers, metal organic frameworks and

ionic liquid modified nanoparticles have been developed with particularly useful applications in analytical chemistry [27]. The common advantages of these materials are their sensitivity, rapidity and efficiency.

In this review, recent development of different types of adsorbent materials and their applications in sample preparation for determination of penicillin are summarized and evaluated. The miniaturized SPE methods have been reviewed previously. The present review primarily addressed the development, from the year 2015 to 2020, of sample preparation method, the materials used, method of extraction, the sensitivity or limit of detection (LOD) and recovery of the compound.

Table 1. MRLs established by Commission Regulation (EU) number 37/2010 for PENs residues in foodstuffs

Analyte	**MRL (µg kg^{-1})**	
	Milk	**Bovine**
Oxacillin	30	300
Cloxacillin	30	300
Dicloxacillin	30	300
Nafcillin	30	300
Penicillin G	4	50
Penicillin V	4	50
Ampicillin	4	50
Amoxicillin	4	50

Adsorbent-based Sample Preparation Technique

Nanoparticles

Over the past few decades, nanoparticles have been extensively used worldwide in many fields such as material sciences, physics, medicine, electronic and chemistry [28]. The shapes and types of nanomaterials such as nanotubes, nanohorns and nanocages can be prepared from organics and inorganics materials [29]. Nanoparticles differ from classical solid particles by their size which is smaller by several orders of magnitude, and by their specific properties due to their high surface area over volume ratio [30]. Nanoparticles are almost zero-dimensional which means all dimensions are in the nanoscale (1-100nm) [31]. Due to the sheer small size, particles in nanoscale often have different physical, chemical and biological properties compared to macro and micro scale [32]. Nanoparticles can be used for further enhancement of SPE methods as they have high surface area-to-volume ratio and provide a surface functionalization which can be tailored depending on applications.

Carbon-based adsorbents

Carbon-based materials are made up carbon atoms in the form of cages, sheets or tubes. Carbon nanotubes (CNTs) are one of such materials in the form of tubes. Due to their structure and adsorption properties, CNTs are considered promising adsorbents for SPE. This allotrope of carbon was first discovered in 1991 by accident during experimental synthesis of fullerene in an electric arc. CNTs are made up of graphene sheets rolled into cylindrical structure, with diameter in the range of nanometer and length up to several micrometers. There are two types of CNTs, single-walled CNTs (SWCNTs) and multi-walled CNTs (MWCNTs). SWCNTs are produced from the rolling of a single graphene sheet, while MWCNTs are composed of multiple SWCNTs arranged compactly together by van der Waals force around an axis. Properties of CNTs like lightness, high

tensile strength, high resistance to mechanical damage, high thermal stability and conductivity and excellent electric conductor make them versatile materials for various applications including extraction. As adsorbents for SPE, CNTs provide large surface area for adsorption, and allow for fast and rapid extraction rate. Their selectivity towards target analytes and sensitivity in various matrices can be enhanced by further functionalization of carbon [33].

In 2016, Ahmadi et al. crown-functionalized a magnetic MWCNTs (MMWCNTs) adsorbent using a supramolecular compound 4,4'-diamindibenzo-18-crown-6 (DADB18C6), for spectrophotometric quantification of amoxicillin [34]. DADB18C6, which was synthesized according to Keypour et al. [35], has excellent host-guest molecular recognition ability. In addition to its high selectivity, the host, with its large cavities, showed better incorporation of guest molecules [35]. In the study, the sensitivity of amoxicillin detection was enhanced spectrophotometrically by treating the amoxicillin containing solution with aryldiazonium ion. This ion reacts with nucleophilic amoxicillin to produce a colored azo derivative of amoxicillin, which is more sensitive towards spectrophotometric detection than pure amoxicillin. The optimized method was validated by analyzing real life samples, amoxicillin capsules and human urine. The method succeeded in detecting amoxicillin in the concentration range of 5.0–1000.0 ng mL^{-1} with the LOD of 3.0 ng mL^{-1} [34].

Following this study, in 2018, Jia et al. developed a disposable SPE membrane for rapid removal and sensitive surface-enhanced Raman scattering (SERS) to detect antibiotics in water samples [37]. The membrane was prepared by trapping the activated carbon modified with silver nanoparticles (Ag NPs/AC) solution on the commercially available SPE column. The activated carbon showed high adsorption ability due to its porous structure and high surface area. In addition, the resulting "hotspots" due to embedded silver nanoparticles amplified Raman signals and thus improving SERS detection by Raman spectrometer. After optimizing the method, penicillin G sodium and ampicillin were analyzed for method validation. Penicillin G sodium was detected in the concentration range of 6.0×10^{-9} to 4.0×10^{-5} M with the LOD of 2.5×10^{-9} M, while ampicillin was detected in the concentration range of 8.0×10^{-9} to 8.0×10^{-5} M with the LOD of 3.2×10^{-9} M. The low relative standard deviation (RSD), which is less than 15% indicated that this disposable SPE membrane is highly reproducible [37].

The most recent study involving PENs detection using carbon-based adsorbents was by Golzari Aqda et al. [38]. They performed SPME using a graphene-oxide-starch-based nanocomposite for the determination of three antibiotic residues (amoxicillin, ampicillin and cloxacillin) in 114 milk samples. The pre-concentrated samples were further analyzed using high-performance liquid chromatography-ultraviolet detection (HPLC-UV). In this method, the synthesis of graphene oxide was initiated based on Hummers method. Then, following the procedure by Pourjava et al. [39], four types of hydrogels were synthesized: graphene oxide-starch-based nanocomposite without calcium carbonate ($CaCO_3$), graphene oxide-starch-based nanocomposite in the presence $CaCO_3$, porous graphene oxide-starch-based nanocomposite after removing $CaCO_3$, and starch-graft-polyacrylamide without $CaCO_3$ and graphene oxide. From the four hydrogels, hydrogels of porous graphene oxide-starch-based nanocomposite after removing $CaCO_3$ showed the highest extraction efficiency compared to the other three hydrogels. This was contributed by the use of graphene oxide and $CaCO_3$ that has increased the surface area of the adsorbent. The subsequent removal of $CaCO_3$ after its entrapment inside the nanocomposite structure resulted in increase in porosity and surface area. The analytes were adsorbed on the porous adsorbent by hydrogen bond interactions. After optimization, the method managed to detect the selected antibiotics in the concentration range of 2.7–5.0 μg kg^{-1} with the LOD of 0.8–1.5μg kg^{-1} [38]. The results of the studies are tabulated in Table 2.

Table 2. Recent applications of miniaturized SPE for the determination of penicillin antibiotics in various matrices (2015-2020)

Type of SPE	Adsorbent Material	Analytes	Matrices	Detection method	Amount detected ($\mu g\ L^{-1}$ or $\mu g\ kg^{-1}$)	Sensitivity (LODs) ($\mu g\ L^{-1}$ or $\mu g\ kg^{-1}$)	Recovery (%)	Ref
MSPE	Crown-MMWCNTs	Amoxicillin	Amoxicillin capsules, human urine	UV-Vis	19.8 – 49.7 48.1 – 510.5	3.0	98.0 – 98.5 96.2 –102.1	[34]
Disposable, highly reproducible SPE membrane	Activated carbon nanocomposite modified with silver nanoparticles	Penicillin G sodium, ampicillin	Standard solution	Raman spectrometer	not recorded	0.9	not recorded	[37]
SPME	Graphene-oxide-starch-based nanocomposite	Amoxicillin, ampicillin, cloxacillin	Cow milk	HPLC-UV	13.8 – 242.9	0.8 – 1.5	83.0 – 105.0	[38]
MISPE	Silica@MIP	Oxacillin, cloxacillin, dicloxacillin	Milk	HPLC	7.5 – 480	1.60 – 1.90	92.0 – 102.0	[49]
SPME	silica@chitosan-glutaraldehyde	Penicillin G	Tap, river, lake, well water, wastewater	HPLC	1 – 300	0.49	91.0 – 123.3	[17]
MISPE	NAFC- MAA-EGDMA-ACN-AIMN	Ampicillin, amoxicillin, oxacillin, penicillin G, penicillin V, cloxacillin, dicloxacillin, nafcillin	Powdered infant formulas	HPLC-MS/MS	Not recorded	0.7 – 23.6	60.0 – 91.0	[3]
MISPE	Sulfaguanidine-imprinted polymer	Penicillin G/procaine	Wellspring water, wastewater	HPTLC	Not detected	5.0	95.0 – 108.0	[54]
SMISPE	Ampicillin-surface-molecularly-imprinted polymer	Ampicillin	Commercial milk, rat blood	HPLC-UV	Not detected Detected, not recorded	50.0 150.0	63.8 – 82.5 67.3 – 79.1	[11]
MISPE	Ampicillin-imprinted polymer	Ampicillin	Cow milk	HPLC-UV	Not recorded	35.8	> 95.0	[55]

Table 2 (cont'd). Recent applications of miniaturized SPE for the determination of penicillin antibiotics in various matrices (2015-2020)

Type of SPE	Adsorbent Material	Analytes	Matrices	Detection method	Amount detected (µg L^{-1} or µg kg^{-1})	Sensitivity (LODs) (µg L^{-1} or µg kg^{-1})	Recovery (%)	Ref
SPME	Aluminium-based MOF polymer monoliths	Penicillin G, penicillin V, oxacillin, cloxacillin, dicloxacillin, nafcillin	River water	UPLC-UV	Not detected	0.06 – 0.26	81.0 – 100.7	[57]
UAMSPE	Copper-based magnetic MOF	Ampicillin	Cow milk	HPLC-UV	Not detected	0.29	95.0 – 100.8	[59]

**Abbreviations:*
MSPE – Magnetic solid phase extraction
SPME – Solid phase microextraction
MISPE – Molecularly imprinted solid-phase extraction
SPME – Solid phase microextraction
SMIPSE – Surface molecularly imprinted solid-phase extraction
SPME– Solid phase microextraction
UAMSPE – Ultrasonic-assisted magnetic solid phase extraction

Silica-based nanoparticle

As a relatively inexpensive, chemically inert, thermally stable, and biocompatible material, silica is very appealing for analytical applications. Over the past two decades, silica nanoparticle (SiNP) has gained much attention on their application in catalysis, separation, biosensors, and adsorption [29] because SiNP is easy to be synthesized and modified by altering the functional groups on their surface [40]. According to Wang et al. [41], there are several physical properties that makes silica an attractive adsorbent, one of them being particle sizes can be tuned from 50 to 300 nm with stable and rigid frame that provides resistance to mechanical stress and degradation. Another desirable property is pore diameters can be tuned between 2 and 10 nm permitting different chemicals or analytes loading. Also, SiNP has a high surface area (> 700 m^2/g) and large pore volume (> 0.9 cm^3/g) allowing high loadings of chemicals. Silica nanoparticles were produced though different methods such as reverse micro emulsion, Stöber process, flame synthesis and widely utilized sol-gel method, in addition to several other novel methods later on [42]. The chemically synthesized silica nanoparticles are more widely used, because the chemical route is easy to comprehend and offers more options for modification of the different parameters of the silica nanoparticle [42].

In recent years, hybrid and composite materials have been extensively studied due to their diverse properties [43]. Their properties combine the advantages of both inorganic and organic materials [44]. In this respect, organically modified silica nanoparticles are a typical class of hybrid materials [45]. Due to the challenges in the detection of penicillin in complex samples such as food, it is crucial to develop sampling and sample preparation procedures for efficient analysis [46]. MSPE with magnetic nanoparticles (MNPs) has generated great interest in the analytical community [47]. However, pure MNPs suffer from an inherent limitation as they tend to agglomerate, which alters their magnetic properties in complex matrices. Therefore, the

modification of these MNPs is essential to overcome such limitation. Among the different materials, silica nanoparticles have been proven to have the proper ability to enhance mechanical and interfacial properties [17]. At present, the Stöber process, sol-gel process, and aerosol pyrolysis seem promising for coating iron oxide nanoparticles with silica [48].

In 2016, Urraca et al. has developed selective molecularly imprinted polymers in the form of microspheres, using porous silica beads (40-75μm) for the analysis of beta-lactamase-resistant penicillins [49]. Molecularly imprinted polymers (MIPs) have been shown to be a useful alternative to immune-affinity columns and other commercially available SPE cartridges for sample clean-up and selective pre-concentration of different analytes in complex matrices, as the so-called molecularly imprinted solid-phase extraction (MISPE) [50]. In the study, the analytical method was validated according to EU guideline 2002/657/EC. The limits of quantification (S/N=10) were in the 5.3-6.3 μg kg^{-1} range and well below the maximum residue limits (MRLs). Interday mean recoveries were in the acceptable range of 99–102% with RSDs below 9% for the analysis of penicillins in milk samples.

Recently, Hassan et al. has synthesized silica@chitosan-glutaraldehyde (Si@Cs-G) for extraction of penicillin G (PG) from the synthetic and real samples followed by HPLC determination [17]. Chitosan (Cs) is a polysaccharide polymer which has bifunctional groups and as a consequence, possesses unique physiological activity and physiochemical properties. Hydrophilicity, harmlessness, biodegradability, low cost, abundance and ease of chemical derivatization result in Cs being regarded as a useful and auspicious material for preparing the adsorbent [51]. However, Cs is easily oxidized or destructed when exposed to high concentration of pollution and low pH, making Cs unstable and unreliable [52]. Therefore, modification with silica is necessary because silica nanoparticles have been proven to have the proper ability to enhance Cs mechanical and interfacial properties [51]. In the study, the following conclusions were observed: the optimized conditions for PG extraction by Si@Cs-G is at pH 6 with contact time 50 minutes and adsorbent dosage 25mg at room temperature. The best desorption rate was associated to acetonitrile solvent at volume of 0.75 mL under 40 minutes. Extraction recovery in synthetic samples was 99.0%, with LOD = 0.49 μg L^{-1}, limit of quantification (LOQ) = 1.64 μg L^{-1} and RSD < 1.95%. The method was successfully applied for determination of PG in real water samples (tap, river, lake and well water) and wastewater samples (hospital effluent). The obtained relative recoveries were in the range of 91.31-123.27% with RSD less than 6.34% for all the real samples. Table 2 shows the summary of silica nanoparticle-based techniques for detection of penicillins in various matrices in the years 2015-2020.

Molecularly imprinted polymers as adsorbents

Molecularly imprinted polymers (MIPs) are macromolecules synthetically produced in the presence of target molecules called template. After removing the template, the imprinted polymer would have binding sites with specific shape and size similar to target molecules. MIPs have higher selectivity and affinity towards target molecules and their analogues due to their prearranged structures and better molecular recognition ability which encourage both covalent and non-covalent bindings. In addition to having good stability, MIPs are easy to prepare and can be used repeatedly without significant loss of activity [53], making them an increasingly popular approach to selective sample preparation.

In January 2015, various MIPs adsorbent with different templates and cross-linkers have been tested for the determination of eight PENs in milk powder formulas for infants [3]. The eight PENs were ampicillin, amoxicillin, oxacillin, penicillin G, penicillin V, cloxacillin, dicloxacillin, and nafcillin. After pre-concentration step, the samples were analyzed with high-performance liquid chromatography coupled to tandem mass spectrometer (HPLC-MS/MS). In the study, oxacillin, amoxicillin, and nafcillin have been selected as template candidates. They were crosslinked to methacrylic acid and either to divinylbenzene 80%, ethylene glycol dimethacrylate or trimethylolpropane trimethacrylate. The loading and washing solvents were chosen between methanol, acetonitrile and

acetonitrile/toluene. After optimization, nafcillin-methylacrylic acid-ethylene glycol dimethacrylate-acetonitrile was decided as the most suitable SPE adsorbent as they exhibit the highest retention capacity of the eight PENs. The PENs were detected in the concentration range of 2.4-78.4 μg kg^{-1} with the LOD of 0.7-23.6 μg kg^{-1} [3].

A study on preparation and application of sulfaguanidine-imprinted polymer was performed in 2015 to monitor eight pharmaceuticals including penicillin G/procaine from wellspring water and wastewater samples [54]. In this study, sulfaguanidine was used as the template molecule, methacrylic acid and 2-hydroxyethyl methacrylate were the functional monomers, ethylene glycol dimethacrylate acted as cross-linker, and 2,2'-azobis-isobutyronitrile served as the initiator. Unlike enzyme, which is completely specific, MIPs can retain more than one molecule. In case of sulfaguanidine-imprinted polymers, they were expected to retain eight other molecules of similar structure to sulfaguanidine, among them was penicillin G/procaine. The optimized method detected penicillin G/procaine from water samples using high-performance thin-layer chromatography (HPTLC) with the LOQ and LOD of 10 μg L^{-1} and 5 μg L^{-1}, respectively [54].

Later in 2016, Wu et al. studied a novel surface MIP (SMIP) for the selective determination of ampicillin sodium from milk and blood samples [11]. Like MIP, it uses silica gels as support. However, instead of using conventional bulk polymerization which resulted in irregular materials shape, poor site accessibility, slow mass transfer, incomplete templates removal, low binding capacity and serious templates leakage, SMIP is synthesized using surface molecular imprinting technique. This technique improves recognition site, binding capacity and mass transfer rate as well as contributing to more uniformly sized morphology. In this study, following the activation of silica gels, the silica gels were amino-functionalized before being surface-molecularly imprinted with ampicillin sodium. After method optimization, the samples were analyzed using HPLC-UV. The optimized method succeeded in detecting ampicillin in the concentration range of 5-200 μg mL^{-1}, with the LOD of 0.2 μg mL^{-1} and 0.5 μg mL^{-1} for milk and blood samples, respectively [11].

The most recent study on MIPs adsorbent for selective pre-concentration of PEN antibiotics was in 2017, where Soledad-Rodríguez et al. prepared MIPs with ampicillin as template for determination of ampicillin drugs in cow milk samples [55]. Through bulk polymerization, the procedure utilized methacrylic acid or methyl methacrylate as functional monomers, ethylene glycol dimethacrylate as crosslinking monomer, acetonitrile as porogen and hydrogen peroxide as initiator. In the study, the ratio of functional monomer to cross-linker was manipulated to achieve the highest binding capacity towards ampicillin drugs. Ratio 1:5 was selected as the most suitable ratio to achieve intended results. The cow milk samples went through quantitative analysis using HPLC-UV. The optimized method's LOQ and LOD were 10.7 μg L^{-1} and 35.8 μg L^{-1}, respectively [55]. Table 2 shows the results of selected studies on MIPs adsorbents.

Metal-organic frameworks as adsorbents

Metal-organic frameworks (MOFs) are crystalline network formed *via* coordination bonds between inorganic metals and multidentate organic ligands. MOFs are synthesized by self-assembly in a one-pot reaction. Varying metals and ligands and reaction conditions allows the pore size of MOFs to be manipulated to suit any specific application. The most common synthetic methods are solvothermal synthesis and hydrothermal synthesis. In both methods, high temperature and pressure result in increased rate of reaction. However, mild reaction conditions are preferred to obtain perfect crystalline formation. For SPE, four types of MOFs are commonly used: isoreticular MOF (IRMOF) series, materials of Institute Lavoisier (MIL) series, zeolitic imidazolate framework (ZIF) series, and University of Oslo (UiO) series [56].

In 2016, a study by Lirio et al. highlighted the application of MIL-53 as aluminium-based MOF (Al-MOF) polymer monolith adsorbents in solid phase microextraction (SPME) of selected penicillins [57]. In this study, MIL-53 was first synthesized according to Loiseau et al. [58] under hydrothermal conditions using

aluminum nitrate nonahydrate as the metal and 1,4-benzenedicarboxylic acid as the ligand. Then, MIL-53 was mixed with butyl methacrylate and ethylene dimethacrylate monomers for co-polymerization, with azobisisobutyronitrile as the initiator. The resulting mixture was pretreated before being sealed into SPE column and underwent microwave-assisted polymerization for five minutes. The optimized method was utilized to analyze river samples for the determination of penicillin G, penicillin V, oxacillin, cloxacillin, dicloxacillin, and nafcillin using ultra-performance liquid chromatography-ultraviolet detection (UPLC-UV). The method managed to detect PENs with the LOQ of 0.20–0.87 μg L^{-1} and LOD of 0.06–0.26 μg L^{-1} [57].

Following that study, in 2020, Bagheri and Ghaedi developed copper-based magnetic MOFs (Cu-MMOF) as adsorbents for ultrasonic-assisted magnetic SPE (UAMSPE) of ampicillin from cow milk samples prior to HPLC-UV [59]. In addition to enhancing the adsorption capacity by MOF, the magnetic properties of the adsorbents decreased extraction time by eliminating the need for filtration, centrifugation and precipitation processes. Firstly, magnetic nanoparticles were synthesized according to their previous work [60]. Then, copper (II) nitrate trihydrate as metal and terepthalic acid as ligand were reacted in a one-pot solvothermal synthesis for 12 hours to obtain the Cu-MMOF adsorbents. After optimization, this method achieved detection in the concentration range of 1–5000 μg L^{-1} with the LOD of 0.29 μg L^{-1} [59]. Results for related studies were shown in Table 2.

Conclusion

Numerous numbers of nanomaterials with chemical composition and properties have been found to be excellent absorbents in sample preparation. In addition, the surface functionalization or modification of different nanomaterials aid the development of versatile approaches for efficient analysis of various analytes. So far, all the methods used have achieved the MRL detection with low LOD between 0.05-150.0 μg L^{-1}. This review paper has established that miniaturized SPE can be a powerful method for sample preparation today. Based on recent studies, miniaturized SPE methods like MSPE and SPME have much potential to trim down preparation time, laborious effort, cost and high chemical usage commonly associated with sample preparation. Miniaturized SPE adsorbent materials like magnetic adsorbents can be recovered and used repeatedly; and they eliminate the problems that come with conventional SPE cartridges. Optimizing the choice of adsorbents and maximizing their adsorption efficiency are the correct approach to solving the difficulties in extracting analytes from complex matrices. However, still much effort is required to improve application of advanced adsorbents so that they can extract analytes with higher selectivity, lower LOD and higher extraction recoveries. All in all, the future of advanced adsorbents as alternative for extraction of antibiotics including PENs is very promising. With collaboration between research institutes and governmental bodies, a facile, robust and economical sample preparation procedure using advanced adsorbents could be established to monitor MRL of antibiotics in our environmental water and food in the future.

Acknowledgement

The authors gratefully acknowledged the financial support from both the Ministry of Higher Education, Malaysia (Fundamental Research Grant Scheme-203.CIPPT.6711630) and Universiti Sains Malaysia (Research University Grant 1001.CIPPT.8011052).

References

1. Samanidou, V. F., Nisyriou, S. A. and Papadoyannis, I. N. (2007). Development and validation of an HPLC method for the determination of penicillin antibiotics residues in bovine muscle according to the European Union Decision 2002/657/EC. *Journal of Separation Science*, 30(18): 3193-3201.
2. Bailón-Pérez, M. I., García-Campaña, A. M., del Olmo-Iruela, M., Gámiz-Gracia, L. and Cruces-Blanco, C. (2009). Trace determination of 10 β-lactam antibiotics in environmental and food samples by capillary liquid chromatography. *Journal of Chromatography A*, 1216(47): 8355-8361.

3. Díaz-bao, M., Barreiro, R., Miranda, J. M., Cepeda, A. and Regal, P. (2015). Fast HPLC-MS/MS Method for determining penicillin antibiotics in infant formulas using molecularly imprinted solid-phase extraction. *Journal of Analytical Methods in Chemistry*, 2015: 959675.
4. Miller, E. L. (2002). The penicillins : A review and update. *Journal of Midwifery & Women's Health,* 47(6): 426-434.
5. Evaggelopoulou, E. N. and Samanidou, V. F. (2013). Development and validation of an HPLC method for the determination of six penicillin and three amphenicol antibiotics in gilthead seabream (*Sparus aurata*) tissue according to the European Union Decision 2002/657/EC Cloxacillin Dicloxacillin. *Food Chemistry*, 136(3–4): 1322-1329.
6. Webb, V. and Davies, J. (1993). Antibiotic preparations contain DNA: A source of drug resistance genes?. *Antimicrobial Agents and Chemotherapy*, 37(11): 2379-2384.
7. Piddock, L. J. V. (1996). Does the use of antimicrobial agents in veterinary medicine and animal husbandry select antibiotic-resistant bacteria that infect man and compromise antimicrobial chemotherapy?. *Journal of Antimicrobial Chemothera*, 38(1–3): 95-95.
8. Lara, F. J., Olmo-iruela, M., Cruces-blanco, C., Quesada-molina, C. and Garcı, A. M. (2012). Advances in the determination of β-lactam antibiotics by liquid chromatography. *TrAC Trends in Analytical Chemistry*, 38: 52-66.
9. Zhi, S., Zhou, J., Liu, H., Wu, H., Zhang, Z., Ding, Y. and Zhang, K. (2020). Simultaneous extraction and determination of 45 veterinary antibiotics in swine manure by liquid chromatography-tandem mass spectrometry. *Journal of Chromatography B*, 1154: 122286.
10. Watanabe, N., Bergamaschi, B. A., Loftin, K. A., Meyer, M. T. and Harter, T. (2010). Use and environmental occurrence of antibiotics in freestall dairy farms with manured forage fields. *Environmental Science & Technology*, 44(17): 6591-6600.
11. Wu, N., Luo, Z., Ge, Y., Guo, P., Du, K., Tang, W. and Fu, Q. (2016). A novel surface molecularly imprinted polymer as the solid-phase extraction adsorbent for the selective determination of ampicillin sodium in milk and blood samples. *Journal of Pharmaceutical Analysis*, 6(3): 157-164.
12. Meetschen, U. and Petz, M. (1990). Capillary gas chromatographic method for determination of benzylpenicillin and other beta-lactam antibiotics in milk. *Journal - Association of Official Analytical Chemists*, 73(3): 373-379.
13. Sahebi, H., Konoz, E., Ezabadi, A., Niazi, A. and Hamid, S. (2020). Simultaneous determination of five penicillins in milk using a new ionic liquid-modified magnetic nanoparticle based dispersive micro-solid phase extraction followed by ultra-performance liquid chromatography-tandem mass spectrometry. *Microchemical Journal*, 154: 104605.
14. Castilla-fernández, D., Moreno-gonzález, D., Beneito-cambra, M. and Molina-díaz, A. (2019). Critical assessment of two sample treatment methods for multiresidue determination of veterinary drugs in milk by UHPLC-MS/MS. *Analytical and Bioanalytical Chemistry*, 411:1433-1442.
15. Rossi, R., Saluti, G., Moretti, S., Diamanti, I. and Galarini, R. (2017). Multiclass methods for the analysis of antibiotic residues in milk by liquid chromatography coupled to mass spectrometry: A review. *Food Additives & Contaminants: Part A*, 2017: 1-17.
16. Alipanahpour Dil, E., Asfaram, A. and Sadeghfar, F. (2019). Magnetic dispersive micro-solid phase extraction with the CuO/ZnO@Fe_3O_4-CNTs nanocomposite sorbent for the rapid pre-concentration of chlorogenic acid in the medical extract of plants, food, and water samples. *Analyst*, 144(8): 2684-2695.
17. Hassan, M., Fazlzadeh, M. and Hazrati, M. (2020). A novel silica supported chitosan/glutaraldehyde as an efficient sorbent in solid phase extraction coupling with HPLC for the determination of Penicillin G from water and wastewater samples. *Arabian Journal of Chemistry*, 13(9): 7147-7159.

18. Arthur, C. L. and Pawliszyn, J. (1990). Solid phase microextraction with thermal desorption using fused silica optical fibers. *Analytical Chemistry*, 62(19): 2145-2148.
19. Fumes, B. H., Silva, M. R., Andrade, F. N., Eduardo, C., Nazario, D. and Lanças, F. M. (2015). Recent advances and future trends in new materials for sample preparation. *Trends in Analytical Chemistry*, 71: 9-25.
20. Xu, M., Liu, M., Sun, M., Chen, K., Cao, X. and Hu, Y. (2016). Magnetic solid-phase extraction of phthalate esters (PAEs) in apparel textile by core – shell structured Fe_3O_4@ silica @ triblock-copolymer magnetic microspheres. *Talanta*, 150: 125-134.
21. Wu, Q., Song, Y., Wang, Q., Liu, W., Hao, L., Wang, Z. and Wang, C. (2020). Combination of magnetic solid-phase extraction and HPLC-UV for simultaneous determination of four phthalate esters in plastic bottled juice. *Food Chemistry*, 339: 127855.
22. Sahebi, H., Konoz, E. and Ezabadi, A. (2019). Synthesis of DABCO-based ionic liquid functionalized magnetic nanoparticles as a novel sorbent for the determination of cephalosporins in milk samples by dispersive solid-phase extraction followed by ultra-performance liquid chromatography-tandem mass spectrometry. *New Journal of Chemistry*, 43(34): 13554-13570.
23. Bader, N. (2018). Stir bar sorptive extraction as a sample preparation technique for chromatographic analysis: An overview. *Asian Journal of Nanosciences and Materials*, 1(2): 56-62.
24. Raynie, D. E. (2006). Modern extraction techniques. *Analytical chemistry*, 78(12): 3997-4004.
25. Yadav, V. K. and Kumar, V. (2015). New approach in extraction process for discovery of herbal drug. *Indo American Journal of Pharmaceutical Research*, 4(8): 14-39.
26. Hemmati, M., Rajabi, M. and Asghari, A. (2018). Magnetic nanoparticle based solid-phase extraction of heavy metal ions: A review on recent advances. *Microchimica Acta*, 185(3): 160.
27. Wan Ibrahim, W. A., Sutirman, Z. A., Qaderi, J., Abu Bakar, K., Md Basir, S. H. and Aouissi, I. E. (2020). A Review on applications of gold and silver-based sorbents in solid phase extraction and solid phase microextraction. *Malaysian Journal of Analytical Sciences*, 24(4): 464-483.
28. Baharin, S. N. A. (2016). Functionalized polythiophene-coated magnetic nanoparticles for solid-phase extraction of phthalates, Doctoral dissertation, University of Malaya.
29. Dios, A. S. De and Díaz-garcía, M. E. (2010). Multifunctional nanoparticles: Analytical prospects. *Analytica Chimica Acta*, 666(1-2): 1-22.
30. Liu, Y., Tourbin, M., Lachaize, S. and Guiraud, P. (2013). Silica nanoparticles separation from water: Aggregation by cetyltrimethylammonium bromide (CTAB). *Chemosphere*, 92(6): 681-687.
31. Ahmadi, M., Elmongy, H. and Madrakian, T. (2017). Nanomaterials as sorbents for sample preparation in bioanalysis: A review. *Analytica Chimica Acta*, 958: 1-21.
32. Alivisatos, P. (2000). Colloidal quantum dots. From scaling laws to biological applications. *Pure and Applied Chemistry*, 72(1-2): 3-9.
33. Bitas, D. and Samanidou, V. (2018). Carbon nanotubes as sorbent materials for the extraction of pharmaceutical products followed by chromatographic analysis. *Fullerens, Graphenes and Nanotubes*: pp. 375-411.
34. Ahmadi, M., Elmongy, H. and Madrakian, T. (2017). Nanomaterials as sorbents for sample preparation in bioanalysis: A review. *Analytica Chimica Acta*, 958: 1-21.
35. Keypour, H., Shayesteh, M., Sharifi-Rad, A., Salehzadeh, S., Khavasi, H. and Valencia, L. (2008). Synthesis and characterization of copper(II) and cobalt(II) complexes with two new potentially hexadentate Schiff base ligands. X-ray crystal structure determination of one copper(II) complex. *Journal of Organometallic Chemistry*, 693(19): 3179-3187.
36. Zhao, F. and Zhao, M. (2007). Supramolecules: The chemical building blocks of the future. *ChemInform*, *38*(23): 89-100.

37. Jia, Q., Geng, Z. Q., Liu, Y., Wang, W., Han, C. Q., Yang, G. H., Li, H. and Qu, L. L. (2018). Highly reproducible solid-phase extraction membrane for removal and surface-enhanced Raman scattering detection of antibiotics. *Journal of Materials Science*, 53(21): 14989-14997.
38. Golzari Aqda, T., Behkami, S., Raoofi, M. and Bagheri, H. (2019). Graphene oxide-starch-based micro-solid phase extraction of antibiotic residues from milk samples. *Journal of Chromatography A*, 1591: 7-14.
39. Pourjavadi, A., Nazari, M., Kabiri, B., Hosseini, S. H. and Bennett, C. (2016). Preparation of porous graphene oxide/hydrogel nanocomposites and their ability for efficient adsorption of methylene blue. *RSC Advances*, 6(13): 10430-10437.
40. Xu, L., Qi, X., Li, X., Bai, Y. and Liu, H. (2016). Recent advances in applications of nanomaterials for sample preparation. *Talanta*, 146: 714-726.
41. Wang, L., Zhao, W. and Tan, W. (2008). Bioconjugated silica nanoparticles: development and applications. *Nano Research*, 1(2): 99-115.
42. Jeelani, P. G., Mulay, P., Venkat, R. and Ramalingam, C. (2020). Multifaceted application of silica nanoparticles: A review. *Silicon*, 12(6): 1337-1354.
43. Ansari, F. (2017). Novel nanostructured electron transport compact layer for efficient and large-area perovskite solar cells using acidic treatment of titanium layer. *Nanotechnology*, 2017: 1-30.
44. Shafqat, S. S., Khan, A. A., Zafar, M. N., Alhaji, M. H., Sanaullah, K., Shafqat, S. R., Murtaza, S. and Pang, S. C. (2019). Development of amino-functionalized silica nanoparticles for efficient and rapid removal of COD from pre-treated palm oil effluent. *Journal of Materials Research and Technology*, 8(1): 385-395.
45. Sun, Y., Zhang, Z. and Wong, C. P. (2005). Study on mono-dispersed nano-size silica by surface modification for underfill applications. *Journal of Colloid and Interface Science*, 292(2): 436-444.
46. Molaei, R., Tajik, H. and Moradi, M. (2019). Magnetic solid phase extraction based on mesoporous silica-coated iron oxide nanoparticles for simultaneous determination of biogenic amines in an Iranian traditional dairy product; Kashk. *Food Control*, 101: 1-8.
47. Abdolmohammad-Zadeh, H., Hassanlouei, S. and Zamani-Kalajahi, M. (2017). Preparation of ionic liquid-modified SiO_2@Fe_3O_4 nanocomposite as a magnetic sorbent for use in solid-phase extraction of zinc(II) ions from milk and water samples. *RSC Advances*, 7(38): 23293-23300.
48. Wu, W., He, Q. and Jiang, C. (2008). Magnetic iron oxide nanoparticles: Synthesis and surface functionalization strategies. *Nanoscale Research Letters*, 3(11): 397-415.
49. Urraca, J. L., Chamorro-Mendiluce, R., Orellana, G. and Moreno-Bondi, M. C. (2016). Molecularly imprinted polymer beads for clean-up and preconcentration of β-lactamase-resistant penicillins in milk. *Analytical and Bioanalytical Chemistry*, 408(7): 1843-1854.
50. Gros, M., Rodríguez-Mozaz, S. and Barceló, D. (2013). Rapid analysis of multiclass antibiotic residues and some of their metabolites in hospital, urban wastewater and river water by ultra-high-performance liquid chromatography coupled to quadrupole-linear ion trap tandem mass spectrometry. *Journal of Chromatography A*, 1292: 173-188.
51. Salari, M., Dehghani, M. H., Azari, A., Motevalli, M. D., Shabanloo, A. and Ali, I. (2019). High performance removal of phenol from aqueous solution by magnetic chitosan based on response surface methodology and genetic algorithm. *Journal of Molecular Liquids*, 285: 146-157.
52. Huang, Y., Zheng, H., Li, H., Zhao, C., Zhao, R. and Li, S. (2020). Highly selective uranium adsorption on 2-phosphonobutane-1,2,4-tricarboxylic acid-decorated chitosan-coated magnetic silica nanoparticles. *Chemical Engineering Journal*, 388: 124349.
53. Li, W. K. and Shi, Y. P. (2019). Recent advances and applications of carbon nanotubes based composites in magnetic solid-phase extraction. *TrAC - Trends in Analytical Chemistry*, 118: 652-665.

54. Mutavdzic Pavlovic, D., Nikšić, K., Livazović, S., Brnardić, I. and Anžlovar, A. (2015). Preparation and application of sulfaguanidine-imprinted polymer on solid-phase extraction of pharmaceuticals from water. *Talanta*, 131: 99-107.
55. Soledad-Rodríguez, B., Fernández-Hernando, P., Garcinuño-Martínez, R. M. and Durand-Alegría, J. S. (2017). Effective determination of ampicillin in cow milk using a molecularly imprinted polymer as sorbent for sample preconcentration. *Food Chemistry*, 224: 432-438.
56. Li, G., Xia, L., Dong, J., Chen, Y. and Li, Y. (2019). Metal-organic frameworks. In *Solid-Phase Extraction*. Elsevier Inc.
57. Lirio, S., Liu, W., Lin, C., Lin, C. and Huang, H. (2016). Aluminum based metal-organic framework-polymer monolith in solid-phase microextraction of penicillins in river water and milk samples. *Journal of Chromatography A*, 1428: 236-245.
58. Loiseau, T., Serre, C., Huguenard, C., Fink, G., Taulelle, F., Henry, M., Bataille, T. and Férey, G. (2004). A rationale for the large breathing of the porous aluminum terephthalate (MIL-53) upon hydration. *Chemistry - A European Journal*, 10(6): 1373-1382.
59. Bagheri, A. R. and Ghaedi, M. (2020). Magnetic metal organic framework for pre-concentration of ampicillin from cow milk samples. *Journal of Pharmaceutical Analysis*, 10(4): 365-375.
60. Bagheri, A. R., Arabi, M., Ghaedi, M., Ostovan, A., Wang, X., Li, J. and Chen, L. (2019). Dummy molecularly imprinted polymers based on a green synthesis strategy for magnetic solid-phase extraction of acrylamide in food samples. *Talanta*, 195: 390-400.

Malaysian Journal of Analytical Sciences (MJAS)
Published by Malaysian Analytical Sciences Society

UNVEILING HOMOGENEOUS CATALYTIC PERFORMANCE OF *N,N'*-BIS-(3,5-DI-*TERT*-BUTYLSALICYLIDENE)-2,2-DIMETHYLPROPANE-1,3-DIAMINEPALLADIUM(II) IN THE MIZOROKI-HECK REACTION

(Menyingkap Prestasi Pemangkinan Homogen *N,N'*-bis-(3,5-di-*tert*-butilsalisilidena)-2,2-dimetilpropana-1,3-diaminapaladium(II) dalam Tindak Balas Mizoroki-Heck)

Siti Kamilah Che Soh*, Mohd Sukeri Mohd Yusof, Wan M. Khairul

Faculty of Science and Marine Environment,
Universiti Malaysia Terengganu, 21030 Kuala Nerus, Terengganu, Malaysia.

**Corresponding author: sitikamilah@umt.edu.my*

Received: 18 September 2020; Accepted: 22 November 2020; Published: 20 February 2021

Abstract

Efficient Mizoroki-Heck coupling reactions were obtained using a homogeneous catalyst of symmetrical square planar *N,N'*-bis-(3,5-di-*tert*-butylsalicylidene)-2,2-dimethylpropane-1,3-diaminepalladium(II), Pd-L_{DDP}. The variables of time (3 and 6 hours), temperature (100, 120 and 140 °C), amount of catalyst loading (0.5, 1.0, 1.5 and 2.0 mmol%), and type of bases (Et_3N, $NaHCO_3$, Na_2CO_3 and NaOAc) were optimised to obtain excellent yield of Mizoroki-Heck coupling products of 4-bromoacetophenone with methyl acrylate. Catalytic results exhibited that the Pd-L_{DDP}/NaOAc/0.5 mmol%/140 °C catalyst system gave the optimum condition and achieved high performance for a wide range of electron withdrawing aryl bromides with the conversion of up to 85% in 6 hours of reaction time. Thus, the proposed phoshine-free catalyst, which is more stable towards air and moisture, significantly provided access towards the organic transformation of Mizoroki-Heck coupling reaction.

Keywords: N_2O_2-tetradentade ligand, palladium(II) complex, Mizoroki-Heck reaction

Abstrak

Tindak balas gandingan Mizoroki-Heck yang efisien telah dihasilkan menggunakan mangkin homogen bersimetri segi empat planar, *N,N'*-bis-(3,5-di-*tert*-butilsalisilidena)-2,2-dimetilpropana-1,3-diaminapaladium(II), Pd-L_{DDP}. Pembolehubah masa (3 dan 6 jam), suhu (100, 120 dan 140 °C), jumlah muatan mangkin yang digunakan (0.5, 1.0, 1.5 dan 2.0 mmol%), dan jenis bes (Et_3N, $NaHCO_3$, Na_2CO_3 dan NaOAc) telah dioptimumkan untuk memberikan hasil yang sangat baik bagi produk gandingan Mizoroki-Heck 4-bromoasetofenon dengan metil akrilat. Hasil kajian pemangkinan menunjukkan sistem mangkin Pd-L_{DDP}/NaOAc/0.5 mmol%/140 °C telah memberikan keadaan yang optimum serta mencapai prestasi tinggi bagi pelbagai aril bromida berpenarik elektron dengan penukaran hasil sehingga 85% dalam masa tindak balas selama 6 jam. Oleh itu, cadangan mangkin bebas-fosfina yang lebih stabil terhadap udara dan kelembapan secara signifikan telah menyediakan capaian terhadap transformasi organik dalam tindak balas gandingan Mizoroki-Heck.

Kata kunci: ligan tetradentat-N_2O_2, kompleks paladium(II), tindak balas Mizoroki-Heck

Introduction

The palladium catalysed Mizoroki-Heck reaction provides a promising route for the formation of C-C bonds in organic synthesis as these coupling reactions are significantly used for the preparation of materials [1], natural products [2], biologically active compounds [3] conducting polymers, and pharmaceutical intermediates [4, 5]. The reaction was discovered by Mizoroki and Heck in year 1972 through independent research which could replace the combination of metalated arenes and reoxidants, thus giving rise to the form of catalytic reaction practised today [6]. Mannepalli et al., reported that palladium is arguably the most versatile and achieved the status of an indispensable tool for organic transformations [7]. There is no doubt that other transition metals cannot compete with the versatility of palladium. The ready accessibility of two stable oxidation states, 0 and +2, as well as the availability of Pd-containing species simultaneously, are mainly responsible for the rich chemistry enjoyed by the palladium complex in the catalytic system.

The improvement of catalytic efficiency also strongly relies on the reactivity of palladium catalyst attached with efficient supporting ligands. Recently, much efforts have been made to search for powerful ligands that could replace common type homogeneous palladium-phosphine complexes which are often air and moisture sensitive [8]. P-C bond degradation sometimes occurs at elevated temperatures, leading to the decomposition of the catalyst and this phenomenon strongly affects the catalytic conversion as well as selectivity [9-11]. In this regard, the development of simple, mild, efficient, and more environmentally N-, O- donor Schiff base ligands have emerged as phosphine-free ligands. Schiff bases have been extensively studied and proved suitable for the palladium species. In an attempt to evaluate the phosphine-free system in the Mizoroki-Heck reaction, tetradentate N_2O_2 chelated palladium(II) complex was chosen for this purpose due to its facile approach, relative tolerance, readily adjusted ancillary ligand, and electronic environment on the metal centre [12].

Inspired by these properties, the tetradentate N_2O_2 chelated palladium(II) complex often act as a catalyst. This study aims to investigate the performance of the synthesised catalyst to be potentially used for carbon cross-coupling reaction. Then, the catalytic of this synthesised complex was evaluated using the Mizoroki-Heck reaction to produce trans alkene with excellent yields. Notably, the use of palladium(II) complex derived from bulky 3,5-di-*tert*-butylsalicylidene has a positive influence on the Mizoroki-Heck reaction which conserved leading to an inexpensive alternative and provide a magical boosting of catalytic activity and efficiency [13].

Materials and Methods

Chemicals and reagents

All reactants, reagents and solvents were of synthetic grade, purchased from various commercial sources and used without prior treatment unless stated otherwise. Chemicals namely sodium acetate (NaOAc), sodium carbonate (Na_2CO_3), sodium bicarbonate ($NaHCO_3$), and triethylamine (Et_3N) were obtained from R&M Supplier, United Kingdom. In addition, 4-bromoacetophenone and methyl acrylate were procured from Sigma-Aldrich (Malaysia) Sdn Bhd. N,N-dimethylacetamide (DMAc) and other solvents were supplied by Merck Sdn Bhd, Malaysia.

Characterisation techniques

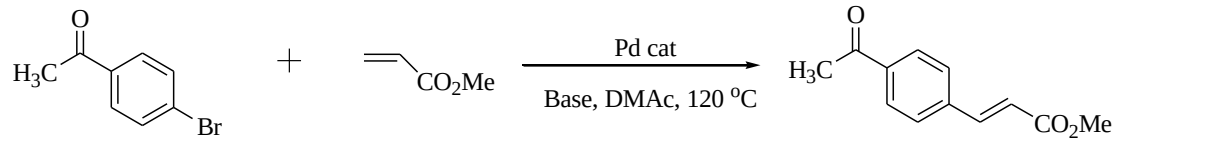
The catalytic Mizoroki-Heck reaction was analysed using a gas chromatography (GC-Hewlett Packard-5890 Series II) with ULTRA-1.0.05, 100% dimethylpolysiloxane capillary column (30 m length and 0.25 mm diameter), and flame ionization detector. The microliter (1 μL) samples were injected at 50 °C and the temperature increment was set at the rate of 15 °C per minute. The final temperature of the analyses was fixed at 300 °C. The catalytic conversion of reactant percentage was calculated using Equation 1:

$$\% \text{ conversion} = \frac{(A_{initial}) - (A_{final})}{(A_{initial})} \times 100 \quad (1)$$

The structure of the isolated catalytic product was elucidated with FTIR, ^{1}H and ^{13}C NMR spectroscopies.

General procedure for catalytic Mizoroki-Heck reaction

The catalytic tests were conducted under a nitrogen atmosphere using Carousel 12 Plus reaction station. In a typical Mizoroki-Heck reaction (Scheme 1), a mixture of 4-bromoacetophenone (1.0 mmol), methyl acrylate (1.5 mmol), base (2.4 mmol), catalyst (approximately 0.5-2.0 mmol%), and DMAc (2.5 mL) was stirred and heated for a given time (3 and 6 hours) and at a given temperature (100, 120 and 140 °C). After the desired reaction time, a small fraction (1 μL) of the liquid sample was taken and analysed by GC-FID. Then, the product was acidified with 2% hydrochloric acid (HCl) solution [14]. The percentage of product conversion was calculated based on the amount of 4-bromoacetophenone consumed. The purified product was determined by Perkin Elmer Spectrum One FTIR spectrometer and Bruker Avance 400 MHz NMR spectroscopy.



4-bromoacetophenone Methyl acrylate 3-(4-acetyl-phenyl)-acrylic acid methyl ester

Scheme 1. The palladium (II) complex catalysed Mizoroki-Heck reaction

Results and Discussion

The synthesised complex, namely *N,N'*-bis-(3,5-di-*tert*-butylsalicylidene)-2,2-dimethylpropane-1,3-diaminepalladium(II) **(**Pd-L_{DDP}) was successfully obtained in 76% yields as orange crystals by the reaction according to the previous methods [15, 16]. The spectroscopic characterisations of the ligand are agreed with literature values [17, 18]. As a preliminary study, the complex was explored as a homogeneous catalyst for the Mizoroki-Heck coupling of 4-bromoacetophenone with methyl acrylate. DMAc was used in this catalytic reaction as polar aprotic solvents give faster reaction rates compared to polar protic and nonpolar solvents [19, 20]. DMAc with a high boiling point has a strong influence on the solubilisation and stabilisation of the palladium catalyst [21, 22]. Reaction conditions were optimised using different types of bases, catalyst loading, and temperature [23, 24]. With the optimised conditions in hand, the catalytic reaction was further investigated for a variety of aryl bromides and the results obtained from the Mizoroki-Heck cross-coupling reaction are discussed in the following section.

Influence of different bases

Inorganic and organic bases were tested in the catalytic Mizoroki-Heck reaction. It should be noted that the choice of the base has been found to have a crucial effect on the rate and the conversion of Mizoroki-Heck product [25, 26]. A study by Dounay and Overman, reported that base plays a significant role in the reductive elimination of hydrogen bromide from the palladium(II) centre in the last step of the Mizoroki-Heck catalytic cycle and also to regenerate the palladium(0) catalyst [27]. Initially, four types of different bases (NaOAc, Na_2CO_3, $NaHCO_3$ and Et_3N) were selected for screening (Figure 1). It was observed that all the bases encouraged yields in the presence of polar DMAc and the increase of reaction time. Notably, NaOAc gave the highest conversion of the coupling product of up to 85% in 6 hours of reaction time. The effectiveness of using NaOAc for Mizoroki-Heck reaction was also reported previously [28]. Other inorganic bases such as $NaHCO_3$ and Na_2CO_3 recorded conversion percentage of 61% and 24%, respectively, due to the relative insolubility effects of the inorganic bases in the organic transformation reaction [29].

However, it is noteworthy that acceptable percentage product conversion of 35% was achieved when Et_3N was used as the base, and this could be explained due to the ligating properties of an organic base that may compete with the substrates and in part to block off free coordination sites on the palladium centre [30].

Influence of catalyst loading

Encouraged by the results of the different bases effect, the catalytic behaviour of palladium(II) complex was further investigated using various catalyst loading. The coupling of 4-bromoacetophenone with methyl acrylate in the presence of DMAc as the solvent, NaOAc as the base at 120 °C were set out in this study. The volume of the solvent, base, temperature, and time was also kept constant. The experiments were repeated for 0.5, 1.5 and 2.0 mmol% of the amount of catalyst used, respectively. As observed in Table 1, by increasing the amount of the palladium catalyst, the conversion percentage also increased [29]. This suggests that palladium functions as an active site for the cross-coupling reaction and the catalyst loads of 1.0 mmol% typically required to achieve a quantitative conversion of the substrates. The amount of catalyst loading tremendously affects the overall catalytic performance and selectivity patterns [1]. It was apparent that 0.5 mmol% recorded the highest TON occurred with 66% of product conversion (Table 1, entry 2). Thus, by controlling the amount of catalyst, an excellent TON was expected to maximise the conversion percentage of the desired products. The Mizoroki-Heck catalytic reaction that can be carried out with a small amount of expensive catalyst is the most efficient feature of synthetic reactions involving palladium(II) complex.

Influence of reaction temperature

After the optimisation of catalyst loading, the experiments with various reaction temperature revealed that the best reaction temperature was found to be at 140 °C, which was suitable for the activation of aryl bromide using the synthesised Pd-L_{DDP}. It could be seen that no conversion of the product was formed when the reaction was carried out at room temperature (Table 2, entries 1 and 5), but as the temperature increased, the constant reaction rate increased due to the increase in average kinetic energy of molecules and more collisions per unit time [19]. The conversion of 4-bromoacetophenone increased from 53% to 90% under the same reaction time. Thus, showed that the Pd-L_{DDP} exhibited stability at high temperature. The high temperature used in the catalytic reaction should be carefully controlled to prevent the possible decomposition of Pd-L_{DDP} by the formation of palladium black, thereby the catalytic cycle of Mizoroki-Heck could be terminated immediately.

Different and diversely substituted aryl bromides

To show the performance efficiency of Pd-L_{DDP}**,** the catalytic Mizoroki-Heck was further investigated using different substrates (Scheme 2). With the favourable results in hand, the optimal reaction conditions: (Pd-L_{DDP} (0.5 mmol), aryl bromides (1.0 mmol), methyl acrylate (1.5 mmol), NaOAc (2.4 mmol), DMAc (5 mL) under thermal conditions at 140 °C, four aryl bromides were tested to study the natural effect of substituents containing electron-donating and electron-withdrawing groups. The activated aryl bromides which have electron-withdrawing groups (Table 3, entries 1 and 2) were beneficial and gave excellent conversion percentage at the reaction time of 6 hours. However, no desirable coupled products were obtained until the end of the reaction for deactivated electron-donating aryl bromides (entries 3 and 4).

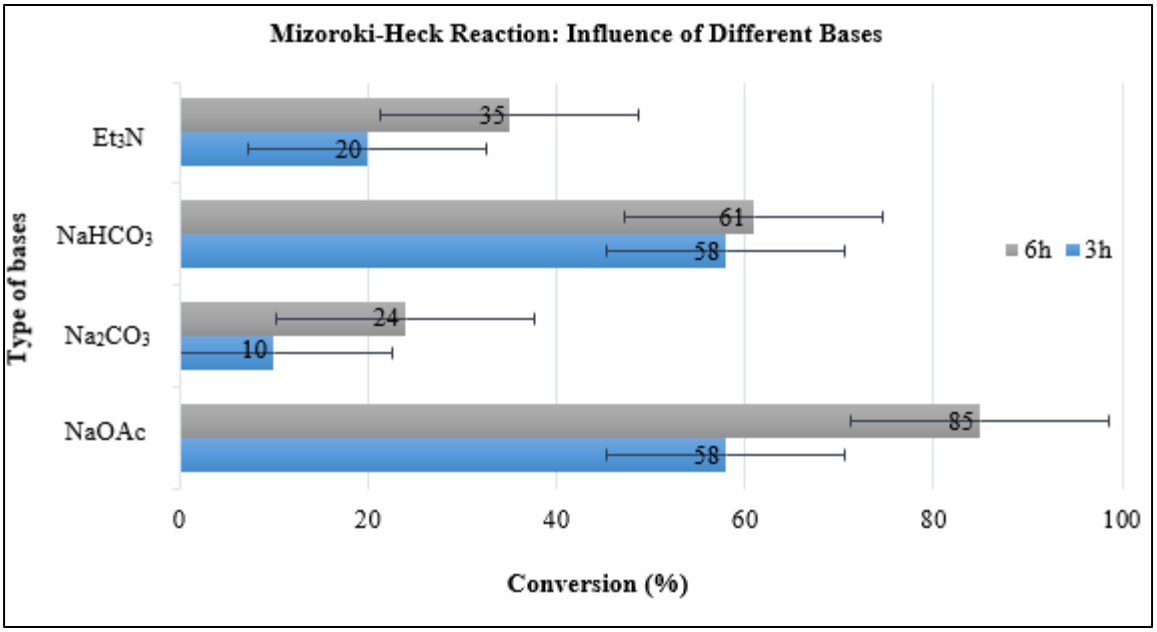


Figure 1. Results obtained for Mizoroki-Heck reaction with a different type of bases

Table 1. Results obtained for Mizoroki-Heck reaction with the effect of different catalyst loading

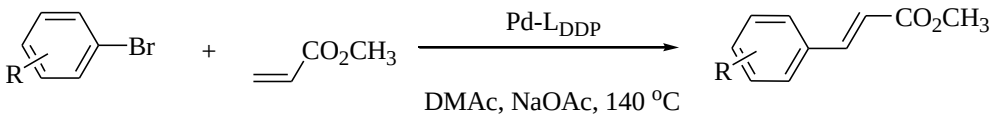
Entry	Catalyst (Pd-L_{DDP}) (mmol%)	Reaction Time (h)	Reaction Temperature (°C)	Product Conversion[b] (%)	TON[c]
1	0.5	3	120	46	92
2	0.5	6	120	66	132
3	1.0	3	120	58	58
4	1.0	6	120	85	85
5	1.5	3	120	62	41
6	1.5	6	120	88	59
7	2.0	3	120	71	36
8	2.0	6	120	92	46

[a]Reaction conditions: 4-bromoacetophenone (1.0 mmol), methyl acrylate (1.5 mmol), NaOAc (2.4 mmol), 5 mL DMAc, Pd(II) catalyst.
[b]Determined by GC-FID.
[c]Turnover number (TON) calculated at the completion of the reaction (mmol of 4-bromoacetophenone transformed/mmol of catalyst used).

Table 2. Results obtained from Mizoroki-Heck reaction with the effect of different reaction temperature

Entry	Catalyst (Pd-L_{DDP}) (mmol%)	Reaction Time (h)	Reaction Temperature (°C)	Product Conversion[b] (%)
1	0.5	3	room temp.	0
2	0.5	3	100	31
3	0.5	3	120	46
4	0.5	3	140	79
5	0.5	6	room temp.	0
6	0.5	6	100	53
7	0.5	6	120	66
8	0.5	6	140	90

[a]Reaction conditions: 4-bromoacetophenone (1.0 mmol), methyl acrylate (1.5 mmol), NaOAc (2.4 mmol), 5 mL DMAc, Pd(II) catalyst
[b]Determined by GC-FID



Scheme 2. Mizoroki-Heck reaction of aryl bromides

Table 3. Results obtained from the Mizoroki-Heck reaction with diversity substituted aryl bromides

Entry	R (mmol%)	Reaction Time (h)	Product Conversion[b] (%)
1	4-COMe	6	90
2	4-NO_2	6	85
3	4-OMe	6	No conversion
4	H	6	No conversion

[a]Reaction conditions: aryl halide (1.0 mmol), methyl acrylate (1.5 mmol), NaOAc (2.4 mmol), 5 mL DMAc, Pd(II) catalyst
[b]Determined by GC-FID

Conclusion

The **Pd-L$_{DDP}$** was successfully tested as a homogeneous catalyst in the Mizoroki-Heck reaction. The catalyst demonstrated good catalytic performances in the Mizoroki-Heck coupling reaction, in which the high conversion of products was obtained. Remarkably, only small amounts of **Pd-L$_{DDP}$** (0.5 mmol%) were required to perform the catalysed reaction at a high temperature of 140 °C. Optimised conditions resulted in up to 80% of product conversion for activated electron-withdrawing groups. Also, the electronic nature of aryl bromides had a dominating effect on the conversion of the product. The activated aryl bromides reacted nearly quantitatively compared to other substituents. We believe these findings were found to be optimum are beginning to merge as set of conditions for **Pd-L$_{DDP}$** catalyst which could be the starting point for most substrates.

Acknowledgement

We gratefully acknowledge the financial support from the Ministry of Higher Education (FRGS/1/2016/STG01/UMT/02/1) for the funding under Grant No. 59456 and Universiti Malaysia Terengganu (UMT) for the use of research facilities. This paper also is dedicated to our wonderful colleague, Professor Dr. Mustaffa Shamsuddin, who recently retired from Universiti Teknologi Malaysia.

References

1. Jagtap, S. (2017). Heck reaction-state of the art. *Catalysts*, 7(9): 267.
2. Ghosh, T. (2019). Reductive Heck reaction: An emerging alternative in natural product synthesis. *ChemistrySelect*, 4(16): 4747-4755.
3. Tarnowicz-Ligus, S. and Trzeciak, A. M. (2018). Heck transformations of biological compounds catalyzed by phosphine-free palladium. *Molecules*, 23(9): 2227.
4. Budarin, V. L., Shuttleworth, P. S., Clark, J. H. and Luque, R. (2010). Industrial applications of C-C coupling reactions. *Current Organic Synthesis*, 7(6): 614-627.
5. Biajoli, A. F. P., Schwalm, C. S., Limberger, J., Claudino, T. S. and Monteiro, A. L. (2014). Recent progress in the use of Pd-catalyzed C-C cross-coupling reactions the synthesis pharmaceutical compounds. *Journal of the Brazilian Chemical Society*, 25(12): 2186-2214.
6. Watson, D. A. (2012). Selected diastereoselective reactions: Heck type cyclizations. Comprehensive Chirality. Elsevier Science, Netherland: pp. 648-684.
7. Mannepalli, L. K., Gadipelly, C., Deshmukh, G., Likhar, P., and Pottabathula, S. (2020). Advances in C-C coupling reactions catalyzed by homogeneous phosphine free palladium catalysts. *Bulletin of the Chemical Society of Japan*, 93(3): 355-372.
8. Mino, T., Shirae, Y., Sasai, Y., Sakamoto, M. and Fujita, T. (2006). Phosphine-free palladium catalyzed mizoroki−heck reaction using hydrazone as a ligand. *The Journal of Organic Chemistry*, 71(18): 6834-6839.
9. Bakherad, M., Keivanloo, A., Amin, A. H. and Jajarmi, S. (2012). Phosphine-free polystyrene-supported palladium(II) complex as an efficient catalyst for the Heck and Suzuki coupling reactions in water. *Comptes Rendus Chimie*, 15(11-12): 945-949.
10. Mingji, D., Liang, B., Wang, C., You, Z., Xiang, J., Dong, G., Chen, J. and Yang, Z. (2004). A novel thiourea ligand applied in the Pd-catalyzed Heck, Suzuki and Suzuki carbonylative reactions. *Advanced Synthesis & Catalysis*, 346 (13-15): 1669-1673.
11. Farina, V. (2004). High-turnover palladium catalysts in cross-coupling and Heck chemistry: A critical overview. *Advanced Synthesis & Catalysis*, 346: 1553-1582.
12. Wang, M., Zhu, H., Jin, K., Dai, D. and Sun, L. (2003). Ethylene oligomerization by Salen-Type zirconium complexes to low-carbon linear α-olefins. *Journal of Catalysis*, 220: 392-398.
13. Ulusoy, M., Birel, Ö., Şahin, O., Büyükgüngör, O. and Centikaya, B. (2012). Structural, spectral, electrochemical and catalytic reactivity studies of a series of N_2O_2 chelated palladium(II) complexes. *Polyhedron*, 38: 141-148.

14. Oberholzer, M. and Frech, C. M. (2014). Mizoroki-Heck cross-coupling reactions catalyzed by dichloro{bis[1,1',1"-(phosphinetriyl)tripiperidine]} palladium under mild reaction conditions. *Journal of Visualized Experiments*, 85(51444): 1-7.
15. Faghih, Z., Neshat, A., Wojtczak, A., Faghih, Z., Mohammadi, Z. and Varestan, S. (2018). Palladium(II) complexes based on schiff base ligands derived from ortho-vanillin; synthesis, characterization and cytotoxic studies. *Inorganica Chimica Acta*, 471: 404-412.
16. Feng, Z. Q., Yang, X. L. and Ye, Y. F. (2013). Pd(II) and Zn(II) based complexes with Schiff base ligands: synthesis, characterization, luminescence, and antibacterial and catalytic activities. *The Scientific World Journal*, 2013: 956840
17. Rao, G. K., Kumar, A., Kumar, B., Kumar, D. and Singh, A. K. (2012). Palladium(II)-Selenated Schiff base complex catalyzed Suzuki-Miyaura coupling: Dependence of efficiency on alkyl chain length of ligand. *Dalton Transactions*, 41: 1931-1937.
18. Kianfar, A. H., Zargari, S. and Khavasi, H. R. (2010). Synthesis and electrochemistry of M(II) N_2O_2 Schiff base complexes: X-ray structure of {Ni[Bis(3-chloroacetylacetone)ethylenediimine]}. *Journal of the Iranian Chemical Society*, 7: 908-916.
19. Nyangasi, L. O., Andala, D. M., Onindo, C. O., Ngila, J. C., Makhubela, B. C. and Ngigi, E. M. (2017). Preparation and characterization of Pd modified TiO_2 nanofiber catalyst for carbon–carbon coupling Heck reaction. *Journal of Nanomaterials*, 2017: 8290892.
20. Djakovitch, L. and Koehler, K. (1999). Heterogeneously catalysed Heck reaction using palladium modified zeolites. *Journal of Molecular Catalysis A: Chemical*, 142(2): 275-284.
21. Nuri, A., Vucetic, N., Smått, J. H., Mansoori, Y., Mikkola, J. P. and Murzin, D. Y. (2020). Synthesis and characterization of palladium supported amino functionalized magnetic-MOF-MIL-101 as an efficient and recoverable catalyst for Mizoroki–Heck cross-coupling. *Catalysis Letters*, 2020: 1-13.
22. Yang, C. and Nolan, S. P. (2001). A highly efficient palladium/imidazolium salt system for catalytic Heck reactions. *Synlett*, 10: 1539-1542.
23. Kumari, S., Maddipoti, K., Das, B. and Ray, S. (2019). Palladium–Schiff base complexes encapsulated in zeolite-Y host: functionality controlled by the structure of a guest complex. *Inorganic Chemistry*, 58(2): 1527-1540.
24. Che Soh, S. K. and Shamsuddin, M. (2018). Synthesis, characterization and catalytic applications of 2,2-dimenthylpropane-1,3-diaminopalladium(II) complex in Mizoroki-Heck reaction. *Asian Journal of Chemistry*, 30(1): 81-84.
25. Xu, H. J., Zhao, Y. Q. and Zhou, X. F. (2011). Palladium-catalyzed Heck reaction of aryl chlorides under mild conditions promoted by organic ionic bases. *The Journal of Organic Chemistry*, 76(19): 8036-8041.
26. Littke, A. F., and Fu, G. C. (2001). A versatile catalyst for heck reactions of aryl chlorides and aryl bromides under mild conditions. *Journal of the American Chemical Society*,123(29): 6989-7000.
27. Dounay, A. B. and Overman, L. E. (2003). The asymmetric intramolecular Heck reaction in natural product total synthesis. *Chemical Reviews*, 103(8): 2945-2964.
28. Beller, M. and Riermeier, T. H. (1996). First efficient palladium-catalyzed Heck reactions of aryl bromides with alkyl methacrylate. *Tetrahedron Letters*, 37(36): 6535-6538.
29. Nasrollahzadeh, M., Azarian, A., Ehsani, A. and Khalaj, M. (2014). Preparation, optical properties and catalytic activity of TiO_2@ Pd nanoparticles as heterogeneous and reusable catalysts for ligand-free Heck coupling reaction. *Journal of Molecular Catalysis A: Chemical*, 394: 205-210.
30. Hahn, F. E., Jahnke, M. C., Gomez-Benitez, V., Morales-Morales, D. and Pape, T. (2005). Synthesis and catalytic activity of pincer-type bis(benzimidazolin-2-ylidene) palladium complexes. *Organometallics*, 24: 6458-6463.

Malaysian Journal of Analytical Sciences (MJAS)
Published by Malaysian Analytical Sciences Society

DUAL-PRODUCTION OF POLYHYDROXYALKANOATE AND RHAMNOLIPID BY *Pseudomonas aeruginosa* UMTKB-5 USING INDUSTRIAL BY-PRODUCTS

(Dwi-Produksi Polihidroksialkanoat dan Ramnolipid oleh *Pseudomonas aeruginosa* UMTKB-5 dengan Penggunaan Hasil Sampingan Industri)

Noor Fazielawanie Mohd Rashid[1], Tan Suet May Amelia[1], Al-Ashraf Abdullah Amirul[2,3,4], Kesaven Bhubalan[1,4,5]*

[1]*Faculty of Science and Marine Environment,*
Universiti Malaysia Terengganu, 21030 Kuala Nerus, Terengganu, Malaysia
[2]*Centre for Chemical Biology,*
Universiti Sains Malaysia, 11900 Bayan Lepas, Penang, Malaysia
[3]*School of Biological Sciences,*
Universiti Sains Malaysia, 11800 Gelugor, Penang, Malaysia
[4]*Malaysian Institute of Pharmaceuticals and Nutraceuticals,*
National Institutes of Biotechnology Malaysia, 11700 Gelugor, Penang, Malaysia
[5]*Institute of Marine Biotechnology,*
Universiti Malaysia Terengganu, 21030 Kuala Nerus, Terengganu, Malaysia

**Corresponding author: kesaven@umt.edu.my*

Received: 9 September 2020; Accepted: 10 November 2020; Published: 20 February 2021

Abstract

The biodegradability and biocompatibility of polyhydroxyalkanoate (PHA) bioplastic and rhamnolipid (RL) biosurfactant have encouraged their application in medicine, packaging, and bioremediation. However, the resources used to produce these two substances contribute to high manufacturing costs. Therefore, we applied the dual-production approach and fed the same renewable and economical carbon and nitrogen sources into singular cultivation media to produce both PHA and RL simultaneously. By-products from oleochemical (glycerol and glycerine pitch) and sugarcane (molasses and sweet water) industries were used to produce mcl-PHA and RL from *Pseudomonas aeruginosa* UMTKB-5. Furthermore, we also attempted the introduction of plasmid pBBR-PC$_{1020}$ into transformant *P. aeruginosa* UMTKB-5 to produce 20-50% scl-mcl PHA with better properties. The PHA and RL yields were compared between wild-type and transformant strains with the use of seven carbon sources and six nitrogen sources. With glycerol as the carbon source and urea [$CO(NH_2)_2$] as the nitrogen source, the wild-type strain had produced the highest amount of PHA and RL at 0.24 ± 0.01 and 2.31 ± 0.01 g/L, respectively. The overall molecular weights (M_w) of the polymers produced ranged from 4 x 10^5 to 5 x 10^5 Da. Characterisation analysis on the RL congeners produced were identified as mono- and di-RL.

Keywords: *Pseudomonas aeruginosa*, polyhydroxyalkanoate, rhamnolipid, glycerine pitch, glycerol, dual-production

Abstrak

Biopolimer polihidroksialkanoat (PHA) dan biosurfaktan ramnolipid (RL) yang mempunyai ciri-ciri biodegradasi dan keserasian bio telah mendorong penggunaannya dalam perubatan, pembungkusan, dan bioremediasi. Walau bagaimanapun, sumber yang digunakan untuk menghasilkan kedua-dua bahan ini menyumbang kepada kos pembuatan yang tinggi. Justeru, kami mengaplikasikan pendekatan dwi-produksi dan memberi sumber karbon dan nitrogen sama yang boleh diperbaharui dan murah ke dalam media kultur tunggal untuk menghasilkan PHA dan RL secara serentak. Hasil sampingan dari industri oleokimia (gliserol dan gliserin) dan tebu (molase dan air manis) digunakan sebagai sumber karbon untuk menghasilkan mcl-PHA dan RL dari *Pseudomonas aeruginosa* UMTKB-5. Selanjutnya, kami juga memperkenalkan plasmid pBBR-PC$_{1020}$ kepada transforman *P. aeruginosa* UMTKB-5 untuk menghasilkan 20-50% scl-mcl PHA dengan sifat yang lebih baik. Hasil PHA dan RL dibandingkan antara strain jenis liar dan transforman dengan penggunaan tujuh sumber karbon dan enam sumber nitrogen. Dengan gliserol sebagai sumber karbon dan urea [CO(NH$_2$)$_2$] sebagai sumber nitrogen, strain jenis liar telah menghasilkan jumlah PHA dan RL tertinggi masing-masing pada 0.24 ± 0.01 dan 2.31 ± 0.01 g/L. Berat molekul (*Mw*) polimer yang dihasilkan secara keseluruhan adalah dari 4 x 10^5 hingga 5 x 10^5 Da. Analisis pencirian atas kongener RL yang dihasilkan telah dikenal pasti sebagai mono- dan di-RL.

Kata kunci: *Pseudomonas aeruginosa*, polihidroksialkanoat, ramnolipid, sisa gliserin, gliserol, dwi-produksi

Introduction

Plastic pollution and the depletion of finite sources, such as natural gas and crude oil, from the manufacturing of fossil-based plastic have urged the research for alternative materials. One of the potential substitutes of plastic, polyhydroxyalkanoate (PHA), is known as a naturally occurring, biodegradable, and biocompatible polymer [1]. Polyhydroxyalkanoate is biosynthesised by microbes, such as fungi, algae, and bacteria, as an energy storage compound in cell cytoplasm [2]. This biopolymer is classified by their branching monomers. Short-chain-length PHA (scl-PHA) consists of 3-5 carbon atoms in the monomer units, such as poly(3-hydroxybutyrate) [P(3HB)] and poly(4-hydroxybutyrate) [P(4HB)]. Medium-chain-length PHA (mcl-PHA) comprises more than 6 carbon atoms, such as poly(3-hydroxyhexanoate) [P(3HHx)] and poly(3-hydroxydecanoate) [(3HD)] [3]. Polyhydroxyalkanoate can also be categorised into a homopolymer PHA that comprises one type of hydroxyalkanoate [e.g. P(3HB)] or a heteropolymer PHA that comprises more than one type of hydroxyalkanoate [e.g. poly(3-hydroxybutyrate-*co*-3-hydroxyvalerate) P(3HB-*co*-3HV)]. The diverse types of PHA allow the polymer to be tailored for multiple applications such as agriculture, packaging, and biomedicine [4]. For example, mcl-PHA is elastomeric; scl-PHA is crystalline, brittle, and stiff; while scl-mcl-PHA, has the combined properties of both types of PHA, is less crystalline, higher toughness, and higher degradation rate [5-7].

Certain bacterial PHA-producers also biosynthesise rhamnolipid (RL), which is the most studied biosurfactant [8-10] with emulsifying and antimicrobial properties. It is commonly composed of rhamnose (Rha) sugar molecules and β-hydroxyl alkanoic acids moieties. The properties of RL depends on homologue composition and distribution, bacterial producer, culture conditions, and medium types. *Pseudomonas* spp. Have been receiving research attention for biosurfactant applications since the RL produced from this genus showed high reduction of surface tension [11]. A marine isolate, *Pseudomonas aeruginosa* UMTKB-5 was previously reported to produce high RL concentration particularly from renewable agro-industrial by-products as substrates, which were molasses and sweetwater [12].

Some strains in the *Pseudomonas* genus have been reported to produce RL and PHA simultaneously [13-16]. Both PHA and RL are produced during imbalanced growth conditions, particularly under excess carbon sources and limitation of multivalent ions, such as nitrogen and phosphorus. Their yield is also influenced by the type of carbon source, type of nitrogen source, pH, and age of culture. The biodegradability, biocompatibility, and low toxicity of both PHA and RL encourage their usage in various industries. For example, RL has been researched in bioremediation, pharmaceuticals, cosmetics, and food industry [17-19], while PHA is widely used in pharmaceuticals, medical, packaging, and aquaculture industries [20-23].

However, low productivity, high downstream processing and raw-material costs caused a bottleneck for the commercialisation of PHA and RL. Carbon source accounts for about 30 to 50% of total production cost [24], hence alternative renewable resources, such as agro-industry by-products, have been researched to replace conventional substrates [25,26]. The renewable resources tested to produce PHA and RL from bacteria were wastes or by-products from biofuel and biochemical (glycerol and glycerine pitch), sugar cane (molasses), frying oil (waste lipids), cheese (whey), water treatment (municipal wastewater), starch (cassava wastewater), and other industries that use lignocellulosic raw materials [8, 13, 27-28]. Therefore, we attempted to construct transformant *P. aeruginosa* UMTKB-5 (harbouring PHA-synthesising gene (*phaC*) from *Cupriavidus* sp. USMAA1020) to biosynthesise scl-mcl PHA, and then compared the PHA and RL yields between wild-type and transformant *P. aeruginosa* UMTKB-5 with the use of seven carbon sources (common sugars and agro-industrial by-products) and six nitrogen sources through simultaneous production in a single production medium (Figure 1).

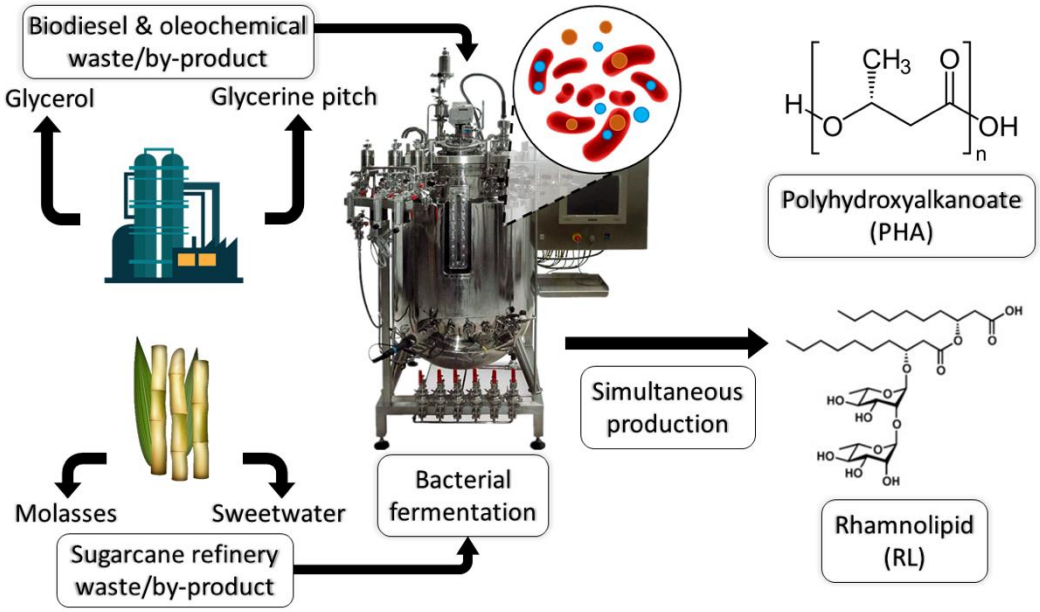


Figure 1. Illustration showing the simultaneous production of PHA and RL from industrial by-products using bacterial fermentation

Materials and Methods

Bacterial strains, plasmids, carbon sources

The wild-type *P. aeruginosa* UMTKB-5 strain (GenBank accession number: KT194193.1), isolated from marine sediment at Pulau Bidong (Terengganu, Malaysia), was obtained from the culture collection of Institute of Marine Biotechnology, Universiti Malaysia Terengganu [12]. Several types of carbon sources were used to produce PHA and RL. Bacteriological-grade sucrose (HiMedia, India) and 100% refined-grade glycerol (Bendosen, Norway) were purchased from commercial supplier. Meanwhile, glycerine pitch, generally comprising glycerol, ash, fatty acids, and organic salts, was obtained from Oleochemicals Industry, Penang, Malaysia [29]. On the other hand, molasses and sweetwater were obtained from cane sugar refinery company Gula Padang Terap Sdn. Bhd. (14006-V), Kuala Nerang, Kedah, Malaysia. Molasses typically consist of dry solids, ash, sugars (fructose and sucrose), and nutrients (phosphorus and nitrogen). Sweetwater is an agricultural by-product that still contains residual sucrose after filtration by a sugar cane refining process.

Biosynthesis of PHA and RL was carried out at a concentration of 20 g/L carbon substrate. The amount of sugars in the molasses and sweetwater used in this study were calculated to be 50.9 and 18.4 wt.%, respectively [12, 25].

Construction of transformant *P. aeruginosa* UMTKB-5

Prior biosynthesis, the *P. aeruginosa* UMTKB-5 transformant strain was constructed using the pBBR-PC_{1020} plasmid, a pBBR1MCS-2 derivative harbouring approximately 1.7 kb fragment of PHA synthase gene from *Cupriavidus* sp. USMAA1020 [30,31]. Transformant *P. aeruginosa* UMTKB-5 was constructed using benchtop- and microcentrifuge-based approaches based on the method proposed by Chuanchuen et al. [32]. The concentration of the plasmid was determined at an absorbance of 260 nm using Biophotometer Plus (Eppendorf, Germany). Transformation was carried out by adding 100 to 400 ng (2-5 µL) of plasmid DNA into 100 µL of prechilled competent cells. Sterile distilled water was used as negative control. The mixture was incubated in ice for 15 minutes, then heat-shock at 37 ºC for 3 minutes, followed by an addition of 500 µL of LB broth. The tubes were incubated on a shaking incubator at 37 ºC for 1 hour. 100 µL of the mixture was plated onto the LB agar containing 50 µg/mL of kanamycin (Merck, Darmstadt, Germany) to maintain plasmid stability. The plates were incubated at 37 °C overnight and observed.

Biosynthesis of PHA and RL

To prepare activated pre-culture, 2 loopfuls of wild-type *P. aeruginosa* UMTKB-5 bacterial cells were inoculated into 50 mL NR broth (HiMedia, India) and cultivated at 30 ºC, 200 rpm using HIMAC CR 22N (Hitachi, Japan) centrifuge machine for 11 hours. The transformant *P. aeruginosa* UMTKB-5 was cultivated for 8 hours with 50 µg/mL kanamycin added for plasmid maintenance. Using one-stage cultivation, biosynthesis of PHA and RL was carried out aerobically at 200 rpm, 30 ºC for 72 hours in a 5-L Biostat® C plus (Sartorius, Germany) bioreactor (2.5-L working volume) with 40% dissolved oxygen and pH 7 [13]. The pH was maintained by adding either 5 M of KOH (R&M, UK) or HCl solutions. Growth profiling was done for 96 hours with sampling at 12-hours intervals. Biosynthesis was carried out and compared between the use of seven types of carbon sources (glucose, fructose, sucrose, glycerol, glycerine pitch, molasses, and sweetwater) and six different types of nitrogen sources [$NH_4H_2PO_4$, $CO(NH_2)_2$, $NaNO_3$, NH_4NO_3, NH_4Cl, $(NH_4)_2SO_4$] to test for the source that produced the highest yield. Carbon sources were added into the mineral salt's medium prior fermentation. The concentration of nitrogen source applied was 2.5 g/L, whereas the carbon source applied was based on a C/N ratio of 50. The mineral salts medium consisted of KH_2PO_4 (R&M, UK), Na_2HPO_4 (R&M, UK), and NH_4Cl (Bendosen, HmbG) [33]. The cells were harvested by centrifugation (9000 rpm, 4 ºC) after 72 hours of fermentation. The collected supernatant was subjected to RL analysis, and the cell pellet was lyophilised using FreeZone 4.5 (Labconco Corporation, USA) freeze dry system for 72 h prior to PHA detection using gas chromatography analysis. The lyophilised cells were weighed using Sartorius CP2245 electronic balance (Sartorius, Germany) to determine cell biomass.

PHA characterisation: **Gas chromatography analysis**

The methanolysis was performed according to the modified method of Braunegg et al. [34]. Approximately 8-10 mg of lipolyzed cells were weighed and filled into screw-capped test tubes. A volume of 2 mL of methanolysis solution and 2 mL of $CHCl_3$ were added into the tube, and then sealed with Teflon tape. The samples were heated at 100 ºC on a heating block for two and a half hours. The tube was slightly inverted at every 30 minutes interval to homogenise the mixture.

After heating, the solution was cooled at room temperature for 15 minutes. A volume of 1 mL distilled water was added into the tubes and vortexed for 30 sec to encourage the formation of two distinct phases. The upper layer consists of water, while the bottom layer consists of $CHCl_3$ and hydroxyalkanoate methyl ester. By using 1endoza pipette, the bottom layer was transferred into tube containing anhydrous sodium sulphate (Na_2SO_4) (R&M, UK) to absorb the remaining water. Prior to injection, 0.5 mL of the solution was then transferred into GC vials containing 0.5 mL of Caprylic acid Methyl Ester (CME) solution.

The GC analysis was run using Trace GC ultra (Thermo Scientific, Italy) equipped with a flame ionisation detector (FID) and a fused silica capillary column (30 m length x 0.32 mm internal diameter, 0.25 µm film (Supelco, SPB-TM1, USA) with conditions: injector temperature 200 °C, detector temperature 280 °C, initial column temperature 50 ºC, final column temperature 280 ºC, air flow 2 mL/min, total flow 10 ºC/min, and analysis time 30 min. The concentration of PHA in the sample was calculated using the formula equation below [35]:

$$\text{Concentration of C6} = \frac{\text{(Area of C6 x concentration IS)}}{\text{(Area IS x } Rf\text{C6)}}$$

where area C6 is peak area for the C6 monomer, area IS is peak area for the internal standard, methyl benzoate, concentration IS is the amount of methyl benzoate per mL dichloromethane (DCM) and *Rf*C6 is the relative response factor for the C6 methyl-ester

Gas permeation chromatography analysis

The molecular weight data was obtained by using GPC (Shimadzu, Japan), refractive index detector (RID-0A) equipped with Plgel 5 µm MIXED-C column, 600 x 7.5 mm (polymer Laboratories, Ltd, UK) [36].

Approximately 1 mg of polymer sample was dissolved in 1 mL of $CHCl_3$ (HPLC grade). The solution was then filtered using 0.45 µm PTFE syringe filter (Sartorius, Germany). The sample was analysed to get the molecular weight (M_w), number average molecular weight (M_n) as well as polydispersity index (M_w/M_n). The $CHCl_3$ at a flow rate of 1.0 mL/min was used. Polystyrene standards with a low polydispersity were used as standard.

Differential scanning calorimetry analysis

DSC was run by using *Perkin-Elmer Pyris I* (Perkin Elmer, USA) equipped with nitrogen cooling accessory. Approximately 5-8 mg of samples was heated from -50 to 200 ºC. The rate of heating applied was 10 ºC/min. The glass transition temperature (T_g), melting temperature I and heat of fusion (ΔH_m) were determined from the graph [36].

Thermogravimetric analysis

TGA was conducted using thermal analysis system TGA/DSC 1 Mettler Toledo according to Guo et al. [37] with modification. Samples of approximately 15 mg were used for each measurement. Samples were heated at a flow rate of 20 mL/min from room temperature to 600 ºC using argon gas.

RL characterisation

Direct amount of RL in the sample were assessed by orcinol assay according to the method described by Koch et al. [38]. The orcinol reagent was prepared by adding the concentrated sulphuric acid, H_2SO_4 (98% w/w) and 0.19% of orcinol (3,5-dihydroxytoluene) to distilled water. The final concentration of acid was 53% w/w. A total of 100 mL of orcinol reagent was prepared by weighing 0.19 g of orcinol powder, 99% purity (R&M, UK), and mixed with 46 mL of distilled water. Finally, 54 mL of 98% w/w of H_2SO_4 was added into the solutions dropwise. For sample preparation, 400 µL of supernatant was added with 750 µL of diethyl ether (Merck, USA). Approximately 900 µL of prepared orcinol reagent was added to 100 µL of sample prior to determination of RL concentration. The optical density of 421 nm wavelengths was determined using spectrophotometer *UV1601PC* (Shimadzu, Japan).

The RL was further extracted using the method as proposed by Yin et al. [39]. The supernatant was mixed with ethyl acetate (Merck, Germany) at a ratio of 1:1 and vigorously shook for 3 minutes. The upper fraction was collected, and the solution was concentrated using rotary evaporator (Buchi, Switzerland) at 40 °C. Crude RL was obtained. A total of 30 mL of 0.05 M sodium bicarbonate was used to dissolve the crude RL. After adjusting to pH 2, the solution was kept overnight before being lyophilised for 72 hours.

The liquid chromatography-mass spectrometry (LC-MS) analysis was run using LCMS-QtoF model 6560 *UPHLC* (Agilent, USA) with a G4220A binary pump, a G4212A diode array detector, a G4226A HiP autosampler and a G1316C column compartment. Column POROSHELL 210 EC-C18 (4.6 mm x 100 mm, internal diameter 2.7 µm) [ChromTech, Inc., Minnesota, USA] was used for LCMS with conditions: gas

temperature 225 °C, gas flow 12 L/min, nebulizer 20 psig, sheath gas temperature 400 °C, sheath gas flow 12 L/min, nozzle voltage 500 V, fragmentor 365 V, mobile phase flow 0.40 mL/min, column temperature 40 °C. For solvent A or aqueous solvent, 2 Mm ammonium acetate in Milli-Q water, pH 8.0–8.5 was prepared. For solvent B or organic solvent, 2 Mm ammonium acetate in acetonitrile, pH 8.0–8.5 was prepared. Different gradient of mobile phase ranged from 30 to 70% was applied. Approximately 32 mg pure RL was dissolved in 1.5 mL of acetonitrile (I). A total of 10 µL of sample was auto injected using the autosampler. The syringe was automatically rinsed with ACN after each injection.

Results and Discussion

Effect of carbon sources on the yield of PHA and RL

The PHA and RL were biosynthesised at an incubation shaking speed of 200 rpm and a temperature of 30 ºC for 72 hours with a fixed concentration of carbon source at 20 g/L. Based on the GC analysis data, the wild-type strain was able to produce PHA from 0.05 to 0.31 g/L for all carbon sources tested, with the exception of sucrose and sweetwater (Figure 2a). Data showed that the highest PHA concentration was obtained when the strain was fed with glycerol as sole carbon source, accounting to 0.31 ± 0.01 g/L. This is approximately 10 wt.% in terms of contents of cell biomass. The PHA concentration obtained in the present study was much better compared to *P. aeruginosa* L2-1 (0.143 g/L) using the same concentration of carbon source [15]. Therefore, it can be concluded that the accumulation of PHA seems to be strain dependent. When the strain was supplemented with sugars, the strain was able to produce PHA with the exception of sucrose. The utilisation of sucrose could have been sufficient for the bacterial growth but not PHA production, which may be due to the energy conversion and lack of a utilisation pathway. In other words, the use of sucrose as a carbon source causing low PHA yield could be explained by bacterial energy conservation where much was used for sucrose conversion, growth, and RL production, hence limited intermediates were channelled for PHA production. In a previous study, *Ralstonia eutropha* was unable to utilise sucrose as a carbon source for PHA production until a sucrose utilisation pathway was introduced through the addition of a gene that encodes b-fructofuranosidase [40]. Also, Ali and Jamil [41] reported that *P. aeruginosa* IFS and 30N produced 0.013 and 0.039 g/L of PHA when the said strains were fed with sucrose as sole carbon sources. Thus, it can be concluded that the utilisation of sucrose as carbon source for PHA production was strain and genome dependent.

On the other hand, when molasses and sweetwater was used, the value was lower compared to other reported strains. For example, *P. aeruginosa* NCIM and *B. megaterium* UMTKB-1 were capable of producing 4.14 ± 0.12 and 0.29 ± 0.01 g/L of PHA, when the strains were supplemented with molasses and sweetwater, respectively [6, 25]. This is the first report of utilisation of sweetwater for PHA production in *Pseudomonas* strain. The lower PHA concentration obtained using molasses and sweetwater as carbon sources could be due to the additional nitrogen and lower glycerol contents. Molasses contains approximately 41% and 32% of sucrose and glycerol, respectively [25]. However, molasses can contain up to approximately 9.5% of nitrogenous compounds [42]. Meanwhile, sweetwater contains approximately 17% and 10% of sucrose and glycerol, respectively [12]. Here, the glycerol present in molasses and sweetwater only supported the growth of cell.

The RL production was also found to vary depending on the carbon sources used. In general, wild-type *P. aeruginosa* UMTKB-5 produced RL ranging from 0.12 ± 0.02 to 1.94 ± 0.03 g/L. The highest RL concentration was obtained when the strain was supplemented with fructose as sole carbon source, accounting for 1.94 ± 0.03 g/L. The performance of *P. aeruginosa* UMTKB-5 with fructose at 20 g/L was much better compared to *P. aeruginosa* PA14 (1.34 ± 0.03 g/L) [43] using the same carbon concentration, thus concluded that RL production was strain dependent. Glycerol was noted to produce the second highest amount of RL, accounting for 1.11 ± 0.03 g/L. However, the value was lesser compared to other *P. aeruginosa* strains as reported by Santos et al. [44] and Rooney *et al*. [45], accounting for 2.0 and 2.3 g/L, respectively.

For transformant strain, it was clearly observed that insertion of *phaC* gene into wild-type *P. aeruginosa* UMTKB-5 resulted in the increasing significantly (p <0.05) of polymer accumulation, with exception for molasses and sweetwater (Figure 2b). When glucose was fed as carbon source, PHA concentration increased fourfold to 0.25 ± 0.02 g/L. The PHA concentration was increased six-fold when sucrose was utilised accounting for 0.35 ± 0.01 g/L. While, using glycerol and glycerine pitch, PHA accumulation increased to 0.78 ± 0.03 and 0.45 ± 0.02 g/L, respectively. In contrast, molasses and sweetwater only accumulated trace amount (<0.05 g/L) of polymer produced. Using glycerol, the transformant *P. aeruginosa* UMTKB-5 was able to produce approximately 24.0 ± 3.0 wt.% of PHA (0.78 ± 0.03 g/L), slightly higher compared to engineered *Pseudomonas putida* KT2440 that produced 21.0 wt.% PHA [46].

On the other hand, RL production was lower significantly (p <0.05) in transformant strain, compared to wild-type strain for all the carbon sources tested. When glucose and fructose were utilised, the RL concentration decreased to 0.170 ± 0.001 g/L (six-fold) and 0.33 ± 0.05 g/L (six-fold). Using glycerol and glycerine pitch, the RL concentrations were reduced to 0.37 ± 0.07 (threefold) and 0.23 ± 0.03 (fourfold) g/L, respectively. Using molasses and sweetwater, RL concentration decreased to 0.03 ± 0.01 and 0.04 ± 0.01 g/L. The introduction of *phaC* gene increased PHA production but decreased RL production. The decrease in RL production clearly indicated competition for intermediates between PHA and RL biosynthesis pathways, since the lipid moieties derived from fatty acid biosynthesis are involved in both pathways [47].

Composition of PHA

The PHA monomers accumulated by wild-type *P. aeruginosa* UMTKB-5 strain was different according to the substrate used, with the chain length (between C_6 and C_{10}) as shown in Table 1(a). 3-hydroxyhexanoate (HHX) [C_6] was the only major type of PHA found when sugars (glucose, fructose) and sugar cane by-products (molasses, sweetwater) were utilised as the sole substrate. The strain was able to accumulate high compositions of 3-hydroxydecanoate (HD) [C_{10}], ranging from 50 to 90 mol% when glycerol and glycerine pitch were used. Besides that, 3-hydroxyoctanoate (HO) [C_8] was also produced using these carbon substrates. The finding of this study agrees with Hori and co-workers [48], such that HHx, HO and HD monomers were accumulated by *P. aeruginosa* utilising decanoate, glucose and ethanol as substrates. On the other hand, Marsudi and co-workers [16] also obtained PHA monomer compositions of HHx, HO and HD when *P. aeruginosa* IFO03924 utilised 13.8 g/L of glycerol as carbon substrate. In addition, *P. aeruginosa* IPT169 was able to produce PHA monomer composition of HHx, HO, HD and HDd when the strain was fed with corn oil as carbon substrate [49].

The PHA monomer composition from transformant *P. aeruginosa* UMTKB-5 was different compared to the wild-type strain. The transformant strain showed successful accumulation of P(3HB) ranging from 20 to 50% for all the carbon sources examined, with exception of molasses and sweetwater [Table 1 (b)]. Glycerine pitch gave the highest P(3HB) monomer composition, accounting for 49%. This was possible because this genetically modified strain harbours the PHA synthase gene (*phaC*) of *Cupriavidus* sp. USM1020, a strain well-known for P(3HB) production.

The reported compositions of PHA monomer were very similar to those provided with glucose and fructose as sole substrates. However, no P(3HB) was detected when molasses and sweetwater were fed. This is mainly due to the low concentration of glycerol contained in both molasses and sweet water to trigger P(3HB) production. In the present study, the glycerol present in molasses and sweetwater supported cell growth. However, it was insufficient to generate intermediate into production of P(3HB).

In the present study, the monomer composition of PHA from the transformant strain was similar to that from the study by Cepades et al. [50], whereby PHA composed mainly of 3HB, 3HHx and 3HD were produced when non-naturally occurring *P. aeruginosa* harbouring PHA synthase gene from *Aeromonas* sp. was provided with glucose as the only carbon source. The type of microorganism, environmental condition, and carbon

substrate affect PHA composition and production of scl or mcl fatty acids [51]. Rehm et al. [52] noted that the *phaC*, carbon sources and metabolic routes play important roles in determining the compositions of PHA.

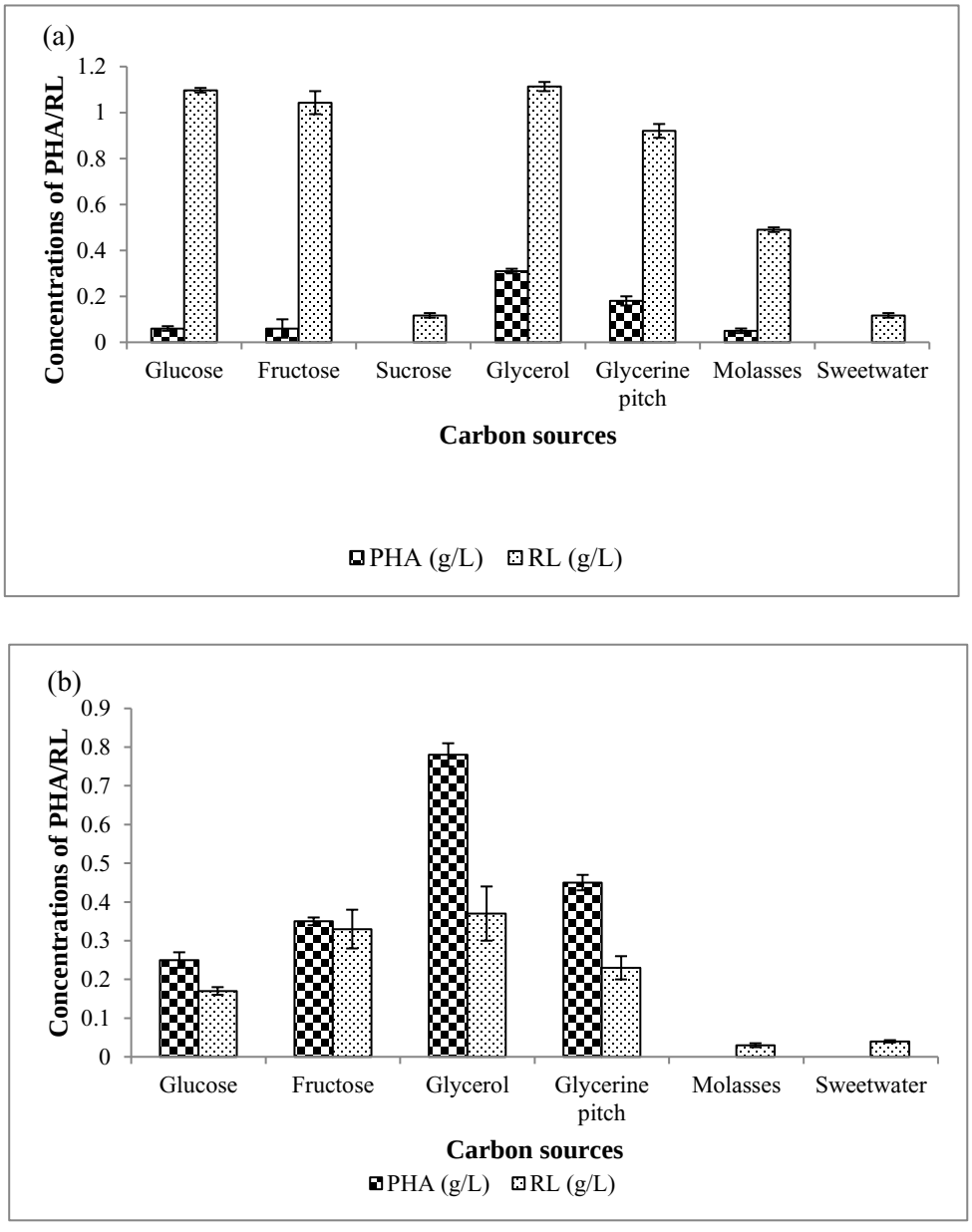


Figure 2. Simultaneous production of PHA and RL by wild-type (a) and transformant (b) *Pseudomonas aeruginosa* UMTKB-5 strains using different carbon sources

Table 1. Composition of PHA produced by (a) wild-type and (b) transformant *P. aeruginosa* UMTKB-5 utilising different carbon sources

Carbon Source (g/L)	[a]Relative Amount of Monomer in PHA (%)		
	HHx	HO	HD
Glucose	100	0	0
Fructose	100	0	0
Glycerol	7.8	4.4	87.8
Glycerin pitch	17.0	24.0	59.0

Carbon sources (g/L)	[b]Relative amount of monomer in PHA (%)			
	HB	HHx	HO	HD
Glucose	27.6	72.4	0	0
Fructose	34.4	65.6	0	0
Glycerol	34.0	46.4	11.8	7.8
Glycerin pitch	49.9	30.3	9.2	10.5

HB: 3-hydroxybutyrate, HHx: 3-hydroxyhexanoate, HO: 3-hydroxyoctanoate, HD: 3-hydroxydecanoate

Effect of nitrogen sources on the yield of PHA and RL

Glycerol at a C/N ratio of 50 was selected as the sole carbon source for subsequent comparison of the production of PHA and RL between different nitrogen sources since it is an economical and renewable resource and has also produced one of the highest PHA yields (Figure 2). The highest production of PHA and RL was achieved when wild-type *P. aeruginosa* UMTKB-5 was supplemented with $CO(NH_2)_2$ as nitrogen source and glycerol as sole carbon source, accounting for 0.242 ± 0.011 and 2.308 ± 0.010 g/L, respectively (Table 2). The nitrogen source that provided the highest PHA concentration of 2.242 g/L was $CO(NH_2)_2$. Our findings agreed with a study by Tripathi *et al*. [6], which also obtained the highest PHA concentration (2.89 g/L) using the same nitrogen source, $CO(NH_2)_2$.

For RL production, $CO(NH_2)_2$ gave the highest RL concentration (2.308 ± 0.010 g/L), where all carbon sources tested had significant difference in the amount of PHA produced (p <0.05). However, Moussa et al. [9] obtained the highest RL concentration at 0.34 g/L when $NaNO_3$ was used compared to $CO(NH_2)_2$, which was 0.3 g/L. The carbon source that yielded the most PHA was different between the two mentioned studies, which could be due to the difference in the concentration and type of carbon source, the concentration of nitrogen source supplemented into the culture medium, and incubation time. $CO(NH_2)_2$ exists as an uncharged polar molecule, which is easily assimilated into *P. aeruginosa* [53].

Characterisation of PHA from wild-type *P. aeruginosa* UMTKB-5

The thermal properties of the polymers produced by *P. aeruginosa* UMTKB-5 utilising glycerol and glycerine pitch as sole carbon sources were shown in Table 3. The T_m of PHA polymers produced by wild-type *P. aeruginosa* UMTKB-5 using glycerol and glycerine pitch was approximately 48 to 50 ºC. The value was almost similar with polymers obtained from *P. aeruginosa* [54]. On the other hand, Guo et al. [37] obtained T_m range of 54 to 55 ºC when *P. mendocina* strains were grown on 20 g/L of glucose as carbon source and 0.7 g/L of $(NH_4)_2SO_4$ as nitrogen source.

Conversely, in this study, the T_g could not be detected from the endothermic peaks in each DSC trace, which indicates that the samples are amorphous.

It is important to determine the physical properties of biopolymer produced to determine its suitability in a particular application. To measure the molecular mass of mcl-PHA produced by *P. aeruginosa* UMTKB-5, both number-average molecular weights (*Mn*) and polydispersity (*Mw/Mn*) were measured using GPC. The *Mn* of the polymer is important in determining its strength as well as ability to be shaped [1].

Using glycerol as carbon source, the weight-average molecular weight (*Mw*) and the number-average molecular weight (*Mn*) were $4.0x10^5$ and $1.4x10^5$ Da, respectively. While when glycerine pitch was utilised, *Mw* and *Mn* of $4.7x10^5$ and $4.19x10^5$ were obtained, respectively. The physical properties produced from glycerol was comparable with the polymer produced by *P. aeruginosa* ATCC, which obtained *Mw* of polymer ranged from $7.7x10^4$ to $1.88x10^5$ Da, when the said strain was grown on odd chain fatty acids as carbon sources [54]. Polydispersity (PI) (*Mw/Mn*) of PHA using glycerol and glycerine pitch obtained in the present study was 2.85 and 4.19, respectively. Hori et al. [48] obtained PI of 2.0 when *P. aeruginosa* IF03924 was grown on glucose as carbon source. On the other hand, PI of 1.8-2.0 was obtained when *P. putida* G016 was grown on Sodium terephthalate (TA) and waste glycerol (WG) in fed-batch fermentation [55]. These values are typical for mcl-PHA polymer. However, in this study, a slightly higher PI was obtained when glycerine pitch was fed as carbon source. However, it was at the same level as that mcl-PHA synthesised by *P. aeruginosa* strains [48].

On the other hand, thermal degradation studies were carried out for mcl-PHA polymers produced by *P. aeruginosa* UMTKB-5 utilising glycerol and glycerine pitch as carbon sources using thermogravimetric analysis (TGA). TGA was used to measure the degradation temperature of polymers [56]. Results obtained in the present study showed that the degradation rate of the polymers was 310 ºC (Table 3). It was higher in comparison with degradation temperatures of mcl-polymers of *P. putida* ranging from 280 to 290 ºC [55]. The different in degradation temperatures probably due to the different in culture condition used in each study such as carbon and nitrogen source, temperature, pH and agitation [57]. Kenny et al. [55] used MSM medium supplemented with Sodium terephthalate (TA) and waste glycerol (WG) from biodiesel manufacture as carbon sources. *P. aeruginosa* 47T2 obtained degradation temperature of 295 ºC when the strain was grown on waste cooking oil supplemented with $CO(NH_2)_2$ as nitrogen source [58]. Different monomers ratios of the polymers and also different in culture conditions used affected the thermal properties of the polymer produced [59]. The properties of produced polymers can be tailored to be applied in various industries ranging including packaging materials or highly elastic ones, because the polymers are produced from renewable carbon sources [60].

Characterisation of RL congener from wild-type *P. aeruginosa* UMTKB-5

Rhamnolipids comprise one or two β-hydroxy fatty acids of varying chain lengths (C_8–C_{22}) linked to one or two rhamnose rings [39]. Common RL congeners (i.e., substance structurally related to RL by origin and function) include di-RL, α-l-rhamnopyranosyl-α-l-rhamnopyranosyl-β-hydroxydecanoyl-β-hydroxydecanoate (RhaRha C10C10) and RhaRhaC10, as well as mono-RL homologs, RhaC10 and RhaC10C10. Other homologs were found to be present within the *m/z* range of 475–677 depending on the number of rhamnose ring, fatty acid chain, and carbon [39].

Mass spectrometry analysis revealed the presence of mono- and di-RL moieties in the RL mixture. Three major components of *m/z* 649, 621 and 675 were detected when using glycerol supplemented with $CO(NH_2)_2$. These corresponded to the congeners $RhaRhaC_{10}C_{10}$, $RhaRhaC_{10}C_8$ and $RhaRhaC_{10}C_{12:1}$ at 38.14%, 25.69%, and 17.14% respectively. The LCMS also detected $RhaRhaC_8$ (*m/z* 451), $RhaRhaC_{10}C_{10:1}$ (*m/z* 647), $RhaC_{10}$ (*m/z* 333) and $RhaRhaC_{12}$ (*m/z* 507) in their biosurfactant mixture (Table 4). On the other hand, when glycerol supplemented with NH_4NO_3 was used, five major components of *m/z* 649, 621, 479, 675, and

677 were detected. These corresponded to $RhaRhaC_{10}C_{10}$, $RhaRhaC_{10}C_8$, $RhaRhaC_{10}$, $RhaRhaC_{10}C_{12:1}$, and $RhaRhaC_{10}C_{12}$ at 25.64%, 21.76%, 12.92%, 10.83%, and 10.49% respectively. A few minor components were also detected, which were $RhaRhaC_8$ (*m/z* 451), $RhaRhaC_{10}C_{10:1}$ (*m/z* 647), $RhaC_{10}$ (*m/z* 333) and $RhaRhaC_{12}$ (*m/z* 507) (Table 4).

The result in Table 4 shows that $RhaRhaC_{10}C_{10}$ was the predominant component in the biosurfactant mixture of glycerol supplemented with $CO(NH_2)_2$) and NH_4NO_3, accounting for relative abundance 38.14% and 25.64% respectively, using negative electrospray ionisation. In addition, the di-RL formed 96.81% and 95.53% in glycerol that respectively utilised $CO(NH_2)_2$) and NH_4NO_3. The result obtained in this study agrees with Siddharta et al. [61], whereby $RhaRhaC_{10}C_{10}$ was found as an abundance mixture (42.6%) when *P. aeruginosa* was provided with glycerol. Another study by Lotfabad et al. [62] also produced $RhaRhaC_{10}C_{10}$ (35.93%) as an abundance mixture when *P. aeruginosa* MR01 was supplemented with glucose as carbon source. On the other hand, Aparna et al. [63] also obtained the same range of *m/z* when *Pseudomonas* sp. 2B was grown on different carbon sources and analysed by negative mode. A mixture of RL with molecular ions at *m/z* 333,479, 504, 505, 532, 650 and 678 were produced. The results obtained were very similar with the RL congener produced in this study.

This study demonstrated that the biosurfactant produced by *P. aeruginosa* UMTKB-5 was indeed RL, in which $RhaRhaC_{10}C_{10}$ and $RhaRhaC_{10}C_8$ were the predominant mixtures compared to mono-RL. Most of the authors reported di-RL as the predominant component of RL biosurfactants from *P. aeruginosa* [15,62]. Déziel et al. [64] found that di-RL has higher CMC concentration, thus having higher surface activity over mono-RL. Having these great properties, di-RL is widely used in the bioremediation of poly-aromatic hydrocarbon (PAH) to treat contaminated sites [62]. The applications of RL depend on the proportion and type of monomers produced by bacterial species [65]. The RL is being produced as a mixture of different molecules [65]. The difference in the proportion of RL mixture produced in this study in comparison with those reported in the literature could be explained by the difference of carbon source, nitrogen source, medium and extraction technique used [8, 63]. In addition, *P. aeruginosa* strains or species can also affect the proportion of RL-congener produced [64, 65].

Table 2. Effect of various nitrogen sources on the production of PHA and RL by wild-type *P. aeruginosa* UMTKB-5[a] using glycerol as sole carbon source at a C/N ratio of 50

Nitrogen Sources	**CDW (g/L)**	**Rhamnolipid (g/L)[b]**	**PHA Content (wt.%)[c]**	**PHA Concentration (g/L)[d]**	**PHA Composition**		
$NH_4H_2PO_4$	1.13 ± 0.12	1.534 ± 0.260	7.10 ± 0.78	0.080 ± 0.001	4.5	25.5	70
$CO(NH_2)_2$	2.48 ± 0.13	2.308 ± 0.010	9.78 ± 0.21	0.242 ± 0.011	4.5	26.9	68.5
$NaNO_3$	1.54 ± 0.04	1.309 ± 0.100	6.10 ± 0.52	0.010 ± 0.001	3.8	25.8	70.4
NH_4Cl	1.84 ± 0.07	0.856 ± 0.110	6.40 ± 0.48	0.115 ± 0.010	3.9	26.2	69.8
$(NH_4)_2SO_4$	1.12 ± 0.06	0.967 ± 0.060	7.47 ± 0.47	0.082 ± 0.012	3.3	27.7	69.1
NH_4NO_3	1.96 ± 0.05	1.541 ± 0.090	4.36 ± 0.81	0.085 ± 0.011	7.9	24	68.1

$NH_4H_2PO_4$, Ammonium dihydrogen phosphate; $CO(NH_2)_2$, urea; $NaNO_3$, Ammonium nitrate; NH_4Cl, Ammonium chloride; $(NH_4)_2SO_4$, Ammonium sulphate; NH_4NO_3, Ammonium nitrate; HHx, 3-hydroxyhexanoate; HO, 3-hydroxyoctanoate; HD, 3-hydroxydecanoate

[a]Incubated for 72 h at 30 ºC at 200 rpm in MSM

[b]RL concentration as determined by orcinol assay

[c]PHA content in freeze-dried cells were determined by gas chromatography

[d]PHA concentration = PHA content x CD

Table 3. Thermal properties and molecular weights of PHA polymers produced by wild-type *P. aeruginosa* UMTKB-5 using glycerol and glycerine pitch

Carbon Sources	Thermal Properties[a]				Molecular Weights[e]		
	T_g (ºC)[b]	T_m (ºC)[c]	ΔH_m (J/g)[d]	T_d (ºC)[e]	M_n (x 10^5 Da)	M_w (x 10^5 Da)	M_w/M_n
Glycerol	ND	48.7	4.3	310	1.4	4.0	2.85
Glycerin pitch	ND	49.8	2.6	310	1.1	4.7	4.19

[a] Thermal properties determined by DSC
[b] *Tg*- glass transition temperature
[c] T_m- melting temperature
[d] ΔH_m, enthalphy of fusion
[e] Determined by TGA
[f] M_w, weight average molecular weight; M_n, number average molecular weight
ND = not detected

Table 4. Structural and relative abundance of RL homologue produced by *P. aeruginosa* UMTKB-5 after 72 h of cultivation determined by LCMS analysis

Congener	Pseudomolecular ion (*m/z*)	Glycerol + $CO(NH_2)_2$[a]		Glycerol + NH_4NO_3[b]	
		Retention Time	Relative Abundance (%)	Retention Time	Relative Abundance (%)
$RhaRhaC_{10}C_8$	621	2.573	25.69	2.563	21.76
$RhaRhaC_8$	451	2.585	9.00	2.568	9.23
$RhaRhaC_{10}C_{10:1}$	647	2.87	2.88	2.833	9.82
$RhaRhaC_{10}C_{10}$	649	3.208	38.14	3.152	25.64
$RhaRhaC_{10}$	479	-	-	3.18	12.92
$RhaC_{10}$	333	3.725	3.19	3.612	4.47
$RhaRhaC_{10}C_{12:1}$	675	3.771	17.14	3.679	10.83
$RhaRhaC_{12}$	507	4.411	3.96	4.347	2.52
$RhaRhaC_{10}C_{12}$	677	-	-	4.387	10.49

[a] The strain was cultured using glycerol supplemented with $CO(NH_2)_2$) as nitrogen source
[b] The strain was cultured using glycerol supplemented with NH_4NO_3 as nitrogen source

Conclusion

Overall, *P. aeruginosa* UMTKB-5 strains have exhibited successful bioconversion of oleo- or agro-industrial by-products into value-added PHA and RL in a single cultivation medium. Glycerol was found to be the most preferred by-product for *P. aeruginosa* UMTKB-5 and it resulted in one of the highest concentrations of PHA and RL simultaneously. However, the mutant strain could not be further tested for PHA and RL production due to the instability of the plasmid. A possible way to overcome this is by homologous recombination of the gene into the bacterial chromosome. The application of dual-production and inexpensive renewable carbon sources will considerably reduce the final production cost for these biomaterials. To make the industrial production of PHA and RL viable, significant efforts in strain optimisation and

bioengineering are needed to produce high yield of biomaterials using economical carbon sources.

Acknowledgement

This study was funded by the Exploratory Research Grant Scheme (ERGS) [ERGS/1/2013/STG07/ UMT/03/02]. We express our sincere gratitude to Gula Padang Terap Sdn. Bhd. for supplying molasses and sweetwater and Biofuel-Oleochemicals Industry, Penang, Malaysia for providing glycerine pitch. The authors are grateful to Prof. Dr. Mohamad Suffian Mohamad Annuar from University of Malaya for his assistance in GC-FID analysis. The authors thank Ms. Amelia Tan Suet May for her constructive comments to improve the manuscript.

References

1. Doi Y. (1990) *Microbial polyesters*. New York, USA, VCH.
2. Muneer, F., Rasul, I., Azeem, F., Siddique, M. H., Zubair, M. and Nadeem, H. (2020). Microbial polyhydroxyalkanoates (PHAs): Efficient replacement of synthetic polymers. *Journal of Polymers and the Environment*, 28: 2301-2323.
3. Sharma, A., Jansen, R., Nimtz, M., Johri, B. N. and Wray, V. (2007). Rhamnolipids from the rhizosphere bacterium *Pseudomonas* sp. GRP3 that reduces damping-off disease in chilli and tomato nurseries. *Journal of Natural Products*, 70(6): 941-947.
4. Amelia, T. S. M., Govindasamy, S., Tamothran, A. M., Vigneswari, S. and Bhubalan, K. (2019). Applications of PHA in agriculture. In Kalia, V. C. (Ed.), *Biotechnological Applications of Polyhydroxyalkanoates*. Singapore: Springer: pp. 347-361.
5. Chan, P. L., Yu, V., Wai, L. and Yu, H. F. (2006). Production of medium-chain-length polyhydroxyalkanoates by *Pseudomonas aeruginosa* with fatty acids and alternative carbon sources. *Applied Biochemistry and Biotechnology*, 129-132: 933-941.
6. Tripathi, A. D., Yadav, A., Jha, A. and Srivastava, A. K. (2012). Utilizing of sugar refinery waste (cane molasses) for production of bio-plastic under submerged fermentation process. *Journal of Polymers and the Environment*, 20: 446-453.
7. Luef, K. P. Stelzer, F. and Wiesbrock, F. (2015). Poly(hydroxyalkanoate)s in medical applications. *Chemical and Biochemical Engineering Quarterly*, 29(2): 287-297.
8. Azemi, M. A. F. M. (2017). Biosynthesis of rhamnolipid by *P. aeruginosa* UMTKB-5 from selected carbon sources and its characterisation for biosurfactant application. Master thesis, Universiti Malaysia Terengganu.
9. Moussa, T. A. A., Mohamed, M. S. and Samak, N. (2014). Production and characterization of di-rhamnolipid produced by *Pseudomonas aeruginosa* TMN. *Brazilian Journal of Chemical Engineering*, 31(04): 867- 880.
10. Luo, Z., Yuan, X. Z., Zhong, H., Zeng, G. M., Liu, Z. F., Ma, X. L. and Zhu, Y. Y. (2013). Optimizing rhamnolipid production by *Pseudomonas aeruginosa* ATCC 9027 grown on waste frying oil using response surface method and batch-fed fermentation. *Journal of Central South University*, 20: 1015-1021.
11. Reis, R. S., Pereira, A. G., Neves, B. C. and Freire, D. M. G. (2011). Gene regulation of rhamnolipid production in *Pseudomonas aeruginosa*-A review. *Bioresource Technology,* 102: 6377-6384.
12. Azemi, M. A. F. M., Fazielawanie, N. M. R., Saidin, J., Mohd Effendy, A. W. and Bhubalan, K. (2016). Application of sweetwater as potential carbon source for rhamnolipid production by marine *Pseudomonas aeruginosa* UMTKB-5. *International Journal of Bioscience, Biochemistry and Bioinformatics*, 6(2): 50-58.
13. Rashid, M. N. F., Azemi, M. A. F. M., Abdullah, A. A., Wahid, M. A. and Bhubalan, K. (2015). Simultaneous production of biopolymer and biosurfactant by genetically modified *Pseudomonas aeruginosa* UMTKB-5. *International Proceedings of Chemical, Biological and Environmental Engineering*, 90(3): 16-21.
14. Cirstea, D. M., Stefanescu, M., Pahonţu, J. M. and Cornea, C. P. (2014). Use of some carbon sources by *Pseudomonas* strains for synthesizing polyhydroxyalkanoates and/or rhamnolipids. *Romanian Biotechnological Letters*, 19(3): 9401.

15. Costa, S. G. V. A. O., Lépine, F. Milot, S., Déziel, E., Nitschke, M. and Contiero, J. (2009). Cassava wastewater as a substrate for the simultaneous production of rhamnolipids and polyhydroxy alkanoates by *Pseudomonas aeruginosa*. *Journal of Industrial Microbiology and Biotechnology*, 36: 1063-1072.
16. Marsudi, S., Unno, H. and Hori, K. (2008). Palm oil utilization for the simultaneous production of polyhydroxyalkanoates and rhamnolipids by *Pseudomonas aeruginosa*. *Applied Microbiology and Biotechnology*, 78: 955-961.
17. Chen, Q., Bao, M., Fan, X., Liang, S. and Sun, P. (2013). Rhamnolipids enhance marine oil spill bioremediation in laboratory system. *Marine Pollution Bulletin*, 71(1-2): 269-75.
18. Laith, A. A. A., Rahman, R. N. Z. A., Basri, M. and Salleh, A. B. (2007). The effects of culture conditions on biosurfactant activity of *Pseudomonas aeruginosa* 181 using response surface methodology. *Journal of Medical and Biological Science*, 1(1): 1-4.
19. Banat, I. M., Makkar, R. S. and Cameotra, S. S. (2000). Potential commercial application applications of microbial surfactants. *Applied Microbiology and Biotechnology*, 53: 459-508.
20. Bhubalan, K., Lee, WH. and Sudesh, K. (2011). Polyhydroxyalkanoate. In Domb, A. J., Kumar, N. and Ezra, A. (Eds.). *Biodegradable polymer in clinical use and clinical development*. New Jersey: Wiley: pp. 249-315.
21. Wu, Q., Wang, Y. and Chen, GO. (2009). Medical application of microbial biopolyesters polyhydroxyalkanoates, artificial cells. *Blood Substitutes, and Biotechnology*, 37(1): 1-12.
22. Ojumu, T. J. and Solomon, B. O. (2004). *African Journal of Biotechnology*, 3(1): 18-24.
23. Situmorang, M. L., Schryver, P. D., Dierckens, K. and Bossier, P. (2016). Effect of poly-β-hydroxybutyrate on growth and disease resistance of Nile tilapia *Oreochromis niloticus* juveniles. *Veterinary Microbiology*, 182: 44-49.
24. Akaraonye, E., Keshavarz, T. and Roy, I. (2010). Production of polyhydroxyalkanoates: the future green materials of choice. *Journal of Chemical Technology and Biotechnology*, 85: 732-743.
25. Yatim, A. F. M., Syafiq, I. M., Huong, K. H., Amirul, A. A. A., Effendy, A. W. M. and Bhubalan, K. (2017). Bioconversion of novel and renewable agro-industry by-products into a biodegradable poly(3-hydroxybutyrate) by marine *Bacillus megaterium* UMTKB-1 strain. *BioTechnologia*, 98(2): 141-151.
26. Thavasi, R., Subramanyam Nambaru, V. R. M., Jayalakshmi, S., Balasubramanian, T. and Banat, I.M. (2011). Biosurfactant production by Pseudomonas aeruginosa from renewable resources. *Indian Journal of Microbiology*, 51(1): 30-36.
27. Fontes, G. C., Ramos, N. M., Amaral, P. F. F., Nele, M. and Coelho, M. A. Z. (2012). Renewable resources for biosurfactant production by *Yarrowia lipolytica*. *Brazilian Journal of Chemical Engineering*, 29(3): 483-493.
28. Dubey, K. and Juwarkar, A. (2011). Distillery and curd whey wastes as viable alternative sources for biosurfactant production. *Journal of Microbiology and. Biotechnology*, 17: 61-69.
29. Hazimah, A. H., Ooi, T. L. and Salmiah, A. (2003). Recovery of glycerol and diglycerol from glycerol pitch. *Journal of Oil Palm Research*, 15(1): 1-5.
30. Friedrich, B., Hogrefe, C. and Schlegel, H. G. (1981). Naturally occurring genetic transfer of hydrogen-oxidizing ability between strains of *Alcaligenes eutrophus*. *Journal of Bacteriology*, 147: 198-205.
31. Syafiq, I. M., Huong, K., Shantini, K., Vigneswari, S., Aziz, N. A., Amirul, A. A. and Bhubalan, K. (2017). Synthesis of high 4-hydroxybutyrate copolymer by *Cupriavidus* sp. transformants using one-stage cultivation and mixed precursor substrates strategy. *Enzyme and Microbial Technology*, 98: 1-8.
32. Chuanchuen, R., Narasaki, C. T. and Schweizer, H. P. (2002). Benchtop and microcentrifuge preparation of *Pseudomonas aeruginosa* competent cells. *Biotechniques*, 33(4): 760-763.
33. Lima, T. M. S., Procópio, L. C., Brandão, F. D., Carvalho, A. M. X., Tótola, M. R. and Borges, A. C. (2011). Biodegradability of bacterial surfactants. *Biodegradation*, 22: 585-592

34. Braunegg, G., Sonnleitner, B. and Laffery, R. M. (1978). A rapid gas chromatographic method for the determination of poly-β-hydroxybutyric acid in microbial biomass. *European Journal of Applied Microbiology and Biotechnology*, 6(1): 29-37.
35. Annuar, M. S. M. (2004). Production of medium-chain-length poly (3-hydroxyalkanoates) from saponified palm kernel oil by *Pseudomonas putida*. Ph.D thesis, University of Malaya, Malaysia.
36. Kenny, S. T., Runic, J. N., Kaminsky, W., Woods, T., Babu, R. P., Keely, C. M., Blau, W. and O'Connor, K.E. (2008). Up-cycling of PET (polyethyleneterephthalate) to the biodegradable plastic PHA (polyhydroxyalkanoate). *Environmental Science & Technology*, 42(20):7696-7701.
37. Guo, W., Duan, J., Geng, W., Feng, J., Wang, S. and Song, C. (2013). Comparison of medium-chain-length polyhydroxyalkanoates synthases from *Pseudomonas mendocina* NK-01 with the same substrate specificity. *Microbiological Research*, 168: 231-237.
38. Koch, A. K., Kappeli, O. and Fiechter, A. (1991). Hydrocarbon assimilation and biosurfactant production in *Pseudomonas aeruginosa* mutants. *Journal of Bacteriology*, 173(3): 4212-4219.
39. Yin, H., Qiang, J., Jia, Y., Ye, J., Peng, H., Qin, H. and He, B. (2009). Characteristics of biosurfactant produced by *Pseudomonas aeruginosa* S6 isolated from oil-containing wastewater. *Process Biochemistry*, 44(3): 302-308.
40. Park, S. J., Jang, Y., Noh, W., Oh, Y. H., Lee, H., David, Y., Baylon, M. G., Shin, J., Yang, J. E., Choi, S. Y., Lee, S. H., Lee, S. Y. (2015). Metabolic engineering of *Ralstonia eutropha* for the production of polyhydroxyalkanoates from sucrose. *Biotechnology and Bioengineering*, 112(3): 638-643.
41. Ali, I. and Jamil, N. (2017). Biosynthesis and genetics of polyhydroxyalkanoates by newly isolated *Pseudomonas aeruginosa* IFS and 30N using inexpensive carbon sources. *International Journal of Environmental Science and Technology*, 14(9): 1879-1888.
42. Clarke, M. A. (2003). Syrups. In Caballero, B. (Ed.). *Encyclopedia of Food Sciences and Nutrition* (Second Edition): pp. 5711-5717.
43. Choi, M. H., Xu, J., Gutierrez, M., Yoo, T., Cho, Y. H. and Yoon, S. C. (2011). Metabolic relationship between polyhydroxyalkanoic acid and rhamnolipid synthesis in *Pseudomonas aeruginosa*: comparative ^{13}C NMR analysis of the products in wild type and mutants. *Journal of Biotechnology*, 151(1): 30-42.
44. Santos, S. C., Fernandez, L. G., Rossi-Alva, J. C. and de Abreu Roque, M. R. (2010). Evaluation of substrates from renewable-resources in biosurfactants production by *Pseudomonas* strains. *African Journal of Biotechnology*, 9(35): 5704-5711.
45. Rooney, A. P., Price, N. P. J., Ray, K. J. and Kuo, T.M. (2009). Isolation and characterization of rhamnolipid-producing bacterial strains from a biodiesel facility. *Research Letter*, 295: 82-87.
46. Meur, S. L., Zinn, M., Egli, T., Thöny-Meyer, L. and Ren, Q. (2012). Production of medium-chain-length polyhydroxyalkanoates by sequential feeding of xylose and octanoic acid in engineered *Pseudomonas putida* KT2440. *BioMed Central Biotechnology*, 12(53): 1472-6750.
47. Abdel-Mawgoud, A. M., Lepine F. and Deziel, E. (2014). A stereospecific pathway diverts β-oxidation intermediates to the biosynthesis of rhamnolipid biosurfactants. *Chemistry and Biology*, 21: 156-165.
48. Hori, K., Marsudi, S. and Unno, H. (2002). Simultaneous production of polyhydroxyalkanoates and rhamnolipids by *Pseudomonas aeruginosa*. *Biotechnology and Bioengineering*, 78(6): 699-707.
49. Silva-Querioz, S. R., Silva, L. F., Pradella, J. G. C., Pereira, E. M. and Gomez, J. G. C. (2009). PHAMCL biosynthesis systems in *Pseudomonas aeruginosa* and *Pseudomonas putida* strains show differences on monomer specificities. *Journal of Biotechnology*, 143: 111-118.

50. Cespedes, L. G., Nahat, R. A. T. P. S., Mendonça, T. T., Tavares, R. R., Oliveira-Filho, E. R., Silva, L. F., Taciro, M. K., Sánchez, R. J. and Gomez, J. G. C. (2018). A non-naturally-occurring P(3HB-*co*-3HAMCL) is produced by recombinant *Pseudomonas* sp. from an unrelated carbon source. *International Journal of Biological Macromolecules*, 114: 512-519.
51. Gomaa, E. Z. (2014). Production of polyhydroxyalkanoates (PHAs) by *Bacillus subtilis* and *Escherichia coli* grown on cane molasses fortified with ethanol. *Brazilian Archives of Biology and Technology*, 57(1): 145-154.
52. Rehm, B. H. A. and Steinbüchel, A. (1999). Biochemical and genetic analysis of PHA synthases and other proteins required for PHA synthesis. *International Journal of Biological Macromolecule*, 25: 3-19.
53. Kulpreecha, S., Boonruangthavorn, A., Meksiriporn, B. and Thongchul, N. (2009). Inexpensive fed-batch cultivation for poly(3-hydroxybutyrate) production by a new isolate of *Bacillus megaterium*. *Journal of Bioscience and Bioengineering*, 107(3): 240-245.
54. Impallomeni, G., Ballistreri, A., Carnemolla, G. M., Rizzo, M. G., Nicolò, M. S. and Guglielmino, S. P. P. (2018). Biosynthesis and structural characterization of polyhydroxyalkanoates produced by *Pseudomonas aeruginosa* ATCC27853 from long odd-chain fatty acids. *International Journal of Biological Macromolecules*, 108: 608-614.
55. Kenny, S. T., Runic, J. N., Kaminsky, W., Woods, T., Babu, R. P. and O'Connor, K. E. (2012). Development of a bioprocess to convert PET derived terephthalic acid and biodiesel derived glycerol to medium chain length polyhydroxyalkanoate. *Applied Microbiology and Biotechnology*, 95: 623-633.
56. Reddy, M. V., Mawatari, Y., Onodera, R., Nakamura, Y., Yajima, Y. and Chang, Y.-C. (2017). Polyhydroxyalkanoates (PHA) production from synthetic waste using *Pseudomonas pseudoflava*: PHA synthase enzyme activity analysis from *P. pseudoflava* and *P. palleronii*. *Bioresource Technology*, 234: 99-105.

Malaysian Journal of Analytical Sciences (MJAS)
Published by Malaysian Analytical Sciences Society

STUDIES ON THE PROPERTIES OF NATURAL RUBBER/POLY-3-HYDROXYBUTYRATE BLENDS PREPARED BY SOLVENT CASTING

(Kajian Mengenai Sifat Campuran Getah Asli/Poli-3-Hidroksibutirat yang Disediakan Melalui Kaedah Acuan Pelarut)

Asmaa' Zainal Abidin, Noor Hana Hanif Abu Bakar*, Mohamad Abu Bakar

Nanoscience Research Laboratory, School of Chemical Sciences,
Universiti Sains Malaysia, 11800 USM Penang, Malaysia

**Corresponding author: hana_hanif@usm.my*

Received: 18 September 2020; Accepted: 28 November 2020; Published: 20 February 2021

Abstract

Bio-based polymer blends constituting of poly(3-hydroxybutyrate) (PHB) and natural rubber (NR), prepared *via* solvent casting technique have been studied. Various ratios of 80:20, 60:40, 40:60 and 20:80 (wt./wt.) of NR/PHB were investigated. The IR spectra of the blend samples did not show any chemical interaction between the components. X-ray diffraction (XRD) confirmed that the crystallinity of the samples increased as the ratio of PHB is increased in the blend. Thermal stability and thermal transition of the blend system were characterized by thermogravimetric analysis (TG and DTG) and differential scanning calorimetry (DSC). Thermal stability of the blend samples showed similar characteristics as the original polymers. Meanwhile, two separate glass transition temperatures were observed for the blends, indicating that NR and PHB are immiscible. Polarized optical microscopy (POM) revealed inconsistent growth of PHB spherulite in the blends after subjected to annealing. The results indicated that NR obstructs the regular arrangement of the ring banded spherulite.

Keywords: natural rubber, poly-3-hydroxybutyrate, blending, solvent casting, miscibility

Abstrak

Campuran biopolimer yang terdiri daripada poli-3-hidroksibutirat (PHB) dan getah asli (NR), telah dikaji dan disintesis melalui teknik acuan pelarut. Pelbagai nisbah 80:20, 60:40, 40:60 dan 20:80 (wt./wt.) NR/PHB telah dikaji. Spektrum IR bagi sampel campuran tidak menunjukkan interaksi kimia antara komponen. Pembelauan sinar-X (XRD) mengesahkan bahawa kristaliniti sampel meningkat apabila nisbah PHB meningkat dalam campuran. Kestabilan terma dan peralihan terma bagi sistem campuran telah dianalisis menggunakan termogravimetri (TG dan DTG) dan perbezaan pengimbasan kalorimetri (DSC). Kestabilan terma untuk sampel campuran menunjukkan ciri yang serupa dengan polimer asal. Sementara itu, terdapat dua suhu peralihan kaca untuk campuran yang menunjukkan bahawa NR dan PHB tidak dapat dicampur. Mikroskop optik polarisasi (POM) menunjukkan pertumbuhan sferulit PHB yang tidak konsisten dalam campuran setelah mengalami penyepuhlindapan. Hasil kajian menunjukkan bahawa NR menghalang susunan biasa sferulit berikat cincin.

Kata kunci: getah asli, poli-3-hidroksibutirat, campuran, acuan pelarut, keterlarutcampura

Introduction

Polymers have been used in all aspects of modern living, such as plastics, paper, textiles and cosmetic products. The production of polymeric materials has reached a quantum of 30 million tons each year [1]. Owing to its promising advantages, such as strength, low cost and durability, polymer science and engineering has rapidly developed as one of the fastest growing industries in the world. Generally, two or more different polymers can be combined to obtain a novel material with desirable features. With this goal, vast systems based on physical and chemical modification of polymer have been developed through polymer blends [2], graft [3], random [4], and block copolymerization [5].

Recently, the demand for bio-based polymers has found a niche in the polymer industry because of increasing environmental concerns. As an example, most disposed plastic materials remain persistent in the environment [6]. This is caused by their resistance to a biological breakdown. Thus, this occurrence has driven the search for biodegradable plastic materials. Poly-3-hydroxybutyrate (PHB) is a thermoplastic polymer belonging to the polyhydroxyalkanotae (PHA) family. It is a good candidate to replace non-biodegradable plastics due to its biodegradability, biocompatibility as well as processability [7]. Unfortunately, PHB is generally labelled as a weak and brittle material, displaying a short break elongation and low mechanical strength [8]. This limits its application. Hence, several approaches have been employed to modify PHB in order to widen its application range.

One of the successful approaches is the incorporation of hydroxyvalerate units into PHB during the fermentation process [9]. Another popular approach is blending PHB with other polymers capable of improving the inherent brittleness. Generally, PHB has been blended with numerous polymers ranging from natural to synthetic polymers. Studies on the blends of PHB with poly-caprolactone (PCL) [2, 10, 11], natural anionic polysaccharides [12], diglycidyl ether of bisphenol A (DGEBA) [8], poly-lactic acid (PLA) [13] and lignin [14] have been carried out. For instance, Cavalcante and co-workers investigated the miscibility and crystallinity of (PHB)/low molecular weight polycaprolactone (PCL), prepared through solvent casting [2]. The strength of PHB/PCL blends increased when compared to that of pristine PHB. Elastomer can also be blended with PHB to improve its properties. Natural rubber (NR) is an important class of natural elastomer which is extracted from rubber trees (*Hevea brasiliensis*) in latex form [15]. NR is an amorphous polymer with hydrophobic characteristic and high elasticity [15]. Bhatt and co-workers studied the blending of medium chain length polyhydroxyalkanoate (mcl-PHA) with different types of rubber such as natural rubber, nitrile rubber and butadiene rubber [16]. It was discovered that the thermal decomposition temperature of the blends increased compared to that of pristine PHA. This shows that the two polymers successfully interacted since there was a shift in the melting point of the newly synthesized polymer blend. This finding was also reported by previous studies which focused mostly on the biodegradation of PHA blend with different rubbers [16, 17]. They show that, the degradation of PHA enhances the degradation rate of natural rubber. Even though some reports were found on the blends of PHA/NR, so far, no studies have reported on the characteristic of NR/PHB blends. Hence, the present work attempted to explore the properties of blends which focus on PHB with NR prepared using different ratios.

Materials and Methods

Materials

Natural rubber latex was obtained from Malaysian Rubber Board, Kuala Lumpur. Poly-3-hydroxybutyrate (PHB) was purchased from BIOCYCLE (Brazil) and purified before use. The following chemicals such as chloroform (QRec, Malaysia) and methanol (QRec, Malaysia) were purchased and used as received. Meanwhile, liquid nitrogen was supplied from Well solution Sdn. Bhd.

Purification method of PHB and NR

PHB was purified by dissolution in chloroform. The mixture was stirred until a clear solution was obtained. It was then filtered and followed by precipitation using methanol. The resultant product was dried in a vacuum oven at 50 °C for 24 hours. Dry natural rubber (NR) was

prepared using natural rubber latex (NRL). Natural rubber latex was dropped into acetone at room temperature, until a cloudy solution was obtained. The solution was removed after a while, leaving the NR coagulants which were washed again using acetone for a few times until a clear solution was achieved. Finally, the NR coagulants was dried in a vacuum oven at 40 ˚C until constant weight was reached.

Preparation of NR/PHB blends

The blends of NR and PHB with various compositions of 100:0, 20:80, 40:60, 60:40, 80:20 and 0:100 (wt./wt.) ratio were prepared via solvent casting technique. As much as 12.5 g of each pristine PHB and NR was dissolved separately in 500 mL chloroform. Subsequently various volumes of the stock solution (according to Table 1) were mixed for 1 hour. It was then cast onto a Teflon mould and dried at room temperature to ensure complete evaporation of the solvent.

Characterization

The as prepared samples (NR, PHB and various ratios of NR/PHB blends) were characterized by FTIR Perkin Elmer 2000 spectrometer. The sample was scanned on Attenuated Total Reflection (ATR) mode ranging from 4000 to 650 cm^{-1}. The samples were analyzed by placing a sample on the surface of a KBr disc surface and subjecting to IR scan. Meanwhile, the thermal behaviour of the samples was investigated using a Mettler Toledo DSC 800. The sample was first heated from 30 to 190 ˚C at a heating rate of 20 ˚C min^{-1} under nitrogen atmosphere and held for 2 minutes. The sample was then quenched to -100˚C at a rate of 20 ˚C min^{-1} and held for another 2 minutes. Finally, the sample was subjected to a second heating scan where it was again heated from -100 ˚C to 190 ˚C at a rate of 20 ˚C min^{-1}. Subsequently, the thermal stability of the as prepared samples was conducted using a Perkin Elmer STA 6000 simultaneous thermal analyser at a heating rate of 20 ˚C min^{-1}. The samples were heated from 30 ˚C to 900 ˚C under nitrogen flow and the weight change of the sample as a function of temperature was monitored.

The diffractogram of the crystalline polymer was obtained using X-ray diffraction (XRD) technique. The X-ray diffraction pattern of the sample was obtained using the Philips X'pert Pro Mrd Pw3040 X-ray diffractometer in the 2θ range 30˚-100˚. A Cu – Kα radiation (λ = 1.54 Å) was employed as the X-ray source. Besides that, the growths of spherulite of the prepared samples were monitored under an Olympus polarizing optical microscope equipped with a Linkam THMS hot stage. A sample was placed on a clean glass slide. Then, the sample was heated from 30 to 190 ˚C at a heating rate of 20 ˚C min^{-1} and held for 2 minutes, before cooling to room temperature. The spherulite were allowed to grow during the cooling step and the images of the growing spherulite were acquired.

Table 1. Preparation of NR/PHB blends

NR/PHB Ratio	Volume of 0.37 M NR Stock Solution (mL)	Volume of 0.25 M of PHB Stock Solution (mL)
100:0	40	0
80:20	32	8
60:40	24	16
40:60	16	24
20:80	8	32
0:100	0	40

Results and Discussion

Fourier Transform Infrared Spectroscopy

Figure 1 shows the FTIR spectra for PHB, NR, and a typical NR/PHB blend with 40:60 ratio, respectively. As can be seen in Figure 1(a), the main peak of PHB occurs at 1720 cm^{-1}, which is attributed to the carbonyl stretching. Besides that, the peak, which appears at 1100 cm^{-1} is ascribed as C-O-C stretching vibration. The peaks at 2975 cm^{-1} and 2937 cm^{-1} correspond to the –C-H asymmetric and symmetric stretching, respectively. Meanwhile, peaks that occur at 1455 cm^{-1}, 1379 cm^{-1}, and 826 cm^{-1} belong to the various CH_3 modes, such as asymmetric deformation, symmetric deformation as well as bending [18].

In contrast, the FTIR spectrum of pristine NR as shown in Figure 1(b) exhibits three significant peaks at 2962 cm^{-1}, 2921 cm^{-1}, and 2853 cm^{-1}. The first peak corresponds to the CH_3 asymmetric vibrations, while the other two depict asymmetry and symmetry -CH_2- as well as CH_3 vibrations. Additionally, the small peak, which appears at 1663 cm^{-1} is due to the C=C stretching while another two sharp peaks at 1446 cm^{-1} and 1376 cm^{-1} correspond to the –CH_2 and CH_3 bending of NR. On the other hand, another significant peak at 836 cm^{-1} represents =CH out of plane bending. The IR spectrum of NR exhibits similar features to those reported in previous works [19, 20].

The comparison of the spectra of NR/PHB blends with that of the pristine PHB and NR, confirms that peaks for both NR and PHB were present in the blends. This is presented in Figure 1(c). As an example, the main peaks attributed to PHB are observed at 1720 cm^{-1}, 1455 cm^{-1}, 1379 cm^{-1}, 2975 cm^{-1}, and 2937 cm^{-1}, respectively. Meanwhile, the peaks for NR are seen at 2853 cm^{-1} as well as at 836 cm^{-1} with no appearance of the C=C peak signal at 1663 cm^{-1}. This may be because the C=C peak overlaps with the C=O peak of PHB. In addition, as can be seen in Figure 1(c), the PHB peaks are more prominent compared to NR due to the PHB rich phase in the blends. No significant peak shifts and additional peaks are seen, suggesting that no interaction between NR and PHB occurred.

X-ray diffraction analysis

The prepared samples were further characterized by the X-ray diffraction technique. As illustrated in Figure 2(a), the pristine PHB exhibits six prominent peaks at 2θ values of 13.6°, 17.3°, 22.5°, 26.8°, 29.8°, and 45.1°. These peaks are indexed to the respective (0 2 0), (1 1 0), (1 0 1), (1 1 1), (1 2 1), (0 0 2), and (2 2 2) planes signifying a face centred cubic (fcc) phase of an orthorhombic unit cell. This is in agreement with previous studies that show PHB commonly crystallizes in an orthorhombic lattice structure [7, 18, 21]. On the other hand, NR displays a broad hump in the 2θ range of 10.0° to 30.0° characteristic of an amorphous polymer. A similar observation has been reported in other studies [22, 23].

For crystalline/amorphous polymer blends, the crystalline behaviour of the crystalline component can be influenced greatly and even prohibited when the content of the amorphous component is increased [24]. The comparison of the neat PHB and NR spectra with the spectra of the NR/PHB blends is shown in Figure 2(b). The results show that all peaks mentioned in NR and PHB are seen in the 80:20, 60:40, 40:60, and 20:80 ratios. In general, NR/PHB blends with ratios 80:20 and 60:40 show a broad pattern, which is similar to NR. Additionally, low intensities of PHB peaks are observed at 13.6°, 17.3°, 26.8°, and 29.8° respectively. This may be attributed to the low amount of PHB in the blends and can be related to the low crystallinity of the samples when compared to the other ratios. The NR/PHB blends with ratios of 40:60 and 20:80, exhibit high intensity diffraction peaks at 2θ of 13.6° and 29.5°. In addition, the broad peak of NR is reduced. This may indicate that crystallinity of the blends increases when PHB is the major phase and decreases when NR is the major phase.

Thermogravimetric analysis

The thermal stability of the polymer blends can be evaluated via the TG and DTG profiles. As can be seen in Figures 3(a) and (b), the TG and DTG profiles of pristine PHB, NR and various compositions of NR/PHB blends. The temperatures that correspond to the onset of weight loss (T_{onset}) and temperature at maximum degradation rate (T_{max}) are summarized in Table 2.

The PHB indicates a single weight loss in the range of 29 to 911 ºC. In addition, pristine PHB was stable up to 271.4 ºC, beyond which, it started to decompose and the T_{max} of PHB occurred at 285 ºC. This is due to the chain scission of PHB. In contrast, NR shows a single step of weight loss with T_{onset} at 359.6 ºC and the T_{max} occurred at 385.0 ºC. This can be attributed to the thermal decomposition of the polymer chain poly(*cis-1,4-isoprene*). After blending, similar weight loss trends were observed in the TG profiles of NR/PHB blends. This indicates the highly immiscible two-phase phenomenon of the blends. For instance, the T_{onset} for the first step of weight loss for 80:20, 60:40, 40:60, and 20:80 ratios occurred at 244.9 ºC, 260.0 ºC, 273.2 ºC and 281.2 ºC. These are ascribed to the degradation of PHB. As can be seen here, low T_{onset} values for 80:20 and 60:40 ratios were observed when compared to that of pure PHB. This trend may be due to the availability of less bulky PHB chains in the blends, which caused T_{onset} to occur earlier. Nevertheless, T_{max1} of NR/PHB blends show a similar trend with the pure PHB as tabulated in Table 2.

In contrast, the T_{onset} for the second stage of weight loss occurred at temperatures 364.4 ºC, 362.6 ºC, 357.0 ºC, and 367.8 ºC for the 80:20, 60:40, 40:60, and 20:80 ratios of NR/PHB blends respectively. These are attributed to the degradation of NR. Additionally, the T_{max2} of the NR/PHB blends show no significant difference with pure NR. It can be seen that the 20:80, 40:60, 60:40, and 80:20 ratios of NR/PHB blends showed T_{max2} values at 385 ºC, 385 ºC, 386 ºC, and 386 ºC respectively. Therefore, based on the results obtained, the thermal stability of NR/PHB blends remained the same as the pure polymer, which confirms that no interaction occurred in this system.

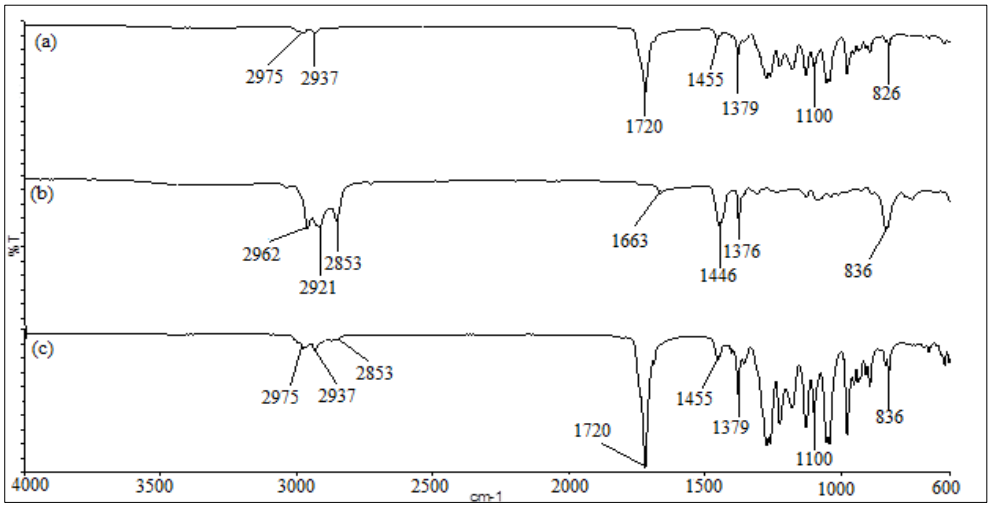


Figure 1. FTIR spectra of (a) purified PHB (b) pristine NR and (c) typical of 40:60 (wt./wt.) NR/PHB

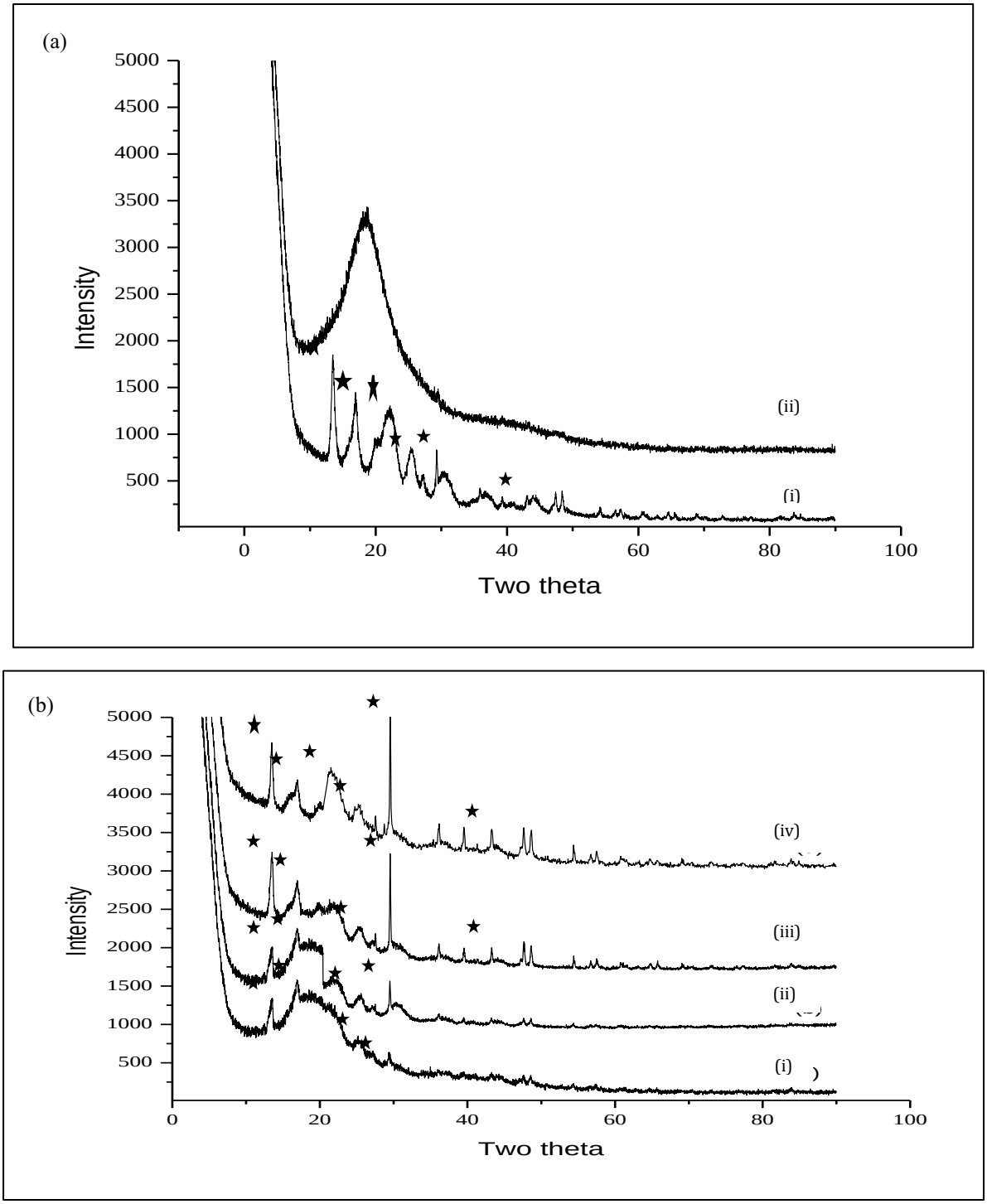


Figure 2. XRD patterns of (a) pristine PHB (i) and NR (ii), while (b) NR/PHB blends with 80:20 (i) 60:40 (ii) 40:60 (iii) and 20:80 (iv) ratios of NR/PHB blends

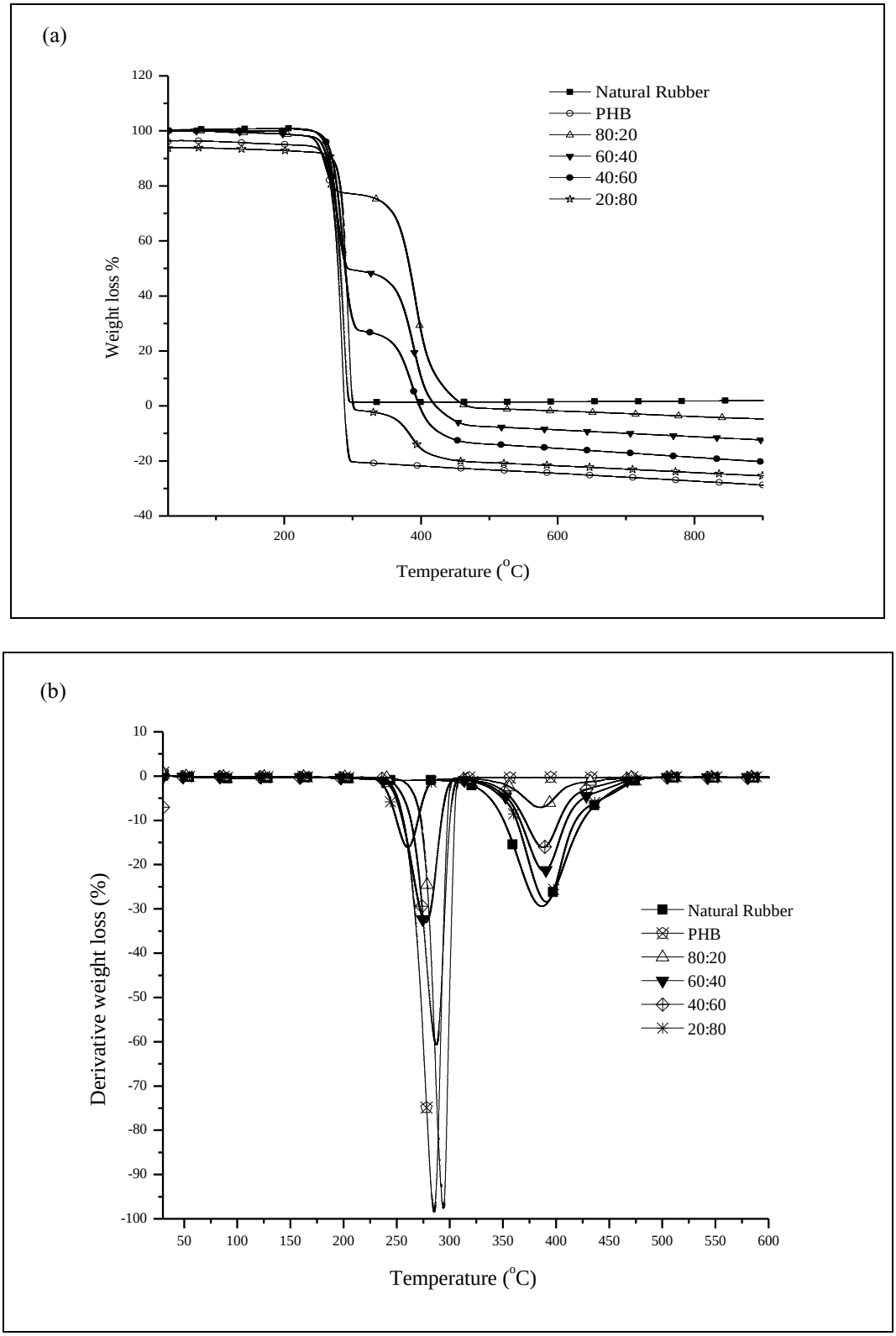


Figure 3. (a) TG and (b) DTG of the NR, PHB, and various composition of NR/PHB blends

Table 2. Thermal degradation of NR, PHB, and various composition of NR/PHB blends

NR/PHB	T_{onset}		T_{max}	
	T_{onset1}	T_{onset2}	T_{max1}	T_{max2}
100:0	359.6	-	385	-
80:20	244.9	364.4	288	385
60:40	260.0	362.6	285	385
40:60	273.2	357.0	286	386
20:80	281.2	367.8	280	386
0:100	271.4	-	285	-

Differential scanning calorimetry

The thermal properties were investigated for pristine NR and PHB as well as the NR/PHB blends with various compositions. The thermograms of the samples are shown in Figure 4, while the thermal data including the glass transition temperature (T_g), crystallization temperature (T_c), melting temperature (T_m) and the calculated polymer's crystallinity (χc) are listed in Table 3.

Pristine NR shows a T_g at -60.9 ^oC with the absence of melting and a crystallization peak. This corresponds to the amorphous nature of NR, which causes the low T_g value. In contrast, the T_g of pristine PHB was clearly observed at 8.6 ^oC with a T_m located at 172.1 ^oC. It is interesting to note that the T_c peaks were undetectable in PHB and all the NR/PHB samples. Only an endothermic peak which is related to the melting of PHB was observed in the thermograms. The disappearance of the T_c peak in the second heating scan is attributed to the complete crystallization process during the cooling step [25]. Therefore, perfect lamellar crystals were formed during the second heating scan [25].

As can be seen in Table 3, the T_m values for 80:20, 60:40, 40:60, and 20:80 of NR/PHB blends occurred at 171.9 ^oC, 169.4 ^oC, 172.4 ^oC, and 171.5 ^oC respectively. These blends reveal a T_m peak similar to that of the neat PHB, which also indicate the non-interacting nature between the components. A contradicting observation was reported by a previous work [16]. The authors discovered that a medium chain length of PHA (mcl-PHA)/NR blends was successfully interacted since there was a shifting in T_m value for 15:85 ratio. This suggests that a variation in ratio of the polymers can promote interaction. This may be related to the long polymer chain of NR.

Subsequently, all the blends exhibited two distinct T_g. The appearance of two T_g values indicates the occurrence of phase separation as a result of the non-interacting nature of the two polymers. Furthermore, the T_g for NR/PHB blends prepared using 80:20, 60:40, 40:60, and 20:80 ratios showed similar T_g values as NR and PHB. It can be observed that, the T_g for 80:20, 60:40, 40:60, and 20:80 of NR/PHB ratio occurred at -60.1 ^oC and 6.3 ^oC, -61.6 ^oC and 5.3 ^oC, -60.2 ^oC and 7.9 ^oC as well as -61.0 ^oC and 8.2 ^oC respectively. As can be seen, T_g of PHB decreases with increasing NR content. This behaviour is possibly due to the disruption of the PHB chain by NR to a limited extent. In the meantime, the apparent T_g associated with NR remained the same across composition. Interestingly, a previous study also reported similar findings with the appearance of two T_g values when blending PHB with poly(ethylene-co-vinyl acetate) (EVA) [26]. However, only a single T_g was detected for PHB/EVA with a 10:90 ratio. Therefore, it can be concluded that the T_g values and miscibility of the polymer blends are strongly dependent on the blend compositions.

The DSC curves as shown in Figure 4, reveal the addition of NR into PHB interrupted the molecular attraction between PHB chains to some extent, thereby it inhibited cold crystallization to occur in all NR/PHB blends. This is depicted by the disappearance of the T_c peaks in the thermograms. Similar observation was reported in another study [27]. The degree of crystallinity (χc) of neat PHB and NR/PHB blends was calculated using Equation 1.

$$\chi c = \Delta H_m/\Delta H_{100} \cdot W_{PHB} \text{ x } 100\% \quad (1)$$

The values are summarized in Table 3. Pristine PHB exerts 55% of χc values, while for NR/PHB blend falls in the range of 47-17%. This trend is due to the amorphous nature of NR in the blends, which reduced the crystallinity of PHB. Similar to the XRD results, the crystallinity of the NR/PHB blends increased with an increase in the PHB content in the samples. For instance, NR/PHB blends with a ratio 20:80 displayed the highest χ_c value which is 47%. This is followed by NR/PHB blends with ratios 40:60, 60:40, and 80:20, which have decreasing χc values of 42%, 35.8%, and 17.8%, respectively.

To summarize, two T_g values with no shifting in the T_m of PHB indicate that phase separation occurred in NR/PHB blends. However, a previous study involving blends of PHB/ polycarbonate (PPC) shows contrary findings with the appearance of a single T_g and no significant change in the T_m peaks of PHB [24]. In general, it is difficult to deduce the miscibility of the blend based on the T_g values. Further confirmation of the miscibility of polymer blends can be carried out using the polarized optical microscopy, since the two polymers have different refractive indices.

Polarized optical microscopy

The morphologies of pristine NR, PHB, and the NR/PHB blends are shown in Figure 5. The properties of the prepared samples directly influence their respective morphologies. Therefore, the interplay between the evaporation of solvent, phase separation composition, and crystallization of PHB directly determines the morphologies of the blends.

As shown in Figure 5(a), the POM image of NR has an even and smooth surface due to its amorphous characteristic. In contrast, a neat PHB (Figure 5(b)) features large spherulites with closely ring bands. These spherulites are attributed to the crystalline properties of PHB. As for the blends, a single phase should be observed if PHB is miscible with NR. Otherwise, two phases are formed. Here, all compositions show heterogeneous phases. The presence of NR in the blends of NR/PHB results in spherulites with various sizes that vary depending on the blend's composition. The addition of NR to PHB influences the crystallinity of PHB as it decreases the mobility of PHB segments and retards the crystal growth.

The morphology of the 80:20 NR/PHB ratio shows the appearance of PHB crystalline phase with no occurrence of spherulites. These globular PHB islands (refer to the arrow in Figure 5(c)) are dispersed in the amorphous phase of NR. This observation has been reported by Zhang and co-workers [24] where the minor droplets of PHB are dispersed in the amorphous polycarbonate (PPC) matrix when PPC is the major phase. Besides that, in this case, the absence of spherulites maybe due to the higher content of NR which covered the surface of the PHB crystal. Further decrease in the NR content, such as in the 60:40, 40:60, and 20:80 NR/PHB blends, reveals different morphologies, which have irregular shape and imperfect spherulites. In addition, the spherulite sizes are smaller and the boarders of the spherulites are not clearly seen compared to pure PHB. This phenomenon can be due to the occurrence of the degradation of PHB after the annealing process.

As can be seen from the 60:40 ratio, the phase separation is obvious with no clear banded structure detected in the spherulite. Since its content is only 40 wt.% in the blend, PHB crystallizes in a pattern as shown in Figure 5(d). In contrast, an uneven surface morphology is seen in the 40:60 ratio with a much denser nucleation and smaller size of spherulites compared to 60:40. This is due to rubber dispersed in the continuous PHB matrix. On the other hand, from Figure 5(f) of the 20:80 ratio, the growth of spherulites seems to have different rates, since there is a coexistence of large and small spherulites. This

phenomenon corresponds to the inhomogeneity of PHB in the blends. Therefore, it can be summarized that, more imperfect spherulites were formed although with a smaller volume shown in 40:60 and 20:80 when the PHB was the major phase. Overall, the morphologies of NR/PHB blends prove a phase separation, which correspond to the immiscibility between NR and PHB. This result agrees well with the DSC findings. The lack of immiscibility between the polymers in this system can be ascribed to the bulkiness of the polymer chains which causes poor chain entanglement between the two polymers.

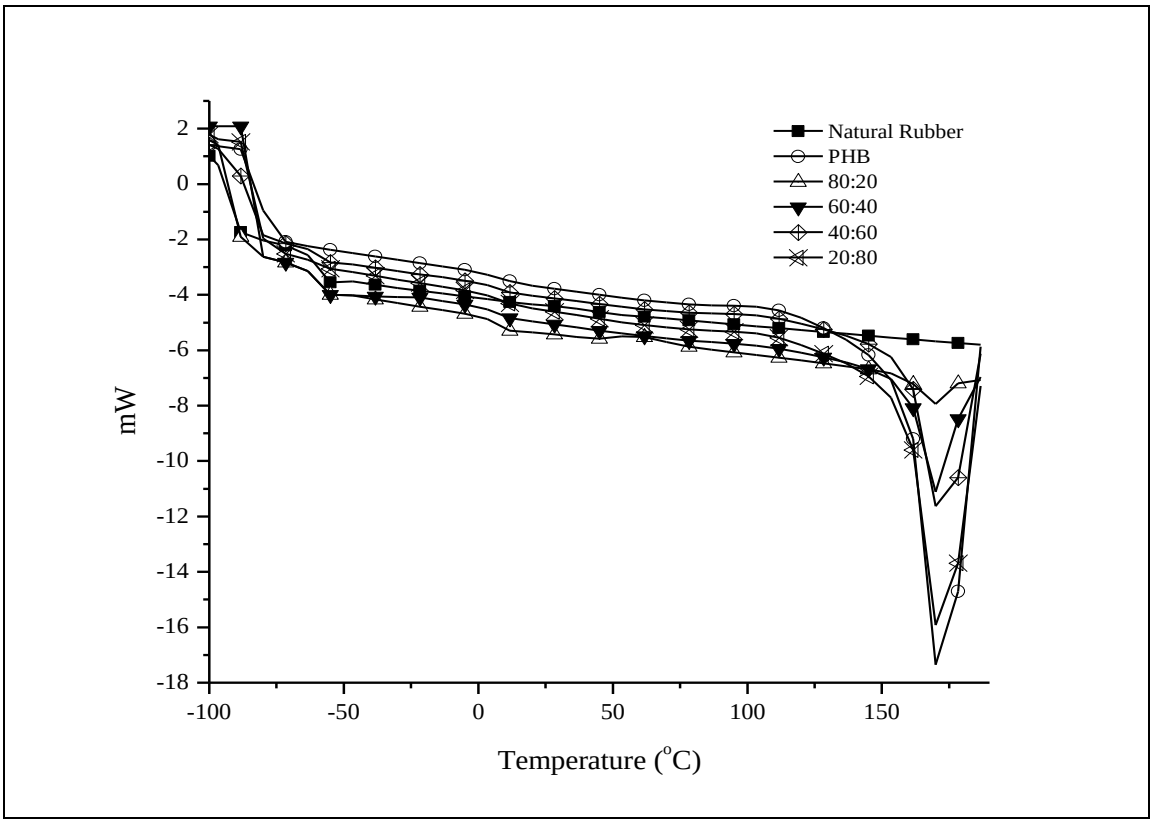


Figure 4. DSC thermogram for NR, PHB and various ratio of NR/PHB blends

Table 3. The thermal transition of NR, PHB and various NR/PHB blend

NR/PHB	2nd Heating Scan				
	T_{g1} (°C)	T_{g2} (°C)	T_m (°C)	T_C (°C)	χ_c
100:0	-60.9	-	-	-	-
80:20	-60.1	6.3	171.9	-	17.8
60:40	-61.6	5.3	169.4	-	35.8
40:60	-60.2	7.9	172.4	-	42.0
20:80	-61.0	8.2	171.5	-	47.0
0:100	-	8.6	172.1	-	55.0

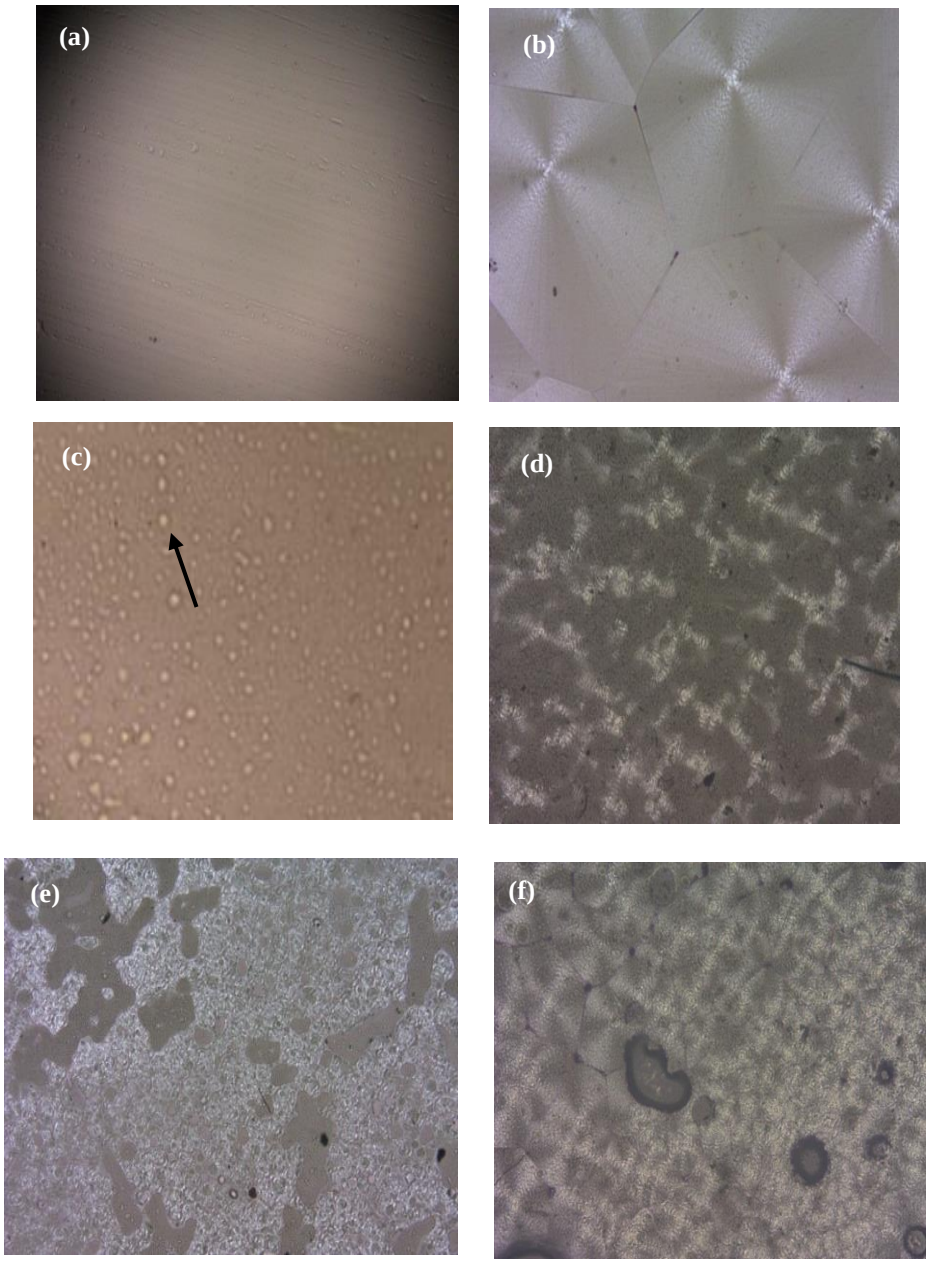


Figure 5. Polarized Optical Micrograph images (10x magnification) of (a) NR (b) PHB (c) 80:20 (d) 60:40 (e) 40:60 and (f) 20:80 of NR/PHB blend

Conclusion

In summary, this work describes a basic study on an amorphous/semi-crystalline blend system focusing on characterization of the blends in terms of morphology, crystallinity as well as thermal behaviour. Blending is the easiest, most effective and economical approach for obtaining new materials with improved physical and mechanical properties. The drawbacks of the parent components can be altered and tailored by choosing and varying the compositions of the blend and preparation parameters. Based on FTIR, blends of NR/PHB

prepared in various compositions ranging from 20 to 80 wt.% of PHB, using solvent casting technique, has revealed that, no interaction occurred between NR and PHB since no shifting and additional peaks are observed. Besides that, the presence of NR has evident influence on the crystallization and spherulite morphology of PHB. The XRD patterns obtained show low crystallinity peaks were observed when the NR amount was increased. These results correlate with the degree of crystallinity from the DSC data. Besides that, DSC results indicated immiscibility of all compositions, due to the two distinct glass transition temperatures that are similar to pristine NR and PHB respectively. In addition, the TG data for NR/PHB blends shows similar characteristic of NR and PHB. Further confirmation of the immiscible system can be seen via the two-phase morphology from POM studies. The occurrence of immiscibility in this system is because of the high molecular weight of NR and PHB, leads to poor interfacial adhesion between the phases.

Acknowledgement

The authors would like to acknowledge the financial support from research grant scheme (FRGS 203/PKIMIA/6711596) and ministry of higher education for scholarship.

References

1. Notario, B., Pinto, J., Rodriguez-Perez, M. A. (2016). Nanoporous polymeric materials: A new class of materials with enhanced properties. *Progress in Materials Science,* 78-79: 93-139.
2. Cavalcante, M. P., Toledo, A. L. M. M., Rodrigues, E. J. R., Neto, R. P. C. and Tavares, M. I. B. (2017). Correlation between traditional techniques and TD-NMR to determine the morphology of PHB/PCL blends. *Polymer Testing,* 58:159-165.
3. Golshaei, P. and Güven, O. (2017). Chemical modification of PET surface and subsequent graft copolymerization with poly(N-isopropylacryl amide). *Reactive Functional Polymer,* 118: 26-34.
4. Mazzocchetti, L., Scandola, M. and Jiang, Z. (2012). Random copolymerization with a large lactone enhances aliphatic polycarbonate crystallinity. *European Polymer Journal,* 48:1883-1891.
5. Ganji, F. and Abdekhodaie, M. J. (2010). The effects of reaction conditions on block copolymerization of chitosan and poly(ethylene glycol). *Carbohydrate Polymer,* 81: 799-804.
6. Murugan, P., Han, L., Gan, C. Y., Maurer, F. H. J. and Sudesh, K. (2016). A new biological recovery approach for PHA using mealworm, *Tenebrio molitor*. *Journal of Biotechnology,* 239: 98-105.
7. Arrieta, M. P., López, J., López, D., Kenny, J. M. and Peponi, L. (2016). Biodegradable electrospun bionanocomposite fibers based on plasticized PLA–PHB blends reinforced with cellulose nanocrystals. *Industrial Crops Products,* 93: 290-230.
8. Tognana, S., Salgueiro, W. and Silva, L. (2016). Spherulitic growth and crystallization kinetics in PHB/DGEBA blends. *Thermochimica Acta,* 623:1-8.
9. Cavalheiro, J. M. B.T., Raposo, R. S., de Almeida, M. C. M. D., Teresa Cesário, M., Sevrin, C., Grandfils, C. and da Fonseca, M. M. R. (2012). Effect of cultivation parameters on the production of poly(3-hydroxybutyrate-co-4-hydroxybutyrate) and poly(3-hydroxybutyrate-4-hydroxybutyrate-3-hydroxy valerate) by *Cupriavidus necator* using waste glycerol. *Bioresource Technology,* 111: 391-397.
10. Hinüber, C., Häussler, L., Vogel, R., Brünig, H., Heinrich, G. and Werner, C. (2011). Hollow fibers made from a poly(3-hydroxybutyrate)/poly-ε-caprolactone blend. *Express Polymer Letter,* 5: 643-652.
11. Garcia-Garcia, D., Ferri, J. M., Boronat, T., Lopez-Martinez, J., Balart, R. (2016). Processing and characterization of binary poly(hydroxybutyrate) (PHB) and poly(caprolactone) (PCL) blends with improved impact properties. *Polymer Bulletin,* 73: 3333-3350.
12. Goonoo, N., Bhaw-Luximon, A., Passanha, P., Esteves, S., Schönherr, H. and Jhurry, D. (2017). Biomineralization potential and cellular response of PHB and PHBV blends with natural anionic polysaccharides. *Materials Science Engineering C,* 76:13-24.
13. Arrieta, M. P., López, J., Rayón, E. and Jiménez, A. (2014). Disintegrability under composting conditions of plasticized PLA–PHB blends. *Polymer Degradation and Stability,* 108: 307-318.

14. Mousavioun, P., Halley, P. J. and Doherty, W. O. S. (2013). Thermophysical properties and rheology of PHB/lignin blends. *Industrial Crops Products,* 50: 270-275.
15. Pongsathit, S. and Pattamaprom, C. (2018). Irradiation grafting of natural rubber latex with maleic anhydride and its compatibilization of poly(lactic acid)/natural rubber blends. *Radiation Physics and Chemistry* 144: 13-20.
16. Bhatt, R., Shah, D., Patel, K. C. and Trivedi, U. (2008) PHA-rubber blends: Synthesis, characterization and biodegradation. *Bioresource Technology,* 99: 4615-4620.
17. Ramsay, B. A., Langlade, V., Carreau, P. J. and Juliana, A. (1993). Biodegradability and mechanical properties of poly-(f3-hydroxybutyrate-co-3-hydroxyvalerate)-starch blends. *Applied and Environmental Microbiology,* 59:1242-1246.
18. Abdelwahab, M. A., Flynn, A., Chiou, B. S., Imam, S., Orts, W. and Chiellini, E. (2012). Thermal, mechanical and morphological characterization of plasticized PLA-PHB blends. *Polymer Degradation and Stability* 97: 1822-1828.
19. Rolere, S., Liengprayoon, S., Vaysse, L., Sainte-Beuve, J. and Bonfils, F. (2015). Investigating natural rubber composition with Fourier transform infrared (FT-IR) spectroscopy: A rapid and non-destructive method to determine both protein and lipid contents simultaneously. *Polymer Testing,* 43:83-93.
20. Li, C., Feng, C., Peng, Z., Gong, W. and Kong, L. (2013) Ammonium-assisted green fabrication of graphene/ natural rubber latex composite. *Polymer Composite,* 34: 88-95.
21. Zhijiang, C., Yi, X., Haizheng, Y., Jia, J. and Liu, Y. (2016). Poly(hydroxybutyrate)/cellulose acetate blend nanofiber scaffolds: Preparation, characterization and cytocompatibility. *Materials Science Engineering C,* 58: 757-767.
22. Abraham, E., Elbi, P. A., Deepa, B., Jyotishkumar, P., Pothen, L. A., Narine, S. S. and Thomas, S. (2012). X-ray diffraction and biodegradation analysis of green composites of natural rubber/nanocellulose. *Polymer Degradation and Stability,* 97: 2378-2387.
23. Pazhooh, H. N., Bagheri, R. and Adloo, A. (2017). Fabrication of semi-conductive natural rubber nanocomposites with low copper nanoparticle contents. *Polymer,* 108:135-145.
24. Zhang, S., Sun, X., Ren, Z., Li, H. and Yan, S. (2015) The development of a bilayer structure of poly(propylene carbonate)/poly(3-hydroxybutyrate) blends from the demixed melt. *Physical Chemistry,* 17: 32225-32231.
25. Tan, W. L., Yaakob, N. N., Zainal Abidin, A., Abu Bakar, M. and Abu Bakar, N. H. H. (2016). Metal chloride induced formation of porous polyhydroxybutyrate (PHB) films: Morphology, Thermal properties and crystallinity. *IOP Conference Series Materials Science Engineering,*133: 1-11.
26. Ma, P., Cai, X., Chen, M., Dong, W. and Lemstra, P. J. (2014). Partially bio-based thermoplastic elastomers by physical blending of poly(hydroxyalkanoate)s and poly(ethylene-co-vinyl acetate). *Express Polymer Letter,* 8: 517-527.
27. Pachekoski, W. M., Agnelli, J. A. M. and Belem, L. P. (2009). Thermal, mechanical and morphological properties of poly (hydroxybutyrate) and polypropylene blends after processing. *Materials Resource,* 12: 159-164.

Malaysian Journal of Analytical Sciences (MJAS)
Published by Malaysian Analytical Sciences Society

DYNAMIC FATTY ACID PROFILES OF ASIAN SEA BASS (*Lates calcarifer)* FROM SETIU WETLANDS, EAST COAST PENINSULAR MALAYSIA

Profil Dinamik Asid Lemak Ikan Siakap Asia (*Lates calcarifer)* Dari Tanah Bencah Setiu, Pantai Timur Semenanjung Malaysia

Chan Yu Bin[1], Loh Saw Hong[2], Yusof Shuaib Ibrahim[2], Zainuddin Bachok[3], Sabiqah Tuan Anuar[2]*

[1]Department of Chemical Science, Faculty of Science,
Universiti Tunku Abdul Rahman, 31900 Kampar, Perak, Malaysia
[2]Faculty of Science and Marine Environment
[3]Marine Ecology Research Program, Institute of Oceanography and Environment
Universiti Malaysia Terengganu, 21030 Kuala Nerus, Terengganu, Malaysia

**Corresponding author: sabiqahanuar@umt.edu.my*

Received: 16 October 2020; Accepted: 4 December 2020; Published: 20 February 2021

Abstract

The oil lipids from the tissue and liver of locally grown Asian sea bass (*Lates calcarifer*) in an aquaculture of Setiu Wetlands, Terengganu, were extracted and analyzed for their fatty acid composition. The obtained fatty acid profiles revealed that both oils consisted of high amounts of saturated and monounsaturated fatty acids (SFA and MUFA, respectively) ranging within 35-54%, while polyunsaturated fatty acid (PUFA) were detected in lower proportions (10-15%). Among the fatty acids detected in the *L. calcarifer* tissue, C24:1 had the highest proportion (31.14%), followed by C16:0, C18:1n9 (*trans*), and C18:0. In contrast, C16:0 was the predominant fatty acid in the liver oil accounting for 33.88%, followed by C18:1n9 (*cis*), C24:1, and C18:0. The higher content of the extracted tissue and liver oils in MUFAs and SFAs was attributed to the salinity and temperature of the estuary water and the different dietary intake during the monsoon season. The fatty acid profiles were also compared with those obtained for *L. calcarifer* grown in other regions, indicating that the growing area of fish can affect the distribution of oil in the fish body as well as the lipid profiles within the same species.

Keywords: Asian sea bass, eicosapentaenoic acid, docosahexaenoic acid, liver, Setiu Wetlands, tissue

Abstrak

Minyak dari tisu dan hati ikan siakap Asia tempatan (*Lates calcarifer*) yang diternak dalam akuakultur di Tanah Bencah Setiu, Terengganu, telah diekstrak dan dianalisis untuk mengetahui komposisi asid lemak mereka. Profil asid lemak yang diperolehi mendedahkan bahawa kedua-dua minyak terdiri daripada jumlah asid lemak tepu dan mono tak tepu yang tinggi (SFAs dan MUFAs, masing-masing) antara 35-54%, manakala asid lemak poli tak tepu (PUFAs) dikesan dalam kadar yang lebih rendah (10-15%). Antara asid lemak yang dikesan dalam tisu *L.calcarifer*, C24:1 mempunyai bahagian tertinggi (31.14%), diikuti C16:0, C18:1n9 (*trans*), dan C18:0. Sebaliknya, C16:0 adalah asid lemak utama dalam minyak hati memberikan 33.88%, diikuti oleh C18:1n9 (*cis*), C24:1, dan C18:0. Kandungan tinggi MUFAs dan SFAs yang diekstrak dari minyak tisu dan minyak hati dalam

adalah disebabkan oleh perbezaan saliniti dan suhu air muara serta tahap pengambilan pemakanan yang berbeza pada musim tengkujuh. Profil asid lemak juga dibandingkan dengan untuk *L. calcarifer* yang didapati di kawasan lain, menunjukkan bahawa kawasan penternakan ikan boleh memberi kesan terhadap kuantiti minyak di dalam badan ikan serta profil lipid dalam spesies yang sama.

Kata kunci: ikan siakap, asid eikosapentaenoik, asid dokosaheksaenoik, hati, Tanah Bencah Setiu, tisu

Introduction

Natural fatty acids are aliphatic (saturated or unsaturated) monocarboxylic acids derived from animal or vegetable fat, oil, or wax, and they consist of a chain of 4-28 commonly unbranched and even-numbered carbons [1]. Fatty acids in animals are formed from carbohydrates during lactation in the liver, adipose tissue, and mammary glands. Polyunsaturated fatty acids (PUFAs), which may contain either omega-6 (n-6) or omega-3 (n-3) double bonds, are essential dietary fatty acids [2]. In fish and fish oils, they are mainly found as long-chain PUFA (LC-PUFA) with docosahexaenoic acid (DHA, 22:6n-3), eicosapentaenoic acid (EPA, 20:5n-3), and docosapentaenoic acid (DPA, 22:5n-3) being the most significant n-3 PUFA [3]. LC n-3 PUFA in fish have gained particular scientific and public interest due to their benefits to animal and human health [4]. According to Yi et al., EPA and DHA are vital for the prevention of cardiovascular diseases, the reduction of the inflammatory rate after surgery, and the growth and functional development of the infant brain, while they can also benefit the therapeutic potential in mental conditions and maintain the normal function of the adult brain [5]. Although n-3 PUFA are the essential nutrient, n-3 fatty acids, they cannot be synthesized by the human body [4].

Lates calcarifer, also known as Barramundi or Asian sea bass (in Malay: Kakap Putih or Siakap), can be normally found in Southeast Asia and Northern Australia. Its abundance in individual nature basins depends on the river morphology and the fishing pressure. In such microhabitats, *L. calcarifer* is much more affected, allowing the collection of more quantitative information. The spawning grounds of *L. calcarifer* are generally complex, but they are most likely determined by the presence of high salinity such as in estuaries, coastal mudflats headlands, and other nearshore waters. In particular, the spawning grounds can be found in shallow (up to 2 m deep) lateral gutters near river mouths, but not close to the main channel to be protected against high tidal sand and/or mud flows—[6-8]. Interestingly, the LC-PUFA biosynthesis in diadromous fish, such as *L. calcarifer*, has caught the attraction of researchers as the dietary PUFA requirement is different and the capabilities of converting PUFA to LC-PUFA are within that of marine and freshwater fish species [9]. Hence, in this study, the fatty acid compositions in fish oil extracted from *L. calcarifer* tissue and liver was analyzed. In addition, the results were compared with those obtained for *L. calcarifer* grown in other regions.

Materials and Methods

Study area and sample collection

Aqua cultured *L. calcarifer* (n = 10) of the same weight (~300 g) were caught during Northeast Monsoon season at a fish farm in Setiu Wetland, Estuary of Terengganu, East Coast Peninsular Malaysia (Figure 1), and stored at 4 °C in the ice box and kept frozen at -8 °C in the laboratory until further analysis.

Lipid extraction

The collected fish were gutted, washed, and dissected. For each sample, 20 g of flesh and liver were weighted and prepared for lipid extraction. The Bligh–Dyer method [10] was used with some modifications for the lipid extraction using a sample/chloroform/methanol mixture of 1:1:2. In brief, each fish flesh or liver sample was homogenized in 20 mL chloroform and 40 mL methanol, forming a monophasic system. The mixture was then homogenized again using 20 mL chloroform, followed by the addition of 20 mL distilled water. After filtration of the mixture, a biphasic system was finally obtained, which was allowed to separate. The lower layer of the mixture was collected, and the remaining sample was mixed with 10 mL chloroform and filtered. The lipid content in each sample was determined

gravimetrically by evaporating the chloroform layer in the presence of nitrogen.

Transesterification of fatty acid methyl ester (FAME)

Transesterification reaction of fish oils was carried out using a one-step reaction using methoxide reagent. In brief, a solution of sodium methoxide (5.402 g) was prepared in 100 mL. *n*-Hexane (1 mL) was then added to 0.1 mL of the oil sample. Afterward, 1 mL of the sodium methoxide solution was added to the oil solution and stirred vigorously for 30-60 s using a vortex stirrer. The mixture was then allowed to stand for 30 min to separate the fatty acid methyl ester (FAME) from the cloudy aqueous layer.

Fatty acid analysis by gas chromatography–flame ionization detector

A Shimadzu GC-2011 gas chromatographic (GC) system equipped with a flame ionization detector (FID) (Shimadzu Corp., Japan) and a BPX 70 capillary column (30 m × 0.25 mm × 0.25 mm i.d.) (SGE Analytical Science, Australia) were used to determine and quantify the FAME chemical composition. The injection volume was 1 µL in split injection mode with a split ratio of 1:20. The total airflow and column flow rates were set at 400 and 0.92 mL/min, respectively, and the hydrogen and helium (carrier gas) gas flow rates were set at 40 and 30 mL/min, respectively. Moreover, the temperatures of the injection port and the detector were set at 250 °C and 255 °C, respectively, while the injector port pressure was set at 75.4 kPa. The oven temperature program involved heating at 40 °C for 1 min, followed by a temperature increase to 140 °C at a rate of 10 °C/min, where it was maintained for 5 min. Finally, the oven temperature was increased to 240 °C at a rate of 4 °C/min, where it was maintained for another 5 min. Supelco 37 Components FAME Mix was used as external standard in determining the identity of the FAME chemical composition obtained from GC-FID.

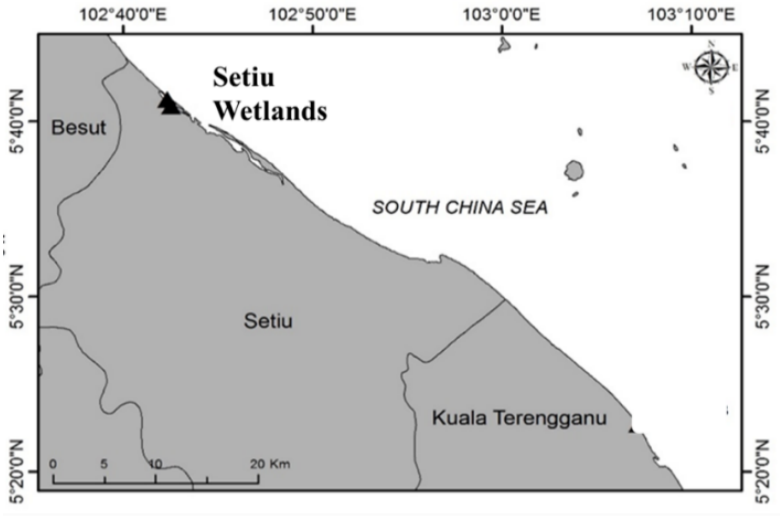


Figure 1. Location of Setiu Wetland, Estuary of Terengganu, East Coast Peninsular Malaysia.

Results and Discussion

Fatty acid composition of the *L. calcarifer* tissue and liver obtained from Setiu Wetlands

Eight types of major fatty acids were detected in the *L. calcarifer* tissue obtained from Setiu Wetlands, Terengganu using a GC-FID system (Figure 2, Table 1). Among them, the highest proportion (31.14%) was found for C24:1, followed by C16:0 (19.42%), C18:1n9 (*trans*) (18.02%), and C18:0 (11.36%). Moreover, in the total content of total fatty acids (TFA) (17.86%) in the *L. calcarifer* tissue, C20:2, C18:2n6 (cis), C24:0, and C20:3n3 accounted for 5.86%, 5.49%, 4.11%, and 2.4%, respectively. In addition, the total content of saturated fatty acids (SFA), monounsaturated fatty acids (MUFA), and PUFA was 35.73 ± 0.01%, 49.81 ± 0.01%, and 14.45 ± 0.01%, respectively, while the n-3/n-6 ratio of PUFAs was 0.43.

Meanwhile, as shown in Figure 3 and Table 1, nine types of major fatty acids were detected in the *L. calcarifer* liver collected from Setiu Wetland, Terengganu. C16:0 was the predominant fatty acid corresponding to 33.88% of the total fatty acid content, followed by C18:1n9 (cis) (16.67%), C24:1 (13.30%), and C18:0 (12.73%). Moreover, in the total content of TFA (15.35%) in the *L. calcarifer* liver, 6.48%, 3.22%, 2.35%, 2.31%, and 0.99% were attributed to C18:2n6 (trans), C16:1, C14:0, C22:1n9, and C22:2, respectively. Moreover, the total content of SFA, MUFA, and PUFA was 53.77%, 35.94%, and 9.74%, respectively, and the n-3/n-6 ratio of PUFA was 0.11.

The fatty acids determined in the *L. calcarifer* tissue and liver were compared, indicating that the tissue of *L. calcarifer* contained the largest amount of MUFA (49.81 ± 0.01%), while the SFA were the predominant fatty acids (53.77%) in the *L. calcarifer* liver. Moreover, large amounts of palmitic acid (C16:0) were found in both fish body parts, whereas α-linoleic acid (C18:3n-3) was the least detectable fatty acid (up to 0.87%). The finding is supported by Daniela in his report in 2015, as he reported that the lipids are stored in the form of SFA and MUFA in fish to generate energy and that both SFA and MUFA can be synthesized de novo [11]. It has also been found that the different lipid classes are affected by the water salinity [12]. Herein, the water salinity of Setiu Wetland was 17.8 ppt, i.e., within the range of fresh water and seawater salinity (0.5–30.0 ppt), as the estuary is a mixture of fresh water and seawater (brackish water). Likewise, when the water salinity is 5–18 ppt, the water is called mesohaline water. Moreover, the water temperature has a significant effect on the fish lipid classes. It suggests that the high water temperature is not suitable for the production of long-chain PUFA, as Malaysia is located near to equatorial with tropical climate. The long-chain PUFA are mainly found in high amounts at low water temperatures [13] and a similar result has been previously reported, where a large amount of UFA was clearly observed in the colder regions [14]. However, *L. calcarifer* from Setiu Wetland live in a mesohaline environment (17.8 ppt) with a warm water temperature (31.7 °C), which explains the predominance of MUFA over PUFA in the *L. calcarifer* tissue. Furthermore, Rabeh et al. have reported that the content of SFA and MUFA is significantly higher in seawater than in freshwater reared fish, while n-3 PUFA predominate in freshwater reared fish [12]. The different fatty acid compositions in freshwater and marine fish may be related to the physiological adaption of fish to the environment. In fresh water, SFA and UFA are used to produce energy or synthesize long chain-PUFA, whereas marine fish need these fatty acids to regulate the osmotic pressure [12, 15].

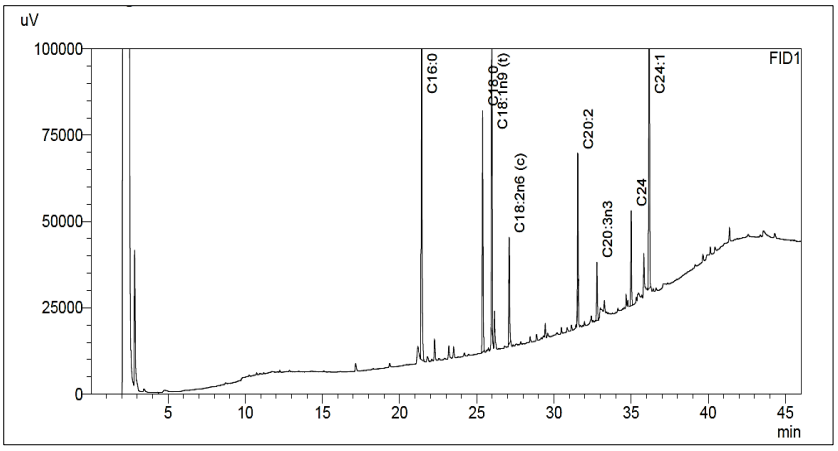


Figure 2. Chromatogram of the *L. calcarifer* tissue oil.

Table 1. Main fatty acids identified in the *L. calcarifer* tissue and liver

Fatty Acids	**Name**	**Percentage (%)**	
		Tissue	**Liver**
C14:0	Myristic acid	n.d.	2.35
C16:0	Palmitic acid	19.42	33.88
C18:0	Stearic acid	11.36	12.73
C24:0	Lignoceric acid	4.11	0.46
Total SFA		35.73	53.77
C16:1	Palmitoleic acid	0.42	3.22
C18:1n9 (*trans*)	Elaidic acid	18.02	n.d.
C18:1n9 (*cis*)	Oleic acid	0.05	16.67
C22:1n9	Erucic acid	0.05	2.31
C24:1	Nervonic acid	31.14	13.30
Total MUFA		49.81	35.94
C18:3n3	α-Linolenic acid	n.d.	0.87
C20:3n3	*cis*-11,14,17-Eicostrienoic acid	2.40	n.d.
C20:5n3	*cis*-5,8,11,14,17-Eicosapentaenoic acid	0.08	n.d.
C18:2n6 (*trans*)	Linolelaidic acid	0.10	6.48
C18:2n6 (*cis*)	Linoleic acid	5.49	n.d.
C20:2	*cis*-11,14-Eicocadienoic acid	5.86	0.56
C22:2	*cis*-13,16-Docosadienoic acid	0.29	0.99
Total PUFA		14.45	9.74
n-3/n-6 PUFA ratio		0.43	0.11

n.d.: not detectabl

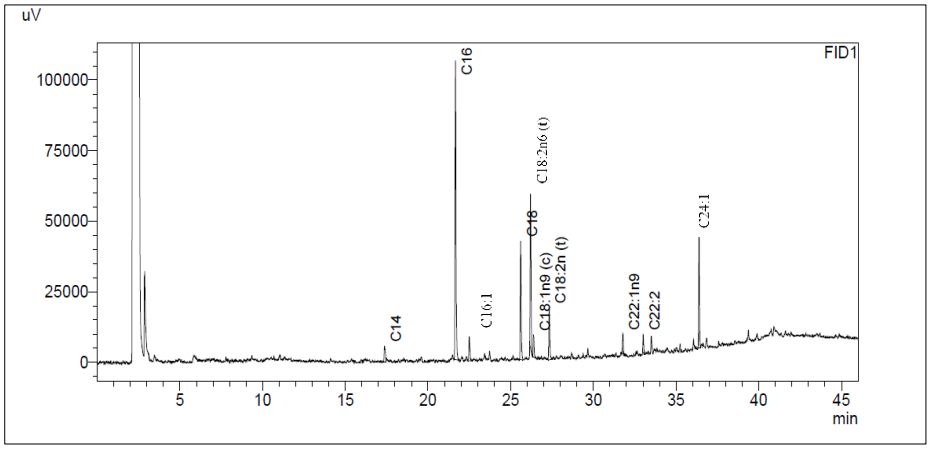


Figure 3. Chromatogram of the *L. calcarifer* liver oil.

Comparison of *L. calcarifer* tissue fatty acid profiles from Setiu Wetland and other regions

The fatty acid profile of the *L. calcarifer* tissue oil obtained from Setiu Wetland were also compared with the corresponding results reported for *L. calcarifer* from other regions. As shown in Table 2, C16:0 dominated in all *L. calcarifer* tissue oils obtained from Setiu Wetland and other regions (9.14-39.41%), except for the oil extracted from the tissue of Kelantan and Australia aqua cultured *L. calcarifer* [8, 16]. In these regions, the major fatty acids were C18:1n-9 and C18:1n-9 (*cis*). Instead, for wild estuary fish species including from Vietnam [16], Sri Lanka [17] and Myanmar [18], C16:0 and C18:0 were the major SFAs, while C18:1 was the major MUFA (Table 2). Moreover, C18:3n-3 was detected in most regions as a minor fatty acid (0.06%–1.9%) but was not detectable in *L. calcarifer* from Setiu Wetland and Selangor. This difference could be attributed to the inability of vertebrates, including fish, to produce PUFAs de novo [13, 15, 19]. Additionally, the lack of Δ12 and Δ15 double bonds in n-3 would reduce the chance to be desaturate C18:1n9 to C18:2n6 and subsequently to C18:3n3 by fatty acid desaturases [20].

Furthermore, *L. calcarifer* from all compared regions had a high content of C18 PUFAs, indicating that despite the growing area, the fatty acid elongase of *L. calcarifer* had a similar pattern to the elongation of very long chain fatty acids protein 5 (known as Elovl5) with similar elongation activity toward C18 and C20 PUFAs, but lower toward C22, as previously reported [8]. Moreover, as already mentioned, C16:0 was the SFA with the highest percentage in the *L. calcarifer* tissue fish oil obtained from Setiu Wetland accounting for 19.42%. A similar trend was also observed in the *L. calcarifer* tissue oils obtained from the other compared areas, which was in line with the results reported by Pervin et al. in 2012 [7]. In contrast, C18:1, which is one of the main substrates for mitochondrial β-oxidation catabolized through the tricarboxylic acid cycle to generate energy, was the major MUFA, in which C16:0 and C18:1n-9 fatty acids are key components for energy production in fish, as reported previously [21]. It is worth to note that the amount of C18 PUFAs was relatively high in the species obtained Setiu Wetlands and Kelantan, whereas both located at the South China Sea region. Nevertheless, this finding was in agreement with previously reported study [21] indicated that *L. calcarifer* obtained from East Peninsular Malaysia had a high total content of C18 PUFAs, indicating the greater amount of C18 PUFAs and the lower content of C20 and C22 fatty acids in local freshwater fish than in seawater fish. Moreover, C16:0 was the most dominant SFA, corresponding to 33.88% and 19.4 ± 0.6% in Setiu Wetland and Kelantan aquacultures, respectively,

complying with the findings of Nath et al. conducted in 2014 [22].

In comparison, C18:3n-3 was the minor fatty acid in the *L. calcarifer* liver oil extracted from all regions (ranging from 0.17% and 1.9%), except for the present study obtained from the Setiu Wetlands. This result was supported by Ackman in his findings in 1967 [14], who reported that the fish cannot synthesize C18:3n-3, and in agreement with Tu and his co-worker results obtained in 2013 [9], who found that the C18:3n-3 level remained low although *L. calcarifer* was fed a C18:3n-3-rich diet. As previously mentioned, the low C18:3n-3 content could be further explained by the lack of Δ12 and Δ15 double bonds in the n-3 PUFA, which serve as initiators of the C18:1n-9 desaturation to C18:2n-6 and C18:3n-3. This earlier study also showed that *L. calcarifer* lacks pathways for long chain-PUFAs biosynthesis, further limiting the amount of C18:3n-3 formed [20]. Thus, it was revealed that the predominant fatty acids in fish tissue oil and in general the lipid content may vary between different growing areas of the same species.

Table 2. Comparison of selected fatty acids identified in the tissue oil of *L. calcarifer* obtained from Malaysia (local) and other (overseas) regions

		Content of Fatty Acids (%)								Total Content (%)			n-3/n-6 PUFAs Ratio
		C16:0	C18:0	C18: 1n-7	C18: 1n-9 (*trans*)	C18: 1n-9 (*cis*)	C18: 3n-3	C20: 5n-3	C22: 6n-3	SFAs	MUFAs	PUFAs	
Present study	Setiu Wetland, Terengganu	19.42	11.36	n.d.	18.02	0.05	n.d.	0.08	n.d.	35.73	49.81	14.45	0.43
Locals	Kelantan[8] (Aquaculture)	19.5 ± 0.6	7.4 ± 0.6	2.6 ± 0.1	19.6 ± 1.1[a]		1.2 ± 0.2	4.4 ± 0.3	10.2 ± 1.6	30.7 ± 1.0	28.7 ± 1.7	40.6 ± 1.6	1.0 ± 0.1
	Selangor[19]	9.14	4.17	-	7.20[b]		n.d.	-	-	14.71	17.97[c]		-
Overseas	Sri Lanka[17] (Wild)	22.90	-	12.44	-	11.53	-	-	27.59	26.67	25.73	47.60	2.67
	India[22]	39.41	13.68	-	12.96	2.76	0.17	0.19	0.21	66.23	28.69	5.05	1.03
	Vietnam[16] (Wild)	26.6 ± 1.13	9.5 ± 0.40	2.5 ± 0.09	-	17.3 ± 2.52	0.5 ± 0.08	2.5 ± 0.20	13.3 ± 1.29	41.0	24.8	25.0	15.80
	Vietnam[16] (Aquaculture)	22.8 ± 2.43	8.3 ± 2.61	3.0 ± 0.58	-	15.6 ± 5.44	1.1 ± 0.34	3.0 ± 1.06	9.2 ± 4.75	36.9	24.6	26.0	12.20
	Australia[16] (Wild)	26.9 ± 0.61	6.7 ± 0.57	2.5 ± 0.06	-	12.8 ± 0.73	1.9 ± 0.07	3.3 ± 0.17	4.1 ± 0.31	28.0	43.6	18.5	7.40
	Australia[16] (Aquaculture)	19.3 ± 0.47	5.4 ± 0.26	2.6 ± 0.04	-	33.7 ± 0.53	1.5 ± 0.06	3.0 ± 0.11	3.1 ± 0.33	43.5	25.6	21.2	6.2
	Myanmar[18] (Wild)	23.69	9.36	3.22	8.09[d]		1.86	2.97	18.68	34.15	18.91	39.64	1.80

n.d.: not detectable; -: not reported; [a,d]Total percentage of C18:1n9; [b]Total percentage of C18:1; [c]Total percentage of U

Conclusion

The lipids of the tissue and liver of *L. calcarifer* grown in an aquaculture in Setiu Wetland were extracted to determine their fatty acid profiles. The results showed that the tissue oil had a high content of MUFA (44.81%), while the highest amount of SFA was found in the *L. calcarifer* liver (53.71%). However, both tissue and liver had the lowest PUFA content, accounting for 14.45% and 9.74%, respectively. Similar lipid composition results have been reported in studies using wild or aqua cultured *L. calcarifer* grown in other regions. The comparison of the findings in the *L. calcarifer* tissue of the current study with those of other regions indicated that most of the compared regions had a high content of either SFA or MUFA. Further comparison of the lipid composition in the *L. calcarifer* liver revealed that fish from Setiu Wetland had the highest amount of MUFA (33.88%) compared to the *L. calcarifer* liver from the Kelantan aquaculture, where PUFA predominated (37%). These differences were attributed to the effect of temperature, different dietary intake, and salinity of estuary water on the fatty acid profiles, as well as on the unique properties of SFA and MUFA. Nevertheless, C18:1n-9 was found to be the predominant MUFA in all regions. Given that C18:1 is one of the main sources for energy production and that C18:1n-9 can decrease the risk of breast cancer and cardiovascular diseases, it could be used to synthetically prepare fish oil with high nutritional value. However, further research studies are needed, as there are some arguments regarding the benefits of C18:1n-9 to human health.

Acknowledgement

The authors would like to thank the Ministry of Higher Education Malaysia, for the financial support (FRGS59327/FRGS/1/2014/SG01/UMT/02/2). The authors acknowledge the technical assistant from Mr. Yuzwan Mohamad especially in providing map for the work. The authors also thank the Faculty of Science and Marine Environment and Centre of Research and Field Service, University Malaysia, Terengganu, for providing technical support and facilities during this research.

References

1. McNaught, A. D. and Wilkinson, A. (1997). IUPAC: Compendium of chemical terminology (the "Gold Book") (2nd edition). *Blackwell Scientific Publications*, Oxford.
2. Cleland, L. G., James, M. J. and Proudman, S. M. (2006). Fish oil: What the prescriber needs to know. *Arthritis Research and Theraphy,* 8(1): 202.
3. Maqsood, S., Benjakul, S. and Kamal-Eldin, A. (2012). Extraction, processing, and stabilization of health-promoting fish oils. FNA Recent Patents on Food. *Nutrition and Agriculture,* 4(2): 141-147.
4. Rudy, M. D., Kainz, M. J., Graeve, M., Colombo, S. M. and Arts, M. T. (2016). Handling and storage procedures have variable effects on fatty acid content in fishes with different lipid quantities. *PLoS ONE,* 11(8): 1-19.
5. Yi, T., Li, S., Fan, J., Fan, L., Zhang, Z., Luo, P., Zhang, X., Wang, J., Zhu, L., Zhao, Z. and Chen, H. (2014). Comparative analysis of EPA and DHA in fish oil nutritional capsules by GC-MS. *Lipids in Health and Disease* 13(1): 190.
6. McGrill, A. S. and Moffat, C. F. (1992). A study of the composition of fish liver and body oil triglycerides. *Lipids,* 27(5): 360-70.
7. Pervin, T., Yeasmin, S., Islam, R. K., Rahman, A. and Sattar, A. (2013). Studies on nutritional composition and characterization of lipids of *Lates calcarifer* (Bhetki). *Bangladesh Journal of Scientific and Industrial Research,* 47(4): 393.
8. Mohd-Yusof, N. Y., Monroig, O., Mohd-Adnan, A., Wan, K. and Tocher, D. R. (2010). Investigation of highly unsaturated fatty acid metabolism in the Asian sea bass, *Lates calcarifer*. *Fish Physiology and Biochemistry*, 36(4): 827-843.
9. Tu, W., Mühlhäusler, B. S., James, M. J., Stone, D. A. and Gibson, R. A. (2013). Dietary alpha-linolenic acid does not enhance accumulation of omega-3 long-chain polyunsaturated fatty acids in barramundi (*Lates calcarifer*). *Comparative Biochemistry and Physiology Part B: Biochemistry and Molecular Biology*, 164(1): 29-37.
10. Bligh, E. G. and Dyer, W. J. (1959). A rapid method of total lipid extraction and purification.

Canadian Journal of Biochemistry and Physiology, 37(8): 911-917.

11. Daniela, C.B. (2005). Fatty acids distribution in marine, backish and freshwater plankton during mesocosm experiments, Dissertation (Ed). University of Kiel., Kiel, Germany: pp. 73.
12. Rabeh, I., Thlahigue, K., Boussoufa, D., Besbes, R. and Cafsi M. E. (2015). Comparative analysis of fatty acids profiles in muscle and liver of at Tunisian thick lipped grey mullet *Chelon labrosus* reared in seawater and freshwater. *Journal of Tunisian Chemical Society*, 17: 95-104.
13. Halver, J. E. (1980). Chapter 4 lipids and fatty acids. In: Fish feed technology, United Nations Development Programme. FAO of USA, ADCP/REP/80/11. Rome, pp. 41-53.
14. Ackman, R. (1967). Characteristics of the fatty acid composition and biochemistry of some fresh-water fish oils and lipids in comparison with marine oils and lipids. *Comparative Biochemistry and Physiology,* 22(3): 907-922.
15. Rabeh, I., Thlahigue, K., Gazali, N., Chetoui, I., Boussoufa, D., Besbes, R. and Cafsi M. E. (2013). Time course of changes in fatty acid composition in the osmoregulatory organs of the thicklip grey mullet (*Chelon labrosus*) during acclimation to low salinity. *Marine and Freshwater Behaviour and Physiology*, 46(2): 59-73.
16. Manthey-Karl, M., Lehmann, I., Ostermeyer, U. and Schröder, U. (2016). Natural chemical composition of commercial fish species: Characterisation of Pangasius, wild and farmed Turbot and Barramundi. *Foods,* 5(3): 58.
17. Ahmad, S. B. N., Jinadasa, B. K. K. K. and Edirisinghe, E. M. R. K. B. (2012). The nutritional composition and fatty acid profile of sea bass (*Lates calcarifer*) in Sri Lanka. In: NARA Scientific Sessions 2012. NARA. Colombo, Sri Lanka.
18. Ho, B. T. and Paul, D. R. (2009). Fatty acid profile of Tra Catfish (*Pangasius hypophthalmus*) compared to Atlantic Salmon (*Salmo solar*) and Asian Seabass (*Lates calcarifer*). *International Food Research Journal,* 16: 501-506.
19. Endinkeau, K. and Tan, K. K. (1993). Profile of fatty acid contents in Malaysian freshwater fish. *Pertanika Journal of Tropical Agricultural Science,* 16(3): 215-221.
20. Monroig, O., Navarro, J. C. and Tocher, D. R. (2011). Long-chain polyunsaturated fatty acids in fish: Recent advances on desaturases and elongases involved in their biosynthesis. In: Proceedings of the XI international symposium on aquaculture. (eds. Cruz-Suarez, L.E., Ricque-Marie, D., Tapia-Salazar, M., Nieto-López, M.G., Villarreal-Cavazos, D.A., Gamboa-Delgado, J., Hernández-Hernández, L.H.) pp 257-283. Universidad Autónoma de Nuevo León, Monterrey, México.
21. Muhamad, N. A. and Mohamad, J. (2012). Fatty acids composition of selected Malaysian fishes. *Sains Malaysiana*, 41(1): 81-94.
22. Nath, A. K., Patra, A., Sen, B., Dey, D., Das, I., Mukherjee, I., Gosh, N. and Paul, S. (2014). Fatty acid compositions of four edible fishes of Hooghly Estuary, West Bengal, India. *International Journal of Current Microbiology and Applied Science,* 3: 208-218.

Malaysian Journal of Analytical Sciences (MJAS)
Published by Malaysian Analytical Sciences Society

THE EXPLOITATION OF UNDERUTILISED *Mangifera indica L.* SEED AS COCOA BUTTER ALTERNATIVE

(Exploitasi Biji *Mangifera indica L.* Yang Tidak Di Gunakan Sebagai Alternatif Mentega Koko)

Nur Rahimah Said[1]*, Nursabrina Munawar[2], Quratul Quswa Amir[1], Siti Norshamshia Abd Hishamuddin[1]

[1]School of Chemistry and Environment, Faculty of Applied Sciences
[2]Alliance of Research and Innovation for Food (ARIF)
Universiti Teknologi MARA, Cawangan Negeri Sembilan, Kampus Kuala Pilah, 72000 Kuala Pilah, Negeri Sembilan, Malaysia

**Corresponding author: nurra1435@uitm.edu.my*

Received: 11 September 2020; Accepted: 30 December 2020; Published: 20 February 2021

Abstract

Cocoa butter, also known as theobroma oil, is a common fat that can be attained from cocoa seeds. It is the main ingredient used in the cosmetic industry for making ointments, toiletries, essential oils, and pharmaceutical products. However, the cocoa price is increasing continuously due to limited supply. Pest attacks, diseases, and ageing plantations are a few causes which reduced the supply of cocoa seeds. Hence, this study is focussed on utilising the mango seed biomass waste as cocoa butter alternative. The oil from the mango seed or kernel part was extracted and its important properties were determined. The mango kernel oil (MKO) was extracted by using the Soxhlet extractor with hexane which reported to have the highest oil yield 7.32% ± 1.25. The presence of triglyceride in the MKO was confirmed by significant peaks of CH_2, CH_3, C=O and C-O in the FTIR spectrum. Meanwhile, the thermal and fatty acid profiles found that the MKO had a high themostability, and had a mixture of triglyceride group with a combination of several fatty acids, such as palmitic acid ($C_{16:0}$), stearic acid ($C_{18:0}$), and linoleic acid ($C_{18:2}$). The physical and chemical properties analysis, such as total carotene content (147.27 µg%), melting point (30-34 °C), refractive index (1.7447), saponification value (191.40 mg KOH/g), and acid value (2.40 mg KOH/g) were compared with the cocoa butter properties. The results showed that the MKO properties were comparable with cocoa butter. Thus, it could be a high industrial potential as an alternative to cocoa butter, to be used as an ingredient in pharmaceutical, cosmetic, and food productions.

Keywords: manggo kernel oil, cocoa butter, physical properties, chemical properties

Abstrak

Mentega koko juga dikenali sebagai minyak tengkawang adalah lemak biasa yang dapat diperoleh daripada biji koko. Mentega koko merupakan ramuan utama digunakan dalam industri kosmetik untuk membuat minyak gosok, peralatan mandian, minyak pati dan produk farmasuetikal. Namun begitu, harga koko terus meningkat kerana bekalan yang terhad. Serangan haiwan perosak, penyakit dan penuaan tanaman adalah beberapa penyebab yang mengurangkan bekalan biji koko. Oleh itu, kajian ini difokuskan pada memanfaatkan sisa biomas mangga sebagai alternatif mentega koko. Minyak daripada biji mangga atau bahagian isirung diekstrak dan sifat pentingnya ditentukan. Minyak isirung biji mangga (MKO) diekstrak dengan menggunakan pengekstrak Soxhlet dengan heksana dilaporkan mempunyai hasil minyak tertinggi 7.32% ± 1.25. Kehadiran trigliserida dalam MKO dibuktikan oleh kehadiran puncak yang penting iaitu CH_2, CH_3, C=O dan C-O dalam spektrum FTIR. Sementara itu, profil haba dan asid lemak mendapati bahawa MKO mempunyai kebolehtahanan haba yang tinggi, dan mengadungi campuran kumpulan trigliserida dengan

gabungan beberapa asid lemak, seperti asid palmitik ($C_{16:0}$), asid stearik ($C_{18:0}$), dan asid linoleik ($C_{18:2}$). Analisis sifat fizikal dan kimia, seperti jumlah kandungan karotena (147.27 µg%), takat lebur (30-34 °C), indeks biasan (1.7447), nilai saponifikasi (191.40 mg KOH/g), dan nilai asid (2.40 mg KOH/g) telah dibandingkan dengan sifat mentega koko. Hasil kajian menunjukkan bahawa sifat MKO setara dengan mentega koko. Oleh itu, MKO berpotensi perindustrian yang tinggi sebagai alternatif bagi mentega koko untuk digunakan sebagai bahan dalam produk farmasi, kosmetik, dan makanan.

Kata kunci: minyak isirung biji mangga, mentega koko, sifat fizik, sifat kimia

Introduction

Mango (*Mangifera indica L.*) is being commercialised in more than 90 countries, including Malaysia. In Malaysia, mango is cultivated widely, and abundantly at the northern states of Peninsular Malaysia due to the suitable climate and favourable soil conditions [1]. It is recognised for its varieties, striking colour, flavourful taste, health benefits, and also high nutritive values [2]. A report estimated about 16,913 million tons of mangoes were exported for domestic and international demands [3]. Apart from direct consumption, mangoes could be converted into various products, such as juices, puree, leather, chutney, jam, slices, powder, and ready-to-serve beverages [4].

It is estimated annually that 35-60% of the total fruit weight was discarded as waste after processing them in the form of peel and seed. As a result, the waste might pose as a threat to environmental pollution if not properly managed [5]. It was reported that the seed or mango kernel had the potential for a sustainable secondary product. The fat content (7-15% of dry matter) from the seed could be a good source for the recovery of edible fats [6]. Researchers found that the mango kernel oil (MKO) from the mango seeds could be an alternative to cocoa butter usage in food, cosmetic, and pharmaceutical industries as it contained common fatty acids, such as palmitic acid, stearic acid, and linoleic acid [7, 8]. Cocoa butter is an important ingredient in such products because it is rich in anti-oxidants, and also has a natural emollient moisturiser that is useful in dealing with dry skin. Due to limited sources, which were only cultivated in a few countries, and had tempering difficulties, the price of cocoa butter increased yearly [9-11]. Therefore, the economical source that has similar properties like cocoa butter is needed as an alternative in the future.

In this study the MKO from Malaysia's variety was extracted through the Soxhlet extraction by using hexane, ethanol, and petroleum ether. The structure of extracted MKO was then analysed by using the Fourier Transform Infrared Spectroscopy (FTIR). The physical and chemical properties of the MKO was analysed and compared with cocoa butter in order to determine its suitability as an alternative to cocoa butter.

Materials and Methods

Materials

The mango kernel sample was prepared as follows. The mangoes were purchased from the NSK supermarket located in Seremban, Negeri Sembilan, Malaysia. The mangoes were supplied directly from the Federal Agricultural Marketing Authority's (FAMA) farm, and known as *Mangga Susu,* in the local name. The mango seeds were obtained from 10 kg of mangoes and cracked after utilising the flesh. Then, the kernel was dried, grounded to powder form, and stored at a temperature of below 4 °C. The storage at low temperature mantained the humidity and prevented the oxidation process on the dried mango kernel where the powder caused a decrease of extracted MKO yield [12].

The chemicals in this research, used without future purification, were hexane (QREC-98%), ethanol absolute (HMBG), petroleum ether (R&M-analytical grade), diethyl ether (R&M-99.5%), methanol (HMBG-analytical grade), phenolphthalein solution 1% (BENDOSEN), sodium hydroxide-50% w/v solution (MERCK), potassium hydroxide (QREC), sulphuric acid (R&M-95%), hydrochloric acid-fuming 37% (R&M), acetone (R&M-analytical grade), acetonitrile (FRIENDEMANN SCHMIDT-analytical grade), and hexane (HPLC grade). Besides, three standards were used, which were palmitic acid ($C_{16:0}$), stearic acid

($C_{18:0}$), and linoleic acid ($C_{18:2}$). All standards were purchased from the R&M chemicals.

Extraction of the MKO

The Soxhlet extraction was performed in triplicate with hexane, ethanol, and petroleum ether, respectively. The mango kernel sample (20 g) was extracted with 200 mL of solvent for 4 hours separately at 60 °C (hexane), 70 °C (petroleum ether), and 50 °C (ethanol). The temperature chosen was different for each solvent to avoid thermal degradation on bioactive components [12]. Finally, the resulting extracts were separated by evaporating the solvents used in a rotary evaporator under low pressure. The significant functional group in the structure of the MKO was confirmed by using the Perkin Elmer Spectrum 100 FTIR over the range 4,000-650 cm^{-1}, performed in attenuated total reflection (ATR) mode.

Physical properties of MKO: Thermal profile

The Perkin-Elmer Diamond Different Scanning Calorimetric (DSC) instrument was calibrated by using indium and zinc. The MKO was purged with 99.99% nitrogen with a flow rate of 100 mL/min and pressured at 20 psi. Frozen oil samples were heated at 40°C in an oven until it completely melted. Thereafter, the MKO was placed in an aluminium volatile pan and cooled to -80 °C and held for 2 minutes. It was heated from -80 °C to 40 °C at a rate of 5 °C/min, and held isothermally for 2 minutes [11, 13].

Melting point

The MKO was inserted around 1 cm in a capillary tube, and was cooled at a temperature of less than 0 °C for 2 hours. The frozen capillary tube was submerged in hot water to make sure the top end of the MKO was 1 cm below the water level. The temperature was recorded when the range of the frozen MKO started to slip until it totally slipped out from the capillary tube [14].

Refractive index

Refractive index indicates the ratio of speed of light at a specific wavelength in the air to the speed of light in the MKO. The determination of the refractive index was carried out by using a refractometer and a sodium lamp. Two to three drops of distilled water were placed on the main prism surface and covered with secondary prism that was visible through an eyepiece. The refractometer was set at 1.3330 when the temperature reaches 20 °C. Then, the 2-3 drops of MKO were inserted at the centre of the main prism. The boundary line was observed by turning the measurement knob slowly. The colour compensator knob was turned to remove the colour of the boundary line, and the refractive index was recorded [14].

Chemical properties of MKO: Total carotene content

The total carotene content in the MKO was analysed by using the Ultraviolet-Visible (UV-Vis) spectrophotometer at 450 nm. The MKO was homogenised by using a homogeniser, and weighed accurately to 0.1 g in the 25 mL volumetric flask, and diluted to the mark with n-hexane solution [15]. The total carotene content of the MKO was calculated as β-carotene in part per million (ppm) by using the equation 1, where V = volume used for analysis (mL), As = absorbance of the sample, Ab = cuvette error, W = weight of MKO used (g), and 2,592 = the extinction coefficient.

$$\text{Carotene content} = \frac{[V \times 2592 \times (As - Ab)]}{(100 \times W)} \quad (1)$$

Saponification value

The MKO was melted at 90 °C and homogenised by using a homogeniser for 2 minutes, and then filtered to remove any impurities. The 2 g of MKO was added into a conical flask which contained 30 mL of 0.5 N ethanolic potassium hydroxide solution. The reaction mixture was refluxed for 1 hours stirring continuously, and cooled at room temperature. Then, the phenolphthalein solution was added to the reaction mixture as an indicator followed by titration with 0.5 N hydrochloric acid until the pink colour disappear. A blank determination was also carried out omitting the MKO, and the saponification value was calculated by using the equation bellow, where a = volume of HCl titrated in reaction mixture (mL), b = volume of HCl titrated in blank solution (mL), M = molarity of HCl, 56.1 = molecular weight of KOH, and w = weight of MKO used (g) [14].

$$\text{Saponification value} = \frac{[(b-a)\times M \times 56.1]}{w} \quad (2)$$

Acid value

The MKO was melted at 90 °C, weighing approximately 5-10 g, and transferred into the Erlenmeyer flask. Similar volume (25 mL) of diethyl ether, and methanol were added followed with a few drops of 1% phenolphthalein solution as an indicator. The temperature of the mixture was controlled at 40 °C and was titrated against 0.1 M NaOH along with a gentle shake until the first permanent pink colour appears. The free fatty acid value was calculated as oleic acid, where 1 ml of 0.1 M NaOH = 0.0282 g of oleic acid [14]. The formula was used, where b = volume of NaOH titrated in the sample (mL), and w = weight of MKO used (g).

$$\text{Acid value} = \frac{b\times 5.61}{w} \quad (3)$$

Fatty acid profile

Fatty acid composition was determined by the conversion of fatty acid to fatty acid methyl ester. The 0.05 g of melted MKO was trans-esterified by using 2 mL of methanol:sulphuric acid (20:80) and heated at 90-100 °C for 30 minutes in a water bath. Then, the solution was cooled at room temperature and added with n-hexane HPLC grade (2 mL), and distilled water (8 mL). The mixture was agitated vigorously for 1 minute, and continued with the separation of hexane soluble and insoluble layer by using centrifuge at 3,500 rpm for 2 minutes. The fatty acid methyl esters (FAME) that was soluble in the hexane was collected and the fatty acid profile of the MKO was determined quantitatively and qualitatively by using a GC-FID. The 0.5 µL of FAME was injected into the system with the injector temperature of 220 °C with helium as gas carrier. The oven temperature was set at 175 °C for 30 min, and gradually increased at 3.0 °C/min up to 220 °C [16].

Results and Discussion

The MKO extract was pale yellow in colour and the percentage yield of extraction for each solvent used was summarised in Table 1. The selection of solvent used in this study were suitable for the extraction of oil from plants [12]. Among the three solvents used, hexane gave the highest percentage yield, followed by petroleum ether, and ethanol. The differences of percentage yield among the solvents were due to the different polarity between solvents and solutes. Since triglyceride is a non-polar compound, the extraction by using hexane, which was the most non-polar solvent compared to petroleum ether and ethanol, gave the highest percentage yield [7]. Thus, hexane was chosen as a preference solvent in the extraction of the MKO for this study.

Table 1. The percentage yield of MKO extract

Solvent	% Yield
Hexane	7.32% ± 1.25
Petroleum Ether	3.40% ± 0.84
Ethanol	1.16% ± 0.21

FTIR spectroscopy

The FTIR spectrometer is an important analysis to determine the presence of triglycerides based on its significant functional group in the MKO. The triglycerides were ester derived from fatty acid, and a trifunctional alcohol-glycerol. The functional group that was found in the triglycerides were CH_2, CH_3, C=O and C-O. The FTIR spectrum of the extracted MKO was illustrated in Figure 1, and showed a similarity of the FTIR at its peak [17]. Significant absorption peaks of CH_2, CH_3, and C-O were observed in the medium intensity at 2921, 2852, and 1260 cm^{-1}, respectively. While the absorption peak of C=O at 1747 cm^{-1} with a high intensity was probably because it contained more than one ester in the molecule.

Thermal profile

The DSC was used to determine the thermal profile of the MKO. The crystallisation and melting profile of the MKO was obtained during the cooling and heating process, respectively. Both thermograms were shown in Figure 2. The crystallisation onset (T_{CO}) and melting completion (T_{MC}) were considered to be the temperature at which the crystallisation began and the melting ended, respectively. The MKO started to crystallise at 26 °C (T_{CO}) which was considered a high temperature because

it consisted of a long-chain fatty acid. The crystallisation was followed by the phase transition at temperatures of 18 °C (T_1), 16 °C (T_2), 11 °C (T_3), 4 °C (T_4), and ended at -10 °C (T_5). Meanwhile, the melting process of the MKO started at -40 °C (T_1) with the phase transition at 1 °C (T_2), 6 °C (T_3), 12 °C (T_4), 20 °C (T_5), and ended at 30 °C (T_{MC}). The transition temperatures observed in the thermogram were an evidence of the complex feature of the MKO and corresponded to the mixture of triglycerides group with a different melting point [18]. The melting behaviour indicated the presence of triglyceride formed by poly unsaturated acid appearing at -40 °C, mono unsaturated at 1 °C, and saturated acid at a temperature above than 12 °C [13]. The melting and crystalline values were slightly higher than the cocoa butter values as reported previously [1]. These may be contributed to the higher saturated fatty acid content in the MKO which comprised of saturated long hydrocarbon chain of palmitic, stearic, and oleic acid. Besides, the higher value of T_{MC} showed that the MKO had higher thermostability [13, 17, 19].

Fatty acid profile

The MKO consisted of both saturated and unsaturated fatty acid. The major difference between saturated and unsaturated fatty acid is the presence of double bond. The double bond is only present in the unsaturated fatty acid which means there are less hydrogen atoms present in the molecule's structure. Three major fatty acid presented were palmitic, stearic, and linoleic acid, similar to studies conducted previously [1]. The separation of the compounds was based on the different strengths of interaction of the compounds with the stationary phase. The stronger the interaction, the longer the compound interacted with the stationary phase, and the more time needed to migrate through the column. Stearic acid took a longer time to separate (13.651) than palmitic acid (11.710), and linoleic acid (13.409), as it contained the longest carbon chain which made them to be less polar than the others [2, 7, 12, 20].

Total carotene content

The total carotene content found in the MKO was 147.27 μg%. The lower value was related to the pale yellow colour of the extracted MKO. Carotene is a natural pigment that represent the orange colour of a substance, mainly found in fruits and vegetables. Carotenoid is a bioactive substance in food with powerful antioxidant activity. However, due to the unsaturated nature of the carotene, it is easily degraded due to the oxidation and severe processing conditions, such as thermal process [14]. In the human body, they could act as a precursor of vitamin A, which is a pigment essential for good vision and healthy eyes. Studies showed that regular consumption of β-carotene in food lowered the risk of certain chronic diseases, such as cataract, cardiovascular diseases, and cancers [2, 15].

Comparative study of MKO and commercial cocoa butter

The physical and chemical properties of extracted MKO was analysed and compared with the commercial cocoa butter. The results of the melting point, refractive index, saponification value, and acid value were summarised in Table 2.

The melting point of the MKO was observed at a range of 30 to 34°C. Meanwhile, cocoa butter had a melting point between 27 to 35°C [21]. This result could classify that the MKO and cocoa butter had comparable melting point. The MKO started to melt at a higher temperature compared to cocoa butter due to the long-chain length of saturated fat in the structure of the MKO, thus increasing the melting point, as well as its thermostability [17, 21].

The refractive index of the MKO was found at a value of 1.7447 at 40 °C. This data showed that the MKO had higher refractive index value compared to commercial cocoa butter which was 1.4540 to 1.4590 [22]. Higher refractive index indicated an increase in the chain length and the number of double bond in the MKO. The value was proportional to the length of carbon chain, the number of double bond presented, and the molecular weight of the substance. However, refractive index was found to decrease linearly with increasing temperature. The correlation concluded that the substance with the higher value of refractive index would have a higher density. The refractive index measured the bending ray of light as it passed from one medium to another that showed the information about the behaviour of light, and intermolecular interaction of the substance [23, 24].

The saponification value data for the MKO and cocoa butter were comparable at 191.41 mg KOH/g, and 194.4 mg KOH/g, respectively [25]. The finding indicated the chain length of the MKO carbon molecule was similar to the chain length of commercial cocoa butter. The saponification value found in the MKO was considered high and showed the indicator that it was suitable for use in the cosmetic industries [26, 27]. It represented the amount of potassium hydroxide, or sodium hydroxide (in mg) required to saponify 1.0 g of fat under specific conditions. The average molecular weight or chain length of all the fatty acid might vary depending on the choice of substance and solvent used in the study [2, 12, 24].

Another parameter measured for the physicochemical study is the acid value. The acid value for the MKO was found as 2.40 mg KOH/g, while for cocoa butter was 1.68 [11]. The higher value of the MKO compared to commercial cocoa butter might indicate the increased susceptibility of fat to oxidation due to high degree of unsaturation. The result was in accordance with the previous finding [21]. Even though the MKO acid value was higher compared to cocoa butter, it was still considered accceptable. The acid value was a measure of the total acidity of the lipid, involving contribution from all the constituent fatty acid that made up the glyceride molecule, and it also measured the free fatty acid. The acid value was defined as the weight of potassium hydroxide (in mg) needed to neutralise the free fatty acid present in 1.0 g of fat, and it was also necessary in determining the quantity of free fatty acid present in fat or oils. It indicated its quality, age, edibility, and its oil suitability for cosmetic usage. The hydrolysis of triglycerides occurred and increased in rancidity when there was an increase in the free fatty acid value in a substance [28].

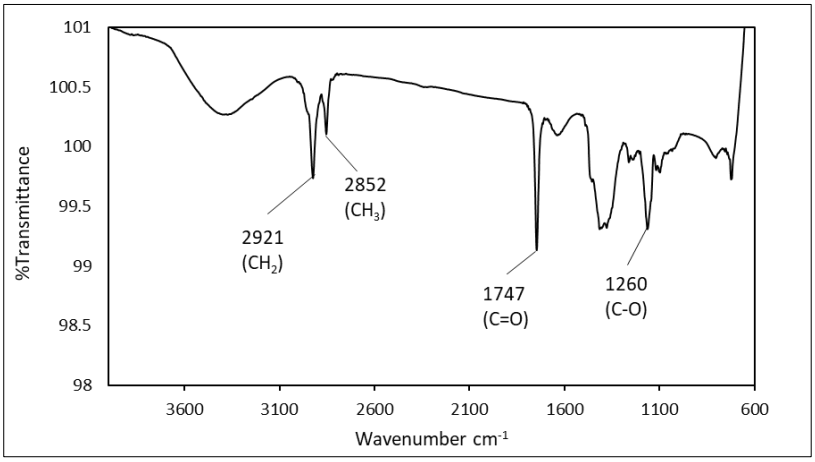


Figure 1. FTIR spectrum of MKO

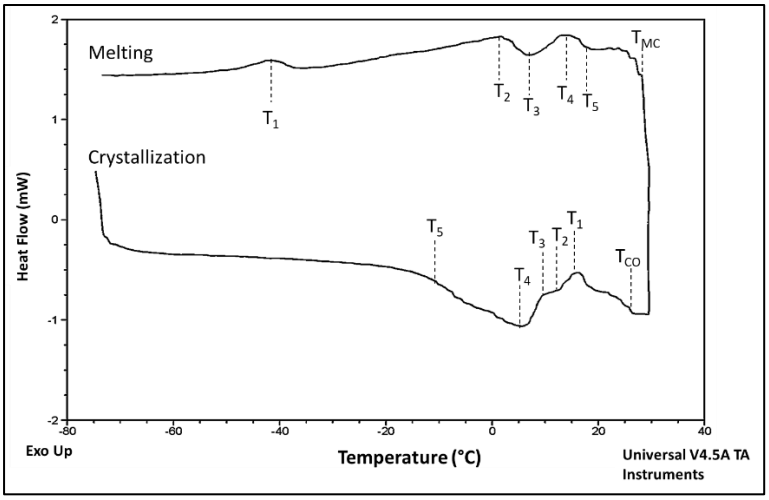


Figure 2. Thermogram of MKO

Table 2. Comparative study between extracted MKO and cocoa butter

Physical or Chemical Properties	**MKO**	**Cocoa Butter [Ref.]**
Melting point (°C)	30-34	27-35 [21]
Refractive index	1.7447	1.4540-1.4590 [22]
Saponification value (mg KOH/g)	191.40	194.40 [25]
Acid value (mg KOH/g)	2.40	1.68 [11]

Conclusion

The data obtained showed a few similarities to cocoa butter properties. Thus, it indicated that extraction of the MKO has a potential as a cocoa butter alternative, and can further be used in food, pharmaceutical, or cosmetic industries. However, a few improvisations, such as chemical and physical refining, and blending with other fats and oils sources can enhance the physicochemical properties of the MKO to be on par, or superior than cocoa butter. In addition, the data from this study could contribute to support the uses, health, and economic benefit of the MKO that is completely unexploited commercially in Malaysia. The exploitation of mango seeds by the industry into a valuable product can thrive the agricultural sector by product segment, increase value-added properties to the by-product, and at the same time help to reduce the environmental pollution.

Acknowledgement

The author wishes to thank Faculty of Applied Sciences, Universiti Teknologi MARA, Cawangan Negeri Sembilan, Kampus Kuala Pilah for the research facilities and financial supported.

References

1. Omar, N. H., Mohd, M., Nor, N. M. I. M., and Zakaria, L. (2018). Characterization and pathogenicity of Fusarium species associated with leaf spot of mango (*Mangifera indica* L.). *Microbial Pathogenesis*, 114: 362-368.

2. Nadeem, M., Imran, M., and Khalique, A. (2016). Promising features of mango (*Mangifera indica* L.) kernel oil: a review. *Journal of Food Science and Technology*, 53(5): 2185-2195.
3. Dardak, R. A. (2019). Trends in production, trade, and consumption of tropical fruit in Malaysia. *FFTC Agricultural Policy Articles*. Access from https://ap.fftc.org.tw/article/1381[Access online 19 April 2020].
4. Lieb, V. M., Schuster, L. K., Kronmüller, A., Schmarr, H. G., Carle, R. and Steingass, C. B. (2019). Fatty acids, triacylglycerols, and thermal behaviour of various mango (*Mangifera indica* L.) kernel fats. *Food Research International*, 116: 527-537.
5. Asif, A., Farooq, U., Akram, K., Hayat, Z., Shafi, A., Sarfraz, F., Sidhua, M. A. I., Rehman, H. And Aftab, S. (2016). Therapeutic potentials of bioactive compounds from mango fruit wastes. *Trends in Food Science & Technology*, 53: 102-112.
6. Pereira, A. D. S., Fontes-Sant'Ana, G. C. and Amaral, P. F. (2019). Mango agro-industrial wastes for lipase production from *Yarrowia lipolytica* and the potential of the fermented solid as a biocatalyst. *Food and Bioproducts Processing*, 115: 68-77.
7. Kittiphoom, S. (2012). Utilization of mango seed. *International Food Research Journal*, 19(4): 1325-1335.
8. Kaphueakngam, P., Flood, A. and Sonwai, S. (2009). Production of cocoa butter equivalent from mango seed almond fat and palm oil mid-fraction. *Asian Journal of Food and Agro-Industry*, 2(4): 441-447.
9. Jahurul, M. H. A., Jing, Y. W., Foong, C. Y., Shaarani, S. M., Zaidul, I. S. M., Jinap, S., Hasmadi, M., Ali, M. E. and Nyam, K. L. (2017). Effect of accelerated storage on chemical compositions of mango seed fat and palm oil mid-fraction blends as cocoa butter replacers. *LWT*, 84: 551-554.
10. Jahurul, M. H. A., Zaidul, I. S. M., Norulaini, N. N., Sahena, F., Abedin, M. Z., Ghafoor, K. and Omar, A. M. (2014). Characterization of crystallization and melting profiles of blends of mango seed fat and palm oil mid-fraction as cocoa butter replacers using differential scanning calorimetry and pulse nuclear magnetic resonance. *Food Research International*, 55: 103-109.
11. Jahurul, M. H. A., Zaidul, I. S. M., Norulaini, N. A. N., Sahena, F., Abedin, M. Z., Mohamed, A. and Omar, A. K. M. (2014). Hard cocoa butter replacers from mango seed fat and palm stearin. *Food Chemistry*, 154: 323–329.
12. Kittiphoom, S., and Sutasinee, S. (2013). Mango seed kernel oil and its physicochemical properties. *International Food Research Journal*, 20(3): 1145-1149.
13. Nzikou, J. M., Kimbonguila, A., Matos, L., Loumouamou, B., Pambou-Tobi, N. P. G., Ndangui, C. B., Abena, A. A., Silou, T., Scher, J. and Desobry, S. (2010). Extraction and characteristics of seed kernel oil from mango (*Mangifera indica*). *Research Journal of Environmental and Earth Sciences*, 2(1): 31-35.
14. Hajar, N., Mohamad, N., Tokiman, A., Munawar, N., Rahim, H. A., Sani, N., Azman, N., Khudzari, N. A. M., Mayuddin, F. K., Nosarimy, I. S., Md Yatim, N. S., Abd Rashid M. I. and Shahrizan, N. S. (2017). Physicochemical properties of rambutan seed fat. *Journal of Academia*, 5(1): 82-91.
15. Haque, S., Begum, P., Khatun, M. and Islam, S. N. (2015). Total carotenoid content in some mango (*Mangifera indica*) varieties of Bangladesh. *International Journal of Pharmaceutical Sciences and Research*, 6(11): 4875-4878.
16. Orsavova, J., Misurcova, L., Ambrozova, J. V., Vicha, R. and Mlcek, J. (2015). Fatty acids composition of vegetable oils and its contribution to dietary energy intake and dependence of cardiovascular mortality on dietary intake of fatty acids. *International Journal of Molecular Sciences*, 16(6): 12871-12890.
17. Awolu, O. O. and Manohar, B. (2019). Quantitative and qualitative characterization of mango kernel seed oil extracted using supercritical CO_2 and solvent extraction techniques. *Heliyon*, 5(12), e03068.
18. Sonwai, S. and Ponprachanuvut, P. (2014). Studies of fatty acid composition, physicochemical and thermal properties, and crystallization behavior of mango kernel fats from various Thai varieties. *Journal of Oleo Science*, 63(7): 661-669.

19. Omar, K. A., Gounga, M. E., Liu, R., Mwinyi, W., Aboshora, W., Ramadhan, A. H.,Sheha, K. A. and Wang, X. (2017). Triacylglycerol composition, melting and crystallization profiles of lipase catalysed anhydrous milk fats hydrolysed. *International Journal of Food Properties*, 20(S2): S1230-S1245.
20. Calder, P. C., and Burdge, G. C. (2012). Fatty acids. *Bioactive Lipids*, 2012: 1-36.
21. Akhter, S., McDonald, M. A. and Marriott, R. (2016). *Mangifera sylvatica* (wild mango): A new cocoa butter alternative. *Scientific Reports*, 6: 32050.
22. Oroian, M., and Ropciuc, S. (2017). Honey authentication based on physicochemical parameters and phenolic compounds. *Computers and Electronics in Agriculture*, 138: 148-156.
23. George, A. K. and Singh, R. N. (2015). Correlation of refractive index and density of crude oil and liquid hydrocarbon. *International Journal of Chemical, Environmental and Biological Sciences*, 3(5): 2320-4087.
24. Fahimdanesh, M. and Bahrami, M. (2013). Evaluation of physicochemical properties of Iranian mango seed kernel oil. *International Proceedings of Chemical, Biological and Environmental Engineering*, 51 (26): 139-142.
25. Manaf, Y. N. A., Marikkar, J. M. N., Long, K. and Ghazali, H. M. (2013). Physico-chemical characterisation of the fat from red-skin rambutan (*Nephellium lappaceum* L.) seed. *Journal of Oleo Science*, 62(6): 335-343.
26. Silva Ferreira, B., Pereira Faza, L. and Le Hyaric, M. (2012). A comparison of the physicochemical properties and fatty acid composition of indaiá (*Attalea dubia*) and babassu (*Orbignya phalerata*) oils. *The Scientific World Journal*, 2012: 532374
27. Che Hamzah, N. H., Khairuddin, N., Siddique, B. M., & Hassan, M. A. (2020). Potential of *Jatropha curcas* L. as biodiesel feedstock in Malaysia: A concise review. *Processes*, 8(7): 786.
28. Michael, A., Fausat, A. and Doyinsola, T. (2014). Extraction and physicochemical analysis of some selected seed oils. *International Journal of Advanced Chemistry*, 2(2): 70-73.

Malaysian Journal of Analytical Sciences (MJAS)
Published by Malaysian Analytical Sciences Society

MEFENAMIC ACID DETERMINATION IN TABLET FORMULATIONS USING A SELECTIVE AND ACCURATE SPECTROPHOTOMETRIC METHOD BASED ON PRUSSIAN BLUE FORMATION

(Penentuan Asid Mefenamik dalam Formulasi Tablet Menggunakan Kaedah Spektrofotometri yang Selektif dan Tepat Berdasarkan Pembentukan Biru Prusian)

Hendri Wasito[1,2]*, Desi Purnamasari[2], Muhamad Salman Fareza[1]

[1]*Department of Pharmacy,*
Faculty of Health Sciences, Jenderal Soedirman University, Purwokerto 53123, Indonesia
[2]*Analytical Chemistry for Pharmaceutical and Health Research Group, Department of Pharmacy, Faculty of Health Sciences, Jenderal Soedirman University, Purwokerto 53123, Indonesia*

[*]*Corresponding author: hendri.wasito@unsoed.ac.id*

Received: 10 November 2020; Accepted: 6 January 2021; Published: 20 February 2021

Abstract

Selective and accurate visible spectrophotometric methods based on Prussian blue formation were successfully developed for the quantitative analysis of mefenamic acid in a tablet. The proposed method showed that visible spectrophotometric measurement at 715 nm under the optimized condition of 15 mmol/L potassium ferricyanide and 2.5 mmol/L ferric chlorides in 0.5 mol/L acetic acids after 15 minutes incubation time. The analytical performance demonstrated good linearity with the squares of correlation coefficient (r^2) more than 0.99 in the concentration ranges of 3.0-14.0 mg/L with a limit of detection and quantification (LOD and LOQ) were found to be 0.31 mg/L and 1.04 mg/L, respectively. The method also seemed to be selective that proven by small interference with various excipients added. The developed and validated method was suitable for routine analysis of mefenamic acid in real samples of the tablet.

Keywords: quantification, mefenamic acid, spectrophotometry, validation

Abstrak

Kaedah spektrofotometri kelihatan selektif dan tepat berdasarkan pembentukan biru Prusian berjaya dibangunkan untuk analisis kuantitatif asid mefenamik dalam penyediaan tablet. Kaedah yang dicadangkan menunjukkan bahawa pengukuran optimum spektrofotometri yang dapat dilihat pada 715 nm di bawah keadaan 15 mmol/L kalium feriksianida dan 2.5 mmol/L ferik klorida dalam 0.5 mol/L asid asetik setelah 15 minit masa inkubasi. Prestasi analitikal menunjukkan kelinearan yang baik dengan pekali korelasi (r^2) lebih besar daripada 0.99 dalam julat kepekatan 3.0-14.0 mg/L dengan had pengesanan dan kuantifikasi (LOD dan LOQ) masing-masing didapati 0.31 mg/L dan 1.04 mg/L. Kaedah ini juga nampaknya selektif yang terbukti dengan campur tangan kecil dengan pelbagai eksipien yang ditambahkan. Kaedah yang dibangunkan dan disahkan sesuai untuk analisis rutin asid mefenamik pada sampel sebenar tablet.

Kata kunci: kuantifikasi, asid mefenamik, spektrofotometri, pengesahan

Introduction

Mefenamic acid (Figure 1) is a non-steroidal anti-inflammatory drug (NSAID) that is pharmaceutically used to reduce mild and moderate pain such as headaches, tooth pain, pain after surgery, dysmenorrhea, osteoarthritis, and rheumatoid arthritis. In higher doses, this compound decreases inflammation [1]. On the other hand, mefenamic acid is formulated in a tablet dosage form for oral administration. Quality control and determination of active substances in pharmaceutical dosage forms must be met the requirement to ensure the quality of drug formulations and support the achievement of expected therapeutic effects. One of the quality requirements is the active compound concentration in the pharmaceutical dosage form that must meet the requirements, as stated in the pharmacopeia or other compendia [2].

Numerous analytical methods were performed to determine mefenamic acid in pharmaceutical dosage forms, such as high-performance liquid chromatography (HPLC), titration method, voltammetry, and potentiometry [3-6]. Spectrophotometric methods were also developed in UV and visible measurements, as well as derivative and flow injection analysis strategies. This spectrophotometric method was proven to be inexpensive, accurate, and fast in determining active compounds in pharmaceutical products [7-12].

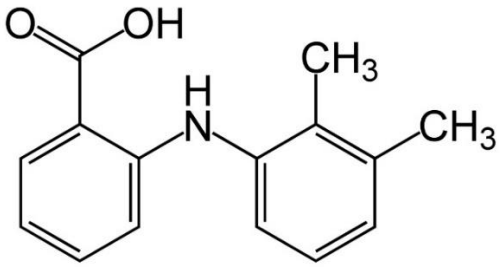


Figure 1. Chemical structure of mefenamic acid

Spectrophotometry is a simple analytical method for the determination of mefenamic acid in pharmaceutical dosage forms. Determination of active ingredient compounds in tablet formulation that contains other excipients that can absorb energy in ultraviolet (UV) became challenging. For instance, sunset yellow dyes can be detected in both UV and visible areas. In the UV region, this excipient gives absorption at wavelengths of 230 nm and 315 nm. At the same time, absorption at wavelengths of 480 nm in the visible area is observed [13]. Therefore, a selective spectrophotometric method is needed to overcome this problem by measuring the absorption in a visible area that not interfering with other excipients.

Selective strategies that can be developed for determining active compounds in complex matrix samples using spectrophotometric methods are based on the formation of colors that can be analyzed in visible regions. Visible spectrophotometric methods based on the formation of red complexes through the reduction of ferric (Fe^{3+}) ions to ferrous (Fe^{2+}) ions by mefenamic acid followed by complex formation with o-phenanthroline was developed for quantification in pharmaceutical products [8]. Another method for mefenamic acid analysis was based on the formation of N-chlorosuccinimide color through the oxidative coupling reaction of mefenamic acid and 4-amminoantipyrine in the acidic medium [14]. However, visible spectrophotometry methods based on Prussian blue formation have not to be reported previously. This approach is not performed yet because other studies use other chemicals to form colored complex compounds and make it more promising to be developed and investigated.

The development of an analytical method for mefenamic acid determination in tablets based on Prussian blue formation is significantly promising because mefenamic acid has the ability to reduce Fe^{3+} to Fe^{2+} ions [8]. The presence of Fe^{2+} ions can be used to form Prussian blue complexes with potassium ferricyanide. The intense blue colored complex afterward analyzed by visible spectrophotometry method at a visible wavelength [15, 16]. This study aimed to develop and validate a visible spectrophotometric method for mefenamic acid determination in tablet formulations based on Prussian blue formation. Optimization of various parameters in terms of reaction conditions and other spectrophotometric parameters was observed.

Comprehensive analytical performances were evaluated based on the guideline for the validation of analytical procedures [17]. Additionally, the proposed method was implemented for the quantitative analysis of mefenamic acid in the real samples. The proposed method was easy to handle due to using simple chemicals and instruments and a fast reaction time of 35 minutes. On the other hand, selectivity for other compounds contributing to the redox reaction may be more challenging. However, the application for the determination of mefenamic acid in tablets showed minor interference. The interference of some excipients that were commonly used in the tablet was evaluated in this study.

Materials and Methods

Chemicals

The analytical grade of mefenamic acid standards (purity ≥ 98.5%), ferric chloride ($FeCl_3$) (purity 99.0%-102.0%), potassium ferricyanide ($K_3(FeCN6)$) (purity ≥ 99.0%), acetic acid (purity ≥ 96.0%), and ethanol (purity ≥ 99.5%) were purchased from Merck (Darmstadt, Germany). The technical grade of distilled water and some excipients, such as talc, starch, and polyvinyl pyrrolidone (PVP), were purchased from Bratachem (Purwokerto, Indonesia). All other chemicals were of analytical grade. Mefenamic acid tablet samples were obtained from the pharmacies in the Purwokerto area.

Instruments

UV-Vis 3000 single-beam spectrophotometer (Cecil CE 3021, Cambridge, England) was used for measurements. Analytical balance, shaker incubator Memmert EN 60529 (Schwabach, Germany), pH meter, and micropipette (Socorex, Switzerland) were used for sample preparations.

Spectrophotometric determination

Mefenamic acid standard solutions and potassium ferricyanide solutions were prepared by accurately weighing each compound, dissolving, and serial dilution into ethanol to obtain appropriate concentration. For instance, 50.0 mg mefenamic acid was dissolved in 50 mL ethanol in a volumetric flask, and then serial dilution was carried out by transferring 1.0 mL solutions into 25 mL volumetric flask, and ethanol was added to obtain 40.0 mg/L mefenamic acid standard solutions. The optimized conditions were performed for measuring mefenamic acid concentration using a spectrophotometer based on Prussian blue formation. In brief, 2.0 mL of mefenamic acid solution was reacted with two mL of 15 mmol/L potassium ferricyanide and two mL of 2.5 mmol/L ferric chlorides in 0.5 mol/L acetic acids in a 10.0 mL volumetric flask. Afterward, 50% ethanol was added to make up the mark. The maximum wavelength was determined using a solution without mefenamic acid to confirm other chemicals and solvents' interference in the measurement. The absorbance of the mixture solution was measured using a spectrophotometer after 35 min incubation at room temperature. The wavelength of 715 nm was used for measuring the absorbance against a reagent blank that contained distilled water.

Analytical method validation

Analytical parameters in terms of linearity, detection limits, quantification limits, accuracy, precision, and selectivity were evaluated for method validation, according to ICH (Q2) R1 guideline [17]. Linearity study was carried out using five series concentrations of mefenamic acid standard solutions in the range of 3.0 mg/L to 14.0 mg/L. Each concentration was prepared in three replicated and then reacted with ferric chloride in acetic acid solution and potassium ferricyanide under optimized conditions. The absorbance was measured with a spectrophotometer at 715 nm. Subsequently, the calibration curve was prepared based on mefenamic acid concentration and their absorbance value. Detection and quantitation limits were calculated based on the residual standard deviation value and the calibration curve slope.

The standard addition method was carried out for accuracy and precision assessments in three concentration levels replicate. Three concentration levels of spiked samples, namely 75%, 100%, and 125%, were processed using 6.0 mg/L, 8.0 mg/L, and 10.0 mg/L of a mefenamic acid standard added to 0.11 mL of the mefenamic acid tablet sample solution, respectively. These levels were selected to cover lower and higher concentrations from the defined concentration. Preparation of the mefenamic acid tablet sample solution was carried out by grinding 20 mefenamic acid tablets, followed by weighed accurately

50.0 mg of homogenized powder and transferred it into a 50 mL volumetric flask. To made up the mark, 50% ethanol was added and mixing until homogeneous, then filtered. An unspiked sample solution that contained only the mefenamic acid tablet sample was prepared with 50% ethanol.

The absorbance values were measured using a visible spectrophotometer after reaction with ferric chloride in acetic acid solution and potassium ferricyanide under optimized conditions. Repeatability (intra-day) and intermediate (inter-day) precision were evaluated from three measurements on the same day and three different days, respectively. Selectivity performance was done by adding separately 8.0 mg/L mefenamic acid standard solutions into common excipients that might be added during formulations, such as talc, starch, and PVP with a concentration of 1000 mg/L for each solution. The absorbance then measured using a spectrophotometer at 715 nm in the optimized condition.

Mefenamic acid determination in tablet

Quantitative determination of mefenamic acid concentrations in the tablet was carried out using three different mefenamic acid tablet brands. First, 20 tablets were pulverized and accurately weighed 50.0 mg of homogenized powder and then dissolved in 25 mL ethanol in a volumetric flask. Following this, the sample solutions were filtered, and afterward, an appropriate sample was transferred into a 25 mL volumetric flask and added 50% ethanol to make the mark. Then, 2.0 mL samples were mixed with ferric chloride in acetic acid solution and potassium ferricyanide under optimized conditions. Finally, the absorbance values were measured using a spectrophotometer at 715 nm.

Data analysis

The concentration of mefenamic acid samples was calculated by interpolating the absorbance value with the mefenamic acid standard calibration curve. The analytical method's linearity was given in the square of the correlation coefficient (r^2), indicating the relationship between the mefenamic acid concentration and their absorbance values. The detection limit and the quantification limit were expressed as the concentration level (mg/L) calculated from three times and ten times the standard residual deviation in the method, respectively. The accuracy was evaluated from the recovery percentage, and the precision was observed from the relative standard deviation (% RSD) of measurements. Also, selectivity assessment was recognized from the percentage of mefenamic acid concentration recovery after adding some excipients tablet samples. Regarding the determination of the real sample tablet, the data were presented descriptively in the form of the percentage of the claimed label for each identified tablet brand.

Results and Discussion

Method development for mefenamic acid determination using visible spectrophotometry

Determination of the spectrophotometric detection wavelength was carried out by measuring the absorption of Prussian blue solutions formed from the reaction of mefenamic acid with ferric chloride in acetic acid solution and potassium ferricyanide in the region wavelength between 500 nm to 800 nm. Figure 2 illustrated the findings of optimized wavelength at 715 nm that shown the higher concentration of mefenamic acid as a reducing agent, the higher intensity of Prussian blue formed. These findings suggested that the reduced agent's increased capacity contributed to the increasing Prussian blue formed, and afterward, the absorbance level gradually increases [18]. The optimized wavelength measurement was obtained at 715 nm. This wavelength region corresponded to the wavelength for a bluish-green color solution in the range of 610 nm to 750 nm [20]. On the other hand, according to Teepoo et al. [15], the Prussian blue wavelength was 700 nm. Another study reported that the slight difference of the optimized wavelength was obtained probably due to the different conditions of the Prussian blue formation such as temperature, pH, differences in solvents, and differences in reaction conditions [21].

To optimize the measurement and reaction conditions for Prussian blue formation, various parameters in terms of operating time measurement and concentration of potassium ferricyanide, ferric chloride, and acetic acid solutions were investigated using a spectrophotometer at 715 nm. The stable measurement time for Prussian blue formation was observed over 75 minutes after reaction

to mefenamic acid with ferric chloride and potassium ferricyanide solutions. The suitable time for measurement was obtained at 35 minutes (Figure 3a) under the conditions of 40.0 mg/L mefenamic acid, 15.0 mmol/L potassium ferricyanide, and 0.5 mmol/L ferric chlorides in 0.5 mol/L acetic acids after 35 min incubation. This finding seemed different from the other research, which reported the operating time for Prussian blue formation derived from reducing Fe^{3+} to Fe^{2+} ions using ascorbic acid as a reducing agent followed by reaction with potassium ferricyanide was 10 minutes [15]. It is reasonable because ascorbic acid is a strong reducing agent that the reaction time needed for the reduction process occurs faster due to the formation of Prussian blue only needs in less time [22].

Various concentration solutions to form optimum Prussian blue was observed using potassium ferricyanide, ferric chloride, and acetic acid. The investigated results obtained that the higher potassium ferricyanide concentration influenced the higher intensity absorbance to 15 mmol/L and became remained constant (Figure 3b). This finding shows that 15 mmol/L potassium ferricyanide was a suitable condition for optimum concentration to form Prussian blue. The measurement was performed using 40.0 mg/L mefenamic acid and 0.5 mmol/L ferric chloride in 0.5 mol/L acetic acids after 35 minutes incubation. This finding was in accordance with the other studies that the addition of potassium ferricyanide in higher concentration increased the absorbance of Prussian blue formed [15, 23]. Evaluation from ferric chloride concentration also gave the same trend. An increase of ferric chloride concentration was gradually followed by increasing the absorbance at 715 nm (Figure 3c). The absorbance remained stable after a concentration value of 2.5 mmol/L, indicated that the optimum concentration of ferric chloride for this measurement was carried out using 0.5 mol/L acetic acid, 40.0 mg/L mefenamic acids, and 15.0 mmol/L potassium ferricyanide, with incubation time 35 minutes.

On the other hand, the optimum concentration of acetic acid was 0.5 mol/L (Figure 3d). Acetic acid was used for dissolving ferric chloride. Increasing acetic acid concentration causes an increase in Prussian blue, which was formed due to acidic conditions that can increase Prussian blue's solubility. In addition, Prussian blue was unstable under alkaline conditions where Prussian blue will form deposits of iron oxide ($Fe(OH)_3$) [24]. In summarize, these results showed that optimum Prussian blue formed using 40 mg/L mefenamic acids under the condition of 15 mmol/L potassium ferricyanide and 2.5 mmol/L ferric chlorides in 0.5 mol/L acetic acids.

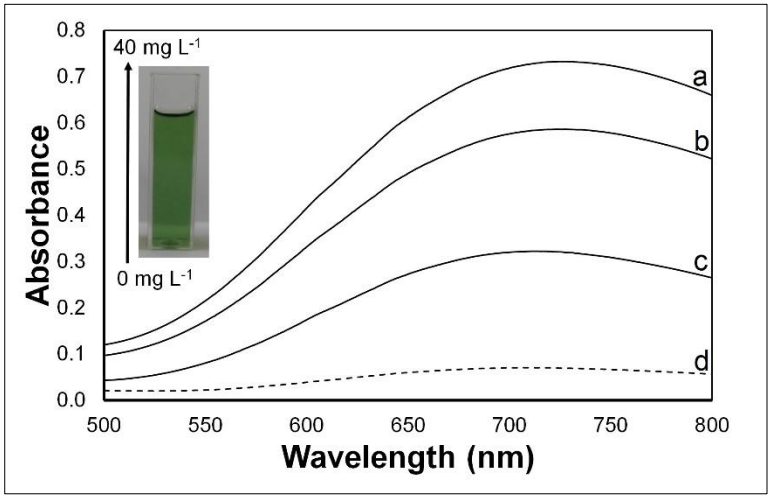


Figure 2. Absorption spectra of soluble Prussian blue formation. Condition: 3.0 mmol/L potassium ferricyanide and 0.5 mmol/L ferric chloride in 0.5 mol/L acetic acid with (a) 40.0 mg/L, (b) 24.0 mg/L, (c) 6.0 mg/L, and (d) 0.0 mg/L mefenamic acid

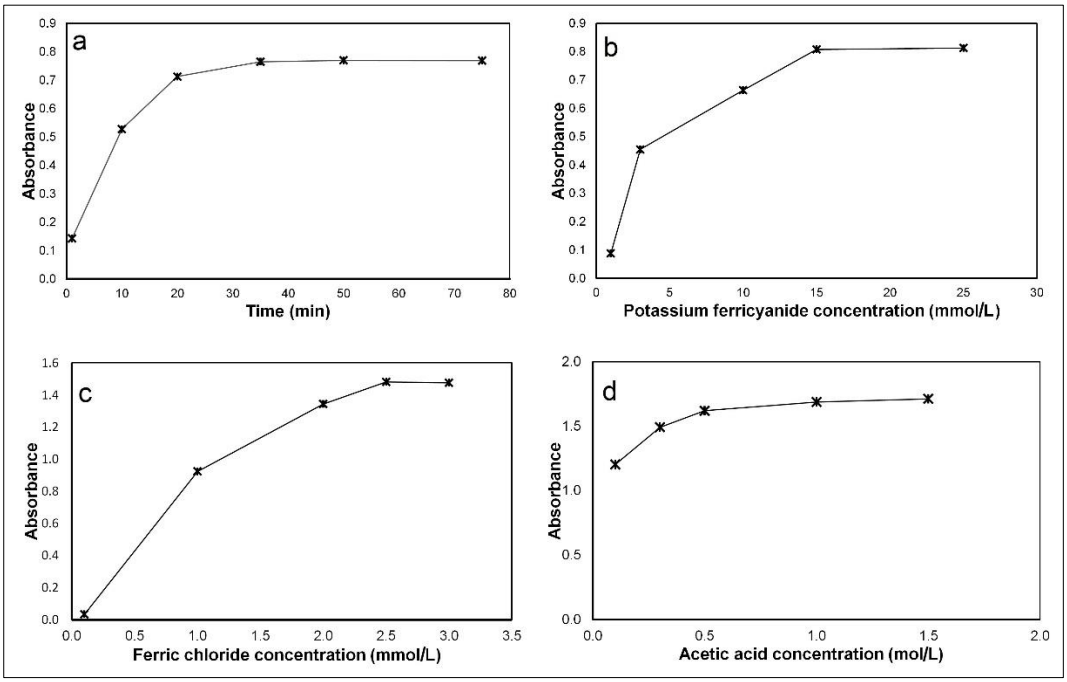


Figure 3. Optimization of Prussian blue color formation measured using spectrophotometry at 715 nm. The effect of (a) incubation time, (b) potassium ferricyanide, (c) ferric chloride, and (d) acetic acid concentrations on color development

Method validation performance

Linearity measurement was performed using five different mefenamic acid concentrations, which gave absorbance in the range of between 0.2 and 0.8 absorbance units with three replicates. The measurement results are presented in Figure 4. It can be seen that the value of the square correlation coefficient (r^2) obtained was 0.9954 in the concentration range of 3.0 mg/L to 14.0 mg/L, which means that there was a good correlation between the concentration and the absorbance measurement. In addition, the high degree of correlation coefficient value of the regression equation showed good linearity following Lambert Beer's law [25, 26]. In other studies, Ahmed and Mufty, who developed an analytical method for determining the concentration of mefenamic acid through oxidation of mefenamic acid by Fe^{3+} and reacted with phenanthroline, gave the degree of correlation coefficient was 0.9993 [8]. Whereas in the research of Raza et al., who developed the method of determining mefenamic acid through the reaction of mefenamic acid with chloranil, which produced violet color, the degree of correlation coefficient was 0.9996 [9].

On the other hand, measuring mefenamic acid based on N-bromosuccinimide's oxidation reaction produced a yellow color with a linear degree of correlation coefficient of 0.9999 [27]. Additionally, the LOD and LOQ calculated based on mefenamic acid standard calibration curves were 0.31 mg/L and 1.04 mg/L, respectively. This result seemed to be better than another report from Raza et al. that obtained the value of 2.16 mg/L for LOD and 7.5 mg/L for LOQ [9].

Accuracy and precision evaluation were done using the standard addition method using three standard

concentration levels with three replicate measurements (Table 1). Accuracy performance was obtained from the recovery value of the mefenamic acid added into the sample. The results of the average recovery for each level of concentration was between 90.00% and 93.79%. On the other hand, this method's precision was less than 1.60% and 3.03% for intra-day and inter-day measurements, respectively. Finally, selectivity performance was obtained by adding 1000 mg/L of talk, starch, and PVP solution to the standard solution of mefenamic acid with a concentration of 8.0 mg/L. The selectivity value was observed from the recovery value. The recovery value obtained was between 99.94% and 102.76% (Table 2). This result indicated an appropriate selectivity of the proposed method in the presence of excipient in the matrix sample commonly used in the tablet dosage form.

Application of mefenamic acid level measurement in tablet

The proposed visible spectrophotometric method was used to determine the concentration of mefenamic acid in the pharmaceutical tablet. Three different samples of commercially mefenamic acid tablets, namely PNT, GMA, and MFL, with the same batch number were determined. The mefenamic acid concentration in the sample was determined by measuring absorbance at 715 nm using external calibration approaches. Relative average concentration comparing with claim labeled measurement for mefenamic acid tablet labels were between 99% and 103% (Table 3). These results suggested that each sample measured using the proposed method was under the requirements. The Indonesian Pharmacopoeia and British Pharmacopeia stated that mefenamic acid tablets should contain mefenamic acid in the range of 95.0% to 105.0% of the amount stated on the label [28, 29].

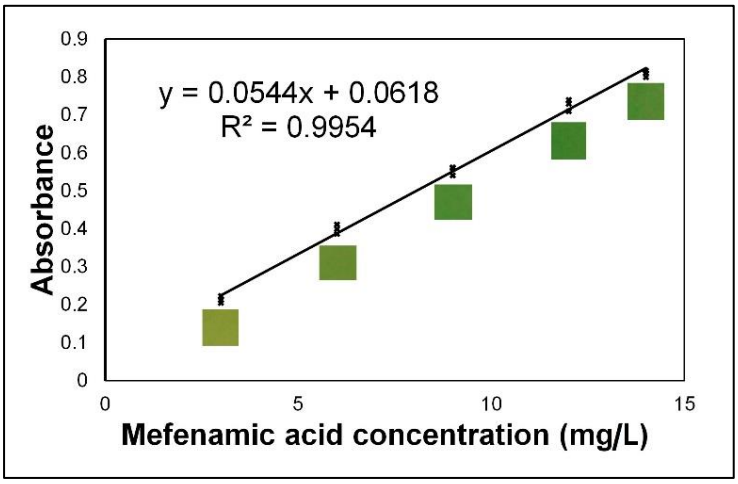


Figure 4. Linear regression calibration curve for mefenamic acid's standard solution in the concentration range of 3.0 mg/L to 14.0 mg/L (n = 3)

Table 1. Accuracy and precision of mefenamic acid spectrophotometric measurement using standard addition method (n = 3)

Level (%)	Sample	Mefenamic acid added	Intra-day		Inter-day	
			Mefenamic acid found	Recovery	Mefenamic acid found	Recovery
		(mg/L)	(mg/L)	(%)	(mg/L)	(%)
75	1	6.00	5.63	93.83	5.41	90.17
	2	6.00	5.59	93.17	5.33	88.83
	3	6.00	5.46	91.00	5.46	91.00
	Average			**92.67**		**90.00**
	% RSD			**1.60**		**1.22**
100	1	8.00	7.44	93.00	7.16	89.50
	2	8.00	7.50	93.75	7.15	89.34
	3	8.00	7.57	94.63	7.44	93.00
	Average			**93.79**		**90.61**
	%RSD			**0.87**		**2.28**
125	1	10.00	9.25	92.50	8.79	87.90
	2	10.00	9.46	94.60	9.31	93.10
	3	10.00	9.21	92.10	9.21	92.10
	Average			**93.07**		**91.03**
	% RSD			**1.44**		**3.03**

Table 2. Method selectivity evaluation in the presence of various excipients in tablet formulations (n = 3)

Excipients	Amount Taken (mg/L)	Mefenamic Acid Added (mg/L)	Recovery (%)	RSD (%)
PVP	1000	8.00	98.38	2.33
Talc	1000	8.00	108.12	3.15
Starch	1000	8.00	104.20	1.38

Table 3. Application of the proposed method for analysis of commercial mefenamic acid formulations in tablet dosage form (n =3)

Sample	Label Claimed in Each Tablet (mg)	Weight of Sample for Each Tablet (Mg)	Mefenamic Acid Found in Each Tablet ($\bar{x}$ ± SD Mg)	Mefenamic Acid Found in Each Tablet ($\bar{x}$ ± SD%)	Percentage of Label Claimed Found in Each Tablet ($\bar{x}$ ± SD %)
PNT	500	728	499.72 ± 1.15	68.68 ± 0.16	99.94 ± 0.23
GMA	500	654	513.78 ± 6.01	78.53 ± 0.92	102.76 ± 1.20
MFL	500	910	507.83 ± 9.99	55.78 ± 6.13	101.57 ± 2.00

Conclusion

A selective and accurate visible spectrophotometric method was successfully developed for mefenamic acid determination in the tablet formulations based on Prussian blue formation. The proposed method can be applied as an alternative method for the routine analysis of mefenamic acid in pharmaceutical raw and dosage forms with a good analytical performance.

Acknowledgment

The authors would like to thank the Jenderal Soedirman University for financial support and the Department of Pharmacy, Faculty of Health Sciences, Jenderal Soedirman University for research facilities.

References

1. Sweetman, S. C. (2009). Martindale The complete drug reference, Pharmaceutical Press, London: pp. 80.
2. Council of Experts and Its Expert Committees (2014). United States Pharmacopeia 37, United States Pharmacopoeial Convention, Rockville: pp. 3672-3673.
3. Ibrahim, H., Boyer, A., Bouajila, J., Couderc, F. and Nepveu, F. (2007). Determination of non-steroidal anti-inflammatory drugs in pharmaceuticals and human serum by dual-mode gradient HPLC and fluorescence detection. *Journal of Chromatography B*, 857(1): 59-66.
4. Kormosh, Z. and Matviychuk, O. (2013). Potentiometric determination of mefenamic acid in pharmaceutical formulation by membrane sensor based on ion-pair with basic dye. *Chinese Chemical Letters*, 24(4): 315-317.
5. Malode, S. J., Shetti, N. P. and Kulkarni, R. M. (2019). Voltammetric detection and determination of mefenamic acid at silver-doped TiO_2 nanoparticles modified electrode. *Materials Today: Proceedings*, 18: 671-678.
6. Poerwono, H., Widyowati, R., Kubo, H., Higashiyama, K. and Indrayanto, G. (2005). Mefenamic acid: analytical profile, profiles of drug substances, excipients and related methodology, Academic Press, Brittain: pp. 281-336.
7. Dinç, E., Yücesoy, C. and Onur, F. (2002). Simultaneous spectrophotometric determination of mefenamic acid and paracetamol in a pharmaceutical preparation using ratio spectra derivative spectrophotometry and chemometric methods. *Journal of Pharmaceutical and Biomedical Analysis*, 28(6): 1091-1100.
8. Al-mufty, M. Z. and Ahmed, N. R. (2009). Indirect spectrophotometric method for the determination of mefenamic acid in pharmaceutical formulations. *Rafidain Journal of Science*, 20(6): 39-47.
9. Raza, A. (2008). Spectrophotometric determination of mefenamic acid in pharmaceutical preparations. *Journal of Analytical Chemistry*, 63(3): 244-247.
10. Zisimopoulos, E. G., Tsogas, G. Z., Giokas, D. L., Kapakoglou, N. I. and Vlessidis, A. G. (2009). Indirect chemiluminescence-based detection of mefenamic acid in pharmaceutical formulations by flow injection analysis and effect of gold nanocatalysts. *Talanta*, 79(3): 893-899.

11. Mofavvaz, S., Sohrabi, M. R. and Heydari, A. (2020). Application of UV/vis spectrophotometry based on using least squares support vector machine and continuous wavelet transform methods for the simultaneous analysis of antibiotics drugs in tablet formulation: Comparison with HPLC method. *Optik*, 220: 165246.
12. Darbandi, A., Sohrabi, M. R. and Bahmaei, M. (2020). Development of a chemometric-assisted spectrophotometric method for quantitative simultaneous determination of Amlodipine and Valsartan in commercial tablet. *Optik*, 218: 165110.
13. Pavanelli, S. P., Bispo, G. L., Nascentes, C. C. and Augusti, R. (2011). Degradation of food dyes by zero-valent metals exposed to ultrasonic irradiation in water medium: Optimization and electrospray ionization mass spectrometry monitoring. *Journal of the Brazilian Chemical Society*, 22(1): 111-119.
14. Othman, N. S. and Awades, L. S. (2008). Spectrophotometric determination of mefenamic acid via oxidative coupling reaction with 4-amminoantipyrine in presence of N-chlorosuccinimide. *Pakistan Journal Analytical Environmental Chemistry*, 9(2): 64-68.
15. Teepoo, S., Chumsaeng, P., Jongjinakool, S., Chantu, K. and Nolykad, W. (2012). A new simple and rapid colorimetric screening test for semi-qualitative analysis of vitamin C in fruit juices based on Prussian blue. *Journal of Applied Sciences*, 12(6): 568-574.
16. Wasito, H., Fatoni, A., Hermawan, D. and Susilowati, S. S. (2019). Immobilized bacterial biosensor for rapid and effective monitoring of acute toxicity in water. *Ecotoxicology and Environmental Safety*, 170: 205-209.
17. Borman, P. and Elder, D. (2017). Q2 (R1) validation of analytical procedures. *ICH Quality Guidelines*, 5: 127-166.
18. Jayanthi, P. and Lalitha, P. (2011). Reducing power of the solvent extracts of Eichhornia crassipes (Mart.) Solms. *International Journal of Pharmacy and Pharmaceutical Sciences*, 3(3): 126-128.
19. Grandjean, F., Samain, L. and Long, G. J. (2016). Characterization and utilization of Prussian blue and its pigments. *Dalton Transactions*, 45(45): 18018-18044.
20. Malacara, D. (2011). Color vision and colorimetry: Theory and applications. SPIE Press, Bellingham: pp. 1-20.
21. Giovannetti, R. (2012). The use of spectrophotometry UV-Vis for the study of porphyrins macro to nano spectroscopy. InTech, China: pp. 87-108.
22. Rao, G. G. and Rao, V. N. (1955). Ascorbic acid as a reducing agent in quantitative analysis. *Fresenius' Zeitschrift Für Analytische Chemie*, 147(5): 338-347.
23. Samain, L., Grandjean, F., Long, G. J., Martinetto, P., Bordet, P. and Strivay, D. (2013). Relationship between the synthesis of Prussian Blue pigments, their color, physical properties, and their behavior in paint layers. *The Journal of Physical Chemistry C*, 117(19): 9693-9712.
24. Adhikamsetty, R. and Jonnalagadda, S. (2009). Kinetics and mechanism of prussian blue formation. *Bulletin of the Chemical Society of Ethiopia*, 23(1): 47-54.
25. El-Didamony, A. M., Saad, M. Z. and Saleem, N. O. (2013). Kinetic spectrophotometry method for the determination of morphine, nalbuphine and naltrexone drugs in bilk and pharmaceutical formulation. *Journal of the Chilean Chemical Society*, 58(3): 1907-1913.
26. Hu, W.-H., Zhai, Q.-Z. and Zhang, X.-M. (2014). Determination of trace amount of IO_3^- with KIO_3-KBr-(DBS-arsenazo) system by spectrophotometry. *Journal of Analytical Chemistry*, 69(5): 438-441.
27. Alarfaj, N., Altamimi, S. and Almarshady, L. (2009). Spectrophotometric determination of mefenamic acid in pharmaceutical preparations. *Asian Journal of Chemistry*, 21(1): 217-226.
28. Panitia Farmakope Indonesia, R. (1995). Farmakope Indonesia Edisi Keempat, Depkes, Jakarta: pp. 1107-1110.
29. British Pharmacopoeia Commission Office (2009). British Pharmacopoeia, Volume I & II, Medicines and Healthcare Products Regulatory Agency (MHRA), London: pp. 4788.

Malaysian Journal of Analytical Sciences (MJAS)
Published by Malaysian Analytical Sciences Society

STUDYING THE PERFORMANCE OF DIAPER CHAR PRODUCED VIA PYROLYSIS AS AN EFFICIENT ADSORBENT FOR LEAD REMOVAL

(Mengkaji Prestasi Char Lampin yang Dihasilkan Melalui Pirolisis Sebagai Penjerap Berkesan untuk Penyingkiran Plumbum)

Najiyatul Munirah Yasin, Siti Nurul Hidayah Badrul Hisham, Najaa Nur Atiqah Rozulan, Nurul Ashraf Razali*

Faculty of Ocean Engineering Technology and Informatics,
Universiti Malaysia Terengganu, 21030 Kuala Nerus, Terengganu, Malaysia

**Corresponding author: Nrazali@umt.edu.my*

Received: 17 August 2020; Accepted: 28 December 2020; Published: 20 February 2021

Abstract

Industrial wastewater contains heavy metal ions that are harmful to the environment. This work aims to study the performance of the adsorbent from diaper char (DC) and activated DC for lead (Pb) removal. The morphology of the adsorbent was characterised using scanning electron microscopy (SEM), X-ray diffraction (XRD), and Fourier transform infrared (FTIR) analysis. DC was prepared *via* pyrolysis and activated using zinc chloride ($ZnCl_2$, 0.5 M) and potassium hydroxide (KOH, 0.5 M). The efficiency of the adsorbent was analysed using synthetic Pb. About 96.6% of Pb^{2+} removal was observed upon the introduction of 1 g/L of DC in 20 mg/L of Pb^{2+} solution for 25 min at pH 7. Also, adsorption occurred rapidly even in 5 min (94%). The efficiency of the adsorbent to remove Pb^{2+} was then tested for DC activated using $ZnCl_2$ and KOH. DC-$ZnCl_2$ (99.8%) showed higher percentage removal of Pb^{2+} than DC-KOH (98.2%). The adsorption behaviour was fixed with the Freundlich isotherm model (R^2 = 0.9202) with the maximum adsorption capacity of 7.626 mg/g, where the results indicated a multilayer adsorption mechanism. The findings showed that DC can be utilised as the adsorbent for Pb removal and also demonstrate excellent alternative use of abundant diaper waste.

Keyword: adsorption, diaper char, isotherm, lead

Abstrak

Air sisa buangan industri mengandungi ion logam berat yang berbahaya kepada alam sekitar. Hasil kajian ini bertujuan mengkaji prestasi penjerap daripada char lampin (DC) dan DC teraktif untuk penyingkiran plumbum. Morfologi penjerap dikategorikan dengan menggunakan analisis mikroskop elektron pengimbas (SEM), belauan sinar-X (XRD), dan inframerah transformasi Fourier (FTIR). Penyediaan DC dilakukan melalui teknik pirolisis dan diaktifkan menggunakan zink klorida ($ZnCl_2$, 0.5 M) dan kalium hidroksida (KOH, 0.5 M). Kecekapan penjerap dianalisis dengan menggunakan plumbum sintetik. Kajian menunjukkan bahawa 96.6% penyingkiran plumbum telah dicatatkan apabila 1 g/L DC ditambah dan kepekatan awal plumbum adalah 20 mg/L dalam 25 minit dan pada pH 7. Kecekapan penjerap juga berlaku pada kadar yang cepat dalam 5 minit (94%). Kecekapan penjerap untuk menyingkirkan plumbum kemudian diuji menggunakan DC yang telah diaktifkan menggunakan $ZnCl_2$ dan KOH. DC-$ZnCl_2$ (99.8%) memberikan peratusan penyingkiran plumbum yang lebih tinggi berbanding DC-KOH (98.2%). Tingkah laku penjerapan diperbaiki dengan model isoterma Freundlich (R^2 = 0.9202) dengan kapasiti penjerapan maksimum 7.626 mg/g, di mana hasilnya menunjukkan mekanisme penjerapan pelbagai lapisan. Hasil kajian menunjukkan bahawa DC boleh digunakan sebagai penjerap untuk penyingkiran plumbum dan juga alternatif terbaik penggunaan sisa lampin yang banyak.

Kata kunci: penjerapan, char lampin, isoterma, plumbum

Introduction

Increasing industrial wastewater pollution from mining, chemical manufacturing, electronics, metallurgical, and electroplating industries has become a global concern [1, 2], in which metal mining and processing contributed to 48% of the total release of contaminants in European industrial sectors [3]. Heavy metals, such as lead, mercury, chromium, and nickel are non-biodegradable, carcinogenic, and tend to accumulate in living organisms. Several techniques have been proposed to remove heavy metal ions from industrial wastewater, including precipitation, adsorption, biological and electrochemical methods, ion exchange, chemical coagulation/flocculation, and membrane filtration methods [4, 5]. Adsorption has high efficiency and selectivity to remove heavy metals, simple to operate, easy recovery, and cost-effective [6, 7]. The United States Environmental Protection Agency and World Health Organization have set the guidelines for maximum allowable levels of heavy metals in water bodies. Malaysia has enacted strict laws to suppress the discharge of heavy metal ions from industrial activities. According to the Environmental Quality Act 1974, the permissible discharge of lead (Pb) in industrial effluent set by the Department of Environment Malaysia under the Fifth Schedule is 0.10 mg/L for Standard A and 0.5 mg/L for Standard B [8].

Recently, the amount of municipal solid waste has been increasing each year throughout the world due to rapid urbanisation, increased economic and population growth, improved living standards, and industrialisation [9, 10]. One of the major problems due to increasing population growth is increased diaper waste. According to the National Solid Waste Management Department Malaysia, disposable diaper waste contributed to approximately 12% of the total waste decomposed in a landfill [11]. In addition, the pathogens from the solid waste of diapers may potentially contaminate water sources and consequently, pollute drinking water. In order to solve this problem, thermochemical processes for converting solid waste into valuable products (e.g., biochar, bio-oil, and gas) have been employed, including pyrolysis [12, 13], gasification [13], carbonisation [14], and torrefaction [15].

Biochar has been widely used as an adsorbent to remove contaminants in wastewater from various sources and the material is economically and environmentally friendly [16]. In this case, baby diapers that consist of biomass and polymer are converted into adsorbents *via* pyrolysis. In their study, Oh and co-worker showed that the pyrolytic solid (char) derived from used disposable diapers has a porous, coarser, and more heterogeneous surface as the pyrolytic temperature increased and also proved that diaper char (DC) has durable adsorption capacity as an adsorbent to adsorb pollutants [17]. However, there are very limited adsorption studies that used DC as an adsorbent.

Biochar synthesised from pyrolysis has high potential to be employed as adsorbents to remove heavy metal ions due to its high porosity, environmentally friendly, and variety of sources [18]. Chemical activation is cost-effective as it requires shorter processing time, lower activation temperature, and high carbon efficiency compared to physical activation [19]. Biochar can be activated using acids, bases, and oxidising agents for expanding its applications and enhancing its performance [16], [20]. According to Heidarinejad et al., various techniques in chemical activation for both acidic and alkaline groups give different surface structures for the char [19]. A study was conducted by Guo and his team using chemical activation methods (potassium hydroxide (KOH), zinc chloride ($ZnCl_2$), and phosphoric acid (H_3PO_4) to prepare activated biochar made from rice husk [21]. Based on their findings, the addition of KOH promoted the development of overlapping pores, the addition of $ZnCl_2$ formed new mesopores, and the addition of H_3PO_4 achieved numerous heterogeneous pore size distribution.

The efficiency of adsorbents to remove heavy metals from wastewater is significantly affected by the initial concentration, pH, adsorbent dosage, particle size, and contact time. Langmuir and Freundlich isotherm models

can be the best methods to describe the adsorption characteristics between adsorbents and heavy metals [22]. Most adsorption studies used adsorbents from feedstock products, but limited studies used raw materials made of synthetic products, such as plastics and diapers. There are limited adsorption studies on diapers and its potential to remove contaminants, such as heavy metals in wastewater. The current study was carried out to better understand the interrelation between DC and activated DC with heavy metals. This study aims to remove Pb^{2+} from synthetic wastewater (aqueous solution) using DC and activated DC as adsorbents. The experiments on the effect of initial concentration, pH, adsorbent dosage, and contact time were followed by Langmuir and Freundlich isotherm models. The findings of this study are important to evaluate the efficiency of DC and activated DC to remove Pb in wastewater.

This work has been proposed for the first time to study the performance of thermally treated DC as an efficient adsorbent for Pb removal from synthetic wastewater containing Pb. Lead is highly toxic and needs to be removed from water bodies as Pb may affect human health, such as brains, lungs, and neurons even at low concentrations [23]. The objectives of this study are to explore (1) the morphology of DC, DC-KOH, and DC-$ZnCl_2$, (2) the optimum reaction conditions for DC, DC-KOH, and DC-$ZnCl_2$ to adsorb Pb, and (3) the maximum adsorption capacity of DC to remove Pb in synthetic wastewater.

Materials and Methods

Chemicals

All chemicals used in the experiments were of analytical reagent grade, including sodium hydroxide (NaOH) (98%, Quality Reagent Chemical), $ZnCl_2$ (97%, R&M Chemical), KOH (85%, Quality Reagent Chemical), and hydrochloric acid (HCl) (37%, Merck). Commercial lead sulphate (HMBG) was also used in this study.

Adsorbent preparation

Char preparation

The DC was produced via the pyrolysis of used baby diapers containing super-absorbent polymer materials, cellulose, and plastic [24]. The inner layer comprised baby excrement (e.g., liquid and urine) that was pre-treated through pyrolysis. The reaction was carried out by the Pyrolysis Technology Research Group, Universiti Malaysia Terengganu. The diapers were pyrolyzed for 30 minutes at 600 W *via* microwave pyrolysis and then crushed and sieved into smaller particle size ranging from 0.8 to 1.0 mm.

Activated diaper char preparation

0.5 M KOH solution was prepared by dissolving KOH in deionised water. 10 g of char was added into KOH solution and stirred at 300 rpm for 12 hours. Then, the char was filtered and dried at 105 °C for 12 hours. Next, the char was calcined for 2 hours at 500 °C in static air with a heating ramp from room temperature of 10 °C min^{-1}. The activated DC was denoted as DC-KOH. The DC was also activated using $ZnCl_2$ by applying similar methods as DC-KOH and denoted as DC-$ZnCl_2$. Both DC-KOH and DC-$ZnCl_2$ were crushed and sieved in a range of 0.8–1.0 mm [25].

Adsorbent characterisation

The morphology of the adsorbent was studied using scanning electron microscopy (SEM, JEOL 6360 LA), where the adsorbent was mounted on carbon and gold-coated prior to examination. The crystalline structure of DC, DC-KOH, and DC-$ZnCl_2$ was studied using X-ray diffraction (XRD). The sample was ground to the size of 10-50 μm and placed onto the specimen holder. The sample was measured from 10 to 90°. Fourier transform infrared (FTIR) spectroscopy (Shimadzu IRTracer-100) was used to study the surface functionalities of the absorbent. The sample was placed in a sample holder (ATR cell) and the spectra were collected over the range of 400-4000 cm^{-1} with a resolution of 4 cm^{-1}.

Preparation of lead stock solution

Synthetic wastewater containing Pb was prepared by mixing lead sulphate in 1,000 mL of deionised water in a 1,000 mL volumetric flask. The samples of synthetic wastewater (standard solution) with the concentrations of 20, 40, 60, and 80 mg/L were prepared.

Batch adsorption experiments

An amount 200 mL of synthetic wastewater was mixed simultaneously at room temperature (24-26 °C) using a jar tester at 150 rpm. The experimental work was

performed in the presence of 1 g/L of DC with the initial concentration of 20 mg/L for 25 minutes. Then, the mixture was filtered to remove DC from the solution, and the final concentration of Pb^{2+} was analysed using inductively coupled plasma-optical emission spectroscopy (ICP-OES) (Optima 8300, Perkin Elmer). The adsorption was then conducted by varying several reaction parameters, including the initial concentration of Pb^{2+} (20-80 mg/L), pH (3-11), adsorbent dosage (0.5-4.0 g/L), and contact time (5-25 minutes). The pH of the solution was adjusted using 0.1 M of HCl and 0.1 M of NaOH according to the designated pH. The adsorption of DC-KOH and DC-$ZnCl_2$ was conducted following the same methodology for DC, and the reaction parameters used were 40 mg/L of initial concentration, pH 7, and 3 g/L of adsorbent.

The percentage removal of Pb, RE (%) can be determined using Eq. 1, where C_0 is the initial concentration of the solution without the adsorbent (mg/L) and C_f is the final concentration of the solution at equilibrium (mg/L).

$$\mathrm{RE} = \frac{(C_0 - C_f)}{C_0} \times 100\% \quad (1)$$

The amount of adsorption at equilibrium, q_e (mg/g) can be determined using Eq. 2, where C_0 is the initial concentration of the solution without the adsorbent (mg/L), C_f is the final concentration of the solution at equilibrium (mg/L), V is the volume of the solution (L), and W is the mass of the adsorbent (g).

$$q_e = \frac{(C_0 - C_f)V}{W} \quad (2)$$

Adsorption isotherm models

The adsorption capacity was determined using Langmuir and Freundlich isotherm models to evaluate the effectiveness of the adsorption process. The Langmuir isotherm assumes that the adsorption of the adsorbent onto the surface occurs in monolayer adsorption, which can be expressed using Eq. 3, where q_e is the adsorption capacity at equilibrium (mg/g), q_{max} is the maximum adsorption capacity per unit weight of the adsorbent (mg/g), C_e is the concentration of adsorbate at equilibrium (mg/L), and K_L is the Langmuir constant relating the affinity of the binding sites (L/mg).

$$\frac{1}{q_e} = \frac{1}{K_L \cdot q_{max}} \bullet \frac{1}{C_e} + \frac{1}{q_{max}} \quad (3)$$

The Freundlich isotherm assumes that the adsorption of the adsorbent onto the surface occurs in multilayer adsorption, which can be calculated using Eq. 4, where q_e is the adsorption capacity at equilibrium (mg/g), C_e is the concentration of adsorbate at equilibrium (mg/L), n is the sorption intensity of the adsorbent, and K_f is the Freundlich constant.

$$\log q_e = \frac{1}{\mathrm{n}} \log \mathrm{C_e} + \log K_f \quad (4)$$

This isotherm model is suitable to describe the sorption of several compounds to a heterogeneous surface or surface supporting sites of varied affinities, assuming the stronger binding sites are occupied first and then the binding strength decreases with increasing degree of site occupation [26].

Results and Discussion

Characterisation of adsorbents

Scanning electron microscopy

The surface morphology of DC, DC-KOH, and DC-$ZnCl_2$ was determined at different magnification levels using SEM. Figure 1 shows the SEM micrographs of DC, DC-KOH, and DC-$ZnCl_2$. From the images, the adsorbents showed rough surfaces. The DC structure was well retained after carbonisation (pyrolysis) and several pores were formed upon activation using KOH and $ZnCl_2$. The surface of DC shown in Figure 1(b) is covered by a fine crystal structure. This provides a better understanding of their functional groups present in FTIR analysis. The presence of a needle crystal-like structure is expected due to the formation of ammonia crystals during pyrolysis. The activation of char with KOH has greatly destroyed the surface structure of the char and overlapped pores have successfully developed [14]. The image of DC-$ZnCl_2$ shows that some spherical particles have developed, which are expected to be the agglomeration of Zn.

X-ray diffraction

The XRD patterns were used to analyse the crystal structures of fresh catalysts, as displayed in Figure 2. The XRD results (Figure 2) were used to confirm the crystalline phase of ZnO and KOH deposited on DC. It is possible to observe the dominant phase of ZnO, as

characterised by the peaks at 2θ = 31.6, 34.2, 36.0, 47.5, 56.7, 62.2, 66.9, and 69.2 [27]. The peaks corresponding to potassium carbonate (K_2CO_3) (PDF 11-0566) were observed in DC-KOH, where KOH reacted with carbon to form K_2CO_3 ($6KOH + 2C \rightarrow 2K + 3H_2 + 2K_2CO_3$) [28].

Fourier transform infrared

FTIR analysis was employed to identify the surface functionalities of the adsorbents. Figure 3 presents the FTIR spectra of DC, DC-KOH, and DC-$ZnCl_2$. The peaks were identified and summarised in Table 1. The peaks observed at 3,300-3,500 cm^{-1} confirmed the presence of the stretching vibration of the O-H group, which disappeared from DC-KOH and DC-$ZnCl_2$ samples [21]. The peak detected at 3,047.57 cm^{-1} was attributed to the O-H stretching. The peak observed at 1,660-1,680 cm^{-1} confirmed the presence of the C=C group, such as alkenes. Meanwhile, the peaks detected at 1,429.25 cm^{-1} for DC and 1,409.96 cm^{-1} for DC-KOH represent the C-N group. The N=H group from baby urine may remain in used baby diapers even after pyrolysis. This finding supports the presence of a needle crystal-like structure from SEM images. The peaks detected at 827.46 cm^{-1} (DC) and 873.75 cm^{-1} (DC-KOH) were assigned to the N-H stretching group.

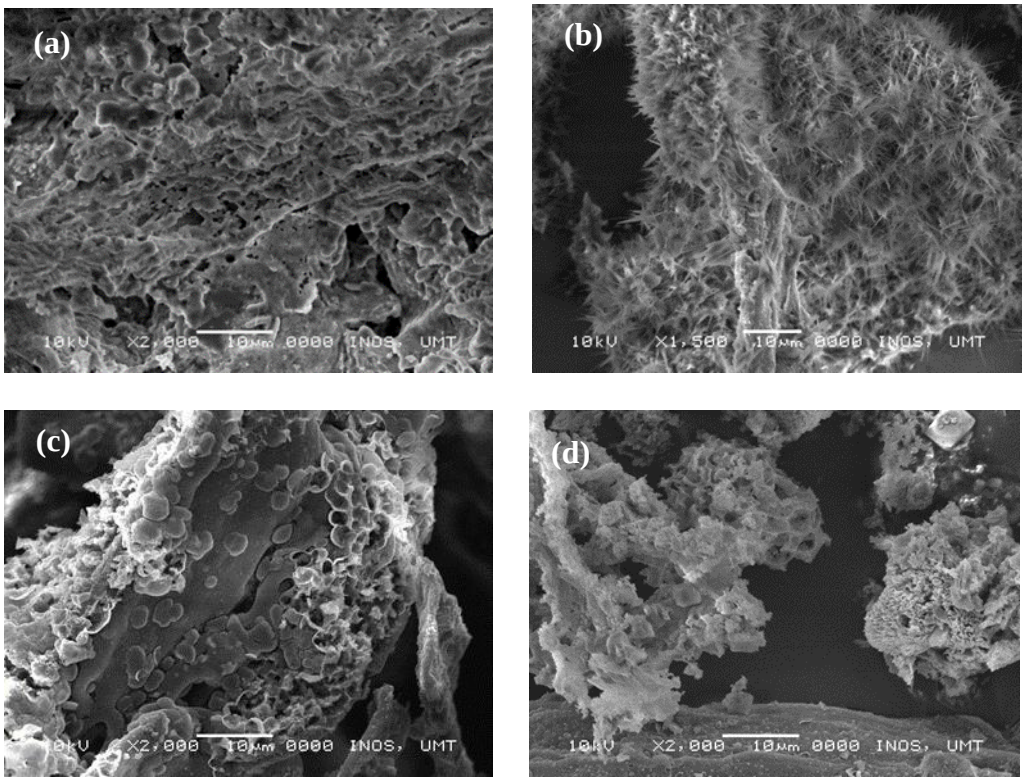


Figure 1. SEM images at different magnification levels: (a) DC: 2,000x, (b) DC: 1,500x, (c) DC-KOH: 2,000x, and (d) DC-$ZnCl_2$: 2,000x

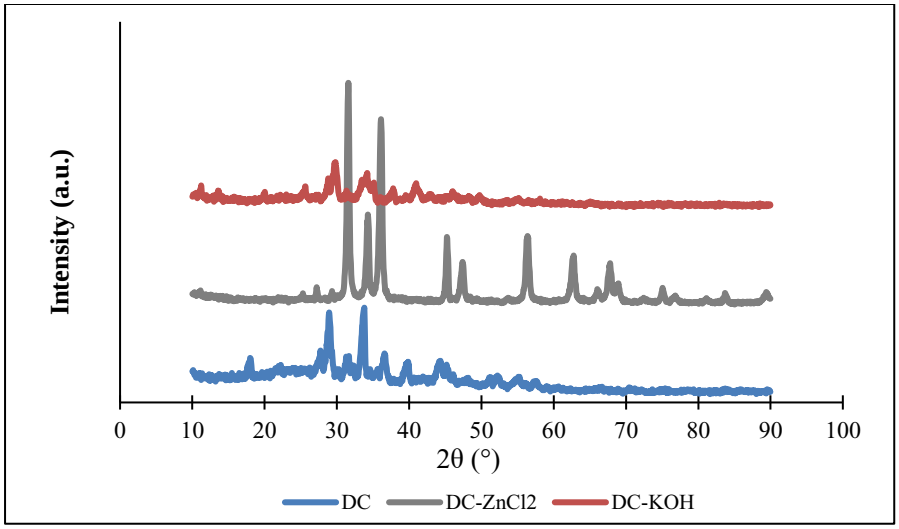


Figure 2. XRD patterns of DC, DC-$ZnCl_2$, and DC-KOH

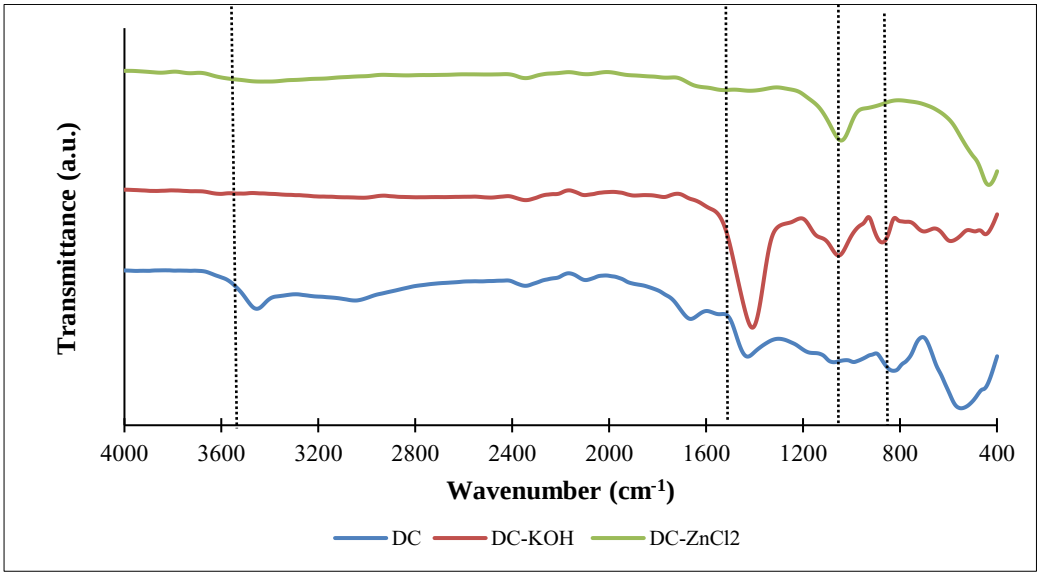


Figure 3. FTIR spectra of DC, DC-KOH, and DC-$ZnCl_2$ before adsorption

Table 1. The wavelength of diaper char from FTIR results

Frequency Ranges (cm^{-1})	Frequency (cm^{-1})			Functional Groups	Compound Class
	DC	DC-KOH	DC-$ZnCl_2$		
3,300–3,500	3,454.51	-	-	O-H stretching	Alcohol, carboxylic acids
3,000–3,100	3,047.57	-	-	O-H stretching	Alcohol
1,620–1,680	1,662.64	-	-	C=C stretching	Alkenes
1,400–1,600	1,429.25	1,409.96	-	C-N stretching	Aromatic
1,000–1,200	-	1,053.13	1,043.49	C-O bending	Alcohol, ether, carboxylic acid
665–910	827.46	873.75	-	N-H stretching	Amines

Batch adsorption studies

Effect of initial concentration of solution

The performance of DC was evaluated for Pb removal and the results are shown in Figure 4. From the results, DC could perform as a good adsorbent as it could remove more than 90% of Pb^{2+} even at a high concentration of Pb^{2+} (80 mg/L). This reaction was carried out with the Pb^{2+} concentrations of 20, 40, 60, and 80 mg/L for 25 minutes with 1 g/L of DC at pH 7. A high percentage of Pb^{2+} removal was observed at 20 mg/L (96.4%), followed by 40, 60, and 80 mg/L, and 80 mg/L achieved the lowest percentage removal of 92.5%. The higher initial concentration causes a higher amount of metal ions in the solution. As there is the same amount of adsorbent dosage for every concentration, thus the affinity of Pb^{2+} to bind with the adsorption sites of DC increases. Once the binding sites are completely filled with Pb^{2+} ions, some Pb^{2+} ions are not adsorbed and suspended in the solution. The abundance of Pb^{2+} ions in the solution is due to the saturated available sites [29]. Singh and co-worker tested the ability of polyethylene (PE), polyethylene terephthalate (PET), and polyvinyl chloride (PVC) char to remove heavy metals from aqueous solution [30]. The char prepared from the pyrolysis of (i) PVC and PE, (ii) PVC and PET, and (iii) PET and PE resulted in 39%, 18%, and 70% of Pb^{2+} removal efficiency, respectively, where the initial Pb^{2+} concentration was 20 ppm, with pH of 6.0, adsorbent dosage of 0.5 g, and contact time of 20 minutes.

Effect of pH of the solution

The pH of wastewater is the main parameter influencing the rate of adsorption between Pb^{2+} and DC. The functional groups of adsorbent and adsorbed molecules are significantly affected by the concentration of hydrogen (H^+) and hydroxide (OH^-) ions in the solution [31]. The experiments for the effect of the pH of the solution were carried out at pH 3, 5, 7, 9, and 11 using 20 mg/L of Pb^{2+} concentration for 25 minutes with 1 g/L of DC.

The pH of Pb solution is important in the adsorption process as the degree of ionisation and speciation of adsorbate is mainly affected by the pH value of solution [32]. Figure 5 shows the percentage removal of Pb^{2+} at different pH values. pH 7 obtained the highest Pb^{2+} percentage removal (96.6%), and only 67% of Pb^{2+} removal was observed at a lower pH value (pH 3). According to Abbar et al., low metal absorption occurred at low pH, which may be ascribed to H^+ competing with metal ions for exchangeable cations on the surface of the adsorbent [33]. As the pH value increased, the negative charge density on the adsorbent surface would increase, thus increasing the attraction of Pb^{2+} by the positive charge, allowing the sorption onto the DC surface [32, 33].

Effect of adsorbent dosage

The amount of adsorbent dosage may also affect the adsorption rate of Pb^{2+}. In this study, 0.5, 1.0, 2.0, 3.0, and 4.0 g/L of DC were employed.

The efficiency of DC for Pb^{2+} removal was tested at different adsorbent dosages from 0.5 to 4.0 g/L, as shown in Figure 6. It was observed that the percentage removal of Pb^{2+} increased from 0.5 until 3.0 g/L and started to decrease after more than 3.0 g/L of DC was added. In this case, only 91.8% of Pb^{2+} could be removed in the presence of 0.5 g/L of DC. 96.2%, 96.6%, and 97.3% of Pb^{2+} removal was achieved upon the introduction of 1.0, 2.0, and 3.0 g/L of DC, respectively. The increasing amount of adsorbent dosage can improve the total number of surface area, and the binding sites of DC consequently improve the chances of Pb^{2+} ions to be bound with the surface of the adsorbent. However, the increasing amount of adsorbent dosage does not improve the adsorption capacity because it has reached the optimum absorption level (i.e., saturation occurred). Increasing the amount of DC from 1.0 to g/L to 4 g/L does not show any significant difference in terms of percentage removal; therefore, only 1 g/L of DC was employed to study the impact of contact time.

Effect of contact time

Figure 7 shows the percentage removal of Pb^{2+} at different contact times. The absorption of Pb^{2+} in the presence of DC occurred in a short period and the saturation occurred in 5 min. The adsorption occurred rapidly in the first 5 min due to a high number of active sites. Increasing the adsorption rate resulted in the increase of concentration gradient of Pb^{2+} ions in the solution onto the char surface. The char surface is almost filled with Pb^{2+} ions and becomes limited as time passes by due to repulsive forces and physical constraints [29]. Thus, the adsorption rate becomes slower and constant.

Adsorption of lead in wastewater using activated diaper char

The performance of DC-KOH (98.2%) and DC-$ZnCl_2$ (99.8%) was tested for Pb^{2+} removal, as shown in Figure 8. From the results, the DC activated with KOH and $ZnCl_2$ demonstrated better removal performance than DC (96.2%). At these reaction conditions (40 mg/L of initial Pb^{2+} concentration, pH 7, and 3 g/L of adsorbent dosage), there is no competition between H^+ or OH^- and Pb^{2+} ions to bind with adsorption sites on the adsorbent surfaces because the solution is in a neutral state, and a higher adsorbent dosage has made the adsorption process becomes more efficient as there are more adsorption sites available for Pb^{2+} ions to attach to. It is expected that the activated char may result in high surface areas. In general, the activation with $ZnCl_2$ yields activated carbons with a heterogeneous pore size and of both micro- and mesopores [34]. Large pore volume will contribute to more Pb^{2+} ions bound to the adsorption sites of the adsorbent surfaces. Hence, DC-$ZnCl_2$ tends to remove more Pb^{2+} ions from wastewater. The XRD analysis was conducted (Figure 2) and confirmed the formation of the crystalline phase of zinc oxide (ZnO) deposited on the DC. In general, ZnO can adsorb several metal cations, including copper, cadmium, manganese, lead, and mercury; thus, the ZnO deposited on the surface of DC would also improve the adsorption of Pb [35].

Adsorption isotherm

The experimental data of DC were analysed using adsorption isotherm models of Langmuir and Freundlich isotherms. Table 2 presents the Langmuir and Freundlich isotherm constants. The results for the Langmuir isotherm were calculated using Eq. 3 to find the values of q_{max} and K_L. Meanwhile, the results for the Freundlich isotherm were calculated using Eq. 4 to determine the values of n and K_F.

The Langmuir isotherm graph, which is a plot of C_e/q_e against C_e, is shown in Figure 9 with the correlation coefficient value of 0.7388. By comparing Eq. 3 and the linear equation based on the graph in Figure 9, the value of q_{max} was obtained from the intercept and the value of K_L was obtained from the slope.

The graph of log q_e against log C_e plotted in Figure 10 shows the Freundlich isotherm of Pb^{2+} ions onto DC. The value of the correlation coefficient based on the graph is 0.9202. By comparing Eq. 4 and the linear equation from the graph in Figure 10, the value of n was obtained from the slope and the value of K_F was obtained from the intercept.

The best-fitted linearity from both isotherm models was selected based on the correlation coefficient value (R^2). The R^2 closer to 1 gives the best fit towards adsorption characteristics. The R^2 value from the Langmuir isotherm is 0.7388, whereas the R^2 value from the Freundlich isotherm is 0.9202. Thus, these experimental results better fit to the Freundlich isotherm model for Pb^{2+} adsorption. It shows that the adsorption of Pb^{2+} onto the surface of the adsorbent has a multilayer adsorption mechanism.

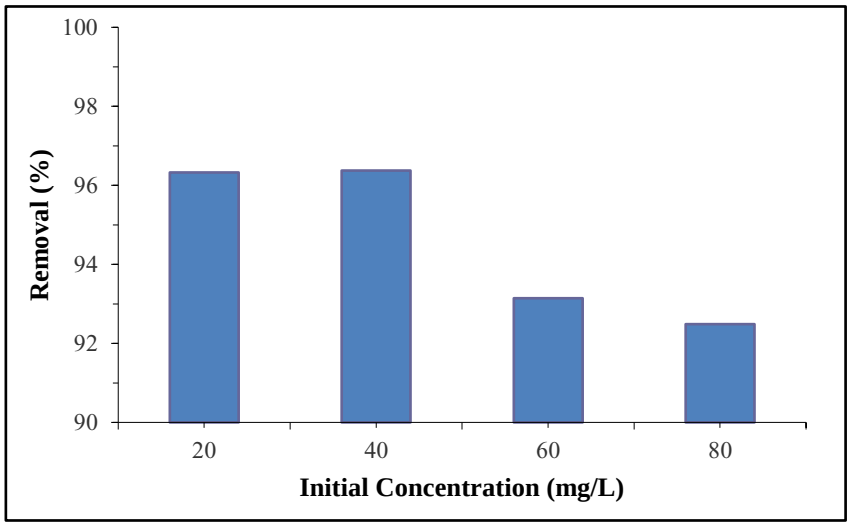


Figure 4. Percentage removal of Pb^{2+} at different initial concentrations (20, 40, 60, and 80 mg/L of lead solution, 1 g/L of DC, 25 min, pH 7)

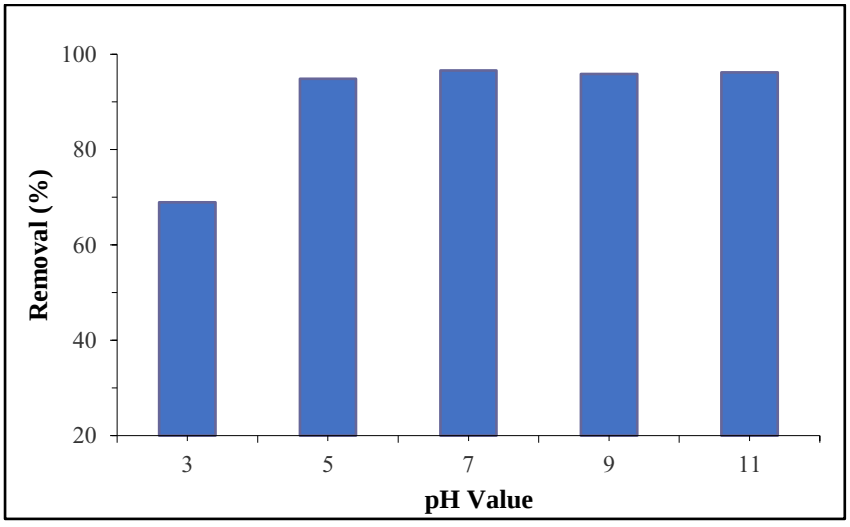


Figure 5. Percentage removal of Pb^{2+} at different pH values (20 mg/L of lead solution, 1 g/L of DC, 25 minutes, pH 3, 5, 7, 9, and 11)

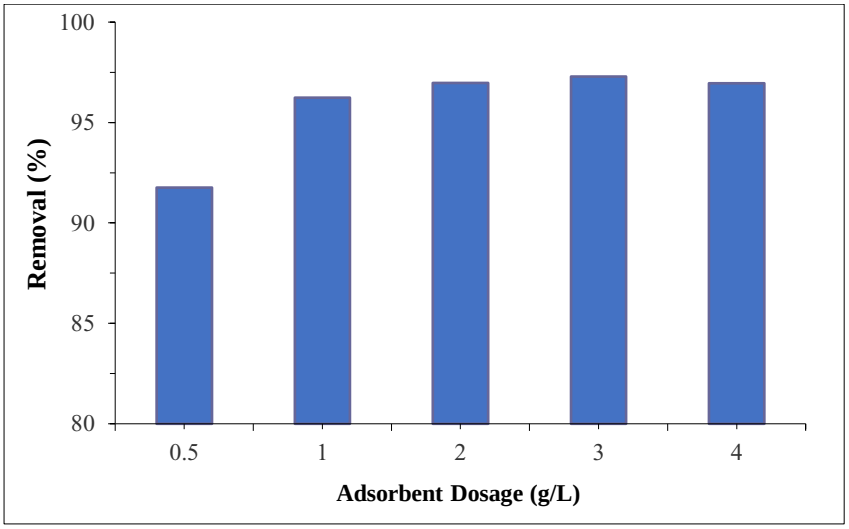


Figure 6. Percentage removal of Pb^{2+} at different adsorbent dosages (20 mg/L of lead solution, 0.5, 1.0, 2.0, 3.0, and 4.0 g/L of DC, 25 min, pH 7)

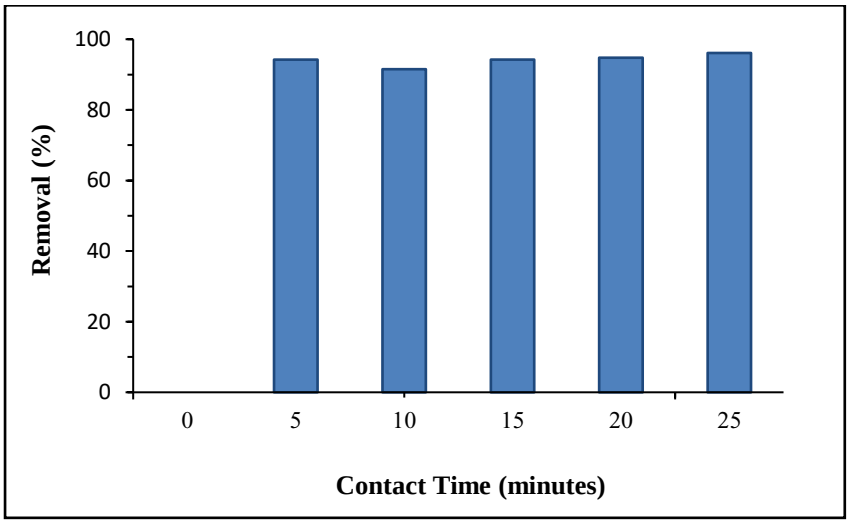


Figure 7. Percentage removal of Pb^{2+} at different contact times (20 mg/L of lead solution, 1 g/L of DC, 5, 10, 15, 20, and 25 minutes, pH 7)

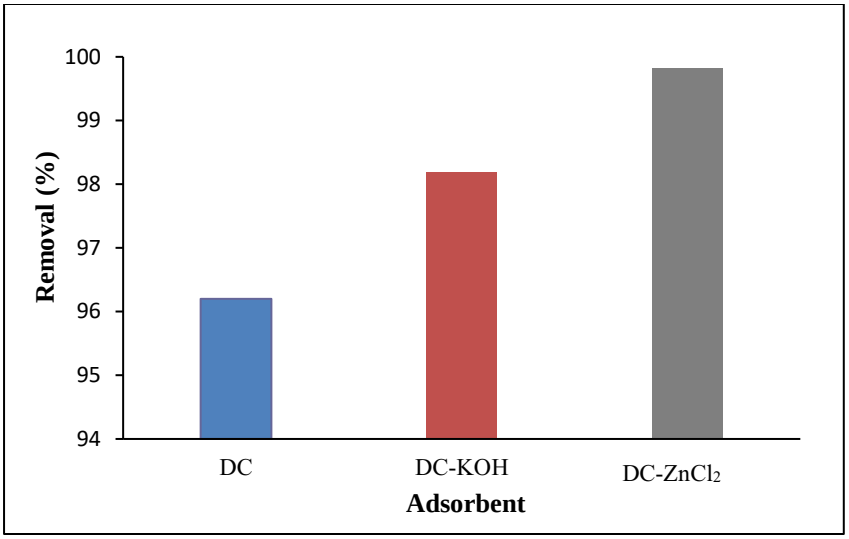


Figure 8. Percentage removal of Pb^{2+} by DC, DC-KOH, and DC-$ZnCl_2$ (40 mg/L of Pb^{2+} initial concentration, pH 7, 3 g/L of adsorbent dosage, 25 min)

Table 2. Langmuir and Freundlich isotherm constants

Langmuir Isotherm			**Freundlich Isotherm**		
q_{max} (mg/g)	**K_L (L/mg)**	**R^2**	**n**	**K_F ((mg/g)(L/mg)$^{1/n}$)**	**R^2**
7.262	-0.055	0.7388	0.714	4.1314	0.9202

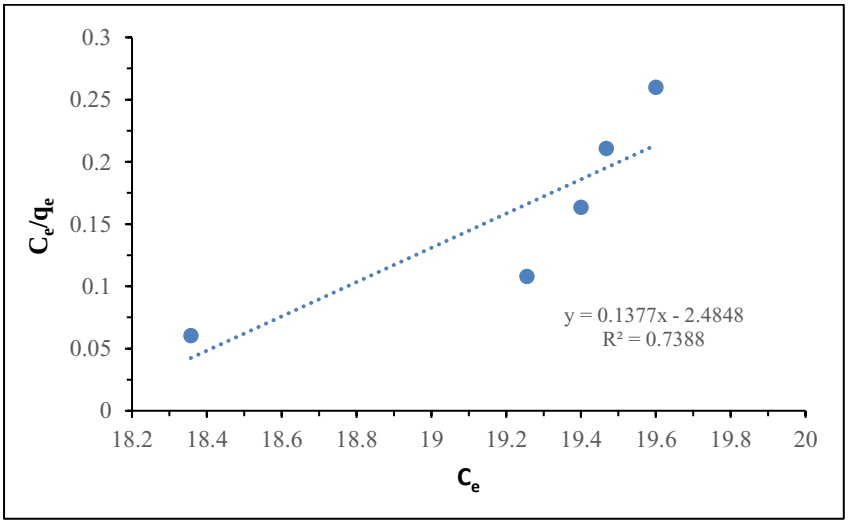


Figure 9. Langmuir isotherm of Pb^{2+} ions onto DC

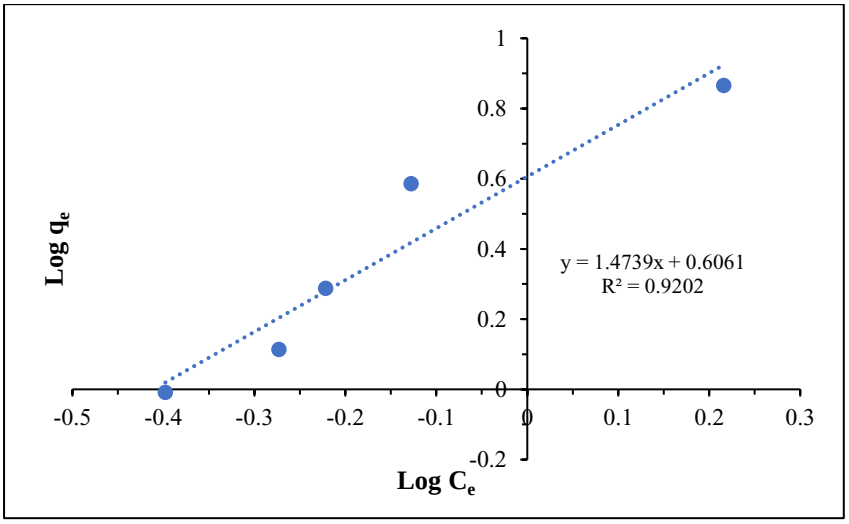


Figure 10. Freundlich isotherm of Pb^{2+} ions onto DC

Conclusion

This study showed that DC successfully removed Pb^{2+} in synthetic wastewater, as more than 90% of Pb^{2+} adsorbed onto the DC. 96.6% of Pb^{2+} removal was observed upon the introduction of 1 g/L of DC in 20 mg/L of Pb^{2+} solution for 25 minutes and at pH 7. The adsorption occurred rapidly within 5 minutes. The activation of DC with KOH and $ZnCl_2$ successfully removed Pb^{2+} for approximately 98% and 99% due to the large pore volume that improved the adsorption performance on the adsorbent surfaces after activation. This adsorption study of DC to remove Pb^{2+} in wastewater better fitted to the Freundlich isotherm model, where the R^2 for the Freundlich isotherm model is 0.9202. Therefore, it can be concluded that DC can be utilised as the adsorbent for Pb removal and also demonstrate excellent alternative use of abundant diaper waste. The ability of both DC and activated DC in removing several types of heavy metals, such as copper, cadmium, and zinc must be studied and tested. This study can be used as the baseline to study the potential of plastic char from several sources (other than DC) as green adsorbents and can simultaneously reduce the amount of plastic waste that will be decomposed in landfills.

Acknowledgements

The authors would like to thank Universiti Malaysia Terengganu for the financial support (RIGS 55192/11). The plastic char was prepared with the support of the Pyrolysis Technology Research Group, Universiti Malaysia Terengganu.

References

1. Chu, B., Amano, Y. and Machida, M. (2020). Preparation of bean dreg derived n-doped activated carbon with high adsorption for Cr(VI). *Colloids and Surfaces A: Physicochemical and Engineering Aspects*, 586: 124262.
2. Lai, K. C., Lee, L. Y., Hiew, B. Y. Z., Thangalazhy-Gopakumar, S. and Gan, S. (2019). Environmental application of three-dimensional graphene materials as adsorbents for dyes and heavy metals: Review on ice-templating method and adsorption mechanisms. *Journal of Environmental Sciences*, 79: 174-199.
3. Vareda, J. P., Valente, A. J. M. and Durães, L. (2019). Assessment of heavy metal pollution from anthropogenic activities and remediation strategies: A review. *Journal of Environmental Management*, 246: 101-118.

4. Joseph, L., Jun, B. M., Flora, J. R. V., Park, C. M. and Yoon, Y. (2019). Removal of heavy metals from water sources in the developing world using low-cost materials: A review. *Chemosphere,* 229: 142-159.
5. Zhang, H., Xu, F., Xue, J., Chen, S., Wang, J. and Yang, Y. (2020). Enhanced removal of heavy metal ions from aqueous solution using manganese dioxide-loaded biochar: Behavior and mechanism. *Scientific Reports,* 10(1): 1-13.
6. Pyrzynska, K. (2019). Removal of cadmium from wastewaters with low-cost adsorbents. *Journal of Environmental Chemical Engineering*, 7(1): 102795.
7. Vardhan, K. H., Kumar, P. S. and Panda, R. C. (2019). A review on heavy metal pollution, toxicity and remedial measures: Current trends and future perspectives. *Journal of Molecular Liquids*, 290: 111197.
8. Malaysia, G. (1974). Environmental Act Quality 1974. Environmental Act Quality 1974: pp. 57.
9. Lestari, P. and Trihadiningrum, Y. (2019). The impact of improper solid waste management to plastic pollution in Indonesian coast and marine environment. *Marine Pollution Bulletin*, 149: 110505.
10. Liu, Y. and Wang, J. (2020). Treatment of fresh leachate from a municipal solid waste incineration plant by combined radiation with coagulation process. *Radiation Physics and Chemistry*, 166: 108501.
11. The Star (2016). Soiled Diapers Stuck in Landfills Access from https://www.thestar.com.my/metro/community/2016/05/23/soiled-diapers-stuck-in-landfills-recycling-is-the-way-forward-says-expert/#:~:text=Malaysians use about 9.72 million, and 0.5kg a piece. [Accessed online 01 December 2020].
12. Uroševic, T. and Pešovski, B. (2018). A review on adsorbents for treatment of water and wastewaters containing copper ions. *Chemical Engineering Science*, 192: 273-287.
13. Gunarathne, V., Ashiq, A., Ramanayaka, S., Wijekoon, P. and Vithanage, M. (2019). Biochar from municipal solid waste for resource recovery and pollution remediation. *Environmental Chemistry Letters*, 17: 1225-1235.
14. Guo, F., Peng, K., Liang, S., Jia, X., Jiang, X. and Qian, L. (2019). Evaluation of the catalytic performance of different activated biochar catalysts for removal of tar from biomass pyrolysis. *Fuel*, 258: 116204.
15. Dacres, O. D., Tong, S., Li, X., Sun, Y., Wang, F., Luo, G., Liu, H., Hu, H. and Yao, H. (2020). Gas-pressurized torrefaction of biomass wastes: the effect of varied pressure on pyrolysis kinetics and mechanism of torrefied biomass. *Fuel*, 276: 118132.
16. Shen, Q., Wang, Z., Yu, Q., Cheng, Y., Liu, Z., Zhang, T. and Zhou, S. (2020). Removal of tetracycline from an aqueous solution using manganese dioxide modified biochar derived from Chinese herbal medicine residues. *Environmental Research*, 183: 109195.
17. Oh, T. K. and Shinogi, Y. (2013). Characterization of the pyrolytic solid derived from used disposable diapers. *Environmental Technology*, 34: 3153-3160.
18. Zhang, J., Shao, J., Jin, Q., Zhang, X., Yang, H., Chen, Y., Zhnag, S. and Chen, H. (2020). Effect of deashing on activation process and lead adsorption capacities of sludge-based biochar. *Science of the Total Environment,* 716: 137016.
19. Heidarinejad, Z., Dehghani, M. H., Heidari, M., Javedan, G., Ali, I. and Sillanpää, M. (2020). Methods for preparation and activation of activated carbon: A review. *Environmental Chemistry Letters*, 18(2): 393-415.
20. Sajjadi, B., Chen, W. Y., Mattern, D. L., Hammer, N. and Dorris, A. (2020). Low-temperature acoustic-based activation of biochar for enhanced removal of heavy metals. *Journal of Water Process Engineering*, 34: 101166.
21. Chen, Y., Zhu, Y., Wang, Z., Li, Y., Wang, L., Ding, L., Gao, X., Ma, Y. and Guo, Y. (2011). Application studies of activated cabon derived from rice husks produced by chemical-thermal process - A review. *Advances in Colloid and Interface Science*, 163(1): 39-52.
22. Burakov, A. E., Galunin, E. V., Burakova, I. V., Kucherova, A. E., Agarwal, S., Tkachev, A. G. and Gupta, V. K. (2018). Adsorption of heavy metals on conventional and nanostructured materials for wastewater treatment purposes: A review. *Ecotoxicology and Environmental Safety,* 148: 702-712.

23. Wani, A. L., Ara, A., and Usmani, J. A. (2015). Lead toxicity: A review. *Interdisciplinary Toxicology,* 8(2): 55-64.
24. Lam, S. S., Wan Mahari, W. A., Ma, N. L., Azwar, E., Kwon, E. E., Peng, W., Chong, T. C., Liu, Z., and Park, Y-K. (2019). Microwave pyrolysis valorization of used baby diaper. *Chemosphere,* 230: 294-302.
25. Khan, M. A., Alemayehu, A., Duraisamy, R., and Berekete, A. K. (2015). Removal of lead ion from aqueous solution by bamboo activated carbon. *International Journal of Water Resource*, 5: 33-46.
26. Syafiuddin, A., Salmiati, S., Jonbi, J. and Fulazzaky, M. A. (2018). Application of the kinetic and isotherm models for better understanding of the behaviors of silver nanoparticles adsorption onto different adsorbents. *Journal of Environmental Management*, 218(20): 59-70.
27. Muhammad, W., Ullah, N., Haroon, M. and Abbasi, B. H. (2019). Optical, morphological and Biological Analysis of zinc oxide nanoparticles (ZnO NPs) using *Papaver somniferum* L. *RSC Advances*, 9: 29541-29548.
28. Nam, H., Wang, S. and Jeong, H. R. (2018). TMA and H_2S gas removals using metal loaded on rice husk activated carbon for indoor air purification. *Fuel,* 213: 186-194.
29. Mahdi, Z., Yu, Q. J. and El Hanandeh, A. (2018). Removal of lead (II) from aqueous solution using date seed-derived biochar: Batch and column studies. *Applied Water Science*, 8: 1-13.
30. Singh, E., Kumar, A., Mishra, R., You, S., Singh, L., Kumar, S. and Kumar, R. (2021). Pyrolysis of waste biomass and plastics for production of biochar and its use for removal of heavy metals from aqueous solution. *Bioresouresource Technology*. 320: 124278.
31. Hamzah, S., Yatim, N. I., Alias, M., Ali, A., Rasit, N. and Abuhabib, A. (2019). Extraction of hydroxyapatite from fish scales and its integration with rice husk for ammonia removal in aquaculture wastewater extraction of hydroxyapatite from fish scales and its integration with rice husk for ammonia removal in aquaculture wastewater. *Indonesia Journal of Chemistry*, 19: 1019-1030.
32. Hamzah, S., Razali, N., Yatim, N. I., Alias, M., Ali, A., Zaini, N. S. and Abuhabib, A. A. (2018). Characterisation and performance of thermally treated rice husk as efficient adsorbent for phosphate removal. *Journal Water Supply Resources Technology,* 67(8): 766-778.
33. Abbar, B., Alema, A., Marcotte, S., Pantet, A., Ahfir, N., Bizet, L. and Duriatti, D. (2017). Experimental investigation on removal of heavy metals (Cu^{2+}, Pb^{2+} and Zn^{2+}) from aqueous solution by flax fibres. *Process Safety and Environmental Protection*, 109: 639-647,
34. Bedia, J., Peñas-Garzón, M., Gómez-Avilés, A., Rodriguez, J. J. and Belver, C. (2020) Review on activated carbons by chemical activation with $FeCl_3$. *Journal of Carbon Research,* 6: 1-25.
35. Rodríguez, C., Tapia, C., Leiva-Aravena, E. and Leiva, E. (2020). Graphene oxide–ZnO nanocomposites for removal of aluminum and copper ions from acid mine drainage wastewater. *International Journal of Environmental Research and Public Health*, 17: 1-18.

Malaysian Journal of Analytical Sciences (MJAS)
Published by Malaysian Analytical Sciences Society

NOVEL AND VALIDATED NON-AQUEOUS TITRIMETRIC METHOD FOR DETERMINATION OF PERSPECTIVE POTASSIUM-SPARING DIURETIC DRUG CANDIDATE IN PURE FORM AND PHARMACEUTICAL FORMULATION

(Kaedah Titrimetrik Bukan Akues Novel dan Ditentusahkan bagi Penentuan Penahanan Kalium-Dadah Diuretik dalam Formulasi Tulen dan Farmaseutikal)

Alexey Ivanov[1]*, Ivan Smırnov[2], Tatyana Murashko[2], Marina Trusova[1], Elena Stepanova[1]

[1]Research School of Chemistry & Applied Biomedical Sciences,
National Research Tomsk Polytechnic University, Tomsk, Russia
[2]The Faculty of Pharmacy,
Altai State Medical University, Barnaul, Russia

**Corresponding author: ivanovaa@tpu.ru*

Received: 31 August 2020; Accepted: 22 November 2020; Published: 20 February 2021

Abstract

4-O-β-D-(glucopyranosyloxy)-benzoic acid sodium salt (4-GBA) is promising potassium-sparing diuretic and anti-inflammatory drug. For the survey of 4-GBA as pharmaceutical substance, a durable method of its quantification is needed. In the present study, a titrimetric method for 4-GBA quantification since it is evident, very simple, fast, applicable for routine analysis and there is no need of using reference standards was developed. Aqueous titration gave unsatisfactory result. Thus, based on the weak basic properties of the 4-GBA, non-aqueous titration was chosen. Glacial acetic acid was used as a solvent, and an anhydrous solution of perchloric acid in glacial acetic acid was used as a titrant. End-point detection was carried out potentiometrically (method A) and visually with violet crystalline as an indicator (method B). Using aqueous titration, we determined pK_a of 4-GBA as 4.27. The developed non-aqueous titration method is of excellent linearity (r^2 = 0.9995 and r^2 = 0.9947 for method A and method B, respectively), accuracy (recovery from 98.8 to 101.1 % and from 98.1 to 103.2 % for method A and method B, respectively) and precision (RSD ≤ 2% for intra- and inter-day analysis). The developed method is fast, simple, cheap and is applicable for the quantitative determination of 4-GBA both in pure form, bulk and pharmaceutical formulations.

Keywords: glucosides, potassium-sparing diuretics, validation methods, non-aqueous titration, quantitative determination.

Abstrak

Garam sodium 4-O-β-D-(glukopiranosiloksi)-asid benzoik (4-GBA) merupakan penahanan diuretik kalium dan dadah anti-radang yang berkesan. Dari tinjauan 4-GBA sebagai bahan farmaseutikal, satu kaedah tahan lasak bagi kuantifikasi adalah diperlukan. Dalam kajian ini, kaedah titrimetrik bagi kuantifikasi 4-GBA telah dibangunkan kerana ia terbukti ringkas, pantas dan aplikasi mudah bagi analisis rutin dan piawai rujukan tidak diperlukan. Pentitratan akues telah memberikan hasil yang tidak memuaskan. Maka berdasarkan sifat bes lemah 4-GBA, pentitratan bukan akues telah dipilih. Asid asetik glasier telah digunakan sebagai pelarut, dan larutan asid perklorik kontang di dalam asid asetik glasier telah digunakan sebagai titran. Pengesanan titik akhir telah

dijalankan secara potentiometrik (kaedah A) dan secara visual dengan kehadiran hablur sebagai penunjuk (kaedah B). Berdasarkan pentitratan akues, nilai pKa 4-GBA ditentukan pada 4.27. Kaedah pentitratan bukan akues yang telah dibangunkan memberi nilai kelinearan baik ($r^2 = 0.9995$ dan $r^2 = 0.9947$ masing-masing bagi kaedah A dan B), ketepatan (perolehan semula dari 98.8 hingga 101.1% dan dari 98.1 hingga 103.2% masing-masing bagi kaedah A dan B) dan kejituan (RSD ≤ 2% bagi analisis intra dan inter-hari). Kaedah yang dibangunkan adalah pantas, mudah, murah dan kebolehgunaan bagi penentuan 4-GBA di dalam formulasi tulen, pukal dan farmaseutikal.

Kata kunci: glukosida, penahanan diuretik kalium, kaedah tentusahkan, pentitratan bukan akues, penentuan kuantitatif

Introduction

Diuretics are extremely important in the management of a wide range of illnesses [1-3] and considered as first-line drugs [4-5]. Among them potassium-sparing diuretics play special role in therapy since they do not increase the secretion of potassium ions into urine and maintain electrolyte balance. However, they have a number of side effects, namely, nephrolithiasis, gynecomastia, hirsutism, hyperchloremic acidosis and etc. [1, 3, 6-7]. In this context, the search for new effective and safe potassium-sparing diuretics is a critical problem of pharmaceutical chemistry.

4-O-β-D-(glucopyranosyloxy)-benzoic acid – is well-known lignin related secondary metabolite of many plants [8-12] and likely responsible for the specific biological activities of plant extracts [13]. 4-O-β-D-(glucopyranosyloxy)-benzoic acid demonstrated antioxidant [14], anti-neuroinflammatory [15] and tyrosinase inhibitory activity [13] with low toxicity in *in vitro* experiments. Recently, we demonstrated *in vivo* diuretic activity of 4-O-β-D-(glucopyranosyloxy)-benzoic acid sodium salt (4-GBA). We found that 4-GBA increases daily diuresis 1.5 and 2.5 times with chronic oral administration (7 days) at a dose of 18 μmol/kg and 54 μmol/kg, respectively. Also, 4-GBA did not increase daily clearance of sodium and potassium ions [16, 17]. We also demonstrated that 4-GBA *in vivo* has an average of two times greater anti-inflammatory activity than aspirin and did not lead to ulcerative activity in chronic oral administration for 7 days [18, 19], compared to aspirin.

The combination of biological effects allows effective treatment of chronic inflammatory and infectious urinary tract diseases. Long-term oral intake of 4-GBA will not lead to electrolyte disturbance, unlike conventional diuretics, and will not damage the digestive tract, unlike commonly used oral anti-inflammatory drugs [20, 21]. Thus, 4-GBA is a promising drug candidate for potassium-sparing diuretic and anti-inflammatory agent. For further survey, we need to develop a reliable method for quantitation of 4-GBA in raw materials, bulk and pharmaceutical formulations.

In the present paper, we developed the titrimetric methods for 4-GBA quantification. Titrimetric methods are evident, very simple, fast, applicable for routine analysis and there is no need of using reference standards [22]. The known methods for quantification of pharmaceutical substances have significant drawbacks such as high cost and multiple steps; they are time-consuming or require costly solvents [22, 23]. The proposed titrimetric method is simple with the short analytical time and good reproducibility, accuracy, durability and cost-effectiveness.

Materials and Methods

Materials

The 4-GBA was obtained from methyl ether of 4-O-β-D-(glucopyranosyloxy)-benzoic acid (ME-4-GBA) by alkaline hydrolysis (Figure 1), according to the method described [24, 25]. Before analysis, 4-GBA was dried at 80°C and 70 mbar for 8 hours. Glacial acetic acid, perchloric acid and crystal violet were obtained from Panreact (Russia). All reagents were of analytical grade. All measurements were carried out at a temperature of 25 °C. All aqueous titrations and the preparation of aqueous solutions were carried out using deionized CO_2-free water.

Instrumental

Potentiometric titration was performed on an AT-510 autotitrator (Kyoto Electronics Manufacturing Co.) equipped with a C-173 combined glass electrode and microburette (resolution 0.025 mL). Visual titration was performed involving glass burette (class A) and crystal violet as indicator (2 drops).

Hydrochloric acid (0.1 M)

A 0.1 hydrochloric acid was prepared by diluting 36% aqueous HCl (8.5 mL) with deionized water to 1 L. The solution was standardized using 0.1 M sodium carbonate (K=1.01) [26].

Perchloric acid (0.1 M)

To glacial acetic acid (900 mL) was added perchloric acid (8.2 mL), well mixed, and acetic anhydride (32 mL) was added and mixed again. The mixture was cooled to room temperature, and glacial acetic acid was added to produce 1000 mL and kept for 24 hours. The solution was standardized using 0.1 M potassium hydrogen phthalate in glacial acetic acid (K=1.09) [26].

Crystal violet indicator solution

A crystal violet indicator solution was prepared by dissolving 5 g of pure dye into 1 L of glacial acetic acid [26].

Potassium bromide solution (0.5 M)

Potassium bromide (59.5 g), was dissolved in 1 L of deionized water and mixed until complete dissolution.

Procedure of aqueous titration

Accurately weighed quantities of 4-GBA (1 g) were dissolved in deionized water (30 mL) to produce the concentration of 4-GBA 0.1 mol\L. Titration was carried out with previously standardized 0.1 M hydrochloric acid solution. End-point determination was potentiometric.

Procedure of non-aqueous titration with potentiometric determination of end-point (Method A)

Accurately weighed quantities of 4-GBA (160-240 mg, Table 1) were dissolved in glacial acetic acid (30 ml). Titration was carried out with a previously standardized 0.1 M $HClO_4$ in glacial acetic acid. The end-point was determined as the maximum on the derivative titration curve in first order. A blank experiment (in the absence of 4-GBA) was carried out in parallel.

Procedure of non-aqueous titration with visual determination of end-point (Method B)

Accurately weighed quantities of 4-GBA (160-240 mg, Table 1) were dissolved in glacial acetic acid (30 ml). Titration was carried out with a previously standardized 0.1 M $HClO_4$ in glacial acetic acid using 2 drops of crystal violet indicator solution until blue end-point.

Calculation of 4-GBA content

The content of the active substance (P) was calculated according to the Equation 1.

$$P = \frac{T \times K \times (V^0 - V^C) \times 100 \times 100}{m \times (100 - W)} \quad (1)$$

T is titer of 0.1 M $HClO_4$ in glacial acetic acid (mg/mL), K is correction factor 0.1 M $HClO_4$ in glacial acetic acid, calculated according to [26], V^0 is volume of titrant in experiment (mL), V^C is volume of titrant in blank experiment (mL), m is mass of 4-GBA (mg), W is loss on drying of 4-GBA (%). 1 mL of 0.1 M $HClO_4$ in glacial acetic acid is equivalent to 32.22 mg of 4-GBA.

The pK_a calculation

The pK_a value was determined as pH value at the half of inflection point (on the titrant volume) of 4-GBA titration curve (Figure 2A) [27]. Inflection point was determined by first and second-derivative method from titration curve (Figure 2B) [28, 29]. The measurements were carried out under the same conditions as the aqueous titration in a 0.5 M potassium bromide solution.

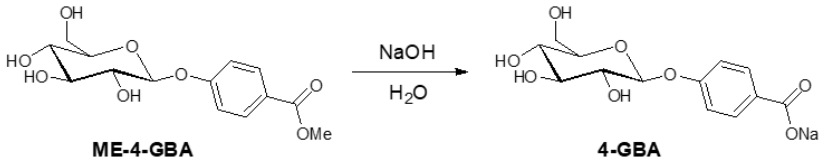


Figure 1. Preparation of 4-GBA from ME-4-GBA

Results and Discussion

The 4-GBA is a water soluble salt of a weak monobasic acid and a strong base (Figure 1). This compound in aqueous solutions is basic, therefore, acidimetry should be used for quantitative determination.

Acid-base properties of 4-GBA in aqueous solutions

The acid-base properties of 4-GBA were studied by potentiometric titration. The resulted curve is shown in Figure 2. The titrimetric analysis demonstrated one low-grade change of the pH value in a wide range from 3.75 to 1.82.

To estimate the quantitative determination of 4-GBA by the titrimetric method in an aqueous solution we calculated the negative logarithm of the dissociation constant (pK_a). There is a wide range of techniques for determining pK_a value, for example, potentiometry, conductometry, calorimetry, nuclear magnetic resonance (NMR), electrophoresis, high-performance liquid chromatography (HPLC), ultraviolet–visible spectroscopy and others [27]. We chose potentiometry for determination of pK_a value because this method is fast, simple, universal, cheap and highly precise [27, 28]. The change of solution ionic strength may influence pK_a determination [27]. Thus, we carried out pK_a measurements in 0.5 N potassium bromide solution in order to maintain constant ionic strength. Optimal concentrations of 4-GBA and hydrochloric acid solutions were determined as 0.1 N [30].

Second-derivative method was chosen for inflection point determination since it is applicable for weak bases and acids and provide accurate determination in case of titration curve has no sharp pH jump. This method is based on plot $\Delta^2pH/\Delta V^2$ vs. volume of titrant (V) (Figure 2b). The inflection point is where $\Delta^2pH/\Delta V^2$ equals 0 [29]. The equivalent titrant volume was 30 mL (Figure 2a). pK_a value was determined as pH value at the point corresponding to half of the titration (15 mL) (Figure 2a). Calculated according to this method 4-GBA $pK_a = 4.27$ indicates that 4-GBA is a very weak base.

Referring to the titration curves (Figure 2) and pK_a value of 4-GBA, the aqueous titration method for quantitative determination is of insufficient accuracy. The maximum of fist-derivative and the inflection point of second-derivative plots are not constant. Results obtained for the samples were not reproducible. Even at high concentrations of 4-GBA (0.1 mol\L) only the wide jump of pH was achieved which significantly complicates the determination of titration end-point.

Non-aqueous titration of 4-GBA

Since aqueous titration gave unsatisfactory result, we developed another strategy for quantification of 4-GBA. Non-aqueous titration is used to quantify weak acids and bases [31] and is widely used for the evaluation of active substances in pharmaceutical substances formulations [22]. Salts of organic acids are typically titrated in solvents which have both protophilic and protogenic properties [32]. Considering this, we chose acetic acid as titrant, because it is non-toxic, cheap, environmentally friendly and readily available [33]. Also, 4-GBA dissolves completely in acetic acid in studied concentrations at room temperature (~ 25 °C) while it is not protonated upon dissolution. The obtained titrimetric curves for non-aqueous titration of 4-GBA are shown in Figure 3.

Non-aqueous titration conditions demonstrate excellent results in comparison to aqueous titration. The non-aqueous titration curve (Figure 3a) has a pronounced jump of potential, which allows uniquely determining

the end-point using acid-base indicators. In addition, excellent results were obtained when determining the equivalence point by the differential potentiometric method (Figure 3b). The increased basicity of 4-GBA is explained by the formation of acetonium ion ($CH_3COOH_2^+$) which results from interaction of perchloric acid and glacial acetic acid. The acetonium ion easily gives up proton to neutralize 4-GBA [33].

Validation

Thus, a conclusion can be made that non-aqueous titration using glacial acetic acid as a solvent and perchloric acid as titrant meets the main requirements for the quantitative determination of 4-GBA in laboratory and industrial conditions: it is express, easily accessible and precise. According to the requirements of world pharmaceutical standards, any quantification procedure must pass the validation process. Titrimetric methods were validated according to the procedures described in ICH guidelines Q2 (R1) for validation of analytical methods [34]. Validation was carried out according to the following indicators: specificity, linearity, accuracy, recovery, intermediate precision.

Specificity

The specificity of the method was examined by the absence of response on the related impurities that can influence the titration result. Methyl ether of 4-GBA (ME-4-GBA) was chosen as a related impurity because it is an intermediate compound in the synthesis of 4-GBA [24]. 4-GBA and its mixtures with ME-4-GBA (25, 50, 75 and 100% of the 4-GBA aliquot) were titrated (Table 1, entries 1-5 for Method A and entries 9-13 for Method B). For identification of possible excipients interference on quantification, 4-GBA was titrated in presence of several typical excipients for oral and injectable formulations of the following composition: talc (50% w/w), calcium gluconate (20% w/w), lactose (28.4% w/w), magnesium stearate (0.5% w/w), kollidon (0.1% w/w), aerosol (1% w/w). The results are shown in Table 1 (entries 6-8 for Method A and entries 14-116 for Method B).

As can be seen from Table 1, the addition of ME-4-GBA up to 100% of 4-GBA aliquot does not affect the result. The presence of excipients does not affect the quantitative determination as well. The latter indicates non-aqueous titration of 4-GBA in acetic acid as excellent method for its quantification in pharmaceutical preparations. Thus, we can conclude that both methods A and B are specific for quantitative determination of 4-GBA.

Linearity

Linearity was studied in the range 80-120% of the test concentration [34]. LOD and LOQ value of method A were detected by signal-to-noise ratio (S/N), which was 3 for LOD and 10 for LOQ. LOD and LOQ for method B was not calculated, because at low concentrations of 4-GBA determination of end-point (color change) accurately is impossible. Obtained data is show in Table 2, both methods demonstrate good linearity with excellent correlation coefficient.

Precision

Precision was determined by repeatability (intra-day) and intermediate precision (inter-day). Repeatability was evaluated by the analysis of three samples during the same day, and the intermediate precision was studied by comparing the analyses on three different days. The analyses were carried out in triplicate and results were expressed as the relative standard deviation (RSD) of the analytical measurements. The results are shown in Table 3. As can be seen from Table 3, both methods A and B are precise because of RSD is more than 2%.

Accuracy

Accuracy was determined by recovery of 80%, 100%, 120% of the test concentration of 4-GBA from a standard solution [34]. The obtained percentages of the drug recovered, and standard deviations of the analysis are shown in Table 4. The percentage range recovery of 4-GBA was from 98.8 to 101.1% and from 98.1 to 103.2% for method A and method B, respectively. These ranges are suitable for the quantitative analysis of pharmaceutical substances.

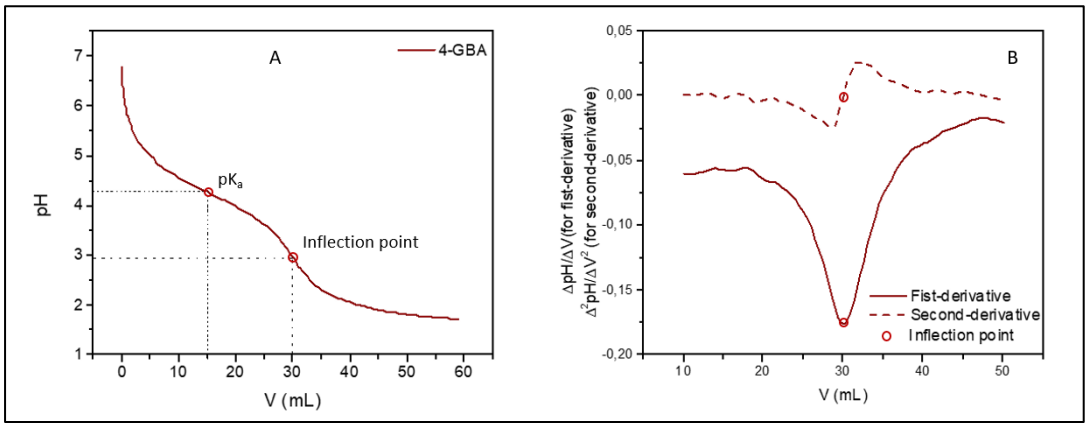


Figure 2. Graphical representation of aqueous titration analysis of 4-GBA with 0.1 N hydrochloric acid as titrant (a) and first (solid line), second (dashed line) derivative plot (b).

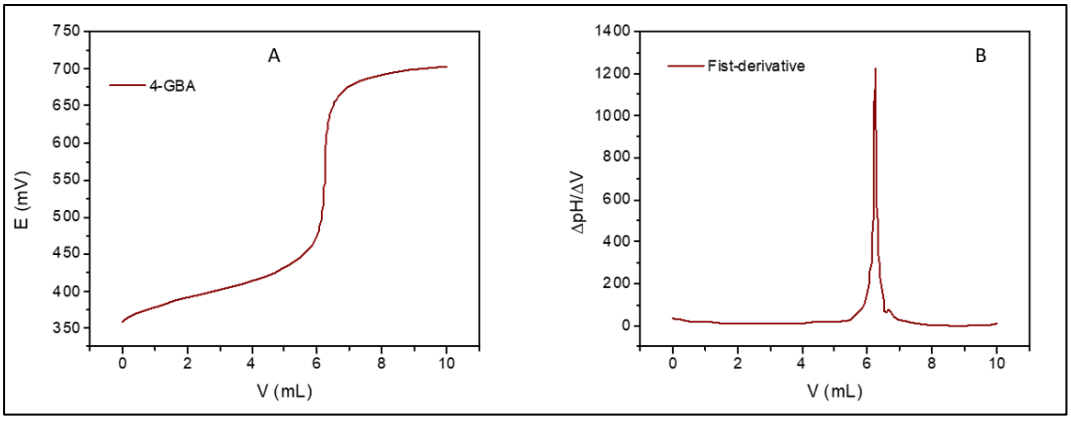


Figure 3. Non-aqueous titration curves of 4-GBA in (a) zero and (a) first order

Table 1. Results of specificity determination

Entry	Method	4-GBA (mg)	ME-4-GBA (mg)	Mix* (mg)	V (mL)	Assay (%)	Mean Assay
1	A	201.5	0.0	0	6.275	99.7	100.08 ± 0.59
2		198.3	50.3	0	6.150	100.1	
3		200.1	103.2	0	6.225	99.8	
4		196.3	154.8	0	6.025	101.1	
5		204.8	201.3	0	6.375	99.7	
6		200.4	0	100	6.335	101.79	100.12 ± 1.18
7		198.4	0	200	6.125	99.41	
8		203.1	0	300	6.255	99.17	

Table 1 (cont'd). Results of specificity determination

Entry	Method	4-GBA (mg)	ME-4-GBA (mg)	Mix* (mg)	V (mL)	Assay (%)	Mean Assay
9	B	200.3	0.0	0	6.2	98.7	100.56 ± 1.43
10		199.6	49.7	0	6.1	101.6	
11		201.7	101.1	0	6.3	99.4	
12		200.4	150.5	0	6.2	102.0	
13		198.8	198.7	0	6.2	101.1	
14		199.4	0	100	6.3	101.7	100.6 ± 1.4
15		200.7	0	200	6.3	101.1	
16		201.9	0	300	6.2	98.9	

* Mixture of excipients

Table 2. Results of linearity determination

Parameter	Results	
	Method A	Method B
Regression equation	y = 0.0312x - 0.005	y = 0.0331x - 0.37
Slope	0.0312	0.0331
Intercept	0.005	0.37
Correlation coefficient (r^2)	0.9995	0.9947
LOD	5.4 µg/mL	N/A*
LOQ	7.5 µg / mL	N/A*

*not applicable

Table 3. Precision of titration experiments

Method	Weight (mg)	Intra-day accuracy and precision (n=3)			Inter-day accuracy and precision (n=3)		
		Measured (mg)	RE (%)	RSD (%)	Measured (mg)	RE (%)	RSD (%)
A	181.4	180.9	0.26	0.61	182.5	0.59	1.56
	200.3	200.9	0.28	0.53	201.0	0.37	1.09
	219.8	218.9	0.39	0.46	219.5	0,15	0.88
B	180.3	181.7	0.79	1.52	181.8	0.81	1.99
	200.1	201.8	0.83	1.28	201.7	0.78	1.55
	220.3	221.3	0.45	1.23	219.8	0.21	1.63

Table 4. Results of accuracy and recovery

Method	Weight (mg)	Measured (mg)	Recovery (%)	Recovery (mean) (%)	RSD (%)
A	160.3	160.14	99.9	100.0	0.21
	160.8	161.12	100.2		
	161.1	160.78	99.8		
	200.4	198.00	98.8	99.8	1.2
	200.9	203.11	101.1		
	201.3	200.09	99.4		
	241.2	243.13	100.8	99.6	1.0
	240.8	238.15	98.9		
	240.3	238.14	99.1		
B	160.1	163.20	98.1	99.2	1.11
	161.7	162.84	99.3		
	160.8	160.32	100.3		
	200.1	202.74	98.7	101.4	1.79
	201.4	197.06	102.2		
	200.8	194.57	101.2		
	241.3	237.73	101.5	101.3	1.16
	240.2	240.92	99.7		
	239.8	235.33	101.9		

Conclusion

Fast, simple and reliable titrimetric method for quantitative determination of 4-GBA was developed and validated. This method allows quantitative determination 4-GBA in each batch of the substance in subsequent preclinical studies without use of standard samples. The aqueous titrimetric assay was unsuccessful and demonstrated insufficient accuracy due to the wide jump of pH. Instead, non-aqueous titrimetric method using glacial acetic acid and perchloric acid was applied to the determination of pure authentic samples and some of their pharmaceutical preparations. The non-aqueous titration demonstrated rather well shaped end-points with high potential jumps both in potentiometric and visual methods. Statistical tests indicate that the proposed titrimetric method appear to be equally suitable for routine determination of 4-GBA in pharmaceutical formulation, bulk and in pure form.

Acknowledgement

Research was carried out using the core facilities of TPU's "Physical and chemical methods of analysis". This work was financially supported by the Tomsk Polytechnic University Competitiveness Enhancement Program grant 203/2020.

References

1. David, H. E. (2019). Clinical pharmacology in diuretic use. *Clinical Journal of the American Society of Nephrology*, 14(8): 1248-1257.
2. Roush, G. C., Kaur, R. and Ernst, M. E. (2014). Diuretics: A review and update. *Journal of Cardiovascular Pharmacology and Therapeutics*, 19(1): 5-13.
3. Wile, D. (2012). Diuretics: a review. *Annals of Clinical Biochemistry*. 49(5): 419-431.

4. Roush, G. C. and Sica, D. A. (2016). Diuretics for hypertension: A review and update. *American Journal of Hypertension*, 29(10): 1130-1137.
5. Weber, M. A., Schiffrin, E. L., White, W. B., Mann, S., Lindholm, L. H., Kenerson, J. G., Flack, J. M., Carter, B. L., Materson, B. J., Ram, C. V. S., Cohen, D. L., Cadet, J-C., Jean-Charles, R. R., Taler, S., Kountz, D., Townsend, R. R., Chalmers, J., Ramirez, A. J., Bakris, G. L., Wang, J., Schutte, A. E., Bisognano, J. D., Touyz, R. M., Sica, D. and Harrap, S. B. (2014). Clinical practice guidelines for the management of hypertension in the community: A statement by the American society of hypertension and the international society of hypertension. *The Journal of Clinical Hypertension,* 16(1): 14-26.
6. Brater, D. C. (2000). Pharmacology of diuretics. *The American Journal of the Medical Sciences*, 319(1): 38-50.
7. Ettinger, B. (1985). Excretion of triamterene and its metabolite in triamterene stone patients. *The Journal of Clinical Pharmacology*, 25(5): 365-368.
8. Chemam, Y., Benayache, S., Marchioni, E., Zhao, M., Mosset, P. and Benayache, F. (2017). On-line screening, isolation and identification of antioxidant compounds of *Helianthemum ruficomum*. *Molecules*, 22(2): 239.
9. Hong, S. S., Choi, C. W., Choi, Y.-H. and Oh J. S. (2016). Coixlachryside A: a new lignan glycoside from the roots of *Coix lachryma-jobi L. var. ma-yuen Stapf*. *Phytochemistry Letters*, 17: 152-157.
10. Yamashita-Higuchi, Y., Sugimoto, S., Matsunami, K., Otsuka, H. and Nakai, T. (2014). Grevillosides J–Q, Arbutin derivatives from the leaves of *Grevillea robusta* and their melanogenesis inhibitory activity. *Chemical and Pharmaceutical Bulletin*, 62(4): 364-372.
11. Tanaka, Y., Yanagida, A., Komeya, S., Kawana, M., Honma, D., Tagashira, M., Kanda, T. and Shibusawa, Y. (2014). Comprehensive separation and structural analyses of polyphenols and related compounds from bracts of hops (*Humulus lupulus L.*). *Journal of Agricultural and Food Chemistry*, 62(10): 2198-2206.
12. Pan, H. and Lundgren, L. N. (1996). Phenolics from inner bark of *Pinus sylvestris*. *Phytochemistry*, 42(4): 1185-1189.
13. Masuda, T., Fujita, N., Odaka, Y., Takeda, Y., Yonemori, S., Nakamoto, K. and Kuninaga, H. (2007). Tyrosinase inhibitory activity of ethanol extracts from medicinal and edible plants cultivated in Okinawa and identification of a water-soluble inhibitor from the leaves of *Nandina domestica*. *Bioscience, Biotechnology, and Biochemistry*, 71(9): 2316-2320.
14. Fiorentino, A., D'Abrosca, B., Pacifico, S., Mastellone, C., Piscopo, V., Caputo, R. and Monaco, P. (2008). Isolation and structure elucidation of antioxidant polyphenols from Quince (*Cydonia vulgaris*) peels. *Journal of Agricultural and Food Chemistry*, 56(8): 2660-2667.
15. Ye, X., Tian, W., Wang, G., Zhang, X., Zhou, M., Zeng, D., Liu, X., Yao, X., Zhang, Y. and Chen, H. (2020). Phenolic glycosides from the roots of *Ficus hirta* Vahl. and their anti-neuroinflammatory activities. *Journal of Agricultural and Food Chemistry*, 68(14): 4196-4204.
16. Smirnov, I. V., Murashko, T. O., Ivanov, A. A., Nemtsev, A. O., Postnikov, P. S., Bondarev, A. A. and Udut, V. V. (2016). Diuretic activity of 4-O-carboxyphenyl-D-glucopyranoside sodium salt administered via different routes. *Eksperimental'naya i Klinicheskaya Farmakologiya*, 79(1): 20-22.
17. Smirnov, I. V., Murashko, T. O., Voloboy, N. L., Ivanov, A. A., Nemtcev, A. O., Bondarev, A. A. and Udut, V. V. (2015). The study of diuretic properties of a new synthetic substance. *Pharmacy*, 64(3): 40-42.
18. Murashko, T. O., Smirnov, I. V., Bondarev, A. A., Ivanov, A. A., Postnikov, P. S., Nemtsev, A. O. and Udut, V. V. (2016). Anti-inflammatory activity of sodium salt of 4-(O-β-d-glucopyranosyloxy) benzoic acid. *Eksperimental'naya i Klinicheskaya Farmakologiya*, 79(4): 26-28.

19. Murashko, T. O., Smirnov, I. V., Ivanov, A. A., Postnikov, P. S., Nemtsev, A. O., Bomdarev, A. A., Udut, V. V., Prisukhin, A. N., Kornaukhov, A. N. and Sergeev, T. S. (2016). Studying gastric ulceration effect of a new drug intended for treatment of chronic inflammatory diseases of kidneys and urinary tract. *Eksperimental'naya i Klinicheskaya Farmakologiya*. 79(5): 26-28.
20. Goldstein, J. L. and Cryer, B. (2015). Gastrointestinal injury associated with NSAID use: A case study and review of risk factors and preventative strategies. *Drug, Healthcare and Patient Safety*, 2015(7): 31-41.
21. García-Rayado, G., Navarro, M. and Lanas, A. (2018). NSAID induced gastrointestinal damage and designing GI-sparing NSAIDs. *Expert Review of Clinical Pharmacology*. 11(10): 1031-1043.
22. Görög, S. (2005). The sacred cow: the questionable role of assay methods in characterising the quality of bulk pharmaceuticals. *Journal of Pharmaceutical and Biomedical Analysis*. 36(5): 931-937.
23. Siddiqui, M. R., Al Othman, Z. A. and Rahman, N. (2017). Analytical techniques in pharmaceutical analysis: A review. *Arabian Journal of Chemistry*, 10: 1409-1421.
24. Smirnov, I., Murashko, T., Ivanov, A., Bondarev, A. and Udut, V. (2016). Study of specific pharmacological activity of sodium salt (4-O-β-glucopyranosyloxy)-benzoic acid. *Jurnal of Teknologi*, 78(6-8): 21-24.
25. Stepanova, E., Nagornaya, M., Belyanin, M. and Filimonov, V. (2017). The first total syntheses of the diglycosides Virgaureoside A, of *Solidago virgaurea L.*, and its analogue iso-Virgaureoside A. *Current Organic Synthesis*, 14(3): 394-397.
26. World Health Organization (2019). International Pharmacopoeia (IP). Reagents, test solutions and volumetric solutions. 9th edition, Geneva, Switzerland.
27. Reijenga, J., van Hoof, A., van Loon, A. and Teunissen, B. (2013). Development of methods for the determination of pK_a Values. *Analytical Chemistry Insights*, 8(1): 53-71.
28. Babic, S., Horvat, A. J. M., Pavlovic, D. M. and Kastelan-Macan, M. (2007). Determination of pK_a values of active pharmaceutical ingredients. *Trends in Analytical Chemistry*, 26(11): 1043-1061.
29. Qiang, Z. and Adams, C. (2004). Potentiometric determination of acid dissociation constants (pK_a) for human and veterinary antibiotics. *Water Research*, 38(12): 2874-2890.
30. Po, H. N. and Senozan, N. M. (2001). The Henderson–Hasselbalch equation: Its history and limitations. *Journal of Chemical Education*, 78(11): 1499-1503.
31. Markunas, P. C. and Riddick, J. A. (1951). Titrimetry in glacial acetic acid. Scope of method. *Analytical Chemistry*, 23(2): 337-339.
32. World Health Organization (2019). International Pharmacopoeia (IP). Methods of analysis: Chemical methods: Non-aqueous titration. 9th edition, Geneva, Switzerland.
33. Byrne, F. P., Jin, S., Paggiola, G., Petchey, T. H. M., Clark, J. H., Farmer, T. J., Hunt, A. J., McElroy, C. R. and Sherwood, J. (2016). Tools and techniques for solvent selection: green solvent selection guides. *Sustainable Chemical Process*. 4(7): 1-24.
34. International Conference on Harmonization, ICH (Q2 (R1)) (2015). Validation of Analytical Procedures: Text and methodology. International Conference on Harmonization, Geneva, Switzerland.

Malaysian Journal of Analytical Sciences (MJAS)
Published by Malaysian Analytical Sciences Society

COPOLYMERISATION OF METHYL METHACRYLATE AND HYDROXYPROPYL METHYLCELLULOSE VIA EMULSION POLYMERISATION TECHNIQUE

(Pengkopolimeran Metil Metakrilat dan Hidroksipropil Metilselulosa Melalui Teknik Pempolimeran Emulsi)

Noor Aniza Harun[1,2]*, Liew Pei Chen[1], Anis Arina Zainudin[1], Tan Yea Tzy[1], Farhanini Yusoff[1]

[1]Faculty of Science and Marine Environment,
[2]Advanced Nano Materials (ANOMA) Research Group, Faculty of Science and Marine Environment,
Universiti Malaysia Terengganu, 21030 Kuala Nerus, Terengganu, Malaysia

**Corresponding author: nooraniza@umt.edu.my*

Received: 22 September 2020; Accepted: 29 November 2020; Published: 20 February 2021

Abstract

Copolymerisation between methyl methacrylate (MMA) and hydroxypropyl methylcellulose (HPMC) to produce poly(methyl methacrylate-*co*-hydroxypropyl methylcellulose) P(MMA-*co*-HPMC) nanoparticles was successfully prepared *via* an emulsion polymerisation technique. The effects of different molar ratios of MMA and HPMC monomers towards the copolymer formation, morphology, thermal stability and solubility were thoroughly discussed. Homopolymerisation of poly(methyl methacrylate) (P(MMA)) and poly(hydroxylpropyl methylcellulose) (P(HPMC)) was also carried out as control *via* emulsion polymerisation. Sodium dodecyl sulphate (SDS) and potassium persulfate (KPS) were used as anionic surfactant and water-soluble initiator, respectively, throughout the emulsion polymerisation process. The formation of copolymer P(MMA-*co*-HPMC) and homopolymers of P(MMA) and P(HPMC) nanoparticles was confirmed by Fourier transform infrared spectroscopy (FTIR). The morphology of copolymer and homopolymer nanoparticles was determined using scanning electron microscopy (SEM). The decomposition rate of homopolymer and copolymer nanoparticles was verified using thermogravimetric analysis (TGA) technique. Meanwhile, the hydrophilicity of homopolymer and copolymer nanoparticles was determined by a simple solubility test to obtain their degree of solubility in aqueous medium. It was found that the copolymers formed with higher molar ratios of MMA monomers were less thermally stable and possessed lower rates of solubility than that of the higher molar ratios of HPMC monomers.

Keywords: methyl methacrylate, hydroxypropyl methylcellulose, copolymerization, emulsion polymerization, hydrophilic nanoparticles

Abstrak

Pengkopolimeran di antara metil metakrilat (MMA) dan hidroksilpropil metilselulosa (HPMC) untuk menghasilkan nanopartikel poli(metil metakrilat-*ko*-hidroksilpropil metilselulosa) (P(MMA-*ko*-HPMC)) berjaya disediakan melalui teknik pempolimeran emulsi. Kesan nisbah molar yang berlainan daripada monomer MMA dan HPMC terhadap pembentukan kopolimer, morfologi, kestabilan haba dan kelarutan telah dibincangkan dengan jelas. Penghomopolimeran poli(metil metakrilat) (P(MMA)) dan poli(hidroksilpropil metilselulosa) (P(HPMC)) juga dijalankan sebagai kawalan melalui pempolimeran emulsi. Sodium dodesil

sulfat dan kalium persulfat digunakan sebagai surfaktan anionik dan agen pemula di sepanjang tindak balas pempolimeran emulsi. Pembentukan nanopartikel kopolimer P(MMA-*ko*-HPMC) dan homopolimer P(MMA) dan P(HPMC) telah disahkan oleh puncak penyerapan spektroskopi infra-merah Fourier (FTIR). Morfologi nanopartikel kopolimer dan homopolimer ditentukan dengan menggunakan mikroskopi pengimbasan elektron (SEM). Kadar penguraian nanopartikel homopolimer dan kopolimer ditentukan dengan menggunakan teknik termogravimetrik (TGA). Manakala keterlarutan homopolimer dan kopolimer nanopartikel ditentukan oleh ujian kelarutan mudah bagi menentukan tahap keterlarutan di dalam medium akues. Ianya didapati bahawa kopolimer yang terbentuk dengan nisbah molar monomer MMA yang lebih tinggi mempunyai kestabilan haba yang lebih rendah dan mempunyai kadar kelarutan yang lebih rendah daripada nisbah molar monomer HPMC yang tinggi.

Kata kunci: metil metakrilat, hidroksilpropil metilselulosa, pengkopolimeran, pempolimeran emulsi, nanopartikel hidrofilik

Introduction

The increase in nano-medicine components in the field of nanotechnology has induced the development of nano-scale materials for drug delivery applications. Amongst the materials, synthetic polymeric nanoparticles (PNPs), which are synthesised from biocompatible and biodegradable monomers, have become favourable. Polymer-based nanoparticles within the size range of 10-500 nm can effectively carry drugs, proteins, and DNA to target cells and organs. This is because their nanometer size can promote effective permeation through cell membranes and stability in the blood stream [1]. Due to the grand bioavailability, better encapsulation, control release, and less toxic properties, biodegradable polymeric nanoparticles are often used to increase the therapeutic value of many water soluble or insoluble medicinal drugs and bioactive molecules by improving bioavailability, solubility, and retention time [2].

PNPs can be easily prepared by several methods, namely preformed polymers and direct polymerisation of monomers. In the preparation of PNPs from preformed polymers, several techniques such as solvent evaporation, salting out, dialysis, and supercritical fluid technology can be utilised. PNPs can also be directly synthesised via polymerisation techniques such as microemulsion [3, 4], miniemulsion [5, 6], emulsion [7, 8], and interfacial polymerisation [9]. The selection of preparation method is based on several factors, such as the type of polymeric system, area of application, and size requirement [10]. Amongst the various methods, emulsion polymerisation is known as the fastest method for nanoparticle preparation because it is readily scalable. In general, emulsion polymerisation is defined as a heterogeneous reaction that consists of dispersed and continuous phases initiated by free radical to prepare dispersions of polymers [11]. The advantage of this technique includes the production of high molecular weight polymers via rapid polymerisation with narrow molecular weight distribution.

Emulsion polymerisation is a common technique used for producing biodegradable polymer that has been utilised in many industries for synthesising large quantities of latex in various applications such as surface coating in paints and adhesives [12]. Several research have been performed on the synthesis of biodegradable polymer by using the emulsion polymerisation technique. Poly(methacrylic acid)-polysorbate 80-grafted starch (PMAA-PS 80-*g*-St) nanoparticles are synthesised by using a one-pot emulsion polymerisation method. This technique enables simultaneous grafting of PMAA and polysorbate 80 onto starch and composite nanoparticles are formed in an aqueous medium. This research is focused on the design of new pH-responsive nanoparticles for controlled delivery of anticancer drug doxorubicin (Dox) [13].

Several studies have been carried out on the preparation and characterisation of HPMC copolymer and MMA monomers via the emulsion polymerisation technique. For example, Baek et al. prepared hydroxypropyl methylcellulose graft poly(ethylacrylate-*co*-methylacrylate) [HPMC-*g*-poly(EA-*co*-MMA)] nano-particles *via* resin-fortified emulsion polymerisation using ceric ammonium nitrate (CAN) as the redox initiator in determining the solubility behaviour of aspirin tablet [14]. In another study, copolymers of methyl methacrylate and butyl acrylate were synthesised

by varying concentrations of methacrylic acid and 2-hydroxy ethyl methacrylate *via* the emulsion polymerisation technique. The copolymers showed good thermal stability on the TGA characterisation and could be applied for coating of textiles without any thickening agent [15].

Biodegradable polymers can be defined as polymers that are able to degrade within the body as a result of natural biological processes due to enzyme-catalysed hydrolysis reactions to produce biocompatible by-products. These polymers can be metabolised and excreted *via* normal physiological pathways. Biodegradable polymers can be classified as natural or synthetic polymers. Natural biodegradable polymers that are commonly used are gelatine and alginate [16]. However, synthetic biodegradable polymers are found to be more versatile and possess diverse biomedical applications through modifications in the polymer structures. Synthetic biodegradable polymers have been widely used in the development of biomedical fields due to their biocompatibility and biodegradability [17].

Methyl methacrylate (MMA) monomer is considered as a hydrophobic monomer since it is only partially soluble in water [18]. Emulsion polymerisation of MMA will produce poly(methyl methacrylate) (P(MMA)) that has the characteristic of partial solubility in water, which is not completely biodegradable [19]. Therefore, to improve the hydrophilicity and biocompability of P(MMA) nanoparticles, it is desirable to combine MMA monomer with another monomer via the copolymerisation method. Hydroxypropyl methylcellulose (HPMC) is a hydrophilic swelling polymer that provides water permeability and solubility [20]. Therefore, this study highlights the synthesis of homopolymer and copolymer of MMA and HPMC monomers and examines the ability of HPMC monomer to improve the hydrophilicity of P(MMA) nanoparticles at different molar ratios. The development of copolymer MMA-HPMC is expected to be further utilised in medical and biological applications. In this particular research, the hydrophilic homopolymer and copolymer nanoparticles are synthesised *via* the emulsion polymerisation technique by using methyl methacrylate (MMA) and hydroxypropylmethyl cellulose (HPMC) monomers. The PNPs obtained are characterised using Fourier transform infrared spectroscopy (FTIR), scanning electron microscopy (SEM), and thermogravimetric analysis (TGA).

Materials and Methods

Materials

Methyl methacrylate (MMA) and hydroxypropylmethyl cellulose (HPMC) monomers, sodium dodecyl sulphate (SDS) as the anionic surfactant, and potassium persulfate (KPS) as the initiator were all commercially obtained from Sigma Aldrich. Distilled water was used throughout the experiment.

Emulsion polymerization of homopolymer P(MMA) and P(HPMC) nanoparticles

Emulsion polymerisation was conducted in a 250 mL two-neck round bottom flask equipped with a magnetic stirrer, reflux-condenser, nitrogen gas inlet, and thermometer. Distilled water (50 mL) and methyl methacrylate (MMA) (0.05 g) were mixed with the anionic surfactant, i.e. sodium dodecyl sulfate (SDS) (8.2 mM), and added into a reactor at room temperature. The solution mixture was purged with N_2 for 15 minutes to remove any dissolved oxygen. The N_2 inlet was removed and the neck of the round bottomed flask was sealed with parafilm. The polymerisation was initiated by adding aqueous potassium persulfate (KPS) (6.95 mM) and the reaction was performed in an oil bath at 80 °C for 2 hours with constant stirring at 400 rpm. The product was cooled for 30 minutes and the remaining solvent was removed by a rotary evaporator. The process was repeated by homopolymerisation of HPMC *via* a similar procedure, whereby the starting amount of HPMC monomer was 0.65 g. Table 1 summarises the ingredients used.

Emulsion polymerization of copolymer P(MMA-*co*-HPMC) nanoparticles

Emulsion copolymerisation between MMA and HPMC was prepared using the similar method as described above. Different molar ratios of MMA and HPMC monomers (1:4) were mixed with the anionic surfactant (SDS) and added into the reactor at room temperature prior to initiation with aqueous KPS solution. The procedure for the preparation of homopolymer P(MMA)

and P(HPMC) nanoparticles and copolymer of P(MMA-*co*-HPMC) nanoparticles is summarised in Table 1.

Fourier transform infrared spectroscopy

The solid samples of polymer nanoparticles were prepared in the form of potassium bromide (KBr) pellet. The polymer nanoparticles were mixed and crushed together with KBr powder in a ratio of 1:7. The KBr powder was heated for 1 hour or more to avoid any moisture that can affect the IR spectra. The pellet was placed on a plate and clamped in the right position. The FTIR spectra was recorded using Perkin-Elmer 100 series Fourier transform instrument covering a scan range between 4000–450 cm^{-1}.

Scanning electron microscopy

The coating of polymer nanoparticles was prepared using JFC-1600 Auto Fine Coater. The particle sizes and morphology polymer nanoparticles were observed using Oxford Instrument attached to JSM-6360 LA Analytical Transmission Electron Microscope at a magnification observation of 5000x, with 50 nm scale bar and acceleration voltage of 15 kV.

Thermogravimetric analyzer

TGA characterisation was performed using Q500 (TA Instrument) with a heating rate of 10 °C/min under nitrogen condition at temperature up to 600 °C. About 10 mg of polymer samples were placed in a TGA pan and utilised in this analysis.

Solubility test

A simple solubility test was conducted to compare the hydrophilicity of homopolymer and copolymer of P(MMA), P(HPMC) and P(MMA-*co*-HPMC) nanoparticles, respectively. About 0.05 g of polymer nanoparticles were weighed and dissolved with 6 mL of distilled water at room temperature. The ability of homopolymer and copolymer nanoparticles to dissolve in aqueous medium was observed.

Results and Discussion

Emulsion Polymerization of Copolymer Poly(MMA-*co*-HPMC) via Emulsion Polymerization Technique

Copolymerisation of methyl methacrylate (MMA) and hydroxypropyl methylcellulose (HPMC) monomers to produce poly(methyl methacrylate-*co*-hydroxypropyl methylcellulose) P(MMA-*co*-HPMC) nanoparticles at different molar ratios was successfully synthesised via the emulsion polymerisation technique in the presence of sodium dodecyl sulphate (SDS), potassium persulfate (KPS), and water as dispersion medium (Table 1).

Homopolymer P(MMA) and P(HPMC) nanoparticles were also synthesised *via* emulsion polymerisation and acted as the control for comparison in this research. P(MMA) nanoparticles were obtained in white powder form (Figure 1a), whereas P(HPMC) nanoparticles were attained as gel-like form (Figure 1b). P(MMA-*co*-HPMC) nanoparticles with molar ratios of MMA and HPMC 1:1 (Figure 1c) and 1:4 (Figure 1d), respectively, appeared as soft white powder. The chemical structures of the synthesised polymeric nanoparticles are shown in Scheme 1 and the proposed mechanism for the copolymerisation of P(MMA-*co*-HPMC) is depicted in Scheme 2.

Fourier transform infrared spectroscopy

Fourier transform infrared spectroscopy (FTIR) was measured to identify the functional group present within the samples. The FTIR spectra were recorded using Perkin-Elmer 100 series Fourier transform instrument, covering a scan range between 4000 - 450 cm^{-1}.

According to the FTIR graph in Figure 2, the large and broad peak at wavenumber around 3200 - 3500 cm^{-1} was present in P(HPMC), and a series of copolymer P(MMA-*co*-HPMC) nanoparticles referred to the *ν*(OH) functional group. It can be seen that as the molar ratios of MMA monomer increased, the *ν*(OH) group peak became less intense. In comparison, when the molar ratios of HPMC monomer increased, the *ν*(OH) group peak became more significant as the HPMC structure itself consisted many *ν*(OH) groups (Scheme 1b). This can clearly be seen in P(MMA-*co*-HPMC)$_{1:2}$ that showed an intense large broad *ν*(OH) peak. However, the *ν*(OH) peak in P(MMA-*co*-HPMC)$_{1:3}$ and P(MMA-*co*-HPMC)$_{1:4}$ were slightly diminished, which justified the expected product at which one of the *ν*(OH) group in HPMC was attacked by radical from the *ν*(C=C) bond in MMA to form a new bond of *ν*(C-O-C). Furthermore, the IR peaks around 1665-1760 cm^{-1} corresponded to

v(C=O) stretching within P(MMA) polymer nanoparticles, which became less sharp in copolymer nanoparticles of P(MMA-*co*-HPMC)$_{1:2,}$ P(MMA-*co*-HPMC)$_{1:3}$, and P(MMA-*co*-HPMC)$_{1:4}$. Additionally, the consistent existence of the *v*(C-O-C) peak at 1000–1320 cm^{-1} eventually suggested that methyl methacrylate (MMA) monomers were successfully copolymerised with hydroxypropyl methylcellulose (HPMC) monomers to form P(MMA-*co*-HPMC). Overall, the most suitable molar ratio for the copolymerisation between MMA and HPMC was observed at 1:4 (MMA:HPMC) with no presence of *v*(C=O) bond.

Scanning electron microscopy

Scanning electron microscopy (SEM) was performed to determine the size and morphology of P(MMA), P(HPMC), and P(MMA-*co*-HPMC) nanoparticles (Figure 3). The SEM images of P(MMA), P(HPMC), and P(MMA-*co*-HPMC) nanoparticles were viewed at 50 nm scale bar under magnification observation of 5000x with acceleration rate of 15 kV. Figure 3a shows that the P(MMA) nanoparticles appeared as spherical-like shape, whereas the P(HPMC) nanoparticles (Figure 3b) appeared as a three-dimensional network. The morphology of P(MMA-*co*-HPMC)$_{1:1}$ (Figure 3c) was observed as an irregular shape with small particles, whereas P(MMA-*co*-HPMC)$_{2:1}$ showed a group of larger particles (Figure 3d). This observation could be due to the increase of molar concentration of MMA monomers. The structure of P(MMA-*co*-HPMC)$_{3:1}$ (Figure 3e) resulted in spherical-like shapes, which could be the effect of high concentration of MMA monomers dominating the polymerisation. In addition, the morphology of P(MMA-*co*-HPMC)$_{4:1}$ (Figure 3f) illustrated the existence of polymer nanoparticle aggregation. P(MMA-*co*-HPMC)$_{1:2}$ (Figure 3g) showed a cluster of large lumps of particles that clumped together, which might be caused by moisture traces within the particles. Meanwhile, P(MMA-*co*-HPMC)$_{1:3}$ (Figure 3h) depicted that the particles were dispersed in polymer matrix. P(MMA-*co*-HPMC)$_{1:4}$ (Figure 3i) showed the existence of particles but with some blurry view. This observation might be due to the drying process of the sample during SEM preparation and the limitation of SEM, which could not observe the particles in nanoscale regimes.

The average particle sizes of P(MMA) and P(HPMC), P(MMA-*co*-HPMC) nanoparticles of varying MMA and HPMC concentrations were determined by randomly measuring the polymer particles obtained from the SEM images. The average particle size of P(MMA) was 455 nm, whereas P(HPMC) had an average particle size of 483 nm. P(MMA-*co*-HPMC)$_{2:1}$ and P(MMA-*co*-HPMC)$_{3:1}$ had average particle sizes of 690 nm and 759 nm, respectively. This finding indicated that the average particle size of copolymer increased as the concentration of MMA increased. As for P(MMA-*co*-HPMC)$_{1:1}$, it was hard to determine its particle size due to the aggregation of particles and the blurry view of the image, caused by the limitation of SEM magnification, which could not focus further to view the morphology of polymer particles. P(MMA-*co*-HPMC)$_{1:2}$ and P(MMA-*co*-HPMC)$_{1:3}$ had average particle sizes of 700 nm and 586 nm, respectively, which depicted that the average particle size of copolymers obtained was smaller when the concentration of HPMC increased.

Table 1. The formulation of P(MMA-*co*-HPMC) nanoparticles prepared *via* emulsion polymerization by varying molar ratios of MMA and HPMC monomers

Polymer Nanoparticles (PNPs)	**Molar Ratios of (MMA:HPMC)**	**SDS (mM)**	**KPS (mM)**
P(MMA)	-		
P(HPMC)	-		
P(MMA-*co*-HPMC)$_{1:1}$	1 (0.01 M) :1 (0.01 M)		
P(MMA-*co*-HPMC)$_{2:1}$	2 (0.02 M) :1 (0.01 M)		
P(MMA-*co*-HPMC)$_{3:1}$	3 (0.03 M) :1 (0.01 M)	8.2	6.95
P(MMA-*co*-HPMC)$_{4:1}$	4 (0.04 M) :1 (0.01 M)		
P(MMA-*co*-HPMC)$_{1:2}$	1 (0.01 M) :2 (0.02 M)		
P(MMA-*co*-HPMC)$_{1:3}$	1 (0.01 M) :3 (0.03 M)		
P(MMA-*co*-HPMC)$_{1:4}$	1 (0.01 M) :4 (0.04 M)		

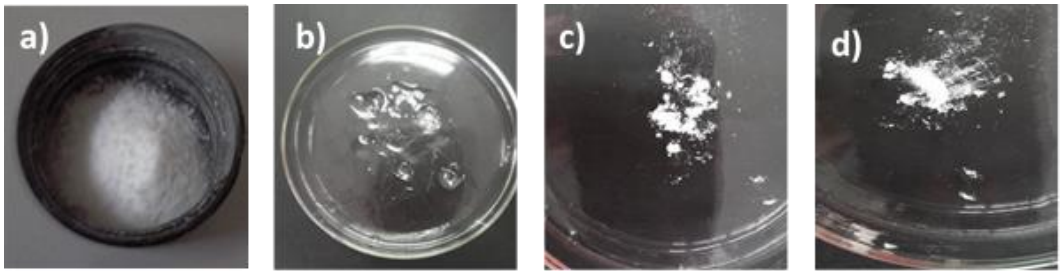
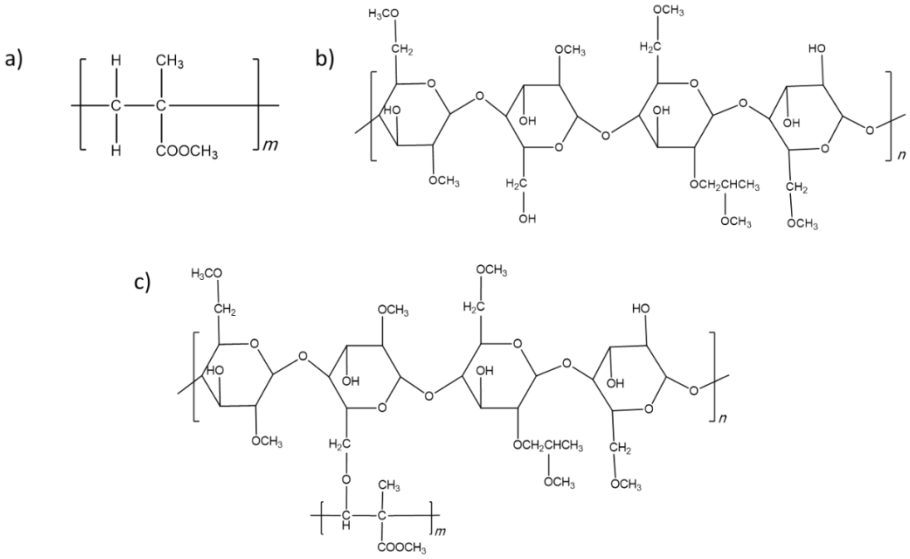
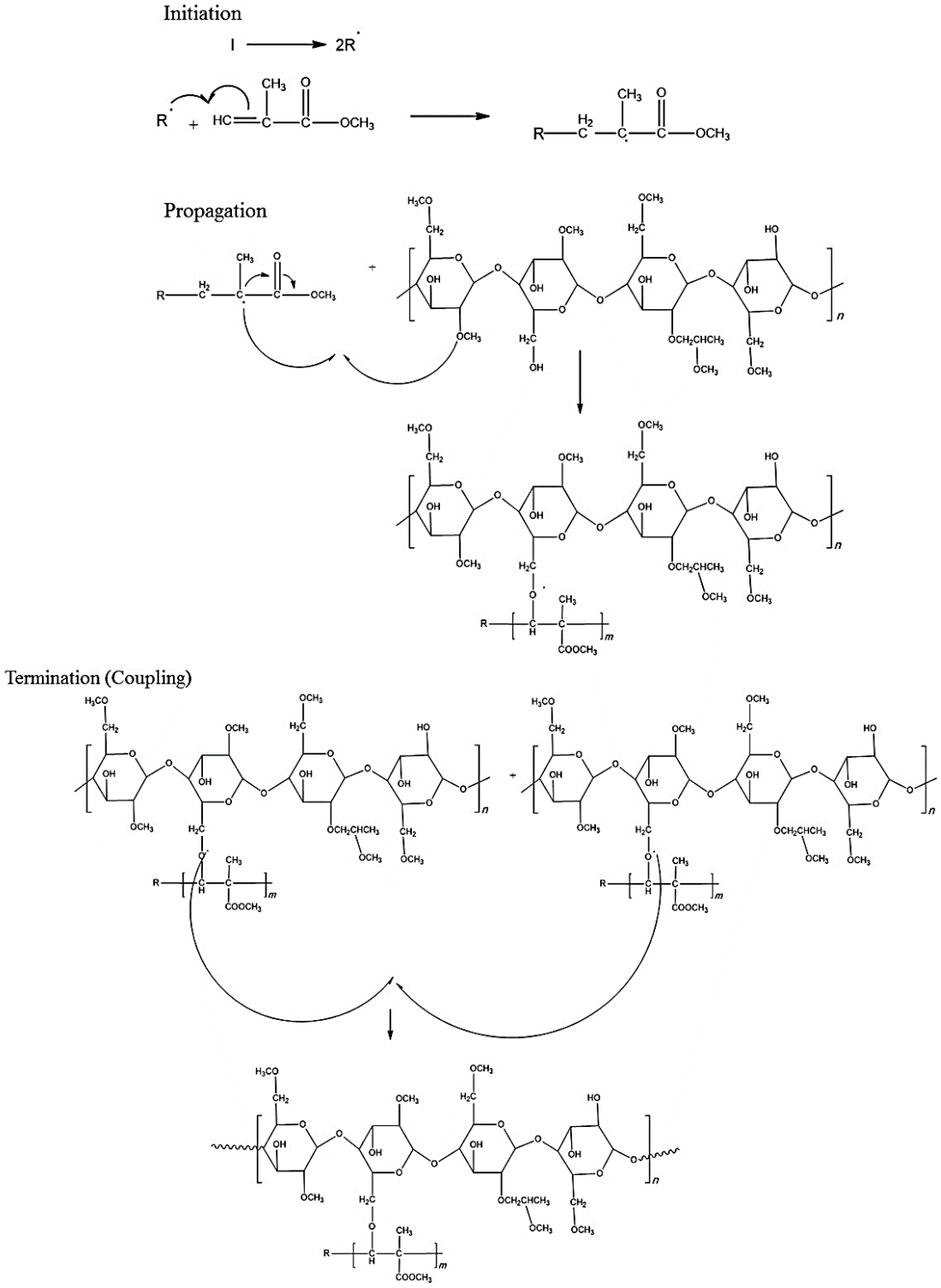


Figure 1. Physical appearances of (a) P(MMA), (b) P(HPMC), (c) P(MMA-*co*-HPMC)$_{1:1}$ and (d) P(MMA-*co*-HPMC)$_{1:4}$



Scheme 1. The chemical structures of (a) P(MMA), (b) P(HPMC) and c) P(MMA-*co*-HPMC)



Scheme 2. The proposed mechanism for copolymerization of P(MMA-*co*-HPMC)

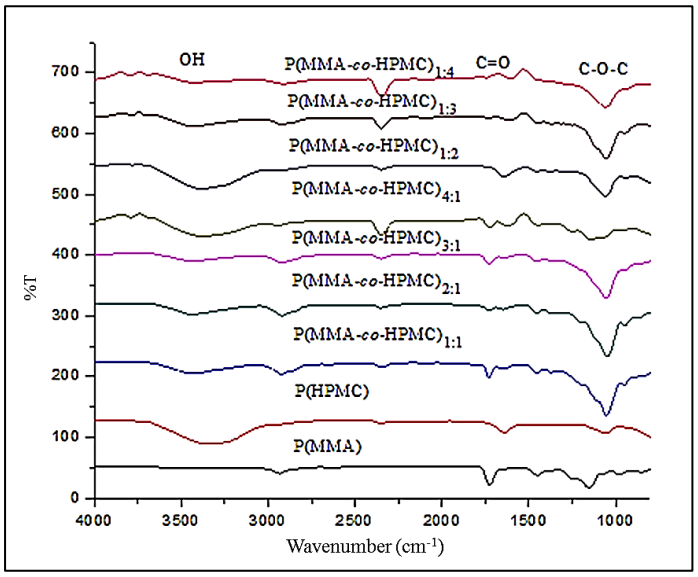


Figure 2. IR spectra of P(MMA), P(HPMC) and P(MMA-*co*-HPMC) nanoparticle

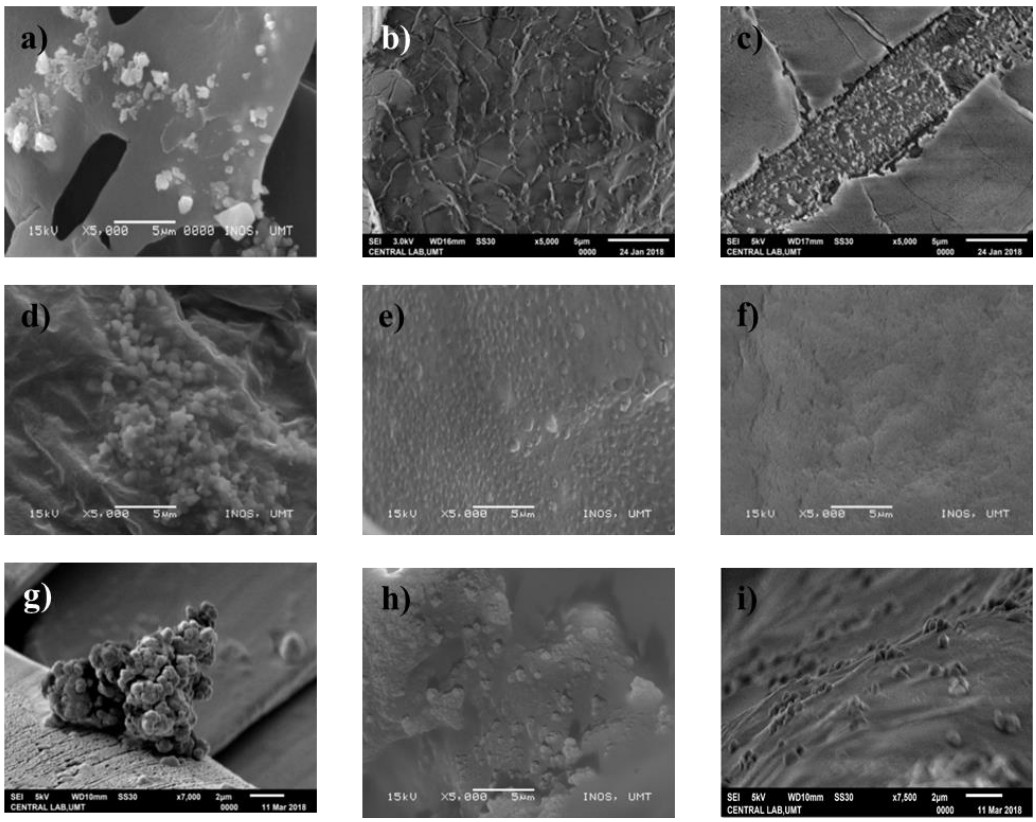


Figure 3. SEM images of (a) P(MMA), (b) P(HPMC), (c) P(MMA-*co*-HPMC)$_{1:1}$, (d) P(MMA-*co*-HPMC)$_{2:1}$, (e) P(MMA-*co*-HPMC)$_{3:1}$, (f) P(MMA-*co*-HPMC)$_{4:1}$, (g) P(MMA-*co*-HPMC)$_{1:2}$, (h) P(MMA-*co*-HPMC)$_{1:3}$, (i) P(MMA-*co*-HPMC)$_{1:4}$ nanoparticles by varying the concentration of MMA and HPMC

Thermogravimetric analysis

Thermogravimetric analysis (TGA) measures the amount of change in a sample mass as a function of temperature and is used to determine thermal stability [21]. The decomposition rates of P(MMA), P(HPMC), and P(MMA-*co*-HPMC) polymer nanoparticles at different molar ratios of MMA and HPMC were investigated. The TGA plots (Figure 4) showed the percentage of mass as a function of sample temperature for P(MMA), P(HPMC) and P(MMA-*co*-HPMC) nanoparticles, which was determined under inert (N_2) conditions. Approximately 10 mg of sample were heated at a rate of 20 °C/min using the PerkinElmer TGA.

P(MMA) nanoparticle samples showed a two-step weight loss in a temperature range of 75 - 350 °C. The first weight loss of around 75 °C might be due to the moisture traces within the samples and the second weight loss of around 350 °C was the result of polymer degradation. P(HPMC) sample also showed a two-step weight loss, whereby the first weight loss was around 110 °C, which was due to moisture traces within the sample. Meanwhile, the second weight loss of P(HPMC) started at a lower temperature of 210 °C, which displayed that P(HPMC) sample possesses less thermal stability than that of P(MMA).

It can be clearly seen that the TGA curves for copolymer nanoparticles of P(MMA-*co*-HPMC) showed the existence of a combination peak between P(MMA) and P(HPMC) nanoparticles, confirming the successful synthesis of copolymer nanoparticles (Figures 4 and 5). There were two distinctive weight loss curves observed for copolymer samples at around 170 °C and 370 °C. For the copolymer samples with high molar ratios of MMA monomer ($P(MMA\text{-}co\text{-}HPMC)_{1:1}$, $P(MMA\text{-}co\text{-}HPMC)_{2:1}$, $P(MMA\text{-}co\text{-}HPMC)_{3:1}$), (Figure 4), the first degradations were observed around 165 °C, while the second degradation happened around 365 °C. $P(MMA\text{-}co\text{-}HPMC)_{4:1}$ (Figure 4) that was prepared using the highest molar concentration of MMA demonstrated a very broad peak in which the degradation temperature was almost similar to the P(MMA) nanoparticles. This observation indicated that at a high concentration of MMA monomer, the MMA segments were significant than HPMC and the degradation according to MMA became dominant.

Moreover, copolymer samples that were prepared using high molar concentrations of HPMC showed a slight difference in terms of degradation temperature. $P(MMA\text{-}co\text{-}HPMC)_{1:2}$, $P(MMA\text{-}co\text{-}HPMC)_{1:3}$, and $P(MMA\text{-}co\text{-}HPMC)_{1:4}$ samples (Figure 5) indicated that the first degradation temperature occurred approximately at 200 °C, which was higher than copolymer nanoparticles prepared using high molar concentration of MMA monomers. On the other hand, the second degradation slope for copolymer nanoparticles prepared using high molar ratios of HPMC monomer was observed at around 370 °C. This observation strongly suggested that the copolymers formed by varying concentrations of HPMC were more thermally stable than that of the varying concentrations of MMA. As the concentration of HPMC increased, the thermal degradation temperature also increased.

Table 2 shows P(MMA) undergoing a significant weight loss of 60%, which might due to the diffusion of water uptake in glassy polymer (P(MMA)). Upon heating, this changed the glassy state to rubbery (soft state), increasing the mobility of the polymer chains [22]. In contrast, P(HPMC) accounted for only 15% of weight loss due to the water retention properties of HPMC. $P(MMA\text{-}co\text{-}HPMC)_{1:1}$, $P(MMA\text{-}co\text{-}HPMC)_{1:2}$, $P(MMA\text{-}co\text{-}HPMC)_{1:3}$, $P(MMA\text{-}co\text{-}HPMC)_{1:4}$, $P(MMA\text{-}co\text{-}HPMC)_{2:1}$, $P(MMA\text{-}co\text{-}HPMC)_{3:1}$, and $P(MMA\text{-}co\text{-}HPMC)_{4:1}$ depicted 35% of weight loss, except for $P(MMA\text{-}co\text{-}HPMC)_{4:1}$, which took up to 70% of weight loss possibly due to the highest molar ratios of MMA monomer. From the observations of percentage weight loss, it could be summarised that copolymer nanoparticles of P(MMA-*co*-HPMC) were more stable than the homopolymer nanoparticles of P(MMA).

Solubility test

A simple solubility test was conducted to confirm the hydrophilicity of P(MMA), P(HPMC), and P(MMA-*co*-HPMC) nanoparticles. Approximately 0.05 g of polymer samples were weighed and dissolved in 6 mL of distilled water at room temperature. The ability of P(MMA), P(HPMC), and P(MMA-*co*-HPMC)

nanoparticles to dissolve in aqueous solution was observed. Figure 6 shows the images of P(MMA), P(HPMC), and P(MMA-*co*-HPMC) at molar concentrations of 1:1 and 1:4 (MMA:HPMC), respectively, which were obtained before and after the solubility test. It was observed that P(MMA) nanoparticles (Figure 6a) were partially soluble after being dissolved in aqueous solution on account of P(MMA) itself is partially soluble in water [23].

As for P(HPMC) nanoparticles, they were soluble after being dissolved in aqueous solution but took 2 to 3 minutes to become completely soluble (Figure 6b). This was because hydroxypropyl methylcellulose is a water-soluble monomer and allows diffusion of water to take place easily in a dispersion medium [24]. Meanwhile, P(MMA-*co*-HPMC)$_{1:1}$ nanoparticle that had a similar monomer ratio of MMA and HPMC was partially soluble in aqueous medium (Figure 6c). Interestingly, copolymer P(MMA-*co*-HPMC)$_{1:4}$ nanoparticles were immediately soluble after being dissolved in water, which proved that the hydrophilicity of P(MMA) nanoparticles increased by the copolymerisation with HPMC monomer (Figure 6d). It was worth to note that the different molar ratios of MMA and HPMC had different rates of solubility. For example, P(MMA-*co*-HPMC) nanoparticles obtained by varying concentrations of MMA with constant concentration of HPMC took a longer duration (after two days) to dissolve as the concentration of MMA was increased in the ratio of 4:1 (Figure 7). On the other hand, P(MMA-*co*-HPMC) nanoparticles obtained by varying concentrations of HPMC with constant concentration of MMA took a shorter time for the copolymer nanoparticles to be dissolved in water when the concentration of HPMC was increased in the ratio of 1:4.

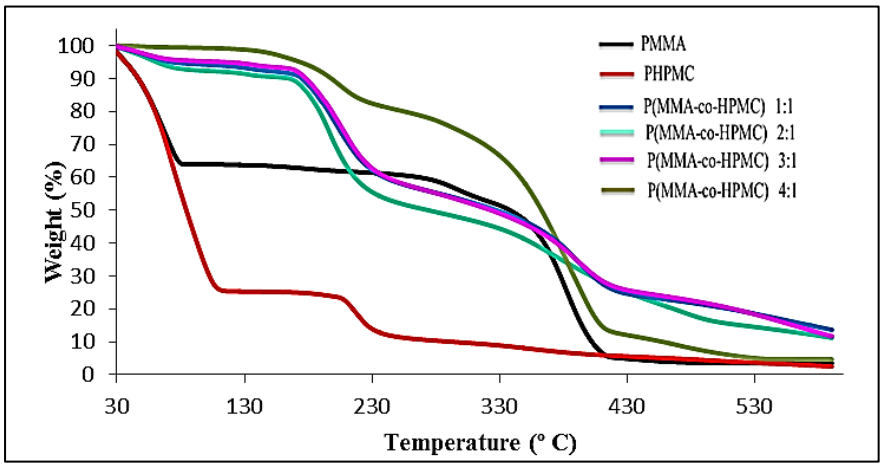


Figure 4. TGA curves obtained for P(MMA), P(HPMC), P(MMA-*co*-HPMC)$_{1:1}$, P(MMA-*co*-HPMC)$_{2:1}$, P(MMA-*co*-HPMC)$_{3:1}$, P(MMA-*co*-HPMC)$_{4:1}$ nanoparticles by varying the concentration of MMA

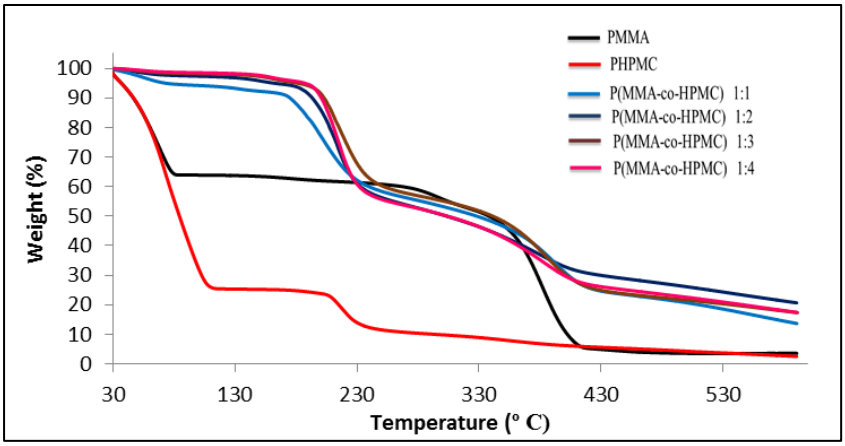


Figure 5. TGA curves obtained for P(MMA), P(HPMC), P(MMA-*co*-HPMC)$_{1:1}$, P(MMA-*co*-HPMC)$_{1:2}$, P(MMA-*co*-HPMC)$_{1:3,}$ P(MMA-*co*-HPMC)$_{4:1}$ nanoparticles by varying the concentration of HPMC

Table 2. The percentage weight loss of P(MMA-*co*-HPMC) of nanoparticles prepared *via* emulsion polymerization by varying molar ratios of MMA and HPMC monomer

PNPs	**Percentage of Weight Loss (%)**
P(MMA)	60
P(HPMC)	15
P(MMA-*co*-HPMC)$_{1:1}$	35
P(MMA-*co*-HPMC)$_{2:1}$	35
P(MMA-*co*-HPMC)$_{3:1}$	35
P(MMA-*co*-HPMC)$_{4:1}$	70
P(MMA-*co*-HPMC)$_{1:2}$	35
P(MMA-*co*-HPMC)$_{1:3}$	35
P(MMA-*co*-HPMC)$_{1:4}$	35

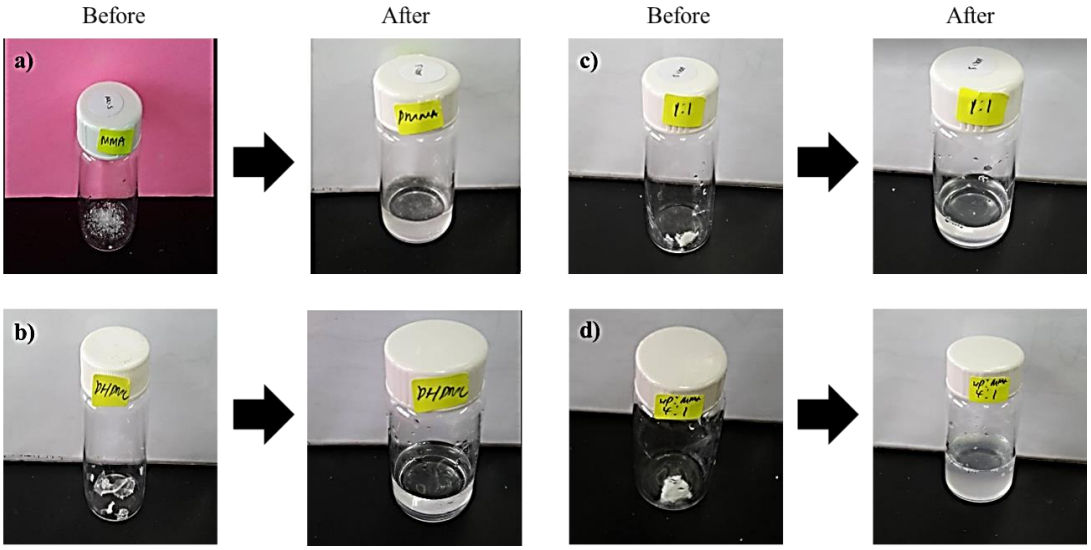


Figure 6. The solubility test of (a) P(MMA), (b) P(HPMC), (c) P(MMA-*co*-HPMC)$_{1:1}$ and (d) P(MMA-*co*-HPMC)$_{1:4}$

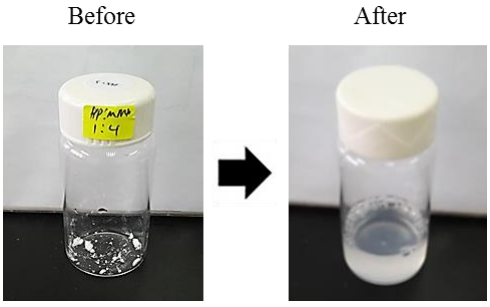


Figure 7. The solubility test of P(MMA-*co*-HPMC)$_{4:1}$ after two days observation

Conclusion

Emulsion copolymerisation of methyl methacrylate (MMA) with hydroxypropyl methylcellulose (HPMC) to produce poly(methyl methacrylate-*co*-hydroxypropyl methylcellulose) (P(MMA-*co*-HPMC)) was obtained successfully, and the formation of P(MMA-*co*-HPMC) nanoparticles was confirmed by FTIR analysis, in which *v*(C=O) diminished when PMMA lost its double bonds. Despite the limitation of SEM that was unable to clearly observe the morphology and structure of the polymer nanoparticles, it showed the existence of aggregation of P(MMA-*co*-HPMC) nanoparticles. Thermograms obtained from the TGA analysis determined that P(MMA-*co*-HPMC) nanoparticles prepared by increasing the molar ratios of HPMC monomers were more thermally stable. This was because copolymer of higher molar ratios of HPMC monomers degraded at higher temperature than that of higher molar ratios of MMA. The effect of different molar ratios of MMA and HPMC concentration could affect the morphology and size of the P(MMA-*co*-HPMC) nanoparticles. When the amount of MMA increased, the average particles size of

P(MMA-*co*-HPMC) nanoparticles tend to become larger. In contrast, an increase in HPMC concentration led to the decrease in the average particle size of P(MMA-*co*-HPMC) nanoparticles. The simple solubility test was carried out to confirm the hydrophilicity of P(MMA-*co*-HPMC) nanoparticles in which the copolymer samples of higher concentrations of MMA took a longer time to be dissolved. In comparison, the copolymer samples of higher concentrations of HPMC took a shorter time to be fully dissolved.

Acknowledgement

We thanked the Ministry of Higher Education, Malaysia for the funding (FRGS/1/2020/STG02/UMT/02/1/ 59633) and Universiti Malaysia Terengganu for the generous support.

References

1. Nagavarma, B. V. N., Hemant, K. S. Y., Ayaz, A., Vasudha, L. S. and Shivakumar, H. G. (2012). Different technique for preparation of polymeric nanoparticles – a review. *Asian Journal of Pharmaceutical and Clinical Research,* 5(3): 16-23.
2. Kumari, A., Yadav, S. K. and Yadav, S. C. (2010). Biodegradable polymeric nanoparticles based drug delivery system. *Colloids and Surfaces B: Biointerfaces,* 75(1): 1-18.
3. Liang, Y., Yun, W., Maozhi, P., Garry, L. R. and Qinmin, P. (2013). Synthesis of poly(methyl methacrylate) nanoparticles via differential microemulsion polymerization. *European Polymer Journal*, 49(1): 41-48.
4. Dusadee, T., Garry, L. R. and Pattarapan, P. (2017) Preparation of poly(methyl methacrylate)-silica nanoparticles via differential microemulsion polymerization and physical properties of NR/PMMA-SiO_2 hybrid membranes. *Polymer Engineering & Science*, 58(5): 759-766.
5. Ismail, Z. and Harun, N. A. (2019). Synthesis and characterizations of hydrophilic PHEMA nanoparticles via inverse miniemulsion polymerization. *Sains Malaysiana*, 48(8): 1753-1759.
6. Kamaruddin, N. N., Kassim, S. and Harun, N. A. (2017). Volume effect of non-polar solvent towards the synthesis of hydrophilic polymer nanoparticles prepares via inverse miniemulsion polymerization. *AIP Conference Proceedings*, 1885: 020056.
7. Harun, N. A., Md Tahier, N., Kamaruddin, N. N., Mamat, M. and Kassim, S. (2018). Emulsion polymerization of poly(methacrylic acid) nanoparticles: Effects of different cationic surfactants. *Asian Journal of Chemistry*, 30 (10): 2299-2304.
8. Harun, N. A., Tzy, T. Y., Chen, L. P. Zainuddin, A. A. and Kassim, S. (2019). Copolymerization of methacrylic acid (MAA) and butyl acrylate (BuA) via emulsion polymerization technique. *Malaysian Journal of Chemistry*, 21(3): 20-28
9. Nopparat, V. and Panya, S. (2020). Synthesis of crosslinked poly(methacrylic acid) shell/ lipid core colloidal nanoparticles via L-in-L_m interfacial polymerization and their pH responsiveness. *Colloids and Surfaces A; Physicochemical and Engineering Aspects*, 603: 125180.
10. Rao, J. P. and Geckeler, K. E. (2011). Polymer nanoparticles: Preparation techniques and size-control parameters. *Progress in Polymer Science,* 36(7): 887-913.
11. José, M. A. (2004). Emulsion polymerization: From fundamental mechanisms to process developments. *Journal of Polymer Science Part A: Polymer Chemistry* 42(5): 1025-1042.
12. Thickett, S. C. and Gilbert, R. G. (2007) Emulsion polymerization: State of the art in kinetics and mechanisms. *Polymer,* 48(24): 6965-6991.
13. Shalviri, A., Raval, G., Prasad, P., Chan, C., Liu, Q., Herrklotz, H., Rauth, A. M. and Wu, X. Y. (2012). pH-dependent doxorubicin release from terpolymer of starch, polymethacrylic acid and polysorbate 80 nanoparticles for overcoming multidrug resistance in human breast cancer cells. *European Journal of Pharmaceutics and Biopharmaceutics,* 82(3): 587-597.

14. Baek, H. H., Lee, J. M., Cho, J. E., Kim, J. H. and Cheong, I. W. (2010). Hydroxypropyl methylcellulose-graft-poly(ethyl acrylate-co-methyl methacrylate) particles by resin emulsion polymerization. *Macromolecule Research,* 18(1): 53-58.
15. Mondal, S., Gupta, B. and Sing, H. (2005). Acrylic monomers based emulsion copolymer for coating application. *Indian Journal of Fibre and Textile Research,* 30: 184-189.
16. Joshi, J. R. and Patel, R. P. (2012). Role of biodegradable polymers in drug delivery. *International Journal of Current Pharmaceutical Res*earch, 4(4): 74.
17. Tian, H. Y., Tang, Z. H., Zhuang, X. L., Chen, X. S. and Jing, X. B. (2012). Biodegradable synthetic polymers: preparation, functionalization and biomedical application. *Progress in Polymer Science,* 37(2): 237-280.
18. Lu, T., Liu, X. Y., Qi, D. M. and Zhao, H. T. (2015). Effect of hydrophobic monomer on the aqueous dispersion polymerization of acrylamide with quaternary ammonium cationic monomer. *Iranian Polymer Journal,* 24(3): 219-227.
19. Wu, B., Lenz, R. W. and Hazer, B. (1999). Polymerization of methyl methacrylate and its copolymerization with ε-caprolactone catalyzed by isobutylalumoxane catalyst. *Macromolecules,* 32(20): 6856-6859.
20. Miranda, A., Mill, M. and Caraballo, I. (2006). Study of the critical points of HPMC hydrophilic matrices for controlled drug delivery. *International Journal of Pharmaceutics,* 311(1-2): 75-81.
21. Ding, C. C., Li, G. Y. and Zhang, M. (2015). Preparation and characterization of collagen/hydroxypropyl methylcellulose (HPMC) blend film. *Carbohydrate Polymer,* 119: 194-201.
22. Wayne, N. A., Stephen, P. D. and Samual, L. E. (2014). Ageing and moisture uptake in polymethyl methacrylate (PMMA) bone cements. *Journal of the Mechanical Behavior of Biomedical Materials*, 32(100): 76-88.
23. Fatimah, A., Amir, H. N. and Francesco, P. (2019). Material encapsulation in poly(methyl methacrylate) shell: A review. *Journal of Applied Polymer,* 136(41): 48039.
24. Wu, H. C., Du, S. Y., Lu, Y., Li, Y. and Wang, D. (2014). The application of biomedical polymer material hydroxy propyl methyl cellulose (HPMC) in pharmaceutical preparations. *Journal of Chemical and Pharmaceutical Research,* 6(5): 155-160.

Malaysian Journal of Analytical Sciences (MJAS)
Published by Malaysian Analytical Sciences Society

PHYTOCHEMICAL AND ANTIBACTERIAL PROPERTIES ON THREE MEDICINAL PLANTS FOR POTENT ANTI-SOFT ROT AGENTS

(Fitokimia dan Sifat Antibakteria Tiga Jenis Pokok Berubat sebagai Agen Anti Reput Buah)

Airiel Daniel Daud[1], Nur Suhada Azman[1], Nur Izni Ainina Alias[1], Norfatihah Syaifudin[1], Aiza Harun[1]*, Noorshilawati Abdul Aziz[2]

[1] Faculty of Applied Science,
[2] Faculty of Plantation and Agrotechnology
Universiti Teknologi MARA Pahang, 26400 Bandar Tun Razak Jengka, Pahang, Malaysia

**Corresponding author: aizaharun@.uitm.edu.my*

Received: 28 September 2020; Accepted: 13 December 2020; Published: 20 February 2021

Abstract

Gynura procumbens, *Murraya koenigii*, and *Cosmos caudatus* are among the readily homegrown medicinal plants possessing ethnomedicinal applications. The lack of studies on the utilisation of these plants against plant pathogen has driven this study to investigate these plants as a potential for plant pathogen soft rot disease and proposed structures. Antibacterial activity of three types of extracts of each plant species was conducted against a gram-positive soft rot disease bacterium of *Erwinia chrysanthemi*. An agar disc diffusion method was used to evaluate antibacterial activity on the extracts against *E. chrysanthemi*. A thin layer chromatographic technique (TLC) was used to screen the presence of phytochemicals. The molecular structures of the anti-soft rot agents were based on the proton nuclear magnetic resonance (NMR), infrared (IR) spectroscopy and comparison with literature. The phytochemicals of alkaloid, terpenoid, and phenolics were detected in all plant species. All extracts exhibited antibacterial activity against *E. chrysanthemi*, and the activity was in a concentration-dependent manner. The highest inhibition zone was recorded as 12 mm from the methanol extract of *C. caudatus*. Infrared analysis recorded functional groups of hydroxyl (OH), carbon double bond (C=C), and carbonyl (C=O) in which these groups of molecules might be retained inside the active compounds. Using TLC, IR, NMR and comparison with the available literature, the anti-soft rot agents were proposed as a phenolic compound known as rutin **(1)**, triterpenoid saponin **(2)**, hydroxycinnamic acid ester **(3)**, caffeic acid **(4)**, quinic acid **(5),** and alkaloid derivatives **(6)**. These results could provide scientific baseline information for the development of natural pesticide to control anti-soft rot disease.

Keywords: antibacterial activity, anti-soft rot, phytochemicals, medicinal plants, *Erwinia chrysanthemi*

Abstrak

Gynura procumbens, *Murraya koenigii*, dan *Cosmos caudatus* merupakan pokok tumbuhan berubat yang sangat dikenali kerana penggunaannya dalam perubatan tradisional. Akibat kekurangan kajian ketiga-tiga pokok ini terhadap patogen tumbuhan, maka fokus kajian adalah untuk melihat potensi sifat antibakteria ketiga-tiga pokok ini terhadap patogen penyakit reput buah dan juga mencadangkan struktur agen anti reput buah. Aktiviti antimikrob ini telah dilakukan ke atas satu bakteria gram positif iaitu *Erwinia chrysanthemi*. Teknik penyerakan cakera agar telah digunakan untuk menilai keberkesanan aktiviti antibakteria untuk semua jenis ekstrak tumbuhan. Teknik pemisahan kromatografi lapisan nipis (KLN) telah digunakan untuk melihat kehadiran bahan fitokimia.

Cadangan struktur kimia agen anti-reput buah telah dilakukan menggunakan spektroskopi nukleus hidrogen teraruh, spektroskopi infra merah dan perbandingan dengan kajian lepas. Fitokimia jenis alkaloid, terpen dan fenolik telah dikesan di dalam ekstrak ketiga-tiga jenis pokok. Kesemua ekstrak menunjukkan aktiviti antimikrob dan aktiviti ini berkadar terus dengan kepekatan ekstrak. Zon perencatan yang tertinggi diperolehi daripada ekstrak methanol *C.caudatus* iaitu sepanjang 12 mm. Analisa infra merah ekstrak ketiga-tiga pokok telah merekodkan kehadiran kumpulan berfungsi jenis hidroksil (OH), karbon ikatan ganda dua (C=C) dan kumpulan karbonil (C=O) di mana ia berkemungkinan berada di dalam struktur aktif ekstrak pokok. Selepas analisa KLN, infra merah dan spektroskopi nukleus magnetik resonan dan perbandingan dengan kajian lepas dijalankan terhadap ekstrak tumbuhan, struktur agen anti reput buah telah dicadangkan sebagai sebatian fenolik jenis rutin **(1)**, terpen saponin **(2)**, ester asid hidroksisinamik **(3),** asid kafeik **(4)**, asid kuinik **(5)**, dan terbitan alkaloid **(6)**. Hasil kajian diharap dapat menyediakan maklumat saintifik asas dalam pembuatan racun makhluk perosak semulajadi untuk mengawal penyakit anti reput buah.

Kata kunci: aktiviti antibakteria, anti reput buah, fitokimia, tumbuhan berubat, *Erwinia chrysanthemi*

Introduction

Plants are able to produce secondary metabolites such as flavonoids, alkaloids, phenols, and saponins that are critical for their survival [1]. These metabolites enable plants to shield themselves from pathogens, herbivory effects, competition with other plants, and to preserve them from unfavourable physical conditions such as harmful UV radiation, water deprivation, and low temperatures. The antimicrobial activity is dependent on the types of pathogen and the presence of the active compounds due to the variation on the results, which could be due to the restriction of the active components inside the extract to cause antimicrobial action [2]. *Cosmos caudatus* was reported to exhibit antimicrobial action against five microbial strains which are *Bacillus subtilis*, *Candida albicans*, *Escherichia coli*, *Pseudomonas aeruginosa*, and *Staphylococcus aureus* with the MIC concentration of the extract ranging from 6.25 mg/mL to 12.5 mg/mL. *M. koenigii* has an antimicrobial effect on *Candida albicans, Aspergillus niger*, and *Trichophyton rubrum.* The antimicrobial effect of could be due to the presence of monoterpenoids and sesquiterpernoids in the *M. koenigii's* leaves [3].

An antibacterial activity using hexane, methanol, and chloroform from *M. koenigii* against *Bacillus subtilis, Staphylococcus aureus*, *Escherichia coli* as well as *Salmonella typhi* was also conducted [4]. The flavonoid compounds in *M. koenigii* were found to be responsible for the remarkable antibacterial activities and the antioxidant activity [5]. *G. procumbens* showed remarkable antimicrobial activity against gram-positive and gram-negative bacteria such as *Bacillus cereus, Pseudomonas aeruginosa, Vibrio parahaemolyticus*, and *Salmonella typhi* as well as antifungal activity against fungi such as *Candida albicans* and *Aspergillus niger*. These antimicrobial effects established the traditional use of *G. procumbens* to treat infections by herpes simplex virus and malaria parasites [6]. However, the limitation of applying these plants species to combat plant pathogen of soft rot disease *in vitro* study is the reason to further this investigation. Therefore, this study aims to evaluate the potency of plant extracts of *C. caudatus*, *M. koenigii*, and *G. procumbens* against *E. chrysanthemi*.

Materials and Methods

Preparation of leave extracts

The plant samples were collected at Herbs Nursery UiTM Pahang. The samples were washed and placed in an oven at a temperature of 40 ˚C until fully dried. The dried samples were then ground into a fine powder using an electric blender. The soaking process of a measured mass of the powdered sample was performed consecutively using three types of solvents with increasing polarities namely hexane, ethyl acetate (EA), and methanol (MeOH). The soaking process was held for three days and repeated three times for each solvent until no colour was detected. Then, the solvent mixture was filtered, evaporated to dryness using a rotary evaporator, and was kept until further use.

Antibacterial activity

The antibacterial work of all extracts of the plant species against *E. chrysanthemi* was conducted based on the previously published study [7]. The strain of the bacteria

was obtained from Biology Laboratory UiTM Pahang. All extracts were two-fold serially diluted from 400 mg/mL until 50 mg/mL and were used to prepare 6 mm impregnated disc. The effectiveness of the extracts was determined by the size of the inhibition zone (in mm) through the disc diffusion method.

Thin layer chromatographic analysis

The TLC analysis of extracts was performed according to the previously published study [8]. The developed TLC was sprayed with chemical reagents such as vanillin/H_2SO_4 reagent, Dragendorff's reagent, or ferric chloride reagent to ascertain any occurrence of phytochemicals such as terpenoid, alkaloid, and phenolic compounds.

Fourier transform infrared analysis

The FTIR analysis of extracts was performed using the same technique as previously described [9]. The information of functional groups recorded from infrared spectrum provided a basic structural formula of phytochemicals.

Proton nuclear magnetic resonance analysis

The proton NMR analysis was conducted to determine the types of proton presents. It was recorded on JEOL FTNMR 400 MHz transformed spectrometer in $CDCI_3$ or acetone-D6 using tetramethylsilane (TMS) as the internal standard at 400 MHz. The data from the proton NMR spectrum provide the type of proton.

Results and Discussion

Table 1 depicted the *in vitro* antibacterial activity for each extract of *C. caudatus*, *M. koeginii*, and *G. procumbens*. The size of the inhibition zone appeared from the antibacterial action reveals the effectiveness of the extracts. The greater the inhibition zone, the more effective the extracts with higher antibacterial activity.

Generally, all types of extracts for all plant species exhibit antibacterial activity in a concentration-dependent manner. As the concentration of the extract increases, the size of the inhibition zone also increases enhancing the antibacterial activity. The accumulation of active compounds in the extracts are sufficient to affect the growth of *E. chrysanthemi* by preventing cell wall synthesis or cell content and inhibit DNA replication, which will then stop the growth of *E. chrysanthemi* [10]. As the polarity of the extracts increases from hexane to methanol, the inhibition zone also increases except for methanol extract of *G. procumbens* stem. Methanol extract from *C. caudatus* leaves was found as the most active extract since it inhibited the growth of *E. chrysanthemi* prominently with an inhibition zone of 12 mm at 400 mg/ml compared to other species and among other extracts from *C. caudatus* itself. However, this extract inhibited the growth of *E. chrysanthemi* in a moderate action in accordance with its inhibition zone at 400 mg/ml. The higher antibacterial activity was methanol extract of *C. caudatus* compared to ethyl acetate and hexane extract, and this is aligned with previous studies [10, 11] that showed antibacterial activity of a plant if methanol extract was used.

Meanwhile, another previous antibacterial study using an ethanol extract of *C. caudatus* recorded promising antibacterial activity against selected human bacteria [2]. According to previous reports, phenolic compounds such as flavonoid was found to take part in suppressing bacterial growth [1, 12, 13] and it was isolated and identified from the polar extract. Therefore, the existence of phenolic compound in *C. caudatus* leaves as tabulated in Table 2 is consistent with previous studies and its presence might be the reason for the antibacterial action revealed by the extracts against *E. chrysanthemi*. However, the trend of antibacterial activity for *G. procumbens* stem does not follow the polarity of the extracts as in other tested species. The extract from nonpolar extract hexane with an inhibition zone of 8.5 mm at 400 mg/ml was recognised as an active extract. These different trends of antibacterial activity may be in part caused by the presence of alkaloid and terpenoid that would be found in the hexane extracts of *G. procumbens* stem as illustrated in Table 2.

Phytochemical investigation of anti-soft rot agents

An active compound such as rutin, which possessed antibacterial properties [14, 15] is one of the phenolic compounds isolated from the leaves extract of *C. caudatus*. Since the phenolic compounds were also found in all extracts of *C. caudatus* leaves (Table 2) and are also an antibacterial agent, it is hence suggested that

rutin is one of the phytochemicals that are responsible for inhibitory action against *E. chrysanthemi*. Based on the structure of rutin (**1**), the common groups or functional groups are phenol rings, which contain C=C, OH groups, C-O-C linkage as well as CH_3 and CH groups (Figure 1).

In accordance with the infrared result in Table 3, functional groups such as OH, benzene ring and C-O-C linkage are also detected in methanol extract of *C. caudatus* leaves. The presence of these functional groups is present in rutin as illustrated from the structure as well as the types of proton present (CH_3, CH_2 and CH) that is depicted in Table 4. Therefore, it is sugges ted that this structure would be one of the phenolic compounds retains in the methanol extract of *C. caudatus* and is responsible to enhance its antibacterial efficacy. Theoretically, the active groups such as OH groups in rutin weakens the cell wall of bacteria by making the lipid bilayer disconformated and disordered hence promoting vesicle leakage [16]. This phenomenon could be one of action mechanism of the phenolic compound from methanol extract of *C. caudatus* causing an inhibitory effect on the growth of *E. chrysanthemi*. Previous reports also claimed that other phenolic compounds such as apigenin, morin, and rhamnetin affect the thickness of lipid bilayer and fluidity level to decrease and increased membrane permeability, leading to the leaking of intracellular proteins in bacterial [17].

Ethyl acetate extract from *M. koenigii* and *G. procumbens* leaves is the active extracts against *E. chrysanthemi* with an inhibition zone of 11 mm and 7 mm, respectively. These inhibitory actions are considered as moderately active for *M. koenigii* leaves and weakly active for *G. procumbens* leaves. According to Table 2, since terpenoid and phenolic are detected in *M. koenigii* leaves and *G. procumbens* leaves as well as terpenoid and alkaloid are detected in *G. procumbens* stem, these might be the sources of inhibitory effect. Table 2 summarises the secondary metabolites or phytochemicals detected in all types of extracts of *C. caudatus, M. koenigii*, and *G. procumbens* through TLC separation. The presence of these compounds is unavoidable as these are the range of phytochemicals content contribute to the enhancement of antibacterial activity.

The antibacterial activity arises in ethyl acetate extract of *M. koenigii* and *G. procumbens* leaves extract might be due to the growth of *E. chrysanthemi* is inhibited by terpenoid and phenolic compound. Previous study [4] reported that the antibacterial activity increased with chloroform extract of *M. koenigii* leaves. Since the polarity index of ethyl acetate and chloroform is almost the same, which is 4.4 for ethyl acetate and 4.1 for chloroform, therefore, the finding in this study agrees with the previous studies. Another study reported that phenolic compounds were the major phytochemical in *M. koenigii* that caused antibacterial activity [5].

Previous study reported that inhibitory action against several human pathogens [18] is influenced by the presence of phenolic compounds in *G. procumbens* leaves. This is in line with the results in this study as tabulated in Table 2 in which the phenolic compound was also found in ethyl acetate and methanol extract of *G. procumbens* leaves. Several phenolic compounds known as flavanone, aurone, isoflavone, benzofuran, xanthone, and stilbene have been reported [19]. The proposed bioactive terpenoid such as terpenoid saponin **(2)** and phenolic compound such as hydroxycinnamic acid ester **(3)** from *M. koenigii* leaves agrees with the structures as previously reported [19]. These suggested that the structures fit with the infrared result of *M. koenigii* as in Table 3 whereby the functional groups of OH, C=O, C-O, and aromatic ring are present. The structures are comparable with the data on the types of the proton as in Table 4 whereby proton methyl ($R\text{-}CH_3$) methylene($R\text{-}CH_2$), methine(R-CH), vinyl proton(H-C=C-), proton hydroxyl (R-OH), and aryl proton (proton benzene) are consistent with the suggested structures in **(2)** and **(3)**.

Polyphenol such as caffeic acid **(4)** and quinic acid **(5)** in Figure 3 was also reported as the bioactive constituents from *G. procumbens* leaves [20] and would possibly dwell in its ethyl acetate extract or methanol extract. The structure of **(4)** and **(5)** of *G. procumbens* might involve in inhibiting the growth of *E. chrysanthemi* although the inhibition zone is smaller

compared with *C. caudatus* and *M. koenigii*. The groups of OH, C=O, and C=C in the proposed structure of **(4)** are consistent with the functional groups from methanol extract of *G. procumbens* leaves. The proposed structure **(5)** contains common functional groups of OH, C=O, C=C, CH_2 groups and the finding of these functional groups in ethyl acetate extract of *G. procumbens* leaves from Table 3 and the types of the proton from Table 4 agrees with the proposed structures. Therefore, it is suggested that both structures could function as antibacterial agents to ensure the feasibility of inhibitory action.

Results in Table 2 illustrate that hexane extract of *G. procumbens* stem may contain an alkaloid, which may be in part responsible for its antibacterial effect against *E. chrysanthemi* although the activity is weaker than *C. caudatus* and *M. koenigii*. FTIR result of hexane extract of *G. procumbens* stem as depicted in Table 3 suggested the appearance of OH, C=O, C=C, and C-N functional groups, which likely consistent with alkaloid derivatives **(6)** [21]. The data on the types of proton such as methane proton, CH_2-N, methylene proton, and vinyl proton depicted in Table 4 are comparable with **(6)** structure. Therefore, the structure **(6)** is proposed as one of the active alkaloids from *G. procumbens* stem that may involve in antibacterial action.

The different profile of antibacterial activity between *C. caudatus*, *M. koenigii*, and *G. procumbens* is unique since they grow from different plant family with a wide range of phytochemicals. However, an assumption can be made in such a way that a powerful synergistic action of terpenoid and phenolic in *C. caudatus* might cause higher antibacterial activity against *E. chrysanthemi* compared to other tested plant extracts.

Table 1. The antibacterial activity on the crude extracts of *C. caudatus*, *M. koenigii*, and *G. procumbens* against *E. chrysanthemi*

Extract	**Concentration (mg/mL)**	***C. caudatus* Leaves**	***M. koenigii* Leaves**	***G. procumbens* Leaves**	***G. procumbens* Stem**
		Inhibition Zone (mm)	**Inhibition Zone(mm)**	**Inhibition Zone (mm)**	**Inhibition Zone (mm)**
Hexane	50	8.0	6.7	6.0	6.0
	100	8.0	6.7	6.0	6.5
	200	11.0	7.0	6.0	7.5
	400	8.0	8.7	6.0	8.5
Ethyl acetate	50	6.0	6.7	7.0	7.0
	100	6.0	6.7	7.0	7.0
	200	7.0	7.7	7.0	7.3
	400	9.0	11.0	7.0	7.7
Methanol	50	6.0	6.0	6.0	6.0
	100	6.3	8.0	6.0	6.0
	200	7.0	6.0	6.0	6.0
	400	12.0	10.0	7.0	6.0
Ampicillin	10 ug/ml	30	30	30	30

6 mm= not active (no inhibition zone); 7-10 mm = weakly inhibited; 11-14 mm = moderately inhibited; > 15 mm = strongly inhibited

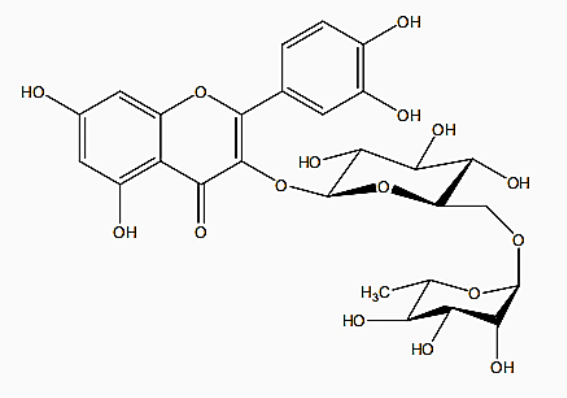


Figure 1. Based on the structure of rutin (**1**)

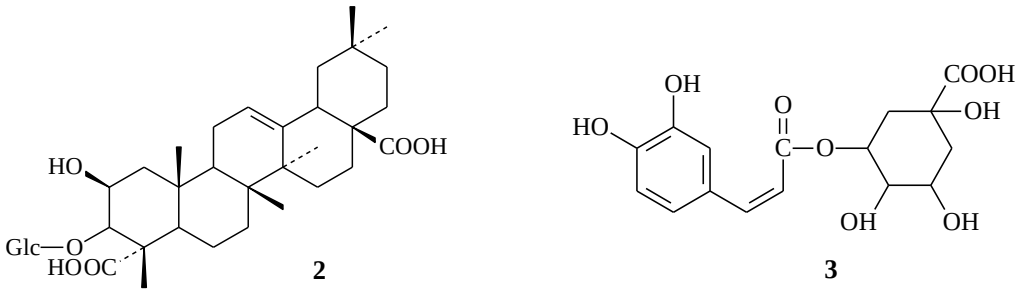
Table 2. TLC analysis of phytochemicals in *C. caudatus*, *M. koenigii*, and *G. procumbens*

Species	Terpenoid*			Alkaloid**			Phenolic***		
	Hex	EA	MeOH	Hex	EA	MeOH	Hex	EA	MeOH
C. caudatus	√	√	√	x	x	x	√	√	√
M. koenigii	√	√	√	x	x	x	√	√	√
G. procumbens leaves	x	x	x	√	x	x	x	√	√
G. procumbens stem	√	√	√	√	x	x	x	x	x

x= not exist; √ = exist

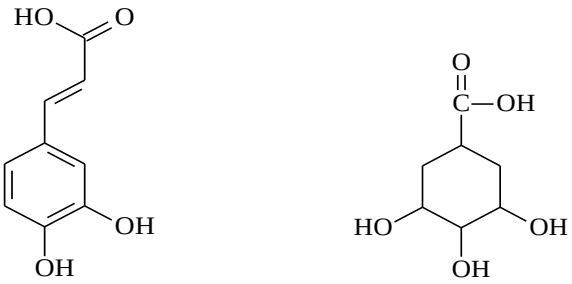
Hex=hexane extract; EA=ethyl acetate extract; MeOH= methanol extract

*using vanillin/H_2SO_4 spraying reagent; **using Dragendorff's spraying reagent; ***Ferric chloride spraying reagent.



2 **3**

Figure 2. The suggested structures for terpenoid saponin (**2**) and hydroxycinnamic acid ester (**3**)



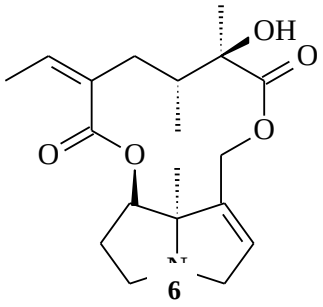
4 **5**

Figure 3. The suggested structures for caffeic acid **(4)** and quinic acid **(5)**

Table 3. FTIR spectroscopy of functional groups present in plant extracts of *C. caudatus*, *M. koenigii*, and *G. procumbens*

Extract	***C. caudatus*** **Leaves**		***M. koenigii*** **Leaves**		***G. procumbens*** **Leaves**		***G. procumbens*** **Stem**	
Hex	WN(cm^{-1})	FG	WN(cm^{-1})	FG	WN(cm^{-1})	FG	WN(cm^{-1})	FG
	3332.65	O-H	3374.79	O-H	3404.20	N-H	3418.62	O-H
	1651.45	C=O	2919.38	sp^3C-H	2850.09	sp^3 C-H	2915.19	sp^3C-H
	1603.23	aromatic	2850.83	sp^3C-H	2917.62	C-H	1740.98	C=O
	1200.69	C-O	1712.37	C=O	1735.12	C=O	1050.95	C-N
					1010.60	C-N		
EA	3334.60	O-H	1619.06	C=C	3383.74	O-H	3385.93	O-H
	2919.73	C-H	2918.89	sp^3C-H	2917.50	sp^3 C-H	2919.56	sp3C-H
	1611.08	aromatic	2850.81	sp^3C-H	2849.79	sp^3 C-H	1710.87	C=O
	1060.58	C-O	3352.25	O-H	1734.75	C=O		
MeOH	3259.13	O-H	3355.09	O-H	3362.10	O-H	3385.57	O-H
	1601.94	aromatic	2924.63	sp^3C-H	2919.14	sp^3 C-H	2919.21	sp^3C-H
	1057.32	C-O	2853.92	sp^3C-H	2851.04	sp^3 C-H	1600.25	C=C
					1632.08	C=C		

Hex = hexane; EA=ethyl acetate; MeOH= methanol; WN=wave number; FG=functional group



6

Figure 4. The suggested structures for alkaloid derivatives **(6)**

Table 4. General information on types of proton from ^{1}H-NMR spectrum

Species	**Range of Chemical Shift (ppm)**	**Types of Proton**
Compound from *C. caudatus*	0.9 - 1.5	R-CH_3
	1.2 - 1.4	R2-CH_2
	1.4 - 1.7	R3-CH
	0.5 - 5.0	R-OH
	4.5 - 5.0	sugar moiety/Ph-OH
Compound from *M. koenigii*	0.7 - 2.1	R-CH_3, R2-CH_2, R3-CH
	4.5 - 5.0	sugar moiety/R-OH
	4.5 - 6.5	C=C-H
	6.5 - 7.5	Benzene proton/ring
Compound from *G. procumbens* leaves	0.7 - 2.1	R-CH_3, R2-CH_2, R3-CH
	3.0 - 4.0	CH_2-O
	4.5 - 6.0	H-C=C-, OH
Compound from *G. procumbens* stem	0.7 - 2.1	R-CH_3, R2-CH_2, R3-CH
	3.0 - 3.5	CH_2-NR_2, CH_2-C=C-
	4.5 - 5.0	OH, CH_2-O

Conclusion

In conclusion, the methanol extract of *C. caudatus* leaves extract is regarded as the most active extract based on its higher inhibition zone against *E. chrysanthemi* compared to other plant extracts. Phenolic compound rutin **(1)** is suggested as the proposed anti-soft rot agent from methanol extract of *C. caudatus*. Other anti-soft rot agents are proposed as terpenoid saponin **(2),** hydroxycinnamic acid **(3),** ester caffeic acid **(4),** quinic acid **(5),** and alkaloid derivatives **(6)** from *M. koenigii* and *G. procumbens*. The establishment of antibacterial activity by evaluating the MIC as well as MBC values needed to be conducted. An extensive structure determination needs to be undertaken in detail such as 2D NMR analysis and LCMS to ascertain the anti-soft rot agent's structures.

Acknowledgement

The author would like to express the warmest gratitude to people who involve directly or indirectly for the completion of this research project.

References

1. Salehan, N. M., Meon, S. and Ismail, I. S. (2013). Antifungal activity of *Cosmos caudatus* extracts against seven economically important plant pathogens. *International Journal of Agriculture and Biology*, 15(5): 864-870.
2. Rasdi, N. H. M., Samah, O. A., Sule, A. and Ahmed, Q. U. (2010). Antimicrobial studies of *Cosmos caudatus* kunth.(compositae). *Journal of Medicinal Plants Research*, 4(8): 669-673.
3. Handral, H. K., Pandith, A. and Shruthi, S. D. (2012). A review on *Murraya koenigii*: Multipotential medicinal plant. *Asian Journal of Pharmaceutical and Clinical Research*, 5: 5-14.
4. Subramanian, P. (2015). *Murraya koenigii* (Curry leave)- a review on its potential. *International Journal of PharmTech Research*, 7(4): 566-572.
5. Kumar, N. S., Simon, N. and Santhoshkumar, R. (2016). Invitro antimicrobial activity and phytochemical analysis of *Murraya koenigii* leaf extracts. *Global Journal of science Frontier Research*, 11(2): 17-20.
6. Tan, H. L., Chan, K. G., Pusparajah, P., Lee, L. H. and Goh, B. H. (2016). *Gynura procumbens*: An overview of the biological activities. *Frontiers in Pharmacology*, 7: 52.
7. Maha Yudden, N. K., Nordin, N. N., Harun, A., Mohd Rosli, N. H., Abdul Aziz, N. and Daud, S. (2019). Comparative study of antioxidant activity of stem and leaves of *Entada spiralis* and their antibacterial properties against *Erwinia chrysanthemi*. *Science Letters*, 13: 37-47.
8. Abdul Majid, N. and Harun, A. (2019). Isolation and tentative identification of antioxidative constituents from dichloromethane extract of *Muraya koenigii* leaves using chromatographic technique. *Gading Journal of Science and Technology*, 2: 31-37.
9. Mohd Padli, N. F. F., Sulaiman, S. N. A., Daud, S., Harith, S. S. and Abdul Aziz. N. (2019). Antioxidative constituents from twig and leaves of *Jasminum Sambac. Gading Journal of Science and Technology*, 2(2): 8-16.
10. Abdullah, E., Ahmad Raus, R. and Jamal, P. (2012). Extraction and evaluation of antibacterial activity from selected flowering plants. *American Medical Journal*, 3(1): 27-32.
11. Caunii, A., Pribac, G., Grozea, I., Gaitin, D. and Samfira, I. (2012). Design of optimal solvent for extraction of bio–active ingredients from six varieties of *Medicago sativa. Chemistry Central Journal*, 6(1): 123.
12. Zongo, F., Ribuot, C., Boumendjel, A. and Guissou, I. (2013). Botany, traditional uses, phytochemistry and pharmacology of *Waltheria indica L.*(syn. *Waltheria americana*): A review. *Journal of Ethnopharmacology*, 148(1):14-26.
13. Cushnie, T. T. and Lamb, A. J. (2011). Recent advances in understanding the antibacterial properties of flavonoids. *International Journal of Antimicrobial Agents*, 38(2): 99-107.
14. Mediani, A., Abas, F., Khatib, A., Maulidiani, H., Shaari, K., Choi, Y. H. and Lajis, N. H. (2012). 1H-NMR-based metabolomics approach to understanding the drying effects on the phytochemicals in *Cosmos caudatus*. *Food Research International*, 49(2): 763-770.

15. Guardia, T., Rotelli, A. E., Juarez, A. O. and Pelzer, L. E. (2001). Anti-inflammatory properties of plant flavonoids. Effects of rutin, quercetin and hesperidin on adjuvant arthritis in rat. *Il farmaco*, 56(9): 683-687.
16. Matijasevic, D., Pantic, M., Raskovic,B., Pavlovic,V., Duvnjak, D., Sknepnek, A, and Niksi, C. M. (2016). The antibacterial activity of *Coriolus versicolor* methanol extract and its efficient on ultrastructural changes of *Staphylococcus aureus* and *Salmonella Enteritidis*. *Frontier Microbiology*, 2016: 7-12.
17. Sanver, D., Murray, B. S., Sadeghpour, A., Rappolt, M. and Nelson, A. L. (2016). Experimental modelling of flavonoid–biomembrane interactions. *Langmuir*, 32: 13234-13243.
18. Zain, I. K. (2017). Effect of Cadmium and Copper Exposure on Growth, Secondary Metabolites and Antioxidant Activity in Cadmium (Cd). *Molecules*, 22(10):1623.
19. Dixon, R. A. (2001). Natural products and plant disease resistance. *Nature*, 411(6839): 843-847.
20. Murugesu, K., Mohammed Saghir, S. A., Sadikun, A., Khaw, K. Y. and Murugaiyah, V. (2020). Exploiting column chemistry for chromatographic separation and quantification of caffeoylquinic acids in *Gynura procumbens*. *Acta Chromatographica*, 2020: 1-9.
21. Schramm, S., Kohler, N. and Rozhon, W. (2019). Pyrrolizidine alkaloids: biosynthesis, biological activities and occurrence in crop plants. *Molecules*, 24: 1-44.

Malaysian Journal of Analytical Sciences (MJAS)
Published by Malaysian Analytical Sciences Society

PREPARATION AND CHEMICAL COMPOSITION OF ALKALINE WATER FROM PLANT COMBUSTION ASH

(Penyediaan dan Komposisi Kimia Air Beralkali dari Abu Loji Pembakaran)

Pairin Pongsa and Napa Tangtreamjitmun*

Department of Chemistry, Faculty of Science,
Burapha University, Bangsaen, Chonburi, 20131 Thailand

**Corresponding author email address: napa@buu.ac.th*

Received: 9 December 2020; Accepted: 18 January 2021; Published: 20 February 2021

Abstract

The alkaline water prepared from burning natural materials into ash and submersing the ash in water was studied. The combustion time and the percentage of ash obtained for each material were different. The major chemical components of the ash were identified by Fourier Transform Infrared Spectroscopy. The main functional groups found were carbonate and hydroxide. The alkaline water which had a pH of 11-12 was filtered and studied for its chemical composition. The alkalinity in terms of hydroxide, carbonate and bicarbonate species was determined by acid titration. The sodium, potassium, calcium and magnesium content were determined by Inductively Coupled Plasma Optical Emission Spectrophotometer. The major cations found were potassium and sodium. The concentrations and pH of the alkaline water that would be obtained after dilution should be suitable for human consumption although further medical testing is required.

Keywords: alkaline water, lye water, ash, alkalinity

Abstrak

Air beralkali telah disediakan dari pembakaran bahan semulajadi kepada abu dan kebolehan tenggelan abu di dalam air telah dikaji. Masa pembakaran dan peratus abu yang diperolehi bagi setiap bahan adalah berbeza. Komponen kimia utama bagi abu telah dikenalpasti menggunakan Spektroskopi Inframerah Transformasi Fourier. Kumpulan berfungsi utama yang ditemui adalah karbonat dan hidroksida. Air beralkali yang mempunyai nilai pH 11-12 telah dituras dan dikaji komposisinya. Sifat kealkalian seperti spesis hidroksida, karbonat dan bikarbonat telah ditentukan melalui pentitratan asid. Kandungan sodium, kaliam, kalsium and magnesium telah di analisis menggunakan Spektrofotometer Sebaran Optikal – Plasma Gandingan Aruhan. Kation utama yang dijumpai adalah kalium dan sodium. Kepekatan dan nilai pH air beralkali diperolehi selepas pencairan sesuai bagi penggunaan manusia meskipun ujian perubatan lanjutan masih diperlukan.

Kata kunci: air beralkali, air abu, abu, kealkalian

Introduction

Alkaline water or lye water is made by submersing plant ash in water for a length of time. The soluble salts in the ash dissolve, resulting in basic water. This is how people in the past used to produce alkaline water for their own consumption in the household. This process has been known since ancient times. The alkaline water was called "Kan Sui" in Cantonese [1]. Kan Sui has been used for making noodles turn into yellow color with a firm and elastic texture. It is also used to refresh dry squid and sea cucumber. In Eastern European region, lye water is used to make a brown surface of breads, such as bagels and pretzels.

Currently, alkaline water can also be produced by electrolysis process. The produced alkaline ionized water (AIW) or alkaline reduced water (ARW) was reported to have clinical effects due to its antioxidant properties in treatment and prevention of diseases [2, 3]. Drinking alkaline water is popular among people, who are concerned about their health. Most consumers believe that the basic properties of alkaline water will help balance the acid-base equilibrium in the body caused by some acidic foods.

Food grade lye water produced from potassium carbonate is commercially available nowadays. But the preferred method of naturally alkaline water making from plant ash is still used in some parts of the world. In Thailand, the bottled alkaline water is sold in the form of concentrated alkaline water produced from coconut husk ash. There is usually a label indicating "Concentrated alkaline water" and the recommended dilution ratio for drinking. Therefore, this research has studied the factors that affect the preparation of alkaline water from different plant ash and its chemical composition which should be useful information for consumers.

Materials and Methods

Ash production and its chemical composition

The leaf samples from six edible trees and coconut husk (shown in Figure 1) were sun dried for 5 days. 50 grams of each dried sample was then combusted in a basin on a gas stove in the fume hood. The time spent in combustion until the leaves turn to ash was recorded. The ash was weighed and the percentage of ash obtained from the dry weight of the leaf sample was calculated. The ash was analyzed for chemical composition by Fourier Transform Infrared Spectrophotometer (FTIR) (System 2000, Perkin Elmer, USA).

Preparation and pH measurement of alkaline water

Deionized water (E-Pure Barnstead 3 column Model D4632, Thermo Fisher Scientific, USA) was used to extract the ash. The ash and water were mixed at ratios of 1:5 and 1:100 (g:mL) and submersed for 12 hours. The suspension was filtered and the pH of the alkaline water was measured.

The ash was mixed with water at a ratio 1:5 and the pH of the suspension was measured at 10, 30, 60, 120 and 720 minutes. The ash was mixed with water at a ratio 1:5. The pH of the suspension was measured after 10 minutes. The suspension was then filtered and the same volume of fresh water was added to the solids. The pH was measured after 10 minutes. This was repeated until the pH value was constant for 3 consecutive times.

The chemical composition of alkaline water

The alkaline water set 1 was obtained from submersion of ash at a ratio 1:5 for 12 hours. After the alkaline water was removed, fresh water was added to re-submerse the ash at the same conditions. The process was repeated twice, in order to obtain alkaline water set 2 and set 3. Then the three sets of prepared alkaline water samples and alkaline water samples sold in health stores were titrated with acid to determine alkalinity using the procedure in Standard Methods for the Examination of Water and Wastewater [4].

Sodium, potassium, calcium, and magnesium were analyzed in purchased alkaline water samples. The samples were digested with 10% HCl in an ultrasonic bath (690D, Crest Ultrasonics Corp., USA) for 20 min. A mixed standard solution of sodium, potassium, calcium, and magnesium (Mono-element standard Solution for AAS, Loba Chemie, India) was prepared to

make a calibration curve. All solutions were analyzed by Inductively Coupled Plasma Optical Emission Spectrophotometer (ICP-OES) (PlasmaQuant® PQ 9000, Analytik Jena AG, Germany).

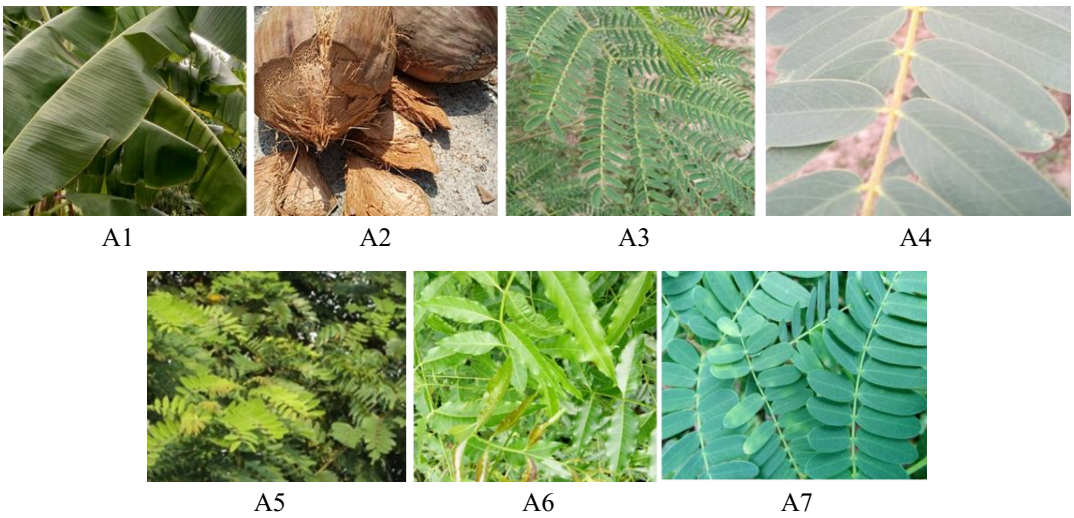


Figure 1. Fresh plant leaves and dry coconut husk used in combustion to produce ash; A1: Banana leaf (*Musa sapientum Linn.*) A2: Coconut husk (*Cocos nucifera Linn.*) A3: Acacia leaf (*Leucaena leucocephala (Lamk.*) de Wit) A4: Sesbania grandiflora leaf (*Sesbania grandiflora (L.) Pres.*) A5: Cassia leaf (*Cassia siamea Britt.*) A6: Neem leaf (*Azadirachta indica var. siamensis Valeton*) A7: Tamarind leaf (*Tamarindus indica Linn.*)

Results and Discussion

Ash production

During the combustion process, the dry sample first turned into a black ash. Then, after a period of time, the black ash turned white to grayish white or light brown depending on the type of plant (as shown in Figure 2).

All leaf samples took less time for combustion than coconut husk. The coconut husk took almost 6 hours for combustion and gave the lowest percentage of ash (4.5%) as shown in Figure 3. The other samples gave a percentage ash between 6.8-10.3. Sesbania grandiflora leaf, cassia leaf, banana leaf and acacia leaf had the lowest combustion time about 1 hour. Sesbania grandiflora leaf gave the highest percentage of ash 10.3. Tamarind and neem leaves took about 1.5 hours to complete combustion. Tamarind leaves gave 10.1% ash, but takes about half an hour more combustion time than Sesbania grandiflora leaves. It can be seen that leaves yield more ash than the stem. Stem combustion yields about 0.2-1% ash but occasionally gave 3-4% [5]. According to past research, bark and leaves produce more ashes than the core of the stem [6].

Chemical composition of ash

Ash was analyzed by FTIR for functional groups. The IR spectra in Figure 4 showed a fairly wide peak of -OH- at about 3400 cm^{-1} and a peak of Si-O at about 1100 cm^{-1}[7]. The 1400 cm^{-1} peak was the C-O stretching and bending bond in the CO_3^{2-} group of calcium carbonate [8]. In addition, the spectrum of all ash, except banana leaves and coconut husk contained a sharp peak at about 900 cm^{-1} due to SO_4^{2-} [7].

Ash from hardwood normally contains 80% of water insoluble constituents. The remaining soluble inorganic compounds are potassium carbonate (K_2CO_3), soda ash (Na_2CO_3), arcanite (K_2SO_4), and calcium hydroxide $Ca(OH)_2$. However, if the temperature is above 600 $^{\circ}C$ potassium carbonate decomposes to potassium oxide

(K_2O) [9]. The gas stove used in this study could only provide a temperature of about 250 °C thus potassium oxide should not be produced in this combustion process.

These soluble compounds are important in the uses of alkaline water from ash. Based on the spectra shown in Figure 4, all ash contains carbonate (CO_3^{2-}) and hydroxide (OH^-) groups as the anion of soluble inorganic components in the ash. It is apparent that ash from the leaves and coconut husk will have an ash component that is similar to that of hardwood ash.

Factors affecting alkaline water preparation: Mixing ratio of ash to water

The pH of alkaline water produced from mixing ratios of 1:5 and 1:100 were between 11.2-12.5 and 10.1-11.3, respectively. Alkaline water is generally sold in concentrated form in bottles with pH 10-12. Therefore, ratios between 1:5 and 1:100 could be used for alkaline water preparation. The consumer would have to dilute concentrated alkaline water about 50-100 times as specified on label typical to prepare it for drinking. The pH of the diluted alkaline water for drinking would be about 8.5 as this is the upper limit of pH for standard drinking water (Ministry of Public Health, Thailand (No. 256; 2000). The 1:5 ratio was used for alkaline water preparation in all experiments in this work.

Optimum submersion time

The pH of alkaline water obtained by ash submersion in water at various times did not vary by more than 0.5 over 12 hours as shown in Figure 5.

However, long submersion times provided good settling of non-soluble ash and resulted in clearer alkaline water, which would be more pleasant to drink. In addition, it was found that alkaline water produced from neem leaf (A6) ash gave the highest pH value of 12.5. The coconut husk (A2) ash produced alkaline water with the lowest pH of 11.2.

Re-submersion of ash

The pH of alkaline water from re-submersion of the ash every 10 minutes gradually decreases. Once the ash has been re-submersed for 35 times, the pH stayed almost constant about 8.6-9.0. Thus the ash can be re-submersed for about 35 times in the production of alkaline water. However, the pH value alone does not indicate the water capacity of alkaline water to neutralize acid. Therefore, the alkalinity of water, which was defined as water capacity to neutralize acid [10] was studied in the next section. The capacity of water in this context indicates the “buffering capacity”.

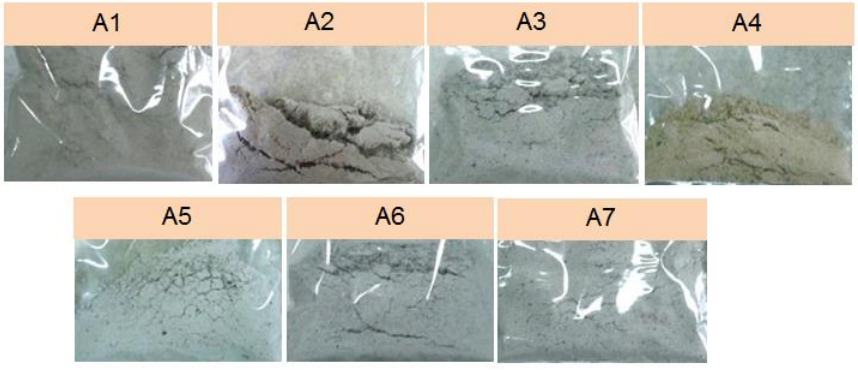


Figure 2. The combustion ash obtained from various leaves and coconut husk

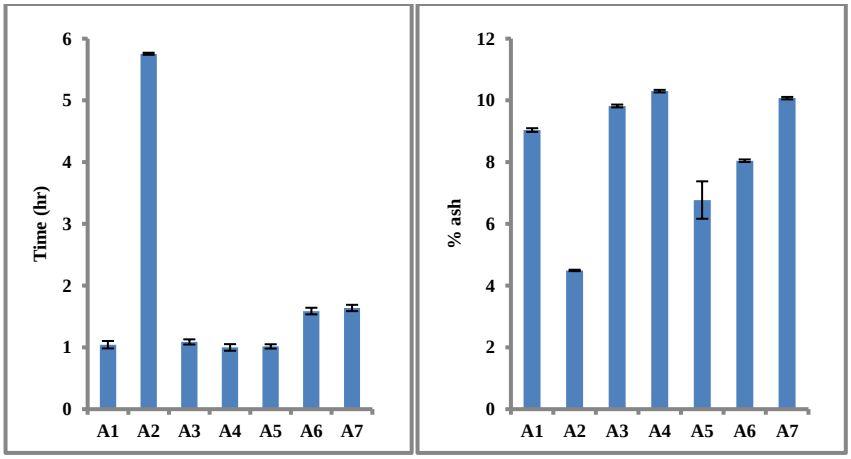


Figure 3. Combustion time (left) and percentage of ash (right) produced from different plant combustion. A1: Banana leaf, A2: Coconut husk, A3: Acacia leaf, A4: Sesbania grandiflora leaf, A5: Cassia leaf, A6: Neem leaf, A7: Tamarind leaf

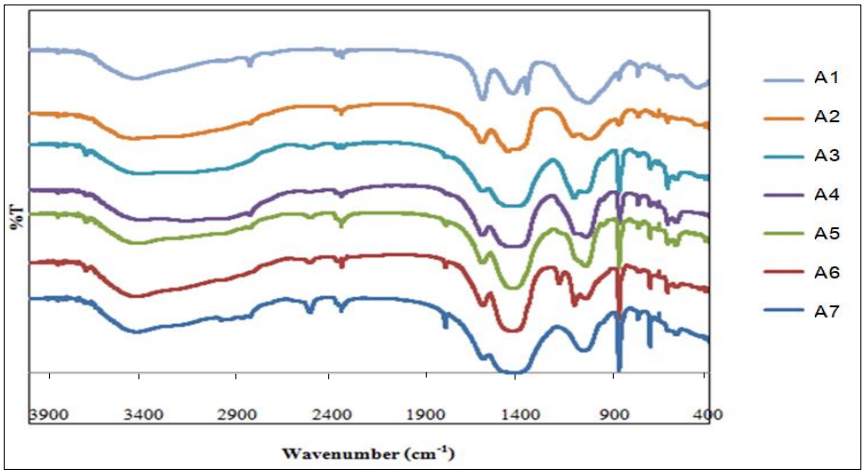


Figure 4. Infrared spectrum of different ash samples. From top to bottom; A1: Banana leaf, A2: Coconut husk, A3: Acacia leaf, A4: Sesbania grandiflora leaf, A5: Cassia leaf, A6: Neem leaf, A7: Tamarind leaf

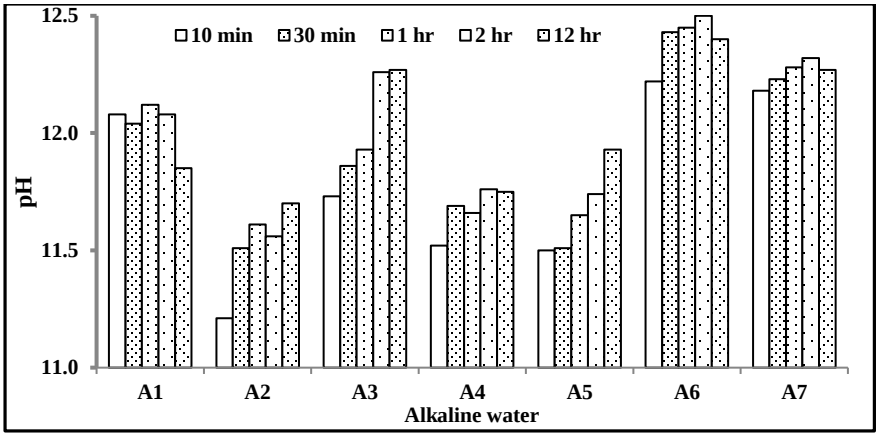


Figure 5. pH of alkaline water using a submersion ratio 1:5 at various submersion time. The alkaline water from different ash samples: A1: Banana leaf, A2: Coconut husk, A3: Acacia leaf, A4: Sesbania grandiflora leaf, A5: Cassia leaf, A6: Neem leaf, A7: Tamarind leaf

Chemical composition of alkaline water: **Alkalinity**

The alkalinity titration for three sets of alkaline water is shown as mg L^{-1} $CaCO_3$ in Table 1. According to the high pH of all alkaline water samples (pH>11), no hydrogen carbonate were found as alkalinity species in these seven samples. Carbonate (CO_3^{2-}) was the main alkalinity species for all samples except A1 (banana leaf) in set 1 (obtained from the first submersion). For the banana leaf ash, hydroxide was the only alkalinity species found in the set 1 alkaline water. The alkaline water from Sesbania grandiflora leaf ash (A4) contained only the weak base carbonate (CO_3^{2-}) in every set, which is a good buffering system for acid neutralization. Therefore, Sesbania grandiflora leaf ash produces the best alkaline water in terms of acid neutralization. The total alkalinity was also high (32,578 mg L^{-1} $CaCO_3$).

For the other leaves, the strong base hydroxide ion (OH^-) was found in alkaline water obtained in the second and third submersion (set 2 and set 3). It can be concluded that, re-submersion of ash should be avoided, in order to exclude hydroxide ions from the alkaline water produced. Because $Ca(OH)_2$ found in ash is a sparingly soluble salt and it will dissolve less in basic solutions of the first submersion. But in re-submersion solution, fresh water (pH 7) will dissolve $Ca(OH)_2$ resulting in release of hydroxide ions. Therefore, hydroxide ions can be found only in A1 and A6 for set 1. For the first submersion, K_2CO_3 or Na_2CO_3 will dissolve first to release carbonate ion. Hydrogen carbonate ion cannot be found in chemical equilibrium with the carbonate ion in high pH solutions.

Banana leaf (A1) is different from the other leaves. The composition of the ash may therefore differ from the other ashes. The strong base hydroxide ion was found in three sets of alkaline water. The carbonate ion was obtained only in the second and third submersion. The total alkalinity obtained from banana leaves were the lowest quantity among all leaves. The hydroxide ion is not a buffer, thus the neutralization reaction was very strong, resulting in a large change of pH. Thus, ash from banana leaf is considered not to be suitable for making alkaline water.

Coconut husk is commonly used in making ash for alkaline water because it can be easily found as a waste in the community. The obtained alkaline water has a very high alkalinity and carbonate concentration. But it is recommended that ash should not be reused to make alkaline water because hydroxide ions will be released.

The alkalinity of alkaline water samples bought from stores is shown in Table 2. Sample B1 and B2 contained hydroxide and carbonate species similar to the re-submersion alkaline water; set 2 and 3 in Table 1 (except

A4; Sesbania grandiflora leaf). Sample B 3contained only carbonate. For sample B4, which is a diluted ready to drink alkaline water produced from an electrolysis machine, contained only hydrogen carbonate in a very low amount.

Cation analysis by ICP-OES

The alkaline water samples bought from stores (B1, B2, B3) were labeled "made from coconut husk ash" and thus should be similar to alkaline water prepared in the laboratory. The amount of cations in alkaline water B1, B2, B3 were determined and compared to alkaline water produced by the electrolysis machine (B4). The results are shown in Table 3.

The highest amount of potassium was detected in concentrated alkaline water samples bought from stores. The potassium ion possibly came from K_2CO_3 and K_2SO_4, the water-soluble salts in ash. Sodium and calcium were also detected but magnesium was present at much lower concentrations. This result agrees to the solubility product constant of $Ca(OH)_2$ (5.0×10^{-6}) compared to $Mg(OH)_2$ (5.6×10^{-12}). The alkaline water produced from an electrolysis machine (sample B4) contained very low levels of Na and K. However, Ca and Mg were found in higher amount than other alkaline samples made from ash. They could have been added during production.

Table 1. Alkalinity values of alkaline water samples prepared from different ash samples (n=3)

Alkaline Water	Alkalinity (±sd) (mg L^{-1} $CaCO_3$)						Total alkalinity (±sd) (mg L^{-1} $CaCO_3$)
	Set 1		Set 2		Set 3		
	OH^-	CO_3^{2-}	OH^-	CO_3^{2-}	OH^-	CO_3^{2-}	
A1	987 (±21)	-	104 (±4.9)	1002 (±0)	430 (±87)	568 (±87)	3091 (±108)
A2	-	25010 (±206)	2527 (±125)	5365 (±170)	982 (±7)	4252 (±27)	38136 (±296)
A3	-	25461 (±2398)	604 (±31)	9671 (±490	572 (±112)	3109 (±151)	39417 (±2454)
A4	-	20040 (±71)	-	6804 (±125)	-	5734 (±23)	32578 (±146)
A5	-	20302 (±1573)	662 (±70)	9625 (±20)	253 (±14)	4252 (±48)	35094 (±1575)
A6	1474 (±41)	21848 (±418)	835 (±47)	13954 (±599)	994 (±45)	4483 (±457)	43588 (±865)
A7	-	15453 (±337)	979 (±101)	5837 (±151)	606 (±13)	2287 (±13)	25162 (±383)

Table 2. Alkalinity of alkaline water bought from stores (n=3)

Sample	Alkalinity (±sd) (mg L^{-1} $CaCO_3$)			Total alkalinity (±sd)
	OH^-	CO_3^{2-}	HCO_3^-	(mg L^{-1} $CaCO_3$)
B1	561 (±51)	803 (±65)	-	1364 (±82)
B2	91 (±6)	750 (±24)	-	841 (±25)
B3	-	1576 (±21)	-	1576 (±21)
B4*	-	-	70 (±9.7)	70 (±9.7)

*B4 is a ready to drink alkaline water

Table 3. The amount of cation (mg L^{-1}) found in alkaline water samples determined by ICP-OES

Sample	Na	K	Ca	Mg
B1	396±13	1367±16	72±8	nd*
B2	494±7	2152±12	19±6	0.064±0.00
B3	693±3	1993±14	64±2	nd*
B4	26±2	90±0.4	163±5	4.07±0.06

* nd = not detected (LOD = 0.30 μg L^{-1})

Conclusion

Analysis of cations and anions detected in alkaline water made from ash confirmed that potash (K_2CO_3) was the major component of soluble salts found in ash. The exception was ash from banana leaves that could contain $Ca(OH)_2$ and K_2CO_3/Na_2CO_3 in similar amounts. Ash from different plants yielded slightly different alkaline species in alkaline water. Re-submersion of ash or boiling ash should not be done, in order to avoid hydroxide ion formation. We concluded that ashes obtained from the different plants studied should be suitable as alkaline water for human consumption or in the production of various food products although further medical testing is required.

Acknowledgement

We would like to thank Analytik Jena Far East (Thailand) Ltd. for their support of the use of ICP-OES instrument. We thank Dr. Ron Beckett for helpful proofreading and suggestions concerning the manuscript.

References

1. Fu, B. X. (2008). Asian noodles: History, classification, raw materials, and processing. *Food Research International,* 41: 888-902.
2. Ignacio, R. M., Joo, K. B., and Lee, K. J. (2012). Clinical effect and mechanism of alkaline reduced water. *Journal of Food and Drug Analysis,* 20(1): 394-397.

3. Shirahata, S., Hamasaki, T. and Yeruya, K. (2012). Advanced research on the health benefit of reduced water. *Trends in Food Science & Technology,* 23: 124-131.
4. APHA. (2012). No. 2320 B: Titration Method. Standard Methods for the Examination of Water and Wastewater. 22nd ed. American Public Health Association, Washington, D.C.
5. Berg, M.G. Fertilizer guide. (1982). Using Wood Ashes in the Home Garden. Oregon state university extension service. https://ir.library.oregonstate.edu/downloads/2j62s561s [Access online 15 May 2019].
6. Rafat, S. (2012). Utilization of wood ash in concrete manufacturing. *Resources Conservation and Recycling,* 67: 27-33.
7. Martins, F. M., Martins J. M., Ferracin L. C. and Cunha, C. J. (2007). Mineral phases of green liquor dregs, slaker grits, lime mud and wood ash of a Kraft pulp and paper mill. *Journal of Hazardous Materials,* 147: 610-617.
8. Adler, H. H. and Kerr, P. F. (1963). Infrared absorption frequency trends for anhydrous normal carbonates. *The American Mineralogist,* 48: 124-137.
9. Misra, M. K., Ragland, K.W. and Baker, A. J. (1993). Wood ash composition as a function of furnace temperature. *Biomass and Bioenergy,* 4(2): 103-116.
10. US-EPA. (1994). EPA's drinking water glossary: A dictionary of technical and legal terms related to drinking water, EPA810-B-94-006, Environmental Protection Agency, Washington, DC. USA.

Malaysian Journal of Analytical Sciences (MJAS)
Published by Malaysian Analytical Sciences Society

SYNTHESIS, CHARACTERIZATION AND ELECTROCHEMICAL STUDIES OF TRANSITION METAL COMPLEXES CONTAINING 3,6-BIS(3,5-DIMETHYLPYRAZOLYL) PYRIDAZINE LIGAND

(Sintesis, Pencirian dan Kajian Elektrokimia bagi Kompleks Logam Peralihan Mengandungi Ligan 3,6-Bis(3,5-Dimetilpirazolil) Piridazina)

Shankary Selvanathan and Woi Pei Meng*

Department of Chemistry, Faculty of Science,
Universiti Malaya, 50603 Kuala Lumpur, Malaysia

**Corresponding author: pmwoi@um.edu.my*

Received: 2 November 2020; Accepted: 21 January 2021; Published: 20 February 2021

Abstract

Four novel coordination complexes were synthesized based on 3,6-bis (3,5-dimethylpyrazolyl) pyridazine ligand with Cu(II), Fe(II), Ni(II) and Co(II) metals. The synthesized complexes were characterized using several analyses. The infrared (IR) spectra for all the complexes showed a significant shift at the ligand methyl group (C-H), pyrazole ring (C=N), pyridazine ring (C-N) and (N-N) at 2926 cm^{-1}, 1137 cm^{-1}, 1162 cm^{-1} and 970 cm^{-1}, respectively. The elemental analyses of the complexes confined to the stoichiometry of 1:2 ratio between the ligand and the metal cation. The presence of the metal in the complexes was confirmed using the FESEM-EDX analysis. The complexation of the metals to the ligand was evidenced when all the complexes exhibit a significant shift in the position of the characteristic ligand band at around 260 nm due to the HOMO → LUMO $\pi \rightarrow \pi^*$ transitions of the pyridazine and pyrazoles groups in the UV-Vis spectrum. Cyclic voltammetry (CV) method was used to explore the redox characteristics of the complexes. The Cu(II), Fe(II) and Ni(II) complexes exhibited quasi-reversible single electron transfer process while no peak was observed in Co(II) complex upon scanning from -1.5 to 1.5 V vs. Ag/AgCl. This observation is speculated to be the effect of poor complexation in between the metal and the ligand. The potential recorded for Cu(II) complex at 0.03 V vs. Ag/AgCl was corresponded to the reduction of Cu(II) to Cu(I) while the potential at 0.75 V was due to the oxidation of Cu(I) to Cu(II). For the Fe(II) complex, the redox couple Fe(II)/Fe(III) was recorded at -0.47 V and -0.67 V during its oxidation and reduction process respectively. Finally, the peak at 0.71 V in the CV of Ni(II) complex is attributed to its oxidation process of Ni(I) to Ni(II) while the peak at 0.12 V is due to its reduction from Ni(II) to Ni(I).

Keywords: pyridazine, transition metal, coordination complex, electrochemical behavior

Abstrak

Empat kompleks koordinatan novel telah disintesis berdasarkan ligan 3,6-bis(3,5-dimetilpirazolil) piridazina dengan logam Cu(II), Fe(II), Ni(II) dan Co(II). Kompleks yang disintesis dicirikan dengan beberapa kaedah analisis. Spektrum IR bagi kesemua kompleks menunjukkan perubahan yang ketara pada kumpulan metil ligan (C-H), lingkaran pirazol (C=N), lingkaran piridazina (C-N) and (N-N) masing-masing pada 2926 cm^{-1}, 1137 cm^{-1}, 1162 cm^{-1} and 970 cm^{-1}. Analisis unsur kompleks membataskan nisbah stoikiometri ligan: logam kepada 1: 2. Kehadiran logam dalam kompleks juga telah disahkan menerusi analisis FESEM-

EDX. Pembentukan kompleks bersama logam dan ligan disahkan lebih lanjut kerana semua kompleks mempamerkan perubahan yang sangat ketara dalam pencirian pada 260 nm kerana peralihan HOMO → LUMO π → π* dalam lingkaran pirazol and piridazina menerusi spektrum UV-Vis. Sifat redoks kompleks telah disiasat dengan kaedah elektrokimia voltammetri kitaran (CV). Kompleks Cu(II), Fe(II) dan Ni(II) mempamerkan proses pemindahan elektron tunggal yang seakan-balik manakala tiada puncak diperhatikan bagi kompleks Co(II) apabila kesemua kompleks ini diimbas pada potensi -1.5 ke 1.5 V vs. Ag/AgCl. Potensi untuk kompleks Cu(II) pada 0.03 V vs. Ag/AgCl sepadan dengan penurunan Cu(II) kepada Cu(I) manakala potensi pada 0.75 V adalah disebabkan oleh pengoksidaan Cu(I) kepada Cu(II). Bagi kompleks Fe(II), pasangan redoks Fe(II)/Fe(III) mencatatkan potensi masing-masing pada -0.47 V dan -0.67 V semasa proses pengoksidaan dan penurunan. Akhirnya, potensi pada 0.71 V dalam voltammogram kitaran kompleks Ni(II) adalah disebabkan oleh proses pengoksidaan Ni(II) kepada Ni(I) manakala potensi pada 0.12 V adalah disebabkan oleh penurunan dari Ni(II) ke Ni(I).

Kata kunci: piridazina, logam peralihan, kompleks koordinatan, tindakan elektrokimia

Introduction

Coordination chemistry is an interesting field of study which assimilates both the traditional inorganic and organic chemistry disciplines by segregating a new class of compounds, comprising a central metallic atom bound to a group of organic molecules, known as metal complexes [1]. These metal complexes possess valuable chemical properties, which pave the way to a variety of applications, particularly as catalysts in various chemical reactions. One of such prospective applications is in the field of electrocatalysis.

Amongst all the other types of metal atoms, transition metals are the commonly used metal center in electrocatalytic metal complexes, namely in catalyzing reaction with having strong interests in environmental conservation such as hydrogen evolution, carbon dioxide reduction and water oxidation processes [2]. The first-row transition metals have been the center of attraction of this research due to a few advantages possessed by them. One of which is their lower toxicity property compared to other row transition metals which makes it a suitable choice of metals in order to pursue a green chemistry method. In addition, the 3d transition metals can be found more abundantly in nature.

The electronic arrangement of transition metals allows them to exist in a variety of oxidation states and they are also able to interchange between the oxidation states, form complexes with the reagent and be a good source for electrons. These characteristics help transition metal complexes to catalyze many redox reactions in nature. The catalytic ability of the transition metal complexes is exploited when it is coupled to an electrochemical cell in which it catalyzes the redox reactions of specific substrate. A fascinating feature in this application is the capacity to alter the potential of the redox reaction by manipulating the metal centers and the corresponding ligands [3].

One of the widely used ligands in coordination chemistry are pyridazines. The two nitrogen atoms in the heterocyclic structure of pyridazine allow it to coordinate with two metal centers close to each other [4]. On the other hand, pyrazole is classified as a five membered aromatic structure comprising three carbons and two nitrogens. The idea of having both the six-membered ring structure such as pyridazine and five-membered ring structure such as pyrazole combined as one ligand provides an interesting dimension and geometry upon binding with metals. In return, the complexes of such ligands are expected to have a different electronic properties [5].

The target ligand in this study, 3,6-bis-(3,5-dimethylpyrazolyl)-pyridazine is one of such unique ligand molecules that contain both pyridazine and pyrazolyl structures. The ability of the ligand to form a metallacycle leads to a stable mononuclear and polynuclear complexes [6]. However, by far in literature, most of the studies employing this ligand are focused on metals from the lanthanide series. An attempt to pair this ligand with first and second row transition metals for the synthesis of metal complexes is the novel idea being the focus in this study. Hence, in this work we aim to explore the effect of coordinating different

transition metal cations to 3,6-bis-(3,5-dimethylpyrazolyl) pyridazine, follows by investigation and characterization on the electrochemical behavior of the resulting metal complexes.

Materials and Methods

Chemicals and reagents

3,5-dimethylpyrazole ($C_5H_8N_2$, 99%, Aldrich), 3,6-dichloropyridazine ($C_4H_2Cl_2N_2$, 97%, Aldrich), copper(II) chloride dihydrate ($CuCl_2 \cdot 2H_2O$, 99%, Aldrich), iron(II) chloride tetrahydrate ($FeCl_2 \cdot 4H_2O$, 99%, Aldrich), nickel(II) chloride hexahydrate ($NiCl_2 \cdot 6H_2O$, 99%, Aldrich), cobalt(II) nitrate hexahydrate ($Co(NO_3)_2 \cdot 6H_2O$, 98%, Aldrich), sodium hydride (NaH, 90%, Aldrich) and anhydrous dimethylformamide (99.8%, Aldrich) were used as such without further purification.

Synthesis of 3,6-bis(3,5-dimethylpyrazolyl) pyridazine

As shown in Figure 1, 3,5-dimethylpyrazole (240.3 mg, 2.5 mmol) and sodium hydride (103.6 mg, 2.5 mmol) were put in the reaction flask under nitrogen gas purging. Anhydrous dimethylformamide (5 mL) was added into the flask. After one hour stirring, the solution was cooled to 0 °C after being kept in an ice bath. 3,6-dichloropyridazine (148.9 mg, 1.0 mmol) was added to the solution and the temperature was maintained at 0 °C for 30 minutes while stirring. The solution was stirred overnight at ambient temperature to yield the desired ligand. The resulting pale-yellow solution was mixed into ice water (100 mL) to obtain white filtrate solid. Synthesis route of the preparation is shown in Figure 2.

Synthesis of transition metal complexes

DPPMe (53.67 mg, 0.20 mmol) was dissolved in chloroform, $CHCl_3$ (5 mL). The appropriate metal salt (0.40 mmol) was dissolved in MeOH (5 mL) separately and was added dropwise into the previous solution. A colored solid precipitated immediately. The solution was continuously stirred for five hours. The precipitate was filtered and washed with methanol followed by drying in oven. Table 1 shows the mass of metal salts used in each complex.

Characterization

The proton nuclear magnetic resonance, ^{1}H-NMR for the ligand was measured by using the Bruker Advance 400. Deuterated chloroform, $CDCl_3$ was used as the solvent. Infrared spectra were obtained using attenuated total reflection (ATR) with model Perkin-Elmer 400 FT in the range of 4000-400 cm^{-1}. Carbon, Hydrogen and Nitrogen (CHN) analyzer of model TrueSpec Micro was used to analyze the ligand and metal complexes to determine respective elemental composition. Energy dispersive X-ray spectrometry was performed using INCAEnergy200 to determine the presence and distribution of the transition metal atoms in the metal complexes.

Solubility test

Solubility test was done on each of the synthesized metal complexes. Approximately 5 mg of the complex was measured and put into the test tubes containing various solvents such as chloroform, dimethyl sulfoxide, acetonitrile, ethanol, methanol, dimethyl formamide and tetrahydrofuran. The solubility of the complexes in each of the solvent was observed. The same procedure was repeated for the DPPMe ligand.

Electrochemical study

The electrochemical measurements were performed using potentiostat (AUTOLAB/PGSTAT 302N) which was run by Analysis of Variance software (ANOVA) installed in the computer. Ag/AgCl, platinum rod, and glassy carbon were used in the setup. Prior to the measurement, the metal complex solution was drop-casted on the glassy carbon electrode and left to dry overnight. A thin film of the metal complex was formed on the electrode. All the measurements were performed at room temperature in the potential range from -1.2 V to +1.6 V vs. Ag/AgCl with a scan rate from 10-100 mV s^{-1} and 0.10 M tetrabutylammonium perchlorate [$Bu_4N(ClO_4)$] was used as supporting electrolyte in dimethylformamide.

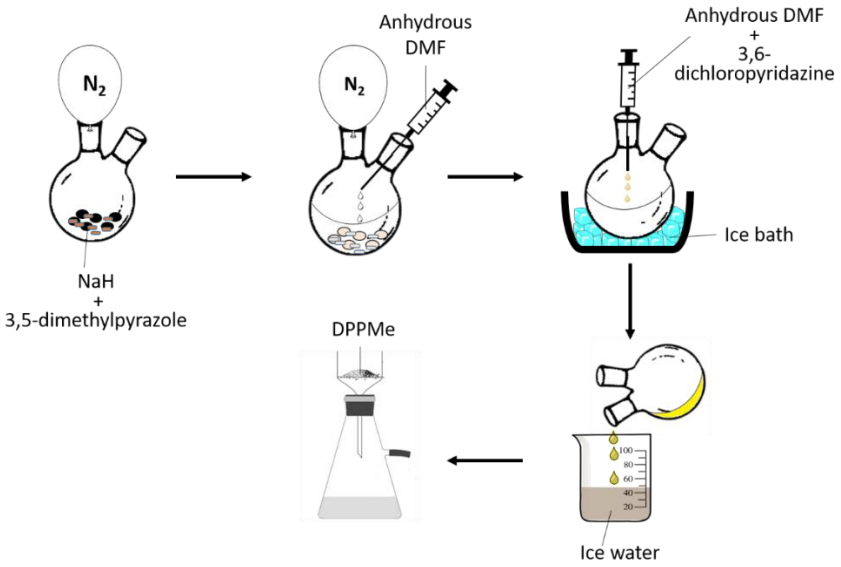


Figure 1. Reaction scheme for synthesis of DPPMe ligand

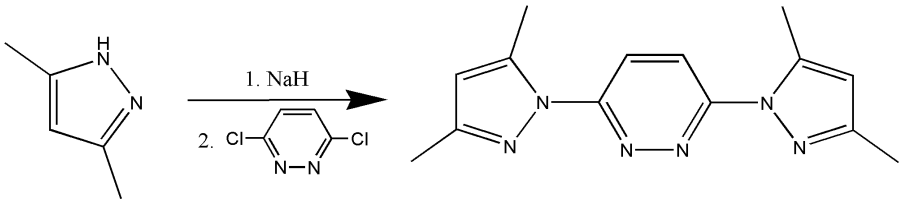


Figure 2. Synthetic route of DPPMe ligand

Table 1. Mass of metal salts used

Metal Salt	Mass (mg)	Yield Color	Designation
$CuCl_2 \cdot 2H_2O$	34.10	Pale green	Complex 1
$FeCl_2 \cdot 4H_2O$	39.76	Dark red	Complex 2
$NiCl_2 \cdot 6H_2O$	47.54	Dark green	Complex 3
$CoNO_3 \cdot 6H_2O$	47.59	Dark orange	Complex 4

Results and Discussion

^{1}H-NMR spectra of DPPMe ligand

The ^{1}H-NMR spectrum of the ligand was analyzed in $CDCl_3$ from δ 0.00 – 12.00 ppm. From the spectrum (Figure 3), it shows that the 3,6-dichloropyridazine has been successfully reacted to 3,5-dimethylpyrazole. The singlet peak attributed to the methyl protons is shifted to the upfield at δ 2.22 ppm (H-1) as they were close to the electrons in the ring structure which creates a deshielding effect from its huge anisotropic field. [7]. Furthermore, the protons in the aromatic ring of the pyridazine appeared as doublets and gave two different signals at δ 7.50 ppm (H-4) and δ 8.11 ppm (H-5). The proton in the pyrazole ring gives rise a singlet peak as

there is no neighboring protons to couple with at δ 6.09 ppm (H-3). The assignation of chemical shifts is summarized in Table 2.

IR spectra of DPPMe ligand and the metal complexes

IR spectroscopy confirmed the introduction of the 3,5-dimethylpyrazole into the pyridazine molecule at position 3 and 6 was confirmed by the appearance of new peaks in the spectrum. Figure 4 shows the IR spectrum of the ligand with each peak assignment color coordinated to its corresponding functional group. The spectrum exhibited new absorption peak at 2926 cm^{-1} which is attributed to the methyl group attached to the pyrazole group [8]. The absorption peaks observed at 1443 cm^{-1} and 1137 cm^{-1} correspond to the C-N and C=N stretching of the pyrazole structure respectively [9]. Besides that, the stretching of N-N in the pyridazine and pyrazole group has its own characteristic absorption peaks at 970 cm^{-1} and 1312 cm^{-1}, respectively. The C=N belonging to the pyridazine group was found at 1162 cm^{-1} [10]. When compared to the spectrum of the ligand as in Figure 5, the band attributed to C=N in the pyrazole ring at around 1125-1129 cm^{-1} in the metal complexes was shifted to lower wavenumber proving that the metal ion did form a bond with the nitrogen atom in the pyrazole structure [11]. The infrared band obtained at 1162 cm^{-1} in the free ligand spectrum corresponding to C=N of the pyridazine ring, has been shifted to a higher frequency region at 1168-1171 cm^{-1} in the metal complexes, indicating the participation of the pyridazine ring nitrogen atom as a possible bonding site. IR band observed at 970 cm^{-1} of N-N in the pyridazine, was also found shifted to a higher frequency region 988-996 cm^{-1} in complexes, which provide further information on the presence of pyridazine ring nitrogen atom in bonding. Table 3 summarized the comparison of infrared bands shifting.

Solubility test of synthesized metal complexes

The coordination of metal ions with the ligand had changed the solubility properties of the complexes as presented in Table 4 which proves that the complexation of the metal with the ligand has been successfully occurred. The solubility studies also help in identifying the suitable solvent used in the electrochemical studies.

Elemental analyses

The complexation of the metal with the ligand resulted in different percentages of carbon, hydrogen and nitrogen of the complexes as tabulated in Table 5. Complex 3 and 4 show a higher deviation in the percentage of the carbon which probably due to the presence of unreacted metal salts in the complex.

UV-Vis spectroscopy spectrum of the metal complexes

Figure 6 displays the UV-Vis spectra for both ligands and its metal complexes 1-4. All the solutions were prepared with the same concentration. From the spectrum, it can be observed that there are three maximum peaks at 246, 259 and 271 nm appearing within the absorption band ranging from 200-300 nm. These three peaks originated from HOMO → LUMO $\pi \rightarrow \pi^*$ transitions of the pyridazine and pyrazoles groups [12]. The absorption pattern portrayed by the metal complexes are significantly different than the free ligand. All the complexes exhibited a shift in the position of the characteristic ligand band at around 260 nm. This shift is significant as it proves that the metal ion successfully coordinates with the pyridazine and pyrazole rings in the ligand structure.

Energy-Dispersive X-ray spectrum of the metal complexes

EDX analysis (Figure 7) was performed to investigate the elements present in the metal complexes. All the materials used in the synthesis of each metal complexes can be observed which further confirms the complexation of the transition metal to the ligand. The presence of higher percentage of Cl atom in all the metal complexes is due to metal salt used in the reaction and the byproduct formed from 3,6-dichoropyridazine compound after the complexation process. All metal complexes were synthesized using their respective chloride salt.

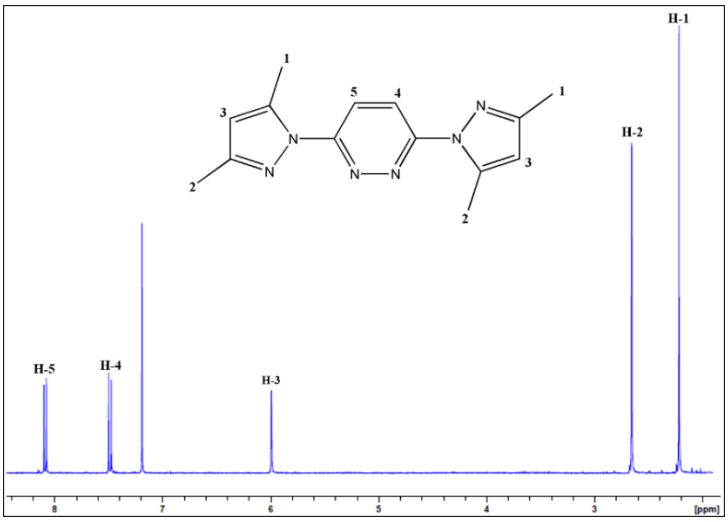


Figure 3. ^{1}H-NMR spectrum of 3,6-bis(3,5-dimethylpyrazolyl) pyridazine

Table 2. ^{1}H-NMR chemical shifts assignation

H-position	Integrations	Chemical shift, δ (ppm)	Multiplicity
1	6H	2.22	s
2	6H	2.66	s
3	2H	6.09	s
4	1H	7.50	d
5	1H	8.11	d

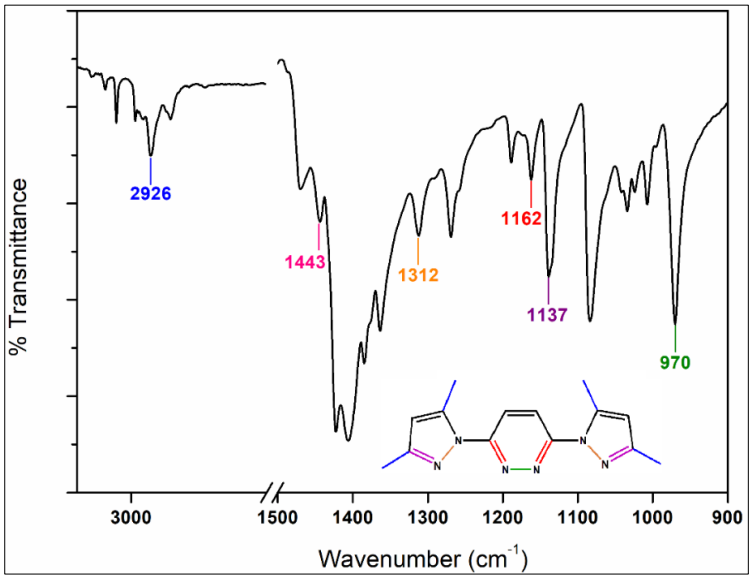


Figure 4. IR spectrum of DPPMe ligand

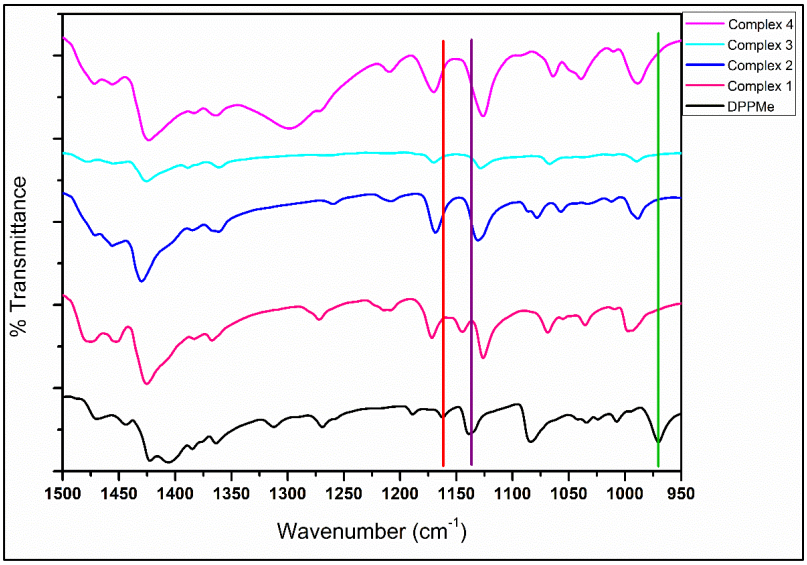


Figure 5. FTIR spectra comparison of DPPMe ligand and its metal complexes

Table 3. FTIR frequencies (in cm^{-1}) of DPPMe and its metal complexes

Compound	Pyrazole Ring (C=N)	Pyridazine Ring (C=N)	Pyridazine Ring (N-N)	Methyl Group (C-H)
DPPMe	1137	1162	970	2926
Complex 1	1125	1171	996	2922
Complex 2	1129	1168	988	2923
Complex 3	1127	1169	989	2922
Complex 4	1126	1170	988	2925

Table 4. Solubility of DPPMe and its metal complexes

Solvent	Solubility of DPPMe	Solubility of Metal Complexes 1-4
Chloroform	✓	✓
Dimethyl sulfoxide (DMSO)	×	✓
Acetonitrile	×	✓
Ethanol	×	✓
Methanol	×	✓
Dimethyl formamide (DMF)	×	✓
Tetrahydrofuran (THF)	×	✓

Table 5. The percentages of carbon, hydrogen, and nitrogen in the complexes

Compound	Proposed Empirical Formula	C%		H%		N%	
		Observed	Calculated	Observed	Calculated	Observed	Calculated
DPPMe	$C_{17}H_{28}N_6$	62.70	64.52	8.58	8.92	32.34	26.56
Complex 1	$[Cu_2(C_{17}H_{28}N_6)\cdot 4Cl$	33.03	34.88	3.12	4.82	14.31	14.36
Complex 2	$[Fe_2(C_{17}H_{28}N_6)\cdot 4Cl$	33.41	35.82	3.87	4.95	14.20	14.75
Complex 3	$[Ni_2(C_{17}H_{28}N_6)\cdot 4Cl$	27.14	35.47	5.87	4.90	14.38	14.60
Complex 4	$[Co_2(C_{17}H_{28}N_6)\cdot 4NO_3$	19.95	47.01	5.50	6.50	18.92	19.35

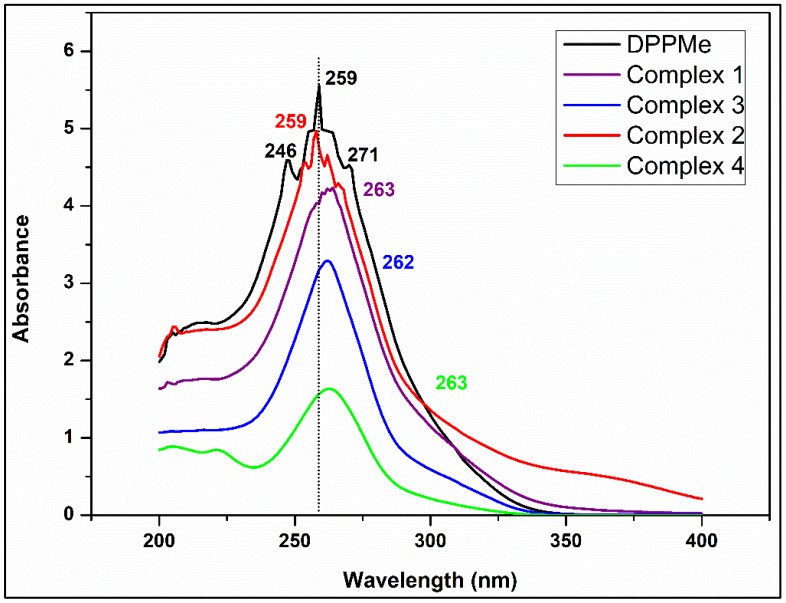
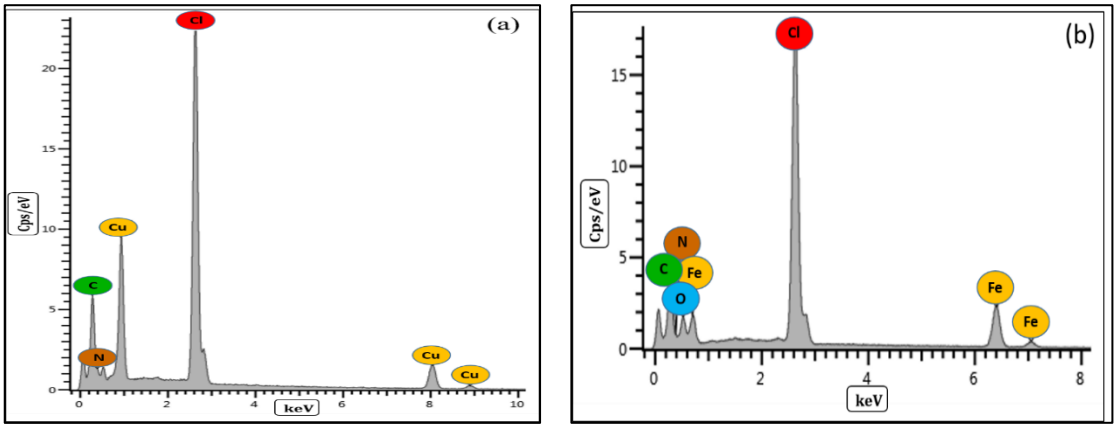


Figure 6. UV-Visible spectra of DPPMe and its metal complexes



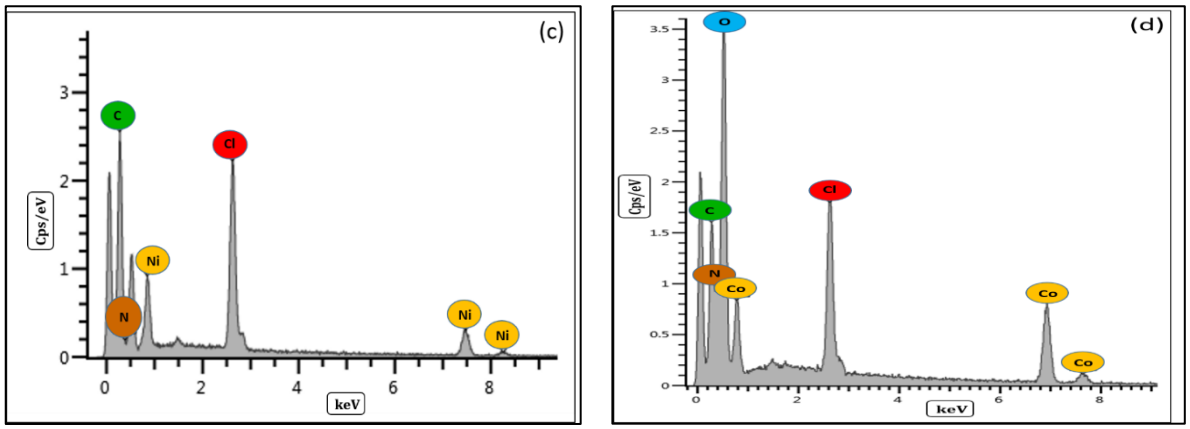


Figure 7. EDX spectrum of the metal complexes (a) Complex 1, (b) Complex 2, (c) Complex 3, (d) Complex 4

Electrochemical studies

From the cyclic voltammogram displayed in Figure 8, complexes 1-3 show a similar pattern which exhibits one electron quasi reversible transfer process with an oxidation peak (E_{pa}) at the forward scan rate and its corresponding reduction peak at the reverse scan rate. The cathodic peak detected in complex 1 at 0.03 V is due to the reduction of Cu(II) to Cu(I). When the scan is reversed, the anodic peak at 0.75 V indicates the oxidation of Cu(I) to Cu(II). Similarly, in complex 2, a cathodic peak is observed at -0.47 V when Fe(II) is oxidized to Fe(III) while its corresponding anodic peak at -0.67 V is formed when Fe(III) is reduced back to Fe(II). Finally, the peak at 0.71 V in complex 3 is attributed to the oxidation of Ni(I) to Ni(II) and the peak at 0.12 V is due to the reduction of Ni(II) to Ni(I). Apart from that, a small reduction peak can be observed at -0.84 V vs. Ag/AgCl at the reverse scan rate for complex 1 while in complex 3 another reduction peak appears at -0.74 V. However, complex 4 did not show any peaks throughout the scan. This could be explained due to the incomplete complexation of cobalt metal and the ligand in complex 4 which can be governed by a few factors such as the metal to ligand ratio, pH and temperature of the synthesis reaction. The alteration in these parameters could lead to a successful complexation in between cobalt and the ligand.

In Figure 9, the cyclic voltammogram of all three complexes in different scan rates were shown in which it can be clearly observed that there was a significant shift in the peak potential during the forward scan towards a more positive potential while in the reverse scan the shift was towards negative value. This behavior is typical for a quasi-reversible system. A significant difference in the quasi reversible voltammogram can be noticed as it displays a large peak-to-peak separation as compared to reversible processes [13]. Theoretically, the process is termed as quasi reversible when the charge transfer and mass transport on the electrode interface does not comply with Nernst equilibrium [14]. There a few properties that shows the cyclic voltammogram is a quasi-reversible such as when the I_p increases with scan rate, it is not proportional to it and the E_{pc} shifts negatively with increasing υ. The peak potentials and peak separation of the metal complexes has been tabulated in Table 6.

The electron transfer process which happened on the electrode for each metal complexes was determined by plotting the peak currents (I_{pa} and I_{pc}) against the scan rates and the square root of the scan rates, respectively. In order to calculate the electrochemical transfer kinetic parameters of the metal complexes, Laviron's Equations (1 and 2) were used.

$$E_{pa} = a + \frac{2.303\,RT}{(1-\alpha)nF}\log \upsilon \quad (1)$$

$$E_{pc} = b + \frac{2.303\,RT}{\alpha nF}\log \upsilon \quad (2)$$

This parameter includes the number of electrons transfer (η) and the electron transfer coefficient (α) [15]. Based on the graph plotted, Figure 10 indicates the complexes 1-3 exhibit a mass diffusion-controlled process as the anodic and cathodic peak current increase linearly to the square root of the scan rate ($\sqrt{\upsilon}$) [16].

The redox peak potentials and scan rates from 20-100 mVs^{-1} in logarithmic scale was plotted in Figure 11. It was found to be linear to each other as depicted in Figure 11. The slopes derived from plot were applied in equation 1 and 2 to extract information on the number of electrons (η) and electron transfer coefficient (α). For complex 1, the number of electrons is estimated to be 0.74 ≈ 1 and the α is 0.38. Hence, the electrochemical redox process of complex 1 ($Cu^{2+} \rightleftharpoons Cu^{+}$) required one electron. The slope of complex 2 shows the number of electrons to be 0.55 ≈ 1 and the α is 0.36. Complex 2 also shows a one electron transfer electrochemical redox process ($Fe^{2+} \rightleftharpoons Fe^{3+}$). Finally, for complex 3, the number of electrons is estimated to be 0.66 ≈ 1 and the α is 0.54. Thus, it also shows a one electron transfers redox process ($Ni^{2+} \rightleftharpoons Ni^{+}$).

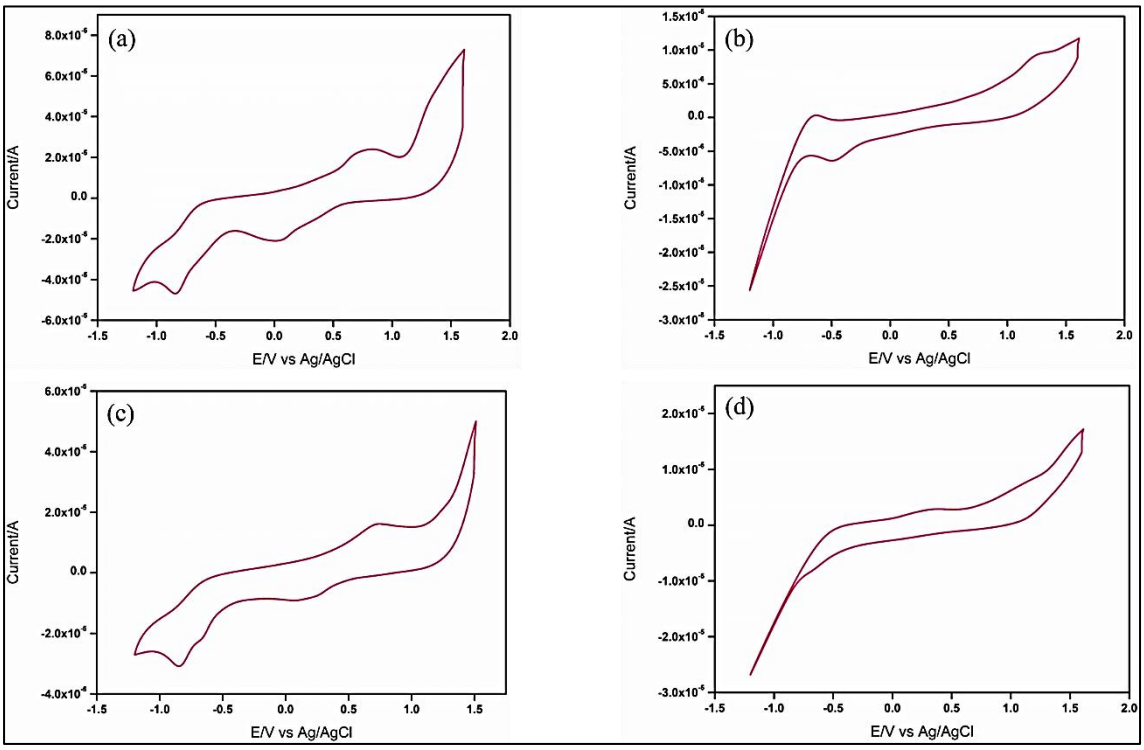


Figure 8. Cyclic voltammograms of the metal complexes (a) Complex 1, (b) Complex 2, (c) Complex 3 and (d) Complex 4 at a scan rate of 100 mV s^{-1} in the presence of 100 mM tetrabutylammonium perchlorate, [Bu4N(ClO4)] in DMF electrolyte solution. Scanning was performed against Ag/AgCl (sat. KCl) reference electrode

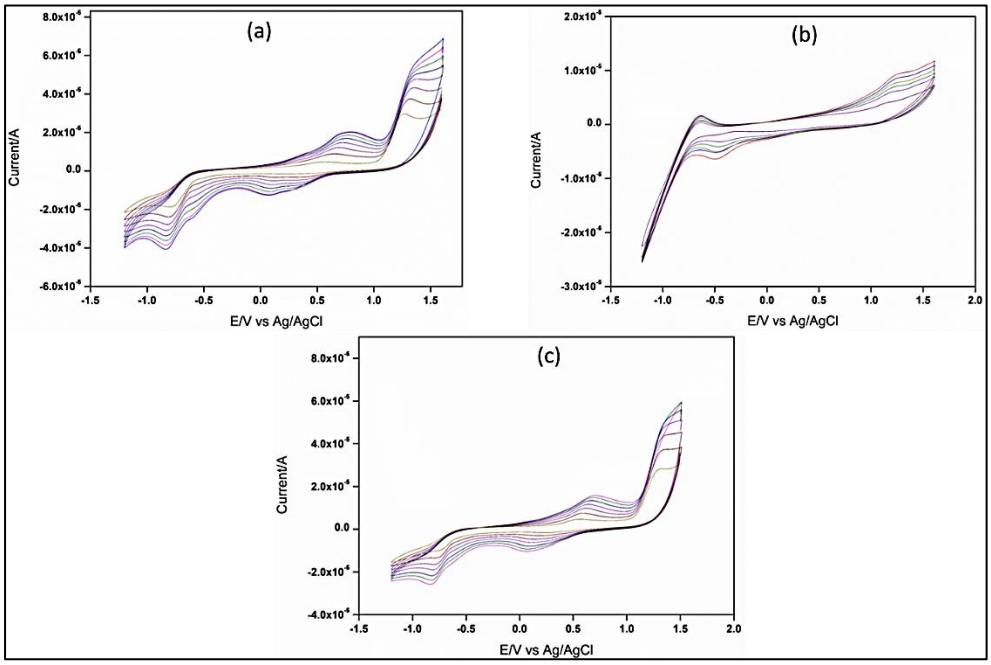


Figure 9. Cyclic voltammograms of the metal complexes (a) Complex 1, (b) Complex 2 and (c) Complex 3 at a scan rates of 20-90 mVs^{-1}

Table 6. Peak potentials and peak separation of complex 1-3

Compound	E_{pa} **(V vs Ag/AgCl)**	E_{pc} **(V vs Ag/AgCl)**	ΔE **(V vs Ag/AgCl)**
Complex 1	0.75	0.03	0.72
Complex 2	-0.67	-0.47	0.20
Complex 3	0.71	0.12	0.59

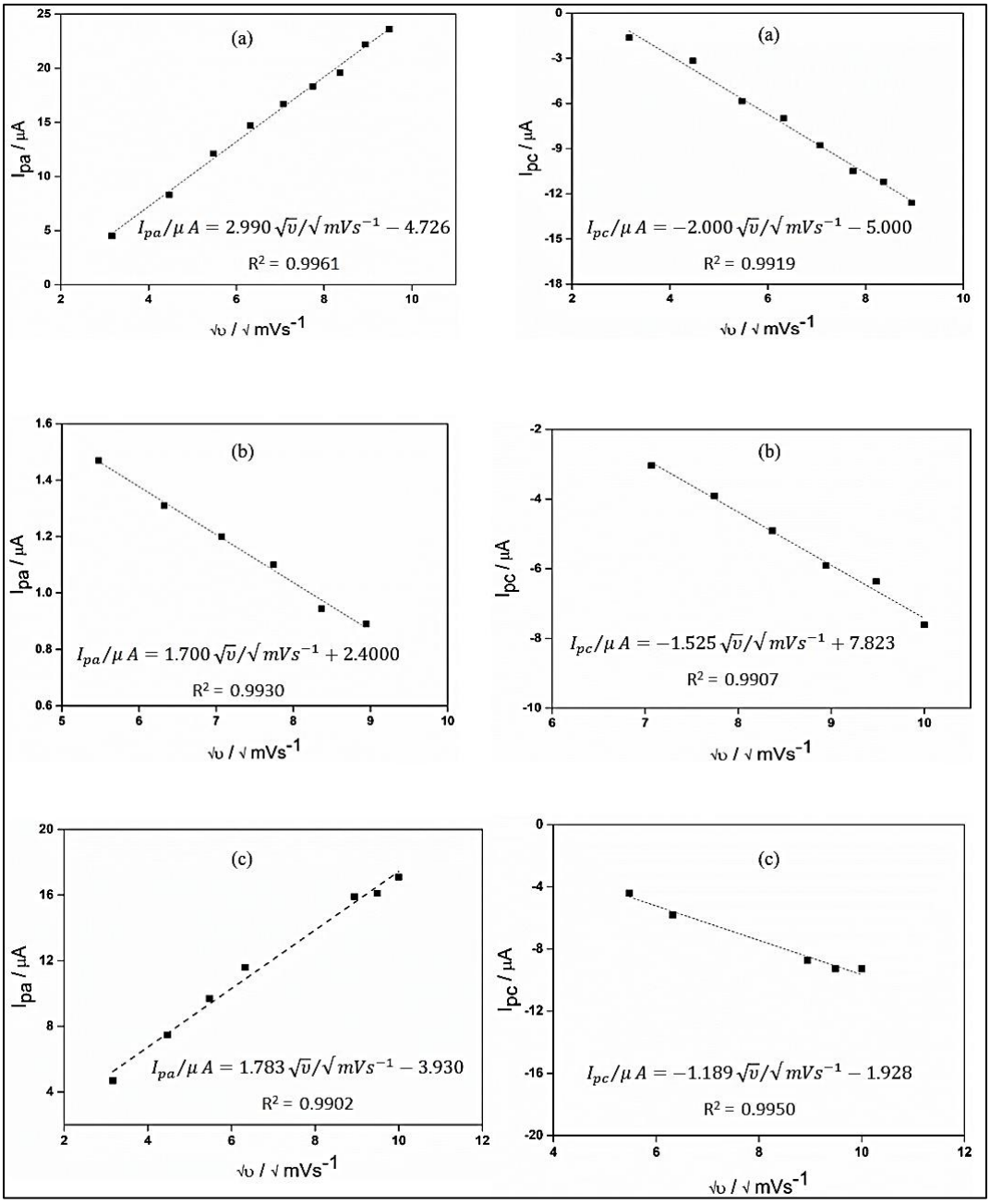


Figure 10. Graph of peak currents against square root of the scan rates: (a) Complex 1, (b) Complex 2 and (3) Complex 3

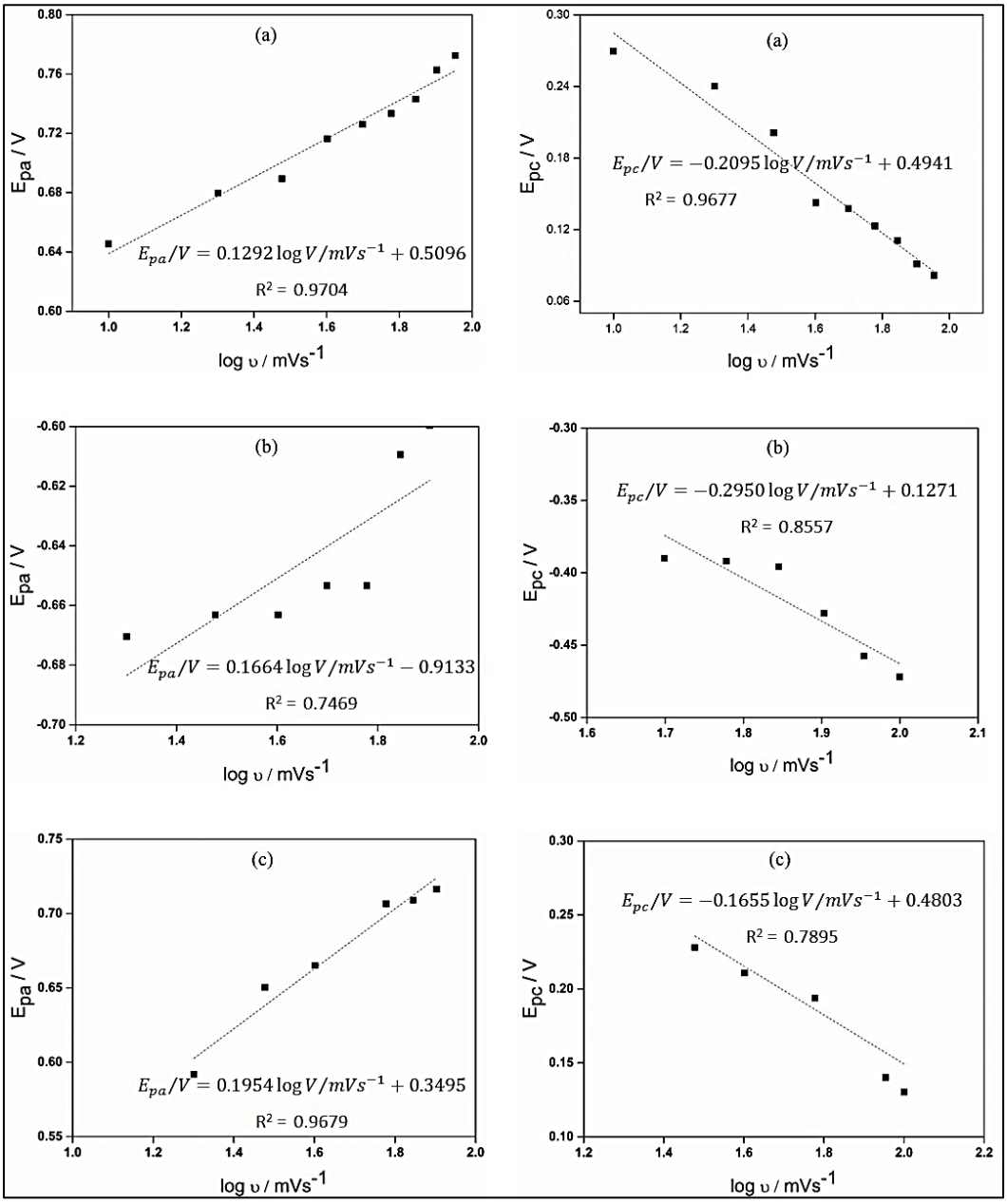


Figure 11. Graph of peak potentials against logarithm of the scan rates: (a) Complex 1, (b) Complex 2 and (3) Complex 3

Conclusion

In this project, 3,6-bis (3,5-dimethylpyrazol-1yl) pyridazine ligand has been successfully synthesized through several steps of reactions. The structure produced through the reaction of 3,5-dimethylpyrazole with 3,6-dichloropyridazine was confirmed by using IR and ^{1}H NMR spectral analyses. The ligand was then complexed with Cu(II), Fe(II), Ni(II) and Co(II) transition metals to form four novel coordinated complexes named as complex 1, complex 2, complex 3

and complex 4 respectively. Subsequently, the complexation of the metals to the ligand was affirmed through several analyses. The IR spectra of the metal complexes displayed significant shifts in several peaks of the functional groups present in the ligand. Furthermore, the UV-Vis analysis confirmed the complexation when the spectrum showed a prominent shift at ligand band characteristic at around 260 nm. The stoichiometry of the complexes was determined based on the elemental analyses and the empirical formula for each complex were proposed as $[Cu_2(C_{17}H_{28}N_6).4Cl]$, $[Fe_2(C_{17}H_{28}N_6).4Cl]$, $[Ni_2(C_{17}H_{28}N_6).4Cl]$ and $[Co_2(C_{17}H_{28}N_6).4NO_3]$, respectively. EDX analysis was used to confirm the presence of the metals in the complexes. Finally, cyclic voltammetry analysis was performed on all the complexes to study its electrochemical properties. Complex 1, 2 and 3 showed quasi-reversible of one electron transfer process with oxidation peaks at 0.75 V, -0.67 V and 0.71 V respectively whereas its corresponding reduction peaks at 0.03 V, -0.47 V and 0.12 V. Complex 4 did not show any peaks throughout the forward and reversed scans. In future, the effect of the complex solubility in different organic solvents on its electrochemical behavior will be studied. The complexes will also be explored in electrochemical applications such as electrocatalytic dye degradation and electrocatalyst for water splitting process.

Acknowledgement

This research is supported by the Interdisciplinary Research Program Grant (IIRG013B-2019) given by the Universiti Malaya. The work was also supported by the IMRC/AISTDF/CRD/2018/000048 (ASEAN-India Collaborative R&D Scheme).

References

1. Cargnelutti, R., Schumacher, R. F., Belladona, A. L. and Kazmierczak, J. C. (2021). Coordination chemistry and synthetic approaches of pyridyl-selenium ligands: A decade update. *Coordination Chemistry Reviews*, 426: 213537.
2. Dubois, D. L. (1997). Development of transition metal phosphine complexes as electrocatalysts for CO_2 and CO reduction. *Comments on Inorganic Chemistry*, 19(5): 307-325.
3. Cheung, K.-C., Wong, W. L., Ma, D. L., Lai, T. S. and Wong, K. Y. (2007). Transition metal complexes as electrocatalysts-Development and applications in electro-oxidation reactions. *Coordination Chemistry Reviews*, 251(17): 2367-2385.
4. Grünwald, K. R., Saischek, G., Volpe, M., Belaj, F. and Mösch-Zanetti, N. C. (2010). Pyridazine-Based ligands and their coordinating ability towards first-row transition metals. *European Journal of Inorganic Chemistry,* (15): 2297-2305.
5. Viciano-Chumillas, M., et al. (2010). Coordination Versatility of Pyrazole-Based Ligands towards High-Nuclearity Transition-Metal and Rare-Earth Clusters. *European Journal of Inorganic Chemistry*, (22): p. 3403-3418.
6. Gao, H., Tanase, S., de Jongh, L. J. and Reedijk, J. (2006). Synthesis, crystal structures and properties of the novel mononuclear copper(II) and tetranuclear cobalt(II) complexes with 3,6-bis-(3,5-dimethylpyrazolyl)-pyridazine. *Transition Metal Chemistry*, 31(8): 1088-1092.
7. Baranac-Stojanović, M. (2014). New insight into the anisotropic effects in solution-state NMR spectroscopy. *RSC Advances*, 4(1): 308-321.
8. Kaddouri, Y., Abrigach, F., Mechbal, N., Karzazi, Y., El Kodadi, M., Aouniti, A. and Touzani, R. (2019). Pyrazole compounds: Synthesis, molecular structure, chemical reactivity, experimental and theoretical DFT FTIR spectra. *Materials Today: Proceedings*, 13: 956-963.
9. Anush, S. M., Vishalakshi, B., Kalluraya, B. and Manju, N. (2018). Synthesis of pyrazole-based Schiff bases of Chitosan: Evaluation of antimicrobial activity. *International Journal of Biological Macromolecules*, 119: 446-452.
10. Figueiredo, H., Silva, B., Raposo, M. M. M., Fonseca, A. M., Neves, I. C., Quintelas, C. and Tavares, T. (2008). Immobilization of Fe(III) complexes of pyridazine derivatives prepared from biosorbents supported on zeolites. *Microporous and Mesoporous Materials*, 109(1): 163-171.

11. Mészáros Szécsényi, K., Leovac, V. M., Jacimovic, Z. K. and Pokol, G. (2003). Transition Metal Complexes with Pyrazole Based Ligands. *Journal of Thermal Analysis and Calorimetry*, 74(3): 943-952.
12. Mezei, G. and Raptis, R. G. (2004). Effect of pyrazole-substitution on the structure and nuclearity of Cu(II)-pyrazolato complexes. *Inorganica Chimica Acta*, 357(11): 3279-3288.
13. Kutluay, A. and Aslanoglu, M. (2013). Modification of electrodes using conductive porous layers to confer selectivity for the voltammetric detection of paracetamol in the presence of ascorbic acid, dopamine and uric acid. *Sensors and Actuators B: Chemical*, 185: 398-404.
14. Beaver, B. D., Hall, L. C., Lukehart, C. M. and Preston, L. D. (1981). Reactions of coordinated molecules. XXVII. Cyclic voltammetry of several transition metal metalla-acetylacetonate complexes. *Inorganica Chimica Acta*, 47: 25-30.
15. Huang, F., Wang, F., Feng, S., Li, Y., Li, S. and Li, Y. (2013). Direct electrochemistry and electrochemical biosensing of glucose oxidase based on CdSe@CdS quantum dots and MWNT-modified electrode. *Journal of Solid State Electrochemistry*, 17(5): 1295-1301.
16. Hamel, C., Chamelot, P. and Taxil, P. (2004). Neodymium(III) cathodic processes in molten fluorides. *Electrochimica Acta*, 49(25): 4467-4476.

Malaysian Journal of Analytical Sciences (MJAS)
Published by Malaysian Analytical Sciences Society

A MINI REVIEW ON SENSOR AND BIOSENSOR FOR FOOD FRESHNESS DETECTION

(Satu Ulasan Mini Sensor dan Biosensor untuk Pengesanan Kesegaran Makanan)

Wan Elina Faradilla Wan Khalid* and Nur Izzatul Afiqah Jais

Universiti Teknologi MARA, Cawangan Negeri Sembilan,
Kampus Kuala Pilah, Pekan Parit Tinggi, 72000 Kuala Pilah, Negeri Sembilan, Malaysia

**Corresponding author: wan_elina@uitm.edu.my*

Received: 11 October 2020; Accepted: 30 December 2020; Published: 20 February 2021

Abstract

The freshness of food is one of the important qualities that need to be considered by consumers while selecting the food. However, many people are having trouble to determine the level of freshness without the presence of devices or instruments. Therefore, the development of food freshness sensor has become one of the promising analytical techniques, which provides more benefits as compared to other instruments such as gas chromatography mass spectrometry (GC-MS), high-performance liquid chromatography (HPLC) and capillary electrophoresis (CE). Food freshness sensors offer faster analysis and most importantly, it is non-destructive to food sample. In this review, we focus on the development and performance of various types of sensors for food freshness detection such as electrochemical sensors, optical sensors, potentiometry sensors and pH sensor. For each type of sensors, there are several main elements that will be emphasized, which include type of samples, reagents used, immobilization matrix and performances of the sensors. A section that discusses the future works, which have the potential for the application in the sensor and biosensor of freshness detection is also highlighted.

Keywords: sensor, biosensor, immobilization matrix, food freshness detection

Abstrak

Kesegaran makanan ialah salah satu kualiti penting yang perlu diambil kira oleh pengguna semasa pemilihan makanan. Walau bagaimanapun, pengguna akan mengalami kesukaran untuk menentukan tahap kesegaran makanan tanpa kehadiran peralatan atau instrumen. Oleh itu, pembangunan sensor kesegaran makanan telah menjadi salah satu teknik analisis yang menjanjikan lebih banyak faedah berbanding instrumen lain seperti kromatografi gas-spektrometri jisim (GC-MS), kromatografi cecair prestasi tinggi (HPLC) dan elektroforesis rerambut (CE). Sensor kesegaran makanan menawarkan analisis yang lebih cepat dan yang paling penting ia tidak merosakkan sampel makanan. Ulasan ini memfokuskan kepada pembangunan dan prestasi pelbagai jenis sensor untuk pengesanan kesegaran makanan seperti sensor elektrokimia, sensor optik dan sensor potensiometri. Bagi setiap jenis sensor, terdapat beberapa elemen penting yang akan ditekankan termasuk jenis sampel, reagen yang digunakan, matrik pemegunan dan prestasi sensor. Bahagian yang membincangkan kajian masa depan yang berpotensi untuk aplikasi sensor dan biosensor untuk penentuan kesegaran juga disorot.

Kata kunci: sensor, biosensor, matrik pemegunan, penentuan kesegaran makanan

Introduction

Food spoilage has become a major problem in our society as it could lead to many health problems. It is a complex ecological phenomenon caused by physical, chemical and microbiological activities [1]. Physical food spoilage occurs when dried food absorbs excessive amounts of moisture or moist foods are excessively dehydrated. Chemical food spoilage happened when various components in the food react with foreign components resulting in the characteristic changes of food such as enzymatic browning, non-enzymatic browning, and oxidation [2]. Microbiological food spoilage is caused by the microorganisms like yeasts, molds and bacteria. These microorganisms will produce enzymes and produce by-products in the food [1]. Pathogens in food have caused severe diarrhoea and meningitis, meanwhile chemical contamination has led to serious food poisoning and cancer in the long-term period. Therefore, the most important quality that needs to be measured is the food freshness. The freshness of food can be detected physically and chemically where it can be identified physically through colours, textures and flavours of the food [3]. Fresh food is the easiest one to be contaminated by microorganisms as compared to dry and processed food. There are several microorganisms that cause food spoilage such as *Pseudomonas* spp, *Acinetobacter* spp and *Botrytis* [4]. There are also a few compounds found in fresh stock such as proteins, carbohydrates, and fat, which are easily degraded by microbial actions [5].

Consumers can determine the food freshness physically, but it could become a problem when the food is chemically or biologically contaminated. There will be some difficulties in identifying the freshness level without using specific instruments and methods like gas chromatography-mass spectrophotometry (GC-MS) and high-performance liquid chromatography (HPLC) [6]. Although all the detection methods are available and very accurate in determining the food spoilage, it has several drawbacks which are time-consuming, expensive and inaccessible to consumers [7]. In addition, the use of these instruments required a trained personnel to handle. Therefore, by developing a handheld sensor that will be able to detect food freshness can aid the consumers to measure the freshness easily in a shorter time as compared to by using the high-end instruments. Many researchers have developed various sensors that can determine the qualities of food. Researchers have found that a real-time monitoring of food quality becomes very important to consumers and also to food manufacturers [8]. There are many sensors that have been developed for food freshness detection by using different sensing methods such as optical and electrochemical techniques. Besides that, there are several indicators or reagents that have been used for food freshness detection, namely bromothymol blue (BB), bromocresol green (BCG), curcumin, anthocyanin and enzymes-based reagents, such as xanthine oxidase (XO) [3, 9-11].

The growing research interest on food freshness detection has been shown by many articles related to food freshness since 2010. Based on Figure 1, it shows that the number of publications on food freshness sensors continue to increase from 2010 to 2020. This shows that over the year, many researchers are interested in food freshness sensors as the number of publications are gradually increased. Moreover, there are also several articles that have been reviewed pertaining to food freshness sensors including the fabrication of electrochemical sensors using various type of indicators [12-14] and biosensor development [15-16]. Interestingly, there are few researchers that reviewed the intelligent packaging used for food freshness detection [17-19]. In this review, we will focus on the development of optical and electrochemical sensors or biosensors for food freshness detection.

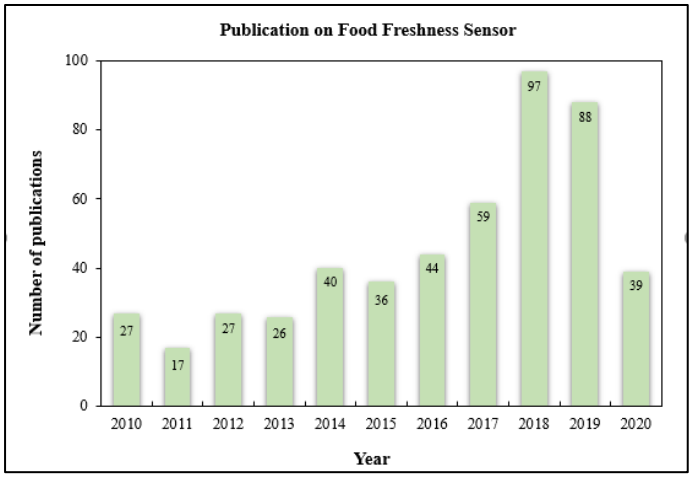


Figure 1. Number of publications on food freshness detection against year. Source taken from Scopus

Sensor and biosensor development for food freshness detection

Many sensors for food freshness detection have been developed by using natural, biological and chemical indicators. The chemical and biological reagents have been immobilized in various types of polymer matrix [20]. Freshness sensors can be defined as sensors that are able to indicate any changes such as pH, temperature, humidity and colour [21]. In addition, a freshness sensor is also sensitive to any changes occurred during degradation of the food, such as colour change, gas produced from food spoilage and bacterial count [20]. Here are two main types of freshness sensors that have been invented, which are direct sensor and indirect sensor. For the direct sensor, it senses the freshness of food directly by indicating the freshness level using ripeness, spoilage and microbial indicators. Meanwhile, the indirect sensors operate indirectly where they measure the freshness of the food by observing the variables such as temperature and storage time [22].

Optical sensor

Optical sensors are analytical devices that have attracted researcher's attention especially in analytical field. Optical sensors are considered a chemical or bio-based sensor that consist of chemical recognition phase (sensing receptors) coupled with optical transducers [23]. Generally, optical sensors are devices that have the capacity to detect and quantify various properties of lights, such as frequency, wavelength, polarization and intensity [24]. Optical sensors have been widely used in the food industries for food quality measurements, such as pH, temperature and spoilage monitoring [25]. Besides the application in the food industries, optical sensors are also used in environmental monitoring, pharmaceuticals, clinical analysis and biotechnology [23].

In sensors development, the main important parts are receptors and transducers. A receptor is either chemical reagent or biomolecule that can react with analytes while transducer convert the chemical or biochemical signal produced from the analyte reaction and receptor [26]. For optical sensors, the receptors could be established by using various natural (biological) or synthetic (chemical) materials. The receptors are integrated on a sensor interface by many techniques, such as immobilization, molecular imprinting and self-assembled monolayers (SAMs) [23]. Moreover, most receptors are in a thin layer formed which are able to interact with the analyte molecules and selectively catalysed or participate in the chemical reaction. The receptors identify the changes that occur on the analytes like pH or temperature and produce the optical signals, such as colour changes. The colour changes will indicate the condition of tested samples. The optical transducers will translate the signal into readable signals that are suitable for the measurement purposes [27]. Optical

sensors give advantages such as high selectivity, inexpensive, non-destructive to analyte, can easily be miniaturized and possibility for multiple analyte detection.

There are several studies that have been done on the development of optical sensors for food freshness detection on different samples, such as milk, fruit, fish, and shrimp. Weston et al. have synthesized zinc oxide (ZnO) solution with conjugated polymers, polydiacetylene (PDAs) to detect freshness of full cream milk. The PDA/ZnO nanocomposite was prepared by using thin film hydration method and has been immobilized in an agarose to form a disc sensor. PDAs have unique colorimetric properties that make them an attractive building block for colorimetric sensors. In this study, the structure of the PDA/ZnO nanocomposite has been optimized to acquire the optimum pH value recorded from the spoiling milk. The colour of PDA/ZnO/agarose film have changed from blue to red with the increasing pH. Moreover, this sensor was able to differentiate between fresh, spoiling and spoiled milk based on the concentration of lactic acid produced by the milk. PDA/ZnO nanocomposite is a great indicator because it is sensitive towards acid where it will change colour due to disruption of steric forces within the nanocomposite. Lastly, PDA/ZnO also exhibited higher stability in a broad range of solvents than pure PDA. Therefore, it can be casted into various types of materials which is ideal to be imposed in food packaging systems [28].

Maftoonazad and Ramaswamy in their study have designed a pH biosensor that can detect fresh date fruit, *Rutab*. In this study, the sensor film was placed in the packaging where the changes in colour of the film was observed according to the pH changes of *Rutab*. Anthocyanin which is very suitable for colorimetric determination of pH has been extracted from the red cabbage and was immobilized inside polyvinyl alcohol (PVA). The use of anthocyanin red cabbage, which is naturally abundant as the indicator in developing the pH biosensor gives an advantage in terms of lower preparation cost. The pH biosensor developed was found to be reversible, stable and sensitive [10]. Hasanah et al. have successfully developed an optical pH sensor to determine the fish freshness by using chromoionophore as the reagent. Chromoionophore was immobilized in pectin hydrogel membrane and the pH change on fish was detected based on the protonation and deprotonation of chromoionophore functional groups. Furthermore, pectin hydrogel membrane is suitable and can be used as sensor matrix due to the non-toxic property. In addition, pectin is a hydrophilic polymer, hence it has a higher permeability than hydrophobic synthetic polymer. The hydrophilicity properties can enhance the adsorption of chromoionophore into the polymer, thus allowing a rapid response towards pH change. The protonation in acidic condition (615 nm) and deprotonation in basic condition (535 nm) were analysed by using UV-Vis spectrophotometer. The changes in protonation and deprotonation processes produced an isosbestic point (Figure 2) where it indicates the optimum absorbance of the optical pH sensor in both conditions. Based on the analytical performance tested, the sensor was able to give a fast response and produce desirable linearity and reproducibility [29].

Additionally, Lee and Shin have developed a freshness indicator to monitor the quality of skate (*Raja kenojei*) during the storage time. Skate is fermented fish with unique smell that produces ammonia gas from the fermentation process. In this research, they indicate the freshness of skates by measuring the ammonia content produced during storage. The sensor was fabricated by using pH indicator, namely bromothymol blue-phenol red (BTB-PR) and immobilized in cellulose acetate solution. The sensor was coated with polyethylene terephthalate (PET) film to allow the gas to pass through. Moreover, the sensor was coated with polytetrafluoroethylene (PTFE) which acted as hydrophobic gas-permeable membrane to protect the indicator from humidity. From this study, they found out that the pH of the skates increased as temperature and storage time increased, thus changed the colour of the sensor film from yellow (fresh food) to purple (spoiled food). In this study the reagents used were free from leaching and the sensor showed a rapid response [30].

Although polyanaline (PANI) is a conductive polymer and widely used for electrochemical sensor, Wang et al.

have used PANI to develop a calorimetric or optical sensor to detect the freshness of tilapia fish by detecting the total volatile basic nitrogen (TVBN) released during the tilapia spoilage. In this study, hydrochloric acid was used to prepare doped-PANI. In the presence of spoiled tilapia, the indicator based on doped-PANI changed colour from green to peacock blue. The sensor developed was reusable for at least three times and offer some advantages such as easy to use and inexpensive for large production scale [31].

In another work, Rukchon et al. have developed a colourimetric sensor to indicate the spoilage of skinless chicken breast by using two types of pH-sensitive indicators, which were bromothymol blue and methyl red. The mixed reagents were then immobilized in polyethylene glycol. The films have been placed in the packaging of the chicken sample. The spoilage of the chicken was observed by the colour changes, which correlated to the amount of CO_2 produced by the spoiled chicken. Moreover, this sensor can also respond towards the temperature changes and microbial growth [11].

Kuswandi et al. reported an optical sensor for monitoring the shrimp spoilage by using curcumin as reagent. The curcumin is a natural dye pigment that is isolated from herbs named *Curcuma longa*. Curcumin was immobilized in the bacterial cellulose membrane polymer matrix by absorption. The curcumin/bacterial cellulose membrane showed a colour change from yellow to orange with the increasing pH and then to reddish orange, which indicated the spoilage of the shrimps. Curcumin which is highly sensitive to acid-base reactions provides a simple method and this has enabled the mass production of low costs sensors [3].

Electrochemical sensor

Electrochemical sensors are one of the oldest chemical sensors that have been developed due to their advantages that can be miniaturized and simple [32, 14]. In general, electrochemical sensors are devices that provide information about composition in analyte by coupling a chemically selective layer (recognition elements/receptors) to an electrochemical transducer [33]. Recent studies have shown that besides using chemical reagents as recognition elements, biological materials like protein and DNA also have become common because usually they are much more specific. Electrochemical sensors have been used in numerous applications due to its sensitivity, selectivity and ability to analyse samples with slight or no pre-treatment. One of the applications of electrochemical sensors in the forensic field where the sensors are developed for drug and poison detection [34]. In addition, the advancement of electrochemical measuring systems and bio-analytical chemistry has led to the development of electrochemical sensors in agricultural, environmental, medical (diagnosis of genetic disorders) and food analysis (genetically modified organism (GMO) content in food and freshness level) [32, 12].

Basically, electrochemical sensors are based on redox reactions where it involves the target analyte and three-electrode configuration which are working electrode, reference electrode and auxiliary electrode [35]. Electrochemical sensors can be divided into several types based on the signal transduction namely amperometric, impedimetric and potentiometric [36]. Therefore, several studies have been reported on the development of electrochemical sensors for measuring the fish freshness. Thandavan et al. have reported the development of iron oxide (Fe_3O_4) nanoparticles-based electrochemical biosensor for quantitative determination of xanthine using amperometry technique. Xanthine is produced from degradation of nucleotides by dead organisms, such as fish. Therefore, the quantification of this molecule is suitable for determining fish freshness. In this study, they have used Xanthine Oxidase (XO) as reagent and it was covalently immobilized onto Fe_3O_4 nanoparticles which act as an interface between the reagent and electrode. The working electrode was fabricated by electropolymerization of XO/Fe_3O_4 on the gold (Au) electrode to promote higher electron transfer. Based on the study, it was found that the biosensor was able to determine the concentration of xanthine in the range of 0.4 to 2.4 nM. This biosensor showed better performance with higher sensitivity, mediator-free and less interference due to excellent electron transfer pathway by XO/Fe_3O_4/Au modified electrode [37].

Dervisevic et al. reported a study on developing amperometric enzyme-based biosensor to detect the fish freshness. In this study, they have developed a polymeric mediator by mixing two redox copolymers which are vinylferrocene (VFc) and glycidyl methacrylate (GMA) with multiwalled carbon nanotube (MWCNT). These polymeric mediators were used due to its excellent electron transfer properties. XO was immobilized in pencil graphite electrode (PGE) coated with GMA-co-VFc and MWCNT, (PGE/P(GMA-co-VFc)/MWCNT). Based on the result, the current response increased with the increasing of xanthine concentration produced by fish in the concentration range of 2-48 μM. The use of MWCNT in the development of this biosensors has offered some advantages such as higher sensitivity and selectivity towards xanthine analysis [38].

Dolmac et al. also reported the fabrication of amperometric biosensor for fish freshness. In their study, XO was immobilized in polypyrrole-polyvinylsulphonate (PPy-PVS) film by entrapment method to determine the level of hypoxanthine (Hx) in fish. In this study, XO/PPy-PVS was electropolymerized on the platinum (Pt) electrode and the electrode act as the working electrode. The level of Hx was electrochemically monitored based on the oxidation of uric acid liberated during enzyme activity on the electrode surface. Based on the finding, this biosensor was able to determine the concentration of Hx from 1.0×10^{-7} to 1.0×10^{-3} M. In general, this biosensor provides a simple and rapid detection with a low detection limit [39].

Bourigua et al. have prepared amperometric and impedimetric biosensors to detect trimethylamine (TMA), a volatile compound that is also one of the parameters to determine fish freshness. In this study, the reagent used was flavin-containing monooxygenase 3 (FMO3). FMO3 is a NADPH-dependant enzyme that catalyses the oxygenation of TMA to trimethylamine N-oxide (TMAO). The conducting polymer (CP), polypyrrole was substituted with ferrocenyl and used for enzyme immobilization. CPs can be considered a good polymer matrix for enzyme biosensor because it can preserve the catalytic activities of enzyme from any alteration. Meanwhile, the ferrocenyl group was used as a redox probe due to its higher sensitivity towards electrochemical response. The copolymer film has been electrodeposited on Au working electrode by chronoamperometry method. This technique was used to control the thickness and reproducibility of the film. In this study, FMO3 was attached to the polymer-modified electrode by covalent immobilization where the amine group from lysine was bound to N-hydroxyphthalamide. This biosensor showed a linear response in the range of 0.4 μg mL^{-1} to 10 μg mL^{-1} and 0.4 μg mL^{-1} to 80 μg mL^{-1} for both amperometric and impedance methods. The charge transfer resistance for impedance was increased while the current response for amperometric has decreased with the increase of TMA concentration. The fabricated biosensor showed high selectivity and exhibited a broad linear range for the evaluation of fish freshness [40].

Potentiometry method is the measurement of potential difference between indicator and reference electrode [41]. Generally, potentiometric method can be considered as a simple method and are suitable for the development of electrochemical sensors to determine the food freshness [33]. Basically, potentiometric sensors consist of ion-selective membrane that measures the changes in membrane potential between two electrodes when in contact with the analyte solution. Ion selective electrodes (ISEs) are electrochemical ion sensor that convert activity of desired ion into electrical signal and coupled with reference electrodes for potentiometry application at zero current condition [42]. The ISEs membranes can be made either from solid, liquid or glass [43]. The most familiar ISEs are glass electrodes for pH measurements, which respond to H^+ concentration in analyte solution. Generally, ISE is a non-destructive method and it is considered inexpensive.

In a study conducted by Park et al., they have developed a flexible potentiometric pH sensor that can measure the pH for a spoiled milk and curved surface apple. The pH sensor has two-electrode configuration which were PANI nanofiber array-based sensing electrode and Ag/AgCl reference electrode. The working (carbon) and reference electrodes were produced by using screen

printing technique on a flexible polyethylene terephthalate (PET) substrate (Figure 3). PANI nanofiber array was deposited on the surface of carbon electrode through chemical polymerization method. The use of PANI as electrode provided higher stability to the pH sensor because it enabled redox reactions to happen. The performance of the pH sensors showed that the pH decreased from pH 7.1 to 6.2 after 48 hours which indicated the spoilage of the milk. This is because spoiled milk contains higher acidity due to amount of lactic acid produced. Meanwhile, for the pH determination of apple showed that the spoiled apple has lower acidity than the fresh apple. The advantage of this sensor is it demonstrated excellent selectivity and flexibility as compared to standard pH meter because it can measure the pH level of dent surface on fruits [44].

Kaneki et al. have developed a potentiometric gas sensor that were used to determine the freshness level of salmon and sardine by measuring the response from volatile gases compound produced from decomposed fish. They have configured a three-sensor system that included oxidation-reduction (ORP) gas sensor, ammonia gas sensor and hydrogen sulphide gas sensor. In this study, the ORP-sensor was developed by themselves meanwhile the other two sensors were obtained commercially. ORP-sensor consists of reference electrode (Ag/AgCl), Au detection electrode and inner solutions (Ce^{3+}, Ce^{4+} and KCl). Based on the study, the gas sensor measured dimethylamine (DMA) and TMA that were produced from decomposed fish. In general, it was found that the potential change between electrodes increased as the storage time increased. This indicates that the emission of volatile compound increases with the deterioration of fish freshness. Potentiometric gas sensor was successfully developed, and it showed high sensitivity towards the product from fish degradation and showed no interference from the humidity [45]. Table 1 shows the summary of the different freshness sensor that have been fabricated.

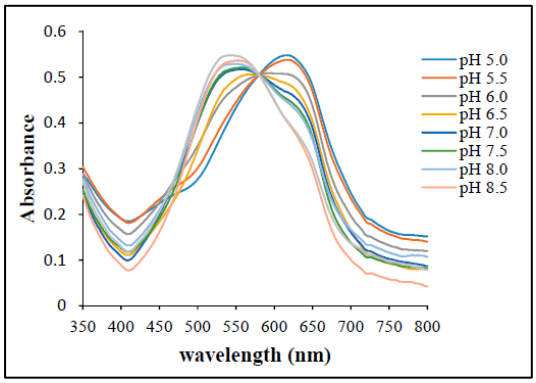


Figure 2. The response of optical pH sensor towards various pH [29]

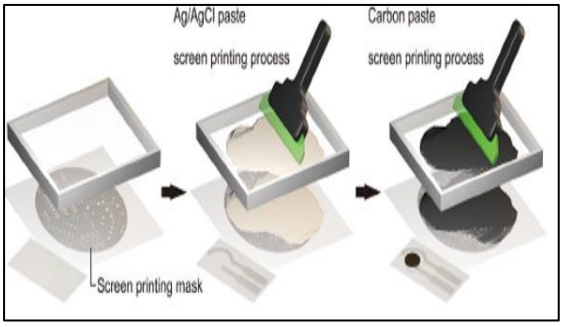


Figure 3. Schematic diagram on the fabrication of potentiometric pH sensor [44]

Table 1. Summary on the various fabrication of freshness sensors

Reagent/ Indicator/Enzyme	Immobilization Matrix	Type of Sensor	Linear Range	Application	Reference
XO	PGE/P(GMA-co-VFc)/MWCNT	Electrochemical Sensor	2 - 48 μM	Monitoring fish freshness	[38]
XO	Fe_3O_4	Electrochemical Sensor	0.4 - 2.4 nM	Monitoring fish freshness	[37]
XO	Polypyrrole-polyvinylsulphonate (PPy-PVS)	Electrochemical Sensor	1.0 x 10^{-7} - 1.0 x 10^{-3} M	Monitoring fish freshness	[39]
FMO3	Polypyrrole-ferrocenyl	Electrochemical Sensor	0.4 μg mL^{-1} - 10 μg mL^{-1} (amperometric) 0.4 μg mL^{-1} - 80 μg mL^{-1} (impedance)	Monitoring fish freshness	[40]
PANI nanofiber	Carbon electrode	Potentiometric pH Sensor	pH 3.9 - 10.1	Monitoring pH of spoiled milk and apple	[44]
ORP, Ammonia and Hydrogen sulphide gas sensors	Gas permeable membrane Teflon	Potentiometric Gas Sensor	-	Monitoring salmon and sardine freshness	[45]
PDA/ZnO nanocomposite	Agarose gel	Optical Sensor	• Fresh (pH 6.8 - 6.0) • Spoiling (pH 6.0 - 4.5) • Spoiled (pH 4.5 - 4.0)	Monitoring milk freshness	[28]
Anthocyanin	PVA	Optical Sensor	pH 2 - 12	Monitoring freshness of date	[10]
Chromoionophore	Pectin hydrogel membrane	Optical Sensor	pH 5 - 9	Monitoring fish freshness	[29]
Bromothymol blue-phenol red (BTB-PR)	Cellulose acetate	Optical Sensor	• 5,000 and 10,000 mg/L of ammonia - early state of fish fermentation • 50,000 mg/L of ammonia – fish fermentation	Monitoring freshness of skate (*Raja kenojei*)	[30]

Table 1 (cont'd). Summary on the various fabrication of freshness sensors

Reagent/ Indicator/Enzyme	Immobilization Matrix	Type of Sensor	Linear Range	Application	Reference
Doped PANI	-	Optical Sensor	• Green-Fresh • Dark peacock blue - Spoilage	Monitoring milk freshness	[31]
Bromothymol blue and methyl red	Polyethylene glycol	Optical Sensor	-	Monitoring freshness of skinless chicken breast	[11]
Curcumin	Bacterial cellulose membrane	Optical Sensor	• Reddish orange - Spoilage	Monitoring freshness of shrimp	[3]

Future works

The development of sensor and biosensor for food freshness detection has attracted many researchers especially in the food sector. Despite of the achievement obtained so far, there are still some improvements needed. The used of computational chemistry to study the binding interaction between sensing agent and the analyte could be carried out to fabricate a more selective sensor. In addition, nanostructured material can be used for enzyme immobilization as it increases the electrochemically active surface area and enhances the efficiency of electron transfer. In addition, the development of e-tongue for food freshness detection has attracted researchers although there are some problems with the stability of the data obtained. Therefore, improvement in the e-tongue system need to be made and also for the development of smartphone-based sensor.

Conclusion

The development of sensors to determine the freshness of food has attracted many interests. In this review, we have discussed a brief overview on the food spoilage. The present review also highlights on the various type of sensors fabrication for food freshness detection. Based on the current trends, the development of electrochemical sensors involves the use of nanomaterials to achieve the low detection limit and enhance the sensitivity of the sensors. Besides that, the use of highly selective reagent is one of the important factors in determining the performance of the sensor. Until now, there has been so much progress in the sensor research, but there is still room for improvement to fabricate sensors with a rapid response, higher sensitivity, renewable and more importantly can be miniaturized. The binding interaction between reagent and the analyte can be predicted using computer simulation to produce a more selective sensor. In addition, the use of mediator-less electrochemical sensor can provide a good sensor response and improve the selectivity. Therefore, more studies on the fabrication of mediator-less sensor or biosensor can be conducted.

Acknowledgement

The authors wish to thank Universiti Teknologi MARA Cawangan Negeri Sembilan for the services and facilities to carry out the work.

References

1. Lianou, A., Panagou, E. Z. and Nychas, G. J. E. (2016). Microbiological spoilage of foods and beverages. *In the Stability and Shelf Life of Food*: pp. 3-42.

2. Petruzzi, L., Corbo, M. R., Sinigaglia, M. and Bevilacqua, A. (2017). Microbial spoilage of foods: Fundamentals. *In the Microbiological Quality of Food: Foodborne Spoilers*: pp. 1-21.
3. Kuswandi, B., Jayus, Larasati, T. S., Abdullah, A., and Heng, L. Y. (2012). Real-time monitoring of shrimp spoilage using on-package sticker sensor based on natural dye of curcumin. *Food Analytical Methods*, 5(4): 881-889.
4. Al-Kharousi, Z. S., Guizani, N., Al-Sadi, A. M., Al-Bulushi, I. M., and Shaharoona, B. (2016). Hiding in fresh fruits and vegetables: Opportunistic pathogens may cross geographical barriers. *International Journal of Microbiology*, 2016: 1-14.
5. Hong, X. and Wang, J. (2012). Discrimination and prediction of pork freshness by E-nose. *IFIP Advances in Information and Communication Technology*, 1: 1-14.
6. Kaczmarek, M., Avery, S. V. and Singleton, I. (2019). Microbes associated with fresh produce: Sources, types and methods to reduce spoilage and contamination. *Advances in Applied Microbiology*, 107: 4-5.
7. Ghasemi-Varnamkhasti, M., Apetrei, C., Lozano, J. and Anyogu, A. (2018). Potential use of electronic noses, electronic tongues and biosensors as multisensor systems for spoilage examination in foods. *Trends in Food Science and Technology*, 80: 71-92.
8. Dudnyk, I., Janeček, E. R., Vaucher-Joset, J. and Stellacci, F. (2018). Edible sensors for meat and seafood freshness. *Sensors and Actuators, B: Chemical*, 259: 1-9.
9. Lee, K., Baek, S., Kim, D. and Seo, J. (2019). A freshness indicator for monitoring chicken-breast spoilage using a Tyvek® sheet and RGB color analysis. *Food Packaging and Shelf Life*, 19: 40-46.
10. Maftoonazad, N. and Ramaswamy, H. (2019). Design and testing of an electrospun nanofiber mat as a pH biosensor and monitor the pH associated quality in fresh date fruit (Rutab). *Polymer Testing*, 75: 76-84.
11. Rukchon, C., Nopwinyuwong, A., Trevanich, S., Jinkarn, T. and Suppakul, P. (2014). Development of a food spoilage indicator for monitoring freshness of skinless chicken breast. *Talanta*, 130: 547-554.
12. Honeychurch, K. C. and Piano, M. (2018). Electrochemical (bio) sensors for environmental and food analyses. *Biosensors*, 8(3): 2-4.
13. Johnson, J., Atkin, D., Lee, K., Sell, M. and Chandra, S. (2019). Determining meat freshness using electrochemistry: Are we ready for the fast and furious? *Meat Science*, 150: 40-46.
14. Zeng, L., Peng, L., Wu, D. and Yang, B. (2019). Electrochemical sensors for food safety. *Nutrition in Health and Disease - Our Challenges Now and Forthcoming Time*: pp. 1-11.
15. Rustagi, S. and Kumar, P. (2013). Biosensor and its application in food industry. *Advance in Bioresearch*, 4(42): 168-170.
16. Thakur, M. S. and Ragavan, K. V. (2013). Biosensors in food processing. *Journal of Food Science and Technology*, 50(4): 625-641.
17. Dobrucka, R. and Przekop, R. (2019). New perspectives in active and intelligent food packaging. *Journal of Food Processing and Preservation*, 43(11): 1-9.
18. Kalpana, S., Priyadarshini, S. R., Maria Leena, M., Moses, J. A. and Anandharamakrishnan, C. (2019). Intelligent packaging: Trends and applications in food systems. *Trends in Food Science and Technology*, 93: 145-157.
19. Müller, P. and Schmid, M. (2019). Intelligent packaging in the food sector: A brief overview. *Foods*, 8(1): 16.
20. Perez de Vargas-Sansalvador, I. M., Erenas, M. M., Martínez-Olmos, A., Mirza-Montoro, F., Diamond, D. and Capitan-Vallvey, L. F. (2020). Smartphone based meat freshness detection. *Talanta*, 216: 1-24.
21. Plumpe, M., Beckers, M., Mecnika, V., Seide, G., Gries, T., and Bunge, C. A. (2017). Applications of polymer-optical fibres in sensor technology, lighting and further applications. *Polymer Optical Fibres*, 2017: 311-335.
22. Kuswandi, B. (2017). Freshness sensors for food packaging. *Reference Module in Food Science*: pp. 1-11.

23. Mujahid, A., and Dickert, F. L. (2012). Molecularly imprinted polymers for sensors: Comparison of optical and mass-sensitive detection. *Molecularly Imprinted Sensors*: pp. 125-159.
24. Peixoto, A. C. and Silva, A. F. (2017). Smart devices: Micro-and nanosensors. *Bioinspired Materials for Medical Applications*: pp. 297-329.
25. Skouteris, G., Webb, D. P., Shin, K. L. F. and Rahimifard, S. (2018). Assessment of the capability of an optical sensor for in-line real-time wastewater quality analysis in food manufacturing. *Water Resources and Industry*, 20: 75-81.
26. Zhang, H., Zhang, H., Aldalbahi, A., Zuo, X., Fan, C. and Mi, X. (2017). Fluorescent biosensors enabled by graphene and graphene oxide. *Biosensors and Bioelectronics*, 89: 96-106.
27. Lobnik, A., Turel, M. and Urek, Š. K. (2012). Optical chemical sensors: Design and applications. *Advances in Chemical Sensors*: pp. 4-28.
28. Weston, M., Kuchel, R. P., Ciftci, M., Boyer, C. and Chandrawati, R. (2020). A polydiacetylene-based colorimetric sensor as an active use-by date indicator for milk. *Journal of Colloid and Interface Science*, 572: 31-38.
29. Hasanah, U., Setyowati, M., Efendi, R., Muslem, M., Md Sani, N. D., Safitri, E. and Idroes, R. (2019). Preparation and characterization of a pectin membrane-based optical pH sensor for fish freshness monitoring. *Biosensors*, 9(2): 2-8.
30. Lee, G. Y. and Shin, H. S. (2016). Development of freshness indicator for quality of skate (Raja kenojei) during storage. *Food Science and Biotechnology*, 25(5): 1485-1489.
31. Wang, W., Xiong, Y. and Li, M. (2017). A renewable intelligent colorimetric indicator based on polyaniline for detecting freshness of tilapia. *Packaging Technology and Science,* 31(3): 133-140.
32. Ahmed, M. U., Hossain, M. M., and Tamiya, E. (2008). Electrochemical biosensors for medical and food applications. *Electroanalysis*, 20(6): 616–626.
33. Antuña-Jiménez, D., Díaz-Díaz, G., Blanco-López, M. C., Lobo-Castañón, M. J., Miranda-Ordieres, A. J. and Tuñón-Blanco, P. (2012). Molecularly Imprinted Electrochemical Sensors: Past, present, and future. *Molecularly Imprinted Sensors*: pp. 1-34.
34. Shaw, L. and Dennany, L. (2017). Applications of electrochemical sensors: Forensic drug analysis. *Current Opinion in Electrochemistry*, 3: 23-28.
35. Dejous, C., Hallil, H., Raimbault, V., Rukkumani, R. and Yakhmi, J. V. (2017). Using microsensors to promote the development of innovative therapeutic nanostructures. *Nanostructures for Novel Therapy: Synthesis, Characterization and Applications*, 539-561.
36. Zuber, A. A., Klantsataya, E., and Bachhuka, A. (2019). Biosensing. *Comprehensive Nanoscience and Nanotechnology*: pp. 105-126.
37. Thandavan, K., Gandhi, S., Sethuraman, S., Rayappan, J. B. B. and Krishnan, U. M. (2013). Development of electrochemical biosensor with nano-interface for xanthine sensing-A novel approach for fish freshness estimation. *Food Chemistry*, 139: 963-969.
38. Dervisevic, M., Custiuc, E., Çevik, E. and Şenel, M. (2015). Construction of novel xanthine biosensor by using polymeric mediator/MWCNT nanocomposite layer for fish freshness detection. *Food Chemistry*, 181: 277-283.
39. Dolmaci, N., Çete, S., Arslan, F. and Yaşar, A. (2012). An amperometric biosensor for fish freshness detection from xanthine oxidase immobilized in polypyrrole-polyvinylsulphonate film. *Artificial Cells, Blood Substitutes, and Biotechnology*, 40(4): 275-279.
40. Bourigua, S., El Ichi, S., Korri-Youssoufi, H., Maaref, A., Dzyadevych, S.and Jaffrezic Renault, N. (2011). Electrochemical sensing of trimethylamine based on polypyrrole-flavin-containing monooxygenase (FMO3) and ferrocene as redox probe for evaluation of fish freshness. *Biosensors and Bioelectronics*, 28(1): 105-111.
41. González, M. and González, V. (2005). Methods for the determination of water and minerals in food. *Food and Nutritional Analysis*: pp. 241-250.
42. Hu, J., Stein, A. and Bühlmann, P. (2016). Rational design of all-solid-state ion-selective electrodes and reference electrodes. *TrAC - Trends in Analytical Chemistry*, 76: 102-114.

43. Amemiya, S. (2007). Potentiometric Ion-Selective Electrodes. *In Handbook of Electrochemistry:* pp. 261-294.
44. Park, H. J., Yoon, J. H., Lee, K. G. and Choi, B. G. (2019). Potentiometric performance of flexible pH sensor based on polyaniline nanofiber arrays. *Nano Convergence*, 6(1): 1-7.
45. Kaneki, N., Tanaka, H., Kurosaka, T., Shimada, K. and Asano, Y. (2003). Measurement of fish freshness using potentiometric gas sensor. *Sensors and Materials*, 15(8): 413-422.

Malaysian Journal of Analytical Sciences (MJAS)
Published by Malaysian Analytical Sciences Society

NATURAL RADIOACTIVITY OF ^{210}Pb IN MUSSELS AT THE SEMI-ENCLOSED WATER OF THE JOHOR STRAIT, MALAYSIA THROUGH STATISTICAL APPROACH

(Radioaktiviti Semulajadi ^{210}Pb dalam Kupang di Perairan Separa-Tertutup Selat Johor, Malaysia Melalui Pendekatan Statistik)

Noor Affizah Bujang Saili and Che Abd Rahim Mohamed*

Department of Earth Sciences and Environment,
Faculty of Science and Technology
Universiti Kebangsaan Malaysia, 43600 UKM Bangi, Selangor, Malaysia

**Corresponding author: carmohd@ukm.edu.my*

Received: 10 August 2020; Accepted: 11 November 2020; Published: 20 February 2021

Abstract

Mussel and seawater samples were collected along the Johor Strait during the northeast monsoon, inter-monsoon, and southwest monsoon. The aim of this study is to determine the allometric relationship of ^{210}Pb and investigate the ^{210}Pb content in mussel tissues where there is semi-enclosed water flow. The statistical tests (ANOVA) indicate an insignificant relationship between mussel condition indexes (C*i*) related to seasons and geography. A high level of ^{210}Pb in mussels (mean: 29.33±6.65 Bq kg^{-1} dry weight) was measured during inter-monsoon with less dissolved oxygen content (< 3.0 mg L^{-1}). The causeway structure disrupts water quality and conditions in the Johor Strait and causes almost hypoxic conditions in its vicinity. That dissolved oxygen in the water column is inversely proportional to ^{210}Pb in mussels proves that oxygen deficiency is influenced the bioaccumulation of ^{210}Pb in mussels.

Keywords: Johor Strait, dissolved oxygen, hypoxia, monsoon, ^{210}Pb

Abstrak

Sampel kupang dan air laut diambil di sepanjang Selat Johor pada musim monsun timur laut, inter-monsun dan monsun barat daya. Matlamat kajian ini adalah untuk menentukan hubungan allometrik ^{210}Pb dan mengkaji kandungan ^{210}Pb dalam tisu kupang khususnya di perairan separa-tertutup. Ujian statistik (ANOVA) menunjukkan hubungan yang tidak signifikan di antara indeks keadaan kupang (C_i) terhadap perubahan musim dan keadaan geografi. Kandungan ^{210}Pb yang tertinggi dalam kupang (min: 29.33±6.65 Bq kg^{-1} berat kering) diperolehi pada musim inter-monsun di mana kandungan oksigen terlarut adalah pada paras yang rendah (< 3.0 mg L^{-1}). Struktur tambak telah menyekat aliran air dan menyebabkan kualiti air di perairan Selat Johor menghampiri keadaan hipoksik. Kandungan oksigen terlarut dalam turus air berkadar sonsang terhadap kandungan ^{210}Pb dalam kupang dan ini membuktikan kekurangan oksigen teralarut mempengaruhi bioakumulasi ^{210}Pb dalam kupang.

Kata kunci: Selat Johor, oksigen terlarut, hipoksia, monsun, ^{210}Pb

Introduction

Lead-210 (^{210}Pb, half-life, $t_{1/2}$: 22.3 years) is well known as a particle reactive radionuclide that is widely utilized as a tracer in marine geochemistry to determine sedimentation rate and particle scavenging in the water column. However, there are limited studies on ^{210}Pb especially on radiological risk to aquatic organisms compared to its progeny ^{210}Po. The ^{210}Pb radionuclide is presumed to be less significant in terms of radiation hazard to aquatic organism health as well as in its effect on humans. The concern arises through the improvement of the established method of chemical speciation which contributed to new findings on ^{210}Pb binding capacity in marine sediments. In anoxic sediments, about 5 to 33% of ^{210}Pb is bound to organic matter [1] and it is reported that more than 50% of organic matter preserved in surface sediments exposed to hypoxic conditions [2]. These findings trigger the question of ^{210}Pb bioavailability in an oxygen deficient environment.

Recently, anoxic, and hypoxic conditions in aquatic environments worldwide have been on the increase due to urbanization. Coastal development activities such as land reclamation are potential pathways and sediment sources which may contribute to anthropogenic support of ^{210}Pb in aquatic environments instead of that which is naturally produced from the *in-situ* decay of radium-226 (^{226}Ra, half-life =1600 years). In addition, the source of unsupported ^{210}Pb in shallow water regions originates largely from the atmospheric deposition results in the exclusive decay of radon-222 (^{222}Rn, half-life =3.82 days). The ^{210}Pb radionuclide is thus introduced into aquatic environments via rainfall into rivers, estuaries, and seas. However, ^{210}Pb is more particle-reactive and eliminated by suspended particulate matters [3]. The distribution of ^{210}Pb in an aquatic environment is subject to the interaction between dissolved and small particulate phases *via* sorption/ desorption as well as reversible ^{210}Pb exchange by small and large particulate phases by aggregation/ disaggregation [4]. Finally, the particulate matter will fall to the seabed and become part of surface sediment.

According to previous studies, radionuclide concentration in mussels significantly decreases with size [5, 6]. However, other factors e.g. local environmental conditions, hypoxia and season changes might also influence the variation of radionuclides in mussels [6]. The Johor Strait has undergone extensive development and has been established as an important site for aquaculture production of marine fishes and mussels as a local source of protein. Unfortunately, the causeway structure and industrial discharge along the Johor Straits are significantly interrupts the status marine water quality [7]. In addition, the strait is located in the tropics, which is affected by seasonal monsoons. Therefore, this study may contribute to new insight on ^{210}Pb behavior in mussels in the tropics in semi-enclosed marine areas and hypoxic conditions which not published by the previous researchers and will be also useful as a comparison with other subtropical regions. The purpose of this study is to investigate the behaviors and level of ^{210}Pb in mussels with the geography of shallow straits through the statistical approach.

Materials and Methods

Study area and sample collection

The Johor Strait is located between Malaysia and Singapore as established as the largest mussel's production in Malaysia [7]. Therefore, the Johor Strait was selected as a study area to understand the behavior of ^{210}Pb in the aquatic organisms. Green mussels (*Perna viridis*) have been established as a good bioindicator due to its sessile and filter feeding habits as well as its abundance in the Johor Strait [8, 9].

Sampling was conducted three times in the periods between 29th to 30th November 2017, 28th to 29th March 2018 and 1st to 2nd August 2018 during the northeast monsoon, inter-monsoon and southwest monsoon, respectively. Sampling stations were identified along the Johor Strait by considering the causeway structure which separates the water body into two regions (Figure 1). On the western half of the Johor Strait (WJS) there were three sample collection stations and six sampling stations on the eastern side of the Causeway (EJS).

Mussels were collected from each station by hand and were usually found attached on vertical ropes tied to floating rafts at 0.5 to 2 m depth in the water column. Samples were washed and separated based on their length as follows: small (< 5 cm), medium (between 5 to 7 cm) and large (> 7 cm). The weight, length and gonad condition of the mussels were recorded individually before the soft tissues were detached from the shell. Female gonad maturation was observed based on > 50% orange gonadal tissues covering the mantle (Figure 2). The soft tissue samples from each size interval were pooled and dried at 60 °C in the oven to constant weight. The soft tissue samples were then homogenized and 3 replicates from the pooled samples were proceeding for acid digestion. The results of the three replicates were averaged for reporting (dry weight) and the standard deviation is based on the replicates.

In-situ surface water quality parameters were recorded using a calibrated YSI (Professional Plus) at 1.0 m depth near the mussel rafts. About 20 L of seawater was taken using a Niskin water sampler at the same point where the water quality measurement was taken. All the samples were brought to the laboratory and filtered before proceeding to chemical extraction. Meanwhile, another 3 L of seawater were kept in opaque PE bottle and immediately filtered within 24 hours upon sampling time for chlorophyll-a analysis.

Chemical extraction

Published analytical procedures were applied [10, 11] where about 0.3 g of homogenized mussel powder was spiked with 20 mg mL^{-1} of lead nitrate, $Pb(NO_3)_2$ as chemical yield. Closed digestion was then performed by mixing 9 mL of nitric acid, HNO_3 and 3 mL of hydrogen peroxide, H_2O_2 (3:1) for 3 hours on a hotplate at 80 °C. The solution was thereafter filtered using 0.45 µm pore size glass fiber filter paper (Advantec), dried and dissolved with 50 mL of 0.5 M HNO_3 for purification. About 20 L of filtered seawater samples were filtered again through 0.45 µm pore size pre-weighted membrane filters following published analytical procedures for purification [12, 13].

Finally, ^{210}Pb was measured using the Gross Alpha-beta Spectrometry (Canberra Tennelec Model Series 5 XLB with Eclipse software) based on the growth of its immediate daughter ^{210}Bi which established equilibrium greater than 98% after 30 days. Analytical quality control was also applied with three replicates of Certified Reference Material IAEA-437 with yield recovery mean value of 72±18%.

Statistical analysis

Statistical Package for the Social Sciences (SPSS) Version 16.0 was used to perform statistical operations. Analysis of Variance (ANOVA) is a parametric test that determines whether there is any statistical significance between the means of ^{210}Pb relative to stations, regions, and sampling periods. In order to perform the ANOVA test, all the pre-requisite protocols are certified with parametric statistics. The deviated data processed under Kruskal-Wallis ANOVA with a statistically significant value of $p < 0.05$.

Follow-up analyses for ANOVA effect size were estimated manually by calculating the eta-square (η^2) which is easily interpreted as the proportion of variance in the dependent variable that can be attributed to the independent variable. The η^2 for omnibus ANOVA effect size was calculated as described in Eq. (1):

$$\eta^2 = \frac{SS_{Between}}{SS_{Total}} \quad (1)$$

where the $SS_{Between}$ is the between-group sum of squares, and the SS_{Total} is the total sum of squares, with both values obtained from the ANOVA summary table. Cohen [14] suggested that the η^2 values of 0.10, 0.59 and 1.38 could be considered as small, medium, and large effect sizes, respectively.

The η^2 was also calculated using the Kruskal-Wallis ANOVA effect size as shown in Eq. (2):

$$\eta^2 = [\chi^2] / (N - 1) \quad (2)$$

where, the chi-square (χ^2) value can be read from the statistic output and N is the total sample size. In this study, the effect size of Kruskal-Wallis ANOVA is represented as Cohen's *f* in Eq. (3):

$$f = \sqrt{\frac{\eta^2}{1-\eta^2}} \quad (3)$$

The f values could be considered as small, medium, and large effect sizes respectively, and were 0.10, 0.25 and 0.40 [14].

PAleontological STatistics (PAST3.26) software was used to perform a Linear Discriminant Analysis (LDA). LDA is a multivariate analysis that can best separate group data and provides more information about underlying dimensions. All the data were log-transformed in order to get normal distribution data ($p > 0.05$) before proceeding to the LDA analysis. A convex hull was selected instead of 95% ellipses to display clear discrimination in a scatter plot.

Mussels allometric

Each mussel's physiological status was determined using the Mussel Condition Index (*Ci*) as described by Lucas & Beniger [15] in Eq. (4):

$$(Ci) = W.L^{-3} \times 10^{6} \quad (4)$$

where W is the average of soft tissues in dry weight (g) and L is the average of shell maximum length (mm). Normally, a mussel's higher body weight and shell length corresponds to its age.

Concentration Factor

The concentration factor (CF) is derived in terms of unit volume and is expressed in L kg^{-1} as described in Eq. (5) at a steady state IAEA [16]:

$$\text{CF (L kg}^{-1}) = \frac{\text{Concentration per unit mass of organism (Bq kg}^{-1})}{\text{Concentration per unit volume of seawater (Bq L}^{-1})} \quad (5)$$

where, ^{210}Pb activities in mussels from each station were the average of small, medium, and large sizes in dry weight as there was no significant difference between sizes. The CF value is a rapid observation to investigate the ability of mussels in the Johor Strait to concentrate ^{210}Pb from their surroundings.

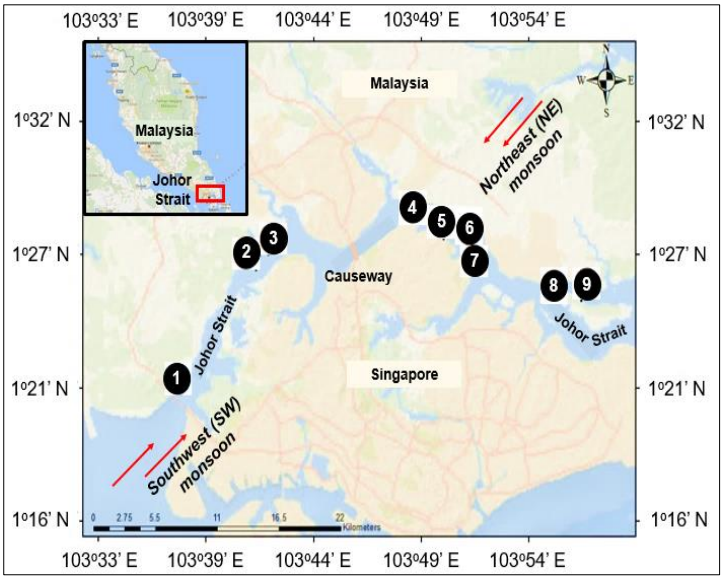


Figure 1. Map of Johor Strait which is separated by a causeway structure that links Malaysia and Singapore with monsoon wind directions. The western part of the Johor Strait (WJS) consists of Station 1 until Station 3, meanwhile the eastern part of the Johor Strait (EJS) region consists of Station 4 until Station 9

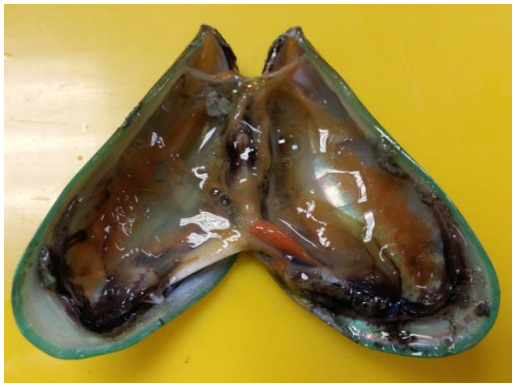


Figure 2. Female gonad maturation with > 50% orange gonadal tissues covering the mantle

Results and Discussion

Allometric relationships of ^{210}Pb in mussels

In order to investigate the effect of mussel sizes on ^{210}Pb activities, the mean biometric parameters of mussels at different time of sampling sessions, regions, and sizes are displayed in Table 1. An analysis of variance (ANOVA) showed significant differences in physiological C_i with regards to different mussel sizes ($F(2,54) = 27.330$, $p = 0.000$, $\eta^2 = 0.503$) which constantly decreases throughout their lifespan with a of mean 4.497 ± 0.789 (small), 3.377 ± 0.682 (medium) and 2.746 ± 0.553 (large). According to previous studies, the physiological C_i was sensitive to reproductive development [17, 18] and the depletion of glycogen as well as a cycle of lipid storage during gonad maturation, which then contributes to low physiological C_i [19]. In general, reproduction was very sensitive to temperature changes and food availability as well discussed by previous researcher [20].

However, this study revealed that there was no significant relationship between physiological C_i and temperature (Pearson's Correlation, $r = -0.131$, $N = 57$, $p = 0.330$ as well as chlorophyll-a content as a food availability indicator (Pearson's Correlation, $r = 0.136$, $N = 57$, $p = 0.312$). This insignificant relationship was also shown in the one-way ANOVA test (95% confident level) which proved that there was no significant physiological C_i changes at different sampling times ($F(2,54) = 1.477$, $p = 0.237$, $\eta^2 = 0.052$) and regions ($F(1,55) = 1.586$, $p = 0.213$, $\eta^2 = 0.028$) and stations ($F(8,48) = 0.818$, $p = 0.591$, $\eta^2 = 0.120$). Both statistical models demonstrate that growth and gonad maturation of mussels did not correspond to the fluctuation of stations and time. Female gonad maturation seems to be all-year-round in the tropical region with 14% to 15% for small sizes, 24% to 42% for medium sizes and 33% to 45% for large sizes (Figure 3). The spawning was similarly reported for *Perna viridis* [21, 22].

Figure 4 displays mussel growth as a function of (a) the maximum shell length and (b) tissue dry weight. Both dependent variables were best expressed as a power function of maximum shell length with high determination of coefficients for shell, wet and dry weight of tissues with R^2 value 0.913, 0.844 and 0.845, respectively. Those variables as a power function of tissue dry weight fit the data of shell and wet weight with R^2 value 0.884 and 0.964, respectively. All these statistics indicated that mussel growth is significantly related to size, where the weight increases proportionately with length throughout their lifespan. In general, mussels gain more energy for growth and gonad development when in its juvenile stages as the metabolism rate is higher than during its adult stages [22]. This is due to the greater energy needed for muscle development and growth than gonad development for reproduction. It is thus believed that small mussels have the potential to accumulate more contaminants such as radionuclides from the environment [23].

The level of ^{210}Pb activities in mussels varied between small, medium and large sizes ranging from 8.87 to 58.58 Bq kg^{-1} (mean = 19.82 ± 3.76 Bq kg^{-1}), 5.59 to 49.85 Bq kg^{-1} (mean = 21.06 ± 11.49 Bq kg^{-1}) and 9.86 to 35.47 Bq kg^{-1} (mean = 21.06 ± 7.51 Bq kg^{-1}), respectively. According to Vives I Battlle et al. [23] and Carvalho et al. [24], the allometric relationship between radionuclide contents with mussel size demonstrated high radionuclide content found in smaller mussels than in large ones. However, as far as the sizes were concerned, the Kruskal-Wallis ANOVA indicated that there was no significant difference in ^{210}Pb activities in mussels related to small (Mean Rank = 24.67), medium (Mean Rank = 29.04) and large sizes (Mean Rank = 31.32), ($\chi^2(2) = 1.247$, N = 57, $p = 0.536$, Cohen's f = 0.150). Therefore, ^{210}Pb activities in mussel soft tissues in the Johor Strait might be dominated by other factors than the physiological.

By comparison, ^{210}Pb activities in mussel soft tissues (5.59 to 58.58 Bq kg^{-1}, d.w. with mean 20.65 ± 7.59 Bq kg^{-1}) at the Johor Strait were higher than the Tejo Estuary in Portugal (10 ± 4 Bq kg^{-1} d.w.) [25] and the Vernice Lagoon, Italy (3 to 16 Bq kg^{-1} d.w.) [26]. However, our findings are still lower than that reported from the Turkish Coast of the Aegean Sea (6 to 135 Bq kg^{-1}, d.w.), which is affected by local pollutants e.g., domestic sewage, industries, etc. [6]. Other studies have also used bivalves for heavy metal and radionuclide pollution monitoring in the temperate region [27] as well as published by on ^{210}Pb [6, 25]. They also found [6, 25, 27] the level activities of ^{210}Pb in bivalves were high during winter season and assuming the unsupported of ^{210}Pb came from the atmospheric deposition. In contrast, the temperature (Table 2) in the tropical region shows no significant difference due to the hot and wet climate all the year ($F(2,24) = 1.375$, $p = 0.273$, $\eta^2 = 0.103$).

Table 1. Mean biometric parameters and ^{210}Pb activities in mussel soft tissues at different sampling times, regions, and sizes

Sampling	Region	Station	Size	N	Shell Length (mm)	Dry Weight Soft Tissues (g)	Condition Index (C_i)	^{210}Pb in Mussels (Bq kg^{-1}) d.w.
Northeast monsoon (29th -30th November 2017)	WJS	1	S	12	45.47	0.378	4.02	16.41 ± 5.06
			M	12	55.51	0.545	3.14	5.59 ± 5.28
			L	3	79.47	1.239	2.37	13.66 ± 4.26
		2	S	6	38.67	0.246	4.30	14.91 ± 4.97
			M	7	57.96	0.505	2.63	8.72 ± 3.02
			L	4	79.09	1.523	3.00	12.07 ± 3.82
		3	S	-	-	-	-	-
			M	15	60.46	0.465	2.12	15.61 ± 7.95
			L	16	74.12	0.772	1.91	12.14 ± 0.61
	EJS	6	S	10	42.77	0.254	3.19	14.87 ± 7.16
			M	7	57.93	0.468	2.43	18.77 ± 4.20
			L	-	-	-	-	-
		8	S	-	-	-	-	-
			M	14	62.44	1.076	4.39	10.81 ± 5.46
			L	14	84.35	2.196	3.76	16.45 ± 7.11
		9	S	-	-	-	-	-
			M	15	63.74	1.061	4.05	14.66 ± 9.78
			L	15	79.46	2.072	3.67	15.15 ± 6.12

Table 1 (cont'd). Mean biometric parameters and ^{210}Pb activities in mussel soft tissues at different sampling times, regions, and sizes

Sampling	Region	Station	Size	N	Shell Length (mm)	Dry Weight Soft Tissues (g)	Condition Index (C_i)	^{210}Pb in Mussels (Bq kg^{-1}) d.w.
Inter-monsoon 28th -29th March 2018)	WJS	1	S	10	42.29	0.381	4.79	30.23 ± 14.35
			M	16	63.34	1.057	4.14	16.85 ± 12.23
			L	16	79.78	1.742	3.42	25.07 ± 10.05
		2	S	15	38.60	0.269	4.61	24.83 ± 10.52
			M	20	61.07	0.803	3.53	33.63 ± 12.30
			L	18	76.41	1.319	2.92	9.86 ± 9.08
		3	S	-	-	-	-	-
			M	18	66.24	0.882	3.07	18.14 ± 8.50
			L	22	77.79	1.123	2.40	25.57 ± 10.58
	EJS	4	S	-	-	-	-	
			M	10	63.99	0.975	3.80	36.88 ± 14.26
			L	20	83.08	1.836	3.16	25.14 ± 18.33
		5	S	-	-	-	-	
			M	20	60.06	0.786	3.65	36.45 ± 14.55
			L	20	78.92	1.413	2.86	29.21 ± 27.46
		6	S	-	-	-	-	-
			M	20	64.00	0.516	1.98	49.85 ± 43.84
			L	20	74.32	0.755	1.84	23.05 ± 15.82
		7	S	17	45.24	0.356	3.80	58.58 ± 3.83
			M	20	57.41	0.576	3.09	34.37 ± 8.07
			L	20	78.50	1.040	2.16	30.36 ± 25.18
		8	S	-	-	-	-	-
			M	20	63.22	0.821	3.25	23.91 ± 21.90
			L	20	79.53	1.263	2.55	34.72 ± 12.75
		9	S	12	45.09	0.372	4.02	21.85 ± 0.60
			M	20	58.32	0.719	3.62	31.27 ± 24.04
			L	20	80.36	1.241	2.35	20.57 ± 23.04
Southwest monsoon (1st-2nd August 2018)	WJS	1	S	-	-	-	-	-
			M	30	57.00	0.701	3.66	13.47 ± 4.58
			L	15	75.56	1.419	3.24	12.42 ± 4.03
		2	S	20	31.66	0.176	5.38	12.18 ± 5.56
			M	30	58.36	0.894	4.39	29.32 ± 15.15
			L	24	75.24	1.461	3.39	12.28 ± 7.28
		3	S	20	31.09	0.188	5.77	12.75 ± 1.73
			M	30	56.19	0.781	4.35	10.68 ± 8.89
			L	13	83.81	1.501	2.60	35.47 ± 6.11
	EJS	5	S	-	-	-	-	-
			M	29	58.61	0.637	3.14	12.34 ± 5.64
			L	10	83.12	1.511	2.62	25.02 ± 12.42
		6	S	-	-	-	-	-
			M	30	60.94	0.871	3.78	15.77 ± 0.74
			L	19	80.71	1.534	2.97	20.64 ± 7.85
		7	S	20	36.40	0.266	5.50	12.72 ± 8.02
			M	20	61.57	0.699	3.02	23.50 ± 8.84
			L	19	79.85	0.949	1.94	23.33 ± 10.64

Table 1 (cont'd). Mean biometric parameters and ^{210}Pb activities in mussel soft tissues at different sampling times, regions, and sizes

Sampling	Region	Station	Size	N	Shell Length (mm)	Dry Weight Soft Tissues (g)	Condition Index (C_i)	^{210}Pb in Mussels (Bq kg^{-1}) d.w.
	EJS	8	S	20	36.17	0.234	4.82	8.87 ± 5.65
			M	20	61.51	0.818	3.49	7.88 ± 0.66
			L	13	74.82	1.050	2.45	22.94 ± 7.62
		9	S	20	36.29	0.181	3.76	9.65 ± 4.84
			M	20	64.52	0.801	2.94	15.97 ± 8.15
			L	15	80.00	1.464	2.84	18.15 ± 8.68

S (small): <5 cm; M (medium): 5-7 cm; L (large): >7 cm

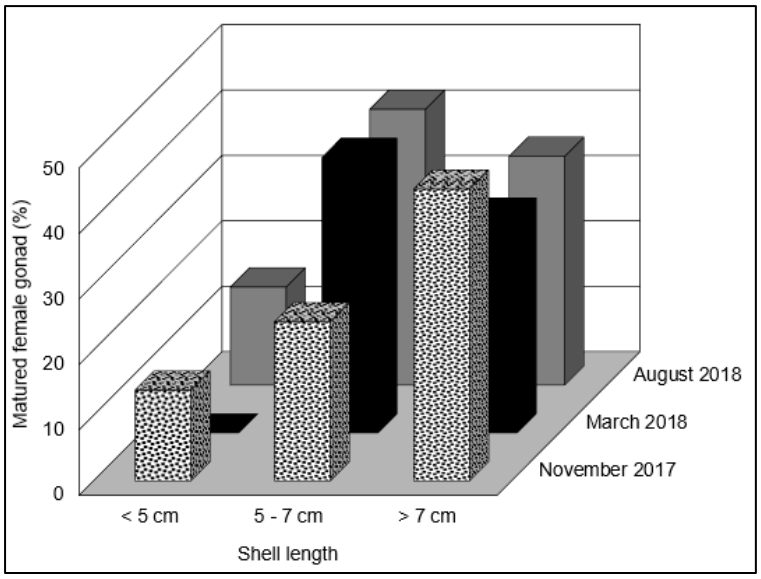


Figure 3. Percentage of matured female gonad at different size intervals and sampling periods

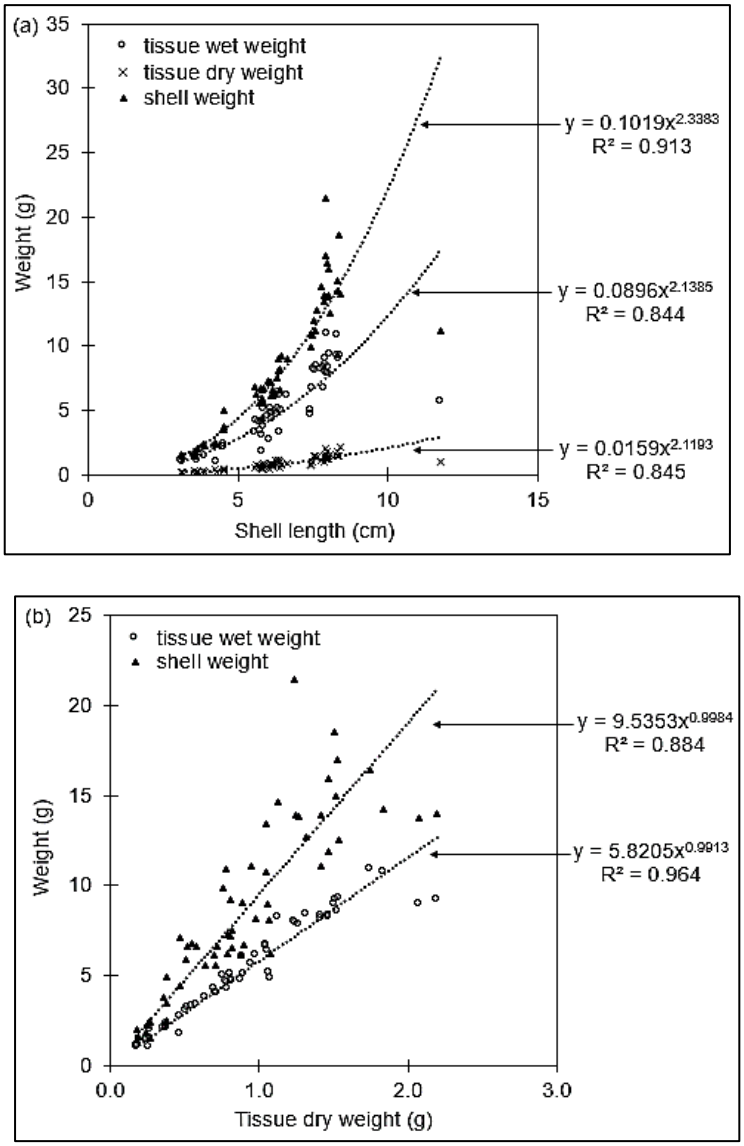


Figure 4. (a) Mussel growth based on shell and tissue weights (d.w. and w.w.) as a function of the maximum shell length and (b) Mussel growth based on shell and tissue weight (w.w.) as a function of tissue weight (d.w.). Each data plot is the average of individual biometric value of N samples as display in Table 1.

Table 2. Water parameter, ^{210}Pb in seawater and mussels along the Johor Strait at different sampling times

	Region	Station	N	Water Parameter				^{210}Pb Activity	
				Depth (m)	Temp (°C)	DO (mg L^{-1})	Chl-a (µg L^{-1})	^{210}Pb in Sea Water (mBq L^{-1})	^{210}Pb in Mussel* (Bq kg^{-1}) d.w.
Northeast monsoon (29th -30th Nov 2017)	WJS	1	27	10.13	29.9	7.32	21.99	4.58 ± 1.99	11.89 ± 5.62
		2	17	6.33	29.8	5.39	25.69	4.61 ± 1.58	11.90 ± 3.10
		3	31	8.33	29.8	7.66	30.81	3.71 ± 1.81	13.87 ± 2.45
	EJS	4	-	11.67	29.8	2.14	-	3.46 ± 1.33	-
		5	-	11.47	29.5	2.16	-	4.10 ± 1.71	-
		6	17	11.07	29.6	3.75	10.49	5.13 ± 2.34	16.82 ± 2.76
		7	-	15.67	29.6	3.65	-	5.25 ± 2.44	-
		8	28	10.10	29.1	6.02	16.73	5.34 ± 2.32	13.63 ± 3.99
		9	30	6.70	29.1	5.96	8.21	4.82 ± 1.87	14.90 ± 0.35
inter-monsoon (28th -29th March 2018)	WJS	1	42	9.70	29.3	4.75	0.53	3.49 ± 1.20	24.05 ± 6.75
		2	53	3.53	29.3	2.78	2.41	3.76 ± 1.66	22.77 ± 12.02
		3	40	4.07	29.9	2.13	0.82	2.83 ± 1.15	21.86 ± 5.25
	EJS	4	30	9.97	29.9	2.10	14.91	3.95 ± 1.62	31.01 ± 8.30
		5	40	15.00	29.9	2.10	4.98	3.74 ± 1.37	32.83 ± 5.12
		6	40	15.70	29.5	2.69	6.82	3.06 ± 1.40	36.45 ± 18.95
		7	57	16.50	29.4	2.96	1.47	3.48 ± 1.60	41.10 ± 15.27
		8	40	6.93	29.1	5.05	11.73	3.07 ± 1.31	29.31 ± 7.64
		9	52	7.53	29.1	6.26	10.20	3.69 ± 1.63	24.56 ± 5.84
Southwest monsoon (1st-2nd Aug 2018)	WJS	1	45	9.40	29.4	4.61	4.57	4.96 ± 2.27	12.95 ± 0.74
		2	74	4.50	29.7	3.55	11.30	3.79 ± 1.68	17.93 ± 9.87
		3	63	4.70	29.7	3.13	11.13	3.86 ± 1.55	19.63 ± 13.75
	EJS	4	-	5.40	30.0	1.63	-	3.25 ± 1.44	-
		5	39	15.30	30.2	4.17	15.05	3.84 ± 1.74	18.68 ± 8.97
		6	49	16.70	30.0	3.29	5.43	3.38 ± 1.59	18.20 ± 3.44
		7	59	15.40	29.9	4.01	5.06	5.28 ± 2.81	19.85 ± 6.18
		8	53	8.70	29.4	4.52	1.68	5.23 ± 2.10	13.23 ± 8.42
		9	55	5.90	29.3	4.64	0.59	3.41 ± 1.67	14.59 ± 4.41

* ^{210}Pb in mussel are in average of all sizes.

November 2017 – Mussel cages at Stations 4, 5 and 7, the line was covered by unidentified mussels which believed as an invasive species.

August 2018 – Mussel cages at Station 4 have been removed due to reclamations activities

Discrimination of ^{210}Pb in mussels by monsoon season

Since the univariate analysis obtained revealed insignificance in the variation of ^{210}Pb activities in mussel tissues at different sizes, a Linear Discriminant Analysis (LDA) was utilized to get a better picture of the data and predict the best discrimination component effect of ^{210}Pb activities in mussels. The LDA will provide the best set of variables into group within the minimum error, where Figure 5 shows the scatter plotted contents of ^{210}Pb in mussels which 87% of data have been classified correctly according to the sampling periods. The highest accuracy of ^{210}Pb activities in mussels was 89% in March 2018 followed by 88% in August 2018 and 83% in November 2017. The Kruskal-Wallis ANOVA test indicated that there was significance in the correlation between ^{210}Pb activities in mussels and time of sampling with the highest mean rank score of about 42.59 in March 2018, followed by 22.76 in August 2018 and 17.00 in November 2017, ($\chi^2(2) = 25.034$, N = 57, $p = 0.000$, Cohen's f = 0.899).

The convex hulls clearly showed that ^{210}Pb activities in March 2018 significantly discriminated from November 2017 and August 2018. Figure 6 illustrates the distribution of ^{210}Pb in mussels, which is consistently higher in March 2018 than November 2017 and August 2018 for all size intervals.

In the Johor Straits, the NE monsoon usually occurs from October to March (sampling conducting in November 2017 represents the effects of the NE monsoon), meanwhile March 2018 represents the inter-monsoon season since sampling was conducted at the end of March. The SW monsoon begins in April and lasts until September (sampling in August 2018 represents the SW monsoon). The NE and SW monsoon seasons experience abundant rainfall from different wind directions compared to the inter-monsoon which has less precipitation (Figure 7). Therefore, the mean activities of ^{210}Pb in seawater during the NE (4.56 ± 0.67 mBq L^{-1}) and SW (4.11 ± 0.27 mBq L^{-1}) monsoons were higher than during the inter-monsoon (3.45 ± 0.38 mBq L^{-1}) (Table 2).

The ^{210}Pb activity in mussels related to seawater demonstrated an inverse relationship significant at 99% confidence level (Pearson's correlation, $r = -0.573$, N = 23, $p = 0.004$) which contradicts the nature of mussels as a bioindicator. In general, high pollutants in mussels indicate a high level of pollution in its environment e.g., the Turkish coast of the Aegean Sea established high ^{210}Pb activities in mussels during winter where high precipitation is believed to be the source of unsupported ^{210}Pb [6]. In contrast to this scenario, we suggest that the lower dissolved oxygen content given the hypoxic environment in the Johor Strait is indirectly related to the inter-monsoon season. Figure 8a shows the distribution of DO along the Johor Strait which decreases constantly towards the causeway during the inter-monsoon season where less rainfall potentially limited water flow resulted from the causeway connecting Johor and Singapore. During the inter-monsoon, ^{210}Pb activity in seawater increases proportionally with DO while ^{210}Pb activities in mussels' increases with a decrease in DO level content (Figure 8b). In the water column, Fe and Mn hydroxide cause the preferential removal of ^{210}Pb to suspended particulate matter *via* unselective co-precipitation [29, 30] which is associated with the changes in physicochemical properties of the water column during the inter-monsoon [31]. Meanwhile the high tolerance mussels established the lowest percentage of gonad maturation during inter-monsoon and contribute to high ^{210}Pb uptake *via* unselective ingestion to restore their energy [21, 22]. These clearly indicate that the distribution content of ^{210}Pb in seawater and mussels in the Johor Straits correspond to a hypoxic environment.

About 87% is true using the LDA statistical test analysis for a classified scatter plot (Table 3) with a misclassified value of only about 13%. Table 3 summarizes the confusion matrix of ^{210}Pb activities in mussels assigned by sampling period. The misclassified values for November 2017, March 2018 and August 2018 were 17%, 11% and 13%, respectively. Specifically, the misclassified values came from Station 6 (Pasir Gudang port), Station 3 (west coast near the Causeway) and Station 1 (close to Tanjung Pelepas port). These misclassified values might due to geographic elements

(e.g., industry, harbour, and causeway) and other similar factors at these specific locations which subsequently influence the ^{210}Pb activities in mussels and the water column. According to Ugur et al. [6], the source of ^{210}Pb could be from local pollution and rivers as well as rainfall input. In this case, we found that all the misclassified stations located near the causeway structure caused hypoxic conditions associated with the status of *in-situ* water parameters (e.g., pH, dissolved oxygen, and total suspended particles).

Environmental effect to bioconcentration of ^{210}Pb in mussels

In order to understand the relationship between ^{210}Pb in mussels related to ambient water in the Johor Straits, the concentration factor (CF) has been utilized as a simple indicator for contaminant substance uptake in mussels from water exposure. Generally, the CF value in this study ranged from 10^3 to 10^4 which exceeds the ^{210}Pb CF recommendation value, 1×10^3 L kg^{-1} [31]. The highest mean of CF values obtained was found during the March 2018 ($8.6 \pm 2.1 \times 10^3$ L kg^{-1}) sampling, followed by August 2018 ($4.2 \pm 1.1 \times 10^3$ L kg^{-1}) and November 2018 ($3.0 \pm 0.5 \times 10^3$ L kg^{-1}). A positive and strong relationship between CF values and ^{210}Pb in mussels at 99% confidence level (Pearson's Correlation, r = 0.9625, N = 23, p = 0.000) was determined (Figure 9). The inter-monsoon season in the Johor Straits caused less water flow, lower levels of dissolved oxygen content and the high decomposition process of suspended particles will affect the water quality and organisms living there. Therefore, high ^{210}Pb activities in mussels during the inter-monsoon is influenced by metabolic transformation, which then increases the uptake of ^{210}Pb *via* ingested food as well as by respiratory uptake *via* gills [24]. Metabolic transformation is a mechanism which is developed by organisms to survive under thermal stress and oxygen deprivation at low tide and is used by most bivalves that inhabit the intertidal zone [32]. However instead of its use to survive under natural environmental changes, these mussels were exposed to anthropogenic activities as well.

Table 2 shows the water parameters along the Johor Strait at different sampling times. There were dramatic changes in dissolved oxygen (DO) content between stations along the Johor Strait (Kruskal-Wallis ANOVA, $\chi^2(8) = 16.214$, N = 27, p = 0.039, Cohen's f = 1.238). This study revealed that the causeway structure interrupts water quality where DO concentrations decrease on both sides of the Straits and becomes almost hypoxic adjacent to the causeway. Figure 8a shows the distribution of DO content in the water column along the Johor Strait and how it decreases toward the causeway structure in both halves of the EJS and WJS. The lowest DO value was recorded at Station 4 which decreases from 2.14 mg L^{-1} > 2.10 mg L^{-1} > 1.63 mg L^{-1} (hypoxic, O_2 < 2 mg L^{-1}) from the November 2017 to the August 2018 sampling. Figure 8b proved that the deficiency of dissolved oxygen content in the water column potentially affects the level of ^{210}Pb in mussels with R^2 value 0.428. The deficiency of oxygen content in the water column potentially influences the bioavailability of ^{210}Pb in mussels and metabolic transformation might be relevant in a build-up of CF values due to environmental changes [33].

In this study, the causeway structure was believed to be an obstruction of the water flow in the Johor Strait. Figure 10a shows the whisker plot of ^{210}Pb in mussels at the WJS and EJS with an outlier of case number 37. The Kruskal-Wallis ANOVA ($\chi^2(1) = 3.952$, N = 57, p = 0.0.047, Cohen's f = 0.2754) proved that, there was significant differences between the two regions where the ^{210}Pb in mussels at the EJS (Mean Rank = 32.73) was much higher than WJS (Mean Rank = 23.88). The outlier of case number 37 with score 58.58 occurred at Station 7 (Kuala Masai) during the inter-monsoon. This outlier was not neglected because the authors found that the Masai River has a 10 year history of pollution issues that is frequently reported in Malaysian mainstream media [34].

Figure 10b illustrates the distribution of ^{210}Pb in mussels and seawater at different stations along the Johor Strait. Besides Station 7, Station 4 is also exposed to higher ^{210}Pb activity. The causeway structure limits water spreading especially at the EJS and thus potentially accumulates more ^{210}Pb as well as other contaminants. Water quality is shown to be poor, especially adjacent to the causeway, which is almost hypoxic, thus

significantly contributing to higher ^{210}Pb in mussels (Figure 7). However, the experiment done by Wang et al. [35] indicated that the reduction of DO content reduced absorption efficiency and respiration rates of the mussels.

We presume that, the higher accumulation of ^{210}Pb in mussels at the hypoxic zone is probably due to its high tolerance to the reduction of DO content and exposes them longer to the ambient water. Furthermore, the behavior of ^{210}Pb in hypoxic environments should be considered instead of the mussel's physiological responses. In marine environments, hypoxic bottom water conditions potentially preserve more than 50% of the organic matter (OM) in surface sediments than oxic conditions, contributing 5 to 33% of total ^{210}Pb bound to OM [2, 36]. Consequently, the authors suggest that the causeway structure potentially exposes the Johor Strait to higher bioavailability of ^{210}Pb due to the hypoxic conditions where organic particle suspension in the water column seems to be a major pathway for ^{210}Pb absorption by mussels [37].

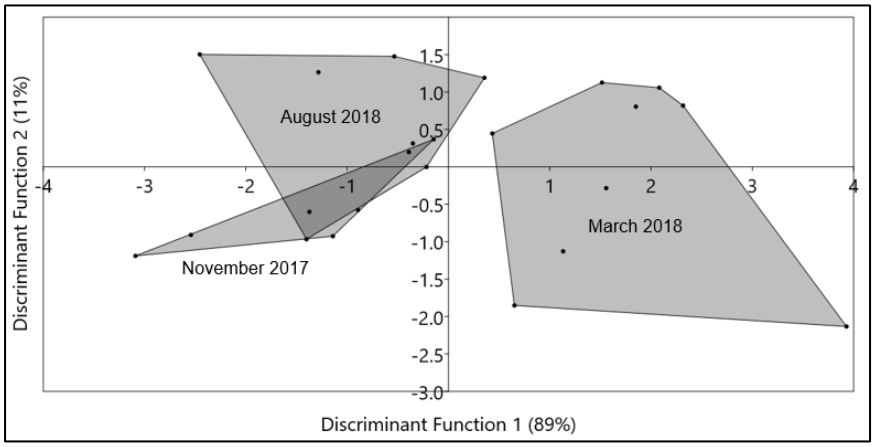


Figure 5. LDA scatter plot of ^{210}Pb activities in mussels' samples (N=23) classified with convex hulls by different time of sampling

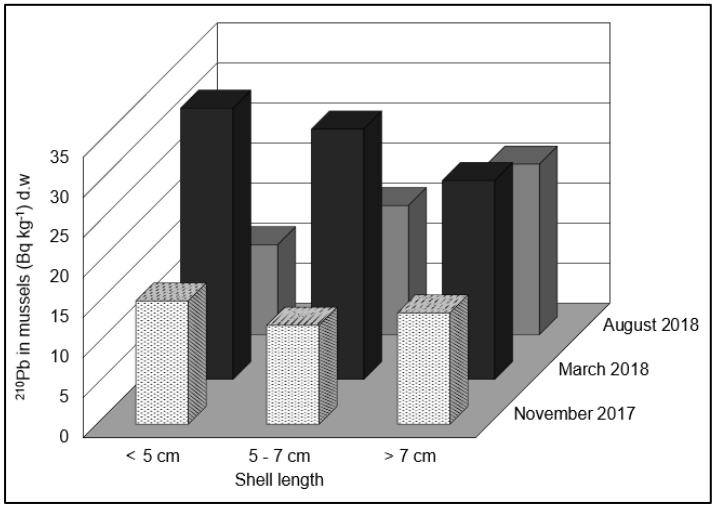


Figure 6. ^{210}Pb in mussels (Bq kg^{-1}) at different size intervals and sampling periods

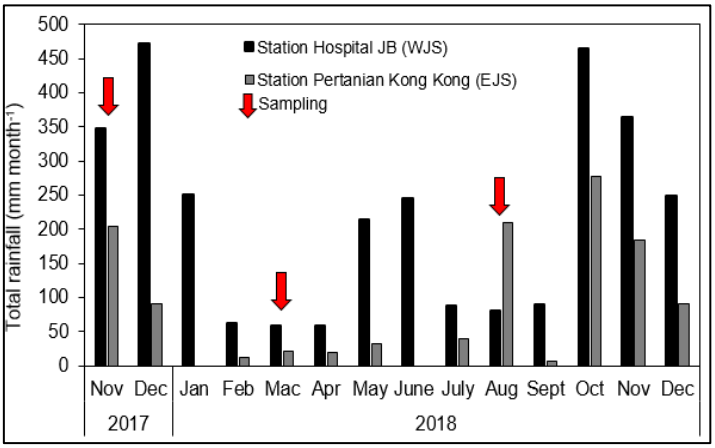


Figure 7. Distribution of total rainfall at the WJS and EJS from November 2017 to December 2018 [28]

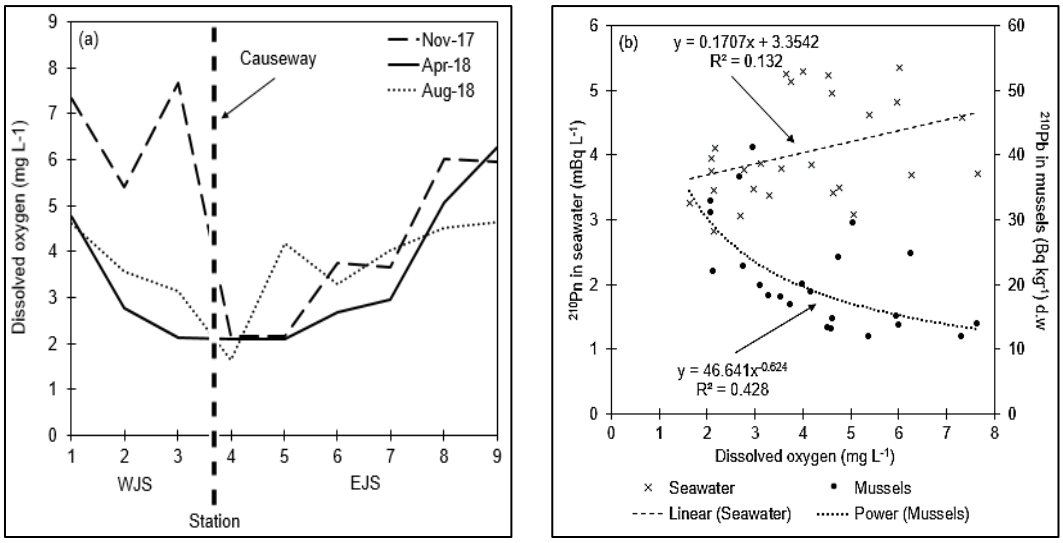


Figure 8. (a) Distribution of Dissolved Oxygen (DO) in water column in the western (WJS) and eastern (EJS) of the Johor Strait, (b) ^{210}Pb in seawater (dissolved phase) proportionate with DO in the water column which contradicts the inverse relationship of ^{210}Pb in mussels as a function of DO

Table 3. Confusion matrix of ^{210}Pb activities in mussels assigned by sampling period

Sampling Time	November 2017	March 2018	August 2018	Total
November 2017	5	0	[c]1	6
March 2018	0	8	[b]1	9
August 2018	[a]1	0	7	8
Total	6	8	9	23

Row: given groups, Column: predicted groups, [a]Station 1, [b]Station 3, [c]Station 6

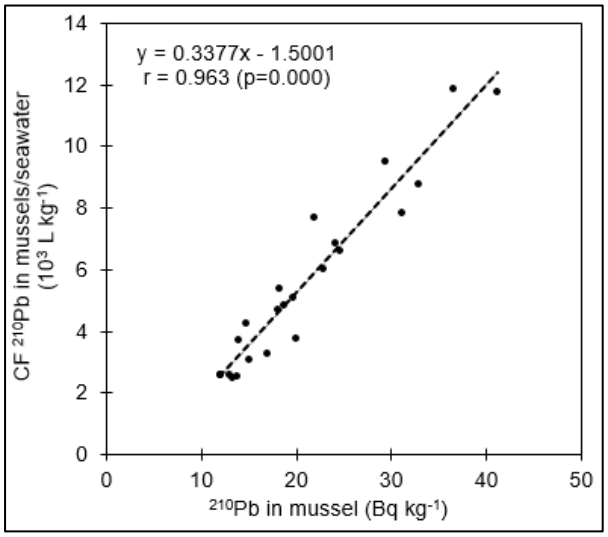


Figure 9. Relationship between concentration factors (CF) of ^{210}Pb in mussels related to seawater and ^{210}Pb in mussels

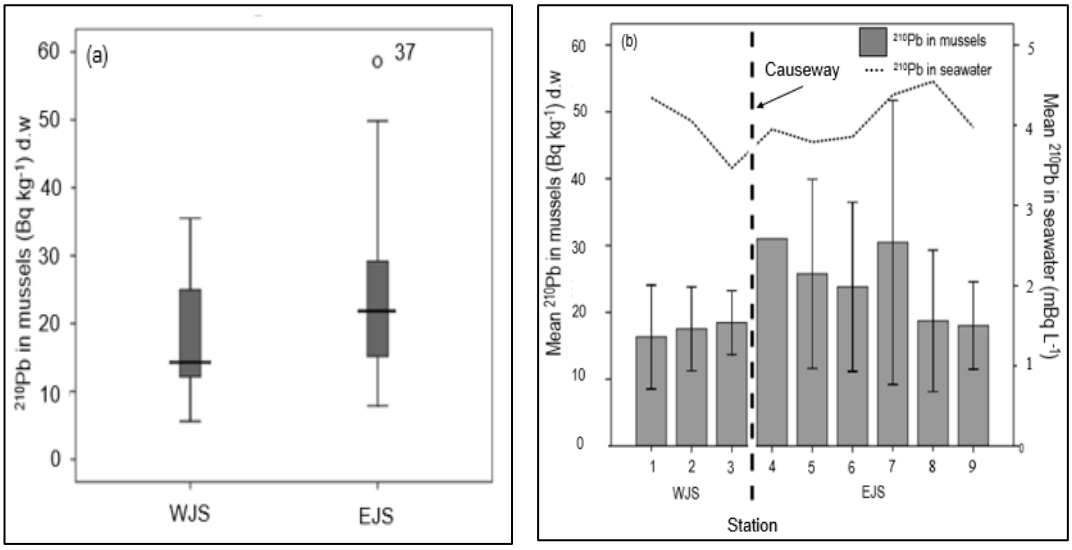


Figure 10. (a) The whisker plot of ^{210}Pb in mussels at the WJS and EJS with an outlier of case number 37 (station 7), and (b) The mean distribution of ^{210}Pb in mussels and seawater along the Johor Strait

Conclusion

The highest ^{210}Pb activity in mussels occurred during the inter-monsoon which there is less precipitation and water flushing. The causeway structure limits water flow and causes the environment to be almost hypoxic especially adjacent to the causeway. The extent of oxygen deficiency was expanded during the inter-monsoon. The inverse relationship between ^{210}Pb in mussels as a function of dissolved oxygen in the water column indicates that the oxygen deficiency potentially influences the bioavailability of ^{210}Pb in mussels. The metabolic transformation as well as unselective ingestion might be relevant in the build-up of CF due to environmental changes. Further works are required to identify the species of ^{210}Pb in order to confirm the percentage of the bioavailability ^{210}Pb in the Johor Strait and comprehensive dose assessment of ^{210}Pb to human *via* mussel consumption.

Acknowledgement

This research is supported by Universiti Kebangsaan Malaysia grant (code: DPK-2017-010). The authors would like to thank all the members of Land-Atmospheric-Ocean Interaction Research (LAOI) group, Faculty of Science and Technology, Universiti Kebangsaan Malaysia for their help during sampling and sample analysis.

References

1. Connan, O., Boust, D., Billon, G., Solier, L., Rozet, M. and Bouderbala, S. (2009). Solid partitioning and solid-liquid distribution of ^{210}Po and ^{210}Pb in marine anoxic sediments: roads of Cherbourg at the northern France. *Journal of Environmental Radioactivity,* 100: 905-913.
2. Jessen, G. L., Lichtschlag, A., Ramette, A., Pantoja, S., Rossel, P. E., Schubert, C. J., Struck, U. and Boetius, A. (2017). Hypoxia causes preservation of labile organic matter and changes seafloor microbial community composition (Black Sea). *Science Advances,* 3: 1-14.
3. Bacon, M. P., Spencer, D. W. and Brewer, P. G. (1976). ^{210}Pb/^{226}Ra and ^{210}Po/^{210}Pb disequilibria in seawater and suspended particulate matter. *Earth Planetary Science Letters,* 32: 277-296.
4. Rigaud, S., Stewart, G., Baskaran, M. and Marsan, D. (2015). ^{210}Po and ^{210}Pb distribution, dissolved-particulate exchange rate, and particulate export along the North Atlantic US GEOTRACES GA03 section. *Deep Sea Research Part II,* 116: 60-78.
5. Carvalho, F. P., Oliveira, J. M., Alberto, G. and Vives I Batlle, J. (2010). Allometric relationship of ^{210}Po and ^{210}Pb in mussels and their application to environmental monitoring. *Marine Pollution Bulletin,* 60: 1734-1742.
6. Ugur, A., Ozden, B. and Filizok, I. (2011). Spatial and temporal variability of ^{210}Po and ^{210}Pb in mussel (*Mytilus galloprovincialis*) at the Turkish of the Aegean Sea. *Chemosphere,* 83: 1102-1107.
7. Ismail, M., Hashim, N. N. and Kazemi, Z. (2016). Estimating dissolved oxygen depletion in inner western Johor Strat, Malaysia using a three dimensional water quality model. *Malaysian Journal of Civil Engineering,* 28(3): 240-251.
8. Yap, C. K., Ismail, A., and Tan, S. G. (2004). Biomonitoring of heavy metal in the west water of Peninsular Malaysia using the green-lipped mussel *Perna viridis*: Present Status and What Next?. *Journal of Tropical Agriculture Science*, 27(2):151-161.
9. Othman, Z., Wahid, M. A., Lee, W. K. and Mohamed Basri, Z. D. (2015). Water quality observation on Johor River Estuary and East Tebrau Strait, Malaysia. *Jurnal Teknolologi*, 72(1): 1-4.
10. Mohamed, C.A.R., Tee, L.T., Zal, U.M., Zaharuddin, A. and Masni, M.A. (2006). Activity concentrations of ^{210}Po and ^{210}Pb in edible tissue of fish caught at Kuala Selangor, Malaysia. *Malaysian Applied Biology Journal* 35(2): 67-73.
11. Zakaria, N., Sarimin, A.S., Sabuti, A.S. and Mohamed, C.A.R. (2013). Assessment activity of ^{210}Po and ^{210}Pb in the edible tissues of cultured seabass (*Lates calcarifer*) at Peninsular Malaysia. *Environmental Asia* 6(1): 66-73.
12. Theng, T. L. and Mohamed, C. A. R. (2005). Activities ^{210}Po and ^{210}Pb in the water column at Kuala Selangor, Malaysia. *Journal of Environmental Radioactivity*, 80(3): 273-286.

13. Sabuti, A. A. and Mohamed, C. A. R. (2010). Lead. In: Radionuclides in the environment (Ed: Atmood DA). John Wiley and Sons Co, Ltd: pp. 139-147.
14. Cohen, J. (1988). Statistical power analysis for the behavioural science (2nd edition) Hillsdale, N.J: Erlbaum
15. Lucas, A. and Beniger, P. G. (1985). The use of physiological condition indices in marine bivalve aquaculture. *Aquaculture,* 44: 187-200.
16. IAEA (2001). Generic models for use in assessing the impact of discharges of radioactive substances to the environment. Vienna, International Atomic Energy Agency.
17. Ojea, J., Pazos, A. J., Martinez, D., Novoa, S. and Sanchez, J. L. (2004). Seasonal variation in weight and biochemical composition of tissue of *Ruditapes decussatus* in relation to the gametogenic cycle. *Aquaculture*, 238: 451-469.
18. Peharda, M., Mladineo, I., Bolotin, J., Kekez, L. and Skaramuca, B. (2006). The reproductive cycle and potential protandic development of the Noah's Arc shell, *Arca noae* L.: Implications for aquaculture. *Aquaculture*, 252: 317-327.
19. Orban, E., Di Lena, G., Nevigato, T., Casini, I., Marzetti, A. and Caproni, R. (2002). Seasonal changes in meat content, condition index and chemical composition of mussels (*Mytilus galloprovincialis*) cultured in two different Italian sites. *Food Chemistry,* 77: 57-65.
20. Gosling, E. (2003). Bivalve molluscs-biology, ecology and culture. Fishing New Books, Oxford Press.
21. Laxmilatha, P. (2013). A review of the green mussel, *Perna viridis* fishery of South West Coast of India. *International Journal of Marine Science,* 3: 408-416.
22. Soon, T. K. and Ransangan, J. (2014). A review of feeding behaviour, growth, reproduction, and aquaculture site selection for green-lipped mussel, *Perna viridis*. *Advances in Bioscience and Biotechnol*ogy, 5: 462-469.
23. Vives I Battlle, J., Wilson, R. C., Watts, S. J., McDOnald, P. and Craze, A. (2009). Derivation of allometric relationships for radionuclides in marine phyla. *Radioprotection,* 44: 47-52.
24. Carvalho, F. P. (2018). Radionuclide concentration process in marine organism: A comprehensive review. *Journal of Environmental Radioactivity,* 186: 124-130.
25. Carvalho, F. P., Oliveira, J. M. and Alberto, G. (2010). Factors affecting ^{210}Po and ^{210}Pb activity concentrations in mussels and implications for environment bio-monitoring programmes. *Journal of Environmental Radioactivity,* 102: 128-137.
26. Jia, G., Belli, M., Sansone, U., Rosamilia, S. and Blasi, M. (2003). ^{210}Pb and ^{210}Po concentration in the Vernice lagoon ecosystem (Italy) and the potential radiological impact to the public and environment. *Journal of Radioanalytical and Nuclear Chemistry,* 256(3): 513-528.
27. Fonolosa, E., Penalver, A., Aguilar, C. and Borrull. (2017). Bioaccumulation of natural radionuclides in molluscs from the Ebro Delta area. *Environmental Science Pollution Research,* 24: 28-214.
28. Malaysian Meteorological Department (2018). Taburan hujan di Stesen Hospital JB dan Stesen Pertanian Kong Kong Johor 2017-2018.
29. Carvalho, F. P. (1995). ^{210}Pb and ^{210}Po in sediment and suspended matter in Targus Estuary. Local enhancement of natural levels by wastes from phosphate ore processing industry. *Science Total Environment Journal,* 159: 201-161.
30. Benoit, G. and Rozan, T. F. (1999). The influence of size distribution on the particle concentration effect and trace metal partitioning in rivers. *Geochemica et Cosmochimica Acta,* 63(1): 113-127.
31. Sanudo-wilhelmy, S. A., Rivera-Duarte, I. and Flegal, A. R. (1996). Distribution of colloidal trace elements in San Fransisco Bay estuary. *Geochemica et Cosmochimica Acta,* 60: 4933-4944.
32. Anestis, A., Portner, H.O. and Michaelidis, B. (2010). Anaerobic metabolic patterns related to stress responses in hypoxia exposed mussels *Mytilus galloprovincialis*. *Journal of Experimental Marine Biology and Ecology,* 394: 123-133.

33. Giannetto, A., Maisano, M., Cappello, T., Olivia, S., Parrino, V., Natalotto, A., Marco, G. D. and Fasulo, S. (2017). Effect of oxygen availability on oxidative stress biomarkers in the Mediterranean mussels *Mytilus galloprovincialis*. *MarineBiotechnology,* 2017: 1-13.
34. Kosmo Online (2018). Sungai Masai Besar tercemar 10 tahun, nelayan minta pembelaan, access from http://www.kosmo.com.my/negara/sungai-masai-besar-tercemar-10-tahun-nelayan-minta-pembelaan1.627 512. [Accessed date 5 September 2019].
35. Wang, Y., Hu, M., Wong, W. H., Shin, P. K. S. and Chueng, S. G. (2011). The combined effects of oxygen availability and salinity on physiological responses and scope for growth in the green-lipped mussel *Perna viridis*. *Marine Pollution Bulletin*, 63: 255-261.
36. Ontiveros-Cuadras, J. F., Ruiz-Ferna´ndez, A. C., Sanchez-Cabeza, J. A., Wee-Kwong, L. L. and Pe´rez-Bernal L. H. (2012). Geochemical fractionation of ^{210}Pb in oxic estuarine sediments of Coatzacoalcos River, Gulf of Mexico. *Journal of Radioanalytical and Nuclear Chemistry,* 292: 947-956.
37. Pan, J. F. and Wang, W. X. (2004). Differential uptake of dissolved and particulate organic carbon by the marine mussel *Perna viridis*. *Limnology and Oceanography*, 49: 1980-1991.

Malaysian Journal of Analytical Sciences Vol 25 No 2 2021

		Page
	Editorial: Utilization Modern Analytical Instruments for Food and Plant Analysis *Wan Mohd Afiq Wan Mohd Khalik and Sabiqah Mohd Anuar* Malaysian Analytical Sciences Society (ANALIS)	i
1.	ELECTROCHEMICAL IMPEDIMETRIC BIOSENSOR BASED ON SILICON-ON-INSULATOR NANOGAP FOR THE DETECTION OF BANANA BLOOD DISEASE BACTERIUM (Biosensor Impedimetrik Elektrokimia Berasaskan Silikon-Pada-Penebat Jurang Nano untuk Pengesanan Bakteria Penyakit Darah Pisang) *Masniza Sairi, Khairul Anuar Shafie, Ahmad Syazwan Ismail, Nur Azura Mohd Said, Noor Azlina Masdor, Nur Humaira Md Salleh, Ten Seng Teik, Siti Noraini Bunawan, Mohd Afendy Abdul Talib, Nur Sulastri Jaffar, Izyani Raship*	184
2.	BIODEGRADATION OF OIL AND GREASE FROM AGRO-FOOD INDUSTRY BY IMMOBILISED *Serratia marcescens* SA30 (Biodegradasi Minyak dan Gris dari Industri Agro-Makanan oleh *Serratia marcescens* SA30 yang Dipegunkan) *Shakila Abdullah, Farhah Husna Mohd Nor, Mohd Hairul Khamidun*	193
3.	OILY SAND CLEANING OPTIMIZATION BY SURFACTANTS INTERFACIAL TENSION SCREENING AND HYDROCYCLONE SEPARATION (Pengoptimuman Pembersihan Pasir Berminyak oleh Saringan Ketegangan antara Muka Surfaktan dan Pemisahan Hidrosiklon) *Akhmal Sidek, Ahmad Faiq Omar, Aizuddin Supee, Amni Haslinda Alpandi, Hazlina Husin, Dewandra Bagus Ekaputra, Shaziera Omar*	203
4.	PERBANDINGAN BIOREAKTOR MEMBRAN DAN BIOREAKTOR MEMBRAN BERELEKTRIK UNTUK RAWATAN AIR SISA KILANG MINYAK KELAPA SAWIT (Comparison of Membrane Bioreactor and Electric Membrane Bioreactor for Wastewater Treatment of The Palm Oil Mill) *Teow Yeit Haan, Sharmila Pragash Sundaram, Najah Hafizah Musa, Syarifah Nornabilah Syed Muaz,Shakir Ahmad Mohamed Sultan, Nur Ameera Rosli*	215
5.	EFFECT OF SODIUM BISULFITE ON CORN STARCH SOLID POLYMER ELECTROLYTE (Kesan Sodium Bisulfit terhadap Elektrolit Polimer Pepejal Kanji) *Fatin Farhana Awang, Khadijah Hilmun Kamarudin, Mohd Faiz Hassan*	224
6.	FORMATION, MORPHOLOGICAL, MOLECULAR INTERACTION AND IONIC CONDUCTIVITY OF SiO_2 FILLED PMMA/PEG ELECTROLYTES (Pembentukan, Morfologikal, Interaksi Molekul dan Kekonduksian Ionik Elektrolit PMMA/PEG Terisi SiO_2) *Nurul Dhabitah Basri, Famiza Abdul Latif, Ruhani Ibrahim, Fazni Susila Abdul Ghani, Sharil Fadli Mohamad Zamri*	234

7. COMPARISON OF PHYSICOCHEMICAL, TOTAL PROTEIN AND ANTIOXIDANT PROFILES BETWEEN MALAYSIAN *Apis* AND *Trigona* HONEYS 243
(Perbandingan Profil Fizikokimia, Jumlah Protin dan Antioksidan antara Madu *Apis* dan *Trigona* Malaysia)
Norjihada Izzah Ismail, Mohammed Rafiq Abdul Kadir, Razauden Mohamed Zulkifli, Mahaneem Mohamed

8. A BRIEF REVIEW ON THE THIAZOLE DERIVATIVES: SYNTHESIS METHODS AND BIOLOGICAL ACTIVITIES 257
(Ulasan Ringkas Terbitan Tiazol: Kaedah Sintesis dan Aktiviti Biologi)
Iswatun Hasanah Abdullah Ripain and Nurziana Ngah

9. VOLTAMMETRIC TECHNIQUE FOR DETERMINATION OF ARSENIC RESIDUES IN CALCIUM CARBIDE RIPENED CLIMACTERIC FRUITS 268
(Teknik Voltammetrik bagi Penentuan Sisa Arsenik dalam Pematangan Buah Klimakterik Menggunakan Kalsium Karbida)
Nurasmat Mohd Shukri, Noor Zuhartini Md Muslim, Nur Fazeera Kamal, Faizuan Abdullah

10. POLYMELAMINE/GOLD NANOPARTICLE-MODIFIED CARBON PASTE ELECTRODE AS VOLTAMMETRIC SENSOR OF URIC ACID 286
(Elektrod Pes Carbon Terubahsuai Polimelamin/Partikel Nano Emas sebagai Sensor Voltametrik bagi Asid Urik)
Muji Harsini, Erna Fitriany, Ainy Nur Farida, Dianita Suryaningrum, Dimas Noor Asy'ari, Bernadeta Ayu Widyaningrum, Denok. Rizky Ayu Paramita, Afaf Baktir, Fredy Kurniawan

11. SENSOR ION Al^{3+} OPTIK BERASASKAN ERIOKROM SIANIN R TERPEGUN DALAM MEMBRAN POLIMER TERANGKUM MENGGUNAKAN PRINSIP PENGUKURAN SERAPAN 296
(An Optical Sensor For Al^{3+} Ion Based on Immobilized Eriochrome Cyanine R in Polymer Inclusion Membrane using Absorption Sensing Principle)
Faiz Bukhari Mohd Suah, Musa Ahmad, Lee Yook Heng

12. INFLUENCE OF MINERALS ON CONTROL MEASUREMENT OF AMMONIUM, NITRITE, NITRATE AND PHOSPHATE USING UV-SPECTROPHOTOMETER 311
(Pengaruh Mineral Terhadap Pengukuran Kawalan bagi Ammonium, Nitrit, Nitrat dan Fosfat Menggunakan Spektrofotometer UV)
Md. Salatul Islam Mozumder, Shehab Shahreyar, Saiful Islam, Md. Delowar Hossain

13. THE REMEDIATION POTENTIAL OF BIOCHAR DERIVED FROM *Morus rubra* LINN. BARK 324
(Potensi Pemulihan oleh Terbitan Arang Bio dari Kulit Kayu Morus rubra Linn.)
Judith Clarisse Jose, Mark Nathaniel Dolina, Maria Carmen Tan

14. MODE OF ACTION OF 5-ACETYL-4-METHYLTHIAZOLE DERIVATIVES AS ANTIMICROBIAL AGENTS 341
(Mod Tindakan Sebatian Terbitan 5-Asetil-4-Metiltiazol Sebagai Agen Antimikrob)
Iswatun Hasanah Abdullah Ripain, Nurziana Ngah, Deny Susanti Darnis

15. DETERMINATION OF METSULFURON METHYL IN CRUDE PALM OIL USING LIQUID CHROMATOGRAPHY TRIPLE QUADRUPOLE MASS SPECTROMETER 352
(Penentuan Metsulfuron Metil dalam Minyak Sawit Mentah Menggunakan Kromatografi Cecair Spektrometri Jisim Caturkutub Ganda Tiga)
Nik Sasha Khatrina Khairuddin, Chee Beng Yeoh, Najwa Sulaiman, Farah Khuwailah Ahmad Bustamam, Halimah Muhamad, Ismail Sahid

Malaysian Journal of Analytical Sciences (MJAS)
Published by Malaysian Analytical Sciences Society

Editorial: Utilization Modern Analytical Instruments for Food and Plant Analysis

Wan Mohd Afiq Wan Mohd Khalik and Sabiqah Tuan Anuar

Malaysian Analytical Sciences Society (ANALIS)

Food or plant analysis is a branch study of scientific procedures to describe the characteristics of foods, plants and their constituents. Major analytical instruments are used to provide knowledge about a variety of food or plant characteristics, including chemical compositions, chemical structures, physicochemical properties or sensory qualities [1]. The development of analytical methods and the selection of the best instrument for food and plant analysis have always been challenging, mostly due to a wide range of their physicochemical properties. Additionally, improper pre-treatment can alter analyte structure or reduce extraction efficiencies. In the latest publication April 2021, we highlight four research works showcasing the use of analytical instrumentation for the intended purpose.

First paper wrote by Sairi et al. [2] describe the application of impedance biosensor for detection of plant disease namely blood disease bacterium, commonly found in banana crops. Research work highlights in detail the capability of electrochemical impedance spectroscopy for the detection of target analyte at low ranging concentrations, 10^1 to 10^3 CFU/mL. Low detection limit for blood disease bacterium measurement was achieved using silicon-on-insulator nanogap sensor. Thus, it was deemed suitable to be used for routine analysis.

Second paper describe the physiochemical protein and antioxidant profile for beneficial uses of *Apis* and *Trigona* honeys [3]. Analytical instrumentation namely liquid chromatography was used to determine the sugar content and hydroxymethylfurfural. Other instruments used include the photometer (colour), refractometer (total soluble solids), and microplate spectrophotometer (total phenolic, flavonoid, protein content), respectively.

Third research work discuss the development of voltametric technique based on gold electrode for determination of arsenic residue in mango and banana samples [4]. The presence of arsenic was believed to be part of the impurities in calcium carbide used to ripen the climacteric fruits. Analysis of real sample and validation of research works were performed using differential pulse anodic stripping voltammetry.

Fourth documented paper by Jose et al. [5] discuss the potential of mulberry bark, *Morus rubra* Linn. for remediation of metal residue in aqueous solution. Characterization of biochar was evaluated using different analytical instruments such as gas chromatography-electron ionization-mass spectrometry (identification of main compounds), scanning electron microscope (surface morphology), energy dispersive X-ray spectroscopy (compositional analysis), Fourier transform infrared spectroscopy (identification of functional group), and atomic absorption spectroscopy (determination of metal content), respectively. Finding from the study reveals the capability of produce biochar's to remove lead pollutant up to 60% of the initial concentration.

Editorial looks forward to receiving new submission on related topics for the forthcoming publication. Innovative research works and review papers on instrumental analytical techniques applied to food and plant analysis are most welcome.

Happy reading and best wishes,

Wan Mohd Afiq Wan Mohd Khalik
Executive Editor
Sabiqah Tuan Anuar
Associate Editor

References

1. McClements, J. (2003). Analysis of food product. Access from McClements homepage for food science course https://people.umass.edu/ ~mcclemen/581Introduction.html
2. Sairi, M., Shafie, K. A., Ismail, A. S., Said, N. A. M., Masdor, N. A., Salleh, N. H. S, Teik, T. S., Bunawan, S. N., Abdul Talib, M. A., Jaffar, N. S., and Raship, I. (2021). Electrochemical impedimetric biosensor based on silicon-on-insulator nanogap for the detection of banana blood disease bacterium. *Malaysian Journal of Analytical Sciences*, 25(2): 184-192.
3. Ismail, N. I., Kadir, M. R. A., Zulkifli, R. M. and Mohamed, M. (2021). Comparison of physicochemical, total protein and antioxidant profiles between Malaysian *Apis* and *Trigona* honeys. *Malaysian Journal of Analytical Sciences*, 25(2): 243-256.
4. Shukri, N. M., Muslim, N. Z. M., Kamal, N. F., and Abdullah, F. (2021). Voltammetric technique for determination of arsenic residues in calcium carbide ripened climacteric fruits. *Malaysian Journal of Analytical Sciences*, 25(2): 268-285.
5. Jose, J. C., Dolina, M. N. and Tan, M. C. (2021). The remediation potential of biochar derived from *Morus rubra* Linn. bark. *Malaysian Journal of Analytical Sciences*, 25(2): 324-340.

Malaysian Journal of Analytical Sciences (MJAS)
Published by Malaysian Analytical Sciences Society

ELECTROCHEMICAL IMPEDIMETRIC BIOSENSOR BASED ON SILICON-ON-INSULATOR NANOGAP FOR THE DETECTION OF BANANA BLOOD DISEASE BACTERIUM

(Biosensor Impedimetrik Elektrokimia Berasaskan Silikon-Pada-Penebat Jurang Nano untuk Pengesanan Bakteria Penyakit Darah Pisang)

Masniza Sairi[1]*, Khairul Anuar Shafie[1], Ahmad Syazwan Ismail[2], Nur Azura Mohd Said[2], Noor Azlina Masdor[2], Nur Humaira Md Salleh[3], Ten Seng Teik[1], Siti Noraini Bunawan[2], Mohd Afendy Abdul Talib[2], Nur Sulastri Jaffar[4], Izyani Raship[5]

[1]*Engineering Research Centre*
[2]*Biotechnology and Nanotechnology Research Centre*
[3]*Director General Office*
[4]*Horticulture Research Centre*
[5]*Industrial Crop Research Centre*
MARDI Headquarters, Persiaran MARDI-UPM, 43400 Serdang, Selangor

**Corresponding author: masniza@mardi.gov.my*

Received: 11 November 2020; Accepted: 2 March 2021; Published: 25 April 2021

Abstract

An impedance biosensor for the detection of blood disease bacterium (BDB) in banana was developed based on a 70 nm nanogap sensor. The nanogap was fabricated using a silicon-on-insulator (SOI) wafer of 190 nm thickness Si layer supported on 350 nm thickness SiO_2 layer via photolithography, Si etching, and electron beam lithography. The sensing area underwent surface modification, antibody immobilization, and blocking agent addition, followed by BDB culture detection. Electrochemical impedance spectroscopy (EIS) analysis was used to detect various concentrations of BDB culture from 10^1 to 10^4 CFU/mL. The working dynamic range for the nanogap sensor was 10^1–10^3 CFU/mL. A limit of detection (LOD) of 6.73 CFU/mL was achieved. The nanogap sensor represents an attractive strategy for a label less immunosensor at low concentration bacteria culture detection, hence useful for plant disease management.

Keywords: blood disease bacterium, nanogap sensor, electrochemical impedance spectroscopy, limit of detection, plant disease management

Abstrak

Biosensor impedans untuk pengesanan bakteria penyakit darah (BDB) pada pisang telah dibangunkan berasaskan penderia jurang nano berjarak 70 nm. Penderia jurang nano difabrikasi menggunakan substrat silikon-pada-penebat (SOI) pada lapisan Si berketebalan 190 nm yang disokong oleh lapisan SiO_2 350 nm melalui proses fotolitografi, goresan Si, dan litografi pancaran elektron. Kawasan penderiaan menjalani pengubahsuaian permukaan, pengikatan antibodi, dan penambahan agen penghalang, diikuti dengan pengesanan kultur BDB. Analisis spektroskopi impedans elektrokimia (EIS) digunakan untuk mengesan kepekatan

kultur BDB yang berbeza dari 10^1 hingga 10^4 CFU/mL. Julat dinamik berfungsi untuk penderia jurang nano adalah 10^1 hingga 10^3 CFU/mL. Had pengesanan (LOD) dicapai pada 6.73 CFU/mL. Penderia jurang nano menunjukkan potensi untuk pengesanan kultur bakteria sensor immuno tanpa label pada kepekatan rendah yang berguna untuk pengurusan penyakit tumbuhan.

Kata kunci: bakteria penyakit darah, penderia jurang nano, spektroskopi impedans elektrokimia, had pengesanan, pengurusan penyakit tumbuhan

Introduction

Banana blood disease is a type of wilting disease affecting banana plants in countries such as India, Indonesia, the Philippines, and Malaysia. This disease is one of the most severe diseases in the banana growth sector that spreads widely and halts banana plant growth, resulting in critical yield losses. Blood disease, in particular, is caused by the blood disease bacterium (BDB), previously known as *Pseudomonas celebensis*, which demonstrates comparable symptoms as Moko disease [1,2]. The blood disease spreads widely across the tropical and subtropical regions through pollination insects, contaminated soil environment, and planting equipment. The symptoms started with the color of young leaves that changes from green to yellow or brown, followed by wilting. Other symptoms are smelly bacterial slime presence, vascular discoloration, bacterial ooze, and reddish-brown fruit rot [2-4]. The disease suppresses banana production globally, in which the loss can be within 10-93%, depending on the infection severity [3]. Thus, efforts to suppress pathogenic bacteria development are essential.

Biosensor technology has been reported in disease diagnostics, drug detection, and food quality control [5]; recently, the technology has been applied in plant disease detection [6]. Detection via biosensors can eliminate or simplify sample preparation steps and detect a broad spectrum of analytes in complex sample matrices. An electrochemical biosensor is favored among other classes of biosensors (e.g., optical and piezoelectric sensors) due to its low cost, ease of use, portability, and simplicity of construction [5-7]. The principle of electrochemical biosensor lies in the coupling of the bioreceptors on a transducer (i.e., electrode) with its specific analytes that convert the binding event to a signal that can be analyzed [8].

An antibody-based biosensor or immunosensor is one of the tools of interest in biosensing and it is remarked to hold great potential for agricultural plant pathogen detection as the biosensor enables pathogen detection in air, water, and seeds with on-site application [9]. Antibody-based electrochemical biosensors can be performed by amperometric, potentiometric, impedimetric, or conductometric techniques. The capability of electrochemical antibody-based biosensors to detect plant pathogens has been reported for tungro virus in rice [10], cucumber mosaic virus [11], rice bacterial leaf streak [12], and citrus bacterial canker [13]. However, most of these detection methods employed amperometric measurement that requires indirect detection format using labeled antibodies. With this regard, electrochemical impedance spectroscopy (EIS) has great advantages in probing detection at the molecular level where it requires no label, thus offering direct detection of the target analyte [14].

The impedance of an interface is usually determined by applying a sinusoidal voltage perturbation while measuring the current response [15, 16]. The impedance or EIS data can be represented and analyzed using various techniques, such as the Bode and Nyquist plots [17, 18]. The Bode plot represents the impedance magnitude |Z| (log scale) versus frequency, f (log scale) of how resistive the system to current flow at the applied frequency. On the other hand, the Nyquist plot represents the out-of-phase or imaginary component (Z_j) versus the in-of-phase or real component (Z_r) contribution to impedance (both in log scales) and the relationship at varying frequencies. In the Nyquist plot, the highest frequency data points are located at lower impedances and vice versa. Since the Nyquist plot masks the impedance dependence on frequency, the Bode plot serves as an alternative approach [5, 17, 19].

This research project investigates the electrochemical behavior of BDB culture with varying concentrations at the fabricated nanogap sensors. Quantitative methods involving the detection of BDB culture using EIS are presented.

Materials and Methods

Reagents

All reagents were used without further purification unless stated otherwise. 2% (3-aminopropyl)triethoxy silane (APTES), 0.4 M 1-ethyl-3-(3-dimethyl amino propyl)carbodiimide (EDC), and 0.1 M N-hydroxy succinimide (NHS) were purchased from Sigma Aldrich Pty. Ltd., Germany and Japan. 0.1 M sodium carbonate bicarbonate (carbonate buffer) was purchased from Merck & Co., Inc., Germany. 0.01 mg/mL antibody blood disease bacterium (BDB ab) was produced at the Animal House, MARDI, Malaysia. Phosphate buffered saline (PBS) solution (pH 7.0, 0.01 M) was prepared by dissolving a PBS tablet in 200 mL of deionized water. All solutions were prepared in deionized water from a Sartorius Arium ® Pro water purification system (Sartorius, Germany).

Fabrication of nanogap sensors

The nanogap sensors used in this study, as depicted in Figure 1(a), were fabricated at the Department of Mechanical Engineering and Institute of Nanotechnology, Southern Taiwan University of Science and Technology, Tainan, Taiwan. The substrate used in the fabrication was a 6-inch p-type silicon-on-insulator (SOI) wafer with 190 nm thickness Si layer supported on 350 nm thickness buried oxide layer. The SOI wafer was selected to reduce the device parasitic element and improve the final performance with higher sensitivity [20]. The 70 nm gap sensors with gold electrodes were fabricated via photolithography, Cr and Au deposition, and Si etching. The depth-to-width ratio of the etching was set to 1:2 (gap: thickness). The fabricated nanogap sensors were randomly sampled and measured the EIS values using a Precision Impedance Analyzer WK 6500B (Wayne Kerr Electronics, UK) for failure testing (electrical characterization to study the potential and stability of the fabricated nanogap sensors).

Prior to detection procedures, the nanogap sensors were plasma-cleaned with Plasma Cleaner PDC-32G-2 (Harrick Plasma, USA) and dried in air to remove any unwanted contamination and particles on the sensing surface area. All experiments were conducted at room temperature (20 °C).

Bacteria culture preparation

BDB was isolated from a diseased banana plant by the Horticultural Research Centre, MARDI. Next, the bacterium was grown in media culture. For sensor study, the BDB was used as antigen at varying concentrations (10^0, 10^1, 10^2, 10^3, and 10^4 CFU/mL) using a serial dilution procedure.

Polyclonal antibody production

Polyclonal antibody against BDB was produced *via* in-vivo immunization in two New Zealand White breed rabbits with the bacteria based on the guidelines by Leenaars and Hendriksen [21]. Prior to the first injection, a batch of blood was collected by bleeding the central auricular artery on the rabbit's ear into a sterilized vacutainer tube (BD Vacutainer System) and this pre-immune blood was assigned as control. Both booster injections and bleeding activities were alternately performed every fortnight until the highest activity of the antibody was achieved. The antibody production protocol was reviewed and approved by the Animal Ethics Committee of Malaysian Agricultural Research and Development Institute, Malaysia (Approval number 20170717/R/MAEC00015).

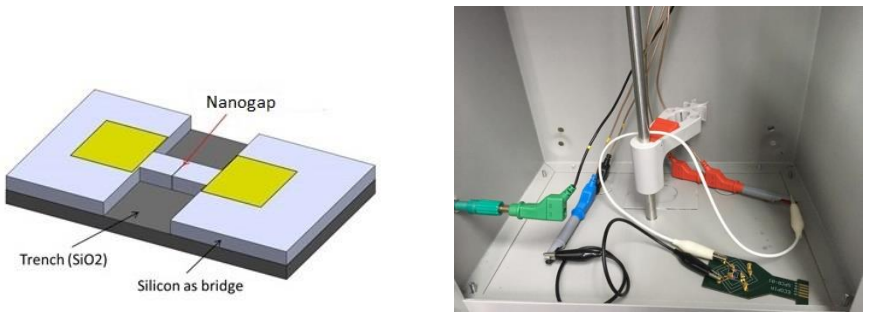
Electrochemical procedure

A two-electrode electrochemical cell (set up) was employed in this study (Figure 1(b)). A four-point probe sample board, model Ecopia SPCB-1 (Aseptec Sdn. Bhd., Malaysia) was used to hold the nanogap sensor in place. The sample board has a gold-plated spring-loaded cell with good Ohmic contact and can mount a board with 2 mm thickness and up to 20 mm on one side. For this setup, only a two-point probe was used for impedance measurement.

Following the assembly of the electrochemical cell (set up), EIS was performed using a Metrohm Autolab PGSTAT 20 (Eco Chemie, The Netherlands) expanded with a frequency response analysis module for EIS, interfaced to a computer, running the Nova 1.10 software package supplied with the instrument. EIS was conducted at the frequencies between 0.1 and 100,000 Hz, where the values are distributed logarithmically through the range. The root mean square (RMS) amplitude of the applied potential was 50 mV. A quiet time of 5 s at the start of each scan was implemented to stabilize and minimize the background charging current. The initial potential for EIS was first determined by the open circuit potential (OCP) procedure. All measurements were performed in triplicate. The electrochemical cell (set up) was housed in a Faraday cage for the duration of the experiment to minimize electrical noise.

Detection procedure

Bare nanogap sensors were first characterized electrochemically *via* EIS. The sensing area underwent surface modification through incubation with 2% APTES for 1 hour at room temperature and then cleaned with deionized water and air-dried with N_2 gas. Next, the sensing area was immobilized with 1 mg/mL polyclonal antibody against BDB coupled with EDC and NHS for 1 hour, and then cleaned with PBS solution and rinsed with deionized water. Finally, BDB culture as the antigen was incubated for 1 hour on the sensing area before EIS measurement.



(a) (b)

Figure 1. (a) Nanogap sensor design and (b) experimental set-up

Results and Discussion

Nanogap sensors characterisation

Nine randomized fabricated nanogap sensors were sampled and measured the impedance spectra. The nanogap sensors demonstrated repeatable and stable impedance values with an average of 30.73 ± 0.78 kΩ at 10.65 kHz (Table 1).

Impedimetric BDB detection

A simplified schematic diagram for EIS analysis of an electrode/electrolyte interface is illustrated in Figure 2. The electrified interface can be modeled by an equivalent circuit known as the Randles circuit. When a potential difference is applied across the interface, the electrical double layer is developed, which is composed of the electrical charge at the electrode surface and the charge of distributed ions in the solution in the immediate vicinity of the electrode. This double layer is equivalent to that of a double-layer capacitor with a capacitance of C_{dl}. The electrolyte side of the double layer is assumed to be made up of several distinct layers, mainly the inner Helmholtz plane (IHP) and the outer Helmholtz plane (OHP) [17, 22].

The electrons transfer to/from the electroactive species by overcoming the activation barrier or polarization

resistance, R_p and electrolyte solution resistance, R_s. The Warburg impedance, Z_w is resulted by the diffusion from the bulk electrolyte to the electrode, while the charge transfer resistance, R_{ct} (R_p at an equilibrium potential) demonstrates the charge transfer-limited process [23]. The interfacial electron transfer kinetics is affected by the distribution of bacterial cells between the electrodes, which increase or decrease electron transfer conductivity in the electrolyte environment [23].

The variation of the impedance spectra of the functionalized nanogap sensor with a fixed concentration of immobilized antibody (0.01 mg/mL) at varying concentrations of BDB culture (from 10^1 to 10^4 CFU/mL) was studied (Figure 3). The surface saturation could be obtained with 0.01 mg/mL of antibody concentration, which was determined prior to the saturation concentration of the antibody in the nanogap sensor study (data not shown). The selection of the antibody saturation concentration is important for high sensitivity detection [5].

It was observed that the semicircle diameter (of the Nyquist plot) increased accordingly with BDB concentration from 10^0 to 10^3 CFU/mL on the sensing surface area. This is likely due to many BDB molecules bound to immobilized antibody, which acts as a definite barrier for the charge transfer between the electrodes. However, the semicircle decreased at the concentration of 10^4 CFU/mL, indicating that the hybridization process between the antibody and BDB culture approached saturation (Figure 3(a)).

At low and high frequencies in the Nyquist plot, bacteria sensing is mass transfer controlled and kinetics controlled, respectively. In the kinetics-controlled region (high frequency), the semicircle diameter indicates the R_{ct} [23]. The R_{ct} is the most applied parameter to estimate bacterial concentration; when bacterial cells bind to the target bioreceptors at the working electrode, WE surface, the redox reaction is hindered and R_{ct} increases [16]. In this research, the ΔR_{ct} increased from 10^1 to 10^3 CFU/mL and then decreased (Figure 3(b)). The linear relationship between ΔR_{ct} responses and BDB culture concentration ($\Delta R_{ct}\ (\Omega) = 8 \times 10^7 x - 5 \times 10^7$; $R^2 = 0.97$) demonstrated the working dynamic range for the nanogap sensor of 10^1 – 10^3 CFU/mL (Figure 4). The R_{ct} increased as the bacteria (*Escherichia coli, E. coli*) concentration increased, as reported previously [25]. In this case, the higher content of *E. coli* cells is linked to the interface, generating a higher content of blocking to the electron transfer of the redox probe. The research group reported a linear response in the electron transfer resistance for the concentration of *E. coli* between 6×10^4 and 6×10^7 cells/mL [25].

On the other hand, the limit of detection (LOD) is the BDB culture concentration that induces a signal variation (in this case, impedance response). The LOD of the nanogap sensor was calculated to be 6.73 CFU/mL, which is sufficiently low for bacterial culture detection. The LOD of 10 bacterial cells/mL has been reported for a microfluidic chip implementing the EIS method to detect *E. coli* in field water [23]. An immunobiosensor chip has reported the LOD of 6×10^3 cells/mL in the detection of *E. coli* O157:H7 using EIS [25]. Furthermore, a label-free impedance immunosensor based on microfluidic technology has reported the LOD of 3×10^3 CFU/mL to detect *Salmonella typhimurium* [16, 26]. The results achieved in this research demonstrated the fabricated impedance nanosensor with antibody-antigen binding that offers attractive future potential for BDB detection in real samples with better sensitivity.

Table 1. Impedance values at the frequency of 10.65 kHz

Sensor	Impedance (kΩ)
1	30.91
2	30.08
3	29.63
4	31.01
5	30.41
6	32.32
7	30.36
8	31.26
9	30.58
Average	30.73
Std. Dev.	0.78

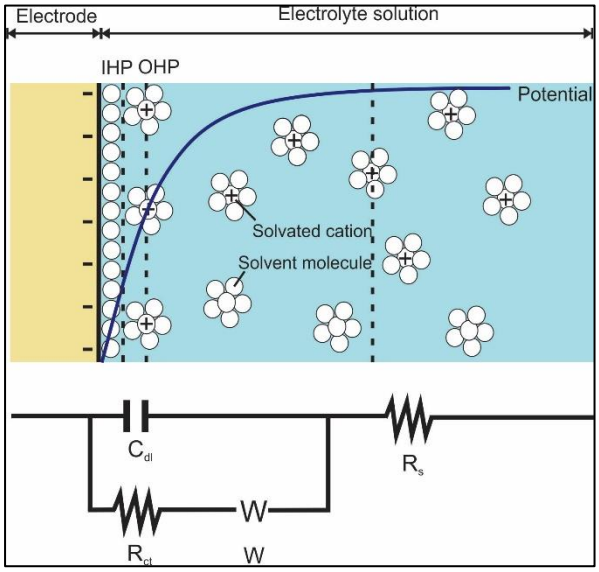


Figure 2. The simplified schematic diagram for EIS analysis of an electrode/electrolyte interface (adapted from [24])

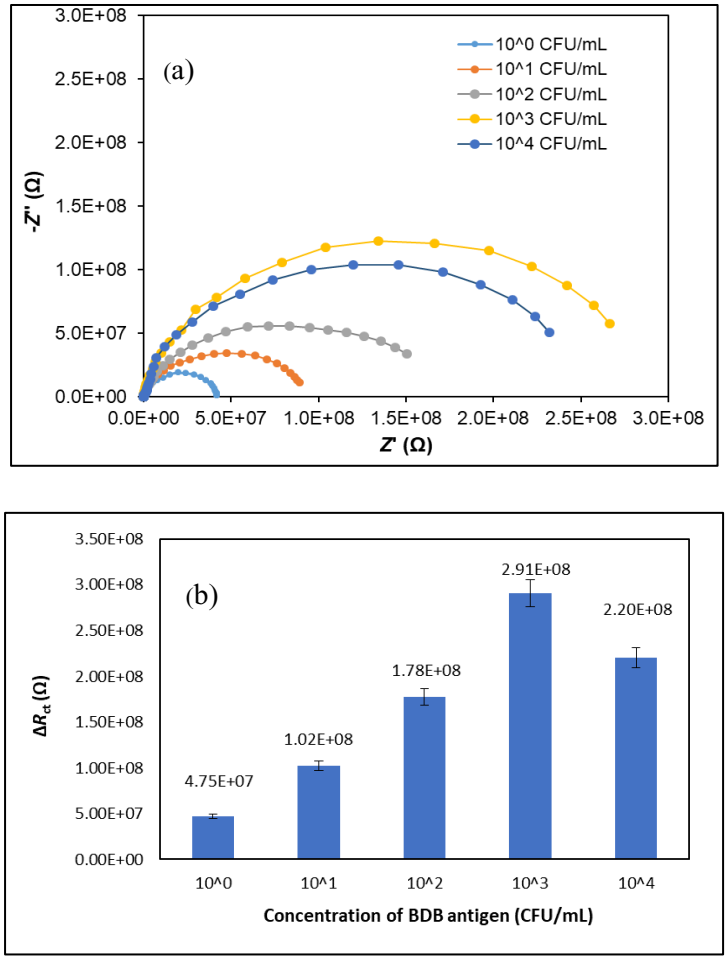


Figure 3. (a) The Nyquist plot for BDB culture detection and (b) the charge transfer resistance (ΔR_{ct}) calculated from the Nyquist plot semicircles using a nanogap sensor with 0.01 mg/mL antibody at varying concentrations of BDB culture

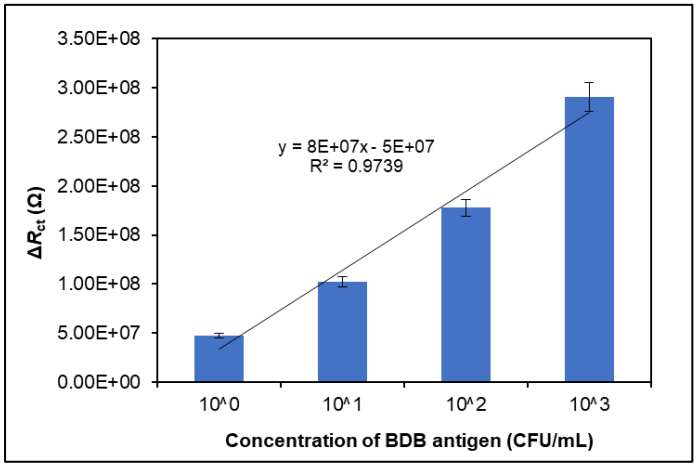


Figure 4. Working dynamic range for nanogap sensor

Conclusion

The electrochemical behavior of BDB culture with various concentrations from 10^1 to 10^4 CFU/mL at the fabricated nanogap sensors was investigated. The results showed that the BDB culture could be detected *via* EIS with the working dynamic range of 10^1–10^3 CFU/mL. The LOD was calculated to be 6.73 CFU/mL, which is suitable for applications of bacteria detection in real samples. In the future, studies on the optimization of detection time, the matrix effect in a real sample, cross-reaction with other plant disease bacteria, nanogap sensors stability, and prediction models are suggested.

Acknowledgment

This research was supported by the Malaysian Agricultural Research and Development Institute (MARDI) *via* the 11th Malaysian Development Plan Fund (P-RH405-1001). The authors would like to express utmost gratitude to the Biotechnology and Nanotechnology Research Centre and Engineering Research Centre at MARDI for the use of facilities for the research. The gratitude is also extended to Southern Taiwan University of Science and Technology, Taiwan for the nanogap sensors fabrication.

References

1. Fegan, M. and Prior, P. (2006). Diverse members of the ralstonia solanacearum species complex cause bacterial wilts of banana. *Australasian Plant Pathology*, 35(2): 93-101.
2. Teng, S.-K., Abd Aziz, N. A., Mustafa, M., Laboh, R., Ismail, I. S., Sulaiman, S. R., Azizan, A. A. and Devi, S. (2016). The occurrence of blood disease of banana in Selangor, Malaysia. *International Journal of Agriculture & Biology*, 18: 92-97.
3. Latupeirissa, Y., Nawangsih, A. A. and Mutaqin, K. H. (2014). Selection and identification of bacteria from tongkat langit banana (*Musa troglodytarun* L.) to control the blood disease bacteria. *Journal of the International Society for Southeast Asian Agricultural Sciences*, 20(2): 110-120.
4. Teng, S.-K., Abd Aziz, N. A., Mustafa, M., Laboh, R., Ismail, I. S. and Devi, S. (2016). In-vitro study on the effect of endogeic earthworm on blood disease bacterium (BDB) in banana - a preliminary observation. *The Asia Journal of Applied Microbiology*, 3(1): 1-11.
5. Adnane, A. (2011). Electrochemical biosensors for virus detection. In P. A. Serra (Ed.), *Biosensors for Health, Environment and Biosecurity*. IntechOpen, London: pp. 321-330.
6. Fang, Y. and Ramasamy, R. P. (2015). Current and prospective methods for plant disease detection. *Biosensors*, 5(3): 537-561.
7. Maalouf, R., Fournier-Wirth, C., Coste, J., Chebib, H., Saïkali, Y., Vittori, O., Errachid, A., Cloarec, J.-P., Martelet, C. and Jaffrezic-Renault, N. (2007). Label-Free detection of bacteria by electrochemical impedance spectroscopy: Comparison to surface plasmon resonance. *Analytical Chemistry*, 79(13): 4879-4886.
8. Silvestrini, M., Habtamu, H. B., Moretto, L. M. and Ugo, P. (2014). Electrochemical biosensors for sensitive molecular diagnostics. *Proceedings of the Cross-Border Italy-Slovenia Biomedical Research*, 2014: 184-190.
9. Skottrup, P. D., Nicolaisen, M. and Justesen, A. F. (2008). Towards on-site pathogen detection using antibody-based sensors. *Biosensors and Bioelectronics*, 24(3): 339-348.
10. Muhammad Nur Aiman, U., Tijjani, A., Hasfalina, C. M., Faridah, S., Zamri, I., Uda, H. and Shahrul, A. B. A. (2014). Reviewed immunosensor format using nanomaterial for tungro virus detection. *Advanced Materials Research*, 832: 410-414.
11. Rafidah, A. R., Faridah, S., Shahrul, A. A., Mazidah, M. and Zamri, I. (2016). Chronoamperometry measurement for rapid cucumber mosaic virus detection in plants. *Procedia Chemistry*, 20: 25-28.
12. Hazana, R., Nur Azura, M. S. and Faridah, S. (2019). Immunosensor development for the detection of *Xanthomonas oryzae* pv. *oryzicola* in rice bacterial leaf streak. *Transactions of the Malaysian Society of Plant Physiology*, 26: 315-320.
13. Haji-Hashemi, H., Norouzi, P., Safarnejad, M. R., Larijani, B., Habibi, M. M., Raeisi, H. and Ganjali, M. R. (2018). Sensitive electrochemical immunosensor for citrus bacterial canker disease detection using fast Fourier transformation square-wave voltammetry method. *Journal of Electroanalytical Chemistry*, 820: 111-117.
14. Lisdat, F. and Schäfer, D. (2008). The use of electrochemical impedance spectroscopy for biosensing. *Analytical and Bioanalytical Chemistry*, 391: 1555-1567.

15. Santos, A., Davis, J. J. and Bueno, P. R. (2014). Fundamentals and applications of impedimetric and redox capacitive biosensors. *Journal of Analytical & Bioanalytical Techniques*, 7(16): 1-15.
16. Grossi, M. and Riccò, B. (2017). Electrical impedance spectroscopy (EIS) for biological analysis and food characterization: A review. *Journal of Sensors and Sensor Systems*, 6: 303-325.
17. Bard, A. J. and Faulkner, L. R. (2001). Electrochemical methods: Fundamentals and applications. John Wiley and Sons Inc., New York: pp. 833.
18. Mitchell, R. A. (2012). Electrical properties of nano-scale liquid/liquid interfaces contained at arrays of solid state nano-pores. Honours Thesis, Curtin University.
19. Orazem, M. E. and Tribollet, B. (2008). Electrochemical impedance spectroscopy. John Wiley and Sons Inc., New Jersey: pp. 523.
20. Usenko, A. Y. and Carr, W. N. (1999). Silicon-on-insulator technology for microelectromechanical applications. *Semiconductor Physics Quantum Electronics and Optoelectronics*, 1(1): 93-97.
21. Leenaars, M. and Hendriksen, C. F. M. (2005). Critical steps in the production of polyclonal and monoclonal antibodies: Evaluation and recommendations. *ILAR Journal*, 46(3): 269-279.
22. Zoski, C. G. (2007). Handbook of electrochemistry. Elsevier B.V., The Netherlands: pp. 892.
23. Jiang, J., Wang, X., Chao, R., Ren, Y., Hu, C., Xu, Z. and Liu, G. L. (2014). Smartphone based portable bacteria pre-concentrating microfluidic sensor and impedance sensing system. *Sensors and Actuators B: Chemical*, 193: 653-659.
24. Park, S.-M. and Yoo, J.-S. (2003). Electrochemical impedance spectroscopy for better electrochemical measurements. *Analytical Chemistry*, 75(21): 455-461.
25. Ruan, C., Yang, L. and Li, Y. (2002). Immunobiosensor chips for detection of *Escherichia coli* O157: H7 using electrochemical impedance spectroscopy. *Analytical Chemistry*, 74(18): 4814-4820.
26. Ghosh Dastider, S., Barizuddin, S., Yuksek, N. S., Dweik, M. and Almasri, M. F. (2015). Efficient and rapid detection of salmonella using microfluidic impedance based sensing. *Journal of Sensors*, 2015: 1-8.

Malaysian Journal of Analytical Sciences (MJAS)
Published by Malaysian Analytical Sciences Society

BIODEGRADATION OF OIL AND GREASE FROM AGRO-FOOD INDUSTRY BY IMMOBILISED *Serratia marcescens* SA30

(Biodegradasi Minyak dan Gris dari Industri Agro-Makanan oleh *Serratia marcescens* SA30 yang Dipegunkan)

Shakila Abdullah[1]*, Farhah Husna Mohd Nor[1], Mohd Hairul Khamidun[2]

[1]*Department of Physics and Chemistry, Faculty of Applied Sciences and Technology, Universiti Tun Hussein Onn Malaysia, Educational Hub Pagoh, 84600 Muar, Johor, Malaysia*
[2]*Department of Civil Engineering, Faculty of Civil Engineering and Built Environment, Universiti Tun Hussein Onn Malaysia, 86400 Batu Pahat, Johor, Malaysia*

**Corresponding author: shakilaa@uthm.edu.my*

Received: 20 July 2020; Accepted: 10 March 2021; Published: 25 April 2021

Abstract

The agro-food industrial wastewater (AFIW) contains high concentrations of oils and grease (O&G), which are significant threats to aquatic environments. In the context of the removal of contaminants from wastewater, the capability of *Serratia marcescens* SA30 immobilized in a packed-bed column reactor (PBCR) of O&G removal from AFIW needs to be verified. This study analyses the *Serratia marcescens* SA30 immobilized on oil palm frond (OPF) in PBCR in order to elucidate its removal ability of O&G from AFIW. The physicochemical parameters of the AFIW samples collected from the agro-food industry were analyzed according to Standard Methods for Examination of Water and Wastewater. The PBCR treatment system was set up using immobilized *Serratia marcescens* SA30 onto OPF for the removal of O&G from AFIW. The AFIW samples were collected at the inlet and outlet of the PBCR, and the respective concentrations of O&G were determined. These values assert that the parameters does not comply the production limit set in Environmental Environment Quality B (Industrial Effluent Regulations, 2009). The performance of the PBCR realized 100% efficiency, with the population ranging from 10^8 – 10^7 with the immobilized *Serratia marcescens* SA30 acting as a biosurfactant-producing bacteria, which was achieved by experiments ran at a volumetric flow rate of 3 mL/min during treatment using concentrations of O&G at 100% v/v after 144 hours operation in the PBCR. The data obtained would provide a green and sustainable pathway for the removal of O&G from water.

Keywords: Agro-food industrial wastewater, packed-bed column reactor, *Serratia marcescens* SA30, oil and grease, immobilized

Abstrak

Sisa air perindustrian agro-makanan (AFIW) mengandungi kepekatan minyak dan gris (O&G) yang boleh memberikan ancaman kepada persekitaran akuatik. Dalam konteks penyingkiran bahan bukan organik dan organik dari air sisa, keupayaan *Serratia marcescens* SA30 yang dipegunkan dalam reaktor turus terpadat tunggal (PBCR) perlu disahkan. Kajian ini menganalisis *Serratia marcescens* SA30 yang dipegunkan di pelepah kelapa sawit (OPF) dalam PBCR untuk menjelaskan kemampuan penyingkiran O&G dari AFIW. Parameter fizikokimia sampel AFIW yang diambil dari industri agro-makanan dianalisis berdasarkan Kaedah Piawai untuk Pemeriksaan Air dan Air Sisa. Sistem rawatan PBCR dibentuk menggunakan *Serratia marcescens* SA30 yang dipegunkan ke OPF untuk penyingkiran O&G dari AFIW. Sampel AFIW dikumpulkan di saluran masuk dan keluar PBCR, dan

kepekatan O&G masing-masing ditentukan. Nilai-nilai tersebut menegaskan bahawa parameter tersebut tidak mencapai limit pengeluaran yang telah ditetapkan dalam Kualiti Persekitaran Lingkungan B (Peraturan Efluen Industri, 2009). Prestasi PBCR mencapai kecekapan 100% dengan populasi antara 10^8-10^7 dengan *Serratia marcescens* SA30 yang dipegunkan bertindak sebagai bakteria penghasil biosurfaktan, yang dicapai dengan eksperimen yang dijalankan pada kadar aliran volumetric 3 mL/min semasa rawatan menggunakan kepekatan O&G pada 100% v/v setelah 144 jam beroperasi dalam PBCR. Kajian ini akan memberikan laluan hijau dan lestari untuk menyingkirkan O&G dari air.

Kata kunci: Sisa air perindustrian agro-makanan, reaktor turus terpadat tunggal, *Serratia marcescens* SA30, minyak dan gris, dipegunkan

Introduction

Agro-food industries are one of the significant contributors to environmental pollution. The rapid expansion of small and medium industries (SMEs) in Malaysia, particularly in rural areas, led to water body pollution due to most of these industries discharging a large amount of untreated wastewater into the environment [1]. Factors such as O&G, chemical oxygen demands (COD), and total suspended solids (TSS) can be minimized *via* proper storage, cleaning, slicing, washing, frying, salting, and coating and packing [2]. However, the lack of prior treatment of wastewater results in pollution, which can be harmful to humans. The current physicochemical and biological processes for the removal of O&G from industrial wastewaters include electrocoagulation, advanced oxidation process, and membrane technologies [3, 4, 5]. However, the processes mentioned above are costly undertakings and result in byproducts, such as excessive gases and sludges. Due to increased environmental awareness and stringent public policies, it is becoming necessary to compel industries to limit their respective discharges [6].

In response to this, industries begin to utilize sustainable technologies for wastewater management. To improve the microbial remediation of an O&G the bacterial cells must be immobilized in a suitable carrier or used of biosurfactant as a biocatalyst has been investigated compared with the free cells in various biotechnological processes. The use of immobilized cells in biodegradation processes enhances the O&G removal rates and provides increased tolerance ability to unfavorable conditions [7]. Parthipan et al. [8] found that biosurfactant producing strain of *Bacillus subtilis* was able to degrade oil about 87% within a short period of time (7 days). A study by Shen et al. [9] elucidated the ability of immobilized microbial consortia in the degradation of different types of petroleum hydrocarbons. A recent study showed the importance of *Bacillus pumilus* isolated from *Chelidonium majus* L. exhibit potential for hydrocarbons degradation and biosurfactant production [10]. The success of biotechnological solutions for bioremediation applications depends on the identification of the indigenous microbial communities having the ability to degrade complex O&G and enhancing their biodegradation potential.

Therefore, the main objective of this present work was to elucidate the ability of immobilized *Serratia marcescens* SA30 onto OPF for the removal of O&G effluent from the agro-food processing industry in a column reactor. The optimal conditions for O&G degradation under the influence of immobilized *Serratia marcescens* SA30 onto OPF, such as inert supporting material, initial concentrations and times, and flow rates were established. The biodegradation potential was determined by evaluating the O&G removal rates and the presence of *Serratia marcescens* SA30 in the column reactor pre and post-treatment. This proposed approach could be an effective and environmentally-friendly biological treatment process that fulfills environmental regulations.

Materials and Methods

Characterization of agro-food industrial wastewater

The agro-food industrial wastewater (AFIW) samples were obtained from the final effluents discharged from an industrial food factory located in Batu Pahat, Johor. The AFIWs served as nutrients to the bacteria. The AFIWs' pH, microbiological count, temperature, color,

chemical oxygen demand (COD), and oil and grease (O&G) concentrations were determined. The samplings and characterizations were performed as per the Standard Methods for Examination of Water and Wastewater [11].

Bacteria

Serratia marcescens SA30 was isolated from the collected AFIW [12]. *Serratia marcescens* SA30 was cultivated in an NB at 30 ºC and 200 rpm for 24 hours. The strain was identified using the PCR-mediated amplification of the 16S rRNA gene sequencing analysis performed by Vivantis (M) Sdn. Bhd. The genes that were 100% similar to *Serratia marcescens* were obtained from the 1398 nucleotide sequence. The nucleotide sequence was deposited into the GenBank and marked with an accession number KF686740. A strain of *Serratia marcescens* SA30 is capable of producing biosurfactants [13].

Laboratory-scale column reactor

The experimental setup for the O&G biodegradation system consists of a tank, peristaltic pump, and a column (reactor), and is shown in Figure 1. The acrylic column reactor has a capacity of 5 L, and is 50 cm in height and has an inner diameter of (i.d) 4.6 cm. An acrylic column, divided into four sections measuring 2 cm each were filled with inert stones with a granular size of ~1-2 cm at the top and the bottom of the column. The stones were utilized to ensure excellent flow distribution within the column while retaining the column's content. The inert stones were soaked in pure water for ~24 hours to remove impurities, then rinsed with distilled water and dried in an incubator (Memmert IN 110) for 24 hours. 35 cm of the column was filled with 90g of inert OPF, while 1-2 cm length range was used as inert supporting materials for bacterial cell immobilization during treatment. A headspace of 0.46 L was retained to ensure the consistent availability of oxygen supply.

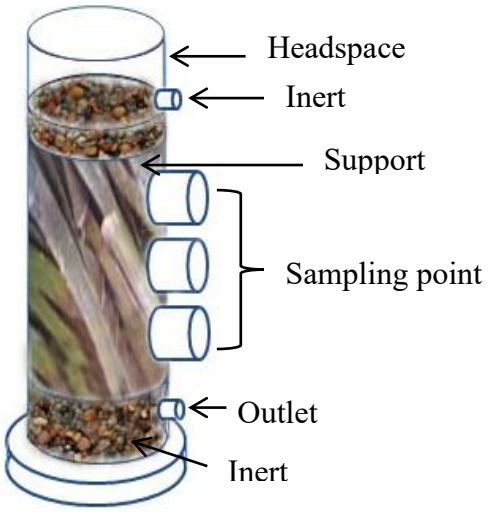


Figure 1. Schematic diagram of laboratory packed-bed column of degradation of oil and grease

Immobilization of *Serratia marcescens* SA30 onto oil palm frond

Serratia marcescens SA30 was used during the immobilization of cells onto OPF packed within the column. OPF was obtained from the oil palm tree in Kulai, Johor, Malaysia, and selected using the coning and quartering method. Fresh OPF was cut into irregular lengths of ~1-2 cm. The OPF was rinsed with deionized water at a constant flow rate of ~0.18L h^{-1} to prevent clogging of the column and allow for the electrostatic charge and hydrophobic interactions necessary for the bacterial adhesion to the supporting material. The *Serratia marcescens* SA30 was pumped at a continuous circulation at similar flow rates to allow initial bacterial attachment for 3 days, followed by 5 L of NB and AFIW to ensure the bacteria used the NB and AFIW as its sole carbon source.

Determination of biodegradation

The microbial degradation of O&G was performed in a column reactor. The samples were analyzed daily for 32 days. To optimize for immobilization and the degradation of O&G, the effect of initial concentrations (25%, 50%, 75%, and 100% (v/v)) and flow rates (1, 3, and 5 mL/min) were determined. At the end of the experiment, the O&G concentration and cell concentration (CFU/mL) were obtained.

Analytical method

The O&G was measured using the O&G determination method APHA 5520B (APHA, 2005) with n-hexane as its oil extraction solvent. The O&G content was determined for each sample pre and post-experiment. The experimental results of the analyses were expressed as mean ± standard deviation from the duplicate. The pH was determined using a pH meter (Eu-Tech), while the microbiological count was determined using the dislodging method via the spread-plate technique. ~1 g of OPF-attached bacteria samples were placed in a Bijou bottle containing 10 mL of sterilized DI and vortexed for 1 minute at high speed. For the quantification of bacteria, an aliquot (1 mL) of the suspension was diluted and spread onto the NA plates. The NA plates were then incubated at 30 ^{o}C for 24 hours in the incubator (Memmert IN110). The actual number of bacteria in the sample were then calculated and enumerated.

Results and Discussion

Characteristics of agro-food industrial wastewater

The results from the characterization of AFIW as shown in Table 1. Most of the parameters did not comply with the regulated discharge limit outlined in Standard B Environmental Quality (Industrial Effluent) Regulation 2009 [14], except for temperature and pH. The presence of high levels of O&G and other contaminants in the AFIW were assumed to be dependent on a series of industrial processes encompassing raw material storing, cleaning, shelling, slicing, washing, frying, salting, picking, coating, and packing due to the runoff water from cleaning of equipment or from fruit-washing, where trace concentrations of contaminants could leach from soil particles [12]. The wastewater was acidic due to the presence of fatty acids in the AFIW. The presence of 10 bacterial colonies indicated the possibility of biosurfactant producing bacteria that used the fatty acid in AFIW as nutrients for bacterial survival and growth [15].

Effect of concentration and time

The amount of O&G degradation at different concentrations onto OPF is shown in Figure 2. It can be seen that the O&G removal rate increases after 144 hours. The quickest O&G removal is observed at higher-level concentrations of 100% (v/v) AFIW, with complete removal being realized, followed by 75% (v/v), at 98% O&G removal. However, when decreasing the O&G concentrations from 50% (v/v) to 25% (v/v), the reactors demonstrated similar removal rate performance of complete degradation, corresponding to values of ~78% and ~72%, respectively. The degradation efficiency of O&G by immobilized cells increases with increasing O&G concentrations, even at a high O&G concentration of AFIW due to the growth of the biomass attached to a support material, rendering it possible for the O&G to be adsorbed on it while functioning as a protective shield against the toxicity of the O&G [16, 17]. Higher concentrations of AFIW encouraged the formation of biofilm while preventing the toxic effects of O&G towards the bacterial cells, which is due to the availability of reaction sites around or within the surface of *Serratia marcescens* SA30. This can be explained by the fact that higher concentrations result in faster transport prompted by the increased mass transfer coefficient of adsorption [18]. The rate of O&G can dictate the rate of O&G uptake transported from the exterior to the interior sites of the adsorbent particles and via the membrane of *Serratia marcescens* SA30 post-adsorption.

The bacteria demonstrated a faster degradation performance due to the adaptation of the isolates to the AFIW. The O&G environment is excellent for the lipolytic microorganisms due to the unrecovered O&G being present in the effluent, which induces the enzymes and biosurfactants to degrade O&G [19]. The yield of the enzyme lipase and biosurfactant increased alongside the concentration, which saturated the uptake system, as observed by the absence of O&G and free fatty acids in the medium. On the other hand, the free fatty acid, released into the medium, supported growth, which is indicated by the absence of the FFA from the growth medium or treated oily wastewater [20].The initial pH of the immobilized cells increased alongside time and became alkaline due to the absorption of the fatty acid present in the AFIW via the alteration to the charges of bacterial cell membranes and pH of ~7-9. The pH also affects the metabolism of microorganisms and its corresponding acceleration, which results in improved biodegradation of O&G [21].

Effect of flow rate

The effect of flow rate on O&G adsorption by AFIE was determined by setting different flow rates on the inlet solution (1, 3, 5, 7, and 9 mL/min) shown in Figure 3, resulting in a >70% of the O&G being removed, with complete reduction achieved after 144 hours of reactor operations. It should be pointed out that a flow rate of 3 mL/min resulted in the effective removal of O&G (100%), followed by ~84% (5 mL/min), ~83% (1 mL/min), ~72% (9 mL/min), and ~70% (7 mL/min). The increases in flow rate significantly affected the removal of O&G due to poor mass transfer, diffusional limitations, and short residence time [22]. Shorter times indicated by the increase flow rates resulted in the complexity of the AFIW, which extended the time it takes to facilitate the uptake process of the complex nutrient into the immobilized cell. When the influent flow rate was increased from 5 to 9 mL/min, the adsorption capacities were lower due to the insufficient residence time of the solute in the column and diffusion of the solute into the pores of the adsorbent, which results in the solute leaving the column before equilibrium [23]. The sorption capacity was smaller when the flow rate was high. It was generally assumed that at high flow rates, the residence period of O&G in the column was transitory, which cannot lead to the equilibrium of the sorption process [24]. The dominating roles of the biodegradation of O&G by the microbes attached to the bio-layer were formed on the surface of the adsorbent, making it one of the factors constituting increased removal rates.

The presence of *Serratia marcescens* SA30 in different parts of the column

The initial bacteria attachment shows a high cell concentration of *Serratia marcescens* SA30 value of $2.95 \times 10^9 \pm 7.07 \times 10^7$ (OD600 = 1.833 ± 0.018), which refers to the growth of *Serratia marcescens* SA30 in a rich medium NB. The cell concentration of *Serratia marcescens* SA30 in the column containing OPF gradually decrease to $3.95 \times 10^8 \pm 4.07 \times 10^7$ (OD600 = 1.377 ± 0.037) after 72 hours of continuous immobilization process. These values show that the *Serratia marcescens* SA30 has been attached to the support materials post-immobilization due to the decrease in cell concentrations.

In this study, the population of *Serratia marcescens* SA30 declined to a certain extent in the community after 32 days of operations at different parts of the column (top, middle, bottom, and effluent), ranging from 10^8 – 10^7 throughout the degradation at different concentrations and flow rates was shown in Figure 4 and Figure 5 respectively. The number of *Serratia marcescens* SA30 on OPF significantly decreased alongside decreasing bacterial concentration in AFIW [25], which could be due to the accumulation of nutrients and the activity of the cells varying from point-to-point along the individual pore channels, which suggests that competitive carbon sources and the exhaustion of nutrients commonly forces bacteria to remain in stationary or death phases, making it easily degradable in the AFIW.

The analysis confirmed that bacterial diversity increased gradually as the reactor is operating. The PBCR was not sterile, which results in the breeding of various microorganisms that could utilize O&G as a carbon source [26]. External microorganisms from the air or the influent could also grow on the OPF in the PBCR. However, the isolated bacteria from viable cell counts revealed that *Serratia marcescens* SA30 was the predominant microorganism on OPF in PBCR throughout the entire operation due to the high levels of colonization in the top, middle, and bottom of the column. The dominant *Serratia marcescens* SA30 in the PBCR is likely to be initiated by the adaptation of the bacteria to its proliferation in the different parts of the column, and the inoculation of the *Serratia marcescens* SA30, which reduces the toxic effects of the AFIW [27]. *Serratia marcescens* SA30 demonstrated a comparative advantage when competing with other microorganisms for habitat due to the strain possessing the highest oil-degrading activity.

Table 1. Characteristics of food industrial wastewater and total bacteria isolated

Parameters	Unit	Values	Standard B
Temperature	°C	28.9 - 34.3	40
pH	-	4.99 - 5.69	5.5 - 9.0
COD	mg/L	8750 - 34000	200
O&G	mg/L	8312 - 128007	10
Color	mg/L	3000 - 17125	200
Total no of bacteria isolated	-	10	-

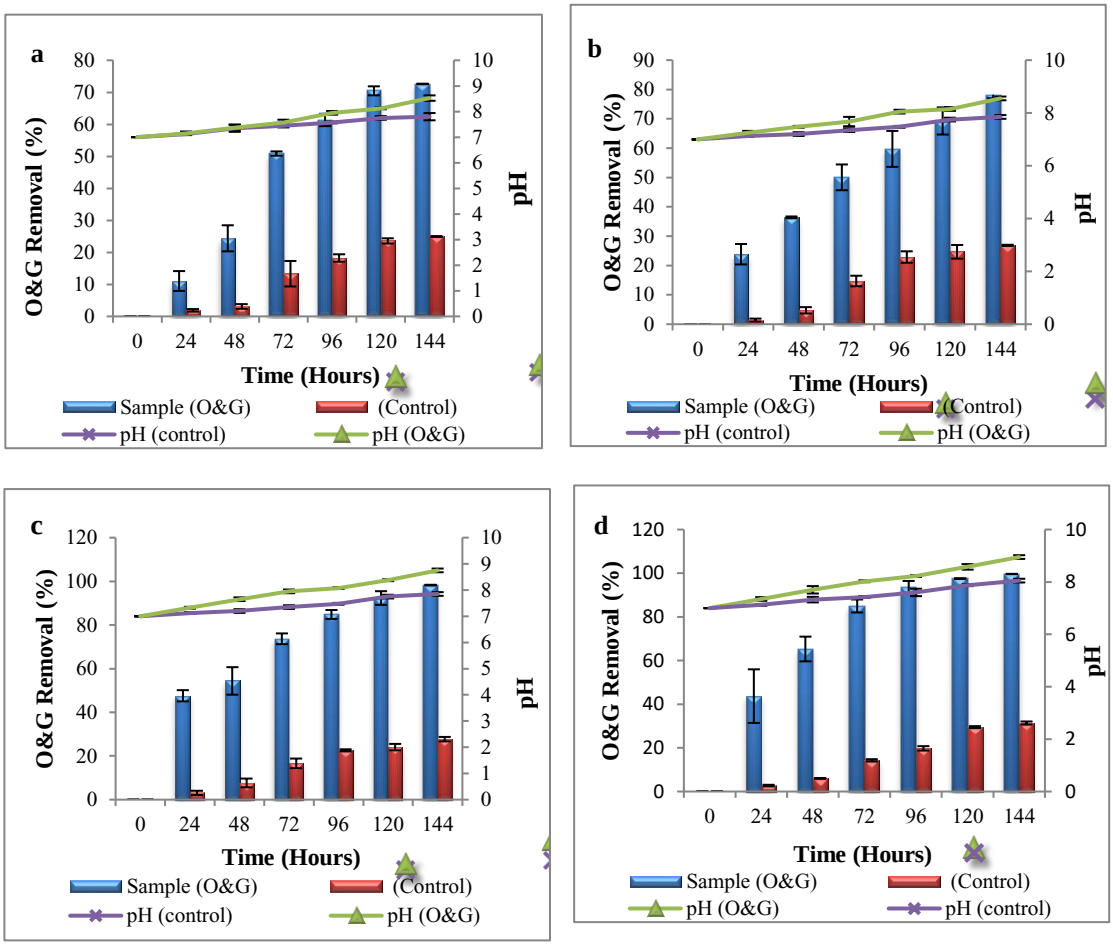


Figure 2. Percentage removal of O&G during biodegradation of AFIW by immobilized *Serratia marcescens* SA30 at different concentration and time intervals:(a) 25% (v/v) (b) 50% (v/v) (c) 75% (v/v) and (d) 100% (v/v)

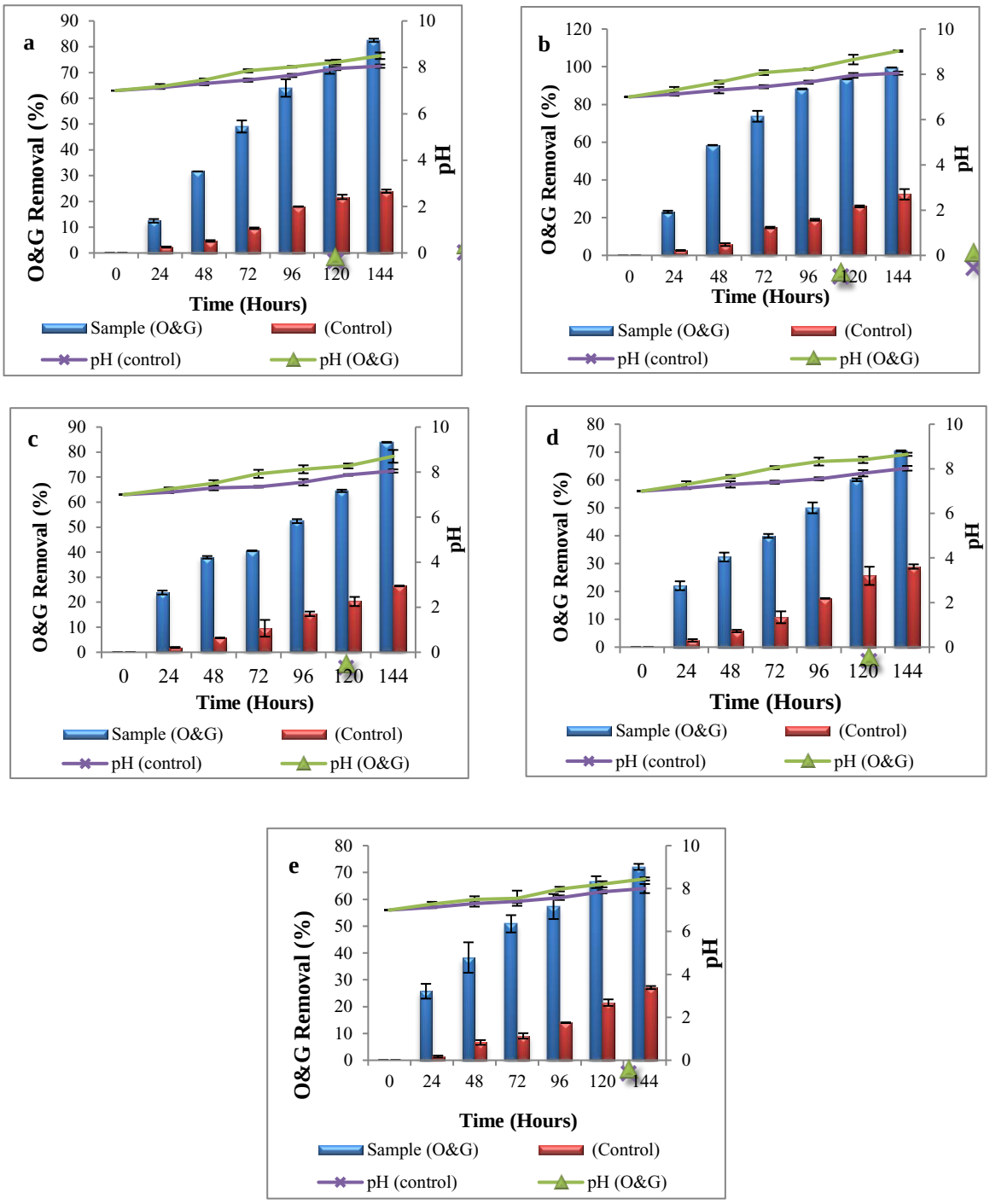


Figure 3. Percentage removal of O&G during biodegradation of AFIE by immobilized *Serratia marcescens* SA30 at different flow rate and time intervals: (a) 1mL/min (b) 3 mL/min (c) 5 mL/min (d) 7 mL/min and (e) 9 mL/m

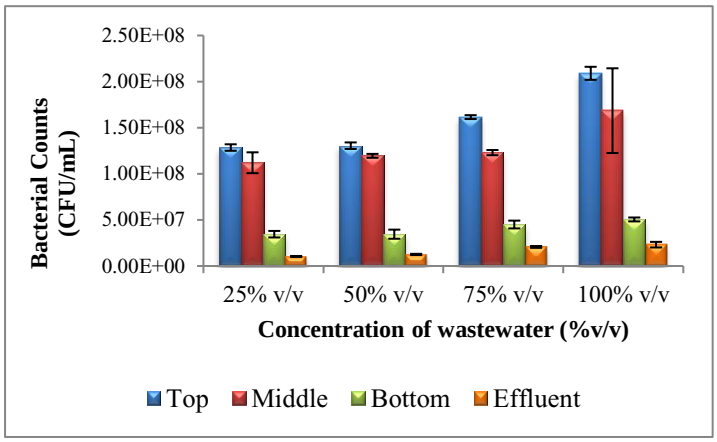


Figure 4. Distribution of *Serratia marcescens* SA30 cells at top, middle and bottom of the column (a) 25%, 50%, 75% and 100% (v/v)

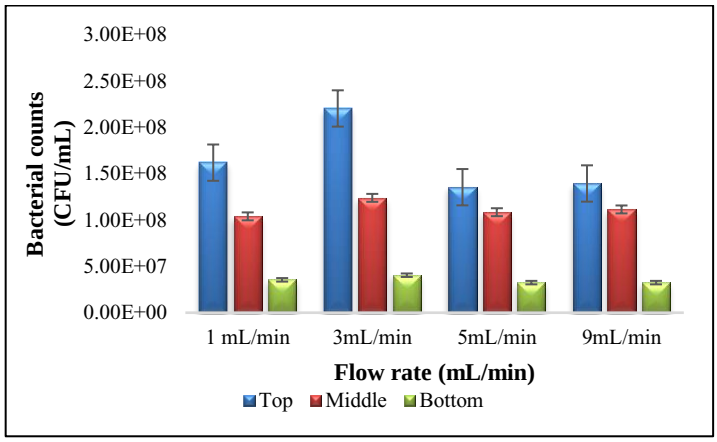


Figure 5. Distribution of *Serratia marcescens* SA30 cells at top, middle and bottom of the column 1, 3, 5 and 9 mL/min

Conclusion

This study assessed the capability of immobilized *Serratia marcescens* SA30 onto OPF to predict the optimum concentrations and flow rates for the removal of O&G from AFIW. It was found that the optimum operating of PBCR treated system realized 100% efficiency condition of 100% v/v concentration, a flow rate of 3 mL/min at a pH 7 after 144 hours operation. The use of *Serratia marcescens* SA30 strain immobilized onto the OPF removed O&G from AFIW, which contributes to the high efficiency of an environmentally-friendly method for treating wastewaters and advanced biotechnology studies.

Acknowledgement

We thank the Universiti Tun Hussein Onn Malaysia (UTHM) for financial support of Tier 1 Grant (Vot. no. U905).

References

1. Preisner, M. (2020). Surface water pollution by untreated municipal wastewater discharge due to a sewer failure. *Environmental Processes*, 7: 767-780.

2. Emara, M. M., El-Razek, M. A. A. and Ahmed, A. A. M. S. (2017). Industrial food processing wastewater treatment by modified moving bed biofilm reactor (MBBR*). International Journal of Scientific & Engineering Research*, 8(1): 929-934.
3. Olajire, A. A. (2020). Recent advances on the treatment technology of oil and gas produced water for sustainable energy industry-mechanistic aspects and process chemistry perspectives. *Chemical Engineering Journal Advances*, 4: 100049.
4. Kuyukina, M. S., Krivoruchko, A.V., Ivshina, I. B. (2020). Advanced bioreactor treatments of hydrocarbon-containing wastewater. *Applied Sciences*, 10: 831.
5. Wei, X., Zhang, S., Han, Y. and Wolfe, F. A. (2019). Treatment of petrochemical wastewater and produced water from oil and gas. *Water Environment Research*, 91: 1025-1033.
6. Dors, G., Mendes, A. A., Pereira, E. B., Castro, H. F. and Furigo, A. (2013). Simultaneous enzymatic hydrolysis and anaerobic biodegradation of lipid-rich wastewater from poultry industry. *Applied Water Science*, 3: 343-349.
7. Zur, J., Wojcieszynska, D and Guzik, U. (2016). Metabolic responses of bacterial cells to immobilization. *Molecules*, 21: 958.
8. Fenibo, E.O., Ijoma, G. N., Selvarajan, R. and Chikere, C. B. (2019). Microbial surfactants: The next generation multifunctional biomolecules for applications in the petroleum industry and its associated environmental remediation. *Microorganism*, 7(581): 1-29.
9. Parthipan, P., Preetham, E., Machuca, L. L., Rahman, P. K. S. M., Murugan, K. and Rajasekar, A. (2017). Biosurfactant and degradative enzymes mediated crude oil degradation by bacterium *Bacillus subtilis* A1. *Frontiers in Microbiology,* 8: 193.
10. Shen, T., Pi, Y., Bao, M., Xu, N., Li, Y. and Lu, J. (2015). Biodegradation of different petroleum hydrocarbons by free and immobilized microbial consortia. *Environmental Science Processes & Impacts*, 17: 2022-2033.
11. Marchut-Mikolajczyk, O., Drożdżyński, P., Pietrzyk, D. and Antczak, T. (2018). Biosurfactant production and hydrocarbon degradation activity of endophytic bacteria isolated from *Chelidonium majus* L. *Microbial Cell Factories*, 17: 171.
12. American Public Health Association (2005). Standard methods for the examination of water and wastewater, 21st edition, APHA, Washington DC.
13. Fulazzaky, M. A., Abdullah, S., Salim, M. R. (2015). Fundamentals of mass transfer and kinetics for biosorption of oil and grease from agro-food industrial effluent by *Serratia marcescens* SA30. *RSC Advances*, 5: 104666-104673.
14. Fulazzaky, M. A., Abdullah, S. and Salim, M. R. (2016). Supporting data for identification of biosurfactant-producing bacteria isolated from agro-food industrial effluent. *Data in Brief*, 7: 834 - 838.
15. Environmental Quality Act and Regulations Handbook (2009). Laws of Malaysia: Details on Environmental Quality Act 1974 and Regulations Amendments up to June 2009: Act 127 with Inde. Kuala Lumpur: MDC Publishers: pp. 34 – 35.
16. Hisham, N. H. M. B., Ibrahim, M. F., Ramli, N. and Abd Aziz, S. (2019). Production of biosurfactant produced from used cooking oil by *Bacillus* sp. HIP3 for heavy metals removal. *Molecules,* 24(2617): 1 - 16.
17. Paşka, O. M., Păcurariu C. and Muntean, S. G. (2014). Kinetic and thermodynamic studies on methylene blue biosorption using corn-husk. *RSC Advances*, 4: 62621-6263.
18. Liu, W-J., Tian, K., Jiang H. and Yu, H-Q. (2014). Harvest of Cu NP anchored magnetic carbon materials from Fe/Cu preloaded biomass: Their pyrolysis, characterization, and catalytic activity on aqueous reduction of 4-Nitrophenol. *Green Chemistry*, 16: 4198-4205.
19. Samuel, J., Pulimi, M., Paul, M.L., Maurya, A., Chandrasekaran, N. and Mukherjee, A. (2013). Batch and continuous flow studies of adsorptive removal of Cr(VI) by adapted bacterial consortia immobilized in alginate beads. *Bioresource Technology,* 128: 423-430.
20. Teixeira, P. D., Silva, V. S. and Tenreiro, R. (2019). Integrated selection and identification of bacteria from polluted sites for biodegradation of lipids. *International Microbiology*, 23(3): 1-14.

21. Ittrat, P., Chacho, T., Pholprayoon, J., Suttiwarayanon, N. and Charoenpanich, J. (2014). Application of agriculture waste as a support for lipase immobilization. *Biocatalysis and Agricultural Biotechnology*, 3: 77-82.
22. Bao, M., Chen, Q., Gong, Y., Li, Y., Wang, H. and Jiang, G. (2013). Removal efficiency of heavy oil by free and immobilised microorganisms on laboratory-scale. *The Canadian Journal of Chemical Engineering*, 91: 1-8.
23. Kathiravan, M. N., Praveen, S. A., Gim, G. H., Han, G. H. and Kim, S. W. (2014). Biodegradation of methyl orange by alginate-immobilized *Aeromonas* sp. in a packed bed reactor: External mass transfer modelling. *Bioprocess and Biosystem Engineering*, 37: 2149-2162.
24. Agarry, S. E. and Aremu, M. O. (2012). Batch equilibrium and kinetic studies of simultaneous adsorption and biodegradation of naphthalene by orange peels immobilized *Pseudomonas aeruginosa* NCIB 950. *Journal of Bioremediation and Biodegradation*, 3(2): 1-12.
25. Xiong, Q., Baychev, T. G. and Jivkov, A. P. (2016). Review of pore network modelling of porous media: Experimental characterisations, network constructions and applications to reactive transport. *Journal of Contaminant Hydrology*, 192: 101-117.
26. Li, L. B., Vorobyov I. and Allen, T. W. (2012). The role of membrane thickness in charged protein-lipid interactions. *Biochimica et Biophysica Acta Biomembranes*, 1818: 135-145.
27. Kureel, M. K., Geed, S. R., Giri, B. S., Shukla, A. K., Rai, B. N. and Singh, R. S. (2016). Removal of aqueous benzene in the immobilized batch and continuous packed bed bioreactor by isolated bacillus sp. M1. *Resources-Efficient Technologies*, 2: S87-S95.
28. Shehzadi, M., Afzal, M., Khan, M. U., Islam, E., Mobin, A., Anwar, S. and Khan, Q. M. (2014). Enhanced degradation of textile effluent in constructed wetland system using *Typha domingensis* and textile effluent-degrading endophytic bacteria. *Water Research*, 58: 152-159.

Malaysian Journal of Analytical Sciences (MJAS)
Published by Malaysian Analytical Sciences Society

OILY SAND CLEANING OPTIMIZATION BY SURFACTANTS INTERFACIAL TENSION SCREENING AND HYDROCYCLONE SEPARATION

(Pengoptimuman Pembersihan Pasir Berminyak oleh Saringan Ketegangan antara Muka Surfaktan dan Pemisahan Hidrosiklon)

Akhmal Sidek[1]*, Ahmad Faiq Omar[1], Aizuddin Supee[2], Amni Haslinda Alpandi[3], Hazlina Husin[3], Dewandra Bagus Ekaputra[4], Shaziera Omar[1]

[1]Petroleum Engineering Department, SCEE, Faculty of Engineering
[2]Energy Management Group, SCEE, Faculty of Engineering
Universiti Teknologi Malaysia, 81310 Skudai, Johor, Malaysia
[3]Petroleum Engineering Department,
Universiti Teknologi PETRONAS, 32610 Seri Iskandar, Perak, Malaysia
[4]Department of Geological Engineering, Faculty of Engineering,
Universitas Islam Riau, Riau 28284, Indonesia

**Corresponding author: akhmalsidek@utm.my*

Received: 30 December 2020; Accepted: 10 February 2021; Published: 25April 2021

Abstract

The oily sand cleaning process should pass the standard discharge requirements so that its impact on the environment can be minimized. This work has used integrated surfactants which includes sodium dodecyl sulfate (SDS, anionic), saponin (plant-based, nonionic), and cetyl trimethylammonium bromide (CTAB, cationic) with hydrocyclone method, for washing oily sand (41 wt.% of paraffin) with fixed cleaning time of 150 minutes. The interfacial tension (IFT) of the surfactants as a cleaning agent was screened based on the critical micelle concentration (CMC) so that the desirable surfactant concentration can be used. Field Emission Scanning Electron Microscopy-Energy Dispersive X-ray (FESEM-EDX) was used to characterize the sand for before and after the cleaning process. As compared to without hydrocyclone, the application of hydrocyclone caused in increasing oil removal efficiency with CTAB exhibits 91%, followed by SDS (87%), and saponin (79%). Based on the FESEM-EDX characterization, besides its primary function of oil removal from the sand, saponin is also capable to remove heavy metal elements. It can be deduced that the integration of hydrocyclone with the surfactants can cause in synergized effects which could then improve the oily sand cleaning efficiency.

Keywords: interfacial tension screening, critical micelle concentration, hydrocyclone, oily sand cleaning, efficiency

Abstrak

Proses pembersihan pasir berminyak perlu melepasi syarat-syarat piawai pelepasan supaya kesannya terhadap alam sekitar boleh dikurangkan. Kajian ini telah menggunakan integrasi surfaktan yang merangkumi sodium dodekil sulfat (SDS, anionik), saponin (sumber tumbuhan, non-ionik) dan cetyl trimetilammonium bromida (CTAB, kationik) dengan kaedah hidrosiklon, bagi

pembersihan pasir berminyak (kandungan paraffin 41 wt.%) dengan masa pembersihan tetap 150 minutes. Ketegangan antara muka (IFT) surfaktan sebagai agen pembersihan telah disaring berdasarkan kepekatan misel kritikal (CMC) supaya kepekatan surfaktan yang diingini dapat digunakan. Mikroskopi Imbasan Electron Pelepasan Medan-Tenaga Serakan sinar-X (FESEM-EDX) telah digunakan untuk mencirikan pasir sebelum dan selepas proses pembersihan. Berbanding dengan tanpa hidrosiklon, penggunaan hidrosiklon telah menyebabkan peningkatan kecekapan penyingkiran minyak dengan CTAB menunjukkan 91%, diikuti oleh SDS (87%), dan saponin (79%). Berdasarkan ciri FESEM-EDX, selain fungsi utama penyingkiran minyak dari pasir, saponin juga mampu menyingkirkan unsur logam berat. Dapat disimpulkan bahawa integrasi hidrosiklon dengan surfaktan menyebabkan kesan sinergi yang kemudian membawa kepada peningkatan kecekapan pembersihan pasir berminyak.

Kata kunci: saringan ketegangan antara muka, kepekatan misel kritikal, hidrosiklon, pembersihan pasir berminyak, kecekapan

Introduction

Sand is commonly produced along with hydrocarbons into the separator. Sand production can severely affect well productivity, damage equipment and surface facilities as well as lead to the risk of a catastrophic failure of the production system [1, 2]. In addition, produced sand may contain hydrocarbons, wax, water, clay, silt, and corrosion products [3]. The production of sand and other reservoir solids can cause major impediment to hydrocarbon production and facility operations [4].

Oily sand (oil-on-sand) discharge rules may limit disposal options and compel storage of some or all of the sand [5]. It may be accumulated in separator vessel and needs to be flushed out at regular intervals with a strict maximum limit discharged of oil content of 10g/1kg (0.01 wt.%) from contaminated materials as stated by the Department of Environment, Malaysia [6]. Despite decades of research, successful bioremediation of hydrocarbon contaminated sand remains a challenge particularly its limited application in the field [7, 8, 9]. The sand cleaning aims to reduce volume of solid wastes by applying several approaches to clean oily sand such as thermo-chemical cleaning [10], electrochemical [11], and ultrasonic washing [12]. Surfactant-enhanced sand de-oiling has long been used as a technique for removing oil from sand as it has a relatively high removal ratio while being cost-effective [13].

The mechanism involves the surfactant ability to enhance the solubility of hydrophobic organic compounds by partitioning them into the hydrophobic cores of surfactant micelles. High solubility of micelles has better efficiency to remove hydrocarbon contaminants [14]. The concentration when the micelle formed is known as the critical micelle concentration (CMC) while simultaneously the decrease in interfacial tension (IFT) influenced by the surfactant concentration which must be higher than or equal to the CMC [15]. The right concentration of surfactant can improve oil recovery by IFT screening which are no further effect when below and under the CMC [16, 17]. Sodium dodecyl sulfate (SDS) is anionic surfactant which is commonly used in the oil and gas industry with characterization of hydrophilic properties derived from the presence of ionic groups in large numbers, such as sulfate or sulfonate groups [18]. In addition, the hydrophobic group is bonded to the hydrophilic portion with an unstable C-O-S bond which can be easily hydrolyzed. The alternatives of the chemical surfactants related plant-based natural surfactants are called as saponin [19]. Saponin is non-ionic surfactant in nature due to the presence of ether or hydroxyl groups. This is the possible reason for the hydrophilic characteristics existence in this surfactant (saponin) [20]. Saponin can be used in heavy metal contaminated material cleaning as it contains hydroxyl or carboxyl [21, 22]. On the other side, cetyl trimethylammonium bromide (CTAB) is one of cationic surfactants types that is widely used particularly to enhance oil recovery [23]. This cationic surfactant contains the hydrophilic group with a positive charge which is generally caused by the presence of natrium sulfates [24].

In the oil and gas industry, cationic surfactants were used with respect to facilitate the wettability of wet oil-water to water-wet which subsequently increase the oil production rate in carbonate reservoir [25]. Additionally, cationic surfactants have the ability to be

used in high temperature environment (up to 100 °C) and salinity up to 200,000 ppm [26]. The concentration of SDS, saponin, CTAB, contaminants, and removal efficiency of oil-sand particles from previous scholars is summarized in Table 1.

The hydrocyclones has been used in numerous separation applications especially for liquid-solid systems (LSS), overcoming conventional technical, mechanical material dispersion by fluid stream that applied centrifugal force [39], and reducing economic operating constraints [40]. This technology is dominantly applied in de-oiling facilities especially in offshore for water treatment with standard rotation speed of 3000 rpm [41, 42]. Although various scholars have applied the surfactants for their oily sand cleaning, none of them have performed the oily sand cleaning process *via* the integration of surfactants interfacial tension screening and LSS hydrocyclone assistance. Thus, this present work attempts to determine the optimum surfactant concentration with the application of LSS hydrocyclone separator in oily sand cleaning process.

Table 1. Types of surfactants with their concentration and oil-based removal from previous scholars

Surfactant	Concentration (wt.%)	Contaminants	Removal (wt.%)	References
SDS	0.04	Crude oil	63.0	[27]
(anionic)	0.08	Diesel	73.7	[28]
	0.5	Pesticide	86.0	[29]
	0.1	Toluene	62.1	[30]
Saponin	0.028	Diesel	45.0	[31]
(non-ionic)	0.14	Paraffin	76.8	[32]
	0.01	Pyrene	52.7	[33]
	0.5	Phenanthrene	87.4	[34]
CTAB (cationic)	0.3	Crude oil	82.5	[35]
	0.02	Cooking oil	64.4	[36]
	0.008	Crude oil	36.9	[37]
	0.3	Paraffin	79.1	[38]

Materials and Methods

Oily sand

The sand was collected from Desaru, Johor and sieved to standardize the sand grain size to the range of 0.1mm to 0.25mm (200/400 mesh) by following the ASTM E11 standard [43], with their total weight set to 1000g. Synthetic paraffin oil (Sigma-Aldrich) was used to represent crude oil with density of 0.83 g/cm^3 and viscosity of 30 cp. Paraffin was mixed with black dye for virtual observation of paraffin movement in compacted sand (Figure 1). After that, the oily sand was prepared by pouring 720g of paraffin oil into the containers to achieve a contamination level of 41 wt.% refer to Zheng et al. [32] and pH of 7.5. The saturated oily sand was obtained after the oily sand undergone mixing process using the FANN multi-mixer for approximately 1 hour and left for stabilize in 3 days.

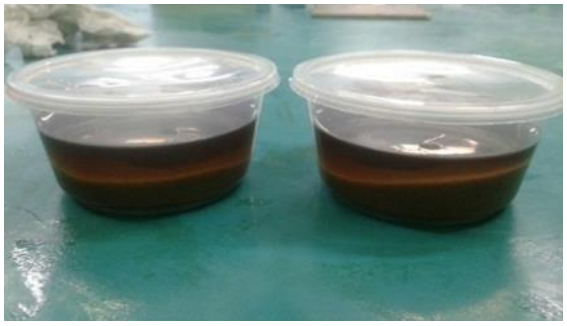


Figure 1. Oily sand preparation

Surfactants

The non-ionic biosurfactant used from saponin (Sigma-Aldrich) is in powder form. This plant based saponin acts as a surface-agent as a solute with various amounts to prepare the surfactant solution. The molecular weight of saponin is 1.5 g/mol with density of 1.02 g/cm^3 and composition of sapogenin of 25%. Meanwhile for the SDS (Sigma-Aldrich), it is a white powder form which possess 85% of active content with anionic charge. For the CTAB (cationic), it was also purchased from Sigma-Aldrich, with 99% purity. All of them were used in the oil removal process.

Solid characterization

The characterization of sand particles for the before and after cleaning process were performed using the Field Emission Scanning Electron Microscopy-Energy Dispersive X-ray (FESEM-EDX):JSM-6701F located at CSNano Laboratory, Ibnu Sina Institute, Universiti Teknologi Malaysia.

IFT of surfactants

The Krüss Tensiometer-K6 (Du Noüy ring method) which is available at the Reservoir Laboratory, School of Chemical and Energy Engineering, Universiti Teknologi Malaysia was used to determine the IFT in liquid-liquid interface. With this equipment, the CMC of surfactants was able to be determined and then used as a mechanism in oily sand cleaning.

Hydrocyclone washing machine

The hydrocyclone Separator-Pilot cyclone EPC100P for LSS was designed and fabricated-in-house by the Environment Laboratory, Universiti Teknologi Malaysia. The machine has 150 cm thickness with diameter of 100 cm together with 50 cm nozzle at discharge valve line. The hydrocyclone was equipped with the pump that can speed up to 6000 rpm. This centrifugal effect (cyclone) was used to wash the oily sand by adding the distilled water and surfactants in the system. After the washing process has been accomplished, the sand was discharged through the discharge valve at the bottom of the container.

Oily sand cleaning process

The concentration for each surfactant which consists of 0.05 wt.%, 0.1 wt.%, 0.3 wt.%, 0.5 wt.%, 0.8 wt.%, and 1.0 wt.% was prepared based on equation 1. Their CMC value can be determined by measuring the IFT between those surfactant concentration and paraffin oil followed by the graph plotting of IFT versus surfactant concentration [17]. After the IFT screening, optimum surfactant concentration at CMC point was opted to clean the oily sand.

$$C_{su}\ (\text{wt}\%) = \frac{W_{su}}{W_{H2O}+W_{sand}+W_{oil}+W_{su}}\ \text{x}\ 100\% \qquad (1)$$

where C_{su} is surfactant concentration in wt.%, W_{su} is weight of surfactant, W_{H20} is weight of water, W_{sand} is weight of sand particles and W_{oil} is weight of paraffin oil.

The method used for this work is summarized in Figure 2. To investigate the effects of surfactant addition and hydrocyclone application, the cleaning process was also performed with the absence of surfactant (only use distilled water) and hydrocyclone. Basically, with the surfactants and hydrocyclone application, the oily sand (with recorded weight) was poured together with 1000 mL of distilled water into hydrocyclone system. After that, the contaminated sand was washed for 60, 90, 120, and 150 min with 3000 rpm and then left for 10 min [44]. Next, the sand was flushed out from the hydrocyclone to the sand collector. Then, the collected sand was filtered, cleansed with distilled water, and heated at 100 °C for 1.5 hour to remove the moisture and the surfactants [45]. After the heating process completed, the clean sand was left for 3 hours in the ambience temperature (27 °C) and then weighted in order to calculate the percentage of oil removed.

The experiment was performed with different CMC surfactant concentration (different type of surfactant) with washing time up to 150 minutes and fixed 3000 rpm centrifugal rotation. The micrographs and elemental analysis obtained from the Field Emission Scanning Electron Microscopy-Energy Dispersive X-ray (FESEM-EDX) was used to describe the sand (before and after the cleaning process). Once the cleaning process has completed, the effluent was filtered and discharged. The efficiency of this cleaning system was referred to different value of samples weighed before and after experiment using a gravimetric method [46]. It can be obtained by comparing the percentage of oil removal on sample weight by using Equation 2.

$$\text{Oil removed (\%)} = \frac{W_b - W_a}{W_{oil}} \times 100\% \quad (2)$$

where W_b is total weight of contaminated sand before washing (g), W_a is total weight of contaminated sand after washing (g) and W_{oil} is initial oil in sand (g).

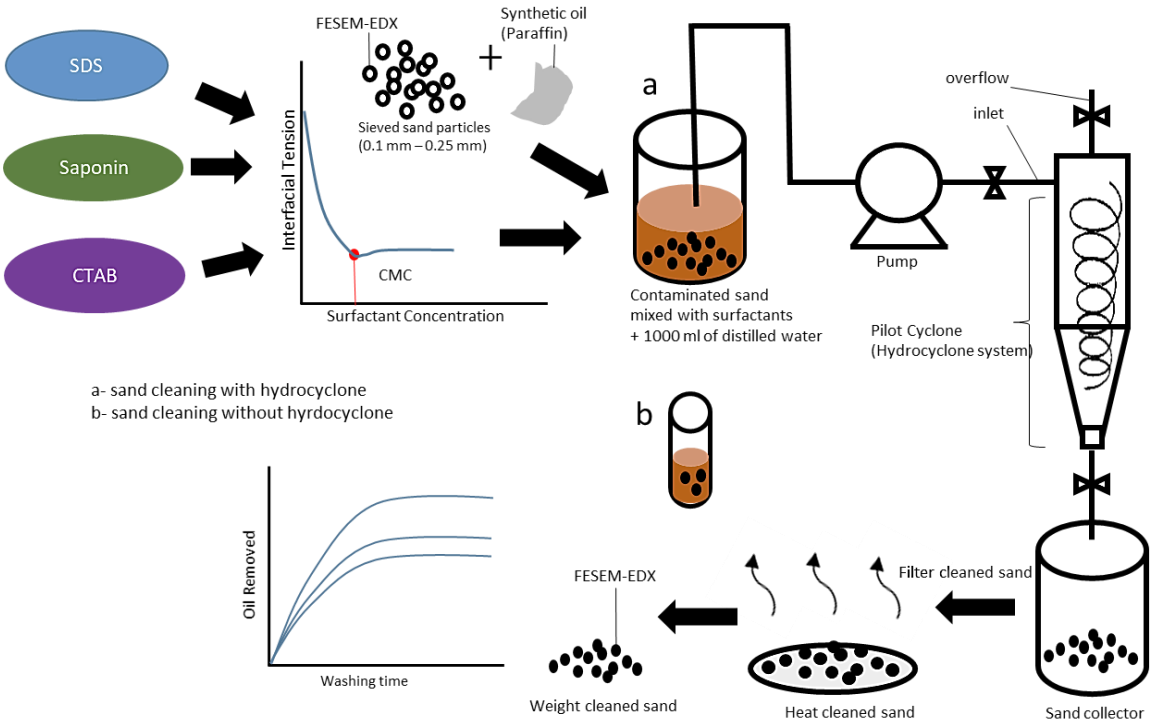


Figure 2. Method used for oily sand cleaning process

Results and Discussion

IFT screening

Surfactant was normally used in cleaning job especially for oil removal in which it can improve the mobility of contaminants from contaminated particles [13]. Thus, it is vital to screen the optimum surfactant concentration so that the cleaning process efficiency become better. The optimum surfactant concentration can be obtained by determining the CMC point of the surfactant. Figure 3 depicts the plot of IFT versus surfactant concentration for different type of surfactant used in this work. The CMC point which denoted by the vertical red line was determined using the meeting-point between two slopes (black line) from the graph. In other word, the CMC point is denoted by the optimum surfactant concentration in which the reduction in IFT is insignificant for the surfactant concentration beyond that point. This concept of selecting the optimum

surfactant concentration for oily solid particles cleaning also corresponded with previous scholars [28, 30, 38]. Based on Figure 3(a-c), the optimum surfactant concentration for SDS, saponin, and CTAB are 0.34 wt.%, 0.58 wt.%, 0.13 wt.%, respectively. These optimum concentrations were then further adopted in our oily sand cleaning process.

Effect of surfactants and hydrocyclone on cleaning process efficiency

Figure 4 summarizes the cleaning process efficiency (oil removal, %) with assistance of hydrocyclone with the surfactants' presence (optimum surfactant concentration) and absence (only use distilled water) at different washing time. Generally, the percentage of oil removal increased with the increase of washing time. Without surfactants, the maximum percentage of oil removal that can be obtained only limited to 46% with total washing time of 150 min. With surfactants, the oil removal percentage increased to greater than 75% with CTAB exhibits the highest percentage (90%), followed by SDS (87%), and saponin (79%). There were two possible mechanisms involved in removing the oil from the sand with the surfactant presence which are the micellar solubilization and mobilization of surfactants by centrifugal force (cyclone) [29, 39]. Based on our work, the cationic CTAB results in the highest performance for sand cleaning and this finding is also parallel with Gu et al. [25] and Nandwani et al. [38], respectively. Even though the distilled water is ineffective in oil removal as compared to the surfactants' application, however, it is recommended to apply the distilled water first before proceeding with the surfactant. By doing this, the consumption of surfactants in the cleaning process can be reduced significantly or in other words, reduce the cost effectively.

The effects of hydrocyclone on cleaning process efficiency has been investigated. The same cleaning solution (distilled water and optimum surfactant concentration) has also been applied to the system without the hydrocyclone. The comparison between them (with and without the hydrocyclone) is shown in Figure 5. Obviously, the percentage of oil removal from the sand was decreased (19-22%) with no hydrocyclone in the cleaning system regardless of the surfactants presence or not. Therefore, it can be concluded that the synergized effects of optimum surfactant concentration and hydrocyclone applications at 150 min washing time results in higher cleaning process efficiency.

Further analysis on the effects of using hydrocyclone on effluent produced from the cleaning process is depicted in Figure 6. Without the hydrocyclone (Figure 6a), the effluent behavior exhibited two separate layers which composed of oil and surfactant solution. Meanwhile with the hydrocyclone (Figure 6b), three distinct layers existed which consist of foam and turbidity (wash layer). All the effluents from the surfactants used in this work exhibit similar layer formation as in Figure 6b with CTAB results in the highest foam and turbidity formation, while the saponin exhibit the least. The least formation of foam for saponin (non-ionic) is due to no surface charge on the foam films and larger surface area of molecules [34]. As the CTAB is a cationic surfactant, it resulted in higher adsorption of oil which then cause in more turbidity as compared to SDS and saponin [23].

Sand analysis for before and after cleaning process with hydrocyclone assistance

The EDX results of the sand for the before and after cleaning process are shown in Table 2. Before the cleaning process, the sand consists of dominance Si-O (quartz-sand) with small traces of Al, Fe, Ca and K which typically found in sandy beaches. The traces of Fe element are possibly due to nature occurrences caused by sedimentation from weathered volcanic rock that precipitate which then influence the composition of the used sand [22]. After the cleaning process, the sand has shown the presence of saponin at optimum surfactant concentration which results in significant reduction of heavy metal elements (Fe, Al, Mg). Thus, in addition to remove oil from the sand, saponin is also capable to reduce heavy metal elements and the results obtained resemble the works by previous scholars [21]. As compared to the sand before the cleaning process, higher C content was found for those three surfactants after the cleaning process. This might be due to the unsettled paraffin component on the sand [31].

Figure 7a shows a FESEM micrograph for the sand before the cleaning process. Obviously, it can be seen

that a relatively small particles attached on sand which possibly due to the clay and iron oxide particles formation. After three cleaning process with the SDS (Figure 7b) and saponin (Figure 7c), white materials on sand were detected and this might be an organic compound that absorbed and precipitate on sand during the cleaning. There are no white materials detected on the sand for the CTAB surfactant in Figure 7d. This might be due to the hydrophilic nature of CTAB which effectively enhance the oil compound absorption on sand and oil removal process.

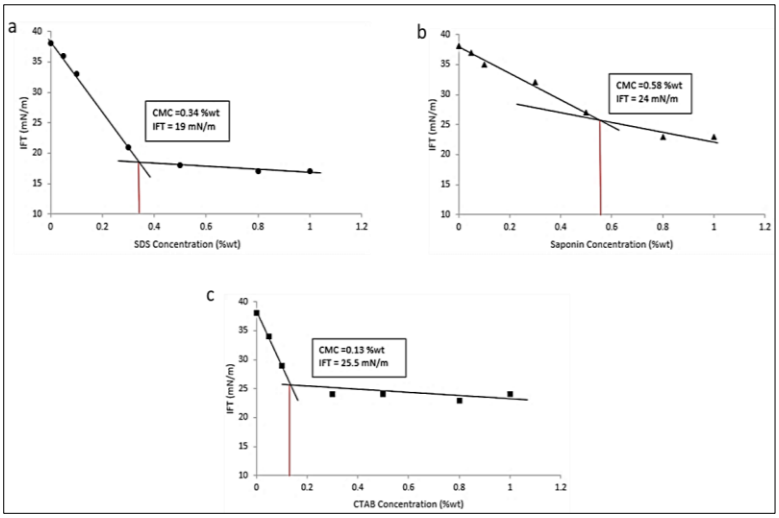


Figure 3. IFT versus surfactant concentration, (a) SDS, (b) Saponin and (c) CTAB

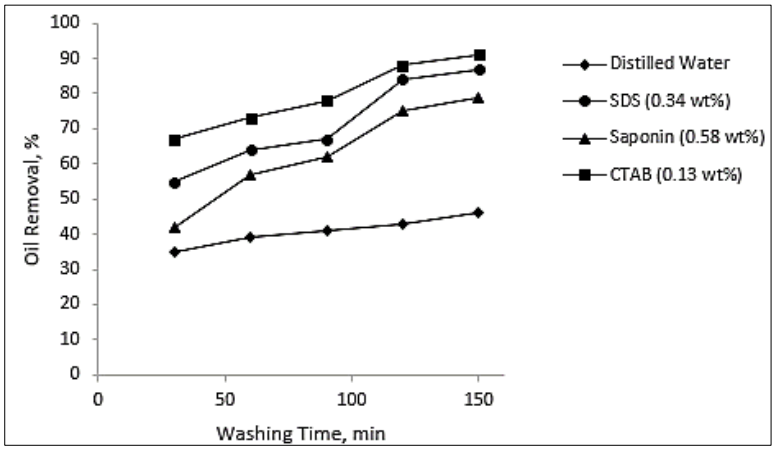


Figure 4. Oil removal percentage versus washing time.

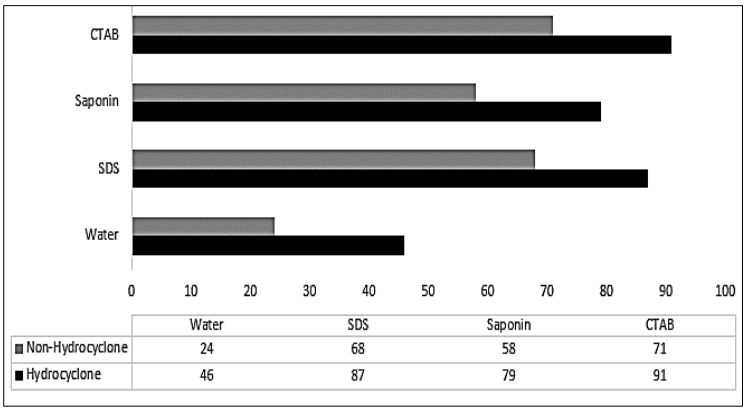


Figure 5. Oil removal percentage with and without LSS hydrocyclone separator for 150 min washing time

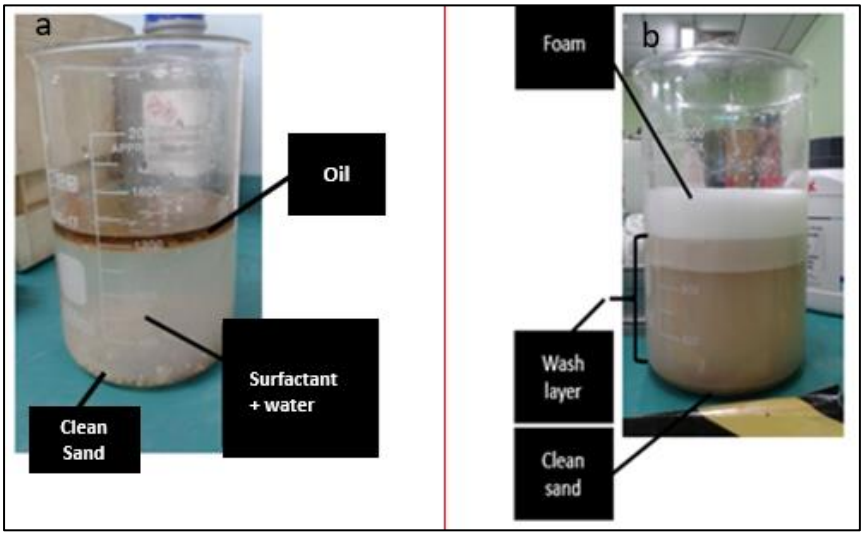


Figure 6. Effluent behaviour from the cleaning process, (a) without hydrocyclone and (b) with hydrocyclone

Table 2. EDX elemental analysis on sand for before and after cleaning process

Element, wt.%	C	O	Na	Mg	Al	Si	K	Ca	Fe
Before	0.1	37.1	1.2	1.2	5.7	28.2	2.2	2.3	4.3
After (SDS)	1.2	35.0	1.0	1.2	5.0	28.0	2.0	2.3	3.2
After (Saponin)	1.3	35.3	0.5	0.7	2.1	28.1	1.2	1.8	1.7
After (CTAB)	0.7	36.0	1.1	1.2	5.2	28.2	2.2	2.2	2.2

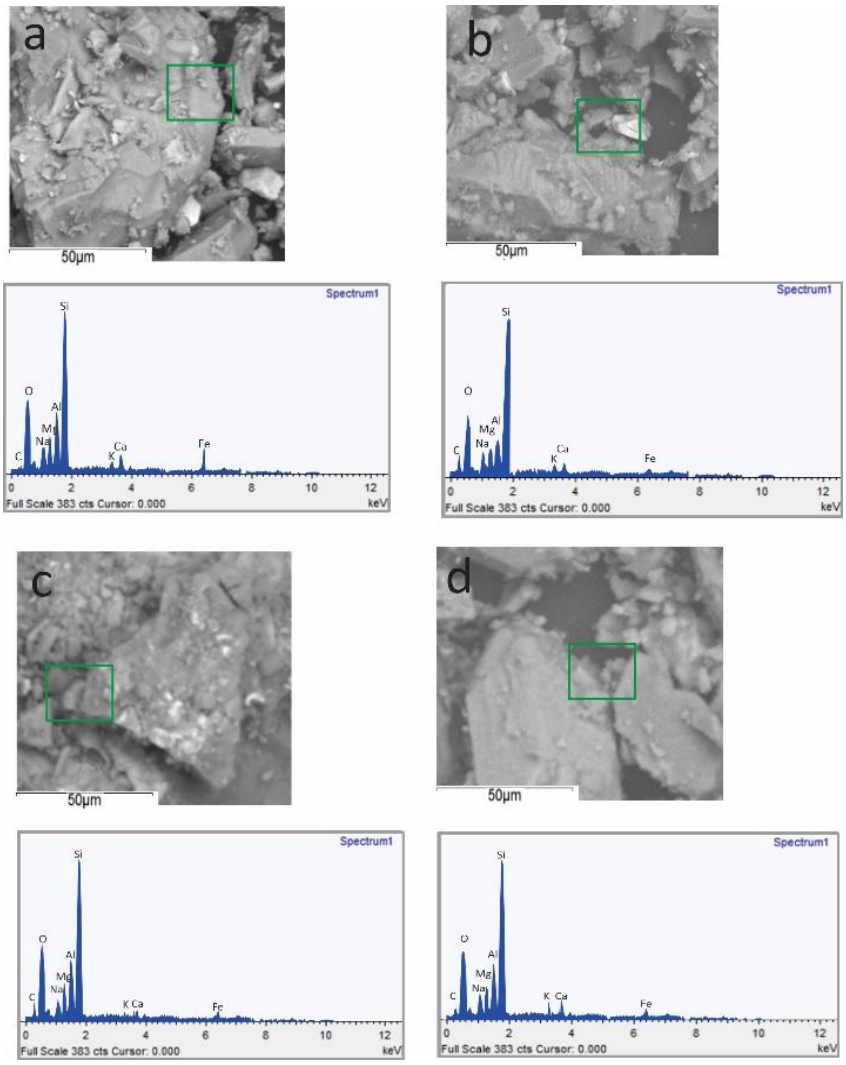


Figure 7. FESEM-EDX micrographs sand particles, (a) before cleaned, and after cleaned by (b) SDS, (c) saponin and (d) CTAB

Conclusion

The IFT screening on surfactants (SDS, saponin, and CTAB) and the oily sand washing through LSS hydrocyclone has been determined systematically. Based on the findings from this work, it can be concluded that the IFT values decreased significantly for the surfactant concentration below the CMC point. Increased in surfactant concentration exceeding the CMC point only results in insignificant IFT reduction. The CTAB at optimum surfactant concentration resulted in higher cleaning process efficiency (greater amount of oil removal) as compared to SDS and saponin. With the hydrocyclone assistance, the efficiency became greater and the improvement was due to the synergized effects (surfactant-IFT and centrifugal force). Saponin surfactant has a binary function whereby it can remove the oil from the sand and reduce heavy metal elements. These binary functions are possibly able to avoid the secondary pollution and reduce the washing time so that the oil sand disposal requirements set by the authority can be fulfilled.

Acknowledgement

We would like to thank the Ibnu Sina Institute and the School of Chemical and Energy Engineering, Universiti Teknologi Malaysia for the laboratory equipment and

sample characterization and this work is funded by UTM Transdiciplinary Research Grant (Q. J130000.3551.07G12).

References

1. Rawlins, H. (2013). Sand management methodologies for sustained facilities operations. *Oil and Gas Facilities*, 2(05): 27-34.
2. Ikporo, B. and Sylvester, O. (2015). Effect of sand invasion on oil well production: a case study of Garon field in the Niger Delta. *The International Journal of Engineering and Science*, 4(5): 64-72.
3. Pichtel, J. (2016). Oil and gas production wastewater: Soil contamination and pollution prevention. *Applied and Environmental Soil Science*, 2016: 1-25.
4. Khamehchi, E., Ameri, O. and Alizadeh, A. (2015). Choosing an optimum sand control method. *Egyptian Journal of Petroleum*, 24(2): 193-202.
5. Jiuxing, Z. H. Y. Y. W. and Dongping, W. (2010). A study on oily sludge (sand) treatment technology. *Environmental Protection of Oil & Gas Fields*, 3: 1-20.
6. Zali, M. A., Ahmad, W. K. W., Retnam, A. and Catrina, N. (2015). Concentration of heavy metals in virgin, used, recovered and waste oil: a spectroscopic study. *Procedia Environmental Sciences*, 30: 201-204.
7. AlSofi, A. M., AlKhatib, A. M., Al-Ajwad, H. A., Wang, Q. and Zahrani, B. H. (2019). Assessment of enhanced-oil-recovery-chemicals production and its potential effect on upstream facilities. *SPE Journal*, 24(3): 1-037.
8. Bahmani, F., Ataei, S. A. and Mikaili, M. A. (2018). The effect of moisture content variation on the bioremediation of hydrocarbon contaminated soils: modeling and experimental investigation. *Journal of Environmental Analytical Chemistry*, 5(2): 236.
9. Liu, P. W. G., Chang, T. C., Whang, L. M., Kao, C. H., Pan, P. T. and Cheng, S. S. (2011). Bioremediation of petroleum hydrocarbon contaminated soil: Effects of strategies and microbial community shift. *International Biodeterioration & Biodegradation*, 65(8): 1119-1127.
10. Jing, G., Chen, T. and Luan, M. (2016). Studying oily sludge treatment by thermo chemistry. *Arabian Journal of Chemistry*, 9: S457-S460.
11. Muñoz-Morales, M., Braojos, M., Sáez, C., Cañizares, P. and Rodrigo, M. A. (2017). Remediation of soils polluted with lindane using surfactant-aided soil washing and electrochemical oxidation. *Journal of Hazardous Materials*, 339: 232-238.
12. Gao, Y. X., Ding, R., Chen, X., Gong, Z. B., Zhang, Y. and Yang, M. (2018). Ultrasonic washing for oily sludge treatment in pilot scale. *Ultrasonics*, 90: 1-4.
13. Arelli, A., Nuzzo, A., Sabia, C., Banat, I. M., Zanaroli, G. and Fava, F. (2018). Optimization of washing conditions with biogenic mobilizing agents for marine fuel-contaminated beach sands. *New Biotechnology*, 43: 13-22.
14. Singh, A. K. and Cameotra, S. S. (2013). Efficiency of lipopeptide biosurfactants in removal of petroleum hydrocarbons and heavy metals from contaminated soil. *Environmental Science and Pollution Research*, 20(10): 7367-7376.
15. Belhaj, A. F., Elraies, K. A., Alnarabiji, M. S., Shuhli, J. A., Mahmood, S. M. and Ern, L. W. (2019). Experimental investigation of surfactant partitioning in pre-CMC and post-CMC regimes for enhanced oil recovery application. *Energies*, 12(12): 2319.
16. Manshad, A. K., Rezaei, M., Moradi, S., Nowrouzi, I. and Mohammadi, A. H. (2017). Wettability alteration and interfacial tension (IFT) reduction in enhanced oil recovery (EOR) process by ionic liquid flooding. *Journal of Molecular Liquids*, 248: 153-162.
17. Duan, M., Wang, X., Fang, S., Zhao, B., Li, C. and Xiong, Y. (2018). Treatment of Daqing oily sludge by thermochemical cleaning method. *Colloids and Surfaces A: Physicochemical and Engineering Aspects*, 554: 272-278.
18. Bahadori, A. (2018). Fundamentals of enhanced oil and gas recovery from conventional and unconventional reservoirs. Gulf Professional Publishing.

19. Saidy, A. R., Smernik, R. J., Baldock, J. A., Kaiser, K. and Sanderman, J. (2013). The sorption of organic carbon onto differing clay minerals in the presence and absence of hydrous iron oxide. *Geoderma*, 209: 15-21.
20. Ferreira, T. M., Bernin, D. and Topgaard, D. (2013). NMR studies of nonionic surfactants. In *Annual Reports on NMR Spectroscopy*. Academic Press, 79: pp. 73-127.
21. Tang, J., He, J., Xin, X., Hu, H. and Liu, T. (2018). Biosurfactants enhanced heavy metals removal from sludge in the electrokinetic treatment. *Chemical Engineering Journal*, 334: 2579-2592.
22. Borghi, C. C., Fabbri, M., Fiorini, M., Mancini, M. and Ribani, P. L. (2011). Magnetic removal of surfactants from wastewater using micrometric iron oxide powders. *Separation and Purification Technology*, 83: 180-188.
23. Dehaghani, A. H. S. and Badizad, M. H. (2018). Effect of magnetic field treatment on interfacial tension of CTAB nano-emulsion: Developing a novel agent for enhanced oil recovery. *Journal of Molecular Liquids*, 261: 107-114.
24. Para, G., Hamerska-Dudra, A., Wilk, K. A. and Warszyński, P. (2010). Surface activity of cationic surfactants, influence of molecular structure. *Colloids and Surfaces A: Physicochemical and Engineering Aspects*, 365(1-3): 215-221.
25. Gu, X., Zhang, F., Li, Y., Zhang, J., Chen, S., Qu, C. and Chen, G. (2018). Investigation of cationic surfactants as clean flow improvers for crude oil and a mechanism study. *Journal of Petroleum Science and Engineering*, 164: 87-90.
26. Negin, C., Ali, S. and Xie, Q. (2017). Most common surfactants employed in chemical enhanced oil recovery. *Petroleum*, 3(2): 197-211.
27. Urum, K., Pekdemir, T. and Gopur, M. (2003). Optimum conditions for washing of crude oil-contaminated soil with biosurfactant solutions. *Process Safety and Environmental Protection*, 81(3): 203-209.
28. Khalladi, R., Benhabiles, O., Bentahar, F. and Moulai-Mostefa, N. (2009). Surfactant remediation of diesel fuel polluted soil. *Journal of Hazardous Materials*, 164(2-3): 1179-1184.
29. Bandala, E. R., Aguilar, F. and Torres, L. G. (2010). Surfactant-enhanced soil washing for the remediation of sites contaminated with pesticides. *Land Contamination & Reclamation*, 18(2): 2.
30. Long, A., Zhang, H. and Lei, Y. (2013). Surfactant flushing remediation of toluene contaminated soil: Optimization with response surface methodology and surfactant recovery by selective oxidation with sulfate radicals. *Separation and Purification Technology*, 118: 612-619.
31. Huang, Z., Wang, D., Befkadu, A. A., Zhou, J., Srivastava, I., Pan, D. and Chen, Q. (2020). Enhancement of auxiliary agent for washing efficiency of diesel contaminated soil with surfactants. *Chemosphere*, 252: 126494.
32. Zheng, C., Wang, M., Wang, Y. and Huang, Z. (2012). Optimization of biosurfactant-mediated oil extraction from oil sludge. *Bioresource Technology*, 110: 338-342.
33. Kobayashi, T., Kaminaga, H., Navarro, R. R. and Iimura, Y. (2012). Application of aqueous saponin on the remediation of polycyclic aromatic hydrocarbons-contaminated soil. *Journal of Environmental Science and Health, Part A*, 47(8), 1138-1145.
34. Zhou, W., Wang, X., Chen, C. and Zhu, L. (2013). Enhanced soil washing of phenanthrene by a plant-derived natural biosurfactant, Sapindus saponin. *Colloids and Surfaces A: Physicochemical and Engineering Aspects*, 425: 122-128.
35. Li, G., Guo, S. and Hu, J. (2016). The influence of clay minerals and surfactants on hydrocarbon removal during the washing of petroleum-contaminated soil. *Chemical Engineering Journal*, 286: 191-197.
36. Trisunaryanti, W., Larasati, S., Bahri, S., lailun Ni'mah, Y., Efiyanti, L., Amri, K. and Sumbogo, S. D. (2020). Performance comparison of Ni-Fe loaded on NH_2-functionalized mesoporous silica and beach sand in the hydrotreatment of waste palm cooking oil. *Journal of Environmental Chemical Engineering*, 8(6): 104477.

37. Zhu, Z., Zhang, B., Chen, B., Cai, Q. and Lin, W. (2016). Biosurfactant production by marine-originated bacteria Bacillus Subtilis and its application for crude oil removal. *Water, Air, & Soil Pollution*, 227(9): 328.
38. Nandwani, S. K., Malek, N. I., Lad, V. N., Chakraborty, M. and Gupta, S. (2017). Study on interfacial properties of Imidazolium ionic liquids as surfactant and their application in enhanced oil recovery. *Colloids and Surfaces A: Physicochemical and Engineering Aspects*, 516: 383-393.
39. Saad, M. A., Kamil, M., Abdurahman, N. H., Yunus, R. M. and Awad, O. I. (2019). An overview of recent advances in state-of-the-art techniques in the demulsification of crude oil emulsions. *Processes*, 7(7): 470.
40. Yurdem, H., Demir, V. and Degirmencioglu, A. (2010). Development of a mathematical model to predict clean water head losses in hydrocyclone filters in drip irrigation systems using dimensional analysis. *Biosystems Engineering*, 105(4): 495-506.
41. Durdevic, P., Pedersen, S., Bram, M., Hansen, D., Hassan, A. and Yang, Z. (2015). Control oriented modeling of a de-oiling hydrocyclone. *IFAC-PapersOnLine*, 48(28): 291-296.
42. Shi, Y., Zhu, H., Zhang, J., Yin, B., Xu, R. and Zhao, J. (2017). Investigation of condition parameters in each stage of a three-stage helico-axial multiphase pump via numerical simulation. *In the 27th International Ocean and Polar Engineering Conference*. International Society of Offshore and Polar Engineers.
43. ASTM E11 (2013). Standard specification for woven wire test sieve cloth and test sieves. West Conshohocken: ASTM
44. Arpornpong, N., Padungpol, R., Khondee, N., Tongcumpou, C., Soonglerdsongpha, S., Suttiponparnit, K. and Luepromchai, E. (2020). Formulation of bio-based washing agent and its application for removal of petroleum hydrocarbons from drill cuttings before bioremediation. *Frontiers in Bioengineering and Biotechnology*, 8: 961.
45. Falciglia, P. P., Giustra, M. G. and Vagliasindi, F. G. A. (2011). Low-temperature thermal desorption of diesel polluted soil: Influence of temperature and soil texture on contaminant removal kinetics. *Journal of Hazardous Materials*, 185(1): 392-400.
46. Villalobos, M., Avila-Forcada, A. P. and Gutierrez-Ruiz, M. E. (2008). An improved gravimetric method to determine total petroleum hydrocarbons in contaminated soils. *Water, Air, and Soil Pollution*, 194(1-4): 151-161.

Malaysian Journal of Analytical Sciences (MJAS)
Published by Malaysian Analytical Sciences Society

PERBANDINGAN BIOREAKTOR MEMBRAN DAN BIOREAKTOR MEMBRAN BERELEKTRIK UNTUK RAWATAN AIR SISA KILANG MINYAK KELAPA SAWIT

(Comparison of Membrane Bioreactor and Electric Membrane Bioreactor for Wastewater Treatment of The Palm Oil Mill)

Teow Yeit Haan[1,2]*, Sharmila Pragash Sundaram[1], Najah Hafizah Musa[1], Syarifah Nornabilah Syed Muaz[1], Shakir Ahmad Mohamed Sultan[1], Nur Ameera Rosli[1]

[1]*Department of Chemical and Process Engineering, Faculty of Engineering and Built Environment*
[2]*Research Centre for Sustainable Process Technology, Faculty of Engineering and Built Environment*
Universiti Kebangsaan Malaysia, 43600 UKM Bangi, Selangor, Malaysia

**Pengarang utama:* yh_teow@ukm.edu.my

Received: 29 January 2021; Accepted: 1 March 2021; Published: 25 April 2021

Abstrak

Perkembangan industri kelapa sawit yang pesat menyebabkan pencemaran alam sekitar yang disebabkan oleh air sisa kilang minyak kelapa sawit (POME) yang terhasil dari proses pengekstrakan minyak sawit. Bioreaktor membran (MBR) dengan gabungan rawatan biologi dan teknologi membran merupakan kaedah yang berkesan untuk rawatan POME. Penerapan ini dapat ditambahbaik dengan pengenalan bioreaktor membran berelektrik (EMBR) dimana daya tolakan yang terhasil antara permukaan membran konduktif GO/MCWNTs dan zarah-zarah dalam POME dijangka akan meningkatkan lagi prestasi sistem EMBR. Objektif kajian ini adalah untuk mengkaji keberkesanan membran konduktif GO/MCWNTs di sistem bioreaktor membran berelektrik (EMBR) untuk rawatan POME dan dibandingkan dengan sistem MBR tanpa medan elektrik. Prestasi sistem MBR dan EMBR dinilai dengan peratusan penyingkiran permintaan oksigen kimia (COD) dan nitrogen amonia (NH_3-N). Manakala, untuk kajian penurasan jangka panjang, penapisan membran konduktif GO/MCWNTs beroperasi selama 32 minit dan diberhentikan. Ia diikuti dengan pembekalan medan elektrik arus terus merentasi membran konduktif GO/MCWNTs selama 6 minit untuk sistem EMBR, dan sistem MBR diberhenti tanpa bekalan medan elektrik. Proses berselang-seli ini diulangi untuk 4 kitaran. Prestasi sistem EMBR yang dialirkan elektrik adalah lebih baik daripada sistem MBR tanpa aliran elektrik dengan peratusan penyingkiran COD dan NH_3-N setinggi 82.07% dan 70.5% untuk sistem EMBR dan 53.63 % dan 43.81% bagi sistem MBR. Hal ini membawa kesimpulan bahawa sistem EMBR mempunyai keberkesanan penyingkiran yang baik and fluks penurasan yang lebih tinggi berbanding sistem MBR untuk rawatan POME.

Kata kunci: bioreaktor membran berelektrik, membran konduktif GO/MCWNTs, membran bioreaktor, rawatan air, air sisa kilang kelapa sawit

Abstract

The rapid development of the palm oil industry results in environmental pollution caused by the wastewater of the palm oil mill (POME) from the palm oil extraction process. Membrane bioreactor (MBR) with a combination of biological treatment and

membrane technology is an effective method for POME treatment. This application can be improved with the use of electromagnetic membrane bioreactors (EMBRs) where the repulsive force form between the surface of GO/MCWNTs conductive membranes and particles in POME can enhance the performance of EMBR system. The objective of this study was to examine the effectiveness of GO/MCWNTs conductive membrane in electric membrane bioreactor (EMBR) system for POME treatment and to compare with the MBR system without an electric field. The performance of MBR and EMBR systems is assessed by the percentage of removal of chemical oxygen demand (COD) and ammonia nitrogen (NH_3-N). Meanwhile, for long-term filtration studies, GO/MCWNTs conductive membrane filtering operates for 32 minutes and discontinued. It was followed by an electric supply across the GO/MCWNTs conductive membrane for 6 minutes for EMBR system, and the MBR system was discontinued without electric supply. This intermittent process is repeated for 4 cycles. The performance of EMBR system with electric supply is better than an electro-free MBR system with COD and NH_3-N removal percentages as high as 82.07% and 70.5% for EMBR system and 53.63% and 43.81% for MBR system. This concluded that the EMBR has good removal efficiency and higher filtration flux than MBR system for POME treatment.

Keywords: **e**lectric membrane bioreactor, GO/MCWNTs conductive membrane, membrane bioreactor, water treatment, wastewater of the palm oil mill

Pengenalan

Industri minyak kelapa sawit merupakan antara penyumbang tertinggi kepada ekonomi Malaysia disebabkan permintaannya yang tinggi di seluruh dunia. Namun, perkembangan industri kelapa sawit yang pesat juga mendatangkan kesan negatif seperti pencemaran alam sekitar yang disebabkan oleh air sisa kilang minyak kelapa sawit (POME) yang terhasil dari proses pengekstrakan minyak sawit [1]. Jumlah air yang banyak diperlukan untuk proses pengekstrakan minyak sawit. Antaranya, lebih daripada separah jumlah air ini akan berakhir sebagai POME. Pengeluaran POME dilapor sekitar 50 juta tan pada kadar tahunan 2017 [2].

POME merupakan salah satu air sisa yang paling banyak dihasilkan di Malaysia dan mempunyai tahap kekotoran yang 100 kali lebih kotor daripada air sisa bandar. Pelepasan POME ke persekitaran tanpa rawatan akan mendatangkan kesan yang buruk terhadap alam sekitar. POME mengandungi asid organik, karbohidrat, mineral, dan protein yang tinggi. Nutrien yang tinggi ini menjadikannya sumber pertumbuhan mikrob dan mendorong kepada eutrofikasi jika dibuang terus ke sumber air seperti sungai tanpa rawatan [3]. POME boleh dirawat melalui rawatan biologi kerana kandungan organiknya tinggi. Rawatan biologi dipromosi kerana penggunaan tenaga elektrik yang rendah dan hasil enapcemar daripada rawatan biologi boleh digunakan sebagai baja untuk tanaman [4]. Walaubagaimanapun, terdapat beberapa kelemahan terhadap rawatan biologi seperti penggunaan ruang yang besar, tidak berkesan untuk menyingkirkan bahan bukan organik yang terkandung dalam air sisa seperti patogen dan jangka masa rawatan yang panjang.

Sistem penapisan membran merupakan teknologi termaju yang dapat menangani kelemahan rawatan biologi. Kualiti air rawatan yang tinggi dan konsisten dapat dihasilkan melalui proses penurasan membran, dimana sistem penapisan membran hanya memerlukan ruang kecil untuk rawatan, dan operasi rawatan secara spontan [5]. Namun pemendapan kotoran seperti bahan organik daripada POME atas permukaan membran merupakan kelemahan teknologi membran, dimana ia akan menyingkatkan jangka hayat membran. Hal ini akan mengenakan kos operasi tambahan untuk pembersihan membran mahupun penggantian membran [6]. Kaedah yang berkesan untuk rawatan POME disamping mengurangkan pemendapan bahan organik daripada POME pada permukaan membran boleh dilakukan dengan menggabungkan kedua-dua rawatan biologi dan teknologi membran. Sistem penggabungan ini dinama sebagai bioreaktor membran (MBR).

Pengubahsuaian permukaan membran dengan ciri hidrofilik merupakan salah satu kaedah yang berkesan untuk mengurangkan kotoran pada membran [7]. Secara amnya, kebanyakan kotoran dalam air sisa seperti bahan organik adalah bercas negatif. Maka, pengubahsuaian permukaan membran bersifat hidrofilik dan bercas negatif dapat meningkatkan prestasi membran

disamping mengelak kotoran pada membran dengan penghasilan daya tolakan elektrostatik antara membran dan kotoran [8]. Kumpulan penyelidikan kami telah berjaya menghasilkan membran konduktif dengan menggunakan grafena oksida (GO) dan nanotiub karbon pelbagai dinding (MWNCTs) melalui kaedah pengadunan fasa songsang. Nisbah GO:MWNCTs yang optimum telah direka pada 1:9 berdasarkan kekonduksian membran. Membran konduktif GO/MCWNTs yang dihasilkan ini berjaya mengurangkan kotoran pada permukaaan membran untuk proses rawatan POME dengan bekalan medan elektrik. Fluks membran dapat dikekalkan untuk jangka masa operasi penurasan yang lebih panjang berbanding dengan membran yang lain [9].

Objektif kajian ini adalah untuk mengkaji keberkesanan membran konduktif GO/MCWNTs di sistem bioreaktor membran berelektrik (EMBR) untuk rawatan POME dan dibandingkan dengan sistem MBR yang tanpa medan elektrik. Daya tolakan yang terhasil antara permukaan membran konduktif GO/MCWNTs dan zarah-zarah dalam POME dijangka akan meningkatkan lagi prestasi teknologi yang menggabungkan kedua-dua rawatan biologi dan teknologi membran ini.

Bahan dan Kaedah

Sintesis membran konduktif

GO disintesis daripada grafin dengan menggunakan kaedah Hummer [10]. Membran konduktif GO/MCWNTs dihasilkan dengan mencampur bahan nano karbon ke dalam larutan polimer membran. Pada permulaannya, GO dan MWNCTs dengan nisbah 1:9 w/w dicampur ke dietilacetamida (DMAc). Campuran tersebut dikacau sehingga sebati dan disonifikasi selama 30 minit pada 40 KHz dan 124 W dengan menggunakan ultrasonikator, WUC-A03H (Wisd. Korea). Seterusnya, polivinilidena fluorida (PVDF) ditambah ke dalam larutan campuran bahan nano karbon secara perlahan-lahan. Larutan polimer membran dikacau pada 250 rpm dan dipanaskan pada suhu 65 °C selama 4 jam [11]. Larutan membran polimer yang terhasil kemudiannya dituang rata di atas kaca. Membran konduktif GO/MCWNTs dihasilkan dengan menggunakan alat aplikasi filem Elcometer 4340 (Elcometer Ltd., UK) pada ketebalan 200 µm. Lapisan membran konduktif GO/MCWNTs seterusnya direndam ke dalam air ultrapure (UP) dengan kadar segera. Membran konduktif GO/MCWNTs yang terhasil dikeluarkan dari air UP selepas rendaman seharian.

Penyesuaian iklim bakteria dalam sistem MBR dan sistem EMBR

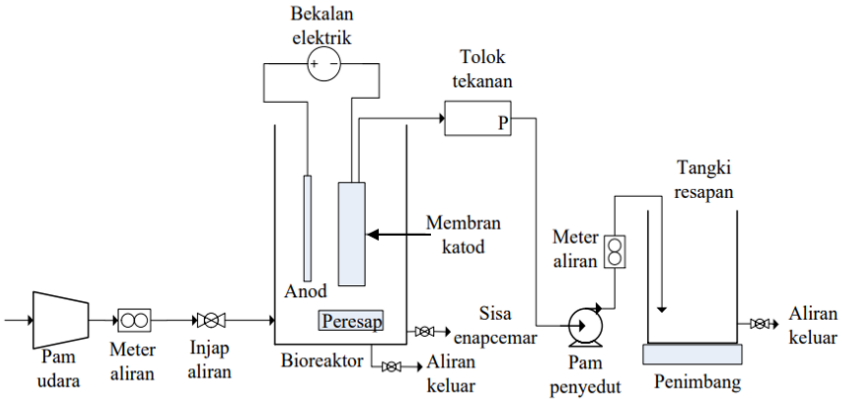
Penyesuaian iklim bakteria dalam EMBR dijalankan dengan mengguna POME mentah dan POME aerobik yang dikumpul dari kilang kelapa sawit yang terletak di Bestari Jaya, Selangor Darul Ehsan, Malaysia. 9.6 L POME aerobik diguna sebagai inokulum (80% daripada isipadu EMBR), Manakala 2.4 L POME aerobik (20% daripada isipadu EMBR) ditambah untuk menjadikan isipada keseluruhan 12 L. Aliran udara disalurkan ke sistem EMBR pada $10 m^3/h$. Parameter seperti pH, oksigen terlarut (DO), permintaan oksigen kimia (COD), permintaan oksigen biokimia (BOD), dan nitrogen amonia (NH_3-N) dipantau untuk mengenalpasti keselesaian proses penyesuaian iklim bakteria dalam sistem EMBR.

Penilaian prestasi sistem MBR dan EMBR

POME aerobik diguna sebagai efluen yang dirawat di sistem MBR dan EMBR. Helaian membran konduktif GO/MCWNTs yang diguna pada katod dalam sistem EMBR, manakala kepingan keluli tahan karat diguna pada anod. Jarakan antara katod dan anod ditetapkan pada 35 mm. Flux sistem MBR dan EMBR ditentukan pada 15 L/m^2 h dan aliran udara disalurkan ke sistem adalah $10 m^3/h$ untuk memastikan kepekatan DO sistem adalah di antara 6 - 8 mg/L [12]. Pam penyedut digunakan untuk menyedut efluen yang ditapis oleh membran konduktif GO/MCWNTs. Untuk kajian penurasan jangka panjang, penapisan membran konduktif GO/MCWNTs beroperasi selama 32 minit dan diberhentikan. Ia diikuti dengan pembekalan medan elektrik arus terus merentasi membran konduktif GO/MCWNTs selama 6 minit untuk sistem EMBR, manakala sistem MBR diberhenti tanpa bekalan medan elektrik. Proses berselang-seli ini diulangi untuk 4 kitaran. Rajah 1 menunjukkan lukisan skematik persediaan sistem MBR dan EMBR.

Analisis kualiti air

Suhu, pH, dan DO diukur dengan menggunakan meter pH, meter suhu PHM4202, dan meter DO, masing-masing (Hanna, UK). Untuk analisis COD, 2 mL sampel air dan air suling dituang kedalam kelalang COD secara berasingan dan dipanaskan kepada 150 °C selama 2 jam di Digital Reactor Block DRB200 (Hach, USA). Selepas pemanasan selama 2 jam, kedua-dua sampel air dan air suling dibiarkan sejuk dan diukur dengan Spectrophotometer DR3900 (Hach, USA). Manakala untuk analisis NH_3-N, 3 titisan penstabil mineral dimasukkan ke dalam silinder penyukat yang mengandungi sampel air dan digoncang. Seterusnya, 3 titisan polivinil alkohol ditambah ke dalam campuran larutan tersebut dan digoncang. Kemudiannya, 1 mL reagen Nessler ditambah, digoncang, dan dibiar selama 1 minit. 10 mL larutan campuran daripada silinder penyukat dimasukkan ke dalam kuvet dan diukur dengan Spectrophotometer DR3900 (Hach, USA).



Rajah 1. Lukisan skematik persediaan sistem MBR dan EMBR

Keputusan dan Perbincangan

Pengesuaian iklim bakteria dalam sistem EMBR

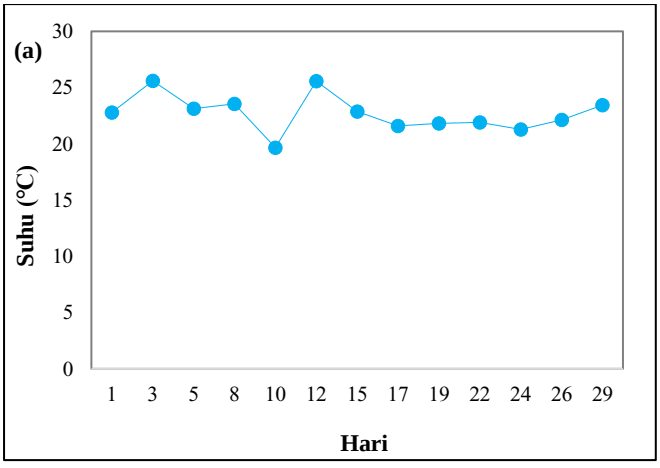
Rajah 2 menunjukkan bacaan parameter seperti suhu, pH, DO, COD, dan NH_3-N yang tercatat semasa proses penyesuaian iklim bakteria selama 4 minggu berturut-turut. Parameter suhu bermula hari pertama ke hari 15 adalah turun naik dan bermula mencapai kestabilan selepas hari ke 15. Manakala parameter pH menaik secara berterusan. Sekitar hari ke 19 hingga ke 29, bacaan pH turut mencapai kestabilan dan berada dalam lingkungan 8 - 10. Bacaan COD dan NH_3-N menunjukkan penurunan secara mendadak pada hari pertama sehingga hari ke 8. Peratusan penurunan sebanyak 95.5% dan 81.4% tercatat oleh parameter COD dan NH_3-N, masing-masing. Manakala, bacaan DO meningkat sebanyak 58%. Menyusul dari hari ke 10 hingga hari ke 19, bacaan bagi ketiga-tiga parameter COD, NH_3-N, dan DO cendurung mencapai kestabilan. Penyesuaian iklim bakteria dalam sistem EMBR selesai pada hari 19 apabila bacaan parameter menjadi stabil. Selepas hari 19, parameter COD dan NH_3-N mula meningkat dan bacaan DO menurun. Peningkatan COD dan NH_3-N adalah sebanyak 68% dan 63%, manakala DO menurun sebanyak 72.8% berbanding dengan hari sebelumnya. Berbanding dengan kajian yang dilakukan oleh Wong et al., 27 hari diperlukan untuk membolehkan kesemua bakteria aerobik menyesuaikan persekitaran baru dengan sempurna [13]. Namun, kajian ini hanya memerlukan 15 hari untuk mencapai penyesuaian iklim bakteria dalam sistem EMBR yang dikenalpasti dengan kestabilan bacaaan parameter.

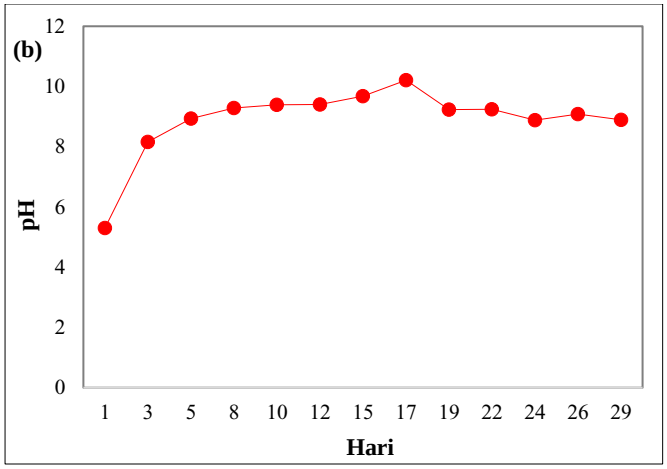
Penilaian prestasi sistem MBR dan EMBR

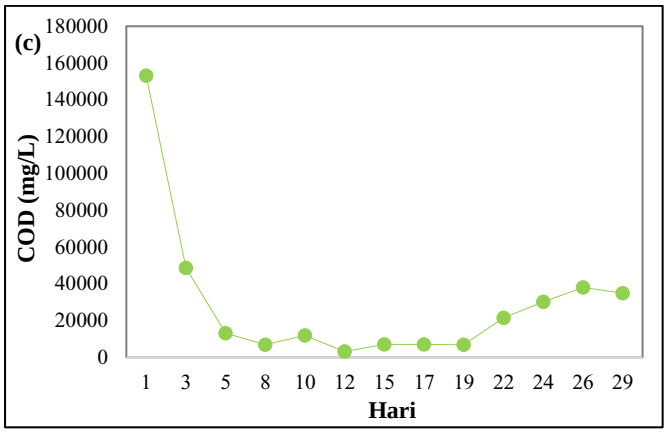
Prestasi membran konduktif GO/MCWNTs di sistem MBR dan EMBR dinilai berdasarkan peratusan penyingkiran COD dan NH_3-N. Rajah 3 menunjukkan

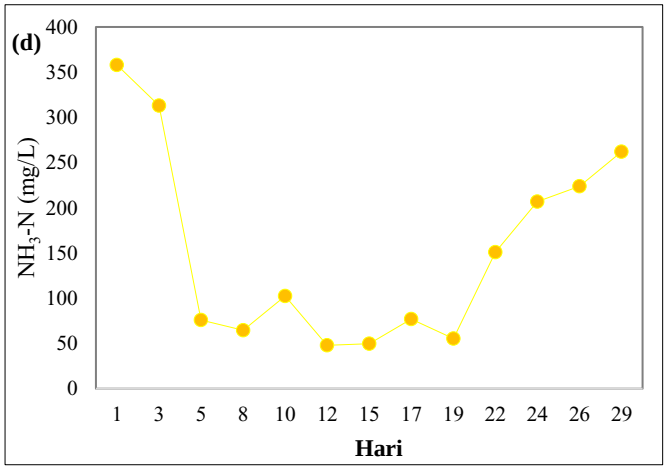
peratus penyingkiran COD dan NH_3-N untuk sistem MBR dan EMBR. Secara amnya, prestasi sistem EMBR yang dialirkan elektrik adalah lebih baik daripada sistem MBR tanpa aliran elektrik dengan peratusan penyingkiran COD dan NH_3-N setinggi 82.07% dan 70.5%. Hal ini kerana aliran elektrik merentasi permukaan membran konduktif GO/MCWNTs di sistem EMBR meningkat kecekapatan sistem EMBR untuk penyingkir COD dan NH_3-N dari POME melalui mekanisme elektroforesis. Bekalan elektrik di sistem EMBR memberi muatan negatif pada permukan membran konduktif GO/MCWNTs. Cas negatif tambahan pada permukaan membran konduktif GO/MCWNTs ini mendorong penolakan molekul makro bercas negatif di POME seperti bahan organik semulajadi, seterusnya mencatat prestasi penyingkiran yang lebih baik untuk sistem EMBR [14].

Rajah 4 menunjukkan fluks penurasan jangka panjang untuk sistem MBR dan sistem EMBR. Secara keseluruhannya, nilai fluks menurun sepanjang proses penurasan untuk keempat-empat kitaran. Namun, fluks sistem EMBR adalah lebih tinggi daripada fluks sistem MBR. Hal ini kerana disebabkan oleh mekanisma elektroforesis yang bertindak pada permukaan membran konduktif GO/MCWNTs apabila disalur dengan medan elektrik. Elektroforesis berlaku apabila pergerakan molekul makro bercas dipengaruh oleh medan elektrik seragam spasial yang terhasil antara elektrod. Medan elektrik yang disalur ke sistem EMBR akan memberi cas negatif kepada membran konduktif GO/MCWNTs yang bertindak sebagai katod. Cas negatif tambahan pada permukaan membran konduktif GO/MCWNTs menolak molekul makro yang bercas negatif dari mendekati permukaan membran melalui mekanisme elektroforesis ini. Tolakan elektrostatik yang kuat antara kotoran dan permukaan membran konduktif GO/MCWNTs mengurangkan pengotoran pada permukaan membran di sistem EMBR dan menjelaskan fluks sistem EMBR yang lebih tinggi daripada fluks sistem MBR [15]. Peratusan pengurangan fluks relatif oleh sistem MBR adalah lebih cenderung berbanding dengan sistem EMBR iaitu sebayak 73.40% bagi sistem MBR dan 40.01% bagi sistem EMBR. Ini membukti bahawa sistem EMBR mempunyai keberkesanan penyingkiran yang baik, fluks penurasan yang lebih tinggi, dan tahap ketahan kotoran yang lebih berkesan berbanding sistem MBR.

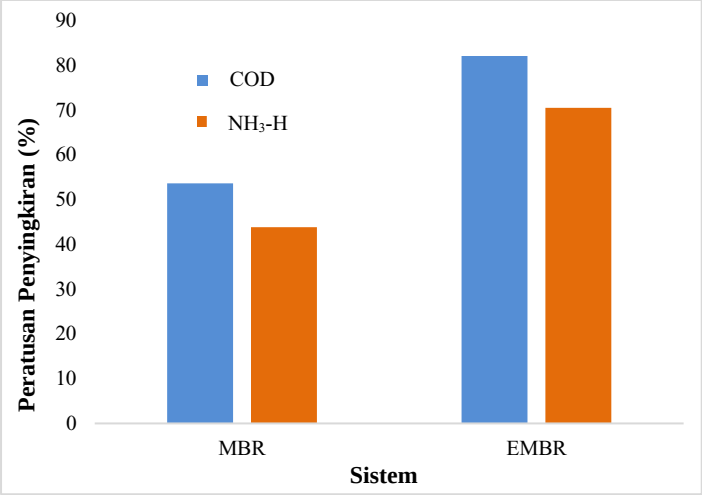




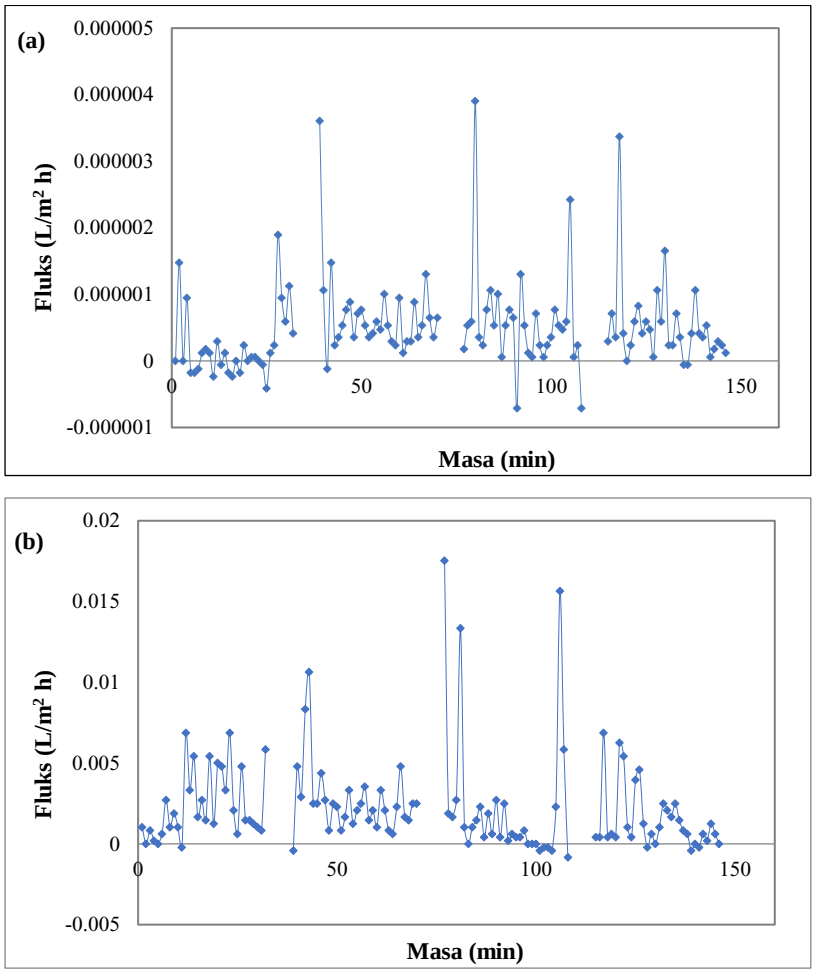




Rajah 2. Bacaan parameter diambil semasa proses penyesuaian iklim bakteria selama 4 minggu berturut-turut (a) suhu (b) pH (c) COD (d) NH_3-N



Rajah 3. Peratusan penyingkiran COD dan NH_3-N untuk sistem MBR dan EMBR



Rajah 4. Fluks penurasan jangka panjang untuk (a) sistem MBR (b) sistem EMBR

Kesimpulan

Prestasi sistem EMBR yang dialirkan elektrik adalah lebih baik daripada sistem MBR tanpa aliran elektrik dengan peratusan penyingkiran COD dan NH_3-N setinggi 82.07% dan 70.5% untuk sistem EMBR dan 53.63% dan 43.81% bagi sistem MBR. Daya tolakan elektrostatik yang kuat antara kotoran dan permukaan membran konduktif GO/MCWNTs berjaya mengurangkan kotoran pada permukaan membran di sistem EMBR sejurusnya mendorong kepada peratusan pengurangan fluks relatif yang sedikit berbanding dengan sistem MBR. Hal ini membawa kesimpulan bahawa sistem EMBR mempunyai keberkesanan penyingkiran yang baik, fluks penurasan yang lebih tinggi, dan tahap ketahan kotoran yang lebih berkesan berbanding sistem MBR untuk rawatan POME.

Penghargaan

Penulis ingin merakamkan penghargaan kepada Dana Padanan Kolaborasi (DPK-2021-002) dan Dana Modal Insan (MI-2019-017) atas sokongan kewangan yang diberi untuk kajian ini.

Rujukan

1. Wan Mohammad Hamdan, W. N. A., Teow, Y. H. and Mohammad, A. W. (2018). Sustainable approach in palm oil industry - green synthesis of palm oil mill effluent based graphene sand composite (P-GSC) for aerobic palm oil mill effluent treatment. *Jurnal Kejuruteraan SI,* 1(7): 11-20.
2. Aziz, N. I. H. A. and Hanafiah, M. M. (2017). The potential of palm oil mill effluent (POME) as a renewable energy source. *Acta Scientifica Malaysia,* 1 (2): 9-11.
3. Subramaniam, M. N., Goh, P. S., Lau, W. J., Tan, Y. H., Ng, B. C. and Ismail, A. F. (2017). Hydrophilic hollow fiber PVDF ultrafiltration membrane incorporated with titanate nanotubes for decolourization of aerobically-treated palm oil mill effluent. *Chemical Engineering Journal,* 316: 101-110.
4. Sajjad, A. A., Teow, Y. H. and Mohammad Hussain, A. W. (2018). Sustainable approach for recycling palm oil mill effluent (POME) using integrated biofilm/membrane filtration system for internal plant usage. *Jurnal Teknologi,* 80(4): 165-172.
5. Teow, Y. H., Ooi, B. S., Ahmad, A. L. and Lim, J. K. (2012). Mixed-matrix membrane for humic acid removal: influence of different types of TiO_2 of membrane morphology and performance. *International Journal of Chemical Engineering and Applications,* 3(6): 374-379.
6. Ghani, M. S. H., Teow, Y. H., Ang, W. L., Mohammad, A. W., Ngteni, R. and Mohamed Yusof, K.M. (2017). Fouling assessment of tertiary palm oil mill effluent (POME) membrane treatment for water reclamation. *Journal of Water Reuse and Desalination,* 8(3): 412-423.
7. Teow, Y. H., Ahmad, A. L., Lim, J. K., Ngang, H. P., Susan, L.Y. and Ooi, B.S. (2015). Hydroxyl functionalized PVDF-TiO_2 ultrafiltration membrane and its antifouling properties. *Journal of Applied Polymer Science,* 132(21): 41844.
8. Huang, J., Wang, Z., Zhang, J., Zhang, X., Ma, J. and Wu, Z. (2015). A novel composite conductive microfiltration membrane and its anti-fouling performance with an external electric field in membrane bioreactors. *Scientific Reports,* 5(1): 9268.
9. Ho, K. C., Teow, Y. H., Ang, W. L. and Mohammad, A. W. (2017). Novel GO/MWCNTs mixed-matrix membrane with enhanced antifouling property for palm oil mill effluent treatment. *Separation and Purification Technology*, 177: 337-349.
10. Ho, K. C., Teow, Y. H. and Mohammad, A.W. (2019). Optimization of nanocomposite conductive membrane formulation and operating parameters for electrically-enhanced palm oil mill effluent filtration using response surface methodology. *Process Safety and Environmental Protection,* 126: 297-308.
11. Teow, Y. H., Ahmad, A. L., Lim, J. K. and Ooi, B. S. (2012). Preparation and characterization of PVDF/TiO_2 mixed matrix membrane via in situ colloidal precipitation method. *Desalination,* 295: 61-69.

12. Zhang, J., Satti, A., Chen, X., Xiao, K., Sun, J., Yan, X. and Liang, P. (2015). Low-voltage electric field applied into MBR for fouling suppression: Performance and mechanisms. *Chemical Engineering Journal*, 273: 223-230.
13. Wong, Y., Ong, S., Lim, K. and Lee, H. (2011). Acclimatization and performance study of acidogenesis anaerobic degradation process for palm oil mill effluent. *International Conference on Environment and Industrial Innovation IPCBEE,* 12: 1-5.
14. Ho, K. C., Teow, Y. H., Mohammad, A.W. and Ang, W.L. (2017). An overview of electrically-enhanced membrane bioreactor (EMBR) for fouling suppression. *Journal of Engineering Science and Technology Review,* 10(3): 128-138.
15. Teow, Y. H., Ooi, B.S. and Ahmad, A. L. (2017). Study on PVDF-TiO_2 mixed-matrix membrane behaviour towards humic acid removal. *Journal of Water Process Engineering,* 15: 99-106.

Malaysian Journal of Analytical Sciences (MJAS)
Published by Malaysian Analytical Sciences Society

EFFECT OF SODIUM BISULFITE ON CORN STARCH SOLID POLYMER ELECTROLYTE

(Kesan Sodium Bisulfit terhadap Elektrolit Polimer Pepejal Kanji)

Fatin Farhana Awang, Khadijah Hilmun Kamarudin, Mohd Faiz Hassan*

Advanced Nano-Materials (ANoMa) Research Group, Faculty of Science and Marine Environment
Ionic State Analysis (ISA) Laboratory, Faculty of Science and Marine Environment
Universiti Malaysia Terengganu, 21030 Kuala Nerus, Terengganu, Malaysia

**Corresponding author: mfhassan@umt.edu.my*

Received: 17 January 2021; Accepted: 25 February 2021; Published: 25 April 2021

Abstract

In this study, solid polymer electrolyte films were prepared using corn starch as polymer doped with various wt.% ratios of $NaHSO_3$ *via* solution casting technique. The SPE films have been characterized using electrical impedance spectroscopy (EIS) and X-ray diffraction (XRD). The plots of conductivity versus $NaHSO_3$ (wt.%) have shown an increasing trend along with $NaHSO_3$ content. It was found that the highest ionic conductivity at room temperature is 2.22×10^{-4} Scm^{-1}. Besides, XRD analysis also indicates that the increase in amorphous content will enhance the conductivity value.

Keywords: electrical impedance spectroscopy, X-ray diffraction, solid polymer electrolyte, corn starch

Abstrak

Dalam kajian ini, filem elektrolit polimer pepejal telah disediakan menggunakan kanji sebagai polimer dan ditambah dengan pelbagai nisbah berat (wt.%) $NaHSO_3$ melalui kaedah penuangan larutan. Filem-filem SPE tersebut telah diuji menggunakan spektrometer elektrokimia impedans (EIS) dan analisa pembelauan sinar-X (XRD). Plot kekonduksian melawan kandungan $NaHSO_3$ menunjukkan peningkatan dengan meningkatnya wt.% $NaHSO_3$. Ia telah dijumpai bahawa kekonduksian tertinggi pada suhu bilik adalah 2.22×10^{-4} Scm^{-1}. Disamping itu, analisis XRD menunjukkan peningkatan kandungan amorphous akan membantu dalam peningkatan nilai kekonduksian.

Kata kunci: spektrometer elektrokimia impedans, pembelauan sinar-X, elektrolit polimer pepejal, kanji

Introduction

In the past few years, solid polymer electrolytes (SPEs) have received much attention due to their wide range of applications in electrochemical devices such as batteries, solar cell, chemical sensors, and supercapacitors [1-5]. The main advantages of SPEs are their high ionic conductivity, leakage proof, simple to prepare and have excellent mechanical strength [6-8]. However, most of the conventional synthetic polymers come from petroleum and are known as non-degradable. This is believed that synthetic-based polymer electrolytes would give an impact on the environment.

To overcome this problem, biodegradable polymer electrolytes were used to replace the traditional ones.

The uses of natural polymers such as starch [9, 10] cellulose and its derivatives [11, 12] and chitosan [13] have attracted attention in previous works due to their mechanical and electrical properties. In this study, starch is chosen as a polymer host due to its characteristics which are naturally in abundance, low cost, biodegradable [14,15] and possess high solubility. This is important to choose a suitable material to ensure it would not give a long-lasting effect on the environment. According to [16], it was mentioned that most of the natural polymers like starch relatively show a very low ionic conductivity. Then, in order to enhance the conductivity, several attempts have been taken such as blending of polymer [17], plasticization [18, 19] and the addition of ceramic fillers [20-22] into a polymer electrolyte.

The addition of salts such as sodium also helps to improve the conductivity of SPE films [23]. The selection of sodium (Na) as a dopant due to its characteristics which are low atomic mass, affordable in price, low toxicity and abundance element in nature [24]. From the previous research, it was reported that the maximum conductivity value of SPE films based on sodium ions was achieved in the range 10^{-3} Scm^{-1} [25]. The low crystallinity nature also would influence to the high conductivity of the film itself. Hence, this study focuses on the results of an investigation on the structural and ionic conductivity of corn starch doped with sodium bisulfite ($NaHSO_3$) using EIS and XRD.

Materials and Method

Preparation of samples

Corn starch ($C_6H_{10}O_5$) and sodium bisulfite ($NaHSO_3$) with a purity of 96% were used to prepare the SPE films by using a solution casting technique (Figure 1). The solvents (distilled water and glycerine) were added with various amounts (5- 40 wt. %) of $NaHSO_3$ as tabulated in Table 1 and stirred until no left residue. The weight percentage was calculated using a formula as expressed in Equation 1. Then, 1 g of corn starch was mixed with the solutions and heated at the temperature of 60-70 ˚C. All solutions were stirred using a magnetic stirrer until it turned homogenous. After that, the homogenous solution was cast into a petri dish and left it dry naturally about three days until electrolyte films are formed. For a further drying process, samples were kept in a desiccator filled with silica gels.

$$\text{wt.}\,\% = \frac{x}{x+y} \times 100 \quad (1)$$

where, wt.% is the varying values for salt in percentage, x is the amount of dopant (g) and y is the amount of polymer.

Characterization techniques

Electrical impedance spectroscopy (EIS) were used to determine the electrical properties of SPE films. The impedance data were measured using HIOKI 3532-50 LCR Hi-Tester which is interfaced with a computer at room temperature in a frequency range of 50 Hz to 1 MHz. The samples were cut into 3.00 cm size of diameter and placed between two blocking electrodes. A digital micrometre screw gauge was used to measure the thickness of SPE films. The ionic conductivity was calculated by using Eq. 2 [26]. Bulk resistance, R_b can be obtained by taking average values from the plot of imaginary impedance ($-Z_i$) against real impedance (Z_r) known as the Cole-cole plot as shown in Figure 2.

$$\sigma = \frac{l}{R_b A} \quad (2)$$

From Equation 2, l is the thickness of SPE films while A is the surface area of blocking electrode contact.

X-ray diffraction (XRD) technique was used to identify the nature of SPE films whether they are crystalline, amorphous or both. Prepared samples were cut into a dimension of 1.00 cm × 1.00 cm and placed onto the glass slides before being measured. A MiniFlex II diffractometer with Cu Kα radiation was used to analyse the samples in a range of $2\Theta = 10^{\circ}$ to 80° with 5°/min of step size. Then, the obtained data were used to analyse the phase identification, crystallinity and/or amorphosity of the SPE films by using Search-Match and Origin software.

$$\text{Crystallinity (\%)} = \frac{A_c}{A_C + A_m} \text{ x } 100 \quad (3)$$

where A_c is peak areas for crystalline and A_m is corresponding to the peak areas for amorphous. Then, to study the phase of the mentioned materials with the d-spacing, it can be obtained by matching the peaks in the given datasheet from Search-Match software.

The percentage of crystallinity for SPE films can be verified by dividing the area under all peaks with the area under the whole diffractogram. Equation 3 shows the formula to calculate the crystalline value of SPE films.

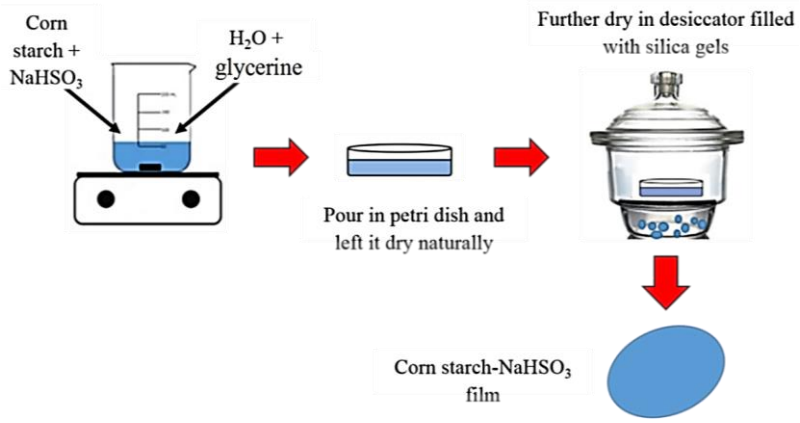


Figure 1. A schematic diagram for preparation of SPE films

Table 1. Composition of corn starch-$NaHSO_3$ SPE films

SPE samples	$NaHSO_3$ (wt. %)	$NaHSO_3$ (g)	Solvent (mL)	
			Distilled water	Glycerine
A	0	0	20	0.6
B	5	0.053	20	0.6
C	10	0.111	20	0.6
D	15	0.176	20	0.6
E	20	0.250	20	0.6
F	25	0.333	20	0.6
G	30	0.429	20	0.6
H	35	0.538	20	0.6
I	40	0.667	20	0.6

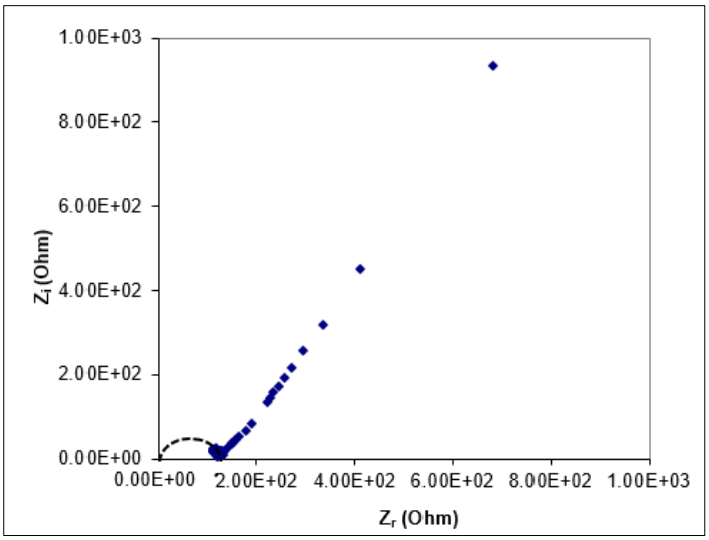


Figure 2. The Cole-cole plot for 15wt. % of $NaHSO_3$ at ambient temperature

Results and Discussion

Figure 3 shows the different images of corn starch films and corn starch doped with $NaHSO_3$ films. The images were taken by using a mobile phone camera that have 8 MP and 5× magnifications. It was observed that the SPE films had changed from transparent to translucent when the amount of salts added is increased. In addition, it is also may alter the structure and morphology of films as well.

The variation of ionic conductivity as a function of $NaHSO_3$ composition at room temperature as shown in Figure 4 while Table 2 presents the value of bulk resistance, R_b and ionic conductivity. The thickness of dried samples is measured in the range between 0.101 mm to 0.293 mm. In Figure 4, the ionic conductivity of free salt SPE is 1.1×10^{-6} Scm^{-1}. The conductivity of the SPE films increased to 7.65×10^{-6} Scm^{-1} when 5 wt.% of $NaHSO_3$ was added and continued the increasing trend until 15 wt.% of $NaHSO_3$ has been added to the corn starch. Then, the addition of 20 wt.% of $NaHSO_3$ into polymer electrolyte causes the conductivity of SPE films started to drop with value 1.06×10^{-4} Scm^{-1}. The decreased trend of conductivity continued in 25 wt.% to 40 wt.% of $NaHSO_3$ until the value is 6.98×10^{-6} Scm^{-1}. It can be said that the increase of ionic conductivity along with the addition of $NaHSO_3$ may be influenced by the amorphous nature and also increase in the number of charge carriers [27]. As expected, from XRD analysis in Figure 4, it was proven that the amorphous nature of SPE films has increased with the addition of $NaHSO_3$. This can be seen through the highest conducting SPE film (15 wt.% of $NaHSO_3$) shows a higher amorphous nature. According to literature, the increase of amorphous state in SPE films will enhance the mobility of free ions through the system and so does the ionic conductivity [28-31]. In contrast, at higher salt concentration there will be an increase in aggregation of ions which lead to the formation of neutral ion pairs, thus limits the movement of freely ions [32]. Hence, decrease in conductivity values.

XRD patterns of corn starch with different $NaHSO_3$ composition is shown in Figure 5. The corn starch diffraction pattern can be identified with a broad peak located at $2\Theta = 15^{\circ}$ to 28°, which known as amorphous hump [35]. This can be assigned as (002) and (112) planes with a tetragonal structure and have a lattice constant of a = 6.07 *Å* and c = 8.60 *Å* (JCPDS 80-31). Then, the presence of peaks at angle $2\Theta = 24.6^{\circ}$, 33.1°, 39.2°, 47.4°, 47.7°, 52.3°, 61.7°, 65° and 69.8° for pure $NaHSO_3$ which correspond to the planes of (101), (103), (110), (006), (200), (115), (107), (008) and (220). It is a well agreement to the orthorhombic structure with a

lattice constant of a = 5.60 *Å*, b = 8.95 *Å* and c = 6.96 *Å* (JCPDS 83-1570). The appearance of a crystalline peak in the polymer-salt system indicates that sodium salts have existed. Table 3 shows the value of *d*-spacing for pure corn starch, $NaHSO_3$ and SPE films with various ratios of $NaHSO_3$. D-spacing values had been obtained using Search-Match software and being compared with the data provided by the datasheet. From the results, it can be concluded that the *d*-spacing values of the mentioned materials are almost well-matched with the values provided in the JCPDS database.

Furthermore, to confirm the crystallinity of SPE films, the percentage of crystalline was calculated by using Equation 3 and it was tabulated in Table 4. Based on the results, the crystalline value was against the conductivity pattern. This is because the decrease in the degree of crystallinity of the SPE films will impart a better ion's diffusion in polymers, thus resulting in increases of conductivity. It also assumed that the association of ions was promoted due to the presence of glycerine as a plasticizer [33, 34]. This happened due to the properties of the plasticizer itself which is a high dielectric constant (ε_r = 78.5) that can weaken the Coulombic force between anion and cation of salt. So, that it can help for the salts to dissociate easily, hence increased the ion's concentration [35, 36].

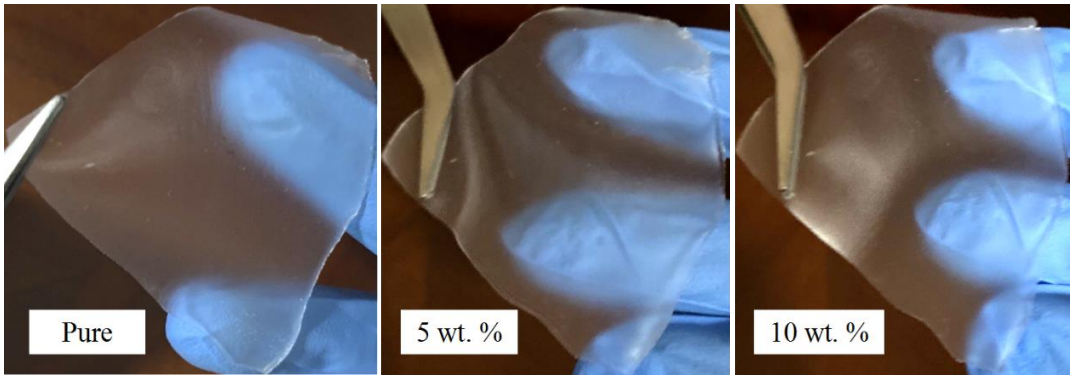


Figure 3. The selected images of corn starch-$NaHSO_3$ SPE films

Table 2. Bulk resistance and ionic conductivity of corn starch-$NaHSO_3$ films

Samples (Content of $NaHSO_3$, wt.%)		**Bulk resistance, R_b (Ω)**	**Ionic conductivity, σ (Scm^{-1})**
A	0	3.00×10^3	1.1×10^{-6}
B	5	4.20×10^2	7.65×10^{-6}
C	10	6.00×10^1	8.96×10^{-5}
D	15	2.50×10^1	2.22×10^{-4}
E	20	4.00×10^1	1.06×10^{-4}
F	25	1.47×10^2	5.43×10^{-5}
G	30	1.60×10^2	3.69×10^{-5}
H	35	7.00×10^2	1.33×10^{-5}
I	40	1.17×10^3	6.98×10^{-6}

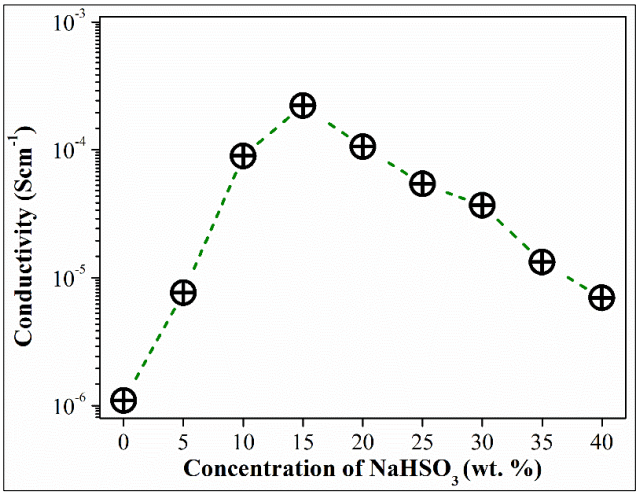


Figure 4. The trend of conductivity SPE films with various compositions of $NaHSO_3$

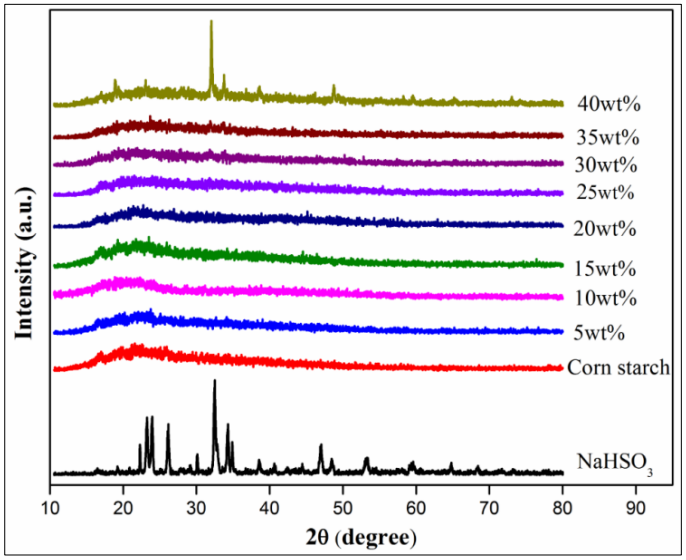


Figure 5. XRD diffraction patterns for corn starch and corn starch-$NaHSO_3$ SPE films

Table 3. The comparison between *d*-spacing values of experimental and theoretical of SPE films

Samples	**Software**	**Experimental Result**	
	d (*Å*)	**d (*Å*)**	**2*Θ* (˚)**
Pure corn starch	4.294	4.295	20.6
(JCPDS 80-31)	3.036	3.037	29.3
$NaHSO_3$	4.752	4.748	18.6
(JCPDS 83-1570)	3.925	3.920	22.6
	3.483	3.481	25.5
	2.803	2.803	31.9
	2.061	2.061	43.8
	1.619	1.618	56.8
	1.294	1.299	72.7
5 wt.%	4.752	4.832	18.3
	2.134	2.138	42.2
10 wt.%	4.752	4.742	18.7
	2.134	3.727	23.8
15 wt.%	1.829	1.816	50.1
	1.742	1.721	53.1
20 wt.%	3.483	3.380	26.3
	2.809	2.816	31.7
	2.749	2.743	32.6
	2.376	2.389	37.6
	1.963	1.926	47.1
	1.883	1.886	48.2
	1.769	1.767	51.6
25 wt.%	2.809	2.818	31.7
	1.963	1.916	47.2
	1.829	1.808	50.4
30 wt.%	4.752	4.948	17.9
	1.218	1.218	78.4
35 wt.%	3.925	3.973	22.3
	3.809	3.820	23.2
	3.483	3.463	25.7
	2.809	2.884	30.9
	2.634	2.689	33.2
40 wt.%	2.634	2.696	33.1
	1.584	1.577	58.4

Table 4. The Percentage crystallinity and amorphosity of complexed SPE films.

Composition of $NaHSO_3$ (wt. %)	Percentage of Crystallinity (%)	Percentage of Amorphosity (%)
0 (Pure corn starch)	10.51	89.49
100 ($NaHSO_3$)	67.39	32.61
5	72.31	27.69
10	61.97	38.03
15	35.88	64.12
20	44.25	55.75
25	48.49	51.51
30	49.83	50.17
35	53.40	46.60
40	44.52	44.52

Conclusion

In summary, solid polymer electrolytes based on corn starch with a varied amount of sodium bisulfite ($NaHSO_3$) is successfully prepared *via* solution casting technique. EIS analysis shows that at 15 wt.% $NaHSO_3$ electrolyte obtains the highest conductivity of 2.22 x 10^{-4} Scm^{-1} and is supported by the amorphous phase. This also shows that the enhancement of conductivity is not only influenced by the concentration of ions but also by the high mobility and diffusion of free ions. Based on the XRD study, the addition of $NaHSO_3$ as a dopant salt also improved the amorphousness of the SPE films.

Acknowledgement

The authors would like to thank the Ministry of Education via the FRGS 2019-1 grant of (Vot. No. 59586), Faculty of Science and Marine Environment and University Malaysia Terengganu for the financial and technical support for this work to be completed.

References

1. Barbosa, P. C., Rodrigues, L. C., Silva, M. M., Smith, M. J., Parola, A. J., Pina, F. and Pinheiro, C. (2010). Solid-state electrochromic devices using pTMC/PEO blends as polymer electrolytes. *Electrochimica Acta,* 55(4): 1495-1502.
2. Dai, S., Chu, Y., Liu, D., Cao, F., Wu, X., Zhou, J., Cheng, Y. and Huang, J. (2018). Intrinsically ionic conductive cellulose nanopapers applied as all solid dielectrics for low voltage organic transistors. *Nature Communication,* 9(1): 1-10,
3. Hassan, M. F. and Azimi, N. S. N. (2019). Conductivity and transport properties of starch/glycerin-$MgSO_4$ solid polymer electrolytes. *International Journal of Advanced and Applied Sciences,* 6(5): 38-43.
4. Misenan, M. S. M. and Khiar, A. S. A. (2018). Conductivity, dielectric and modulus studies of Methylcellulose-NH_4TF polymer electrolyte. *Eurasian Journal of Biological and Chemical Sciences,* 1(2): 59-62.
5. Deraman, S. K., Mohamed, N. S. and Subban, R. H. Y. (2013). Conductivity and electrochemical studies on polymer electrolytes based on poly vinyl (chloride)- ammonium triflate -ionic liquid for proton battery. *International Journal Electrochemical Science,* 6(1): 1459-1468.
6. Chandra, A., Agrawal, R. C. and Mahipal, Y. K. (2009). Ion transport property studies on PEO–PVP blended solid polymer electrolyte membranes. *Journal of Physics D: Applied Physics,* 42(13): 135107.

7. Hema, M., Selvasekarapandian, S., Arunkumar, D., Sakunthala, A. and Nithya, H. (2009). FTIR, XRD and ac impedance spectroscopic study on PVA based polymer electrolyte doped with NH_4X (X=Cl, Br, I). *Journal of Non-Crystalline Solids,* 355(2): 84-90.
8. Hassan, M. F., Zainuddin, S. K., Kamarudin, K. H., Sheng, C. K. and Abdullah, M. A. A. (2018). Ion-conducting polymer electrolyte films based on poly (sodium 4-styrenesulfonate) complexed with ammonium nitrate: studies based on morphology, structural and electrical spectroscopy. *Malaysian Journal of Analytical Science,* 22(2): 238-248.
9. Ramesh, S., Liew, C.-W. and Ramesh, K. (2011). Evaluation and investigation on the effect of ionic liquid onto PMMA-PVC gel polymer blend electrolytes. *Journal of Non-Crystalline Solids*, 357(10), 2132-2138.
10. Marcondes, R. F. M. S., D'Agostini, P. S., Ferreira, J., Girotto, E. M., Pawlicka, A. and Dragunski, D. C. (2010). Amylopectin-rich starch plasticized with glycerol for polymer electrolyte application. *Solid State Ionics*, 181(13-14): 586-591.
11. Harun, N. I., Ali, R. M., Ali, A. M. M. and Yahya, M. Z. A. (2011). Dielectric behaviour of cellulose acetate-based polymer electrolytes. *Ionics,* 18(6): 599-606.
12. Lopes, L. V. S., Machado, G. O., Pawlicka, A. and Donoso, J. P. (2005). Nuclear magnetic resonance and conductivity study of hydroxyethylcellulose based polymer gel electrolytes. *Electrochimica Acta*, 50(19): 3978-3984.
13. Pawlicka, A., Mattos, R. I., Tambelli, C. E., Silva, I. D. A., Magon, C. J. and Donoso, J. P. (2013). Magnetic resonance study of chitosan bio-membranes with proton conductivity properties. *Journal of Membrane Science*, 429: 190-196.
14. Xu, Y., Miladinov, V. and Hanna, M. A. (2004). Synthesis and characterization of starch acetates with high substitution. *Cereal Chemistry,* 81(6): 735-740.
15. Hassan, M. F., Azimi N.S.N, Kamarudin, K. H. and Sheng, C. K. (2018). Solid polymer electrolytes based on starch- magnesium sulphate: study on morphology and electrical conductivity. *ASM Science Journal*, 2018: 17-28.
16. Shahrudin, S. and Ahmad, A. H. (2017). Electrical analysis of corn starch-based polymer electrolyte doped with NaCl. *Solid State Phenomena*, 268: 347-351.
17. Sivakumar, M., Subadevi, R., Rajendran, S., Wu, H. C. and Wu, N. L. (2007). Compositional effect of PVdF–PEMA blend gel polymer electrolytes for lithium polymer batteries. *European Polymer Journal*, 43(10): 4466-4473.
18. Seng, L. K. (2018). Preparation and characterization of solid polymer electrolyte based on carboxymethyl chitosan, ammonium nitrate and ethylene carbonate. *The Eurasia Proceedings of Science, Technology, Engineering & Mathematics (EPSTEM)*, 2: 10-16.
19. He, R. and Kyu, T. (2016). Effect of plasticization on ionic conductivity enhancement in relation to glass transition temperature of crosslinked polymer electrolyte membranes. *Macromolecules,* 49(15): 5637-5648.
20. Liew, C. W. and Ramesh, S. (2015). Electrical, structural, thermal, and electrochemical properties of corn starch-based biopolymer electrolytes. *Carbohydrate Polymers*, 124: 222-228.
21. Teoh, K. H., Ramesh, S. and Arof, A. K. (2012). Investigation on the effect of nanosilica towards corn starch–lithium perchlorate-based polymer electrolytes. *Journal of Solid State Electrochemistry*, 16(10): 3165-3170.
22. Rathod, S. G., Bhajantri, R. F., Ravindrachary, V., Pujari, P. K. and Sheela, T. (2014). Ionic conductivity and dielectric studies of $LiClO_4$ doped poly (vinylalcohol)(PVA)/chitosan(CS) composites. *Journal of Advanced Dielectrics,* 4(4); 1450033.
23. Mohd Asnawi, A. S. F., Mohd Azli, A. M., Hamsan, M. H., Abdul Kadir, M. F. Z. and Mohamed Yusof, Y. (2020). Electrical and infrared spectroscopic analysis of solid polymer electrolyte based on polyethylene oxide and graphene oxide blend. *Malaysian Journal of Analytical Sciences,* 24: 682-697.
24. Shahrudin, S. A., A. H. (2016). Corn starch based biopolymer electrolyte doped with Na_3PO_4. *Science Letters,* 10(2): 26-30.

25. Hassan, N. and Ahmad, A. H. (2016). Conductivity and FTIR Studies of NaI-Na_3PO_4-PLL electrolyte for solid state batteries. *Materials Science Forum*, 846: 505-509.
26. Khairul, W. M., Isa, M. I. N., Samsudin, A. S., Adli, H. K. and Ghazali, S. R. (2014). Conductive biodegradable film of N-N-octyloxyphenyl-N -(4 methylbenzoyl)thiourea. *Bulletin of Materials Science*, 37(2): 357-369.
27. Hirankumar, G. and Mehta, N. (2018). Effect of incorporation of different plasticizers on structural and ion transport properties of PVA-$LiClO_4$ based electrolytes. *Heliyon*, 4(12): 00992.
28. Osman, Z., Md Isa, K. B., Ahmad, A. and Othman, L. (2010). A comparative study of lithium and sodium salts in PAN-based ions conducting polymer electrolytes. *Ionics*, 16(5): 431-435.
29. Fonseca, C. P., Rosa, D. S., Gaboardi, F. and Neves, S. (2006). Development of a biodegradable polymer electrolyte for rechargeable batteries. *Journal of Power Sources*, 155(2): 381-384.
30. Hafiza, M. N., Bashirah, A. N. A., Bakar, N. Y. and Isa, M. I. N. (2014). electrical properties of carboxyl methylcellulose/chitosan dual-blend green polymer doped with ammonium bromide. *International Journal of Polymer Analysis and Characterization*, 19(2), 151-158.
31. Samsudin, A. S., Lai, H. M. and Isa, M. I. N. (2014). Biopolymer materials based carboxymethyl cellulose as a proton conducting biopolymer electrolyte for application in rechargeable proton battery. *Electrochimica Acta*, 129: 1-13.
32. Ramya, C. S., Selvasekarapandian, S., Savitha, T., Hirankumar, G. and Angelo, P. C. (2007). Vibrational and impedance spectroscopic study on PVP–NH_4SCN based polymer electrolytes. *Physica B: Condensed Matter*, 393(1-2): 11-17.
33. Kadir, M. F. Z., Majid, S. R. and Arof, A. K. (2010). Plasticized chitosan–PVA blend polymer electrolyte based proton battery. *Electrochimica Acta*, 55(4): 1475-1482.
34. Phetwarotai, W., Potiyaraj, P. and Aht-Ong, D. (2012). Characteristics of biodegradable polylactide/gelatinized starch films: Effects of starch, plasticizer, and compatibilizer. *Journal of Applied Polymer Science*, 126(S1): 162-172.
35. Arof, A. K., Shuhaimi, N. E. A., Alias, N. A., Kufian, M. Z. and Majid, S. R. (2010). Application of chitosan/iota-carrageenan polymer electrolytes in electrical double layer capacitor (EDLC). *Journal of Solid State Electrochemistry*, 14(12): 2145-2152.
36. Sekhar, P., Naveen Kumar, P. and Sharma, A. K. (2012). Effect of plasticizer on conductivity and cell parameters of (PMMA+$NaClO_4$) polymer electrolyte system. *IOSR Journal of Applied Physics*, 2(4): 1-6.

Malaysian Journal of Analytical Sciences (MJAS)
Published by Malaysian Analytical Sciences Society

FORMATION, MORPHOLOGICAL, MOLECULAR INTERACTION AND IONIC CONDUCTIVITY OF SiO_2 FILLED PMMA/PEG ELECTROLYTES

(Pembentukan, Morfologikal, Interaksi Molekul dan Kekonduksian Ionık Elektrolit PMMA/PEG Terisi SiO_2)

Nurul Dhabitah Basri[1], Famiza Abdul Latif[1,2], Ruhani Ibrahim[1,2], Fazni Susila Abdul Ghani[1,2], Sharil Fadli Mohamad Zamri[1,2]*

[1]Faculty of Applied Sciences
[2]Synthesis and Application of Conducting Polymer Research Group
Universiti Teknologi MARA, 40450 Shah Alam, Selangor, Malaysia

**Corresponding author: sharil7240@uitm.edu.my*

Received: 20 November 2020; Accepted: 16 February 2021; Published: 25 April 2021

Abstract

In this study, silicon dioxide (SiO_2) was used as a filler in the preparation of polymer electrolytes (PEs) containing poly(methyl methacrylate) (PMMA) and poly(ethylene glycol) (PEG). The role of SiO_2 as a filler in the formation, morphology molecular interaction, and ionic conductivity of PMMA/PEG electrolytes films was investigated. PMMA/PEG blends were doped with lithium tetrafluoroborate ($LiBF_4$) with incorporation of various weight percentages of SiO_2 as a filler. The samples were prepared via the solvent casting method with tetrahydrofuran (THF) as a solvent. PMMA/PEG electrolyte films were characterised using Fourier transform infrared (FTIR) spectroscopy, optical microscopy (OM), and electron impedance spectroscopy (EIS). It was observed that the opacity of the PE films increased as the weight percentage of SiO_2 increased. Meanwhile, it was noted that the intensity of FTIR peaks at 1723 cm^{-1}, 1386 cm^{-1}, and 1239 cm^{-1} which corresponded to C=O and O-CH_3 of PMMA, and C-O-C of PEG, respectively, decreased with increased SiO_2 weight percentage. Furthermore, phase separation was observed in OM analysis between PMMA and PEG in the PMMA/PEG blends. Interestingly, the dispersion of PEG-rich phase in the polymer films increased with increased SiO_2 weight percentage. EIS analysis showed that the ionic conductivity of PMMA/PEG electrolyte films increased with increased SiO_2 weight percentage up to 3% with maximum ionic conductivity of 5.55 x 10^{-6} S cm^{-1}. However, the ionic conductivity of PMMA/PEG electrolyte films decreased when the weight percentage of SiO_2 increased beyond 3%.

Keywords: lithium tetrafluoroborate, poly(ethylene glycol), poly(methyl methacrylate), silicon dioxide, polymer electrolytes

Abstrak

Dalam kajian ini, silikon dioksida (SiO_2) telah digunakan sebagai pengisi dalam penyediaan elektrolit polimer (PEs) yang mengandungi poli(metil metakrilat) (PMMA) dan poli(etilena glikol). Peranan SiO_2 sebagai pengisi dalam pembentukan, morfologikal, interaksi molekul, dan kekonduksian ionik elektrolit PMMA/PEG filem telah dikaji. Adunan PMMA/PEG telah dicampurkan dengan litium tetrafluoroborat ($LiBF_4$) dengan tambahan pelbagai peratusan berat SiO_2 sebagai pengisi. Sampel telah disediakan dengan kaedah larutan tuang dengan tetrahidrofuran (THF) sebagai pelarut. Filem elektrolit PMMA/PEG telah dicirikan menggunakan spektroskopi inframerah transformasi Fourier (FTIR), mikroskop optikal (OM) dan spektroskopi elektron impedan

(EIS). Pemerhatian menunjukkan bahawa kelegapan filem PE meningkat dengan peratusan berat SiO_2 meningkat. Sementara itu, diperhatikan bahawa keamatan puncak FTIR pada 1723 cm^{-1}, 1386 cm^{-1} dan 1239 cm^{-1} sepadan C=O dan O-CH_3 bagi PMMA, dan C-O-C bagi PEG berkurang dengan peratusan berat SiO_2 meningkat. Selanjutnya, analisis OM menunjukkan bahawa terdapat fasa pemisahan antara PMMA dan PEG dalam adunan PMMA/PEG. Menariknya, fasa serakan PEG dalam filem polimer telah meningkat dengan peratusan berat SiO_2 meningkat. Analisis EIS menunjukkan bahawa kekonduksian ionik daripada filem telah meningkat dengan penambahan peratusan berat SiO_2 sehingga 3% dengan kekonduksian ionik tertinggi 5.55 x 10^{-6} S cm^{-1}. Walau bagaimanapun, kekonduksian ionik filem telah menurun apabila peratusan SiO_2 telah tambah melebihi 3%.

Kata kunci: litium tetrafluoroborat, poli(etilena glikol), poli(metil metakrilat), silikon dioksida, elektrolit polimer

Introduction

PEs have attracted the attention of many researchers in recent years due to their applicability in electrochemical devices, such as supercapacitors [1], lithium batteries [2], and solar cells [3]. This is due to the superior features of PEs over liquid electrolytes, such as easy processability [4], safe, non-flammable, and non-leakage property [5]. PEs can be divided into three major categories, namely solid polymer electrolytes (SPEs), gel polymer electrolytes (GPEs), and nanocomposite polymer electrolytes (NCPEs) [6]. The advantages of SPEs are that they give no issue of corrosive solvent leakage and are long lasting, [7] while GPEs have high flexibility and are leakage free [8]. However, both systems are unable to give adequate ionic conductivity at ambient temperature, which limits their application in various electric and electronic devices [8, 9].

Recently, several studies have been carried out by many researchers to subdue this limitation. Many improvements have been embraced, such as adding plasticiser [10], polymer blends [11], and nano-filler [12]. Vignarooban et al. [13] declared that the addition plasticiser in PE systems has the ability to increase the amorphous region, which decreased crystallinity of PE. In addition, the incorporation of plasticiser gives better physical and mechanical properties of electrolytes in the form of flexibility and elasticity [14]. It also encourages the augmentation of the segmental movement of the polymer backbone, which subsequently helps ionic transport along the polymer chains [14]. Examples of plasticisers that have been used in previous studies are ethylene carbonate (EC) [15], dimethylformamide (DMF) [16], and propylene carbonate (PC) [17].

From all the proposed strategies, polymer blend system is very interesting to be explored since it is wisely adjustable. In a polymer blending system, a mixture of two or more different polymers is mixed homogenously in a suitable solvent. The technique will not produce new covalent bonds between the polymers [18]. It is the most decent technique to be used [19] because polymer blend systems offer superior characteristics, such as good conductivity [11], and better thermal and mechanical properties compared to single polymer systems. Examples of polymer electrolytes prepared via polymer blend technique are polyethylene oxide(PEO)/PMMA/poly(vinylidene fluoride hexafluoropropylene)(P(VDF-HFP)) [20], P(VDF-HFP)/poly(vinyl alcohol)(PVA) [21], and PMMA/poly(methyl methacrylate grafted natural rubber)(PMMA-g-NR) [18] electrolytes.

Dispersions of nano-particle filler with a high dielectric constant being in polymeric system [22] help to enhance the conductivity of the polymer blend. Stephan and Nahm [23] studied the presence of filler in PE, usually also known as nanocomposite polymer electrolytes (NCPEs), and found that it could enhance ionic conductivity and provide a better interfacial property in lithium batteries. In addition, one of the significant discoveries of Gozdz and Tarascon was that the expansion of highly dispersed silica to P(VDF-HFP) matrix significantly improved solvent absorption ability, thus led to the improvement of measured conductivities [24]. Since then, a number of nanoparticle fillers have been investigated including aluminium oxide (Al_2O_3) [11], silicon dioxide (SiO_2) [25], and titanium dioxide (TiO_2) [26].

The polymer host is a major component in the PE because it acts as a polymer matrix that prompts a net dipole moment [27]. Some of the polymer hosts that have been explored for preparation of PE are poly(vinyl chloride) (PVC) [28], PMMA [29], PEO [30], and poly(vinylidene fluoride) (PVDF)[11]. PMMA has been receiving the most attention from researchers due to its high ionic conductivity [31], reasonable wettability, and chemical and thermal stability [32]. PMMA is considered as an ideal polymer host for PEs owing to its transparent polymer that has a high degree of amorphous [19] and non-tacking characteristics [29].

This study investigated the effects of various weight percentage of SiO_2 filler on NCPE films of PMMA/PEG electrolytes. The effects of the filler on the formation, morphology, molecular interaction, and ionic conductivity of the films are reported.

Materials and Methods

Materials

Preparation of PEs film were PMMA (Mw = 350 000 $gmol^{-1}$) (Aldrich), PEG (Mw = 5800 $gmol^{-1}$) (Aldrich), SiO_2 (15 nm) (Aldrich), $LiBF_4$ (Sigma Aldrich), and THF (Sigma Aldrich) as a solvent.

Preparation of polymer stock solutions

PMMA (5.0 g) and PEG (2.5 g) were dissolved separately in 250 mL of tetrahydrofuran (THF) under stirring condition at ambient temperature for 24 hours.

Preparation of PMMA/PEG electrolyte films containing SiO_2 filler

PMMA (25 mL) and PEG (5 mL) solutions were mixed in 250 mL screw cap bottles. Then, specific amounts of SiO_2 (0-7%) were added into the solutions under continuous stirring for another 24 hours. Next, 0.2 g of $LiBF_4$ salt was added into each of the solutions as shown in Table 1. The solutions containing SiO_2 and $LiBF_4$ were stirred again for 24 hours.The resultant polymer blend solutions were then casted into petri dishes and left overnight under nitrogen gas flow. Finally, the obtained films were peeled off using forceps and dried in an oven at 50 °C for 24 hours.

Characterisation

Fourier transform infrared spectroscopy

FTIR was used to investigate the presence of PMMA and PEG functional groups. The samples were analysed using ATR Nicolet 6100 with frequency range of 4000 to 400 cm^{-1} at 16 times scanning rate.

Optical microscopy

The phase separation between PMMA and PEG in PMMA/PEG electrolytes was examined by Nikon ECLIPSE ME 600 at 20× magnification.

Electronic impedance spectroscopy

The ionic conductivity of PMMA/PEG electrolyte films was analysed using a Hioki 3532-01 LCR High Tester. The frequency range from 100Hz to 1MHz was used to measure the conductivity at room temperature. The ionic conductivity equation is shown below [1, 7]:

$$\boldsymbol{\sigma} = t/R_bA \quad (1)$$

where $\boldsymbol{\sigma}$ is ionic conductivity, t is the thickness of the samples, R_b is bulk resistance, A is the surface area of the sample.

Table 1. Materials composition of PEs

Film Samples (%)	PMMA (g)	PEG (g)	Mass of Filler (g)	Weight of $LiBF_4$ (g)
0	0.5	0.05	0.000	0.2
1	0.5	0.05	0.005	0.2
3	0.5	0.05	0.015	0.2
5	0.5	0.05	0.025	0.2
7	0.5	0.05	0.035	0.2

Results and Discussion

The formation of PMMA/PEG electrolyte films containing various weight percentages of SiO_2 filler is shown in Figure 1. It was observed that the opacity of films increased as the weight percentage of SiO_2 increased. Furthermore, the films visually changed to yellowish-brown after being dried overnight in an oven. This phenomenon was due to interaction between the salt, filler, and polymers in the system. Singh et al. [34] reported that the same observation was observed when potassium iodide was doped into starch.

FTIR spectra of the PE films (Figure 2) show the peaks at 1723 cm^{-1} [35] and 1386 cm^{-1} [36] corresponded to C=O and O−CH_3 of PMMA, respectively. Meanwhile, the peaks recorded at 1239 [4, 37] and 728 cm^{-1} [38] corresponded to C−O−C of PEG and BF_4^- of $LiBF_4$, respectively. It was observed that the intensity of FTIR peaks, which corresponded to C=O and O−CH_3 of PMMA, C−O−C of PEG, and BF_4^- of $LiBF_4$ decreased as the weight percentage of SiO_2 increased. This is possibly due to the complexation between polymers and salt with filler. A similar observation was reported by Farheen et al. [39] in PEO/PMMA/$LiClO_4$ electrolyte containing TiO_2. Besides that, Sharma et al. (2012) also reported the same observation when Al_2O_3 was added in PEO/PMA/EC electrolyte [35].

The suggested interactions between O atoms in C=O and O−CH_3 of PMMA, C−O−C of PEG with Li^+ ion of $LiBF_4$ are depicted in Figure 3. The lower intensity of FTIR peaks was observed for sample with 0% of SiO_2 filler probably due to the strong interactions of Li^+ ions in $LiBF_4$ with O atoms in the functional groups, which restricted their vibration bonds [40].

The intensity of C=O, O−CH_3, C−O−C, and BF_4^- increased when the weight percentage of SiO_2 filler was increased up to 3%, probably due to the interaction between O atoms in the functional groups and H atoms of silanol group (Si-OH) of SiO_2 with Li^+ ion of $LiBF^4$ (Figure 4). Interestingly, the intensity of FTIR peaks, which corresponded to C=O, O−CH_3, C−O−C, and BF_4^- decreased when the weight percentage of SiO_2 was beyond 3%.

Figure 5 shows OM micrographs of PMMA/PEG electrolyte films at various weight percentages of SiO_2. Figure 5(a) shows that phase separation was observed between PMMA rich-phase and PEG rich-phase, indicated by brownish-orange colour background and numerous dark brown patches, respectively. The phase separation indicated that PMMA and PEG were incompatible. PEG was recognised as dark brown patch colour because 10% of PMMA/PEG electrolytes was made up of PEG.

Interestingly, Figures 5(b) - (e) show that the dark brown spots were accumulated and became darker compared to Figure 5(a). This indicated that the dispersion of PEG-rich phase improved when the weight percentage of SiO_2 increased by up to 7%. This observation proved that SiO_2 filler could interact with PEG-rich phase *via* hydrogen bond as claimed by Yuan et al. [41]. However, Figure 5 shows that the phase separation between the polymers still existed although higher weight percentage of SiO_2 in the system indicated that PMMA/PEG blend was an immiscible system. A similar observation was reported by Elmér and Jannasch [43].

Ionic conductivity of PMMA/PEG electrolyte films at ambient temperature is depicted in Table 2. The result indicated that the ionic conductivity increased with the increased weight percentage of the SiO_2 filler up to 3% with the maximum ionic conductivity value of 55.5×10^{-7} Scm^{-1}. The ionic conductivity then decreased when the weight percentage of the SiO_2 filler was added beyond 3%. The same observation was reported by Latif et al. [44]. They found that the highest ionic conductivity of PMMA/50% epoxidized natural rubber (ENR 50) electrolytes was at 3% of SiO_2 filler.

The ionic conductivity is associated with the interaction between Li^+ ion from $LiBF_4$ and O atoms from PMMA and PEG as shown in Figure 3 and Figure 4. At 0% of SiO_2, Li^+ ion tends to attach strongly to the O atoms in C=O and O−CH_3 of PMMA and C−O−C of PEG. Therefore, the strong interaction resulted in low free ion

and restrict ionic movement in the PMMA/PEG electrolyte. Interestingly, the dissociation of $LiBF_4$ was higher in the polymer system when the weight percentage of SiO_2 was increased up to 3%. This phenomenon resulted in increased ionic conductivity due to the formation of hydrogen bonding between H atom in Si-OH of SiO_2 and O atom of PMMA (Figure 4) that weakened the Li^+ - O interaction. As a consequence, the Li+ ions detached easily from the O atom [45] and the number of free ion increased. Unfortunately, further increase in the weight percentage of SiO_2 filler beyond 3% led to the gradual decrement of ionic conductivity of the system. This was probably because the system was congested with a high amount of SiO_2 [46]. In other words, SiO_2 particles dispersed in polymer films and got close to each other, causing agglomeration. Previous studies stated that congestion of filler led to the obstacle effect and restricted the movement of the polymer chains, hence reduced ionic conductivity [14, 39].

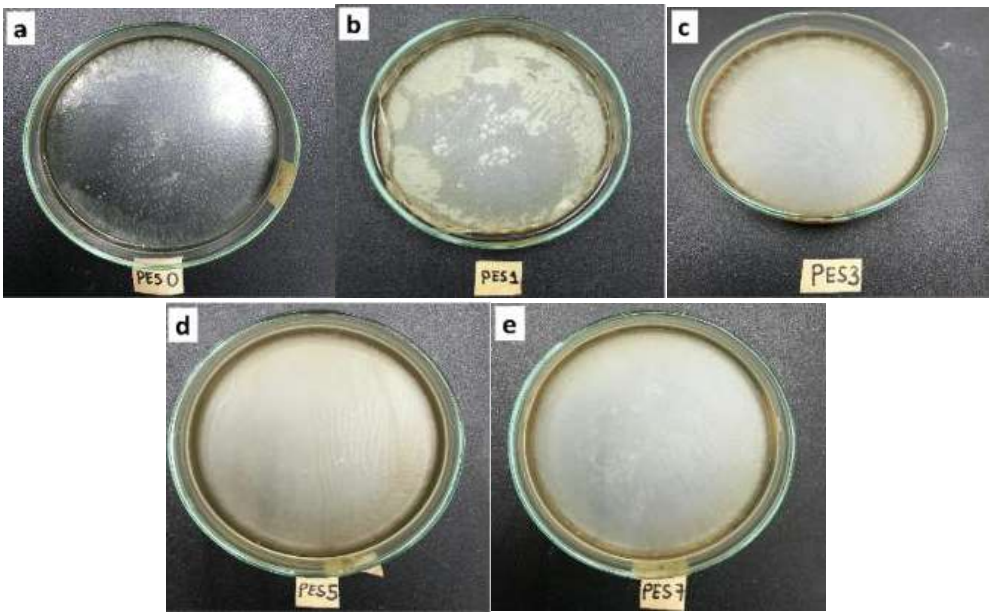


Figure 1. Formation of PMMA/PEG electrolytes films containing different weight percentages of SiO_2 of (a) 0%, (b) 1%, (c) 3%, (d) 5%, and (e) 7%

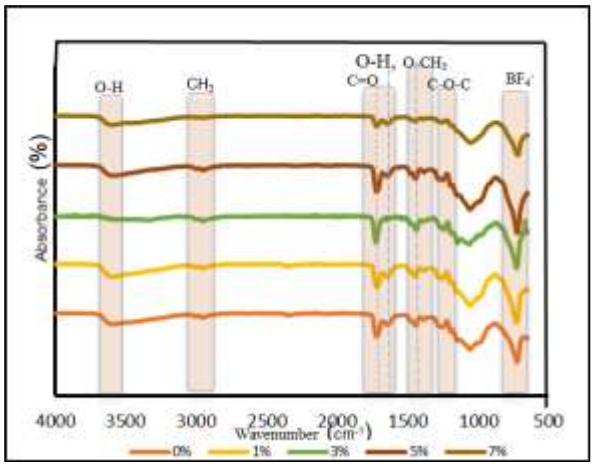


Figure 2. FTIR spectra of PMMA/PEG at different weight percentages of SiO_2

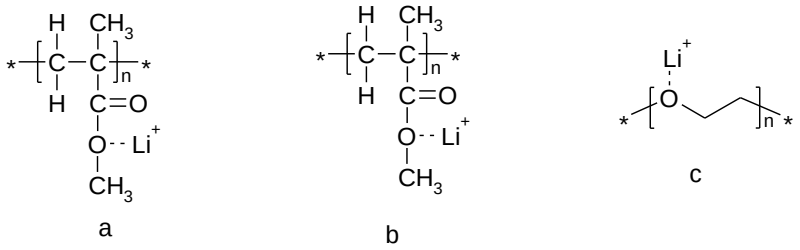


Figure 3. Suggested interaction between PMMA/PEG with Li^+ ion

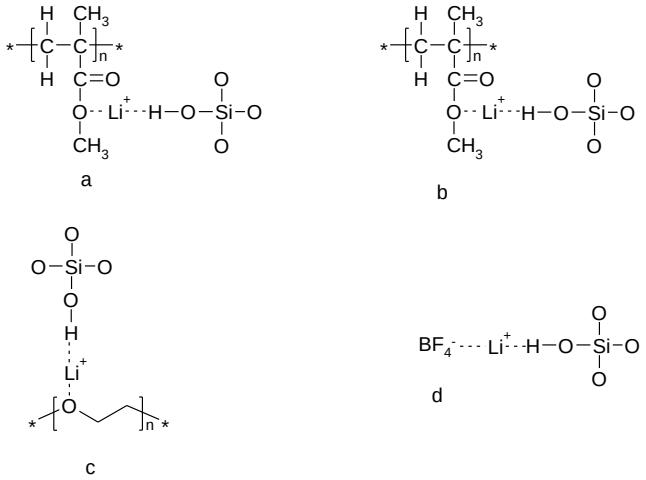


Figure 4. Suggested interaction between PMMA/PEG with Li^+ ion and SiO_2

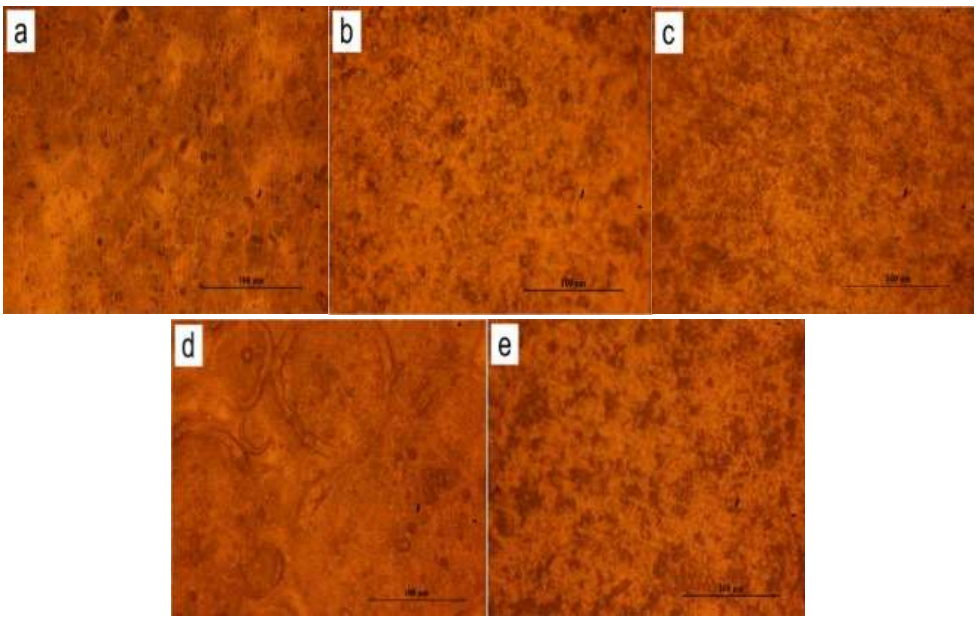


Figure 5. OM micrographs of PMMA/PEG electrolytes films at different weight percentages of SiO_2 filler: (a) 0%, (b) 1%, (c) 3%, (d) 5%, and (e) 7% at 20× magnification

Table 2. Ionic conductivity of PMMA/PEG electrolytes with different weight percentages SiO_2 filler at room temperature

SiO_2 (%)	0	1	3	5	7
Ionic Conductivity (Scm^{-1}) ($x10^{-7}$)	11.4	13.8	55.5	22.2	2.65

Conclusion

SiO_2 filled PEG/PMMA electrolytes were successfully prepared *via* the solvent casting method. The addition of SiO_2 in PEG/PMMA electrolyte improved the formation and morphology of the film. Molecular interactions between polymers, salt, and filler were successfully proven. The phase separation of polymer films improved but conduced the opacity of the polymer films. Interestingly, the incorporation of SiO_2 filler fluctuated the ionic conductivity of the PMMA/PEG electrolyte films. The highest ionic conductivity was recorded at 55.5×10^{-7} S cm^{-1} at 3% SiO_2. This finding is important to conduct further research on the physical and thermal properties of SiO_2 filled PMMA/PEG electrolytes.

Acknowledgement

The authors would like to acknowledge Universiti Teknologi MARA for the technical support for this study.

References

1. Aziz, S. B., Woo, T. J., Kadir, M. F. Z. and Ahmed, H. M. (2018). A conceptual review on polymer electrolytes and ion transport models. *Journal of Science: Advanced Materials and Devices*, 3: 1-17.
2. Marcinek, M., Syzdek, J., Marczewski, M., Piszcz, M., Niedzicki, L., Kalita, M. and Wieczorek, W. (2015). Electrolytes for Li-ion transport – Review. *Solid State Ionics*, 276: 107-126
3. Mohd, S., Zulazlan, A., Zulkifli, S., Akmal, M., Mainal, A., Subramanian, B. and Sabirin, N. (2015). Polymer electrolyte liquid crystal system for improved optical and electrical properties. *European Polymer Journal*, 66: 266-272.
4. Xiao-Yuan, Y., Xiao, M., Shuang-Jin, W., Qi-Qiang, Z. and Yue-Zhong, M. (2010). Fabrication and characterization of PEO/PPC polymer electrolyte for lithium-ion battery. *Journal of Applied Polymer Science*, 115(5): 2718-2722
5. Wang, A., Xu, H., Liu, X., Wang, S., Zhou, Q., Chen, J. and Zhang, L. (2017). High electrochemical performances of solid nano-composite star polymer electrolytes enhanced by different carbon nanomaterials. *Composites Science and Technology*, 152: 68-75.
6. Stephan, A. M. (2006). Review on gel polymer electrolytes for lithium batteries. *European Polymer Journal*, 42: 21-42.
7. Ngai, K. S., Ramesh, S., Ramesh, K. and Juan, J. C. (2018). Electrical, dielectric and electrochemical characterization of novel poly(acrylic acid)-based polymer electrolytes complexed with lithium tetrafluoroborate. *Chemical Physics Letters*, 692: 19-27.
8. Xiao, W., Wang, Z., Zhang, Y., Fang, R., Yuan, Z., Miao, C. and Jiang, Y. (2018). Enhanced performance of P(VDF-HFP)-based composite polymer electrolytes doped with organic-inorganic hybrid particles PMMA-ZrO_2 for lithium ion batteries. *Journal of Power Sources*, 382: 128-134.
9. Kumar, S., Prajapati, G. K., Saroj, A. L. and Gupta, P. N. (2019). Structural, electrical and dielectric studies of nano-composite polymer blend electrolyte films based on (70–x) PVA–x PVP–NaI–SiO_2. *Physica B: Condensed Matter*, 554: 158-164.
10. Ganesan, S. V, Mothilal, K. K., Selvasekarapandian, S. and Ganesan, T. K. (2017). Studies on conductivity, morphology and thermal stability of PMMA-PSAN based Solid Polymer Electrolytes using SiO_2 as nanofiller. *International Journal of ChemTech Research*, 10(7): 55-65.
11. Kuppu, S. V., Jeyaraman, A. R., Guruviah, P. K. and Thambusamy, S. (2018). Preparation and characterizations of PMMA-PVDF based polymer composite electrolyte materials for dye sensitized solar cell. *Current Applied Physics*, 18(6): 619-625.

12. Salman, A. L. I. D., Jani, G. H. and Fatalla, A. A. (2017). Comparative study of the effect of incorporating SiO_2 nano-particles on properties of polymethyl methacrylate denture bases. 10(3): 1525-1535.
13. Vignarooban, K., Dissanayake, M. A. K. L., Albinsson, I. and Mellander, B. (2014). Effect of TiO_2 nano-filler and EC plasticizer on electrical and thermal properties of poly(ethylene oxide) (PEO) based solid polymer electrolytes. *Solid State Ionics*, 266: 25-28.
14. Ataollahi, N., Ahmad, A., Hamzah, H., Rahman, M. Y. A. and Mohamed, N. S. (2015). Comparative study of the properties of plasticized (PVDF-HFP)-MG49-$LiBF_4$ blend polymer electrolytes. *Russian Journal of Electrochemistry*, 51(3): 227-235.
15. Johan, M. R., Shy, O. H., Ibrahim, S., Mohd Yassin, S. M. and Hui, T. Y. (2011). Effects of Al_2O_3 nanofiller and EC plasticizer on the ionic conductivity enhancement of solid PEO-$LiCF_3SO_3$ solid polymer electrolyte. *Solid State Ionics*, 196(1): 41-47.
16. Sekhar, P. C., Kumar, P. N. and Sharma, A. K. (2012). Effect of plasticizer on conductivity and cell parameters of (PMMA+$NaClO_4$) polymer electrolyte system. J*ournal of Applied Physics*, 2(4): 01-06.
17. Das, S. and Ghosh, A. (2015). Ionic conductivity and dielectric permittivity of PEO-$LiClO_4$ solid polymer electrolyte plasticized with propylene carbonate. *AIP Advances*, 5(2): 1–9.
18. Shukur, M. F., Kadir, M. F. Z., Ahmad, Z. and Ithnin, R. (2012). Transport properties of chitosan/PEO blend based proton conducting polymer electrolyte. *Advanced Materials Research*, 488–489: 114-117.
19. Ngai, K. S., Ramesh, S., Ramesh, K., and Juan, J. C. (2016). A review of polymer electrolytes: Fundamental, approaches and applications. *Ionics*, 22(8): 1259-1279.
20. Shi, J., Yang, Y. and Shao, H. (2017). Co-polymerization and Blending based PEO/PMMA/P(VDF-HFP) gel polymer electrolyte for rechargeable lithium metal batteries. *Journal of Membrane Science*, 547: 1-10.
21. Tiautit, N., Puratane, C., Panpinit, S. and Saengsuwan, S. (2014). Effect of SiO_2 and TiO_2 nanoparticles on the performance of dye-sensitized solar cells using PVDF-HFP/PVA gel electrolytes. 56: 378-385.
22. Srivastava, N. and Tiwari, T. (2009). New trends in polymer electrolytes a reviews. *E-Polymers*, 146: 1-17.
23. Stephan, A. M. and Nahm, K. S. (2006). Review on composite polymer electrolytes for lithium batteries. *Polymer*, 47: 5952-5964.
24. Kurc, B. (2014). Precipitated silica as filler for polymer electrolyte based on poly(acrylonitrile)/ sulfolane. *Journal of Solid State Electrochemistry*, 18(7): 2035-2046.
25. Zhu, A., Shi, Z., Cai, A., Zhao, F. and Liao, T. (2008). Synthesis of core-shell PMMA-SiO_2 nanoparticles with suspension-dispersion-polymerization in an aqueous system and its effect on mechanical properties of PVC composites. *Polymer Testing*, 27(5): 540-547.
26. Cao, J., Wang, L., Shang, Y., Fang, M., Deng, L., Gao, J. and He, X. (2013). Dispersibility of nano-TiO_2 on performance of composite polymer electrolytes for Li-ion batteries. *Electrochimica Acta*, 111: 674-679.
27. Zhang, R., Chen, Y. and Montazami, R. (2015). Ionic liquid-doped gel polymer electrolyte for flexible lithium-ion polymer batteries. *Materials*, 2015: 2735-2748.
28. Ramesh, C. H., Reddy, M. J., Kumar, J. S. and Reddy, K. N. (2014). Structural and transport properties of PVC blend PEG doped with $Mg(ClO_4)_2$ solid polymer electrolyte. *AIP Conference Proceedings*, 1391: 1389-1391.
29. Mohamad Zamri, S. F. and Abdul Latif, F. (2015). Effects of acid modified SiO_2 on ionic conductivity and blend properties of $LiBF_4$ doped PMMA/ENR 50 electrolytes. *Advanced Materials Research*, 1107: 187-193.
30. Choudhary, S. (2017). Dielectric dispersion and relaxations in (PVA-PEO)-ZnO polymer nanocomposites. *Physica B: Condensed Matter*, 522: 48-56.

31. Muchakayala, R., Song, S., Wang, J., Fan, Y., Bengeppagari, M., Chen, J. and Tan, M. (2017). Development and supercapacitor application of ionic liquid-incorporated gel polymer electrolyte films. *Journal of Industrial and Engineering Chemistry*, 59: 79-89
32. Cheng, X., Pan, J., Zhao, Y., Liao, M. and Peng, H. (2018). Gel polymer electrolytes for electrochemical energy storage. *Advanced Energy Materials*, 8(7): 1-16.
33. Zamri, S. F. M., and Latiff, F. A. (2013). SiO_2 filler as interface modifier in PMMA/ENR 50 electrolytes. *Advanced Materials Research*, 812: 120-124.
34. Singh, R., Bhattacharya, B., Rhee, H. and Singh, P. K. (2014). New biodegradable polymer electrolyte for dye sensitized solar cell. *International Journal of Electrochemical Sciences*, 9: 2620-2630.
35. Sharma, P., Kanchan, D. K., and Gondaliya, N. (2012). Effect of nano-filler on structural and ionic transport properties of plasticized polymer electrolyte. *Open Journal of Organic Polymer Materials*, 2(2): 38-44.
36. Alias, Y., Ling, I., and Kumutha, K. (2005). Structural and electrochemical characteristics of 49% PMMA grafted polyisoprene-$LiCF_3SO_3$-PC based polymer electrolytes. *Ionics*, 11(5–6): 414-417.
37. Soydan, A. M. and Akdeniz, R. (2017). Polymer electrolytes based on borane/poly(ethylene glycol) methyl ether for lithium batteries. *Journal of Chemistry*, 2017: 1-7.
38. Sharil Fadli, M. Z., Famiza, A. L., and Siti Izzati Husna, M. A. (2019). Morphology, ionic-molecular interaction and ionic conductivity behavior of PMMA/ENR 50 electrolytes containing carboxylic acids modified SiO_2 fillers. *Key Engineering Materials*, 821: 419-425.
39. Farheen, S., and Mathad, R. D. (2015). Effect of nano filler on conductivity in PEO-PMMA-$LiClO_4$ polymer electrolyte. *International Journal of Advanced Science and Technology*, 81: 49-52.
40. Wang, H., Li, H., Xue, B., Wang, Z., Meng, Q. and Chen, L. (2005). Solid-state composite electrolyte LiI/3-hydroxypropionitrile/SiO_2 for dye-sensitized solar cells. *Journal of the American Chemical Society*, 127(17): 6394-6401.
41. Yuan C. Y., Chen S. Y., Tang J. C., Yang H. C. and Chen-Yang Y. W. (2006). Physical and electrochemical properties of low molecular weight poly(ethylene glycol)-bridged polysilsesquioxane organic–inorganic composite electrolytes via sol–gel process. *Journal of Applied Polymer Science*, 116(5): 2658-2667.
42. Sun, Z., Li, Y., Zhang, S., Shi, L., Wu, H., Bu, H. and Ding, S. (2019). G-C_3N_4 nanosheets enhanced solid polymer electrolytes with excellent electrochemical performance, mechanical properties, and thermal stability. *Journal of Materials Chemistry A*, 7(18): 11069-11076.
43. Elmér, A. M. and Jannasch, P. (2006). Solid electrolyte membranes from semi-interpenetrating polymer networks of PEG-grafted polymethacrylates and poly(methyl methacrylate). *Solid State Ionics*, 177(5–6): 573-579.
44. Latif, F., Mohamad Zamri, S. F., and Aziz, M. (2015). Anions effect on the electrical properties of PMMA/ENR 50 blend electrolytes. *Advanced Materials Research*, 1107: 145-150.
45. Silakul, P. and Magaraphan, R. (2019). Polymer electrolyte developed from natural rubber-polyacrylic acid cotrimethoxysilyl propyl methacrylate grafted fumed silica and its application to dye sensitized solar cell. *Polymer Composites*, 40(1): 304-314.
46. Ahmad, A., Rahman, M. Y. A., Low, S. P. and Hamzah, H. (2011). Effect of $LiBF_4$ salt concentration on the properties of plasticized MG49-TiO_2 based nanocomposite polymer electrolyte. *ISRN Materials Science*, 2011: 1-7.
47. Zamri, S. F. M., Latif, F. A., Ali, A. M. M., Ibrahim, R., Azuan, S. I. H. M., Kamaluddin, N., and Hadip, F. (2017). Exploration on effects of 15 nm SiO_2 filler on miscibility, thermal stability and ionic conductivity of PMMA/ENR 50 electrolytes. *AIP Conference Proceedings*, 1809: 020049.

Malaysian Journal of Analytical Sciences (MJAS)
Published by Malaysian Analytical Sciences Society

COMPARISON OF PHYSICOCHEMICAL, TOTAL PROTEIN AND ANTIOXIDANT PROFILES BETWEEN MALAYSIAN *Apis* AND *Trigona* HONEYS

(Perbandingan Profil Fizikokimia, Jumlah Protin dan Antioksidan antara Madu *Apis* dan *Trigona* Malaysia)

Norjihada Izzah Ismail[1,2]*, Mohammed Rafiq Abdul Kadir[1], Razauden Mohamed Zulkifli[3], Mahaneem Mohamed[4]

[1]*School of Biomedical Engineering and Health Sciences, Faculty of Engineering*
[2]*Medical Devices and Technology Centre*
[3]*Department of Biosciences, Faculty of Science*
Universiti Teknologi Malaysia, 81310 Skudai, Johor, Malaysia
[4]*Department of Physiology, School of Medical Sciences,*
Universiti Sains Malaysia, 16150 Kubang Kerian, Kelantan, Malaysia

**Corresponding author: norjihada@utm.my*

Received: 24 November 2020; Accepted: 25 February 2021; Published: 25April 2021

Abstract

The properties of honeys are highly influenced by botanical sources, geographical origins, seasonal, processing, and bee species. The aims of this study are to characterize and compare the physicochemical, total phenolic, total flavonoids, total protein and antioxidant profiles between several Malaysian *Apis* and *Trigona* honeys. pH, free acidity, total soluble solids, ash content, electrical conductivity, density, colour, hydroxymethylfurfural and sugar content were the observed physicochemical parameters. All honey samples were also analyzed for their total phenolic (TPC), flavonoid (TFC) and protein contents, DPPH radical scavenging and total antioxidant activities. The physicochemical results of Malaysian *Apis* and *Trigona* honeys were noticeably different in terms of free acidity and electrical conductivity (EC), with extremely high free acidity (271.1 – 553.2 meq/kg) and higher EC (0.92 – 1.29 mS/cm) were observed for the latter. The results from TPC (60.21 mg GAE/100 g), TFC (65.86 mg QE/100 g), DPPH radical scavenging IC_{50} (10.57 mg/mL) and total antioxidant activities (713.82 µM Fe(II)) revealed that *Trigona* K1 honey was rich with polyphenols and other antioxidants compared to other *Trigona* and *Apis* honeys. It can be concluded from the present study that Malaysian *Trigona* honeys have distinguished physicochemical and antioxidant profiles than *Apis* honeys.

Keywords: *Apis* honey, *Trigona* honey, stingless bee, physicochemical, total phenolic content, antioxidant

Abstrak

Sifat-sifat madu adalah sangat dipengaruhi oleh sumber botani, asal geografi, musim, pemprosesan dan jenis lebah. Matlamat kajian ini adalah untuk mencirikan dan membandingkan profil fizikokimia, jumlah fenolik, jumlah flavonoid, jumlah protin dan antioksidan antara beberapa madu *Apis* dan *Trigona* Malaysia. pH, asid bebas, jumlah pepejal larut, kandungan abu, kekonduksian elektrikal, ketumpatan, warna, kandungan hidroksimetilfurfural dan kandungan gula adalah parameter-parameter yang dilihat. Kesemua sampel madu juga dianalisa untuk jumlah kandungan fenolik (TPC), kandungan flavonoid (TFC) dan kandungan protin,

aktviti memerangkap radikal DPPH dan aktiviti jumlah antioksidan. Keputusan fizikokimia bagi madu *Apis* dan *Trigona* Malaysia telah menunjukkan perbezaan yang ketara dari segi asid bebas dan kekonduksian elektrikal (EC), dengan asid bebas yang amat tinggi (271.1 – 553.2 meq/kg) dan EC yang tinggi (0.92 – 1.29 mS/cm) diperhatikan untuk jenis madu kedua. Keputusan TPC (60.21 mg GAE/100 g), TFC (65.86 mg QE/100 g), IC_{50} memerangkap radikal DPPH (10.57 mg/mL) dan aktiviti jumlah antioksidan (713.82 µM Fe(II)) mendedahkan bahawa madu *Trigona* K1 adalah kaya dengan polifenol-polfenol dan antioksidan-antioksidan lain berbanding dengan madu *Trigona* dan *Apis* yang lain. Dapat disimpulkan daripada kajian ini bahawa madu *Trigona* Malaysia mempunyai profil fizikokimia dan antioksidan yang berbeza daripada madu *Apis*.

Kata kunci: madu *Apis*, madu *Trigona*, lebah kelulut, fizikokimia, jumah kandungan fenolik, antioksidan

Introduction

Honey composition is greatly influenced by its botanical and geographical origins [1, 2], therefore justifying the presence of a variety of honey in the global market. Known to have carbohydrates and water as its major compositions, honey also comprises of other constituents including enzymes, amino acids, organic acids, vitamins, minerals, polyphenols (phenolic compounds), carotenoids and Maillard reaction products which are contributed by plants and bees themselves [1, 2]. Enzymes such as catalase, glutathione-*S*-transferase and superoxide dismutase are among antioxidant enzymes found in honeybees *A. mellifera* [3]. During their visit on flowering plants, bees could have visit various different plants and thus take up the antioxidant compounds produced by the plants in the form of nectar and/or pollen. Due to this, honey exhibits a wide range of free-radical scavenging phytochemicals such as flavonoids, phenolic acids, ascorbic acid, α-tocopherol, carotenoids-like substances as well as other non-enzymatic antioxidants such as Maillard reaction products, organic acids, amino acids and proteins [2, 4-7]. Particularly, polyphenols mainly flavonoids and phenolic acids have been directly linked to the antioxidant activities in honey through both direct and indirect scavenging of free radicals [2, 6, 8].

Sensory properties of honey (i.e. colour, texture, flavor, odor) may influence consumption predisposition and commercialization. In fact, other than sensory, honey quality can be determined through its physical, chemical and microbiological characteristics [9]. Considering the importance of ensuring quality of honey, two guidelines namely Codex Alimentarius Standard 1981/2001 [10] and European Union (EU) Directive 2001/110 [11] have outlined several honey physicochemical quality criteria to evaluate honey quality including moisture content, free acidity, ash content, electrical conductivity, reducing and non-reducing sugars, diastase activity and hydroxymethylfurfural (HMF) content. Although microbiological properties can also be used to evaluate honey quality, lacks of specifications with regard to microbial contamination and hygiene of honey except for *Clostridium botulinum* making physicochemical analysis of honey is the most frequently studied all over the world [9].

Even though honey can be produced by honey bee (Apidae, Apini) and stingless bee (Apidae, Meliponini), physicochemical properties of honeys were shown to differ between different bee genera (e.g. *Apis*, *Melipona*, *Trigona*) [12-14]. Specifically, higher moisture content, lower diastase activity and reducing sugars, higher electrical conductivity and acidity were the characteristics observed in sour-sweet (acidic) taste stingless bee honey as compared to *Apis mellifera* honey [15]. Considering the difference in the physicochemical properties of stingless bee honeys, the influence of bee species on honey composition and properties should be considered when assessing honey quality [12, 13, 16, 17]. However, there are no or limited published quality control regulations pertaining to stingless bee honey are made available. The two mentioned guidelines Codex Alimentarius and EU Directive particularly address honey produced by honeybees (*Apis* spp.) and *A. mellifera* (European or western honeybees), respectively [10, 11]. Thus, it is noteworthy that honey produced from different bee genera than specified in EU Directive and Codex Alimentarius may not meet the outlined criteria.

Insufficient information pertaining to honeys from stingless bee could be the reason it is not included in the international standards for honey (Codex Alimentarius) [15]. The aims of this study are to characterize the physicochemical, total phenolic, total flavonoids, total protein and antioxidant properties of several Malaysian *Apis* and *Trigona* honeys and to differentiate these profiles between these two bee genera. The information from this study is useful and can be considered for the establishment of national and international standards for stingless bee honey.

Materials and Methods

Chemicals

D(-)-Fructose, D(+)-sucrose, analytical and HPLC-grade methanol were purchased from Merck (Darmstadt, Germany). Bovine serum albumin was procured from Vivantis Inc. (USA). D(+)-glucose and 5-hydroxymethylfurfural (HMF) were supplied by Sigma Chemicals Co. (St. Louis, MO, USA). Folin & Ciocalteu's phenol reagent, sodium nitrite, sodium carbonate, aluminum chloride, iron (III) chloride hexahydrate, iron (II) sulfate heptahydrate, Bradford reagent, 2,2-diphenyl-1-picrylhydrazyl (DPPH) and 2,4,6-Tris(2-pyridyl)-*s*-triazine (TPTZ) were purchased from Sigma-Aldrich Co. (Steinheim, Germany).

Collection of honey samples

Seventeen natural honeys from *Apis* spp. and *Trigona* spp. were collected from several areas in Malaysia. Three types of unifloral honey (gelam, nanas and acacia) and two types of multifloral honey (tualang and kelulut) were analyzed. Details of honey samples are provided in Table 1. All honey samples were identified by authorized bee keepers and personnel from Johor Department of Agriculture, Terengganu Honey Collector Corporation, as well as Sabah Rural Development Corporation. All honey samples were kept in the dark at room temperature between 24-28 °C prior to analysis. All physicochemical analyses were conducted in less than nine months. Samples were tested for biochemical and antioxidant analyses within one year of storage.

Physicochemical profiles

pH and free acidity

pH of samples was measured in a solution prepared with 10 g of sample in 75 mL of distilled water using a pH meter (Delta 320, Mettler Toledo, USA) whereas free acidity was determined by dissolving 10 g of samples in 75 mL of distilled water and titrated with 0.1 M NaOH to pH 8.3 [18].

Total soluble solids and density

Total soluble solids (TSS) of 20% (w/v) samples were measured using a refractometer (E-line ATC 44-803, Bellingham-Stanley, UK). TSS measurements were further corrected for a standard temperature of 20 °C by including the correction factor 0.00023/°C [19]. Density was calculated using Equation 1.

Table 1. Honey samples

Sample	Bee species	Botanical origin	Location
A1	*Apis mellifera*	*Acacia mangium*	Johor, Peninsular Malaysia
A2, A3, A4	*Apis cerana indica*	*Acacia mangium*	Sabah, West Malaysia
G1, G2, G3	*Apis mellifera*	*Melaleuca cajuputi*	Terengganu, Peninsular Malaysia
N1, N2, N3	*Apis mellifera*	*Ananas comosus*	Johor, Peninsular Malaysia
T1	*Apis dorsata*	Mixed source	Sabah, West Malaysia
T2, T3	*Apis dorsata*	Mixed source	Terengganu, Peninsular Malaysia
K1	*Trigona spp.*	Mixed source	Sabah, West Malaysia
K2, K3, K4	*Trigona itama*	Mixed source	Kelantan, Peninsular Malaysia

A = acacia, G = gelam, N = nanas, T = tualang, K = kelulut

$$\text{Density} = \frac{[(\text{weight of sample+cylinder}) - \text{weight of cylinder}]}{\text{volume of sample}} \quad (1)$$

Ash content and electrical conductivity

One gram of samples was ignited until completely dried. The sample crucibles were then placed in a furnace (Thermolyne-Barnstead, USA) and incinerated at 600 °C for 6 hours. Ash content (g ash/100 g of honey) was calculated using the following formula [18]:

$$\text{Ash} = \frac{[(m_1 - m_2)]}{m_0}\ x\ 100 \quad (2)$$

where m_0 = sample weight, m_1 = weight of crucible + ash, and m_2 = weight of empty crucible. Electrical conductivity (EC) of 20% w/v (dry weight basis) sample was determined using a conductivity meter (HI 98311, Hanna Instruments, Mauritius) in ultrapure water [18].

Hydroxymethylfurfural content

HMF content was determined using a HPLC according to methods described by the IHC [18]. Ten grams of sample was dissolved in 50 mL ultrapure water, filtered through 0.45 µm nylon membrane filter, and injected into an HPLC system (Agilent 1100, Agilent Technologies, USA) equipped with a photodiode array detector. The analytical column was a ZORBAX Eclipse XDB-C18 (4.6 x 150 mm, 5 µm; Agilent Technologies, USA). The mobile phase was methanol: water (90:10, v/v) at a flow rate of 1.0 mL/min. The detection wavelength was set at 285 nm. The standard curve was prepared using standard HMF (0 – 10 mg/L, Y = 145.77x + 0.8048, R^2 = 0.999). Results were expressed as mg of HMF/1000 g of honey (mg/kg).

Colour

Colour of samples was measured using a colour photometer (Hanna HI 96785, Hanna instruments, Romania) with reference to analytical grade glycerol and classified according to United States Department of Agriculture (USDA) colour standard designation [20].

Sugar content

Sugar content of honey samples was determined using HPLC system (Agilent 1100, Agilent Technologies, USA) equipped with a refractive index detector [18]. Honey solution 5% (w/v) was prepared, filtered through 0.45 µm nylon membrane filter and 20 µL was injected into the HPLC system equipped with Phenomenex NH_2 column (5 µm, 250 mm x 4.6 mm) kept at 30 ºC. Mobile phase was ultrapure water maintained at a flow rate 0.6 mL/min. Calibration curves were produced for glucose, fructose, and sucrose solutions (0 - 10 mg/ mL, R^2 = 0.999). Results were expressed as mg of saccharide/100 g of honey (mg/100 g).

Total protein and antioxidant profiles

Determination of total phenolic content

One milliliter of Folin-Ciocalteu reagent was mixed with 1 mL of diluted honey samples (0.2 g/mL). After 3 min, 1 mL of 10 % sodium carbonate solution was added to the reaction mixture, and the volume was adjusted to 10 mL with distilled water [21]. The mixture was incubated in the dark for 90 min at ambient temperature and the absorbance was read at 725 nm (Epoch, BioTek Instruments Inc., USA). The standard curve was prepared using gallic acid (0 - 140 µg/mL, Y = 0.0066x - 0.0098, R^2 = 0.999). Results were expressed as mg of gallic acid equivalents (mg GAE)/100 g of honey.

Determination of total flavonoid content

Four milliliters of distilled water were added to 1 mL of diluted honey (0.2 g/mL), followed by addition of 0.3 mL of 5 % w/v sodium nitrite. After 5 minutes, 0.3 mL of 10 % w/v aluminum chloride was added. After 6 minutes, 2 mL of 1 M NaOH was added, and the volume was increased to 10 mL by adding 2.4 mL of distilled water [21]. The solution was mixed well and read at 510 nm. A calibration curve was prepared using standard solutions of quercetin (0 - 100 µg/mL, Y = 0.0004x + 0.0007, R^2 = 0.998). Results were expressed as mg of quercetin equivalents (mg QE)/100 g of honey.

Determination of total protein content

Honey sample (5 µL, 50 % w/v) was mixed with 250 µL of Bradford reagent [22]. The mixture was incubated for 5 minutes and the absorbance was taken at 595 nm. Bovine serum albumin (0 - 1.4 mg/mL, Y = 0.3739x – 0.0183, R^2 = 0.997) was used as a standard for preparing

the calibration curve. Results were expressed as mg of protein/kg of honey.

DPPH radical scavenging activity

The DPPH radical scavenging activity was measured as described by [23] and with some modifications as made by Ferreira et al. [24]. Pure honey samples in different concentrations (0.98 - 62.5 mg/mL), ascorbic acid (0.24 - 31.25 µg/mL) and DPPH (0.04 mg/mL) were prepared in methanol. In 96-well plates, 100 µL of sample was mixed with 100 µL of methanolic solution containing DPPH radical. The mixture was homogenized and left to stand in the dark for 30 minutes. Absorbance was measured at 517 nm against a blank to eliminate the influence of honey colour. The blank was honey sample without DPPH radical. Ascorbic acid was used as a control. Radical scavenging activity (RSA) was calculated using the following formula:

$$\text{RSA}\ (\%) = \frac{[(A_{DPPH} - A_S)]}{A_{DPPH}}\ x\ 100 \qquad (2)$$

where A_S is the absorbance of the solution when the sample has been added at a particular level and A_{DPPH} is the absorbance of the DPPH solution. IC_{50} is the concentration of sample at which 50% of DPPH radicals were scavenged. IC_{50} was calculated from the relationship curve of RSA (%) against sample concentrations.

Estimation of total antioxidant activity

Total antioxidant activity was determined using ferric reducing antioxidant power (FRAP) assay. FRAP reagent was freshly prepared by mixing 300 mM acetate buffer (pH 3.6), 10 mM TPTZ solution in 40 mM HCl and 20 mM $FeCl_3.6H_2O$ at the volume of 10:1:1 and pre-warmed to 37 ˚C prior to use. Diluted honey (200 µL, 0.2 g/mL) was mixed with 1.5 mL of FRAP reagent. The absorbance of the reaction mixture was measured at 593 nm after incubation at 37 ˚C for 4 minutes [21]. Aqueous standard solution of $FeSO_4.7H_2O$ (0 - 1000 µM, R^2 = 0.997) were used for the calibration curve. Results were expressed as the FRAP value (µM Fe (II)) of the 20% honey solution.

Statistical analysis

Results were presented as mean values ± standard deviation (SD). All physicochemical, total protein and antioxidant analyses were conducted in three independent experiments in triplicates (n = 9) except for HMF (two independent experiments, n = 2) and sugar content (three independent experiments, n = 3). The statistical differences represented by letters were obtained through one-way analysis of variance (ANOVA) followed by Tukey's honestly significant difference (HSD) post hoc test ($p < 0.05$). These were carried out using SPSS version 16.0 program (IBM Corporation, New York, USA).

Results and Discussion

Physicochemical profiles

Trigona honeys showed lower pH but higher free acidity and EC than *Apis* honeys (Table 2). Similarly, earlier study reported that *Trigona* (*Heterotrigona and Geniotrigona spp*.) honey had lower pH but higher free acidity than *A. mellifera* honey [17]. pH of all honey samples (2.88 - 3.65) were lower compared to the range set for blossom honeys (pH 3.5 - 4.5) and none fall within honeydew honey classification (pH 4.5 - 6.5) (Table 2). pH of Malaysian *Apis* honeys obtained in this study were comparable to those reported by literatures [25-27] with pH ranged from 3.44 - 3.89, 3.21 - 3.50, and 3.53 - 4.03, respectively. Evidence also pointed out that some Malaysian and Thailand *Trigona* honeys exhibited slightly higher pH (3.70 - 4.05) [15, 28, 29] than observed in this study. pH values of some Indian and Algerian honeys ranged from 3.7 - 4.4 and 3.49 - 4.43, respectively [19, 30]. pH differences in honey could be affected by harvest and storage conditions [31] and bee species [15-17]. The acidic pH contributes to honey antibacterial properties [32] and subsequently prolongs the shelf-life of honey due to stability against microbial spoilage [27]. It was reported by Al-Kafaween [33] that 25% (w/v) *Trigona* honey was the minimum bactericidal concentration (MBC) needed to kill bacteria *Pseudomonas aeruginosa* and *Streptococcus pyogenes*, thus indicating the antibacterial activity of *Trigona* honey.

Free acidity of honeys ranged from 10.80 - 553.20 meq/kg (Table 2). Gelam (G1) sample was the only honey sample that showed free acidity within limit 50 meq/kg which indicates absence of undesirable fermentation [10]. Honeys from Portugal were reported to contain free acidity between 16 - 32 meq/kg [9]. The higher free acidity in nearly all analyzed Malaysian honey samples could possibly be the results of increased glucose oxidation and fermentation activity. Considered the seasonal factor, diluted honey resulted in activation of glucose oxidase, the enzyme that converts glucose to gluconic acid which is the major organic acid in honey [17, 32]. Fermentation is also expected to occur within the naturally higher moisture content Malaysian honeys upon storage. This condition favors action of yeasts that convert glucose and fructose into ethyl alcohol and carbon dioxide. The alcohol is then converted into acetic acid and water in the presence of oxygen, resulting in a sour taste [19, 25]. On top of that, this study suggested that the extremely high free acidity seen in *Trigona* honeys (Table 2) is most likely be due to the influence of bee species and floral composition. Similar findings were observed by Chuttong et al. [15] in which their honey samples from three *Trigona* spp. exhibited total acidity between 440 and 592 meq/kg. Another study by Shamsudin et al. [17] pointed out that free acidity between *Heterotrigona itama and Geniotrigona thoracica* honeys differ between nectar sources. Also, their *Trigona* honey samples showed higher free acidity than *A. mellifera* honey with four organic acids namely gluconic, lactic, acetic and citric acids were found in all these stingless bee honey samples.

Total soluble solids (TSS) of honeys was in the range of 63.33 - 84.11 ˚Brix (Table 2), in accordance to the values of 60.9 - 76.7 ˚Brix, 76.2 - 80.4 ˚Brix, 79.0 - 82.2 ˚Brix and 70.0 - 85.0 ˚Brix found in some Malaysian, Indian, Portugal and Saudi Arabia honeys, respectively [17, 19, 34, 35]. Earlier study demonstrated that the TSS values found in stingless bee honey were lower than in *A. mellifera* honey [17]. However, two *A. mellifera* honeys (gelam G2 and G3) also showed lower TSS values (Table 2). It was reported that Saudi Arabia honeys with low TSS contents showed low density values and high water content [35]. The Brix values are related to the sugar content in honey [17]. Density of analyzed honey samples ranged from 1.27 - 1.57 g/mL (Table 2) whereas some Saudi Arabia honeys demonstrated density between 1.35 - 1.44 [35]. Kelulut (K3 and K4) and gelam (G2) honeys showed lower density than other samples (Table 2). Honeys with lowest density have high moisture content and vice versa [30, 35]. Due to the high moisture content, stingless bee honeys such as *Melipona subnitida* honeys appear more fluid [14]. In fact, several factors are known to affect the honey water content including harvesting season, climatic factors and degree of maturity reached in the hive [34].

Ash content and EC showed some interrelation with mineral content of honey [26]. Ash content of samples ranged from 0.03 - 0.45 g/100 g (Table 2). Some Algerian, Portugal and Indian honeys exhibited ash content between 0.06 - 0.23%, 0.07 - 0.35% and 0.03 - 0.43%, respectively [9, 19, 30]. Similar to earlier findings, all analyzed honey samples were of nectar origin where the ash content ≤ 0.6% [26]. A number of mineral elements were reported to be present in Malaysian honeys including potassium (70%), sodium, magnesium, iron, aluminium, zinc, chromium, etc. [26]. The ash content of *Trigona* honeys (0.13 - 0.45 g/100 g) measured in this study was in accordance to the previous study which reported ash content in between 0.15 and 0.67 g/100 g [36]. Some Thailand stingless bee honeys were shown to have ash content ranged from 0.04 - 3.1 g/100g [15]. Trigonini are known as the most generalized bees due to the wide spectrum of pollen they collect, possibly due to their small size that gives them more flexibility in collective sampling as well as living in populous to very populous colonies [37, 38], thus could explain the higher ash contents observed for some *Trigona* honeys in this study. Amazingly, it was reported that *Trigona* bees were shown to collect a very high number of total pollen (3289 - 58,994) compared to *A. mellifera* bees (53 - 485) [29].

EC values of samples ranged between 0.25 and 1.29 mS/cm (Table 2). EC relies on ash and acid contents of honey. Specifically, the higher their contents, the higher the resulting conductivity [9, 19]. Higher EC values ranged from 1.07 - 1.80 mS/cm and > 2.0 mS/cm have been reported for respective Malaysian *Apis* honeys and

Thailand stingless bee honeys [15, 26]. Similarly, some *Apis* honeys and all *Trigon*a honeys in this study exhibited high EC values (> 0.8 mS/cm), which do not fall within the guideline for nectar honey by previous studies [10,11].

HMF content in honey samples ranged from 0.70 to 163.15 mg/kg honey (Table 2). HMF is normally absent in fresh honeys but tends to increase during processing and/or due to aging, thus it is widely recognized as a parameter of honey freshness [9]. According to Codex Alimentarius Commission [10], honey originated from countries or regions with tropical ambient temperatures and blends of these honeys shall contain HMF not more than 80 mg/kg honey. However, honeys acacia (A1) and kelulut (K1) showed HMF values higher than permitted limit of 80 mg/kg honey. This indicates that these two honey samples have lost their freshness due to much longer storage time compared to other samples prior to analysis. Samples with low HMF values indicate freshness of samples [35] and proven unheated as claimed by the honey suppliers. Higher HMF content could also be the results of heating where acid-catalyzed dehydration of hexose sugars such as fructose and glucose takes place [25]. Singh and Bath [39] stated that fructose is highly susceptible to the acid-catalyzed dehydration reaction as it is found unstable at pH 4.6 and is five times more reactive than glucose in its most stable acid environment. Earlier study by Khalil et al. [25] reported that five Malaysian honey samples stored for up to six months at room temperature yielded low HMF values ranged from 2.80 - 24.87 mg/kg honey, which is within the permitted maximum level of 40 mg/kg honey as recommended by [10] for honey after processing and/or blending. The study also revealed that two tualang honey samples stored for 24 months at room temperature had the highest HMF values (986.57 - 1131.76 mg/kg honey) regardless of low pH content. Their study demonstrated that storage duration had a strong positive correlation with HMF formation whereas pH showed only moderate correlation with HMF content. Thus, HMF content in honey could be influenced by poor storage conditions (e.g. temperature), higher temperature and longer duration of heating process, pH and floral sources.

Colour of honeys ranged from 51 - 150 mm Pfund (Table 2). Darker colour was observed for *Trigona* honeys, dissimilar to most of monofloral *Apis* honeys (Table 2). Dark-colored honeys were reported to have higher mineral content [26], however, this pattern was inconsistent in this study. Earlier study revealed that dark honeys exhibited higher phenolic contents and were rich in pigments such as carotenoids than the light ones [24, 35].

The sugar content in analyzed honey samples are shown in Figure 1. It can be seen that all *Apis* honeys exhibited higher concentration of sugars (43.5 - 61.15 g/100 g) than *Trigona* honeys (12.15 - 38.00 g/100 g). This could explain the less sweetness taste of *Trigona* honeys and one of the reasons for their low sugar content could be due to the conversion of sugars into organic acids [32] resulting in a sour taste. Similarly, these findings were supported by Omar et al. [28] who reported low concentrations of fructose and glucose (4.5 - 24.6%) and sucrose (0.5 - 2.2%) in four Malaysian stingless bee honeys. Much recent study also demonstrated low reducing sugars [fructose and glucose] (15.4 - 24.7%) in Malaysian *Trigona* honeys compared to *A. mellifera* honey (51.0%) [17].

EU Council [11] pointed out that total fructose and glucose (reducing sugars) content in blossom honey must not be less than 60 g/100 g of honey. Higher reducing sugars were reported in some Malaysian *Apis* honeys between 61.17 - 63.89% [27], Algerian honeys between 67.83 - 80.25% [30] and Portugal honeys between 67.7 - 73.7% [9]. Nonetheless, the lower reducing sugar values of *Apis* honeys seen in this study were supported by Saxena et al. [19] who demonstrated variations in the reducing sugar content of some Indian honey samples ranging from 43.3 - 65.5%. Comparisons between all honey samples revealed that Acacia (A2) and gelam (G1) honeys exhibited highest fructose (29.6 %) and glucose (30.2 %), respectively (Figure 1). Sucrose contents in analyzed honey samples ranged from 0.3 - 5.6 g/100 g (Figure 1). Codex Alimentarius Commission [10] specified that sucrose content in honey should be less than 5%. Except for acacia (A1), other samples showed lower sucrose content within the permitted limit. The higher sucrose content observed in

acacia (A1) honey sample could be due to the early harvest of honey where sucrose conversion to fructose and glucose by the bees' invertase enzymes has not completely taken place [19]. Additionally, nanas honeys (N1-N3) exhibited nearly equivalent composition of reducing sugars (Figure 1). It is suggested that bee species and sources of nectar are most likely to have some influence on these observed results.

Total protein and antioxidant profiles

Apis honeys showed total phenolic content (TPC) between 12.6 - 47.1 mg GAE/100 g of honey (Table 3). These results were comparable to the earlier studies by Khalil et al. [21] (22.32 - 41.99 mg GAE/100 g), Moniruzzaman et al. [27] (18.67 - 35.27 mg GAE/100 g) and Ranneh et al. [40] (13.94 - 18.39 mg GAE/100 g) for Malaysian *Apis* honeys. In contrast, other studies reported higher (110.39 - 196.50 mg GAE/100 g) [41] and lower TPC (1.52 – 4.22 mg GAE/100 g) [42] for some Malaysian *Apis* honeys. *Trigona* honeys showed higher TPC than *Apis* honeys in the range of 33.2 – 60.2 mg GAE/100 g (Table 3), in accordance to the TPC results reported by Bakar et al. [36]. Foraging differences between these bee species on multiple plant sources could possibly be one of the reasons [16]. Also, it is noteworthy that the TPC results for *Trigona* honeys in this study were much higher than reported by Ranneh et al. [40] (22.81 - 23.53 mg GAE/100 g). This observation may be due to the influence of several factors including floral origin and seasonal factors. Floral origin affects concentration and type of phenolic compounds found in honey [8, 19]. Seasonal factors such as monsoon season may restrict the norm of bee foraging activities [16].

Estimated total flavonoid content (TFC) obtained for *Apis* honeys in this study (Table 3) were higher (14.5 - 70.3 mg QE/100 g of honey) than other reported studies for Malaysian *Apis* honeys by Khalil et al. [21] (13.53 – 31.89 mg catechin equivalent (CE)/100 g), Moniruzzaman et al. [27] (2.20 – 6.57 mg CE/100 g), Ranneh et al. [40] (6.47 – 6.70 mg CE/100 g) and Chua et al. [41] (18.51 – 32.89 mg rutin equivalent (RE)/100 g). *Trigona* honeys in this study exhibited TFC in the range of 43.2 - 65.9 mg QE/100 g of honey (Table 3). These results were higher than TFC values of *Trigona* honeys demonstrated by earlier studies which were in the range of 5.38 - 30.86 mg RE/100 g [36], 9.79 - 10.15 mg CE/100 g [40] and 2.38 - 9.31 mg QE/100 g [17]. Variations between the present and previous findings could be due to different floral origins, seasonal factors, and bee species preference [4, 16, 17].

The protein contents ranged from 274.4 - 1058.9 μg/g (Table 3). Protein in honeys can be attributed to the presence of enzymes as the main contributors from introduction by bees or from nectar of plants [19, 27]. In fact, total protein and amino acid in honey are also influenced by the geographical and botanical origins as well as storage time [27]. Normally, honey contains less than 5 mg protein/g honey and amino acid proline dominates in honey [1]. Moniruzzaman et al. [27] reported that the protein content in their Malaysian *Apis* honey samples ranged from 2040 - 4830 μg/g, higher than observed in this study.

The IC_{50} for honey samples ranged from 10.6 – 52.7 mg/mL, lowest in kelulut (K1) and highest in gelam (G1) samples, respectively (Table 3). Earlier findings reported that IC_{50} of Malaysian *Apis* honeys were between 5.24 and 17.51 mg/mL [42] whereas Malaysian *Trigona* honeys exhibited IC_{50} between 32.58 and 105.53 mg/mL [17]. The lower IC_{50} for some *Apis and Trigona* honeys in this study indicated the high radical scavenging activity of these honeys (Table 3). From Table 3, it can be seen that monofloral acacia (A1 and A2), multifloral kelulut (K1-K4) and tualang (T1) showed 50% DPPH inhibition at less than 20 mg/mL honey. The unpaired electron of DPPH forms a pair with an electron donated by antioxidants (e.g. from honey), causing a colour changes from deep purple to yellow as a result of conversion of DPPH radical to its reduced form (1,1-diphenyl-2-picryl-hydrazine) [19]. However, DPPH only measures the activity of water-soluble antioxidants [43]. Radical scavenging activity of phenolics is positively correlated with the number of OH groups [44]. Thus, it is assumed that honeys with lower IC_{50} may contain phenolics with more OH groups in addition to other water-soluble antioxidants.

Reducing power of honeys ranged from 196.3 – 713.8 μM Fe(II) (Table 3). FRAP assay is a simple, fast and precise assay [45] that gives a direct estimation of the

antioxidants (reductants) present in a sample based on their ability to reduce ferric 2,4,6-tripyridyl-s-triazine complex (Fe^{3+}-TPTZ) to its ferrous form (Fe^{2+}-TPTZ) which resulted in a blue product [21, 27]. Aljadi et al. [5] reported that the FRAP values for Malaysian gelam and coconut honeys were 1350 and 961 µM Fe(II), respectively. These values are higher than those obtained in this study. Variations in the antioxidant activities of honeys are likely due to the different types and concentrations of polyphenols in each honey sample [16, 44]. However, total antioxidant activity is not solely contributed by the polyphenols where the presence of constituents other than the phenolic compounds such as vitamin C (ascorbic acid), E (α-tocopherol) and carotenoids may as well have some contributions [2, 4].

Table 2. Physicochemical profiles of honey samples

Sample	**pH**	**Free Acidity (meq/kg)**	**TSS (°Brix)**	**Density (g/mL)**	**Ash (g/100 g)**	**EC (mS/cm)**	**HMF (mg/kg)**	**Colour[c] (mm Pfund)**
A1	3.24 ± 0.01	84.00 ± 0.53	82.11 ± 1.90	1.40 ± 0.00	0.22 ± 0.03	0.84 ± 0.02	117.73 ± 9.60	150.00 ± 0.00
A2	3.64 ± 0.03	64.93 ± 4.27	77.67 ± 0.58	1.38 ± 0.00	0.17 ± 0.03	0.74 ± 0.01	5.55 ± 0.23	81.00 ± 1.00
A3	3.59 ± 0.02	61.27 ± 5.83	74.78 ± 2.04	1.39 ± 0.00	0.21 ± 0.06	0.81 ± 0.01	4.08 ± 2.18	80.00 ± 1.00
A4	3.40 ± 0.04	77.93 ± 4.46	77.00 ± 1.00	1.36 ± 0.00	0.17 ± 0.03	0.74 ± 0.02	6.11 ± 0.42	81.00 ± 1.00
G1	3.65 ± 0.06	10.80 ± 0.35	84.11 ± 0.19	1.55 ± 0.00	0.03 ± 0.02	0.25 ± 0.03	45.42 ± 0.02	51.00 ± 1.00
G2	3.12 ± 0.02	88.67 ± 0.83	63.33 ± 2.08	1.28 ± 0.00	0.04 ± 0.03	0.46 ± 0.00	nd	64.00 ± 2.00
G3	3.38 ± 0.02	76.13 ± 4.57	68.56 ± 1.26	1.35 ± 0.00	0.15 ± 0.04	0.57 ± 0.01	0.70	120.00 ± 1.00
N1	3.33 ± 0.01	57.60 ± 1.44	77.89 ± 0.84	1.57 ± 0.00	0.10 ± 0.03	0.37 ± 0.01	13.97 ± 1.52	101.00 ± 5.00
N2	3.31 ± 0.01	56.20 ± 0.00	77.67 ± 0.58	1.39 ± 0.00	0.11 ± 0.02	0.41 ± 0.02	13.20 ± 0.93	66.00 ± 4.00
N3	3.26 ± 0.04	59.87 ± 2.16	79.67 ± 1.15	1.32 ± 0.00	0.11 ± 0.03	0.40 ± 0.02	14.42 ± 0.76	67.00 ± 4.00
T1	3.29 ± 0.01	84.67 ± 0.42	75.67 ± 1.15	1.35 ± 0.00	0.13 ± 0.01	0.84 ± 0.02	46.54 ± 3.56	130.00 ± 1.00
T2	3.30 ± 0.02	70.00 ± 1.22	73.33 ± 1.53	1.47 ± 0.00	0.16 ± 0.02	0.89 ± 0.02	nd	75.00 ± 1.00
T3	3.28 ± 0.02	73.83 ± 0.98	74.33 ± 1.34	1.46 ± 0.00	0.16 ± 0.01	0.75 ± 0.01	nd	107.00 ± 2.00
Mean *Apis*	3.37 [a]	66.61 [a]	75.85 [a]	1.41 [a]	0.13 [a]	0.62 [a]	-	90.00 [a]

Table 2 (cont'd). Physicochemical profiles of honey samples

Sample	pH	Free Acidity (meq/kg)	TSS (˚Brix)	Density (g/mL)	Ash (g/100 g)	EC (mS/cm)	HMF (mg/kg)	Colour[c] (mm Pfund)
K1	2.98 ± 0.02	271.13 ± 1.51	70.00 ± 1.73	1.35 ± 0.00	0.13 ± 0.01	0.92 ± 0.00	163.15 ± 14.08	118.00 ± 0.00
K2	3.24 ± 0.02	466.60 ± 4.87	72.45 ± 0.69	1.36 ± 0.00	0.45 ± 0.01	1.29 ± 0.02	5.87 ± 1.26	91.00 ± 3.00
K3	2.88 ± 0.01	553.20 ± 6.04	68.67 ± 0.58	1.27 ± 0.00	0.15 ± 0.01	0.93 ± 0.00	8.66 ± 1.28	100.00 ± 2.00
K4	3.02 ± 0.03	501.47 ± 4.17	67.33 ± 1.15	1.27 ± 0.00	0.25 ± 0.01	1.08 ± 0.01	6.03 ± 2.26	121.00 ± 1.00
Mean *Trigona*	3.03 [b]	448.10 [b]	69.61 [b]	1.31 [b]	0.25 [b]	1.05 [b]	-	107.00 [a]

[a] A = acacia, G = gelam, N = nanas, T = tualang, K = kelulut, TSS = total soluble solids, EC = electrical conductivity, HMF = hydroxymethylfurfural, nd = not detected

[b] Values are means ± SD of three independent experiments in triplicates (n = 9) except for HMF (two independent experiments, n = 2)

[c] USDA colour standard for honey; 51 – 85 = light amber, 86 - 114 = amber, > 114 = dark amber

[d] Values with different letters (superscripts) indicate significant differences ($p < 0.05$)

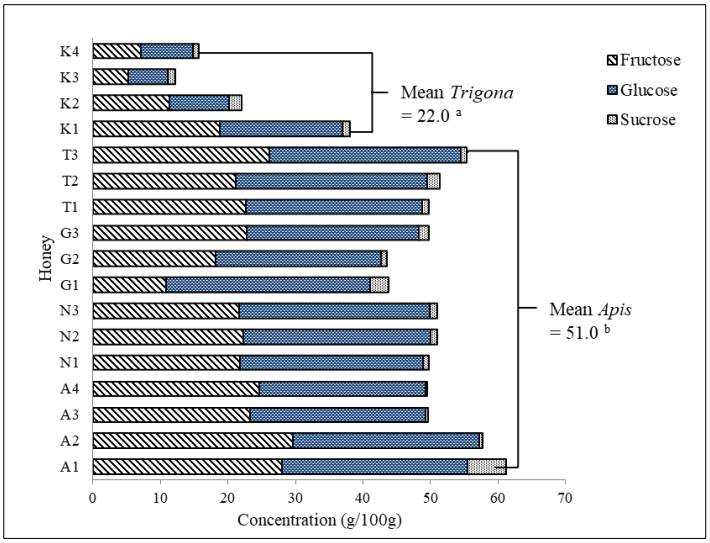


Figure 1. Sugar content of honeys: acacia (A), nanas (N), gelam (G), tualang (T) and kelulut (K). Values with different letters (superscripts) indicate significant differences ($p < 0.05$)

Table 3. Total protein and antioxidant profiles of honey samples

Sample	TPC (mg GAE/100 g)	TFC (mg QE/100 g)	Protein (µg/g)	IC_{50} (mg/mL)	FRAP (µM Fe(II))
A1	47.1 ± 2.3	48.1 ± 0.7	577.5 ± 21.6	12.9 ± 1.0	529.8 ± 6.4
A2	23.2 ± 1.3	34.2 ± 1.3	556.1 ± 47.9	12.2 ± 3.9	285.3 ± 1.9
A3	24.8 ± 0.8	32.3 ± 3.6	556.1 ± 34.4	21.9 ± 0.2	285.6 ± 10.2
A4	24.6 ± 0.8	29.3 ± 4.5	543.6 ± 66.5	26.8 ± 3.4	276.8 ± 2.8
G1	12.6 ± 0.1	14.5 ± 0.5	274.4 ± 32.5	52.7 ± 2.1	196.3 ± 3.3
G2	20.5 ± 0.9	30.0 ± 0.4	1058.9 ± 103.2	44.8 ± 8.4	201.6 ± 43.5
G3	20.1 ± 1.6	41.4 ± 2.1	598.9 ± 31.3	32.8 ± 3.9	234.2 ± 47.7
N1	25.6 ± 3.1	20.5 ± 1.6	481.2 ± 31.3	34.6 ± 2.4	263.0 ± 4.1
N2	27.6 ± 0.3	19.3 ± 0.8	491.9 ± 22.3	33.8 ± 3.4	263.5 ± 2.1
N3	24.8 ± 2.2	18.9 ± 1.4	468.8 ± 6.2	35.7 ± 3.3	265.4 ± 1.2
T1	46.3 ± 1.6	70.3 ± 1.1	495.5 ± 42.9	13.9 ± 1.2	529.8 ± 16.9
T2	26.9 ± 0.3	26.8 ± 2.4	351.1 ± 18.8	29.1 ± 0.7	269.1 ± 8.5
T3	22.3 ± 0.4	24.4 ± 1.3	352.9 ± 29.5	33.6 ± 2.3	253.3 ± 13.1
Mean *Apis*	26.6 [a]	31.5 [a]	523.6 [a]	29.6 [a]	296.4 [a]
K1	60.2 ± 2.2	65.9 ± 4.8	335.0 ± 21.6	10.6 ± 0.6	713.8 ± 20.1
K2	41.8 ± 1.2	53.4 ± 2.7	461.6 ± 42.5	11.2 ± 0.6	624.7 ± 4.3
K3	33.2 ± 1.2	43.2 ± 3.3	440.2 ± 14.2	19.7 ± 1.6	334.9 ± 4.4
K4	35.0 ± 1.1	46.6 ± 2.6	682.7 ± 40.5	14.8 ± 0.5	428.7 ± 1.0
Mean *Trigona*	42.6 [b]	52.3 [b]	479.9 [a]	14.1 [b]	525.5 [b]

[a] A = acacia, G = gelam, N = nanas, T = tualang, K = kelulut, TPC = total phenolic content, TFC = total flavonoid content, IC_{50} = concentration of sample at which 50% of DPPH radicals were scavenged, FRAP = ferric reducing antioxidant power assay, GAE = gallic acid equivalent, QE = quercetin equivalent.

[b] Values are means ± SD of three independent experiments in triplicates (n = 9).

[c] Values with different letters (superscripts) indicate significant differences ($p < 0.05$).

Conclusion

The physicochemical properties of Malaysian honeys were influenced by many factors including bee species, floral sources, seasonal factors, processing, geographical distribution, etc. The Malaysian *Apis* and *Trigona* honeys were remarkably different in several physicochemical parameters and therefore this study strongly supported the establishment of different standards for stingless bee honeys as a guideline for the consumers as well as the authorities in assessing honey quality. Considering the limited number of samples analyzed in this study, it is suggested that more studies should be conducted in the future with variety of honeys from different bee genera to obtain comprehensive information. It was observed from the antioxidant profiling that *Trigona* honeys exhibited significantly higher TPC, TFC and reducing power as well as lower IC_{50} than *Apis* honeys. However, two of the studied *Apis* honeys namely monofloral acacia (A1) and multifloral tualang (T1) honeys showed resemblance to *Trigona* honeys, indicating the influence of other factors such as floral sources to the honeys' antioxidant properties. It can be concluded from this study that both Malaysian *Apis* and *Trigona* honeys exhibited antioxidant activities at varying levels and thus can serve as good sources of natural antioxidants.

Acknowledgement

We gratefully acknowledge the financial support from the Ministry of Higher Education Malaysia and research university grant from Universiti Teknologi Malaysia (UTM) (PY/2014/03300 [7845.4F581]). Our sincere appreciation is extended to Prof. Dr. Siti Amrah Sulaiman and Prof. Dr. Gan Siew Hua (Universiti Sains Malaysia, USM) for their kind assistance. We thank UTM as well as School of Medical Sciences and School of Health Sciences, USM for the provided equipment. The first author expresses her gratitude to UTM for the awarded Zamalah Scholarship during her study.

References

1. Anklam, E. (1998). A review of the analytical methods to determine the geographical and botanical origin of honey. *Food Chemistry,* 63(4): 549-562.
2. Gheldof, N., Wang, X. H. and Engeseth, N. J. (2002). Identification and quantification of antioxidant components of honeys from various floral sources. *Journal of Agricultural and Food Chemistry*, 50(21): 5870-5877.
3. Weirich, G. F., Collins, A. M. and Williams, V. P. (2002). Antioxidant enzymes in the honey bee, *Apis mellifera*. *Apidologie*, 33(1): 3-14.
4. Al-Mamary, M., Al-Meeri, A. and Al-Habori, M. (2002). Antioxidant activities and total phenolics of different types of honey. *Nutrition Research*, 22(9): 1041-1047.
5. Aljadi, A. M. and Kamaruddin, M. Y. (2004). Evaluation of the phenolic contents and antioxidant capacities of two Malaysian floral honeys. *Food Chemistry*, 85(4): 513-518.
6. Beretta, G., Granata, P., Ferrero, M., Orioli, M. and Facino, R. M. (2005). Standardization of antioxidant properties of honey by a combination of spectrophotometric/fluorimetric assays and chemometrics. *Analytica Chimica Acta*, 533(2): 185-191.
7. Baltrušaitytė, V., Venskutonis, P. R. and Čeksterytė, V. (2007). Radical scavenging activity of different floral origin honey and beebread phenolic extracts. *Food Chemistry*, 101(2): 502-514.
8. Tenore, G. C., Ritieni, A., Campiglia, P. and Novellino, E. (2012). Nutraceutical potential of monofloral honeys produced by the Sicilian black honeybees (*Apis mellifera* ssp. sicula). *Food and Chemical Toxicology*, 50 (6): 1955-1961.
9. Gomes. S., Dias, L. G., Moreira, L. L., Rodrigues, P. and Estevinho, L. (2010). Physicochemical, microbiological and antimicrobial properties of commercial honeys from Portugal. *Food and Chemical Toxicology*, 48(2): 544-548.
10. Codex Alimentarius Commission (2001). Codex Standard for Honey: CODEX STAN 12-1981, Rev. 1 (1987), Rev. 2 (2001). FAO, Rome: pp. 1-8.
11. EU (European Union) Council. (2002). Council Directive 2001/110/EC of 20 December 2001 relating to honey. *Official Journal of the European Union*, L10: pp. 47-52.
12. Vit, P., Bogdanov, S. and Kilchenmann, V. (1994). Composition of Venezuelan honeys from stingless bees (Apidae : Meliponinae) and *Apis mellifera* L. *Apidologie*, 25(3): 278-288.
13. Bogdanov, S., Vit, P. and Kilchenmann, V. (1996). Sugar profiles and conductivity of stingless bee honeys from Venezuela. *Apidologie*, 27(6): 445-450.
14. Silva, T. M. S., dos Santos, F. P., Evangelista-Rodrigues, A., da Silva, E. M. S., da Silva, G. S., de Novais, J. S., dos Santos, F. d. A. R. and Camara, C. (2013). A phenolic compound, melissopalynological, physicochemical analysis and antioxidant activity of jandaíra (*Melipona subnitida*) honey. *Journal of Food Composition and Analysis*, 2 (1): 10-18.
15. Chuttong, B., Chanbang, Y., Sringarm, K. and Burgett, M. (2016). Physicochemical profiles of stingless bee (Apidae: Meliponini) honey from South East Asia (Thailand). *Food Chemistry*, 192: 149-155.
16. Ismail, N. I., Kadir, M. R. A., Mahmood, N. H., Singh, O. P., Iqbal, N. and Zulkifli, R. M. (2016). Apini and Meliponini foraging activities influence the phenolic content of different types of Malaysian honey. *Journal of Apicultural Research*, 55(2): 137-150.

17. Shamsudin, S., Selamat, J., Sanny, M., Razak, S. B. A., Jambari, N. N., Mian, Z. and Khatib, A. (2019). Influence of origins and bee species on physicochemical, antioxidant properties and botanical discrimination of stingless bee honey. *International Journal of Food Properties*, 22(1): 239-264.
18. Bogdanov, S. (2009). Harmonised method of the international honey commission. Access from http://www.bee-hexagon.net/en/network.htm. [Access online 20 January 2013].
19. Saxena, S., Gautam, S. and Sharma, A. (2010). Physical, biochemical and antioxidant properties of some Indian honeys. *Food Chemistry*, 118(2): 391-397.
20. United States Department of Agriculture (1985). United States standards for grades of extracted honey. Washington D.C., United States of America: Agricultural Marketing Service.
21. Khalil, M. I., Sulaiman, S. A., Alam, N., Ramli, N., Mohamed, M., Bai'e, S. and Hua G. S. (2012). Content and antioxidant properties of processed tualang honey (Agromas®) collected from different regions in Malaysia. *International Journal of Pharmacy and Pharmaceutical Sciences*, 4: 214-219.
22. Bradford, M. M. (1976). A rapid and sensitive method for quantification of microgram quantities of protein utilizing the principle of protein-dye binding. *Analytical Biochemistry*, 72(1-2): 248-254.
23. Wang, H., Gao, X. D., Zhou, G. C., Cai, L. and Yao, W. B. (2008). In vitro and in vivo antioxidant activity of aqueous extract from *Choerospondias axillaris* fruit. *Food Chemistry*, 106(3): 888-895.
24. Ferreira, I. C. F. R., Aires, E., Barreira, J. C. M. and Estevinho, L. M. (2009). Antioxidant activity of Portuguese honey samples: Different contributions of the entire honey and phenolic extract. *Food Chemistry*, 114(4): 1438-1443.
25. Khalil, M. I., Sulaiman, S. A. and Gan, S. H. (2010). High 5-hydroxymethylfurfural concentrations are found in Malaysian honey samples stored for more than one year. *Food and Chemical Toxicology*, 48(8-9): 2388-2392.
26. Chua, L. S., Abdul-Rahaman, N. L., Sarmidi, M. R. and Aziz, R. (2012). Multi-elemental composition and physical properties of honey samples from Malaysia. *Food Chemistry*, 135(3): 880-887.
27. Moniruzzaman, M., Khalil, M. I., Sulaiman, S. A. and Gan, S. H. (2013). Physicochemical and antioxidant properties of Malaysian honeys produced by *Apis cerana*, *Apis dorsata* and *Apis mellifera*. *BMC Complementary and Alternative Medicine*, 13(1): 43.
28. Omar, S., Enchang, F. K., Nazri, M. U. I. A., Ismail, M. M. and Ismail, W. I. W. (2019). Physicochemical profiles of honey harvested from four major species of stingless bee (kelulut) in north east peninsular of Malaysia. *Malaysian Applied Biology*, 48(1): 111-116.
29. Selvaraju, K., Vikram, P., Soon, J. M., Krishnan, K. T. and Mohammed, A. (2019). Melissopalynological, physicochemical and antioxidant properties of honey from West Coast of Malaysia. *Journal of Food Science and Technology*, 56(5): 2508-2521.
30. Ouchemoukh, S., Louaileche, H. and Schweitzer, P. (2007). Physicochemical characteristics and pollen spectrum of some Algerian honeys. *Food Control*, 18(1): 52-58.
31. Terrab, A., Díez, M. J. and Heredia, F. J. (2002). Characterisation of Moroccan unifloral honeys by their physicochemical characteristics. *Food Chemistry*, 79(3): 373-379.
32. Tan, H. T., Rahman, R. A., Gan, S. H., Halim, A. S., Hassan, S. A., Sulaiman, S. A. and Kirnpaul-Kaur, B. S. (2009). The antibacterial properties of Malaysian tualang honey against wound and enteric microorganisms in comparison to manuka honey. *BMC Complementary and Alternative Medicine*, 9 (34): 1-8.
33. Al-Kafaween, M. A., Hilmi, A. B. M., Jaffar, N., Al-Jamal, H. A. N., Zahri, M. K. and Jibril, F. I. (2020). Antibacterial and antibiofilm activities of Malaysian *Trigona* honey against *Pseudomonas aeruginosa* ATCC 10145 and *Streptococcus pyogenes* ATCC 19615. *Jordan Journal of Biological Sciences*, 13(1): 69-76.

34. Silva, L. R., Videira, R., Monteiro, A. P., Valentão, P. and Andrade, P. B. (2009). Honey from Luso region (Portugal): physicochemical characteristics and mineral contents. *Microchemal Journal*, 93(1): 73-77.
35. Alqarni, A. S., Owayss, A. A. and Mahmoud, A. A. (2016). Physicochemical characteristics, total phenols and pigments of national and international honeys in Saudi Arabia. *Arabian Journal of Chemistry*, 9(1): 114-120.
36. Bakar, M. F. A., Sanusi, S. B., Bakar, F. I. A., Cong, O. J. and Mian, Z. (2017). Physicochemical and antioxidant potential of raw unprocessed honey from Malaysian stingless bees. *Pakistan Journal of Nutrition*. 16(11): 888-894.
37. Roubik, D. W. (1979). Nest and colony characteristics of stingless bees from French Guiana (Hymenoptera: Apidae). *Journal of the Kansas Entomological Society*, 52(3): 443-470.
38. Sommeijer, M. J., De Rooy, G., Punt, W. and De Bruijn, L. L. M. (1983). A comparative study of foraging behavior and pollen resources of various stingless bees (Hym., Meliponinae) and honeybees (Hym., Apinae) in Trinidad, West-Indies. *Apidologi*e, 14(3): 205-224.
39. Singh, N. and Bath, P. K. (1997). Quality evaluation of different types of Indian honey. *Food Chemistry*, 58(1-2): 129-133.
40. Ranneh, Y., Ali, F., Zarei, M., Akim, A. M., Hamid, H. A. and Khazaai, H. (2018). Malaysian stingless bee and Tualang honeys: A comparative characterization of total antioxidant capacity and phenolic profile using liquid chromatography-mass spectrometry. *LWT-Food Science and Technology*, 89: 1-9.
41. Chua, L. S., Rahaman, N. L. A., Adnan, N. A. and Tan, T. T. E. (2013). Antioxidant activity of three honey samples in relation with their biochemical components. *Journal of Analytical Methods in Chemistry*, 2013: 313798.
42. Khalil, M. I., Alam, N., Moniruzzaman, M., Sulaiman, S. A. and Gan, S. H. (2011). Phenolic acid composition and antioxidant properties of Malaysian honeys. *Journal of Food Science*, 76(6): 921- 928.
43. Frankel, S., Robinson, G. E. and Berenbaum, M. R. (1998). Antioxidant capacity and correlated characteristics of 14 unifloral honeys. *Journal of Apicultural Research*, 37(1): 27-31.
44. Ismail, N. I., Sornambikai, S., Kadir, M. R. A., Mahmood, N. H., Zulkifli, R. M. and Shahir, S. (2018). Evaluation of radical scavenging capacity of polyphenols found in natural Malaysian honeys by voltammetric techniques. *Electroanalysis*, 30(12): 2939-2949.
45. Benzie, I. F. F. and Strain, J. J. (1999). Ferric reducing/antioxidant power assay: Direct measure of total antioxidant activity of biological fluids and modified version for simultaneous measurement of total antioxidant power and ascorbic acid concentration. *Methods in Enzymology*, 299: 15-27.

Malaysian Journal of Analytical Sciences (MJAS)
Published by Malaysian Analytical Sciences Society

A BRIEF REVIEW ON THE THIAZOLE DERIVATIVES: SYNTHESIS METHODS AND BIOLOGICAL ACTIVITIES

(Ulasan Ringkas Terbitan Tiazol: Kaedah Sintesis dan Aktiviti Biologi)

Iswatun Hasanah Abdullah Ripain and Nurziana Ngah*

Department of Chemistry, Kulliyyah of Science,
International Islamic University Malaysia, Kuantan Campus Bandar Indera Mahkota, 25200 Kuantan, Pahang, Malaysia

**Corresponding author: nurziana@iium.edu.my*

Received: 27 January 2021; Accepted: 24 March 2021; Published: 25 April 2021

Abstract

Thiazole is one of the leading heterocyclic five-membered ring compounds that contain sulphur atoms at position 1 and nitrogen atoms at position 3. Many of its natural and synthetic derivatives possess diverse biological activities. In drug research development, the substituent at thiazole ring was modified to generate new molecules with potent biological activities. This review describes the chemistry of thiazole, the synthetic pathway of thiazole, and their biological activities that could benefit other researchers to design new molecules of thiazole derivatives with more potent biological activities.

Keywords: thiazole, chemistry, synthetic pathway, biological activities

Abstrak

Tiazol merupakan sebatian heterosiklik bergelang lima yang mempunyai atom sulfur dan nitrogen pada kedudukan masing-masing 1 dan 3 pada gelang tersebut. Sebatian ini, samada semulajadi atau sintetik banyak diaplikasikan dalam pelbagai bidang biologi. Di dalam kajian penghasilan ubatan baru, banyak terbitan baru sebatian tiazol dapat dicipta dengan menukarkan pelbagai penukarganti yang sesuai terhadap gelang tiazol tersebut supaya mempunyai potensi dalam aktiviti biologi. Di dalam kajian ini, kimia sebatian tiazol, laluan sintetik tiazol dan aplikasi sebagai bahan antibiologi dibincangkan. Diharap, ulasan ini dapat memberi manfaat kepada penyelidik yang ingin mengkaji dengan lebih mendalam potensi sebatian tiazol sebagai agen biologi.

Kata kunci: tiazol, kimia, laluan sintetik, aktiviti biologi

Introduction

The exploration of new compounds with multifunctional biological behaviour is an interest research area due to its cruciality and significance. Several inorganic [1], polymer [2], and organic compounds [3] were synthesised and the isolation of natural products [4] have been proved to possess biological activities. Among these compounds, the organic compound appears to be the most favourable in the biological field due to its facile synthesis methods [5] and a high percentage yield [6]. One of the main research areas that focuses on organic chemistry to develop an antimicrobial drug is the synthesis of heterocyclic compounds. Heterocyclic compound is a cyclic

compound with at least two different atoms as the members in the ring and has been extensively applied in medicinal and biological applications. For example, benzimidazole, pyrimidine and oxazole were claimed to possess antimicrobial [7], antifungal [8], anti-inflammatory as well as antitumor [9] properties.

Over the years, research on a small molecule of heterocyclic ring integrated with nitrogen and sulphur such as thiazole [10, 11] and triazole [12,13] have been extensively studied based due to their synthetic and biological applications. Thiazole is the most commonly reported compound in the literature. Thiazole is a 5-membered ring moiety containing nitrogen and sulphur at position 1 and 3, respectively. The structural pattern of thiazole derivatives as active compounds is predominantly focused on the substitution of hydrogen atoms with desired moieties at position 2, 4, 5 [14,15]. The derivatives were reported to demonstrate anti-inflammatory [14], antifungal [17], anticancer [14, 20], antibacterial [14, 16], anticonvulsant [19], antiviral [17], and antitumor [14, 20] activities. This has generated an urge to extend the study by synthesising new thiazole derivatives as potential candidates for drug discovery prospect.

Methods

The search for literature related to thiazole derivatives and their application in biological activities were retrieved from PUBMED, Science Direct, Scopus, Springer, and Google Scholar databases. The articles chosen for this study were articles published from 2009 to 2018 covering thiazole and its derivatives, synthesis, and applications.

Chemistry of thiazole

Thiazole employs both an electron-donating group (-S-) and an electron accepting group (C=N) and these create a stable heterocyclic compound [21]. Thiazole and its analogue such as oxazole are considered as an important group of heterocycles possessing several biological properties [22]. Thiazole compound is isomeric with an azole compound such as isothiazole that comprises similar atoms compound (nitrogen and sulphur) but at a different position. Thiazole is a clear pale-yellow liquid with a boiling point of 116 -118 ºC [17], soluble in alcohol and ether but moderately soluble in water [23]. The heterocyclic ring of thiazole contains a delocalisation of 6 π electrons corresponding to Huckel's rule from the lone pair electrons, which is the sulphur atom [24]. Figure 1 shows the resonance forms of thiazole **(1)**. Thiazole derivatives are desirable model compounds for chemistry study due to its planar and aromatic structure that exhibits larger π-electron delocalisation compared to oxazole [23].

The aromatic behaviour of the thiazole ring was verified using ^{1}H NMR spectroscopy whereby the chemical shift of the protons is spotted between 7.27 and 8.77 ppm [21]. The reactivity of the thiazole derivatives ring was strained due to the addition of different substituents at C-2, C-4, and C-5 positions, which could lead to further structural consideration [25]. For example, the effect of the methyl group (electron donating group) substituent was recognised when it was located at any position of the thiazole ring, leading to an increase in its basicity and nucleophilicity properties. However, the basicity and nucleophilicity reductions occur when a strong electron withdrawing group such as a nitro group was incorporated into the molecule [26, 27].

The molecular frame of thiazole is unique due to its versatile building blocks as bioactive compounds [28]. Several studies have reported that the thiazole ring is present in most natural and synthetic products with an extensive range of biological properties [29, 30]. One of the examples is vitamin B1 or known as thiamine involving thiazole moiety where it naturally supports the nervous system by connecting its role in acetylcholine synthesis [31]. Moreover, thiazole derivatives **(2)** that are shown in Figure 2 possessed amphiphilic character due to having both hydrophobic (lipophilic) and hydrophilic (lipophobic) parts. This property increases its potential to diffuse facilely into the cell membrane of bacteria for inhibition activity [32]. Compound with both hydrophilic and lipophilic sections is beneficial against both Gram-negative and Gram-positive bacteria [33] by breaking through the cell membrane of bacteria for an inhibition process. This penetration leads to cytoplasmic materials leakage, cell physiology disturbance, and apoptosis [34].

Synthetic approach of thiazole derivatives

The explorations of thiazole derivatives have emerged as an important topic throughout the years due to its various applications. The most appealing characteristic is the derivatives can be synthesised with a good yield from the starting material by a simple synthesis method [35]. The unique structure and significance of thiazole compounds have led to the expansion of methods by applying various conditions, catalysts, and approaches.

Hantzsch synthesis

The most notable method to synthesise thiazole is the Hantzsch thiazole synthesis [36, 37], which was invented in 1887 by a German chemist named Hantzsch. This method utilises the condensation reaction of α-haloketone with nucleophilic reagents such as thioamide, thiourea, ammonia thiocarbamate or dithiocarbamate derivatives [38,39]. Moreover, Hantzsch thiazole synthesis was suggested to be the most productive method for the synthesis of thiazole derivatives [40]. In this method, four thiazole derivatives were prepared by employing the Hantzsch reaction of thionicotinamide (**3**) with four types of α-haloketone namely chloroacetone (**5**), 3-chloroacetylacetone (**6**), 3-bromoacetylcoumarin (**7**), and p-chloroacetylacetanilide (**8**) in the presence of catalytic triethylamine (**4**). The reaction produced 2-(3-pyridyl) thiazole derivatives (**9**-**12**) as shown in Scheme 1.

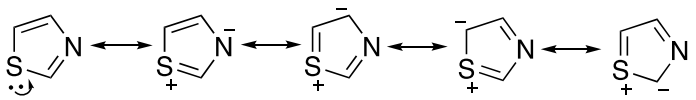
Several studies reported that this method has major drawbacks such as low percentage yields, harsh reaction condition, prolonged reaction time, and employs expensive catalysts [5, 41, 42, 43]. In contrast, it was reported by another researcher that this method gives high yields *via* dehalogenation of the haloketone during the reaction [44]. The nature of halide as a good leaving group has promoted the vacant site for a nucleophilic attack to furnish the reaction. The Hantzsch cyclisation method was proposed by synthesising thiazole derivatives, in which the tetrafluroethoxy moiety was directly attached to the carbon atom of the heterocyclic ring [45]. In their research, α-bromo-α-tetrafluoroethoxyacetophenone (**13**) was heated with thiobenzamide (**14**) at 60 °C in dioxine that led to the formation of 2,4-diphenyl-5-(1,1,2,2-tetrafluorethoxy)-thiazole (**15**) (Scheme 2). However, the percentage of yield is low (18-20%) due to the unstable thiobenzamide in an acidic medium.

Cook-Heilbron synthesis

In addition, thiazole ring can also be synthesised from α-aminonitriles or α-aminoamides and carbon disulfide as the reactants, known as Cook-Heilbron synthesis that is discovered by Cook and Heilbron [26]. The Cook-Heilbron method produced 5-aminothiazoles in which substitution occurred at position 2 by the reaction of aminonitrile with salt and esters of thioacids, carbon disulfide or isothiocyanates under mild conditions [46]. Scheme 3 depicts the reaction of α-aminonitriles (**16**) with carbon disulfide (**17**) to form 5-amino-2-mercapto-thiazole (**18**).

Gabriel synthesis

Another alternative of a synthetic approach to synthesise thiazole derivatives is Gabriel synthesis. This method focuses on the closure of the thiazole ring by reacting acylamino-ketone with phosphorus pentasulfide producing 2,5- disubstituted thiazole derivatives [47]. This study was promoted by Kotadiya [48] whereby the synthesis of the desired compound involved heating of acylamino compounds namely *N*-(2-oxopropyl) acetamide (**19**) with phosphorus pentasulfide (**20**) to produce 2,5-dimethylthiazole (**21**) as shown in Scheme 4.



1

Figure 1. Resonance forms of thiazole compound

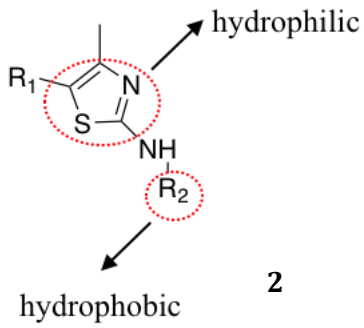
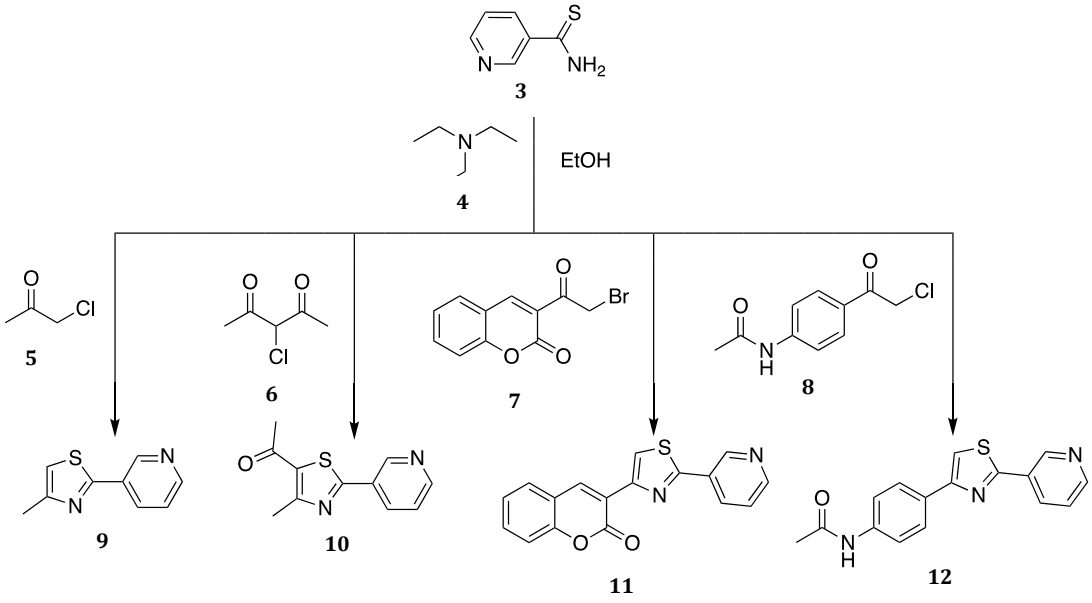
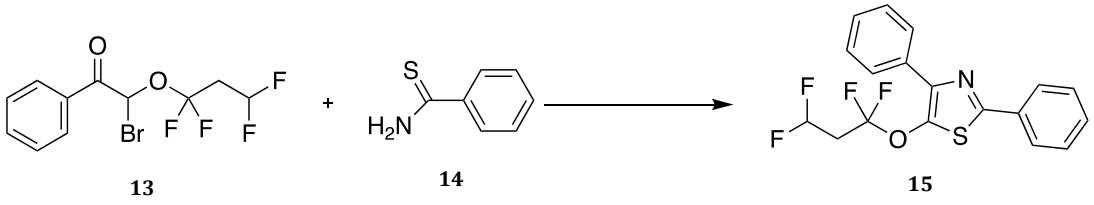


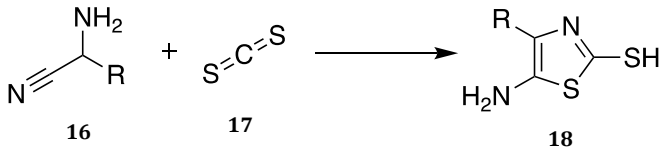
Figure 2. Structure of thiazole derivatives



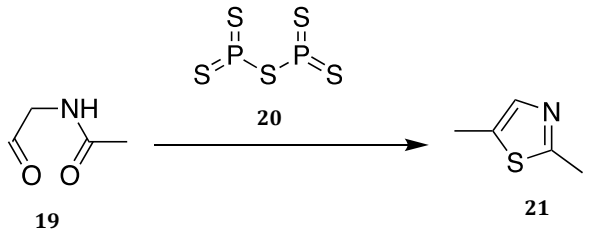
Scheme 1. Reaction synthesis of 2-(3-pyridyl) thiazole derivatives [40]



Scheme 2. Hantzsch type synthesis of 2,4-diphenyl-5-(1,1,2,2-tetrafluorethoxy)-thiazole



Scheme 3. The Cook-Heilbron thiazole synthesis [26]



Scheme 4. Synthesis of thiazole compound *via* Gabriel reaction [48]

However, Hantzsch cyclisation, Cook-Heilbron, and Gabriel synthesis methods have major drawbacks in terms of time consuming and unsatisfactory percentage yields. Hence, several studies have improved the method. For example, the synthesis of thiazole derivatives by occupying the chemoenzymatic organic reactions or known as an enzymatic synthesis of heterocyclic compounds were designed [49]. In the study, a medium condition of chemoenzymatic was applied in a one-pot multicomponent reaction. The reaction of the starting materials such as secondary amine (**22**), benzoyl isothiocyanate (**23**), and dimethyl acetylenedicarboxylate (**24**) was catalysed by α-amylase derived from *Aspergillus oryzae* in ethanol (Scheme 5).

Furthermore, the synthetic pathway improvement of thiazole synthesis coping with environmental-friendly and practical methods has been also investigated. The designation of *N*-substituted 2-aminothiazole analogue namely *N*-(4-phenyl-1,3-thiazol-2-yl)-benzamide (**30**) comprises two stages of reaction synthesis was developed [50] whereby phenylthiazole was reacted with benzoyl chloride with continuous stirring at room temperature. Scheme 6 displays the synthetic routes to synthesise the thiazole compound in ethanol with continuous heating and stirring for 8 hours.

A simple but potent synthetic route of thiazole derivatives is still under investigation and improvement. The prominent method should exert low energy consumption, less waste generated, high percentage yield, and involve a one-pot reaction.

Biological application of thiazole derivatives

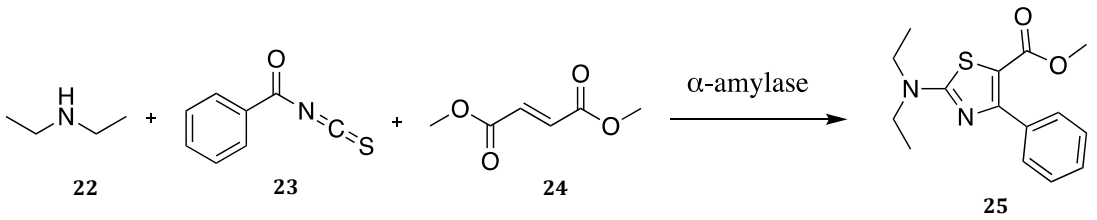
Thiazole derivatives have been comprehensively applied in the field of biology as well as pharmacology with a well-established ability in pharmaceutical drugs. They were reported to exhibit antimicrobial [51,53], antioxidant [52], anticancer [53], and antitubercular [53] behaviour. Thiazole compound namely bis-(4-phenylthiazol-2-yl) amine **(31)** and 1-(4-methyl-2-(2-(1-phenylethylidene) hydrazineyl)-4,5-dihydrothiazol-5-yl) ethenone **(32)** as shown in Figure 3 possess anti-inflammatory due to the presence of nitrogen and sulphur atoms in the molecules [53].

Besides that, a compound with thiazole as the core structure demonstrated an antioxidant agent [54]. The antioxidant properties of the synthesised thiazole derivatives (**33**, **34** and **35**) were evaluated using DPPH (1,1-diphenyl-2-picyrylhydrazyl) scavenging capacity test. The results showed that the DPPH radical inhibition for compound **33** and **34** were 18.73% and 15.62%, respectively. No antioxidant activity was seen from compound **35**, which could be due to the lack of several active atoms leading to a decrease in possible resonance in the structure. The chemical structures of compound **33**, **34,** and **35** are shown in Figure 4.

In another application, thiazole compounds have also been explored as a drug candidate for an antibacterial agent. The appearance of antibiotic (drug) resistance against bacterial strains has captivated outstanding concern in the discovery and development of a new suited antimicrobial drug. Since thiazole moiety is widely known in biological activity, investigations on thiazole derivatives as an antimicrobial agent have been vigorously conducted. Introduction of various substituents in the main molecular framework of thiazole showed optimistic result towards the tested bacterial strains [10]. A number of studies have been extensively performed to improve the chemical structures of thiazole derivatives for antimicrobial applications. In particular, trichlorophenyl thiazole compound exhibited considerable inhibitory effect against numerous Gram-positive and Gram-negative strains such as *Bacillus subtilis*, *Escherichia coli*, *Staphylococcus epidermidis*, *Staphylococcus aureus*, and *Pseudomonas fluorescens* [26].

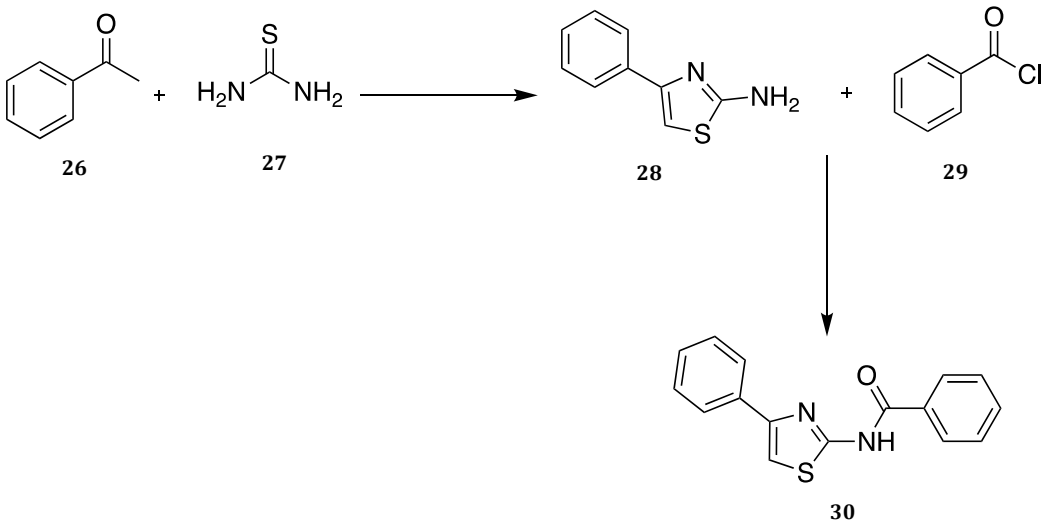
Prolongation synthesis of active antimicrobial agents resulted in a series of 2,4-disubstituted-1,3-thiazole derivatives (Figure 5) designation with identifiable *in-vitro* antimicrobial activities [55]. The synthesised analogues of **36** and **37** comprising nitro group at phenyl substituents exhibited active results towards *B. subtilis*, *S. aureus* and *E. coli* with MIC values of 3.92-4.01, 3.39-4.11 and 3.59-4.23 µM/mL, respectively compared to compound **38** with values of 4.51, 4.60 and 4.32 µM/mL, respectively. This is a result of the existence of nitro moiety at the para position, which makes a strong hydrogen bonding with the amino acid residue in the tested microorganisms. Therefore, it can be concluded that the thiazole ring with nitro at position 4 played crucial roles to inhibit microorganism activities as well as the optimisation of the substituent at the ring [26].

In another study, the -C=N spacer in the thiazole was reported to be the advantageous factor for the antifungal behaviour of the compounds [56]. The synthesised compounds of **39** and **40** (Figure 6) demonstrated high antifungal activity against *U. tritici* and *P. striiformis.*



22 **23** **24** **25**

Scheme 5. One-pot multicomponent synthesis of thiazole derivatives using derived enzyme [49]



Scheme 6. Synthesis of thiazole derivatives in two stages of reaction

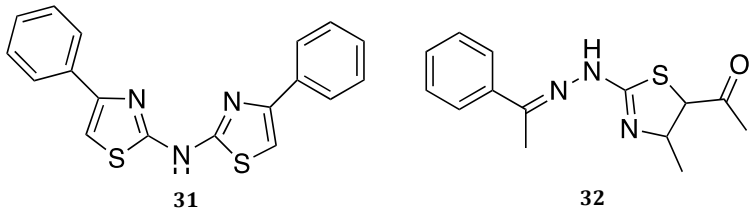


Figure 3. Chemical structures of 2-aminothiazole derivatives as an anti-inflammatory agent

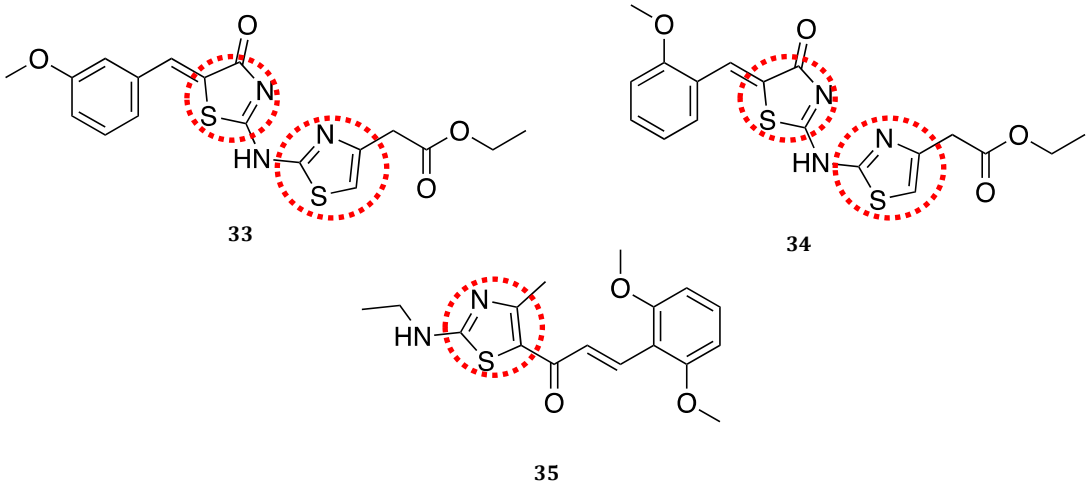


Figure 4. Chemical structures of thiazole derivatives possess antioxidant activities

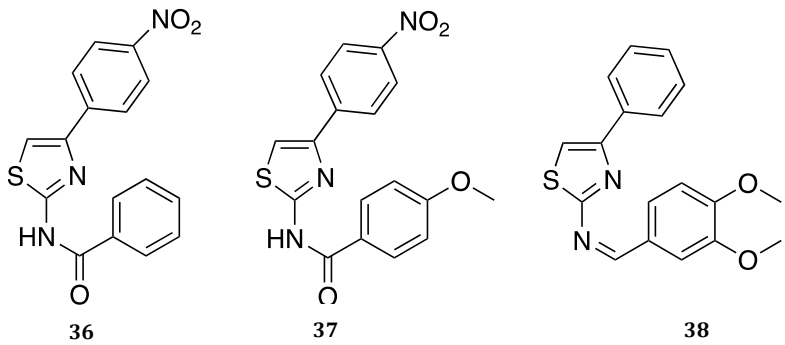


Figure 5. Series of 2,4-disubstituted thiazole derivatives as antimicrobial agents

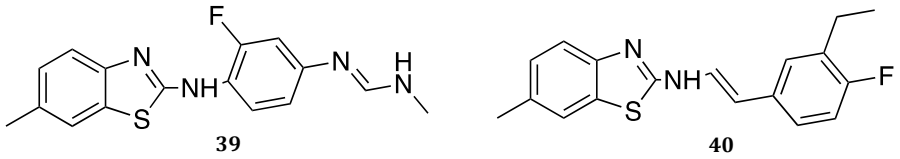


Figure 6. Chemical structures of fluorinated benzothiazole-2-yl-1,2,4-triazoles derivatives

Conclusion

In summary, there were numerous methods reported on the synthetic pathway of thiazole derivatives. A new practical method can be designed to synthesise thiazole derivatives with a high yield. In biological application, several new structures were designed and synthesised by modifying the substituent at thiazole ring with suitable substituent groups in order to improve the biological activities. Therefore, research on thiazole derivatives can be the focal point for future exploration due to its special attributes and potential.

Acknowledgement

We gratefully acknowledge grants from the Ministry of Education Malaysia FRGS14-15-0392 and the Department of Chemistry, Kulliyyah of Science, International Islamic University Malaysia (IIUM).

References

1. Ejideke, I. P. and Ajinade, P. A. (2015). Synthesis, characterization, antioxidant and antibacterial studies of some metal (ii) complexes of tetradentate schiff base ligand: (4E)-4-[(2{(E)-[1-(2,4-Dihydroxyphenyl)ethylidene] amino}imino]penta-2-one. *Bioinorganic Chemistry and Applications* 9: 1-9.
2. Gaballah, S. T., Khalil, A. M. and Rabie, S. T. (2018). Thiazole derivatives-functionalized polyvinyl chloride nanocomposites with photostability and antimicrobial properties. *Journal of Vinyl & Additive Technology*, 25(S1): 137-146.
3. Hussein, W. and Turan-Zitouni, G. (2018). Synthesis of new thiazole and thiazolyl derivatives of medicinal significant-a short review. *MOJ Bioorganic & Organic Chemistry*, 2(2): 52-55.
4. Davyt, D. and Serra, G. (2010). Thiazole and oxazole alkaloids: Isolation and synthesis. *Marine Drugs*, 8: 2755-2780.
5. Bodireddy, M. R., Mohinuddin, P. M. K., Gundala, T. R. and Reddy, G. (2016). Lactic acid-mediated tandem one-pot synthesis of 2-aminothiazole derivatives: A rapid, scalable and sustainable process. *Organic Chemistry* 2: 1-13.
6. Kołazcek, A., Fusiarz, I., Ławecka, J. and Branowska, D. (2014). Biological activity and synthesis of sulfonamide derivatives: A brief review. *Chemik Er Zeitung* 68(7): 620-628.

7. Alasmary, F. A. S., Snelling, A. M., Zain, E. M., Alafeefy, A. M., Awaad, A. S. and Karodia, N. 2015. Synthesis and evaluation of selected benzimidazole derivatives as potential antimicrobial agents. *Molecules,* 20: 15206-15223.
8. Shahi, M., Foroughifar, N. and Mobinikhaledi, A. (2015). Synthesis and antimicrobial activity of some tetrahydro quinolone diones and pyrano[2,3-d] pyrimidine derivatives. *Iranian Journal of Pharmaceutical Research,* 14(3): 757-763.
9. Das, D., Sikdar, P. and Bairagi, M. (2016). Recent developments of 2-aminothiazoles in medicinal chemistry. *European Journal of Medicinal Chemistry,* 109: 89-98.
10. Catalano, A., Carocci, A., Defrenza, I., Muraglia, M., Carrieri, A., Bambeke, F. V., Rosato, A., Corbo, F. and Franchini, C. (2013). 2-aminobenzothiazole derivatives: search for new antifungal agents. *European Journal of Medicinal Chemistry,* 64: 357-364.
11. Yurttaş, L., Özkay, Y., Gençer, H. K. and Acar, U. (2015). Synthesis of some new thiazole derivatives and their biological activity evaluation. *Journal of Chemistry,*10: 1-7.
12. Floros, M. C., Bortolatto, J. F., Oliveira, O. B., Salvador, S. L. S. and Narine, S. S. (2016). Antimicrobial activity of amphiphilic triazole-linked polymers derived from renewable sources. *ACS Biomaterials Science & Engineering,* 2(3): 336-343.
13. Hu, B., Zhao, H., Chen, Z., Xu, C., Zhao, J. and Zhao, W. (2018). Efficient synthesis and bioactivity of novel triazole derivatives. *Molecules,* 23(709): 1-14.
14. Al-Saadi, M. S., Faidallah, H. M. and Rostam, S. A. F. (2008). Synthesis and biological evaluation of some 2,4,5-trisubstituted thiazole derivatives as potential antimicrobial and anticancer agents. *Archiv der Pharmazie-Chemistry in Life Sciences,* 341: 424-434.
15. Zamigajlo, L. L., Vinnyk, A. O., Turov, O. V. and Kolos, N. M. (2013). A new approach to 2,4,5-trisubstituted thiazoles from ß-dicarbonylic compounds, arylglyoxals and thioamides. *Ukrainica Bioorganica Acta*, 1: 37-43.
16. El-Sayed, W. A., Abdel-Monem, Y. K., Yousif, N. M., Tawfek, N., Shaaban, M. T. and Abdel-Rahman, A. A. H. (2009). Antimicrobial activity of new 2,4-disubstituted thiazolidinone derivatives. *International Journal of Pharmacy and Pharmaceutical Sciences,* 64: 785-789.
17. Siddiqui, N., Arshad, M. F., Ahsan, W. and Alam, M. S. (2009). Thiazoles: A valuable insight into the recent advances and biological activities. *International Journal of Pharmaceutical Sciences and Drug Research,* 1(3): 136-143.
18. Hassan, F. A. (2012). Synthesis, characterization, anti-inflammatory and anti-oxidant activities of some new thiazole derivatives. *International Journal of Applied Science and Technology,* 2(7): 180-187.
19. Nalawade, A. M., Nalawade, R. A., Patange, S. M. and Tase, D. R. (2013). Thiazole containing Schiff base and their transition metal complexes. *International Journal of Engineering Science Invention,* 2(7):1-4.
20. Cai, W. X., Liu, A. L., Li, Z. M., Dong, W. L., Liu, X. H. and Sun, N. B. (2015). Synthesis and anticancer of novel thiazole-5-carboxamide derivatives. *Applied Sciences,* 6(8): 2-10.
21. Mishra, C. B., Kumari, S. and Tiwari, M. (2015). Thiazole: A promising heterocycle for the development of potent CNS active agents. *European Journal of Medicinal Chemistry,* 92: 1-34.
22. Ansari, A., Ali, A., Asif, M., Rauf, M. A. and Owais, M. S. (2018). Facile one-pot multicomponent synthesis and molecular docking studies of steroidal oxazole/thiazole derivatives with effective antimicrobial, antibiofilm and hemolytic properties. *Steroids,* 134: 22-36.
23. Gupta, V. and Kant, V. (2013). A review on biological activity of imidazole and thiazole moieties and their derivatives. *Science International,* 1: 253-260.
24. Khan, K. M., Qurban, S., Salar, U., Taha, M., Hussain, S., Perveen, S., Hameed, A., Ismail, N. H., Riaz, M. and Wadood, A. (2016). Synthesis, in vitro α-glucosidase inhibitory activity and molecular docking studies of new thiazole derivatives. *Bioorganic Chemistry,* 68: 245-258.

25. Abdel-Sattar, N. E. A., El-Naggar, A. M. and Abdel-Mottaleb, M. S. A. (2017). Novel thiazole derivatives of medicinal potential: Synthesis and modelling. *Journal of Chemistry*, 2017: 1-11.
26. Ayati, A., Emami, S., Asadipour, A., Shafiee, A. and Foroudi, A. (2015). Recent application of 1,3-thiazole core structure in the identification of new lead compounds and drug discovery. *European Journal of Medicinal Chemistry*, 97: 699-718.
27. Mallia, C. J., Englert, L., Walter, G. C. and Baxendale, I. R. (2015). Thiazole formation through a modified gewald reaction. *Beilstein Journal of Organic Chemistry*, 11: 875-883.
28. Weiß, K. M., Wei, S. and Tsogoeva, S. B. (2011). Novel one-pot process for the synthesis of 1,3-thiazoles via organocatalysed epoxidation of nitro-olefin. *Organic & Biomolecular Chemistry*, 9: 3457-3461.
29. Gupta, R., Fuloria, N. K. and Fuloria, S. (2012). Synthesis and antimicrobial activity evaluation of some schiff bases derived from 2-aminothiazole derivatives. *Indonesian Journal of Pharmacy*, 4(5): 2626-2630.
30. Sauer, A. C., Leal, J. G., Stefanello, S. T., Leite, M. T. B., Souza, M. B., Soares, F. A. A., Rodrigues, O. E. D. and Dornelles, L. (2017). Synthesis and antioxidant properties of organosulfur and organoselenium compounds derived from 5-substitued-1,3,4-oxadiazole/thiadiazole-2-thiols. *Tetrahedron Letters*, 58(1): 87-91.
31. Rouf, A. and Tanyeli, C. (2015). Bioactive thiazole and benzothiazole derivatives. *European Journal of Medicinal Chemistry*, 97: 911-927.
32. Sharshira, E. M. and Hamada, N. M. M. (2012). Synthesis, characterization and antimicrobial activities of some thiazole derivatives. *American Journal of Organic Chemistry* 2(3): 69-73.
33. Liu, C., Shan, B., Bai, H., Tang, J., Yan, L. and Ma, Y. (2015). Hydrophilic/hydrophobic characters of antimicrobial peptides derived from animals and their effects on multidrug resistant clinical isolates. *Zoological Research* 36(1): 41047.
34. Expósito, J. A. C. (2006). Studies on antimicrobial activity of arginine-based surfactants and chemo-enzymatic synthesis of novel amphiphiles based on l-arginine and d-fagomine. Dissertation Doctor of Philosophy. Universidad Autónoma De Barcelona Facultad De Química.
35. Grozav, A., Găină, L. I., Pileczki, V., Crisan, O., Silaghi-Dumitrescu, L., Therrien, B., Zaharia, V. and Berindan-Neagoe, I. (2014). The synthesis and antiproliferative activities of new arylidene-hydrazinyl-thiazole derivatives. *International Journal of Molecular Sciences*, 231(15): 22059-22072.
36. Dawane, B. S., Konda, S. G., Kamble, V. T., Chavan, S. A., Bhosale, R. B. and Basheer, S. M. (2010). Multicomponent one-pot synthesis of substituted hantzsch tiazole derivatives under solvent free conditions. *E-Journal of Chemistry* 6(S1): S358-S362.
37. Depti, V., Kumari, M. A., Harikrishna, N., Ramesh, G. and Rao, V. (2013). Synthesis of novel 2-amino thiazole derivatives. *Der Pharma Chemica*, 5(2):181-184.
38. Yu, Y., Chen, H., Wang, L., Chen, X. and Fu, B. (2009). A facile synthesis of 2,4-disubstituted thiazoles using MnO_2. *Molecules*, 14(12): 4858-4865.
39. Mickevičius, V., Voskienė, A., Jonuškienė, I., Kolosej, R., Šiugždaitė, J., Venskutonis, P. R., Kazernavičiūtė R., Brazienė, Z. and Jakienė, E. (2013). Synthesis and biological activity of 3-[phenyl(1,3-thiazol-2-yl)-amino] propanoic acids and their derivatives. *Molecules*, 18(12): 15000-15018.
40. Bondock, S., Naser, T. and Ammar, Y. A. (2013). Synthesis of some new 2-(3-pyridyl)-4,5-disubstituted thiazoles as potent antimicrobial agents. *European Journal of Medicinal Chemistry*, 62: 270-279.
41. Jain, K. S., Bariwal, J. B., Kathuravan, M. K., Raskar, V. K., Wankhede, G. S., Londhe, N. A. and Dighe, S. N. (2011). An efficient and rapid synthesis of 2-amino-4-arylthiazole employing microwave irradiation in water. *Green and Sustainable Chemistry*, 1: 36-40.
42. Mishra, D., Fatima, A., Rout, C. and Singh, R. (2015). An efficient one-pot synthesis of 2-aminothiazole derivatives. *Der Chemica Sinica*, 6(8): 14-18.

43. Zhou, W., Ni, S., Mei, H., Han, J. and Pan, Y. (2015). Cyclization reaction of *n*-allylbenzothioamide for direct construction of thiazole and thiazoline. *Tetrahedron Letters*, 56 (27): 4128-4130.
44. Joybari, M. R. S. and Hossaini, Z. (2016). Synthesis of thiazole derivatives *via* multicomponent reaction of tetramethyl thiourea using water as a safe solvent. *Journal of Applied Chemical Research*, 10(2): 7-12.
45. Sokolenko, T. M., Davydova, Y. A. and Yagupolskii, Y. L. (2012). Efficient synthesis of 50-fluoroalkoxythiazoles *via* a-bromo-a-fluoroalkoxyacetophenones hantzsch type cyclization with thioureas or thioamides. *Journal of Fluorine Chemistry*, 136: 20-25.
46. Frija, L. M. T., Pombeiroa, A. J. L. and Kopylovicha, M. N. (2016). Coordination chemistry of thiazole, isothiazoles and thiadiazoles. *Coordination Chemistry Reviews*, 308(1): 32-55.
47. Kumar, S. V., Parameshwarappa, G. and Ila, H. (2013). Synthesis of 2,4,5-trisubstituted thiazole *via* lawesson's reagent mediated chemoselective thionation-cyclization of functionalized enamides. *The Journal of Organic Chemistry*, 78(14): 7362-7369.
48. Kotadiya, M. (2017). Thiazoles: Past, present and future. *International Journal of Advancement in Engineering Technology, Management and Applied Science*, 4(1): 24-44.
49. Zheng, H., Mei, Y. J., Du, K., Cao, X. T. and Zhang, P. F. (2013). One-pot chemoenzymatic multicomponent synthesis of thiazole derivatives. *Molecules*, 18(11): 13425-13433.
50. Fatima, A., Kulkarni, R. and Mantipragada, B. (2015). Design and synthesis of *n*-substituted aminothiazole compounds as anti-inflammatory agents. *Der Pharma Chemica*, 7(3): 212-220.
51. Darwish, E. S., Fattah, A. M. A., Attaby, F. A. and Al-Shayea, O. N. (2014). Synthesis and antimicrobial evaluation of some novel thiazole, pyridone, pyrazole, chromene, hydrazone derivatives bearing a biologically active sulfonamide moiety. *International Journal of Molecular Sciences*, 15: 1237-1254.
52. Jha, A. K., Shukla, P. K., Soni, N. and Verma, A. (2015). Synthesis, characterization and biological evaluation of thiazole incorporated triazole compounds. *Scholars Research Library*, 7(1):67-74.
53. Khalifa, M. E. (2018). Recent developments and biological activities of 2-aminothiazole derivatives. *Journal of The Slovenian Chemical*, 65: 1-22.
54. Djukic, M., Fesatidou, M., Xenikakis, I., Geronikaki, A., Angelova, V. T., Savic, V., Pasic, M., Krilovic, B., Djukice, D., Gobeljika, B., Pavlicae, M., Djurica, A., Stanojevicf, I., Vojvodicf, D. and Saso, L. (2018). *In-Vitro* antioxidant activity of thiazolidinone derivatives of 1,3-thiazole and 1,3,4-thiadiazole. *Chemico-Biological Interactions*, 286(3): 119-131.
55. Arora, P., Narang, R., Bhatia, S., Nayak, S. K., Singh, S. K. and Narasimnhan, B. (2015). Synthesis, molecular docking and QSAR studies of 2,4-disubstituted thiazole as antimicrobial agents. *Journal of Applied Pharmaceutical Science*, 5(2): 28-42.
56. Sidhu, A. and Kukreja, S. (2015). Synthesis of novel fluorinated benzothiazol-2-yl-1,2,4-triazoles: molecular docking, antifungal evaluation and *in silico* evaluation for SAR. *Arabian Journal of Chemistry*, 12(8): 2118-2127.

Malaysian Journal of Analytical Sciences (MJAS)
Published by Malaysian Analytical Sciences Society

VOLTAMMETRIC TECHNIQUE FOR DETERMINATION OF ARSENIC RESIDUES IN CALCIUM CARBIDE RIPENED CLIMACTERIC FRUITS

(Teknik Voltammetrik bagi Penentuan Sisa Arsenik dalam Pematangan Buah Klimakterik Menggunakan Kalsium Karbida)

Nurasmat Mohd Shukri[1], Noor Zuhartini Md Muslim[1]*, Nur Fazeera Kamal[1], Faizuan Abdullah[2]

[1]*School of Health Sciences,*
Universiti Sains Malaysia, 16150 Kubang Kerian, Kelantan, Malaysia
[2]*Department of Chemistry, Faculty of Science,*
Universiti Teknologi Malaysia, 81310 Johor Bahru, Malaysia

**Corresponding author: zuhartini@usm.my*

Received: 13 December 2020; Accepted: 9 February 2021; Published: 25 April 2021

Abstract

Calcium carbide (CaC_2) often being used as one of the fruit ripening agents due to cheaper cost and readily available in the market. However, it is not recommended to use CaC_2 in Malaysia, because the arsenic (As) residues which present as impurities in this fruit ripening agents can cause serious adverse effect to human consumption. Voltammetric measurement using a gold electrode in acidic medium (2 M HCl) was developed to determine the As residues in the fruit samples. This technique observed the electrochemical behaviour and quantitative analysis of the As(V) species at the gold electrode. It was found that As(V) undergone irreversible oxidation process at the gold electrode. The working parameters validated for differential pulse anodic stripping voltammetry (DPASV) were E_i = -0.20 V, E_f = +0.30 V, v = 0.02 V/s, E_{acc1} = -1.10 V, t_{acc1} = 120 s, E_{acc2} = +0.04V, t_{acc2} = 10 s and pulse amplitude = 0.05 V which produced peak potential at +0.10 V. The LOD and LOQ using statistical method were 1.3 ppb and 4 ppb, respectively. While by visual observation were 0.7 ppb and 2 ppb, respectively. The method successfully applied for the estimation of As residue in fruit ripening that was used CaC_2 as a ripening agent and also As(V) in fruits bought from local market. Therefore, the developed voltammetry method can be a great potential instrument to measure As(V) in fruit sample.

Keywords: differential pulse anodic stripping voltammetry, gold electrode, arsenic, calcium carbide, climacteric fruits

Abstrak

Kalsium karbida (CaC_2) sering digunakan sebagai salah satu agen pematangan buah kerana harganya yang lebih murah dan mudah didapati di pasaran. Walau bagaimanapun, tidak digalakkan menggunakan CaC_2 di Malaysia, kerana sisa arsenik (As) yang hadir sebagai kekotoran pada agen pematangan buah ini boleh menyebabkan kesan buruk yang serius terhadap penggunaan manusia. Pengukuran voltammetrik menggunakan elektrod emas dalam medium berasid (2 M HCl) dikembangkan untuk menentukan sisa As dalam sampel buah. Teknik ini memerhatikan tingkah laku elektrokimia analisis kuantitatif spesies As(V) pada elektrod emas. Didapati bahawa As(V) menjalani proses pengoksidaan yang tidak berbalik pada elektrod emas. Parameter kerja yang disahkan untuk voltammetri denyut pembeza pelucutan anodik (DPASV) adalah E_i = -0.20 V, E_f = +0.30 V, v = 0.02 V/s, E_{acc1} = -1.10 V, t_{acc1} = 120 s, E_{acc2} = +0.04V, t_{acc2} = 10 s dan nadi amplitud = 0.05 V yang menghasilkan potensi puncak pada +0.10 V. LOD dan

LOQ menggunakan kaedah statistik masing-masing adalah 1.3 ppb dan 4 ppb, sementara dengan pemerhatian visual masing-masing 0.7 ppb dan 2 ppb. Kaedah ini berjaya digunakan untuk perkiraan sisa As dalam pematangan buah yang mengunakan CaC_2 sebagai agen pematangan dan As(V) pada buah-buahan yang dibeli di pasar tempatan. Oleh itu, kaedah voltammetri yang dikembangkan dapat menjadi instrumen berpotensi besar untuk mengukur As(V) dalam sampel buah.

Kata kunci: voltammetri denyut pembeza pelucutan anodik, elektrod emas, arsenik, kalsium karbida, buah klimaterik

Introduction

The ripening of fruits after storage has shown many commercial advantages since it effectively lengthens the season fruits may be kept without the need to undergo canning processes [1]. Fruits generally store better if they are picked before they are mature. The ripening process will soften the cell wall substances and digest the starch and other constituents of the fruit, making the ripe fruit subject to bruising and effective medium for fungal growth [2]. The transportation of the unripe fruit can be handled easier as fruits that are green and firmer so the injury can be reduced as compared to ripe fruits [3].

According to Prasanna et al. [3], ripe fruit cannot be kept as well as green fruits due to the digestion and chemical transformation occurred at a high rate in ripe fruits. Thus, unripe fruits are preferable to be stored as to lengthen the period of availability and get to regulate the supply in the market. Therefore, the use of artificial fruit ripening agents has become prevalent mostly due to the commercial purposes of unripen fruit. Artificial ripening agent is used for fruits supply in the market to make it available for the customer during off-season [1].

Nowadays, several artificial ripening agents are available and used, such as calcium carbide, ethylene gas, carbon monoxide, potassium sulphate, ethephon, potassium dihydrogen orthophosphate, putrisein, oxytocin and protoporphyrinogen [4]. They are used during pre-harvest, post-harvest, transportation, capping and storage [4]. They accelerate fruits for ripening and inducing colour changes in unripe fruits. However, artificial fruit ripening is considered as a matter of concern because of various health-related issues [5]. There are direct and indirect health hazards associated with artificial ripening agents and their impurities.

One of the artificial ripeners that are far more concerned in this research is calcium carbide (CaC_2). Calcium carbide is a chemical compound which is used in the production of acetylene and calcium cyanamide [6]. It is also produced industrially in an electric arc furnace from a mixture of lime and coke at an extreme temperature which generally had around 80% of CaC_2 by weight [7].

Calcium carbide has been used extensively in Asian countries for fruits ripening [8]. The extensive use of this chemical is due to its low price and availability [5]. In Malaysia, for example, it can easily purchase from rural shops for RM5.50/kg [9]. The dose recommended for CaC_2 to be applied onto fruits is about 0.3-10 g for each kilogram of yields [8]. However, not all farmers obey to this recommended level because of the higher amount of CaC_2 is required to wholly ripened the fruits.

The CaC_2 content of the product is assessed by measuring the amount of acetylene produced during hydrolysis. Calcium carbide not only changed the skin colour of the fruits, but it also initiates the enzymatic action that breaks down the glucose resulting in a quick ripening of the fruits [10]. Use of CaC_2 sometimes gives ripening colour to raw fruit. It also increases the shelf life and maintains the ripened colour [10].

Calcium carbide leave behind residues of heavy metals like arsenic (As) and phosphorus on the fruit surface, which are potentially carcinogenic. Arsine gas released from CaC_2 combines with oxygen and other elements to form inorganic arsenic compounds [11]. As a rule, inorganic arsenic exhibit more significant toxicity than organic arsenicals. Intentional or unintentional ingestion of As can lead to serious health issues or sometimes can be vital. Since the commercial CaC_2 contains As and phosphorus as impurities, concurrently the detected As residues in the ripened fruits can be used as a tool to identify fruits ripened by using carbide gas. However, it

is not recommended to used CaC_2 in Malaysia as this artificial ripening agent can cause severe adverse effect to human consumption. Some of the imported artificial ripened fruit went through the border of Malaysia and sold to the local market. The information on the detection and determination of As residue in CaC_2 ripened fruit can therefore serve as an indicator for the presence of CaC_2 used in artificial fruit ripening in the local market.

Thus, the present study is carried out to detect the As residues from the CaC_2 ripened fruits using voltammetry of the electrochemical technique. The use of electrochemical techniques is of considerable importance in analytical techniques due to their high degree of sensitivity, accuracy, precision, and selectivity as well as large linear dynamic range, with relatively low-cost instrumentation [12, 13]. The stripping voltammetry technique involves two main steps. The first step is a controlled potential electrolysis enough to deposit the analyte on the electrode. The second step consists of the application of a voltage scan to the electrode that causes an electrolytic dissolution [14]. The observation from this study can be used as an indicator that the local or imported fruit trader has utilized the CaC_2 for their fruits ripening. The result from this study is compared with the limit of total arsenic proposed by Food Regulations of 1985 and FDA/WHO which is not more than one ppm.

Materials and Methods

Apparatus, materials and reagent

A VA 797 Computrace Metrohm Voltammetric Analyser interfaced with multi-mode electrode stand model 663 VA (Metrohm) was used for all voltammetric measurements, composed of a stationary gold working electrode, an Ag/AgCl (KCl 3 M) as a reference electrode, platinum as the auxiliary electrode, a purge tube for purging (nitrogen) and stirring the solution during the deposition step. The software used to control the whole system, and the acquisition and processing of the data was VA Computrace software (Metrohm) installed in a computer.

Reagents were of pro-analysis grade (Merck or R&M chemicals) and deionized water (18.2 MΩ cm resistivity) by Sartorius Atrium pro DI ultrapure water system. All the glassware's were cleaned by soaking in 10% nitric acid (HNO_3) and rinsed thoroughly using deionized water prior to use. 0.1 M of sodium hydroxide (NaOH) solution was prepared by dissolving 40 mg of NaOH pellet with deionized water. 0.5 M sulphuric acid (H_2SO_4) was prepared from H_2SO_4 solution diluted with deionized water. 3 mL of concentrated HCl (37% w/w) added with deionized water into 10 mL of the volumetric flask to get a total concentration of 2 M HCl.

The 1000 ppm As(V) stock solution was commercially available and bought from Agilent technologies. The solution was stored at room temperature. The required working and standard solutions of 10 ppm, 1 ppm, and 50 ppb of As(V) were prepared daily by diluting the stock solutions with deionized water.

Voltammetric techniques: Electrode pre-treatment

The electrode must be kept in 0.1 M NaOH when not in used or at least 30 minutes for cleaning purposes. Then, it was rinsed thoroughly with ethanol and deionized water alternatively and electrochemically activated. The gold electrode must be electrochemically conditioned in order to obtain reproducible curves for each determination. This step should be done every day before starting the measurements and when the background current varies enormously from measurement to measurement.

The electrochemical activation of the electrode surface carried out by cyclic voltammetry with 0.5 M H_2SO_4 as supporting electrolyte. The electrode was polarized between 0 to +1.5 V at 0.1 V/s by applying 10 cycles. Linear potential sweep CV was performed daily to monitor the electrode surface electrochemical activation, and this conditioning must be performed several times if the background was still not consistent yet.

Electrochemical behaviour of As

The electrochemical behaviour of As was studied using cyclic voltammetry experiment in an electrochemical cell to ascertain the peak potential for As element in the fruit sample. 0.4 mL of 1 ppm of As(V) standard solution was spiked using micropipette into a

voltammetric cell with supporting electrolyte, 2 M of HCl. The resulting concentration of the stock solution in the cell was 20 ppb of As(V) standard. The CV was performed by scanning from anodic direction and then switched to the cathodic direction. The instrument parameters used for the analysis of arsenic were sweep rate of 0.1 V/s with initial purge time of 200 s, start potential and second vertex potential, +0.5 V, switch potential or first vertex potential, -0.3 V at voltage step of 0.018 V.

Determination of As(V) by differential pulse anodic stripping voltammetry

All solutions (samples and standards) were prepared to a final volume of 20 mL, starting the analysis with the blank solution. The blank corresponded to 2 M HCl and was purged for two minutes with nitrogen gas. The determination was carried out in 10 mL of sample or standards added with 3 mL of concentrated HCl dilute to 10 mL total volume to obtain 2 M HCl in the solution.

In the validation of the chemical conditions, the standard addition method was employed for the determination of As(V). The aliquots of the reagents or known concentration of standards were spiked manually to the blank in the cell and purge of two minutes was used. Each scan has undergone triplicate measurement to ensure that the peak current was constant.

The DPASV procedure was employed by starting the determination of As(V) standard with the purging of the solution with purified nitrogen gas for 300 s to avoid contamination with oxygen. The electrode was pre-treated with cleaning potential of -1.10 V for 120 s and deposition potential at +0.04 V for 10 s, with an equilibration time of 5 s after stirring. The gold electrode scanned in the anodic direction from -0.2 V to +0.3 V with differential pulses at a speed rate of 0.02 V/s, a potential step of 6 mV and an amplitude of 50 mV. The working method parameters were adjusted from recommended parameters given in the operating instruction manual of the instrument or application bulletin 226/2e [15].

Validation

In order to confirm if the method was suitable for this analysis, a validation was required for observing the overall performances of the developed method. Different validation methods were employed to ensure that the results obtained were accurate and reliable for the intended use. The validation method involved precision, linearity range response, the limit of detection (LOD), the limit of quantification (LOQ) and the accuracy [16].

The precision and sensitivity of the instrument responses were evaluated from six independent measurements of As(V) standard. 20 mL of 2 M HCl were analyzed before and after five additions of 0.4 mL of 50 ppb As(V) standard solution. The precision was calculated as the relative standard deviation (RSD) of the total of six measurements for each addition. The linear range of response was examined based on calibration curves exploring a range of As(V) concentrations between 1 to 5 ppb.

LOD and LOQ were determined for analyte concentration giving a signal to the blank solution, yB, plus three or ten standard deviations of the blank, respectively [17]. In addition to the statistical methods for accessing LOD and LOQ, another practical approach on determining the LOD and LOQ of the ASV method was through visual evaluation of the produced output. This method involved by diluting 4 ppb initial concentration of As(V) with 1.7 mL of 2 M HCl (supporting electrolyte) until the minimum detectable level. In contrast, LOQ is calculated as three times the LOD value.

The recovery test to evaluate the accuracy of the method was performed by using spiked sample added with As(V) concentration of 10 ppb and 20 ppb. For each spiked sample at different concentrations, the analyte concentration was obtained in triplicate measurement to calculate the mean concentration.

Fruits samples analysis

Four uniforms, mature green but unripe mangoes were randomly procured from the private compound around Health Campus of Universiti Sains Malaysia and brought to the analytical laboratory for experimentation. Nine samples believed to be ripened mangoes also procured from the local fruit market in Kota Bharu and Kubang Kerian, Kelantan to compare and authenticate the results for the presence of arsenic residues in traditionally ripened fruits. Besides, for detection of As residues in randomly chosen fruits, there were two sets of fruits; local fruits and imported fruits were collected. The origin of the fruits was known based on the seller information or displayed on the price label.

Meanwhile, a hand of banana was bought from the local market, and only one finger was used for each treatment. Three sets of bananas were also purchased from two different fruit markets where each group contained four fingers of banana. Only two fingers of banana from each batch were analyzed for As(V) detection. One set of bananas was from a local orchard, and another two bunches of bananas were imported from other countries. The fruits that need to undergo treatment with CaC_2 were washed with water to remove the latex and left dried until no moisture was visible on the fruit surfaces. The fruits were then packed into a container and kept at room temperature for further treatment. Commercial grade CaC_2 was bought from an online store to be used as the ripening agent.

Treatments of fruits using calcium carbide

The extent of residues of As present on the mango fruit ripened by using CaC_2 was determined on the fruit surface only. For conducting these studies, the harvested fruits were ripened by using commercial grade CaC_2 in the form of solution and powdered sachet. Calcium carbide was crushed into small pieces and weighed using analytical weighing balance. Each fruit was subjected to three levels of CaC_2 treatment as followed: 2% solution, 5 and 10 g CaC_2 per average of 230 g fruit to induce ripening. T_1 being the controls (without CaC_2) as per following treatment schedule (Table 1).

These treatments of fruit using CaC_2 were adapted from a study done by Chandel et al. [11]. The fruit from each treatment was labelled into eight respective samples, where M1, M2, M3 and M4 referred to mangoes while B1, B2, B3, and B4 were for bananas. Each of the fruit was washed using distilled water, and the resultant wash water was introduced into glass bottles, which then appropriately labelled and preserved in a refrigerator at 15°C for other sample digestion process.

Sample preparation for wet digestion

For estimation of As(V) on the fruit surface, the fruit of each treatment was washed in 0.5 L of deionized water by allowing it to dip for one hour. The fruit surface then washed thoroughly to collect all the adhering residues in the wash water which later used for estimation of As residues on the fruit surface.

Wet digestion method

The wet digestion method was modified from the standard analytical method established by AOAC [18] to meet the sample requirement. 10 mL of washed water of the fruit was placed into the Erlenmeyer flask. 5 mL of H_2SO_4 and 5 mL of HNO_3 were added in the Erlenmeyer flask and were allowed to digest the sample fluid. The sample was then heated gently on a hot plate at low temperature for the destruction of organic matter. The Erlenmeyer flask was covered with a watch glass to avoid massive loss due to evaporation of the solution.

Heating was continued until the liquid appear darkened in color. Further, HNO_3 was added in small proportions and heated to fuming for 20 to 30 minutes until the solution failed to dim. When the organic matters were merely oxidized, the solution was allowed to cool. Then, the solution was boiled gently to fuming after addition of 10 mL of deionized water. Finally, the digest was cooled at ambient temperature and made to a known volume of 50 mL by using deionized water. The digested sample was transferred into a capillary tube, and aliquots of digest sample were taken for determination of As residues by using voltammetric analysis.

Voltammetric determination of washed water fruit samples

Differential pulse anodic stripping voltammetry (DPASV) was carried out by adding 10 mL of digested

sample into an electrochemical cell containing 10 mL of 2 M HCl solution. The peak for As(V) was appeared after adding 0.1 mL of 1 ppm As(V) standard solution into the voltammetry cell.

The amounts of As residues in washed water were calculated according to the obtained regression equation derived from the calibration curve from the analysis of the sample. The 10 mL sample introduced into the 20 mL of the volumetric cell only represented one part out of 50 mL of total wash water of fruit samples. The total concentration of As residues in the sample were calculated as following Equation 1:

10 mL of fruit wash water contains arsenic = X ppb

$$50 \text{ mL of fruit wash water contain arsenic} = \frac{X \times 50 \text{ mL}}{10 \text{ mL}} = 5X \text{ ppb} \quad (1)$$

Table 1. Treatments schedule for ripening of fruits

Treatment No.	Details
T1	The fruit was allowed ripening naturally without using CaC_2. The fruit was placed inside a plastic container and allowed to ripen at ambient temperature (30-37°C).
T2	The fruit was dipped in 2% CaC_2 solution (10 g/ 0.5 litres water) and kept for 1 hour. After the treatment, the fruit was removed from the solution and air-dried to remove adhering moisture. The treated fruits were then placed in a plastic container and allowed to ripen at ambient temperature (30-37°C).
T3	Fruit ripened by using 5 g of CaC_2 sachet placed in a single layer. Fruit packed in a plastic container to which the sachet made up from 5 g of powdered CaC_2 weighted and put inside a folded paper. The fruit left in the closed box was kept at ambient temperature (30-37°C) to allow the fruit to ripen.
T4	Fruit ripened by using 10 g of CaC_2 sachet placed inside a closed plastic container. Total of 10 g CaC_2 sachet placed in two layers to which 5 g per layer of powdered CaC_2 was put inside folded paper (below and above the fruit). The container after closing was kept at ambient temperature (30-37°C) to allow the fruit to ripen.

Results and Discussion

Treatments of the gold electrode surface

In electroanalytical procedures with solid electrodes, it is necessary to employ pre-treatment or activation steps. This pre-treatment step is essential to maintain the electrode surface reproducibility and applicable state for the electrochemical measurement [19]. As claimed by other researchers [20, 21] quality and reproducibility of the As(V) signal were improved after a proper electrode conditioning was done. The voltammograms in Figure 1 obtained from cyclic voltammetry during electrochemical activation and polarization in 0.5 M H_2SO_4 as supporting electrolyte (Figure 1(a)) was used for daily monitoring of the electrode surface. A gradually decreased peak height was observed if the gold electrode surface was still unsatisfactory clean.

In order to identify the reproducible state of the gold electrode for each determination, particular voltammogram was obtained as in Figure 1 (a), also known to several works which referred them as clean gold electrode surface [21, 22, 23]. The electrode was scanned in positive direction giving anodic peak formation at +1.30 V. A constant anodic peak formed after several repeated cycles were due to the oxidation of gold electrode.

The nature of species that adhered on the gold surface during oxidation is not known. However, some of the authors suggested that the peak formation on the surface is from the presence of monolayer of oxides or hydrated oxides (Au_2O_3/Au couple) [22, 23]. A monolayer of oxide was utterly formed at about +1.5 V corresponding to this potential.

Figure 1 (b) shows the cyclic voltammogram when the electrode was not cleaned adequately after several analyses of samples were completed. The presence of additional peaks; anodic peak at +1.15 V and cathodic peak at +0.80 V probably due to the electrochemistry of the gold electrode. Gold can exist in different oxidation states (Au^0, Au^I and Au^{III}); thus, it could form into multilayers of oxides which caused the formation of the additional peak. According to Burke et al. [24], the presence of these multilayer oxides could reduce the electrode performance and might affect the As signal in subsequent determination.

The electrode needs to be sufficiently soaked into 0.1 M of NaOH for at least 30 minutes and alternately rinsed with ethanol and water before chemically activated. It was mentioned by Giacomino et al. [21] that the sequence of cleaning processes has its function on cleaning the deposited layer to improve the electrode performance. The researchers believed that complete or in part hydration layer of the gold surface might be replaced by forming a layer of hydroxides with the presence of NaOH. Ethanol was utilized to remove the electrode's surface covered with hydroxides and solubility of ethanol with water able to removes traces of ethanol at the gold surfaces [21]. After proper cleaning processes, cyclic voltammogram in Figure 1(a) was able to be retrieved.

Figure 1(c) shows the development of cyclic voltammogram that appeared to be relatively different with the Figure 1(a) as there was no peak of oxidation and decreased in the current charge for reduction peak of the gold electrode. The electrode also started at a slow sweep rate over the potential. Giacomino et al. [21] claimed that the possibility of this outcome might come from the formation of many layers of oxides (passivating layer) on the electrode surface which causes the electron transfer to be inefficient and reduce the analyte deposition on the electrode. The gold electrode should be polished with aluminum oxide if rinsing with NaOH and ethanol as well, because electrochemically conditioning has no longer provide satisfactory results [15].

Determination of As(V) standard using voltammetry

To investigate the suitable parameters that supported the instrument conditions, a few test runs were conducted. The position of the purging tube for nitrogen flows should be placed near the auxiliary electrode to minimize the gas bubbles adhered to the auxiliary electrode during determination. Deaeration with nitrogen was necessary for the removal of the oxygen to reduce the background due to oxygen reduction for about 200 s or 300 s, working respectively with CV or differential pulse (DP).

In the determination of As using a gold electrode, supporting electrolyte serves as a medium used to maintain the migration of ions in solution by electrons transfer from the electrode to the analyte [25]. With regard that As(V) characteristic has traditionally been observed as poorly electroactive in alkaline, neutral or acidic media, many studies have successfully demonstrated the excellent ability of As(V) in reaction with a high concentration of acid [15, 26]. HCl is the most suitable and widely used supporting electrolyte in which able to avoid the formation of hydrolyzed species during stripping step of As [27]. The presence of chloride acts as a bridge that reacts with arsenic to form $AsCl_3$, which can be indicated based on the positive shift of peak potential and As signal was observed as the digested sample added concurrently increased resistant in migration of ions.

Although in the bulletin of Metrohm [15] has recommended the usage of concentrated HCl as supporting electrolyte, this study has proved 2 M HCl was enough to provide well-defined As(V) signal in ASV determination. This parameter was supported by previous studies which employed 2 M of HCl in their studies [28]. Thus, higher concentrations of HCl was not necessarily in this study because it offered a similar sensitivity to detect the signal of As metal and able to

minimize the amount of acidic waste generated. This phenomenon explained that at this concentration of acid, it could provide good sensitivity and narrow arsenic peaks which indicated the fast charge-transfer reaction occurred in 2 M HCl supporting electrolyte.

Cyclic voltammetry studies for As(V) standard

Cyclic voltammetry analysis usually employed to acquire qualitative information about electrochemical reactions. In this study, CV analysis of 20 ppb As(V) standard at gold electrode offers a rapid location of redox potentials of this species and convenient evaluation of the effects of 2 M HCl as the supporting electrolyte upon the redox process. Five cycles of repetitive CV were carried out to obtain the information of As(V) electrochemical behavior by scanning in anodic direction and switch in cathodic order to measure the current resulting from the applied potential.

In acidic medium, the redox process of As(V) possessed one well-defined oxidation peak potential at +0.15 V, as shown in Figure 2. There was also anodic current at a positive potential more than +0.5 V and large cathodic current at negative potentials than -0.1 V. According to Wei and Somasundaran [29], the large cathodic current at the negative potential was believed to cause by hydrogen development or possibly arsine gas.

As(III) was easily oxidized to As(V) which is electro inactive except in an extreme condition of high acid concentration or at very negative potentials like -1.20 V [30]. No cathodic peak for As(V) reduction was observed, which suggested that it was irreversible at the gold electrode. This result supported by Giacomino et al. [21] finding where As(V) has not reduced back to As(III) in the reverse scan.

From this information, the electrochemical behaviour of As(V) at cyclic voltammetry was known and noted. Subsequent analysis on As(V) determination using DPASV was then employed. Any anodic peak presence around the potential +0.15 V could be recognized as peak potential for As(V) and needed to confirm by addition of As(V) standard using DPASV.

Validation of the differential pulse anodic stripping voltammetry method in As(V) analysis

The validation of the DPASV method for analysis of As(V) was evaluated based on the precision, linearity, LOD, LOQ and accuracy by recovery test [16].

Precision and linearity

Figure 3 shows the voltammogram for As(V) which indicated that the measurements had good repeatability. The six analyses for each concentration; 1, 2, 3, 4, and 5 ppb of As(V) standard obtained RSD values of 9.23%, 6.11%, 3.59%, 3.41% and 2.46%, respectively. The RSD value of less than 10% believed to give good precision, as mentioned by Taşdemir [31].

Dependence of peak current (in terms of peak height) on the concentration of As(V) was studied using DPASV method. Inset in Figure 3 illustrates the calibration curve for the standard addition of As(V) using DPASV on rotating gold electrode up to five standard addition. The results showed that the anodic peak current has a linear relationship with the concentration in the range of 1 to 5 ppb. The regression equation is: Ip (µA) =0.2225 [As(V)] + 0.0524 having the R^2 value of 0.9983, which close to 1 signified that the model fitted the data obtained.

Limit of detection and limit of quantification

Based on the Miller and Miller [17] approach, the limit of detection (LOD) and limit of quantification (LOQ) were calculated to be 1.3 ppb and 4 ppb, respectively. The LOD obtained was in good agreement with that reported on validation for As(V) determination by Garlaschelli et al. [16]. Another approach on the determination of LOD by visual detection was taken to confirm the lowest peak signal could be detected. Table 2 records the previous studies that focused on detecting As(III) and As(V) in different types of samples by using gold-based electrode which applied different voltammetric techniques. The previous studies obtained different LOD and LOQ values of 0.08 – 0.7 µg/L and 0.5- 0.93 µg/L, respectively [30, 32-37].

In this study, by visually observed the voltammogram, undetectable peak illustrated at 0.5 ppb. Having the initial concentration of 4 ppb of As(V), 1.7 mL of supporting electrolyte added for each dilution addition giving the particular final concentration of As(V). The LOD from visual determination showed significantly lower LOD by the minimum detectable peak present at 0.7 ppb While; the LOQ was three times the LOD by means; the LOQ was 2 ppb [16, 17, 38]. This data indicated that by practical, the DPASV method using gold as electrode could be considered one of the sensitive methods for detecting As species in climacteric fruit as the lower values of LOD and LOQ produced.

Accuracy

The accuracy of the determination was investigated based on the recovery tests of the spiked sample on a randomly selected sample at two different concentrations (10 ppb and 20 ppb). The actual amount of As(V) in the sample was calculated by using the regression equation derived from the calibration curve and was subtracted with the original amount in the sample before spiked. The percentage recoveries for As(V) spiked at a concentration of 10 ppb, and 20 ppb were 101.43 ± 0.84% and 98.12 ± 0.24%, respectively. The per cent showed high accuracy of recovery, and these values fall within an acceptable range of the standard per cent recovery between 70 to 120% [39].

Fruit samples analysis: Physical characteristic of fruit treated using calcium carbide

Fruit naturally ripens on trees and fruit harvested when green (let to ripe) has quite different physicochemical changes between them. From the previous study, artificial ripening agent (CaC_2) could affect the ripening process [40]. Physical changes of fruit ripened with different treatment of CaC_2 are recorded in Table 3 for mango (M1-M4) and banana (B1-B4) samples.

In brief, a total of four mangoes of the same type (apple mango) and banana (*Rastali*) were treated using different amounts of CaC_2 which were kept to ripe for five and three days, respectively. Color development is a vital maturity index of many fruits and associated with ripening [41]. By day five, all the mangoes were ripened shown by color changes from green to yellow.

Sample M1 was let to be naturally ripened without any CaC_2 added in the closed container. Observation of sample labelled as M1 showed that there were slight changes in surface color, but the green color was still prominent. Hence, the pulp of M1 was still raw. This observation indicated that for naturally ripened mango, a longer time (more than five days) was needed for the fruit to be fully matured.

Calcium carbide, when mixed with water, will produce acetylene gas and generates heat which fastened the ripening process. The uniformity of surface color was distinguishable for CaC_2 sachet and CaC_2 dip treatment. For instances, M2 showed uniform yellow color distribution on the surface as compared to M3 and M4, where there was a part of the fruit surface did not turn color to yellow. The reasons behind this phenomenon might happen because the heat from CaC_2 solution was able to cover the total surface area of the fruit when dipped. Meanwhile, for sample M3 and M4, the convection of hot gas spreading upwards; thus, the upper position of fruits was observed to be ripened faster than the bottom part.

For banana samples, all the samples changed color from green to yellow within three days. There was not much difference of ripening time for banana either it was naturally ripened or treated with CaC_2. It was also difficult to differentiate between uniformity of color changes for all the samples. Somehow, CaC_2 ripened banana was subjected to bruising and darker patches and black spots and eventually presence on the surface of banana as seen in Table 3.

In addition to the color changes, it was observed that the application of CaC_2 to the fruit accelerates senescence of the fruit and the fruit become rotten faster. Moisture from the product of CaC_2 reacted with water to promote the formation of fungi or black molds on the fruit surface. Thus, the CaC_2 ripened fruit ripened faster but did not have a longer shelf life as compared to naturally ripened fruit. It is worth mentioning that it is essential to choose healthy fruit and the proper cutting technique of the fruit for the sake of this experiment. For example, to avoid fungus formed on the fruit before the experiment, banana needs to cut right at the stalk away from the

upper finger, so the pulp was not exposed to the surrounding.

After visual observations of the fruit samples were recorded, the fruit wash water was subjected to perform acid digestion. The digested wash water sample was used for subsequent analysis of As determination using DPASV method.

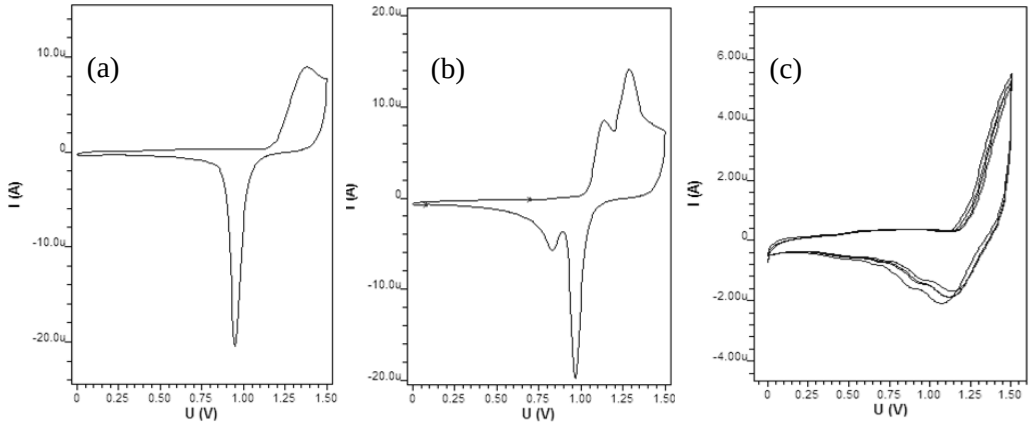


Figure 1. Voltammograms of electrochemical behavior for gold electrode by cyclic voltammetry in 0.5 M H_2SO_4; (a) clean surface, (b) presence of multilayer of oxides at the surface and (c) the passivating layer covered the electrode surface

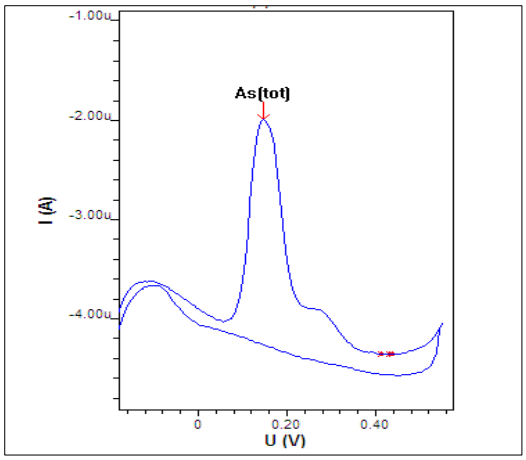


Figure 2. Cyclic voltammogram of 20 ppb As(V) in 2 M HCl at a sweep rate of 0.018 V/s

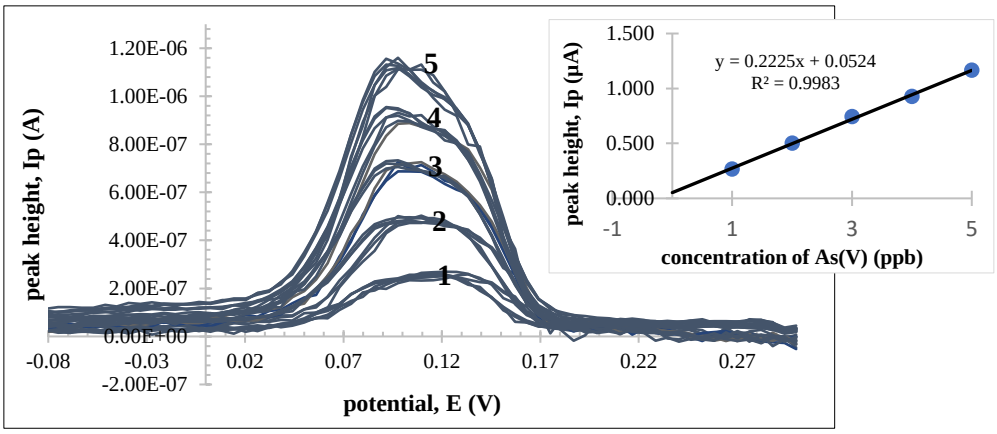


Figure 3. DPASV voltammogram and linear curve of Ip against concentration of As(V) standard additions: 0.4 mL of As(V) 50 ppb in 2 M HCl at **1**: first addition, **2**: second addition, **3**: third addition, **4**: fourth addition and **5**: fifth addition (n = 6)

Table 2. Previous studies on detection of As species in different kind of samples using gold based electrodes with different voltametric techniques

Electrode/Substrate	**As Species**	**Sample type**	**Technique(s)**	**LOD (µg/L)**	**LOQ (µg/L)**	**Reference**
gold-disk electrode	As(III)	Natural waters and biomaterials	DPASV, Linear sweep anodic stripping voltammetry (LS ASV)	0.15	0.5	[32]
gold microelectrode	As(III) As(V)	Sea water	Square wave anodic stripping voltammetry (SW ASV)	0.3	1.0	[30]
gold nanowires	As(III) As(V)	River water	ASV	0.08	0.24	[33]
GC, modified gold-Pt nanoparticles	As(III)	Natural waters	LS ASV	0.20	0.93	[34]
GC, modified with gold film	As(III) As(V)	Drinking water and Natural water	ASV	0.55	1.7	[35]

Table 2 (cont'd). Previous studies on detection of As species in different kind of samples using gold based electrodes with different voltametric techniques

Electrode/Substrate	As Species	Sample type	Technique(s)	LOD (µg/L)	LOQ (µg/L)	Reference
gold microelectrode	As(III) As(V)	Drinking water and groundwater	SW ASV	0.39	13.0	[36]
gold electrode	As(III)	Environmental waters	ASV	0.7	2.54	[37]

Table 3. Physical changes of climacteric fruits before and after treated with CaC_2

Sample	Before Treatment	After Five Days of Treatment	Treatment No.	Sample	Before Treatment	After Three Days of Treatment
M1			T1: Without CaC_2	B1		
M2			T2: Dipping in 2% CaC_2 solution	B2		
M3			T3: 5g of CaC_2 sachet	B3		
M4			T4: 10g of CaC_2 sachet	B4		

Voltammetry determination of washed water fruit samples

The data related to the residual arsenic presence on mango surface by applying different treatments of ripening fruits using CaC_2 are presented in Table 4. After five days of treatment with CaC_2, the ripened mango fruits were analyzed to detect the presence of As residues. The residual effect on the fruit surface was determined by analyzing the digested wash water of the fruits. 10 mL of wash water sample was added with 10 mL of HCl (supporting electrolyte) and taken for interpretation to represent the digested sample. Total As on fruit surface was calculated by multiplying the dilution factor of five with the represented sample concentration. Amount of As by weight in 500 mL of wash water was also calculated in Table 4.

From the data above, the average value of the total concentration of As residues in mangoes ripened by different treatments of CaC_2 varied from 6.5 to 10.32 ppb. The peak of As in voltammogram for fruit matured without using CaC_2 (T1) was not detected, it might

indicate that there was no As presence or perhaps the arsenic content was too small to be detected. Among the treatments, mangoes ripened by dipping in 2% CaC_2 solution (T2) recorded the maximum average value of total As residues in fruit surface which was 10.32 ppb followed by the fruits ripened by fruits ripened in 10 g of CaC_2 solution (T4) that gave a concentration of 8.89 ppb.

The lowest total average value of fruit treated with CaC_2 was observed in fruit ripened by using the lowest concentration of CaC_2, which was 5 g CaC_2 sachet (T3) that found to be 6.5 ppb. The data showed that higher As residues found in mangoes that dipped into CaC_2 solution as compared to sachet. It was believed that As residues were transferred to the fruit surface, which had the most contact with the CaC_2 solution.

For all market samples that were analyzed as in Table 5, the range concentration of As residues in fruit surface was between 4.42 to 10.81 ppb. Sample MS1, MS2, MS3 and MS5 did not show visual peak detected using DPASV. However, having the assumption of no As presence in the mango sample could not be deduced as the sample peak might be lowered than the LOD of As determination (0.7 ppb). Thus, this study considered the presumption of the minute amount of As that might be presented but could not be detected using DPASV in the mango sample. Further, the level of As residues found in the market sample was compared to other methods of CaC_2 ripening. Presence of high level of As residues in the market sample than the CaC_2 treated fruit indicated that traders use a much higher level of CaC_2 for the maturation of the mangoes.

The highest concentration of As residues found in mango fruits collected from the market was MS6 with a value of 10.81 ppb indicated that mangoes are ripened by traders using a very high concentration of CaC_2, for example, more than 10 g CaC_2 sachet or the traders might dip it into more than 2% of CaC_2 solution (10 g/ 0.5 L). Market sample for MS4, MS7 and MS8 showed the total concentration As residue presence at the fruit surface with 9.87, 6.96 and 7.27 ppb, respectively. From this data, it could be estimated that fruit traders utilized some amount of CaC_2 as their fruit ripening agent for instances more than 5 to 10 g of CaC_2 sachet for sample MS4, MS7 and MS8. While the lowest concentration of As found in the local market was MS9 with a concentration of 4.42 ppb.

Among the mango samples bought at the market, it showed that most of the imported mangoes had detected the presence of As except for MS5. This observation implied that imported mangoes had utilized the application of CaC_2 in their fruit ripening process. A harsh condition during road transportation and long hour of the journey might cause deterioration to the fruit. In contrast, green ripened mangoes using CaC_2 during the transport and reached the market was fully matured and ready to be sold [3]. On the other hand, As in local mangoes (MS1, MS2 and MS3) was not detected. The application of CaC_2 on local mangoes was seemed unpopular, as the local fruit sellers preferred to let their fruit ripened naturally or they used other fruit ripening method.

The same treatment of CaC_2 application on mango was done for banana samples. The ripened bananas were analyzed for the presence of As(V) residues after three days of treatment with CaC_2 using the DPASV. The results of the residual arsenic from different treatments of ripening fruits using CaC_2 present on banana fruit are presented in Table 6.

Among the different ripening treatments using CaC_2, the most As residues amount recorded on the banana surface in 500 mL of wash water was sample B4 (9.96 ppb of As concentration) which undergone T1, followed by T2 for sample B3 which As concentration obtained was 7.16 ppb and sample B4 (6.10 ppb of As) for T3. Similar treatment with mango (T1), no peak of As(V) presence for sample B1 was detected as well. Hence, the treatment on control fruit without CaC_2 which absence of arsenic residues in comparison with fruits ripened with CaC_2 suggested that As(V) detected might exist as impurities in commercial CaC_2.

The results for the highest As residues found on the banana surface was contradictory with the mango sample as 10 g of CaC_2 sachet measured as the highest amount of As found at the fruit surface than dipping in

CaC_2 solution. Chandel et al. [11] believed that the As present in CaC_2 solution settles down at the bottom because of the properties of As which has a molecular weight (74.92 g/mol) heavier than water (18 g/mol) [11]. Besides, the size of container used to dip the fruit might correspond to this result, as the larger surface area of the box which spread the As at the bottom of the container and caused the lesser surface area of the fruit in contact with the As. Hence, the fruit dipped in CaC_2 solution has less transfer of As on to the surface of the banana.

Furthermore, as mentioned in the literature, arsine gas released when the CaC_2 reacts with water and combined with oxygen to form inorganic arsenic [11]. With the molecular weight of arsine gas (77.95 g/mol) higher than average dry air (28.97 g/mol), the As released from the sachet settles at the bottom layer of air in the container and kept covered to the fullest of fruit surface area for five days treatment, unlike when dipped in the CaC_2 solution, where the probability of contact reduces when the banana was only treated for one hour before being removed and kept in the container. Plus, during the mixture with water, most of the arsine gas had evaporated thus lesser As residues in fruits ripened by using CaC_2 solution.

For all banana samples bought from the market, there was no peak could be detected using DPASV. The inference of these results probably due to the concentration of As residues were smaller than the LOD concentration, or there might be no CaC_2 used by the trader to ripen the banana. Perhaps, the traders used another method of ripening such as smoke in the ethylene gas chamber, methyl jasmonate or ethephon, which proven by another study not to contain arsenic residues [4].

It is worth noting that, voltammetry analysis on different fruit parts such as peel and pulp of the fruit were not successfully being measured as there was broad peak interfered which masked the arsenic peak so it cannot be detected. This phenomenon happened due to voltammetry determination is sensitive towards the organic matter. The matrix effect from the organic matter has interfered the deposition of the analyte of interest at the gold electrode.

Table 4. Concentration of As residues found on the surface of mangoes by different treatments of CaC_2 application

Treatments	**Samples No.**	**Average As Residues in Mango's Wash Water ± SD (ppb)**	
		Represented Sample Concentration, X (10 mL)	**Total Concentration, 5X (50 mL)**
T1: without CaC_2	M1	ND	ND
T2: dipping in 2% CaC_2 solution	M2	2.06 ± 0.12	10.32 ± 0.62
T3: 5 g of CaC_2 sachet	M3	1.30 ± 0.08	6.50 ± 0.25
T4: 10 g of CaC_2 sachet	M4	1.78 ± 0.05	8.89 ± 0.38

* ND refers to no peak detected; (n = 3)

Table 5. Concentration of As residues detected on the surface of mango bought at the market

Market Samples No.	Average Residual Arsenic in Mango's Wash Water ± SD (ppb)	
	Represented Sample Concentration (10 mL)	Total Concentration (50 mL)
MS1	ND	ND
MS2	ND	ND
MS3	ND	ND
MS4	1.97 ± 0.08	9.87 ± 0.38
MS5	ND	ND
MS6	2.16 ± 0.05	10.81 ± 0.25
MS7	1.39 ± 0.11	6.96 ± 0.53
MS8	1.45 ± 0.06	7.27 ± 0.32
MS9	0.88 ± 0.02	4.42 ± 0.09

* ND refers to no peak detected; (n = 3)

Table 6. Concentration of arsenic residues found at the fruit surface of bananas by different treatments of CaC_2 application

Treatments	Samples No.	Average Residual Arsenic in Bananas' Wash Water ± SD (ppb)	
		Represented Sample Concentration (10 mL)	Total Concentration (50 mL)
T1: without CaC_2	B1	ND	ND
T2: dipping in 2% CaC_2 solution	B2	1.43 ± 0.02	7.16 ± 0.11
T3: 5 g of CaC_2 sachet	B3	1.22 ±0.07	6.10 ± 0.34
T4: 10 g of CaC_2 sachet	B4	1.99 ± 0.05	9.96 ± 0.26

* ND refers to no peak detected; (n = 3)

Conclusion

CV and DPASV method of electrochemical behaviour and quantitative determination of As(V) standards and samples have been successfully studied in this research. The electrode pre-treatment was required to be employed every day before any electrochemical measurement of As(V) standard and fruit samples (mango and banana), to maintain the gold electrode surface reproducibility and appropriate state. The CV analysis of 20 ppb As(V) standard at gold electrode proved that in acidic medium (2 M HCl), redox process of As(V) has irreversible nature which possessed one oxidation peak potential at +0.15 V.

Physical changes of fruit ripened using CaC_2 was also recorded and compared between fruits of different CaC_2 treatment. The fruits surface color changed from green to yellow upon ripening. It was observed that fruits with CaC_2 ripened faster and have a shorter shelf life. The DPASV technique for As(V) in fruit wash water samples has been successfully applied after sample preparation in wet acid digestion.

Based on the observation of determination of As(V) on different treatments of CaC_2 using DPASV, the presence of As(V) in the samples could be used as an indicator for application of CaC_2 in fruit ripening. The concentration of As in fruit for different treatments of CaC_2 could be used to estimate the amount of CaC_2 applied on the sample bought from the market. The concentration of As(V) found in fruit purchased from the market (range between 4.42 to 10.81 ppb) below the maximum limit of As level in Food Act 1983 and FDA/WHO which is 1 ppm.

Acknowledgement

The authors greatly appreciate the instrumental and financial supports received from School of Health Sciences, Universiti Sains Malaysia (USM).

References

1. Islam, Md. N., Imtiaz, M. Y., Alam, S. S., Nowshad, F., Shadman, S. A. and Khan, M. S. (2018). Artificial ripening on banana (Musa Spp.) samples: Analyzing ripening agents and change in nutritional parameters Yildizlez, F., (Ed.). *Cogent Food & Agriculture*, 4: 1–16.
2. Bouzayen, M., Latché, A., Nath, P. and Pech, J.C. (2010). Mechanism of fruit ripening. In: Pua, E.C. And Davey, M.R., (Eds.) Plant developmental biology - biotechnological perspectives. Springer Berlin Heidelberg. Berlin, Heidelberg: pp. 319-339.
3. Prasanna, V., Prabha, T. N. and Tharanathan, R. N. (2007). Fruit ripening phenomena–an overview. *Critical Reviews in Food Science and Nutrition*, 47: 1-19.
4. Dhembare, A.J. (2013). Bitter truth about fruit with reference to artificial ripener. *Archives of Applied Science Research*, 5: 45-54.
5. Siddiqui, W. and Dhua, R. S. (2010). Eating artificially ripened fruits is harmful. *Current Science*, 99: 1664-1668.
6. Mondal, P., Balo Majumder, C. and Mohanty, B. (2007). Removal of trivalent arsenic (As(III)) from contaminated water by calcium chloride ($CaCl_2$)-impregnated rice husk carbon. *Industrial & Engineering Chemistry Research*, 46: 2550-2557.
7. Kjuus, H., Andersen, A. and Langard, S. (1986). Incidence of cancer among workers producing calcium carbide. *Occupational and Environmental Medicine*, 43: 237-242.
8. Rohani, M., (1999). Proses pemasakan dan penyahhijauan. In: pengendalian lepas tuai buah-buahan dan sayur-sayuran tropika. Institut Penyelidikan dan Kemajuan Pertanian Malaysia (Mardi): pp. 70-76.
9. Consumers Association of Penang (2011). Ban the Use of Carbide Gas to Ripen Fruits. Access from http://www.consumer.org.my/index.php/food/safety/502-ban-the-use-of-carbide-gas-to-ripen-fruits.
10. Ur-Rahman, A., Chowdhury, F. R. and Alam, M. B. (2008). Artificial ripening: What we are eating. *Journal of Medicine*, 9(1): 42-44.
11. Chandel, R., Sharma, P. C. and Gupta, A. (2018). Method for detection and removal of arsenic residues in calcium carbide ripened mangoes. *Journal of Food Processing and Preservation*, 42: 1-6.
12. Benhadria, N., Attar, T. and Messaoudi, B. (2020). Understanding the link between the detection limit and the energy stability of two quercetin–antimony complexes by means of conceptual DFT. *South African Journal of Chemical*, 73: 120-124.
13. Behadria, N., Messaoudi, B. and Attar, T. (2020). The study of the correlation between the detection limit and the energy stability of two antimony complexes by means of conceptual DFT. *Malaysian Journal of Chemistry*, 22: 111-120.
14. Attar, T., Messaoudi, B. and Benhadria, N. (2020). DFT theoretical study of some thiosemicarbazide derivatives with copper. *Chemistry & Chemical Technology*, 14: 20-25.
15. Metrohm, (2019). Determination of arsenic by stripping voltammetry at the rotating gold electrode. https://www.metrohm.com/sv-se/applications/ab-226 [Accessed online 16 April 2019].
16. Miller, J. N. and Miller, J. C. (2000). Statistics and chemometrics for analytical chemistry. 4th Edition, Pearson Education.

17. Garlaschelli, F., Alberti, G., Fiol, N. and Villaescusa, I. (2017) Application of anodic stripping voltammetry to assess sorption performance of an industrial waste entrapped in alginate beads to remove As(V). *Arabian Journal of Chemistry*, 10: 1014-1021.
18. Association of Official Analytical Chemists (1990). AOAC: Official Methods of Analysis (Volume 1). In: *Official Methods of Analysis of The Association Of Official Analytical Chemists*. Association of Official Analytical Chemists, Inc, Virginia, USA: pp. 1-771.
19. Izumi, T., Yokohama, Y. and Watanabe, I. (1991). Activation of a gold electrode by electrochemical oxidation-reduction pretreatment in hydrochloric acid. *Journal of Electroanalytical Chemistry and Interfacial Electrochemistry*, 303: 151-160.
20. Fischer, L. M., Tenje, M., Heiskanen, A., Masuda, N., Castillo, J., Bentien, J., Emneus, J., Jakobsen M. H. and Boisen, A. (2009). Gold cleaning methods for electrochemical detection applications. *Microelectronic Engineering*, 86: 1282-1285.
21. Giacomino, A., Abollino, A., Lazzara M., Malandrino, M. and Mentasti, E. (2011). Determination of As(III) by anodic stripping voltammetry using a lateral gold electrode: Experimental conditions, electron transfer and monitoring of electrode surface. *Talanta*, 83: 1428-1435.
22. Susteric, M. G., Almeida, N. V., Von Mengershausen, A. E. and Esquenoni, S. M. (2012). Hydrogen oxidation on gold electrode in sulphuric acid solution. *International Journal of Hydrogen Energy*, 37: 14747-14752.
23. Zhang, W., Bas, A.D., Ghali, E. and Choi, Y., (2015). Passive behavior of gold in sulfuric acid medium. *Transactions of Nonferrous Metals Society of China*, 25: 2037-2046.
24. Burke, L. D., Moran, J. M. and Nugent, P. F. (2003). Cyclic voltammetry responses of metastable gold electrodes in aqueous media. *Journal of Solid State Electrochemistry*, 7: 529-538.
25. Elgrishi, N., Rountree, K. J., McCharty, B. D., Rountree, Eisenhart, T. S. and Dempsey, J. R. (2018). A practical beginner's guide to cyclic voltammetry. *Journal of Chemical Education*, 95: 197-206.
26. Yilmaz, S., Baba, B., Baba, A., Yagmur, S. and Citak, M. (2009). Direct quantitative determination of total arsenic in natural hotwaters by anodic stripping voltammetry at the rotating lateral gold electrode. *Current Analytical Chemistry*, 5: 29-34.
27. Cavicchioli, A., La-Scalea, M. A. and Gutz, I. G. R. (2004). Analysis and speciation of traces of arsenic in environmental, food and industrial samples by voltammetry: A review. *Electroanalysis*, 16: 697-711.
28. United State Environmental Protection Agency (1996). Arsenic in aqueous samples and extracts by anodic stripping voltammetry: pp. 1-9.
29. Wei, Z. and Somasundaran, P. (2004). Cyclic voltammetric study of arsenic reduction and oxidation in hydrochloric acid using a Pt RDE. *Journal of Applied Electrochemistry*, 34: 241-244.
30. Salaün, P., Planer-Friedrich, B. and Van Den Berg, C. M. G. (2007). Inorganic arsenic speciation in water and seawater by anodic stripping voltammetry with a gold microelectrode. *Analytica Chimica Acta*, 585: 312-322.
31. Taşdemir, İ. H. (2014). Electrochemistry and determination of cefdinir by voltammetric and computational approaches. *Journal of Food and Drug Analysis*, 22: 527-536.
32. Kopanica, M. and Novotný, L. (1998). Determination of traces of arsenic(III) by anodic stripping voltammetry in solutions, natural waters and biological material. *Analytica Chimica Acta*, 368(3): 211-218.
33. Mardegan, A., Scopece, P., Ugo, P. and Moretto, L. M. (2015). Ensembles of gold nanowires for the anodic stripping voltammetric determination of inorganic arsenic. *Journal of Nanoscience and Nanotechnology*, 15(5): 3417–3422.
34. Bu, L., Liu, J., Xie, Q. and Yao, S. (2015). Anodic stripping voltammetric analysis of trace arsenic(III) enhanced by mild hydrogen-evolution at a bimetallic Au-Pt nanoparticle modified glassy carbon electrode. *Electrochemistry Communications*, 59: 28-31.

35. Jedryczko, D., Pohl, P. and Welna, M. (2016). Inorganic arsenic speciation in natural mineral drinking waters by flow-through anodic stripping chronopotentiometry. *Talanta*, 150: 265-271.
36. Zhou, C., Yang, M., Li, S. S., Jiang, T. J., Liu, J. H., Huang, X. J. and Chen, X. (2017). Electrochemically etched gold wire microelectrode for the determination of inorganic arsenic. *Electrochimica Acta*, 231: 238-246.
37. Tupiti, W., Chandra, S. and Prasad, S. (2018). Sensitive inorganic arsenic speciation on a voltammetric platform in environmental water samples. *Microchemical Journal*, 139: 301-305.
38. Caseiro, A. Bauer, H., Schmidl, C., Pio, C. A. and Puxbaum, H. (2009). Wood burning impact on PM_{10} in three Austrian regions. *Atmospheric Environment*, 43: 2186-2195.
39. Unsworth, J. (2010). Guidance on residue analytical methods. Access from http://agrochemicals.iupac.org/.
40. Noor Shaeda, I., Irniza, R., Sarva, M. P. and Emilia, Z.A. (2018). Calcium carbide (CaC_2) exposure from fruit ripening process and health effects among fruit farmers: A research review. *International Journal of Public Health and Clinical Sciences*, 5: 91-101.
41. Asif, M. (2012). Physico-chemical properties and toxic effect of fruit-ripening agent calcium carbide. *Annals of Tropical Medicine and Public Health*, 5: 150-156.

Malaysian Journal of Analytical Sciences (MJAS)
Published by Malaysian Analytical Sciences Society

POLYMELAMINE/GOLD NANOPARTICLE-MODIFIED CARBON PASTE ELECTRODE AS VOLTAMMETRIC SENSOR OF URIC ACID

(Elektrod Pes Carbon Terubahsuai Polimelamin/Partikel Nano Emas sebagai Sensor Voltametrik bagi Asid Urik)

Muji Harsini[1]*, Erna Fitriany[1,2], Ainy Nur Farida[1], Dianita Suryaningrum[1], Dimas Noor Asy'ari[1], Bernadeta Ayu Widyaningrum[1], Denok. Rizky Ayu Paramita[3], Afaf Baktir[1], Fredy Kurniawan[4]

[1]Department of Chemistry, Faculty of Science and Technology, Universitas Airlangga, Surabaya, Indonesia
[2]Akademi Farmasi Mitra Sehat Mandiri, Sidoarjo, Indonesia
[3]Akademi Farmasi Jember, Jember, Indonesia
[4]Department of Chemistry, Faculty of Natural Science, Institut Teknologi Sepuluh Nopember, Surabaya, Indonesia

**Corresponding author: muji-h@fst.unair.ac.id*

Received: 25 December 2020; Accepted: 25 February 2021; Published: 25 April 2021

Abstract

Uric acid (UA), a vital biological substance, should be accurately detected in clinical monitoring and diagnosis. An electrochemical sensor was developed for UA determination based on polymelamine/gold nanoparticle-modified carbon paste electrode (AuNPs/PM/CPE). Carbon paste electrode (CPE) was made by mixing carbon and paraffin powder at a ratio of 7:3. PM/CPE was made using 1 mM melamine electropolymerisation in 0.1 M NaOH solution on the CPE surface with the cyclic voltammetry (CV) technique with a potential range of 0 to +1.6 V, and a scan rate of 100 mV/s. AuNPs/PM/CPE electrodes were made using Au electrodeposition on the PM/CPE surface using a 1 mM $HAuCl_4$ solution containing 0.1 M Na_2SO_4. Electrodeposition was performed by CV in the potential range of -0.6 to +1.5 V, with a scan rate of 50 mV/s. The electrocatalytic activity towards UA was systematically studied by CV techniques on the surface of CPE, PM/CPE, AuNPs/CPE, and AuNPs/PM/CPE in phosphate-buffered solution (PBS) at pH 7 with the potential of 0 V to + 1 V, and a scan rate of 100 mV/s. The effect of pH and the analysis of real samples using baby urine that had been diluted and spiked with UA were also studied. The results for bare CPE, and AuNPs/PM/CPE showed a 5-fold increase in anodic peak currents for UA. The optimum conditions were pH 5 (PBS 0.1 M) with the scan rate of 100 mV/s. Under this optimised condition, the modified electrode demonstrated high catalytic activity of UA oxidation. The differential pulse voltammetry (DPV) technique was used for quantitative analysis. The performance of AuNPs/PM/CPE electrodes has a linearity range, detection limit, sensitivity, precision, and accuracy of 0.1-11 µM, 0.0647 µM, 7.8592 µA/µM, 0.1107-0.3930%, and 82.45-107.23%, respectively. The results of the UA analysis in the baby urine show that the recovery of the disposed sample was 99.41 ± 0.06%, indicating that these electrodes have good accuracy.

Keywords: voltammetry, uric acid, polymelamine, gold nanoparticles, modified carbon electrode

Abstrak

Asid urik (UA), bahan biologi penting, mesti dikesan dengan tepat dalam pemantauan dan diagnosis klinikal. Penderia elektrokimia telah dibangunkan untuk pengesanan UA berdasarkan elektrod pes karbon terubahsuai nano partikel emas/polimelamin (AuNPs/PM/CPE). Elektrod pes karbon (CPE) disediakan dengan mencampurkan karbon dan serbuk parafin pada nisbah 7:3. PM/PCE dihasilkan menggunakan 1 mM elektropolimerisasi melamin dalam larutan 0.1 M NaOH pada permukaan CPE melalui teknik voltametri berkitar (CV) pada julat potensi 0 hingga +1.6 V dan kadar imbasan 100 mV/s. Elektrod AuNPs/PM/CPE dihasilkan menggunakan pengelektroendapan Au pada permukaan PM/CFE menggunakan larutan 1 mM $HAuCl_4$ yang mengandungi 0.1 M Na_2SO_4. Pengelektroendapan dilakukan menggunakan CV dalam julat potensi −0.6 hingga +1.5 V, dengan kadar imbasan 50 mV/s. Aktiviti elektropemangkinan UA dikaji secara sistematik menggunakan teknik CV pada permukaan CPE, PM/CPE, AuNPs/CPE, dan AuNPs/PM/CPE dalam larutan penimbal fosfat (PBS) pada pH 7 dengan julat potensi 0 hingga +1 V dan kadar imbasan 100 mV/s. Kesan pH dan analisis sampel sebenar menggunakan air kencing bayi yang dicairkan dan dicampur dengan UA juga dikaji. Keputusan bagi CPE terdedah dan AuNPs/PM/CPE menunjukkan peningkatan 5 kali ganda dalam arus puncak anodik bagi UA. Keadaan optimum adalah pada pH 5 (PBS 0.1 M) dengan kadar imbasan 100 mV/s. Pada keadaan optimum tersebut, elektrod terubah suai menunjukkan aktiviti pemangkinan pengoksidaan UA yang tinggi. Teknik voltametri denyut pembezaan (DPV) digunakan untuk analisis kuantitatif. Prestasi elektrod AuNPs/PM/CPE masing-masing mempunyai julat kelinearan, had pengesanan, kepekaan, kejituan, dan ketepatan pada 0.1–11 μM, 0.0647 μM, 7.8592 μA/μM, 0.1107%–0.3930%, dan 82.45%–107.23%. Keputusan analisis UA dalam bayi air kencing menunjukkan bahawa perolehan sampel dilupuskan pada 99.41 ± 0.06%, menunjukkan elektrod ini mempunyai ketepatan yang baik.

Kata kunci: voltametri, asid urik, polimelamin, nano partikel emas, elektrod karbon terubahsuai

Introduction

Uric acid (UA) is the main product of purine metabolism in the human body [1]. The normal UA content in healthy human blood serum is in the range of 1.5 to 6.0 mg/dL for women and 2.5 to 7.0 mg/dL for men [1, 2]. Normal UA levels in human urine ranged from 1400-4000 μM [3]. Abnormalities of UA levels in the body can be used as an indication of various diseases such as gout, hyperuricemia, Lesch-Nyhan, arthritis, kidney, neurological, cardiovascular, and kidney disease [4, 5]. Therefore, research analysis and monitoring of UA levels in biological fluids are vital.

Various UA analysis methods and techniques have been developed, including the UV-Vis technique [6-8], chromatography [9-11], and voltammetry with modified electrodes [12-19]. Although some work has been performed on the development method of the UA voltammetry analysis, it is still necessary to innovate the modification of electrodes that are easy to produce, low-cost, but still prioritise excellent electrode performance. Compared to other analytical techniques, the advantages of voltammetry include instrumentation and cost analysis of inexpensive, fast, sensitive, and broad linear concentration ranges for simultaneous determination of analyte mixtures. Meanwhile, the basic principles involved are oxidation and reduction processes, surface adsorption processes, electron transfer, and reaction mechanisms [20].

Modification of carbon paste electrodes (CPE) is very extensive in its use to increase its sensitivity, selectivity, and reproducibility. Various conductive polymers have been developed as voltammetry sensor modifiers [18-28]. In addition, electrode modification can also be done using gold nanoparticles (AuNPs). Gold nanoparticles have good electrocatalytic activity, conductivity, and biocompatibility for electrochemical applications, allowing them to be used as chemical and biochemical sensors [32, 33]. The combination of polymelamine (PM) with gold nanoparticles (AuNPs) on the surface of CPE has been used as a dopamine sensor (DA) [34], ascorbic acid sensor (AA) [35], and hydroquinone (HQ) [36], with all three compounds, provide different anodic peak potential (*Epa*). In this study, these electrodes were used as voltammetric UA sensors in the hope of obtaining different peak potentials from the two previous analytes, so that they are selective, sensitive, and accurate. The following Scheme 1 is the preparation of AuNPs/PM/CPE electrodes and their use as UA sensors. In Step 1, CPE is prepared from a mixture of carbon powder and 7:3 (w/w) solid paraffin. The surface

of CPE is coated with PM using melamine (M) electropolymerisation by cyclic voltammetry (CV) with 0.1 M NaOH solution as supporting electrolyte, to form PM/CPE. In the final step, AuNPs are coated on the surface of PM/CPE with sodium sulphate (Na_2SO_4) and sulfuric acid (H_2SO_4) as an electrolyte supporting material by electrodeposition of $HAuCl_4$ solution, so that AuNPs/PM/CPE will be formed. In Stage 2, AuNPs/PM/CPE electrodes are used as UA sensors, in both CV and differential pulse voltammetry (DPV).

Materials and Methods

Materials and instrumentation

The main materials used in the study were carbon (obtained from the Bogor Research Centre for Forest Products, Indonesia), uric acid (Fluka), melamine (Aldrich), and tetrachloroauric acid ($HAuCl_4$; obtained by dissolving 0.1 g of 24-carat pure gold in aqua regia, then diluted with ultra-high water to obtain the desired concentration). Other chemicals were sodium hydroxide (NaOH, Merck), sulfuric acid (H_2SO_4, Merck), sodium sulphate (Na_2SO_4, Merck), and phosphate-buffered solution (PBS, pH 3-9) made from a mixture of phosphoric acid (H_3PO_4), sodium dihydrogen phosphate (NaH_2PO_4), and disodium hydrogen phosphate (Na_2HPO_4) solution. These materials have a degree of pro-analysis purity (p.a.). The water used was ultra-high pressure (UHP) water.

The main instrument used in this study was a set of Edaq e-corder 201 (Model ed 201) potentiostats with Echem software version 1.5 and equipped with three electrodes, namely working electrodes AuNPs/PM/CPE, Ag/AgCl as reference electrodes, and platinum wire as auxiliary electrodes.

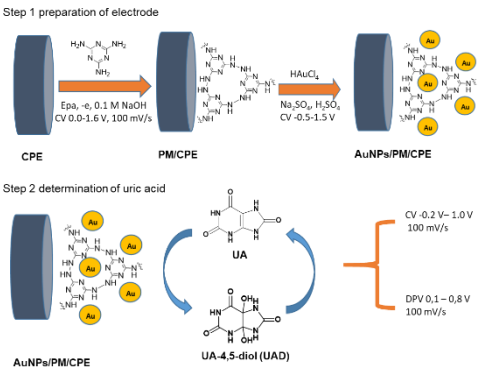
Preparation of AuNPs/PM/CPE electrode

Carbon paste electrode (CPE) is made by mixing carbon powder and solid paraffin with a ratio of 7:3. These electrodes were activated by cleaning the surface using CV in the potential range of 0 to 1.0 V by 30 cycles, with a scan rate of 100 mV/s using a 0.5 M H_2SO_4 solution. PM/CPE was made using 1 mM melamine electropolymerisation in 0.1 M NaOH solution on the CPE surface with CV technique of 0 to +1.6 V, a scan rate of 100 mV/s in 20 cycles [1].

AuNPs/PM/CPE electrodes were made using Au electrodeposition on the PM/CPE surface using a 1 mM $HAuCl_4$ solution containing 0.1 M Na_2SO_4. Electrodeposition was performed by CV in the potential range of -0.6 to +1.5 V, with a scan rate of 50 mV/s, in as many as 12 cycles. Furthermore, the surface of the AuNPs/PM/CPE was rinsed using ultra-high pressure (UHP) water and dried at room temperature [2].

Voltammetric analysis of UA by using AuNPs/PM/CPE

Qualitative analysis of UA was determined by CV technique using 3 µM UA solution in PBS pH 7 at a potential of 0 V to + 1 V, with a scan rate of 100 mV/s. Quantitative analysis was carried out by DPV technique with variations in UA concentration in the potential range of +0.1 V to +0.7 V and scan rate of 100 mV/s.



Scheme 1. Proposed electropolymerisation of melamine and electrodeposition of AuNPs on the surface of CPE as UA sensor

Results and Discussion

Cyclic voltammogram of UA

Figure 1 shows a cyclic voltammogram of a 3 μM UA solution that has higher anodic peak currents (Ipa) than a cathodic peak, indicating that UA is easier to undergo an oxidation reaction than a reduction. The Ipa are 3.292, 9.134, 10.491, and 15.041 μA on the surface of CPE electrodes, PM/CPE, and AuNPs/PM/CPE, respectively. This shows that the modification of electrodes can improve catalytic activity. The highest UA current peak is obtained using AuNPs/PM/CPE electrodes with increasing current approximately five times greater than the CPE electrode.

AuNPs/PM/CPE electrodes provide the highest current response due to the synergistic effect of PM, which is rich in amine groups and AuNPs with high surface area and excellent catalytic activity[3]. PM can prevent aggregation of gold nanoparticles because N atoms surround gold nanoparticles; therefore, avoiding gold aggregation process [4].

The effect of pH was studied using PBS with a concentration of 0.1 M, which varied with a pH range of 3 to 9. Besides assisting in maintaining the pH of the solution, buffer solution also functions as electrolyte support to reduce current migration, so that high peak current values will be obtained. The analysis was carried out using a scan rate of 100 mV/s and the potential range between 0 V to + 1.0V. Figure 2 is a curve of the relationship between the pH of the solution and the value of anodic peak current (Ipa) UA. Based on Figures 2 and 3, the UA analysis at various pH has the optimum anodic peak value at pH 5.

Based on these images, the anodic peak currents increase to pH 5 and then decreased sharply at pH 6, before appearing to be flat towards pH 9. UA has the pKa of 5.4, in the pH range 3 to 4. At this point, UA is in the form of a neutral molecule that is difficult to be oxidised, causing a small peak current. Whereas at pH 5, this value is almost close to the pKa value, so the character of UA at this pH will increase, whereby it is easier to experience a redox reaction. Decreasing peak currents occurs in the pH range 6 to 9, where UA will be in the form of a salt (anionic), and more challenging to experience an oxidation reaction. Hence, the decrease of the peak current value [5]. Figure 4 is a UA redox reaction that is influenced by the pH of the solution.

Differential pulse voltammogram of UA

Quantitative analysis was carried out by varying dopamine concentrations from 0.1 to 11 μM in PBS pH 5 and the scan rates of 100 mVs^{-1}. The DPV UA voltammogram at various concentrations can be seen in Figure 5, while the linear curve is shown in Figure 6.
Based on the curve of the relationship between concentration and anodic peak current in the UA analysis, R^2 was obtained at 0.9998, which approached the value of 1. The concentration that gave linear relations was in the concentration range of 0.1 μM to 11 μM. The slope produced from the UA standard curve shows the sensitivity of the analysis method. Based on the standard curve obtained a slope value of 7.8592, which indicates that the sensitivity of the UA analysis used AuNPs/PM/CPE electrodes of 7.8952 μA/μM. The limit of detection (LOD) was calculated statistically through the regression equation from the standard curve obtained 0.0647 μM (6.5×10^{-8} M). Table 1 is a comparison of UA detection limits in some literature. AuNPs/PM/CPE electrodes in references [14, 16, 18, 19] have lower LOD. However, when compared to the electrodes in references [12, 15], and [17] which have lower LOD, AuNPs/PM/CPE electrodes have the advantage of being easy to produce, cheaper, and nontoxic.

Determination of method accuracy was carried out at a concentration of 0.1 μM to 11 μM with three replications of measurements. The error range permitted in analysing 1 μA was 80-110% [12], while the accuracy value obtained in the UA analysis in this study is 82.45-107.23%, indicating an accurate method.

Precision is determined as the coefficient of variation, with good accuracy being ≤2%. In this study, the precision values meet the acceptability requirements for concentrations of 0.1 μM and 11 μM at 22.6% and

11.3%. Based on the calculation results, the value of KV in the UA analysis was 0.1107-0.3930%, indicating that this method has a good precision value.

The analysis of real samples utilised the urine of 21-day-old infants. Urine samples were diluted 50 times using PBS pH 5 solution. The determination of UA was checked by adding UA compounds to ensure the concentration in urine as 1 µM, which is the minimum level in infants [13]. The results of the UA analysis in the baby urine are shown in Table 2, with the disposed sample recovery of 99.41 ± 0.06%. This shows that the AuNPs/PM/CPE electrode can be used as a sensor in the UA analysis of urine samples with good accuracy.

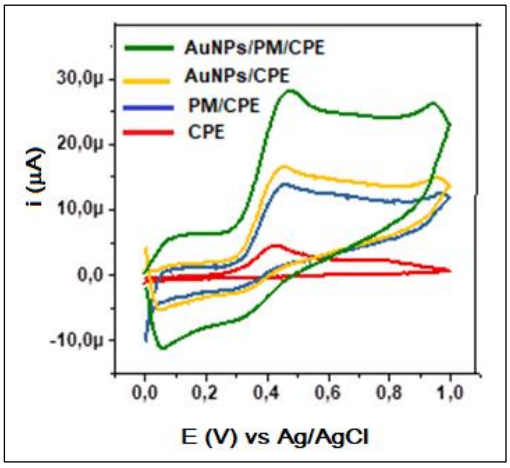


Figure 1. Cyclic 3 µM UA voltammogram in the scan rate of 100 mV/s using various electrodes

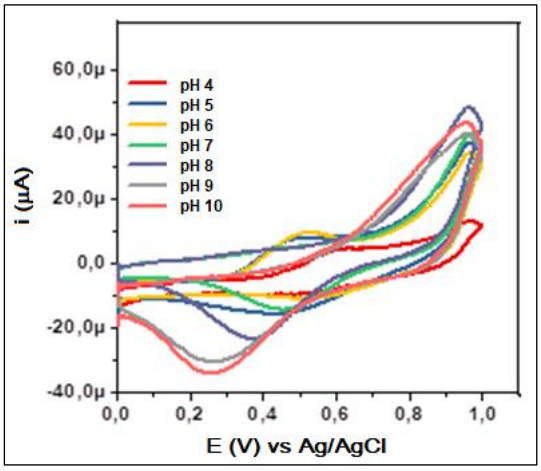


Figure 2. Cyclic voltammograms of 2 µM UA with pH variation using PBS with scan rate of 100 mV/s

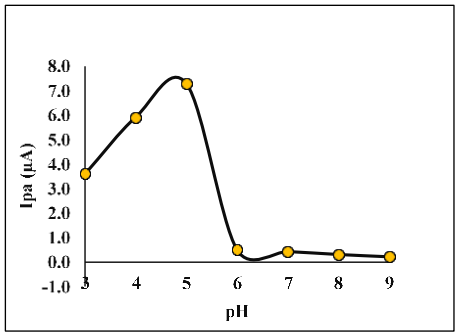


Figure 3. Relationship curve between pH vs. Ipa UA cyclic voltammogram

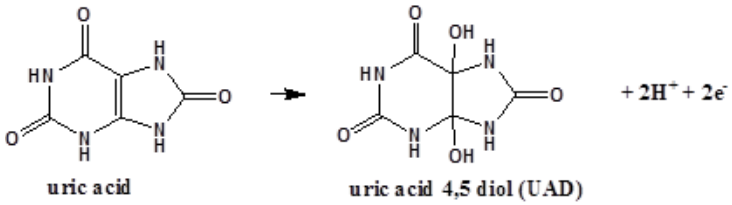


Figure 4. Oxidation-reduction reaction of UA

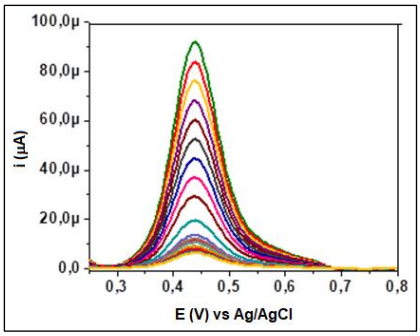


Figure 5. Differential pulse voltammogram of UA in PBS pH 5 with the scan rate 100 mV/s

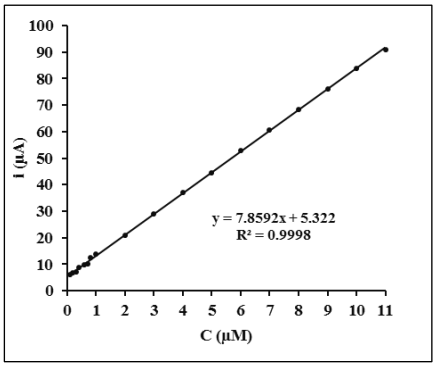


Figure 6. Calibration curve of UA from the DPV voltammogram

Table 1. Comparison of UA detection limit data in several literature

Electrode	Limit of Detection (M)	References
Diamond Film	1.5×10^{-8}	[12]
Poly(p-toluene sulfonic acid) Modified Electrode	5.0×10^{-7}	[14]
MIP/HMDE	6.0×10^{-10}	[15]
Poly(p- Aminobenzene Sulfonic Acid)-Modified Glassy Carbon Electrode	5.0×10^{-7}	[16]
Carbon paste/cobalt Schiff base composite electrode	8.0×10^{-9}	[17]
Fe_3O_4/Graphene	7×10^{-5}	[18]
SPCEs	1.9×10^{-7}	[19]
AuNPs/PM/CPE	6.5×10^{-8}	This work

Table 2. Analysis of UA in infant urine samples using AuNPs/PM/CPE electrodes

Sample	UA Concentration Added (µM)	Concentration Obtained (µM)	Average Recovery (%)
Urine	0.00	-	-
	1.00	0.9947	99.41±0.06
	1.00	0.9934	
	1.00	0.9942	

Conclusion

Voltammetric analysis of UA has been developed using CPE modified with PM and AuNPs. The synergistic effect of PM, which is rich in amine groups and AuNPs with a high surface area and excellent catalytic activity, can increase the anodic peak current approximately five times greater than the bar electrode. These electrodes have excellent performance, including accuracy, precision, and detection limits. The results of the UA analysis in the baby urine showed that these electrodes have good accuracy. However, these electrodes still need to be improved for the analysis of UA samples in blood.

Acknowledgement

The authors gratefully acknowledge the financial support of this work by the Directorate of Research and Community Service of the Republic of Indonesia and the Ministry of Research, Technology and Higher Education in the 2019 fiscal year.

References

1. Maiuolo, J., Oppedisano, F., Gratteri, S., Muscoli, C. and Mollace, V. (2016). Regulation of uric acid metabolism and excretion. *International Journal of Cardiology*, 213: 8-14.
2. Atta, N. F., El-kady, M. F. and Galal, A. (2010). Simultaneous determination of catecholamines, uric acid and ascorbic acid at physiological levels using poly (N-methylpyrrole)/Pd-nanoclusters sensor. *Analytical Biochemistry*, 400(1): 78-88.

3. Kong, D., Zhuang, Q., Han, Y., Xu, L., Wang, Z. and Jiang, L. (2018). Simultaneous voltammetry detection of dopamine and uric acid in human serum and urine with a poly (procaterol hydrochloride) modified glassy carbon electrode. *Talanta,* 185(3): 203-212.
4. Rana, L., Gupta, R., Tomar, M. and Gupta, V. (2018). Highly sensitive Love wave acoustic biosensor for uric acid. *Sensors & Actuators: B. Chemical*, 261: 169-177.
5. El, R. and Tallima, H. (2017). Physiological functions and pathogenic potential of uric acid: A review. *Journal of Advanced Research*, 8(5): 487-493.
6. Norazmi, N., Rasad, Z. R. A., Mohamad, M. and Manap, H. (2017). Uric acid detection using UV-Vis spectrometer. *IOP Conference Series: Materials Science and Engineering*, 257(1): 1-6.
7. Norazmi, N., Rasat, Z. R. A., Mohamad, M. and Manap, H. (2018). UV detection on artificial uric acid using UV-Vis spectrometer. *Journal of Lasers, Optics & Photonics*, *5*(179): 2.
8. Jeliki, M., Djurdjevi, P. and Stankov, D. (2003). Determination of uric acid in human serum by an enzymatic method using N-methyl-N-(4-aminophenyl)-3-methoxyaniline reagent. *Journal Serbian Chemical Society*, 68: 691-698.
9. Kock, R., Seitz, S., Delvoux, B. and Greiling, H. (1995). A method for the simultaneous determination of creatinine and uric acid in serum by high-performance-liquid-chromatography evaluated versus reference methods. *Clinical Chemistry and Laboratory Medicine*, 33(1): 23-30.
10. Wijemanne, N., Soysa, P., Wijesundara, S. and Perera, H. (2018). Development and validation of a simple high performance liquid chromatography/UV method for simultaneous determination of urinary uric acid, hypoxanthine, and creatinine in human urine. *International Journal of Analytical Chemistry*, 2018: 1-7.
11. Honeychurch, K. (2018). The Determination of uric acid in human saliva by liquid chromatography with electrochemical detection. *Journal of Analytical, Bioanalytical and Separation Techniques*, *2*(1): 47-51.
12. Popa, E., Kubota, Y., Tryk, D. A. and Fujishima, A. (2000). Selective voltammetric and amperometric detection of uric acid with oxidized diamond film electrodes. *Analytical Chemistry,* 72(7): 1724-1727.
13. Kumar, S. S., Mathiyarasu, J., Phani, K. L., Jain, Y. K. and Yegnaraman, V. (2005). Determination of uric acid in the presence of ascorbic acid using poly (3, 4-ethylenedioxythiophene)-modified electrodes. *Electroanalysis: An International Journal Devoted to Fundamental and Practical Aspects of Electroanalysis*, 17(24): 2281-2286.
14. Wang, L., Huang, P., Bai, J., Wang, H., Wu, X. and Zhao, Y. (2006). Voltammetric sensing of uric acid and ascorbic acid with poly (p-toluene sulfonic acid) modified electrode. *International Journal of Electrochemical Science,* 1: 334-342.
15. Khasanah, M., Mudasir, M., Mada, U. G. and Kuncaka, A. (2012). Development of uric acid sensor based on molecularly imprinted polymethacrylic acid-modified hanging mercury drop electrode. *Journal of Chemistry and Chemical Engineering*, 6: 209-214.
16. Sadikoglu, M., Taskin, G., Demirtas, F. G., Selvi, B. and Barut, M. (2012). Voltammetric determination of uricacid on poly (p-aminobenzene sulfonic acid)-modified glassy carbon electrode. *International Journal of Electrochemical Science,7*: 11550-11557.
17. Amiri, M. and Bezaatpour, A. (2012). Simultaneous voltammetric determination of uric acid and ascorbic acid using carbon paste/cobalt Schiff base composite electrode, *Journal Solid State Electrochemistry,* 16: 2187-2195.
18. Movlaee, K., Norouzi, P., Beitollahi, H., Rezapour, M. and Larijani, B. (2017). Highly selective differential pulse voltammetric determination of uric acid using modified glassy carbon electrode. *International Journal of Electrochemical Science,*12: 3241-3251.
19. Metto, M., Eramias, S., Gelagay, B. and Washe, A. P. (2019). Voltammetric determination of uric acid in clinical serum samples using DMF modified screen printed carbon electrodes, *International Journal of Electrochemistry,* 2019: 1-8.

20. Kounaves, S. P. (1997). Voltammetric techniques, handbook of instrumental techniques for analytical chemistry: pp. 709-726.
21. Sroysee, W., Chairam, S. and Amatatongchai, M. (2016). Poly (m-ferrocenylaniline) modified carbon nanotubes-paste electrode encapsulated in nafion film for selective and sensitive determination of dopamine and uric acid in the presence of ascorbic acid. *Journal of Saudi Chemical Society*, 22(2): 173-182.
22. Chitravathi, S., Swamy, B. E. K., Mamatha, G. P. and Sherigara, B. S. (2012). Electrochemical behavior of poly (naphthol green B)-film modified carbon paste electrode and its application for the determination of dopamine and uric acid. *Journal of Electroanalytical Chemistry*, 667: 66-75.
23. Atta, N. F. and El-kady, M. F. (2010). Novel poly (3-methylthiophene)/Pd, Pt nanoparticle sensor: Synthesis, characterization and its application to the simultaneous analysis of dopamine and ascorbic acid in biological fluids. *Sensors & Actuators: B. Chemical*, 145(1): 299-310.
24. Wang, C., Li, J., Shi, K., Wang, Q., Zhao, X., Xiong, Z. and Wang, Y. (2016). Graphene coated by polydopamine/multi-walled carbon nanotubes modified electrode for highly selective detection of dopamine and uric acid in the presence of ascorbic acid. *Journal of electroanalytical Chemistry*, 770: 56-61.
25. Chandrashekar, B. N., Lv, W. and Jayaprakash, G. K. (2019). Cyclic voltammetric and quantum chemical studies of a poly (methionine) modified carbon paste electrode for simultaneous detection of dopamine and uric acid. *Chemosensors*, 7(24):1-18.
26. Hou, S., Zheng, N., Feng, H., Li, X. and Yuan, Z. (2008). Determination of dopamine in the presence of ascorbic acid using poly (3, 5-dihydroxy benzoic acid) film modified electrode, 179: 179-184.
27. Xiongwei, X. U., In, Q. L., Iu, A. L., Hen, W. C., Eng, X. W. and Ang, C. W. (2010). Simultaneous voltammetric determination of ascorbic acid, dopamine and uric acid using polybromothymol blue film-modified glassy. *Chemical and Pharmaceutical Bulletin,* 58(6): 788-793.
28. Baskar, S., Liao, C., Chang, J. and Zen, J. (2013). Electrochemical synthesis of electroactive poly (melamine) with mechanistic explanation and its applicability to functionalize carbon surface to prepare nanotube – nanoparticles hybrid. *Electrochimica Acta*, 88: 1-5.
29. Goyal, R. N. (2015). Gold nanoparticles decorated poly-melamine modi fi ed glassy carbon sensor for the voltammetric estimation of domperidone in pharmaceuticals and biological fl uids. *Talanta*, 141: 53-59.
30. Peng, J., Feng, Y., Han, X. and Gao, Z. (2016). Simultaneous determination of bisphenol A and hydroquinone using a poly (melamine) coated graphene doped carbon paste electrode. *Microchimica Acta*, 183: 2289-2296.
31. Gupta, P., Yadav, S. K. and Goyal, R. N. (2015). A sensitive polymelamine modified sensor for the determination of lomefloxacin in biological fluids. *Journal of The Electrochemical Society*, 162(1): 86-92.
32. Tadayon, F., Vahed, S. and Bagheri, H. (2016). Au-Pd/reduced graphene oxide composite as a new sensing layer for electrochemical determination of ascorbic acid, acetaminophen and tyrosine. *Materials Science & Engineering C*, 68: 805-813.
33. Amidi, S., Ardakani, Y. H., Amiri-Aref, M., Ranjbari, E., Sepehri, Z. and Bagheri, H. (2017). Sensitive electrochemical determination of rifampicin using gold nanoparticles/poly-melamine nanocomposite. *RSC Advances,* 7(64): 40111-40118.
34. Widyaningrum, B. A. (2018). Modifikasi elektroda pasta karbon dengan polimelamin/nanopartikel emas secara elektrokimia sebagai sensor voltammetri dopamin. Tesis Magister, Universitas Airlangga, Surabaya-Indonesia.
35. Farida, A. N., Fitriany, E., Baktir, A., Kurniawan, F. and Harsini, M. (2019). Voltammetric study of ascorbic acid using polymelamine/gold nanoparticle modified carbon paste electrode. *IOP Conference Series: Earth and Environmental Science*, 217(1): 012004.
36. Paramita, D. R. A. (2018). Modifikasi elektroda pasta karbon menggunakan polimelamin/ nanopartikel emas secara elektrokimia sebagai sensor voltammetri hidrokuinon. Tesis Magister, Universitas Airlangga, Surabaya-Indonesia.

37. Zen, J. and Chen, P. (1997). A selective voltammetric method for uric acid and dopamine detection using clay-modified electrodes. *Analytical Chem*istry, 69(24): 5087-5093.
38. Harmita (2004). Petunjuk pelaksanaan validasi metode dan cara perhitungannya, *Majalah Ilmu Kefarmasian,* 1(3): 117-135.
39. Association for Clinical Biochemistry (2013). Dopamine (plasma, urine). Retrieved from http://www.acb.org.uk/Nat Lab Med Hbk/ Dopamine.pdf.

Malaysian Journal of Analytical Sciences (MJAS)
Published by Malaysian Analytical Sciences Society

SENSOR ION Al^{3+} OPTIK BERASASKAN ERIOKROM SIANIN R TERPEGUN DALAM MEMBRAN POLIMER TERANGKUM MENGGUNAKAN PRINSIP PENGUKURAN SERAPAN

(An Optical Sensor For Al^{3+} Ion Based on Immobilized Eriochrome Cyanine R in Polymer Inclusion Membrane using Absorption Sensing Principle)

Faiz Bukhari Mohd Suah[1]*, Musa Ahmad[2], Lee Yook Heng[3]

[1]Green Analytical Chemistry Laboratory, School of Chemical Sciences, Universiti Sains Malaysia, 11800 Minden, Pulau Pinang, Malaysia
[2]Faculty of Science and Technology, Universiti Sains Islam Malaysia, 71800 Nilai, Negeri Sembilan, Malaysia
[3]School of Chemical Sciences and Food Technology, Faculty of Science and Technology, Universiti Kebangsaan Malaysia, 43600 UKM Bangi, Selangor, Malaysia

**Pengarang Utama: fsuah@usm.my*

Received: 7 February 2021 ; Accepted: 18 March 2021; Published: 25 April 2021

Abstrak

Sensor optik bagi pengesanan ion aluminium (Al^{3+}) berasaskan reagen terpegun dalam membran polimer terangkum (PIM) telah dibangunkan dalam kajian ini. Sensor ini menggunakan eriokrom sianin R (ESR) sebagai reagen dan prinsip pengukuran serapan sebagai kaedah pengesanan ion Al^{3+}. Bahan sensor PIM yang digunakan dalam kajian ini mengandungi selulosa triasetat 60% berat (m/m): Aliquat 336 30% berat (m/m): dioktil ftalat 10% berat (m/m) dan ESR dengan kepekatan 5.00×10^{-4} mol L^{-1}. Sensor berasaskan PIM ini menghasilkan rangsangan yang lebih tinggi berbanding sensor tidak berasaskan PIM. Masa optimum rangsangan sensor ialah pada lima minit dengan nilai pH optimum 6.0. Sensor ini memberikan julat rangsangan linear pada julat kepekatan ion Al^{3+} 7.41×10^{-6} - 4.44×10^{-4} mol L^{-1}, dengan had pengesanan terendah 5.63×10^{-6} mol L^{-1}. Sifat kepilihan yang tinggi kepada ion Al^{3+} turut ditunjukkan oleh sensor ini kecuali gangguan minima daripada ion Be^{2+} dan Fe^{3+}. Akhir sekali, sensor ini telah digunakan bagi penentuan ion Al^{3+} dalam beberapa sampel air semula jadi. Keputusan analisis menunjukkan sensor ini mampu menghasilkan keputusan yang setara dengan spektrofotometer serapan atom konvensional.

Kata kunci: sensor Al^{3+}, Aliquat 336, eriokrom sianin R, membran polimer terangkum

Abstract

An optical sensor for aluminium ion (Al^{3+}) based on immobilized reagent in polymer inclusion membrane (PIM) was developed in this study. This sensor utilized eriochrome cyanine R (ECR) as its reagent and absorption sensing principle as the method for Al^{3+} ion sensing. PIM's sensing material used in this study consists of cellulose triacetate 60% mass (m/m): Aliquat 336 30% mass (m/m): dioctyl phthalate 10% mass (m/m) and ECR with concentration of 5.00×10^{-4} mol L^{-1}. This sensor which based on immobilized PIM produced higher response compared to sensor based on non-immobilized PIM. Optimum response time of this sensor was five minutes with an optimum pH value of 6.0. This sensor also produced a linear response range for Al^{3+} ion

concentration of 7.41×10^{-6} - 4.44×10^{-4} mol L^{-1}, with detection limit of 5.63×10^{-6} mol L^{-1}. High selectivity towards Al^{3+} ion was also demonstrated by this sensor, except minimal interferences from Be^{2+} and Fe^{3+} ions. Finally, this sensor was applied for the determination of Al^{3+} ion in natural water samples. Results shows this sensor is capable of producing comparable output to conventional atomic absorption spectrophotometer.

Keywords: Al^{3+} sensor, Aliquat 336, eriochrome cyanine R, polymer inclusion membrane

Pengenalan

Dalam tiga dekad yang lepas, pencemaran ion aluminium(III) (Al^{3+}), dalam sumber air semula jadi dan air minuman telah mendapat perhatian daripada banyak pihak kerana kesan toksik dan biologi yang berpunca daripada ion Al^{3+} [1]. Kehadiran ion Al^{3+} adalah sangat rendah di dalam sumber air semula jadi, namun sejumlah ion Al^{3+} telah digunakan sebagai agen penggumpalan bagi proses rawatan air bagi tujuan kegunaan domestik yang seterusnya meningkatkan kandungan ion Al^{3+} di dalam air terawat. Sebelum ini, ion Al^{3+} telah dikategorikan sebagai logam yang tidak toksik kepada kesihatan manusia, namun beberapa kajian yang dijalankan dalam jangka masa yang panjang telah mendedahkan bahawa ion Al^{3+} berpotensi meningkatkan risiko penyakit saraf dan pelembutan tulang, penyakit Alzheimer, penyakit Parkinson, masalah buah pinggang, kelahiran pra-matang bagi ibu mengandung dan kecacatan kepada bayi semasa dilahirkan [2,3]. Justeru, satu pendekatan baharu perlu dilakukan bagi mengesan kehadiran ion Al^{3+} pada peringkat awal bagi mengelakkan kesan toksik ion Al^{3+} kepada manusia khususnya.

Dalam kajian ini, sensor kimia optik berasaskan reagen eriokrom sianin R (ESR) terpegun dalam membran polimer terangkum (PIM) untuk analisis kuantitatif ion Al^{3+} menggunakan prinsip pengukuran serapan telah dibangunkan. Tindak balas ini adalah berasaskan kepada pembentukan kompleks antara ESR terpegun dalam PIM dengan ion Al^{3+} dan disertai kehadiran pengekstrak, Aliquat 336. Pemegunan reagen mengunakan polimer selulosa triasetat (CTA) pemplastik, dimana molekul ESR serta Aliquat 336 diperangkap ke dalam matrik polimer yang telap dan hidrofobik bagi membolehkan analit menyerap masuk dan bertindak balas dengan reagen dengan pantas.

Diketahui bahawa antara masalah utama pembangunan sensor kimia optik adalah larut resap reagen daripada penyokong. Bagi mengelakkan ESR melarut resap ke dalam larutan akueus, reagen ini dipegunkan ke dalam matrik polimer pemplastik. Selain itu, masalah ini turut diatasi dengan penambahan Aliquat 336 ke dalam matrik polimer tersebut. Artikel ini membincangkan analisis kuantitatif ion Al^{3+} dengan menggunakan sensor kimia optik yang dibina. Akhir sekali, sensor kimia ini diaplikasikan untuk menentukan kandungan ion Al^{3+} di dalam sampel air semula jadi, iaitu air tasik dan air sungai.

Bahan dan Kaedah

Bahan kimia yang digunakan dalam eksperimen ini adalah aluminium (Fluka), ESR (BDH), Aliquat 336 (Aldrich), dioktil ftalat (DOP) (Fluka), poli(vinil klorida) (PVC) (berat molekul 200000) (Sigma-Aldrich), etanol 95% (Hmbg. Chem.), asid asetik (CH_3COOH), asid nitrik (HNO_3) dan diklorometana (DCM) (Aldrich) dan natrium asetat (Analar). Manakala reagen lain seperti natrium klorida, asid etilenadiaminatetraasetik (EDTA), kalium sulfat dodekahidrat, berilium klorida, barium nitrat, kadmium sulfat, kobalt klorida, ferum(II) klorida, ferum(III) sulfat, magnesium sulfat, merkuri klorida, plumbum klorida dan zink sulfat diperoleh daripada Merck.

Peralatan yang digunakan dalam eksperimen ini ialah spektrofotometer UL-nampak dengan aksesori optik model Cary 100 (Varian) yang digunakan bagi semua pengukuran serapan PIM. Peralatan lain yang turut digunakan ialah pengacau magnet (Stuart Sci. SM 22 dan Wiggen Hauser) dan neraca penimbang (Sartorius). Pengukuran pH untuk penyediaan larutan penimbal dilakukan dengan menggunakan pH meter (Hanna Instrument HI2211) dan dikalibrasi menggunakan larutan penimbal piawai pH 4.0, 7.0 dan 10.0 (Hamilton). Spektrofotomer serapan atom (Perkin

Elmer AAnalyst 700) telah digunakan untuk tujuan validasi.

Bagi penyediaan PIM, larutan PVC disedia dengan melarutkan 300 mg PVC di dalam 10 mL DCM. Satu larutan berasingan yang mengandungi 150 mg Aliquat 336 dan 50 mg DOP juga disediakan dengan melarutkannya di dalam 5 mL DCM. Kemudian kedua-dua set larutan dicampur dan dikacau selama 2 jam dengan pengacau magnet sehingga homogen. Campuran homogen ini dituangkan ke dalam piring petri berdiameter 9 cm yang mempunyai permukaan bawah yang rata. Selepas itu, piring petri ini diletakkan di atas permukaan meja yang rata bagi membolehkan membran yang seragam terbentuk. Selepas DCM dibiarkan tersejat daripada larutan tuangan selama 48 jam, membran yang lutsinar dan homogen dikeluarkan daripada piring petri. Membran ini dibilas dengan air ternyahion sebanyak tiga kali. Kemudian membran dicelup dan dikacau di dalam 20 mL larutan ESR yang berkepekatan 5.00×10^{-4} mol L^{-1} selama dua jam bagi membolehkan penghasilan warna yang seragam. Membran dibilas sekali lagi dengan air ternyahion sebanyak tiga kali untuk menyingkirkan reagen dan pelarut yang tidak terperangkap di dalam membran. Membran dipotong dan disediakan pada luas 2 cm × 1 cm bagi tujuan analisis dan kajian pencirian.

Pada awalnya, PIM berukuran 2 cm × 1 cm dicelupkan ke dalam 25 mL larutan ion Al^{3+} yang ditimbal pada pH 6.0 dan dikacau selama lima minit. Selepas itu, PIM dibilas dengan air ternyahion, dikeringkan dengan tisu dan diletakkan ke dalam dinding sel kuartza (3 cm × 1 cm × 1 cm) bagi proses pengukuran serapan. Spektrum serapan bagi PIM dengan kehadiran ion Al^{3+} dalam larutan penimbal pH 6.0 direkod dengan menggunakan spektrofotometer UL-nampak pada panjang gelombang 400-700 nm. Spektrum serapan bagi sensor tersebut sebelum dan selepas bertindak balas dengan ion Al^{3+} direkodkan untuk mendapatkan perbezaan serapan. Rangsangan bagi sensor yang dibangunkan telah dikaji pada panjang gelombang 618 nm untuk setiap pencirian yang dilakukan.

Pengoptimuman parameter penting lain seperti komposisi optimum PIM, kesan kepekatan Aliquat 336, kesan kepekatan morin, kesan pH, masa rangsangan keadaan mantap, julat dinamik sensor, kestabilan foto sensor, kebolehan dan kebolehasilan sensor, penjanaan semula dan kesan gangguan ion turut dijalankan.

Kajian validasi dilakukan untuk menguji kebolehan sensor bagi analisis kuantitatif ion Al^{3+} dalam sampel sebenar, iaitu air semula jadi. Analisis dilakukan menggunakan dua sampel air semula jadi, iaitu air tasik dan air sungai. Sampel air tersebut diperolehi dari Tasik Presint 18 dan Tasik Presint 2, Putrajaya dan Sungai Langat, Bandar Baru Bangi. Pada awalnya, semua sampel diambil dan disimpan terus ke dalam botol polietilena 1000 mL. Selepas itu, 2 mL HNO_3 70% (v/v) ditambahkan ke dalam botol sampel bagi tujuan pengawetan. Proses analisis sampel dilakukan terus, iaitu sekurang-kurangnya 2 jam daripada sampel diambil bagi mengurangkan perubahan fisiokimia sampel air tersebut. Sebanyak 50 mL sampel air diambil dan dituras dengan kertas turas. Kemudian 15 mL sampel air yang telah dituras ini ditambahkan dengan larutan penimbal pH 6.0 dan dicairkan ke dalam kelalang isipadu 25 mL. Sampel kemudiannya ditindakbalaskan dengan PIM yang disedia dan bacaan serapan direkodkan. Proses penyediaan sampel air ini dilakukan pada suhu bilik 25˚C. Perolehan semula nilai kepekatan ion Al^{3+} menggunakan sensor yang dibangunkan dalam sampel air semula jadi dibandingkan dengan nilai kepekatan sebenar ion Al^{3+} yang ditambah untuk mendapatkan peratus perolehan semula.

Keputusan dan Perbincangan

ESR adalah reagen yang akan memberikan perubahan warna apabila membentuk kompleks dengan kation seperti Al^{3+}, Fe^{3+}, Be^{2+} dan Cu^{2+} dalam julat pH 4.0 - 6.0 [4]. Apabila PIM yang dibangunkan ini dimasukkan ke dalam larutan ion Al^{3+}, perubahan warna daripada hijau kepada biru dapat diperhatikan. Rajah 1 menunjukkan spektrum serapan sensor kawalan PIM (mengandungi CTA: Aliquat 336: DOP: ESR) tanpa kehadiran ion Al^{3+}, sensor bukan PIM (mengandungi CTA: DOP: ESR) dengan kehadiran ion Al^{3+} dan sensor menggunakan PIM (mengandungi CTA: Aliquat 336: DOP: ESR) dengan kehadiran ion Al^{3+}. Serapan maksimum sensor kawalan PIM tanpa kehadiran ion

Al^{3+}, sensor bukan PIM dan sensor menggunakan PIM dengan kehadiran ion Al^{3+} masing-masing ialah pada 458 nm, 535 nm dan 618 nm.

Daripada Rajah 1, dapat diperhatikan bahawa satu perubahan batokromik berlaku dalam spektrum serapan sensor kawalan dan spektrum serapan sensor menggunakan PIM yang bertindak balas dengan ion Al^{3+}, iaitu daripada panjang gelombang 535 nm kepada 618 nm. Fenomena yang unik ini berpunca daripada kehadiran Aliquat 336 di dalam sensor menggunakan PIM tersebut. Kehadiran Aliquat 336 ini telah mengubah persekitaran mikro berlaku tindak balas antara ion Al^{3+} dan ESR yang akhirnya akan menyebabkan berlakunya perubahan panjang gelombang berlaku tindak balas, sama seperti yang telah dilaporkan oleh Mohd Suah et al. [5]. Perubahan panjang gelombang tindak balas ini sebenarnya membuktikan bahawa satu kompleks ternari yang baharu terbentuk iaitu kompleks ESR – Al^{3+} – Aliquat 336 [6].

Selain daripada itu, serapan sensor menggunakan PIM dengan kehadiran ion Al^{3+} adalah hampir dua kali lebih tinggi berbanding serapan sensor bukan PIM. Fenomena ini adalah pemerhatian penting yang diperoleh dalam kajian ini. Perkara ini berlaku disebabkan oleh peranan yang dilakukan oleh Aliquat 336. Interaksi elektrostatik antara reagen anionik (ESR) dengan pengekstrak kationik (Aliquat 336) berlaku pada kumpulan yang bercas negatif yang hadir pada reagen ESR iaitu kumpulan SO_3^- dan COO^-. Interaksi elektrostatik yang berlaku secara berterusan ini serta kesan pelarutan tambahan yang turut berlaku telah menyumbang kepada berlakunya peningkatan serapan maksimum kompleks ternari ini [7, 8].

Pengekstrak yang digunakan dalam kajian ini iaitu Aliquat 336 adalah pengekstrak yang sering digunakan bagi kajian ekstraksi dan pengangkutan ion logam [4]. Dalam kajian ini, reagen ESR akan membentuk ikatan ionik yang kuat dengan Aliquat 336 disebabkan oleh pemasangan ion antara cas negatif kumpulan sulfonik ESR dengan cas positif kumpulan ammonium kuaternari Aliquat 336. Apabila PIM didedahkan kepada larutan ion Al^{3+}, proses pertukaran dan pengekstrakan ion Al^{3+} ke dalam fasa membran PIM berlaku serentak di mana proton daripada membran dilepaskan ke dalam larutan Al^{3+}. Persamaan tindak balas ini ditunjukkan dalam persamaan 1:

$$[L^+ Ind^-]_{(mem)} + Al^{3+}_{(ak)} + H^+_{(ak)} \rightleftharpoons [Al^{3+} - L^+ - Ind^-]_{(mem)} + H^+_{(ak)} \quad (1)$$

dimana L adalah Aliquat 336, Ind adalah reagen ESR dan subskrip mem dan ak masing-masing merujuk kepada fasa membran dan fasa akueus.

Sebagai tambahan, kepekaan sensor ini turut didorong oleh penggunaan CTA sebagai matriks penyokong. Pemegunan reagen penunjuk di dalam matriks penyokong seperti hydrogel, poli (vinil klorida) (PVC) dan CTA akan menyumbang kepada peningkatan kepekaan sensor kimia optik tersebut. Kepekaan sensor kimia optik ini sebenarnya disumbang oleh sifat CTA itu sendiri iaitu mempunyai liang yang banyak dan boleh dikawal saiznya dengan menggunakan pemplastik yang sesuai. Liang ini kemudiannya akan dipenuhi oleh reagen serta pengekstrak. Penambahan kuantiti reagen dan pengekstrak terpegun akan membolehkan lebih banyak analit membentuk kompleks ternari dengannya dan seterusnya akan meningkatkan bacaan serapan sensor [9].

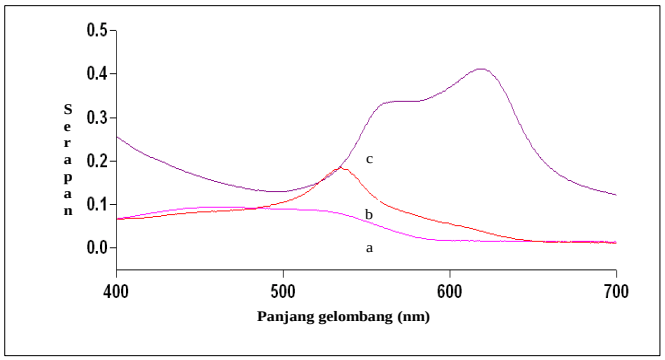
Keputusan daripada Jadual 1 menunjukkan bahawa PIM IV, yang mempunyai komposisi CTA 60% berat (m/m): Aliquat 336 30% berat (m/m): DOP 10% berat (m/m) dan ESR 5.00×10^{-4} mol L^{-1} memberikan bacaan serapan tertinggi berbanding PIM lain. Menurut Makowka dan Pospiech (2019) dalam kajian pengangkutan ion lanthanum(III) menggunakan PIM, komposisi pengekstrak yang optimum bagi membran menggunakan CTA adalah sekitar 30 - 40% berat (m/m) daripada jisim PIM [10]. CTA yang mempunyai kumpulan hidroksil dan asetil dalam strukturnya mampu membentuk ikatan hidrogen yang kuat dengan Aliquat 336. Pembentukan ikatan hidrogen ini seterusnya akan menyumbang kepada keupayaan CTA untuk menampung komposisi Aliquat 336 sehingga kepada 40% berat (m/m) daripada jisim PIM selain daripada turut mendorong kepada pembentukan membran yang homogen dan lutsinar.

Selain daripada itu, dapat diperhatikan juga bahawa PIM yang disediakan dalam kajian ini juga boleh disediakan tanpa menggunakan pemplastik (PIM I dan III). Keputusan ini membuktikan bahawa Aliquat 336 mampu berfungsi sebagai pemplastik walaupun menggunakan penyokong yang berlainan, sama ada PVC atau CTA. Aliquat 336 berupaya bertindak sebagai pemplastik dalam PIM yang mempunyai CTA sebagai penyokong kerana ia memiliki sifat seperti sifat lipofilik yang tinggi, berupaya untuk membentuk ikatan hidrogen dengan CTA serta keupayaan CTA untuk mengambil bahagian dalam interaksi dwikutub-dwikutub [11].

Jadual 1 turut menunjukkan bahawa komposisi jisim Aliquat 336 di dalam PIM amat mempengaruhi bacaan serapan sensor. Dapat diperhatikan bahawa apabila komposisi jisim Aliquat 336 bertambah sehingga kepada 30% berat (m/m), bacaan serapan sensor turut bertambah kecuali bagi PIM III dan IX. Penjelasan yang boleh diberikan oleh penurunan bacaan serapan sensor bagi PIM III adalah kerana Aliquat 336 dengan komposisi jisim 30% berat (m/m) adalah komposisi yang optimum bagi membolehkan proses pertukaran ion dan ko-pengekstrakan ion Al^{3+} ke dalam PIM berlaku. Komposisi jisim Aliquat 336 yang melebihi 30% berat (m/m) pula tidak akan menyumbang kepada peningkatan bacaan serapan kerana kuantiti Aliquat 336 yang terdapat di dalam PIM adalah tepu. Manakala bagi PIM IX pula, komposisi jisim Aliquat 336 yang terlalu tinggi menyebabkan membran yang homogen, fleksibel dan lutsinar langsung tidak terbentuk. Pemerhatian yang hampir sama juga pernah dilaporkan oleh Radzyminska-Lenarcik et al. (2020) dalam kajian pengangkutan ion Zn^{2+} merentasi PIM yang menggunakan CTA sebagai penyokong. Mereka melaporkan bahawa CTA hanya mampu membentuk membran yang homogen dan memberikan bacaan kadar pengangkutan ion Zn^{2+} yang maksimum apabila komposisi jisim pengekstrak yang digunakan adalah kurang daripada 50% berat (m/m) [12]. Perkara ini berlaku kerana liang CTA tidak mampu untuk menampung kuantiti Aliquat 336 yang berlebihan.

Selain daripada jenis penyokong dan reagen, teknik pemegunan dan nilai pH optimum tindak balas sensor, satu lagi parameter utama iaitu kuantiti reagen terpegun perlu juga diberi perhatian. Dalam kajian ini, didapati kuantiti ESR terpegun amat mempengaruhi rangsangan sensor ion Al^{3+} optik yang dibina. Rajah 2 menunjukkan satu corak keputusan yang menarik iaitu apabila kepekatan awal ESR meningkat, rangsangan sensor terhadap ion Al^{3+} turut meningkat sehingga kepekatan ESR awal mencapai 5.00×10^{-4} mol L^{-1}. Apabila kepekatan awal ESR ditingkatkan lagi, diperhatikan rangsangan sensor tidak mengalami sebarang perubahan. Perkara ini sudah dijangka kerana reagen terpegun lebih cenderung untuk bertembung sesama sendiri pada kepekatan yang terlalu tinggi [13]. Oleh itu, kepekatan ESR 5.00×10^{-4} mol L^{-1} telah dipilih bagi proses pemegunan reagen di dalam PIM.

Perubahan serapan sensor berasaskan PIM terhadap perubahan nilai pH pada panjang gelombang 618 nm turut dikaji. Kesan perubahan nilai pH terhadap rangsangan sensor pada kepekatan ion Al^{3+} 7.41×10^{-5} mol L^{-1} dijalankan dengan mengukur serapan sensor pada julat pH 3.0 - 7.5. Keputusan kajian menunjukkan bahawa serapan maksimum sensor berlaku pada nilai pH 6.0 (Rajah 3). Pada nilai pH yang tinggi, iaitu pada pH neutral dan beralkali, bacaan serapan sensor didapati menurun. Perkara ini berlaku disebabkan oleh kecenderungan kompleks ESR - Al^{3+} untuk membentuk kompleks ESR – Al^{3+} – OH, kesan daripada kehadiran ion OH^- dalam larutan beralkali. Menurut Abdullah et al. (2017), fenomena ini dikenali sebagai pemendakan hidroksida atau hidrolisis ion [14]. Bagi nilai pH yang rendah iaitu kurang daripada pH 4.0 bacaan serapan sensor didapati turut menurun. Bacaan serapan sensor yang menurun ini menunjukkan kepekaan rangsangan sensor juga berkurangan. Perkara ini berlaku kerana reagen cenderung untuk mengalami protonasi ion yang menyebabkan reagen kurang reaktif untuk membentuk ikatan dengan ion logam [4]. Oleh itu, pH 6.0 telah dipilih sebagai nilai pH tindak balas bagi kajian seterusnya.

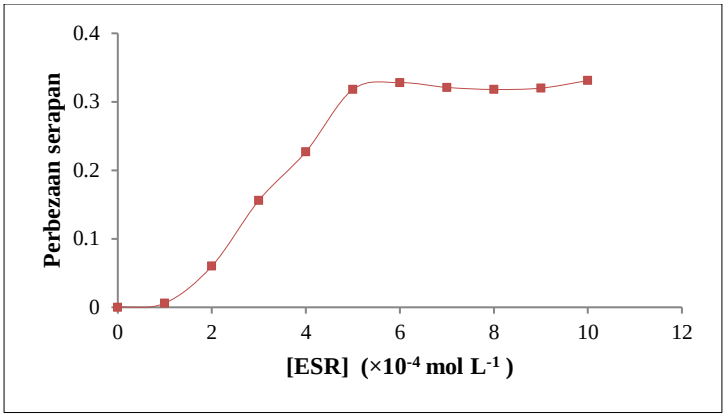


Rajah 1. Spektrum serapan (a) sensor kawalan PIM (mengandungi CTA: Aliquat 336: DOP: ESR) tanpa kehadiran ion Al^{3+}, (b) sensor bukan PIM (mengandungi CTA: DOP: ESR) dengan kehadiran ion Al^{3+} dan (c) sensor menggunakan PIM (mengandungi CTA: Aliquat 336: DOP: ESR) dengan kehadiran ion Al^{3+}. Keadaan eksperimen: $[Al^{3+}] = 7.41 \times 10^{-5}$ mol L^{-1}, [ESR] = 5.00×10^{-4} mol L^{-1}, pH = 6.0

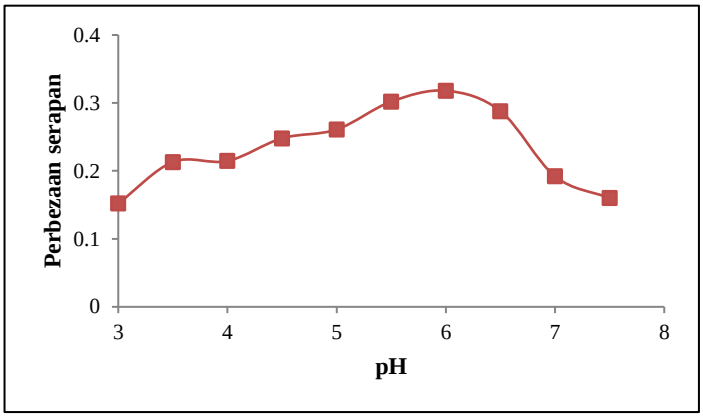
Jadual 1. Komposisi PIM yang disediakan dalam kajian ini

Membran	**CTA (mg)**	**Aliquat 336 (mg)**	**DOP (mg)**	**Komposisi (% Berat)**	**Serapan Maksimum[a]**
I	350	150	-	70:30:00	0.33
II	350	100	50	70:20:10	0.27
III	300	200	-	60:40:00	0.36
IV	300	150	50	60:30:10	0.41
V	300	100	100	60:20:20	0.28
VI	300	50	150	60:10:30	0.24
VII	250	150	100	50:30:20	0.36
VIII	250	100	150	50:20:30	0.34
IX	250	250	-	50:50:00	Membran tidak terhasil
X[b]	300	-	200	60:00:40	0.18[c]

[a]Serapan diukur pada 618 nm, $[Al^{3+}]= 7.41 \times 10^{-5}$ mol L^{-1}, pH = 6.0
[b]Sensor bukan PIM (mengandungi CTA: DOP: ESR)
[c]Serapan diukur pada 535 nm, $[Al^{3+}] = 7.41 \times 10^{-5}$ mol L^{-1}, pH = 6.0



Rajah 2. Kesan kepekatan awal ESR untuk pemegunan terhadap rangsangan sensor apabila ditindak balas dengan ion Al^{3+}. Keadaan eksperimen: $[Al^{3+}] = 7.41 \times 10^{-5}$ mol L^{-1}, pH 6.0



Rajah 3. Kesan pH terhadap rangsangan sensor apabila ditindak balas dengan ion Al^{3+}. Keadaan eksperimen: $[Al^{3+}] = 7.41 \times 10^{-5}$ mol L^{-1}

Keputusan yang ditunjukkan dalam Rajah 4 membuktikan masa rangsangan keadaan mantap bagi tindak balas sensor ini amat bergantung kepada kepekatan ion Al^{3+} yang dikaji. Masa rangsangan keadaan mantap bagi ion Al^{3+} berkepekatan rendah mengambil masa yang lebih lama berbanding kepekatan yang tinggi. Bagi ion Al^{3+} berkepekatan 7.41×10^{-5} mol L^{-1}, masa rangsangan mantap yang diperoleh adalah selepas 7 minit tindak balas manakala bagi ion Al^{3+} berkepekatan 5.50×10^{-5} mol L^{-1} pula masa rangsangan mantap yang dicerap adalah selepas 9 minit tindak balas. Oleh kerana masa rangsangan keadaan mantap bagi tindak balas sensor ini agak panjang, penentuan masa rangsangan berasaskan kaedah kinetik telah digunakan. Kaedah kinetik dalam kajian sensor adalah suatu kaedah dimana bacaan serapan direkodkan selepas satu tempoh masa yang ditetapkan [15]. Pada kebiasaannya, tindak balas kimia antara reagen dan analit telah berlaku dan hampir mencapai tahap optimum tindak balas. Kelebihan penggunaan kaedah kinetik dalam pemilihan masa rangsangan keadaan mantap telah digunakan oleh beberapa penyelidik sebelum ini. Menurut Du dan Xie (2021), penggunaan kaedah kinetik dalam aplikasi sensor kimia optik memberikan kelebihan seperti tempoh pengesanan analit yang lebih singkat serta sesuai digunakan bagi sensor optik yang melibatkan penggunaan teknik pelindapan pendarfluor [15]. Berdasarkan keputusan yang diperoleh, masa

pengukuran serapan sensor yang dipilih adalah selepas 5 minit masa rangsangan tindak balas.

Keputusan ujikaji menunjukkan serapan sensor yang bertindak balas dengan ion Al^{3+} berkepekatan 7.41×10^{-5} mol L^{-1} meningkat hampir sekali ganda apabila larutan ion Al^{3+} dikacau berbanding dengan serapan sensor bagi larutan ion Al^{3+} yang tidak dikacau (Rajah 5). Diperhatikan juga bacaan serapan oleh sensor menjadi malar selepas larutan analit dikacau selama 5 minit. Perkara ini berlaku kerana semua reagen ESR terpegun telah bertindak balas dengan ion Al^{3+}. Oleh itu, semua ujikaji dijalankan selepasa PIM dikacau di dalam larutan ion Al^{3+} selama 5 minit.

Diketahui bahawa kesan penguraian foto boleh menyumbang kepada pengurangan kepekaan sensor [16]. Oleh itu, kajian kesan kestabilan foto PIM dilakukan dengan merekodkan bacaan serapan PIM yang ditindak balas dengan ion Al^{3+} berkepekatan 7.41×10^{-5} mol L^{-1} untuk tempoh dua minggu. Hasil kajian menunjukkan PIM yang digunakan dalam kajian ini adalah stabil secara foto kerana tiada penurunan nilai serapan yang ketara diperhatikan (Rajah 6). Nilai RSD yang diperoleh ialah 2.32%.

Kestabilan foto sesuatu reagen terpegun di dalam penyokong polimer bergantung kepada beberapa faktor seperti struktur molekul reagen, jenis penyokong polimer yang digunakan dan teknik pemegunan reagen tersebut. Bagi PIM yang digunakan dalam kajian ini, kestabilan fotonya disumbang oleh teknik pemegunan reagen dan penggunaan pengekstrak yang bercas, iaitu Aliquat 336. Pemegunan reagen ESR secara pemerangkapan reagen di dalam PIM dengan menggunakan DOP sebagai pemplastik telah membolehkan ESR dipegun dan digunakan berulang kali tanpa mengalami masalah kelunturan reagen yang signifikan. DOP akan berfungsi untuk mengikat dan memerangkap reagen di dalam penyokong PVC supaya ia mempunyai ketahanan kimia dan fizikal yang kuat [17]. Sebagai tambahan, kehadiran Aliquat 336 turut menyumbang kepada kestabilan foto sensor yang dibina. Aliquat 336 ini akan berperanan untuk menstabilkan cas reagen penunjuk (ESR) serta turut bertindak sebagai pemplastik [13].

Keputusan kajian kebolehulangan dan kebolehasilan sensor adalah seperti yang ditunjukkan dalam Rajah 7. Nilai RSD bagi kebolehulangan dan kebolehasilan sensor ini masing-masing ialah 1.82% dan 3.63%. Kedua-dua nilai RSD yang rendah ini membuktikan bahawa sensor yang dibina ini boleh memberikan bacaan yang konsisten dan tepat apabila proses pengukuran dilakukan pada keadaan yang sama [18]. Sebagai tambahan, tiada sebarang perubahan dilakukan terhadap struktur sensor yang digunakan dalam kajian ini iaitu semasa proses penyediaannya. Struktur sensor yang tidak mengalami perubahan ini akan turut menyumbang kepada penghasilan nilai RSD yang rendah bagi sifat kebolehasilan sensor.

Keputusan yang diperoleh dalam kajian ini menunjukkan larutan F^- 0.5 mol L^{-1} berupaya untuk menjana semula sensor ion Al^{3+} optik yang telah dibina. Rajah 8 menunjukkan purata masa yang diambil untuk proses penjanaan semula sensor bagi satu kitaran lengkap adalah sekitar 15 minit. Walaupun masa penjanaan semula sensor ini agak lama, namun dapat diperhatikan penggunaan larutan F^- sebagai larutan penjana telah berjaya mendorong sensor mencapai kembali rangsangan garis dasarnya. Keputusan nilai RSD kebolehasilan sensor selepas dijana semula sebanyak tiga kali ialah 3.58%. Nilai RSD yang rendah ini membuktikan bahawa sensor ini masih berupaya untuk menghasilkan bacaan yang konsisten dan tepat walaupun telah dijana secara berulang kali.

Dalam kajian ini, had toleransi telah didefinasikan sebagai kepekatan ion yang menyebabkan berlakunya ralat relatif yang kurang daripada ± 5% nilai serapan sensor [19]. Oleh itu, beberapa jenis ion pengganggu telah ditambah kepada larutan ion Al^{3+} berkepekatan 7.41×10^{-5} mol L^{-1} bagi mengkaji kesan gangguan ion terhadap prestasi sensor.

Keputusan seperti yang ditunjukkan dalam Jadual 2 membuktikan masih terdapat beberapa ligan dan ion yang boleh menghasilkan gangguan kepada sensor tersebut. Seperti yang dijangka, EDTA dan fosfat menghasilkan ralat relatif yang lebih tinggi daripada ion F^-. Perkara ini berlaku kerana kedua-dua ligan ini mempunyai lebih daripada dua tapak yang boleh

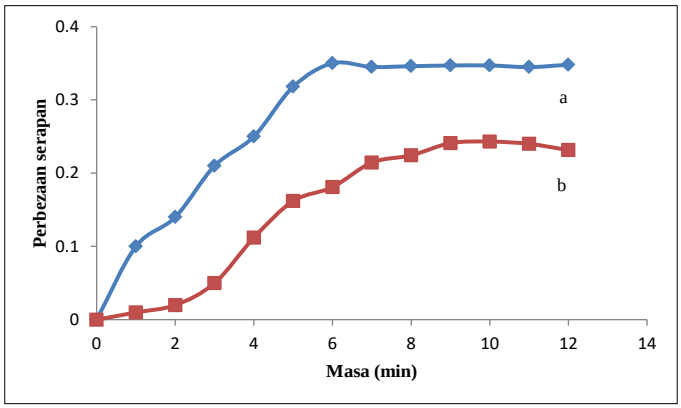
membentuk ikatan dengan ion Al^{3+} dan seterusnya membolehkan lebih banyak ion Al^{3+} membentuk ikatan dengannya [20]. Gangguan daripada kation yang signifikan hanya disumbang oleh kehadiran ion Be^{2+} dan Fe^{3+} yang hadir pada kepekatan yang tinggi. Kesan gangguan ini sememangnya sudah dijangkakan kerana ESR turut mampu membentuk kompleks yang stabil dengan kedua–dua kation tersebut [21]. Namun begitu, gangguan daripada ion pengganggu Be^{2+} dan Fe^{3+} ini masing-masing boleh diatasi dengan menggunakan agen penopeng [13-14, 22-23]. Manakala gangguan daripada kation lain adalah rendah dan tidak menghasilkan gangguan yang ketara walaupun hadir pada nisbah kepekatan yang lebih tinggi daripada ion Al^{3+}.

Tahap kepilihan sensor yang tinggi ini turut disumbang oleh kesan daripada pemegunan ESR di dalam PIM. Tahap kepilihan ini sebenarnya disumbang oleh beberapa faktor hasil daripada pemegunan reagen. Faktor tersebut adalah seperti pengurangan kebolehan ESR untuk membentuk kompleks dengan kation selain daripada ion Al^{3+} dan peningkatan tahap penelapan yang disediakan oleh CTA pemplastik [17].

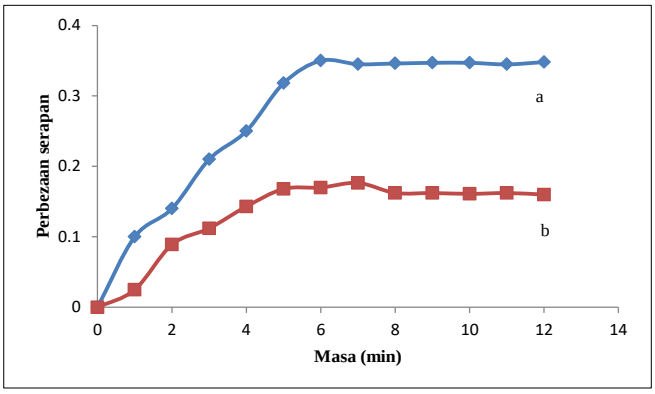
Rangsangan sensor terhadap kepekatan ion Al^{3+} yang berbeza ditunjukkan dalam Rajah 9. Graf perbezaan serapan sensor melawan kepekatan ion Al^{3+} menunjukkan rangsangan sensor adalah linear dalam julat kepekatan ion Al^{3+} 7.41×10^{-6} - 4.44×10^{-4} mol L^{-1}. Nilai LOD yang dikira berdasarkan kepekatan yang diberikan oleh purata isyarat pengukuran keamatan serapan reagen tanpa analit dan dicampurkan dengan tiga kali sisihan piawai bagi isyarat tersebut ialah 5.63×10^{-6} mol L^{-1}.

Keputusan ini membuktikan sensor menggunakan PIM ini adalah peka dan setanding dengan sensor ion Al^{3+} optik yang pernah dibangunkan oleh Nguyen et al. [24]. Rangsangan sensor tersebut adalah linear dalam julat 2-54 ppm (100 μM - 1 mM) ion Al^{3+}. Peningkatan kepekaan ini sebenarnya disumbang oleh kehadiran Aliquat 336 di dalam PIM. Aliquat 336 yang berfungsi sebagai pengekstrak telah berjaya menarik lebih banyak ion ion Al^{3+} di dalam larutan untuk membentuk kompleks berwarna dengan ESR di dalam PIM. Penambahan kuantiti kompleks ESR - ion Al^{3+} akan meninggikan lagi keamatan spektrum serapan sensor dan seterusnya mendorong kepada peningkatan kepekaan sensor.

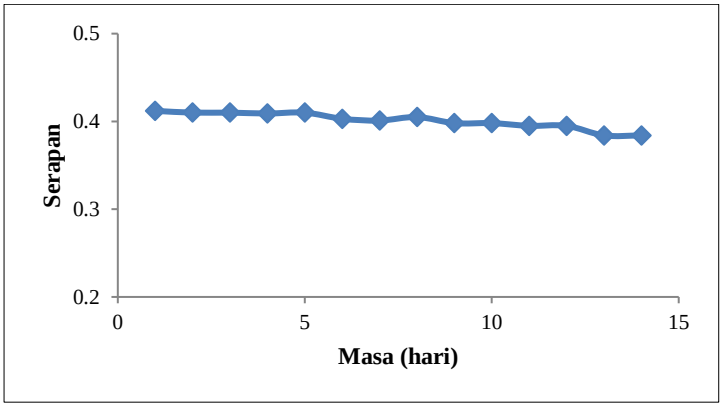
Untuk mengkaji prestasi sensor bagi penentuan ion Al^{3+} dalam sampel sebenar, ujian perolehan semula telah dijalankan. Jadual 3 menunjukkan keputusan peratus perolehan semula ion Al^{3+} oleh sensor ion Al^{3+} optik yang dibina. Bagi sampel air tasik di Presint 18 dan Presint 2 Putrajaya serta air Sungai Langat, purata peratus perolehan semula masing-masing ialah 104.9%, 106% dan 109.42%. Keputusan daripada jadual tersebut turut menunjukkan peratus perolehan semula bagi semua sampel adalah menghampiri 100%. Keputusan yang diperoleh membuktikan bahawa sensor yang dibangunkan ini tidak mengalami gangguan daripada ion pengganggu dengan ketara dengan peratus perolehan semula sensor kurang daripada 10% [25].



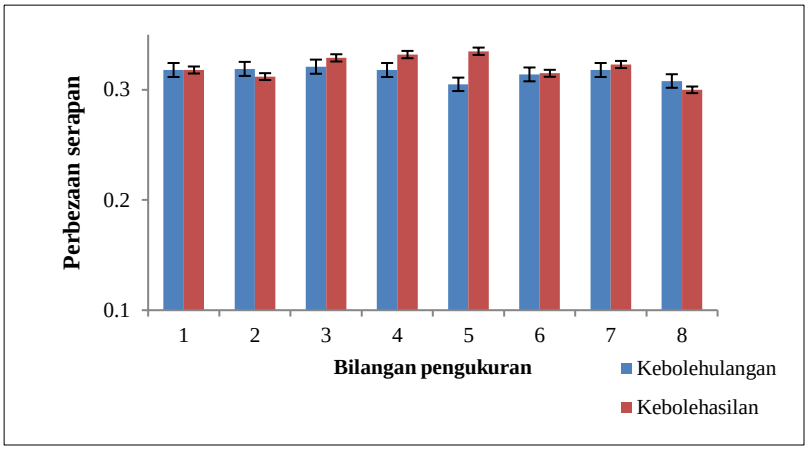
Rajah 4. Masa rangsangan keadaan mantap untuk sensor terhadap kepekatan ion Al^{3+} yang berbeza iaitu (a) 7.41×10^{-5} mol L^{-1} dan (b) 5.50×10^{-5} mol L^{-1}



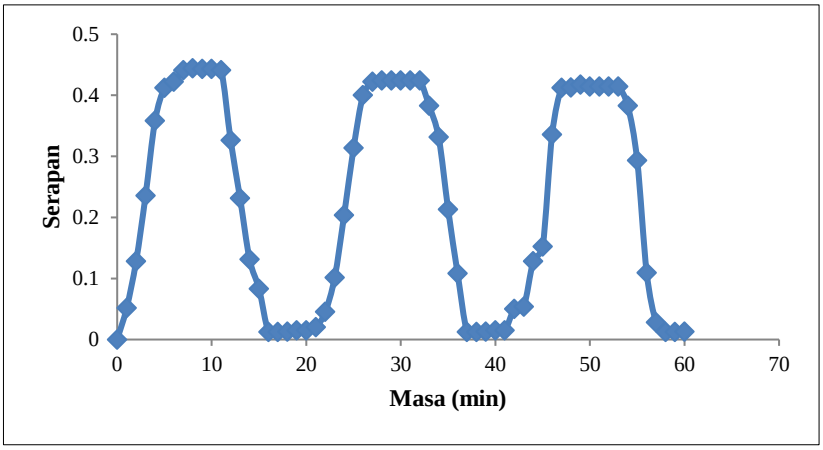
Rajah 5. Masa rangsangan mantap sensor bagi tindak balas dengan (a) larutan ion Al^{3+} yang dikacau dan (b) larutan ion Al^{3+} yang tidak dikacau



Rajah 6. Kestabilan foto sensor yang didedahkan kepada cahaya untuk tempoh 14 hari



Rajah 7. Kajian kebolehulangan dan kebolehasilan sensor terhadap ion Al^{3+} berkepekatan 7.41×10^{-5} mol L^{-1}



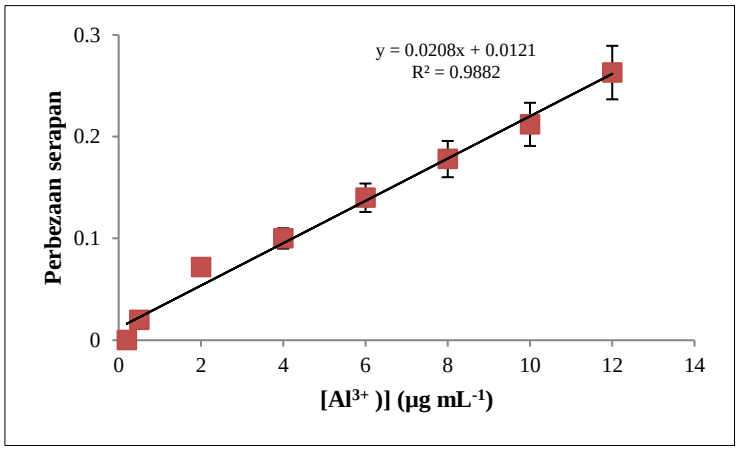
Rajah 8. Rangsangan serapan sensor pada panjang gelombang 618 nm apabila dijana semula dengan larutan F^- 0.5 mol L^{-1}.

Jadual 2. Kesan gangguan ion terhadap prestasi rangsangan serapan sensor

Ion	**Nisbah Mol (Ion Al^{3+}:Ion)**	**Serapan**	**Ralat Relatif (%)**
EDTA	1:1	± 0.30	- 27.18
	1:5	± 0.26	- 37.86
F^-	1:1	± 0.35	- 14.80
	1:5	± 0.34	- 17.48
PO_4^{-2}	1:1	± 0.31	- 24.27
	1:5	± 0.24	- 41.74
Be^{2+}	1:1	± 0.43	+ 5.22
	1:5	± 0.51	+ 24.22

Jadual 2 (cont'd). Kesan gangguan ion terhadap prestasi rangsangan serapan sensor

Ion	Nisbah Mol (Ion Al^{3+}:Ion)	Serapan	Ralat Relatif (%)
Ca^{2+}	1:1	± 0.44	+ 7.48
	1:5	± 0.46	+ 12.53
Cd^{2+}	1:1	± 0.42	+ 1.86
	1:5	± 0.43	+ 3.79
Co^{3+}	1:1	± 0.42	+ 2.48
	1:5	± 0.43	+ 4.13
Cu^{2+}	1:1	± 0.43	+ 4.80
	1:5	± 0.45	+ 9.06
Fe^{2+}	1:1	± 0.43	+ 3.64
	1:5	± 0.44	+ 6.21
Fe^{3+}	1:1	± 0.44	+ 6.30
	1:5	± 0.50	+ 21.40
Hg^{2+}	1:1	± 0.42	+ 1.74
	1:5	± 0.43	+ 4.51
Mg^{2+}	1:1	± 0.43	+ 4.80
	1:5	± 0.43	+ 5.41
Pb^{2+}	1:1	± 0.43	+4.60
	1:5	± 0.43	+520
Zn^{2+}	1:1	± 0.42	+ 2.41
	1:50	± 0.43	+ 5.08



Rajah 9. Julat dinamik ion Al^{3+} yang memberikan rangsangan sensor yang linear pada panjang gelombang 618 nm dan pH 6.0

Jadual 3. Prestasi rangsangan sensor terhadap sampel air semula jadi yang ditambah dengan ion Al^{3+}

Sampel	**Ion Al^{3+} Ditambah ($\mu g\ mL^{-1}$)**	**Ion Al^{3+} Yang Diperoleh AAS ($\mu g\ mL^{-1}$)(n=3)**	**Ion Al^{3+} Yang Diperoleh Sensor ($\mu g\ mL^{-1}$)(n = 3)**	**Perolehan Semula (%) (n = 3)**
Tasik Presint 18	-	0.24 ± 0.03	-	-
	2.0	-	2.35 ± 5.08	104.90
Tasik Presint 2	-	0.29 ± 0.05	-	-
	4.0	-	4.33 ± 2.68	106.00
Sungai Langat	-	0.45 ± 0.03	-	-
	10.0	-	11.43 ± 0.05	109.40

Kesimpulan

Daripada kajian ini, boleh disimpulkan bahawa kepekaan sensor kimia optik untuk pengesanan ion ion Al^{3+} berasaskan prinsip pengukuran serapan boleh ditingkatkan dengan menggunakan sensor menggunakan PIM. Komposisi optimum PIM diperoleh dengan kandungan CTA 60% berat (m/m): Aliquat 336 30% berat (m/m): DOP 10% berat (m/m) dan dengan kepekatan ESR 5.00×10^{-4} mol L^{-1}. Masa rangsangan sensor yang ditetapkan selepas 5 minit. Rangsangan sensor yang maksimum diperoleh pada nilai pH 6.0. Sensor ini berjaya menghasilkan rangsangan linear terhadap kepekatan ion Al^{3+} dalam julat 7.41×10^{-6} - 4.44×10^{-4} mol L^{-1} dengan nilai LOD yang dikira ialah 5.63×10^{-6} mol L^{-1}. Sensor ini boleh dijana semula dengan menggunakan larutan penjana F^- berkepekatan 0.5 mol L^{-1}. Sensor ini juga kepilihan kerana hanya kation Be^{2+} dan Fe^{3+} yang hadir pada nisbah molar yang tinggi sahaja didapati benar-benar mengganggu rangsangan sensor terhadap ion Al^{3+}. Kajian validasi prestasi sensor menunjukkan peratus perolehan semula sensor adalah dalam julat 104 - 109% dalam penentuan sampel air semula jadi dan ia membuktikan sensor ini boleh digunakan bagi aplikasi penentuan ion Al^{3+} di dalam sampel sebenar.

Penghargaan

Penulis ingin mengucapkan terima kasih kepada Universiti Sains Malaysia kerana membiaya penyelidikan ini melalui *Short Term Grant* (304 / PKIMIA / 6315197) dan *Bridging Grant* (304 / PKIMIA / 6316215).

Rujukan

1. Shetty, R., Vidya, C. S. N., Prakash, N. B, Lux, A. and Vaculik, M. (2021). Aluminium toxicity in plants and its possible mitigation in acid soils by biochar: A review. *Science of the Total Environment*, 765: 142-744.
2. Yokel, R. A. (2020). Aluminum reproductive toxicity: a summary and interpretation of scientific reports. *Critical Reviews in Toxicology*, 50: 551-593.
3. Dórea, J. G. (2020). Neurotoxic effects of combined exposures to aluminum and mercury in early life (infancy). *Environmental Research*, 188: 109734.
4. Gürses, A., Açıkyıldız, M., Güneş, K. and Gürses, M. S. (2016). Dyes and pigments. Springer, Berlin: pp 13-29.
5. Mohd Suah, F. B., Ahmad, M. and Lee, Y. H. (2016). Kesan penambahan surfaktan tak-ionik kepada kompleks Al(III)-ESR dalam penentuan aluminium(III) akues secara spektrofotometri. *Sains Malaysiana*, 45: 1807-1814.
6. Nizar, S. A., Satar, N. S. A., Amar, S. A. S., Abdullah, F. H., Mehamod, F. S., Suah, F. B. M. (2019). Fluorescence enhancement of Al^{3+} - sodium morin-5-sulfonate complex by imidazolium ionic liquid and its application in determination of Al^{3+} ions in an aqueous solution. *Jurnal Teknologi*, 81: 175-180.

7. Mohd Suah, F. B., Ahmad, M. and Lee, Y. H. (2014). Highly sensitive fluorescence optode based on polymer inclusion membranes for determination of Al(III) ions. *Journal of Fluorescence*, 24: 1235-1243.
8. Chebotaryov, A. N., Snigur, D.V., Duboviy, V. P., Scherbakova, T. M., Bevziuk, K. V. and Nevmerjitcaia, K. S. (2017). The features of pyrocatechol violet complexation with Mo(VI) and W(VI) in solutions. The spectrophotometric determination of Mo(VI) in multivitamins. *Methods and Objects of Chemical Analysis*, 12: 12-16.
9. Wang, X. D. and Wolfbeis, O. S. (2020). Fiber-optic chemical sensors and biosensors (2015-2019). *Analytical Chemistry*, 92: 397-430.
10. Makowka, A. and Pospiech, B. (2019). Synthesis of polymer inclusion membranes based on cellulose triacetate for recovery of lanthanum(III) from aqueous solutions. *Autex Research Journal*, 19: 288-292.
11. Ncib, S., Barhoumi, A., Bouguerra, W., Larchet, C., Dammak, L., Hamrouni, B. and Elaloui, E. (2018). Preparation and characterization of cellulose triacetate polymer inclusion membrane blended with acetylated kraft lignin: Effect of akl and application to the copper(II) extraction from acidic media. *Desalination and Water Treatment*, 104: 263-272.
12. Radzyminska-Lenarcik, E., Pyszka, I. and Ulewicz, M. (2020). Separation of Zn(II), Cr(III), and Ni(II) ions using the polymer inclusion membranes containing acetylacetone derivative as the carrier. *Membranes*, 10: 88.
13. Mohd Suah, F. B. and Ahmad. M. (2017). Preparation and characterization of polymer inclusion membrane based optode for determination of Al^{3+} ion. *Analytica Chimica Acta*, 951: 133-139.
14. Abdullah, F. H., Latif, N. A. A., Suah, F.B.M. and Mehamod, F.S. (2017). Sensitive fluorimetric determination of Al^{3+} ion based on the formation of ternary complex containing room temperature ionic liquid. *Journal of Luminescence*, 188: 267-274.
15. Du, X. and Xie, X. (2021). Ion-selective optodes: alternative approaches for simplified fabrication and signaling. *Sensors Actuators B: Chemical*, 335: 129368.
16. Mohd Suah, F. B. (2017). Preparation and characterization of a novel Co(II) optode based on polymer inclusion membrane. *Analytical Chemistry Research*, 12: 40-46.
17. Denna, M. C. F. J., Camitan, R. A. B., Yabut, D. A. O., Rivera, B. A. and Coo, L. D. (2018). Determination of Cu(II) in environmental water samples using polymer inclusion membrane-TAC optode in a continuous flow system. *Sensors Actuators B: Chemical*, 260: 445-451.
18. Khajehsharifi, H., Bordbar, M. M. and Esfandiary, P. (2018). Design and evaluation of a novel bismuth optical sensor using PC-ANN application. *Analytical and Bioanalytical Chemistry Research*, 5: 159-169.
19. Miller, J. N., and Miller, J. C. (2018). Statistics and chemometrics for analytical chemistry. 7th Edition. Pearson/Prentice Hall, Harlow: pp 1-30.
20. Mohd Suah, F. B., Mehamod, F. S. and Ahmad, M. (2017). Effect of non-ionic surfactants to the Al(III)-morin complex and its application in determination of Al(III) ions: a preliminary study. *Malaysian Journal of Analytical Sciences*, 21: 793–800.
21. Ramadan, M. S., El-Mallah, N. M., Nabil, G. M. and Abd-Elmenem, S. M. (2019). Hydrophobic effect for anionic dye - cationic surfactant interaction in aqueous and mixed solvent. *Journal of Dispersion Science and Technology*, 40: 1110–1120.
22. Anwar, Z. M., Ibrahim, I. A., Kamel, R. M., Abdel-Salam, E. T. and El-Asfoury, M. H. (2018). New highly sensitive and selective fluorescent terbium complex for the detection of aluminium ions. *Journal of Molecular Structure*, 1154: 272-279.
23. Yıldız, E., Saçmacı, Ş., Saçmacı, M. and Ülgen, A. (2017). Synthesis, characterization and application of a new fluorescence reagent for the determination of aluminum in food samples. *Food Chemistry*, 237: 942-947.

24. Nguyen, M. P., Kelly, S. P., Wydallis, J. B. and Henry, C. S. (2020). Read-by-eye quantification of aluminum (III) in distance-based microfluidic paper-based analytical devices. *Analytica Chimica Acta*, 1100: 156-162.
25. Harris, D. C. and Lucy, C. A. (2020). Quantitative chemical analysis. 10th Edition. Freeman WH, New York: pp 99-126.

Malaysian Journal of Analytical Sciences (MJAS)
Published by Malaysian Analytical Sciences Society

INFLUENCE OF MINERALS ON CONTROL MEASUREMENT OF AMMONIUM, NITRITE, NITRATE AND PHOSPHATE USING UV-SPECTROPHOTOMETER

(Pengaruh Mineral Terhadap Pengukuran Kawalan bagi Ammonium, Nitrit, Nitrat dan Fosfat Menggunakan Spektrofotometer UV)

Md. Salatul Islam Mozumder*, Shehab Shahreyar, Saiful Islam, Md. Delowar Hossain

Department of Chemical Engineering and Polymer Science,
Shahjalal University of Science and Technology, Sylhet-3114, Bangladesh

**Corresponding author: salatul-cep@sust.edu*

Received: 12 February 2021; Accepted: 30 March 2021; Published: 25 April 2021

Abstract

Interference of different minerals on UV-spectrophotometric determination of ammonium nitrogen (NH_4^+-N), nitrite-nitrogen (NO_2^--N), nitrate-nitrogen (NO_3^--N) and phosphate (PO_4^{3-}) was investigated in this study. Iron, magnesium and sodium acetate had significant interference in Nesslerization of NH_4^+-N which was needed to adopt standard protocol for the accurate determination of NH_4^+-N. However, adding 5 times higher Nessler reagent compared to standard method was used to overcome the limitations due to interference of minerals. In determination of NO_2^--N through sulphanilmide method, magnesium and iron did not show any significant affect. Presence of 5 g/L sodium acetate reduced the slope of calibration curve of NO_2^--N from 0.603 to 0.224. Presence of sodium, either in form of sodium acetate or sodium chloride, reduced the absorbance of sulphanilmide method for NO_2^--N determination. Increasing sodium acetate concentration from 2 to 10 g/L, the absorbance of 4 mg/L NO_2^--N was reduced by 5 times: 1.50 to 0.34. Identical absorbance for 4 mg/L NO_2^--N was found in the presence of 0.84 g/L NaCl (≈ 0.33 g/L Na^+) and 2 g/L Na-acetate (≈ 0.56 g/L Na^+) which indicated that chlorine also had interference on NO_2^--N measurement. The complex formed by nitration of salicylic acid was not interfered by the presence of potassium, phosphate, sodium, magnesium, iron and sodium acetate; almost the same slope (0.0095) was observed for both with and without presence of minerals. In addition, Ammonium molybdate method for the determination of PO_4^{3-} was a robust method since the measurement was not affected in the presence of minerals.

Keywords: UV-spectrophotometer, Nesslerization, sulphanilmide method, salicylic acid method, ammonium-molybdate method

Abstrak

Gangguan mineral berbeza dalam penentuan ammonium nitrogen (NH_4^+-N), nitrit-nitrogen (NO_2^--N), nitrat-nitrogen (NO_3^--N) dan fosfat (PO_4^{3-}) melalui spektrofotometrik-UV telah disiasat dalam kajian ini. Ferum, magnesium dan natrium asetat menghasilkan gangguan yang signifikan tindak balas Nessler bagi NH_4^+-N yang perlu di adaptasi dalam protokol piawai bagi penentuan tepat NH_4^+-N. Walau bagaimanapun, penambahan 5 kali ganda reagen Nessler berbanding kaedah piawai telah digunakan untuk mengatasi kelemahan iaitu gangguan dari mineral. Dalam penentuan NO_2^--N menggunakan kaedah sulfanilmida, magnesium dan ferum tidak menunjukkan kesan yang signifikan. Kehadiran 5 g/L natrium asetat mengurangkan cerun lengkung

kalibrasi NO_2^--N dari julat 0.603 hingga 0.224. Kehadiran sodium, sama ada dalam bentuk natrium asetat atau natrium klorida, mengurangkan serapan bagi kaedah sulfanilmida dalam penentuan NO_2^--N. Peningkatan kepekatan natrium asetat dari julat 2 hingga 10 g/L, serapan 4 mg/L NO_2^--N menurun sebanyak 5 kali ganda: 1.50 hingga 0.34. Serapan sama bagi 4 mg/L NO_2^--N diperolehi dengan kehadiran 0.84 g/L NaCl (≈ 0.33 g/L Na^+) dan 2 g/L Na-asetat (≈ 0.56 g/L Na^+) telah menjelaskan klorin memberi gangguan kepada pengukuran NO_2^--N. Kompleks yang terhasil melalui penitratan oleh asid salisilik tidak diganggu oleh kehadiran kalium, fosfat, natrium, magnesium, ferum dan natrium asetat, kecerunan yang sama (0.0095) telah diperhatikan bagi kehadiran mineral atau sebaliknya. Selanjutnyam kaedah ammonium molibidat bagi penentuan PO_4^{3-} diketahui kaedah teguh kerana pengukuran tidak diganggu dengan kehadiran mineral.

Kata kunci: spektrofotometer UV, tindak balas Nessler, kaedah sulfanilmida, kaedah asid salisilik, kaedah ammonium-molibdat

Introduction

Trace elements in the surface water play a key role in the development of analytical method for the determination of water quality. Nutrient contents, specifically ammonium-nitrogen (NH_4^+-N), nitrite-nitrogen (NO_2^--N), and nitrate-nitrogen (NO_3^--N), are increasing in environmental water with the change of food habit and economic growth across the world. Albeit nutrients are essential trace elements in the surface water, concentrations of nutrients above certain levels can be hazardous to both life and earth [1]. Therefore, NH_4^+-N, NO_2^--N and NO_3^--N need to be analyzed and determined accurately for the proper treatment of wastewater considering the environmental and biological concern.

Phosphorus, commonly found as phosphate, is one of the abundant elements on the earth surface, while high concentrations of NH_4^+-N and PO_4^{3-} in the stream or lake avail massive algae blooming (eutrophication) which subsequently contributes to depleting the dissolved oxygen level in the water that is destroying aquatic life [2,3]. Furthermore, plants and animals use phosphate to conduct photosynthesis and respiration. Hence, plant growth rate is linked with increasing the phosphate concentrations [4]. For microorganisms and photosynthetic organisms in different environments, NH_4^+-N, NO_2^--N and NO_3^--N are available forms of N which need to be accurately measured for examining N cycling and their existence in terrestrial as well as in aquatic ecosystems [5].

With the improvement of environmental quality control and monitoring system in different countries, aqueous NH_4^+-N, NO_2^--N, NO_3^--N and PO_4^{3-} are being controlled due to the strict regulation [6]. In addition, a number of in-plant processes is going to treat wastewater containing NH_4^+-N, NO_2^--N, NO_3^--N and PO_4^{3-} following the recently advanced wastewater treatment technology where the ions need to be determined accurately and more easily. For instance, several determination methods, specifically spectrophotometric, fluorescence, chemiluminescence, and electrochemical detections, have been investigated by researchers for ammonium, nitrate, nitrite and phosphate ions [7]. Besides these, capillary zone electrophoresis, high performance liquid chromatography and ion chromatography methods have also been used for the aforementioned ions determination [8,9]. However, most of the above-mentioned methods reflect complexity either in determination steps or in pretreatment of samples. Hence, UV-spectrophotometric methods are most commonly used technique for the determination of NH_4^+-N, NO_2^--N, NO_3^--N and PO_4^{3-} due to its simplicity, easy measurement, low fixed and operating cost [10].

Nowadays vials with reagents of different companies such as HACH, HANNA, BEKA Scientific GmbH, Lovibond etc. are widely used for the direct and automatic measurement of NH_4^+-N, NO_2^--N, NO_3^--N and PO_4^{3-} using spectrophotometer [11,12,13]. In spectrophotometric method, in-built calibration mostly accomplished with distilled water is embedded within the program of spectrophotometer for automatic determination. During the quantitative analysis of the sample following UV-spectrophotometric method, the sample shows error measurements when the samples contain different minerals which have interference on

color forming complex. Therefore, real sample in spectrophotometer shows a different value from the actual one since the calibration of spectrophotometer has been accomplished with distilled water.

In this study, UV-spectrophotometric determination methods were adopted from the standard EPA method for real case scenario, i.e. in presence of minerals. In the experiment, the calibration curves were made with the standard method using distilled water as well as mineral medium for the determination of NH_4^+-N, NO_2^--N, NO_3^--N and PO_4^{3-} aiming to assess the effect of minerals on UV-spectrophotometric determination. The study intended to develop the accurate UV-spectrophotometric determination methods of NH_4^+-N, NO_2^--N, NO_3^--N and PO_4^{3-} ions concentration in the presence of common minerals like iron, magnesium, sodium acetate by overcoming the interference of these minerals on the determination.

Materials and Methods

Standard method of ammonium-nitrogen (NH_4^+-N) determination

The Nessler method is the widely applied analysis for the determination of NH_4^+-N in water using UV-spectrophotometer, specifically with the use of the concentration range 0.4 - 1.0 mg NH_4^+-N/L [14]. At the NH_4^+-N determination phase, yellow to brown color complex was produced through the Nessler ammonium reaction which strongly absorbed at 400 to 425 nm.

To prepare Nessler Reagent, 4.4 g $HgCl_2$ (Merck, India) was dissolved in 70 mL distill water and heated for complete dissolution. Besides the saturated solution of $HgCl_2$ Preparation, 11 gm KI (Sigma-Aldrich, Germany) was dissolved separately in the minimum amount of water to produce saturated solution of KI. Subsequently, saturated solution of KI was added drop wise to the saturated solution of $HgCl_2$ to form abundant precipitation of orange HgI_2. Maximum quantity of HgI_2 precipitate formation was observed at 1:2 molar ratio of the two reagents $HgCl_2$ and KI respectively. Further addition of KI led to the dissolution of orange precipitate of the HgI_2 by transforming into water soluble complex $K_2[HgI_4]$. At 1:4 molar ratio of the two reagents ($HgCl_2$ and KI), the total dissolution of HgI_2 precipitate and consequent yellowish color complex solution formation were observed. The yellowish color complex solution was taken in 250 mL beaker and mixed with 40 mL of 5 M NaOH solution (Merck, India) where NaOH concentration could be slightly higher than 5 M but not lower than 5 M. Finally, distilled water was added to make the solution 200 mL.

An amount 50 mL of standard (dissolving $(NH_4)_2SO_4$ (Merck, Germany)) or sample of NH_4^+-N solution with concentration of 0.4 - 8 mg/L was uniformly mixed with 1 mL of 0.5 g/L K-Na Tartarate (Rochelle salt solution) (Merck, India) and 1 mL of Nessler's reagent. The solution stagnant was kept for five minutes to complete the reaction; then absorbance was taken at 390 nm (where the maximum absorbance was found) using UV-spectrophotometer (SHIMADZU, UV-1800, Japan).

Standard method of nitrite-nitrogen (NO_2^--N) determination

In this method, sulphanilmide reagent (10 g/L) (Merck, India) (Reagent SA) was prepared by dissolving 5 g sulphanilamide in a mixture of 50 mL, 37% concentrated HCl and approximately 300 mL distilled water and then diluted to 500 mL. 0.2 mL of sulphanilmide reagent was mixed with 10 mL standard sample prepared by dissolving $NaNO_2$ (Merck, India) in distilled water and was allowed 8 minutes to complete the reaction. 0.3 mL of 1 g/L 1-naphthyl ethylenediamine dihydrochloride (Merck, India) solution (Reagent ED) was then mixed and kept for 10 minutes to complete the reaction before taking absorbance at 543 nm using UV-spectrophotometer. The stock solution of N-(1-naphthyl)-ethylenediamine dihydrochloride (Reagent ED) was stored in dark bottle as well as in refrigerated condition. It was needed to prepare fresh N-(1-naphthyl)-ethylenediamine dihydrochloride solution in every week or sooner if a strong brown coloration was observed.

Standard method of nitrate-nitrogen (NO_3^--N) determination

According to rapid determination method of nitrate-N, a complex molecule was formed by reacting with salicylic acid under highly acidic conditions and maximum absorbance was observed in basic (pH > 12) condition

at 410 nm wavelength [15]. Salicylic acid-H_2SO_4 reagent was prepared by dissolving 5 g of salicylic acid (Merck, Germany) in 100 mL of conc. H_2SO_4 (Merck, India), while the reagent was important to store in a brown bottle at 4^0 C. 0.25 mL standard or sample was mixed thoroughly with 0.8 mL of 5% (w/v) salicylic acid-H_2SO_4 reagent. The mixture was kept for 20 minutes at room temperature to complete the reaction and then, 19 mL of 2 N NaOH was added to raise the pH above 12 that ensured the formation of color forming complex. Finally, the absorbance of sample was taken at 410 nm using UV-Spectrophotometer.

Standard method for phosphate (PO_4^{3-}) determination

To determine the PO_4^{3-} concentration, a combined reagent was prepared by mixing 500 mL of 2.5 M H_2SO_4, 50 mL of 2.75 g/L potassium antimony tartrate ($K(SbO)C_4H_4O_6.5H_2O$) solution, 150 mL of 40 g/L ammonium molybdate ($(NH_4)_6Mo_7O_6.4H_2O$) solution and 300 mL of 17.6 g/L ascorbic acid solution. A fresh mixture of this reagent mixture was needed to make every day. 13 mL combined reagent was mixed with 50 mL sample, and it shook thoroughly and made up to the mark 100 mL with distilled water. The solution was kept in rest for 30 minutes to develop color. After color formation in the sample solution, the absorbance of the sample solution was measured at 710 nm.

Evaluation of effect of minerals on determination

To assess the effect of minerals on determination of NH_4^+-N, NO_2^--N, NO_3^--N and PO_4^{3-}, a combined mineral medium commonly used in bioprocess, biological nitrogen removal and phosphate recovery process, was considered in this study. The mineral medium, consisting of KH_2PO_4, K_2HPO_4, $MgSO_4$, $Na_3C_6H_5O_7$, $FeSO_4$ etc., together with NH_4-N, was significant and widely used for the proper growth of different organisms. The composition of the mineral medium used in this study is shown in Figure 1. The calibration curves of NH_4^+-N, NO_2^--N, NO_3^--N and PO_4^{3-} were prepared by following the standard method discussed above but, in this case, mineral medium was used instead of distilled water.

Beside these, the concentration of CH_3COONa, Mg and Fe were varied within the mineral medium to find out the effect on measurement. The stability of the color forming complex in presence of minerals was measured by keeping the color solution for an hour and measuring the absorbance in a regular interval.

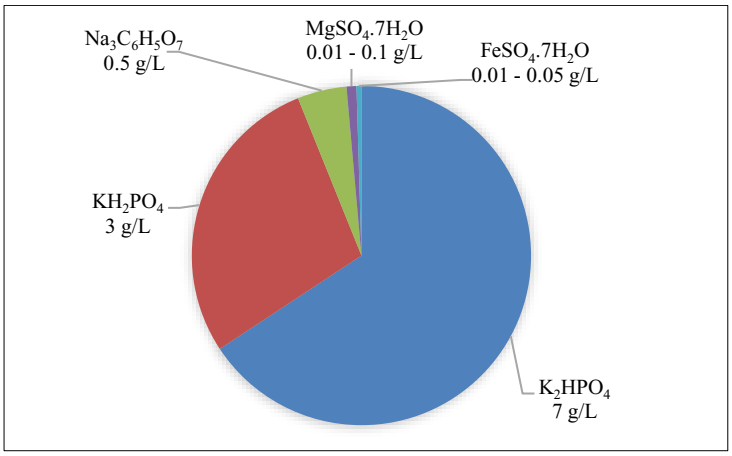


Figure 1. Mineral medium composition

Results and Discussion

NH_4^+-N determination in presence of mineral medium

Initially a calibration curve was made for NH_4^+-N using standard Nessler method. In this standard measurement, NH_4^+-N solution and reagents were prepared using distilled water. With varying NH_4^+-N concentrations from 0.4 to 8.0 mg/L, absorbance was measured by repeating each measurement for three times to ensure the accuracy. The produced calibration curve with standard deviation is shown in Figure 2a. A straight line relationship with slope 0.2152 and R^2 0.9993 ensured the accuracy of the measurement.

In the evaluation of interference of mineral medium (following the composition shown in Figure 1) on determination of NH_4^+-N, all the reagents were prepared with distilled water and the standard NH_4^+-N solution, but the dilutions were made using mineral medium. At the beginning of this measurement, absorbance was taken as per standard procedure; in the standard method, 1mL of Nessler solution and 1 mL of K-Na Tartarate were added in 50 mL sample (Figure 2b). It revealed that the low ammonium concentration (< 2 mg/L) did not produce sufficient color for the UV-spectrophotometric determination and subsequently the relation became non-linear. If water contained other color inducing substances mainly alkali ions like HS^-, Mg^{2+}, Fe^{2+} and Ca^{2+}. the Nessler method was not suitable for ammonium determination. These ions react with Nessler reagent and they should be removed through treatment with Rochelle solution or ethylenediamine-tetra-acetic acid (EDTA) or $ZnSO_4$, to overcome the interference of HS^-, Mg^{2+}, Fe^{2+} and Ca^{2+} [16]. In fact, stabilizer could be applied to remove hardness from water while it was collected from anaerobic digester for analyzing the NH_4^+-N [17]. Moreover, to increase the sensitivity of Nessler method the polyvinyl alcohol (PVA) could be added that increased the light absorbance [18,19].

In case of using 1 mL each reagent (as standard method), the Rochelle solution was not sufficient enough to remove the interfering substances. Due to the establishment of two equilibrium relationships; mineral medium with reagents and NH_4^+-N with reagents made an exponential relationship between absorbance and concentration. The interference for the reaction between mineral medium and reagents was overcome by increasing the amounts of reagents. The linearity of the relationship between NH_4^+-N concentration and absorbance increased with increasing amounts of reagents, specifically 3 to 5 mL each reagent in 50 mL sample (shown in Figure 2b). A linear relation passing through the origin was observed while 5 mL of Nessler and 5 mL of K-Na tartarate were used in 50 mL sample with minerals. To ensure the accuracy of the developed protocol for the determination of NH_4^+-N present in mineral medium, it was repeated for five times; the calibration curve with standard deviation is shown in Figure 2b. The slope of the calibration curve was found 0.207 with R^2 value 0.9917.

Effect of Fe and CH_3COONa on NH_4^+-N determination

In order to evaluate the effect of Fe concentration on UV-spectrophotometric determination of NH_4^+-N concentration, absorbance was taken using the same mineral medium following the composition shown in Figure 1 but changing Fe concentration (0.02 - 0.10 g/L). In the modified Nessler method, 5 mL of Nessler solution and 5 mL of 10 g/L K-Na Tartarate (Rochelle salt solution) solution in 50 mL of 6 mg/L NH_4^+-N solution were used. The stability of the color forming complex was evaluated by taking absorbance for the period of an hour (Figure 3a). Increasing Fe concentration from 0.02 g/L to 0.10 g/L, absorbance was decreased from 1.35 to 1.10. The brown color solution, which was produced by the reaction between ammonium and Nessler reagent, was stable during one-hour experimental period. Accurate analysis of NH_4^+-N could not be possible using original Nessler method due to strong interference of Fe^{2+} when Fe^{2+} content became more than 1.0 mg/L [16]. Fe^{2+} reacted with the Nessler reagents and formed a complex and turbid compound that increased the absorbance. However, five times higher Rochelle salt was used in this study that acted to minimize the interference of substances, like Fe, Mg and Ca which helped to measure NH_4^+-N accurately (within 3% variation).

Presence of sodium acetate had a significant effect on NH_4^+-N determination following Nessler method.

Addition of 2 g/L sodium acetate decreased the absorbance by 6 - 7%. However, when 10 g/L sodium acetate was used, an unstable color forming complex was formed. Initial absorbance was much lower compared to the presence of 2 g/L sodium acetate, but the color intensity as well as absorbance increased over time (shown in Figure 3b). Mechanism behind increasing the color intensity is still unknown. However, to measure the NH_4^+-N in presence of sodium acetate, a fixed time was essential to consider for both the calibration curve preparation and sample analysis.

Effect of Mg concentration on NH_4^+-N determination

Water samples with Mg^{2+} concentration of 0.01 to 0.10 g/L were analyzed with modified Nessler method and the results were compared in Figure 3c. Initial absorbance at time, t = 0 was not changed significantly with changing Mg^{2+} concentration. While 0.01 g/L Mg^{2+} was present in mineral medium, absorbance for 5 mg/L NH_4^+-N was not deviated from its initial value. Increasing Mg^{2+} concentration, the absorbance was randomly deviated from its initial value. It was due to the formation of precipitate by the reaction of Mg^{2+} with Nessler reagents [20]. A high turbidity was formed at 0.10 g/L Mg^{2+} that increased the absorbance and later turbid compound was settled down that produced a clear solution as well as decreased the absorbance. Other researchers observed similar behavior using original Nessler method, following the findings of the researches; an accurate measurement of NH_4^+-N could not be possible in presence of Mg^{2+} [16,20]. 0.122 g/L Mg^{2+} (≈ 0.5 g/L Mg^{2+} as $CaCO_3$) concentration augmented the absorbance more than double; consequently, large overestimation of NH_4^+-N concentrations was noticed. In fact, the absorbance varied proportionally to the Mg^{2+} concentration [16]. To overcome the interference of complex formation of Mg^{2+}, it was better to determine the absorbance immediately after mixing the reagents.

NO_2^--N determination in presence of minerals

To determine the NO_2^--N present in distilled water and in mineral medium following the composition shown in Figure 1, calibration curves were compared using sulphanilamide method in both conditions (Figure 4). To prepare the calibration curves, 10 mL of standard NO_2^--N solution either in distilled water or in mineral medium was mixed with 0.2 mL sulphanilamide (SA) and 0.3 mL 1-naphthyl ethylenediamine dihydrochloride (ED). Finally, the solution was kept stagnant for 10 minutes to complete the reaction. The results showed that mineral medium did not have any effect on the determination of NO_2^--N where the slope was identical for both the cases, specifically 0.6075 and 0.6032 (Figure 4a and b). Sodium acetate, which was used as carbon source in many bioprocesses, had a significant effect on NO_2^--N determination. Absorbance and slope of calibration curves decreased with the presence of sodium acetate (Figure 4c). It showed a straight-line relationship for 0 - 2 mg/L NO_2^--N concentration, while the maximum absorbance was around 0.5. Above 2 mg/L NO_2^--N concentration, the absorbance remained steady due to the limitation of reagent to produce more color forming complex. This limitation was confirmed by increasing the amount of reagents that ultimately increased the detection limit of NO_2^--N (Figure 5). The absorbance and slope of calibration curves increased with the increasing amount of reagents.

The ratio of sulphanilamide (SA) and 1-naphthyl ethylenediamine dihydrochloride (ED) used in NO_2^--N determination was crucial for the accuracy. Between the two reagents, 1-naphthyl ethylenediamine dihydrochloride was mainly responsible to develop the color forming complex through the reaction with reaction product of NO_2^--N and reagent SA. Increasing reagent ED from 1 to 2 mL in 10 mL sample (mineral medium and 5 g/L sodium acetate) and 1 mL reagent A, the slope increased from 0.38 to 1.72 (Figure 5c and d). The slope increased with the increasing amounts of reagents. Higher slope increased the accuracy of the measurement but decreased the detection limit or narrowed the concentration range for the determination. However, the amount of reagents used for the determination of NO_2^--N must be balanced between the slope of calibration curve and measurement limit.

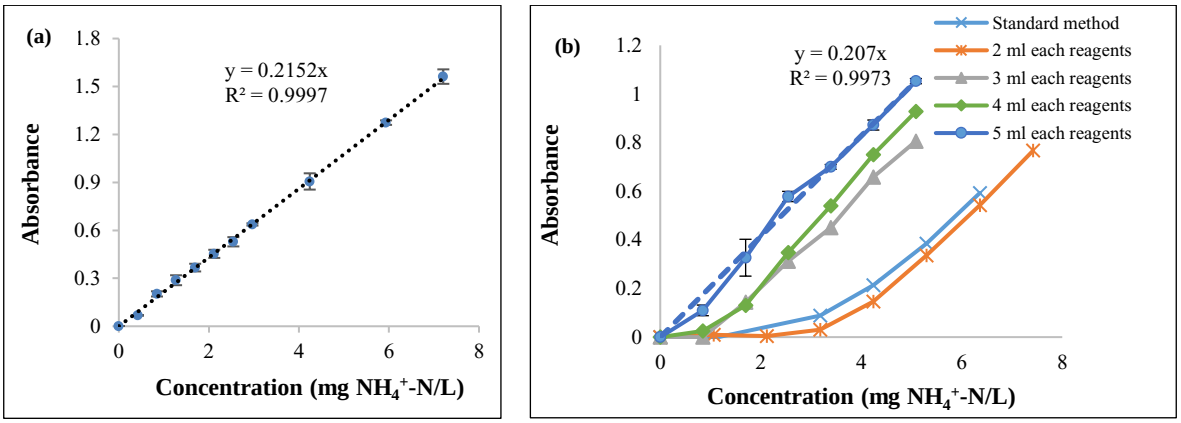


Figure 2. Relationship between the concentration and absorbance for NH_4^+-N determination: (a) using distilled water, and (b) using mineral medium with varying the amount of reagents

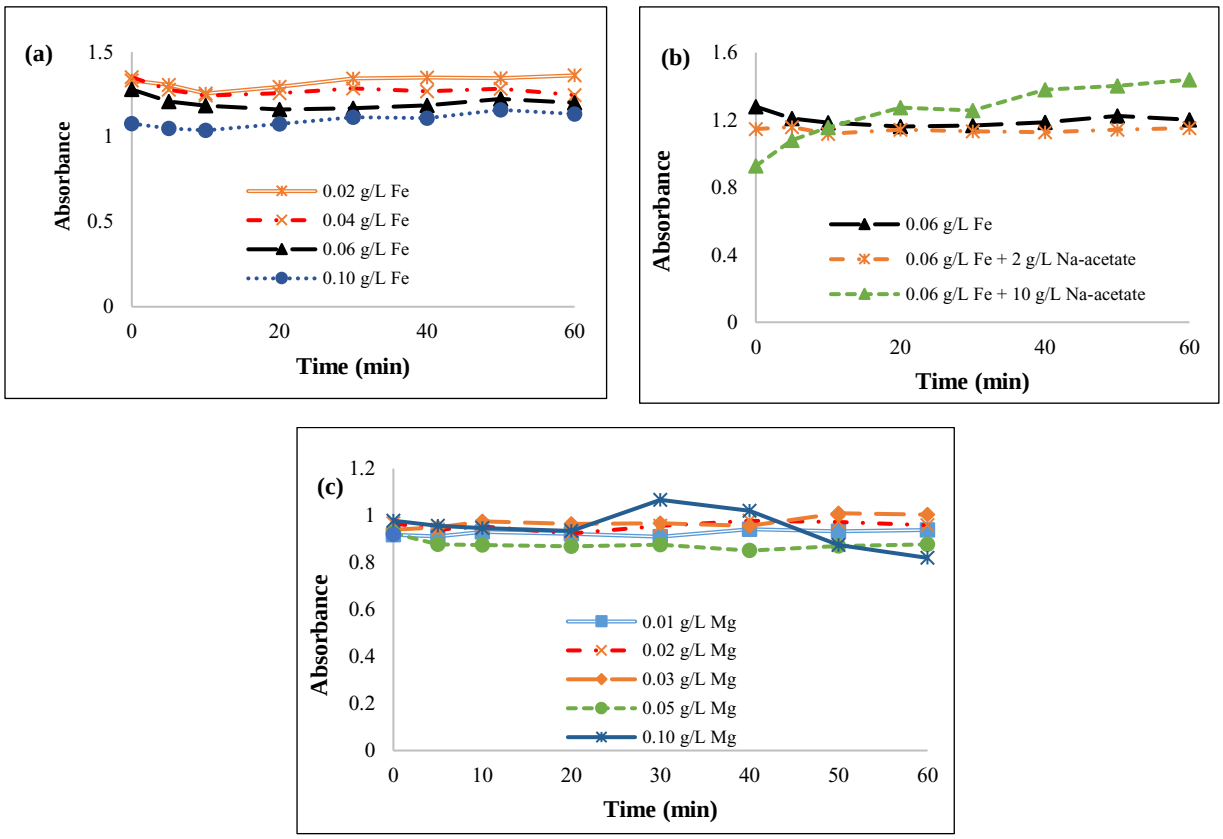


Figure 3. UV-Spectrophotometer absorbance of 5 mg/L NH_4^+-N in mineral medium as per Figure 1 but varying: (a) Fe^{2+} concentration, (b) sodium acetate, and (c) Mg^{2+} concentration

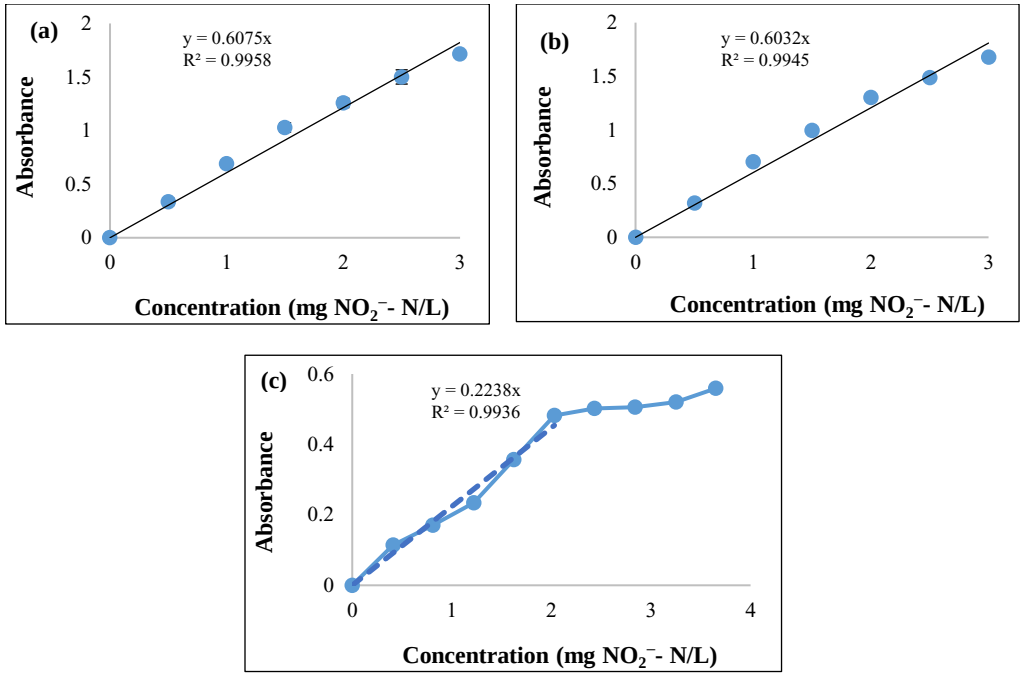


Figure 4. Calibration curves of NO_2^-- N using sulphanilamide method; standard was made with: (a) distilled water, (b) mineral medium, and (c) mineral medium and 5 g/L sodium acetate

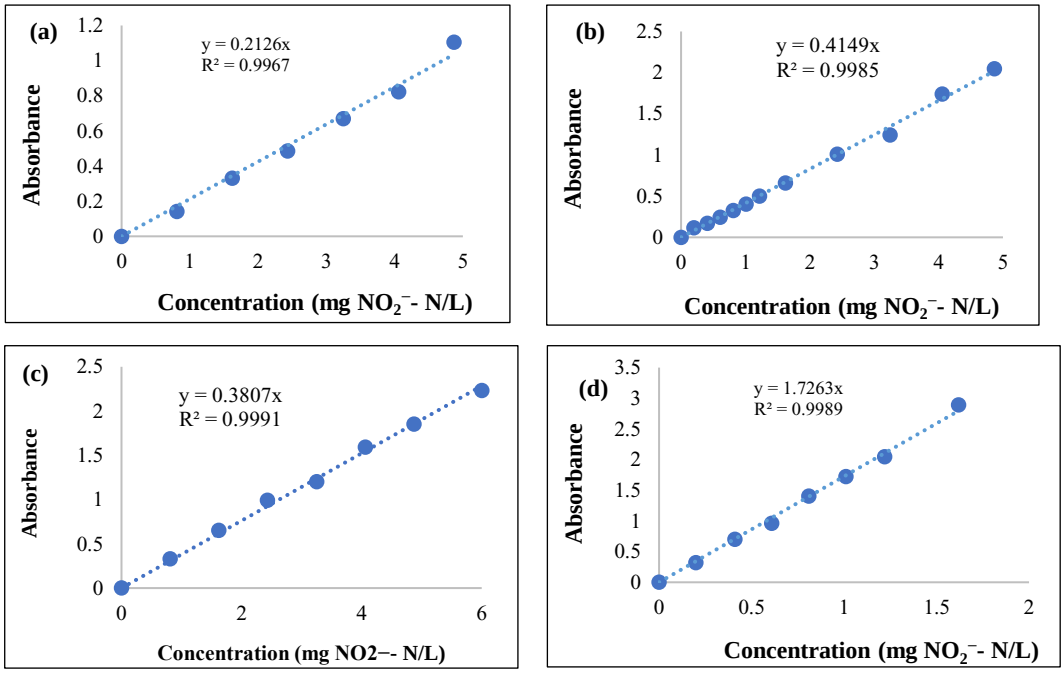


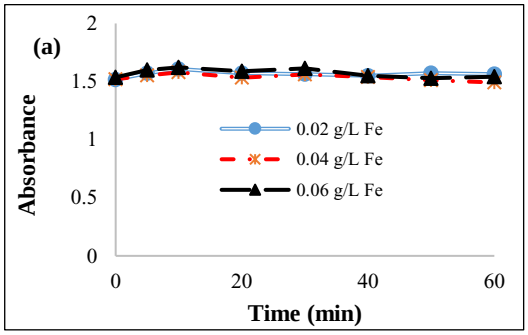
Figure 5. Calibration curves of NO_2^-- N using mineral medium and 5 g/L sodium acetate with varying amounts of color forming reagents: (a) 10 mL Sample + 0.3 mL SA + 0.4 mL ED, (b) 10 mL Sample + 0.5 mL SA + 0.75 mL ED; (c) 10 mL Sample + 1 mL SA + 1 mL ED, and (d) 10 mL Sample + 1 mL SA + 2 mL EB

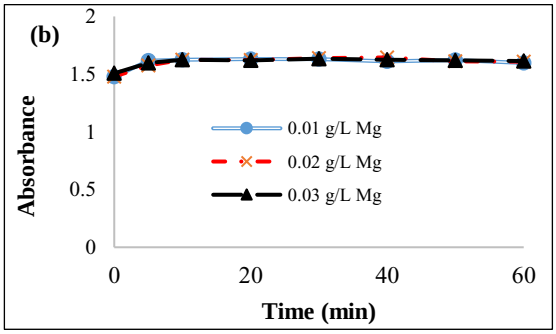
Effect of Fe and Mg on NO_2^--N determination

To assess the Fe^{2+} interference in the measurement of NO_2^--N, absorbance was taken for 4 mg/L NO_2^--N dissolved in mineral medium, following the composition shown in Figure 1, but varying Fe^{2+} concentration from 0.02 g/L to 0.06 g/L. In this case, 0.5 mL sulphanilamide (SA) and freshly prepared 0.75 mL 1-naphthyl ethylenediamine dihydrochloride (ED) were used in 10 mL sample to develop the color forming complex. Finally, the results showed that Fe^{2+} did not have any interference on NO_2^--N determination (Figure 5a). In this regard, more than 95% reduction of color formation was noticed while Fe^{2+} was present in the determination of NO_2^--N [21]. Through a simultaneous addition of sulfanilamide and 1-naphthyl ethylenediamine to the sample that already contains iron, the limitations were minimized. Low tolerance of iron on determination of NO_2^--N was observed in azo dye method [22]. Following the evaluation of the iron interference (Fe^{2+} and Fe^{3+}) experiment, Fe^{2+} concentration below 20 mg/L and Fe^{3+} concentration below 100 mg/L did not make any interference to NO_2^--N determination (within 2% error) [23]. Almost similar result was observed in this study since no interference of Fe^{2+} up to 60 mg/L on NO_2^--N determination was noticed (Figure 6a). Similarly, Mg^{2+} concentration also did not have any effect on NO_2^--N determination (Figure 6b).

Effect of CH_3COONa on NO_2^--N determination

Absorbance was taken for 4 mg/L NO_2^--N in mineral medium following the composition shown in Figure 1 with varying sodium acetate concentration from 0 to 10 mg/L. The absorbance decreased with increasing sodium acetate concentration (Figure 6c). Sodium presence in sodium acetate was mainly responsible for the interaction and subsequent formation of color forming complex in sulphanilamide method. Interaction of sodium was ensured by decreasing absorbance using NaCl. Identical absorbance for 4 mg/L NO_2^--N was found in the presence of 0.84 g/L NaCl (≈ 0.33 g/L Na^+) and 2 g/L Na-acetate (≈ 0.56 g/L Na^+) which indicated that chlorine also had interference on NO_2^--N measurement. A permissible concentration of both sodium and chlorine was found 4 g/L in the measurement of NO_2^--N (with less than 2% error) [23]. But in this study, a very strong interference of sodium and chloride was observed even in a low concentration. However, in all cases (Figure 6a-c), initial absorbance at time, t = 0 min was little lower, a stable color forming complex formed within 10 minutes. For this reason, original sulphanilamide method guided to wait 10 minutes to complete the reaction before measuring the absorbance.





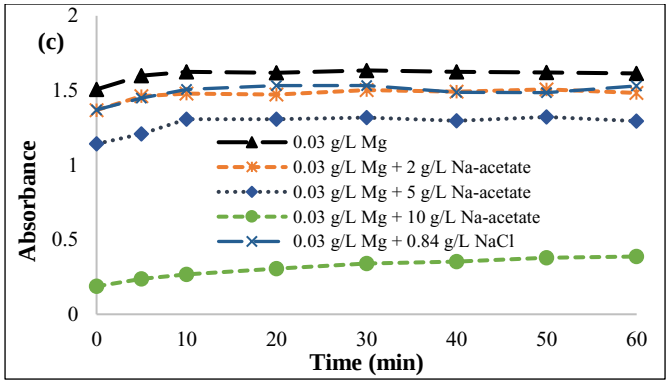


Figure 6. Effect of (a) iron (Fe^{2+}), (b) magnesium (Mg^{2+}), and (c) sodium acetate on NO_2^-- N determination using sulphanilamide method

NO_3^--N determination in presence of mineral medium

The method that was used to measure NO_3^--N in this study is well-known as salicylic-acid method [24]. Calibration curves were prepared with the use of the standard solution with distilled water and also with the use of the mineral medium, following the composition shown in Figure 1, with 5 g/L sodium acetate. While the stock solution and dilution were conducted using mineral medium, all the reagents were prepared with distilled water. Both calibration curves showed a straight line relationship with R^2 value above 98% and almost similar slopes, specifically 0.0094 and 0.0095 (Figure 7(ia) and 7(ib)). It indicated that mineral medium did not have any significant interference on NO_3^--N measurement in UV-spectrophotometer. Similarly, presence of ammonium-N, nitrite-N and chloride did not interfere on determination of NO_3^--N [24]. Albeit interference of iron (iron > 10 mg/L) was found on the colorimetric determination of NO_3-N using a standard method that involved reduction of NO_3^--N to NO_2^--N using cooperized cadmium followed by NO_2^--N determination by sulfanilamide method [21]. Sulfanilamide method for NO_2^--N determination has interference with some minerals. However, in this study, NO_3^--N was directly determined without reduction of NO_3^--N to NO_2^--N and found no interference of minerals.

PO_4^{3-} determination in presence of minerals

The calibration curve for the determination of PO_4^{3-} was prepared using either distilled water or mineral medium following the composition shown in Figure 1. The results were shown in Figure 7(iia) and 7(iib) where both the calibration curves showed a straight line with R^2 value above 99%. The slope of these straight-lines was close to each other, for instance 0.4315 and 0.4242, which indicated that minerals present in medium did not have any interference on PO_4^{3-} measurement for the use of ammonium molybdate method. Following the analysis of soil sample, metal ions such as Cr, Al, Fe, Hg, Pb, Cd, Zn, Ni, Co, Mn, Ca, Mg and etc. did not show any interference in phosphate determination [25]. A high tolerance of foreign ions in the UV-Spectrophotometric determination of PO_4^{3-} with ammonium molybdate solution was found, and it was coincided with this study [26].

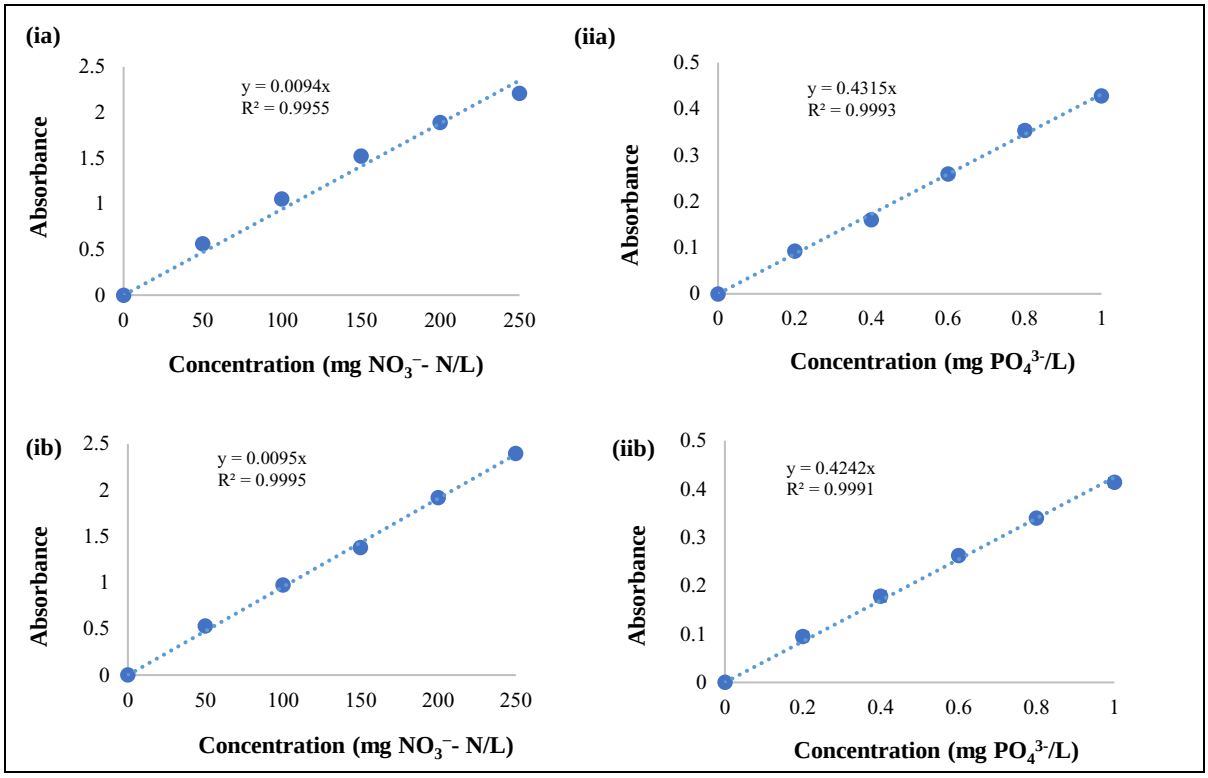


Figure 7. Calibration curves of (i) NO_3^--N and (ii) PO_4^{3-} where the standard was made with: (a) distilled water, and (b) mineral medium and 5 g/L sodium acetate

Conclusion

Mineral medium had a significant interference on original Nessler method of NH_4^+-N measurement which need to be adopted with the standard protocol for an accurate measurement of ammonium in water. On NH_4^+-N measurement, presence of Fe^{2+} reduced the absorbance but overestimated the NH_4^+-N concentration in Nessler method, whereas Mg^{2+} generated precipitation through the reaction with Nessler reagents which interfered on measurement. To overcome the interference of sodium acetate and Mg^{2+} in Nessler method, it would be better to take the absorbance immediately after mixing the reagents. However, for accurate measurement of NH_4^+-N in real sample, presence of other cations has to be measured where the calibration curve will be in the presence of those cations. On NO_2^--N determination, iron and magnesium did not have a significant effect, while sodium and chlorine showed a significant interference where a clear decrease of absorbance was observed due to the presence of sodium either in sodium acetate or other form. 1-naphthyl ethylenediamine was mainly responsible for the development of the color forming complex through reaction with the product of NO_2^--N and sulphanilamide. During the measurement of NO_2^--N, the concentration of sodium in the medium has to be measured initially and then the calibration curve will be made with the same sodium concentration. For the determination of NO_3^--N, salicylic acid method was more robust compared to copperised cadmium reduction method. Moreover, iron, magnesium, and sodium as sodium acetate did not have a significant effect on NO_3^--N and PO_4^{3-} determination.

Acknowledgement

The authors gratefully acknowledge the Bangladesh Bureau of Educational Information and Statistics (BANBEIS), Bangladesh for financial support to conduct this research (Project ID: SD2017530) and Dr. Mohammad Shafiqul Islam (Associate Professor,

Department of English, Shahjalal University of Science and Technology) for the Proofread of this manuscript.

References

1. Rezende, D., Nishi, L., Coldebella, P. F., Silva, M. F., Vieira, M. F., Vieira, A. M. S., Bergamasco, R. and Fagundes-Klen, M. R. (2016). Groundwater nitrate contamination: assessment and treatment using moringa oleifera lam. Seed extract and activated carbon filtration. *The Canadian Journal of Chemical Engineering,* 94: 725-732.
2. Ramos, A. C., Regan, S., McGinn, P. J. and Champagne, P. (2019). Feasibility of a microalgal wastewater treatment for the removal of nutrients under non-sterile conditions and carbon limitation. *The Canadian Journal of Chemical Engineering,* 97: 1289-1298.
3. Foulon, E., Rousseau, A. N., Benoy, G. and North, R. L. (2020). A global scan of how the issue of nutrient loading and harmful algal blooms is being addressed by governments, non-governmental organizations, and volunteers. *Water Quality Research Journal,* 55 (1): 1-23.
4. Yaqoop, M., Nabi, A. and Worsfold, P. J. (2004). Determination of nanomolar concentrations of phosphate in freshwaters using flow injection with luminol chemiluminescence detection. *Analytica Chimica Acta,* 510: 213-218.
5. Gamon, F., Tomaszewski, M. and Ziembińska-Buczyńska, A. (2019). Ecotoxicological study of landfill leachate treated in the ANAMMOX process. *Water Quality Research Journal,* 54 (3): 230-241.
6. Brezinski, K., Gorczyca, B. and Sadrnourmohammadi, M. (2019). Ion-exchange for trihalomethane control in potable water treatment - a municipal water treatment case study in Rainy River, Ontario, Canada. *Water Quality Research Journal,* 54(2): 142-160.
7. Moorcroft, M. J., Davis, J. and Compton, R. G. (2001). Detection and determination of nitrate and nitrite: a review. *Talanta,* 54: 785-803.
8. Fukushi, K., Tada, K., Takeda, S., Wakida, S., Yamane, M., Higashi, K. and Hiiro, K. (1999). Simultaneous determination of nitrate and nitrite ions in seawater by capillary zone electrophoresis using artificial seawater as the carrier solution. *Journal of Chromatography A*, 838: 303-311.
9. Okemgbo, A. A., Hill, H. H. and Siems, W. F. (1999). Reverse polarity capillary zone electrophoretic analysis of nitrate and nitrite in natural water samples. *Analytical Chemistry,* 71: 2725-2731.
10. American Public Health Association (2005). Standard methods for the examination of water and wastewater. Access from https://www.standardmethods.org/
11. He, X., Sun, Q., Xu, T., Dai, M. and Wei, D. (2019). Removal of nitrogen by heterotrophic nitrification–aerobic denitrification of a novel halotolerant bacterium Pseudomonas mendocina TJPU04. *Bioprocess Biosystems Engineering,* 42: 853-866.
12. Mozumder, M. S. I., De Wever, H., Volcke, E. I. P. and Garcia-Gonzalez, L. (2014). A robust fed-batch feeding strategy independent of the carbon source for optimal polyhydroxybutyrate production. *Process Biochemistry,* 49: 365-373.
13. Zhao, J., Wang, X., Li, X., Jia, S., Wang, Q. and Peng, Y. (2019). Improvement of partial nitrification endogenous denitrification and phosphorus removal system: balancing competition between phosphorus and glycogen accumulating organisms to enhance nitrogen removal without initiating phosphorus removal deterioration. *Bioresource Technology,* 281: 382-391.
14. Crosby, N. T. (1968). Determination of ammonia by the Nessler method in waters containing hydrazine. *Analyst,* 93: 406-408.
15. Cataldo, D. A., Haroon, M., Schrader, L. E. and Youngs, V. L. (1975). Rapid colorimetric determination of nitrate in plant-tissue by nitration of salicylic-acid. *Communications in Soil Science and Plant Analysis,* 6(1): 71-80.
16. Jeong, H., Park, J. and Kim, H. (2013). Determination of NH_4^+ in environmental water with interfering substances using the modified nessler method. *Journal of Chemistry,* 2013: 1-9.
17. Boopathy, R. (2003). Use of anaerobic soil slurry reactors for the removal of petroleum hydrocarbons in soil. *International Biodeterioration and Biodegradation,* 52: 161-166.

18. Hach, C. C., Brayton, S. V. and Kopelove, A. B. (1985). A powerful kjeldahl nitrogen method using peroxymonosulfuric acid. *Journal of Agricultural & Food Chemistry,* 33: 1117-1123.
19. Gulsoy, G., Tayanc, M. and Erturk, F. (1999). Chemical analyses of the major ions in the precipitation of Istanbul, Turkey. *Environmental Pollution,* 105: 273-280.
20. Foyn, E. (1950). Ammonia determination in sea water. *ICES Journal of Marine Science,* 16: 175-178.
21. Colman, B. P. (2010). Understanding and eliminating iron interference in colorimetric nitrate and nitrite analysis. *Environmental Monitoring and Assessment,* 165: 633-641.
22. Norwitz, G. and Keliher, P. N. (1985). Study of interferences in the spectrophotometric determination of nitrite using composite diazotisation - coupling reagents. *Analyst,* 110: 689-694.
23. Tarafder, P. K. and Rathore, D. P. S. (1988). Spectrophotometric determination of nitrite in water, *Analyst,* 113: 1073-1076.
24. Cataldo, D. A., Maroon, M., Schrader, L. E. and Youngs, V. L. (1975). Rapid colorimetric determination of nitrate in plant tissue by nitration of salicylic acid. *Communications in Soil Science and Plant Analysis,* 6(1): 71-80.
25. Ganesh, S., Khan, F., Ahmed, M. K., Velavenda, P., Pandey, N. K. and Mudali, U. K. (2012). Spectrophotometric determination of trace amounts of phosphate in water and soil. *Water Science and Technology,* 66(12): 2653-2658.
26. Mahadevaiah, Kumar, M. S. Y., Galil, M. S. A., Suresha, M. S., Sathish, M. A. and Nagendrappaa, G. (2007). A simple spectrophotometric determination of phosphate in sugarcane juices, water and detergent samples. *E-Journal of Chemistry,* 4(4): 467-473.

Malaysian Journal of Analytical Sciences (MJAS)
Published by Malaysian Analytical Sciences Society

THE REMEDIATION POTENTIAL OF BIOCHAR DERIVED FROM *Morus rubra* LINN. BARK

(Potensi Pemulihan oleh Terbitan Arang Bio dari Kulit Kayu *Morus rubra* Linn.)

Judith Clarisse Jose[1], Mark Nathaniel Dolina[2], Maria Carmen Tan[2]*

[1]*Biology Department*
[2]*Chemistry Department*
De La Salle University, 2401 Taft Avenue, Manila 0922, Philippines

**Corresponding author: maria.carmen.tan@dlsu.edu.ph*

Received: 15 December 2020; Accepted: 27 March 2021; Published: 25 April 2021

Abstract

Morus rubra L., commonly known as red mulberry, contains a myriad of phytochemical compounds. Mulberry plants have been previously studied for their potential in the phytoremediation process of potentially toxic elements (PTEs). In this study, biochars of red mulberry bark were produced by hydrothermal carbonization using a hydrothermal autoclave reactor (HAR) with PTFE liner and a Parr oxygen combustion vessel (POCV). These biochars were chemically characterized and their remediation potential were also investigated. Solvent extraction using dichloromethane was performed on the bark and biochars derived therefrom and the subsequent samples were evaluated using gas chromatography – electron ionization– mass spectrometry (GC–EI–MS). Scanning electron microscopy (SEM) provided the exterior characterization of these biochars, together with the dried red mulberry bark. Compositional analyses were determined by an energy dispersive X-ray spectrometer (EDX) and a Fourier transform infrared spectrometer (FT-IR). The biochar's remediation potential of toxic heavy metals was discerned by atomic absorption spectroscopy. Phytochemical analyses revealed the constituents of red mulberry bark which included phytosterol, triterpenes, and triterpenoids, whereas, biochars contained esters, alkanes, alkenes, alkaloids, diene, and fatty alcohol. Comparing the two carbonization processes, the Parr oxygen combustion vessel (POCV) was able to carbonize red mulberry bark more than the hydrothermal autoclave reactor (HAR) with PTFE liner, as observed in their GC-EI-MS and SEM profiles. Elemental analysis showed high percentages of oxygen and carbon in red mulberry bark due to the presence of carbohydrates. Both biochar products effectively absorbed lead (Pb) by almost 60% and minimally absorbed cadmium (Cd) and iron (Fe) in the heavy metal solution. Copper (Cu) and chromium (Cr) were not remediated from the heavy metal solution by both biochar samples.

Keywords: *Morus rubra* L., gas chromatography-electron ionization-mass spectrometry, scanning electron microscopy, Fourier transform infrared spectroscopy, energy dispersive X-ray analysis

Abstrak

Morus rubra L. umum dikenali sebagai mulberi merah, kaya dengan kandungan sebatian fitokimia. Pokok mulberi pada kajian terdahulu melihat potensinya dalam proses fitoremediasi terhadap unsur toksik (PTEs). Dalam kajian ini, arang bio dari kulit kayu mulberi merah telah dihasilkan melalui pengkarbonan hidrotermal menggunakan reaktor autoklaf hidrotermal (HAR) dengan liner PTFE dan vesel pembakaran oksigen Parr (POCV). Arang bio yang terhasil dicirikan secara kimia dan potensi pemulihannya turut dikaji. Pengekstrakan pelarut diklorometana digunakan terhadap kulit kayu dan terbitan arang bio dan diikuti analisis menggunakan spektrometri jisim-pengionan elektron-kromatografi gas (GC-EI-MS). Mikroskopi imbasan elektron (SEM) menjelaskan pencirian

luar arang bio bersama kayu kulit mulberi merah yang telah dikeringkan. Analisis komposisi telah ditentukan melalui spektometer sinar-X serakan tenaga (EDX) dan spektrometer inframerah transformasi Fourier (FT-IR). Potensi pemulihan arang bio terhadap ketoksikan logam berat telah dianalisa menggunakan spektroskopi serapan atom. Analisis fitokimia menjelaskan jujukan kimia bagi kulit kayu mulberi merah termasuklah fitosterol, triterpene, dan triterpenoid, manakala arang bio mengandungi ester, alkana, alkena, alkaloid, diena dan lemak alkohol. Perbandingan dua proses pengkarbonan vesel pembakaran oksigen Parr (POCV) mampu menghasilkan karbon yang lebih tinggi kandungannya berbanding reaktor autoklaf hidrotermal (HAR) dengan liner PTFE, diperhatikan dalam profil GC-EI-MS dan SEM. Analisis unsur telah menunjukkan peratusan tinggi kehadiran oksigen dan karbon di dalam kulit kayu mulberi merah disebabkan oleh kandungan karbohidrat. Produk arang bio berkesan menyerap plumbun (Pb) sehingga 60% dan serapan minima bagi kadmium (Cd) dan ferum (Fe) di dalam larutan logam berat. Kuprum (Cu) dan kromium (Cr) tidak dapat dipulihkan dari larutan logam berat oleh kedua-dua sampel arang bio.

Keywords: *Morus rubra* L., spektrometri jisim-pengionan elektron-kromatografi gas, mikroskopi imbasan elektron, spektrometer inframerah transformasi Fourier, spektometer sinar-X serakan tenaga

Introduction

The notable attention that is being given to timber-derived resources as a substitute of activated carbon for commercial adsorbent purposes is largely due to its efficient loading function, high availability, and low production expenditure [1]. Biochar is a high-carbon solid residue formed from pyrolysis processes. Biochar efficiency is largely dependent on the type of feedstock used, and the conditions of pyrolysis [2]. Apart from remediation of soil that has been contaminated by potentially toxic elements (PTEs), biochar can also remove other pollutants like organic substances, improve soil quality for agricultural productivity, and reduce greenhouse gases [3]. The macroporosity in granular wood-based hydrochar has been found to result in high sorption capacities [1].

Morus rubra L. (MR) is known as the scarlet mulberry which is indigenous to Eastern as well as Central North America. Additionally, MR is regarded as an endangered tree species in some parts of the United States and Canada, prompting its conservation [4]. MR has been established to be part of the Moraceae family along with the *Morus* genus, MR is classified as a perennial, deciduous, and woody plant [5]. The foliage of MR has been observed to be morphologically similar to black mulberry greenery (*Morus nigra*), although MR tends to possess thicker, lobed, and larger leaves [4]. *Morus* berries have also been in traditional medicine as a laxative, dewormer, emetic, anthelmintic, hypoglycemic agent, and to treat dysentery [6].

Numerous phytochemical compounds with antidiabetic properties such as flavonoids, alkaloids, triterpenes, saponins, sterols, glycosides, and phenolics have been found in the different parts as per *Morus* species [7]. It is the presence of these phytochemical compounds that give the mulberry plant its reported antidiabetic, anticorpulence, anti-inflammatory, carcinopreventive, bactericidal, free radical scavenging, prophylactic for viruses, cytoprotectant and neuroprotectant capacities [8]. Comparative studies among different mulberry species have been done to investigate possible differences in bioactivities found in their leaves, fruit, and bark. In one study, leaves and bark samples from *Morus alba* and MR were collected to evaluate their antioxidant and antibacterial activity. The results showed all extracts displaying significant antioxidant activity, with aqueous extracts from stem bark exhibiting greater antioxidant activity. The highest IC_{50} value reported among the samples was of MR, at 4.78 mg/ml. On the other hand, hydromethanolic extracts were found to have higher antimicrobial activity than aqueous extracts [9]. Another study involved aqueous MR leaf extracts being administered to rats, and it was found that at least 400 mg/kg of the MR extract were able to control hyperglycemia and dyslipidemia. Its exceptional antioxidant properties were propositioned to help ease complications arising from diabetes [7]. The cytotoxic effects of DMSO extracts of MR trials on homo sapiens colon adenocarcinoma (WiDr) were also investigated. MR extracts were found to exhibit moderate selective toxicity on colon cancer cells and significantly repress telomerase. The IC_{50} value was found to be 297.4 +/- 9.6 μg/mL [10]

Amino acid content analysis of black, white, and red mulberry leaves found fifteen different aminoalkanoic acids, namely glutamic acid, glycine, methionine, and tyrosine, with superior concentrations of amino acid groups detected in *M. alba* foliage. Extractions using 40% ethanol as the solvent yielded different micronutrients (phenolic acids) such as gallic acid, caffeic acid, chlorogenic acid, as well as tannin acid. Chlorogenic acid generated a quantitative content of 0.14% and rutin having a value of 0.058% [11]. Fatty acid analysis of *M. alba*, MR, and *M. nigra* revealed varying concentrations of unsaturated fatty acids which was mostly made up of linoleic acid, palmitic acid, and oleic acid [6]. Statistically significant differences in total anthocyanin content have been found between *M. nigra* and MR. Black mulberry berries were reported to have higher anthocyanin content (674-787 Cy 3-glu μg/g) compared to the content found in red mulberry samples (81-132 Cy 3-glu μg/g) [12]. Red mulberry and black mulberry have been noted for their high nutritional value which is largely attributed to their mineral content, though MR has been shown to have a higher Ca content than *M. nigra*, *M. nigra* has less Mg and K in its plant matrix. Moreover, *Morus* species were distinguished to have noteworthy mineral content which was higher than that of other cultivated and harvested fruits [12].

Hitherto, studies have only been limited to the absorption phytoremediation potential of mulberry plants. *Morus* species plants are known for their notable characteristics of swift development of plant growth, rapid proliferation, healthy leaves, and an extensive vascular network which render them appropriate for mitigation of polluted soils [13] especially for cadmium (Cd) and zinc (Zn) phytoextraction [14]. Only a few studies have been done on the remediation potential of its biochar. One study found that biochar derived from *M. alba* was found to have significantly removed Pb from solution, which was attributed to the biochar's chemical properties, namely the presence of organic functional groups (which are rich in electronegative groups), which can act as potential sequestrants [15]. However, the remediation potential of biochar derived from red mulberry bark has yet to be studied. After extensive literature search, the authors presuppose that this work is unique in its endeavor in the characterization and the investigation of the remediation potential of the biochar produced from the dried bark of the red mulberry species.

Materials and Methods

Materials

M. rubra bark was collected from Abucay, Bataan, Philippines (14.7128° N, 120.4934° E) on well cultivated arable land. The plant identity was substantiated and authenticated by the Bureau of Plant Industry (BPI) in Malate, Manila, National Capitol Region, Philippines.

Sample preparation

Dried MR bark was cut and ground into finer pieces. The crude extract was prepared by incubating 100 mg of dried red mulberry bark in dichloromethane (DCM) for 3 hours. The extract was filtered using Whatman filter paper No. 1 (11 μm pore size) and dried over nitrogen gas. The accumulated dried extract (1.3 mg) was diluted in DCM before filtering into a vial using a 0.45 μm syringe filter with a final volume of 1 mL. The sample was analyzed and characterized using gas chromatography – electron ionization – mass spectrometry (GC-EI-MS).

Hydrothermal carbonization of red mulberry bark

Hydrothermal carbonization (HTC) of dried MR bark was done using a hydrothermal autoclave reactor (HAR) with PTFE liner and a Parr oxygen combustion vessel (POCV). One gram of the outer covering of the MR plant was placed in both HAR and POCV, and both were heated using a furnace at 180 °C for 4 hours, increased at 260 °C for 120 minutes, and at 400 °C for 120 minutes. The temperature was increased until the samples were carbonized. The resulting biochar, a product of HTC obtained from both HAR and POCV, was prepared for GC – EI – MS analyses. One hundred milligrams (100 mg) of each biochar from HAR and POCV were incubated in DCM for 3 hours. The samples were filtered into a beaker by means of a 0.45 μm syringe membrane and were dried over nitrogen gas. The dried samples (1.4 mg for HAR and 1.2 mg for POCV) were concentrated over nitrogen gas and diluted in 1 mL DCM. Each subsequent eluate was then

prefiltered using a 0.45 µm membrane, with a total final volume of 1 mL in each vial (1.5 capacity vial).

Gas chromatography - electron ionization - mass spectrometry

All samples obtained from DCM extraction of dried red mulberry bark and hydrothermal carbonization of dried MR bark using HAR and POCV at 400 °C were analyzed using an Agilent gas chromatograph in tandem with a mass spectrometer (7890B) with a HP-5ms (5%-phenyl)-methylpolysiloxane Ultra Inert column (30 m x 250 mm x 0.25 mm). Ultrapure helium gas served as the mobile phase (1 mL/min), maintained pressure at 8.2 psi, rate of 36.62 cm/s, and holdup period of 1.37 minutes. The injection inlet (split less) was maintained at 250 °C, with a pressure of 8.2 psi, a flow rate of 24 mL/min, and a septum purge stream velocity of 3 mL/min. The temperature gradient was initially set at 70 °C after which the temperature was incrementally augmented to 2 °C/min to reach 135 °C for 10 minutes. Another temperature ramp was programmed to raise the temperature to 220 °C at 4 °C/min and was held at this temperature for 10 minutes. The final temperature ramp gradually raised to 270 °C at 3.5 °C/min and was held at 37 minutes. The compounds were identified via the National Institute of Standards and Technology (NIST) Archive 2.0. The computation of the % peak area average was derived from the subsequent total ion chromatograms (TIC). Identification was verified by the assessment of the individual constituents based on their order of elution with their relative retention indices on a gas chromatography column (mid-polar). Calculations of retention indices for all the compounds were evaluated using a standard consisting of multiple *n*-alkanes. All tests were performed in triplicates.

Scanning electron microscopy

A JSM 5310 Scanning Microscope (JEOL, Japan) was used to examine the morphology of the dried MR bark and biochar samples. This instrument uses a focused beam of electrons to scan the surface of the samples. A small amount of each sample was mounted in a metal stub using a conductive carbon adhesive tape and all samples were coated with gold ions for 65 seconds using JFC-1200 Fine Coater (JEOL, Japan). Analyses were done using SemAfore V.5.2 to analyze the produced image.

Energy dispersive X-ray analysis

An AMETEK-EDAX Z2e Analyzer was used to collect and analyze the energy dispersive spectroscopy (EDS) data and compositional characterization of the dried MR bark. The EDAX system which is attached to a JSM 5310 Scanning Microscope wherein the imaging ability of SEM identifies the specimen to be analyzed by EDAX. Analyses were done using EDAX APEX™ Review software.

Fourier transform infrared spectroscopy

A Thermo Scientific Nicolet 6700 FT-IR (Thermo Fisher Scientific, USA) with a DTGS potassium bromide detector (KBr), Csl beamsplitter, and transmission accessory were utilized for the characterization of the samples. Analytical grade KBr was employed to collect the background. Each sample was scanned 16 times from 400-4000 cm^{-1} with a spectral resolution of 4 cm^{-1}. Omnic Spectra software 8.0.342 (Thermo Fisher Scientific, USA) was used to analyze the data.

Atomic absorption spectroscopy

The AA-6300 Atomic Absorption Spectrophotometer, operated with an air-acetylene flame, was utilized for the detection of absorbance of heavy metals of dried MR bark and biochar samples. Copper, iron, lead, cadmium, and chromium were the heavy metals used to create a stock solution of 10 ppm. Working solutions were also prepared with final dilutions of 10 ppm, 5 ppm, 1 ppm, and 0.5 ppm. Three milligrams of each sample were placed in a plastic container and were incubated in 25 mL of different concentrations of working solutions of heavy metals for 72 hours at room temperature. Each trial was then prefiltered using Whatman filter paper No. 1 (11 µm pore size) to remove particulate matter. Standard concentrations of 10 ppm, 5 ppm, 1 ppm, 0.5 ppm, and 0.25 ppm were used for the analyses. Measurement of absorbances were set at the following wavelengths: 324.8 nm for copper [Cu], 248.3 nm for iron [Fe], 283.3 nm for lead [Pb], 228.8 nm for cadmium [Cd], and 357.9 nm for chromium [Cr]. All tests were performed in triplicates.

Results and Discussion

GC-MS analyses of dried red mulberry bark and biochar samples

Dried red mulberry bark was extracted using dichloromethane as the extracting solvent. GC-EI-MS identified six eluents from the crude extract. The constituents are enumerated in Table 1 and presented in Figure 1A based on their elution succession using the HP-5ms column. Characterization of the constituents was verified using their retention index based on the NIST Archive 2.0. The extract was mainly composed of triterpenes and phytosterols: α-amyrin (8.56%), lanosterol (2.61%) and γ-sitosterol (4.11%).

α-Amyrin is a pentacyclic triterpene found to be synthesized by several cultivars of plants. This is known to be usually found with its isomer β-amyrin in plant extracts [16]. These triterpenes have been stated to cover a wide spectrum of biological activities. Reported bioactivities involved anti-hyperglycemic [17], anti-microbial [18], and anti-inflammatory properties [19], among others. They are also known to have weak anti-cancer activity, but newly synthesized derivatives of the compounds improved the anticancer activity of α, β-amyrin [20]. Contrastingly, α-amyrin was shown to stimulate the proliferation of human keratinocytes by up to 18% [16].

Lanosterol was also observed to be present in the extract. It is a tetracyclic triterpenoid from which all steroids are derived [21]. It has been reported that lanosterol could be used as an alternative treatment in human cataracts. The study reported that lanosterol treatment significantly decreased the protein aggregates of various cataract-causing mutant crystallins and could reduce cataract severity [22]. However, another study had shown contradicting results wherein both lanosterol and 25-hydroxycholesterol were found to be unable to counteract lenticular opacities or avert advancements of cataracts [23]. Furthermore, age-related cataractous nuclei also showed progression and no changes even when under treatment with lanosterol for 6 days [24].

Another compound found from the extract is γ-sitosterol. It is a phytosterol that has the potential to be employed as an antidiabetic agent [25]. γ-Sitosterol, purified and separated from *Strobilanthes crispus*, was also tested for its cytotoxicity on several cancer cell lines revealing IC_{50} values of 8.3, 21.8, and 28.8 μg/mL for Caco-2, HepG2, and MCF-7 cell lines, correspondingly. γ-Sitosterol also suppressed *c-myc* gene, a cancer-causing gene, and induced apoptosis in Caco-2, HepG2 cell lines [26].

Meanwhile, six volatile constituents were identified from the biochar extract produced from HAR (Table 2). The extract was mostly composed of triterpenes, diene, and ester. β-amyrin (31.35%) had the highest peak area, followed by octadecane, 3-ethyl-5-(2-ethylbutyl)- (18.56%), and a-neooleana-3(5),12-diene (17.03%). Other notable compounds like 10-octadecenoic acid, methyl ester (14.83%), olean-13(18)-ene (13.87%) and 4,4,6a,6b,8a,11,11,14b-octamethyl-1,4,4a,5,6,6a,6b,7, 8,8a,9,10,11,12,12a,14,14a,14b-octadecahydro-2H-picen-3-one (10.03%) were also identified. Figure 1B presents the mass spectrum of the analyzed biochar obtained from HAR.

β-amyrin, which is the major peak in the HAR extract, is a pentacyclic triterpenoid. Pentacyclic triterpenes are acknowledged to be beneficial in metabolic disorders. A mixture of pentacyclic triterpenes α,β-amyrin was investigated and revealed an antihyperglycemic and hypolipidemic effect in mice. α, β-Amyrin considerably reduced streptozotocin –stimulated augmentations in blood sugar, cholesterol levels, and triacylglycerols at 10, 30, and 100 mg/kg. However, the mixture did not reduce normal blood sugar levels but exhibited hypolipidemic effects at 100 mg/kg [17]. Most of the components present in the extract were also triterpenes including olean-13(18)-ene and 4,4,6a,6b,8a,11,11,14b-octamethyl-1,4,4a,5,6,6a,6b,7,8,8a,9,10,11,12,12a,14, 14a,14b-octadeca hydro-2H-picen-3-one, which is also known as β-amyrone. Both mentioned triterpenes are β-amyrin derivatives [27, 28].

The biochar obtained from POCV was also analyzed via GC-EI-MS. A total of nine (9) eluents were observed and identified as listed in Table 3. The major peaks in the extract were composed of mostly esters, alkaloids, and fatty alcohol. 10-octadecenoic acid, methyl ester

had the highest peak area of 31.89% among all eluents, followed by 1,3-benzenedicarboxylic acid, bis(2-ethylhexyl) ester (21.01%). 10-Octadecanoic acid, methyl ester was reported to have antibacterial, antifungal, and antioxidant properties, and was found to decrease blood cholesterol [29].

It is worth mentioning that although GC-MS analysis of biochar from POCV (Figure 1c) identified more peaks (9 peaks) from the extract compared with the extract of biochar obtained from HAR (6 peaks), there is a great difference in their abundance numbers. The highest peak from HAR analysis had an abundance of 2 800 000 compared to the highest peak from POCV analysis which had only an abundance of 650 000. This could imply that POCV had carbonized the dried red mulberry bark more than HAR. The retention time (RT) of the major peaks from POCV coincided with the RT of the minor peaks from the chromatogram of HAR analyses.

SEM analyses

The surface morphology of dried MR bark and biochar products of HAR and POCV were analyzed using SEM. Scans of dried red mulberry bark seemingly showed square to rectangular patterns with dimensions of 10.29 ± 3.46 x 14.13 ± 1.85 µm (mean ± standard deviation) as shown in Figure 2 (a-b). Flakes and small particles measuring 3.10 ± 1.25 µm can also be observed. At 2000x magnification (Figure 2a) other regions of dried red mulberry bark appeared similar to rounded microparticles measuring 2.30 ± 0.67 µm which was prominent at the surface of the sample.

SEM photographs of biochars produced from HAR (Figure 2, c-d) and POCV (Figure 2, e-f) revealed a more distinct patterns similar to cork wood. Porous channels measuring 7.77 ± 0.65 µm were visible at 2000x magnification (Figure 2d) of biochar produced by HAR. However, it can be noticed that the biochar product of POCV did not display distinct geometrical patterns as compared to HAR with pores measuring 5.42 ± 1.08 µm (Figure 2e). This could also be an indication that POCV had a greater carbonization effect on the dried red mulberry bark than using HAR upon pyrolysis.

The patterns of both biochars from HAR and POCV SEM images were similar to the pattern of cork derived from the outer covering of the tree *Quercus suberus* L., which was described as honeycomb-shaped cells. The cork of *Quercus suberus* L. was used as a natural sustainable template to synthesize a highly porous ZnO-based biomorphic materials. The cork template was infiltrated with an aerosol to prepare ZnO with zinc acetate and nitrate used as precursors. Heating the infiltrated experiments at 350 °C maintained the honeycomb-shaped cells of the original structure of cork template. This methodology produced a graphite-comprising material that had dual physical adsorption and photocatalytic potential, which made it suitable for environmental remediation [30]. In this research, the dried red mulberry bark was heated multiple times with temperatures ranging from 180 °C to 400 °C. The SEM images of both biochars shown in Figure 2 (C–F) were the result of the pyrolysis of the bark at 400 °C. The biochar of HAR produced a well-defined cork structure compared to the biochar produced by POCV. However, the observance of the presence of porosity in both biochars could indicate that both carbonization processes were suitable for the production of environmental remediation materials.

EDX analysis

The elemental composition of dried red mulberry bark was investigated using the AMETEK-EDAX Z2e Analyzer. The EDAX APEXTM Review software revealed six elements present in the bark including oxygen (O) 52.76%, carbon (C) 33.82%, calcium (Ca) 7.92%, potassium (K) 3.21%, magnesium (Mg) 1.24%, and copper (Cu) 1.05%. Fresh sample of *M. alba* fruit also revealed similar elemental compositions with high potassium following carbon and oxygen content [31]. The scanning image and elemental analysis of MR is shown in Figure 3.

Carbon and oxygen are integral elements that can be found in plants, particularly in the form of carbon dioxide, which plays a significant role in the process of photosynthesis together with water to form simple sugars or carbohydrates [32]. These carbohydrates, such as cellulose, hemicelluloses, and polysaccharides covalently bonded to lignin, whether for structural or

storage purposes, are crucial to the development of the plant. The bark or outer covering is most made up of starch, a non-soluble sugar, although other plant species have been found to store other soluble plant sugars as well, such as glucose and fructose [33]. Calcium, in the form of Ca^{2+} ions, is an element collected by plants through the soil, and commonly transported through the xylem for the purpose of influencing plant enzymes such as phospholipase and other proteins which aid in plant growth [34]. The recommended dietary allowance for calcium can vary from 1,000 to 1,300 mg/day for adults [35]. Potassium is also essential to both cellular and reaction mechanisms in human physiology. In fact, potassium and sodium are the primary electrolytes that control the water equilibrium and the acid-base equilibrium in bodily homeostasis [36]. Adequate intakes (AIs) for potassium are within the range of 2,600 mg/day for adult females and 3,400 mg/day for adult males [37].

Magnesium, an essential element in biochemical functions of several metabolic processes, is used in therapeutics of various commonplace illnesses specifically migraines, metabolic disorders, diabetes, hyperlipidemia, asthma, premenstrual syndrome, preeclampsia, and differing cardiac arrhythmias [38]. The current recommended dietary allowance (RDA) for magnesium is 320 mg/day for adult females and 420 mg/day for adult males [39]. On the other hand, copper is considered a necessary element but has been found to be detrimental if it accumulates in living systems. The tolerable upper intake level for copper sourced from food and supplements is at 10,000 mcg for individuals older than 19 years old [40]. The WHO (World Health Organization) advocates the consumption of 30 µg per kg of body weight per day of copper to ensure sufficient health requirements. Cardiovascular integrity, lung elasticity, neovascularization, neuroendocrine function, and iron metabolism is also dependent on the presence of copper. Conversely, high intake of copper may induce toxicity and eventual onset of disease [41].

FTIR analyses

The dried red mulberry bark and biochars produced from HAR and POCV were characterized by FTIR. Figure 4 presents the FTIR patterns of all the samples. The peak patterns of the three samples were almost like one another. The mid infrared (IR) absorptions, with a wavenumber range of 4,000 to 400 cm^{-1} (wavelengths 2.5 to 25 µm), of the dried red mulberry bark is represented in Table 4. The peak obtained at 3416.65 cm^{-1} has been ascribed to the stretching of O – H bands implicating the presence of an alcohol. The peaks within at 3000 – 2840 cm^{-1} has been corresponded to C – H stretching of an alkane, whereas the peak at 1629.04 cm^{-1} has been correlated to the stretching of C = C bands of a conjugated alkene. Meanwhile, the peak obtained at 11427.61 cm^{-1} corresponded to the O – H bending from a carboxylic acid. Peaks within 1390 – 1310 cm^{-1} has been associated with the presence of phenols because of the O – H bending. The presence of an alkyl aryl ether has been correlated to the C – O stretching of peak obtained at 1246.45 cm^{-1}. The peak obtained at 1060.13 cm^{-1} corresponded to the stretching of C – O bands of a primary alcohol.

Similar observations were also exhibited in the FTIR spectrum patterns of the biochar produced from HAR (Table 5). The peak acquired at 3430.31 cm^{-1} has been linked to the O – H stretching of an alcohol. Peaks obtained within 3000 – 2840 cm^{-1} can be attributed to the C – H stretching of an alkane. A cyclic alkene may perhaps be present due to the C = C stretching of the peak seen at 1555.05 cm^{-1}. Peaks obtained at 1445.30 cm^{-1} can be attributed to the bending of O – H bands from a carboxylic acid, while the peaks shown within 1390 – 1310 cm^{-1} may possibly correspond to O – H bending of phenol compounds. The peak at 1087.67 cm^{-1} has been connected to the stretching of C – O bands of an aliphatic ether.

Occurrences of C – H stretching and methylene bending in the FTIR analyses revealed the possible presence of aliphatic and olefinic hydrocarbons in the dried red mulberry bark and biochars produced from HAR and POCV [42] as well as aromatic breakdown products associated with pyrolysis [43].

Table 6 presents the FTIR correlations because of the biochar generated from POCV. The peaks obtained are most likely to be attributed to the presence of alcohols by the stretching of O – H bands and C – O bands. The

peak at 2920.87 cm^{-1} corresponded to the C – H stretching of an alkane, while the peak at 1625.45 cm^{-1} was correlated to the C = C stretching from a conjugated alkene. The peak ascribed at 1427.71 cm^{-1} was assigned to the bending of O – H bands from a carboxylic acid. The peak at 1380.92 cm^{-1} was attributed to the C – H bending representing an alkane.

Table 1. Volatile constituents of dichloromethane crude extract of dried red mulberry bark

	Compound	RT (min)	RI[(a)]	% Peak Area	Functionality
1	γ-sitosterol	100.56	3487	4.11	Phytosterol
2	lanosterol	102.51	3426	2.61	Triterpenoid
3	α-amyrin	103.98	3453	8.56	Triterpene
4	12-oleanen-3-yl acetate, (3α)-	108.35	3448	15.58	Triterpene
5	lanosta-8,24-dien-3-ol, acetate, (3β)-	109.46	3470	8.44	Triterpenoid
6	12-oleanen-3-yl acetate, (3α)-	111.59	3466	58.70	Triterpene

[(a)]Retention Index (HP 5ms column)

Table 2. Volatile constituents of biochar obtained using HAR

	Compound	RT (min)	RI[(a)]	% Peak Area	Functionality
1	10-octadecenoic acid, methyl ester	60.47	2101	14.83	Ester
2	octadecane, 3-ethyl-5-(2-ethylbutyl)-	83.03	2899	18.56	Alkane
3	a-neooleana-3(5),12-diene	85.44	2892	17.03	Diene
4	β-amyrin	89.53	3064	31.35	Triterpene
5	olean-13(18)-ene	90.37	3099	13.87	Triterpene
6	4,4,6a,6b,8a,11,11,14b-octamethyl-1,4,4a,5,6,6a,6b,7,8,8a,9,10,11,12,12a,14,14a,14b-octadecahydro-2H-picen-3-one	102.45	3425	10.03	Triterpene

[(a)]Retention Index (HP 5ms column)

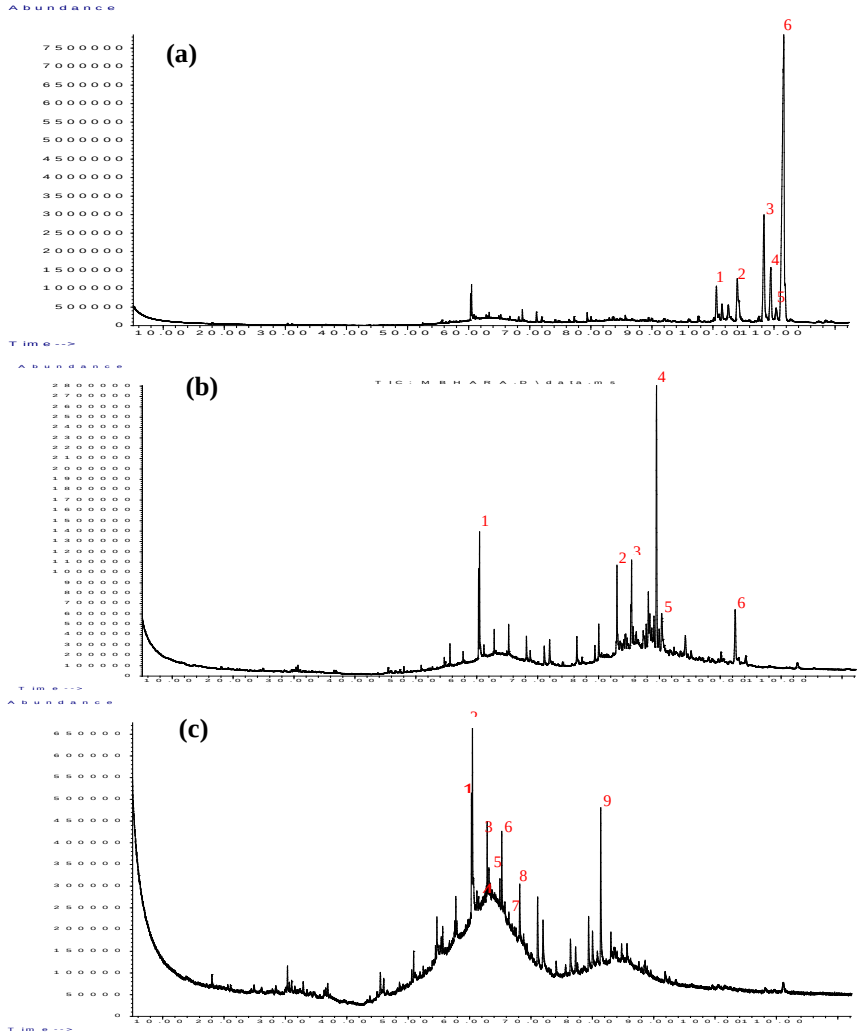


Figure 1. Total ion chromatograms of (A) dried MR bark, (B) hydrochar from HAR, and (C) hydrochar from POCV

Table 3. Volatile constituents of biochar obtained using POCV

	Compound	RT (min)	RI[(a)]	% Peak Area	Functionality
1	8,11-octadecadienoic acid, methyl ester	60.32	2095	12.56	Ester
2	10-octadecenoic acid, methyl ester	60.48	2101	31.89	Ester
3	ethyl iso-allocholate	60.65	2108	9.58	Alkaloid
4	2,7-Diphenyl-1,6-dioxopyridazino[4,5:2',3']pyrrolo[4',5'-d]pyridazine	61.48	2143	10.64	Alkaloid
5	1-Heptatriacotanol	63.16	2112	8.78	Fatty alcohol

Table 3 (cont'd). Volatile constituents of biochar obtained using POCV

	Compound	RT (min)	RI[(a)]	% Peak Area	Functionality
6	17-Pentatriacontene	65.25	2300	14.33	Alkene
7	Ethyl iso-allocholate	65.77	2318	8.37	Alkaloid
8	octadecane, 3-ethyl-5-(2-ethylbutyl)-	68.18	2400	12.86	Alkane
9	1,3-benzenedicarboxylic acid, bis(2-ethylhexyl) ester	81.38	2844	21.01	Isophthalate

[(a)]Retention Index (HP 5ms column)

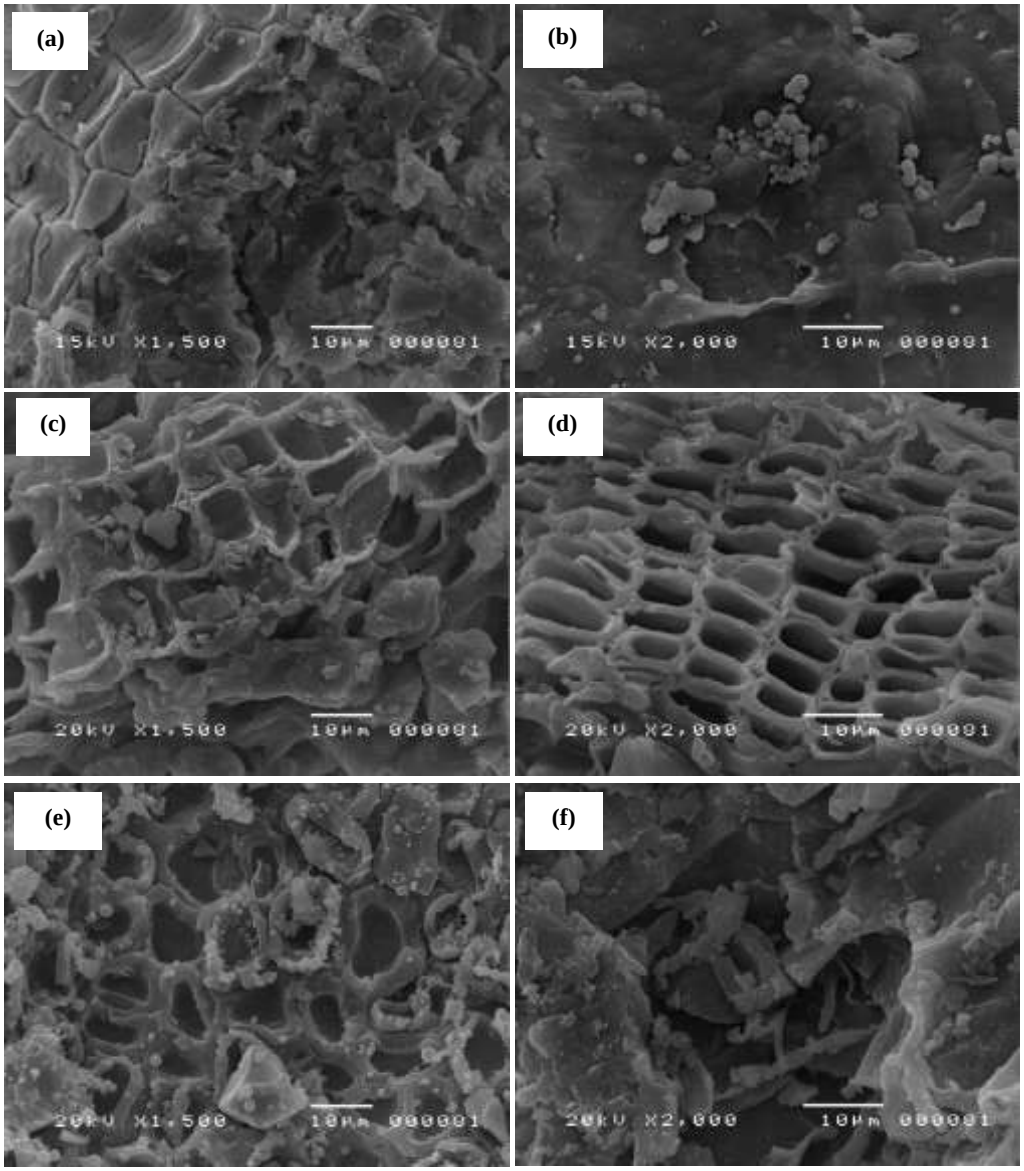


Figure 2. SEM images of MR bark (a-b), biochar product of *M. rubra* bark from HAR (c-d) and POCV (e-f)

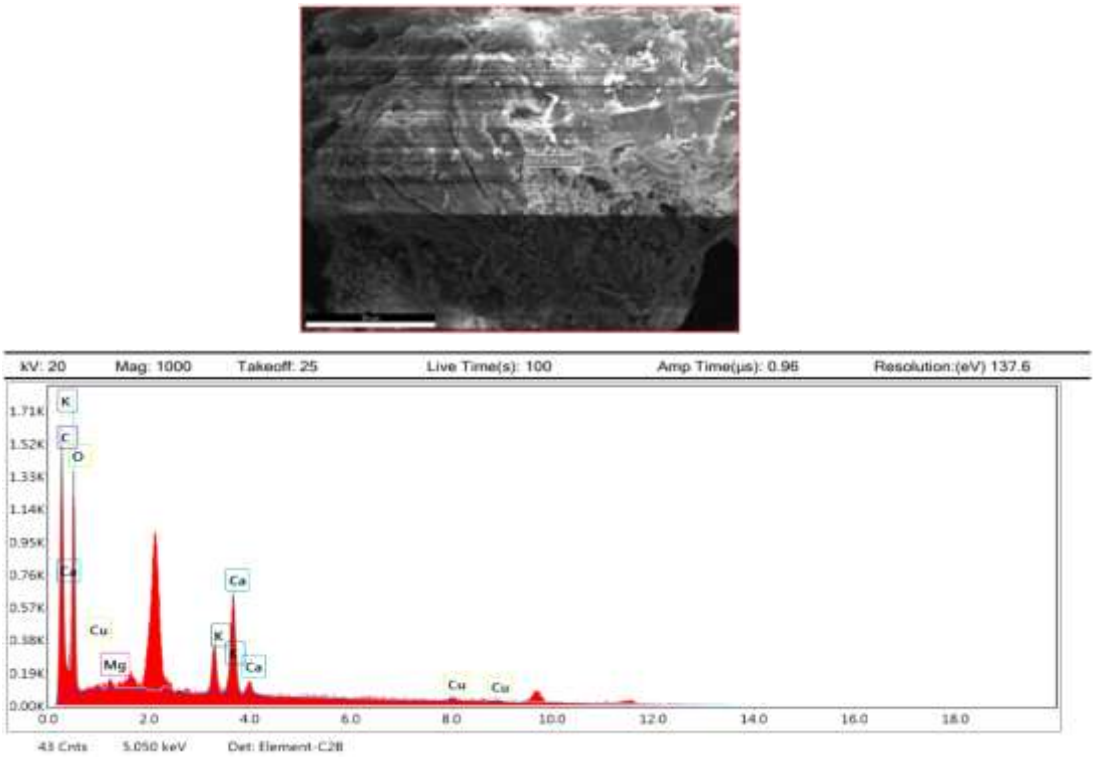


Figure 3. Image captured from the EDAX software and elemental analysis spectrum of dried bark of MR

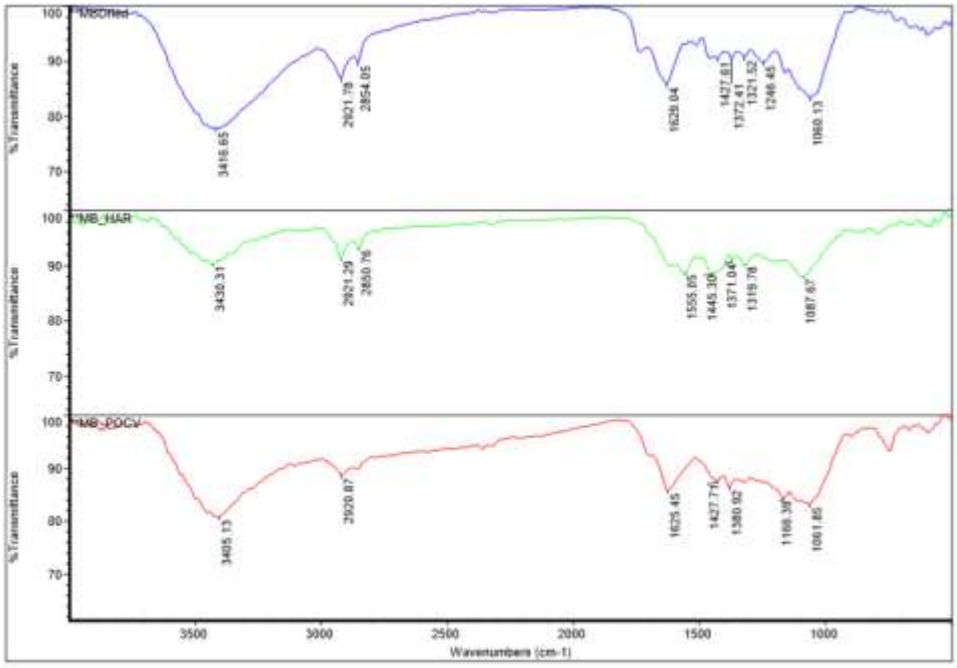


Figure 4. FTIR analysis of dried red mulberry bark (top) and biochars produced using HAR (middle) and POCV (bottom)

Table 4. IR absorptions of dried red mulberry bark

Wavenumber (cm^{-1})	**Functional Group**	**Description**
3416.65	O – H stretching	Alcohol
2921.78	C – H stretching	Alkane
2854.05	C – H stretching	Alkane
1629.04	C = C stretching	Conjugated alkene
1427.61	O – H bending	Carboxylic acid
1372.41	O – H bending	Phenol
1321.52	O – H bending	Phenol
1246.45	C – O stretching	Alkyl aryl ether
1060.13	C – O stretching	Primary alcohol

Table 5. IR absorptions of biochar of red mulberry bark produced from HAR

Wavenumber (cm^{-1})	**Functional Group**	**Description**
3430.31	O – H stretching	Alcohol
2921.29	C – H stretching	Alkane
2850.76	C – H stretching	Alkane
1555.05	C = C stretching	Cyclic alkene
1445.30	O – H bending	Carboxylic acid
1371.04	O – H bending	Phenol
1319.78	O – H bending	Phenol
1087.67	C – O stretching	Aliphatic ether

Table 6. IR absorptions of biochar of red mulberry bark produced from POCV

Wavenumber (cm^{-1})	**Functional Group**	**Description**
3405.13	O – H stretching	Alcohol
2920.87	C – H stretching	Alkane
1625.45	C = C stretching	Conjugated alkene
1427.71	O – H bending	Carboxylic acid
1380.92	C – H bending	Alkane
1166.39	C – O stretching	Tertiary alcohol
1061.85	C – O stretching	Primary alcohol

Flame AAS analysis

Both biochars were analyzed for their ability to absorb heavy metals. After 72 hours, all samples under different test concentrations were analyzed using atomic absorption spectrophotometry. Results showed that both biochars absorbed lead (Pb) by more than 60%, with only 3.8 ppm of Pb remaining after incubating in 10 ppm of heavy metal solution (Table 7). On the other hand, the biochar samples absorbed only a minimal amount of cadmium (Cd) and iron (Fe) from the solution. Other heavy metals (Cr and Cu) were not effectively absorbed by both biochars.

Pb was absorbed the most among the metals tested in the prepared solution by both hydrochars derived from the bark of MR. Pb is considered as a highly poisonous environmental hazard affecting mostly plants. Moreover, Pb has been reported as second to the most hazardous substance, arsenic, with regards to frequency of occurrence, toxicity, and human exposure [44]. The oral lethal dose (LD) for humans is reported to be 714 mg/kg of lead acetate or about 450 mg/kg of Pb [45]. Pb can be easily bioremediated by different parts of the plant, although it is identified as a non-essential element. Excess lead can result to curbed growth, chlorosis, and darkening of the underground vascular network of the plant [46]. Mulberry plants are popularly cultivated as nourishment for silkworms in several nations [6]. One study reported the use of mulberry plant (*M. alba*) – silkworm system in a Pb-polluted soil detoxification process. The experiment revealed that the mulberry underground vascular systems of the plant adsorbed a significant amount of the Pb in the soil, where more than 90% of the Pb in the aerial parts built up in their cell walls [47].

Another study dedicated in the investigation of the absorbed metals in mulberry berries, *M. alba*, MR and *M. nigra*, was performed which revealed that Fe was highly accumulated, and that Cd was minimally accrued in all three mulberry fruits [48]. Cd is a non-essential element that may induce damage or toxicity to plants when accumulated which can cause stunted growth, chlorosis, and leaf rolls in plants [49]. White mulberry (*M. alba*) was reported to be suitable in phytoextracting Cd and Ni. Different organs of *M. alba* were treated with varying levels of heavy metals such as Cd, Cr, and Ni. Green leaves were observed to contain higher amounts of Cd while fallen leaves had higher amounts of Cr and Ni compared to the roots and stem of white mulberry [14]. A dose of 0.5 mg/m^3 of Cd would result in respiratory distress from an 8-hour exposure, whereas a dose of 1-5 mg/m^3 of Cd is already reported as "immediately dangerous" for humans causing facial edema, hypotension, dysrhythmias, confusion and others [50]. In this study, the biochar samples absorbed nominal amounts of Cd and Fe from the heavy metal solution.

Fe is considered as a micronutrient for its minimal requirement for normal plant growth. Plants may suffer iron deficiency causing chlorosis and stunted growth. However, excessive intake of iron or iron overload may also induce toxicity. Fe toxicity has been one of the perceived problems affecting lowland rice plantation resulting in stunted growth and complete yield loss [51]. In humans, serum iron concentrations exceeding or equivalent to 350 μg/dl in 2- and 6-hours post-ingestion intervals suggested that serum iron content greater than 500 μg/dl would pose a dangerous hazard leading to acute liver malfunction [52]. In this study, minimal fluctuations in the content of Fe were observed in the heavy metal solution at 5 -10 ppm concentrations. However, at lower concentrations (0.5 - 1 ppm), both biochars absorbed most of Fe.

Unfortunately, Cr was not effectively absorbed by both biochars. This heavy metal is considered as a serious environmental pollutant which can induce toxicity and deleterious effects to plants including alterations in the germination process that can affect total dry matter and yield production [53]. Likewise, Cu concentration was not reduced significantly in the solutions.

Table 7. Total concentration of heavy metals absorbed by biochars of mulberry bark at different test concentrations after 72 hours of incubation

	Concentration (ppm)				
	Cd	**Pb**	**Cr**	**Cu**	**Fe**
HAR					
10 ppm	8.62 ± 0.01	3.84 ± 0.01	9.25 ± 0.03	9.76 ± 0.01	9.68 ± 0.01
5 ppm	*	4.27 ± 0.03	*	*	4.30 ± 0.02
1 ppm	*	*	*	*	0.33 ± 0.04
0.5 ppm	*	*	*	*	0.00 ± 0.00
POCV					
10 ppm	8.60 ± 0.04	3.74 ± 0.01	*	9.89 ± 0.02	9.99 ± 0.01
5 ppm	*	3.65 ± 0.01	*	*	4.65 ± 0.07
1 ppm	*	*	*	*	0.46 ± 0.10
0.5 ppm	*	*	*	*	0.00 ± 0.00

Data reported as mean ± standard deviation. **no remediation observed*

Conclusion

Characterization of dried red mulberry bark (MR) revealed the presence of several phytosterols, triterpenes, triterpenoids, esters, alkanes, alkenes, alkaloids, diene, and fatty alcohols. POCV seemed to induce greater carbonization in biochars as reflected in the GC-EI-MS profile. Surface characterization of dried red mulberry bark and biochars revealed the presence of cork wood patterns typical in all woody plants, which are known to aid in the remediation process. Though the POCV samples displayed a less distinct pattern of cork wood in the SEM images compared to the regular patterns seen in HAR trials, both biochars of *M. rubra* L. bark effectively absorbed almost 60% of Pb in the heavy metal solution and minimal amounts of Cd and Fe. However, both biochars showed no effect in removing Cu and Cr in the solution. Based on the findings of this work, future research could be focused in the use of *M. rubra* biochar in water purification systems for both rural and commercial development, especially in areas where Pb contamination is evident.

Acknowledgement

A research grant from De La Salle University Science Foundation, through the University Research Coordination Office, is gratefully acknowledged.

References

1. Shaheen, S. M., Niazi, N. K., Hassan, N. E. E., Bibi, I., Wang, H., Tsang, D. C. W., Ok, Y. S., Bolan, N. and Rinklebe, J. (2019). Wood-based biochar for the removal of potentially toxic elements in water and wastewater: a critical review. *International Materials Reviews*, 64(4): 216-247.
2. Oni, B., Oziegbe, O. and Olawole, O. (2019). Significance of biochar application to the environment and economy. *Annals of Agricultural Sciences*, 64(2): 222-236.
3. Yang, X., Zhang, S., Ju, M. and Liu, L. (2019). Preparation and modification of biochar materials and their application in soil remediation. *Applied Sciences*, 9(7): 1365.

4. Vijayan, K., Tikader, A., Weiguo, Z., Nair, C., Ercisli, S. and Tsou, C. (2011). Morus. *Wild Crop Relatives: Genomic and Breeding Resources*: 75-95.
5. Jiang, Y., Huang, R., Yan, X., Jia, C., Jiang, S. and Long, T. (2017). Mulberry for environmental protection. *Pakistan Journal of Botany*, 49: 781-788.
6. Ercisli, S. and Orhan, E. (2007). Chemical composition of white (*Morus alba*), red (*Morus rubra*), and black (*Morus nigra*) mulberry fruits. *Food Chemistry*, 103: 1380-1384.
7. Sharma, S. B., Gupta, S., Ac, R., Singh, U. R., Rajpoot, R. and Shukla, S. K. (2010). Antidiabetogenic action *of Morus rubra* L. leaf extract in streptozotocin-induced diabetic rats. *Journal of Pharmacy and Pharmacology*, 62: 247-255.
8. Dhiman, S., Kumar, V., Mehta, C., Gat, Y. and Kaur, S. (2019). Bioactive compounds, health benefits and utilisation of *Morus* spp.– a comprehensive review. *The Journal of Horticultural Science and Biotechnology*, 95(1): 8-18.
9. Thabti, I., Elfalleh, W., Tlili, N., Ziadi, M., Campos, M. and Ferchichi, A. (2013). Phenols, flavonoids, and antioxidant and antibacterial activity of leaves and stem bark of *Morus* species. *International Journal of Food Properties*, 17(4): 842-854.
10. Demir, S., Turan, I., Aliyazicioglu, Y., Kilinc, K., Yaman, S. and Ayazoglu Demir, E. (2016). *Morus rubra* extract induces cell cycle arrest and apoptosis in human colon cancer cells through endoplasmic reticulum stress and telomerase. *Nutrition and Cancer*, 69(1): 74-83.
11. Selina, I. I. (2014). A comparative study of the amino acid composition of black mulberry *(Morus nigra* L.), white mulberry (*Morus alba* L.) and red mulberry (*Morus rubra* L.). *Basic Research*, 3(4): 770-774.
12. Ercisli, S., Tosun, M., Duralija, B., Voća, S., Sengul, M. and Turan, M. (2010). Phytochemical content of some black (*Morus nigra* L.) and purple (*Morus rubra* L.) mulberry genotypes. *Food Technology & Biotechnology*, 48(1): 102-106.
13. Nikolova, T. (2015). Absorption of Pb, Cu, Zn, and Cd type *Morus alba* L. cultivated on soils contaminated with heavy metals. *Bulgarian Journal of Agricultural Science*, 21(4): 747-750.
14. Rafati, M., Khorasani, N., Moattar, F., Shirvany, A., Moraghebi, F. and Hosseinzadeh, S. (2011). Phytoremediation potential of *Populus alba* and *Morus alba* for cadmium, chromium and nickel absorption from polluted soil. *International Journal of Environmental Research*, 5: 961-970.
15. Zama, E., Zhu, Y., Reid, B. and Sun, G. (2017). The role of biochar properties in influencing the sorption and desorption of Pb(II), Cd(II) and As(III) in aqueous solution. *Journal Of Cleaner Production*, 148: 127-136.
16. Biskup, E., Gołębiowski, M., Gniadecki, R., Stepnowski, P. and Łojkowska, E. (2012). Triterpenoid α-amyrin stimulates proliferation of human keratinocytes but does not protect them against UVB damage. *Acta Biochimica Polonica*, 59(2): 255-260.
17. Santos, F., Frota, J., Arruda, B., de Melo, T., da Silva, A. and Brito, G. (2012). Antihyperglycemic and hypolipidemic effects of α, β-amyrin, a triterpenoid mixture from *Protium heptaphyllum* in mice. *Lipids in Health and Disease*, 11(1): 98.
18. Vázquez, LH., Palazon, J. and Navarro-Ocaña, A. (2012). The pentacyclic triterpenes α, β-amyrins: A review of sources and biological activities. In V. Rao (Ed), *Phytochemicals – A Global Perspective of Their Role in Nutrition and Health*. InTech: pp. 487-502.
19. Melo, C., Morais, T., Tomé, A., Brito, G., Chaves, M., Rao, V. and Santos, F. (2011). Anti-inflammatory effect of α, β-amyrin, a triterpene from *Protium heptaphyllum*, on cerulein-induced acute pancreatitis in mice. *Inflammation Research*, 60(7): 673-681.
20. Victor, M., David, J., dos Santos, M., Barreiros, A., Barreiros, M. and Andrade, F. (2017). Synthesis and evaluation of cytotoxic effects of amino-ester derivatives of natural α, β-amyrin mixture. *Journal of The Brazilian Chemical Society*, 28(11): 2155-2162.

21. National Center for Biotechnology Information. PubChem Database. Lanosterol, CID=246983, https://pubchem.ncbi.nlm.nih.gov/compound/Lanosterol [Access online 10 July 2020].
22. Zhao, L., Chen, X., Zhu, J., Xi, Y., Yang, X. and Hu, L. (2015). Lanosterol reverses protein aggregation in cataracts. *Nature*, 523(7562): 607-611.
23. Daszynski, D., Santhoshkumar, P., Phadte, A., Sharma, K., Zhong, H., Lou, M. and Kador, P. (2019). Failure of oxysterols such as lanosterol to restore lens clarity from cataracts. *Scientific Reports*, 9(1): 8459.
24. Shanmugam, P., Barigali, A., Kadaskar, J., Borgohain, S., Mishra, D., Ramanjulu, R. and Minija, C. (2015). Effect of lanosterol on human cataract nucleus. *Indian Journal of Ophthalmology*, 63 (12): 888.
25. Tripathi, N., Kumar, S., Singh, R., Singh, C., Singh, P. and Varshney, V. (2013). Isolation and identification of γ- sitosterol by GC-MS from the leaves of *Girardinia heterophylla* (Decne). *The Open Bioactive Compounds Journal*, 4(1): 25-27.
26. Endrini, S., Rahmat, A., Ismail, P. and Taufiq-Yap, Y. (2015). Cytotoxic effect of γ-sitosterol from Kejibeling (*Strobilanthes crispus*) and its mechanism of action towards *c-myc* gene expression and apoptotic pathway. *Medical Journal of Indonesia*, 23(4): 203-208.
27. Corey, E., Hess, H. and Proskow, S. (1963). Synthesis of a β-amyrin derivative, olean-11,12;13,18-diene. *Journal of The American Chemical Society*, 85(24): 3979-3983.
28. de Almeida, P., Boleti, A., Rüdiger, A., Lourenço, G., da Veiga Junior, V. and Lima, E. (2015). Anti-inflammatory activity of triterpenes isolated from *Protium paniculatum* oil-resins. *Evidence-Based Complementary and Alternative Medicine*, 2015: 1-10.
29. Belakhdar, G., Benjouad, A. and Abdennebi, E.H. (2015). Determination of some bioactive chemical constituents from *Thesium humile* vahl. *Journal of Materials and Environmental Science*, 6(10): 2778-2783.
30. Quarta, A., Novais, R., Bettini, S., Iafisco, M., Pullar, R. and Piccirillo, C. (2019). A sustainable multi-function biomorphic material for pollution remediation or UV absorption: Aerosol assisted preparation of highly porous ZnO-based materials from cork templates. *Journal of Environmental Chemical Engineering*, 7(2): 102936.
31. Yashvanth, S., Shobha Rani, S. and Madhavendra, SS. (2015). *Morus alba* L., A New Perspective: Scan-ning electron microscopic, micro chemical, GC-MS and UPLC-MS characterisation. *International Journal of Research in Pharmacy and Chemistry*, 5(1): 106-115.
32. InfoPlease (2020). Carbon (element): Biological importance. Access from https://www.infoplease.com/encyclopedia/science/chemistry/elements/carbon/biological-importance. [Access online 13 July 2020].
33. Chantuma, P., Lacointe, A., Kasemsap, P., Thanisawanyangkura, S., Gohet, E. and Clement, A. (2009). Carbohydrate storage in wood and bark of rubber trees submitted to different level of C demand induced by latex tapping. *Tree Physiology*, 29(8): 1021-1031.
34. Krutul, D., Zielenkiewicz, T., Radomski, A., Zawadzki, J., Antczak, A., Drożdżek, M. and Makowski, T. (2011). Metals accumulation in scots pine (*Pinus sylvestris* L.) wood and bark affected with environmental pollution. *Wood Research*, 2017(62): 353-364.
35. Ross, A., Taylor, C., Yaktine, A. and Cook, H. (2011). Dietary reference intakes for calcium and vitamin D. The National Academies Press, Washington, DC.
36. Haas, E. (2011). Role of potassium in maintaining health. Access from https://hkpp.org/patients/potassium-health [Access online 13 July 2020].
37. National Academies of Sciences, Engineering, and Medicine (2019). Dietary reference intakes for sodium and potassium. The National Academies Press, Washington, DC.
38. Schwalfenberg, G. and Genuis, S. (2017). The importance of magnesium in clinical healthcare. *Scientifica*, 2017: 1-14.

39. Institute of Medicine (1997). Dietary reference intakes: Calcium, phosphorus, magnesium, vitamin D and fluoride. National Academy Press, Washington, DC.
40. Institute of Medicine Panel (US) on Micronutrients (2001). Dietary reference intakes for vitamin A, vitamin K, arsenic, boron, chromium, copper, iodine, iron, manganese, molybdenum, nickel, silicon, vanadium, and zinc. The National Academies Press, Washington, DC.
41. National Research Council (US) Committee on Copper in Drinking Water (2000). Copper in drinking water. National Academy Press, Washington, DC.
42. Jose, J. C., Oyong, G., Ajero, M. D., Chiong, I., Cabrera, E., Tan, M. C. S. (2020). Insights on the chemical constituents and hydrothermal carbonization of *Crescentia cujete* L.. *Malaysian Journal of Analytical Sciences,* 24(1): 134-145.
43. Naron, D., Collard, F., Tyhoda, L. and Görgens, J. (2019). Production of phenols from pyrolysis of sugarcane bagasse lignin: Catalyst screening using thermogravimetric analysis – thermal desorption – gas chromatography – mass spectroscopy. *Journal of Analytical and Applied Pyrolysis*, 138: 120-131.
44. Pourrut, B., Shahid, M., Dumat, C., Winterton, P. and Pinelli, E. (2011). Lead uptake, toxicity, and detoxification in plants. *Reviews of Environmental Contamination and Toxicology,* 213:113-136.
45. Centers for Disease Control and Prevention (2020). CDC - immediately dangerous to life or health concentrations (IDLH): Lead compounds (as Pb) - NIOSH publications and products. Access from https://www.cdc.gov/ niosh/idlh/7439921.html. [Accessed online 16 July 2020].
46. Sharma, P. and Dubey, R. S. (2005). Lead toxicity in plants. *Brazilian Journal of Plant Physiology*, 17(1): 35-52.
47. Zhou, L., Zhao, Y., Wang, S., Han, S. and Liu, J. (2015). Lead in the soil–mulberry (*Morus alba* L.)–silkworm (*Bombyx mori*) food chain: Translocation and detoxification. *Chemosphere,* 128: 171-177.
48. Mićić, R., Dimitrijević, D., Kostić, D., Stojanović, G., Mitić, S. and Mitić, M. (2013). Content of heavy metals in mulberry fruits and their extracts-correlation analysis. *American Journal of Analytical Chemistry*, 4(11): 674-682.
49. Benavides, M. P., Gallego, S. M. and Tomaro, M. L. (2005). Cadmium toxicity in plants. *Brazilian Journal of Plant Physiology*, 17(1): 21-34.
50. Bull, S. (2010). Cadmium toxicological overview. Access from https://assets.publishing.service.gov.uk/ government/uploads/system/uploads/attachment_data/file/337542/hpa_cadmium_toxicological_overview_v3.pdf [Accessed online 16 July 2020].
51. Baruah, K. K. and Bharali, A. (2015). Physiological basis of iron toxicity and its management in crops. In: Amrit L.S. Recent advances in crop physiology. Daya Publishing House®, New Delhi, India
52. Abhilash, K., Arul, J. and Bala, D. (2013). Fatal overdose of iron tablets in adults. *Indian Journal of Critical Care Medicine*, 17(5): 311-313.
53. Shanker, A., Cervantes, C., Lozatavera, H. and Avudainayagam, S. (2005). Chromium toxicity in plants. *Environment International*, 31(5): 739-753.

Malaysian Journal of Analytical Sciences (MJAS)
Published by Malaysian Analytical Sciences Society

MODE OF ACTION OF 5-ACETYL-4-METHYLTHIAZOLE DERIVATIVES AS ANTIMICROBIAL AGENTS

(Mod Tindakan Sebatian Terbitan 5-Asetil-4-Metiltiazol Sebagai Agen Antimikrob)

Iswatun Hasanah Abdullah Ripain, Nurziana Ngah*, Deny Susanti Darnis

Department of Chemistry, Kulliyyah of Science,
International Islamic University Malaysia, Kuantan Campus, Bandar Indera Mahkota, 25200 Kuantan, Pahang, Malaysia

**Corresponding author: nurziana@iium.edu.my*

Received: 5 February 2021; Accepted: 29 March 2021; Published: 25 April 2021

Abstract

Thiazole derivatives have been widely known to possess antimicrobial behaviour. The purpose of this study is to investigate the mode of antimicrobial actions of synthesised thiazole compounds on Gram-positive bacteria (*Staphylococcus aureus*), Gram-negative bacteria (*Salmonella typhimurium*), and fungus (*Candida albicans*). Three synthesised thiazole compounds namely 5-acetyl-4-methyl-2-(3,4-dichloroaniline)-1,3-thiazole (**T1**), 5-acetyl-4-methyl-2-(4-aminophenol)-1,3-thiazole (**T2**), and 5-acetyl-4-methyl-2-(methyl-4-aminobenzoate)-1,3-thiazole (**T3**) were evaluated in the mode of action assays such as salt tolerance, time-killing, crystal violet and leakage 260/280 nm absorbing materials. The result showed that the **T3** compound exhibited the best performance for all tested assays at a concentration equal to 4 × MIC compared to **T1** and **T2**.

Keywords: thiazole, mode of action, antimicrobial

Abstrak

Terbitan tiazol telah dikenali umum sebagai sebatian yang mempunyai sifat antimikrob. Justeru, kajian ini dijalankan untuk mengkaji mod tindakan sebatian tiazol yang disintesis sebagai agen antimikrob terhadap bakteria Gram-positif (*Staphylococcus aureus*), Gram-negatif (*Salmonella typhimurium*) and fungus (*Candida albicans*). Tiga sebatian tiazol yang telah disintesis iaitu 5-asetil-4-metil-2-(3,4-dikloroanilina)-1,3-tiazol (**T1**), 5-asetil-4-metil-2-(4-aminofenol)-1,3-tiazol (**T2**) dan 5-asetil-4-metil-2-(metil-4-aminobenzoat)-1,3-tiazol (**T3**) telah dikaji dan dinilai secara toleransi garam, masa pembunuhan, violet kristal dan kebocoran bahan serapan 260/280 nm. Keputusan kajian mendapati sebatian **T3** menunjukkan kebolehan sebagai agen antimikrob yang terbaik pada kepekatan 4 × MIC berbanding **T1** dan **T2**.

Kata kunci: tiazol, mod tindakan, antimikrob

Introduction

Serious diseases such as diarrhoea, infections to intravascular organ, nausea, inflammation, and abdominal pain caused by bacterial infection have led to the growing research trend in the development of treatment system [1, 2]. One of the main related research areas is antibiotic development [3]. The synthesised organic compound is known to be the most suitable

candidate compared to inorganic and natural product extract due to its easy structural modification, high percentage yield, and prevention of natural resources depletion [4-8]. The main challenge for this option is to design an efficient compound that can solve the rising concern on antibiotic resistance. In recent years, thiazole has emerged as the subject of considerable interest in the field of pharmacology among researchers due to its excellent properties in biological fields since it can act as anti-inflammatory, antifungal, anticancer, antibacterial, anticonvulsant, and antiviral [9]. The manifestation of nitrogen and sulphur atoms in thiazole moiety has significantly increased its physiochemical properties to be biologically active in most biological areas [10]. A continuous effort from our previous work on synthesis, preliminary biological screening and molecular docking [11] has led to the evaluation of three thiazole derivatives. The mode of action assays such as salt tolerance, time-killing, crystal violet, and leakage 260/280 nm absorbing materials was performed on the derivatives.

Materials and Methods

Preparation of thiazole derivatives

Synthesis and characterisation of thiazole derivatives namely 5-acetyl-4-methyl-2-(3,4-dichloroaniline)-1,3-thiazole (**T1**), 5-acetyl-4-methyl-2-(4-aminophenol)-1,3-thiazole (**T2**), and 5-acetyl-4-methyl-2-(methyl-4-aminobenzoate)-1,3-thiazole (**T3**) were performed as previously described [11]. The chemical structure of T1, T2, and T3 is shown in Figure 1.

Test microorganisms

The cultured microorganisms that were used in this study include Gram-positive bacteria, Gram-negative bacteria, and fungus. The Gram-positive bacteria used was *Staphylococcus aureus* (ATCC25923) while *Salmonella typhimurium* (IMRS1406/08A) was selected as the Gram-negative bacteria. The fungus species used was *Candida albicans* (ATCC10231).

Preparation of Inoculum

Stock cultures of bacteria and fungus were grown in Nutrient Agar (NA) at 37 °C for 24 hours and Potato Dextrose Agar (PDA) at 27 °C for 48 hours, respectively. A sub-culturing process was carried out on both microbes to get single colonies at the stationary phase. After the formation of single colonies, the top of each colony was swabbed using a cotton swab and transferred into a Falcon tube containing 10 mL of Nutrient Broth (NB) and Potato Dextrose Broth (PDB) for bacterial strains and fungus, respectively. Incubation process was then performed for the bacterial strains at 37 °C for 24 hours and fungus at 27 °C for 48 hours before the measurement of optical density (OD) using a spectrophotometer.

Salt tolerances assay

The capability of cultured bacteria and fungus treated with **T1**, **T2,** and **T3** on agar appended with sodium chloride (NaCl) at 50g/L was studied by applying a previously published method [12] with some modification. The microbes suspension was treated with compounds and standard drugs (streptomycin and tetracycline for bacteria and clotrimazole for fungus) at the respective MIC and 2 × MIC values concentration. Meanwhile, untreated cultures were used as control (blank). Next, both treated and untreated cultures were incubated for 30 minutes at 37 ºC. The samples were then serially diluted and inoculated onto an agar plate of NA and PDA or NA-NaCl and PDA-NaCl. After the incubation process, the number of CFU of bacteria per millilitre (CFU/mL) on each NA/PDA-NaCl plate was counted and compared to the NA/PDA plate. The tests were done in triplicate and data were computed using Microsoft Excel 2013 and the results were expressed as mean ± standard deviation (S.D) with p <0.05 is considered as statistically significant.

(Note: NA and NA-NaCl for bacteria; PDA and PDA-NaCl for fungus)

Time-killing assay

Ammonium assay for the killing rate of bacteria and fungus by the compounds was carried out using a plating method [13] with Clinical and Laboratory Standards Institute (CLSI). The effect of the compounds on killing ability over the time intervals of 0, 30, 60, and 120 minutes of treatment was measured [14]. The test compound was added into 10 mL of inoculum suspension that is equal to 4 × MIC. As a control, suspension of microorganism without test compound

was included in each trial. After each time interval, 100 µL of treated and untreated cultures were transferred onto an agar plate. The plate was then incubated at 37 °C for 24 hours (for bacteria) at room temperature for 48 hours (for fungus). After the incubation period, the growth of the colonies on the agar plate was counted at each time interval and compared with control. The experiments were performed in triplicates.

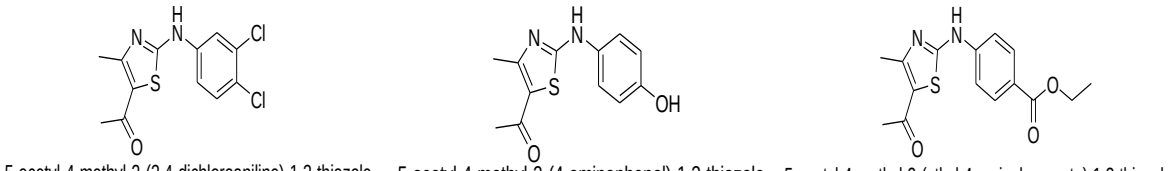
Crystal violet assay

The effect on membrane permeability of microorganism treated with **T1**, **T2,** and **T3** was assessed *via* crystal violet assay [15] using a staining method with some modification. Briefly, the cells were harvested upon exponential growth via centrifugation at 4500 × g for 5 minutes at 4 °C and washed twice prior to resuspension in phosphate buffer saline (pH 7.4) solution. Next, the compound was added into the cell suspension with different concentration of 2 × MIC and 4 × MIC values. The cell suspension without compound was marked as control whereas cells treated with 0.25M EDTA was used as the positive control. The antibiotics (Streptomycin: 0.62 µg/mL; Clotrimazole: 0.16 µg/mL) were also used in the treatment as standards. After incubated for 30 minutes at 37 ºC, the cells were harvested *via* centrifugation at 9300 × g for 5 minutes. Then, the cells were suspended in PBS containing 10 µg/mL of crystal violet and re-incubated for another 10 minutes. After that, the suspension was centrifuged at 13,400 × g for 15 minutes. Finally, the optical density (OD) value of the supernatant was measured using a UV-Vis spectrophotometer at 600 nm for bacteria and 494 nm for fungus [16]. The percentage of crystal violet uptake of all cells was calculated using the following formula in equation 1[17]:

$$\frac{\text{OD value of the sample}}{\text{OD value of crystal violet solution}} \text{ X } 100\% \qquad (1)$$

Leakage of 260 and 280nm-absorbing material assay

The assays were conducted to evaluate the leakage of materials into the microorganisms when exposed to thiazole compounds at a wavelength of 260 nm and 280 nm using a UV spectrophotometer [12] with some modification. The difference in absorption values used in this test was to estimate the release of metabolites of nucleic acid and protein [18]. Firstly, the cultured microorganism was centrifuged at 10,000 × g for 12 minutes at 4 °C prior to the twice washing step and resuspended with PBS (pH 7.4). Then, different concentrations of compounds at 2 × MIC and 4 × MIC values were added into 1 mL of cell suspension. Untreated cells were discernible as negative control and standard drugs were used as positive controls. All cells suspension was incubated for 60 minutes before centrifuged at 13,400 × g for 15 minutes. Finally, the optical density (OD) values of the supernatant measured at 260 and 280 nm were reflected as a percentage of cellular UV-absorbing materials released by the cells. The tests were performed in triplicates and the mean values were determined.



T1 **T2** **T3**

Figure 1. The chemical structures of **T1**, **T2**, and **T3**

Results and Discussion

Salt tolerances assay

The effect of **T1**, **T2,** and **T3** compounds on the osmotic potential of bacteria and fungus cells was studied by investigating their ability to grow on agar plate supplemented with NaCl. In this assay, the antimicrobial effect of the compounds against the tested bacterial and fungal strains was investigated in treated and untreated agar with the salt solution. To conduct this assay, the concentration of MIC and 2 × MIC, which was able to inhibit the microbes were applied. The results of the salt tolerance assay of untreated and treated microbial are tabulated in Figure 2. The number of colonies was found to be reduced in all treated cells as the treatment concentration doubled. The sub-lethal damage of the cell membrane was seen by the reduction in the ability to form colonies on the agar supplemented with NaCl. Moreover, all treated cells showed a decreasing colony-forming ability as the treatment concentration increases. However, there was a slight difference in the number of survived colonies on NA/PDA and NA/PDA-NaCl agar. The range number of colonies survived on NA/PDA agar by seeing both concentrations applied for tested compounds towards all microbes were from 94×10^3 to 12×10^4 CFU/mL compared to untreated blank culture (control) at the range of 14×10^4 to 86×10^4 CFU/mL. In contrast, the range number of colonies that survived on NA/PDA-NaCl for both concentrations against microbial tested were 23×10^4 to 11×10^4 CFU/mL compared to control that was in the range of 78×10^4 to 13×10^4 CFU/mL.

From Table 1, it can be concluded that NaCl supplemented agar reduced the formation of the microbial colony. The addition of salt has affected the growth of microorganism by disturbing the metabolic process of microbial strains by changing the membrane arrangement and reducing their cell division [19]. Based on the assay, **T3** was found to be the most active compound towards all microbial tested on both media at MIC and 2 × MIC values. The number of colonies survived on NA/PDA-NaCl by *S. aureus, S. typhi*, and *C. albicans* treated with 2 × MIC value of **T3** were observed to be 54×10^3, 48×10^3 and 11×10^4 CFU/mL, respectively. In addition, **T1** displayed the weakest activity with a greater number of colonies survived equally to 18×10^4, 62×10^3, 13×10^4 CFU/mL, respectively.

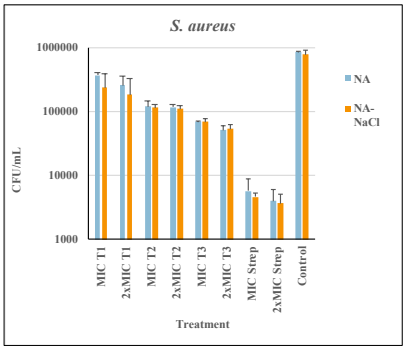
Time-killing assay

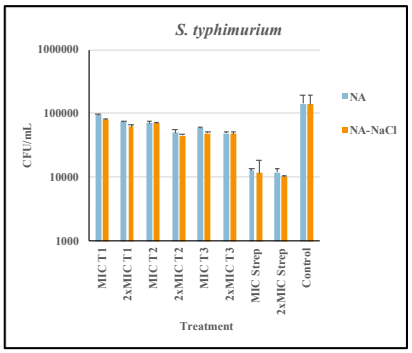
A time-killing assay was performed to determine the bactericidal and fungicidal effect of thiazole compounds as described in the previous literature [13]. This assay was widely applied for *in-vitro* analysis of new antimicrobial agents by delivering qualitative data on the pharmacodynamics relationships between bioactive compounds and their effects on microbes. The killing rate of the tested microbes by the compounds was determined by measuring the reduction in the number of colony-forming units (CFU/mL). A bactericidal effect can be defined as 99.9% killing of the final inoculums by observing the absence of colony growth. The results of the time-killing assay of the compounds were compared to the control towards microbial strains are shown in Figure 3 and Table 2. The results showed that all compounds exhibited similar patterns of killing kinetic profiles against all tested microbes. All growth reduction of treated cultured microbe significantly increased over time from 0 to 120 minutes as matched to the control. A treatment of microbial growth for compounds was observed to reach the endpoint at 60 minutes after incubation. The **T3** compound was found to be the most active compound with a significant killing ability towards all tested microbes by showing the lowest number of colonies survived after 30 minutes at a range of 23×10^2 to 60×10^2 CFU/mL. The highest number of colonies of 57×10^2 to 88×10^2 CFU/mL was recorded when treated with **T1,** which indicates a weak killing performance. In contrast, the control exhibited a different pattern by showing an increasing number of survived colonies ranging from 59×10^6 to 25×10^7 CFU/mL signifying a continuous growth of microbes after 30 minutes of treatment.

Crystal violet assay

The formation of a biofilm layer with a community of sessile bacterial cells and hydrated matrix provides a beneficial surface of planktonic bacteria by attracting nutrient and colonisation of macromolecules [20, 21]. Therefore, to study the ability of **T1**, **T2,** and **T3** to demolish the membrane of microbial strains or biofilms was performed using crystal violet assay [15] with some modification. In principle, the crystal violet solution has a weak ability in penetrating the outer membrane, but it can easily enter when the membrane is disrupted [22]. To conduct the experiment, all microbes were cultured before treated with the compounds and stained with crystal violet solution. The membrane permeability properties of the compounds were evaluated by measuring the percentage of crystal violet solution uptake after treatment. Figure 4 shows the percentage of CV uptake by microbial strains at a concentration of 2 × MIC and 4 × MIC. From the graphs, all compounds inhibited the formation of membrane for all tested microbes. It can be seen that the percentage of CV uptake by the microbial strains increased as the concentration of the compounds increased. In this assay, EDTA solution was used as a chelating agent that could modify the permeability of the outer membrane layer of a bacterial cell wall [22] and as external positive control. Streptomycin (for bacteria) and Clotrimazole (for fungus) were used as the internal positive control.

The results of the crystal violet assay were also matched with the untreated culture as a negative control. The results showed that the membrane layer of the microbial cell walls significantly increased in the crystal violet uptake after treated with the compounds compared to the negative control (untreated culture). Besides that, both external and internal positive controls also showed an increase uptake of crystal violet after treatment. **T3** showed the highest percentage of CV uptake towards all microbial strains tested such as *S. aureus*, *S. typhi*, and *C. albicans* at 4 × MIC with percentages of 49.4 %, 67.2 % and 67.9 %, respectively. Next, **T2** also exhibited good antibiofilm activity against microbes tested at similar concentration with percentage values of 47.1%, 65.0% and 65.7%, respectively. In contrast, **T1** showed the weakest CV uptake at a similar concentration of 4 × MIC against microbes with percentage values of 34.7 %, 51.4 % and 60.6 %, respectively. It can be concluded that the difference in the uptake of CV from the microbial cell walls is due to the destructive cell wall as their permeability changes [23].





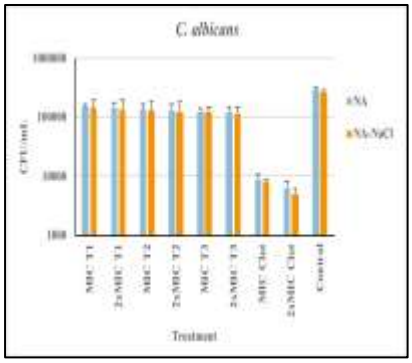


Figure 2. Salt tolerance by untreated (control) and untreated *S. aureus*, *S. typhi*, and *C. albicans* at a concentration equal to MIC and 2 × MIC of **T1**, **T2,** and **T3**

Table 1. Salt tolerance results of synthesised thiazole and antibiotics

Compound	Agar Condition	*S. aureus*	*S. typhi*	*C. albicans*
MIC **T1**	NA	37×10^4	94×10^3	15×10^4
	NA-NaCl	23×10^4	80×10^3	14×10^4
2 × MIC **T1**	NA	26×10^4	72×10^3	14×10^4
	NA-NaCl	18×10^4	62×10^3	13×10^4
MIC **T2**	NA	12×10^4	70×10^3	13×10^4
	NA-NaCl	11×10^4	69×10^3	12×10^4
2 × MIC **T2**	NA	11×10^4	50×10^3	13×10^4
	NA-NaCl	10×10^4	44×10^3	12×10^4
MIC **T3**	NA	70×10^3	59×10^3	12×10^4
	NA-NaCl	69×10^3	48×10^3	11×10^4
2 × MIC **T3**	NA	55×10^3	49×10^3	12×10^4
	NA-NaCl	54×10^3	48×10^3	11×10^4
MIC Strep	NA	56×10^2	12×10^3	-
	NA-NaCl	46×10^2	11×10^3	-
2 × MIC Strep	NA	40×10^2	11×10^3	-
	NA-NaCl	36×10^2	10×10^3	-
MIC Clot	PDA	-	-	90×10^2
	PDA-NaCl	-	-	78×10^2
2 × MIC Clot	PDA	-	-	65×10^2
	PDA-NaCl	-	-	52×10^2
Control	NA	86×10^4	14×10^4	-
	NA-NaCl	78×10^4	13×10^4	-
	PDA	-	-	30×10^4
	PDA-NaCl	-	-	27×10^4

Note. Strep: Streptomycin; Clot: Clotrimazole

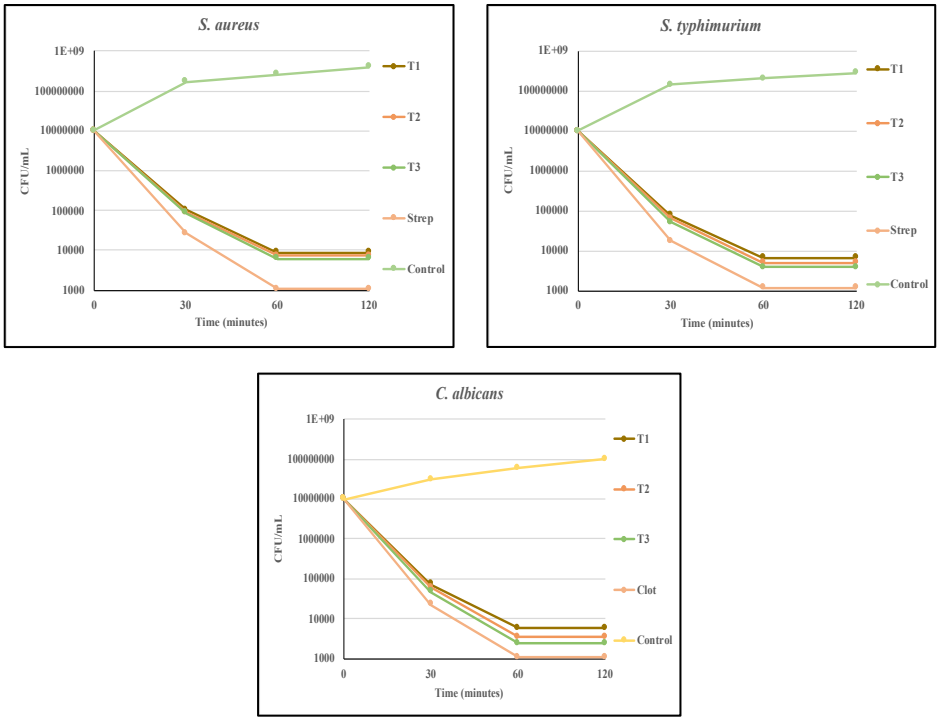


Figure 3. Time-killing curves of untreated (control) and treated *S. aureus*, *S. typhi*, and *C. albicans* at a concentration equal to 4 × MIC of thiazole compounds

Table 2. Time-killing results of synthesised thiazole and antibiotics

Compounds	**Time (Minutes)**	***S. aureus***	***S. typhi***	***C. albicans***
T1	30	10×10^4	79×10^3	73×10^3
	60	88×10^2	68×10^2	57×10^2
	120	88×10^2	68×10^2	57×10^2
T2	30	89×10^3	65×10^3	59×10^3
	60	73×10^2	51×10^2	34×10^2
	120	73×10^2	51×10^2	34×10^2
T3	30	85×10^3	53×10^3	46×10^3
	60	60×10^2	39×10^2	23×10^2
	120	60×10^2	39×10^2	23×10^2
Streptomycin	30	27×10^3	17×10^3	-
	60	11×10^2	12×10^2	-
	120	11×10^2	12×10^2	-
Clotrimazole	30	-	-	22×10^3
	60	-	-	10×10^2
	120	-	-	10×10^2
Control	30	17×10^7	14×10^7	30×10^6
	60	25×10^7	20×10^7	59×10^6
	120	39×10^7	28×10^7	99×10^6

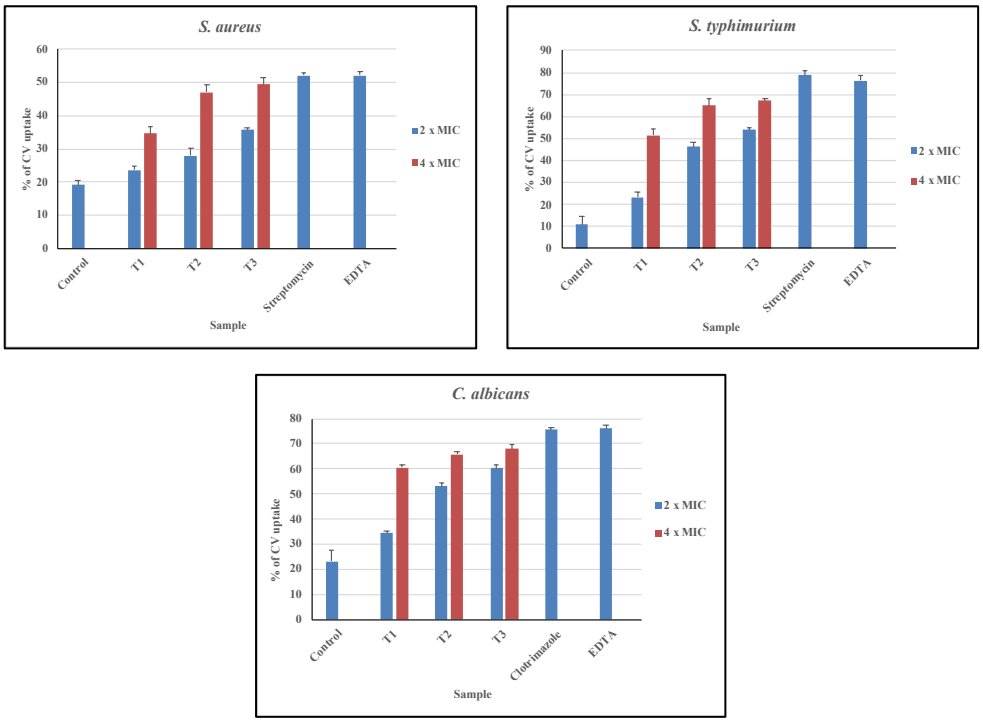


Figure 4. Percent of crystal violet uptake by untreated (control) and treated microbes at a concentration equal to 2 × MIC and 4 × MIC of **T1**, **T2** and **T3**, 0.25 M EDTA, and standard drugs

Leakage of 260 and 280nm-absorbing material assay

The assay was carried out to investigate material loss from the microbial strains when treated with the compounds. The leakage of material cells of nucleic acid and protein were analysed using a UV spectrophotometer at a wavelength of 260 and 280 nm, respectively. The results showed that higher absorption values indicate more loss of material cells from the microbial strains tested. Figure 5 shows the absorbance values of material cells (nucleic acids) of all microbes at 260 nm.

From Figure 5, doubled the concentration of the compounds, a greater leakage was observed due to the loss of absorbing material of nucleic acid. Among all compounds, the highest absorbance values of OD260 were recorded at 0.77, 0.65 and 0.74 of *S. aureus*, *S. typhi* and *C. albicans*, respectively when exposed to **T3** at a concentration of 4 × MIC. Whilst **T3** compound also showed the highest absorbance values at a concentration of 2 × MIC compared to **T1** and **T2** towards microbial strains tested, which were 0.62, 0.57 and 0.67, respectively. Moreover, the second highest absorbance values were recorded for **T2** against similar microbial strains of *S. aureus*, *S. typhi*, and *C. albicans* were 0.62, 0.57 and 0.67, respectively but at 4 × MIC concentration. In contrast, when compared with **T1** at the concentration of 4 × MIC, the lowest absorbance values were analysed at 0.66 (*S. aureus*), 0.57 (*S. typhi*) and 0.58 (*C. albicans*), respectively. It can be assumed that the highest values of OD_{260} were recorded with **T3** whereas the lowest OD_{260} values were seen for **T1**, indicating that **T3** treatment released the highest amounts of nucleic acids.

Next is the results of the leakage of proteins materials at 280 nm-absorbing materials of microbial strains. The findings of the assay are shown in Figure 6. A similar trend to 260 nm-absorbing material results was observed when the concentrations of the compounds doubled. The

higher absorbance values were detected due to the greater leakage of proteins. From the graphs, **T3** showed the greatest OD_{280} absorbance values, which were 0.79, 0.78 and 0.83 towards *S. aureus*, *S. typhi* and *C. albicans*, respectively at a concentration of 4 × MIC. **T1** also showed the weakest absorbance values of 0.65, 0.68 and 0.74, respectively at a similar concentration.

It can be concluded that microbial suspension treated with **T1**, **T2,** and **T3** lost their absorbing materials significantly at 260 and 280 nm through a destroyed cytoplasmic membrane that released nucleic acids and proteins. This could be explained by the chemical structure of compounds that comprise of two parts. The first group is heterocyclic thiazole containing nitrogen and sulphur atoms that are attached to the amine at the 2-position to another group linked to an aryl group that plays a role in the mode of action of the assay. The heterocyclic thiazole and aryl groups possess hydrophilic and hydrophobic properties, respectively. Therefore, the compounds can be considered as amphiphilic molecules with two parts of hydrophilic (polar group) and hydrophobic (non-polar group) possibly to interrupt the microbes cell membrane resulting in cell lysis.

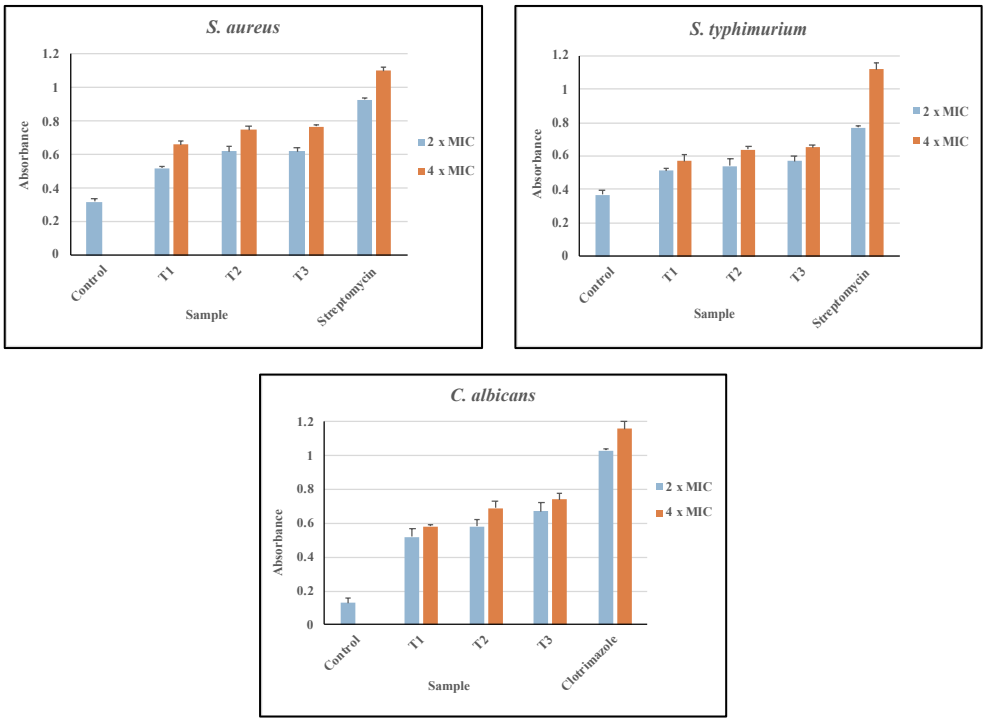


Figure 5. Leakage of extracellular 260 nm-absorbing material from untreated and treated microbial strains with compounds and standard drugs at a concentration equal to 2 × MIC and 4 × MIC

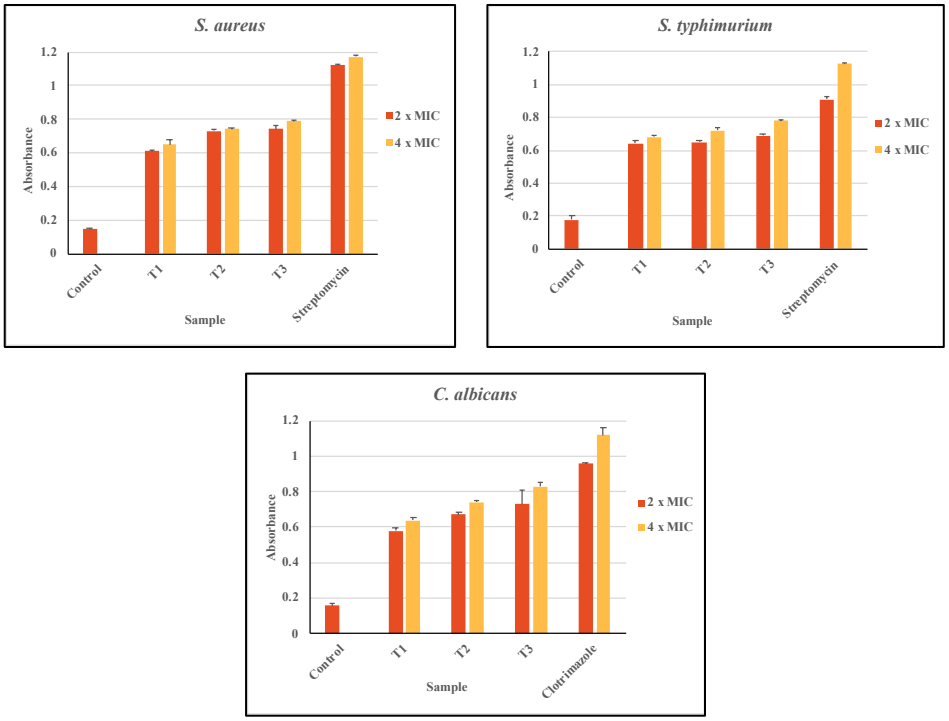


Figure 6. Leakage of 280 nm-absorbing materials from untreated and treated microbial strains with compound and standard drugs at a concentration equal to 2 × MIC and 4 × MIC

Conclusion

In conclusion, this work has demonstrated that 5-acetyl-4-methylthiazole derivatives (**T1-T3**) were successfully evaluated for their mode of action assays. From the experimental data, **T3** exhibited the best performance against tested bacterial and fungal strains compared to **T1** and **T2** in all tested assays.

Acknowledgement

We gratefully acknowledge grants from the Ministry of Education Malaysia FRGS14-15-0392, and Department of Chemistry and Biotechnology, Kulliyyah of Science, International Islamic University Malaysia (IIUM) for providing the essential laboratory facilities.

References

1. Tran, T., Nguyen, T., Do, T., Huynh, T., Tran, C. and Thai, K. (2012). Synthesis and antibacterial activity of some heterocyclic chalcone analogues alone and in combination with antibiotics. *Molecules*, 17(6): 6684- 6696.
2. Kotb, E. R., Anwar, M. M., Abbas, H. S. and El-Moez, S. I. A. (2013). A concise synthesis and antimicrobial activity of a novel series of naphthylpyridine-3-*carbonitrile compounds. Acta Poloniae Pharmaceutica-Drug Research*, 70(4): 667-679.
3. Nalawade, A. M., Nalawade, R. A., Patange, S. M. and Tase, D. D. (2013), Thiazole containing Schiff base and their transition metal complexes. *International Journal of Engineering Science Invention*, 2(7): 1-4.
4. Edijeke, I. P. and Ajibade, P. A. (2015). Synthesis, characterization, antioxidant and antibacterial studies of some metal (II) complexes of tetradentate Schiff base ligand: (4E)-4-[(2-{(E)-[1-(2,4-dihydroxyphenyl) ethylidene] amino} ethyl) imino]penta-2-one. *Bioinorganic Chemistry and Applications*, 9: 1-9.
5. Dayt, D. and Serra, G. (2010). Thiazole and oxazole alkaloids: Isolation and synthesis. *Marine Drugs*, 8: 2755-2780.

6. Penta, S. and Vedula, R. R. (2012). A facile one-pot synthesis of thiazole-pyrazole derivatives *via* multicomponent approach. *Organic Communications*, 5(3): 143-149.
7. Bodireddy, M. R., Mohinuddin, P. M. K., Gundala, T. R. and Reddy, G. (2016). Lactic acid-mediated tandem one-pot synthesis of 2-aminothiazole derivatives: A rapid, scalable and sustainable process. *Organic Chemistry*, 2: 1-13.
8. Kołazcek, A., Fusiarz, I., Ławecka, J. and Branowksa, D. (2014). Biological activity and synthesis of sulfonamide derivatives: A brief review. *Chemik Er Zeitung*, 68(7): 620-628.
9. Kushwara, N., Kushwara, S. K. S. and Rai, A. K. (2012). Biological activities of thiadiazole derivatives: A review. *International Research of Chemtech Research*, 4(2): 517-531.
10. Kaur, K., Kaur, R. and Dhir, G. N. (2014). Synthesis and biological of amino acid and peptide conjugates of Rhein derivatives. *Journal of Advanced Pharmaceutical Education and Resource*, 4(3): 311-318.
11. Ripain, I. H. A., Roslan, N., Norshahimi, N. S., Salleh, S. S. M., Bunnori, N. M. and Ngah, N. (2019). Synthesis and molecular docking of 2,4,5-trisubstituted-1,3-thiazole derivatives as antibacterial agents. *Malaysian Journal of Analytical Sciences*, 23(2): 237-246.
12. Carson, C. F., Mee, B. J. and Riley, T. V. (2002). Mechanism of action of *Melaleuca Alternifolia* (Tea Tree) oil on *Staphylococcus Aureus* determined by time-kill, leakage and salt tolerance assay and electron microscopy. *Antimicrobial Agents and Chemotherapy*, 46(6): 1914-1920.
13. Balouiri, M., Sadiki, M. and Ibnsouda, S. K. (2016). Methods for in-vitro evaluating antimicrobial activity: A review. *Journal of Pharmaceutical Analysis*, 6(2): 71-79.
14. Culafic, D. M., Gacic, B. V., Vukcevic, J. K., Stankovic, S. and Simic, D. (2005). Comparative study on the antibacterial activity of volatiles from Sage (*Salvia Officinalis* L.). *Archives of Biological Sciences*, 57: 173-178.
15. Guo, N., Gai, Q., Jiao, J., Wang, W., Zu, Y. and Fu, Y. (2016). Antibacterial activity of *Fructus Forsythia* essential oil and the application of EO-loaded nanoparticles to food-borne pathogens. *Foods*, 5(73): 1-13.
16. Qarallleh, H., Idid, S., Saad, S., Susanti, D., Taher, M. and Khleifat, K. (2010). Antifungal and antibacterial activities of four Malaysian sponge species (Petrosiidae). *Journal de Mycologie Médicale*, 20(4): 315-320.
17. Devi, K. P., Nisha, S. A., Sakthivel, R. and Pandian, S. K. (2010). Eugenol (An essential oil of clove) acts as an antibacterial agent against *Salmonella typhi* by distrupting the cellular membrane. *Journal of Ethnopharmacology*, 130(1): 107-115.
18. Miksusanti, M., Jenie, B. S. L., Priosoeryanto, B. P., Syarief, R. and Rekso, G. T. (2008). Mode of action Temu Kunci (Kaempferia pandurate) essential oil on *E.coli* K1.1 cell determined by leakage of material cell and salt tolerance assays. *HAYATI Journal of Biosciences*, 15(2): 56-60.
19. Mendrapa, J., Parekh, V., Vaghela, S., Makasana, A., Kunjadia, P. D., Sanghvi, G., Vaishnav, D. and Dave, G. S. (2013). Isolation and characterization of high salt tolerance bacteria from agricultural soil. *European Journal of Experimental Biology*, 3(6): 351-358.
20. Gittens, J. E., Smith, T. J., Suleiman, R. and Akid, R. (2013). Current and emerging environmentally-friendly systems for fouling control in the marine environmental. *Biotechnology Advances*, 31(8): 1738-1753.
21. Chapman, J., Hellio, C., Sullivan, T., Brown, R., Russell, S., Kiterringham, E., Nor, L. L. and Regan, F. (2014). Bioinspired synthetic macroalgae: examples from nature for antifouling applications. *International Biodeterioration & Biodegradation*, 65: 1-8.
22. Ahmad, S. J., Lian, H. H., Basri, D. F. and Zin, N. M. (2015). Mode of action of endophytic *Streptomycin sp*., SUK 25 extracts against MRSA; microscopic, biochemical and time-kill analysis. *International Journal of Pharmaceutical Sciences Review and Research*, 30(1): 11 – 17.
23. Babii, C., Mihalache, G., Bahrin, L. G., Neagu, A., Gostin, I., Mihai, C. T., Sa, L., Birsa, L. M. and Stefan, M. (2018). A novel synthetic flavanois with potent antibacterial properties: in-vitro activity and proposed mode of action. *Plos One*, 13(4): 1-5.

Malaysian Journal of Analytical Sciences (MJAS)
Published by Malaysian Analytical Sciences Society

DETERMINATION OF METSULFURON METHYL IN CRUDE PALM OIL USING LIQUID CHROMATOGRAPHY TRIPLE QUADRUPOLE MASS SPECTROMETER

(Penentuan Metsulfuron Metil dalam Minyak Sawit Mentah Menggunakan Kromatografi Cecair Spektrometri Jisim Caturkutub Ganda Tiga)

Nik Sasha Khatrina Khairuddin[1]*, Chee Beng Yeoh[1], Najwa Sulaiman[1], Farah Khuwailah Ahmad Bustamam[1], Halimah Muhamad[1], Ismail Sahid[2]

[1]Malaysian Palm Oil Board,
No. 6, Persiaran Institusi, Bandar Baru Bangi, 43000 Kajang, Selangor, Malaysia
[2]School of Environmental Science and Natural Resources, Faculty Science and Technology,
Universiti Kebangsaan Malaysia, 43600 Bangi, Selangor, Malaysia.

**Corresponding author: sashakhatrina@mpob.gov.my*

Received: 23 December 2020 ; Accepted: 16 February 2021; Published: 25 April 2021

Abstract

A simple and fast method for the determination of metsulfuron methyl (MSM) in crude palm oil (CPO) was developed and validated in-house. The analytical method developed involved a liquid-liquid extraction of MSM with the incorporation of a heating step that has been found to enhance the extraction efficiency and stability. This is followed by clean-up using solid phase extraction (SPE), concentration and reconstitution of the analyte prior to injection into the liquid chromatography triple quadrupole mass spectrometer (LC/MS/MS). Using this method, good linearity with good coefficient correlation (r^2) of >0.999 was obtained for matrix-matched calibration. Results showed that the average recoveries obtained for MSM in CPO samples at different levels of concentration (ultra-low, low, and high) are in the range between 84-98% with a relative standard deviation (RSD) of less than 5% for all samples. The limit of detection (LOD) and limit of quantification (LOQ) for analysis of residual MSM in CPO was estimated to be 1.0 and 5.0 ng/g, respectively. An experiment determining the repeatability resulted in an RSD of less than 5% for all samples and intermediate precision at spiking level at 10 ng/g and 50 ng/g showed RSD of 6.93% and 4.07%, respectively. A very low % RSD indicates good precision and suitability of this method for use in the analysis of residual MSM in CPO. Quick monitoring of Malaysian CPO was also carried out by analyzing 10 samples obtained from various mills throughout Malaysia. Results from the CPO monitoring showed that all samples were free from residual MSM.

Keywords: method development, metsulfuron methyl, pesticides, crude palm oil, liquid chromatography triple quadrupole mass spectrometer

Abstrak

Satu kaedah yang mudah dan pantas bagi penentuan kandungan metsulfuron metil (MSM) dalam minyak sawit mentah telah dibangunkan dan telah ditentusahkan. Kaedah analitikal yang telah dibangunkan melibatkan kaedah pengekstrakan MSM jenis cecair-cecair, dengan penambahan langkah pemanasan yang didapati dapat meningkatkan kecekapan dan kestabilan

pengekstrakan, diikuti dengan langkah pembersihan menggunakan pengekstrakan jenis fasa pepejal (SPE), serta pemekatan dan pelarutan semula analit sebelum disuntik ke dalam instrumen kromatografi cecair spektrometri jisim caturkutub ganda tiga (LC/MS/MS). Melalui kaedah ini, kelinearan dan korelasi pekali penentuan yang baik, dengan nilai (r^2) >0.999 bagi kalibrasi padanan matriks telah diperolehi. Keputusan menunjukkan purata perolehan semula yang diperolehi bagi MSM dalam sampel minyak sawit mentah pada kepekatan yang berbeza (sangat rendah, rendah dan tinggi) adalah pada julat antara 84-98% dengan nilai sisihan piawai relatif (RSD) kurang daripada 5% bagi kesemua sampel. Had pengesanan (LOD) dan had pengkuantitian (LOQ) bagi analisis sisabaki MSM dalam minyak sawit mentah masing-masing adalah 1.0 dan 5.0 ng/g. Eksperimen bagi penentuan kebolehulangan menunjukkan nilai RSD yang kurang daripada 5% untuk kesemua sampel dan kejituan pertengahan pada kepekatan 10 ng/g dan 50 ng/g menunjukkan nilai RSD masing-masing 6.93% and 4.07%. Nilai RSD yang sangat rendah menunjukkan kejituan yang baik dan kesesuaian penggunaan kaedah ini untuk analisis sisabaki MSM dalam minyak sawit mentah. Satu kajian pemantauan kandungan MSM dalam minyak sawit mentah di Malaysia juga telah dijalankan terhadap 10 sampel minyak sawit mentah yang diperolehi daripada beberapa kilang pemprosesan minyak sawit di Malaysia. Hasil keputusan pemantauan ini menunjukkan bahawa semua sampel minyak sawit mentah yang dianalisa adalah bebas dari sisabaki MSM.

Kata kunci: pembangunan kaedah, metsulfuron metil, pestisid, minyak sawit mentah, kromatografi cecair spektrometri jisim caturkutub ganda tiga

Introduction

Oil palm is one of the most important crops in the global market and Malaysia is the world's second largest producer and exporter [1]. In 2019, the total of Malaysian palm oil and the exported products was 27.98 million tonnes [2]. Like any other crops, oil palm is also threatened by various types of weeds such as *Asystasia gangetica, Chromolaena odorata, Mikania micrantha, Hedyotis verticillate, and Peperomia pellucida*. These threats have caused a fair amount of losses to the production of palm oil, which led to an increase in maintenance cost. There are a large number of herbicides registered globally to be used for weeds management. The chemical and physical properties of these chemical compounds vary considerably. It is noted that continuous and extensive application of herbicides or any type of pesticides contaminates the water, soil, and food, and this leads to compromising human health and polluting the environment. The growing number of pesticides usage has increased the demands for the development of new laboratory methods applicable to their effective detection and control [3]. Therefore, the development of methods for all registered pesticides to be used in oil palm plantations is important to monitor residual pesticides to ensure that the trade and market of palm oil can be sustained.

MSM is one of the herbicides currently used in Malaysian oil palm plantation for weed management (Figure 1). It is a residual sulfonylurea compound used as a selective pre- and post-emergence herbicide. It has a high herbicidal activity even at low application rate and is widely used including Malaysia for effective control of a wide range of weeds such as annual grasses, pasture, and plantation crops. It is a systemic compound with foliar and soil activity that inhibits cell division in shoots and roots through the inhibition of acetolactate synthase (ALS), which is a key enzyme in the biosynthesis of branched amino acids (valine, isoleucine, and leucine) in plant and micro-organisms. ALS, however, is not present in animals [4]. MSM can be applied alone or in tank mixture with other herbicides for weed control such as glyphosate, paraquat, and others [5]. It is common to add MSM to increase the efficacy of mix herbicides [6].

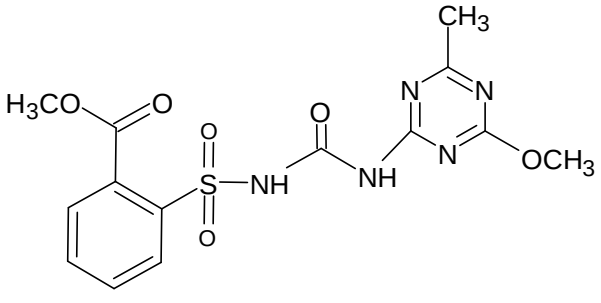


Figure 1. Molecular structure of MSM

Various methods have been described for the determination of MSM herbicide residue in soil and water [7-10]. However, there are only a few reports on

its determination in oil or fatty matrices despite the various analytical methods described for the determination of various pesticides in oil crops such as olive oil, palm oil, sunflower oil and other oils [11-17].

Nageswara Rao et al. [18] reported a dispersive extraction method for the determination of MSM in groundnut oil. In the developed method, the author homogeneously dispersed (1:1, (w/w)) groundnut oil in C18 adsorbent prior to the elution using (1:1, v/v) 20 mL of ethyl acetate-dichloromethane. This resulted in average recoveries ranging from 90–97% and RSD of less than 3%. In another study by Maldaner [19], matrix solid phase dispersion extraction followed by C_8 co-column clean-up for the determination of MSM in soybeans was reported. For oil palm application, research on MSM in soil has been carried out [20, 21], however, lack of research was performed for CPO. Although there are several studies reported on pesticide multiresidue analysis in oil matrices including palm oil, MSM residue was not included [16, 22-23]. Therefore, the applicability of the method for residual MSM analysis is unknown. In another study by Kostelac and Anastassiades [24], residual analysis of MSM was included in the multiresidue analysis using the Quick, Easy, Cheap, Effective, Rugged and Safe (QuEChERS) technique. The method described is only limited to be used for non-fatty matrices such as cucumber, lemon, raisins, and wheat flour. Due to the lack of literature concerning residues of MSM in palm oil, there is a need to carry out a study on the development of an analytical method for MSM in palm oil matrix. In this study, the method was developed based on a paper published by Yeoh et al. [25] and Yeoh and Chong [16]. However, in that method, the chlorinated solvent was used as a diluent in sample extraction. Reported in this study is a modified method for MSM residue determination in palm oil matrix that omits the use of halogenated solvent but maintaining the effectiveness of the method.

Materials and Methods

Chemicals, materials and apparatus

All chemicals and reagents used in this study were of analytical or liquid chromatographic grade. Methanol (MeOH) was obtained from Merck whereas acetic acid (LC/MS grade) was obtained from Sigma Aldrich. Deionized water used in this experiment was from a Milli-Q water purification system (Millipore Corp., USA). Both MSM (99% purity) and ethametsulfuron methyl (EMSM, 98% purity) standard materials were purchased from Dr. Ehrenstorfer (Ausburg, Germany). Carbograph SPE columns (500 mg/8 mL) used for sample clean-up were obtained from Alltech™. Nitrogen evaporator (Horizon Technology, USA) was used for samples drying.

Preparation of stock and working standard solution

A stock solution of MSM with a concentration of 100 µg/mL was prepared by dissolving 10.1 mg of the MSM standard in 100 mL of MeOH. A similar procedure was carried out for the preparation of the EMSM stock solution (100 µg/mL). Working standard solutions for MSM (5, 10, 20, 30, 50 and 70 µg/mL) were then prepared by dilution with the appropriate MeOH volume. The prepared standard solutions were stored at -20ºC. For EMSM, a suitable amount of stock solution was used to prepare EMSM working standard solution (500 µg/mL) in order to spike in the final extract as an internal standard before injecting into the LC/MS/MS system.

Spiking sample preparation

200 g of blank CPO obtained from a nearby palm oil mill was melted in a 500 ml beaker (tall form) using water bath controlled at 60ºC. Before conducting the experiment, the oil samples were analyzed to ensure the absence of any MSM residual. For the preparation of spiked CPO samples at 10 ng/g, 20 µL of MSM stock solution (100 µg/mL) was spiked into the blank CPO followed by stirring using a magnetic bar for 30 minutes. This is important to ensure that the spiking of MSM into the oil sample is well distributed and homogenized. While ensuring the stirring using the magnetic bar is continuous, 5 g each of CPO samples spiked with MSM at 10 ng/g level were weighed. A total of 30 spiked samples were obtained and stored in a freezer controlled at -20ºC. These samples were taken out for analysis when required. The same procedure was repeated for the preparation of spiked CPO samples at 5 and 50 ng/g levels.

Liquid-liquid extraction and SPE Clean-up

As shown in Figure 2, 5.0 g of CPO sample and 5 mL of MeOH extraction solvent were mixed in a 30 mL self-standing Falcon tube. The sample was shaken using a vortex mixer for 2 minutes and was left in the water bath (60°C) for a subsequent 2 minutes. The same process (shaking and heating) was repeated until a total of 10 minutes shaking time was achieved. Then, the samples were tilted at approximately 45-60° in the freezer (-20°C) for 1 hour prior to centrifugation at 2655 x g for 5 minutes to allow phase separation. The placement of samples in a tilted position was found to give better phase separation [17].

For SPE clean-up (Figure 3), the carbograph SPE cartridge was first conditioned using 8 mL of MeOH. Then, 1 mL aliquot of the extracted sample (from the liquid-liquid extraction section) was transferred into the SPE cartridge. Elution of MSM was carried out using 6 mL of MeOH solvent under gravity flow. The collected SPE eluate was dried using nitrogen evaporator followed by reconstitution with 1 mL of MeOH, and the addition of 25 µL internal standard. The sample was shaken with a vortex mixer for a few seconds prior to LC/MS/MS injection.

LC/MS/MS analysis

LC/MS/MS analysis was conducted using AB Sciex QTRAP® 4500 (Foster City, CA, USA) triple quadrupole MS/MS with ESI in the positive ion mode. The system was equipped with Analyst® Instrument Control and Data Processing version 1.6.2 software. Kinetex C18 100A capillary column (50 mm x 2.1 mm x 2.6 µm) attached to the guard column (SecurityGuard™ ULTRA cartridges for UHPLC C_{18}, with an internal diameter of 2.1 mm) were both provided by Phenomenex™. The column compartment temperature was set at 40°C. Mobile phase A and B were 10mM aqueous acetic acid solution and 100% MeOH, respectively at the flow rate of 0.2 mL/min using a gradient elution profile depicted in Table 1. A volume of 10 µL of the sample was injected into the LC/MS/MS system with a total analysis time of 15 min for each sample. The determination of the respective compounds (MSM and EMSM) was carried out according to the multiple reaction monitoring experiment parameters as shown in Table 2.

In-house validation

In-house method validation was carried out and the parameters tested were linearity, LOD, LOQ, and method precision.

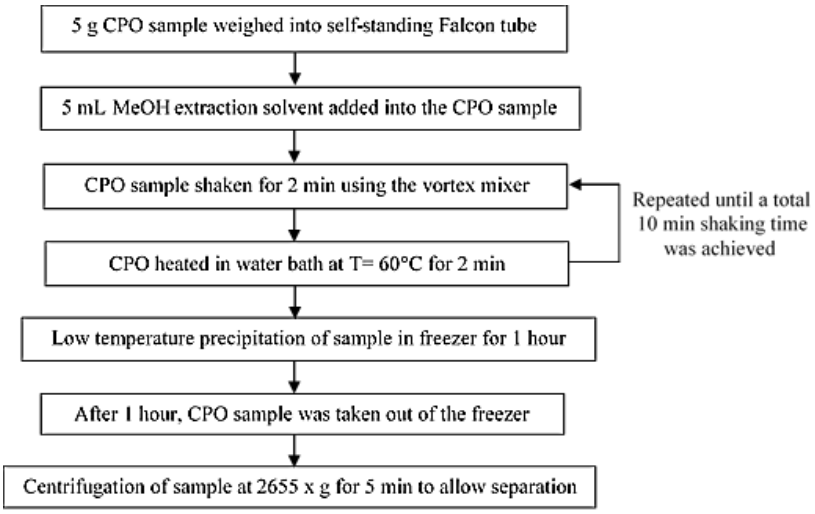


Figure 2. Liquid-liquid extraction steps for residual analysis of MSM in CPO using LC/MS/MS

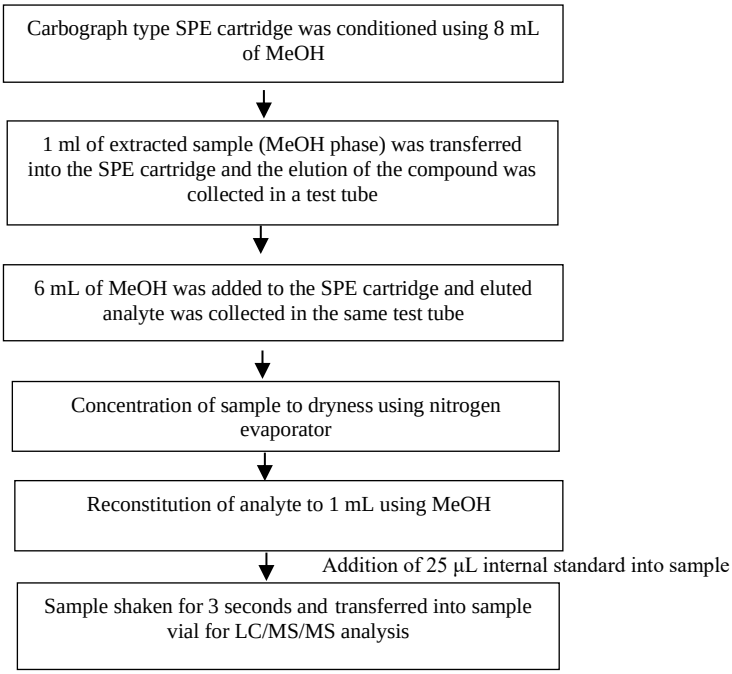


Figure 3. SPE clean-up steps for residual analysis of MSM in CPO using LC/MS/MS

Table 1. Mobile phase gradient system used in the residual MSM analysis using LC/MS/MS

Time (min)	**Flow Rate (mL/min)**	**A (%)**	**B (%)**
0.00	0.20	95	5
5.00	0.20	5	95
10.00	0.20	5	95
10.50	0.20	95	5
15.00	0.20	95	5

Table 2. Optimum parameter for MSM and EMSM obtained by manual tuning

Term Used	**Transition (m/z)**	**DP**	**EP**	**CE**	**CXP**
MSM 1	382/167	91	10	19	8
MSM 2	382/199	91	10	32	8
EMSM 1	411/196	86	10	24	10
EMSM 2	411/168	86	10	42	10

DP=Declustering Potential, EP=Entrance Potential, CE=Collision Energy, CXP=Collision Cell Exit Potential

Results and Discussion

Heating technique versus no heating technique

It is known that palm oil contains approximately 1:1 ratio of saturated and unsaturated fatty acids in its composition. Palm oil tends to solidify at room temperature. In this experiment, cloudiness was observed during the extraction process (Figure 4). It was believed that the formation of crystals during the extraction process may reduce the extraction efficiency. In order to optimize the extraction of MSM residue in this experiment, the extraction was carried out with an addition of intermittent heating step at constant and consistent intervals (every one-minute interval for five minutes). The intermittent heating step was found to yield better and consistent recovery compared to without heating (Figure 5). This observation is in agreement with the observation reported by Yeoh et al. [26]. In that paper, it was noted that there was an increase of ~20% recovery when a heating step was included possibly due to the melting of micro crystals in palm oil matrix with the presence of heat. Thus, increases the extraction efficiency that leads to improving the recovery percentage.

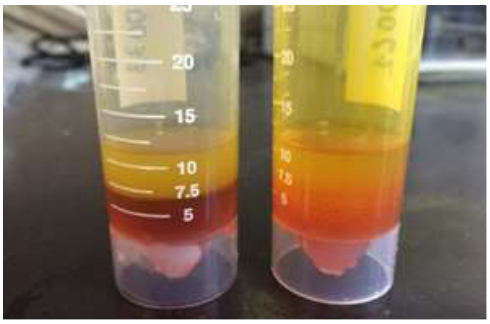


Figure 4. Comparison of physical condition of CPO sample with the addition of intermittent heating step (left) versus CPO sample without intermittent heating step which resulted cloudiness (right)

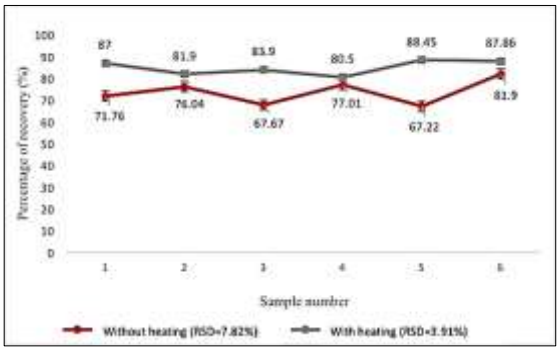


Figure 5. Comparison of recovery percentage for samples that underwent heating step versus samples without the addition of heating step

Linearity and matrix effect

From Figure 6, it was noted that the signals obtained for MSM are linear in the concentration ranging from 5-70 ng/g. This is true for both calibration curves plotted for MSM prepared in both pure solvent and blank CPO extract (matrix-matched). It could also be observed that the MSM signal suffers from serious suppression effect due to the matrix. Determination of this matrix effect was carried out by comparing the slope of both calibration curves according to Pano-Farias et al. [27] in which the matrix effect was found to be approximately -1956% (matrix suppression effect). Therefore, it was decided that further work on method development of residual MSM in CPO would be based on the matrix-matched calibration curve.

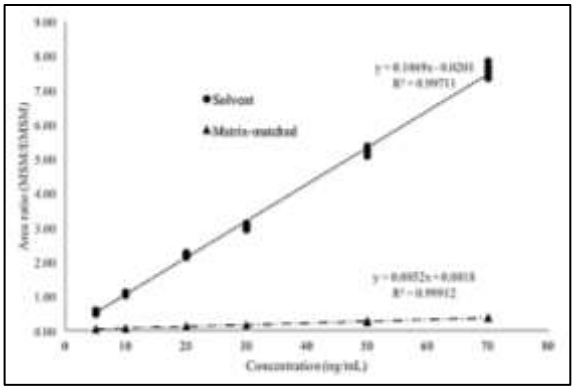


Figure 6. Comparison of MSM calibration curve prepared in pure solvent versus blank CPO extract (matrix-matched)

LOD and LOQ

The LOD value was estimated based on 3 times the y-residual standard deviation of the calibration curve. The LOQ value was estimated based on 10 times the y-residual standard deviation [28]. In this study, both the LOD and LOQ were estimated to be 1.0 and 5.0 ng/g, respectively.

Method recovery

The method recovery was examined by analyzing six replicates of spiked samples at ultra-low (5 ng/g), low (10 ng/g), and high (50 ng/g) spiking levels. Based on the results, the range of recoveries obtained was within 84-98% with RSD <5% for all levels. Results for the recovery analysis of residual MSM in CPO is summarized in Table 3. Low RSD % obtained from this recovery study also indicated that the method has good repeatability. Figure 7 shows a typical chromatogram of blank CPO sample, MSM working standard solution at 10 ng/mL concentration, and CPO sample spiked at 10 ng/g of MSM.

Method precision study: Repeatability

Repeatability of the analysis was verified through recovery experiment using the method that was developed for the analysis of residual MSM in CPO (n=6) at low and high spiking level (10.0 and 50 ng/g) carried out by two different analysts (Analyst 1 and Analyst 2). It could be observed from Table 4 that the average recovery for all sample replicates on each day (Day 1 and Day 2) by Analyst 1 and Day 2 for Analyst 2 were between 84-108%. Despite the lack of experience in performing the analysis using this newly developed analytical method, method repeatability study performed by Analyst 2 was comparable to those by Analyst 1. The method RSD % calculated from recovery experiment datasets were all below 5% and were considered to be excellent according to the literature [29, 30].

Method precision study: Intermediate precision

Intermediate precision is the measurement of method repeatability over a short period with possible minor variations in the experimental conditions such as different batches of reagents used, different analyst, different column efficiency and others. Therefore, a comparison study of method recovery was conducted by two different analysts in two days for CPO samples analysis (n=6) spiked at 10 and 50 ng/g of MSM, respectively. From Table 4, the calculation of RSD % for both 10 ng/g and 50 ng/g spiking levels taking into account variations in terms of analyst's skill and time of analysis resulted in 6.93% and 4.07% of RSD, respectively. These values confirm that the method precision (repeatability and intermediate precision) is within the acceptable levels [29, 30].

Monitoring of CPO samples

10 CPO samples obtained from selected licensed palm oil mills with incoming fresh fruit bunches (FFB) from plantations with known MSM usage history in Peninsular Malaysia, Sabah and Sarawak were analyzed for possible residual MSM using the developed method (liquid-liquid extraction followed by SPE clean-up) in three replicates. Based on the monitoring, no residual MSM was detected in any of the CPO samples. This gives a preliminary indication that the usage of MSM in oil palm plantations was based on the recommended dosage by the manufacturer and also follow the good agricultural practice. However, more CPO samples need to be analyzed in the future to obtain more comprehensive data for the production of palm oil in Malaysia.

Table 3. studies for analysis of MSM in CPO at the concentration of 5, 10 and 50 ng/g

Sample Replication	Spiking Level		
	5 ng/g	10 ng/g	50 ng/g
1	93.02	92.40	91.02
2	86.86	94.78	90.23
3	93.84	96.17	98.00
4	84.11	96.43	89.06
5	88.37	96.83	88.19
6	85.52	92.01	87.06
Average	88.62	94.77	90.59
Standard Deviation	4.00	2.11	3.55
RSD %	4.51	2.22	3.92

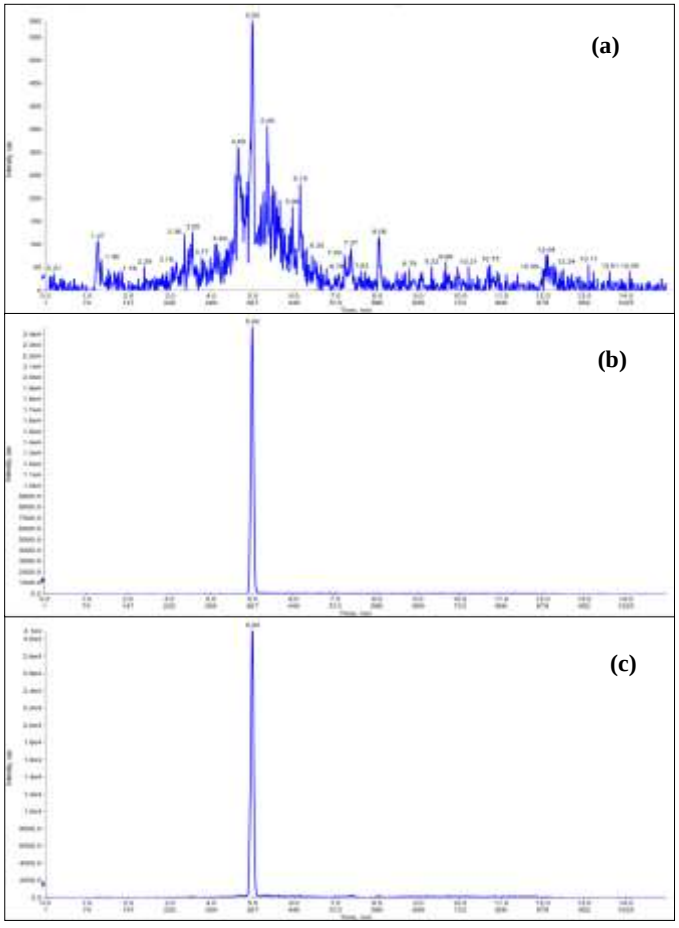


Figure 7. Representative chromatogram of (A) blank CPO sample, (B) MSM working standard solution (in MeOH) at the concentration of 10 ng/mL and (C) CPO sample spiked at 10 ng/g of MSM

Table 4. Intermediate precision study of residual MSM determination in CPO at 10 and 50 ng/g spiking levels

Sample Replication	10 ng/g Spiking Level			50 ng/g Spiking Level		
	Analyst 1		Analyst 2	Analyst 1		Analyst 2
	Day 1	Day 2	Day 2	Day 1	Day 2	Day 2
1	92.40	99.83	105.16	91.02	84.68	84.16
2	94.78	95.52	117.29	90.23	83.89	89.23
3	96.17	97.16	108.27	98.00	85.13	86.08
4	96.43	91.57	107.50	89.06	85.74	84.74
5	96.83	97.10	101.19	88.19	84.34	87.22
6	92.01	100.34	108.26	87.06	83.17	88.08
Average	94.77	96.92	107.95	90.59	84.49	86.59
Standard Deviation	2.11	3.19	5.31	3.55	0.83	1.96
RSD %	2.22	3.29	4.92	3.92	0.98	2.26

Conclusion

A new method was developed and optimized for the analysis of residual MSM in CPO matrix. Results from the experiment showed that the extraction technique using MeOH followed by heating of the samples, low temperature precipitation technique, and sample clean-up using SPE (carbograph) gave good recovery rates (84-98%) with RSD of less than 5% for all samples. The method was also in-house validated and passed the important validation parameters such as linearity, recovery, and precision (repeatability and intermediate precision). LOD and LOQ for the developed method were estimated to be 1.0 and 5.0 ng/g, respectively.

Acknowledgement

The authors would like to thank the Director-General of MPOB for granting permission to publish the findings from this study. Special thanks also go to the Analytical Research laboratory assistants for their continuous technical support.

References

1. Kushairi, A., Loh, S. K., Azman, I., Elina, H., Meilina, O.-A., Mohd Noor Izudin, Z. B., Razmah, G., Shamala, S. and Ahmad Parveez, G. K. (2018). *Journal of Oil Palm Research*, 30: 163-195.
2. Parveez, G. K. A., Elina, H., Loh, S. K., Ong-Abdullah, M., Kamalrudin, M. S., Zanal Bidin, M. N. I., Sundram, S., Hasan, Z. A. A. and Zainab, I. (2020). Oil palm economic performance in Malaysia and R&D progress in 2019. *Journal of Oil Palm Research,* 32(2): 159-190.
3. Lacina, O., Zachariasova, M., Urbanova, J., Vaclavikova, M., Cajka, T. and Hajslova, J. (2012). Critical assessment of extraction methods for the simultaneous determination of pesticide residues and mycotoxins in fruits, cereals, spices and oil seeds employing ultra-high performance liquid chromatography-tandem mass spectrometry. *Journal of Chromatography A*, 1262: 8-18.
4. Zanardini, E., Negri, M., Boschin, G., D'Agostina, A., Valle, A., Arnoldi, A. and Sorlini, C. (2002). Biodegradation of chlorsulfuron and metsulfuron-methyl by *Aspergillus niger*. *The Scientific World Journal*, 2: 1369-1374.
5. Bazzigalupi, O. and Cepeda, S. (2005). Relations between soil moisture and the metsulfuron methyl effects on the seedling growth of soybean (*Glycine max* L. Merr.) *Revista de Investigaciones Agropecuarias*, 34(1): 101-110.
6. Wibawa, W. and Sugandi, D. (2013). The effectiveness of three herbicides mixed with metsulfuron methyl in controlling weeds on two types of soil in smallholders oil palm plantation. *International Journal of Current Research*, 5(9): 2487-2493.

7. Ghani, A. and Wardle, D. A. (2001) Fate of ^{14}C from glucose and the herbicide metsulfuron–methyl in a plant–soil microcosm system. *Soil Biology and Biochemistry*, 33: 777-785.
8. Pons, N. and Barriuso, E. (1998). Fate of metsulfuron-methyl in soils in relation to pedo-climatic conditions. *Pesticide Science*, 53: 311-323.
9. Sondhia, S. (2008). Persistence of metsulfuron-methyl in wheat crop and soil. *Environmental Monitoring and Assessment*, 147: 463-469.
10. Sondhia, S. (2009). Persistence of metsulfuron-methyl in paddy field and detection of its residues in crop produce. *Bulletin of Environmental Contamination and Toxicology*, 83: 799-802.
11. Ferrer, C., Gómez, M. J., García-Reyes, J. F., Ferrer, I., Thurman, E. M. and Fernández-Alba, A. R. (2005). Determination of pesticide residues in olives and olive oil by matrix solid-phase dispersion followed by gas chromatography/mass spectrometry and liquid chromatography/tandem mass spectrometry. *Journal of Chromatography A*, 1069: 183-194.
12. Muhamad, H., Tan, Y. A. and Ismail, B. S. (2008). Determination of the herbicide fluroxypyr in oil matrices. *Journal of Environmental Science and Health B*, 43: 134-140.
13. Li, L., Zhou, Z., Pan, C., Qian, C., Jiang, S. and Liu, F. (2007) Determination of organophosphorus pesticides in soybean oil, peanut oil and sesame oil by low-temperature extraction and GC-FPD. *Chromatographia*, 66: 625-629.
14. Nageswara Rao, T., Ramasubbih A.V. and Parvathi, T. (2012). Development and validation of a HPLC-UV method for simultaneous determination of five sulfonylurea herbicide residues in soybean oil followed by matrix solid-phase dispersion. *International Journal of Chemical, Environmental and Pharmaceutical Research*, 3(2): 117-121.
15. Ramli, M. I., Zakaria, Z., Sahid, I., Tan, Y. A. and Muhamad, H. (2012). Determination of herbicide diuron levels in palm oil matrices using HPLC-UV. *Sains Malaysiana*, 41: 1451-1459.
16. Yeoh, C. B. and Chong, C. L. (2012). LC–MSMS analysis of acetamiprid residue in crude palm oil. *European Journal of Lipid Science and Technology*, 114(12): 1358-1361.
17. Zainudin, B. H., Bakar, N. K. A. and Muhamad, H. (2009). Determination of cypermethrin in palm oil matrices. *European Journal of Lipid Science and Technology*, 111: 1014-1019.
18. Nageswara Rao, T., Ramesh, A. and Parvathamma, T. (2012). Development and validation of a HPLC-UV method for simultaneous determination of five sulfonylurea herbicide residues in groundnut oil followed by matrix solid-phase dispersion. *ISRN Analytical Chemistry*, 2012: 1-5.
19. Maldaner, L., Santana, C. C. and Jardim, I. C. S. F. (2008). HPLC determination of pesticides in soybeans using matrix solid phase dispersion. *Journal of Liquid Chromatography and Related Technologies*, 31(7): 972-983.
20. Ismail, B. S. and Ooi, K. E. (2012). Adsorption, desorption and mobility of metsulfuron-methyl in soils of the oil palm agroecosystem in Malaysia. *Journal Environmental Biology*, 33(3): 573-577.
21. Mohd Tahir, N. and Jee Sing, N. Y. (2006). Adsorption of metsulfuron-methyl on soils under oil palm plantation: A case study, *1st International Conference on Natural Resources Engineering & Technology*, Putrajaya, Malaysia. p.591-596.
22. Lászlo Polgár, Béla Kmellár, Juan F. García-Reyes and Péter Fodor. (2012). Comprehensive evaluation of the clean-up step in the QuEChERS procedure for the multi-residue determination of pesticides in different vegetable oils using LC-MS/MS. *Analytical Methods*, 4(4): 1142-1148.
23. Sobhanzadeh, E., Bakar, N. K. A., Abas, M. R. B., & Nemati, K. (2012). A simple and efficient multi-residue method based on QuEChERS for pesticides determination in palm oil by liquid chromatography time-of-flight mass spectrometry. *Environmental Monitoring and Assessment*, 184(9): 5821-5828.
24. Kostelac, D. and Anastassiades. (2007). Access from QuEChERS validation method for acidic pesticides. https://www.eurl-pesticides.eu/library/docs/fv/2ndtr2007_AcidicKostelac.pdf [accessed October 2019].

25. Yeoh, C. B., Kuntom, A., Dorasamy, S., Omar, M. R., Nor, M.Y. M., and Noh, M. R. M. (2006). Determination of acephate, methamidophos, and monocrotophos in crude palm oil. *European Journal of Lipid Science and Technology*, 108: 960-964.
26. Yeoh, C. B., Ahmad Bustamam, F. K., Sulaiman, N., Khairuddin, N. S. K., Tay, M. G. and Saw, M. H. (2019). Development of analytical method for determination of thiosultap-disodium residue in palm oil matrix. *Journal of Oil Palm Research*, 3: 634-640.
27. Pano-Farias, N. S., Ceballos-Magaña, S. G., Muñiz-Valencia, R. and Gonzalez, J. (2017). Validation and assessment of matrix effect and uncertainty of a gas chromatography coupled to mass spectrometry method for pesticides in papaya and avocado samples. *Journal Food Drug Analysis*, 25: 501-509.
28. Vial, J. and Jardy, A. (1999). Experimental comparison of the different approaches to estimate LOD and LOQ of an HPLC method. *Analytical Chemistry*,71: 2672-2677.
29. European Commission, Sante/11813/2017-Guidance document on analytical quality control and validation procedures for pesticide residues and analysis in food and feed, 2017: pp 1-46.
30. Huber, L. (2007). Validation and qualification in analytical laboratories. 2nd Edition. CRC Press, Boca Raton: pp 1-288.

Malaysian Journal of Analytical Sciences Vol 25 No 3 2021

1. THE ELECTROCHEMICAL BEHAVIOUR OF Au-PEDOT/rGO MODIFIED ELECTRODE IN URIC ACID (Sifat Elektrokimia Elektrod Bermodifikasi Komposit Au-PEDOT/rGO dalam Asid Urik) 363
Farhanini Yusoff, Mohd Faris Rosdidi, Azleen Rashidah Mohd Rosli, Syara Kassim, Noor Aniza Harun, Noorashikin Md Saleh

2. SITE-SELECTIVE CARBOXYMETHYLATION OF CHITOSAN UNDER HETEROGENEOUS CONDITIONS 376
(Penentuan Tapak bagi Proses Pengkarboksimetil pada Kitosan dalam Keadaan Heterogen)
Nur Ellina Annisa Salehuddin, Nurul Adilah Rodzali, Ku Halim Ku Bulat, Nadhratun Naiim Mobarak

3. CLASSIFICATION MODEL FOR DETECTION AND DISCRIMINATION OF INEDIBLE PLASTIC ADULTERATED PALM COOKING OIL USING ATR-FTIR SPECTROSCOPY COMBINED WITH PRINCIPAL COMPONENT ANALYSIS 388
(Model Pengkelasan bagi Pengesanan dan Pengasingan Produk Cemaraduk Plastik dalam Minyak Masak Sawit Menggunakan Spektroskopi ATR-FTIR dengan Gabungan Analisis Komponen Prinsipal)
Dzulkiflee Ismail, Aliyalina Rahimi, Wan Rosli Wan Ishak, Naji Arafat Mahat, Wan Nur Syuhaila Mat Desa

4. ADDITION OF GLYCEROL AND SODIUM CHLORIDE INTO *Garcinia atroviridis* CHITOSAN FILM, AND ITS APPLICATION FOR WRAPPING OF CHICKEN MEAT 399
(Penambahan Gliserol dan Natrium Klorida Pada *Garcinia atroviridis* Filem Kitosan dan Aplikasinya Pada Pembungkusan Daging Ayam)
S-Navin Sivanasvaran, Ianne Kong, Hui-Ling Tan, Liew-Phing Pui

5. RECENT ADVANCES IN AGRICULTURAL WASTE-BASED ADSORBENTS FOR THE REMOVAL OF POLLUTANTS IN WATER (2017-2020) 415
(Kemajuan Terkini dalam Penjerap Berasaskan Sisa Pertanian untuk Penyingkiran Bahan Pencemar dalam Air (2017-2020))
Lim Yen Yee, Norsahirutiara Mohd Asrul, Fatin Farhanim Kamarulzaman, Timothy Gandu Ali, Nur Shahz Ereena Zulkifli, Amirah Farhan Kamaruddin, Nursyafreena Attan, Mohamad Afiq Mohamed Huri, Aemi Syazwani Abdul Keyon

6. CO_2-EFFERVESCENT TABLET-ASSISTED DISPERSIVE LIQUID-LIQUID MICROEXTRACTION WITH CENTRAL COMPOSITE DESIGN FOR PRE-CONCENTRATION OF ACETAMINOPHEN DRUG: METHOD DEVELOPMENT, VALIDATION AND GREEN ASSESSMENT PROFILE 432
(Tablet Berbuak-CO_2 Berbantukan Sebaran Pengekstrakan Mikro Cecair-Cecair dengan Reka Bentuk Komposit Berpusat untuk Kepekatan Awalan Dadah Acetaminophen: Pembangunan Kaedah, Validasi dan Profil Penilaian Hijau)
Priya Murugan, Sarveishwhary Rajendran, Saw Hong Loh, Marinah Mohd Ariffin, Wan Mohd Afiq Wan Mohd Khalik

7. PREPARATION AND CHARACTERIZATION OF COGON GRASS NATURAL FIBER AS A CONCRETE FILLER FOR GAMMA RADIATION SHIELDING 446
(Penyediaan dan Pencirian Serat Semula Jadi Rumput Cogon sebagai Pengisi Konkrit untuk

Perisai Sinar Gama)
Yusrina Mohd Yusof and Siti Amira Othman

8. RECENT TRENDS IN THE QUANTIFICATION OF VITAMIN B 466
(Kaedah Terkini dalam Pengkuantitian Vitamin B)
Nurul Hafawati Hashim, Rozita Osman, Nurul Auni Zainal Abidin, Nur Sofiah Abu Kassim

9. SIMPLE METHOD DETERMINATION OF SATURATED AND UNSATURATED FATTY ACIDS SOURCES FOR DIESEL-BIODIESEL BLENDS 483
(Kaedah Mudah untuk Penentuan Sumber Asid Tepu dan Taktepu bagi Campuran Diesel-Biodiesel)
Nurul Hazwah Mohd Kamarulzaman, Siti Norhafiza Mohd Khazaai, Muhammad Nor Fazli Abd Malek, Mohd Hasbi Ab. Rahim, Gaanty Pragas Maniam

10. APPLICATION OF WASTE CATALYST, $CaO\text{-}SiO_2$ IN THE TRANSESTERIFICATION OF PALM OIL 490
(Aplikasi Mangkin Bahan Buangan, $CaO\text{-}SiO_2$ dalam Transesterifikasi Minyak Sawit)
Siti Norhafiza Mohd Khazaai, Sih Yiting, Mohd Hasbi Ab. Rahim, Mohd Lokman Ibrahim, Gaanty Pragas Maniam

11. ^{210}PO DETERMINATION IN URINE SAMPLES AMONG RADIATION WORKERS BY ALPHA SPECTRUM ANALYSIS 498
(Penentuan ^{210}Po dalam Sampel Urin di Kalangan Pekerja Sinaran Melalui Analisis Spektrum Alpha)
Nurrul Assyikeen Md. Jaffary, Nurul Zakila Azlan, Jalal Sharib @ Sarip, Mohd Tarmizi Ishak, Zulkifli Daud, Mohd Izwan Abdul Adziz

12. THE EFFECTS OF STORAGE TEMPERATURE AND TIME ON THE LEVELS OF PHTHALATES IN COMMERCIAL PET-BOTTLED WATER 508
(Kesan Suhu dan Masa Penyimpanan Terhadap Kandungan Ftalat dalam Air Berbotol PET Komersial)
Nur Amira Syazwan Razali, Ungku Fatimah Ungku Zainal Abidin, Nur Hanani Zainal Abedin, Syaliza Omar, Jinap Selamat, Maimunah Sanny

13. PREPARATION OF CERIUM DOPED NICKEL OXIDE FOR LOWER REDUCTION TEMPERATURE IN CARBON MONOXIDE ATMOSPHERE 521
(Serium yang Didopkan ke atas Nikel Oksida untuk Suhu Penurunan Lebih Rendah dalam Atmosfera Karbon Monoksida)
Norliza Dzakaria, Azizul Hakim Lahuri, Tengku Shafazila Tengku Saharuddin, Alinda Samsuri, Fairous Salleh, Wan Nor Roslam Wan Isahak, Muhammad Rahimi Yusop, Mohd Ambar Yarmo

14. DEVELOPMENT OF EDIBLE CHITOSAN FILM INCORPORATED WITH POMEGRANATE PEEL EXTRACT FOR THE PACKAGING OF BEEF 532
(Penghasilan Filem Kitosan yang Boleh Dimakan yang Digabungkan dengan Ekstrak Kulit Buah Delima untuk Pembungkusan Daging Lembu)
Seah Jia Min, Ianne Kong, Enis Mudiliar Rajan, Pui Liew Phing, Yus Aniza Yusof

Malaysian Journal of Analytical Sciences (MJAS)
Published by Malaysian Analytical Sciences Society

THE ELECTROCHEMICAL BEHAVIOUR OF Au-PEDOT/rGO MODIFIED ELECTRODE IN URIC ACID

(Sifat Elektrokimia Elektrod Bermodifikasi Komposit Au-PEDOT/rGO dalam Asid Urik)

Farhanini Yusoff[1]*, Mohd Faris Rosdidi[1], Azleen Rashidah Mohd Rosli[1], Syara Kassim[2], Noor Aniza Harun[2], Noorashikin Md Saleh[3]

[1]Faculty of Science and Marine Environment
[2]Advanced Nano Materials (ANoMa) Research Group, Faculty of Science and Marine Environment
Universiti Malaysia Terengganu, 21030 Kuala Nerus, Terengganu, Malaysia
[3]Research Centre for Sustainable Process Technology, Department of Chemical Engineering,
Faculty of Engineering and Built Environment,
Universiti Kebangsaan Malaysia, 43600 UKM Bangi, Selangor, Malaysia

**Corresponding author: farhanini@umt.edu.my*

Received: 28 March 2021; Accepted: 23 May 2021; Published: 27 June 2021

Abstract

The development of gold nanoparticle/poly(3,4-ethylene dioxythiophene)/reduced graphene oxide (denoted as Au-PEDOT/rGO) sensor is necessary for the detection of UA as the irregular amount of UA in the human body may cause several diseases such as gout, heart disease, kidney stone and hypertension. In this work, Au-PEDOT/rGO nanocomposite was synthesized by a facile chemical technique. The morphology, composition, and structure of Au-PEDOT/rGO composite were confirmed by FTIR, SEM, and XRD characterization. FTIR spectrum showed the presence of C-O-C stretching and C-S stretching of the thiophene ring. The attachment of Au with PEDOT and rGO was confirmed by SEM. XRD analysis showed the presence of Au(111), Au(200), Au(220), Au(311) and Au(222) corresponding to Au-PEDOT/rGO composite. This proved that Au-PEDOT/rGO has been successfully synthesized. The electrochemical behavior of Au-PEDOT/rGO/GCE was evaluated by cyclic voltammetry (CV) in 1.0 M KCl with 5 mM $K_4[Fe(CN)_6]$ and the results demonstrated that Au-PEDOT/rGO/GCE has a better electrical conductivity for detection of UA in the real sample. DPV measurements showed a linear relationship between oxidation peak current and concentration of UA in phosphate buffer (pH 7) over the concentration range 0.10 µM until 25.0 µM. The limit of detection of UA is 0.05 µM, and the limit of quantification of UA is 0.22 µM. Thus, Au-PEDOT/rGO electrode composite is a worthy alternative for the detection of UA in human's urine.

Keywords: conducting polymer, gold nanoparticles, reduced graphene oxide, uric acid

Abstrak

Pembangunan sensor buat zarah nano aurum/poli(3,4-etilenadioxitiofena/grafin oksida terturun (dilabel sebagai Au-PEDOT/rGO) adalah diperlukan untuk pengesanan UA kerana jumlah UA yang tidak normal dalam tubuh manusia boleh menyebabkan beberapa kondisi penyakit seperti gout, penyakit jantung, batu ginjal dan darah tinggi. Dalam kajian ini, komposit nano Au-PEDOT/rGO

telah disinthesis melalui teknik kimia mudah. Morfologi, komposisi, dan struktur komposit Au-PEDOT/rGO telah disahkan melalui teknik pencirian FTIR, SEM, dan XRD. Spektrum FTIR menunjukkan kehadiran regangan C-O-C dan regangan C-S bagi ikatan tiofena manakala penggabungan Au kepada lembaran PEDOT dan rGO telah dibuktikan melalui SEM. Analisis XRD menunjukkan kehadiran Au(111), Au(200), Au(220), Au (311) dan Au(222) sepadan dengan komposit Au-PEDOT/rGO. Keputusan tersebut telah mengesahkan bahawa Au-PEDOT/rGO telah berjaya disintesis. Sifat elektrokimia Au-PEDOT/rGO telah dinilai melalui voltammetri berkitar (CV) di dalam 1.0 M KCl bersama dengan 5 mM $K_4[Fe(CN)_6]$ dan hasil kajian menunjukkan bahawa Au-PEDOT/rGO memiliki konduksi elektrik yang bagus untuk pengesanan UA di dalam sample nyata. Analisis DPV menunjukkan hubungan linear antara puncak pengoksidaan arus dan kepekatan UA di dalam penimbal fosfat (pH 7) diantara julat kepekatan 0.10 μM hingga 25.0 μM. Had pengesanan yang diukur bagi UA ialah 0.05 μM manakala had pengukuran UA adalah 0.22 μM. Oleh itu, komposit Au-PEDOT/rGO merupakan alternatif yang berbaloi untuk mengesan UA dalam air kencing manusia.

Kata kunci: polimer pengalir, zarah nano aurum, grafin oksida terturun, asid urik

Introduction

Uric acid (UA) is a purine end product formed by xanthine dehydrogenase in humans, and it has been discovered to play a significant role in the physiology of living organisms [1]. The two types of purine are exogenous and endogenous. The exogenous pool of purine is related to diet and animal proteins, while the endogenous purine metabolism that produces UA is from the liver, intestines, and other body tissues [2]. In theory, UA has either benefit or drawback effect toward the human body depending on concentration intake. Hyperuricemia that refers to overproduction or under-excretion of UA can lead to serious health issues such as heart disease, kidney stone, and gout [3]. These diseases are linked to chronic diseases such as hypertension, diabetes, metabolic syndrome, and renal failure [4]. The most common clinical features of hyperuricemia are associated with crystallization and uric acid deposition in surrounding joints and tissues. However, the precise mechanism of tissue injury caused by uric acid remains indefinite. Overproduction of UA also causes oxidative stress. Thus, this detection of UA will benefit not only the field of clinical diagnosis but also the human health.

Several methods of sensing UA in the human body have been discovered over the past years such as High Performance Liquid Chromatography (HPLC) [5], enzymatic [6], electrochemical [7] and phosphor-tungstic acid deoxidizing methods [8]. However, the electrochemical method is most favorable due to its fast analysis, low detection limit, sensitivity, and also high in accuracy compared to the other methods. UA often coexists with the presence of ascorbic acid (AA), and dopamine (DA) in the human urine sample and these substances are electrochemically active substances that will interfere in the process of UA detection [9]. Thus, electrode surface modification is an effective alternative to overcome these problems as the bare electrode is found to have challenges in separating the peak of interference substance [10].

Graphene which is a thin sheet of hexagonally arranged carbon has captivate significant attention because of its exclusive thermal, optical and also its electrical characteristics. Graphene undergoes oxidation and exfoliation forming graphene oxide, which contains some reactive oxygen [11]. The immensely improved graphene oxide's surface ability makes it easier to bind with other compounds due to the oxygen-containing group [12].

Meanwhile, poly(3,4-ethylene dioxythiophene), also known as PEDOT, is one of the electroactive polymers that is widely studied because of its stability in the environment and enormous conductivity of its polycationic form [13]. This polymer is used for numerous applications as it possesses a simple synthesis process, superior biocompatibility and relatively wide electrical conductivity [10,14]. Recently, researches on noble metal nanoparticles such as platinum, gold, and silver were actively conducted due to their properties in conductivity and electrocatalyticity [15]. Gold (Au) nanoparticle has good prospects in the application of the detection of electroactive species [16]. Its specific structure, low toxicity, and biocompatibility make it compatible in sensing application [17].

Herein, we reported an electrocatalyst of Au decorated PEDOT functionalized with rGO (Au-PEDOT/rGO) which was synthesized by the facile synthesis technique. Then, the modified electrode was prepared via the drop-casting of the composite onto the surface of a glassy carbon electrode (GCE). The performance of the electrode as an electrochemical sensor for the detection of UA was evaluated using Cyclic Voltammetry (CV). The unique Au-PEDOT/rGO sensor is revealed to have a wide linear response over the concentration range from 0.1 to 25.0 μM UA. Additionally, detection of UA in a human urine sample is found to exhibit high accuracy. This newly developed sensor is expected to offer high accuracy, high sensitivity with fast analysis towards the determination of UA.

Materials and Methods

Materials

3,4-ethylenedioxythiophene (EDOT), gold(III) chloride hydrate ($HAuCl_4$), sodium borohydride ($NaBH_4$), sodium nitrate ($NaNO_3$), graphite, Uric acid (UA), ethanol absolute (EtOH), potassium chloride (KCl) and potassium hexacyanoferrate(II) 3-hydrate ($K_4Fe(CN)_6$) powder were purchased from Sigma-Aldrich, USA. Meanwhile, di-potassium hydrogen phosphate (K_2HPO_4), potassium dihydrogen phosphate (KH_2PO_4), potassium permanganate ($KMnO_4$), and aluminium oxide (Al_2O_3) were purchased from Merck, Germany. The UA standard solution was prepared in the 0.1 M of phosphate buffer solution.

Synthesis of rGO

Graphene oxide (GO) was synthesized from graphite powder via a modified Hummer's method, which was previously reported by Kaur *et al.,* 2018 [18]. Then, 200 mg of GO solution from the previous product was added into 200 ml of deionized water (DI) and sonicated for 2 hours. Next, 66.8 μL of hydrazine hydrate was added into the mixture with ratio of 1:3 (hydrazine: GO). The beaker was immersed in an oil bath at 80˚C under cooled condenser for 12 hours. The solution was then transferred into 50 mL centrifuge tube and centrifuged at 3500 rpm for 10 minutes. The supernatant from the centrifuge process was removed and EtOH was added into the centrifuge tube to further centrifuge the solution. This step was repeated for three times and product was then washed with DI water to remove excess impurities. Lastly, the product was filtered by a vacuum pump and dried at 60˚C for 12 hours.

Preparation of Au/rGO

About 4 mL of rGO was added into 25 mL of $HAuCl_4$ solution (0.2 mg mL^{-1}). The mixture was stirred for 1 hour in order to encourage the interaction between the graphene surface with the gold ions. 0.2 mol/mL of sodium citrate was dropped gradually into the mixture. Next, the solution was heated at 80˚C for 2 hours [19]. The solution was then transferred into 50 mL centrifuge tube for centrifugation process at 3500 rpm for 10 minutes. The supernatant was removed then EtOH was added and centrifuge at 3500 rpm for 10 minutes. After 3 times removal of the excess supernatant, the product was resuspended by washing with deionized water via centrifugation. The product was filtered by vacuum pump and dry in oven at 60˚C for 12 hours.

Preparation of Au-PEDOT/rGO

Approximately 70 mL of 0.65 mM $HAuCl_4$ solution was added into the mixture of 5 mL ethanol solution and 22.5 mM EDOT while stirred at the normal room temperature. The formation of PEDOT was occurred when the mixture colour changes from black-colored solution to dark blue and $AuCl_4^-$ ions as the oxidant was reduced to form Au nanparticles [10]. The reaction was then kept stir for 4 hours. Later, the 0.5 mg/mL rGO suspension was mixed into the solution and then, the mixture was sonicated for 2 hours in order to disperse the Au-PEDOT and rGO. Lastly, the obtained solution was centrifuged by transfer the solution into the centrifuge tube and washed with EtOH and distilled water repeatedly until a neutral pH.

Characterization of Au-PEDOT/rGO

The characterization of Au-PEDOT/rGO was determined by using Fourier Transform Infrared Spectrometer (FTIR) for determination of the functional group and Scanning Electron Microscopy (SEM) was used to study the surface morphology and structure of the composite samples. Meanwhile, X-ray Diffractometry (XRD) was practiced for determation of the atomic and molecular structure of a crystal and UV-Vis spectroscopy is used to indicate the bond

transition of the sample. A standard three electrode electrochemical cell was used to carry out the electrochemical measurements in which a platinum wire act as auxiliary electrode, glassy carbon electrode (GCE) as working electrode and reference electrode of Ag/AgCl. The cyclic voltammetry was obtained in 5μM $K_4[Fe(CN)_6]$ and 1 M KCl at different scan rates in the potential range of -0.2 to 0.8 V at room temperature.

Fabrication of Au-PEDOT/rGO/GCE

Before the surface modification of the bare glassy carbon electrode (3 mm in diameter), the surface was polished with fine alumina slurry (0.05 μm) and rinse thoroughly with deionized water. The GCE was then ultra-sonicated in the acetone and deionized water successively and dry under ambient condition. The Au-PEDOT/rGO (1.0 mg) was added into 1 mL of deionized water and produced a homogeneous suspension after completion of one-hour sonication. Finally, 5 μL of the Au-PEDOT/rGO homogenized solution was drop-casted on the pretreated GCE and allowed to dry in a vacuum desiccator for 2 hours.

Determination of UA

0.05 M of phosphate buffer solution (PBS saline) was prepared by mixing the two substance of 8.41 g of potassium dihydrogen phosphate (KH_2PO_4) and 6.63 g of di-potassium hydrogen phosphate (K_2HPO_4). The UA standard solution was then prepared by dissolving the UA standard powder with the PBS saline prepared previously. Then, differential pulse voltammetry (DPV) technique was practiced to obtain the oxidation peak of the UA (concentration ranging from 0.1 μM to 25.0 μM) through voltammograms. The voltammogram analysis were then used to plot a calibration curve, and the analysis was used as an indicator to determine the lowest detection of UA.

Results and Discussion

FTIR and XRD analyses

Figure 1 shows the FTIR spectra of graphite powder, GO, rGO, Au/rGO, and Au-PEDOT/rGO. From the figure, no significant peaks are observed for raw graphite. However, the GO spectrum showed a peak at 1051cm^{-1}, which is attributed to the C-O bond, indicating that GO was successfully oxidized by the graphite. The peak at 1620 cm^{-1} was appointed to the alkene group C=C stretching and the 1724 cm^{-1} indicated C=O stretching. A broad peak at 3392 cm^{-1} indicated O-H stretching vibrations of C-OH groups. As expected, rGO bands are relatively weaker as it was reduced from GO to rGO by hydrazine hydrate. The intensities of oxygen-containing functional group absorption bands such as C-O at 1564 cm^{-1} and O-H stretchings at 3417 cm^{-1} are dramatically reduced. Also found to have disappeared from the rGO composites were the C=O and C=C stretchings. This shows that after the reduction process, rGO was successfully obtained.

Accordingly, the intent for the reduction of GO was to remove the epoxy and hydroxyl groups on the spectra, while other functional groups such as carbonyl, carboxyl and ester groups present on the edges of the carbon plane do not interfere with the conductivity of the rGO sheet. For the FTIR spectrum of Au/rGO, the peak present at 3466 cm^{-1} is linked to the stretching of O-H. The 1575 cm^{-1} absorption peak represents epoxide C-O vibration. There are no additional Au peaks detected, but due to Au doping on rGO, the intensity is increased. Therefore, the spectrum of Au/rGO should correspond to rGO composite. However, for the FTIR spectrum of Au-PEDOT/rGO, the vibrational band at 1512 cm^{-1} was due to the formation of C=C and the absorption peak at 1346 cm^{-1} is assigned to the C-C stretching in the ethylene dioxy group of the thiophene ring structure [20]. The C-S bond in the thiophene ring appeared at the wavenumber of 975 cm^{-1} and 840 cm^{-1}.

The XRD patterns for GO, rGO, Au/rGO, and Au-PEDOT/rGO are illustrated in Figure 2. The diffractogram of characteristic peak of GO was observed at 10.25° that represents a wider interlayer distance between the GO layers. This is the result of the oxidation of graphite during the synthesis process and also due to the formation of certain functional groups such as epoxy, carboxyl and hydroxyl which is supported in the FTIR results [21]. Meanwhile, the XRD pattern of rGO showed a broad diffraction peak at $2\theta = 23.0^{o}$ due to the removal of oxygen functional group from GO which indicated that the rGO was successfully obtained. According to the XRD pattern of Au/rGO composites,

diffraction peaks at 2θ = 38.2°, 44.45°, 65.61°, 77.61°, and 82.61° are indexed to the (111), (200), (220), (311), and (222) planes of well crystalline Au with cubic phase. The diffraction peak corresponds to 002 from rGO layers and is complimented by a broad graphitic peak that appears at 2θ = 23°. The diffractogram of AuNP-PEDOT/rGO showed similar pattern and diffraction peaks with Au/rGO showed more intense 2θ peak. The 2θ peak appeared at 38.05º, 44.17º, 64.52º, 77.30º and 81.84º, which corresponded to the reflection planes of Au (111), Au (200), Au (220), Au (311) and Au (222), respectively. Furthermore, a broad diffraction peak at 23.0º belonging to C (002) from PEDOT and rGO was also observed [22]. This proved that metallic gold appeared in AuNPs/PEDOT/rGO sheets.

SEM analysis

SEM was utilized to observe the morphology of graphite, GO, rGO, Au/rGO, and Au-PEDOT/rGO. It provided a highly magnified image of the composite surface. Figure 3a shows the image of graphite (at 5000X magnification) which is as platelet-like crystalline form of carbon. It could be clearly seen that graphite was arranged and presented as a typical multilayer structure in agglomerates. However, GO (Figure 3b) showed the wrinkled aggregates composite with multiple folds which is related to the oxidation process to promote oxygen-containing functional groups on the graphite sheets. The formation of rGO (Figure 3c) produced more rough wrinkles compared to GO. This is due to the reduction process by hydrazine hydrate. In Figure 3d, Au particles were uniformly distributed across the rGO. As compared to the rGO micrograph, the Au nanoparticles were seen to be successfully incorporated and covered the rGO surface. Meanwhile, the bubble-like shape (Figure 3e) indicates that the Au/PEDOT particle displayed an irregular shape and uniformly wrapped the rGO sheet. The wrinkled sheet of rGO provided an attachment site for Au along with PEDOT particle [23].

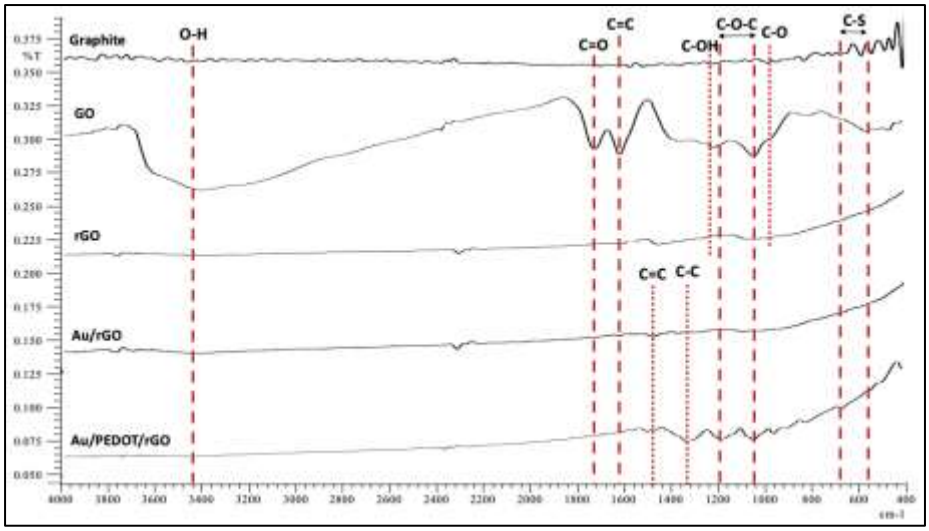


Figure 1. FTIR spectra measured of graphite, GO, rGO, Au/rGO and Au-PEDOT/rGO electrocatalyst

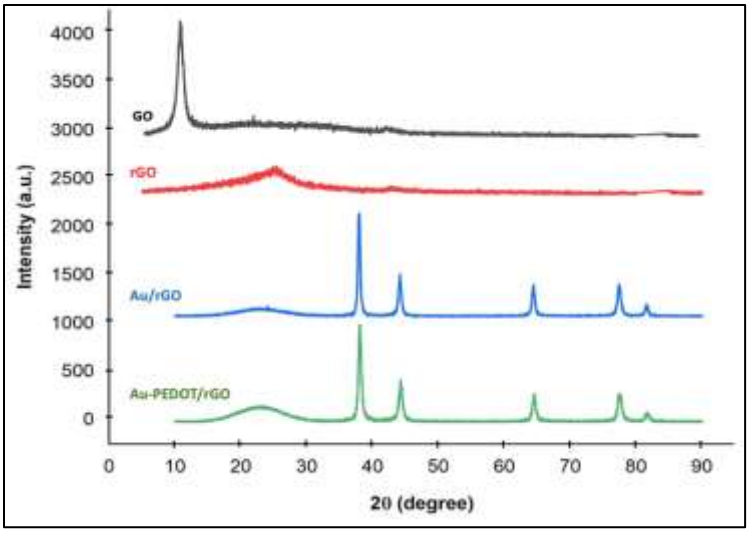


Figure 2. XRD pattern of GO, rGO, Au/rGO and Au-PEDOT/rGO

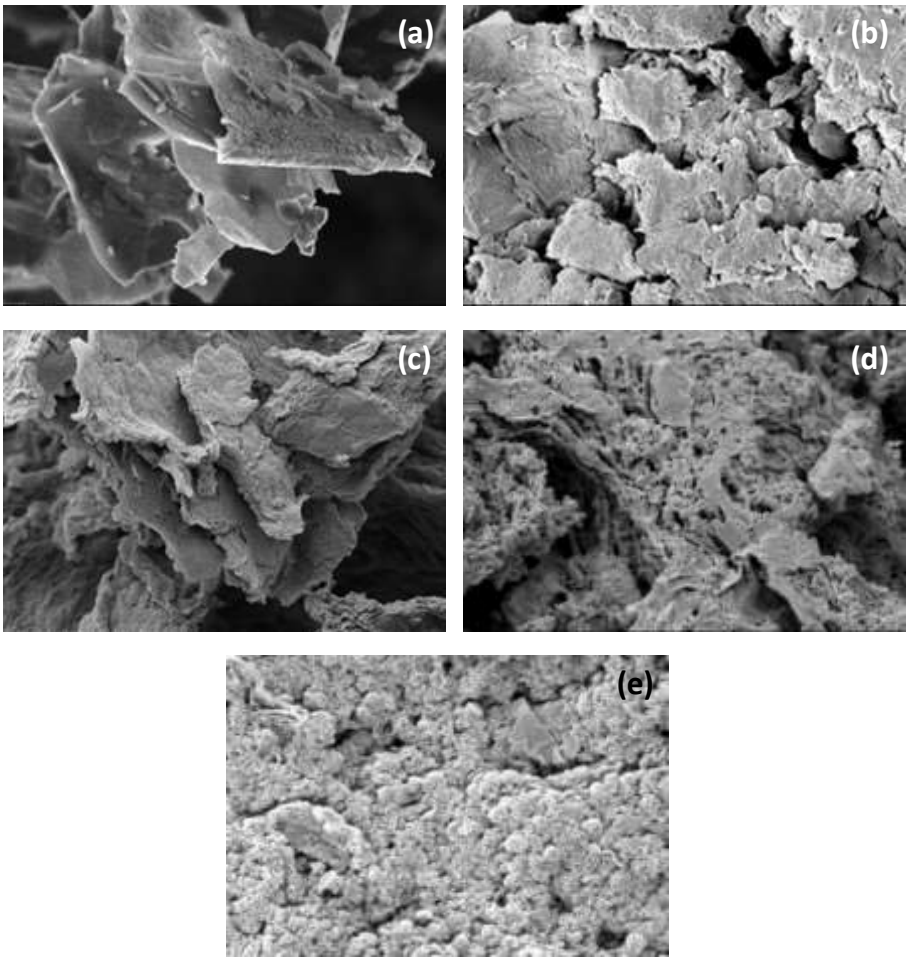


Figure 3. SEM images of (a) graphite, (b) GO, (c) rGO, (d) Au/rGO and (e) Au-PEDOT/rG

UV-Vis analysis

Figure 4 shows the UV-visible spectra of rGO, Au/rGO, and Au-PEDOT/rGO while Figure 4: Inset shows the comparison of UV spectrum of all composites with the presense of GO. The UV-visible spectrum of GO had the highest absorption peak at 228 nm indicating the π-π* transition C=C aromatic bonds [24]. As for rGO, the absorption peak had been reduced which proves the reduction process of rGO by hydrazine hydrate. Au/rGO had absorption peaks at 268 nm and 525 nm, while Au-PEDOT/rGO showed an absorption peaks of 226 nm and 510 nm. The formation of gold nanoparticles decorated on the rGO surface was demonstrated by the broad absorption peak observed for Au/rGO and Au-PEDOT/rGO at 510 nm and 525 nm, respectively, due to the active surface plasmon resonance of Au particle. The lowest absorbance represents the simultaneous reduction of Au^{3+} to Au as well as reduction of GO to rGO resulting in Au/rGO and Au-PEDOT/rGO.

Electrochemical characterization

A cyclic voltammetry technique exploiting the solution based redox probe $[Fe(CN)_6]^{4-}$ was used to analyze the electrochemical features of the modified electrode as shown in Figure 5a. In theory, the CVs of all four modified electrodes (GO/GCE, rGO/GCE, Au/rGO/GCE, and Au-PEDOT/rGO/GCE) were expected to show higher in redox peak current and smaller peak separation compared to bare GCE. In these cases, Au-PEDOT/rGO showed the higher redox peak current than bare, GO, rGO and Au/rGO modified electrodes and enhanced electron transfer between the electrode surface and electrolyte that showed a high electron transfer of composite Au-PEDOT/rGO compared to other modified electrodes studied.

To further investigate the behaviour of Au-PEDOT/rGO modified electrode, the effect of current toward different scan rates was also examined (Figure 5b). From this figure, the oxidation peak current increased proportionally with scan rate. This finding can be explained by the limited electron transfer process of the system. The diffusion layer in a slow voltage scan rate will grow much farther from the electrode in comparison to a fast scan rate. Furthermore, the peak separation remaining at the same value shows a perfect reversibility of electrode [12]. The result obtained also shows that the redox peak current increased linearly with the square root of scan rate (Figure 5c) indicating that redox reaction was controlled by the diffusion of $[Fe(CN)6]^{-3/-4}$ towards the electrode surface. According to the Randles-Sevcik formula (Equation 1), it can be clearly seen that the I_{pa} and I_{pa} increases against square roots of scan rate with a linear correlation coefficient of (r^2) = 0.9893 and 0.9887, respectively where I_p is the oxidation peak current (A), n is the number of transferred electrons per mole, A is the active surface area of the electrode (cm^2), D is the diffusion coefficient (cm^2/sec), C is concentration (mol/cm^3) and ν is the scan rate (V/s). These results indicated that the redox reaction of $[Fe(CN)6]^{-3/-4}$ on Au-PEDOT/rGO/GCE surface is a diffusion-controlled electrochemical processes.

$$I_p=(2.69\times10^5)n^{3/2}AD^{1/2}C\nu^{1/2} \quad (1)$$

Electrochemical oxidation of UA at Au-PEDOT/rGO modified GCE

Electrochemical oxidation of 1 mM of UA was conducted on a bare GCE and Au-PEDOT/rGO modified GCE by CV to elucidate their electron transfer behavior in the presence of PBS (0.1 M) at a scan rate of 50 mVs^{-1} and potential range in -0.2 V to 0.8 V (Figure 6). The Au-PEDOT/rGO/GCE demonstrated an immensely enhanced oxidation peak at potential of 0.45 V. In contrast, oxidation at the bare GCE showed a lower oxidation peak current at the same potential. It was obvious that Au-PEDOT/rGO/GCE produced highly enhanced catalytic current of UA oxidation compared to the bare GCE which can be attributed to the synergistic effect of the individual component in the nanocomposite, promoting the electron transfer between the redox probe and the electrode surface. This establishes that Au-PEDOT/rGO/GCE exhibit high electro-catalytic activity useful for UA detection. Figure 6 (inset) depicts a potential reaction for the oxidation of UA at the Au-PEDOT/rGO/GCE modified GCE. The oxidation of UA is a direct two-electron transfer mechanism where the 1H-purine-2,6,8 (9H)-trione was converted by 1H-purine-2,6,8 (3H,7H,9H)-trione which is also known as uric acid.

Determination of UA by DPV

DPV has much higher current sensitivity than the CV and therefore, lower UA concentrations can be analysed more accurately. The concentrations of UA ranging from 0.1 µM to 25.0 µM at the Au-PEDOT/rGO /GCE modified electrode in 0.1 M PBS solution are shown in Figure 7a. It was observed that the peak current increased with the increase in concentration. Figure 7b represents a linear calibration plot between peak current and concentration for the uric acid in the given range and gave the linear regression equation of y = 0.8915x + 2.647, with an r^2 value of 0.9974. The limit of detection (LOD) for UA sample by using Au-PEDOT/rGO/GCE was calculated to be 0.05 µM while the limit of quantification (LOQ) was determined to be 0.22 µM. The synergistic effect of Au-PEDOT and rGO for the sensitive detection of UA could be contributed to the outstanding electrocatalytic performance. For UA detection, this potential modified electrode was compared to other similar electrodes, as shown in Table 1.

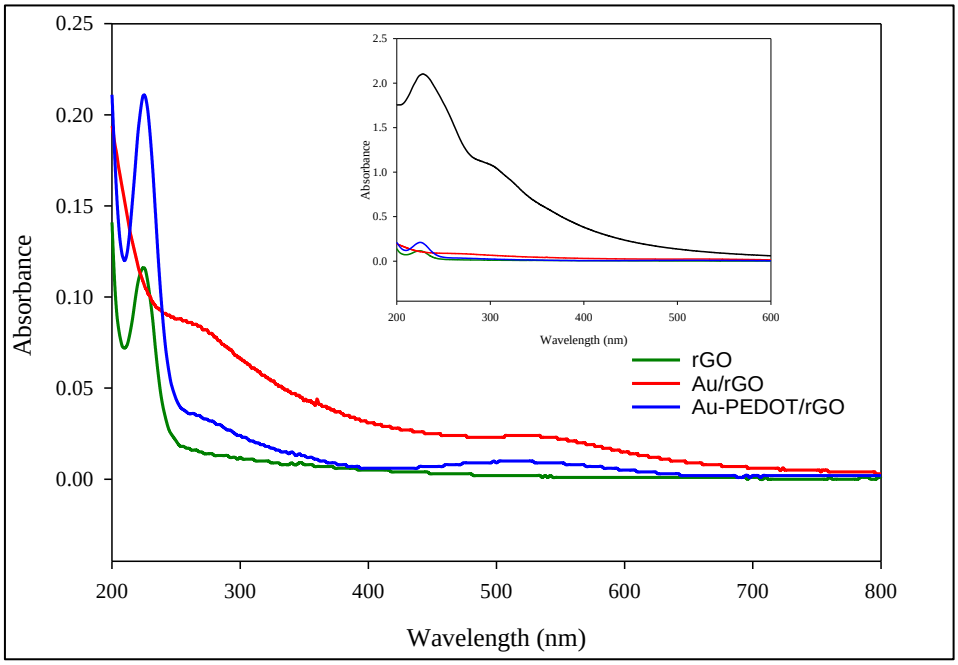


Figure 4. UV spectra of rGO, Au/rGO and Au-PEDOT/rGO. Inset: Comparison of UV spectra of all composites with the presence of GO (black line)

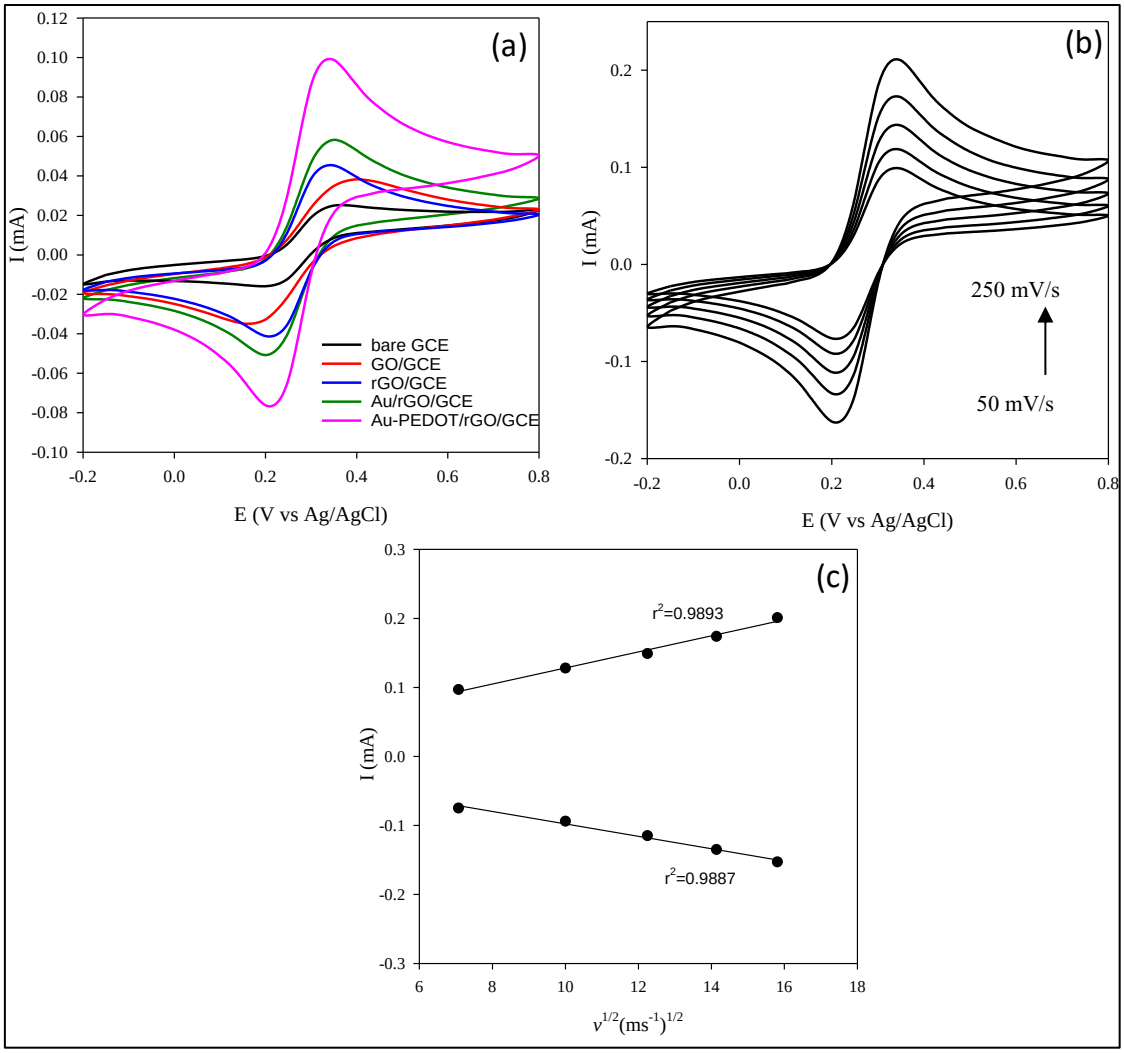


Figure 5. (a) Cyclic voltammogram of modified electrode in 5µM $K_4[Fe(CN)_6]$ and 1 M KCl electrolyte solution with scan rate of 100 mV/s, (b) Cyclic voltammograms of Au-PEDOT/rGO/GCE at different scan rate in 5µM $K_4[Fe(CN)_6]$ and 1 M KCl electrolyte solution and (c) The plot of square root of scan rate vs. current

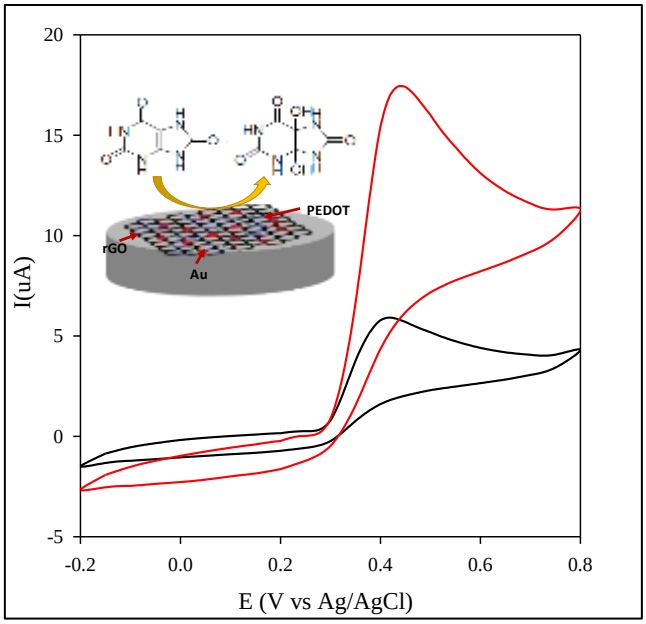


Figure 6. (a) Cyclic voltammograms obtained at the bare GCE (black line) and Au-PEDOT/rGO/GCE (red line) in 0.1 M of PBS (pH 7) containing 1.0 mM of UA. Inset : Electrocatalytic oxidation of UA at Au-PEDOT/rGO/GCE

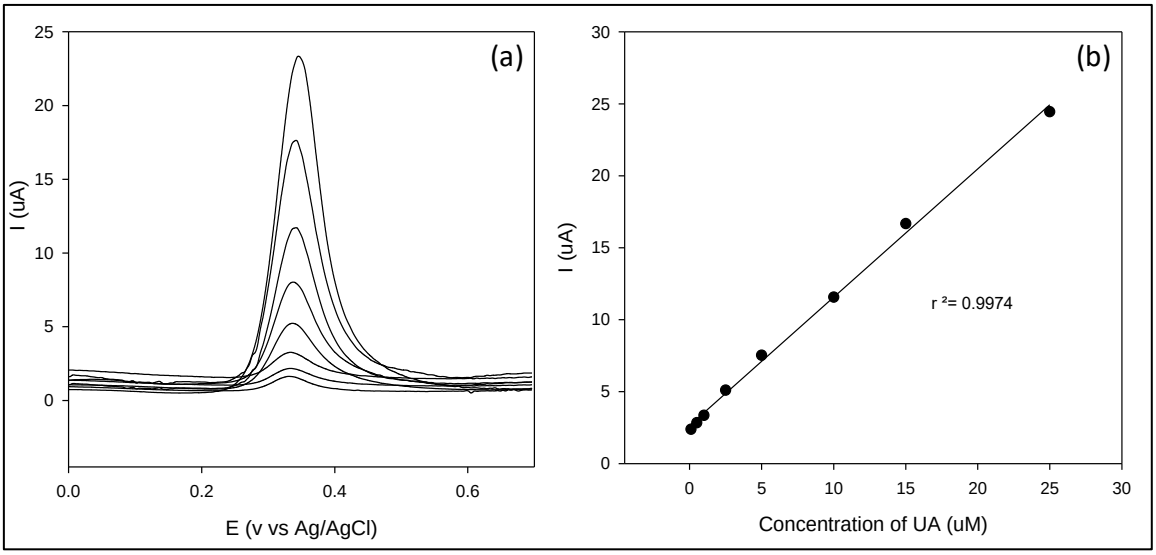


Figure 7. (a) DPV response measured over a range of UA concentration from 0.1 µM to 25.0 µM and (b) The relationship between the oxidation peaks current against UA concentration

Table 1. Comparison of various type of modified electrode for detection of uric acid in human urine sample

Modified electrode	Type of Detection	Linear Range	Limit of Detection (μM)	Ref
PEDOT/Au	DPV	2.0-600 μM	1.50	[25]
Au/rGO/GCE	DPV	6.8-41 μM	1.40	[26]
Au/rGO	SWV	0.5-60 μM	0.21	[27]
3D Electrochemically rGO	DPV	0.1-10 μM	0.10	[28]
PEDOT/Au hollow nanosphere	DPV	0.15-330 μM	0.08	[22]
Au nanocoral/PET	Amperometry	0.2-600 μM	0.06	[29]
Au-PEDOT/rGO/GCE	DPV	0.1-25.0 μM	0.05	This work

Conclusion

In summary, Au-PEDOT/rGO modified electrode has been synthesized by a facile method. The product was characterized by FTIR that observed C-O-C and C-S stretching indicates the PEDOT has successfully presenced in the composite. The morphology of Au-PEDOT/rGO by SEM shows the Au along with PEDOT has attached to rGO sheets. Glassy carbon electrode was modified with Au-PEDOT/rGO and underwent electrochemical characterization by using CV for the detection of UA and shows excellent electrical properties. The detection limit of UA by Au-PEDOT/rGO/GCE in PBS solution is calculated to be 0.05 μM over a linear range of 0.1μM to 25.0 μM via a DPV studies. The results suggested the great potential use of Au-PEDOT/rGO in selectively non-enzymatic sensing of UA.

Acknowledgments

The authors are grateful to Research Acculturation Grant Scheme (RAGS) RAGS/1/2015/ST0/UMT/03/ for financial support as well as Universiti Malaysia Terengganu for providing facilities for undertaking this research.

References

1. Yu, H., Zhang, Z., Shen, T., Jiang, J., Chang, D. and Pan, H. (2018). Sensitive determination of uric acid by using graphene quantum dots as a new substrate for immobilisation of uric oxidase. *IET Nanobiotechnology*, 12(23): 191-195.
2. Soares, F., Paula, F. D. S., Franco, D. L., Torres, W. and Ferreira, L. F. (2017). Electrochemical detection of uric acid using graphite screen-printed electrodes modified with prussian blue/poly(4-aminosalicylic acid)/uricase. *Journal of Electroanalytical Chemistry*, 806: 172-179.
3. Ndrepepa, G. (2018) Uric acid and cardiovascular disease. *Clinica Chimica Acta*, 484(3): 150-163.
4. Black, C. N., Bot, M., Peter, G., Snieder, H. and Penninxm B. W. J. H. (2017). Uric acid in major depressive and anxiety disorders. *Journal of Affective Disorders*, 225: 684-690.
5. Kand, R., Drábková, P. and Hampl, R. (2011). The determination of ascorbic acid and uric acid in human seminal plasma using an HPLC with UV detection. *Journal of Chromatography B*, 879: 2834-2839.
6. Long, Q., Fang, A., Wen, Y., Li, H., Zhang, Y. and Yao, S. (2016). Biosensors and bioelectronic rapid and highly-sensitive uric acid sensing based on enzymatic catalysis-induced upconversion inner filter effect. *Biosensors and Bioelectronic*, 86: 109-114.
7. Wei, Y., Liu, Y., Xiu, Z., Wang, S., Chen, B., Zhang, D. and Fang, Y. (2020). Simultaneous detection of ascorbic acid, dopamine, and uric acid using a novel electrochemical sensor based on palladium nanoparticles/reduced graphene oxide nanocomposite. *International Journal of Analytical Chemistry*, 1-13.

8. Su, C. H., Sun, C. L. and Liao, Y. L. (2017). Printed combinatorial sensors for simultaneous detection of ascorbic acid, uric acid, dopamine and nitrite. *ACS Omega*, 2(8): 4245-4252.
9. Tukimin, N., Abdullah, J. and Sulaiman, Y. (2018). Electrodeposition of poly(3,4-ethylenedioxy thiophene)/reduced graphene oxide/manganese dioxide for simultaneous detection od uric acid, dopamine and ascorbic acid. *Journal of Electroanalytical Chemistry*, 820: 74-81.
10. Muhamad, N. B., Khairul, W. M. and Yusoff, F. (2019). Synthesis and characterization of poly(3,4-ethylenedioxythiophene) functionalized graphene with gold nanoparticles as a potential oxygen reduction electrocatalyts. *Journal of Solid State Chemistry*, 275(4): 30-37.
11. Li, Y., Du, Y., Dou, Y., Cai, K. and Xu, J. (2017). PEDOT-based thermoelectric nanocomposites- a mini review. *Synthetic Metals*, 226: 119-128.
12. Lawal, A. T. (2019). Graphene-based nano composites and their applications. A review. *Biosensors and Bioelectronics*, 2019: 111384.
13. Rosli, A. R., Loh, S. H. and Yusoff, F. (2019). Synthesis and characterization of magnetic fe_3o_4/reduced graphene oxide and its application in determination of dopamine. *Asian Journal of Chemistry*, 31(12): 2785-2792.
14. Berisha, L., Shabani, E., Maloku, A., Jashari, G. and Arbneshi, T. (2020). Electrochemical determination of dopamine and uric acid in blood serum using anionic surfactants at carbon paste electrodes. *Malaysian Journal of Analytical Sciences*, 24(1): 97-106.
15. Jin W. and Maduraiveeran, G. (2017). Electrochemical detection of chemical pollutants based on gold nanomaterials. *Trends in Environmental Analytical Chemistry*, 14(4): 28-36.
16. Harun, N. A., Kassim, S., Tahrin, R. A. A. and Rusdi, N. F. (2018). Bimetallic (Au-Ag) in 3D hot spots as highly sensitive substrate for high performance surface-enhanced raman scattering (SERS). *ASM Science Journal*, 11(1): 86-95.
17. Kassim, S., Padmanabhan, S. C., Salaun, M. and Pemble, M. E. (2011). PMMA gold metallodielectric photonic crystals and inverse opals: preparation and optical properties. *AIP Conference Proceeding*, 263: 1-4.
18. Kaur, M., Kaur, H., and Kukkar, D. (2018). Synthesis and characterization of graphene oxide using modified Hummer's method. *AIP Conference Proceeding*, 1953(1): 030180.
19. Johra, F. T. and Jung, W. (2016). Low temperature synthesis of RGO-Au nanocomposite for apparently reduced time and its application as a chemical sensor. *Applied Surface Science*, 362: 169-175.
20. Liu, Z., Xu, J., Yue, R., Yang, T. and Gao, L. (2016). Facile one-pot synthesis of Au-PEDOT/rGO nanocomposite for highly sensitive detection of caffeic acid in red wine sample. *Electrochimica Acta*, 196: 1-12.
21. Yan, Q., Zhi, N., Yang, L., Xu, G., Feng, Q., Zhang, Q. and Sun, S. (2020). A highly sensitive uric acid electrochemical biosensor based on a nano-cube cuprous oxide/ferrocene/uricase modified glassy carbon electrode. *Scientific Reports*, 10: 10607.
22. Ali, A., Zhang, Y., Jamal, R., and Abdiryim, T. (2017). Solid-state heating synthesis of poly(3,4-ethlylenedioxythiophene)/gold/graphene composite and its application for amperometric determination of nitrite and iodate. *Nanoscale Research Letter*, 12(568): 1-10.
23. Muhammad, N. B., and Yusoff, F. (2018). The physical and electrochemical characteristic of gold nanoparticles supported PEDOT/graphene composite as potential cathode material in fuel cells. *Malaysian Journal of Analytical Sciences*, 22(6): 921–930.
24. Gualandi, I., Tonelli, D., Mariani, F., Scavetta, E., Marzocchi, M. and Fraboni, B. (2016). Selective detection of dopamine with an all PEDOT:PSS organic electrochemical transistor. *Scientific Reports*, 6 (10): 1-10.
25. Sekli-belaidi, F., Temple-boyer, P. and Gros, P. (2010). Voltammetric microsensor using PEDOT-modified gold electrode for the simultaneous assay of ascorbic and uric acids. *Journal of Electroanalytical Chemistry*, 647(2): 159-168.

26. Wang, C., Du, J. and Wang, H. (2014). A facile electrochemical sensor based on reduced graphene oxide and Au nanoplates modified glassy carbon electrode for simultaneous detection of ascrobic acid, dopamine and uric acid. *Sensors & Actuators: B. Chemical*, 204: 302-309.
27. Tian, X., Cheng, C. and Yuan H. (2012). Simultaneous determination of L-ascorbic acid, dopamine and uric acid with gold nanoparticles-–β-cyclodextrin–graphene-modified electrode by square wave voltammetry. *Talanta*, 93: 79-85.
28. Yu, X., Sheng, K. and Shi, G. (2014). A Three-dimensional interpenetrating electrode of reduced graphene oxide for selective detection of dopamine.*The Analyts*, 139: 4525-4531.
29. Hsu, M., Chen, Y., Lee, C., and Chiu, H. (2012). Gold nanostructures on flexible substrates as electrochemical dopamine sensors. *Applied Material and Interface,* 4(10): 5570-5575.

Malaysian Journal of Analytical Sciences (MJAS)
Published by Malaysian Analytical Sciences Society

SITE-SELECTIVE CARBOXYMETHYLATION OF CHITOSAN UNDER HETEROGENEOUS CONDITIONS

(Penentuan Tapak bagi Proses Pengkarboksimetil pada Kitosan dalam Keadaan Heterogen)

Nur Ellina Annisa Salehuddin[1], Nurul Adilah Rodzali[1], Ku Halim Ku Bulat[2], Nadhratun Naiim Mobarak[1]*

[1] *Department of Chemical Sciences, Faculty of Science and Technology*
Universiti Kebangsaan Malaysia, 43600 Bangi, Selangor, Malaysia
[2]*School of Fundamental Science*
Universiti Malaysia Terengganu, 21030 Kuala Nerus, Terengganu, Malaysia

**Corresponding author: nadhratunnaiim@ukm.edu.my*

Received: 11 March 2021; Accepted: 22 May 2021; Published: 27 June 2021

Abstract

The substitution sites on chitosan are affected by the presence of a base. Herein, the effects of pH on the site-selective carboxymethylation of chitosan were investigated. Carboxymethyl chitosan was synthesized by reacting chitosan with monochloroacetic acid at different pH under heterogeneous conditions. Fourier transform infrared-attenuated total reflectance (FTIR-ATR) spectroscopy confirmed that carboxymethylation was successful, with the appearance of peaks around 1326-1320 cm^{-1} (C–N groups) and 1257-1253 cm^{-1} (C–O–C groups) and allowed differentiation between the carboxymethyl substitution sites on chitosan. Additionally, the peaks at approximately 3.28 and 4.12 ppm in the ^{1}H nuclear magnetic resonance (NMR) spectra confirmed that substitution occurred at amine and hydroxyl groups, respectively. Overall, the carboxymethylation of chitosan under heterogeneous conditions at pH 8.5-11 gave O-substitution, at pH 12-13 gave N,O-substitution, and at pH 14 gave N-substitution. This pH dependence of the site-selective substitution of chitosan is important for polymer electrolyte application.

Keywords: carboxymethyl chitosan, pH effect, substitution site, heterogeneous conditions

Abstrak

Tapak penggantian kitosan dipengaruhi oleh kehadiran bes. Dalam kajian ini, kesan pH terhadap tapak penggantian pengkarboksimetil kitosan telah dikaji. Karboksimetil kitosan disintesis melalui tindak balas kitosan dengan asid monokloroasetik pada pH berbeza dalam keadaan heterogen. Spektroskopi inframerah transformasi Fourier (ATR-FTIR) mengesahkan bahawa karboksimetilasi telah berjaya dilakukan dengan kemunculan puncak sekitar 1326–1320 cm^{-1} (kumpulan C–N) dan 1257–1253 cm^{-1} (kumpulan C–O–C), yang menunjukkan perbezaan tapak penggantian karboksimetil pada kitosan. Selain itu, puncak sekitar 3.28 dan 4.12 ppm dalam spektrum resonans magnetik nukleus (^{1}H NMR) mengesahkan bahawa penggantian berlaku pada kumpulan amina dan hidroksil. Secara keseluruhan, karboksimetilasi kitosan dalam keadaan heterogen pada pH 8.5-11 memberikan penggantian pada tapak O, pH 12-13 memberikan penggantian pada tapak N dan O, dan pH 14 memberikan penggantian pada tapak N. Kebergantungan tapak pemilihan untuk penggantian kitosan dengan pH ini adalah penting untuk aplikasi elektrolit polimer.

Kata kunci: karboksimetil kitosan, kesan pH, tapak penggantian, keadaan heterogen

Introduction

Chitosan has been widely studied for various applications in the biomedical field owing to its biocompatible, biodegradable, nontoxic, and antimicrobial properties [1]. However, the limited solubility of chitosan in water and other organic solvents has restricted its potential in drug delivery and tissue engineering [2]. As a water-soluble derivative of chitosan, carboxymethyl chitosan (CM-chitosan) has better biological and physicochemical properties [3]. Furthermore, CM-chitosan is easy to synthesize and can be used for many applications in cosmetic, biomedical, environmental, food industry, and polymer electrolyte systems [4].

Several researchers have claimed that substitution occurs preferentially at the hydroxyl group at C6 in the chitosan structure rather than at the hydroxyl group at C3 and the amine group [4]. This selectivity is influenced by the steric hindrance at the hydroxyl group at C3 and the amine group. However, the choice of the appropriate reaction conditions and reagents allows the preparation of CM-chitosan derivatives with site-selective substitution at either the primary hydroxyl or amine group of chitosan to produce O-carboxymethyl chitosan (O-CM-chitosan), N-carboxymethyl chitosan (N-CM-chitosan), N,O-carboxymethyl chitosan (N,O-CM-chitosan), or N,N-carboxymethyl chitosan (N,N-CM-chitosan), as shown in Figure 1 [3-5].

The selection of a particular substitution site is important, as it influences the performance of chitosan derivatives for specific applications. According to a previous study, O-CM-chitosan has a higher moisture retention–absorption ability than N-CM-chitosan [6]. High moisture retention-absorption properties are crucial for applications in cosmetics, such as moisturizing skincare [7]. In contrast, low moisture retention–absorption properties are important for applications such as battery membranes [8].

O-CM-chitosan can be synthesized through direct alkylation by reacting chitosan, sodium hydroxide (NaOH), and monochloroacetic acid ($ClCH_2COOH$) at different temperatures and reactant ratios under heterogeneous conditions [9, 10]. Meanwhile, N-CM-chitosan can be obtained through a reductive N-alkylation reaction [11]. The N-alkylation of chitosan can be carried out in the presence of various bases. The pK_a of the reaction condition should be higher than 6.3 [12]. Previously, N-CM-chitosan and N,N-CM-chitosan have been prepared at pH 8 and pH 8.5, respectively. These reactions were carried out under homogeneous conditions and the pH was adjusted to 8 or 8.5 after the addition of $ClCH_2COOH$ [13, 14]. Other than these N-alkylation reactions, a prior study reported the unsuccessful preparation of N-octylchitosan under heterogeneous conditions, likely due to the high steric hindrance caused by using chitosan with a degree of deacetylation (DD) lower than 90% [15]. To the best of our knowledge, there have been no reports on the successful synthesis of N-CM-chitosan under heterogeneous conditions.

Therefore, in the present study, the effect of pH under heterogeneous conditions for the synthesis of N-CM-chitosan have been investigated. We also discussed the effect of pH on the degree of substitution (DS), as research has shown that the DS is influenced by the reaction conditions, with low DS values obtained for heterogeneous reactions and high DS values for homogeneous conditions [16]. We used Fourier transform infrared-attenuated total reflectance (FTIR-ATR) spectroscopy, ^1H nuclear magnetic resonance spectroscopy (NMR), and the DS to characterize and analyze the synthesized CM-chitosan derivatives. Computational modeling was also performed to understand the charges in all the structures.

Materials and Methods

Materials

Chitosan (DD = 89%, as calculated by ^1H NMR spectroscopy) was commercially obtained from ChitoChem. NaOH and $ClCH_2COOH$ were purchased from Sigma-Aldrich. Isopropanol (IPA), ethanol (EtOH), and acetic acid (CH_3COOH) were purchased from Systerm. All materials were used without further purification.

Preparation of CM-chitosan derivatives

The carboxymethylation of chitosan was carried out based on previously reported work with minor modifications [17]. Briefly, 5 g of chitosan was suspended in 25 mL of IPA in a flask. Then, a mixture of 5 g of NaOH in 25 mL of water was added to the flask. The resulting mixture was stirred with a magnetic stirrer at 50 °C for 1 hour on a hot plate. The pH of the mixture (pH 8.5-14) was adjusted by adding NaOH dropwise using a micropipette. Subsequently, 7.5 g of $ClCH_2COOH$ dissolved in 25 mL of IPA was added to the reaction mixture. After stirring for 4 hours at 50 °C, the reaction was terminated by adding 70% EtOH (100 mL). The precipitate was filtered and rinsed with 70%, 80%, and 90% EtOH to obtain the final product. The final product, which was obtained as the Na-salt of CM-chitosan, was stored in a desiccator for 3-5 days. The obtained products were denoted as CM-chitosan-8.5 (pH 8.5), CM-chitosan-9 (pH 9), CM-chitosan-10 (pH 10), CM-chitosan-11 (pH 11), CM-chitosan-12 (pH 12), CM-chitosan-13 (pH 13), and CM-chitosan-14 (pH 14). The masses of the obtained products were 7.8375 g (CM-chitosan-8.5), 7.0290 g (CM-chitosan-9), 6.2343 g (CM-chitosan-10), 6.4860 g (CM-chitosan-11), 6.1240 g (CM-chitosan-12), 6.2510 g (CM-chitosan-13), and 6.562 g (CM-chitosan-14).

FTIR-ATR spectroscopy

FTIR-ATR spectra were recorded using a PerkinElmer Spectrum 2000 spectrometer in the range of 4000–650 cm^{-1} with a scanning resolution of 2 cm^{-1}. The FTIR-ATR analysis was conducted to observe the changes in the functional groups before and after chitosan modification.

^{1}H NMR spectroscopy

NMR analysis was performed to confirm the N- and O-substitution of the CM-chitosan derivatives. ^{1}H NMR spectra were recorded using a Bruker Avance 111 spectrometer (400 MHz). Chitosan and the CM-chitosan derivatives were dissolved in a mixture of 1% CD_3COOD in D_2O [18].

DS of CM-chitosan derivatives

To determine the DS of each CM-chitosan derivatives, the Na form was changed to the H-form [19, 20]. First, 1.5 g of Na-form CM-chitosan was suspended in 80% EtOH (100 mL) and then 37% hydrochloric acid (10 mL) was added. After stirring the mixture was with a magnetic stirrer for 30 min, the precipitate was filtered and rinsed with 70–90% EtOH. The products were stored in a desiccator for 2–3 days.

The DS represents the average number of substitutions per anhydroglucose unit (AGU). The DS values of the CM-chitosan derivatives were determined by the standard ASTM D1439 method, as previously reported [21]. First, 0.5 g of dry H-form CM-chitosan was dispersed in 100 mL of distilled water in a flask. Then, 25 mL of NaOH solution (0.3 M) was added to the suspension and the resulting mixture was stirred for 15 min at 40 °C. Three drops of phenolphthalein were then added to the mixture as an indicator. Finally, the mixture was titrated with 0.3 M HCl until the indicator changed from pink to colorless. A blank test also was carried out using the same procedure without adding a CM-chitosan derivative.

The percentage of CM groups (%CM) and the DS were calculated using equations (1) and (2), respectively.

$$\%CM = \frac{[(Vo-Vn)M \times 0.059 \times 100]}{m} \quad (1)$$

$$DS = \frac{162 \times \%CM}{[5900-(58 \times \%CM)]} \quad (2)$$

where V_o is the volume of HCl used for the blank test (mL), V_n is the volume of HCl used for sample titration (mL), M is the molar concentration of HCl (M), m is the amount of sample (g), 162 is the molar mass of the AGU, and 59 is the molar mass of a CM group (–CH_2COOH).

The differences between means were analyzed for statistical significance using Student's t-test. A value of $p < 0.05$ was considered significant [22].

Computational modeling studies

Density functional theory (DFT) calculations implemented in Gaussian 09 were used to investigate the Mulliken charge and stability of all the CM-chitosan structures. The GaussView 5.0 program was used for

molecular visualization. The gas-phase molecular structure of chitosan and all the CM-chitosan derivatives in the ground state were optimized by DFT in its restricted form without any symmetry constraint. To produce accurate ground state geometries, chitosan and the CM-chitosan derivatives were modeled using two monomers. The chitosan monomer consists of glucosamine and *N*-acetylglucosamine. For O-CM-chitosan, the hydroxyl groups on the chitosan chain were substituted with CM groups (–CH_2COOH). For N-CM-chitosan, the CM groups were substituted at the amine groups. For N,O-CM-chitosan, both the hydroxyl and amine groups were substituted with CM groups. All the structures were minimized using the B3LYP/6-31++G (d,p) basis set.

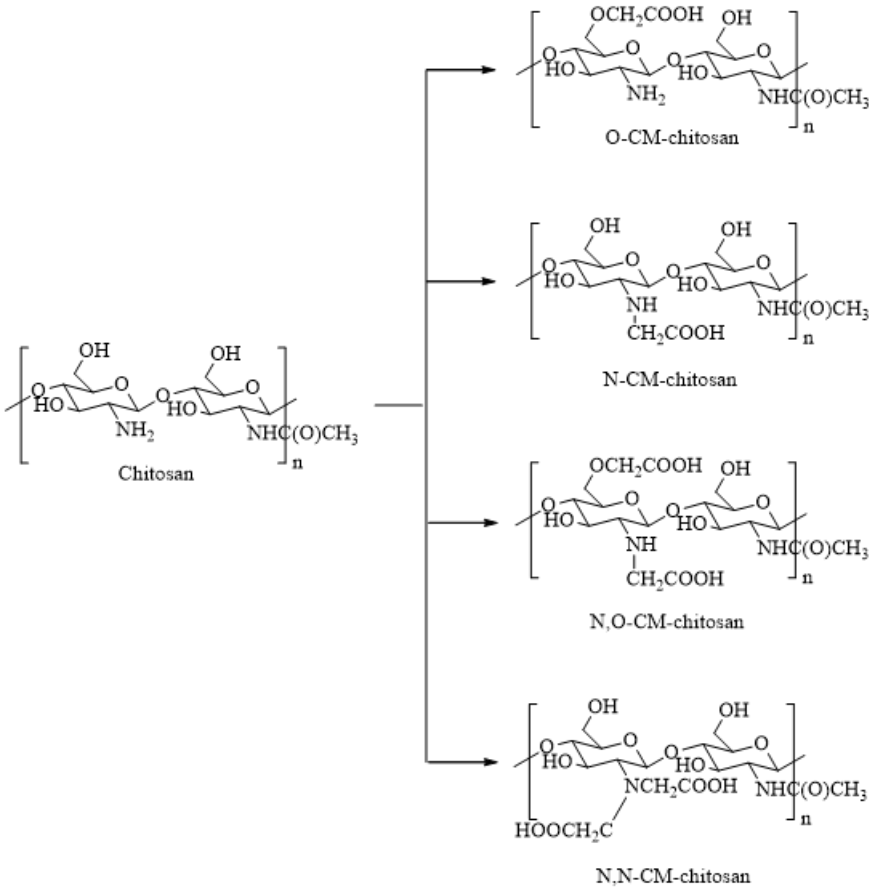


Figure 1. Structures of chitosan and CM-chitosan derivatives

Results and Discussion

Characterization by FTIR-ATR spectroscopy

CM-chitosan can be synthesized through a direct alkylation process. Figure 2 shows the FTIR-ATR spectra of chitosan and the various CM-chitosan derivatives. In the FTIR-ATR spectrum of chitosan, the peaks at 3283, 2868, 1644, 1585, and 1060 cm^{-1} represent O–H stretching, C–H stretching, the N–C(O)–CH_3 carbonyl, N–H bending, and C–O stretching, respectively. The positions of these peaks are similar to those reported in a previous study [23]. In contrast, in the FTIR-ATR spectra of all the CM-chitosan derivatives, a new peak appears around 2922–2954 cm^{-1}, corresponding to the methylene of the CM group,

which confirmed the carboxymethylation of chitosan. Additional new peaks at 1648-1634 cm^{-1} and 1588-1585 cm^{-1} correspond to the N-acetyl and carboxylate of the CM group, respectively.

However, intense peaks around 1533-1529 cm^{-1}, 1386-1379 cm^{-1}, and 1257-1253 cm^{-1} are only observed for CM-chitosan-8.5 to CM-chitosan-13. These peaks can be assigned to the amide II group, symmetrical $–COO^-$ stretching, and ether groups, respectively. In contrast, the intense peaks observed around 1326-1320 cm^{-1} for CM-chitosan-12 and CM-chitosan-13 correspond to C–N stretching. In addition, CM-chitosan-14 exhibits peaks around 1414, 1376, and 1327 cm^{-1}, representing symmetrical $–COO^-$ stretching, the amide III group, and C–N stretching, respectively. These peaks have also been reported in a previous study [24]. As well as confirming that carboxymethylation occurred, these observations provided an initial indication that the CM groups had been substituted at hydroxyl groups for CM-chitosan-8.5 to CM-chitosan-13 and at amine groups for CM-chitosan-12 to CM-chitosan-14. These findings were further confirmed by ^{1}H NMR analysis and determination of the DS.

Characterization by ^{1}H NMR spectroscopy

Figure 3 shows the ^{1}H NMR spectra of chitosan and the CM-chitosan derivatives obtained under different pH conditions. The proton assignments for chitosan are as follows. ^{1}H NMR (400 MHz, 1% CD_3COOD/D_2O), δ (ppm): 2.17 (H7), 3.11 (H2), 3.66–3.84 (H3, H4, H5, H6), 4.81 (H1). The DD was calculated based on the intensity of the ^{1}H NMR peaks using Equation (3) [25].

$$DD(\%) = \{1 - \left(\frac{1}{3} I_{CH3} / \frac{1}{6} I_{H2-H6}\right)\} \times 100 \quad (3)$$

Following the substitution of CM groups, new peaks, assigned as H8a and H8b, should be observed. Furthermore, the H1 peak should appear at approximately 4.80 ppm as reported by previous study [26–28] but this peak was not apparent owing to overlap with the solvent signals.

The proton assignments for the CM-chitosan derivatives are as follows: CM-chitosan-8.5. ^{1}H NMR (400 MHz, 1% CD_3COOD/D_2O), δ (ppm): 2.18 (H7), 3.13 (H2), 3.67–3.84 (H3, H4, H5, H6), 4.11 (H8a), 4.81 (H1). CM-chitosan-9. ^{1}H NMR (400 MHz, 1% CD_3COOD/D_2O), δ (ppm): 2.17 (H7), 3.13 (H2), 3.67–3.85 (H3, H4, H5, H6), 4.12 (H8a), 4.81 (H1). CM-chitosan-10. ^{1}H NMR (400 MHz, 1% CD_3COOD/D_2O), δ (ppm): 2.17 (H7), 3.12 (H2), 3.67–3.87 (H3, H4, H5, H6), 4.12 (H8a), 4.81 (H1). CM-chitosan-11. ^{1}H NMR (400 MHz, 1% CD_3COOD/D_2O), δ (ppm): 2.17 (H7), 3.12 (H2), 3.67–3.85 (H3, H4, H5, H6), 4.13 (H8a), 4.81 (H1). CM-chitosan-12. ^{1}H NMR (400 MHz, 1% CD_3COOD/D_2O), δ (ppm): 2.16 (H7), 3.11 (H2), 3.28 (H8b), 3.66–3.84 (H3, H4, H5, H6), 4.12 (H8a), 4.81 (H1). CM-chitosan-13. ^{1}H NMR (400 MHz, 1% CD_3COOD/D_2O), δ (ppm): 2.17 (H7), 3.12 (H2), 3.27 (H8b), 3.64–3.84 (H3, H4, H5, H6), 4.11 (H8a), 4.81 (H1). CM-chitosan-14. ^{1}H NMR (400 MHz, 1% CD_3COOD/D_2O), δ (ppm): 2.17 (H7), 3.11 (H2), 3.66–3.84 (H3, H4, H5, H6), 3.23 (H8b), 4.81 (H1).

Based on the ^{1}H NMR spectra in Figure 3, peaks at 4.11–4.12 ppm are observed for CM-chitosan-8.5, CM-chitosan-9, CM-chitosan-10, CM-chitosan-11, CM-chitosan-12, and CM-chitosan-13. Furthermore, peaks at 3.23–3.28 ppm are observed for CM-chitosan-12, CM-chitosan-13, and CM-chitosan-14. The peaks in the region of 4.05–4.55 ppm correspond to protons of CM groups ($–OCH_2–COOD$) substituted at the hydroxyl groups at the C3 and C6 positions, as described in the previous study [27, 28]. In contrast, the peaks in the region of 3.25 ppm correspond to the protons of $N–CH_2–COOH$ groups, which are confirmed by the previous study that reported the substitution of CM groups at the amine groups at around 3.2 ppm [26, 29]. These results indicate that O-CM-chitosan can be attained at pH 8.5-11, whereas pH 12-13 gives N,O-CM-chitosan, and N-CM-chitosan can only be obtained at pH 14.

DS of CM-chitosan derivatives

The DS indicates the number of substituent groups attached per monomeric unit. Because chitosan has two hydroxyl groups and one amine group, the maximum DS value is 3 [20,21]. As depicted in Table 1, the DS values are close to 1 for all the CM-chitosan derivatives. Based on the NMR spectra, at pH 8.5–11, substitution occurred

at the hydroxyl groups. However, as the pH increases in this range, the DS decreases. Thus, the deprotonated hydroxyl group is expected to play an important role in producing O-CM-chitosan, as shown in Scheme 1.

Although the NMR spectra showed that substitution occurred at both the amine and hydroxyl groups at pH 12 and 13, DS values of 2 were not observed under these conditions. The DS values of 0.80 and 0.66 at pH 12 and 13, respectively as reported in Table 1, indicates that incomplete substitution occurred at both functional groups at these pH values. However, it is possible that the degree of substitution at each site differed depending on the pH. Finally, at pH 14, the NMR spectrum confirmed that substitution only occurred at the amine group with a DS of 0.75. At such a high pH, the amine group should act as a stronger nucleophile than the hydroxyl group [30], and a plausible mechanism for N-CM-chitosan formation is shown in Scheme 2.

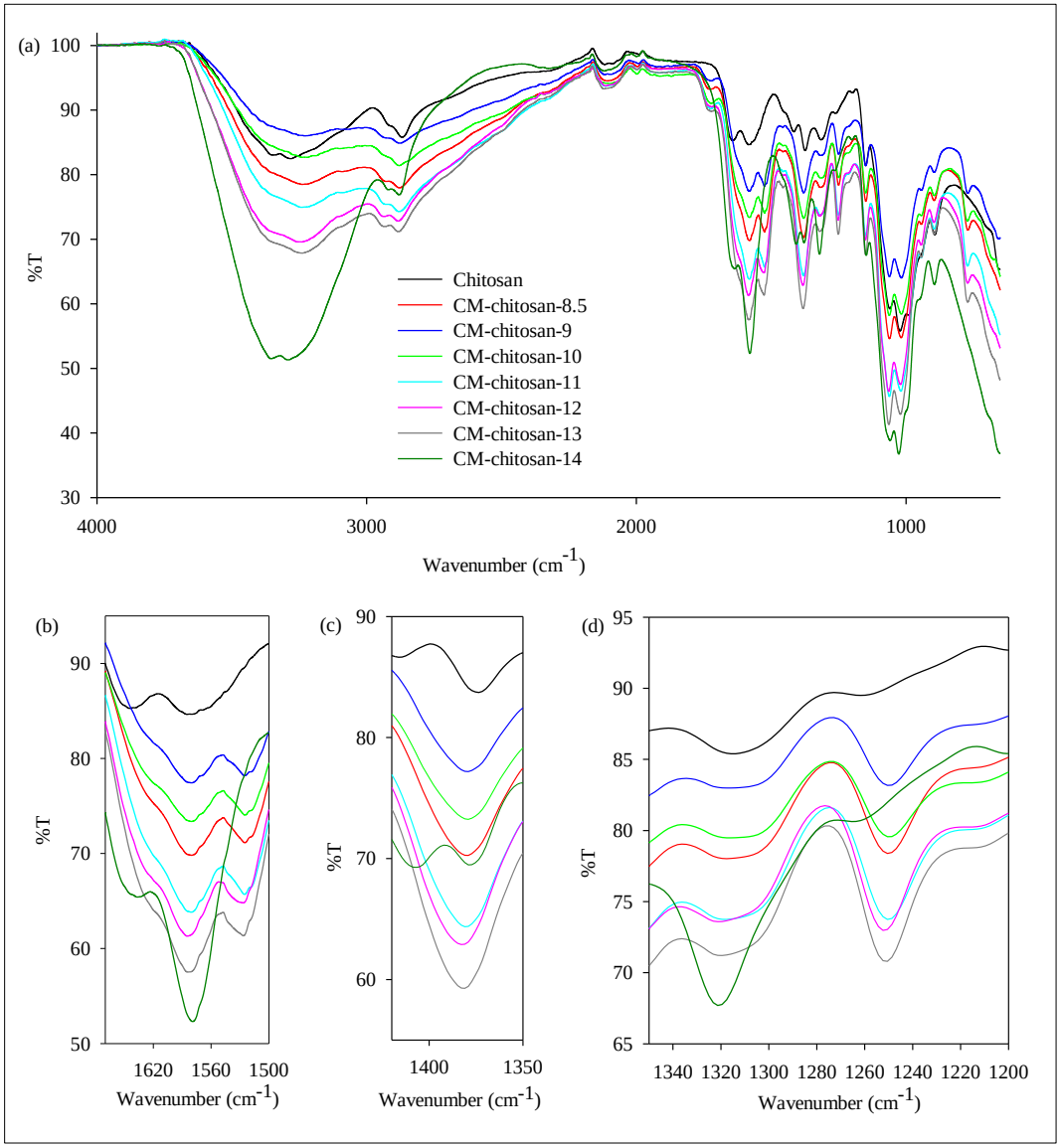


Figure 2. (a) Full FTIR-ATR spectra of chitosan and CM-chitosan derivatives. Enlarged spectra in the regions of (b) 1680–1500 cm^{-1}, (c) 1420–1350 cm^{-1}, and (d) 1360–1200 cm^{-1}

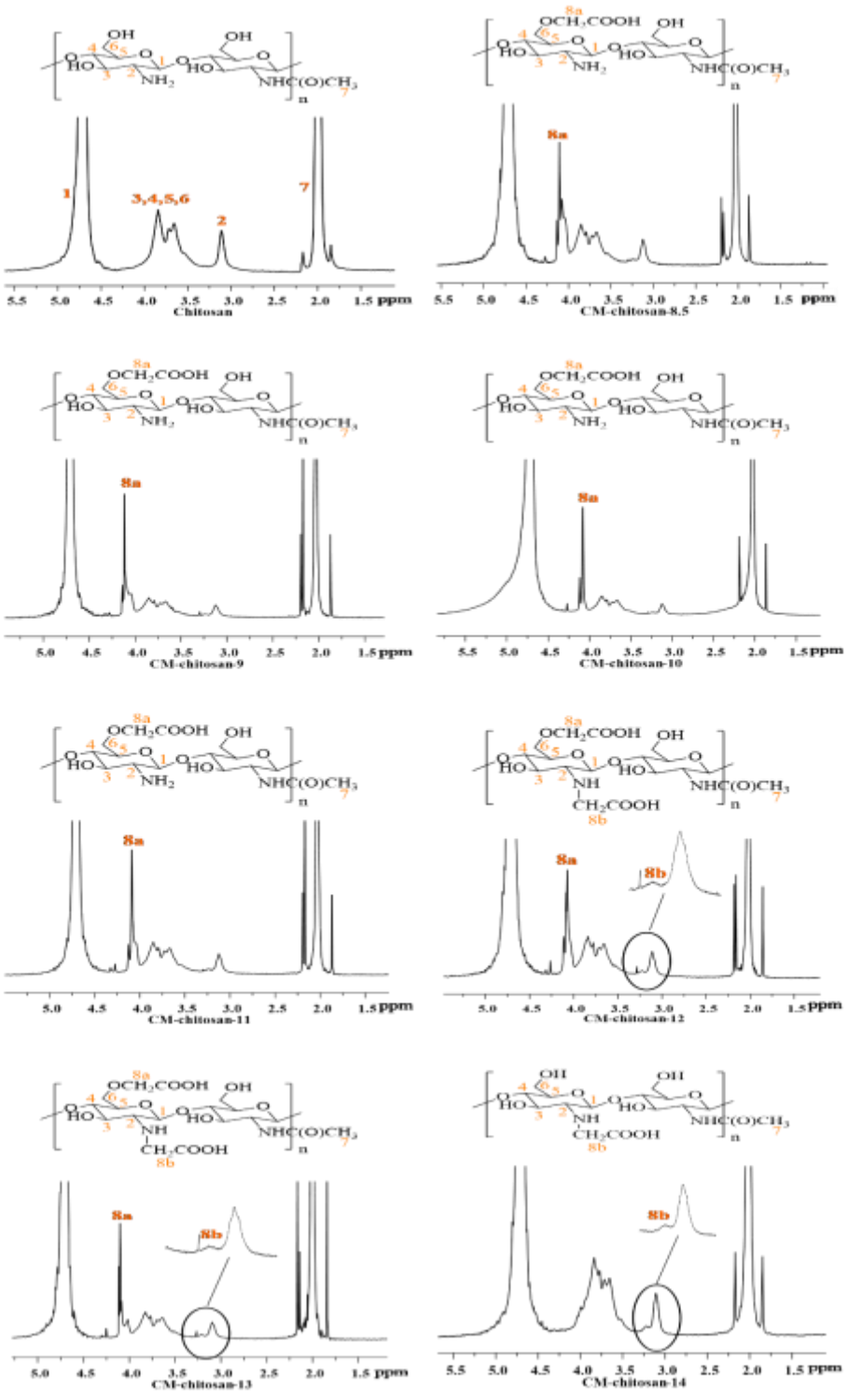
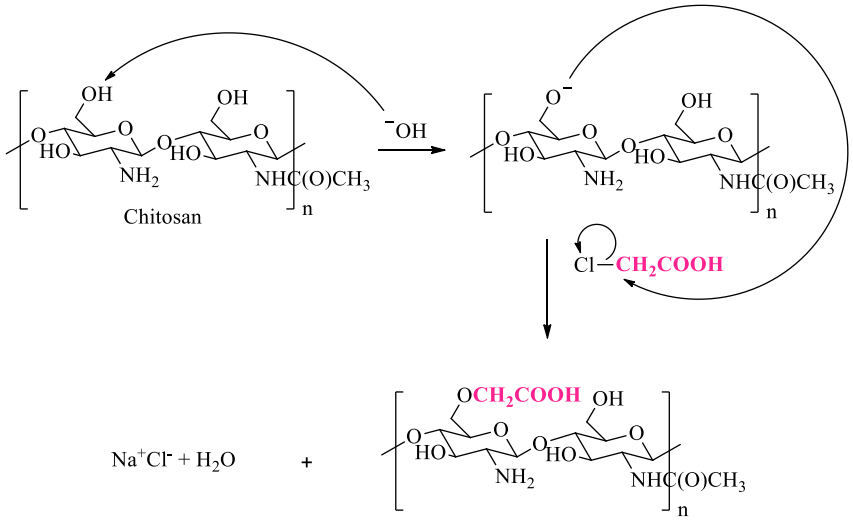


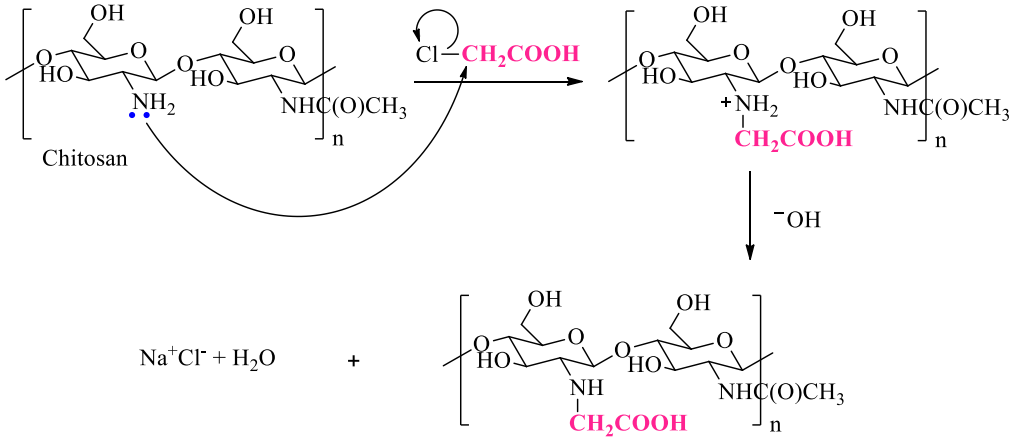
Figure 3. ^{1}H NMR spectra of chitosan and CM-chitosan derivatives

Table 1. DS values for CM-chitosan derivative synthesized at various pH values

Sample	DS
CM-chitosan-8.5	0.80 ± 0.10
CM-chitosan-9	0.81 ± 0.12
CM-chitosan-10	0.78 ± 0.12
CM-chitosan-11	0.70 ± 0.10
CM-chitosan-12	0.80 ± 0.10
CM-chitosan-13	0.66 ± 1.10
CM-chitosan-14	0.75 ± 0.26



Scheme 1. Plausible mechanism for the synthesis of O-CM-chitosan from chitosan



Scheme 2. Plausible mechanism for the synthesis of N-CM-chitosan from chitosan

The student's *t*-test was used to observe the significance between pH selection and substitution site. pH values of 8.5-11 and pH 12-13 were selected as substitutions occurred at hydroxyl and amine groups, respectively. Based on the results, there were no significant differences in the DS values ($p > 0.05$), which showed that CM substitution can be carried out at the hydroxyl groups at pH 8.5-11 and the amine group at pH 12-13.

Computational modeling studies

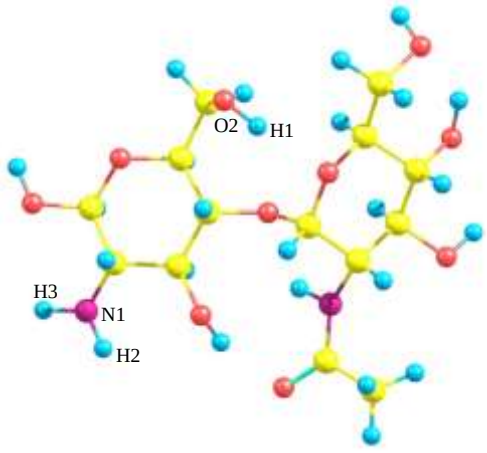
The optimized structures of chitosan, O-CM-chitosan, N,O-CM-chitosan, and N-CM-chitosan are depicted in Figure 4. The structural optimization was performed at the B3LYP/6-31++G (d,p) level.

The Mulliken charges at O2, H1, N1, H2, and H3 of chitosan are shown in Table 2. The hydrogen atom at O2, which is H1, has a higher positive value than both the hydrogen atoms at N1, which are H2 and H3, because the oxygen atom is more electronegative than the nitrogen atom. As a result, the oxygen has a greater ability than the nitrogen atom to pull electrons from a hydrogen atom towards it.

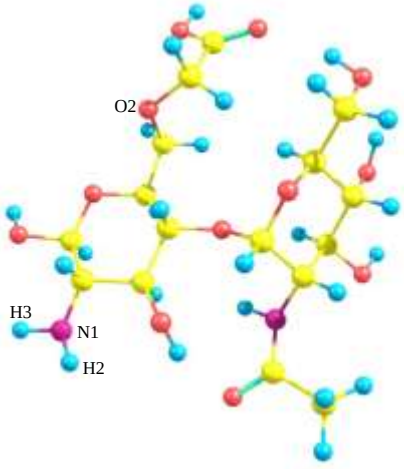
Furthermore, the pK_a of oxygen is higher than that of nitrogen. The pK_a is a measure of how tightly a proton is held by an acid. Therefore, the electron density of the hydrogen bonded to oxygen decreased and the resulting increase in electropositivity made nucleophilic substitution of H1 easier than that of H2 or H3.

In addition, Mulliken charge values became more positive after CM group substitution. A similar outcome had been reported in a previous study. The study showed an increase of Mulliken charges for the structure with electron withdrawing substituents [31]. The Mulliken charge of O2 in O-CM-chitosan increased from −0.6334 to −0.2080, and a similar increase occurred for N1 in N-CM-chitosan (from −0.7153 to −0.2295). As shown in Table 2, the values for N,O-CM-chitosan were more positive, likely because the carboxylate groups, which are electron-withdrawing groups, were able to pull electrons from both the oxygen and nitrogen atoms [31]. However, the Mulliken charge not only affected the substituted atom, as the other atoms in the molecule also became more positive. Similar effects were observed for all the CM-chitosan derivatives. Previous study reported that this was due to the weakening of inter- and intramolecular hydrogen bonds after the introduction of CM groups [32].

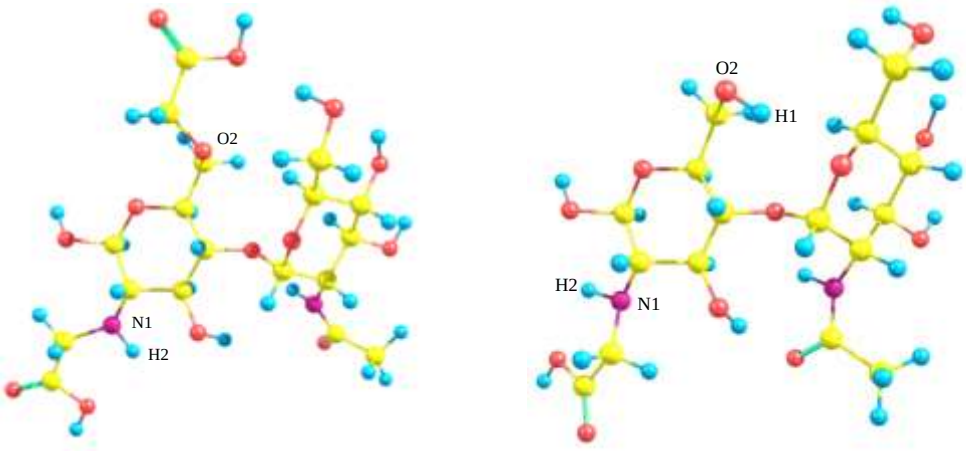
The total energies of the chitosan and CM-chitosan derivative structures are illustrated in Figure 5. N,O-CM-chitosan has the lowest energy (−50796.31 eV) compared with chitosan, N-CM-chitosan, and O-CM-chitosan (−38378.67, −44595.38, and −44595.38 eV, respectively). Thus, among these structures, N,O-CM-chitosan is the most stable, likely because both the nucleophilic sites in N,O-CM-chitosan were substituted with a CM group, which made the structure less reactive and simultaneously increased the stability.



Chitosan



O-CM-chitosan



N,O-CM-chitosan N-CM-chitosan

Figure 4. Optimized structures of chitosan and CM-chitosan derivatives (yellow: carbon; blue: hydrogen; red: oxygen; purple: nitrogen)

Table 2. Mulliken charges of atoms in chitosan and CM-chitosan derivative structures

Atom	Mulliken charges			
	Chitosan	**O-CM-chitosan**	**N,O-CM-chitosan**	**N-CM-chitosan**
O2	−0.6334	−0.2080	−0.1871	−0.4152
H1	0.3977	-	-	0.4555
N1	−0.7153	−0.4480	−0.1356	−0.2295
H2	0.2918	0.3002	0.3880	0.3755
H3	0.2984	0.3376	-	-

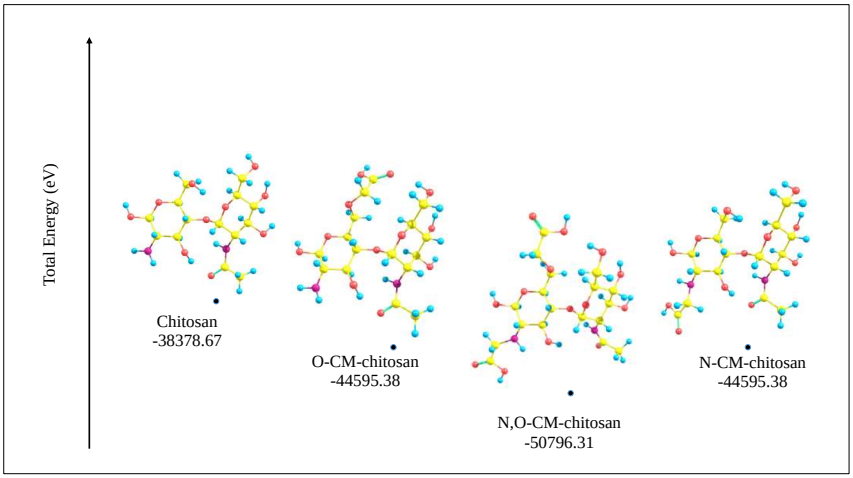


Figure 5. Total energies of chitosan and CM-chitosan derivative structures

Conclusion

In this study, CM-chitosan was successfully prepared under various pH conditions, as confirmed by FTIR-ATR spectroscopy, ^{1}H NMR spectroscopy, and DS calculations. Furthermore, computational modeling showed that the N,O-CM-chitosan structure was more stable than the O-CM-chitosan and N-CM-chitosan structures. The findings from this study make a noteworthy contribution to understanding the site-selectivity of chitosan substitution reactions under heterogeneous conditions. Under heterogeneous conditions, O-CM-chitosan was successfully obtained at pH 8.5–11, N,O-CM-chitosan at pH 12–13, and N-CM-chitosan at pH 14.

Acknowledgement

The authors would like to thank Universiti Kebangsaan Malaysia (UKM) for providing the facilities and research grant GGPM-2017-093.

References

1. Zhao, D., Yu, S., Sun, B., Gao, S., Guo, S. and Zhao, K. (2018). Biomedical applications of chitosan and its derivative nanoparticles. *Polymers*, 10(4): 462.
2. Wang, W., Meng, Q., Li, Q., Liu, J., Zhou, M., Jin, Z. and Zhao, K. (2020). Chitosan derivatives and their application in biomedicine. *International Journal of Molecular Sciences*, 21(2): 487.
3. Kalliola, S., Repo, E., Srivastava, V., Zhao, F., Heiskanen, J. P., Sirviö, J. A., Liimatainen, H. and Sillanpää, M. (2018). Carboxymethyl chitosan and its hydrophobically modified derivative as pH-switchable emulsifiers. *Langmuir*, 34(8): 2800-2806.
4. Rayung, M., Aung, M. M., Azhar, S. C., Abdullah, L. C., Su'ait, M. S., Ahmad, A., and Jamil, S. N. A. M. (2020). Bio-based polymer electrolytes for electrochemical devices: Insight into the ionic conductivity performance. *Materials*, 13(4): 838.
5. Zhang, E., Xing, R., Liu, S., Li, K., Qin, Y., Yu, H., and Li, P. (2017). Comparison in docetaxel-loaded nanoparticles based on three different carboxymethyl chitosans. *International Journal of Biological Macromolecules*, 101: 1012–1018.
6. Aranaz, I., Acosta, N., Civera, C., Elorza, B., Mingo, J., Castro, C., Gandía, M. D. L. L. and Caballero, A. H. (2018). Cosmetics and cosmeceutical applications of chitin, chitosan and their derivatives. *Polymers*, 10(2): 213.
7. Jimtaisong, A. and Saewan, N. (2014). Utilization of carboxymethyl chitosan in cosmetics. *International Journal of Cosmetic Science*, 36(1): 12–21.
8. Zhong, H., He, A., Lu, J., Sun, M., He, J. and Zhang, L. (2016). Carboxymethyl chitosan/conducting polymer as water-soluble composite binder for $LiFePO_4$ cathode in lithium ion batteries. *Journal of Power Sources*, 336: 107-114.
9. Sun, S. and Wang, A. (2006). Adsorption kinetics of Cu(II) ions using N,O-carboxymethyl-chitosan. *Journal of Hazardous Materials*, 131(1–3): 103-111.
10. Mi, Y., Su, R., Fan, D., Zhu, X. and Zhang, W. (2013). Preparation of N,O-carboxymethyl chitosan coated alginate microcapsules and their application to *Bifidobacterium Longum* BIOMA 5920. *Materials Science and Engineering: C*, 33(5): 3047-3053.
11. Muzzarelli, R. A. A., Tanfani, F., Emanuelli, M. and Mariotti, S. (1982). N-(carboxymethylidene)chitosans and N-(carboxymethyl)chitosans: Novel chelating polyampholytes obtained from chitosan glyoxylate. *Carbohydrate Research*, 107(2): 199-214.
12. Nudga, L. A., Plisko, E. A. and Danilov, S. N. (1973). N-alkylation of chitosan. *Zhurnal Obshchei Khimii*, 43(12): 2756-2760.
13. An, N. T., Dung, P. L., Thien, D. T., Dong, N. T. and Nhi, T. T. Y. (2008). An improved method for synthesizing N,N′-dicarboxymethylchitosan. *Carbohydrate Polymers*, 73(2): 261-264.
14. An, N. T., Dung, P. L., Thien, D. T., Dong, N. T. and Nhi, T. T. Y. (2009). Water-soluble N-carboxymethylchitosan derivatives: preparation, characteristics and its application. *Carbohydrate Polymers*, 75(3): 489-497.

15. Nikmawahda, H. T., Sugita, P., and Arifin, B. (2015). Synthesis and characterization of n-alkylchitosan as well as its potency as a paper coating material. *Advances in Applied Science Research*, 6(2): 141-149.
16. Sashiwa, H., Shigemasa, Y., and René, R. (2000). Novel N-alkylation of chitosan via michael type reaction. *Chemistry Letters*, 29(8): 862-863.
17. Sun, G., Chen, X., Li, Y., Zheng, B., Gong, Z., Sun, J., Chen, H., Li, J. and Lin, W. (2008). Preparation of H-oleoyl-carboxymethyl-chitosan and the function as a coagulation agent for residual oil in aqueous system. *Frontiers of Materials Science in China*, 2(1): 105-112.
18. Leong, K. H., Chung, L. Y., Noordin, M. I., Mohamad, K., Nishikawa, M., Onuki, Y., Morishita, M., and Takayama, K. (2011). Carboxymethylation of kappa-carrageenan for intestinal-targeted delivery of bioactive macromolecules. *Carbohydrate Polymers*, 83(4): 1507-1515.
19. Singh, R. K. and Khatri, O. P. (2012). A scanning electron microscope based new method for determining degree of substitution of sodium carboxymethyl cellulose. *Journal of Microscopy*, 246(1): 43-52.
20. Elomaa, M., Asplund, T., Soininen, P., Laatikainen, R., Peltonen, S., Hyvärinen, S. and Urtti, A. (2004). Determination of the degree of substitution of acetylated starch by hydrolysis, ^{1}H NMR and TGA/IR. *Carbohydrate Polymers*, 57(3): 261-267.
21. Aggeryd, I., and Olin, Å. (1985). Determination of the degree of substitution of sodium carboxymethylcellulose by potentiometric titration and use of the extended henderson-hasselbalch equation and the simplex method for the evaluation. *Talanta*, 32(8A): 645-649.
22. Liu, J., Zhang, X., Kennedy, J. F., Jiang, M., Cai, Q. and Wu, X. (2019). Chitosan induces resistance to tuber rot in stored potato caused by *Alternaria tenuissima*. *International Journal of Biological Macromolecules*, 140: 851-857.
23. Mobarak, N. N., Ahmad, A., Abdullah, M. P., Ramli, N. and Rahman, M. Y. A. (2013). Conductivity enhancement via chemical modification of chitosan based green polymer electrolyte. *Electrochimica Acta*, 92: 161-167.
24. Lusiana, R. A., Siswanta, D. and Mudasir, M. (2014). Modifying surface charge of chitosan membrane by N,O-carboxymethyl chitosan blended with poly(vinyl alcohol). *International Journal of Advances in Chemical Engineering and Biological Sciences*, 1(1): 16-20.
25. Hirai, A., Odani, H. and Nakajima, A. (1991). Determination of degree of deacetylation of chitosan by ^{1}H NMR spectroscopy. *Polymer Bulletin*, 26(1): 87-94.
26. Muzzarelli, R. A. A., Ilari, P., and Petrarulo, M. (1994). Solubility and structure of N-carboxymethylchitosan. *International Journal of Biological Macromolecules*, 16(4): 177-180.
27. Prabaharan, M. and Gong, S. (2008). Novel thiolated carboxymethyl chitosan-g-β-cyclodextrin as mucoadhesive hydrophobic drug delivery carriers. *Carbohydrate Polymers*, 73 (1): 117-125.
28. Chen, X. G. and Park, H. J. (2003). Chemical characteristics of o-carboxymethyl chitosans related to the preparation conditions. *Carbohydrate Polymers*, 53(4): 355-359.
29. Bukzem, A. L., Signini, R., Dos Santos, D. M., Lião, L. M. and Ascheri, D. P. R. (2016). Optimization of carboxymethyl chitosan synthesis using response surface methodology and desirability function. *International Journal of Biological Macromolecules*, 85: 615-624.
30. Mourya, V. ., Inamdar, N. N. and Tiwari, A. (2010). Carboxymethyl chitosan and its applications. *Advanced Materials Letters*, 1(1): 11-33.
31. Pranowo, H. D., Mulya, F., Aziz, H. A, and Santoso, G. A. (2018). Study of substituent effect on properties of platinum(II) porphyrin semiconductor using density functional theory. *Indonesian Journal of Chemistry*, 18(4): 742-748.
32. Lu, X., Xue, J. Q., Wang, Y. J., Mao, W. B., Wu, M. and Li, J. X. (2010). Theoretical studies on the chemical structure of carboxymethyl chitosan. *Advanced Materials Research*, 160-162: 1822-1827.

Malaysian Journal of Analytical Sciences (MJAS)
Published by Malaysian Analytical Sciences Society

CLASSIFICATION MODEL FOR DETECTION AND DISCRIMINATION OF INEDIBLE PLASTIC ADULTERATED PALM COOKING OIL USING ATR-FTIR SPECTROSCOPY COMBINED WITH PRINCIPAL COMPONENT ANALYSIS

(Model Pengkelasan bagi Pengesanan dan Pengasingan Produk Cemaraduk Plastik dalam Minyak Masak Sawit Menggunakan Spektroskopi ATR-FTIR dengan Gabungan Analisis Komponen Prinsipal)

Dzulkiflee Ismail[1], Aliyalina Rahimi[1], Wan Rosli Wan Ishak[2], Naji Arafat Mahat[3], Wan Nur Syuhaila Mat Desa[1]*

[1] Forensic Science Programme, School of Health Sciences
[2] Nutrition Programme, School of Health Sciences
Universiti Sains Malaysia, Health Campus, 16150 Kubang Kerian, Kelantan, Malaysia
[3]Department of Chemistry, Faculty of Science,
Universiti Teknologi Malaysia, 81310 Skudai, Johor, Malaysia

**Corresponding author: wannurs@usm.my*

Received: 17 March 2021; Accepted: 28 May 2021; Published: 27 June 2021

Abstract

Adulteration of edible oil by replacing or admixing cheaper or waste oil is an irresponsible act motivated by profiteering. A more sinister act of dissolving inedible plastic materials in hot oil during frying to enhance the crispiness and prolong the shelf life of deep-fried snacks has been alleged. In this study, a protocol using ATR-FTIR spectroscopy combined with principal component analysis (PCA) for detection of inedible plastic materials in palm cooking oil is presented. To achieve this, palm cooking oil samples purchased from convenience stores were heated and adulterated either with low-density polyethylene (LDPE), high-density polyethylene (HDPE) or polypropylene (PP). The resultant spectra from 4000-600 cm^{-1} were subjected to direct visual examinations prior to PCA. Detection of plastic materials in the samples from direct visual examinations of the resultant spectra was difficult as all samples revealed similar spectra dominated by major absorption bands at 2922 cm^{-1}, 2853 cm^{-1}, 1740 cm^{-1}, 1465 cm^{-1}, 1377 cm^{-1} and 721 cm^{-1}, which were typical of triacylglycerols. Despite the similarities, the detection was possible when the resultant spectra were subjected to PCA. The results demonstrated the potential of ATR-FTIR spectroscopy combined with PCA for the detection of inedible plastic adulterated palm cooking oil.

Keywords: ATR-FTIR spectroscopy, cooking oil, adulteration, polyethylene, polypropylene

Abstrak

Cemaraduk minyak makan dengan menggantikan atau mencampurkan bersama minyak murah atau minyak sisa adalah tindakan tidak bertanggungjawab didorong oleh sikap meraih keuntungan. Tindakan yang lebih tidak bertanggungjawab adalah melarutkan plastik tidak boleh dimakan ke dalam minyak panas semasa menggoreng bertujuan untuk meningkatkan kerangupan dan

memanjangkan jangka hayat makanan gorengan telah diperkatakan. Kajian ini membentangkan protokol menggunakan kaedah spektroskopi ATR-FTIR yang digabungkan bersama analisis komponen prinsipal (PCA) untuk mengesan bahan plastik tidak boleh dimakan dalam minyak sawit goreng. Untuk mencapai matlamat ini, sampel minyak masak sawit dibeli dari kedai serbaneka telah dipanaskan dan diadukkan bersama polietilena ketumpatan rendah (LDPE), polietilena ketumpatan tinggi (HDPE) atau polipropilena (PP). Spektra inframerah yang diperoleh dari 4000-600 cm^{-1} telah diperiksa terlebih dahulu melalui kaedah pemeriksaan visual langsung sebelum PCA. Pengesanan bahan plastik tidak boleh dimakan dalam semua sampel melalui kaedah pemeriksaan visual dari spektra inframerah yang dihasilkan adalah sukar berikutan kesemua sampel menghasilkan spektra serupa dengan jalur penyerapan utama tipikal triasilgliserol pada 2922 cm^{-1}, 2853 cm^{-1}, 1740 cm^{-1}, 1465 cm^{-1}, 1377 cm^{-1} dan 721 cm^{-1}. Walaupun terdapat persamaan, pengesanan dilakukan dengan jayanya menggunakan PCA. Hasil kajian menunjukkan potensi penggabungan spektroskopi ATR-FTIR bersama PCA untuk pengesanan plastik tidak boleh dimakan teraduk dalam minyak masak sawit.

Kata kunci: spektroskopi ATR-FTIR, minyak masak, pengadukan, polietilena, polipropilena

Introduction

Palm cooking oil is a popular choice for deep frying due to its excellent and versatile techno-economic advantages for almost all frying activities [1]. In certain South East Asia countries, deep-fried snacks such as deep-fried banana, deep-fried fish fritter and fried chicken are commonly found in street stalls sold by hawkers. Recently, the practise of adding and dissolving inedible plastic materials such as used plastic carrier bags, used plastic packaging and used straws into hot oil by irresponsible street hawkers prior to frying is rumoured. Purportedly, this practise helps to enhance the crispiness, as well as prolong the freshness and the shelf-life of deep-fried snacks [2]. If this allegation is true, such malpractice is undoubtedly alarming as it poses serious health implications to the consumers since a wide range of chemicals used in the manufacture of plastics such as bisphenol-A (BPA), melamine, thalates, antiminitroxide, brominated flame retardants and poly-fluorinated chemicals are known to be toxic [3,4]. Among health problems associated with toxins found in plastics are liver dysfunction, cancers, skin diseases, neuro-toxicity, lung problems and gastrointestinal issues [3, 4]. This malicious practice which is undoubtedly a serious food safety issue warrants the development of a sensitive detection technique, capable of detecting dissolved inedible plastic materials.

Infrared (IR) spectroscopy has emerged as one of the useful analytical tools for monitoring food safety issues. In order to further enhance its detection ability, it is often combined with chemometrics techniques [5, 6]. This hybrid approach has been used, among others to detect the adulteration of extra virgin olive oil with sunflower, peanut, canola, corn, sunflower and soybean oil [7], the adulteration of high-priced walnut oil with low-priced sunflower and soybean oil [8], the presence of chicken fat in butters [9], the adulteration of rapeseed oil with waste cooking oil [10], the presence of lard in French fries pre-fried in palm oil adulterated with lard [11] and the adulteration of *pekmez*, a Turkish sweet with glucose syrup, high fructose corn syrup and other sugars [5].

IR spectroscopy is a spectroscopy technique that uses the electromagnetic radiation within the IR region. When transmitted through a sample, this electromagnetic radiation stimulates vibrational motions of the molecules within the sample [6, 12]. When the vibration of a molecule matches with the frequency of the transmitted IR radiation, a spectral band or peak is produced. Different molecules absorb IR radiation at different frequencies, hence producing different spectral bands characteristic which are useful for identification. Early IR spectrophotometers require tedious sample preparation. With the advancement of technology, attenuated total reflectance (ATR) attachment is introduced. This attachment has revolutionized FTIR spectroscopy which allows for direct *in-situ*, straightforward sample analysis with minimal to no sample pre-treatment requirement.

Principal Component Analysis (PCA) is one of the chemometrics techniques that has been used to monitor and detect adulterants in food. This particular

chemometrics technique allows large sample of data sets to be described using a much smaller number of principal components or PCs. The first PC, known as PC1 describes the gross average features of the data sets while the second PC, or PC2, and the subsequent PCs introduce further specific features of decreasing significance [13, 14]. PCA is a suitable tool for simplification, data reduction, outlier detection and pattern recognition highlighting the variance or differences within a dataset. In the case of PCA performed on a FTIR spectra, it allows the investigation of trends in the studied samples and relationships or differences between samples.

As far as this study is concerned, no work has been done focussing on the detection of plastic adulterated cooking oil using ATR-FTIR spectroscopy combined with PCA. Therefore, in this study, the authors intend to demonstrate the use of this hybrid approach for the detection and discrimination of inedible plastic in palm cooking oil.

Materials and Methods

Sample collection

New and unused 1 kg refined palm cooking oils (RCO) (n = 6) of similar brand were purchased from a local convenience store over a period of 6 months while low-density polyethylene (PE1), high-density polyethylene (PE2) and polypropylene (PP) plastic bags were purchased directly from a plastic bag retail store to reflect the alleged field practice. Fresh bananas purchased from the local market were selected as the item to fry because it was an easy local snack to prepare compared to other processed foods such as chicken meats. The heating and cooking procedures were conducted using a stainless-steel frying pan (Zebra Inc., Thailand) and a portable cooking stove (Power Plus, China) equipped with a portable butane gas canister (Chelstar, Korea).

Sample preparation

Each packet of 1 kg (equivalent to approximately 1200 mL) (n=6) RCO was divided to five equal portions to prepare for control unadulterated (URCO), heated refined oil (HRCO), heated with food (HRCOB), adulterated without food (ARCO, referred as RCO-PE1, RCO-PE2 and RCO-PP according to the plastic materials used to adulterate them) and adulterated with food (ARCOB, referred as ARCO-B-PE1, ARCO-B-PE2 and ARCO-B-PP according to the plastic materials used to adulterate them) oil sets.

HRCO (n=5) was prepared by heating approximately 400 mL of control cooking oil to approximately 200 °C (K-type digital thermocouple, MYPIN, China) until small bubbles and thin white smoke were released. The heating time to achieve the condition was about 2 minutes. Once heating was completed, sample was allowed to stand to cool off at room temperature at approximately 25 ^{o}C.

Adulterated oil samples without food (ARCO) (n=5) were prepared by gradually dissolving approximately four grams of PE1 strips into hot RCO as previously described. The amount of plastic incorporated reflects the average weight of one plastic bag. Similar procedures were repeated for PE2 and PP plastic materials.

For HRCOB (n=5) and ARCOB (n=5) samples, slices of banana were fried for 2 minutes each under a similar set-up. Upon cooling, the oil samples from each set were filtered using a filter paper (Whatman, Merck, Germany). Approximately 2 mL of the filtered oil was then transferred into a separate half dram glass vial (Bischem, Malaysia) and kept at 4°C in refrigerator prior to subsequent ATR-FTIR analysis.

ATR-FTIR analysis

The IR spectra were obtained using a Bruker Tensor 27 FTIR spectrometer (Bruker Technologies, USA) equipped with a zinc selenide (ZnSe) ATR sampling interface. The instrument control and data acquisition were operated by OPUS Ver. 7.0.122 software (Bruker, Germany). To check for detection accuracy, the FTIR spectrometer was calibrated against a standard polystyrene film (Bruker Optics, Germany). All IR spectra were obtained in the frequency region of 4000-600 cm^{-1} where 16 scans were collected at a resolution of 4 cm^{-1}.

Sample IR spectra acquisition was performed by placing a drop of oil sample on the surface of the ZnSe sampling interface. Once measurement had been completed, the oil sample was removed from the interface using dry tissues (Kimberly Clark, UK) and subsequently was wiped again using a clean tissue soaked with methanol before and after each analysis. The plastic materials were also measured in ATR mode. Confirmation of the IR profiles of the plastic materials used as the adulterants were accomplished by comparison with literature references [15]. Spectrum acquisition for each sample was performed in six replicates at room temperature (25 ^{o}C).

Sample variations

In this study, variations within and between samples were assessed through repeatability and reproducibility measurements respectively using the URCO as the samples. The former was measured by conducting six consecutive measurements or spectra acquisitions on one of the URCO samples while the latter was measured by conducting one measurement to each of the six batches of the URCO samples. Both repeatability and reproducibility were expressed using relative standard deviation (%RSD) which is defined as the percentage ratio of standard deviation over mean or average of below than 5% as stated by international analytical guidelines [15].

Data pre-processing and principal component analysis

The resultant IR spectra were converted to comma-separated values (.CSV) format prior to importing to the Excel spreadsheet (Microsoft, USA) for further data preparation and pre-processing. A series of data pre-processing strategies which were auto-scaling, column centring and square root transformation were applied to the IR data matrices. Once the series of data pre-processing were completed, the pre-processed IR data matrices were imported to Minitab Version 16.2.3 statistical software (Minitab Inc., USA) environment for principal component analysis (PCA). Assessment of the ability of PCA to detect and discriminate the non-plastic adulterated oil from its non-adulterated counterparts was made based on score plots observations in which the principal component (PC) score plots were constructed using the first two resultant principal components.

Results and Discussion

In this study, the %RSD for both repeatability and reproducibility were computed using the absorbances recorded by six prominent peaks manually selected from the IR spectra of the URCO oil samples. The %RSD for repeatability recorded for the six prominent peaks at 2922.01 cm^{-1}, 2852.27 cm^{-1}, 1743.56 cm^{-1}, 1463.89 cm^{-1}, 1159.16 cm^{-1} and 721.34 cm^{-1} were 0.45%, 0.44%, 0.28%, 0.27%, 1.77% and 0.24% respectively while their %RSD for reproducibility were 0.57%, 0.63%, 0.44%, 0.57%, 0.66% and 0.88%, respectively. Following the analytical guideline mentioned earlier, the low percentage of these %RSD values indicated good repeatability and reproducibility of the analyses.

ATR-FTIR spectral analysis of the plastic materials

The IR spectra of PE1, PE2 and PP used as the adulterants are shown in Figure 1 to Figure 3 respectively. Close manual visual examinations of PE1 and PE2 IR spectra in Figure 1 and Figure 2 revealed similar absorption peaks occurring at ~2910 cm^{-1} which corresponds to C-CH_3 and ~2843 cm^{-1} corresponding to CH_2. Methylene deformations i.e. CH_2 vibrations were observed at ~1460 cm^{-1} and ~720 cm^{-1} due to their bending vibrations [16]. The difference in the degree of branching within PE1 and PE2 structures could possibly accounts for different proportions of peak intensity. The spectrum of PP shown in Figure 3 revealed characteristic absorption bands in the functional group with a more complicated absorption band in the fingerprint regions in comparison to PE due to different monomer build-up of propene (C_3H_6) in PP plastic such as the addition of a methyl side group. Characteristic split peaks at ~2954 cm^{-1} and ~2914 cm^{-1} correspond to methyl groups while ~2866-2835 cm^{-1} designates the CH groups within the sample. The complicated PP fingerprint region with weak absorption band within ~1160 cm^{-1} and ~790 cm^{-1} regions showed vibration characteristic of polypropylene. Table 1 to Table 3 detail out the absorption peaks and the corresponding functional groups recorded for PE1, PE2 and PP respectively. These absorption peaks are in conformance

to those described by Asensio et al. [14] and Moinuddin [17].

ATR-FTIR spectral analysis of the cooking oil samples

Triacylglycerols (TAGs) are the major organic compounds of oils and fats of plant origin including palm oil, therefore they dominate the spectra as seen in Figure 4. The IR spectra of the samples including those adulterated with the plastic materials show that there were several absorption bands in the functional group regions compared to the absorption bands in the fingerprint region. Strong absorption bands were observed in the region of 3000-2800 cm^{-1} caused by C-H stretching vibrations. Bands at 3009 cm^{-1} correspond to the stretching vibration of C=H. The stretching vibration of methylene ($-CH_2-$) and methyl ($-CH_3$) functional groups can be seen at 2922 cm^{-1} and 2853 cm^{-1}, respectively. Methylene and methyl groups were also observed at 1465 cm^{-1} and 1377 cm^{-1} due to their bending vibrations [16] The sharp peak around 1740 cm^{-1} was due to C=O double bond stretching vibration. Deformation and bending of C-H and stretching vibration of C-O result in peaks at 1500-650 cm^{-1} region [17-19]. The functional groups associated with the absorption peaks identified from the spectra of the cooking oil samples are summarised in Table 4.

In general, the oil spectra in Figure 4 did not show any major differences between them. Further examination on the fingerprint regions (between 1500-600 cm^{-1}) also revealed a similar spectral pattern with a very minimal shift of absorption band positions and intensity across the samples despite the inclusion of plastic adulterants and further subdued under different conditions. These samples may have undergone a different degree of chemical reactions after adulteration. Furthermore, during cooking, hydrolysis, oxidation, polymerisation and isomerisation reactions are inevitable thus may have resulted in the multitude of assorted by-products [14, 17]. Hence, it is postulated that those chemical reactions may bring evident changes to the spectra especially between the unadulterated cooking oils (URCO and HRCO) and the plastic adulterated cooking oils (ARCO-PE1, ARCO-PE2 and ARCO-PP), however this is not the case. Perhaps the changes due to those reactions are significantly small which explain the subtle differences between the spectra which have hampered the differentiation of the samples by direct visual examination and recognition. Furthermore, since the manual visual examination is subjective, it is therefore practical to incorporate statistical methods which can aid in explaining the differences between the cooking oil samples or in other words, capture the differences between the samples.

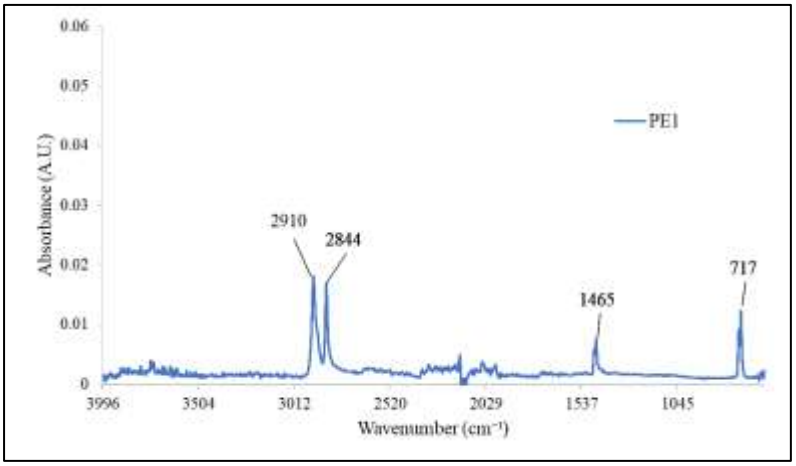


Figure 1. IR spectrum of PE1 (LDPE)

Table 1. The functional groups associated with absorption peaks identified in PE1

Absorption Peak (cm^{-1})	**Functional Group**
2910	$C\text{-}CH_3$
2844	CH_2
1465	CH_3
717	-CH=CH-(cis)

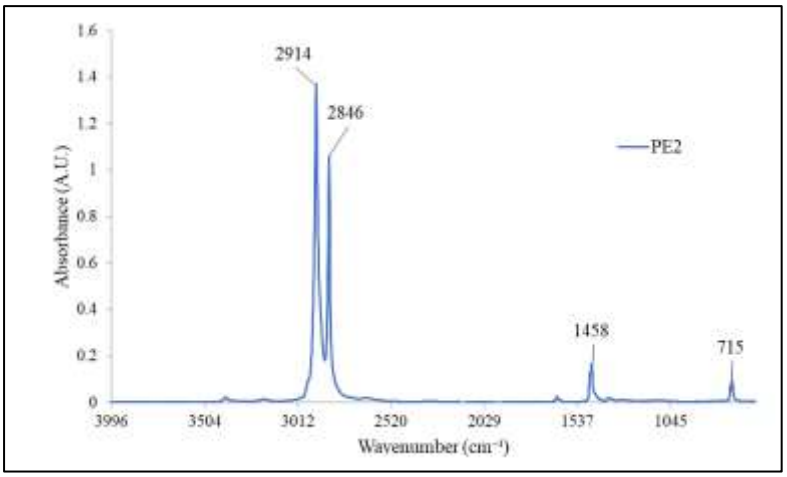


Figure 2. IR spectrum of PE2 (HDPE)

Table 2. The functional groups associated with absorption peaks identified in PE2

Absorption Peak (cm^{-1})	**Functional Group**
2914	$C\text{-}CH_3$
2846	CH_2
1458	CH_3
715	-CH=CH-(cis)

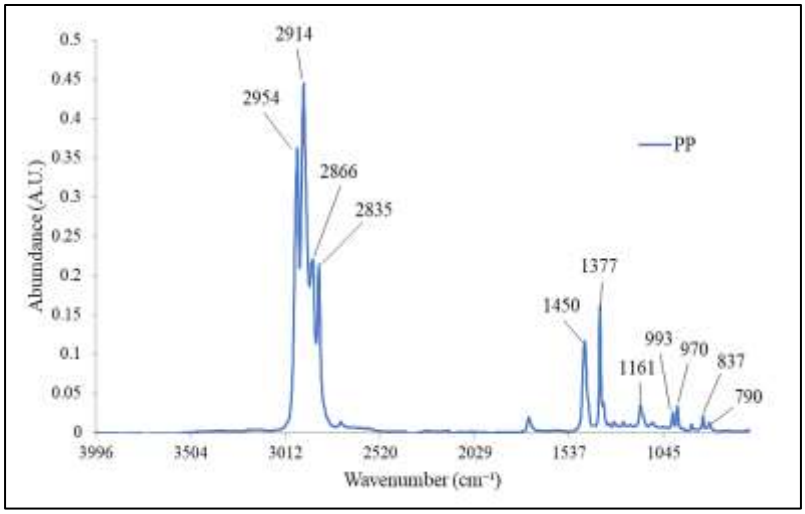


Figure 3. IR Spectrum of PP

Table 3. The functional groups associated with absorption peaks identified in PP

Absorption Peak (cm^{-1})	**Functional Group**
2954	$C\text{-}CH_3$
2914	$C\text{-}CH_3$
2866	CH_2
2835	CH_2
1450	CH_3
1377	CH_3
1161	Acetates
993	$\text{-}CH{=}CH_2$
970	-CH=CH- (trans)
837	$C{=}CH_2$
790	-CH=CH-(cis)

Data pre-processing and principal component analysis

Prior to applying PCA, the IR spectra of the oil samples were pre-processed using a series of pre-processing techniques previously mentioned in the pre-processing section, aiming to minimise data variation due to run-to-run variation and to overcome the dominating effect of strong peak absorbance over weaker absorbance intensity. The entire IR spectrum region from 4000-600 cm^{-1} with 3401 variables would be the best option for performing PCA, however due to its extremely large number of variables, it limits the software's ability to execute the principal component analysis. Since the frequency region from 4000 cm^{-1}-1501 cm^{-1} did not carry much information as evident in Figure 4, and to overcome the limitation associated with the software, it was decided to focus only on the characteristic fingerprint region (from 1500-600 cm^{-1}). This approach was sensible as unlike the frequency region, the fingerprint region carries more useful information as

evident in Figure 4 which corroborates with prior information [13,14]. Additionally, it has a much lower number of variables (901 variables), which has proven to be beneficial in reducing the computational burden of the software. Subsequently, pre-processing and PCA were performed on the fingerprint regions.

A large number of PCA score plots had been generated in this study from the pairwise combinations of specific fingerprint region with different pre-processing strategies. However, for simplicity of discussion, only PCA score plot that has generated the easiest interpretable outcome i.e. score plot of square root transformed is reported here. Figure 5 shows the PCA score plot of the square root transformed dataset plotted using the first two principal components, namely PC1 and PC2. The former PC explains 67.2% of the variation or variability in the dataset while the second PC explains 14.8% of the variation in the dataset. The combination of these two PCs hence explains 81.8% (PC1 = 67.2% + PC2 = 14.6% = 81.8%) of the variation in the dataset which means that the PCA has adequately captured relevant information within the dataset.

Close examinations of the PCA score plot reveal nine neat clusters or groupings (designated as cluster A, B, C, D, E, F, G, H and I) associated with each of the nine cooking oil samples in this study which can be divided into two hyperplanes. Cooking oil samples without plastic materials are clustered into three separate clusters, identified as cluster A (U-RCO), B (H-RCO) and C (H-RCO-B) at the lower region of the score plot. The cooking oil samples which contained or were adulterated with plastic materials only are also clustered into three clusters as shown by cluster D (RCO-PE1), E (RCO-PE2) and F (RCO-PP) at the upper region of the score plot spanning from left to the upper centre of the plot. It is particularly interesting to note that cooking oil samples containing plastic materials which were used to fry the bananas are also clustered into three separate clusters as cluster G (ARCO-B-PE1), H (ARCO-B-PE2) and I (ARCO-B-PP) at a position away from the rest of the cooking oil samples. This rather interesting finding indicates the capability of this hybrid approach for monitoring cooking oil adulterated with plastic materials which are not intended for human consumption.

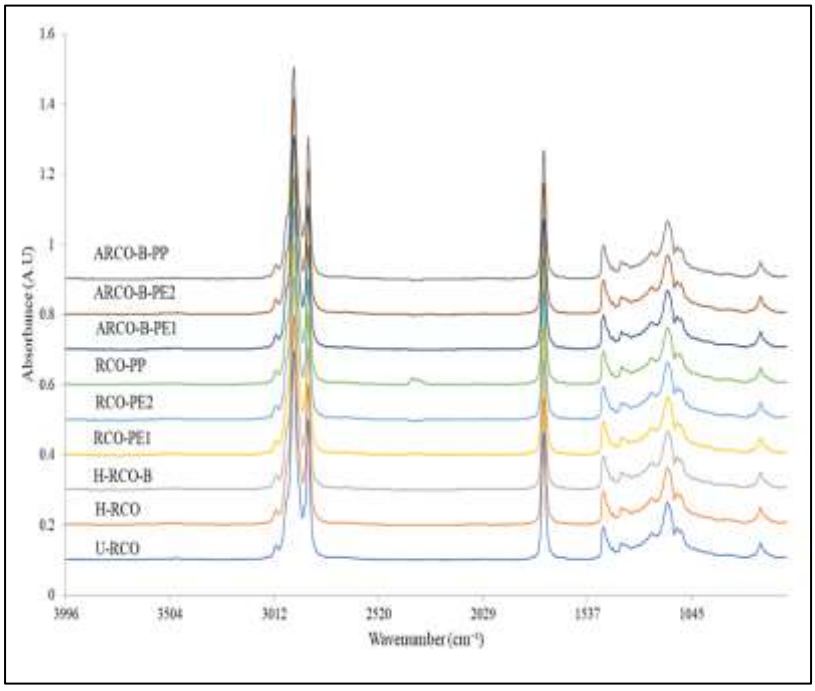


Figure 4. FTIR spectra of the cooking oil samples.

Table 4. The major peaks found in the spectra of the cooking oil samples and their corresponding functional groups [17]

Wavenumber (cm^{-1})	**Peak Assignment**
3009	C-H stretching vibration of the cis-double bond (=CH)
2960	Symmetric and asymmetric stretching vibration shoulder of the aliphatic CH_3 group
2852, 2920	Symmetric and asymmetric stretching vibration of the aliphatic CH_2 group
1743	Ester carbonyl functional group of the triglycerides
1465	Bending vibrations of the CH_2 and CH_3 aliphatic groups
1377	Bending vibrations of CH_2 groups
1098, 1117, 1160, 1236	Stretching vibration of the C-O ester groups
721	Overlapping of the CH_2 rocking vibration and the out-of- plane vibration of cis-disubstituted olefins

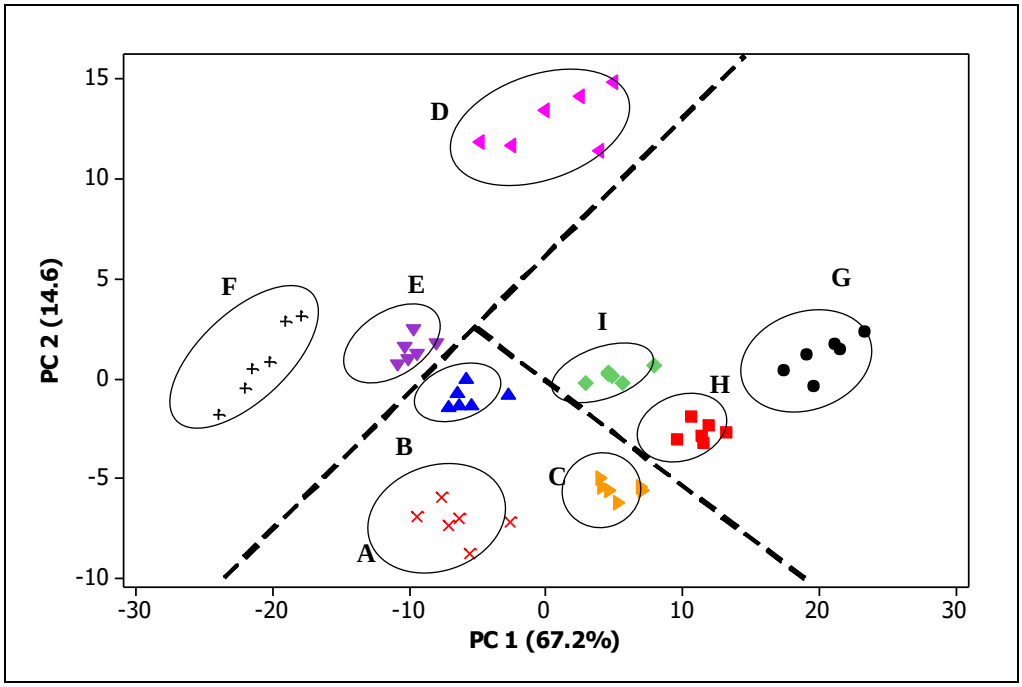


Figure 5. PCA score plot of the square root transformed dataset for the cooking oil samples

Conclusion

ATR-FTIR spectroscopy in combination with PCA can be successfully used for initial detection and discrimination of cooking oil adulterated with inedible plastic materials. Using specific IR information, PCA was able to discriminate between unadulterated and plastic adulterated cooking oil despite the dominant effect and high degree of the chemical profile similarities of TAG against the minute amount of plastic adulterants. As this study serves as an approach to simple and fast detection of inedible plastic in cooking oil, the characterisation of adulterated compounds from such activities indeed warrants further investigation.

Acknowledgements

The authors greatly acknowledged the funding provided by the Universiti Sains Malaysia under the Short-Term Grant Scheme (304/PPSK/61313030) which has enabled this work to be conducted.

References

1. Almeida, D. T., Viana, T. V., Costa, M. M., Silva, C. S. and Feitosa, S., (2019). Effects of different storage conditions on the oxidative stability of crude and refined palm oil, olein and stearin (*Elaeis guineensis*). *Food Science and Technology*, 39 (Suppl. 1): 211-217.
2. Daily Express, (2014), Plastic Materials used in frying banana fritters? http://www.dailyexpress.com.my/news.cfm?NewsID=94247. [Accessed online 23 November 2020].
3. Ram, P., Tapos, K., Md.Saiful, I., Mohammad, A. H., Md. Mahfuzar, R. and Mahabubur, R. M. (2018). Toxic effects of plastic on human health and environment: A consequences of health risk assessment in Bangladesh. *International Journal of Health*, 6(1): 1-5.
4. Zuleyha, E. (2021) Melamine exposure from the weaning period causes apoptosis, inflammation and damage to the blood-brain barrier. *Journal of Chemical Neuroanatomy*, 113(1): 1-9.
5. Yaman, N. and Velioglu, S. D. (2019). Use of attenuated total reflectance—Fourier transform infrared (ATR-FTIR) spectroscopy in combination with multivariate methods for the rapid determination of the adulteration of grape, carob and mulberry Pekmez. *Foods*, 8(7): 231-233.
6. Smith, R. (2019), Food fraud and adulteration detection using FTIR spectroscopy, food safety tech., https://foodsafetytech.com/feature_article/food-fraud-and-adulteration-detection-using-ftir-spectroscopy /2/ [Access online 12 November 2020].
7. Meng, P., Suqin, S. and Qun, Z., (2018) a simple and portable screening method for adulterated olive oils using the hand-held FTIR spectrometer and chemometrics tools. *Journal of Food Science*, 83(6): 1605-1612.
8. Bingning L., Haixia W., Qiaojiao Z., Ouyang J. and Wu, Y., (2015), Rapid detection of authenticity and adulteration of walnut oil by FTIR and fluorescence spectroscopy: A comparative study. *Food Chemistry*, 181 (1): 25-30.
9. Nurrulhidayah, A., Rohman, A., Amin, I., Shuhaimi, M., Khatib, A. (2013). Analysis of chicken fat as adulterant in butter using Fourier transform infrared spectroscopy and chemometrics. *Grasas y Aceitas*, 64 (4): 395-355.
10. Wu, Z., Li, H. and Tu, D. (2015). Application of Fourier transform infrared (FT-IR) spectroscopy combined with chemometrics for analysis of rapeseed oil adulterated with refining and purificating waste cooking oil. *Food Analytical Methods*, 8(10): 2581-2587.
11. Rohman, A., Che Man, Y. B., Hashim, P. and Ismail, A. (2011). FTIR spectroscopy combined with chemometrics for analysis of lard adulteration in some vegetable oils. *CyTA - Journal of Food,* 9(2): 96-101.
12. Skoog, D. A., West, D. M, Holler, F. M. and Crouch, S. R. (2020). Fundamentals of Analytical Chemistry: 10th Ed., Saunders College Publications. Philadelphia: pp 746-759.
13. Nur Farah Dina, A., Foo K. H, Naji A. M., Wan Nur Syuhaila M. D, Mohd Rahim K., Mohammad Afiq M. H., Hasmerya M. and Dzulkiflee I., (2021). Counterfeit one hundred Malaysian ringgit banknotes discrimination using chemical imaging inspection and pattern recognition. *Australian Journal of Forensic Sciences*, 53(3); 1-15.

14. Asensio, R.C., Moya, M. S. A., Roja, J. M., and Gomez, M. (2009). Analytical characterization of polymers used in conservation and restoration by ATR-FTIR spectroscopy. *Analytical and Bioanalytical Chemistry*, 395(7): 2081-2096.
15. Association of Official Analytical Chemists, AOAC (2019). Official Methods of Analysis., 21st edition USA: AOAC International.
16. Pavia, D. L., Lampman, G. M., Kriz, G. S. and Vyvyan J. A. (2008). Introduction to spectroscopy. Cengage Learning, Stamford: pp. 31-35.
17. Moinuddin S. (2011). Municipal waste plastic conversion into different category liquid hydrocarbon fuel, chemistry, emission control, radioactive pollution and indoor air quality, Nicolas Mazzeo, IntechOpen https://www.intechopen.com/books/chemistry-emission-control-radioactive-pollution-and-indoor-air-quality/municipal-waste-plastic-conversion-into-different-category-liquid-hydrocarbon-fuel [Access online 20 February 2021].
18. Lerma-García, M. J., Ramis-Ramos, G., Herrero-Martínez, J. M. and Simó-Alfonso, I. E. F. (2010). Authentication of extra virgin olive oils by Fourier-transform infrared spectroscopy. *Food Chemistry*, 118 (1): 78-83.
19. Rohman, A. and Che Man, Y. B. (2011). The use of Fourier transform mid infrared (FT-MIR) Spectroscopy for detection and quantification of adulteration in virgin coconut oil. *Food Chemistry*, 129(2): 583-588.

Malaysian Journal of Analytical Sciences (MJAS)
Published by Malaysian Analytical Sciences Society

ADDITION OF GLYCEROL AND SODIUM CHLORIDE INTO *Garcinia atroviridis* CHITOSAN FILM, AND ITS APPLICATION FOR WRAPPING OF CHICKEN MEAT

(Penambahan Gliserol dan Natrium Klorida Pada *Garcinia atroviridis* Filem Kitosan dan Aplikasinya Pada Pembungkusan Daging Ayam)

S-Navin Sivanasvaran, Ianne Kong, Hui-Ling Tan, Liew-Phing Pui*

Department of Food Science and Nutrition, Faculty of Applied Sciences, UCSI University, 56000 Cheras, Kuala Lumpur, Malaysia

**Corresponding author: puilp@ucsiuniversity.edu.my*

Received: 28 February 2021; Accepted: 22 May 2021; Published: 27 June 2021

Abstract

Glycerol and sodium chloride (NaCl) have a strengthening effect that can be incorporated into edible films to enhance their mechanical properties. This study evaluates the effects of glycerol (0.5-2.0% v/v) and NaCl (5.0-10.5 mM w/v) on the physical, mechanical, and antimicrobial properties of chitosan film incorporated with *Garcinia atroviridis*. Storage tests were conducted on chicken meat that were wrapped with and without the film. The moisture content, water solubility, and elongation at break of film with 1.5% (v/v) glycerol and 10 mM (w/v) NaCl was the highest. The increment of glycerol and NaCl reduced thickness, tensile strength, and Young's modulus. The total color difference of the film with 0.5% (v/v) glycerol and 0 mM (w/v) NaCl was highest and showed the greatest inhibition against *Pseudomonas aeruginosa* and *Staphylococcus aureus*. The pH of the control increased whereas the pH of chicken meat wrapped with the film decreased as the number of storage days increased. In conclusion, film with 1.5% (v/v) glycerol and 10 mM (w/v) NaCl might be a suitable film because it demonstrated the highest elongation at break and a prolonged shelf life for the chicken meat of at least 15 days, which was longer than of the control.

Keywords: glycerol, sodium chloride, edible film, chitosan, *Garcinia atroviridis*

Abstrak

Gliserol dan natrium klorida (NaCl), yang mempunyai kesan pengukuhan, dapat dimasukkan ke dalam filem yang boleh dimakan, untuk meningkatkan sifat mekanikal filem yang boleh dimakan. Tujuan kajian ini adalah untuk menilai kesan gliserol (0.5-2.0% v/v), dan NaCl (5.0-10.5 mM w/v) terhadap sifat fizikal, mekanikal, dan antimikrob filem kitosan yang diperbadankan dengan *Garcinia atroviridis*. Ujian penyimpanan dilakukan pada daging ayam yang dibungkus dengan dan tanpa filem. Kandungan kelembapan, kelarutan air, dan pemanjangan pada pemecahan filem dengan gliserol 1.5% (v/v), NaCl 10 mM (w/v) adalah yang tertinggi. Peningkatan gliserol dan NaCl mengurangkan ketebalan, kekuatan tegangan, dan pekali Young. Perbezaan warna keseluruhan filem dengan 0.5% (v/v) gliserol dan 0 mM (w/v) NaCl adalah tertinggi dan ia menunjukkan penghambatan terbesar terhadap *Pseudomonas aeruginosa* dan *Staphylococcus aureus*. Pengawalan pH meningkat sedangkan pH daging ayam yang dibungkus dengan filem menurun ketika hari penyimpanan meningkat. Kesimpulannya, filem dengan gliserol 1.5% (v/v) dan NaCl

10 mM (w/v) mungkin merupakan filem yang sesuai kerana ia mempunyai pemanjangan tertinggi pada pemecahan dan jangka hayat daging ayam yang berpanjangan sekurang-kurangnya 15 hari yang lebih lama daripada kawalan.

Kata kunci: gliserol, natrium klorida, filem boleh dimakan, kitosan, *Garcinia atroviridis*

Introduction

In Malaysia, chicken meat is one of the most consumed foods. Statistics show the poultry consumption per person in Malaysia was approximately 49 kg in 2019 (https://www.statista.com/statistics/756920/malaysia-meat-consumption-per-capita-by-type/). Chicken meat had a shelf life of 6 days when in refrigerated storage at 4 °C. Common pathogens that were reported in chicken meat are *Campylobacter*, *Salmonella*, *Staphylococcus aureus,* and *Pseudomonas aeruginosa* [1]. Food packaging was invented to preserve foods from external contamination [2]. Edible packaging is gaining greater interest due to the disadvantages associated with petroleum-based food packaging and how they deplete non-renewable natural resources [3]. This study focuses on consumable films or coatings that are applied onto food products [4]. Edible packaging provides mechanical protection and extends shelf life of foods [5].

Chitosan is widely used to produce edible films because it possesses good antimicrobial and gas barrier properties that give it a film forming ability [6]. Several researchers have found that chitosan has a proven antibacterial effect towards gram-positive and gram-negative bacteria [7-8]. The incorporation of 20% (v/v) *Piper nigrum* leaf extract increased the inhibition zone of chitosan and polyvinyl alcohol blended films against *Escherichia coli* [9]. On the other hand, chitosan film incorporated with grape seed extract extended the shelf life of chicken breast fillets and inhibited lipid oxidation [10]. Additionally, chitosan film incorporated with cinnamon oil inhibited lipid oxidation and reduced microbial growth on chicken breast fillets [11].

Garcinia atroviridis is known as *'*asam keping*'* or 'asam gelugur'. It is commonly used to make pickles, in tea, and as a seasoning in curries. Al-Mansoub et al. [12] found that *Garcinia atroviridis* extract had antioxidant, antimicrobial, and antitumor-promoting properties. According to Basri et al. [13], *Garcinia atroviridis* extracts inhibited gram-positive bacteria (*Staphylococcus aureus*, *Staphylococcus epidermis, Bacillus subtilis*) and gram-negative bacteria (*Salmonella enterica, Salmonella typhimurium, Escherichia coli* and *Pseudomonas aeruginosa*). Chitosan film incorporated with *Garcinia atroviridis* extracts showed promising characteristics for use as food packaging [6]. From their study, it was found that the film increased the shelf life of Indian mackerel during storage and inhibited the microbial growth of *Pseudomonas aeruginosa*, *Bacillus subtilis,* and *Staphylococcus aureus*. However, the tensile strength and elongation at the break of film were low.

The mechanical properties of packaging materials are important to ensure product safety and security until it reaches the consumer. Glycerol improves the elongation at the break of edible film [14, 15]. Another study, Choi et al. [16] reported that addition of NaCl increased the elongation at break of pea starch films by adjusting formation and strength of intermolecular hydrogen bonds of starch molecules. Further, increasing the NaCl concentration enhanced the hydration effect of chitosan films. More hydrated chloride ions impeded the hydrophobic interactions between chitosan molecules and disrupted hydrogen bonding on the chitosan film [17].

Since studies on enhancing the mechanical properties of chitosan film incorporated with *Garcinia atroviridis* are scarce, the study of addition levels of glycerol and NaCl on chitosan films with *Garcinia atroviridis* can provide further insights into the application of film for chicken meat. This research evaluates the effects of physical, mechanical, and antimicrobial analysis of chitosan film incorporated with *Garcinia atroviridis* by optimizing the additional levels of glycerol and NaCl. The optimized film shall be applied to chicken meat for storage tests. The chicken meat slices will be wrapped

with the optimized chitosan film incorporated with *Garcinia atroviridis* and stored in a chiller at 4 °C for 15 days for further analysis.

Materials and Methods

Materials

Garcinia atroviridis and chicken breast meat (*Gallus gallus domesticus*) were purchased from a local market (Petaling Jaya, Malaysia). Chitosan analytical grade, glycerol (≥99.5%), and sodium chloride analytical grade were purchased from Sigma-Aldrich (M) Sdn Bhd, Petaling Jaya, Malaysia. Glacial acetic acid (≥99.99%) and Tween-80 analytical grade were purchased from LGC Scientific Sdn Bhd, Malaysia. Ethanol (≥99.8%) (Synertec Enterprise Sdn Bhd, Malaysia), barium chloride (≥99.99%) (Sigma Aldrich, USA), and sulphuric acid (≥96%) (Fisher Scientific, Malaysia), Mueller-Hinton agar (Synertec Enterprise Sdn Bhd, Malaysia), plate count agar (Chemolab, Malaysia), peptone water (Synertec Enterprise Sdn Bhd, Malaysia), stomacher bags (LGC Scientific Sdn Bhd, Malaysia), and petri dishes (90 mm × 15 mm) (Synertec Enterprise Sdn Bhd, Malaysia) were purchased.

Preparation of *Garcinia atroviridis* extracts

The *Garcinia atroviridis* was cut into smaller pieces and dried in an oven (1350 FX, Sheldon Manufacturing, Oregon, USA) overnight at 60 °C. After drying, it was ground into powder with a grinder (8011G, Waring, USA) to increase the total surface area of the *Garcinia Atrovidis* to obtain a higher yield during extraction. The powder was then placed into a sealed pack and kept in a chiller at 4 °C for further analysis.

The extraction was conducted as previously described by Zaman et al. [6] in which 80 g of *Garcinia atroviridis* powder was added to 800 mL of 99.8% (v/v) ethanol in a 1 L beaker. The mixture was then mixed for 24 h with a magnetic stirrer (MS-H280-Pro, DLAB Scientific, Beijing, China) at 1500 rpm at room temperature. After 2 h, a vacuum filter (WP6222050, Milipore, MA, USA) and filter paper (Whatman No. 3, Thermoline, NSW, Australia) were used to filter out the residue in the mixture. The filtrate then underwent evaporation using a rotary evaporator (R-000, BÜCHI, Flawil, Switzerland) at 60 °C under vacuum condition and the *Garcinia atroviridis* extracts were poured into a universal bottle and kept at 4 °C until future use.

Preparation of film

Film formation was conducted following the casting procedure of Zaman et al. [6]. To prepare the film solution, 1.5 g of chitosan (CH) powder was added in 100 mL of 1% (v/v) acetic acid to form (1.5%, w/v) CH solution. The CH solution was magnetically stirred for 24 h at room temperature. It was then filtered using a vacuum filter with filter paper to filter out insoluble residue.

For film formation, 25 mL of the CH solution was poured into a 50 mL beaker. After that, 5% (v/v) *Garcinia atroviridis* extract and 0.01% (v/v) Tween-80 were added to the solution with additional levels of glycerol (0.5, 1.0, 1.5, 2.0%, v/v) and NaCl (5, 10, 10.5 mM, w/v) as shown in Table 1. The solutions were homogenized using a homogenizer (HG-15D, Daihan Scientific, South Korea) at 9000 rpm for 4 min. After homogenization, the solution was transferred to a petri dish and placed into the oven for 24 h at 50°C. Once the films were dried, they were peeled and transferred into a zip-lock plastic bag and stored in a desiccator for further analysis.

Physical properties of film: Moisture content

The film moisture content was analyzed according to the method described by Lee et al. [3]. Films with a size of 2 × 2 cm were placed in a desiccator overnight. Then, the initial mass of the film was weighed (M_i). The film was then placed into an oven at 90°C until there were no changes in the final mass (M_f). Moisture content was determined using the equation below:

$$\text{Moisture content} = \frac{M_i - M_f}{M_i} \times 100\% \quad (1)$$

where M_i and M_f refer to the mass of the initial dried film and final dried film (g), respectively.

Water solubility

The film water solubility was measured following procedures from Chan et al. [18] with some modifications. The final mass of the dried films from the

moisture content determination were taken as the initial mass (W_1). The dried films were placed into a boiling tube filled with 30 mL of distilled water for 3 h. After immersion, they were taken out and underwent drying again in an oven for 24 h at 60°C. The final dry mass of the film was measured (W_2). The water solubility was determined using the following equation:

$$Water\ solubility = \frac{W_1 - W_2}{W_1} \times 100\% \quad (2)$$

where $W1$ and $W2$ refer to the mass of the initial dried film and final dried film (g), respectively.

Color profile

The film color profile was measured according to the method described by Chan et al. [18]. A colorimeter (ColourFlex EZ, Hunterlab, Virginia, USA) was used to determine the color. The values, L^* (luminosity), a^* (green-red) and b^* (blue-yellow) were used to express the film color. The total color difference (ΔE) of the film was determined using the following equation:

$$\Delta E = \sqrt{(L - L^*)^2 + (a - a^*)^2 + (b - b^*)^2} \quad (3)$$

where the color parameters of the white plate are expressed by L, a, and b and the color of the *Garcinia atroviridis* films are expressed as L^*, a^* and b^*.

Thickness

A manual micrometer (QB420100, JY, China) was used to measure the film thickness as described by the method from Kuan et al. [4]. Measurements were made at five random places of the film for which an average value was determined.

Mechanical properties

The measurements of tensile strength and elongation at break were conducted according to the procedures demonstrated by Lim et al. [19] with some modifications. A universal testing machine (CS4921, Lloyd Instrument, UK) was pre-set with the specifications for speed, gauge length, thickness, width, units, and tension mode. Film strips of 20 × 50 mm were held parallel to the grip of the machine. The separation of the grip was adjusted to 30 mm. The speed of the crosshead was adjusted to 20 mm/min. The values from the machine called peak load and peak extension were taken as tensile strength (*MPa*) and elongation at break (%), respectively. Young's modulus was determined using the following equation:

$$Young's\ modulus\ MPa = \frac{Stress}{Strain} \quad (4)$$

where stress is determined as the tensile force (F) / cross-sectional area (A) while strain is the length of film extension (e) / original film length (l_o).

Antimicrobial properties

The film antimicrobial properties were analyzed using the agar disk diffusion method described by Chan et al. [18]. Antimicrobial activities of the film were examined against two bacteria (*Pseudomonas aeruginosa* and *Staphylococcus aureus*). The bacterial suspension was prepared with reference to the 0.5 McFarland standard. Then, 100 µL of the suspension was inoculated on a Mueller-Hinton Agar and spread aseptically with a glass hockey stick.

Films were shaped into 6 mm diameter discs and aseptically placed onto the Mueller-Hinton Agar plates that were previously inoculated. The positive control for *Pseudomonas aeruginosa* was Streptomycin (10 mg/mL). For the *Staphylococcus aureus,* penicillin (10 mg/mL) was used as the positive control. Ethanol was used as the negative control. The plates were then put into the incubator at 37°C for 24 h. The inhibition zone diameter including the edible film disk (6 mm) was determined with a vernier caliper.

Storage test of chicken meat

The chicken meat for storage test was prepared according to the method described by Higueras et al. [20]. After purchasing the chicken meat from the market, it was placed in an icebox and brought to the laboratory. It was cleaned with distilled water and lightly tamped with tissue paper. The chicken meat was cut into 2 cm × 2 cm size, 10 ± 1 g, and placed in the chiller at 4°C for further use.

The slices of chicken meat were then wrapped with the optimized film , which was based on the results of a previous analysis. They were then placed into a zip-lock bag. The chicken meat without film was also placed into a zip-lock bag and served as the control in this test. The chicken meat wrapped with film and the control were placed in the chiller at 4°C until analysis. They were stored for 15 days and the analysis on the chicken meats were conducted on day 0, 3, 6, 9, 12, and 15 of storage.

pH changes of chicken meat

The pH of the chicken meat wrapped with film and control were measured following procedures described in Tantasuttikul et al. [21]. The films were peeled off the chicken meat and the chicken meat were put into a stomacher bag. Then, the stomacher bag was filled with 100 mL of distilled water. Then it underwent homogenization for 2 min using a stomacher (BagMixer 400, Interscience, France). The pH reading was measured by dipping the pH meter (pH700, EUTech Instruments, Singapore) into the mixture.

Microbial changes of chicken meat

The total colony count was analyzed according to the procedures outlined in Remya et al. [46] with slight modifications. The films were peeled off the chicken meat and the chicken meat were put into a stomacher bag. Then, 90 mL of peptone water was poured into the stomacher bag, which underwent homogenization for 2 min using a stomacher. The homogenized chicken mixture underwent serial dilutions from 10^{-1} up until 10^{-6} using peptone water. After homogenization, 100 µL of each serial dilution was inoculated on a plate count agar and a glass hockey stick was used to spread the inoculations evenly. The plates were incubated for 24 h at 37°C. After incubation, the colonies were counted with the results expressed as $\log_{10}$ (CFU/mL).

Statistical analysis

Results were expressed as mean ± standard deviation of three determinations. The results were statistically analyzed using Minitab version 17 ($p \leq 0.05$) (Minitab, USA). The comparison of means was performed by one-way analysis of variance followed by Tukey's test. The Paired T-test was conducted to analyze results of total colony count and pH reading between the chicken meat wrapped with film and chicken meat without film (control).

Table 1. Formulation of chitosan film incorporated with *Garcinia atroviridis* extract

Film Formulation	Glycerol Concentration (%)	Sodium Chloride Concentration (mM)
A	0.0	0.0
B	0.5	0.0
C	1.0	5.0
D	1.5	10.0
E	2.0	10.5

Results and Discussion

Physical properties of films

Moisture content

Dehghani et al. [22] showed that low moisture content is usually favorable for edible films as it reduces the risk of microbial growth. Table 2 presents the moisture content of each chitosan film with *Garcinia atroviridis* extract with different addition levels of glycerol and NaCl.

The increment of glycerol and NaCl increased the moisture content of the film from 15.42% to 27.29%. This might be due to the glycerol's hygroscopicity whereby it tended to absorb and retain moisture from its surrounding [23]. Additionally, as a humectant, the hydroxyl groups in glycerol formed hydrogen bonds in the water [24]. The addition of glycerol also elevated the viscosity and allowed for film matrix interaction with

water to increase [25]. These results are also similar to Peng et al. [26] and Dick et al. [27] in which the increment of glycerol caused the moisture content of a film to increase.

Water solubility

Water solubility is an important attribute because it determines biodegradability, integrity, and water resistance [28]. Table 2 shows that the increment of additional levels of glycerol and NaCl increased the water solubility of the films from 46.40% to 59.30%. The increment in water solubility might be due to the hydrophilic behavior of glycerol. The incorporation of glycerol increased the affinity of the film matrix to bind to water thus increasing the solubility of the film [29].

Additionally, Yang et al. [30] suggested that glycerol increased the hydrogen bonds in the chitosan film matrix and leads to a higher availability for it to interact with water molecules. Furthermore, it could be explained that glycerol disrupted the chitosan network interaction density. The presence of a polar molecule, glycerol would increase the interaction with water. It caused a decrease in intermolecular forces by interacting with the functional groups of the chitosan, causing an increase in solubility. This led to the elevation of the water solubility of the film [23]. This trend of increasing water solubility was also observed by Cerqueira et al. [28], whereby the water solubility of chitosan films increased from 51.86% to 69.94% when the glycerol was increased from 0.5% (v/v) to 2.0% (v/v).

Color profile

Color plays a significant part in the consumer's perception of food as it is one of the first characteristics that the customer will evaluate [4]. Figure 1 shows the appearance of the films. As seen in the figure, the films were yellowish-brown in color. According to Zaman et al. [6], the yellowish-brown film color was mainly due to the presence of pigments in *Garcinia atroviridis* called xanthonoids.

The overall color profile of the films is best described using the total color difference (ΔE) (Table 3). The range of the ΔE of the films was from 0.00–1.37. The results showed that the ΔE of the film with 0.5% (v/v) glycerol and 0 mM (w/v) NaCl was highest. However, there was no significant difference between the color profile of the films. The ΔE of the film reduced when the addition level of glycerol and NaCl increased. This could be attributed to the fact that glycerol and NaCl was colorless and it did not have the color imparted into the film. Peng et al. [26] and Dick et al. [27] observed the increment of glycerol had not changed the ΔE of film in combination with tea polyphenols. Another factor to consider is the concentration of chitosan used that influences the color of the edible film. However, in this study, the concentration of chitosan was kept constant. Therefore, it did not influence the color of the films**.**

Thickness

Thickness is a key characteristic in an edible film because thicker films provide more security for the food product. Figure 2 shows the results of the film thickness analysis. The thickness of the films ranged from 0.097–0.122 mm. The thickness value of film with 2% (v/v) glycerol and 10.5 mM (w/v) NaCl was the lowest. The concentration of NaCl in the film with 2% (v/v) glycerol and 10.5 mM (w/v) allowed the permeation of hydrated chloride ions (Cl^-) into the chitosan films, which disrupted the hydrogen bonds and hydrophobic interactions. This led to the loss of cohesion capacity of chitosan films. As a result, water molecules were squeezed out from hydrated ions and reduced the film's thickness [17]. Similar results were reported for chia mucilage films [27].

Mechanical properties of film

Tensile strength measures the amount of tensile stress the film can withstand until it breaks. Conventional standards state that food packaging should have a tensile strength greater than 3.5 MPa to be deemed as satisfactory [31]. Table 4 presents the tensile strength of the films was in the range of 4.03–9.24 MPa. Hence, based on this standard, all the film formulations in this study fulfilled this criterion.

Further, the tensile strength reduced as the additional levels of glycerol and NaCl increased. The increment in the additional levels of glycerol in the film caused a plasticizing effect for which the chitosan network chains became weaker [31]. Furthermore, more mobile regions

were created due to the interference caused by glycerol. High additional levels of glycerol elevated the film water content. This could be attributed to the hygroscopic behavior of glycerol that led to the reduction in the interactions between adjacent macromolecules [29].

Several studies showed that the increment in the additional levels of glycerol reduced the tensile strength of the film [33, 34]. Apart from that, the results from this study showed an improvement in tensile strength when compared to the results of Zaman et al. [6]. The authors detected that at 5% (v/v) addition level of *Garcinia atroviridis* extract, the tensile strength was 3.28 MPa, which was lower than for films in this study. This indicated that the addition of glycerol and NaCl improved the tensile strength of the film.

Elongation at break is the film's capability to resist changes in shape without breaking. For edible films, a high elongation is favorable as it enhances the ability of the film to wrap and package food. Table 4 shows the range of the elongation at break was from 59.32–123.35%. The film with 1.5% (v/v) glycerol and 10 mM (w/v) NaCl had the highest elongation at break. Additionally, the increment in additional levels of glycerol and NaCl in the film showed increments on the elongation at break except for the film with 2% (v/v) glycerol and 10.5 mM (w/v) NaCl.

The increment in elongation of the film can be due to the interactions of the glycerol with the chitosan chains. The plasticizing effect of glycerol reduced the acting forces between the molecules leading to the sliding of the polymer chain. Thus, the flexibility and ductility of the film were increased [33]. Apart from that, the addition of NaCl enhanced elongation of the film. The NaCl ions may cause an increase of electrostatic repulsion among chitosan chains leading to the formation of stretched chitosan chains from coiled chitosan chains [35]. Prateepchanachai et al. [48] demonstrated that salt produces a counter-ion effect that depresses the third electroviscous effect and renders the chitosan molecules more flexible with a random, coiled shape. Coiled molecules will result in less inter-molecular entanglements. The ability of the film to stretch was increased, increasing the elongation of the film. The results of this study are similar to Liu et al. [36] in that the elongation of chitosan-starch blended films had an incorporation of 2.5-10% (v/v) glycerol increased from 13.5-18.0%, accordingly.

However, the elongation of the film decreased from 123.35% to 70.45% when the additional levels was increased to 2% (v/v) glycerol and 10.5 mM (w/v) NaCl. This was probably associated to the anti-plasticizing effect exhibited by glycerol at high additional levels [36]. Souza et al. [38] found that at high additional levels, plasticizers exhibited strong interactions with biopolymers. This led to the decrement in the macromolecular mobility and elongation at break of the film. This explained why, at higher plasticizer concentrations, such as the anti-plasticization phenomena were associated with stronger interactions between plasticizer and chitosan molecules, which impedes macromolecular mobility. When the amount of plasticizer molecules in a plasticized chitosan-based film exceeded a critical value, anti-plasticization occurred. As a result, the film's elongation at the break was reduced [47].

Young's modulus measures the ability of a film to withstand elastic deformation when under elongation or compression. Table 4 shows that the range of the values of Young's modulus was from 0.046–0.146 MPa. The increment in additional levels of glycerol and NaCl decreased the Young's modulus of the film. The decreasing trend of Young's modulus might be due to the effect of glycerol in increasing the elasticity of the film and reducing the interactions among the chitosan chain. This resulted in the film becoming less stiff [32]. Similarly, Kusumaningtyas et al. [39] detected that the increment in glycerol lowered the Young's modulus of films as well.

Antimicrobial properties of film

Figures 3 and 4 show the inhibition zone of the different film formulations on selected pathogens. The findings showed that film with 0.5% (v/v) glycerol and 0 mM (w/v) NaCl, which showed the highest inhibition zone

against *Pseudomonas aeruginosa* (10.50 mm) and *Staphylococcus aureus* (11.00 mm).

The inhibition zone of the films ranged from 9.67–10.50 mm for *Pseudomonas aeruginosa* and 10.17–11.00 mm for *Staphylococcus aureus*. The results indicated that the films exhibited antimicrobial properties towards these pathogens. The antimicrobial properties of the film could be attributed to the chitosan film and the *Garcinia atroviridis* extract. Chitosan has been widely known to exhibit antimicrobial properties because it possessed charged groups and has ionic interactions with bacterial cell walls. The antibacterial action of chitosan was done via the binding of the amino group with the membrane of the bacterial cell. This led to the disruption of the cell membrane, followed by the intracellular leakage that led to cell death [8].

The extracts from *Garcinia atroviridis* are known to exhibit antibacterial properties against various bacteria due to flavonoids and other phenolic compounds [13]. Zhang et al. [40] demonstrated that chitosan film with 10% (w/v) mangosteen rind powder was able to inhibit *Salmonella* and *Staphylococcus aureus*. Additionally, Zaman et al. [6] observed that chitosan film incorporated with 5% (v/v) *Garcinia atroviridis* extract was able to inhibit *Pseudomonas aeruginosa* and *Bacillus subtilis*.

Table 2. Moisture content (%) and water solubility (%) of the different formulations of chitosan films incorporated with *Garcinia atroviridis* extract

Film Formulation	Moisture Content, (%)	Water Solubility (%)
A	15.42 ± 1.84^{a}	46.40 ± 1.31^{a}
B	18.64 ± 2.10^{b}	49.60 ± 1.94^{ab}
C	22.31 ± 1.96^{c}	52.13 ± 2.43^{b}
D	24.15 ± 1.64^{c}	55.77 ± 1.64^{c}
E	27.29 ± 1.37^{d}	59.30 ± 2.04^{d}

Results are presented as mean value ± standard deviation of three replicates.

Different letters superscripted denote significant difference ($p \leq 0.05$) between samples for each parameter in the same column.

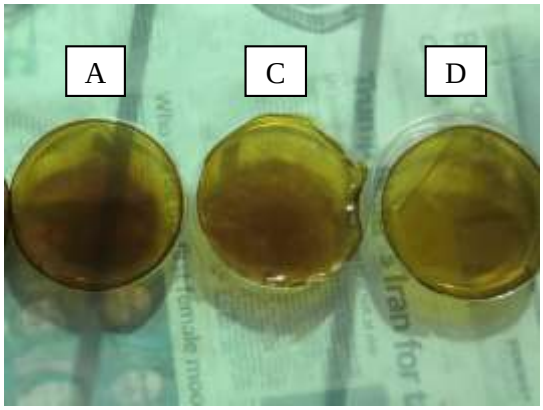


Figure 1. The appearance of the films made from formulation A, C and D

Table 3. Color parameters of the different formulations of chitosan film incorporated with *Garcinia atroviridis* extract

Film Formulation	L*	a*	b*	ΔE
A	8.50 ± 1.03^{ab}	0.39 ± 0.65^{a}	8.70 ± 0.62^{ab}	0.00 ± 0.00^{a}
B	8.30 ± 0.64^{a}	-1.43 ± 0.40^{b}	8.37 ± 1.46^{a}	1.37 ± 0.93^{b}
C	9.19 ± 0.72^{ab}	0.77 ± 0.94^{a}	8.40 ± 0.67^{a}	0.78 ± 0.61^{a}
D	8.46 ± 0.21^{ab}	1.20 ± 0.38^{a}	9.16 ± 0.51^{b}	0.27 ± 0.91^{a}
E	9.31 ± 1.07^{b}	1.12 ± 0.25^{a}	8.81 ± 0.06^{ab}	0.63 ± 0.78^{a}

Results are presented as mean value ± standard deviation of three replicates.

Different letters superscripted denote significant difference ($p \leq 0.05$) between samples for each parameter in the same column

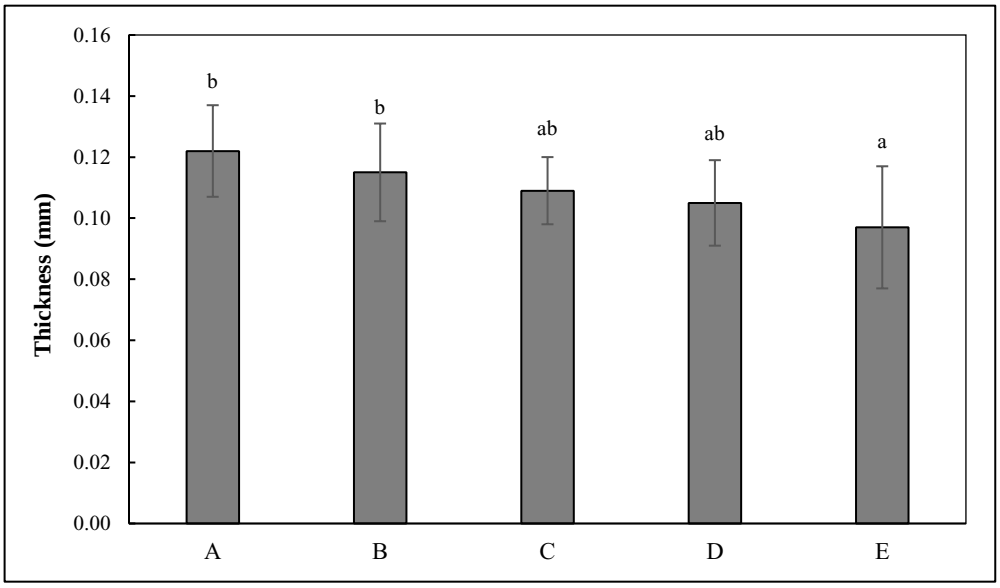


Figure 2. The thickness (mm) of the different film formulations of chitosan film incorporated with *Garcinia atroviridis* extract. A represents film containing 0% glycerol and 0 mM NaCl; B represents film containing 0.5% glycerol and 0 mM NaCl; C represents film containing 1.0% glycerol and 5 mM NaCl; D represents film containing 1.5% glycerol and 10 mM NaCl; and E represents film containing 2.0% glycerol and 10.5 mM NaCl. Error bars indicate mean ± standard deviation of three replicates. Bars with different letters denote significant difference ($p \leq 0.05$) between samples.

Table 4. Mechanical properties of the different film formulations of chitosan film incorporated with *Garcinia atroviridis* extract

Film Formulation	Tensile Strength (MPa)	Elongation at Break (%)	Young's Modulus (MPa)
A	9.24 ± 0.77^{d}	59.32 ± 2.50^{a}	0.156 ± 0.011^{c}
B	7.44 ± 0.55^{c}	93.77 ± 2.85^{c}	0.080 ± 0.005^{b}
C	6.17 ± 0.72^{b}	109.63 ± 3.36^{d}	0.056 ± 0.006^{a}
D	5.66 ± 0.64^{b}	123.35 ± 3.73^{e}	0.046 ± 0.054^{a}
E	4.03 ± 0.62^{a}	70.45 ± 1.69^{b}	0.057 ± 0.009^{a}

Results are presented as mean value ± standard deviation of three replicates

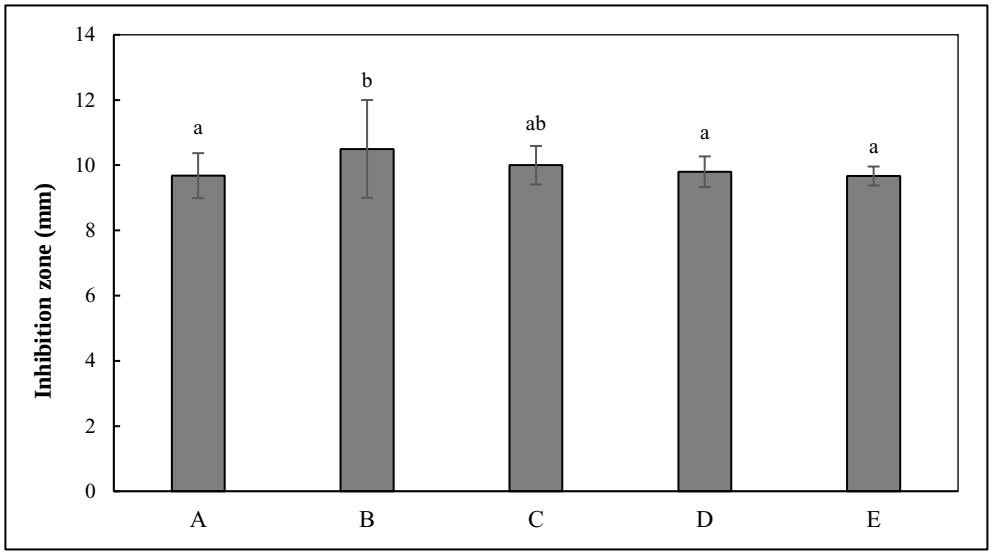


Figure 3. The antibacterial activity of the different film formulations of *Garcinia atroviridis* extract incorporated into chitosan film on *Pseudomonas aeruginosa*. A represents film containing 0% glycerol and 0 mM NaCl; B represents film containing 0.5% glycerol and 0 mM NaCl; C represents film containing 1.0% glycerol and 5 mM NaCl; D represents film containing 1.5% glycerol and 10 mM NaCl; and E represents film containing 2.0% glycerol and 10.5 mM NaCl. Error bars indicate mean ± standard deviation of three replicates

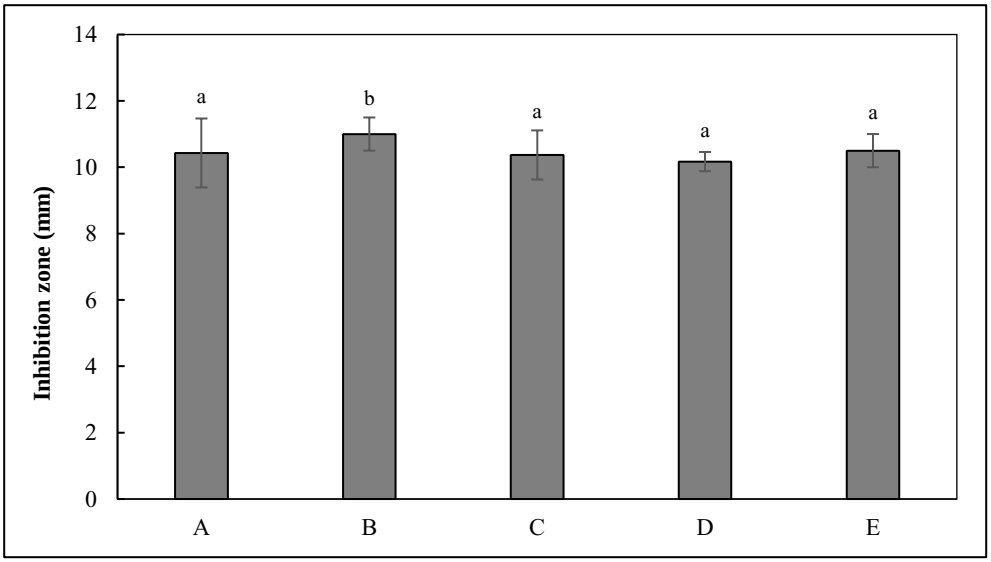


Figure 4. The antibacterial activity of the different film formulations of *Garcinia atroviridis* extract incorporated into chitosan film on *Staphylococcus aureus*. A represents film containing 0% glycerol and 0 mM NaCl; B represents film containing 0.5% glycerol and 0 mM NaCl; C represents film containing 1.0% glycerol and 5 mM NaCl; D represents film containing 1.5% glycerol and 10 mM NaCl; and E represents film containing 2.0% glycerol and 10.5 mM NaCl. Error bars indicate mean ± standard deviation of three replicates

Storage test of chicken meat: Optimized film

The film formulation that was used for the storage test was chosen through the evaluation of physical, mechanical, and antimicrobial properties of the films. Each film formulation showed antimicrobial properties. Hence, films with optimum additional levels of glycerol and NaCl were selected based on its mechanical properties. The elongation at break of the film with 1.5% (v/v) glycerol and 10 mM (w/v) NaCl was the highest (123.35%) and had an acceptable tensile strength (5.66 MPa) and Young's Modulus (0.046 MPa). The film with incorporation of 1.5% (v/v) glycerol and 10 mM (w/v) NaCl was applied to the chicken meat for the storage tests.

pH changes of chicken meat

Figure 5 presents the pH values of the chicken meat wrapped with the film and chicken meat without film (control) during storage. The pH of the chicken meat at the beginning of the storage test was 5.86. The pH of the control increased as the number of storage days increased whereas the pH of the chicken meat wrapped with film decreased as the number of storage days increased (Figure 5). The increment in the pH value of the control might be caused by the accumulation of amines and ammonia due to the growth of bacteria. The bacteria broke down amino acids, which produced an accumulation of ammonia that increased the pH value of the chicken meat [41]. The studies on chicken breast meat storage have shown that pH and bacterial growth had a positive correlation [42]. Further, it was suggested by Bazargani-Gilani et al. [43] that the rise in pH value of chicken meat during storage because of a rise in volatile bases caused by the activity of endogenous enzymes such as protease and lipase.

Krishnan et al. [41] showed that the pH of raw chicken meat increased after 15 days of storage at 4 °C, which agrees with our findings. On the other hand, the decrease of the pH value of the chicken meats wrapped with film may be caused by the reduction of bacterial activity and the production of volatile base compounds in the chicken meats [44].

Microbial changes of chicken meat

The total colony count of the chicken meat wrapped with film and control during storage was calculated and expressed in log (CFU/mL) as shown in Figure 6. The black dotted lines in the line graph represents the safe microbial limits for consumption of chicken meat, which was less than log 6.0 [10]. The chicken meat was considered to be unsafe for consumption when its total colony count exceeded log 6.0. The total colony count of the chicken breast meat at beginning of the storage test was log 3.48.

The total colony count increased as the number of storage days increased for the controls and the chicken meats wrapped with film. The total colony count for the controls reached a value of log 8.17 after 15 days of storage. Conversely, the chicken meats wrapped with the film reached a total colony count of log 6.10 after 15 days. The total colony count for the chicken meats wrapped with the film was lower than the control for all days of the storage period.

In addition, from Figure 6, the colony-forming unit (CFU) for the control exceeded log 6.0 on the 6th day of storage; whereas, the chicken meats wrapped with the film only exceeded log 6.0 on the 15th day of storage. Hence, we deduced that the control was safe for consumption up to day 5 of storage while the chicken meats wrapped with the film were safe for consumption up to day 14 of storage. It can be concluded that the chitosan film incorporated with 5% (v/v) *Garcinia atroviridis* extract can extend the shelf life of chicken meat from 5 days to 14 days when stored at 4°C. The ability of the film to prolong the shelf life of the chicken meat might be due to the presence of antimicrobial properties in the film. Figures 3 and 4 show that the films inhibited the growth of *Pseudomonas aeruginosa* and *Staphylococcus aureus*.

Basri et al. [13] showed that *Garcinia atroviridis* extract can inhibit the growth other pathogenic bacteria such as *Bacillus subtilis*, *Salmonella enteritidis* and *Escherichia coli*. Hence, the films can reduce the total colony count of the chicken meat and consequently extended its shelf life. Several studies have similarly reported on the ability of edible films to increase the shelf life of food

products. Chitosan film incorporated with clove essential oil and nisin increased the shelf life of pork patties from 6 days to 12 days [45]. In another study, the shelf life of Indian mackerel fish was extended when the fish was wrapped with chitosan film incorporated with 5% (v/v) *Garcinia atroviridis* [6].

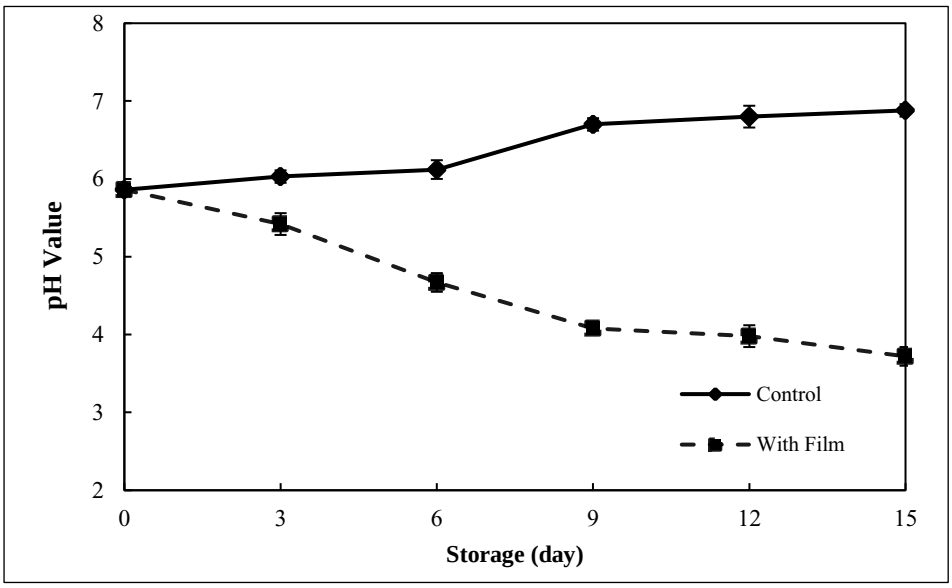


Figure 5. Changes in pH value throughout the storage period

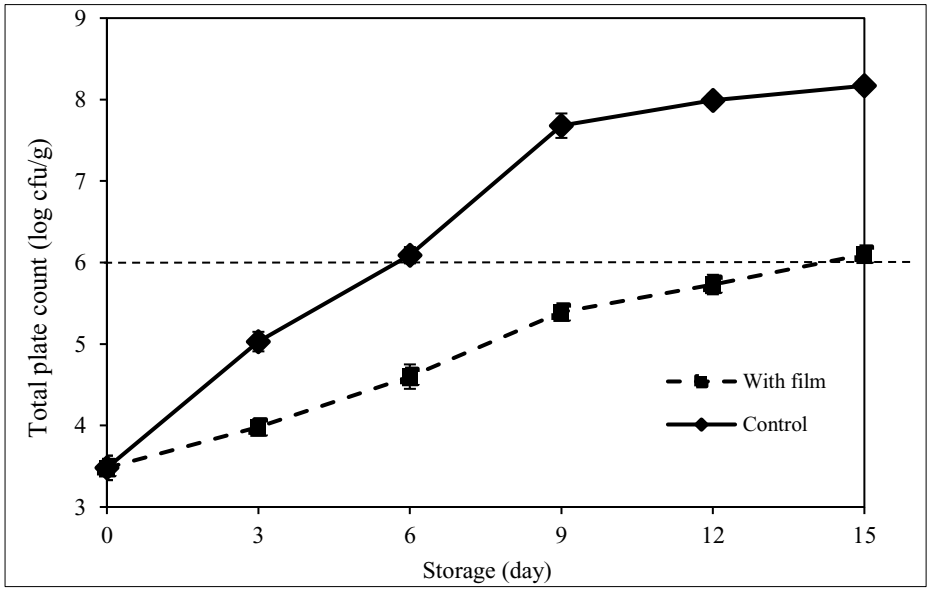


Figure 6. Changes in total plate count in log (CFU/mL) throughout the storage period

Conclusion

This study has demonstrated the incorporation of 1.5% (v/v) glycerol and 10 mM (w/v) NaCl into chitosan film incorporated with *Garcinia atroviridis* extract had the highest elongation at break and tensile strength that fulfilled the conventional standard. Therefore, glycerol and NaCl improved the mechanical properties of film. Storage tests showed that that the chicken meat wrapped with the film had a shelf life less than 14 days whereas the controls had a shelf life of 5 days. Additionally, the results from the storage test indicated that applying the film onto meat products such as chicken meat can extend its shelf life. Hence, edible films with better mechanical properties are able to extend shelf life of food products and were developed in this study.

Acknowledgement

This work was supported by UCSI University Pioneer Scientist Incentive Fund (Proj-In-FAS-056) from UCSI University and UCSI Fundamental Research Grant Scheme (FRGS/1/2020/STG01/UCSI/02/3) from the Ministry of Education Malaysia.

References

1. Voidarou, C., Vassos, D., Rozos, G., Alexopoulos, A., Plessas, S., Tsinas, A., Skoufou, M., Stavropoulou, E. and Bezirtzoglou, E. (2011). Microbial challenges of poultry meat production. *Anaerobe*, 17(6): 341-343.
2. Mihindukulasuriya, S. D. F. and Lim, L. T. (2014). Nanotechnology development in food packaging: A review. *Trends in Food Science & Technology*, 40(2): 149-167.
3. Lee, Y. Y., Yusof, Y. A. and Pui, L. P. (2020). Development of milk protein edible films incorporated with *Lactobacillus rhamnosus* GG. *BioResources*, 15(3): 6960-6973.
4. Kuan, Y. L., Sivanasvaran, S. N., Pui, L. P., Yusof, Y. A. and Senphan, T. (2020). Physicochemical properties of sodium alginate edible film incorporated with mulberry (*Morus australis*) leaf extract. *Pertanika Journal of Tropical Agricultural Science*, 43(3): 359-376.
5. Okcu, Z., Yavuz, Y. and Kerse, S. (2018). Edible film and coating in fruits and vegetables. *Alinteri Journal of Agriculture Sciences*, 33(2): 221–226.
6. Zaman, N. B. K., Lin, N. K. and Phing, P. L. (2018). Chitosan film incorporated with *Garcinia atroviridis* for the packaging of Indian mackerel (*Rastrelliger kanagurta*). *Ciência e Agrotecnologia*, 42(6): 666-675.
7. Ahmed, S., Ahmad, M. and Ikram, S. (2014). Chitosan: A natural antimicrobial agent-a review. *Journal of Applicable Chemistry*, 3(2): 493-503.
8. Tan, H., Ma, R., Lin, C., Liu, Z. and Tang, T. (2013). Quaternized chitosan as an antimicrobial agent: antimicrobial activity, mechanism of action and biomedical applications in orthopedics. *International Journal of Molecular Sciences*, 14(1): 1854-1869.
9. Kasai, D., Chougale, R., Masti, S., Chalannavar, R., Malabadi, R. B., Gani, R. and Gouripur, G. (2019). An investigation into the influence of filler *Piper nigrum* leaves extract on physicochemical and antimicrobial properties of chitosan/poly (vinyl alcohol) blend films. *Journal of Polymers and the Environment*, 27(3): 472-488.
10. Sogut, E. and Seydim, A. C. (2018). The effects of chitosan and grape seed extract-based edible films on the quality of vacuum packaged chicken breast fillets. *Food Packaging and Shelf Life*, 18: 13-20.
11. Khare, A. K., Abraham, R. J., Rao, V. A., Babu, R. N. and Ruban, W. (2017). Effect of chitosan and cinnamon oil edible coating on shelf life of chicken fillets under refrigeration conditions. *Indian Journal of Animal Research*, 51(3): 603-610.
12. Al-Mansoub, M. A., Asmawi, M. Z. and Murugaiyah, V. (2014). Effect of extraction solvents and plant parts used on the antihyperlipidemic and antioxidant effects of *Garcinia atroviridis*: A comparative study. *Journal of the Science of Food and Agriculture*, 94(8): 1552-1558.
13. Basri, D. F., Sharif, R., Morat, P. and Latip, J. (2005). Evaluation of antimicrobial activities of the crude extracts from *Garcinia atroviridis* and *Solanum torvum*. *Malaysian Journal of Science*, 24(1): 233-238.

14. Nordin, N., Othman, S. H., Rashid, S. A. and Basha, R. K. (2020). Effects of glycerol and thymol on physical, mechanical, and thermal properties of corn starch films. *Food Hydrocolloids*, 106: 105884-105892.
15. Tonny, W., Tuhin, M. O., Islam, R. and Khan, R. A. (2014). Fabrication and characterization of biodegradable packaging films using starch and chitosan: Effect of glycerol. *Journal of Chemical Engineering and Chemistry Research*, 1(5): 343-352.
16. Choi, W. S., Patel, D. and Han, J. H. (2016). Effects of pH and salts on physical and mechanical properties of pea starch films. *Journal of Food Science*, 81(7): 1716-1725.
17. Tan, Q., Kan, Y., Huang, H., Wu, W. and Lu, X. (2020). Probing the molecular interactions of chitosan films in acidic solutions with different salt ions. *Coatings*, 10(11): 1052-1066.
18. Chan, H. M., Nyam, K. L., Yusof, Y. A. and Pui, L. P. (2020). Investigations of properties of polysaccharide-based edible film incorporated with functional *Melastoma malabathricum* extract. *Carpathian Journal of Food Science & Technology*, 12(1): 120-133.
19. Lim, L.I., Tan, H.L. and Pui, L.P. (2021). Development and characterization of alginate-based edible film incorporated with hawthorn berry (*Crataegus pinnatifida*) extract. *Journal of Food Measurement and Characterization*, 15: 2540-2548.
20. Higueras, L., López-Carballo, G., Hernández-Muñoz, P., Gavara, R. and Rollini, M. (2013). Development of a novel antimicrobial film based on chitosan with LAE (ethyl-Nα-dodecanoyl-L-arginate) and its application to fresh chicken. *International Journal of Food Microbiology*, 165(3): 339-345.
21. Tantasuttikul, A., Kijroongrojana, K. and Benjakul, S. (2011). Quality indices of squid (*Photololigo duvaucelii*) and cuttlefish (*Sepia aculeata*) stored in ice. *Journal of Aquatic Food Product Technology*, 20 (2): 129-147.
22. Dehghani, S., Hosseini, S. V. and Regenstein, J. M. (2018). Edible films and coatings in seafood preservation: A review. *Food Chemistry*, 240: 505-513.
23. Rangel Marrón M, Montalvo Paquini C, Palou E. and Lopez Malo A. (2013). Optimization of the moisture content, thickness, water solubility and water vapor permeability of sodium alginate edible films. *Recent Advances in Chemical Engineering, Biochemistry and Computational Chemistry*, 72-78.
24. Arham, R., Salengke, S., Metusalach, M. and Mulyati, M. T. (2018). Optimization of agar and glycerol concentration in the manufacture of edible film. *International Food Research Journal,* 25(5): 1845-1851.
25. Singh, T. P., Chatli, M. K. and Sahoo, J. (2015). Development of chitosan based edible films: Process optimization using response surface methodology. *Journal of Food Science and Technology*, 52(5): 2530-2543.
26. Peng, Y., Wang, Q., Shi, J., Chen, Y. and Zhang, X. (2020). Optimization and release evaluation for tea polyphenols and chitosan composite films with regulation of glycerol and tween. *Food Science and Technology*, 40(1): 162-170.
27. Dick, M., Costa, T. M. H., Gomaa, A., Subirade, M., de Oliveira Rios, A. and Flôres, S. H. (2015). Edible film production from chia seed mucilage: Effect of glycerol concentration on its physicochemical and mechanical properties. *Carbohydrate Polymers*, 130: 198-205.
28. Cerqueira, M. A., Souza, B. W., Teixeira, J. A. and Vicente, A. A. (2012). Effect of glycerol and corn oil on physicochemical properties of polysaccharide films–A comparative study. *Food Hydrocolloids*, 27(1): 175-184.
29. Yang, M., Shi, J. and Xia, Y. (2018). Effect of SiO_2, PVA, and glycerol concentrations on chemical and mechanical properties of alginate-based films. *International Journal of Biological Macromolecules*, 107: 2686-2694.
30. Basiak, E., Lenart, A. and Debeaufort, F. (2018). How glycerol and water contents affect the structural and functional properties of starch-based edible films. *Polymers*, 10(4): 412-430.

31. Kang, H. J. and Min, S. C. (2010). Potato peel-based biopolymer film development using high-pressure homogenization, irradiation, and ultrasound. *LWT-Food Science and Technology*, 43(6): 903-909.
32. Arham, R., Mulyati, M. T., Metusalach, M. and Salengke, S. (2016). Physical and mechanical properties of agar based edible film with glycerol plasticizer. *International Food Research Journal*, 23(4): 1669-1675.
33. Adamu, A. D., Jikan, S. S., Talip, B. H. A., Badarulzaman, N. A. and Yahaya, S. (2017). Effect of glycerol on the properties of tapioca starch film. *Materials Science Forum*, 888: 239-243.
34. Leceta, I., Guerrero, P. and De La Caba, K. (2013). Functional properties of chitosan-based films. *Carbohydrate Polymers*, 93(1): 339-346.
35. Prateepchanachai, S., Thakhiew, W., Devahastin, S. and Soponronnarit, S. (2017). Mechanical properties improvement of chitosan films via the use of plasticizer, charge modifying agent and film solution homogenization. *Carbohydrate Polymers*, 174: 253-261.
36. Liu, H., Adhikari, R., Guo, Q. and Adhikari, B. (2013). Preparation and characterization of glycerol plasticized (high-amylose) starch–chitosan films. *Journal of Food Engineering*, 116(2): 588-597.
37. Aguirre, A., Borneo, R. and León, A. E. (2013). Properties of triticale protein films and their relation to plasticizing–antiplasticizing effects of glycerol and sorbitol. *Industrial Crops and Products*, 50: 297-303.
38. Souza, A. C., Benze, R. F. E. S., Ferrão, E. S., Ditchfield, C., Coelho, A. C. V. and Tadini, C. C. (2012). Cassava starch biodegradable films: Influence of glycerol and clay nanoparticles content on tensile and barrier properties and glass transition temperature. *LWT-Food Science and Technology*, 46(1): 110-117.
39. Kusumaningtyas, R. D., Putri, R. D., Badriah, N. and Faizah, F. E. (2018). Preparation and characterization of edible film from sorghum starch with glycerol and sorbitol as plasticizers. *Journal of Engineering Science and Technology*, 13: 47-55.
40. Zhang, X., Liu, J., Yong, H., Qin, Y., Liu, J. and Jin, C. (2020). Development of antioxidant and antimicrobial packaging films based on chitosan and mangosteen (*Garcinia mangostana* L.) rind powder. *International Journal of Biological Macromolecules,* 145: 1129-1139.
41. Radha krishnan, K., Babuskin, S., Azhagu Saravana Babu, P., Sasikala, M., Sabina, K., Archana, G., Sivarajan, M. and Sukumar, M. (2014). Antimicrobial and antioxidant effects of spice extracts on the shelf life extension of raw chicken meat. *International Journal of Food Microbiology*, 171: 32-40. Cortez-Vega, W. R., Pizato, S. and Prentice, C. (2012). Quality of raw chicken breast stored at 5C and packaged under different modified atmospheres. *Journal of Food Safety*, 32(3): 360-368.
42. Cortez-Vega, W. R., Pizato, S. and Prentice, C. (2012). Quality of raw chicken breast stored at 5C and packaged under different modified atmospheres. *Journal of Food Safety*, 32(3): 360-368.
43. Bazargani-Gilani, B., Aliakbarlu, J. and Tajik, H. (2015). Effect of pomegranate juice dipping and chitosan coating enriched with *Zataria multiflora* Boiss essential oil on the shelf-life of chicken meat during refrigerated storage. *Innovative Food Science & Emerging Technologies*, 29: 280-287.
44. Yasin, R., Samiullah, K., Fazal, R. M., Hussain, S., Mahboob, S., Al-Ghanim, K. A., Al-Misned, F. A. and Ahmed, Z. (2020). Combined effect of probiotics on prolonging the shelf life of GIFT tilapia fillets. *Aquaculture Research*, 51(12): 5151-5162. Venkatachalam, K. and Lekjing, S. (2020). A chitosan-based edible film with clove essential oil and nisin for improving the quality and shelf life of pork patties in cold storage. *RSC Advances*, 10(30): 17777-17786.
45. Venkatachalam, K. and Lekjing, S. (2020). A chitosan-based edible film with clove essential oil and nisin for improving the quality and shelf life of pork patties in cold storage. *RSC Advances*, 10(30): 17777-17786.

46. Remya, S., Mohan, C. O., Bindu, J., Sivaraman, G. K., Venkateshwarlu, G. and Ravishankar, C. N. (2016). Effect of chitosan based active packaging film on the keeping quality of chilled stored barracuda fish. *Journal of Food Science and Technology*, 53(1): 685-693.
47. Sanyang, M., Sapuan, S., Jawaid, M., Ishak, M. and Sahari, J. (2015). Effect of plasticizer type and concentration on tensile, thermal and barrier properties of biodegradable films based on sugar palm (*Arenga pinnata*) starch. *Polymers*, 7(6): 1106-1124.
48. Prateepchanachai, S., Thakhiew, W., Devahastin, S. and Soponronnarit, S. (2017). Mechanical properties improvement of chitosan films via the use of plasticizer, charge modifying agent and film solution homogenization. *Carbohydrate Polymers*, 174: 253-261.

Malaysian Journal of Analytical Sciences (MJAS)
Published by Malaysian Analytical Sciences Society

RECENT ADVANCES IN AGRICULTURAL WASTE-BASED ADSORBENTS FOR THE REMOVAL OF POLLUTANTS IN WATER (2017-2020)

(Kemajuan Terkini dalam Penjerap Berasaskan Sisa Pertanian untuk Penyingkiran Bahan Pencemar dalam Air (2017-2020))

Lim Yen Yee[1], Norsahirutiara Mohd Asrul[1], Fatin Farhanim Kamarulzaman[1], Timothy Gandu Ali[1], Nur Shahz Ereena Zulkifli[1], Amirah Farhan Kamaruddin[1,2,3], Nursyafreena Attan[1], Mohamad Afiq Mohamed Huri[1], Aemi Syazwani Abdul Keyon[1,4]*

[1]Department of Chemistry, Faculty of Science,
Universiti Teknologi Malaysia, 81310 UTM, Johor Bahru, Johor, Malaysia
[2]Department of Materials,
University of Manchester, Sackville Street Building, Manchester, M1 3BB
[3]Manchester Institute of Biotechnology,
University of Manchester, 131 Princess Street, Manchester, M1 7DN
[4]Centre for Sustainable Nanomaterials, Ibnu Sina Institute for Scientific and Industrial Research,
Universiti Teknologi Malaysia, 81310 UTM, Johor Bahru, Johor, Malaysia

**Corresponding author: aemi@utm.my*

Received: 11 March 2021; Accepted: 31 May 2021; Published: xx June 2021

Abstract

Rapid human activities result in the increasing production of pollutants from both industrial processes and agricultural practices, which negatively impact the environment and human health. Most of chemical pollutants are discharged either intentionally or accidentally via water bodies. Therefore, various pollutants removal techniques have been developed including utilization of agricultural waste as adsorbents. Agricultural waste-based adsorbents are easily prepared, cheap and moderately to highly efficient. A good understanding of agricultural waste-based adsorbents would be beneficial for future research improvements as well as industrial applications. Thus, this review aims at shedding light on recent advancements (from year 2017-2020) in the preparation, characterizations and application of agricultural waste-based adsorbents for removal of different types of chemical pollutants in water and wastewater.

Keywords: agriculture waste, adsorbent, pollutants removal, water, wastewater

Abstrak

Kegiatan manusia yang giat mengakibatkan peningkatan penghasilan bahan pencemar dari kedua-dua proses industri dan amalan pertanian yang memberi kesan negatif terhadap alam sekitar dan kesihatan manusia. Kebanyakan bahan pencemar kimia disingkir secara sengaja atau tidak sengaja melalui takungan air. Oleh itu, pelbagai teknik penyingkiran bahan pencemar telah dikembangkan termasuk penggunaan sisa pertanian sebagai penjerap. Penjerap berasaskan sisa pertanian mudah disediakan, murah dan daripada sederhana hingga sangat cekap. Pemahaman yang baik tentang bahan penjerap berasaskan sisa pertanian akan bermanfaat untuk peningkatan penyelidikan masa hadapan dan juga aplikasi industri. Oleh itu, tinjauan ini bertujuan untuk menjelaskan kemajuan

terkini (dari tahun 2017-2020) dalam penyediaan, pencirian dan penggunaan penjerap berasaskan sisa pertanian untuk penyingkiran pelbagai jenis bahan pencemar kimia di dalam air dan air sisa.

Kata kunci: sisa pertanian, penjerap, penyingkiran bahan pencemar, air, air sisa

Introduction

Several of the most relevant categories of environmental pollutants are the one caused by heavy metals, pesticides, herbicides, dyes and phenolic compounds, which are present in large amount in wastewater from various industry activities. The release of these pollutants into water bodies is alarmingly causing severe effects to the environment and human health, whereby the latter happens due to the accumulation since they are non-biodegradable [1]. World Health Organization (WHO) has set a standard of 10 μg/L of arsenic (As) content in drinking water for the public safe consumption worldwide [2]. Human will suffer in skin lesions and skin coloration upon contact, while prolonged consumption of high level as drinking water may cause skin cancer [3]. The maximum allowable level of copper (Cu) and nickel (Ni) in drinking water set by WHO are 2.0 [4] and 0.07 mg/L [5], respectively. Paulino *et al.* [6] reported that high level of ingested Cu may cause vomiting, cramps and even death. Ni accumulated in human body can decrease the level of red blood cells, leading to the dysfunction of immune and cardiovascular systems. Human are at risk to suffer osteoporosis and kidney failure if ingestion of cadmium (Cd) is above 3 μg/L as stated by WHO [7]. Furthermore, lead (Pb) level above permissible level of 10 μg/L also affect in neurological system, kidney function and synthesis of red blood cells [8]. In addition, significant impairment of intellectual ability is reported to be the consequence of even low level of Pb concentration in children's blood [9]. Removal can be done by chemical precipitation and physical treatments (i.e., ion exchange, solvent extraction and reverse osmosis) from water and wastewater. However, these methods provide some disadvantages due to incomplete removal, low selectivity, high costs, and large amount of waste [10]. Among these techniques, adsorption is thought to be the most promising because of its high efficiency, simplicity, relatively low quantities of residue, and ability to isolate a wide variety of chemical compounds. Moreover, this is the most widely used technique for removing organic and inorganic pollutants from aqueous solutions [11].

Dye production industry and other industries (e.g. printing, paper and textile, cosmetics and pharmaceuticals, and food industries) that involve dyes and pigments in their processes generate large amount of waste water [12]. Every year, there are about 10,000 types of dyes and over $7x10^5$ tonnes of dyes are produced around the world [13]. Due to this variation, dyes wastewater is difficult to be treated. Dyes are stable and resistant towards heat, light, oxidizing agent and aerobic digestion [14]. They can absorb sunlight and cause intensity of sunlight in water bodies to decrease, thus reducing photosynthesis and concentration of dissolved oxygen. Consequently, level of chemical oxygen demand (COD) increases [14]. Dyes can cause irritation to the skin and respiratory tract [15]. For example, malachite green (MG) and leucomalachite green, that present in tissues of treated fish can cause severe effect to human consuming the fish due to genotoxity and carcinogenicity of dyes. However, cheaper cost, availability and its effectiveness cause the usage of these dyes still continue [16].

Phenolic compounds are another type of pollutants released into water bodies from various industries such as petroleum refineries, coal, production of dye, pharmaceuticals, pesticides and others [17]. Some examples of phenolic compounds are phenol, chlorophenol, catechol and chlorocatechols, nitrophenols, methylphenols, alkylphenols, bisphenols and aminophenols. On top of that, the production and decomposition (e.g., photo-oxidation, leaching, comminution and mineralization) [18] of organic matters (e.g., dead plants and animals) also lead to the formation of phenols in ecosystem [19]. Radical reaction which can damage cell membrane takes place easily with donation of free electrons from phenols. For example, 2,4,6-trichlorophenol (2,4,6-TCP), a yellow colour and sweet smell phenolic pollutant that is listed

in Group B2 by Environmental Protection Agency (EPA) [20] is probable to bring carcinogenicity effect to human and animals. Its usage and production are already banned in the United States of America. 2,4,6-TCP is difficult to be removed due to its stable structure. Therefore, removal of phenolic compounds prior discharge to water bodies is pertinent.

Conventional pesticides can be divided into six types which are insecticides, herbicides, rodenticides, bactericides, fungicides and larvicides [21]. Pesticides can be classified by components of active ingredients, for examples organochlorines, carbamates, organophosphorus pyrethrin and pyrethroids [22]. They can be categorized as extremely hazardous, highly hazardous, moderately hazardous, slightly hazardous and acute hazard [23]. Pesticides make a great contribution in production and growing of crops by controlling the pest. However, high toxicity of pesticides brings negative effect to human health. Moreover, pesticides are difficult to be treated using biological treatment due to their non-biodegradable properties and abundancy [24]. Improper usage of pesticides causes residual effect in food chain, pollution and eventually affect the ecosystem. Prolonged exposure of pesticides in environment through ingestion, inhalation and skin contact increase the risk of cancer, severe renal failure, serious effect to immune system, reproductive system, nervous system, endocrine system and behavioural disorder [25]. Therefore, removing them from industrial effluents has become a big environmental concern in recent years. There are some conventional methods being used to remove these pollutants, however they may have come with several significant limitations. For example, coagulation and flocculation which are usually used to treat high concentration of phenol in wastewater have issue with large amount of sludge disposal [26]. Biological treatment is both environmentally friendly and energy saving but it cannot treat phenol effluents with high concentrations. Hence, chemical oxidation can usually be used for most of the time. [27]. In the case of pesticides, ozonation [28], photocatalytic degradation [29], advanced oxidation processes [30], nanofiltration and photo-Fenton oxidation [24] are all commonly used methods. Although some of these methods shown to be effective, some of them suffered some drawbacks and limitations such as using excess amount of chemical solvent, having high operating costs, and producing a lot of sludge, which has serious disposal issue [31].

Adsorbents made from agricultural waste, or usually called as biosorbents are reported able to reduce the disposal amount, avoid on-site burning and save disposal cost. They are low-cost, high-efficient, environmentally friendly and becoming increasingly important in the removal of pollutants mentioned above as an alternative to conventional methods. It manipulates biomass's natural ability to immobilise dissolved elements on its surface. Thus, discovering efficient adsorbents made from waste biomass is of great interest. Waste produced from different agricultural operations may consist constituents of lignin, cellulose, hemicellulose, extractives, lipids, proteins, sugars, water and different functional groups. Carboxyl, amine and hydroxyl group are ionizable functional group that build up potential binding sites for adsorption [32]. Several researchers modified adsorbent materials by functionalizing them with other chemical and substances to enhance their capacity to adsorb pollutants. The adsorption of pollutants by these low-cost adsorbents were usually evaluated under various conditions such as pH, pollutants' concentration, contact time, mixing speed and adsorbent dose through kinetic and/or isotherm studies. The optimum removal condition was also identified for each metal ion. This review paper highlights the recent advancements (from year 2017-2020) in the preparation, characterizations and application of agricultural waste-based adsorbents for removal of different types of chemical pollutants in water and wastewater. Removal characteristics of heavy metals, dyes, pesticide, herbicides and phenolic compounds in water or wastewater using coir pith ash, carnauba straw powder, banana peels, tea and coffee ground waste, coconut shell, rice straw, pine bark powder and etc were reviewed. Where available, information was given about their adsorption capacity, isotherm and/or kinetic model and adsorption mechanism. Table 1 represents all adsorption parameters of different agricultural waste-based adsorbent for the adsorption of different classes of pollutants; pertinent methods are detailed in the next sections.

Table 1. Adsorption parameters of different agriculture waste for the adsorption of different classes of pollutants in water

No.	Agriculture Waste	Pollutant	Contact Time	Adsorbent Dosage	Adsorption Capacity	Isotherm Model and/or Kinetic Model	Ref.
1	Coir pith ash	As	60 min	5 g/L	36.5 mg/g	Langmuir isotherm model	[33]
2	Natural pine sawdust	Cu, Pb	5 min	10 g/L	9.59 mg/g	Freundlich isotherm model	[34]
3	Carnauba straw powder	Cu	5 min	10 g/L	9.5 mg/g	Langmuir isotherm model	[35]
4	Rice husk	Pb, Crystal violet	90 min	0.1 g/20mL	93.5 mg/g	Langmuir isotherm model and Lagergren pseudo-second order kinetic model	[36]
5	Fern plant-cyclosorus interruptus	Pb	12 h	30 mg	133 mg/g	Langmuir isotherm model and pseudo-second order kinetic model	[37]
6	Pulp lignin	Cr(III)	30 min	0.2 g	44.5 mg/g	Langmuir and Dubinin-Radushkevich isotherm models, pseudo-first and second order kinetic models	[38]
7	Tea waste	As, Cr	1 h	NA	21.2-38 mg/g	Langmuir Isotherm model	[39]
8	Coffee ground powder	Rhodamine dyes	3 h	50 mg/50mL	5.26-17.4 mmol/g	Langmuir isotherm model	[40]
9	Wood apple shell	MG dye	3.30 h	0.4 g	80.7 mg/g	Langmuir isotherm model	[41]
10	Coffee waste	MCPA	5 min	0.825 g/L	340 mg/g	Langmuir isotherm model	[42]

Table 1 (cont'd). Adsorption parameters of different agriculture waste for the adsorption of different classes of pollutants in water

No.	Agriculture Waste	Pollutant	Contact Time	Adsorbent Dosage	Adsorption Capacity	Isotherm Model and/or Kinetic Model	Ref.
11	Switchgrass	Phenoxy herbicides	6 h	1 -2 g/L	50-134 mg/g	Freundlich or Redlich-Peterson isotherm model	[43]
12	Pine bark powder	2,4,6-TCP	120 min	0.4 g	88 mg/g	Langmuir isotherm model	[44]
13	Pinecone powder	Phenol, 2-CP, 4-CP	60 min	0.6 g/0.1 L	165 - 220 mg/g	Langmuir isotherm model	[45]
14	Coconut shell	Phenol	120 min	100 g (fluidized-bed reactor)	58.1 -415 mg/g	Langmuir, Freundlich and Redlich Peterson isotherm models	[26, 46]
15	Coconut spathe	Phenol, 2-CP, 4-CP	15 min	100 mg/L	120-275 mg/g	Langmuir isotherm model	[47]
16	Avocado seed	15 phenolic compounds	120 min	1.5 g/L	99.5- 327 mg/g	NA	[31, 48]
17	Tucuma seed	2-nitrophenol	30 min	1.5 g/L	1382 mg/g	Liu isotherm model and general order kinetic model	[49]
18	Rice straw	Phenol	24 h	2.5 g	5.78 mg/g (Langmuir)	Freundlich and Langmuir isotherm models	[50]
19	Rice husk	Cd	60 min	0.5 g/L	139 mg/g	NA	[51]
20	Corn cob	Cr(III) and Cr(VI)	120 min	0.1 g	277 mg/g	Langmuir isotherm model and the pseudo-second order model	[52]
21	Corn	Phosphate and Cd	75 min	0.1 g	57.5 mg/g	Langmuir isotherm model and pseudo-first-order kinetic model	[53]
22	Banana peel	MB dye	150 min	0.05 g	222 mg/g	Pseudo-second kinetic order	[54]

Table 1 (cont'd). Adsorption parameters of different agriculture waste for the adsorption of different classes of pollutants in water

No.	Agriculture Waste	Pollutant	Contact Time	Adsorbent Dosage	Adsorption Capacity	Isotherm Model and/or Kinetic Model	Ref.
23	Indian almond shell, ground nutshell, areca nutshell, tamarind shell, cashew nutshell	Azure A dye	30 min	2.0 g/L	21.9 -834 g/g (based on Langmuir)	Freundlich, Langmuir, Temkin, Redlich–Peterson and Dubinin–Radushkevich isotherm models.	[55]
24	Black and green olive stones	MB dye	24 h	0.05 g	714 and 769 mg/g	Freundlich isotherm model	[56]
25	Barley and wheat	Ni	65 min	0.01 g	303 mg/g	Freundlich isotherm model and pseudo-first-order kinetic model	[57]
26	Alfalfa hays	Tetracycline	1818 min (fixed bed)	1 g	302 mg/g	Elovich and Freundlich isotherm models	[58]
27	Grape stalk	Basic Blue 41 dye	NA	0.5-5.0 g/L	205 mg/g	Pseudo-second order kinetic model	[59]

Abbreviations:

2-CP	2-chlorophenol	MG	Malachite green
4-CP	4-chlorophenol	MPC	Magnetic porous carbonaceous
As	Arsenic	Ni	Nickel
Cd	Cadmium	NPs	Nanoparticles
CGP	Coffee ground waste	NA	Not available
Co	Cobalt	Pb	Lead
CSAC	Coconut shell activated carbon	PBP	Pine bark powder
Cu	Copper	PCP	Pinecone powder
Fe	Iron	Rh6G	Rhodamine 6G
Hg	Mercury	RhB	Rhodamine B
MB	Methylene blue	Zn	Zinc

Advances on the adsorbents for the removal of toxic heavy metals

The adsorption of heavy metals by low-cost agricultural waste materials has attracted much attention since the 1980s [60-64]. Because heavy metals are positively charge in nature, removal studies would require deep investigation of adsorbents' functional groups and physical properties to understand the mechanism for efficient adsorption. It was found that coir pith ash [33], pine sawdust [34], carnauba straw powder [35], rice husk [36], banana peel [65], corn [53] and fern plant[37] were utilized for the past four years. A heat-treated natural coir pith ash (CPA) was prepared by Bahar et al. [33] as biosorbent to remove As ions in contaminated water. As(III) was oxidised to As(V) in order to remove it from water. The characterization of the biosorbent showed the presence of S-H and C=O functional groups in CPA that aid in the adsorption of As(V) onto the surface of the adsorbent for effective removal. The conditions obtained via batch sorption reported that the adsorption of As(V) could be done in a wide pH range (pH 2–12) and the best adsorbent dose was 5 g/L. The data fitted Langmuir isotherm with maximum adsorption capacity As of 36.5 mg/g at 25°C. In addition, the mean free energy obtained from Dubinin–Radushkevich (D–R) isotherm was 8.64 kJ/mol, showing that the adsorption of As(V) was based on ion-exchange mechanism. On top of that, the studies of desorption and recovery of As(V) proved that hydrochloric acid could be used as a solvent to replace toxic As(V) ions from the biosorbent for full recovery of As(V), and sodium hydroxide for the regeneration of CPA. These findings show that the alkaline-in-nature CPA biosorbent has great potential for removing As(V) from contaminated water, particularly acidic wastewater. Semerjian et al. [34] directly utilized natural pine sawdust as a biosorbent to remove Pb and Cu in water. The biosorbent was only sifted, washed and dried, and did not undergo any chemical pre-treatment to maintain its status as green biosorbent. The removal of metal ions was based on the presence of polyphenolic groups of various organic compounds (i.e., lignin, cellulose, and hemicellulose) within the pine sawdust. The factors influencing the metals adsorption were studied through batch sorption experiments to obtain the highest removal efficiency. From the result, optimum pH levels for Cu and Pb removal were 7 and 5, respectively with the adsorbent concentration of 10 g/L and contact times of 5 min for both Cu and Pb using initial concentration of 1 mg/L [34]. The adsorption capacity was 9.59 mg/g. Equilibrium adsorption for Cu fitted with Freundlich isotherm, while Pb data fitted equally both Freundlich and generalized isotherm models. The adsorption kinetics were best described by the pseudo second-order model. They implied that removal involved valance forces through sharing or exchange of electrons between pine sawdust and metals. The author reported that the equilibrium adsorption capacity of sawdust improved at higher temperature (~60 °C) and the adsorption was an endothermic chemical process (as proven by positive values of standard entropy of adsorption ($\Delta S°$)). Similarly, Ferreira *et al.* [35] explored the potential of carnauba straw powder (CSP) as adsorbent to remove Cu in water. CSP possessed lignocellulosic components consisted of functional groups available for adsorption site for Cu. The adsorption of Cu was maximised at pH 6 due to the increase of negatively charged surface of CSP functional groups resulting in better sorption of metal ions via electrostatic attraction of cation and anion binding sites. At optimum conditions (adsorbent dosage of 10 g/L, removal at pH 6 at 50 °C for 1 hour), the efficiency of Cu adsorbed was reported to improve with the decrease of granule size of biosorbent. The smaller the size, the higher the surface area for the sorption of Cu onto the CSP surface. The obtained adsorption capacity was 9.5 mg/g at 50 °C, where it fitted both the pseudo-second order and Langmuir adsorption models [35]. As compared to pine sawdust biosorbent developed by Semerjian [34], the carnauba-based biosorbent was comparable in removing Cu as both adsorption capacity was ~ 10 mg/g. However, both adsorbents were not yet tested with real wastewater, therefore further studies are required.

Masoumi and co-workers [36] developed a nanoparticle adsorbent based on the modification of rice husk and a copolymer to remove Pb from water. The mechanical and physical properties of the adsorbent were improved through the addition of poly-methylmetacrylate and

poly-maleic anhydride. On top of that, the interaction between tartaric acid and rice husk enhanced the binding capacity of metal. The removal efficiency of Pb could be as high as 98% when using the modified nanoparticles rice husk as compared to the untreated rice husk and copolymer individually. This might be due to the presence of various chelating sites of carboxylic acid and amine from the backbone of the synthesised polymer resulting in more adsorption mechanism of metal ions on the surface of adsorbent. The maximum sorption capacity of Pb was 93.5 mg/g that fitted the Langmuir isotherm. Based on the kinetic data, the increase of temperature enhanced the adsorption of Pb as the values of ΔG, ΔH and ΔS favoured to be spontaneous, more disorder and endothermic physical adsorption. Mahindrakar et al. [65] explored the potential of banana peels waste for removal of strontium, Sr(II) from water. The presence of anionic groups of hydroxyl, carbonyl and carboxyl in the adsorbent were responsible to bind with the cationic metal of interest. The optimum pH was at pH 7, giving more adsorption sites on the surface of adsorbent for the binding Sr(II). Within 10 min of contact time, the adsorbent achieved 99% removal of Sr(II). The maximum adsorption of Sr(II) was 41.5 mg/g, which fitted with the pseudo-second order model. The authors found out that the adsorbent could be reused up to 5 cycles and still maintained the 90% range removal. In 2020, Faheem et al. [53] developed a corn-based multifunctional biochar adsorbent to remove phosphate and Cd in wastewater in a two-stage adsorption set-up. They successfully grafted and introduced multiple functionalities with both amino and carboxylic functional groups on biochar surface after chemical modification route was applied. The uptake capacity of phosphate was 57.50 mg/g P g in acidic conditions. Then, as-obtained multifunctional biochar loaded with phosphate could adsorb Cd ion up to 61.4 mg/g when it was further applied for second-stage adsorption. Both residual carboxylic group and phosphate loaded on the biochar surface were responsible for Cd^{2+} sorption. The synergistic effects between phosphate and Cd^{2+} ions helped phosphate removal up to 95% in the presence of Cd^{2+}. Both Langmuir and Freundlich models were implemented, however Langmuir isotherm fitted data the best (R^2 >0.992).

Magnetic-based adsorbent was one of the current trendy techniques in removing heavy metal efficiently in aqueous media. Zhou et al. [37] reported a fast removal of Pb in water using magnetic multi-porous biosorbent after modification with amino siloxane. A comparison of this magnetic adsorbent was also reported for its capability to adsorb other metals, i.e. Zn, Ni and cobalt (Co). The adsorbent was prepared from a fern plant-cyclosorus interruptus (CI) which has an abundant amount of porous structure with crinkled morphology and then assimilated with Fe_3O_4 nanoparticles. The uppermost part of activated cyclosorus (ACI) was coated with a layer of 3-aminopropyltriethoxysilane (AS). The highest Pb adsorbed was 133.3 mg/g using AS-ACI-2.0 (2 g of ACI) based on Langmuir isotherm model at 323K which showed a favourable and feasible adsorption process (separation factor, R_L was 0.02-0.10). Furthermore, the Pb adsorption kinetics followed a pseudo-second-order model ($R^2 \geq 0.995$) and Pb was adsorbed onto this bio-based magnetic adsorbent through both chemical (chelation) and physical adsorption (from the multi-porous structure and puckered morphology) (E_a was 23.9 kJ/mol). Pb showed the greatest adsorption capacity as the adsorbent portrayed higher selectivity towards Pb. This might be due to the nitrogen atoms present on the adsorbent that able to bind with Pb in water. Based on Pearson acid-base theory, the interaction of Pb with amine and hydroxyl groups on the adsorbent had precedence over other metals. The adsorbent was reusable up to five cycles, keeping >90% of the original adsorption capacity. In 2019, Dai et al. [38] prepared a magnetic alkaline lignin−dopamine nanoparticle adsorbent. Alkaline lignin was a type of waste from pulping and bio-energy industry. It was functionalized by the conjugation with dopamine molecules and nano-precipitation method to make a candidate adsorbent for removal of Cr(III) from wastewaters. Furthermore, this magnetic adsorbent possessed sensitive magnetic responsiveness up to 24.6 emu/g, which is beneficial for magnetic recovery (>90% recycled within 2 min), and reusability for subsequent adsorption–desorption cycles. The maximum adsorptive capability of the adsorbent was 44.6 mg/g, thanks for the three-dimensional network and catechol structure of lignin and dopamine within the adsorbent. The sorption isotherms suited

Langmuir and Dubinin-Radushkevich models. The initial (<0.5 h) and the following stages (> 0.5 h) of Cr(III) adsorption onto the adsorbent followed pseudo-first ($R^2 = 0.9995$) and second order kinetic model ($R^2 = 0.9996$), respectively.

Advances on the adsorbents for the removal of dyes

Dye pollution is one of the major concerns in environmental problems. Hence, high quality wastewater treatment towards these toxic and carcinogenic dyes is necessary before they are discharged into water bodies. Water quality criteria used to evaluate quality of dye-related effluent are pH 5.5-9.0, BOD level below 50 mg/L and COD level below 100 mg/L [66]. It was found that tea waste [39], coffee waste [40], wood apple waste [41, 67] were utilized as adsorbents for the past four years. Tea production in China produced large amount of tea wastes annually. Thus, tea wastes were usually chosen as raw materials for synthesizing magnetic porous carbonaceous (MPC). Wen et al. [39] synthesized MPC (MPC-300, MPC-400, MPC-500) material using tea waste for the removal of dyes and other contaminants (i.e. arsenic (As), chromium (Cr) and humic acid). Thermal pyrolysis of $FeCl_3$ in treated tea waste caused embedding of nanosized γ-Fe_2O_3 nanoparticles (NPs) into porous structures. Chemical composition in tea waste prevented agglomeration of γ-Fe_2O_3 NPs and promoted the growth of γ-Fe_2O_3. BET surface area for MPC underwent pyrolysis at 300°C was 63 m^2/g, which was higher than MPC pyrolyzed at 400 °C (34 m^2/g) and 500 °C (31 m^2/g). Adsorption capacities of MPC-300 towards methyl orange, methylene blue (MB) and rhodamine B (RhB) were 73.12 mg/g, 45.74 mg/g and 31.94 mg/g, respectively. MPC-300 had better adsorption ability towards MO as compared to MB and RhB because the anionic MO had strong electrostatic attraction towards positive charge of γ-Fe_2O_3 surface.

Coffee ground waste has been used for environmental remediation, adsorption of toxic pollutants from aqueous and gas phase and removal of salt from effluents [68]. World annual coffee manufacture is projected to be 165 million bags (60 kg bag) in 2020 [69]. Thus, wide application and high abundant coffee ground are gaining popularity to be utilized as raw material for adsorbents synthesis. Shen and Ghondal [40] reported that non-modified coffee ground powder (CGP) could remove rhodamine dyes (RhB and Rhodamine 6G (Rh6G)) from wastewater. Acidic condition was more favourable for the adsorption process as compared to alkaline condition [40]. Positive surface charge of CGP existed with any pH <3.5. Thus, pH played an important role on degree of ionization of dye molecule. Rh6G and RhB experienced highest adsorption under acidic condition at pH 2, resulting to adsorption capacity of 25.1 and 7.18 μmol/g, respectively. These two cationic dyes exhibit electrostatic interaction with the negatively charged CGP surface. However, Rh6G showed a higher adsorption capacity compared to RhB. The presence of ester group in Rh6G might be responsible in the uptake on the CGP surface. Meanwhile, RhB comprised carboxylate ion, which could attribute to the repulsion forces between RhB and the negatively charged CGP surface. On the other hand, under alkaline condition of pH 10, Rh 6G and Rh B achieved adsorption capacities of 9.1 and 1.7 μmol/g only. The adsorption process was reversible for both dyes and this was proven through positive value of ΔS^o. Adsorption process for RhB and Rh6G were non-spontaneous and spontaneous, respectively (based on standard Gibbs energy of adsorption (ΔG^o)).

Wood apple (*Feronia acidissima*) commonly found in India, Sri Lanka, and Pakistan contains functional group of alcoholic, carboxylic and ether [67]. Bark, leaves and fruits of wood apple have been reported to be used as medicinal biosource. However, disposal of plenty of shells as agricultural waste may lead to environmental pollution because the decomposition of shell waste can produce various unwanted chemical compounds and microorganism [70]. Sartape et al.[41] prepared adsorbent from wood apple shell to remove MG dye. They reported that adsorbent's surface and MG dye (pKa 10.3) experienced positive charge under acidic condition. Consequently, electrostatic repulsion formed between the surface of wood apple shell and MG dye, thus weakened the adsorption of MG towards wood apple shell. Alternatively, removal conducted under alkaline condition (pH 10-12) resulted in the

accumulation of OH- ion at adsorbent surface, forming negative layer. Adsorption capacity was strengthened due to electrostatic attraction between surface and cationic MG [41, 71]. They reported that 98.9% of MG dye removal was achieved with initial dye concentration 100 mg/L at pH 7-9 shaking with 150 rpm for 3.30 h at room temperature. Increasing initial dye concentration from 100 to 700 mg/L led to a better adsorption with the evidence of adsorption capacity increased from 12.35 to 80.645 mg/g. Higher MG concentration provided a driving force of mass transport and hence strengthened the interaction between adsorbates and adsorbent. They reported maximum adsorption capacity of 80.645 mg/g with Langmuir isotherm model.

Advances on the adsorbents for the removal of pesticides/herbicides

The presence of pesticides in water bodies has increased considerably for the past few years, therefore, it was important to develop methods in order to minimize and prevent pollution of water bodies due to leaching of pesticides [72]. There are several techniques developed to remove pesticides in water including adsorption [72], ozonation [73], hydrostatic pressure [74] and ultrasonic treatment [75]. The phenomenon of adsorption was where the molecules of pesticides attracted to the surface of a solid and linked together by physical or chemical bonds. Adsorption used low cost agricultural waste has been explored because of eco-friendly nature, cost effectiveness, easy operation and integration opportunity with the present system of water treatment [76]. From the survey of literatures, coffee waste [42] and switchgrass [43] were utilized as adsorbents for the past four years. Coffee waste-based adsorbent was investigated by Al Zaben et al. [42] to remove 4-chloro-2-methyl phenoxy acetic acid (MCPA) pesticide in aqueous solution. The adsorbent was prepared only by washing and boiling coffee waste to eliminate chemicals adherences like acid and metal ions. The synthesized adsorbent was known to have equal size and shape for the nanoparticles' distribution, which was proved by the dynamic light scattering measurement and transmission electron microscopy. Based on zeta potential analysis, the biosorbent showed negatively charged particles due to the presence of carboxylate and hydroxylate anions. These anions were responsible to provide binding sites for the adsorption of MPCA onto the surface of the biosorbent. The author reported that there was no significant change on the adsorption capacity of MCPA with the change of pH since the coffee waste charge was pH independent.

In addition, kinetic study conducted showed a rapid adsorption in the first few minutes (5 min), then decreased gradually due to the lesser adsorption sites available. The maximum adsorption recorded was 340 mg/g that fits Langmuir isotherm. The authors suggested that the coffee waste biosorbent was a great alternative to remove MCPA in wastewater [42]. Next, an agricultural waste based on switchgrass was prepared by Essandoh et al. [43] by fast pyrolysis to remove phenoxy herbicides in aqueous solutions. They aimed to remove MCPA and 2,4-dichlorophenoxyacetic acid (2,4-D) due to the highest usage and their significant detrimental effect towards environment. Switchgrass possessed 3-D swollen solid structure after heating at high temperature, exposing more adsorption sites throughout the biochar to adsorb MCPA and 2,4-D effectively. In addition, the silica content in switchgrass improved the biochar surface with Si-OH groups, resulting the adsorbent to be hydrophilic in nature. The hydrophilicity of the surface was able to adsorb analytes of interest and ease water diffusion within the solid structure of biochar. Low pH of solution increased electrostatic attraction for the adsorption to occur due to the presence of hydrogen bonding from carboxylic acid group of the biochar. The maximum adsorption for MCPA and 2,4-D were 50 mg/g and 134 mg/g, respectively. Despite the low surface area (1.1 m^2/g) portrayed by the synthesized biochar based on BET analysis, both analytes still adsorb effectively over a wide pH range (pH 2-10) [43].

Advances on the adsorbents for the removal of phenolic compounds

Trend is showing researchers utilizing agricultural wastes to synthesize adsorbents for removal of phenolic contaminants. Examples of wastes used were pine bark powder [44], coconut shell [26, 46], pine cone biomass [45], coconut spathe [47], avocado seed [31], tucuma seed [31] and rice straw [50]. Unmodified adsorbent is the easiest to prepare as not many chemicals are needed. While for activated carbon, chemical, physical

activation or pyrolysis are involved. This is reflected by studies by Siva Kumar *et al.* [44, 45]. They utilized both unmodified and chemical modification routes to prepare their adsorbents. Only used distilled water to wash dirt and impurities on pine bark and pine cone, followed by drying process for 48 h. Samples were grounded to obtain fine powder with particle size varied from 55 to 75 µm for pine bark power (PBP) and 53 to 74 µm for pine cone powder (PCP). PCP was placed in desiccator before used while PBP was soaked in 0.1 M NaOH and followed by 0.1 M H_2SO_4 to remove lignin compound. After that, PBP was washed and dried. Siva Kumar et al. [44] synthesized pine bark powder (PBP) to remove 2,4,6-trichlorophenol (2,4,6-TCP) from aqueous media. After washing, drying and grinding to the size of 55 to 75 µm, PBP was soaked in 0.1 M NaOH and followed by 0.1 M H_2SO_4 to remove lignin compound. After that, PBP was washed and dried. The PBP had maximum adsorption of 289.09 mg/g, which was as predicted by using Langmuir isotherm model and could achieve 97% of removal percentage. BET surface area for PBP was only 0.1 m^2/g. Adsorption capacity of 88 mg/g could be achieved at pH 6. 2,4,6-TCP was a weak acid with pKa value of 6.23. Acidic pH favoured for adsorption process as protonated form of chlorophenols were easier to be adsorb. However, electrostatic repulsion existed between negatively charge adsorbent surface and chlorophenolate anions at pH greater than 6. Percentage removal increased from 45% to 97% with increment of adsorbent dosage from 0.05 to 0.40 g but no further increment with higher adsorbent dosage. Biosorption capacity was improved from 50 to 325 mg/g with increased of initial adsorbate concentration from 100 ppm to 400 ppm. Optimum conditions to remove 2,4,6-TCP were pH 6, 0.4 g of PBP, and 120 minutes contact time [44]. Pine cone powder (PCP) produced by the same group [45] was used to remove phenol, 2-chlorophenol (2-CP) and 4-chlorophenol (4-CP). They only used distilled water to wash dirt and impurities on pine cone, followed by drying process for 48 h. Samples were grinded to obtain fine powder with particle size varied from 53 to 74 µm. BET surface area for PCP was 7.1 m^2/g. Phenol, 2-CP and 4-CP had pKa values of 9.9, 8.8, and 9.2, respectively. These compounds existed as phenolate anions under alkaline condition and predominant as molecular form under acidic condition. Biosorption capacities increased at pH < 5 and decreased with further increased in pH. Repulsion force formed between negatively charge PCP surface and phenolate anions at higher pH. At pH 5, maximum adsorption for phenol, 2-CP, and 4-CP were 70.41, 79.12, and 84.84 mg/g, respectively. Increment of adsorbent dosage 0.05 to 0.6 g improved biosorption ability with greater percentage removal but no significant improvement after 0.6 g. Maximum removal percentage for phenol, 2-CP, and 4-CP with 0.6 g adsorbent used were 86%, 93% and 95% respectively. Optimum conditions to remove phenol, 2-CP, and 4-CP were pH 5, only 60 minutes contact time needed and 0.6 g/0.1 L PCP used [45]. The optimum adsorption capacities were 164.51 mg/g, 189.44 mg/g and 220.12 mg/g, respectively. Both adsorption PBP and PCP on phenolic compounds favoured acidic condition. However, PCP with shorter contact time was more applicable in industry as compared to PBP.

Karri et al. [26, 46] and Prashanthakumar et al. [47] both used coconut as raw material for their adsorbents. Karri *et al.* [26, 46] synthesized activated carbon from coconut shell to remove phenol while Prashanthakumar et al. [47] used coconut spathe to remove phenol, 2-CP and 4-CP. Coconut shell activated carbon (CSAC) synthesized by Karri et al. [26, 46] underwent chemical and physical activations. After that, samples were rinsed with 0.5 N HCl and distilled water with pH maintained at pH 6, while last step of synthesis involved drying process at 110 °C. From Karri's study [46], adsorption of phenol increased with increasing of adsorbent dosage and decreasing of initial phenol concentration. Percentage removal up to 96% was achieved with 100 g of adsorbent used. 78% of percentage removal increased to 96% when initial phenol concentration reduced from 100 mg/L to 25 mg/L. Equilibrium was reached after 95 minutes. They reported the chemisorption mechanism since it was observed that pseudo second order model, fits the experimental phenol adsorption data as compared to the pseudo first order model.

Prashanthakumar et al.[47] reported that their pre-carbonized coconut spathe material was treated with potassium hydroxide (KOH) that acted as activating agent to produce KOH-treated activated carbon (KAC).

Hydrochloric acid was added to unclog pores from chemical residues. Through SEM analysis, the KAC showed smooth surface texture and pores could be observed appeared on the top surface. The pore opening provided access into the internal pores. Due to the interaction between phenolic compounds and the functional groups present in the adsorbent, some of the pores became widened. Highest removal of 98% was achieved for phenol by using 100 mg of adsorbent. BET surface area for KAC was a staggering 1705 m^2/g. Percentage removal increased with initial adsorbate concentration from 10 ppm to 100 ppm. Adsorption for phenol, 2-CP and 4-CPat 100 ppm were 120, 262, 275 mg/g respectively. Equilibrium was reached after 30 minutes. Optimum pH to remove adsorbate was pH 7. Adsorption ability was weak at higher pH due to electrostatic repulsion between adsorbent surface and adsorbates. However, adsorption performance at strong acidic condition (<pH 3) decreased as well because proton in solution competed with adsorbates for active site. From pH 3-7, percentage removal increased from 74% to 80% for phenol, 87% to 90% for 2-CP and 94% to 95% for 4-CP. Both Karri et al. [26, 46] and Prashanthakumar et al. [47] used coconut waste as precursor for their adsorbent. KAC could be concluded as a more effective adsorbent for phenol as compared to CSAC due to its shorter contact time, lower adsorbent dosage and highest removal percentage. The adsorption mechanism was reported to be largely dependent on the −OH and −Cl functional groups and their interaction with the adsorbent surface. For removal of phenol, 2-CP and 4-CP, Siva Kumar et al. [45] and Prashanthakumar et al. [47] reported that removal percentage of adsorbates increased with more amount of adsorbent but could not improve adsorption density or amount of adsorbate adsorbed per unit mass. This was due to agglomerations and overlapping of high amount of adsorbent that led to decreasing of surface area. 4-CP and 2-CP had higher adsorption capacities as compared to phenols. This was because driving force for phenols from bulk solution to adsorbent surface decreased when small-sized phenols molecules diffused easily into internal pores [47].

Activated carbon from avocado seed had different synthesis procedure. Leite et al. [31, 48] grinded 100 g of avocado seed to obtain particle size < 250 μm and followed by mixing of water and $ZnCl_2$ as activating agent. The paste was put in furnace for heating under nitrogen flow (150 mL/min). Final heating temperature (500-700 °C) and heating time (30,45,60 min) were determined by using a 2^2 full-factorial design of experiment. Pyrolysis step was done when samples cooled down under nitrogen atmosphere with temperature < 150 °C. Samples were refluxed at 80 °C with concentrated HCl. Adsorption process involved 1.5 g/L of ASAC adsorbent, contact time of 120 min and temperature of 25 °C. Activated carbon had adsorption capacity of 99.5 to 327 mg/g towards 15 phenolic compounds. Specific surface area for adsorbent was a staggering 1584 m^2/g. In the ASAC, they found out the surface contained large amounts–OH, –COO, –O and –NH which exhibit hydrophilic behaviour for adsoprtion. Umpierres et al. [49] synthesized activated carbon from tucuma seed (palm family) to remove 2-nitrophenol from aqueous solution. Tucuma seed was added with water and $ZnCl_2$ that acted as activating agent until a homogeneous paste was formed. Later, the paste was subjected to microwave-assisted pyrolysis. Pyrolyzed materials were then refluxed at 75 °C with concentrated HCl solution. Specific surface area of adsorbent was 1318 m^2/g. Optimum conditions to remove 2-nitrophenol were pH 7, contact time of 30 minutes, adsorbent dosage 1.5 g/L and temperature of 50 °C. Maximum adsorption capacity for adsorbent (TMAC-2.0) based on the most suitable isotherm model (Liu model) was 1382 mg/g at elevated temperature (50°C). Adsorption of 2-nitrophenol onto adsorbent was exothermic and spontaneous.

Both Leite et al. [31, 48] and Umpierres et al. [49] synthesized activated carbon from seed using pyrolysis method with $ZnCl_2$ as activating agent. Adsorption ability of avocado seed activated carbon towards 2-nitrophenol was better than tucuma seed activated carbon due to greater specific surface area and lower operating temperature. However, contact time of 120 minutes was too long to be utilized in industry. Rice straw is lignocellulosic waste after harvesting paddy. Alternative to in-situ burning, piling and dumping, the waste can be converted into other useful environmental friendly products because it is a carbon-neutral

renewable resource [77]. Sarker et al. [50] prepared raw rice straw without activation and synthesized 2 activated carbon from rice straw through physical activation and thermal activation methods. For physical activation, rice straw was boiled for 2 h and dried until a constant weight was achieved. While for thermal activation, rice straw was heated in high temperature until ash was formed. Phenol removal efficiency of 84.07 % was achieved using 2.5 g thermally activated rice straw ash having size <1 mm. Adsorbent with smaller particle size (<1 mm) could remove more phenol as compared to 1 mm particles that had percentage removal of 76.67%. Equilibrium was reached after 1 hour of contact. Thermally activated rice straw ash had greater removal efficiency (84.1%) as compared to physically activated and raw rice straw (<30%). This was because organic matrix in rice straw could be destructed by thermal treatment and thus increased the adsorption surface area.

Conclusion

Safe water supply and effective treatment of wastewater remain as one of the worldwide environmental concern. It is found that for the past four years, there has been significant advances in development of adsorbents from agricultural waste for the removal of pollutants in water or wastewater. Removal characteristics of heavy metals, dyes, pesticide, herbicides and phenolic compounds in water or wastewater using various adsorbents (e.g., coir pith ash, carnauba straw powder, banana peels, tea and coffee ground waste, coconut shell, rice straw, pine bark powder etc) were reviewed. The adsorbent preparation and mechanism of adsorption (e.g., ion-exchange, chemisorption, chelation, electrostatic attraction and hydrophilicity) were specifically discussed. The effect of physicochemical factors on the performance of these adsorbents were reviewed. It can be concluded that the surface area and type of functional groups play a big role in removing pollutants. In most of the research, good removal percentages and adsorption capacities were obtained. The adsorption of the pollutants either follow Langmuir, Freundlich or other linearized isotherms. However, most of the research were developed in synthetic aqueous solutions, which contain the pollutants of interest without the real sample matrix interferences. Thus, it is deemed necessary for future works to conduct experiments in real samples as well as in industrial setup. Subsequently, economic analysis to know the overall cost of the process applicable to industrial setup is also predicted to be inevitable.

Acknowledgement

The Ministry of Higher Education Malaysia (MOHE) and Universiti Teknologi Malaysia (UTM) are thanked for funding A.S.A.K through Fundamental Research Grant Scheme (FRGS/1/2018/STG01/UTM/02/4, R.J130000.7854.5F010) and UTM Fundamental Research grant (UTMFR, Q.J130000.2554.20H98). The authors have declared no conflict of interest.

References

1. Fu, F. and Wang, Q. (2011). Removal of heavy metal ions from wastewaters: A review. *Journal of Environmental Management*, 92(3): 407-418.
2. World Health Organization (2003). Arsenic in Drinking-Water: Background Document for Development of Who Guidelines for Drinking-Water Quality, in Background Document for Development of WHO Guidelines for Drinking-Water Quality: Geneva.
3. Hill, M.K. (2010). Understanding Environmental Pollution. Cambridge University Press: pp. 425.
4. World Health Organization (2004). Copper in Drinking-Water. Background Document for Preparation of Who Guidelines for Drinking-Water Quality, in Background Document for Development of WHO Guidelines for Drinking-Water Quality: Geneva.
5. World Health Organization (2005). Nickel in Drinking-Water Background Document for Preparation of Who Guidelines for Drinking-Water Quality, in Background Document for Development of WHO Guidelines for Drinking-Water Quality: Geneva.
6. Paulino, A. T., Minasse, F. A., Guilherme, M. R., Reis, A. V., Muniz, E. C. and Nozaki, J. (2006). Novel adsorbent based on silkworm chrysalides for removal of heavy metals from wastewaters. *Journal of Colloid and Interface Science*, 301(2): 479-487.

7. World Organization (2004). Cadmium in Drinking-Water: Background Document for Development of Who Guidelines for Drinking-Water Quality, in Background Document for Development of WHO Guidelines for Drinking-Water Quality: Geneva.
8. World Health Organization (2003). Lead in Drinking-Water: Background Document for Development of Who Guidelines for Drinking-Water Quality. World Health Organization., in Background Document for Development of WHO Guidelines for Drinking-Water Quality: Geneva.
9. Canfield, R. L., Henderson Jr, C. R., Cory-Slechta, D. A., Cox, C., Jusko, T. A. and Lanphear, B. P. (2003). Intellectual impairment in children with blood lead concentrations below 10 μg per deciliter. *New England Journal of Medicine*, 348(16): 1517-1526.
10. Witek-Krowiak, A., Szafran, R. G. and Modelski, S. (2011). Biosorption of heavy metals from aqueous solutions onto peanut shell as a low-cost biosorbent. *Desalination,* 265(1-3): 126-134.
11. Mittal, A., Kurup, L. and Gupta, V. K. (2005). Use of waste materials—bottom ash and de-oiled soya, as potential adsorbents for the removal of amaranth from aqueous solutions. *Journal of Hazardous Materials*, 117(2-3): 171-178.
12. Viswanathan, B. (2009). Pollution control strategies: A chemist's perspective, in pollution control in dye industry. National Centre For Catalysis Research Indian Institute of Technology: Chennai. p. 1-16.
13. Campos, R., Kandelbauer, A., Robra, K. H., Cavaco-Paulo, A. and Gübitz, G. M. (2001). Indigo degradation with purified laccases from *Trametes hirsuta* and *Sclerotium rolfsii*. *Journal of Biotechnology*, 89(2-3): 131-139.
14. Rangabhashiyam, S., Anu, N. and Selvaraju, N. (2013). Sequestration of dye from textile industry wastewater using agricultural waste products as adsorbents. *Journal of Environmental Chemical Engineering,* 1(4): 629-641.
15. Nestmann, E. R., Douglas, G. R., Matula, T. I., Grant, C. E. and Kowbel, D. J. (1979). Mutagenic activity of rhodamine dyes and their impurities as detected by mutation induction in Salmonella and DNA damage in Chinese hamster ovary cells. *Cancer Research,* 39(11): 4412-4417.
16. Srivastava, S., Sinha, R. and Roy, D. (2004). Toxicological effects of malachite green. *Aquatic Toxicology*, 66(3): p. 319-329.
17. Dos Reis, G. S., Adebayo, M. A., Sampaio, C. H., Lima, E. C., Thue, P. S., de Brum, I. A., Dias, S. I. P. & Pavan, F. A. (2016). Removal of phenolic compounds from aqueous solutions using sludge-based activated carbons prepared by conventional heating and microwave-assisted pyrolysis. *Water, Air, & Soil Pollution*, 228(1): 33.
18. Schowalter, T. D. (2016). Insect ecology: An ecosystem approach. Massachusetts: Academic press.
19. Anku, W.W., Mamo, M. A. and Govender, P. P. (2017). Phenolic compounds in water: Sources, reactivity, toxicity and treatment methods. Phenolic compounds-natural sources, importance and applications, ed. M. Soto-Hernández, M. Palma-Tenango, and R. García-Mateos. InTechOpen: London. 420-443.
20. USEPA (2000). Integrated Risk Information System (Iris) on 2,4,6-Trichlorophenol. Available from: https://iris.epa.gov/static/pdfs/0122_summary.pdf. [Access online 23/5/2021].
21. Harcombe, G., Harrington, S., Lester, M., Lindsay, M., Mak, D., Neaves, K., Philippe, D. and Tan. H. (2010). Environmental health practitioner manual: A resource manual for environmental health practitioners working with aboriginal and Torres Strait Islander communities. Department of Health: Perth.
22. Li, Z. and Jennings, A. (2017). Worldwide regulations of standard values of pesticides for human health risk control: A review. *International Journal of Environmental Research and Public Health,* 14(7): 826.
23. World Health Organization and I.P.o.C. Safety. (2010). The WHO recommended classification of pesticides by hazard and guidelines to classification 2009. World Health Organization: Geneva.
24. Zhang, Y. and Pagilla, K. (2010). Treatment of malathion pesticide wastewater with nanofiltration and photo-fenton oxidation. *Desalination*, 263(1-3): 36-44.

25. Blair, A., Ritz, B., Wesseling, C. and Beane Freeman, L. (2015). Pesticides and human health. *Occupational and Environmental Medicine*, 72(2): 81-82.
26. Karri, R. R., Sahu, J. and Jayakumar, N. (2017). Optimal isotherm parameters for phenol adsorption from aqueous solutions onto coconut shell based activated carbon: Error analysis of linear and non-linear methods. *Journal of the Taiwan Institute of Chemical Engineers*, 80: 472-487.
27. Ramírez, E. E. P., de la Luz Asunción, M., Rivalcoba, V. S., Hernández, A. L. M. and Santos, C. V. (2017). Removal of phenolic compounds from water by adsorption and photocatalysis. Phenolic compounds-natural sources, importance and applications, ed. Soto-Hernández, M., Palma-Tenango, M. and García-Mateos, R. IntechOpen: London.
28. Chen, J., Lin, Y. and Kuo, W. (2013). Pesticide residue removal from vegetables by ozonation. *Journal of Food Engineering*, 114(3): 404-411.
29. Lhomme, L., S. Brosillon, and D. Wolbert. (2008). Photocatalytic degradation of pesticides in pure water and a commercial agricultural solution on TiO_2 coated media. *Chemosphere*, 70(3): 381-386.
30. Quiroz, M. A., Bandala, E. R. and Martínez-Huitle, C. A. (2011). Advanced oxidation processes (AOPs) for removal of pesticides from aqueous media. Pesticides-formulations, effects, fate, ed. Stoytcheva, M. IntechOpen: London.
31. Leite, A. B., Saucier, C., Lima, E. C., Dos Reis, G. S., Umpierres, C. S., Mello, B. L., Shirmardi, M. Dias, S . L. P. and Sampaio, C. H. (2018). Activated carbons from avocado seed: optimisation and application for removal of several emerging organic compounds. *Environmental Science and Pollution Research*, 25(8): 7647-7661.
32. Yuvaraja, G., Krishnaiah, N., Subbaiah, M. V. and Krishnaiah, A. (2014). Biosorption of Pb(II) from aqueous solution by *Solanum melongena* leaf powder as a low-cost biosorbent prepared from agricultural waste. *Colloids and Surfaces B: Biointerfaces*, 114: 75-81.
33. Bahar, M.M., Mahbub, K. R. Naidu, R. and Megharaj, M. (2018). As(V) removal from aqueous solution using a low-cost adsorbent coir pith ash: Equilibrium and kinetic study. *Environmental Technology & Innovation*, 9: 198-209.
34 Semerjian, L. (2018). Removal of heavy metals (Cu, Pb) from aqueous solutions using pine (*Pinus halepensis*) sawdust: Equilibrium, kinetic, and thermodynamic studies. *Environmental Technology & Innovation*, 12: 91-103.
35. da Silva, A. J. F., de Alencar Moura, M. C. P., da Silva Santos, E., Pereira, J. E. S. and de Barros Neto, E. L. (2018). Copper removal using carnauba straw powder: Equilibrium, kinetics, and thermodynamic studies. *Journal of Environmental Chemical Engineering*, 6(6): 6828-6835.
36. Masoumi, A., Hemmati, K. and Ghaemy, M. (2016). Low-cost nanoparticles sorbent from modified rice husk and a copolymer for efficient removal of Pb(II) and crystal violet from water. *Chemosphere*, 146: 253-262.
37. Zhou, J., Liu, Y., Zhou, X., Ren, J. and Zhong, C. (2018). Magnetic multi-porous bio-adsorbent modified with amino siloxane for fast removal of Pb(II) from aqueous solution. *Applied Surface Science*, 427: 976-985.
38. Dai, L., Li, Y., Liu, R., Si, C. and Ni. Y. (2019). Green mussel-inspired lignin magnetic nanoparticles with high adsorptive capacity and environmental friendliness for chromium(III) removal. *International Journal of Biological Macromolecules*, 132: 478-486.
39. Wen, T., Wang, J., Yu, S., Chen, Z., Hayat, T. and Wang, X. (2017). Magnetic porous carbonaceous material produced from tea waste for efficient removal of as (V), Cr (VI), humic acid, and dyes. *ACS Sustainable Chemistry & Engineering*, 5(5): 4371-4380.
40. Shen, K. and Gondal. M. (2017). Removal of hazardous rhodamine dye from water by adsorption onto exhausted coffee ground. *Journal of Saudi Chemical Society*, 21: 120-127.
41. Sartape, A. S., Mandhare, A. M., Jadhav, V. V., Raut, P. D., Anuse, M. A. and Kolekar, S. S. (2017). Removal of malachite green dye from aqueous solution with adsorption technique using *Limonia acidissima* (wood apple) shell as low cost adsorbent. *Arabian Journal of Chemistry*, 10: S3229-S3238.

42. Al-Zaben, M. I. and Mekhamer. W. K. (2017). Removal of 4-chloro-2-methyl phenoxy acetic acid pesticide using coffee wastes from aqueous solution. *Arabian Journal of Chemistry*, 10: S1523-S1529.
43. Essandoh, M., Wolgemuth, D., Pittman, C. U., Mohan, D. Jr. and Mlsna, T (2017). Phenoxy herbicide removal from aqueous solutions using fast pyrolysis switchgrass biochar. *Chemosphere*, 174: 49-57.
44. Siva Kumar, N., Asif, M., Al-Hazzaa, M. I. and Ibrahim, A. A. (2018). Biosorption of 2,4,6-trichlorophenol from aqueous medium using agro-waste: Pine (*Pinus densiflora Sieb*) bark powder. *Acta Chimica Slovenica*, 65(1): 10.
45. Siva Kumar, N., Asif, M. and Al-Hazzaa, M. I. (2018). Adsorptive removal of phenolic compounds from aqueous solutions using pine cone biomass: Kinetics and equilibrium studies. *Environmental Science and Pollution Research*, 25(22): 21949-21960.
46. Karri, R. R., Jayakumar, N. and Sahu, J. (2017). Modelling of fluidised-bed reactor by differential evolution optimization for phenol removal using coconut shells based activated carbon. *Journal of Molecular Liquids*, 231: 249-262.
47. Prashanthakumar, T., Kumar, S. A. and Sahoo, S. K. (2018). A quick removal of toxic phenolic compounds using porous carbon prepared from renewable biomass coconut spathe and exploration of new source for porous carbon materials. *Journal of Environmental Chemical Engineering*, 6(1): 1434-1442.
48. Leite, A. J., Sophia A, C., Thue, P. S., dos Reis, G. S., Dias, S. L., Lima, E. C., Vaghetti, J. C. P. and de Alencar, W. S. (2017). Activated carbon from avocado seeds for the removal of phenolic compounds from aqueous solutions. *Desalination and Water Treatment*, 71: 168-181.
49. Umpierres, C. S., Thue, P. S., Lima, E. C., Reis, G. S. D., de Brum, I. A., Alencar, W. S. D. and Dotto, G. L. (2018). Microwave-activated carbons from tucumã (astrocaryum aculeatum) seed for efficient removal of 2-nitrophenol from aqueous solutions. *Environmental Technology*, 39(9): 1173-1187.
50. Sarker, N. and Fakhruddin. A. N. M. (2017). Removal of phenol from aqueous solution using rice straw as adsorbent. *Applied Water Science*, 7(3): 1459-1465.
51. Qu, J., Meng, X., You, H., Ye, X. and Du, Z.(2017). Utilization of rice husks functionalized with xanthates as cost-effective biosorbents for optimal Cd(II) removal from aqueous solution via response surface methodology. *Bioresource Technology*, 241: 1036-1042.
52. Manzoor, Q., Sajid, A., Hussain, T., Iqbal, M., Abbas, M. and Nisar, J. (2019). Efficiency of immobilized zea mays biomass for the adsorption of chromium from simulated media and tannery wastewater. *Journal of Materials Research and Technology*, 8(1): 75-86.
53. Faheem, Du, J., Bao, J., Hassan, M. A., Irshad, S., Talib, M. A. and Zheng, H. (2020). Efficient capture of phosphate and cadmium using biochar with multifunctional amino and carboxylic moieties: Kinetics and mechanism. *Water, Air, & Soil Pollution*, 231(1): 25.
54. Abu Bakar, A. A., Wan Mazlan, W. N. R., Akbar, N. A., Badrealam, S. and Muhammad Ali, K. A. (2019). Agriculture Waste from Banana Peel as Low Cost Adsorbent in Treating Methylene Blue from Batik Textile waste water effluents. *Journal of Physics: Conference Series*, 1349: 012078.
55. Sivakumar, S., Muthirulan, P. and Meenakshi S. M. (2019). Adsorption kinetic and isotherm studies of azure a on various activated carbons derived from agricultural wastes. *Arabian Journal of Chemistry*, 12(7): 1507-1514.
56. Al-Ghouti, M. A. and Sweleh, A. O. (2019). Optimizing textile dye removal by activated carbon prepared from olive stones. *Environmental Technology & Innovation*, 16: 100488.
57. Akhayere, E., Essien, E. A. and Kavaz, D. (2019). Effective and reusable nano-silica synthesized from barley and wheat grass for the removal of nickel from agricultural wastewater. *Environmental Science and Pollution Research*, 26(25): 25802-25813.
58. Jang, H. M. and Kan, E. (2019). Engineered biochar from agricultural waste for removal of tetracycline in water. *Bioresource Technology*, 284: 437-447.

59. Benvenuti, J., Giraldi Fisch, A., Zimnoch Dos Santos, J. H. and Gutterres, M. (2020). Hybrid sol–gel silica adsorbent material based on grape stalk applied to cationic dye removal. *Environmental Progress & Sustainable Energy*: e13398.
60. Bhattacharya, A. K. and Venkobachar, C. (1984). Removal of cadmium (II) by low cost adsorbents. *Journal of Environmental Engineering*, 110(1): 110-122.
61. Ferro-García, M. A., Rivera-Utrilla, J., Rodríguez-Gordillo, J. and Bautista-Toledo, I. (1988). Adsorption of zinc, cadmium, and copper on activated carbons obtained from agricultural by-products. *Carbon*, 26(3): 363-373.
62. Deshicar, A. M., Bokade, S. S. and Dara, S. S. (1990). Modified *Hardwickia binata* bark for adsorption of mercury (II) from water. *Water Research*, 24(8): 1011-1016.
63. Okieimen, F.E. and Onyenkpa, V. U. (1989). Removal of heavy metal ions from aqueous solutions with melon (*Citrullus vulgaris*) seed husks. *Biological Wastes*, 29(1): 11-16.
64. Gosset, T., Trancart, J.-L. and Thévenot, D. R. (1986). Batch metal removal by peat. kinetics and thermodynamics. *Water Research*, 20(1): 21-26.
65. Mahindrakar, K.V. and Rathod, V. K. (2018). Utilization of banana peels for removal of strontium (II) from water. *Environmental Technology & Innovation*, 2018: 371-383.
66. Ahmad, A. and Hameed. B. (2009). Reduction of COD and color of dyeing effluent from a cotton textile mill by adsorption onto bamboo-based activated carbon. *Journal of Hazardous materials*, 172(2-3): 1538-1543.
67. Jain, S. and Jayaram. R. V. (2010). Removal of basic dyes from aqueous solution by low-cost adsorbent: wood apple shell (*Feronia acidissima*). *Desalination*, 250(3): 921-927.
68. Plaza, M., González, A., Pevida, C., Pis, J., and Rubiera, F. (2012). Valorisation of spent coffee grounds as CO_2 adsorbents for postcombustion capture applications. *Applied Energy*, 99: 272-279.
69. Agriculture, U.S.D. (2019). Coffee: World Markets and Trade [Access online 1/3/2020].
70. Suresh, C., Reddy, D. H. K., Harinath, Y., Naik, B. R., Seshaiah, K. and Reddy, A. V. R. (2014). Development of wood apple shell (*Feronia acidissima*) powder biosorbent and its application for the removal of Cd(II) from aqueous solution. *Scientific World Journal*, 2014: 154809-154809.
71. Das, S., Dash, S. K.and Parida, K. M. (2018). Kinetics, isotherm, and thermodynamic study for ultrafast adsorption of azo dye by an efficient sorbent: Ternary Mg/(Al + Fe) layered double hydroxides. *ACS Omega*, 3(3): 2532-2545.
72. Mandal, A., Singh, N. and Nain, L. (2017). Agro-waste biosorbents: Effect of physico-chemical properties on atrazine and imidacloprid sorption. *Journal of Environmental Science and Health, Part B: Pesticides, Food Contaminants and Agricultural Wastes*, 52(9): 671-682.
73. Chen, J.Y., Lin, Y. J. and Kuo, W. C. (2013). Pesticide residue removal from vegetables by ozonation. *Journal of Food Engineering*, 114(3): 404-411.
74. Iizuka, T., Yahata, M. and Shimizu, A. (2013). Potential mechanism involved in removal of hydrophobic pesticides from vegetables by hydrostatic pressure. *Journal of Food Engineering*, 119(1): 1-6.
75. Zhu, Y., Zhang, T., Xu, D., Wang, S., Yuan, Y., He, S. and Cao, Y. (2019). The removal of pesticide residues from Pakchoi (*Brassica Rape* L. Ssp. Chinensis) by ultrasonic treatment. *Food Control*, 95: 176-180.
76. Ramrakhiani, L., Ghosh, S., Mandal, A. K. and Majumdar, S. (2019). Utilization of multi-metal laden spent biosorbent for removal of glyphosate herbicide from aqueous solution and its mechanism elucidation. *Chemical Engineering Journal*, 361: 1063-1077.
77. Nguyen, H.V., Nguyen, C. D., Tran, T. V., Hau, H. D., Nguyen, N. T. and Gummert, M. (2016). Energy efficiency, greenhouse gas emissions, and cost of rice straw collection in the Mekong River Delta of Vietnam. *Field Crops Research*, 198: 16-22.

Malaysian Journal of Analytical Sciences (MJAS)
Published by Malaysian Analytical Sciences Society

CO_2-EFFERVESCENT TABLET-ASSISTED DISPERSIVE LIQUID-LIQUID MICROEXTRACTION WITH CENTRAL COMPOSITE DESIGN FOR PRE-CONCENTRATION OF ACETAMINOPHEN DRUG: METHOD DEVELOPMENT, VALIDATION AND GREEN ASSESSMENT PROFILE

(Tablet Berbuak-CO_2 Berbantukan Sebaran Pengekstrakan Mikro Cecair-Cecair dengan Reka Bentuk Komposit Berpusat untuk Kepekatan Awalan Dadah Acetaminophen: Pembangunan Kaedah, Validasi dan Profil Penilaian Hijau)

Priya Murugan, Sarveishwhary Rajendran, Saw Hong Loh, Marinah Mohd Ariffin, Wan Mohd Afiq Wan Mohd Khalik*

Faculty of Science and Marine Environment,
Universiti Malaysia Terengganu, 21030 Kuala Nerus, Malaysia

**Corresponding author: wan.afiq@umt.edu.my*

Received: 15 April 2021; Accepted: 2 June 2021; Published: 27 June 2021

Abstract

This study discovered the extraction procedure of acetaminophen from water samples using the effervescent tablet-assisted dispersive liquid-liquid microextraction (DLLME) method. The effervescent tablet that is composed of sodium dihydrogen phosphate (proton donor) and sodium carbonate (CO_2 source) was formulated using the wet granulation technique. In this study, high performance liquid chromatography coupled with ultraviolet visible detection (HPLC-UV) was used for qualitative and quantitative analysis of the targeted analyte. The chromatographic separation was conducted in less than 6 min (R_t 5.10 min) using a non-polar C_{18} column and an isocratic elution (methanol: water of 40: 60 (v/v)) at a controlled flowrate of 1 mL min^{-1}. Optimum wavelength was set at 264 nm. Main variables that influenced the extraction efficiency namely the amount of extraction solvent (X_1), the number of tablets consumed (X_2) and the effect of extraction temperature (X_3) were tested during optimization work. Operation setting for extraction procedure was optimized using a 2^3 full factorial central composite design, CCD (STATISTICA Version 10). The values of optimum extraction condition were set as 215 µL of extraction solvent, 5 pieces of tablets and 47 °C extraction temperature. Under optimal condition, a good linearity with determination coefficient R^2 = 0.995 was obtained. Extraction recoveries at spiked concentrations (500 ng mL^{-1} and 100 ng mL^{-1}) were recorded ranging from 83% to 94.1%. The detection and quantification limits of the proposed method were calculated at 8.62 ng mL^{-1} and 28 ng mL^{-1}, respectively. In terms of the precision method, the relative standard deviation was recorded < 5%. Real analysis samples were performed, which fortified with commercial drugs dissolved in 80 mL of deionized water. The concentration levels were determined at 5.60 mg L^{-1} (sample A) and 5.47 mg L^{-1} (sample B) respectively.

Keywords: analgesic drug, CO_2-effervescence, central composite design, liquid phase microextraction

Abstrak

Kajian ini meneroka prosedur pengekstrakan bagi acetaminophen dari sampel air mengunakan kaedah tablet berbuak berbantukan sebaran pengekstrakan mikro cecair-cecair (DLLME). Tablet berbuak terdiri dari sodium dihidrogen fosfat (penderma proton) dan sodium karbonat (sumber CO_2) di formulasi mengunakan teknik penggranulan basah. Dalam kajian ini, kromatografi cecair berprestasi tinggi gabungan pengesan ultralembayung nampak (HPLC-UV) telah digunapakai bagi analisis kuantitatif dan kualitatif terhadap analit sasaran. Pemisahan kromatografi berlaku dalam masa kurang 6 min (R_t 5.10 min) mengunakan turus tak berkutub C_{18} dan elusi isokratik (metanol: air 40:60 (v/v)) pada kawalan aliran 1 mL min^{-1}. Panjang gelombang optimum ditetapkan pada 264 nm. Pemboleh ubah utama yang mempengaruhi keberkesanan pengekstrakan seperti jumlah pelarut pengekstrak (X_1), bilangan tablet yang digunakan (X_2) dan kesan perubahan suhu (X_3) diuji semasa kerja pengoptimuman. Tetapan operasi bagi prosedur pengekstrakan bagi pengoptimuman mengunakan reka bentuk komposit berpusat, CCD (STATISTICA versi 10). Nilai yang diperolehi bagi keadaan optimum ialah pelarut pengekstrakan 215 µL, 5 biji tablet dan tetapan suhu 47 °C. Kelinearan yang baik dengan pekali regresi R^2 = 0.995 telah diperolehi pada keadaan optimum. Perolehan semula pengekstrakan pada kepekatan yang dipaku (500 ng mL^{-1} dan 100 ng mL^{-1}) telah merekodkan nilai julat 83%-94.1%. Had pengesanan dan pengkuantitian bagi kaedah yang dibangunkan dihitung masing-masing pada 8.62 ng mL^{-1} dan 28 ng mL^{-1}. Bagi aspek kejituan kaedah, sisihan piawai relatif telah direkodkan < 5%. Analisis sampel sebenar telah dijalakan dengan penambahan dadah komersial yang dilarut dalam 80 mL air ternyah ion. Kepekatan telah ditentukan masing-masing pada 5.60 mg L^{-1} (sampel A) dan 5.47 mg L^{-1} (sampel B).

Kata kunci: dadah analgesik, CO_2-berbuak, reka bentuk komposit berpusat, pengekstrakan mikro fasa cecair

Introduction

Effervescent reaction is one of the disperser-solvent-free techniques in DLLME. This novel work was first introduced by Lasarte-Aragones et al. [1] for the extraction of herbicides in water. Once the tablet is mixed with an aqueous solution, a simple reaction between the proton donor and carbon source (i.e. sodium carbonate) induces the formation of gas microbubbles (CO_2). The effervescence occurs from the bottom to top of the container and the extractant solvent is uniformly distributed [2]. This method accelerates the dispersion of the extraction solvent without additional energy. Large contact surface area between the target analyte and the extractant promotes mass transfer, which can vastly improve extraction efficiency [3]. Indeed, it reduces the partition coefficients of the hydrophobic analytes into the extraction solvent [4]. Other advantages include rapid, effective, reproducible, eliminating multi-stage operation, and low cost [2-6]. The effervescent tablets are easy to formulate because the proton donor, and carbon source are all solid substances that can be simply mixed and compressed using a tablet machine. The extraction solvent functions as a binder when it solidifies at low temperature.

Microextraction method uses effervescence reaction generated by a tablet for preconcentration of drugs include antibiotics [7, 8], nonsteroidal anti-inflammatories [9], steroid hormones [10], and stimulants [11]. Selection of extraction solvents varies from supramolecular to switchable hydrophilicity solvents. Supramolecular solvent is relatively cheap, low freezing points, and less volatile which has recently been used in microextraction especially for the effervescence method [12]. Meanwhile, switchable hydrophilicity solvents offer tunable properties like miscible liquid or biphasic mixture with water and easily ionized by adjustment the pH values [13, 14]. The extraction solvent can be efficiently dispersed into the aqueous sample owing to the use of effervescent tablets, which improves the effective mass transfer of target analytes, and reflects through high enrichment factors [15]. The extraction process needs a shorter time to complete and the utilization of extractant is always minimal.

Acetaminophen (N-acetyl-p-aminophenol; $C_8H_9NO_2$) is a mild analgesic that is effectively used to treat headaches, minor aches or pains [16]. This drug is considered as a first-line therapy due to its relatively low

adverse side effects, efficacy and low price [17]. It has been reported that human urine excretes 58-68% of acetaminophen, a considerable low concentration of residue but frequently detected in the municipal wastewater systems, ranging between ng L^{-1} to µg L^{-1} [18, 19]. Development of the microextraction method for the preconcentration of acetaminophen drugs from waters includes solid phase (i.e., fiber coating, in-tube, molecularly imprinted polymer) or liquid phase (i.e., hollow fiber, dispersive) [20-24]. In the present work, dispersive liquid-liquid microextraction with the acceleration of dispersion mode by effervescent tablets was aimed for the extraction of acetaminophen (analgesic drug) in the water samples. To construct the experimental work, a full factorial central composite design was applied to optimize the microextraction procedure. Method validation and green profile assessment were also carried out.

Materials and Methods

Reagents and materials

Acetaminophen standard was purchased from Sigma-Aldrich (St. Louis, USA) with purity of 98%. HPLC-grade acetonitrile and methanol were purchased from Merck (Darmstadt, Germany). Analytical-grade sodium bicarbonate, sodium hydrogen phosphate, glycerin, 1-dodecanol were acquired from Merck. Due to its high enrichment factors and low price, 1-dodecanol was chosen as the extractant. Stock standard solution was initially prepared in methanol with a concentration of 5 µg mL^{-1} and stored in the dark at 4 °C. The working standard solutions of the acetaminophen drug were prepared by appropriate dilution of the stock standard solution with methanol. The purified deionized water was obtained from a Millipore Milli-Q reference water purification system that has a resistivity of 18.2 MΩ.cm at 25 °C (Bedford, MA, USA). An analytical balance 210G/D.1MG HC-A Smith Model HC-A 210 was used for weighing. A stainless-steel tablet machine (Henan, China) was used to prepare the flat face radius edge effervescent tablets.

Instrumental and analytical conditions

HPLC–UV analysis was performed using a Shimadzu HPLC system (Kyoto, Japan) equipped with an autosampler (SIL-20A HT), vacuum degasser (DGU-20A 5R), system controller (LC-20AT), quaternary pump (LC-10ATVP), oven (CTO-10AS VP), and series multiple wavelength UV detector (SPD-20A). An Apollo C_{18} column (250 mm x 4.6 mm, 5 µm Hichrom Limited) was used for the separation. The mobile phase was a mixture of methanol-water (40:60 v/v) at a flow rate of 1 mL min^{-1}, and the column temperature was held at 30 °C. The UV detection wavelength was set at 264 nm. The injection volume was set at 10 µL per analysis. Peak identification was observed in less than 6 min (Figure 1). Shimadzu Class VP version 6.41 SP1 software was used to control the HPLC–UV system and to perform the data analysis.

Preparation of the effervescent tablet

In this study, the effervescent tablets were produced using the wet granulation method. Sodium bicarbonate and sodium hydrogen phosphate salt (effervescence precursors), glycerin (binder) and 1-dodecanol (extraction solvent) were formulated in a tablet form. The effervescent precursors were dried in an oven at 60 °C overnight before mixing the materials. Sodium bicarbonate (1.0 g) and sodium hydrogen phosphate (1.0 g) salt were weighed into a glass mortar, and sufficiently ground to achieve homogeneous mixing. Then, a few drops of glycerin and a desired volume of 1-dodecanol (X_1) were added into the mixture. The homogenous mixture was transferred into a tablet mold with the dimension of 2.5 cm × 3.7 cm and subsequently compressed for 60 s to produce an effervescent tablet using a tablet press hammer. The effervescent tablets (dimension 2.5 cm (width) × 3.7 cm (height)) were stored in a 30 mL plastic bottle with a screw cap at 4°C to maintain the tablets' shape.

Physical and chemical analysis

The morphology of effervescent tablet was observed using a Jeol JSM-6360LV (Tokyo, Japan) scanning electron microscope (SEM). The scanning electron microscope operated at an accelerating voltage of 10 kV with a probe current of ≈ 1 pA - 1 µA having a resolution of 3.0 nm. Prior to examination, the effervescent tablet was prepared by mounting approximately 0.1 to 1.0 g of powder onto a 10 mm × 10 mm SEM specimen aluminum stub via double-sided adhesive tape to permit a quick mounting of samples on a stub. The effervescent

tablet was made electrically conductive by coating it with a thin layer of gold about 30 µm thickness using an auto fine coater (Jeol JFC-1600, Japan). The samples were coated for 60 s at a beam current of 30 mA. Attenuated total reflectance Fourier transform infrared (ATR-FTIR) Shimadzu IRTracer-100, (Kyoto, Japan) spectra equipped with a temperature controlled DLATGS detector were applied to study the occurrence of different functional groups in effervescent tablets. The spectra were recorded in transmittance mode at 40 scans and a resolution of 4 cm^{-1} over the wavenumber region ranging between 4000 cm^{-1} to 400 cm^{-1}.

Microextraction procedure

Eighty mL of water sample was transferred in a 150 mL glass volumetric flask prior spiked with 1 mL of working standard solution. Then, the flask was placed in a water bath and the water temperature was adjusted to the desired setting (X_3) as listed in Table 1. Once the temperature was achieved, the effervescent tablet was released into water samples and the ETA-DLLME was implemented. Number of the effervescent tablet (X_2) used was subject to design matrix. The effervescent tablets disintegrated in the aqueous solution when microbubbles started to form due to the releasing of CO_2 gas. The reaction was considered complete once no microbubbles were released from the tablet. Next, the top organic phase containing analyte was collected using a 1 mL syringe and placed into a 3 mL microcentrifuge tube. The extracted solution was centrifuged for 1 min at 3000 rpm. Then, the organic phase, 1-dodecanol was mixed with 1 mL of HPLC grade methanol prior injected into a HPLC-UV system.

Central composite design

Three variables, namely volume of extraction solvent (X_1), number of effervescent tablets (X_2), and extraction temperature (X_3), were subjected to optimization in this study (Table 1). A 2^3 full factorial design of CCD was generated with STATISTICA version 10 (TIBCO software, Germany). For optimization of extraction conditions, peak area was used in the data processing. Profiling the desirability of responses involved specifying DF for each dependent variable, by assigning predicted values a scale ranging from 0.0 to 1.0 [25]. Three-dimensional graphs were used to evaluate the interactive effect of two variables on the response.

Method validation

The analytical figure of merits is investigated in terms of linearity, detection limit, recovery, and repeatability. A calibration curve was obtained by a series of 6 standard solutions ranging from 0.01 to 0.50 µg mL^{-1} spiked into water samples. Detection and quantification limits were calculated using the linear regression method. The lowest concentration spiked was 0.01 µg mL^{-1}, and triplicate analysis was performed. The precision was evaluated through the repeatability (intra-day) and (inter-day) assay of the method with water samples spiked with acetaminophen. Both assays were calculated as %RSD with respect to the measurements made in triplicate (n=3). Extraction recovery was calculated by the following mathematical expression in equation 1:

$$ER = EF \times \frac{V_{org}}{V_{aq}} \times 100\% \quad (1)$$

where V_{Org}, and V_{aq} are the volume of acetaminophen in organic and aqueous phases, respectively. EF is calculated value from ratio between concentration of acetaminophen in organic phase and in aqueous phase, respectively.

Green assessment profile

The green profile of the proposed method was tested subject to analytical eco-scale and AGREE tools. Analytical eco-scale is a semi-quantitative tool, in which the calculation is based on maximum score of 100. Penalty points were subtracted from a base 100 for non-green aspects, which were linked to four parameters, namely amount of reagent used, hazardousness, energy consumption, and waste production. Eco-scale score was classified as ideal (100), excellent (> 75), acceptable (50-75) and inadequate (< 50), respectively [26-28]. AGREE: Analytical Greenness Calculator v. 0.5 beta (Universidade de Vigo, Gdańsk University of Technology) downloaded from https://mostwiedzy.pl/ en/wojciech-wojnowski,174235-1/AGREE. The evaluation metrics were extracted from the 12 principles of green analytical chemistry and

converted score into a unified 0-1 scale. The overall score is depicted in the center of the pictogram, with values close to 1 and dark green color indicating that the evaluated method is greener. Through this metric, highlighting the weakest points in analytical techniques that require further improvements in terms of greenness is possible [29, 30].

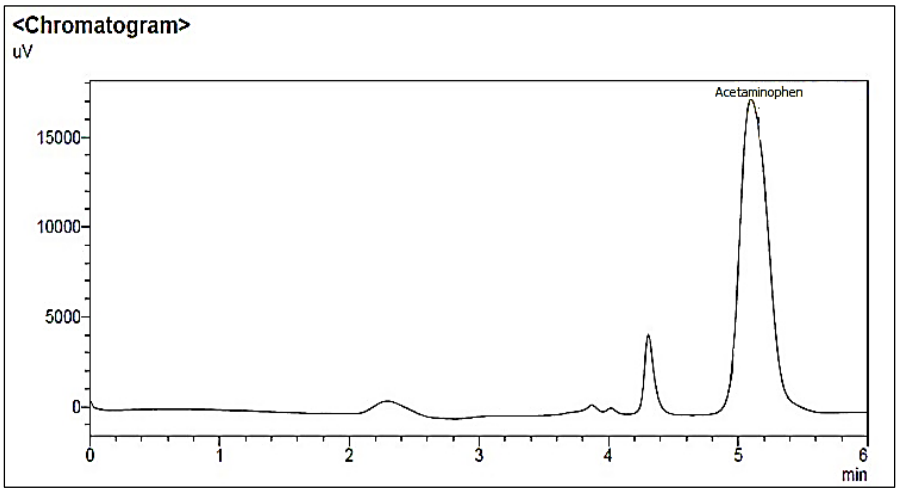


Figure 1. Peak identification of acetaminophen using standard spiked in water sample (Rt 5.10 min)

Table 1. Experimental variable and their levels

Parameter	**Code**	**Unit**	**Range**
Effect of extraction solvent	X_1	µL	132 – 468
Effect number of tablets	X_2	Pieces	1 – 5
Effect of temperature	X_3	°C	13 – 47

Parameter	**-α**	**-1**	**0**	**+1**	**+α**
Extraction solvent (X_1)	132	200	300	400	468
Number of tablets (X_2)	1	2	3	4	5
Temperature (X_3)	13	20	30	40	47

Results and Discussion

Physical and chemical characterization

Under varied magnification, the rough surface was imaged link to the presence of both salt (citric acid and sodium bicarbonate) even after grind to produce small particles. In addition to extraction solvent, the precursor composition seemed agglomerate compared to auxiliary blank tablet samples, observed at x 100 magnification (Figure 2). Solidification of tablets in low temperature helped to compress the structure of effervescent tablet and provide good surface area. Tablets made by the wet granulation method well coated with a binder had a

smaller number of void spaces in matrix structures. The targeted functional groups such as single C-O stretching (1043 cm^{-1}), O-H stretching (3236 cm^{-1}) and CH_2 (2930 cm^{-1}) were observed in spectra but the intensity of the main peaks was kept at medium. Band assignment was compared to literature documented by Zeng et al. [31] Thus, the appearance of main functional group for 1-dodecanol prove that the solution did not lose properties during wet granulation.

Method development: Microextraction procedure

The linear, interaction, and quadratic effects were optimized and evaluated using central composite design. A *P*-value in the ANOVA table indicates the statistical significance of an effect at 95% confidence level (Table 2). The second order polynomial regression equation gained for the optimized parameters is shown by Equation (2).

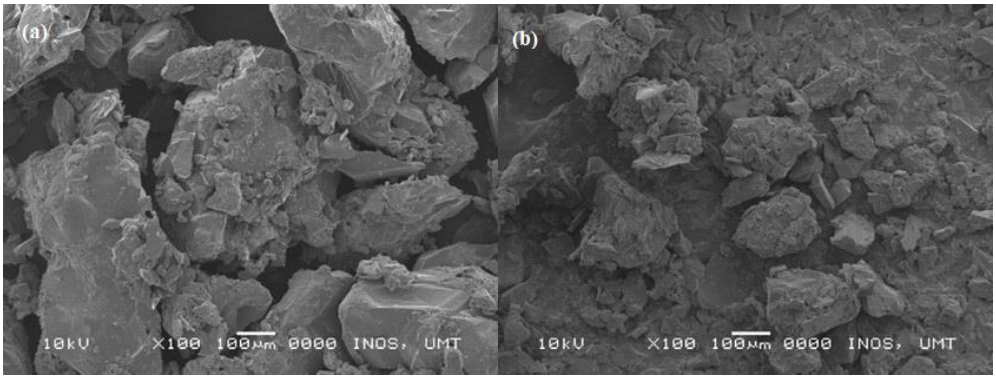


Figure 2. Morphology of surface tablet under x100 magnification (a) precursor only and (b) 1-dodecanol

Table 2. The analysis of variance (ANOVA) for the second-order regression model

Factor	SS	df	MS	F	P
Extraction solvent (L)	22816	1	22816	6.050	0.049*
Extraction solvent (Q)	10734	1	10734	2.846	0.142
No. of tablet (L)	3899	1	3899	1.034	0.348
No. of tablet (Q)	591	1	591	0.156	0.705
Effect of temperature (L)	13368	1	13368	3.545	0.108
Effect of temperature (Q)	16237	1	16237	4.306	0.038*
1L by 2L	3087	1	3087	0.818	0.400
1L by 2L	12276	1	12276	3.255	0.121
2L by 3L	702	1	702	0.186	0.681
Error	22625	6	37708		
Total SS	100641	15			

L is linear, Q is quadratic, **p*-value <0.05

$$\text{Peak height} = 57.34 + 0.41X_1 + 177.09X_2 - 23.49X_3 + 0.01X_1^2 + 25.26X_2^2 + 1.32X_3^2 - 0.62X_1X_2 - 0.12X_1X_3 - 2.96X_2X_3 \quad (2)$$

Variables namely extraction solvent (X_1) and number of tablets (X_2) have positive linearity values in the regression model. A positive symbol in front of terms denotes a synergistic effect, while a negative symbol represents an antagonistic effect. The optimization plot (Figure 3) showed the predicted conditions for the optimum point and desirability of prediction. The R^2 statistic indicated that the model explained 88% of the variability. R^2 is a calculation of the sum of variance around the mean explained by the model [32]. In this model, a desirability function of 1.0 was recorded. The desirability of 1 was assigned for maximum response of peak height (1145), 0.5 for middle (196), and 0 for minimum (140). In this study, the lack-of-fit recorded *P*-value of 0.049, indicated that the lack-of-fit in the model is not significantly relative to pure error, good predictive model. The optimum variables for the extraction procedure were proposed by the model as follows: volume of extraction solvent, X_1 (215 µL), effect of temperature, X_2 (47 °C), and number of tablets, X_3 (5 pieces), respectively. The total contribution of each variables on the extraction yield of acetaminophen was calculated at 56.93% (X_1), 33.36% (X_2) and 9.73% (X_3), respectively.

The normal probability plot demonstrated in Figure 4 signifies the values towards a constant straight line, which demonstrated normal distribution and no evidence of non-normality, skewness, outlier, or undefined variable. The dot (refer as datasets) present along the straight line indicated the ideal fitting of the modal, meanwhile the data deviated from the straight line was the least. The graph describes that the consistency of the variance in errors through equal scatter of the residual data close to 0 value on the y-axis. Residual is the vertical distance between data point and regression line. Each data point has one residual. The point is positive when it lies above the regression line and it is negative when it lies below the regression line. There is no discernible trend in the residual versus predicted response (Figure 5).

Effect volume of extraction solvent

Acetaminophen has low log K_{ow} 0.46, a relative indicator of high solubility in water. Although paracetamol is soluble in alcohols, its solubility decreases as the length of the carbon chain increases [33]. The immiscible property of 1-dodecanol in water helps the extraction of acetaminophen from an aqueous to organic phase. The acetaminophen molecules were extracted by the extraction solvent due to the hydrophobic interaction. The effect of the 1-dodecanol volume was investigated in the range of 132 - 468 µL. The effect on the volume of extraction solvent was dominant than the number of tablets. The extractant could not well disperse in the sample solution due to the low volume, so 1-dodecanol was added sufficiently to aid the mass transfer of analyte to complete the extraction. Other leverage of 1-dodecanol can form a biphasic system with methanol, and the target compound peak is unaffected during chromatographic analysis [34]. Surface shown in Figure 6 shows that the maximum point is outside the range studied, its recommended to re-run the experimental work. Nonetheless, additional experiment performed reveals the volume of extraction solvent has no significant difference in the range of 400-500 µL. The percentage of contribution for extraction solvent versus the number of tablets consumed in the study was calculated at 56.93%.

Effect number of tablets

Sodium dihydrogen phosphate and sodium bicarbonate were selected as proton donor and carbon dioxide source, respectively. With a sufficient number of effervescent tablets added into the aqueous sample, it can produce a larger amount of bubbles, which helps the acceleration of the targeted analyte towards the upper phase of the solution. The production of CO_2 microbubbles with gentle release creates good contact time between microbubbles and organic droplet, 1-dodecanol. The in-situ production of CO_2 microbubbles is responsible for breaking down the emulsion and promoting the phase separation process. Bicarbonate has shorter effervescence time [35], thus consumption of the five tablets seemed suitable to complete the extraction. The percentage of contribution by the number of tablets in the extraction process of acetaminophen was calculated at 9.73% (Figure 7).

Effect adjustment of temperature

A suitable temperature can allow the extraction solvent (1-dodecanol) to be fully dispersed into the aqueous solution and ensure a rapid acceleration of acetaminophen (mobility of analyte) from water phase into the extraction solvent. The percentage of contribution by the effect of water temperature towards the extraction efficiency was calculated at 33.36% (Figure 8). There is no significance on this relationship, but temperature must be maintained above 24 °C to hold the solvent in liquid form. For 1-dodecanol, the melting point near the room temperature (24 °C), tunable properties make easier change from liquid to solid or vice versa. Extractant droplets can be easily collected after solidifying at low temperatures due to their tunable properties. The floated extraction solvent (d = 0.8309 $g \cdot mL^{-1}$) was much easier to collect and the extract was cleaner, compared to high density solvent. Besides, solidified floating phase was easily transferred, which avoided the loss of the analyte ensuring a high precision.

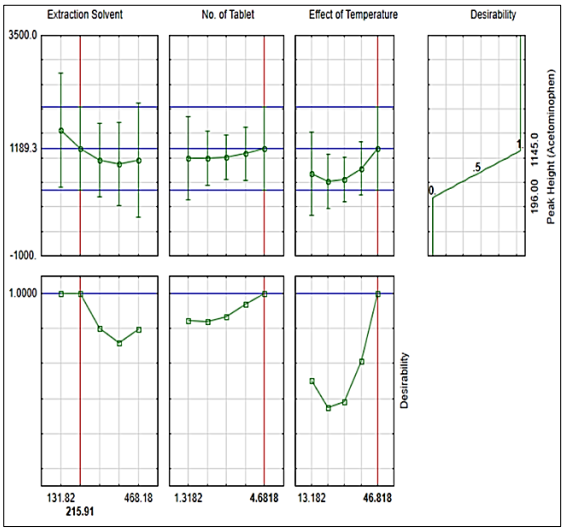


Figure 3. Optimizer plots for variables studied

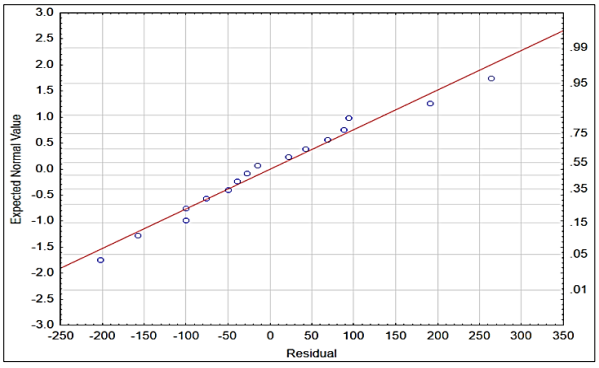


Figure 4. The normal probability plot

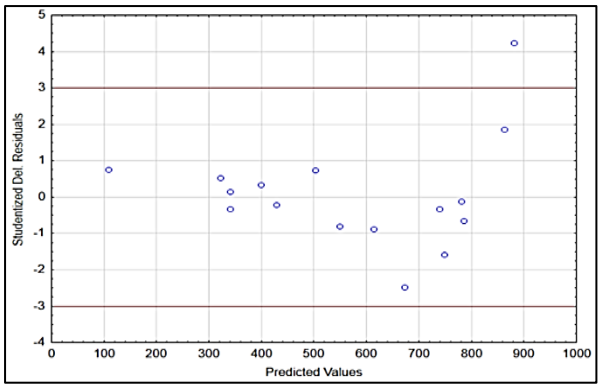


Figure 5. The residuals versus fitted data set

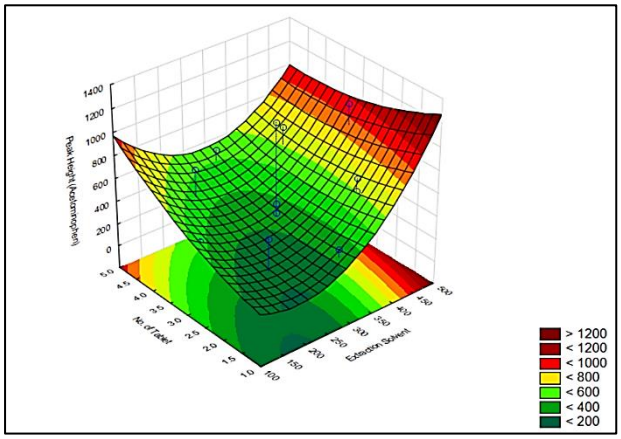


Figure 6. The 3D response shows the relationship between the number of tablet *vs* the extraction solvent

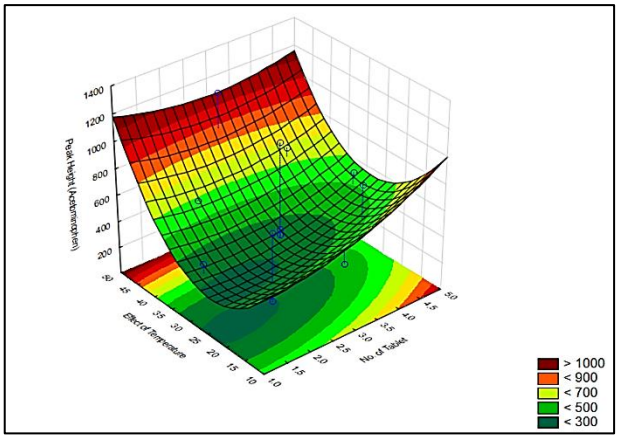


Figure 7. The 3D response shows the relationship between the effect of the temperature *vs* the number of tablets

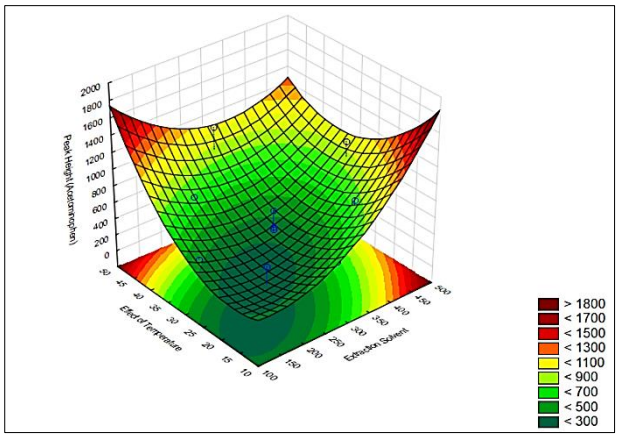


Figure 8. The 3D response shows the relationship between the effect of temperature *vs* the extraction solvent

Validation of the proposed method

A good linearity range was achieved at a satisfactory level of $R^2 \geq 0.995$ (Table 3). The sensitivity of the proposed method was shown by calculating the limit of detection and quantification (LOD and LOQ), which were recorded at 0.008 µg mL^{-1} and 0.028 µg mL^{-1}, respectively. Good extraction recovery of 85%-94% was recorded when two concentrations of spiked acetaminophen (500 and 100 ng mL^{-1}) were introduced into the matrix samples. Recovery of the proposed method was comparable with other liquid phase microextraction such as hollow fiber (96.8-127.8%), and dispersive using ionic liquid (95-96%), respectively [20-21]. The repeatability test indicated low bias measurement (i.e., <5% RSD), which was below the acceptable value proposed by AOAC guidelines.

Green assessment profile

The proposed method was a green methodology, which falls under excellent score (Table 4). On the eco-scale it recorded a high score of 88 and used low energy, either for extraction or chromatographic analysis. The deduction point was attributed by consumption of a reagent (methanol, dodecanol, glycerin), instrument and waste generation post analysis. The AGREE metric score of the proposed method was 0.65 (Figure 9). The AGREE metric showed that the proposed microextraction procedure was a green method based on criteria such as (4) integration of analytical processes for synchronous step (preparation, extraction and retrieval), (6) no derivatization agent used during extraction and analysis (7) minimal waste generation post analysis (8) high number of consecutive samples that can be analyzed in one hour due to reach fast equilibrium phase, (11) consumption of less toxic reagents and (12) minimal threats to operator and environment due to reagent used. Two criteria namely (2) minimal sample size and (3) *in-situ* measurement represented by red color received a low score. Thus, improvement on both criteria may be considered for future works.

Table 3. Analytical performance of extraction method

Analytical Assay	**Figure of Merit**
Linearity, r^2	0.995
LOD (µg mL^{-1})	0.008
LOQ (µg mL^{-1})	0.028
ER, %	85-94
RSD (Intra-day), n = 3	0.70-1.02
RSD (Inter-day), n = 3	0.95-1.42
Real sample (µg mL^{-1})	Fortified with brand A (5.60)
	Fortified with brand B (5.47)

Table 4. The penalty points calculated for the proposed method

Assessment Criteria	**Sub-Criteria**	**Consumption**	**Penalty Points**
Reagents	Type (Hazard)		
	Methanol (3)	10-100 mL	6
	1-dodecanol (2)	< 10 mL	2
	Glycerin (1)	< 10 mL	1
	Sodium bicarbonate (1)	< 10 g	1
	Sodium hydrogen phosphate (0)	< 10 g	0
Instruments	Energy		
	HPLC-UV		1
	Occupational hazard		0
Waste		< 1 mL	1
Total Penalty Point			12
Eco-scale score			88

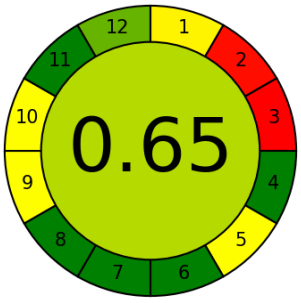


Figure 9. Generic result of AGREE assessment for the proposed method

Conclusion

The research work illustrated the successful application of the dispersive liquid-liquid microextraction combined with the effervescent tablet as a dispersive agent. The optimized method shows good performance to extract acetaminophen drugs in water samples at low-level concentration. This work provides some benefits in terms of method performance, including the short time required for sample preparation, extraction, and instrumental analysis. Low bias values obtained in calculated data suggest that the method is comparable to other developed liquid phase microextraction methods. It is worth to note that the method seems suitable for routine analysis. Analytical eco-scale and AGREE metric score have given concrete evidence about the greenness profile of the proposed method.

Acknowledgements

The authors acknowledge the Ministry of Higher Education, Malaysia and Universiti Malaysia Terengganu for providing financial support under the research grant FRGS/1/2019/STG01/UMT/03/3 (Vot 59585).

References

1. Lasarte-Aragonés, G., Lucena, R., Cárdenas, S. and Valcárcel, M. (2014). Effervescence assisted dispersive liquid–liquid microextraction with extractant removal by magnetic nanoparticles. *Analytica Chimica Acta*, 807: 61-66.
2. Jiang, W., Chen, X., Liu, F., You, X. and Xue, J. (2014). Effervescence-assisted dispersive liquid–liquid microextraction using a solid effervescent agent as a novel dispersion technique for the analysis of fungicides in apple juice. *Journal of Separation Science*, 37(21): 3157-3163.
3. Piao, H., Jiang, Y., Qin, Z., Tao, S., Ma, P., Sun, Y. and Song, D. (2020). Development of a novel acidic task-specific ionic liquid-based effervescence-assisted microextraction method for determination of triazine herbicides in tea beverage. *Talanta*, 208: 120414.
4. Shishov, A., Sviridov, I., Timofeeva, I., Chibisova, N., Moskvin, L. and Bulatov, A. (2017). An effervescence tablet-assisted switchable solvent-based microextraction: On-site preconcentration of steroid hormones in water samples followed by HPLC-UV determination. *Journal of Molecular Liquids*, 247: 246-253.
5. Wang, X., Wu, L., Cao, J., Hong, X., Ye, R., Chen, W. and Yuan, T. (2016). Magnetic effervescent tablet-assisted ionic liquid dispersive liquid–liquid microextraction of selenium for speciation in foods and beverages. *Food Additives & Contaminants: Part A*, 33(7): 1190-1199.
6. Zhou, P., Zheng, R., Zhang, W., Liu, W., Li, Y., Wang, H. and Wang, X. (2019). Development of an effervescent tablet microextraction method using $NiFe_2O_4$-based magnetic nanoparticles for preconcentration/extraction of heavy metals prior to ICP-MS analysis of seafood. *Journal of Analytical Atomic Spectrometry*, 34(3): 598-606.
7. Vakh, C., Pochivalov, A., Andruch, V., Moskvin, L. and Bulatov, A. (2016). A fully automated effervescence-assisted switchable solvent-based liquid phase microextraction procedure: liquid chromatographic determination of ofloxacin in human urine samples. *Analytica Chimica Acta*, 907: 54-59.
8. Gao, M., Wang, J., Song, X., He, X., Dahlgren, R. A., Zhang, Z. and Wang, X. (2018). An effervescence-assisted switchable fatty acid-based microextraction with solidification of floating organic droplet for determination of fluoroquinolones and tetracyclines in seawater, sediment, and seafood. *Analytical and Bioanalytical Chemistry*, 410(11): 2671-2687.
9. Fadzil, F. N. I. M., Loh, S. H., Ariffin, M. M. and Khalik, W. M. A. W. M. (2020). Development of effervescent-assisted liquid phase microextraction using 1-dodecanol for determination of ketoprofen drug in water. *ASM Science Journal*, 13: 1-8.
10. Shishov, A., Gerasimov, A., Nechaeva, D., Volodina, N., Bessonova, E. and Bulatov, A. (2020). An effervescence-assisted dispersive liquid–liquid microextraction based on deep eutectic solvent decomposition: Determination of ketoprofen and diclofenac in liver. *Microchemical Journal*, 156: 104837.

11. Tazulazhar, N., Loh, S. H., Ariffin, M. M. and Khalik, W. M. A. W. M. (2021). Optimization of effervescent tablet-assisted dispersive liquid-liquid microextraction with central composite design for preconcentration of stimulant drug. *Sains Malaysiana*, 50(1): 109-121.
12. Liu, X., Shen, Z., Wang, P., Liu, C., Zhou, Z. and Liu, D. (2014). Effervescence assisted on-site liquid phase microextraction for the determination of five triazine herbicides in water. *Journal of Chromatography A*, 1371: 58-64.
13. Moghadam, A. G., Rajabi, M., Hemmati, M. and Asghari, A. (2017). Development of effervescence-assisted liquid phase microextraction based on fatty acid for determination of silver and cobalt ions using micro-sampling flame atomic absorption spectrometry. *Journal of Molecular Liquids*, 242: 1176-1183.
14. Jing, X., Cheng, X., Zhao, W., Wang, H. and Wang, X. (2020). Magnetic effervescence tablet-assisted switchable hydrophilicity solvent-based liquid phase microextraction of triazine herbicides in water samples. *Journal of Molecular Liquids*, 306: 112934.
15. Medinskaia, K., Vakh, C., Aseeva, D., Andruch, V., Moskvin, L. and Bulatov, A. (2016). A fully automated effervescence assisted dispersive liquid–liquid microextraction based on a stepwise injection system. Determination of antipyrine in saliva samples. *Analytica Chimica Acta*, 902: 129-134.
16. Villaroel, E., Silva-Agredo, J., Petrier, C., Taborda, G. and Torres-Palma, R. A. (2014). Ultrasonic degradation of acetaminophen in water: effect of sonochemical parameters and water matrix. *Ultrasonics Sonochemistry*, 21(5): 1763-1769.
17. Montaseri, H. and Forbes, P. B. (2018). Analytical techniques for the determination of acetaminophen: A review. *TrAC Trends in Analytical Chemistry*, 108: 122-134.
18. Lima, D. R., Hosseini-Bandegharaei, A., Thue, P. S., Lima, E. C., de Albuquerque, Y. R., dos Reis, G. S., and Tran, H. N. (2019). Efficient acetaminophen removal from water and hospital effluents treatment by activated carbons derived from Brazil nutshells. *Colloids and Surfaces A: Physicochemical and Engineering Aspects*, 583: 123966.
19. Mashayekh-Salehi, A., Moussavi, G. and Yaghmaeian, K. (2017). Preparation, characterization and catalytic activity of a novel mesoporous nanocrystalline MgO nanoparticle for ozonation of acetaminophen as an emerging water contaminant. *Chemical Engineering Journal*, 310: 157-169.
20. Salvatierra-stamp, V., Muñiz-Valencia, R., Jurado, J. M. and Ceballos-Magaña, S. G. (2018). Hollow fiber liquid phase microextraction combined with liquid chromatography-tandem mass spectrometry for the analysis of emerging contaminants in water samples. *Microchemical Journal*, 140: 87-95.
21. Yao, C., Li, T., Twu, P., Pitner, W. R. and Anderson, J. L. (2011). Selective extraction of emerging contaminants from water samples by dispersive liquid–liquid microextraction using functionalized ionic liquids. *Journal of Chromatography A*, 1218(12): 1556-1566.
22. Yu, H., Merib, J. and Anderson, J. L. (2016). Faster dispersive liquid-liquid microextraction methods using magnetic ionic liquids as solvents. *Journal of Chromatography A*, 1463: 11-19.
23. Moeder, M., Schrader, S., Winkler, M. and Popp, P. (2000). Solid-phase microextraction–gas chromatography–mass spectrometry of biologically active substances in water samples. *Journal of Chromatography A*, 873(1): 95-106.
24. Moliner-Martínez, Y., Prima-Garcia, H., Ribera, A., Coronado, E. and Campíns-Falcó, P. (2012). Magnetic in-tube solid phase microextraction. *Analytical Chemistry*, 84(16): 7233-7240.
25. Asati, A., Satyanarayana, G. N. V. and Patel, D. K. (2017). Comparison of two microextraction methods based on solidification of floating organic droplet for the determination of multiclass analytes in river water samples by liquid chromatography tandem mass spectrometry using central composite design. *Journal of Chromatography A*, 1513: 157-171.
26. Gałuszka, A., Migaszewski, Z. M., Konieczka, P. and Namieśnik, J. (2012). Analytical eco-scale for assessing the greenness of analytical procedures. *TrAC Trends in Analytical Chemistry*, 37: 61-72.

27. Mohamed, H. M. and Lamie, N. T. (2016). Analytical eco-scale for assessing the greenness of a developed RP-HPLC method used for simultaneous analysis of combined antihypertensive medications. *Journal of AOAC International*, 99(5): 1260-1265.
28. Tobiszewski, M., Marć, M., Gałuszka, A. and Namieśnik, J. (2015). Green chemistry metrics with special reference to green analytical chemistry. *Molecules*, 20(6): 10928-10946.
29. Pena-Pereira, F., Wojnowski, W. and Tobiszewski, M. (2020). AGREE—Analytical GREEnness Metric Approach and Software. *Analytical Chemistry*, 92(14): 10076-10082.
30. Gamal, M., Naguib, I. A., Panda, D. S. and Abdallah, F. F. (2021). Comparative study of four greenness assessment tools for selection of greenest analytical method for assay of hyoscine N-butyl bromide. *Analytical Methods*, 13(3): 369-380.
31. Zeng, H., Qiao, K., Li, X., Yang, M., Zhang, S., Lu, R. and Zhou, W. (2017). Dispersive liquid–liquid microextraction based on the solidification of deep eutectic solvent for the determination of benzoylureas in environmental water samples. *Journal of Separation Science*, 40(23): 4563-4570.
32. Khodadoust, S. and Ghaedi, M. (2013). Optimization of dispersive liquid–liquid microextraction with central composite design for preconcentration of chlordiazepoxide drug and its determination by HPLC-UV. *Journal of Separation Science*, 36(11): 1734-1742.
33. Granberg, R. A. and Rasmuson, Å. C. (1999). Solubility of paracetamol in pure solvents. *Journal of Chemical & Engineering Data*, 44(6): 1391-1395.
34. Ojeda, C. B. and Rojas, F. S. (2011). Separation and preconcentration by dispersive liquid–liquid microextraction procedure: recent applications. *Chromatographia*, 74(9-10): 651.
35. Jafarinejad, M., Ezoddin, M., Lamei, N., Abdi, K., Babhadi-Ashar, N., Pirooznia, N. and Akhgari, M. (2020). Effervescent tablet-assisted demulsified dispersive liquid–liquid microextraction based on solidification of floating organic droplet for determination of methadone in water and biological samples prior to GC-flame ionization and GC-MS. *Journal of Separation Science*, 43(16): 3266-3274.

Malaysian Journal of Analytical Sciences (MJAS)
Published by Malaysian Analytical Sciences Society

PREPARATION AND CHARACTERIZATION OF COGON GRASS NATURAL FIBER AS A CONCRETE FILLER FOR GAMMA RADIATION SHIELDING

(Penyediaan dan Pencirian Serat Semula Jadi Rumput Cogon sebagai Pengisi Konkrit untuk Perisai Sinar Gama)

Yusrina Mohd Yusof and Siti Amira Othman*

Department of Physics and Chemistry, Faculty of Applied Sciences and Technology
Universiti Tun Hussein Onn Malaysia, 84600 Pagoh, Johor, Malaysia

**Corresponding author: sitiamira@uthm.edu.my*

Received: 3 April 2021; Accepted: 2 June 2021; Published: 27 June 2021

Abstract

Concrete is a combination of cement, fine aggregate, coarse aggregate, and water. Concrete has a high shielding potential against gamma radiation from radioactive source. Concretes having a higher attenuation coefficient may be produced by varying the additives of various specific densities to increase the shielding performance. This study uses a cogon grass fiber, an invasive and unwanted grass due to their ability to grow, and disrupt desirable vegetation efficiently as a reinforcement material mixed into the concrete composite to observe its performance in radiation shielding. Natural fiber is known to have a tolerance to post splitting, high energy absorption and increased fatigue resistance of cement-based composites. Cogon grass fibers are use with different percentages of 0%, 0.5%, 1.0% and 1.5% fiber content with four different thicknesses. In this study, the chemical and physical properties of cogon grass were characterized by the hydrolysis process (Chesson Method) and Atomic Force Microscopy (AFM), respectively. The effect of different percentage of cogon grass fiber in concrete with different thickness to linear attenuation coefficient, the difference of linear attenuation coefficient value between lead concrete and cogon grass fiber concrete and half value layer (HVL) were also investigated. The possibility of using cogon grass natural fiber as a block of concrete for gamma radiation shielding was also evaluated based on the results obtained in this study. The results show that the hemicellulose, cellulose and lignin content of raw cogon grass fiber were 27.60%, 36.62% and 6.11%, respectively. AFM micrograph of cogon grass showed a blocky and rough surface. The calculated linear attenuation coefficient of cogon grass fiber showed an increase with the increase of fiber content and thickness. However, lead concrete showed a higher attenuation coefficient and lower HVL value compared to cogon grass fiber. Despite that, cogon grass fiber concrete may have the potential to be used as shielding material with some improvement.

Keywords: cogon grass, fiber, concrete, filler, gamma radiation

Abstrak

Konkrit adalah campuran dari simen, agregat halus, agregat kasar, dan air. Konkrit mempunyai potensi pelindung yang tinggi terhadap sinaran radioaktif gama daripada sumber radioaktif. Konkrit yang mempunyai pekali pelemahan yang lebih tinggi dapat dihasilkan dengan mengubah bahan tambahan dari pelbagai ketumpatan tertentu untuk meningkatkan kadar pelindung. Kajian ini

menggunakan serat semula jadi rumput lalang, sejenis rumput invasif dan tidak diingini kerana kemampuan mereka untuk tumbuh, dan mengganggu tumbuh-tumbuhan yang diinginkan dengan cekap sebagai bahan tambahan yang dicampurkan dalam komposit konkrit untuk menilai kemampuannya dalam pelindung radiasi. Serat semula jadi diketahui mempunyai toleransi terhadap pemisahan pasca, penyerapan tenaga yang tinggi dan peningkatan ketahanan komposit berasaskan simen. Serat rumput lalang yang digunakan dengan peratusan 0%, 0.5 %, 1.0% dan 1.5% kandungan serat dengan empat ketebalan yang berbeza. Dalam kajian ini, sifat fizikal dan kimia rumput lalang dicirikan dengan menjalankan proses hidrolisis (Kaedah *Chesson*) dan Mikroskop Daya Atom (AFM). Kesan peratusan serat rumput cogon yang berbeza terhadap pekali pelemahan linear konkrit, kesan ketebalan berbeza dari konkrit serat rumput lalang terhadap pekali pelemahan linear dan perbezaan pekali pelemahan linear antara konkrit plumbum dan konkrit serat rumput lalang juga disiasat. Potensi menggunakan serat semula jadi rumput lalang sebagai blok konkrit sebagai pelindung radiasi gamma juga dinilai berdasarkan hasil kajian ini. Kajian menunjukkan kandungan hemiselulosa, selulosa dan lignin dari serat rumput lalang masing-masing adalah 27.60%, 36.62% dan 6.11%. Mikrograf AFM rumput lalang menunjukkan permukaan yang tersekat dan kasar. Pekali pelemahan linear yang dikira dari konkrit serat rumput lalang menunjukkan peningkatan dengan peningkatan kandungan serat dan ketebalan konkrit. Walau bagaimanapun, konkrit plumbum menunjukkan pekali pelemahan yang lebih tinggi dan nilai HVL yang lebih rendah berbanding dengan serat rumput cogon. Walaupun begitu, konkrit serat rumput cogon mungkin berpotensi digunakan sebagai bahan pelindung dengan sedikit peningkatan.

Kata kunci: rumput cogon, serat, konkrit, pengisi, sinaran gama, perisai

Introduction

Radiation shielding effectiveness has always been a concern and priority for many engineers and scientists as radioactive materials are extremely dangerous materials that can lead to a harmful effect when exposed to them. Radiation shielding is very important in protecting people from harmful radiation effects that can cause damage to the human body system. Primarily, radiation is a process where energy travels through space as particles or electromagnetic (EM) waves from the atoms of a radioactive material and can potentially penetrate various materials.

There are two types of radiation which is ionizing and non-ionizing radiation. Non-ionizing radiations like light, microwaves and radio waves are less harmful as they have less energy compared to ionizing radiation since ionizing radiations can only cause the movement of molecules in an atom but not the electrons. On the other hand, common ionizing radiation comes from radioactive materials and also X-ray machines, including alpha radiation (α), beta radiation (β), neutron radiation, X-rays radiation, and gamma radiation (γ). Ionization can be produced by charged particles or ions in matter. This type of radiation can remove the electrons in an atom at the same time creating ions that contain a high amount of energy particles which makes it an extremely dangerous radiation. Thus, methods of shielding against these types of ionizing radiations that are harmful to humans need to be explored.

Fundamentally, shielding is when a source of radiation is blocked or shielded by barrier of solid or liquid material at which this material absorbs the energy from the radiation emitted by the source. Lead and concrete are the common materials used to shield radiation. However, according to AbuAlRoos et al. [1], in their review, indicate that lead exposure is a significant environmental disease that may harm the environment and has serious consequences for the human body. A suitable radiation shielding material is therefore desperately required to avoid the harmful effects of radiation on human beings and the environment. The most effective features of radiation shielding materials are high atomic numbers and high-density materials, such as tungsten and concrete. Hence, through this study, concrete is the choice to be used as a radiation shielding material. Basically, according to Ekolu et al. [2], concrete is a durable substance and most commonly used in construction material. The structures of the reinforced concrete can also be built to be resilient in extreme environmental conditions to withstand harsh winds, fire and earthquakes.

According to Gencel et al. [3], concrete is an ideal and appropriate shielding material for nuclear reactors, particulate accelerators, research reactors, hot laboratories and medical facilities. This material is commonly used as a shielding material. Concretes are a fairly low-cost material, easily treated and casted into complex shapes. It contains a mix of different light and heavy elements and a photon and neutron mitigation capability. According to Han et al. [4], the composite of cement, water and heavyweight aggregates are the materials in the radiation shielding concrete. Due to its high density and large content of crystal water, it can resist radiations including alpha rays, beta rays, gamma rays, x-rays and neutrons. The ability of concrete to be used in many fields that required shielding of radiation sources is well recognized and acknowledged by most researchers.

Radiation sources are integral parts of human daily lives and these sources exist in different forms and intensities. To maintain and protect the high quality of our everyday lives for instance, smoke sensors are used to alert people when the fire occurs, x-ray devices are used to detect concealed weapons, as well as other kinds of imaging techniques that are to identify diseases. However, without proper shielding, the ineptitude in handling the radiation emitting devices, or the failure to provide protective equipment to a person who handles these devices will likely cause permanent injuries and deaths due to prolonged or even brief exposures to radiations. This is where radiation shielding concrete plays a role to prevent such harmful and lethal radiation effects.

In this study, the natural fiber used as reinforcement in concrete to enhance the radiation shielding performance is "*Imperata Cylindrica*", usually known as Cogon grass or "*Lalang*" in Malaysia. Among natural fibers, cogon grass is classified as a type of grass fiber together with bamboo, bagasse, Napier, corn and others [5]. According to Jumaidin et al. [6], cogon grass is one of the ten worst weeds in the world because it is capable of quickly colonizing, spreading and desirable attractive species. The weed comes from the Poaceae family, native to the temperate and tropical Old World areas. It is a persistent rhizomatized grass native to East and Southeast Asia, Micronesia, Australia, India, Melanesia and Africa.

Cogon grass is known as an invasive species in several countries beyond its native range. The plant is typically used for flood control and other cultivars are grown as ornamentals. Approximately 2 cm in diameter, it can grow up to 3 meters or between 2 and 10 feet tall. Cogon grass has historically been commonly used only in papermaking and making of bags and mats as well as in traditional Chinese medicine. However, the growth of this exotic invasive species is unstoppable and might have a major influence on either ecological or economic consequences in some area. So, the use of cogon grass needs to be redefined whether in construction, manufacturing, or any other fields so that the existence of this plant-life is not wasted. Therefore, cogon grass may be beneficial as it can be proposed as an alternative fiber to reinforced concrete as a radiation shielding material and at the same time enhance the shielding performance of concrete.

Concrete credibility and performance as a radiation shielding structure have been improved and upgraded from time to time by researchers that found new solutions to acquire better properties of concrete as it is also a better choice of material compared to lead where its toxicity is detrimental to the environment and the human body. Natural fiber will be used as an additive as reinforcement in the concrete proportion to increase the quality of concrete for radiation shielding performance and at the same time it can lead to environmental protection purposes. Moreover, natural fibers which refer to plant or vegetable fibers are the most utilized and applied in different engineering tools. Furthermore, cogon grass does not have any economic value and is commonly treated as waste by many.

Moreover, the breeding of cogon grass is also unstoppable as it continues to grow aggressively and may become a disturbance to new seedlings of desirable vegetations. Farmers and planters also may have difficulty in controlling cogon grass population as it costs a lot of energy, effort and money. Therefore, cogon grass breeding can be controlled by using it to reinforce concrete. This study will evaluate the

practicality of adding cogon grass fiber in concrete to achieve a better radiation shielding performance based on the use of natural fiber guided by the literature. Concurrently, this study will also strive to establish beneficial usage cogon grass so that it may play a small part in the local economy development.

In Malaysia, the authority that license any ionizing radiation activities and industries is the Atomic Energy Licensing Board (AELB), which covers both medical and non-medical uses. Radiation safety and radiation control are being constantly boosted and challenged. Many agencies and organizations are involved in developing radiation protection policies. They also contribute to the new legislation for protection against risks caused by the ionizing radiation. Furthermore, the problem of cogon grass or "*lalang"* grass in this country can be overcome by using it in the construction field. Cogon grass can be an alternative fiber that can easily be found in Malaysia to improve the strength of concrete that can be used as radiation shielding materials in medical and non-medical purposes in Malaysia.

The potential of natural fiber especially cogon grass as reinforcement in concrete will be studied and determined in this study. Moreover, the ability of the fiber reinforced concrete in improving the radiation shielding performance will also be evaluated so that its feasibility can be used as an effective radiation protection in Malaysia can be determined.

Materials and Methods

Sample collection

Cogon grass is an abundantly inexpensive weed growing in Malaysia that can be easily cultivated through seeds and large rhizome systems [7]. Production of these grass fibers can turn the wasted leaves into a renewable and low-cost natural fiber that will be integrated into the concrete mixes. Cogon grass as seen in Figure 1, is often visible as a luxurious yellowish-green grass on the roadsides. The cogon grass for this study was collected from the field area in Klang, Selangor.

Preparation of the fiber sample

A multiple-step procedure is performed to prepare the samples of the cogon grass fiber. Firstly, the cogon grass was cleaned with water to eliminate dust, waste, and any harmful materials and then left to dry under the sunlight for a week. Secondly, the dried grasses were cut manually and sieved to ensure that each cut piece of fibers is about 1 mm to 2 mm in size. Next, they are placed in the airtight glass container and labelled as cogon grass (CGF). For further analyses, the cogon grass fibers were later analyzed for their physical and chemical characteristics. Then, they are chemically treated to improve their strength performance [8]. After that, the cut and dried cogon grasses were weighed using an analytical weighing balance according to 0.5%, 1.0% and 1.5% volume dosage of fiber.

Cogon grass characterization

Chemical properties

Natural fibers consist of some basic chemical compositions such as cellulose, hemicellulose, pectin, lignin, and others. Determination of chemical compositions such as the amount of lignin, cellulose, and hemicellulose in natural fiber can be accomplished by conducting a hydrolysis test. Therefore, in this study, the hydrolysis process is carried out using the Chesson method. To begin, approximately 1 g of dry cogon grass fiber (W1) was mixed with 150 mL of distilled water at a temperature of about 90 to 100 °C for an hour. Then, a filter was used to separate the residue fibers which were then cleaned with 300 mL of hot water. After that, the residual fibers were dried in an oven at 120 °C until a constant weight is observed (W2).

The process continued with a mixture of dry residue (W2) with 150 mL of 1 N H_2SO_4 which after that being heated as previously done with the same temperature and period. To prepare 150 mL of 1 N H_2SO_4, formula and steps below were followed.

Volume of sulphuric acid + Volume of distilled water = 150 ml

1. Determine the gram of sulphuric acid

$$\text{Gram of } H_2SO_4 = \frac{\text{molar mass of } H_2SO_4}{\text{number of moles}} \quad (1)$$
$$= \frac{98.08 \text{ g/mol}}{2}$$
$$= 49.04 \text{ g}$$

2. Determine the gram of compound needed

Compound needed = (N desired) (equivalent mass) (volume in litre desired)
= (1) (49.04g) (0.15 litre)
= 7.356 g

3. The volume of concentrated acid needed

$$\text{Concentrated acid needed} = \frac{\text{gram of compund needed}}{(\text{percent of conc. acid})(\text{specific gravity})} \quad (2)$$
$$= \frac{7.356 \text{ g}}{(0.97)(1.84)}$$
$$= 4.12 \text{ mL}$$

Therefore, 4.12 ml concentrated H_2SO_4 diluted into 145.88 mL of distilled water.

Then, the residues were filtered and washed again with 300 mL of distilled water then dried and weighed (W3). Next, the dried residues were soaked in 10 mL of 72% H_2SO_4 at room temperature for about four hours. About 150 mL of N H_2SO_4 was added to the mixture and refluxed at a constant temperature of between 90° to 100°C for an hour. Then, the fibers were again washed with 400 mL of distilled water and being later heated in an oven at 120°C after which the weight is taken (W4). As for the final step, the fibers (W4) were heated until ashes were formed and the weight of ashes was recorded (W5).

Later on, the amount of cogon grass fiber's chemical compositions (hemicellulose, cellulose and lignin) can be calculated using equation (3), equation (4) and equation (5) as below:

$$\text{Hemicellulose, He} = \frac{W2 - W3}{W1} \times 100\ \% \quad (3)$$

$$\text{Cellulose, Ce} = \frac{W3 - W4}{W1} \times 100\ \% \quad (4)$$

$$\text{Lignin, Li} = \frac{W4 - W5}{W1} \times 100\ \% \quad (5)$$

Hence, using all the weights taken and the equations above, the percentage of hemicellulose (He), cellulose (Ce) and lignin (Li) in the cogon grass fiber can be obtained.

Chesson method

Determination of chemical compositions such as the amount of lignin, cellulose, and hemicellulose in natural fiber can be accomplished by conducting a hydrolysis test also known as Chesson Method. In this experiment, five different weights needed to be obtained as they were crucial for this test. These five weights are the weight of dry natural fiber labeled as W1, the weight of dry residue of fiber after being mixed with distilled water (W2), the weight of dry residue after being mixed with N H_2SO_4 (W3), the weight of solid after being mixed with 72% H_2SO_4 and N H_2SO_4 (W4), and lastly, the weight of the fibers that were heated to ashes labeled as W5. All the weights recorded can be seen as shown in Table 1.

After that, the amount of cogon grass fiber's chemical compositions (hemicellulose, cellulose and lignin) can be calculated using the equations below.

1. Hemicellulose content

$$\text{Hemicellulose, He} = \frac{W2 - W3}{W1} \times 100\%$$
$$\text{He} = \frac{0.9351 - 0.6584}{1.0024} \times 100\%$$
$$\text{He} = 0.2760 \times 100\%$$
$$\text{He} = 27.60\%$$

2. Cellulose content

$$\text{Cellulose, Ce} = \frac{W3 - W4}{W1} \times 100\%$$
$$\text{Ce} = \frac{0.6584 - 0.2909}{1.0024} \times 100\%$$
$$\text{Ce} = 0.3662 \times 100\%$$
$$\text{Ce} = 36.62\%$$

3. Lignin content

$$\text{Lignin, Li} = \frac{\text{W4} - \text{W5}}{W1} \times 100\%$$

$$\text{Li} = \frac{0.2909 - 0.2296}{1.0024} \times 100\%$$

$$\text{Li} = 0.0611 \times 100\%$$

$$\text{Li} = 6.11\%$$

Hence, using all the weights taken and the equations above, the percentage of hemicellulose (He), cellulose (Ce) and lignin (Li) in the cogon grass fiber can be obtained.

Table 1. All the weights recorded in the hydrolysis test

Sample of Cogon Grass Fiber	Weight of Cogon Grass Fiber Sample (±0.0001 g)
Weight 1 (W1)	1.0024
Weight 2 (W2)	0.9351
Weight 3 (W3)	0.6584
Weight 4 (W4)	0.2909
Weight 5 (W5)	0.2296

Physical properties

In this study, cogon grass specimens (Figure 1) were studied using Atomic Force Microscopy (AFM) (Bruker, United States) for their microstructural and surface characteristics where there were two locations were observed in this study, point 1 and point 2. A small piece of the specimen was placed onto a double-sided tape of the specimen stub. Nano scope Analysis Software was used to analyze the microstructural characteristics of cogon grass fiber.

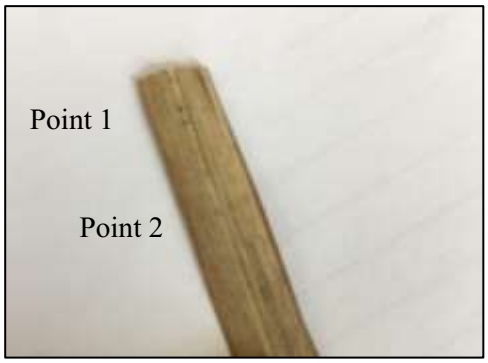


Figure 1. Cogon grass specimen used in Atomic Force Microscopy (AFM)

Chemical treatment of cogon grass fiber

In this study, the fibers were immersed in 4% of NaOH concentration with the soaking duration of these fibers being 24 hours as shown in Figure 2(a). This could partially remove the hemicellulose, waxes and lignin present on the surface of the fibers. This immersion led to an increase in thermal decomposition temperature and mechanical properties of the fibers themselves [17]. After the soaking process, the fibers were immersed in distilled water for one hour to remove excess sodium hydroxide. Then the fibers were dried for another week and kept in sealed plastic bags to help avoid any exposure to moisture (Figure 2(b)).

Preparation of concrete specimen

One (1) normal conventional concrete specimen, three (3) concrete sample sets utilizing different quantities of cogon grass fiber (0.5 %, 1.0 % and 1.5 %) and three (3) concrete sample sets utilizing different quantities of lead powder (Figure 3) (0.5 %, 1.0 % and 1.5 %) were prepared. All the samples had the same thickness of 2 centimeters. The percentage values of 0.5 %, 1.0 % and 1.5 % were chosen to see the trend and relationship between material. Later on, the same set of concrete specimens were produced with a thickness of 4 cm,

6cm, and 8 cm. Table 2 below shows the constituent of each sample according to concrete mixes ratio of 1:2:3.5.

Materials used in concrete preparation

Ordinary Portland Cement (OPC) (Figure 4a) was used to prepare the samples tested. Fine sand (Figure 4b), which passes by 4.75 mm to 63μm sieve size, while gravel (coarse aggregate) of 6.3 mm to 20 mm thickness has also been used.

Frame construction

Four sets of plywood frames with measurement of 10 cm × 10 cm were constructed to cast the concrete slabs with 2 cm, 4 cm, 6 cm, and 8 cm thickness (Figure 5).

Concrete mix design

Suggest mixing cement, fine sand (fine aggregate), gravel (coarse aggregate) and water at a ratio of 1:2:3.5:0.55 to produce the concrete specimens. Later on, a different percentage of reinforcement/ additive was added to the mixture.

Mixing process

Once the materials were fully organized according to specified weights in trays, the dried cogon grass fiber, cement, sand and rough aggregates were manually mixed. Dry mixing of the materials was carried out where cement was applied, followed by the addition of sand, coarse aggregates and fiber. Every component was applied gradually and uniformly so that the uniform distribution of the fibers through the concrete could be verified. The calculated quantity of water was then applied and gradually poured into the dry mixture until uniformity was accomplished. Then, the freshly mixed concrete was poured and spread out in a molds frame previously constructed. After that, the specimens were left to set for 24 hours. After the casts were set, the concrete slabs were de-molded from the plywood frames. The figure of concrete specimens with 2 cm (Figure 6a), 4 cm (Figure 6b), 6 cm (Figure 6c) and 8 cm (Figure 6d) thickness can be seen below.

Curing process

The concrete slabs were completely immersed and cured in a pool of water (Figure 7) for a day to achieve ultimate compressive strength. It is well understood that proper curing of concrete is very necessary not only to obtain the required compressive strength, but also needed in designing strong concrete. Finally, at the end of the curing phase, the specimens were left to be dried under the sun for 24 hours before being tested for gamma radiation shielding.

Gamma-ray linear attenuation coefficient measurement

The linear attenuation coefficients are often used to analyze the performance of radiation shielding of any type of materials. In this study, the developed radiation shielding concrete slabs as shown in Figure 8a were tested to determine the measurement of exposure dose rate using a survey meter (Figure 8b). The survey meter used was OD-02 survey meter with mode operation of H*(10). The type of radiation detector for this survey meter was an air-opened ionization chamber. Measurements were performed on gamma-rays emitted from Cobalt-60, ^{60}Co radioactive source.

The experimental setup used in this study is shown in Figure 8c. As shown in the figure, the concrete previously produced was placed between the radioactive source (in the container) and the survey meter and the distance between the detector and the radioactive source was fixed at 10 cm for all concrete samples. The measurements were taken at 20 minutes intervals for each sample.

After the exposure dose rate was recorded, the linear attenuation coefficients were determined by a calculation of I and I_o, which are the count rates recorded by the survey meter, with and without the thickness absorber x, using equation (6) below.

$$I = I_o e^{-\mu x} \quad (6)$$

where I is the intensity of radiation transmitted through the material of thickness x, I_0 is the incoming radiation intensity, and μ is a linear attenuation coefficient.

Besides that, through this study, the half value layer (HVL) was also calculated according to various concrete thickness. HVL is the thickness at which an absorber will reduces the radiation to half of its original

intensity. The equation used to calculate the HVL value is as below.

$$HVL = \frac{0.693}{\mu} \quad (7)$$

where μ is a linear attenuation coefficient.

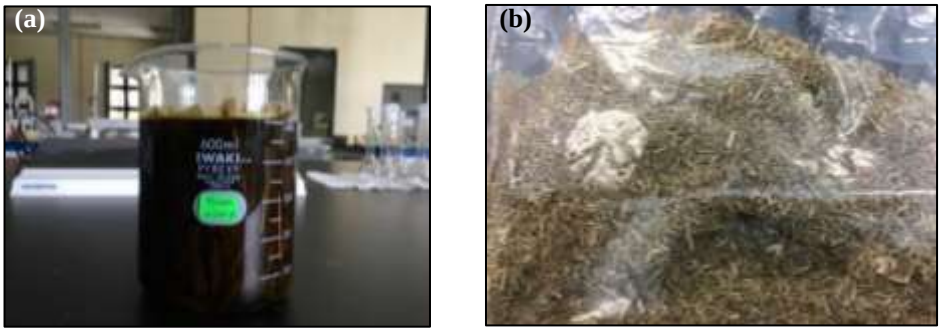


Figure 2. (a) Cogon grass fibers immersed in 4% of NaOH concentration for 24 hours (b) Cogon grass fibers were kept in sealed plastic bags



Figure 3. Lead powder used as a reinforcement in concrete

Table 2. Constituent of each sample according to concrete mixes ratio of 1:2:3.5

Percentage of Reinforcement in Concrete (%)	**Thickness (cm)**	**Mass (± 0.01 g)**					
		Water	**Cement**	**Sand**	**Aggregate**	**Fiber**	**Lead**
0	2	37.53	68.23	137.42	248.77	-	-
	4	75.05	136.47	274.83	497.54	-	-
	6	112.59	204.70	412.25	746.31	-	-
	8	150.11	272.94	549.66	995.08	-	-
0.5	2	37.53	68.23	137.42	248.77	1.54	1.54
	4	75.05	136.47	274.83	497.54	3.08	3.08
	6	112.59	204.70	412.25	746.31	4.62	4.62
	8	150.11	272.94	549.66	995.08	6.16	6.16

Table 2 (cont'd). Constituent of each sample according to concrete mixes ratio of 1:2:3.5

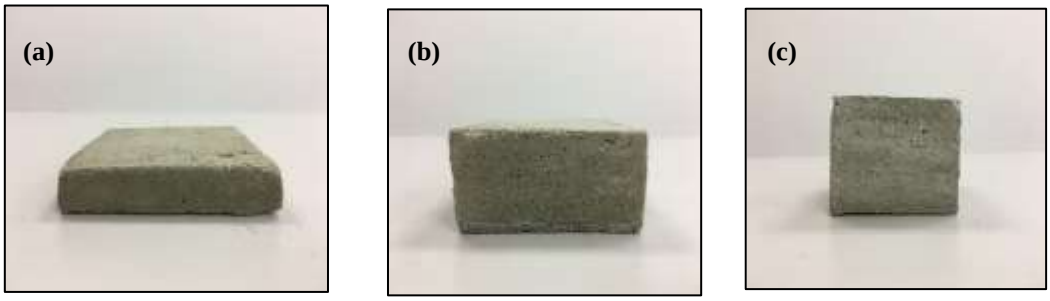
Percentage of Reinforcement in Concrete (%)	Thickness (cm)	Mass (± 0.01 g)					
		Water	Cement	Sand	Aggregate	Fiber	Lead
1.0	2	37.53	68.23	137.42	248.77	3.08	3.08
	4	75.05	136.47	274.83	497.54	6.16	6.16
	6	112.59	204.70	412.25	746.31	9.24	9.24
	8	150.11	272.94	549.66	995.08	12.32	12.32
1.5	2	37.53	68.23	137.42	248.77	4.62	4.62
	4	75.05	136.47	274.83	497.54	9.24	9.24
	6	112.59	204.70	412.25	746.31	13.86	13.86
	8	150.11	272.94	549.66	995.08	18.48	18.48



Figure 4. (a) Ordinary Portland cement (OPC) (b) Fine sands (fine aggregates) (c) Gravel (coarse aggregates)



Figure 5. Constructed frame using plywood



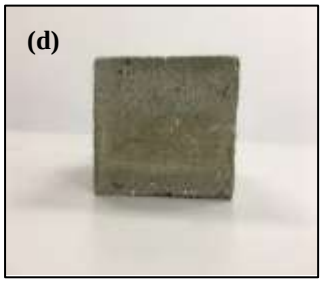


Figure 6. (a) 2 cm thickness of concrete specimen (b) 4 cm thickness of concrete specimen (c) 6 cm thickness of concrete specimen (d) 8 cm thickness of concrete specimen



Figure 7. Soaking of slab into the water

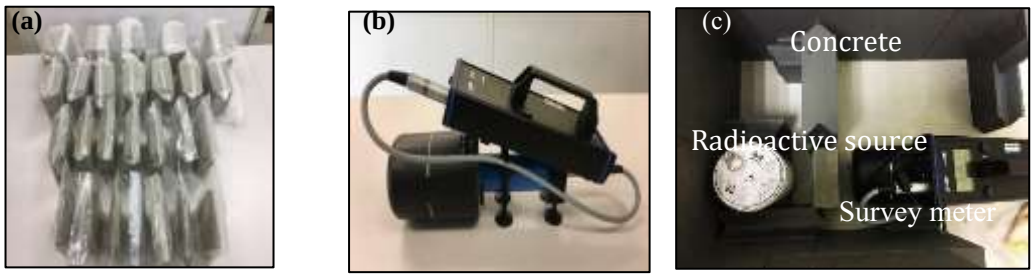


Figure 8. (a) Developed radiation concrete slabs (b) Survey meter (c) Experimental setup in this study

Results and Discussion

Chemical properties

Analysis using hydrolysis test

The percentage of chemical compositions in cogon grass natural fiber can be summarized in Table 3.

Table 3 above shows the chemical properties of cogon grass fiber which consist of cellulose, hemicellulose and lignin. For cellulose, this study shows that cogon grass contains 36.66% of cellulose, which is approximately similar with the result reported by Mohd Kassim et al. [9, 10] (37.1% of cellulose). Cellulose is a significant constituent because the increased cellulose content provides better quality and stronger materials. As for hemicellulose, cogon grass is characterized by a relatively low content of hemicellulose that is 27.60% where this amount could make a significant contribution to the product's strength. Lastly, the lignin content in cogon grass is 6.11% which is considered low. Different from the previous study, inaccuracies in

composition percentage obtained from this study may have been influenced by several factors such as preparation of the solutions and how the method was carried out.

Physical properties analysis

The physical properties of cogon grass fiber were observed using atomic force microscopy (AFM).

Atomic force microscopy analysis

Atomic force microscopy images of raw cogon grass fiber can be observed as shown in Figure 9. Figure 9(a) and 9(b) show AFM images of cogon grass fiber at two different places. The images are shown in two-dimensional (2D) image. Whilst, Figure 9(c) and Figure 9(d) illustrated AFM images of cogon grass fiber in three-dimensional (3D). Surface roughness of this fiber can be seen from image size 6 × 6 μm^{-1} scan area.

All figures above illustrated are AFM images of ultra-structural cogon grass fiber that appears to have a blocky and rough surface. In a three-dimensional image, cogon grass fiber is shown to have very obvious rough surface. Meanwhile, a blocky surface is due to the cuticular waxy layer which contains long chains of fatty acids, lipids and phenolic compounds [11]. *Imperata* cuticular waxy layer has very low permeability to cellulose-degrading enzymes, and it was expected that the alkaline NaOH pre-treatment can remove the outer granular waxy layer sufficiently and to allow direct contact with a digestive enzyme. Non-cellulosic materials on the surface of the *Imperata* can be seen in phase images in AFM as grains. Granules or grain surfaces consisted mostly of lignin but also hemicellulose and possible hemicellulose extractives.

Radiation shielding performance of fiber-reinforced concrete by measuring the gamma-ray linear attenuation coefficient

The radiation shielding performance of materials can be evaluated by determining the linear attenuation coefficient. The linear attenuation coefficient was calculated from the measurement of dose rate taken from the survey meter to analyze the effect of fiber reinforcement in concrete for radiation shielding performance as the amount of fiber increases. However, there are also other factors that affect linear attenuation coefficient including absorber thickness, x and density of the material. In this study, half value layer (HVL) was also calculated.

Effect of different percentage of cogon grass fiber reinforced in concrete to the linear attenuation coefficient

In this study, cogon grass fibers were added in concrete mixture with four different percentages of fiber content (0%, 0.5%, 1.0% and 1.5%). The obtained results of calculated linear attenuation coefficients for cogon grass natural fiber concrete were presented in Table 4 and Figure 10.

From the line graph, it can be observed that the linear attenuation coefficient slightly increases as the increase of the percentage of the fiber for all tested absorber thickness, x. At 2 cm thickness, the value of the linear attenuation coefficient for 0 percent concrete fiber content is 0.1256 cm^{-1} compared to 0.1479 cm^{-1} for 0.5 percent fiber content, 0.1590 cm^{-1} for 1 percent fiber content and 0.1736 cm^{-1} for 1.5% concrete fiber content.

Next, at 4 cm thickness, the value of the linear attenuation coefficient for 0 percent concrete fiber content is 0.1479 cm^{-1} which is similar to the value for concrete with 0.5 percent fiber content, 0.1736 cm^{-1} for 1 percent fiber content and 0.2168 cm^{-1} for 1.5% concrete fiber content. As for the 6 cm thick concrete sample, 0% concrete fiber content indicate 0.1327 cm^{-1} linear attenuation coefficient, 0.5 percent concrete fiber content with 0.159 cm^{-1} linear attenuation coefficient, 0.1884 cm^{-1} for 1 percent concrete fiber content and 0.2218 cm^{-1} for 1.5% concrete fiber content. Lastly, for the 8 cm concrete, the value of the linear attenuation coefficient for 0 percent concrete fiber content is 0.1742 cm^{-1} compared to 0.2177 cm^{-1} for 0.5 percent fiber content, and 0.2653 cm^{-1} for both 1.0 % and 1.5% concrete fiber content.

Overall, this line graph, indicates that the increase in the percentage of cogon grass fiber content in concrete can influence and increase the value of the linear

attenuation coefficient for any absorber thickness, *x*. The linear attenuation coefficient shows and characterizes how easily a volume of material can be penetrated by a beam of light, sound, particles, or other energy or matter. A higher value of linear attenuation coefficient means that the beam or gamma radiation is quickly attenuated or weakened as it passes through the medium, in this case, cogon grass natural fiber. It can be observed that cogon grass natural fiber absorbed and attenuated the gamma radiation in a way that the fibers may affect of the radiation as it passes through the concrete. It is also found that the linear attenuation coefficient measured increases with the increase of fiber content, congruent to similar studies [12]. This also shows that the linear attenuation coefficient depends on the percentage of fiber content in concrete.

Effect of different thickness of cogon grass fiber reinforced concrete to the linear attenuation coefficient

Cogon grass fibers concretes were cast with four different thickness (2 cm, 4 cm, 6 cm and 8 cm). The obtained results of calculated linear attenuation coefficients for cogon grass natural fiber concrete were presented in Table 5 and Figure 11.

From the line graph, it can be observed that the linear attenuation coefficient slightly increases as the thickness of fiber concrete increases for all different percentages of cogon grass fiber. At 0% fiber content, the value of linear attenuation coefficient for 2 cm concrete is 0.1256 cm^{-1} compared to 0.1479 cm^{-1} for 4 cm concrete, 0.1327 cm^{-1} for 6 cm concrete and 0.1742 cm^{-1} for 8 cm concrete thickness.

At 0.5% fiber content, the value of linear attenuation coefficient for 2 cm concrete thickness is 0.1479 cm^{-1} which is similar to the value for the concrete with 4 cm thickness, 0.1590 cm^{-1} for 6 cm concrete and 0.2177 cm^{-1} for 8 cm concrete thickness. As for 1.0% fiber content, 2 cm thick concrete indicates a 0.1590 cm^{-1} linear attenuation coefficient, 4 cm concrete with 0.1736 cm^{-1} linear attenuation coefficient, 0.1884 cm^{-1} for 6 cm concrete and 0.2653 cm^{-1} for 8 cm concrete thickness. Lastly, for 1.5% fiber content, the value of the linear attenuation coefficient for 2 cm thick concrete is 0.1736 cm^{-1} compared to 0.2168 cm^{-1} for 4 cm concrete, 0.2218 cm^{-1} for 6 cm concrete and 0.2653 cm^{-1} for 8 cm concrete.

Overall, this line graph, indicates that the increase in concrete thickness did influence and increase the value of the linear attenuation coefficient. It can be observed that the calculated linear attenuation coefficient increases with the increasing of concrete thickness [13]. Therefore, the greater the thickness of the attenuating material, the greater is the attenuation.

Table 3. Chemical compositions of cogon grass fiber

Chemical Composition of Cogon Grass Fiber	**Percentage of Chemical Composition (% w/w)**
Hemicellulose	27.60
Cellulose	36.62
Lignin	6.11

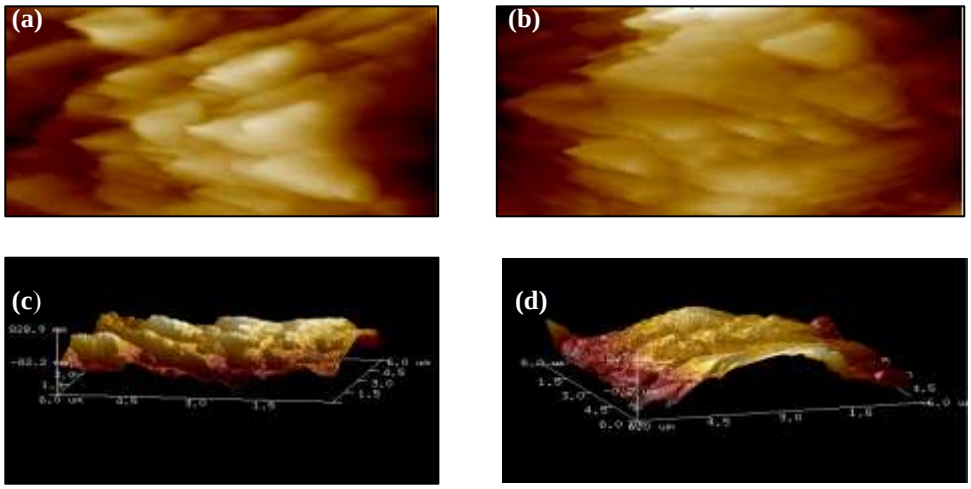


Figure 9. (a) AFM 2D image of cogon grass fiber at point 1 (b) AFM 2D image of cogon grass fiber at point 2 (c)AFM 3D image of cogon grass fiber at point 1 (d) AFM 2D image of cogon grass fiber at point 2

Table 4. Calculated linear attenuation coefficients (cm^{-1}) for cogon grass fiber concrete

Percentage of Fiber Reinforced in Concrete (%)	**Thickness, *x* (cm)**			
	2	**4**	**6**	**8**
0	0.1256	0.1479	0.1327	0.1742
0.5	0.1479	0.1479	0.159	0.2177
1.0	0.159	0.1736	0.1884	0.2653
1.5	0.1736	0.2168	0.2218	0.2653

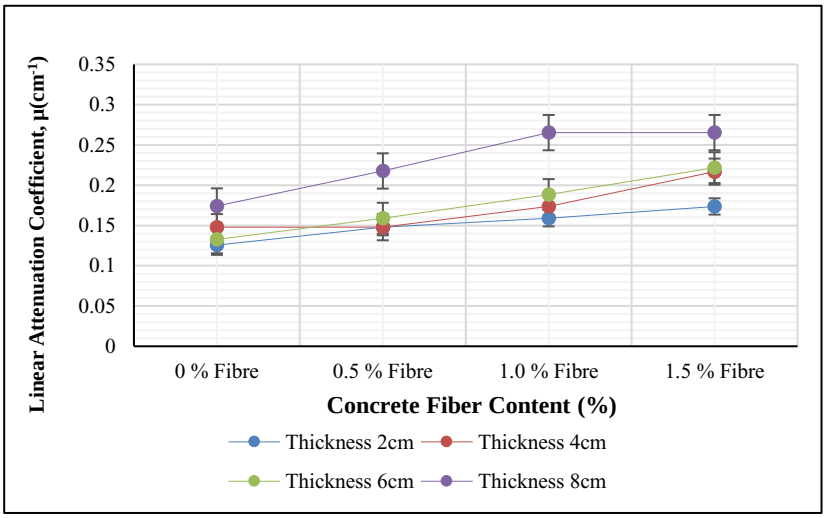


Figure 10. Line graph of linear attenuation coefficient (cm^{-1}) against the percentage of concrete fiber content (%)

Table 5. Calculated linear attenuation coefficients (cm^{-1}) for cogon grass fiber concrete for different thickness

Thickness (cm)	Percentage of Fiber Reinforced in Concrete (%)			
	0	0.5	1.0	1.5
2	0.1256	0.1479	0.159	0.1736
4	0.1479	0.1479	0.1736	0.2168
6	0.1327	0.1590	0.1884	0.2218
8	0.1742	0.2177	0.2653	0.2653

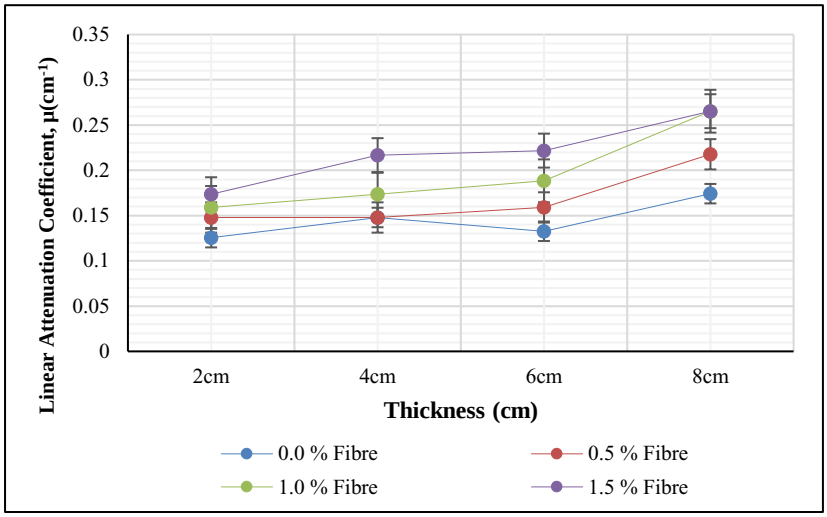


Figure 11. Line graph of linear attenuation coefficient (cm^{-1}) against the concrete thickness, x (cm)

Half value layer of concrete made with cogon grass fiber

Half value layer (HVL) is calculated using the equation of HVL $=\frac{0.693}{\mu}$. In this study, the obtained results of half layer value were presented as in Table 6 and Figure 12.

The results of half value layer (HVL) of concrete containing different percentage of cogon grass natural fiber can be seen in Table 6 and Figure 12, respectively. As shown in in Figure, the half value layer (HVL) values of concrete with 0 %, 0.5 %, 1.0% and 1.5% cogon grass fiber decrease with the increase of concrete thickness. This shows that the increase in concrete thickness decreases the HVL values. The lower the values of HVL, the better are the radiation shielding materials in term of the thickness requirements. For instance, for concrete with 1.0% fiber, the HVL values decrease with the increase of concrete thickness where the values are 4.3585 cm, 3.9919 cm, 3.6783 cm, and 2.6121 cm for the concrete thickness of 2 cm, 4 cm, 6 cm, and 8 cm, respectively. Figure 12 also shows that the half value layer (HVL) values of concrete with 1.5 % fiber are lower compared to concrete made with 0% fiber. Additionally, the figure also indicates that the half value layer (HVL) decreases with the increase of cogon grass fiber in the concrete.

Difference of linear attenuation coefficient between lead powder reinforced concrete and cogon grass fiber reinforced concrete

Concrete containing lead is commonly used to shield radiation. Therefore, in this study, the comparison between concrete containing cogon grass fiber and

concrete containing lead at 2 cm concrete thickness was done. The comparison results of calculated linear attenuation coefficients between concrete containing lead concrete and concrete containing cogon grass natural fiber were presented in Table 7 and Figure 13.

As shown in the table and figure above, the average trend line of the linear attenuation coefficient of concrete containing lead powder is higher than the concrete sample made with cogon grass natural fiber. At 0 percent reinforcement content, cogon grass fiber concrete recorded 0.1256 cm^{-1} of attenuation coefficient compared with 0.1316 cm^{-1} recorded for lead concrete. Next, at 0.5% reinforcement content, cogon grass concrete also shows a lower value of linear attenuation coefficient which is 0.1479 cm^{-1} than recorded by lead concrete which is 0.1756 cm^{-1}.

However, at 1 percent content, lead concrete recorded 0.1552 cm^{-1} which is lower than fiber concrete which recorded 0.1590 cm^{-1}. Lastly, at 1.5% content, the linear attenuation coefficient of lead concrete rose much higher than fiber concrete which is 0.2359 cm^{-1} compared to 0.1736 cm^{-1}. Overall, shows that lead concrete has a higher attenuation coefficient and shielding effectiveness compared to concrete containing cogon grass fiber. Lead is generally known to have a higher density compared to cogon grass fiber which has a much lower density. Therefore, this experiment also shows that the linear attenuation coefficient depends on the density of the shielding material.

Difference of half value layer between lead powder reinforced concrete and cogon grass fiber reinforced concrete

In this study, the comparison of half value layer (HVL) between concrete containing cogon grass fiber and concrete containing lead at 1.5 % content was done. The comparison results of calculated half value layer (HVL) were presented in Table 8 and Figure 14.

As shown in the Table 8 and Figure 14, the trend line of the half value layer (HVL) values of concrete containing lead powder are lower than the concrete sample made with cogon grass natural fiber. At 2 cm thickness, cogon grass fiber concrete recorded HVL value of 3.9919 cm which was higher than lead concrete with 2.9377 cm. At 4 cm, cogon grass concrete also showed a higher value of HVL which was 3.1965 cm than recorded by lead concrete which was 2.7472 cm. The 6 cm, lead concrete recorded lower HVL than the 6 cm fiber concrete with the HVL being 2.4623 and 3.1244 cm respectively. At 8 cm, the HVL values of lead concrete was lower than fiber concrete with 2.1289 cm compared to 2.6121 cm.

Overall, this graph indicates that the HVLs for both lead concrete and fiber concrete decrease as the concrete thicknesses increase of. However, lead concrete has a lower HVL value compared to concrete containing cogon grass fiber. The decrease of HVL value indicates a better radiation shielding materials in terms of thickness. It shows that concrete containing lead powder has better shielding properties compared to cogon grass fiber concrete. Despite that, cogon grass fiber concrete still exhibits the potential to decrease the HVL value with the increase of concrete thickness.

A higher value of linear attenuation coefficient means that the beam or gamma radiation is quickly attenuated or weakened as it passes through the medium. This study shows that the increase of cogon grass fiber content in concrete has increase the value of the linear attenuation coefficient for any absorber thickness, *x*. This study also indicates that the increase of concrete thickness also influences and increase the value of the linear attenuation coefficient. Linear attenuation coefficient is greater with the increase of concrete thickness. Besides that, the HVL of concrete containing cogon grass fiber decreases with the increase in concrete thickness. Furthermore, this study also shows that the HVL decreases with the increase of cogon grass fiber in the concrete.

By comparing the linear attenuation coefficient of cogon grass concrete and lead concrete, the results show that lead concrete has a higher attenuation coefficient and shielding effectiveness compared to cogon grass concrete. In gamma-ray shielding, lead contained in concrete increases the density of concrete compared to concrete containing cogon grass fiber.

Therefore, this shows that the linear attenuation coefficient depends on the density of the shielding material, and the lead concrete are more effective materials for shielding gamma rays compared to cogon grass fibers. As for HVL, lead concrete has higher HVL values compared to cogon grass fiber concrete since. Lead has a higher density compared to cogon grass fiber which has a much lower density. This study shows that the values of HVL are inversely proportionate to the concrete density. Therefore, this result further consolidates that the HVL depends on the thickness and also the density of the materials. It is also found that lead concrete is superior to cogon grass concrete in gamma radiation shielding.

The results obtained in this study, indicate that adding fiber in the concrete can increase the gamma-ray linear attenuation coefficient. A higher attenuation coefficient of a material shows a better performance as a gamma-ray radiation shielding. The linear attenuation coefficient slightly increases as the increase of the percentage of the fiber for all tested absorber thickness, x where x is 2 cm, 4 cm, 6 cm and 8 cm. It can be assumed that cogon grass natural fiber can absorb and attenuate the gamma radiation by decreasing the intensity of the radiation as it passes through the concrete. This also shows that linear attenuation coefficient can be increased with the percentage increase of fiber content in concrete. Besides that, the HVL value of cogon grass fiber concrete decreases with the percentage increase of fiber content and thickness. Therefore, through this study, it can be assumed that cogon grass has the potential to be used as reinforcement in concrete in enhancing the radiation shielding with the right amount of fiber in appropriate concrete thickness.

Unfortunately, by comparing the linear attenuation coefficient of concrete containing cogon grass fiber and concrete containing lead powder, this study shows that lead concrete is still far better as a shielding material compared to cogon grass fiber concrete due to its high density. However, although lead concrete has a much higher linear attenuation coefficient, the study shows that cogon grass fiber concrete can also attenuated and reduce the intensity of incoming radiation from a radioactive source as the percentage of fiber content increases [14]. Nevertheless, cogon grass fiber concrete has shown its potential to be commercialized and used as a shielding material and its performance can be improved by adding other materials in concrete composite that has higher density such as heavyweight aggregate. This improvement may reduce the use of lead as a shielding material as its toxicity may harm and affect the environment.

Furthermore, natural fiber can be obtained from nature and the use of these fibers are safer and more environment friendly. Moreover, nowadays, we are trying to reduce the use of non-biodegradable materials to keep our environment free from pollution [15]. Hence, natural fibers are the potential candidate to be used as additives in the concrete to improve the performance of radiation shielding at the same time reduce the environmental pollution. Thus, it can be said that cogon grass fiber which is in the class of natural fiber may have the possibility for use in shielding. Cogon grass is embedded with silica and contains a durable fiber in which silica is usually used as an additive in concrete to add strength to it [16]. Additionally, natural fiber is becoming important materials for building construction due to its lightweight, high strength to weight ratio, corrosion resistance, and other benefits. Furthermore, cogon grass has an economic advantage an additive in the radiation shielding concrete since its growth rampantly and abundantly in nature.

Table 6. Half value layer (HVL) (cm) for cogon grass fiber concrete

Percentage of Fiber Reinforced in Concrete (%)	**Thickness, *x* (cm)**			
	2	**4**	**6**	**8**
0	5.5175	4.6856	5.2223	3.9782
0.5	4.6856	4.6856	4.3585	3.1833
1.0	4.3585	3.9919	3.6783	2.6121
1.5	3.9919	3.1965	3.1244	2.6121

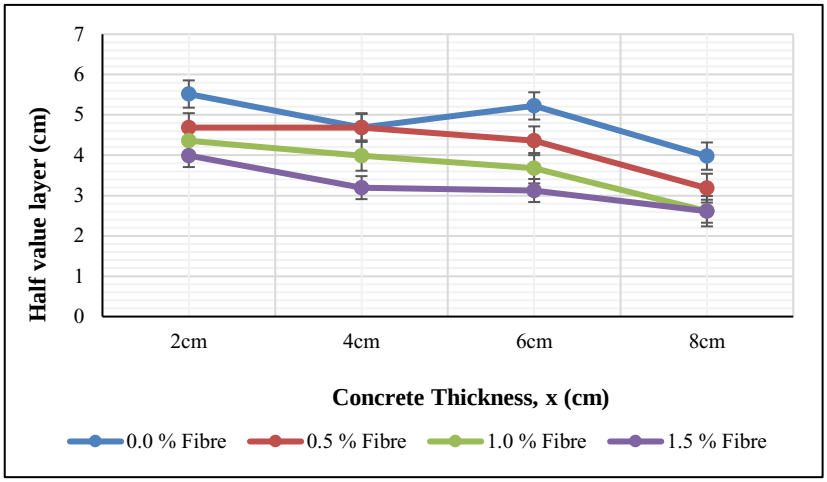


Figure 12. Line graph of half layer value (cm) of cogon grass fiber concrete against the concrete thickness (cm)

Table 7. Calculated linear attenuation coefficients (cm^{-1}) for two types of concrete

Percentage of Reinforcement in Concrete (%)	**Type of Concrete**	
	Fiber	**Lead**
0	0.1256	0.1316
0.5	0.1479	0.1756
1.0	0.159	0.1630
1.5	0.1736	0.2359

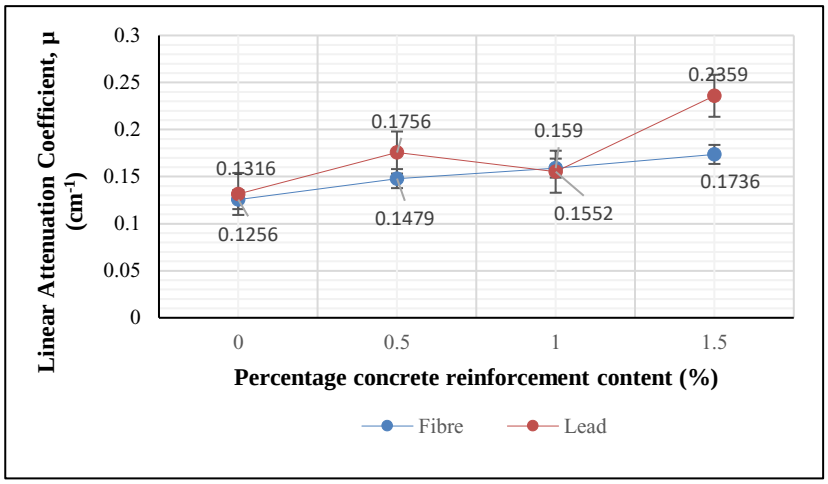


Figure 13. Line graph of linear attenuation coefficient (cm^{-1}) against the percentage of concrete reinforcement for two types of concrete (%)

Table 8. Half value layer (HVL) (cm) for two types of concrete

Thickness, *x* (cm)	Type of Concrete	
	Fiber	Lead
2	3.9919	2.9377
4	3.1965	2.7472
6	3.1244	2.4623
8	2.6121	2.1289

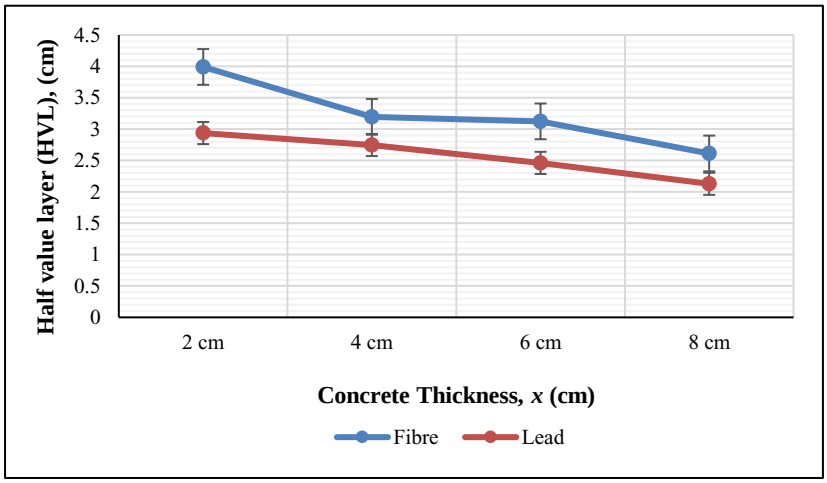


Figure 14. Line graph of half value layer (HVL) (cm) against Concrete thickness (cm) for two types of concrete

Conclusion

As a conclusion, this study revealed that the chemical properties of cogon grass fiber are made up of 36.62% cellulose, 27.60% hemicellulose and 6.11% lignin content. AFM indicated that physically cogon grass fiber appears to have a blocky and rough surface due to the cuticular waxy layer which contains a long chain of fatty acids, lipids and phenolic compounds. More importantly, by comparing the results of the measurement of gamma-ray linear attenuation coefficient of concrete with different percentages of fiber, it is indicated that adding fiber into the concrete mixture can increase the gamma-ray linear attenuation coefficient with appropriate thickness in which at the same time, improves the performance of radiation shielding. Furthermore, it can be assumed that natural fiber has the potential for use as reinforcement in concrete in enhancing the radiation shielding. Therefore, cogon grass natural fiber can be used as an additive in the concrete to improve the performance of radiation shielding at the same time reduce the environmental pollution. Finally, the improvement with this product not only can be commercialize as a shielding material used in nuclear reactors, but also in the laboratory, medical purposes or any other purposes in Malaysia.

Acknowledgement

The authors would like to thanks Universiti Tun Hussein Onn Malaysia for facilities provided during research works.

References

1. AbuAlRoos, N., Amin, N. B. and Zainon, R. (2019). Conventional and new lead-free radiation shielding materials for radiation protection in nuclear medicine: A review. *Radiation Physics and Chemistry*, 165: 108439.
2. Ekolu, S. O., Dundu, M. and Gao, X. (2014). Construction materials and structures. Amsterdam Netherlands: IOS Press BV: p. 3.
3. Gencel, O., Bozkurt, A., Kam, E. and Korkut, T. (2010). Determination and calculation of gamma and neutron shielding characteristics of concretes containing different hematite proportions. *Annals of Nuclear Energy*, 38(12): 2719-2723.
4. Han, B., Zhang, L. and Ou, J. (2017). Smart and multifunctional concrete toward sustainable infrastructures. Springer, Singapore.
5. Jamir, M. R. M., Majid, M. S. A. and Khasri, A. (2018). Natural lightweight hybrid composites for aircraft structural applications. Composites science and engineering, sustainable composites for aerospace applications. Woodhead Publishing: pp. 155-170.
6. Jumaidin, R., Khiruddin, M., Asyul Sutan Saidi, Z., Salit, M. and Ilyas, R. (2019). Characteristics of cogon grass fibre reinforced thermoplastic cassava starch biocomposite: Water absorption and physical properties. *Experimental Thermal and Fluid Science*, 62: 43-52.
7. Ibrahim, S., Baharuddin, S., Ariffin, B., Hanafiah, M. and Kantasamy, N. (2018). Cogon grass for oil sorption: Characterization and sorption studies. *Key Engineering Materials*, 775: 359-364.
8. Hu, B., Zhang, N., Liao, Y., Pan, Z., Liu, Y., and Zhou, L. (2018). Enhanced flexural performance of epoxy polymer concrete with short natural fibers. *Science China Technological Sciences*, 61(8): 1107-1113.
9. Mohd Kassim, A. S., Mohd Aripin, A., Ishak, N. and Zainulabidin, M. (2015). Cogon grass as an alternative fibre for pulp and paper-based industry: On chemical and surface morphological properties. *Applied Mechanics and Materials*, 773-774: 1242-1245.
10. Mohd Kassim, A.S., Mohd Aripin, A., Ishak, N., Hairom, N. H. H., Fauzi, N. A., Razali, N. F. and Zainulabidin, M. H. (2016). Potential of cogon grass (*Imperata cylindrica*) as an alternative fibre in paper-based industry. *Journal of Engineering and Applied Sciences*. 11: 2681-2686.
11. Haque, M., Barman, D., Kim, M., Yun, H. and Cho, K. (2015). Cogon grass (*Imperata cylindrica*), a potential biomass candidate for bioethanol: Cell wall structural changes enhancing hydrolysis in a mild alkali pretreatment regime. *Journal of the Science of Food and Agriculture*, 96(5): 1790-1797.

12. Çakıroğlu, M. (2016). Investigation of radiation shielding properties of polypropylene fiber reinforced shotcrete. *Acta Physica Polonica A*, 129(4): 705-706.
13. Ouda, A. (2014). Development of high-performance heavy density concrete using different aggregates for gamma-ray shielding. *Advances in Materials Research*, 3(2): 61-75.
14. Abdo, A., Ali, M. and Ismail, M. R. (2003). Natural fibre high-density polyethylene and lead oxide composites for radiation shielding. *Radiation Physics and Chemistry*. 66: 185-195.
15. Shahriar Kabir, M., Hossain, M., Mia, M., Islam, M., Rahman, M., Hoque, M. and Chowdhury, A. (2018). Mechanical properties of gamma-irradiated natural fiber reinforced composites. *Nano Hybrids and Composites*, 23: 24-38.
16. Tagal, J. A. and Cataytay, J. D. (n.d.) Production and evaluation of cement-bonded particle board using cogon grass as constituent: pp. 9.
17. Ruksakulpiwat, C., Wanasut, W., Singkum, A. and Yupaporn, R. (2013). Cogon grass fiber-epoxidized natural rubber composites. *Advanced Materials Research*, 747: 375-378.

Malaysian Journal of Analytical Sciences (MJAS)
Published by Malaysian Analytical Sciences Society

RECENT TRENDS IN THE QUANTIFICATION OF VITAMIN B

(Kaedah Terkini dalam Pengkuantitian Vitamin B)

Nurul Hafawati Hashim[1], Rozita Osman[1], Nurul Auni Zainal Abidin[2], Nur Sofiah Abu Kassim[2]*

[1]Faculty of Applied Sciences,
Universiti Teknologi MARA, 40450 Shah Alam, Selangor, Malaysia
[2]School of Chemistry and Environment,
Faculty of Applied Science, Universiti Teknologi MARA,
Cawangan Negeri Sembilan, Kampus Kuala Pilah, 72000, Kuala Pilah, Negeri Sembilan, Malaysia

**Corresponding author: nursofiah@uitm.edu.my*

Received: 28 April 2021; Accepted: 31 May 2021; Published: 27 June 2021

Abstract

Numerous analytical methods have been developed for a variety of matrices to quantify vitamin B compounds. It is important to establish a method with great accuracy and precision of chromatographic separation. This review provides a wide-ranging search of the vitamin B extraction methods developed during the last five years in all applications. Particular emphasis is given to sample extraction and chromatography analysis for vitamin B compounds' extraction in different applications such as biological fluids, food, and pharmaceuticals. Hence, this review will elaborate the properties of vitamin B and its metabolites, and the extraction and quantification of water-soluble vitamin B content in foods for compliance monitoring and for their particular application.

Keywords: review, sample preparation, extraction, vitamin B, chromatography analysis

Abstrak

Terdapat pelbagai kaedah analitikal telah digunakan untuk menentukan kandungan vitamin B dalam pelbagai sampel matriks. Ia adalah penting untuk membangunkan sesuatu kaedah yang mempunyai ketepatan dan kejituan yang tinggi dalam pemisahan kromatografik. Ulasan ini mengandungi carian menyeluruh untuk semua kaedah penentuan vitamin B yang telah dibangunkan sepanjang lima tahun terkini dalam semua aplikasi. Fokus diberikan kepada analisis pengekstrakan sampel dan analisis kromatografi untuk sebatian vitamin B dalam pelbagai aplikasi seperti cecair biologi, makanan, dan farmaseutikal. Oleh itu, ulasan ini akan menjelaskan ciri-ciri vitamin B dan metabolitnya, dan pengekstrakan dan pengkuantitian kandungan vitamin B larut air bagi tujuan pemantauan pematuhan kepada peraturan dan juga aplikasi tertentu.

Kata kunci: ulasan, penyediaan sampel, pengekstrakan, vitamin B, analisis kromatografi

Introduction

Vitamins B compounds differ in chemical structure and biological roles, which are essential for health. The deficiency of vitamin B, will have negative consequences for the catabolic process because one or more vitamin B compounds are involved in every

aspect of the essential process for generating energy within cells [1]. A study showed that vitamin B performed essential and closely interrelated roles in cellular functioning, acting as co-enzymes in a vast array of catabolic and anabolic enzymatic reactions [2]. Typically, it is synthesised by plants, which is in chloroplast, mitochondria, and cytosol that are regulated to the plant's fluctuating requirements. On the other hand, there is an exception for vitamin B_{12} which is synthesised by bacteria and is typically sequestered from animal-derived food. Although most vitamins are derived from plants, they are often consumed indirectly from the higher up food chain in foods of animal origin including meat, dairy, and eggs [3]. Most experts agreed that vitamin B concentration between 200 and 900 ng/mL is considered sufficient, whereas a concentration below 200 ng/mL indicates insufficiency. Daily intake of 4 to 7 µg dietary vitamin B_{12} is associated with sufficient concentrations of vitamin B_{12} related as biomarkers in the healthy and young population.

Early detection of vitamin B deficiency is of key importance to identify affected individuals who can then receive adequate and appropriate treatment. Therefore, there are a lot of methods have been used in previous studies to determine vitamin B compounds such as UV-Visible spectrophotometry, chemiluminescence, fluorimetry, microbiological, capillary electrophoresis, and high performance liquid chromatography (HPLC). Besides, a few comprehensive reviews of pre-treatment and determination of vitamins had been published. The most common sample preparation methods such as solid-phase extraction, ultrasonic-assisted extraction (UAE), supercritical fluid extraction (SFE), liquid–liquid extraction (LLE), and dispersive liquid–liquid microextraction (DLLME) using different analysis methods such as chromatography, immunoassay, electrophoretic methods, and biosensors for analysis of vitamins since 2010 had been reviewed [4]. Therefore, this review includes method development in different matrices including food, plants, biological fluids, and pharmaceutical preparations published during the last five years. Emphasis was given to various vitamin B compounds that were measured including sample preparation and extraction methods developed. Hence, this review will provide a valuable addition to the literature and will enable other researchers to access developments across several applications and to select or develop the optimal method for their particular application. This review on all vitamin B extraction methods includes comprehensive databases from previous literature which has been published from 2015 to 2020.

Vitamin B metabolites

Vitamins represent a group of various compounds, where they may be present in several chemically-diversed but biologically interconvertible forms. Besides, they are essential dietary components for humans and animals. They are needed in relatively small amounts to maintain good health and sustain life [5]. Therefore, lack of a sufficient amount of vitamins can lead to serious illnesses. Furthermore, the amount of vitamins that is required for normal development and maintenance of body functions is not always contained in the human diet and it might be lost through chemical reactions or even by extraction and leaching during storage and processing of food which is often the case with water-soluble vitamins [6]. Thus, to confirm the percentage of the recommended dietary allowance (RDA) which present in the final food products, a rapid, efficient, and reliable analytical determination of the vitamin content in food is needed for manufacturers, food laboratories, and also regulatory authorities. The B-group is a big family which consists of vitamins B_1 (thiamine), B_2 (riboflavin), B_3 (niacin), B_5 (pantothenic acid), B_6 (pyridoxine), B_8 (biotin), B_9 (folic acid), and B_{12} (cyanocobalamin). Several vitamin B compounds play significant roles and act mainly as coenzymes to produces energy. The biological roles, dietary sources, RDA, and chemical structures of vitamin B_1, B_2, B_3, B_5, and B_{12} are presented in Table 1.

Table 1. The biological roles, dietary sources, RDA, and chemical structures of vitamin B_1, B_2, B_3, B_5, and B_{12}. [2,4]

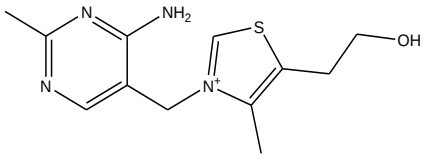
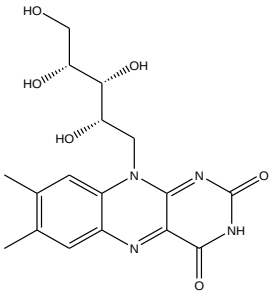
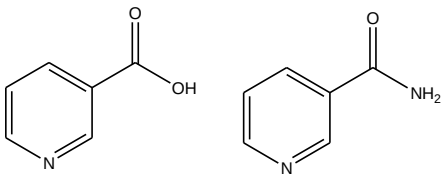
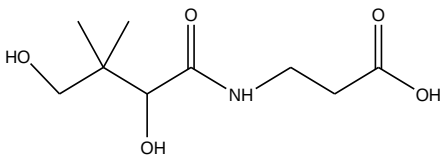
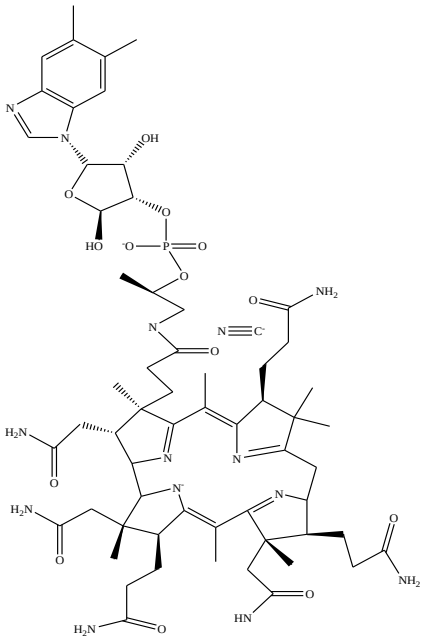
Vitamin B Forms	**Benefits**	**Dietary source**	**RDA**
Thiamine (B_1) 	Thiamine is a portion of an enzyme that is required for energy metabolism and significant for nerve function.	Moderate amounts in all nutritious foods: wholegrain/enriched cereals, breads, nuts, and seeds.	1.2/1.1 mg
Riboflavin (B_2) 	Riboflavin is a portion of an enzyme that is required for energy metabolism and important for skin health and normal vision.	Enriched, wholegrain cereals and breads, milk products, and leafy green vegetables.	1.3/1.1 mg
Niacin ($B_{3)}$ 	Niacin is a portion of an enzyme that is required for energy metabolism and important for digestive, nervous systems, and skin health.	Fish, meat, peanut butter, asparagus, and also mushrooms.	16/14 mg
Pantothenic acid (B_5) 	Pantothenic acid is a portion of an enzyme that is required for energy metabolism.	It is widespread in foods.	5 mg

Table 1 (cont'd). The biological roles, dietary sources, RDA, and chemical structures of vitamin B_1, B_2, B_3, B_5, and B_{12}. [2,4]

Vitamin B Forms	Benefits	Dietary source	RDA
Cyanocobalamin (B_{12}) 	Cyanocobalamin is a portion of an enzyme required for the production of new cells and important to the function of nerves.	Milk, eggs, seafoods, meats, and not present in plant foods.	2.4 µg

Sample pre-treatment methods

Analysing water-soluble compounds such as vitamin B compounds provides a great challenge to ensure an efficient extraction followed by sample clean-up to remove the interfering substances prior to analyte separation and/or detection. Thus, sample preparation is crucial to allow the detection of compounds especially at a low concentration level in a complex matrix. During the sample preparation process, different substances can be pre-concentrated and separates, thus able to improve the analytical performance such as accuracy, sensitivity, and also selectivity. Besides, many effective sample preparation technologies have emerged and give advantages such as reduce the personnel costs and time consumption.

The sample preparation method will be depending on the type of sample matrix used, either liquid or solid samples [4]. In brief, the extraction process is basically based on enzymatic treatment or acid hydrolysis and protein precipitation to extract the analyte of interest from the other complex matrix.

Solid-phase extraction

Solid-phase extraction (SPE) is among the commonly used methods for the extraction of vitamin B in aqueous sample [4]. Conventional SPE procedure consists of four basic steps which are conditioning, sample adsorption, washing, and elution. However, the extraction and clean-up of analytes in samples using this type of SPE is time-consuming and error-prone. Therefore, an improvement method called online solid-phase extraction liquid chromatography (online SPE-

LC) is getting more attention. Online SPE follows the same steps and is governed by the same principles in extraction and clean-up process. In online SPE-LC, the eluted analytes are directly transferred into the analytical column for separation and quantitation [7]. Thus, the online SPE method has the advantages of the significant reduction in sample preparation time and human handling which leads to high sensitivity and accuracy of the produced result. Besides, online SPE has advantages of which the column can be washed and reuse due to the high-pressure pump. Thus, a cycle of SPE column's enrichment, impurity removal, and column equilibrium could be achieved consistently [7].

Online SPE techniques have made faster methods possible by increasing sample throughput. Besides, other important advantages of online coupling techniques are the ability to eliminate analyte losses by evaporation or degradation during sample preconcentration, improve precision and accuracy, and also reduce risks of contamination of samples and sample extracts [7]. Furthermore, higher sensitivity also can be achieved due to the transfer and analysis of the entire extracted sample on the analytical system. It was reported that smaller sample volumes sufficiently sensitive to analyse large number of compounds with lower limit of detection (LOD) [4]. On the other hand, online SPE consumes smaller amount of solvents compared to conventional SPE, thus reduces the cost of organic solvents waste disposal. Besides, SPE coupled online to HPLC does not require all residual water to be removed from cartridges due to the elution solvents used are compatible with the liquid chromatography (LC) separation methods [8].

Usually, a method based on SPE is used as preconcentration and clean-up step before the determination of vitamin B. A SPE based on the dispersion of a solid sorbent in liquid samples which called dispersive solid-phase extraction (d-SPE) is a more environmental, economical, and faster method compared to conventional SPE due to the lower usage of solvent and no conditioning of sorbent. Besides, d-SPE sorbents are not a single usage, unlike SPE sorbents. Thus, d-SPE techniques have been successfully performed as a clean-up method for vitamin B by using graphene oxide (GO) [9] and hydrophilic multi-template molecularly imprinted biopolymers (mt-MIBP) as novel adsorbents [10]. GO has hydrophilic and polar character due to the large quantities of oxygen atoms on its surface as carbonyl, hydroxyl group, epoxy, and polar group. These characteristics make it appropriate for the extraction of vitamin B_{12} [9].

Meanwhile, ultrasound-assisted dispersive solid-phase extraction (UA-DSPME) was used to extract vitamin B from juices. Based on a previous study, glucose was used to replace carbon sphere and deposit hydrophilic chitosan onto d-SPE sorbents for a green synthesis approach [10]. Satisfactory recoveries of 75.8%-92.7%, 83.3%-92.5%, and 84.7%-93.8% for B_2, B_3, and B_6, respectively, were obtained in this study [10]. Besides that, nanofibers have been used oftenly as adsorbents for packed-fibre SPE (PF-SPE) to extract three water-soluble vitamin B compounds from urine simultaneously with 84.9%–125.4% recovery range. Xie et al. in 2018 published a strategy employing polypyrrole nanofibers as the sorbent for PF-SPE. Diphenylboronic acid 2-aminoethyl ester (DPBA) was used as a complexing agent to enhance retention of three vitamins on the SPE column due to its multi-interaction with vitamins [11]. The main advantage of SPE is its stability of modification according to a compound of interest. However, the disadvantage of SPE in the vitamin analysis is low recoveries for highly polar vitamins on the C_{18} column [12].

Protein precipitation

Protein precipitation is one of the common methods used to release all the peptide-vitamin linkages. Protein precipitation was used for samples such as serum, urine, milk, and blood for extraction of water-soluble vitamins such as vitamin B. This is due to the samples being complex mixture compounds that biologically and actively bond to the analyte of interest, interfere, and have a negative impact on the stability of the analyte [4]. In a study on the determination of the native form of vitamin B_1 in bovine milk, different acids for the acidic protein precipitation were compared. Perchloric acid (7%), acetic acid (2.5 mol/L or 5.0 mol/L), hydrochloric acid (1.0 mol/L), and

trichloroacetic acid (4%) were used for the preparation of the same commercial milk sample. The result showed that acetic acid at a pH level of 3.5 performed the best, resulting in 0.58 ± 0.03 μmol/L thiamine monophosphate (TMP) and 0.83 ± 0.03 μmol/L thiamine, yielding 0.43 ± 0.02 mg/L of total vitamin B_1 which represented as 100%. Meanwhile, for the protein precipitation of the milk sample, at pH levels of 4.5 and 5.0 proved to be insufficient because of high standard deviations. Furthermore, at all pH levels, hydrochloric acid and acetic acid performed significantly better than trichloroacetic acid and perchloric acid [13].

There are different solvents been used in the protein precipitation method for the determination of vitamin B in human milk. Study conducted by Ren *et al*. compared to the removal of protein by using methanol, acetonitrile with diethyl ether, and ethyl acetate were applied to remove the non-polar constituents and to assure the efficiency of the analysis [14]. The extraction recovery rates were 80.31%–118.63% for using either methanol or acetonitrile (ACN) for B_1, B_2, B_3, B_9, and B_6. However, the recovery percentage showed the best result by using methanol (80.7%-93.9%) compared to ACN (22.0%-66.7%) for the determination of pantothenic acid, nicotinic acid, pyridoxamine, and pyridoxal. Thus, methanol was selected in removing the protein. Furthermore, other step for pre-treatment was extracting the non-polar constituents and the response of using ethyl acetate was nearly twice lower than using diethyl ether [14].

Ultrasonic-assisted extraction

Ultrasonic-assisted extraction (UAE) is one of the methods that have high efficiency. Compared to soxhlet extraction and maceration, UAE has advantages not only in reducing the usage of solvent, but it also has high reproducibility and reduces the extraction time. This is due to the ultrasonic energy that is able to enhance the efficiency of extraction through induced cavitation. Moreover, this pre-treatment method produces high amount of yield and quality of an extract and fast mass transfer. Figure 1 shows the information block diagram of UAE process [4].

A previous study found that the efficiency of UAE of cyanocobalamin was greater than that of heat extraction [15]. Overall, the mean cyanocobalamin in the heat-treated ones with the added sugar alcohols was lower than in ultrasonic-treated samples (without and with added sugar alcohols). This was due to the formation of cavitation bubbles by ultrasound which caused mechanical and chemical effects. Thus, it led to the supplement's matrix broke down and cyanocobalamin was released. Furthermore, the appearance of very fine emulsions from immiscible liquid because of sonication and significant improvement in the interfacial contact areas between the liquids and a dramatic accelerate in the mass transfer among them. On the other hand, cavitation which appears following ultrasound exposure causes more available surface area and improves the procedure extraction efficiency, and also assists the release of interesting extractable compounds. Furthermore, efficiency can be increased based on the best selection of adsorbent and method [16].

The mechanical effects of ultrasound cause higher penetration of the solvent into cellular materials and also improve mass transfer. The ultrasound in the extraction can also disrupt the cell walls, helping the release of the content. There were a few studies where it gives the impact of pre-treatment steps such as drying and particle size in evaluating extraction efficiency. Mannaï *et al.* reported used instant controlled pressure drop (DIC) as a pre-treatment prior to ultrasonic extraction for the preservation of vitamin B_1 and B_6 [17]. It will helps to preserve heat-sensitive molecules because of short time during heating and lower the thermal degradation of the biological components. DIC is a process that has an effect of structure expansion to improve the technological aptitude of raw material which has been proved that the greater the expansion rate, the better the diffusivity constant [17].

Dispersive liquid–liquid microextraction (DLLME)

There is another miniaturised pre-treatment techniques of LLE which is known as dispersive liquid-liquid microextraction (DLLME). The significance of DLLME is that it is a powerful pre-treatment technique

due to its simplicity, requires small amount of sample and low solvent consumption, has high enrichment factor, and short analysis time [12]. The DLLME method was compared with the traditional LLE methods in a study, results showed that the abundant contact surface of analytes and fine droplets increase the mass transferring processes of analytes from the aquatic phase to the organic phase in a DLLME process. Thus, it not only solved the time-consuming problem but also enhanced the extraction efficiency [4].

The new version of DLLME, which is known as ion pair-based dispersive liquid–liquid microextraction (IP-DLLME) has been used as a pre-concentration technique for five folate and B_9 derivatives from complex food matrix with enrichment factor ranged from 108 to 135 due to problem transfer of hydrophilic vitamins into the organic phase. Ethanol is usually used as the dispersion solvent meanwhile 1-octanol as the extraction solvent. In order to assist the transfer of hydrophilic folates into the organic phase in the extraction process due to the anionic structure of folates ions, quaternary ammonium salt (aliquot-336) is used as a cationic surfactant [18]. However, there are only a few applications of DLLME for the extraction of hydrophilic vitamins due to the use of chlorinated solvents as extraction solvents, which make these techniques less suitable for the extraction of vitamin B [12].

Summary of sample pre-treatment methods

Among all the pre-treatment methods, solid-phase extraction (SPE) is preferred for vitamin B analysis. SPE sequence with its online coupling with LC followed by various detectors show advantages of the less human handling which results in high sensitivity and accuracy. Moreover, multiple vitamin compounds can be quantified simultaneously in a single run by SPE; thus, a significant reduction in the sample preparation time. Therefore, the optimisation of the parameter is very important in a sample preparation. In order to confirm the optimised conditions, the fractional factorial design has been used in some studies to investigate the effect of the extraction conditions that are able to produce efficient extraction or clean-up of the target analytes from the sample matrix. The disadvantages of conventional SPE method used for extraction of vitamin B is relatively expensive because the SPE cartridges are intended for single-use, tedious, and require a long time and effort in method development. The pre-treatment methods used in previous studies are summarised in Table 2.

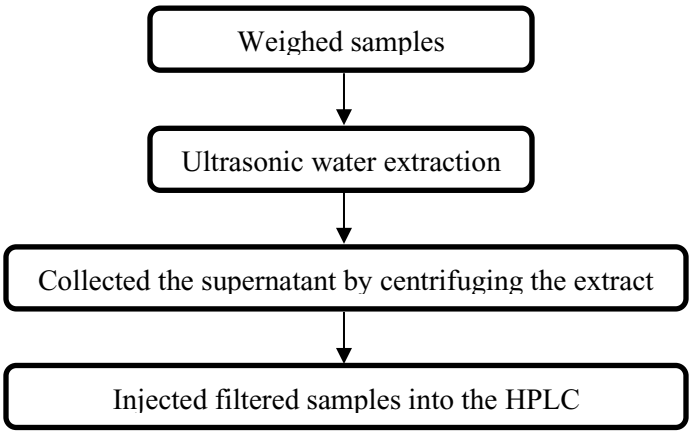


Figure 1. Ultrasonic-assisted extraction process [4]

Table 2. Pre-treatment methods, sample matrices and analytes of the recent articles

Pre-treatments	**Sample Matrices**	**Analytes**	**References**
Ultrasonic-assisted extraction (UAE)	Energy drinks.	Caffeine and water-soluble vitamins.	[19]
Hydrolysis	Fortified food and nutritional supplements.	Vitamin B_{12}.	[20]
Dilution	Pharmaceutical and biological fluids.	Thiamine hydrochloride, vitamin B_1.	[21]
UAE	Pharmaceuticals and urine samples.	Vitamin B_6, pyridoxine.	[22]
Dilution	Dietary supplements.	Vitamin B_{12}.	[23]
Enzymatic digestion, hydrolysis	Infant formulas	Vitamin B_1, B_2, B_3, and B_6.	[24]
Dilution (isotope)	Human plasma	Vitamin B_2.	[25]
Dilution	Oral powder for veterinary consumption.	Vitamin B_1, B_2, B_3, B_6, and C.	[26]
Centrifugation, filtration	Infant and toddler milk formulas.	Vitamin B_{12}.	[27]
Protein precipitation	Cow milk	Vitamin B_2 and B_6.	[28]
Enzymatic digestion	Cereal-based baby foods.	Vitamin B_1, B_2, and B_3.	[29]
Protein precipitation	Fresh milk from cow, goat, buffalo and pasteurised cow milk.	Vitamin B.	[3]
Enzymatic treatment	*Faba* bean seeds.	Vitamin B.	[30]
Ultrasound-assisted dispersive solid-phase microextraction (UA-DSPME)	Human urine and milk samples.	Nicotinamide.	[31]
Immunoaffinity	Mealworm, cricket, grasshopper, cockroach.	Vitamin B_{12}.	[32]

Table 2 (cont'd). Pre-treatment methods, sample matrices and analytes of the recent articles

Pre-treatments	Sample Matrices	Analytes	References
SPE (Graphene oxide)	Pharmaceutical formulations.	Vitamin B_{12}.	[9]
Dilution	Pharmaceutical products and urine sample.	Antidepressant drugs and vitamin B_{12}.	[33]
Acid hydrolysis, enzymatic digestion	Bovine milk.	Vitamin B_1.	[13]
Protein precipitation and enzymatic treatment	Breast milk.	B-vitamers.	[34]
SPE (polypyrrole as sorbent)	Urine sample.	Vitamin B.	[11]
Protein precipitation	Human milk	Vitamin B.	[14]
UAE (DIC)	*Steviarebaudiana* bertoni	Vitamin B_1 and B_6	[17]
Ion pair based dispersive liquid–liquid microextraction (IP-DLLME)	Food matrix	Vitamin B_9	[18]

Analysis methods

Although a few studies have used HPLC and mass spectrometry (MS) detectors due to their high specificity and sensitivity, UV, PDA, DAD detections are still being used as they are less expensive. Based on the chemical structure of vitamin B compounds, these compounds absorb at approximately 256 nm. There are many different methods such as electrophoretic, biosensor, and microbiological assay. The development of such methods; sensors and biosensors for food freshness detection has attracted many researchers, especially in the food sector. Despite the achievement obtained so far, there are still some improvements needed.

Liquid chromatography

Liquid chromatography (LC) has been widely used due to its high sensitivity and broad linear range. Nowadays, reversed-phase high performance liquid chromatography (RP-HPLC) has been used in analytical methods to determine water-soluble vitamins such as vitamin B. This method with the combination of a polar mobile phase and non-polar stationary phase becomes popular due to some advantages over normal phase such as better peak shape, its compatibility with MS detection, the robustness of chromatographic columns, and also fast equilibrium. Furthermore, there are several types of stationary phase that have been used in RP-HPLC but the one that being used widely is C_{18} for the separation of vitamin B by eluting with a mixture of water and organic solvents such as methanol, acetonitrile and ethanol and also small percentage of acids such as trichloroacetic acid, hexane, sulfuric acid, and formic acid [3, 10, 25, 28, 35, 36, 37]. Simultaneous extractions of different analytes of vitamin B such as B_1, B_2, nicotinic acid, nicotinamide, B_5, and B_{12} was successfully done by

using the C_{18} column as a stationary phase [10, 24, 33, 38, 39].

LC coupled with MS and multiclass analyses

HPLC–MS/MS has become the main analytical technique used for the determination of vitamin B due to its higher selectivity and sensitivity compared to other instrumental methods. Furthermore, the basic principle of this method is the measurement of the mass-to-charge (m/z) ratios of ionised molecules, and it is used to quantify and identify a substance where it can confirm a compound's molecular structure. Usually, this detection technique is applied by using a triple quadrupole analyser and a selected reaction monitoring mode, which allows the confirmation of the composition of compounds and gives structural information. Besides, the advantage of MS/MS is the fact that a complete HPLC separation of the target analytes is not necessary for selective detection. Instead, it is advisable to have a good chromatographic separation to reduce matrix effects which result in the suppression or less frequently in the enhancement of analyte signals. Thus, to consider speeding up the analysis, short HPLC columns are often used [4].

The method was established to determine simultaneously total vitamins B_1, B_2, B_3, and B_6 in infant formula and related nutritional foods. This method uses acid phosphatase to dephosphorylate the phosphorylated vitamin forms and then measures thiamine, riboflavin, nicotinamide, nicotinic acid, pyridoxine, pyridoxal, and pyridoxamine from digested sample extract by LC-tandem MS. In addition, the presence of modern MS instrumentation with electrospray ionisation (ESI) helps simultaneous determination by removing remaining hurdles associated with the detection. In this study, prepared samples and standard solutions were injected onto an ultra-high pressure liquid chromatography (UHPLC) which then interfaced to a triple-quadrupole mass spectrometer for analysis, where the function is to monitor parent-daughter (precursor-fragment) ion pairs for each analyte and internal standard. Intermediate precision average was 3.9% and over-spike recovery was generally 95%-105% for all four vitamins [24].

LC–MS/MS method was established for the determination of nicotinamide, nicotinic acid, B_1, B_6, B_2, B_5, B_7, B_9, and B_{12} in fish. Baseline separation of the vitamins was achieved in a hydrophilic interaction of LC condition. LOQ values ranged from 0.4 to 50 ng/g for the different vitamins while the spike recovery ranged from 87.5 to 97.5% at values 50 and 100 ng/g [40].

Liquid chromatography coupled with other techniques

Usually, RP-HPLC will be used with ultraviolet (UV), fluorescence (FLD), or photodiode array (DAD) in process of quantification of vitamins in different types of samples. However, they are not able to provide direct evidence of the structure or composition of a substance even if these approaches are quantitative. UV detection has the least selective and sensitive, but it is the most affordable and versatile method. Meanwhile, FLD is found to be more selective and sensitive compared to UV.

The separation and quantification of ten B vitamins in pretreated human milk samples have been successfully performed within 11 minutes by using the UPLC–MS/MS method with an Acquity UPLC HSS T3 column (2.1 × 100 mm, 1.8 μm). The homogenised human milk samples were deproteinised by using methanol and unknown contaminants were extracted using diethyl ether then, the hydrophobic phase was discarded. The analytes were monitored by using ESI+ ionisation and with three acquisition functions, it was detected in multiple reaction monitoring (MRM) [14].

A previous study established an isotope dilution method for determination of riboflavin in human plasma by using LC–MS/MS where separation performance was obtained with an Agilent 1290 UHPLC combine with Poroshell 120 SB-Aq column (100 mm × 2.1 mm × 2.7 μm) and was operated in positive ion mode. This method required a short execution time (2.5 min) and the average recovery was 90.5%–99.5%. Thus, it is reliable to be applied in clinical diagnosis of deficiency and supplementation monitor of riboflavin [25].

A simple and rapid method for determination of thiamine in red wine by using HPLC coupled to fluorescence detector was conducted. Polyvinylpolypyrrolidone was used to remove phenolic compounds from red wines and allow a spike recovery of thiamine vitamers (101% for thiamine, 104% for TMP, and 100% for TDP) in a wide range of red wines [39]. Unfortunately, this method encountered a problem where the interaction of polyphenols with ferricyanide had caused the effectiveness of ferricyanide oxidation in the derivation process to decrease. Thus, polyvinylpolypyrrolidone was used to remove polyphenols so that it allows the accurate determination of thiamin vitamers by calculating its mean of HPLC with fluorescence detection (HPLC-FLD).

Electrophoretic methods

Capillary electrophoresis (CE) is also a good quantitative analytical method that usually used when there are only small amounts of a sample available. It has several advantages such as highly efficient, low solvent consumption, and also fast techniques where the sample components are separated according to their sizes and charges. Furthermore, this method also ables to analyse several samples simultaneously in multicapillary systems and consume low volume of reagents and accessories (packaged columns are not required). However, chromatographic techniques are more sensitive for the determination of vitamin B compared to CE methods, even though it has greater efficiency when compared to LC methods.

Mostly the analysis of vitamins used the CE method by employing capillary zone electrophoresis (CZE) or micellar electrokinetic chromatography (MEKC) modes where they are coupled with laser-induced fluorescence (LIF), UV, electrochemical (EC), and MS detectors. Vitamin B is in the category of water-soluble vitamins and as charged molecules, it can be separated by using CZE whereby their separation efficiency can be improved by applying MEKC to simultaneously separate fat-soluble and water-soluble vitamins [41].

In MEKC, when micelles of surfactants in the background electrolyte (BGE) acts as a pseudo-stationary phase, electrostatic and hydrophobic interactions occur with analytes. A MEKC method was established in a study to analyse eight water-soluble vitamins by using HP3D CE system with DAD in energy and sports drinks. Sodium dodecyl sulphate (SDS) gave the best separation in this study because it was able to resolve the B_5–C vitamin pair as compared to other tested surfactants including sodium deoxy-cholate (SDC) and sodium cholate (SC). However, this technique was not suitable for the determination of vitamin B_{12} due to the very low concentration below the LOQ [42].

Biosensors

Optical biosensors is one of the excellent tools to detect vitamins in different matrices due to their advantages which are simplicity, the possibility to be used in field analyses, and low cost. For example, electrochemical sensors that are based on the use of receptors fabricated through different imprinting approaches have been developed for the detection of vitamin B [22, 43-46]. Furthermore, electrochemical techniques have shown interest in the recent research development because of their advantages such as high sensitivity, easy operation, low cost, and also the portability of the equipment used.

A study proposed an electrochemical method for the determination of vitamin B_{12} where the Co(I/II) redox pair was monitored by using a boron-doped diamond electrode for the analysis of supplementation products, where its surface was characterised by electrochemical impedance spectroscopy and cyclic voltammetry. The results were compared with those provided by UV-Vis spectrometry and the statistical analysis showed no critical difference between these two methods in terms of the precision and accuracy of the data. The electrode was sensitive to vitamin B_{12} sensing in the linear range from 0.25 to 5.0 μmol^{-1} with a value of LOD of 86.0 $nmolL^{-1}$ [44].

Meanwhile, another study had established the electrocatalytic method for the determination of vitamin B_6 by using vanadium (III) Schiff base complex that was electrochemically polymerised using glassy carbon electrode (GCE) as the working

electrode. This method gives a faster response, cost-effective, good accuracy, and simple procedure. They utilised vanadium (III) Schiff base complex for the GCE active surface modification. Furthermore, vanadium complexes show a good electrochemical redox behaviour because of their different oxidation states (+3, +4, +5). Thus, poly-V-SBC/GCE shows better electrocatalytic sensing activity for the determination of vitamin B_6 [46].

Other methods

On the other hand, there is also an effective method such as a microbiological assay that has been developed to determine vitamin B. This method is justified when it needs to carry out quality control routine of relatively simple sample compositions. However, this method is challenging when applied to newer, more diversed nutritional products and is no longer considered the gold standard. Newer methods such as chromatographic methods, especially with mass spectral detection, becomes the new standard due to their specificity that enable accurate quantitation across more complex and diverse matrixes.

Summary of analysis methods

Among all of the analytical methods, LC is the most popular due to its advantages. LC methods can meet the requirements of the qualitative and quantitative analyses of vitamins in different matrices, such as foods and biological samples, especially when they are combined with MS. However, UV and FLD detectors suffer overlapping peaks when dealing with complex samples, while matrix effects and high costs are necessary when using LC–MS. CE is an alternative method for the determination of vitamins which is highly efficient, low solvent-consuming, and fast, but its separation reproducibility needs to be enhanced. The main advantages of biosensors include their low cost, technical simplicity, and the possibility of being used in field analyses, while their relatively short lifespan restrict the development of technology. Spectrometry is cheap and easy to promote, but its sensitivity does not quite meet requirements sometimes. In conclusion, with the development of equipment of HPLC and MS, this technology will surely be broadly used, while other technologies, such as electrophoresis and spectrometry, are seen as supplementary methods to be used when necessary. Table 3 presents a selection of analytical methods used for the detection of vitamin B reported since 2015.

Table 3. Summary of separation, detection, and quantification methods used for the analysis of vitamin B

Vitamin B forms	Mobile phase	Column	Instrument analysis method	LOD	LOQ	Ref
Vitamins B_1, B_2, B_3, B_6, B_9, B_{12}, and C	A: 5.84 mM hexane-1-sulfonic acid sodium: acetonitrile (95:5) with 0.1 % triethylamine B: 5.84 mM hexane-1-sulfonic acid sodium: acetonitrile (50:50) with 0.1 % triethylamine	C_{18} BDS column (10 cm × 4.6 mm; 3 µm)	HPLC with UV-DAD/FLD detection	0.0032–0.0267 mg/L	0.0097 – 0.0810 mg/L	[38]

Table 3 (cont'd). Summary of separation, detection, and quantification methods used for the analysis of vitamin B

Vitamin B forms	**Mobile phase**	**Column**	**Instrument analysis method**	**LOD**	**LOQ**	**Ref**
Vitamins B_1, B_2, B_3, B_5, B_6, B_9, B_{12}, and C	A: 0.01% formic acid B: methanol	Phenomenex Synergi, C_{18} (4.6 × 150 mm; 4.0 µm particles)	HPLC	0.03 – 0.23µg/mL	0.18 – 0.67 µg/mL	[47]
Vitamins B_2, B_3, and B_6.	Water:methanol:acetic acid (72%:27 %:1%, v/v)	Agilent C_{18} column (4.6 × 250 mm; 5 µm)	HPLC	1.2 – 5.5 µg/L	4.0 – 18.4 µg/L	[10]
Vitamin B_{12}	A: 20 mM ammonium formate in H_2O B: Acetonitrile (ACN)	:UG120V C_{18} (1.5 × 250 mm; 5 µm)	LC–MS/MS	0.03 µg/L	0.1 µg/L	[27]
B-vitamins	A: 2.5mmol/L Ammonium formate aqueous solution. B: ACN	Acquity UPLC HSS T3 (2.1 × 100 mm; 1.8 µm)	UPLC–MS/MS	0.05 – 1.50 µg/L	0.25 – 3 µg/L	[14]
B-vitamins	A: 10 mM ammonium acetate, 0.1% acetic acid in water B: methanol	Agilent Zorbax SB-Aq column (100 × 2.1 mm; 1.8 µm particle size), SB-Aq guard column (5 × 2.1 mm; 1.8 µm)	UPLC–SRM MS	0.01 – 0.625 µM	0.1 – 26.3 µM	[30]
Vitamin B_1 and B_6	A: 25 mmol/L potassium phosphate buffer pH 7 B: Methanol	YMC meteoric core C_{18} column (100 × 4.6 mm; 2.6 µm particle size) protected by guard column C_{18} (10 × 4.6 mm)	HPLC-PDA and fluorescence	1.28 – 2.50 nmol/L	4.27 – 8.32 nmol/L	[48]
Vitamin B_{12}	A: 20 mmol/L potassium phosphate monobasic (adjusted to pH 3 with phosphoric acid) B: ACN	Express C_8 column (2.7 µm; 3 × 100 mm), guard column (2.7 mm; 3 × 5 mm)	HPLC-DAD	0.16 µg/mL	0.52 µg/mL	[23]

Table 3 (cont'd). Summary of separation, detection, and quantification methods used for the analysis of vitamin B

Vitamin B forms	Mobile phase	Column	Instrument analysis method	LOD	LOQ	Ref
Water-soluble vitamins	A: 25 mM $NaH_2PO_4.H_2O$, pH adjusted to 4.0 B: Methanol	XSelect ESH C_{18} column (150 × 4.6 mm; 3.5 µm particle size)	UHPLC-DAD	0.02 – 1.7 mg/L	0.05 – 5.1 mg/L	[49]
Vitamin B_{12}	A: UHQ water modified with 0.025% trifluoroacetic acid B: Methanol	Acquity UPLC column (BEH C_{18}, 50 × 2.1 mm)	UHPLC	0.12 – 1.61 nM	0.40 – 5.34 nM	[32]

Conclusion

The development of analytical methods for the accurate determination of vitamin B and its metabolites is an important area in analytical chemistry because of the importance of these vitamins in the human body. In this review, the methods published during the last five years (2015–2020) were evaluated for vitamin B determination. The key roles of these methods are played by sample preparation techniques, and the main efforts in this field have been focused on the optimisation of the preparation, extraction, and clean-up steps and on the enhancement of the environmental safety of these procedures. Based on current trends, the method with the most promise in achieving these goals is the SPE sequence with its online coupling with LC followed by various detectors. The main advantages of this approach are its good compatibility with high throughput multi-residue analytical procedures and its relatively low cost.

The currently proposed analytical approaches for the detection of vitamin B are mainly based on HPLC–MS or HPLC–MS/MS. Great advances in HPLC–MS/MS have made it a key technique for the determination of not only vitamins but also other targets. The main trend in this field is the combination of MS detectors with modern chromatographic approaches such as UHPLC. Therefore, this technique is expected to have the most pronounced development in the future.

Furthermore, the development of new sample preparation methods using various novel materials, green solvents and miniaturised devices for improving the sensitivity, robustness and effectiveness of analytical methods, and the method standardisation should also be emphasised in the future.

Acknowledgement

The authors would like to thank the Ministry of Higher Education, Malaysia for the Graduate Research Assistance (GRA) allowances (RACER/1/2019/ STG01/UITM//2) and (RACER/1/2019/STG01/ UITM//5) to N. H Hashim. The authors would like to acknowledge Faculty of Applied Sciences, Universiti Teknologi Mara (UiTM) Negeri Sembilan (Kuala Pilah Campus) and Universiti Teknologi Mara (UiTM), Selangor for the facilities provided.

References

1. Kirkland, J. B., Zempleni, J., Buckles, L. K. and Christman, J. K. (2007). *Handbook of vitamins*. Taylor & Francis: Boca Raton.
2. Kennedy, D. O. (2016). B vitamins and the brain: Mechanisms, dose and efficacy-A review. *Nutrients*, 8(2): 68.

3. Shetty, S. A., Young, M. F., Taneja, S. and Rangiah, K. (2020). Quantification of B-vitamins from different fresh milk samples using ultra-high performance liquid chromatography mass spectrometry/selected reaction monitoring methods. *Journal of Chromatography A*, 1609: 460452.
4. Zhang, Y., Zhou, W. E., Yan, J. Q., Liu, M., Zhou, Y., Shen, X. and Li, G. H. (2018). A review of the extraction and determination methods of thirteen essential vitamins to the human body: An update from 2010. *Molecules*, 23(6): 1-25.
5. Khaneghah, A. M., Hashemi, S. M. B., Es, I., Gholamhosseinpour, A., Loizzo, M. R., Giardinieri, A. and Ferreira, D. S. (2019). Water-soluble vitamins. In *Innovative Thermal and Non-Thermal Processing, Bioaccessibility and Bioavailability of Nutrients and Bioactive Compounds*. Woodhead Publishing: pp. 241- 266.
6. Zhu, Y., Thakur, K., Feng, J., Cai, J., Zhang, J. and Hu, F. (2020). Trends in food science and technology B-vitamin enriched fermented soymilk : A novel strategy for soy-based functional foods development. *Trends in Food Science & Technology*, 105(June): 43-55.
7. Ibrahim, N., Osman, R., Abdullah, A. and Saim, N. (2014). Determination of phthalate plasticisers in palm oil using online solid phase extraction-liquid chromatography (SPE-LC). *Journal of Chemistry*, 2014: 682975
8. Kataoka, H. (2012). Recent advances in online column-switching sample preparation. In *Chemistry Molecular Sciences and Chemical Engineering*: pp. 649-676
9. Moradi, M., Zenouzi, S., Ahmadi, K., and Aghakhani, A. (2014). Graphene oxide-based solid phase extraction of vitamin B_{12} from pharmaceutical formulations and its determination by X-ray fluorescence. *X-ray Spectrometry*, 2014: 1-8.
10. Ostovan, A., Ghaedi, M., Arabi, M., Yang, Q., Li, J. and Chen, L. (2018). Hydrophilic multi-template molecularly imprinted biopolymers based on a green synthesis strategy for determination of B-family vitamins *Applied Materials & Interfaces*, 10: 4140-4150.
11. Xie, L., Huang, J., Han, Q., Song, Y., Liu, P. and Kang, X. (2018). Determination of three water-soluble vitamins in urine. *Journal of Chromatography A*, (1589): 30-38.
12. Fatima, Z., Jin, X., Zou, Y., Yeong, H., Quinto, M. and Li, D. (2019). Recent trends in analytical methods for water-soluble vitamins. *Journal of Chromatography A*, 1606: 360245.
13. Schmidt, Anatol, Pratsch, H., Schreiner, M. G. and Mayer, H. K. (2017). Determination of the native forms of vitamin B_1 in bovine milk using a fast and simplified UHPLC method. *Food Chemistry*, 229: 452-457.
14. Ren, X. N., Yin, S. A., Yang, Z. Y., Yang, X. G., Shao, B., Ren, Y. P. and Zhang, J. (2015). Application of UPLC-MS/MS Method for analyzing B-vitamins in human milk. *Biomedical and Environmental Sciences*, 28(10): 738-750.
15. Chandra-hioe, M. V, Xu, H. and Arcot, J. (2020). The efficiency of ultrasonic-assisted extraction of cyanocobalamin is greater than heat extraction. *Heliyon*, 6(July 2019): e03059.
16. Roosta, M., Ghaedi, M., Daneshfar, A. and Sahraei, R. (2015). Ultrasound assisted microextraction-nano material solid phase dispersion for extraction and determination of thymol and carvacrol in pharmaceutical samples: Experimental design methodology. *Journal of Chromatography B*, 975: 34-39.
17. Mannaï, A., Jableoui, C., Hamrouni, L., Allaf, K. and Jamoussi, B. (2019). DIC as a pretreatment prior to ultrasonic extraction for the improvement of rebaudioside A yield and preservation of vitamin B1 and B6. *Journal of Food Measurement and Characterization,* 13: 2764-2772.
18. Nojavan, Y., Kamankesh, M., Shahraz, F., Hashemi, M. and Mohammadi, A. (2015). Ion pair-based dispersive liquid-liquid micro-extraction followed by high performance liquid chromatography as a new method for determining five folate derivatives in Food-stuffs. *Talanta*, 137: 31-37.
19. Hampel, D. and Allen, L. H. (2015). Analyzing B-vitamins in human milk : Methodological approaches. *Critical Reviews in Food Science and Nutrition*, 56(3): 37-41.

20. Sobczyńska-Malefora, A. (2019). Methods for assessment of folate (Vitamin B_9). *Journal of Clinical Pathology*, 71(11): 949-956.
21. Yaman, M. and Faruk, Ö. (2019). Determination and evaluation of in vitro bioaccessibility of the pyridoxal, pyridoxine and pyridoxamine forms of vitamin B_6 in cereal-based baby foods. *Food Chemistry,* 298: 125042.
22. Antakli, S., Sarkees, N. and Sarraf, T. (2015). Determination of water-soluble vitamins B_1, B_2, B_3, B_6, B_9, B_{12} and C on C_{18} column with particle size 3 μm in some manufactured food products by HPLC with UV-DAD/FLD detection. *International Journal of Pharmacy and Pharmaceutical Sciences*, 7(6): 219-224.
23. Liddicoat, C., Hucker, B., Liang, H. and Vriesekoop, F. (2015). Thiamin analysis in red wine by fluorescence reverse phase-HPLC. *Food Chemistry*, 177: 325-329.
24. Chatterjee, N., Kumar, A., Ajeshkumar, K. K., Kumari, K. R., Vishnu, K V., Anandan, R., Matthew, S. and Ravishankar, C. (2017). Screening natural content of water-soluble B vitamins in fish: Enzymatic extraction, HILIC separation, and tandem mass spectrometric determination. *Journal of AOAC International*, 100(3): 579-585.
25. Hernández-Mesa, M., Moreno-González, D., Lara, F. J. and García-Campaña, A. M. (2019). Electrophoresis capillary electrophoresis: Food chemistry applications. In *Encyclopedia of Analytical Science* (3rd edition), Elsevier.
26. Navarro-pascual-ahuir, M., Lerma-garcía, M. J. and Sim, E. F. (2016). Determination of water-soluble vitamins in energy and sport drinks by micellar electrokinetic capillary chromatography. *Food Control*, 63: 110-116.
27. Muthusankar, G., Rajkumar, C., Chen, S. M., Karkuzhali, R., Gopu, G., Sangili, A. and Sankar, R. (2019). Sonochemical driven simple preparation of nitrogen-doped carbon quantum dots/SnO_2 nanocomposite: A novel electrocatalyst for sensitive voltammetric determination of riboflavin. *Sensors and Actuators, B: Chemical*, 281: 602-612.
28. Pereira, D. F., Santana, E. R., Piovesan, J. V. and Spinelli, A. (2020). A novel electrochemical strategy for determination of vitamin B_{12} by Co(I/II) redox pair monitoring with boron-doped diamond electrode. *Diamond & Related Materials*, 2020: 107793.
29. Sharma, A., Arya, S., Chauhan, D., Solanki, P. R., Khajuria, S. and Khosla, A. (2020). Synthesis of Au–SnO_2 nanoparticles for electrochemical determination of vitamin B_{12}. *Journal of Materials Research and Technology*, 9(6): 14321-14337.
30. Supriya Prasad, P., Praveen Kumar, S., Bharathi, K. and Narayanan, V. (2018). Determination of vitamin B_6 by vanadium (III) schiff base complex modified GCE. *Materials Today: Proceedings*, 5(2): 9026-9032.
31. Abibu, M. A., Takuwa, D. T. and Sichilongo, K. (2019). Quantification of eight water soluble vitamins in *Sutherlandia frutescen*s species from Botswana using a validated reversed phase HPLC method. *Separation Science Plus,* 2(6): 1-10.
32. Jenčo, J., Kujovská, L., Sobotka, L., Bláha, V. and Solich, P. (2020). Development of novel liquid chromatography method for clinical monitoring of vitamin B_1 metabolites and B_6 status in the whole blood. *Talanta*, 211: 120702.
33. Rakuša, Ž. T., Grobin, A. and Roškar, R. (2021). A comprehensive approach for the simultaneous analysis of all main water- soluble vitamins in multivitamin preparations by a stability-indicating HPLC-DAD method. *Food Chemistry*, 337: 127768.
34. Redeuil, K., Bénet, S., Affolter, M., Thakkar, S. K. and Campos-giménez, E. (2017). A novel methodology for the quantification of B-vitamers in breast milk. *Journal of Analytical & Bioanalytical Techniques,* 8(1): 1-10.
35. Hampel, D. and Allen, L. H. (2015). Analyzing B-vitamins in human milk : Methodological approaches. *Critical Reviews in Food Science and Nutrition*, 56(3): 37-41.
36. Sobczyńska-Malefora, A. (2019). Methods for assessment of folate (Vitamin B_9). *Journal of Clinical Pathology*, 71(11): 949-956.

37. Yaman, M. and Faruk, Ö. (2019). Determination and evaluation of in vitro bioaccessibility of the Antakli, S., Sarkees, N. and Sarraf, T. (2015). Determination of water-soluble vitamins B_1, B_2, B_3, B_6, B_9, B_{12} and C on C_{18} column with particle size 3 µm in some manufactured food products by HPLC with UV-DAD/FLD detection. *International Journal of Pharmacy and Pharmaceutical Sciences*, 7(6): 219-224.
38. Liddicoat, C., Hucker, B., Liang, H. and Vriesekoop, F. (2015). Thiamin analysis in red wine by fluorescence reverse phase-HPLC. *Food Chemistry*, 177: 325-329.
39. Chatterjee, N., Kumar, A., Ajeshkumar, K. K., Kumari, K. R., Vishnu, K V., Anandan, R., Matthew, S. and Ravishankar, C. (2017). Screening natural content of water-soluble B vitamins in fish: Enzymatic extraction, HILIC separation, and tandem mass spectrometric determination. *Journal of AOAC International*, 100(3): 579-585.
40. Hernández-Mesa, M., Moreno-González, D., Lara, F. J. and García-Campaña, A. M. (2019). Electrophoresis capillary electrophoresis: Food chemistry applications. In *Encyclopedia of Analytical Science* (3rd edition), Elsevier.
41. Hernández-Mesa, M., Moreno-González, D., Lara, F. J. and García-Campaña, A. M. (2019). Electrophoresis capillary electrophoresis: Food chemistry applications. In *Encyclopedia of Analytical Science* (3rd edition), Elsevier.
42. Navarro-pascual-ahuir, M., Lerma-garcía, M. J. and Sim, E. F. (2016). Determination of water-soluble vitamins in energy and sport drinks by micellar electrokinetic capillary chromatography. *Food Control*, 63: 110-116.
43. Muthusankar, G., Rajkumar, C., Chen, S. M., Karkuzhali, R., Gopu, G., Sangili, A. and Sankar, R. (2019). Sonochemical driven simple preparation of nitrogen-doped carbon quantum dots/SnO_2 nanocomposite: A novel electrocatalyst for sensitive voltammetric determination of riboflavin. *Sensors and Actuators, B: Chemical*, 281: 602-612.
44. Pereira, D. F., Santana, E. R., Piovesan, J. V. and Spinelli, A. (2020). A novel electrochemical strategy for determination of vitamin B_{12} by Co(I/II) redox pair monitoring with boron-doped diamond electrode. *Diamond & Related Materials*, 2020: 107793.
45. Sharma, A., Arya, S., Chauhan, D., Solanki, P. R., Khajuria, S. and Khosla, A. (2020). Synthesis of Au–SnO_2 nanoparticles for electrochemical determination of vitamin B_{12}. *Journal of Materials Research and Technology*, 9(6): 14321-14337.
46. Supriya Prasad, P., Praveen Kumar, S., Bharathi, K. and Narayanan, V. (2018). Determination of vitamin B_6 by vanadium (III) schiff base complex modified GCE. *Materials Today: Proceedings*, 5(2): 9026-9032.
47. Abibu, M. A., Takuwa, D. T. and Sichilongo, K. (2019). Quantification of eight water soluble vitamins in *Sutherlandia frutescen*s species from Botswana using a validated reversed phase HPLC method. *Separation Science Plus,* 2(6): 1-10.
48. Jenčo, J., Kujovská, L., Sobotka, L., Bláha, V. and Solich, P. (2020). Development of novel liquid chromatography method for clinical monitoring of vitamin B_1 metabolites and B_6 status in the whole blood. *Talanta*, 211: 120702.
49. Rakuša, Ž. T., Grobin, A. and Roškar, R. (2021). A comprehensive approach for the simultaneous analysis of all main water- soluble vitamins in multivitamin preparations by a stability-indicating HPLC-DAD method. *Food Chemistry*, 337: 127768.

Malaysian Journal of Analytical Sciences (MJAS)
Published by Malaysian Analytical Sciences Society

SIMPLE METHOD DETERMINATION OF SATURATED AND UNSATURATED FATTY ACIDS SOURCES FOR DIESEL-BIODIESEL BLENDS

(Kaedah Mudah untuk Penentuan Sumber Asid Tepu dan Taktepu bagi Campuran Diesel-Biodiesel)

Nurul Hazwah Mohd Kamarulzaman[1], Siti Norhafiza Mohd Khazaai[1,2]*, Muhammad Nor Fazli Abd Malek[1], Mohd Hasbi Ab. Rahim[1], Gaanty Pragas Maniam[1,3]

[1]Faculty of Industrial Sciences & Technology,
Universiti Malaysia Pahang, Lebuhraya Tun Razak, 26300 Gambang, Kuantan, Pahang, Malaysia
[2]Faculty of Applied Sciences,
Universiti Teknologi MARA Pahang, 26400 Jengka, Pahang, Malaysia
[3]Biotropic Centre Laboratory,
Universiti Malaysia Pahang, Lebuhraya Tun Razak, 26300 Gambang, Kuantan, Pahang, Malaysia

**Corresponding author: ctnorhafiza03@yahoo.com*

Received: 30 April 2021; Accepted: 6 June 2021; Published: 27 June 2021

Abstract

Biodiesel is one of the fuel alternatives made from vegetable oils and animal fats that have low emission and biodegradable profiles that are currently being used to reduce pollutions. The optimum parameters for alkali-catalyzed transesterification is 1.5 wt.% of catalyst within 2 hours at 65 ℃, molar ratio methanol to the oil of 9:1. A series of diesel-biodiesel blends of B5, B7, B10, B15 and B20 was prepared by mixing the pure diesel with biodiesel produced. Each of the blends was analyzed using UV-Visible spectroscopy to identify and differentiate the absorbance of the blends. The characterization of diesel-biodiesel (acid value, peroxide value, density, viscosity, moisture content, flash point and refractive index) was performed according to the ASTM method. The UV-Vis analysis of saturated fatty acid and unsaturated fatty acid was compared to prove the suitability of the method used. All the parameters values for the blends meet the requirement of the American Standard Testing Material (ASTM) D6751 except for the moisture content. Rapid determination of blending for both types of fatty acids by UV-Vis analysis was obtained. This may benefit the related industries as well as monetary gain in countering any false claim on the percentage blend with a simple and low-cost method.

Keywords: biodiesel, UV-Vis analysis, rapid analysis

Abstrak

Biodiesel merupakan salah satu alternatif bahan bakar yang diperbuat daripada minyak sayuran dan lemak haiwan yang mempunyai tahap penyingkiran yang rendah dan profil biodegradasi bagi mengurangkan pencemaran. Parameter optimum bagi transesterifikasi bermangkin alkali adalah 1.5 wt.% mangkin dalam masa 2 jam pada suhu 65 ℃, dan nisbah metanol kepada minyak ialah 9:1. Suatu siri campuran diesel-biodiesel B5, B7, B10, B15 dan B20 telah disediakan dengan mencampurkan diesel dengan biodiesel

yang terhasil. Setiap campuran tersebut dianalisa dengan menggunakan spektroskopi Ultralembayung-nampak (UV-Vis) untuk mengenali dan membezakan penyerapan setiap campuran. Pencirian bagi diesel-biodiesel seperti keasidan, nilai peroksida, ketumpatan, kelikatan, kelembapan, titik cahaya dan indeks refraktif telah dijalankan mengikut kaedah ASTM. Analisa UV-Vis antara asid tepu dan asid tak tepu digunakan untuk melihat kesesuaian kaedah tersebut untuk jenis asid yang berbeza. Semua parameter mematuhi keperluan "American Standard Testing Material" (ASTM) D6751 kecuali kelembapan. Penentuan pantas bagi campuran diesel-biodiesel daripada dua jenis asid yang berbeza telah dijalankan. Ini dapat memberi manfaat kepada industri serta menghalang sebarang kesalahan dalam penentuan peratusan minyak campuran dengan kaedah yang mudah dan murah.

Kata kunci: biodiesel, analisa UV-Vis, analisis pantas

Introduction

Biodiesel is one of the alternative fuels that can be produced using vegetable oils or animal fats by reacting it chemically with alcohol. Biodiesel is defined as fuels that make up of mono-alkyl esters of long chain fatty acids, for example fatty acid methyl ester (FAME), obtained from renewable sources that can be produced by transesterification under mild conditions with the presence of a base catalyst [1]. According to the news article of The Star on 21 February 2020 [2], Malaysia will adopt the use of B20 starting June 2021 with a little modification to the car engine to avoid biodiesel absorbing too much moisture [3]. The petroleum diesel percent used in the blending process has a significant influence on the properties of biodiesel. To compromise with the engine performance, a specific level of biodiesel is needed. Therefore, an analysis of the data and blend level of petroleum diesel-biodiesel is required. Every percentage of diesel-biodiesel blended may affect its properties, such as viscosity, density and may also make the market price changes at any time. If the blend level decreases, its price becomes higher. Therefore, it is important to validate each of the blend properties to ensure the diesel-biodiesel in the market meets its specification according to its label and to counter the false claims on biodiesel ratio by biodiesel producers. To validate each blend levels, a rapid method needs to be establishing to determine the blend level of diesel-biodiesel. The rapid method also needs to be applicable for both saturated and unsaturated fatty acids as different countries produce biodiesel from different types of vegetable oils. The development of methods for determining or verifying the content of the diesel/ biodiesel blend level is therefore of interest and need.

Different approaches have been used to determine the amount of blend in diesel/biodiesel. Nuclear Magnetic Resonance (NMR) spectroscopy is one the powerful techniques to elucidation the structure of chemical compound. NMR is one of a fast measurement and automatically setup that can allow large amount sample can be analyzed in short time [4]. However, the use of NMR spectroscopy to detect a blend is prohibitively costly based on the instrumentation price and maintenance costs. In addition, NMR cannot readily be implemented at point-of-sale locations. Another method can be used is Gas Chromatography (GC) by using a high-temperature capillary column and a flame ionization detector (FID) [5]. GC has the purpose of detecting the fatty acid, tri-, di- and monoglycerides in the oil from transesterification reaction. However, the limitation of using GC is the compound existing in the vapor phase at a temperature that can be produced by the GC and withstood by the column.

High Performance Liquid Chromatography (HPLC) is also the method to predict the blend level of diesel/biodiesel. HPLC is less energy intensive but the isolation of long-chain fatty acids and their glycerides requires different types of columns [5]. Meanwhile, UV spectroscopy is a reliable and affordable technology to detect blend level biodiesel based on absorption pattern of aromatic compound. In UV, the feedstock does not affect the absorbance of diluted biodiesel thus it shows in 245-305 nm range. The blend level biodiesel can be detected at 254 to 281 nm absorbance. When the diesel is known, blend level can be detected by using the single wavelength [6]. UV spectroscopy provides the easier and faster result analysis due to reduction analysis time and lower reagent consumption. In fact, UV

spectroscopy has the potential to quantify biodiesel content [7].

Materials and Methods

The research was conducted in several stages; the first stage is the optimization of biodiesel, the parameters involved are catalyst concentration, reaction time and methanol to oil ratio (9:1) at constant reaction temperature (65 °C). The range catalyst used (1.2-2 wt.%) is sodium hydroxide (NaOH) with 5 g of oil to determine the highest percent yield of FAME within 60 minutes, 90 minutes and 120 minutes. The transesterification reaction was conducted to produce fatty acid methyl ester (FAME) for blending of diesel-biodiesel. 1.5 wt.% of catalyst was dissolved in the methanol then was added into three neck round-bottomed flask that contained olive oil using the ratio of 9:1. Transesterification reaction was carried out with the aid of magnetic stirrer for continuous stirring. The materials used for transesterification reaction were olive oil (Basso: Extra Virgin) that was bought in nearby supermarket.

The second stage is the preparation of the biodiesel in a large batch using the optimized condition. The mixture was cooled overnight in the fume hood and was separated into two layers using a separating funnel. The last two steps are washing and drying the biodiesel. The washing of biodiesel was done using water washing several times until the water becomes clearer or the pH of biodiesel is 7. After that, the biodiesel undergoes a drying process by heating it on a hotplate at 90-100 °C until its appearances become clear. The third stage is the blending of diesel-biodiesel. The biodiesel of olive oil will be split to produce five different concentrations of diesel-biodiesel with a ratio of blend levels as B5 (5% biodiesel, 95% petroleum diesel), B7 (7% biodiesel, 93% petroleum diesel), B10 (10% biodiesel, 90% petroleum diesel), B15 (15% biodiesel, 85% petroleum diesel) and B20 (20% biodiesel, 80% petroleum diesel). The last stage is the characterization of the diesel-biodiesel blends. Other properties of diesel-biodiesel blends that were analyzed are the viscosity, refractive index, moisture content, flash point, acid value, peroxide value and density of each blend. Each data from every analysis was then tabulated before the conclusion was made from the overall outcome of the research.

Results and Discussion

The transesterification process was carried out at a constant temperature (65 °C) and the same methanol to oil ratio (9:1). The parameters optimized were including the concentration of catalyst and reaction time to obtain the highest methyl ester yield. For the optimization of catalyst concentration, the variables used were 1.2 wt.%, 1.5 wt.% and 1.8 wt.% for the weight of the oil used in the transesterification process. Pullen & Saeed [8] stated that NaOH was the most potent catalyst in converting the oil to FAME and produced the highest FAME yield within the shortest time. The highest yield of FAME is 88.37% using 1.5 wt.% of catalyst. At first, the percent yield increased until 1.5 wt.%, which is the optimum amount of catalyst for this reaction. This showed that when the catalyst concentrations increase, the conversion of triglycerides also increases. After 1.5 wt.%, the FAME yield decreased due to the lesser conversion of triglycerides to FAME. If the amount of catalyst is insufficient, it will lead to incomplete conversion of triglycerides but exceeded the amount of catalyst, which will form more soap as the catalyst reacts with triglycerides [9].

Meanwhile, the reaction times used for the analysis were 60, 90, 120 and 150 minutes. FAME yield increases with the reaction time. The maximum yield was reached at a reaction time lower than 90 minutes and remained constant even though the reaction time increases [10]. The reaction time at 120 min produced the highest percent yield of FAME. This proves that the transesterification requires time for the reaction to occur, where the amount of FAME increases as the reaction time increases. However, a longer reaction time may reduce the FAME yield due to the reversible reaction of transesterification and the formation of the soap, resulting in loss of esters [9].

Acid value refers to the amount of potassium hydroxide in milligrams needed to neutralize the free fatty acids in 1 gram of sample. Based on ASTM D7467, the maximum acid value is 0.50 mgKOH/. The free fatty acid concentration is one of the direct measures of the

quality of oil [11]. The volume of KOH decreases as the biodiesel blends increase as stated in Figure 1(a). The highest acid value is the B100 with the value of 0.2827 mgKOH/kg while the lowest acid value is pure diesel that was 0.0673 mgKOH/g. The correlation coefficient is strong between the acid value and biodiesel content with $r^2 = 0.8187$. Meanwhile, peroxide value is defined as the amount of peroxide oxygen per 1 kilogram of fat or oil. Based on Figure 1(b), the highest peroxide value is pure biodiesel (B100) which is 15.9000 meq/kg while the lowest peroxide value is pure diesel, which is 1.4000 meq/kg. Other peroxide values are 1.9000 meq/kg, 2.4000 meq/kg, 4.4000 meq/kg, 6.9000 meq/kg and 8.4000 meq/kg. The result shows that increasing the biodiesel amount in blended fuel will also increase the peroxide value. Generally, the oxidation rate increases when the temperature increases. The change in the partial pressure of the oxygen might affect the reaction rate of oxidation because the oxygen becomes less soluble in lipids and water [12]. The correlation is a strong coefficient between peroxide value and biodiesel content with r^2 equal to 0.8411.

Density can be described as the quantity of mass per unit volume of a substance. The density of biodiesel is slightly higher than petroleum diesel and it is directly proportional to the concentration of blending. FAME density is commonly affected by the unsaturation of the fatty acids; higher unsaturation will increase the density [9]. Based on Figure 1(c), pure biodiesel is denser than the other blends and pure diesel due to the higher chain length of biodiesel. Compared to pure diesel, the longer chain will decrease the density of the biodiesel. The density of pure biodiesel is 0.8699 while the density of pure diesel is 0.8400. The correlation coefficient between density and biodiesel content is 0.6905, which is a moderate correlation.

Based on Figure 1(d), the viscosity of pure biodiesel is the highest, which is 4.3677 mm^2/s while the lowest is pure diesel at 1.6120 mm^2/s. As for B5, B7, B10, B15 and B20, the viscosity is 2.3748 mm^2/s, 2.3984 mm^2/s, 2.5399 mm^2/s, 2.5581 mm^2/s and 2.5758 mm^2/s, respectively. The viscosity of the biodiesel blends slightly increased but for B100, it increased sharply. The correlation coefficient relationship is moderate between viscosity and biodiesel content with r^2 equal to 0.6643. The nature and number of double bonds are the factors that strongly affect the kinematic viscosity of unsaturated fatty compounds as the presence of double bond will less affecting the viscosity of the biodiesel [13].

Flash point can be defined as the lowest temperature at which a liquid can give off vapor to form an ignitable mixture in air near the surface of the liquid. The lower the flash point, the easier it is to ignite the material. Pure biodiesel has the highest flash point at 170-175°C and pure diesel has the lowest flash point at 70-75 °C. For blends of B5, B7 and B10, the range of flash point is the same at 90-95 °C while the flash points for B15 and B20 are 95-100 °C. The value of the flash point increases along with the increase in the blend level (Figure 2(a)). The production of biodiesel was affected by a high flash point value. The high flash point in biodiesel is due to the presence of predominate unsaturated acid chain length of C18:1 and C18:2 in the oil [14]. Biodiesel has a higher tendency to absorb water than pure diesel and this can cause problems, such as water accumulation and microbial growth. This is due to the hygroscopic character of biodiesel that can cause corrosion to the fuel tank components [15].

Based on Figure 2(b), the highest moisture content percentage was 0.06% for B20 while pure diesel has the lowest percentage which was 0.03%. The correlation coefficient of the relationship between moisture content and biodiesel content is strong with a value of r^2 equal to 0.8601. The moisture content for pure biodiesel was 0.06 %. B5 and B7 shared the same percentage of moisture content, which was 0.04% while for B10 and B15; the moisture content percentages were 0.05% and 0.06%, respectively. The parameter of the refractive index (RI) usually relates to molecular weight, fatty acid chain length, degree of conjugation and degree of saturation. The lowest RI value is for pure biodiesel, which was 1.4522 while the highest value was 1.4645 for pure diesel as shown in Figure 2(c). For B5, B7, B10, B15 and B20, the RI value is 1.4640, 1.4641, 1.4636, 1.4629 and 1.4623. The RI value for each blend slightly decreased and gave a moderate correlation coefficient with a value of $r^2 = 0.5412$. It is notable that the RI value

of biodiesel blends decreased as the amount of biodiesel contents increased.

Zawadzki et al. [6] stated that there is a possibility to distinguish between diesel and biodiesel due to the presence of aromatic compounds in diesel but is absent in biodiesel. The range for absorbance in biodiesel is 240 nm to 350 nm. As shown in Figure 3(a), the highest absorbance was by B15, which were 3.992 while the lowest is B20 that is 3.788 at 287 nm. The different values in absorbance were due to the presence of the aromatic compound in diesel fuel [16]. When the biodiesel content decreases, the aromatic compound in diesel increase, which makes the absorbance, becomes higher as the aromatic compound absorbs more ultraviolet light. For B15, an error must be occurring during the dilution. In addition, Figure 3(b) shows the saturated fatty acid analysis where B5 has the highest absorbance, which is 0.686. Meanwhile, the absorbance of B7 is 0.439, B10 is 0.132, B15 is 0.054 and B20 is 0.038, respectively. The absorbance of B5, B7 and B10 clearly showed a big different while B15 and B20 only showed a slightly different absorbance. Compared to the unsaturated fatty acid, the fluctuation data recorded with the highest absorbance is 4.652 for B15 and lowest absorbance is 3.910 for B7 while B5, B10 and B20 has the absorbance of 4.053, 3.944, and 4.229 respectively. The comparison between saturated and unsaturated fatty acid showed that the method used in this research is more suitable for saturated fatty acid as the UV-Vis spectra showed a decrease in absorbance as the biodiesel content increased and not suitable for unsaturated fatty acid like olive oil, since the degree of unsaturation is higher compare to palm oil.

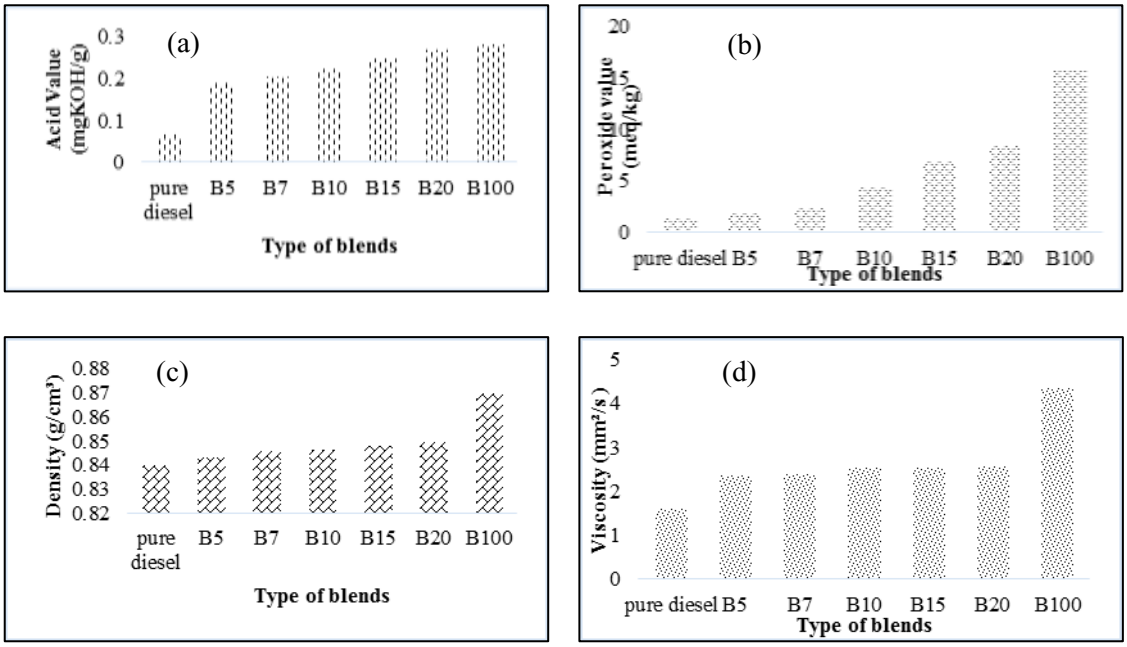


Figure 1. (a) acid value of each blends; (b) peroxide value of each blends; (c) density of each blends; (d) viscosity of each blends

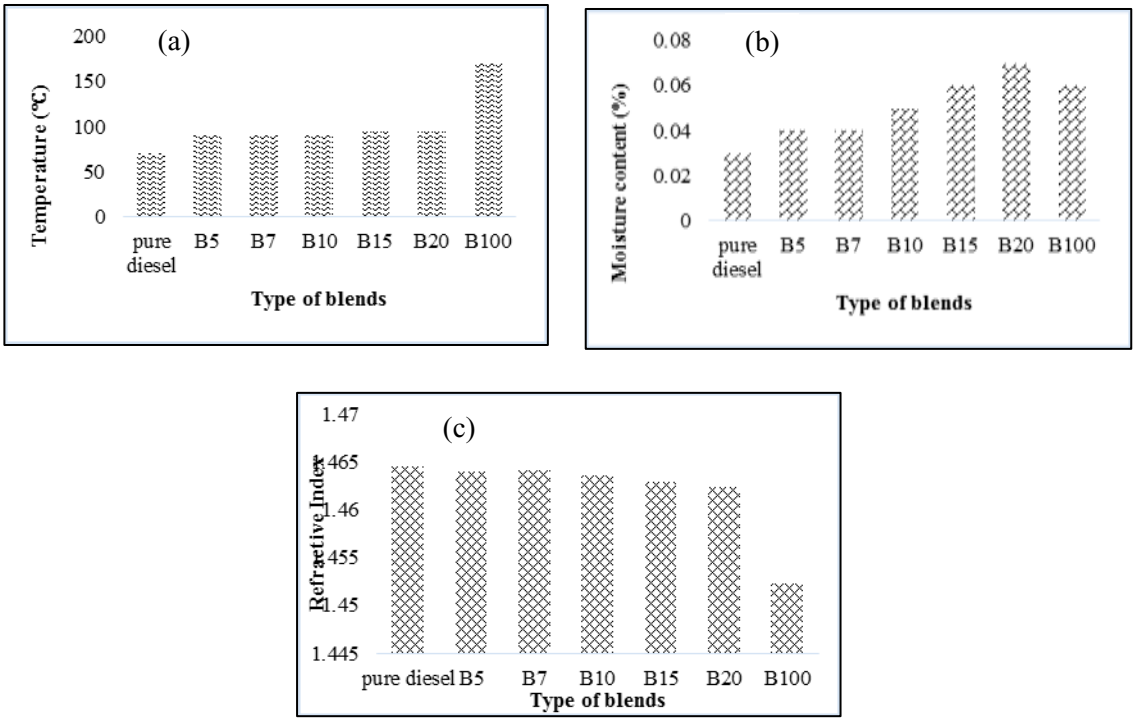


Figure 2. (a) flash point of each blend, (b) moisture content of each blends, (c) refractive index of each blends

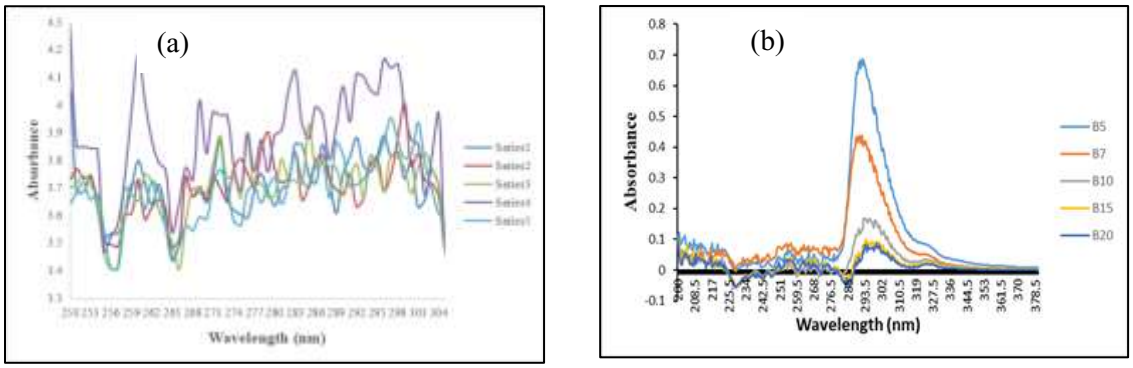


Figure 3. a) UV-Vis absorbance for unsaturated fatty acids b) UV-Vis absorbance spectra for saturated fatty acid

Conclusion

The focus of this research is the transesterification of olive oil to produce biodiesel. The optimization of the catalyst concentration and reaction time was conducted in order to obtain the highest percent yield of biodiesel. The absorbance of the blend levels increased as the percentage of biodiesel in each blend decreased. The characterization of biodiesel was done to observe the quality of the diesel-biodiesel blends and the parameter involved were acid value, peroxide value, density, viscosity, refractive index, flash point and moisture content. The correlation coefficient for each parameter was determined and the result showed that the higher the correlation coefficient, the better the quality of biodiesel.

Acknowledgement

The authors would like to thank Ministry of Higher Education, Malaysia, Universiti Malaysia Pahang and Universiti Teknologi MARA Pahang for research project (600-TNCPI 5/3/DDN (06)(001/2020) and (FGRS/1/2019/STG01/UMP/02/2).

References

1. Knothe, G. (2010). Biodiesel and renewable diesel: A comparison. *Progress in Energy and Combustion Science*, 36(3): 364–373.
2. The Star (2020). Bumps expected from B20 rollout. https://www.thestar.com.my/news/nation/2020/02/21/bumps-expected-from-b20-rollout. [Access online 20 Mac 2020].
3. Chong, C. T., Jo-HanNg, B. T., Fan, L., Ni, S., Wong, K. Y. and Hochgreb, S. (2020). Quantification of carbon particulates produced under open liquid pool and prevaporised flame conditions: Waste cooking oil biodiesel and diesel blends. *Fuel*. 270: 117469.
4. Silitonga, A. S., Masjuki, H. H., Mahlia, T. M. I., Ong, H. C., Chong, W. T., and Boosroh, M. H. (2013). Overview properties of biodiesel diesel blends from edible and non-edible feedstock. *Renewable and Sustainable Energy Reviews*, 22: 346-360.
5. Chattopadhyay, S., Das, S. and Sen, R. (2011). Rapid and precise estimation of biodiesel by high performance thin layer chromatography. *Applied Energy*, 88(12): 5188-5192.
6. Zawadzki, A., Shrestha, D. S. and He, B. (2007). Biodiesel blend level detection using ultraviolet absorption spectra. *Transactions of The Asabe*, 50(2): 1349-1353.
7. Monteiro, M. R., Ambrozin, A. R. P., Lião, L. M. and Ferreira, A. G. (2009). Determination of biodiesel blend levels in different diesel samples by 1H NMR. *Fuel*, 88(4): 691-696.
8. Pullen, J. and Saeed, K. (2015). Investigation of the factors affecting the progress of base-catalyzed transesterification of rapeseed oil to biodiesel FAME. *Fuel Processing Technology*, 130: 127-135.
9. Mathiyazhagan, M. and Ganapathi, A. (2011). Factors affecting biodiesel production. *Research in Plant Biology*, 1(2): 1-5.
10. Leung, D. Y. C., Wu, X. and Leung, M. K. H. (2010). A review on biodiesel production using catalyzed transesterification. *Applied Energy*, 87(4): 1083-1095.
11. Nierat, T. H., Al-Smadi, D., Musameh, S. M. and Abdel-Raziq, I. R. (2014). Storage age dependence of olive oil acidity in different locations in Palestine. *Journal of Physical Science*, 25(1): 33-43.
12. Popa, M., Glevitzky, I., Dumitrel, G.-A., Glevitzky, M. and Popa, D. (2017). Study on peroxide values for different oils and factors affecting the quality of sunflower oil. *Series E. Land Reclamation Earth Observation & Surveying, Environmental Engineering,* 6: 137-140.
13. Saxena, P., Jawale, S. and Joshipura, M. H. (2013). A review on prediction of properties of biodiesel and blends of biodiesel. *Procedia Engineering*, 51: 395-402.
14. Knothe, G. and Steidley, K. R. (2005). Kinematic viscosity of biodiesel fuel components and related compounds. Influence of compound structure and comparison to petrodiesel fuel components. *Fuel*, 84(9): 1059-1065.
15. Silitonga, A. S., Masjuki, H. H., Mahlia, T. M. I., Ong, H. C., Chong, W. T. and Boosroh, M. H. (2013). Overview properties of biodiesel diesel blends from edible and non-edible feedstock. *Renewable and Sustainable Energy Reviews*, 22: 346-360.
16. Delfino, J. R., Pereira, T. C., Costa Viegas, H. D., Marques, E. P., Pupim Ferreira, A. A., Zhang, L., Zhang, J. and Brandes Marques, A. L. (2017). A simple and fast method to determine water content in biodiesel by electrochemical impedance spectroscopy. *Talanta*, 179: 753-759.

Malaysian Journal of Analytical Sciences (MJAS)
Published by Malaysian Analytical Sciences Society

APPLICATION OF WASTE CATALYST, CaO-SiO_2 IN THE TRANSESTERIFICATION OF PALM OIL

(Aplikasi Mangkin Bahan Buangan, CaO-SiO_2 dalam Transesterifikasi Minyak Sawit)

Siti Norhafiza Mohd Khazaai[1,2]*, Sih Yiting[1], Mohd Hasbi Ab. Rahim[1], Mohd Lokman Ibrahim[4], Gaanty Pragas Maniam[1,5]

[1]*Faculty of Industrial Sciences & Technology,*
Universiti Malaysia Pahang, Lebuhraya Tun Razak, 26300 Gambang, Kuantan, Pahang, Malaysia
[2]*Faculty of Applied Sciences,*
Universiti Teknologi MARA Pahang, 26400 Jengka, Pahang, Malaysia
[3]*Faculty of Applied Sciences,*
Universiti Teknology MARA, 40450 Shah Alam, Selangor, Malaysia
[4]*Centre of Nanomaterial Research, Institute of Sciences,*
Universiti Teknologi MARA, Shah Alam 40450, Selangor, Malaysia
[5]*Biotropic Centre,*
Universiti Malaysia Pahang, Lebuhraya Tun Razak, 26300 Gambang, Kuantan, Pahang, Malaysia

**Corresponding author: ctnorhafiza03@yahoo.com*

Received: 30 April 2021; Accepted: 7 June 2021; Published: 27 June 2021

Abstract

The increment of global demand for energy resources and peaking of atmospheric carbon dioxide level have gained researcher's attention to study the alternative energy from renewable resources. In this work, biodiesel were produced by utilizing waste catalysts in converting palm oil into biodiesel. The waste eggshell and sea sand (sources of calcium oxide (CaO) and silicon oxide (SiO_2)) were used to produce CaO-SiO_2 heterogeneous solid catalyst. The effects of different ratio of both sources of catalysts and reaction variables such as reaction time, methanol to palm oil ratio and catalyst loading were studied. Surprising, the analysis using FTIR showed similar functional groups detected before and after the calcination process. Thus, uncalcined SiO_2 was chosen to assist the transesterification process. It was found that 93.01% biodiesel yield were produced at the optimal conditions studied: 65 ± 3 °C, 12:1 methanol to oil ratio within 1 hour 30 minutes, and the application of 5 wt.% catalysts. In conclusion, the CaO-SiO_2 heterogeneous solid catalyst derived from waste eggshell and sea sand showed high potential for biodiesel production from palm oil.

Keywords: biodiesel, eggshell, sea sand, calcium oxide

Abstrak

Peningkatan ke atas sumber tenaga secara global dan tahap kenaikan karbon dioksida dalam udara yang semakin meruncing mendapat perhatian para penyelidik untuk mengkaji sumber alternatif yang boleh diperbaharui. Di dalam kajian ini, biodiesel terhasil melalui penggunaan mangkin daripada bahan buangan untuk tindakbalas bersama minyak sawit. Di sini, bahan buangan

seperti kulit telur dan pasir pantai merupakan sumber bagi kalsium oksida (CaO) dan silika oksida (SiO_2) yang digunakan untuk menghasilkan mangkin pepejal heterogenos CaO-SiO_2. Kesan terhadap nisbah yang berbeza oleh dua bahan tersebut serta parameter tindakbalas seperti masa tindakbalas, nisbah minyak sawit terhadap metanol dan jumlah mangkin telah dijalankan. Menariknya, analisis FTIR menunjukan kehadiran kumpulan berfungsi yang sama sebelum dan selepas berlakunya proses kalsin. Maka SiO_2 tanpa dikalsin telah dipilih untuk membantu dalam proses transesterifikasi. Optimal keadaan yang dihasilkan adalah 65 ± 3 °C dan 12:1 nisbah metanol kepada minyak sawit dalam 1 jam 30 minit dengan penggunaan mangkin sebanyak 5 wt.% menghasilkan 93.01% biodiesel. Kesimpulan, mangkin pepejal heterogenos CaO-SiO_2 yang terhasil dari bahan buangan kulit telur dan pasir pantai menunjukan potensi sebagai mangkin bagi menghasilkan biodiesel daripada minyak sawit.

Kata kunci: biodiesel, kulit telur, pasir pantai, kalsium oksida

Introduction

The growth of renewable energy has attracted significant attention due to increasing concern towards air pollution, global warming, and limited supplies of fossil fuels. Apart from global warming, carbon dioxide (CO_2) emission may trigger ocean acidification, hence reducing the ocean's pH. Marine organisms such as corals and seashells become thinner and begin to dissolve. Losses of these species undoubtedly affecting the food chain, fishes, and marine mammals [1]. Therefore, a comprehensive approach is required to keep Earth habitable throughout the coming years. Substitution of conventional diesel with biodiesel may fulfill the environment mandate and regulation.

Biodiesel is also known as fatty acid methyl esters (FAME), can be produced from various animal fats and vegetable oils through transesterification reaction between the triglycerides and the short-chain alcohols, such as methanol and ethanol. Biodiesel has the highest potential in replacing petroleum diesel fuel as biodiesel is environmentally friendly, non-toxic, biodegradable, lower harmful exhaust emissions, as well as lower risk for fire than diesel [2].

Malaysia is the second-largest palm oil producer in the world and the production of palm oil is considered as the primary economic source of Malaysia. Statistically, 1.48 million hectares were planted with oil palm trees in 1985, increased to 4.85 million hectares of plantation in 2010, and surged up to about 5.74 million hectares in 2016 as reported by Malaysian Palm Oil Board (MPOB) [3]. Therefore, the total production of palm oil has achieved 25.64 million tonnes, a promising potential feedstock to produce biodiesel. To obtain the biodiesel from the palm oil, transesterification is recommended as stated in many types of research. There have few types of catalytic reaction that can be applied such as homogeneous transesterification, heterogeneous transesterification and enzymatic transesterification. However, there are certain limitations that existed in acid and enzyme catalyst. Onoji et al. [4] had proposed that the used of homogeneous base catalyst will lead to the formation of soap during transesterification due to the high content of free fatty acid (FFA). Therefore, homogeneous transesterification is not the best method to carry out. Heterogeneous catalyst has the potential to be reused and recovered quickly compared to homogeneous catalyst as the homogeneous catalytic reaction requires multi-purification and high amount of wastewater being produced. These create additional constraints to the industries. High production cost is the major obstacle of biodiesel industrial production which majorly contributed from the expensive feedstock and processes. The price for commercial biodiesel is about 1.5 times higher than the conventional petroleum diesel [5].

Ultimately, there is demand for a cost-effective and reliable catalyst in biodiesel production. The utilization of waste source helps to reduce wastes which create more economical and eco-friendly processes. Moreover, CaO extracted from eggshells, snail shells, clamshells, and mollusk shells is speculated to produce higher yield in the reaction when mixed with other oxides. The catalyst has been reported reusable almost three times and the percentage of methyl esters was higher than 90% [6]. In this study, the solid base

catalyst CaO-SiO_2 was optimized for the transesterification of palm oil into methyl esters. The abundant and low cost sources of calcium oxide and silica from eggshells and sea sand were used as the alternative approach in exploring new avenues for the development of highly active, stable, and cost-effective solid base catalyst.

Materials and Methods

Palm oil (Saji) was bought in from a supermarket located at Kuantan, Pahang. Meanwhile, the sea sand and eggshells were collected from Pantai Teluk Cempedak, Kuantan and restaurants respectively. Analytical grade of methanol (99.8%), n-hexane (>95%), n-heptane (99.9%), petroleum ether (100%), and chloroform (99.8%) were obtained from Merck. Analytical grade of methyl heptadecanoate, phenolphthalein, 4-nitroaniline, and 2,4-dinitroaniline were purchased from Sigma Aldrich company (Switzerland).

The eggshells were washed with hot water to remove impurities and dried for 24 hours at 100 °C. The dried shells were pulverized using grinder and ball mill to obtain finer powders, and later calcined at 900 °C for 2 hours to produce CaO [7]. Silicon dioxide (SiO_2) was prepared by drying the sea sand in the oven until constant weight was obtained prior to grinding process using ball mill to obtain finer powders of SiO_2. Then, 20 g of SiO_2 was calcined at 900 °C for 2 hours. The CaO-SiO_2 catalysts were prepared by mixing both CaO and SiO_2 through ball milling method at different ratios (1:1, 2:1, and 1:2). The CaO-SiO_2 catalyst was analyzed via Fourier Transform Infrared (FTIR) spectrophotometer, in combination with Brunauer-Emmett-Teller (BET) analysis.

The reaction of transesterification was carried out in open system reflux technique equipped with a thermometer, magnetic stirrer, condenser, and 50 mL round bottom flask that were immersed in a water bath. The reaction was controlled at 65 ± 3 °C under the aid of constant magnetic stirring. Various reaction parameters such as duration of reaction, ratio of methanol to oil, and catalyst loading were tested for optimum conditions. Separation of products and layers of byproduct were conducted by centrifugation (4000 rpm) for 10 min to obtain pure methyl esters. These procedures were repeated for three different ratios of catalysts. The produced biodiesel was mixed with the 10 mg/mL (in heptane) internal standard of methyl heptadecanoate (C17) and analyzed with Gas Chromatography-Flame Ionization Detector (GC-FID) (Agilent 7890A). The HP-INNOWax (30 m length × 0.25 mm internal diameter × 0.25 µm film thickness) was used as a polar capillary column.

Results and Discussion

The physical and chemical properties of palm oil were evaluated using standard test methods (ASTM D1298; ASTM D1298) in order to determine the quality of the oil. The results obtained were as follows: density at 25 °C was 0.9087 g/cm3, kinematic viscosity at 25 °C was 79.34 mm^2/s, and free fatty acid and moisture content were 0.13% and 0.11%, respectively. The palm oil used in the present work consists of 50.4% saturated fatty acids while the remaining 49.6% were unsaturated components as determined by chromatographic analysis. The most abundant fatty acid was palmitic acid which similar to [8].

The functional groups of the catalyst were determined by using FTIR analysis. Surprisingly, the absorption peaks for SiO_2 from sea sand (before and after calcination) were almost the same. The primary compound in sea sand was quartz (SiO_2 –Si-O symmetric) at the wavenumber of 796.89 cm^{-1}, 778.74 cm^{-1}, 796.38 cm^{-1}, and 778.19 cm^{-1}. Besides, the aliphatic stretch of Si–O–C was observed at the peaks of 1085.21 cm^{-1} and 1084.83 cm^{-1}. Uncalcined sea sand was chosen to be incorporated with CaO as a catalyst (almost the same functional groups) compared to the calcined sea sand [9]. In fact, according to [10], significant components such as quartz in the sea sand will not change into other substances below 1000°C. Moreover, result obtained in Figure 2(c) depicted same observations, before and after calcination process. Hence, the uncalcined catalyst may reduce the preparation time and eco-environmental friendly. The vibration of O-H bond in the calcium hydroxide, $Ca(OH)_2$ was recorded at the absorption band of 3643 cm^{-1} and this justified that CaO can be hydrolyzed into

$Ca(OH)_2$ when exposed to air [5, 11]. The absorption bands at 1064.78 cm^{-1} and 873.66 cm^{-1} corresponded to the C=O stretching that occurred in CaO. The stretching of C=O in amides appeared at 1636.23 cm^{-1}. Besides, the spectra observed for uncalcined SiO_2 and the mixed catalysts were within the same absorption bands [12].

The identification phase of calcined CaO and CaO-SiO_2 in X-ray diffraction (XRD) profiling as presented in Figure 2 with the characteristic peaks at 2θ ranging from 10° to 80°. It demonstrated the CaO reflection at 32.484°, 37.635°, 54.109°, 64.404°, and 67.644°, respectively as shown in Figure 2(a) meanwhile 21.128°, 26.921°, 36.787°, 42.777°, 50.946°, and 55.542° for the composition of quartz, SiO_2 and confirmed the existing of CaO-SiO_2. Referring to Figure 2(b), there were no peaks of calcium carbonate ($CaCO_3$) since the eggshells were subjected to calcination process and converted to CaO. Meanwhile, a small reflection of diffraction peaks from CaO and SiO_2 suggested that the compound diffused well on the surface of the supported catalyst [13]. The average crystallite size of the catalysts were mathematically calculated using Debye-Scherrer equation based on the highest intensity in the XRD diagram [5], where 1.2295 nm and 0.95207 nm were obtained for calcined CaO and CaO-SiO_2, respectively. The crystallite size was inversely proportional to the surface area of the catalyst.

Table 1 shows the tabulated surface area, pore-volume, and pore size form BET analysis. The calcined CaO had higher surface area compared to CaO-SiO_2 due to the transformation process of the composition in the calcined CaO which may increase the surface area and the existing of close-packed arrangement to each other [12]. As expected, CaO-SiO_2 had the lower surface area due to the uncalcined SiO_2 and reflected by the catalyst alteration on the metal oxide. Meantime, the lower pore volume of CaO-SiO_2 indicates that SiO_2 was successfully impregnated with CaO.

The X-ray fluorescence (XRF) analysis was conducted to confirm the elemental compositions of sea sand (before and after calcination). The values obtained were almost identical. Remarkably, the uncalcined sea sand revealed a higher differential of percentage (5.73%) compared to calcined sea sand. Thus, it was chosen for the transesterification process. Similar observation was reported by other researchers [9].

In this study, the transesterification reaction of palm oil catalyzed by CaO-SiO_2 was successfully carried out. Figure 3 shows the effect of time on the methyl ester production. It was observed that at the initial first hour, the conversion yield obtained was only 62.05%, which gradually increased to 93.01% within 1 hours 30 minutes, and slowly decreased with the increasing reaction time. The triglyceride and methanol reacted in a lower rate of conversion with longer duration as they are immiscible [5]. It can be observed that after a particular reaction time, the intermediate products (mono- and diglycerides) present in the mixture and facilitated the diffusion between reactants and products. Consequently, the conversion yield showed increasing trend in achieving incredibly high conversion and later reduced with increasing reaction time. This is related to the reversible reaction of transesterification. As the reaction reached equilibrium, the reverse reaction took place, leading to the formation of soap, and reduced the conversion of methyl ester [14]. In order to determine the optimum amount of methanol to oil ratio, the range of 3:1 to 13:1 (methanol: oil) were used, and the highest conversion yield obtained was 93.01% at 12:1 methanol to oil ratio with catalyst amount, 5 wt.% at 65 ± 3 °C.

The Le Chatelier's principle (Scheme 1) can be applied to explain the reversible process of the reaction. There are two reactions involved: (i) reverse reaction and (ii) forward reaction, shifting the equilibrium to the left and promoted the reaction of fatty acids and glycerol. Meanwhile, the reverse reaction leads to the formation of triglycerides. Hence, the conversion of methyl esters will obviously reduce [7]. Excess of methanol is not preferable as higher energy is required to recover and may increase the industrial production cost of methyl esters [5]. Catalyst with high amount of active sites will play an important role to facilitate the reaction. Therefore, 5 wt.% of the catalyst loading was used to

obtain the highest conversion of methyl ester (93.01%). Nevertheless, addition of more catalyst loading reduced the conversion yield due to the difficulties in mixing the solvent homogeneously. Furthermore, emulsion from the soap formation may also increase the viscosity of the mixture [15].

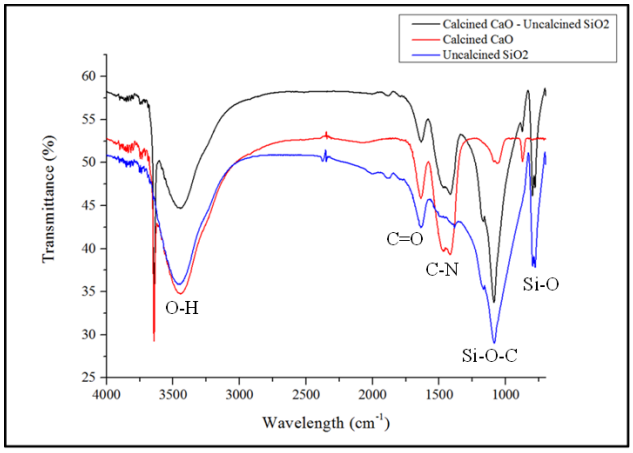


Figure 1. FTIR spectra of CaO-uncalcined SiO_2, Calcined CaO and Uncalcined SiO_2

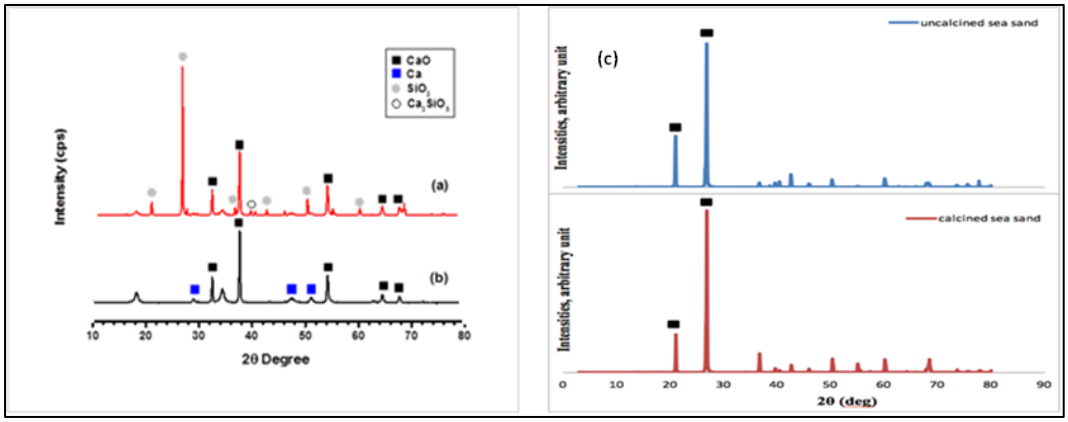


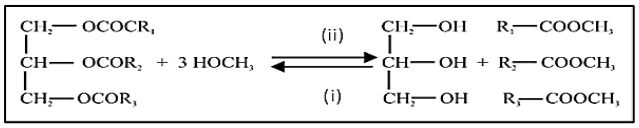
Figure 2. XRD patterns of (a) CaO-SiO_2 and (b) calcined CaO (c) Uncalcined and calcined SiO_2

Table 1. The Brunauer-Emmett-Teller (BET) result for calcined CaO and CaO-SiO_2

Characteristics	**Calcined CaO**	**CaO-SiO_2**
BET Surface Area (m^2/g)	9.11	2.73
Pore Volume (cm^3)	0.0358	0.0106
Pore Size (nm)	15.7129	15.5863

Table 2. Elemental compositions of sea sand (before and after calcination)

Compounds	Percentage (%)	
	Before Calcination	After Calcination
Silicon Dioxide	43.37	37.64
Calcium Oxide	2.51	2.38
Iron Oxide (Fe_2O_3)	0.31	1.76
Aluminium Oxide (Al_2O_3)	0.56	1.01
Phosphorus Pentoxide (P_2O_5)	0.45	0.49



Scheme 1. Le Chatelier's principle for the reaction of fatty acids and glycerol

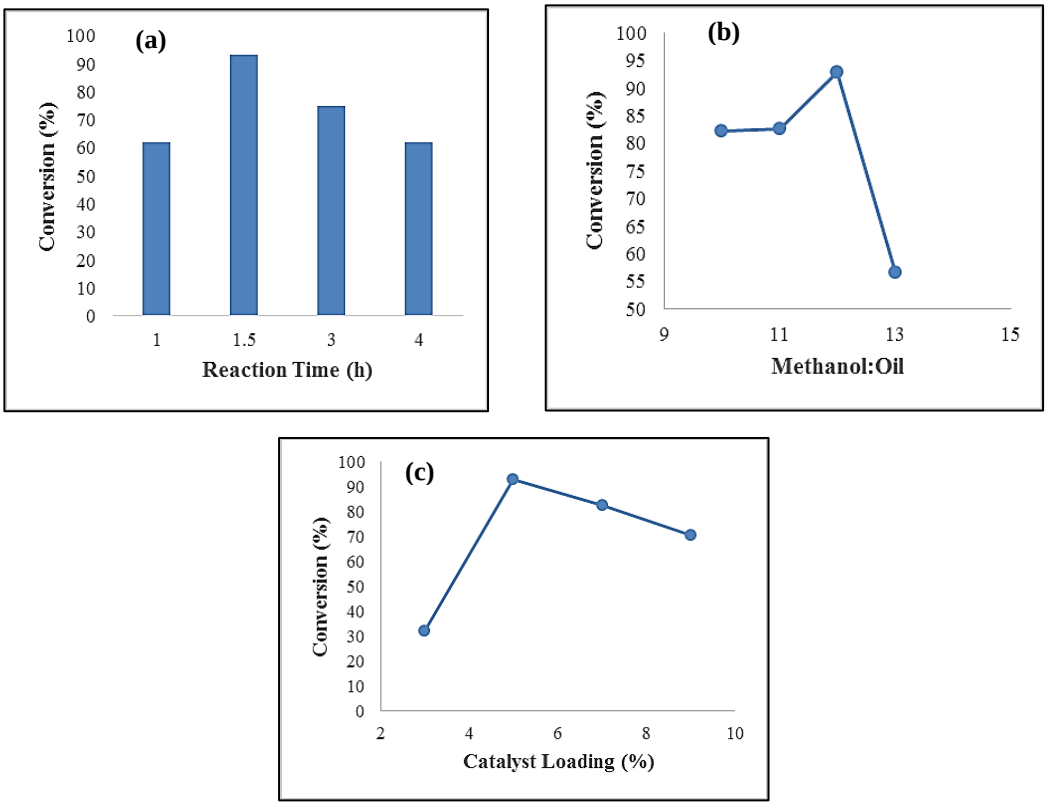


Figure 3. Effect of (a) reaction duration (b) methanol/oil molar ratio and (c) catalyst loading on the methyl ester yield

Conclusion

As a summary, heterogeneous catalyst from waste biomass, eggshell (CaO) and sea sand (SiO_2) were capable in producing methyl ester. Analyses using FTIR and XRF revealed successful preparation of $CaOSiO_2$ catalyst to assist the transesterification process of palm oil. It was reported that the prepared catalyst was able to produce 93.01% of methyl ester in 1 hour 30 minutes at 65 ± 3°C with MeOH/oil mass ratio of 12:1 and catalyst amount of 5 wt.%. This type of catalyst is a good potential than the existing catalyst for biodiesel production and more affordable as a cost-efficient and eco-friendly catalyst.

Acknowledgement

The authors would like to thank Ministry of Higher Education, Malaysia, Universiti Malaysia Pahang and Universiti Teknologi MARA Pahang for research project (600-TNCPI 5/3/DDN (06)(001/2020) and (FGRS/1/2019/STG01/UMP/02/2).

References

1. Terhaar, J. Kwiatkowski, L. and Bopp, L. (2020). Emergent constraint on Arctic Ocean acidification in the twenty-first century, *Nature*, 582: 379-383.
2. Bello, E. I. and Out, F. (2015). Physicochemical properties of rubber (*Hevea brasiliensis*) seed oil, its biodiesel and blends with diesel. *British Journal of Applied Science & Technology*, 6: 261-275.
3. Sukiran, M. A., Abnisa, F., Daud, W. M. A. W., Bakar, N. A. and Loh, S. K. (2017). A review of torrefaction of oil palm solid wastes for biofuel production. *Energy Conversion Management*, 149: 101-120.
4. Onoji, S. E., Iyuke, S. E., Igbafe, A. I. and Nkazi, D. B. (2016). Rubber seed oil: A potential renewable source of biodiesel for sustainable development in sub-Saharan Africa. *Energy Conversion and Management*, 110: 125-134.
5. Syazwani, O. N., Teo, S. H., Islam, A. and Taufiq-Yap, Y. H. (2017). Transesterification activity and characterization of natural CaO derived from waste Venus clam (*Tapes belcheri S*.) material for enhancement of biodiesel production. *Process Safety and Environmental Protection*, 105: 303-315.
6. Ngamcharussrivichai, C. P., Totarat, P. and Bunyakiat, K. (2008). Ca and Zn mixed oxide as a heterogeneous base catalyst for transesterification of palm kernel oil. *Applied Catalysis A: General*, 341: 77-85.
7. Boey, P. L., Maniam, G. P. and Hamid, S. A. (2011). Performance of calcium oxide as a heterogeneous catalyst in biodiesel production: A review. *Chemical Engineering Journal*, 168: 15-22.
8. Muthusamy, K., Nordin, N., Vesuvapateran, G., Ali, M., Mohd Annual, N. A., Harun, H. and Ullap, H. (2014). Exploratory study of rubber seed shell as partial coarse aggregate replacement in concrete. *Research Journal of Applied Sciences, Engineering and Technology*, 7: 1199-1202.
9. Sanuzi, A. I., Tahir, S. M. and Khazaai, S. N. M. (2018) Clamshell and sea sand as heterogeneous catalysts for waste cooking oil-based biodiesel production via transesterification reaction. *Malaysian Journal of Analytical Sciences*, 22: 107-114.
10. Mechri, M. L., Chihi, S., Mahdadi, N. and Beddiaf, S. (2017). Diagnosis of the heating effect on the electrical resistivity of Ouargla (Algeria) dunes sand using XRD patterns and FTIR spectra. *Journal of African Earth Sciences*, 125: 18-26.
11. Jindapon, W., Jaiyen, S. and Ngamcharussrivichai, (2016). Seashell-derived mixed compounds of Ca, Zn and Al as active and stable catalysts for the transesterification of palm oil with methanol to biodiesel. *Energy Conversion Management*, 122: 535-543.
12. Mutalib, A. A. A., Ibrahim, M. L., Matmin, J., Kassim, M. F., Sufri Mastuli, M., Taufiq-Yap, Y. H., Shohaimi, N. A. M., Islam, A., Tan, Y. H. and Kaus, N. H. M. (2020). SiO_2-rich sugar cane bagasse ash catalyst for transesterification of palm oil. *Bioenergy Resources*, 13: 986-997.
13. Farooq, M., Ramli, A. and Subbarao, D. (2013). Biodiesel production from waste cooking oil using bifunctional heterogeneous solid catalysts. *Journal of Cleaner Production*, 59: 131-140.

14. Boro, J., Thakur, A. J. and Deka, D. (2011). Solid oxide derived from waste shells of *Turbonilla striatula* as a renewable catalyst for biodiesel production. *Fuel Processing Technology*, 92: 2061-2067.

15. Jaiyen, S., Naree, T. and Ngamcharussrivichai, (2015). Comparative study of natural dolomitic rock and waste mixed seashells as heterogeneous catalysts for the methanolysis of palm oil to biodiesel. *Renewable Energy*, 74: 433-440.

Malaysian Journal of Analytical Sciences (MJAS)
Published by Malaysian Analytical Sciences Society

^{210}PO DETERMINATION IN URINE SAMPLES AMONG RADIATION WORKERS BY ALPHA SPECTRUM ANALYSIS

(Penentuan ^{210}Po dalam Sampel Urin di Kalangan Pekerja Sinaran Melalui Analisis Spektrum Alpha)

Nurrul Assyikeen Md. Jaffary*, Nurul Zakila Azlan, Jalal Sharib @ Sarip, Mohd Tarmizi Ishak, Zulkifli Daud, Mohd Izwan Abdul Adziz

Radiochemistry and Environmental Laboratory, Waste and Environmental Technology Division, Malaysian Nuclear Agency, Bangi, 43000 Kajang, Malaysia

**Corresponding author: assyikeen@nuclearmalaysia.gov.my*

Received: 26 April 2021; Accepted: 11 June 2021; Published: 27 June 2021

Abstract

The radioactivity of ^{210}Po in the urine sample of radiation workers working in radiochemical laboratory, Malaysian Nuclear Agency, was determined. Collected urine samples have to go through the hot acid dissolution process followed by the auto-deposition technique using HCl as the solution. Measurements using the alpha spectrometry system showed good ^{209}Po retrieval, while ^{210}Po determination has no interference by other natural radionuclides. The specific radioactivity of ^{210}Po was determined from 1.33 mBqL^{-1} to 49.84 mBqL^{-1}. This preliminary study was conducted to obtain reference data as part of methods development for further investigations in emergencies. The assessment of the data findings in terms of radiation safety was done. Such radioactivity measurement procedure would also be applying for the routine ^{210}Po analysis in the urine.

Keywords: polonium isotopes, radioactivity, radiochemical separation, alpha spectrometry, bioassay

Abstrak

Radioaktiviti ^{210}Po dalam sampel urin pekerja radiasi yang bekerja di makmal radiokimia, Agensi Nuklear Malaysia telah ditentukan. Sampel urin yang dikumpulkan mesti melalui proses pembubaran asid panas diikuti dengan teknik pemendapan-auto menggunakan HCl sebagai medium larutan. Pengukuran menggunakan sistem spektrometri alpha menunjukkan dapatan semula ^{209}Po yang baik, sementara penentuan ^{210}Po tiada gangguan daripada kehadiran radionuklida semula jadi yang lain. Radioaktiviti spesifik ^{210}Po telah ditentukan dari 1.33 mBqL^{-1} hingga 49.84 mBqL^{-1}. Kajian awal ini dilaksanakan untuk mendapatkan data rujukan sebagai sebahagian dari pengembangan kaedah bagi situasi kecemasan. Penilaian ke atas dapatan data dari segi keselamatan radiasi telah dilakukan. Prosedur pengukuran radioaktif seperti ini juga digunakan untuk aktiviti analisis rutin ^{210}Po dalam sampel urin.

Kata kunci: isotop polonium, radioaktiviti, pemisahan radiokimia, spektrometri alfa, bioasai

Introduction

^{210}Pb and ^{210}Po are associated with the ^{238}U decay chain, a naturally occurring radionuclide. ^{210}Pb and its daughter ^{210}Bi are beta sources with a half-life of 22.3 years and 5.0 days, respectively. Meanwhile, ^{210}Po, the granddaughter of ^{210}Pb, is an alpha transmitter. The half-life of ^{210}Po is only 138.4 days, and it is the lengthiest polonium radioisotope. ^{210}Po occurrences have been continually supplied in the environment by ^{210}Pb, which is technologically enhanced from natural radioactive materials (TENORM) [1].

Owing to the natural background radiation, ^{210}Po contributes significantly to human internal dosage when absorbed into the body by inhalation or ingestion and is therefore essential to be monitored [1]. An excessive dose of ^{210}Po may cause acute radiation syndrome (ARS), which includes nausea, vomiting, diarrhea in the prodromal period, and later symptoms, including hair loss and bleeding. A lower dose can cause long-term organ failure, which could lead to death. The medical sequence can be defined when intake of ^{210}Po more than 1 GBq (109 Bq) occurs [2].

Historically, ^{210}Po has also been linked to the death of Mr. Alexande Litvinenko, a former Soviet spy. He died on 23rd November 2006, 22 days after consuming a cup of tea laced with ^{210}Po. The assassins left radioactive traces all over London. Following this attack, London Health officials used alpha spectrometry to track hundreds of urine samples from internally infected individuals [2, 3]. Despite the fact that ^{210}Po can be easily determined by measuring alpha radiation emissions, there is a shortage of reference on ^{210}Po in human tissues and body fluids used as a baseline in determining whether or not the individual would be contaminated [4].

The bioassay technique was used to measure the amount of actinide present in the body based on the rate of excretion of body fluids. In an emergency of high ^{210}Po activity spread, urine samples of individuals dealing specifically with ^{210}Po from open sources should be analysed. It is critical to act rapidly in an emergency to identify radiological threats, particularly to the general public. Urine bioassays are often used to assess internal ^{210}Po exposure [2], which can be separated into two types; spontaneous plating [5] and micro-precipitation technique [6]. However, the pre-concentration approach is tedious and time-consuming, which may not be appropriate in an emergency. Therefore, to measure ^{210}Po in urine samples, new and quick analysis methods are needed.

In this study, sample selection from the radiochemical laboratory of the Malaysian Nuclear Agency was used as a reference group to determine ^{210}Po. This paper defines the procedure used for determining ^{210}Po in urine samples, which involved wet decomposition followed by automated deposition for alpha spectrometry. Furthermore, this research focuses on the factors that affect polonium determination and the need to improve the method. Finally, the study results of ^{210}Po value will be used as the primary baseline reference data, and assessment in terms of radiation safety were done.

Materials and Methods

Materials

^{209}Po was purchased from Perkin Elmer and was diluted to 30Bq. The diluted concentration was calibrated by preparing a set of a known amount of standards and using a calibration curve to create a radioactivity relationship between the amount spiked and an instrument response. Nitric acid (65% purity) and hydrogen peroxide (30% purity) were purchased from MERCK, used for acid dissolution. Hydrochloric acid (37% purity) was supplied by Scharlau, and distilled water was used for acid dilution in preparing final solution of 2M HCl for auto-deposition process. Mixed standard alpha reference sources (^{238}U, ^{234}U, ^{239}Pu and ^{241}Am) were obtained from ANALYTICS used to calibrate the alpha spectrum energy for the alpha spectrometry system.

Sampling and sample analysis

A 24-hour urine specimen obtained from 6 radiochemical workers were used to examine. 50 mL of the obtained urine sample, moved to a 100 mL glass beaker and diluted with 50 mL of distilled water. Each

sample was made in triplicate and heated to just below 90 ºC until almost dry. The known amount (approximately 6 Bq) of ^{209}Po as the tracer was added. In the urine bioassay method, ^{210}Po has often been corrected using a ^{208}Po tracer or ^{209}Po to assess the recovery due to any depletion or cross contamination of ^{210}Po during the sample analysis. In this study, ^{209}Po was used as a tracer due to the advantage in energy isolation from the ^{210}Po peak. The ^{208}Po is not widely used as a tracer since its peak energy is closed to ^{210}Po and can be interference in mistake (Table 1).

Complete dissolution was carried out with 10 mL of 65% nitric acid and 1 mL of 30% hydrogen peroxide until all the organics had been decomposed. The solution was evaporated until almost dry after dissolution, and the digestive residue was converted to chloride form by applying 10 mL 37% hydrochloric acid. Once the evaporation process was completed, 3.5 mL of 37% hydrochloric acid was applied directly to dissolve the residue. The solution was then rendered to 0.5M hydrochloric acid medium by adding 80 mL of distilled water.

Auto plating

In each sample, hydroxylamine chloride and Bi carrier were added, which were then gently heated on a hot plate and dissolved before being placed on the silver disk as seen in
Figure 1. ^{210}Pb and its daughter ^{210}Bi must be entirely separated to maintain the secular equilibrium between ^{210}Bi and ^{210}Po with no interference of ^{210}Pb [3]. 4 hours of plating is needed to achieve optimum recovery [8]. Reducing the plating time (at room temperature) to speed up sample processing throughput could be an alternative, but it will reduce the recovery and increase the MDA. In this case, the volume of tracer used must be adjusted to account for the reduction of recovery.

Active source measurement using alpha spectrometry system

The 450 mm^2 silver discs active surface was then measured using an alpha spectrometry system consisting of Alpha Passivated Implanted Planar Silicon (PIPS) detectors, as shown in
Figure **2**(a). Compared to other radiometric methods, such as γ-ray spectrometry, alpha spectrometry has a distinct advantage: the background is very low. The efficiency of more than 20% was measured based on efficiency measurement of ANALYTICS mixed standard alpha reference sources for a source to the sensor distance less than 1 cm (shelve number 1 in the alpha detector chamber), as shown in
Figure **2**(b). The detector efficiency does not vary with energy (4 MeV to 9 MeV) due to the small distance of α-peak energy. Because of this efficiency's freedom from energy (i.e. the intrinsic efficiency of one), the precise non-standard alpha activity ratio for peak energy's efficiency calibration may be determined [9].

The duration of the active source measurements in this study was 24 hours. Due to its volatility, the polonium atoms readily exit the source disc in the vacuum counting chamber, allowing a significant fraction drift to the detector. Because of the drawback of the long half-life of ^{209}Po, extra care was taken on sample handling to prevent detector contamination. Figure 3. shows the overall ^{210}Po analysis in the urine by wet decomposition for alpha analysis.

The polonium alpha spectrum with ^{209}Po viewed in Alpha Vision software is shown in Figure 4. A particular amount of ^{209}Po was added to the sample to be used as an internal isotope tracer, making it possible to calculate the results of the radiochemical analysis. The result was calculated from the peak area of ^{209}Po using equation (1), while ^{210}Po activity was calculated from equation (2).

$$\eta_{\mathrm{chem}} = \frac{\mathrm{Area}_{209\mathrm{Po}}}{\mathrm{A}_{209\mathrm{Po}} \cdot \mathrm{tm}209_{Po} \cdot \varepsilon_{\mathrm{det}}} \quad (1)$$

$$\mathrm{A}_{210\mathrm{Po}} = \frac{\mathrm{Area}_{210\mathrm{Po}}}{t\eta_{\mathrm{chem}} \cdot \varepsilon_{\mathrm{det}} \cdot m_s} \quad (2)$$

where, A^{210}Po is activity of ^{210}Po in the sample, Bqkg^{-1}, A^{209}Po is activity of ^{209}Po in the sample, Bqkg^{-1}, Area^{210}Po is peak area of ^{210}Po, counts, Area^{209}Po is peak area of ^{209}Po, counts, t is measurement time, s, η_{chem} is yield of ^{209}Po tracer,%, ε_{det} is counting efficiency, %, m^{209}Po is tracer mass, g, and m_s is sample mass, kg.

Table 1. ^{208}Po, ^{209}Po, and ^{210}Po decay data

Radionuclides	Half-life (t1/2)	Disintegration Modes	Eα (MeV)	Intensity (%)
^{208}Po	2.898y	α:99.99777%	5.1149	99.9956
			4.220	4.220
^{209}Po	102y	α:99.52%	4.885	19.7
			4.883	79
			4.622	0.551
			4.310	$1.5x10^{-4}$
			4.110	$5.6x10^{-4}$
^{210}Po	138.376	α:100	5.40746	99.99876
			4.60436	$1.24x10^{-3}$

References: [7]



Figure 1. Image of an auto-deposition setup

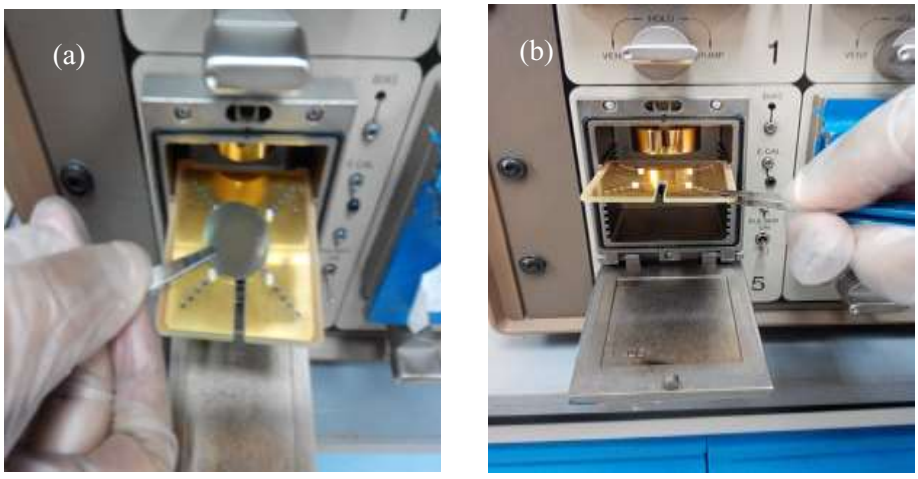


Figure 2. a) Active source placed paralleled to the detector b) Shelve placed at the same calibrated mixed alpha standard ANALYTICS source

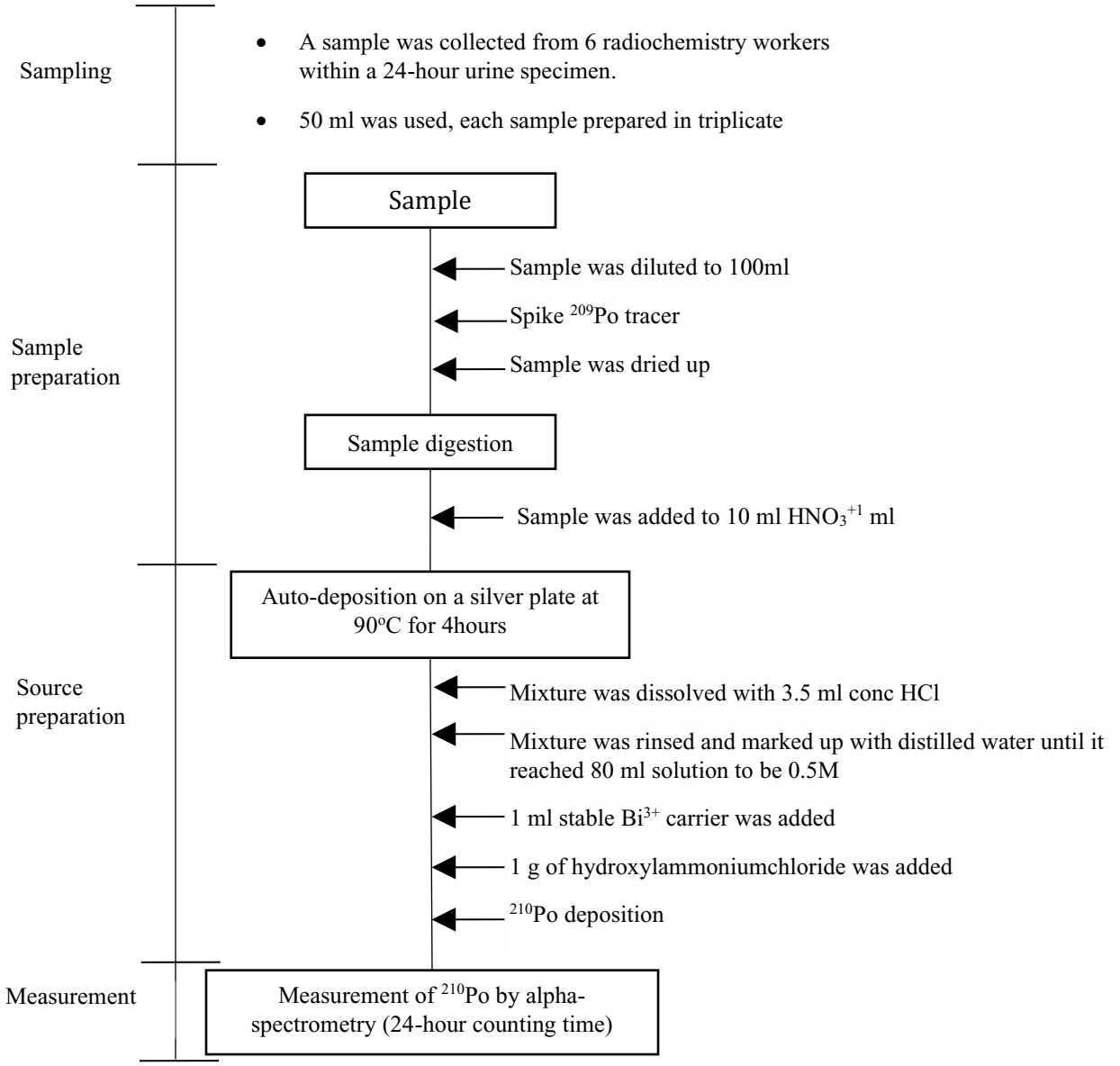


Figure 3. A flow chart for determination of ^{210}Po in urine samples using alpha spectrometry system

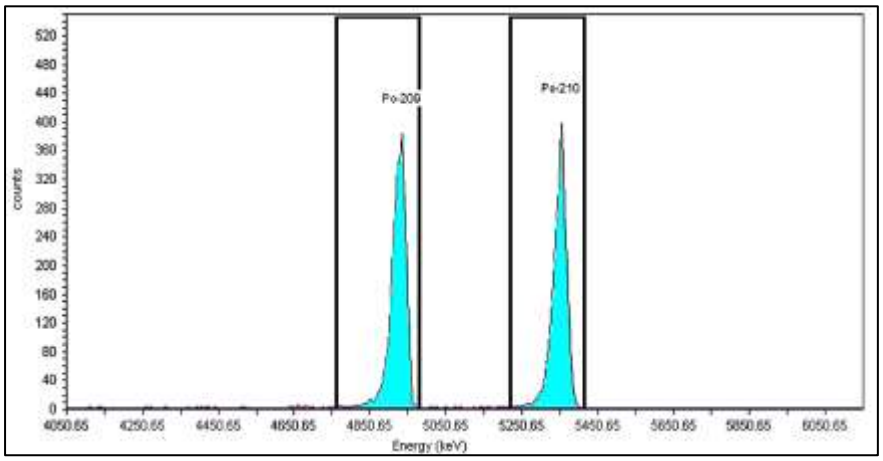


Figure 4. Polonium alpha, ^{210}Po spectrum with ^{209}Po yield tracer from this study

Results and Discussion

Urine samples

Table 2 shows the ^{210}Po concentrations in the urine samples relative to blank samples. The average specific radioactivity measured is 17.93 mBqL^{-1}, with an estimated relative uncertainty of 0.80 mBqL^{-1}. The recovery data is quite good and comparable to other research [6,8]. The varies of ^{210}Po of each individual is greatly dependent upon the daily excretion rates between individuals. Individual variations in urine volume provided to the laboratory for examination may imply that specific urine samples can lead to a collection period of less than or more than 24 hours.

The results of the ^{210}Po bioassay are compared to those of the preceding sample in Table 3. In comparison to previous investigations, the data has showed that the specific radioactivity is slightly greater than other reported research [4, 10]. The variation of ^{210}Po in urine is influenced by the targeted person, with ^{210}Po in urine acquired from radiation workers in this study being more susceptible to internal exposure. Radiation workers who work with TENORM should wear personal protective equipment (PPE) such as a respiratory mask to prevent inhalation or ingestion of the radioactive gas or dust to avoid serious health effects due to external and or internal exposure on workers [12]. Considering the ^{238}U decay series from TENORM activity, workers may internally expose to the radioactive ^{226}Ra gas by inhalation if without applying radiation protection principles. The ^{226}Ra then decays to its granddaughter of ^{210}Po in particulate form and is trapped and accumulated inside the body. The alpha particle will ionize the individual's cell and cause damage to the cell and tissue. The considering pathway may give an acute health risk to the radiation worker. The reported data in this study, however, is still within the background levels of ^{210}Po in urine which has been examined and assessed for almost 550 measurements of the general public [11].

Assessment on the detection level

The ^{210}Po concentration in urine samples from the current study was computed into the daily excretion rate determined in mBq.d^{-1}, as shown in Table 4. Based on the UK Health Protection Agency's experience in assessing ^{210}Po contamination of members of the public in London areas, the maximum committed effective dose to be considered is below 1 mSv.y^{-1}, which is computed by ^{210}Po daily excretion rate determined at or below 30 mBqd^{-1} [4]. It is well known that the ^{210}Po levels in urine differed from person to person based on environmental and lifestyle variables [6]. Studies have indicated that more than 80% of the contribution from ^{210}Po to the total annual background dose is derived from ^{210}Po associated with seafood consumption [14, 15]. The accumulation of ^{210}Po in various environmental products, including fish and shrimp, is

well-reported [16, 17]. Hence, food intake across the district can also affect the data, while uptake through inhalation of air and cigarette smoke gives smaller contributions [18].

According to the category of public, occupational, and emergency, the level of exposure is tabulated in Table 5. According to the findings of the current report, the following screening thresholds were deemed to be of no significance in terms of radiation safety. The required detection level (RDL) for assessing background levels in human urine and chronic exposures is $3mBqd^{-1}$ for the general public, indicating that the Malaysian Nuclear Agency's Radiochemistry Laboratory has been far from the criteria for the assessment of ^{210}Po in urine. Based on this study, we would like to emphasise that the suitability of experimental procedures can be ascertained as ^{210}Po measurements with alpha spectrometry are given in a standardised manner and have been extensively used for various biological samples such as marine samples, body fluids like urine and blood [4, 19].

Table 2. Results of determination ^{209}Po in urine sample

Sample	**^{210}Po Determination ($mBqL^{-1}$±1SD)**	**Recovery (%)**
Blank	2.85	77.59
P 1	12.67±0.44	72.78
P 2	38.42±0.26	74.93
P 3	41.46±0.51	79.08
P 4	12.48±0.18	76.32
P 5	10.78±0.23	80.61
P 6	17.86±0.57	78.48

Table 3. Comparison of ^{210}Po in urine with the previous study measured using alpha spectrometry system

Concentration ($mBqL^{-1}$)	**Sample**	**References**
Average: 23.27 Min: 1.33 Max: 49.84	Radiochemistry laboratory worker	This study
Min: 0.5 Max: 4.8	Reference group of Portuguese citizens	[4]
	Saudi Arabia Volunteer public	[10]
5.9	• Non-smokers	
8.9	• Smokers	
8.1	• Shisha smokers	
Min: 0.6 Max: 69.6	550 measurements from the general public were examined	[11]

Table 4. ^{210}Po daily excretion rate compared with other studies measured using alpha spectrometry system

Country	**Sample /Country**	**Average Daily Excretion Rate (mBqd^{-1})**	**References**
Malaysia	Radiochemistry laboratory worker	Average:1.16 Min: 0.07 Max: 2.49	This study
Brazil	Monazite plant workers		[13]
	• Non-smokers	5.2	
	• Smokers	9.9	
Italy	Volunteer public		[5]
	• Non-smokers	11.8	
	• Smokers	12	
Portugal	Portuguese citizen potentially exposed to ^{210}Po in London	3.06	[4]
United Kingdom	UK residents acquired internal contamination	30 mBq in 24 hours (when computed to committed effective dose is below 1mSvyr^{-1})	[2]

Table 5. Level of exposure according to category

Category	**Level of Exposure**	**Committed Effective Dose**	**References**
1	Public	0-1 mSvyr-1	
2	Occupational	1-20 mSv yr-1	[6]
3	Emergency	>20mSv	

Conclusion

The proposed method provided an easy way to determine ^{210}Po concentration in a urine sample. The most common method for measuring ^{210}Po in urine is sample digestion, Po isolation, and auto deposition, accompanied by α spectrometric counting. Urine samples are conventionally digested and evaporated in an open beaker on a hotplate in the presence of oxidising agents (acids and hydrogen peroxide). Since radioactive compounds like ^{210}Po are present in nature, they can also be found in the human body. To assess any contaminants, a clearer understanding of the population's baseline level is needed. The ^{210}Po excretion rate can be used to estimate doses resulting from ^{210}Po or a combination of ^{238}U chain radionuclides that comprises ^{210}Po. The ^{210}Po of radiochemistry laboratory's worker in this study were measured between 1.33 mBqL^{-1} to 49.84 mBqL^{-1}. Finally, further research should be conducted to increase the precision and accuracy of ^{210}Po determination on urine samples significantly. The RAS laboratory must always get ready with ^{210}Po and other radionuclides on hand for bioassay research. This method should allow to measure low levels of ^{210}Po and a fast turnaround for screening. In an emergency,

this preliminary study was suggested for further review, considering continuous method development.

Acknowledgments

The authors thank the management of the Waste and Environmental Technology Division for supporting the implementation of this project, and the staff of Alpha Laboratory, Radiochemistry and Environmental Laboratory for their assistance in this work.

References

1. Vreček, P., Benedik, L. and Pihlar, B. (2004). Determination of ^{210}Pb and ^{210}Po in sediment and soil leachates and in biological materials using a Sr-resin column and evaluation of column reuse. *Applied Radiation and Isotopes*, 60(5): 717-723.
2. Maguire, H., Fraser, G., Croft, J., Bailey, M., Tattersall, P., Morrey, M. and Troop, P. (2010). Assessing public health risk in the London polonium-210 incident, 2006. *Public Health*, 124(6): 313-318.
3. Li, C., Sadi, B., Davis, K., Wyatt, H., Cornett, J., Kramer, G. and Canada, P. E. (2011). Is alpha spectrometry reliable for ^{210}Po urine bioassay? *Radiation Protection Dosimetry*, 143(1): 106-108.
4. Carvalho, F. P. and Oliveira, J. M. (2009). Bioassay of ^{210}Po in human urine and internal contamination of man. *Journal of Radioanalytical and Nuclear Chemistry*, 280(2): 359-362.
5. Meli, M. A., Desideri, D., Roselli, C. and Feduzi, L. (2009). ^{210}Po determination in urines of people living in Central Italy. *Journal of Environmental Radioactivity*, 100(1): 84-88.
6. Manickam, E., Sdraulig, S. and O'Brien, R. (2010). An improved and rapid radiochemical method for the determination of polonium-210 in urine. *Australian Journal of Chemistry*, 63(1): 38-46.
7. IAEA (2009). A procedure for the determination of Po-210 in water samples by alpha spectrometry. IAEA Analytical Quality in Nuclear Applications Series No. 12.
8. Guérin, N. and Dai, X. (2015). An emergency bioassay method for ^{210}Po in urine. *Applied Radiation and Isotopes*, 103: 179-184.
9. Aggarwal, S. K. (2016). Alpha-particle spectrometry for the determination of alpha emitting isotopes in nuclear, environmental and biological samples: Past, present and future. *Analytical Methods*, 8(27): 5353-5371.
10. Al-Arifi, M. N., Alkarfy, K. M., Al-Suwayeh, S. A., Aleissa, K. A., Shabana, E. I., Al-Dhuwaili, A. A. and Al-Hassan, M. I. (2006). Levels of ^{210}Po in blood, urine and hair of some Saudi smokers. *Journal of Radioanalytical and Nuclear Chemistry*, 269(1): 115-118.
11. Hodgson, A. (2018). Natural levels of Polonium-210 in urine. *Journal of Radiological Protection*. 38: 393.
12. Jaffary, N. A., Khoo, K. S., Mohamed, N. H., Yusof, M. A. W. and Mohd Fadzil, S. (2019). Malaysian monazite and its processing residue: chemical composition and radioactivity. *Journal of Radioanalytical and Nuclear Chemistry*, 322(2): 1097-1105.
13. Lipsztein, J. L., Melo, D. R., Sousa, W., Dias da Cunha, K. M., Azeredo, A. M. G., Julião, L. and Santos, M. (2003). Norm workers: A challenge for internal dosimetry programmes. *Radiation Protection Dosimetry*, 105(1–4), 317-320.
14. Alonso-Hernandez, C., Diaz-Asencio, M., Munos-Caravaca, A., Suarez-Morell, E. and Avila-Moreno, R. (2002). ^{137}Cs and ^{210}Po dose assessment from marine food in Cienfuegos Bay (Cuba). *Journal of Environmental Radioactivity*, 61(2): 203-211.
15. Noshkin, V. E., Robison, W. L. and Wong, K. M. (1994). Concentration of ^{210}Po and ^{210}Pb in the diet at the Marshall Islands. *Science Total of Environment*, 155: 87-104.
16. UNSCEAR (2000). Sources and effects of ionizing radiation, New York: pp 1.
17. Alam, L. and Mohamed, C. A. R. (2011). Natural radionuclide of Po210 in the edible seafood affected by coal-fired power plant industry in Kapar coastal area of Malaysia. *Environmental Health: A Global Access Science Source*, 10(1): 1-10.
18. Carvalho, F. P. (1995). Origins and concentrations of ^{222}Rn, ^{210}Pb, ^{210}Bi and ^{210}Po in the surface air at Lisbon, Portugal, at the Atlantic edge of the European continental landmass. *Atmospheric*

Environment, 29(15): 1809-1819.

19. García-Orellana, I. and García-León, M. (2002). An easy method to determine ^{210}Po and ^{210}Pb by alpha spectrometry in marine environmental samples. *Applied Radiation and Isotopes*, 56(4): 633-636.

Malaysian Journal of Analytical Sciences (MJAS)
Published by Malaysian Analytical Sciences Society

THE EFFECTS OF STORAGE TEMPERATURE AND TIME ON THE LEVELS OF PHTHALATES IN COMMERCIAL PET-BOTTLED WATER

(Kesan Suhu dan Masa Penyimpanan Terhadap Kandungan Ftalat dalam Air Berbotol PET Komersial)

Nur Amira Syazwan Razali[1], Ungku Fatimah Ungku Zainal Abidin[2,3], Nur Hanani Zainal Abedin[1,3], Syaliza Omar[4], Jinap Selamat[1,5], Maimunah Sanny[1,5]*

[1]Department of Food Science, Faculty of Food Science and Technology
[2]Department of Food Service Management, Faculty of Food Science and Technology
[3]Halal Products Research Institute,
Universiti Putra Malaysia, 43400 Serdang, Selangor, Malaysia
[4]Faculty of Pharmacy,
Universiti Sultan Zainal Abidin, Besut Campus, 222000, Besut, Terengganu, Malaysia
[5]Laboratory of Food Safety and Food Integrity, Institute of Tropical Agricultural and Food Security,
Universiti Putra Malaysia, 43400 Serdang, Selangor, Malaysia

**Corresponding author: s_maimunah@upm.edu.my*

Received: 5 April 2021; Accepted: 22 May 2021; Published: 27 June 2021

Abstract

This study was conducted to determine the effects of storage temperature and time on the levels of phthalates in commercial PET-bottled water. Freshly-produced water samples consisted of drinking, mineral, and sparkling in PET bottles were collected from a manufacturing site and subjected to different storage temperatures (refrigeration temperature of 4 °C, room temperature of 25 °C, and 40 °C) and times (0 month as control, 1.5 months, 3 months, and 6 months). Six different phthalates were analyzed using LC-MS/MS with deuterated bis(2-ethylhexyl)phthalate (DEHP) as internal standard. DEHP in the PET-bottled water was detected in the range from 2.32 to 27.6 ng/mL for 3- and 6-month storage samples; higher than di-n-octyl phthalate (DnOP) detected in the range from 1.57 to 12.6 ng/mL. Higher levels of DEHP and DnOP in PET-bottled mineral water were detected at room temperature of 25 °C when compared to refrigeration temperature of 4 °C, and 40 °C at 6-month storage. Higher level of DEHP and DnOP in drinking water was found at 6 months compared to 3 months in refrigeration temperature of 4 °C. The pronounced effects of storage temperatures on the levels of phthalates was observed only after 6 months of storage in which DEHP levels exceeded the maximum established limit of 6 ng/mL.

Keywords: PET-bottled water, phthalates, storage temperature, storage time, liquid chromatography-mass spectrometry/mass spectrometry.

Abstrak

Kajian ini dilakukan untuk mengetahui kesan suhu dan masa penyimpanan terhadap kandungan phthalates dalam air berbotol PET komersial. Sampel air yang baharu dihasilkan di pusat pengilangan terdiri daripada air minuman, air mineral, dan air soda yang dibotolkan dengan menggunakan botol PET telah dikumpulkan dan disimpan di dalam suhu (suhu penyejukan 4 °C, suhu

bilik 25 °C, dan 40 °C) dan masa (0 bulan sebagai kawalan, 1.5 bulan, 3 bulan, dan 6 bulan) yang berbeza. Enam jenis ftalat dianalisa dengan menggunakan LC-MS/MS dan bis(2-etilheksilt)ftalat (DEHP) deuterasi sebagai piawai dalaman. DEHP dalam air botol PET dikesan dalam julat 2.32 hingga 27.6 ng/mL untuk sampel penyimpanan 3- dan 6 bulan; lebih tinggi daripada di-n-oktil ftalat (DnOP) yang dikesan dalam julat 1.57 hingga 12.6 ng/mL. Tahap DEHP dan DnOP yang lebih tinggi dalam air mineral botol PET dikesan pada suhu bilik 25 °C jika dibandingkan dengan suhu penyejukan 4 °C, dan 40 °C pada penyimpanan 6 bulan. Tahap DEHP dan DnOP yang lebih tinggi dalam air minuman didapati pada 6 bulan berbanding 3 bulan pada suhu penyejukan 4 °C. Kesan suhu penyimpanan yang ketara kepada kandungan ftalat diperhatikan hanya selepas penyimpanan selama 6 bulan di mana tahap DEHP melebihi had maksimum yang ditetapkan iaitu 6 ng/mL.

Kata kunci: air berbotol PET, ftalat, masa penyimpanan, suhu penyimpanan, kromatografi cecair-spektrometri jisim/spektrometri jisim

Introduction

Changes in human lifestyle have affected the development and innovation of food packaging [1]. Bottled water are mostly obtainable in two major forms of packaging material: plastic and glass [2, 3]. About 80% of plastic bottles made today are of polyethylene terephthalate (PET) due to the desired characteristics of its chemical and physical properties such as lightweight, clarity, strength, and easy recyclability [4]. A class of compounds named phthalates are utilised extensively as a plasticiser in the manufacturing of various plastics such as consumer products, including food contact applications [5, 6]. Phthalates cause severe health risks such as endocrine disruption, cancers and development and reproductive effects [7,8]. United States Environmental Protection Agency regulates bis(2-ethylhexyl)phthalate (DEHP) and bis(2-ethylhexyl)adipate (DEHA) as National Primary Drinking Water Regulations under the Safe Drinking Water Act. The maximum contaminant level of DEHP in drinking water was set at 6.0 ng/mL [9]. In addition, World Health Organization stated a guideline of 8.0 ng/mL of DEHP in fresh and drinking waters [10,11].

Malaysia is a tropical country with a fairly constant temperature of 28 – 32 °C all year round [12]. Storing plastic bottled water outdoor or exposing them to sun light by some markets are a very common practice in countries such as Iraq [13] and China [14], including Malaysia. Phthalates are not covalently bound to plastics and therefore, they can be easily migrated from packaging materials into foods in extreme conditions (e.g. high temperature) over time [15, 16]. Numerous research have reported that time and temperature [17,18], fat content [19,20], pH [17,21-23], contact surface [17], and exposure to sunlight [24-26] highly influence the migration of phthalates. Storage time besides the temperature are considered as the most important factors [17, 18, 27].

Keresztes et al. [17] detected DEHP after keeping PET-bottled mineral water at 22 °C for 44 days and further reported that the leaching of DEHP was the highest on samples that were kept over 1200 days. However, Al-Saleh et al. [28] observed higher levels of phthalates (i.e., DEHP, Benzyl butyl phthalate (BBP), Diethyl Phthalate (DEP), and Dimethyl phthalate (DMP)) in bottled water stored at 4 °C (1-month storage) than samples kept in room temperature (2-month storage) and outdoors (40-45 °C for 3 months). In addition, Amiridou and Voutsa [29] did not detect DMP, di-n-octyl phthalate (DnOP), and BBP in PET-bottled drinking and mineral water samples stored outdoors and directly exposed to sunlight up to 40 °C for up to 30 days. Literature reported indistinct effects of storage temperature and time on the migration of phthalates. Thus, it is worth to be further studied. Additionally, Erythropel et al. [30] cited regional differences as one of the factors that might cause the variability in the levels of phthalates reported in literature. Therefore, the prevalence in PET-bottled water in Malaysia needs to be determined.

Moreover, recent literature have predominantly reported migration of phthalates from PET bottles into acidic liquids such as verjuice, lemon juice, and vinegar [23], sparkling water [22], drinking water [28,

29], soft drink [21, 31] and mineral water [11, 17, 21, 22, 29, 32]. All the aforementioned samples were either randomly gathered from the market [11, 14, 17, 21, 22, 28, 29, 32] or prepared in the laboratory [23] or using food stimulants [24, 33, 34] and treated to different temperatures and time conditions. Studies that purchased PET-bottled water from the market were likely to suffer from limitations such as passed shelf life, therefore the results did not accurately represent the migration.

Most manufacturers recommend the shelf life for bottled water of no more than two years for non-carbonated water, and one year for sparkling water [35]. Accelerated stability test is one of the methods to estimate shelf life in which a product is subjected to elevated stress surroundings that induces the chemical and biochemical changes in shorter time [36]. It is known that phthalate migration is accelerated by heat [2, 3]. Therefore, accelerated stability test was conducted in this study to determine the extent of phthalate migration in bottled water when subjected to different storage temperatures. Furthermore, studies pertaining to the phthalates' migration from PET-bottled into drinking, mineral, and sparkling water, particularly those freshly-produced and collected from a manufacturing site and subsequently kept sealed in their original packaging throughout storage study, are in scarcity. Therefore, this study's aim to evaluate the effects of storage temperature and time on the levels of phthalates in commercial PET-bottled water.

Materials and Methods

Characteristics of samples

Seventy-two samples of different types of water, i.e., freshly-produced drinking, mineral, and sparkling water in PET bottles were collected from a manufacturing site. For each type of PET-bottled water, two different batches of production were collected from Company A. In addition, two samples of mineral water in glass bottles of the same batch number manufactured by Company B commercially available in the market were also collected. The two batches of mineral water in PET bottles were in 600-mL containers. The size of mineral water in glass bottles from company B was 325 mL. On the day of sampling at the manufacturing site, drinking and sparkling water in PET bottles of different batches of the same size were not available. Therefore, drinking water of 1 L for the first batch and 600 mL for the second batch were sampled. Similarly, sparkling water of 325 mL for the first batch and 1 L for the second batch were sampled. Company A is located in Taiping, Perak, Malaysia whereas Company B is located near Evian-les-Bains, France (46°23' 00.0"N 6°35' 00.0"E). Mineral water in glass bottles manufactured by Company B that commercially available in the market were collected since none of the manufacturers of bottled-water in Malaysia is producing this product. The 0-month control samples and mineral water in glass bottles were analyzed a soon as the samples reached the laboratory. PET-bottled water samples were subjected to different storage temperatures (4 °C refrigeration temperature, 25 °C room temperature, and 40 °C) and times (0 month as control, 1.5 months, 3 months, and 6 months). The collected mineral water in glass bottles however, were not subjected to storage study. A chiller was used to maintain the refrigeration temperature of 4 °C, whereas an oven was used to keep the storage temperature of 40 °C. Room temperature of 25 °C was attained by keeping the bottled water samples in an air-conditioned room in which the temperature of the air-conditioner was set at 25 °C. Samples were kept sealed in their original packaging and stored at room temperature, not exceeding one week prior to the time of analysis. Phthalates analysis was performed on every batch of PET-bottled water and on replicate samples of mineral water in glass bottles to obtain the levels of phthalates in the mean of duplicate determination.

Phthalates analysis

Reagent and materials

EPA 606-M Phthalate Esters Mix (DEHP, DEP, DMP, DnOP, Dibutyl Phthalate (DBP), and BBP) at the 200 µg/mL concentration was obtained from Supelco (Bellefonte, PA, USA). Bis(2-ethylhexyl)phthalate-3,4,5,6-d4 analytical standard (DEHP d4) that was used as internal standard throughout the study was purchased from Sigma-Aldrich Chemicals (St. Louis, USA). High purity analytical grade of methanol was

purchased from Sigma-Aldrich Chemicals (St. Louis, USA).

Phthalate Esters Mix (1 µg/mL) and DEHPd4 (1000 mg/L) stock solutions were prepared by dissolving the compound in methanol. Intermediate standard for Phthalate Esters Mix was prepared by diluting the stock solution to concentrations of 50 ng/mL and 100 ng/mL with methanol. Intermediate standard for DEHPd4 was prepared by diluting the stock solution to the concentration of 1 µg/mL with methanol. All stock solutions and intermediate standards were stored in refrigerator at 4°C for maximum of 1 year.

Analysis methods

The scheme described by Schreiber et al. [37] was followed. One mL of water sample was added into a 10-mL volumetric flask, and made into volume with methanol. Internal standard with concentration of 100 ng/mL was spiked into the volumetric flask and mixed well. The mixture was then allowed to stand for 5 minutes before being transferred into vial for LC-MS/MS analysis.

Phthalates in bottled water were detected using PerkinElmer Flexar UHPLC AS system (PerkinElmer, Waltham, Massachusetts, US) coupled with Q TRAP® 3200 Linear Ion Trap Quadrupole LC-MS/MS performed in Multiple Reaction Monitoring (MRM) mode (AB Sciex, Framingham, Massachusetts, USA). Phthalates standards were prepared in concentrations of 0.5, 1.0, 5.0, 10.0, 20.0, and 50.0 ng/mL. Phthalate internal standard ($DEHP_{D4}$) was prepared at the concentration of 10.0 ng/mL. Volume of injection was 20 µL.

Phthalates separation was achieved under gradient conditions using Phenomenex Synergi Fusion RP C_{18} (100 mm x 2.0 mm x 2 µm) column and mobile phase of fast gradient water with 0.1% formic acid and acetonitrile with 0.1% formic acid used at flow rate of 400 µL/min. The MS/MS transition monitored was m/z 279>205 for DBP, 223>177 for DEP, 195>163 for DMP, 391>261 for DnOP, 313>205 for BBP, 391>279 for DEHP, and 395>171 for $DEHP_{D4}$.

The transition m/z values of 279>205 for DBP, 223>177 for DEP, 195>163 for DMP, 391>261 for DnOP, 313>205 for BBP, 391>279 for DEHP, and 395>171 for $DEHP_{D4}$ were used for quantification. For confirmation of peak identity, m/z values of 279>149 for DBP, 223>149 for DEP, 195>133 for DMP, 391>149 for DnOP, 313>149 for BBP, 391>167 for DEHP, and 395>153 for $DEHP_{D4}$ were used. A calibration graph was constructed by plotting peak area of phthalates relative to the internal standard against corresponding ratios of amounts of analyte. Calibration curves of phthalates were linear (R^2 > 0.999). Phthalates levels in samples were calculated from the calibration slope and intercept value. The limit of detection (LOD) and quantitation (LOQ) were 0.5 ng/mL and 1.5 ng/mL respectively. The recoveries were in the range between 80 and 120%.

Statistical analysis

All data obtained were analysed by using SPSS Version 21.0 (SPSS Inc., Chicago, IL). Two-way ANOVA with Tukey's Test was utilized to determine the differences in the means of phthalates levels when treated at different storage time and temperature. P-value of 0.05 or less was considered significant.

Results and Discussion

Freshly-produced drinking, mineral, and sparkling water samples in PET bottles were collected from a manufacturing site and subjected to different storage temperatures and times. Table 1 shows that all types of phthalates were not detected in the freshly produced water (0-month storage) for all types of PET bottles. The findings are in contrast with Amiridou and Voutsa [29] who detected DEHP at median level of 0.350 ng/mL, while DBP and DEP were found at lower levels of 0.044 and 0.033 ng/mL respectively. The researchers however did not detect DMP, BBP, and DnOP in PET-bottled drinking and mineral water samples in Greece that were analyzed immediately upon purchase. Similarly, Zaki and Shoeib [38] reported DEHP was the most abundant phthalate compounds, ranging from 0.062 to 0.298 ng/mL, while DBP was the second-most abundant, detected at levels ranging from 0.043 to 0.071 ng/mL. The researchers also did not detect DEP, DMP, BBP, and DnOP in

PET-bottled water samples in Egypt analyzed immediately after purchasing (~2 weeks after production). The presence of DEHP, DBP, and DEP in cited studies and absence of the contaminants in the freshly-produced samples (0-month storage) for all types of PET-bottled water in the present study may be due to different production facilities and different brands tested as observed by other researchers [28,38].

Although all types of phthalates were not detected in the 1.5-month storage samples, DEHP in PET-bottled water was detected in the range of 2.32 to 27.6 ng/mL for 3- and 6-month storage samples; higher than DnOP detected in the range of 1.57 to 12.6 ng/mL. The findings are in agreement with numerous authors who reported high levels of phthalates in PET-bottled water upon storage, especially DEHP [17,28,29]. European Authorities banned Low Molecular Weight (LMW) phthalates such as DEHP (1B Category) for use in cosmetics, children articles, toys, and medical devices as it is considered as toxic to human's reproduction system [39]. However, High Molecular Weight (HMW) phthalates such DnOP has only been prohibited on items that toddlers can suck & chew on such as children articles and toys (1999/815/EC and directive 2005/84/EC). It appears that present study detected higher levels of LMW (i.e., DEHP) phthalates when subjected to 3- and 6-month storage than HMW (i.e., DnOP) phthalates in the PET-bottled water of drinking, mineral, and sparkling samples. To protect human health, the European Food Safety Authority (EFSA) has set Tolerable Daily Intakes (TDI) for DEHP at 50 μg kg^{-1} body weight (bw) [40]. Different authors discussed that the presence of phthalates in bottled water can be attributed to several factors; among them are (i) the quality of the raw material and the technology used in bottle production [29], or the chemicals used in the production process [41] and (ii) the use of recycled PET [42].

Table 1 indicates that higher levels of DEHP and DnOP in PET-bottled mineral water (room temperature of 25 °C) were detected when compared to refrigeration temperature of 4 °C, and 40 °C at 6-month storage; the difference however, was not significant. Similarly, no significant difference in DEHP and DnOP levels was detected among different storage temperatures for drinking and sparkling water at 6-month storage. These findings are presented in Figure 1 for DEHP and Figure 2 for DnOP. The findings are consistent with the work of Leivadara et al. [25] who reported higher DEHP levels (up to 2 ng/mL) when bottled water was kept at room temperature (24 °C for 3 months in dark) as compared with DEHP was not detected when stored outdoor (30 °C for 3 months). In addition, Al-Saleh et al. [28] observed that the levels of DEHP in bottled water samples stored at 4 °C for 1 month were significantly higher than those stored at room temperature for 2 months and outdoors (> 45 °C) for 3 months. However, Schmid et al. [24] reported DEHP levels escalated in PET-bottled water kept at a higher temperature (direct sunlight, up to 34 °C for 17 hours) compared to lower temperature (room temperature in the dark). In general, high temperature accelerates the migration [2,3]. However, no clear patterns was observed with regards to storage temperature's effect on DEHP's level have been generated, with reports of contradictory observations on increasing concentrations [2, 24] and decreasing concentrations of DEHP [25, 28].

Table 1 indicates that higher levels of DEHP and DnOP in PET-bottled mineral water at room temperature of 25 °C were detected when compared to refrigeration temperature of 4 °C, and 40 °C at 6-month storage; the difference however, was not significant. Similarly, no significant difference in DEHP and DnOP levels was detected among different storage temperatures for drinking and sparkling water at 6-month storage. These findings are presented in Figure 1 for DEHP and Figure 2 for DnOP. The findings are consistent with the work of Leivadara et al. [25] who reported higher DEHP levels (up to 2 ng/mL) when bottled water was stored at room temperature (24 °C in the dark for 3 months) as compared with storage at 30 °C under outdoor conditions for 3 months (DEHP was not detected). In addition, Al-Saleh et al. [28] reported that the levels of DEHP in bottled water samples stored at 4 °C for 1 month were significantly higher than those stored at room temperature for 2 months and outdoors (> 45 °C) for 3 months. However, Schmid et al. [24] reported an increase in DEHP levels in PET-

bottled water stored at a higher temperature (a maximum of 3 4°C for 17 hours under direct sunlight) compared to lower temperature (room temperature in the dark). In general, high temperature accelerates the migration [2, 3]. However, no clear or consistent trends regarding the effects of storage temperature on DEHP concentration have been produced, with reports of contradictory observations on increasing concentrations [2, 24] and decreasing concentrations of DEHP [25, 28]. Different research stated that the increase or decrease of phthalates due to different storage conditions depends mainly on the bottle's country of origin [17, 24] due to different production facilities or brands tested as mentioned above [28, 38]. Furthermore, Keresztes et al. [17] showed that different brands of PET-bottled mineral water subjected to different storage temperatures demonstrate different patterns in the increase of phthalates. The researchers performed a storage study at 22 °C, 40 °C, 50 °C, and 60 °C, and reported that the concentrations of DiBP, DBP, BBP, and DEHP for PET-bottled mineral water brand C increased by factors of 1.6, 1.4, 2.6, and 2.5, respectively, at 60 °C after 24 hours compared to the initial concentration values. This is in contrast to brand A characterized by undetectable phthalate levels at 22 °C. DEHP was the only phthalate that could be determined in significant concentration after 24 hours of storage at 60 °C.

Table 1 also shows higher levels of DEHP and DNOP in drinking water at 6 months compared to 3 months in refrigeration temperature of 4 °C; the difference however, was not significant. The findings are in agreement with Casajuana and Lacorte [43] who reported higher concentration of DEHP after storage in PET-bottled water at 30 °C for 10 weeks while it could not be quantified in the initial samples. Furthermore, Leivadara et al. [25] observed the level of DEHP increased from the initial of less than 0.5 to 2 ng/mL when bottled water was stored at 24 °C in the dark for 3 months. The present study shows that the increase in storage time of PET-bottled drinking water stored in refrigeration temperature of 4 °C affects phthalates (i.e., DEHP and DnOP) migration. PET plastics can be subjected to various types of degradation, leading to potential leaching of phthalates [29]. Rahman and Brazel [44] also suggested that ageing and breakdown of plastic packaging might accelerate the migration process.

Table 1 shows that the levels of DEHP in the PET-bottled mineral water at 6-month storage that ranged from 9.35 to 27.6 ng/mL were the highest, followed by PET-bottled sparkling water (ranging from 6.70 to 9.75 ng/mL) and drinking (ranging from 6.63 to 7.19 ng/mL). Similarly, the levels of DnOP in the PET-bottled mineral water at 6-month storage that ranged from 4.14 to 12.6 ng/mL were the highest, followed by PET-bottled sparkling water (ranging from 2.78 to 3.76 ng/mL) and drinking (ranging from 1.94 to 2.34 ng/mL). The findings are consistent with Montuori et al. [22] who also observed slightly higher DEHP levels for PET-bottled mineral and drinking water than the sparkling water samples. Sparkling is an example of carbonated water whereas drinking and mineral are examples of non-carbonated ones. One of the differences between carbonated and non-carbonated waters is pH, which plays an important role in the acid- or base-catalysed ester hydrolysis, a slow equilibrium process at room temperature [45]. However, Lertsirisopon et al. [46] showed that there is no significant effect on the efficiency of abiotic degradation of DEHP via hydrolysis at neutral pH, acidic, or alkaline solution. It might explain why the levels of DEHP and DnOP in PET-bottled sparkling water lower than are not higher in comparison to drinking and mineral water.

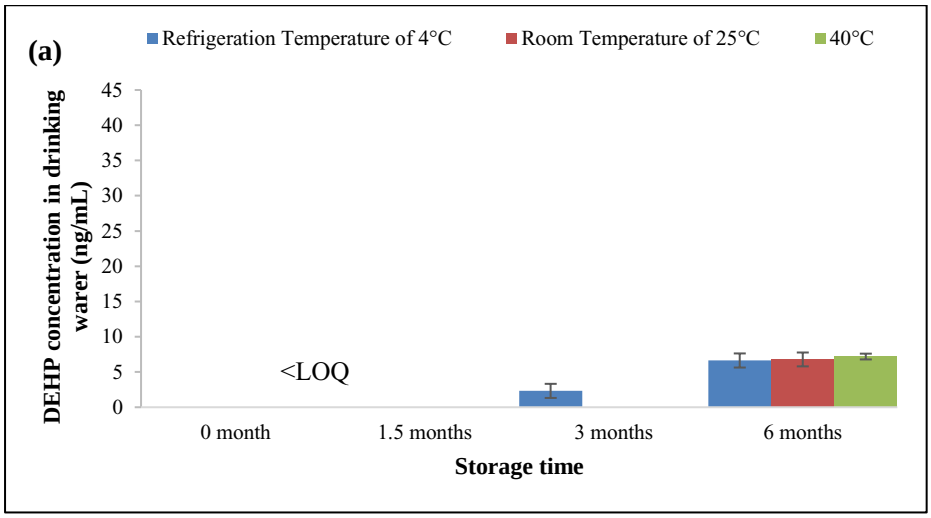
Mineral water samples in glass bottles commercially available in the market were also collected to compare the migration of phthalates from two different food contact materials; PET and glass bottles. The present study found all types of phthalates were not detected in the glass-bottled mineral water samples (data not shown). Similarly, Montuori et al. [22] did not detect DMP, DEP, or DEHP in glass-bottled water samples. Although DEHP was not detected for all types of PET-bottled water in 0-month storage and 1.5-month storage, the levels were above the maximum established limit (6 ng/mL) after 6-month storage for all temperatures. Similar results were obtained by Yousefi et al. [18] who reported the DEHP levels in

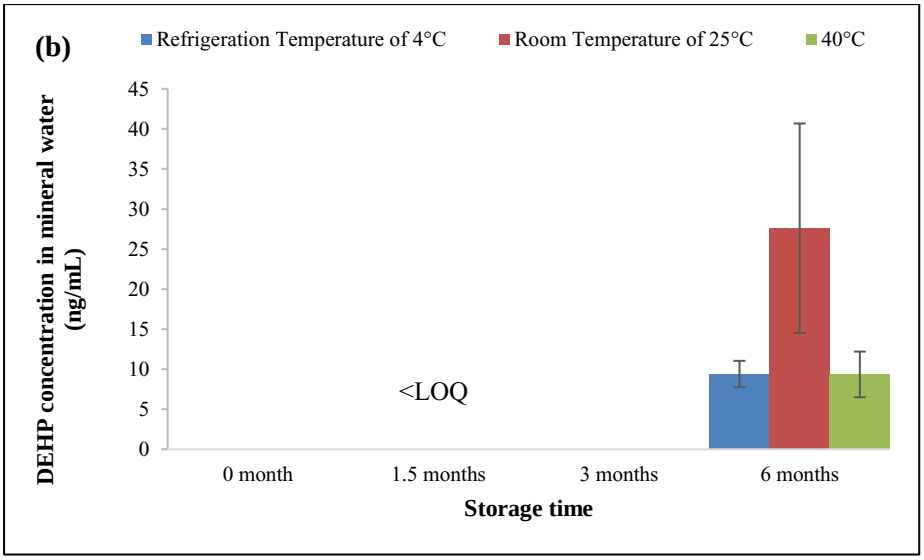
PET-bottled drinking water subjected to storage temperature of 42 °C for 15 days and 25 °C for 75 days were 10.33 and 9.62 ng/mL, respectively, higher than the established limit. It should be noted that the typical shelf life for commercial bottled water is 24 months. Thus, consumption of bottled water after expiry date may increase the dietary exposure of phthalates from bottled water.

Table 1. Concentration of phthalates in drinking, mineral, and sparkling PET-bottled water at different storage temperature and time (ng/mL)

Phthalate esters	Type of water	Drinking			Mineral			Sparkling		
	Storage Time (Month) / Temp.	Refrigeration Temp. of 4 °C	Room Temp. of 25 °C	40 ˚C	Refrigeration Temp. of 4 °C	Room Temp. of 25 °C	40 ˚C	Refrigeration Temp. of 4 °C	Room Temp. of 25 °C	40 ˚C
[2]BBP	0	ND	ND	ND	ND	ND	ND	ND	ND	ND
	1.5	ND	ND	ND	ND	ND	ND	ND	ND	ND
	3	ND	ND	ND	ND	ND	ND	ND	ND	ND
	6	ND	ND	ND	ND	ND	ND	ND	ND	ND
[3]DBP	0	ND	ND	ND	ND	ND	ND	ND	ND	ND
	1.5	ND	ND	ND	ND	ND	ND	ND	ND	ND
	3	ND	ND	ND	ND	ND	ND	ND	ND	ND
	6	ND	ND	ND	ND	ND	ND	ND	ND	ND
[4]DEHP	0	ND^{B}	ND	ND	ND	ND	ND	ND	ND	ND
	1.5	ND^{B}	ND	ND	ND	ND	ND	ND	ND	ND
	3	2.32 ± 1.68^{AB}	ND	ND	ND	ND	ND	ND	ND	ND
	6	6.63 ± 1.93^{Aa}	6.78 ± 0.04^{a}	7.19 ± 0.22^{a}	9.40 ± 1.89^{a}	27.6 ±18.9^{a}	9.35 ±6.85^{a}	9.75 ± 3.36^{a}	6.70 ±0.43^{a}	8.63 ±0.18^{a}
[5]DEP	0	ND	ND	ND	ND	ND	ND	ND	ND	ND
	1.5	ND	ND	ND	ND	ND	ND	ND	ND	ND
	3	ND	ND	ND	ND	ND	ND	ND	ND	ND
	6	ND	ND	ND	ND	ND	ND	ND	ND	ND
[6]DMP	0	ND	ND	ND	ND	ND	ND	ND	ND	ND
	1.5	ND	ND	ND	ND	ND	ND	ND	ND	ND
	3	ND	ND	ND	ND	ND	ND	ND	ND	ND
	6	ND	ND	ND	ND	ND	ND	ND	ND	ND
[7]DNOP	0	ND^{A}	ND	ND	ND	ND	ND	ND	ND	ND
	1.5	ND^{A}	ND	ND	ND	ND	ND	ND	ND	ND
	3	1.57 ± 1.03^{A}	ND	ND	ND	ND	ND	ND	ND	ND
	6	2.28 ± 1.26^{Aa}	2.34 ± 0.26^{a}	1.94 ± 0.27^{a}	4.65 ± 0.27^{a}	12.6 ±9.92^{a}	4.14 ±3.46^{a}	3.76 ±1.95^{a}	2.78 ±0.16^{a}	3.38 ±0.3^{a}

[1]LOQ = 1.5 ng/mL
[2]Benzylbutyl phthalate
[3]Dibutyl phthalate
[4]Di-2-ethylhexyl phthalate
[5]Diethyl phthalate
[6]Dimethyl phthalate
[7]Di-n-octyl phthalate
$^{A-B}$ Values within the same column with different letters are significantly different ($p \leq 0.05$).
$^{a-b}$ Values within the same row with different letters are significantly different ($p \leq 0.05$).
Values are means of duplicate determination ± SD


(a)
Refrigeration Temperature of 4°C
Room Temperature of 25°C
40°C
DEHP concentration in drinking warer (ng/mL)
45
40
35
30
25
20
15
10
5
0
<LOQ
0 month
1.5 months
3 months
6 months
Storage time


(b)
Refrigeration Temperature of 4°C
Room Temperature of 25°C
40°C
DEHP concentration in mineral water (ng/mL)
45
40
35
30
25
20
15
10
5
0
<LOQ
0 month
1.5 months
3 months
6 months
Storage time

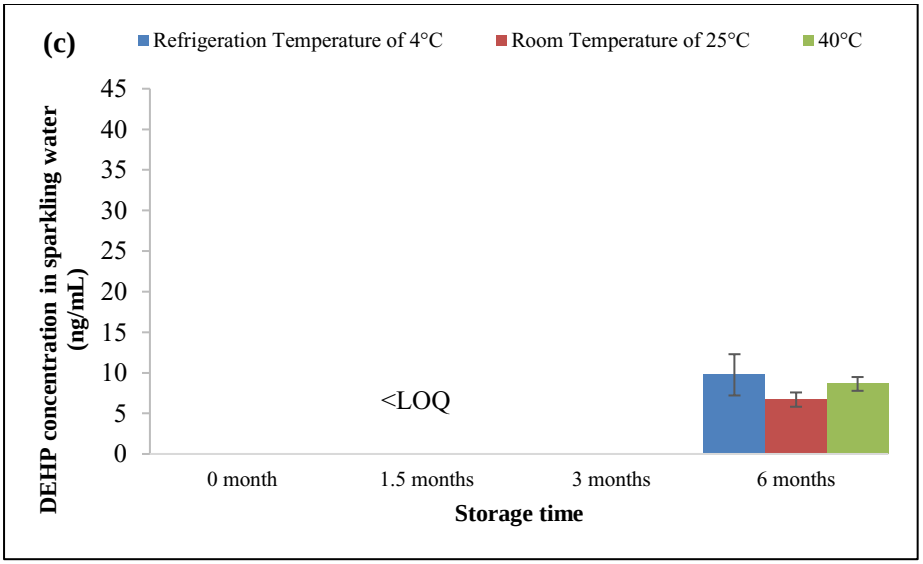
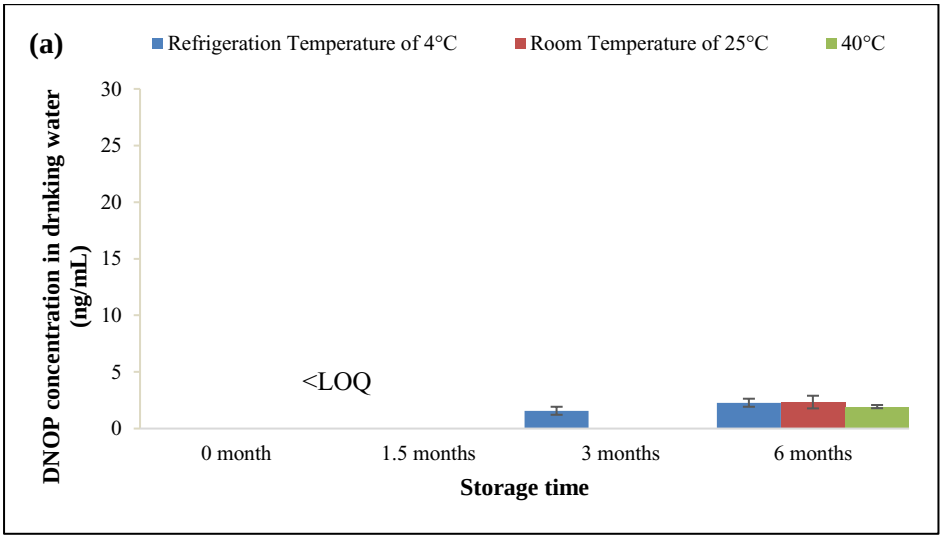


Figure 1. The effect of storage temperature (refrigeration temperature of 4 °C, room temperature of 25 °C, and 40 °C) and storage time (0 month as control, 1.5 months, 3 months, and 6 months) on DEHP concentration in different types of bottled water (A: drinking, B: mineral, C: sparkling). Data are means of duplicate (n = 2) determination with bars indicating standard error (± SE)



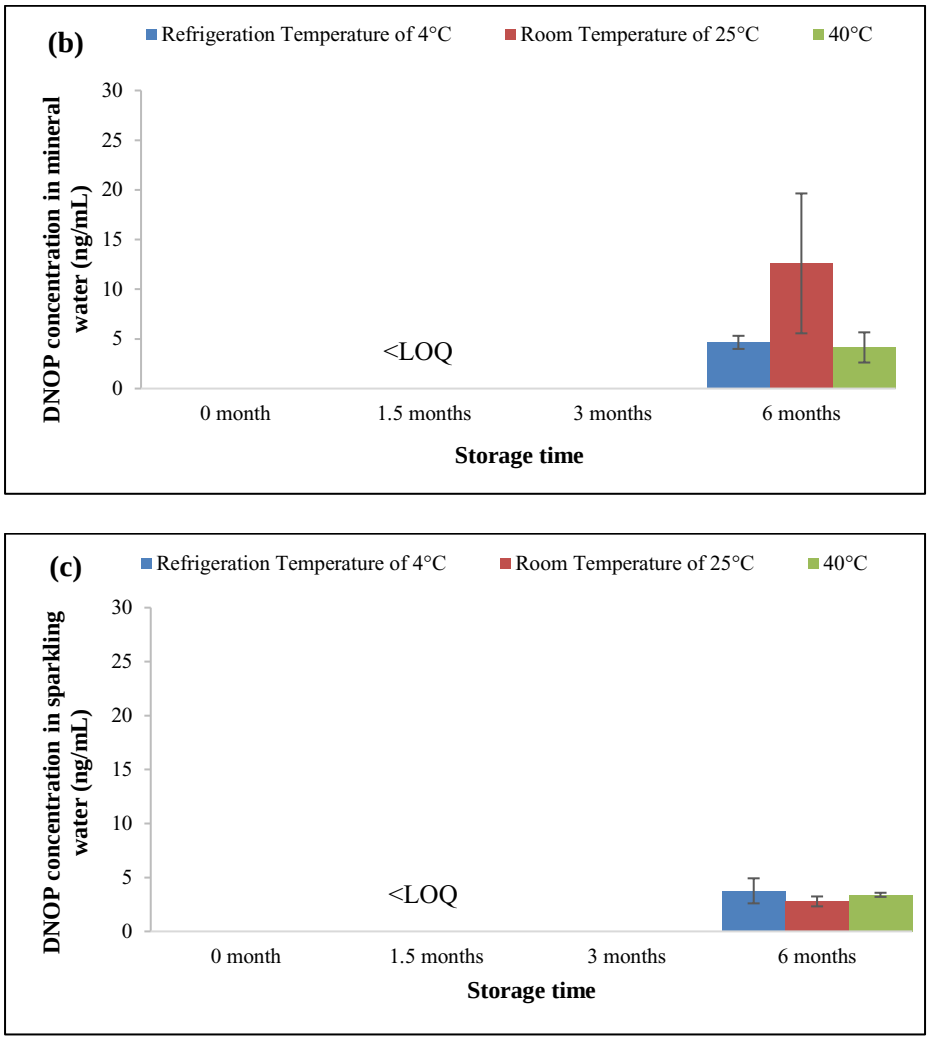


Figure 2. The effect of storage temperature (refrigeration temperature of 4 °C, room temperature of 25 °C, and 40 °C) and storage time (0 month as control, 1.5 months, 3 months, and 6 months) on DNOP concentration in different types of bottled water (A: drinking, B: mineral, C: sparkling). Data are means of duplicate (n = 2) determination with bars indicating standard error (± SE)

Conclusion

The present study shows that all types of phthalates were not detected in the 0 and 1.5 months of storage at different storage temperatures for all types of PET-bottled water. However, DEHP in the PET-bottled water was detected in the range between 2.32 and 27.6 ng/mL for 3- and 6-month storage samples; higher than DnOP detected in the range from 1.57 to 12.6 ng/mL. Higher levels of DEHP and DnOP in PET-bottled mineral water were detected at room temperature of 25°C when compared to refrigeration temperature of 4°C, and 40°C at 6-month storage. Similarly, higher

level of DEHP in drinking water was found at 6 months compared to 3 months in refrigeration temperature of 4°C. The pronounced effects of different storage temperatures on the levels of phthalates was not observed in the first one and the half month of storage but rather after 6 months of storage in which DEHP levels were exceeded the maximum established limit of 6 ng/mL. The findings from this study may be utilized in future research that could determine the dietary exposure of phthalates from bottled water, especially in Malaysia population.

Acknowledgement

The authors gratefully acknowledge Universiti Putra Malaysia under Insentif Putra Siswazah [Grant number: GP-IPS/2017/9525800] funding received, and Higher Institution Centers of Excellence (HICOE) environment set by the Ministry of Education of Malaysia at Institute of Tropical Agriculture and Food Security, Universiti Putra Malaysia.

References

1. Majid, I., Ahmad Nayik, G., Mohammad Dar, S. and Nanda, V. (2018). Novel food packaging technologies: Innovations and future prospective. *Journal of the Saudi Society of Agricultural Sciences,* 17: 454-462.
2. Jeddi, M. Z., Rastkari, N., Ahmadkhaniha, R. and Yunesian, M. (2016). Endocrine disruptor phthalates in bottled water: Daily exposure and health risk assessment in pregnant and lactating women. *Environmental Monitoring and Assessment,* 188: 534.
3. Pourzamani, H., Falahati, M., Rastegari, F. and Ebrahim, K. (2017). Freeze-melting process significantly decreases phthalate ester plasticizer levels in drinking water stored in polyethylene terephthalate (PET) bottles. *Water Science and Technology: Water Supply,* 17: 745-751.
4. Welle, F. (2011). Twenty years of PET bottle to bottle recycling - An overview. *Resources, Conservation & Recycling,* 55: 865-875.
5. Choi, K., Joo, H., Campbell, J. L., Andersen, M. E. and Clewell, H. J. (2013). In vitro intestinal and hepatic metabolism of Di(2-ethylhexyl) phthalate (DEHP) in human and rat. *Toxicology in Vitro,* 27: 1451-1457.
6. Rowdhwal, S. S. S. and Chen, J. (2018). Toxic effects of di-2-ethylhexyl phthalate: An overview. *BioMed Research International,* 1750368: 1-10.
7. Wang, Y., Zhu, H. and Kannan, K. (2019). A review of biomonitoring of phthalate exposures. *Toxics,* 7: 21.
8. Nowak, K., Jabłońska, E. and Ratajczak-Wrona, W. (2019). Immunomodulatory effects of synthetic endocrine disrupting chemicals on the development and functions of human immune cells. *Environment International,* 125: 350-364.
9. US EPA. National Primary Drinking Water Regulations. Available online: https://www.epa.gov/ground-water-and-drinking-water/national-primary-drinking-water-regulations [Accessed on August 30 2020].
10. WHO. Guidelines for drinking water quality. Available online: https://apps.who.int/iris/bitstream/handle/10665/204411/9789241547611_eng.pdf;jsessionid=2F9904A829F426314A3F34407D3CFB84?sequence=1 [Accessed on 30 August 2020].
11. Khatib, A. J. A., Habib, I.Y., Muhammad, M., Danladi, F. I., Bala, S. S. and Adamu, A. (2014). Analysis of phthalate plasticizer in Jordanian bottled waters by liquid chromatography-tandem mass spectrophotometry (LC-MS/MS). *European Scientific Journal,* 10: 271-282.
12. Oldeman, L. R., Frere, M. (2021). A study of the agroclimatology of the humid tropics of Southeast Asia: Technical Report. Available online: https://library.wmo.int/doc_num.php?explnum_id=1084 [Accessed on 20 April 2021].
13. Muhamad, S. G., Esmail, L. S. and Hasan, S.H. (2011). Effect of storage temperature and sunlight exposure on the physicochemical properties of bottled water in Kurdistan region-Iraq. *Journal of Applied Structural Equation Modeling,* 15: 147-154.

14. Xu, X., Zhou, G., Lei, K., LeBlanc, G.A., An, L. (2019). Phthalate esters and their potential risk in PET bottled water stored under common conditions. *International Journal of Environmental Research and Public Health,* 17: 1-13.
15. Halden, R. U. (2010). Plastics and health risks. *Annual Review of Public Health,* 31: 179-194.
16. Srinivasan, K. (2016). Phthalate leachates in selected plastic packed food products - A GC-MS. *International Journal of Research in Chemistry and Environment,* 6: 18-21.
17. Keresztes, S., Tatar, E., Cazegeny, Z., Zaray, G. and Mihucz, V. G. (2013). Study on the leaching of phthalates from polyethylene terephthalate bottles into mineral water. *Science of the Total Environment,* 458-460: 451-458.
18. Yousefi, Z., Babanezhad, E., Mohammadpour, R. A. and Ala, A. (2018). Concentration of phthalate esters in polyethylene terephthalate bottled drinking water in different storage conditions. *Journal of Mazandaran University of Medical Sciences,* 28: 110-120.
19. Xu, Q., Yin, X., Wang, M., Wang, H., Zhang, N., Shen, Y., Xu, S., Zhang, L. and Gu, Z. (2010). Analysis of phthalate migration from plastic containers to packaged cooking oil and mineral water. *Journal of Agricultural and Food Chemistry,* 58: 11311-11317.
20. Ibrahim, N., Osman, R., Abdullah, A. and Saim, N. (2014). Determination of phthalate plasticisers in palm oil using online solid phase extraction-liquid chromatography (SPE-LC). *Journal of Chemistry,* 682975: 1-9.
21. Bosnir, J., Puntaric, D., Galic, A., Skes, I., Dijanic, T., Klaric, M., Grgic, M., Curkovic, M. and Smit, Z. (2007). Migration of phthalates from plastic containers into soft drinks and mineral water. *Food Technology and Biotechnology,* 45: 91-95.
22. Montuori, P., Jover, E., Morgantini, M., Bayona, J. M. and Triassi, M. (2008). Assessing human exposure to phthalic acid and phthalate esters from mineral water stored in polyethylene terephthalate and glass bottles. *Food Additives & Contaminants: Part A: Chemistry, Analysis, Control, Exposure & Risk Assessment,* 25, 511-518.
23. Rastkari, N., Zare, J. M., Yunesian, M. and Ahmadkhaniha, R. (2017). The effect of storage time, temperature and type of packaging on the release of phthalate esters into packed acidic liquids. *Food Technology and Biotechnology,* 55: 562-569.
24. Schmid, P., Kohler, M., Meierhofer, R., Luzi, S. and Wegelin, M. (2008). Does the reuse of PET bottles during solar water disinfection pose a health risk due to the migration of plasticisers and other chemicals into the water? *Water Research,* 42: 5054-5060..
25. Leivadara, S. V., Nikolaou, A. D. and Lekkas, T. D. (2008). Determination of organic compounds in bottled waters. *Food Chemistry,* 108: 277-286.
26. Abtahi, M., Dobaradaran, S. and Torabbeigi, M. (2019). Health risk of phthalates in water environment: Occurrence in water resources, bottled water, and tap water, and burden of disease from exposure through drinking water in Tehran, Iran. *Environmental Research,* 173: 469-479.
27. Greifenstein, M., White, D. W., Stubner, A., Hout, J. and Whelton, A. J. (2013). Impact of temperature and storage duration on the chemical and odor quality of military packaged water in polyethylene terephthalate bottles. *Science of the Total Environment* 456-457: 376-383.
28. Al-Saleh, I., Shinwari, N. and Alsabbaheen, A. (2011). Phthalates residues in plastic bottled waters. *The Journal of Toxicological Sciences,* 36: 469-478.
29. Amiridou, D. and Voutsa, D. (2011). Alkylphenols and phthalates in bottled waters. *The Journal of Hazardous Materials,* 185: 281-286.
30. Erythropel, H. C., Maric, M., Nicell, J. A., Leask, R. L. and Yargeau, V. (2014). Leaching of the plasticizer di(2-ethylhexyl)phthalate (DEHP) from plastic containers and the question of human exposure. *Applied Microbiology and Biotechnology,* 98: 9967-9981.
31. Yin, S., Yang, Y., Yang, D., Li, Y., Jiang, Y., Wu, L. and Sun, C. (2019). Determination of 11 phthalate esters in beverages by magnetic solid-phase extraction combined with high-performance liquid chromatography. *Journal of AOAC International,* 102: 1624-1631.

32. Ceretti, E., Zani, C., Zerbini, I., Guzzella, L., Scaglia, M., Berna, V., Donato, F., Monarca, S. and Feretti, D. (2010). Comparative assessment of genotoxicity of mineral water packed in polyethylene terephthalate (PET) and glass bottles. *Water Research,* 44: 1462-1470.
33. Guart, A., Bono-Blay, F., Borrell, A. and Lacorte, S. (2011). Migration of plasticizers phthalates, bisphenol A and alkylphenols from plastic containers and evaluation of risk. *Food Additives & Contaminants: Part A: Chemistry, Analysis, Control, Exposure & Risk Assessment,* 28, 676-685.
34. Moreira, M. A., André, L. C. and Cardeal, Z. L. (2013). Analysis of phthalate migration to food simulants in plastic containers during microwave operations. *International Journal of Environmental Research and Public Health,* 11, 507-526.
35. Petersen, A. A (2020). Little secret about bottled water. Available online: https://www.wsj.com/articles/SB10764606307932 6366 [Accessed on 31 August 2020].
36. Haouet, M. N., Tommasino, M., Mercuri, M. L., Benedetti, F., Bella, S. D., Framboas, M., Pelli, S. and Altissimi, M. S. (2018). Experimental accelerated shelf life determination of a ready-to-eat processed food. *Italian Journal of Food Safety,* 7: 6919-6919.
37. Schreiber, A., Fu, F., Yang, O., Wan, E., Gu, L., LeBlanc, Y. (2015). Increasing selectivity and confidence in detection when analyzing phthalates by LC-MS/MS. Available online: http://sciex.com/Documents/brochures/Phthalates_ QTRAP5500%20SelexION_3690411.pdf [Accessed on 2 Sept 2015].
38. Zaki, G. and Shoeib, T. (2018). Concentrations of several phthalates contaminants in Egyptian bottled water: Effects of storage conditions and estimate of human exposure. *Science of the Total Environment* 618: 142-150.
39. Ventrice, P., Ventrice, D., Russo, E. and De Sarro, G. (2013). Phthalates: European regulation, chemistry, pharmacokinetic and related toxicity. *Environmental Toxicology and Pharmacology,* 36: 88-96.
40. Vittorio, S., Jose Manuel, B. B., Claudia, B., Andrew, C., Pier, S. C., Riccardo, C., David, M. G., Konrad, G., Evgenia, L., Alicja, M. (2019). Update of the risk assessment of di-butylphthalate (DBP), butyl-benzyl-phthalate (BBP), bis(2-ethylhexyl)phthalate (DEHP), di-isononylphthalate (DINP) and di-isodecylphthalate (DIDP) for use in food contact materials. *EFSA Journal,* 17: 5838.
41. Plotan, M., Frizzell, C., Robinson, V., Elliott, C. T., Connolly, L. (2013). Endocrine disruptor activity in bottled mineral and flavoured water. *Food Chemistry,* 136: 1590-1596.
42. Bach, C., Dauchy, X., Chagnon, M. C. and Etienne, S. (2012). Chemical compounds and toxicological assessments of drinking water stored in polyethylene terephthalate (PET) bottles: A source of controversy reviewed. *Water Research,* 46, 571-583.
43. Casajuana, N. and Lacorte, S. (2003). Presence and release of phthalic esters and other endocrine disrupting compounds in drinking water. *Chromatographia,* 57: 649-655.
44. Rahman, M. and Brazel, C. S. (2004). The plasticizer market: An assessment of traditional plasticizers and research trends to meet new challenges. *Progress in Polymer Science* 29: 1223-1248.
45. Boudreaux, K. A. (2020). Chapter 5 carboxylic acids and esters. Available online: https://www.angelo.edu/faculty/kboudrea/index_2 353/Chapter_05_2SPP.pdf [Accessed on 31 August 2020].
46. Lertsirisopon, R., Soda, S., Sei, K. and Ike, M. (2009). Abiotic degradation of four phthalic acid esters in aqueous phase under natural sunlight irradiation. *Journal of Environmental Sciences,* 21: 285-290.

Malaysian Journal of Analytical Sciences (MJAS)
Published by Malaysian Analytical Sciences Society

PREPARATION OF CERIUM DOPED NICKEL OXIDE FOR LOWER REDUCTION TEMPERATURE IN CARBON MONOXIDE ATMOSPHERE

(Penyediaan Serium yang Didopkan ke atas Nikel Oksida untuk Suhu Penurunan Lebih Rendah dalam Atmosfera Karbon Monoksida)

Norliza Dzakaria[1]*, Azizul Hakim Lahuri[2], Tengku Shafazila Tengku Saharuddin[3], Alinda Samsuri[4], Fairous Salleh[5], Wan Nor Roslam Wan Isahak[6], Muhammad Rahimi Yusop[5], Mohd Ambar Yarmo[5]

[1]*Advanced Material for Environmental Remediation (AMER) Research Group, Faculty of Applied Science, Universiti Teknologi MARA, Cawangan Negeri Sembilan, Kampus Kuala Pilah, 72000 Kuala Pilah, Negeri Sembilan, Malaysia*
[2]*Department of Science and Technology, Universiti Putra Malaysia Bintulu Campus, 97008 Bintulu, Sarawak, Malaysia*
[3]*Faculty of Science and Technology, Universiti Sains Islam Malaysia, Bandar Baru Nilai, 71800, Nilai, Negeri Sembilan, Malaysia*
[4]*Department of Chemistry, Centre for Defence Foundation Studies, Universiti Pertahanan Nasional Malaysia, Kem Sungai Besi, 57000 Kuala Lumpur, Malaysia.*
[5]*Catalysis Research Group, School of Chemical Sciences and Food Technology, Faculty of Science and Technology*
[6]*Department of Chemical and Process Engineering, Faculty of Engineering & Built Environment Universiti Kebangsaan Malaysia, 43600 UKM Bangi, Selangor Darul Ehsan, Malaysia*

**Corresponding author: norliza864@uitm.edu.my*

Received: 11 May 2021; Accepted: 17 June 2021; Published: 27 June 2021

Abstract

The reduction behavior of cerium nickel oxide (Ce/NiO) catalyst was investigated by using temperature programmed reduction (TPR) with exposure of 40% (v/v) carbon monoxide (CO) in nitrogen atmosphere as a reductant agent. The Ce/NiO catalysts were prepared by using the conventional impregnation method. The reduction characteristics of NiO to Ni were examined up to 700 ºC and followed by isothermal reduction. The TPR profiles of doped NiO slightly shifted to a lower temperature from 375 to 366 ºC when Ce loading was increased from 3% to 10% (wt./ wt.), respectively. Whereas the undoped NiO was reduced at a higher temperature of 387 ºC. XRD diffractogram of the catalysts showed a complete reduction of NiO to Ni. The interaction between cerium and nickel ions for Ce/NiO series leads to a slight decrease in the reduction temperature. Fine sharp particles of Ce deposited on the NiO surfaces were observed through the FESEM images indicating some morphology modification occurred on NiO. It was found that the addition of 10% (w/w) of Ce on NiO also exhibited a larger BET surface area (11.31 m^2g^{-1}) and a smaller average pore diameter (17.7 nm). Based on these results, it is interesting to note that the addition of Ce to NiO has a remarkable influence in reducing the temperature of the reduction process. The 5% Ce/NiO was found sufficient to enhance the reducibility of NiO at a lower temperature.

Keywords: reduction, nickel oxide, cerium, carbon monoxide

Abstrak

Sifat penurunan nikel oksida (NiO) dan serium (Ce) yang didopkan ke atas NiO (Ce/NiO) telah dikaji menggunakan aturcara suhu penurunan (TPR) dengan kehadiran 40% (v/v) karbon monoksida (CO) dalam nitrogen sebagai penurun. Sampel Ce/NiO disediakan menggunakan kaedah impregnasi. Sifat penurunan NiO kepada Ni dikaji dengan peningkatan suhu sehingga 700 ºC dan diikuti dengan penurunan isoterma. TPR bagi sampel NiO yang telah didop menunjukkan anjakan isyarat penurunan pada suhu yang lebih rendah daripada 375 ºC (3% (bt/bt) Ce/NiO) kepada 365 ºC (10% (bt/bt) Ce/NiO). Manakala NiO sahaja diturunkan pada suhu lebih tinggi 387 ºC. Difraktogram XRD membuktikan penurunan lengkap bagi NiO kepada Ni. Interaksi di antara ion serium dan nikel bagi siri Ce/NiO menyebabkan suhu penurunan yang lebih rendah. Partikel tajam halus Ce yang terenap pada permukaan NiO diperhatikan melalui imej-imej FESEM menunjukkan terdapat pengubahsuaian morfologinya. Penambahan 10% (bt/bt) Ce pada NiO juga mempamerkan luas permukaan BET yang lebih tinggi (11.31 m^2g^{-1}) dan purata diameter liang yang lebih kecil (17.7 nm). Berdasarkan keputusan yang diperolehi, amat menarik untuk menekankan bahawa penambahan Ce ke atas NiO mempunyai pengaruh yang berkesan dalam merendahkan suhu penurunan. Sampel 5% Ce/NiO (bt/bt) didapati mencukupi untuk memperolehi penurunan NiO pada suhu yang lebih rendah.

Kata kunci: penurunan, nikel oksida, serium, karbon monoksida

Introduction

Metal oxides are widely used in technological applications such as coating, catalysis, electrochemistry, optical fibers, and sensors [1, 2]. Nickel oxide (NiO) is an earth-abundant transition metal oxide with superior redox property, electrochemical performance and gas sensing property. Several researchers who studied NiO catalysts with various morphologies for CO oxidation found that ring-like and flower-like NiO demonstrated high activity. Ni is the best catalyst for the reaction by the virtue of its life, high activity and selectivity towards CO oxidation at a lower cost. The partial reduction of nickel oxide under hydrogen at elevated temperature is the most effective method for the preparation of active oxide catalysts [3-6].

Meanwhile, cerium oxide (CeO_2) usually acts as promising materials for chemical transformation mainly for environmental applications and energy conversion systems and sole support or an additive to enhance the catalytic activity of metal oxide catalyst [7-9]. The wide range of properties of CeO_2 such as redox properties, dielectric behavior and thermal stability has seen considerable attention by the researchers [10]. CeO_2 increases the oxygen storage capacity buttresses the metal dispersion of the three ways auto catalysts and enhances CO to CO_2 conversion [11-17]. The presence of transition metal or metal oxides can further enhance their properties. Catalyst performance such as improving the surface area and dispersion of the active phase was attributed by the presence of transition metal, Ce [18, 19]. The transition metal showed interesting redox properties when cerium is combined with nickel [18]. This material has been widely used for many applications such as a catalyst in automobile engines [20], electrodeposition process [22], water gas shift reaction, CO_2 reforming of methane, water splitting reactions, methane oxidation, hydrogen storage and hydrogen emission [23-26]. The co-deposition of CeO_2 and NiO can improve the corrosion resistance compared to that of pure Ni [27]. A comparison from our previous work showed that NiO as a bimetal catalysts of zirconia doped nickel oxide and cobalt doped nickel oxide gave high reduction temperature in the CO atmosphere as the percentage of zirconia and cobalt increased [28, 29].

The usage of reductant of CO in this work was from the idea of the Boudouard reaction. Instead of using precious H_2 as a reductant, CO can perform the same role in reducing metal oxides. The Boudouard reaction has been known since 1905, it occurs during the gasification of coal and other carbon-rich sources [30]. This reaction is highly endothermic with the equilibrium lies far to the right according to the Le Chatelier's principle. Hence, CO_2 is the favored product (Equation 1).

$$2CO \rightleftharpoons C + CO_2 \qquad \Delta H = -172 \text{ kJ/mol} \qquad (1)$$

The free energy of the formation of CO_2 is relatively insensitive to temperature, while the entropy is positive. At high temperatures above 700 °C as typically cited, the free energy change becomes negative, making CO formation progressively more favored. The reaction only plays a significant role in high-temperature (>900 °C) gasification and smelting processes [31, 32]. This reaction has potentially represented a means of CO_2 remediation by converting it to a more synthetically flexible CO. Besides, the reaction has been proposed as part of "clean coal" schemes that convert the CO_2 product gas to CO, which can then be used to produce hydrogen via the water−gas shift reaction or hydrocarbons through the Fischer−Trøpsch process [33].

In this paper, we present a study regarding the reduction behavior of cerium as an additive to nickel oxide at different percentage 3%, 5%, 10% cerium doped (Ce-NiO) and undoped NiO in carbon monoxide by standard wet impregnation method.

Materials and Methods

Catalyst preparation

The NiO (97.0%) and Ce (99.0%) were purchased from Acros Organics Chemical Company and Merck respectively. The ethanol was obtained from ChemAr. The Ce/NiO was prepared by the wet impregnation method. 3 mol % Ce of the total metal cation was dissolved in 5 mL distilled water and 5 mL ethanol. The NiO powder was added corresponding to the metal cation additives in the above proportion. The mixture was stirred vigorously for 2 hours at room temperature. The mixtures were dried at 120 °C overnight and subsequently calcined at 400 °C for 4 hours. The catalysts were denoted as xCe/NiO NiO with x representing the percentage of Ce loading.

Characterization

Temperature programmed reduction (TPR) measurements was performed using a Micromeritic Autochem 2920 Chemisorption Analyzer (Micromeritic, USA). The 50 mg of catalysts were heated up with non-isothermal reduction until 700 °C at 10 °C/ min and followed by isothermal reduction at 700 °C for 60 minutes with 40% CO in N_2 flow at 20 mL/ min (STP) as reducing gas. The carbon monoxide consumption was monitored using a thermal conductivity detector (TCD). Phase characterization was carried out by X-ray diffraction (XRD) Bruker AXS D8 (Bruker, Germany) Advance type with X-ray radiation source of Cu Kα (40 kV, 40 mA) to record the 2θ diffraction angle from 10-80 degree at the wavelength λ = 0.154 nm to observe the lattice of the structures. For identification purposes of crystalline phase composition, diffraction patterns obtained were matched with standard diffraction (JCPDS) files.

The N_2 adsorption-desorption isotherms and textural properties were obtained using a static volumetric technique instrument (gas sorption analyzer, Micromeritics ASAP 2020, USA). The Brunauer–Emmett–Teller (BET) surface area was calculated from the isotherms. Approximately 500 mg of catalysts were degassed at 300 °C for 4 hours under vacuum to remove moisture content and humidity gases prior to measurement. The measurement was conducted in a circulating bath of liquid N_2 of nitrogen (77 K). The Field Emission Scanning Electron Microscope (FESEM-EDX) technique was used for morphological investigation of the catalysts. A ZEISS MERLIN Compact microscope (MERLIN, Germany) equipped with a field emission gun and EDX probe was employed. The measurements were carried out at an accelerating voltage of 20 kV.

Results and Discussion

Temperature programmed reduction

The reduction process of 3%, 5%, 10% (wt./wt.) Ce/NiO and undoped NiO in the CO atmosphere were studied by using CO-TPR as shown in Figure 1. The TPR profile for NiO exhibited a narrower peak compared to Ce/NiO series with one reduction peak ranging from 350 - 400 °C with a maximum peak at 387 °C. The Ce/NiO catalysts exhibited a wider peak due to the addition of Ce on NiO. Nevertheless, the reducing trends were shifted toward lower temperatures. The chemical shift was assumed from the interaction of Ce and Ni particles that led to lower reduction temperature. As the percent of Ce was increased, the reduction temperature was reduced. However, at 10% Ce/NiO was a wider peak among all Ce/NiO series with a maximum reduction

peak at 365 °C. Thus, 5% Ce/NiO was found to be sufficient to reduce the NiO with a maximum reduction temperature of 366 °C. From the result, it was found that the reduction reaction process performed better at a lower percentage of Ce loading. The lower percentage of Ce loading caused Ce particles to be more likely to disperse evenly on the NiO surfaces. Inversely, the Ce particles would be more likely to form larger Ce clusters as the percentage of Ce loading increased. Besides, this might lead to the competition between isolated/fine particle Ce, Ce clusters and NiO to be reduced at the same time. Thus, the reduction temperature did not differ significantly between 10 % and 5 %. For the CeO_2 alone, no reduction peak was observed indicating that there was no reduction process.

Crystallinity analysis using XRD

XRD patterns of calcined 3%, 5%, 10% Ce/NiO and undoped NiO catalysts are shown in Figure 2. All catalysts displayed well-defined diffraction peaks that were matched with NiO peaks with JCPDS file number 03-065-5745. Nonetheless, all peak intensities for Ce/NiO series were notably lower than NiO. The addition of Ce on NiO affected the nucleation process and then decreased the crystallinity of the catalysts. The increment of Ce loading is believed to affect the intensity of the crystalline peaks of NiO. The highest loading of Ce for 10% Ce/NiO exhibited peaks that were less than half of undoped NiO. Thus, the 10% loading of Ce on NiO led to a decrease in NiO crystallinity. None of Ce peak was observed indicating the Ce particles were well dispersed on the NiO surfaces.

Figure 3 shows XRD patterns of reduced 3% Ce/NiO, 5% Ce/NiO,10% Ce/NiO and undoped NiO catalysts. The complete reduction was observed from NiO to Ni throughout all catalysts. All peaks were matched with Ni with JCPDS file number 01-071-4654. The diffraction peaks were also consistent with the undoped NiO, but it possessed the same trends of the peaks intensity for Ce/NiO series, which were notably lower than NiO catalyst.

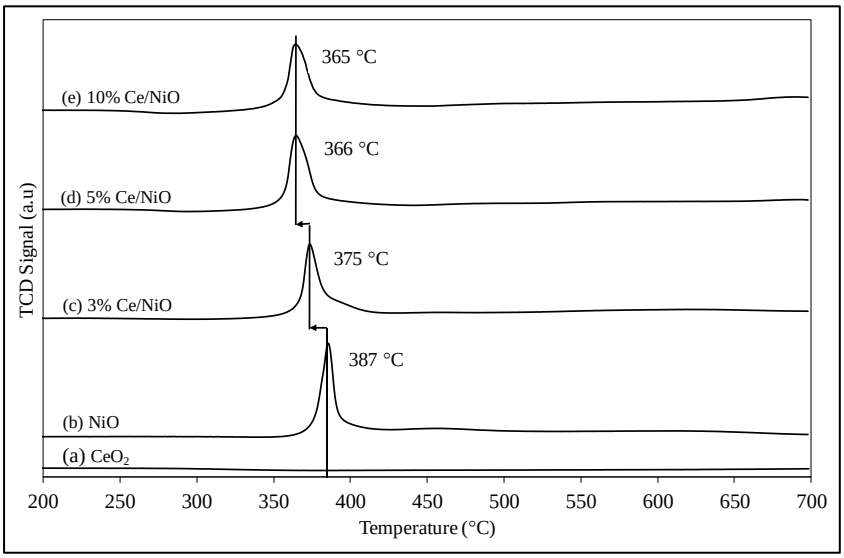


Figure 1. TPR profile of (a) CeO_2, (b) NiO, (c) 3% Ce/NiO, (d) 5% Ce/NiO and (e) 10% Ce/NiO in CO atmosphere

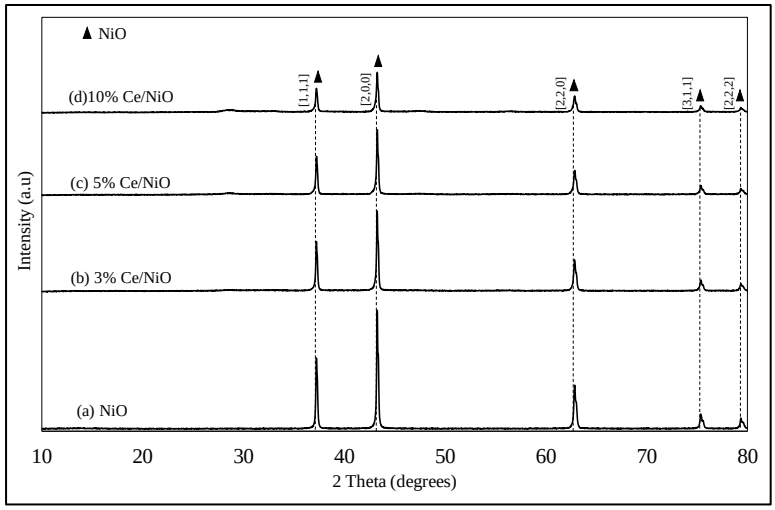


Figure 2. XRD diffractogram of (a) NiO, (b) 3% Ce/NiO, (c) 5% Ce/NiO and (d) 10% Ce/NiO after calcined at 400 ºC for 4 hours.

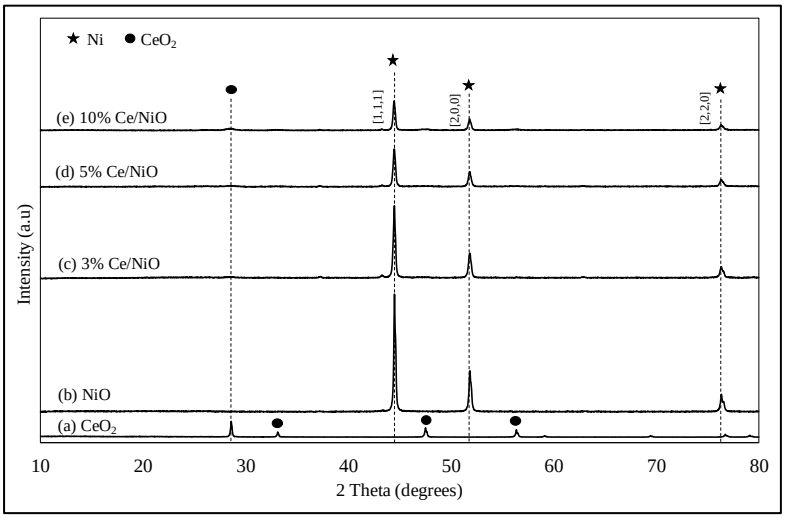


Figure 3. XRD diffractogram (a) NiO, (b) 3% Ce/NiO, (c) 5% Ce/NiO and (d) 10% Ce/NiO after reduction at 700 ºC

Physical surface analysis

The textural properties of the catalysts were studied through N_2 adsorption-desorption isotherms (Figure 4) and its parameters such as BET surface area, pore volume and average pore diameter (Table 1). The catalysts showed typical isotherms for bimetals catalysts obtained by Lahuri et al. [34,35]. The isotherms are referring to type III according to IUPAC classification of isotherms, with H3 type hysteresis of desorption branches covering a large range of relative pressure (P/Po) where the adsorbent−adsorbate, interaction is weak but could be obtained with certain porous adsorbents [36]. The hysteresis is proven based on the isotherms ascribed from plate-like particles giving rise

to slit-shaped pores from the adsorbent with large ranges of pore diameters, which does not exhibit any limiting adsorption at high P/Po [37].

The parameters of BET surface area, pore volume and average pore diameter for the catalysts are shown in Table 1. NiO exhibited the smallest specific BET surface area (4.57 m^2g^{-1}) and the largest average pore diameter (40.6 nm). The additional percentage of Ce led to the increase of surface area and the decrease of pore diameter. The addition of different percent of Ce reduced the pore diameter [30]. For 10% Ce/NiO, the BET surface area obtained were the highest (11.31 m^2g^{-1}) among all catalysts. It was ascribed to the addition of Ce deposited on NiO surfaces that contributed to the increment of mesopore, which resulted in the reduction of the average pore diameter (17.7 nm). It is believed the modification of Ce/NiO improved the textural properties by increasing the BET surface area, hence, a higher active site could be exposed for any desirable reaction.

Pore size distribution curve of the catalysts is illustrated in Figure 5. Another evidence that Ce loading on NiO contributed to BET surface area significantly was the Ce particles that possessed mesopore structure as shown in the inset of Figure 5. The pore size distribution depended on the distribution of the available pore for each sample. Besides the NiO pore size distribution, the addition of the Ce metal also has its own pore size distribution that alter the overall distribution. Thus, the pore size distribution would change accordingly when the catalyst was loaded with the different percentages of Ce metal loading. It is noteworthy to observe that 3% Ce/NiO exhibited bimodal distribution with high pore size distribution at the region of 450 Å (45 nm) and 810 Å (85 nm). Furthermore, the improvement on the pore size distribution curve for Ce/NiO series catalysts at around 20-50 Å (2 - 5 nm) compared to NiO alone which flattened at this region, is shown in the inset of Figure 5. At above 3% of Ce metal loading, the pore size distribution at the range of 400-1100 Å (40-110 nm) was lower than NiO alone. It was attributed to the agglomeration of Ce metal which reduced available pores.

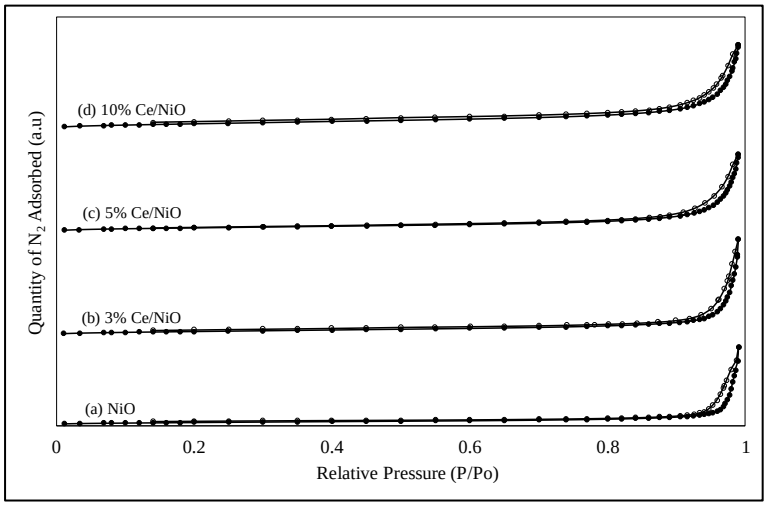


Figure 4. N_2 adsorption-desorption isotherms

Table 1. The surface area and pore characterization of the catalysts

Catalyst	S_{BET} (m^2g^{-1})	V_{pore} (cm^3g^{-1})	D_{pore} (nm)
10% Ce/NiO	11.31	0.053	17.7
5% Ce/NiO	8.52	0.049	22.8
3% Ce/NiO	6.82	0.059	32.1
NiO	4.60	0.047	40.6

[a] S_{BET}: BET surface area; V_{pore}: total pore volume; D_{pore}: average pore diameter

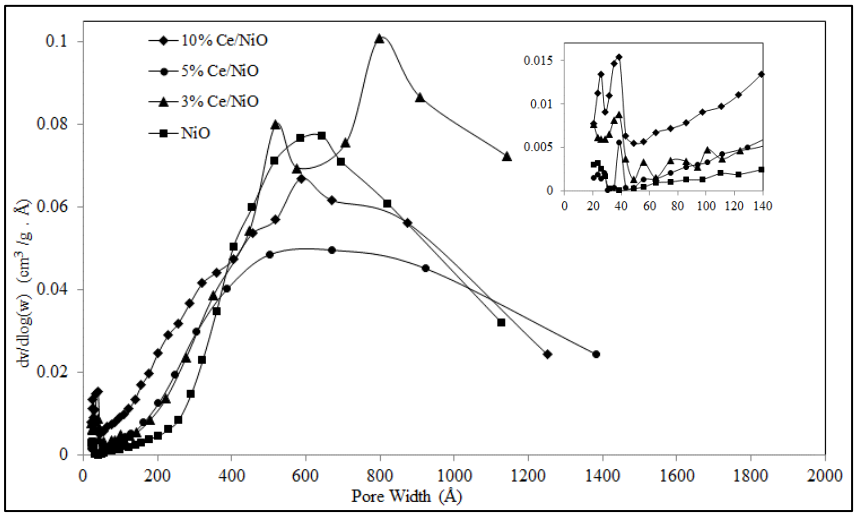


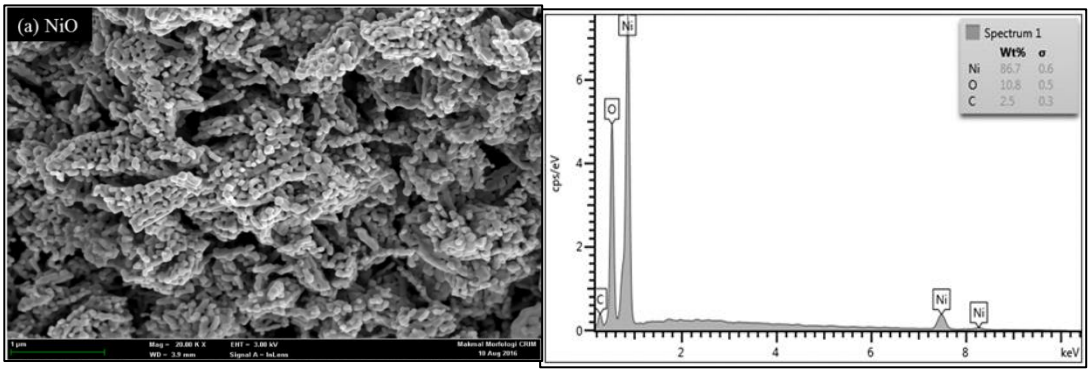
Figure 5. Pore size distribution

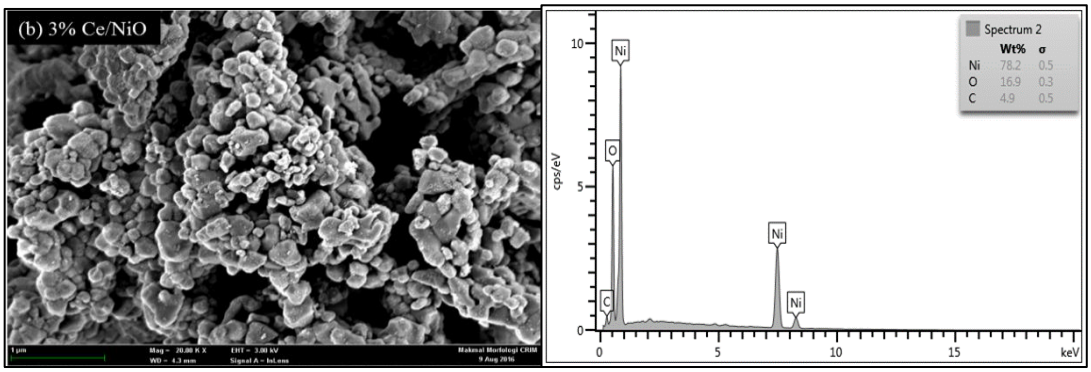
Surface morphology by FESEM-EDX

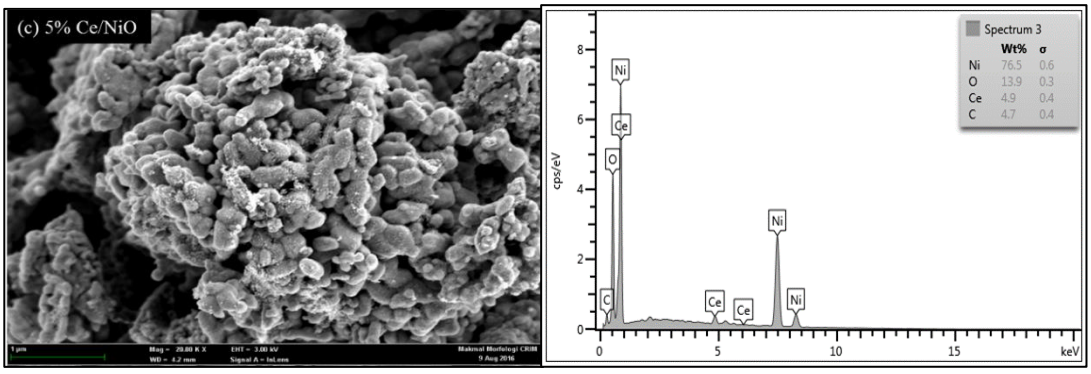
Catalyst morphology was investigated by FESEM and the results are shown in Figure 6. The NiO catalyst showed a rod structure. The addition of Ce to NiO altered the morphology significantly. Besides, the morphologies of NiO catalysts were influenced by Ce. The 3% Ce/NiO exhibited irregular shape and non-uniform particle size distribution of NiO particles with agglomeration forming the bulky size of NiO. For the 5% Ce/NiO catalyst, the NiO was generated in clearer particles. It was believed at 5% Ce addition caused a disturbance in between NiO particles. The 10% Ce/NiO catalyst exhibited more regular spherical particles, smaller particle size and more uniform particle size distribution. The Ce particles deposited on NiO also can be seen with fine sharp particles shape. Hence, these results explain and support the BET surface area results. The NiO catalysts showed different specific surface areas, crystallinity, morphology and surface nickel valence distribution with the different cerium percentages. The experimental temperature, precursor, surfactants and pH control the crystallization of metal oxides with controlled sizes and shapes [31]. Cerium loading on NiO could affect the crystal phase, pore structure and nickel dispersion and then influence oxidative activity [32]. Finally, it could result in a different structure, morphology, surface composition and surface elemental valence for the catalysts. The NiO catalyst showed different structural properties from the Ce/Ni oxide catalysts. The doped metal oxide influenced the structure and morphology of the catalyst [33]. The 10% Ce/NiO catalysts showed regular spherical particles with the highest specific surface area ascribed from the Ce was well dispersed on NiO resulted in

prevention of NiO particles agglomeration. Therefore, the 10% Ce/NiO catalyst showed the highest specific surface area, the lowest crystallinity, the most evenly distributed particle size and the most surface-active Ni^{2+}.

The XRD diffractogram did not detect the presence of Ce elements due to the well-dispersed particles on the NiO surface. Nonetheless, according to EDX results, the Ce particles can be detected at 5% loading. The 5% Ce/NiO was the catalysts that contained enough Ce loading to obtain a lower reduction temperature. Hence, it was proven that the presence of Ce particles could enhance the NiO reduction. The EDX result exhibited a higher weight percentage of Ce for 10% Ce/NiO compared to 5% Ce/NiO due to the EDX was scanned only at a certain targeted area which did not represent the whole sample. It also might be attributed to agglomeration of Ce particles at above 5% of Ce loading which resulted in an uneven distribution of the Ce particles. Nevertheless, this result indicates the presence of Ce on each catalyst.







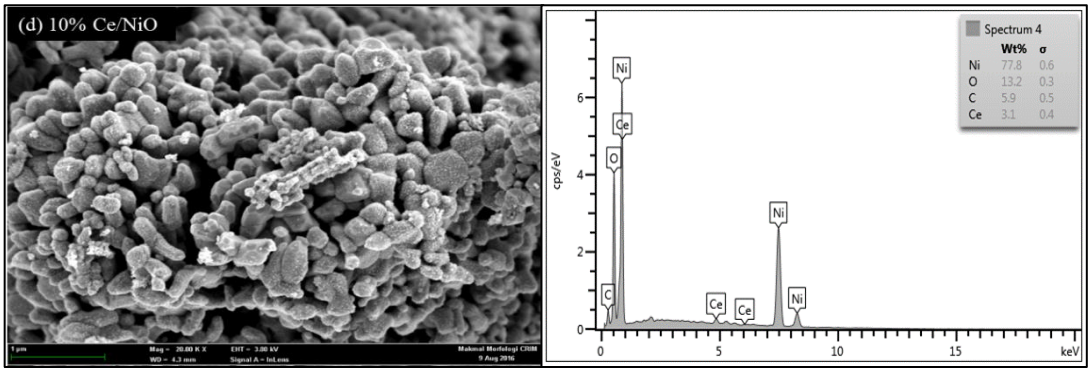


Figure 6. FESEM images and EDX values for (a) NiO, (b) 3% Ce/NiO, (c) 5% Ce/NiO, and (d) 10% Ce/NiO

Conclusion

The reduction behavior of undoped NiO and Ce/NiO catalysts were investigated and compared using the TPR technique and characterized by XRD, BET and FESEM-EDX analysis. The findings in this research revealed that the reduction reaction of NiO obeyed the consecutive mechanism, NiO was reduced to Ni completely. The Ce/NiO also possessed a higher surface area and for FESEM it was clearly shown the Ce was well dispersed on the surface of NiO. Furthermore, the addition of Ce to NiO enhanced a lower reduction temperature. The addition of Ce to the NiO shifted the TPR peaks to the lower temperature. It can be concluded that the reduction temperature of NiO decreases by increasing Ce addition with 5% Ce loading, which is sufficient to reduce NiO to Ni at 366 °C. The Ce changes the coordination environment of nickel and the strength of Ni-O bonds, leading to a decrease in the reduction temperature of doped NiO.

Acknowledgement

The authors wish to thanks Universiti Kebangsaan Malaysia (UKM) for funding this project under research grant number FRGS/1/2015/SG01/UKM/02/2 and GUP-063-2016 from the Ministry of Higher Education (MOHE) Malaysia and Centre of Research and Innovation Management (CRIM) UKM for the instruments facilities.

References

1. Heinrich, V. E. and Cox, P. A. (1994). The surface science of metal oxides. Cambridge University Press, Cambridge.
2. Pacchioni G. (2000). Ab initio theory of point defects in oxide materials: Structure, properties, chemical reactivity. *Solid State Sciences*, 2: 161-179.
3. Maity, A., Ghosh, A. and Majumder, S. B. (2016). Engineered spinel-perovskite composite sensor for selective carbon monoxide gas sensing. *Journal of Sensors and Actuators B: Chemical*, 15: 1-23.
4. Moncada, N. G., Navarro, J. C., Odriozola, J. A., Lefferts, L. and Faria, J. A. (2021). Enhanced catalytic activity and stability of nanoshaped Ni/CeO_2 for CO_2 methanation in micro-monoliths. *Catalysis Today*, In Press.
5. Dey, S. and Mehta, N. S. (2020). Oxidation of carbon monoxide over various nickel oxide catalysts in different conditions: A review. *Chemical Engineering Journal Advances*, 1: 100008.
6. Janković, B., Adnađević, B. and Mentus, S. (2008). The kinetic study of temperature-programmed reduction of nickel oxide in hydrogen atmosphere. *Chemical Engineering Science*. 63: 567-575.
7. Roy, B. and Leclerc, C. A. (2015). Study of preparation method and oxidization/reduction effect on the performance of nickel-cerium oxide catalysts for aqueous-phase reforming of ethanol. *Journal of Power Sources*, 299: 114-124.

8. Montini, T., Melchionna, M., Monai, M. and Fornasiero, P. (2016). Fundamentals and catalytic applications of CeO_2-based materials. *Chemical Reviews*, 116: 5987-6041.
9. Vita A. (2020). Catalytic applications of CeO_2-based materials. *Catalysts*, 10: 576-580.
10. Gangopadhyay, S., Frolov, D., Masunov, A. E. and Seal, S. (2014). Structure and properties of cerium oxides in bulk and nanoparticulate forms. *Journal of Alloys and Compounds*, 584: 199-208.
11. Taylor, K. C. (993), Nitric oxide catalysts in automotive systems. *Catalysis Reviews Science Engineering*, 35: 457-481.
12. Yao, H. C. and Yao, Y. F. Y. (1984). Ceria in automotive exhaust catalysts: I. Oxygen storage. *Journal of Catalysis*, 86: 254-265.
13. Kummer, J. T. (1986). Use of noble metals in automobile exhaust catalysts. *Journal Physical Chemistry*, 90: 4747-4752.
14. Oh, S. H. (1990). Effect of cerium addition on the CO-RO reaction kinetics over alumina-supported rhodium catalysts. *Journal of Catalysis*, 124: 477-485.
15. Oh, S. H. and Eickel, C. C. (1988). Effects of cerium addition on CO oxidation kinetics over alumina-supported rhodium catalysts. *Journal of Catalysis*. 112: 543-555.
16. Loof, P., Kasemo B. and Keck, K. E. (1989). Oxygen storage capacity of noble-metal car exhaust catalysts containing nickel and cerium. *Journal of Catalysis*. 118: 339-348.
17. Bera, P., Patil, K. C., Jayaram, V., Subbanna, G. N. and Hegde, M. S. (2000). Ionic dispersion of Pt and Pd on CeO_2 by combustion method: Effect of metal–ceria interaction on catalytic activities for NO reduction and CO and hydrocarbon oxidation. *Journal of Catalysis*. 196: 293-301.
18. Deraz, N. M. (2012). Effect of NiO content on structural, surface and catalytic characteristics of nano-crystalline NiO/CeO_2 system. *Ceramics International*. 38: 747-753.
19. Castano, C. E., O'Keefe, M. J. and Fahrenholtz, W. G. (2015). Cerium-based oxide coatings. *Current Opinion in Solid State & Materials Science*, 19: 69-76.
20. Ashif, H. T., Avinash, A. C., Faheem, A. S., Jin, C. W. and Kim, H. (2015). Synthesis and application of CeO_2/NiO loaded TiO_2 nanofiber as novel catalyst for hydrogen production from sodium borohydride hydrolysis. *Energy*. 89: 568-575.
21. Wang, J., Shen, M., Wang, J., Yang, M., Wang, W., Ma, J. and Jia, L. (2010). Effects of Ni-doping of ceria-based materials on their micro-structures and dynamic oxygen storage and release behaviors. *Catalysis Letter*. 140: 38-48.
22. Zeng, Y. B., Qu, N. S. and Hu, X. Y. (2014). Preparation and characterization of electrodeposited Ni-CeO_2 nanocomposite coatings with high current density. *International Journal of Electrochemical Science*, 9: 8145-8155.
23. Du, X., Zhang, D., Shi, L., Gao, R. and Zhang, J. (2012). Morphology dependence of catalytic properties of Ni/CeO_2 nanostructures for carbon dioxide reforming of methane. *Journal of Physical Chemistry C*, 116: 10009-10016.
24. Lin, X., Zhang, Y., Wang, Z., Wang, R., Zhou, J. and Cen, K. (2014). Hydrogen production by HI decomposition over nickel–ceria–zirconia catalysts via the sulfur–iodine thermochemical water-splitting cycle. *Energy Conversion Management*, 84: 664 – 670.
25. Shao, S., Shi, A., Liu, C. L., Yang, R. Z. and Dong, W. S. (2014). Hydrogen production from steam reforming of glycerol over Ni/CeZrO catalysts. *Fuel Processing Technology*, 125: 1-7.
26. Makarshin, L. L., Sadykov, V. A., Andreev, D. V., Gribovskii, A. G., Privezentsev, V. V. and Parmon, V. N. (2015). Syngas production by partial oxidation of methane in a microchannel reactor over a $Ni–Pt/La_{0.2}Zr_{0.4}Ce_{0.4}O_x$ catalyst. *Fuel Processing Technology*, 131: 21-28.
27. Hasannejad, H., Shahrab, T. and Jafarian, M. (2012). Synthesis and properties of high corrosion resistant Ni-cerium oxide nano-composite coating. *Material Corrosion*, 63: 9999-10005.
28. Dzakaria, N., Abu Tahari, M. N., Saidin, S., Tengku Saharuddin, T. S., Salleh, F., Lahuri, A. H. and Yarmo, M. A. (2020). Effect of cobalt on nickel oxide toward reduction behaviour in hydrogen and carbon monoxide atmosphere. *Material Science Forum*, 1010: 373-378.

29. Dzakaria, N., Samsuri, A., Abdul Halim, A., M., Tengku Saharuddin, T. S., Abu Tahari, M. N., Salleh, F., Yusop, M. R., Wan Isahak, W. N. R., Mohamed Hisham, M. W., and Yarmo, M. A. (2020). Chemical reduction behavior of zirconia doped to nickel at different temperature in carbon monoxide atmosphere. *Indonesian Journal of Chemistry*, 20(1): 105-112.
30. Bielowicz, B. and Misiak, J. (2020). The impact of coal's petrographic composition on its suitability for the gasification process: The example of polish deposits. *Resources*, 9(9): 111.
31. Van Deventer, J. S. J. (1987). The effect of additives on the reduction of chromite by graphite: An isothermal kinetic study. *Thermochim. Acta*, 111: 89.
32. Walker Jr, P. L., Rusinko Jr, F. and Austin, L. G. In Advances in Catalysis (1959). Eds.; Academic Press, Volume 11: pp 133.
33. Hunt, J. Ferrari, A. Lita, A. Crosswhite, M. Ashley, B. and Stiegman, A. E. (2013). Microwave-specific enhancement of the carbon–carbon dioxide (Boudouard) reaction. *Journal of Physical Chemistry C*, 117 (51): 26871-26880.
34. Lahuri, A. H., Yarmo, M. A., Marliza, T. S., Abu Tahari, M. N., Samad, W. Z., Dzakaria, N. and Yusop, M. R. (2016). Carbon dioxide adsorption and desorption study using bimetallic calcium oxide impregnated on iron (III) oxide. *Materials Science Forum*, 888: 479-484.
35. Lahuri, A. H., Yarmo, M. A., Abu Tahari, M. N., Marliza, T. S., Tengku Saharuddin, T. S., Mark Lee, W. F. and Dzakaria, N. (2020). Comparative adsorption isotherm for beryllium oxide/iron(III) oxide toward CO_2 adsorption and desorption studies. *Materials Science Forum*, 1010: 361-366.
36. Sing, K. S. W., Everett, D. H., Haul, R. A. W., Moscou, L., Pierotti, R. A. and Rouquerol, J. (1985). Reporting physisorption data for gas/solid systems with special reference to the determination of surface area and porosity. *Pure & Applied Chemistry*, 57(4): 603-619.
37. Condon, J. B. (2006). Surface area and porosity determinations by physisorption measurements and theory, first edition, Elsevier, Netherland.

Malaysian Journal of Analytical Sciences (MJAS)
Published by Malaysian Analytical Sciences Society

DEVELOPMENT OF EDIBLE CHITOSAN FILM INCORPORATED WITH POMEGRANATE PEEL EXTRACT FOR THE PACKAGING OF BEEF

(Penghasilan Filem Kitosan yang Boleh Dimakan yang Digabungkan dengan Ekstrak Kulit Buah Delima untuk Pembungkusan Daging Lembu)

Seah Jia Min[1], Ianne Kong[1], Enis Mudiliar Rajan[1], Pui Liew Phing[1]*, Yus Aniza Yusof[2,3]

[1]*Department of Food Science with Nutrition, Faculty of Applied Sciences, UCSI University, 56000 Kuala Lumpur.*
[2]*Department of Process and Food Engineering, Faculty of Engineering*
[3]*Laboratory of Halal Services, Halal Products Research Institute Universiti Putra Malaysia, 43400 Selangor, Malaysia.*

**Corresponding author: puilp@ucsiuniversity.edu.my*

Received: 20 May 2021; Accepted: 17 june 2021; Published: 27 June 2021

Abstract

The aim of this research was to produce a chitosan-based edible film with pomegranate peel extract. Different chitosan concentration (1-2% w/v) and pomegranate peel extract (0%-6% w/v) were used to produce an edible film, and physical (thickness, moisture content, water-solubility, and total color change), mechanical (tensile strength and elongation at break), chemical (Fourier Transform Infrared) and antimicrobial properties of the edible films were investigated. The optimized edible film was applied to beef samples for a 7 days storage at 4 °C. When the concentration of the pomegranate peel extract increases from 1 to 6% (w/v), the thickness, water solubility, and total color difference of the film also increases. The chitosan film added with pomegranate peel extract was effective in inhibiting the *Streptococcus aureus* (SA) growth as compared to *Pseudomonas aeruginosa* (PA). In addition, an increasing in chitosan concentration (from 1% to 2%) reduced the water solubility of pomegranate peel extract film from 41.42% to 33.02%. Films with 2% (w/v) chitosan have the highest tensile strength (12.67 MPa) while the highest elongation at break (10.21%) was exhibited by the film with 1.5% (w/v) chitosan and 4% (w/v) pomegranate peel extract. The optimal concentration of chitosan and pomegranate peel extract of the film was 1.5% (w/v) and 4% (w/v), respectively. Moreover, shelf life of the beef sample was increased from 4 days to 7 days with the application of the pomegranate peel extract chitosan film.

Keywords: film, antimicrobial, chitosan, pomegranate peel extract, beef

Abstrak

Tujuan penyelidikan ini adalah untuk menghasilkan plastik yang boleh dimakan berasaskan kitosan dengan ekstrak kulit buah delima. Kepekatan kitosan yang berbeza (1-2% w/v) dan ekstrak kulit buah delima (0%-6% w/v) digunakan untuk menghasilkan plastik yang boleh dimakan, dan fizikal (ketebalan, kandungan kelembapan, kelarutan air, dan jumlah perubahan warna), mekanikal (kekuatan tegangan dan pemanjangan maksima), sifat kimia (inframerah Fourier transformasi) dan antimikrob plastik yang boleh dimakan telah dikaji. Plastik yang dioptimum, telah digunakan untuk sampel daging lembu untuk simpanan 7 hari pada 4 °C. Apabila kepekatan ekstrak kulit buah delima meningkat dari 1 hingga 6% (w/ v), ketebalan, kelarutan air, dan jumlah

perbezaan warna plastik juga meningkat. Plastik kitosan yang ditambah dengan ekstrak kulit buah delima berkesan dalam menghalang pertumbuhan *Streptococcus aureus* (SA) berbanding *Pseudomonas aeruginosa* (PA). Di samping itu, peningkatan dalam kepekatan kitosan (dari 1% hingga 2%) mengurangkan kelarutan air plastik ekstrak kulit buah delima daripada 41.42% kepada 33.02%. Plastik dengan 2% (w/v) kitosan mempunyai kekuatan tegangan tertinggi (12.67 MPa) manakala pemanjangan maksima (10.21%) dipamerkan oleh plastik 1.5% (w/v) kitosan dan 4% (w/v) ekstrak kulit buah delima. Kepekatan optimum kitosan dan ekstrak kulit buah delima adalah 1.5% (w/v) dan 4% (w/v), masing-masing. Selain itu, jangka hayat sampel daging lembu telah ditingkatkan dari 4 hari kepada 7 hari dengan aplikasi plastik kitosan-ekstrak kulit buah delima.

Kata kunci: plastik, antimikrob, kitosam, ekstrak kulit buah delima, daging lembu

Introduction

Food packaging is intentionally designed as a tool to transport, store and protect foods and goods [1]. As technologies advanced, it is utilized as a preventive measure to maintain or extend product shelf life [2]. Recent advancement such as active food packaging system has offered a great opportunity in improving food safety, quality and convenience [3]. It utilizes bioactive agents, like antioxidants and antimicrobial, to enhance product safety and quality by allowing those agents to interact with the internal environment within the package [3]. Ever since the environmental issues had become a major concern globally, researches on replacing petroleum-based packaging materials with biodegradable or edible materials have been conducted in a wide range [4]. As a result, active packaging, which is edible and biodegradable, has received much concern in the food application and packaging industries.

Edible packaging materials can be classified into three various types namely polysaccharide, protein, and lipid [5, 6, 7, 8]. Chitosan (CH) is a polysaccharide that derivate from crustaceans' shell and it is actually biodegradable as well as non-toxicity [9]. Chitosan film incorporated with essential oils such as oregano, extract of *Garcinia atroviridis* (asam keeping), and musk lime extract increased the film's antibacterial properties, potentially inhibiting the growth of microorganisms which are commonly contained in seafood especially in fish and also in meat products [10].

As an alternative to maintaining food quality, the invention of an antimicrobial edible packaging method has been proposed [7, 8]. Constitutes of fruits and plants that possess antimicrobial properties have also been studied in the development of edible packaging [5]. Whey protein edible film added with 6.0% anise oils was inhibit the growth of the molds (*Aspergillus flavus* and *Penicillium* sp.) which is found on dried fish [11]. To summarise, edible films containing an antimicrobial compound extracted from fruits and plants can help food products last longer [12].

Pomegranate is an ancient fruit that has been cultivated for over a thousand years [13]. Pomegranate fruit is a rounded shape with dark reddish skin [14]. It is normally consumed as fresh or in commercial products, whereby peels are usually disposed of as waste. Pomegranate extracts have been used for millennia for their anti-infective properties, with activity more recently being attributed to their rich composition of ellagitannins and other secondary polyphenolic compounds [15]. It has an antimicrobial effect against *Staphylococcus aureus*, and *Pseudomonas aeruginosa* which are commonly found in fresh meat, especially on beef [16].

Fresh meat, such as beef, is an important protein source. The shelf life of fresh beef is 3 to 5 days at 4˚C [17]. Beef is highly susceptible to microbial degradation and lipid oxidation attribute to its intrinsic parameters, such as high moisture and fat content, availability of nutrients, and optimal pH range [18, 19]. The degradation of meat quality causes a heavy off-odour, discoloration, and slime development, which cause a major problem with customer acceptance [17]. Reduction of microbial spoilage has been a challenge in the meat industry as the contamination can be originated from the animal or processing environment [20]. In the retail shop, the common preservation of

fresh beef is kept in the chill condition and wrapped with a polyethylene bag. Currently, there is scarce information on the application of edible film incorporated with plant extract as a preservation method on fresh beef.

Hence, the present study aims at developing a chitosan film which will be incorporated with pomegranate peel extract (PPE). Based on mechanical, physical, chemical, and antimicrobial activity, the optimal concentration of chitosan and pomegranate peel extract will be determined. The optimal film will be proceeding to the storage test in order to determine the effect of chitosan-pomegranate peel extract edible film on fresh beef meat samples.

Material and Methods

Extraction of pomegranate peel

The drying method of pomegranate peel was conducted with some modification [21]. Pomegranate fruits were washed with water before being sliced in half with a knife. Arils were then removed manually from the peel. The peels were cut into small pieces and dried in a hot air oven at 55 °C for 22 to 24 hours. The dried peels were then sieved after being ground into a fine powder with a food grinder. The extraction method of pomegranate peel extract was conducted with some modifications [22]. Pomegranate peel powder was firstly soaked in 80% methanol in a 1:4 ratio at room temperature for 24 hours. This is because methanol is more widely used than ethanol and has a boiling point of 78.4 °C compared to 64.7 °C for ethanol. Methanol extract needs a lower temperature in the rotary evaporator to evaporate the solvent, resulting in less damage to the extract. Methanol is safe to consume since it evaporates during the process. Subsequently, the solution was filtered with cotton wool and collected in a conical flask. Then, a rotary evaporator was used to evaporate the filtrates at 50 °C. All the condensation of waste was collected in a waste collector. The process of evaporation was completed when no excess condensed vapour. Finally, the extract was stored in a glass bottle at 0 °C until further analysis.

Preparation of CH-PPE edible film

The solvent casting method was used to produce the chitosan-pomegranate peel extract edible film [23]. Chitosan powder (1%, 1.25%, 1.5%, 1.75% and 2% (w/v)) was dissolved in 1% acetic acid to prepare 30 g for each solution. Chitosan solution was then left to stir overnight using magnetic stirrer at low speed. Followed by filtration with the use of a vacuum filter and Whatman No.3 filter paper. Glycerol (0.5% v/v) has been added as a plasticizer into the chitosan solution and stirred for 15 minutes to get a homogenous suspension. Tween 80 (0.05% v/v) was incorporated as an emulsifying agent. After stirring for 15 minutes, pomegranate peel extract was incorporated into chitosan solution and the final concentrations of 0%, 1%, 2%, 3%, 4%, 5% and 6% (w/v) were achieved. The chitosan-pomegranate peel extract (CH-PPE) film-forming solution was subjected to homogenization at 9,000 rpm for 4 minutes. Lastly, 25 mL of homogenous film-forming solution were cast on a sterile petri dishes (90 mm × 15 mm) and dried in a ventilated oven for 22-24 hours at 40˚C. Once the films dried, peeled off from the petri dishes and kept in desiccators at room temperature for further experimental analysis.

Physical properties of CH-PPE edible film

Thickness

Edible film's thickness was determined with minor modifications [24]. The thickness (mm) of the chitosan-pomegranate peel extract edible film was determined using a hand-held micro-meter at five random locations of each film.

Moisture content

The moisture content of chitosan-pomegranate peel extract (CH-PPE) edible film was measured [10]. The obtained film was first cut into a square with a 2 cm x 2 cm diameter and its initial mass was weighed (W_0). It was subsequently placed in a plastic cup and placed in a 60°C oven for 24 hours to remove moisture before a constant mass was reached. After drying, films were cooled to room temperature, and the final mass (W_1) of edible films was determined, and its weight was recorded. The calculation of moisture content of the edible film was determined as the following equation 1.

$$Moisture\ content\ =\ (W0\ -\ W1)/W0\ x\ 100\% \quad (1)$$

Water solubility

The water solubility of CH-PPE edible film was obtained, with modifications [25]. At room temperature, each dried edible film was immersed in 25 mL distilled water for 2 hours. The free water was removed, and the films were dried for 24 hours at 60°C in an oven. The final mass of dried edible films (W_2) was measured after it was brought to room temperature. Calculation of water solubility was determined as the following equation 2.

$$Water\ solubility = \frac{W1-W2}{W1} \times 100\% \quad (2)$$

Color

The edible film's color was determined [26]. Colorimeter was firstly calibrated with a white and black calibrate plate. After calibration, 64 mm diameter of CH-PPE edible film was placed on the ColorFlez sample cup. The sample was rotated 90° after each reading. The film color was expressed in L*, a*, and b* values. L* represents the darkness of black at L=0 and the brightness of white at L=100; a* indicates red and green hue whereby the negative value signifies green hue and the positive value signifies red hue; the value of b* represents yellow/blue whereby yellow at the positive value and blue at a negative value. The color index (ΔE) that identifies the total color differences between each sample was determined as the following equation.

$$\Delta E = \sqrt{(\Delta L^*)^2\ +(\Delta a^*)^2\ +(\Delta b^*)^2} \quad (3)$$

Mechanical properties of CH-PPE edible film

Tensile strength and elongation at the breakpoint of CH-PPE edible film were determined using the method of which conformance to ASTM D882-02 method [27]. The film was cut into 20 mm × 70 mm strips. The strips were placed into the film-extension grips and clamped with a 50 mm initial grip distance. The crosshead was set to a speed of 20 mm/min.

Chemical properties of CH-PPE edible film

The absorbance spectra of CH-PPE edible film were measured using Fourier Transform Infrared (FTIR) spectrometry (Nicolet^{tm} iS^{tm} 5 Spectrometer, Thermo Scientific, Malaysia**)** connected to OMNIC Specta Software in transmission mode, which was slightly modified [28]. A tiny probe was used to fix the films to the sample holder. All spectra were then obtained with a resolution of 4 cm^{-1} as the average of 20 scans in the range of 4000 cm^{-1} to 500 cm^{-1} against a background spectrum from an empty cell.

Antimicrobial properties of CH-PPE edible film

The antimicrobial activity of the chitosan-pomegranate peel extract edible film against *Pseudomonas aeruginosa* (PA) and *Staphylococcus aureus* (SA) was determined using the agar disc diffusion method [29]. *Pseudomonas aeruginosa* (PA) and *Staphylococcus aureus* (SA) were pre-cultured overnight at 37°C in sterile nutrient broth. The turbidity of the bacterial suspensions was adjusted to 0.5 Mcfarland standard in a final inoculum density of 1.5×10^8 CFU/ml [30]. A 100 µL inoculum of each bacteria strain was spread evenly on Mueller-Hilton Agar (MHA) under aseptic conditions.

CH-PPE edible film was cut into 6mm diameter disc, then placed on the prepared MHA plate. A 6mm sterile paper disc (Whatman No.3 filter paper) was dipped in 80% methanol and dried in laminar flow as a negative control. Positive controls for *Pseudomonas aeruginosa* (PA) and *Staphylococcus aureus* (SA) were streptomycin and chloramphenicol, respectively. Finally, plates were incubated for 24 hours at 37°C. A ruler was used to measure the total diameter of inhibition, and the inhibition zone was measured in millimetres (mm).

Storage test of beef

Pre-treatment of beef

Freshly cut sirloin tip side of beef was acquired at a local supermarket. The beef meat was roughly cut into 10 g with 2 cm × 3 cm. These pieces were then wrapped with chitosan-pomegranate peel extract (CH-PPE) edible film (10 cm × 2 cm) and covered the entire meat surface. Beef meats without wrapping of CH-PPE edible film was controlled sample while beef meats wrapped with 1.5% CH + 4.0% PPE edible film was treatment sample. All meat samples were wrapped in a

polyethylene plastic bag and kept in 4˚C until further experimental analysis.

pH value of beef

The pH value of beef samples was obtained with slight modification [31]. Before the test, the pH meter was calibrated with pH 4, 7, and 10 buffer solutions. A stomacher was used to homogenise a beef sample of about 10 g in 100 mL sterile peptone water for 1 minute. The test was carried out during each day of storage (day 0, 1, 2, 3, 4, 5, 6, and 7).

Total plate count

The total plate count (TPC) test was conducted with some modifications [32]. To make the stock solution, a 10 g beef from treatment sample was homogenised for 1 minute in 100 mL sterile peptone water using a stomacher. Serial dilutions (10^{-1}-10^{-6}) were prepared in the test tube to enumerate the colonies in the range of 30 to 300. A 100 µL of bacteria inoculum of each dilution was spread evenly on plate count agar (PCA) by using the spread plate technique. All plates were incubated for 18 to 24 hours at 37°C. The TPC was conducted during each day of storage (day 0, 1, 2, 3, 4, 5, 6, and 7). The colony count was expressed in log CFU/mL.

Statistical analysis of data

All analyses were carried out in triplicate forms (n=3) except the storage test, which was conducted in duplicate (n=2). All results were reported as mean ± standard deviation. Tukey test was conducted to determine the significant differences among all treatments of CH-PPE films. All significant differences were set as 95% interval ($p \leq 0.05$). A pair T-test was performed to analyse the significant difference of total plate count and pH value between the two treatment groups of the beef sample from the three independent trials.

Results and Discussion

Physical properties of films

Thickness is an essential parameter in characterization of film because it affects the mechanical properties of films. The thickness of CH-PPE edible film was affected by concentration of the pomegranate peel extract (PPE), as shown in Table 1. The addition of PPE increased the thickness of CH-PPE edible film from 0.05 mm to 0.16 mm, as shown in Table 1. The thickness of 1.5% CH + 5% PPE edible film was 0.16 mm, and there was no statistical difference ($p > 0.05$) to a thickness of 1.5% CH + 6% PPE edible film.

This observation was consistent with the findings who discovered that the incorporation of antimicrobial agent increased the thickness of the chitosan film [25]. The CH-PPE edible film was thicker compared to the films used in previous research. The film-forming methods used in the research have an effect on the difference in film thickness 30 g of 1% (w/v) CH film-forming solution was cast on a 17.8 cm x 17.8 cm glass plate, produced 0.01 mm chitosan film [25]. The thickness of chitosan films was increased from 0.017 mm to 0.020 mm by adding lauric arginate and cinnamon oil in concentrations ranging from 0.1% (v/v) to 1% (v/v). 25 mL of film-forming solution was poured into a 90 mm 15 mm sterile petri dish in this experiment. Thus, as a smaller container was used for film casting in this analysis, a thicker film may result.

To prevent moisture transfer, it is important to maintain the edible film's moisture content at a similar level to the product's [33]. The moisture level and total soluble solid content of edible film affect its application on food. Table 1 shows the moisture content of CH-PPE film with various concentration of pomegranate peel extract ranging from 1% to 6%. The moisture content of the chitosan film was reduced from 28.01% to 7.47% after the addition of PPE (1% to 6%). A similar analysis revealed that when carvacrol and grape seed essence are applied to chitosan film, the moisture content decreases [34].

The film’s moisture content can be determined by total void volume filled by water molecules in the polymeric structure of the chitosan film [35]. From the result in Table 1, the presence of pomegranate peel extract lowered the film’s moisture content. It is suggested that the addition of PPE has occupied the space between the microstructural networks of chitosan film. As a result, lesser hydrogen bonds were formed between a water molecule and a functional group of chitosan, such as

amino and hydroxyl groups that represent water molecule binding sites [36]. Thus, it leads to low retention of water within the polymeric matrix.

Water solubility is an essential parameter that indicates the film's integrity in an aqueous environment. It is also one of the essential factors that determines the edible film's biodegradability [25]. Films with high-water solubility possess lower water resistance and vice versa. The requirement of film water solubility is different in various food applications. A film with a high-water solubility is better for releasing antimicrobial agents into the surrounding food, while a film with a low water solubility is better for longer storage periods, particularly for food products with a lot of moisture or water activity [37]. The chitosan film's water solubility is influenced by the functional group in the chitosan and water holding capacity of plasticizer [38].

The addition of bioactive compounds disrupts the polymer chain's positioning and hydrogen bonding of chitosan film, resulting in a change in the film's solubility [39]. Table 1 also presented the effect of PPE concentration on the water solubility of CH-PPE edible film. From the observation of the result shown in Table 1, the increasing order of water solubility on CH-PPE edible film resulted from the increase of PPE concentration. Additional PPE from 0% to 6% has caused a significant change of water solubility that increased from 27.29% to 41.68%. The addition of PPE to chitosan can cause bonding to break and the structure of the molecule to change, and the increasing water solubility [25]. The hydrophilic compound in PPE contributed to the increased hydrophilicity of the film. By increasing hydrophilic properties, the affinity of polymeric molecules to water could be improved [40].

The appearance of a product can affect the consumer's acceptance. Color is one of the main parameters that affect product appeal. Thus, the determination of the film's color profile is critical in this case. Table 2 showed the effect of PPE concentration on the color profile of CH-PPE edible film in terms of its lightness (L*), red-green (a*) and yellow-blue (b*), and total color difference (ΔE). The lightness (L*) value of CH-PPE edible films was reduced when PPE was added from 0% to 6%. An increment in both the a* parameter and decrement of b* parameter was observed, indicating an increase of redness and a reduction of yellowness of CH-PPE edible film, respectively, with an increasing PPE concentration when compared to control film (1.5% CH + 0% PPE).

The reduction of lightness (L*), from 31.16 to 14.18, may be attributed to the color nature of PPE, which showed dark reddish-brown color visually. The a* parameter of the control film has shown in negative value (-0.77), which indicated the exhibition of green color. The polyphenol in PPE, anthocyanins that exhibits red color is suggested to the contribution of the increment of a* parameter, which intensifies redness to the film [41]. As the concentration of PPE increased, the color of PPE masks the original color of chitosan film and leads to the decrement of yellowness of CH-PPE edible film. With the addition of PPE from 0 to 6% in 1.5% CH film, the total color difference (E) has increased from 0 to 17.56. It reduced the transparency and yellowness but intensified the redness of CH-PPE edible film.

Table 1. The effect of pomegranate peel extract concentration on the thickness, moisture content, water-solubility of CH-PPE edible film

PPE (%) in Chitosan Film	Thickness, Mm	Moisture Content (%)	Water Solubility (%)
0	0.05 ± 0.01^{a}	28.01 ± 0.12^{f}	27.29 ± 0.66^{a}
1	0.08 ± 0.01^{b}	15.03 ± 0.78^{e}	33.28 ± 1.82^{b}
2	0.09 ± 0.01^{b}	13.79 ± 0.11^{d}	34.18 ± 1.94^{b}
3	0.12 ± 0.01^{c}	11.84 ± 0.39^{c}	36.86 ± 2.50^{cd}
4	0.13 ± 0.01^{c}	10.66 ± 0.25^{b}	37.62 ± 1.95^{cd}
5	0.16 ± 0.01^{d}	9.70 ± 0.02^{b}	40.40 ± 2.15^{d}
6	0.16 ± 0.01^{d}	7.47 ± 0.12^{a}	41.68 ± 2.40^{d}

[a-f]Means ± standard deviations with different superscript letters within the same column indicate significant difference between formulations ($p \leq 0.05$) according to Tukey's test.

Table 2. The effect of pomegranate peel extract concentration on the color, and mechanical properties of CH-PPE edible film

PPE (%) in Chitosan Film	*L**	*a**	*b**	Δ*E*	Tensile Strength, MPa	Elongation at Break, %
0	31.16 ± 0.31^{e}	-0.77 ± 0.02^{a}	4.75 ± 0.05^{e}	0.00 ± 0.00^{a}	5.02 ± 0.08^{a}	15.60 ± 0.87^{e}
1	27.06 ± 0.25^{d}	0.04 ± 0.05^{b}	4.73 ± 0.09^{e}	5.36 ± 0.65^{b}	7.78 ± 0.15^{b}	14.30 ± 0.10^{d}
2	27.01 ± 0.30^{d}	0.75 ± 0.04^{c}	3.90 ± 0.03^{d}	5.78 ± 0.43^{b}	10.07 ± 0.35^{c}	11.77 ± 0.35^{c}
3	25.93 ± 0.62^{c}	1.14 ± 0.02^{d}	3.50 ± 0.06^{c}	4.75 ± 0.43^{b}	10.54 ± 0.07^{c}	10.84 ± 0.32^{bc}
4	25.65 ± 0.26^{c}	1.68 ± 0.01^{e}	3.28 ± 0.08^{c}	4.96 ± 0.36^{b}	11.93 ± 0.4^{d}	10.21 ± 0.36^{c}
5	19.56 ± 0.11^{b}	1.82 ± 0.05^{e}	1.99 ± 0.02^{b}	12.21 ± 0.32^{c}	10.83 ± 0.69^{c}	7.57 ± 0.15^{b}
6	14.18 ± 0.11^{a}	2.14 ± 0.05^{f}	1.34 ± 0.17^{a}	17.56 ± 0.31^{d}	5.10 ± 0.77^{a}	5.83 ± 0.35^{a}

[a-f]Means ± standard deviations with different superscript letters within the same column indicate significant difference between formulations ($p \leq 0.05$) according to Tukey's test.

Mechanical properties of films

The mechanical properties of a film can be used to determine its ability to protect product samples during storage, transportation, and handling. The films' tensile strength and elongation at break were tested at various PPE concentrations. The tensile strength (TS) and elongation at break (% E) of 1.5% CH-PPE edible film with varying PPE concentrations from 0 to 6% were

shown in Table 2. Tensile strength of CH-PPE edible film was also improved significantly from 5.02 MPa to 10.54 MPa with the increasing concentration of PPE from 0% to 4%. Moreover, 1.5% CH + 4.0% PPE edible film showed the highest tensile strength (11.93 MPa) at all films. However, the films' tensile strength started to drop from 11.93 MPa to 5.10 MPa when the concentration of the PPE increase from 4% to 6%.

The addition of PPE into the film has improved the tensile strength of the edible film by enhancing the formation of the hydrogen bonds between pomegranate peel extract and chitosan and yielded a compact structure of the films. Besides, a brittle film and uneven surface of the film may result from low tensile strength. It may due to the higher content of PPE was difficult to disperse and form homogenous CH-PPE edible film, therefore, reduced its intermolecular interaction. The tensile strength of 1.5% CH + 6% PPE film was similar to the tensile strength of 1.5% CH + 0% PPE film (5.02 MPa).

On the other hand, a reduction of %E was revealed by the increment of PPE concentration ranging from 1% to 6%, which reduced %E from 15.60% to 5.83%. Among all films, the results of %E were all significantly difference from each other. However, the %E of 1.5% CH + 3% PPE (10.84%) edible film had no significantly different to the %E of 1.5% CH + 2% PPE (11.77%) edible film and 1.5% CH + 4% PPE (10.21%) edible film. Thus, as the concentration of the PPE increases, the value of the elongation factor decreases. The optimal concentration of chitosan and pomegranate peel extract of the edible film was 1.5% (w/v) and 4.0% (w/v), respectively.

Elongation at breakpoint accounts for the extensibility and elasticity of material [42]. The value of elongation at breakpoint might relate to the moisture content of the film. The decrease of %E resulted from the increasing concentration of plant extracts incorporated in chitosan films may be owing to the decreasing moisture content in the films [12].

Chemical properties of films

The interaction between chitosan and pomegranate peel extract (PPE) was studied using FTIR analysis [28]. Figure 1 has depicted the spectra of CH-PPE edible film incorporated with PPE at varying levels. At the peaks of 1021 cm^{-1}, 2154 cm^{-1}, and 2874 cm^{-1}, all spectra showed similar patterns. The absorption peak at (i) 1350 cm^{-1} to 1000 cm^{-1} represented the C=O and C-N stretching vibrations [33], (ii) the peak around 2154 cm^{-1} indicated the stretching of alkyne bond (-C=C-), (iii) a weak band 2874 cm^{-1} represent the stretching of C-H and O-H bond [43] (iv) absorption peak at 1550 cm^{-1} corresponded to N-H stretching of amide I, (v) peak at 1400 cm^{-1} was assigned as a carboxylic group (-COO--) [28], (vi) broadband at 3500 cm^{-1} to 3200 cm^{-1} indicated the stretching vibration of N-H and O-H bond, as well as intermolecular hydrogen bonding of chitosan molecules [28].

The intensification of the absorption peak at the region of 1350 cm^{-1} to 1000 cm^{-1} be may be owing to the high content of PPE that contain a considerable amount of polyphenols, such as punicalagin and punicalin, which consists of hydroxyl, carbonyl, and aromatic group [44]. CH-PPE edible film with concentration between 4% to 6% PPE showed absorption peaks at 1400 cm^{-1} and 1550 cm^{-1}. This may due to the phenolic compounds were insufficient to be detected when PPE concentration was at 3% and below.

Glycerol has intensified the absorption peak of flaxseed mucilage film in the region of 3500 cm^{-1} to 3200 cm^{-1}, which represents O-H bond stretching [45]. Two new peaks at 2883.1 cm^{-1} and 1100 cm^{-1} to 920 cm^{-1} region that signifies that stretching vibration of C-H bond and C=O group appeared upon the incorporation of glycerol into flaxseed mucilage-based film. These three peaks indicated the vibration of the functional group in glycerol. Besides, the stretching vibration of methyl and methylene group ($-CH_2$) of Tween 80 shared the same absorption peak with glycerol at 2800-2960 cm^{-1} region [46].

By comparing the FTIR spectra to the result of the present study, a similar absorption band and peak were observed at 3281 cm^{-1}, 2874 cm^{-1}, and 1350 cm^{-1} to 1000 cm^{-1} region. However, the amplitude of the absorption band and peak at 3281 cm^{-1} and 2874 cm^{-1} region were similar among all CH-PPE edible films. This may vary due to the concentration of glycerol, and Tween 80 added into the CH-PPE edible films was fixed at 0.5% (v/v). As a result, the fixed concentration of glycerol and Tween 80 did not contribute to the intensification or shift or absorption band and peak.

Polar functional groups in organic compounds, such as hydroxyl, amines, carbonyl, and carboxylic groups, can increase their water solubility [47]. These compounds enhance the polarity of water and thus improved the hydrophilicity of film when incorporated in. From the result, the higher amplitude of absorption peak in the hydroxyl group, carbonyl group, amide group, and the carboxylic group were obtained as the concentration of PPE was increased.

Antimicrobial properties of films

An anti-microbial activity of chitosan film incorporated with pomegranate peel extract (PPE) at various concentrations against predominant bacteria found on beef meat sample was assessed using circular discs of the chitosan-pomegranate peel extract edible film with a diameter of 6 mm. Table 3 has shown the inhibitory effect of CH-PPE film against *Pseudomonas aeruginosa* (PA) and *Staphylococcus aureus* (SA). According to the findings, CH-PPE edible film was more effective at inhibiting SA growth. Control film (1.5% CH + 0% PPE) has similar inhibitory properties against the growth of tested microorganisms. The highest antimicrobial effect of CH-PPE film against PA was recorded at the 1.5% CH + 6% PPE edible film, of which the inhibition zone reached 12.16 mm. This was followed by 1.5% CH + 5% PPE edible film and 1.5% CH + 4% PPE edible film that exhibited an inhibition diameter of 12.06 mm and 11.56 mm, respectively.

In the case of *Staphylococcus aureus* (SA), the inhibition zones fell in the range of 12.39 mm to 15.33 mm as the PPE concentration increased. The highest effective concentration of PPE against *Staphylococcus aureus* (SA) was 6% (15.33). The inhibition zone is given by 4%, and 5% PPE incorporated film was 14.89 mm and 15.11 mm, respectively. However, there was no significant difference ($p > 0.05$) among the addition of 4%, 5%, and 6% PPE into chitosan film.

Chitosan exhibits antimicrobial effect on several Gram-negative bacteria such as *Salmonella typhimurium, Escherichia coli, Vibrio parahaemolyticus,* and *Pseudomonas fluorescens*, as well as Gram-positive bacteria such as *Listeria monocytogenes, Staphylococcus aureus, Bacillus cereus, Bacillus megaterium, Lactobacillus brevis and, Lactobacillus bulgaricus* and *Lactobacillus plantarum* [48, 49]. The inhibitory effect of chitosan was attributed to the cationic amino group of chitosan to bind to the anionic groups of these microorganisms [50]. Also, the antimicrobial effect of pomegranate peel extract (PPE) has been investigated and reported in the literature.

Gallic acid, flavonols, ellagitannins, anthocyanin, procyanidins, and ellagic acid are among the polyphenol compounds contained in pomegranate peel [41]. This phenolic compound has a number of biological functions, including antimicrobial, antioxidant, anti-inflammatory, and anticancer. Among them, ellagitannins (punicalagins and punicalin) are particularly high in amount. Punicalagins have remarkable antimicrobial activity against SA and PA [51]. By disrupting the bacterial cell membranes, phenolic compounds can inhibit the survival and proliferation of bacteria. Additionally, phenolic compounds can deactivate pathogenic microorganisms through adhesive binding, protein and cell wall adhesion, enzyme deactivation, and migration into the cell wall and/or DNA [6].

Storage of beef

The pH value is crucial in determining the quality of meat. Before slaughtering process, initial pH value of the meat is between the values of pH 6.8 to pH 7.3. An unstressed animal would have a pH value of 5.4 to 5.8 at rigor mortis, while a stressed animal would result in DFD (dark, firm, dry) meat with a higher pH value of 5.9 to 6.5 [52]. Figure 2 has indicated the pH change of both the control and sample groups during the storage

period. The pair T-test value was 0.001 ($p<0.05$), indicating that the pH values in the control and sample groups were significantly different.

Initial pH value of beef in the present study was 5.59. The finding which reported the initial pH value of fresh beef at 5.87 [31]. During the 7 days of storage at 4 °C, the pH of beef meat increased significantly ($p <0.05$). The pH of beef sample in the control group was risen faster than the pH of beef in the treatment group. The pH value of beef samples in the control group varied from the value of 5.59 to 7.45 whereas the pH value of treatment beef sample at day 7 was 6.25. However, the findings of the current study were in line with the observation of [31], where an increment of pH value at both control and treatment group during the storage period.

The total plate count of beef meat in both the control and treatment beef samples were illustrated in Figure 3. The perforated black line represented the maximum limit of acceptable microbial load on fresh beef meat. Both control and treatment beef samples showed an increasing trend from 3.77 log CFU/mL to 8.06 log CFU/mL and 3.77 log CFU/mL to 7.02 log CFU/mL in microbial load during the storage period at 4 °C from day 0 to day 7. On day 0, initial value of the total plate count (TPC) on beef meat was 3.77 log CFU/mL. As expected, the treatment beef sample showed a reduction ($p \leq 0.05$) in total plate count than control group. The antimicrobial effect of CH-PPE edible film was attributed to the punicalagins in PPE. By inhibiting the growth of PA and SA, the total plate count can be reduced partly.

Beef meat with > 7 log CFU/mL of spoilage microorganisms is unacceptable and unsafe for human consumption [54]. For the control beef sample, the total plate count has reached the limit point at day 4 and unfit for consumption. With the application of CH-PPE edible film, the TPC of beef sample was 4.17 log CFU/mL at day 4 where a 2.8 log reduction was achieved, and the shelf life of beef has been effectively extended from day 4 to day 7. A similar study has reported that milk protein-based film incorporated pimento essential oil has shown a reduction of *E. coli* counts on beef meat on day 5 [32]. In comparison, CH-PPE edible film is an effective tool in retaining the quality and prolonging the shelf life of beef.

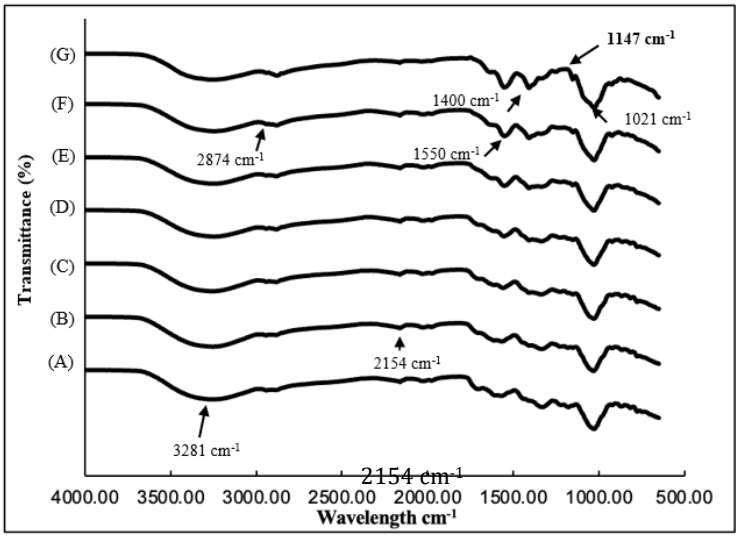


Figure 1. Spectra of CH-PPE edible films (A) 1.5%CH+0%PPE (B) 1.5%CH+1%PPE (C) 1.5%CH+2%PPE (D) 1.5%CH+3%PPE (E) 1.5%CH+4%PPE (F) 1.5%CH+5%PPE (G) 1.5%CH+6%PPE

Table 3. Antimicrobial activity of CH-PPE edible film

PPE (%) in Chitosan Film	Inhibition Zone (mm)	
	***Pseudomonas aeruginosa* (PA)**	***Staphylococcus aureus* (SA)**
0	6.07 ± 0.04^{a}	6.12 ± 0.06^{a}
1	10.28 ± 0.20^{b}	12.39 ± 0.10^{b}
2	10.38 ± 0.14^{b}	13.72 ± 0.27^{c}
3	10.56 ± 0.20^{b}	14.11 ± 0.10^{c}
4	11.56 ± 0.10^{c}	14.89 ± 0.20^{d}
5	12.06 ± 0.10^{cd}	15.11 ± 0.10^{d}
6	12.16 ± 0.17^{d}	15.33 ± 0.16^{d}

[a-e]Means ± standard deviations followed by different superscript letters within the same column indicate a significant difference between formulations ($p \leq 0.05$) according to Tukey's test.

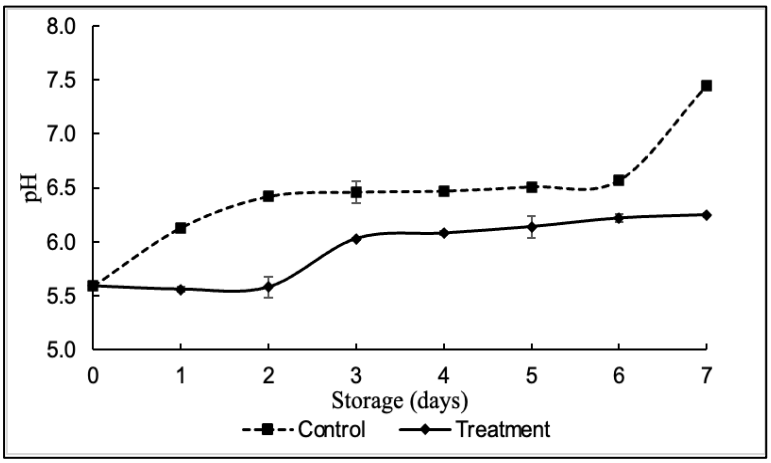


Figure 2. The change of pH throughout the 7 storage days at 4 °C

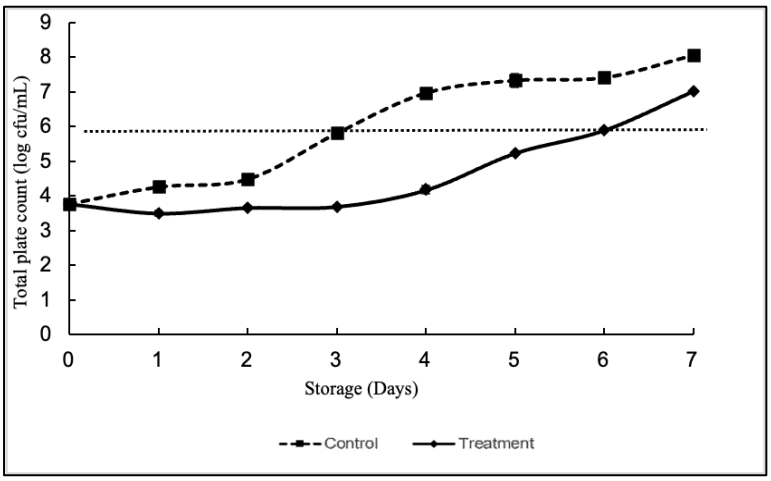


Figure 3. Total plate count of beef meat at both control and treatment samples during 7 storage days at 4 °C

Conclusion

The pomegranate peel extract and chitosan concentration had a significant impact on the edible film's physical, mechanical, chemical, and antimicrobial properties. The best combination of the pomegranate peel extract and chitosan in this study was 4.0% PPE and 1.5% chitosan. Increasing concentration of pomegranate peel extract enhance film's thickness, water solubility, and antimicrobial properties against *Pseudomonas aeruginosa* and *Staphylococcus aureus* while the addition of chitosan improved film's thickness and moisture content, but decrease film's water solubility. The CH-PPE edible film is an important tool for preserving the quality of beef and extending its shelf life. With the application of CH-PPE edible film, the TPC of beef meat was 4.17 log CFU/mL at day 4 where a 2.8 log reduction was achieved, and the shelf life of beef has been effectively extended from day 4 to day 7. The edible film with enhanced mechanical and antimicrobial properties had the potential to be developed for active food packaging applications. Furthermore, additional research should be conducted to investigate other applications to various meat products and microorganisms for the strength and effectiveness of chitosan-based edible film containing pomegranate peel extract.

Acknowledgement

This work was supported by UCSI University Pioneer Scientist Fund (Proj-In-FAS-056).

References

1. Ghaani, M. (2016). An overview of the intelligent packaging technologies in the food sector. *Trends in Food Science & Technology*, (51): 1-11.
2. Brunazzi, G., Parisi, S. and Pereno, A. (2014). The importance of packaging design for the chemistry of food products. *Springer Briefs in Molecular Science*: pp. 1-3.
3. Rizzolo, A. (2016). Volatile compound composition and antioxidant activity of cooked ham slices packed in propolis- based active packaging. *Food Packaging and Shelf Life*, 8(16): 41-49.
4. Maisanaba, S. (2016). A new advance in active packaging incorporated with essential oils or their main components for food preservation. *International Journal of Molecular Sciences,* 33(5): 447-515.
5. Ponce, A. G. (2008). Antimicrobial and antioxidant activities of edible coatings enriched with natural plant extracts: *In vitro* and *In vivo* studies. *Postharvest Biology and Technology,* 49(2): 294-300.
6. Sivarooban, T., Hettiarachchy, N. and Johnson, M. (2008). Physical and antimicrobial properties of grape seed extract, nisin, and EDTA incorporated soy protein edible films. *Food Research International,* 41(8): 781-785.
7. Alkan, D. and Yemenicioğlu. (2015). A potential application of natural phenolic antimicrobials and edible film technology against bacterial plant pathogens. *Food Hydrocolloids*, (55): 1-10.
8. Alexandre, E. (2016). Gelatin-based films reinforced with montmorillonite and activated with nanoemulsion of ginger essential oil for food packaging applications. *Food Packaging and Shelf Life,* 10 (10): 87-96.
9. Rinaudo, M. (2006). Chitin and chitosan: Properties and applications. *Progress in Polymer Science*, 31(7): 603-632.
10. Lee, Y. Y. and Phing, P. L. (2020). Development of milk protein edible films incorporated with *Lactobacillus rhamnosus* GG. *Bioresources,* 15: 6960-6973.
11. Matan, N. (2012). Antimicrobial activity of edible film incorporated with essential oils to preserve dried fish (*Decapterus maruadsi*). *International Food Research Journal,* 19(4): 1733-1738.
12. Choong, K. Y. (2019). Antibacterial properties of chitosan edible films incorporated with musk lime extract for the preservation of squids. *Malaysian Journal of Analytical Sciences*, 23(6): 914-925.
13. Jaiswal, V., Dermarderosian, A. and Porter, J. (2010). Anthocyanins and polyphenol oxidase from dried arils of pomegranate (*Punica Granatum* L.). *Food Chemistry*, 118(1): 11-16.

14. Masci, A. (2016). Evaluation of different extraction methods from pomegranate whole fruit or peels and the antioxidant and antiproliferative activity of the polyphenolic fraction. *Food Chemistry*, 202 (4):59-69.
15. Celiksoy, V. and Heard, C. (2021). Antimicrobial potential of pomegranate extracts. Access from https://www.intechopen.com/online-first/ antimicrobial-potential-of-pomegranate-extracts. [Access online 14 April 2021].
16. Dahham, S. S. (2010). Studies on antibacterial and antifungal activity of pomegranate (*Punica Granatum* L.). *American-Eurasion Journal Agriculture and Environmental Science*, 9(3): 273-281.
17. Reid, R. (2017). The microbiology of beef carcasses and primals during chilling and commercial storage. *Food Microbiology*, 61(9): 50-57.
18. Kerry, J. (2012). Advances in meat, poultry, and seafood packaging. *Woodhead Publishing, Cambridge*. 1-4.
19. Buncic, S. (2014). Microbial pathogen control in the beef chain: Recent research advances. *Meat Science*, 97(3): 288-297.
20. Radha K. K. (2014). Antimicrobial and antioxidant effects of spice extracts on the shelf life extension of raw chicken meat. *International Journal of Food Microbiology*, 171(14): 32-40.
21. Panichayupakaranant, P., Tewtrakul, S. and Yuenyongsawad, S. (2010). Antibacterial, anti-inflammatory, and anti-allergic activities of standardised pomegranate rind extract. *Food Chemistry,* 123(2): 400-403.
22. Al-zoreky, N. (2009). Antimicrobial activity of pomegranate (*Punica Granatum* L.) fruit peels. *International Journal of Food Microbiology*, 134(3): 244-248.
23. Remya, S. (2015). Effect of chitosan based active packaging film on the keeping quality of chilled stored barracuda fish. *Journal of Food Science and Technology*, 53(1): 685-693.
24. Chan, H. M. (2020). Investigation of properties of polysaccharide-based edible film incorporated with functional *Melastoma malabathricum* extract. *Carpathian Journal of Food Science & Technology*, 12(1): 120-133.
25. Ma, Q., Zhang, Y. and Zhong, Q. (2016). Physical and antimicrobial properties of chitosan films incorporated with lauric arginate, cinnamon oil, and ethylene diamine tetraacetate. *Food Science and Technology*, 65(6): 173-179.
26. Kuan, Y. (2020). Physicochemical properties of sodium alginate edible film incorporated with mulberry (*Morus australis*) leaf extract. *Pertanika Journal of Tropical Agricultural Science,* 43(3): 359-376.
27. Dick, M., Costa, T. M. H., Gomaa, A., Subirade, M., Rios, A. de O. and Flores, S. H. (2015). Edible film production from chia seed mucilage: Effect of glycerol concentration on its physicochemical and mechanical properties. *Materials Science and Engineering,* 33(4): 1819-1841.
28. Pranoto, Y., Rakshit, S. and Salokhe, V. (2005). Enhancing the antimicrobial activity of chitosan films by incorporating garlic oil, potassium sorbate and nisin. *Food Science and Technology*, 38(8): 859-865.
29. Fernandez-pan, I., Royo, M. and Ignacio Mate, J. (2012). Antimicrobial activity of whey protein isolate edible films with essential oils against food spoilers and foodborne pathogens. *Journal of Food Science*, 77(7): 383-390.
30. Remya, S. (2015). Effect of chitosan based active packaging film on the keeping quality of chilled stored barracuda fish. *Journal of Food Science and Technology*, 53(1): 685-693.
31. Emiroglu, Z. (2010). Antimicrobial activity of soy edible films incorporated with thyme and oregano essential oils on fresh ground beef patties. *Meat Science*, 86(2): 283-288.
32. Oussalah, M. (2004). Antimicrobial and antioxidant effects of milk protein-based film containing essential oils for the preservation of whole beef muscle. *Journal of Agricultural and Food Chemistry,* 52(18): 5598-5605.
33. Singh, T., Chatli, M. and Sahoo, J. (2014). Development of chitosan based edible films: process optimization using response surface methodology. *Journal of Food Science and Technology*, 52(5): 2530-2543.

34. Rubilar, J. (2013). Physico-mechanical properties of chitosan films with carvacrol and grape seed extract. *Journal of Food Engineering*, 115(4): 466-474.
35. Pereda, M. (2011). Chitosan-gelatin composites and bi-layer films with potential antimicrobial activity. *Food Hydrocolloids*, 25(7): 1372-1381.
36. Bourtoom, T. and Chinnan, M. S. (2008). Preparation and properties of rice starch-chitosan blend biodegradable film. F*ood Science and Technology*, 41(9): 1633-1641.
37. Laohakunjit, N. and Noomhorm, A. (2004). Effect of plasticizers on mechanical and barrier properties of rice starch film. *Starch Starke*, 56(8): 348-356.
38. Ojagh, S. (2010). Effect of chitosan coatings enriched with cinnamon oil on the quality of refrigerated rainbow trout. *Food Chemistry,* 120(1): 193-198.
39. Maizura, M. (2007). Antibacterial activity and mechanical properties of partially hydrolyzed sago starch/alginate edible film containing lemongrass oil. *Journal of Food Science,* 72(6): 324-330.
40. Zhang, P., Zhao, Y. and Shi, Q. (2016). Characterization of a novel edible film based on gum ghatti: Effect of plasticizer type and concentration. *Carbohydrate Polymers,* 153(3): 345-355.
41. Jurenka, J. (2008). Therapeutic applications of pomegranate (*Punica Granatum* L.): A review*: Alternative Medicine Review*, 13(2): 128-144.
42. Rivero, S., García, M. A. and Pinotti. (2010). A crosslinking capacity of tannic acid in plasticized chitosan films. *Carbohydrate Polymers*, 82(2): 270-276.
43. Zivanovic, S., Li, J., Davidson, P. and Kit. (2007). Physical, mechanical, and antibacterial properties of Chitosan/PEO blend films. *Biomacromolecules,* 8(5): 1505-1510.
44. Ashassi-sorkhabi, H. (2015). Pomegranate (*Punica Granatum*) peel extract as a green corrosion inhibitor for mild steel in hydrochloric acid solution. *International Journal of Corrosion,* 2015: 1-6.
45. Tee, Y. B. (2017). Chemical, physical, and barrier properties of edible film from flaxseed mucilage. *Bioresources*, 12(3): 6656-6664.
46. Huang, Y. (2014). Effect of carbon coating on cycle performance of lifepoc composite cathodes using tween80 as carbon source. *Electrochimica Acta*, 130(14): 740-747.
47. Ghosh, T. and Jasti, B. (2005). Theory and practice of contemporary pharmaceutics. *CRC Press Boca Raton:* pp. 68-69.
48. Liu, N. (2006). Effect of MW and concentration of chitosan on antibacterial activity of *Escherichia coli*. *Carbohydrate Polymers*, 64(1): 60-65.
49. Jung, E. (2010). Antibacterial activity of chitosan with different degrees of deacetylation and viscosities. *International Journal of Food Science & Technology*, 45(4): 676-682.
50. Kumar, M. N. R. (2000). A review of chitin and chitosan applications. *Reactive and Functional Polymer***s**, 46(1): 1-27.
51. Pagliarulo, C. (2016). Inhibitory effect of pomegranate (*Punica Granatum L.*) polyphenol extracts on the bacterial growth and survival of clinical isolates of pathogenic *Staphylococcus aureus* and *Escherichia coli*. *Food Chemistry*, 190(2): 824-831.
52. Bender, A. (1992). Meat and meat products in human nutrition in developing countries. *FAO Food and Nutrition Paper*; 53: 1-91.
53. Kenawi, M., Aghlul, M. and Abdel-salam, R. (2011). Effect of two natural antioxidants in combination with edible packaging on the stability of low-fat beef product stored under frozen condition. *Biotechnology in Animal Husbandry*, 27(3): 345-356.
54. Hayrapetyan, H., Hazeleger, W. and Beumer, R. (2012). Inhibition of *Listeria monocytogenes* by pomegranate *(Punica Granatum L.*) peel extract in meat pate at different temperatures. *Food Control*, 23(1): 66-72.

Malaysian Journal of Analytical Sciences Vol 25 No 4 2021

		Page
1.	A SHORT REVIEW ON THE SYNTHESIS OF AZAMACROCYCLIC LIGAND: CONVENTIONAL AND NON-TEMPLATE METHODS (Ulasan Pendek Sintesis Ligan Aza Makrosilik: Kaedah Konvensional dan Tanpa Templat) *Nur Halimatus Saadiah Abdullah, Lailatun Nazirah Ozair, Bohari Mohd Yamin*	547
2.	SYNTHESIS AND CHARACTERIZATION OF RUBBER SEED SHELL IMPREGNATED WITH CALCIUM OXIDE AS CATALYST FOR BIODIESEL PRODUCTION (Sintesis dan Pencirian Kulit Biji Getah dengan Resapan Kalsium Oksida Sebagai Bahan Pemangkin Untuk Penghasilan Biodiesel) *Nurul Farhanah Zakaria, Sarah Laila Mohd Jan, Siti Norhafiza Mohd Khazaai, Mohd Lokman Ibrahim, Mohd Hasbi Ab. Rahim, Gaanty Pragas Maniam*	561
3.	EXTRACTION OF POMEGRANATE PEEL AND GREEN TEA LEAVES AND THEIR EFFECTS ON THE MICROBIAL, PHYSICOCHEMICAL, MICROSTRUCTURAL AND SENSORIAL PROPERTIES OF CHILLED-STORED CHICKEN MEAT (Pengekstrakan Kulit Buah Delima dan Daun Teh Hijau dan Kesannya Terhadap Sifat-Sifat Mikroorganisma, Fizikokimia, Mikrostruktur dan Deria Rasa Daging Ayam yang Disimpan pada Suhu Sejuk) *Safiullah Jauhar, Mohammad Rashedi Ismail-Fitry, Gun Hean Chong, Mahmud Ab Rashid Nor-Khaizura, Wan Zunairah Wan Ibadullah*	569
4.	FORENSIC DISCRIMINATION OF BLUE PEN INKS: EMERGENCE OF HYBRID PEN INKS (Diskriminasi Forensik Bagi Dakwat Pen Biru: Kemunculan Dakwat Pen Hibrid) *Linthini Gannetion, Siti Nur Musliha Mohamad Noor, Poh Ying Lim, Kah Haw Chang, Ahmad Fahmi Lim Abdullah*	584
5.	PRODUCTION OF BIODIESEL FROM WASTE COOKING OIL USING POTASSIUM HYDROXIDE SUPPORTED ON ALUMINA CATALYST (Penghasilan Biodiesel daripada Minyak Masak Terpakai Menggunakan Kalium Hidroksida Disokong oleh Mangkin Alumina) *Shahida Hanum Kamarullah, Zainal Kifli Abdul Razak, Norshahidatul Akmar Mohd Shohaimi, Nailul Amal Zakariah*	596
6.	HARDNESS REMOVAL OF GROUNDWATER THROUGH SAND, ZEOLITE AND RICE HUSK ACTIVATED CARBON (Rawatan Air Bawah Tanah Menggunakan Pasir, Zeolit dan Karbon Reaktifdari Sekam Padi bagi Penyingkiran Keliatan Air) *Nor Izzah Abdul Aziz, Norzila Othman, Wahid Ali Hamood Altowayti, Zalilah Murni Yunus, Marlinda Malek, Nurina Fitriani, Muhammad Tahir, Firhat Muhammad Fikri*	605
7.	PHYSICOCHEMICAL PROPERTIES OF SAGO BARK BIOCHAR AND ITS POTENTIAL AS PLANT GROWTH MEDIA (Sifat Fizikokimia Bio-Arang Sisa Kulit Sagu dan Potensinya Sebagai Media Pertumbuhan Tanaman) *Nor Khairunnisa Mohamad Fathi, Sharifah Mona Abd Aziz Abdullah, Mohamad Fhaizal Mohamad Bukhori, Rafeah Wahi, Mohd Alhafiizh Zailani*	622

8.	CHEMICAL CONSTITUENTS OF THE MOSS *Calyptothecium ramosii* BROTH. (Juzuk Kimia bagi Lumut *Calyptothecium ramosii* Broth.) *Consolacion Y. Ragasa, Virgilio C. Linis, Chien-Chang Shen, Mary Stephanie Carranza, Maria Carmen Tan*	637
9.	COLOUR STRENGTH AND WASH FASTNESS OF SILK FABRIC DYED WITH METHANOLIC EXTRACTED RANGOON CREEPER USING INFRA-RED DYEING MACHINE (Kekuatan Warna dan Ketahanan Cucian Kain Sutera Diwarnakan dengan Akar Dani yang Diekstrak dengan Pelarut Metanol Menggunakan Mesin Pencelup Infra-Merah) *Suhaidi Ariffin, Wan Syazehan Ruznan, Muhammad Nurkhairunizam Yazid, Suraya Ahmad Suhaimi, Mu'adz Ahmad Mazian, Muhammad Mu'az Mustamam*	642
10.	OPTIMIZATION OF EXTRACTION TEMPERATURE AND TIME ON PHENOLIC COMPOUNDS AND ANTIOXIDANT ACTIVITY OF MALAYSIAN PROPOLIS *Trigona Spp.* AQUEOUS EXTRACT USING RESPONSE SURFACE METHODOLOGY (Pengoptimuman Suhu dan Masa Pengekstrakan pada Sebatian Fenolik dan Aktivikiti Antioksidan daripada Ekstrak Akues Propolis Kelulut (*Trigona Spp.*) Malaysia menggunakan Kaedah Gerak Balas Permukaan) *Abdullah Hagar, Nurlisa Fatihah Abd Rani, Muhammad Ibrahim, Norazsida Ramli,Idris Adewale Ahmed, Abbe Maleyki Mhd Jalil, Mohd Nur Nashriq Anuar*	649
11.	CHEMICAL COMPOSITION OF KASTURI TOBACCO RESINOID DETERMINED BY GAS CHROMATOGRAPHY-MASS SPECTROMETRY (Komposisi Sebatian Kimia Resinoid Tembakau Kasturi Menggunakan Kromatografi Gas-Spektrometri Jisim) *Larissa Tania, Ari Satia Nugraha, Tri Handoyo, Banun Kusumawardani*	661
12.	SYNTHESIS AND CHARACTERIZATION OF ACETOL FROM PALM-BASED GLYCEROL (Sintesis dan Pencirian Asetol daripada Gliserol Berasaskan Sawit) *Roila Awang and Mohamad Hanif Mohamed*	669
13.	PHYTOCHEMICAL INSIGHTS ON PALM OILS AND EXTRA VIRGIN OLIVE OIL (Tinjauan Fitokimia Minyak Sawit dan Pati Minyak Zaitun) *Noor Idayu Tahir, Nurul Liyana Rozali, Nadirah Zakaria, Abrizah Othman, Umi Salamah Ramli*	678
14.	EFFECT OF DRYING TIMES AND TEMPERATURES ON THE QUALITY OF TRADITIONAL SPICY SAUCE CUBE (Kesan Masa dan Suhu Pengeringan Terhadap Kualiti Kiub Sambal Tradisional) *Nur Huda Mohd Masseri, Norhayati Muhammad, Nur Fazira Abdul Rahim*	695

Malaysian Journal of Analytical Sciences (MJAS)
Published by Malaysian Analytical Sciences Society

A SHORT REVIEW ON THE SYNTHESIS OF AZAMACROCYCLIC LIGAND: CONVENTIONAL AND NON-TEMPLATE METHODS

(Ulasan Pendek Sintesis Ligan Aza Makrosilik: Kaedah Konvensional dan Tanpa Templat)

Nur Halimatus Saadiah Abdullah[1], Lailatun Nazirah Ozair[1]*, Bohari Mohd Yamin[2]

[1]Faculty of Science and Technology,
Universiti Sains Islam Malaysia, 71800 Bandar Baru Nilai, Negeri Sembilan, Malaysia
[2]Faculty of Science and Technology
Universiti Kebangsaan Malaysia, 43600 UKM Bangi, Selangor, Malaysia

**Corresponding author: lailatunnazirah@usim.edu.my*

Received: 21 June 2021; Accepted: 26 July 2021; Published: 29 August 2021

Abstract

Various methods have been developed for the synthesis of azamacrocyclic ligands and their derivatives, which varies from the selection of amino group, ionic compound, and solvent. Among the popular methods include the rigid group method, high dilution method, and the template metal effect method. Recently, researchers have considered the non-template method as a promising and effective approach to produce a higher yield of metal-free azamacrocyclic ligands compared to the conventional approaches. Hence, this review presented an overview of the synthesis and structure of azamacrocyclic compounds through conventional methods and the newly developed non-template method. The advantages and disadvantages related to each technique were also highlighted.

Keywords: azamacrocyclic ligand, non-template method, cyclisation, metal ion

Abstrak

Pelbagai kaedah dikembangkan untuk sintesis ligan aza makrosilik dan terbitannya yang berbeza daripada pemilihan kumpulan amino, sebatian ion dan pelarut. Antara pelbagai kaedah yang terkenal termasuklah kaedah kumpulan tegar, kaedah percairan tinggi, dan kaedah kesan templat logam. Baru-baru ini, penyelidik telah mengenal pasti kaedah tanpa templat sebagai pendekatan berkesan untuk menghasilkan ligan aza makrosilik yang bebas logam dengan hasil yang tinggi, berbanding dengan kaedah konvensional. Oleh itu, ulasan ini membincangkan sintesis dan struktur sebatian aza makrosilik dengan kaedah konvensional dan tanpa templat. Di samping itu, kelebihan dan kekurangan setiap teknik juga dibincangkan untuk penambahbaikan pada masa hadapan.

Kata kunci: ligan aza makrosilik, kaedah tanpa templat, perkitaran, logam ion

Introduction

A macrocyclic ligand is defined as a cyclic compound with a minimum of nine heteroatoms and consists of three or more potential donor atoms for ligating. To date, donor atoms found in macrocycles include nitrogen, oxygen, and sulphur. Since its discovery by Busch and

Curtis in the 1960s [1], studies on macrocyclic ligand has undergone tremendous development and progress in various field of application. The pioneering work has also been adopted in the synthesis of oxygen-based ligand for biological processes by Pedersen where cyclic polyether showed good interaction towards alkali and alkaline earth metal ions [2].

Macrocyclic ligands are classified based on their donor types (Figure 1) and chemical structures (Figure 2). The aza crowns class is the most diverse and studied macrocyclic compound compared to the crown ethers and thiacrowns [3]. This is because nitrogen is available naturally in many common groups, including pyridine, porphyrins, ammonium, thiourea, amino, and others, which forms the basic structure of azamacrocyclic ligands [4-10]. Moreover, ligand containing nitrogen atoms has a high possibility to interact and form a coordination bond with transition metal ion to produce complex compounds [11].

The utilisation of azamacrocyclic ligand has been studied by chemists thoroughly by focusing on its complexation towards a variety of metal ions [12]. In addition, they have been applied in various fields, such as biomimetics, the removal of heavy metal in waste treatment, as a contrasting agent in medical imaging, and also as an anti-cancer agent [13-15].

Realising the significance of azamacrocyclic ligand, various methods were proposed for the synthesis of macrocyclic compounds. The most crucial and difficult step in the synthesis of azamacrocyclic ligand is the assemblymen of the macrocyclic compound. As the research field expands, continuous efforts and progress have led to the establishment of simpler and cheaper methods with higher yield. Currently, there are three established methods for the synthesis of azamacrocyclic ligand [16]. The first approach, known as the rigid group method, restricts the rotation of the open-chain precursors [17]. Secondly, the high dilution method is performed under high temperature and inert atmosphere [18]. The third method is the selective metal template effect method, which introduces transition metal ions to promote the formation of macrocyclic compounds [19].

The non-template method is a newly introduced method to synthesis macrocyclic compounds in the absence of metal ions during cyclisation. Recently, Borisova et al. stated that the suitable selection of reaction conditions such as solvent, concentration, and temperature in the non-template method plays a vital role in obtaining the target product with various structures at a considerable yield [33]. Therefore, this study aimed to analyse and discuss the process and speciality of the non-template method for the synthesis of azamacrocyclic ligand compared to the conventional approaches. The fundamental understanding of the macrocyclisation process is important towards the synthesis of a diverse range of ligands as artificial cationic, anionic, and neutral guest receptors.

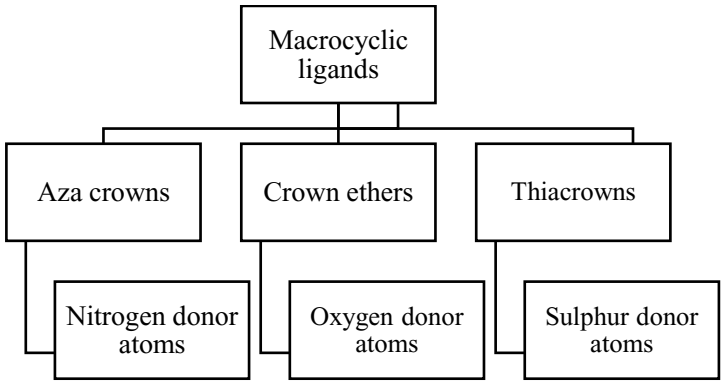


Figure 1. Classification of predominantly macrocyclic ligands

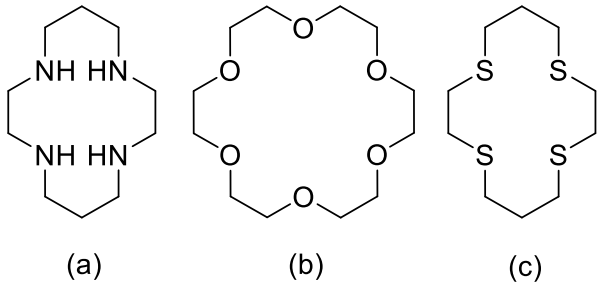


Figure 2. Chemical structures of a) azacrowns b) crown ethers c) thiacrowns

Rigid Group Method

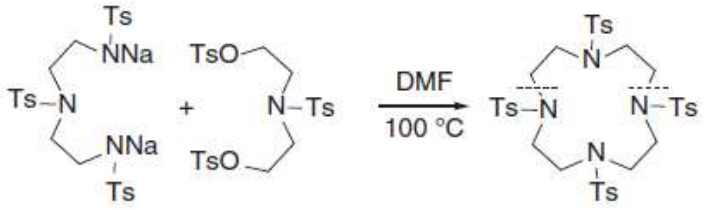
The Richman-Atkins reaction is reaction of dimetal salts of sulphonamide with a terminal dihalide in preparation of polyamines with a yield of up to 90% [20]. The cyclisation process is performed in a low dilution medium through the condensation of a tosylamide and tosylated alcohol in dimethyl formamide (DMF) (Scheme 1). Each precursor compound has two reactive functional groups at the end. The use of the tosyl group is more complicated because it requires the preparation of arduous reagents with a limited scope of substrates [21].

The rigid group method is used of condensation catalysts such as dicyclohexylcarbodiimide (DCC) and 4-(dimethylamino) pyridine (DMAP) for the condensation of primary amines. Previously, this technique was applied using different rigid groups, including DCC and DMAP in Richman-Atkins reaction. The study reported the successful synthesis of 14-22-membered tetraoxomacrocyclic tetramines with 50% yield from dicarboxylic acids and primary diamines [22]. The presence of rigid groups serves as a good condensing agent to reduce the number of conformational degree of freedom by preventing bond rotation. Hence, minimising the condensation pathway allows the formation of macrocyclic compounds. This method is still widely used but only limited to the synthesis of macrocyclic polyamines and alkyl halides because sometimes difficult to obtain the desired pure product [23].

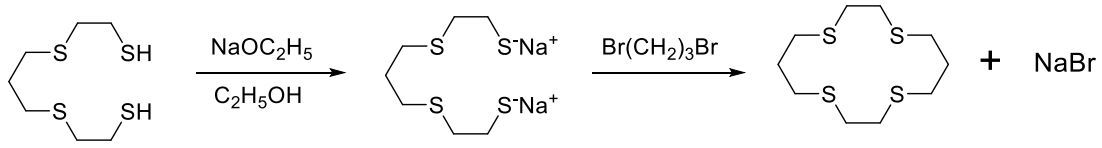
High Dilution Technique

The rate of formation of linear polymers is higher in a concentrated solution due to the presence of many active sites and frequent contacts between polymers and reagents. Therefore, diluting the solution to achieve an exceedingly low concentration of the reacting reagents subsequently reduces the rate of contact between polymers and additional reagent. This process, known as the high dilution technique, enhances intramolecular reactions and increases the possibility of the formation of macrocyclic ligands.

Rosen and Busch first reported the synthesis of 14-thiacrown-4 (14aneS_4) with a very low yield of 7.5% as a result of the competitive formation of polymeric compounds [24]. However, when Travis applied the high dilution technique, the yield recorded an increase up to 50% as more sulphur donor atoms were available in the reaction, as shown in Scheme 2 [25]. This remarkable discovery demonstrated that the production of the macrocyclic ligand was improved with the increasing dilution of the solution. However, certain drawbacks of the method remain a concern, particularly the long reaction time and the ability to synthesis many ring system [46]. For example, many-membered ring ketones should be synthesized on different reaction paths such as the dinitrile reaction and acyloin condensation [46].



Scheme 1. The Richman-Atkins reaction [20]



Scheme 2. High dilution method for the synthesis of 14-thiacrown-4 [25]

Metal Template Effect Method

The term template is broadly used in coordination chemistry to indicate a substance that acts as a mould to amplify the chemical reaction. The transition metal templates are commonly used as a guide for the cyclisation process and are a powerful tool in inorganic chemistry [26]. In this method, the synthetic route of macrocyclic ligands involves the use of a metal ion template to orient the reacting groups of ligands in the desired conformation for optimum ring closure. The favourable enthalpy for the formation of the metal-ligand bonds dominated over the unfavourable entropy from the ordering of the multidentate ligand around the metal ion, thereby enhancing the cyclisation reaction [27]. Hence, the synthesis of macrocyclic compounds through the template effect method is contributed by the combination of pre-ligand and metal ions, as illustrated in Scheme 3 [28]. The macrocyclic product is electrophilically alkylated with 1,2-bis(bromomethyl) benzene, while [Ni(L4)] acts as the template.

In terms of template synthesis, the macrocyclic complex can be useful to remove or replace the templated metal with different transition metal ions. The metal complex can be demetallated using specific reagents for the release of metal-free macrocyclic ligand [30]. For example, a hydrated hexaaza macrocyclic ligand was prepared through the demetallation of nickel [Ni(II)] complex of 6,6'-dihydrazino-2,2'-bipyridil using sodium cyanide in methanol to provide a free macrocyclic ligand, as presented in Scheme 4 [29].

However, the template cyclisation technique lacks the consistency to isolate azamacrocycles. The major drawback of the technique is contributed by the demetallation process in which the macrocycles become unstable in the uncoordinated state or the complex formation is too strong for the decomplexation process [31]. The high stability of the metal-ligand coordination and macrocyclic effect maintains the metal complex from releasing the free ligand. Thus, the direct synthesis or non-template method offers the best approach to overcome this problem.

Non-Template Method

In contrast to the metal template reaction, the ligand is synthesised first in the direct or non-template method, followed by the combination with a transition metal to form the complex compound. In 1971, Holm reported the first straightforward non-template synthesis of a basic macrocyclic 14-membered tetraaza ring system [32]. The moderate yield of 50% crystalline product from reaction of carbonyl-containing group and ketone group inspired other researchers to further explore this technique.

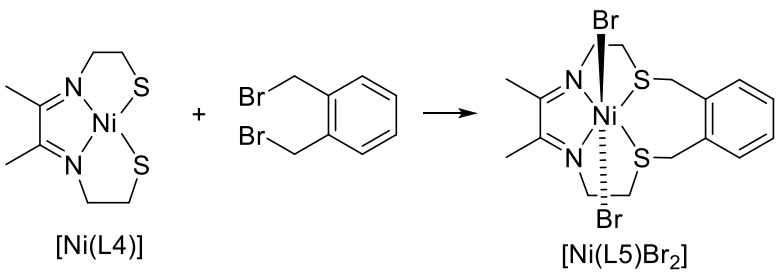
In 1980, Owston and co-workers proposed the preparation of a metal-free tetraaza macrocycle under various condensation conditions [34]. The selected solvents allowed the free ligands to separate from the solution and structure formation based on the stability of the imine bond during the cyclisation process. However, the reaction of dialdehyde group with 1,2-diaminoethane, 1,2-diaminobenzene, and 1,3-diaminopropane produced different arrangements of linear products instead of macrocyclic di-imines. This due to the absence of aniline-hydrogen in the reactant that affecting the stabilization of the imine bond by hydrogen-bonding.

Swamy et al. carried out further studies by reacting to different groups of amines with diacid chlorides and diesters in the presence of anhydrous sodium carbonate during the isolation of pure macrocycles [35]. The results obtained revealed the formation of 14-, 15-, or 16-membered rings with four amide nitrogen atoms in Figure 3 (left). In addition, the diamines-diamides also reacted with alkyl dichlorides to form two amide and two secondary amine nitrogen atoms in the ring in Figure 3 (right). The success of the cyclisation process indicates that the lone pair repulsions were reduced in the presence of at least two secondary amine hydrogen atoms, as shown in Figure 3 (right).

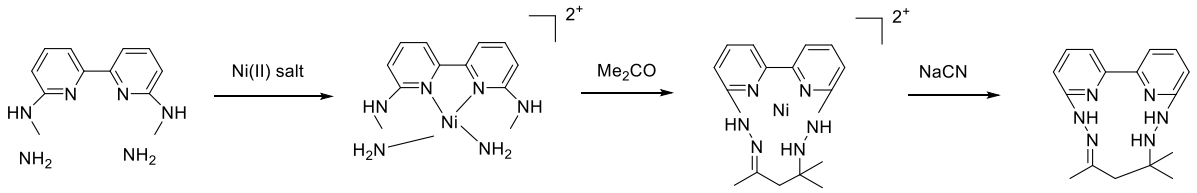
Alternative steps for the synthesis of novel tetraaza macrocyclic ligand were proposed by Swamy et al. through the non-template condensation reaction between ethylenediamine and ethyl acetoacetate, as in Scheme 5 [35]. The formation of crystalline ligand at an approximate yield of 75% was contributed by the effective coordination of amide nitrogen with metal chlorides from the *d*-block elements, including ruthenium [Ru(III)], platinum [Pt(II)], and palladium [Pd(II)] metal ions. These interactions were demonstrated through the presence of peaks of medium bands in the Infra-Red (IR) spectra around the region of 450–470 cm^{-1}, which were assigned to the metal-nitrogen vibrations.

Besides, Ni(II) complex was synthesised using the same non-template condensation technique in the presence of acetic acid [11]. Tetraaza cyclotetradeca ligand was obtained from the reaction of diaminoethane in ethanol with ethyl acetoacetate, resulting in a high yield of 75% crystalline product. Moreover, the presence of nitrogen with lone pairs in macrocyclic makes it a versatile coordinating agent with a high possibility to form stable complexes with transition metals. Hence, Ni(II) ion was able to fit in the centre of the ring while attached to the $(CH_3COO)_2$ groups in an octahedral configuration.

In addition, a tetraaza macrocyclic nitrogen donor ligand, $C_{24}H_{28}N_4$ was prepared by Chandra et al. [3] through a simple two-step synthesis. Firstly, the 2,3-hexanedione reacts with *m*-phenylenediamine in the presence of hydrochloric acid (HCl) to develop a macrocyclic moiety. This is followed by the complexation of Co(II), Cu(II), and Ni(II) complexes for antibacterial and antifungal screening activity. The study also used different types of counter anion, X = chloride (Cl^-), nitrate (NO^{3-}), and isothiocyanate(NCS^-), resulting in the formation of different geometry due to the metal-ligand interaction. The magnetic moment values corresponded to the high spin configuration, indicating the tetrahedral square pyramidal with anions occupied the axial positions and octahedral geometry of complexes (Figure 4).



Scheme 3. The preparation of $[Ni(L5)Br_2]$ through kinetic coordination template effect [28]



Scheme 4. Demetallation of Ni(II) to obtain metal-free macrocyclic ligand [29]

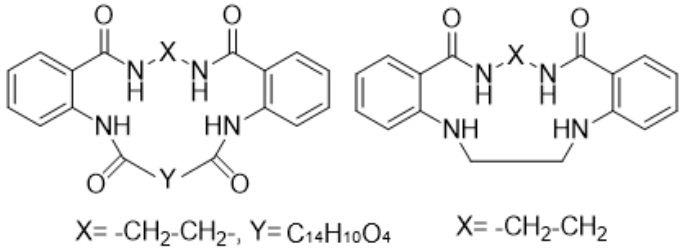
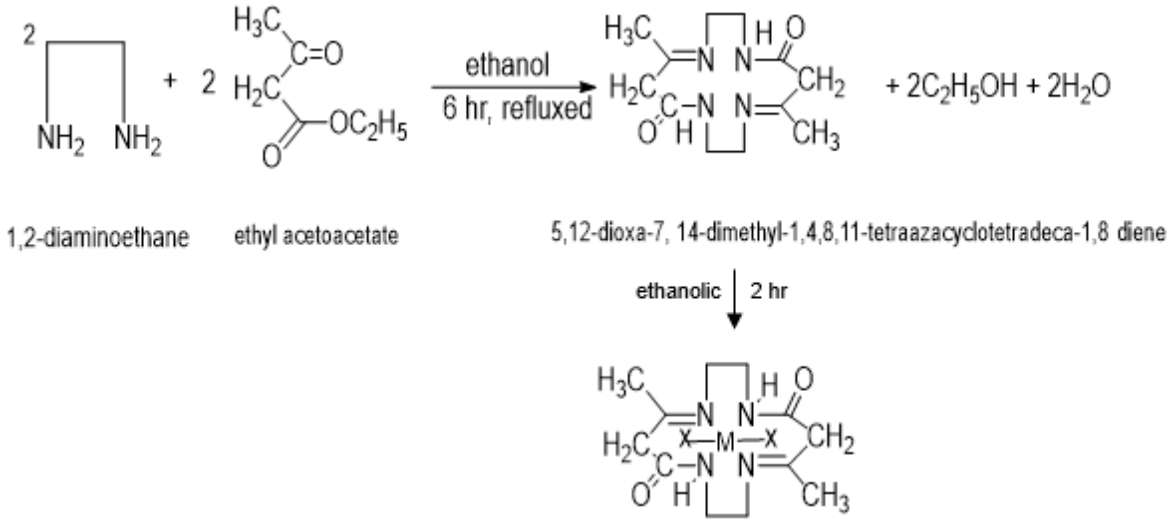


Figure 3. 14-, 15-, or 16-membered rings with four amide nitrogen atoms (left) with two amide and two secondary amine nitrogen atoms in the ring (right) [35]



Scheme 5. Synthesis of tetraaza macrocyclic ligand and its complexes where M= Ru(III), Pt(II) and Pd(II) and X= Cl^- [35]

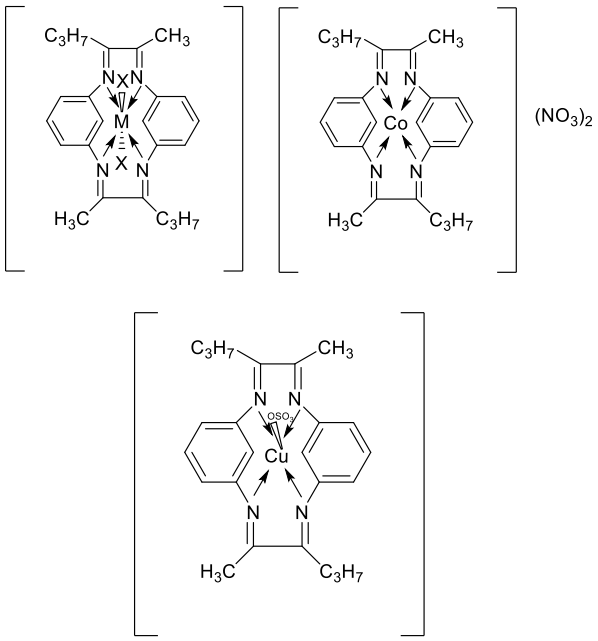


Figure 4. Structures of the tetradentate macrocyclic nitrogen donor ligand complexes where M = Co(II), Ni(II), and Cu(II) and X = Cl^-, NO_3^-, and NCS^- [3]

The successful development in the previous research [3] has facilitated other studies to investigate different diamines groups for the synthesis of tetraaza macrocyclic ligands. Recently, a hot ethanolic solution of benzyl was mixed with 2,6-diaminopyridine, *o*-phenylenediamine, and ethylenediamine, respectively [45]. An IR band corresponding to C=N at a range of 1650–1660 cm^{-1} in the ligands, which was referred to as the azomethine linkage, was observed to shift to the lower band due to the complex formation [30]. The ligands provided the binding sites towards the Pd(II) and Pt(II) metal ions through four nitrogen atoms of the azomethine groups. The structure of the complexes was diamagnetic and exhibited a square-planar geometry of *N,N,N,N*-pattern.

In another study, the reaction between *o*-phenylenediamine and benzoylacetone in ethanolic solution led to the formation of tetraazacyclotetradecine [36]. The Hydrogen-1 Nuclear Magnetic Resonance (^{1}H-NMR) spectrum confirmed the existence of imine methyl and methylene protons of benzoyl acetone ranging at 2.20–2.64 ppm, suggested the free ligand is formed. The antifungal screening action was evaluated by performing complexation with Co(II), Ni(II), and Cu(II) metal ions attached to four nitrogen donor. Co and Cu atoms were formulated as $[M(L)Cl_2]$, while Ni atoms were formulated as $[M'(L)]Cl_2$ due to their non-electrolytic and electrolytic nature, respectively. Based on the spectral studies, each metal complex displayed different coordination, as depicted in Figure 5. The Co(II) complex exhibited octahedral geometry with chlorine atoms at the axial position, whereas Ni(II) and Cu(II) complexes were arranged in a square-planar and tetragonal geometry, respectively.

The type and ring size of macrocyclic ligands are very useful in the application of biological process, which is termed as the metalloenzymes. Previously in 2010, Patil and Akkasali reported the non-template synthesis of tetraaza macrocyclic compound with variable ring sizes and higher yield [37]. The starting materials were prepared by reacting diketone with ethylenediamine, *o*-phenylenediamine, and diaminopropane. As a result of the ring closure reaction, 14- and 16-membered nitrogen groups of tetraaza macrocycles were successfully

isolated. All the free ligands exhibited moderate biological activity, thus, signifying the stability and effectiveness of this method.

Furthermore, Sen et al. synthesised a novel tetraaza macrocyclic ligand ranging from 14 to 15 rings [38]. The study involved the reaction of diethyl malonate with three different amino groups comprising 1,2-Bis{(2-aminobenzoyl)amino}propane, 2-amino-N-[3-(2-aminobenzoilamino)propil] benzamide, and 1,4-Bis{(2-aminobenzoil)amino}butane. The results were in agreement with Swamy et al. where three ligands with particular macrocyclic members were obtained through the non-template condensation reaction [35]. The reaction between various amino groups is summarized in Table 1.

Recently, the metal complexes comprising Mn(II), Co(II), Ni(II), Cu(II), and Zn(II) were reported to exhibit as ionic compounds in the presence of chloride ions [39]. The tetraaza macrocyclic ligands were synthesised from *N,N'*-bis(2-aminoethyl)hexanediamide, which served as the starting material that originated from the reaction between adipic acid and ethylenediamine, followed by diethyloxalate and diethylmalonate, respectively (Scheme 6). This new approach was focused on antimicrobial activity against various microorganisms. The results showed that all metal complexes displayed efficient functionality compared to their parent ligands under the same experimental conditions due to the polarity of the metal ion.

According to Scheme 7, the cyclocondensation of ethylenediamine with acetone produced isomeric macrocyclic compounds [40]. The isomeric macrocycles were formed when ethylenediamine reacted with methyl ethyl ketone, which was 2a and 2b. Further reactions of 1a and 1b with monoperchlorate salt of ethylenediamine and acetone produced the stable free ligand in addition to the perchlorate salt. Further studies were performed based on the insights of this study, which involved the synthesis of an 18- and 22-membered azamacrocyclic compound containing two azomethine and amine nitrogen atoms in the ring. The ability of α,ω-diamine to develop azamacrocyclic mixture depended on the length of the carbon chain since the 16-membered compound only recorded a low yield of 25% [41]. In contrast, the reaction of 1,3-diaminopropane with acetone achieved a 100% yield.

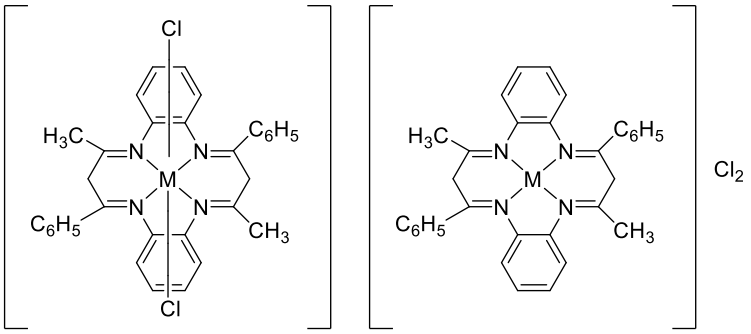
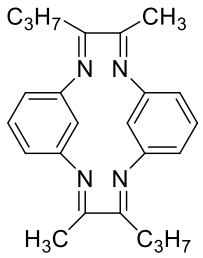
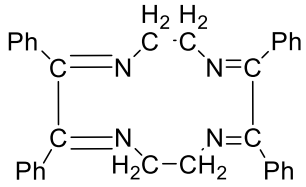
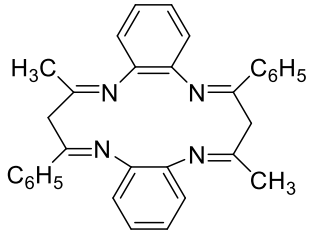
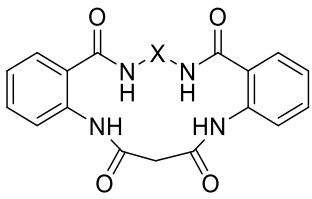
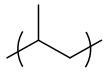
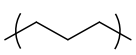
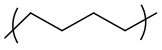
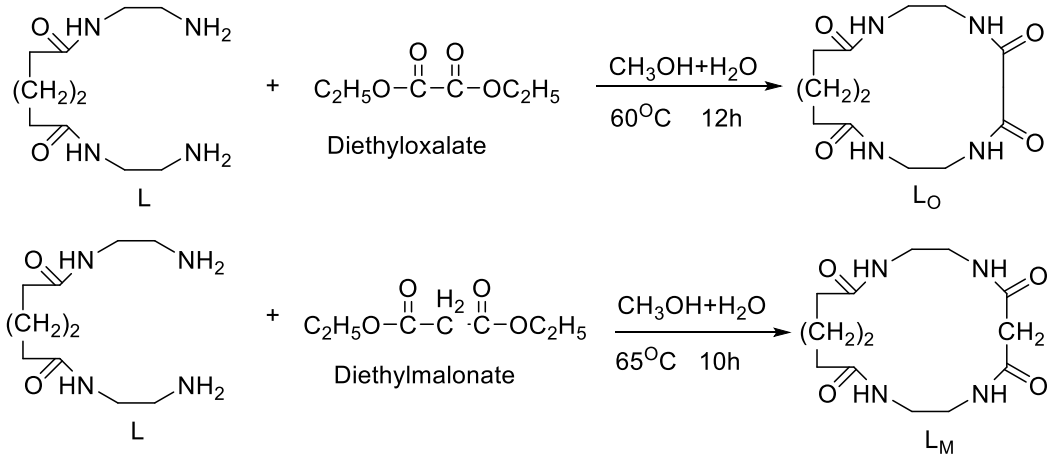


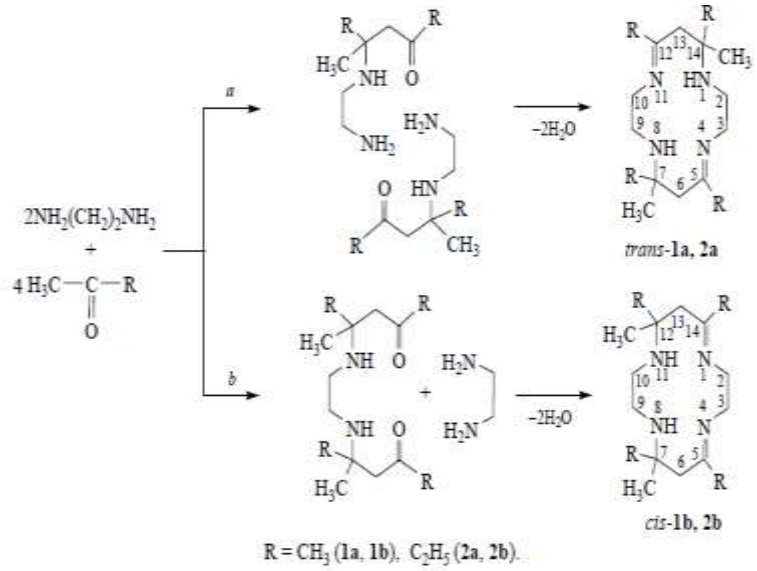
Figure 5. Proposed structures of the metal complexes, where M = Co(II), Cu(II) and M' = Ni(II) [36]

Table 1. Structural compounds of tetraaza macrocyclic ligand by non-template synthesis

Structural Compounds	Experiment Condition	Wavenumber (cm^{-1})	References
	Hot ethanolic solution of 2,3-hexanedione and hot ethanolic solution of *m*-phenylenediamine were mixed at 75°C for 9 hr in the presence of few drops of concentrated hydrochloric acid (pH~3)	1618 730-768 1441-1590	[3]
	Hot ethanolic solution of benzil and hot ethanolic solution of ethylene diamine were mixed at 75 °C for 8 hr in the presence of few drops of concentrated hydrochloric acid (pH~3)	1650-1660	[45]
	Hot ethanolic solution of benzoylacetone and hot ethanolic solution of *o*-phenylenediamine were mixed at 85 °C for 15 hr in the presence of few drops of concentrated hydrochloric acid (pH~3)	1594 1566	[36]
 -X- =  -X- =  -X- = 	Diethyl malonate in methanol was mixed with three different amino groups: 1,2-Bis{(2-aminobenzoyl)amino}propane,2-amino-N-[3-(2-aminobenzoilamino)propil] benzamide, 1,4-Bis{(2-aminobenzoil)amino}butane respectively at 60-70 °C for 4-5 hr	3468-3480 3292-3053 1603-1626 1532-1579 1433-1489	[38]



Scheme 6. The final step of synthesis of macrocyclic ligands [39]



Scheme 7. *Trans*- and *cis*-isomers of tetraaza macrocycles [40]

Furthermore, the condensation between 1,4-diaminobutane and 1,6-diaminohaxane with acetone obtained a 75-85% yield of *trans*-azamacrocyclic compound [41]. In comparison with the cyclocondensation process, the outcome of the experiment was similar in the reaction of α, ω-diamine using acetone or hydrated/dehydrated alcohol and ketone. Nonetheless, an exothermic effect was detected when anhydrous alcohol and ketone reacted with the α, ω-diamine.

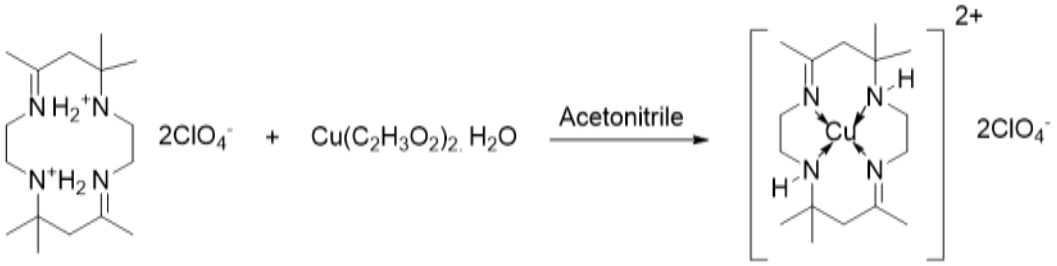
A preliminary study conducted by Yamin et al. [42] showed that tetraaza macrocyclic ligands were successfully synthesised via the non-template method at a higher yield. Scheme 8 shows the path of synthesis of the Cu(II) complex from its macrocyclic ligand. The technique to produce the tetraaza ligand and non-template complexation was considered a novel approach through the application of ammonium perchlorate that reacts with ethylenediamine to produce a free ionic tetraaza ligand and ClO_4^- counter anion. In addition, the

utilisation of this new method for the synthesis of ligand demonstrated a potentially simple and cheap alternative pathway for large scale production of macrocyclic ligand since the yield was recorded at 78%.

Based on the results from the magnetic moment, electronic spectral studies, and X-ray crystallography, the Cu(II) complex exhibited a square-planar geometry. However, when the same method was applied in the ionic liquid [Bmim] [PF_6], which is a different solvent, the complex displayed a different structural agreement where the Cu(II) complex exhibited an octahedral geometry bonded to two ethylenediamine ligands and two oxygen from the perchlorate ion with 79% yield [43]. These phenomena were strongly associated with the interaction or mechanism between metal/ligands during the synthesis reaction.

The discovery of new and simple method of preparation of 5,5,7,12,12,14-hexamethyl-1,4,8,11-tetraazacyclo tetradeca-7,14-dienium salts ligand has enabled the detailed study on the complexation reaction with various transition metal ions such as copper, nickel, and zinc complexes were carried out [44]. The analytical and physical data showed that up to 88% yield of the complexes were generated. In addition, the ultraviolet (UV)-visible spectrometric analysis indicated the existence of the azomethine chromophore and the *d-d* transition intensely indicate that the metal complex was successfully maintained in its original tetraaza ligand structure. The biological activity studies of the complexes were also reported.

The emerging non-template method using the various reaction of amino groups under several conditions shows significant results where free neutral and ionic ligands with their complexes are successfully synthesized. The presence of at least two secondary amine hydrogen atoms help to alleviate the lone pair repulsion on nitrogen donor atoms during cyclisation process. Apart from that, the cyclisation process of the tetraaza macrocyclic ligand has advantages which are inexpensive starting materials, high overall yield and desired product can be obtained easily since not involving difficult process of removing nitrogen-protecting groups [35].



Scheme 8. Synthetic route of Cu(II) complex from metal-free tetraaza ligand [42]

Conclusion

Several modifications and improvements have been conducted to prepare and provide an efficient mechanism for the synthesis of tetraaza macrocyclic ligand and its complexes. Based on the brief comparison of conventional method synthesis and the elaborative discussion on the new direct technique for the preparation of free tetraaza macrocyclic ligand, this paper highlighted the non-template method as the efficient method for the production of tetraaza macrocyclic ligands in the absence of metal ions during cyclisation with significantly high yield. In addition, the response between amide nitrogen atoms and alcohol functional group with the solvent provided a guideline for various ring size and ligand/complex nature. Given the limited studies of complexation reaction in the non-template method, future studies should focus on investigating the effect of various metal salts in the

complexation reaction at different conditions for a potential application such as catalyst in industrial activity and biomedical application.

Acknowledgement

This research was funded by the Ministry of Higher Education of Malaysia through the Fundamental Research Grant Scheme (USIM/FRGS/FST/ 055002/53419).

References

1. Curtis, N. F. (1968). Macrocyclic coordination compounds formed by condensation of metal-amine complexes with aliphatic carbonyl compounds. *Coordination Chemistry Reviews*, 3(1): 3-47.
2. Pedersen, C. J. (1967). Cyclic polythers and their complexes with metals salts. *Journal of the American Chemical Society*, 89(I): 2495-2496.
3. Chandra, S. and Gupta, L. K. (2005). Spectroscopic studies on Co(II), Ni(II) and Cu(II) complexes with a new macrocyclic ligand: 2,9-dipropyl-3,10-dimethyl-1,4,8,11-tetraaza-5,7:12,14-dibenzocyclotetradeca-1, 3,8,10-tetraene. *Spectrochimica Acta - Part A: Molecular and Biomolecular Spectroscopy*, 61(6): 1181-1188.
4. Tseberlidis, G., Demonti, L., Pirovano, V., Scavini, M., Cappelli, S., Rizzato, S. and Caselli, A. (2019). Controlling selectivity in alkene oxidation: anion driven epoxidation or dihydroxylation catalysed by [iron(iii)(pyridine-containing ligand)] complexes. *ChemCatChem*, 11(19): 4907-4915.
5. Chizhova, N. V., Ivanova, Y. B., Rusanov, A. I., Khrushkova, Y. V. and Mamardashvili, N. Z. (2019). Synthesis and spectral and fluorescent properties of metal complexes of octakis(4-flurophenyl)tetraazaporphyrins. *Russian Journal of Organic Chemistry*, 55(5): 655-661.
6. Yamazaki, S. Ichi, Asahi, M., Taguchi, N. and Ioroi, T. (2019). Electrochemical analysis of the porphyrazine-induced enhancement of orr activity of pt catalysts for the development of porphyrazine-adsorbed Pt catalysts. *Journal of Electroanalytical Chemistry*, 848(113321): 3-10.
7. Tahir, M. N., Abdulhamied, E., Nyayachavadi, A., Selivanova, M., Eichhorn, S. H. and Rondeau-Gagné, S. (2019). Topochemical polymerization of a nematic tetraazaporphyrin derivative to generate soluble polydiacetylene nanowires. *Langmuir*, 35(47):15158-15167.
8. Boudebouz, I., Arrous, S., Plotnikov, E., Voronova, O. and Bakibaev, A. (2019). Synthesis and antioxidant activity of some new thioglycoluril derivatives. *Journal of Sulfur Chemistry*, 40(4): 389-399.
9. Khabibullina, G. R., Zaynullina, F. T., Tyumkina, T. V., Yanybin, V. M. and Ibragimov, A. G. (2019). Catalytic aminomethylation of α,ω-diacetylenes with secondary diamines and aldehydes as an efficient approach to diaza alkatetraynes and tetraaza tetraacetylenic macrocycles. *Russian Chemical Bulletin*, 68(7): 1407-1413.
10. Chen, J., Zhang, T., Liu, X. and Shen, L. (2019). Enantioselective synthesis of (S)-Γ-amino alcohols by Ru/Rh/Ir catalyzed asymmetric transfer hydrogenation (ATH) with tunable chiral tetraaza ligands in water. *Catalysis Letters*, 149(2): 601-609.
11. Panchbhai, M. A. and Bhave, N. S. (2009). Novel Ni (II) tetraaza macrocyclic complex: Synthesis and characterization. *International Journal of Chemical Sciences*, 7(2): 997-1003.
12. Savastano, M., Arranz-Mascarós, P., Bazzicalupi, C., Clares, M. P., Godino-Salido, M. L., Guijarro, L. and López-Garzón, R. (2017). Polyfunctional tetraaza-macrocyclic ligands: Zn(II), Cu(II) binding and formation of hybrid materials with multiwalled carbon nanotubes. *ACS Omega*, 2(7): 3868-3877.
13. El-boraey, H. A., El-Salamony, M.E. and Hathout, A. A. (2016). Macrocyclic [N5] transition metal complexes: Synthesis, characterization and biological activities. *Journal of Inclusion Phenomena and Macrocyclic Chemistry*, 86: 153-166.
14. Ramadan, A. E. M. M., Shaban, S. Y., Khalil, S. M. E., Shebl, M. and El-Naem, R. A. S. (2017). Synthesis and characterization of N_3S_2 donors macrocyclic copper (II) complexes. Catechol oxidase and phenoxazinone synthase biomimetic catalytic activity. *Journal of the Chinese Advanced Materials Society*, 5(4): 215-240.

15. Yusuf, M. M. and Salga, M. S. (2019). Synthesis and study of the efficacies of tetraaza macrocyclic ligand for the adsorption of heavy metals from wastewater. *Bayero Journal of Pure and Applied Sciences*, 11(1): 126.
16. Chaudhary, A. and Rawat, E. (2014). Macrocyclic assembly: A dive into the pecking order and applied aspects of multitalented metallomacrocycles. *International Journal of Inorganic Chemistry*, 2014: 1-30.
17. Wankhede, D. S., Wagh, P. B. and Hangirgekar, S. P. (2015). Synthesis and characterization of tetraazamacrocyclic complexes using silica supported perchloric acid ($HClO_4$:SiO_2) as catalyst. *Journal of Chemical and Pharmaceutical Research*, 7(12): 1153-1159.
18. Knops, P., Sendhoff, N., Mekelburger, H. B. and Vögtle, F. (1992). Cyclophanes I. Springer Berlin Heidelberg, Berlin. 161: pp. 1-36.
19. Bhake, A., Shastri, S. and Limaye, N. (2014). A review on macrocyclic complexes. *Chemical Science Review and Letters*, 2(6): 449-455.
20. Cole, R. J., Kirksey, J. W., Hill, R. K., Carlson, R. M. and Isidor, J. L. (1974). Nitrogen analogs of crown ethers. *Journal of the American Chemical Society*, 1(1): 2268-2270.
21. Hoye, R. C., Hoye, R. C., Richman, J. E., Dantas, G. A., Lightbourne, M. F. and Scott Shinneman, L. (2001). Synthesis of polyazamacrocyclic compounds via modified richman-atkins cyclization of β-trimethylsilylethanesulfonamides. *Journal of Organic Chemistry*, 66(8): 2722-2725.
22. Shakir, M. and Varkey, S. P. (1995). A new synthetic route for the preparation of a new series of 14-22-membered tetraoxomacrocyclic tetraamines and their transition metal complexes. *Polyhedron*, 14(9): 1117-1127.
23. Yu, X. and Zhang, J. (2018). Macrocyclic polyamines: Synthesis and applications. Wiley-VCH Verlag GMbH & Co. KGaA: pp. 7-44.
24. Rosen, W. and Busch, D. H. (1969). Nickel (II) complexes of cyclic tetradentate thioethers. *Journal of the American Chemical Society*, 91(17): 4694-4697.
25. Travis, K. and Busch, D. H. (1974). Cobalt(III) and Rhodium(III) complexes of cyclic tetradentate thioethers. *Inorganic Chemistry*, *13*(11), 2591-2597.
26. Sues, P. E., Cai, K., Mcintosh, D. F. and Morris, R. H. (2014). Template effect and ligand substitution methods for the synthesis of iron catalysts: A two-part experiment for inorganic chemistry. *Journal of Chemical Education*, 92(2): 378-381.
27. Cameron, J. H. (1995). Template synthesis of macrocyclic complexes: A laboratory project for advanced undergraduate students. *Journal of Chemical Education*, 72(11): 1033-1036.
28. Arion, B. (1999). Template synthesis of macrocyclic compounds. Wiley-VCH Verlag GMbH: pp. 1-27.
29. Haque, A., Ilmi, R., Al-Busaidi, I. J. and Khan, M. S. (2017). Coordination chemistry and application of mono- and oligopyridine-based macrocycles. *Coordination Chemistry Reviews*, 350: 320-339.
30. Alam, M. M. (2011). Template synthesis of new type of macrocyclic molecule derived from pyridine-2, 6-decarboxaldehyde and 1,2-bis(2-aminoethoxy) ethane. *Journal of Bangladesh Academy of Sciences*, 35(1): 61-65.
31. Edwards. F. and Hahn, P.G. (2011). Synthesis and coordination chemistry of macrocyclic ligands featuring NHC donor groups. *The Royal Society of Chemistry*, 40: 10278-10288.
32. Truex, T. J. and Holm, R. H. (1971). Nontemplate synthesis of an unsaturated tetraaza[14] macrocycle and its metal(II) complexes. *Journal of the American Chemical Society*, 93(1): 285-286.
33. Borisova, N. E., Reshetova, M. D. and Ustynyuk, Y. A. (2007). Metal-free methods in the synthesis of macrocyclic Schiff bases. *Chemical Reviews*, 107(1): 46-79.
34. Owston, P. G., Peters, R., Ramsammy, E., Tasker, P. A. and Trotter, J. (1980). Non-template synthesis of "N4" macrocyclic imine ligands with variable ring sizes: The importance of intramolecular hydrogen-bonding. X-ray crystal structures of three macrocyclic and two open-chain ligands. *Journal of the Chemical Society, Chemical Communications*, (24): 1218-1220.

35. Swamy, S. J., Veerapratap, B., Nagaraju, D., Suresh, K. and Someshwar, P. (2003). Non-template synthesis of "N4" di- and tetra-amide macrocylic ligands with variable ring sizes. *Tetrahedron*, 59(50): 10093-10096.
36. Chandra, S., Tyagi, M. and Agrawal, S. (2010). Synthesis and characterization of a tetraaza macrocyclic ligand and its cobalt(II), Nickel(II) and Copper(II) complexes. *Journal of the Serbian Chemical Society*, *75*(7): 935-941.
37. Patil, N. and Akkasali, R. (2010). Non-template synthesis and antimicrobial activities of tetraazamacrocyclic ligands with variable ring sizes. *International Journal of Pharma and Bio Sciences*, 1(2): 1-6.
38. Sen, I., Yildiz, C. B. and Azizoglu, A. (2013). Non template synthesis, characterization and theoretical study of tetraazamacrocycles. *Ovidius University Annals of Chemistry*, 23(1): 121-127.
39. Nishat, N., Bhat, S. A., Kareem, A., Dhyani, S., Mohammad, A. and Mirza, A. U. (2018). Synthesis, characterization and biological analysis of transition metal complexes with macro cyclic ligands derived from adipic acid, ethylenediamine with diethyloxalate and diethylmalonate. *Journal of Inclusion Phenomena and Macrocyclic Chemistry*, 92(3–4): 395-409.
40. Anisimova, N. A., Khristoforova, E. I. and Trishin, Y. G. (2015). Cyclocondensation of ethylenediamine with acetone and methyl ethyl ketone as a synthetic route to 14-membered azamacrocyclic compounds. *Russian Journal of General Chemistry*, 85(9): 2080-2086.
41. Anisimova, N. A., Khristoforova, E. I. and Trishin, Y. G. (2016). Synthesis of azamacrocyclic compounds by cyclocondensation of aliphatic α,ω-diamines with acetone. *Russian Journal of General Chemistry*, 86(9): 2047-2051.
42. Hassan, N. H., Ali, N. M., Yamin, B. M., Karim, N. H. A. and Ghani, N. A. A. (2014). Synthesis and characterization of 5,5,7,12,12,14-hexamethyl-1,4,8,11-tetraazacyclotetradeca-7,14-dienium diperchlorate copper(II) complex. *Malaysian Journal of Analytical Sciences*, 18(3): 562-571.
43. Ali, N. M., Zaid, N. A. M., Karim, N. H. A., Yamin, B. M. and Hassan, N. H. (2018). Pengkompleksan 5,5,7,12,12,14-heksametil-1,4,8,11-tetraazasiklo tetraazadeka-7,14-dienium diperklorat dengan kuprum(II) asetat monohidrat dalam cecair ionik. *Malaysian Journal of Analytical Sciences*, 22(1): 27-34.
44. Fairus, S., Yusoff, M., Yamin, B. M. and Leng, O. W. (2015). Synthesis, characterization, and antibacterial activity of Cu(II), Ni(II), and Zn(II) complexes of 14-membered macrocyclic tetraaza ligand. *Oriental Journal of Chemistry*, 31(3): 1751-1758.
45. Chandra, S., Raizada, S. and Rani, S. (2008). Structural and spectral studies of palladium(II) and platinum(II) complexes derived from N,N,N,N-tetradentate macrocyclic ligands. *Spectrochimica Acta - Part A: Molecular and Biomolecular Spectroscopy*, 71(2): 720-724.
46. Rossa, L. and Vögtle, F. (1983). Cyclophanes I. Springer Berlin Heidelberg, Berlin. 113: pp. 1-86.

Malaysian Journal of Analytical Sciences (MJAS)
Published by Malaysian Analytical Sciences Society

SYNTHESIS AND CHARACTERIZATION OF RUBBER SEED SHELL IMPREGNATED WITH CALCIUM OXIDE AS CATALYST FOR BIODIESEL PRODUCTION

(Sintesis dan Pencirian Kulit Biji Getah dengan Resapan Kalsium Oksida Sebagai Bahan Pemangkin Untuk Penghasilan Biodiesel)

Nurul Farhanah Zakaria[1], Sarah Laila Mohd Jan[1]*, Siti Norhafiza Mohd Khazaai[1,2], Mohd Lokman Ibrahim[2,4], Mohd Hasbi Ab. Rahim[3] , Gaanty Pragas Maniam[3]

[1]Faculty of Applied Sciences,
Universiti Teknologi MARA Cawangan Pahang, Kampus Jengka, 26400 Jengka, Pahang, Malaysia
[2]Faculty of Applied Sciences,
Universiti Teknologi MARA, 40450 Shah Alam, Selangor, Malaysia
[3]Faculty of Industrial Sciences & Technology,
Universiti Malaysia Pahang, Lebuhraya Tun Razak, 26300 Gambang, Kuantan, Pahang, Malaysia
[4]Centre of Nanomaterial Research, Institute of Sciences,
Universiti Teknologi MARA, 40450 Shah Alam, Selangor, Malaysia

**Corresponding author: sarahlaila@uitm.edu.my*

Received: 30 April 2021; Accepted: 13 July 2021; Published: 29 August 2021

Abstract

Biomass can be manipulated as a promising heterogeneous catalyst that provides greener synthesis route for sustainable production of biodiesel. The oven-dried rubber seed shell (RSS) biomass was ground, and calcined at 700 °C for 4 hours. Later, RSS/CaO catalysts were prepared using the wet impregnated method with 1:4 ratios and calcined at 450 °C for 4 hours. The physicochemical properties were characterized by using thermogravimetric analysis (TGA), Fourier-transform infrared spectroscopy (FTIR) and scanning electron microscopy-energy dispersive X-ray (SEM-EDX). Methyl ester yield obtained was 68.6% by employing 10 wt.% of catalyst loading with 1:12 oil to methanol molar ratio at a temperature of 70 °C within 3 hours. Therefore, the present study verified that the RSS/CaO catalyst was one of the suitable catalysts for methyl ester production.

Keywords: methyl ester, biomass, waste cooking oil

Abstrak

Biojisim boleh dimanipulasi sebagai bahan pemangkin heterogen harapan yang boleh menyediakan laluan sintesis lebih mesra alam sekitar untuk pengeluaran biodiesel yang lebih mampan. Kulit biji getah yang telah dikering dalam oven kemudiannya dikisar dan dikalsinasi pada suhu 700 ˚C selama 4 jam. Bahan pemangkin RSS/CaO disediakan dengan menggunakan kaedah resapan basah dengan nisbah 1:4 dan dikalsinasi pada suhu 450 °C selama 4 jam. Sifat fizikokimia dicirikan dengan menggunakan analisis termogravimetrik (TGA), spektoskopi infrmerah transformasi Fourier (FTIR) dan mikroskopi imbasan elektron-tenaga serakan sinar-X (SEM-EDX). Hasil metil ester yang diperoleh adalah 68.6% dengan menggunakan 10% berat pemangkin dengan nisbah

molar minyak dan metanol 1:12 pada suhu 70 °C dalam 3 jam. Oleh itu, kajian ini mengesahkan bahawa bahan pemangkin RSS/CaO adalah salah satu pemangkin yang sesuai untuk pengeluaran metil ester.

Kata kunci: metil ester, biojisim, sisa minyak masak

Introduction

Green catalyst refers to the catalyst synthesized from biomass, and many researchers are progressively developing low cost of biomass-derived catalyst to reduce the cost of biodiesel production as well as to solve the problems of biomass waste disposal [1]. An abundance of biomass residue resulted mainly from various human and agricultural activities. The biomass waste produced by the agricultural sector in Malaysia was predicted to reach 110 million tons in 2020. The biomass waste such as empty fruit bunch, peels, kernels, seeds, trunk, shell and many more can be recycled into a new valuable product for various applications rather than be disposed at landfill or burned into ashes [2]. Biomass can be converted into the solid base catalyst by direct carbonization or combustion at high temperature [3].

The utilization of biomass-derived solid heterogeneous catalyst is a lot cheaper due to high abundance and availability of biomass, able to reduce the problem regarding solid waste disposal, pollution free [4], low production cost and highly efficient catalytic ability [5]. The reviews from various researchers had explored and listed several catalysts derived from various biomass such as waste egg shell, waste coral, animal bones, ashes, agricultural waste, mollusk shell, palm and coconut shell, peanut hull, sea sand, bamboo, sugarcane, banana trunk, rice husk, cocoa pod husk, wood, sewage sludge and snail shell that showcased excellent catalytic ability in transesterification of feedstock with high yield of methyl ester [1, 2].

About 1.3 million hectares of land in Malaysia is devoted for rubber plantation and produce approximately 150 kg of RSS per hectares every season that only regarded as waste as it is not edible [6]. The RSS falls naturally from the rubber tree and left to rot on the soil [7]. In order to reduce the solid waste generated from rubber plantation in our country, the research of raw RSS as a potential basic and acidic heterogeneous catalyst in biodiesel production is much needed. Solid biomass-derived catalyst can function as basic or acidic catalyst support by firstly converted into carbonaceous materials then functionalized with active group. The acidity and basicity of the catalyst depends on the chemicals used during the chemical impregnation (CI) of active sites [8].

Currently, in order to accomplish the concept of green chemistry, there has been a great shift in focus towards producing solid biomass-derived catalyst as the precursor for transesterification of biodiesel. An intense research of cost-efficient green technology for biodiesel production is much needed. Biodiesel is nominated as the promising alternative of fuel due to properties such as free of toxic, biodegradable, compatible with environment, low greenhouse gas emission, low viscosity, excellent lubricity, high flash point and cetane number [9]. To manufacture biodiesel, extensive study has been conducted on renewable resources, the majority of which are plant-based oil (sunflower oil, palm oil, rice bran oil) and waste cooking oil (WCO). WCO was selected as a biodiesel resource in this study because it is considered environmentally friendly due to the recycling act and good management of improper dumping of WCO. Date pits [10], coconut husk [11], Tucuma peel [3], and fly ash [12] are just a few examples of the biomass-derived catalysts that have been studied and have shown tremendous results in biodiesel production with 98–70% yield.

In this present study, rubber seed shell (RSS) of *Hevea brasiliensis* is chosen as the biomass to synthesis the heterogeneous catalyst for biodiesel production. Previous studies reported that apart from carbon, the RSS has mineral composition of calcium, magnesium; sodium and potassium thus fulfill the criteria worthy of biomass-derived heterogeneous catalyst [13].

Materials and Methods

Materials

Rubber seed was collected in local estate and it is consisting of the outer shell and inner kernel. Later, the

kernel was separated from the seed in order to obtain the biomass sample, rubber seed shell (RSS). Waste cooking oil (WCO) was obtained from a local household kitchen. WCO was filtered to remove the impurities and heated at 120 °C for 2 hours to eliminate the moisture content [14]. An analytical grade of methanol, n-heptane, petroleum ether, and chloroform were obtained from Merck. An analytical grade of methyl heptadecanoate, phenolphthalein, 4-nitroaniline and 2,4-dinitroaniline were purchased from Sigma Aldrich company (Switzerland).

Preparation of RSS/CaO catalyst

RSS was washed with distilled water to remove any dirt and impurities. Then, the RSS sample was placed in fan-assisted drying oven at 80 °C for 12 hours to remove any moisture. The oven-dried RSS biomass was ground, placed in crucibles and calcined at 700 °C for 4 hours in a muffle furnace. The resulted RSS-derived carbon material was impregnated with an aqueous solution of $Ca(NO_3)_2•4H_2O$ at constant temperature and stirring rate for 2 hours with the ratio of 1:4 [3, 12]. The dried sample was then calcined at 450 °C for 4 hours to transform the impregnated $Ca(NO_3)_2•4H_2O$ into active calcium oxide group [10].

Characterization of RSS/CaO catalyst

Thermo gravimetric analysis (TGA) using TGA-SDTA 851 Mettler Toledo was carried out to find the minimum calcination temperature of converting RSS into a stable carbon material [11]. The functional group of calcined RSS and RSS/CaO catalyst were identified using Perkin Elmer SpectrumTM 400 FTIR Spectrometer. The surface morphology of calcined RSS and RSS/CaO catalyst were also examined under scanning electron microscopy (SEM) followed by EDX Oxford Instrument for elemental analysis.

Evaluation of catalytic analysis

The transesterification temperature, time and methanol-to-oil ratio was kept constant at 70 °C, 3 hours and 12:1 to investigate the effect of catalyst loading. The WCO and methanol was refluxed in a water bath with the presence of various RSS/CaO catalyst loading (6, 8, 10, 15 and 20 wt.%). The reaction mixture was cooled down at room temperature and left overnight to remove the residual methanol. The catalyst was separated from the liquid phase using centrifugation at 3000 rpm for 20 minutes. The biodiesel yield was calculated by following equation 1 [13].

$$\text{Biodiesel yield (\%)} = \frac{\text{upper biodiesel layer weight}}{\text{WCO weight}} \times 100 \qquad (1)$$

The collected upper biodiesel layer was analyzed using gas chromatography equipped with mass spectrometry (GC-MS) to identify the type of FAME content that present [15]. Agilent 7890B gas chromatographer equipped with 5977A MSD and Zebron ZB-Wax capillary column with diameter 30m x 0.2mm x 0.25µm was used. The probability of each chromatogram peaks were indeed methyl ester were confirmed by matching the unknown spectra with the mass spectra in the National Institute of Standards and Technology (NIST) library database. Equation 1 was used to calculate the reaction yield as the internal standard was not employed when analyzing the collected upper layer using the GC-MS.

Results and Discussion

Characterization of RSS/CaO catalyst: Thermo-gravimetric analysis ((TGA)

The calcination temperature was chosen at 700°C for dried RSS based on the TGA result in Figure 1. Apart from achieving thermal stability, high calcination temperature is preferable as shorter calcination time is required to produce catalyst with uniform surface [16]. Biomass that was calcined at high temperature can be directly used as catalyst for biodiesel production [3, 17]. Unfortunately, the firstly calcined RSS at 700 °C in the present study does not exhibit any catalytic activity as there was no conversion observed during transesterification reaction due to the low number of active sites. Therefore, the calcined RSS was further treated with aqueous solution of $Ca(NO_3)_2•4H_2O$ to functionalized the carbonaceous material with CaO active sites. $Ca(NO_3)_2•4H_2O$ was chosen as the precursor due to lower calcination temperature was required to form CaO as compared to other precursor such as calcium carbonate [11]. Widely known CaO have excellent catalytic ability, it is still very important to anchor CaO on RSS carbon support to avoid Ca^{2+} ion leaching into the reactants [17]. Furthermore, the

oxygen ion on the CaO surface easily reacts with methanol and glycerol forming hydrogen bonds [18]. As a result, the viscosity of glycerol increases leading to strenuous separation. Anchoring CaO on a fixed carbon support can solve the discussed issues. Another function of RSS carbon support is to provide larger surface area for better catalytic ability [11].

Fourier-transform infrared spectroscopy

Calcined RSS does not exhibit any peak indicating there is no functional group present apart from the carbonaceous residue according to Figure 2. After anchoring the calcined RSS with CaO, four prominent peaks were observed on the infrared spectrum. RSS/CaO spectrum exhibited a broad peak at 1469 cm^{-1} due to the bending vibration of Ca-O thus confirmed the attachment of CaO onto the carbon support. The sharp peak observed at 3640 cm^{-1} belongs to the hydroxyl group (-OH) stretching vibration of $Ca(OH)_2$ due to the interaction of CaO with moisture when exposed to the surrounding. The peak at 875 cm^{-1} is due to the stretching vibration of carbonate ion $(CO_3)^{2-}$ [16]. The presence of carbonate ion furthers proven with the occurrence of weak band at 1085 cm^{-1} that belongs to C-O stretch [19].

Scanning electron microscopy-energy dispersive X-ray

Based on Figure 3(a) and (b), the calcined RSS at 700°C exhibited smooth and protruding bead-like agglomerated surfaces that able to provide high surface area for attachment of active sites. The EDX elemental analysis of calcined RSS shows that carbon (86.16 wt.%) dominates the composition followed by oxygen (13.56 wt.%) and trace amount of calcium (0.28 wt.%). The soil and climate condition are factors that determine the mineral content of grown biomass [19]. Similarly reported, a trace element of calcium in RSS biomass was found [13]. Meanwhile, according to Figure 4(a) and (b), the attachment of CaO active sites had modified the surface morphology of RSS. After activation, the catalyst exhibited more regular flakes-like flat surface structure. The particle sizes reduction was also observed for RSS/CaO that further increases the surface area which is a very significant feature of heterogeneous catalyst [16]. RSS/CaO catalyst consist of higher amount of calcium (35.18 wt.%) and oxygen (47.04 wt.%) due to activation process followed by the carbon support (17.79 wt.%). The RSS/CaO elements mapping also shown that carbon and calcium are superimposed. Superimposed images are due to formation of mixed phases of elements proving that CaO is definitely attached onto the carbon support [20]. The regular spatial distribution as observed in Figure 4(d) showed that the impregnated CaO was well scattered over the RSS carbon support.

Catalytic activity of RSS/CaO for biodiesel production

The transesterification reaction of WCO to produce biodiesel was successfully conducted using the synthesized RSS/CaO catalyst. As shown in Figure 5, the minimum concentration (6 wt.%) of RSS/CaO catalyst required to convert WCO to FAME within 3 hours. The most optimum catalyst loading is 10 wt.% that shows the best catalytic activity with highest biodiesel yield at 68.6%. Similarly, fly ash/CaO catalyst achieved slightly higher biodiesel yield at 71.1% by employing 6 wt.% catalysts [11]. The result trend is consistent with several studies that suggested higher catalyst concentration contained a lot more active sites thus provide better catalytic activity [3, 5, 15, 16]. In addition, higher CaO sites leads to higher formation of calcium methoxide, $Ca\text{-}(CH_3O)_2$ that amplified the reaction rates [16]. Meanwhile, decrease in biodiesel yield at catalyst concentration exceeding optimum load is due to increase in viscosity of reactant that declines the mass transfer rate between reactant and catalyst surface [3]. The FAME composition was qualitatively determined using GC-MS. The chromatogram peaks reflect all kinds of compounds that exist in the biodiesel. Out of ten prominent peaks that appeared, six peaks were verified as FAME using mass spectral NIST library (dodecanoic acid methyl ester, methyl tetradecanoate, hexadecanoic acid methyl ester, methyl stearate, eicosanoic acid methyl ester, octadecatrienoic acid methyl ester). Four of them were similar to the previous study [15]. Slight variations in type of FAME produced may be due to the different sources of WCO were employed.

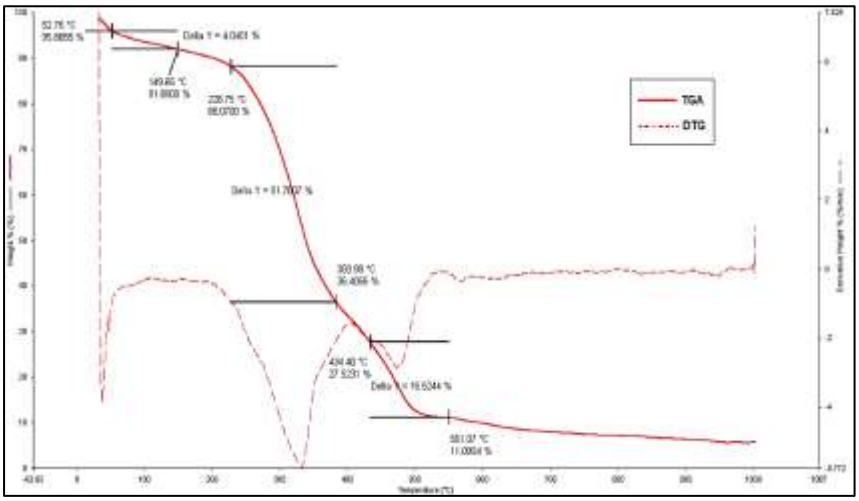


Figure 1. TGA-DTG curve for raw dried RSS

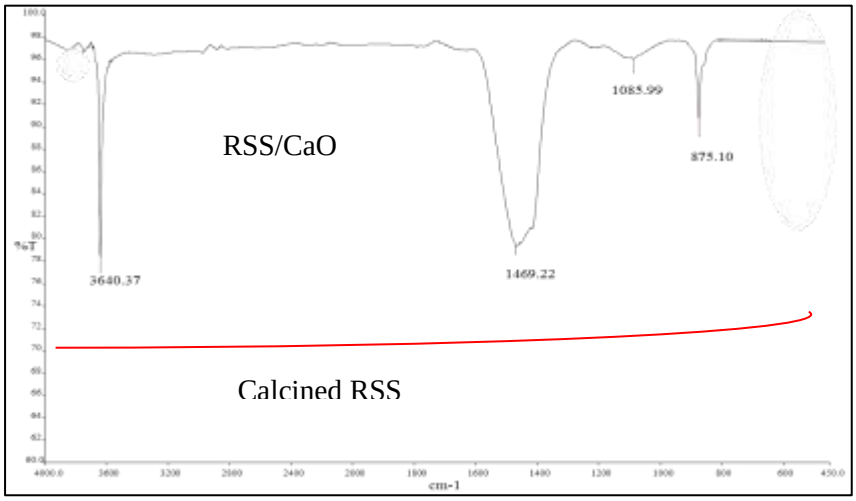


Figure 2. IR spectrum of calcined RSS and RSS/CaO catalyst

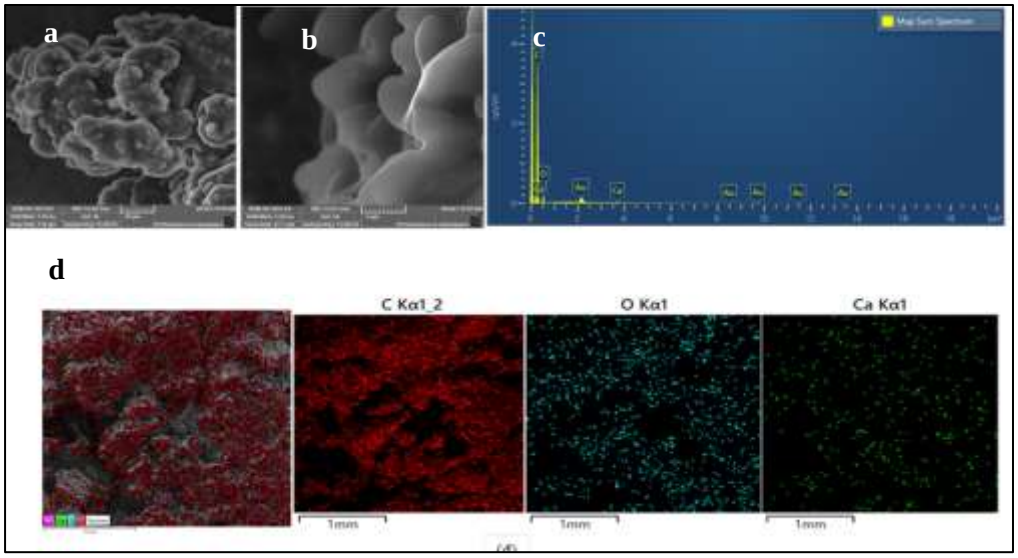


Figure 3. Calcined RSS at 700°C (a) 1000x magnification (b) 5000x magnification (c) element spectrum (d) element mapping

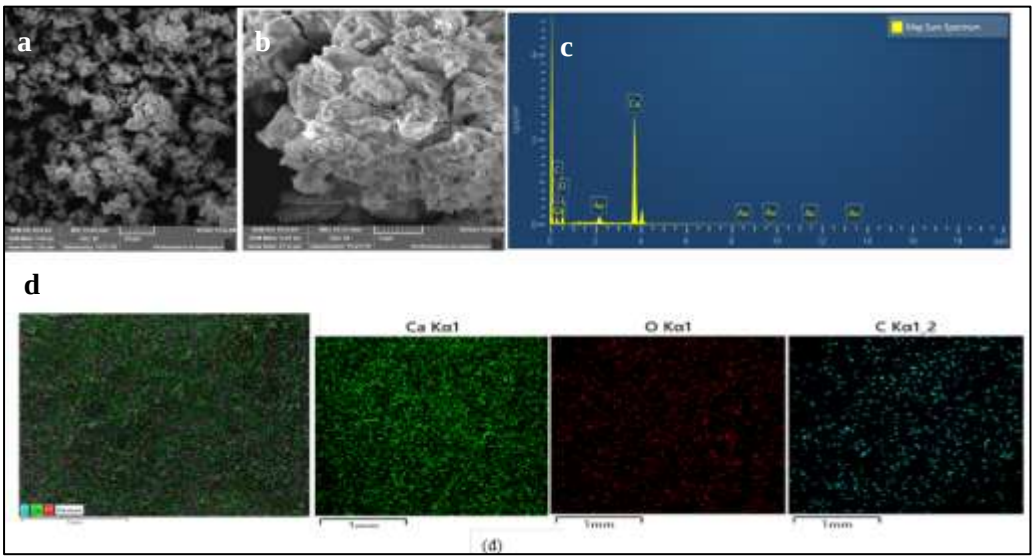


Figure 4. Calcined CaO/RSS at 700°C (a) 1000x magnification (b) 5000x magnification (c) element spectrum (d) element mapping

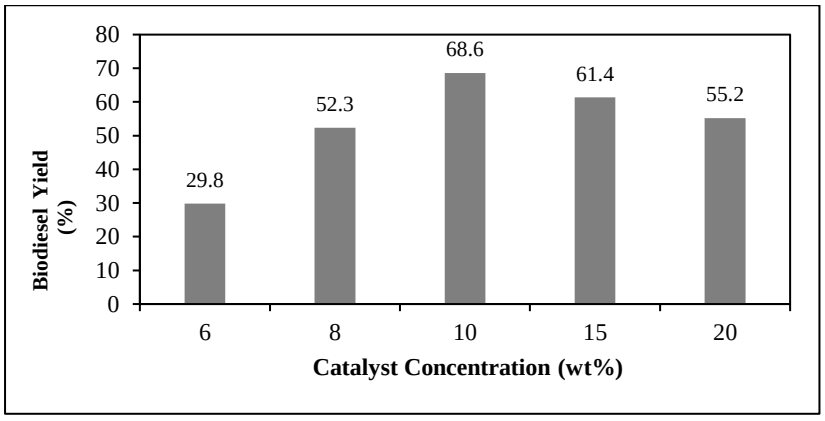


Figure 5. The effect of catalyst loading on the biodiesel yield

Conclusion

RSS is an attractive carbon source for catalyst support as thermal analysis conducted by TGA showed that RSS had high thermal stability. Impregnation of CaO active sites had modified and improved the RSS carbon structure thus increased the catalytic ability of the catalyst. The attachment of CaO onto carbon support was confirmed by the presence of significant functional group bands on IR spectrum as well as SEM-EDX morphological and elemental analysis. Certify the catalyst capable of yielding 68.8% of methyl ester within 3 hours of reaction time at 70 °C with MeOH/oil mass ratio, 12:1; catalyst amount, 10 wt.%. Qualitative analysis of collected upper layer by GC-MS also confirmed that WCO was successfully transformed into FAME.

Acknowledgement

The authors would like to thank Ministry of Higher Education, Malaysia, Universiti Malaysia Pahang and Universiti Teknologi MARA Pahang for research project (600-TNCPI 5/3/DDN (06)(001/2020) and (FGRS/1/2019/STG01/UMP/02/2).

References

1. Abdullah, S. H. Y. S., Hanapi, N. H. M., Azid, A., Umar, R., Juahir, H., Khatoon, H. and Endut, A. (2017). A review of biomass-derived heterogeneous catalyst for a sustainable biodiesel production. *Renewable and Sustainable Energy Reviews*, 70: 1040-1051.
2. Tang, Z. E., Lim, S., Pang, Y. L., Ong, H. C. and Lee, K. T. (2018). Synthesis of biomass as heterogeneous catalyst for application in biodiesel production: State of the art and fundamental review. *Renewable and Sustainable Energy Reviews*, 92: 235-253.
3. Mendonça, I. M., Paes, O. A. R. L., Maia, P. J. S., Souza, M. P., Almeida, R. A., Silva, C. C. S., Duvoisin Jr. and de Freitas, F. A. (2019). New heterogeneous catalyst for biodiesel production from waste tucumã peels (*Astrocaryum aculeatum* meyer): Parameters optimization study. *Renewable Energy*, 130: 103-110.
4. Chellappan, S. and Nair, V. (2018). Synthesis, optimization and characterization of biochar based catalyst from sawdust for simultaneous esterification and transesterification. *Chinese Journal of Chemical Engineering*, 26: 2654-2663.
5. Mazaheri, H., Ong, H. C., Masjuki, H. H., Amini, Z., Harrison, M. D., Wang, C. T., Kusumo, F. and Alwi, A. (2018). Rice bran oil based biodiesel production using calcium oxide catalyst derived from chicoreus brunneus shell. *Energy*, 144: 10-19.
6. Hassan, S. N. A. M., Ishak, M. A. M., Ismail, K., Ali, S. N. and Yusop, M. F. (2014). Comparison study of rubber seed shell and kernel (*Hevea brasiliensis*) as raw material for bio-oil production. *Energy Procedia*. 52: 610-617.

7. Khazaai, S. N. M., Maniam, G. P., Rahim, M. H. A., Yusoff, M. M. and Matsumura, Y. (2017). Review on methyl ester production from inedible rubber seed oil under various catalysts. *Industrial Crops and Production*, 97: 191.
8. Muthusamy, K., Nordin, N., Vesuvapateran, G., Ali, M., Mohd Annual, N. A., Harun, H. and Ullap, H. (2014). Exploratory study of rubber seed shell as partial coarse aggregate replacement in concrete. *Research Journal of Applied Sciences, Engineering and Technology*, 7: 1199-1202.
9. Shah, B., Sulaimana, S., Jamal, P. and Alam, M. Z. (2014). Production of heterogeneous catalysts for biodiesel synthesis. *International Journal Chemical Environmental Engineering*, 5(2): 73-75.
10. Al-Muhtaseb, A. A. H., Jamil, F., Al-Haj, L., Zar Myint, M. T., Mahmoud, E., Ahmad, M. N., Hasan, A. O. and Rafiq, S. (2018). Biodiesel production over a catalyst prepared from biomass-derived waste date pits. *Biotechnology Reports*, 20: 00284.
11. Vadery, V., Narayanan, B. N., Ramakrishnan, R. M., Cherikkallinmel, S. K., Sugunan, S., Narayanan, D. P. and Sasidharan, S. (2014). Room temperature production of jatropha biodiesel over coconut husk ash. *Energy*, 70: 588-594.
12. Helwani, Z., Fatra, W., Saputra, E. and Maulana, R. (2018). Preparation of CaO/fly ash as a catalyst inhibitor for transesterification process off palm oil in biodiesel production. *IOP Conference Series: Materials Science and Engineering*, 334: 012077.
13. Ekebafe, L., Imanah, J. and Okieimen, F. (2010). Physico-mechanical properties of rubber seed shell carbon-filled natural rubber compounds. *Chemical Industry and Chemical Engineering Quarterly*, 16: 149-156.
14. Shohaimi, N. A. M. and Marodzi, F. N. S. (2018). Transesterification of waste cooking oil in biodiesel production utilizing CaO/Al_2O_3 heterogeneous catalyst. *Malaysian Journal Analytical Sciences*, 22: 157-165.
15. Onoji, S. E, Iyuke, S. E., Igbafe, A. I. and Daramola, M. O. (2017). Transesterification of rubber seed oil to biodiesel over a calcined waste rubber seed shell catalyst: Modeling and optimization of process variables. *Energy Fuels*, 31: 6109-6119.
16. Abbaszaadeh, A., Ghobadian, B., Omidkhah, M. R. and Najafi, G. (2012). Current biodiesel production technologies: A comparative review. *Energy Conversion Managment*, 63: 138-148.
17. Lv, C., Liu, P., Yuan Z., Yan, F. and Luo, W. (2010). The nanometer magnetic solid base catalyst for production of biodiesel. *Renewable Energy*, 35: 1531-1536.
18. Khan, N. B. A. and Yacob, A. R. (2017). Potassium hydroxide and calcium oxide activated carbon for transesterification reaction of biodiesel. *eProceedings Chemistry*, 2: 63-69.
19. Reshad, A. S., Tiwari, P. and Goud, V. V. (2018). Thermo-chemical conversion of waste rubber seed shell to produce fuel and value-added chemicals. *Journal Energy Insdustry*, 91: 940-950.
20. Neri, G., (2003). K- and Cs-FeV/Al_2O_3 soot combustion catalysts for diesel exhaust treatment. *Applied Catalysis B: Environmental*, 42(4): 381-391.

Malaysian Journal of Analytical Sciences (MJAS)
Published by Malaysian Analytical Sciences Society

EXTRACTION OF POMEGRANATE PEEL AND GREEN TEA LEAVES AND THEIR EFFECTS ON THE MICROBIAL, PHYSICOCHEMICAL, MICROSTRUCTURAL AND SENSORIAL PROPERTIES OF CHILLED-STORED CHICKEN MEAT

(Pengekstrakan Kulit Buah Delima dan Daun Teh Hijau dan Kesannya Terhadap Sifat-Sifat Mikroorganisma, Fizikokimia, Mikrostruktur dan Deria Rasa Daging Ayam yang Disimpan pada Suhu Sejuk)

Safiullah Jauhar[1,3], Mohammad Rashedi Ismail-Fitry[1]*, Gun Hean Chong[1], Mahmud Ab Rashid Nor-Khaizura [2], Wan Zunairah Wan Ibadullah [2]

[1]Department of Food Technology, Faculty of Food Science and Technology
[2]Department of Food Science, Faculty of Food Science and Technology
Universiti Putra Malaysia, 43400 UPM Serdang, Selangor, Malaysia
[3]Department of Food Technology, Faculty of Veterinary Science,
Afghanistan National Agriculture Science and Technology University, Dand District, Kandahar Province, Afghanistan

**Correspondence: ismailfitry@upm.edu.my*

Received: 19 June 2021; Accepted: 27 July 2021; Published: 29 August 2021

Abstract

Pomegranate (*Punica granatum* L.) peel extracts (PPE) and green tea (*Camellia sinensis*) leaves extracts (GTE) have the potential to be the natural preservatives to prolong the chicken meat quality stored in chilling temperature. The first part of this work aimed to determine the effects of solid-liquid extraction (SLE) and ultrasound-assisted extraction (UAE) in extracting the pomegranate peel and green tea leaves. The second part was to determine the microbial, physicochemical, microstructural and sensorial properties of chicken meat applied with the PPE, GTE or PPE+GTE and stored in chill temperature for seven days. UAE method resulted in higher antioxidant activity in PPE and GTE at 74.3% and 70.4%, respectively compared to SLE method at 48.2% and 41.5%, respectively. The GTE inhibited the microbial growth with 5.47 and 5.96 log CFU/g of the chicken meat at the third and seventh day of chilled-storage, respectively. The water holding capacity, pH, lipid peroxidation and texture were not affected by the extracts. GTE affected the chicken meat by increasing the yellowness (*b**), changing the microstructure, and reducing the sensory acceptability. Overall, GTE can to be used as a natural preservative for chilled chicken meat, however, further additional treatments are needed to overcome the negative effect on the chicken meat characteristics.

Keywords: chicken meat, green tea leaves, natural antioxidants, pomegranate peel, solid-liquid extraction, ultrasound-assisted extraction

Abstrak

Ekstrak kulit buah delima (*Punica granatum* L.) (PPE) dan ekstrak daun teh hijau (*Camellia sinensis*) (GTE) berpotensi menjadi pengawet semula jadi untuk mengekalkan kualiti daging ayam yang disimpan dalam suhu sejuk. Bahagian pertama kerja ini bertujuan untuk mengenalpasti kesan pengekstrakan pepejal-cecair (SLE) dan pengekstrakan secara-ultrabunyi (UAE) dalam mengekstrak kulit buah delima dan daun teh hijau. Bahagian kedua adalah untuk menentukan sifat mikroorgnisma, fizikokimia, mikrostruktur dan deria rasa daging ayam yang diaplikasikan dengan PPE, GTE atau PPE+GTE dan disimpan dalam suhu sejuk selama tujuh hari. Kaedah UAE menghasilkan aktiviti antioksida yang lebih tinggi pada PPE dan GTE masing-masing pada 74.3% dan 70.4% berbanding kaedah SLE masing-masing pada 48.2% dan 41.5%. GTE menghalang pertumbuhan mikroorganisma masing-masing dengan 5.47 dan 5.96 log CFU/g daging ayam pada hari ketiga dan ketujuh penyimpanan sejuk. Kebolehan memegang air, pH, peroksidaan lipid dan tekstur tidak dipengaruhi oleh ekstrak. GTE mempengaruhi daging ayam dengan meningkatkan warna kekuningan (*b**), mengubah struktur mikro, dan mengurangkan penerimaan analisa deria rasa. Secara keseluruhan, GTE dapat digunakan sebagai pengawet semula jadi untuk daging ayam sejuk, namun, pengolahan tambahan lebih lanjut diperlukan untuk mengatasi kesan negatif kepada ciri daging ayam.

Kata kunci: daging ayam, daun teh hijau, aktioksidan semulajadi, kulit buah delima, pengekstrakan pepejal-cecair, pengekstrakan secara-ultrabunyi

Introduction

Meat, especially chicken meat possesses high percentage of water and abundant nutrients on its surface and is highly susceptible to microbial decay [1]. The spoilage occurs through microbial activities, oxidation of meat protein and lipid [2], especially when stored for a longer time in chilled or room temperature. Recently, plant phenolic compounds which contain natural antioxidant have shown remarkable results when used as food preservative and free radical scavenging agent and at the same time containing health benefits against several diseases [3, 4]. Several abundant plants such as pomegranate fruits and green tea contain high phenolic compounds and may be used as an agent to preserve chicken meat.

Pomegranate fruit (*Punica granatum* L.) is known to be a high source of antioxidants, its peel, in particular, has much higher phenolic compounds compared to other parts [5]. Recent investigations have shown that the pomegranate peel has high phenolic compounds with remarkable medicinal importance [6]. Green tea (*Camellia Sinensis*) is considered the second most consumed beverage around the world after plain water. It has up to 36% phenolic compounds, the amount of which is related to season, variety, and climate [7]. Mitsumoto et al. [8] applied tea catechins and vitamin C on cooked/raw beef and chicken meat patties and showed that green tea was more potent than vitamin C and extended the shelf life of the meat products even longer. Green tea has also been applied as a preservative in Turkish dry-fermented sausage [9].

Several extraction methods have been used to extract phenolic compounds from these types of plants. These methods vary according to the nature of the plants and their antioxidant activities; the methods can be divided into simple (or conventional) methods and advanced methods [10]. Solid-liquid extraction (SLE) has been used for a long time to extract phenolic compounds from various types of plants [11]. Some important variables in SLE must be considered. For instance, the solvents used in the process such as ethanol, methanol, water or ethyl acetate are strongly dependent on contact time, stirring, and temperature [12]. Of the advanced extraction methods, ultrasound-assisted extraction (UAE) is the most commonly used and preferred in the field of food science because it can easily be used and is more economical compared to other methods [13]. The method uses ultrasound waves to change the properties of the target plant, interrupt its cell walls and its cavity creation mechanism, causing the release of all the compounds in the cell that cannot be easily extracted. Moreover, UAE uses less solvent, produces a high-quality product, is easy to use, and results in a highly purified product [14].

The methods used could influence the phenolic compounds extractions and the extracts obtained could be applied as a natural preservative of raw chicken meat. Therefore, the objectives of this study were 1) to compare the effectiveness of the solid-liquid extraction (SLE) and ultrasound-assisted extraction (UAE) in extracting pomegranate peel and green tea extracts and 2) to determine the physicochemical, microbial and sensorial properties of raw chicken meat applied with the best extract, either pomegranate peel extract (PPE) or green tea extract (GTE) or a combination of both and then stored at 4 °C for seven days.

Materials and Methods

Chemicals and materials

Analytical grade chemicals were obtained from Sigma Aldrich (St. Louis, MO, USA), including the Folin-Ciocalteu reagent, quercetin, gallic acid, 2,2-diphenyl-1-picrylhydrazyl (DPPH), methanol, ethanol, ethyl acetate, sodium carbonate, potassium acetate, and aluminium chloride. The pomegranate (*Punica granatum* L.) variety native to India, natural dried green tea (*Camellia sinensis*) native to Taiwan, and sodium hypochlorite were purchased from a local market in Seri Kembangan, Selangor. The raw breast chicken meat was purchased from Azli Chicken Meat Whole seller and shipped at 4 °C, 3 hours after slaughter to the laboratory.

Plant samples drying processes

The pomegranate received from the local market was manually peeled and washed with flowing water. The peels were then washed with 20 ppm sodium hypochlorite solution for 15 minutes [15], followed by washing with deionized water. The peels were cut into approximately 1 cm^2, placed on an aluminium tray with some distance between the peel slices and dried in an air-circulated oven at 45 °C. After that, the dried peel was ground with a Panasonic MX-GM1011 grinder followed by sieving through a 0.425 mm stainless steel sieve. Following that, the sample was immediately stored at -21 °C [16]. Dried green tea was received from the market and then ground using a grinder followed by sieving via a 40 mm mesh stainless steel sieve at room temperature [17, 18].

Solid-liquid extraction process

The phenolic compounds from the dried pomegranate peels and the green tea leaves were extracted using a thermostatic water bath shaker (WNB 14 c/w sloping). The extraction of the pomegranate peel extract was carried out using an ethyl acetate solvent at a 15:1 (w/w) ratio of solvent to sample (dry weight) at 40 °C for 4 hours. The green tea was extracted in 80% acetone solution for 15 minutes at room temperature in a conical flask followed by filtration using a Whatman No. 1 filter. The supernatants of both extracts were vacuum-dried in a rotary evaporator at 40 °C in a dark room until 95% evaporation was reached and the remaining 5% solution was then freeze-dried and stored at -21 °C for further usage. [18,19]. The yield was obtained using equation (1).

Ultrasound-assisted extraction process

The phenolic compounds from dried pomegranate peel (4 g) were extracted using 200 mL of 70% ethanol solution in an ultrasound bath set to 60 °C for 30 minutes followed by centrifugation at 4500 rpm for 10 minutes and then filtered using a Whatman No. 1 filter. The supernatant was vacuum-dried in a rotary evaporator at 40 °C in a dark room until 95% evaporation was reached [16, 20]. The remaining 5% solution was then freeze-dried and stored at -21 °C for further usage. The extraction of green tea phenolic compounds was done using an electronic ultrasound bath at 35 kHz set to 160/640 W input power. Green tea (4 g) was extracted with 400 ml double distilled water at 70 °C. Then, the green tea was placed in an ultrasound cleaner bath at 80 °C for 20 minutes. After that, it was filtered through Whatman No. 1 filter paper and the extract was cooled at room temperature (25 °C) [17]. Next, centrifugation was done at 4500 rpm for 10 minutes and the tea filtered through a Whatman No. 1 filter. The supernatant was vacuum-dried in a rotary evaporator in a dark room at 40 °C until 95% evaporation was achieved [16]. The remaining 5% solution was then freeze-dried and stored at -21 °C for further usage.

Total antioxidant activity

Antioxidant activity was measured using 2, 2- Diphenyl-1-picrylhydrazyl (DPPH) scavenging activity. The DPPH (1 mg) was dissolved in 1 mL methanol to

prepare a 1 mg/mL DPPH solution. As the control absorbent, the DPPH solution was further dissolved with 5 mL MeOH solution and observed at 517 nm using a UV-Spectrophotometer. Both PPE and GTE samples (0.05 g each) were dissolved in 5 ml methanol solution. Then, 100 µL of prepared DPPH (1 mg/ml) solution was added to 100 µL of the prepared sample solution. This was followed by dilution in 5 mL methanol and incubation at room temperature for 30 minutes and then absorbance at 517 nm UV-Spectrophotometer (Thermo-10D) [21]. The radical scavenging activity can be expressed using equation (2).

Estimation of total phenolic content

The Folin-Ciocalteu colourimetric method was used to determine the phenolic compounds. Samples of PPE and GTE (0.125 g each) were dissolved in 100 mL water. An aliquot of 70 µL of the prepared sample, 759 µL of 1.9M sodium carbonate, and 250 µL of Folin-Ciocalteu were added to a 10 mL test tube. The test tube was filled with distilled water up to 5 mL and vortexed for one minute. It was then incubated for 2 hours in a dark room. The absorbance was detected at 765 nm using a UV-visible spectrophotometer. Gallic acid standard solutions were used to prepare the calibration curve and the result stated in mg/g dry solid [22].

Estimation of total flavonoid content

Calorimetric method of aluminium chloride was used to determine the flavonoid compound. An aliquot (1.25 mL/mg) of the PPE and (3.5 mg/mL) of the GTE were prepared in methanol solution. An aliquot (0.5 mL) of the prepared sample was further dissolved in 1.5 mL of methanol followed by mixing with 0.1 mL of 1 M potassium acetate, 0.1 mL of 10% aluminium chloride and 2.8 mL of distilled water. It was incubated for 30 minutes in dark at room temperature. The absorbance was detected at 415 nm by using UV-visible spectrophotometer. Quercetin standard solution was used for the preparation of a calibration curve and the result was stated as mg/g dry solids [23].

Chicken meat sample preparation and treatment

Under an aseptic condition, raw chicken breast meat, 3 hours after slaughter, was sliced into sizes of 1.5 cm thick, 2 cm long and 8 cm high portions. The extracts were prepared at 0.02% concentration using sterilized distilled water and applied to the chicken meat at the ratio of 1: 2 (meat: extract). Four treatments were prepared as follows: 1) control (meat: sterilized distilled water), 2) (meat: PPE), 3) (meat: GTE), and 4) (meat: PPE+GTE). The samples were marinated for one minute each, and then wiped using sterilized tissue paper, packed in the aerobic condition in low-density polyethylene bags and stored at 4 °C under aseptic conditions [24]. The analyses were carried out on the zero-day, third-day and seventh-day. The appearance of the chicken meat changed drastically by the higher concentration and longer time of the marination based on the preliminary study. Therefore, lower concentration and shorter time of marination were justified to minimize changes in the appearance of the chicken meat.

Microbial quality evaluation

A plate count agar (PCA) and potato dextrose agar (PDA) were used to measure the total count of bacteria, yeast, and mould. The samples were homogenized (Seward™ Stomacher™, Model 400 Circulator Lab Blender, 110V, England) with sterile peptone water in 10 mg/90 mL, meat/sterile peptone water. The mixture was further diluted with 0.1% peptone water before inoculation to PCA and PDA. Four serial dilutions (10^{-2}-10^{-5}) were used for each sample in triplicate. After incubation at 35-37 °C for 24-48 hours (PCA) and 25 °C for 72-120 hours (PDA), both plates were read [24].

Determination of water holding capacity

An aliquot of 1 cm long cylinders of the meat sample was weighed and enfolded in filter paper. Then, the sample was centrifuged at 10000 × g for 10 min at 10 °C and the sample was weighed again [25]. The water holding capacity was calculated using the equation (3).

Yield (%) = Total weight of the extract/ Sample total weight before extraction × 100 (1)

$$\text{Inhibition (\%)} = (\text{Control absorbance} - \text{Sample absorbance})/ (\text{Control absorbance}) \times 100 \quad (2)$$

$$\text{Water loss (\%)} = (\text{Pre-weight} - \text{Post-weight})/ (\text{Pre-weight}) \times 100 \quad (3)$$

pH analysis

The chicken meat sample (10 g) was homogenized (Seward™ Stomacher™, Model 400 Circulator Lab Blender, 110V, England) in 100 mL distilled water. After filtration, the mixture pH was measured using a pH meter (SevenMulti, Mettler-Toledo GmbH 8603 Scherzenbach, Switzerland) [26].

Lipid peroxidation measurement

A 5 g meat sample was mixed with 25 mL of 7.5% trichloroacetic acid (w/v) including 0.1% ethylenediaminetetraacetic acid (EDTA). It was integrated into a Panasonic grinder MX-GM1011, at 15000 rpm. Later, at room temperature, it was centrifuged at 3600 g for 20 minutes, and purified via a Whatman 4 filter. Then, the Supernatant was combined in a boiling bath for 30 minutes with 5 mL TBA 0.02 mol/L reagent. It was subsequently cooled to room temperature, and the absorbance recorded against a blank sample at 532 nm (5 mL TBA mixed with 5 mL distilled water). In the mg malondialdehyde per kg of meat sample, the result of thiobarbituric acid reactive substances (TBARS) (mg MDA/kg) was shown [26].

Colour analysis

The colour of meat was measured vertically in triplicates on the surface of the meat using a Chroma Meter (CR-410, Japan) to obtain an average value. The results were described as lightness (L^*), redness (a^*) or yellowness (b^*) [26].

Texture profile analysis

The texture profiles (hardness, chewiness, springiness and cohesiveness) of the samples were evaluated using a texture analyzer (Stable Micro Analyzer TA-XT2i, UK). The samples were kept in a closed plastic container and allowed to reach to 25 ± 1 °C before the analysis. A 50 mm flat-bottom aluminium cylindrical probe P/50 SMP was used at 25 °C. All the samples were formed into a cylindrical shape (24 mm diameter, 20 mm height) and compressed by 40% using a double compression cycle test. The pre-test speed was 1 mm/s, the test speed was 1 mm/s, and the post-test speed was 2 mm/s [27].

Microstructure of meat

The samples were cut into 1 cm × 1 cm × 0.5 cm. dehydrated at 45 °C for 24 hours. Next, the sample was attached to aluminium stubs and then coated with gold. A scanning electron microscope (JEOL JSM-T100 model) was then used to photograph the sample using an accelerated voltage of 1, the micrograph and the video print of the specimen were captured at 300x magnification [28].

Sensory analysis

Every sample was assessed by 30 untrained panellists using a 9-point hedonic scaling test in terms of colour, aroma, flavor, tenderness, juiciness, springiness and overall satisfaction. The ratings were as follows: 1-disliked very much, 2-disliked, 3-moderately disliked, 4-slightly disliked, 5-indifferent, 6-liked slightly, 7-liked moderately, 8-liked, and 9-liked a lot. The chicken meat samples were cooked for 40 minutes at an internal temperature of 120 °C in an electric oven (NN-8655, Panasonic, Osaka, Japan) cooled up to 25 °C, cut into dices (1.0 cm^3). The samples were then marked with the three-digit number randomly selected and randomly distributed to all panellists. The panellists tasted the sample one at a time and cleared their mouths with water between each sample [29].

Statistical analysis

A triplicate system was used to examine the meat samples and the Minitab 17.0 (Minitab Inc., State College, PA, USA) software was used for significant differences ($p < 0.05$). The comparison was made using one-way ANOVA for each factor separately without considering the interaction between factors.

Results and Discussion

Extraction yield, total antioxidant activity, total phenolic content and total flavonoid content of the extracts

The SLE is a simple method for the extraction of phenolic compounds using polar solvents such as methanol, ethanol, acetone, chloroform, and ethyl acetate. Without advanced technologies, it can be applied easily and less expensive, however, due to the chemicals used, this method is less preferred. The UAE method is derived from the technology of ultrasound processing which uses as an innovative technology in the food industry. It allows sonication through the process of food extraction, which is created by sound waves. Ultrasound wave sound is produced through a process of rarefaction and compression that produces 2 MHz or greater high-frequency sound. It generates cavitation bubbles near the sample tissue, thus disrupting the walls of plant cells and releasing their cell content [30].

Table 1 shows the extraction yield, total antioxidant activity, total phenolic content and total flavonoid content of pomegranate peel extracts (PPE) and green tea extracts (GTE) via the SLE and UAE methods. The UAE method showed significantly ($p < 0.05$) higher yield compared to SLE, i.e., 22.9% and 28.1% yield for PPE and GTE, respectively. The PPE yield in this study is higher than the 22% yield obtained in a previous study, which used pulsed ultrasound-assisted extraction [31], but it is lower than the 45% yield obtained in a similar study [16]. The reason for this quantitative decrease might be that the freeze-drying method used in this study. Because it resulted in a dry product, however, the other study used rotary evaporator for obtaining the final extract, which normally produces a sticky product and is weighty compared to freeze-drying, which contains less water.

The SLE method yielded 1.6% and 22.6% phenolic compounds for PPE and GTE, respectively. The PPE yield in this research is comparable to that of Wang et al. [19], who obtained a 1.04% yield. However, the use of ethyl acetate caused less extraction of phenolic yield in comparison to other solvents such as methanol and water, albeit with higher antioxidant activity. The GTE yield in the current finding is double that (9.8%) of a previous study [18]. Perva-Uzunalić et al. [32] also extracted a high phenolic yield from GTE using acetone compared to other polar solvents as part of SLE. The UAE method resulted in 74.3% and 70.4% antioxidant activity in PPE and GTE, respectively, which were significantly ($p < 0.05$) higher than the 48.2% and 41.5% antioxidant activity for PPE and GTE, respectively obtained via SLE. The antioxidant activity of PPE in this study is much higher than that of similar studies by Ali et al. [21], i.e., 68.66% and Tabaraki et al. [16] i.e., 67.94%. The antioxidant activity of GTE in this research was less than the 92% obtained by Das and Eun [17], but it was higher than the extraction using ethyl acetate from a study by Gadkari et al. [33], who obtained 42% yield.

The phenolic content of PPE extracted using UAE was significantly higher ($p < 0.05$) than that of GTE, which was 328.7 mg GAE/g sample and 268.8 mg GAE/g sample, respectively. The TPC result of PPE in this work was much higher than the result of similar research i.e., 86 mg GAE/g sample [16], 131.1 mg/g and 161.25 mg/g [20] and 276 mg/g [5]. The TPC result of GTE in this research was also higher than the GTE obtained by Das and Eun [17], i.e. 167 ± 3 g. The SLE method resulted in 389.5 mg GAE/g and 708.7 mg GAE/g of TPC for PPE and GTE, respectively. This value is higher than similar research previously carried out by Drużyńska et al. [18] and Wang et al. [19]. Different cultivars of the same plants could be one of the factors for the different amounts of TPC obtained [5].

The UAE method produced a significantly higher ($p < 0.05$) TFC level compared to SLE, while PPE showed a notably higher ($p < 0.05$) TFC level than GTE. The TFC amount obtained using UAE was 30.0 mg and 6.3 mg QE/g of PPE and GTE, respectively, whereas SLE obtained 7.9 mg and 0.4 mg QE/g for PPE and GTE, respectively. Kanatt et al. [20] reported that PPE extracted via UAE produced of 7.57 mg/g dry weight flavonoids, about three times less than the current research. However, Das and Eun [17], reported 62 mg/g

dry weight of flavonoid in GTE, which was higher than the results of this work. The SLE method resulted in significantly higher TPC from GTE correlated to UAE and the reason might be due to different solutions and methods for the extraction purpose, however, based on the results collected from the antioxidant activity, TPC (from PPE) and TFC analyses, the PPE and GTE extracted using UAE were the best overall, since the target is higher antioxidant treats hence the UAE method was therefore applied on the raw chicken meat for further investigation.

Application of the phenolic extracts on raw chicken meat: Microbial evaluation

Table 2 shows the total bacteria, yeast, and mould counts of raw chicken meat treated with PPE and GTE measured during storage for seven days at 4 ± 1 °C. No changes were observed between treatments on the zero-day of storage, most probably due to immediate analysis after the application of the extracts. The log counts for all the samples were quite high because no pre-treatments were carried out on the samples, which could be contaminated during the slaughtering and handling. On the third day, the GTE notably decreased ($p < 0.05$) the bacterial count to 5.47 log CFU/g, while, PPE decreased it to 5.89 log CFU/g and GTE mixed with PPE reduced the bacterial count to 6.50 log CFU/g compared to the control (6.81 log CFU/g). It showed that GTE and PPE had the potential to slow down the microbial growth, however, the combination of both could trigger the antagonistic effect as compared to individual treatment. On the seventh day, the bacteriostatic effect of the extracts showed no functionality on the chicken meat, however, the GTE still was able to keep the chicken meat below log 6. In common practice, to keep chicken meat at the chilling temperature more than three days is considered as not safe due to the fragility of the chicken meat, however, this study proved otherwise by the addition of GTE, specifically. The yeast and mould analyses on the treated chicken meat showed no significant changes except for an increment on the third day of storage when both PPE and GTE were combined and applied together. As the yeast and mould are more difficult to be inhibited compared to the bacteria, the antagonistic effect of PPE and GTE, and the uneven distribution of microbial load that occurred naturally in the chicken meat could be affecting the results.

Similar research on some plant extracts (rosemary and cloves) applied on beef also showed significant inhibition of bacteria after 9 days of refrigerated storage, however, the sample used was cooked [34]. Likewise, GTE has been claimed to decrease microbial spoilage of raw beef meat stored at 4 °C for 9 days [35]. Malviya et al. [36] also proved the antibacterial activities of pomegranate extract and hypothesized its antibacterial effects against gram-positive and gram-negative bacteria. They declared that the antibacterial effects of PPE targeted metabolic toxins or broad-spectrum antimicrobial compounds. Kanatt et al. [20] applied different concentrations (0.01%, 0.05% and 0.1%) of the PPE on the chicken products and found that it is effective against the well-known food inhibitors such as *E. coli*, *S. typhimurium*, *Pseudomonas* spp., *S. aureus* and *B. cereus*. The PPE was also claimed to be effective against Gram-positive bacteria and showed significant result only against *Pseudomonas* spp. of Gram-negative.

The natural phenolic compound has certain antibacterial activity *in vitro* [35], several factors affecting the antimicrobial traits of natural antioxidants and the existing of these factors decrease its efficiencies such as low pH and low solubility. Generally, the phenolic compounds showed their antimicrobial effects when tested on the media, however, their antimicrobial effects are decreased when applied to food [34]. Microbial spoilage usually limits the shelf life of the raw meat. Raw patties have a shelf life of around 7 days based on hygiene and pre-evasion conditions of refrigeration and aerobiosis [35]. The reason for no significant increase in log CFU/g of the control sample on the seventh day of storage time might be proper hygiene and proper refrigeration condition. The fluctuation of microbes is related to appropriate conditions (nutrient, temperature, pH, and water activity), so the growth of bacteria also changes when the optimal condition is altered [37].

Water holding capacity, pH and lipid peroxidation

Table 3 shows the impact of PPE and GTE on the water holding capacity, pH and lipid peroxidation of raw chicken meat stored at 4 ± 1 °C for seven days. The

extracts did not significantly ($p > 0.05$) affect the water holding capacity of meat samples compared to the control. Similar studies confirm the result of this research [38]. However, Morsy et al. [39] found that the nanoparticles of pomegranate peel extract improved the water holding capacity of meatballs during refrigerated storage, however, the pomegranate peel extract was mixed in the meatballs' emulsion, where else in this study the extracts were only applied on the surface. The application of the extracts significantly reduced ($p < 0.05$) the pH of the meat on zero-day compared to the control but did not have any notable effects ($p > 0.05$) on the third and seventh days of storage. The treated meat sample with GTE (5.65 ± 0.05) showed the lowest pH followed by PPE + GTE (5.88 ± 0.04), PPE (6.01 ± 0.11), and the control (6.18 ± 0.08). A similar study confirms the result of this research, i.e., Qin et al. [40], found that pomegranate peel extracts significantly decreased the pH of raw ground pork from pH 5.88 to 5.61. Low pH can inhibit microbial growth, as the optimal level for bacteria to grow is around pH 7.0 [34, 41]. This could be one of the factors that helped in controlling the bacteria growth especially for the sample treated with GTE.

The application of the extracts, however, did not significantly change ($p > 0.05$) the TBARS values of the chicken meats compared to the control and during storage time. Vaithiyanathan et al. [24], claimed that dipping samples in PPE had little effect on the TBARS values of the treated samples, but significant ($p < 0.05$) changes were observed on the fourth day of storage. A study on meat products also declared the significant effects of green tea on the inhibition of TBARS value [9]. Turgut et al. [42] stated that PPE inhibited the TBARS value of beef meatball. The less significant results of the TBARS value in this study might be due to the lower percentage of phenolic extracts used, as some mentioned studies applied up to 1% phenolic extract, which is much higher than the 0.02% used in this research. Selection of low concentrate phenolic (0.02%) in this research was considered due to the effect on the chicken meat sensory attributes.

Colour of the chicken meat

Table 4 shows the effects of PPE and GTE on the colour of raw chicken meat stored at 4 ± 1 °C. The result reveals that the phenolic extracts from different sources did not have any significant effect ($p > 0.05$) on the lightness (L^* value) and redness (a^* value) of the chicken meat except a lower L^* value for PPE+GTE-treated sample and higher a^* value for PPE-treated sample. Both changes most probably occurred due to the effect of storage time as the results were detected on the seventh day of storage. The chicken meat had some notable increments ($p < 0.05$) on the yellowness (b^* value) at the zero-day, especially when treated with GTE due to the green tea colour. On the third and seventh day of storage, no changes were observed for the b^* values, however, the values were still higher compared to the control. The colour changes might be minimal but it can influence the panellists' perceptions. Since the TBARS values of this research indicated no significant difference, therefore, it can also be concluded that oxidation did not affect the meat colour.

Texture properties of the chicken meat

Table 5 shows the texture profile analysis (TPA) of the raw chicken meat samples treated with PPE and GTE and stored at 4 ± 1 °C for seven days. In general, no changes ($p > 0.05$) were observed for the hardness, chewiness, springiness and cohesiveness of the treated chicken meats and control within the zero-day and third day of the storage. However, on the seventh day, the hardness values were increased, while the cohesiveness values were decreased for all the samples. The results most probably were affected by the storage time rather than the extracts applied, where it is uncommon to keep raw chicken meat for more than three days in chilling temperature as mentioned earlier. A study supported the finding where plant extracts including green tea extract applied on chicken breast meat resulted in no significant ($p > 0.05$) changes on hardness, cohesiveness, and chewiness [43]. However, uneven results were observed for the chewiness GTE-treated chicken meat and the springiness of the untreated chicken meat, again, most probably due to the effect of the seven days of storage. Nevertheless, it can be concluded that the extracts did not influence the texture profiles of the chicken meat as the applications were only on the surfaces.

Table 1. Comparison between ultrasound-assisted and solid-liquid extraction methods

Measurements	**Extracts**	**Extraction Methods**	
		Ultrasound	**Solid-Liquid**
Extraction yield (%)	PPE	22.9 ± 2.7^{Aa}	1.6 ± 0.25^{Bb}
	GTE	28.1 ± 2.05^{Aa}	22.6 ± 3.5^{Ab}
Total antioxidant activity (%)	PPE	74.3 ± 2.26^{Aa}	48.2 ± 0.02^{Ab}
	GTE	70.4 ± 1.8^{Aa}	41.5 ± 2.6^{Bb}
Total phenolic content (mg GAE/g)	PPE	328.7 ± 1.6^{Aa}	389.5 ± 0.4^{Ba}
	GTE	268.8 ± 1.8^{Bb}	708.7 ± 10.5^{Aa}
Total flavonoid content (mg QE/g)	PPE	30.0 ± 2.5^{Aa}	7.9 ± 0.4^{Ab}
	GTE	6.3 ± 1.8^{Ba}	0.4 ± 0.4^{Bb}

PPE = Pomegranate peel extracts, GTE = Green tea leaves extracts. Means with different small letters of the same measurement are significantly different ($p < 0.05$) between rows, means with different capital letters of the varied extraction methods are significantly different ($p < 0.05$) between columns

Table 2. Effects of PPE and GTE on total plate count and total Yeast and Mould count of raw chicken meat stored at 4 ± 1 °C for seven days

Parameters	**Treatments**	**Day 0**	**Day 3**	**Day 7**
Total Plate Count (Log CFU/g)	Control	5.45 ± 0.29^{Ab}	6.81 ± 0.68^{Aa}	6.02 ± 0.14^{Aab}
	PPE	5.37 ± 0.4^{Aa}	5.89 ± 0.54^{ABa}	6.21 ± 0.22^{Aa}
	GTE	5.27 ± 0.57^{Aa}	5.47 ± 0.32^{Ba}	5.96 ± 0.13^{Aa}
	PPE+GTE	5.5 ± 0.3^{Ab}	6.50 ± 0.31^{ABa}	6.26 ± 0.34^{Aab}
Total Yeast and Mould (Log CFU/g)	Control	5.11 ± 0.32^{Aa}	5.16 ± 0.4^{Aa}	5.65 ± 0.47^{Aa}
	PPE	5.2 ± 0.26^{Aa}	5.84 ± 0.55^{Aa}	5.95 ± 0.1^{Aa}
	GTE	5.23 ± 0.42^{Aa}	5.2 ± 0.13^{Aa}	5.24 ± 0.47^{Aa}
	PPE+GTE	5.19 ± 0.29^{Ab}	6.16 ± 0.39^{Aa}	5.4 ± 0.16^{Ab}

PPE = Pomegranate peel extracts, GTE = Green tea leaves extracts. Means with different small letters of the same treatment (effect of the day) are significantly different ($p < 0.05$), Means with different capital letters of the varied treatment (effect of treatment) are significantly different ($p < 0.05$)

Table 3. Effects of PPE and GTE on the water holding capacity, pH and lipid peroxidation of raw chicken meat stored at 4 ± 1 °C for seven days

Parameters	**Treatments**	**Day 0**	**Day 3**	**Day 7**
Water Holding Capacity	Control	31.52 ± 4.98^{Aa}	22.47 ± 5.10^{Aa}	21.27 ± 3.12^{Aa}
	PPE	27.17 ± 5.82^{Aa}	21.76 ± 2.68^{Aa}	18.55 ± 3.75^{Aa}
	GTE	27.56 ± 6.38^{Aa}	28.53 ± 1.67^{Aa}	28.37 ± 3.39^{Aa}
	PPE+GTE	29.75 ± 4.37^{Aa}	28.33 ± 2.67^{Aa}	31.09 ± 4.34^{Aa}
pH	Control	6.18 ± 0.08^{Aa}	5.86 ± 0.20^{Aa}	6.03 ± 0.04^{Aa}
	PPE	6.01 ± 0.11^{ABa}	6.11 ± 0.34^{Aa}	6.02 ± 0.01^{Aa}
	GTE	5.65 ± 0.05^{Cb}	5.71 ± 0.07^{Ab}	5.92 ± 0.05^{Aa}
	PPE+GTE	5.88 ± 0.04^{Ba}	5.84 ± 0.04^{Aa}	5.80 ± 0.26^{Aa}

Table 3 (cont'd). Effects of PPE and GTE on the water holding capacity, pH and lipid peroxidation of raw chicken meat stored at 4 ± 1 °C for seven days

Parameters	Treatments	Day 0	Day 3	Day 7
Lipid Peroxidation (TBARS, mg MDA/kg)	Control	0.30 ± 0.10^{Aa}	0.23 ± 0.10^{Aa}	0.35 ± 0.11^{Aa}
	PPE	0.24 ± 0.10^{Aa}	0.18 ± 0.10^{Aa}	0.33 ± 0.02^{Aa}
	GTE	0.34 ± 0.10^{Aa}	0.23 ± 0.10^{Aa}	0.31 ± 0.11^{Aa}
	PPE+GTE	0.21 ± 0.05^{Aa}	0.26 ± 0.11^{Aa}	0.20 ± 0.10^{Aa}

PPE = Pomegranate peel extracts, GTE = Green tea leaves extracts. Means with different small letters of the same treatment (effect of day) are significantly different ($p < 0.05$), Means with different capital letters of the varied treatment (effect of treatment) are significantly different ($p < 0.05$).

Table 4. The effects of PPE and GTE on the *L**, *a** and *b** values of raw chicken meat stored at 4 ± 1 °C for seven days

Parameters	Treatments	Day 0	Day 3	Day 7
*L**	Control	61.00 ± 4.15^{Aa}	58.82 ± 1.63^{Aa}	58.04 ± 2.50^{Aa}
	PPE	63.58 ± 3.89^{Aa}	60.15 ± 2.40^{Aa}	56.23 ± 3.38^{Aa}
	GTE	58.93 ± 1.07^{Aa}	59.57 ± 3.12^{Aa}	55.65 ± 3.11^{Aa}
	PPE+GTE	63.16 ± 3.32^{Aa}	58.80 ± 2.01^{Aab}	54.88 ± 1.11^{Ab}
*a**	Control	10.69 ± 2.22^{Aa}	10.60 ± 1.75^{Aa}	9.96 ± 2.25^{Aa}
	PPE	9.59 ± 2.03^{Ab}	11.21 ± 0.59^{Aab}	13.28 ± 0.91^{Aa}
	GTE	12.91 ± 0.58^{Aa}	10.21 ± 1.86^{Aa}	12.28 ± 1.71^{Aa}
	PPE+GTE	10.33 ± 1.50^{Aa}	10.90 ± 1.35^{Aa}	12.98 ± 1.05^{Aa}
*b**	Control	7.85 ± 2.70^{Ba}	11.42 ± 3.42^{Aa}	11.00 ± 4.21^{Aa}
	PPE	12.45 ± 1.02^{ABa}	15.40 ± 1.33^{Aa}	15.81 ± 2.91^{Aa}
	GTE	14.15 ± 1.65^{Aa}	14.78 ± 0.61^{Aa}	15.19 ± 1.88^{Aa}
	PPE+GTE	11.63 ± 1.86^{ABa}	13.44 ± 2.16^{Aa}	13.84 ± 0.80^{Aa}

PPE = Pomegranate peel extracts, GTE = Green tea leaves extracts. Means with different small letters of the same treatment (effect of the day) are significantly different ($p < 0.05$), Means with different capital letters of the varied treatment (effect of treatment) are significantly different ($p < 0.05$)

Table 5. The effects of PPE and GTE on the texture profile of raw chicken meat stored at 4 ± 1 °C for seven days

Parameters	Treatments	Day 0	Day 3	Day 7
Hardness (g)	Control	1546 ± 482^{Ab}	1882 ± 998^{Ab}	19434 ± 4004^{Aa}
	PPE	2946 ± 2121^{Ab}	3969 ± 1376^{Ab}	23930 ± 2498^{Aa}
	GTE	2638 ± 938^{Ab}	2774 ± 15^{Ab}	24035 ± 57^{Aa}
	PPE+GTE	2480 ± 10^{Ab}	2978 ± 91^{Ab}	16377 ± 46^{Aa}
Chewiness (g.mm)	Control	816 ± 236^{Aa}	762 ± 332^{Aa}	1244 ± 980^{Aa}
	PPE	1072 ± 695^{Aa}	1421 ± 465^{Aa}	2680 ± 891^{Aa}
	GTE	1042 ± 339^{Ab}	1125 ± 36^{Ab}	3282 ± 555^{Aa}
	PPE+GTE	1001 ± 231^{Aa}	1288 ± 248^{Aa}	1446 ± 508^{Aa}

Table 5 (cont'd). The effects of PPE and GTE on the texture profile of raw chicken meat stored at 4 ± 1 °C for seven days

Parameters	Treatments	Day 0	Day 3	Day 7
Springiness (mm)	Control	0.74 ± 0.08^{Aa}	0.64 ± 0.08^{Aa}	0.20 ± 0.04^{Bb}
	PPE	0.62 ± 0.05^{ABab}	0.63 ± 0.02^{Aa}	0.30 ± 0.05^{Aa}
	GTE	0.50 ± 0.05^{Bb}	0.60 ± 0.001^{Aa}	0.30 ± 0.003^{ABab}
	PPE+GTE	0.65 ± 0.04^{ABa}	0.60 ± 0.004^{Aa}	0.30 ± 0.03^{ABab}
Cohesiveness	Control	0.71 ± 0.02^{Aa}	0.66 ± 0.03^{Aa}	0.20 ± 0.08^{Ab}
	PPE	0.60 ± 0.08^{Aa}	0.56 ± 0.03^{Aa}	0.30 ± 0.04^{Ab}
	GTE	0.60 ± 0.05^{Aa}	0.66 ± 0.06^{Aa}	0.30 ± 0.03^{Ab}
	PPE+GTE	0.64 ± 0.06^{Aa}	0.66 ± 0.07^{Aa}	0.28 ± 0.03^{Ab}

PPE = Pomegranate peel extracts, GTE = Green tea leaves extracts. Means with different small letters of the same treatment (effect of day) are significantly different ($p < 0.05$), Means with different capital letters of the varied treatment (effect of treatment) are significantly different ($p < 0.05$)

The microstructure of the chicken meat

Figure 1 reveals the microstructure of the raw chicken meat treated with the extracts on the zero-day. The results showed changes in the microstructure of the chicken meat surfaces treated with phenolic compared to the control. The black holes visible in the control meat sample were filled by the extracts via the marinating process through which the phenolic compounds were absorbed. The surface of the sample treated with PPE appeared to be smoother and clearer than the GTE-treated sample, which looks rough and uneven. The structure of the sample treated with both PPE and GTE was observed to be a little bit rougher similar to the sample treated with GTE but it also had a smooth surface similar to the sample treated with PPE only. It can be concluded that PPE might had smaller particle sizes compared to GTE due to the presence of catechin in GTE. In addition, a study on the effects of marination of grilled chicken with some ingredients on the microstructure of the meat found the same results as this research [28].

Sensory evaluation

The results of sensory evaluation of the treated meat sample using GTE and PPE are shown in Table 6. Thirty untrained panellists evaluated the cooked chicken meat on the third day of storage using a 9-point hedonic scale. Selection of the third day for the sensory evaluation was due to the safety of panellists based on the microbial results obtained. The data revealed that all samples were not significantly ($p > 0.05$) different in terms of colour, aroma, flavor, tenderness, juiciness, and springiness. However, the overall acceptance scores of the samples were significantly different ($p > 0.05$) where the control sample had the highest score, followed by the samples treated with PPE, PPE + GTE and GTE. Similar research that had studied the effect of applying tea catechins on raw patties of beef and chicken found that the sample treated with tea catechins had significantly decreased sensory scores, especially colour [8]. The reason for the GTE's lowest score might be due to the yellow colour of the green tea, which normally affects the food and alters its normal colour. In addition, the distribution of the particles of the GTE as observed in the microstructure analysis could also influence the panellists. This result also justified the decision of applying lower concentration of the extracts on the chicken meat as sensory results play important roles towards the acceptability of the products.

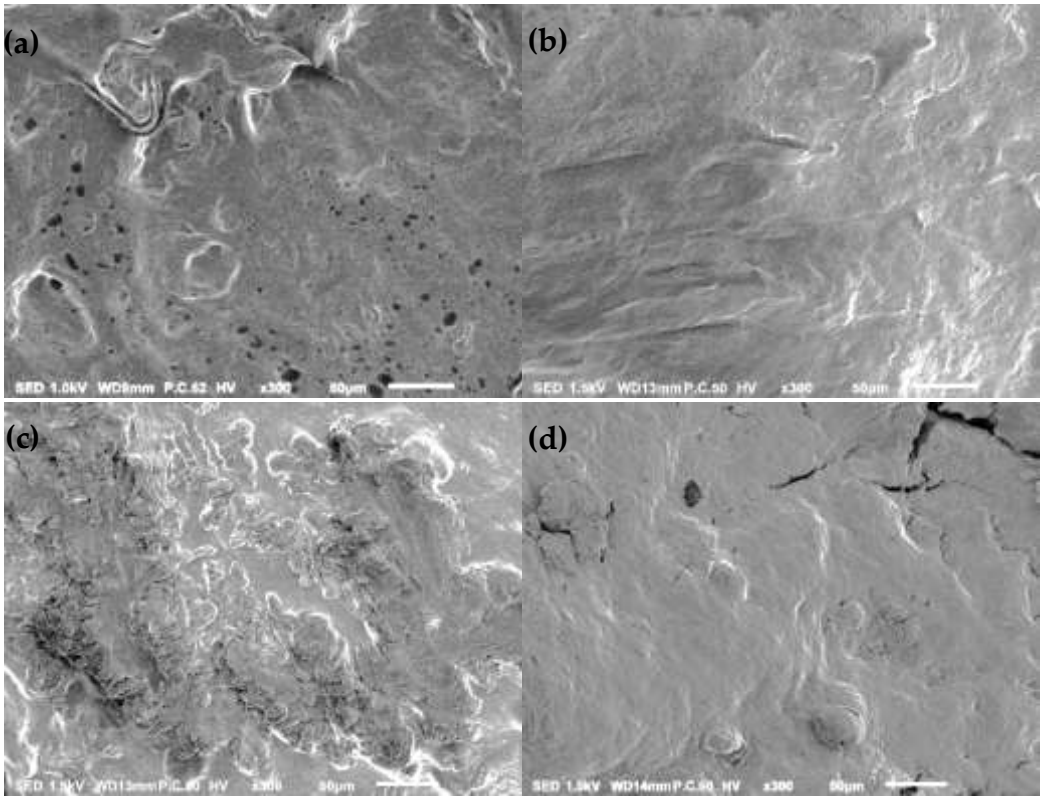


Figure 1. The effects of PPE and GTE on the microstructure of raw chicken meat (300 x): (a) control, (b) chicken meat treated with pomegranate peel extracts (PPE), (c) chicken meat treated with green tea extracts (GTE), (d) chicken meat treated with pomegranate peel extracts and green tea extracts (PPE+GTE)

Table 6. The effects of PPE and GTE on the sensory analysis of raw chicken meat stored at 4 ± 1 °C for three days

Attributes	Treatments			
	Control	PPE	GTE	PPE+GTE
Colour	5.75 ± 1.50^{A}	5.16 ± 1.40^{A}	4.91 ± 1.90^{A}	5.16 ± 2.10^{A}
Aroma	5.5 ± 1.60^{A}	5.33 ± 1.6^{A}	6.08 ± 1.4^{A}	4.83 ± 1.4^{A}
Flavor	5.20 ± 1.20^{A}	4.91 ± 1.80^{A}	5.00 ± 1.50^{A}	4.70 ± 1.60^{A}
Tenderness	6.50 ± 1.60^{A}	5.91 ± 1.50^{A}	5.00 ± 1.40^{A}	5.08 ± 2.00^{A}
Juiciness	5.16 ± 1.50^{A}	4.91 ± 1.80^{A}	4.91 ± 1.40^{A}	4.91 ± 1.30^{A}
Springiness	5.75 ± 1.70^{A}	5.58 ± 1.30^{A}	5.00 ± 1.40^{A}	5.08 ± 1.30^{A}
Overall acceptability	6.41 ± 1.30^{A}	5.66 ± 1.30^{AB}	4.83 ± 1.20^{B}	5.58 ± 1.50^{AB}

PPE = Pomegranate peel extracts, GTE = Green tea leaves extracts. Means with different capital letters of the varied treatments (row-wise) are significantly different ($p < 0.05$), Means ± standard deviation (n=30)

Conclusion

The extracts of pomegranate (*Punica granatum* L.) peel and green tea (*Camellia sinensis*) leaves extracted using ultrasound-assisted extraction (UAE) and solid-liquid extraction (SLE) were confirmed of containing phenolic compounds based on their TPC, TFC, and total antioxidant activity. The UAE method is considered a better method because it resulted in a high capacity of radical scavenging activity, the best production of total flavonoids, and the best total yield compared to SLE, even though the total phenolic compounds extracted via SLE were higher than that of UAE. Green tea extract (GTE) was better in inhibiting the microbial growth over seven days of chilled storage compared to pomegranate peel extract (PPE) or a combination of both. However, other physicochemical properties of the chicken meat treated with the extracts such as water holding capacity, pH, lipid peroxidation and texture were not much affected, most probably due to the lower concentration used. The yellowness (*b**) of the chicken meat were higher compared to the control. The microstructure of the treated chicken meat surface also changed significantly especially when GTE was applied. This can also be related to the lower overall acceptability of the GTE-treated chicken meat in the sensory analysis. Therefore, future work should consider this matter as increasing the concentration of the GTE might produce better microbial and physicochemical properties results of the treated chicken meat, however, further additional treatments could help to cater the negative impact on the appearance and acceptance.

References

1. Casaburi, A., Di Martino, V., Ercolini, D., Parente, E. and Villani, F. (2015). Antimicrobial activity of *Myrtus communis* L. water-ethanol extract against meat spoilage strains of *Brochothrix thermosphacta* and *Pseudomonas fragi* in vitro and in meat. *Annals of Microbiology*, 65: 841-850.
2. Giatrakou, V. and Savvaidis, I. N. (2012). Bioactive packaging technologies with chitosan as a natural preservative agent for extended shelf-life food products, modified atmosphere and active packaging technologies. Taylor & Francis, Boca Raton: pp. 685-730.
3. Ameer, K., Shahbaz, H. M. and Kwon, J. H. (2017). Green extraction methods for polyphenols from plant matrices and their byproducts: A review. *Comprehensive Reviews in Food Science and Food Safety*, 16: 295-315.
4. Pinelo, M., Ruiz-Rodríguez, A., Sineiro, J., Señoráns, F. J., Reglero, G. and Núñez, M. J. (2007). Supercritical fluid and solid-liquid extraction of phenolic antioxidants from grape pomace: A comparative study. *European Food Research and Technology*, 226: 199-205.
5. Hasnaoui, N., Wathelet, B. and Jiménez-Araujo, A. (2014). Valorization of pomegranate peel from 12 cultivars: Dietary fibre composition, antioxidant capacity and functional properties. *Food Chemistry*, 160: 196-203.
6. Al-Rawahi, A. (2014). Phenolic constituents of pomegranate peels (*Punica granatum L.*) cultivated in Oman. *European Journal of Medicinal Plants*, 4: 315-331.
7. Sinija, V. R. and Mishra, H. N. (2009). Green tea: Health benefits. *Journal of Nutritional and Environmental Medicine*, 17: 232-242.
8. Mitsumoto, M., O'Grady, M. N., Kerry, J. P. and Joe Buckley, D. (2005). Addition of tea catechins and vitamin C on sensory evaluation, colour and lipid stability during chilled storage in cooked or raw beef and chicken patties. *Meat Science*, 69: 773-779.
9. Bozkurt, H. (2006). Utilization of natural antioxidants: Green tea extract and *Thymbra spicata* oil in Turkish dry-fermented sausage. *Meat Science*, 73: 442-450.
10. Cong-Cong, X., Bing, W., Yi-Qiong, P., Jian-Sheng, T. and Tong, Z. (2017). Advances in extraction and analysis of phenolic compounds from plant materials. *Chinese Journal of Natural Medicines*, 15: 721-731.
11. Ismail, T., Sestili, P. and Akhtar, S. (2012). Pomegranate peel and fruit extracts: A review of potential anti-inflammatory and anti-infective effects. *Journal of Ethnopharmacology*, 143: 397-405.

12. Pinelo, M., Del-Fabbro, P., Manzocco, L., Nuñez, M. J. and Nicoli, M. C. (2005). Optimization of continuous phenol extraction from *Vitis vinifera* byproducts. *Food Chem*istry, 92: 109-117.
13. Díaz-de-Cerio E., Tylewicz U., Verardo V., Fernández-Gutiérrez A. and Segura-Carretero A., (2017). Design of sonotrode ultrasound-assisted extraction of phenolic compounds from *Psidium Guajava* L. leaves. *Food Analytical Methods*, 10(8): 2781-2791.
14. Chemat, F. and Zill-E-Huma and Khan, M. K. (2011). Applications of ultrasound in food technology: Processing, preservation and extraction. *Ultrasonics Sonochemistry*, 18: 813-835.
15. Marchi, L. B., Monteiro, A. R. G., Mikcha, J. M. G., Santos, A. R., Chinellato, M. M., Marques, D. R., Dacome, A. S. and Costa, S. C. (2015). Evaluation of antioxidant and antimicrobial capacity of pomegranate peel extract (*Punica granatum*. L.) under different drying temperatures. *Chemical Engineering Transactions*, 44: 121-126.
16. Tabaraki, R., Heidarizadi, E. and Benvidi, A. (2012). Optimization of ultrasonic-assisted extraction of pomegranate (*Punica granatum L.*) peel antioxidants by response surface methodology. *Separation and Purification Technology*, 98: 16-23.
17. Das, P. R. and Eun, J. B. (2018). A comparative study of ultra-sonication and agitation extraction techniques on bioactive metabolites of green tea extract. *Food Chemistry*, 253: 22-29.
18. Drużyńska, B., Stępniewska, A. and Wołosiak, R. (2007). The influence of time and type of solvent on efficiency of the extraction of polyphenols from green tea and antioxidant properties obtained extracts. *ACTA Scientiarum polonorum Technologia Alimentaria*, 6: 29-40.
19. Wang, Z., Pan, Z., Ma, H. and Atungulu, G. G. (2011). Extract of phenolics from pomegranate peels. *Open Food Science Journal*, 5: 17-25.
20. Kanatt, S. R., Chander, R. and Sharma, A. (2010). Antioxidant and antimicrobial activity of pomegranate peel extract improves the shelf life of chicken products. *International Journal of Food Science Technology*, 45: 216-222.
21. Ali, U. and Kumar, P. (2015). Effect of Soxhlet and ultrasound assisted extraction on antioxidant activity of pomegranate peel extract. *International Journal of Food and Nutritional Science*, 3: 265-270.
22. Al-Rawahi, A. S., Rahman, M. S., Guizani, N. and Essa, M. M. (2013). Chemical composition, water sorption isotherm, and phenolic contents in fresh and dried pomegranate peels. *Drying Technology*, 31: 257-263.
23. Ghosh, M., Sinha, B. N., Seijas, J. A., Vázquez-Tato, M. P. and Feás, X. (2014). Flavonoids and phenolic compounds from *Litsea polyantha* juss. bark. *The 18th International Electronic Conference on Synthetic Organic Chemistry*, 2014: pp. 1-5.
24. Vaithiyanathan, S., Naveena, B. M., Muthukumar, M., Girish, P. S. and Kondaiah, N. (2011). Effect of dipping in pomegranate (*Punica granatum*) fruit juice phenolic solution on the shelf life of chicken meat under refrigerated storage (4°C). *Meat Science*, 88: 409-414.
25. Zheng, H., Han, M., Yang, H., Xu, X. and Zhou, G. (2018). The effect of pressure-assisted heating on the water holding capacity of chicken batters. *Innovative Food Science and Emerging Technologies*, 45: 280-286.
26. Jauhar, S., Ismail-Fitry, M. R., Chong, G. H., Nor-Khaizura, M. A. R. and Ibadullah, W. Z. W. (2020). Application of supercritical carbon dioxide (SC-CO^2) on the microbial and physicochemical quality of fresh chicken meat stored at chilling temperature. *International Food Research Journal*, 27(1): 103-110.
27. Zheng, H., Xiong, G., Han, M., Deng, S., Xu, X. and Zhou, G. (2015). High pressure/thermal combinations on texture and water holding capacity of chicken batters. *Innovative Food Science and Emerging Technologies*, 30: 8-14.
28. Komoltri, P. and Pakdeechanuan, P. (2012). Effects of marinating ingredients on physicochemical, microstructural and sensory properties of golek chicken. *International Food Research Journal*, 19: 1449-1455.

29. Saengphol, E. and Pirak, T. (2018). Hoary basil seed mucilage as fat replacer and its effect on quality characteristics of chicken meat model. *Agriculture and Natural Resources*, 52(4): 382-387.
30. Jauhar, S., Ismail-Fitry, M. R., Chong, G. H., Nor-Khaizura, M. A. R. and Ibadullah, W. Z. W. (2018). Polyphenol compounds from pomegranate (*Punica Granatum*) extracted via various methods and its application on meat and meat products: A review. *Journal of Advanced Research in Applied Sciences and Engineering Technology*, 12: 1-12.
31. Pan, Z., Qu, W., Ma, H., Atungulu, G. G. and McHugh, T. H. (2012). Continuous and pulsed ultrasound-assisted extractions of antioxidants from pomegranate peel. *Ultrasonics Sonochemistry*, 19: 365-372.
32. Perva-Uzunalić, A., Škerget, M., Knez, Ž., Weinreich, B., Otto, F. and Grüner, S. (2006). Extraction of active ingredients from green tea (*Camellia sinensis*): Extraction efficiency of major catechins and caffeine. *Food Chemistry*, 96(4): 597-605.
33. Gadkari, P. V., Kadimi, U. S. and Balaraman, M. (2014). Catechin concentrates of garden tea leaves (*Camellia sinensis L.*): Extraction/isolation and evaluation of chemical composition. *Journal of the Science of Food and Agriculture*, 94: 2921-2928.
34. Ahn, J. and Grün, I. U. and Mustapha, A. (2007). Effects of plant extracts on microbial growth, colour change, and lipid oxidation in cooked beef. *Food Microbiology*, 24: 7-14.
35. Bañón, S., Díaz, P., Rodríguez, M., Garrido, M. D. and Price, A. (2007). Ascorbate, green tea and grape seed extracts increase the shelf life of low sulphite beef patties. *Meat Science*, 77: 626-633.
36. Malviya, S., Arvind, Jha, A. and Hettiarachchy, N. (2014). Antioxidant and antibacterial potential of pomegranate peel extracts. *Journal of Food Science and Technology*, 51: 4132-4137.
37. Chavasit, V., Photi, J., Purttiponthanee, S. and Saekoo, P. (2018). Use of bacterial growth curve for assessing risk of microbiological pathogens in food products, microbial contamination and food degradation. Academic Press, Massachusetts: pp. 341-365.
38. El-Nashi, H. B., Abdel Fattah, A. F. A. K., Abdel Rahman, N. R. and Abd El-Razik, M. M. (2015). Quality characteristics of beef sausage containing pomegranate peels during refrigerated storage. *Annals of Agricultural Sciences*, 60: 403-412.
39. Morsy, M. K., Mekawi, E. and Elsabagh, R. (2018). Impact of pomegranate peel nanoparticles on quality attributes of meatballs during refrigerated storage. *LWT - Food Science and Technology*, 89: 489-495.
40. Qin, Y. Y., Zhang, Z. H., Li, L., Xiong, W., Shi, J. Y., Zhao, T. R. and Fan, J. (2013). Antioxidant effect of pomegranate rind powder extract, pomegranate juice, and pomegranate seed powder extract as antioxidants in raw ground pork meat. *Food Science and Biotechnology*, 22: 1063-1069.
41. Jay, J. M. (1998). Modern food microbiology (Fifth Edition). Aspen Publishers, Inc., Maryland: pp. 38-41.
42. Turgut, S. S., Soyer, A. and Işıkçı, F. (2016). Effect of pomegranate peel extract on lipid and protein oxidation in beef meatballs during refrigerated storage. *Meat Science*, 116: 126-132.
43. Rababah, T. M., Ereifej, K. I., Al-Mahasneh, M. A. and Al-Rababah, M. A. (2006). Effect of plant extracts on physicochemical properties of chicken breast meat cooked using conventional electric oven or microwave. *Poultry Science*, 85(1): 148-154.

Malaysian Journal of Analytical Sciences (MJAS)
Published by Malaysian Analytical Sciences Society

FORENSIC DISCRIMINATION OF BLUE PEN INKS: EMERGENCE OF HYBRID PEN INKS

(Diskriminasi Forensik Bagi Dakwat Pen Biru: Kemunculan Dakwat Pen Hibrid)

Linthini Gannetion[1], Siti Nur Musliha Mohamad Noor[2], Poh Ying Lim[3], Kah Haw Chang[1], Ahmad Fahmi Lim Abdullah[1]*

[1]Forensic Science Programme, School of Health Sciences, Universiti Sains Malaysia, 16150 Kubang Kerian, Kelantan, Malaysia
[2]Document Examination Division, Forensic Science Analysis Centre, Department of Chemistry, Jalan Sultan, 46661 Petaling Jaya, Selangor, Malaysia
[3]Department of Community Health, Faculty of Medicine and Health Sciences, Universiti Putra Malaysia, 43400 Serdang, Selangor, Malaysia

**Corresponding author: fahmilim@usm.my*

Received: 18 May 2021; Accepted: 22 July 2021; Published: 29 August 2021

Abstract

Pens are frequently used to make alterations to documents during forgery. Comparing to conventional inks, hybrid pen ink brings a different challenge to forensic document examiners in differentiating ink entries on a questioned document. Therefore, this study aims to investigate the characteristics of different blue pen inks using non-destructive approaches followed by destructive techniques. Twenty blue pens consisting of ten ballpoint pens and ten gel pens of various brands were subjected to microscopic examination, video spectral comparator examination, attenuated total reflectance-Fourier transform infrared (ATR-FTIR) spectroscopy, and thin layer chromatography (TLC) using two different solvent systems. The microscopic examination showed significant different optical features on handwritten samples produced by ballpoint and gel pens. Luminescence behaviour of certain inks allowed discrimination, and ATR-FTIR coupled with principal component analysis clustered ink samples of similar compositional profiles in a score plot. TLC allowed further discrimination of ink samples from ballpoint and hybrid pens. The proposed analysis scheme had categorised the ink samples into 11 groups. To conclude, the hybrid pen labelled as gel pen appeared optically like gel pen. However, it possesses chemical characteristics similar to a ballpoint pen. Therefore, its emergence deserves attention during forensic questioned document examination, particularly for the determination of pen inks.

Keywords: forensic science, questioned document, ink, hybrid pen, discrimination, alteration.

Abstrak

Pen sering digunakan untuk membuat pindaan ke atas dokumen ketika pemalsuan. Berbanding dengan dakwat yang lazim, kemunculan dakwat pen hibrid mendatangkan suatu cabaran yang berbeza kepada pemeriksa dokumen forensik dalam membezakan entri dakwat pada suatu dokumen yang dipertikaikan. Justeru, kajian ini bermatlamat untuk menyiasat ciri-ciri dakwat pen biru yang berbeza dengan menggunakan pendekatan bukan-pemusnah diikuti dengan teknik pemusnah. Dua puluh pen biru yang terdiri daripada sepuluh pen mata bulat dan sepuluh pen gel dari pelbagai jenama telah dikenakan kepada pemeriksaan mikroskop, pemeriksaan perbanding spektrum video, spektroskopi infra merah transformasi Fourier dengan

pantulan penuh pengecilan (ATR-FTIR) dan kromatografi lapisan nipis (TLC) dengan menggunakan dua sistem pelarut berbeza. Pemeriksaan mikroskop menunjukkan perbezaan ciri-ciri optik yang bererti pada sampel bertulis yang dihasilkan oleh pen mata bulat dan pen gel. Perilaku pendarcahaya pada sebahagian dakwat membenarkan pembezaan dan ATR-FTIR bersama dengan analisis komponen utama mengelompokkan sampel dakwat dengan profil kandungan yang serupa dalam suatu plot skor. TLC membolehkan diskriminasi sampel-sampel seterusnya daripada dakwat pen mata bulat dan dakwat pen hibrid. Skema analisis yang dicadangkan telah mengumpulkan sampel dakwat kepada 11 kumpulan. Secara kesimpulan, pen hibrid yang dilabelkan sebagai pen gel kelihatan serupa seperti pen gel secara optik. Namun, dakwat tersebut membawa ciri-ciri kimia serupa dengan dakwat pen mata bulat. Dengan itu, kemunculannya perlu diberi perhatian ketika pemeriksaan forensik dokumen yang dipertikaikan, terutamanya bagi penentuan dakwat pen.

Kata kunci: sains forensik, dokumen yang dipertikaikan, dakwat, pen hibrid, diskriminasi, pindaan.

Introduction

A written document can be forged or altered by over-writing, extending, or interlining pre-existing handwriting on the document. Such acts are frequently done by the fraudsters to gain monetary profit or other illegal purposes [1, 2]. Usually, these types of alterations are made intentionally in ways that do not create suspicion to the recipients or victims. Therefore, the newly pen entries must appear optically similar to the original entries on the altered document as much as possible. For investigation of forged document, both optical and chemical characterisation of writing inks can help establish whether an alteration was made, the types of ink used, and the probable source of pen [2, 3].

Writing inks are generally complex homogenous medium made up of colourants, either dyes or pigments, with various combinations of solvents, resins, surfactants, lubricants, emulsifiers and/or additives [1, 4]. Different ink compositions would be used by the manufacturers to achieve the desired property or to fulfil the market trend [5]. Therefore, ink compositions for a particular colour would vary between manufacturers. Variations can occur between batches even by the same manufacturers. These variations could provide important evidential values for the discrimination of inks upon forensic examination on the suspected ink entry in a document [1-3]. Of the common pens available, ballpoint pens and gel pens are widely used where ink from gel pens could be easily distinguishable than other pen types [6]. Hybrid pen was also recently available at the marketplace. This type of pen provides solid entries as demonstrated in conventional gel pen, but with fast drying and non-smudging characteristics of a ballpoint pen. Innovations on ink formulation and pen product variations have certainly posed a different challenge to forensic document examiners in differentiating ink entries on questioned documents.

Previous studies have suggested the utilisation of a wide range of analytical techniques to analyse and further distinguish the ink composition. The techniques included thin-layer chromatography (TLC) [7, 8], capillary electrophoresis [9], Raman spectroscopy [10, 11], gas chromatography–mass spectrometry [12-14], attenuated total reflectance-Fourier transform infrared (ATR-FTIR) spectroscopy [15, 16], as well as high performance liquid chromatography [16, 17]. These analytical techniques possessed respective advantages to provide useful information on ink compositions [18], especially when the ink samples are available in bulk. Nonetheless, unlike bulk ink analysis, ink analysis in forensic document examination shall, as much as possible, be non-destructive to preserve its inherent value in the court of law [19].

As part of our continuous research in forensic document examination, this research aims to characterise the characteristics of pen inks labelled with ballpoint and gel pens. Analysis of ink components from the selected samples began with non-destructive techniques followed by the application of destructive TLC for discriminative purpose. It is hoped that through a combination of analytical techniques commonly used in a forensic context, we can provide useful insights on the characteristics of pen inks,

especially with the emergence of new pen types and formulations.

Materials and Methods

Sample preparation

Twenty blue pens, consisting of ten ballpoint pens (labelled as BP) and ten gel pens (labelled as GP) were purchased from the local market. Note that the types of pen were classified according to the label on each pen, as shown in Table 1.

This study was carried out at the Questioned Document Examination Laboratory of Department of Chemistry Malaysia and the Forensic Laboratory of Royal Malaysian Police College, Kuala Lumpur. Before writing, each pen was tested by gently scribbling on a piece of paper to ensure it was functioning before sampling. Then, using each pen, a straight horizontal line of 1 mm thickness was drawn on a piece of white A4 paper (PaperOne™, Copier 70 gsm, Singapore). On a separate piece of paper, the words "Blue Pen Inks" were written using each pen by the same person to ensure standardised writing. The written samples were properly labelled for traceability. Note that the papers used were of the same type from the same rim. Prior to examination and analysis, samples were kept in a hardcover envelope in between two pieces of white A4 papers to avoid any possible two-way smudging of ink materials.

Chemicals and materials

Analytical grade methanol, ethyl acetate, ethanol, n-butanol, and 2 M hydrochloric acid (HCl) were purchased from Sigma-Aldrich (St. Louis, MO). Silica gel 60 F254 TLC plates (20 cm x 20 cm) from Merck (Kenilworth, NJ) and developing chambers were used to carry out TLC analysis.

Microscopic examination

Ink samples written on paper were firstly examined under a Leica MZ16 stereomicroscope (Leica Microsystems, Leica MZ16, Heerbrugg, Switzerland) to investigate the general morphological characteristics of pen ink deposited on the paper. The TL RC 1 external cold light source (Leica Microsystems, Heerbrugg, Switzerland) was set at 2650 K and the written ink lines were studied under the magnification of 16×. Images of ink samples were then captured using Leica FC 290 digital camera (Leica Microsystems, Heerbrugg, Switzerland) attached to the stereomicroscope and saved as TIFF files. The microscopic system was supported by Leica Application Suite software (Leica Microsystems, Heerbrugg, Switzerland).

Video spectral comparator examination

A VSC-6000 video spectral comparator (Foster + Freeman, Worcestershire, United Kingdom) was used to examine the written ink lines and to identify differences in inks. The VSC was connected to a digital camera and a high-resolution grating spectrometer integrated with various light sources and optical filters. Written ink samples were viewed by multispectral light sources from ultraviolet to infrared regions. Barrier filters with wavelengths ranging from 400-730 nm were used to investigate the luminescence properties of ink samples. All digital images were captured, and any luminescence characteristic of inks was recorded.

Attenuated total reflectance-Fourier transform infrared spectroscopy and principal component analysis

Infrared spectra of ink samples were also obtained using Bruker FTIR Tensor 27 (Bruker Corporation, Billerica, MA) equipped with a single reflection zinc selenide attenuated total reflectance (ATR) sampling accessory. Absorbance was measured in the wavelength ranging from 600 to 4000 cm^{-1} while the resolution was set at 4 cm^{-1}. Sixteen scans were performed for each sample. OPUS 7.0.122 software (Bruker Corporation, Billerica, MA) was utilised for spectra acquisition.

Each written ink sample on paper was positioned in contact with ATR on the crystal plate at controlled ambient temperature (≈25 ºC). Before scanning each sample, a reference background spectrum was taken at a spot close to the written line. The spectrum of each sample was taken in duplicates, compared, and evaluated. All the absorbance values of the spectrum were recorded as data points and saved to Microsoft Excel® (Redmond, WA). The data points of regions

with noticeable variations ranging between 1800 and 600 cm^{-1} were normalised and subjected to principal component analysis (PCA) using Minitab 18 software (Minitab Inc., State College, PA). The experimental data were decomposed into a manageable form for the multivariate analysis. The normalised data point was transformed into principal components (PC), and a score plot of the first two PCs was used to generate a score plot to explore the pattern of sample clustering.

Thin layer chromatography

Six strips of respective ink samples applied on white paper were cut into a dimension of 1 mm × 5 mm and placed in separate 1 mL glass tubes. Prior to TLC, an additional solubility test was carried out. In a separate glass tube with ink samples, 100 µL of methanol was added, respectively. Each glass tube was vigorously shaken for 1 minutes and the solubility characteristics of ink samples in methanol were recorded.

For TLC analysis, supernatant methanolic solutions were used for spot application on the TLC plate. Note that only the methanol-soluble ink samples were subjected to TLC. Negative control with the blank white paper of the same dimension was also prepared. Two solvent systems, namely ethyl acetate: ethanol: distilled water (14:7:6) and n-butanol: ethanol: distilled water (4:1:1) were used in this study [8]. TLC plates were heated at 100 ˚C for 1 hour and cooled before spotting with the methanolic ink extracts. Spotted TLC plates were developed in two separate TLC chambers containing different solvent systems. The developed TLC plate was examined under white and ultraviolet lights. R_f values of different visible bands and their respective colours were recorded.

Table 1. Labelling of ballpoint pen and gel pen ink samples

Sample	Types	Brand	Specific Name
BP01	Ballpoint Pen	G'Soft®	BP-GS-56
BP02	Ballpoint Pen	G'Soft®	Ballpoint 5566
BP03	Ballpoint Pen	Pilot	Super-GP
BP04	Ballpoint Pen	Pilot	BP-S
BP05	Ballpoint Pen	Paper Mate®	Fine Blue
BP06	Ballpoint Pen	Paper Mate®	Kilometrico 100
BP07	Ballpoint Pen	Paper Mate®	Kilometrico 80%
BP08	Ballpoint Pen	Faber-Castell	1422
BP09	Ballpoint Pen	Faber-Castell	Speedx 7
BP10	Ballpoint Pen	Stabilo	Excel 828N F
GP01	Gel Pen	Faber-Castell	True Gel
GP02	Gel Pen	Pilot	Super Gel
GP03	Gel Pen	Pilot	Wing Gel
GP04	Gel Pen	Pilot	G-1
GP05	Gel Pen	Carera	Soft-gel S-Fine
GP06	Gel Pen	Carera	V-gel
GP07	Gel Pen	Carera	Soft-gel Fine
GP08	Gel Pen	M&G	K3
GP09	Gel Pen	Test Good	Zhi Xin
GP10	Gel Pen	Reynolds	Racer Gel

Results and Discussion

Microscopic examination

In general, based on microscopic examination, the distribution of ink onto the paper substrate upon writing was found different where ten written samples using gel pens have shown more even and smoother ink distribution with visible ink diffusing into the paper substrate. Ink bleedings from gel pen inks were observed, as demonstrated in Figure 1(a). In comparison, the written ink using ballpoint pens was found to exhibit poorer and less smooth ink distribution with features of halo, Figure 1(b) and fine striations, Figure 1(c). Halo and fine striations had been absent in those handwritten samples produced by gel pen in this study.

During writing, ink is deposited onto the substrate and the solvents are subsequently evaporated leaving behind the coloured particles [20]. In this study, the paper used as the substrate was a porous surface, and it allows the diffusion of liquid ink into the paper. Therefore, a less viscous characteristic of ink reserved in a pen could potentially produce a more even appearance of trace on a paper upon writing as demonstrated by gel pen ink. On the other hand, a relatively thicker or paste-like consistency ballpoint pen ink could have contributed to less diffused writing features on the paper substrate making the inked-trace appear as being stained on the surface of the paper.

In our written ink samples using ballpoint pens, the formation of a halo as a small gap that discontinued smooth writing was observed in eight out of ten handwriting samples and it could be due to the inadequate ink flow from the pen reservoir [21]. This feature was found along with fine striations on the handwriting samples as a distinctive pattern [3]. Accumulation of dried ink might cause uneven distribution of ink on the rollerball of a ballpoint pen [21]. Note that in our case, the functionality of all pens was tested before writing. Observation of halos and gaps could be due to the restriction of the smooth flow of more viscous ink from the reservoir onto a substrate, leading to a tendency of ink to be retained on the surface of roller ball.

The mechanism of ink deposition has contributed to different morphological features on written samples produced by different types of pens. In general, the microscopic examination could suggest the types of pens of different ink type, in this case, ballpoint pen and gel pen inks. However, microscopy alone could not confidently help to discriminate traces written with two pens of very similar type, and therefore more detailed physical and chemical examinations are required.

Hyperspectral Imaging using Video Spectral Comparator-6000

Under UV light examination, all 20 samples revealed no luminescence characteristics. However, certain ink samples luminesced with the application of different barrier filters to the light sources, and the luminescence characteristics of written ink samples in this study were demonstrated in Table 2.

Based on VSC analysis, the ink samples could be categorised into three different luminescent categories, namely (i) inks that contained no luminescent component, (ii) inks that contained luminescent components and (iii) inks that luminesce at certain wavelength exposure [18]. Out of 20 samples, ten of them (i.e., 7 ballpoint pen inks and 3 gel pen inks) showed no luminescence regardless of the filter barriers. Based on the luminescence characteristic, both filters of respective wavelength values ranging from 400 – 535 nm and 485 – 610 nm did not show much difference in luminescence output, except in three samples (i.e., GP02, GP03 and GP04) that demonstrated bluish glows when applied with the latter. The filter of longer wavelength (i.e., 605-730 nm) provided only limited information, where only five samples (i.e., BP02, BP05, BP08, BP09 and BP10) luminesced in white and another three in blue (i.e., GP02, GP03 and GP04) against dark backgrounds. However, a combination of filters of varying wavelengths was found to be useful for ink discrimination. Based on the results, four different groups of ink characters could be established, firstly by 485 – 610 nm wavelength filter to determine the presence of luminescence characteristic as well as their respective colours, followed by the filter of longer wavelength (605- 730 nm) to differentiate the bluish

and whitish glowed samples as ballpoint pen and gel pen inks, respectively. It was also important to note that the luminescence characteristic of a pen was not determined by the types of pens. In this study, both ballpoint and gel pen inks might luminesce.

Attenuated total reflectance- Fourier transform infrared spectroscopy

Through ATR-FTIR spectroscopy, complex interacting vibrations were observed in the 'fingerprint' region (1800- 600 cm^{-1}). It is worth noting that no attempt was made to predict the compounds since the aim of this study is to relatively compare the ATR-FTIR spectra to establish the possible similarities among the ink samples. Figure 2 illustrates the general pattern of ATR-FTIR profiles of representative pen inks. ATR-FTIR spectra patterns of the ink samples were observed to be different, particularly between the different types of pen inks. Detailed comparison demonstrated the variations in the respective ATR-FTIR profiles even though the ink samples were originated from the same types.

For more objective comparison, the data points of ATR-FTIR spectra were normalised to the total area of the spectrum to correct the multiplicative scaling effect and subjected to PCA, in a situation where information on ink sample classification is needed, such as to investigate unknown origins of ink samples. Figure 3 illustrates the score plot generated through PCA. Note that the score plot was developed with the first two PCs, accounting for 76.9% of the explained variance. Generally, two main clusters of ink samples were evident in the score plot. Cluster A was mainly constituted by ballpoint pen ink samples, and Cluster B mainly consisted of only gel pen ink samples. Note that there were two gel pen ink samples (i.e., GP03 and GP04) found to be located within Cluster A with a majority of ballpoint pen ink samples. In other words, these two samples could have contained composition more similarly to ballpoint pen inks.

Through PC1 (56.3%), it was observed that three samples (i.e., BP01, BP09 and GP02) were justified to be away from the two main clusters, where one sample located at the left upper quadrant and the other two situated at the left lower quadrant of the score plot. On the contrary, samples in Cluster A showed positive score while those in Cluster B reported with the negative score on PC2 (20.6%). It is possible that closely located samples in the respective clusters could have produced from very similar ingredients.

Duplicate samples, namely GP10a and GP10b as indicated by the dotted line, were located very closely in the score plot to suggest the distance between two points that could be arisen from the same sample. Samples, such as BP03 and BP04, which were also very close to each other, therefore could not be differentiated through the score plot, possibly due to their very similar ink compositions between samples. Note that only the first two PCs were considered and interpreted in this study, where PC3 (9.2%) did not demonstrate any influence over the separation in PCA.

Thin layer chromatography

The solubility of ink samples in methanol was investigated before TLC, where 13 samples were found soluble in methanol. Of these samples, 10 were the ballpoint pens while three were gel ink samples, namely GP02, GP03 and GP04. It is interesting to find that these three ink samples were luminesced under VSC observation, distinguishing them from other gel pen inks. It was also noted that they were clustered closer to the cluster consisting of ballpoint pen inks in ATR-FTIR score plot. Conventionally, only dye-based inks are found soluble in methanol while pigment-based inks previously found in gel pens are generally insoluble [7, 22, 23]. Gel pens made up of pigments are reported to be more resistant to strong organic solvents [4]. Our results showed that the three ink samples with different observations could be made up of dye, although they exhibited gel pen ink characteristics upon writing and marketed as gel pens. Table 3 shows the outcome upon TLC using two different solvent systems on 13 methanolic samples.

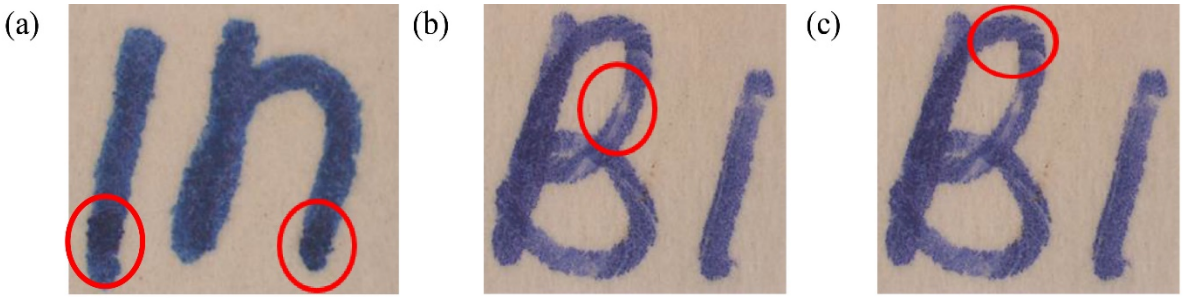


Figure 1. Microscopic images of handwriting samples showing special characteristics

Table 2. Luminescence characteristic of 20 ink samples

Sample	Wavelength of Filter Barrier		
	400 – 535 nm	485 – 610 nm	605 – 730 nm
BP01	Yellowish glow	Yellowish glow	Whitish glow
BP02	Yellowish glow	Yellowish glow	Whitish glow
BP03	ND	ND	ND
BP04	ND	ND	ND
BP05	Bluish glow	Bluish glow	Whitish glow
BP06	Bluish glow	Bluish glow	Whitish glow
BP07	ND	ND	ND
BP08	Bluish glow	Bluish glow	Whitish glow
BP09	Yellowish glow	Yellowish glow	Whitish glow
BP10	Bluish glow	Bluish glow	Whitish glow
GP01	ND	ND	ND
GP02	ND	Bluish glow	Bluish glow
GP03	ND	Bluish glow	Bluish glow
GP04	ND	Bluish glow	Bluish glow
GP05	ND	ND	ND
GP06	ND	ND	ND
GP07	ND	ND	ND
GP08	ND	ND	ND
GP09	ND	ND	ND
GP10	ND	ND	ND

*ND-Not detected

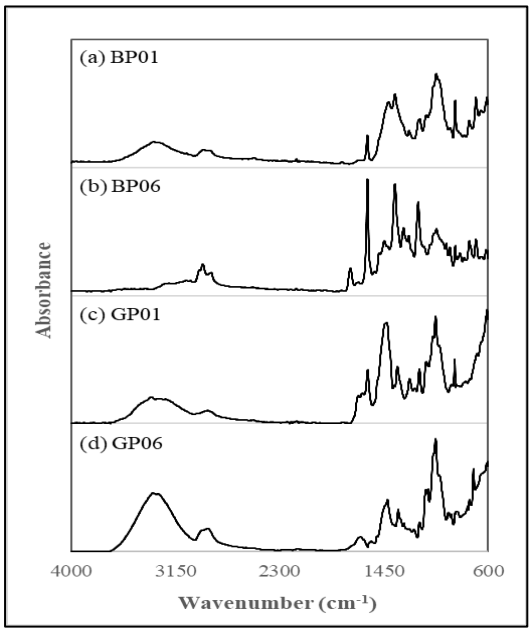


Figure 2. Representative ATR-FTIR profiles of ballpoint pen inks (a-b) and gel pen inks (c-d)

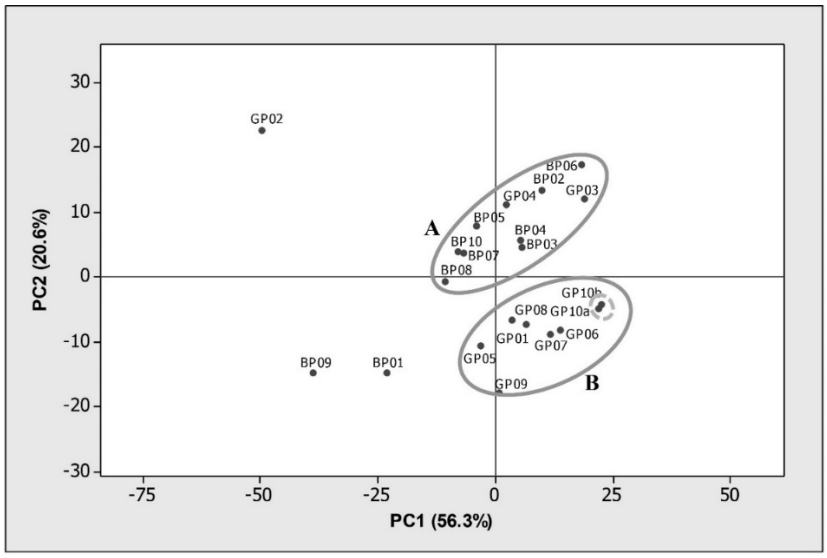


Figure 3. Score plot of 20 ink samples upon PCA

Table 3. Separation of ink components with respective R_f values

Solvent System	Methanolic Sample												
	BP01	**BP02**	**BP03**	**BP04**	**BP05**	**BP06**	**BP07**	**BP08**	**BP09**	**BP10**	**GP02**	**GP03**	**GP04**
A	0.59	0.73	0.62	0.73	0.57	0.57	0.57	0.58	0.58	0.53	0.57	0.58	0.58
	0.73	0.77	0.72	0.77	0.75	0.73	0.78	0.75	0.73	0.62	0.77	0.74	0.73
	0.78	0.82	0.77	0.81	0.79	0.78	0.82	0.78	0.78	0.76	0.81	0.84	0.83
	0.83	0.83	0.81	0.85	0.82	0.82	0.85	0.82	0.82	0.81	0.83	0.86	0.85
	0.85	0.87	0.85	0.89	0.85	0.87		0.84	0.85	0.83	0.87	0.89	0.88
	0.89		0.89		0.88	0.90		0.87	0.88	0.88		0.92	0.91
B	0.19	0.27	0.20	0.28	0.28	0.28	0.28	0.19	0.19	0.29	0.28	0.28	0.29
	0.26	0.49	0.26	0.51	0.49	0.49	0.49	0.24	0.26	0.35	0.49	0.50	0.49
	0.49	0.55	0.49	0.57	0.52	0.52	0.52	0.47	0.50	0.39	0.51	0.52	0.52
	0.55	0.64	0.54	0.65	0.58	0.58	0.58	0.53	0.55	0.56	0.57	0.60	0.60
	0.60	0.71	0.60	0.72	0.61	0.60		0.58	0.60	0.60	0.59	0.61	0.62
	0.65		0.66		0.67	0.67		0.64	0.65	0.64		0.67	0.68

From the 13 methanolic soluble samples subjected to TLC analysis, the solvent system consisting of ethyl acetate: ethanol: distilled water in a ratio of 14:7:6 allowed for the grouping of 13 samples into seven different groups. The number and colour of bands from these samples were observed to vary from four to six in red and blue shades in addition to several spots which fluoresced under UV light. The result suggested the possible utilisation of different or a combination of different colouring agents by manufacturers to give the desired colours that appear hardly distinguishable under naked-eye visualisation. On the other hand, the solvent system consisting of n-butanol: ethanol: distilled water in a ratio of 4:1:1 needed a longer separation time. One ink sample (BP08) exhibited the same band number and band pattern as the other two ink samples (i.e., BP05 and BP06) with the former solvent system, was successfully distinguished by this solvent system.

The separation of a compound or ink mixture highly depends on the type of absorbent and solvent system used [16]. Hence, a particular solvent system is not adequate to separate all dye substance [16]; therefore, different solvent systems could result in varying dye separation. Despite resulting in relatively poor separation, the second solvent system still helped in discriminating the inks which are indistinguishable by the first solvent system and vice versa. Therefore, it is essential to employ different solvent systems for better discrimination of pen inks, if a sufficient sample is available for such analysis.

Comparison of ink samples

Under most circumstances, non-destructive visual microscopic examination and comparison against respective ink samples are preferred to avoid any further damage on the disputed documents, particularly for those stand exhibit in court. Undoubtedly, destructive methods, including TLC analysis in this study, provided much detailed information although it could impose irreversible damage to the documents, but shall only be attempted whenever sufficient samples are available and allowed for such analysis. In this study, a series of different analytical techniques, initiated by microscopic examination, VSC observation, ATR-FTIR spectroscopy, and TLC analysis has successfully created possible discrimination among ink samples. A schematic diagram summarising how the samples were

successively distinguished by each technique is presented in Figure 4.

In many instances, microscopic examination alone allowed the differentiation of two main types of pen inks, namely the ballpoint pen inks and gel pen inks, in line with the label on each pen. Based on luminescence behaviour, not all ink samples luminescence to establish sample-to-sample linkage but could assist in the exclusion of an ink sample from a source of origin. ATR-FTIR showed that ink samples from the same types tend to locate closer in the score plot, as they could have contained very similar compositional profiles. However, it was also found that two ink samples labelled as gel pens in the study were also clustered together with other ballpoint pen ink samples, and thus required careful interpretation during forensic document examination on their ATR-FTIR profiles. The use of ATR-FTIR data point and PCA score plot clustering is useful to include or exclude a group of pen samples suspected to have been used in an alteration.

Dye-based ballpoint pen inks were found soluble in methanol, supporting the microscopic examination demonstrating ballpoint pen morphological features. The three ink samples, namely GP02, GP03 and GP04, that showed gel pen ink characteristics through microscopic examination were also found to be dissolved in methanol and luminesced under 485-610 and 605-730 nm light sources. These samples exhibited hybrid characteristics from both ballpoint pen and gel pen inks. By TLC, inks samples could be further discriminated from the rest, given that they were priorly dissolved in methanol. It was worth noting that TLC analysis was only restricted to ballpoint pen and hybrid pen inks. The technique is necessary in some cases where samples are sufficient and other non-destructive techniques were not able to discriminate among the samples.

In brief, the 20 ink samples were categorised into 11 different groups upon analyses. The presence of hybrid pen ink possessing both ink characteristics of ballpoint and gel pens as found in our study demonstrated that careful interpretation during the forensic investigation against written document related to ink is required, especially when alteration involves gel pen inks. Under one analytical technique, a hybrid pen may resemble the characteristics of either gel pen ink or a ballpoint pen ink and could lead to false positive or false negative results. This may make even an unauthentic document seem authentic if not carefully interpreted. Nonetheless, further analytical work is necessary for defensible characterisation of the source of pens, including identification of specific compounds in the ink composition.

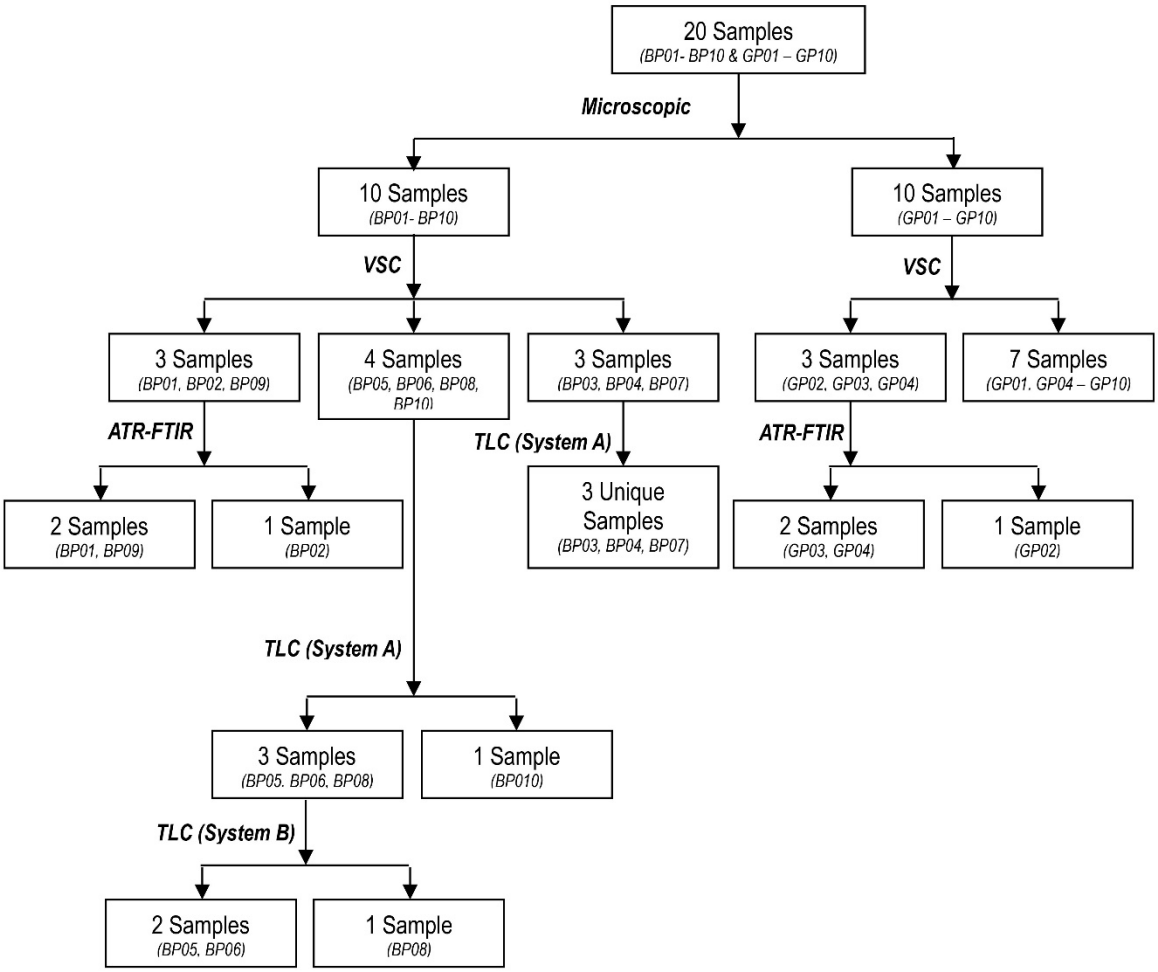


Figure 4. Discrimination of pen samples by a series of analytical techniques

Conclusion

Based on a combination of analytical techniques, the ink from pen samples tested in this study could be discriminated from the others, especially between a ballpoint pen and gel pen inks. Marked differences between the characteristics of these inks were evidently making them readily distinguishable. Nevertheless, a conclusion should not be made solely based on microscopic findings as gel pen inks could show characteristics similar to ballpoint pen inks according to their chemical compositions. The experimental protocol used in this study can be used for the exclusion of different sources of pen inks by comparing the profiles on suspected samples and crime scene samples. We also highlighted the characteristics of hybrid pen that worth serious attention during a forensic investigation, especially when it is widely used in the future.

Acknowledgement

The authors thank the financial support via the Fundamental Research Grant Scheme (FRGS) from the Ministry of Education Malaysia (203/PPSK/6171208).

References

1. Calcerrada, M. and García-Ruiz, C. (2015). Analysis of questioned documents: A review. *Analytica Chimica Acta,* 853: 143-166.

2. Hammand, D. L. (2013). Encyclopedia of forensic sciences. Overview of forensic document examination. Elsevier, London: pp. 391-394.
3. Lindblom, B. S. (2006). Scientific examination of questioned document. Pens and pencils. CRC Press, Baco Raton: pp. 147-158.
4. Bell, S. (2008). Encyclopedia of forensic science. Infobase Publishing, New York: pp. 375-379.
5. Allen, M. (2015). Foundations of forensic document analysis: Theory and practice. John Wiley & Sons, Oxford: pp. 163-175.
6. Gernandt, M. N. and Urlaub, J. J. (1996). An introduction to the gel pen. *Journal of Forensic Sciences*, 41 (3): 503-504.
7. Djozan, D., Baheri, T., Karimian, G. and Shahidi, M. (2008). Forensic discrimination of blue ballpoint pen inks based on thin layer chromatography and image analysis. *Forensic Science International,* 179 (2–3): 199-205.
8. Barker, J., Ramotowski, R. and Nwokoye, J. (2016). The effect of solvent grade on thin layer chromatographic analysis of writing inks. *Forensic Science International,* 266: 139-147.
9. Cruces-Blanco, C., Gámiz-Gracia, L. and García-Campaña, A. M. (2007). Applications of capillary electrophoresis in forensic analytical chemistry. *Trends in Analytical Chemistry,* 26(3): 215-226.
10. Braz, A., López-López, M. and García-Ruiz, C. (2013). Raman spectroscopy for forensic analysis of inks in questioned documents. *Forensic Science International,* 232(1-3): 206-212.
11. de Souza Lins Borba, F., Honorato, R. S. and de Juan, A. (2015). Use of Raman spectroscopy and chemometrics to distinguish blue ballpoint pen inks. *Forensic Science International,* 249: 73-82.
12. Bügler, J. H., Buchner, H. and Dallmayer, A. (2005). Characterization of ballpoint pen inks by thermal and desorption and gas chromatography-mass spectrometry. *Journal of Forensic Sciences,* 50(5): 1209-1214.
13. Bügler, J. H., Buchner, H. and Dallmayer, A. (2008). Age determination of ballpoint pen ink by thermal desorption and gas chromatography-mass spectrometry. *Journal of Forensic Sciences,* 53(4): 982-988.
14. Weyermann, C., Kirsch, D., Vera, C. C. and Spengler, B. (2007). A GC/MS study of the drying of ballpoint pen ink on paper. *Forensic Science International,* 168 (2–3): 119-127.
15. Harris, J. (2013). A preliminary report on the nondestructive examination of ballpoint pen ink on questioned documents by FT-IR spectroscopy. *The Canadian Society of Forensic Science Journal,* 24(1): 5-21.
16. Sharma, V. and Kumar, R. (2017). Fourier transform infrared spectroscopy and high performance thin layer chromatography for characterization and multivariate discrimination of blue ballpoint pen ink for forensic applications. *Vibrational Spectroscopy,* 92: 96-104.
17. Abdul Halim, M. I., Saim, N., Osman, R., Jasmani, H. and Zainal Abidin, N. N. (2013). Discrimination of black ballpoint pen inks by high performance liquid chromatography (HPLC). *Malaysian Journal of Analytical Sciences,* 17(2): 230-235.
18. Chen, H-S., Meng, H-H. and Cheng, K-C. (2002). A survey of methods used for the identification and characterization of inks. *Forensic Science Journal,* 1: 1-14.
19. Neumann, C. and Margot, P. (2009). New perspectives in the use of ink evidence in forensic science. Part III: Operational applications and evaluation. *Forensic Science International,* 192(1–3): 29-42.
20. Bell, S. (2013). How to identify a forgery: A guide to spotting fake art, counterfeit currencies and more. Skyhorse Publishing Inc, New York: pp. 43-52.
21. Ellen, D., Day, S. and Davies, C. (2018). Scientific examination of documents: Methods and techniques. CRC Press, Baco Raton: pp. 128-136.
22. Mazella, W. D. and Buzzini, P. (2005). Raman spectroscopy of blue gel pen inks. *Forensic Science International,* 152(2-3): 241-247.
23. Reed, G., Savage, K., Edwards, D. and Daeid, N. N. (2014). Hyperspectral imaging of gel pen inks: An emerging tool in document analysis. *Science and Justice,* 54(1): 71-80.

Malaysian Journal of Analytical Sciences (MJAS)
Published by Malaysian Analytical Sciences Society

PRODUCTION OF BIODIESEL FROM WASTE COOKING OIL USING POTASSIUM HYDROXIDE SUPPORTED ON ALUMINA CATALYST

(Penghasilan Biodiesel daripada Minyak Masak Terpakai Menggunakan Kalium Hidroksida Disokong oleh Mangkin Alumina)

Shahida Hanum Kamarullah*, Zainal Kifli Abdul Razak, Norshahidatul Akmar Mohd Shohaimi, Nailul Amal Zakariah

Faculty of Applied Sciences,
Universiti Teknologi MARA Pahang, Jengka Campus, 26400 Bandar Tun Abdul Razak Jengka, Pahang, Malaysia

**Corresponding author: shahidahanum@uitm.edu.my*

Received: 19 May 2021; Accepted: 26 July 2021; Published: xx August 2021

Abstract

In this study, waste cooking oil (WCO) was used to produce biodiesel using KOH supported on alumina (KOH/Al_2O_3) as the catalyst. Three parameters were studied to find the optimum conditions which are catalyst loading, reaction time and the reusability of the catalyst. Al_2O_3 was impregnated with KOH and characterized using thermogravimetric analyzer (TGA) before the catalyst was calcined at 700 ˚C for 3 hours. The reaction was refluxed with constant conditions at the temperature of 65 ˚C, 10% of $KOH-Al_2O_3$, and methanol to oil ratio of 12:1 for 3 hours. The reaction time was studied using optimum catalyst loading which was 7 wt.% of catalyst amount and the reaction varied from 1-hour to 4-hour reaction. The highest yield of biodiesel obtained was 73.7% in 2 hours of reaction. At the end of the study, the reusability of the catalyst was studied. Three cycles of reaction were done using the used catalyst from the previous 2-hours reaction of yield determination and the result found a decreasing pattern of yield after 4 cycles of reaction. Hence, the optimal conditions for this catalyst were reaction temperature of 65 ˚C, 10% of $KOH-Al_2O_3$, methanol to oil ratio of 12:1, and 7 wt.% of catalyst loading at 2 hours of reaction. The highest yield of biodiesel was 73.7%.

Keywords: potassium hydroxide supported on alumina, biodiesel, waste cooking oil, transesterification

Abstrak

Dalam kajian ini, sisa minyak masak (WCO) digunakan untuk menghasilkan biodiesel menggunakan kalium hidroksida yang disalutkan atas sokongan alumina (KOH/Al_2O_3) sebagai mangkin. Tiga parameter telah dikaji untuk mencari keadaan optimum iaitu berat mangkin digunakan, masa tindak balas dan kebolehgunaan semula mangkin. KOH telah diintegrasikan dengan Al_2O_3 dan diuji menggunakan penganalisis termogravimetrik (TGA) sebelum mangkin itu dibakar pada suhu 700 ˚C selama 3 jam. Tindak balas itu di refluks dalam keadaan malar pada suhu 65 ± 2 ˚C, 10% $KOH-Al_2O_3$, nisbah metanol kepada minyak 12:1 selama 3 jam. Waktu tindak balas dikaji menggunakan mangkin optimum iaitu 7 wt.% dan tindak balasnya di ubah dari 1-4 jam dan hasil tertinggi diperolehi adalah 73.3% pada tindak balas 2 jam. Pada akhir kajian ini, kebolehgunaan semula mangkin telah dikaji. 3 kitaran tindak balas telah dilakukan menggunakan mangkin yang telah digunakan untuk tindak balas sebelumnya semasa penentuan hasil untuk 2 jam dan hasil kajian mendapati corak hasil biodiesel menurun selepas 4 kitaran tindak balas.

Oleh itu, keadaan optimum untuk mangkin ini ialah suhu tindak balas pada suhu 65 ˚C, 10% KOH-Al_2O_3, nisbah metanol kepada minyak 12:1, 7 wt.% jumlah mangkin pada masa tindak balas jam dan hasil tertinggi biodiesel ialah 73.7%.

Kata kunci: kalium hidroksida, biodiesel, minyak masak terpakai, transesterifikasi

Introduction

Biodiesel is one of the alternatives for petroleum which has the potential to replace the fossil fuels which are produced partially from parts of dead organisms such as plants and animals. It is defined as the mono alkyl esters of long chain fatty acids [1, 2] formed from biolipids through transesterification of vegetable oils such as palm oil [3, 4] canola oil [5], castor oil [6] and waste oil from the food industry [7, 8] in reaction with methanol under either acidic or basic conditions. Waste Cooking Oil (WCO) has been used in studies since it is available in the lowest price because it is 2-3 times cheaper than virgin vegetable oil and the supply of vegetable oil is abundant in the Malaysian market [9].

There are some studies [10, 11, 12, 13] which investigated the production of biodiesel using homogeneous base catalysts such as potassium hydroxide and sodium hydroxide as well as homogeneous acid catalyst using sulfuric acid. However, such processes have many disadvantages such as they could reduce the yield of biodiesel production, homogeneous base could not be reused or regenerated after a reaction and toxic wastewater might also be produced [14]. Besides, the production cost due to the separation of catalyst from products in hydrolysis and saponification reactions of transesterification is also higher because the elimination of the catalysts from the biodiesel product requires a large amount of water which could contaminate the products [15], thus resulting in the loss of useful material [16]. Moreover, the separation between the catalysts and glycerol is difficult [17]. In the same case, even if the separation process succeeds, a huge amount of wastewater is still produced [3] which is not economically and environmentally friendly [2]. In addition, some soap would be produced with the presence of too much FFAs in the process that would reduce the yield of FAME production [3]. A high content of FFAs (>1% w/w) would lead to these phenomena which increase the viscosity of the solution and difficulty to separate the glycerol [18].

In that case, heterogeneous catalysts were thus used in this study as they were separable and produce high quality methyl ester and glycerol, resulting in a lowered cost of processing operations. Hence, the use of heterogeneous base catalysts was proven to be effective due to their reusability, widespread availability, easy separation process from the product and longer lifetime [14]. Furthermore, for active species like potassium hydroxide (KOH), attaching catalysts to support such as alumina increases the contact area and number of pores [19]. Alumina had been investigated as the most frequently used catalyst support to produce biodiesel due to its high thermal and mechanical stability, high contact area (can exceed to 300 m^2 /g), large pore diameter (5-15 nm), bigger pore volume (1.07 cm^3 /g) and the ability to form and extrude the pellets. The aim of this study was to investigate the effect of catalyst loading and reaction time on biodiesel production from waste cooking oil (WCO) using potassium hydroxide supported on alumina as a heterogeneous catalyst. The reusability of the catalyst was also investigated over several consecutive runs as it is a major advantage for industrial biodiesel development.

Materials and Methods

Materials

Waste cooking oil was collected from a household in Jengka. Aluminium oxide, Al_2O_3, was obtained from Sigma-Aldrich (commercial grade). Potassium hydroxide (K_2CO_3, 99%) was obtained from Merck and methanol (CH_3OH, 99%) was that of analytical grade (AR). The chromatographic standards were methyl heptadecanoate as the internal standard and the FAME standard mixture GLC-10 from Sigma-Aldrich. GLC-10 consists of methyl palmitate, methyl stearate, methyl oleate, as well as methyl linoleate and methyl linolenate.

Pre-treatment of waste cooking oil

The waste cooking oil was first filtered to remove traces of suspended particles followed by heating at 100 ℃ for 1 hour to remove moisture. The pre-treated waste cooking oil was then stored in a closed container before proceeding with the transesterification reaction.

Catalyst preparation

A 5 g of alumina powder was dissolved in 10 mL of distilled water and stirred until it became a suspended mixture. The alumina suspended solution was heated and stirred using a magnetic stirrer and 2.15 g of KOH solution was then added to the mixture dropwise. The paste was then dried in an oven at 90 ˚C for 24 hours to remove excess water [20, 21]. Next, this impregnated catalyst was calcined in a muffle furnace at 700 ˚C for 3 hours with a ramp rate of 5 ˚C/min. The catalyst was characterized using thermogravimetric analysis (TGA) to determine the thermal transition and the decomposition of the catalyst [2].

Transesterification reaction

WCO, methanol and catalyst were the main components in this process. The selected parameter in this study was catalyst loading on the percentage yield of biodiesel. The transesterification reaction was conducted in a 500 mL round bottom flask equipped with a reflux condenser, thermometer, and magnetic stirrer [22] submerged in a steel basin with paraffin oil and the reaction was done at the boiling point of methanol (65˚C). Then, 10 g of WCO was mixed with 4.3 g of methanol together with a series of catalyst loading (1 wt.%, 3wt.%, 5 wt.%, 7 wt.% and 9 wt.%) added into the flask. A magnetic stirrer was used to mix the oil, catalyst, and methanol together [3] and the reaction was carried out for 3 hours while the external temperature (temperature of paraffin oil) was maintained at 75 ˚C. After the reaction completed, the mixture was poured into a centrifuge tube and then was centrifuged at 4000 rpm in 5 minutes. The mixture formed two layers by which the methyl ester obtained was on the top layer while the glycerol was at the lower layer. The glycerol was discarded and the removal of excess methanol on the upper part and catalyst at the bottom layer was done by washing the methyl ester using warm distilled water (80-100 ˚C) in a separatory funnel. The mixture was then shaken gently and left for about 3 minutes until two layers were formed by which the lower layer was then removed again [8]. After that, the washed methyl ester was transferred into a 100 mL beaker and heated to remove any existing moisture/methanol for about half an hour while being stirred. All these procedures were repeated for other reaction mixtures at different reaction time (1 hour, 2 hour and 4 hour).

Reusability test

This test was conducted only for the catalyst with the highest yield of biodiesel using the same reaction conditions stated previously. The catalyst was isolated from the reaction product after the first reaction. To eliminate the non-polar compounds attached to the catalyst, it was washed with methanol three times and filtered using filter paper. The catalyst was then dried for 1 hour in the oven and used in the transesterification reaction. With the same optimum condition, the procedures were repeated three times and the composition of the biodiesel was tested with gas chromatography (GC) analysis.

Gas chromatography analysis

The GC-MS is a library-built instrument that offers a complete list of elements in the sample [21]. The purity of methyl ester produced was determined by using gas chromatography. The analysis was done by Agilent 7890B gas chromatographer equipped with 5977A MSD and Zebron ZB-FAME capillary column (60 m x 0.20 mm x 0.25 µm). The instrument was set up as the following: Split ratio of 100:1 and initial oven temperature of 60˚C to 240˚C at 14˚C/min. The temperature of the injection was set at 250˚C while the MS transfer line temperature was 280˚C. The sample was injected to reach reproducible peaks where methyl heptadecanoate was used as an internal standard. After the ester content was obtained, the percentage of pure biodiesel was then calculated.

Results and Discussion

Characterization of KOH/Al_2O_3 catalyst

Figure 1 shows the thermal degradation pattern of KOH/Al_2O_3 catalyst. From the figure, it was observed that there were three stages of weight loss process

within the temperature range of 32.50˚C to 926.39˚C. The first level of weight loss was about 7.9% which took place at the temperature of 32.50˚C to 135.42˚C pointing that water had evaporated and was removed from the catalyst surface. Meanwhile, the second level of weight loss was about 1.18% at the temperature of 201.20˚C to 314.76˚C which indicated a complete removal of water surface on the catalyst. The amount of mixture content and slight weight loss were observed below 200˚C due to the catalyst being subjected to oven drying at 80˚C overnight before the analysis was conducted. At the end of the analysis, about 2.57% of catalyst became decomposed at 767.41˚C to 926.39˚C. This shows that the removal of hydroxyl group (-OH) and formation of K_2O phase was due to the decomposition at the end of the analysis. It can be concluded that water and impurities were removed after the thermal treatment at the temperature of 700˚C.

Effect of catalyst loading

The effect of wt.% of catalyst loading on the yield of biodiesel produced is summarized in Figure 2. In this study, the catalyst loading varied within the range of 1 wt.% to 9 wt.% to catalyze the reaction. Referring to the figure, the yield of each loading did not show a significant difference except for 1 wt.% and 3 wt.%. For the first two catalyst loading (1 wt.% and 3 wt.%), there was no biodiesel produced on both due to the formation of emulsions. The production of FAME could not be achieved in an insufficient catalyst loading amount [6]. This might be due to a slow reaction rate resulting from a low amount of catalyst in a short reaction time. The highest pure biodiesel obtained was 9 wt.% which is 58.52% while at catalyst loading of 7 wt.% and 5 wt.%, they are 58.38% and 51.5% respectively. Since there were no obvious differences between 7 wt.% and 9 wt.%, the 7 wt.% was considered as the optimum catalyst loading.

Larger catalyst loading triggered high resistance to mass transfer because of the viscous mixture [23]. When the excess catalyst was used, the reaction mixture became more viscous, resulting in poor dispersion of reactants in the three phase systems. This brought about reduced yield and conversion, thus consuming more costs and time [24].

Effect of reaction time

The effect of reaction time was studied as it had a significant impact on the transesterification of waste cooking oil. The reaction time varied from 1 to 4 hours in 7 wt.% of catalyst loading. As summarized in Figure 3, the FAME yield increased from 58.35% to 73.7% in the first two hours. However, the yield declined as the reaction continued further than 2-hour reaction. It is concluded that when the temperature increased during the 2 hours of reaction, the rate of reaction increased, and the yield of biodiesel became optimal (73.7%) before the yield decreased due to methanol evaporation [25] as well as the loss of solvent and by-product formation such as olefins and fatty alcohol [9]. The methyl ester favored a backward reaction in a longer reaction time, producing more glycerol than methyl ester [11]. In addition, high molar ratio required a shorter time as it had enough methanol to produce high yield reaction. Hence, 2-hour reaction time was selected as the optimum reaction time as it provided the highest biodiesel yield. In a previous work [26], WCO was converted to biodiesel and it achieved a higher yield of 95% after 2 hours of reaction with methanol to oil ratio of 9:1 and catalyst loading of 5%. The catalyst used was also KOH/alumina, but it was calcined at 700^{o}C for 7 hours, compared to the catalyst in this research which was calcined for only 3 hours at the same temperature. Therefore, it could be regarded that increasing the calcination time would increase the catalytic activity of the catalyst.

Reusability test

Catalyst reusability is an important aspect in the development of biodiesel. The reusability of KOH/Al_2O_3 was determined at the optimum state of the conditions for 3 cycles as shown in Figure 4. It was noticed that after cycle 1 with yield of 73.7%, the cycle demonstrated a declining pattern of yield of pure biodiesel which was 72.12%, 70.86% and 68.75% for cycle 2, 3 and 4 respectively. This decreasing trend caused by the deactivation of the catalyst due to the loss of almost half of the original weight after the third cycle. The loss of catalyst due to the partial solubility

of the catalyst in methanol (leaching) eventually affected the glycerol recovery [2] and disrupted the reaction mixture.

Qualitative analysis of gas chromatography

Figure 5 shows the GC-MS chromatogram of biodiesel for 2-hour reaction. Four peaks of methyl esters were observed in Table 1 which consisted of methyl palmitate, methyl stearate, methyl oleate and methyl linoleate. The main components of biodiesel were methyl palmitate and methyl oleate which showed high peak of GC. This GC-MS chromatogram was comparable to the fatty acid profile of palm oil. Thus, it indicated the formation of biodiesel from the oil used [2]

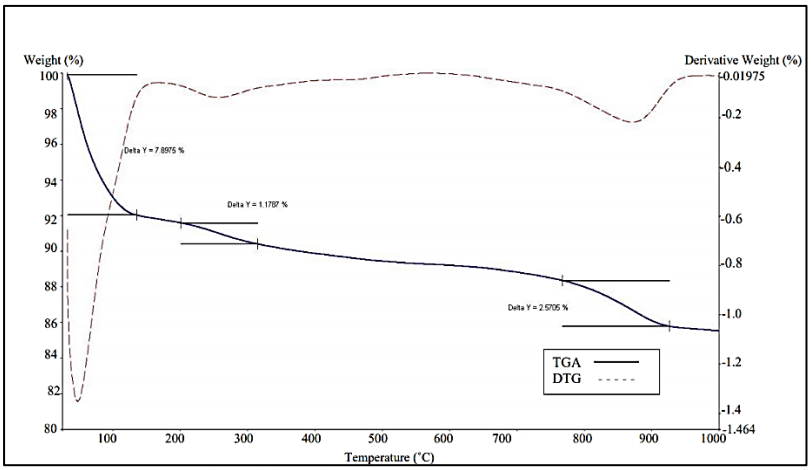


Figure 1. TGA and DTG curve for KOH/Al_2O_3 catalyst

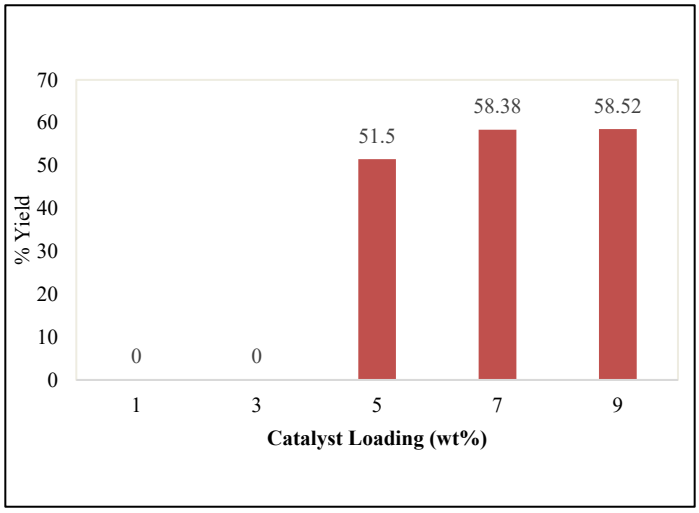


Figure 2. The effect of the catalyst loading on the yield (10% of $KOH-Al_2O_3$, 12:1 MeOH: oil, 65 ˚C temperature and 3-hour reaction.

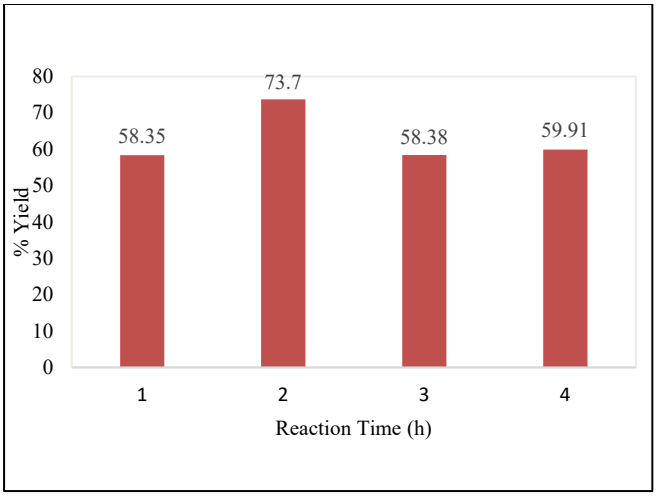


Figure 3. Effect of reaction time on the yield (12:1 MeOH: oil, 65˚C temperature and 7 wt.% catalyst)

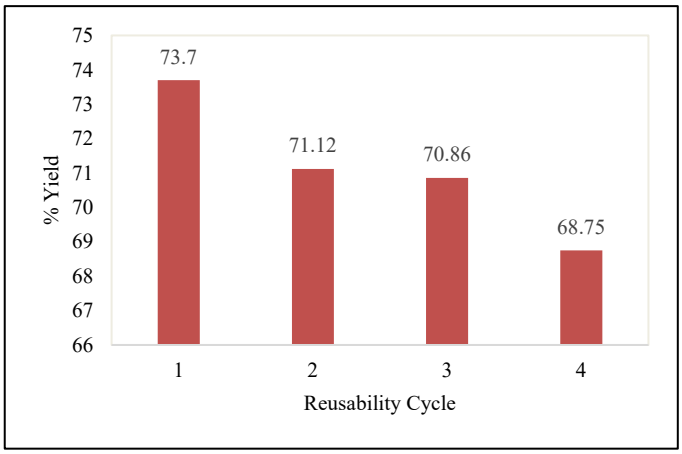


Figure 4. The reusability of the catalyst

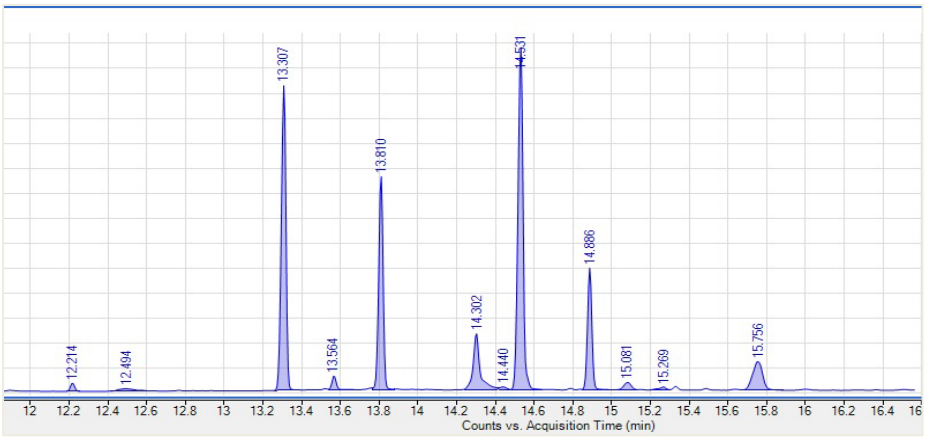


Figure 5. GC-MS chromatogram of biodiesel for 2-hour reaction (10% KOH-Al_2O_3, 12:1 MeOH: oil, 65˚C temperature and 7 wt.% catalyst)

Table 1. Retention time and FAME of biodiesel obtained using 7 wt.% catalyst

Retention Time (min)	**Common Name**
13.307	Methyl palmitate
13.810	Methyl heptadecanoate (Internal standard)
14.302	Methyl stearate
14.531	Methyl oleate
14.886	Methyl linoleate

Conclusion

In this study, the maximum biodiesel yield achieved was 73.7% with the reaction temperature of 65 ˚C, 10% of KOH-Al_2O_3, catalyst loading of 7 wt.%, reaction time of 2 hours and methanol to oil ratio of 12:1. After the reaction was done in 4 cycles, the yield of biodiesel became reduced to 68.75% as the catalyst was deactivated because almost half of the weight was lost. The GC-MS chromatogram confirmed the presence of two main components of methyl ester which were methyl palmitate and methyl oleate. For future research, it is suggested that the preparation of the catalyst is to be studied in more detail, for example, optimizing the ratio of KOH: alumina, the calcination temperature, and the calcination time for preparing the catalyst, as these might improve the catalytic activity.

Acknowledgement

Authors would like to express gratitude to all staff of the chemistry laboratory of UiTM Jengka Pahang, Malaysia, for their assistance in the completion of this research.

References

1. Alkabbashi, A. N., Alam, M. Z., Mirghani, M. E. S. and Al-Fusaiel, A. M. A. (2009). Biodiesel production from crude palm oil by transesterification process. *Journal of Applied Sciences*, 9: 3166-3170.
2. Aqliliriana, C. M., Ernee, N., M. and Irmawati, R. (2016). Preparation and characterization of modified calcium oxide from natural sources and their application in the transesterification of palm oil. International *Journal of Scientific & Technology Research*, 4(11): 168-175.

3. Noiroj, K., Intarapong, P., Luengnaruemitchai, A. and Jai-In, S. (2009). A comparative study of KOH/Al_2O_3 and KOH/NaY catalysts for biodiesel production via transesterification from palm oil. *Renewable Energy*, 34, 1145-1150.
4. Sulaiman, S. and Ramli, N. S. (2017). Biodiesel production from palm oil using KOH supported polyvinyl alcohol as the catalyst. *Energy Sources*, 39(18): 1948-1953.
5. Ilgen, O. G. and Akin, A. S. N. U. (2009). Development of alumina supported alkaline catalysts used for biodiesel production. *Turkish Journal Chemistry*, 33: 281-287.
6. Keera, S. T., Sabagh, S. M. E. and Taman, A. R. (2018). Castor oil biodiesel production and optimization. *Egyptian Journal of Petrol*, 27: 979-984.
7. Ghasemi, M. and Molaei Dehkordi, A. (2014). Transesterification of waste cooking oil to biodiesel using KOH/γ-Al_2O_3 catalyst in a new two-impinging-jets reactor. *Industrial & Engineering Chemistry Research*, 53(31): 12238-12248.
8. Taslim, Andika Sinaga, B., Nathalia Sihaloho, M., Iriany, and Bani, O. (2019). Biodiesel synthesis from waste cooking oil using heterogeneous catalyst from corncob ash impregnated with KOH. *Journal of Physics: Conference Series*, 1175: 012281.
9. Ma, G., Hu, W., Pei, H., Jiang, L., Ji, Y. and Mu, R. (2015). Study of KOH/Al_2O_3 as heterogeneous catalyst for biodiesel production via in situ transesterification from microalgae. *Environmental Technology*, 36:5, 622-627.
10. Jitputti, J., Kitiyanan, B. and Rangsunvigit, P. (2006). Transesterification of crude palm kernel oil and crude coconut oil by different solid catalysts. *Chemical Engineering Journal*, 116: 61–6.
11. Renganathan, S. V., Narashimhan, S. L., and Muthukumar, K. (2008). An overview of enzymatic production of biodiesel. *Bioresource Technology*, 99: 3975-3981.
12. Zhang, J., Liu, J. and Ma, H. (2012). Esterification of free fatty acids in *Zanthoxylum bungeanum* seed oil for biodiesel production by stannic chloride. *Journal American Oil Chemical Society*, 89:1647-1653.
13. Zhang, L., Wu, H. T. and Yang, F. X. (2015). Evaluation of Soxhlet extractor for one-step biodiesel production from *Zanthoxylum bungeanum* seeds. *Fuel Process Technology*, 131: 452–457.
14. Modiba, E., Enweremadu, C., and Rutto, H. (2014). Production of biodiesel from waste vegetable oil using impregnated diatomite as heterogeneous catalyst. *Chinese Journal of Chemical Engineering*, 2014: 1-9.
15. Roschat, W., Siritanon, T., Yoosuk, B., and Promarak, V. (2016). Biodiesel production from palm oil using hydrated lime-derived CaO as a low-cost basic heterogeneous catalyst. *Energy Conversion and Management*, 108: 459-467.
16. Kansedo, J., Lee, K. T. and Bhatia, S. (2009). Biodiesel production from palm oil via heterogeneous transesterification. *Biomass and Bioenergy*, 33: 271-276.
17. Buasri, A., Chaiyut, N., Loryuenyong, V., Rodklum, C., Chaikwan, T. and Kumphan, N. (2012). Continuous process for biodiesel production in packed bed reactor from waste frying oil using potassium hydroxide supported on *Jatropha curcas* fruit shell as solid catalyst. *Applied Science*, 2: 641-653.
18. Refaat, A. A. (2010). Different techniques for the production of biodiesel from waste vegetable oil. *International Journal of Environment, Science & Technology*, 7(1): 183-213.
19. Uprety, B. K., Chaiwong, W., Ewelike, C. and Rakshit, S. K. (2016). Biodiesel production using heterogeneous catalysts including wood ash and the importance of enhancing byproduct glycerol purity. *Energy Conversion and Management,* 115: 191-199.
20. Shohaimi, N. A. M., Bakar, W. A. W. A. and Jaafar, J. (2014). Catalytic neutralization of acidic crude oil utilizing ammonia in ethylene glycol basic solution. *Journal of Industrial and Engineering Chemistry*, 20(4): 2086-2094.

21. Shohaimi, N. A. M., and Marodzi, F. N. S. (2018). Transesterification of waste cooking oil in biodiesel production utilizing CaO/Al_2O_3 heterogeneous catalyst. *Malaysian Journal of Analytical Sciences*, 22(1): 157-165.
22. May, C. Y. (2004). Transesterification of palm oil: Effect of reaction parameters. *Journal of Oil Palm Research,* 16(2): 1-11.
23. Mahesh, S. E., Ramanathan, A., S.Begum, K. M. M., and Narayanan, A. (2015). Biodiesel production from waste cooking oil using KBr impregnated CaO as catalyst. *Energy Conversion and Management*, 91: 442-450.
24. Maneerung, T., Kawi, S., Dai, Y. and Wang, C.-H. (2016). Sustainable biodiesel production via transesterification of waste cooking oil by using CaO catalysts prepared from chicken manure. *Energy Conversion and Management*, 123: 487-497.
25. Daniyan, A., Adeodu, A. O., Dada, O. M., and Adewumi, D. F. (2015). Effect of reaction time on biodiesel yield. *Journal of Bioprocessing and Chemical Engineering*, 3(2): 1-4.
26. Madhu, A., Garima, C., Chaurasia, S. P. and Kailash, S. (2012). Study of catalytic behavior of KOH as homogeneous and heterogeneous catalyst for biodiesel production. *Journal of the Taiwan Institute of Chemical Engineers,* 43: 89-94.

Malaysian Journal of Analytical Sciences (MJAS)
Published by Malaysian Analytical Sciences Society

HARDNESS REMOVAL OF GROUNDWATER THROUGH SAND, ZEOLITE AND RICE HUSK ACTIVATED CARBON

(Rawatan Air Bawah Tanah Menggunakan Pasir, Zeolit dan Karbon Reaktifdari Sekam Padi bagi Penyingkiran Keliatan Air)

Nor Izzah Abdul Aziz[1], Norzila Othman[1]*, Wahid Ali Hamood Altowayti[1], Zalilah Murni Yunus[2], Nurina Fitriani[3], Mohd Fadhil Md Din[4], Firhat Muhammad Fikri[5]

[1]Faculty of Civil Engineering and Built Environment
[2]Faculty of Science Technology & Human Development
Universiti Tun Hussein Onn Malaysia, 86400, Batu Pahat Johor, Malaysia
[3]Faculty of Science and Technology,
Universitas Airlangga, Surabaya, Jawa Timur 60115, Indonesia
[4]Faculty of Engineering,
Universiti Teknologi Malaysia, 81310 Skudai, Johor, Malaysia
[5]Bendang Afwa Enterprise Sdn Bhd
Bukit Tembaga, Kuala Nerang, Kedah, Malaysia

**Corresponding authors: norzila@uthm.edu.my*

Received: 10 June 2021; Accepted: 16 July 2021; Published: 29 August 2021

Abstract

Recently the treatment for hard water was by using a technique that will give an impact on the environment and consumer. Sand, zeolite and rice husk-activated carbon can be used as a media for water hardness treatment by adsorption process. Performance of sand, zeolite and rice husk activated carbon (RHAC) for removal of Ca^{2+} and Mg^{2+} in hard water was investigated by employing a batch experimental set-up. The study considered X-ray fluorescence (XRF) spectroscopy analysis for the evaluation of the chemical composition of the media and Fourier transform infrared (FTIR) spectroscopy for the surface functional group. Experimental adsorption data were modelled by Langmuir, Freundlich and BET. The adsorption process followed the Langmuir isotherm model with high coefficients of correlation R^2 (0.9888) for Ca^{2+} and R^2 (0.9662) for Mg^{2+}. The R_L value in this study was less than one for both Ca^{2+} and Mg^{2+}, indicating that the absorption of the metal ion onto all the media is favourable. The pseudo-second-order fitted well in correlation to the experiment results. The results indicate that sand, zeolite, and RHAC have chemisorption mechanisms and can be alternative media for hard water treatment using the adsorption process. Furthermore, there will be an advantage in terms of economic and environment-friendly media.

Keywords: adsorption, kinetic study, filter media, groundwater treatment, hard water, isotherm study

Abstrak

Rawatan keliatan air yang sedia ada memberi kesan kepada pengguna dan alam sekitar. Pasir, zeolit dan karbon teraktif dari sekam padi boleh digunakan sebagai media bagi rawatan air liat. Semua media ini akan bertindak sebagai penyerap. Eksperimen kaedah kelompok digunakan bagi menyiasat keberkesanan pasir, zeolit dan karbon teraktif dari sekam padi dalam menyerap dan merendahkan nilai bagi ion Ca^{2+} dan Mg^{2+} di dalam air bawah tanah. Analisis spektroskopi pendaflour sinar-X (XRF) ke atas

komposisi bahan kimia dan spektroskopi infra merah transformasi Fourier (FTIR) pada setiap media turut dijalankan. Hasil dapatan daripada ekperimen kaedah kelompok, keputusannya disuaipadan dengan kaedah permodelan Langmuir, Freundlich and BET bagi mengenalpasti sifat kebolehserapan semua media. Proses penjerapan adalah memenuhi kriteria permodelan Langmuir dengan nilai pekali R^2 (0.9888) untuk Ca^{2+}, dan R^2 (0.9662) untuk Mg^{2+}. Nilai bagi R_L bagi kajian ini adalah adalah kurang dari nilai satu, maka menunjukkan semua media berfungsi sebagai agen penjerap bagi ion Ca^{2+} dan Mg^{2+}. Kajian kinetik mekanisme penjerapan dikategorikan sebagai tertib pseudo-kedua, ini membuktikan media pasir, zeolit dan karbon teraktif dari sekam padi mempunyai mekanisme penjerapan secara tindakbalas kimia. Maka dengan itu kaedah penjerapan dengan menggunakan media ini dapat digunakan sebagai rawatan kepada keliatan air. Media pasir, zeolit dan karbon teraktif dari sekam padi mudah didapati adalah merupakan kelebihan untuk dipilih sebagai media rawatan bagi keliatan air.

Kata kunci: penjerapan, kajian kinetik, media penapis, rawatan air bawah tanah, keliatan air, kajian isoterm

Introduction

Particularly in Malaysia, drinking water is mainly supplied through surface water treatment plants and distributed to the public by a centralised piping system. The implication of water scarcity in Malaysia has been increased widely and demand for other water supply sources has been increased such as groundwater [1]. Groundwater is being utilized for drinking purposes in some Malaysian states like Kelantan, Terengganu, Pahang, Perlis, Kedah, Sabah, and Sarawak [2]. Demands for groundwater as an alternative source for water supply are also increasing due to surface water pollution. However, groundwater is a fresh source of water, which is available beneath the Earth's surface. But its quality is a problem in terms of hardness, salinity and presence of iron, manganese, ammonium, fluoride and rarely nitrate and arsenic [3].

The hardness of groundwater is determined mainly by its content of Ca^{2+} and $Mg^{2+.}$ High concentrations in Ca^{2+} and Mg^{2+} also increase total dissolved solids (TDS) levels in groundwater [3]. Although Ca^{2+} and Mg^{2+} contents in groundwater do not have any dangerous health impacts, it creates a scaling problem for household utensils and poses problems in cleaning through detergents [4]. Hardness can be classified as temporary hardness and permanent hardness. Dissolved bicarbonate minerals cause temporary hardness in the water like calcium bicarbonate and magnesium bicarbonate. The temporary hardness of water can be removed by boiling it or by adding lime. However, the permanent hardness of water cannot be treated by boiling. Permanent hardness is due to dissolved sulphate and chloride ions like calcium sulphate and magnesium sulphate [5]. Recently, there are a few techniques for the removal of hardness of water such as ion exchange, adsorption, filtration, precipitation by lime soda and softening process. Water softening is defined as a treatment process where the Ca^{2+} and Mg^{2+}. ions are removed from water [6]. Table 1 describes the technique for hard water treatment and the comparison of advantages and disadvantages. Therefore, it is essential to establish an efficient, rapid, and eco-friendly technique to remove Ca^{2+} and $Mg^{2+.}$ ions from groundwater.

Low-cost media which is also easy to handle, and the media's capability to be regenerated are the main factors that will decrease the operating and maintenance cost [11, 12]. Among the hard water treatment techniques, the absorption process is more reliable whereby adsorbent techniques can be employed. Adsorption brings advantages economically has good efficiency and promising good metal binding [8]. In this study sand, zeolite and activated carbon are selected as filtration media due to their performance and ability according to previous researches on hard water treatment, whereby every media has its ability and advantages. Table 2 describes the function of the selected media based on the previous studies.

Recently, the batch experiment was used to determine the adsorption isotherm and kinetic by doing the analysis based on every media separately. Therefore, the objective of this study was to investigate the hard water treatment efficiency of sand, zeolite and rice husk activated carbon (RHAC) as filter media for Ca^{2+} and Mg^{2+} removal from groundwater using batch experiment. The analysis from the batch experiment was based on all media and the result will be compared

with individual media. This will be the novelty of this study.

Table 1. Advantages and disadvantages for hard water treatment technique

Technique	Materials and Method	Advantages	Disadvantages	Reference
Ion exchange	Ion-exchange resin, (sodium as a softening salt with chlorine)	The resin can be automated control. Resins could remove all hardness from the water	More power feeding and periodical revival of saturated ion-exchanger resin are required. Regeneration process effluent has possible hazards.	[7]
Adsorption	Activated carbon	It can be formed from any carbonaceous materials that are rich in elemental carbon and a low proportion of inorganic components, natural materials like agricultural by-products have the potential to be utilized as precursors of activated carbon.	The carbon adsorption process is controlled by the diameter of pores in the carbon media and by the diffusion rate of organics via pores (based on activated carbon precursors)	[8]
Filtration (membrane)	Membrane	Easy removal of bacteria, microorganisms, particulates, and natural organic materials, but can impart colour, tastes, add odours to water and react with disinfectants to form disinfection by-products.	Fouling creates problems in the membrane for the treatment of water. High operation and maintenance cost	[9]
Precipitation using lime-soda	Lime as hydroxide and soda ash as carbonate ion	Rich source, high efficiency of removal. Economic and easy to operate	It could produce a large amount of sludge which will relate to the increased cost of dewatering the sludge and it will also take a long time to settle	[10]

Table 2. The function of sand, zeolite and rice husk activated carbon

Media	Function	Reference
Sand	Sand filtration units can remove up to 99% of bacteria and other unnecessary contaminants from the water supply.	[13]
Rice husk activated carbon (RHAC)	RHAC adsorbents are proved to have magnificent removal capabilities for most heavy metal ions furthermore it will save disposal costs and alleviate potential environmental problems	[14]
Zeolite	It is an active sorbent and ion–exchange media for metal ions which could be used as ion exchange for the removal of heavy metals from wastewater	[15]

Materials and Methods

Groundwater sample

Raw groundwater containing high Ca2+ and Mg2+ was collected at Bukit Tembaga, Kuala Nerang, Kedah. A high level of hardness in Bukit Tembaga was possibly due to the geological formation of the area that consists of main alluvium, gravel and sand layers and hard limestone rock [3]. The samples were taken directly from the well, which was equipped with a pump for 9 months from April 2016 until January 2017. The chosen period will cover all the climate conditions, rainy and dry seasons, and was collected at different times, morning, noon, and evening. Every sample must be in triplicate, and the result was from the average data. The preliminary data of groundwater on site were observed after the sampling is done. The water samples were analysed using atomic adsorption spectroscopy (AAS) to determine the concentration of Ca2+ and Mg2+ ions.

Media preparation

Activated carbon was prepared from rice husk with impregnation method by nitric acid and carbonization process. Impregnation is the process where rice husk was impregnated in nitric acid (HNO3) of 10% concentration. Nitric acid with low concentration was used as this water will be treated for drinking purposes [16]. The impregnation process will enhance the development of the pore size of activated carbon [17]. The rice husk was carbonized at the temperature of 450 oC for 20 minutes. The carbonization process produces a distribution of interval pores and affects the carbon surface, which generally enhances its absorptive capacity [18].

Raw sand was cleaned with distilled water. Next, it was dried in an oven for 24 hours. The optimal sieve size of 0.7 mm was chosen in preparing the filtration media. The effective size for the filtration sand range between 0.15 to 0.20 mm, uniformity coefficient < 2.5 and the maximum quantity of fine sand grains of 4% < 0.1 mm passing through a 150 sieve [19]. The chiloptilolite zeolite which in the range of 0.3 – 1.0 mm in size were purchased from Syarikat Scientific Bersatu. The raw zeolite was cleaned with distilled water and dried in an oven for 24 hours to clean any dirt.

Media characterization

The study of the surface chemistry of solids is possible by using X-ray fluorescence (XRF) spectroscopy analysis. Sample preparation involved sequence works; grinding the media, pulverizing the media to less than 150 micrometres, weighted 8.0 g of the sample and mixed with 2.0 g of binder to make a homogenous pellet. The PE-MAN Manual Hydraulic Press was used to form the mixture into a pallet. FTIR spectrometer (PE Spectrum 100, USA) was employed to determine the presence of a surface functional group for each media.

Batch adsorption experiment

Adsorption is mainly affected by initial ion concentration, temperature, pH, and mass media [8]. A batch adsorption experiment was performed to investigate all factors. Adsorption isotherm is designated to an adsorbent capacity, solute-solution contact and the degree of accumulation of adsorbed materials on the surface of the adsorbent [20]. In addition, adsorption isotherm was considered at various

initial concentrations of Ca^{2+} (45, 60, 75, 90, 105 and 120 mg/L) and Mg^{2+} cations (45, 112, 180, 247, 283 and 344 mg/L). Optimum pH of 7 was applied. The mass of sand, zeolite and RHAC of 4, 3.6 and 1 g was suspended in groundwater of 100 mL volume. The flasks were located on an orbital shaker and agitated at 125 rpm at room temperature. Next, the suspension was filtered through a 0.45 µm nylon membrane filter and the filtrate was analysed for the residual concentration using Atomic absorption spectrophotometry (AAS). The data from the batch adsorption experiment were collected and analysed using Langmuir, Freundlich and BET adsorption isotherm.

Langmuir isotherm

The Langmuir isotherm is widely used for homogeneous surfaces. The model assumes that the adsorption energy is the same for all surface sites, indicating monolayer adsorption by the substrates. The Langmuir isotherm as shown in equation 1 [21, 22]:

$$q_e = \frac{q_m K_L C_e}{1+K_L C_e} \quad (1)$$

where qm is maximal adsorption capacity, K_L is a constant related to free energy adsorption. The essential characteristics of Langmuir isotherm can be expressed by a dimensionless constant called separation factor (or equilibrium parameter), R_L, which is defined by the following equation:

$$R_L = \frac{1}{1+K_L C_0} \quad (2)$$

where, C_0 is highest initial concentration of metal ions (mg/L) and R_L provides the important indication whether the isotherm is either unfavourable (R_L > 1), linear (R_L = 1), favourable (0 > R_L > 1), or irreversible (R_L = 0) [23].

Freundlich isotherm

Freundlich isotherm assumes that the adsorption process takes place on a heterogeneous surface. The Freundlich exponential equation as in equation 3 [24, 25]:

$$q_e = K_F C_e^{\frac{1}{n}} \quad (3)$$

where K_F and 1/n are Freundlich isotherm constant related to adsorption capacity and intensity of adsorption. A larger value for 1/n points out a larger change in effectiveness over different equilibrium concentrations and describes that the change in adsorbed concentration was greater than the change in solute concentration [20, 26].

To linearize the equation, as in equation 4.

$$log q_e = log K_F + n_F log C_e \quad (4)$$

where *qe* = quantity adsorbed per unit mass (mol/g); C_e = equilibrium solution concentration (mol/L); K_F = L/g and *1/n* = nF = is empirical Freundlich constant. K_F (mg/g (L/mg)1/n) is defined as the adsorption capacity of the adsorbent *1/n* is heterogeneous as its value gets to closer to zero [27].

Brunauer Emmett and Teller

Adsorbate molecules generally procedure multilayer, in which, few molecules adsorbed on already adsorbed molecules and thus, the Langmuir isotherm is not valid. However, Stephan Brunner, Paul Emmett and Edward Teller developed an isotherm model in 1938 that could be considered more appropriate and named it as BET isotherm model. As an extension of the Langmuir model, this model changes the assumption from a monolayer to several molecular layers. The additional layer of adsorbate molecules above the monolayer is likely to equilibrate with the layer below it and layers of different thicknesses can coexist and take the following equation 5.

$$\frac{C_e}{(C_i - C_e)q_m} = \frac{1}{K_B q_m} + \left[\frac{K_B - 1}{K_B q_m}\right]\left[\frac{C_e}{C_i}\right] \quad (5)$$

Adsorption kinetic experiment

The kinetic experiment was conducted by mixing 4 g sand, 3.6 g zeolite and 1 g RHAC with the optimum initial concentration of Ca^{2+} or Mg^{2+} of 308.8 mg/L and 405 mg/L each in a conical flask. The flasks were placed on an orbital shaker and agitated at 125 rpm with different contact times (15, 30, 45, 60 and 75 minutes) [28]. The samples were directly filtered after each interval through a 0.45µm nylon membrane filter and the filtrate was analysed for the residual concentration using

atomic absorption spectrophotometry (AAS). The data collected were modelled using pseudo-first-order and pseudo-second-order.

The pseudo –first order is described as an equation 6 below [29]:

$$\ln (q_e - q_t) = \ln q_e - k1t \quad (6)$$

This equation posited that the adsorption rate is based on the adsorption capacity, where q_e and q_t (mg/g) are the amounts of adsorbate adsorbed at equilibrium and any time, t (h), respectively and k1(1/h) is the constant adsorption rate. The plot of ln ($q_e - q_t$) versus t gives the slope of k1 and intercept of ln q_e. The pseudo-second-order kinetic expression for adsorption system has been applied in earlier studies including those concerning the adsorption of anions [30]. In this study, the kinetics for the Ca^{2+} and Mg^{2+} ion adsorption was described using a pseudo-second-order mechanism. Pseudo – second-order kinetic model, which is based on the equilibrium adsorption is described in equation 7 below:

$$\frac{t}{q_t} = \frac{1}{k_2 q_e^2} + \frac{1}{q_e} t \quad (7)$$

whereas, k_2 is the constant rate of pseudo-second-order biosorption (g mg^{-1} min^{-1}). Pseudo-second order constant rate k_2 and qe values were calculated from the slope and intercept of the plots t/q versus t. Adsorption experiments for the kinetic study were carried out by shaking a 250 mL conical flask with 100 mL groundwater filled with 4 g sand, 3.6 g zeolite and 1g RHAC. The Ca^{2+} and Mg^{2+} anions concentration in groundwater solutions are 303.8 mg/L and 405mg/L. The pre-determined contact times for the experiments were 30, 45, 60, and 75, 90, 105 and 120 minutes. The groundwater pH was maintained at 7.

Results and Discussion

Groundwater characterization

Table 3 presents the result for groundwater from the study area. From the Table 3, only a certain element in the groundwater is above the permittable value by WHO. Turbidity values are higher due to suspended sediments, such as particles of clay, soil, and silt commonly entered the water from disturbed sites and the effect of the water quality. It is important to note that a higher turbidity level will not influence the groundwater quality. The content in total dissolved solids (TDS) is ion and cations, which are calcium, magnesium, sodium, potassium, hydrogen carbonate, chloride sulphate and nitrate anion in groundwater. From the Table 3, the amount of Ca^{2+}, Mg^{2+} and potassium is higher than the permittable value by WHO. This could be attributed to the water movement through soil and rock which will dissolve small amounts of naturally occurring minerals and carries them into it. Furthermore, water has a great tendency to dissolve calcium and magnesium [3].

Groundwater with higher content of Calcium and Magnesium can be classified as hard water [4]. Hard water has serious consequences on the human health and environment, and increase potential health risks caused by hard water like a kidney stone, dermatitis, a reproductive health issue and pancreatic cancer [31]. Ion exchange, filtration using membrane, precipitation using lime soda and adsorption are among treatment methods in water softening. According to Sepehr et al. [32] adsorption is an important method that could be used effectively for softening of water and it has great potential to replace expensive conventional softening approaches other than reducing the usage of extra chemicals. Therefore, in this study, sand, zeolite and RHAC were selected as filtration media.

Characterization of media

The result for the chemical composition of sand, zeolite, and RHAC are tabulated in Table 4. A previous study on RHAC by Ghosh and Bhattacherjee [33] had proved its possibility to be used in wastewater treatment. The main components of an adsorbent such as silica oxide, ferric oxide, calcium oxide and magnesium oxide were found in all media (sand, zeolite and RHAC). This factor will be contributing to the media showing a high possibility of metals removal. The chemical compositions of sand and zeolite are comparable to previous findings of Abdolahnejad et al. [6], where he considered sand and zeolite as filtration media for the purpose of water softening.

Figure 1 shows rice husk activated carbon spectra with 450 °C firing temperature and impregnated with 10% of HNO_3. Based on the FTIR analysis of RHAC, the result indicated the presence of a broad spectrum of important functional groups such as alcohol, phenol and carboxylic groups. The maximum spectrum at 3353 cm^{-1} is usually the characteristic of stretching vibration of the hydrogen-bonded hydroxyl group of water adsorbed in RHAC. The bands between 2220-2300cm^{-1} corresponded to the vibration in the alkane group which corresponded (C=N) strength to the vibration in alkanes and alkyl groups. Band 700-1755cm^{-1} correspond to carbonyl stretching. The carbonyl stretching absorption is one of the strongest IR absorptions. It is very useful in structure determination as one can determine the number of carbonyl groups. It also originated from a C-O single bond in functional groups such as carboxylic acids, alcohols and others [8].

The presence of hydroxyl groups, carbonyl group, ethers and aromatic compounds is evidence of the lignocellulosic structure rice husk and is also observed in other materials such as Brazilian coconut shell [34], and jackfruit peel waste [35] which were used as activated carbon precursor.

FTIR analysis result of zeolite as in Figure 2 displays bands between 1640-1500 cm^{-1} which were attributed to the flexion vibration of alkenes (C- C=C) symmetric stretch. Wavenumber 1060-895 cm^{-1} indicate the characteristic of asymmetric stretching of C-N bonds from substitute amines. Finally, typical stretching broadband of zeolite is present around 3361 cm^{-1}, the same as RHAC, which relate to the hydroxyl (O-H) group such as alcohol and phenols [36]. The hydroxyl and carboxyl groups, among the most common functional groups, found to contribute widely to the adsorption of heavy metals, such as Pb(II), Hg(II), Cr(II), Cd(II) and Ni(II) ions onto various adsorbents [37].

Figure 3 shows the characteristic of sand spectra between 1300-1000 cm^{-1}. The sand surface is composed of a plan of oxygen atoms bound to the silica tetrahedral layer and hydroxyl groups that are associated with the edge of the silicate structure units. These functional groups provide surface sites for the chemisorption of metal ions. The surface hydroxyl groups dissociate in water and serve as Lewis bases towards metal ions. The metals favor the metal surface bonding (adsorption) reaction due to their hydrolysis properties [38]. This shows that the presence of silica in sand contributes to the removal. On the other hand, Mg^{2+} and Ca^{2+} removal through physical adsorption or ion exchange were dominant in anthracite and quartz sand [30]. The identified group for sand was similar to research by Guchi [39], which shows that sand is a suitable filtration technology to remove waterborne pathogens and reducing turbidity. The sand can improve the physical, chemical, and microbiological quality of water in a single treatment process without the addition of chemicals and can produce an effluent low in turbidity and free of bacteria, parasites and viruses.

Table 3. Groundwater parameter for the study area

Parameter	**Value in mg/L (unless otherwise stated)**	**Drinking Water Standard (WHO2006)**
Turbidity	120 NTU	0.1 NTU
Total dissolved solids (TDS)	450	500
Dissolved oxygen (DO)	9.5	NA
pH	6.23	6.5-8.5
Chloride (Cl^-)	32.97	250
Sulphate (SO_4^{2-})	20.05	250
Potassium (K^+)	288.2	200
Calcium (Ca^{2+})	308.8	NA
Magnesium (Mg^{2+})	450	30

NA is not available

Table 4. Chemical composition for filter media

Chemical Composition	**Sand (%)**	**Zeolite (%)**	**RHAC (%)**
SiO_2	0.77	65.7	78.79
Al_2O_3	0.11	13.5	NIL
Fe_2O_3	0.36	1.3	1.29
Na_2O	NIL	1.16	0.01
K_2O	NIL	3.14	0.06
CaO	54.71	3.10	2.61
MgO	0.21	0.63	1.41
SO_3	NIL	NIL	9.00
Total	56.17	88.58	93.16
Loi	43.83	11.42	6.84

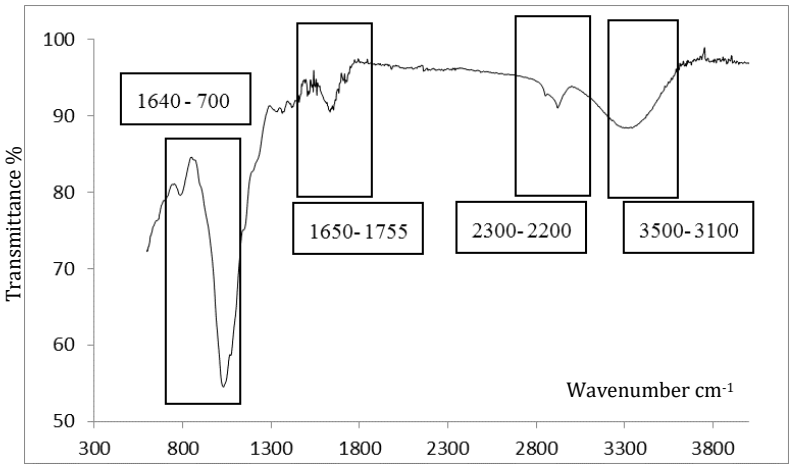


Figure 1. FTIR spectra for RHAC

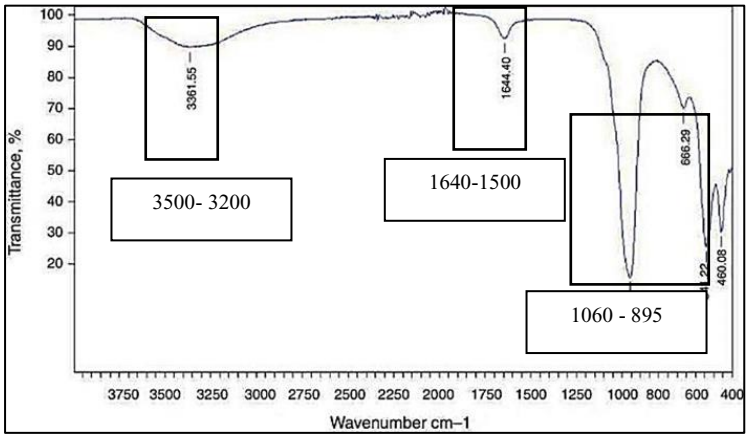


Figure 2. FTIR spectra for zeolite

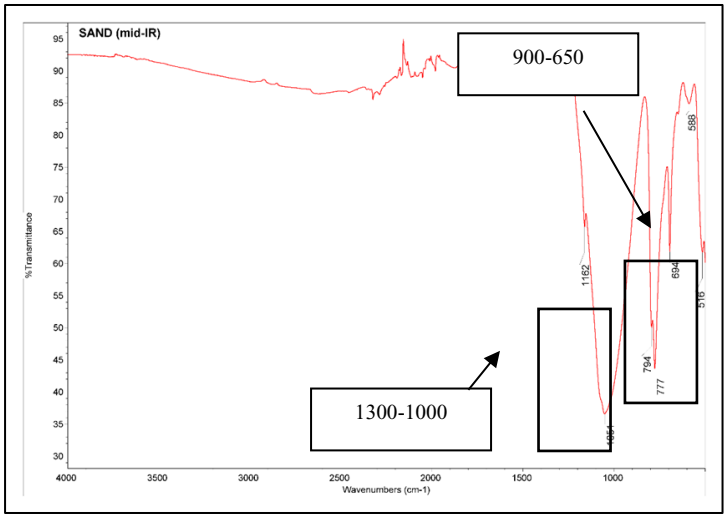


Figure 3. FTIR spectra for sand

Adsorption isotherms

BET isotherm of Mg^{2+} and Ca^{2+} showed linear correlation coefficient, R^2 of 0.9662 and 0.9888 respectively (Figure 4 and Figure 5).

Freundlich adsorption of all media resulted in a linear correlation coefficient, R^2 of 0.4734 and 0.9831. The values of n for Mg^{2+} and Ca^{2+} were 0.317 and -270.27 respectively as in Figure 6 and Figure 7.

The Langmuir isotherm constant b and q_{max} were calculated from the slope and intercept of the plot C_e/q_e versus C_e (Figure 8 and Figure 9).

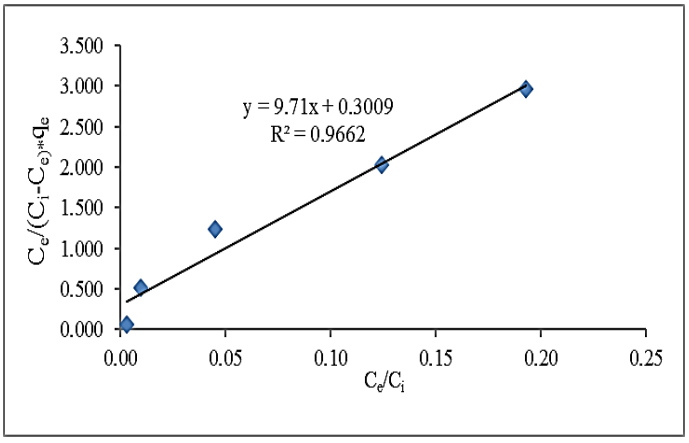


Figure 4. BET sorption isotherm of Mg^{2+}

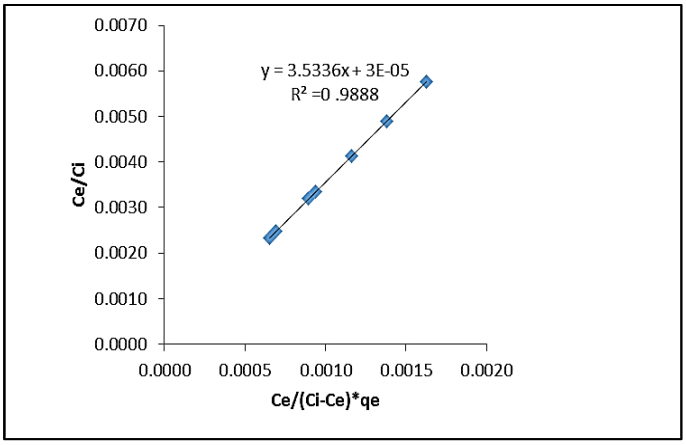


Figure 5. BET sorption isotherm of Ca^{2+}

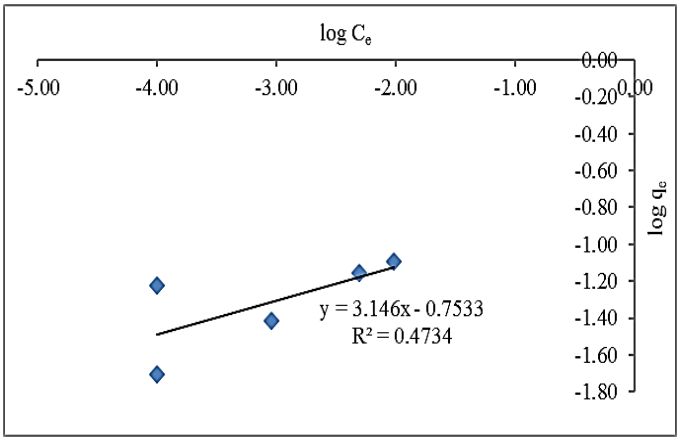


Figure 6. Freundlich sorption isotherm of Mg^{2+}

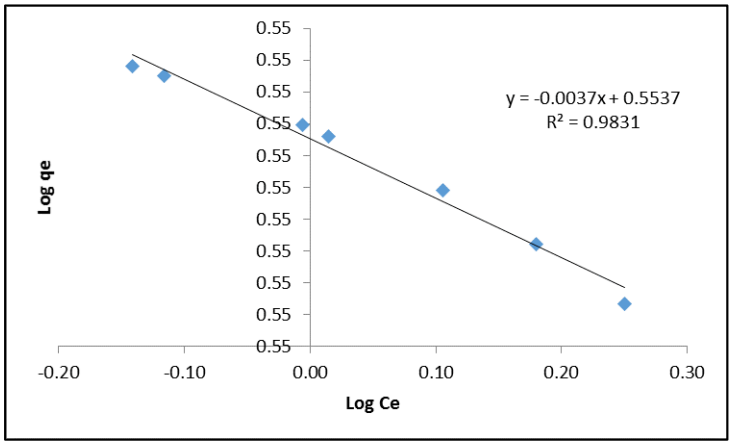


Figure 7. Freundlich sorption isotherm of Ca^{2+}

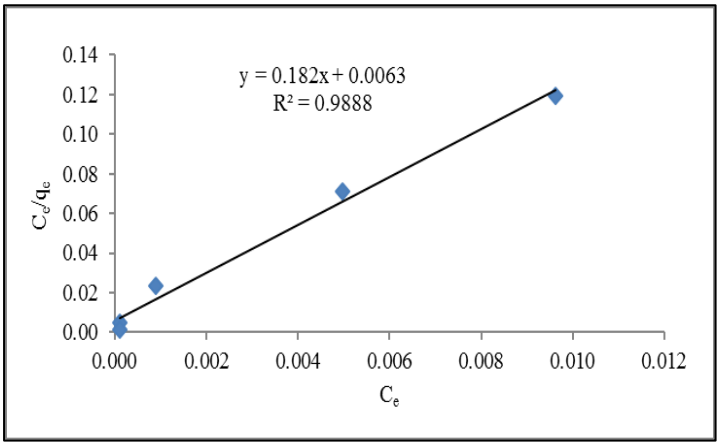


Figure 8. Langmuir sorption isotherm of Mg^{2+}

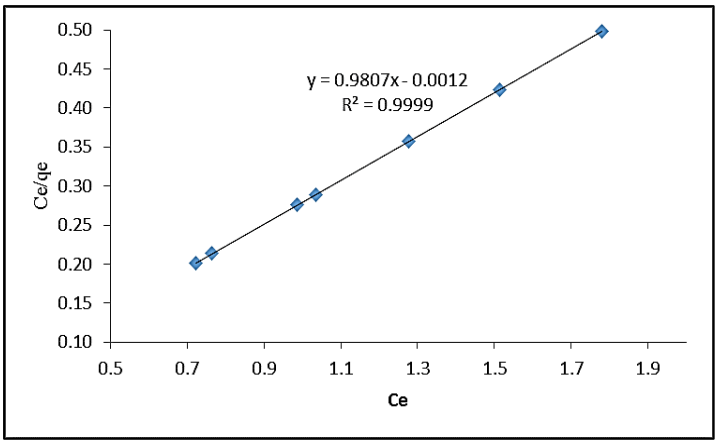


Figure 9. Langmuir Freundlich sorption isotherm of Ca^{2+}

The equilibrium adsorption of Langmuir, Freundlich and BET for all media are summarized in Table 5. The Langmuir isotherm constant b and q_{max} were calculated from the slope and intercept of the plot C_e/q_e versus C_e. It demonstrates a linear correlation coefficient, R^2 of 0.9888 and 0.999 and the sorption capacity q_{max} were 5.49 mg/g for Mg^{2+} and 1.02mg/g for Ca^{2+}, respectively.

Freundlich adsorption of Mg^{2+} and Ca^{2+} resulted from linear correlation coefficient, R^2 of 0.4734 and 0.9831 respectively. The value of n of Mg^{2+} and Ca^{2+} are 0.317 and -270.27 respectively. BET isotherm of all media showed that the linear correlation coefficient, R^2 were 0.9662 and 0.9888 respectively. The sorption capacity, q_{max} were 5.49 mg/g for Mg^{2+} and 1.02 mg/g for Ca^{2+} as in Table 5.

From Table 5, it can be concluded that all the media were best fitted with Langmuir isotherm which refer to monolayer adsorption. The sorption capacity, q_{max}, which was the indicator of maximum sorption capacity conforming to comprehensive monolayer coverage that

defines the metal uptake for Ca^{2+} and Mg^{2+} were close to experimental sorption capacity. Sorption of Ca^{2+} and Mg^{2+} by all media give the R_L values of 0.00323 mg/l and 0.00077 mg/l as in Table 6 which indicate that all the media are favourable and effective for the adsorption process.

Furthermore, Langmuir's assumption of Ca^{2+} and Mg^{2+} revealed the simultaneous occurrence of both physisorption and chemisorption onto sand, zeolite and RHAC. The result obtained from the present study was compared to previous research. It was noted that the performance of combined media in the absorption experiment is still in line with the previous findings that used single media for the experiment as tabulated in Table 7. Langmuir isotherm assumes that the number of adsorption sites is fixed and that adsorption is reversible. Adsorption cannot occur beyond monolayer coverage and each site can hold only one adsorbate molecule.

Kinetics adsorption study

The mechanism of adsorption not only depends on the physical and chemical characteristics of the adsorbent but also the mass transfer process [28]. From Table 8, the R^2 value suggests that the adsorption of Mg^{2+} and Ca^{2+} onto the sand, zeolite, and RHAC does not follow the pseudo-first-order kinetics model.

In a conclusion, the continuous reaction follows the pseudo-second-order mechanism rather than a pseudo-first-order mechanism. The best fit of pseudo-second-order kinetics also suggests that the rate-limiting step of the sorption process could be chemisorption involving valence forces through sharing the exchange of electrons. Similar phenomena of sorption of other metal onto the sand [30], zeolite [42] and RHAC [43] was also noticed.

Table 5. Adsorption isotherm constants sorption of Ca^{2+} and Mg^{2+} onto all media

Isotherm	Parameter	Magnesium (Mg)	Calcium (Ca)
BET	R^2	0.9662	0.9888
	K_B	31.2	7.106
	Q_m(mg/g)	9.40	0.28
Freundlich	R^2	0.4734	0.9831
	K_F	0.176	1.13
	N	0.317	-270.27
Langmuir	R^2	0.9888	0.9999
	b	28.91	0.00122
	q_{max} (mg/g)	5.49	1.02

Table 6. R_L value all media

Metal	R_L	Condition
Ca^{2+}	0.00323	Favourable
Mg^{2+}	0.00077	Favourable

Table 7. Adsorption isotherm constants sorption onto single media

Langmuir Isotherm Model	Removal	Estimated Isotherm Parameters			Reference
		q_{max} (mg/g)	k_L (L/mg)	R^2	
Sand	Phosphorus	0.169	0.242	0.991	[30]
	Uranyl ions	25	0.052	0.992	[38]
	Ca^{2+}	1.03	0.1114	0.999	[15]
Zeolite	Cd^{2+}	54.05	0.114	0.999	[40]
Activated Carbon	Mg^{2+}	0.207	4.25	0.999	[41]
	Phenol	1.152	14.47	0.996	[27]

Table 8. Kinetic parameters of biosorption of Ca^{2+} Mg^{2+} onto all media

Kinetic	Parameter	Magnesium
Pseudo 1st order	R^2	0.7161
	k_1	1.001
	q_e	442.48
Pseudo 2nd order	R^2	0.9495
	K_2	-0.00333
	q_e	5.03

Conclusion

This study concluded that the ability of sand, zeolite and RHAC as a filter media for hard water treatment was proven based on the experimental results. Moreover, the following conclusions were made based on the investigation; i) the adsorption isotherms can be well fitted by the Langmuir model representing monolayer sorption on a homogenous surface, ii) this study noticed that R_L value was less than one, which shows that the adsorption of Ca^{2+} and Mg^{2+} onto the sand, zeolite, and RHAC is favourable, and iii) the kinetics of the adsorption process followed the pseudo-second-order kinetic model, which indicates chemisorption.

Furthermore, it was observed that all the media is greatly available locally, therefore, making an economic adsorbent, abundantly available with substantial-high adsorption capacity. It could be treated as an economic filter media for hard water treatment.

Acknowledgment

This research was supported by Ministry of Higher Education (MOHE) through Fundamental Research Grant Scheme (FRGS)(FRGS/1/2019/WAB05/UTHM/02/7) and Universiti Tun Hussein Onn Malaysia through GPPS Vot U569

References

1. Ahmed, F., Siwar, C. and Begum, R. A. (2014). Water resources in Malaysia: Issues and challenges. *Journal of Food Agriculture Environment,* 12(2): 1100-1104.

2. Ab Razak, N. H., Praveena, S. M., Aris, A. Z. and Hashim, Z. (2015). Drinking water studies: A review on heavy metal, application of biomarker and health risk assessment (a special focus in Malaysia). *Journal of Epidemiology and Global Health*, 5(4): 297-310.
3. Aziz, N. I. A. and Othman, N. (2017). Groundwater quality and soil characterization: A case study at Bukit Tembaga, Kuala Nerang, Kedah. In *MATEC Web of Conferences*, 103, p. 05011.
4. Mahasti, N. N., Shih, Y. J., Vu, X. T. and Huang, Y. H. (2017). Removal of calcium hardness from solution by fluidized-bed homogeneous crystallization (FBHC) process. *Journal of the Taiwan Institute of Chemical Engineers*, 78: 378-385.
5. Ojo, O. I., Otieno, F. A. and Ochieng, G. M. (2012). Groundwater: Characteristics, qualities, pollutions and treatments: An overview. *International Journal of Water Resources and Environmental Engineering,* 4(6): 162-170.
6. Abdolahnejad, A., Ebrahimi, A. and Jafari, N. (2014). Application of Iranian natural zeolite and blast furnace slag as slow sand filters media for water softening. *International Journal of Environmental Health Engineering,* 3(1): 26.
7. Gomelya, M., et al., *Research into ion exchange softening of highly mineralized waters.* 2016. Gomelya, M., Hrabitchenko, V., Trokhymenko, A., & Shabliy, T. (2016). Research into ion exchange softening of highly mineralized waters. *European of Enterprise Technologies,* 4(10): 4-9.
8. Othman, N., Mohd-Asharuddin, S. and Azizul-Rahman, M. F. H. (2013). An overview of fruit waste as sustainable adsorbent for heavy metal removal. *Applied Mechanics and Materials*, 389: 29-35).
9. Gando-Ferreira, L. M., Gaspar, C. S. S., Monteiro, M. and Moreira, M. J. A. (2017). Studies on integration of ion exchange and nanofiltration for water desalination. *Separation Science and Technology,* 52(16): 2600-2610.
10. Abdullahi, M. E., Folorunsho, A. D., Agaie, B. G. and Jibril, M. (2012). Predictive model for lime dosage in water treatment plant. *International Journal of Scientific and Research Publications*, 2(12): 1-5.
11. Ayob, S., Othman, N., Altowayti, W. A. H., Khalid, F. S., Bakar, N. A., Tahir, M. and Soedjono, E. S. (2021). A review on adsorption of heavy metals from wood-industrial wastewater by oil palm waste. *Journal of Ecological Engineering,* 22(3): 249-265.
12. Hess, A. F., Rachwa, A. and Chipps, M. J. (2002). Filter maintenance and operations guidance manual. American Water Works Association.
13. Yongabi, K. A. (2013). A sustainable low-cost phytodisinfectant-sand filter alternative for water purification. Doctoral dissertation, University of Adelaide.
14. Chowdhury, S., Chakraborty, S. and Saha, P. (2011). Biosorption of basic green 4 from aqueous solution by *Ananas comosus* (pineapple) leaf powder. *Colloids and surfaces B: Biointerfaces,* 84(2): 520-527.
15. Rahman, M. M., Awang, M. B. and Yusof, A. M. (2012). Preparation, characterization and application of zeolite-Y (Na-Y) for water filtration. *Australian Journal of Basic and Applied Sciences,* 6(1): 50-54.
16. Allwar, A., Hartati, R. and Fatimah, I. (2017). Effect of nitric acid treatment on activated carbon derived from oil palm shell. In *AIP Conference Proceedings*, 1823(1): 020129.
17. Nahil, M. A. and Williams, P. T. (2012). Pore characteristics of activated carbons from the phosphoric acid chemical activation of cotton stalks. *Biomass and Bioenergy,* 37: 142-149.
18. Yunus, Z. M., Al-Gheethi, A., Othman, N., Hamdan, R. and Ruslan, N. N. (2020). Removal of heavy metals from mining effluents in tile and electroplating industries using honeydew peel activated carbon: A microstructure and techno-economic analysis. *Journal of Cleaner Production,* 251: 119738.
19. Xin-Hui, D., Srinivasakannan, C., Jin-Hui, P. E. N. G., Li-Bo, Z. and Zheng-Yong, Z. (2011). Preparation of activated carbon from Jatropha hull with microwave heating: optimization using response surface methodology. *Fuel Processing Technology*, 92(3): 394-400.

20. Ayawei, N., Ebelegi, A. N. and Wankasi, D. (2017). Modelling and interpretation of adsorption isotherms. *Journal of Chemistry*, 201: 3039817.
21. Altowayti, W. A. H., Allozy, H. G. A., Shahir, S., Goh, P. S. and Yunus, M. A. M. (2019). A novel nanocomposite of aminated silica nanotube (MWCNT/Si/NH_2) and its potential on adsorption of nitrite. *Environmental Science and Pollution Research,* 26(28): 28737-28748.
22. Altowayti, W. A. H., Othman, N., Goh, P. S., Alshalif, A. F., Al-Gheethi, A. A. and Algaifi, H. A. (2021). Application of a novel nanocomposites carbon nanotubes functionalized with mesoporous silica-nitrenium ions (CNT-MS-N) in nitrate removal: Optimizations and nonlinear and linear regression analysis. *Environmental Technology & Innovation*, 22: 101428.
23. Altowayti, W. A. H., Algaifi, H. A., Bakar, S. A. and Shahir, S. (2019). The adsorptive removal of As (III) using biomass of arsenic resistant *Bacillus thuringiensis* strain WS3: Characteristics and modelling studies. *Ecotoxicology and Environmental Safety*, 172: 176-185.
24. Allozy, H. G. A. and Abd Karim, K. J. (2020). Removal of copper ions from aqueous solutions using poly (vinylbenzyl chloride). *Malaysian Journal of Analytical Sciences,* 24(6): 978-991.
25. Altowayti, W. A. H., Haris, S. A., Almoalemi, H., Shahir, S., Zakaria, Z. and Ibrahim, S. (2020). The removal of arsenic species from aqueous solution by indigenous microbes: Batch bioadsorption and artificial neural network model. *Environmental Technology & Innovation*, 19: 100830.
26. Haris, S. A., Altowayti, W. A. H., Ibrahim, Z. and Shahir, S. (2018). Arsenic biosorption using pretreated biomass of psychrotolerant Yersinia sp. strain SOM-12D3 isolated from Svalbard, Arctic. *Environmental Science and Pollution Research,* 25(28): 27959-27970.
27. Liu, Q. S., Zheng, T., Wang, P., Jiang, J. P. and Li, N. (2010). Adsorption isotherm, kinetic and mechanism studies of some substituted phenols on activated carbon fibers. *Chemical Engineering Journal,* 157(2-3): 348-356.
28. Aljeboree, A. M., Alshirifi, A. N. and Alkaim, A. F. (2017). Kinetics and equilibrium study for the adsorption of textile dyes on coconut shell activated carbon. *Arabian Journal of Chemistry*, 10: S3381-S3393.
29. Bahari, Z. M., Altowayti, W. A. H., Ibrahim, Z., Jaafar, J. and Shahir, S. (2013). Biosorption of As (III) by non-living biomass of an arsenic-hypertolerant Bacillus cereus strain SZ2 isolated from a gold mining environment: Equilibrium and kinetic study. *Applied Biochemistry and Biotechnology,* 171(8): 2247-2261.
30. Jiang, C., Jia, L., Zhang, B., He, Y. and Kirumba, G. (2014). Comparison of quartz sand, anthracite, shale and biological ceramsite for adsorptive removal of phosphorus from aqueous solution. *Journal of Environmental Sciences,* 26(2): 466-477.
31. Ab Kadir, N. N., Shahadat, M. and Ismail, S. (2017). Formulation study for softening of hard water using surfactant modified bentonite adsorbent coating. *Applied Clay Science,* 137: 168-175.
32. Sepehr, M. N., Zarrabi, M., Kazemian, H., Amrane, A., Yaghmaian, K. and Ghaffari, H. R. (2013). Removal of hardness agents, calcium and magnesium, by natural and alkaline modified pumice stones in single and binary systems. *Applied Surface Science,* 274: 295-305.
33. Ghosh, R. and Bhattacherjee, S. (2013). A review study on precipitated silica and activated carbon from rice husk. *Journal of Chemical Engineering Process Technology,* 4(4): 1-7.
34. Vargas, A. M., Cazetta, A. L., Garcia, C. A., Moraes, J. C., Nogami, E. M., Lenzi, E. and Almeida, V. C. (2011). Preparation and characterization of activated carbon from a new raw lignocellulosic material: Flamboyant (*Delonix regia*) pods. *Journal of Environmental Management*, 92(1): 178-184.
35. Prahas, D., Kartika, Y., Indraswati, N. and Ismadji, S. J. C. E. J. (2008). Activated carbon from jackfruit peel waste by H_3PO_4 chemical activation: Pore structure and surface chemistry characterization. *Chemical Engineering Journal,* 140(1-3): 32-42.

36. Gopalakrishnan, Y., Al-Gheethi, A., Abdul Malek, M., Marisa Azlan, M., Al-Sahari, M., Radin Mohamed, R. M. S. and Noman, E. (2020). Removal of basic brown 16 from aqueous solution using durian shell adsorbent, optimisation and techno-economic analysis. *Sustainability,* 12(21): 8928.
37. Yang, X., Wan, Y., Zheng, Y., He, F., Yu, Z., Huang, J. and Gao, B. (2019). Surface functional groups of carbon-based adsorbents and their roles in the removal of heavy metals from aqueous solutions: A critical review. *Chemical Engineering Journal,* 366: 608-621.
38. Elhefnawy, O. A. and Elabd, A. A. (2017). Natural silica sand modified by calcium oxide as a new adsorbent for uranyl ions removal from aqueous solutions. *Radiochimica Acta,* 105(10): 821-830.
39. Guchi, E. (2015). Review on slow sand filtration in removing microbial contamination and particles from drinking water. *American Journal of Food and Nutrition,* 3(2): 47-55.
40. Selim, M. M., EL-Mekkawi, D. M., Aboelenin, R. M., Sayed Ahmed, S. A. and Mohamed, G. M. (2017). Preparation and characterization of Na-A zeolite from aluminum scrub and commercial sodium silicate for the removal of Cd^{2+} from water. *Journal of the Association of Arab Universities for Basic and Applied Sciences,* 24(1), 19-25.
41. Lestari, A. Y. D., Malik, A., Ilmi, M. I. and Sidiq, M. (2018). Removal of calcium and magnesium ions from hard water using modified Amorphophallus campanulatus skin as a low cost adsorbent. In *MATEC Web of Conferences*, 154: 01020.
42. Xue, Z., Li, Z., Ma, J., Bai, X., Kang, Y., Hao, W. and Li, R. (2014). Effective removal of Mg^{2+} and Ca^{2+} ions by mesoporous LTA zeolite. *Desalination,* 341: 10-18.
43. Yao, S., Zhang, J., Shen, D., Xiao, R., Gu, S., Zhao, M. and Liang, J. (2016). Removal of Pb(II) from water by the activated carbon modified by nitric acid under microwave heating. *Journal of Colloid and Interface Science,* 463: 118-127.

Malaysian Journal of Analytical Sciences (MJAS)
Published by Malaysian Analytical Sciences Society

PHYSICOCHEMICAL PROPERTIES OF SAGO BARK BIOCHAR AND ITS POTENTIAL AS PLANT GROWTH MEDIA

(Sifat Fizikokimia Bio-Arang Sisa Kulit Sagu dan Potensinya Sebagai Media Pertumbuhan Tanaman)

Nor Khairunnisa Mohamad Fathi[1], Sharifah Mona Abd Aziz Abdullah[2]*, Mohamad Fhaizal Mohamad Bukhori[2], Rafeah Wahi[1], Mohd Alhafiizh Zailani[2]

[1]Faculty of Resources Science and Technology,
[2]Centre for Pre-University Studies,
Universiti Malaysia Sarawak, 94300 Kota Samarahan, Sarawak, Malaysia

**Corresponding author: aaasmona@unimas.my*

Received: 23 June 2021; Accepted: 2 August 2021; Published: xx August 2021

Abstract

Biochar application as a soil amender can alter soil physical properties with its effects on soil aeration, water holding capacity, soil workability and plant growth. Sago biochar (SBB) was produced through carbonization of the sago bark waste in an oxygen free environment. This study aims to improve the morphological characteristics and physicochemical properties of SBB. The SBB was chemically treated using HCl and NaOH. The morphological characteristics of samples were analysed using SEM and BET. Meanwhile, the physicochemical analysis was performed using FTIR, CHN analyser and AAS. The treated sago biochar (TSB) showed the highest surface area (158.82 m^2/g) and can be classified as macropores (53.4 nm). This indicates that the TSB has large pores influencing the cohesiveness of soil particles, water storage, and increase in water holding capacity (97.63%). It also had the highest Ca and Mg (6.67% and 4.37%, respectively) which can assist in the production of chlorophyll in plant. TSB also showed a higher micronutrient concentration (Mn, Cu, and Fe) particularly the Fe concentration (2.00 mg/kg). The findings suggested that TSB could be used to improve soil qualities such as water holding and nutrients content, indicating that it has a good potential as a soil amender.

Keywords: chemical modification, plant growth study, biochar, soil amender, *Metroxylon sagu* Rottb

Abstrak

Bio-arang diaplikasikan sebagai bahan pembaikpulih tanah di mana ia dapat mengubah sifat fizikal tanah dan memberi pengaruh terhadap pengudaraan tanah, daya tahan air, kemampuan kerja tanah dan pertumbuhan tanaman. Bio-arang sisa kulit sagu (SBB) dihasilkan melalui pengkarbonan sisa kulit sagu dalam persekitaran bebas oksigen. Kajian ini bertujuan untuk menambahbaik ciri morfologi dan sifat fizikokimia SBB. SBB dirawat secara kimia menggunakan HCl dan NaOH. Ciri morfologi pada sampel dianalisis menggunakan SEM dan BET. Sementara itu, analisis fizikokimia dilakukan dengan menggunakan FTIR, CHN dan AAS. SBB yang dirawat (TSB) mempunyai luas permukaan tertinggi (158.82 m^2/g) dan boleh dikelaskan sebagai makropori (53.4 nm). Ini menunjukkan bahawa TSB mempunyai liang besar yang akan mempengaruhi kejelekitan zarah tanah, penyimpanan air, dan peningkatan daya tahan air (97.63%). TSB mempunyai kandungan Ca dan Mg tertinggi (masing-masing sebanyak 6.67% and 4.37%) yang dapat membantu dalam penghasilan klorofil dalam tumbuhan. TSB juga menunjukkan

kepekatan mikronutrien yang lebih tinggi (Mn, Cu, dan Fe) terutamanya kepekatan Fe (2.00 mg/kg). Hasil kajian mendedahkan bahawa TSB dapat digunakan untuk memperbaiki kualiti tanah seperti daya tahan air dan kandungan nutrien, sekaligus menunjukkan pontesinya sebagai pembaikpulih tanah.

Kata kunci: penguahsuaian kimia, kajian pertumbuhan tumbuhan, bio-arang, pembaikpulih tanah, *Metroxylon sagu* Rottb

Introduction

Sago (*Metroxylon sagu* Rottb) is a species from the genus *Metroxylon* which is under the Palmae family. Sago palm is one of the oldest tropical plants which has been domestically and commercially exploited for its stem starch [1]. Sago is distributed in many countries including Indonesia, Malaysia, Papua New Guinea, Philippines, Thailand, and Brunei [2]. According to Ehara et al. [2], sago distribution worldwide spreads 6.5 million ha^{-1} and the Papua area has led the distribution of around 4.7 million ha. Meanwhile, the distribution of sago in Malaysia was primarily in Sarawak (67%), Sabah (22%), and West Malaysia (11%). There are over 40 operational sago factories in Sarawak, primarily in Mukah and Dalat [3]. Domestically, Sarawak is annually exporting about 25,000 to 40,000 tons of sago products to several countries [1]. Sago products has multiple usages including food (biscuit and sago pearl) and manufacturing (biodegradable plastic, alcohol, citric acids, and biochar) [4].

Generally, most of the sago factories which are located near riverbanks are lack of waste management plan. Most of the waste was improperly disposed into the rivers which become a potential threat to the environment, biological, and aquatic life [3]. Approximately 0.75 tonnes of sago bark waste are generated from every tonne of sago flour processing. These wastes undergo carbonization in a closed furnace for the generation of heat for the drying process of sago flour [5]. This process produces biochar as the by-product which is beneficial for soil improvement.

Biochar is a carbon-rich product that acquired from the heating of biomass (wood, leaves, or manure) in a controlled condition and temperature above 250^{o}C with practically or completely absence of oxygen [6]. Application of biochar as soil amender is reported can alter the physical and chemical properties of soils such as the texture, structure, pore size distribution, bulk density, pH, and organic matter. This influences the aeration, water holding capacity, and available nutrients which will affect the plant performance [7]. Meanwhile, Piash et al. [6] reported that besides as a carbon-rich substance, biochar contains other main minerals such as calcium (Ca), magnesium (Mg), and inorganic carbonates. In addition, biochar also contains organic matter and nutrients which could influence the fertility of agricultural growth media by affecting the soil pH, electric conductivity (EC), organic carbon (OC), total nitrogen (TN), available phosphorus (P), and the cation-exchange capacity (CEC) [8].

Chemical treatment using acids on biochar was reported to enhance the adsorption capacity, increase water solubility, and plant availability of nutrients [9]. On that note, to enhance the properties of biochar, chemical modification using acid-base is reported to increase the pore volume of biochar while increases the acidic property and produces a positive charge on the surface which is favourable for the adsorption of negatively charged species [10]. According to Alzaydien [11], chemical modification of biochar using acid can develop more pores and cavities resulting in an enhanced adsorption capability. Chemically modified biochar was also reported to have a high tendency to adsorb inorganic contaminants through surface adsorption and retention of carboxyl functional group [12].

Past researchers have published numerous articles and review papers on the effect of biochar on soil structure and soil aggregation in plant growth performance including, maize (*Zea mays* L.) [13]; red chilli (*Capsicum annum* L.) [14]; lettuce and cabbage (*Lactusa sativa* and *Brassica chinensis*) [7]; and cowpea and peanut (*Vigna unguiculata* L., and *Arachis hypogaea* L.) [15]. Study reported by Carter et al. [7], the rice-husk biochar was slightly alkaline, improved

the pH of the soil, and had higher quantities of several trace metals and exchangeable cations (K, Ca, and Mg). Furthermore, water holding capacity of soil increased depending on type of biochar feedstock [16]. The same author also reported that the quantities of macropores and micropores in biochar attributed to a higher water holding capacity. Therefore, biochar could be a promising material for boosting acid soil productivity due to its liming effect, water and nutrient retention capability, and carbon sequestration capacity [17]. On top of this, the application of biochar as potential agricultural growth media fertility and soil amender would significantly reduce the cost and usage of commercial fertilizer which will be turned into cost-effective farming. Therefore, the current study aims to analyse the raw material of sago bark waste (SBW), sago biochar (SBB) and chemically treated sago biochar (TSB) properties. The biochar characterisation included the surface morphology, surface area measurements, water holding capacity, infrared spectra analysis, proximate and elemental analysis. Lastly, this study also evaluates the potential of SBB and TSB as soil amendments.

Materials and Methods

Samples preparation

The SBW and SBB were collected from sago factory in Mukah, Sarawak. Samples were oven-dried at 60 ^{o}C, 24 hours, grounded and sieved using No. 10 mesh (2 mm sieve size) prior to analysis. TSB was prepared from SBB via acid base treatment, as follows: SBB sample (5 g) was soaked in NaOH solution (2 M, mL) at 60 ^{o}C for 2 hours prior to oven-drying (105 ^{o}C, 24 hours). Sample was subjected under reflux with HCl (5 M, 25 mL) at 95 ^{o}C for 2 hours. The sample was washed with hot distilled water to obtain TSB of pH 7 and oven-dried (105 ^{o}C, 24 hours) [18, 19]. The prepared sample in this study is shown in Figure 1.

Physical characterisation

The surface morphology of sample was studied at magnification of 500× using Field Emission Scanning Electron Microscopy (FESEM) (JSM-6390LA, JEOL). Meanwhile, the elements presence on the surface of samples were determined by Energy Dispersive X-ray (EDX) (JSM-IT500HR, JEOL) [20]. The Brunauer, Emmet and Teller (BET) surface area and pore volume analysis was carried out using Surface Area Analyzer (Quantachrome® ASIQwin™). Prior to gas adsorption measurements, the solid products were vacuum degassed at 200 ^{o}C for 8 hours under vacuum conditions. Nitrogen gas was used as adsorptive gas at 77K. The N_2 adsorption isotherm was measured and interpreted using BET theory [19]. Water holding capacity (WHC) was conducted following [21]. Samples were oven-dried (105 ^{o}C, 24 hours), weighed (W_1) followed by 48 hours immersion in water. Samples were then vacuum-filtered and the wet sample mass was recorded (W_2). The WHC was calculated using equation 1:

$$\text{WHC}\ (\%) = \frac{(W_2 - W_1)}{W_1} \times 100\% \quad (1)$$

Chemical characterisation

The samples were characterised by proximate analysis and ultimate analysis (CHNS Elemental Analyzer Flash EA1112 series, ThermoScientific) [22]. The Fourier Transform Infrared Spectroscopy (Nicolet iS10 FTIR Spectrometer, ThermoScientific) was used for samples functional group and identification of structural changes analysis. The samples' pH and conductivity were determined using CyberScan pH/Conductivity/TDS meter (Eutech Instrument) from a prepared solution with a ratio of 1:2.5 (sample: distilled water) [22]. For the total macro- and micronutrient element content analysis, samples were ashed in a closed muffle furnace at 900 ^{o}C for 4 hours. An amount of 2 mL of concentrated HCl and 10 mL of 20% HNO_3 were added and allowed to digest in water bath for 1 hour. Finally, the solution was filtered into a 100 mL volumetric flask for further analysis [23]. The phosphorus content analysis was carried out by UV/Vis spectrometer (Cary 60 UV-Vis, Agilent) at a wavelength of 410 nm with a mixture of 10 mL of ash solution and 25 mL of working molybdovanate reagent. Meanwhile, the total macro- and micronutrient element content of further dilution of ash solutions were analysed using atomic absorption spectrometer (Cary 500 AnalytikJena, ThermoScientific).

Statistical analysis

The SPSS 26 software (SPSS for Windows, SPSS IBM, Armonk, Nueva York, USA) was used for statistical analysis. One-way ANOVA analysis was used for analysing the significance of the differences between the means. Treatment means were compared by Tukey's test at $p \leq 0.05$.

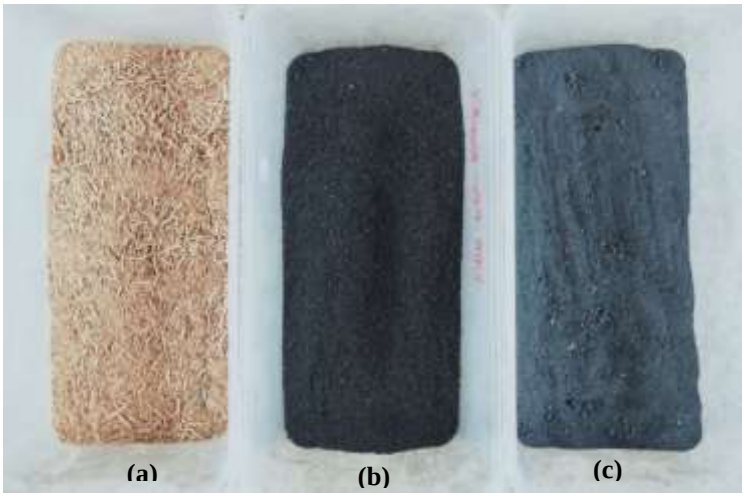


Figure 1. Sample of SBW (a), SBB (b), and TSB (c) with particle size < 2 mm

Results and Discussion

SEM analysis

From the SEM image in Figure 2**,** there are oval-shaped structures were observed on SBW which represent the starch granules. It also shown that natural cavities or porous structure were present in SBW cells. Functionally, these structures allow the release of volatile matter during the carbonisation process [10]. As compared with previous work by Hedge et al. [24] on the same feedstock (SBW), similar results were recorded on the carbon (55.03%), oxygen (43.43%), potassium (0.53%) and calcium (0.57%) composition. Meanwhile, a higher content of silicon (3.02%) was detected in this study compared to the previously reported by Hegde et al. [24].

There were differences on the SBB micrograph when compared with SBW in term of the porous surface structure with irregular cavities due to the pyrolysis. As reported by Zhang and You [21], the biochar pores are quite large, cylindrical-like and have a same direction in their arrangement. The starch granules had been diminished due to high heating temperature. The formation of porous holes in biochar has causes the devolatilization of sago bark. According to Gondim et al. [16], the fewer amount of micropores and thick lignified cell walls of biochar will result in the decrease in water holding capacity. The SBB had the highest carbon content (88.76 ± 0.06%) than the SBW and TSB because of the degree of carbonization applied on SBW [25]. Liang et al. [26] reported that an EDX spectra of carbonize furfural residue at 500oC showed the presence of carbon (82.4%) and oxygen (13.9%) which demonstrate that the carbon was the main skeleton in the biochar. Comparing with Suárez et al. [27] work, similar results on the carbon content (>80%) in three different biochar samples (*Eucalyptus grandis, Acacia magnium,* and *Gmelia arborea*) are reported. This is due to the high degree of carbonization and a decrease in oxygen suggesting the possible increase in the surfaces' hydrophobicity of the biochar [27].

An increase in porosity for the TSB sample was due to the volatile compounds escaping the structure during the thermochemical degradation. The homogenous type of pore structures was well developed on the surface of

the TSB, thus, resulting a larger surface area which represent the best development of pores compared to the SBW and SBB samples. The diffusion of sodium (Na) species into the biochar help to enhance the pore sizes and the formation of new pores. According to Tan et al. [10], there was an inconsistent pore structure on the surface of the activated carbon after the treatment using a high concentration of acid (5 M). The high concentration of acid resulting in the decrease in the BET surface area and produces the honeycomb structure. The higher amounts of micropores can increase the plant available water and improving the soil water retention [16]. Spectra image of EDX for the TSB showed a high content in oxygen (40.55±0.10%), silicon (16.64±0.07%), sodium (1.63±0.02%), magnesium (2.40±0.02%), calcium (4.16±0.04%), and potassium (2.34±0.04%) compared to the SBW and SBB. The high oxygen content in TSB surface is possibly due the increase number of oxygen-containing functional group after the acid and base modification. Meanwhile, high Si content may be attributed to the high ash content in the biochar [28] which is consistent with the ash content result (Table 2) for TSB in the current study. However, study reported by Ibrahim et al. [29] is in contrast with the current result where the Si content decreased after acid modification of biochar which might be due to the removal of silica bodies on the surface of untreated biochar. Therefore, the acid and base treatment in current study might affect the percentage of soluble organic component and thus relatively increased the percentage of inorganic component in TSB. Si content is recognized as a functional nutrient in all plant growth because it can increase the pathogen resistance and essential for sustainable crop production [30] while the higher Ca, Mg and K content making TSB suitable as a component of a plant growth media [31].

Surface area, total pore volume, and average pore diameter analysis

The main surface analysis was performed to measure the BET surface area, total pore volume, and average pore size of all samples (SBW, SBB, and TSB) (Table 1). The BET surface area increases in the following manner, SBW (10.964 m2/g), SBB (64.140 m2/g), and TSB (158.817 m2/g). The surface area of TSB was increased by 59.61% after the chemical modification of SBB. This shows that the TSB could provide a greater adsorption capacity due to the pore enlargement and surface destruction during the acid-base modification [27, 32]. According to Tan et al. [10], treatment of activated carbon with 1 M NaOH has reduces the surface area which is mainly attributed by the reduce in the micropore volume. The average pore diameter of SBW, SBB and TSB were 26.77, 15.40 and 53.40 nm, respectively. The porous media pore size can be categorised as follows; micropores (<2 nm), mesopores (2-50 nm), and macropores (>50 nm) [21]. Hence, the TSB can be classified as macropores due to the presence of large pores which can significantly improve the cohesiveness of soil particles, water storage, and water holding capacity in soil [33].

Water holding capacity (WHC) analysis

Several studies have shown that greater water holding capacity is caused by high surface area of the biochar [34, 35, 36]. In this study, the WHC of TSB (97.63%) was significantly higher than SBB (86.34%) (Table 1). The results demonstrate that the SBB and TSB both has a good water retention in soil which improves the soil water content, reducing the mobility of water and subsequently decrease the water stress in plant [34]. In addition, the high ash content of SBB and TSB which were reported in different section of this study also contributed to the high micro porosity of the biochar. This will result in hydrophobicity which influences the water retention of soil [37]. Meanwhile, the soil aggregates will create pores which can store water for plants to access. The fine-textured material of TSB results in a rapid water drainage due to its large pore size. Therefore, the SBB and TSB will potentially enhance the fertility of the agricultural growth media and subsequently the crop yield by providing a good soil water holding capacity.

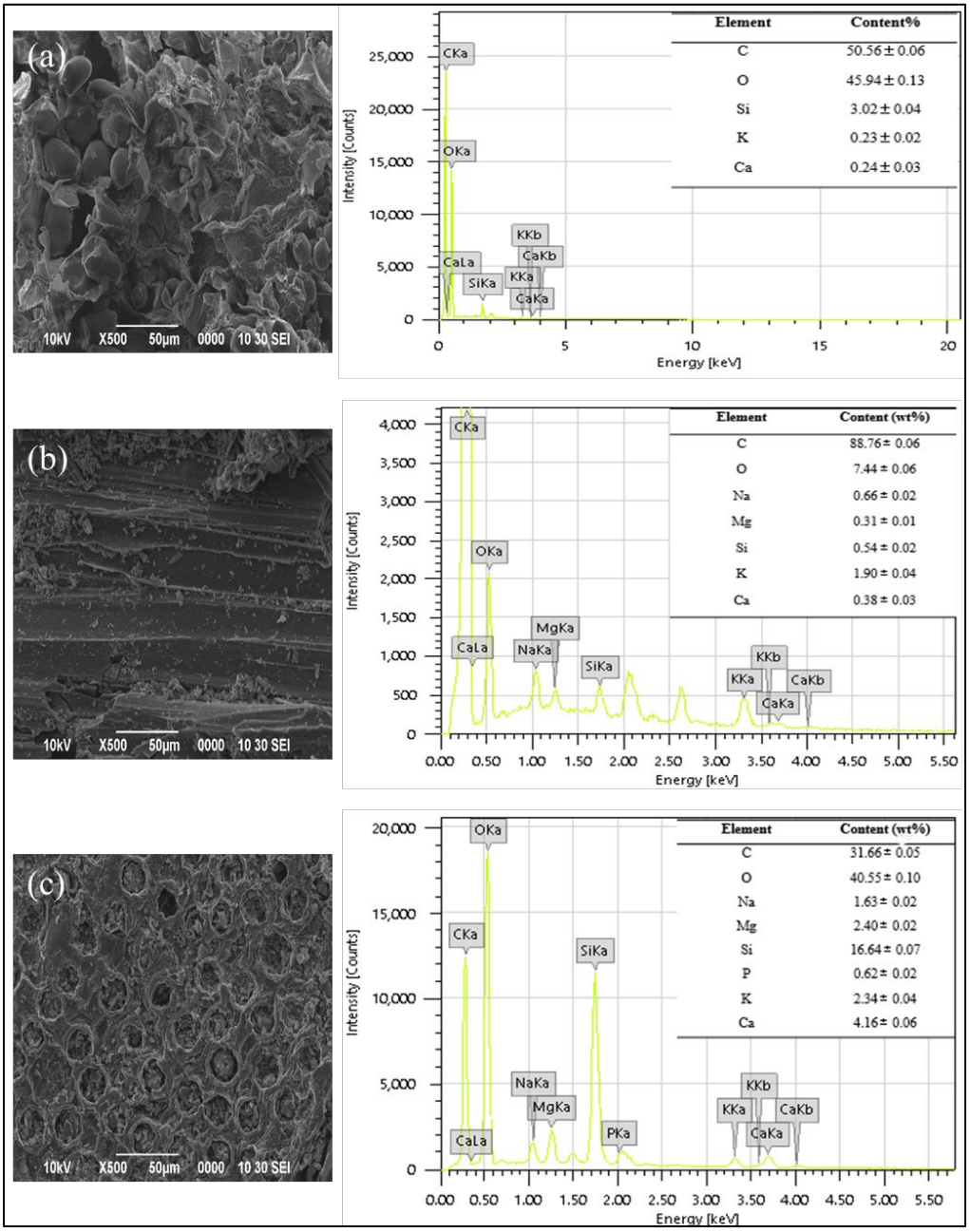


Figure 2. SEM and EDX spectra images of (a) SBW, (b) SBB, and (c) TSB at 500x magnification

Table 1. Physical properties of the SBW, SBB, and TSB

Sample	BET Surface Area (m^2/g)	Total Pore Volume (cc/g)	Average Pore Size (nm)	WHC (%)
SBW	10.964	1.467×10^{-2}	26.77	117.39 ± 0.54^{a}
SBB	64.140	4.943×10^{-2}	15.40	86.34 ± 0.38^{c}
TSB	158.817	4.24×10^{-1}	53.40	97.63 ± 0.14^{b}

The numbers to the right of each value represent the standard deviation of the mean. Significant differences between treatments are indicated by different letters abc in superscript to the right of each value

Proximate analysis

The proximate analysis was done to measure the moisture content, volatile matter, ash content, and fixed carbon of samples. Generally, all of the samples (SBW, SBB, and TSB) was significantly different from each other at $p < 0.05$ (Table 2). The result shows that the SBB (3.76%) and TSB (6.27%) have recorded a lower moisture content compared to its feedstock, SBW (8.82%). The lower moisture content was due to water dehydration during the carbonisation of SBW. Meanwhile, the volatile matter content of SBB (37.14%) and TSB (33.61%) was decreased ~ 50% as compared to SBW. According to Gunamantha & Widana [38], biochar with a high volatile matter content is less stable and has a higher amount of labile carbon, which provides energy for microbial activity while limiting the nitrogen available for plant growth, resulting in plant growth suppression. Biochar with volatile matter content more than 35% is considered high (causing nitrogen deficiency) whereas volatile matter below 10% is considered low [38], hence, TSB in this study is not predicted to limit plant growth. The ash content of SBB and TSB is higher than that of its feedstock, SBW at 28.81% and 30.55% respectively. This is related to the accumulation of inorganic constituents which is also related to high nutrient contents in both SBB and TSB [39]. The fixed carbon content in both SBB (30.38%) and TSB (29.57%) showed a similar trend as the ash content. According to Gunamantha & Widana [38], higher fixed carbon content of biochar compared to its feedstock, implies a reduction in carbon emissions and may have a critical influence due to their mineral content.

Ultimate analysis

The ultimate analysis was conducted to measure the composition of carbon, hydrogen, oxygen, sulphur, and nitrogen in the samples. Generally, the analysis of all samples (SBW, SBB, and TSB) was significantly different at $p < 0.05$ (Table 3). The percentage of carbon content was the highest in the SBW followed by SBB and TSB. The carbon content recorded in this study was lower compared to Wahi et al. [19]. It could be manifested that the carbonisation of the SBW was exposed to oxygen that causes high measurement of oxygen in the SBB. A decreasing trend was observed in the hydrogen contents from the SBB (2.37%) and TSB (1.26%) due to the carbonisation process. This also indicate the increased in the aromaticity which agrees with previous work by Zhao et al. [41]. The amount of nitrogen (< 1%) was almost absent in all samples. The lowest N availability was by the TSB (0.18%) that gives a high C/N ratio which effects the N immobilization due to the adsorption of NH_4^+ by the biochar [40]. An increase in oxygen (77.27%) and a decrease in carbon (21.22%) in the TSB were due to a crosslinking reaction on the surface of biochar and the modifying agents [43]. The TSB had the highest O/C ratio (4.88%) indicating the decrease in hydrophobicity, increase in cation exchange capacities (CECs), and the presence of more carbonyl, hydroxyl, and carboxylate groups [34, 43].

Fourier Transform Infrared Spectroscopy (FTIR) analysis

The comparison of IR absorption spectra between the samples are shown in Figure 3 and Table 4. The FTIR spectra shows the presence of OH bonds at a frequency

range between 3600 cm^{-1} and 3200 cm^{-1}. The SBW sample shows strong intensity of O-H stretching which indicates the presence of alcohols and phenols at 3426 cm^{-1}. The same result was displayed by previous research on the raw empty fruit bunch which a broad characteristics peak at 3259.38 cm^{-1} was spotted in the SBW that indicates the presence of O-H stretching [40]. The bands between 3700-3400 cm^{-1} was slightly diminished for both SBB and TSB when compared with SBW. However, some of the functional group of O-H at 3423 cm^{-1} was spotted in TSB. The same result was shown for HCl treated of empty fruit bunch biochar where the O-H stretching was further reduced as some volatile matter was released during the washing pre-treatment [38]. According to Figuerado et al. [44], the presence of carboxyl and phenol groups in the soil can contribute to the formation of soil charges. The presence of medium broad band at 3423 cm^{-1} in the TSB shows the presence of new hydroxyl group which probably due to the modification process of the biochar with NaOH. The treatment might improve the number of –OH groups in the surface of the SBB. Meanwhile, new bands were observed for the SBB which is due to the carbonization of SBW in the closed furnace [45]. Both the SBW and SBB showed the presence of aliphatic functional groups at the range of 2850-2970 cm^{-1} [27]. The C=O stretching of aldehydes and ketones functional groups was spotted at 1654 cm^{-1}. Suárez et al. [27] reported that this functional groups are formed by the dissociation of cellulose and hemicellulose which can be found in the raw wood material. Based on a previous report, the variable peaks observed at 1462 cm^{-1} in the TSB showed the presence of aromatic quinones associated with lignin in the biochar. This feature could improve the biochar-soil amendment [27]. The presence of a band at 1048.32 cm^{-1} indicated the presence of CO-O-CO bond in the SBB compared to SBW. It can be observed that all samples have O=C=O bond (carbon dioxide) and CO-O-CO anhydride group which are typically found in the IR spectra of biochar's [45, 46, 47].

Table 2. Proximate analysis of the SBW, SBB, and TSB

Sample	Moisture	Volatile Matter (wt. %)	Ash Content	Fixed Carbon
SBW	8.82 ± 0.22^{a}	70.71 ± 1.16^{a}	18.86 ± 0.66^{a}	1.61 ± 0.06^{a}
SBB	3.76 ± 0.25^{b}	37.14 ± 0.94^{b}	28.81 ± 0.72^{b}	30.38 ± 0.96^{b}
TSB	6.27 ± 0.04^{c}	33.61 ± 0.41^{c}	30.55 ± 0.34^{c}	29.57 ± 0.57^{c}

The numbers to the right of each value represent the standard deviation of the mean. Significant differences between treatments are indicated by different letters abc in superscript to the right of each value in each column

Table 3. Ultimate analysis (C, H, N, O, S) by weight (%) of SBW, SBB and TSB

Sample	C	H	N	O	S	O/C
SBW	42.97 ± 1.39^{a}	6.13 ± 0.27^{a}	0.28 ± 0.03^{a}	50.62 ± 1.50^{a}	0^{a}	1.57 ± 0.10^{a}
SBB	25.11 ± 1.37^{b}	2.37 ± 0.67^{b}	0.58 ± 0.66^{b}	71.94 ± 0.60^{b}	0^{a}	3.72 ± 0.17^{b}
TSB	21.22 ± 1.51^{c}	1.26 ± 0.46^{b}	0.18 ± 0.01^{b}	77.27 ± 1.48^{c}	0.07 ± 0.01^{b}	4.88 ± 0.42^{c}

The numbers to the right of each value represent the standard deviation about the mean. Significant differences between treatments are indicated by different letters abc in superscript to the right of each value in each column

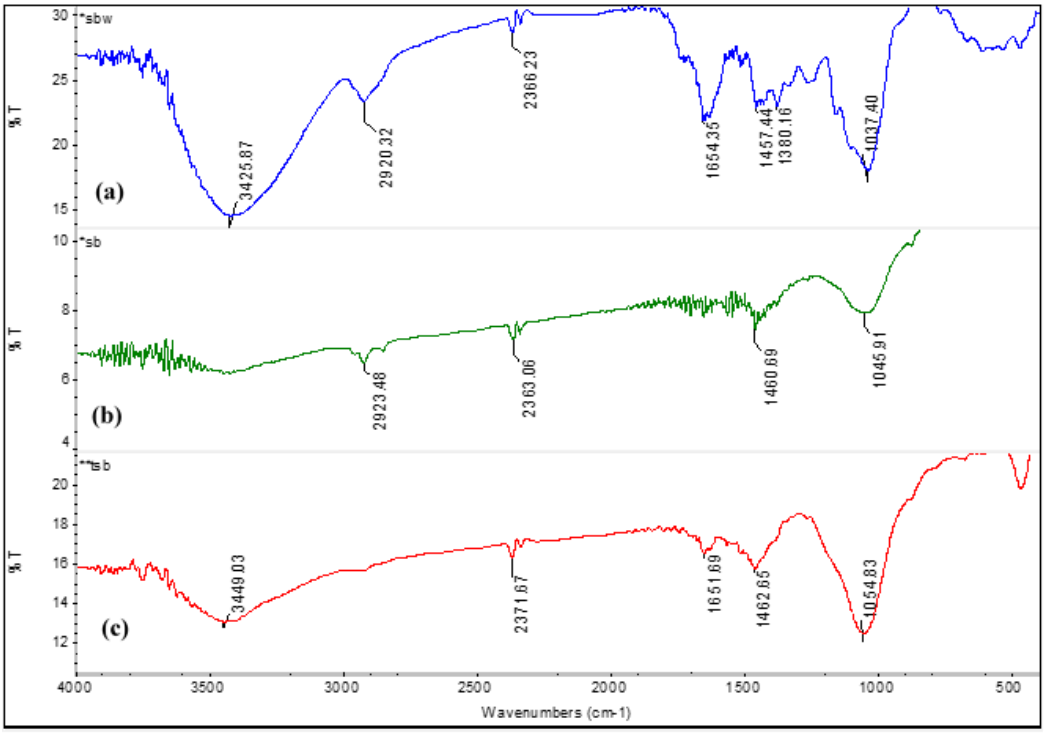


Figure 3. The FTIR spectra for the (a) SBW, (b) SBB, and (c) TSB

Table 4. Functional group observed in FTIR spectra for the SBW, SBB and TSB

Absorption (cm^{-1})	**SBW (cm^{-1})**	**SBB (cm^{-1})**	**TSB (cm^{-1})**	**Vibration Characteristic**
3550-3200	3426	-	3423	O-H stretching (alcohol & phenols)
2970-2850	2920	2923	-	C-H stretching
2349	2366	2366	2363	O=C=O stretching (carbon dioxide)
1750-1650	1654	-	-	C=O (aldehyde and ketones)
1500	-	-	1462	C=C stretching (aromatic)
1050-1040	1037	1046	1055	CO-O-CO stretching (anhydride)

- means not detected

pH and electrical conductivity (EC) analysis

Based on the pH values recorded (Table 5), SBB has the highest pH value of 10.41 while TSB has a relatively lower pH value of 8.98. Both biochars are alkaline implying that they could be utilised as liming agents to remediate soil acidity. According to Berek [17], the presence of carbonates and oxides (basic cations) in biochar will neutralize the excess H^+ ions from the acidic soil causing an increase in soil pH. Meanwhile, according to Ding et al. [48], biochar with a high pH value has the ability to hold the NH_4^+ and K-fertilizers in the soil. In this study, the SBW recorded the lowest value of 2.86 mS, followed by TSB (5.17 mS), and SBB (18.78 mS) for the EC. EC is a measure

of the amount of salt and its ability to conduct electricity. The result indicates the existence of more water soluble salts in SBB than in TSB. The higher EC in SBB might be attributed to the higher concentration of residues or ash induced by the loss of volatile matter during pyrolysis. Meanwhile, lower EC in TSB is possibly due to the removal of soluble salts during acid and base treatment. The EC results for SBB and TSB is comparable with the EC value of biochars reported from previous studies which is ranging from 0.04 mS cm^{-1} to 54.2 mS cm^{-1} [49]. In this study, the SBB had the highest value in pH and conductivity which imply the ionic concentration in the SBB was higher compared to the SBW and TSB.

Macronutrient and micronutrient content

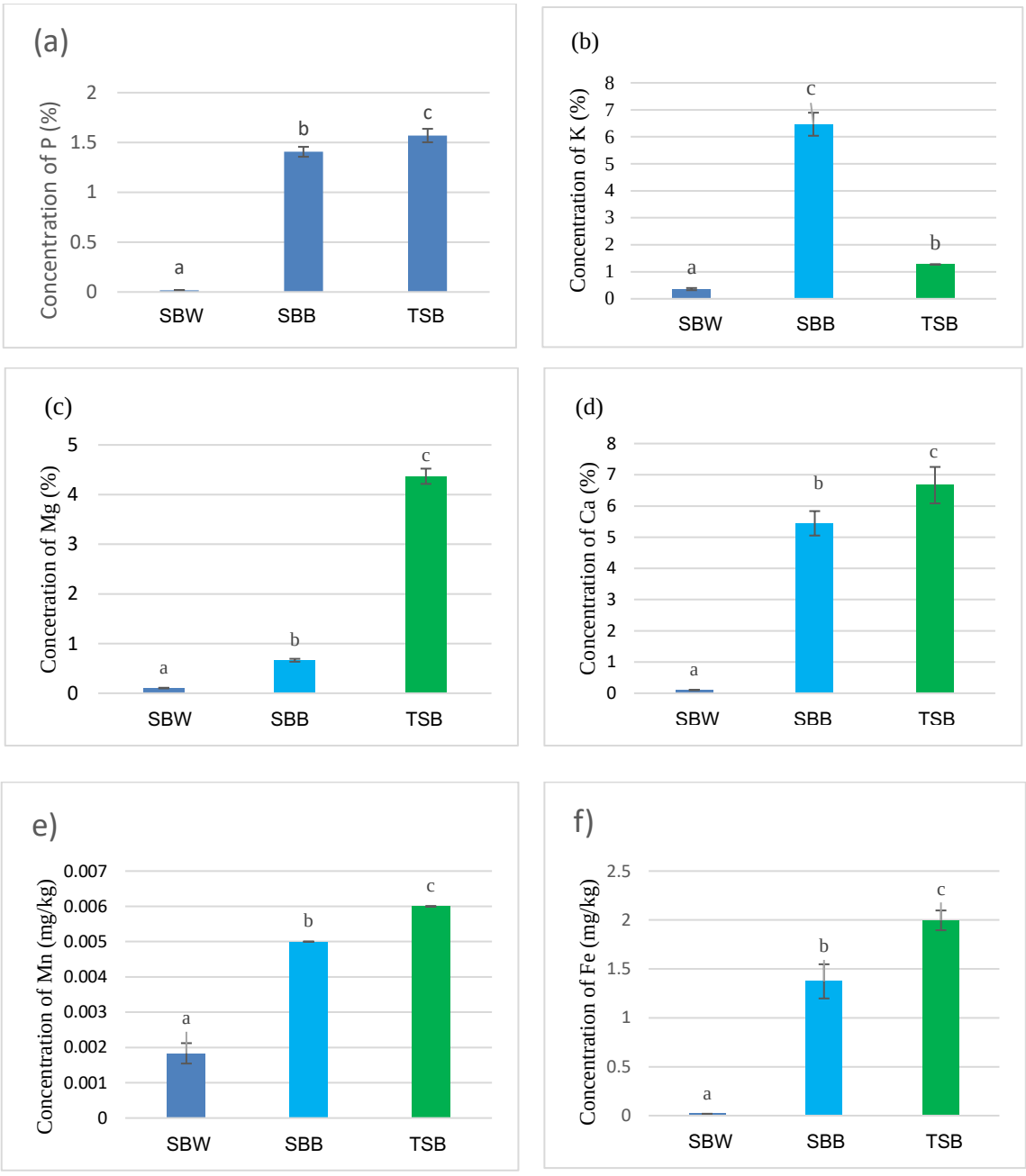
The macronutrient phosphorus (P), potassium (K), calcium (Ca), and magnesium (Mg) and micronutrient iron (Fe), manganese (Mn), copper (Cu) contents of the SBW, SBB, and TSB samples is shown in Figure 4. Generally, all samples were significantly different at a $p<0.001$. The macronutrient contents in both the SBB and TSB showed a higher concentration compared to the SBW. During pyrolysis, cation elements present in feedstock forming metal oxides in the ash that were merged with the biochar [50]. According to Karimi et al. [51], the high ash contents of biochar as well as soluble alkaline components released from the biochar, contributed to increased nutrient values. The available P for both the SBB and TSB samples (1.41±0.05% and 1.57±0.07%, respectively) were almost similar. This indicates that P availability in both samples would affect in the increase of soil pH and consequently will improve retention of exchangeable anion [42]. According to Hussain et al. [52], biochar can provide a P nutrient source which is similar to the commercial P fertilizer. This suggesting that biochar application in agricultural practices would significantly reduce the cost and usage of commercial fertilizer.

The K (6.47±0.43%) was recorded the highest in the SBB meanwhile the Ca (6.67±0.58%) and Mg (4.37± 0.15%) were recorded as the highest in the TSB. Significantly, the K helps to regulate the stomatal conductance in the plant leaf and water used efficiency which is important for plant growth performance [53]. According to Novak et al. [50], pecan shell-based biochar can improve K, Ca and P concentration in a loamy sand soil. The Mg is assisting in major constituent of the chlorophyll molecule which actively involved in photosynthesis, and the Ca has a key role in the development of the cell wall membrane in plant cell [52].

For micronutrient content, the TSB showed a higher concentration compared to the SBW and SBB especially for the Fe concentration (2.00 ± 0.10 mg/kg). The Fe was the highest available metals in micronutrients content. Significantly, the Fe element is essential for the processes in plants, especially in the photosynthesis and the chloroplast development [54]. The results for the Mn and Cu contents for both SBB (0.005±0 and 0.010±0 mg/kg) and TSB (0.006±0 and 0.013±0 mg/kg) were relatively similar. Cu and Mn are essential for the plant development which only requires a small amount in which their range of critical deficiency levels are 1-5 mg/kg of plant dry mass [55]. Biochar also has been reported to reduce the bioavailability of heavy metals in soil particularly the soil with high pH value and amounts of lime [56].

Table 5. pH and electrical conductivity (EC) value of the SBW, SBB, and TSB

Sample	pH	EC (mS cm^{-1})
SBW	4.29	2.86
SBB	10.41	18.78
TSB	8.98	5.17


(a)
Concentration of P (%)
2
1.5
1
0.5
0
a
b
c
SBW
SBB
TSB
(b)
Concentration of K (%)
8
7
6
5
4
3
2
1
0
a
c
b
SBW
SBB
TSB
(c)
Concetration of Mg (%)
5
4
3
2
1
0
a
b
c
SBW
SBB
TSB
(d)
Concentration of Ca (%)
8
7
6
5
4
3
2
1
0
a
b
c
SBW
SBB
TSB
e)
Concentration of Mn (mg/kg)
0.007
0.006
0.005
0.004
0.003
0.002
0.001
0
a
b
c
SBW
SBB
TSB
f)
Concentration of Fe (mg/kg)
2.5
2
1.5
1
0.5
0
a
b
c
SBW
SBB
TSB

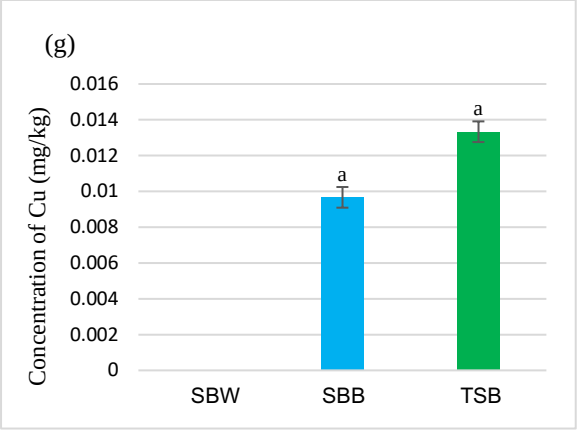


Figure 4. Total macronutrient a) P, b) K, c) Mg, d) Ca, and micronutrient e) Mn, f) Fe, g) Cu element contents of the SBW, SBB and TSB. The error bars represent standard deviation of the mean (n=3) and bars with different letters abc indicate statistically significant ($p < 0.001$) differences.

Conclusion

The SBB and TSB were analysed for their characteristics which contribute to the soil amender properties in promoting plant growth. The SBB had recorded a pH value of 10.41 which is suitable for crops cultivated on acidic soil. Meanwhile, the TSB is suitable for crops cultivated on slightly acidic soil. From the BET analysis, the surface area of the TSB had increased by 59.61% compared to the SBB which potentially to have a higher water holding capacity in soil due to the high storage capacity. The FESEM-EDX spectra images showed that the TSB had developed a new porous structure and has a high content of silicon which essential for the sustainable of crop production. Both SBB and TSB had a slightly diminished bands between 3700-3400 cm^{-1} compared to the SBW. However, the O–H functional group, at 3423 cm^{-1} was spotted in the TSB due to the present of new hydroxyl groups after the modification process of the biochar in the presence of NaOH. Finally, the TSB had the highest Ca and Mg (6.67% and 4.37%, respectively) contents which these elements can assist in the production of the chlorophyll molecules in plant. These results imply the potential of acid-base treatment in improving the characteristics of the biochar as a good soil amender. Future research needs to address the impact of the wide range of biochar applications on the other plant growth media and plant growth.

Acknowledgement

The authors thank the Universiti Malaysia Sarawak for financial support to conduct this work through the Tun Openg Chair grant (Grant No.: C09/TOC/1753/2018).

References

1. Lim, L.W. K., Chung, H. H., Hussain, H. and Bujang, K. (2019). Sago palm (*Metroxylon sagu* Rottb.): Now and beyond. *Pertanika Journal Tropical Agricultural Science*, 42(2): 435-451.
2. Ehara, H., Toyoda, Y. and Johnson, D.V. (2018). Sago palm: Multiple contributions to food security and sustainable livelihoods. In sago palm: multiple contributions to food security and sustainable livelihoods. Springer, Singapore.
3. Jong, F. S. (2018). *An Overview of Sago Industry Development, 1980s–2015*. In: Ehara H, Toyoda Y, Johnson D. (eds) Sago Palm. Springer, Singapore.
4. Singhal, R. S., Kennedy, J. F. and Gopalakrishnan, S. M. (2017). Industrial production, processing, and utilization of sago palm-derived products. *Carbohydrate Polymer*, 72: 1-20.
5. Rasyid, T. H., Kusumawaty, Y. and Hadi, S. (2020) The utilization of sago waste: prospect and challenges. *IOP Conference Series: Earth and Environmental Science*, 415: 12-23.

6. Piash, M. I., Hossain, M. F. and Zakia, P. (2019). Effect of biochar and fertilizer application on the growth and nutrient accumulation of rice and vegetable in two contrast soils. *Acta Scienctific Agriculture*, 3(2): 74-83.
7. Carter, S., Shackley, S., Sohi, S., Suy, T. B. and Haefele, S. (2013). The impact of biochar application on soil properties and plant growth of pot grown lettuce (*Lactuca sativa*) and cabbage (*Brassica chinensis*). *Agronomy*, 3: 404-418.
8. Bayu, D., Tadesse, M. and Amsalu, N. (2016). Effect of biochar on soil properties and lead (Pb) availability in a military camp in South West Ethiopia. *African Journal of Environmental Science and Technology*, 10(3): 77-85.
9. Sahin, O., Taskin, M. B., Kaya, E. C. and Gunes, A. (2017). Effect of acid modification of biochar on nutrient availability and maize growth in a calcareous soil. *Soil Use and Management*, 33: 447-456.
10. Tan, I. A. W., Abdullah, M. O., Lim, L. L. P. and Yeo, T. H. C. (2017). Surface modification and characterization of coconut shell-based activated carbon subjected to acidic and alkaline treatments. *Journal of Applied Science & Process Engineering*, 4(2): 186-194.
11. Alzaydien, A. S. (2016). Physical, chemical and adsorptive characteristics of local oak sawdust based activated carbons. *Asian Journal of Scientific Research*, 9(2): 45-56.
12. Zhao, S. X., Ta, N. and Wang, X. D. (2017). Effect of temperature on the structural and physicochemical properties of biochar with apple tree branches as feedstock material. *Energies*, 10(9): 1293.
13. Sukartono, W. H., Kusuma, Z. and Nugrobo, W. H. (2011). Soil fertility status , nutrient uptake , and maize (*Zea mays* L .) yield following biochar and cattle manure application on sandy soils of Lombok, Indonesia. *Journal of Tropical Agriculture*, 49(1-2): 47-52.
14. Wisnubroto, E.I., Utomo, W.H. and Indrayatie, E.R. (2017). Residual effect of biochar on growth and yield of red chili (*Capsicum annum* L.). *Journal of Advanced Agricultural Technologies* 4(1): 28-31.
15. Yamato, M., Okimori, Y., Wibowo, I. F., Anshori, S. and Ogawa, M. (2006). Effects of the application of charred bark of *Acacia mangium* on the yield of maize, cowpea and peanut, and soil chemical properties in South Sumatra, Indonesia. *Soil Science and Plant Nutrition*, 52(4): 489-495.
16. Gondim, R. S., Muniz, C. R., Eduardo, C. and Lima, P. (2018). Explaining the water-holding capacity of biochar by scanning electron microscope images. *Revista Caatinga*, 31(4): 972-979.
17. Berek, A. K. (2019). The potential of biochar as an acid soil amendment to support Indonesian food and energy security - A review. *Tropical Agricultural Science*, 42(2): 745-759.
18. Tan, G., Xu, N., Xu, Y., Wang, H. and Sun, W. (2016). Sorption of mercury(II) and atrazine by biochar, modified biochars and biochar based activated carbon in aqueous solution. *Bioresource Technology*, 2016: 1-43.
19. Wahi, R., Zuhaidi, N. F. Q., Yusof, Y., Jamel, J. and Kanakaraju, D. (2018). Chemically treated microwave biochar from sago bark waste. *Proceedings of ISER 119th International Conference, Kuala Lumpur, Malaysia, 1st-2nd April 2018*: 52–54.
20. Hamzah, Z. and Shuhaimi, S. N. A. (2018). Biochar : effects on crop growth. *IOP Conference Series: Earth and Environmental Science*, 215: 1-8.
21. Zhang, J. and You, C. (2013). Water holding capacity and absorption properties of wood chars. *Energy & Fuels*, 27: 2643-2648.
22. Ahmad, N.F., Alias, A.B., Talib, N. and Rashid, Z. (2018). Characteristics of rice husk biochar blended with coal fly ash for potential sorption material. *Malaysian Journal of Analytical Sciences*, 22(2): 326-332.
23. Estefan, G., Sommer, R. and Ryan, J. (2013). *Methods of soil, plant, and water analysis: A manual for the West Asia and North Africa region* (3rd edition). International Center for Agricultural Research in the Dry Areas (ICARDA). Beirut, Lebanon.

24. Hegde, G., Abdul Manaf, S. A., Kumar, A., Ali, G. A. M., Chong, K. F., Ngaini, Z. and Sharma, K. V. (2015). Biowaste sago bark based catalyst free carbon nanospheres: waste to wealth approach. *American Chemical Society Sustainable Chemistry and Engineering*, 3(9): 2247-2253.
25. Ma, X., Zhou, B., Budai, A., Jeng, A., Hao, X., Wei, D., Zhang, Y. and Rasse, D. (2016). Study of biochar properties by scanning electron microscope-energy dispersive x-ray spectroscopy (SEM-EDX). *Communications in Soil Science and Plant Analysis*, 47(5): 593-601.
26. Liang, H., Chen, L., Liu, G. and Zheng, H. (2016). Surface morphology properties of biochars produced from different feedstocks. *Proceedings of the 2016 International Conference on Civil, Transfortation and Environment*, pp. 1205-1208.
27. Suárez, H. L., Alba N., A. A. and Barrera, Z. R. (2017). Morphological and physicochemical characterization of biochar produced by gasification of selected forestry species. *Revista Facultad de Ingeniería*, 26(46): 123-130.
28. Palniandy, L. K., Yoon, L. W., Wong, W. Y., Yong, S. T. and Pang, M. M. (2019). Application of biochar derived from different types of biomass and treatment methods as a fuel source for direct carbon fuel cells. *Energies*, 12(2477): 1-15.
29. Ibrahim, I., Tsubota, T., Hassan, M. A. and Andou, Y. (2021). Surface functionalization of biochar from oil palm empty fruit bunch through hydrothermal process. *Processe*, 9(149): 1-14.
30. Varela, M. O., Rivera, E. B., Huang, W. J., Chien, C. C. and Wang, Y. M. (2013). Agronomic properties and characterization of rice husk and wood biochars and their effect on the growth of water spinach in a field test. *Journal of Soil Science and Plant Nutrition*, 13(2): 251–266.
31. Prasad, M., Chrysargyris, A., McDaniel, N., Kavanagh, A., Gruda, N. S. and Tzortzakis, N. (2019). Plant nutrient availability and pH of biochars and their fractions, with the possible use as a component in a growing media. *Agronomy*, 10(10): 1-17.
32. Li, L., Liu, S. and Liu, J. (2011). Surface modification of coconut shell based activated carbon for the improvement of hydrophobic VOC removal, *Journal of Hazardous Materials*, 192(2): 683-690.
33. Lu, S., Sun, F. and Zong, Y. (2014). Catena effect of rice husk biochar and coal fly ash on some physical properties of expansive clayey soil (Vertisol). *Catena*, 114: 37-44.
34. Batista, E. M. C. C., Shultz, J., Matos, T. T. S., Fornari, M. R., Ferreira, T. M., Szpoganicz, B., De Freitas, R. A. and Mangrich, A. S. (2018). Effect of surface and porosity of biochar on water holding capacity aiming indirectly at preservation of the Amazon biome. *Scientific Reports*, 8(1): 1-9.
35. Mukherjee, A. and Lal, R. (2013). Biochar impacts on soil physical properties and greenhouse gas emissions. *Agronomy*, 3(2): 313-339.
36. Southavong, S., Preston, T. R. and van Man, N. (2012). Effect of biochar and biodigester effluent on growth of water spinach (*Ipomoea aquatica*) and soil fertility. *Livestock Research for Rural Development*, 24(2): 1-15.
37. Pühringer, H. (2016). Effects of different biochar application rates on soil fertility and soil water retention in on-farm experiments on smallholder farms in Kenya. In Department of Soil and Environment, Swedish University of Agricultural Sciences.
38. Gunamantha, I. M. and Widana, G. A. B. (2018). Characterization the potential of biochar from cow and pig manure for geoecology application. *International Conference Series:Earth and Environmental Science*, 131(012055) :1-6.
39. Zhao, S. X. Z., Ta, N. and Wang, X. D. (2017). Effect of temperature on the structural and physicochemical properties of biochar with apple tree braches as feedstock material. *Energies*, 10(1293): 1-15.
40. Meri, N. H., Alias, A. B., Talib, N., Rashid, Z. A. and Ghani, W. A. (2018). Effect of chemical washing pre-treatment of empty fruit bunch (EFB) biochar on characterization of hydrogel biochar composite as bioadsorbent. *IOP Conference Series: Materials Science and Engineering*, 358: 1–7.

41. Zhao, B., O'Connor, D., Shen, Z., Tsang, D. C. W., Rinklebe, J. and Hou, D. (2020). Sulfur-modified biochar as a soil amendment to stabilize mercury pollution: An accelerated simulation of long-term aging effects. *Environmental Pollution*, 264: 114687.
42. Ndor, E., Ogara, J. I., Bako, D. A. and Osuagbalande, J. A. (2016). Effect of biochar on macronutrients release and plant growth on degraded soil of Lafia, Nasarawa State, Nigeria. *Asian Research Journal of Agriculture*, 2(3): 1–8.
43. Godwin, P. M., Pan, Y., Xiao, H. and Afzal, M. T. (2019). Progress in preparation and application of modified biochar for improving heavy metal ion removal from wastewater. *Journal of Bioresources and Bioproducts*, 4(1): 31-42.
44. Figuerado, N. A., Costa, L. M., Melo, L. C. A., Siebeneichlerd, E. A. and Tronto, J. (2017). Characterization of biochars from different sources and evaluation of release of nutrients and contaminants. *Revista Ciencia Agronomica*, 48(3): 1–10.
45. Tomczyk, A., Sokołowska, Z. and Boguta, P. (2020). Biochar physicochemical properties: Pyrolysis temperature and feedstock kind effects. *Reviews in Environmental Science and Biotechnology*, 19(1): 191-215.
46. Ghani, W.A., Mohd, A., Silva, S, G., Bachmann, R.T., Taufiq, Y.H., Rashid, U. and Al-Muhtaseb, A. H. (2013). Biochar production from waste rubber-wood-sawdust and its potential use in C sequestration: Chemical and physical characterization. *Industrial Crops & Products*, 44: 18-24.
47. Liu, Y., He, Z. and Uchimiya, M. (2015). Comparison of biochar formation from various agricultural by-products Using FTIR spectroscopy, *Modern Applied Science*, 9(4): 246-253.
48. Ding, A. Y., Liu, Y., Liu, S., Huang, X. and Li, Z. (2017). Potential benefits from biochar application for agricultural use: A review. *Pedosphere: An International Journal*, 2017: 1-20.
49. Singh, B., Dolk, M. M., Shen, Q. and Arbestain, M. C. (2017). Biochar: A guide to analytical methods chapter 3 biochar pH, electrical conductivity and liming potential. CSIRO Publishing. Access from https://biochar-international.org/wpcontent/uploads/2019/11/2017_Biochar_pH_electrical_conductivity_and_liming_potential_Singhetal.pdf
50. Novak, J. M., Busscher, W. J., Laird, D. L., Ahmedna, M., Watts, D. W. and Niandou, M. A. S. (2009). Impact of biochar amendment on fertility of a southeastern coastal plain soil. *Soil Science*, 174(2): 105-112.
51. Karimi, A., Moezzi, A., Chorom, M. and Enayatizamir, N. (2019). Application of biochar changed the status of nutrients and biological activity in a calcareous soil. *Journal of Soil Science and Plant Nutrition.* (20): 450-459.
52. Hussain, M., Farooq, M., Nawaz, A., Al-Sadi, A. M., Solaiman, Z. M., Alghamdi, S. S., Ammara, U., Ok, Y. S. and Siddique, K. H. M. (2017). Biochar for crop production: potential benefits and risks. *Journal of Soils and Sediments*, 17(3): 685-716.
53. Abdul, N. F. and Abdul, N. S. (2017). Microbial & biochemical technology the effect of biochar application on nutrient availability of soil planted with MR219. *Journal of Microbial & Biochemical Technology*, 9(2): 583–586.
54. Mukhti, G. (2014). Heavy metal stress in plants. *International Journal Advance Residual*, 2(6): 1043-1055.
55. Ducic, T. and Polle, A. (2005). Transport and detoxification of manganese and copper in plants. *Brazillian Journal of Plant Physiology*, 17(1): 1-16.
56. Salmani, M. S., Khorsandi, F., Yasrebi, J. and Karimian, N. (2014). Biochar effects on copper availability and uptake by sunflower in a copper contaminated calcareous soil. *International Journal of Plant, Animal and Environmental Sciences*, 4(3): 389-394.

Malaysian Journal of Analytical Sciences (MJAS)
Published by Malaysian Analytical Sciences Society

CHEMICAL CONSTITUENTS OF THE MOSS *Calyptothecium ramosii* BROTH.

(Juzuk Kimia bagi Lumut *Calyptothecium ramosii* Broth.)

Consolacion Y. Ragasa[1, 2], Virgilio C. Linis[3], Chien-Chang Shen[4], Mary Stephanie Carranza[1], Maria Carmen Tan[1]*

[1]*Chemistry Department,*
De La Salle University, 2401 Taft Avenue, Manila 1004, Philippines
[2]*Chemistry Department,*
De La Salle University Science & Technology Complex Leandro V. Locsin Campus, Biñan City, Laguna 4024, Philippines
[3]*Biology Department,*
De La Salle University, 2401 Taft Avenue, Manila 1004, Philippines
[4]*National Research Institute of Chinese Medicine,*
Ministry of Health and Welfare, 155-1, Li-Nong St., Sec. 2, Taipei, Taiwan

**Corresponding author: maria.carmen.tan@dlsu.edu.ph*

Received: 5 July 2021; Accepted: 10 August 2021; Published: 29 August 2021

Abstract

Calyptothecium ramosii Broth. of the moss family Pterobyaceae is a species indigenous to the Philippines. Chemical investigation of the dichloromethane extract of *C. ramosii* has led to the isolation of γ-polypodatetraene (**1**), cinnamic acid (**2**) and saturated long-chain hydrocarbons (**3**). The structure of **1** was elucidated by extensive 1D and 2D nuclear magnetic resonance spectroscopy (NMR) and confirmed by comparison of its NMR data with literature data. The structures of **2** and **3** were identified by comparison of their NMR data with literature data.

Keywords: *Calyptothecium ramosii* Broth., cinnamic acid, long-chain hydrocarbons, γ-polypodatetraene, Pterobyaceae

Abstract

Calyptothecium ramosii Broth. ialah lumut dari famili Pterobyaceace merupakan spesies asli bagi Filipina. Kajian juzuk kimia dilakukan ke atas ekstrak *C. ramosii* menggunakan diklorometana untuk memisahkan γ-polipodatetraen (**1**), asid sinamik (**2**) dan hidrokarbon tepu rantaian panjang (**3**). Struktur 1 telah dicirikan melalui spektroskopi nuklear magnetik resonan 1D dan 2D dan ditentusahkan melalui perbandingan data kajian literatur dan data NMR.

Kata kunci: *Calyptothecium ramosii* Broth., asid sinamik, hidrkarbon rantaian panjang, γ-polipodatetraen, Pterobyaceae

Introduction

Calyptothecium ramosii Broth. in the moss family Pterobryaceae, is a species indigenous to the Philippines having several gatherings from the islands of Luzon, Mindoro, and Samar [1]. The species is also documented in southern China [2]. Its genus, *Calyptothecium* Mitt.,

is a large group of Bryophytes characterized by having a primary axis in the form of a creeping, conspicuous stoloniform shoot attached to the substratum by rhizoids that arise in the leaf axils [3]. Diagnostic characteristics include secondary axes (stems) diverging from these stoloniform shoots, which are typically pinnately branched with crowded, apiculate leaves and small auricles forming at the leaf bases [4]. The most obvious and most easily seen feature in *C. ramosii* is its large and rugose auricles [5, 6]. Similar auricles may also occur in another species of Philippine *Calyptothecium*, the *C. urvilleanum* (Müll.Hal.) Broth. [7]. In *C. ramosii*, the stem leaves are observed to be smooth with sharply acuminate apices compared to the undulate appearance of the stem leaves of *C. urvilleanum*, with abruptly acute or obtuse leaf apices [5]. *Calyptothecium ramosii* is primarily considered a corticolous epiphyte but saxicolous populations have been documented [5]. Published literature has revealed the antioxidant characteristics of the bryophyte due to the major presence of the constituents: phytol, phytol acetate, 7,9-di-tert-butyl-1-oxaspiro-4,5-deca-6,9-diene-2,8-dione, and 4,8,12,16-tetramethylheptadecan-4-olide, detected by gas chromatography spectroscopy [8].

There are no reported studies on faster screening and larger surveying of the chemical constituents and biological activities of *C. ramosii*. Nuclear magnetic resonance (NMR) spectroscopy allows for the differentiation of optical and geometric isomers, as well as the presence of hydrocarbons with similar ions. We report herein the isolation of γ-polypodatetraene (**1**), cinnamic acid (**2**), and saturated long-chain hydrocarbons (**3**) from *C. ramosii*. The chemical structures of **1** and **2** are presented in Figure 1.

Materials and Methods

Sample collection

The moss species, *Calyptothecium ramosii* Broth. was collected and authenticated by one of the authors (Dr. Virgilio C. Linis, VCL). The moss was gathered from a large boulder inside a residual lowland forest along the lower slope of Pantingan peak at 400 m elevation on November 13, 2017. Collection locality is in the Municipality of Bagac, Province of Bataan in Luzon Island, Philippines, with coordinates 14° 33' 32.08" N 120° 27' 3.93" E.

Isolation of the Chemical Constituents of *C. ramosii*

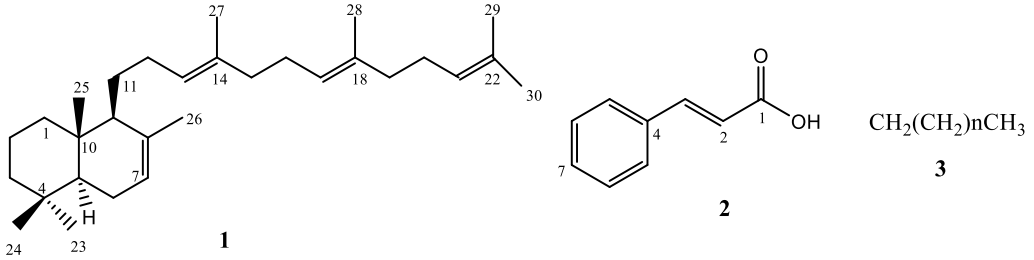
The freeze-dried moss (37.27 g) was ground in a blender and then soaked in dichloromethane (CH_2Cl_2) for 3 days and filtered. The filtrate was concentrated in vacuo to afford a crude extract (71.9 mg) which was chromatographed by gradient elution using increasing proportions of acetone in CH_2Cl_2 at 10% increment by volume. The CH_2Cl_2 fraction was re-chromatographed using petroleum ether. The less polar fractions were combined and re-chromatographed in petroleum ether to yield **3** (0.2 mg) after washing with petroleum ether. The more polar fractions were re-chromatographed (2×) using 1% ethyl acetate (EtOAc) in petroleum ether to afford **1** (2.2 mg) after washing with petroleum ether. The 50% acetone in CH_2Cl_2 fraction was re-chromatographed (3×) using acetonitrile (CH_3CN): diethyl ether (Et_2O): CH_2Cl_2 (0.5:0.5:9, v/v) to obtain **2** (1.0 mg) after washing with petroleum ether.

General isolation procedure

Pasteur pipette was used for the fractionation of the crude extract. Fractions of 1 mL volumes were collected and monitored by thin layer chromatography (TLC). Fractions containing spots with similar R_f values were combined and re-chromatographed using the appropriate solvent. TLC-pure isolates were combined, and after evaporation of the solvent, were subjected to NMR analysis.

General experimental procedure

Nuclear magnetic resonance (NMR) spectra were recorded on a Varian VNMRS spectrometer in deuterated chloroform ($CDCl_3$) at 600 MHz for hydrogen proton magnetic resonance (1H NMR) and 150 MHz for carbon-13 nuclear magnetic resonance (13C NMR) spectra. Column chromatography was performed with silica gel 60 (70-230 mesh). Thin layer chromatography was performed with plastic backed plates coated with silica gel F254 and the plates were visualized by spraying with vanillin/ sulfuric acid (H_2SO_4) solution followed by warming.



1 **2** **3**

Figure 1. Chemical structures of γ-polypodatetraene (**1**), cinnamic acid (**2**) and saturated long-chain hydrocarbons (**3**) from *C. ramosii*

Results and Discussion

Silica gel chromatography of the dichloromethane extract of *C. ramosii* afforded γ-polypodatetraene (**1**), cinnamic acid (**2**) and saturated long-chain hydrocarbons (**3**).

γ-polypodatetraene (1)

^{1}H NMR (600 MHz, $CDCl_3$): δ 0.94, 1.84 (m, H_2-1), 1.42, 1.52 (m, H_2-2), 1.14, 1.40 (m, H_3-3), 1.16 (m, H-5), 1.84, 1.94 (m, H_2-6), 5.37 (br s, H-7), 1.61 (m, H-9), 1.20, 1.42 (m, H_2-11), 1.94, 2.15 (m, H_2-12), 5.12 (m, H-13), 1.98 (m, H_2-15), 2.06 (m, H_2-16), 5.10 (m, H-17), 1.98 (m, H_2-19), 2.06 (m, H_2-20), 5.09 (m, H-21), 0.83 (s, H_3-23), 0.85 (s, H_3-24), 0.72 (s, H_3-25), 1.69 (s, H_3-26), 1.58 (s, H_3-27, H_3-29), 1.59 (s, H_3-28), 1.66 (s, H_3-30); ^{13}C-NMR (150 MHz, $CDCl_3$): δ 39.2 (C-1), 18.8 (C-2), 42.4 (C-3), 33.0 (C-4), 50.2 (C-5), 23.8 (C-6), 122.0 (C-7), 135.6 (C-8), 54.2 (C-9), 36.7 (C-10), 27.3 (C-11), 30.2 (C-12), 124.8 (C-13), 135.0 (C-14), 39.7 (C-15), 26.8 (C-16), 124.3 (C-17), 135.0 (C-18), 39.7 (C-19), 26.7 (C-20), 124.4 (C-21), 131.3 (C-22), 33.2 (C-23), 21.9 (C-24), 13.5 (C-25), 22.2 (C-26), 16.2 (C-27), 16.0 (C-28), 17.7 (C-29), 25.7 (C-30).

***Trans*-cinnamic acid (2)**

^{1}H NMR (600 MHz, $CDCl_3$): δ 6.42 (d, *J* = 16.2 Hz, H-2), 7.65 (d, *J* = 16.2 Hz, H-3), 7.51 (m, H-5, H-9), 7.36 (m, H-6, H-7, H-8).

Hydrocarbons (3)

^{1}H NMR (600 MHz, $CDCl_3$): δ 1.23 (br s, -CH_2-), 0.86 (t, *J* = 7.2 Hz, terminal CH_3).

The ^{1}H NMR spectrum of **1** gave resonances for three methyl singlets at δ 0.72, 0.83 and 0.85; five allylic methyl singlets at δ 1.58 (2×), 1.59, 1.66, 1.69; four olefinic protons at δ 5.37 (1H, br s) and 5.08-5.12 (3H, m); allylic methylene protons (δ 1.81-2.15); and shielded methylene protons (δ 0.95-1.52). The ^{13}C NMR data of **1** indicated resonances for four protonated olefinic carbons at δ 122.04, 124.26, 124.40, 124.82, four non-protonated olefinic carbons at δ 131.25, 134.95 (2×), 135.62. The remaining twenty-two carbons were attributed to methyl, methylene and methine carbons in **1**. The structure of **1** was elucidated by 2D NMR spectroscopy (COSY, HSQC and HMBC). The COSY spectrum of **1** indicated five isolated spin systems as follows: H_2-1/H_2-2/H_2-3; H-5/H_2-6/H-7; H-9/H_2-11/H_2-12/H-13; H_2-15/H_2-16/H-17; H_2-19/H_2-20/H-21. Protons attached to carbons were assigned from HSQC data. The structure of **1** was determined by analysis of the HMBC correlations of H_3-23, H_3-24/C-3, C-4, C-5, H_3-25/C-1, C-5, C-9, C-10, H_3-26/C-7, C-8, C-9, H_3-27/C-13, C-14, C-15, H_3-28/C-17, C-18, C-19, H_3-29/C-21, C-22, C-30 and H_3-30/C-21, C-22, C-29. All long-range correlations are consistent with the structure of **1**, which was further confirmed by comparison of data collected with γ-polypodatetraene [9, 10].

γ-Polypodatetraene was the first example of a bicyclic triterpenoid hydrocarbon which was isolated from *Polystichum polyblepharum* leaflets [11]. Previous literature has demonstrated that the triterpene may be one of many triterpenes with cytotoxic activities against neoplastic cell lines and with anti-inflammatory

properties [12, 13]. Another study reported that **2** was also found in the moss *Floribundaria aurea* subsp. nipponica [14]. Cinnamic acid was found to exhibit antibacterial and are particularly cytotoxic for bacteria and cancer cells [15]. Published reports of compound **3** suggested that the hydrogen-carbon links are generally used as chief components of fuel and everyday products which may be very toxic in its handling [16]. The potential utilization of these compounds are not limited to their uses in a clinical setting, but as well as in industrial and manufacturing applications.

The NMR data of **2** and **3** were in accordance with the data reported in the literature for cinnamic acid [17] and saturated long-chain hydrocarbons [18], respectively.

Conclusion

Calyptothecium ramosii Broth., a moss endemic to the Philippines, was investigated for its chemical constituents. Fractions analyzed by NMR analysis revealed the presence of: (**1**) γ-polypodatetraene, (**2**) cinnamic acid, and (**3**) saturated long-chain hydrocarbons, isolated for the first time from *C. ramosii*.

Acknowledgement

A project endowment (Project Number: (10 IR U 2TAY16-3TAY17) from the De La Salle University Science Foundation *via* the University Research Coordination Office (URCO) is thankfully recognized.

References

1. Tan, B. C. and Iwatsuki, Z. (1991) A new annotated Philippine moss checklist. *Harvard Papers in Botany*, 1(3): 1-64.
2. Linis, V. C. (2006) A review of intra-Philippine distribution patterns of Philippine mosses based on recent evidence of tectonic evolution of the archipelago: Insights and problems. *Banwa*, 3(1&2): 31-64.
3. Mitten, W. (1868) A list of the Musci collected by the Rev. Thomas Powell in the Samoa or Navigator's Islands. *Journal of the Linnean Society*, 10: 166-195.
4. Noguchi, A. (1986) Notulae bryologicae, XII. *Journal of the Hattori Botanical Laboratory*, 60: 149-158.
5. Bartram, E. B. (1939). Mosses of the Philippines. *Philippine Journal of Science*, 68(1–4):1-437.
6. Brotherus, V. F. (1913). Contributions to the bryological flora of the Philippines IV. Philippine Journal of *Science*, 8:65-98.
7. Hyvönen, J. (1989). Bryophyte flora of the Huon Peninsula, Papua New Guinea. XXVI. Pterobryaceae (Musci). *Acta Botanica Fennica*, 137: 1-40.
8. Carranza, M.S., Linis, V., Ragasa, C. and Tan, M. (2019). Chemical constituents and antioxidant potentials of seven Philippine mosses. *Malaysian Journal of Analytical Sciences*, 23(6):950-962.
9. Shiojima, K., Arai, Y., Masuda, K., Kamada, T. and Ageta, H. (1983). Fern constituents: Polypodatetraenes, novel bicyclic triterpenoids, isolated from polypodiaceous and aspidiaceous plants. *Tetrahedron Letters*, 24(51): 5733-5736.
10. Kinoshita, M., Ohtsuka, M., Nakamura, D. and Akita, H. (2002). First synthesis of (+)-α- and (+)-γ-polypodatetraenes. *Chemical and Pharmaceutical Bulletin*, 50(7): 930-934.
11. Shiojima, K., Arai, Y., Masuda, K., Kamada, T., Suzuki, M. and Ageta, H. (1997). Chemotaxonomy of fern plants. (V). Japanese *Polystichum* species. *Nature Medicine*, 51(6): 523-527.
12. Chudzik, M., Korzonek-Szlacheta, I. and Krol, W. (2015). Triterpenes as potentially cytotoxic compounds. *Molecules*, 20: 1610-1625.
13. Kushiro, T., Ebizuka, Y. (2010). Chapter 1.18: Triterpenes. comprehensive natural products II. Reference module in chemistry, molecular sciences and chemical engineering. vol 1: pp. 673-708.
14. Toyota, M., Masuda, K. and Asakawa, Y. (1998). Triterpenoid constituents of the moss *Floribundaria aurea* subsp. *nipponica*. *Phytochemistry*, 48(2): 297-299.
15. Zolfaghari, B., Yazdiniapour, Z., Sadeghi, M., Akbari, M., Troiano, R. and Lanzotti, V. (2020). Cinnamic acid derivatives from welsh onion (*Allium fistulosum*) and their antibacterial and cytotoxic activities. *Phytochemical analysis*, 32(1): 84-90.
16. Curtis, J., Metheny, E., Sergeant, S.R. (2021). Hydrocarbon toxicity. *StatPearls*. Treasure Island (FL): StatPearls Publishing.

17. Ragasa, C. Y., Biona, K. and Shen, C.-C. (2014). Chemical constituents of *Sechium edule* (Jacq.) Swartz. *Der Pharma Chemica*, 6(5): 251-255.

18. Ragasa, C. Y., Medecilo, M. P. and Shen, C.-C. (2015). Chemical constituents of *Moringa oleifera* Lam. leaves. *Der Pharma Chemica*, 7(7): 395-399.

Malaysian Journal of Analytical Sciences (MJAS)
Published by Malaysian Analytical Sciences Society

COLOUR STRENGTH AND WASHFASTNESS OF SILK FABRIC DYED WITH METHANOLIC EXTRACTED RANGOON CREEPER USING INFRA-RED DYEING MACHINE

(Kekuatan Warna dan Ketahanan Cucian Kain Sutera Diwarnakan dengan Akar Dani yang Diekstrak dengan Pelarut Metanol Menggunakan Mesin Pencelup Infra-Merah)

Suhaidi Ariffin[1], Wan Syazehan Ruznan[1]*, Muhammad Nurkhairunizam Yazid[2], Suraya Ahmad Suhaimi[1], Mu'adz Ahmad Mazian[2], Muhammad Mu'az Mustamam[2]

[1]Clothing Innovation and Textile Research Association (CITRA),
[2]Faculty of Applied Sciences,
Universiti Teknologi MARA Cawangan Negeri Sembilan, Kampus Kuala Pilah, 72000 Kuala Pilah, Negeri Sembilan, Malaysia

**Corresponding author: syazehan@uitm.edu.my*

Received: 21 June 2021; Accepted: 11 August 2021; Published: 29 August 2021

Abstract

Extracting dyes from plant sources is one of the eco-friendly ways to reduce environmental pollution. Since the discovery of synthetic dyes back in 1856, the use of natural dyes in the textile industry has become lessen. This work focuses on the determination of new colours from Rangoon creeper petals through the methanolic extraction method and dyed by using an Infra-Red dyeing machine to generate a new colour pallet that is similar to PANTONE® colour and to study its washfastness properties. Silk fabric was used and dyeing was carried out with calamansi and vinegar as the mordanting agents. Dyed silk samples were measured by using X-rite RM2000 Capsure to get the commercial PANTONE® colour code. The CIELAB colours coordinates were retrieved from the PANTONE® website and the L*a*b* values plotted indicates that all dyed silks were in the yellow-red quadrant. Colourfastness to washing shows an excellent rating i.e., 4/5, indicating outstanding stability. Thus, it was found that the colour produced from Rangoon creeper petals is suitable as a natural dye and also established high commercial value because the colour obtained is commensurate with the colour displayed by PANTONE® colours.

Keywords: rangoon creeper, natural dye, methanol extraction, infra-red dyeing

Abstrak

Mengekstrak pewarna daripada tumbuhan adalah salah satu kaedah mesra alam untuk mengurangkan pencemaran alam sekitar. Sejak penemuan pewarna sintetik pada tahun 1856, penggunaan pewarna semula jadi dalam industri tekstil semakin berkurangan. Kajian ini memfokuskan kepada penemuan warna baharu daripada kelopak bunga Akar Dani melalui kaedah pengekstrakan metanol dan diwarnakan dengan menggunakan mesin pencelup Infra-Merah bagi menghasilkan palet warna baharu yang serupa dengan warna PANTONE®, serta mengkaji sifat ketahanan warna. Kain sutera digunakan dan pencelupan dilakukan dengan limau kasturi dan cuka sebagai agen pengikat. Sampel sutera yang dicelup diukur dengan menggunakan X-rite RM2000 Capsure untuk mendapatkan kod warna PANTONE® yang komersial. Koordinat warna CIELAB diambil dari laman web PANTONE dan nilai L*a*b* yang ditunjukkan menunjukkan bahawa semua sutera yang dicelup berada di kuadran kuning-

merah. Ketahanan warna terhadap cucian menunjukkan tahap cemerlang iaitu 4/5. Oleh itu, didapati bahawa warna yang dihasilkan daripada kelopak Akar Dani sesuai sebagai pewarna semula jadi dan juga memiliki nilai komersial yang tinggi kerana warna yang diperolehi setara dengan warna yang ditunjukkan oleh warna PANTONE®.

Kata kunci: akar dani, pewarna semula jadi, pelarut metanol, pencelupan infra-merah

Introduction

Textile industry is one of the biggest industries in the world. This industry is not only producing textile materials and garments, but also the products that people use in their daily lives. This growing industry is now becoming a major contributor in strengthening the economic scale. However, activities from the textile industry were reported to generate a large number of industrial effluents contributing to water pollution [1, 2]. Most of the dyes disposed to the environment were synthetic dyes, and these synthetic substances are typically carcinogenic. If the effluent treatment plant is not well controlled, the chemicals released will cause water pollution and also harm the water ecosystems [3, 4]. A few approaches can be implemented to overcome the problem, and one of them is by using dye extracted from natural sources.

Nowadays, the extraction process of dye compounds from natural sources especially plants has become an alternative strategy by many industrial practices. In general, natural dyes are inexpensive, biodegradable, non-toxic and have higher compatibility with the environment. Hence, the utilization of plants as raw material for natural dye has been applied on textile substrates. Natural dyes from flowers are not new in textile dyeing, with a few researches works in dyeing and printing conducted using natural dyes from flowers [5, 6, 7]. However, experimentation of Rangoon creeper flowers as a natural dye is scarce. Rangoon creeper or its botanical name, *Quisqualis indica* (*Q. indica* L.) belongs to the family of Combretaceae (Figure 1). It is indigenous in Africa, Indo Malaysian region and cultivated all over India. This flowering plant which is known as Akar Dani in Malaysia is largely grown as an ornamental plant and was reported to have many phytoconstituents in each part of the plant, also showing different bioactivities as well [8]. The flower is unique with a nice fragrant, which normally blooms in abundance. Moreover, the flowers are very attractive with white petals, which turns to pink and red when matured and borne in clusters. Anthocyanins are chemical compounds that are responsible to give pigment colours of red, pink, blue and purple for flowers.

This work aimed to explore the local-wild Rangoon creeper flowers for dye production by using solvent extraction techniques. The shades obtained were compared with the PANTONE® colour chart to establish the commercial value of the colour. A replacement for synthetic dyes is much in need, thus it is important to produce the colour that matches global colour references such as PANTONE® colours. Colours produced from Rangoon creeper with matching shade to PANTONE® colours are expected to have great commercial value in the colouration industry.

Materials and Methods

Sources

The flower of *Q. indica* L. (Rangoon creeper) was collected at Kampong Beting, Kuala Pilah, Negeri Sembilan, which wildly grow along the roadside in the village. Fresh samples were immediately transported to the laboratory to be processed. The petals were plucked and dried at room temperature for 5 days to remove water content. Then, the dried petals were ground into powder form by using a mixer grinder for better extraction.

Textile substrates used in this research work is 100% silk fabric. Fabrics made of natural protein fibre was selected to have a better affinity with natural dyes. Sodium chloride was used as a fixator agent, while vinegar and calamansi were used as mordanting agents, which work not only as a fixator but also as a catalyst in dyeing textile substrates using natural dyes. Natural mordants were selected in this work to make the dyeing more sustainable.

Extraction

Alcoholic extraction method was applied in which precisely 200 g of fine dried powder sample were infused in 2.0 L methanol solvent for 2 days at room temperature (25±2 °C) [9]. The solvent-containing extract was then decanted and filtered using Whatman filter paper no.1 by gravity filtration. The filtrate was evaporated under reduced pressure at 40°C using a rotary evaporator and dried at room temperature to give viscous concentrated crude methanolic dye extract.

Preparation for dyeing

Preparation for dyeing was done using MLR of 1:100, 10 g/L of mordant and 10 g/L of sodium chloride salt on the amount of solutions. Dye solution with 1% concentration was prepared by adding 2 g of extracted colorants in the 200 mL of distilled water.

Simultaneous mordanting

Simultaneous or meta mordanting was conducted by immersing the fabric sample in the dye bath containing mordant, dye extract and sodium chloride salt. Dyeing took place at 80 ^{o}C for 60 minutes using the MLR of 1:100.

Dyeing

Dyeing was carried out by using an Infra-Red dyeing machine. Three samples of 100% silk fabric were prepared with a standard weight of 2 g each. Infra-Red dyeing machine rotated for 3 minutes clockwise and changed the rotational direction to anti-clockwise with an interval of 3 seconds. The dyeing process started at 40 ^{o}C then raised to 80 ^{o}C with a gradient of 5 ^{o}C/min. When it reached 80 ^{o}C, it was held for 60 minutes before cooled down to 40 ^{o}C. The fabrics were then removed after dyeing and rinsed with cold distilled water before drying under shade.

Colour value

All dyed samples were evaluated for colour shade using X-rite RM2000 Capsure. This shade is similar to the standard PANTONE® colour. This hand-held colour measurement tool kept the PANTONE® library and will match the PANTONE® colour shade to the dyed fabric sample. The colours obtained were also measured using CIELAB colour space.

Colourfastness to washing

Colourfastness to washing is a test to identify how strong the colour molecules stay and are bound in the fibre after washing. The test was carried out for 30 minutes at 60 ^{o}C in accordance with MS ISO 105-C03–1996. The fabric samples were then rinsed and dried prior to evaluation under the lighting cabinet. Greyscales for assessing colour change were used to analyse the colour change of the dyed fabric samples, and also the staining of adjacent white fabrics. Change in colour and staining were rated using greyscales standard ranging from 1 to 5, where 1 is poor and 5 is excellent in accordance with ISO 105-A02:1993.



Figure 1. *Quisqualis indica* flowers

Results and Discussion

Extraction of Rangoon creeper flowers

Colours extracted from Rangoon creeper flowers were documented in several articles, and most of them used aqueous extraction techniques [10]. Extracting colour from creeper's flowers using chemical solvent was scarcely found in Malaysia. This work has successfully extracted Rangoon creepers flowers using methanol as solvent extraction medium to obtain dark brown viscous concentrated crude methanolic dye extract with a concentration of 21.142 g/L. The whole process is shown in Figure 2.

Colour measurement

Colour measurement was successfully done by capturing the shades of the dyed samples. Silk fabric samples dyed using vinegar as mordanting agent showed earthy shades. Basically, all dyed samples were categorised using a type of mordant as the dye is the same. There are grouped as non-mordanted, vinegar and calamansi. Principally, all samples have the same colour hue. The lightest shades were displayed by silk samples dyed using calamansi as mordant (Figure 3a), followed by darker shades by non-mordanted dyed samples (Figure 3b). The darkest shades were showed by samples dyed using vinegar as mordants (Figure 3c).

The colours plotted using CIELAB colour space showed that all dyed samples were plotted in the yellow-red space as shown in Figure 4 below. Colour values i.e., RGB, L*a*b* and Delta E were stated in Table 1. All measured colours were plotted in the 2D colour plot and all dyed fabrics have the same shade. Fabric dyed with Rangoon creeper flowers using calamansi as mordanting agent give ore reddish shade as compared to fabric with vinegar as mordant and non-mordanted fabric.

Colourfastness to washing

Colourfastness to washing shows good results for all mordanted and non-mordanted samples. Non-mordanted samples gave slightly different shades but were acceptable, which give a rating of 4 (good). Although the mordanted samples are slightly different before and after washing, the hue is still the same. Mordanted samples show excellent ratings i.e., 4/5, which is almost similar to the unwashed samples. The excellent ratings obtained for both mordanting agents show that calamansi and vinegar are suitable to be used in natural dyeing. Both mordants are able to hold the colour on the textile substrates after washing. The results also show that there is almost no stain of the dye on the adjacent fabrics for both mordanted samples.



Figure 2. Methanolic dye extract process: (1) raw sample, (2) drying, (3) soaking with methanol, (4) filtered, (5) evaporate to dryness, and (6) dye extract

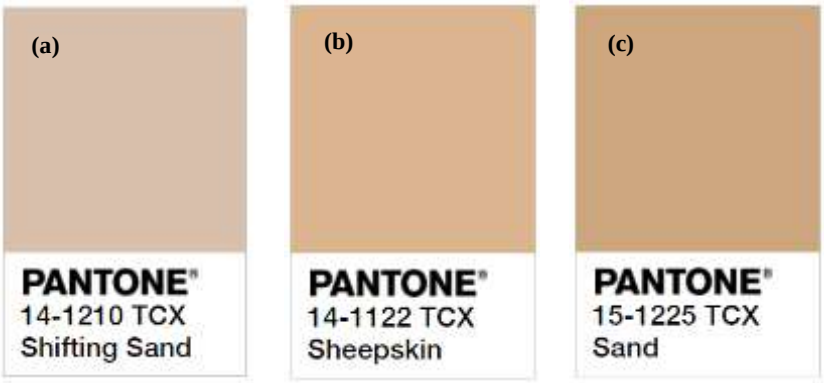


Figure 3. Dyed silk fabric samples with different mordant (a) calamansi, (b) non-mordanted, (c) vinegar

Table 1. RGB and L*a*b* data for non-mordanted and mordanted samples

Mordants	**R**	**G**	**B**	**L***	**a***	**b***
Non-mordanted	204	166	127	70.62	8.57	25.45
Calamansi	216	185	152	77.01	6.24	20.87
Vinegar	182	149	116	63.91	7.62	22.08

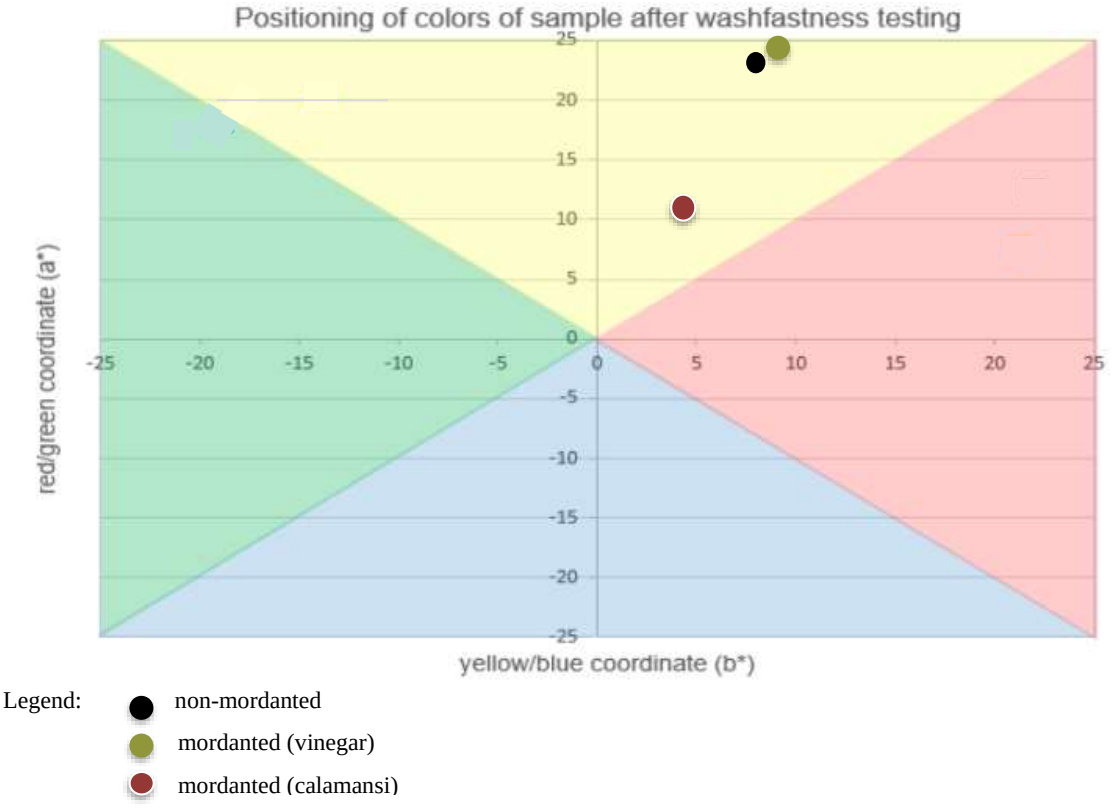


Figure 4. 2D plot for fabrics dyed with Rangoon creeper flower

Table 2. Rating for colourfastness to washing

Mordants	Change in Colour	Staining on White Fabrics		Indicator
		100% silk	100% cotton	
Non-mordanted	4	4	4	Good
Calamansi	4/5	5	4/5	Excellent
Vinegar	4/5	5	4/5	Excellent

Conclusion

Natural dyes show substantial growth for the past few years due to their non-toxicity of natural and sustainable sources with minimal environmental impact characteristics. The application of natural dye on textile substrates using alcoholic extraction has created attention to the scientific community to use this large diversity of natural dye sources in the textile dyeing industry. In the current study, emphasis has been laid on the extraction and colourimetry of natural dye from the flower. Natural colourants extracted from the Rangoon creeper demonstrate good colour strength and are comparable with PANTONE®. The colour yield has shown different shades of brown, with excellent colourfastness to washing. Infra-Red dyeing technique used also make the dyeing process more sustainable with more even colour on textile substrates.

Acknowledgement

This is a self-funded study by the collaboration of teaching practitioners of different fields. The authors would like to thanks UiTM Negeri Sembilan Branch, Kuala Pilah Campus for providing facilities for this study.

References

1. Kishor, R., Purchase, D. Saratale, G. D., Saratale, R. G., Ferreira, L. F. R., Bilal, M., Chandra, R. and Bharagava, R. N. (2020). Ecotoxicological and health concerns of persistent coloring pollutants of textile industry wastewater and treatment approaches for environmental safety. *Journal of Environmental Chemical Engineering*, 9(2): 1-18.
2. Hassaan, A., M. (2017). Health and environmental impact of dyes: Mini review. *American Journal of Environmental Science and Engineering* 1(3): 64-67.
3. Behera, M., Nayak, J., Banarjee, S., Chakrabortty, S. and Tripathy, S. K. (2021). A review on the treatment of textile industry waste effluents towards the development of efficient mitigation strategy: An integrated system design approach. *Journal of Environmental Chemical Engineering* 9(4): 1-21.
4. Tkacyzk, A., Mitrowska, K. and Posyniak, A. (2020). Synthetic organic dyes as contaminants of the aquatic environment and their applications for ecosystems: A review. *Science of the Total Environment* 717: 1-19.
5. Ludin, N. A., Al-Alwani, M.A.M., Mohamad, A. B., Kadhum, A. A. H., Hamid, N. H., Ibrahim, M. A., Teridi, M. A. M., Al-Hakeem, A., Mukhlus, A. and Sopian, K. (2018). Utilization of natural dyes from *Zingiber officinale* leaves and *Clitoria ternatea* flowers to prepare new photosensitiser for dye-sensitised solar cells. *International Journal of Electrochemical Science*, 13(2018): 7451-7465.
6. Kim, H. J., Bin, Y.T., Karthick, S. N., Hemalatha, K. V., Raj, C. J., Venkatesan, S., Park, S. and Vijaykumar, G. (2013). Natural dye extracted from rhododendron species flowers as a photosensitizer in dye-sensitized solar cell. *International Journal of Electrochemistry Science*, 8: 6734-6743.

7. Singh, S., Bothara, S. B. and Singh, S. (2011). Acid-base indicator properties of dye from local flowers: *Cassia anugostifolia* Linn., *Thevetia peruviana* (Pers.) K. Schum and *Thevetia thvetiodes* (Kunth) K. Schum. *Pharmacognosy Journal*, 3(19): 35-39.
8. Sahu, J., Patel, P. K. and Dubey, B. (2012). *Quisqualis indica* Linn: A review of its medicinal properties. *International Journal of Pharmaceutical and Phytopharmacological Research*, 1(5): 313-321.
9. Voon, Ching, H., Bhat, R. and Rusul, G. (2012). Flower extracts and their essential oils as potential antimicrobial agents for food uses and pharmaceutical applications. *Comprehensive Reviews in Food Science and Food Safety*, 11(1): 34-55.
10. Soniya, M. and Anitha, D. (2018). Microwave extraction of dye from Madhumalti flower. *Journal of Research Angrau*, 46(4): 61-66.

Malaysian Journal of Analytical Sciences (MJAS)
Published by Malaysian Analytical Sciences Society

OPTIMIZATION OF EXTRACTION TEMPERATURE AND TIME ON PHENOLIC COMPOUNDS AND ANTIOXIDANT ACTIVITY OF MALAYSIAN PROPOLIS *Trigona Spp*. AQUEOUS EXTRACT USING RESPONSE SURFACE METHODOLOGY

(Pengoptimuman Suhu dan Masa Pengekstrakan pada Sebatian Fenolik dan Aktivikiti Antioksidan daripada Ekstrak Akues Propolis Kelulut (*Trigona Spp.*) Malaysia menggunakan Kaedah Gerak Balas Permukaan)

Abdullah Hagar[1], Nurlisa Fatihah Abd Rani[1], Muhammad Ibrahim[1]*, Norazsida Ramli[2], Idris Adewale Ahmed[3], Abbe Maleyki Mhd Jalil[4], Mohd Nur Nashriq Anuar[1]

[1]*Department of Nutrition Sciences, Kulliyyah of Allied Health Sciences*
[2]*Department of Biomedical Science, Kulliyyah of Allied Health Sciences*
International Islamic University Malaysia, Jalan Istana, Bandar Indera Mahkota, 25200 Kuantan, Pahang, Malaysia
[3]*Centre for Natural Products Research and Drug Discovery (CENAR), Level 3, Research Management & Innovation Complex,*
University of Malaya, 50603 Kuala Lumpur, Malaysia
[4]*School of Nutrition and Dietetics,*
Universiti Sultan Zainal Abidin, 21030 Kuala Terengganu, Terengganu, Malaysia

**Corresponding author. abumaisarah@iium.edu.my*

Received: 8 July 2021; Accepted: 8 August 2021; Published: 29 August 2021

Abstract

Propolis is a natural product with rich bioactive constituents for medicinal, pharmaceutical, food, and cosmetic uses. It is considered a diet supplement to enhance health and prevent disease. The optimum extraction conditions used to obtain the highest yield of total phenolic content (TPC), total flavonoid content (TFC), and antioxidant capacities for Trigona propolis aqueous extract was analyzed using response surface methodology and the central composite design. The effects of extraction temperature (X_1: 30 - 60 °C) and extraction time (X_2: 24 - 72 hours) on TPC (Y_1), TFC (Y_2), and antioxidant activities (DPPH (Y_3), $ABTS^{\bullet+}$ radical scavenging assay (Y_4), and ferric reducing antioxidant power (Y5) were investigated. The experimental data were satisfactorily fitted into a second-order polynomial model with regard to TPC ($R^2 = 0.9461$, $p = 0.0003$), TFC ($R^2 = 0.9110$, $p = 0.0015$), DPPH ($R^2 = 0.9482$, $p < 0.0001$), ABTS ($R^2 = 0.9663$, $p < 0.0001$), and FRAP ($R^2 = 0.9058$, $p = 0.0018$). The optimum extraction temperature and time were 43.75 °C and 52.85 hours. The predicted response values for TPC, TFC, DPPH, ABTS, and FRAP were 104.30 mg GAE/100g, 6.95 mg QE/g, 3.24 mMTE/g, 2.59 mMTE/g, and 4.34 mMTE/g, respectively. The experimental values were close to the predicted values 100.41 ± 2.74 mg GAE/100g, 6.74 ± 0.08 mg QE/g, 3.17 ± 0.08 mMTE/g, 2.76 ± 0.14 mMTE/g, and 4.60 ± 0.14 mMTE/g. As a result, the models generated are suitable, and RSM was successful in

optimizing the extraction conditions. Consequently, in this study, it was observed that the optimum extraction temperature and time provided the highest antioxidant yield of aqueous propolis extract which can be used as functional food ingredients.

Keywords: phenolic, antioxidant, propolis

Abstrak

Propolis merupakan hasil semulajadi yang kaya bahan bioaktif bagi perubatan, farmaseutikal, makanan dan kosmetik. Ia dianggap diet tambahan bagi kesihatan dan mencegah penyakit. Keadaan pengekstrakan optimum yang telah digunakan untuk hasil jumlah kandungan fenolik (TPC), jumlah kandungan flavonoid (TFC), dan kapasiti antioksidan tertinggi dianalis menggunakan pengekstrakan akues propolis kelulut melalui kaedah gerak balas permukaan, reka bentuk komposit berpusat. Kesan suhu pengekstrakan (X_1: 30 - 60 °C) dan masa pengekstrakan (X_2: 24 - 72 jam) pada aktiviti TPC (Y_1), TFC (Y_2) dan aktiviti antioksidan DPPH (Y_3), $ABTS^{\bullet+}$ (Y_4), dan FRAP (Y_5) telah diselidik. Data eksperimen diperolehi adalah sepadan bagi model polinomial peringkat kedua terhadap TPC (R^2 = 0.9461, p = 0.003), TFC (R^2 = 0.9110, p = 0.0015), DPPH (R^2 = 0.9482, p <0.0001), ABTS (R^2 = 0.9663, p <0.0001), dan FRAP (R^2 = 0.9058, p=0.0018). Suhu dan masa pengekstrakan yang optimum ialah 43.75 °C dan 52.85 jam. Nilai tindak balas yang diramalkan untuk TPC, TFC, DPPH, ABTS, dan FRAP adalah 104.30 mg GAE/100g, 6.95 mg QE/g, 3.24 mMTE/g, 2.59 mMTE/g, dan 4.34 mMTE/g. Nilai eksperimen hampir dengan nilai yang diramalkan iaitu 100.41 ± 2.74 mg GAE/100g, 6.74 ± 0,08 mg QE/g, 3.17 ± 0.08 mMTE/g, 2.76 ± 0,14 mMTE/g, dan 60 ± 0,14 mMTE/g. Dalam kajian ini, diperhatikan bahawa suhu dan masa pengekstrakan yang optimum memberikan hasil antioksidan tertinggi ekstrak propolis dan dapat digunakan sebagai bahan makanan

Kata kunci: fenolik, antioksida, propolis

Introduction

Propolis is a resinous material collected by bees from plant exudates and the nectar of buds, tree gum, combined with wax and bee enzymes [1]. It is a natural product with rich bioactive constituents for medicinal, pharmaceutical, food, and cosmetic uses [2-4]. Propolis is considered a diet supplement to enhance health and prevent diseases [5, 6]. It has also been used as natural preservatives and is considered healthier and safer than synthetic preservatives [7, 8]. Propolis prolongs the shelf life, improves the quality of various food product compositions, and prevents undesirable changes in the physical and chemical characteristics of food [4, 9, 10]. Propolis extract is used as an antioxidant to enhance the antioxidant properties of honey, fruit, and juices during storage [4]. Thus, using ethanolic propolis extract or aqueous propolis extract is more economical. Alcoholic extraction, however, has certain disadvantages, such as heavy residual taste and alcohol sensitivity in some clients [7].

There is, however, limited data on the use of propolis aqueous solutions [4]. The issue of poor solubility of propolis in water at room temperature and lower amounts of the phenolic compounds are a disadvantage of aqueous extraction techniques compared to ethanol extraction [7, 11]. Nonetheless, higher solubility and diffusion coefficient of phenolic compounds can be achieved by increasing the extraction temperature [7, 12, 13]. The amount of total phenolic content increased with the increment in the extraction temperature. Higher extraction temperature leads to increased material transfer and therefore, increased penetration of solvent into propolis. Furthermore, when the temperature increased, the viscosity of propolis decreased and the entire process accelerated [14, 15].

A prolonged extraction time enhances polyphenolic compound extraction [15, 16]. However, extremely high temperatures may cause the degradation and/or volatilization of certain composites, resulting in decreased process efficiency [17, 18]. Mostly, a longer extraction period with high temperatures might lead to more polyphenol losses [14, 19]. Thus, extraction temperature and time are important factors that should be optimized to protect the active compounds, save process cost, and obtain extract rich in phenolic compounds and antioxidant activities [16, 19]. However, studies on the optimum temperature and time for the aqueous extraction of Malaysian Trigona bee

propolis are still limited. Thus, this study aims to use the response surface methodology (RSM) method for optimizing the extraction temperature and time to maximize the yield of total phenolic, total flavonoid content, and antioxidant capacities from Trigona propolis aqueous extract.

Materials and Methods

Chemicals and reagents

In the current study, analytical grade chemicals were utilized. Folin- Ciocalteu (FC) reagent, sodium carbonate, Iron(III) Chloride Hexahydride, aluminum chloride ($AlCl_3$), ethanol, methanol, were bought from Merck (Darmstadt, Germany). While, 2,2-diphenyl-1-picrylhydrazyl hydrate (DPPH), 2,4,6-tripyridyl-s-triazine (TPTZ), HCl, 2,2'-azino-bis(3-ethylbenzothiazoline-6-sulphonic acid) (ABTS) were bought from Sigma-Aldrich Co. (St. Louis, MO, USA). Potassium persulfate and tetramethylchromane-2-carboxylic acid (Trolox) were purchased from Acros (New Jersey, USA). Gallic acid was from Merck (Hohenbrunn, Germany). Quercetin was bought from Nacalai-Tesque (Kyoto, Japan). Sodium Acetate Trihydrate was purchased from fisher scientific Loughborough, UK. Glacial Acetic Acid, was from MP Biomedicals, LLC, Parcd'innovation, IIIkirch, France.

Sample collection

In September 2017, 200 kg of Trigona propolis was collected from "TriBrothers Kelulut Farm", Kampung Kubang Kiat, Ketereh, Kota Bharu, Kelantan, Malaysia, and protected from the light and frozen at -20 °C until extraction.

Sample preparation and extraction

Propolis extraction was done using the method reported by Thusheva et al. [20], with some modifications. First, propolis was washed and cut using a knife. The cut samples were ground using mortar, pestle, and laboratory blender (Waring). Then 5 g of the ground propolis were extracted in 50 mL of distilled water (1:10 w/v) at different temperatures (23.79 - 66.21 °C), and various soaking times (14.06 - 81.94 hours) using RSM, central composite design (CCD), Design-Expert Version 6.0.10 (Minneapolis, MN) software for the optimization studies. The extracts were separated from the sediment through centrifugation at 1500 g for 5 minutes. The sediment was washed twice with 10 mL of the extract solution, then centrifuged at 1500 g for 5 minutes and added to the initial supernatant. The extracted propolis was concentrated by a rotary evaporator (Buchi, Flawil, Switzerland), under reduced pressure (72) at 60 °C and 50 rpm. Then the extracted soft propolis samples were preserved at 4 °C until analysis [21].

Estimation of total phenolic content

The FC reagent was utilized to evaluate the total phenolic content (TPC) in the various aqueous extracts of propolis (AEP) and standard [22]. About 20 µL of AEP (10 mg/mL) were mixed with 100 µL of FC reagent (1:10 v/v, reagent: water) in each well of a 96-well plate. This was followed by adding 75 µL of sodium carbonate (7.5%) to the mixture, then incubated for 40 minutes at room temperature in the dark and the absorbance recorded at 740 nm against a blank (distilled water) using a spectrophotometer [microplate reader (Nano Quant Infinite M 200, Tecan, Grodig, Austria)]. Gallic acid was used as a standard to plot the calibration curve at concentrations ranging from 20 to 160 µg/mL, R^2 = 0.9951. The mean and standard deviation of the triplicate (n = 3) were used, and the results were expressed as mg of gallic acid equivalents per 100 g of sample weight (mg GAE/100g).

DPPH free radical scavenging assay

The DPPH assay was conducted as stated by [23] with modifications using a 96-well microplate. Aliquots of 100 µL of the AEP (10 mg/mL), control, and standard were added to the wells, followed by 100 µL of 100 µM methanol solution of DPPH (3.94 mg in 100 mL methanol). The plate was incubated in the dark for 30 minutes and the absorbance was measured at 517 nm in a spectrophotometer [microplate reader (Nano Quant Infinite M 200, Tecan, Grodig, Austria)]. Aqueous (distilled water) was used as a blank (negative control) and Trolox was applied as a positive control. DPPH scavenging effect was calculated by DPPH discoloration percentage, using the equation 1:

$$DPPH\ radical\ scavenging\ activity\ (\%) = \frac{A_{blank} - A_{sample}}{A_{blank}} \times 100 \quad (1)$$

A_{blank} is the blank's absorbance (extraction solvent + DPPH solution) and the A_{sample} is the sample's absorbance (extracts + DPPH solution).

The decolorization is expressed as a percentage of absorbance inhibition, then plotted as a function of the antioxidant concentration in the sample. A standard curve of Trolox (5 - 60 µmol TE /mL, $R^2 = 0.9919$) was observed. The mean and standard deviation of the triplicate were used, and the outcomes were expressed as mmol Trolox equivalents per g of sample weight (mmol TE/g).

$ABTS^{\bullet+}$ radical scavenging assay

In the $ABTS^{\bullet+}$ radical scavenging assay (an electron transfer-based assay), the 2,2′-azino-bis(3-ethylbenzo thiazoline-6-sulfonate) radical cation ($ABTS^{\bullet+}$) was conducted to evaluate the antioxidant capacity in various AEP according to [25], with modifications. $ABTS^{\bullet+}$ radical stock solution was made by reacting 7 mM ABTS solution and 2.45 mM potassium persulfate solution in equal volumes and reacted for 16 hours in the dark at room temperature. Then 2 mL of $ABTS^{\bullet+}$ radical stock solution was diluted by 50 mL ethanol to get an absorbance of 0.706 ± 0.01 units at 734 nm using a spectrophotometer [microplate reader (Nano Quant Infinite M 200, Tecan, Grodig, Austria)]. Aliquots of 20 µL of standard Trolox, blank and AEP (10 mg/mL), and 180 µL of $ABTS^{\bullet+}$ radical solution were added to microplate wells and kept at room temperature in the dark. The absorbance was recorded 5 min after starting the oxidation at 734 nm. Distilled water was used as a blank. $ABTS^{\bullet+}$ scavenging influence was calculated by $ABTS^{\bullet+}$ discoloration percentage using equation 2 as follows:

$$\text{ABTS radical scavenging activity (\%)} = \frac{[\text{A blank} - \text{A sample}]}{\text{A blank}} \times 100 \quad (2)$$

where the blank was the mixture of distilled water and ABTS+ solution and the sample is the mixture of sample extract and ABTS+ solution. Trolox was employed as standard at concentrations ranging from 2.5 to 40µM/mL ($R^2 = 0.9931$). The mean and standard deviation (SD) of the triplicate were used and the results were expressed as mmol Trolox equivalents per g of sample weight (mmol TE/g).

Ferric reducing antioxidant power (FRAP)

The FRAP assay was modified from [26]. The fresh working solution of FRAP reagent (10:1:1) was prepared by mixing 25 mL of 0.3 M acetate buffer (pH 3.6), 2.5 mL of 10 mM TPTZ, and 2.5 mL of 20 mM $FeCl_3.6H_2O$, and incubated in the dark at 37 °C. Then aliquots of 20 µL of AEP were added to 180 µL of FRAP reagent and the plate was incubated at 37 °C for 10 minutes. The absorbance was recorded using a spectrophotometer [microplate reader (Nano Quant Infinite M 200, Tecan, Grodig, Austria)] at 593 nm against a blank (distilled water). A calibration curve was created using Trolox (200 - 600 µM Trolox/mL, $R^2 = 0.9921$). The average and standard deviation of the three readings (n = 3) were used and expressed as mM Trolox equivalent (mM TE/g sample weight).

Experimental design

The central composite design was utilized to determine the optimum levels of temperature and extraction time for maximizing the antioxidant capacity of AEP on five responses, namely TPC, TFC, and antioxidant activities (DPPH, ABTS, and FRAP). Two factors, namely temperature (X_1: 23.79–66.21 °C) and extraction time (X_2: 14.06 - 81.94 hours) were coded into five levels (-1.414, -1, 0, 1, 1.414), from the lowest to the highest, respectively [21]. Thirteen different experiments were examined in terms of their responses (antioxidant properties). The coded and non-coded factors applied in the RSM design are presented in Table 1.

Table 1. Coded and actual values levels of factors used in the RSM design

	Factors **Coded Levels**	**−1.414**	**−1**	**0**	**1**	**1.414**
X_1	Temperature (°C)	23.79	30.00	45.00	60.00	66.21
X_2	Extraction time (hour)	14.06	24	48	72	81.94

Statistical analysis

The statistical analysis was implemented using the Design-Expert Version 6.0.10 software. The results for TPC, TFC, DPPH, ABTS, and FRAP were indicated as mean values of three replicates. The response surface analysis was carried out to validate the regression coefficients and the model statistical significance and for fitting the mathematical models of the experimental data to optimize the dependent variables. A second-order polynomial model was used to fit the data. As presented in the following equation 3:

$$Y = b_0 + b_1X_1 + b_2X_2 + b_1^2X_1^2 + b_2^2X_2^2 + b_1 b_2 X_1X_2 \quad (3)$$

where the expected response is Y, while b_0 is a constant, the linear influence regression coefficients are b_1 and b_2, the quadratic impact is b_1^2 and b_2^2 and interaction influences are b_1 and b_2, respectively. The model quality was predicted by the ANOVA analysis (p <0.05) and the regression analysis (R^2). From the ANOVA analysis, only the significant coefficients were included. While the non-significant coefficients were omitted from the initial model. The relationship between the factors (X_1 and X_2) and the responses (Y_1, Y_2, Y_3, Y_4, and Y_5) is illustrated by the three-dimensional model graph. The desired aim was set in numerical optimization to produce the optimum condition and point predicted values of the responses.

Model verification

The experimental data for TPC, TFC, and antioxidant activities were determined according to optimum conditions predicted by the software. The experimental values were compared to the predicted values from the optimized model to confirm the validity of the model.

Results and Discussion

Fitting the model

The experimental values of TPC (Y_1), TFC (Y_2), and DPPH• scavenging ability (Y_3), ABTS•+ inhibition activity (Y_4), and FRAP (Y_5) were used in multiple regression analysis by applying response surface analysis to fit the second-order polynomial equations. The experimental values were close to the predicted values, demonstrating an adequate model (Table 2). The regression coefficients of determination (R^2), adjusted R^2 values, probability values (p), and lack-of-fit values for all dependent variables are shown in Table 3. The quality of fit to the second-order polynomial models was established based on the coefficients of determination (R^2), which were 0.9461, 0.9110, 0.9482, 0.9663, and 0.9058 for TPC, TFC, and antioxidant activities (DPPH, ABTS, FRAP), respectively; thus, indicating that approximately 91 to 97% of the variations were determined by the model. The fitness of the model was verified by the lack-of-fit test for all the responses but was insignificant (p >0.05).

Effect of extraction parameters on TPC, TFC, and Antioxidant activity

The effect of the two factors (X_1 and X_2) on the dependent variables (Y_1, Y_2, Y_3, Y_4, and Y_5) was established by the significant (p<0.05) coefficient of the second-order polynomial regression equation. For TPC (Y_1) and ABTS scavenging capacity (Y_4), the effect of extraction temperature and extraction time was significant (p <0.05) in the first-order linear effect (X_2), second-order quadratic effect (X_1^2, X_2^2), and interaction effect (X_1X_2), with a good regression coefficient (R^2 =

0.9461 and R^2 = 0.9663, respectively). The predicted models obtained for Y_1 and Y_4 are given in Table 3. Based on the polynomial equations for (Y_1) and (Y_4), both temperature and time affected TPC and ABTS scavenging capacity. The temperature was, however, the most important factor contributing to the increase in the extraction efficiency in terms of TPC and ABTS scavenging capacity. This is because increasing extraction temperature enhances the solubility of solute and increases the extraction coefficient, the TPC, and ABTS scavenging capacity. According to the literature [19], the extraction temperature plays a more critical role in comparison to the extraction time.

For TFC (Y_2) and FRAP (Y_5), the effect of temperature and time was significant (p <0.05) in the second-order quadratic effect (X_1^2, X_2^2) and no interaction effect, with a high regression coefficient of R^2 = 0.9110 and R^2 = 0.9058, respectively. The predicted models obtained for Y_2 and Y_5 are given in Table 3. Both the temperature and time affected TFC and FRAP, with the temperature affecting more than the time. The result is in agreement with the work of Yim et al. [19]. The extraction temperature plays a more critical role than the extraction time. The increasing temperature enhances the solubility of solute and higher TFC and FRAP.

However, for DPPH scavenging capacity (Y_3), the effect of temperature and time was significant (p <0.05) in the first-order linear effect (X_1) and second-order quadratic effect (X_1^2, X_2^2), with the regression coefficient (R^2 = 0.9482). The predicted model found for Y_3 is given in Table 3. High temperatures enhance phenolic compound recovery [15, 16, 32]. However, a quadratic influence was discovered with a longer extraction time and a higher temperature. Higher polyphenol losses may arise from longer extraction periods at high temperatures [13, 14, 19].

Figures 1a and 1d show the 3D response surface, with a quadratic effect of temperature, and linear increase, and a quadratic effect of extraction time, as well as a significant interaction impact between time and temperature on Y_1 and Y_4. Overall, a combination of moderate points of temperature (40.98 °C and 43.05 °C) and moderate time (58.09 and 55.13 hours) gave maximum yield (104.88 mg GAE/100g and 2.59 mMTE/g) of TPC contents and ABTS•+ inhibition activity, respectively. The TPC and ABTS•+ inhibition activity increased with an increase in temperature from 30 °C up to a certain point (40.98 and 43.05 °C) and time from 24 hours to 58.09 and 55.13 hours, respectively. It then decreased with further increase in temperature and prolonged time, producing a TPC and ABTS• scavenging capacity that ranged from 66.23 to 104.88 mg GAE /100g and 1.41 to 2.59 mMTE/g, respectively.

Similarly, Figures 1b and 1e show a 3D response, with a quadratic effect of both temperature and time on TFC and FRAP value. Generally, a combination of a moderate point of temperature (44.21 and 45.83 °C) and moderate time (53.14 and 51.70 hours) gave maximum values of TFC and FRAP (6.95 mg QE/g and 4.35 mMTE/g, respectively).

Figure 1c shows the response surface of the effect of temperature and time on DPPH• scavenging capacity. Overall, a combination of a moderate point of extraction temperature (42.65 °C) and moderate extraction time (49.72 hours) yielded a maximum DPPH• scavenging capacity value (3.24 mMTE/g). The antioxidative compounds may be subjected to decomposition and degradation upon longer extraction time and higher temperature [19].

The results are in agreement with previously reported studies. It illustrates that the increase in extraction temperature promotes higher solubility and diffusion coefficient of phenolic compounds and allows more phenolic extraction rate [7, 12, 27]. Higher extraction temperatures result in more material transfer and, as a result, more solvent penetration into propolis. Furthermore, when the temperature increased, the viscosity of propolis decreased, speeding up the entire process [14, 15]. However, extremely high temperatures might cause degradation and/or volatilization of some chemicals, resulting in a decreased process efficiency [17, 18]. Interestingly, there was a significant (p <0.05) negative interaction between extraction temperature and time for total phenolic contents and ABTS, which can be attributed to the decomposition of anti-oxidative compounds because of longer extraction time at higher

temperatures [14, 19]. The findings of this study are in line with the literature [14, 18]. The results are also consistent with previous studies on the beneficial effects of temperature on polyphenol extraction from various matrices [19, 28-31].

Concerning the effects of extraction time on TPC, TFC, DPPH, ABTS, and FRAP, the yield increased linearly with the increase in extraction time. A prolonged extraction time enhances polyphenolic compound extraction, giving enough time for solute exposure to the release medium. Moreover, the high temperature was known to enhance the capability of improving phenolic compound recovery [15, 16, 32]. A quadratic effect was observed with a more prolonged extraction time and a high temperature. A longer extraction period with high temperatures might lead to more polyphenol losses [13, 14, 19]. The result of the time effect on phenolic extracts is also in line with the literature [21]. The variations in the extraction conditions such as time and temperature should, however, be properly monitored and controlled to protect the active compounds from damage and to practically save the process cost. At optimum temperature, a longer extraction time should be avoided to prevent the loss, decomposition, and degradation of antioxidant compounds.

Table 2. Experimental design and responses of the dependent variables to extraction conditions

Extraction Parameters			**Responses**									
Standard Order	**Temperature (˚C)**	**Time (hour)**	**TPC (mgGE/100g) Y_1**		**TFC (mgQE/g) Y_2**		**DPPH (mMTE/g) Y_3**		**ABTS (mMTE/g) Y_4**		**FRAP (mMTE/g) Y_5**	
			Exp.	**Pred.**	**Exp.**	**Pred.**	**Exp.**	**Pred.**	**Exp.**	**Pred.**	**Exp.**	**Pred.**
1	-1	-1	62.15	66.23	4.01	3.88	2.22	2.35	1.34	1.41	3.06	3.26
2	1	-1	77.37	77.71	4.39	4.07	2.37	2.33	1.70	1.77	3.17	3.44
3	-1	1	92.57	97.65	4.79	5.16	2.58	2.67	2.16	2.21	3.43	3.45
4	1	1	69.52	70.86	4.35	4.54	2.24	2.18	1.59	1.65	3.48	3.57
5	-1.414	0	84.65	79.29	4.34	4.17	2.69	2.55	1.77	1.71	3.02	2.92
6	1.414	0	68.52	68.46	3.76	3.87	2.11	2.19	1.64	1.57	3.33	3.13
7	0	−1.414	75.67	73.66	3.85	4.18	2.39	2.34	1.71	1.64	3.99	3.71
8	0	1.414	94.47	91.04	5.81	5.43	2.47	2.46	2.18	2.12	3.96	3.94
9a	0	0	100.86	103.10	6.87	6.90	3.25	3.24	2.52	2.56	4.53	4.35
10a	0	0	98.16	103.10	7.55	6.90	3.42	3.24	2.76	2.56	4.23	4.35
11a	0	0	106.95	103.10	6.50	6.90	3.13	3.24	2.51	2.56	4.16	4.35
12a	0	0	101.61	103.10	6.12	6.90	3.08	3.24	2.46	2.56	4.49	4.35
13a	0	0	107.90	103.10	7.45	6.90	3.32	3.24	2.54	2.56	4.32	4.35

a Centre point.

Y_1 (TPC) = Total phenolic content, Y_2 (TFC) = Total flavonoid content

Y_3 (DPPH) = 2, 2-diphenyl-1-picrylhydrazyl radical scavenging ability,

Y_4 (ABTS) = 2, 2′-azino-bis (3-ethylbenzthiazoline-6-sulfonic acid) radical cation inhibition,

Y_5 (FRAP) = Ferric Reducing Antioxidant power, GAE = Gallic acid equivalent, QE = Quercetin equivalent,TE = Trolox equivalent, Exp. = Experimental value, Pred. =Predicted va--

Table 3. Polynomial equation and statistical parameters calculated after implementation of two-factor central composite experimental design

Regression Coefficient	Polynomial Equation	R^2	R^2 (Adjusted)	Regression (*p* value)	Lack Of Fit
TPC (Y_1)	$+ 103.10 + 6.14X_2 - 14.61X_1^2 - 10.37X_2^2 - 9.5724X_1X_2$	0.9461	0.9075	0.0003	0.3029
TFC (Y_2)	$+ 6.90 - 1.44\ X_1^2 - 1.05X_2^2$	0.9110	0.8474	0.0015	0.6822
DPPH (Y_3)	$+ 3.24 - 0.13\ X_1 - 0.44\ X_1^2 - 0.42\ X_2^2$	0.9482	0.9112	< 0.0001	0.4619
ABTS (Y_4)	$+ 2.56\ + 0.17\ X_2\ - 0.46X_1^2 - 0.34X_2^2 - 0.23X_1X_2$	0.9663	0.9422	< 0.0001	0.5495
FRAP (Y_5)	$+ 4.35 - 0.66\ X_1^2 - 0.26\ X_2^2$	0.9058	0.8385	0.0018	0.1498

TPC (Y_1) = Tot al phenolic content, TFC (Y_2) = Total flavonoid content,
DPPH (Y_3) = 2, 2-diphenyl-1- picrylhydrazyl (DPPH) radical scavenging ability,
ABTS (Y_4) =2, 2′-azino-bis (3-ethylbenzthiazoline-6-sulfonicacid) (ABTS) radical cation inhibition,
FRAP (Y_5) = Ferric Reducing antioxidant power

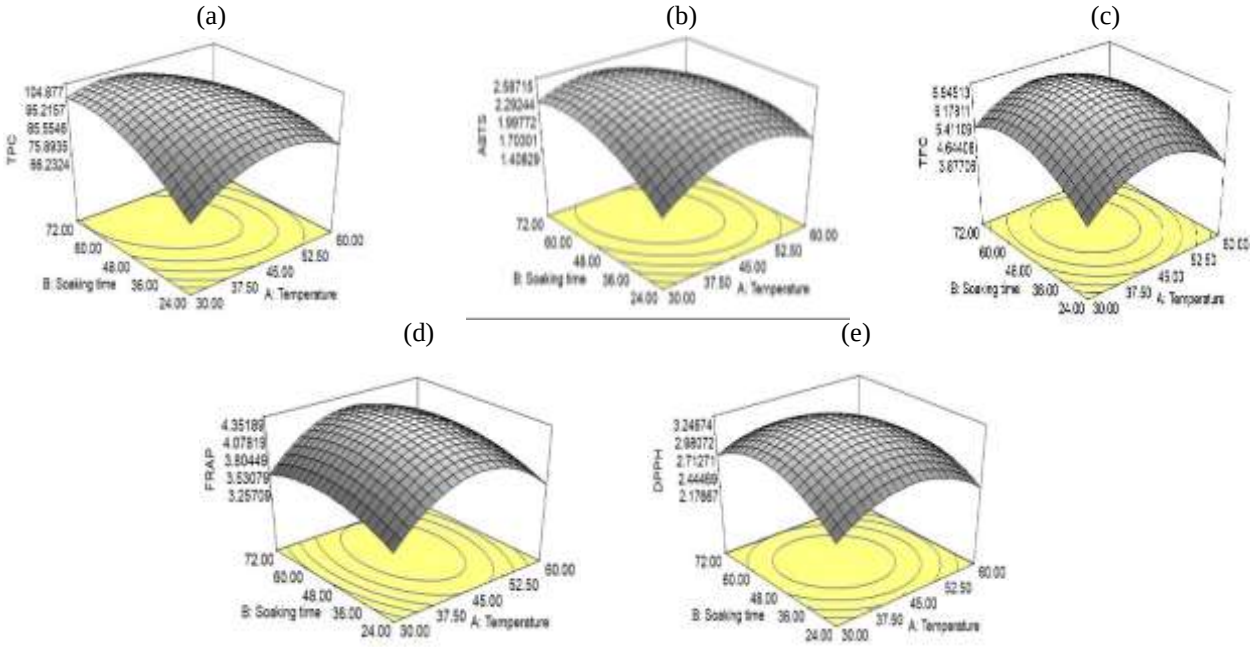


Figure 1. Response surface plot of temperature and extraction time on; (a) total phenolic content (mg GAE/100 g), (b) total flavonoid content (mg QE/g), (c) the DPPH (mM TE/g), (d) ABTS (mM TE/g), and (e) FRAP (mM TE/g) of Trigona propolis samples

Optimization of response and verification of model

In numerical optimization, the optimum covering criteria of temperature and time were 43.75 °C and 52.86 hours, respectively for propolis extraction (Figure 2). The predicted TPC, TFC, DPPH, ABTS, and FRAP were 104.30 mg GAE/100g, 6.95 mg QE/g, 3.24 mMTE/g, 2.58 mMTE/g, and 5.29 mMTE/g, respectively while the experimental values obtained were 100.41 ± 2.74 mg GAE/100g, 6.74 ± 0.08 mg QE/g, 3.17 ± 0.08 mMTE/g, 2.76 ± 0.14 mMTE/g, and 5.54 ± 0.14 mMTE/g, respectively. The experimental and predicted values were compared to verify the response surface model. The experimental values were close to the predicted values. The differences for TPC, TFC, DPPH, ABTS, and FRAP were 3.73%, 3.01%, 2.17%, 6.90%, 6.02%, respectively, as shown in Table *4*.

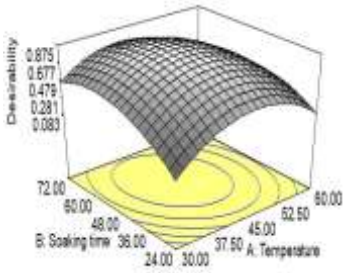


Figure 2. Response surface plot of the desirability as a function of extraction time and temperature

Table 4. Experimental data of the verification of predicted extraction parameters

Factors (Optimum)	**Temperature (ºC)**	**Time (hour)**	**Predicted Value**	**Experimental Value**	**% Difference**
Response	43.75	52.85			
TPC(mgGAE/100g)			104.30	100.41± 2.74	3.73
TFC (mgQE/g)			6.94	6.74±0.08	3.01
DPPH(mMTE/g)			3.24	3.17±0.08	2.17
ABTS(mMTE/g)			2.59	2.76±0.14	6.90
FRAP(mMTE/g)			4.34	4.60±0.14	6.02

TPC = Total phenolic content, TFC = Total flavonoid content,
DPPH =2, 2- diphenyl-1-picrylhydrazyl radical scavenging ability,
ABTS = 2, 2′-azino-bis (3- ethylbenzthiazoline-6-sulfonic acid) radical cation inhibition,
FRAP = Ferric reducing antioxidant power,
Results were expressed as mean ± standard deviation (n=3).

Conclusion

The optimum extraction time and temperature that yielded the highest TPC, TFC, and antioxidant activities from Trigona propolis aqueous extract were determined using central composite design, response surface methodology. Adequate model equations were obtained to predict the influences of the extraction temperature and time for aqueous propolis extraction. The high antioxidant capacity of the propolis aqueous extract was successfully verified through TPC, TFC, and DPPH

radical-scavenging assays, ABTS•+ inhibition activity, and FRAP. The extraction conditions for the optimized high antioxidant aqueous extract propolis were determined as extraction temperature and time at 43.75 °C and 52.86 hours, respectively. The optimum extraction conditions would ensure efficient energy use and process cost. The phenolic-rich extract with a high antioxidant capacity also provides many benefits for various potential applications. Though both temperature and time affect TPC, TFC, and antioxidant activities of Trigona propolis aqueous extract, the extraction temperature, however, plays a more critical role than the extraction time because the increasing temperature enhances the solubility of the solute. Future studies are suggested to evaluate the role of green solvents like natural deep eutectic solvents.

Acknowledgment

The authors would like to thank the Kulliyyah of Allied Health Sciences, and Central Research and Animal Facility, IIUM for the technical support.

References

1. Oryan, A., Alemzadeh, E. and Moshiri, A. (2018). Potential role of propolis in wound healing: Biological properties and therapeutic activities. *Biomedicine and Pharmacotherapy*, 98(2017): 469-483.
2. Freires, I. A., Queiroz, V. C. P. P., Furletti, V. F., Ikegaki, M., de Alencar, S. M., Duarte, M. C. T. and Rosalen, P. L. (2016). Chemical composition and antifungal potential of Brazilian propolis against Candida spp. *Journal de Mycologie Medicale*, 26(2): 122-132.
3. Freires, Irlan Almeida, De Alencar, S. M. and Rosalen, P. L. (2016). A pharmacological perspective on the use of Brazilian Red Propolis and its isolated compounds against human diseases. *European Journal of Medicinal Chemistry*, 110: 267-279.
4. Pobiega, K., Kraśniewska, K. and Gniewosz, M. (2019). Application of propolis in antimicrobial and antioxidative protection of food quality – A review. *Trends in Food Science and Technology*, 83(2018): 53-62.
5. Farooqui, T. (2012). Beneficial effects of propolis on human health and neurological diseases. *Frontiers in Bioscience*, E4(1): 779.
6. Salas, A., Mercado, M. I., Zampini, I. C., Ponessa, G. I. and Isla, M. I. (2016). Determination of botanical origin of propolis from Monte Region of Argentina by histological and chemical methods. *Natural Product Communications*, 11(5): 627-630.
7. Kubiliene, L., Laugaliene, V., Pavilonis, A., Maruska, A., Majiene, D., Barcauskaite, K., Kubilius, R., Kasparaviciene, G. and Savickas, A. (2015). Alternative preparation of propolis extracts: Comparison of their composition and biological activities. *BMC Complementary and Alternative Medicine*, 15(1): 1-7.
8. Yang, W., Wu, Z., Huang, Z. Y. and Miao, X. (2017). Preservation of orange juice using propolis. *Journal of Food Science and Technology*, 54(11): 3375-3383.
9. Luis-Villaroya, A., Espina, L., García-Gonzalo, D., Bayarri, S., Pérez, C. and Pagán, R. (2015). Bioactive properties of a propolis-based dietary supplement and its use in combination with mild heat for apple juice preservation. *International Journal of Food Microbiology*, 205: 90-97.
10. Viera, V. B., Piovesan, N., Moro, K. I. B., Rodrigues, A. S., Scapin, G., Rosa, C. S. da. and Kubota, E. H. (2016). Preparation and microbiological analysis of Tuscan sausage. *Food Science and Technology*, 36: 37-41.
11. Mello, B. C. B. S., Petrus, J. C. C. and Hubinger, M. D. (2010). Concentration of flavonoids and phenolic compounds in aqueous and ethanolic propolis extracts through nanofiltration. *Journal of Food Engineering*, 96(4): 533-539.
12. Bachir Bey, M., Meziant, L., Benchikh, Y. and Louaileche, H. (2014). Deployment of response surface methodology to optimize recovery of dark fresh fig (*Ficus carica* L., var. Azenjar) total phenolic compounds and antioxidant activity. *Food Chemistry*, 162: 277-282.
13. Durling, N. E., Catchpole, O. J., Grey, J. B., Webby, R. F., Mitchell, K. A., Foo, L. Y. and Perry, N. B. (2007). Extraction of phenolics and essential oil from dried sage (*Salvia officinalis*) using ethanol-water mixtures. *Food Chemistry*, 101(4): 1417-1424.

14. Erdogan, S., Ates, B., Durmaz, G., Yilmaz, I. and Seckin, T. (2011a). Pressurized liquid extraction of phenolic compounds from Anatolia propolis and their radical scavenging capacities. *Food and Chemical Toxicology*, 49(7): 1592-1597.
15. Yusof, N., Munaim, M. S. A. and Veloo Kutty, R. (2021). Optimization of total phenolic compounds extracted from propolis by ultrasound- assisted extraction. *Chemical Engineering Communications*, 208(4), 564-572.
16. Oldoni, T. L. C., Oliveira, S. C., Andolfatto, S., Karling, M., Calegari, M. A., Sado, R. Y., Maia, F. M. C., Alencar, S. M. and Lima, V. A. (2015). Chemical characterization and optimization of the extraction process of bioactive compounds from propolis produced by selected bees Apis mellifera. *Journal of the Brazilian Chemical Society*, 26(10): 2054-2062.
17. González-Montelongo, R., Lobo, M. G. and González, M. (2010). The effect of extraction temperature, time and number of steps on the antioxidant capacity of methanolic banana peel extracts. *Separation and Purification Technology*, 71(3): 347-355.
18. Olczyk, P., Komosinska-Vassev, K., Ramos, P., Mencner, L., Olczyk, K. and Pilawa, B. (2017). Free radical scavenging activity of drops and spray containing propolis - An EPR examination. *Molecules*, 22(1): 128.
19. Yim, H. S., Chye, F. Y., Rao, V., Low, J. Y., Matanjun, P., How, S. E. and Ho, C. W. (2013). Optimization of extraction time and temperature on antioxidant activity of Schizophyllum commune aqueous extract using response surface methodology. *Journal of Food Science and Technology*, 50(2): 275-283.
20. Trusheva, B., Trunkova, D. and Bankova, V. (2007). Different extraction methods of biologically active components from propolis; A preliminary study. *Chemistry Central Journal*, 1(1): 1–4.
21. Margeretha, I., Suniarti, D. F., Herda, E. and Alim, Z. (2012). Optimization and comparative study of different extraction methods of biologically active components of Indonesian propolis Trigona spp. *Journal of Natural Products*, 5: 233-242.
22. Tiveron, A. P., Rosalen, P. L., Franchin, M., Lacerda, R. C. C., Bueno-Silva, B., Benso, B., Denny, C., Ikegaki, M. and De Alencar, S. M. (2016). Chemical characterization and antioxidant, antimicrobial, and anti-inflammatory activities of South Brazilian organic propolis. *PLoS ONE*, 11(11): 1-18.
23. Ahmed, I. A., Mikail, M. A., Bin Ibrahim, M., Bin Hazali, N., Rasad, M. S. B. A., Ghani, R. A., Wahab, R. A., Arief, S. J. and Yahya, M. N. A. (2015). Antioxidant activity and phenolic profile of various morphological parts of underutilised Baccaurea angulata fruit. *Food Chemistry*, 172: 778-787.
24. Meda, A., Lamien, C. E., Romito, M., Millogo, J. and Nacoulma, O. G. (2005). Determination of the total phenolic, flavonoid and proline contents in Burkina Fasan honey, as well as their radical scavenging activity. *Food Chemistry*, 91(3): 571-577.
25. Hatano, A., Nonaka, T., Yoshino, M., Ahn, M. R., Tazawa, S., Araki, Y. and Kumazawa, S. (2012). Antioxidant activity and phenolic constituents of red propolis from Shandong, China. *Food Science and Technology Research*, 18(4): 577-584.
26. Alvarez-Suarez, J. M., Tulipani, S., Díaz, D., Estevez, Y., Romandini, S., Giampieri, F., Damiani, E.,Astolfi, P., Bompadre, S. and Battino, M. (2010). Antioxidant and antimicrobial capacity of several monofloral Cuban honeys and their correlation with color, polyphenol content and other chemical compounds. *Food and Chemical Toxicology*, 48(8–9): 2490-2499.
27. Spigno, G., Tramelli, L. and De Faveri, D. M. (2007). Effects of extraction time, temperature and solvent on concentration and antioxidant activity of grape marc phenolics. *Journal of Food Engineering*, 81(1), 200-208.
28. Baharuddin, N. A. F., Nordin, M. F. M., Morad, N. A., Aris, N. I. A. and Yunus, M. A. C. (2018). Total phenolic, flavonoid content and antioxidant activity of *Clinacanthus nutans* leaves by water-based ultrasonic assisted extraction. *Malaysian Journal of Analytical Sciences*, 22(4): 659-666.

29. Dent, M., Dragović-Uzelac, V., Penić, M., Brñić, M., Bosiljkov, T. and Levaj, B. (2013). The effect of extraction solvents, temperature and time on the composition and mass fraction of polyphenols in dalmatian wild sage (*Salvia officinalis* L.) extracts. *Food Technology and Biotechnology*, 51(1): 84-91.
30. Dranca, F. and Oroian, M. (2017). Total monomeric anthocyanin, total phenolic content and antioxidant activity of extracts from eggplant (*Solanum Melongena* L.) peel using ultrasonic treatments. *Journal of Food Process Engineering*, 40(1): 12312.
31. Miron, T. L., Plaza, M., Bahrim, G., Ibáñez, E. and Herrero, M. (2011). Chemical composition of bioactive pressurized extracts of Romanian aromatic plants. *Journal of Chromatography A*, 1218(30): 4918-4927.
32. Gan, C. Y. and Latiff, A. A. (2011). Optimisation of the solvent extraction of bioactive compounds from *Parkia speciosa* pod using response surface methodology. *Food Chemistry*, 124(3): 1277-1283.

Malaysian Journal of Analytical Sciences (MJAS)
Published by Malaysian Analytical Sciences Society

CHEMICAL COMPOSITION OF KASTURI TOBACCO RESINOID DETERMINED BY GAS CHROMATOGRAPHY-MASS SPECTROMETRY

(Komposisi Sebatian Kimia Resinoid Tembakau Kasturi Menggunakan Kromatografi Gas-Spektrometri Jisim)

Larissa Tania[1,5], Ari Satia Nugraha[2,5], Tri Handoyo[3,5], Banun Kusumawardani[4,5]*

[1]*Graduate School of Biotechnology, Postgraduate Program,*
[2]*Drug Utilisation and Discovery Research Group, Faculty of Pharmacy,*
[3]*Department of Agronomy, Faculty of Agriculture,*
[4]*Department of Biomedical Sciences, Faculty of Dentistry,*
[5]*Center for Development of Advance Science and Technology,*
University of Jember, Jember 68121, East Java, Indonesia

**Corresponding author: banun_k.fkg@unej.ac.id*

Received: 19 July 2021; Accepted: 8 August 2021; Published: 29 August 2021

Abstract

In Indonesia, Kasturi tobacco is widely cultivated in Jember and Bondowoso Districts. This local tobacco planted in dry season and sundried processed which the leaves were used as the raw material of premium cigarettes. The leaves constitute of diverse molecules with various biological or pharmacological activities that have been widely used in medical treatments in form of natural based medicament. This study aimed to determine the chemical composition in the Kasturi tobacco leaves using gas chromatography-mass spectrometry (GC-MS). Kasturi tobacco leaves were air-dried prior extraction using stirred assisted maceration method for 24 hours in methanol. Less polar components was extracted using *n*-hexane and vacuum dried before fractionation under a silica column chromatography. Fractions were analyzed using gas chromatography-mass spectrometry resulted in detection of esters, hydrocarbons, alcohol, nitrogenous compounds and terpenoids including, two unique tobacco resinoids α-CBT (4,8,13-cyclotetradecatriene-1,3-diol) and the labdanoid (11*E*, 13*Z*)-labdadien-8-ol and (12*Z*)-abienol.

Keywords: diterpenoid, fractionation, gas chromatography-mass spectrometry, Kasturi tobacco leaves, resinoid

Abstrak

Di Indonesia, tembakau Kasturi ditanam secara meluas di daerah Jember dan Bondowoso. Tembakau tempatan ini di tanam pada musim kering dan proses pengeringan di mana daun digunakan sebagai bahan mentah dalam pembuatan rokok premium. Bahagian daun yang kaya dengan aktiviti biologi dan farmakologi telah digunakan secara meluas bagi rawatan perubatan dalam bentuk ubatan semulajadi. Kajian ini bertujuan mengkaji komposisi kimia di dalam daun tembakau Kasturi menggunakan kromatografi gas-spektrometri jisim (GC-MS). Daun tembakau Kasturi terlebih dahulu dikeringkan sebelum pengekstrakan kaedah maserasi berbantukan pengacauan selama 24 jam di dalam larutan metanol. Sebatian tak berkutub diekstrak mengunakan n-heksana dan pengeringan vakum sebelum pemisahan dilakukan melalui kromatografi turus silika. Hasil analisis kromatografi gas-spektrometri jisim mengesan kehadiran ester, hidrokarbon, alkohol, sebatian nbernitrogen dan terpenoids termasuklah resinoids unik iaitu α-CBT (4,8,13-siklotetradekatrien-1,3-diol) and the labdanoid (11*E*, 13*Z*)-labdadien-8-ol and (12*Z*)-abienol.

Keywords: diterpenoid, pemisahan, kromatografi gas-spektrometri jisim, daun tembakau Kasturi, resinoid

Introduction

Tobacco (*Nicotiana tabacum* L.) is one of the industrial plants that is widely cultivated throughout the world due to its social and economic value [1]. Medicinal uses have also driven tobacco as one of the largest studied crops globally [2]. Tobacco leaves are the major components in cigarettes and cigars production. Sundried-tobacco leaves have been also a source of aroma products including tobacco concrete, tobacco resinoids and tobacco absolute which is an re-extraction product from tobacco concrete or tobacco resinoids using polar solvents at low temperature [2-4]. Tobacco leaves contain various chemical compounds with diverse biological or pharmacological activities such as alkaloids, isoprenoids, phenolics, and terpenoids [5, 6]. Tobacco leaves or its extract have been part of traditional medicine as sedative, anesthetic, emetic, expectorant, diuretic, antispasmodic, anticonvulsant, anti-rheumatic, anti-inflammatory and wound healing agents [7]. Recent studies found tobacco leaves to have potential as source for an anticancer agent [8].

One of the tobacco varieties cultivated in Indonesia is Kasturi in which this local tobacco was planted in dry season (Voor Oogst) in Jember and Bondowoso Districts. Kasturi tobacco used as a blending component for premium cigarettes [9]. Only selected Kasturi tobacco leaves were largely used as the raw material of cigarettes or cigars resulting low quality leaves as waste which used as source for medicinally important molecules.

Several methods for the analysis of chemical compounds in tobacco leaveswere reported including gas chromatography (GC) [10], gas chromatography-mass spectrometry (GC-MS) [11], and high-performance liquid chromatography (HPLC) [12]. Analysis by gas chromatography-mass spectrometry (GC-MS) has high sensitivity and selectivity so it is widely used in quantitative analysis [13]. This study aimed to determine the volatile chemotype composition in the Kasturi tobacco leaves using gas chromatography-mass spectrometry (GC-MS).

Materials and Methods

Chemicals, materials and instrumentations

Chemical methanol, *n*-hexane, dichloromethane, ethyl acetate and HCl were obtained from Merck (Darmstadt, Germany). Dragendorff reagent and silica gel (70-230 mesh) for the column chromatography (CC) were purchased from Sigma-Aldrich (St. Louis, MO, USA). Gas chromatography was performed in a Shimadzu GCMS-QP2010 Plus gas chromatograph with a mass selective detector (Shimadzu Corporation, Kyoto, Japan) and DB-5ms UI column (0.25 µm film thickness, 30mx0.25mm) (J&W Scientific, Folsom, CA). Instrument and data collection controlled with Shimadzu LabSolutions GC/MS solution software. The commercial mass spectral libraries (NIST 08 and Wiley7) database was employed to search chemical similarity.

Preparation of tobacco resinoid

Kasturi tobacco leaves obtained from Ledokombo Village, Jember District, East Java Province-Indonesia. The tobacco leaves used are tobacco leaves waste at the post-harvest processing stage. Voucher sample was kept in Graduate School of Biotechnology, Postgraduate Program, University of Jember, East Java-Indonesia under accession number KT01J. Kasturi tobacco leaves (1000 g) are air-dried then ground and sieved with 80 mesh to produce tobacco leaves powder (50 g). Tobacco leaves powder was then macerated with methanol (500 mL) and stirred for 24 hours followed by filtration. To the filtrate, *n*-hexane (250 mL) was added and was stirred for 25 minutes. The *n*-hexane was separated and treated with HCl solution (10%, 0.5 mL). After acid layer removal, the hexane fraction was tested against dragendorff reagent for alkaloid clearance indication. HCl treatment was repeated until dragendorff test was negative. Finally, alkaloid free *n*-hexane fraction was evaporated using a rotary vacuum evaporator (1.13 g).

Fractionation of tobacco resinoid

Tobacco resinoid (1 g) was fractionated through a silica column chromatography (2.5x30 cm) containing silica gel using 5 solvents, *n*-hexane 100% (50 mL), dichloromethane 50% (25 mL): *n*-hexane 50% (25 mL), dichloromethane 100% (50 mL), ethyl acetate 50% (25 mL): dichloromethane 50% (25 mL) and ethyl acetate 100% (50 mL). Further, the fractions were analyzed using gas chromatography-mass spectrometry (GC-MS).

GC-MS analysis

The sample solution was prepared by dissolving 10 mg tobacco resinoid in dichloromethane in a 10 mL volumetric flask. Sample (1.0) µL was injected into a GC-MS with a method with initial temperature at 160 °C for 2 minutes, increased at 10 °C min^{-1} to 210 °C and held for 35 minutes. Then increased at 10 °C min^{-1} until it reaches 250 °C and held for 15 minutes. Helium was used as a carrier gas at a flow of 1.2 mL min^{-1} [14]. The data obtained was analyzed using GC-MS software which is equipped with a library of NIST 08 and Wiley7.

Results and Discussion

Tobacco (*Nicotiana tabacum* L.) belongs to the Nicotiana genus which is the most commercial species among the Solanaceae members. Tobacco leaves are used as materials for various tobacco products although they have harmful effects on human health [15]. On the other hand, several secondary metabolites in tobacco were developed for medicinal uses. The utilisation of tobacco plant metabolites attracts researchers to developed innovation through extraction and fractionation of tobacco, to obtain its beneficial constituents [1].

The GC-MS chromatogram indicated various peaks of individual compounds at 60 minutes of running time (Figure 1). Kasturi tobacco resinoids fraction number 2 has highest numbers of individual compound peaks, followed by fraction number 1, fraction number 3, fraction number 4, and fraction number 5 Kasturi tobacco resinoids. The chemical composition of Kasturi tobacco resinoids were grouped according to the class of chemical compounds and presented in percent of the total number of compounds identified in Figure 2 and Table 1. In this study, the predominant class of chemical compounds in Kasturi tobacco resinoid were 22% esters, followed by 17% hydrocarbons, 15% alcohol, 10% nitrogenous compound and 7% terpenoids. The hydrocarbon affect the color of the Kasturi tobacco resinoids, while the presence of esters and diterpene contributes to the Kasturi tobacco resinoids's odor [1].

In the fraction number 1 Kasturi tobacco resinoid using *n*-hexane solvent contained 38% ester compounds, 36% hydrocarbon compounds, 14% alcohol, 8% ether, and 4% phenol. The fraction number 2 of Kasturi tobacco resinoid with *n*-hexane:dichloromethane contained 20% hydrocarbon compounds, 22% esters, 12% terpenoids, 10% alcohol, 4% haloalkanes, 6% phenols, 4% ether, and 22% other compounds. In the fraction number 3 of Kasturi tobacco resinoid with dichloromethane solvent contained 30% ester compounds, 22% alcohol, 16% hydrocarbons, 14% carboxylic acids, 8% ether, 4% haloalkanes, 4% terpenoids, and 2% nitrogenous compounds. In the fraction number 4 of Kasturi tobacco resinoid with dichloromethane:ethyl acetate contained 18% phenol, 16% alcohol, 14% esters, 14% carboxylic acids, 14% nitrogenous compound, 12% hydrocarbons, 6% terpenoids, 2% haloalkanes, and 2% ketone. While in the fraction number 5 of Kasturi tobacco resinoid with ethyl acetate, there were 34% nitrogenous compounds, 16% carboxylic acids, 14% alcohol, 12% phenol, 8% esters, 4% terpenoid, 2% ketone, 2% aldehyde, and 8% other compounds. In the Virginia, Burley and Oriental tobacco resinoid have dominant chemical composition, were the aliphatic hydrocarbons, oxygenated aliphatic compounds, diterpenes and triterpenes. The differences in chemical composition from tobacco were likely impacted by the types and varieties, climatic condition, the location where the plant is grown and the parts of plant extracted [1, 15].

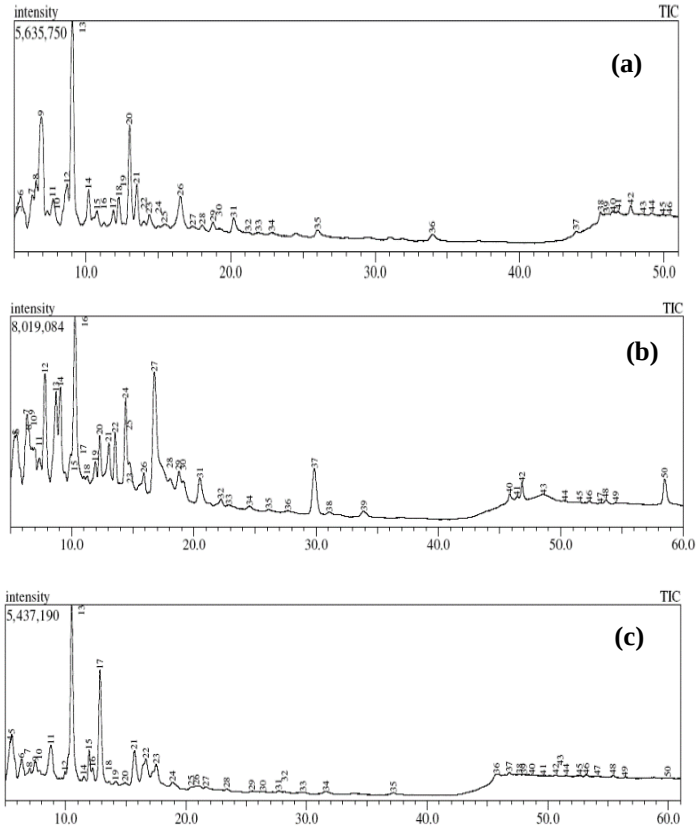
On tobacco leaves, there is a trichome gland that contains important biochemical compounds in large quantities, such as sucrose esters, waxes, microelements, and diterpenoid [16]. Depending on their genetic background, tobacco cultivars produce macrocyclic cembranoids, carbocyclic labdanoids, or both [17, 18]. Bioconversion and biodegradation of these compounds lead to a large number of derivatives

of diterpenoids and norterpenoids that play an important role as a tobacco fragrance [19].

In tobacco was found two main classes of diterpenoids which are the cembranoid and labdanoid, an analysis of terpenoid classes found in the Kasturi tobacco resinoid (Figure 3). The results were found the presence of diterpene compounds with the chemical structure of the cembranoid and labdanoid in fraction number 2 and fraction number 3 of Kasturi tobacco resinoid.

There are many cembranoid in tobacco that has been reported, α- and β- 2,7,11-cembratriene-4,6-diol (CBT) are the most widely distributed, and showed potential as anticancer agent [8]. α-CBT structure namely, 4,8,13-cyclotetradecatriene-1,3-diol was found in fraction 2 of Kasturi tobacco resinoid. Biodegradation during the preservation of tobacco leaves leads to the formation of various flavor compounds with the C8-C19 chemical framework. Labdanoid diterpenes namely, (11*E*, 13*Z*)-labdadien-8-ol and (12*Z*)-abienol were found in the fractions 2 and 3 of Kasturi tobacco resinoid. *Z*-abienol is the main labdanoid found in oriental tobacco. Labdanoid concentrations decrease significantly during the drying process with air or sunlight [20].

The biochemical profile of diterpenoid differs between types of tobacco has been reported. Oriental tobacco usually contains both types of diterpenoids, while Burley tobacco only contains cembranoids. Diterpenoid is an essential precursor of substance aroma of tobacco and affects insect resistance, thus, identify factors involved in the synthesis of diterpenoid and glandular trichomes secretion can help to increase the aroma of tobacco and resistance to biotic stress [21].



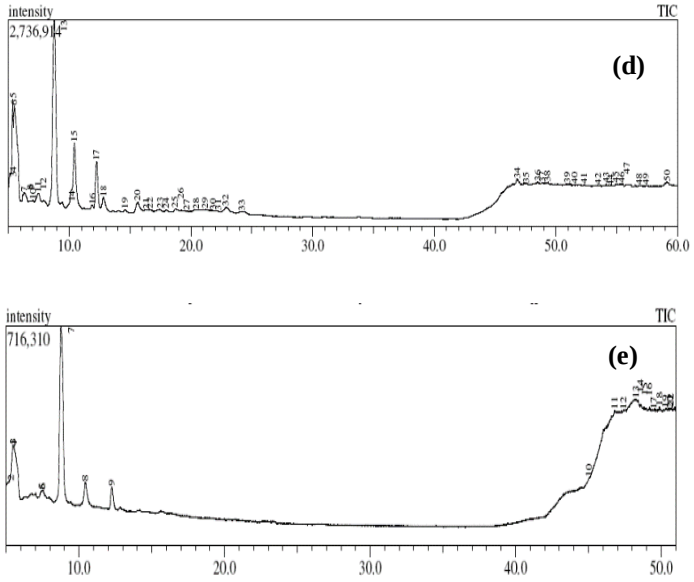


Figure 1. Chromatogram of Kasturi tobacco resinoid (a) fraction 1, (b) fraction 2, (c) fraction 3, (d) fraction 4, (e) fraction 5

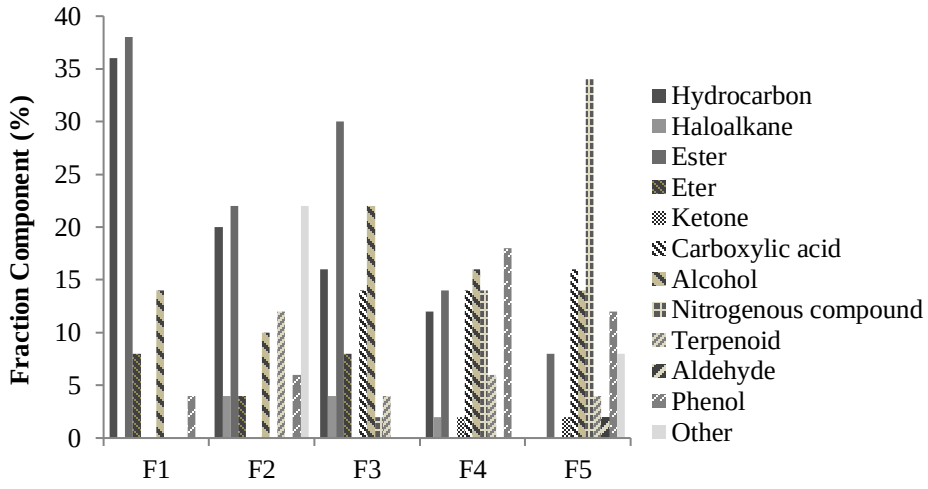


Figure 2. Chemical composition of Kasturi Tobacco Resinoid

Table 1. Kasturi tobacco resinoid composition by classes of chemical compounds

Chemical Compounds	% Fraction Component				
	F1	F2	F3	F4	F5
Hydrocarbon	36	20	16	12	0
Haloalkane	0	4	4	2	0
Ester	38	22	30	14	8
Eter	8	4	8	0	0
Ketone	0	0	0	2	2
Carboxylic acid	0	0	14	14	16
Alcohol	14	10	22	16	14
Nitrogenous compound	0	0	2	14	34
Terpenoid	0	12	4	6	4
Aldehyde	0	0	0	0	2
Phenol	4	6	0	18	12
Other	0	22	0	0	8

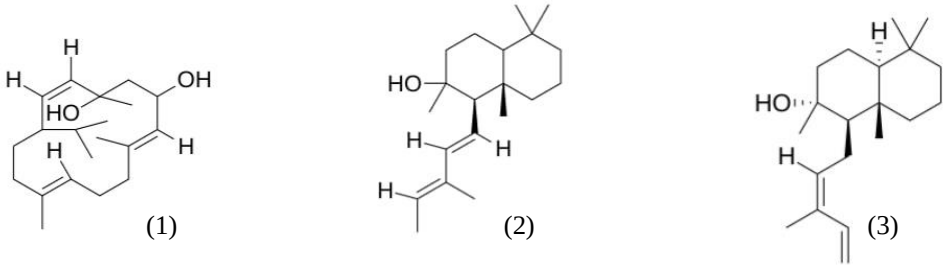


Figure 3. Chemical structure of (1) 4,8,13-cyclotetradecatriene-1,3-diol, (2) (11*E*,13*Z*)-labdadien-8-ol, (3) (12*Z*)-abienol

Conclusion

In the Kasturi tobacco resinoid contained ester compounds, followed by hydrocarbons, alcohol, nitrogenous compounds, terpenoids, and other chemical compounds. The hydrocarbon compound is affect the color of the product, while the presence of esters and diterpenes contribute to the Kasturi tobacco resinoids's odor. The presence of two main classes of diterpenoid found in tobacco, which are the cembranoid and labdanoid, in Kasturi tobacco resinoid there are known compounds with the structure of α-CBT (4,8,13-cyclotetradecatriene-1,3-diol and a labdanoid compound, (11*E*, 13*Z*)-labdadien-8-ol and (12*Z*)-abienol. The existence of two diterpene compounds in tobacco can be influenced by the type of tobacco. Not in all types of tobacco can find both of these diterpenoid compounds, sometimes it only contains one of them. In Oriental tobacco usually contains both of diterpenoid compound, while Burley tobacco only contains cembranoid. This study could provide an early information for the use of Kasturi tobacco leaves as source for bioactive compounds. This benefited the industry which produced biomass waste from under quality leaves and non-industrial usage part of tobacco crops.

Acknowledgement

This research has been supported by Research Institute of University of Jember, Indonesia (Grant No. 3240/UN25.3.1/LT/2019)

References

1. Popova, V., Tumbarski, Y., Ivanova, T., Hadjikinova, R. and Stoyanova, A. (2019). Tobacco resinoid (*Nicotiana tabacum* L.) as an active ingredient of cosmetic gels. *Journal of Applied Pharmaceutical Science*. 9(09): 111-118.
2. Antonova, D., Ivanova, D., Antonov, L. and Abe, I. (2016). Insight into the aroma profile of bulgarian tobacco absolute oil. *Industrial Crops and Products*, 94: 226-232.
3. Baser, K. H. C., and Buchbauer, G. (2010). Handbook of essential oils: Science, technology, and applications. CRC Press, Boca Raton: pp. 42-85.
4. Bauer, K., Garbe, D. and Surburg, H. (2001). Common fragrance and flavor materials. Preparation, properties and uses, 4th edition. Wiley-VCH, Weinheim, New York: pp. 177-238.
5. Banožić, M., Banjari, I., Jakovljević, M., Šubarić, D., Tomas, S., Babić, J. and Jokić, S. (2019). Optimization of ultrasound-assisted extraction of some bioactive compounds from tobacco waste. *Molecules*, 24(8): 1-14.
6. Rodgman, A. and Perfetti, T. (2013). The chemical components of tobacco and tobacco smoke, 2nd edition. CRC Press, Boca Raton: pp. 28.
7. Kishore, K. (2014). Monograph of tobacco (*Nicotiana tabaccum*). *Indian Journal of Drugs*, 2(1): 5-23.
8. El Sayed, K. A. and Sylvester, P. W. (2007). Biocatalytic and semisynthetic studies of the anticancer tobacco cembranoids. *Expert Opinion on Investigational Drugs*, 16: 877-887.
9. Balai Penelitian Tanaman Pemanis dan Serat. http://balittas.litbang.pertanian.go.id/index.php/id/tentang-kami/komoditas/pemanis/60-info-teknologi/104-kasturi [Access online 15 May 2020].
10. Saunders, J. A. and Blume, D. E. (1981). Quantitation of Major Tobacco Alkaloids by High Performance Liquid Chromatography. *Journal of Chromatography A*, 205: 147-154.
11. Severson, R. F., Ellington, J. J. and Schlotzhauer, P. F. (1977). Gas chromatographic method for the determination of free and total solanesol in tobacco. *Journal of Chromatography A*, 139: 269-282.
12. Qian, X. B., Ye, J. P., Chen, X. M., Zhang, C. H., Liang, Y.J., Li, Z. H. and Yang, J. (2014). Analysis of cembranoids in flue-cured tobacco by accelerated solvent extraction and gas chromatography-mass spectrometry-selected ion monitoring. *Journal of the Chinese Chemical Society*, 61: 1133-1140.
13. Pizzuti, I. R., de Kok, A., Cardoso, C. D., Reichert, B., de Kroon, M., Wind, W., Righi, L. W. and da Silva, R. C. (2012). A multi-residue method for pesticides analysis in green coffee beans using gas chromatography–negative chemical ionization mass spectrometry in selective ion monitoring mode. *Journal of Chromatography A*, 1251: 16-26.
14. Zhou, Y., Yang, Y., Li, X. L., Chen, Z. Y., Liu, Q. B., Zhu, X. L. and Yang, J. (2016). Determination of cembrenediols in tobacco by gas chromatography–mass spectrometry-selected ion monitoring with precolumn derivatization. *Acta Chromatographica*, 28(4): 513-524.
15. Popova, V., Ivanova, T., Stoyanova, A., Georgiev, V., Hristeva, T., Nikolova, V., Docheva, M.., Nikolov, N. and Damianova, S. (2018). Phytochemicals in leaves and extracts of the variety "plovdiv 7" of bulgarian oriental tobacco (*Nicotiana tabacum* L.). *Trends in Phytochemical Research*, 2: 27-36.
16. Johnson, A.W., Severson, R. F. and Hudson, J. (1985). Tobacco leaf trichomes and their exudates. *Tobacco Science*, 29: 67-72.
17. Colledge, A., Reid, W. W. and Russel, R. (1975). The diterpenoids of nicotiana species and their potential technological significance. *Chemistry & Industry*, 5(13): 570-571.
18. Reid, W.W. (1974). The phytochemistry of the genus nicotiana. *Ann. Tabac*, SEITA 2: 145-178.
19. Enzell, C. R. and Wahlberg, I. (1990). Tobacco isoprenoids - precursors of important aroma constituents. *Pure and Applied Chemistry*, 62(7): 1353-1356.

20. Leffingwell, J.C. (1999). Tobacco: Production, chemistry, and technology. Blackwell Science, London: pp. 265-284.

21. Huang, M., Zhang, H., Wang, Z., Niu, D., Li, Y. and Cui, H. (2018). Comparative studies of leaf surface chemical biosynthesis in different tobacco cultivars. *Acta Physiologiae Plantarum*, 40: 67.

Malaysian Journal of Analytical Sciences (MJAS)
Published by Malaysian Analytical Sciences Society

SYNTHESIS AND CHARACTERIZATION OF ACETOL FROM PALM-BASED GLYCEROL

(Sintesis dan Pencirian Asetol daripada Gliserol Berasaskan Sawit)

Roila Awang[1]* and Mohamad Hanif Mohamed[2]

[1]Engineering and Processing Division,
Malaysian Palm Oil Board No.6, Persiaran Institusi, Bandar Baru Bangi, 43000 Kajang, Selangor, Malaysia
[2]Department of Chemistry, Faculty of Science,
Universiti Putra Malaysia, 43400 Serdang, Selangor, Malaysia

**Corresponding author: roila@mpob.gov.my*

Received: 10 July 2021; Accepted: 20 August 2021; Published: 29 August 2021

Abstract

Glycerol conversion to value-added product, acetol was studied through the dehydration reaction of glycerol catalyzed by copper chromite in a single step reactive distillation. The physical properties of the synthesized acetol such as its appearance, density and viscosity were compared with those of a commercial product. The effects of reaction temperature (190 ºC and 200 ºC), reaction period (1.5-7 hours), catalyst loading (0.63-7.0%) and water content (2-20% w/w) in the glycerol feedstock were studied to optimize its production. The results show conversion of glycerol increased with the increase of reaction period and catalyst loading while the presence of water in the glycerol feedstock decreased the conversion and also reduced the residue which provided ease of removal and recycles the catalyst. Optimum conditions for the conversion of glycerol to acetol was at a reaction period of 3.5 hours with 2.5% catalyst concentration and 200 ºC reaction temperature without dilution where 64.47% of the product was obtained. Fourier transform infrared (FTIR), gas chromatography (GC) and nuclear magnetic resonance (NMR) were used to characterize and validate the product from the dehydration reaction of glycerol. FTIR spectrum of the product showed stretching of the carbonyl group which suggested that acetol had been successfully synthesized. All of the analyses (GC and NMR) validate that acetol was successfully synthesized.

Keywords: acetol, dehydration, glycerol, palm-based, synthesis

Abstrak

Penukaran gliserol kepada produk bernilai tinggi, asetol telah dikaji melalui tindak balas nyah-hidrat gliserol dimangkin oleh kuprum kromit dalam penyulingan reaktif satu langkah. Ciri-ciri fizikal asetol yang dihasilkan seperti penampilan, ketumpatan dan kelikatan telah dibandingkan dengan produk komersil. Kesan suhu tindak balas (190 ºC and 200 ºC), tempoh tindak balas (1.5-7jam), kuantiti mangkin (0.63-7.0%) dan kandungan air (2-20% w/w) dalam stok suapan gliserol dikaji untuk mengoptimumkan penghasilannya. Hasil kajian menunjukkan penukaran gliserol meningkat dengan peningkatan tempoh tindak balas dan kuantiti mangkin manakala kehadiran air dalam stok suapan gliserol merendahkan penukaran dan juga mengurangkan sisa dimana memudahkan pengasingan dan kitar semula mangkin. Keadaan optimum untuk penukaran gliserol kepada asetol adalah pada tempoh tindak balas sebanyak 3.5 jam dengan kuantiti mangkin 2.5% dan 200 ºC suhu tindak balas tanpa pencairan stok suapan dimana ia memperolehi 64.4% produk. Inframerah transformasi Fourier (FTIR), kromatografi gas (GC) dan resonans magnetik

nuklear (NMR) telah digunakan untuk mencirikan dan mengesahkan produk daripada tindak balas nyah-hidrat gliserol. Spektrum IR produk menunjukkan regangan kumpulan karbonil menunjukkan asetol telah berjaya dihasilkan. Semua analisis (GC dan NMR) mengesahkan bahawa asetol berjaya disintesis.

Kata kunci: acetol, dehidrasi, gliserol, berasaskan sawit, sintesis

Introduction

Glycerol is a clear, odorless and viscous liquid that is the main component of triglycerides. It is derived from soap or biodiesel processing and can be found in animal fats, vegetables oils or petrochemical feedstock. Despite its many uses as an ingredient or processing aid in cosmetics, toiletries, personal care and food products, glycerol is usually used in a highly refined and purified form [1]. The accumulation of the biodiesel by-product/unrefined glycerol has caused an oversupply and consequently a fall in glycerol price. This scenario has created new markets for polymers, ethers and other fine chemicals. Because of its multifunctional structure and properties, glycerol can be converted into a variety of products through various reaction pathways such as dehydration, oxidation, etherification and esterification reaction. Glycerol can be used to make a wide range of chemicals, including ethylene glycol, acetol, dihydroxyacetone, propylene glycol and many others [2].

Acetol is a ketone compound that acts as an organic synthesis intermediate. It is widely used in food, textile and in cosmetics industry as its unique structure allows the promotion of a variety of reactions including dehydration, hydrogenation, oxidation and polymerization [3]. A review on the application and production of acetol has been published [4]. Acetol could be obtained through multiple ways [5] but due to some reasons stated, the best method in producing acetol is by using glycerol as a feedstock. In the absence of hydrogen, glycerol can be dehydrated to acetol *via* a reactive distillation technique. In this study, acetol was isolated from the dehydration of palm-based glycerol as an intermediate for propylene glycol synthesis and the effect of various reaction parameters were also investigated.

Materials and Methods

Materials

Glycerol (98%) was purchased from an oleochemical company in Malaysia. Crude glycerol was obtained from a palm biodiesel plant. Acetol (technical grade, 90%) and copper chromite (catalyst grade, 100%) were purchased from Sigma-Aldrich. Analytical grade methanol was obtained from JT Baker. All other reagents were of analytical grade and were used as received.

Dehydration of glycerol to acetol

The general procedure was according to Dasari [6]. The experiments were carried out in a 150 mL fully agitated glass reactor. A desired amount of glycerol and catalyst were added into the glass reactor. The reaction flask was then attached to the condenser and vacuum pump to obtain a reduce pressure. The reaction mixture was stirred throughout the experiments at 200 rpm using magnetic stirrer. The glass reactor was immersed in a constant temperature oil bath, the temperature of which was maintained within ± 5 °C of the desired temperature. The catalyst was first heated at 100 °C overnight before being charged into the reactor. The percentage conversion of glycerol is defined as the ratio of moles of glycerol consumed in the reaction to the initial moles of glycerol before the reaction. All experiments were repeated twice.

Effect of reaction period on dehydration reaction

The mixture of 50 g glycerol and 1.25 g of copper chromite catalyst was placed in a three-necked round bottom flask. The reaction mixture was heated at the minimum reaction temperature of 190 ^{o}C and 200 ^{o}C. The reaction was then stirred throughout the chosen reaction periods- 1.5, 2.5, 3.5, 4.0, 5.0 and 7.0 hours. The percentage of conversion was defined as number of mole glycerol reacted as compared to number of mole initial glycerol used.

Effect of catalyst concentration on dehydration reaction

The optimum reaction period was then selected to undergo catalyst concentration study. The reaction mixture of 50 g glycerol and a chosen amount of copper chromite catalyst (0.63, 1.25, 2.5, 5.0 and 7.0 % (w/w)) was placed in a three-necked round bottom flask. The reaction mixture was heated at selected reaction temperature (190 ºC and 200 ºC) and stirred for 3.5 hours. The percentage conversion was determined as described earlier.

Effect of glycerol concentration as a feedstock on dehydration reaction

The reaction was carried out using a chosen dilution of 2%, 5%, 7%, 10%, 15% and 20% water concentration of glycerol as feedstock with 1.25 g copper chromite at different reaction temperature (190 ºC and 200 ºC) for 3.5 hours. The percentage conversion was determined as described earlier.

Analytical method

The products obtained were tested for different physical and chemical properties. Hydroxyl value was determined according to AOCS method [7]. Sample was weighed into a 250 mL Erlenmeyer flask, followed by the addition of 25 mL of acetic anhydride-pyridine reagent (1:3 v/v). Then, the flask was placed in a water bath maintained at 98 ºC for 1 hour. After that, the flask was removed from the water bath and cooled to room temperature before titration. Titration was conducted using a 0.5 N standardize NaOH solution and phenol-phthalein as indicator. Density was determined using digital Densitometer, DE 40 (Metler Toledo) according to ASTM D 4052. Fourier transform infrared (FTIR) spectra were recorded on a Perkin Elmer *Spectrum One* model spectrophotometer. Carbon NMR (^{13}C-NMR) and proton NMR (^{1}H-NMR) were recorded on a JOEL ECA-400 spectrometer at 400 MHz. The chemical shifts are expressed in ppm with tetramethylsilane as internal standard.

GC analysis was carried out using a Shimadzu GC-17A, fitted with a non-polar BPX-5 (30m×0.25mm×0.25µm film thickness) capillary column. The samples had undergone silylation process before being injected into the GC. The initial oven temperature was set at 60 °C, followed by ramping at 60-300 °C and held at this temperature for 5 min. The injector and detector were set at 300 °C. Helium was used as the carrier gas.

Results and Discussion

The development of products from the dehydration of glycerol catalyzed by copper-chromite was monitored by thin layer chromatography (TLC) in a solvent system containing chloroform and methanol of 7:3 ratio. The spot representing the raw material appeared at a retention factor (R_f) value of 0.46, while an additional spot which appeared at a R_f value of 0.80 represented the product (Figure 1). The formation of acetol was then confirmed using FTIR spectroscopy, GC and NMR analyses (Figures 2-4).

In the FTIR spectrum of the product (Figure 2), the prominent carbonyl peak centered at 1720 cm^{-1} wave number. The transmittance peak of the hydroxyl group (OH) can still be observed at 3200-3400 cm^{-1} but the peak is broader than the starting material due to the presence of water as a by-product. Meanwhile, the-OH bending bands were observed at 1653 and 1040 cm^{-1}, suggesting that the compound still possessed its primary OH group.

Formation of acetol was confirmed by GC analysis. The identification of the product mixture was based on the comparison of retention time (RT) of the peaks with commercially available acetol. As shown in Figure 3, the chromatogram of the product mixture after conversion to trimethylsilyl (TMS) derivatives revealed the presence of other compounds along with acetol.

The NMR spectra for the commercially available acetol and the product mixture were very similar. The spectrum showed a single peak at 2.18 ppm for -CH_3. This is due to CH_3CO- which rotates freely around the bond between CH_3CO- and -CH_2OH, while the signal at 4.27 ppm represents hydrogen from the hydroxyl group. As for ^{13}C-NMR, the existence of the C=O for ketone compound was observed at 207.6 ppm. The signal resonating at 65.67 ppm showed the presence of the

hydroxyl group. -CH_3 for the product appeared at 21.66 ppm (Figures 4a-b).

Properties of the starting material, crude product and purified product are shown in Table 1. The reaction progress can be described by means of the changes in substrate concentration. In this study, the change in glycerol concentration was monitored. In order to optimize the reaction, the effect of the following variables was investigated (i) reaction time (ii) catalyst concentration and (iii) initial water content.

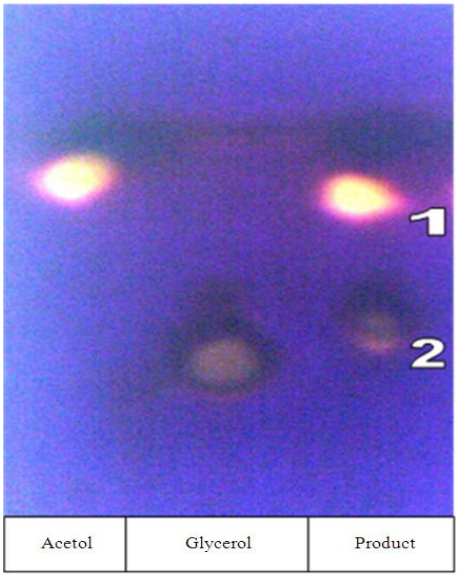


Figure 1. Thin layer chromatography of commercial sample, glycerol and reaction product (1) acetol; (2) glycerol

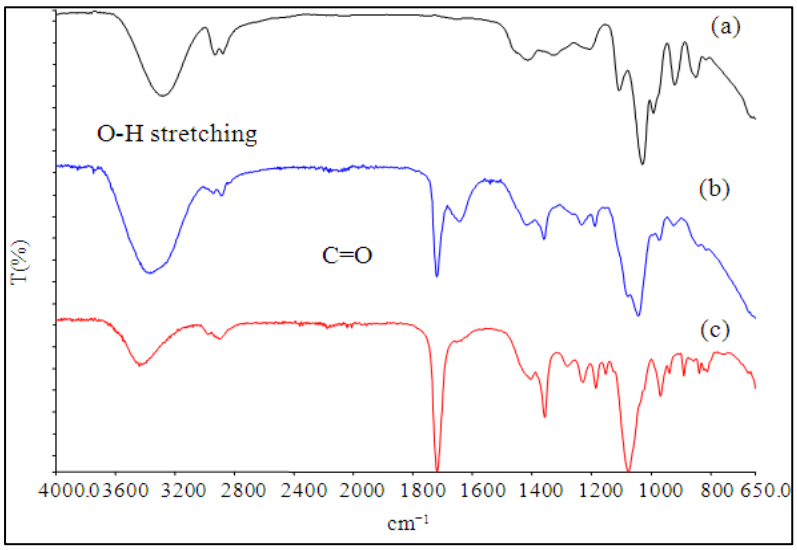


Figure 2. Overlay FTIR spectrum of (a) glycerol; (b) crude product and (c) purified product

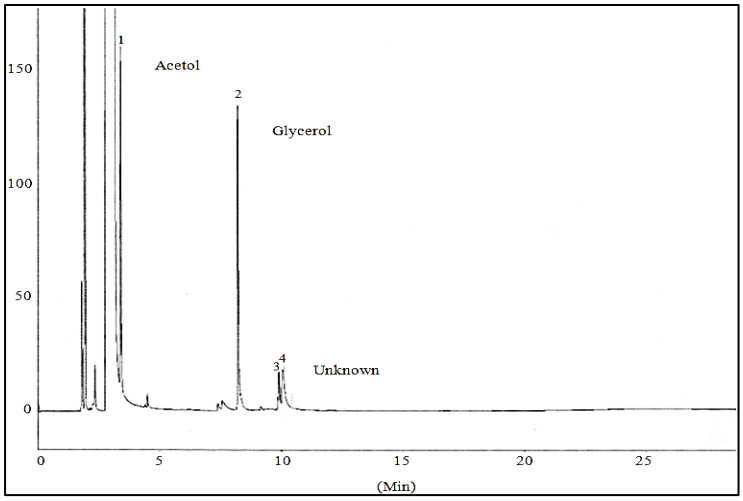


Figure 3. GC chromatogram of the reaction product

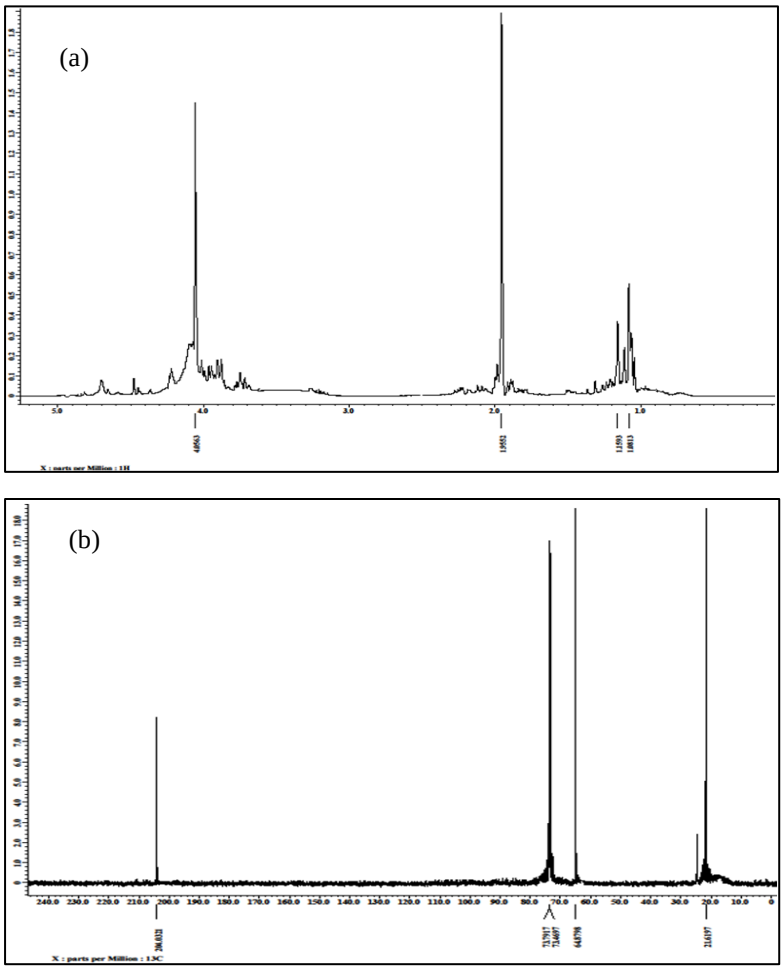


Figure 4. ^{1}H-NMR (a) and ^{13}C-NMR; (b) spectra of the reaction product

Table 1. Properties of glycerol, crude product, purified product and commercial sample

	Glycerol	Crude	Purified	Standard
Colour	Colorless	Light yellow	Yellowish	Colourless-yellowish
Hydroxyl value (mg KOH/g)	1827.6	980-1400	790-843	757.2
Density (g/cm^3)	1.26	1.04	1.08	1.08
Viscosity (mm^2/s)	186.87	2.35	2.58	2.50

Effect of reaction time and temperature

Time course is an excellent predictor of catalyst performance and reaction progress. It can pin point the shortest or sufficient time required to achieve good yields and reduce process costs. Figure 5 showed the conversion of glycerol to acetol increases as the reaction time increased for both temperatures. The dehydration process proceeded rapidly within 3 hours, after which, not much difference in the percentage conversion was observed. This observation might be due to catalyst deactivation. The percentage conversion of the reaction carried out at 200 °C was always higher than the reaction at 190 °C. The behavior and stability of the catalyst, as well as the rate of reaction, are affected by changes in reaction temperature. Chiu and his colleagues [8] stated that the batch mode reactive distillation at higher temperature of 240 ^oC achieved up to 86.6% with 5% copper chromite as catalyst but no total reaction time was mentioned. The highest conversion obtained in this study is 77% with 6 hours reaction period. Based on this data, it is suggested that the reaction at 200 ^oC with half of the catalyst concentration, (2.5%, w/w), is better in term of economic value due to lower catalyst concentration and temperature used as the difference of the conversion is only 10%. In addition, reaction at 200 ^oC prevents the formation of propylene glycol and acrolein compared to that of at 240 ^oC reaction temperature.

Effect of catalyst concentration

The influence of varying the amount of catalyst on the dehydration process was investigated by carrying out the reaction in various amounts of catalyst ranging from 0.63-7.5% by weight of reactant. In most reactions, catalyst content influences the total reaction time required to reach the desired conversion. In this study, increasing the catalyst content from 0.63-2.5% (3.97-fold) increases the percentage conversion of glycerol by 2.52-fold for the reaction carried out at 190 °C and 3.35-fold for the reaction carried out at 200 °C. Further increase to 7.5% (3-fold) of the amount of catalyst only gave an increase in percentage conversion to 1.33-fold for the reaction at 190 °C and 1.23-fold at a temperature of 200 °C (Figure 6). When a higher level of catalyst was used, the rate of reaction increased and up to a point where the percentage conversion was unchanged. In this case substrate limitation or/and catalyst deactivation might be a reason.

Effect of initial water content

In this study, water was added to the glycerol at concentrations of 2, 5, 10, 15 and 20% by weight. The reactions were carried out at 200 °C for 3.5 hours in the presence of 2.5% w/w catalyst. Under test conditions, Figure 7 depicts the influence of initial water content on total glycerol conversion. The glycerol conversion decreases as the amount of initial water in the reaction mixture increases. The accumulation of the water-insoluble residue showed an inverse relationship with increasing initial water content. This was in agreement with the results reported by Chiu et al. [8]. The initial water content prevents residue formation by removing acetol and water vapors from the reaction mixture until it can degrade or polymerize into residue [9].

Reusability of catalyst

Catalyst reuse provides a number of cost advantages, which are often essential prerequisites for establishing

an economically viable process. In this study, the catalyst recovery was done according to literatures [6, 9]. After each cycle, the catalyst was washed with methanol until the wash was clear, and then dried overnight in an oven at 100 ˚C for catalyst activation as well as methanol removal. Figure 8 demonstrated that the catalyst can be reused up to five cycles. The conversion of glycerol was maintained above 58% after repeated runs. However, after 5 cycles of use, the residue began to foam on the catalyst. Once the reaction mixture started foaming, the catalyst could not be recovered anymore.

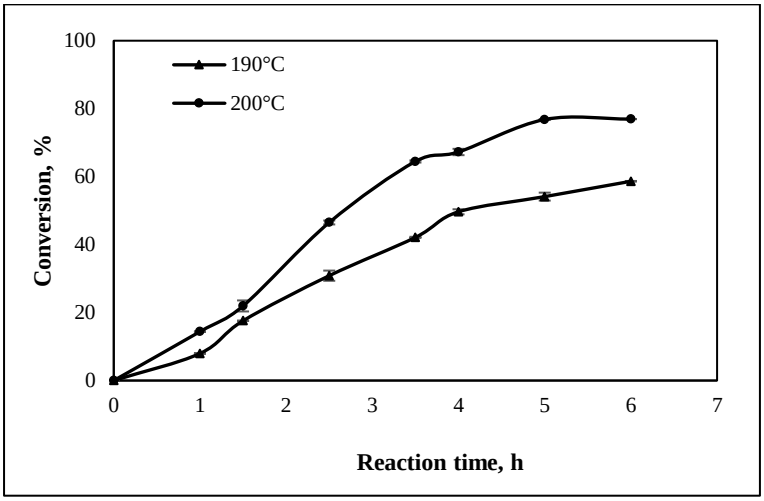


Figure 5. Effect of reaction time on % conversion

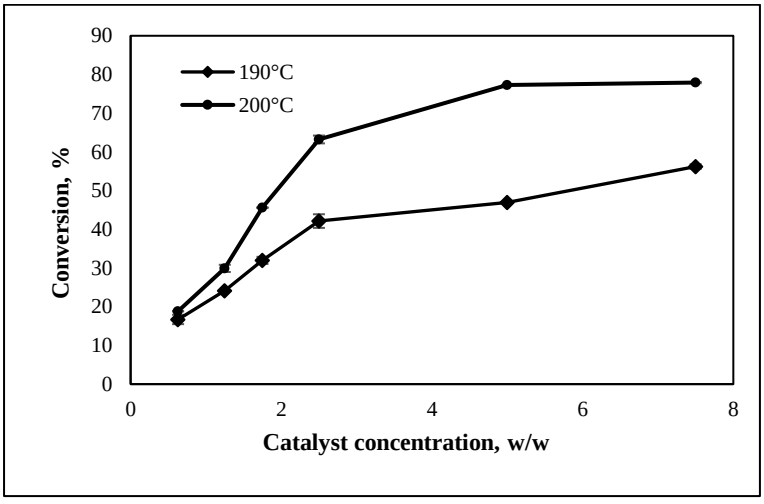


Figure 6. Effect of catalyst concentration on % conversion

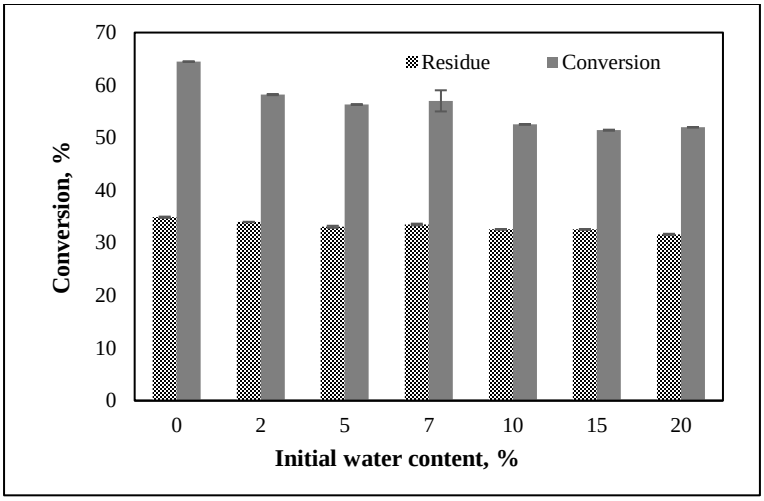


Figure 7. Effect of initial water content on % conversion

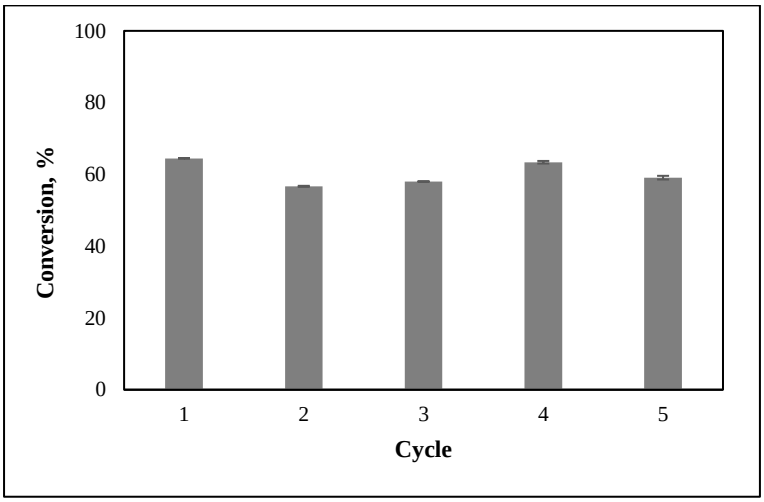


Figure 8. Reusability of catalyst

Conclusion

Acetol was successfully synthesized through dehydration of glycerol catalyzed by copper catalyst under reduced pressure. The acetol from this reaction can be hydrogenated to form propylene glycol. Further study on the synthesis of acetol should be carried out using other type of glycerol available in market particularly crude glycerol which is biodiesel by-product.

Acknowledgement

The researchers would like to thank Director General of MPOB for his permission to publish this paper.

References

1. Choi, W. J. (2008). Glycerol-based biorefinery for fuels and chemicals. *Recent Patents Biotech*. 2: 173-180.

2. Pathak, K., Reddy, K. M., Bakhshi, N. N. and Dalai, A. K. (2010). Catalytic conversion of glycerol to value added liquid products. *Applied Catalysis A: General*, 372: 224-238.
3. Dasari, M. A., Kiatsimkul, P., Sutterlin, W. R and Suppes, G. J. (2005). Low-pressure hydrogenolysis of glycerol to propylene glycol. *Applied Catalyst A: General*, 281: 225-231.
4. Mohamad, M. H., Awang, R. and Yunus, W. M. Z. W. (2011). A review of acetol: Application and production. *American Journal of Applied Sciences*, 8: 1135-1139.
5. Kinage, A. K., Upare, P. P., Kasinathan, P., Hwang, Y. K. and Chang, J. S. (2010). Selective conversion of glycerol to acetol over sodium-doped metal oxide catalysts. *Catalysis Communications*, 11: 620-623.
6. Dasari, M. A. (2006). Catalytic conversion of glycerol and sugar alcohol to value-added products. PhD Thesis, University of Missouri-Columbia.
7. American Oil Chemical Society (1993). Official methods and recommended practices. 4th Edition. AOCS Press, Champaign.
8. Chiu, C. W., Dasari, M. A., Suppes, G. J. and Sutterlin, W. R. (2006). Dehydration of glycerol to acetol via catalytic reactive distillation. *American Institute Chemical Engineers Journal*, 52: 3543-3548.
9. Chiu, C. W., Tekeei, A., Sutterlin, W. R., Roncho, J. M. and Suppes, G. J. (2008). Low-pressure packed-bed gas phase conversion of glycerol to acetol. *American Institute Chemical Engineers Journal*, 54: 2456-2463.

Malaysian Journal of Analytical Sciences (MJAS)
Published by Malaysian Analytical Sciences Society

PHYTOCHEMICAL INSIGHTS ON PALM OILS AND EXTRA VIRGIN OLIVE OIL

(Tinjauan Fitokimia Minyak Sawit dan Pati Minyak Zaitun)

Noor Idayu Tahir[1]*, Nurul Liyana Rozali[1], Nadirah Zakaria[2], Abrizah Othman[1], Umi Salamah Ramli[1]

[1]Advanced Biotechnology and Breeding Centre (ABBC),
Malaysian Palm Oil Board, Bandar Baru Bangi, 43000 Kajang, Selangor, Malaysia
[2]Faculty of Applied Sciences,
Universiti Teknologi MARA Kampus Arau, 02600 Perlis, Malaysia

**Corresponding author: idayu@mpob.gov.my*

Received: 20 July 2021; Accepted: 20 August 2021; Published: 29 August 2021

Abstract

Plants are a major source of oils for food and oleochemicals. Oftentimes, plant oils are highly processed prior to consumer access to achieve certain criteria of appearance and adaptability at the expense of valuable natural components or phytochemicals. Palm oil is refined and fractionated into various end products and is one of the most globally consumed plant oils due to its versatility. In comparison, extra virgin olive oil (EVOO) is prized for its phytonutrients. Refined palm cooking oils, laboratory cold-pressed palm oil (CPPO) and EVOO were subjected to phytochemical analysis to detect the presence of phenolics and flavonoids and to assess their antioxidant activities. The extracts from oils with minimum treatment such as CPPO and EVOO showed higher phytochemicals presence of total flavonoid and phenolic contents, consistent with their chemical profiles observed in the liquid- and gas chromatography-mass spectrometry (LC-MS and GC-MS) analyses. The finding calls for more exploration on the palm oil phytochemical constituents and ultimately the enhancement of refining processes to seek balance between the industrial feasibility and the availability of valuable phytochemicals with potential health benefit.

Keywords: phytochemicals, palm oil, extra virgin olive oil, liquid and gas chromatography, mass spectrometry

Abstrak

Tumbuhan adalah sumber utama minyak untuk makanan dan bahan oleokimia. Sering kali, ianya menjalani pelbagai pemprosesan sebelum menemui pengguna untuk mencapai kriteria dan penampilan produk hiliran. Faktor ini menyebabkan hilangnya komponen semula jadi atau bahan fitokimia yang berharga daripada minyak tumbuhan tersebut. Minyak sawit ditapis dan mengalami pemeringkatan sebelum menjadi pelbagai produk akhir dan merupakan salah satu minyak tumbuhan yang paling banyak digunakan di dunia kerana ciri serba gunanya. Sebagai perbandingan, pati minyak zaitun (EVOO) mempunyai permintaan tinggi kerana kandungan fitonutriennya. Minyak masak sawit diproses, minyak dari perahan sejuk dari mesokarpa sawit (CPPO) dan EVOO dianalisis secara fitokimia untuk mengesan kehadiran fenolik dan flavonoid dan menilai aktiviti antioksidan mereka. Ekstrak dari minyak dengan proses yang minimum seperti CPPO dan EVOO menunjukkan kehadiran fitokimia flavonoid dan fenolik yang lebih tinggi, selaras dengan profil kimia mereka melalui analisis kromatografi cecair dan gas yang digabungkan dengan spektrometri jisim (LC-MS dan GC-MS). Penemuan ini menggalakkan lebih banyak penerokaan terhadap bahan fitokimia sawit dan seterusnya penambahbaikkan berterusan terhadap pemprosesan minyak sawit untuk

mendapatkan keseimbangan di antara kehendak industri dan keperluan bahan fitokimia yang bermanfaat untuk kesihatan pengguna.

Kata kunci: bahan fitokimia, minyak sawit, pati minyak zaitun, kromatografi cecair dan gas, spektrometer jisim

Introduction

The natural chemical components of plants are responsible for their notable colour and organoleptic properties. These metabolites are of biological importance to plants; providing defence against pathogens, herbivores and solar radiation, and function as signalling molecules and regulators in addition to their role as structural components. Flavonoids (phytochemicals with 2-phenyl-1,4-benzopyrone backbone) and phenolics (natural chemicals with aromatic ring(s) with attached hydroxyl groups) are among the known plant chemicals that are bioactive against free radicals, cancerous cells, bacteria and viruses and possess therapeutic functions of anti-inflammatory, antimutagenic, antitumor and many other beneficial effects on human health [1, 2]. They are also the source of valuable commercial products of drugs, dyes, fragrances and flavours.

Plants oils and fats are consumed globally and are essential food supplies for the world's rising population. Among all the vegetable oils, palm oil ranks as the most widely produced and traded crop product [3]. It is extracted from the mesocarp flesh of the oil palm drupes and in its natural presence, contains phytochemicals such as pigments, flavonoids and other lipophilic compounds of tocols, carotenoids, phytosterols and squalene [4]. The oil palm fruit bunch undergoes mechanical processes of sterilization, fruit loosening, oil extraction and clarification to produce crude palm oil (CPO). It is further treated physically and chemically into refined, bleached and deodorized palm oil (RBDPO) or neutralized, bleached, and deodorized palm oil (NBDPO) before fractionation to obtain solid (stearin) and liquid (olein) phases for end use or downstream applications [5]. As a result, some natural components were removed in the pursuit of the versatility of colourless and odourless refined cooking oil. Olive oil is another important vegetable oil especially in the European market and is available in the market in several grades. The extra virgin olive oil (EVOO) is obtained from the first pressing and is untreated chemically during the oil extraction, allowing it to retain its phenolic compounds such as tyrosol, hydroxytyrosol, oleuropein and natural vitamins [6].

A holistic evaluation on palm oil natural chemical profile is warranted as previous investigations mainly focused on the palm oil industry waste valorization by harnessing phytochemicals from oil palm biomass and processing wastewater [7, 8, 9]. Thus, this work was undertaken to investigate and compare the phytochemical profiles of refined and unrefined palm oils using the EVOO as a benchmark, based on the phytochemical screening and liquid and gas chromatography-mass spectrometry (LC- and GC-MS) analyses. The information could promote substantial improvement in the palm oil processing efficiency and in due course encourage the palm oil industry to retain the natural phytonutrients in the palm oil and increase their value and significance for human consumption.

Materials and Methods

Chemicals

Solvents and acetic acid of high performance liquid chromatography (HPLC) grade, SeccoSolv dried pyridine (max. 0.0075% H2O), perfluorotributylamine (PFTBA), methoxyamine hydrochloride, 2-(3,4-dihydroxyphenyl)-3,5,7-trihydroxy-4H-1-benzopyran-4-one (quercetin) (≥95%), 2,3-dihydrobenzoic acid (DHBA) (≥99%), 3,4,5-trihydroxybenzoic acid (gallic acid) (≥98.0%), 2,6-di-tert-butyl-4-methylphenol (BHT) (≥99.0%), Folin & Ciocalteu's phenol reagent and 2,2-diphenyl-1-picrylhydrazyl (DPPH) radical were purchased from Merck (Darmstadt, Germany). N-methyl-N-(trimethylsilyl) trifluoroacetamide (MSTFA) plus 1% trimethylchlorosilane (TMCS) was obtained from Thermo Scientific (Bellefonte, PA, USA) while water was prepared from Milli-Q system water purification unit (Millipore Lab, Bedford, MA, USA).

Oil samples and extraction of phytochemicals

Palm cooking oil (refined, bleached and deodorized (RBD) palm olein), commercial red palm oil (RPO) and extra virgin olive oil (EVOO) (first mechanically pressed olive oil) were purchased from a supermarket shelf well within their production and expiry dates. Palm cooking oil spiked with 1 mg of quercetin and DHBA chemical standards was used as positive control after observation of their appropriate peak heights in mass spectrometry detection. Cold-pressed palm oil (CPPO) was prepared in the laboratory from *Elaeis guineensis* (oil palm) fresh fruit bunch harvested from the Malaysian Palm Oil Board (MPOB) Kluang Research Station, Malaysia. The flesh (mesocarp tissue) was removed from the kernel and cut into smaller pieces before being pressed in a stainless-steel manual oil extractor. The resulting oil was filtered and centrifuged at room temperature for 5 minutes at 4000 rotation per min (rpm) to separate the oil from mesocarp debris. These processes did not involve heating or the usage of chemicals. Each of the oil samples of 5 mL volume were extracted in triplicates with 30 mL methanol with 4 hours, 250 rpm shaking at room temperature based on previous works [10,11]. The mixture was then centrifuged for 10 min at 3000 rpm after which the supernatant was dried using N-EVAP nitrogen evaporator (Organomation, MA, USA). The dried residue was suspended in 10 mL acetonitrile and washed twice with hexane to remove lipid components. The mixture was vortexed and centrifuged for 10 min to discard the upper layer hexane and the lower layer of acetonitrile was again dried over nitrogen stream. The dried extract was reconstituted in the solvent of choice based on the assay(s) or the chromatographic mobile phase.

Phytochemical and 2,2-diphenyl-1-picrylhydrazyl (DPPH) radical scavenging assays

All assays were conducted in triplicates for reproducibility. Alkaline reagent test indicated the presence of flavonoids with the change of sample colour to colourless based on previous works [12,13]. The appearance of dark green colour for ferric chloride test performed according to Raaman [12] and Usman et al. [14] indicated the presence of phenols in the sample solution. For quantitation, aluminium chloride colorimetric technique modified from Aryal et al. [15] was used for flavonoid content estimation equivalent to quercetin while Folin-Ciocalteu assay was modified from Dudonne et al. [16] for phenol quantitation expressed in terms of gallic acid equivalent, GAE (mg/mL of dry mass). The antioxidant activity percentage (AA%) for DPPH radical scavenging was calculated from the absorbance values (Abs) recorded at 517 nm [17] as follows:

$$AA\% = [(Abs_{control} - Abs_{sample}) / Abs_{control}] \times 100 \quad (1)$$

The extract samples and BHT concentrations were prepared in a series of 50, 100, 150, 200 and 250 ppm concentrations. The absorbance of an analyte solution is proportional to the concentration of the absorbing species in the solution [18].

Statistical analysis

One-way ANOVA followed by Tukey's Honestly Significant Difference (HSD) post hoc test were performed using IBM SPSS Statistics Version 20 for the total flavonoids, phenolics, and antioxidant assays. Statistical p values (set at a threshold of $p < 0.01$) indicate levels of significant difference between the sets of data being analyzed.

Liquid chromatography-mass spectrometry (LC-MS) analysis

The dried extracts were reconstituted in methanol and 1 µL volume were injected and separated on a Thermo Fisher Scientific (MA, USA) C18 Reversed-Phase Acclaim® 120Å column of 4.6 mm internal diameter (ID), 150 mm length and 5 µm particle size at 35°C on a Thermo Scientific Ultimate 3000 HPLC. Gradient elution was performed with water containing 0.1% acetic acid (solvent A) and 100% methanol (solvent B) with the following gradient: 0-1.5 min: 5% solvent B, 1.5-15.0 min: B eluted up to 95%, 15.0-24.0 min: 95% B, 24.0-37.0 min: B eluted down to 5% and 37.0-39.5 min: 5% B. MS analysis was performed on MicrOTOF-Q™ quadrupole-time-of-flight (Q/TOF) MS (Bruker Daltonik GmbH, Bremen, Germany) for accurate mass measurement with 3.5 bar nebulizer gas (N2), 8.0 L/min dry gas, 200°C dry temperature, -3500 V capillary voltage and -500 V end plate offset in the

negative electrospray ionization (ESI) mode for a reduced background noise [19] in the mass-to-charge ratio (*m/z*) range of 50-1000. Data processing, molecular formula candidate computation and identity matching to available chemical public databases were performed on Data Analysis 3.4 and Compound Crawler 2.0 (Bruker Daltonik GmbH).

Gas chromatography-mass spectrometry (GC-MS) analysis

For derivatization, the dried samples were dissolved in 80 µL of 20 mg/mL methoxamine hydrochloride in pyridine and incubated at 37 °C for 90 minutes. The mixtures were added with 80 µL MSTFA, incubated for another 30 minutes at 37 °C and allowed to equilibrate at room temperature for an hour. Both the derivatized and underivatized samples in methanol of 1 µL volume were analysed on the 7200B Agilent GC Q/TOF MS with electron ionization (EI) at 70 eV energy, 1 mL/min constant helium carrier gas flow on Agilent J&W Scientific (CA, USA) HP5-MS UI column (0.25 mm ID, 30 m length, 0.25 µm film thickness). The oven temperature began at 50 ˚C, held for 1 minute, followed by an increase of 11˚C/min to 180˚C, held again for 3 minutes, ramped to 300 ˚C and maintained for 18 minutes with solvent delay set at 3.75 minutes. The raw data from 50-1000 atomic mass unit (amu) scanning range were deconvoluted on Mass Hunter Workstation Qualitative Analysis Software B.07.00. Peak identification was by mass spectra matching at ≥70% similarity to the National Institute of Standards and Technology (NIST, US) Library using MS Search 2.2 Software (John Wiley & Sons, Inc., NJ, USA) and G1676AA Agilent Fiehn 2013 GC-MS Metabolomics Library. The acquisition method was locked to the derivatized ribitol commercial standard at 17.44 min and *m/z* 319.1684 at 1 mL/min helium using the Retention Time Locking (RTL) setup.

Results and Discussion

Flavonoids and phenolics screening

The extracts of extra virgin olive oil (EVOO), cold-pressed palm oil (CPPO), palm cooking oil spiked with quercetin and DHBA as positive control and red palm oil (RPO) showed positive changes for flavonoids and phenolics compared to palm cooking oil (Table 1). These results from manual observation exhibited colours and lucidity ranges and were further ascertained by their concentration equivalent to quercetin (flavonoid) and gallic acid (phenolic) chemical standards (Figure 1). The extract of CPPO was recorded with the highest total flavonoid content of 0.0984 quercetin equivalents (QE) mg/mL followed by EVOO with 0.0904 QE mg/mL flavonoids, RPO at 0.0489 QE mg/mL, positive control at 0.0417 QE mg/mL and lastly the palm cooking oil extract with 0.0324 QE mg/mL total flavonoids. The extract from EVOO was recorded to contain the highest phenolic compounds of 0.2771 mg/mL equivalent to gallic acid (GAE) compared to other samples, surpassing the positive control with 0.1449 GAE mg/mL total phenolics. This was followed by CPPO of 0.0774 GAE mg/mL phenolics, palm cooking oil with 0.0695 GAE mg/mL phenolics and lastly the RPO extract with 0.0651 GAE mg/mL total phenolics. In brief, for these tests, EVOO followed by CPPO demonstrated the highest phytochemical content among the oil extracts.

2,2-Diphenyl-1-picrylhydrazyl (DPPH) radical scavenging assay

Table 2 lists the average antioxidant activity (AA%) for the oil sample extracts and the antioxidant standard of BHT in a series of concentration ranging from 100 to 1000 ppm.

Among the oil sample extracts, the positive control sample recorded the overall highest antioxidant activity (AA%) of 27.82 to 80.60% across the series of concentration. At 100 ppm, EVOO extract recorded the second highest antioxidant activity after positive control while RPO extract had the lowest. At 250 and 500 ppm, EVOO maintained its high activity and CPPO and palm cooking oil exhibited the lowest activity among the oil extracts. At 750 ppm, RPO surpassed that of EVOO extract after positive control and lastly, at 1000 ppm, RPO extract topped the other oil extracts at 62.01% antioxidant activity. Overall, EVOO displayed a constant and high antioxidant activity among all samples up to 750 ppm concentration. Despite its lowest activity at 100 ppm concentration, RPO extract rose to high antioxidant capacity parallel to that of EVOO at 750 ppm and

exhibited the highest activity at 1000 ppm, with two-fold value compared to the rest of the samples. Antioxidant activities of CPPO were low, comparable to that of palm cooking oil extract. The fact that the antioxidant activity of CPPO extract was lower than the other oils require some deliberation as illustrated by several studies of flavonoids that exert both antagonistic and synergistic activities in a tested oxidation system [20, 21]. The average antioxidant activity (AA%) values across the series of concentration were plotted into a graph in Figure 2.

Table 1. Flavonoid and phenolic contents in extra virgin olive oil (EVOO), cold-pressed palm oil (CPPO), red palm oil (RPO) and palm cooking oil extracts

Sample	Flavonoids				Phenolics			
	Visual screening	**Concentration (mg QE/mL)**	**Average (ppm) ±SD**	**Relative Standard Deviation (RSD)**	**Visual screening**	**Concentration (mg GAE/mL)**	**Average (ppm) ±SD**	**Relative Standard Deviation (RSD)**
EVOO	+	0.0904^{b}	90.38 ±4.31	4.77	Cloudy light green solution	0.2771^{a}	277.07 ±10.71	3.86
CPPO	Colourless solution with a top layer of precipitate	0.0984^{a}	98.44 ±1.31	1.33	Cloudy orange solution with a top layer of precipitate	0.0774^{c}	77.38 ±7.89	10.20
RPO	+	0.0489^{c}	48.91 ±0.72	1.46	Cloudy yellow solution	0.0651^{c}	65.13 ±7.52	11.54
Palm cooking oil	White cloudy solution	0.0324^{e}	32.35 ±0.66	2.03	Cloudy light yellow solution	0.0695^{c}	69.47 ±4.88	7.02
Positive control	+	0.0417^{d}	41.74 ±0.28	0.68	+	0.1449^{b}	144.90 ±8.17	5.64

*+ = positive change; QE = quercetin equivalents; GAE = gallic acid equivalents, SD = standard deviation (n=3)
*Flavonoids ($F_{4,\ 10}$ = 642.01, $p < 0.0001$), phenolics ($F_{4,\ 10}$ = 366.24, $p < 0.0001$), superscript letters a, b, c, d and e denote significance ($p < 0.01$) from highest to lowest at each subset at $\alpha = 0.05$ according to Tukey's HSD

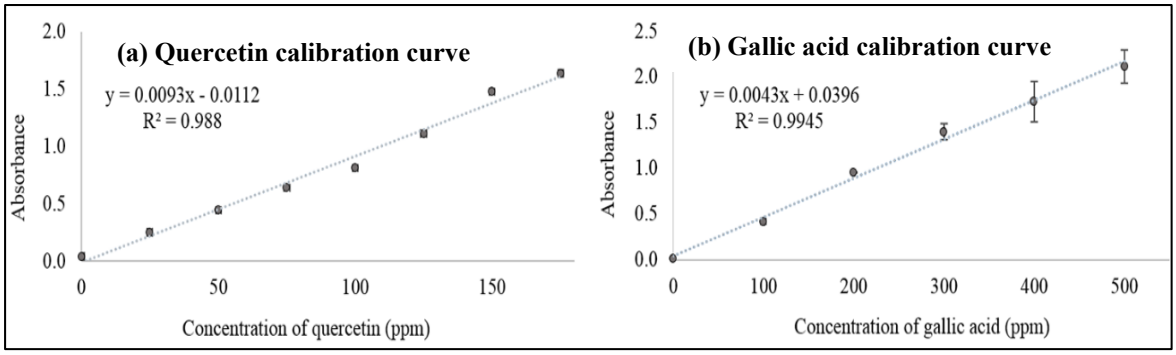


Figure 1. (a) Quercetin and (b) gallic acid standards calibration curves for flavonoid and phenolic quantitation.

Table 2. Average antioxidant activity (AA%±SD) according to sample concentration (ppm)

Sample	100 ppm	250 ppm	500 ppm	750 ppm	1000 ppm
BHT	36.95 ±0.69[a]	44.31 ±0.80[a]	59.10 ±7.77[a]	86.14 ±0.17[a]	96.61 ±1.14[a]
Positive control	27.82 ±0.00[b]	43.66 ±0.57[a]	56.60 ±4.23[a]	70.17 ±2.40[a]	80.60 ±0.69[a]
EVOO	24.18 ±1.37[c]	27.90 ±6.40[b]	30.41 ±3.77[b]	35.10 ±1.26[b]	39.22 ±4.12[c]
RPO	16.08 ±0.03[d]	22.24 ±4.80[b]	26.29 ±8.00[b]	35.50 ±9.37[b]	62.01 ±1.37[b]
CPPO	17.90 ±0.48[d]	19.25 ±1.26[b]	25.70 ±2.20[b]	29.55 ±1.65[b]	31.62 ±3.43[c]
Palm cooking oil	16.16 ±0.13[d]	19.02 ±0.22[b]	26.04 ±7.89[b]	28.28 ±9.45[b]	29.52 ±11.20[c]

*Superscript letters a, b, c, and d denote significant different activities ($p < 0.01$) from highest to lowest at each subset at $\alpha = 0.05$ according to Tukey's HSD

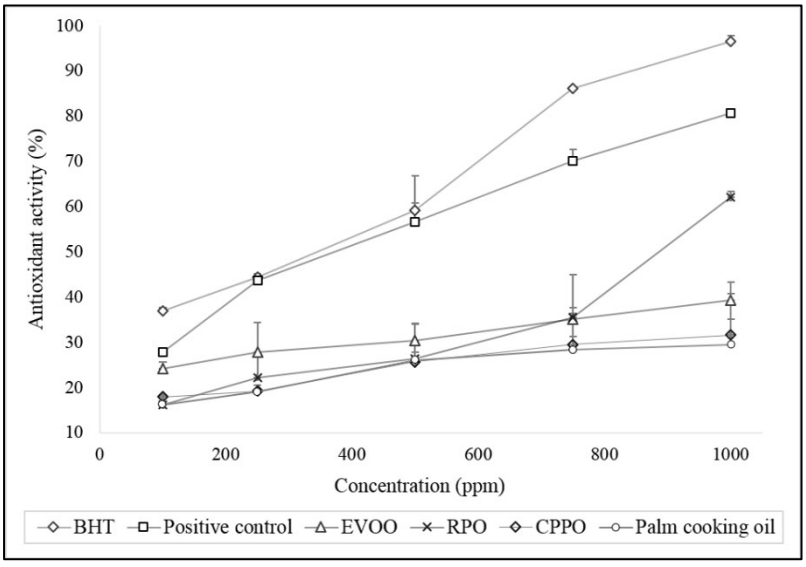


Figure 2. Average antioxidant activities (AA%) of BHT standard, EVOO and palm oil extracts

Liquid chromatography-mass spectrometry (LC-MS) analysis of palm oil extracts

Figure 3(a) shows the LC-MS chromatograms of the investigated oil extracts with numbered peaks and identities of the phytochemicals. The details of retention times (t_R), molecular formulae, molecular ion masses (*m/z*, $[M-H]^-$) with mass errors (mDa), ESI MS/MS fragments for the numbered phytochemical peaks and references to previous investigations are listed in Table 3. The availability of accurate mass measurement by TOF mass spectrometers with resolving power from 8,000 to 20,000 (m/Δm, full width at half maximum; FWHM) allows the determination of elemental composition of monoisotopic mass [22,23]. The identity of peak **1** (*m/z* 187.0992 $[M-H]^-$, $C_9H_{15}O_4$, err [mDa] 1.6) and its tandem MS (MS/MS) fragments of *m/z* 169.0894 ($[M-H]^-$, $C_9H_{13}O_3$, err [mDa] 2.4) and 125.0970 ($[M-H]^-$, $C_8H_{13}O$, err [mDa] 0.2) matched that of nonanedioic acid (azelaic acid) [24], a natural dicarboxylic acid plant signalling metabolite [25]. Peak **2** of *m/z* 171.1048 ($[M-H]^-$, $C_9H_{15}O_3$, err [mDa] 2.1) was identified as oxononanoic acid, a medium-chain fatty acid also found in Camellia (tea seed) oil and grapes [26,27]. Peak **3** (*m/z* 285.0794 $[M-H]^-$, $C_{16}H_{13}O_5$, err [mDa] 2.5) was fragmented by MS/MS into *m/z* 165.0209, 119.0463 and 93.0296, consistent to those of sakuranetin ((2S)-5-hydroxy-2-(4-hydroxyphenyl)-7-methoxy-2,3-dihydrochromen-4-one) [28, 29].

Peak **4** (*m/z* 329.2344 $[M-H]^-$, $C_{18}H_{33}O_5$, err [mDa] 1.0) corresponded to trihydroxyoctadecenoic acid, which was discovered using LC-MS in olive oil [30]. This trihydroxy fatty acid was also screened in Japanese elm and proposed as one of the anti-inflammatory compounds tested [31]. Peak **5** of *m/z* 283.0637 ($[M-H]^-$, $C_{16}H_{11}O_5$, err [mDa] 2.5) was fragmented into *m/z* 268.0405 with 15 amu neutral loss, denoting a loss of methyl group (CH_3) from the molecular ion. A multitude of candidates from flavone and isoflavone classes of flavonoids correspond to the generated molecular formula of $C_{16}H_{12}O_5$, but the loss of CH_3 observed in the MS/MS spectra of peak **5** narrowed the candidates to those with *O*-methylated group. Based on earlier reports of LC-MS and MS/MS data, peak **5** was proposed as 5,7-dihydroxy-8-methoxy-2-phenyl-4H-chromen-4-one or wogonin, an *O*-methylated flavone [32,33]. Flavonoids with methyl and methoxy groups found in the CPPO are known to exhibit the least antioxidant properties compared to other flavonoids with hydroxyl groups [34,35], consistent with the results of the DPPH radical scavenging assay. Nevertheless, flavonoids with these functional groups are of superior bioavailability and their beneficial properties are well introduced into human systemic circulation [36].

Peak **6** (*m/z* 311.2254 $[M-H]^-$, $C_{18}H_{31}O_4$, err [mDa] 2.6) was a hydroxy-oxooctadecenoic acid oxylipin, a group of plant oxygenated fatty acids. The loss of HO-$CH{=}CH(CH_2)_3CH_3$ side-group from the oxylipin molecule during MS/MS as illustrated in Figure 4 can be detected by monitoring 100 amu neutral loss in the LC/MS chromatogram as shown in Figure 5. This deduction was ascertained with the observation of the three common oxylipin molecular ions of *m/z* 329 (as found for peak **4**), *m/z* 311 (as recorded for peak **6**) and *m/z* 295 (peak **8,** *m/z* 295.2319 $[M-H]^-$, $C_{18}H_{31}O_3$, err [mDa] 4.0) that were all fragmented to yield *m/z* 171, a fragment that contains a carboxyl and an OH-group which are characteristics to oxylipins -ESI MS/MS fragments [37]. These natural hydroperoxides were found in several plants such as barley and wheat and are involved in plant development and growth, and protection against stressors [38, 37, 39].

Peak **7** (*m/z* 171.1401 $[M-H]^-$, $C_{10}H_{19}O_2$, err [mDa] 1.0) was identified as decanoic acid, a saturated fatty acid also known as capric acid [40]. Peaks **9** (*m/z* 199.1734 ($[M-H]^-$, $C_{12}H_{23}O_2$, err [mDa] 3.0), **11** (*m/z* 277.2145 $[M-H]^-$, $C_{18}H_{29}O_2$, err [mDa] 2.8), **12** (*m/z* 253.2204 $[M-H]^-$, $C_{16}H_{29}O_2$, err [mDa] 3.1), **13** (*m/z* 279.2310 $[M-H]^-$, $C_{18}H_{31}O_2$, err [mDa] 1.9), **14** (*m/z* 255.2307 $[M-H]^-$, $C_{16}H_{31}O_2$, err [mDa] 2.2), **15** (*m/z* 281.2466 $[M-H]^-$, $C_{18}H_{33}O_2$, err [mDa] 2.0) and **16** (*m/z* 283.2610 $[M-H]^-$, $C_{18}H_{35}O_2$, err [mDa] 3.3) were deduced as acids of dodecanoic (lauric), octadecatrienoic (linolenic, ALA), (9Z)-hexadec-9-enoic (palmitoleic, POA), (9Z,12Z)-octadeca-9,12-dienoic (linoleic, LA), hexadecanoic (palmitic, PA), (9Z)-octadec-9-enoic (oleic, OA) and octadecanoic (stearic, SA) respectively as previously discovered by LC-MS analyses while

peak **10** (*m/z* 413.2909 $[M-H]^-$, $C_{23}H_{41}O_6$, err [mDa] 3.6) was identified as glyceryldiacetate 2-palmitate with MS/MS fragment of acetate ion of $[C_2H_3O_2]^-$ (*m/z* 59.0139 $[M-H]^-$, err [mDa] 2.2) [41,42]. Similar to the CPPO extract, peaks **1** and **10** in the palm cooking oil and RPO extracts LC-MS chromatograms in Figure 3(b) was identified as nonanedioic acid and glyceryldiacetate 2-palmitate. The processed palm oil extracts also contain linolenic, linoleic, palmitic, oleic and stearic acids.

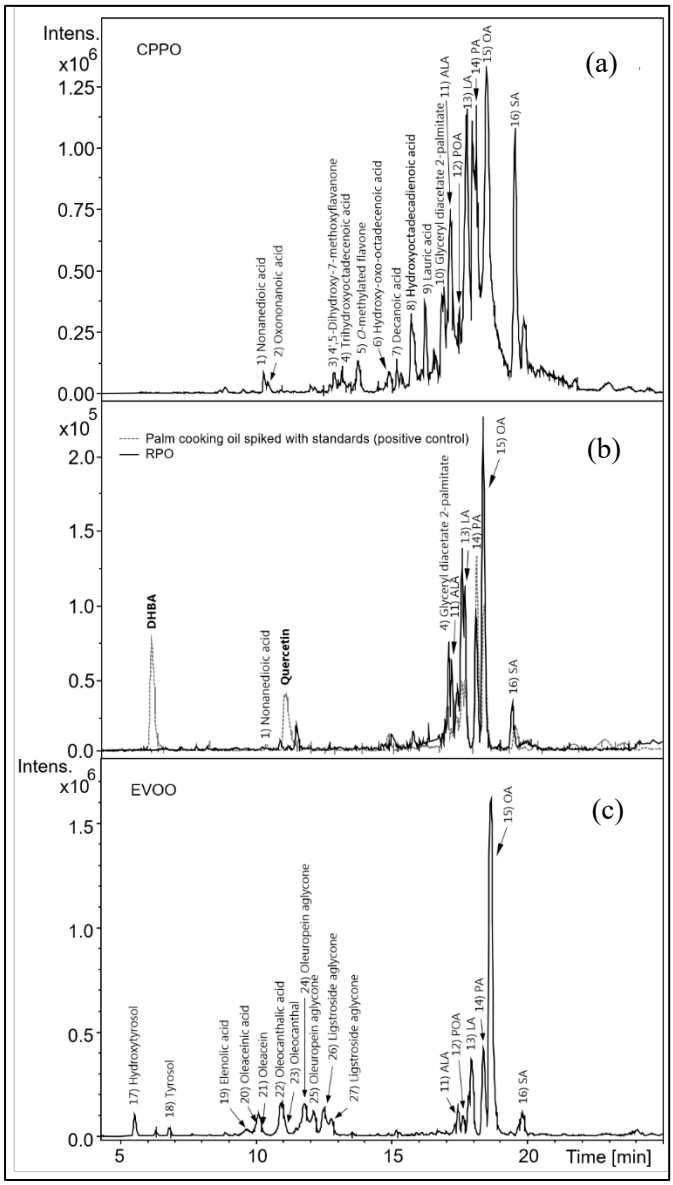


Figure 3. LC-MS chromatograms of CPPO (a), palm cooking oil spiked with DHBA and quercetin, overlapped with RPO extracts (b) and EVOO extract (c). Abbreviation: DHBA, 2,3-dihydrobenzoic acid; ALA, linolenic acid; POA, palmitoleic acid; LA, linoleic acid; PA, palmitic acid; OA, oleic acid; SA, stearic acid).

Table 3. Identified phytochemicals in palm oils and extra virgin olive oil using LC-MS/MS

Peak	Phytochemicals	t_R (min)	Molecular Formula	Measured mass-to-charge Ratio (*m/z*), $[M-H]^-$	Mass Error [mDa]	MS/MS Fragments (*m/z*)	Classification Details	CPPO	Palm Cooking Oil	RPO	EVOO	Ref.
1	Nonanedioic acid (azelaic acid)	10.8	$C_9H_{16}O_4$	187.0992	1.6	169.0894, 125.0970	Dicarboxylic acid, plant signalling metabolite	√	√	√		[24,25]
2	Oxononanoic acid	10.9	$C_9H_{16}O_3$	171.1048	2.1	127.1163	Medium-chain oxo-fatty acid	√				[26,27]
3	Dihydroxy-methoxyflavanone (sakuranetin)	13.3	$C_{16}H_{14}O_5$	285.0794	2.5	165.0209, 119.0463, 93.0296	Methoxyflavanone	√				[28,29]
4	Trihydroxy-octadecenoic acid	13.6	$C_{18}H_{34}O_5$	329.2344	1.0	229.1504, 171.1023	Trihydroxy fatty acid	√				[30,31]
5	Dihydroxy-methoxyflavone (wogonin)	14.2	$C_{16}H_{12}O_5$	283.0637	2.5	268.0405	*O*-methylated flavone	√				[32,33]
6	Hydroxy-oxooctadecenoic acid	15.3	$C_{18}H_{32}O_4$	311.2254	2.6	293.2152, 211.1358, 171.1043	Plant oxygenated fatty acid, natural hydroperoxide (oxylipin)	√				[37,38,39]
7	Decanoic acid (capric acid)	15.6	$C_{10}H_{20}O_2$	171.1401	1.0	153.1436, 127.0374	Saturated fatty acid	√				[40]
8	Hydroxyoctadecadienoic acid	16.2	$C_{18}H_{32}O_3$	295.2319	4.0	277.2198, 195.1421, 171.1048	Plant oxygenated fatty acid, natural hydroperoxide (oxylipin)	√				[37,38,39]
9	Dodecanoic acid (lauric acid)	16.6	$C_{12}H_{24}O_2$	199.1734	3.0	181.0247	Saturated fatty acid	√				[40]
10	Glyceryldiacetate 2-palmitate	17.1	$C_{23}H_{42}O_6$	413.4420	3.6	59.0117	Diglyceride derivatives	√	√	√		[41,42]
11	Octadecatrienoic acid (linolenic, ALA)	17.5	$C_{18}H_{30}O_2$	277.2145	2.8	233.2288	Polyunsaturated omega-3 fatty acid	√	√	√	√	[41,42]
12	Hexadecenoic acid (palmitoleic, POA)	17.6	$C_{16}H_{30}O_2$	253.2204	3.1	209.1381	Monounsaturated omega-7 fatty acid	√			√	[41,42]
13	Octadecadienoic acid (linoleic, LA)	18.0	$C_{18}H_{32}O_2$	279.2310	1.9	261.2226	Polyunsaturated omega-6 fatty acid	√	√	√	√	[41,42]
14	Hexadecanoic acid (palmitic, PA)	18.4	$C_{16}H_{32}O_2$	255.2307	2.2	211.2005	Saturated fatty acid	√	√	√	√	[41,42]
15	Octadecenoic acid (oleic, OA)	18.6	$C_{18}H_{34}O_2$	281.2466	2.0	237.3641	Monounsaturated omega-9 fatty acid	√	√	√	√	[41,42]
16	Octadecanoic acid (stearic, SA)	19.8	$C_{18}H_{36}O_2$	283.2610	3.3	239.2309	Saturated fatty acid	√	√	√	√	[41,42]

Table 3 (cont'd). Identified phytochemicals in palm oils and extra virgin olive oil using LC-MS/MS

Peak	Phytochemicals	t_R (min)	Molecular Formula	Measured mass-to-charge Ratio (*m/z*), $[M-H]^-$	Mass Error [mDa]	MS/MS Fragments (*m/z*)	Classification Details	CPPO	Palm Cooking Oil	RPO	EVOO	Ref.
17	Hydroxytyrosol	5.6	$C_8H_{10}O_3$	153.0567	1.0	123.0454	Phenylethanoid phenolic compound				√	[43,44]
18	Tyrosol	6.8	$C_8H_{10}O_2$	137.0619	1.1	119.0484, 106.0420	Phenylethanoid phenolic compound				√	[44]
19	Elenolic acid	9.7	$C_{11}H_{14}O_6$	241.0726	0.9	165.0736, 139.0079, 127.0422	Phenolic compound				√	[45]
20	Oleaceinic acid	10.1	$C_{17}H_{20}O_7$	335.1160	2.4	181.0520, 155.0716, 111.0836	Phenolic secoiridoids				√	[46]
21	Oleacein	10.1	$C_{17}H_{20}O_6$	319.1187	2.6	275.1028, 249.0820, 183.0694, 165.0572, 69.0333	Phenolic secoiridoids				√	[47,48]
22	Oleocanthalic acid	10.9	$C_{17}H_{20}O_6$	319.1246	1.4	199.0646, 181.0531, 111.0105	Phenolic secoiridoids				√	[46]
23	Oleocanthal	11.1	$C_{17}H_{20}O_5$	303.1243	0.5	285.1155, 217.0054, 183.0693, 165.0605, 141.0183	Phenolic secoiridoids				√	[47,48]
24	Oleuropein aglycone isomer	11.8	$C_{19}H_{22}O_8$	377.1252	1.0	307.0874, 275.0870, 149.0267, 139.0371	Phenolic secoiridoids				√	[49,50]
25	Oleuropein aglycone isomer	12.1	$C_{19}H_{22}O_8$	377.1249	0.7	307.0874, 275.0855, 149.0268, 139.0371	Phenolic secoiridoids				√	[49,50]
26	Ligstroside aglycone	12.5	$C_{19}H_{22}O_7$	361.1304	1.1	291.0920, 259.0954	Phenolic secoiridoids				√	[47,50,51]
27	Ligstroside aglycone	12.8	$C_{19}H_{22}O_7$	361.1329	3.6	291.0924, 259.1012	Phenolic secoiridoids				√	[47,50,51]

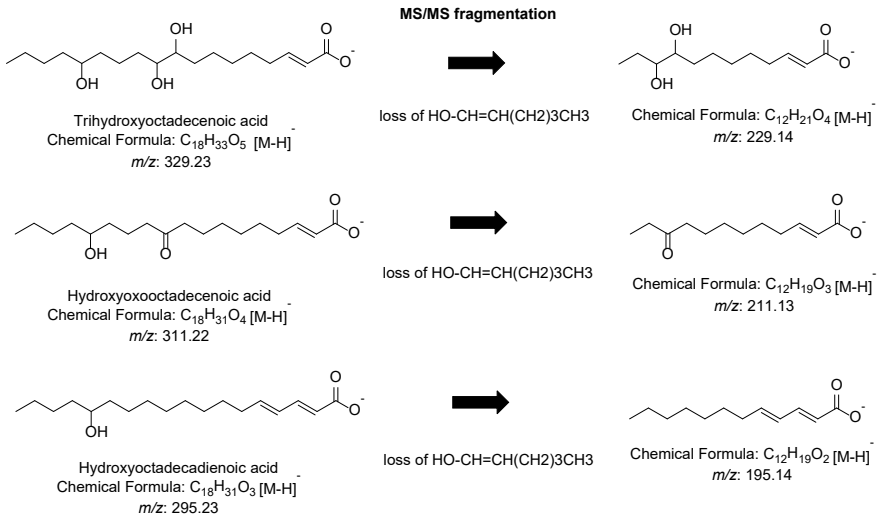


Figure 4. Proposed MS/MS fragmentation of peaks 4, 6 and 8 with the neutral loss of 100 atomic mass unit (amu) corresponding to HO-CH=CH(CH_2)$_3$$CH_3$ moiety

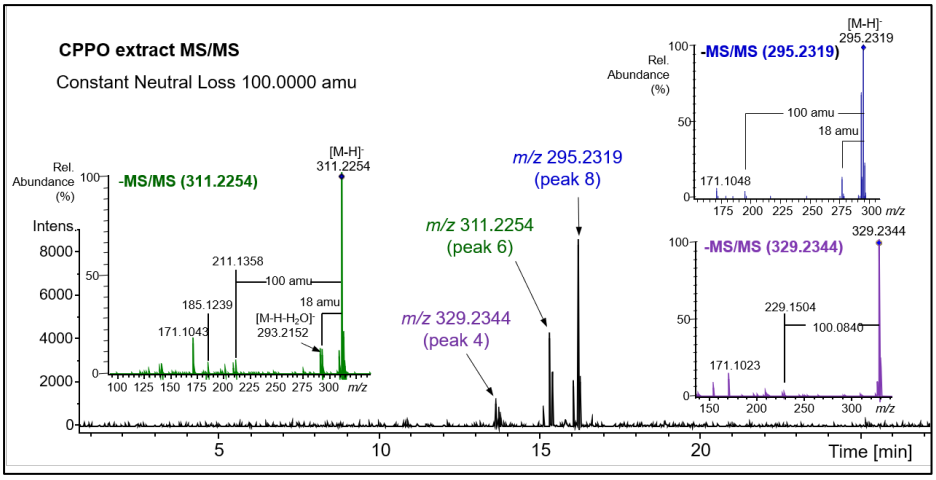


Figure 5. CPPO extract 100.000 amu neutral loss chromatogram and MS/MS spectra of peaks 4, 6 and 8

LC-MS/MS analysis of extra virgin olive oil (EVOO) extract

Peak **17** of *m/z* 153.0567 ([M-H]$^-$, $C_8H_9O_3$, err [mDa] 1.0) observed in the EVOO chromatogram in Figure 3(c) was identified as hydroxytyrosol (4-(2-hydroxyethyl)-1,2-benzenediol), a phenylethanoid phenolic compound with MS/MS fragment of *m/z* 123.0454 ($C_7H_7O_2$, err [mDa] 0.2) after losing CH_2O from its molecular structure [43,44]. Peak **18** (*m/z* 137.0619 [M-H]$^-$, $C_8H_9O_2$, err [mDa] 1.1) that was fragmented into *m/z* 119.0484 after loss of H_2O and *m/z* 106.0420 due to removal of methoxy radical (CH_3O•) was none other than tyrosol (4-(2-hydroxyethyl)phenol), another significant phenolic constituent of olive oil [44]. Peak **19** (*m/z* 241.0726 [M-H]$^-$, $C_{11}H_{13}O_6$, err [mDa] 0.9) was elenolic acid (2-

[(2S,3S,4S)-3-formyl-5-methoxycarbonyl-2-methyl-3, 4-dihydro-2H-pyran-4-yl]acetic acid), a phytochemical indicator for olive ripening with its common MS/MS fragments of *m/z* 165, 139 and 127 [45]. Peak **20** (*m/z* 335.1160 $[M-H]^-$, $C_{17}H_{19}O_7$, err [mDa] 2.4) together with peak **21** (*m/z* 319.1187 $[M-H]^-$, $C_{17}H_{19}O_6$, err [mDa] 2.6), and also peaks **22** (*m/z* 319.1246 $[M-H]^-$, $C_{17}H_{19}O_6$, err [mDa] 1.4) and **23** (*m/z* 303.1243 $[M-H]^-$, $C_{17}H_{19}O_5$, err [mDa] 0.5) were coeluting respectively with both peaks **21** and **22** were of equivalent *m/z* 319. However, peak **21** yielded different MS/MS spectra with fragment ions of *m/z* 275.1028, 249.0820, 183.0694, 165.0572 and 69.0333, while peak **22** was fragmented into *m/z* 199.0646, 181.0531 and 111.0105. Based on their molecular formulae and respective MS/MS fragments, peaks **20** and **22** were coherent to those of oleaceinic acid ((E)-3-(2-(3,4-dihydroxyphenethoxy)-2-oxoethyl)-4-formylhex-4-enoic acid) and oleocanthalic acid ((E)-4-formyl-3-(2-(4-hydroxyphenethoxy)-2-oxoethyl)hex-4-enoic acid) discovered recently [46].

Peak **21** was deduced as oleacein (2-(3,4-dihydroxyphenyl)ethyl (Z)-4-formyl-3-(2-oxoethyl) hex-4-enoate) and peak **23** was identified as oleocanthal (2-(4-hydroxyphenyl)ethyl (3S,4E)-4-formyl-3-(2-oxoethyl)hex-4-enoate) [47,48]. The molecular ion mass of peaks **24** (*m/z* 377.1252 $[M-H]^-$, $C_{19}H_{21}O_8$, err [mDa] 1.0) and **25** (*m/z* 377.1249 $[M-H]^-$, $C_{19}H_{21}O_8$, err [mDa] 0.7) were of similar mass-to-charge (*m/z*) ratio of 377 in addition to their analogous MS/MS fragments of *m/z* 307, 275, 149 and 139. These molecular and fragment ions were identical to those found for oleuropein aglycone isomers (methyl (2R,4S,E)-4-(2-(3,4-dihydroxyphenethoxy)-2-oxoethyl)-3-ethylidene-2-hydroxy-3,4-dihydro-2H-pyran-5-carboxylate) [49]. Peaks **26** (*m/z* 361.1304 $[M-H]^-$, $C_{19}H_{21}O_7$, err [mDa] 1.1) and **27** (*m/z* 361.1329 $[M-H]^-$, $C_{19}H_{21}O_7$, err [mDa] 3.6) were another pair of molecular ion mass of *m/z* 361 with similar MS/MS fragments. These metabolites are secoiridoid isomers known as ligstroside aglycone (methyl(2R,E)-3-ethylidene-2-hydroxy-4-(2-(4-hydroxyphenethoxy)-2-oxoethyl)-3,4-dihydro-2H-pyran-5-carboxylate) which always yield *m/z* 291 and *m/z* 259 MS/MS fragments as exemplified in the olive and ash tree from the Oleaceae family [47,51]. Peaks 11-16 in Figure 3(c) were of linolenic, palmitoleic, linoleic, palmitic, oleic and stearic acids similar to those observed in LC-MS chromatogram of palm oil extracts.

Gas chromatography-mass spectrometry (GC-MS) analysis of oil extracts

The identified phytochemicals from the oil extracts analysed using GC-Q/TOF are listed in Table 4. In the shotgun GC-MS analysis of underivatized oil extracts, phytochemical **28** of 1,2-benzenediol was detected only in EVOO extract possibly from the breakage of catechol moiety in the olive oil, e.g., oleuropein, hydroxytyrosol, during the analysis. The aromatic 2,4-decadienal (phytochemical **29**) was identified in palm cooking oil, EVOO and RPO, with significant abundance in the RPO extract. Phytochemical **30** was observed only in the CPPO and was identified as 2-phenylethan-1-ol or benzeneethanol, a natural chemical found in plant essential oils and is suggested to possess medicinal properties [52]. Another important phytochemical detected only in the CPPO extract is squalene (phytochemical **31, (**6E,10E,14E,18E)-2,6,10,15,19,23-hexamethyltetracosa-2,6,10,14,18,22-hexaene). Squalene is a triterpene involved in the synthesis of plant sterols and was comprehensively investigated for anticancer activity [53]. The detection of all these natural chemicals in the CPPO and not in the refined palm oil extracts suggests that they were unavailable after refining.

Another batch of the oil extracts were derivatized to improve the GC-MS detection and more constituents were found to be abundance in CPPO and EVOO extracts compared to that of refined oils. Several phenolics were uniquely detected in EVOO namely tyrosol (phytochemical **18**), hydroxytyrosol (phytochemical **17**) which were also observed in the LC-MS analysis, and 4-ethenylphenol or 4-vinylphenol (phytochemical **32**). Coniferyl alcohol (phytochemical **33,** 4-[(E)-3-Hydroxyprop-1-enyl]-2-methoxyphenol), an important monolignol for the synthesis of lignin and lignans in plants was only detected in the CPPO extract indicating that the unrefined palm oil contains phytochemicals that could indirectly improve human health by lowering blood pressure, reducing

cardiovascular risk and suppressing the development of diabetes by its ingestion [54]. Tetradecanoic (myristic) (phytochemical **34**), palmitic, linoleic and oleic acids were detected in all of the oil extracts along with xanthoxin (phytochemical **35, (**2Z,4E)-5-[(1S,4S,6R)-4-hydroxy-2,2,6-trimethyl-7-oxabicyclo[4.1.0]hept-1-yl]-3-methyl penta-2,4-dienal), 2-palmitoylglycerol (phytochemical **36**, 1,3-dihydroxypropan-2-yl hexadecanoate), monopalmitin (phytochemical **37**, 2,3-dihydroxypropyl hexadecanoate) and glyceryl monooleate (phytochemical **38**, 2,3-dihydroxypropyl octadecanoate).

Table 4. Phytochemicals detected in palm cooking oil, CPPO, RPO and EVOO extracts by GC-Q/TOF

No.	Phytochemicals*	t_R (min)	Molecular Formula	Palm Cooking Oil	CPPO	RPO	EVOO	Classification
Underivatized extract								
28	1,2-Benzenediol	8.40	$C_6H_6O_2$	-	-	-	√	Phenol
29	2,4-Decadienal	9.71	$C_{10}H_{16}O$	√	-	√	√	Aromatic compound
30	Benzeneethanol	11.26	$C_8H_{10}O$	-	√	-	-	Alcohol and terpene
31	Squalene	24.07	$C_{30}H_{50}$	-	√	-	-	Triterpene
Derivatized extract								
18	Tyrosol	15.11	$C_8H_{10}O_2$	-	-	-	√	Phenolic
17	Hydroxytryrosol	18.14	$C_8H_{10}O_3$	-	-	-	√	Phenolic
34	Myristic acid	19.47	$C_{14}H_{28}O_2$	√	√	√	√	Fatty acid
33	Coniferyl alcohol	20.80	$C_{10}H_{12}O_3$	-	√	-	-	Phenolic
14	Palmitic acid	22.26	$C_{16}H_{32}O_2$	√	√	√	√	Fatty acid
13	Linoleic acid	24.39	$C_{18}H_{32}O_2$	√	√	√	√	Fatty acid
15	Oleic acid	24.46	$C_{18}H_{34}O_2$	√	√	√	√	Fatty acid
35	Xanthoxin	24.76	$C_{12}H_8O_4$	√	√	√	√	Furocoumarin
36	2-Palmitoylglycerol	28.31	$C_{19}H_{38}O_4$	√	√	√	√	Diglycerol
37	Monopalmitin	28.68	$C_{19}H_{38}O_4$	√	√	√	√	Monoglyceride
32	4-Vinylphenol	29.54	C_8H_8O	-	-	-	√	Phenolic
38	Glyceryl monooleate	30.46	$C_{21}H_{40}O_4$	√	√	√	√	Monoacylglycerol

*≥70% similarity to the NIST Library and Agilent Fiehn 2013 GC-MS Metabolomics RTL Library

Conclusion

The constituents of palm cooking oil (RBDO), red palm oil (RPO), cold-pressed palm oil (CPPO) and extra virgin olive oil (EVOO) were examined and compared using phytochemical screening and also liquid and gas chromatography-mass spectrometry. The total flavonoid and phenolic quantitation were encouraging for EVOO and CPPO extracts albeit direct correlation could not be drawn from the results of DPPH radical scavenging assay. From the LC- and GC-MS profiling, EVOO followed by CPPO extracts exhibited more content and metabolite peaks compared to the processed palm oil extracts. A total of 38 phytochemicals were identified from all the oil samples in this investigation. As the total phytochemical content is not accurately reflective of the bioactivities

in a complex mixture for instance its antioxidant activity, more efficient assessment of individual identification and assay of specific metabolite component need to be carried out to fully grasp the status, stability and optimum potential of the palm oil constituents. In the long run, to attain the gold standard of edible oil packed with phytonutrients as attained by the EVOO, the palm oil processing methodologies requires a revisit. Nevertheless, the change or improvement in the physical extraction and milling technology to obtain premium grade palm oil may only be achieved after the phytochemical composition of the unprocessed palm oil is fully profiled and identified.

Acknowledgement

The authors would like to thank the Director General of MPOB for permission to publish this article. We also thank Dr Azmil Haizam AT of Product Development and Advisory Services Division of MPOB for valuable insights on palm oil analysis and Mohamad Faiz Abdullah of ABBC for his technical assistance.

References

1. Holopainen, J. K., Kivimäenpää, M. and Julkunen-Tiitto, R. (2018). New light for phytochemicals. *Trends in Biotechnology,* 36: 7-10.
2. Cotes, S., Cotuá, J. and Muñoz, A. (2018). Calculated antioxidant activity of selected phenolic compounds. *Canadian Journal of Chemistry,* 96: 345-350.
3. Kushairi, A., Ong-Abdullah, M., Nambiappan, B., Hishamuddin, E., ZanalBidin, M. N. I., Ghazali, R., Subramaniam, V., Sundram, S. and Parveez G. K. A. (2019). Oil palm economic performance in Malaysia and R&D progress in 2018. *Journal of Oil Palm Research,* 31: 165-194.
4. Loganathan, R., Subramaniam, K. M., Radhakrishnan, A. K., Choo, Y. M. and Teng, K. T. (2017). Health-promoting effects of red palm oil: evidence from animal and human studies. *Nutrition Reviews,* 75: 98-113.
5. Abdullah, F., Ismail, R., Ghazali, R. and Idris, R. (2018). Total phenolic contents and antioxidant activity of palm oils and palm kernel oils at various refining processes. *Journal of Oil Palm Research,* 30: 682-692.
6. Rizwan, S., Benincasa, C., Mehmood, K., Anjum, S., Mehmood, Z., Alizai, G. H., Azam, M., Perri, E., Sajjad, A. (2019). Fatty acids and phenolic profiles of extra virgin olive oils from selected Italian cultivars introduced in southwestern province of Pakistan. *Journal of Oleo Science,* 68: 33-43.
7. Syarifah-Noratiqah, S. B., Zulfarina, M. S., Ahmad, S. U., Fairus, S. and Naina-Mohamed, I. (2019). The pharmacological potential of oil palm phenolics (OPP) individual components. *International Journal of Medical Sciences,* 16(5): 711-719.
8. Selby-Pham, S. N. B., Siow, L. F. and Bennett, L. E. (2020). Characterising absorption and health-related properties of phytochemicals extracted from Malaysian palm fruit biomass after oil extraction. *Food Function,* 11: 907-920.
9. Zain, M. S. C., Lee, S. Y., Sarian, M. N., Fakurazi, S. and Shaari, K. (2020). In vitro wound healing potential of flavonoid C-glycosides from oil palm (*Elaeis guineensis* Jacq.) leaves on 3T3 fibroblast cells. *Antioxidants,* 9: 326.
10. Xiu-Qin, L., Chao, J., Yan-Yan, S., Min-Li, Y. and Xiao-Gang, C. (2009). Analysis of synthetic antioxidants and preservatives in edible vegetable oil by HPLC/TOF-MS. *Food Chemistry,* 113: 692-700.
11. Atawodi, S. E., Yusufu, L. M., Atawodi, J. C., Asuku, O. and Yakubu, O. E. (2011). Phenolic compounds and antioxidant potential of Nigerian red palm oil (*Elaeis guineensis*). *International Journal of Biology,* 3: 153-161.
12. Raaman, N. (2006). Phytochemical Techniques. New India Publishing Agency, India: pp. 19-23.
13. Gul, R., Jan, S. U., Faridullah, S., Sherani, S. and Jahan, N. (2017). Preliminary phytochemical screening, quantitative analysis of alkaloids and antioxidant activity of crude plant extracts from *Ephedra intermedia* indigenous to Balochistan. *Scientific World Journal*, 2017: 5873648.

14. Usman, H., Abdulrahman, F. I. and Usman, A. (2009). Qualitative phytochemical screening and in vitro antimicrobial effects of methanol stem bark extract of *Ficus thonningii* (Moraceae). *African Journal of Traditional, Complementary and Alternative Medicines,* 6(3): 289-295.
15. Aryal, S., Baniya, M. K., Danekhu, K., Kunwar, P., Gurung, R. and Koirala, N. (2019). Total phenolic content, flavonoid content and antioxidant potential of wild vegetables from Western Nepal. *Plants,* 8: 1-12.
16. Dudonne, S., Vitrac, X., Coutiere, P., Woillez, M. and Merillon, J. M. (2009). Comparative study of antioxidant properties and total phenolics content of 30 plant extract of industrial interest using DPPH, ABTS, FRAP, SOD and ORAC assays. *Journal of Agricultural and Food Chemistry,* 57(5): 1768-1774.
17. Garcia, E. J., Oldoni, T. L. C., De Alencar, S. M., Reis, A., Loguercio, A. D. and Grande, R. H. M. (2012). Antioxidant activity by DPPH assay of potential solutions to be applied on bleached teeth. *Brazilian Dental Journal,* 23: 22-27.
18. Shams-Nateri, A. (2010). Prediction of dye concentrations in a three-component dye mixture solution by a PCA-derivative spectrophotometry technique. *Color Research & Application*, 35(1): 29-33.
19. Liigand, P., Kaupmees, K., Haav, K., Liigand, J., Leito, I., Girod, M., Antoine, R. and Kruve, A. (2017). Think negative: finding the best electrospray ionization/MS mode for your analyte. *Analytical Chemistry,* 89: 5665-5668.
20. Hidalgo, M., Sánchez-Moreno, C. and De Pascual-Teresa, S. (2010). Flavonoid-flavonoid interaction and its effect on their antioxidant activity. *Food Chemistry,* 121: 691-696.
21. Procházková, D., Boušová, I., and Wilhelmová, N. (2011). Antioxidant and prooxidant properties of flavonoids. *Fitoterapia,* 82: 513-523.
22. Werner, E., Heilier, J. F., Ducruix, C., Ezan, E., Junot, C. and Tabet, J. C. (2008). Mass spectrometry for the identification of the discriminating signals from metabolomics: current status and future trends. *Journal of Chromatography* B, 871(2): 143-63.
23. De Vijlder, T., Valkenborg, D., Lemière, F., Romijn, E. P., Laukens, K. and Cuyckens, F. (2018). A tutorial in small molecule identification via electrospray ionization-mass spectrometry: The practical art of structural elucidation. *Mass Spectrometry Review,* 37: 607-629.
24. Wang, X., Zhang, A., Zhou, X., Liu, Q., Nan, Y., Guan, Y., Kong, L., Han, Y., Sun, H. and Yan, G. (2016). An integrated chinmedomics strategy for discovery of effective constituents from traditional herbal medicine. *Scientific Reports,* 6: 18997.
25. Zoeller, M., Stingl, N., Krischke, M., Fekete, A., Waller, F., Berger, S. and Mueller, M. J. (2012). Lipid profiling of the Arabidopsis hypersensitive response reveals specific lipid peroxidation and fragmentation processes: Biogenesis of pimelic and azelaic acid. *Plant Physiology,* 160: 365-378.
26. Zhou, Y. S., Gu, C. M. and Gu, H. (2012). Supercritical CO_2 extraction of tea seed oil from Camellia seeds and composition analysis of tea seed oil extracts. *Advanced Materials Research,* 538-541: 2372-2376.
27. De Ferron, P., Thibon, C., Shinkaruk, S., Darriet, P., Allamy, L. and Pons, A. (2020). Aromatic potential of Bordeaux grape cultivars: Identification and assays on 4-oxononanoic acid, a γ-nonalactone precursor. *Journal of Agricultural and Food Chemistry,* 68(47): 13344-13352.
28. Chen, G., Li, X., Saleri, F. and Guo, M. (2016). Analysis of flavonoids in *Rhamnus davurica* and its antiproliferative activities. *Molecules,* 21: 1-14.
29. Shen, S., Wang, J., Chen, X., Liu, T., Zhuo, Q. and Zhang, S. (2019). Evaluation of cellular antioxidant components of honeys using UPLC-MS/MS and HPLC-FLD based on the quantitative composition-activity relationship. *Food Chemistry,* 293: 169-177.
30. Olmo-García, L., Kessler, N., Neuweger, H., Wendt, K., Olmo-Peinado, J. M., Fernández-Gutiérrez, A., Baessmann, C. and Carrasco-Pancorbo, A. (2018). Unravelling the distribution of secondary metabolites in *Oleae uropaea* L.: Exhaustive characterization of eight olive-tree derived matrices by complementary platforms (LC-ESI/APCI-MS and GC-APCI-MS). *Molecules,* 23(10): 2419.

31. Choi, H. G., Park, Y. M., Lu, Y., Chang, H. W., Na, M. And Lee S. H. (2012). Inhibition of prostaglandin D2 production by trihydroxy fatty acids isolated from *Ulmus davidiana* var. japonica. *Phytotherapy Research* 27: 1376-1380.
32. Wang, D., Liang, J., Yang, W., Hou, J., Yang, M., Da, J., Wang, Y., Jiang, B., Liu, X., Wu, W. and Guo, D. (2014). HPLC/qTOF-MS-oriented characteristic components data set and chemometric analysis for the holistic quality control of complex TCM preparations: Niuhuang Shangqing pill as an example. *Journal of Pharmaceutical and Biomedical Analysis,* 89: 130-141.
33. Li, F., Zhang, Y., Wei, X., Song, C., Qiao, M. and Zhang, H. (2016). Metabolic profiling of Shu-Yu capsule in rat serum based on metabolic fingerprinting analysis using HPLC-ESI-MSn. *Molecular Medicine Reports,* 13: 4191-4204.
34. Halake, K., Birajdar, M. and Lee, J. (2016). Structural implications of polyphenolic antioxidants. *Journal of Industrial and Engineering Chemistry,* 35: 1-7.
35. Sarian, M. N., Ahmed, Q. U., Mat So'ad, S. Z., Alhassan, A. M., Murugesu, S., Perumal, V., Syed Mohamad, S. N. A., Khatib, A. and Latip, J. (2017). Antioxidant and antidiabetic effects of flavonoids: a structure-activity relationship based study. *BioMed Research International*, 2017: 1-14.
36. Chen, L., Teng, H., Xie, Z., Cao, H., Cheang W. S., Skalicka-Woniak, K., Georgiev, M. I. and Xiao, J. (2018). Modifications of dietary flavonoids towards improved bioactivity: An update on structure-activity relationship. *Critical Reviews in Food Science and Nutrition,* 58: 513-527.
37. Levandi, T., Püssa, T., Vaher, M., Toomik, P. and Kaljurand, M. (2009). Oxidation products of free polyunsaturated fatty acids in wheat varieties. *European Journal of Lipid Science and Technology,* 111: 715-722.
38. Hübke, H., Garbe, L. A. and Tressl, R. (2005). Characterization and quantification of free and esterified 9- and 13-hydroxyoctadecadienoic acids (HODE) in barley, germinating barley, and finished malt. *Journal of Agricultural and Food Chemistry,* 53(5): 1556-1562.
39. Holková, I., Rauová, D., Mergová, M., Bezáková, L. and Mikuš, P. (2019). Purification and product characterization of lipoxygenase from opium poppy cultures (*Papaver somniferum* L.). *Molecules* 24(23): 4268.
40. Horai, H., Arita, M., Kanaya, S., Nihei, Y., Ikeda, T., Suwa, K., Ojima, Y., Tanaka, K., Tanaka, S., Aoshima, K., Oda, Y., Kakazu, Y., Kusano, M., Tohge, T., Matsuda, F., Sawada, Y., Hirai, M. Y., Nakanishi, H., Ikeda, K., Akimoto, N., Maoka, T., Takahashi, H., Ara, T., Sakurai, N., Suzuki, H., Shibata, D., Neumann, S., Iida, T., Tanaka, K., Funatsu, K., Matsuura, F., Soga, T., Taguchi, R., Saito, K. and Nishioka, T. (2010). MassBank: a public repository for sharing mass spectral data for life sciences. *Journal of Mass Spectrometry,* 45(7): 703-14.
41. Baker, P. R. S., Armando, A. M., Campbell, J. L., Quehenberger, O. and Dennis, E. A. (2014). Three-dimensional enhanced lipidomics analysis combining UPLC, differential ion mobility spectrometry, and mass spectrometric separation strategies. *Journal of Lipid Research,* 55: 2432-2442.
42. Mok, H. J., Lee, J. W., Bandu, R., Kang, H. S., Kim, K. and Kim, K. P. (2016). A rapid and sensitive profiling of free fatty acids using liquid chromatography electrospray ionization tandem mass spectrometry (LC/ESI-MS/MS) after chemical derivatization. *RSC Advances* 6: 32130-32139.
43. Mazzotti, F., Benabdelkamel, H., Di Donna, L., Maiuolo, L., Napoli, A. and Sindona G. (2012). Assay of tyrosol and hydroxytyrosol in olive oil by tandem mass spectrometry and isotope dilution method. *Food Chemistry,* 135: 1006-1010.
44. Bartella, L., Mazzotti, F., Napoli, A., Sindona, G. and Di Donna, L. (2018). A comprehensive evaluation of tyrosol and hydroxytyrosol derivatives in extra virgin olive oil by microwave-assisted hydrolysis and HPLC-MS/MS. *Analytical and Bioanalytical Chemistry,* 410: 2193-2201.

45. Martini, S., Cavalchi, M., Conte, A. and Tagliazucchi, D. (2018). The paradoxical effect of extra-virgin olive oil on oxidative phenomena during in vitro co-digestion with meat. *Food Research International,* 109: 82-90.
46. Angelis, A., Antoniadi, L., Stathopoulos, P., Halabalaki, M. and Skaltsounis, L. A. (2018). Oleocanthalic and oleaceinic acids: New compounds from extra virgin olive oil (EVOO). *Phytochemistry Letters,* 26: 190e194.
47. Kanakis, P., Termentzi, A., Michel, T., Gikas, E., Halabalaki, M. And Skaltsounis, A. (2013). From olive drupes to olive oil. An HPLC-Orbitrap-based qualitative and quantitative exploration of olive key metabolites. *Planta Medica,* 79: 1576-1587.
48. Sánchez de Medina, V., Miho, H., Melliou, E., Magiatis, P., Priego-Capote, F. and Luque de Castro, M. D. (2017). Quantitative method for determination of oleocanthal and oleacein in virgin olive oils by liquid chromatography-tandem mass spectrometry. *Talanta,* 162: 24-31.
49. Li, H., Yao, W., Liu, Q., Xu, J., Bao, B., Shan, M., Cao, Y., Cheng, F., Ding, A. and Zhang, L. (2017). Application of UHPLC-ESI-Q-TOF-MS to identify multiple constituents in processed products of the herbal medicine Ligustri Lucidi Fructus. *Molecules* 22: 1-14.
50. Luque-Muñoz, A., Tapia, R., Haidour, A., Justicia, J. and Cuerva, J. M. (2019). Direct determination of phenolic secoiridoids in olive oil by ultra-high performance liquid chromatography-triple quadruple mass spectrometry analysis. *Scientific Reports,* 9: 15545.
51. Sanz, M., Fernández de Simón, B., Cadahía, E., Esteruelas, E., Muñoz, A. M., Hernández, T., Estrellac, I. and Pinto, E. (2012). LC-DAD/ESI-MS/MS study of phenolic compounds in ash (*Fraxinus excelsior* L. and *F. americana* L.) heartwood. Effect of toasting intensity at cooperage. *Journal of Mass Spectrometry,* 47: 905-918.
52. Ansari, E., Karami, A. and Ebrahimie, E. (2019). Isolation of 2-phenylethanol biosynthesis related gene and developmental patterns of emission of scent compounds in Persian musk rose (*Rosa moschata* Herrm.). *Biocatalysis and Agricultural Biotechnology,* 19: 1-6.
53. Garcia-Bermudez, J., Baudrier, L., Bayraktar, E. C., Shen, Y., La, K., Guarecuco, R., Yucel, B., Fiore, D., Tavora, B., Freinkman, E., Chan, S. H., Lewis, C., Min, W., Inghirami, G., Sabatini, D. M. and Birsoy, K. (2019). Squalene accumulation in cholesterol auxotrophic lymphomas prevents oxidative cell death. *Nature* 567: 118-122.
54. Prasad, K. (2019). Importance of flaxseed and its components in the management of hypertension. *International Journal of Angiology,* 28: 153-160.

Malaysian Journal of Analytical Sciences (MJAS)
Published by Malaysian Analytical Sciences Society

EFFECT OF DRYING TIMES AND TEMPERATURES ON THE QUALITY OF TRADITIONAL SPICY SAUCE CUBE

(Kesan Masa dan Suhu Pengeringan Terhadap Kualiti Kiub Sambal Tradisional)

Nur Huda Mohd Masseri, Norhayati Muhammad*, Nur Fazira Abdul Rahim

Department of Technology and Natural Resources,
Faculty of Applied Sciences and Technology,
Universiti Tun Hussein Onn Malaysia, 84600 UTHM – Pagoh Campus, Muar, Johor, Malaysia

**Corresponding author: norhayatim@uthm.edu.my*

Received: 12 July 2021; Accepted: 21 August 2021; Published: 29 August 2021

Abstract

Food drying is a food preservation method to inhibit bacterial, yeast and mold growth through the water removal technique. This study aims to analyze the effects of different drying temperatures and durations on the traditional spicy sauce cubes' qualities (moisture content, water activity, texture, color, disintegration time and sensory analysis). Different drying temperatures for the cubes consisted of three different stages temperatures were used to compare with the control cube's quality. The production of traditional spicy sauce cubes involved the preparation of fresh ingredients, cooked into a paste, drying, grinding the paste into powder and compacted into a cube molder (3.3×1.5 cm). It was found that the cubes with high initial temperature had lower moisture content than those with low initial temperature. The three-stage temperature cubes exhibited a lower water activity compared to other cubes and had higher hardness and lower fracturability but their color is still retained. All the traditional cubes had a disintegration time below 60 seconds which indicated the good quality of cubes. The different cyclic temperatures regime showed no significant difference to the aftertaste and overall acceptance among all prepared cubes. Overall, the significant differences in cubes' qualities were affected by varying the cyclic drying temperatures.

Keywords: traditional spicy sauce cube, cyclic drying temperatures, drying times

Abstrak

Pengeringan makanan adalah satu kaedah pegawetan makanan untuk mencegah pertumbuhan bakteria, ragi dan kulat melalui teknik penyingkiran air. Kajian ini bertujuan untuk menganalisis kesan suhu dan jangka masa pengeringan yang berbeza terhadap kualiti kiub sambal tradisional (kandungan kelembapan, aktiviti air, tekstur, warna, masa perlarutan dan penilaian sensori). Suhu pengeringan untuk kiub sambal tradisional yang terdiri daripada tiga tahap yang berbeza telah dibandingkan dengan kualiti kiub kawalan. Penghasilan kiub sambal tradisional merangkumi penyediaan bahan-bahan segar, dimasak menjadi pes, pengeringan dan pengisaran pes menjadi serbuk dan dipadatkan ke dalam acuan kiub (3.3×1.5 cm). Kiub sambal tradisional dengan suhu awal pengeringan yang tinggi didapati mempunyai kandungan kelembapan yang lebih rendah daripada suhu awal pengeringan yang rendah. Kiub dengan suhu tiga-tahap menunjukkan aktiviti air yang lebih rendah berbanding dengan kiub-kiub lain serta lebih keras dan tidak mudah pecah, tetapi warnanya masih dapat dikekalkan. Semua kiub sambal tradisional mempunyai masa perlarutan di bawah 60 saat yang membuktikan kualiti kiub yang baik. Kitaran suhu pengeringan yang berbeza menunjukkan tiada perbezaan

yang signifikan terhadap kesan rasa dan penerimaan keseluruhan antara semua kiub sambal tradisional yang disediakan. Kesimpulannya, perbezaan ketara kualiti kiub sambal tradisional telah dipengaruhi oleh pelbagai kitaran suhu pengeringan.

Kata kunci: kiub sambal tradisional, kitaran suhu pengeringan, masa pengeringan

Introduction

Spicy sauce or known as *sambal* is an Indonesian chili sauce or paste usually made from a combination of a variety of secondary ingredients such as shrimp paste, garlic, ginger, shallot, scallion, palm sugar, and lime juice from a variety of chili peppers. In Malaysia, the spicy sauce had been known as one of the compulsory foods that were often served alongside the main meal such as *nasi lemak, nasi ayam,* and *asam pedas* [1]. The hot, sweet or a combination exhibited by chili or spicy sauce may differ from hot sauce in that many sweet or mild varieties exist, usually lacking in hot sauces. However, Malaysians also have their own interest in making the spicy sauce with spiciness or sweetness to be served in their meal. In contrast to hot sauces, the chili sauce can have a thicker texture and viscosity, while chili paste commonly refers to a paste where the chili pepper is the main ingredient. Some are used chili paste as a cooking ingredient, and some are used after preparation to season a sauce.

In this sophisticated era, the making of spicy sauce may be troublesome for certain individuals especially working spouses or individuals as its conventional cooking process is time-consuming which could affect their busy schedule. This is because the ingredients preparation and cooking process of chili paste requires expertise and reliability particularly, in flavor adjustment. In addition, this modern world had established bouillon cubes that growing consumers' demand in the market. These cubes have some beneficial factors such as convenient, easy-to-use, long shelf life without refrigeration storage, instantly add flavor and can balance almost any dish or soup for a short time. However, to the best of our knowledge, there is no standard method available in preparation of the cube that could mimic the original physical properties and sensory. Thus, this research is conducted to obtain the optimal physical and sensory characteristics of traditional spicy sauce cube.

For food products, it is important to ensure the drying rate is eligible as it can affect food quality. This is supported to a research conducted by Heldman and Hartel, that found the drying temperature, air velocity, relative humidity, pressure and features of food products (concentration and composition) are the key factors that may influence the drying process [2]. Moreover, based on the drying kinetics of tomato paste researched by Jumah et al., the increase in the temperature of the inlet air in the 60-100 °C range greatly increased the drying rate of tomato paste [3]. This indicates that the drying time would be decreased as the air temperature increased. For that reason, the drying time should be properly adjusted according to the air temperature to keep the good quality and nutritional composition of food products. Besides that, it has been reported that improving drying energy efficiency by only 1% could result in a profit increase of up to 10% [4]. The process of food dehydration corresponds to reduce the food moisture to low levels by adding one or more types of energy to the food can prolong the shelf life. This can be concluded that a good quality of product can be achieved with a reasonable drying period and lower consumption of energy. Hence, the factors of drying time and temperatures were highlighted in this study as they can be significant factors in the production of the best spicy sauce cube product.

In this study, the effect of drying times and temperatures in the process of making traditional spicy sauce cube were evaluated to provide the best solution in the product drying process which induced the optimal result of physical properties. The physical properties that were being conducted consist of moisture content, water activity, texture, color and disintegration time which these properties were related to the ability of cubes to withstand the environmental impact from the surroundings. Besides that, the sensory analysis will be conducted to evaluate the most consumer acceptance among the different samples. Based on the sensory analysis, the quality attributes entailing taste, aroma,

appearance and texture are the most important aspects in the products to meet the requirements or demands of the consumer.

Materials and Methods

Materials

The fresh ingredients which consisted of dried chilies, onions, garlic and anchovies were purchased from L&L Mini Market, Pagoh Jaya, Johor while the commercial bouillon cube was bought from Green Apple Store, Pagoh, Johor. The preservative (sodium benzoate) was purchased from Tong Sheng Food Technology Sendirian Berhad, Pulau Pinang while the potato starch was bought from TF Value-Mart, Muar, Johor. All the ingredients used have been food grade acquired from local sources.

Production of traditional spicy sauce paste and cube

For the initial step, the preparation of fresh ingredients was started by cleaning dried chilies, fresh onion, garlic and anchovies to remove unwanted waste and excess dirt. The amount of the ingredients used is shown in Table 1. After that, the dried chilies were sliced to remove the seeds to ensure the smooth chili paste was produced as well as to reduce the spiciness of chilies. Next, the sliced chilies were soaked in hot water (100 °C) for 10 minutes. This process is to soften the chilies and facilitate the blending process. The dried chilies with the addition of 350 mL of water were blended thoroughly by using a kitchen blender (Toshiba, BL-60PHNMY, Japan) for about five (5) minutes at medium speed until forming a smooth chili paste. The minced onion, garlic and anchovies were blended by a kitchen blender. The cooking process of spicy sauce paste started with the addition of cooking oil into a frying pan and was heated at medium temperature (70-80 °C). Then, the chili pastes and the blended ingredients (onion, garlic and anchovies) were added to the same frying pan and stir-fried for 10 minutes. Next, the water was added to the mixture, slowly stirred and continues cooked for another 15 minutes. Lastly, the starch and sodium benzoate (preservative) were added to the paste. The amount of ingredients used has produced approximately 400 g of spicy sauce paste without the removal of oil.

Prior to drying, the paste was spread on the baking paper which formed a thin layer to deliver the efficiency of paste drying in the food dehydrator (Yisino, SX-770, Malaysia). Thus, the paste had been dried until the moisture content below 12% as it is significant to produce the cubes with low moisture content. The low moisture content of the cubes led to adequate textural properties as it induced higher hardness and lower fracturability [5]. Next, the dried paste was grounded into a smaller size using the dry blender (Panasonic, MX-SM1031, Japan) and molded into cubes form by using a 3.3×1.5×1.0 cm (long × width × thickness) molder.

Table 1. Ingredients used in the production of the traditional spicy sauce cube

Ingredients	Amount
Dried chilies	27 g
Fresh onion	260 g
Garlic	19 g
Anchovies	10 g
Starch	10 g
Sodium benzoate	0.1 g
Chilli paste	83 g
Cooking oil	15 mL

Drying times and temperatures variation profile

The minimum and maximum limit of the parameter in drying times and temperatures were according to some previous studies in the cubing process with modification [3, 6]. There are five (5) variations were made in drying temperatures which include the one-stage, two-stage and three-stage temperatures varied between 60 ˚C and 70 ˚C. One-stage temperature drying process consists of 60 ˚C for 12 hours which represented cube (a), two-stage temperature drying process consists of 60 ˚C (4 hours) + 70 ˚C (8 hours) represented as cube (b) and 70 ˚C (4 hours) + 60 ˚C (8 hours) represented as cube (c) while the three-stage temperature consists of 60 ˚C (4 hours) + 70 ˚C (5 hours) + 60 ˚C (3 hours) which represented cube (d) and 70 ˚C (4 hours) + 60 ˚C (5 hours) + 70 ˚C (3 hours) represented as cube (e). The approximate drying time was according to Wiriya et al. with modification to obtain the moisture content below 12% [6]. The spicy sauce paste was spread on a tray as a single layer and this drying process was carried out by using 150-200 g of paste for each variation. However, the traditional spicy sauce cube qualities were also being compared to commercial bouillon cube (brand *Tomyam Knorr*) to observe any differences in response analysis.

Determination of moisture content

The moisture content of cubes was determined by using a moisture analyzer (A & D, MX-50, USA). About five (5) grams of the sample was put on a dish and heated at 120 ˚C in the analyzer [7]. The experimental data was obtained with three (3) replications.

Analysis of water activity

The water activity of the spicy sauce cubes was analyzed by using a dew point equipment (Decagon Devices Inc, Aqualab 4TE, USA). This analysis was required approximately two (2) grams of the sample that was placed into a small cylindrical container with a diameter of 3 cm before the measurement at an ambient temperature of 25 ˚C [8].

Texture analysis

The texture of cubes in terms of fracturability and hardness were tested using a texture analyzer (TA. XT Plus, Stable Micro System, UK) which has been calibrated with 5000 g load cell before analyzing. Then, the texture analyzer mode was set respective to the cubes sample. The probe used was a 0.5'' spherical probe and the platform was set to 10 mm from the probe [8].

Color measurements

Surface color measurement was conducted using the L*a*b* system (Universal HunterLab, Model 45/0 S/N CX-0413), calibrated to a standard black and white tile, prior to sample color measurement. L* corresponds to lightness, a* refers to red (+)/ green (-) and b* represents yellow (+)/ blue (-). The sample was weighed about five (5) grams, placed into the petri dish and covered. Three (3) measurements were conducted for each variation [8].

Analysis of disintegration time of cubes

The cubes were weighed at approximately five (5) grams and dissolved in hot water space. Then, stir the cubes manually to enhance the disintegration process. The time taken for the cubes to break down into smaller particles or granules was recorded by a timer/stopwatch [9].

Sensory analysis

Each variation of cubes (control cube, a, b, c, d and e) was dissolved in 10 mL of hot water and cooled for about five (5) minutes before being presented to the untrained panelist. The selection of panelists in Universiti Tun Hussein Onn Malaysia was random and should be complied to 50 respondents and above as according to Sharif et al. [10]. Therefore, a total of 50 untrained panelists have participated in this test to evaluate the acceptability of the cubes. For this sensory test, a 9-point hedonic scale was used ranging from 'extremely dislike' to 'extremely like'. The score sheets were provided with the product and panelists were requested to rate the product according to the degree of their liking. Then, the average scores of the panelists were computed for different characters [11].

Statistical analysis of spicy sauce cube

One-way analysis of variance (ANOVA) was conducted to compare the means of two or more or more independent groups to determine whether there is statistical evidence that the associated population means

are significantly different. One-way ANOVA, (IBM SPSS Statistics Version 26, USA) was used followed by Tukey honest significant difference (HSD) and least significant difference (LSD) multiple comparison test and p values ≤ 0.05, considered significantly different.

Results and Discussion

Spicy sauce cube prototype production

There are five (5) variations of different drying times and temperatures of the traditional spicy sauce cube and a commercial bouillon cube that acts as a control between groups of the physical properties' analysis. Figure 1 shows the traditional spicy sauce cubes and a commercial bouillon cube that have been obtained as a final desired product in this study. The production of cubes was initiated by the preparation of fresh ingredients, followed by, cooking the mixture of the ingredients into a paste and drying the paste according to the five (5) variations. After that, the dried paste was grounded into powder form prior to the cubing process by the molder. The drying temperature was in the range from 60 ºC to 70 ºC and the drying time was a total of 12 hours according to some previous research with modifications [3, 6]. This modification was made and accomplished to ensure the final product of spicy sauce cubes capable to achieve the desired moisture content which has to be beyond 12%. The dimensions (33 mm × 15 mm × 10 mm) and weight (10 g) as the homogeneity of traditional spicy sauce cubes attributed the good quality parameters.

In addition, the color of the cubes can be affected by the different drying times and temperatures due to browning reaction, therefore the lightness (L*), redness (a*) and yellowness (b*) of cubes have been studied to observe the homogeneity of the traditional spicy sauce cube production. However, the traditional spicy sauce cubes exerted almost the same brown-reddish color and had slightly different in lightness. Besides, the texture of the cubes also has been studied in terms of hardness and fracturability to observe which cubes had resulted in the higher hardness and lower fracturability. The higher hardness of cubes is more preferred in this study as it is related to the lower moisture content and provides a longer shelf life of cubes, while the lower fracturability also impeding the cubes to break easily [5]. Also, the fast-dissolving of the traditional spicy sauce cubes in hot water that was below 60 seconds is also more preferred as it is convenient to the consumers and showed the good quality of cubes.

Moisture content

The results of all tested physical properties of the cubes are shown in Table 2. It was found that the control cube (0.57%) recorded the lowest percentage in moisture than all traditional spicy sauce cubes prepared. The range of moisture content for all traditional spicy sauce cubes were in between 7.35-11.20%. This result was probably due to the higher water retention of the fresh ingredients used in traditional spicy sauce cubes and different cyclic drying temperatures [12]. The fresh ingredients tend to have higher amounts of water, thus, required more drying time or higher drying temperature. Cube (a) which implemented the one cyclic temperature indicated the highest moisture content due to dry out of all mixture at one time at a high temperature which leads to a hardened surface and hinders the evaporation of water inside from the center of the product to the surface [6]. However, the moisture content of traditional cubes in the present study obtained was in the range of ideal moisture content (below 12.00%) even though the result was quite higher than ideal moisture content from other studies [5].

Results also found that cube (c) and cube (e) had a lower moisture content than other traditional spicy sauce cubes, probably due to the higher initial stage temperature during the drying process. Then, the tempering time of the cubes was allowed with an acceptable high temperature during this period for the diffusion of moisture from the center to the cube surface. Therefore, during the second and third stages of drying without excessive heating, moisture removal of cubes can still be achieved, especially on the surface of the cubes. Based on the previous study by Chua et al., during the initial drying period, the effect of temperature tempering on the drying curves is important and is gradually less profound towards the later drying stage. This effect can be attributed to the rapid transfer of moisture and migration in the initial drying stage to the sample surface as a result of higher sensitive heat obtained due to higher air temperature [12]. Thus, the

increase in the evaporation rate of moisture from the sample surface can contribute to the lower moisture content of the traditional spicy sauce cubes.

Water activity

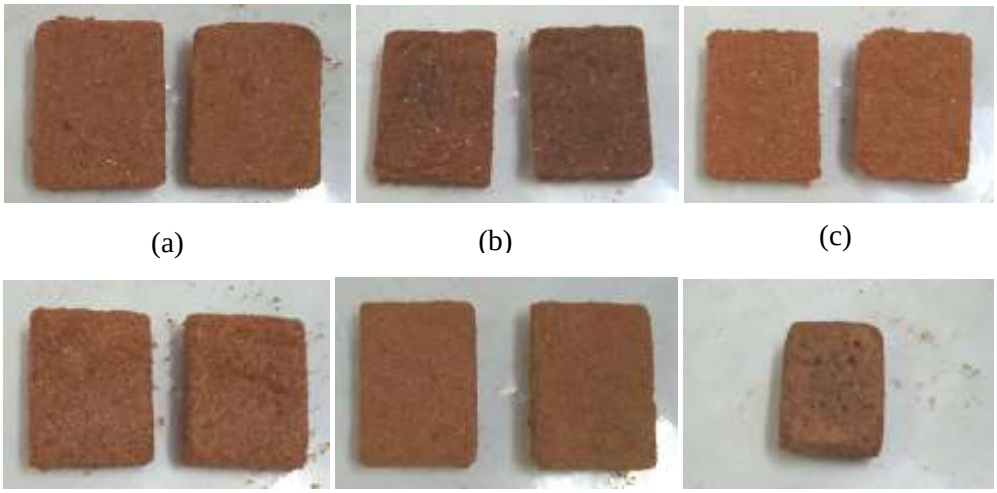
From Table 2, the results showed that overall cubes samples were in the range of 0.47-0.59 as the highest of water activity was the control cube (A_w = 0.59) and the lowest was cube (e) (A_w = 0.47). The water activity of the control cube was significantly different from other cube samples. The three cyclic drying temperatures which complied to both cubes (d) and (e) indicated no significant different ($p < 0.05$) between them but both had lower water activity when compared to the control cube and two cyclic drying temperature cubes which represented by cube (b) and cube (c). The lower water activity in a cube might be due to the tightly bound of water to a protein or carbohydrate molecule which corresponds to lowering and increasing drying temperature [13]. Based on previous research by Smorenburg and Yamson, the recommended water activity of a well-established bouillon cube is below 0.65 [14]. Nevertheless, the range of water activity of cubes can be within the range 0.413 to 0.505. A good flowability of powders in a bouillon cube can be indicated by low water activity [15]. In this study, the lower water activity is more preferably which is denoted by cube (d) and cube (e) to attribute the well-established with good flow-ability of powders of traditional spicy sauce cubes and attain the ambient stability as well as inhibit the survival of microorganisms.

Texture

The result of cubes' texture was shown in Table 2 regarding the hardness and fracturability obtained at 4.0 seconds. Cube (e) showed the highest hardness (0.632 kg) and fracturability (3.99 mm) among other traditional spicy sauce cubes. The good strength of cubes can be denoted due to higher hardness and lower fracturability, impeding the cubes to break easily [5]. According to prior research by Ansari et al., the moisture content was inversely proportional to the hardness of dried figs at a constant drying temperature [16]. On the other hand, the hardness of dried figs decreased with an increase in moisture content. This was possibly due to the lower resistance of the higher moisture content provided to crack the sample. Therefore, the lower rupturing force was required to rupture the dried figs. In overview, the highest hardness that was recorded by the cube (e) might be due to the lower water activity and moisture content as it required more force to break the cube. Thus, the formation of the cracks because the strength of cube (e) was the lowest which contributed to lower fracturability compared to the other cubes.

Color analysis

From Table 3, it presented that the lowest value of L* (lightness) was cube (b) (L*= 28.13) and the highest L* value was cube (d) (L*= 37.13). The two cyclic temperatures of cube (b) showed the darkest brown compared to others due to high temperatures with a long time as its temperature was elevated from 60 ^oC (4 hours) to 70 ^oC (8 hours). Those observations agreed with the results of Lee et al., who have suggested that a dark–brown color due to the non-enzymatic browning reaction was attributed to the use of high temperatures for drying air [17]. For three cyclic temperatures, both cubes of (d) and (e) showed more pure light than the one-stage temperature of cube (a) (L*= 31.77) but cube (e) exerted slightly darker than the control cube (L*= 34.64). The color of traditional spicy sauce cubes was influenced by many factors including the browning reaction of spicy sauce paste during cooking, the natural colors exhibited from the fresh ingredients and the Maillard reaction occurs in different cyclic drying temperatures. The fixed amount of the ingredients used in the cubes production were similar and according to the research methodology, however, the color of onion and garlic that contributed to brownish color may be differed due to the addition of water during paste preparation. According to Gupta et al., the enzymatic and non-enzymatic browning reactions are the main reactions that occur during drying [18]. On the other hand, the higher temperatures and intermediate levels of humidity in food contributed to the increases in the rate of non-enzymatic reactions [19].



(a) (b) (c)

(d) (e) (f)

Note:
(a) 60 ºC (12 hours); (b) 60 (4 hours) +70 ºC (8 hours); (c) 70 (4 hours) +60 ºC (8 hours); (d) 60 (4 hours) +70 (5 hours) +60 ºC (3 hours); (e) 70 (4 hours) +60 (5 hours) +70 ºC (3 hours); (f) Commercial bouillon cube

Figure 1. Traditional spicy sauce cube and commercial bouillon cube

Table 2. Physical properties of traditional spicy sauce and control cubes

Cube Samples	**Physical Properties**			
	Moisture Content (%)	**Water Activity**	**Texture**	
			Hardness (kg)	**Fracturability (mm)**
Control	0.57 ± 0.03^{a}	0.59 ± 0.007^{c}	0.424 ± 0.05^{b}	1.862 ± 0.05^{cd}
(a)	11.20 ± 1.03^{d}	0.52 ± 0.01^{ab}	0.121 ± 0.02^{e}	2.132 ± 0.63^{bc}
(b)	8.46 ± 0.47^{bc}	0.52 ± 0.005^{ab}	0.223 ± 0.02^{cd}	2.860 ± 0.24^{b}
(c)	7.66 ± 0.14^{bc}	0.55 ± 0.05^{bc}	0.254 ± 0.03^{c}	2.093 ± 0.20^{bcd}
(d)	8.93 ± 0.06^{c}	0.48 ± 0.03^{a}	0.130 ± 0.01^{de}	1.157 ± 0.22^{d}
(e)	7.35 ± 0.30^{b}	0.47 ± 0.005^{a}	0.632 ± 0.04^{a}	3.99 ± 0.02^{a}

^{a,b,c,d} Values with different letters in the same row are significantly different ($p < 0.05$)

Note:
(a) 60 ºC (12 hours); (b) 60 (4 hours) +70 ºC (8 hours); (c) 70 (4 hours) +60 ºC (8 hours); (d) 60 (4 hours) +70 (5 hours) +60 ºC (3 hours); (e) 70 (4 hours) +60 (5 hours) +70 ºC (3 hours); (f) Commercial bouillon cube

Table 3. Disintegration time and color analysis of the spicy sauce cubes

Cube Samples	Color			Disintegration Time (seconds)
	L*	a*	b*	Mean ± SD
Control	34.64±0.88^{b}	16.08±0.36^{c}	24.64±0.58^{b}	247.00±6.25^{d}
(a)	31.77±1.12^{c}	19.99±1.81^{b}	31.65±4.21^{a}	42.09±1.67^{c}
(b)	28.13±0.62^{d}	19.30±1.05^{b}	26.78±4.54^{b}	30.30±0.84^{c}
(c)	29.38±0.09^{d}	21.77±1.40^{a}	28.13±3.82^{ab}	20.03±0.42^{b}
(d)	37.13±0.80^{a}	13.88±0.50^{d}	19.66±1.06^{c}	29.89±0.30^{b}
(e)	33.18±0.59^{c}	13.91±0.41^{d}	14.78±0.82^{d}	16.02±0.09^{a}

^{a,b,c,d} Values with different letters in the same row are significantly different ($p < 0.05$)

Note:
(a) 60 ^{o}C (12 hours); (b) 60 (4 hours) +70 ^{o}C (8 hours); (c) 70 (4 hours) +60 ^{o}C (8 hours);
(d) 60 (4 hours) +70 (5 hours) +60 ^{o}C (3 hours); (e) 70 (4 hours) +60 (5 hours) +70 ^{o}C (3 hours)

Disintegration time

From Table 3, it indicates that all traditional spicy sauce cubes had disintegration time below 60 seconds, however, the control cube denoted the longest time to be disintegrated (247 seconds). All the traditional spicy sauce cubes dissolve rapidly in hot water due to the water heat that melts the fat which holds the cubes together. Nevertheless, it was observed that there was a separation of cubes powder and water that contributed to the sedimentation of powder at the bottom layer. The easily dissolving low-fat bouillon cube requires the provision of a free-flowing bouillon powder to a molder with a surface water residue [9]. A rapidly dissolving bouillon cube can be formed when the bouillon powder is compressed at low pressure. For cube (e), it showed the lowest disintegration time which is only 16.09 seconds compared to other cubes as well as denoted the best quality of fast-dissolving cube. Apart from that, the disintegration time of cubes can be related to the amount of moisture content as the higher moisture content possibly improved plastic deformation [20].

The higher moisture present decreased the compact force as it was capable of lowering the hydrodynamic resistance and thus increased elastic recuperation after dissolution [20]. In addition, the moisture content also corresponds to the disintegration time and porosity of cubes. As the increase in moisture content induced a substantial increase in porosity and a decrease in disintegration time, porosity was found to be consistent with disintegration time performance. Therefore, it was suggested that the high amount of moisture content probably contributed to the formation of a particle's freely moving environment, whereas the most acceptable compact configuration was attained. Meanwhile, the disintegration period was extended at low moisture content as the reduction of pores decreased the capacity of water to enter and break up the cubes [21]. In this study, the fast dissolution of the traditional spicy sauce cubes that below 60 seconds when compared to the control cube possibly attributed to the higher moisture content which contributed to the increasing of pores leads to improve the ability of water to enter and deform the cubes.

Sensory evaluation

Meanwhile, for the sensory analysis, the mean scores data of the hedonic test of cubes gravy by 50 panelists was presented in Table 4. Results from this study showed that the preference of cubes corresponding to

the aftertaste and overall acceptance had the highest mean scores for the control cube compared to the traditional spicy sauce cubes, demonstrating the panelists preferred the control cube in the market. The mean scores of attributes aftertaste and overall acceptance of control cube were 6.18 and 7.24 respectively. However, the color for control cube was the least preferred by panelists due to the dark brown color compared to reddish-orange color of traditional spicy sauce cubes, which resulted from the mean scores of only 3.92. The reddish-orange color due to dried chili as the basic ingredients denoted the more pleasant color by panelists than dark brown color. Among the traditional spicy sauce cubes, cube (d) had the highest mean scores (6.58) of overall acceptances which showed a significant difference compared to others. Results obtained that cube (c) had the lowest mean scores for the taste properties which was only 3.72, indicated the most undesirable to the panelists.

Besides, the aftertaste of cube (a) (4.98), cube (b) (4.32), cube (d) (4.94) and cube (e) (4.44) were in the range of 4.32-4.98 which had significant different compared to cube (c) and control cube (6.18). Concerning the range of mean scores for the sensory assessment, the panelist did not notice remarkable differences in the final attributes of traditional spicy sauce cubes that were included of color, aroma, spiciness and aftertaste. The previous research has been shown that the decrease in drying air temperature from 70 ˚C to 50 ˚C resulted in less darkening of the tomatoes and an increase in the sugar or acid ratio, the impact of temperature can be linked to color and flavor changes [22]. Thus, the cyclic drying temperature for cubes provided a better condition of drying process additionally in consider of the sensory preferences in terms of color and aftertaste, the cube (e) which in compliance of three-stage temperature accompanied by the fastest dissolving (16.02 seconds) and low in moisture content (7.35%) was the most recommended for the production traditional spicy sauce cubes.

Table 4. Sensory evaluation of traditional spicy sauce cubes and control cube

Cube Samples	Sensory Attributes				
	Color	**Aroma**	**Spiciness**	**Aftertaste**	**Overall acceptance**
Control	3.92 ± 0.69^{c}	5.24 ± 0.77^{c}	4.7 ± 0.81^{bc}	6.18 ± 0.80^{a}	7.24 ± 0.65^{a}
(a)	5.58 ± 0.86^{b}	6.30 ± 0.65^{a}	4.96 ± 0.92^{b}	4.98 ± 0.62^{b}	5.46 ± 0.93^{c}
(b)	6.72 ± 0.99^{a}	5.16 ± 0.82^{c}	4.44 ± 0.64^{c}	4.32 ± 0.99^{c}	4.44 ± 1.09^{d}
(c)	5.88 ± 0.82^{b}	5.80 ± 0.78^{b}	5.94 ± 0.71^{a}	3.72 ± 1.07^{d}	5.64 ± 0.85^{c}
(d)	4.42 ± 1.03^{c}	5.18 ± 0.89^{c}	4.82 ± 1.10^{bc}	4.94 ± 1.02^{b}	6.58 ± 0.86^{b}
(e)	6.46 ± 0.86^{b}	6.34 ± 0.66^{a}	4.66 ± 0.79^{bc}	4.44 ± 1.11^{bc}	4.24 ± 0.71^{d}

^{a,b,c,d} Values with different letters in the same row are significantly different ($p < 0.05$)

Note:

(a) 60 ºC (12 hours); (b) 60 (4 hours) +70 ºC (8 hours); (c) 70 (4 hours) +60 ºC (8 hours);
(d) 60 (4 hours) +70 (5 hours) +60 ºC (3 hours); (e) 70 (4 hours) +60 (5 hours) +70 ºC (3 hours)

Conclusion

The experimental results showed that the two-stage and three-stage cyclic drying temperatures exhibited a lower moisture content than one-stage temperature of traditional spicy sauce cubes. The cubes of three-stage drying temperatures had a lower water activity than the one-stage and two-stage temperatures might be due to the more efficiency of water removal during the drying

process. Moreover, the hardness and fracturability of three-stage temperature that complied to cube (e) exhibited the best result compared to other traditional spicy sauce cubes as it had the highest hardness and the lowest fracturability. Moreover, the color of the cubes characterized in three-stage temperature was being improved in terms of lightness, redness in two-stage temperature and yellowness in one-stage temperature. Apart from that, the disintegration times of all traditional spicy sauce cubes are below 60 seconds which denoted the fast-dissolving and good quality of cubes. The one-stage drying temperature attained the most preferably aroma and taste among the traditional spicy sauce cubes probably due to the lower drying temperature which decreased the aroma volatile compounds to be evaporated. In conclusion, it is suggested that the temperature applied to have to be lowered to 70 °C and increase the drying time to achieve qualities and consumer acceptability of traditional spicy sauce cubes that could be comparable to the commercial bouillon cube.

Acknowledgement

The authors are grateful and would like to thank the Faculty of Applied Sciences and Technology, Universiti Tun Hussein Onn Malaysia for permitting the use of laboratory facilities and apparatus as well as financially supporting this project.

References

1. Hui, Y. H., Ghazala, S., Graham, M., Murrell, K. D. and Nip, W. K. (2003). Canned chilli sauce. Handbook of vegetable preservation and processing. CRC Press, United States: pp. 162-164.
2. Heldman, D. R. and Hartel, R. W. (1997). Principles of food processing. Chapman and Hall, New York: pp. 309-339.
3. Jumah, R., Banat, F., Al-Asheh S. and Hammad, S. (2004). Drying kinetics of tomato paste. *International Journal of Food Properties*, 7(2): 253-259.
4. Beedie, M. (1995). Energy savings-a question of quality. *South Africa Journal Food Science Technology*, 48(3): 14-16.
5. Paula, A. M. and Conti-Silva, A. C. (2014). Texture profile and correlation between sensory and instrumental analyses on extruded snacks. *Journal of Food Engineering*, 121: 9-14.
6. Wiriya, P., Paiboon, T. and Somchart, S. (2009). Effect of drying air temperature and chemical pretreatments on quality of dried chilli. *International Food Research Journal*, 16: 441-454.
7. Association of Official Analytical Chemists (1984). Official methods of analysis 14th edition. Association of Official Analytical Chemists. Washington, D.C.
8. Ismail, N. and Sahibon, N. S., (2018). Evaluation of bouillon cube prepared with the addition of threadfin bream (*Nemipterus japonicus*) hydrolysate. *Journal of Tropical Agricultural Science*, 41(3):1315-1328.
9. Herreid, R. M. and Lippert, V. E. (2000). Method for making fast dissolving bouillon cubes. United States. Patent No: 6126979.
10. Sharif, M. K., Butt, M. S. Sharif, H. R. and Nasir, M. (2017). Sensory evaluation and consumer acceptability. In book: Handbook of food science and technology. Wiley, United Kingdom: pp. 362-386.
11. Ahmad, N., Shafi'i, S. N., Hassan, N. H., Rajab, A. and Othman, A. (2018). Physicochemical and sensorial properties of optimised roselle-pineapple leather. *Malaysian Journal of Analytical Sciences*, 22(1): 35-44.
12. Chua, K. J., Chou, S. K., Ho, J. C., Mujumdar, A. S. and Hawlader, M. N. A. (2000). Cyclic temperature drying of guava pieces: effect on moisture and ascorbic acid contents. *Food and Bioproducts Processing*, 78(2): 72-78.
13. Sandulachi, E. (2012). Water activity concept and its role in food preservation. In chapter 3 - General considerations for preservation of fruits and vegetables: pp. 41-48.
14. Smorenburg, H.E, and Yamson, T.A. (2009). Fortified bouillon cube. Patent No: WO2009068378A1.
15. Gupta, S., and Bongers, P. (2011). Bouillon cube process design by applying product driven process synthesis. *Chemical Engineering and Processing: Process Intensification*, 50(1): 9-15.

16. Ansari, S., Maftoon-Azad, N., Hosseini, E., Farahnaky, A. and Asadi, G. (2014). Modeling the rehydration behavior of dried figs. *Journal of Agricultural Science and Technology*, 17(1): 133-144.
17. Lee, D. S., Chung, S. K., Kim, H. K. and Yam, K. L. (1991). Nonenzymatic browning in dried red pepper products. *Journal of Food Quality*, 14(2): 153-163.
18. Gupta, P., Ahmed, J., Shivhare, U. S. and Raghavan, G. S. V. (2002). Drying characteristics of red chilli. *Drying Technology*, 20(10): 1975-1987.
19. Sigge, G. O., Hansmann, C. F. and Joubert, E. (1999). Optimizing the dehydration conditions of green bell peppers (*Capsicum annuum* L.): Quality criteria. *Journal of Food Quality*, 22: 439-452.
20. Markl, D. and Zeitler, J. (2017). A review of disintegration mechanisms and measurement techniques. *Pharmaceutical Research*, 34(5): 890–917.
21. Alyami, H., Koner, J., Dahmash, E., Bowen, J., Terry, D. and Afzal, R. (2017). Microparticle surface layering through dry coating: Impact of moisture content and process parameters on the properties of orally disintegrating tablets. *Journal of Pharmacy and Pharmacology*, 69(7): 807-822.
22. Purkayastha, M. D., Nath, A., Deka, B. C. and Mahanta, C. L. (2013). Thin layer drying of tomato slices. *Journal of Food Science Technology*, 50(4)*:* 642-653.

Malaysian Journal of Analytical Sciences Vol 25 No 5 2021

Articles 11 - 15 are selected papers from the "International Virtual Symposium on Environmental and Green Chemistry for Sustainable Development (EnvChem 2021), 9 June 2021; organized by the School of Chemistry and Environment, Faculty of Applied Sciences, Universiti Teknologi MARA Shah Alam, Selangor, Malaysia."

Guest Editor: Sabiha Hanim Saleh

1. A FACILE SYNTHESIS OF N-ALKYLATED DAIBUCARBOLINE A DERIVATIVES VIA PICTET-SPENGLER CONDENSATION OF TRYPTAMINE 706
(Sintesis Mudah Terbitan Daibukarbolin A Melalui Kondensasi Pictet-Spengler Daripada Triptamin)
Nur Ain Nabilah Ash'ari, Noor Hidayah Pungot, Zurina Shaameri, Nor Akmalazura Jani

2. EFFECT OF PLANT ORGANS OF *Ficus deltoidea* IN THE SYNTHESIS OF SILVER NANOPARTICLES 716
(Kesan Organ Tumbuhan *Ficus deltoidea* dalam Mensintesis Nanopartikel Perak)
Shahrulnizahana Mohammad Din, Nik Ahmad Nizam Nik Malek, Mustaffa Shamsuddin, Juan Matmin

3. EXTRACTION SOLVENTS IN MICROALGAL LIPID EXTRACTION FOR BIOFUEL PRODUCTION: A REVIEW 728
(Pelarut Pengekstrakan dalam Pengekstrakan Lipid Mikroalgal untuk Penghasilan Bahan Api Bio: Satu Tinjauan)
Tan Yeong Hwang, Chai Mee Kin, Wong Ling Shing

4. SPECTROPHOTOMETRIC DETERMINATION OF TOTAL FLAVONOID CONTENTS IN TEA PRODUCTS AND THEIR LIQUORS UNDER VARIOUS BREWING CONDITIONS 740
(Penentuan Spektrofotometrik bagi Kandungan Jumlah Flavonoid di dalam Produk Teh dan Arak di Bru pada Keadaan Berbeza)
Nguyen Cong-Hau, Le-Thi Anh-Dao, Le Nhon-Duc, Nguyen Thanh-Nho

5. QUALITY ASSESSMENT OF MANGOSTEEN IN DIFFERENT MATURITY STAGES BY HAND-HELD NEAR-INFRARED SPECTROSCOPY 751
(Penilaian Kualiti Manggis dalam Tahap Kematangan yang Berbeza dengan Genggam Spektroskopi Inframerah Dekat)
Low Shuang Yao, Mahmud Iwan Solihin, Pavalee Chompoorat, Lim Lee Ying, Pui Liew Phing

6. EFFECT OF CARBON FIBER LOADING IN GAPHITE-POLYPROPYLENE COMPOSITE PROPERTIES AS BIPOLAR PLATE FOR POLYMER ELECTROLYTE MEMBRANE FUEL CELL 766
(Kesan Penyebaran Serat Karbon Dalam Gaphit- Polipropilena Komposit Sebagai Plat Dwikutub Untuk Sel Fuel Membran Elektrolit Polimer)
Mohd Zulkefli Selamat, Noor Ashikin Jamil, Rafidah Hasan, Sivakumar Dharmalingam

7. VOLATILE CHEMICAL PROFILING OF UNBURNT AND BURNT RON 95 PETROL FROM THREE OIL STATIONS: A PRELIMINARY STUDY 776
(Pemprofilan Sebatian Kimia Meruap bagi Petrol RON 95 yang Tidak Dibakar dan Dibakar daripada Tiga Stesen Minyak: Satu Kajian Awal)
Dheephikha Kumaraguru, Wan Nur Syuhaila Mat Desa, Khairul Osman, Noor Hazfalinda Hamzah, Gina Francesca Gabriel

8. METAL-ORGANIC FRAMEWORKS AS SORBENT- BASED EXTRACTION: A REVIEW 791
(Rangka Kerja Logam-Organik Sebagai Penjerap Berasaskan Pengekstrakan: Satu Ulasan)
Siti Sufiana Kamni, Karimah Kassim, Nur Sofiah Abu Kassim, Nurul Auni Zainal Abidin

9. CHROMATOGRAPHIC PROFILING OF *Syzygium cumini* LEAVES USING HIGH-PERFORMANCE THIN LAYER CHROMATOGRAPHY AND GAS CHROMATOGRAPHY-MASS SPECTROMETRY TECHNIQUES 808
(Profil Kromatografi bagi daun *Syzygium cumini* mengunakan Teknik Kromatografi Lapisan Nipis Prestasi Tinggi dan Kromatografi Gas-Spektrometri Jisim)
Joshi Vivek, Mer Sagar, Bhagat Keyuri, Savalia Vaibhavi, Dhalani Jayesh, Pandya Mayank, Pandya Devang

10. AIR POLLUTION ASSESSMENT IN SOUTHERN PENINSULAR MALAYSIA USING ENVIRONMETRIC ANALYSIS 821
(Penilaian Pencemaran Udara Di Selatan Semenanjung Malaysia Menggunakan Analisis Environmetrik)
Haslinda Ab Malek, Nurul Nabila Natasha Jalaluddin, Sharifah Nadia Syed Hasan,Umi Amira Hassni, Isnewati Ab Malek

11. ANALYTICAL COMPARATIVE STUDIES OF ADSORPTION EFFICIENCY OF MCM-41 AND SBA-15 ON REMOVAL OF ANIONIC-AZO AND CATIONIC DYES FROM AQUEOUS SAMPLE 831
(Kajian Perbandingan Analisis Keberkesanan Penjerapan MCM-41 dan SBA-15 untuk Penyingkiran Pewarna Anionik-Azo dan Kationik Dari Sampel Akueus)
Nur Zabirah Zabi, Wan Nazihah Wan Ibrahim, Nur Husna Zainal Abidin, Siti Syairah Mat Salleh, Farah Amira Shahrul Effendi, Isna Fazliana Mohamed Idrus, Hamizah Md Rasid, Nursyamsyila Mat Hadzir, Nor Suhaila Mohamad Hanapi, Mazhani Muhammad

12. CHITOSAN-LIGNIN COMPOSITE FOR RECOVERY OF LANTHANUM (III) IONS FROM AQUEOUS SOLUTIONS 848
(Kitosan-Lignin Komposit untuk Perolehan Semula Lanthanum (III) Ion Dari Larutan Akueus)
Shariff Ibrahim, Nur Shuhaidah Shamsul Kamal, Megat Ahmad Kamal Megat Hanafiah, Noorul Farhana Md Ariff, Sabiha Hanim Saleh

13. PHYSICOCHEMICAL AND DYEING CHARACTERISTICS OF COTTON FABRIC DYEING FROM THE EXTRACT OF ANGSANA (*Pterocarpus indicus*) BARK 858
(Fiziko Kimia dan Ciri Pencelupan Pewarnaan Kain Kapas dengan Menggunakan Ekstrak dari Kulit Kayu Angsana (*Pterocarpus indicus*))
Mukmin Sapto Pamungkas, Edia Rahyuningsih, Taranipa Marfitania, Wachid Siti Fatimah

14. EXTRACTION AND ISOLATION OF HIGH QUANTITIES OF CANNABIDIOL, CANNABINOL, AND DELTA-9-TETRAHYDROCANNABINOL FROM *Cannabis sativa* L. 867
(Pengekstrakan dan Pengasingan Kuantiti Tinggi bagi Cannabidiol, Cannabinol dan Delta-9-Tetrahidrocannabinol dari *Cannabis sativa* L.)
Fameera Madaka, Natawat Chankana, Nanthaphong Khamthong, Athip Maha, Thanapat Songsak

15. APPLICATION OF ZINC OXIDE NANOPARTICLES AND NANOCHITOSAN TO ENHANCE THE LIGHT FASTNESS OF COTTON DYED WITH NATURAL INDIGO 882
(Aplikasi Zink Oksida Nanopartikel dan Nano Kitosan untuk Meningkatkan Ketahanan Pudar Kain yang Diwarnai Indigo Asli)
Renung Reningtyas, Edia Rahayuningsih, Yuni Kusumastuti, Indriana Kartini

Malaysian Journal of Analytical Sciences (MJAS)
Published by Malaysian Analytical Sciences Society

A FACILE SYNTHESIS OF *N*-ALKYLATED DAIBUCARBOLINE A DERIVATIVES VIA PICTET-SPENGLER CONDENSATION OF TRYPTAMINE

(Sintesis Mudah Terbitan Daibukarbolin A Melalui Kondensasi Pictet-Spengler Daripada Triptamin)

Nur Ain Nabilah Ash'ari[1], Noor Hidayah Pungot[1]*, Zurina Shaameri[1], Nor Akmalazura Jani[2]

[1]Organic Synthesis Laboratory, Institute of Science,
Universiti Teknologi MARA, 43200 Bandar Puncak Alam, Selangor, Malaysia
[2]Faculty of Applied Sciences,
Universiti Teknologi MARA, 72000 Kuala Pilah, Negeri Sembilan, Malaysia

**Corresponding author: noorhidayah977@uitm.edu.my*

Received: 27 July 2021 ; Accepted: 31 August 2021 ; Published: 25 October 2021

Abstract

A brief and facile approach towards β-carboline and its derivatives is described through a simple three step synthesis. The key reaction involves the construction of β-carboline framework by Pictet-Spengler condensation of tryptamine with various substituted aldehydes. Subsequent aromatization of the resulting tetrahydro-β-carboline intermediates is achieved via iodine-mediated oxidative dehydrogenation reaction. Thereafter, insertion of alkyl subunit at N-1 position afforded a series of corresponding N-alkylated β-carboline derivatives. The structures of all synthesized intermediates and derivatives of β-carboline, including three new structures (**2k**, **2l** and **3e**), were confirmed by NMR, FTIR and GC-MS spectroscopy.

Keywords: β-carboline, Pictet-Spengler condensation, tetrahydro-β-carboline

Abstrak

Pendekatan ringkas dan mudah terhadap β-karbolin dan derivatifnya dijelaskan melalui sintesis tiga langkah mudah. Tindak balas utama melibatkan pembinaan kerangka β-karbolin daripada triptamin melalui kondensasi Pictet-Spengler dengan pelbagai aldehid yang diganti. Aromatisasi seterusnya dari tetrahidro-β-karbolin yang dihasilkan dicapai melalui tindak balas dehidrogenasi oksidatif yang dimediasi iodin. Selepas itu, penyisipan subunit alkil pada kedudukan N-1 menghasilkan satu siri turunan N-alkilasi β-karbolin yang sepadan. Struktur semua perantara yang disintesis dan turunan β-karbolin disahkan oleh spektroskopi NMR, FTIR dan GC-MS dan tiga kompaun (**2k**, **2l**, dan **3e**) adalah baru.

Kata kunci: β-karbolin, kondensasi Pictet-Spengler, tetrahidro-β-karbolin

Introduction

Over the past few decades, wild Syrian rue (*Peganum harmala*) from the family *Zygophyllaceae*, which is common in Iran, has elicited much interest due to its wide pharmaceutical and biological applications. Discoveries in the past few decades have demonstrated

different pharmacological and therapeutic effects associated with various parts of this plant including the seed, bark, and root [1]. Extensive studies on *Peganum harmala* confirm that the most essential constituent in its chemical composition is the β-carboline alkaloid [2], which is responsible for the pharmacological diversity of neuroprotection [3], antiviral [4], anti-allergic [5], antimalarial [6], anti-leishmania [7], antitumor [8], antiplasmodial [9] and anti-HIV [10]. This bioactive β-carboline is widely distributed in human tissues and body fluids, marine creatures, insects, mammalians and plants. Thus, its potential therapeutic activities are very much aligned with the varied health benefits as described [11].

Of the many β-carboline derivatives, daibucarboline A (Figure 1) is recognized as a potential anti-inflammatory agent. This tetracyclic compound is originally isolated from the roots of *Neolitsea daibuensis* by Wong and co-workers, which also led to the isolation of daibucarboline B, C and 20 other known compounds. Anti-inflammatory assessment using inducible nitric oxide synthase (iNOS) assay revealed that daibucarboline A exhibited moderate inhibitory activity with IC_{50} values of 18.41 μM [12]. Jani and co-workers later isolated trace amounts of daibucarboline A from the stems of *Neolitsea kedahensis* [13]. The aromatic β-carboline scaffolds are important synthetic intermediates in the total synthesis of many natural products, including the daibucarboline A and compounds exhibiting strong bioactivities. Their importance demands efficient synthetic methodologies, both for the construction of the heterocyclic system and its functionalization [14].

Owing to the diversity in the field of biology, numerous efforts have been devoted to prepare simple β-carbolines as well as a range of synthetic β-carboline derived compounds. Pictet-Spengler is one of the prominent reactions reported to synthesize β-carboline. In brief, it is a chemical reaction in which a β-arylethylamine undergoes condensation with an aldehyde or a ketone followed by ring closure [15]. Strong Brønsted acids are most commonly employed to promote the Pictet-Spengler reaction [16], involving the cyclization of an electron-rich aromatic ring onto an imine. The few recent examples of Lewis acid catalyzed Pictet-Spengler reaction involved highly reactive species such as nitrone [17], or ionic liquid and microwave irradiation [18] to enhance the reactivity. However, in this study, the researchers attempted a more practical and convenient synthesis of the aromatic β-carbolines using tryptamine and various substituted aldehydes for the desired Pictet-Spengler reaction, followed by oxidative dehydrogenation reaction using molecular iodine under simple reaction conditions. Hence, this report details the efficient Pictet-Spengler condensation catalyzed by TFA, without the use of expensive metal catalysts, prolonged reaction hours or critical reaction conditions.

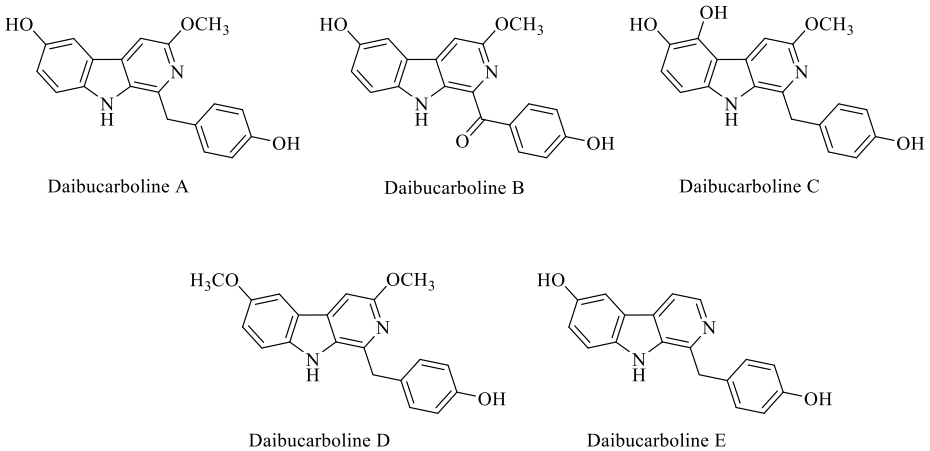


Figure 1. The structures of daibucarboline A analogue

Materials and Methods

General procedure for the synthesis of compounds 2a-n:

Phenylglyoxal monohydrate (0.657 mmol, 1.0 equiv.) was added to a stirred suspension of tryptamine (0.854 mmol, 1.0 equiv.) and TFA (0.657 mmol, 1.5 equiv.) in MeOH. The resulting solution was stirred for 24 hours, and the phenylglyoxal was shown by TLC analysis to be completely consumed. The reaction mixture was added with 10% K_2CO_3 and extracted with EtOAc. The combined organic layer was concentrated and purified by silica gel column chromatography eluted with a gradient of n-hexane and EtOAc (20:80) to afford compounds **2a-n**.

General procedure for the synthesis of compounds 3a-e:

To a solution of compounds **2a-e** (1.0 equiv.) in DMSO, iodine, I_2 (0.5 equiv.) was added followed by H_2O_2 (1.0 equiv.) and the resulting mixture was stirred at 60°C. Once TLC analysis confirmed a complete consumption of the starting material, the reaction mixture was quenched with cold sodium thiosulfate and extracted with EtOAc. The organic layer was evaporated and purified by silica gel column chromatography eluted with a gradient of n-hexane and EtOAc (20:80) to obtain compounds **3a-e**.

General procedure for the synthesis of compounds 4a-b:

NaH (60% dispersion in mineral oil, 75 mmol, 1.5 equiv.) was added to a solution of compounds 3a-b (50 mmol, 1.0 equiv.) in THF at 0°C. The heterogeneous mixture was stirred at 0°C for 15 minutes and 1 hour at room temperature. The mixture was then cooled to 0°C, treated with iodomethane (65 mmol, 1.3 equiv.), and allowed to warm to room temperature. After 30 minutes, the reaction mixture was cooled to 0°C, quenched with saturated NH_4Cl, and extracted with ether. The combined organic layer was washed with brine, dried over anhydrous Na_2SO_4, concentrated and purified by column chromatography eluted with a gradient of n-hexane and EtOAc (30:70) to provide derivatives **4a-b**.

Results and Discussion

1-phenyl-2,3,4,9-tetrahydro-1H-pyrido[3,4 b]indole (2a). Yield: 517 mg (90% yield, dark brown solid). IR *v* cm^{-1}: 3475, 3354, 2483, 1612 cm^{-1}. ^{1}H NMR (400 MHz, MeOD) δ (ppm): 7.63 (d, 1H, *J* = 7.9 Hz), 7.54-7.49 (m, 3H), 7.43-7.40 (m, 2H), 7.32 (d, 1H, *J* = 7.9 Hz), 7.19 (td, 1H, *J* = 7.9 Hz, 1.1 Hz), 7.09 (td, 1H, *J* = 7.9 Hz, 1.1 Hz), 5.79 (s, 1H), 3.65-3.58 (m, 1H), 3.55-3.48 (m, 1H), 3.29-3.22 (m, 1H), 3.15 (dt, 1H, *J* = 8.1 Hz, 5.5 Hz). ^{13}C NMR ($CDCl_3$, 100 MHz): 142.3, 137.2, 134.7, 129.9, 128.1, 127.0, 123.1, 120.8, 118.2, 111.9, 105.4, 65.2, 43.4, 22.6. MS m/z: 248.1.

1-(4-methoxyphenyl)-2,3,4,9-tetrahydro-1H-pyrido[3,4-b]indole (2b). Yield: 336 mg (73% yield, yellow solid). IR *v* cm^{-1}: 3400, 3356, 2835, 2664, 1635 cm^{-1}. ^{1}H NMR (400 MHz, $CDCl_3$) *δ* (ppm): 7.52 (d, 1H, *J* = 7.8 Hz), 7.47 (br s, 1H), 7.28-7.21 (m, 2H), 7.20-7.11 (m, 2H), 6.95-6.87 (m, 3H), 5.18 (s, 1H), 3.73 (s, 3H), 3.43-3.35 (m, 1H), 3.18-3.11 (m, 1H), 2.98-2.91 (m, 1H), 2.86-2.78 (m, 1H). ^{13}C NMR ($CDCl_3$, 100 MHz): 158.4, 138.2, 135.8, 133.3, 129.4, 127.1, 123.9, 120.0, 118.1, 114.8, 112.3, 105.7, 64.1, 55.4, 43.7, 22.9. MS m/z: 278.1.

4-(2,3,4,9-tetrahydro-1H-pyrido[3,4-b]indol-1-yl)phenol (2c). Yield: 148 mg (25% yield, light yellow solid). IR *v* cm^{-1}: 3535, 3474, 3339, 2483, 1742 cm^{-1}. ^{1}H NMR (400 MHz, $CDCl_3$) *δ* (ppm): 7.55 (d, 1H, *J* = 7.8 Hz), 7.52 (br s, 1H), 7.29-7.22 (m, 2H), 7.16-7.09 (m, 2H), 6.92-6.86 (m, 3H), 5.16 (s, 1H), 4.33 (br s, 1H), 3.43-3.38 (m, 1H), 3.19-3.12 (m, 1H), 2.98-2.90 (m, 1H), 2.85-2.79 (m, 1H). ^{13}C NMR ($CDCl_3$, 100 MHz): 157.9, 137.4, 135.2, 133.8, 129.4, 127.4, 122.7, 119.9, 118.2, 115.5,111.6, 105.8, 64.8, 44.1, 23.8. MS m/z: 264.1.

1-(3,4-dimethoxyphenyl)-2,3,4,9-tetrahydro-1H-pyrido[3,4-b]indole (2d). Yield: 366 mg (65% yield, brown solid). IR *v* cm^{-1}: 3445, 3351, 2869, 2672, 1634 cm^{-1}. ^{1}H NMR (400 MHz, $CDCl_3$) *δ* (ppm): 7.54 (d, 1H, *J* = 7.8 Hz), 7.46 (br s, 1H), 7.27-7.22 (m, 2H), 7.16-7.09 (m, 2H), 6.93-6.85 (m, 3H), 5.18 (s, 1H), 3.79 (s, 3H), 3.73 (s, 3H), 3.43-3.35 (m, 1H), 3.18-3.11 (m, 1H), 2.98-2.91 (m, 1H), 2.86-2.78 (m, 1H). ^{13}C NMR

($CDCl_3$, 100 MHz): 158.4, 138.2, 135.8, 133.3, 129.4, 127.1, 123.9, 120.0, 118.1, 114.8, 112.3, 105.7, 64.1, 56.9, 55.4, 43.7, 22.9. MS m/z: 308.1.

2-bromo-4-(2,3,4,9-tetrahydro-1H-pyrido[3,4-b]indol-1-yl)phenol (2e). Yield: 68 mg (20% yield, light brown solid). IR ν cm^{-1}: 3475, 3379, 2513, 1622, 535 cm^{-1}. ^1H NMR (400 MHz, $CDCl_3$) δ (ppm): 7.58-7.55 (m, 1H), 7.52 (br s, 1H), 7.36-7.33 (m, 2H), 7.30-7.27 (m, 2H), 7.26-7.24 (m, 1H), 7.20 (qd, 2H, J = 7.1 Hz, 1.4 Hz), 5.17 (s, 1H), 3.40-3.34 (m, 1H), 3.20 (ddd, 1H, J = 12.5 Hz, 8.8 Hz, 4.8 Hz), 3.02-2.91 (m, 1H), 2.87-2.81 (m, 1H). ^{13}C NMR ($CDCl_3$, 100 MHz): 141.6, 138.0, 134.6, 133.1, 130.4, 129.4, 127.8, 124.6, 123.7, 119.6, 117.7, 113.8, 105.5, 61.0, 42.5, 24.1. MS m/z: 326.0.

4-(2,3,4,9-tetrahydro-1H-pyrido[3,4-b]indol-1-yl)benzonitrile (2f). Yield: 732 mg (91% yield, dark brown solid). IR ν cm^{-1}: 3475, 3379, 2513, 2234, 1622 cm^{-1}. ^1H NMR (400 MHz, $CDCl_3$) δ (ppm): 7.56-7.54 (m, 1H), 7.53 (br s, 1H), 7.33-7.29 (m, 3H), 7.27-7.21 (m, 2H), 7.18 (dtd, 1H, J = 15.8 Hz, 7.1 Hz, 1.4 Hz), 5.15 (s, 1H), 3.38-3.33 (m, 1H), 3.18-3.11 (m, 1H), 3.00-2.89 (m, 1H), 2.85 (dtd, 1H, J = 15.3 Hz, 4.5 Hz, 1.9 Hz). ^{13}C NMR ($CDCl_3$, 100 MHz): 147.9, 138.5, 135.7, 134.8, 129.3, 128.3, 122.1, 120.8, 119.3, 111.5, 106.8, 65.2, 43.3, 21.6. MS m/z: 273.1.

1-(2-fluorophenyl)-2,3,4,9-tetrahydro-1H-pyrido[3,4-b]indole (2g). Yield: 238 mg (55% yield, light yellow solid). IR ν cm^{-1}: 3443, 3385, 2518, 2255, 1676 cm^{-1}. ^1H NMR (400 MHz, $CDCl_3$) δ (ppm): 7.52 (br s, 1H), 7.50 (d, 1H, J = 7.0 Hz), 7.37 (dd, 1H, J = 8.0 Hz, 1.2 Hz), 7.29-7.19 (m, 2H), 7.14-7.10 (m, 4H), 5.90 (s, 1H), 3.26-3.23 (m, 1H), 3.18-3.15 (m, 1H), 2.81-2.76 (m, 2H). ^{13}C NMR ($CDCl_3$, 100 MHz): 160.5, 137.2, 134.1, 129.7, 128.8, 127.2, 125.6, 123.8, 119.0, 118.1, 117.2, 115.9, 106.9, 58.9, 43.2, 22.6. MS m/z: 266.1.

1-(2-Chlorophenyl)-2,3,4,9-tetrahydro-1*H*-β-carboline (2h). Yield: 329 mg (57% yield, dark brown solid). IR ν cm^{-1}: 3475, 3379, 2513, 1622, 826 cm^{-1}. ^1H NMR (400 MHz, MeOD) δ (ppm): 7.63 (br s, 1H), 7.57 (d, 1H, J = 7.0 Hz), 7.47 (dd, 1H, J = 8.0 Hz, 1.2 Hz), 7.27-7.23 (m, 2H), 7.18-7.10 (m, 4H), 5.70 (s, 1H), 3.29-3.23 (m, 1H), 3.18-3.12 (m, 1H), 2.95-2.81 (m, 2H). ^{13}C NMR ($CDCl_3$, 100 MHz): 138.2, 136.4, 134.4, 129.7, 128.6, 127.4, 126.7, 122.1, 119.1, 117.2, 113.1, 107.4, 59.9, 45.9, 23.7. MS m/z: 282.0.

1-(3-bromophenyl)-2,3,4,9-tetrahydro-1H-pyrido[3,4-b]indole (2i). Yield: 371 mg (74% yield, yellow solid). IR ν cm^{-1}: 3436, 3378, 2513, 1622, 541 cm^{-1}. ^1H NMR (400 MHz, MeOD) δ (ppm): 7.58-7.55 (m, 1H), 7.55 (br s, 1H), 7.36-7.33 (m, 2H), 7.30-7.23 (m, 2H), 7.28-7.24 (m, 1H), 7.25 (qd, 2H, J = 7.1 Hz, 1.4 Hz), 5.19 (s, 1H), 3.34-3.24 (m, 1H), 3.25 (ddd, 1H, J = 12.5 Hz, 8.8 Hz, 4.8 Hz), 3.14-2.98 (m, 1H), 2.83-2.78 (m, 1H). ^{13}C NMR ($CDCl_3$, 100 MHz): 142.6, 138.5, 134.8, 132.1, 130.4, 129.2, 127.6, 125.6, 124.7, 119.8, 117.9, 113.1, 107.5, 66.0, 42.7, 24.4. MS m/z: 326.0.

1-(4-Nitrophenyl)-2,3,4,9-tetrahydro-1*H*-β-carboline (2j). Yield: 369 mg (95% yield, light yellow solid). IR ν cm^{-1}: 3478, 3372, 2516, 1622, 1509 cm^{-1}. ^1H NMR (400 MHz, $CDCl_3$) δ (ppm): 8.21 (d, 2H, J = 8.8 Hz), 7.58 (d, 1H, J = 8.5 Hz), 7.53 (d, 2H, J = 8.8 Hz), 7.49 (br s, 1H), 7.27-7.24 (m, 1H), 7.20 (dtd, 2H, J = 8.5 Hz, 7.0 Hz, 1.5 Hz), 5.28 (s, 1H), 3.34 (dt, 1H, J = 8.8 Hz, 5.1 Hz), 3.21 (ddd, 1H, J = 12.7 Hz, 7.8 Hz, 4.8 Hz), 2.98-2.90 (m, 1H), 2.88 (dtd, 1H, J = 7.8 Hz, 4.8 Hz, 1.6 Hz). ^{13}C NMR ($CDCl_3$, 100 MHz): 148.5, 146.6, 136.2, 134.7, 129.7, 128.5, 124.5, 122.3, 118.5, 117.8, 115.2, 109.6, 65.9, 43.5, 25.6. MS m/z: 293.1.

3-(2,3,4,9-tetrahydro-1H-pyrido[3,4-b]indol-1-yl)benzoic acid (2k). Yield: 68 mg (69% yield, brown solid). IR ν cm^{-1}: 3374, 2925, 2849, 1629 cm^{-1}. ^1H NMR (400 MHz, $CDCl_3$) δ (ppm): 7.62 (s, 2H), 7.58-5.53 (d, 1H, J = 7.8 Hz), 7.42-7.40 (d, 2H, J = 8.8 Hz), 7.24-7.22 (m, 1H), 7.16-7.12 (m, 2H), 5.21 (s, 1H), 3.28-3.15 (m, 1H), 3.14-3.13 (m, 1H), 2.93-2.89 (m, 1H), 2.84-2.83 (m, 1H). ^{13}C NMR ($CDCl_3$, 100 MHz): 192.9, 162.4, 151.4, 137.1, 136.7, 136.1, 135.8, 133.5, 131.4, 128.7, 121.2, 118.7, 117.7, 114.6, 112.6, 105.5. MS m/z: 292.1.

1-(4-ethylphenyl)-2,3,4,9-tetrahydro-1H-pyrido[3,4-b]indole (2l). Yield: 165 mg (54% yield, yellow solid). IR ν cm^{-1}: 3013, 2949, 2842, 1572 cm^{-1}. ^{1}H NMR (400 MHz, $CDCl_3$) δ (ppm): 8.16 (s, 1H), 7.57 (br s, 1H), 7.16 (s, 4H), 7.14-7.10 (m, 4H), 5.05 (s, 1H), 3.31-3.26 (m, 1H), 3.08-3.04 (m, 1H), 2.91-2.89 (m, 1H), 2.83-2.82 (m, 1H), 2.70-2.64 (q, 2H), 1.25 (t, 3H). ^{13}C NMR ($CDCl_3$, 100 MHz): 144.1, 138.7, 136.5, 133.6, 128.5, 127.7, 127.0, 120.8, 118.3, 117.3, 110.5, 108.6, 57.1, 41.4, 28.2, 21.4, 14.9. MS m/z: 276.1.

1-(4-ethoxyphenyl)-2,3,4,9-tetrahydro-1H-pyrido[3,4-b]indole (2m). Yield: 148 mg (33% yield, yellow solid). IR ν cm^{-1}: 3400, 3356, 2835, 2664, 1635 cm^{-1}. ^{1}H NMR (400 MHz, $CDCl_3$) δ (ppm): 7.64 (br s, 1H), 7.58-7.55 (m, 1H), 7.27-7.16 (m, 4H), 7.15-7.10 (m, 3H), 5.37 (s, 1H), 4.44 (q, 2H), 3.46-3.38 (m, 1H), 3.16-3.12 (m, 1H), 2.99-2.89 (m, 1H), 2.87-2.81 (m, 1H), 2.41 (t, 3H). ^{13}C NMR ($CDCl_3$, 100 MHz): 144.1, 139.7, 137.4, 133.2, 127.6, 126.8, 119.5, 116.2, 113.7, 105.8, 67.27, 42.3, 28.9, 21.7, 15.4. MS m/z: 292.1.

2,3,4,9-tetrahydro-1H-pyrido[3,4-b]indole (2n). Yield: 229 mg (56% yield, yellow solid). IR ν cm^{-1}: 3474, 3329, 2801, 1681 cm^{-1}. ^{1}H NMR (400 MHz, MeOD) δ (ppm): 10.08 (br s, 1H), 7.31 (d, 1H, J= 7.8 Hz), 7.37 (d, 1H, J=7.8 Hz), 7.04-6.99 (m, 1H), 6.95-6.87 (m, 1H), 3.29 (s, 2H), 3.11 (t, 2H), 2.67 (t, 2H). ^{13}C NMR ($CDCl_3$, 100 MHz): 135.9, 134.2, 127.6, 120.7, 118.6, 117.6, 111.2, 107.3, 43.7, 42.9, 22.4. MS m/z: 172.1.

1-phenyl-9H-pyrido[3,4-b]indole (3a). Yield: 243 mg (72% yield, dark brown solid). IR ν cm^{-1}: 3474, 2361, 1623, 1559, 1233, 736 cm^{-1}. ^{1}H NMR (400 MHz, MeOD) δ (ppm): 10.54 (s, 1H), 8.44 (d, J = 4.8 Hz, 1H), 8.29 (d, J = 7.8 Hz, 1H), 8.12 (d, J = 4.8 Hz, 1H), 8.07−7.98 (m, 2H), 7.67 (d, J = 8.4 Hz, 1H), 7.52 (t, J = 7.8 Hz, 2H), 7.31 (dt, J = 14.8, 7.8 Hz, 2H), 7.24 (t, J = 7.2 Hz, 1H). ^{13}C NMR ($CDCl_3$, 100 MHz): 142.5, 141.7, 138.1, 133.6, 129.5, 128.1, 127.2, 126.4, 125.2, 121.8, 120.5, 119.1, 113.7, 111.4. MS m/z: 244.1.

1-(4-methoxyphenyl)-9H-pyrido[3,4-b]indole (3b). Yield: 156 mg (54% yield, yellow solid). IR ν cm^{-1}: 3474, 2361, 1623, 1559, 1233, 736 cm^{-1}. ^{1}H NMR (400 MHz, MeOD) δ (ppm): 11.27 (s, 1H), 8.32 (d, J = 4.8 Hz, 1H), 8.19 (d, J = 4.8 Hz, 1H), 8.10−8.02 (m, 2H), 7.64 (d, J = 8.4 Hz, 1H), 7.48 (t, J = 7.8 Hz, 2H), 7.31 (dt, J = 14.8, 7.8 Hz, 2H), 7.22 (t, J = 7.2 Hz, 1H), 3.73 (s, 3H). ^{13}C NMR ($CDCl_3$, 100 MHz): 158.2, 138.8, 135.8, 133.3, 129.1, 127.1, 123.9, 120.9, 118.1, 114.8, 112.3, 104.7, 64.5, 52.4, 44.6, 22.7. MS m/z: 274.1.

4-(9H-pyrido[3,4-b]indol-1-yl)phenol (3c). Yield: 124 mg (43% yield, yellow solid). IR ν cm^{-1}: 3535, 3474, 3339, 2483, 1742 cm^{-1}. ^{1}H NMR (400 MHz, $CDCl_3$) δ (ppm): 10.63 (s, 1H), 7.55 (d, 1H, J = 7.8 Hz), 7.52 (br s, 1H), 7.29-7.22 (m, 2H), 7.16-7.09 (m, 2H), 6.92-6.86 (m, 3H), 5.16 (s, 1H), 4.33 (br s, 1H). ^{13}C NMR ($CDCl_3$, 100 MHz): 156.6, 135.4, 134.7, 133.8, 130.7, 127.4, 122.7, 119.9, 118.2, 115.9,111.4, 103.8, 64.8, 43.9, 22.5. MS m/z: 260.0.

1-(3,4-dimethoxyphenyl)-9H-pyrido[3,4-b]indole (3d). Yield: 87 mg (22% yield, light brown solid). IR ν cm^{-1}: 3445, 3351, 2869, 2672, 1634 cm^{-1}. ^{1}H NMR (400 MHz, $CDCl_3$) δ (ppm): 9.46 (s, 1H), 7.54 (d, 1H, J = 7.8 Hz), 7.27-7.22 (m, 2H), 7.16-7.09 (m, 2H), 6.93-6.85 (m, 3H), 5.18 (s, 1H), 3.77 (s, 3H), 3.72 (s, 3H). ^{13}C NMR ($CDCl_3$, 100 MHz): 159.4, 138.7, 135.8, 133.3, 130.6, 127.1, 125.3, 120.0, 117.6, 114.1, 112.3, 104.8, 64.1, 56.9, 55.4, 43.5, 21.5. MS m/z: 304.1.

3-(9H-pyrido[3,4-b]indol-1-yl)benzoic acid (3e). Yield: 76 mg (19% yield, dark brown solid). IR ν cm^{-1}: 3456, 3263, 1640, 1465 cm^{-1}. ^{1}H NMR (400 MHz, $CDCl_3$) δ (ppm): 7.54 (d, 2H, J = 7.8 Hz), 7.32 (d, 2H, J = 4.8 Hz), 7.08-7.04 (m, 4H), 6.99-6.95 (m, 2H). ^{13}C NMR ($CDCl_3$, 100 MHz): 194. 8, 151.5, 137.7, 137.0, 136.2, 136.1, 132.0, 131.7, 130.6, 127.2, 121.1, 118.8, 118.3, 112.7, 105.5. MS m/z: 288.0.

1-phenyl-9H-pyrido[3,4-b]indole (4a). Yield: 132 mg (81% yield, dark brown solid). IR ν cm^{-1}: 3474, 2361, 1623, 1559, 1233, 736 cm^{-1}. ^{1}H NMR (400 MHz, MeOD) δ (ppm): 8.47 (d, J = 4.8 Hz, 1H), 8.35 (d, J = 7.8 Hz, 1H), 8.28 (d, J = 4.8 Hz, 1H), 8.07−7.98 (m, 2H), 7.69 (d, J = 8.4 Hz, 1H), 7.56 (t, J = 7.8 Hz, 2H), 7.31 (dt, J = 14.8, 7.8 Hz, 2H), 7.24 (t, J = 7.2 Hz, 1H), 3.82 (s, 3H). ^{13}C NMR ($CDCl_3$, 100 MHz): 142.5, 141.1,

138.6, 133.8, 129.2, 128.6, 127.8, 126.3, 125.6, 121.8, 120.5, 118.6, 115.3, 112.8. MS m/z: 258.1.

1-(4-methoxyphenyl)-9H-pyrido[3,4-b]indole (4b). Yield: 99 mg (79% yield, light brown solid). IR ν cm^{-1}: 3474, 2361, 1623, 1559, 1233, 736 cm^{-1}. ^{1}H NMR (400 MHz, MeOD) δ (ppm): 8.32 (d, J = 4.8 Hz, 1H), 8.19 (d, J = 4.8 Hz, 1H), 8.10−8.02 (m, 2H), 7.64 (d, J = 8.4 Hz, 1H), 7.48 (t, J = 7.8 Hz, 2H), 7.31 (dt, J = 14.8, 7.8 Hz, 2H), 7.22 (t, J = 7.2 Hz, 1H), 3.85 (s, 3H), 3.84 (s, 3H). ^{13}C NMR ($CDCl_3$, 100 MHz): 158.2, 138.8, 135.8, 133.3, 129.1, 127.1, 123.9, 120.9, 118.1, 114.8, 112.3, 104.7, 64.5, 52.4, 44.6, 22.7. MS m/z: 288.1.

The synthetic studies described in this paper were directed at a series of β-carboline derivatives in which tetrahydro-β-carboline (THβC) was the key intermediate. In order to explore the reactivity of different substituted aldehydes towards the efficiency of Pictet-Spengler reaction, a series of compounds containing different electron-donating and electron-withdrawing substituents attached to the β-carboline skeleton, starting from tryptamine, were synthesized. The reaction was carried out in the presence of acid catalyst TFA, under 24 hours of stirring to give the THβC intermediates in their corresponding yields (Scheme 1).

This approach is concise and yet most preferred due to its simplicity since no heat is involved to drive the reaction. The yields vary accordingly due to inductive and resonance effects of the substituents attached to the benzaldehyde **(2a-2m)** and aliphatic aldehyde **(2n)**. Having electron-donating groups as the substituents **(2b, 2c, 2l, 2m)** activated the ring, making the carbonyl carbon less electrophilic, which resulted in a weaker reactivity and gave lower product yields than that of using standard benzaldehyde **(2a)**. Using dimethoxy-substituted benzaldehyde **(2d)**, the yield is much reduced. On the contrary, benzaldehyde bearing electron-withdrawing group **(2f, 2j, 2k)** gave much higher product yields as anticipated. Despite being an inductively electron-withdrawing group, halogens are activators since their ability to donate electrons into the aromatic ring *via* resonance is much greater. Thus, as expected, halogenated derivatives **(2g, 2h, 2i)** were obtained in much lower yields.

The reaction mechanism occurs by the initial formation of iminium ion followed by electrophilic addition at the C-2 position to directly yield the six-membered ring intermediate. However, both carbon-2 and -3 of tryptamine are nucleophilic. Therefore, the reaction can also proceed by the attack of carbon-3 to yield a spiroindolenine intermediate that would then undergo a 1,2-alkyl shift to form the product as depicted in Scheme 2. Both mechanisms have been proven to be true, yet the prevailing mechanism is still unknown [19].

The pathway proceeded with removal of hydrogen on the B-ring by oxidative dehydrogenation reaction to promote both aromatization and construction of the β-carboline frameworks. Literature survey outlined a few methods for the aromatization of THβC, which generally involve the following drawbacks in driving the reaction; (i) palladium-mediated reactions need high temperature, long reaction hours, along with the possibility of C-N bond cleavage [20], (ii) sulphur-mediated reactions deliver aromatized product in two days with low yields [21], and (iii) selenium-mediated reactions require large quantity of SeO_2 (10 equiv.) offering less yield [22]. It is also reported that peroxide promotes dehydrogenation reaction [23]. Therefore, we employed the THβC and H_2O_2 along with 25 mol% I_2 in DMSO, resulting in 19-91% yields of the oxidized products **(3a-e)** as summarized in Scheme 3.

The reaction occurs by the initial formation of imine intermediate through N-iodination of THβC, followed by dehydroiodination of the N-iodotetrahydro-β-carboline. Further N-iodination of the imine gives ammonium intermediate. Subsequent deprotonation and dehydro-iodination afforded the targeted β-carboline derivatives **(3a-e)**. The purpose of employing DMSO in this reaction is to regenerate the molecular iodine, along with dimethyl sulfide (DMS) by further reaction with the generated HI. The regeneration of molecular I_2 is important to maintain the cycle and the formed DMS is oxidized to DMSO in the presence of H_2O_2 to speed up the reaction time [24]. The mechanism of reaction is as depicted in Scheme 4.

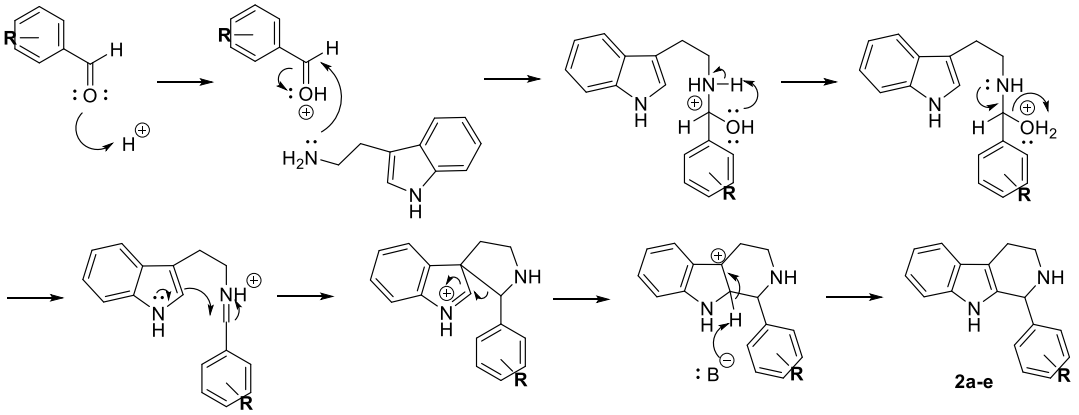
In the final step, β-carbolines **(3a-b)** were converted to N-alkyl derivatives by the reaction of alkylating reagents, R_2-I with indole moiety in the presence of sodium hydride as the base. The use of sodium offers the advantage of the reaction being carried out in a non-hydrolytic solvent. It was thought that the employment of sodium hydride would also offer this advantage and at the same time would be safer and easier to handle than the metal. With this in mind, the preparation of N-substituted β-carbolines by the general reaction shown in Scheme 5 was undertaken.

Scheme 1. Scope of the reaction of tryptamine with different substituted aldehydes



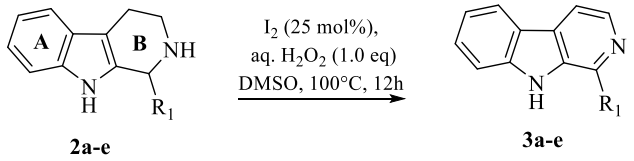
1 **2a-n**

Entry	R_1	Yield (%)
2a	Phenyl	90
2b	*p*-methoxyphenyl	73
2c	*p*-hydroxyphenyl	25
2d	*m*, *p*-dimethoxyphenyl	65
2e	*m*-bromo-*p*-hydroxyphenyl	20
2f	*p*-cyanophenyl	91
2g	*o*-flurophenyl	55
2h	*o*-chlorophenyl	57
2i	*m*-bromophenyl	74
2j	*p*-nitrophenyl	95
2k	*m*-carboxyphenyl	69
2l	*p*-ethylphenyl	54
2m	*p*-ethoxyphenyl	33
2n	H	56

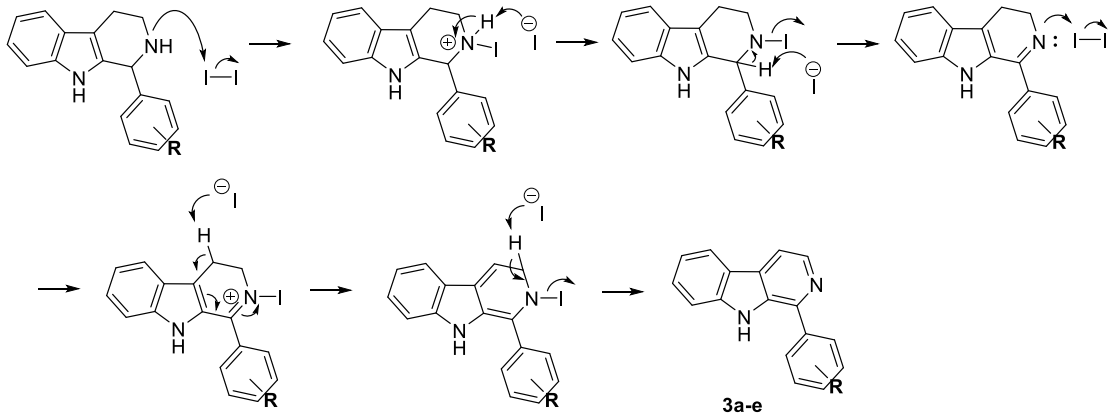


Scheme 2. Mechanism of Pictet-Spengler reaction with electrophilic addition at carbon-3

Scheme 3. Aromatization of tetrahydro-β-carboline intermediates

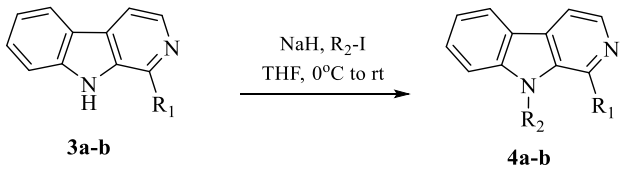


Entry	R_1	Yield (%)
3a	Phenyl	72
3b	*p*-methoxyphenyl	54
3c	*p*-hydroxyphenyl	43
3d	*m*, *p*-dimethoxyphenyl	22
3e	*m*-carboxyphenyl	19



Scheme 4. Mechanism of oxidative dehydrogenation

Scheme 5. N-alkylation of β-carboline derivatives



3a-b **4a-b**

Entry	R_1	R_2	Yield (%)
3a	Phenyl	methyl	81
3b	*p*-methoxyphenyl	methyl	79

Conclusion

In summary, we have successfully synthesized a series of β-carboline derivatives using simple, metal-free iodine-mediated method. In this reaction, the β-carboline skeleton is constructed by cyclization and a subsequent oxidation reaction, followed by N-alkylation reaction. Further application of the scope and mechanism of reaction in the study towards total synthesis of daibucarboline A and other additional biologically active natural products is currently in progress.

Acknowledgement

The authors acknowledge the generous support of Institute of Science, Universiti Teknologi MARA in providing required chemicals and instrumentations, as well as the financial support of Ministry of Higher Education Malaysia (FRGS grant 600-IRMI/FRGS 5/3 (399/2019).

References

1. John, A. J., George, V., Pradeep, N. S. and Sethuraman, M. G. (2008). Chemical composition and antibacterial activity of the leaf, bark and fruit oils of Neolitsea fischeri Gamble. *Journal of Essential Oil Research,* 20(3): 279-282.
2. Jin, H., Zhang, P., Bijian, K., Ren, S., Wan, S., Alaoui-Jamali, M. A. and Jiang, T. (2013). Total synthesis and biological activity of marine alkaloid Eudistomins Y1–Y7 and their analogues. *Marine drugs*, 11(5): 1427-1439.
3. Maria Miranda Santos, C. (2012). New agents promote neuroprotection in Parkinson's disease models. *CNS & Neurological Disorders-Drug Targets*, 11(4): 410-418.
4. Rinehart Jr, K. L., Kobayashi, J., Harbour, G. C., Gilmore, J., Mascal, M., Holt, T. G. and Lafargue, F. (1987). Eudistomins A-Q, beta.-carbolines from the antiviral Caribbean tunicate Eudistoma olivaceum. *Journal of the American Chemical Society*, 109(11): 3378-3387.
5. Sun, B., Morikawa, T., Matsuda, H., Tewtrakul, S., Wu, L. J., Harima, S. and Yoshikawa, M. (2004). Structures of new β-carboline-type alkaloids with antiallergic effects from *Stellaria dichotoma*. *Journal of Natural Products*, 67(9): 1464-1469.
6. Ashok, P., Ganguly, S. and Murugesan, S. (2013). Review on in-vitro anti-malarial activity of natural β-carboline alkaloids. *Mini Reviews in Medicinal Chemistry*, 13(12): 1778-1791.
7. Rahimi-Moghaddam, P., Ebrahimi, S. A., Ourmazdi, H., Selseleh, M., Karjalian, M., Haj-Hassani, G. and Shafiei, M. (2011). In vitro and in vivo activities of *Peganum harmala* extract against Leishmania major. *Journal of Research in Medical Sciences*, 16(8): 1032.
8. Dong, X. C., Wen, R. and Zheng, J. B. (2004). Synthesis of 1-indole substituted beta-carboline alkaloid and its derivatives and evaluation of their preliminary antitumor activities. *Acta Pharmaceutica Sinica*, 39(4): 259-262.

9. Gorki, V., Singh, R., Walter, N. S., Bagai, U. and Salunke, D. B. (2018). Synthesis and evaluation of antiplasmodial efficacy of β-carboline derivatives against murine malaria. *ACS omega*, 3(10): 13200-13210.
10. Wang, Y. H., Tang, J. G., Wang, R. R., Yang, L. M., Dong, Z. J., Du, L. and Zheng, Y. T. (2007). Flazinamide, a novel β-carboline compound with anti-HIV actions. *Biochemical and Biophysical Research Communications*, 355(4): 1091-1095.
11. Patel, K., Gadewar, M., Tripathi, R., Prasad, S. K. and Patel, D. K. (2012). A review on medicinal importance, pharmacological activity and bioanalytical aspects of beta-carboline alkaloid "Harmine". *Asian Pacific journal of tropical biomedicine*, 2(8): 660-664.
12. Wong, S. L., Chang, H. S., Wang, G. J., Chiang, M. Y., Huang, H. Y., Chen, C. H. and Chen, I. S. (2011). Secondary metabolites from the roots of Neolitsea daibuensis and their anti-inflammatory activity. *Journal of Natural Products*, 74(12): 2489-2496.
13. Jani, N. A., Sirat, H. M., Ahmad, F., Abed, S. A. and Aminudin, N. I. (2018). Chemical constituents of the stems of *Neolitsea kedahensis* Gamble. *Phytochemistry Letters*, 26: 12-15.
14. Love, B. E. (1996). Synthesis of β-carbolines. A review. *Organic Preparations and Procedures International*, 28(1): 1-64.
15. Cox, E. D. and Cook, J. M. (1995). The Pictet-Spengler condensation: a new direction for an old reaction. *Chemical Reviews*, 95(6): 1797-1842.
16. Mangalaraj, S. and Ramanathan, C. R. (2012). Construction of tetrahydro-β-carboline skeletons via Brønsted acid activation of imide carbonyl group: syntheses of indole alkaloids (±)-harmicine and (±)-10-desbromoarborescidine-A. *RSC Advances*, 2(33): 12665-12669.
17. Lynch-Colameta, T., Greta, S. and Snyder, S. A. (2021). Synthesis of aza-quaternary centers via Pictet–Spengler reactions of ketonitrones. *Chemical Science*, 12(17): 6181-6187.
18. Srinivasan, N. and Ganesan, A. (2003). Highly efficient Lewis acid-catalysed Pictet–Spengler reactions discovered by parallel screening. *Chemical Communications*, (7): 916-917.
19. Maresh, J. J., Giddings, L. A., Friedrich, A., Loris, E. A., Panjikar, S., Trout, B. L. and O'Connor, S. E. (2008). Strictosidine synthase: Mechanism of a pictet− spengler catalyzing enzyme. *Journal of the American Chemical Society*, 130(2): 710-723.
20. Eagon, S. and Anderson, M. O. (2014). Microwave-assisted synthesis of tetrahydro-β-carbolines and β-carbolines. *European Journal of Organic Chemistry*, 2014(8): 1653-1665.
21. Cain, M., Weber, R. W., Guzman, F., Cook, J. M., Barker, S. A., Rice, K. C. and Skolnick, P. (1982). Beta-carbolines: synthesis and neurochemical and pharmacological actions on brain benzodiazepine receptors. *Journal of Medicinal Chemistry*, 25(9): 1081-1091.
22. Chen, H., Gao, P., Zhang, M., Liao, W. and Zhang, J. (2014). Synthesis and biological evaluation of a novel class of β-carboline derivatives. *New Journal of Chemistry*, 38(9): 4155-4166.
23. Jiang, H., Huang, H., Cao, H. and Qi, C. (2010). TBHP/I2-mediated domino oxidative cyclization for one-pot synthesis of polysubstituted oxazoles. *Organic Letters*, 12(23): 5561-5563.
24. Chu, J. W. and Trout, B. L. (2004). On the mechanisms of oxidation of organic sulfides by H_2O_2 in aqueous solutions. *Journal of the American Chemical Society*, 126(3): 900-908.

Malaysian Journal of Analytical Sciences (MJAS)
Published by Malaysian Analytical Sciences Society

EFFECT OF PLANT ORGANS OF *Ficus deltoidea* IN THE SYNTHESIS OF SILVER NANOPARTICLES

(Kesan Organ Tumbuhan *Ficus deltoidea* dalam Mensintesis Nanopartikel Perak)

Shahrulnizahana Mohammad Din[1,2], Nik Ahmad Nizam Nik Malek[1,3]*, Mustaffa Shamsuddin[4], Juan Matmin[4]

[1]Department of Biosciences, Faculty of Science,
Universiti Teknologi Malaysia, 81310 UTM Johor Bahru, Johor, Malaysia
[2]Department of Chemistry Malaysia,
Johore Branch, Jalan Abdul Samad, 80100 Johor Bahru, Johor, Malaysia
[3]Centre for Sustainable Nanomaterials (CSNano), Ibnu Sina Institute for Scientific and Industrial Research (ISI-SIR)
[4]Department of Chemistry, Faculty of Science
Universiti Teknologi Malaysia, 81310 UTM Johor Bahru, Johor, Malaysia

**Corresponding author: niknizam@utm.my*

Received: 8 September 2021 ; Accepted: 26 September 2021 ; Published: 25 October 2021

Abstract

The effect of different plant organ extracts (leaf, stem, fig and root) of *Ficus deltoidea* var. *kunstleri* (King) Corner (Mas Cotek) in the synthesis of silver nanoparticles (AgNP) was studied. The plant analysis using liquid chromatography-mass spectrometry (LCMS) yielded more than 100 phytochemical compounds in each organ, of which around 50 % belong to the phenolics, flavonoids and polyphenols compounds. The chemical marker compounds (vitexin and isovitexin) were only found in the leaf, and Total Phenolic Content (TPC), as well as Total Flavonoid Content (TFC) were observed to be the highest in fig compared to other organs. The localized surface plasmon resonance (LSPR) of the biosynthesised AgNP using all organs was found at 409 to 428 nm. The capping and stabilization of AgNP by phytochemical compounds were verified by Fourier transform infrared (FTIR) spectroscopy as the vibration and stretching of -NH, $-CH_3$, $-CH_2$, -CH, C=O and -OH functional groups were found. There was a high abundance of phytochemical compounds in each organ: gallic acid, kaempferol-3-(6"-caffeoylglucoside), quercetin-3-O-rhamnoside and kaempferol 3-(3",4"-diacetylrhamnoside) in leaf, stem, fig and root, respectively. These compounds belong to the phenolics, flavonoids and polyphenols groups responsible for reducing Ag^+ to Ag^0 (AgNP). The results indicated that the fig which contained the highest TPC and TFC formed the highest LSPR peak for the formation of AgNP. The most important finding was the ability of each plant organ of *F. deltoidea* in the AgNP biosynthesis.

Keywords: plant organs, *Ficus deltoidea*, biosynthesis, nanoparticles

Abstrak

Kesan ekstrak organ tumbuhan yang berbeza (daun, batang, ara dan akar) dari pokok *Ficus deltoidea* var. *kunstleri* (King) Corner (Mas Cotek) dalam mensintesis nanopartikel perak (AgNP) dianalisis dalam kajian ini. Analisis pokok menggunakan spektometri jisim kromatografi cecair (LC-MS) menemui lebih dari 100 sebatian fitokimia di setiap organ, di mana sekitar 50% tergolong dalam sebatian fenolik, flavonoid dan polifenol. Sebatian penanda kimia (vitexin dan isovitexin) hanya terdapat pada daun, dan kandungan jumlah fenolik (TPC) serta kandungan jumlah flavonoid (TFC) diperhatikan pada bahagian ara adalah

tertinggi berbanding organ lain. Resonans plasmon permukaan setempat (LSPR) bagi AgNP biosintesis menggunakan semua organ didapati dalam lingkungan 409 hingga 428 nm. Pembatasan dan penstabilan AgNP oleh sebatian fitokimia disahkan oleh spektroskopi inframerah transformasi Fourier (FTIR) sebagai getaran dan perenggangan kumpulan berfungsi -NH, -CH_3, -CH_2, -CH, C=O dan -OH di kesan. Terdapat sebilangan besar bahan fitokimia di setiap organ iaitu galik asid, kaempferol-3-(6"-kafeglukosida), quersetin-3-O-ramnosida dan kaempferol 3-(3",4"-diasetilramnosida) di bahagian daun, batang, ara dan akar masing-masing. Sebatian ini tergolong dalam kumpulan fenolik, flavonoid dan polifenol yang bertanggungjawab untuk penurunan Ag^+ ke Ag^0 (AgNP). Hasil kajian menunjukkan bahagian ara yang mengandungi TPC dan TFC tertinggi membentuk puncak LSPR tertinggi untuk pembetukan AgNP. Penemuan yang paling penting adalah kemampuan setiap organ pokok *F. deltoidea* dalam biosintesis AgNP.

Kata kunci: organ tumbuhan, *Ficus deltoidea*, biosintesis, partikel-nano

Introduction

Plant organs such as leaves, stems, roots, flowers, fruits, and seeds have diverse phytochemical compounds [1]. The type and concentration of the phytochemical compounds depend on the metabolism and the functions of the plant organs [2]. Diversity of the growing climate, different harvesting times and stress conditions affect the concentration of the phytochemical compound in the same species or source of the plant [3, 4, 5]. Phytochemical compounds are plant-part specific and vary extensively among different plant populations [5]. It usually consists of tannins, saponins, alkaloids, terpenoids, steroids, proteins, amino acids, phenolic and flavonoid compounds [6]. These phytochemicals give colour and odour for protection and reproduction, serve as phytoalexins for pathogen resistance, are involved in hormonal functions for growth and signalling, act as antifeedants or toxins for pests protection, and allelochemicals for defence against herbivorous animals [7].

Furthermore, plant phenolics and flavonoids can reduce Ag^+ to Ag^0 producing silver nanoparticles (AgNP) because of their functional groups being rich in electrons, forming complexes that are disunited to form AgNP. It is acknowledged that the hydroxyl group (O-H) of the phenolics and flavonoids firmly hold the Ag^+ in an oligomeric cluster, resulting in the formation of aggregates that stabilise into AgNP [8].

For many years, plants with high phytochemicals have been used as medicinal herbs due to their high nutritional values, rich sources of antioxidants that may slow down ageing processes, reduce inflammation and prevent certain diseases [1, 9]. One of the native medicinal plants available in Malaysia is *Ficus deltoidea* Jack var. *kunstleri* (King) Corner, which is also known as Mas Cotek. Traditionally, this plant has been developed as an alternative treatment for diabetes, hypertension, blood flow, gout, pneumonia, cardiac problems, diarrhoea and skin infection [10]. The chemical marker of this plant which are vitexin and isovitexin (flavonoid group) have many medicinal benefits to human. Previous studies have shown that these substances exhibit anti-tumour, anti-inflammatory, and antinociceptive properties [7, 8].

Typically, *F. deltoidea* can reach a height of 2 m, possesses whitish-grey stems and bark when mature. It has broadly spoon-shaped leaves, The leaves range in sizes from 4 to 8 cm with bright green colour on top and rust-red to olive-brown at the bottom. Furthermore, this plant produces yellow to orange figs with a width of about 1.0 to 1.5 cm [12] and also has fibrous brown roots. The different organs of *F. deltoidea* like the leaf, stem, fig and root may contain different phytochemical compounds. In the biosynthesis of AgNP, the reducing ability of any plant organ strongly depends on the presence of a phytochemical compound. However, there are still limited studies on the effect of plant organs on the synthesis of AgNP. This study focused on the analysis of phytochemical compounds of different organs of *F. deltoidea* and its initial effect on the formation of AgNP.

Materials and Methods

Chemical and reagents

Silver nitrate ($AgNO_3$) ≥ 99.0% was purchased from Vchem. Aluminum chloride ($AlCl_3$) ≥ 98.0%, sodium nitrite ($NaNO_2$) ≥ 99.0%, sodium hydroxide (NaOH) 99%, nitric acid (HNO_3) 69%, potassium bromide for infrared (IR) spectroscopy, methanol ≥ 99.8% for liquid chromatography usage, ethanol ≥ 99.9% for liquid chromatography usage, formic acid 97.5-98.5% and quercetin ≥ 95% were procured from Merck. Both vitexin ≥ 95.0% and isovitexin ≥ 98.0% were acquired from Sigma-Aldrich. Gallic acid was purchased from R&M Chemical.

F. deltoidea plant extract

The *F. deltoidea,* with the age of about four years, was provided by the Department of Agriculture Malaysia, Pontian, Johor Branch. The plant was segregated according to its organs: leaf, stem, fig and root. They were cleaned with deionised water to remove unwanted impurities like sand, gravel, insects, bugs, and other contaminants. After that, the plant organs were dried in a 60 °C oven. The dried plant organs were then ground and sieved with a mesh size of 0.45 µm. The dried powdered biomasses were stored in a chiller at 4 °C for later use. Figure 1 shows the illustration of the process flow to obtain the dried plant biomasses.

The process involved mixing 2 g of the dried biomass with 100 ml of boiled deionised water. A hotplate with a magnetic stirrer was used to stir the mixture for 30 minutes at 100 °C [13]. The plant extracts were then filtered with Whatman No 1 filter paper, and the filtrate was stored at 4°C for future use.

Screening of Phytochemical Compounds using Liquid Chromatography Mass Spectrometer (LC-MS)

Ethanol 96% was used as a maceration solvent to macerate 45 g of dried biomass. This procedure took three days to complete. The maceration solvent was replaced for every 24 hours. The ratio of the dried biomass powder weight (g) to solvent (ethanol 96%) volume (L) was 500:6. The maceration solution was collected, and an evaporator was used to separate the solvent and dissolved chemicals generated from the dried biomass. The evaporation procedure was used to generate a paste of approximately 45 g, which was then considered to be at 100% concentration. The LCMS analysis was performed using the Shimadzu LCMS 2010 EV and a reverse phase LC system. The mobile phase of acetonitrile distillation to water ratio was 7:3, and the ammonium acetate concentration was 10 mmol/L. The LC pump gradient system with a vacuum pump flow velocity of 1 mL/min and C-18 column (150 mm × 2.1 mm) with a column temperature of 40 °C were used in this analysis. Only 10 µL of the sample was injected in a single run using a gas nitrogen generator at 250 °C. Positive Ion Electroscopy was used with a Mass Spectrometry Detector (SPD-10 AVP).

Analysis of Vitexin and Isovitexin using High-Performance Liquid Chromatography (HPLC)

Vitexin and isovitexin were selected as chemical markers for F. deltoidea varietal identification [10]. A round bottom flask was filled with 5.0 g of dried biomass and added with 80 mL of ethanol 96%. The sample was allowed to cool after being refluxed for 30 minutes. Thereafter, the sample was filtered with Whatman No. 1 filter paper and the filtrate was evaporated. Methanol (HPLC grade) was used to dissolve 50.0 mg of the dried extracts. It was then injected into the High-Performance Liquid Chromatography (HPLC) column after being filtered with a 0.45 µm syringe filter using HPLC Agilent 1260 Infinity. The injection volume was 10 µl, and the isocratic mobile phase that carried the sample to be separated was a mixture of six volumes of 1% formic acid and four volumes of methanol. The flow rate was set to 1.0 mL/min and the sample was separated in a C-18 column with 250 mm × 4.6 mm and an oven temperature of 30 °C. For each sample, the run time was 15 minutes.

Total Phenolic Content and Total Flavonoid Content

Total phenolic content (TPC) was determined by mixing 1.0 mL of the sample with 0.5 mL of Folin-Ciocalteu reagent and 1.5 mL of Na_2CO_3 20% solution. The mixture was then incubated for half an hour at 40

°C before being measured with a Jenway 7200 Visible spectrophotometer at 750 nm. For Total Flavonoid Content (TFC) analysis, 0.3 mL $NaNO_2$ solution 5% was mixed with 1 mL sample and the mixture was left for five minutes. After that 0.3 mL of $AlCl_3$ 10% solution was added to the sample and the solution was makeup to 10 mL. The sample was measured using the visible spectrophotometer at 510 nm. TPC and TFC values were calculated based on the formula (Equation 1 and 2) obtained from the literature [13], which were expressed in mg of Gallic acid per 1g dry extract (Gallic Acid Equivalent; GAE) and mg of Quercetin equivalent (QE) per gram of dry mass (g), respectively.

$$\text{Total phenolic compound, (GAE)} \left(\frac{\text{mg}}{\text{g}}\right), = \frac{C_1 V}{M} \quad (1)$$

$$\text{Total Flavonoid Content, (QE)} \left(\frac{\text{mg}}{\text{g}}\right), = \frac{C_1 V}{M} \quad (2)$$

where, GAE is gallic acid equivalent, QE is quercetin equivalent, C_1 is concentration gained from calibration curve, V is volume of extract, mL and M is mass of plant biomass (g).

Formation of AgNP using Organs of *F. deltoidea*

For the formation of the AgNP, the aqueous plant extracts were added to 10 ml of $AgNO_3$ 1 mM according to the synthesis conditions as shown in Table 1. The synthesis parameters were selected based on our experiment on optimizing the AgNP synthesis method (Data not shown and will be published elsewhere). The formation of AgNP was monitored using a Jenway 7200 Visible Spectrophotometer in the visible range of 350 to 750 nm. This is due to the fact that AgNP exhibited a localized Surface Plasmon Resonance (LSPR) band at this range based on its free electron excitation [14]. The functional groups of *F. deltoidea* extracts and biosynthesised AgNP (powder form) were analyzed using Fourier Transform Infrared Spectroscopy (FTIR). This analysis was performed on a Perkin Elmer FTIR 1600 using the KBr technique in the range of 4000 – 400 cm^{-1}.

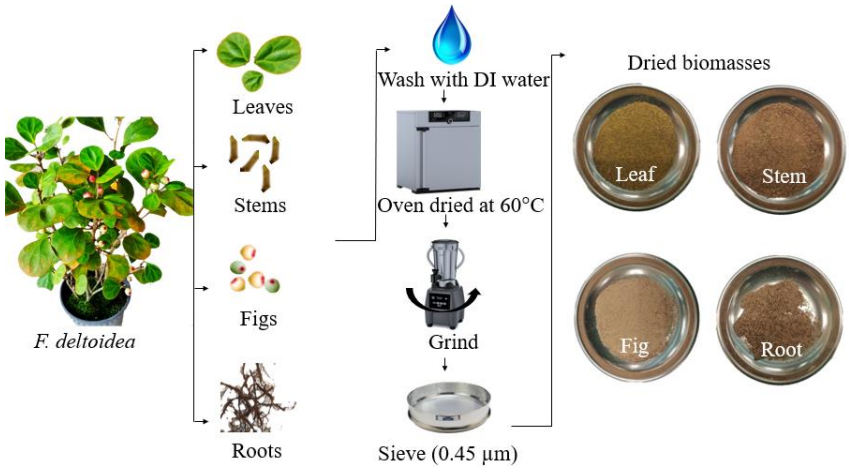


Figure 1. Illustration of the process flow of preparing dried plant biomasses of different organ

Results and Discussion

The LCMS results in Figure 2 indicated that the leaf, stem, fig, and root produced signals at different retention times (RT) of 127, 129, 104, and 119 peaks, respectively. The RT signals could be attributed to the presence of phytochemical compounds. Based on the chromatogram, it can be said that more than 50% of them were phenolics, flavonoids and polyphenol compounds. Among the phytochemical compounds found in *F. deltoidea* are rutin, quercetin, naringenin, vitexin, and isovitexin. The selected phytochemical

compounds content (in percentage) is shown in Table 2.

Notably, these phytochemical compounds act as biological defenses for unicellular and multicellular plants, protect biological cells, tissues and organs of plants from damages caused by oxidative stress, and as plant metabolites, they prevent inflammation and promote carbohydrate metabolism [14-19]. The highest phytochemical compounds identified in each organ are tabulated in Table 2. On that note, gallic acid was identified in the leaf, kaempferol-3-(6"-caffeoylglucoside) in the stem, quercetin-3-O-rhamnoside in fig and kaempferol 3-(3",4"-diacetylrhamnoside) in the root. The molecular structures of these phytochemical compounds are shown in Figure 3.

To validate the chromatogram, the retention time (RT) of a specific flavonoid of vitexin and isovitexin at 7.4 and 8.7 minutes, respectively was used in the HPLC analysis (Figure 4). Notably, these compounds were found at 17.84 ± 2.57 ppm of vitexin and 13.92 ± 0.44 ppm of isovitexin in the leaves of *F. deltoidea*. It was abundantly found in the leaf organ. This finding is in line with the study that has been conducted by Abdullah et al. [17], which found that the concentration of vitexin was higher than that of isovitexin in the leaf of *F. deltoidea*. He at al. [18] mentioned that in *Lemna minor* plant, vitexin was found to be converted to isovitexin and not in reverse direction. These phytochemical compounds serve as siderophores, attractants and feeding deterrents in plant [17]. From previous studies, these compounds also found in various plants such as mung beans, wheat leaves and bamboo [18].

Figure 5 shows the TPC and TFC values of the extracts of *F. deltoidea* measured using the Folin-Ciocalteu method and Aluminium chloride colourimetric assay, respectively. It is important to determine both compounds composition in the plants as the formation of AgNP highly depends on their presence. This was emphasised by Asmat-Campos et al. as they stated that the presence of polyphenol promotes the reduction and capping of nanoparticles [19]. In the Folin-Ciocalteu method, the reagent used was composed of a mixture of phosphotungstic acid and phosphomolybdic acid, which were reduced to a mixture of blue oxides of tungsten and molybdenum once the phenols were oxidised. The blue colour produced had a maximum absorption in the 750 nm range and was proportionate to the total amount of phenolic compounds present in the sample [20]. To determine the TFC, the Aluminium chloride reacted with the flavone, flavanol and hydroxyl/dihydroxyl group in the flavonoids [21]. From the result, the leaf organ of *F. deltoidea* contains 28.56 ± 0.87 (GAE) mg/g TPC and 761.32 ± 13.00 (QE) mg/g. These results are lower than the leaf of *Vigna Unguiculate* Dhawala which contains 508.7 (GAE) mg/g and 1303.1 (QE) mg/g, respectively [22]. Meanwhile, the fig organ of *F. deltoidea* had the highest TPC and TFC values compared to other organs. Even though the number of phytochemical compounds in fig is the lowest, this organ has the highest TPC and TFC values.

Table 1. AgNP synthesizing conditions

Plant Organs	Plant Extract Volume (mL)	Reaction Time (Hours)	Reaction Temperature (°C)	pH of Plant Extract
Leaf	1.0	30	60	10
Stem	1.0	21	90	12
Fig	0.8	33	100	10
Root	3	21	90	12

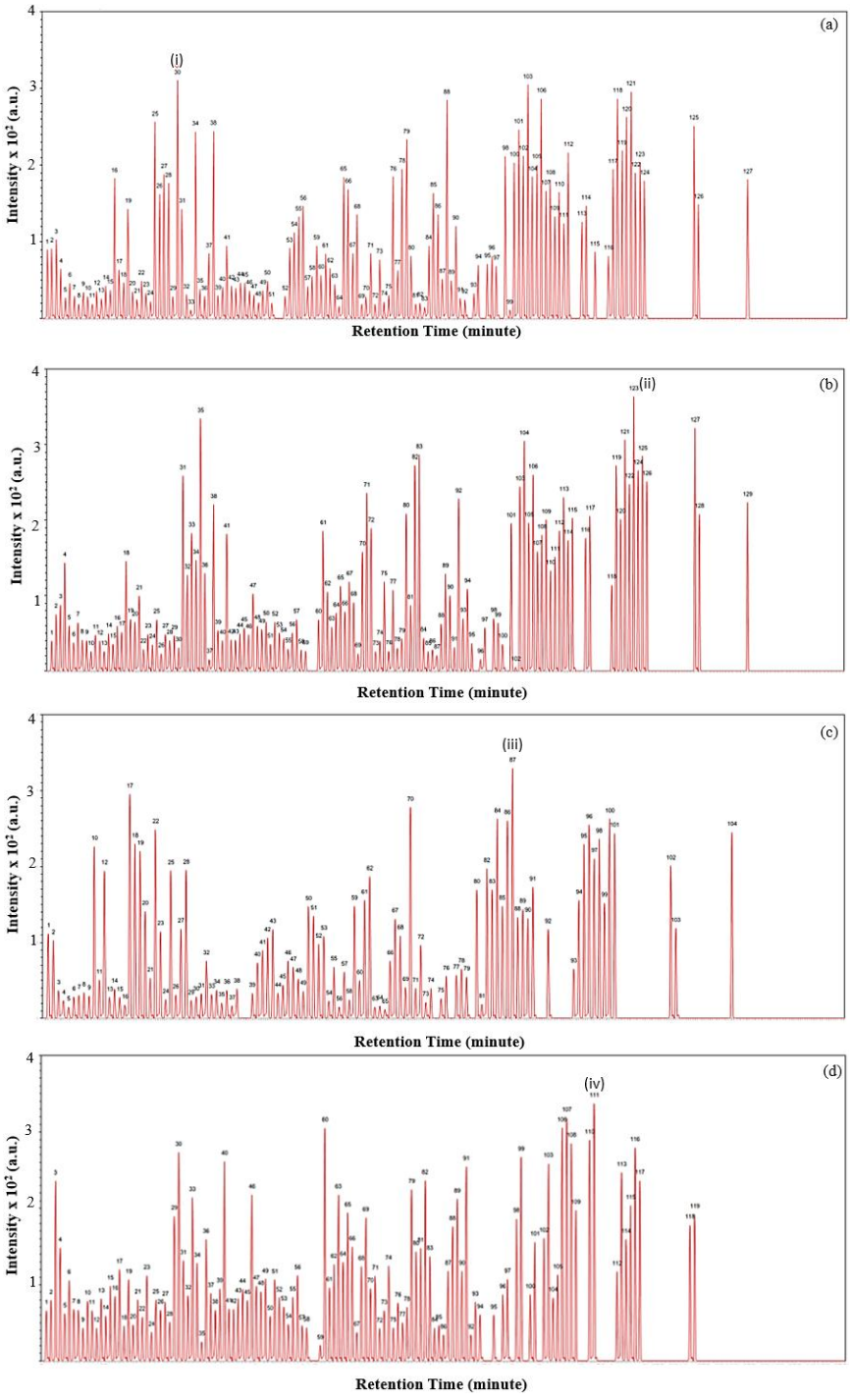


Figure 2. LCMS chromatogram of the phytochemical compounds found in (a) leaf, (b) stem, (c) fig and (d) root of *F. deltoidea*. The labelled peaks are the highest phytochemical compounds contained in each organ which are (i) gallic acid was identified in the leaf, (ii) kaempferol-3-(6"-caffeoylglucoside) in the stem, (iii) quercetin-3-O-rhamnoside in fig and (iv) kaempferol 3-(3",4"- diacetylrhamnoside) in the root.

Table 2. The percentage of phytochemical compounds in *F. deltoidea*

Phytochemical Compounds	Retention Time (min)	Mass to Ion Ratio (m/z)	% Compound			
			Leaf	Stem	Fig	Root
P-coumaric acid	1.859	164.05	1.91	1.79	2.71	1.28
Gallic acid[i]	3.042	170.02	2.32	2.32	2.28	1.45
Chlorogenic acid	12.421	354.10	2.12	1.58	2.55	1.72
Luteolin-7-glucoside	22.628	448.10	2.15	1.80	2.41	1.05
Quercetin-3-O-rhamnoside[iii]	24.003	432.11	2.14	1.39	3.02	1.75
Kaempferol 3-(3"-acetylrhamnoside)	24.77	75.03	1.23	1.60	1.21	2.15
Kaempferol 3-(3",4"-diacetylrhamnoside)[iv]	28.208	516.13	1.10	1.42	1.08	2.28
Kaempferol-3-(6"-caffeoylglucoside)[ii]	35.508	610.13	2.21	2.52	2.17	1.89

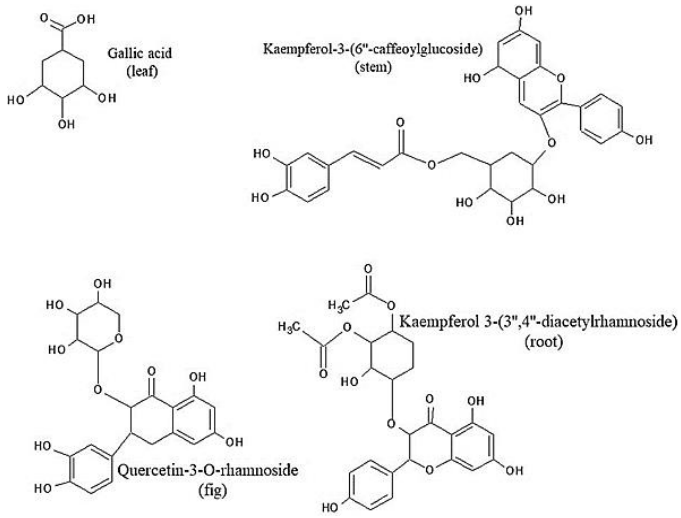


Figure 3. Molecular structures of main phytochemicals compounds in each *F. deltoidea* organs

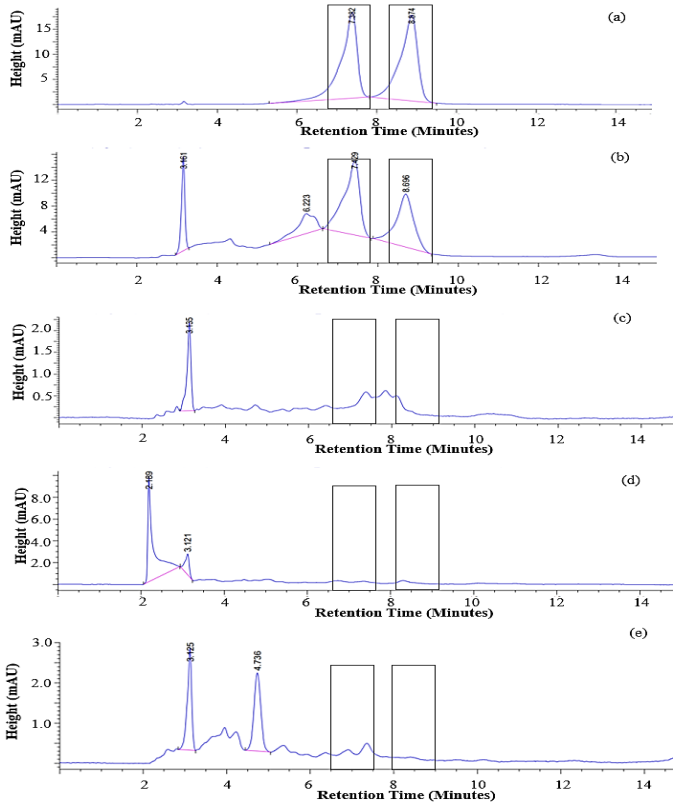


Figure 4. HPLC chromatograms of vitexin and isovitexin in (a) mixed standards, (b) leaf, (c) stem, (d) fig and (e) root

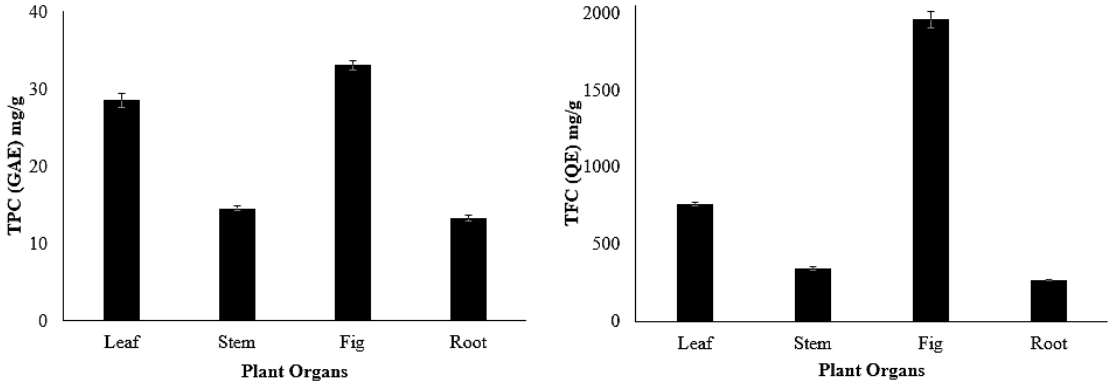


Figure 5. TPC and TFC values of different plant organs of *F. deltoidea*

In this study, different organs of the plant extract were used in the biosynthesis of AgNP. As shown in Figure 6(a), the formation of AgNP was conducted by monitoring the LSPR peak in the range of 350 to 750 nm. The FTIR spectra of the plant biomass and the biosynthesised AgNP using each plant organ can be seen in Figure 6(b and c).

In Figure 6(a), the LSPR absorbance peak of the biosynthesised AgNP using *F. deltoidea* was observed in the visible region between 409 and 428 nm. Based on the LCMS result, the stem had the highest number of phytochemical compounds while fig recorded the lowest percentages; however, the TPC, TFC and capability to form AgNP according to LSPR peak did not follow this trend. This means that the phenolics, flavonoids and polyphenol compound greatly influenced the ability to synthesis AgNP compared to the number of phytochemical compounds in the plant organ. According to Beer-Lambert's Law, it can be deduced that the formation of AgNP was highest when using the fig organ. This aligns with the works of Lavola et al. [5], where they discovered that phenolic content in the fruit of *Empetrum hermaphroditum* was the highest compared to other organs. Nonetheless, the role of each organ in plant physiology could be attributed to the presence of different phenolics content [23]. This also leads to different organ capabilities in the biosynthesis of AgNP. Moreover, the complexity and massive amounts of different phytochemicals in any plant extract is the major challenge in determining the exact phytochemical responsible for the biosynthesis of AgNP [22, 23]. Taking this into account, it is safe to suggest that the oligomeric cluster may comprise one or more phytochemicals that capped and stabilised the AgNP [26].

In the FTIR spectra of *F. deltoidea* plant extract, the peak at 3430 cm^{-1} revealed stretching of the amide (N–H) bond and hydroxyl (–OH) groups. From the IR spectra, the absorption peak at 2920 cm^{-1} could be attributed to $–CH_3$ and $–CH_2$ stretching vibrations. C-H stretching from the alkane group causes the absorption peak at 2830 cm^{-1}. The C=O stretching had a peak at 1735 cm^{-1}, whereas C=C stretching had a peak at 1620 cm^{-1}. The O-H bending from the carboxylic acid functional group is represented by the peak at 1430 cm^{-1}. All of these functional groups corroborated the phytochemical compounds identified by LCMS. The same stretching and vibration bands were observed in the biosynthesised AgNP, indicating the presence of phytochemical compounds from *F. deltoidea* in the AgNP samples, which acted as a capping and stabilising agent in Figure 6(b and c).

From the plant analysis, *F. deltoidea* can be interpreted as a herbal plant that is rich in phenolics, flavonoids and polyphenols compounds. Its organs (leaf, stem, fig and root) have unique functions and metabolisms that make the amount and variety of phytochemical compounds differ from one another. Hence, they have the ability and capability of synthesising AgNP. It can be expected that the AgNP produced has distinct characteristics. The high TPC and TFC values impacted the formation of AgNP tremendously. This was reflected by the fact that the plant organ (fig) that had the highest phenolics and flavonoids exhibited the highest LSPR peak. This composition contributed to the highest formation of biosynthesis AgNP by the fig organ. In this study, phytochemical compounds are not only used as a reducing agent but also proved to be the stabilising agent for AgNP.

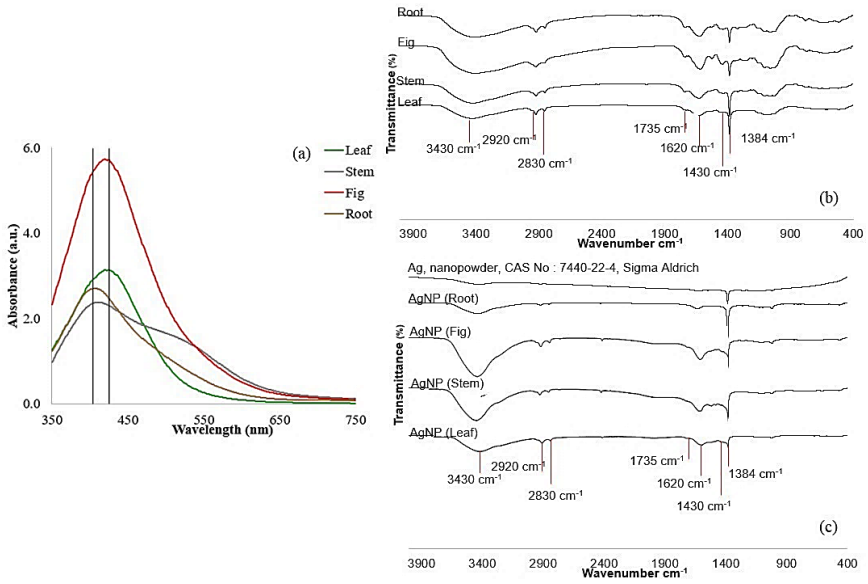


Figure 6. (a) LSPR absorbance for AgNP, (b) FTIR spectra of plant biomasses (b) and (c) biosynthesised AgNP

Conclusion

F. deltoidea Jack var *kunstleri* (King) Corner is a native herb that is rich in phytochemical compounds. From the LC-MS analysis, more than half of the phytochemicals belong to the phenolics, flavonoids and polyphenols group. The validation analysis also revealed that a specific flavonoid of vitexin and isovitexin were only detected in the leaf organ. The phytochemical compounds in plant extracts have the capability in the biosynthesis of AgNP by assisting the LSPR absorbance peak formed at 409 to 428 nm. The FTIR result revealed that the phytochemical compounds also served as a capping and stabilising agent for the formation of AgNP due to the diverse composition and high content of phytochemical compounds in *F. deltoidea*. In conclusion, this study adds to the body of knowledge on phytochemical compounds in plant organs spectrum in biosynthesising AgNP. Thus, this information could be used to manufacture AgNP from suitable plant organs.

Acknowledgement

The Author would like to give thanks to the Ministry of Higher Education and Universiti Teknologi Malaysia for funding and supporting this research project under Fundamental Research Grant Scheme (FRGS/1/2020/STG04/UTM/02/3) with Vot No: 5F291 and UTM-TDR project (Vot No: 06G71 and 06G72).

References

1. Muhamad I. I, Hassan N. D, Mamat S. N. H., Nawi N. M., Rashid W. A. and Tan N. A. (2017). Extraction technologies and solvents of phytocompounds from plant materials: Physicochemical characterization and identification of ingredients and bioactive compounds from plant extract using various instrumentations. *Ingredients Extraction by Physico-Chemical Methods in Food*, pp. 523-560.
2. Deepak K., Shirsat R. and Kawale M. (2016). An overview of major classes of phytochemicals: Their types and role in disease prevention. *Hislopia Journal,* 9: 1-11.
3. Ou B., Huang D., Hampsch-Woodill M., Flanagan J. A. and Deemer E. K. (2002). Analysis of antioxidant activities of common vegetables employing oxygen radical absorbance capacity (ORAC) and ferric reducing antioxidant power (FRAP) assays: A comparative study. *Journal of Agricultural and Food Chemistry*, 50 (11): 3122-3128.

4. Rao B. N. (2003). Bioactive phytochemicals in Indian foods and their potential in health promotion and disease prevention. *Asia Pacific Journal of Clinical Nutrition*, 112(1): 9-22.
5. Lavola A., Salonen A., Virjamo V. and Julkunen-Tiitto R. (2017). Phytochemical Variation in the plant-part specific phenols of wild crowberry (*Empetrum hermaphroditum Hagerup*) populations. *Phytochemistry Letter*, 21: 11-20.
6. Alim A., Ghazali W. A. S. W., Ali N. A. M. and Ponnuraj K. T. (2017). Phytochemical properties and traditional uses of selected medicinal plants in Malaysia: A review. *Journal of Biomedical Science,* 2(2): 4–25.
7. Huang Y., Xiao D., Burton-freeman B. M. and Edirisinghe I. (2016). Chemical changes of bioactive phytochemicals during thermal processing, pp. 1-9.
8. Goswami M., Baruah D. and Das A. M. (2018). Green synthesis of silver nanoparticles supported on cellulose and their catalytic application in the scavenging of organic dyes. *New Journal of Chemistry,* 42(13): 10868–10878.
9. Altemimi A., Lakhssassi N., Baharlouei A., Watson D. G. and Lightfoot D. A. (2017). Phytochemicals: Extraction, isolation, and identification of bioactive compounds from plant extracts. *Plants,* 6 (4): 1-23.
10. Afzan A., Kasim N., Hadiani N., Norfaizura I., Abdul A., Ali M. and Mat N. (2019). Differentiation of *Ficus deltoidea* varieties and chemical marker determination by UHPLC-TOFMS metabolomics for establishing quality control criteria of this popular Malaysian medicinal herb. *Metabolomics,* 15(3): 1–11.
11. Nasma A., Aishath N., Azilah A., and Sulaiman A. Z. (2018). Optimization of vitexin and isovitexin compounds extracted from dried mas cotek leaves using one-factor-at-a-time (OFAT) approach in aqueous extraction. *International Food Research Journal,* 25(6): 2560-2571.
12. Bunawan H., Amin N. M., Bunawan S. N., Baharum S. N. and Noor N. M. (2014). *Ficus deltoidea* Jack: A review on its phytochemical and pharmacological importance. *Evidence-Based Complementary and Alternative Medicine,* 2014: 1-8.
13. Singhal A., Singhal N., Bhattacharya A. and Gupta A. (2017). Synthesis of silver nanoparticles (AgNPs) using *Ficus retusa* leaf extract for potential application as antibacterial and dye decolourising agents. *Inorganic and Nano-Metal Chemistry,* 47(11): 1520-1529.
14. He Y., Wei F., Ma Z., Zhang, H., Yang Q., Yao B. and Zhang Q. (2017). Green synthesis of silver nanoparticles using seed extract of *Alpinia katsumadai,* and their antioxidant, cytotoxicity, and antibacterial activities. RSC Advances, 7 (63): 39842-39851.
15. Labeeuw L., Martone P. T., Boucher, Y. and Case R. J. (2015). Ancient origin of the biosynthesis of lignin precursors. *Biology Direct,* 10 (23): 1–21.
16. Mierziak J., Kostyn K., and Kulma A. (2014). Flavonoids as important molecules of plant interactions with the environment. *Molecules,* 19 (10): 16240-16265.
17. Abdullah F. I. and Chua L. S. (2017). Prediction of c-glycosylated apigenin (Vitexin) biosynthesis in Ficus deltoidea based on plant proteins identified by LC-MS/MS. *Frontiers in Biology,* 12(6): 448-458.
18. He M., Min J. W., Kong W. L., He X. H., Li J. X. and Peng B. W. (2016). A review on the pharmacological effects of Vitexin and Isovitexin. *Fitoterapia,* 115:74–85.
19. Asmat-Campos D., Abreu A. C., Romero-Cano M. S., Urquiaga-Zavaleta J., Contreras-Cáceres R., Delfín-Narciso D., Juárez-Cortijo L., Nazario-Naveda R., Rengifo-Penadillos R. and Fernández I. (2020). Unraveling the active biomolecules responsible for the sustainable synthesis of nanoscale silver particles through nuclear magnetic resonance metabolomics. *ACS Sustainable Chemistry & Engineering,* 8(48): 17816-17827.
20. Kamtekar S., Keer V. and Patil V. (2014). Estimation of phenolic content, flavonoid content, antioxidant and alpha amylase inhibitory activity of marketed polyherbal formulation. *Journal of Applied Pharmaceutical Science,* 4 (9): 1–65.
21. Arifin R. N. A. R. and Jumal J. (2021). Antioxidant activity of *Averrhoa bilimbi* Linn. leaves extract using two different types of solvents. Malaysian Journal of Science, Health & Technology, 7: 76–82.
22. Perera B. R. and Kandiah M. (2018). Microwave assisted one-pot green synthesis of silver nanoparticles using leaf extracts from *Vigna unguiculate*: evaluation of antioxidant and antimicrobial activities. *International Journal of Interdisciplinary and Multidisciplinary Studies*, 5(2): 62-78.

23. Karalija E., Muratović E., Tarkowski P., and Zeljković S. Ć. (2017). Variation in phenolic composition of *Knautia arvensis* in correlation with geographic area and plant organ. *Natural Product Communications*, 12(4): 545-548.
24. Kalia A., Manchanda P., Bhardwaj S. and Singh G. (2020). Biosynthesized silver nanoparticles from aqueous extracts of sweet lime fruit and callus tissues possess variable antioxidant and antimicrobial potentials. *Inorganic and Nano-Metal Chemistry,* 50(11): 1053-1062.
25. Ovais M., Khalil A., Islam N., Ahmad I., Ayaz M., Saravanan M., Shinwari Z. and Mukherjee S. (2018). Role of plant phytochemicals and microbial enzymes in biosynthesis of metallic nanoparticles. *Applied Microbiology and Biotechnology,* 102(16): 6799–6814.
26. Borhamdin S., Shamsuddin M. and Alizadeh A. (2016). Biostabilised icosahedral gold nanoparticles: synthesis, cyclic voltammetric studies and catalytic activity towards 4-nitrophenol reduction. *Journal of Experimental Nanoscience,* 11(7): 518-530.

Malaysian Journal of Analytical Sciences (MJAS)
Published by Malaysian Analytical Sciences Society

EXTRACTION SOLVENTS IN MICROALGAL LIPID EXTRACTION FOR BIOFUEL PRODUCTION: A REVIEW

(Pelarut Pengekstrakan dalam Pengekstrakan Lipid Mikroalgal untuk Penghasilan Bahan Api Bio: Satu Tinjauan)

Tan Yeong Hwang[1]*, Chai Mee Kin[1], Wong Ling Shing[2]

[1]College of Engineering,
University Tenaga Nasional, Jalan Ikram-Uniten, 43000 Kajang, Selangor, Malaysia
[2]Faculty of Health and Life Science, INTI International University,
Persiaran Perdana BBN Putra Nilai, 71800 Nilai, Negeri Sembilan, Malaysia

**Corresponding author: yeonghwang_113@hotmail.com*

Received: 28 July 2021; Accepted: 22 September 2021; Published: 25 October 2021

Abstract

Oleaginous microalgae biomass has gained noteworthy attention as feedstock for biofuel production due to its fast growth rate and capability of growing in non-arable land with high lipid content. Among biofuels, biodiesel has been a prevailing area of interest to many researchers. Prior to transformation of microalgae lipid into biodiesel, a lipid extraction step needs to be performed to disrupt the microalgal cell walls in order to extract the lipid. Hence, selecting an appropriate extraction solvent is of the utmost importance to ensure the efficient extraction of desired lipid content which can then be transformed into high quality biodiesel. Conventional organic solvents such as chloroform, dichloromethane and methanol are usually used in lipid extraction due to its high extraction efficiency. However, toxicity and environmental issues related to these solvents are of major concerns. Hence, many recent studies have focused on the use of green solvents such as bio-based solvents, supercritical carbon dioxide and ionic liquids. This review discusses the use of conventional organic solvents and green solvents in microalgae lipid extraction. Advantages and shortcomings of these solvents are also discussed. In addition, the future perspective for extraction solvents used in lipid extraction is also discussed.

Keywords: extraction solvent, microalgae lipid extraction, green solvent, biofuel

Abstrak

Biojisim mikroalga berminyak dinilai sebagai bahan mentah yang terkenal untuk penghasilan bahan api bio kerana kadar pertumbuhannya yang cepat dan keupayaan bertumbuh di dalam tanah yang tidak sesuai untuk pertanian dengan kandungan lipid yang tinggi. Antara bahan api bio, biodiesel telah menarik minat ramai penyelidik. Sebelum transformasi mikroalgae ke dalam biodiesel, langkah pengekstrakan lipid perlu dilakukan untuk melemahkan dinding sel mikroalga untuk mengekstrak lipid. Oleh itu, memilih pelarut pengekstrakan yang sesuai adalah sangat penting untuk pengekstrakan kandungan lipid yang dikehendaki yang boleh diubah menjadi biodiesel berkualiti tinggi. Pelarut organik konvensional seperti kloroform, diklorometana dan metanol biasanya digunakan dalam pengekstrakan lipid kerana kecekapan pengekstrakan yang tinggi. Namum, ketoksikan dan isu-isu alam sekitar pelarut-pelarut ini adalah kebimbangan utama. Oleh itu, banyak kajian baru-baru ini telah memberi tumpuan kepada penggunaan pelarut hijau seperti pelarut berasaskan bio, karbon dioksida superkritikal dan cecair ionik. Tinjauan ini

membincangkan pelarut organik konvensional dan pelarut hijau yang digunakan dalam pengekstrakan lipid microalga. Kelebihan dan kelemahan pelarut-pelarut tersebut juga dibincangkan. Di samping itu, perspektif masa depan untuk pelarut-pelarut pengekstrakan yang digunakan dalam pengekstrakan lipid juga dibincangkan.

Kata kunci: pelarut pengekstrakan, pengekstrakan lipid mikroalga, pelarut hijau, bahan api bio

Introduction

The increasing demand for sustainable energy resources has spurred the intensive research into biofuels derived from microalgae. Several types of biofuels can be transformed from microalgae biomass such as biodiesel, biogas and biochar [1]. Among them, biodiesel has gained massive interest from many researchers [2]. Compared to plant-based feedstock, microalgae have higher photosynthetic efficiency and a rapid growth rate [3]. The lipid content of microalgae can be up to 80% and their fatty acid profiles are similar to plant-based biodiesel but with low sulphur content and particulate matter [4-5]. In addition, many microalgae can thrive well in non-arable lands such as saline water [6] and wastewater [7]. Hence, microalgae do not compete for the land required for producing food. For biodiesel production, a lipid extraction step is essentially performed to rupture the microalgal cell wall and separate the desired lipids from the complex. Several parameters have been identified as factors that impact the extraction efficiency of lipids from microalgae biomass including types of extraction solvents [8-9], cell disruption techniques [10], biomass-to-solvent ratio [11], extraction time [12], extraction temperature [13] and solvent mixture ratio [14].

Microalgae are covered with rigid cell wall which impedes the extraction efficiency. Therefore, several cell disruption techniques such as the use of microwave, ultrasonics, osmotic shock and high-pressure homogenization are employed to break the cell wall. Then, the extraction solvent gains entry into the cell and extracts out the desired components. Therefore, selecting an appropriate extraction solvent is of utmost importance to ensure the efficient extraction of the desired lipid content which can then be transformed into high-quality biodiesel. This paper reviews the conventional extraction solvents and green solvents used in microalgal lipid extraction. In addition, future perspectives of extraction solvents are also discussed.

Conventional extraction solvents for microalgal lipid extraction

Based on the polarity, lipids in microalgae can be classified into polar and nonpolar (or neutral) lipids. With respect to different factors such as cultivation conditions and microalgae species, the lipids profiles can vary [18-19]. Polar lipids such as phospholipids and glycolipids are main constituents of the cell or organelle membrane whereas non-polar lipids such as triglycerides (TAGs) are important energy reserves [18-19]. In common extraction procedures (Figure 1), after the microalgae biomass is harvested and dried, extraction solvent will be added to the biomass. The mixture is then shaken for a certain period of time followed by separation into organic and aqueous phases. Organic phase contains extracted lipids whereas aqueous phase contains polar molecules such as proteins and carbohydrates. Finally, the organic phase will be collected followed by vacuum evaporation and transesterification.

As a rule of thumb, the extraction solvent should be able to penetrate the cell membrane and should be highly specific to the desired lipids to enable the dissolving of these lipids into the solvent while minimizing the co-extraction of undesired contaminants. Besides that, the ideal extraction solvent should also have properties of being insoluble in water and a low boiling point to ease the evaporation of the extraction solvent from lipids [20]. Various types of organic solvents such as chloroform, diethyl ether, acetone, hexane and methylene chloride [21-24] have been investigated to extract lipids from microalgae.

Nevertheless, using a single solvent alone might not be strong enough to break the strong interaction between neutral lipids and other biomolecules in the cell

membrane [25-26]. To overcome this interaction, a nonpolar solvent is often employed simultaneously with a polar solvent. Polar solvents can break the lipid-protein interaction by forming strong hydrogen bonds with neutral lipid in the complex [27]. However, the use of a polar solvents might result in the co-extraction of undesired polar biomolecules [28]. Previous studies [29-30] have indicated that total lipid extraction can be increased by using polar and nonpolar solvent mixtures, however, it does not necessary increase the quantity of extracted esterifiable lipid. In many cases, the type and ratio of nonpolar and polar solvents must be determined to ensure that the extracted lipid profile is suitable for high-quality biodiesel production.

Various solvent systems have been proposed as potential extracting solvents such as chloroform/methanol [32-33], chloroform/ethanol [21], dichloromethane/methanol [34], hexane/ methanol [35] and hexane/ethanol [14]. Among these solvent systems, chloroform/methanol and n-hexane/methanol mixtures are mostly applied in lipid extraction processes due to their high extraction efficiency and easy recovery [36-37]. However, these organic solvents exhibit toxicity, high volatility and are hazardous to both the operator and the environment. The summary of microalgae lipid extraction efficiency using various conventional solvents is summarized in Table 1.

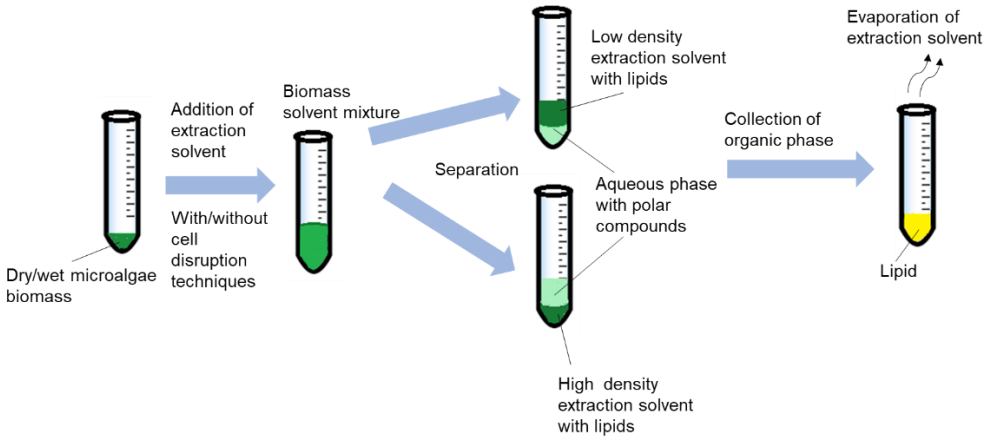


Figure 1. Common method for microalgae lipid extraction

Table 1. Microalgae lipid extraction efficiency of conventional solvents

Extraction Solvent (Volume/Volume)	Microalgae	Cell Disruption Techniques	Lipid Extracted (%)	Ref
Chl: Met (2:1)	*Oedogonium*	Soxhlet extraction	14	[32]
Chl: Met (2:1)	*Oedogonium*	Bligh and Dyer	11.5	[32]
Chl: Met (2:1)	*Chlorella vulgaris* UTEX 395	Accelerated solvent extraction	25.1	[33]
Chl: Met (2:1)	*Chlorella sorokiniana*	Accelerated solvent extraction	25.8	[33]
Chl: Met (2:1)	*Nannochloropsis gaditana*	Accelerated solvent extraction	29.8	[33]
Chl: Met (2:1)	*Chlorella vulgaris*	Chemical extraction	25.33	[31]

Table 1 (cont'd). Microalgae lipid extraction efficiency of conventional solvents

Extraction Solvent (Volume/Volume)	Microalgae	Cell Disruption Techniques	Lipid Extracted (%)	Ref
Chl: Met (1:2)	*Chlorella vulgaris*	Chemical extraction	38.57	[31]
Chl: Eth (2:1)	*Chlorella sp.*	Soxhlet extraction	11.76	[21]
Chl: Met (2:1)	*Scenedesmus obliquus*	Microwave-assisted extraction	19.25	[34]
Chl: Eth (1:1)	*Scenedesmus obliquus*	Microwave-assisted extraction	10.08*	[34]
Chl: Met (2:1)	*Tetraselmis sp. KCTC12429BP*	Chemical extraction	5.51	[35]
Chl: Met: Water (5:10: 4)	*Acutodesmus obliquus*	Bligh and Dyer	7.41	[14]
DCM: Met (2:1)	*Scenedesmus obliquus*	Microwave-assisted extraction	19.00	[34]
Hex: Met (1:1)	*Tetraselmis sp. KCTC12429BP*	Chemical extraction	5.16	[35]
Hex: Met (1:2)	*Chlorella vulgaris*	Chemical extraction	25.17	[31]
Hex: Eth (1:2)	*Acutodesmus obliquus*	Soxhlet extraction	6.82	[14]
Hex: Eth (1:2)	*Acutodesmus obliquus*	Ultrasonic-assisted extraction	4.28	[14]

Chl: chloroform; DCM: dichloromethane; Eth: Ethanol; Hex: n-Hexane; Met: Methanol;
*The lipid was extracted from wet microalgae biomass.

Green solvents for microalgal lipid extraction

With the rising concern of environmental pollution, health impacts and the development of green chemistry, finding suitable green solvents to replace petroleum-based solvents has become a major task of chemists. An ideal green solvent should meet the twelve criteria proposed in the principles of green chemistry [38]. Different solvents such as bio-based solvents, ionic liquid, supercritical carbon dioxide and switchable solvents have been classified as green solvent. The advantages and disadvantages of these solvents are summarized in Table 2.

Bio-based solvents are derived from agricultural biomass such as lignocellulosic biomass [39] and fruit peels [40]. The research evinced that 2-methyltetrahydrofuran [39], terpenes [40], ethyl lactate and ethyl acetate [41] possess similar characteristics to those in chloroform and n-hexane therefore they can be used to extract neutral lipids efficiently with high-quality lipid profiles. Compared to chloroform and hexane, terpenes are less hazardous due to its higher flash point and low toxicity [39-41]. Moreover, due to similar characteristics, the extraction process using bio-based solvents is as easy as conventional solvent extraction methods. However, the application of bio-based solvents for lipid extraction is not extensively evaluated probably due to the limited choice of bio-based solvents. Furthermore, the prices for some bio-based solvents are very expensive which is a limiting for economical industrial-scale extraction [39].

Ionic liquids (ILs) are defined as salt solution constituting organic cations and smaller inorganic or organic anions which they are maintained as liquids at temperatures between 0 and 140 °C [42]. ILs are considered as "designer solvents" due to their ability to accommodate different types of anions and cations [42]. In other words, polarity and properties of ILs can be specifically tailored to achieve the desired extraction

efficiency. In addition, ILs have some common characteristics which render them as ideal green solvents for lipid extraction including non-volatile properties, low viscosity and low vapor pressure [43]. Many studies have shown that lipid extraction process and recovery efficiency using ILs has resulted in high yield of lipids (>70%) [44-46]. Nevertheless, ILs exhibit high viscosity in low temperature therefore lipid extraction is mostly processed with co-solvent addition or at the temperatures ranging from 100 to 120 °C [44]. To date, most studies have focused on investigation of imidazolium-based ionic liquids for lipid extraction. Wahidin et al. [46] reported that 1-ethyl-3-methylimmidazolium methyl sulphate with methanol can be simultaneously used for lipid extraction and direct transesterification of wet microalgae which reduces energy consumption. Although ILs are considered as green solvents, their "greenness" of synthesis process is still questionable and the environmental impact generated by these solvents needs to be investigated [47]. Several studies showed that some cations and anions in ILs are poorly biodegradable and toxic to organisms [47-49], hence, cations and anions of ILs should be chosen carefully with this consideration in mind.

Another promising green solvent called deep eutectic solvent (DES) has been emerged as an alternative to overcome the disadvantages of ILs. DESs generally consist of a hydrogen-bond acceptor and a hydrogen-bond donor compound that often interacts through the formation of hydrogen bonds to form eutectic mixtures [50]. DES has similar characteristics to ILs, which is highly desirable including low vapor pressure, non-flammable, and low volatility. Furthermore, the price of DES is lower than ILs [50] and some DES are reported to be nontoxic [51]. There are limited studies that have investigated the effectiveness of DES on lipid extraction from microalgae [52-55]. Tommasi et al. [53] reported that although DES formed by choline chloride and oxalic acid extracted lower lipid content from *Phaeodactylum tricornutum* compared to conventional solvents, the selectivity of desired fatty acids was better. Nevertheless, DES possess several disadvantages such as high viscous and difficulty of separating the target components from DES [55]. Obluchinskaya et al. [56] pointed out that highly viscous nature of DES may complicate the extraction and separation process. This problem can be overcome by combining with mechanical methods, adding extra water into the mixture, increasing the temperature [53, 56].

Several studies also indicated that some DES are toxic or become toxic at certain concentrations [57-58]. Hence, other alternatives such as supercritical carbon dioxide and switchable solvents should be considered and are gaining wide interest as green solvents. Although these solvents have been extensively used in environmental, food, industrial, pharmaceutical and biological research, there are limited studies on lipid extraction from microalgae using these solvents [59-60]. It should be noted that although these solvents are suggested as potential green solvents, there is no clear evidence indicating their "greenness" in term of biodegradability, biocompatibility and toxicity. Table 3 shows the summary of extraction efficiency for microalgae lipid extraction using various green solvents.

Table 2. Advantages and disadvantages of extraction solvent for lipid extraction

Solvents	Advantages	Disadvantages	Ref
Petroleum-based solvent (Conventional solvent)	• Low cost • High extraction efficiency	• Highly toxic to environment and health	[36]
Bio-based solvent	• higher flash point • low toxicity	• High production cost • Some are highly viscous • Less available choice	[36]

Table 2 (cont'd). Advantages and disadvantages of extraction solvent for lipid extraction

Solvents	Advantages	Disadvantages	Ref
Ionic liquid	• Properties can be tailored • Has varieties of cations and anions	• High cost • Some are toxic to environment and health	[43, 47]
Deep eutectic solvent (DES)	• Low cost • Properties are designable • Has different components which may be derived from biological resources • Some of them are nontoxic	• Some are toxic or become toxic at high concentration • highly viscous • Difficult to separate target components and DES	[50, 55-57]
Supercritical carbon dioxide	• Non-toxic solvent • Easy recyclable	• High processing cost for its infrastructure and operation	[59]
Switchable solvent	• Polarity can be changed abruptly using CO_2 • Simple process	• Tertiary amine which are usually used as extraction solvent are environmentally toxic	[59, 60]

Table 3. Green solvent employed for microalgae lipid extraction

Extraction Solvent	Microalgae	Cell Disruption Techniques	Lipid Extracted (%)	Ref
Bio-based solvent				
2-MeTHF: isoamyl alcohol (2:1, v/v)	*Chlorella pyrenoidosa*	Chemical extraction	99.6 mg/g	[39]
d-limonene	*Chlorella vulgaris*	Soxhlet method	1.29	[40]
α-pinene	*Chlorella vulgaris*	Soxhlet method	0.91	[40]
ρ-cymene	*Chlorella vulgaris*	Soxhlet method	1.52	[40]
Ethyl lactate	*Nannochloropsis sp.*	Soxhlet method	31.1	[41]
2-MeTHF	*Nannochloropsis sp.*	Soxhlet method	19.1	[41]
Ionic liquid				
Butyrolactam hexanoate	*Chlorella sp.*	Chemical extraction	70.90 mg/g*	[45]
Butyrolactam hexanoate	*Chlorococcum sp.*	Chemical extraction	19.86 mg/g*	[45]
[EMIM][$MeSO_4$]	*Nannochloropsis sp.*	Microwave-assisted extraction	40.9*	[46]
[EMIM]Cl	*Nannochloropsis gaditana*	Microwave-assisted extraction	13.9	[57]

Table 3 (cont'd). Green solvent employed for microalgae lipid extraction

Extraction Solvent	Microalgae	Cell Disruption Techniques	Lipid Extracted (%)	Ref
Deep eutectic solvent				
Ch-Aa: methanol-H_2SO_4 (60:40, v/v)	*Chlorella sp.*	Autoclave	13.91	[51]
Ch-Ca: DMC	*Phaeodactylum tricornutum*	Microwave-assisted extraction	11.00	[52]
ChCl: oxalic acid (1:2 v/v)	*Phaeodactylum tricornutum*	Microwave-assisted extraction	12.5%	[52]
ChCl: oxalic acid (1:2 v/v)	*Chlorella* sp.	-	12.5%	[53]
TMG: menthol (3:1, M/M)	*Nannochloropsis* sp.	Ultrasonic	172.3 mg/g	[54]
Supercritical CO_2	*Phaeodactylum tricornutum*	-	0.3	[52]
Switchable solvent				
TEPDA	*Nannochloropsis oceanica*	-	22.67*	[68]

Ch-Aa : Choline chloride-acetic acid; Ch-Ca: choline chloride- carboxylic acids; DMC : dimethyl carbonate; 2-MeTHF: 2-Methyltetrahydrofuran; [EMIM]Cl: 1-ethyl-3-methyl imidazolium chloride; [EMIM][MeSO4]: 1-ethyl-3-methylimmidazolium methyl sulphate; Isoamyl alcohol: 3-methyl-1-butanol; TEPDA: N, N, N', N'-tetraethyl-1,3-propanediamine. TMG: methnol: Tetramethylguanidine: methnol
*The lipid was extracted from wet microalgae biomass

Future perspectives for development of extraction solvents

Replacing conventionally used solvents in lipid extraction by green solvents is not an easy task. Although different lipid extraction methods using various green solvents have been proposed, no green solvent to date can successfully replace conventional solvents in industrial production as the toxicity, biodegradability and biocompatibility of some these green solvents remains questionable. Environmental assessments and toxicity tests must be conducted prior to the scale-up of the extraction process. Some of the green solvents such as 2-methyltetrahydrofuran and ILs are not suitable for large-scale used due to high production cost [39, 42]. In this context, the synthesis process of green solvents should be designed so that it is sustainable and the price is reasonable for scale-up. Researchers should also focus on the techniques that could reduce energy, volume of green solvent required and time taken for lipid extraction. Studies have showed that green solvents combined with mechanical processes can increase the lipid yield which is a promising avenue in this research field [52, 62].

Many researchers tried to search for the best solvent that for the lipid extraction with the lowest environmental impact. Notwithstanding, green solvents are just one of the aspects of green chemistry, the involved reactions in extraction should also be sustainable and have low environment impact [63]. Current processes probably could be improved to minimize environmental and health impact. For instance, Mustapha and Isa [64] devised the commonly used chloroform-methanol mixture to low toxic solvent mixture by modifying the composition and volume of each solvent.

In addition to lipids, microalgae also contained bioactive compounds such as carotenoids. These bioactive compounds have high global market demand and they are expected to grow in the future [65]. Therefore, the transformation of the single product approach to an integrated metabolite production system may help to enhance the production of microalgae biodiesel.

As some of the extraction solvents are toxic and may not easy to biodegrade, hence 3Rs (reuse, recycle and reduce) concept probably could be another consideration to minimize the exposure of these solvents to environment. Recent studies have shown some ILs [66-67], DES and switchable solvents [68] have the recycle and reuse capability, with a slightly decrease on extraction efficiency after several time consecutive cycles.

Conclusion

Microalgae biodiesel is a potential candidate to substitute conventional fossil fuels. Selecting an appropriate extraction solvent for lipid extraction is extremely important to achieve efficient extraction of the desired lipid content that can be transformed into high quality biodiesels. Several types of extraction solvents such as conventional chlorinated solvents, bio-based solvents and ionic liquids have been discussed in this paper, each with their plus points and disadvantages. In addition, the future perspectives for development of extraction solvents were also intensively discussed. Overall, the environmental assessments of green extraction solvents, using integrated metabolite production and improvement of extraction processes based on green chemistry should be the main focus in future research and development of biofuels.

Acknowledgement

The authors would like to acknowledge Ministry of Higher Education Malaysia, MOHE: FRGS/1/2020/STG02/UNITEN/02/1 (60%) and UNITEN BOLD Research Grant 2020: RJO10517844/044 (40%) for the financial support.

References

1. Javed, F., Aslam, M, Rashid, N., Shamair, Z., Khan, A. L., Yasin, M., Fazal, T., Hafeez, A., Rehman, F., Rehman, M. S. U., Khan, Z., Iqbal, J. and Bazmi, A. A. (2019). Microalgae-based biofuels, resource recovery and wastewater treatment: A pathway towards sustainable biorefinery. *Fuel,* 255: 115826.
2. Catone, C. M., Ripa, M., Geremia, E. and Ulgiati, S. (2021). Bio-products from algae-based biorefinery on wastewater: A review. *Journal of Environmental Management,* 293:112792.
3. Sun, S., Zhao, W., Mao, X., Li, Y., Wu, T. and Chen, C. (2018). High-value biomass from microalgae production platforms: Strategies and progress based on carbon metabolism and energy conversion. *Biotechnology for Biofuels,* 11: 1-23.
4. Lin, T. S. and Wu, J. Y. (2015). Effect of carbon sources on growth and lipid accumulation of newly isolated microalgae cultured under mixotrophic condition. *Bioresource Technology,* 184: 100-107.
5. Calixto C. D., Santana, J. K. S., Lira, E. B., Sassi, P. G. B., Rosenhaim, R., Sassi C. F. C, Conceição, M. M. and Sassi, R. (2016). Biochemical compositions and fatty acid profiles in four species of microalgae cultivated on household sewage and agro-industrial residues. *Bioresource Technology,* 221: 438-446.
6. Ridley, C. J. A., Parkera, B. M., Norman, L., Schlarb-Ridley, B., Dennis, R., Jamieson, A. E., Clark, D., Skill, S. C., Smith, A. G. and Davey, M. P. (2018). Growth of microalgae using nitrate-rich brine wash from the water industry *Algal Research,* 33: 91-98.
7. Nagarajan, D., Kusmayadi, A., Yen, H. W., Di Dong, C., Lee, D. J. and Chang, J. S. (2019). Current advances in biological swine wastewater treatment using microalgae-based processes. *Bioresource Technology*, 289: 121718.
8. Balasubramanian, R. K., Doan, T. T. Y and Obbard, J. P. (2013). Factors affecting cellular lipid extraction from marine microalgae. *Chemical Engineering Journal,* 215–216: 929-936.

9. Kuan, D., Du, W., Dai, L., Ma, G. and Liu, D. (2016). Effect of solvent on the extraction of microalgae lipid for biodiesel production. *Chemical Research in Chinese Universities* 32: 625-629.
10. Pohndorf, R. S., Camara, Á. S., Larrosa, A. P. Q., Pinheiro, C. P., Strieder, M. M. and Pinto, L. A. A. (2016). Production of lipids from microalgae *Spirulina* sp.: Influence of drying, cell disruption and extraction methods. *Biomass and Bioenergy,* 93: 25-32.
11. Shin, H.Y., Shim, S. H., Ryu, Y. J. Yang, J. H., Lim, S .M. and Lee, C. G. (2018). Lipid extraction from *Tetraselmis* sp. microalgae for biodiesel production using hexane-based solvent mixtures. *Biotechnology and Bioprocess Engineering,* 23: 16-22.
12. Vieira, B. B., Soares, J., Amorim, M. L., Bittencourt, P. V. Q., Superbi, R. C., Oliveira, E. B., Coimbra, J. S. R. and Martins, M. A. (2021). Optimized extraction of neutral carbohydrates, crude lipids and photosynthetic pigments from the wet biomass of the microalga *Scenedesmus obliquus* BR003. *Separation and Purification Technolog,y* 269:118711.
13. Silitonga, A. S. Masjuki, H. H., Ong, H. C., Mahlia, T. M. I and Kusumo, F. (2017). Optimization of extraction of lipid from *Isochrysis galbana* microalgae species for biodiesel synthesis. *Energy Sources, Part A: Recovery, Utilization and Environmental Effects*, 39: 1167-1175.
14. Escorsim, A. M., Rocha, G., Vargas, J. V. C., Mariano, A. B., Ramos, L. P., Corazza, M. L. and Cordeiro, C. S. (2018) Extraction of *Acutodesmus obliquus* lipids using a mixture of ethanol and hexane as solvent. *Biomass and Bioenergy,* 108: 470-478.
15. Singh, R., Kumar, A. and Sharma, Y. C. (2020). Evaluation of various lipid extraction techniques for microalgae and their effect on biochemical components. *Waste and Biomass Valorization,* 11: 2603-2612.
16. Bernaerts, T. M. M., Verstreken, H., Dejonghe, C., Gheysen, L., Foubert, I., Grauwet, T. and Loey, A. M. V. (2019). Cell disruption of *Nannochloropsis* sp. improves in vitro bioaccessibility of carotenoids and ω3-LC-PUFA. *Journal of Functional Foods,* 65: 103770.
17. González-González, L. M., Astals, S., Pratt, S., Jensen, P. D. and Schenk, P. M. (2019). Impact of osmotic shock pre-treatment on microalgae lipid extraction and subsequent methane production. *Bioresource Technology Reports,* 7: 100214.
18. Yao, L., Gerde, J. S., Lee, S., Wang, T. and Harrata, K. A. (2015). Microalgae lipid characterization. *Journal of Agricultural and Food Chemistry*, 63(6): 1773-1783.
19. Penga, Z., Feng, L., Wang, X. and Miao, X. (2019). Adaptation of *Synechococcus* sp. PCC 7942 to phosphate starvation by glycolipid accumulation and membrane lipid remodeling. *Biochimica et Biophysica Acta - Molecular and Cell Biology of Lipids*, 1864: 158522.
20. Cooney, M., Young, G. and Nagle, N. (2009). Extraction of bio-oils from microalgae. *Separation & Purification Reviews*, 38: 291-325
21. Ramluckan, K., Moodley, K. G. and Bux, F. (2014). An evaluation of the efficacy of using selected solvents for the extraction of lipids from algal biomass by the Soxhlet extraction method. *Fuel*, 114: 103-108.
22. Anthony, R and Stuart, B. 2015. Solvent extraction and characterization of neutral lipids in *Oocystis* sp. *Frontiers in Energy Research*, 3: 1-5.
23. Byreddy, A. R., Gupta, A., Barrow, C. J. and Puri, M. (2015). Comparison of cell disruption methods for improving lipid extraction from *Thraustochytrid* strains. *Marine Drugs*, 13: 5111-5127.
24. Supaporn, P. and Yeom, H. S. (2016). Optimization of a two-step biodiesel production process comprised of lipid extraction from blended sewage sludge and subsequent lipid transesterification. *Biotechnology and Bioprocess Engineering*, 21: 551-560.

25. Xia, A., Sun, C. Fu, Q., Liao, Q., Huang, Y., Zhu, X. and Li. Q. (2020). Biofuel production from wet microalgae biomass: Comparison of physicochemical properties and extraction performance. *Energy*, 212: 118581.
26. Escorsim, A. M., Rocha, G., Vargas, J. V. C., Mariano, A. B., Ramosa, L. P., Corazzac, M. L. and Cordeiro, C. S. (2018). Extraction of *Acutodesmus obliquus* lipids using a mixture of ethanol and hexane as solvent. *Biomass and Bioenergy*, 108: 470-478.
27. Dvoretsky, D., Dvoretsky, S. Temnov, M., Akulinin, E. and Peshkova, E. (2016). Enhanced lipid extraction from microalgae *chlorella vulgaris* biomass: Experiments, modelling, optimization. *Chemical Engineering Transactions*, 49: 175-180.
28. Ryckebosch, E, Bruneel, C., Termote-Verhalle, R., Muylaert, K. and Foubert, I. (2014). Influence of extraction solvent system on extractability of lipid components from different microalgae species. *Algal Research*, 3: 46-43.
29. Mahmood, W. M. A. W, Theodoropoulos, C. and Gonzalez-Miquel, M. (2017). Enhanced microalgal lipid extraction using bio-based solvents for sustainable biofuel production. *Green Chemistry*, 19: 5723-5733.
30. Hidalgo, P., Ciudad, G. and Navia, R. (2016). Evaluation of different solvent mixtures in esterifiable lipids extraction from microalgae *Botryococcus braunii* for biodiesel production. *Bioresource Technology*, 201: 360-364.
31. Moradi-kheibari, N., Ahmadzadeh, H. and Hosseini, M. (2017). Use of solvent mixtures for total lipid extraction of *Chlorella vulgaris* and gas chromatography FAME analysis. *Bioprocess and Biosystems Engineering*, 40: 1363-1373.
32. Ramola, B., Kumar, V., Nanda, M., Mishra, Y., Tyagi, T., Gupta, G. and Sharma, N. (2019). Evaluation, comparison of different solvent extraction, cell disruption methods and hydrothermal liquefaction of *Oedogonium* macroalgae for biofuel production. *Biotechnology Reports*, 22: e00340.
33. Tang, Y., Zhang, Y., Rosenberg, J. N., Sharif, N., Betenbaugh, M. J. and Wang, F. (2016). Efficient lipid extraction and quantification of fatty acids from algal biomass using accelerated solvent extraction (ASE). *RSC Advances*, 6: 29127-29134.
34. Ansari, F. A., Gupta, S. K., Shriwastav, A., Guldhe, A., Rawat, I. and Bux, F. (2017). Evaluation of various solvent systems for lipid extraction from wet microalgal biomass and its effects on primary metabolites of lipid-extracted biomass. *Environmental Science and Pollution Research*, 24: 15299-15307.
35. Shin, H. Y, Shim, S. H., Ryu, Y. J., Yang, J. H., Lim, S. M. and Lee, C. G. (2018). Lipid extraction from *Tetraselmis* sp. microalgae for biodiesel production using hexane-based solvent mixtures. *Biotechnology and Bioprocess Engineering*, 23: 16-22.
36. Kapoore, R. V., Butler, T. O., Pandhal, J. and Vaidyanathan, S. (2018). Microwave-assisted extraction for microalgae: from biofuels to biorefinery. *Biology*, 7: 18.
37. Khoo, K. S. Chew, K. W., Yew, G. Y., Leong, W. H., Chai, Y. H., Show, P. L. and Chen, W. H. (2020). Recent advances in downstream processing of microalgae lipid recovery for biofuel production. *Bioresource Technology*, 304: 122996.
38. Schuur, S., Brouwer, T., Smink, D. and Sprakel, L. M. J. (2019). Green solvents for sustainable separation processes. *Current Opinion in Green and Sustainable Chemistry*, 18: 57-65.
39. Jesus, S. S., Ferreira, G. F., Fregolente, L. V. and Filho, R. M. (2018). Laboratory extraction of microalgal lipids using sugarcane bagasse derived green solvents. *Algal Research*, 292: 292-300.
40. Tanzi, C. D., Vian, M. A., Ginies, C., Elmaataoui, M. and Chemat, F. (2012). Terpenes as green solvents for extraction of oil from microalgae. *Molecules*, 17: 8196-8205.
41. Mahmood, W. M. A. W, Theodoropoulos, C. and Gonzalez-Miquel, M. (2017). Enhanced microalgal lipid extraction using bio-based solvents for sustainable biofuel production. *Green Chemistry*, 19: 5723-5733.

42. Yoo, C. G., Pu, Y. and Ragauskas, A. J. (2017). Ionic liquids: Promising green solvents for lignocellulosic biomass utilization. *Current Opinion in Green and Sustainable Chemistry*, 5: 5-11.
43. Pan, J., Muppaneni, T., Sun, Y., Reddy, H. K., Fu, J., Lu, X. and Deng, S. (2016). Microwave-assisted extraction of lipids from microalgae using an ionic liquid solvent [BMIM][HSO_4]. *Fuel*, 178: 49-55.
44. Valerie C. A. and Rehmann, O. R. (2016). Ionic liquids for the fractionation of microalgae biomass. *Current Opinion in Green and Sustainable Chemistry*, 2: 22-27.
45. Shankara, M., Chhotaray, P. K., Agrawal, A., Gardasd, R. L., Tamilarasan, K. and Rajesh, M. (2017). Protic ionic liquid-assisted cell disruption and lipid extraction from fresh water *Chlorella* and *Chlorococcum* microalgae. *Algal Research*, 25: 228-236.
46. Wahidin, S., Idris, A., Yusof, N. M., Kamis, N. H. H. and Shaleh, S. R. M. (2018). Optimization of the ionic liquid-microwave assisted one-step biodiesel production process from wet microalgal biomass. *Energy Conversion and Management*, 171: 1397–1404.
47. Jordana, A. and Gathergood, N. (2015). Biodegradation of ionic liquids – a critical review. *Chemical Society Reviews*, 44: 8200-8237.
48. Sydow, M., Owsianiak, M., Framski, G., Woźniak-Karczewska, G., Piotrowska-Cyplik, A., Ławniczak, Ł., Szulc, A., Zgoła-Grześkowiaka, A., Heipiepere, H. J. and Chrzanowski, Ł. (2018). Biodiversity of soil bacteria exposed to sub-lethal concentrations of phosphonium-based ionic liquids: Effects of toxicity and biodegradation. *Ecotoxicology and Environmental Safety*, 147: 157-164.
49. Biczak, R., Pawłowska, B., Telesiński, A. and Kapuśniak, J. (2017). Role of cation structure in the phytotoxicity of ionic liquids: growth inhibition and oxidative stress in spring barley and common radish. *Environmental Science and Pollution Research*, 24: 18444-18457.
50. Chen, C. and Mu, T. C. (2021). Revisiting greenness of ionic liquids and deep eutectic solvents. *Green Chemical Engineering*, *2*: 174-186.
51. Chen. J., Wang, Q., Liu, M. and Zhang, L. (2017). The effect of deep eutectic solvent on the pharmacokinetics of salvianolic acid B in rats and its acute toxicity test. *Journal of Chromatography B*, 1063: 60-66.
52. Pan, Y., Alam, A., Wang, Z. Huang, D., Hu, K., Chen, H. and Yuan, Z. (2017). One-step production of biodiesel from wet and unbroken microalgae biomass using deep eutectic solvent. *Bioresource Technology*, 238: 157-163.
53. Tommasi, E., Cravotto, G., Galletti, P., Grillo, G., Mazzotti, M., Sacchetti, G., Samorì, C., Tabasso, S., Tacchini, M. and Tagliavini, E. (2017). Enhanced and selective lipid extraction from microalgae *P. tricornutum* by dimethyl carbonate and supercritical CO_2 using deep eutectic solvents and microwaves as pre-treatment. *ACS Sustainable Chemistry and Engineering*, 5: 8316-8322.
54. Lu, W., Alam, M. A., Pan, Y., Wu, J., Wang, Z. and Yuan, Z. (2016). A new approach of microalgal biomass pretreatment using deep eutectic solvents for enhanced lipid recovery for biodiesel production. *Bioresource Technology*, 218: 123-128.
55. Cai, C., Chen, X., Li, D. and Tan, Z. (2021). Three-phase partitioning based on CO_2-responsive deep eutectic solvents for the green and sustainable extraction of lipid from *Nannochloropsis* sp. *Separation and Purification Technology*, 279: 119685.
56. Obluchinskaya, E. D., Pozharitskaya, O. N., Zakharova, L.V., Daurtseva, A.V., Flisyuk, E.V. and Shikov, A.N. (2021). Efficacy of natural deep eutectic solvents for extraction of hydrophilic and lipophilic compounds from *Fucus vesiculosus*. *Molecules*, 26: 4198.

57. Torregrosa-Crespo, J., Marset, X., Guillen, G., Ramón, D. J. and Martínez-Espinosa, R. M. (2020). New guidelines for testing ‘‘Deep eutectic solvents” toxicity and their effects on the environment and living beings. *Science of the Total Environment*, 704: 135382.
58. Hayyan, M., Hashim, M. A., Al-Saadi, M. A., Hayyan, A., AlNashefc, I. M. and Mirghani, M. E. S. (2013). Assessment of cytotoxicity and toxicity for phosphonium-based deep eutectic solvents. *Chemosphere*, 93: 455-459.
59. Du, Y., Schuur, B., and Brilman, D. W. F. (2017). Maximizing lipid yield in *Neochloris oleoabundans* algae extraction by stressing and using multiple extraction stages with n-ethylbutylamine as switchable solvent. *Industrial & Engineering Chemistry Research*, 56: 8073-8080.
60. Du, Y., Schuur, B., Kersten, S. R. A. and Brilman, D. W. F. (2015). Opportunities for switchable solvents for lipid extraction from wet algal biomass: An energy evaluation. *Algal Research*, 11: 271-283.
61. Bazel, Y., Rečlo, M. and Chubirka, Y. (2020). Switchable hydrophilicity solvents in analytical chemistry. Five years of achievements. *Microchemical Journal*, 157: 105115.
62. Motlagh, S. R., Harun, R., 1, Biak, D. R. A. and Hussain, S. A. (2020). Microwave assisted extraction of lipid from *Nannochloropsis gaditana* microalgae using [EMIM]Cl. *IOP Conf. Series: Materials Science and Engineering*, 778: 012164.
63. Poliakoff, M. and Licence, P. (2007). Green chemistry. *Nature*, 450: 810–812.
64. Mustapha, S. I. and Isa, Y. M. (2020). Utilization of quaternary solvent mixtures for extraction of lipids from Scenedesmus obliquus microalgae. *Chemical Engineering*, 7: 1788877.
65. Molino, A., Mehariya, S., Sanzo, G. D., Larocca, V., Martino, M., Leone, G. P., Marino, T., Simeone Chianese, S., Roberto Balducchi, R. and Musmarr, D. (2020). Recent developments in supercritical fluid extraction of bioactive compounds from microalgae: Role of key parameters, technological achievements and challenges. *Journal of CO2 Utilization*, 36: 196-209.
66. Malekghasemi, S., Kariminia, H. R., Plechkova, N, K. and Ward, V. C. A. (2021). Direct transesterification of wet microalgae to biodiesel using phosphonium carboxylate ionic liquid catalysts. *Biomass and Bioenergy*, 150: 106126.
67. Orr, V. C. A., Plechkova, N. V., Seddon, K. R. and Rehmann, L. (2016). Disruption and wet extraction of the microalgae *Chlorella vulgaris* using room-temperature ionic liquids. *ACS Sustainable Chemistry and Engineering*, 4: 591-600.
68. Jun Cheng, Guo, H., Qiu, Y., Zhang, Z., Mao, Y., Qian, L., Yang, W. and Park, J. Y. (2020). Switchable solvent N, N, N′,N′-tetraethyl-1, 3-propanediamine was dissociated into cationic surfactant to promote cell disruption and lipid extraction from wet microalgae for biodiesel production. *Bioresource Technology*, 312: 123607.

Malaysian Journal of Analytical Sciences (MJAS)
Published by Malaysian Analytical Sciences Society

SPECTROPHOTOMETRIC DETERMINATION OF TOTAL FLAVONOID CONTENTS IN TEA PRODUCTS AND THEIR LIQUORS UNDER VARIOUS BREWING CONDITIONS

(Penentuan Spektrofotometrik bagi Kandungan Jumlah Flavonoid di dalam Produk Teh dan Arak di Bru pada Keadaan Berbeza)

Nguyen Cong-Hau[1], Le-Thi Anh-Dao[1], Le Nhon-Duc[2], Nguyen Thanh-Nho[1]*

[1]*Faculty of Environmental and Food Engineering, Nguyen Tat Thanh University, Ho Chi Minh City, Vietnam*
[2]*Warrantek Joint Stock Company-Testing Center, Can Tho City, Vietnam*

[*]*Corresponding author: ntnho@ntt.edu.vn*

Received: 31 July 2021; Accepted: 7 September 2021; Published: 25 October 2021

Abstract

Tea (*Camellia sinensis* L.) has been considered among the most common beverages consumed worldwide, primarily due to its medical properties and sensory attributes. Flavonoids are the most abundant type of phenolic compounds found in tea leaves, and the flavonoid contents vary according to tea variety and processing method. In this study, we proposed and validated a spectrophotometric method for determining the total flavonoid contents (TFCs) in tea products and their liquors. Quercetin was used as the standard to build the calibration curve with $AlCl_3$ as the color reagent, to measure the absorbance of the formed complex at 510 nm for quantification purposes. The reaction time in the colorimetric assay was investigated, and immediate spectrophotometric measurement after adding enough reagent was applied. The linear range was from 50 to 700 milligrams of quercetin equivalents per liter (mg QE L^{-1}), and the regression equation was $y = 0.0013x + 0.0872$ ($R^2 = 0.9981$). Repeatability and reproducibility ($RSD_r = 1.1$ and $RSD_R = 1.2\%$) were favorable regarding Appendix F. AOAC (2016). Trueness was assessed through the spiked samples, and recoveries ranged from 98 to 102%. The analytical method was applied to determine the TFCs in several tea products collected from tea plantation regions in the North and South of Vietnam. The TFCs in tea products followed the descending order of green (140.1-155.3 mg QE g^{-1}) > Pu'erh (108.5-141.8 mg QE g^{-1}) > white (95.3-99.0 mg QE g^{-1}) > black (60.8-89.7 mg QE g^{-1}) > oolong (42.0 to 59.8 mg QE g^{-1}). Moreover, the effect of brewing conditions on the release of TFCs into tea liquors was assessed. The results indicate that the highest extraction percentage of flavonoid for most tea products was recorded at 90 °C within the infusion time of 40 minutes.

Keywords: *Camellia sinensis* L., flavonoids, quercetin, tea products, tea liquors

Abstrak

Teh (*Camellia sinensis* L.) merupakan minuman yang sering kali diambil di seluruh dunia, terutama disebabkan sifat perubatannya dan aromanya. Flavonoids merupakan jenis sebatian fenolik yang sering dijumpai di dalam daun teh, dan kandungan flavonoids berbeza mengikut varieti teh dan kaedah pemprosesan. Melalui kajian ini, kami mencadangkan dan validasi kaedah spektrofotometrik bagi penentuan kandungan jumlah flavonoids (TFCs) di dalam produk teh dan arak. Quercetin telah di guna sebagai piawai dalam penghasilan lengkung piawai Bersama $AlCl_3$ sebagai reagen warna, untuk mengukur serapan

yang membentuk kompleks pada 510 nm bagi tujuan kuantifikasi. Masa tindak balas ujian kolorimetrik telah dikaji, dan pengukuran spektrofotometrik segera dilakukan selepas penambahan reagen dilakukan. Julat kelinearan dari 50 hingga 700 miligram quertin setiap liter (mg QE L^{-1}), dan pekali persamaan diperolehi ialah y = 0.0013x + 0.0872 (R^2 = 0.9981). Kebolehulangan dan kebolehasilan semula (RSD_r = 1.1 dan RSD_R = 1.2%) adalah baik berdasarkan Appendix F. AOAC (2016). Ketepatan kaedah diuji menggunakan sampel yang dipaku, dan perolehan semula pada julat 98 hingga 102%. Kaedah analisis telah digunapakai bagi penentuan TFCs di dalam pelbagai produk teh yang di ambil dari kawasan ladang teh terletak di utara dan selatan Vietnam. TFCs di dalam produk teh mengikut tertib menurun seperti berikut hijau (140.1-155.3 mg QE g^{-1}) > Pu'erh (108.5-141.8 mg QE g^{-1}) > putih (95.3-99.0 mg QE g^{-1}) > hitam (60.8-89.7 mg QE g^{-1}) > oolong (42.0-59.8 mg QE g^{-1}). Tambahan lagi, kesan bru yang pelbagai terhadap TFCs di dalam teh arak juga telah dikaji. Hasil menunjukkan peratus kesan pengekstrakan flavonoids bagi kebanyakkan teh telah direkod pada 90 °C dengan masa rendaman ialah 40 minit.

Kata kunci: *Camellia sinensis* L., flavonoids, quercetin, produk teh, teh arak

Introduction

Tea plants have a long history of cultivation and utilization worldwide, and tea is considered among the most popular beverages, besides water, coffee, and cocoa. According to Chinese mythology, tea plants were discovered thousands of years ago in South-East Asia, and mankind has been drinking tea for more than 5 000 years for its health and medicinal benefits to prevent and treat diseases, especially cancer (respiratory, digestive, and urinary) and cardiovascular disorder [1]. Tea leaves are used to produce tea infusions, and there are many types of tea products depending on the degree of oxidation, such as white tea (young tea leaves or new growth buds, withered, uncured, baked dry), green tea (not oxidized), oolong tea (partially oxidized), black tea (fully oxidized), and many other commercial products made from tea leaves [2, 3]. Green or raw Pu-erh, processed similarly to green tea: picked, quickly roasted, but then sun-dried under uncontrolled temperature and humidity and allowed to ripen for several weeks or months (not drying with hot air as green tea in order to deactivate oxidases). The enzyme deactivation is not complete for Pu'erh, therefore, the oxidation could still occur during its long storage, which makes for a smooth-tasting tea [4].

Flavonoids are the most abundant component of phenolic compounds in tea and considered the most important constituent because they act as bioactive ingredients to enhance tea's therapeutic properties. Flavonoids are in the primary group of polyphenols and can be divided into six main groups, including flavones (apigenin, luteolin, baicalein, chrysin), flavanones (eriodictyol, hesperetin, naringenin), isoflavones (daidzein, genistein, glycitein, biochanin A, formononetin), flavonols (isorhamnetin, kaempferol, myricetin, quercetin), anthocyanidins (cyanidin, delphinidin, malvidin, pelargonidin, peonidin, petunidin) and flavan-3-ols (monomers, dimers or oligomers). The flavonoid contents in tea products vary regarding the differences in many criteria, including geographical origins, cultivation, and processing methods. White, green, or oolong teas contain mono-catechins such as (+)-catechin, (-)-epicatechin, (-)-epigallocatechin, (+)-gallocatechin, and gallate derivatives. For black tea, catechins are oxidized by the enzyme polyphenol oxidase to form dimer compounds such as theaflavin and thearubigin. Besides the compounds in the flavan-3-ol group mentioned above, tea also contains compounds belonging to the flavonol group. Tea has relatively high flavan-3-ol content, making up the characteristics of tea [5-7]. There has been increasing interest in the positive health effects of tea, which are believed to be related to tea flavonoids, particularly their antioxidant capacities, anticancer, and anti-inflammatory [8-11].

There have been various studies related to the procedures for the determination of flavonoids in many sample matrices. In particular, the analysis of total flavonoid contents (TFCs) based on the principle of molecular absorption spectrophotometry (UV-Vis) is one of the simplest analytical methods to evaluate variations in the TFCs. However, the selection of the colorimetric assay and the standard substances depends

on the compositional nature of the significant existing flavonoids in the sample. For tea, quercetin has been used as the standard for the quantification of TFCs, expressed in milligrams of quercetin equivalents per gram of dry weight (mg QE g^{-1} DW). Although there are many methods used to determine the TFCs, all are based on the ability to form chelate complexes with aluminum ions with the addition of several other reagents such as $NaNO_2$, CH_3COOH, CH_3COONa. The complexes formed with $NaNO_2$ in an alkaline medium for rutin, luteolin, and catechin have significant absorbance at 510 nm. Thus, the procedure using $NaNO_2$ would be suitable for the tea sample in the presence of substantial concentrations of catechin compounds [12].

The study of Qhairul et al. [13] analyzed the TFCs in green and black teas, and the results showed that green tea had higher TFCs, especially green tea produced from tea buds (from 20.90 to 35.17 mg QE g^{-1} DW and from 19.07 to 33.70 mg QE g^{-1} DW for green and black tea samples, respectively). In 2012, Bansal et al. conducted a study on the TFCs in green tea [14] and reported the TFCs in green tea as 130.5 mg 100 g^{-1}. Another study by Putri et al. showed that for the extraction condition of 100 °C within 45 minutes, the extraction of flavonoid content from tea samples into the liquid reached the highest (41.68 ± 1.25 mg L^{-1}) [15]. The publication of Kılıç et al. investigated the infusion temperature values of 60 °C, 80 °C, and 100 °C in 10 minutes, indicating that at 100 °C, the release of flavonoids into tea liquors was the highest [16].

To our knowledge, despite the high production and exportation of tea products in Vietnam, the publications related to chemical profiles for Vietnamese tea products are limited. For most of previous studies, authors mainly focused on determining total polyphenol contents and DPPH radical scavenging as antioxidant activity in tea products among different regions when applying spectrophotometric methods. Meanwhile, flavonoid contents reflect and contribute to the antioxidant capacities of tea products. In the present study, we proposed and validated a spectrophotometric method for determining the total flavonoid contents in various tea products and their liquors. The tea products were of different processing methods, including green, white, black, Pu'erh, and oolong. The effects of temperature and infusion time on the extraction of flavonoid in tea liquors were evaluated to discover the most favorable brewing condition (temperature and infusion time) to achieve the highest total flavonoid content. This study will enrich the scientific data for chemical profiles of Vietnamese tea products.

Materials and Methods

Chemicals and reagents

A stock standard solution of 1000 mg L^{-1} quercetin was prepared by dissolving 10.00 mg of quercetin (Sigma, Germany) in 10.00 mL of methanol (Merck, Germany). Working quercetin standard solutions of 50, 100, 200, 300, 400, 500, 600, and 700 mg L^{-1} was prepared by appropriate dilution of the stock standard solution by deionized (DI) water (Millipore, USA). Other chemicals and reagents were of analytical grade (Merck, Germany) and were used to prepared 10% w/v aluminum chloride, 5% w/v sodium nitrite, and 1 mol L^{-1} sodium hydroxide.

Sample collection, flavonoid extraction, and coloring procedure

This study was conducted in two tea growing regions in Vietnam. The first region was Ha Giang Province located in the high mountainous area in North Vietnam, where 12 old, wild tea products of the green, white, black, and Pu'erh types were collected. The second region was Lam Dong Province in the South-Central Highland of Vietnam, where 6 green and oolong tea products were collected. The green tea plants were believed to be from the old, wild tea in the North of Vietnam which were grown in Lam Dong Province since 1927 (almost 100 years prior). The oolong tea belonged to young tea plants (10-year-old tea). The specific sampling information is presented in Table 1.

Before analysis, tea samples underwent a pre-treatment procedure following ISO 1572:1980 for homogenization purposes [17]. Samples were stored at 25 °C, 70% humidity, and in a shaded space away from direct sunlight.

The well-homogenized tea products were subjected to the extraction procedure referenced from ISO 14502-1:2005 with some modifications [18]. Briefly, a quantity of 0.200 g ± 0.001 g of dried tea sample was weighed into a reaction tube. Then, 10.00 mL of MeOH 70% (v/v) in DI water was added to this tube. The mixture was vortexed for 1 minute and transferred to a 70 °C water bath where the extraction may proceed for 30 minutes. After that, the tube was centrifuged at 4000 rpm for 10 minutes. The supernatant was transferred to another tube and diluted for 5-10 times prior to the colorimetric assay (Figure 1). The calibration curves were established by plotting the milligrams quercetin mass equivalents (mg QE) at various concentrations from 50 to 700 mg QE L^{-1} versus their UV-Vis absorbance values measured at 510 nm in the format of the linear calibration curve ($y = ax + b$) as referenced from Kim et al. [19].

Determination of total flavonoid content in tea products and their liquor

The analytical method for determining total flavonoid contents in tea products (expressed in mg QE g^{-1} dry weight) was validated, following the requirements in Appendix F of AOAC [20]. The evaluated performance characteristics included the calibration curve, limit of detection and quantification (LOD and LOQ) estimation, repeatability/intra-day and reproducibility/inter-day (% RSD_r and % RSD_R), and recovery testing for trueness evaluation. The method limits of detection and quantification (LOD and LOQ) were determined by simultaneous analysis of 11 blank samples. The estimated average concentration value ($\bar{x}$) and standard deviation (SD) were calculated to apply in the following relationships: LOD = $\bar{x}$ + 3SD and LOQ = 3LOD [21]. The method accuracy and precision were evaluated from the recovery study conducted by green tea samples spiked at levels of 40, 80, and 160 mg QE g^{-1}.

The proposed analytical method was applied in determining the TFCs of various tea products and their liquors, with the aim of evaluating the effects of brewing conditions (temperature and infusion time) on the release of flavonoids from tea products into the water. For the preparation of tea liquors, 0.200 g ± 0.001 g of dried tea sample and 10.00 mL of DI water were used for each brewing condition. The surveyed temperature and infusion time varied from 10 °C to 90 °C and 3 minutes to 60 minutes, respectively. The infusion time was kept at 60 minutes to assess the effects of temperature and 90 °C was used as the temperature for evaluating the influences of infusion time. The releasing percentage of TFCs was calculated as the ratio of TFCs between the tea liquors and products at different brewing conditions.

All the analytical data were carried out in three replicates (n = 3) to ensure the repeatability and analyzed by Microsoft Office Excel 2016, then expressed as mean value ± standard deviation (SD).

Table 1. Sampling information

Tea Types	Quantities	Sample Code	Sampling Location
Green	3	Green-1, Green-2, Green-3	Ha Giang Province, mountainous regions in the North (Vietnam)
White	3	White-1, White-2, White-3	
Pu'erh	3	Pu'erh-1, Pu'erh-2, Pu'erh-3	
Black	3	Black-1, Black-2, Black-3	
Green	3	Green-4, Green-5, Green-6	Lam Dong Province, Central Highland in the South (Vietnam)
Oolong	3	Oolong-1, Oolong-2, Oolong-3	

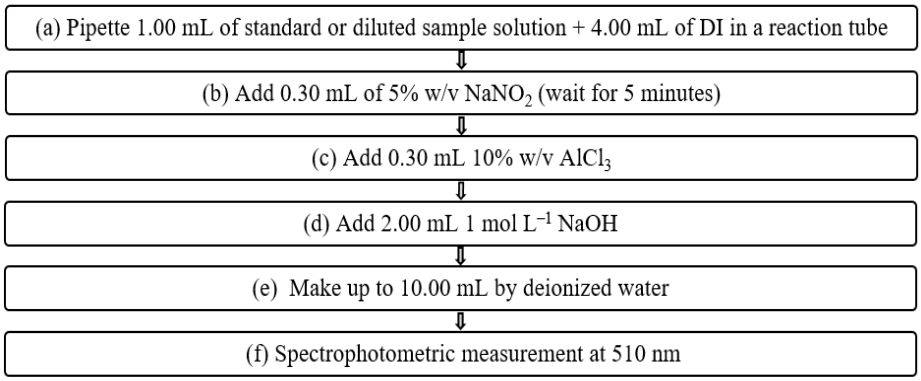


Figure 1. Coloring procedure for determining the total flavonoid content

Results and Discussion

Effect of reaction time on the determination of TFCs

The coloring procedure for TFCs (Figure 1) employed the basic principle of aluminium chloride colorimetric method, in which aluminium chloride formed acid-stable complexes with the C-4 keto group and either the C-3 or C-5 hydroxyl group of flavones and flavonols. Moreover, aluminium chloride also formed acid-labile complicated compounds with the *ortho*-dihydroxyl group in the A- or B- rings of flavonoids. For tea samples, quercetin has been reported to be a suitable standard for determining TFCs [19, 22, 23]. Therefore, the conditions for chemical reactions to form certain complexes during the coloring procedure were remarkably important for quantification purposes to guarantee the accuracy of the analytical results. After adding 1 mol L^{-1} NaOH and volumetric calibration (step (d) and (e) in Figure 1), the pH of the reaction solution would change to be favorable for complex formation, affecting the measured absorption signals. Therefore, the reaction duration before the spectrophotometric measurement was investigated to obtain the optimized coloring procedure. The absorbance was recorded at each reaction duration for 300 mg L^{-1} quercetin standard solution (Figure 2).

As can be seen in Figure 2, the measured absorbance values remained unchanged in the first minute (0-1 minute) and showed a descending trend from 1 to 120 minutes. However, the absorbance declined faster in the first 20 minutes (from 0.5434 to 0.2005). The absorbance continued to decrease in the next 40 minutes (from 0.1811 to 0.1325), but not as much as in the first 20 minutes. From the 60th minute onward, the signals still showed a descending trend but at a very slow rate (from 0.1327 to 0.1075). Therefore, to ensure the highest sensitivity and save analysis time, the spectrophotometric measurement should be carried out right after the addition of NaOH and volumetric calibration or in the first 60 seconds.

Moreover, in this study, we employed the manual measurement; therefore, we could follow the procedure separately for each sample solution. However, in the case of simultaneous measurement of various cells simultaneously (e.g., ELISA method), we could choose the reaction time above 60 minutes with smaller dilution factors.

Analytical method performance for determining TFCs in tea products and their liquors

The proposed analytical method was validated before application on real samples. The results for method performance are shown in Table 2. LOD and LOQ values were estimated as 1.4 and 4.1 mg QE g^{-1}, respectively, which were low compared to the TFCs in tea products. The calibration curve for determining the TFCs in various tea samples and their liquors was established from 50 to 700 mg L^{-1} and is shown in Figure 3.

The regression equation was $y = 0.0013x + 0.0872$ and $R^2 = 0.9981$, exhibiting goodness of linearity. The $\%RSD_r$ and RSD_R were used to evaluate the repeatability (within one day) and reproducibility (for three separate days) of the analytical method. These values were favorable according to Appendix F.

AOAC (2016) for the concentrations from 10 to 100% (RSD_r less than 1.3% and RSD_R less than 2 %) [20]. Besides, the recoveries varied from 98 to 102%, assuring the method's accuracy. Therefore, the validated analytical method could be applied for determining TFCs in tea products and their liquors during routine daily analysis and further research.

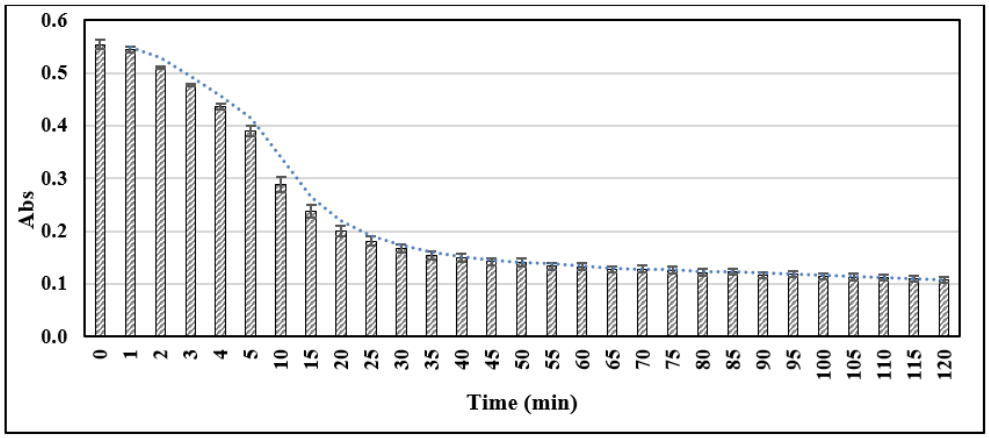


Figure 2. Investigation of reaction durations before spectrophotometric measurement

Table 2. Analytical method performance for the determination of TFCs

Parameter	LOD (mg QE g^{-1})	LOQ (mg QE g^{-1})	Linear range (mg L^{-1})	RSD_r (%)	RSD_R (%)	Recoveries (%)
Values	1.4	4.1	50-700	1.1	1.2	98-102

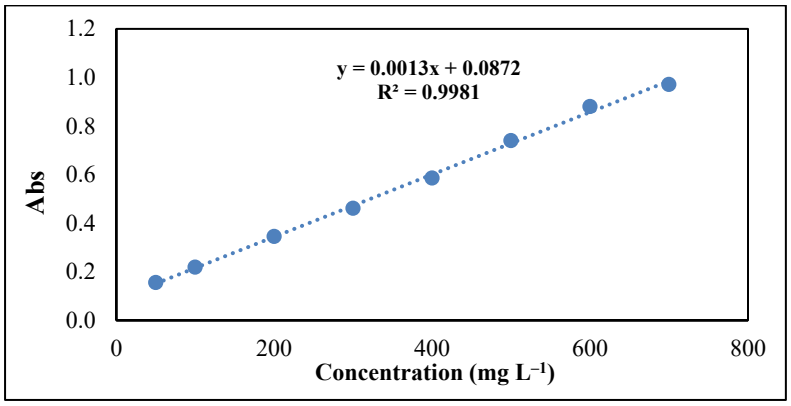


Figure 3. Calibration curve of TFCs

Variations of TFCs in different tea products

For plants in general and tea specifically, flavonoids have been known as the most popular, important, and mostly distributed single group of phenols with strong antioxidant properties [24, 25]. Flavonoids could inhibit metal-initiated lipid oxidation through the formation of complexes with metal ions. The TFC in dried tea products were determined, and their values are presented in Figure 4.

Among the available tea products, green-3 and oolong-2 had the highest (155.3 ± 1.3 mg QE g^{-1}) and lowest (42 ± 0.7 mg QE g^{-1}) TFCs, respectively. For the samples collected from the mountainous regions in North Vietnam, the TFCs were found in the descending order of green tea (140.1 ± 1.0 to 155.3 ± 1.3 mg QE g^{-1}) > Pu'erh tea (108.5 ± 0.8 to 141.8 ± 1.5 mg QE g^{-1}) > white tea (95.3 ± 1 to 99.0 ± 1.0 mg QE g^{-1}) > black tea (60.8 ± 1.1 to 89.7 ± 1.1 mg QE g^{-1}). The same order was reported by Peterson et al. [26] and Unachukwu et al. [27].

The differences in TFCs among various tea products could be explained by their oxidation levels. Non-fermented tea and very lightly fermented tea (green, white, and Pu'erh) contained simple flavonoids (catechins). During fermentation, the polyphenol oxidase enzyme oxidized simple catechins to form low molecular weight dimers (theaflavins) or high-molecular-weight polymers (thearubigins), leading to lower measured TFCs [13, 28]. The oxidation of catechins to theaflavins during the fermentation contributed to the dark color and distinctive flavor of the tea [29, 30]. In this study, the Pu'erh tea products possessed relatively high TFCs, not much different from those of green tea (the most extensive variation of 24 mg QE g^{-1}). It might be due to the similarity in the processing of green tea and Pu'erh tea products. However, oxidation is known to continue during storage for Pu'erh tea products due to the incomplete deactivation of enzymes in its processing, unlike green tea which undergoes heat treatment to remove bitterness and stop fermentation. Therefore, the TFCs for the three Pu'erh tea samples fluctuated in a wider range than other tea types, even though they originated from the same cultivar and variety. Moreover, the TFCs could change during storage, as reported by Chen et al. [31] and Zhou et al. [32].

For green and oolong tea products collected in the Central Highland (the southern Vietnam), they also exhibited a similar trend for non-fermented and fermented tea, in which green tea exhibited higher TFCs than oolong tea (85.2 ± 1.3 to 96.2 ± 1.8 mg QE g^{-1} vs. 42 ± 0.7 to 59.8 ± 0.4 mg QE g^{-1}). However, the difference in TFCs between green tea products of the North and South might be due to the difference in tea cultivar, soil types, altitude of cultivation, planting conditions, post-harvest storage, leaf quality, processing conditions, and ontogenetic effects [22, 33-36]. For fermented teas in this study, the black tea products showed higher TFCs than oolong tea (60.8 ± 1.1 mg QE g^{-1} to 89.7 ± 1.1 mg QE g^{-1} vs. 42 ± 0.7 mg QE g^{-1} to 59.8 ± 0.4 mg QE g^{-1}), which was also reported by Hertog et al. [37] and Zayadi et al. [38] for most oolong and black tea samples.

Effects of temperature and infusion time on TFCs in tea liquors

The effects of brewing conditions, including temperature and infusion duration, on TFCs in several tea liquors were evaluated. A quantity of 12 investigated samples belonging to four tea types of white, green, black, and Pu'erh from the same tea plantation area in Ha Giang Province were evaluated for their average extraction percentage for each brewing condition, as presented in Figure 5. There were no results for green and oolong tea samples in Lam Dong Province here due to the limitation of sample availability and experiment time.

As can be seen from Figure 5, higher brewing temperature led to the higher extraction percentage of TFCs for the four tea types and reached the highest at 90 °C. Black tea showed the most apparent increasing trend (1.02 to 42.8% from 10 °C to 90 °C) and required higher temperature to release the flavonoids from the tea leaves to the water. The temperature accelerated the extraction of internal compounds, especially the easily soluble substances such as flavonoids, catechins, and metal(loid)s from the tea products into their liquors, as reported in several publications [7, 39-42].

For infusion time effects, the extraction percentage of TFCs in tea liquors reached the highest at the infusion time of 40 minutes, then decreased in the next 20 minutes (from 40 to 60 minutes). The longer infusion time could have caused the thermal oxidation or decomposition of flavonoid compounds, leading to lower TFCs recorded in tea liquors [43, 44]. As in the situation of brewing time experiment, black tea exhibited the largest variation in the extraction percentage within the investigated infusion time from 3 to 60 minutes (29.93-43.23%). Meanwhile, the recorded fluctuation was smaller for white, green, and Pu'erh tea types with higher extraction percentages

(59.49%, 55.49%, and 51.74%). Besides the TFCs, a longer infusion time at high temperatures might draw out more undesirable compounds, especially potentially toxic metal(loid)s, into the tea liquors. Therefore, tea drinkers could choose a shorter infusion time without much effect on the TFCs released into tea liquors. For example, green tea had the TFC extraction percentage of 54.31% ± 0.74%, only 8% lower than the most favorable condition (62.29 ± 0.59%).

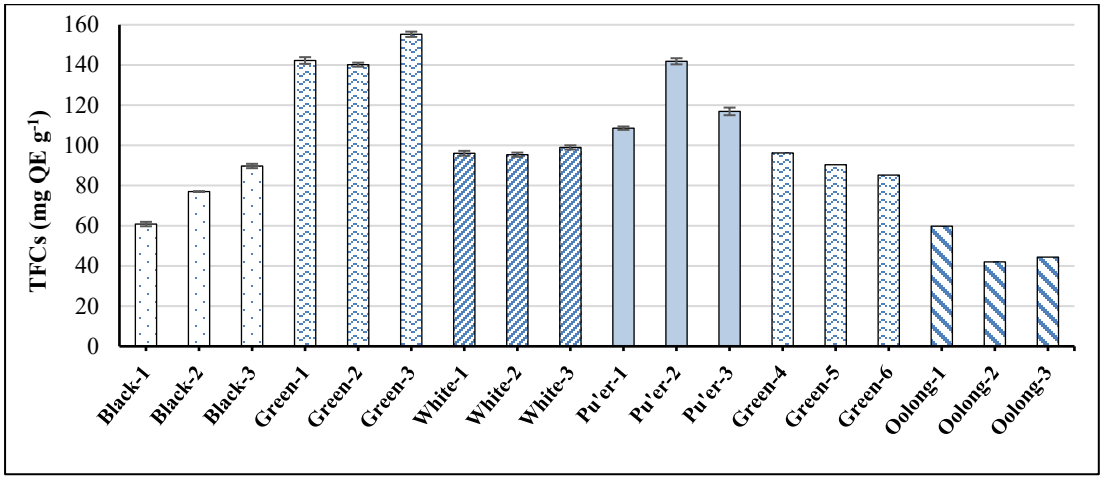
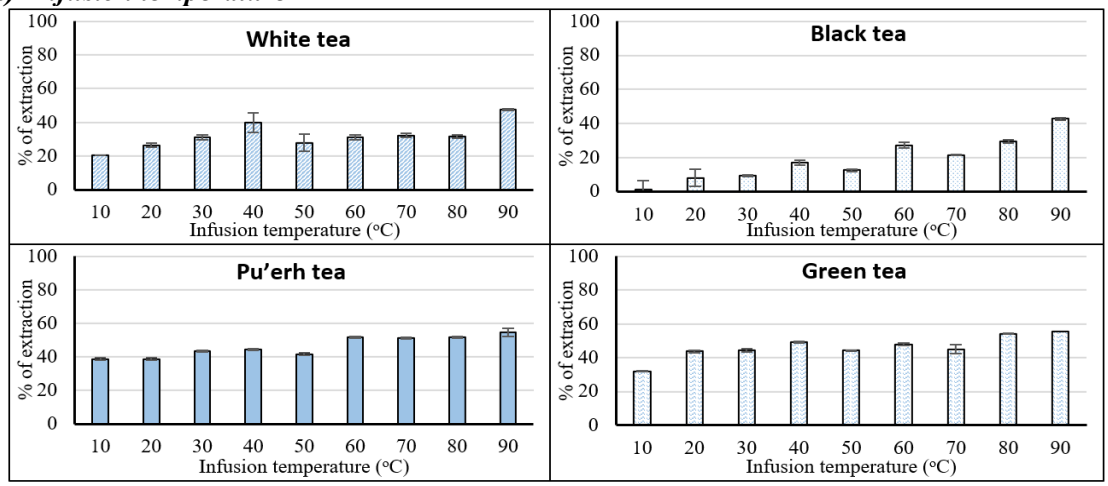


Figure 4. Flavonoid contents in tea samples

(a) Infusion temperature



(b) Infusion time

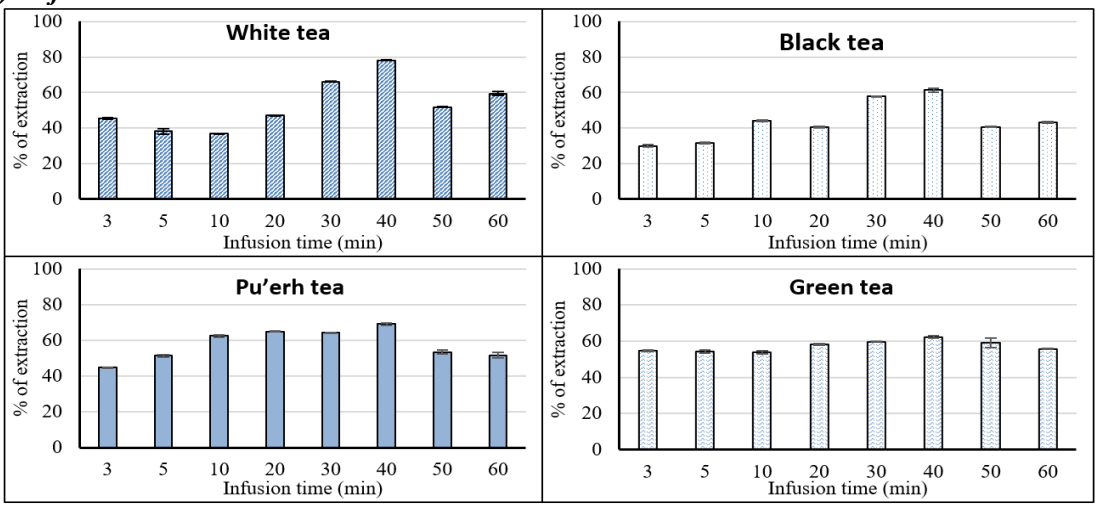


Figure 5. Effect of (a) temperature and (b) infusion time on TFCs in tea liquors

Conclusion

The analytical method for determining the total flavonoid content in different tea products and their liquors, based on the principle of spectrophotometric assay after forming complexes with $AlCl_3$ in alkaline medium, was validated according to the requirements in Appendix F. AOAC (2016). The estimated limit of detection and quantification values were low compared to the TFCs present in tea samples. The calibration curve was built from 50 to 700 mg QE L^{-1} with R^2 = 0.9981, exhibiting goodness of linearity. Non-fermented and lightly-fermented tea products exhibited higher TFCs than fermented ones, whereby TFCs followed the descending order of green (140.1-155.3 mg QE g^{-1}) > Pu'erh (108.5-141.8 mg QE g^{-1}) > white (95.3-99.0 mg QE g^{-1}) > black (60.8-89.7 mg QE g^{-1}) > oolong (85.2-96.2 mg QE g^{-1}).

The temperature and infusion time affected the TFCs in tea liquors. The highest TFCs in tea liquor were recorded at 90 °C within the infusion time of 40 minutes for most tea products. However, for a better assessment, more samples belonging to different tea types should be collected, and we could carry out further investigation for catechins, antioxidant capacities, and elemental analysis to discover the most favorable brewing condition for each tea type.

Acknowledgment

The authors would like to express our thanks and appreciation to Nguyen Tat Thanh University for the assistance and support during this study. This research is funded by Nguyen Tat Thanh University, Ho Chi Minh city, Vietnam, under grant number 2021.01.21/HĐ-KHCN.

References

1. Yan, Z., Zhong, Y., Duan, Y., Chen, Q. and Li, F. (2020). Antioxidant mechanism of tea polyphenols and its impact on health benefits. *Animal Nutrition*, 6(2): 115-123.
2. Zhang, L., Li, N., Ma, Z.-Z. and Tu, P.-F. (2011). Comparison of the chemical constituents of aged pu-erh tea, ripened pu-erh tea, and other teas using HPLC-DAD-ESI-MS. *Journal of Agricultural and Food Chemistry*, 59 (16): 8754-8760.
3. Kosińska, A. and Andlauer, W. (2014). Antioxidant capacity of tea: Effect of processing and storage. *Processing and impact on antioxidants in beverages*. Elsevier: pp. 109-120.
4. Ahmed, S., Unachukwu, U., Stepp, J. R., Peters, C. M., Long, C. and Kennelly, E. (2010). Pu-erh tea tasting in Yunnan, China: correlation of drinkers' perceptions to phytochemistry. *Journal of Ethnopharmacology*, 132 (1): 176-185.
5. Chen, S., Li, M., Zheng, G., Wang, T., Lin, J., Wang, S., Wang, X., Chao, Q., Cao, S. and Yang, Z. (2018). Metabolite profiling of 14 Wuyi Rock tea cultivars using UPLC-QTOF MS and UPLC-QqQ MS combined with chemometrics. *Molecules*, 23(2): 104.

6. Kodama, D. H., Gonçalves, A. E. d. S. S., Lajolo, F. M. and Genovese, M. I. (2010). Flavonoids, total phenolics and antioxidant capacity: comparison between commercial green tea preparations. *Food Science and Technology*, 30: 1077 – 1082.
7. Tao, W., Zhou, Z., Zhao, B. and Wei, T. (2016). Simultaneous determination of eight catechins and four theaflavins in green, black and oolong tea using new HPLC–MS–MS method. *Journal of Pharmaceutical and Biomedical Analysis*, 131: 140-145.
8. Higdon, J. V. and Frei, B. (2003). Tea catechins and polyphenols: health effects, metabolism, and antioxidant functions. *Critical Reviews in Food Science and Nutrition*, 43(1): 89-143.
9. Yokozawa, T., Dong, E., Nakagawa, T., Kashiwagi, H., Nakagawa, H., Takeuchi, S. and Chung, H. Y. (1998). In *vitro* and in *vivo* studies on the radical-scavenging activity of tea. *Journal of Agricultural and Food Chemistry*, 46(6): 2143-2150.
10. Ahmad, N., Cheng, P. and Mukhtar, H. (2000). Cell cycle dysregulation by green tea polyphenol epigallocatechin-3-gallate. *Biochemical and Biophysical Research Communications*, 275(2): 328-334.
11. Kundu, J. K., Na, H.-K., Chun, K.-S., Kim, Y.-K., Lee, S. J., Lee, S. S., Lee, O. -S., Sim, Y.-C. and Surh, Y.-J. (2003). Inhibition of phorbol ester–induced COX-2 expression by epigallocatechin gallate in mouse skin and cultured human mammary epithelial cells. *The Journal of nutrition*, 133 (11): 3805S-3810S.
12. Pękal, A. and Pyrzynska, K. (2014). Evaluation of aluminium complexation reaction for flavonoid content assay. *Food Analytical Methods*, 7(9): 1776-1782.
13. Izzreen, N. Q. and Mohd Fadzelly, A. (2013). Phytochemicals and antioxidant properties of different parts of *Camellia sinensis* leaves from Sabah Tea Plantation in Sabah, Malaysia. *International Food Research Journal*, 20(1): 307-312.
14. Bansal, S., Syan, N., Mathur, P. and Choudhary, S. (2012). Pharmacological profile of green tea and its polyphenols: A review. *Medicinal Chemistry Research*, 21(11): 3347-3360.
15. Putri, T. (2015). In *vitro* anti-gout activity and phenolic content of "black tea" soursop (*Annona muricata* L.) leaves brew. *Journal of Chemical and Pharmaceutical Research*, 7(11): 735-743.
16. Kılıç, C., Can, Z., Yılmaz, A., Yıldız, S. and Turna, H. (2017). Antioxidant properties of some herbal teas (green tea, senna, corn silk, rosemary) brewed at different temperatures. *International Journal of Secondary Metabolite*, 4(3): 142-148.
17. ISO 1572 (1980). Tea-Preparation of ground sample of known dry matter content.
18. ISO 14502-1 (2005). Determination of substances characteristic of green and black tea-Part 1: Content of total polyphenols in tea-Colorimetric method using Folin-Ciocalteu reagent.
19. Kim, D.-O., Jeong, S. W. and Lee, C. Y. (2003). Antioxidant capacity of phenolic phytochemicals from various cultivars of plums. *Food Chem*istry, 81(3): 321-326.
20. Appendix F. AOAC (2016). Guidelines for Standard Method Performance Requirements.
21. Konieczka, P. and Namiesnik, J. (2016). Quality assurance and quality control in the analytical chemical laboratory: A practical approach, CRC Press.
22. Shannon, E., Jaiswal, A. K. and Abu-Ghannam, N. (2018). Polyphenolic content and antioxidant capacity of white, green, black, and herbal teas: a kinetic study. *Food Research*, 2(1): 1-11.
23. Akbay, P., Basaran, A. A., Undeger, U. and Basaran, N. (2003). In *vitro* immunomodulatory activity of flavonoid glycosides from *Urtica dioica* L. *Phytotherapy Research: An International Journal Devoted to Pharmacological and Toxicological Evaluation of Natural Product Derivatives*, 17(1): 34-37.
24. Pokorny, J., Yanishlieva, N. and Gordon, M. H. (2001). Antioxidants in food: Practical applications: CRC press.
25. Abdeltaif, S. A., SirElkhatim, K. A. and Hassan, A. B. (2018). Estimation of phenolic and flavonoid compounds and antioxidant activity of spent coffee and black tea (processing) waste for potential recovery and reuse in Sudan. *Recycling*, 3(2): 27.
26. Peterson, J., Dwyer, J., Bhagwat, S., Haytowitz, D., Holden, J., Eldridge, A., Beecher, G. and Aladesanmi, J. (2005). Major flavonoids in dry tea. *Journal of Food Composition and Analysis*, 18(6): 487-501.
27. Unachukwu, U. J., Ahmed, S., Kavalier, A., Lyles, J. T. and Kennelly, E. J. (2010). White and green teas (*Camellia sinensis* var. *sinensis*): variation in phenolic, methylxanthine, and antioxidant profiles. *Journal of Food Science*, 75 (6): C541-C548.

28. Rusak, G., Komes, D., Likić, S., Horžić, D. and Kovač, M. (2008). Phenolic content and antioxidative capacity of green and white tea extracts depending on extraction conditions and the solvent used. *Food Chemistry*, 110(4): 852-858.
29. Harbowy, M. E., Balentine, D. A., Davies, A. P. and Cai, Y. (1997). Tea chemistry. *Critical Reviews in Plant Sciences*, 16(5): 415-480.
30. Graham, H. N. (1992). Green tea composition, consumption, and polyphenol chemistry. *Preventive Medicine*, 21(3): 334-350.
31. Chen, M., Zhu, Y., Zhang, H., Wang, J., Liu, X., Chen, Z., Zheng, M. and Liu, B. (2017). Phenolic compounds and the biological effects of Pu-erh teas with long-term storage. *International Journal of Food Properties*, 20(8): 1715-1728.
32. Zhou, B., Ma, C., Wu, T., Xu, C., Wang, J. and Xia, T. (2020). Classification of raw Pu-erh teas with different storage time based on characteristic compounds and effect of storage environment. *LWT Food Science and Technology*, 133: 109914.
33. Imran, A., Butt, M. S., Sharif, M. K. and Sultan, J. I. (2013). Chemical profiling of black tea polyphenols. *Pakistan Journal of Nutrition*, 12 (3): 261.
34. Lee, J.-E., Lee, B.-J., Chung, J.-O., Kim, H.-N., Kim, E.-H., Jung, S., Lee, H., Lee, S.-J and Hong, Y.-S. (2015). Metabolomic unveiling of a diverse range of green tea (*Camellia sinensis*) metabolites dependent on geography. *Food Chemistry*, 174: 452-459.
35. Yang, J. and Liu, R. H. (2013). The phenolic profiles and antioxidant activity in different types of tea. *International Journal of Food Science & Technology*, 48(1): 163-171.
36. Pacheco-Coello, F., Peraza-Marrero, M., Orosco-Vargas, C., Ramirez-Azuaje, D. and Pinto-Catari, I. (2020). Determination of total phenolic compounds and evaluation of the antioxidant activity of commercial and artisanal green tea traded in Maracay, Venezuela. *Revista Boliviana de Química*, 37(1): 28-33.
37. Hertog, M. G., Hollman, P. C. and Van de Putte, B. (1993). Content of potentially anticarcinogenic flavonoids of tea infusions, wines, and fruit juices. *Journal of Agricultural and Food Chemistry*, 41(8): 1242-1246.
38. Zayadi, R. A., Rahim, N. A. and Bakar, F. A. (2016). Determination of flavonoid and caffeine content in black and oolong teas. *Journal of Science and Technology*, 8(2): 18-24.
39. Chang, M.-Y., Lin, Y.-Y., Chang, Y.-C., Huang, W.-Y., Lin, W.-S., Chen, C.-Y., Huang, S.-L. and Lin, Y.-S. (2020). Effects of infusion and storage on antioxidant activity and total phenolic content of black tea. *Applied Sciences*, 10(8): 2685.
40. Kelebek, H. (2016). LC-DAD–ESI-MS/MS characterization of phenolic constituents in Turkish black tea: Effect of infusion time and temperature. *Food Chemistry*, 204: 227-238.
41. Jamshidpour, S., Faramarzi, E., Mahmoudi, M. and Varmira, K. (2016). The effect of the duration and temperature of infusion on the heavy metal content of green tea. *European Online Journal of Natural and Social Sciences*, 5 (4): 980-987.
42. Asil, M. H., Rabiei, B. and Ansari, R. H. (2012). Optimal fermentation time and temperature to improve biochemical composition and sensory characteristics of black tea. *Australian Journal of Crop Science*, 6(3): 550-558.
43. Ioannou, I., Chekir, L. and Ghoul, M. (2020). Effect of heat treatment and light exposure on the antioxidant activity of flavonoids. *Processes*, *8* (9): 1078.
44. Buchner, N., Krumbein, A., Rohn, S. and Kroh, L. (2006). Effect of thermal processing on the flavonols rutin and quercetin. *Rapid communications in mass spectrometry,* 20: 3229-3235.

Malaysian Journal of Analytical Sciences (MJAS)
Published by Malaysian Analytical Sciences Society

QUALITY ASSESSMENT OF MANGOSTEEN IN DIFFERENT MATURITY STAGES BY HAND-HELD NEAR-INFRARED SPECTROSCOPY

(Penilaian Kualiti Manggis dalam Tahap Kematangan yang Berbeza dengan Genggam Spektroskopi Inframerah Dekat)

Low Shuang Yao[1], Mahmud Iwan Solihin[2], Pavalee Chompoorat[3], Lim Lee Ying[1], Pui Liew Phing[1]*

[1]*Department of Food Science and Nutrition, Faculty of Applied Sciences*
[2]*Dpartment of* Mechanical and Mechatronics Engineering, Faculty of Engineering, Technology and Built Environment,
Faculty of Engineering, Technology and Built Environment
UCSI University, 56000 Kuala Lumpur, Malaysia
[3]*Faculty of Engineering and Agro-Industry,*
Maejo University, Chiang Mai 50290, Thailand.

**Corresponding author: puilp@ucsiuniversity.edu.my*

Received: 11 August 2021 ; Accepted: 18 September 2021; Published: 25 October 2021

Abstract

Quality loss of mangosteen, a tropical fruit, is caused by improper post-harvest handling. A method that can evaluate mangosteen color along with its physical and chemical properties quickly and conveniently should be developed. In this study, 90 mangosteen samples were collected and scanned by the hand-held micro near-infrared (NIR) spectrometer in the wavelength from 900–1700 nm. The mangosteen samples were tested with destructive methods such as color, total soluble solids, reducing sugar content, titratable acidity, and pH to obtain the reference data for the predictive model. Spectral data collected has undergone several pre-processing techniques. The enhanced spectral data are regressed using the regression model. Partial least square (PLS) regression and Principal Component Regression (PCR) are used as the regression method for predicting mangosteen attributes with the help of Orange data mining software. The results showed that color of the sample was not ideal and stage 5 maturity had the lowest L* (27.99), a* (9.03) and b* (7.22). Maturity of stage 6 mangosteen have the highest amount of reducing sugar (10.70×10^{-6} g/100g) and total soluble solids (7.18%). Pearson's correlation was used to determine the relationship between the chemical and physical properties of the mangosteen samples. The PLS and PCR predictive models for reducing sugars were obtained with accuracy as $R^2 = 0.56$ and $R^2 = 0.50$ for the training and testing data, respectively. This achieved accuracy may not be good, but it can be improved in the future by using nonlinear machine learning and ensemble methods such as PLS and PCR. Overall, this study indicated that the NIR spectroscopy technique combined with several pre-processing methods and the predictive model by PLS and PCR could be a rapid and non-destructive method for evaluating the quality and maturity of the mangosteen fruit.

Keywords: hand-held near-infrared spectroscopy, mangosteen, color analysis, total soluble solids, non-destructive quality assessment

Abstrak

Kehilangan kualiti manggis, buah tropika, disebabkan oleh pengendalian pasca tuai yang tidak betul. Kaedah yang dapat menilai warna manggis, sifat manggis fizikal dan kimia dengan kelajuan dan kemudahan yang pantas harus dikembangkan. Dalam kajian ini, 90 sampel manggis dikumpulkan dan diimbas oleh spektrometer mikro dekat inframerah (NIR) genggam. Sampel manggis diuji dengan kaedah yang merosakkan seperti warna, pepejal larut total, pengurangan kandungan gula, keasidan yang dapat ditetrasi dan pH untuk mendapatkan data rujukan untuk model ramalan. Data spektral yang dikumpulkan telah menjalani beberapa teknik pra-pemprosesan. Data spektrum yang ditingkatkan mundur menggunakan model latihan regresi. Regresi Separa Sekurang Persegi (PLS) dan Regresi Komponen Utama (PCR) digunakan sebagai kaedah regresi untuk meramalkan atribut manggis dengan bantuan perisian perlombongan data Orange. Hasil kajian menunjukkan bahawa warna sampel tidak sesuai untuk kematangan tahap 5 yang mempunyai terendah L* (27.99), a* (9.03) dan b* (7.22). Kematangan manggis tahap 6 mempunyai jumlah gula pengurangan tertinggi (10.70 × 10-6 g/100g) dan jumlah perpejal larut (7.18%). Korelasi Pearson digunakan untuk menentukan hubungan antara sifat kimia dan fizikal sampel manggis. Model ramalan PLS dan PCR diperoleh dengan ketepatan masing-masing R^2=0.56 dan R^2=0.50. Secara kesuluruhan, kajian ini menunjukkan bahawa teknik spektroskopi transmisi NIR digabungkan dengan beberapa kaedah pra-pemprosesan dan model ramalan yang dibandingkan dengan PLS dan PCR dapat menjadi kaedah yang cepat dan tidak merosakkan untuk menilai kualiti dan kematangan buah manggis.

Kata kunci: genggam spektroskopi inframerah dekat, manggis, analisis warna, jumlah pepejal larut, penilaian kualiti yang tidak merosakkan

Introduction

Mangosteen (*Garcinia mangostana* L.) is one of the most important tropical fruits in Southeast Asia, and it is under the family of Clusiacaea [1]. The white edible aril of the mangosteen is juicy and has a sweet and slightly sour taste. The peel color of the mangosteen is the major criteria for determining the maturity of the mangosteen. The mangosteen is typically harvested according to color at various stages, from the peel color is greenish yellow with red until blackish purple [2, 3]. Mangosteen is a climacteric fruit. It will begin to ripen as the peel color will turn into a dark purple color after maturation [4]. To obtain the best quality mangosteen, it should be harvested when the peel color is randomly bright with pink to red spots all over the fruit [3]. Near-infrared (NIR) can be used in quantity analysis, where real data was collected to calibrate and validate the predictive model's accuracy in determining the maturity level of mangosteen.

Two types of regression, partial least square (PLS) regression and principal component regression (PCR), were used to construct a model for predicting maturity non-destructive [5]. Near-infrared (NIR) spectrum data from the mangosteen were collected at the maturity level stage 2, stage 5, and stage 6 using a hand-held NIR spectrometer. Several pretreatment methods for the collected NIR spectrum data were applied to eliminate data that were unrelated or irrelevant and incorporated multivariate analysis. These techniques were used to classify the internal attributes, chemical properties, physical properties, and cell structures of the mangosteen [6].

In Malaysia, it is common human visual inspection that is used to determine the maturity stage of mangosteen. The fruit should not be harvested before stage 2 to obtain a high fruit quality [7]. Fruit harvested before stage 2 does not ripen to full flavor, and the excessive latex will flow at the detach point, causing undesirable stains [8]. Destructive techniques require complex sample preparation, which is time consuming [9]. As a result, a fast and accurate method is needed to determine the stage of maturity for mangosteen. NIR was chosen to collect the spectrum data from mangosteen as a near-infrared spectrometer that is characterized by a fast and non-destructive approach. Moreover, nowadays, NIRs are portable because of advances in optical sensor technology.

This study identifies the feasibility to predict mangosteen quality and maturity with a hand-held NIR. This study also determines the physical properties and chemical composition of mangosteen.

Materials and Methods

Raw materials

Mangosteen fruits without any surface defects and with uniform size were obtained from a local farm in Pahang, Malaysia at the end of August 2020. The diameter of the mangosteen fruit ranged from 38 - 62 cm. The mangosteens were categorized into maturity stages by using peel color according to the color index from Tongdee and Suwanagul [8] (Table 1).

There are seven stages defined by the extent of red or purple coloration on the peel. Mangosteens were selected in three different stages, i.e., stage 2, 5, and 6. According to Osman and Milan [10], the harvest standard for mangosteen export in Malaysia was reddish yellow with red spots. Mangosteen at stage 2 in this study displayed a yellowish pink peel with 51–100% scattered pink spots. Meanwhile, mangosteen at stage 5 and 6 were selected to examine the differences in quality assessments. Mangosteen at stage 5 in this study presented with a dark purple color and mangosteen at stage 6 presented with a purple-black color.

Each maturity level was randomly collected for 30 fruits. Mangosteens were cleaned and stored at ambient temperature for analysis. It was then cut in half along the equatorial section after the spectral data was taken. The peels were stored in a ziplock bag. The pulps were ground by the grinder (MX-GM1011, Panasonic, Japan) and filtered by coffee filters to extract the filtrates. The filtrates were stored in the ziplock bag and kept in a freezer for further analysis. Mangosteens at different maturity stages were stored separately for measurement. The samples were kept for 10 days in a storage temperature of 4 - 10 °C.

Table 1. Characteristics of peel color of mangosteen at different maturity stages [8]

Stage	Characteristics of Pericarp
0	Uniformly yellowish-white or with greyish spots
1	Light greenish yellow with scattered pink spots
2	Light greenish yellow or yellowish pink with apparent pink spots all over the fruit
3	Background pinkish, the spots are not as apparent as in stage 2
4	Red or reddish brown with some purple tint
5	Darkened to reddish purple
6	Dark purple to black with little or no red color remaining

Determination of physicochemical properties of mangosteen

Peel color analysis

The color of mangosteens was measured by using Hunter Lab ColorFlex colorimeter (Hunter Associate Laboratory Inc., Reston, USA) [11]. Calibration was done with black and white piles. The value of L*, a* and b* should be 50.87, -25.11 and 14.98, respectively, after calibration.

The sample cup was cleaned with tap water and with no undesirable stain remaining in the cup. A peeler was used to peel the mangosteen's rind, and the peels of mangosteen were placed in the sample cup. The peels of mangosteen completely covered the bottom surface of the sample cup. The sample cup was put into the sensor after it was closed with a cup-like cover to measure the sample and take readings. The button with a lightning bolt would be pressed to reveal the L*, a*, b* values. The L*, a*, b* values were recorded. Chroma (C*) was used to determine the hue's degree of difference compared to grey with the same lightness.

$$C* = \sqrt{a*^2 + b*^2} \quad (1)$$

Hue angle (h*) was used to determine the differences of a certain color in relation to a grey color with the same lightness.

$$h* = \tan^{-1}\left(\frac{b*}{a*}\right) \quad (2)$$

Total soluble solids

The total soluble acid analysis was done using a digital refractometer (MA887, Milwaukee Instruments, Inc., North Carolina, USA) [12]. After the refractometer was calibrated, around two drops of the filtrate sample were put in the refractometer's sample well with a Pasteur pipette. The read button was pressed, and the reading was recorded as total soluble solids (%Brix).

Reducing sugar

Reducing sugar test was done using the Nelson-Somogyi method [13]. Approximately 1 mL of filtrate sample was poured into a test tube and mixed with 9 mL of water. Then, 1 mL of the diluted sample was taken and transferred to another test tube. The diluted sample was added to 9 mL of distilled water for further dilution. Approximately 1 mL of the diluted sample was transferred to the boiling tube and mixed with 1 mL of Nelson mixture.

The mixture would be heated at 100 °C for 20 minutes in the water bath with a boiling tube rack. After heating, the sample was left to cool down on the lab bench. When the sample completely cooled down, the sample was added with 1 mL of arsenomolybdate reagent and 7 mL distilled water. The sample was shaken to make sure the mixture was mixed well. The sample was poured into the glass cuvette. The absorbance of the sample was measured at 510 nm with the spectrometer (UviLine 9400, United Kingdom).

Titratable acidity

The titratable acidity analysis of the pulp was done by titrating sodium hydroxide with the mangosteen sample [12]. Sodium hydroxide with 0.1 M was prepared by dissolving 4 g of sodium hydroxide into 1 L of distilled water. A clamp stand with a pipette was put on the lab bench. The pipette was rinsed with the distilled water and 0.1 M sodium hydroxide. It was then filled with 0.1 M sodium hydroxide until 50 mL and held by the clamp stand. The conical flask was filled with 5 mL of the liquid sample and placed below the pipette. Two drops of phenolphthalein were added to the conical flask as an indicator. The stopcock was twisted open slowly, allowing the 0.1 M NaOH to drop into the conical flash drop by drop until a permanent pink color appeared. The remaining volume of the pipette was recorded for further calculation.

$$\%Titratable\ acidity = \frac{NxVxE}{Wx\ 1000} \text{ x } 100 \quad (3)$$

N was the normality of sodium hydroxide (NaOH), V was the volume made up, E was the acid's equivalent weight, and W was the sample's weight.

pH

The pH of mangosteen was obtained by a pH meter (Metler-Toledo, China) [12]. The mangosteen aril was blended and filtered by a cloth filter. The filtrates were stored in the 30 mL sample bottles. The sample bottle filtrates were measured using a calibrated pH meter with the electrode's bulb fully submerged in the filtrates. The reading of the pH meter was recorded.

NIR spectral data collection

A total of 90 samples were scanned by using the Near Infrared Spectrometer DLP NIRscan Nano EVM (Texas Instrument, USA). The wavelength ranged from 900-1700 nm [15]. The fruit samples were placed directly on the detector window of the instrument. Each sample was scanned at 3 different spots using the reflectance mode. The reflectance mode was the most suitable for mangosteen samples because it has the light level required for radiation to enter the fruit without altering its properties and the reflected light was detected by the detector [16]. The spectra acquired was then averaged and used for further processing [17].

Pre-processing of spectral data

To have a high signal-to-noise ratio, after the spectra of the mangosteen samples were collected, they underwent several pre-processing techniques that eliminated the noise and scattering effects in the spectra data [17]. Cutting, Gaussian smoothing, Savitzky-Golay (SG) smoothing, Multiplicative scatter correction (MSC), and standard normal variate (SNV) were the different techniques used in this study as effective methods of eliminating noise and scattering effects for the spectra data by using the software Orange Data Mining v. 3.26 (Bioinformatics Lab, University of Ljubljana, Slovenia). The spectra (900 - 980.943 and 1621.240–1700) were

cut out, and Gaussian smoothing with a standard deviation of 10 was used to reduce the noise.

Regression models development

All regression training models were done with Orange v. 3.26 (Bioinformatics Lab, University of Ljubljana, Slovenia) [19-22]. Each regression training model had its optimized setting, and each of them was provided with 80% spectra data for training and 20% spectra data for testing. The training model's prediction ability will evaluate the correlation coefficient, and the root means square error between the predicted value and the validation set's measured value. The prediction performance is better when the correlation coefficient is higher, and the root means the square error is lower.

Principal component regression (PCR)

Principal component regression (PCR) is a linear regression model based on principal component analysis (PCA) [23]. PCR regresses the target based on the spectral data matrix, which may reproduce the original data. In PCR, the first step is to decompose data matrix X into a new latent variable by using PCA. The next step, multiple linear regression (MLR), is used between the score obtained in the first step and the interesting property of interest, y. Hence, PCR consists of a linear regression of the scores and y. The linear model of the PCR is expressed as the equation below.

$$Y = Ab + e \quad (4)$$

Partial least square (PLS)

Partial least square (PLS) is a multivariate regression method used in quantitative NIR analysis. PLS is useful when a set of dependent variables from a large set of independent variables must be predicted. PLS is constructing the regression model between two latent variables: the independent X and the dependent Y. The best number of latent variables can be found most commonly through cross-validation based on the minimal prediction error determination.

$$X = TP^T + E \quad (5)$$

$$Y = UQ^T + F \quad (6)$$

T and U are the score matrices for the data set of X and Y, respectively. On the other hand, P and Q are the loading matrices for X and Y, respectively. E and F are the residual matrices [24].

Statistical analysis

All the tests were conducted in triplicate (n=3), and all of the results were presented in the form of mean ± standard deviation. One-way ANOVA was conducted for the comparing means for the three maturity stages of the mangosteen. Tukey HSD test was conducted because the sample size in the experiment is equal. The significant mean differences for all tests were set at 95% interval, which means when $p>0.05$, there were no significant differences. All the data was interpreted by using SPSS Statistics 26 (IBM, Chicago).

Results and Discussion

Color analysis

Color is a significant external quality attribute, and it is often used as a standard for grading the quality of mangosteen [25]. Table 2 shows maturity stage 2 of mangosteen has the highest value of L* (35.39), followed by maturity stage 6 (31.09) and maturity stage 5 (27.99). For a*, there are no significant differences ($p > 0.05$) between stage 2 and stage 6 mangosteen. Maturity stage 5 mangosteen had the lowest value of a* (9.03). For b*, stage 2 mangosteen had the highest value (22.75), and maturity stage 5 had the lowest value (7.22).

L*'s value decreased from maturity stage 2 to maturity stage 5 and increased from maturity stage 5 to maturity stage 6. This means that stage 2 mangosteen had the lightest color and stage 5 mangosteen had the darkest color. The same goes for the a* value and b* value. The a* value and b* values were decreasing from maturity stage 2 to maturity stage 5 and increasing from stage 5 to stage 6. Stage 2 has the reddest and yellowest color among the three maturities. The outer pericarp color of the mangosteen does not meet with the maturity stages of the mangosteen; stage 6 should have the reddest color among the three maturities. The result was contrary to Palapol et al. [26]. The reason may be because the storing of the rind in the freezer for too long. Internal defects of the mangosteen may cause the color on the rind's surface to not match with the proper maturity stage of the mangosteen [27].

Table 2. Color index, %Brix and reducing sugar and acidity of mangosteen in three maturity stages

Stage	L*	a*	b*	Brix (%)	Reducing Sugar Content (g/100g)	Titratable Acidity (%)	pH
2	35.39 ± 4.93 [a]	11.54 ± 3.51 [a]	22.75 ± 3.49 [a]	2.14 ± 0.54 [c]	$5.07 \times 10^{-6} \pm 0.11 \times 10^{-7}$ [c]	2.03 ± 0.41 [a]	3.49 ± 0.18 [c]
5	27.99 ± 2.07 [c]	9.03 ± 1.37 [c]	7.22 ± 2.94 [c]	4.54 ± 0.99 [b]	$8.93 \times 10^{-6} \pm 0.11 \times 10^{-7}$ [b]	1.27 ± 0.26 [b]	3.86 ± 0.18 [b]
6	31.09 ± 2.76 [b]	10.57 ± 1.59 [b]	12.59 ± 2.69 [b]	7.18 ± 0.82 [a]	$10.70 \times 10^{-6} \pm 0.01 \times 10^{-7}$ [a]	0.78 ± 0.21 [c]	4.34 ± 0.45 [a]

*Data collected are calculated in mean ± standard deviations. Different superscripts are indicating the data is significant at $p < 0.05$ by analysis of the Tukey HSD test

Brix and reducing sugar

Brix is usually used to measure the total soluble solids in the fruit, indicating the fruit's sweetness. Table 2 shows the %Brix value of different maturity stages for mangosteen and ranged from 2.14 - 7.18%. The %Brix values in mangosteen with maturity stage 6 were the highest (7.18%); whereas the %Brix values in mangosteen with maturity stage 2 had the lowest (2.14%).

The %brix value increased from maturity stage 2 to maturity stage 6. The results are supported by Castro et al. [28], which has the %brix value ranging from 15.2 - 19.1 due to the prolonged storage and maturation process. %Brix values increased from stage 2 to stage 6, because the accumulated starch in the mangosteen has been converted to sucrose during maturation [29].

Reducing sugar is one of the metrics for determining the maturity level of fruit. The maturity stage 6 mangosteen had the highest amount of reducing sugar content (10.70×10^{-6} g/100 g), and the maturity stage 2 had the lowest amount of reducing sugar content (5.07×10^{-6} g/100 g). The reducing sugar of mangosteen and increase from stage 2 to stage 6 (5.07×10^{-6} g/100 g) and (10.70×10^{-6} g/100 g), respectively. The reducing sugar increased as the maturity level increased, which indicates that the starch accumulated became hydrolyzed into glucose, fructose, and sucrose during the ripening progress [30].

Titratable acidity and pH value

Titratable acidity measured the total concentration of acid in the fruit, and pH values were used to measure hydrogen ionic concentrations in the solution, referred to as the degree of acidity or alkalinity [31]. Both pH and titratable acidity measure the number of organic acids in a fruit [32]. Maturity stage 2 mangosteen had the highest percentage of reducing sugar (2.03), followed by stage 5 mangosteen (1.27) and stage 6 mangosteen (0.78). The mangosteen's pH value of maturity stage 2, 5, and 6 ranged from 3.49 - 4.34. The highest pH of the mangosteen is the maturity stage 6 mangosteen with a value of 4.34. The lowest pH of the mangosteen is the maturity stage 2 mangosteens with a value of 3.49.

The amount of titratable acidity was decreased from 2.03% for stage 2 mangosteens to 0.78% for stage 6 mangosteen. A previous study showed that mangosteen's titratable acidity decreased from 0.74 of maturity stage 1 - 0.60 of maturity stage 4 [3]. The values of pH ranged from 3.49 - 4.34. This showed that an increase of pH corresponded to a decrease in titratable acidity as observed by Islam et al. [33]. The phenomenon was due to the organic acids used in respiration and conversion to sugars during the maturation process. The titratable acidity value was inversely proportional to the pH value. With lower titratable acidity and increases in the pH value at an

elevated maturity level, the mangosteen fruit will be more palatable [34].

Correlation coefficient

Pearson's correlation determined the interdependences of the variable. Table 3 shows the relationship among mangosteen properties such as color (L*, a*, b*), pH, %brix, titratable acidity, and reducing sugars. L* showed a positive correlation to b* and titratable acidity and a* negative correlation to %brix, pH and reducing sugar content. L* represents the intensity of light. L increases indicated that the lightness increases, which means the fruit is immature and immature fruit is acidic and lower in sugar content.

There is a strong positive correlation between pH, %brix and reducing sugar and a strong negative correlation to titratable acidity. This indicates when the titratable acidity increases, pH, %brix and reducing sugar content decreased. The correlation of pH, %brix, reducing sugar content, and titratable acidity has been supported by Ayaz et al. [35]. The explanation for the correlation between pH, %brix, reducing sugar, and titratable acidity were that the organic acids of the fruit will be converted into sugar during ripening, i.e., the sugar content inside the fruit increased [36].

Spectral data

Figure 1 shows the near-infrared reflectance spectra of 90 mangosteen samples. The absorbance of 90 spectral data gathered from the 90 mangosteen samples in the wavelength range from 900–1700 nm. Figure 1 shows the 90 spectral data were the combined wavelength patterns of three maturity stages of mangosteen (Stage 2, 5, and 6).

Figure 1 shows that all the wavelengths can be seen in its distinguished patterns and absorbance number, which varies depending on their maturity stages. The blue wavelengths (maturity stage 2 mangosteen samples) are occupying the top places of the wavelengths as they have the highest absorbance from 900–1700 nm, while the green wavelengths (maturity stage 6 mangosteen samples) occupied the places at the bottom of the wavelengths as it has the lowest absorbance. As for the red wavelength (maturity stage 5 mangosteen samples), they are inconsistent. Most of the red wavelengths have a similar absorbance with the green wavelength, and some have a similar absorbance with the blue wavelengths.

Spectral pre-processing

In this study, pre-processing plays a vital role in improving prediction accuracy and robustness. Spectral data collected will contain noises and unnecessary background information caused by light scattering, over-heated sensors, etc. Noise produced influence and alter the quality information in the spectral data. Hence, it is suggested to pre-process the spectral data before constructing a prediction model.

Five pre-processing techniques will be used in the spectral data. Cutting removes the unnecessary spectral data from the start and the end and only keeps the spectral data's informative part. Savitzky–Golay and gaussian smoothing can reduce or eliminate the noise produced by the background. SNV will remove the scatter effect caused by baseline and pathlength changes with centering and scaling each spectrum. MSC is achieved by regressing each spectrum to an ideal spectrum with the slope and intercept of this linear fit [37]. Figure 2a, b, c, and d, show the changes in the raw spectral data after the four pre-processing methods, start from Cutting followed by Gaussian and Savitzky-Golay smoothing, SNV and EMSC. After several pre-processing uses, the spectral data becomes neat and condense as most of the noises had been removed from the data (Figure 3).

Table 3. Pearson correlation between different attributes, physical and chemical properties

	L*	a*	b*	pH	%Brix	TA
a*	-0.200					
b*	0.709**	0.273**				
pH	-0.219*	-0.120	-0.353**			
%Brix	-0.371**	-0.109	-0.542**	0.723**		
TA	0.382**	0.164	0.562**	-0.664**	-0.792**	
Reducing sugar	-0.480**	-0.241*	-0.692**	0.668**	0.928**	-0.820**

*A double asterisk (**) indicates the correlation is significant at the level of $p \leq 0.01$. A single asterisk (*) indicates the correlation is significant at the level of $p \leq 0.05$. Abbreviations: TA represents Titratable Acidity.

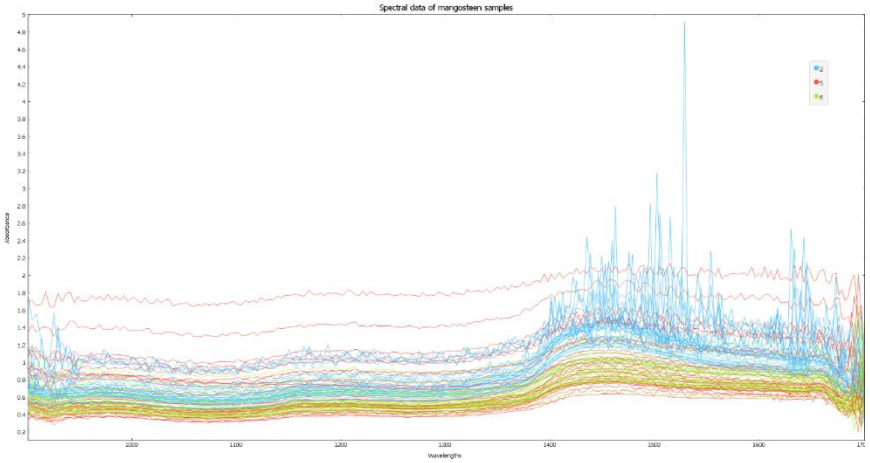
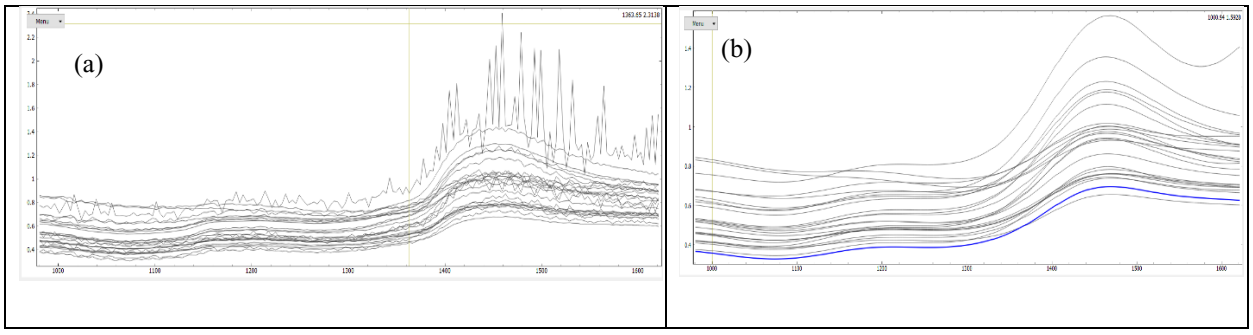


Figure 1. Spectral data collected from the 90 mangosteen samples before pre-processing



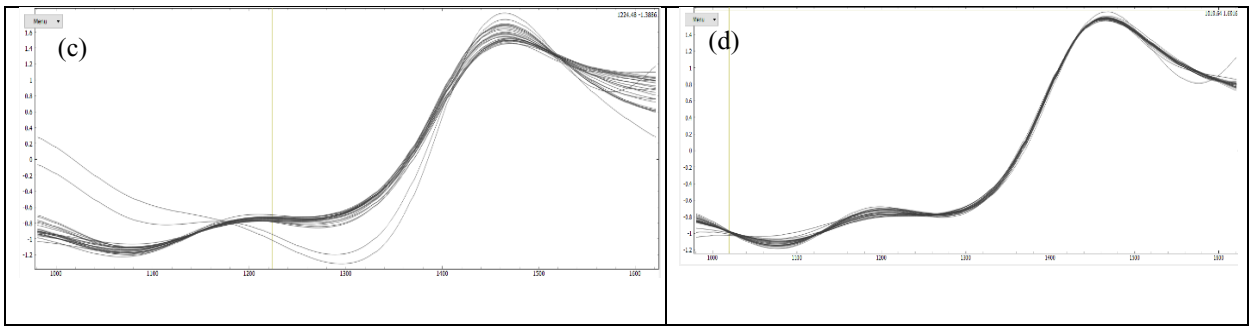


Figure 2. Spectral data after pre-processing; (a) Cut, (b) Smoothing, (c) SNV, (d) EMSC

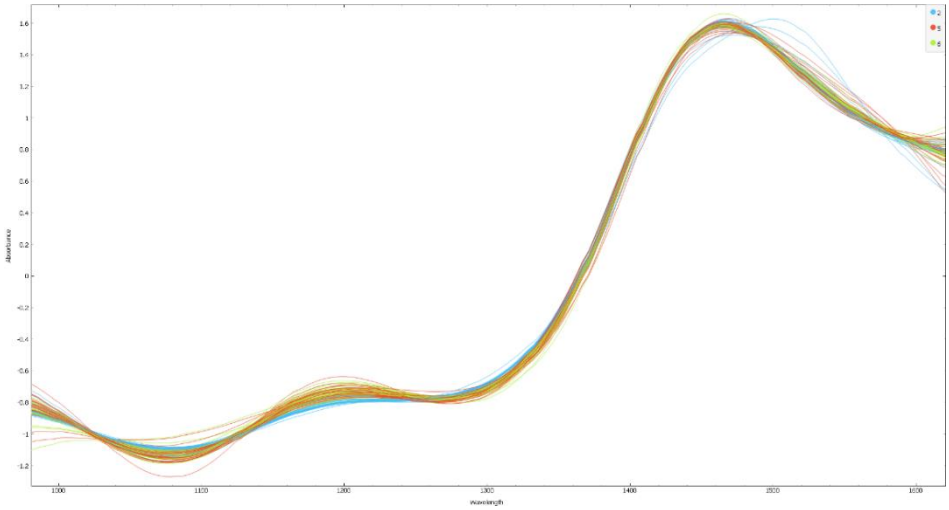


Figure 3. Spectral data after the combination of all pre-processing (Cut, Smoothing, SNV and MSC)

Prediction models for regression

Partial Least Square Regression and Principal Component Regression were used to construct predictive models [38]. The predictive models were developed to acquire information about the attributes of mangosteen buried in the spectral data. Both methods regressed with actual measured value (X-axis) and predicted value from spectra data (Y-axis). Figure 4 shows the graph of predicted and actuals values of the training set of mangosteen's chemical and physical properties with PLS predictive model and PCR predictive model. The pattern of the graph represents the accuracy of the models. The circle mark indicates stage 2, cross indicates stage 5, and triangular indicates stage 6.

From Figure 4a, b, c, d, g, h, i and j, the curve with a slope that is near 45° was compared to the remaining figures. This indicated the predicted value of b, reducing sugar, %brix, and titratable acidity was nearer the actual value [39]. The dot that represented the value for scattering far away from the slopes indicated that the model's predictive performance from PLS and PCR were weak and had a lowered accuracy. The pattern for the scatter graphs was weak, positive, and linear.

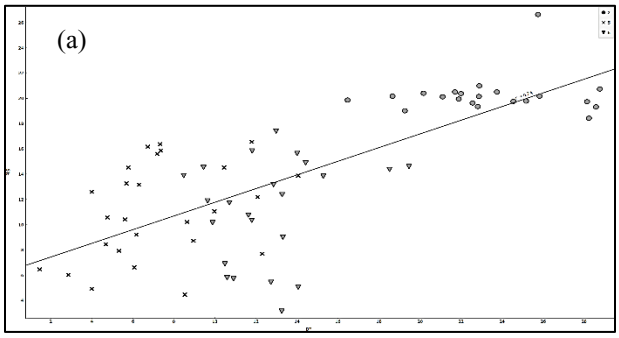
Table 4 shows the p-value = 1 and the standard deviation was high for every property of mangosteen. The predictive model for PLS and PCR was able to determine color, %brix, reducing sugar, titratable acidity, and pH due to $p > 0.05$ in the paired t-test and the high standard deviation showed the data points were away from the mean, which indicated less reliability.

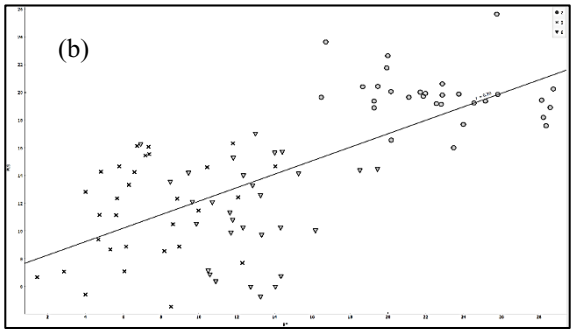
Model evaluation

The indicators for determining the performance prediction models in this experiment were R^2 and RMSE [39]. R^2 is the coefficient of determination, representing the percentages of the explained variance of the result in the dataset. Root mean square error (RMSE) is used to measure the prediction error of the model [41]. The prediction performance will be better when there is a high coefficient of determination, and low root means square error. Table 5 shows the evaluation results for the predictive models using PLS and PCR in determining the attributes of mangosteen.

Table 5 shows L*'s prediction accuracy with the PCR predictive model was very low (R^2 = 0.253). PLS predictive model was slightly better (R^2 = 0.286) than the PCR predictive model but it still was not feasible to predict L*. The prediction results for a* was even lower than L*. The results of PLS and PCR predictive model for a* were (R^2 = 0.155) and (R^2 = 0.165), respectively. The prediction results of the b* with PLS predictive model was over 50% of the coefficient of determination (R^2 > 0.5), but the RMSE was high. It is still not applicable in predicting the b* value as the prediction error was too high. The prediction results of pH for PLS regression were slightly better than PCR regression. The coefficient of determination obtained from PLS for the training set was 0.332 and RMSE of 0.286, while the coefficient of determination obtained from PCR for the testing set was 0.329 and RMSE of 0.390. Hence, the PLS model performed slightly better than PCR in predicting pH.

Moreover, the coefficient of determination for reducing sugar and TSS's training set was 0.563 and 0.325 with RMSE 0 and 1.704 in the PLS predictive model. The PCR predictive model's coefficient's determination was 0.503 in reducing sugar and 0.417 in total soluble solid with RMSE of 0 and 1.648, respectively. PCR predictive model has better predictive performance in determining TSS, and PLS predictive model has better predictive performance in determining reducing sugar. The prediction result of TA in the PLS predictive model was R^2 = 0.440 with RMSE of 0.434, whereas PCR predictive model was R^2 = 0.456 with RMSE of 0.434. PCR predictive model was better at predicting TA. Although PLS had slight advantages in predicting pH and PCR in predicting total soluble solute and TA, they were still not suggested for predicting these attributes due to the low coefficient of determination ($R^2 \leq 0.5$). The only exception is the reducing sugar test as the coefficient of determination was over 50% ($R^2 > 0.5$) and the RMSE was low. Hence, both models are feasible in determining the reducing sugar content in mangosteen; and PLS was a better model for this prediction.





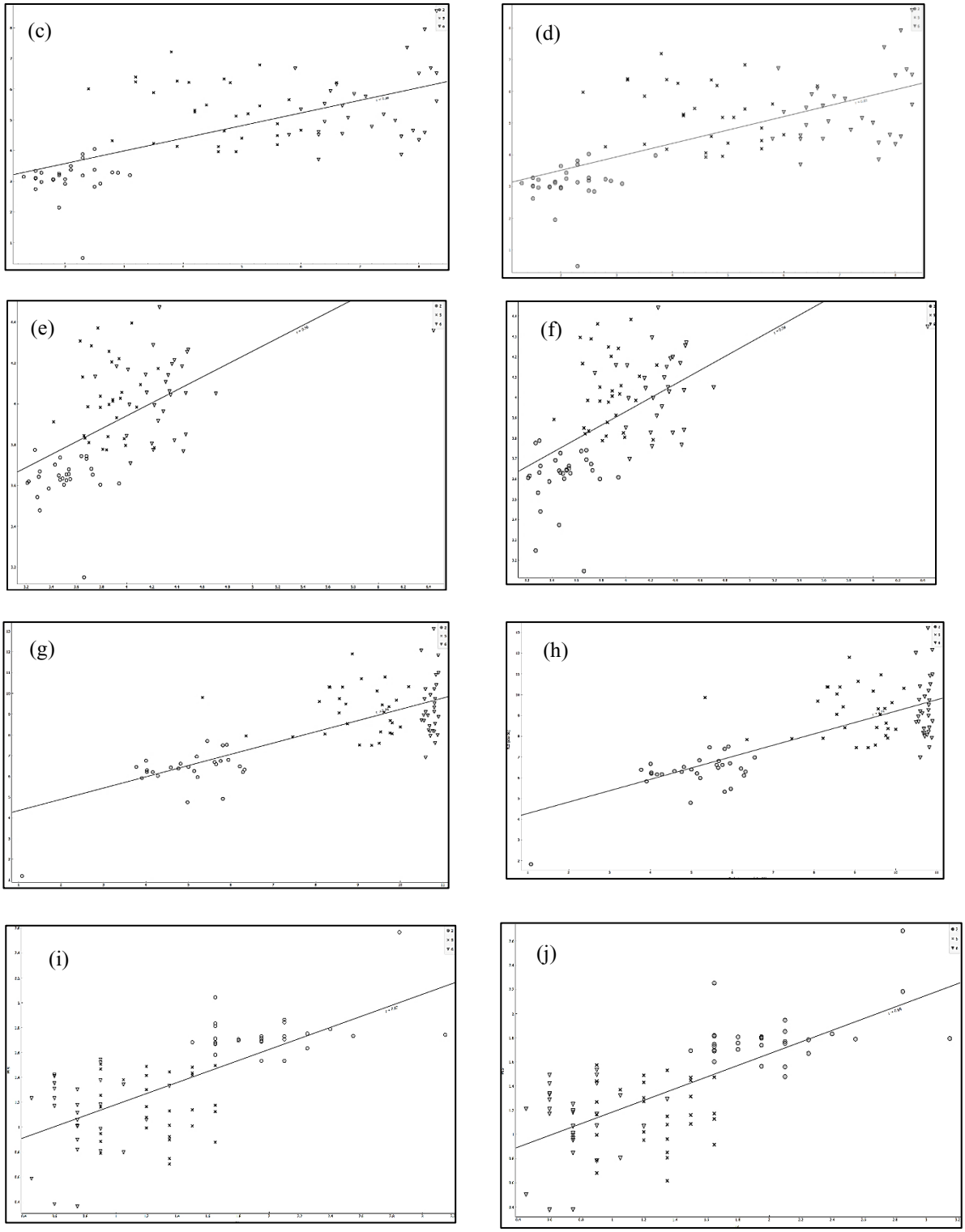


Figure 4. Actual values against predicted values of properties of mangosteen in PLS and PCR predictive model, (a) b* with PLS, (b) b* with PCR, (c) %Brix with PLS, (d) %Brix with PCR, (e) pH with PLS, (f) pH with PCR, (g) reducing sugar with PLS, (h) reducing sugar with PCR, (i) titratable acidity with PLS, and (j) titratable acidity with PCR

Table 4. Actual and predicted values of color, %brix, reducing sugar content, titratable acidity and pH

Value	L*	a*	b*	Brix (%)	Reducing Sugar Content (g/100 g)	Titratable Acidity	pH
Actual	31.49 ± 4.59	10.38 ± 2.56	14.18 ± 7.15	4.62 ± 2.22	$8.24 \times 10^{-6} \pm 2.5 \times 10^{-6}$	1.36 ± 0.60	3.89 ± 0.05
Predicted	31.49 ± 2.31	10.38 ± 1.04	14.18 ± 4.98	4.62 ± 1.44	$8.24 \times 10^{-6} \pm 1.88 \times 10^{-6}$	1.36 ± 0.35	3.89 ± 0.03
P-value	1.00	1.00	1.00	1.00	1.00	1.00	1.00

*Data collected are calculated in mean ± standard deviations. P-values are determined by analysis of Paired T-test

Table 5. Regression results for attributes of mangosteen by using PLS and PCR

Quality Attribute	Methods	R^2 (Training & Testing)	RMSE (Training & Testing)
L*	PLS regression	0.286 & 0.245	3.857 & 4.007
	PCR regression	0.253 & 0.291	3.950 & 3.738
a*	PLS regression	0.155 & 0.143	2.315 & 2.347
	PCR regression	0.165 & 0.127	2.323 & 2.379
b*	PLS regression	0.542 & 0.500	4.931 & 5.020
	PCR regression	0.486 & 0.484	5.095 & 5.046
pH	PLS regression	0.332 & 0.436	0.286 & 0.545
	PCR regression	0.329 & 0.353	0.390 & 0.267
Reducing Sugar	PLS regression	0.563 & 0.495	0.000 & 0.000
	PCR regression	0.503 & 0.727	0.000 & 0.000
Total soluble solids (TSS)	PLS regression	0.409 & 0.503	1.704 & 1.530
	PCR regression	0.417 & 0.478	1.648 & 1.172
Titratable Acidity (TA)	PLS regression	0.440 & 0.599	0.434 & 0.340
	PCR regression	0.456 & 0.669	0.434 & 0.345

*Abbreviations: PLS represents Partial Least square; PCR represents Principal Component Regression; R^2 represents correlation coefficient; RMSE represents Root Mean Square Error.

Conclusion

Nowadays, methods in determining the quality of mangosteen fruit are usually destructive. Farmer and the mangosteen industry workers often harvest the mangosteen at the wrong maturity, which produces poor quality fruit that can't be exported. Hence, NIRS was used as one of the significant non-destructive techniques to determine quality and the maturity stages of the fruit. In this study, the physical and chemical properties of mangosteen were tested. NIRS coupled with pre-processing, PLS and PCR predictive modal were able to feasibly identify the maturity stage of mangosteen by determining the reducing sugar content. From the present results, mangosteen attributes such as %brix, reducing sugar, pH, and titratable acidity were followed by a ripening process for the mangosteen. Brix, reducing sugar, and pH increased while titratable acidity decreased along with the ripening process as sugar content inside the mangosteen increased due to the sugar conversion of organic acid. The maturity stage 5 mangosteen had the darkest color, whereas maturity 2 mangosteen had the lightest color. The %brix of the mangosteen samples ranged from 2.14–7.18%. Maturity stage 2 mangosteen revealed the lowest reducing sugar content ($5.07 \times 10^{-6} \pm 0.11 \times 10^{-7}$) and pH (3.49). In addition, maturity stage 2 mangosteen showed the highest titratable acidity (2.03%) among the three different maturity mangosteens. However, maturity

stage 6 mangosteen had the lowest titratable acidity (0.78%). In conclusion, NIRS was only feasible in determining the reducing sugar content with acceptable accuracy (R^2 > 50%) in both predictive models. This achieved accuracy may not be excellent, but it can be improved in the future by using nonlinear machine learning and ensemble methods as PLS and PCR.

Acknowledgements

The authors would like to express the gratitude to the Centre of Excellence for Research, Value Innovation, and Entrepreneurship (CERVIE) – UCSI University for supporting this project, under PSIF project code: Proj-2019-ln-FETBE-063.

References

1. Ayman, E. L., Hassan, S. M. and Osman, H. E. H. (2019). Mangosteen (*Garcinia mangostana* L.). In Nonvitamin and Nonmineral Nutritional Supplements. Academic Press, Massachusetts: pp. 313-319.
2. Ketsa, S. and Paull, R. E. (2011). Postharvest biology and technology of tropical and subtropical fruits, ed. E.M. Yahia, Woodhead Publishing Series in Food Science, Technology and Nutrition, Amsterdam: pp. 1-32.
3. Sumiasih, I. H., Poerwanto, R. and Efendi, D. (2019). Study of several stages of maturity and storage temperature on color changes and shelf life of mangosteen (*Garcinia mangostana* L.). *International Journal of Applied Biology*, 3(1): 45-54.
4. Manurakchinakorn, S., Chainarong, Y. and Sawatpadungkit, C. (2016). Quality of mangosteen juice colored with mangosteen pericarp. *International Food Reseach Journal*, 23: 1033-1034.
5. Jha, S. N., Narsaiah, K., Jaiswal, P., Bhardwaj, R., Gupta, M., Kumar, R. and Sharma, R.. (2014). Non-destructive prediction of maturity of mango using near infrared spectroscopy. *Journal of Food Engineering*, 124: 152-157.
6. Hayati, R., Munawar, A. A. and Fachruddin F. (2020). Enhanced near infrared spectral data to improve prediction accuracy in determining quality parameters of intact mango. *Data in Brief*, 2020: 105571-105572 .
7. Yahia E. M. (2011). Post-harvest biology and technology of tropical and subtropical fruits: mangosteen to white sapote. Elsevier, Amsterdam.
8. Tongdee, S. C. and Suwanagul A. (1989). Post-harvest mechanical damage in mangosteens. *ASEAN Food Journal Malaysia*.
9. Prabasari, I., Utama, N. A., Hasanah, N. A. U., Riyadi, S. and Hariadi, T. K.. (2016). Non-destructive method for maturity index determination of *Garcinia mangostana* L. using image processing technology. *International Society for Horticultural Science*, pp. 1-10.
10. Osman, M. B. and Milan, A. R. (2006) Mangosteen: *Garcinia mangostana* L. Southampton Centre for Underutilised Crops. University of Southampton, Southampton, UK.
11. Chang, L. S, Tan, Y. L., and Pui, L. P. (2020). Production of spray-dried enzyme-liquefied papaya (*Carica papaya* L.) powder. *Brazilian Journal of Food Technology*, 23: e2019181.
12. Pui, L. P., Karim, R., Yusof, Y. A., Wong, C. W. and Ghazali, H. M. (2018). Physicochemical and sensory properties of selected 'cempedak' (*Artocarpus integer* L.) fruit varieties. *International Food Research Journal*, 25(2): 861-869.
13. Sadasivam, S. (1996). Biochemical Methods. New age international, India.
14. AOAC. (2000). Official Methods of Analysis of AOAC International, 17th edn. Association of Official Analytical Chemists, Arlington.
15. Abdullah Al-Sanabani, D. G., Solihin,M. I., Pui, L. P., Astuti, W., Ang, C. K. and Hong, L. W. (2019). Development of non-destructive mango assessment using handheld spectroscopy and machine learning regression. *Journal of Physics: Conference Series,* 1367(1): 012030.
16. Pissard, A., Fernández Pierna, J. A., Baeten, V., Sinnaeve, G., Lognay, G., Mouteau, A., Dupont, P., Rondia, A. and Lateur, M. (2013). Non-destructive measurement of vitamin C, total polyphenol and sugar content in apples using near-infrared spectroscopy. *Journal of the Science of Food and Agriculture*, 93(2): 238- 244.

17. Yan, H., Xu, Y. C., Siesler, H. W., Han, B. X. and Zhang, G. Z. (2019). Hand-held near-infrared spectroscopy for authentication of fengdous and quantitative analysis of mulberry fruits. *Frontiers in Plant Science*, 10: 1548- 1549.
18. Wang, H., Peng, J., Xie, C., Bao, Y. and He, Y. (2015). Fruit quality evaluation using spectroscopy technology: a review. *Sensors*, 15: 11889-11927.
19. Solihin, M. I., Zekui, Z., Ang, C. K., Heltha, F. and Rizon, M. (2021). Machine learning calibration for near infrared spectroscopy data: A visual programming approach. Springer, Singapore: pp. 577-590.
20. Irfan, U. Bin, Pui, L. P. and Solihin, M. I. (2020). Feasibility study of detecting palm oil adulteration with recycled cooking oil using a handheld NIR spectroscopy. *AIP Conference Proceedings*, 2306(1): 020019.
21. Ting, D. F., Pui, L. P. and Solihin, M. I. (2020). Feasibility of fraud detection in milk powder using a handheld near-infrared spectroscopy. *AIP Conference Proceedings*, 2306(1): 020017.
22. Liew, K. T., Pui, L. P. and Solihin, M. I.. (2020). Feasibility of fraud detection in rice using a handhelf near-infrared spectroscopy. *AIP Conference Proceedings*, 2306(1): 020018.
23. Hanrahan, G.. (2009). Modelling of pollutants in complex environmental systems. ILM Publications, USA.
24. Salleh, N. A. M. and Hassan, M. S. (2019). principal component regression (PCR) and linear support vector machine regression (SVMR). *Journal of Physics: Conference Series*, 1366: 1- 12114.
25. Yahaya, O. K. M., MatJafri, M. Z., Aziz, A. A. and Omar, A. F. (2014). Non-destructive quality evaluation of fruit by color based on RGB LEDs system. *In 2014 2nd International Conference on Electronic Design (ICED)*: pp. 230-233.
26. Palapol, Y., Ketsa, S., Stevenson, D., Cooney, J. M., Allan, A. C. and Ferguson, I. B. (2009). Color development and quality of mangosteen (*Garcinia mangostana* L.) fruit during ripening and after harvest. *Postharvest Biology and Technology*, 51(3): 349-353.
27. Jarimopas, B., Pushpariksha, P. and Singh, S. P. (2009). Postharvest damage of mangosteen and quality grading using mechanical and optical properties as indicators. *International Journal of Food Properties*, 12(2): 414-426.
28. Castro, M. F. P. P. M., Anjos, V. D., Rezende, A. C. B., Benato, E. A. and Valentini, S. R. T. (2012). Post-harvest technologies for mangosteen (*Garcinia mangostana* L.) conservation. *Journal of Food Science and Technology*, 32: 668-672.
29. Yamaki, S. (2010). Metabolism and accumulation of sugar translocated to fruit and their regulation. *Journal of the Japanese Society for Horticultural Science*., 79: 1-15.
30. Tadesse, T., Workneh, T. S. and Woldetsadik, K. (2012). Effect of varieties on changes in sugar content and marketability of tomato stored under ambient conditions. *African Journal of Agricultural Research*, **7**(14): 2024-2030.
31. Trick, J. K., Stuart, M. and Reeder, S. (2008). Contaminated groundwater sampling and quality control of water analyses. *Environmental Geochemistry*, 29-57.
32. Susan, F. (2016). Complete Course in Canning and Related Processes. Woodhead, USA.
33. Islam, M., Khan, M. Z. H., Sarkar, M. A. R., Absar, N. and Sarkar, S. K. (2013). Changes in acidity, TSS, and sugar content at different storage periods of the post-harvest mango (*Mangifera indica* L.) influenced by Bavistin DF. *International Journal of Food Science*, 2013: 1-8.
34. Rooban, R., Shanmugam, M., Venkatesan, T. and Tamilmani, C. (2016). Physiochemical changes during different stages of fruit ripening of climacteric fruit of mango (*Mangifera indica* L.) and non-climacteric of fruit cashew apple (*Anacardium occidentale* L.). *Journal of Applied and Advanced Research*, 1(2): 53-58.
35. Ayaz, F. A., Kadioglu, A. S. İ. M., Bertoft, E., Acar, C. and Turna, I. (2001). Effect of fruit maturation on sugar and organic acid composition in two blueberries (*Vaccinium arctostaphylos* and *V. myrtillus*) native to Turkey. *New Zealand Journal of Crop and Horticultural Science*, 29: 137-141.

36. Batista-Silva, W., Nascimento, V. L., Medeiros, D. B., Nunes-Nesi, A., Ribeiro, D. M., Zsögön, A. and Araújo, W. L.(2018). Modifications in organic acid profiles during fruit development and ripening: correlation or causation?. *Frontiers in Plant Science*, 9: 1689-1690.
37. Huang, J., Romero-Torres, S. and Moshgbar, M.. (2010). Practical Considerations in Data Pre-treatment for NIR and Raman Spectroscopy. *American Pharmaceutical Review*, 2010: 2-10.
38. Wentzell, P. D. and Montoto, L. V. (2003). Comparison of principal components regression and partial least squares regression through generic simulations of complex mixtures. *Chemometrics and Intelligent Laboratory Systems*, 65(2): 257-279.
39. Jaiswal, P., Jha, S. N., and Bharadwaj, R. (2012). Non-destructive prediction of quality of intact banana using spectroscopy. *Scientia Horticulturae*, 135: 14-22.
40. Richter, K., Hank, T. B., Atzberger, C. and Mauser, W. (2011). Goodness-of-fit measures: what do they tell about vegetation variable retrieval performance from Earth observation data. *Remote sensing for agriculture, ecosystems, and hydrology XIII. International Society for Optics and Photonics*, 8174: 81740- 81741.
41. Ait-Amir, B., Pougnet, P. and El Hami, A. (2020). Meta-model development in embedded mechatronic systems 2. *International Society for Technology in Education*: pp. 157-187.

Malaysian Journal of Analytical Sciences (MJAS)
Published by Malaysian Analytical Sciences Society

EFFECT OF CARBON FIBER LOADING IN GAPHITE-POLYPROPYLENE COMPOSITE PROPERTIES AS BIPOLAR PLATE FOR POLYMER ELECTROLYTE MEMBRANE FUEL CELL

(Kesan Penyebaran Serat Karbon Dalam Gaphit- Polipropilena Komposit Sebagai Plat Dwikutub Untuk Sel Fuel Membran Elektrolit Polimer)

Mohd Zulkefli Selamat*, Noor Ashikin Jamil, Rafidah Hasan, Sivakumar Dharmalingam

Centre of Advanced Research on Energy (CARe),
Faculty of Mechanical Engineering,
Universiti Teknikal Malaysia Melaka, Hang Tuah Jaya, 76100 Durian Tunggal, Melaka, Malaysia

**Corresponding author: zulkeflis@utem.edu.my*

Received: 8 August 2021; Accepted: 30 September 2021; Published: 25 October 2021

Abstract

The performance of Polymer Electrolyte Membrane Fuel Cells (PEMFC) is dependent on the properties of bipolar plates (BP). In this research, the BP had been developed using hybrid fillers; graphite (G) as the main filler and carbon fiber (CF) as the second filler while polypropylene (PP) as a binder in G/CF/PP composite. All materials were in powdered form and the composition of this composite was fixed at 80% (fillers) and 20% (PP). The contents of CF was varied from 5% up to 20% of the total weight of fillers (80%). Ball mill was used to mix the fillers and binder together before being pressed by compression molding (hot press) in a rectangular shape (140 mm x 60 mm) mould. The electrical and mechanical properties of the developed composite were measured to investigate its suitability of BP to be used as PEMFC. The result showed that the electrical and mechanical properties decreased as the loading of CF was increased. The composite with 5% of CF loading showed the highest value of electrical conductivity (262.75 S/cm) and flexural strength (40.2 Mpa). Images of the fractured surface for G/CF/PP composites for various CF contents was determined by Scanning Electron Microscope (SEM). This finding shows that the properties G/CF/PP composite is suitable for BP of PEMFC in the future.

Keywords: graphite, carbon fiber, polypropylene, electrical conductive polymer composite, bipolar plate

Abstrak

Prestasi Sel Bahan Bakar Membran Polimer Elektrolit (PEMFC) bergantung pada sifat plat dwikutub (BP). Dalam penyelidikan ini, BP telah dikembangkan menggunakan pengisi hibrid; grafit (G) sebagai pengisi utama dan serat karbon (CF) sebagai pengisi kedua sementara polipropilena (PP) sebagai pengikat dalam komposit G/CF/PP. Semua bahan dalam bentuk serbuk dan komposisi komposit ini ditetapkan pada 80% (pengisi) dan 20% (PP). Kandungan CF divariasi dari 5% hingga 20% dari jumlah berat bahan pengisi (80%). Kempa bebola digunakan untuk mencampurkan pengisi dan pengikat bersama sebelum ditekan dengan acuan mampatan (tekan panas) dalam bentuk segi empat tepat (140 mm x 60 mm). Sifat elektrikal dan mekanikal komposit yang dihasilkan diukur untuk mengkaji kesesuaiannya untuk digunakan sebagai BP untuk PEMFC. Hasilnya menunjukkan bahawa sifat elektrik dan mekanikal telah menurun apabila kandungan CF meningkat. Komposit dengan

kandungan CF 5% menunjukkan nilai tertinggi bagi kekonduksian elektrik (262.75 S/cm) dan kekuatan lenturan (40.2 Mpa). Imej permukaan patah untuk komposit G/CF/PP untuk pelbagai kandungan CF ditentukan oleh Mikroskop Elektron Pengimbas (SEM). Dapatan ini menunjukkan bahawa sifat komposit G/CF/PP sesuai untuk BP PEMFC pada masa akan datang.

Kata kunci: grafit, serat karbon, polipropilena, komposit polimer konduktif elektrik, plat bipolar

Introduction

Fuel cell which only uses hydrogen and oxygen from the air offers environmentally beneficial energy sources to generate electricity through an electrochemical reaction that converts chemical energy into electrical energy with high efficiency [1]. Polymer Electrolyte Membrane Fuel Cell (PEMFC) or also called proton exchange membrane fuel cells are widely applied in automobiles and BP is one of the most important components in the PEMFC stack [2-5]. The functions of BP in the PEM Fuel Cell system are [6]:

a. To separate the individual components of fuel cells from each other.
b. To electrically connect them in series
c. To distribute the process gases (hydrogen and oxygen) to the positive and negative electrodes, respectively.
d. As a cooling system of the fuel cells.

There is a strong relationship between the material employed in the manufacturing of the bipolar plate and its final properties. The most commonly used material for a bipolar plate is Gaphite which has good electrical conductivity and excellent corrosion resistance with a low density [7]. However, it is very brittle and lacks mechanical strength and has poor ductility, and causes the fuel cell stack to be heavy and voluminous [4, 8-9]. The other materials such as metal-based require a proper machining process, special coating, have extra weight, and have a high tendency to corrode, even though they have good electrical conductivity [10, 11]. Hence, conductive polymer composite (CPC) with carbon-based BP is an attractive option to be used for PEMFC [8, 9]. On the other hand, Gaphite/polymer composites can be considered as an ideal material for producing BP [11, 12, 14]. Thus, in this research graphite and carbon fiber were used as fillers for BP in order to improve the electrical and mechanical properties and ease to manufacture, besides reducing the weight and fabrication cost [2, 9, 12, 15].

Moreover, CF has a high tensile and compressive strength, and have a high resistance to corrosion, creep, and fatigue [10,16-17]. The main material for filler in this research was G powder which can be obtained either naturally or synthetically [18]. While CF was being used as a second filler. The other material used in producing this composite was the polymeric binder or matrix. The main function of the binder is to provide greater strength and geometric stability. In this research, the PP was selected as the binder. G/CF/PP composite that being produced must achieve the required target specified by the United States of America Department of Energy (DOE) for the BP as shown in Table 1 [5,11]. The objective of this research is to study the effect of CF loading on G/CF/PP composite properties such as electrical conductivity and mechanical properties.

Table 1. Requirement properties for the bipolar plate (DOE target) [6, 11]

Property	Value
Electrical conductivity	> 100 [Scm^{-1}]
Thermal conductivity	> 10 [$W(mK)^{-1}$]
Flexural strength	> 25 [MPa]
Shore Hardness	> 50
Bulk Density	< 5 [g/cm3]

Materials and Methods

Materials of composites

The polymer matrix used in this research was PP Grade Titan 600 which was purchased from Polypropylene Malaysia Sdn. Bhd. The main conductive filler was G powder and the second filler was chopped CF purchased from Zoltek Industries. Comparison of the properties between PP, CF, and G are shown in Table 2. Figure 1 shows the materials involved in this research.

Preparation of composites

A ball mill machine was used to mix the fillers and binder. Firstly, the PP granular was pulverized into a powdered form. The amount of fillers in one composition was fixed at about 80% and another 20% was the binder. CF loading was varied from 0% to 20% respectively from the filler content as shown in Table 3. The mixed composite was poured into a steel mould and pressed in the hot compression molding machine at 185 °C with 70 tonnes to produce a rectangular specimen (140 mm x 60 mm). After being pressed, the mould was cooled by air until it reached room temperature. A 200 Tonne high precision hydraulic compression molding machine was used to prepare the specimen.

Testing

The in-plane conductivity, flexural strength, shore hardness, and bulk density were determined to study the effect of CF loading on the properties of G/CF/PP composite. The in-plane conductivity was measured using Jandel Multi Height Four Point Probes as shown in Figure 1. Shore hardness was measured by using Shore Durometer (Type D) and bulk density was measured by using Densimeter according to ASTM D792. While the flexural strength was determined using Universal Testing Machine according to ASTM D790.

Microstructure

SEM micrograph of the fractured surface for G/CF/PP composites for various CF content with the same total binder was determined by using Joel Scanning Electron Microscope (SEM). The sample had been cut with the height not more than 1 cm and the surfaces of all the samples were coated with a thin film of platinum. The Polaron SC 7640 Sputter machine was used for about 5 minutes to improve the conductivity and avoid electron charging effects during the examination.

Table 2. Properties of G, CF and PP

Material	G	CF	PP
Gade	3243	Chop Flake	Titan
Density [g/cm^3]	1.74	1.72	0.91
Thermal stability [°C]	350-400	2000	175-220
Size	≤60[μm]	7.2 [μm]	250 [μm]
Resistivity	1295 [10^8Ωm]	0.00155 [Ωcm]	1[10^{14}Ωm]

Table 3. Composition of G/CF/PP composite by weight percentage

Fillers [%]		Binder [%]
G	CF	PP
80	0	20
75	5	20
70	10	20
65	15	20
60	20	20

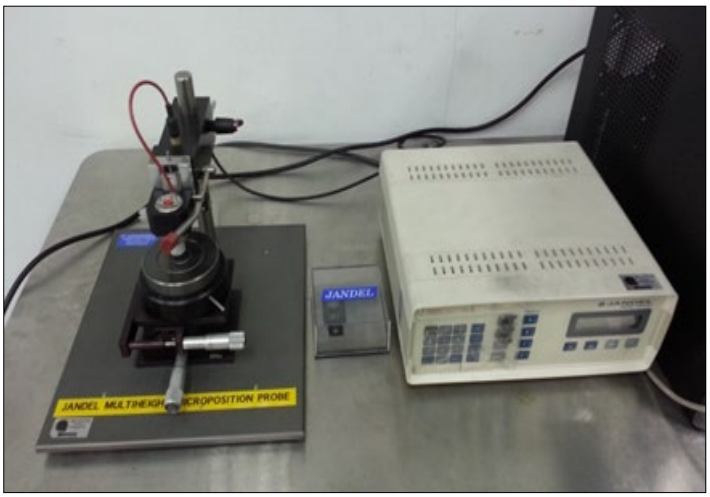


Figure 1. Jandel Multi Height Four Point Probes

Results and Discussion

Physical observation of composites

Based on the images shown in Table 4, there are lumps of materials that can be seen on the surface of 15 % CF and 20 % CF specimens. Besides that, the specimens of 15 % CF and 20 % CF have uneven and bumpy surfaces. This is due to the mixture of G/CF/PP composite that tends to agglomerate when the quantity of CF content is higher. The surface conditions of these composites affect the final properties and the test result of the G/CF/PP composites.

Effects of in-plane conductivity on G/CF/PP composite

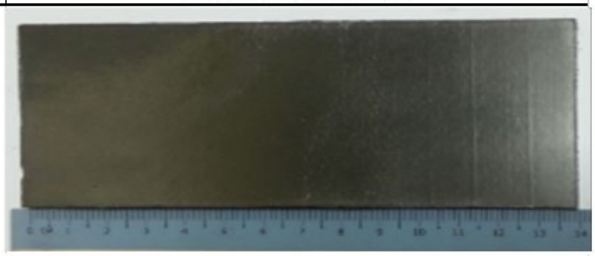
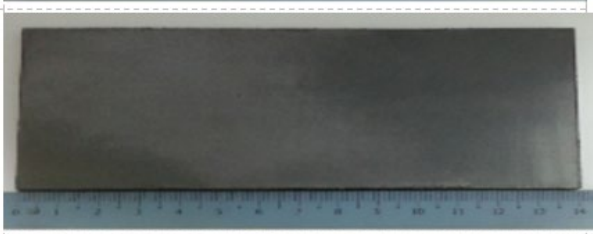
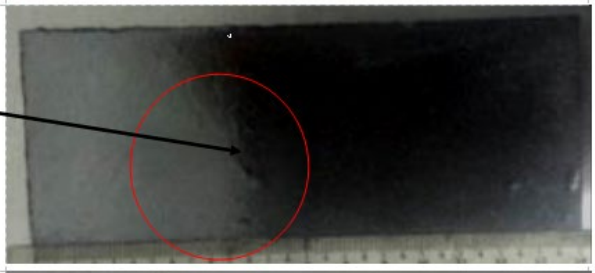
In-plane electrical conductivity of G/CF/PP composites with various CF loadings was shown in Figure 2. The electrical conductivity of G/CF/PP composite has increased with the increase of CF loading from 116.29 S/cm (0% CF) to 262.75 S/cm (5% CF). However, when the CF content is further increased, the electrical conductivity has decreased to 105.10 S/cm (10% CF). This is due to the presence of voids in the G/CF/PP composite and the volume has increased with the increment of CF content. Voids have become obstacles or barriers on the network and interaction of conductive fillers. This has affected the in-plane electrical conductivity of G/CF/PP composites [8, 19-20]. The percentage of increment between G/PP composite and G/CF/PP composites with 5% CF content is about 125.94 %. As compared to the DOE target, the value of electrical conductivity of 5% CF content is higher than the target value, which is 100 S/cm. The results are supported by Lee et al. and Mathur et al., in which the electrical conductivity increases with the increasing of carbon fiber loading until the maximum loading and then decreases with further increase in carbon fiber content [7, 8, 18]

The effect of flexural strength of G/CF/PP composite

The flexure strength result is shown in Figure 3. The highest flexural strength of G/CF/PP composite of 40.2 MPa is observed at the CF loading of 5% and it is more than 100% enhancement as compared to the gear/PP composite with no CF content. The value of flexural strength is decreased with a further increment of CF content of 10% to 20%. CF acts as a reinforcement material as CF has a high aspect ratio and its fibrous characteristic can improve the electrical conductivity and flexural strength [8, 9, 22]. Lee et al. also reported the same behaviour of G/CF composites. The flexural strength for 10% and 15% of CF content decreases and later increases with the increasing of CF loading. During the test run for 20% of CF content, the samples

did not break in the middle as they should be. It is due to the uneven and rough surface of the specimen and agglomeration between the three materials. This finding shows that there is imperfect bonding between the fibers and binders [8]. This explains the unstable trend in the flexural strength of the composites with high filler loadings. All the composition of G/CF/PP composites achieve higher than the DOE target, which is 25 MPa.

Table 4. Photographs of G/CF/PP composite for each composition

CF [wt %]	Photo of G/CF/PP composites
0	
5	
10	
15 Lumps and uneven surface	
20 Lumps	

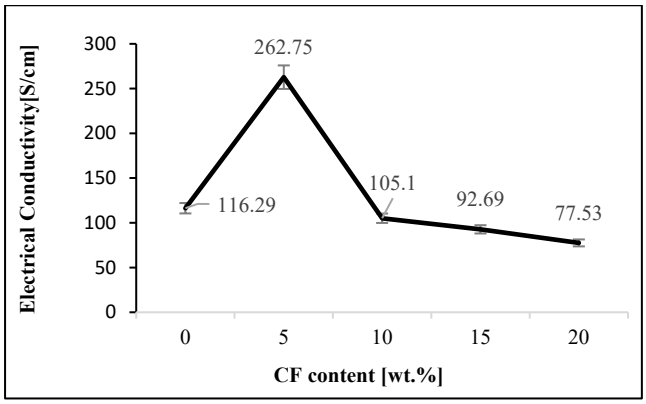


Figure 2. Electrical conductivity and flexural strength against CF content in G/CF/PP composite

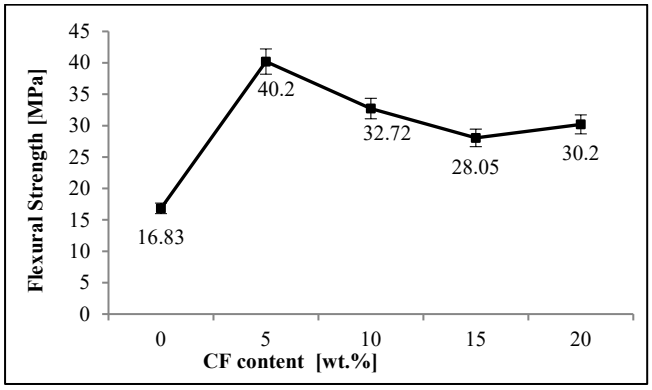


Figure 3. Flexural strength against CF content in G/CF/PP composite

The effect of hardness of G/CF/PP composite

The hardness of the composite plate shows a significant improvement from 58.56 (0% CF) to 64.33 (5% CF) although it decreases with the continuing of the CF content as shown in Figure 4. The increment in hardness of the specimens with the addition of CF content can be attributed to the well-known ribbon or glassy carbon structure of PAN based carbon fibers [9]. The increment of hardness value is due to the application of pressure during compression moulding, which increases the interconnectivity and interactions between the reinforcing constituent [10]. Furthermore, the surface's condition of the composites has highly influenced the result of shore hardness. With more CF content the composite tends to agglomerate, it affects the result of the hardness test. The hardness value is reduced with more CF content. As compared to DOE target, all value of the shore hardness of G/CF/PP are higher than target value, which is 50. According to the result, the composition for a bipolar plate of G/CF/PP composites with 5% CF content is highly recommended.

The effect of bulk density of G/CF/PP composite

Figure 5 shows that the value of bulk density for G/CF/PP composites. It decreases with the increasing of CF contents. Initially, at 0% of CF, the value of bulk density is 1.718 g/cm^3 and it drops with the loading of 5% of CF (1.700 g/cm^3) and until 1.634 g/cm^3 for 20% of CF. The minimum value of bulk density is 1.630

g/cm^3 for 15% of CF loading. G has the highest value of density, so when the value of G decreases, the value of bulk density of the specimens also decreases. Besides that, the bulk density for all compositions meets the DOE target, which is lower than 1.9 g/cm^3. The density of the specimens decreases with the additional CF contents due to their lower density as compared to G and PP.

Microstructure

Table 5 shows the fractured surface of G/CF/PP composites captured by SEM for various CF content. The scanning electron micrograph shows that the CF is evenly distributed in G/PP composites. Based on the images in Table 5, the CF distribution in each percentage has been distributed well and no agglomeration of CF can be observed. More pulled out fibers are observed than broken fibers as the CF content is increased. Previous research by Lee et al. stated that this indicates that there is incomplete bonding between the fibers and binder, thus making the fibers are easy to pull out. Thus, it explains the decreasing value of the flexural strength with higher CF contents. The voids that occurred during the fabrication process affect the electrical conductivity and mechanical properties result of the composites [23-24]. Moreover, when the CF content increases, the voids also increase. When the voids increase, the result for electrical conductivity and mechanical properties such as flexural strength and hardness decrease. It is proven by the result discussed previously.

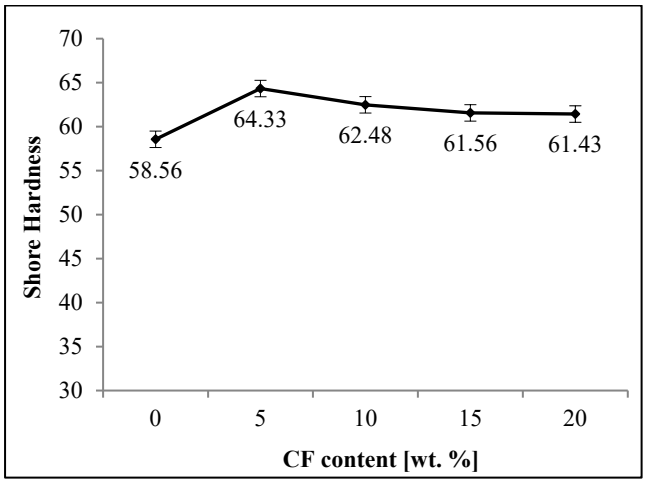


Figure 4. Shore hardness versus CF content in G/CF/PP composite

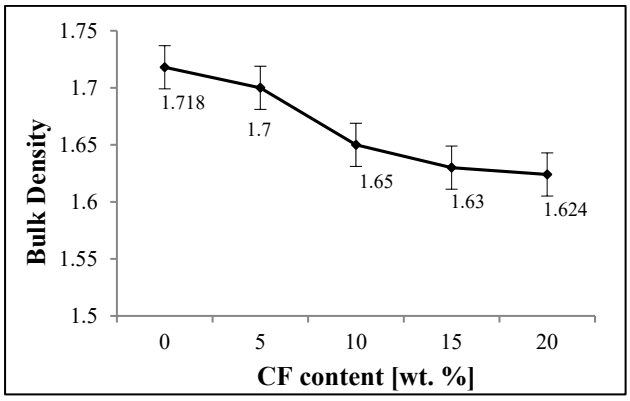
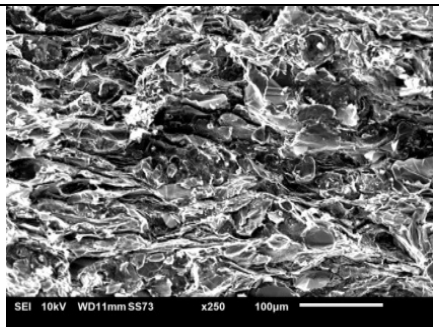
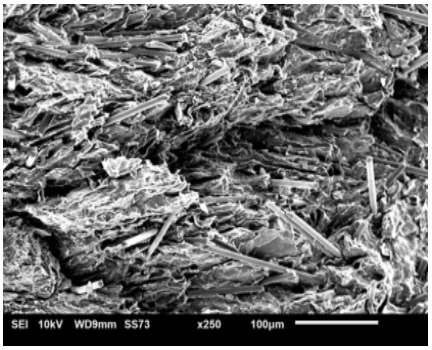
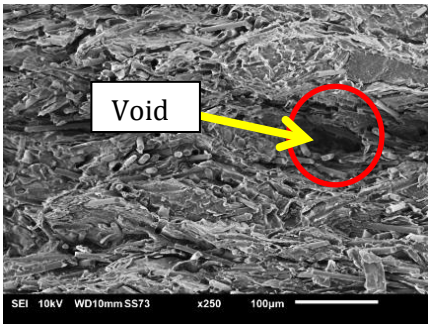
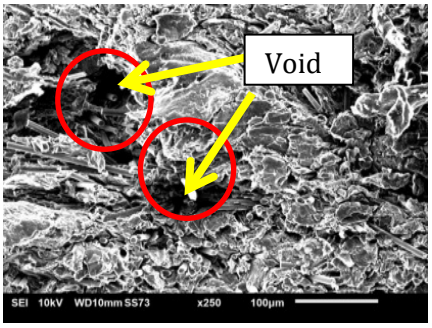
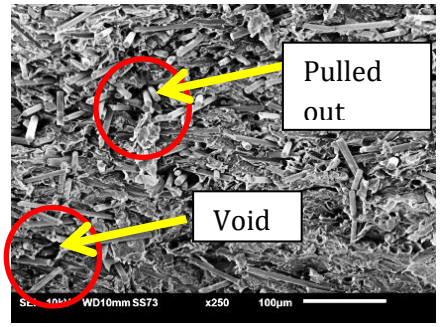


Figure 5. Bulk density versus CF content in G/CF/PP composite

Table 5. Scanning Electron Micrographs of fractured surfaces of G/CF/PP composites for various CF content

CF [wt%]	SEM micrograph of G/CF/PP composites
0	
5	
10	
15	

20



Conclusion

This research has shown that CF as a second filler with polypropylene as a binder had improved the strength and mechanical properties of BP. The addition of CF to the G/PP composite affected the electrical, hardness, strength, and density of G/CF/PP composites. By adding 5 % of CF to the G/PP composite, the in-plane conductivity, flexural strength, and hardness increased and achieved the DOE target for BP. However, by increasing the CF content in the G/PP composite, the in-plane conductivity, flexural strength and hardness were decreased. On the other hand, the density of G/CF/PP composite was decreased with the CF content. The scanning electron micrograph also showed that the material especially CF was distributed evenly in the G/CF/PP composites. It was found that the composite with 5 % of CF content was highly suitable as a bipolar plate for PEMFC. The addition of CF in the G/PP composite can offer a high opportunity in the production of high conductive composites, especially for PEMFC bipolar plates.

Acknowledgement

The authors would like to thank the Malaysia Ministry of Higher Education, Malaysia, and Ministry of Science, Technology, and Innovation for sponsoring this work under Grant PJP/(2013)/FKM(6A)/S01181 and Universiti Teknikal Malaysia Melaka (UTeM) for the financial sponsor of this research.

References

1. Sadelil, Y., Soedarsono, J.W., Prihandoko, B. and Harjanto, S. (2012). The effects of gompression pressure applied on the manufacture of carbon composite bipolar plate for PEMFC by utilizing gaphite waste products. *Advanced Materials Research*, 42: 6-66.
2. Besmann, T. M., Henry, J. J. and Klett, J.W. (2002). Carbon composite bipolar plate for PEM fuel cells. National Laboratory R&D Review DOE Fuel Cells for Transportation Program Denver, Colorado.
3. Brief, T. (2008). Carbon-filled polymer blend based bipolar plates for PEM fuel cell stack. Chapter in Polymer membranes for fuel cells. Springer: pp 281-305.
4. Hwang, I. U., Yu, H. N., Kim, S. S., Lee, D. G., Suh, J. Do, Lee, S. H., Ahn, B. K., Kim, S. H. and Lim, T.W. (2008). Bipolar plate made of carbon fiber epoxy composite for polymer electrolyte membrane fuel cells. *Journal of Power Sources*, 184(1): 90-94.
5. Yean D. K., Chong K. W., Cheng Y., Po C. L., Yu S. S. and Cheng Y. L. (2020). Fuel cell stack design using carbon fiber composites. *Sensors and Materials*, 32(12): 4233-4244.
6. Stauffer, D. B., Hirschenhofer, J. H., Klett, M. G. and Engleman, R. R. (1998). Fuel cell handbook (No. DOE/FETC-99/1076). Federal Energy Technology Center (FETC), Morgantown, WV, and Pittsburgh, PA.
7. Selamat, M. Z., Ahmad, M. S., Daud, M. A. M., Jusoff, K., and Saparudin, M. F. (2013). The hybrid conductive filler in the bipolar plate for polymer electrolyte membrane fuel cells. *Australian Journal of Basic and Applied Sciences*, 7(3): 72-77.

8. Lee, J. H., Jang, Y. K., Hong, C. E., Kim, N. H., Li, P. and Lee, H. K. (2009). Effect of carbon fillers on properties of polymer composite bipolar plates of fuel cells. *Journal of Power Sources*, 193(2): 523-529.
9. Mathur, R. B., Dhakate, S. R., Gupta, D. K., Dhami, T. L. and Aggarwal, R. K. (2008). Effect of different carbon fillers on the properties of Gaphite composite bipolar plate. *Journal of Materials Processing Technology*, 203(1-3): 184-192.
10. Dicks, A. L. (2006). The role of carbon in fuel cells. *Journal of Power Sources*, 156(2): 128-141.
11. Ahmad, M. S., Selamat, M. Z., Daud, M. A. M., Yunus, I. K. M. and Azman, M. S. (2013). Effect of different filler materials in the development of bipolar plate composite for polymer electrolyte membrane fuel cell (PEMFC). *Applied Mechanics and Materials,* (315): 226-230.
12. Antunes, R. A., Lopes de Oliveira, M. C. and Ett, G. (2011). Investigation on the corrosion resistance of carbon black–Gaphite-poly(vinylidene fluoride) composite bipolar plates for polymer electrolyte membrane fuel cells. *International Journal of Hydrogen Energy*, 36(19): 12474-12485.
13. Selamat, M. Z., Ahmad, M. S., Daud, M. A. M. and Ahmad, N. (2013). Effect of carbon nanotubes on properties of gaphite/carbonblack/poly-propylene nanocomposites. *Advanced Materials Research,* 795: 29-34.
14. Zulfiqar A., Yuan G., Bo T., Xinfeng W., Ying W., Maohua L., Xiao H., Linhong L., Nan J. and Jinhong Y. (2021). Preparation, properties and mechanisms of carbon fiber/polymer composites for thermal management applications. *Polymers,* 13:169.
15. Blunk, R., Abd Elhamid, M. H., Lisi, D. and Mikhail, Y. (2006). Polymeric composite bipolar plates for vehicle applications. *Journal of Power Sources*, 156(2): 151-157.
16. Bourell, D. L., Leu, M. C., Chakravarthy, K., Guo, N. and Alayavalli, K. (2011). Gaphite-based indirect laser sintered fuel cell bipolar plates containing carbon fiber additions. *CIRP Annals - Manufacturing Technology*, 60(1): 275-278.
17. Brocks, T., Cioffi, M. O. H. and Voorwald, H. J. C. (2013). Effect of fiber surface on flexural strength in carbon fabric reinforced epoxy composites. *Applied Surface Science*, 274: 210-216.
18. Selamat, M. Z., Sahari, J., Muchtar, A. and Muhamad, N. (2011). Simultaneous optimization for multiple responses on the compression moulding parameters of composite gaphite - polypropylene using Taguchi method. *Key Engineering Materials*, 471-472: 361-366.
19. Selamat, M. Z., Sahari, J., Muhamad, N. and Muchtar, A. (2011). The effects of thickness reduction and particle sizes on the properties gaphite - polypropylene composite. *International Journal of Mechanical and Materials Engineering*, 6(2): 194-200.
20. Iswandi, Sulong, A. B. and Husaini, T. (2019). Effects of graphite/polypropylene on the electrical conductivity of manufactured bipolar plate. *Malaysian Journal of Analytical Sciences,* 23(2): 355-361.
21. Suherman, H., Sulong, A. B. and Sahari, J., 2013. Effect of the compression molding parameters on the in-plane and through-plane conductivity of carbon nanotubes/graphite/epoxy nanocomposites as bipolar plate material for a polymer electrolyte membrane fuel cell. *Ceramics International*, 39(2): 1277-1284.
22. Dweiri, R. and Sahari, J. (2007). Electrical properties of carbon-based polypropylene composites for bipolar plates in polymer electrolyte membrane fuel cell (PEMFC). *Journal of Power Sources*, 171(2): 424-432.
23. Zakaria, M. Y., Sulong, A. B., Sahari, J. and Suherman, H. (2015). Effect of the Addition of Milled Carbon Fiber as a Secondary Filler on the Electrical Conductivity of Gaphite/Epoxy Composites for Electrical Conductive Material. *Composites Part B: Engineering,* 83: 75-80.
24. Alol, A., Otunniyi, I. O. and Pienaar H.C.V.Z. (2019). Prospects of graphite - polypropylene/epoxy blend composite for high performance bipolar plate in polymer electrolyte membrane fuel cell. *IOP Conference Series: Material Science and Engineering,* 655: 012035.

Malaysian Journal of Analytical Sciences (MJAS)
Published by Malaysian Analytical Sciences Society

VOLATILE CHEMICAL PROFILING OF UNBURNT AND BURNT RON 95 PETROL FROM THREE OIL STATIONS: A PRELIMINARY STUDY

(Pemprofilan Sebatian Kimia Meruap bagi Petrol RON 95 yang Tidak Dibakar dan Dibakar daripada Tiga Stesen Minyak: Satu Kajian Awal)

Dheephikha Kumaraguru[1], Wan Nur Syuhaila Mat Desa[2], Khairul Osman[1], Noor Hazfalinda Hamzah[1], Gina Francesca Gabriel[1]*

[1]Forensic Science Programme, Faculty of Health Sciences,
Universiti Kebangsaan Malaysia, Jalan Raja Muda Abdul Aziz, 50300 Kuala Lumpur, Malaysia
[2]Forensic Science Programme, School of Health Sciences, Health Campus,
Universiti Sains Malaysia, 16150, Kubang Kerian, Malaysia

**Corresponding author: ginafgabriel@ukm.edu.my*

Received: 27 July 2021; Accepted: 30 September 2021; Published: 25 October 2021

Abstract

Commercially available petrol is often used as fire accelerants in arson cases, and the determination of petrol residues are instrumental in fire investigations. When subjected to heat, changes occur to the chemical fingerprint of petrol, resulting in differences between petrol in post-fire and pre-fire. This study aimed to identify the differences in the volatile chemical fingerprints of unburnt and burnt petrol (RON 95) from three different oil stations, X, Y and Z, in Malaysia. Unburnt petrol was prepared by diluting 1 mL of petrol with 1 mL of pentane. Burnt petrol was prepared by burning 30 mL of petrol in an aluminium can for 1 minute. All samples were analysed using the gas chromatography-mass spectrometry (GC-MS). Results revealed that a range of *n*-alkanes, *n*-alkylbenzenes, alcohol, *n*-cycloalkanes and indane were detected from unburnt petrol. In contrast, only *n*-alkylbenzenes were present in the burnt petrol samples across the three oil stations. The majority of the volatile chemical of unburnt petrol were similar across all three oil stations. Some specific volatiles were identified in unburnt petrol, including 3,7-dimethyl-1-octene and 2,2,4-trimethylpentane in X, 2-methyl-1-butene in Y and 2-hexene in Z. Principal Component Analysis (PCA) plot (with 80.1% total variation) supported the discrimination of the three unburnt petrol samples. Conversely, PCA plot (with 91.2% total variation) of burnt petrol samples were indistinguishable due to the loss of lighter volatile compounds, including the specific volatiles. This preliminary profiling study explains the characterisation of specific petrol volatiles, which potentially impart valuable information to the forensic ignitable liquid reference database.

Keywords: petrol, gas chromatography-mass spectrometry, activated carbon tablet, RON 95, principal component analysis

Abstrak

Petrol merupakan bahan api yang biasa digunakan dalam kes-kes arson. Oleh itu, pengenalpastian petrol di tempat kejadian kebakaran amat penting dalam penyiasatan kebakaran. Apabila dibakar, perubahan akan berlaku pada komposisi petrol yang menyebabkan perbezaan antara petrol yang tidak dibakar dan dibakar. Dengan itu, kajian ini bertujuan untuk mengenalpasti perbezaan antara petunjuk utama petrol yang dibakar dengan petrol yang tidak dibakar dari tiga stesen minyak yang berlainan di Malaysia. Sampel petrol yang tidak dibakar disediakan dengan melarutkan 1 mL pentana dengan 1 mL petrol. Sampel petrol

terbakar pula disediakan dengan membakar 30 mL petrol dalam tin aluminium selama 1 minit. Semua sampel dianalisis dengan kromatografi gas-spektrometri jisim (GC-MS). Hasil kajian menunjukkan bahawa sebatian *n*-alkana, *n*-alkilbenzena, alkohol, *n*-sikloalkana dan indana dikesan dalam petrol yang tidak terbakar manakala hanya *n*-alkilbenzena dikesan dalam sampel petrol yang terbakar daripada ketiga-tiga stesen minyak. Sebilangan besar sebatian meruap dalam sampel petrol tidak dibakar dari ketiga-tiga stesen minyak adalah sama. Beberapa sebatian meruap spesifik telah dikenalpasti dalam petrol tidak dibakar iaitu 3,7-dimetil-1-oktena dan 2,2,4-trimetilpentana dari X, 2-metil-1-butena dari Y dan 2- heksena dari Z. Plot analisis komponen utama (PCA) (dengan 80.1% total varians) mengukuhkan diskriminasi antara ketiga-tiga sampel petrol tidak dibakar. Sebaliknya, plot PCA (dengan 91.2% total varians) bagi sampel-sampel petrol dibakar tidak dapat dibezakan disebabkan oleh kehilangan sebatian mudah meruap termasuklah sebatian-sebatian meruap spesifik tersebut. Kajian pemprofilan di peringkat permulaan ini menjelaskan bahawa pencirian sebatian meruap yang spesifik dalam petrol berpotensi memberi maklumat tambahan kepada pangkalan data bahan mudah bakar forensik.

Kata kunci: petrol, kromatografi gas-spektrometri jisim, karbon tablet teraktif, RON 95, analisis komponen utama

Introduction

Petrol is a petroleum product that contains a combination of hydrocarbons ranging from 4 to 12 carbon atoms, namely olefinic, naphthenic, paraffinic, and aromatic hydrocarbons with boiling points ranging from 30-225 ºC [1]. The properties of petrol are influenced by the origin of the crude oil, the refining process, and the presence of additives [2], which leads to the generation of a specific formulation of petrol among the different oil stations. Most of the world's largest refineries are situated in the Asia Pacific region, with India hosting the largest refinery complex, followed by Venezuela and South Korea [3]. In Malaysia, refineries are located in Kertih, Port Dickson, Kemaman, and Melaka, to name a few [4].

The refining process includes the addition of additives to the fuel. Examples of petrol additives include ether oxygenates, such as methyl tert-butyl ether (MTBE), detergent dispersant additives, antiknock agents, and antioxidants compounds [5-7]. In Asia pacific region, MTBE is added as additives to reduce harmful exhaust emissions from motor vehicles by helping petrol burn completely, although several other regions have banned its use due to environmental issues [8]. Detergent dispersant additives function as cleaning agents that polish the engine, which improves engine performance, whereas antiknock agents increase the octane rating of petrol to prevent engine damage, which is indicated by Research Octane Number (RON) [9]. Petrol with a high RON has a lower tendency to cause engine damage when compared to petrol with a lower RON [10]. On the other hand, antioxidants inhibit the radical chain oxidation of petrol; thus, they contribute to the fuel chemical stability. Generally, these additives ensure that the vehicle engine runs smoothly during use, generates clean-burning, and maintains the chemical and thermal stability of the fuel.

Oil and gas (O&G) stations are known to have used several different additives in petrol production. For example, the national O&G station Petronas petrol Primax 97 launched a new additive package that includes the world's first Advanced Dual Friction Modifier in 2020 [11]. Others, such as Shell, provides Shell FuelSave petrol which contains Dynaflex technology to help reduce engine friction [12]. However, the exact additives used has not been disclosed as it serves as their proprietary formulation. Despite each station offering the same type of RON 95 fuel in its entirety, minute composition variations may exist, which can potentially help fire debris analysts for discrimination or classification to the respective stations, which is immensely useful in forensic fire investigations.

Petrol is undoubtedly the most common ignitable liquid used in illegal fire settings or arson cases as it is readily available, reasonably cheap and easy to conceal [13]. Arson cases using petrol was reported to increase from 2016 (4 cases) to 2018 (12 cases) in Malaysia [14]. In fire scenes, it becomes a priority for forensic investigators to collect, detect, and identify the ignitable liquid used, if any, from fire debris samples [15]. The fire debris samples are not only limited to burnt substrates. Seldom, pristine ignitable liquids can

also be present [16], likely to have been left behind by the arsonist in its transporting container. Therefore, it is vital to analyse liquid petrol to investigate if the oil stations can be distinguished based on their volatile composition, which can be immensely helpful in scene reconstruction. Petrol that has been burnt on its own (without being doused in other substances) in natural outdoor conditions also needs to be investigated to identify the volatiles present before other compounds mask them. This is especially important in hot climate countries like Malaysia, where daily temperatures can go up to 32ºC [17]. It is postulated that petrol can experience higher evaporation rates at such temperatures, accelerating the loss of volatiles. Therefore, it will be beneficial to observe the volatility of petrol compounds in outdoor tropical climates as the related discussion is limited.

The study on petrol pertaining to fire investigation in Malaysia has been a topic of interest. Few studies have presented petrol residue recovery within a specific period. Pei wen et al. [18] performed controlled burning of petrol on carpet substrate in a metal can and suggested that the maximum recoverable time of petrol in fire residue is preferably within 9 hours and not more than seven days. Samri and Chang [19] discovered that the chromatographic profiles of unburnt petrol were similar to the burnt ones if burnt for 30 seconds or less in a controlled metal container. Discrimination of different types of ignitable liquid with statistical aid was also reported. Kunashegaran utilised principle component analysis (PCA) to classify different unburnt ignitable liquids; petrol, diesel, kerosene and thinner [20]. Similarly, Jais et al. [21] differentiated petrol and diesel in fire debris (burnt cloths) using a similar approach. These works, however, showed less attention or explanation on the discrimination between different oil stations in Malaysia.

Abu Hassan [22] pioneered the analysis of unburnt petrol from three local stations using gas chromatography-flame ionisation detector (GC-FID) using supervised QUEST modelling analysis where they identified that discrimination is possible among the unburnt petrol from three oil stations. However, the limitation is reflected with the use of GC-FID due to its inability to ascertain the exact volatiles responsible for discrimination. The discrimination in Abu Hassan's work was solely based on retention times. Thus the findings only presented limited information in terms of forensic investigation. In this work, GC-MS will be employed to identify the discriminating volatiles based on their *m/z* ratio. This allows for the profiling of the volatile compounds present in RON 95 petrol from three different oil stations in Malaysia for unburnt petrol, particularly performed within Malaysian climate settings. Although forensic fire investigations in Malaysia only require classification of the ignitable liquid classes, knowledge on the volatile organic compound of unburnt and burnt petrol that are produced and distributed in Malaysia may enable brand identification, thus offer additional information during the course of an investigation.

Materials and Methods

Sample

Two litres of unleaded RON 95 petrol were purchased from three different oil stations in Malaysia, X, Y and Z, on the same day. The petrol samples from each station were used for both unburnt and burnt analysis. This was to ensure the continuity of volatile composition from each oil station. The petrol samples were stored in separate tightly sealed aluminium fuel storage containers at room temperature.

Instrumentation

The analysis was carried out with a Shimadzu Series-QP2010 PLUS Gas Chromatography (GC) system coupled with a Mass Selective Detector (MSD) using the ASTM E1618-06 standard method as a guideline. The injector was set at 250 ˚C with 1 µL of the sample being injected into the GC. A split ratio of 5:1 was applied to the instrument with a split flow of 32.7 mL/min. Helium was used as a carrier gas, flowing at a constant rate of 1 mL/min. The column used was a 128-0122 DB-1MS column (25 m × 0.2 mm inner diameter and 0.33 µm film thickness). The initial oven temperature was set to 40 ˚C and held for 5 minutes before ramped at 15 ˚C/min to 280 ˚C and held for 2 minutes. The detector was maintained at 250 ˚C. The MS Quad was set at 150 ˚C and the Ion Source (70 eV)

at 230 ˚C. The chromatographic system was controlled using Hewlett Packard Chemstation software to facilitate data acquisition, peak integration and data manipulation.

Sample preparation of unburnt petrol

One millilitre of petrol RON 95 from X was diluted with 1 mL of pentane. Ten microlitres of tetrachloroethylene were used as the internal standard. Tetrachloroethylene (C_2Cl_4) was chosen as the internal standard as it does not interfere with the analysis and elutes approximately in the middle of the chromatogram. Each sample was analysed six times into the GC-MS. The entire process was repeated with petrol RON 95 from Y and Z.

Thermal decomposition

Pilot study

Six replicates containing 30 mL of petrol were completely burned to identify the most suitable burning duration that will prevent the total loss of volatiles. The time taken for 30 mL of petrol to burn off completely ranged from 2 min 15 s to 2 min 40 s. Therefore, several burning durations were tested to identify the duration where all volatiles were not completely consumed. The burning was carried out for 1 min, 1 min 30 s and 2 mins. For both the 1 min 30 s and 2 min burning duration, no volatiles were detected, but volatiles were detected in the 1 min burning duration. Therefore, the burning process was set to 1 min to yield detectable volatiles. The maximum temperatures for all three burning durations were 530 ˚C (X), 582 ˚C (Z) and 562.5 ˚C (X) as depicted in Figure 1, Figure 2 and Figure 3, respectively.

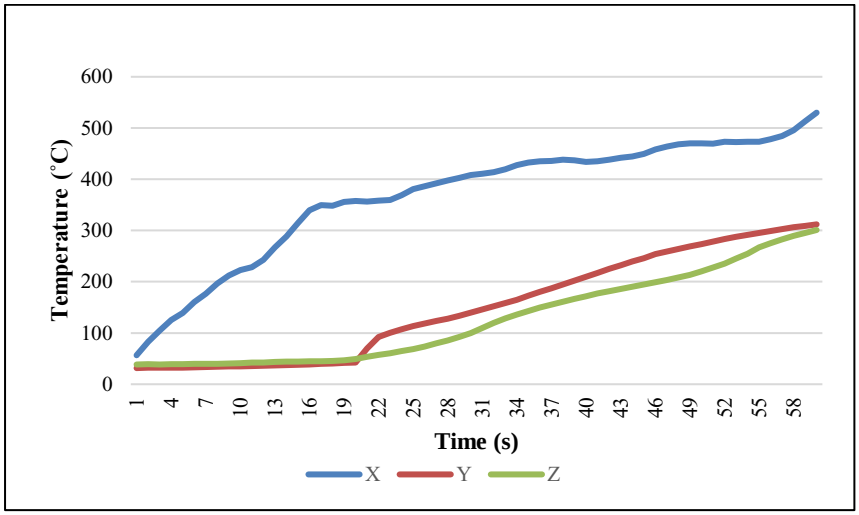


Figure 1. The time-temperature chart for the 1-minute burning of petrol from X, Y and Z

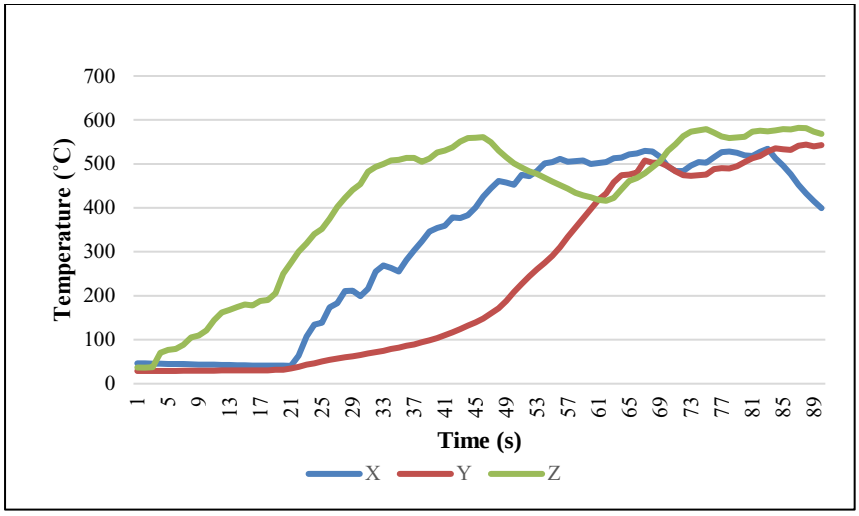


Figure 2. The time-temperature chart for the 1-min 30 sec burning of petrol from X, Y and Z

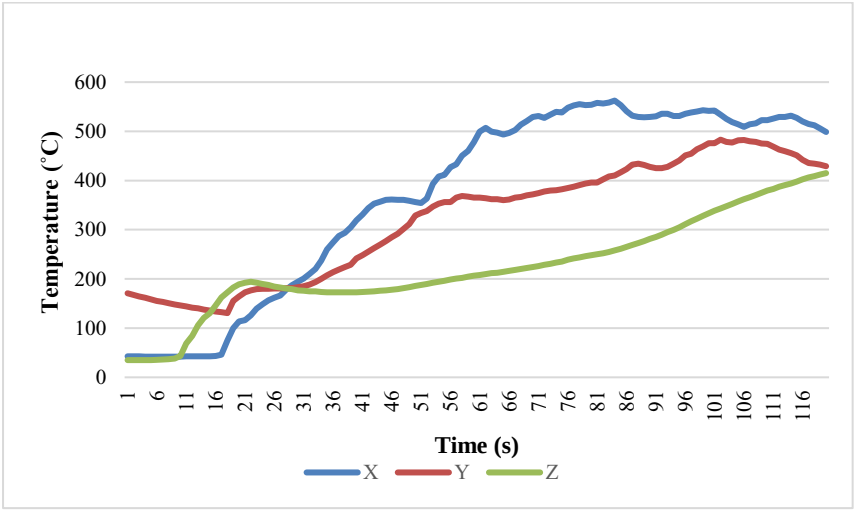


Figure 3. The time-temperature chart for the 2-minute burning of petrol from X, Y and Z

Generation of petrol volatiles

The experiment was set in an outdoor setting. A retort stand was placed on flat ground, and an aluminium can (Scene Safe, United Kingdom) without its lid was placed on a tripod stand for the burning process. Thirty millilitres of petrol were poured into the aluminium can and heated using a Bunsen burner flame underneath the aluminium can for one minute, which was measured from the moment the Bunsen burner was lighted. The temperature of burning was monitored using K-thermocouple (Fluke 80PK-22, United States of America) connected to a digital thermometer model 51 II (Fluke). After one minute, the Bunsen burner was turned off, and the can was closed with a lid to suppress the fire and left to cool before fixing it with an activated carbon tablet (ACT) (250mg, Dyna, Malaysia). Six replicates were carried out for each sample of petrol from X, Y and Z.

Sample extraction

The ACT was fixed using a paperclip and thread in the container headspace. The lid was then secured tightly to the aluminium can. The aluminium can was placed in an oven for 16 hours at 80 ºC for headspace extraction of volatile compounds. After 16 hours, the ACT was removed from the aluminium can and placed in a glass bottle (Fisher Scientific, 50 mL) to be desorbed with 2 mL of pentane (Fisher Scientific, >99%, United Kingdom). The desorbed solution was then filtered using a Polytetrafluorethylene (PTFE) syringe filter, pore size 1.0 µm (Sartorius, Germany) to remove ACT particles and placed into a 2 mL GC vial (Fisher Scientific, United Kingdom). Tetrachloroethylene (EMPLURA, >99%, Germany) was added to the vial as the internal standard (5% v/v).

Sample analysis and detection

Desorbed sample solutions were analysed using the GC-MS method as aforementioned. Identification of the volatile products was conducted on the total ion chromatogram (TIC) of each sample by comparing the mass-to-charge (*m/z*) ratio of the peaks to that of the National Institute of Standards and Technology (NIST) library (acceptable similarity percentage was set at 70% and above), standard test mixture, and database from previous researches identifying key indicators of petrol such as aliphatic hydrocarbons, aromatic hydrocarbons, and alcohols [23-25]. Table 1 shows the functional groups and their respective characteristic *m/z* values that was used as a reference in this study [16].

Data analysis

TIC of the unburnt samples was aligned, and the peak area of identified volatile compounds was acquired. The size of the data matrix for PCA analysis was 18x34, whereby each analysis was theoretically treated as one independent sample due to sampling limitation. Data were normalised to the internal standard and standardised with the power root approach according to the previous work [26-27]. PCA was performed using Minitab Ver. 17.0 (Minitab Inc., USA) with an acceptable total variance of 70% or more. A similar procedure was also performed for chromatographic data of the burnt samples.

Table 1. The functional groups commonly encountered in petrol and their characteristic *m/z* values

Functional Group	*m/z* Value
Alkane	29, 43, 57, 71, 85, 99
Cycloalkane	41, 55, 69, 83
Alkene	41, 55, 69, 83, 97
Alkylbenzene	91, 92, 105, 106, 119, 120
Naphthalene	128, 142, 156, 170
Indane	117, 118, 131, 132
Terpene	93, 136
Alcohol	31, 45, 59

Results and Discussion

Analysis of unburnt petrol samples

Six replicates of petrol samples from each of the three oil stations generated a range of expected volatiles such as *n*-alkanes, *n*-cycloalkanes, benzenes, *n*-alkylbenzenes, and indane. Table 2 displays a summary of the volatiles detected from the three oil stations.

The number of petrol volatiles detected from stations X, Y, and Z differed. Unburnt petrol X had 27 volatiles whereas petrol Y and Z had 32 volatiles and 31

volatiles respectively. Although the number of volatiles detected varied, the majority of functional groups detected were similar to each other, namely *n*-alkanes, *n*-cycloalkanes, alcohol, *n*-alkylbenzenes, and indane. While similar volatiles were detected across the three oil stations, a few of them were specific to each oil station. The compounds were highlighted in bold text in Table 2. The volatile 3,7-dimethyl-1-octene, an alkyl-α-olefin, was detected in the petrol sample from X and was not detected in both Y and Z. Another specific volatile detected from petrol samples from X was 2,2,4-trimethylpentane, an isomer of octane. For samples from Y, 2-methyl-1-butene was a specific volatile, whereas 2-hexene, a linear alkene, was detected exclusively in Z. Figures 4 illustrates the total ion chromatograms (TIC) for petrol samples from X, Y and Z, respectively.

The alkyl-α-olefin. 3,7-dimethyl-1-octene, detected in the petrol sample from X, was not detected in both Y and Z. This specific volatile was also found in a fuel called NSR (Natural State Research Inc) that was created from waste plastics to replace petrol. The NSR fuel burns more efficiently in comparison to commercial petrol as well as being environmentally friendly [29-31]. The presence of 3,7-dimethyl-1-octene in petrol obtained from X could indicate that oil station X utilised additives or refining techniques similar to those used in NSR fuel to make the petrol more energy-efficient and environmentally friendly.

Another specific volatile detected from oil station X was 2,2,4-trimethylpentane, an isomer of octane. This volatile is an additive that is usually added to petrol to increase resistance to auto-ignition or also known as an antiknock index [32]. An antiknock index is indicated by the research octane number (RON), which is measured relative to a reference mixture of 2,2,4-trimethylpentane and *n*-heptane [33]. Petrol with a higher-octane number can withstand high temperatures without auto-igniting, thus enabling more power to be discharged by a higher compression ratio [34]. Therefore, 2,2,4-trimethylpentane could have been added to increase the antiknock index of petrol. The presence of 3,7-dimethyl-1-octene and 2,2,4-trimethylpentane in X's petrol indicates the use of these compounds in X's petrol formulation.

The compound 2-methyl-1-butene was a volatile specific to fuel Y. It is a reactive isoamylene compound which is an olefin of the C_5 fraction of oil [35], with an undesirably high Reid vapour pressure (RVP) reading. Based on ASTM D323-56, the RVP test is a test used to evaluate petroleum fractions for their evaporation rate [36]. Petrol with lower RVP reduces evaporation loss, and this is especially important in hot regions like Malaysia [37], where temperatures can go up to 32ºC [17]. Therefore, the presence of 2-methyl-1-butene can cause petrol to evaporate at a faster rate. This compound also has high atmospheric reactivity and a high potential for tropospheric ozone formation, which is known to have detrimental effects on the environment [38]. Thus, it is usually treated with primary alcohols to produce oxygenates such as *tert*-amyl methyl ether (TAME), which in turn produces a more suitable fuel for the environment [39]. TAME is catalytically produced in the liquid phase by the reaction of isoamylenes; 2-methyl-1-butene, 2-methyl-2-butene, and methanol [40]. TAME works as an octane enhancing additive in petrol which reduces pollution [41]. The presence of 2-methyl-1-butene in the petrol from Y could indicate that the petrol was not treated with primary alcohols, possibly explaining its detection in this study.

A specific compound in Z, 2-hexene, is a linear alkene that has a RON of 92.7. RON is often related to antiknock properties where higher octane numbers are known to have a higher antiknock index, as discussed earlier. Octane numbers are influenced by the position of the double bond on linear alkenes [42]. For example, 1-hexene (double bond on the first carbon-carbon bond) has a lower RON compared to 2-hexene (double bond on the second carbon-carbon bond). Therefore, it is pivotal to convert 1-hexene (RON 76.4) in petrol into 2-hexene (RON 92.7). The conversion of 2-hexene can be done using CoMo/ γ-Al_2O_3, which is a catalyst used in the hydrotreatment of different oil distillates during the refining process [42]. The presence of 2-hexene in the petrol sample from Z gives an insight

into the possible refining techniques that were used as well as the catalyst that may have been used.

The chromatographic data of the volatiles are further explored statistically. PCA method simplifies the differentiation among the unburnt samples, which are demonstrated in a three-dimensional (3D) score plot in Figure 5. Petrol from each station is grouped according to their chemical compositions which accounts for 80.1% total variation (PC1 = 58.3%, PC2 = 12.2%, PC3 = 9.6%). It is important to note that the sample was obtained once from each oil station. Therefore, intra and inter-location variation may occur. More rigorous sampling is planned to determine if the specific compounds detected in this study are found only in their respective oil stations or if they are specific to the location of the oil station.

Nonetheless, the identification of specific volatiles has facilitated the discrimination of these samples. Another study corroborated the importance of characterising additives for petrol discrimination [43]. Additives identified using DART-MS coupled with PCA and varified using partial least squares discriminant analysis (PLS-DA) proved that petrol from different brands can be differentiated using proprietary additives blended in each petrol sample as markers. The ability to discriminate between oil stations will prove to be fruitful in cases where pristine petrol samples are collected from the fire scenes.

Table 2. Summary of volatiles detected in unburnt petrol samples from X, Y and Z

No	Retention Time (min)	Volatiles	X	Y	Z
1	1.15	isobutane	/	/	/
2	1.19	butane	/	/	/
3	1.29	**2-methyl-1-butene**		/	
4	1.58	2,2-dimethylbutane	/	/	/
5	1.66	cyclopentene		/	/
6	1.75	2,4-dimethyl-3-pentanol	/	/	/
7	1.90	3-methylpentane	/	/	/
8	2.06	hexane	/	/	/
9	2.12	2-methyl-2-pentene		/	/
10	2.19	**2-hexene**			/
11	2.27	3-methyl-2-pentene	/	/	/
12	2.35	methylcyclopentane	/	/	/
13	2.41	2,4-dimethylpentane	/	/	/
14	2.68	benzene	/	/	/
15	2.78	3,3-dimethylpentane	/	/	/
16	2.83	cyclohexane	/	/	/
17	3.05	2-methylhexane	/	/	/
18	3.21	3-methylhexane	/	/	/
19	3.33	cis-1,3-dimethylcyclopentane	/	/	/
20	3.40	**3,7-dimethyl-1-octene**	/		
21	3.45	**2,2,4-trimethylpentane**	/		
22	3.80	heptane	/	/	/
23	4.28	methylcyclohexane	/	/	/
24	5.48	toluene	/	/	/
25	5.79	2,3-dimethylhexane	/	/	/
26	6.0	2-methylheptane	/	/	/

Table 3 (cont'd). Summary of volatiles detected in unburnt petrol samples from X, Y and Z

No	Retention Time (min)	Volatiles	X	Y	Z
27	6.20	3-methylheptane	/	/	/
28	7.82	ethylbenzene	/	/	/
29	8.00	p-xylene	/	/	/
30	8.37	o-xylene	/	/	/
31	9.52	ethyltoluene	/	/	/
32	9.97	1,2,3-trimethylbenzene	/	/	/
33	9.98	1,2,4-trimethylbenzene	/	/	/
34	10.47	indane		/	/

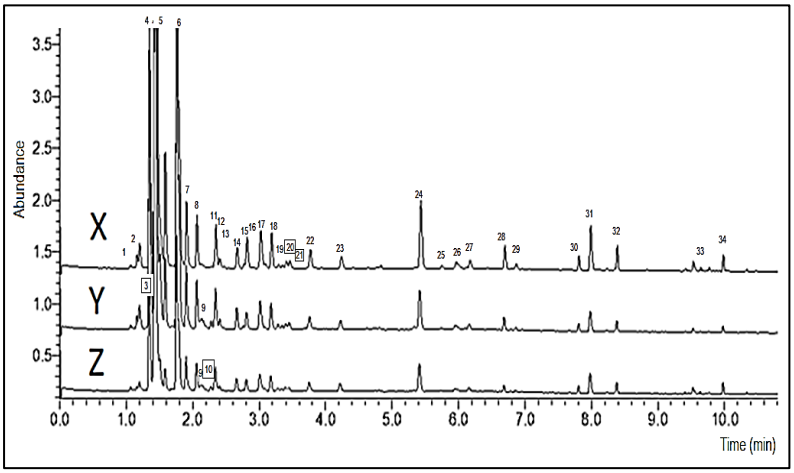


Figure 4. TIC for unburnt petrol samples from X, Y and Z. Peak number corresponds to compound listed in Table 2

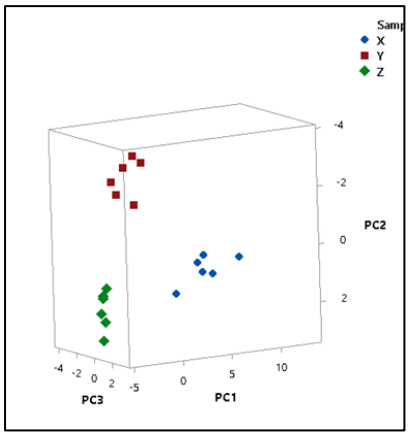


Figure 5. 3D score plot of unburnt petrol from X, Y and Z

Analysis of burnt petrol samples

A small range of *n*-alkylbenzene volatiles were detected in burnt petrol, as listed in Table 3. Figures 6 illustrates the TIC for burnt petrol from X, Y and Z, respectively.

Six *n*-alkylbenzene volatiles, namely toluene, ethylbenzene, *p*-xylene, *o*-xylene, ethyltoluene and 1,2,3-trimethylbenzene were detected across petrol samples from X, Y and Z, showing that outdoor burning of petrol in a hot climate would still leave characteristic compounds consistent with petrol residue. These *n*-alkylbenzenes which are subsets of aromatic hydrocarbons, are common volatiles found in burnt petrol [55] and can be used to distinguish petrol from other petroleum distillates [25] as *n*-alkylbenzenes are one of the dominant components to classify petrol in addition to indanes [15]. However, in this study, indane was not detected in the burnt samples. Several other studies also shared similar outcomes in terms of the absence of indanes [23-24]. The possible reason for this being that some petrol samples tend to have a very low abundance of indane, causing it to be nearly imperceptible during analysis [44]. Indane is also a heavier molecular compound in comparison to the other *n*-alkylbenzenes detected in this study. The evaporation of petrol begins with the lightest volatile and proceeds to the heavier volatiles, and since the burning duration in this study was only 1 minute, it was probably not sufficient to release indane, accounting for its absence. Thus, the use of these ranges of *n*-alkylbenzenes; toluene, ethylbenzene, *p*-xylene, *o*-xylene, ethyltoluene, and 1,2,3-trimethylbenzene, to identify petrol at fire scenes is more robust, and the absence of indane does not necessarily conclude the absence of petrol.

The specific compounds detected in unburnt petrol from each oil station, namely 3,7-dimethyl-1-octene, 2,2,4-trimethylpentane, 2-methyl-1-butene, and 2-hexene, were not detected after the burning process. This entails that these specific compounds can no longer be used to differentiate oil stations in burnt petrol. This was supported by PCA (Figure 7), where no apparent grouping was displayed among the three stations for burnt petrol. The presence of the volatile compounds from burnt petrol sufficiently classified the sample as petrol. However, discrimination based on its respective station could not be done as shown in the 3D score plot of burnt petrol compounds (accounts for 91.2% total variation, PC1 = 59.2%, PC2 = 20.9% and PC3 = 10.6%) in Figure 7. No apparent grouping is displayed among the three stations. Petrol X is largely scattered around a large group which is predominantly comprised of petrol Y and Z, while petrol X and Y were inseparable, as seen at the upper and lower region of the PC2 axis.

Table 4. Summary of volatiles detected in burnt petrol samples from X, Y and Z

No	Retention Time (min)	Volatiles	X	Y	Z
1	5.49	toluene	/	/	/
2	7.83	ethylbenzene	/	/	/
3	8.01	*p*-xylene	/	/	/
4	8.40	*o*-xylene	/	/	/
5	9.54	ethyltoluene	/	/	/
6	9.99	1,2,3-trimethylbenzene	/	/	/

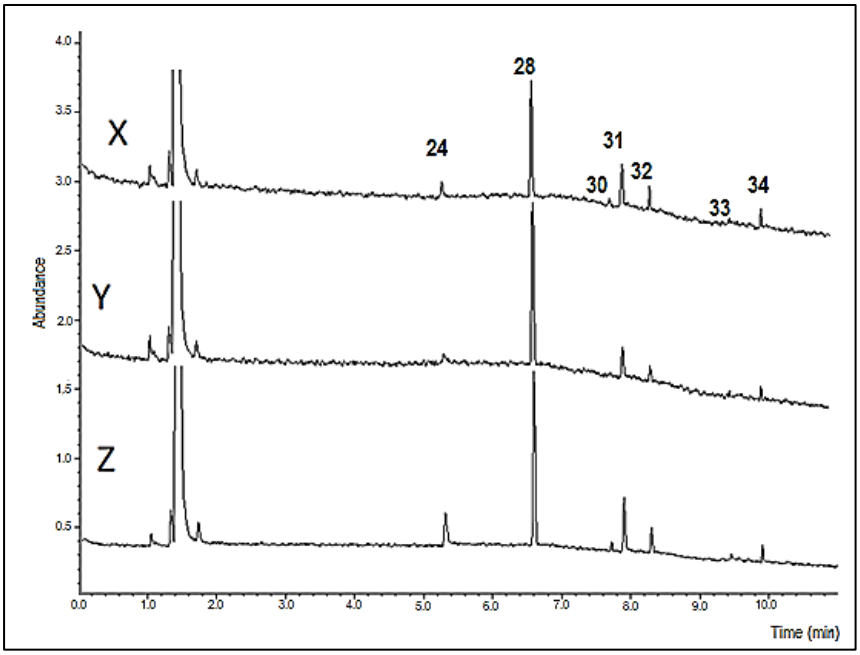


Figure 6. TIC for burnt petrol from X, Y and Z

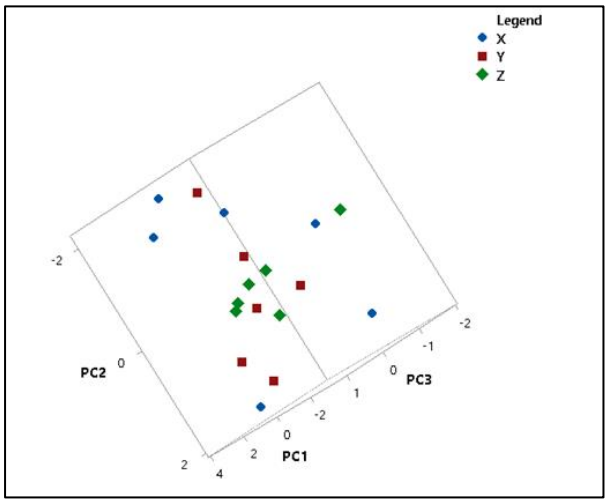


Figure 7. 3D score plot of residual petrol compounds for X, Y and Z

Comparison between unburnt and burnt petrol

In comparison to unburnt petrol, the number of compounds detected from burnt petrol was very small. In each unburnt sample that was analysed from the three oil stations, at least 27 to 32 compounds (*n*-alkanes, *n*-cycloalkanes, alcohol, benzenes, *n*-alkylbenzenes, and indane) were detected, whereas, in burnt samples, only six remaining compounds (*n*-alkylbenzenes) were detected.

This is mainly because compounds in petrol are known to undergo rapid loss during burning [23-24]. Due to the burning that occurred at high temperatures up to 580 ºC, some hydrocarbons have potentially

evaporated and were no longer detected after the one-minute burning. Compounds with high vapour pressures tend to evaporate faster at high temperatures compared to compounds with low vapour pressures. The vapour pressure of a compound can be related to its molecular weight; the lower the molecular weight of a compound, the higher its vapour pressure [45]. Hence, *n*-alkanes, *n*-cycloalkanes, and alcohols that have lower molecular weight compared to *n*-alkylbenzenes will evaporate faster due to their higher vapour pressure which explains why they were no longer detected in the burnt petrol samples.

This can also be related to the strength of the bonds in the molecule. The bond that is most easily broken will be favoured [46]. An alkane or cycloalkane is known to have weaker bonds compared to *n*-alkylbenzenes. *n*-Alkylbenzenes also have higher stability due to the presence of the benzene ring in its backbone and, therefore, is not easily broken [47]. At high temperatures, the volatiles with the weaker bond will break and evaporate first, leaving behind volatiles like *n*-alkylbenzenes, which has stronger bonds. *n*-Alkylbenzenes are known to be persistent, particularly at high temperatures and readily detectable at fire scenes [48].

Although undetected in burnt petrol, the lighter hydrocarbons (*n*-alkanes and *n*-cycloalkanes) were detected in the unburnt petrol sample. Comparable differences were observed between unburnt and burnt petrol samples because during the burning process, the temperature of petrol increases which causes the residues of burnt petrol to have different chemical properties compared to unburnt petrol [49]. This is because when the temperature increases, the complex mixture of volatile hydrocarbons in petrol do not burn at the same rate. It is a blended product that covers the boiling point of 40ºC to 190ºC. The evaporation starts with the lightest and most volatile compound and progresses to the heavier, lesser volatile compounds as the temperature increases [49]. Therefore, after a burning process, heavier compounds like *n*-alkylbenzenes have a higher tendency to remain in the burnt petrol compared to lighter *n*-alkanes, *n*-cycloalkanes, and alcohols.

Due to their high volatility, the specific volatiles (3,7-dimethyl-1-octene and 2,2,4-trimethylpentane in X, 2-methyl-1-butene in Y and 2-hexene in Z) detected in unburnt petrol did not manifest in burnt petrol, possibly affecting the discrimination of burnt petrol (Figure 7). For the unburnt petrol where specific volatiles were detected, PCA score plots (Figure 5) have shown the ability to group unburnt petrol samples accurately. Therefore, these initial findings suggest that even though the majority of the volatiles were the same across the oil stations, distinguishment between oil stations can still be made due to the specific volatiles that were detected in the unburnt samples. However, when more than 70% of the volatiles were lost after burning, discrimination between different oil stations was difficult. Identification of specific volatiles and additive compounds is advantageous as supplemental data for pristine petrol samples comparison if collected in fire investigation.

Conclusion

The analysis of unburnt petrol samples from three different oil stations detected a range of similar volatiles: *n*-alkanes, cycloalkanes, alcohol, benzenes, *n*-alkylbenzenes, and indane. Additionally, specific volatiles were also detected, namely 3,7-dimethyl-1-octene and 2,2,4-trimethylpentane in X, 2-methyl-1-butene in Y and 2-hexene in Z, which potentially contributed to meaningful differentiation of petrol from these three oil stations. Petrol samples that were burnt generated only *n*-alkylbenzenes namely toluene, 1,2,3-trimethylbenzene, *p*-xylene, *o*-xylene, ethyltoluene, and ethylbenzene. The other functional groups were not detected. The chromatographic output of unburnt and burnt petrol samples also differed vastly. Data subjected to PCA revealed that unburnt petrol could be distinguished to each oil station. However, burnt petrol could not be distinguished. This is largely attributed to temperature and burning duration. As this preliminary study involved limited sampling, variation studies to ascertain intra and inter variation of more oil stations are planned. Besides that, a percentage degradation study in outdoor settings under the influence of the two factors to study the volatiles of petrol is planned. Perhaps, investigators could consider the identification of specific volatiles in liquid petrol examination to

serve as intelligent information that may aid the investigation.

Acknowledgement

This study was fully funded by Faculty Health Sciences, Universiti Kebangsaan Malaysia, project code GGPM-2017-014.

References

1. Ré-Poppi, N., Almeida, F. F. P., Cardoso, C. A. L., Raposo Jr, J. L., Viana, L. H., Silva, T. Q., Souza, J. L. C. and Ferreira, V. S. (2009). Screening analysis of type C Brazilian petrol by gas chromatography–flame ionisation detector. *Fuel,* 88(3): 418-423
2. Dabbagh, H. A., Ghobadi, F., Ehsani, M. R. and Moradmand, M. (2013). The influence of ester additives on the properties of petrol. *Fuel,* 104:216-223
3. World's Largest Oil Refineries by Processing Capacity (2021). Available at: https://www.listnbest.com/11-worlds-largest-oil-refineries-processing-capacity/ [Accessed: 22 March 2021]
4. Chong, C., Ni, W., Ma, L., Liu, P. and Li, Z., (2015). The use of energy in Malaysia: Tracing energy flows from primary source to end-use. *Energies*, 8(4): 2828-2866.
5. Westphal, G.A., Krahl, J., Brüning, T., Hallier, E. and Bünger, J. (2010). Ether oxygenate additives in petrol reduce the toxicity of exhausts. *Toxicology,* 268(3):198-203.
6. Pinto, V. S., Gambarra-Neto, F. F., Flores, I. S., Monteiro, M. R. and Lião, L. M. (2016). Use of 1H NMR and chemometrics to detect additives present in the Brazilian commercial petrol. *Fuel*, 182:27-33.
7. Brito, L. R., da Silva, M. P., Rohwedder, J. J., Pasquini, C., Honorato, F. A. and Pimentel, M. F. (2015). Determination of detergent and dispersant additives in petrol by ring-oven and near-infrared hyperspectral imaging. *Analytica Chimica Acta*, 863: 9-19.
8. Demirbas, A., Balubaid, M. A., Basahel, A. M., Ahmad, W. and Sheikh, M. H. (2015). Octane rating of petrol and octane booster additives. *Petroleum Science and Technology,* 33(11):1190-1197.
9. Mohamad, T. I. and How, H. G. (2014). Part-load performance and emissions of a spark-ignition engine fueled with RON95 and RON97 petrol: Technical viewpoint on Malaysia's fuel price debate. *Energy Conversion and Management,* 88: 928-935.
10. Hamadi, A. S. (2010). Selective additives for improvement of petrol octane number. *Tikrit Journal of Engineering Sciences,* 17(2): 22-35.
11. Lim, A. (2020). Petronas Primax 97 with Pro-Race launched - world's first Advanced Dual Friction Modifier for more power - paultan.org. [Accessed 13 May 2021].
12. DYNAFLEX Technology (2021). [Accessed 13 September 2021].
13. Gabriel, G. F., Ismail,Osman, K. and Noor Hazfalinda, H. (2017). The analysis of thermal decomposition products generated from porcine tissues exposed to outdoor burning conditions. *Malaysian Journal of Analytical Sciences,* 21(3): 585-596.
14. Jabatan bomba dan Penyelamat (2018). Laporan tahunan 2018, Malaysia.
15. Gonzalez-Rodriguez, J., Sissons, N. and Robinson, S. (2011). Fire debris analysis by Raman spectroscopy and chemometrics. *Journal of Analytical and Applied Pyrolysis,* 91(1): 210-218.
16. Stauffer, E., Dolan, J. A. and Newman, R. (2007). *Fire debris analysis*. Academic Press. Amsterdam.
17. Malaysian Meterology Department Official Website (2021). Available at: https://www.met.gov.my/?lang=en# (Accessed: 20 March 2020).
18. Lim, P. W., Abdullah, A. F. L., Chang, K. H. (2018). Forensic gas chromatography analysis of time elapsed petrol in fire scene investigation. *Malaysian Journal of Analytical Sciences*, *22*(1): 72-79.
19. Samri, M. A. S. and Chang, K. H. (2016). Gas chromatography based forensic analysis of petrol from burnt carpets retrieved using different fire extinguishing methods. *Malaysian Journal of Forensic Sciences*, 7(1): 39-44.

20. Kunashegaran, H. (2010) Chemometric approach for the discrimination of petroleum-based accelerants from fire debris. Thesis of Master degree, Faculty of Science, Universiti Teknologi Malaysia.
21. Jais, F. I., Mastura, S., Mahat, N.A., Ismail, D. and Mohamad, M. N, (2020). Forensic analysis of accelerant on different fabrics using attenuated total reflectance-fourier transform infrared spectroscopy (ATR-FTIR) and chemometrics techniques. *Malaysian Journal of Medical Health Sciences*, 16(2): 1-6.
22. Abu Hassan @ Mohamad, R. (2013). Determination of chemical fingerprint of RON 95 commercial petrol in Malaysia by chemometric analysis, Thesis of Masters degree, Universiti Kebangsaan Malaysia.
23. Dhabbah, A. M. (2018). Detection of petrol residues in natural and synthetic textiles before and after burning using SPME and GC-MS. *Australian Journal of Forensic Sciences* 52(2): 194-207.
24. Cacho, J. I., Campillo, N., Aliste, M., Viñas, P. and Hernández-Córdoba, M. (2014). Headspace sorptive extraction for the detection of combustion accelerants in fire debris. *Forensic science international* 238: 26-32.
25. Xiao, L., Stern, W. and Maynard, P. (2014). Ignitable liquids in fire debris investigation: A GC-MS practical for forensic chemistry. *Australian Journal of Education in Chemistry* 73: 29.
26. Desa, W. N. M., Daéid, N. N., Ismail, D. and Savage, K. (2010). Application of unsupervised chemometric analysis and self-organising feature map (SOFM) for the classification of lighter fuels. *Analytical Chemistry*, 82(15): 6395-6400.
27. Mat-Desa, W. N., Ismail, D. and NicDaeid, N. (2011). Classification and source determination of medium petroleum distillates by chemometric and artificial neural networks: A self-organising feature approach. *Analytical Chemistry*, 83(20): 7745-7754.
28. Krüger, S., Deubel, J. H., Werrel, M., Fettig, I. and Raspe, T. (2015). Experimental studies on the effect of fire accelerants during living room fires and detection of ignitable liquids in fire debris. *Fire and Materials* 39(7): 636-646.
29. Sarker, M. (2011). Alternative fuels derived from solid waste plastics. *Journal of Environmental Science and Engineering* 5(3): 316-322.
30. Sarker, M., Rashid, M. M., Zaman, A. and Molla, M. (2011). Generation of transportation fuel from solid municipal waste plastics. *Journal of Environmental Science and Engineering,* 5(1): 57-62.
31. Sarker, M., Rashid, M. M. and Molla, M. (2011). New alternative vehicle hydrocarbon liquid fuels from municipal solid waste plastics. *Journal of Fundamentals of Renewable Energy and Applications,* 1: 1-9.
32. Mack, J. H., Rapp, V. H., Broeckelmann, M., Lee, T. S. and Dibble, R.W. (2014). Investigation of biofuels from microorganism metabolism for use as antiknock additives. *Fuel,* 117: 939-943.
33. Oseev, A., Zubtsov, M. and Lucklum, R. (2012). Octane number determination of petrol with a photonic crystal sensor. *Procedia Engineering* 47: 1382-1385.
34. Xin, J., Yan, D., Ayodele, O., Zhang, Z., Lu, X. and Zhang, S. (2015). Conversion of biomass-derived valerolactone into high octane number petrol with an ionic liquid. *Green Chemistry,* 17(2):1065-1070.
35. Soto, R., Fité, C., Ramírez, E., Bringué, R. and Cunill, F. (2014). Equilibrium of the simultaneous etherification of isobutene and isoamylenes with ethanol in liquid-phase. *Chemical Engineering Research and Design,* 92(4):644-656.
36. Vazquez-Esparragoza, J. J., Iglesias-Silva, G.A., Hlavinka, Soto, R., Fité, C., Ramírez, E., Bringué, R. and Cunill, F. (2014). Equilibrium of the simultaneous etherification of isobutene and isoamylenes with ethanol in liquid-phase. *Chemical Engineering Research and Design,* 92(4): 644-656.
37. Hajipour, S., Satyro, M. A. and Foley, M. W. (2014). Uncertainty analysis applied to thermodynamic models and fuel properties–natural gas dew points and petrol reid vapor pressures. *Energy & Fuels* 28(2): 1569-1578.

38. Vazquez-Esparragoza, J. J., Iglesias-Silva, G. A., Hlavinka, M.W. and Bullin, JA (1992). How to estimate Reid vapour pressure (RVP) of blends. *Bryan Research & Engineering, Inc., website, Encyclopedia of Chemical Processing and Design,* 47: 415-424.
39. Finlayson-Pitts, B. J. and Pitts Jr, J. N. (1993). Atmospheric chemistry of tropospheric ozone formation: scientific and regulatory implications. *Air & Waste,* 43(8): 1091-1100.
40. Rihko-Struckmann, L. K., Linnekoski, J. A., Krause, A. O. I. and Pavlov, O. S. (2000). Vapour-liquid and chemical reaction equilibria in the synthesis of 2-methoxy-2-methylbutane (TAME). *Journal of Chemical & Engineering Data,* 45(6):1030-1035.
41. Bumbac, G., Plesu, V., Ciornei, C. and Plesu, A.E. (2014). Modelling and simulation the process in a reactive dividing wall column for petrol additive TAME synthesis in the oil refinery. *Klemes, J. (Ed.), Chemical Engineering Transactions,* 12: 1-6.
42. Nadeina, K. A., Klimov, O.V., Pereima, V. Y., Koryakina, G. I., Danilova, I. G., Prosvirin, I. P., Gerasimov, E.Y., Yegizariyan, A. M. and Noskov, A. S. (2016). Catalysts based on amorphous aluminosilicates for selective hydrotreating of FCC petrol to produce Euro-5 petrol with minimum octane number loss. *Catalysis Today,* 271: 4-15.
43. Barnett, I. and Zhang, M. (2018). Discrimination of brands of petrol by using DART-MS and chemometrics. *Forensic Chemistry,* 10: 58-66.
44. Baerncopf, J. M., McGuffin, V. L. and Smith, R.W. (2011). Association of ignitable liquid residues to neat ignitable liquids in the presence of matrix interferences using chemometric procedures. *Journal of Forensic Sciences,* 56(1): 70-81.
45. Liu, S.J., Wang, Y. H. and Yu, L. L. (2013). Study on timeliness of petrol analysis adsorbed in cotton cloth carrier. *Advanced Materials Research,* 616: 881-884.
46. Sandercock, P. M. L. (2008). Fire investigation and ignitable liquid residue analysis - a review: 2001–2007. *Forensic Science International* 176(2-3):93-110
47. Price, D. and Horrocks, A. R. (2013). *Combustion Processes of Textile Fibres*, in Handbook of Fire-Resistant Textiles. 1st ed.:Woodhead Publishing.
48. Kilinc, F. S. (2013). *Handbook of Fire-Resistant Textiles*. 1st edition: Woodhead Publishing Limited.
49. Pert, A. D., Baron, M. G. and Birkett, J.W. (2006). Review of analytical techniques for arson residues. *Journal of Forensic Sciences,* 51(5): 1033-1049.

Malaysian Journal of Analytical Sciences (MJAS)
Published by Malaysian Analytical Sciences Society

METAL-ORGANIC FRAMEWORKS AS SORBENT- BASED EXTRACTION: A REVIEW

(Rangka Kerja Logam-Organik Sebagai Penjerap Berasaskan Pengekstrakan: Satu Ulasan)

Siti Sufiana Kamni[1], Karimah Kassim[1,2], Nur Sofiah Abu Kassim[3], Nurul Auni Zainal Abidin[3]*

[1]*Faculty of Applied Science*
[2] *Institute of Science*
Universiti Teknologi MARA, 40450 Shah Alam, Selangor, Malaysia
[3] *School of Chemistry and Environment, Faculty of Applied Science,*
Universiti Teknologi MARA, Cawangan Negeri Sembilan,
Kampus Kuala Pilah, 72000 Kuala Pilah, Negeri Sembilan, Malaysia

**Corresponding author: nurulauni@uitm.edu.my*

Received: 27 July 2021; Accepted: 2 October 2021; Published: 25 October 2021

Abstract

Metal-organic frameworks (MOFs) are highly ordered porous crystalline structures and full of cavities. They are formed by inorganic centers (metal ion atoms or metal clusters) and organic linkers connected by covalent coordination bonds. Depending on the ratio of such precursors and the synthetic conditions, the characteristics of the resulting MOFs vary significantly, thus drifting into a countless number of interesting materials with unique properties. This review offers an overview on the current state of the use of MOFs in different microextraction configurations, in all cases covering extraction devices coated with (or incorporating) MOFs, with particular emphasis in their preparation. Moreover, recent analytical applications reported from 2018 to 2020 will be discussed critically.

Keywords: metal-organic framework, microextraction method, sorbent, extraction

Abstrak

Rangka kerja logam-organik (MOFs) adalah struktur kristal berliang yang sangat tersusun dan berongga. MOFs dibentuk oleh logam pusat tak organik (atom ion logam atau kluster logam) dan penghubung organik yang dihubungkan oleh ikatan koordinasi kovalen. Bergantung pada nisbah bahan pemula dan keadaan sintetik, ciri-ciri MOFs yang dihasilkan berbeza-beza, sehingga menjadikan MOFs sebagai penarik kepada bahan penyerap dan bersifat unik. Ulasan ini memberikan gambaran umum mengenai keadaan semasa penggunaan MOFs yang berbeza-beza dalam konfigurasi pengekstrakan mikro yang meliputi kaedah pengekstrakan yang disaluti dengan (atau menggabungkan) MOFs, dengan penekanan khusus dalam penyediaannya. Tambahan pula, aplikasi analisis terkini yang dilaporkan dari tahun 2018 sehingga 2020 akan dibincangkan secara kritikal.

Kata kunci: rangka kerja logam-organik, kaedah pengekstrakan mikro, bahan penyerap, pengekstrakan

Introduction

Metal-organic frameworks (MOFs) are a new class of crystalline materials with three-dimensional (3D) organic inorganic complexes and highly porous nanostructures comprising metal ions/clusters and organic linkers [1]. They may be defined as supra-molecular solids but they consist of strong bonding and linking units that are available for modification by organic synthesis, a geometrically well-defined structure and robustness [2, 3]. In one-dimensional (1D) MOFs, coordination bonds are spread over the polymer in one direction. In two-dimensional (2D) MOFs, the single type layers are superimposed through either edge to edge or staggered type of stacking by weak interactions and guest species can be accommodated in the space between grids of the layers and the space between the layers. 3D MOFs are highly porous and stable since coordination bonds spread in three directions. According to Zhang et al. [4], these intriguing porous crystalline materials have been studied as promising candidates for various applications including gas separation and chemical sensing [5], energy storage [6, 7], homogenous and heterogeneous catalysis [8] and drug delivery [9]. Emam et al. [2] stated that in the last 20 years, a great variety of MOFs were widely designed due to main advantages such as their well-known features of large surface areas [10], high micropore volumes and the tunable pore sizes [11], uniform nanoscale cavity, specific adsorption affinities [12], good thermal and chemical stability [7], and the availability of post-synthetic modification. Overall, MOFs have been attractive candidates as advanced sorbents in sample preparation due to the unique-microenvironment and have been proved to be good catalysts [13]. Consequently, MOFs have been preferably recommended as a reliable and novel sorbent material in sample preparations, including pollutants, large molecules, and heavy metals and others which have led to a rise in the number of published papers [14, 15].

Until now, various MOF materials have been used in different extraction modes, for example, solid-phase extraction (SPE) [16], dispersive-micro solid phase extraction (D-μSPE) [17], solid-phase microextraction (SPME), thin-film solid-phase microextraction (tf-SPME), in-tube solid-phase microextraction (it-SPME) [18], stir-bar solid-phase microextraction (sb- SPME), and lastly, needle trap device [19]. Therefore, MOFs have been applied in many different scientific fields and applications of MOFs have been reported, whereby the most popular applications of the use of MOFs in analytical chemistry are in the field of sample preparation as absorbents for the extraction of a wide range of analytes in different matrices [20]. Other applications of MOFs include MOFs in chromatography and as a sensor in spectroscopic and electro analytical methods [3], MOFs as therapeutic agents, drug carriers, imaging agents and biosensors in cancer biomedicine [21], hydrogen storage in MOFs [10], MOFs in applications like catalysis or separation, and MOFs as substrates for paper spray mass spectrometry (MS) [22].

Metal-organic framework design in analytical separation

There are many kinds of MOFs used in various sample preparation strategies such as metal-organic framework (MOF) family, University of Oslo (UiO) [7], zeolite imidazolate frameworks (ZIF), Matériaux de l'Institut Lavoisier (MIL) and isoreticular metal-organic framework (IRMOF). Among all, IRMOF is the most widely studied as an excellent drug carrier material [7,23].

According to Li et al. [24], the first appearance was reported in the middle of the 1990s by the Yaghi group [25], who claim that MOFs have attracted extensive attentions due to their fascinating structures and unique properties. As a milestone in the history of MOFs, MOF-5 is known for its robust and open framework structure [24]. This material comprises Zn_4O $(CO_2)_6$ octahedral secondary building units (SBUs), each linked by 1,4-benzenedicarboxylate (BDC_2-) units to give a cubic framework. Its Brunauer-Emmett-Teller (BET) surface area reaches 2320 m^2/g. MOF-199 (also called HKUST-1) and is composed of Cu paddle wheel $[Cu_2(CO_2)_4]$ SBUs and a tropic organic linker benzene-1,3,5-tricarboxylate (BTC_3) [23]. This material shows merits in good stability against moisture, relatively easy synthesis procedure, and excellent thermal stability [14].

The UiO family has a Zr-based cuboctahedral SBU building block. As a representative member of this family, UiO-66 composes zirconium clusters and terephthalate ligands [26]. Zirconium is highly resistant to corrosion and has a strong affinity for hard oxygen donor ligands, therefore it is very stable even in strong acid and base solutions. In other words, this MOF UiO-66 exhibits extraordinary thermal stability even at 540 °C [8].

The ZIF family is built by metal ions with imidazolate ligands through nitrogen atoms. Among the ZIFs family members, ZIF-8 (Zn atoms coordinated tetrahedrally with 2-methylimidazolate (MeIM)) is the most studied because it exhibits a large surface area, high porosity, and exceptional chemical stability in organic solvents or boiling sodium hydroxide solution [27]. Recently, Emam et al. [2] in their research on the adsorptive performance of MOFs and MOF containing composites for clean energy and safe environment show that other members (e.g. ZIF-8 (Zn), ZIF-68 (Co)) have been utilised in hydrothermal/in-situ and infrared/in-situ techniques.

As for IRMOF-1, also known as MOF-5 to IRMOF-16 is synthesized with expanded and various functionalized organic linkers with zinc while keeping the same topology [7]. In hydrothermal synthesis, different ditopic carboxylate linkers would yield the same type of framework under closely related conditions. IRMOF-74-I to XI is synthesized from its original linker of one phenylene ring (I) to eleven (XI), respectively, with pore apertures increasing from 14 Å to 98 Å [28]. Different pore sizes of IRMOF could be used to conduct size-exclusion extraction according to the kinetic diameters of analytes.

As for the MIL family, it is constructed by trivalent metal centers and carboxylic acid bridging ligands. Among the MIL family members, MIL-53(Cr) MIL-100(Fe) and MIL-101(Cr) are widely studied in solid-phase extraction (SPE). Meanwhile, [5] stated that MIL-53(Cr) is built up with trimeric chromium octahedral clusters and terephthalate ligands, which exhibits unique pore expansion or contraction behavior with guest molecules. Both MIL-101 (Cr)-SO_3H and MIL-101 (Cr) were functionalized by post-treating them with ethylene diamine and tris (2-aminoethyl) amine (TAEA), ethanolamine (EA), receptively to produce MIL-101 (Cr)-SO_3H-TAEA, MIL-101 (Cr)-EA, and MIL-101 (Cr)-ED [2].

In addition, there are hundreds of novel MOFs reported and named by different researchers, such as PCN [29], BCF [30], NOTT [31], and BioMOF [32], and so on. Even for the same topology, mixed-metal and mixed-ligand MOFs greatly multiplied their diversity. For example, MOF-74 could contain 10 different metal ions (Mg, Ca, Sr, Ba, Mn, Fe, Co, Ni, Zn, and Cd) coordinated with the same ligand in one framework [7]. Goyal, 2019 in his study stated that the most flexible MOF (named MOF-5) have a neutral framework of composition Zn_4O(BDC) in which Zn_4O groups are linked by terephthalate where BDC means 1,4-dicarboxylate has been synthesized and its name has been taken from a known zeolite ZSM-5. Figure 1 shows several representative examples of MOFs structures and their respective SBUs. One of the most representative examples is the family of isoreticular metal–organic frameworks (IRMOFs). This group of MOFs present the same topology and skeleton but different functionalization and pore dimensions to provide new perspectives for developing highly functional flexible MOFs.

MOFs as sorbent for small organic analytes

According to Sajid et al. [34], the following features of metal-organic frameworks (MOFs) include high porosity, designable and tunable structures, ultra-high surface area, utilization of functionalities as well as outer space, high thermal stabilities, and structural cavities that justify their use as sorbents in analytical chemistry as shown in Figure 2.

Relying on metal ion geometry and bridging ligands, different topologies and dimensionalities of MOFs can be attained. MOFs have been widely employed in analytical extractions [3]. Other than polycyclic aromatic hydrocarbons (PAHs), polychlorinated biphenyls (PCBs), polybrominated diphenyl ethers (PBDEs), volatile organic compounds (VOC), pharmaceuticals, herbicides, pesticides, toxins, dyes,

endocrine-disrupting chemicals (EDCs) are the examples of MOFs in small organic analyte. MIL-101 (Cr) has been widely used as an adsorbent [35]. Magnetic MIL-100(Fe) microspheres also showed excellent performance for extraction of (PAHs), and the adsorbent can be used150 times without significant loss in extraction [36].

The magnetization (Fe_3O_4 MNPs) of the MOFs makes their dispersion as well as retrieval easier in the extraction process. A facile method based on the mixing of MOF (MIL-101) and silica-coated magnetic microparticles in the sample solution was suggested for in situ magnetization and micro solid-phase extraction (MSPE) applications. In this case, hydrophobic and π-π interactions with the framework terephthalic acid molecules, and the π -complexation with the Lewis acid sites in the pores of MIL-101 contributed towards extraction of PAHs [2]. In another work, the magnetization of ZIF-7 was achieved through polydopamine (PDA) coating of Fe_3O_4 MNPs, where the NH_2 groups on PDA can form noncovalent and covalent interactions with ZIF-7 giving it magnetization as well as stability and reusability as sorbents. High surface area, accessible internal pores, unsaturated π -complextion, and π-π interactions of bridging ligand benzimidazolate with PAHs contribute toward extraction [4].

MOFs can also be employed in combination with magnetic nanoparticles (MNPs) to enhance their retrieval after extraction [3]. HKUST-1 and MNPs were prepared separately and used together in the extraction of PAHs from water samples. This work does not involve any chemical reaction between HKUST-1 and MNPs to ensure chemical binding. MOF and MNPs were taken in a vial before the addition of the water sample. Ultrasound dispersed the mixture in a sample solution that was retrieved with the help of the magnet after extraction. This simplified the synthesis as well as magnetic extraction [3].

Similar to PAHs, PCBs in environmental samples are usually difficult to determine for their low concentration and to overcome this issue, MIL-101(Cr) was packed into hollow fiber to prepare a novel μ-SPE device where this fiber device was robust and could prohibit the leakage of sorbents and due to the thermal stability of this MOF, it could be used for more than 80 extractions without performance loss and shape change [37].

PBDEs were another aromatic persistent organic pollutants and one type of widely used flame retardants and the application of MOFs as sorbents in PBDEs was quite limited. Su *et al.* [38] stated that $Cd_3(L)_2(bpy)_2.5(H_2O)_2$ was prepared as a sorbent for the dispersive SPE of seven PBDEs in environmental water samples and the Box-Behnken design was used through response surface methodology in method development to get optimum extraction parameters where the limit of detection (LODs) for seven PBDEs were in the range of 0.08–0.15 ng/L.

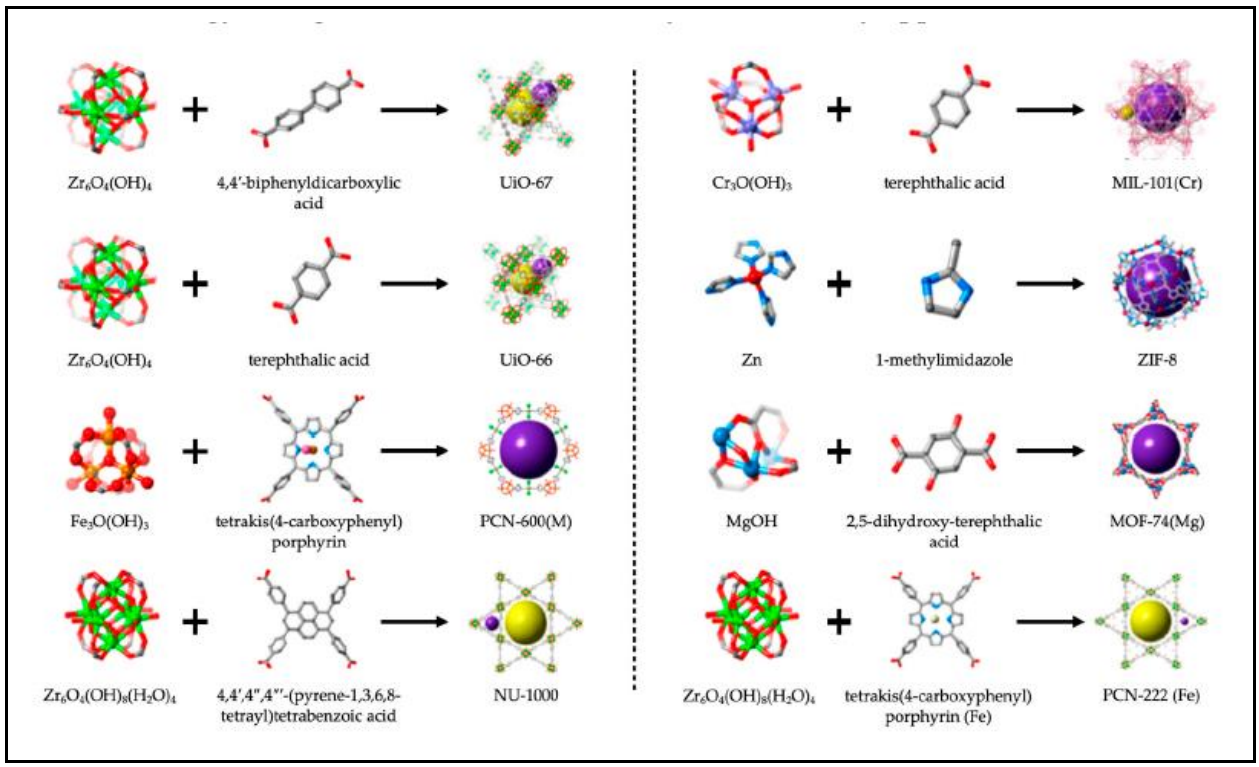


Figure 1. Schematic representation of different metal-organic frameworks structures with their corresponding metallic clusters and organic linkers [33]



Figure 2. Features of metal-organic frameworks (MOFs)

MOF in solid phase extraction

In recent years, applications of MOFs in separation science have been investigated intensively. One of the most important advantages of MOFs is that they can be designed to pertain to preferable (either chemical or physical) properties [16]. Generally, several factors (including flexibility and porosity of the framework, shape, and size of the pores) are considered as the most crucial factors determining the selective adsorption of guest molecules into the bulk structure of these solid materials in the solid-phase extraction (SPE) procedure. Therefore, the selective sorption of target compounds by MOFs is possible based on their shape, size, hydrophilic, and hydrophobic properties. It is important to note that many conventional sorbents used in SPE had either limited selectivity or adsorption capacity towards environmental pollutants such a Å s octadecyl-modified silica (C_{18}), graphitized carbon black (GCB), porous graphitic carbon (PGC), and activated carbon (AC) [39]. In this respect, MOFs are quite flexible to overcome such drawbacks through modification of the pore surface (for different adsorption preferences) against different target molecules [18], for example, MOF DUT-60 holds the world record regarding the highest surface area and pore volume. This MOF has a pore volume of 5.02 $cm^3 \cdot g^{-1}$ and a surface area of 7,800 $m^2 \cdot g^{-1}$ where it is formed by $Zn_4O_6^+$ clusters and an expanded topic ligand 1,3,5-tris(4′-carboxy[1,1′-biphenyl]-4-yl)benzene in combination with a ditopic linker 1,4-bis-p-carboxyphenylbuta-1,3-diene [40]. In general, MOFs with surface areas over 6,000 $m^2.g^{-1}$ are termed ultrahigh porosity crystalline frameworks.

In 2006, Zhou and co-workers stated the first example of using MOF in solid phase extraction was demonstrated by using an on-line flow injection SPE system using copper (II) isonicotinate (Cu (4-C_5H_4N-$COO)_2$ $(H_2O)_4$) as sorbent followed by HPLC-UV for trace determination of polycyclic aromatic hydrocarbons (PAHs) where these target PAHs contained in environmental samples (coal fly ash and local water samples) were concentrated and extracted onto the surface of copper isonicotinate coordination polymer based on the pore size of the hydrophobicity and polymer of the guest molecules.

In another case, an SPE procedure based on a magnetic porous carbon derived from an MIL-53-C was developed for pre-concentration of three steroid hormones (methyltestosterone, testosterone propionate, and nandrolone) from both urine samples and water where MIL-53-C with a good magnetic behavior and large surface area was prepared through its direct carbonization which it was exposed to 100 mL of sample solution containing steroid hormones to remove the target compounds from either human urine samples (LODs: 0.1-0.3 μg L^{-1}) and water (LODs: 0.005-0.01 μg L^{-1}) [36].

Furthermore, pure MOFs can be used as efficient sorbents for SPE of inorganics such as, Zn (II)-MOFs (TMU-4, TMU-5, and TMU-6) for the extraction of heavy metals (Cu (II), Cd (II), Pb (II), Cr (II), and Co (II)) from environmental water samples and TMU-5 was selected for the subsequent SPE analysis of heavy metals because it exhibited the maximum extraction efficiencies [36]. The proposed SPE procedure is known to possess several advantages including high extraction efficiency, simplicity, and low organic waste while, MOFs maintained either high water stability or wide pH range stability, it was recognized as the suitable sorbent for the extraction and pre-concentration of the target analytes from water samples [16].

MOF in dispersive-micro solid phase extraction

Chisvert et al. [17] in their research stated that sorbents used in dispersive-micro solid phase extraction (D-μSPE) play a crucial role in the overall extraction procedure. Both efficient clean-up and enrichment depend on the affinity they present concerning the target analytes, i.e., the facility to entrap them. Nevertheless, as important as the entrapping step is for desorption, the interaction sorbent-analytes should be reversible under different conditions to desorb them readily. This last step could be obviated in case the determination is carried out directly on the sorbent surface.

As mentioned before, the efficiency of both sorption and desorption processes depends on the contact surface area between the sample and the sorbent, and between it and the desorption solvent. In this sense, nanostructured

sorbents with a high surface area to volume ratio provide higher adsorption capacity compared with micro-scale materials [41].

To this regard, the development of new materials as sorbents has a great impact in micro extraction techniques, including D-μSPE, to improve the efficiency and selectivity, and their chemical or physical stability and consequently their lifetime. Many of the sorbents used in D-μSPE, which could be classified by attending to several criteria. Here, they have been divided into three groups: firstly, the micro materials, basically conformed by (but not limited to) the classic sorbents coming from SPE (e.g., the well-known octadecyl silica (C_{18})) that were proposed at the beginning of D-μSPE, and other more selective materials used later; secondly, nanostructured sorbents, especially nanoparticles (NPs) with special emphasis in magnetic NPs (MNPs); and finally, hybrid materials (composites) [42].

Boontongto and Burakham [6] stated that (NH_2-MIL-101(Fe)) has been proposed as a sorbent for dispersive micro-solid phase extraction (D-μSPE) of ten priority phenolic pollutants and the entire D-μSPE process was optimized by studying the effect of experimental parameters affecting the extraction recovery of the target analytes. Meanwhile, MOF functionalised with amino groups, was employed as the sorbent for D-μSPE to pre-treat eight nitrobenzene compounds from environmental water samples [42]. According to Ghorbani *et al.*[43], regarding trends in sorbent development for D-μSPE, it was stated that the most widely used MOFs was D-μSPE sorbent including HKUST-1 and MIL-101, respectively. Furthermore, Ghaemi & Amiri also stated that (MCC/MOF-199) was applied as a sorbent for the (D-μSPE) of chlorophenols, where the D-μSPE method combined with high-performance liquid chromatography-ultraviolet detection (HPLC-UV) was employed to determine four chlorophenols including 2-chlorophenol (2-CP), 4-chlorophenol (4-CP), 2,3-dichlorophenol (2,3-DCP), and 2,5-dichlorophenol (2,5-DCP) in aqueous [44].

MOF in solid phase microextraction

Solid-phase microextraction (SPME), developed in the early 1990s by Arthur and Pawliszyn, is a novel sample preparation method that is fast, highly sensitive, and less solvent consumptive. When it is comparable with other conventional sample preparation methods and can be coupled with gas chromatography (GC) or high-performance liquid chromatography (HPLC). SPME has been successfully used in biological, food, and environmental analyses [27]. In the past two decades, great progress has been made in the thermal and chemical stability of prepared SPME materials as well as the sensitivity, selectivity, and reproducibility of specific analytes. In addition, substantial effort has been made to explore novel SPME coating materials [45].

More recently, MOF-based SPME fibres have garnered increasing interest for efficient extraction and determination of different compounds such as, PAHs, VOCs, and penicillin while in 2009, Cui and co-workers have introduce the first example of using MOFs as SPME coating where hydrothermal procedure was applied to produce a thin film of MOF-199 on the surface of SPME fiber with result offered large enhancement factors (19,613-1,10,880), wide linearity (36-23,000 ng L^{-1}), and low LODs (8.3-23.3 ng L^{-1}) for SPME of benzene homologues. The outstanding efficiency of SPME-based MOF-199 resulted from such features as porous structure and large surface area of MOF-199, π-π interactions between aromatic rings of target compounds and Lewis acid sites of MOF-199 pores.

Furthermore, developing novel fibre materials on Cd (II)-MOF, MOF-199, and MIL-101 have been applied to analyze volatile polycyclic aromatic hydrocarbons and benzene homologs using headspace SPME [13,24,46]. While, Venna et al. stated that SPME fibres coated with some MOFs such as MOF-199, ZIF-7, and ZIF-8 were applied to investigate the selectivity of these adsorbents in separation procedure of n-alkenes [47]. Composite of MOFs with graphite oxide (GO) has been introduced as a new fibre coating for SPME-based separation of organochlorine pesticides (OCPs) and this composite was formed by reaction between the oxygen groups of GO and copper sites in MOF-199 where it provided

large surface area, high porosity, strong dispersive forces and good thermal stability (above 300 ℃) [48].

MOF in thin film solid phase microextraction

According to Gutiérrez-serpa et al.[18], while it is clear that the enlargement of the thickness of the sorbent material in film solid-phase microextraction (tf-SPME) devices implies an increase in the amount of extracted analyte, it also comes with long extraction times to reach the equilibrium due to the radial diffusion of the analytes. Thin-film solid-phase microextraction (tf-SPME) appears as a solution to increase the sensitivity (using larger sorbent amounts) without increasing the extraction time. Wilcockson and Gobas, were the first to propose the tf-SPME configuration. This first device consisted of a glass coverslip coated with a 0.33 µm thin film of ethylene- vinyl acetate (acting as sorbent coating) [49]. The device was tested in the analysis of toxic organic chemicals in aqueous extracts of fish samples.

In tf-SPME, the sorbent material covers the surface of flat material or forms a free membrane with a reduced thickness, with the increasing amount of sorbent being related to the extension of the surface, thus maintaining a high surface area to volume ratio. In this mode, higher sensitivities can be reached given the increased amount of sorbent but requiring shorter times (similar to those of tf- SPME) because there were no extra difficulties in diffusion (same as those in tf-SPME) [50]. Figure 3 below shows a schematic of the tf-SPME configuration reported in the literature.

The main challenge for the different sampling formats of tf-SPME is to avoid film folding. Among formats, it is possible to cite free-membrane, stainless steel rods, cotter pin, and mess holder configurations. Furthermore, it is possible to automate this extraction technique using 96-blades, which is a variety of the commercial 96-well plates system [52].

It is possible to distinguish two different kinds of tf-SPME devices attending to their thermal stability: thermostable and non-thermostable films. Thermostable films can be coupled to a temperature desorption unit and directly injected into the GC. As a disadvantage, there is a limited number of thermostable films reported in the literature and most of them are the same as the polymeric coatings used in conventional tf-SPME. Regarding thermo-labile films, they are used in solvent-assisted desorption applications (implying longer sample preparation times due to the slower diffusion of the analytes in the liquid phase). In addition, the increased size of the tf-SPME device requires the use of higher amounts of eluent solvent (in turn requiring a final step of solvent removal and reconstitution) [53]. Solvent desorption from tf-SPME is more challenging compared to thermal desorption which is related to the lack of conventional interfaces for on-line coupling of tf-SPME device to the workflow of the analytical instrument. This would facilitate the direct introduction of the extracted analytes into the analytical instrument. Furthermore, during the desorption process, the relatively large tf-SPME device requires a larger volume of eluent. According to Olcer et al. [53], only a small portion of the solution is introduced to the instrument after solvent desorption and this does not take full advantage of the large extractive phase, unless reconstitution steps and additional evaporation are employed to generate a smaller, more concentrated sample volume to account for the extra dilution.

The tf-SPME modality recently benefited from the introduction of MOFs. The preparation of MOF-based tf-SPME is easier than other SPME configurations because the increased surface facilitates the MOF growing. MOFs reported in tf-SPME devices include MIL-53(Al) and ZIF-67(Co) [54-55]. Other MOFs studied as sorbent material in tf-SPME are UiO-66(Zr), MIL-53(Fe), MIL-100(Fe), MIL-101(Cr), and ZIF-8(Zn) but presented poor analytical performance when compared with the abovementioned MOFs) [54]. Other thin films incorporate MOFs reported in the literature, but they are used as sorbent material in µ-SPE applications instead of tf-SPME strictly [56-57].

In the case of MIL-53(Al), it is incorporated in the thin-films by embedding the MOF which is previously synthesized in a polymer. This method involves the dispersion of the MOF in a volatile solvent (i.e., acetone), and the addition of such suspension to a polyvinylidene difluoride (PVDF) solution in

dimethylformamide under sonication to ensure homogeneity. Then, the volatile solvent is evaporated, and a dense ink is obtained [54]. The bar coating technique forms the thin film by spreading the ink over a surface. It requires an applicator with an adjustable gap to control the thickness of the film, followed by the ageing of the film and solvent removal to ensure the solidification of the film [53]. The final shape of the tf-SPME device can be easily modulated by proper cutting of the solid membrane obtained. These composites combine the flexibility of the polymers and the high porosity offered by MOFs. The amount of MOF powder cannot be extremely high in the film because it becomes more fragile and flakier. The highest charge reported for a MOF into a membrane for tf-SPME application is 67% (w/w) [54].

Recently, Mohammadi et al. [55], have proposed a method that combines electrospinning and the in-situ solvothermal growth to prepare a ZIF-67(Co)-based tf-SPME device. The electrospinning implies forming a composite of polyacrylonitrile and Co_3O_4 nanofibers. By heating, the polyacrylonitrile suffers calcination and the polymer is removed from the film structure. Afterwards, this film gets in contact with the organic linker required for the preparation of the ZIF-67(Co) (2-methylimidazole) at adequate conditions to ensure formation of the nanofibers. The main advantage of this method is that the MOF is self-supported without the use of a mesh or a polymer, while still maintaining a flexible membrane.

Regarding the applicability of the MOF-based tf-SPME devices, just the self-supported ZIF- 67(Co) film permitted a thermal desorption. In this last case, the application was the determination of pesticides [55]. In terms of analytical performance, they present adequate intra- and inter-device precision, with reported relative standard deviation values lower than 11.4%. Samples analyzed include water and biological fluids for the determination of estrogens and pesticides [54-55].

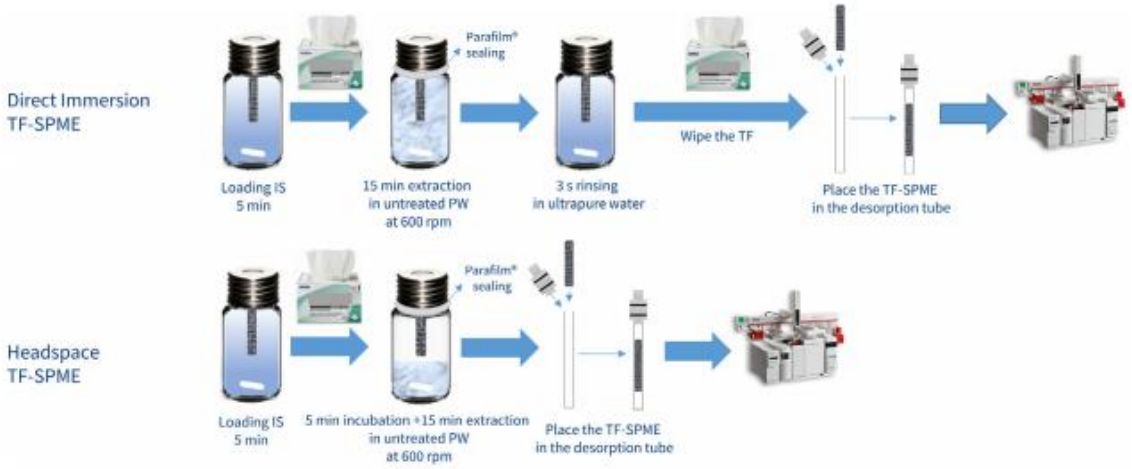


Figure 3. Scheme of the tf-SPME configuration [51]

MOF in in-tube solid phase microextraction

The in-tube solid-phase microextraction configuration (it-SPME) was developed practically after the development of the conventional tf-SPME, mainly to improve the drawbacks related to the coupling of the technique with liquid chromatography (LC). Although the high success of tf-SPME devices in many analytical applications, the extraction of non-volatile, semi-

volatile, and or thermo-labile compounds (not adequate for GC) was a significant hurdle to overcome.

The introduction of it-SPME devices facilitates the online and direct injection in a LC system, and even more importantly, its automation [58]. The first it-SPME devices consisted of 60 cm sections of a GC capillary column, with an internal diameter of 0.25 mm and an internal thin film of the stationary phase coating the capillary. Depending on the nature of the stationary phase, the film thickness varies, exhibiting slightly different internal volumes among the devices. Nevertheless, the nature of the film is the main factor responsible for the difference in behavior [58]. Nowadays, most developed it-SPME devices use open tubular fused-silica capillaries, with a thin film of the extractant material on the inner walls. The development of other capillary modes shifts to the incorporation of novel materials and the improvement of the technique. Other capillary modes include sorbent-packed, fibre-packed, and monolithic phases [59-61].

There are several operational modes for it-SPME depending on the number of pumps and valves. Nevertheless, they can be divided mainly into two configurations attending to the introduction of the sample: the flow-through system and the draw or eject system. In the first one, the injection of the sample can be performed manually or automated, and the sample is continuously injected into the device following a unique direction. In the draw/eject mode, it requires an automatic sample introduction system (programmable). The sample is injected, flows through the device, and goes back to the sample vial through the device again completing a cycle. In this modality, it is important not only to optimize the sample flow, but also the number of required cycles to obtain the maximum extraction efficiency [59, 61]. Up to date, the use of MOFs as sorbent material in it-SPME is not extended, and only few studies have been reported so far using MIL-101(Cr), MIL-53(Al) [62-63] and ZIF-8(Zn), in all cases for the determination of environmental pollutants in water.

In the cases of MIL-101(Cr) and MIL-53(Al), the devices consist of a glass capillary filled with a monolith composed of a polymer and the MOF. Thus, the glass capillary was cut in sections of 4-10 cm length, followed by washing with concentrated NaOH to activate the silanol groups. Then, the inner walls of the capillary were vinylated to guarantee the attachment of the monolith [62]. Afterwards, the mixture suspension containing the necessary amount of MOF (as prepared and already activated), butyl methacrylate as monomer, ethylene dimethacrylate as cross-linker agent, azo-bis-isobutyronitrile as radical initiator, and a porogenic solvent fills the capillary. Once the sides of the capillary are sealed, a microwave-assisted polymerization takes place. It is important to ensure the correct dispersion and homogenization of the mixture suspension before filling the capillary to get a homogenous it-SPME device. Finally, there is a clean-up step to remove the unreacted chemicals from the device) [63]. One of the most important factors to optimize in this kind of device is the amount of MOF in the monolith. If large amounts of MOF are used, the monolith structure would be more compact, thus making the diffusion of the sample and solvents difficult (and in turns resulting in a decreasing of the extraction efficiency of the final device) [63].

Regarding the ZIF-8-based it-SPME device proposed by Ling and Chen, it consisted of a fiber-packed capillary [64]. In this case, the incorporation of the MOF requires an electrodeposition step followed by an *in-situ* crystal growth. The general procedure starts by using a strong acid and a base in order to activate the surface of carbon fibers (bundle of 13 cm). Then, the electrodeposition of ZnO takes place by immersing the carbon fibers (as the working electrode on a three-electrodes system) in a solution of zinc nitrate. The deposition of the oxide takes place by cyclic voltammetry. Once the ZnO is formed all over the surface of the fibers, the cyclic voltammetry is stopped, and the fibers bundle is washed and heated at 100 °C to ensure the immobilization of the oxide. This strategy renders supported ZnO crystals of 30-80 nm. Consecutively, the solvothermal synthesis ensures the growth of the MOF ZIF-8 by immersing the ZnO-based carbon fibers bundle into a solution of the organic linker under adequate growing conditions, followed by packing it in a polyetheretherketone (PEEK) tube. The analytical applications involved the determination of Sudan dyes in environmental waters [64].

MOF in stir-bar solid-phase microextraction

Baltussen et al. [65] introduced the stir-bar solid-phase microextraction (sb-SPME) configuration as an alternative to conventional f-SPME, particularly useful for compounds with low octanol/water partitioning coefficient (non-polar compounds). The device consisted of a magnetic stir bar coated with PDMS. The sample was stirred with the bar at an adequate agitation rate. The bar was removed after proper extraction time, and a direct thermal desorption step took place in a specific GC injection port called a thermal desorption unit. In this configuration, part of the sorbent was in contact with the bottom of the sample container thus blocking possible interactions between the analytes and a portion of the extractant material. Stir-cake solid-phase microextraction (sc-SPME) emerged as a solution to this problem. The sorbent (in general a monolith) was located in a cylindrical device avoiding the contact between the sorbent and the bottom of the vessels thus improving the entire extraction efficiency [66].

Both configurations followed the same extraction fundamentals as conventional SPME. However, the amount of the sorbent material in both modes sb-SPME and sc-SPME were ~50–200 times bigger than the amount used in conventional f-SPME, thus permitting not only an increase of the extraction capacity towards target analytes but also an increase in the extraction time [67].

Currently, there are only two commercially available sb-SPME devices distributed by Gerstel: one coated with PDMS and the other with a PDMS/ethylene glycol copolymer. Although these coatings possessed many merits such as high sensitivity and good reproducibility, they also had low selectivity and required long extraction times to reach the equilibrium conditions. In addition, recoveries for polar compounds are poor due to the non-polar nature of the sorbent, being necessary a derivatization step for their extraction. Given these drawbacks, recent developments of sb-SPME devices focused on the development of more selective coatings with faster extraction kinetics, with MOFs not being an exception [68].

MOFs used as sorbents in sb-SPME include IRMOF-3(Zn), MIL-53(Al)-NH_2, MOF-5(Zn and Fe), ZIF-8, MIL-101(Cr) and it is amino- functionalised version, MIL-68(Al), ZIF-67(Co), and UiO-66-NH_2 [45, 67, 69-73]. The main procedure followed incorporation of MOFs in sb-SPME devices that followed the sol–gel approach. The devices prepared by this procedure have three components which are an iron wire or metallic rod of ~1-3 cm length, a glass jacket, and the sorbent. The iron wire or metallic rod is responsible for the agitation under the magnetic field while the glass jacket isolates the metallic wire from the water sample, avoiding its corrosion. The glass jacket also offers a homogeneous tunable surface for the immobilization of the coating when immersing the bar into the sol–gel solution containing the MOF dispersed into a polymeric solution. Then, the device is removed from the sol–gel solution and the self-assembly of the coating finishes by heating [67].

An alternative to sol-gel is the synthesis of monoliths by polymerization. The general procedure implies filling a template with a pre-polymeric solution (containing the MOF powder dispersed or its precursors), polymerization, removal of the template, and a final wash to clean the monolith [5,74]. Thus, the shape and dimension of the devices depends on the template and not on the support. Even the use of support is not required if magnetic nanoparticles are dispersed in the pre- polymeric suspension [31]. Recently, Du et al. [75] took advantage of this strategy for the preparation of the first MOF-based sc-SPME device by dispersing Fe_3O_4 @HKUST-1 core-shell particles in a pre-polymeric solution of 2-ethylhexylacrylate/divinylbenzene/methyl methacrylate. Although the MOF composite monolith does not utilize classical sc-SPME support, its visual geometry and shape resemble that of the classical sc-SPME device.

Another option is the in-situ solvothermal growth of the crystals onto other types of supports. Hu et al. [45] used this strategy with a porous copper foam as support. The foam is immersed in the solution containing the precursors of MOF-5(Zn) and, after impregnation, the support and the solution are set on the Teflon-lined autoclave, which is heated to form the MOF. In this case,

the sb-SPME device is used in the headspace solid (HS) mode and uses a lab-made rotor to stir the device. As the direct growth of crystals over the support surface is not easy in terms of ensuring homogeneity, a similar approach to atomic layer deposition (ALD) strategy was used, to promote the crystal growth out of the metal nanoparticles previously electrodeposited all over the surface of the support [73]. The main disadvantage of these devices is the weak union MOF-support. The friction between the stir bar and the sample container causes a progressive loss of the MOFs, thus reducing the lifetime of the device. Wang et al. developed the use of a dumbbell-shaped PEEK jacket to improve mechanical strength. However, PEEK material is a highly inert material, requiring several aggressive pre-treatment steps to obtain an activated surface before the in-situ growth [74].

MOF in needle trap device

Needle trap device (NTD) is a microextraction technique that was first introduced by Pawliszyn et al. in 2001 [76]. In recent years, NTD has attracted much scientific interest from many researchers, due to its advantages [77]. In this regard, in previous researches, a wide variety of commercial and synthetic adsorbents have been used in NTD for the determination of different compounds [78]. These adsorbents, compared to other commercial adsorbents, have unique specifications like controllable pore sizes, super porosity, high selectivity, uniform cavities, high thermal stability, high specific surface area (>1000 m^2/g) with regular and uniform cavities, and various functional groups and sorbent flexibility to design and prepare a new adsorbent with desired specifications consistent with the target analytes [79].

Due to the possibility of using various organic linkers and metals, these types of adsorbents have been recently used in the extraction of a wide variety of analytes (like sulphonamides, polychlorinated biphenyls, volatile compounds, and polycyclic aromatic hydrocarbons) from various matrices (water and air) at different concentrations [46]. Until now, MOFs have been used in SPE and SPME for the extraction of phenolic derivatives [74]. The use of needle packed with Zn-MOF as a sorbent in sampling a number of PAHs including naphthalene, anthracene, phenanthrene, and pyrene in the air was conducted in the present study and the performance of this method was assessed using the gas chromatography-flame ionization detector (GC-FID) while to determine the temperature and time of desorption, storage time of the sample, and breakthrough volume (BTV) was exploited by using response surface methodology (RSM) [19].

Furthermore, the NTD packed with MIL-125 was used for extraction of phenol derivatives such as phenol, o-cresol, p-cresol, and 2-chlorophenol followed by gas chromatography analysis which shown the proposed of NTD offered was a high repeatability and accuracy. Also, the values of LOD and LOQ indicated a high sensitivity for the suggested sampler that proved the NTD packed withMIL-125 adsorbent can be used as a sensitive, accurate and fast method for determination phenolic derivatives from workplace air [77].

Conclusion

MOFs are known as well-established sorbents due to their advantages such as robustness, high surface area (provide large adsorption capacity), and highly ordered pores with specific size (selective adsorption for target analytes) over other alternatives. Currently, MOF examples, especially for analytical applications (various sample preparations and chromatographic separations), are limited to UiO-n, MIL-n, ZIF-n and MOF-n series, and a few other MOFs. Overall, MOFs or MOF-based composites with excellent properties as sorbents provide many new opportunities for sample pretreatment in the analytical extraction field. Finally, applications of MOFs and their composites as sorbents in SPE, D-μSPE, SPME, tf-SPME, it-SPME, sb-SPME, and MOF in needle trap device are highlighted. These developments and sustained research efforts will spark more interest in expanding the application of MOFs in sample pretreatment methods. Given the extensive knowledge about MOFs and their composites, we believe that this subject will become of great interest and continue to improve performance in analytical applications and beyond.

Acknowledgements

The authors would like to thank the Ministry of Higher Education, Malaysia for FRGS-RACER grants

(RACER/1/2019/STG01/UITM//5) and (RACER/1/ 2019/STG01/UITM//2). The authors would like to acknowledge the Faculty of Applied Sciences, Universiti Teknologi Mara (UiTM), Cawangan Negeri Sembilan, Kampus Kuala Pilah Campus and Faculty of Applied Sciences, Universiti Teknologi MARA, Shah Alam, Selangor, Malaysia for facilities and services provided for the analysis.

References

1. Xu, G. R., An, Z. H., Xu, K., Liu, Q., Das, R. and Zhao, L. H. (2020). Metal organic framework (MOF)-based micro/nanoscaled materials for heavy metal ions removal : the cutting-edge study on designs, synthesis, and applications potential of zero charge. *Journal of Coordinantion Chemistry*, 427: 2-32.
2. Emam, H. E., Abdelhameed, R. M., A. and Ahmed, H. B. (2020). Adsorptive performance of MOFs and MOF containing composites for clean energy and safe environment. *Journal of Environmental Chemical Engineering*, 8(5): 1-13.
3. Rocio-Bautista, P., Taima-Mancera, I., Pasan, J. and Pino, V. (2019). metal-organic frameworks in green analytical chemistry. *Separation*, 6: 1-21.
4. Zhang, K. D., Tsai, F. C., Ma, N., Xia, Y., Liu, H. L., Zhan, X. Q., Yu, X. Y., Zheng, X. Z., Jiang, T., Shi, D., and Chang, C. J. (2017). Adsorption behavior of high stable Zr-based MOFs for the removal of acid organic dye from water. *Journal of Materials*, 10(205): 1-11.
5. Yang, S., Karve, V. V., Justin, A., Kochetygov, I., Espin, J., Asgari, M., Trukhina, O., Sun, D. T., Peng, L. and Queen, W. L. (2020). Enhancing MOF performance through the introduction of polymer guests. *Coordination Chemistry Reviews*, 427: 1-37.
6. Salunkhe, R. R., Kaneti, Y. V., Kim, J., Kim, J. H. and Yamauchi, Y. (2016). Nanoarchitectures for metal-organic framework-derived nanoporous carbons toward supercapacitor applications. *Accounts of Chemical Research,* 49(12): 2796-2806.
7. Li, X., Ma, W., Li, H., Bai, Y., A. and Liu, H. (2019). Metal-organic frameworks as advanced sorbents in sample preparation for small organic analytes. *Coordination Chemistry Reviews*, 397: 1-13.
8. Ahmad, K., Nazir, M. A., Qureshi, A. K., Hussain, E., Najam, T., Javed, M. S., Shah, S. S. A., Tufail, M. K., Hussain, S., Khan, N. A., Shah, H. R. and Ashfaq, M. (2020). Engineering of zirconium based metal-organic frameworks (Zr-MOFs) as efficient adsorbents. *Materials Science & Engineering B*, 262: 114766.
9. Dahl, J., Maddux, A. B. L. S., and Hutchison, J. E. (2017). Toward greener nano-synthesis. *Chemical Reviews,* 107: 2228-2269.
10. Ge, J., Wu, Z., Huang, X., A. and Ding, M. (2019). An effective microwave-assisted synthesis of MOF235 with excellent adsorption of acid chrome blue K. *Journal of Nanomaterials*, 2019: 1-8.
11. Boontongto, T. and Burakham, R. (2019). Evaluation of metal-organic framework NH_2-MIL-101(Fe) as an efficient sorbent for dispersive micro-solid phase extraction of phenolic pollutants in environmental water samples. *Heliyon*, 5(11): e02848.
12. Goyal, A. (2019). Metal organic frameworks. *Journal of Chemistry*, 8(1): 9-16.
13. Zhang, X. F., Feng, Y., Wang, Z., Jia, M. and Yao, J. (2018). Fabrication of cellulose nanofibrils/UiO-66-NH_2 composite membrane for CO_2/N_2 separation. *Journal of Membrane Science*, 568: 10-16.
14. Wu, H. B. Wen, X. and Lou, D. (2017). Metal-organic frameworks and their derived materials for electrochemical energy storage and conversion : promises and challenges. *Science Advances*, *3*: 1-16.
15. Perez-Cejuela, H. M., Herrero-Martinez, J. M. and Simo-Alfonso, F. E. (2020). Recent advances in affinity MOF-based sorbents with sample preparation purposes. *Molecules*, 25(4216): 1-21.
16. Hashemi, B., Zohrabi, P., Raza, N. and Hashemi, B., Zohrabi, P., Raza, N., and Kim, K. H. (2017). Metal-organic frameworks as advanced sorbents for the extraction and determination of pollutants from environmental, biological, and food media. *Trends in Analytical Chemistry*, 97(September): 65-82.
17. Chisvert, A., Cardenas, S. and Lucena, R. (2019). Dispersive micro-solid phase extraction. *The Turkish Journal of Pediatrics,* 112: 226-233.

18. Gutiérrez-serpa, A., Pacheco-fernández, I., Pasán, J. and Pino, V. (2019). Metal-organic frameworks as key materials for solid-phase microextraction devices - a review. *Separation*, 6(47): 1-29.
19. Soury, S., Bahrami, A., Alizadeh, S., Shahna, F. G., A. and Nematollahi, D. (2019). Development of a needle trap device packed with zinc based metal-organic framework sorbent for the sampling and analysis of polycyclic aromatic hydrocarbons in the air. *Microchemical Journal,* 148(2019): 346-354.
20. Manousi, N., Zachariadis, G. A., Deliyanni, E. A. and Samanidou, V. F. (2018). Application of metal-organic frameworks in food sample preparation. *Molecules*, 23: 1-21.
21. Bieniek, A., Terzyk, A. P., Wiśniewski, M., Roszek, K., Kowalczyk, P., Sarkisov, L. and Keskin, S. and Kaneko, K. (2020). MOF materials as therapeutic agents, drug carriers, imaging agents and biosensors in cancer biomedicine: Recent advances and perspectives. *Progress in Materials Science*, 117: 100743.
22. Wang, X., Chen, Y., Zheng, Y. and Zhang, Z. (2017). Study of adsorption and desorption performances of Zr-based metal-organic frameworks using paper spray mass spectrometry. *Materials*, 10(7): 769.
23. Cai, M., Qin, L., Pang, L., Ma, B., Bai, J., Liu, J., Dong, X., Yin, X. and Ni, J. (2020). Amino-functionalized Zn metal -organic frameworks as antitumor drug curcumin carriers. *New Journal of Chemistry*, 44(41):17693-17704.
24. Li, L., Chen, Y., Yang, L., Wang, Z. and Liu, H. (2020). Recent advances in applications of metal–organic frameworks for sample preparation in pharmaceutical analysis. *Coordination Chemistry Reviews*, 411: 213235.
25. Yaghi, O. M., Li, G. and Li Hailian. (1995). Yaghi-selective binding and removal of guests in a microporous metal-organic framework. *Nature*, 378(December): 703-706.
26. Cavka, J. V., Jakobsen, S., Olsbye, U., Guillou, N., Carlo Lambertis, C. and Silvia. C. (2008). A new zirconium inorganic building brick forming metal organic frameworks with exceptional stability. *Journal American Chemical Society,* 130(42): 13850-13851.
27. Abolghasemi, M.M.; Yousefi, V. and Piryaei, M. (2015). Synthesis of a metal-organic framework confined in periodic mesoporous silica with enhanced hydrostability as a novel fiber coating for solid-phase microextraction. *Journal of Separation Sciences,* 38: 1187-1193.
28. Zhu, J., Wu, L., Bu, Z., Jie, S. and Li, B. G. (2019). Polyethyleneimine-Modified UiO-66-NH_2 (Zr) metal− organic frameworks: Preparation and enhanced CO_2 selective adsorption. *American Chemical Society Omega*, 2019(4): 3188-3197.
29. Kesuma, R. F., Patah, A., A., and Permana, Y. (2019). Microwave-assisted synthesis of DUT-52 and investigation of its photoluminescent properties. *Bulletin of Chemical Reaction Engineering & Catalysis*, 14(1): 124-129.
30. Rada, Z. H., Abid, H. R., Sun, H., Shang, J., Li, J. and He, Y. (2018). Effects of -NO_2 and -NH_2 functional groups in mixed-linker Zr-based MOFs on gas adsorption of CO_2 and CH_4. *Progress in Natural Science: Materials International*, 28(2):160-167.
31. Yang, J. H., Cui, C. X., Qu, L. B., Chen, J., Zhou, X. M. and Zhang, Y. P. (2018). Preparation of a monolithic magnetic stir bar for the determination of sulfonylurea herbicides coupled with HPLC. *Microchemical Journal,* 141: 369-376.
32. Kahkha, M. R. R., Oveisi, A. R., Kaykhaii, M. and Kahkha, B. R. (2018). Determination of carbamazepine in urine and water samples using amino-functionalized metal-organic framework as sorbent. *Chemistry Central Journal*, 12(77): 1-12.
33. Howarth, A. J., Peters, A. W., Vermeulen, N. A., Wang, T. C., Hupp, J. T. and Farha, O. K. (2017). Best practices for the synthesis, activation, and characterization of metal−organic frameworks. *Chemical Materials,* 29: 26-39.
34. Sajid, M., Nazal, M. K. and Ihsanullah, I. (2021). Novel materials for dispersive (micro) solid-phase extraction of polycyclic aromatic hydrocarbons in environmental water samples: A review. *Analytica Chimica Acta,* 1141: 246-262.
35. Zhao, X., Wang, Y., Li, D. S., Bu, X. and Feng, P. (2018). Metal–organic frameworks for separation. *Advances Materials*, 30: 869-932.

36. Ma, M., Lu, L., Li, H., Xiong, Y. and Dong, F. (2019). Functional metal organic framework/SiO_2 nanocomposites: From versatile synthesis to advanced applications. *Polymers*, 11(11): 1823.
37. Lin, S., Gan, N., Cao, Y., Chen, Y. and Jiang, Q. (2016). Selective dispersive solid phase extraction-chromatography tandem mass spectrometry based on aptamer-functionalized Uio-66-NH_2 for determination of polychlorinated biphenyls. *Journal of Chromatography A,* 1446: 34-40.
38. Su, H., Wang, Z., Jia, Y., Deng, L., Chen, X., Zhao, R. and Chan, T. W. D. (2015). A cadmium (II)-based metal-organic framework material for the dispersive solid-phase extraction of polybrominated diphenyl ethers in environmental water samples. *Journal of Chromatography A,* 1422: 334-339.
39. Mavumengwana-Khanyile, B., Katima, Z., Songa, E. A., A. and Okonkwo, J. O. (2019). Recent advances in sorbents applications and techniques used for solid-phase extraction of atrazine and its metabolites deisopropylatrazine and deethylatrazine: A review. *International Journal of Environmental Analytical Chemistry,* 99(11): 1017-1068.
40. Islas, G., Ibarra, I. S., Hernandez, P., Miranda, J. M. and Cepeda, A. (2017). Dispersive solid phase extraction for the analysis of veterinary drugs applied to food samples: A review. *International Journal of Analytical Chemistry*, 2017:1-16.
41. Lawal, A., Wong, R. C. S. Tan, G. H., Abdulra'Uf, L. B. and Alsharif, A. M. A. (2018). Recent modifications and validation of QuEChERS-DSPE coupled to LC-MS and GC-MS instruments for determination of pesticide/agrochemical residues in fruits and vegetables: Review. *Journal of Chromatographic Science,* 56(7): 656-669.
42. Dou, Y., Guo, L., Li, G., Lv, X. and Xia, L. J. (2019). Amino group functionalized metal-organic framework as dispersive solid-phase extraction sorbent to determine nitrobenzene compounds in water samples. *Microchemical Journal*, 146: 366-373.
43. Ghorbani, M., Aghamohammadhassan, M., Ghorbani, H. and Zabihi, A. (2020). Trends in sorbent development for dispersive micro-solid phase extraction. *Microchemical Journal*, 158: 105250.
44. Ghaemi, F. and Amiri, A. (2020). Microcrystalline cellulose/metal-organic framework hybrid as a sorbent for dispersive micro-solid phase extraction of chlorophenols in water samples. *Journal of Chromatography A*, 1626: 1-7.
45. Hu, Y., Lian, H., Zhou, L. and Li, G. (2015). *In situ* solvothermal growth of metal-organic framework-5 supported on porous copper foam for noninvasive sampling of plant volatile sulfides. *Analytical Chemistry,* 87: 406-412.
46. Xie, L., Liu, S., Han, Z., Jiang, R., Liu, H., Zhu, F., Zeng, F., Su, C. and Ouyang, G. (2015). Preparation and characterization of metal-organic framework MIL-101(Cr)-coated solid-phase microextraction fiber. *Analytica Chimica Acta*, 853: 303-310.
47. Venna, S. R., Lartey, M., Li, T., Spore, A., Kumar, S., Nulwala, H., B., Luebke, D. R., Rosi, N. L. and Albenze, E. (2015). Fabrication of mmms with improved gas separation properties using externally-functionalized MOF Particles. *Journal of Materials Chemistry A,* 3(9): 5014-5022.
48. Seo, P. W., Bhadra, Bi. N., Ahmed, I., Khan, N. A. and Jhung, S. H. (2016). Adsorptive removal of pharmaceuticals and personal care products from water with functionalized metal-organic frameworks: Remarkable adsorbents with hydrogen-bonding abilities. *Scientific Reports,* 6: 1-11.
49. Wilcockson, J. B. and Gobas, F. A. P. C. (2001). Thin-film solid-phase extraction to measure fugacities of organic chemicals with low volatility in biological samples. *Environmental Science and Technology,* 35: 1425-1431.
50. Carasek, E. and Merib, J. (2015). Membrane-based microextraction techniques in analytical chemistry: A review. *Analytica Chimica Acta,* 880: 8-25.
51. Emmons, R. V., Liden, T., Schug, K. A. and Gionfriddo, E. (2020). Optimization of thin film solid phase microextraction and data deconvolution methods for accurate characterization of organic compounds in produced water. *Journal of Separation Science,* 43(9-10): 1915-1924.

52. Tascon, M., Gómez-Ríos, G. A., Reyes-Garcés, N., Poole, J., Boyacl, E. and Pawliszyn, J. (2017). High-throughput screening and quantitation of target compounds in biofluids by coated blade spray-mass spectrometry. *Analytical Chemistry,* 89: 8421-8428.
53. Olcer, Y. A., Tascon, M., Eroglu, A. E. and Boyacı, E. (2019). Thin film microextraction: Towards faster and more sensitive microextraction. *Trends Analytical Chemistry,* 113: 93-101.
54. Gao, G., Li, S., Li, S., Zhao, L., Wang, T. and Hou, X. (2018). Development and application of vortex-assisted membrane extraction based on metal-organic framework mixed-matrix membrane for the analysis of estrogens in human urine. *Analytica Chimica Acta,* 1023: 35-43.
55. Mohammadi, V., Jafari, M. T. and Saraji, M. (2019). Flexible/self-supported zeolitic imidazolate framework-67 film as an adsorbent for thin-film microextraction. *Microchemical Journal,* 146: 98-105.
56. Ghani, M., Font Picó, M. F., Salehinia, S., Palomino Cabello, C., Maya, F., Berlier, G., Saraji, M., Cerdà, V. and Turnes Palomino, G. (2017). Metal-organic framework mixed-matrix disks: Versatile supports for automated solid-phase extraction prior to chromatographic separation. *Journal Chromatography A,* 1488: 1-9.
57. Wang, S., Wang, X., Ren, Y. and Xu, H. (2015). Metal–organic framework 199 film as a novel adsorbent of thin-film extraction. *Chromatographia,* 78: 621-629.
58. Eisert, R. and Pawliszyn, J. (1997). Automated in-tube solid-phase microextraction coupled to high-performance liquid chromatography. *Analytical Chemistry,* 69: 3140-3147.
59. Costa Queiroz, M. E., Donizeti de Souza, I. and Marchioni, C. (2019). Current advances and applications of in-tube solid-phase microextraction. *Trends Analytical Chemistry,* 111: 261-278.
60. Moliner-Martinez, Y., Herráez-Hernández, R., Verdú-Andrés, J., Molins-Legua, C., Campíns-Falcó, P. (2015). Recent Advances of In-Tube Solid-Phase Microextraction. *Trends Analytical Chemistry, 71: 205-213.*
61. Fernández-Amado, M., Prieto-Blanco, M. C., López-Mahía, P., Muniategui-Lorenzo, S. and Prada-Rodríguez, D. (2016). Strengths and weaknesses of in-tube solid-phase microextraction: A scoping review. *Analytica Chimica Acta,* 906: 41-57.
62. Shih, Y. H.,Wang, K. Y., Singco, B., Lin, C. H. and Huang, H. Y. (2016). Metal-organic framework-polymer composite as a highly efficient sorbent for sulfonamide adsorption and desorption: Effect of coordinatively unsaturated metal site and topology. *Langmuir,* 32: 11465-11473.
63. Lirio, S., Liu,W. L., Lin, C. L., Lin, C. H. and Huang, H. Y. (2016). Aluminum based metal-organic framework-polymer monolith in solid-phase microextraction of penicillins in riverwater and milk samples. *Journal of Chromatography A,* 1428: 236-245.
64. Ling, X. and Chen, Z. (2019). Immobilization of zeolitic imidazolate frameworks with assist of electrodeposited zinc oxide layer and application in online solid-phase microextraction of sudan dyes. *Talanta,* 192: 142-146.
65. Baltussen, E., Sandra, P., David, F. and Cramers, C. (1999). Stir bar sorptive extraction (SBSE), a novel extraction technique for aqueous samples: Theory and principles. *Journal of Microcoloumn Separations,* 11: 737-747.
66. Płotka-Wasylka, J., Szczepa´ nska, N., de la Guardia, M. and Namie´snik, J. (2015). Miniaturized solid-phase extraction techniques. *Trends Analytical Chemistry,* 73: 19-38.
67. Xiao, Z., He, M., Chen, B. and Hu, B. (2016). Polydimethylsiloxane/metal-organic frameworks coated stir bar sorptive extraction coupled to gas chromatography-flame photometric detection for the determination of organophosphorus pesticides in environmentalwater samples. *Talanta,* 156–157: 126-133.
68. David, F., Ochiai, N. and Sandra, P. (2019). Two decades of stir bar sorptive extraction: A retrospective and future outlook. *Trends Analytical Chemistry,* 112: 102-111.

69. Lin, S., Gan, N., Qiao, L., Zhang, J., Cao, Y. and Chen, Y. (2015). Magnetic metal-organic frameworks coated stir bar sorptive extraction coupled with GC-MS for determination of polychlorinated biphenyls in fish samples. *Talanta,* 144:1139-1145.
70. You, L., He, M., Chen, B. and Hu, B. (2017). One-pot synthesis of zeolitic imidazolate framework-8/poly(methyl methacrylate-ethyleneglycol dimethacrylate) monolith coating for stir bat sorptive extraction of phytohormones from fruit samples followed by high performance liquid chromatography-ultraviolet detection. *Journal of Chromatography A,* 1524: 57-65.
71. Wang, Y., Jia, M., Wu, X., Wang, T., Wang, J. and Hou, X. (2019). PEG modified column MIL-101(Cr)/PVA cryogel as a sorbent in stir bar solid phase extraction for determination of non-steroidal anti-inflammatory drugs in water samples. *Microchemical Journal,* 146: 214-219.
72. Wang, Y., Rui, M. and Lu, G. (2018). Recent applications of metal–organic frameworks in sample pretreatment. *Journal of Separation Sciences*, 41: 180-194.
73. Ghani, M., Ghoreishi, S. M. and Azamati, M. (2018). *In-Situ* growth of zeolitic imidazole framework-67 on nanoporous anodized aluminum bar as stir-bar sorptive extraction sorbent for determining caffeine. *Journal of Chromatography A,* 1577: 15-23.
74. Wang, C., Zhou,W., Liao, X., Wang, X. and Chen, Z. (2018). Covalent immobilization of metal organic frameworks onto chemical resistant poly(ether ether ketone) jacket for stir bar extraction. *Analytica Chimica Acta,* 1025: 124-133.
75. Du, F., Sun, L., Tan,W., Wei, Z., Nie, H., Huang, Z., Ruan, G. and Li, J. (2019). Magnetic stir cake sorptive extraction of trace tetracycline antibiotics in food samples: preparation of metal–organic framework-embedded polyhipe monolithic composites, validation and application. *Analytical Bioanalytical Chemistry,* 411: 2239-2248.
76. Koziel, J. A., Odziemkowski, M. and Pawliszyn, J. (2001). Sampling and analysis of airborne particulate matter and aerosols using in-needle trap and SPME fiber devices. *Analytical Chemistry,* 73: 47-54.
77. Firoozichahak, A., Bahrami, A., Ghorbani Shahna, F., Alizadeh, S., Nematollahi, D. and Farhadian, M. (2019). UIO-66-NH_2 packed needle trap for accurate and reliable sampling and analysis of the halogenated volatile organic compounds in air. *International Journal of Environmental Analytical Chemistry*, 2019: 1-18.
78. Biagini, D., Lomonaco, T., Ghimenti, S., Bellagambi, F. G., Onor, M., Scali, M. C., Barletta, V., Marzilli, M., Salvo, P., Trivella, M. G., Fuoco, R. and Di Francesco, F. (2017). Determination of volatile organic compounds in exhaled breath of heart failure patients by needle trap micro-extraction coupled with gas chromatographytandem mass spectrometry. *Journal of Breath Research*, 11: 047110.
79. Feng, D. and Xia, Y. (2018). Comparisons of glyphosate adsorption properties of different functional Cr-based metal–organic frameworks. *Journal of Separation Sciences*, 41: 732-739.

Malaysian Journal of Analytical Sciences (MJAS)
Published by Malaysian Analytical Sciences Society

CHROMATOGRAPHIC PROFILING OF *Syzygium cumini* LEAVES USING HIGH-PERFORMANCE THIN LAYER CHROMATOGRAPHY AND GAS CHROMATOGRAPHY-MASS SPECTROMETRY TECHNIQUES

(Profil Kromatografi bagi daun *Syzygium cumini* mengunakan Teknik Kromatografi Lapisan Nipis Prestasi Tinggi dan Kromatografi Gas-Spektrometri Jisim)

Joshi Vivek[1]*, Mer Sagar[1], Bhagat Keyuri[1], Savalia Vaibhavi[1], Dhalani Jayesh[2], Pandya Mayank[2], Pandya Devang[1]

[1]School of Pharmacy
[2]Department of Chemistry, School of Science
RK University, Rajkot - 360020, Gujarat, India

**Corresponding author: vjoshi850@rku.ac.in*

Received: 15 June 2021; Accepted: 16 September 2021; Published: 25 October 2021

Abstract

Global use of traditional medicinal plants has increased logarithmically in the past few decades. Leaves of *Syzygium cumini* (*S. cumini*) contain important classes of pharmacologically active phytoconstituents like alkaloids, flavonoids, saponins, tannins, glycosides, phenols, fixed oils, monoterpenoids, steroids, and triterpenoids. Since community health is at risk due to improper knowledge and unenforced standardization parameters for herbal formulations, the focus of the study was to develop high-performance thin layer chromatography (HPTLC) fingerprinting and to identify phytoconstituents through gas chromatography and mass spectrometry (GC-MS). HPTLC fingerprinting of the methanolic extract of the leaves of *S. cumini* was performed using the mobile phase chloroform: methanol: ethyl acetate (6:4:6) after several pilot thin layer chromatography (TLC) analyses, which revealed 14 peaks at 254 nm and 10 peaks at 366 nm. Also, qualitative analysis of the same was performed using GC-MS, which revealed 9 phytoconstituents, some of them possessing known pharmacological activity. Such fingerprint analysis using sophisticated chromatographic and spectral techniques can contribute to the quality control in herbal industries; help in assuring purity, efficacy, and safety of the formulations by detection of adulteration; as well as broaden the horizon of phytochemical research, including the isolation of a marker therefrom.

Keywords: *Syzygium cumini*, adulteration, fingerprinting, gas chromatography mass spectrometry, high-performance thin layer chromatography, standardization

Abstrak

Pengunaan tumbuhan bagi perubatan traditional secara global telah meningkat bagi tempoh beberapa dekad yang lepas. Daun *Syzygium cumini* (*S. cumini*) mengandungi jujukan fito aktif secara farmakologi merupakan kelas utama seperti alkaloid, flavonoid, saponin, tannin, glikosida, fenol, minyak, monoterpenoids, steroids, dan triterpenoids. Semenjak kesihatan komuniti berada pada keadaan berisiko disebabkan oleh maklumat yang kurang tepat dan tidak peguatkuasaan piawaian parameter bagi formulasi herbal, maka fokus kajian ini untuk membangunkan pencapjarian kromatografi lapisan nipis prestasi tinggi (HPTLC) dan mengenalpasti jujukan fito melalui kromatografi gas dan spektrometri jisim (GC-MS). Pencapjarian HPTLC terhadap

ekstrak metanol bagi daun *S. cumini* telah dijalankan mengunakan fasa bergerak klorofom: metanol: etil asetat (6:4:6) selepas beberapa analisis pilot kromatografi lapisan nipis (TLC), ia menjelaskan terdapat 14 puncak pada 254 nm dan 10 puncak pada 366 nm. Juga, analisis kualitatif telah dijalankan mengunakan GC-MS, dimana ia menjelaskan 9 jujukan fito, sebahagian dikenalpasti mempunyai aktiviti farmakologi. Analisis capjari mengunakan teknik kromatografi dan spekta boleh menyumbang kepada kawalan kualiti dalam industri herba; membantu dalam jaminan ketulenan, kejituan dan keselamatan dalam formulasi dengan cara mengenal pemalsuan; juga pengembangan bidang kajian fitokimia, termasuklah pemencilan penanda kimia.

Kata kunci: *Syzygium cumini*, pemalsuan, pencapjarian, kromatografi gas dan spektrometri jisim, kromatografi lapisan nipis prestasi tinggi, pemiawaian

Introduction

Syzygium cumini also known as *Eugenia cumini, Eugenia jambolana, Myrtus cumini*, *Syzygium jambolana, Syzygium jambolanum,* and *Eugenia caryophyllifolia*, is a tree belonging to the Myrtle family, Myrtaceae. It is found in India, Bangladesh, Nepal, Sri Lanka, and Myanmar and throughout south-east Asia and the Pacific Islands while it is also grown in Indonesia, Thailand, Australia, Malaysia, Kenya, Zimbabwe, Madagascar, Colombia, Zambia, Cuba, Mexico, Brazil, and some parts of the USA particularly Florida and Hawaii. It is commonly known as Indian blackberry, Java Plum, Jambolan while Surabhipatra (in Ayurveda); Jamun (in Hindi); Jambudo (in Gujarati); Brahaspati, Mahajambu, and Ksudrajambu (in Sanskrit)[1, 2, 3].*S. cumini* leaves, shown in Figure 1, contain various classes of secondary metabolites: glycosides, alkaloids, triterpenoids, flavonoids, saponins, tannins, phenols, proteins, steroids, and fixed oils and fats. Major phytoconstituents of the leaves include sitosterols, crategolic (maslinic) acid, myricetin, quercetin, ellagic acid, and betulinic acid. Essential oils from leaves are rich in pinocarveol, cineole, α-terpeneol, ellagic acids, myrtenol, eucarvone, α-myrtenal, geranyl acetone, α-cadinol, kaempferol, pinocarvone, quercetin, isoquercetin [4, 5, 6].



Figure 1. Leaves of *Syzygium cumini*

Its leaves are found to be useful in diabetes, hepatitis, and dental disorders as well to be an anticancer, anti-diarrheal, cardioprotective, diuretic, gastroprotective, and hepatoprotective agent. The leaves possess anti-allergic, antipyretic, antibacterial, anti-inflammatory, antimicrobial, and antioxidant properties. The leaves are also used to treat stomachache, dermopathy, leucorrhoea, constipation, fever, reduce DNA damage induced by radiation, and in inhibition of blood discharges in the feces [7-11].

S. cumini leaves are pharmacologically useful. However, the standardization of herbal formulations is always an issue. Additionally, government bodies have also levied certain regulations for the quality control and standardization of herbal products. However, chromatographic analysis of Indian medicinal plants using globally accepted sophisticated techniques is scarcely available.

This research may provide the HPTLC and GC-MS fingerprints of *S. cumini* leaves to herbal industries and society. It may facilitate standardization and quality control for the prevention of adulteration in *S. cumini* leaves formulations, thereby benefitting the end-user. It shall give an insight into the phytochemical composition of the leaves, which can be further worked upon.

Materials and Methods

Collection and sampling

Leaves of *S. cumini* were obtained from the Medicinal Garden of RK University in February (Figure 1). The sample was then authenticated by comparing it with standard literature. Its herbarium SOP/COG/91/2013 was prepared and submitted at the School of Pharmacy, RK University, and certified by the botanist of School of Science, RK University.

Extraction of *S. cumini* leaves

Leaves of *S. cumini* were dried in a hot air oven at 50 ºC and powdered using a mixer grinder. Maceration of 50.0 g dry powder of the leaves with 100 mL methanol was carried out at room temperature for 24 hours. After filtration, on evaporating the excess solvent from the filtrate at room temperature, 7.2 g sticky, dry and solid extract was obtained.

Pilot TLC studies and HPTLC fingerprinting

Several pilot TLCs were developed for methanolic extract using various proportions of chloroform, methanol, and ethyl acetate. Highly non-polar petroleum ether extract and highly polar water extract were not used, as we had expected to obtain chemical constituents of medium polarity. After observing the results, many TLCs of methanolic extract was developed by adding ethyl acetate and formic acid for removal of tailing. The mobile phase Chloroform: Methanol: Ethyl acetate (6: 4: 6) showed the best resolution in TLC studies. Hence, it was further used for HPTLC fingerprinting.

Methanolic extract of *S. cumini* leaves was analyzed to obtain HPTLC fingerprinting using Chloroform: Methanol: Ethyl acetate (6: 4: 6) at the Department of Pharmaceutical Sciences, Saurashtra University, Rajkot, Gujarat, India. The HPTLC fingerprinting was obtained on HPTLC plates containing silica gel C_{60} F_{254} as stationary phase, manufactured by E.MERCK KgaA. CAMAG Linomat 5 “Linomat5_171010” S/N 171010 (2.01.02) was used for a sample application. Peak height and area were selected for evaluation, while the measurement was done using the principle of absorption. The sample was dissolved in Methanol. CAMAG TLC Scanner 3 “Scnner_171010” S/N 171010 (2.01.02) was used for scanning the plates in daylight as well as at 254 nm and 366 nm.

GC-MS analysis

The sample containing methanolic extract of *S. cumini* leaves was named Jambudo (local name of *S. cumini*). Qualitative GC-MS analysis of the sample was performed at the Department of Chemistry, School of Science, RK University, Rajkot, Gujarat, India. Agilent GC-7820A/MS-5977 with HP-5ms column containing (5%-phenyl)-methylpolysiloxane as stationary phase and helium as carrier gas was used for this purpose following the GC-MS protocol from authentic standard works of literature [12,13,14,15,16]. National Institute of Standards and Technology (NIST) library was used for the precise identification of phytoconstituents.

Results and Discussion

Pilot TLC studies and HPTLC fingerprinting

After several pilots, TLC analyses, an HPTLC fingerprinting of the methanolic extract of the leaves of *S. cumini* was performed using the mobile phase Chloroform: Methanol: Ethyl Acetate (6: 4: 6). The HPTLC plates were scanned at 254 nm (Figure 2), 366 nm (Figure 3), and daylight (Figure 4) that revealed 14 spots (Figure 5) at 254 nm and 10 spots (Figure 6) at 366 nm. The distinct R_f values of the spots at 254 nm and 366 nm are as provided in Table 1 and Table 2 respectively.

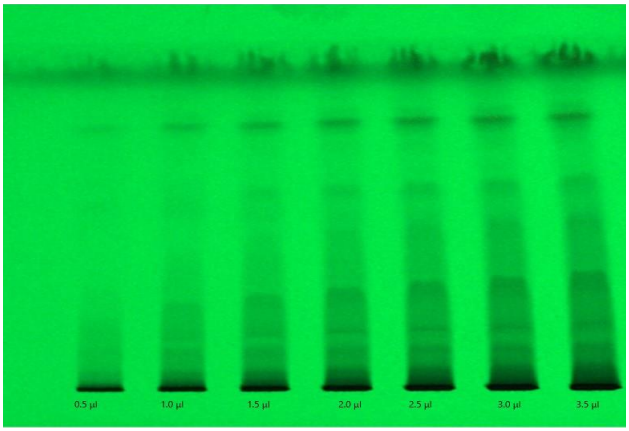


Figure 2. HPTLC plate at 254 nm

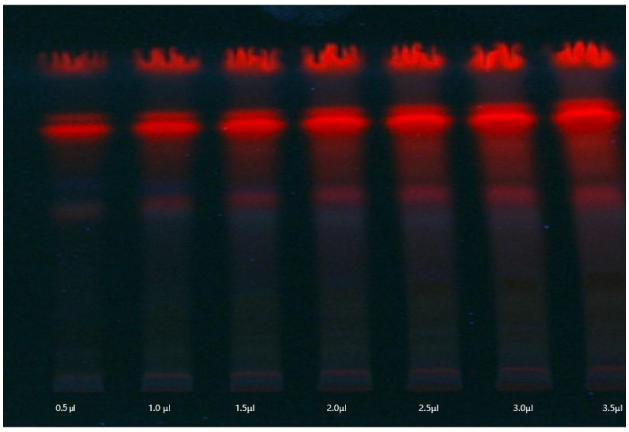


Figure 3. HPTLC plate at 366 nm

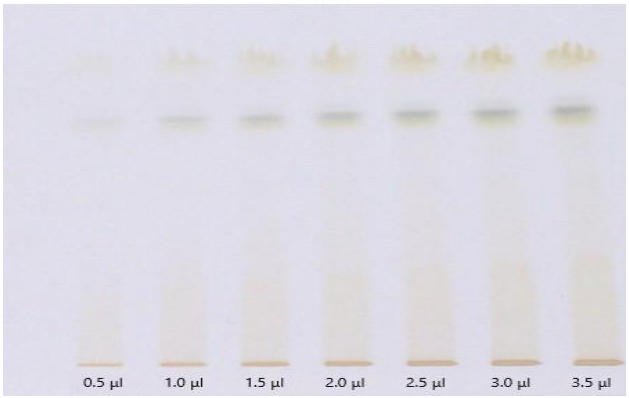


Figure 4. HPTLC plate at daylight

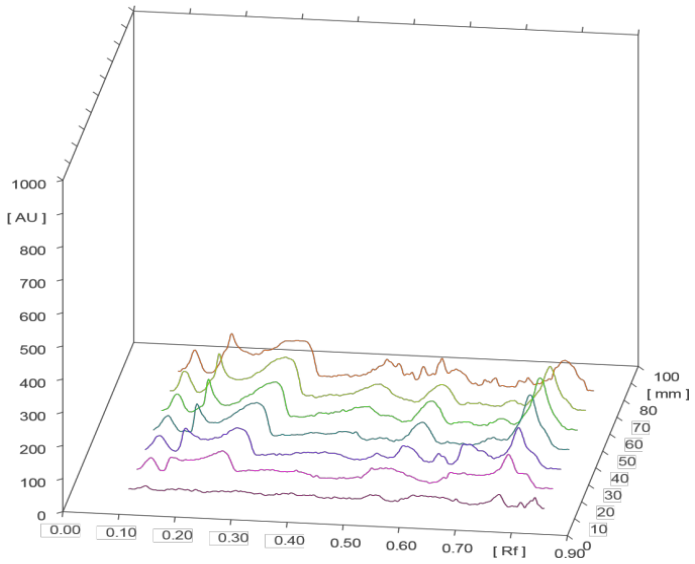


Figure 5. Densitometric chromatogram of methanolic extract of *S. cumini* leaves at 254 nm

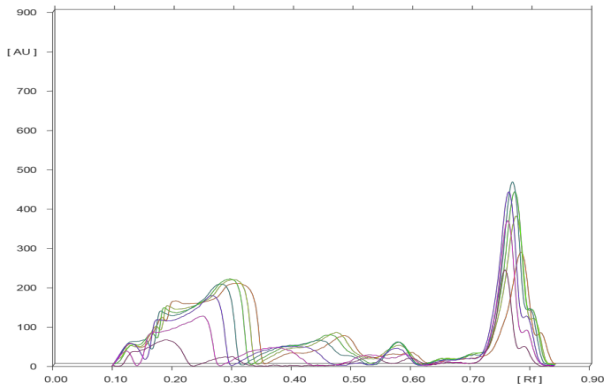


Figure 6. Densitometric chromatogram of methanolic extract of *S. cumini* leaves at 366 nm

Table 1. Maximum R_f and Area under curve at 254 nm

Peak	Max R_f	AUC (ng μL^{-1})
1	0.13	1071.2
2	0.19	3841.1
3	0.31	6786.7
4	0.47	1727.1
5	0.49	548.9
6	0.52	367.7
7	0.54	535.1
8	0.57	1254.4
9	0.60	1081.0
10	0.65	167.0
11	0.67	218.9
12	0.71	188.0
13	0.72	314.9
14	0.79	3410.2

Table 2. Maximum R_f and Area under curve at 366 nm

Peak	Max R_f	AUC (ng μL^{-1})
1	0.13	1304.5
2	0.18	2726.1
3	0.20	3751.8
4	0.30	15174.9
5	0.40	981.2
6	0.49	3995.0
7	0.60	735.7
8	0.67	298.7
9	0.78	9574.9
10	0.81	1127.4

GC - MS analysis

The GC-MS spectrum of methanolic extract of *S. cumini* leaves (Figure 7) revealed a confirmatory structure match of the nine chemical compounds when compared with the NIST database. The following compounds (as shown in Table 3) were identified from the analysis.

Compound 1: (1R)-2,6,6-trimethylbicyclo [3.1.1]hept-2-ene, Mol. formula - $C_{10}H_{16}$, Mol. wt. - 136.2340, RT - 2.31. GC-MS fragment: The peak at 2.31 minutes had a mass [M^+] 136.2340. The daughter ion spectra of compound 1 revealed the characteristic fragments m/z (as shown in Figure 8) 53, 55, 77.1, 78.1, 79.1, 80.1, 91.1, 92.1, 93.1, 105.1.

Compound 2: 2,5,5-trimethyl-cyclopentadiene; Mol. formula - C_8H_{12}; Mol. wt. - 108.18, RT - 4.416. GC-MS fragment: The peak at 4.416 minutes had a mass [M^+] 108.18. The daughter ion spectra of compound 2 revealed the characteristic fragments m/z (as shown in Figure 9) 51, 77, 78, 79, 91, 92, 93.1, 105, 107, 108.

Compound 3: α-terpineol; Mol. formula - $C_{10}H_{18}O$; Mol. wt. - 154.25; RT - 8.27. GC-MS fragment: The peak at 8.27 minutes had a mass [M^+] 154.25. The daughter ion spectra of compound 3 revealed the characteristic fragments m/z (as shown in Figure 10) 59.1, 77.1, 79, 81.1, 91.1, 92.1, 93.1, 94, 121.1, 136.1.

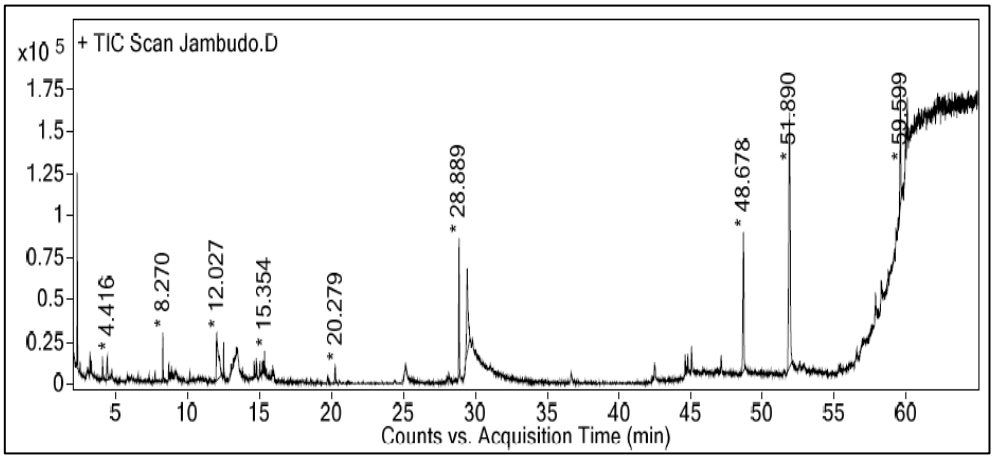


Figure 7. Gas chromatogram of methanolic extract of *S. cumini* leaves

Table 3. Phytoconstituents identified from methanolic extract of *S. cumini* leaves

Peak	RT	Name of Compound	Molecular Formula	Molecular Weight (gm/mol)	Peak Area %
1	2.31	(1R)-2,6,6-trimethylbicyclo[3.1.1]hept-2-ene	$C_{10}H_{16}$	136.2340	7.54
2	4.416	2,5,5-trimethyl-cyclopentadiene	C_8H_{12}	108.18	1.87
3	8.27	α-terpineol	$C_{10}H_{18}O$	154.25	1.95
4	12.027	1,2,3-benzenetriol	$C_6H_6O_3$	126.11	9.24
5	12.499	1,4-methanocycloocta[d]pyridazine,1,4,4a,5,6,9,10,10a-octa hydro-11,11-dimethyl-(1.alpha,4.alpha,4a.alpha,10a.alpha)	$C_{13}H_{20}N_2$	204.15	1.2
6	28.889	3,7,11,15-tetramethyl-2-hexadecen-1-ol	$C_{20}H_{40}O$	296.5310	7.28
7	29.451	9,12,15-octadecatrienoic acid, methyl ester (Z, Z, Z)	$C_{19}H_{32}O_2$	292.4562	10.45
8	48.678	Vitamin E	$C_{29}H_{50}O_2$	430.7061	13.23
9	51.89	γ-sitosterol	$C_{29}H_{50}O$	414.7067	34.01

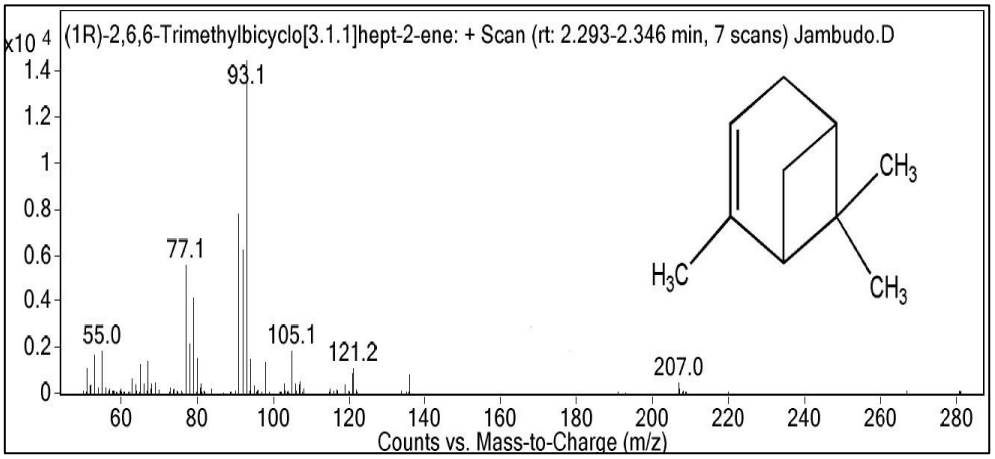


Figure 8. Mass spectrogram of Compound 1

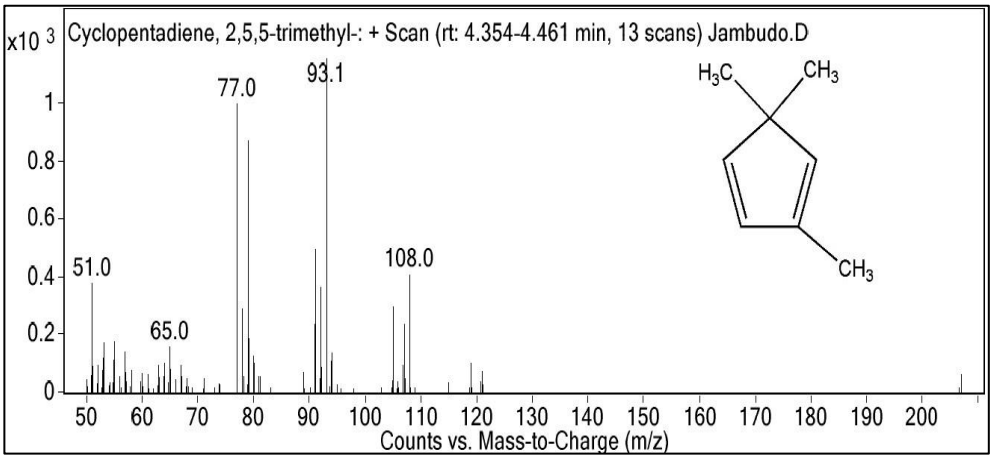


Figure 9. Mass spectrogram of Compound 2

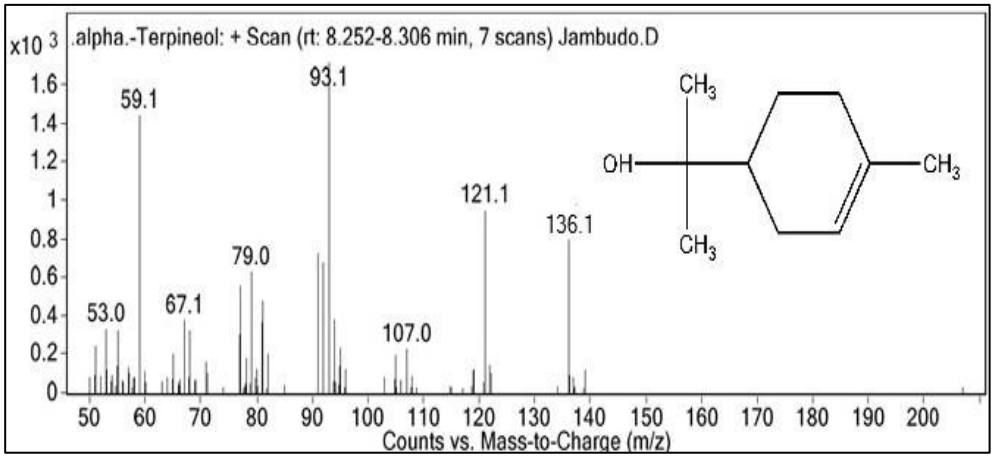


Figure 10. Mass spectrogram of Compound 3

Compound 4: 1,2,3-benzenetriol; Mol. formula - $C_6H_6O_3$; Mol. wt. - 126.11; RT - 12.027. GC-MS fragment: The peak at 12.027 minutes had a mass [M^+] 126.11. The daughter ion spectra of compound 4 revealed the characteristic fragments m/z (as shown in Figure 11) 51, 52, 52.1, 52.9, 53.1, 79, 80, 97, 108, 126.

Compound 5: 1,4-methanocycloocta[d]pyridazine,1, 4,4a,5,6,9,10,10a-octahydro-11,11dimethyl(1.alpha, 4.alpha,4a.alpha,10a.alpha); Mol. formula - $C_{13}H_{20}N_2$; Mol. wt. - 204.15; RT - 12.499. GC-MS fragment: The peak at 12.499 minutes had a mass [M^+] 204.15. The daughter ion spectra of compound 5 revealed the characteristic fragments m/z (as shown in Figure 12) 55.1, 67, 69.1, 77.1, 79.1, 91, 93.1, 105.1, 119.1, 133.

Compound 6: 3,7,11,15-tetramethyl-2-hexadecen-1-ol; Mol. formula - $C_{20}H_{40}O$; Mol. wt. - 296.5310; RT - 28.889. GC-MS fragment: The peak at 28.889 minutes had a mass [M^+] 296.5310. The daughter ion spectra of compound 6 revealed the characteristic fragments m/z (as shown in Figure 13) 55.1, 57.1, 68.1, 69.1, 71.1, 79.1, 81.1, 82.1, 95.1, 123.1.

Compound 7: 9,12,15-octadecatrienoic acid, methyl ester (Z, Z, Z); Mol. formula - $C_{19}H_{32}O_2$; Mol. wt. - 292.4562; RT - 29.451. GC-MS fragment: The peak at 29.451 minutes had a mass [M^+] 292.4562. The daughter ion spectra of compound 7 revealed the characteristic fragments m/z (as shown in Figure 14) 55.1, 60, 67.1, 77.1, 79.1, 80.1, 81.1, 91.1, 93.1, 95.1.

Compound 8: Vitamin E; Mol. formula - $C_{29}H_{50}O_2$; Mol. wt. - 430.7061; RT - 48.678. GC-MS fragment: The peak at 48.678 minutes had a mass [M^+] 430.7061. The daughter ion spectra of compound 8 revealed the characteristic fragments m/z (as shown in Figure 15) 73, 121, 164, 164.1, 165.1, 166.1, 205.1, 430.4, 431.3, 431.4.

Compound 9: γ-sitosterol; Mol. formula - $C_{29}H_{50}O$; Mol. wt. - 414.7067; RT - 51.89. GC-MS fragment: The peak at 51.89 minutes had a mass [M^+] 414.7067. The daughter ion spectra of compound 9 revealed the characteristic fragments m/z (as shown in Figure 16) 55.1, 57.1, 79, 81.1, 91.1, 95.1, 105.1, 145.1, 207, 396.3.

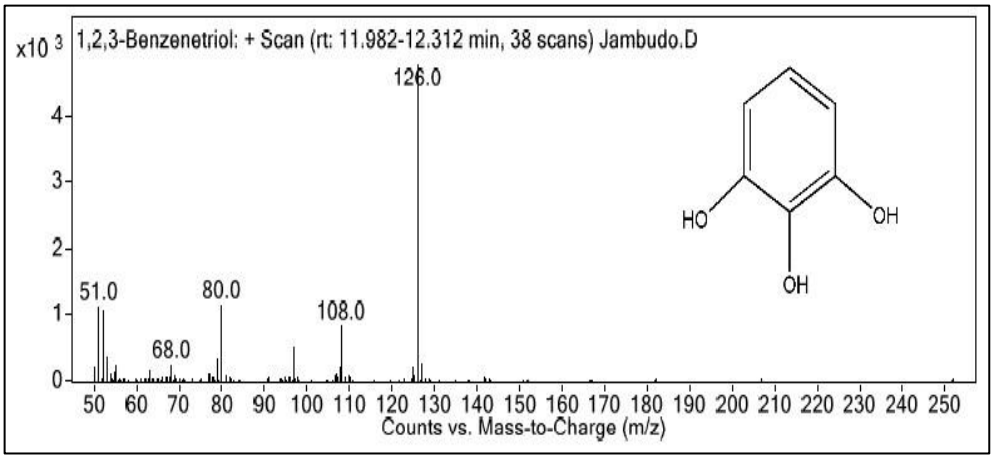


Figure 11. Mass spectrogram of Compound 4

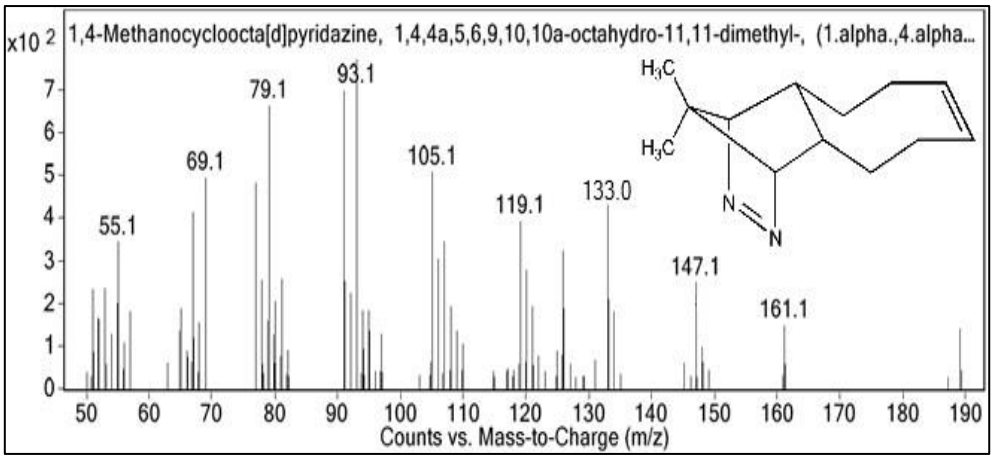


Figure 12. Mass spectrogram of Compound 5

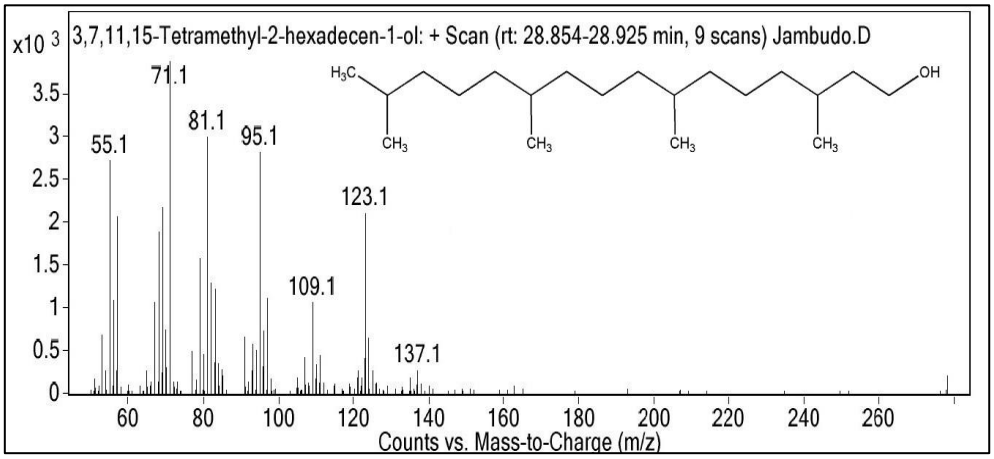


Figure 13. Mass spectrogram of Compound 6

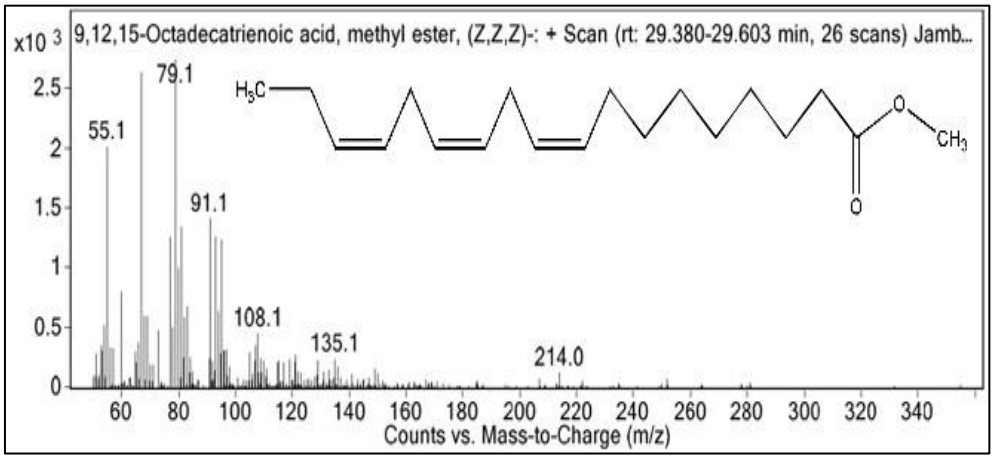


Figure 14. Mass spectrogram of Compound 7

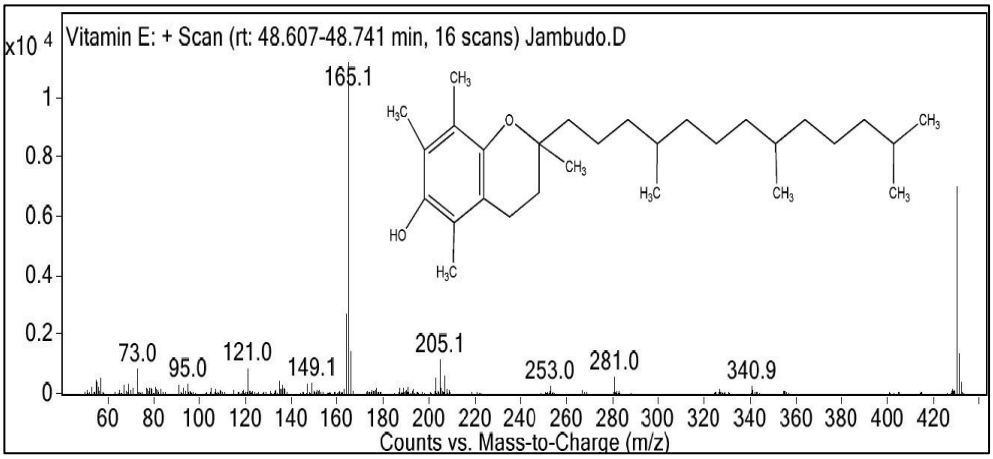


Figure 15. Mass spectrogram of Compound 8

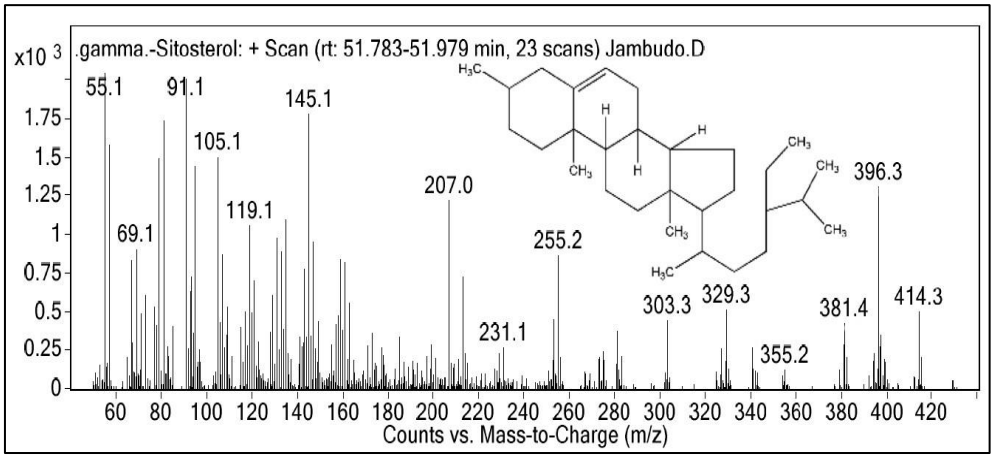


Figure 16. Mass spectrogram of Compound 9

The following phytochemicals detected from the GC-MS analysis of a methanolic extract of *S. cumini* leaves (Table 4) were reported with significant biological activities:

It was found that many of the compounds detected in the GC-MS analysis possessed significant pharmacological activity. Few of them were antimicrobial and specifically antibacterial as well. The presence of Vitamin E explains a lot of health benefits as given in the table. Some of them were found anticancer, anticonvulsant, antinociceptive, antioxidant as well as anti-inflammatory, while one of them was detected possessing antidiabetic activity.

It is noteworthy that Jaleel et al. (2019) have reported 10 different compounds through GC-MS analysis of *S. cumini* seeds extract in hexane [29]. In addition to that, Sharma et al. (2015) had identified and quantified 8 monoterpenoids by GC-MS in volatile oil of unripe

fruit pulp of *S. cumini*[30]. Chitnis et al. (2012) reported HPTLC analysis of available formulations containing *S. cumini* seeds using Toluene: Ethyl acetate: Formic acid (2: 7: 1) [31]. However, general HPTLC analysis by Kharat et al. revealed 12 peaks in ethanolic, 15 in methanolic, 14 in ethyl acetate, 11 in chloroform, and 3 in aqueous extract of *S. cumini* leaves using Toluene: Methanol: Diethylamine (30: 4: 4) solvent system using sonication method [32].

This exclusive method for HPTLC fingerprint and GC-MS analysis of *S. cumini* leaves may help to determine the quality of formulations as well as to detect adulteration by other materials in those formulations, thereby helping in standardization. It paves way for the isolation of the detected compounds. It also opens options for exploring other pharmacological uses of *S. cumini* leaves based on the reported biological properties of the detected compounds.

Table 4. Compounds detected from GC-MS of *S. cumini* leaves and their biological activities

Name of Compound	Reported Biological Activities
(1R)-2,6,6-trimethylbicyclo[3.1.1]hept-2-ene (commonly known as α-pinene)	✓ Anti-inflammatory[17] ✓ Antinociceptive[18] ✓ Inhibits hepatoma carcinoma cell proliferation[19]
α-terpineol	✓ Anticancer agent[20] ✓ Inhibits IL-1β, IL-6 & IL-10 production[21] ✓ Antimicrobial in dental problems[22]
3,7,11,15-tetramethyl-2-hexadecen-1-ol (commonly known as Phytol)	✓ Anticonvulsant[23] ✓ Antinociceptive and antioxidant[24]
9,12,15-octadecatrienoic acid, methyl ester, (Z, Z, Z) (commonly known as α-methyl linolenate)	✓ Antimicrobial and antibacterial[25] ✓ Downregulate melanogenesis[26]
Vitamin E (commonly known as α-tocopherol)	✓ Prevents loss of spermatogenesis and lipid peroxidation, antioxidant, inhibits smooth muscle proliferation, decreases protein kinase C activity, enhances prostacyclin release, upregulates cytosolic phospholipase A2 and cyclooxygenase activities, and facilitates natriuresis.[27]
γ-sitosterol	✓ Antidiabetic[28]

Conclusion

This preliminary fingerprint analysis of *S. cumini* leaves using sophisticated techniques may provide a starting point for quality control of its formulations; assuring purity, efficacy, and safety of the formulations; detecting adulteration; in standardization and ensuring isolation of a marker compound, thereby helping government regulatory agencies, herbal industries, and consumers. It may also broaden the horizon for further phytochemical and pharmacological research, and the development of more sophisticated methods for standardization purposes.

Acknowledgments

The authors especially thank Mr. Rahim Dhanani for providing his expert skills in English editing and Proofreading of this research manuscript, also to Ms. Anjali Patadiya for assistance in linguistics as well as RK University for providing the required facilities and technical support.

References

1. Khare, C. P. (2007). Indian medicinal plants. Springer, Berlin: pp. 637.
2. Kirtikar, K. R. and Basu, B. D. (1935). Indian medicinal plants (2nd Edition). Lalit Mohan Basu, Allahabad, 2: pp. 1052-1054.
3. Bandiola, T. M. B., Ignacio, G. B., Yunson, E. G. A. and Bandiola, P. D. B. (2017).*Syzygium cumini* (L.) Skeels: a review of its phytochemical constituents, toxicity studies, and traditional and pharmacological uses.*International Journal of Applied Pharmaceutical and Biological Research*, 2(6): 15-23.
4. Ayyanar, M. and Subash-Babu, P. (2012). *Syzygium cumini* (L.) Skeels: A review of its phytochemical constituents and traditional uses.*Asian Pacific Journal of Tropical Biomedicine*, 2(9): 240-246.
5. Ramos, I. L. and Bandiola, T. M. B. (2017). Phytochemical screening of *Syzygium cumini* (Myrtaceae) leaf extracts using different solvents of extraction.*Der Pharmacia Lettre*, 9(2): 74-78.
6. Ramya, S., Neethirajan, K. and Jayakumararaj, R. (2012). Profile of bioactive compounds in *Syzygium cumini* - a review.*Journal of Pharmacy Research*, 5(8): 4548-4553.
7. Kumar, A., Ilavarasan, R., Jayachandran, T., Deecaraman, M., Aravindan, P., Padmanabhan, N. and Krishan, M. R. V. (2013).Anti-diabetic activity of *Syzygium cumini* and its isolated compound against streptozotocin-induced diabetic rats.*Journal of Medicinal Plants Research*, 2(9): 246-249.
8. Veeram, A., Sindhu, G. and Girish, C. (2017). A review on pharmacology and phytochemistry of *Syzygium cumini*. *Indian Journal of Pharmaceutical and Biological Res*earch, 5(4): 24-28.
9. Katiyar, D., Singh, V. and Ali, M. (2016). Recent advances in the pharmacological potential of *Syzygium cumini*: A review. *Advances in Applied Science Research*, 7(3): 1-12.
10. Brito, F. A., Lima, L. A., Ramos, M. F. S., Nakamura, M. J., Cavalher-Machado, S. C., Siani, A. C., Henriques, M. G. M. O. and Sampio, A. L. F. (2007). Pharmacological study of the anti-allergic activity of *Syzygium cumini* (L.) Skeels. *Brazilian Journal of Medical and Biological Research*, 40(1): 105-115.
11. Gowri, S. S. and Vasantha, K. (2010). Phytochemical screening and antibacterial activity of *Syzygium cumini* (L.) (Myrtaceae) leaves extracts. *International Journal of PharmTech Research*, 2(2): 1569- 1573.
12. Dhalani, J., Dubal, G., Rathod, C. and Nariya, P. (2020). Evaluation of non-polar composition in *Plumbago zeylanica* leaves by gas chro-matography and mass spectrometry.*Folia Medica*, 62(2): 308-313.
13. Dhalani, J., Kapadiya, K., Pandya, M., Dubal, G., Imbraj, P. and Nariya, P. (2018). An approach to identify sterol entities from *Abrus Pretorius*'s seeds by GC-MS.*Journal of Scientific and Industrial Research*, 77: 297-300.
14. Dhalani, J., Parmar, R., Rajpara, R. and Nariya, P. (2020). Rapid identification of fatty acids from *Leptadenia reticulata* areal parts by GC-MS.*Journal of Scientific and Industrial Research*, 79(8): 709- 711.
15. Dhalani, J., Chandegara, B. and Pathak, V. (2019). Rapid investigation of sterols from *Plumbago zeylanica* stem. *International Research Conference and summit on Innovations, Startups& Investments*: 69-72.
16. Dhalani, J., Dubal, G., Patel, A. and Nariya, P. (2019). Isolation and identification of non-polar chemical entity from *Leptadenia reticulata* aerial parts.*Asian Journal of Pharmaceutical and Clinical Research*, 12(2): 226-229.
17. Kim, D. S., Lee, H. J., Jeon, Y. D., Han, Y. H., Kee, J. Y., Kim, H. J., Shin, H. J., Kang, J. W., Lee, B. S., Kim, S. H., Kim., S. J., Park, S. H., Choi, B. M., Park, S. J., Um, J. Y. and Hong, S. H. (2015). *Alpha pinene* exhibits anti-inflammatory activity through the suppression of MAPKs and the NF-κB pathway in mouse peritoneal macrophages.*American Journal of Chinese Medicines*, 43(4): 731-742.
18. Him, A., Ozbek, H., Turel, I. and Oner, A. C. (2008). Antinociceptive activity of alpha-pinene and fenchone. *Pharmacologyonline* 3: 363-369.

19. Chen, W. Q., Xu, B., Mao, J. W., Wei., F. X., Li, M., Liu, T., Jin, X. B. and Zhang, L. R. (2014). Inhibitory effects of α-pinene on hepatoma carcinoma cell proliferation.*Asian Pacific Journal of Cancer Prevention*, 15(7): 3293-9297.
20. Hassan, S. B., Hala, G. M., Goransson, H. and Larsson, R. (2010). Alpha terpineol: a potent anticancer agent which acts through suppressing NF-κB signaling.*Anticancer Research*,30(6): 1911 – 1919.
21. Noguiera, M. N. M., Aquino, S. G., Rossa Junior, C. and Spolidorio, D. M. P. (2014). Terpinen-4-ol and alpha-terpineol (tea tree oil components) inhibit the production of IL-1β, IL-6, and IL-10 on human macrophages.*Inflammation Research*, 63(9): 769-778.
22. Park, S. N., Lim, Y. K., Freire, M. O., Cho, E., Jin, D. and Kook, J. K. (2012). Antimicrobial effect of linalool and α-terpineol against periodontopathic and cariogenic bacteria. *Anaerobe,*18(3): 369-372.
23. Costa, J. P., Ferreira, P. B., De Sousa, D. P., Jordan, J. and Freitas, R. M. (2012). Anticonvulsant effect of phytol in a pilocarpine model in mice.*Neuroscience Letters*, 523(2): 115-118.
24. Santos, C. C. D. M. P., Salvadori, M. S., Mota, V. G., Costa, L. M., De Almeida, A. A. C., De Oliveira, G. A. L., Costa, J. P., De Sousa, D. P., De Freitas, R. M. and De Almeida, R. N. (2013). Antinociceptive and Antioxidant activities of Phytol *In vivo* and *In vitro* models.*Neuroscience Journal*, 2013: 1-9.
25. Singab, A. N. B., Mostafa, N. M., Eldahshan, O. A., Ashour, M. L. and Wink, M. (2014). Profile of volatile components of Hydrodistilled and extracted leaves of *Jacaranda acutifolia* and their antimicrobial activity against foodborne pathogens. *Natural Product Communications*, 9(7): 1007-1010.
26. Ko, G. A., Shrestha, S. and Kim Cho, S. (2018). *Sageretia thea* fruit extracts rich in methyl linoleate and methyl linolenate downregulate melanogenesis via the Akt/GSK3β signaling pathway. *Nutrition research and practice*, 12(1): 3-12.
27. Brigelius-Flohe, R. and Traber, M. G. (1999). Vitamin E: function and metabolism. *FASEB Journal*, 13(10): 1145-1155.
28. Balamurugan, R., Duraipandiyan, V. and Ignacimuthu, S. (2011). Antidiabetic activity of γ-sitosterol isolated from *Lippia nodiflora* L. in streptozocin induced diabetic rats. *European Journal of Pharmacology*, 667(1–3): 410-418.
29. Jaleel, A. A. H., Mahdi, J. F., Farooqui, M. and Shaikh, Y. H. (2019). Gas chromatography-mass spectroscopic analysis of black plum seed (*Syzygium cumini*) extract in hexane. *Asian Journal of Pharmaceutical and Clinical Research*, 12(2): 219-222.
30. Sharma, R. J., Gupta, R. C., Bansal, A. K. and Singh, I. P. (2015). Metabolite fingerprinting of *Eugenia jambolana* fruit pulp extracts using NMR, HPLC-PDA-MS, GC-MS, MALDI-TOF-MS and ESI-MS/MS spectrometry. *Natural Product Communications*, 10(6): 969-976.
31. Chitnis, K. S., Palekar, S. B., Koppar, D. R. and Mestry, D. Y. (2012). Evaluation of *Syzygium cumini* Linn. seed formulations available in the market using spectrophotometric and chromatographic techniques. *International Journal of Pharmaceutical Sciences and Research*, 3(2): 556-560.
32. Kharat, S. N., Ansari, N. and Mendhulkar, V. D. (2020). HPTLC screening for flavonoids content in leaf extracts of *Syzygium cumini* (Linn.) and its antimicrobial activity. *Research Journal of Pharmacy and Technology*, 13(6): 2720-2726.

Malaysian Journal of Analytical Sciences (MJAS)
Published by Malaysian Analytical Sciences Society

AIR POLLUTION ASSESSMENT IN SOUTHERN PENINSULAR MALAYSIA USING ENVIRONMETRIC ANALYSIS

(Penilaian Pencemaran Udara Di Selatan Semenanjung Malaysia Menggunakan Analisis Environmetrik)

Haslinda Ab Malek, Nurul Nabila Natasha Jalaluddin, Sharifah Nadia Syed Hasan,Umi Amira Hassni, Isnewati Ab Malek*

Faculty of Computer and Mathematical Sciences
Universiti Teknologi MARA, Cawangan Negeri Sembilan, Kampus Seremban,
70300 Seremban, Negeri Sembilan, Malaysia

**Corresponding author: isnewati@uitm.edu.my*

Received: 31 August 2021; Accepted: 2 October 2021; Published: 25 October 2021

Abstract

Air pollution can be defined as the presence of toxic chemicals at levels that pose a health risk. Air quality plays an important role as polluted air could affect the environment. The air pollution problem has become a major issue in Malaysia for the past two decades. Thus, this study focused on the air pollution assessment in Southern Peninsular Malaysia based on the data obtained from the Department of Environment Malaysia. Six major air pollutants (PM_{10}, $PM_{2.5}$, SO_2, NO_2, CO and O_3) in five monitoring stations were measured hourly for the year 2018. Factor Analysis was used to identify the most dominant air pollutant to the air quality. It is found that PM_{10} and $PM_{2.5}$ were the most dominant air pollutants that contribute to the degradation of the air quality in Southern Peninsular Malaysia due to industrial activities. It is hoped that this study could help the authorities in controlling air pollution by determining the most dominant air pollutants involved.

Keywords: air pollution, air pollutant, air quality, factor analysis, dominant

Abstrak

Pencemaran udara dapat didefinisikan sebagai kehadiran bahan kimia beracun pada tahap yang menimbulkan risiko kesihatan. Kualiti udara memainkan peranan penting kerana udara yang tercemar dapat mempengaruhi persekitaran. Masalah pencemaran udara telah menjadi isu utama di Malaysia sejak dua dekad yang lalu. Oleh itu, kajian ini memfokuskan pada penilaian pencemaran udara di Selatan Semenanjung Malaysia berdasarkan data yang diperoleh dari Jabatan Alam Sekitar Malaysia. Enam pencemar udara utama (PM_{10}, $PM_{2.5}$, SO_2, NO_2, CO and O_3) di lima stesen pemantauan diukur setiap jam untuk tahun 2018. Analisis Faktor digunakan untuk mengenal pasti bahan pencemar udara yang paling dominan terhadap kualiti udara. Didapati bahawa PM_{10} dan $PM_{2.5}$ adalah bahan pencemar udara yang paling dominan menyumbang kepada penurunan kualiti udara di Selatan Semenanjung Malaysia kerana aktiviti perindustrian. Diharapkan kajian ini dapat membantu pihak berkuasa dalam mengawal pencemaran udara dengan menentukan bahan pencemar udara yang paling dominan.

Kata kunci: pencemaran udara, bahan pencemar udara, kualiti udara, analisis faktor, dominan

Introduction

Air is the unseen gaseous material that covers the earth, primarily a mixture of oxygen and nitrogen. Air pollution can be characterized as a situation in which high concentrations of air pollutants are present in the atmosphere above their normal ambient levels. In a broader sense, air pollution means the presence of chemicals or compounds in the air which are usually not present and lower the quality of the air that cause detrimental changes to the quality of life [1]. Air pollution sources include contaminants (such as ammonia, carbon monoxide, sulphur dioxide, nitrous oxides, methane and chlorofluorocarbons), particulate matter (both organic and inorganic), and biologic molecules. This can cause human diseases, allergies and even death. This can also damage other living creatures such as livestock and food crops and can affect the natural environment. In Malaysia, Air Pollution Index (API) is a simple and generalized way of describing air quality. The API was introduced as an index system for classifying and reporting the ambient air quality. The API for a given period is calculated based on the sub-index value (sub-API) for all the six air pollutants, namely particulate matter (PM_{10}) and ($PM_{2.5}$), nitrogen dioxide (NO_2), sulphur dioxide (SO_2), carbon monoxide (CO), and ozone (O_3), which are included in the Malaysia API system. The API reference value has been based on the Recommended Malaysian Ambient Air Quality Guidelines (RMAQG) of 1989 as shown in Table1 [2].

$PM_{2.5}$ can cause long term and short-term health impacts, such as irritation in the eyes, sneezing and shortness of breath while the worst scenarios can cause respiratory problems, such as asthma, chronic bronchitis, and heart disease. China is one of the countries listed as the most polluted by $PM_{2.5}$ [3]. This is supported by a case study in Beijing, which indicates $PM_{2.5}$ is one of the air pollutants which becomes an emerging public health issue, especially in China's mega-cities. Moreover, PM_{10} is the main component of dust fall, which comes from industrial activities and construction sites, the transportation exhaust emission and soil dust [4]. Other than that, NO_2 is a gaseous air pollutant formed when a high temperature consumes fossil fuels such as coal, oil, gas or diesel. NO_2 is one of the major indicators of outdoor air pollution in Shah Alam [5]. This is supported by the research done in the Northern Region of Peninsular Malaysia which concluded that NO_2 is one of the major pollutants that have contributed to degrading air quality in that area due to the combustion process from vehicles and industries [6].

Other than that, according to Ismail et al. [6], carbon monoxide (CO) is a poisonous gas made from incomplete combustion of vehicles, industries, and open burning activities. Moreover, research done by Zakaria et al. [5] has found that there is an association between CO and NO_2 which can be demonstrated by their source that came from industrial and traffic activities.

In addition, a study done by Isiyaka and Azid [7] has found that ozone (O_3) and particulate matter (PM_{10}) are the significant parameters influencing the value of the air pollution index (API) in Peninsular Malaysia. High concentration ozone in ambient air may adversely affect individuals and ecosystems. This is supported by Núñez-Alonso et al. [8] who claimed that ozone pollution appears to be the highest in rural areas outside the metropolitan region due to certain chemical that is more common in urban areas, such as nitrogen oxides which are found at lower concentration levels.

Sulphur dioxide (SO_2) is also one of the air pollutants. SO_2 is created when fuel containing sulphur, such as coal and oil is burnt which eventually may lead to air pollution. This gas can also be emitted by trains, large ships, lorries and other diesel equipment. A study done by Kamaruzzaman et al. [9] used multivariate statistics to identify the spatial variation of air quality in selected monitoring stations in Putrajaya, Wilayah Persekutuan, Malaysia. Principal Component Analysis (PCA) together with Factor Analysis indicated that only five parameters (wind speed, wind direction, SO_2, NO_2 and CO) had strong positive loadings (>0.75). Moreover, according to Isiyaka and Azid [7], who indicated that SO_2 was one of the most parameters with a p-value less than 0.0001, which can be discriminated as the best in polluting the air. By using the principal component

analysis, this research shows that SO_2 is one of the major possible air pollutants, which the total variance accounted for more than 58% and proves that SO_2 has a strong influence on the source of air pollution.

Air pollution in Southern Peninsular Malaysia is mainly due to rapid urbanization and industrialization as the region is surrounded by developing areas. The Southern region is mostly encircled by residential area which is nearby to major roads and industrial. This would potentially increase the exposure of the states in the Southern region with pollutants emitted from motor vehicles and industrial that surround the area. Hence, the urban area is considered as a prone zone to experience air quality problems, which would eventually affect human health, wildlife and plants as well as the global environment. A study done by Mohtar et al. [10] found that from 2005 to 2015, the ozone levels have generally increased in suburban areas. Air pollution is a serious issue which all relevant authorities around the globe need to give immediate and serious attention. Therefore, this study focuses on finding the most dominant air pollutant to the air quality in Southern Peninsular Malaysia. Air pollution research is an effort to create awareness in reducing emissions. Hence, it is hoped that this study could help the authorities in controlling the air pollution in Malaysia by determining the most dominant air pollutants involved.

Table 1. API Status Indicator

API	Alert Level	Health Effect Descriptor
0 – 50	No alert	Good
51 – 100	No alert	Moderate
101 – 150	Early alert	Unhealthy
151 – 200	Early alert	Unhealthy
201 – 300	On alert	Very unhealthy
301 – 500	Warning	Hazardous
>500	Emergency	Hazardous

Materials and Methods

Study area

This study used secondary data obtained from the Department of Environment (DOE) Malaysia, under supervision and control by Alam Sekitar Malaysia Berhad (ASMA). The data consists of hourly observations of the average concentration of air pollutants such as PM_{10}, $PM_{2.5}$, NO_2, SO_2, CO, and O_3 from January to December 2018. Five air quality monitoring sites in Table 2 were selected to give a general representation of the air pollution status in Southern Peninsular Malaysia.

Factor Analysis

Factor analysis is a multivariate analytical technique, which derives a subset of uncorrelated variables called factors that explain the variance observed in the original dataset [11]. The inter-correlation between air pollutants needs to be checked before conducting a factor analysis. It can be done by constructing the correlation matrix. With respect to the correlation matrix, the variables must be intercorrelated, but no multicollinearity exists and it should be a singularity. Multicollinearity can be detected via the determinant of the correlation matrix. If the determinant is greater than 0.00001, then there is no multicollinearity [12].

Meanwhile, Bartlett's test of sphericity determines whether the correlation matrix is an identity matrix, which would indicate that the factor model is inappropriate [13]. PCA can perform compression of the available information only if we reject the null

hypothesis. The test statistic of Bartlett's test of sphericity is given in equation (1):

$$\chi^2 = -\left(n - 1 - \frac{2p+5}{6}\right) \times \ln |R| \quad (1)$$

where n is number of samples, p is number of variables and R is correlation matrix of variables.

There are two main issues to take into consideration to determine whether a particular set of data is appropriate for factor analysis: the number of samples size should be a large sample (300 sample sizes) and the strength of the relationship between variables [14]. According to Kaiser [15], the adequacy of sampling is tested through Kaiser-Meyer-Olkin (KMO) as given by equation (2):

$$KMO = \frac{\sum\sum_{j \neq k} r^2_{jk}}{\sum\sum_{j \neq k} r^2_{jk} + \sum\sum_{j \neq k} p^2_{jk}} \quad (2)$$

The Kaiser-Meyer-Olkin criterion is calculated and values between 0 and 1 is obtained. Here, r_{jk} is the correlation between the air pollutant and P_{jk} is the partial correlation.

Moreover, Factor Extraction is the best approach to apply to a large amount of complex environmental monitoring data because they can avoid misinterpretation of results produced during data analysis [16]. The application of environmetric techniques such as PCA has been extensively applied in many scientific studies over the last few years, especially in air quality monitoring [16, 17]. In this study, the extraction of principal components or factors takes place by calculating the eigenvalues of the matrix. According to Rietveld and Hout [18], the number of positive eigenvalues determines the number of factors or components to be extracted. After constructing the factors, it is possible to determine the factor loadings by calculating the correlations between the original variables and the newly obtained factors or components.

In addition, Factor Rotation is used in this study in defining a small number of factors that can be used to best signify the whole relationship between air pollutants. Kaiser's criteria help in deciding to determine the smaller number of factors that should be retained. Under this criterion, components with an eigenvalue larger than 1 are retained [19]. In practice, only factor loading with absolute values greater than 0.5 is selected for the principal component interpretation. The higher the factor loading value, the more the air pollutant contributes to the variation attributed to the principal component [20].

Table 2. Location, coordinates, and area status of a monitoring station

Station ID	Location	Coordinates		Area Status
		Latitude	Longitude	
S1	Nilai, Negeri Sembilan	2.82	101.81	Industrial
S2	Seremban, Negeri Sembilan	2.72	102.24	Urban
S3	Bandar Melaka, Melaka	2.22	102.24	Urban
S4	Kota Tinggi, Johor	1.56	104.23	Urban
S5	Pasir Gudang, Johor	1.47	103.91	Industrial

Source: Department of Environment (DOE) Malaysia

Results and Discussion

Descriptive analysis

Descriptive statistics including minimum, maximum and mean of six air pollutants studied have been carried out. Table 3 shows that the maximum concentration of SO_2, NO_2, and CO are 0.020 ppm, 0.077 ppm and 4.229 ppm respectively. The value of these three pollutants did not exceed the approved level of air pollutants concentration limit based on RMAQG which are 0.13 ppm, 0.17 ppm and 30.00 ppm respectively. However,

the concentration of PM_{10} and O_3 overshoot the approved level of RMAQG. The maximum value of PM_{10} is 319.871 µg/m3, which is greater than the RMAQG approved level of 150.00 µg/m3. Even though the value is quite high from the permitted level, but it does not exceed the hazardous level of PM_{10} that is 600 µg/m3. Meanwhile, the maximum value of O_3 is 0.12 ppm which surpass the approved level by RMAQG, 0.10 ppm.

Correlation analysis

The intercorrelation between the concentration of air pollutants needs to be checked before the factor analysis can be carried out. The top half of Table 4 contains the correlation coefficient between air pollutants whereas the bottom half contains the p-value of each coefficient. The p-value that is less than 0.05 indicated that the correlation is significant with each other. The value of correlation coefficient for all pair of air pollutants are below 0.9 except for PM_{10} and $PM_{2.5}$ with strong correlation coefficient (r = 0.944). Hence, the determinant of the correlation matrix is needed to check the existence of multicollinearity in the data. Since the determinant value is 0.043 which is greater than 0.00001, therefore multicollinearity is not a problem for this data. Factor Analysis seems to be appropriate and suitable for this study as there is an inter-correlation between the air pollutants and no multicollinearity exists.

The strong correlation between PM_{10} and $PM_{2.5}$ illustrated that the dispersion of PM_{10} from the industrial activities in the study area also affected $PM_{2.5}$. PM_{10} and $PM_{2.5}$ concentrations are highly correlated (r = 0.944) because emission sources are mainly the same for the different measures (mobile sources and agricultural activities) [21].

Sampling adequacy

Table 5 shows the value of the Kaiser-Meyer-Olkin (KMO) and Bartlett's test. The value of KMO is 0.646 which is greater than 0.5. According to Kaiser [15], the acceptance value for KMO is greater than 0.5. Hence, it can be concluded that factor analysis is appropriate for this data. In addition, Bartlett's test of sphericity is measured to ensure that the R-matrix is not equal to the identity matrix. Since the p-value (0.000) is less than the significant value (α=0.05), it can be indicated that the R-matrix is not equal to the identity matrix and factor analysis is appropriate.

Table 3. Summary statistics of the air pollutants concentrations

	Minimum	**Maximum**	**Mean**
PM_{10}	0.874	319.871	26.7888
$PM_{2.5}$	0.066	305.648	18.511
SO_2	0.000	0.020	0.001
NO_2	0.000	0.077	0.010
O_3	0.000	0.122	0.019
CO	0.040	4.229	0.633

Table 4. Correlation Matrix

		PM_{10}	**$PM_{2.5}$**	**SO_2**	**NO_2**	**O_3**	**CO**
Correlation	PM_{10}	1.000	0.944	0.130	0.489	-0.168	0.364
	$PM_{2.5}$	0.944	1.000	0.104	0.488	-0.119	0.343
	SO_2	0.130	0.104	1.000	0.132	0.108	0.024
	NO_2	0.489	0.488	0.132	1.000	-0.516	0.479
	O_3	-0.168	-0.119	0.108	-0.516	1.000	-0.418
	CO	0.364	0.343	0.024	0.479	-0.418	1.000
Sig.	PM_{10}		0.000	0.000	0.000	0.000	0.000
	$PM_{2.5}$	0.000		0.000	0.000	0.000	0.000
	SO_2	0.000	0.000		0.000	0.000	0.000
	NO_2	0.000	0.000	0.000		0.000	0.000
	O_3	0.000	0.000	0.000	0.000		0.000
	CO	0.000	0.000	0.000	0.000	0.000	

a. Determinant = .043

Table 5. Kaiser-Meyer-Olkin and Bartlett's test

Kaiser-Meyer-Olkin Measure of Sampling Adequacy		0.646
Bartlett's Test of Sphericity	**Approx. Chi-Square**	120603.42
	df	15
	Sig.	000

Factor Extraction

Total Variance Explained in Table 6 represents the lists of eigenvalues associated with each linear component before and after extraction as well as after rotation. Before extraction, there are six linear components identified within the dataset. The number of linear components identified is similar to the number of variables in the dataset (PM_{10}, $PM_{2.5}$, SO_2, NO_2, CO, and O_3). The initial eigenvalues represent the variance explained by that specific linear component of each factor. It shows that factor 1 explains 46.003% of the total variance.

The Extraction Sums of Squared Loadings extract all factors with eigenvalues greater than 1 based on Kaiser's criterion. The extracted factor with eigenvalues over 1 specifies that the three factors should be retained in the model. Therefore, in this factor analysis, only the first three linear components are extracted and contribute most to the total variance. Meanwhile, the Rotation Sums of Squared Loadings optimize the factor structure and equalize the relative importance of the three factors. Before rotation, Factor 1 accounted for relatively more variance than the remaining two with 46.003% compared to 20.491% and 16.682%, respectively. However, after rotation, it accounts for only 35.859% of the variance for Factor 1 followed by 29.456% and 17.862% for the other two factors, respectively.

The output of Communalities in Table 7 shows the proportion of each variable's variance that can be explained by the underlying factors. The initial value of all communalities is 1, which demonstrates that all variance is common with the work of PCA. The communalities value after extraction (PM_{10} = 0.947, $PM_{2.5}$ = 0.954, SO_2 = 0.968, NO_2 = 0.744, O_3 = 0.779, and CO = 0.599) indicate that the amount of variance in

each variable explained by the included factors. Thus, it can be concluded that 94.7% of the variance correlated with PM_{10} is a common variance.

Table 8 represents the factor loading before and after rotation. This study uses varimax rotation to redistribute the factor loading that reflects the variables common characteristics. It finds that the rotation minimizes the complexity of the factor loadings to make the structure simpler to interpret within each component. These factors loading of each variable are supposed to measure each factor precisely. There are three factors extracted as shown in Table 8. The blank spaces denote the loading that is less than 0.4. Loading less than 0.4 is suppressed in the output to increase a value reflecting the expected value of a significant factor loading.

In the factor loading after rotation, the first component is most highly correlated with $PM_{2.5}$ and PM_{10} with the correlation of 0.967 and 0.957, respectively. These pollutants come from a variety of sources such as all modes of transportation, factories, construction sites and open burning. Generally, PM_{10} and $PM_{2.5}$ are mainly from industrial activities and construction sites [22].

The second component is most highly correlated with O_3, CO and NO_2 with a correlation coefficient of 0.861, 0.701 and 0.697, respectively. O_3 is not emitted directly from automobiles, the unstable compound is formed in the atmosphere through a complex set of chemical reactions involving hydrocarbons, oxides of nitrogen, and sunlight. The rate at which the reactions proceed is related to both the temperature and intensity of the sunlight. Because of this, problematic ozone levels occur most frequently during afternoons [23]. CO is the pollutant that comes from the incomplete combustion of vehicles, industries, and open burning activities [24]. Meanwhile, NO_2 is made up of the largest sources of emissions released by cars, trucks, buses and many of which come from indoor and outdoor. NO_2 emission in Malaysia proves that power stations and industrial activities released about 69% of this pollutant to the air, while 28% is from motor vehicles and the remaining 3% is from other sources [25].

However, the third component is the most highly correlated with SO_2 with a strong correlation of 0.983. These sources of the pollutant are emitted by trains, large ships, lorries and other diesel equipment resulting in the high combustion of sulphur. In addition, the sources of SO_2 are resulted from the motor vehicles combustions, coal-powered power plants and uncontrolled burning of forests and dust storms from the neighboring country due to various activities [16]. According to Minnesota Pollution Control Agency [26], diesel vehicles and equipment have long been a major source of SO_2. Based on this finding, it shows that the most dominant air pollutant that affects the air quality in Southern Peninsular Malaysia are from the $PM_{2.5}$ and PM_{10}. These findings are in line with the result obtained in the research of assessment on air quality patterns in Putrajaya, Malaysia, which said that the major contributions are from automobiles, industries, power plants, transboundary sources and construction sites [9].

Table 6. Total Variance Explained

Factors	Initial Eigenvalues		Extraction Sum of Squared Loadings		Rotation Sum of Squared Loadings	
	Total	Variance (%)	Total	Variance (%)	Total	Variance (%)
1	2.760	46.003	2.760	46.003	2.152	35.859
2	1.229	20.491	1.229	20.491	1.767	29.456
3	1.001	16.682	1.001	16.682	1.072	17.862
4	0.572	9.532				
5	0.379	6.310				
6	0.059	0.981				

Table 7. Communalities

Variables	Initial	Extraction
PM_{10}	1.000	0.947
$PM_{2.5}$	1.000	0.954
O_3	1.000	0.968
CO	1.000	0.744
NO_2	1.000	0.779
SO_2	1.000	0.599

Table 8. Factors Loading for the air pollutants observations

Variables	Factor Loading Before Rotation			Factor Loading After Rotation		
	1	2	3	1	2	3
$PM_{2.5}$	0.862			0.967		
PM_{10}	0.846	0.405		0.957		
O_3	0.797				-0.861	
CO	0.682				0.701	
NO_2	-0.416	0.776		0.433	0.697	
SO_2			0.888			0.983

Conclusion

Air pollution can be defined as the presence of toxic chemicals or substances in the air which pose a health risk. It is one of the most serious environmental phenomena facing our society. This air pollution issue is usually caused by human activities, such as mining, construction, transport, factory work, agriculture, and smelting, which directly or indirectly affect the quality of air. The air pollutants including $PM_{2.5}$, PM_{10}, NO_2, SO_2, CO, and O_3 were obtained hourly from January to December 2018 by five air quality monitoring sites. This study is focused on determining the most dominant air pollutant in Southern Peninsular Malaysia by using Factor Analysis.

The descriptive analysis was used to describe the analysis of the hourly air quality concentration of major air pollutants. It found that the concentration of PM_{10} and O_3 overshoot the approved level of RMAQG. Based on the factor analysis, the most dominant air pollutant that affects the air quality in Southern Peninsular Malaysia are $PM_{2.5}$ and PM_{10} with a strong correlation of 0.967 and 0.957 respectively. The major contribution sources to these pollutants are from induced emission of industrial activities and construction sites. It is hoped that this research will help the authorities in controlling air pollution in Malaysia.

For further study, it is necessary to address a wider suite of components on a larger sample by covering more stations in identifying different sources of air pollution. Moreover, it is recommended that the study be replicated using PCA or Cluster Analysis to identify the correlation between different pollutants and to classify the different monitoring stations based on the different variables. In addition, the chemometric technique is a meaningful tool to disclose and justify significant spatial variability for the assessment of large and complex air quality data.

Acknowledgement

The authors gratefully acknowledge the Department of Environment (DOE) Malaysia for providing data on air pollutants in Southern Peninsular Malaysia.

References

1. Centers, E. P. (2017). What is air pollution? https://www.environmentalpollutioncenters.org/air/. [Access online 29 January 2021].
2. Afroz R., Hassan M. N. and Ibrahim N. A. (2003). Review of air pollution and health impacts in Malaysia. *Environmental Research*, 92(2): 71-77.
3. Airveda (2017). What is $PM_{2.5}$ and why is it important? https://www.airveda.com/ blog/what-is-pm2-5-and-why-is-it-important. [Access online 22 March 2021].
4. Arsene, C., Olariu, R. I., & Mihalopoulos, N. (2007). Chemical composition of rainwater in the Northeastern Romania, Iasi Region (2003–2006). *Atmospheric Environment*, 41(40): 9452-9467.
5. Zakaria, U., Saudi, A., Abu, I., Azid, A., Balakrishnan, A., Amin, N. and Rizman, Z. (2017). The assessment of ambient air pollution pattern in Shah Alam, Selangor, Malaysia. *Journal of Fundamental and Applied Sciences,* 9(4S): 772-788.
6. Ismail, A. S., Abdullah, A. M. and Samah, M. A. A. (2017). Environmetric study on air quality pattern for assessment in northern region of Peninsular Malaysia. *Journal Environmental Science Technology,* 10: 186-196.
7. Isiyaka, H. A. and Azid, A. (2015). Air quality pattern assessment in Malaysia using multivariate techniques. *Malaysian Journal of Analytical Sciences,* 19(5): 966-978.
8. Núñez-Alonso, D., Pérez-Arribas, L. V., Manzoor, S. and Cáceres, J. O. (2019). Statistical tools for air pollution assessment: Multivariate and spatial analysis studies in the Madrid region. *Journal of Analytical Methods in Chemistry,* 9: 1-9.
9. Kamaruzzaman, A., Saudi, A., Azid, A., Balakrishnan, A., Abu, I., Amin, N. and Rizman, Z. (2017). Assessment on air quality pattern: A case study in Putrajaya, Malaysia. *Journal of Fundamental and Applied Sciences,* 9(4S): 789-800.
10. Mohtar, A. A. A, Latif M. T, Baharudin, N. B, Ahmad, F., Chung J. X., Othman, M. and Juneng, L. (2018) Variation of major air pollutants in different seasonal conditions in an urban environment in Malaysia. *Geoscience Letters,* 5: 21.
11. Anazawa, K. and Ohmori, H. (2005). The hydrochemistry of surface waters in Andesitic volcanic area, Norikura Volcano, Central Japan. *Chemosphere,* 59(5): 605-615.
12. Field, A. P. (2013). Discovering statistics using SPSS for windows. Academic Internet Publish: pp. 444.
13. Bartlett, M. S. (1954). A note on the multiplying factors for various χ^2 approximations. *Journal of the Royal Statistical Society: Series B (Methodological),* 1954: 296-298.
14. Pallant, J. (2020). SPSS survival manual: A step-by-step guide to data analysis using IBM SPSS. Routledge: pp. 20.
15. Kaiser, K. L. (1974). On the optical activity of polychlorinated biphenyls. *Environmental Pollution*, 7(2): 93-101.
16. Mutalib, S. N. S. A., Juahir, H., Azid, A., Sharif, S. M., Latif, M. T., Aris, A. Z. and Dominick, D. (2013). Spatial and temporal air quality pattern recognition using environmetric techniques: A case study in Malaysia. *Environmental Science: Processes & Impacts,* 15(9): 1717-1728.
17. Singh, K. P., Malik, A., Mohan, D. and Sinha, S. (2004). Multivariate statistical techniques for the evaluation of spatial and temporal variations in water quality of Gomti River (India)—A case study. *Water Research,* 38(18): 3980-3992.
18. Rietveld, T. and Hout, R. V. (2011). Statistical techniques for the study of language and language behaviour. Meuchen: De Gruyter: pp. 259.
19. Cattell, R. B. (1966). The scree test for the number of factors. *Multivariate Behavioral Research,* 1(2): 245-276.
20. Juahir, H., Zain, S. M., Yusoff, M. K., Hanidza, T. T., Armi, A. M., Toriman, M. E. and Mokhtar, M. (2011). Spatial water quality assessment of Langat River Basin (Malaysia) using environmetric techniques. *Environmental Monitoring and Assessment,* 173(1- 4): 625-641.

21. Janssen, N. A. H., van Vliet, P. H. N., Aarts, F., Harssema, H. and Brunekreef, B. (2001). Assessment of exposure to traffic related air pollution of children attending schools near motorways. *Atmospheric Environment,* 35(22): 3875-3884.
22. Rosman, P. S., Abu Samah, M. A., Yunus, K. and Mohd Hussain, M. R. (2019). Particulate matter ($PM_{2.5}$) at construction site: A review. *International Journal of Recent Technology and Engineering* (IJRTE), 8: 255-259.
23. Arkansas Department of Energy & Environment (2021). Cars and air pollution. https:// www.adeq.state.ar.us/air/planning/ozone/cars.aspx . [Access online 21 September 2021].
24. Isiyaka H., Juahir, H., Toriman, M. E., Gasim, B. M., Azid, A., Amri, M. K., Ibrahim, A., Usman, U. N., Rano, A. R. and Garba, M. A. (2014). Spatial assessment of air pollution index using environmetric modeling techniques. *Advances in Environmental Biology*, 8(24):244-256.
25. Department of Environment Malaysia (2009) A guide to air pollutant index (API) in Malaysia. Putrajaya: Ministry of Natural Resources and Environment. https://www.doe.gov.my. [Access online 21 September 2021].
26. Minnesota Pollution Control Agency (2021). Sulfur dioxide (SO_2). https://www.pca.state.mn.us/ air/sulfurdioxide-so2. [Access online 21 September 2021].

Malaysian Journal of Analytical Sciences (MJAS)
Published by Malaysian Analytical Sciences Society

ANALYTICAL COMPARATIVE STUDIES OF ADSORPTION EFFICIENCY OF MCM-41 AND SBA-15 ON REMOVAL OF ANIONIC-AZO AND CATIONIC DYES FROM AQUEOUS SAMPLE

(Kajian Perbandingan Analisis Keberkesanan Penjerapan MCM-41 dan SBA-15 untuk Penyingkiran Pewarna Anionik-Azo dan Kationik Dari Sampel Akueus)

Nur Zabirah Zabi[1], Wan Nazihah Wan Ibrahim[1]*, Nur Husna Zainal Abidin[1], Siti Syairah Mat Salleh[1], Farah Amira Shahrul Effendi[1], Isna Fazliana Mohamed Idrus[1], Hamizah Md Rasid[1], Nursyamsyila Mat Hadzir[1], Nor Suhaila Mohamad Hanapi[1], Mazhani Muhammad[2]

[1] School of Chemistry and Environment, Faculty of Applied Sciences, Universiti Teknologi MARA, 40450 Shah Alam, Selangor, Malaysia
[2]Centre of Foundation Studies (CFS), Universiti Teknologi MARA, 438000 Dengkil Campus, Selangor, Malaysia

**Corresponding author: wannazihah@uitm.edu.my*

Received: 29 June 2021; Accepted: 15 August 2021; Published: 25 October 2021

Abstract

Mobil Composition of Matter No. 41 (MCM-41) and Santa Barbara Amorphous (SBA-15), a type of mesoporous adsorbents, were successfully prepared via mixed cationic-neutral templating route and sol-gel method, respectively. Analytically, the prepared materials were compared to remove anionic azo (methyl orange) and cationic dyes (methylene blue) from highly colored solutions. Both adsorbents were characterized using Fourier transform infrared (FTIR), field emission scanning electron microscopy (FESEM), and nitrogen adsorption/desorption to enhance the understanding of structure and surface properties. To assess the efficiency of the prepared adsorbents, the pH of the sample, the initial concentration of the dyes, and contact time were studied. At optimum conditions, maximum adsorption capacities for methyl orange (MO) and methylene blue (MB) using MCM-41 were 4.757 mg/g and 16.00 mg/g and for SBA-15 the maximum adsorption capacities were 20.212 mg/g and 10.45 mg/g, respectively. Furthermore, Langmuir and Freundlich isotherm models were selected to describe the adsorption process while pseudo-first-order and pseudo-second-order kinetics equations were applied to determine the adsorption kinetics. The obtained results showed that SBA-15 can remove both dyes 38.53% better than MCM-41 due to higher surface area, which was 507 m^2/g compared to 436 m^2/g for MCM-41.

Keywords: cationic dyes, anionic dyes, adsorption, mesoporous silica

Abstrak

Komposisi Mobil Perkara 41 (MCM-41) dan Santa Barbara Amorfous (SBA-15) jenis penjerap mesopori berjaya disediakan melalui kaedah templat neutral kationik-neutral dan kaedah sol-gel. Bahan yang disediakan dibandingkan secara analitikal untuk mengeluarkan pewarna azo anionik (oren metil) dan pewarna kationik (biru metilena) dari larutan yang sangat berwarna. Kedua-dua penjerap dicirikan menggunakan inframerah jelmaan Fourier (FTIR), mikroskopi elektron pengimbasan pelepasan medan

(FESEM) dan penjerapan/penyahjerapan nitrogen untuk meningkatkan pemahaman mengenai sifat struktur dan permukaan. Untuk menilai kecekapan penjerap yang telah disediakan, tiga parameter telah dikaji iaitu pH sampel, kepekatan awal pewarna dan masa penyentuhan. Pada keadaan optimum, kapasiti penjerapan maksimum untuk metil oren (MO) dan metilena biru (MB) menggunakan MCM-41 ialah 4.757 mg/g dan 16.00 mg/g dan untuk SBA-15 kapasiti penjerapan maksimum ialah 20.212 mg/g dan 10.45 mg/g masing-masing. Selanjutnya, model isoterm Langmuir dan Freundlich dipilih untuk menggambarkan proses penjerapan sementara persamaan kinetik turutan-pseudo-pertama dan turutan-pseudo-kedua digunakan untuk menentukan kinetik penjerapan. Hasil perolehan menunjukkan bahawa SBA-15 dapat menyerap kedua-dua pewarna 38.53% lebih baik daripada MCM-41 kerana luas permukaannya yang lebih tinggi iaitu 507 m^2/g berbanding dengan 436 m^2/g untuk MCM-41.

Kata kunci: pewarna kation, pewarna anion, penjerapan, silika mesopori

Introduction

Dye molecules contain chromophore and auxochrome structures. Chromophore group contains a double bond that oscillates to absorb light and causes a dye to have a visible colour [1]. Natural dyes gave dull colors and were commonly used in the European textile industry before synthetic dyes were produced in 1856 [2]. Dyes are widely used in foods, medicines, and clothes resulting in an increase in dye production [3]. Acid dyes, basic dyes, direct dyes, disperse dyes, reactive dyes and vat dyes are commonly used in textile industrial products [4]. MO is an example of acid or anionic dye that belongs to azo dye which consists of one or more azo groups (-N=N-) between the carbons [5, 6]. Azo dyes are also commonly used in food and could cause bladder cancer when consumed, due to the presence of benzidine, a known carcinogenic agent [7, 8] MB is a basic or cationic dye with a structure of heterocyclic aromatic chemical compound [9]. MB can cause a burning sensation leading to permament injury when in contact with the eyes [10]. In addition to the health effect, the environment could also be affected by the pollution of dyes as this water-soluble compound cannot be easily removed through a filtration method. As a result, it can affect the symbiotic process due to the prevention of light penetration, which leads to low photosynthetic activity in the water [11]. Besides that, a large number of synthetic dyes are released into wastewater during coloration process due to illegal and improper waste management [3].

Various techniques have been developed to remove dye from water including nanofiltration [12], electrochemical coagulation [13], reverse osmosis [14], photochemical degradation [15], ion exchange [16] and adsorption. However, adsorption is more beneficial compared to other techniques due to the simplicity of design, case of operation, initial cost, and insensitivity to toxic substances [17]. The efficiency of the adsorption technique is based on the adsorbent properties, which are high adsorption capacity and selectivity, good mechanical stability, resource abundance, and environmental friendly [18]. Therefore, scientists have developed various kinds of adsorbent from coffee wastes [5], banana plant-derived sorbents [19], calcined and uncalcined Mg/Al layered double hydroxide [20], cellulose-based porous adsorbents [21], activated carbons [22, 23], magnetic lignin-based adsorbent [24], anionic clay-layered double hydroxide [25], amino-cross linked hypromellose [26], and layered double hydroxide/polyacrylamide nanocomposite hydrogels [27] to increase the efficiency of removing a dye. Nonetheless, these types of adsorbents may have their drawbacks such as, expensive to synthesize, difficult to dispose, low adsorption efficiency or difficult, and costly to regenerate [28, 29]. The discovery of mesoporous silica has garnered a lot of attention from researchers since it has high surface areas and well-defined pore structures [30]. The first mesoporous material was created through hydrothermal reaction using aluminisilicate gel with the presence of surfactants [31].

Mobil Composition of Matter No. 41 (MCM-41) and Santa Barbara Amorphous (SBA-15) are a member of the mesoporous family and are suitable for dye removal due to their high specific surface area ranging from 500 to 1000 m^2/g [32]. The pore sizes of SBA-15 and MCM-41 are in the range of 60 to 110 Å and 15 to 100 Å, respectively [33, 34]. Furthermore, the hydroxyl group

(-OH) on their surface area offer ease functionalization to enhance their selectivity [33, 35, 36]. These two adsorbents are preferable compared to other adsorbents because the surface and pores of these materials can be altered to target specific analytes, regenerated, and reused with high capacity at low cost [29]. The objectives of this study are to prepare and characterize mesoporous silica MCM-41 via mixed cationic-neutral templating route using cationic cetyl trimethylammonium bromide and SBA-15 via sol-gel method. This is performed; to assess the performance of prepared adsorbent for removal of anionic MO and cationic MB dyes using ultraviolet -visible spectroscopy.

Materials and methods

Chemicals and reagents

The chemicals that were used in this study are cetyltrimethylammonium bromide (CTABr, 99%, Sigma-Aldrich), 1.0 M aqueous hydroxide (NaOH, Sigma-Aldrich) and Ludox colloidal silica (SiO_2, 30%, Sigma-Aldrich), ammonium hydroxide (NH_4OH, 25%), MB ($C_{16}H_{18}C_1N_3S$, 90%, Sigma-Aldrich), MO ($C_{14}H_{14}N_3NaO_3S$, 90%, Sigma-Aldrich), and distilled water.

Preparation of MCM-41 and SBA-15

The method used to synthesize MCM-41 was adapted with slight modification from a previous study [37]. Sodium silicate (solution A) was firstly prepared by mixing 33.80 mL of Ludox (30%) with 3.03 g of sodium hydroxide (NaOH) in 37.5 mL double distilled water at 80 ℃ with 2 hours stirring at a medium speed using magnetic stirrer. Then, another solution (solution B) was separately prepared by mixing 9.60 g of cetyltrimethylammonium bromide (CTABr) and 0.50 g of ammonium hydroxide (NH_4OH) in 75.0 mL of distilled water with stirring at 80 ℃ until a clear solution was obtained. Both A and B solutions were mixed in a polypropylene bottle to give a gel with a composition of 6 SiO_2: CTABr: 1.5 Na_2O: 0.15 $(NH_4)_2O$: 250H_2O followed with vigorous stirring. The resulting gel was then kept in an oven for crystallization at 100 ℃ for 24 hours. The following day, the gel was then cooled to room temperature for 3 hours, and the pH was adjusted to 10.2 by adding 25 wt.% of acetic acid. The heating and pH adjustments were repeated twice in order to complete the polymerization process of silica monomers. The white conducts were filtered, washed, neutralized, and dried overnight at 100 ℃ in an electrical oven. Finally, the solid product went through a calcination process at 550 ℃ in a furnace for 10 hours to remove the organic template.

The preparation of SBA-15 was referred to previous study with minor modifications [38]. Firstly, distillate water (30 mL), 2.0 M HCl (120 mL), and Pluronic P123 (4.0 g) were dissolved by stirring at 35 ℃ for 20 hours. Then, 8.5 g of tetraethyl-orthosilicate (TEOS) was added dropwise under constant vigorous stirring for 15 minutes. The mixture was kept under static conditions at 35 ℃ for 20 hours. The milky mixture was then placed in an oven at 90 ℃ for 24 hours. The solid product was filtered, washed, and dried at 45 ℃ for 72 hours. Lastly, the product was calcined for 6 hours at 500 ℃ and stored in a proper container.

Characterization of MCM-41 and SBA-15

The functional groups that are present in both adsorbents were determined using FTIR (Perkin Elmer 8300, Massachusetts, USA). Each adsorbent was ground with KBr powder to turn it into a pellet before obtaining the FTIR spectrum. The surface morphology of both adsorbents was identified using FESEM (JEOL JEM-2300, Tokyo, Japan) after it was coated with gold film at 20kV voltage. In addition, the specific surface area and averaged pore size were analyzed using Brunauer-Emmett-Teller (BET) surface analyser (Belsorp-mini II, Japan). The samples were displaced at 300 ℃ with nitrogen flow for 6 hours. The surface area of each adsorbent was discovered from the linear BET method with rapid nitrogen uptake, P/P_O = (0.4-1.0).

Batch studies on MO and MB removal

The batch studies were carried out to investigate the adsorption reaction of MO and MB onto MCM-41 and SBA-15 by varying the pH values of the sample, the initial concentration of both dyes, and contact time. Each parameter gave an effect on the adsorption capacity of the dyes using MCM-41 and SBA-15 as the adsorbent. The adsorbent dosage was kept constant at 0.05 g. The removal process was obtained by placing a

conical flask containing dye solution (10 mL) and 0.05 g adsorbent onto a shaker with a constant speed at 160 rpm. The adsorbent was separated from the dye solution through centrifugation. The residual MO and MB concentrations were then determined by collecting aliquots from the supernatant and measuring them with a UV-Vis spectrophotometer (Lambda 35-Perkin Elmer) at a wavelength of 463 nm for MO and 660 nm for MB [39].

Adsorption isotherm

Adsorption equilibrium provides the fundamental physicochemical data to evaluate the applicability of the adsorption process [40]. The adsorption data of the experiment were fitted according to the two isotherm models, which were Langmuir and Freundlich models. Langmuir model predicts that each adsorbate molecule is located at a single site of identical energy onto the surface of the adsorbent that leads to a formation of a monolayer [41]. The equation for this model is presented in Equation (1).

$$\frac{C_e}{q_e} = \frac{1}{Q_m b} + \frac{C_e}{Q_m} \quad (1)$$

where C_e is equilibrium concentration of adsorbate, q_e is amount of dye adsorbed (mg/g), Q_m = adsorption capacity (mg/g), and b is Langmuir constant (L/mg) which were determined through intercept value from $\frac{C_e}{q_e}$ against C_e graph.

Freundlich model is an empirical equation utilized to define equilibrium on heterogenous surfaces and hence does not assume monolayer capacity [42]. The equation used to represent this model is stated in Equation (2).

$$\log q_e = logK_f + \frac{1}{n} logC_e \quad (2)$$

where k_f is adsorption capacity, n is Freundlich constant, C_e is equilibrium concentration of adsorbate, q_e is capacity of equilibrium adsorption and n were determined from the intercept and slope of graph $\ln(q_e)$ against $\ln(C_e)$.

Adsorption kinetics

The experimental data were fitted by implementing pseudo-first-order and pseudo-second-order kinetic models [41]. The equation for pseudo-first-order and pseudo-second-order is stated in Equation (3) and (4), respectively.

$$\log_{10}(q_e - q_t) = \log_{10}(q_e) - \frac{k_1}{2.303} \quad (3)$$

where q_t is amount of dye adsorbs at certain time equilibrium, k_1 is equilibrium rate constant of pseudo-first constant and t = time (min).

$$\frac{t}{q_t} = \frac{1}{k_2 q_e^2} + \frac{t}{q_e} \quad (4)$$

where K_2 is pseudo-second-order rate constant, q_e is capacity of equilibrium adsorption, q_t is adsorption amount of dye at certain time equilibrium, t is contact time (min), q_e and K_2 were calculated using $\frac{t}{q_t}$ against t graph.

Results and Discussion

Characterization of MCM-41 and SBA-15

FTIR-ATR spectra of MCM-41 and SBA-15 are shown in Figure 1. The broad peak around 3500 and 1639 cm^{-1} in both spectra are mainly due to the bending vibration of the adsorbed water. The bands present around 1030 – 1080 and 450 - 464 cm^{-1} indicate siloxane bond (Si-O-Si) and Si-O bond in both samples, respectively. The peaks representing silanol group (Si-OH) in MCM-41 and SBA-15 are present around 800 - 970 cm^{-1} [43, 44, 45, 47, 48]. These four bonds confirm the silica framework of MCM-41 and SBA-15 [45]. However, SBA-15 contains two extra bonds, which are stretching vibration of C=O (the peak is present at 1701 cm^{-1}) and C-H bending (the peak is present at 1370 cm^{-1}) [45, 46]. Both adsorbents have similar bonds but there are slight differences in their wavenumbers.

FESEM micrographs of both adsorbents are shown in Figure 2. The morphology of each adsorbent is different. On the surface of MCM-41, the presence of pores could be observed after the removal of the CTABr template and the shape appeared as small agglomerated spheres and small rods [49]. SBA-15 shows a perfect sphere due to the removal of triblock copolymer surfactant [50].

The specific surface area, pore volume and pore diameter parameters of the synthesized materials were calculated using the BET method based on the N_2 adsorption and desorption isotherms. N_2 adsorption/desorption isotherms of MCM-41 and SBA-15 are shown in Figure 3. According to the International Union of Pure and Applied Chemistry (IUPAC), the isotherms of both MCM-41 and SBA-15 exhibit typical type IV physisorption curves thus, confirming that both adsorbents are mesoporous and the adsorption process can either be monolayer or multilayer [51]. As for the type of hysteresis loop, both adsorbents show type H1 that often relate to porous materials with well-defined cylindrical-like pore channels or agglomerates of approximately uniform spheres [34]. The specific surface area, pore volume, and pore diameter for MCM-41 are 436 m^2/g, 0.533 cm^3/g and 11.27 nm while for SBA-15 are 507 m^2/g, 0.688 cm^3/g and 7.2 nm, respectively.

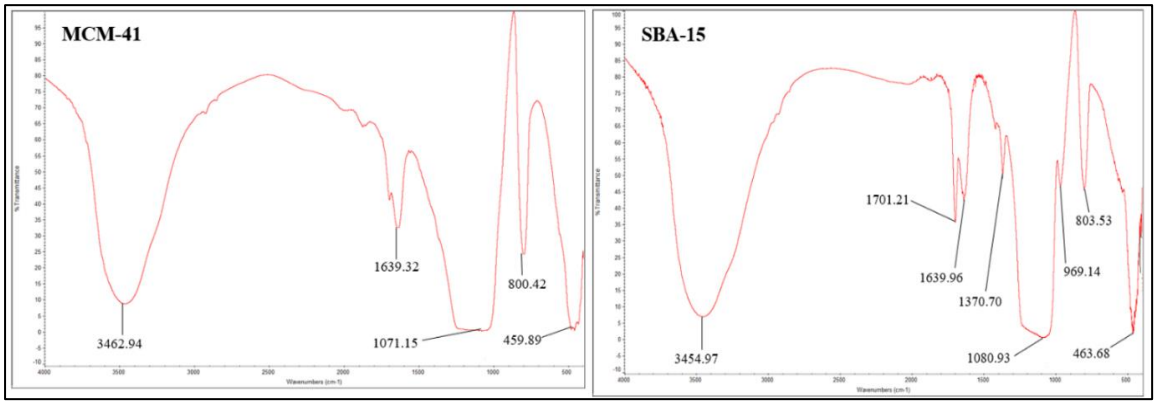


Figure 1. FTIR spectra of (a) MCM-41 and (b) SBA-15

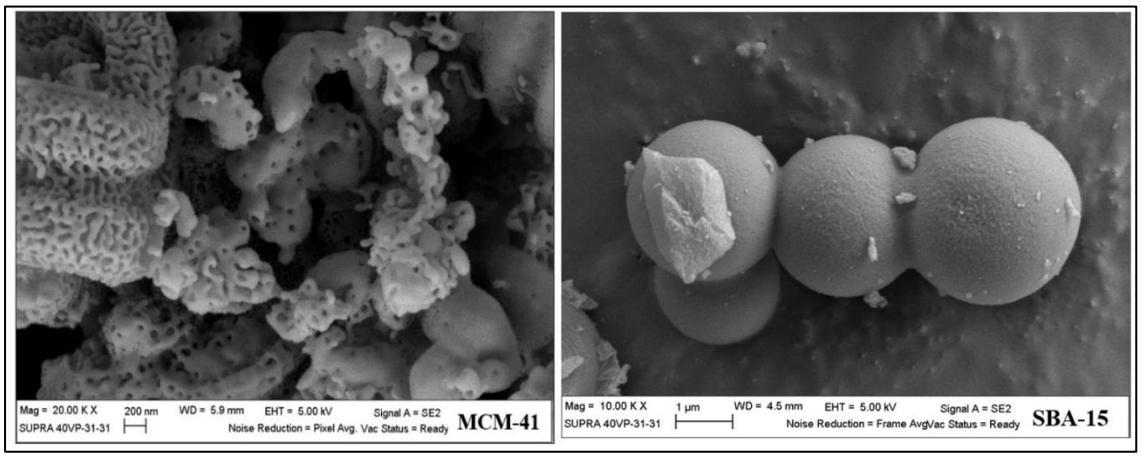


Figure 2. FESEM micrographs of (a) MCM-41 and (b) SBA-15

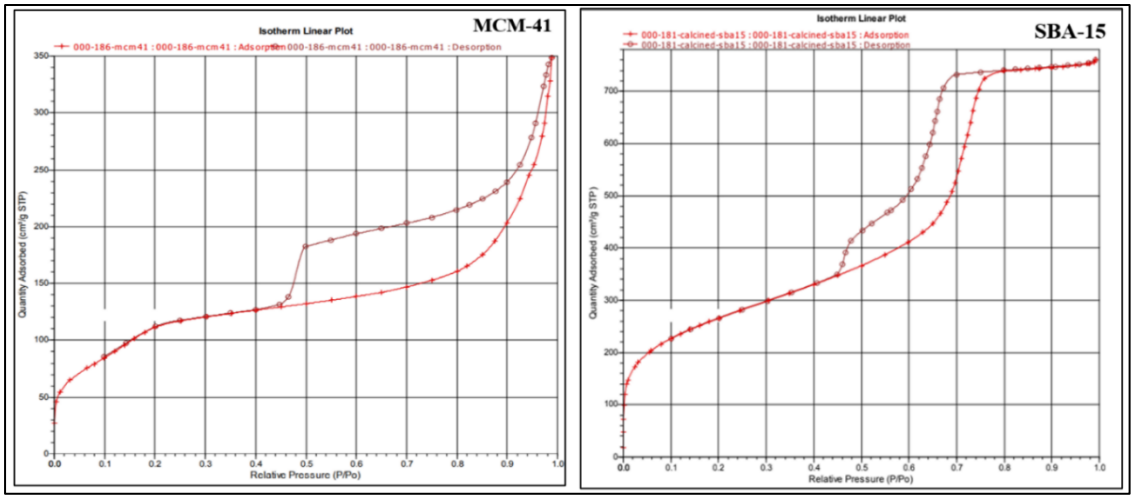


Figure 3. N_2 Adsorption-Desorption Isotherms of MCM-41 and SBA-15

Batch adsorption studies of MO and MB using calcined MCM-41 and SBA-15

Effect of sample pH

The pH of the sample affects every adsorption process especially for dyes since pH controls the magnitude of electrostatic charges on the surface of the adsorbent. When optimized pH is obtained, the adsorbent can adsorb more dye molecules since the surface of the adsorbent have the suitable electrostatic charge to interact with the anionic and cationic dye molecules that have negative and positive charge once the dyes dissolved and partially ionized in water [52]. To study the effect of pH (3, 5, 7, 9, and 11), the pH of the dye solution was adjusted in a beaker before being transferred to a conical flask. In this experiment, 0.01 M NaOH, 0.1 M NaOH, 0.01 M HCl, and 0.1 M HCl was used to adjust the pH systematically. The other variables were set at constant values including sample volume (10 mL), the mass of adsorbent (0.05 g), shaker speed (160 rpm), dye concentration (80 ppm), and contact time (30 mins).

Figure 4, shows that the optimum pH for removal of MO using MCM-41 is pH 3 while SBA-15 is pH 5 with a percentage removal of 58% (MCM-41) and 55.17% (SBA-15). Under an acidic condition, there is a high concentration of H^+ that will change the surface of the adsorbents to be slightly positively charged and increase its ability to adsorb MO that has a negative charge once it dissolves in water [53]. For removal of MB, the optimum pH using MCM-41 and SBA-15 are pH 7 and pH 11, respectively with a percentage removal of 100.24% (MCM-41) and 99.95% (SBA-15). Cationic dyes such as MB gives positively charged ions when dissolved in water and due to this acidic medium (pH<7), the surface of the adsorbent becomes positively charged and tends to oppose the adsorption of the MB molecules. At higher pH (pH ≥ 7), the electrostatic repulsion between the positively charged MB and the surface of the adsorbent was lowered since there were less H^+ ions to compete with cation groups on dye for adsorption sites hence, increasing the removal efficiency of the dye molecules [54-56]. Another study, stated that increasing the pH of the sample will increase the number of hydroxyl (OH^-) ions thus, increasing the number of negatively charged sites on the surface of the adsorbent and enlarges the attraction between MB and adsorbent surface [57] Based on the percentage removal, both MCM-41 and SBA-15 adsorbed more MB compared to MO. This might be due to the presence of silanol groups that have acidic character and are able to form hydrogen bonds with MB molecules compared to MO molecules [30]. It was also found that there is a slight difference in percentage removal of MB between these two adsorbents. However, both adsorbents are still considered efficient adsorbents [39]. Figure 5 shows the

adsorption mechanism under basic and acidic conditions. Based on Figure 5, it shows that the silanol group on the surface of the adsorbents interacts with the dye molecules. In an acidic condition, the silanol groups become slightly positive when it reacts with H^+ ions and become $Si\text{-}OH_2^+$ that enable the adsorbents to adsorb the MO molecules and in basic condition, the silanol groups become slightly negative when OH^- ions react with the group and become $Si\text{-}O^-$ and enable the adsorbents to adsorb MB molecules [53].

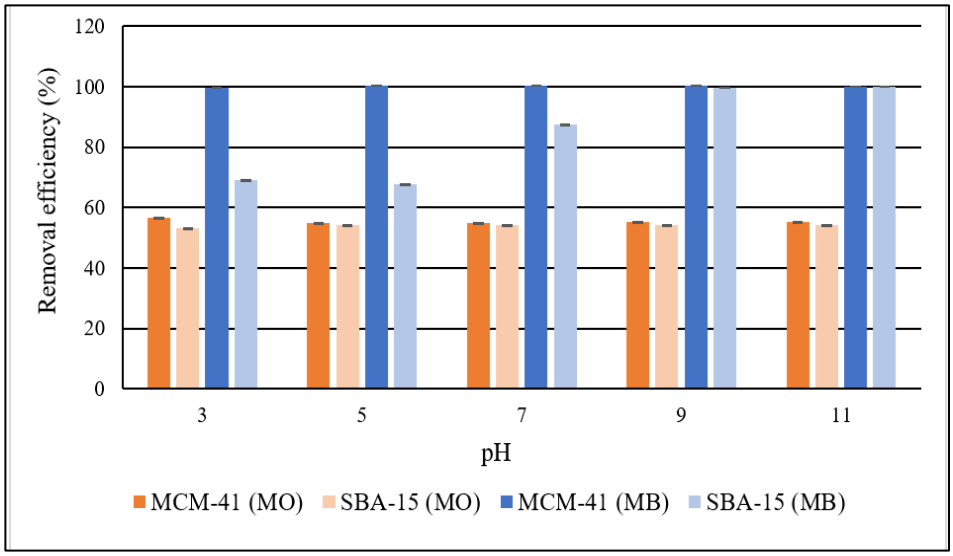


Figure 4. Percentage removal of MO and MB using MCM-41 and SBA-15 at a different range of pH

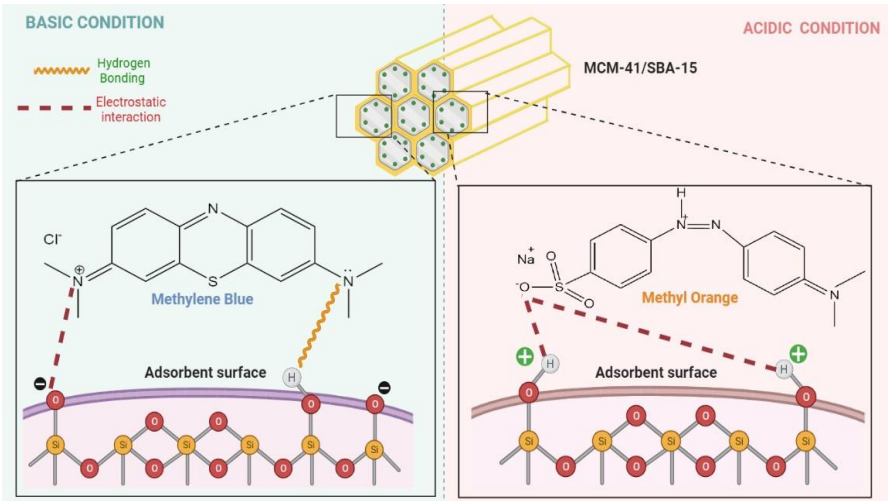


Figure 5. Adsorption mechanism under basic and acidic conditions

Effect of initial concentration

The study on the initial concentration of MO and MB was carried out to determine the adsorption capacity of each adsorbent. The initial concentration used was 60 ppm, 80 ppm, 100 ppm, 120 ppm, and 140 ppm with an adsorbent dosage of 0.05 g. For MCM-41, the pH value of MO solution was set to 3 with a contact time of 30 minutes while for MB, the pH was set to pH 7 with the same contact time. As for SBA-15, the pH value of the MO solution was set to pH 5 with a contact time of 30 minutes while for MB, the pH was set to pH 11 with the same contact time. The initial concentration of the dye will affect the amount of adsorption for dye removal. The amount of dye adsorbed onto the adsorbent is highly dependant on the available sites of the adsorbent surface. As seen in Figure 6, the optimum initial concentration for removal of MO using MCM-41 and SBA-15 is 60 ppm and 140 ppm respectively with a percentage removal of 100% (MCM-41) and 72.54% (SBA-15). As for the removal of MB, the optimum initial concentration using MCM-41 and SBA-15 are 80 ppm (99.98%) and 100 ppm (99.77%), respectively.

As the concentration increases, the percentage removal of dye will decrease because the adsorption site is already concentrated with the dye [58]. This is because, at low concentrations, the ratio of the initial amount of dye molecules to the unoccupied adsorption sites was low and this causes more adsorption sites to be available hence, increasing the percentage removal. At higher concentrations, the ratio of the initial amount of dye to the unoccupied adsorption sites is high, therefore, there are less adsorption sites available hence, decreasing the percentage removal [59]. However, the removal percentage for SBA-15 increases with an increase of initial MO concentration. The adsorption capacity may increase due to the high driving force for mass transfer at a high initial dye concentration [58].

Effect of contact time

An optimum contact time can predict the mechanism of the removal process and the efficiency of the adsorbent to remove the dyes [60]. In the early stage, it is more towards the displacement of dye molecules from the bulk solution to the outer surface of the adsorbent. Consequently, at a longer contact time, the adsorption process occurs due to the interaction between the dye molecules and the adsorption sites in the inner surface of the adsorbent. Finally, the diffusion and interpenetration of the dye molecules will take place in the pores of the adsorbent [61]. In this batch of study, 0.05 g of adsorbent was used and the controlled parameters are pH and initial concentration. For MCM-41(MO), the pH and initial concentration that was chosen are pH 3 and 60 ppm. As for MCM-41 (MB), pH 7 and 80 ppm was chosen as the optimum value and for SBA-15 (MO), pH 5 was chosen with an initial concentration of 140 ppm. Lastly, for SBA-15 (MB), pH 9 and 100 ppm was chosen as the optimum values.

Figure 7 shows the optimum contact time on the removal of MO using MCM-41 and SBA-15, which is 30 min and 40 min, respectively with a percentage removal of 53% (MCM-41) and 56.39% (SBA-15). The removal of MB using MCM-41 and SBA-15 is 10 min and 30 min, respectively with percentage removal of 99.94% (MCM-41) and 92.66% (SBA-15). The efficiency of removing dye increases to a certain extent along with increasing the contact time but further increase in contact time does not increase the adsorption rate between adsorbent and dye molecules. This is due to the decrease of unoccupied surface sites

Adsorption isotherm

Adsorption isotherm determines whether the adsorption reaction occurs in monolayer or multilayer. It determines how the dye molecules cover the surface and internal surface of the adsorbent after the adsorption process reach equilibrium [63]. Graphs for each isotherm model are plotted to obtain linear regression correlation coefficient (R^2) value that is used to define which model is suitable to explain the behavior of the adsorption occuring throughout the adsorption process. R^2 value that is close to 1 is chosen. Figures 8 and 9 show the graph on the Langmuir and Freundlich isotherm model on the removal of MO and MB using MCM-41 and SBA-15, respectively. Based on the graph, the adsorption process for removal of MO (R^2= 0.9742) and MB (R^2= 0.9933) for MCM-41 is described as monolayer adsorption whereby the Langmuir model

is best fitted for both studies [64, 65]. As for SBA-15, adsorption of MO (R^2= 0.7214) is best described as the Freundlich model. Based on the previous study [66], the Langmuir model better fitting on adsorption of acidic dye, however, the result in this study does not come to an agreement. This is because the adsorbent surface during the adsorption process was heterogenous and the adsorption sites have different adsorption energy hence, causes multilayer adsorption [41]. The adsorption data on removal of MB (R^2= 0.9787) using SBA-15 fits the Langmuir model [67]. Figures 8 and 9 show the graphs on the Langmuir and Freundlich isotherm model on the removal of MO and MB using MCM-41 and SBA-15, respectively.

Adsorption kinetic

There are two common kinetic models used in the kinetic study, which are pseudo-first-order or pseudo-second-order. These two kinetic models were used to investigate the mechanism of adsorption and the rate of adsorption that occurred during the adsorption process. The determination of types of kinetic model is based on the linear regression correlation coefficient, R^2 value that is obtained from graphs. The R^2 value close to 1 determines the kinetic model of the adsorption process. The adsorption studies in removing MO and MB using MCM-41 and SBA-15 fit better with pseudo-second-order. This shows that the preferable mechanism of the reaction is chemisorption instead of physisorption [65, 66, 67, 68]. The graphs for t/q_t against contact time for MCM-41 and SBA-15 are shown in Figure 10 and 11, respectively.

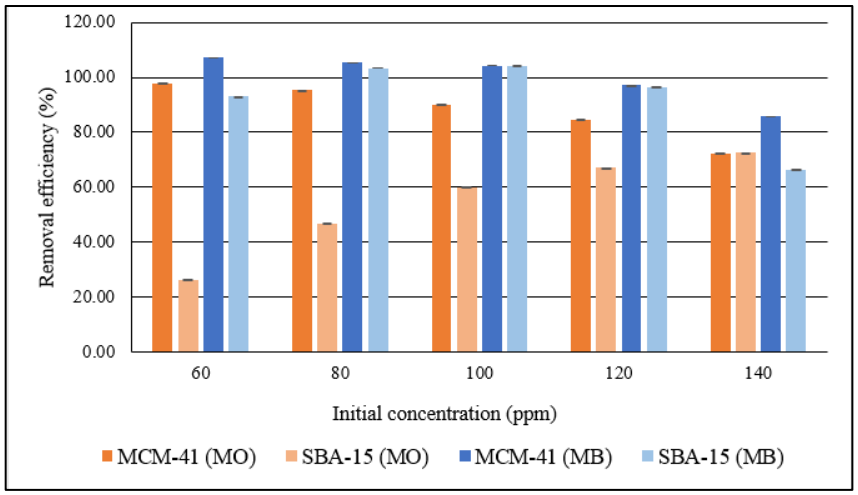


Figure 6. Percentage removal of MO and MB using MCM-41 and SBA-15 at a different range of initial concentration

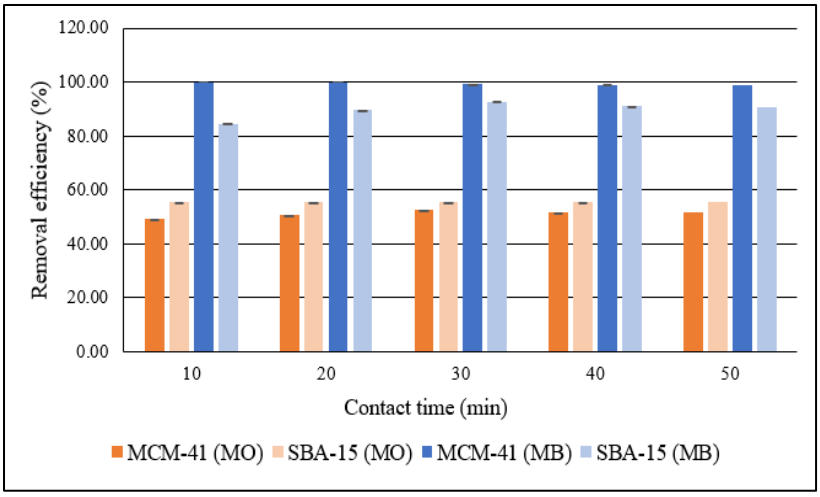


Figure 7. Percentage removal of MO and MB using MCM-41 and SBA-15 at a different range of contact time

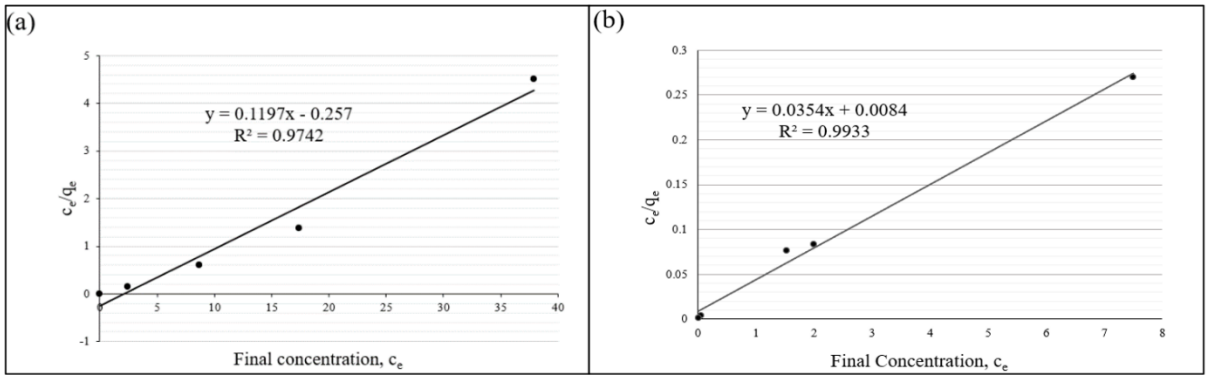


Figure 8. Langmuir adsorption isotherm on the removal of (a) MO and (b) MB using MCM-41

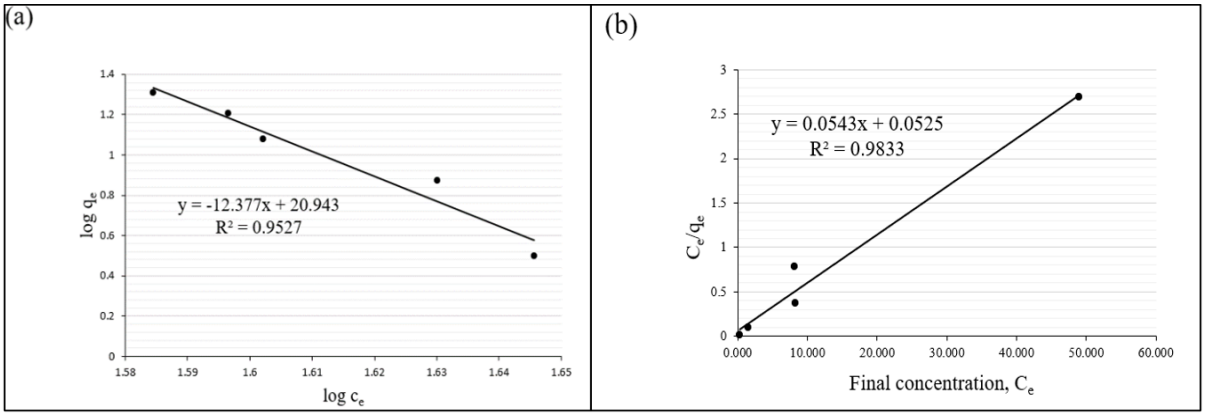


Figure 9. Freundlich adsorption isotherm on the removal of (a) MO and Langmuir isotherm on the removal of (b) MB using SBA-15

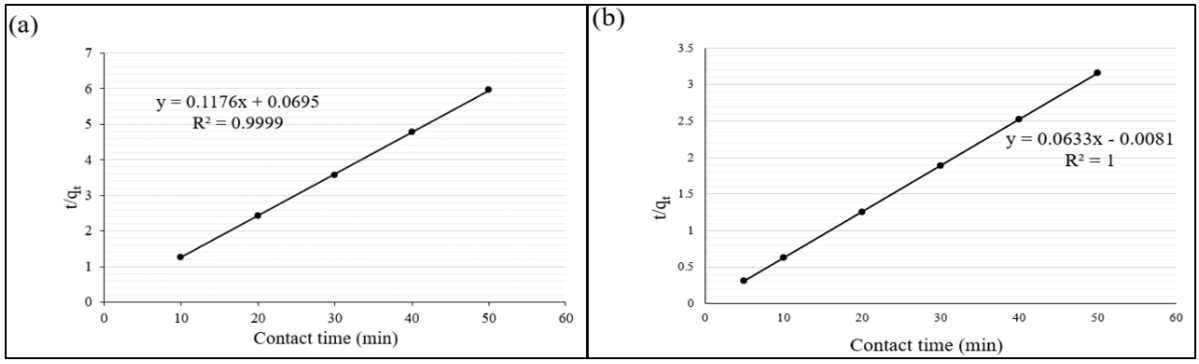


Figure 10. Pseudo-second-order for MCM-41 on removal of (a) MO and (b) MB

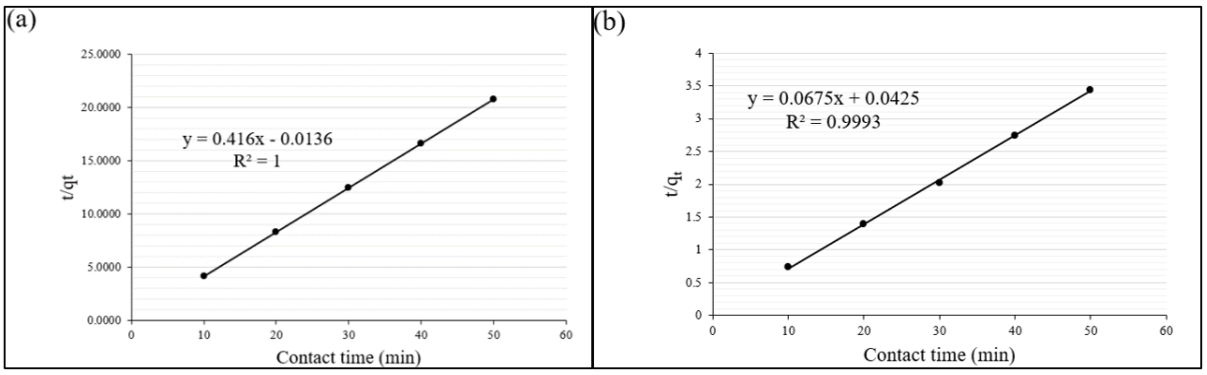


Figure 11. Pseudo-second-order for SBA-15 on removal of (a) MO and (b) MB

Comparison of dye removal efficiency

The removal efficiencies of MCM-41 and SBA-15 were compared with other types of adsorbents for removal of the MO and MB from an aqueous solution. The maximum adsorption capacity of MO and MB dyes on different types of adsorbent are listed in Table 1. According to the table, this study showed the highest adsorption capacity for both dyes.

Table 1. Maximum adsorption capacity of MO and MB using other types of adsorbents

Mesoporous Silica Adsorbent	**Dyes**	**pH**	**Maximum Adsorption Capacities, (mg/g)**	**References**
Mesopore silica composite from rice husk with activated carbon from coconut shell	MO	2.0	0.470	[69]
Non-porous silica	MB	-	9.5	[70]

Table 1 (cont'd). Maximum adsorption capacity of MO and MB using other types of adsorbents

Mesoporous Silica Adsorbent	Dyes	pH	Maximum Adsorption Capacities, (mg/g)	References
Green iron oxides/MCM-41	MO	4.5	1.9	[71]
Calcined magnesite	MB	-	0.39	[72]
	MO	-	0.64	
Zinc metal organic frameworks	MB	-	0.75	[73]
Brazil nut shells	MB	7.0 -10.0	7.81	[74]
MCM-41	MO	3.0	4.757	**This study**
SBA-15	MO	5.0	20.212	**This study**
MCM-41	MB	7.0	16.00	**This study**
SBA-15	MB	11.0	10.45	**This study**

Conclusion

Mesoporous silica MCM-41 and SBA-15 with a specific surface area of 436 m^2/g and 507 m^2/g were applied for removal of anionic and cationic dye from an aqueous solution. At optimum conditions, the maximum adsorption capacities of MO using MCM-41 (pH = 3, initial concentration = 60 ppm, contact time = 30 minutes) and SBA-15 (pH = 5, initial concentration = 140 ppm, contact time = 40 minutes) are 4.757 mg/g and 20.212 mg/g respectively. As for the removal of MB, the maximum adsorption capacities obtained by MCM-41 (pH = 7, initial concentration = 80 ppm, contact time = 10 minutes) and SBA-15 (pH = 11, initial concentration = 100 ppm, contact time = 30 minutes) are 16.00 mg/g and 10.45 mg/g respectively. This study showed that the proposed mesoporous silicates removed a considerable amount of MB cationic dye compared to the MO anionic dye. Since cationic dyes contain positive sites, they can interact with the silanol groups and form strong hydrogen bonds for longer retention on the surface of the adsorbents. Besides that, SBA-15 removes MO better compared to MCM-41, which is due to the higher surface area and pore size. The adsorption data for the removal of MO using MCM-41 and SBA-15 fits Langmuir and Freundlich models respectively, while for the removal of MB, both adsorbents fit the Langmuir model. The adsorption kinetics of MO and MB onto MCM-41 and SBA-15 is best described as pseudo-second-order showing that the adsorption mechanism of MO and MB is chemisorption. It is concluded that MCM-41 and SBA-15 can also be used as adsorbents to efficiently remove the anionic MO and cationic MB from water.

Acknowledgement

The authors would like to thank Universiti Teknologi MARA for the facilities provided and the Technical Secretariat of the Organization for the Prohibition Chemical Weapons (OPCW) for financial aid through the research grant: 100-TNCPI/INT 16/6/2 (022/2021).

References

1. Liang, C. Z., Sun, S. P., Li, F. Y., Ong, Y. K. and Chung, T. S. (2014). Treatment of highly concentrated wastewater containing multiple synthetic dyes by a combined process of coagulation/flocculation and nanofiltration. *Journal of Membrane Science,* 469: 306-315.
2. Forster, S. V. and Christie, R. M. (2013). The sifnificance of the introduction of synthetic dyes in the mid 19th century on the democratisation of western fashion. *Journal of the International Colour Association,* 11: 1-17.

3. Ratna nd Padhi, B. S. (2012). Pollution due to synthetic dyes toxicity and carcinogenecity studies and remediation. *International Journal of Environmental Sciences,* 3(3): 940-947.
4. Kausar, A., Iqbal, M., Javed, A., Aftab, K., Nazli, Z.-i.-H., Bhatti, H. N. and Nouren, S. (2018). Dyes adsorption using clay and modified clay: A review. *Journal of Molecular Liquids,* 256: 395-407.
5. Lafi, R. and Hafiane, A. (2016). Removal of methyl orange (MO) from aqueous solution using cationic surfactants modified coffee waste (MCWs). *Journal of the Taiwan Institute of Chemical Engineers,* 58: 424-433.
6. Elbanna, K., Sarhan, O. M., Khider, M., Elmogy, M., Abulreesh, H. H. and Shaaban, M. R. (2017). Microbiological, histological, and biochemical evidence for the adverse effects of food azo dyes on rats. *Journal of Food and Drug Analysis,* 25(3): 667-680.
7. Weglarz-Tomczak, E. and Gorecki, L. (2012). Azo dyes-biological activity and synthetic strategy. *Chemik Science-Technique-Market,* 66(12): 1298-1307.
8. Percy, A. J., Moore, N. and Chipman, J. K. (1989). Formation of nuclear anomalies in rat intestine by benzidine and its biliary metabolites. *Toxicology,* 57: 217-233.
9. Nasuha, N., Hameed, B. H. and Din, A. T. (2010). Rejected tea as a potential low-cost adsorbent for the removal of methylene blue. *Journal of Hazardous Materials,* 175(1-3): 126-132.
10. Rafatullah, M., Sulaiman, O., Hashim, R. and Ahmad, A. (2010). Adsorption of methylene blue on low-cost adsorbents: a review. *Journal of Hazardous Materials,* 177(1-3): 70-80.
11. Nidheesh, P. V., Zhou, M. and Oturan, M. A. (2018). An overview on the removal of synthetic dyes from water by electrochemical advanced oxidation processes. *Chemosphere,* 197: 210-227.
12. Moradi, G., Zinadini, S. and Rajabi, L. (2020). Development of high flux nanofiltration membrane using para-amino benzoate ferroxane nanoparticle for enhanced antifouling behavior and dye removal. *Process Safety and Environmental Protection*, 144: 65-78.
13. Hussein, T. K. and Jasim, N. A. (2021). A comparison study between chemical coagulation and electro-coagulation processes for the treatment of wastewater containing reactive blue dye. *Materials Today: Proceedings,* 42(5): 1946-1950.
14. Abid, M. F., Zablouk, M. A. and Abid-Alameer, A. M. (2012). Experimental study of dye removal from industrial wastewater by membrane technologies of reverse osmosis and nanofiltration. *Iranian Journal of Environmental Health Science & Engineering*, 9(1): 17.
15. Chen, W., Sun, F., Zhu, Z., Min, Z. and Li, W. (2014). Nanoporous SnO2 prepared by a photochemical strategy: Controlling of specific surface area and photocatalytic activity in degradation of dye pollutants. *Microporous and Mesoporous Materials*, 186: 65-72.
16. Yang, Z., Asoh, T. A. and Uyama, H. (2019). Removal of cationic or anionic dyes from water using ion exchange cellulose monoliths as adsorbents. *Bulletin of the Chemical Society of Japan*, 92(9): 1453-1461.
17. Pathania, D., Sharma, S. and Singh, P. (2013). Removal of methylene blue by adsorption onto activated carbon developed from *Ficus carica* bast. *Arabian Journal of Chemistry,* 10: S1445-S1451.
18. Wang, J. and Zhuang, S. (2017). Removal of various pollutants from water and wastewater by modified chitosan adsorbents. *Critical Reviews in Environmental Science and Technology*, 47(23): 2331-2386.
19. Abdul Karim, S. K., Lim, S.-F., Chua, D., Shanti Faridah, S. and Puong Ling, L. (2018). Removal of crystal violet and acid green dye in aqueous solution using banana plant-derived sorbents. *Malaysian Journal of Analytical Sciences*, 22(1): 115-122.
20. Sumari, S. M., Hamzah, Z. and Kantasamy, N. (2016). Adsorption of anionic dyes from aqueous solutions by calcined and uncalcined Mg/Al layered double hydroxide. *Malaysian Journal of Analytical Science*, 20(4), 777-792.

21. Wang, Y., Zhang, C., Zhao, L., Meng, G., Wu, J. and Liu, Z. (2017). Cellulose-based porous adsorbents with high capacity for methylene blue adsorption from aqueous solutions. *Fibers and Polymers*, 18(5): 891-899.
22. Guo, F., Jiang, X., Li, X., Jia, X., Liang, S. and Qian, L. (2020). Synthesis of MgO/Fe_3O_4 nanoparticles embedded activated carbon from biomass for high-efficient adsorption of malachite green. *Materials Chemistry and Physics*, 240: 122240.
23. Islam, M. A., Ahmed, M. J., Khanday, W. A., Asif, M. and Hameed, B. H. (2017). Mesoporous activated coconut shell-derived hydrochar prepared via hydrothermal carbonization-NaOH activation for methylene blue adsorption. *Journal of Environmental Management,* 203: 237-244.
24. Jiang, C., Wang, X., Qin, D., Da, W., Hou, B., Hao, C. and Wu, J. (2019). Construction of magnetic lignin-based adsorbent and its adsorption properties for dyes. *Journal of Hazardous Materials*, 369: 50-61.
25. Kantasamy, N. and Sumari, S. M. (2016). Equilibrium and thermodynamic studies of anionic dyes removal by an anionic clay-layered double hydroxide. *Malaysian Journal of Analytical Sciences*, 20(2): 358-364.
26. Qu, W., He, D., Huang, H., Guo, Y., Tang, Y. and Song, R. J. (2020). Characterization of amino-crosslinked hypromellose and its adsorption characteristics for methyl orange from water. *Journal of Materials Science*, 55(17): 7268-7282.
27. Yang, X. J., Zhang, P., Li, P., Li, Z., Xia, W., Zhang, H., Di, Z., Wang, M., Zhang, H. and Niu, Q. J. (2019). Layered double hydroxide/polyacrylamide nanocomposite hydrogels: Green preparation, rheology and application in methyl orange removal from aqueous solution. *Journal of Molecular Liquids*, 280: 128-134.
28. Wang, D., Shen, H., Guo, L., Wang, C. and Fu, F. (2016). Porous BiOBr/Bi2MoO6 heterostructures for highly selective adsorption of methylene blue. *ACS Omega*, 1(4): 566-577.
29. Gibson, L. T. (2014). Mesosilica materials and organic pollutant adsorption: part B removal from aqueous solution. *Chemistry Society Reviews*, 43(15): 5173-5182.
30. Boukoussa, B., Hakiki, A., Moulai, S., Chikh, K., Kherroub, D. E., Bouhadjar, L., Guedal, D., Messaoudi, K., Mokthar, F. and Hamacha, R. (2018). Adsorption behaviors of cationic and anionic dyes from aqueous solution on nanocomposite polypyrrole/SBA-15. *Journal of Materials Science*, 53(10): 7372-7386.
31. Kresge, C. T., Leonowicz, M. E., Roth, W. J., Vartuli, J. C. and Beck, J. S. (1992). Ordered mesoporous sieves synthesised by a liquid-crystal template mechanism. *Nature,* 359: 710-712.
32. Björk, E. M. (2016). Synthesizing and characterizing mesoporous silica SBA-15: A hands-on laboratory experiment for undergraduates using various instrumental techniques. *Journal of Chemical Education*, 94(1): 91-94.
33. Sabri, A. A., Albayati, T. M. and Alazawi, R. A. (2015). Synthesis of ordered mesoporous SBA-15 and its adsorption of methylene blue. *Korean Journal of Chemical Engineering,* 32(9): 1835-1841.
34. Alothman, Z. (2012). A review: Fundamental aspects of silicate mesoporous materials. *Materials*, 5(12): 2874-2902.
35. Xiao, X., Zhang, F., Feng, Z., Deng, S. and Wang, Y. (2015). Adsorptive removal and kinetics of methylene blue from aqueous solution using NiO/MCM-41 composite. *Physica E: Low-dimensional Systems and Nanostructures,* 65: 4-12.
36. Diagboya, P. N. E. and Dikio, E. D. (2018). Silica-based mesoporous materials; emerging designer adsorbents for aqueous pollutants removal and water treatment. *Microporous and Mesoporous Materials,* 266: 252-267.
37. Kamaruzaman, S., Sanagi, M. M., Endud, S., Wan Ibrahim, W. A. and Yahaya, N. (2013). MCM-41 solid phase membrane tip extraction combined with liquid chromatography for the determination of non-steroidal anti-inflammatory drugs in human urine. *Journal of Chromatography B,* 940: 59-65.

38. Ab Rahman, N. B., Rashid, H. M., Hassan, H. M. and Jalil, M. N. (2016). Synthesis and characterization of mesoporous silica MCM-41 and SBA-15 from power plant bottom ash. *Malaysian Journal of Analytical Sciences*, 20(3): 539-545.
39. Yuan, N., Cai, H., Liu, T., Huang, Q. and Zhang, X. (2019). Adsorptive removal of methylene blue from aqueous solution using coal fly ash-derived mesoporous silica material. *Adsorption Science & Technology*, 37(3-4): 333-348.
40. Rizzi, V., Romanazzi, F., Gubitosa, J., Fini, P., Romita, R., Agostiano, A., Petrella, A., Cosma, P. (2019). Chitosan film as eco-friendly and recyclable bio-adsorbent to remove/recover diclofenac, ketoprofen, and their mixture from wastewater. *Biomolecules*, 9(10): 571.
41. Rizzi, V., Gubitosa, J., Fini, P., Nuzzo, S. and Cosma, P. (2020). Amino-grafted mesoporous MCM-41 and SBA-15 recyclable adsorbents: Desert-rose-petals-like SBA-15 type as the most efficient to remove azo textile dyes and their mixture from water. *Sustainable Materials and Technologies*, 26: e00231.
42. Morsi, R. E. and Mohamed, R. S. (2018). Nanostructured mesoporous silica: influence of the preparation conditions on the physical-surface properties for efficient organic dye uptake. *Royal Society Open Science*, 5(3): 172021.
43. Shu, Y., Shao, Y., Wei, X., Wang, X., Sun, Q., Zhang, Q. and Li, L. (2015). Synthesis and characterization of Ni-MCM-41 for methyl blue adsorption. *Microporous and Mesoporous Materials,* 214: 88-94.
44. Loganathan, S., Tikmani, M. and Ghoshal, A. K. (2013). A novel pore-expanded MCM-41 for CO_2 capture: Synthesis and characterization. *Langmuir*, 29(10): 3491-3499.
45. He, R., Wang, Z., Tan, L., Zhong, Y., Li, W., Xing, D., Wei, C. and Tang, Y. (2018). Design and fabrication of highly ordered ion imprinted SBA-15 and MCM-41 mesoporous organosilicas for efficient removal of Ni^{2+} from different properties of wastewaters. *Microporous and Mesoporous Materials*, 257: 212-221.
46. Ruthstein, S., Frydman, V., Kababya, S., Landau, M. and Goldfarb, D. (2003). Study of the formation of the mesoporous material SBA-15 by EPR spectroscopy. *The Journal of Physical Chemistry B*, 107(8): 1739-1748.
47. Ghorbani, F., Habibollah, Y., Mehraban, Z., Çelik, M. S., Ghoreyshi, A. A. and Anbia, M. (2013). Preparation and characterization of highly pure silica from sedge as agricultural waste and its utilization in the synthesis of mesoporous silica MCM-41. *Journal of the Taiwan Institute of Chemical Engineers,* 44(5): 821- 828.
48. Veregue, F. R., de Lima, H. H. C., Ribeiro, S. C., Almeida, M. S., da Silva, C. T. P., Guilherme, M. R. and Rinaldi, A. W. (2020). MCM-41/chondroitin sulfate hybrid hydrogels with remarkable mechanical properties and superabsorption of methylene blue. *Carbohydrate Polymers*, 247: 116558.
49. Akpotu, S. O. and Moodley, B. (2018). Application of as-synthesised MCM-41 and MCM-41 wrapped with reduced graphene oxide/graphene oxide in the remediation of acetaminophen and aspirin from aqueous system. *Journal of Environmental Economics and Management,* 209: 205-215.
50. Björk, E. M. (2013). Mesoporous building blocks – synthesis and characterization of mesoporous silica particles and films. Doctoral dissertation, Linköping University, Sweden.
51. Thommes, M., Kaneko, K., Neimark, A. V., Olivier, J. P., Rodriguez-Reinoso, F., Rouquerol, J. and Sing, K. S. W. (2015). Physisorption of gases, with special reference to the evaluation of surface area and pore size distribution (IUPAC Technical Report). *Pure and Applied Chemistry*, 87(9-10): 1051-1069.
52. Zhu, C., Xia, Y., Zai, Y., Dai, Y., Liu, X., Bian, J., Liu, Y., Liu, J. and Li, G. (2019). Adsorption and desorption behaviors of HPEI and thermoresponsive HPEI based gels on anionic and cationic dyes. *Chemical Engineering Journal*, 369: 863-873.
53. Alkan, M., Demirbas, O. and Dogan, M. (2004). Removal of Acid Yellow 49 from aqueous solution by adsorption. *Fresenius Environmental Bulletin*, 13(11): 1121.

54. Fil, B. A., Ozmetin, C. and Korkmaz, M. (2012). Cationic dye (methylene blue) removal from aqueous solution by montmorillonite. *Bulletin of the Korean Chemical Society*, 33(10): 3184-3190.
55. Ansari, R. and Mosayebzadeh, Z. (2010). Removal of basic dye methylene blue from aqueous solutions using sawdust and sawdust coated with polypyrrole. *Journal of the Iranian Chemical Society*, 7(2): 339-350.
56. Bharathi, K. S. and Ramesh, S. T. (2013). Removal of dyes using agricultural waste as low-cost adsorbents: a review. *Applied Water Science*, 3(4): 773-790.
57. Özdemir, Y., Doğan, M. and Alkan, M. (2006). Adsorption of cationic dyes from aqueous solutions by sepiolite. *Microporous and Mesoporous Materials*, 96(1-3): 419-427.
58. Yagub, M. T., Sen, T. K., Afroze, S. and Ang, H. M. (2014). Dye and its removal from aqueous solution by adsorption: A review. *Advances in Colloid and Interface Science,* 209: 172-184.
59. Huang, R., Liu, Q., Huo, J. and Yang, B. (2017). Adsorption of methyl orange onto protonated cross-linked chitosan. *Arabian Journal of Chemistry*, 10(1): 24-32.
60. El-Gamal, S. M. A., Amin, M. S. and Ahmed, M. A. (2015). Removal of methyl orange and bromophenol blue dyes from aqueous solution using Sorel's cement nanoparticles. *Journal of Environmental Chemical Engineering,* 3(3): 1702-1712.
61. Melo, B. C., Paulino, F. A. A., Cardoso, V. A., Pereira, A. G. B., Fajardo, A. R. and Rodrigues, F. H. A. (2018). Cellulose nanowhiskers improve the methylene blue adsorption capacity of chitosan-g-poly (acrylic acid) hydrogel. *Carbohydrate Polymers*, 181, 358–367.
62. Albayati, T. M., Alwan, G. M. and Mahdy, O. S. (2016). High performance methyl orange capture on magnetic nanoporous MCM-41 prepared by incipient wetness impregnation method. *Korean Journal of Chemical Engineering*, 34(1), 259–265.
63. Brdar, M., Šćiban, M., Takači, A. and Došenović, T. (2012). Comparison of two and three parameters adsorption isotherm for Cr(VI) onto Kraft lignin. *Chemical Engineering Journal*, 183: 108-111.
64. Qin, Q., Ma, J. and Liu, K. (2009). Adsorption of anionic dyes on ammonium-functionalized MCM-41. *Journal of Hazardous Materials,* 162(1): 133-139.
65. Juang, L. C., Wang, C. C. and Lee, C. K. (2006). Adsorption of basic dyes onto MCM41. *Chemosphere,* 64(11): 1920-1928.
66. Mirzaie, M., Rashidi, A., Tayebi, H.-A. and Yazdanshenas, M. E. (2017). Removal of anionic dye from aqueous media by adsorption onto SBA-15/polyamidoamine dendrimer hybrid: Adsorption equilibrium and kinetics. *Journal of Chemical & Engineering Data*, 62(4): 1365-1376.
67. Bardajee, G. R., Hooshyar, Z. and Shahidi, F. E. (2015). Synthesis and characterization of a novel Schiff-base/SBA-15 nanoadsorbent for removal of methylene blue from aqueous solutions. *International Journal of Environmental Science and Technology*, 12(5): 1737-1748.
68. Jalil, M. N. (2011). The preparation and characterisation of mesoporous films for electrochemical applications. Doctoral dissertation, University of Manchester, United Kingdom.
69. Yusmaniar, Y., Erdawati, E., Ghifari, Y. F. and Ubit, D. P. (2020). Synthesis of mesopore silica composite from rice husk with activated carbon from coconut shell as absorbent methyl orange color adsorbent. *IOP Conference Series: Materials Science and Engineering*, 830: 032078.
70. Ge, S., Geng, W., He, X., Zhao, J., Zhou, B., Duan, L., Wu, Y. and Zhang, Q. (2018). Effect of framework structure, pore size and surface modification on the adsorption performance of methylene blue and Cu^{2+} in mesoporous silica. *Colloids and Surfaces A: Physicochemical and Engineering Aspects*, 539: 154-162.
71. Nazar de Souza, A. P., Licea, Y. E., Colaço, M. V., Senra, J. D. and Carvalho, N. M. F. (2021). Green iron oxides/amino-functionalized MCM-41 composites as adsorbent for anionic azo dye: Kinetic and isotherm studies. *Journal of Environmental Chemical Engineering*, 9(2): 105062.

72. Ngulube, T., Gumbo, J. R., Masindi, V. and Maity, A. (2018). Calcined magnesite as an adsorbent for cationic and anionic dyes: characterization, adsorption parameters, isotherms and kinetics study. *Heliyon*, 4(10): e00838.
73. Sun, C. Y., Wang, X. L., Qin, C., Jin, J. L., Su, Z. M., Huang, P. and Shao, K. Z. (2013). Solvatochromic behavior of chiral mesoporous metal-organic frameworks and their applications for sensing small molecules and separating cationic dyes. *Chemistry - A European Journal*, 19(11): 3639-3645.
74. de Oliveira Brito, S. M., Andrade, H. M. C., Soares, L. F. and de Azevedo, R. P. (2010). Brazil nut shells as a new biosorbent to remove methylene blue and indigo carmine from aqueous solutions. *Journal of Hazardous Materials*, 174 (1-3): 84-92.

Malaysian Journal of Analytical Sciences (MJAS)
Published by Malaysian Analytical Sciences Society

CHITOSAN-LIGNIN COMPOSITE FOR RECOVERY OF LANTHANUM (III) IONS FROM AQUEOUS SOLUTIONS

(Kitosan-Lignin Komposit untuk Perolehan Semula Lanthanum (III) Ion Dari Larutan Akueus)

Shariff Ibrahim[1]*, Nur Shuhaidah Shamsul Kamal[1], Megat Ahmad Kamal Megat Hanafiah[2], Noorul Farhana Md Ariff[1], Sabiha Hanim Saleh[1]

[1]School of Chemistry and Environment, Faculty of Applied Sciences, Universiti Teknologi MARA, 40450 Shah Alam, Selangor, Malaysia
[2]Faculty of Applied Sciences, Universiti Teknologi MARA, 264000 Jengka, Pahang, Malaysia

**corresponding author: sha88@uitm.edu.my*

Received: 5 July 2021; Accepted: 6 October 2021; Published: 25 October 2021

Abstract

A chitosan-lignin composite was prepared, characterised, and applied as an effective adsorbent to recover precious rare earth La(III) ions. The characterisation studies revealed that the chitosan-lignin composite consisted of slightly acidic groups, as both pH_{ZPC} and pH of the slurry were 6.17 and 5.47, respectively. The specific surface area of the composite was found to be 1.41 m^2 g^{-1} using Brunauer Emmett Teller (BET), which was lower than the raw chitosan surface area. The FTIR spectrum showed the disappearance of the primary amine peak of chitosan at 1648 cm^{-1} due to interaction with the benzene ring in lignin. Factors influencing La(III) adsorption behaviour include the pH of the solution, adsorbent dosage, concentration, and contact time. The maximum adsorption of La(III) was at pH 4 with an adsorbent dosage of 0.5 g L^{-1}. The Langmuir isotherm model fitted well to the experimental isotherm data, with R^2 = 0.99. The maximum adsorption capacity of the chitosan-lignin composite was 500 mg g^{-1} at 300 K. A competitive ion experiment revealed Ce(III) ions, another lanthanide group member, adsorbed more than La(III) when both metal ions were mixed in a binary system. Maximum desorption of 90% La(III) was noted with Na_2EDTA as the desorbing agent.

Keywords: adsorption, composite, chitosan, lignin, kinetics

Abstrak

Komposit kitosan-lignin disediakan, dicirikan, dan digunakan sebagai penjerap yang berkesan untuk pengambilan semula ion La(III) nadir bumi. Kajian pencirian menunjukkan bahawa komposit kitosan-lignin terdiri daripada kumpulan yang sedikit berasid kerana kedua-dua pH_{zpc} dan pH buburan masing-masing adalah 6.17 dan 5.47. Luas permukaan komposit yang spesifik didapati 1.41 m^2 g^{-1} menggunakan Brunauer Emmett Teller (BET), iaitu lebih rendah daripada luas permukaan kitosan mentah. Spektrum FTIR menunjukkan hilangnya puncak kitosan amina primer pada 1648 cm^{-1} kerana interaksi dengan cincin benzena di lignin. Faktor-faktor yang mempengaruhi tingkah laku penjerapan La(III) termasuk pH larutan, dos penjerap, kepekatan, dan masa sentuhan. Penjerapan maksimum La(III) berlaku pada pH 4 dengan dos penjerap 0.5 g L^{-1}. Model isoterma Langmuir sesuai dengan data isoterma eksperimen dengan pekali regresi R^2 = 0.99. Kapasiti penjerapan maksimum komposit kitosan-lignin ialah 500 mg g^{-1} pada 300 K. Eksperimen persaingan ion mendedahkan Ce(III), iaitu ahli kumpulan lantanida lain, dijerap

lebih banyak berbanding La(III) ketika kedua-dua ion logam tersebut bercampur dalam sistem binari. Nyahjerapan maksimum La(III) mencatatkan 90% dengan Na_2EDTA sebagai agen penyahjerapan.

Kata kunci: penjerapan, komposit, kitosan, lignin, kinetik

Introduction

The extensive use of lanthanides in various high technology industries, such as chemical engineering, electronics, metallurgy, and medicine, is due to their unique properties, making them one of the most demanding metals worldwide [1]. Lanthanum (La), a member of the lanthanide group, is categorised as a much sought-after metal. It is a crucial component in making catalysts, ceramics, glass, metal products, and battery alloys. Lanthanum is found in allanite, monazite, cerite, and bastnaesite, which are rare earth compounds [2]. With increasing industrial demand for La, environmental pollution has become a significant issue, particularly water supplies. Efficient management is critical for maintaining a healthy environment, and wastewater recovery can offer a steady supply of La by optimising its use. Numerous techniques for resolving this problem have been investigated, including co-precipitation, ion exchange, and solvent extraction [3]. These techniques, however, are inefficient and expensive to operate and maintain [4]. Due to high-affinity metal adsorption and environmentally acceptable methods, adsorption seems to be the most effective technique for removing lanthanides from aqueous solutions [1].

The use of chitosan as a biosorbent medium has been extensively studied for various applications [5]. Chitosan is a biodegradable biopolymer that may be modified chemically to enhance its physicochemical characteristics [6]. It is effective in removing a variety of inorganic and organic pollutants [7]. However, the high cost of chitosan and a number of its poor characteristics, including mechanical strength, chemical strength, porosity, and surface area, restrict its performance [8, 9]. Thus, modification methods should be used to enhance chitosan's adsorptive capacity. As a result, the possibility of combining chitosan with other adsorbents, such as lignin is discussed in this section.

Apart from its accessibility, lignin has been studied for its polyphenol structure and physicochemical characteristics [10]. Lignin comprises propyl-phenolic subunits that serve as potential active sites for dye and metal adsorption [11]. Numerous investigations into the efficacy of chitosan–alkali lignin composites in removing various kinds of pollutants have been conducted [12, 13]. Researchers discovered that adding lignin to chitosan enables the use of renewable by-products while also lowering the total cost of obtaining the chitosan precursor [14, 15]. They concluded that combining chitosan and lignin may reduce the use of chitosan since lignin is considered a universal waste by-product of the paper and cellulosic bioethanol industries. This is because lignin accounts for about 15-35% of the dry biomass [16].

This article discusses the use of chitosan-lignin composites for removing rare earth metals from aqueous solutions and desorbing them from metal-loaded adsorbents. To better understand the adsorbent/desorption behaviour of the chitosan-lignin composites, they were characterised. Batch parameters, such as the influence of the pH solution, the adsorbent dosage, and the ions competition experiment, were investigated. The data was then applied to determine their fitness for various isotherm models. Desorption with several solvents examined the possible recovery of adsorbed La(III) ions from chitosan-lignin composites. Despite many works on the utilisation of chitosan lignin as an adsorbent material, to the best of our knowledge, the application for La(III) adsorption was scarce [1]. As a result, this work served as a valuable foundation for future research.

Materials and Methods

Materials

Chitosan high molecular weight (95% deacetylated), lignin alkali, and acetic acid reagent (≥99.7%) were purchased from Aldrich. The standard solution used in this work was Lanthanum nitrate hexahydrate,

analytical grade ($La(NO_3)_3.6H_2O$, 96%), purchased from Merck. Deionised water was utilised throughout the adsorption experiments.

Preparation of chitosan-lignin adsorbent

The adsorbent preparation was taken from a previous study [14]. A weight of 2.0 g of chitosan was dissolved using acetic acid (2%, v/v) and left overnight. The lignin solution was set up by dissolving 2.0 g of lignin powder in 100 mL of deionised water. Finally, chitosan and lignin solutions were mixed homogeneously by an orbital shaker at 300 rpm for 3 h. The mixture was then left to dry overnight at 100°C. Lastly, the dried adsorbent was sieved to a size of <500 µm.

Characterisation of chitosan-lignin

The aqueous slurry pH was obtained by mixing 1.0 g of chitosan-lignin adsorbent into 50 mL of deionised water, stirring for 24 hours, filtering, and measuring the final pH. The pH of zero-point charge (pH_{ZPC}) was measured by mixing 0.15 g of chitosan-lignin with 50 mL (0.01 M) of NaCI solution into a series of beakers. The initial pH values of these solutions were arranged from 4 to 12, using 0.10 M of NaOH or HCl solutions and left to agitate at 150 rpm for 48 hours at room temperature before measuring the final pH of the solutions. The Fourier transform infrared (FTIR) spectra were recorded using an FTIR spectrophotometer (PerkinElmer 2000, USA). The samples were analysed in the range of 4000-450 cm^{-1}. Finally, the specific surface area and pore size were evaluated using Brunauer Emmett Teller (BET) and Barrett Joyner Halenda (BJH) methods.

Batch adsorption studies

The adsorption experiments were carried out at room temperature (300 K) using 50 mL of 100 mg L^{-1} La(III) solution with continuous stirring at 250 rpm for 45 minutes. These solutions were then eventually filtered using Whatman 42 filter paper. The filtrate was then analysed using an inductively coupled plasma-optical emission spectrometer (ICP-OES, Perkin Elmer DV5300, USA). The effect of pH was determined by adjusting the pH of La(III) solution from 2 to 6. The dosage effect was measured by varying the dosage of chitosan-lignin adsorbent from 0.5 to 2.0 g L^{-1}. For the ionic competition experiments, 0.05 g of chitosan-lignin adsorbent was added to a mixture of 50 mL (100 mg L^{-1}) La(III) and Ce(III) binary systems. The amount of La(III) and Ce(III) adsorbed, q_e (mg g^{-1}) was determined using Eq. (1). Unless stated, all the experiments were replicated, and the results are reported in mean with relative standard deviations of less than 5%.

$$q_e = \frac{C_o - C_e}{m} V \quad (1)$$

where C_o and C_e are the initial and equilibrium concentrations (mg L^{-1}) of La(III)/Ce(III), respectively; V is the volume of the La(III)/Ce(III) solution (L), and m is the weight of chitosan-lignin composite (g).

Desorption studies

La(III) loaded sorbents were put in an oven at 320 K for 2 h. These were then collected and stirred with 50 mL of deionised water, 0.01 and 0.1 M Na_2EDTA solutions, and 0.01, 0.10, and 1.0 M of NaOH, HCl, and HNO_3, respectively, for 2 h. After stirring, the mixtures were filtered and analysed using ICP-OES. The percentage of desorption can be calculated using equation 2:

$$\text{Percentage of desorption (\%)} = \frac{C_{e(des)}}{C_{e(ads)}} \times 100 \quad (2)$$

where $C_{e(des)}$ is the concentration of metal ion desorbed from the adsorbent (mg L^{-1}), and $C_{e(ads)}$ is the concentration of adsorbed metal ion (mg L^{-1}).

Results and Discussion

Characterisation of chitosan-lignin

The pH_{ZPC} was observed as 6.17, thus, reflecting the net positive charge of the surface below this pH. The pH value of chitosan-lignin at 5.47 indicates that this adsorbent carries slightly acidic groups. The surface area of the chitosan-lignin composite was 1.41 m^2 g^{-1}, lower than the surface area of raw chitosan, 2.26 m^2 g^{-1}. The finding here is consistent with the work of Sohni et al. [17]. They explained that the lignin attachment to the internal framework of raw chitosan resulted in blockage of chitosan porosities. The FTIR spectra of the functional groups of raw chitosan, raw lignin, and the chitosan-lignin composite are presented in Figure 1. The chitosan spectrum shows the presence of -OH and

-NH groups at 3000 – 3500 cm^{-1}. The wavenumbers at 1651 and 1035 cm^{-1} represent Amide I and C-O-C groups, respectively. The lignin spectrum reveals the following information: there is a broad peak from 2500 to 3500 cm^{-1}, suggesting carboxylic acid and -OH (aliphatic and aromatic) groups. The peak at 1710 cm^{-1} could be assigned to the C=O of the carboxylic group. The wavenumber from 1500 to 1600 cm^{-1} represents the C=C group in the aromatic ring. It can be observed that few significant changes occur in the spectrum of the chitosan-lignin composite compared to the spectrum of raw chitosan and raw lignin. The band of chitosan at 1651 cm^{-1} for the amide I group is shifted to 1602 cm^{-1}; meanwhile, the C-O-C stretching band assigned at 1035 cm^{-1} is shifted to 1030 cm^{-1}. Chen et al. [18] suggested that the measurable changes at these wavenumbers were due to the possible hydrogen bonding between the -OH groups of the lignin phenolic ring and the 1,4-glycoside oxygen atom of chitosan. Another possible interaction could involve the electrostatic attraction between the chitosan amino group and the carboxylic group of lignin, as indicated by the peak at 1599 cm^{-1}.

Effect of pH

The pH of the solution affects the amount of La(III) adsorption. Thus, studying the different conditions of pH solution is crucial as it can influence the properties of the adsorbent surface and the adsorbate species. According to Iftekhar et al. [19], La(III) ions are dominant in solutions with a pH below 6, while in solutions with a pH above 6, $La(OH)_3$ precipitation would form. Therefore, adsorption was conducted at pH solutions below 6. In Figure 2, the amount of La(III) adsorbed was almost constant from pH 2 to 6. A slight decrease in adsorption at pH 2 was probably due to the competition between the La^{3+} and H^+ ions for the adsorption sites [20]. Upon increasing pH to 4, the adsorption of La(III) shows a slight improvement with the highest adsorption capacity of 84.2 mg g^{-1}. Overall, good replicate data was observed, as the standard deviation was below 0.43.

Effect of dosage

It is widely known that the increased percentage of adsorption with increasing dosage was attributable to the existence of more active sites. However, a decreasing quantity of adsorbed La(III) was observed when the dosage was raised in Figure 3. At constant metal concentrations, increasing the dosage of the chitosan-lignin composite increased the number of unsaturated active sites and particulate interaction, such as aggregation, from a small quantity of dosage. Oyewo et al. [21] found a similar effect of aggregation, in which the adsorbent's surface area decreased, and the diffusion route length increased. Yanfei et al. [22] hypothesised that particle contact might desorb certain adsorbates that are only weakly and reversibly attached to the adsorbent surface. In general, excellent replication data was obtained, with a standard deviation of less than 1.54.

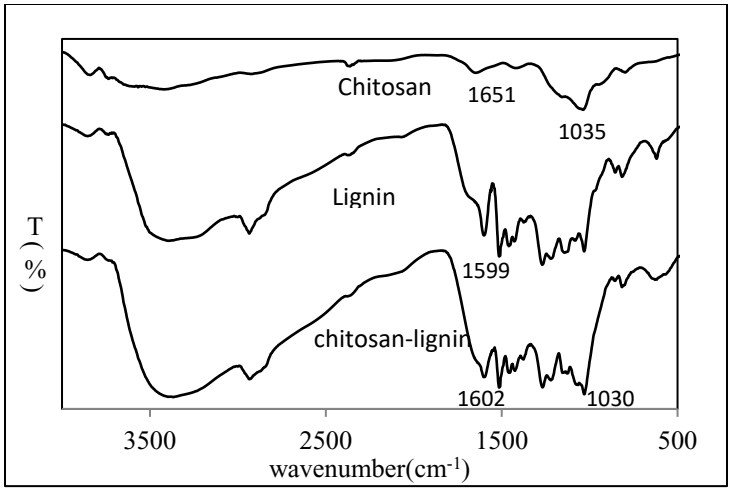


Figure 1. FTIR spectra of chitosan, lignin and Chitosan-lignin

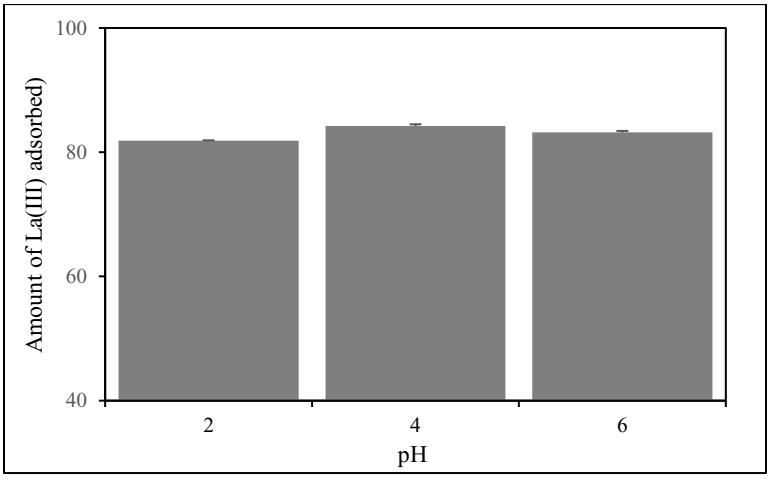


Figure 2. Effect of initial pH on adsorption of La(III) on chitosan-lignin composite

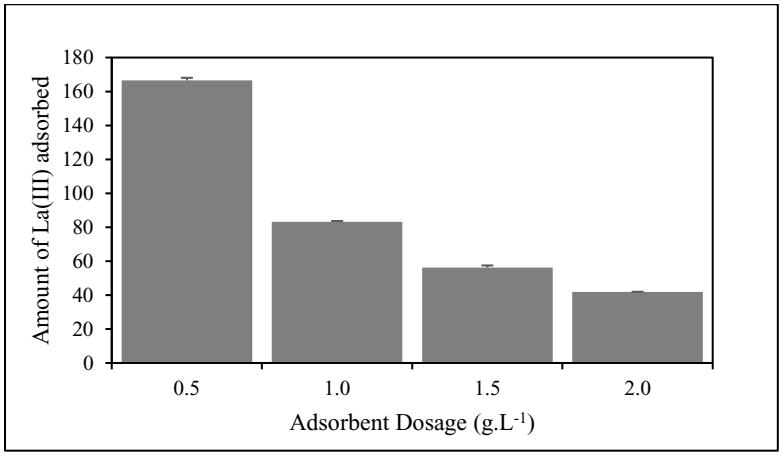


Figure 3. Effect of adsorbent dosage on adsorption of La(III) on chitosan-lignin composite

Adsorption isotherms

The linearised Langmuir equation [23] and Freundlich equation [24] are given in Equations 4 and 5, respectively:

$$\frac{1}{q_e} = \frac{1}{q_m K_L} \cdot \frac{1}{c_e} + \frac{1}{q_m} \quad (4)$$

$$\log q_e = \log K_F + \frac{1}{n} \log C_e \quad (5)$$

where, in the Langmuir equation, C_e is the equilibrium La(III) concentration (mg L^{-1}), q_e is the sum of La(III) adsorbed at equilibrium (mg g^{-1}), q_m is the highest adsorption capacity (mg g^{-1}), and K_L is a constant (L mg^{-1}). The value of K_L mirrors the bonding strength between La(III) and chitosan-lignin surfaces. As for the Freundlich model, K_F addresses the Freundlich constant (mg g^{-1}), and n is thought of as the heterogeneity of the adsorbent outer layer and its affection for the adsorbate.

The plot for Langmuir and Freundlich isotherm models for La(III) adsorption onto the chitosan-lignin are presented in Figures 4 and 5, respectively. Table 1 tabulated data for both models of the isotherm model. Both models showed R^2 values > 0.99, with the Langmuir model recording a maximum adsorption capacity of 500 mg g^{-1}. The value of n above 1 in Table 1 reflects the favourable adsorption. Table 2 compares the adsorption capacity of chitosan-lignin in adsorbing La(III) with other adsorbents. It can be concluded that the chitosan-lignin composite is a promising adsorbent for use in industries for the recovery of La(III) ions.

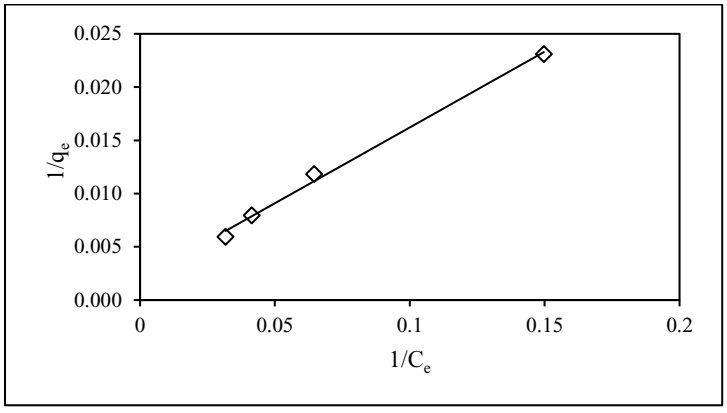


Figure 4. Langmuir isotherm for adsorption of La(III) on chitosan-lignin composite

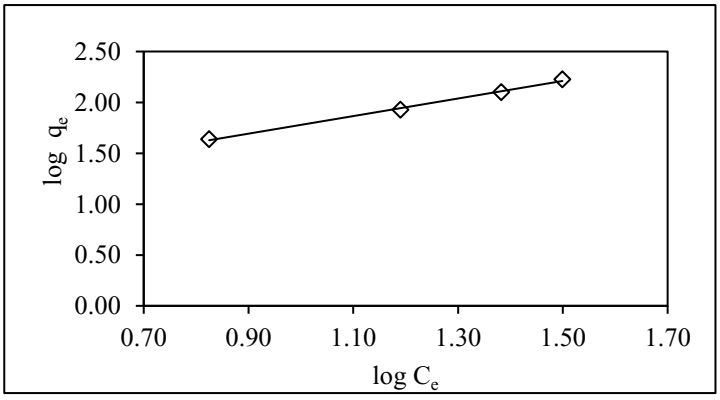


Figure 5. Freundlich isotherm for adsorption of La(III) on chitosan-lignin composite

Table 1. Langmuir and Freundlich parameters for adsorption of La(III) on chitosan-lignin composite

Langmuir			Freundlich		
q_m (mg g^{-1})	K_L (L mg^{-1})	R^2	K_F (mg g^{-1})	n	R^2
500	0.014	0.995	8.228	1.15	0.96

Table 2. Comparison of maximum adsorption capacity (q_m) values for adsorption of La(III) onto various types of adsorbents

Adsorbents	q_m (mg g^{-1})	References
Chitosan-lignin composite	**500.00**	**This study**
Ammonium citrate-modified biochar	362.32	[26]
Poly(vinyl alcohol) & mercaptopropyltrimethoxysilane modified chitosan	460.94	[27]
MgFe-LDH-Cyanex272	480.80	[28]
Pseudomonas sp.	950.00	[29]

Competition between ions

The adsorption effect among lanthanide ions was obtained using a binary system consisting of La(III) and Ce(III) ions. The understanding of competition between ions is essential as one should consider the multi-case component for industrial practice. In binary systems, adsorption consists of light rare earth elements (LREEs) and heavy rare earth elements (HREEs), favouring HREEs. However, in the same group of REEs of the metal system, the system favours higher than lower atomic numbers [25]. As shown in Figure 6, Ce(III) ions were more adsorbed than La(III). Higher Ce(III) sorption was due to Ce(III) having a higher atomic number (58) compared to La(III) (57) as described by Ogata et al. [25]. In this case, both lanthanide ions are competing to occupy the same binding sites on the adsorbent surface, as explained by Vijayaraghavan et al. [26]. Overall, good replicate data was observed, as the standard deviation was low at below 0.25.

Desorption studies

The ideal adsorbent is the one that has high efficiency in adsorption and efficient desorption behaviour [27]. The ability to desorb La(III) ions from the chitosan-lignin composite surface was evaluated using different desorbing agents with varying concentrations, namely distilled water, NaOH, HCl, HNO_3 and Na_2EDTA solutions. Distilled water is reported to have the ability to desorb La(III) ions, which are not strongly bonded to the adsorbent surface, or adsorption occurs via physisorption [28]. This is due to some small portion of La(III), superficially adsorbed to the adsorbent surface, most likely physical adsorption, thus explaining the low desorption amount. Anastopoulos et al. [28] observed the same phenomena in their desorption study of Pb^{2+} and Ni^{2+} from renewable lignocellulosic materials. They concluded that some physisorbed metals are easily released into the aqueous solution.

In Figure 7, only 4.26% of La(III) ions were desorbed by distilled water, explaining why La(III) ions were bonded by a strong chemical bond such as chemisorption. The NaOH desorbing agent failed to desorb La(III) due to the stability of La(III) ions in a basic solution [28]. In an acidic solution of HCl and HNO_3, La(III) ions were observed to be desorbed at a low percentage, ranging from 3.41 to 9.74% for HCl

and 3.10 to 4.16% for HNO_3, respectively. In general, a much higher concentration of acid (1.0 M) used would introduce more protons (H^+) into the solution than at lower acid concentrations. Therefore, more adsorbates were desorbed from the adsorbent surface by an ion-exchange mechanism [29]. The highest desorption percentage was observed using Na_2EDTA, as it desorbs about 90% of La(III) ions. The ability of EDTA to desorb a large quantity of La(III) ions from the surface of chitosan-lignin proves that desorption of La(III) happens by complexation [30]. However, further increasing the concentration of EDTA results in a lower desorption percentage due to precipitation caused by the formation of La(III)-EDTA complexes, as suggested by Awwad, et al. [31]. The desorption study using Na_2EDTA concentration of 1.0 M was not conducted, as Na_2EDTA was difficult to dissolve at this concentration.

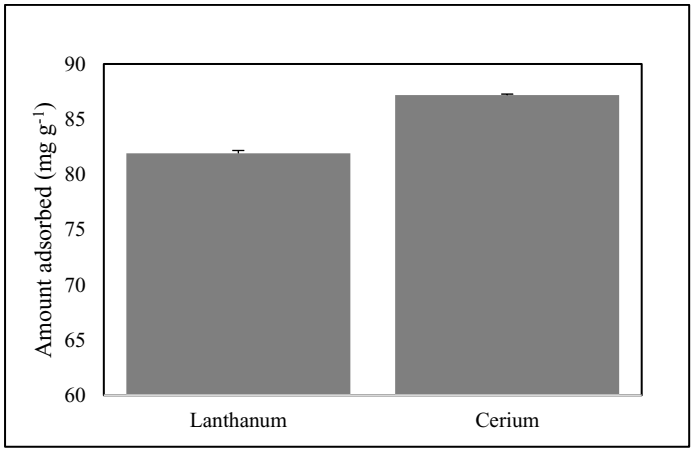


Figure 6. Adsorption of La(III) on chitosan-lignin composite in a binary system

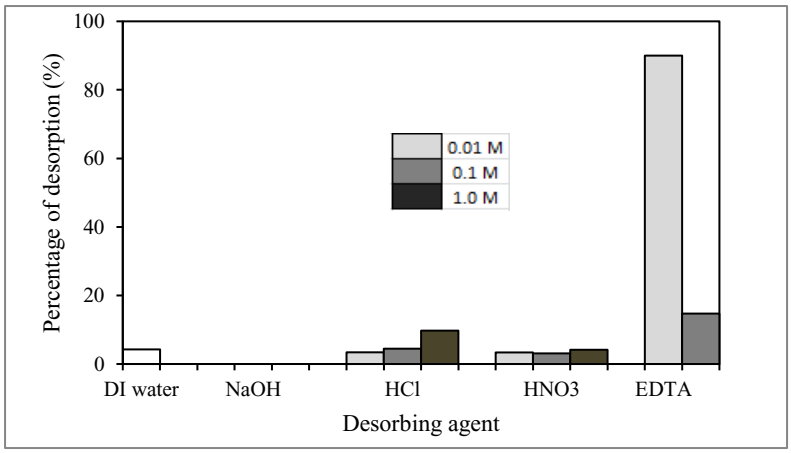


Figure 7. Desorption percentage of La(III) from chitosan-lignin composite using different desorbing agents

Conclusion

The present study demonstrated that the chitosan-lignin composite is a promising–adsorbent for recovering La(III) ions from aqueous solutions. Characterisation experiments reveal that the prepared adsorbent was acidic with a pH of 5.47. BET surface area at 1.41 $m^2\ g^{-1}$ indicates reduced surface area compared to raw chitosan at 2.26$m^2\ g^{-1}$. FTIR spectra showed successful

integration between chitosan and lignin. The experiments indicate that adsorption was affected by adsorbent dosage and La(III) concentration. However, the amount of La(III) adsorbed was slightly affected by pH, with the highest amount of 84.2 mg g^{-1} observed at pH 4. The Langmuir isotherm recorded a maximum adsorption capacity of 500 mg g^{-1}. Na_2EDTA was the best desorbing agent to strip La(III) ions from the chitosan-lignin composite surface. In ionic competition studies, the higher atomic number of rare earth elements would favour their adsorption.

Acknowledgement

The authors are grateful to the Universiti Teknologi MARA for the financial support under the Bestari Perdana Research Grant, vote no. 600-IRMI/PERDANA 5/3 BESTARI (037/2018).

References

1. Iftekhar, S., Ramasamy, D. L., Srivastava, V., Asif, M. B. and Sillanpää, M. (2018). Understanding the factors affecting the adsorption of Lanthanum using different adsorbents: A critical review. *Chemosphere* 204: 413-430.
2. Awwad, N., Gad, H., Ahmad, M. and Aly, H. (2010). Sorption of lanthanum and erbium from aqueous solution by activated carbon prepared from rice husk. *Colloids and Surfaces B: Biointerfaces,* 81(2): 593-599.
3. Zhao, F., Repo, E., Meng, Y., Wang, X., Yin, D. and Sillanpää, M. (2016). An EDTA-β-cyclodextrin material for the adsorption of rare earth elements and its application in preconcentration of rare earth elements in seawater. *Journal of Colloid and Interface Science,* 465: 215-224.
4. Srivastava, V. and Sillanpää, M. (2017). Synthesis of malachite@ clay nanocomposite for rapid scavenging of cationic and anionic dyes from synthetic wastewater. *Journal of Environmental Sciences,* 51: 97-110.
5. Zhang, D., Crini, G., Lichtfouse, E., Rhimi, B. and Wang, C. (2020). Removal of mercury ions from aqueous solutions by crosslinked chitosan-based adsorbents: A mini review. *The Chemical Record,* 20(10): 1220-1234.
6. Kyzas, G. Z. and Bikiaris, D. N. (2015). Recent modifications of chitosan for adsorption applications: A critical and systematic review. *Marine Drugs,* 13(1): 312-337.
7. Vakili, M., Rafatullah, M., Salamatinia, B., Abdullah, A. Z., Ibrahim, M. H., Tan, K. B., Gholami, Z. and Amouzgar, P. (2014). Application of chitosan and its derivatives as adsorbents for dye removal from water and wastewater: A review. *Carbohydrate Polymers,* 113: 115-130.
8. Begum, S., Yuhana, N. Y., Saleh, N. M., Kamarudin, N. N. and Sulong, A. B. (2021). Review of chitosan composite as a heavy metal adsorbent: Material preparation and properties. *Carbohydrate Polymers,* 259: 117613.
9. Karimi-Maleh, H., Ayati, A., Davoodi, R., Tanhaei, B., Karimi, F., Malekmohammadi, S., Orooji, Y., Fu, L. and Sillanpää, M. (2021). Recent advances in using of chitosan-based adsorbents for removal of pharmaceutical contaminants: A review. *Journal of Cleaner Production* 291: 125880.
10. Ge, Y. and Li, Z. (2018). Application of lignin and its derivatives in adsorption of heavy metal ions in water: a review. *ACS Sustainable Chemistry & Engineering,* 6(5): 7181-7192.
11. Guo, X., Zhang, S. and Shan, X. Q. (2008). Adsorption of metal ions on lignin. *Journal Of Hazardous Materials,* 151(1): 134-142.
12. Albadarin, A. B., Collins, M. N., Naushad, M., Shirazian, S., Walker, G. and Mangwandi, C. (2017). Activated lignin-chitosan extruded blends for efficient adsorption of methylene blue. *Chemical Engineering Journal,* 307: 264-272.
13. Fouda-Mbanga, B., Prabakaran, E. and Pillay, K. (2021). Carbohydrate biopolymers, lignin based adsorbents for removal of heavy metals (Cd^{2+}, Pb^{2+}, Zn^{2+}) from wastewater, regeneration and reuse for spent adsorbents including latent fingerprint detection: A review. *Biotechnology Reports*, 2021: e00609.
14. Nair, V., Panigrahy, A. and Vinu, R. (2014). Development of novel chitosan–lignin composites for adsorption of dyes and metal ions from wastewater. *Chemical Engineering Journal,* 254: 491-502.

15. Zhang, D., Wang, L., Zeng, H., Rhimi, B. and Wang, C. (2020). Novel polyethyleneimine functionalized chitosan–lignin composite sponge with nanowall-network structures for fast and efficient removal of Hg(II) ions from aqueous solution. *Environmental Science: Nano,* 7(3): 793-802.
16. Lourenço, A. and Pereira, H. (2018). Compositional variability of lignin in biomass. In lignin—trends and applications (Poletto, M. ed). IntechOpen: pp. 65-98.
17. Sohni, S., Hashim, R., Nidaullah, H., Lamaming, J. and Sulaiman, O. (2019). Chitosan/nano-lignin based composite as a new sorbent for enhanced removal of dye pollution from aqueous solutions. *International Journal of Biological Macromolecules,* 132: 1304-1317.
18. Chen, L., Tang, C.-Y., Ning, N.-Y., Wang, C.-Y., Fu, Q. and Zhang, Q. (2009). Preparation and properties of chitosan/lignin composite films. *Chinese Journal of Polymer Science,* 27(05): 739-746.
19. Iftekhar, S., Srivastava, V., Hammouda, S.B. and Sillanpää, M. (2018). Fabrication of novel metal ion imprinted xanthan gum-layered double hydroxide nanocomposite for adsorption of rare earth elements. *Carbohydrate Polymers,* 194: 274-284.
20. Shojaei, Z., Iravani, E., Moosavian, M. and Torab, M. M. (2016). Removal of cerium from aqueous solutions by amino phosphate modified nano TiO_2: kinetic, and equilibrium studies. *Iranian Journal of Chemical Engineering*, 13(2): 3-21.
21. Oyewo, O., Onyango, M. and Wolkersdorfer, C. (2018). Lanthanides removal from mine water using banana peels nanosorbent. *International Journal of Environmental Science and Technology,* 15(6): 1265-1274.
22. Yanfei, X., Huang, L., Zhiqi, L., Zongyu, F. and Liangshi, W. (2016). Adsorption ability of rare earth elements on clay minerals and its practical performance. *Journal of Rare Earths,* 34(5): 543-548.
23. Langmuir, I. (1918). The adsorption of gases on plane surfaces of glass, mica and platinum. *Journal of the American Chemical Society,* 40(9): 1361-1403.
24. Freundlich, H. (1907). Über die adsorption in lösungen. *Zeitschrift für physikalische Chemie,* 57(1): 385-470.
25. Ogata, T., Narita, H. and Tanaka, M. (2015). Adsorption behavior of rare earth elements on silica gel modified with diglycol amic acid. *Hydrometallurgy,* 152: 178-182.
26. Vijayaraghavan, K., Sathishkumar, M. and Balasubramanian, R. (2011). Interaction of rare earth elements with a brown marine alga in multi-component solutions. *Desalination,* 265(1-3): 54-59.
27. Awual, M.R., Kobayashi, T., Shiwaku, H., Miyazaki, Y., Motokawa, R., Suzuki, S., Okamoto, Y. and Yaita, T. (2013). Evaluation of lanthanide sorption and their coordination mechanism by EXAFS measurement using novel hybrid adsorbent. *Chemical Engineering Journal,* 225: 558-566.
28. Anastopoulos, I., Bhatnagar, A. and Lima, E. C. (2016). Adsorption of rare earth metals: A review of recent literature. *Journal of Molecular Liquids,* 221: 954-962.
29. Ngah, W.W. and Hanafiah, M. (2008). Biosorption of copper ions from dilute aqueous solutions on base treatedrubber (*Hevea brasiliensis*) leaves powder: kinetics, isotherm, and biosorption mechanisms. *Journal of Environmental Sciences,* 20(10): 1168-1176.
30. Fang, L., Zhou, C., Cai, P., Chen, W., Rong, X., Dai, K., Liang, W., Gu, J.-D. and Huang, Q. (2011). Binding characteristics of copper and cadmium by cyanobacterium *Spirulina platensis*. *Journal of Hazardous Materials,* 190(1-3): 810-815.
31. Awwad, N., Daifuallah, A. and Ali, M. (2008). Removal of Pb^{2+}, Cd^{2+}, Fe^{3+}, and Sr^{2+} from aqueous solution by selected activated carbons derived from date pits. *Solvent Extraction and Ion Exchange,* 26(6): 764-782.

Malaysian Journal of Analytical Sciences (MJAS)
Published by Malaysian Analytical Sciences Society

PHYSICOCHEMICAL AND DYEING CHARACTERISTICS OF COTTON FABRIC DYEING FROM THE EXTRACT OF ANGSANA (*Pterocarpus indicus*) BARK

(Fiziko Kimia dan Ciri Pencelupan Pewarnaan Kain Kapas dengan Menggunakan Ekstrak dari Kulit Kayu Angsana *(Pterocarpus indicus)*)

Mukmin Sapto Pamungkas[1,2], Edia Rahyuningsih[1,2]*, Taranipa Marfitania[2], Wachid Siti Fatimah[2]

[1]Department of Chemical Engineering, Faculty of Engineering
[2]Indonesia Natural Dye Institute, Integrated Research and Testing Laboratory
Universitas Gadjah Mada, Sleman 565223, Daerah Istimewa Yogyakarta, Indonesia

**Corresponding author: edia_rahayu@ugm.ac.id*

Received: 12 July 2021; Accepted: 7 October 2021; Published: 25 October 2021

Abstract

Herein, the Angsana bark (*Pterocarpus indicus*) extract was studied for its potential as a natural dye for cotton fabrics. Angsana bark was extracted using water solvent at 70 °C with a ratio of solid-water of 70 g/L, for 1 hour, with a yield of 20.08% (w/w). The Angsana bark extract has acidic pH, a tannin content of 11.90%, and a density of 1.015 g/mL. Visible spectrophotometry results showed the highest peak of 395 nm, which indicated a high tannin content. FTIR revealed the presence of hydroxyl (-OH) (indicating an auxochrome group), aromatic (C-H) (indicating an aromatic group), carbonyl (C=O), and ether (C-O-C) groups. Cotton fabrics were premordanted using alum and soda ash prior to dyeing. Dyeing of the cotton fabrics was done by immersion for 15 minutes in the Angsana extract repeatedly and postmordanted using alum, lime, and iron sulfate. The colors produced by the alum and lime fixatives were different variations of brown, whereas that for the iron sulfate fixative was dark green. The highest K/S value of 8.554 was found for the iron sulfate fixative. Overall wash and light fastness scores were presented on the scale of 4 (good) and 4/5 (excellent). Thus, Angsana bark in water can be used as a source of natural dye for cotton fabrics, showing potential as a new material for application in cotton fabrics.

Keywords: Angsana extract, cotton fabrics, natural dye, *Pterocarpus indicus*

Abstrak

Di sini, potensi ekstrak kulit kayu Angsana (*Pterocarpus indicus*) sebagai pewarna semula jadi untuk kain kapas dikaji. Kulit kayu Angsana diekstrak menggunakan pelarut air pada suhu 70 °C dengan nisbah air pepejal sebanyak 70 g/L, selama 1 jam, dengan hasil sebanyak 20.08% (b/b). Ekstrak kulit kayu Angsana mempunyai pH berasid, kandungan tanin sebanyak 11.90%, dan ketumpatan 1.015 g/mL. Penelitian menggunakan spektrofotometri menunjukkan puncak tertinggi dicapai pada 395 nm, iaitu menunjukkan kandungan tanin yang tinggi. FTIR mendedahkan kehadiran hidroksil (-OH) (menunjukkan kumpulan auxochrome), aromatik (C-H) (menunjukkan kumpulan aromatik), karbonil (C=O), dan kumpulan eter (C-O-C). Sebelum pencelupan, kain kapas akan di pra-mordant menggunakan alum dan abu soda. Pencelupan kain kapas dilakukan dengan merendamkannya ke dalam ekstrak Angsana secara berulang kali dan di post-mordant menggunakan alum, kapur dan besi sulfat.

Warna yang dihasilkan oleh fiksasi alum dan kapur adalah variasi warna coklat yang berbeza, manakala warna untuk fiksasi besi sulfat adalah hijau tua. Didapati fiksasi besi sulfat mempunyai nilai K/S tertinggi iaitu 8.554. Keseluruhan skor pencucian dan ketahanan cahaya ditunjukkan pada skala 4 (baik) dan 4-5 (cemerlang). Demikian, kulit kayu Angsana dapat digunakan sebagai sumber pewarna semula jadi untuk kain kapas, yang menunjukkan potensi sebagai bahan baru untuk aplikasi kain kapas.

Kata kunci: ekstrak Angsana, kain kapas, pewarna semula jadi, *Pterocarpus indicus*

Introduction

Dyes can be classified based on their origin: synthetic dyes are obtained from chemical reactions [1], while natural dyes are produced through solvent extraction of natural sources [2], including various parts of plant, such as roots, stems, bark, leaves, fruit, seeds, and flowers [3]. Synthetic dyes are often chosen for their low cost, sharper color, good fastness properties, and wide range of colors. However, azo dyes, a class of synthetic dye containing stable and difficult-to-degrade R-N=N-R' functional groups, are carcinogenic [4]. Thus, the exploration and use of natural dyes can help in the conservation of environment to achieve the 2030 Sustainable Development Goals.

Angsana, which belongs to the Fabaceae family, is a wood-producing tree species that can grow up to 30–40 m in various tropical regions, with a trunk width of 4 m [5]. Its bark contains tannins that can be used as a source of natural dye, as shown in Figure 1. Tannins are polyphenol compounds with high molecular weight that are soluble in water and organic solvents [6], have diverse chemical structures, and consist of hydroxyl and carboxyl groups [7]. Studies on the utilization of barks from different tree species, such as mahogany, soga tingi, mango, *Rhizophora mucronata*, and Angsana, as a source of natural textile dyes have been carried out previously [8-11]. However, a prior study on the use of Angsana bark as natural dye was limited solely to its application to silk fiber [12], thus opening opportunities to explore other applications of the natural dye produced from Angsana bark extract.

Cotton fabrics are derived from cotton fibers formed by cellulose polymer [13]. Due to the high degree of polymerization of cellulose polymers, cotton fibers have excellent properties such as strength, air permeability, and absorbency [14]. These properties of cotton fiber make it more widely used as a textile material, compared to the other natural fibers (e.g., silk, wool, etc.) [15]. In this study, Angsana bark extract was analyzed for its potential as natural dye for cotton fabrics with the use of different mordants, namely alum, lime, and iron sulfate. For that purpose, the color strength test (K/S value), L*a*b* value test, and color fastness test were performed.

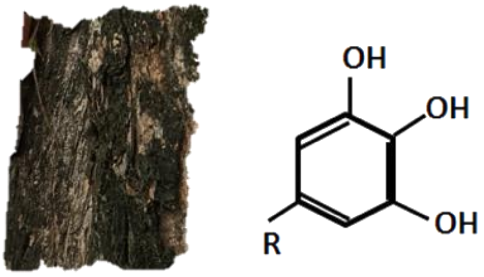


Figure 1. Angsana bark (left) and the main structure of tannin (right)

Materials and Methods

Materials

The Angsana bark analyzed in this study was from Angsana tree that grows in the vicinity of the Faculty of Engineering, Universitas Gadjah Mada, Yogyakarta. Cotton fabrics (100% cotton) used for the dyeing were obtained from PT Primissima Yogyakarta, with the thickness of 0.35 mm and a weight per area of 192 g/m^2. Aquadest was chosen as a solvent for extracting natural dyes. Potassium permanganate, oxalic acid, and indigo carmine were utilized as reagents in volumetric analysis. Alum, limestone, and iron sulfate were employed as fixating agents or also known as mordant.

Extraction of the Angsana bark

First of all, Angsana bark was weighed to obtain 140 g of bark. Then, 2 l of water was heated in a pot to reach a temperature of 70 °C. The Angsana bark was put into

heated water afterwards and stirred every 10 minutes for 1 hour. The addition of solids and extraction were carried out until the sample measured by a hydrometer showed the optimum Baume value. After 1 hour, the solids and extracts were separated; the extract was taken as a dye product.

Evaluation of the Angsana bark extract

The pH value of Angsana bark extract was determined using a pH meter, while a pycnometer was utilized to find out the density of the extract. The yield of the dye was determined by drying 5 mL of the sample in an oven at 65 °C until a constant weight was achieved. The total tannin content was measured by the AOAC method. An amount 10 mL of Angsana bark extract and the solution indicator of indigo carmine were added to the volumetric flask and diluted up to the limit mark with aquadest. After that, 50 mL of the solution was titrated with $KMnO_4$ solution, standardized with oxalic acid ($H_2C_2O_4 \cdot 2H_2O$) until the color changed from blue to golden yellow. The titration was carried out in triplicate. In addition, a blank titration was conducted to determine how much $KMnO_4$ reacted to indigo carmine. One milliliter of 0.1125 N $KMnO_4$ is equivalent to 0.0415 g of tannin.

The visible spectra were recorded using a Logger-lite spectro-visible portable. The Angsana bark extract was characterized by tannic acid, which was also used as a control sample. The concentration of the tannic acid solution was 10 ppm. The color coordinate test was performed using a Konica Minolta Color CR-400. The Fourier transform infrared (FTIR) spectrum of Angsana bark extract powder was recorded from 4000 to 400 cm^{-1} using a Shimadzu Prestige 21 FTIR spectrometer. The Angsana bark extract was transformed into powder by drying it in an oven at a temperature of 65 °C.

Dyeing of cotton fabric

The pre-mordant stage was carried out by soaking the cotton fabric in alum solution and hanging it to dry. Afterward, the dried fabric weighing 1 g in an unfolded state was immersed in 10 ml of the extract solution heated at 60 °C for 20 minutes in a shaker bath and then dried at room temperature. Finally, fixation was performed by heating the cotton fabric to reach a temperature of 60 °C at a ratio of 1:10 (w/v) for 10 minutes using alum, lime, and iron sulfate fixative solutions prepared by dissolving the solids at a ratio of 1:10 (w/w), heating and allowing them to settle overnight, and then filtering them using filter paper. The obtained fabric was then rinsed in running water and dried at room temperature.

Color strength (K/S) value

The color strength value test was carried out at a wavelength range of 350–750 nm using a Shimadzu UV-2401PC spectrophotometer, and the results are expressed in reflectance (%R). The maximum wavelength can be determined with the lowest % R-value. The reflectance value was then converted to a K/S value based on the Kubelka–Munk equation, as follows:

$$\frac{K}{S} = \frac{(1-R)^2}{2R} \quad (1)$$

where K is the light absorption coefficient, S is the light scattering coefficient, and R is the percentage of reflectance. After determining the K/S value of the dyed material, the K/S value was corrected with the K/S value of the white cotton fabric before the dyeing process.

Color fastness

The color fastness to washing was determined according to ISO 105-C06:2010. The cotton fabric (5x10 cm) was placed between the upholsteries, namely a 100% white fabric and a 100% white polyester fabric. The three fabrics were sewn on one of their shortest sides and placed in 150 mL of the washing solution prepared by dissolving 4 g/L of AATCC soap and 1 g/L of sodium perborate and then heating it at 40 °C. The washing process was done in Launder O Meter machine run for 30 minutes. The fabric was then rinsed with 0.2 g/L of glacial acetic acid solution, wrung out, dried at room temperature, and checked for color changes using grayscale and staining scales. The rating scale was expressed in 0 (poor) to 5 (excellent).

The light fastness test was carried out by irradiating Xenon Arc lamp (48 W/m^2) under certain conditions and spaces. After exposure, the color differences between the exposed and protected parts of the fabric were compared to the AATCC grayscale. The rating scale was stated in 0 (poor) to 5 (excellent).

Results and Discussion

Evaluation of the Angsana bark extract

The physicochemical results revealed that an aqueous extract of Angsana bark was dark brown in color and had an acidic pH, 1.015 g/mL density, 11.90% of total tannin, and 20.08% of yield of dyestuff (Table 1). These properties showed the potential of Angsana bark extract as dyeing agent due to its high natural tannin content.

The visible spectrum of the tannic acid solution reached a peak at 391 nm. As for the Angsana bark extract, it showed a sharp increase at 395 nm, indicating high tannin content (Figure 2). Figure 3 displays the FTIR spectrum of the Angsana bark extract, presenting a broad peak at 3425.58 cm^{-1}. In addition, other increases were seen at 1635.64 cm^{-1} and 1064.71 cm^{-1}, caused by the presence of hydroxyl (-OH) stretching vibration of flavonoids [16], C=O stretching of hydrolysable tannin esters [17], and etheric groups of tannins (C-O-C) [18]. Therefore, it can be inferred from the FTIR results (Figure 3) that Angsana bark extract contains flavonoids, polyphenols, and tannins.

Table 1. Physical characteristics of Angsana bark extract

Data	Average	Standard deviation
pH	6.5	0.041
Density (g/mL)	1.015	0.002
Tannin contents (%)	11.90	0.248
The yield of extract (% w/w)	20.08	0.724
CIE L* value	20.73	0.000
CIE a* value	0.85	0.006
CIE b* value	2.25	0.006

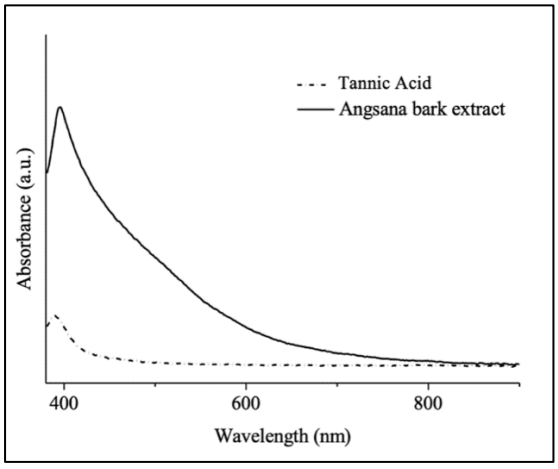


Figure 2. Visible spectra of Angsana bark extract and tannic acid

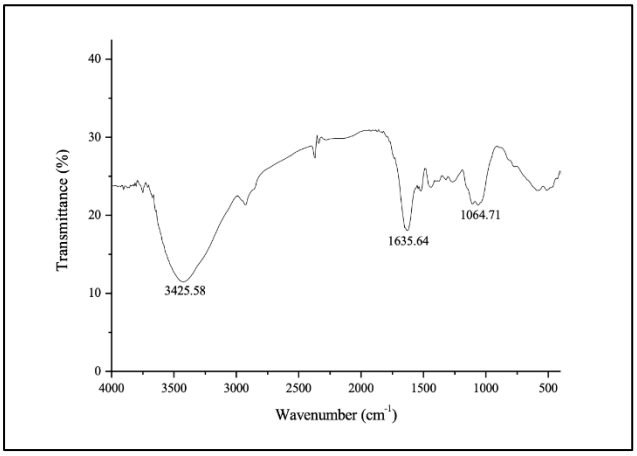


Figure 3. Fourier transform infrared spectrum of Angsana bark extract

Dyeing cotton fabric

The dyeing process of cotton fabric was done after the pre-mordant process. A pre-mordant agent was applied to open the hydroxyl bonds in the cotton fabric to bind to the mordant ions. Dry cotton fabric was dipped in Angsana bark extract with various extract concentrations of 70 and 140 g/l. The mordant ions, namely Al^{3+}, Ca^{2+}, and Fe^{3+} with a coordination number of +6, increased the color intensity of the fabric. The mordant ions can be considered as a bridge between the dye and the cotton fabric. Principally, mordant ions are required for cotton fabrics that will be dyed in natural dyes; otherwise, the color intensity will be low. In the absence of a mordant, hydrogen bonds will be formed between the cellulose fibers and the hydroxyl groups in the auxochromes of the tannin molecule. Hydrogen bonds are relatively weak and produce low fastness. To overcome this problem, mordant ions are needed. Mordant ions will form ionic and coordination bonds between dye-mordant and the mordant-cellulose of the cotton fabrics, as illustrated in Figure 4 below.

Negatively charged electrons can fill the empty orbitals in metal ions. The bonding complex that occurs in the d orbitals gives a distinct color. The number of orbitals that can be filled indicates the value of the coordination number. Al^{3+} ion hybridization occurs in a 3s orbital, three 3p orbitals, and two 3d orbitals. This arrangement forms stability with the same energy value, taking into account the steric resistance that may arise. Similarly, for mordant ions Ca^{2+} and Fe^{2+}, the orbitals were stable at the same energy value.

The color strength (K/S) value identifies the quality of the dyeing parameters. The higher the K/S value, the more the tannin dyes are absorbed by the cotton fabric. Conversely, the lower the K/S value, the lighter the color. Based on the experimental results, the concentration of Angsana bark extract significantly affected the K/S value. The increase in K/S by 6 to 13 means that the concentrated extract of Angsana bark could provide better color strength. The type of mordant was also proven to affect color strength, with the order of alum<lime<iron sulfate. The highest K/S value of 8.554 was obtained for iron sulfate mordant with an extract concentration of 140 g/l. The exact test values are shown in Table 2.

The identification of color types was modeled with the CIELAB color space. The L* value indicates the lightness of the color, which is 0 for black and 100 for white. The a* value describes a green-red color type, where a positive value means red and a negative value means green. The b* value represents the color yellow (+) and blue (-). Overall, the L* value decreased along

with the increase in extract concentration. The lowest L* value of 28.91 implies that the fabric was dyed more. It can be seen that iron sulfate mordant gave a darker color orientation, while alum mordant contributed to a lighter color orientation. The colors produced were in the brown area, namely the burlywood color for Al^{3+} mordant, saddle brown color for Ca^{2+} mordant, and dark olive-green color for Fe^{2+} mordant. The resulting color character was unique under the peculiarities of natural dyes, in which the post-mordant process played a significant role. The Fe^{2+} ion had an empty orbital in the d subshell, creating a specific characteristic of color.

Color fastness properties

Fastness to washing and light is vital in dye applications to fabrics. The washing fastness test was carried out by washing a sample of fabric with certain detergents and sewing it on two white cloths based on ISO 105-C06:2010. Meanwhile, the light fastness test was conducted according to American Association of Textile Chemists and Colorists (AATCC) 16.

The fastness value can be increased by using a mordant in the pre-mordant and post-mordant processes. The illustration in Figure 4 shows that a mordant with metal ions can provide a bridge to bind the dye to the cellulose fibers of the fabric. These bonds can increase the size of the dye molecules so that they can be well-absorbed and it will be difficult for them to get out of the pores of the cotton fibers. At the end of the dyeing process, the fixation process can make the bonds stronger to increase the fastness value. The results of the fastness evaluation are presented in Table 3.

The value of washing fastness was obtained on scales of 3–4 (fairly good) and 4 (good). This value has met the minimum requirements (3–4 scale) for textile fabric products based on SNI 0051:2008. The highest value of washing fastness was in alum mordant at an extract concentration of 140 g/l as well as in lime mordant at 70 g/L and 140 g/L of extract concentrations. This was because Ca^{2+} ions can firmly bind tannin molecules; calcium ions can increase the affinity of tannins for cellulose in cotton fabrics and lock the dye into the fiber molecules [19]. This is in contrast to Fe^{2+} ion, where coordination complex bonds occur to reduce the solubility of the dye, thus reducing the color fastness [20].

The light fastness test obtained an overall score on a scale of 4–5 (excellent). This was due to the complex bond between the dye and the metal ion of the mordant. As seen in Figure 4, the empty orbital diagram in the s, p, and d subshells can be filled by free electrons in the tannin molecules. The subshells protect the chromophore groups from photolytic degradation. The d orbitals can form ligand complexes with the chromophore groups of the dye. The d orbital can be a resonance site on the tannin chromophore, thereby stabilizing the absorbed photon energy irradiated with UV light.

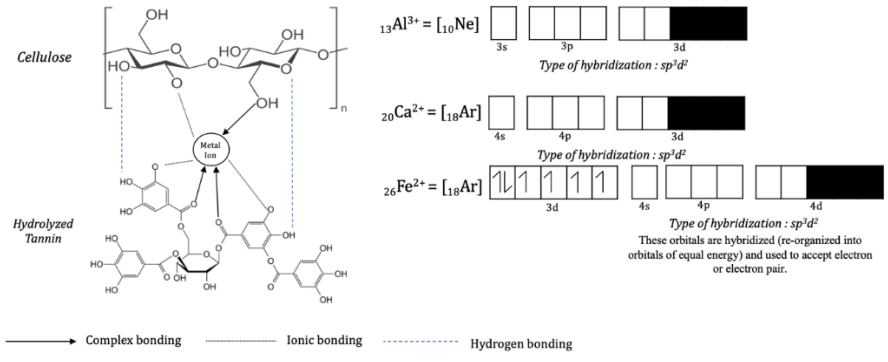


Figure 4. Possible structure of hydrolyzed tannin in Angsana bark extract with the mordant ions on cotton fabrics

Table 2. Results of fabric dyeing test with Angsana bark extract

Fixative	Concentration (g/L)	Color	K/S Value	L*a*b* Value
Alum	70		0.358 ± 0.049	L* 76.63 ± 5.309 a* 10.62 ± 1.084 b* 25.54 ± 1.067
	140		4.017 ± 0.154	L*49.51 ± 1.103 a* 13.62 ± 0.307 b*19.42 ± 0.525
Lime	70		0.823 ± 0.112	L* 67.29 ± 1.236 a* 15.08 ± 0.233 b* 23.23 ± 0.874
	140		5.840 ± 0.285	L*41.33 ± 0.577 a*16.74 ± 0.419 b*21.05 ± 0.750
Iron sulfate	70		1.428 ± 0.215	L* 54.00 ± 0.603 a* 4.543 ± 0.613 b* 15.70 ± 1.306
	140		8.554 ± 0.377	L*28.91 ± 0.485 a*2.277 ± 0.106 b*9.817 ± 1.218

Table 3. Fastness quality testing of cotton fabrics

Fixative	Concentration (g/L)	Washing Fastness	Light fastness
Alum	70	3–4	4–5
	140	4	4–5
Lime	70	4	4–5
	140	4	4
Iron Sulfate	70	3–4	4–5
	140	3–4	4–5

Conclusion

Exploration of potential alternative sources of natural dyes from Angsana bark waste has yielded significant results. This is in line with the mission of environment conservation to reduce the use of synthetic dyes that are not environmentally friendly. From the results of this study, it can be seen that Angsana bark extract produced brown dye. The dyeing results for cotton fabric with extract solutions in low concentration (70 g/L) and high concentration (140 g/L) gave different color changes in the post-mordant solution. The types of color generated by alum and lime mordants were in the variations of brown color, while iron sulfate mordant produced dark green color. The highest K/S value was found in the use of iron sulfate mordant. Overall, the washing fastness scores were on the scale of 4 (good) and the light fastness scores were on the scale of 4-5 (excellent). Thus, Angsana bark extract can be used as a source of natural dye for cotton fabrics.

Acknowledgement

The author would like to express the deepest gratitude to LPDP (Indonesian Endowment Fund for Education) for the funds provided in the RISPRO Commercial Funding scheme and to Chemical Engineering Department, Universitas Gadjah Mada for the supporting facilities made available for this study.

References

1. Booth, G. (2000). Dyes, general survey in Ullman n's encyclopedia of industrial chemistry. Wiley-V CH Verlag GmbH & Co. KGaA, Weinheim: pp. 6 76-678.
2. Gulrajani, M. L. and Gupta, D. (1992). Natural dye s and their application to textiles. Department of T extile Technology, New Delhi: pp. 38–42.
3. Krizova, H. (2013). Textile dyeing theory and appl ication -chapter 2. Natural Dyes. Liberec TUL. Cz echia: pp. 15-25.
4. Bruna, C. V. and Maria, A. M. M. (2013). Azo dye s: Characterization and toxicity – A review. *Textile s and Light Industrial Science and Technology*, 2(2): 85-103.
5. Thomson, L. A. J. (2006). Specifies profiles for Pa cific Island agroforestry: *Pterocarpus indicus* (Nar ra). *Permanent Agriculture Resources, Hawaii*: pp. 1-5.
6. Smith, B. and Swain (1962). Flavonoid compound s: Comparative biochemistry. III. Academic Press, New York: pp. 75-809.
7. Sieniawska, E. and Baj, T. (2017). Pharmacognosy . Tannins. Elsevier, Amsterdam: pp. 199-232.
8. Prayanto, Nur, A. and Nurcahyanti, D (2018). Prod uksi dan aplikasi zat warna alami dari kulit kayu m ahoni dan kulit kayu tingi untuk batik di desa Kuw iran, Kecematan Banyudono, Kabupaten Boyolali. *Jurnal Ilmiah Momentum*, 14(2): 1-7.
9. Handayani, P. A. and Maulana, I. (2013). Pewarna alami batik dari kulit soga tingi (*Ceriops tagal*) de ngan metode ekstraksi. *Jurnal Bahan Alam Terbar ukan*, 2(2): 1-6.
10. Win, Z. M. and Swe, M. M. (2008). purification of natural dyestuff extracted from mango bark for the application on protein fibres. *World Academy of Sc ience, Engineering and Technology*, 46: 536-540.
11. Dewi, L. F., Pringgenies, D., and Ridlo, A. (2018). Pemanfaatan mangrove *Rhizophora mucronata* seb agai pewarna alami katun. *Journal of Marine Rese arch*, 7(2): 79-98.
12. Lestari, D. W. and Satria, Y. (2017). Pemanfaatan kulit kayu Angsana (*Pterocarpus indicus*) sebagai sumber zat warna alami pada pewarnaan kain batik sutera. *Dinamika Kerajinan Dan Batik*, 34(1): 35-4 2.
13. Dochia, M., Sirghie, C., Kozłowski, R.M. and Ros kwitalski, Z. (2012). Handbook of natural fibres: c otton fibres. Woodhead Publishing, Cambridge: pp . 11-23.
14. Ismail, S. and Azha, S. F. (2018). Cotton cloth: Di versified applications beyond fashion and wearabl e cloth. *Current Trend in Fashion Technology & T extile Engineering*, 2(3): 39-45.
15. IHS Markit (2019). Natural and man-made fibers o verview. https://ihsmarkit.com/products/fibers-che mical-economics-handbook.html. [Access online 4 September 2021].
16. Oliveira, R. N., Mancini, M. C., Oliveira, F. C. Sd, Passos, T. M., Quilty, B., Thiré, R. MdS. M., and McGuinness, G. B. (2016). FTIR analysis and qua

ntification of phenols and flavonoids of five commercially available plants extracts used in wound healing. *Matéria (Rio de Janeiro)*, 21(3): 767–779.

17. Okonkwo, S. N., Ohanuzua, C. B. C., Onuegbu, G. C., Obasi, H. C. and Nnorom, O. O. (2019). Extraction of natural dyes from *Whitfieldia lateritia* plant and its application on cotton fabric. *International Journal of Textile Science and Engineering*, 9(1): 1-4.
18. Anburaj, R. and Jothiprakasam, V. (2017). Bioassay of tannin rich fraction and identification of compounds using UV–Vis, FTIR, and RP-HPLC. *Research Journal of Pharmaceutical, Biological and Chemical Sciences*, 8(1): 432-445.
19. Pujilestari, T. (2014). Pengaruh ekstraksi zat warna alam dan fiskasi terhadap ketahanan luntur warna pada kain batik katun. *Dinamika Kerajinan Dan Batik*, 31(1): 31-40.
20. Uddin, M. G. (2015). Extraction of eco-friendly natural dyes from mango leaves and their application on silk fabric. *Textiles and Clothing Sustainability*, 1(1): 1-7.

Malaysian Journal of Analytical Sciences (MJAS)
Published by Malaysian Analytical Sciences Society

EXTRACTION AND ISOLATION OF HIGH QUANTITIES OF CANNABIDIOL, CANNABINOL, AND DELTA-9-TETRAHYDROCANNABINOL FROM *Cannabis sativa* L.

(Pengekstrakan dan Pengasingan Kuantiti Tinggi bagi Cannabidiol, Cannabinol dan Delta-9-Tetrahidrocannabinol dari *Cannabis sativa L.*)

Fameera Madaka[1,2]*, Natawat Chankana[2,3], Nanthaphong Khamthong[4], Athip Maha[2], Thanapat Songsak[2,5]

[1]*Drug and Herbal Product Research and Development Center*
[2]*Medicinal Cannabis Research Institute*
[3]*Sun Herb Thai-Chinese Manufacturing*
[4]*College of Oriental Medicine*
[5]*Department of Pharmacognosy*
College of Pharmacy, Rangsit University, Thailand

**Corresponding author: fameera.m@rsu.ac.th*

Received: 4 August 2021; Accepted: 7 October 2021; Published: 25 October 2021

Abstract

This study aimed to develop the extraction and isolation methods of cannabinoids including cannabidiol (CBD), cannabinol (CBN), and delta-9-tetrahydrocannabinol (THC), from *Cannabis sativa* L. using supercritical fluid extraction (SFE) and flash chromatography, respectively. SFE was performed at different pressures (190-300 bar), temperatures (42-50 ºC), and ethanol as co-solvent (0-4%). The effect of SFE parameters on the yield, and the contents of CBD, CBN, and THC in the crude extracts were investigated. Among the seventeen samples, the highest extraction yields of 7.02, 6.90, and 4.61% were obtained, respectively. Under the setting pressure of 250 bar, the temperature of 50 ºC, and the co-solvent of 1-2%, high- performance liquid chromatography (HPLC) analysis showed the highest contents of CBD (14.53% w/w), CBN (26.75% w/w), and THC (3.21% w/w). Three extracts with high CBD, CBN, and THC contents were selected and further purified by flash chromatography, and the three isolated cannabinoids were analyzed by nuclear magnetic resonance (NMR) and HPLC. Our sequential SFE and flash chromatography process could be employed to obtain a high quantity of cannabinoids which proved that a high purity could be achieved for CBD, CBN, and THC.

Keywords: *Cannabis sativa* L., cannabidiol, cannabinol, delta-9-tetrahydrocannabinol, supercritical fluid extraction

Abstrak

Kajian ini bertujuan untuk mengembangkan kaedah pengekstrakan dan pengasingan kanabinoid termasuk cannabidiol (CBD), cannabinol (CBN), dan delta-9-tetrahidrocannabinol (THC), dari *Cannabis sativa* L. menggunakan masing-masing pengekstrakan cecair supergenting (SFE) dan kromatografi kilat. SFE dilakukan pada tekanan yang berbeza (190-300 bar), suhu (42-50ºC), dan etanol sebagai pelarut bersama (0-4%). Pengaruh parameter SFE terhadap hasil, dan kandungan CBD, CBN, dan THC dalam ekstrak mentah disiasat. Di antara tujuh belas sampel, hasil pengekstrakan tertinggi masing-masing adalah 7.02, 6.90, dan 4.61%.

Di bawah tekanan penetapan 250 bar, suhu 50ºC, dan pelarut bersama 1-2%, analisis kromatografi cecair berprestasi tinggi (HPLC) menunjukkan kandungan CBD tertinggi (14.53% w/w), CBN (26.75% w/w), dan THC (3.21% w/w). Tiga ekstrak dengan kandungan CBD, CBN, dan THC yang tinggi dipilih dan selanjutnya dimurnikan dengan kromatografi kilat, dan tiga kanabinoid yang diasingkan dianalisis mengunakan magnetic resonan nukleus (NMR) dan HPLC. Proses kromatografi kilat dan SFE berurutan kami dapat digunakan untuk mendapatkan jumlah kanabinoid yang tinggi yang membuktikan bahawa kemurnian tinggi dapat dicapai untuk CBD, CBN, dan THC.

Kata kunci: *Cannabis sativa* L., cannabidiol, cannabinol, delta-9-tetrahidrocannabinol, pengekstrakan cecair supergenting

Introduction

There is a growing interest in herbal compounds in medicine. Cannabis (*Cannabis sativa* L.) belongs to the Cannabaceae family and is one of the most popular known medicinal plants. In Thailand, Cannabis is illegal. However, there are limited laws that allow the use of hemp (*Cannabis sativa* subsp. *sativa*) containing high cannabidiol (CBD) and low delta-9-tetrahydrocannabinol (THC). Cannabis contains over 60 cannabinoids [1]. It is well known that THC and CBD are the most prevalent cannabinoids as well as those with the most useful medicinal properties in the cannabis plant and its associated products [2]. CBD is a non-psychoactive cannabinoid with antiepileptic properties. THC, however, is predominantly known for its psychotropic effects [3]. Prior to quality control of high quantities of active compounds from *Cannabis*, crude plant material must undergo effective extraction. Several methods for the extraction of cannabinoids from cannabis have been reported in numerous studies, such as ultrasonic-assisted solvent extraction, soxhlet extraction, derivatization, and microwave-assisted extraction. Each method requires an appropriate selection of specific conditions, such as type of the solvent, temperature, pressure, and some of the methods require long extraction times or large volumes of flammable solvents, many of which are toxic. Recently, supercritical fluid extraction (SFE) with carbon dioxide (CO_2) has been presented as a good alternative for the extraction-separation of cannabinoids, which utilizes an inexpensive GRAS (generally recognized as safe) solvent with very well-known physicochemical properties. CO_2 reaches a supercritical state at 304.25 K and 7.39 MPa and returns to a gas state under an ambient condition, allowing a simple solute to recover, thus providing a solvent-free product. Besides, sensitive changes in pressure and temperature the CO_2 solvent strength can be tuned, this change in the medium provides to some extent, selectivity to the extraction process [4]. However, the low polarity of supercritical carbon dioxide requires that small amounts of alcohol, water, and acids be used in SFE to improve the yields and in some cases the selectivity of the extraction. For example, ethanol (EtOH) can be used in SFE to increase extraction yield for some cannabinoids.

Also, several analytical techniques have been developed for the identification, quantification, and isolation of the extracted cannabinoids, which include a screening test based on colorimetric reactions, like the Fast Blue salt test and the Duquenois-Levine test, radioimmunoassay (RIA), ion mobility mass spectrometry (IMS), thin-layer chromatography (TLC), high-performance liquid chromatography (HPLC), gas chromatography (GC), infrared spectroscopy (IR), mass spectrometry (MS), and nuclear magnetic resonance spectroscopy (NMR) [5]. Some of these have disadvantages such as the need for multiple isolation steps, the use of toxic and polluting organic solvents, and the low purity of obtained substances. In this study, the researchers aimed to develop SFE process (e.g. pressure, temperature, and ethanol as co-solvent) to obtain a high quantity of cannabinoids, including CBD, CBN, and THC from *Cannabis sativa* L., as well as a means to develop the isolation method using flash chromatography to obtain a high purity of CBD, CBN, and THC.

Materials and Methods

Chemicals

Cannabinoid standards (CBD, CBN, and THC) with a purity of over 98% were isolated and purified from the Medicinal Cannabis Research Institute, College of Pharmacy, Rangsit University, Thailand. They were prepared by flash chromatography and prep-HPLC and

certificated through spectroscopy. Carbon dioxide was supplied by Lor Ching Tong Oxygen & Acetylene Co. Ltd. Hexane (AR grade), dichloromethane (AR grade), ethyl acetate (AR grade), methanol (AR grade), 2-propanol (AR grade), methanol (HPLC grade), water (HPLC grade), and ethanol (commercial grade) were purchased from RCI Labscan Ltd. FlashPure Silica and C18 (ID 40 and 120 g; 40 μm) were supplied by Buchi (Thailand) Ltd. TLC Silica gel 60 F_{254} and TLC Silica gel 60 RP-18 $F_{254}S$ were purchased from Merck (Germany). P-Anisaldehyde (98%, 100 g) was obtained from Sigma-Aldrich Chemical Co. (Seelze, Germany).

Sample preparation

An amount 12 kg of dried cannabis samples (*Cannabis sativa* L.) were supplied from illegal narcotic drugs in Thailand arrested by the Narcotics Suppression Bureau and legally authorized representatives in research by the Office of the Narcotics Control Board and the Food and Drug Administration, Thailand. They were deposited at the College of Pharmacy, Rangsit University, Thailand. The samples of cannabis were pulverized with the water content controlled at 5-10% and then kept in a desiccator cabinet at room temperature until they were used for extractions.

Supercritical fluid extraction

A 5L*1Supercritical CO_2 Machine (Model HA120-50-05-C) from Nantong Huaan Supercritical Extraction Co. Ltd. was used in these experiments and is represented schematically in Figure 1. The main technical parameters included the highest extraction pressure (50MPa) possible with a single-cylinder extraction volume (5L), a normal extraction temperature of ~75 ºC, a maximum flow of 0~50 L/h adjustable, and a three-phase five-wire system, 380 V/50HZ, 10KW power supply. Ethanol as a co-solvent was supplied by a liquid pump and mixed with the main CO_2 stream before at the extraction kettle. The researchers optimized process parameters including sample particle size, pressure, temperature, co-solvent, and extraction time. The particle sizes of the sample were set at 14 and 20-40 mesh, with the amount ranging from 420 to 920 g within a 5-L material tank. The samples were loaded into the barrel such that each was not too full, 2-3 cm away from the filter. SFE was performed at different pressures and temperatures of extraction kettle (190-300 bar and 42-50 ºC), separation kettle I (80-90 bar and 55 ºC), and separation kettle II (40-50 bar and 35-40 ºC), co-solvent (0-4%), and extraction times (60-120 min) according to the experiment design outlined in Table 1. Following the extraction, ethanol was removed under vacuum and the extracts were weighed and analyzed using HPLC to quantify their cannabinoid (CBD, CBN, and THC) content.

HPLC analysis of cannabinoids from cannabis extract

Analysis of cannabinoids and the quantification of CBD, CBN, and THC were carried out using an HPLC instrument (Agilent 1260 Infinity, Agilent, USA). The methodology followed Saingam and Sakunpak [6]. A reverse-phase Zorbax C-18 column of 4.6 mm × 100 mm and 3.5 μm was used for the isocratic separation. It was eluted by using a mixture (85:15) of methanol and ultrapure water as the mobile phase with the flow rate set to 1.0 mL/min and an injection volume of 10 μL. The column temperature was controlled at 25 ± 0.5 ºC. The response signal was coupled to a UV detector set to 220 nm. UV spectra scanning from 190 to 400 nm were recorded online for peak identification. The total analysis time for each injection was 10 min. Peak identification was carried out by comparing the retention times and UV absorption spectra of the samples with those of the standard solutions of CBD, CBN, and THC.

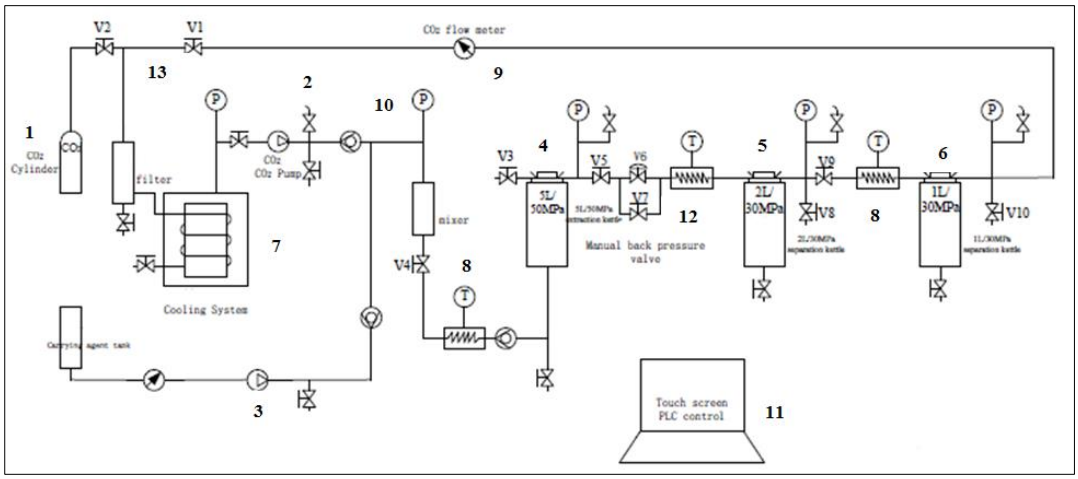


Figure 1. Schematic diagram of SFE (Model HA120-50-05-C) apparatus. (1) CO_2 cylinder, (2) CO_2 pump, (3) carrying agent pump, (4) extraction kettle, (5) separation kettle I, (6) separation kettle II, (7) cooling system, (8) temperature control, (9) CO_2 flow meter, (10) pressure control measurement system, (11) touch screen PLC control, (12) manual back pressure valve, (13) valves

Table 1. Parameters for the extraction of SFE from *Cannabis sativa* L.

Samples (g)	Sieve (Mesh)	Extraction Kettle		Co-Solvent (%)	Separation Kettle I		Separation Kettle II		Extraction Time (min)	
		Pressure (Bar)	Temp. (°C)		Pressure (Bar)	Temp. (°C)	Pressure (Bar)	Temp. (°C)	Separation Kettle I	Separation Kettle II
1. 750	14	290-300	50	-	60-70	55	40-50	35-40	60	-
2. 750	14	290-300	50	1%	60-70	55	40-50	35-40	60	-
3. 480	20-40	250	50	1%	80-90	55	40-50	35-40	60	-
3a. 480	20-40	250	50	1%	80-90	55	40-50	35-40	-	60
3b. 480	20-40	250	50	1%	80-90	55	40-50	35-40	-	60
4. 900	20-40	190-200	50	1%	80-90	55	40-50	35-40	60	-
4a. 900	20-40	190-200	50	1%	80-90	55	40-50	35-40	-	110
4b. 900	20-40	190-200	50	1%	80-90	55	40-50	35-40	-	110
5. 920	20-40	250	50	2%	80-90	55	40-50	35-40	60	-
5a. 920	20-40	250	50	2%	80-90	55	40-50	35-40	-	120
5b. 920	20-40	250	50	2%	80-90	55	40-50	35-40	-	120
6. 420	20-40	250	42	3%	80-90	55	40-50	35-40	60	-
6a. 420	20-40	250	42	3%	80-90	55	40-50	35-40	-	90
6b. 420	20-40	250	42	3%	80-90	55	40-50	35-40	-	90
7. 500	20-40	250	42	4%	80-90	55	40-50	35-40	60	-
7a. 500	20-40	250	42	4%	80-90	55	40-50	35-40	-	60
7b. 500	20-40	250	42	4%	80-90	55	40-50	35-40	-	60

Isolation of cannabinoids and the purification process

The SFE result was used to analyze, using the previously described HPLC method, and select the extract with a good extraction yield and the highest CBD, CBN, and THC content. 30 g of the extract (sample no. 5) from separation kettle I in 90% methanol was partitioned with hexane. Each partition and the obtained extracts (samples no. 4b and 5b) from separation kettle II were evaporated to dryness in a vacuum to produce residues of hexane, methanol, and ethanol, respectively. These extracts underwent isolation and purification by flash chromatography in the Reveleris®PREP Purification System. The normal-phase and reverse-phase flash chromatography methods were used to purify CBD, CBN and, THC within the range of parameters presented in Tables 2 and 3. 13.70 g of the methanol extract (sample no. 5) were dissolved in dichloromethane, sonicated for 10 minutes then filtered through 0.45 µm pore-size filters and separated by an approach that used normal-phase flash chromatography. The parameters of the flash purification of CBD, CBN, and THC from other substances were optimized on a cartridge (FlashPure ID Silica120 g; 40 µm and 40 g respectively). The fractions were collected, by which each was analyzed by thin-layer chromatography (TLC) and separated by an approach that used reverse-phase flash chromatography with a cartridge (FlashPure ID C18 120 g; 40 µm). Finally, three major peaks were collected and identified by nuclear magnetic resonance (NMR) to confirm the purity of the CBD, CBN, and THC. Other extracts (samples no. 5, 4b, and 5b) were separated for each run. The parameters used were similar to sample no. 5 but used multiple isolation steps. The methodology of the isolation and purification of CBD, CBN, and THC are shown in Figures 2-4.

Table 2. Parameters of normal-phase flash chromatography

Cartridge	FlashPure ID Silica 40 g and 120 g
Particle size	40 µm
Sample loader	Liquid sample
Sample loop	5-10 mL
Mobile phase	Dichloromethane/hexane gradient (70-50%)
	Hexane/ethyl acetate isocratic (95:5%)
Flow rate	5-50 mL/min
Detector	UV detector: 254, 220 and 280 nm
	ELSD
Collect	Peaks
Pre-vial volume	7-25 mL

Table 3. Parameters of reverse-phase flash chromatography

Cartridge	FlashPure ID C18 120 g
Particle size	40 µm
Sample loader	Liquid sample
Sample loop	5-10 mL
Mobile phase	Methanol /water isocratic (90:10%)
Flow rate	10-30 mL/min
Detector	UV: 254, 220, and 280 nm
	ELSD
Collect	Peaks
Pre-vial volume	10-25 mL

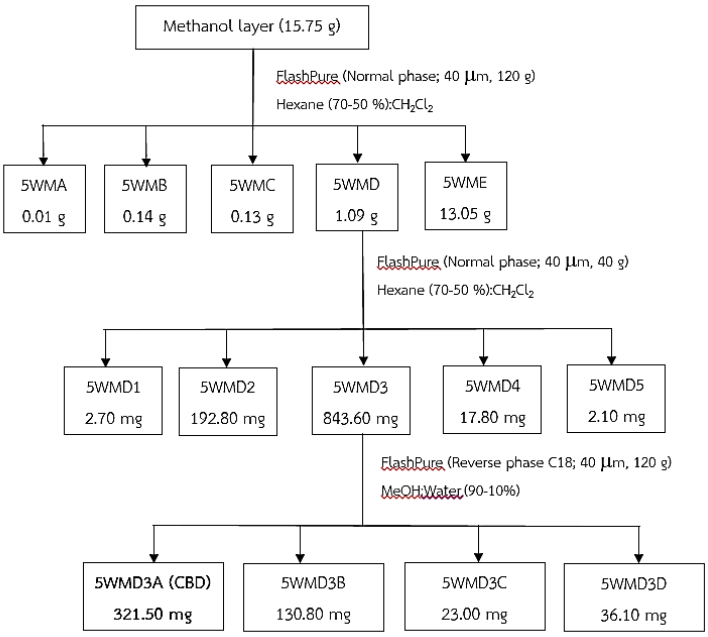


Figure 2. The methodology employed for the purification of the methanol layer (sample no. 5) using flash chromatography

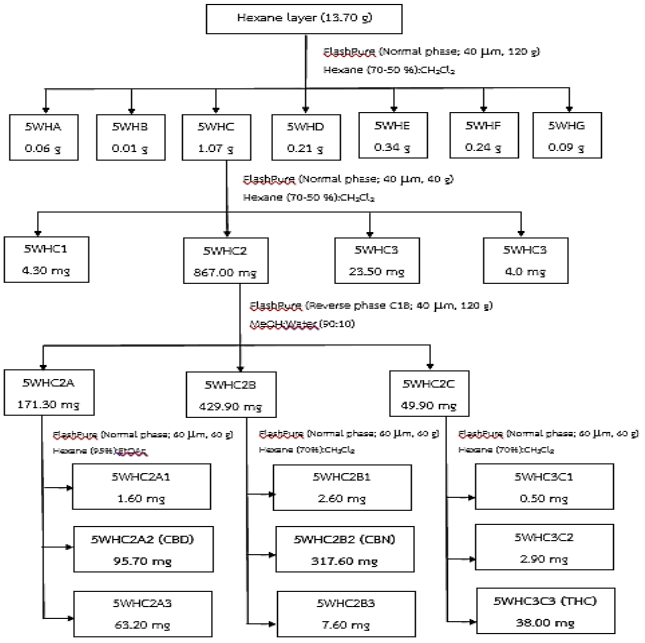


Figure 3. The methodology employed for purification of the hexane layer (sample no. 5) using flash chromatography

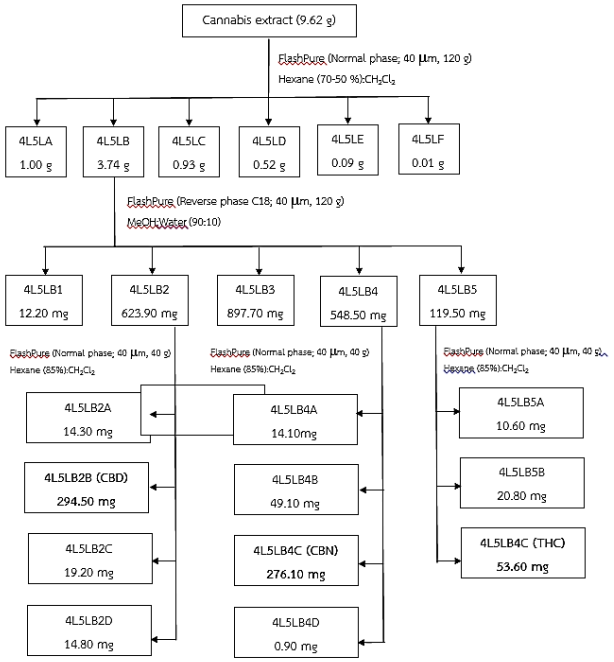


Figure 4. The methodology employed for the purification of the cannabis extract (samples no. 4b and 5b) using flash chromatography

Results and Discussion

Extraction yield

The development of the SFE extraction method was carried out by examining several factors, including pressure, temperature, co-solvent, and extraction time, together with sample particle size. The results of the extraction are shown in Table 4. Among the seventeen samples, the highest extraction yield was 7.02% (sample no. 3), followed by sample no. 5 (6.90%). Each was obtained with the pressure and temperature of the extraction kettle, separation kettle I, and separation kettle II set at 250 bar and 50 ºC, 80-90 bar and 55 ºC, and 40-50 bar and 35-40 ºC, respectively, with the co-solvent of 1-2% and the extraction time (60 min). The third highest is sample no. 4 (4.61%), obtained at 190-200 bar and 50 ºC, 80-90 bar and 55 ºC, and 40-50 bar and 35-40 ºC, respectively, with the co-solvent (1%) and extraction time (60 min). Other extracts with a low extraction yield below 4.61% were samples no.1, 2, 3a-3b, 4a-4b, 5a-5b, 6, 6a-6b, 7, and 7a-7b (between 0.34-3.24%). These factors directly affect the yield of cannabinoid compounds at the end of the extraction process. It is worth noting that similar results were previously reported by Richard [7]. These results suggest that the pressure and temperature of the extraction kettle (250 bar and 50 ºC), co-solvent (1-2%), and extraction time (60 min) favor the highest extraction yield from the dried cannabis plant. Moreover, Gallo-Molina et al. [8] reported a maximum extraction yield of 26.36%, which was obtained at 330 bar, 80 ºC, and 5% EtOH (extract number 6) using the highest levels of extraction pressure, temperature, and co-solvent. At these conditions, the high pressure and temperature can enhance the extraction yield. Another extract with a high yield was number 4 (23.36%) that was obtained at 150 bar, 40 ºC, and 5% EtOH using the lowest levels of extraction pressure, temperature, and co-solvent. Extract numbers 4 and 6 showed a higher extraction yield than those from samples no. 3, 5, and 4. However, these extracts were obtained using different levels of pressure and temperature. Omar et al. [9] reported that for SFE with CO_2/EtOH the extraction of cannabinoids from the cannabis plant was better at low temperatures.

HPLC analysis

In the HPLC analysis, the retention times of CBD, CBN, and THC were observed at 3.18, 5.42, and 6.80 minutes, respectively (Figure 5). The HPLC chromatograms of samples no. 5, 4b, and 5b in the extracts showed that CBD, CBN, and THC eluted at the same retention time as those of the standards (Figure 6). Table 4 shows the results of the experiment. The CBD content of extracts ranged from 4.03 to 14.53% w/w, with the highest at 14.53, 12.51, and 10.43 % w/w (samples no. 4b, 4, and 5 respectively). CBN content ranged from 4.32 to 26.75% w/w, with the highest at 26.75, 25.22, and 23.58 % w/w (samples no. 5b, 1, and 2 respectively). Finally, THC content ranged from 0.55 to 3.21% w/w, with the highest at 3.21, 2.14, and 1.96% w/w (samples no. 3, 5b, and 1 respectively). In the present study, the THC content of extracts is lower compared with those of Gallo-Molina et al., Omar et al., and Rovetto and Aieta (24.73- 37.85%, 0.45-32.4%, and 64.2-76.2%) [4, 8, 9]. The cannabis raw material used in this study was supplied from illegal narcotic drugs in Thailand arrested by the Narcotics Suppression Bureau. Further, degradation of THC will result in CBN. These results showed the cannabinoid content of the CBN is also higher than that of the THC. Therefore, the THC content of extracts can thus be very different despite using the same extraction method, co-solvent, and similar conditions. Previously, Rovetto and Aieta reported that the addition of ethanol as a co-solvent in SFE enhanced the cannabinoids extraction efficiency, including THC. Gallo-Molina et al. also suggested that the co-solvent levels between 2-5% favor the extraction of THC from the cannabis plant. It is worth mentioning that a similar result in this study was obtained using the concentration of the co-solvent of between 1-4%.

Table 4. Extraction yields and the CBD, CBN and THC content of SFE extracts from *Cannabis sativa* L.

Samples	Separation Kettle I	Separation Kettle II	Separation Kettle I	Separation Kettle II	Cannabinoid Content [B]		
	Extracts (g)		Extraction Yields [A] (% w/w)		CBD (% w/w)	CBN (% w/w)	THC (% w/w)
1.	17.20	-	2.29	-	7.68 ± 0.01	25.22 ± 0.01	1.96 ± 0.01
2.	5.30	-	0.71	-	5.30 ± 0.00	23.58 ± 0.02	1.43 ± 0.01
3.	33.69	-	7.02	-	8.44 ± 0.01	19.28 ± 0.01	3.21 ± 0.02
3a.	-	6.47	-	1.35	1.53 ± 0.00	6.81 ± 0.02	0.55 ± 0.01
3b.	-	5.68	-	1.18	4.58 ± 0.01	15.63 ± 0.01	1.81 ± 0.02
4.	41.49	-	4.61	-	12.51 ± 0.06	18.83 ± 0.03	1.82 ± 0.01
4a.	-	3.66	-	0.41	8.13 ± 0.14	18.93 ± 0.01	1.36 ± 0.02
4b.		3.44	-	0.38	14.53 ± 0.00	22.40 ± 0.25	1.90 ± 0.02
5.	63.44	-	6.90	-	10.43 ± 0.00	19.67 ± 0.01	1.81 ± 0.01
5a.	-	4.70	-	0.51	5.52 ± 0.01	11.34 ± 0.00	0.84 ± 0.00
5b.	-	8.60	-	0.93	10.30 ± 0.01	26.75 ± 0.01	2.14 ± 0.01
6.	16.85	-	4.01	-	4.03 ± 0.01	13.33 ± 0.02	0.89 ± 0.02
6a.	-	1.49	-	0.35	6.21 ± 0.02	16.11 ± 0.01	1.00 ± 0.02
6b.	-	6.57	-	1.56	7.18 ± 0.02	18.41 ± 0.01	1.08 ± 0.01
7.	16.18	-	3.24	-	5.91 ± 0.01	21.75 ± 0.01	1.41 ± 0.01
7a.	-	3.34	-	0.67	7.49 ± 0.01	4.38 ± 0.00	1.23 ± 0.02
7b.	-	1.72	-	0.34	7.39 ± 0.01	4.32 ± 0.01	1.09 ± 0.01

[a] in dry cannabis samples
[b] in dry extracts

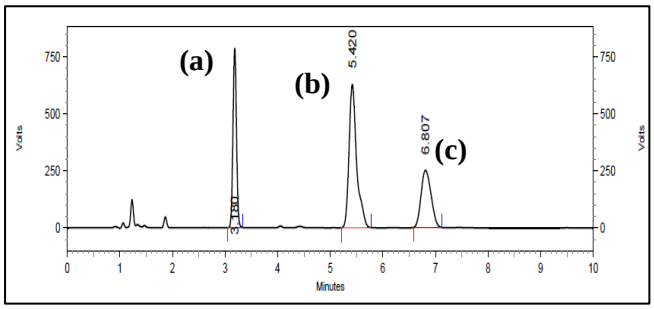
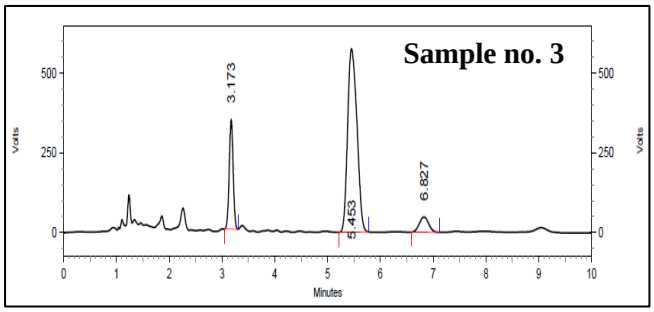
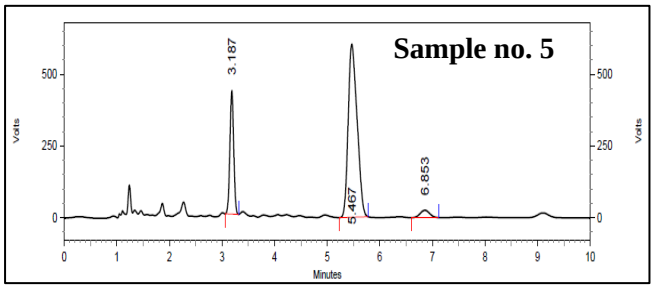
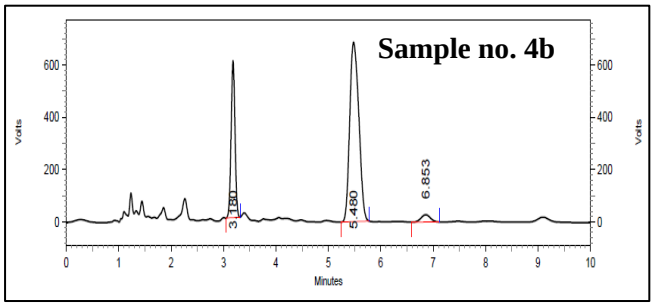


Figure 5. HPLC chromatogram of standard solution (a) CBD, (b) CBN, and (c) THC at a concentration of 100 µg/mL







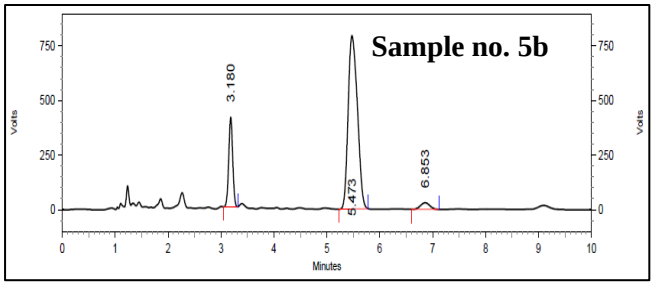


Figure 6. HPLC chromatogram of the cannabis extracts

Isolation and purification of cannabinoids

The results shown in the previous section indicated that samples no. 5, 4b, and 5b are candidates for further purification. These extracts underwent isolation and purification by flash chromatography in the Reveleris®PREP Purification System. The results from the normal-phase flash chromatography method with a 70-50% dichloromethane/hexane gradient showed a good separation with one major peak, which was cannabinoids, and a few minor peaks (Figure 7). After evaporation, each normal-phase fraction was dissolved in MeOH, which was then injected on the reverse-phase flash cartridge. The reverse-phase purification of normal-phase fractions with a methanol/water isocratic (90:10%) was performed on each fraction composing the three major peaks (Figure 8), a much cleaner chromatogram than that in Figure 6. Each one was analyzed by TLC to detect the purity and presence of CBD, CBN, and THC. The dried final fractions thus obtained were weighed and subjected to NMR analysis to confirm the purity of CBD, CBN, and THC. Tables 5-7 compare the ^{1}H-NMR and ^{13}C-NMR signals of the final fractions with CBD, CBN, and THC signals reported in the literature. The ^{1}H-NMR and ^{13}C-NMR signals observed for the final fractions are very similar to those reported for CBD, CBN, and THC by Choi et al. [10] and Leite et al. [11]. The ^{1}H-NMR signals of CBD were observed in the final fraction **1** spectra (Figure 9): the aromatic protons H-2′ and H-3′ of two distinct broad singlets at 5.99 and 6.27 ppm, respectively. The multiplet centered at 3.87 ppm was assigned to the H-1 proton. The singlet at 5.57 ppm was generated by terpenic H-2 and the other broad singlet at 4.85 ppm resulted from the resonance of the aromatic OH groups. The ^{1}H-NMR spectrum of final fraction **2** showed a signal at 8.19 ppm (singlet) due to aromatic hydrogen H-2 of CBN, and two other characteristic signals of CBN appear at 7.07 ppm (doublet, J = 8.0 Hz) and 7.15 ppm (doublet, J = 8.0 Hz). They are due to aromatic hydrogens H-4 and H-5, (Figure 10) respectively. The ^{1}H-NMR spectrum confirmed that final fraction **3** was THC, showing signals due to the olefinic H-2 proton at 6.31 ppm; H-9 and H-8 protons of angular methyl groups at 1.09 and 1.41 ppm (singlet), respectively; H-6 proton at 1.68 ppm; the aromatic H-5′ proton at 6.27 ppm (doublet, J = 1.5 Hz); and the H-5a and H-5b proton at 1.91 and 1.40 ppm (Figure 11), respectively.

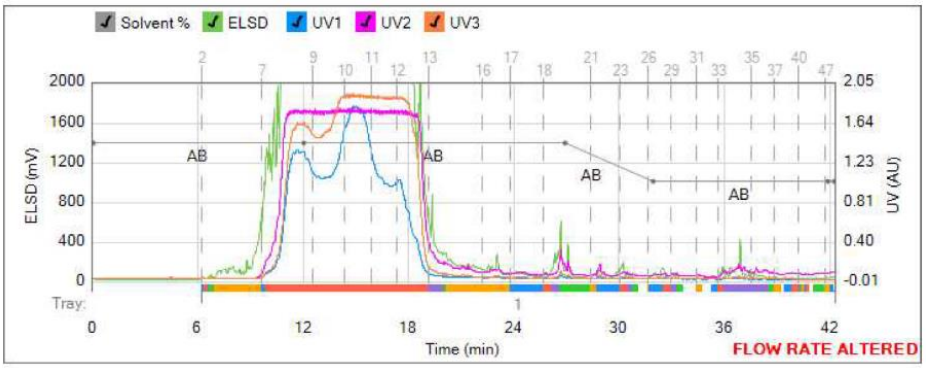


Figure 7. Separation of the extracted cannabinoids using the normal-phase flash chromatography

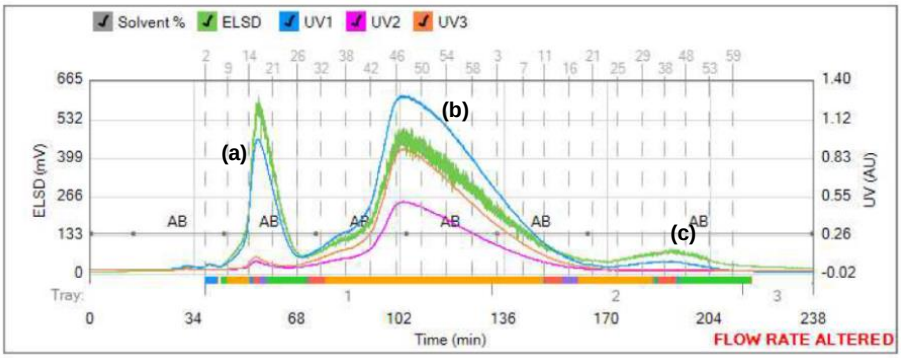


Figure 8. Separation of (a) CBD, (b) CBN, and (c) THC using the reverse-phase flash chromatography

Table 5. ^{1}H-NMR and ^{13}C-NMR spectroscopy data for final fraction 1 and CBD

Position	**^{1}H-NMR (δ ppm, J Hz)**		**^{13}C-NMR (δ ppm)**	
	Final Fraction (1) (500MHz)	**CBD[a] [10]**	**Final Fraction (1) (100MHz)**	**CBD[b] [10]**
1	3.87 (1H, *dm*, *J* = 10.5 Hz)	3.90 (1H, *dm*, *J* = 11.1 Hz)	37.14	37.50
2	5.57 (1H, *s*)	5.57 (1H, *s*)	124.12	127.30
3	-	-	139.98	134.20
4	2.23 (1H, *m*, H_a-4), 2.09 (1H, *m*, H_b-4)	2.21 (1H, *m*), 2.09 (1H, *m*)	30.36	30.70
5	1.83 (1H, *m*)	1.84 (*m*)	28.36	31.70
6	2.40 (1H, *td*, *J* = 11.0, 3.0 Hz)	2.40 (*m*)	46.14	46.40
7	1.79 (3H, *s*)	1.79 (3H, *s*)	23.63	23.70
8	-	-	149.25	150.3
9	4.65 (1H, *m*, H_a-9), 4.55 (1H, *m*, H_b-9)	4.64 (*trans*, 1H, *m*), 4.54 (*cis*, 1H, *m*)	110.81	110.50
10	1.66 (3H, *s*)	1.66 (3H, *s*)	20.39	19.50

Table 5 (cont'd). ^{1}H-NMR and ^{13}C-NMR spectroscopy data for final fraction 1 and CBD

Position	**^{1}H-NMR (δ ppm, J Hz)**		**^{13}C-NMR (δ ppm)**	
	Final Fraction (1) (500MHz)	**CBD[a] [10]**	**Final Fraction (1) (100MHz)**	**CBD[b] [10]**
1'	-	-	113.75	115.90
2′-OH	5.99 (1H, *brs*)	5.99 (1H, *s*)	156.08	157.50
3'	6.27 (1H, *brs*, H-3′)	6.26 (1H, *brs*, H-3′)	107.95	108.30
4'	-	-	142.99	142.70
5'	6.17 (1H, *brs*, H-5′)	6.16 (1H, *brs*, H-5′)	109.67	108.30
6'-OH	4.85 (1H, *brs*)	5.02 (1H, *s*)	153.90	150.30
1"	2.43 (2H, *t*, *J* = 7.5 Hz)	2.43 (2H, *t*, *J* = 7.5 Hz)	35.45	36.60
2"	1.55 (2H, *q*, *J* = 7.5 Hz)	1.55 (2H, *q*, *J* = 7.6 Hz)	30.60	32.00
3"	1.29 (4H, *m*, H_2-3″)	1.29 (4H, *m*)	31.46	32.60
4"	1.29 (4H, *m*, H_2-4″)	1.29 (4H, *m*)	22.50	23.60
5"	0.88 (3H, *t*, *J* = 7.0 Hz)	0.88 (3H, *t*, *J* = 6.8 Hz)	14.00	14.40

δ (ppm): Chemical shift.

J (Hz): Nuclear spin-spin coupling constant.

[a] Reported data obtained using 400 MHz NMR equipment

[b] Reported data obtained using 100 MHz NMR equipment

Table 6. ^{1}H-NMR and ^{13}C-NMR spectroscopy data for final fraction 2 and CBN

Position	**^{1}H-NMR (δ ppm, J Hz)**		**^{13}C-NMR (δ ppm)**	
	Final Fraction (2) (500MHz)	**CBN[a] [11]**	**Final Fraction (2) (100MHz)**	**CBN[b] [10]**
1	-	-	108.67	108.70
2	8.19 (1H, *s*)	8.16 (1H, *s*)	126.41	126.30
3	-	-	136.85	136.90
3-Me	2.39 (3H, *s*)	2.38 (3H, *s*)	21.50	21.50
4	7.07 (1H, *d*, *J* = 8.0 Hz)	7.07 (1H, *d*, *J* = 7.9 Hz)	127.54	127.60
5	7.15 (1H, *d*, *J* = 8.0 Hz)	7.14 (1H, *d*, *J* = 7.9 Hz)	122.56	122.60
6	-	-	136.81	136.90
7	-	-	77.30	77.50
8	1.61 (6H, *s*,)	1.60 (6H, *s*,)	27.08	27.10
9	1.61 (6H, *s*)	1.60 (6H, *s*)	27.08	27.10
1'	-	-	110.67	110.80
2'	-	-	154.57	154.70
3'	6.29 (1H, *d*, *J* = 1.5 Hz)	6.29 (1H, *d*, *J* = 1.1 Hz)	109.84	109.80
4'	-	-	144.49	144.50
5'	6.44 (1H, *d*, *J* = 1.5 Hz)	6.44 (1H, *d*, *J* = 1.1 Hz)	110.67	110.80
6'	-	-	153.11	153.00
1"	2.50 (2H, *t*, *J* = 7.5 Hz)	2.50 (2H, *t*, *J* = 7.5 Hz)	35.58	35.60

Table 6 (cont'd). ^{1}H-NMR and ^{13}C-NMR spectroscopy data for final fraction 2 and CBN

Position	^{1}H-NMR (δ ppm, J Hz)		^{13}C-NMR (δ ppm)	
	Final Fraction (2) (500MHz)	**CBN[a] [11]**	**Final Fraction (2) (100MHz)**	**CBN[b] [10]**
2"	1.63 (2H, *m*)	1.63 (2H, *m*)	30.43	30.40
3"	1.32 (4H, *m*)	1.32 (4H, *m*)	31.45	31.50
4"	1.32 (4H, *m*)	1.32 (4H, *m*)	22.51	22.50
5"	0.90 (3H, *t*, *J* = 7.0 Hz)	0.89 (3H, *t*, *J* = 6.8 Hz)	14.00	14.00
2'-OH	5.47 (1H, *s*)	5.13 (1H, *s*)	-	-

δ (ppm): Chemical shift.

J (Hz): Nuclear spin-spin coupling constant.

[a] Reported data obtained using 400 MHz NMR equipment

[b] Reported data obtained using 100 MHz NMR equipment

Table 7. ^{1}H-NMR and ^{13}C-NMR spectroscopy data for final fraction 3 and THC

Position	^{1}H-NMR (δ ppm, J Hz)		^{13}C-NMR (δ ppm)	
	Final Fraction (3) (500MHz)	**THC[a] [11]**	**Final Fraction (3) (100MHz)**	**THC[b] [10]**
1	3.21 (1H, *d*, *J* = 11.5 Hz)	3.20 (1H, *dm*, *J* = 10.9 Hz)	33.56	33.60
2	6.31 (1H, *brs*)	6.31 (1H, *q*, *J* = 16.0 Hz)	123.73	123.70
3	-	-	134.34	134.30
3-Me	1.68 (3H, *s*)	1.68 (3H, *s*)	23.35	23.40
4	2.16 (2H, *m*)	2.16 (2H, *m*)	31.15	31.20
5	1.91(1H, *m*), 1.40 (1H, *m*)	1.90 (1H, *m*), 1.40 (1H, *m*)	25.00	25.00
6	1.68(1H, *m*)	1.69 (1H, *m*)	45.79	45.80
7	-	-	77.19	76.70
8	1.41 (3H, *s*)	1.41 (3H, *s*)	27.55	27.60
9	1.09 (3H, *s*)	1.09 (3H, *s*)	19.25	19.30
1'	-	-	110.04	110.80
2'	-	-	154.74	154.70
3'	6.14 (1H, *d*, *J* = 1.5 Hz)	6.14 (1H, *d*, *J* = 1.6 Hz)	107.53	107.50
4'	-	-	142.78	142.80
5'	6.27 (1H, *d*, *J* = 1.5 Hz)	6.27 (1H, *d*, *J* = 1.6 Hz)	109.02	110.10
6'	-	-	154.18	154.20
1"	2.43 (2H, *td*, *J* = 7.5, 2.5 Hz)	2.42 (2H, *td*, *J* = 7.3, 1.6 Hz)	35.46	35.50
2"	1.56 (2H, *q*, *J* = 7.5 Hz)	1.55 (2H, *q*, *J* = 7.8 Hz)	30.63	30.60
3"	1.30 (4H, *m*)	1.29 (*m*)	31.50	31.50
4"	1.30 (4H, *m*)	1.29 (*m*)	22.52	22.50
5"	0.88(3H, *t*, *J* = 7.0 Hz)	0.87 (3H, *t*, *J* = 7.0 Hz)	13.99	14.00
2'-OH	4.88 (1H, brs)	4.87 (1H, s)	-	-

δ (ppm): Chemical shift.

J (Hz): Nuclear spin-spin coupling constant.

[a] Reported data obtained using 400 MHz NMR equipment

[b] Reported data obtained using 100 MHz NMR equipment

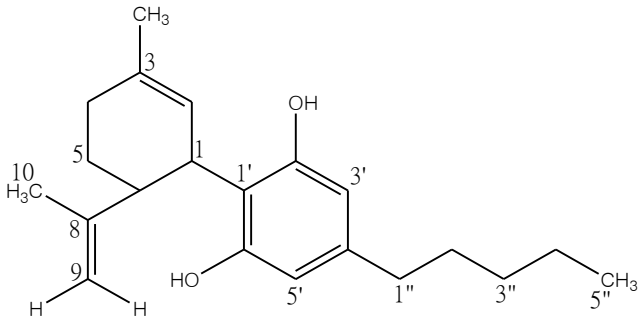


Figure 9. The structure of cannabidiol (CBD)

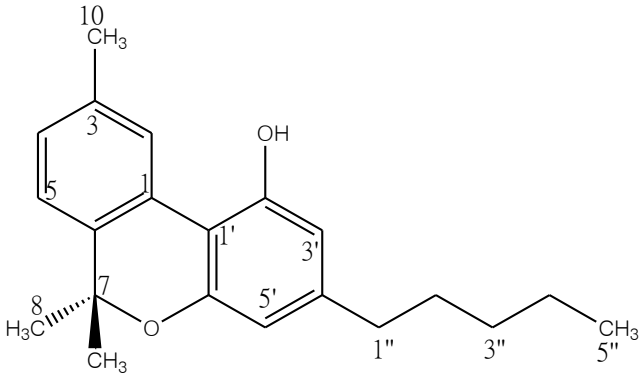


Figure 10. The structure of cannabinol (CBN)

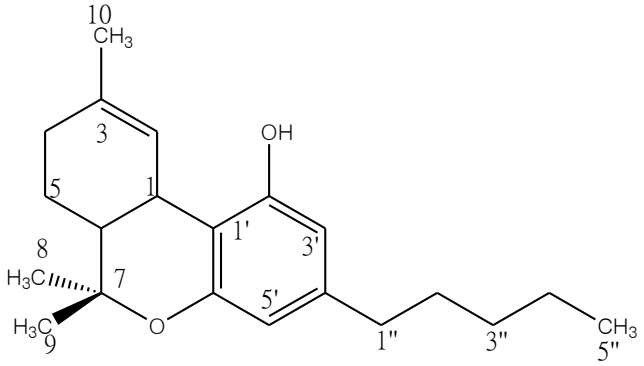


Figure 11. The structure of delta-9-tetrahydrocannabinol (THC)

Conclusion

The researchers developed SFE process, which is a viable technology for the extraction of cannabinoids from *Cannabis Sativa* L., with high yield. Additionally, the chosen operation parameters (e.g. pressure, temperature, and co-solvent) need to be safe, efficient, and capable of maximizing the yield (minimum CBD, CBN, and THC loss). SFE provided one with the highest

extraction yield, sample no. 3 obtained at 250 bar and 50 ºC of pressure and temperature of the extraction kettle, co-solvent (1-2%), and extraction time (60 min). Additionally, using this optimal condition with the pressure and temperature of the extraction kettle (190-200 bar and 50 ºC), co-solvent (1%), and extraction time (110 min) gave the highest amount of CBD at 14.53% w/w. However, the highest amounts of CBN (26.75% w/w, sample no. 5b) and THC (3.21% w/w, sample no. 3) were obtained when the pressure and temperature of the extraction kettle, separation kettle I, and separation kettle II were set to 250 bar and 50 ºC, 80-90 bar and 55 ºC, and 40-50 bar and 35-40 ºC, respectively, with co-solvent of 1-2%. Samples no. 5, 4b, and 5b were selected and further purified by flash chromatography in the Reveleris®PREP Purification System, which together with the structural elucidation of isolated cannabinoids by spectroscopy gave three cannabinoids including CBD, CBN, and THC. The researchers have shown that the usefulness of combining SFE and flash chromatography process could be yield a high quantity of cannabinoids, which proved that a high purity could be achieved for CBD, CBN, and THC. Finally, the cannabinoid extracts and active compounds (CBD, CBN, and THC) produced in our study could be used for ongoing research at the College of Pharmacy, Rangsit University, for future medical benefits.

Acknowledgment

We are grateful to the Research Institute of Rangsit University (Grant No. 106/2561) for financial support. We also wish to thank the Medicinal Cannabis Research Institute of the College of Pharmacy, Rangsit University, Thailand, for providing laboratory facilities.

References

1. Elsohly, M. A. (2007). Marijuana and the Cannabinoids. Totowa, New Jersey, Humana Press Inc: pp. 17-27.
2. Gaoni, Y. and Mechoulam, R. (1964). Isolation, structure, and partial synthesis of an active constituent of Hashish. *Journal of the American Chemical Society,* 86: 1646-1647.
3. Ben Amar, M. (2006). Cannabinoids in medicine: a review of their therapeutic potential. *Journal of Ethnopharmacol,* 105: 791-802.
4. Rovetto, L. J. and Aieta, N. V. (2017). Supercritical carbon dioxide extraction of cannabinoids from *Cannabis sativa* L. *The Journal of Supercritical Fluids,* 129: 16-27.
5. Hazekamp, A., Peltenburg, A., Verpoorte, R. and Giroud, C. (2005). Chromatographic and spectroscopic data of cannabinoids from *Cannabis sativa* L. *Journal of Liquid Chromatgraphy,* 28: 2361-2382.
6. Saingama, W. and Sakunpak, A. (2008). Development and validation of reverse phase high performance liquid chromatography method for the determination of delta-9-tetrahydrocannabinol and cannabidiol in oromucosal spray from cannabis extract. *Brazilian journal of Pharmacognosy,* 28: 669-672.
7. Richard, P. F. (1982). Carbon dioxide as a solvent application of fat, oil and other materials. *Chemistry and Industry,* 20 (12): 394.
8. Gallo-Molina, A. C., Castro-Vargas, H. I., Garzon-Mendez, W. F., Garzon-Mendez, J. A., Martinez Ramirez., Rivera Monroy, Z. J., King, J. W. and Parada-Alfonso, F. (2019). Extraction, isolation and purification of tetrahydrocannabinol from the *Cannabis sativa* L. plant using supercritical fluid extraction and solid phase extraction. *The Journal of Supercritical Fluids,* 146: 208-216.
9. Omar, J., Olivares, M., Alzaga, M. and Etxbarria, N. (2013). Optimisation and characterisation of marihuana extracts obtained by supercritical fluid extraction and focused ultrasound extraction and retention time locking GC-MS. *Journal of Separation Science,* 36: 1397-1401.
10. Choi, Y. H., Hazekamp, A., Peltenburg-Looman, A. M. G., Frederich, M., Erkelens, C., Lefeber, A.W. M. and Verpoorte, R. (2004). NMR Assignments of the major cannabinoids and cannabiflavonoids isolated from flowers of *Cannabis sativa*. *Phytochemical analysis,* 15: 345-354.
11. Leite, J. de A., Oliveira, M. V. L, Conti, R., Borges, W. de S., Rosa, T. R., Filgueiras, P. R. and Alvaro, C. N. (2018). Extraction and isolation of cannabinoids from marijuana seizures and characterization by ^{1}H NMR allied to chemometric tools. *Science & Justice,* 58: 355-365.

Malaysian Journal of Analytical Sciences (MJAS)
Published by Malaysian Analytical Sciences Society

APPLICATION OF ZINC OXIDE NANOPARTICLES AND NANOCHITOSAN TO ENHANCE THE LIGHT FASTNESS OF COTTON DYED WITH NATURAL INDIGO

(Aplikasi Zink Oksida Nanopartikel dan Nano Kitosan untuk Meningkatkan Ketahanan Pudar Kain yang Diwarnai Indigo Asli)

Renung Reningtyas[1,2], Edia Rahayuningsih[1,3]*, Yuni Kusumastuti[1], Indriana Kartini[3,4]

[1]Department of Chemical Engineering, Faculty of Engineering,
Universitas Gadjah Mada, 55281 Yogyakarta, Indonesia
[2] Department of Chemical Engineering, Faculty of Industrial Engineering,
Universitas Pembangunan Nasional "Veteran" Yogyakarta, 55283 Yogyakarta, Indonesia
[3]Indonesia Natural Dye Institute, Integrated Research and Testing Laboratory
[4]Department of Chemistry, Faculty of Mathematics and Natural Sciences
Universitas Gadjah Mada, 55281 Yogyakarta, Indonesia

**Corresponding author: edia_rahayu@ugm.ac.id*

Received: 15 July 2021; Accepted: 11 October 2021; Published: 25 October 2021

Abstract

The use of eco-friendly natural dyes with lower environment impact is getting more interest. Indigo dye is one of the most popular natural dyes and has been used for textile dyeing since ages. The lower light fastness of natural indigo dye compared with blue synthetic dye has been a major disadvantage of its use in the textile industry. In this study, zinc oxide nanoparticles (ZnONPs) synthesized using simple precipitation method were applied as an anti-UV agent to protect the color of natural indigo dyed cotton. To increase the adsorption of ZnONPs in cotton, nanochitosan coating was applied before ZnONPs coating. X-ray diffraction (XRD) and transmission electron microscopy (TEM) were conducted to characterize the crystallinity, shape and size of the produced ZnO. The particle size distribution of ZnONPs and nanochitosan was measured using the dynamic light scattering technique. The amount of ZnO adsorbed in cotton, coated with and without nanochitosan were measured using energy-dispersive X-ray spectroscopy (EDS) and X-ray fluorescence (XRF). Applying nanochitosan coating before ZnONPs coating could increase the amount of ZnO adsorbed in cotton up to fourfold. The ability of ZnONPs as anti-UV agent to protect color of dyed cotton was measured by the photofading test. The photofading test was performed under UV-A light exposure and the color difference of cotton samples before and after 144 h irradiation was measured based on CIELAB value. Cotton dyed with natural indigo and coated with nanochitosan and ZnONP has a lowest color difference, indicating the increasing of light fastness provided by ZnONPs.

Keywords: zinc oxide nanoparticles, nanochitosan, natural indigo dye, adsorption, fading

Abstrak

Penggunaan pewarna asli dengan kesan yang lebih rendah terhadap alam sekitar semakin menarik dikembangkan. Pewarna indigo adalah salah satu pewarna asli yang popular dan telah digunakan untuk pewarnaan tekstil sejak zaman dahulu. Ketahanan cahaya pewarna indigo yang lebih rendah berbanding dengan pewarna sintetik telah menjadi kelemahan utama penggunaannya dalam industri tekstil. Dalam kajian ini, Zink oksida nanopartikel (ZnONPs) yang disintesis dengan kaedah pemendakan sederhana digunakan sebagai agen anti-UV untuk melindungi warna indigo pada kain kapas. Untuk meningkatkan penjerapan ZnONP, lapisan nano kitosan digunakan sebelum lapisan ZnONPs. Pembelauan sinar-X (XRD) dan mikroskop elektron transmisi (TEM) digunakan untuk mencirikan penghabluran, bentuk dan ukuran ZnO yang dihasilkan. Taburan ukuran zarah ZnONP dan nano kitosan diukur dengan teknik penyebaran cahaya dinamik (DLS). Jumlah ZnO yang diserap dalam kapas, dilapisi dengan dan tanpa nano-kitosan diukur menggunakan sinar-X pendafluoran (XRF). Salutan nano kitosan sebelum pelapisan ZnONP dapat meningkatkan jumlah ZnO yang diserap dalam kain kapas hingga empat kali. Ujian pudar dilakukan di bawah cahaya UV-A dan hasil sebelum dan setelah penyinaran selama 144 jam diukur dengan nilai CIELAB. Kain kapas yang diwarnai dengan indigo asli dan telah dilapisi nano-kitosan dan ZnONP mempunyai perbezaan warna yang paling rendah. Hal ini menunjukkan peningkatan daya tahan cahaya dapat disediakan oleh ZnONPs.

Kata kunci: zink oksida nanopartikel, nano-kitosan, indigo asli, jerapan, pudar

Introduction

Eco-friendly natural dye is re-emergencing in the textile industries. This tendency grows with the soaring popularity of the back-to-nature lifestyle [1]. Currently, numerous small enterprise textile industry in Indonesia, especially the Batik industry have moved to the use of natural dye in textile coloring. Natural indigo dye is a popular dye used in different parts of the world, especially in Europe, Japan, India and Indonesia. The unique blue color of indigo mainly comes from indigotin pigment, which can be extracted through fermentation, reduction and oxidation process from indigoid plant leaves such as *Indigofera tinctoria*, *Indigofera sumatrana*, *Indigofera. arecta*, *Indigofera galegoides*, *Indigofera enncaphylla*, *Strobilanthes flaccidifollus*, *Marsdenia tinctoria*, *Isatis tinctoria*, and *Polygonum tinctorium*, and etc. [2]. *Indigofera tinctoria* leaves and the chemical structure of indigotin are shown in Figure 1.

The application of natural indigo dye in textile fabrics has its limitations such as low to moderate light fastness properties [3]. Indigo is prone to fading because of exposure to light. Fading occurs when the energy of light breaks the double bond in the dye structure; hence, dye molecules cannot reflect the original color. A shorter wavelength of light has higher energy; therefore, UV light with higher energy than visible light can cause undesired degradation [4].

Recently, inorganic nanomaterial has received more attention in the textile research industry; to provide multifunctional textile like textiles with anti-UV, anti-microorganism, self-cleaning and anti-odor properties. Particle with a diameter below 20 nm cannot scatter light in the visible range and therefore are not opaque when applied in fiber [5]. Zinc oxide (ZnO), titanium oxide (TiO_2) and silicon oxide (SiO_2) are among the good inorganic UV protection agents [6]. Zinc oxide nanoparticles are metal oxide semiconductors that have a large energy band gap, biocompatibility and relatively low cost. The photocatalytic activity of ZnONPs is also less than that of TiO_2, making it suitable for application in textile. Zinc oxide in nanosize has received considerable attention in numerous studies as an anti UV finishes in textiles [7-9]. However, research on the anti-UV properties in textile was mainly focused on its effect on skin protection. Moreover, ZnONPs were applied in undyed fabric or fabric dyed with synthetic dye. Unlike previous work, our present study is focused on the application of ZnONPs as an anti UV finish on cotton fabrics dyed with natural indigo to protect color from photofading.

The main barrier to nanoparticle application in the textile surface is their low adsorption and durability. To increase nanoparticle adsorption and to maintain nanoparticle durability, the addition of a binder agent is usually employed. Chitosan is a great candidate for an

ecofriendly textile finishing material because of its biodegradability, biocompatibility and nontoxic properties. Chitosan is a functional biopolymer that can be obtained by partial de-N-acetylation of chitin. Chitosan also possesses antimicrobial properties that can be beneficial to protect fabrics as well as the wearer [10]. To create the homogenous coating on the cotton surface, chitosan can be produced in nanosize. To enhanced cellulose and chitosan bonding, the addition of a crosslinking agent like butane tetracarboxylic acid (BTCA), Arcofix NEC [11] and citric acid [12] has been reported. Citric acid is food grade material, has high availability and low cost, and therefore it is suitable to be applied in textile industries.

Several studies combined nanochitosan and ZnO to enhance anti-UV properties of textiles. However, the chitosan and ZnONPs was produced as nanocomposites. Moreover, the study of anti-UV properties in fabrics were focused on skin protection, as measured by the UV protection factor (UPF) [13-16]. Tangkawanit applied nanochitosan and ZnONPs in cotton prior indigo dyeing and the result showed the improvement in color fastness and anti-UV properties [17]. There are few publications in the literature regarding the application of nanochitosan-ZnONPs in dyed fabrics that focused on the color protection.

This research aims to protect color of cotton fabrics dyed with natural indigo from photofading by the application of ZnONPs as an anti-UV finish. Nanochitosan was used to enhance ZnONPs adsorption and durability in cotton fabrics. Impregnation of chitosan and ZnONPs was done in a series process after dyeing the cotton with natural indigo. Nanochitosan was produced by an ionic gelation method using sodium trypolyphosphate. Citric acid was used as a crosslinking agent to provide chemical linking between cellulose and chitosan. A characterization of ZnONP and nanochitosan was conducted and the amount of ZnONP adsorbed in treated cotton was analyzed. The effect of nanochitosan and ZnONP coating on light fastness of cotton dyed with natural indigo was also investigated by the photofading test.

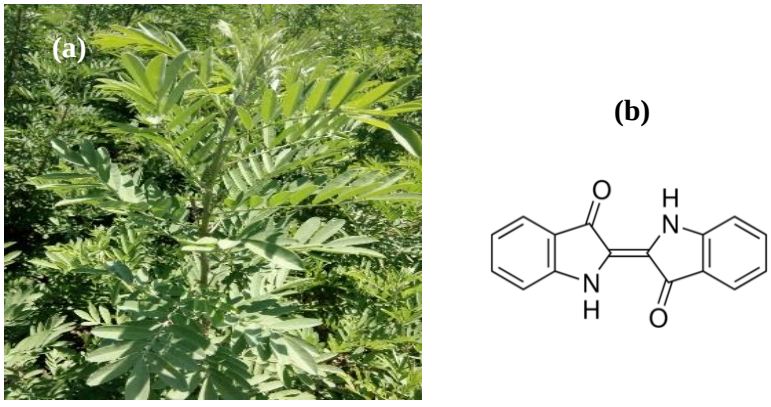


Figure 1. *Indigofera tinctoria* leaves (a) and chemical structure of indigotin (b)

Materials and Methods

Chemicals and materials

Chitosan powder with a 90% degree of deacetylation was purchased from PT. Biotech Surindo, West Java, Indonesia. Zinc nitrate tetrahydrate ($Zn(NO_3)_2.4H_2O$) and sodium hydroxide (NaOH), were purchased from Merck. Natural indigo dye powder, sodium dithionite and sodium carbonate as reduction agent in indigo

dyeing were obtained from Gama Indigo (Indonesia). Cotton fabric (mercerized sanforized with warp 106 and weft 92, Ne1 50) was purchased from PT. Primatexo. The cotton fabric was soaked with 2% non-ionic detergent, washed several times and air dried before further treatment.

Methods: Cotton dyeing

Indigo powder (50 g), sodium carbonate (14 g), and sodium dithionite (18 g) were dissolved in 1 L of water at 70 °C. The solution was allowed to stand for 15 minutes under closed conditions to prevent oxidation. After 15 minutes the solution was mixed with a 9 L solution containing sodium carbonate (3.5 g) and sodium dithionite (4.5 g). The mixture was allowed to stand for 1 hour under closed conditions. The coating of fabrics was performed in a 1:20 mass-to-liquid ratio. Cotton fabric was dipped for 5 minutes in dyebath and air dried for 5 minutes to obtain contact with oxygen. The dipping process was repeated seven times to maximize dye uptake. Dyed cotton was washed with tap water to remove the unreacted dye in fabric surface and air dried.

Synthesis of ZnONPs

Zinc oxide nanoparticles were synthesized using precipitation method reported by Talam et al. with some modifications [18]. An aqueous solution of zinc nitrate at a concentration of 0.05 M (500 mL) was placed in beaker glass under continuous stirring. Sodium hydroxide solution (0.1 M, 500 mL) was added dropwise. The reaction occurred in room temperature (±30 °C) for 2.5 hours and left under constant stirring for 30 minutes to reach completion. The particles were separated from supernatant by sedimentation. The supernatant solution was discharged carefully and the white precipitate remaining were washed 3 times with 100 mL of deionized water, dried in an oven at 100 °C for 3 hours, and ground to a fine powder. ZnONPs powder was kept in air-tight storage for further use.

Synthesis of nanochitosan

Nanochitosan was prepared by the ionic gelation method. Briefly, 0.2% (w/v) chitosan was made by dissolving 1 g of chitosan powder in 500 mL of 1% (v/v) acetic acid solution under constant stirring for 2 hours. After this solution had completely dissolved, 0.84% (w/v) sodium tripolyphosphate (STPP) solution was added dropwise under constant stirring. The volume ratio of chitosan and STPP solution was 5:2 and therefore the chitosan concentration in the dispersion was reduced to 0.14% (w/v). The dispersion of nanochitosan was kept air tight in glass bottle until further use.

Coating of cotton with nanochitosan

Cotton samples of 10 cm × 10 cm (±1 gr) were dip-coated for 5 minutes in a mixture of 100 mL nanochitosan dispersion with the combination of citric acid (0.8 g) as a crosslinking agent and sodium dihydrogen phosphate (0.6 g) as a catalyst. The coated cotton was then dried in oven with the temperature of 80°C for 5 minutes, followed by curing at 150°C for 3 minutes (Figure 2).

Coating of Cotton with ZnONPs

ZnONPs (1 g/L) were dispersed in water using probe sonicator (Vibracell, 750 W). The 100 mL dispersion was irradiated for 5 minutes. The dispersion temperature was raised from room temperature up to 40°C due to sonication process. Cotton samples of 10cm x 10cm (±1 g) were dip-coated for 5 min in the dispersion right after sonication and air dried (Figure 2).

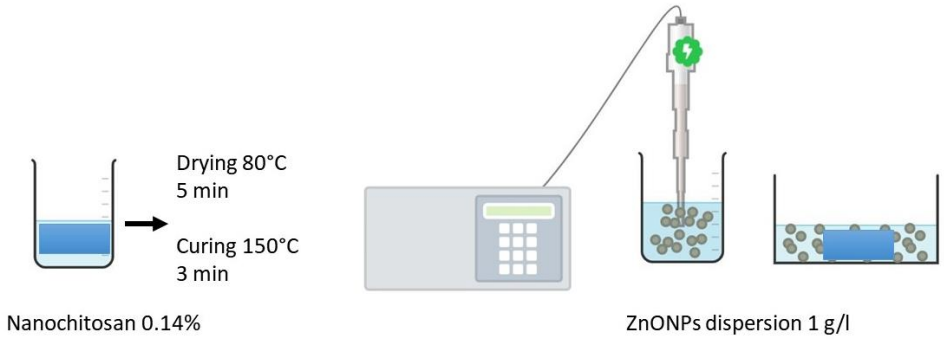


Figure 2. Coating process

Durability test

The coated samples were washed with demineralized water under constant stirring for 5 minutes and air dried. The mass to liquid ratio of washing was 1: 200. All samples were kept in dark chamber before further analysis.

Photofading test

Fading of natural indigo dye in cotton samples was tested using UV-A irradiation (Sankyo Denki, 20 W) for 144 hours. A photoreactor chamber with the dimensions of 60 cm × 50 cm × 30 cm was equipped with a fan to make the temperature inside the chamber uniform. A cotton sample were placed 25 cm below the lamp. The radiant flux was measured at 0.206 mW/cm^2 using a Lutron UV light meter YK-35UV.

Analysis

The shape and size of synthesized ZnONPs were determined by TEM (JEOL JEM 1400). The sample was previously dispersed in ethanol medium.

The X-ray diffraction (XRD) patterns of the ZnO powder were determined using Rigaku Smartlab with Cu Kα radiation of 40 kV, 30 mA, a scan speed 3 deg/min, a step width of 0.01° and a scan range of 3-90°. An estimation of the crystal size was calculated using Scherrer's formula, equation 1, where D is the crystalline size, K is a dimensionless shape factor (0.89), λ is the wavelength of the X-ray (0.154 nm) and β is the full width at half maximum, while θ is the half diffraction angle.

$$D = \frac{k\lambda}{\beta \cos\theta} \quad (1)$$

The size distribution of the ZnONPs dispersion was determined using the dynamic light scattering technique (Zetasizer Nano ZS, Malvern Instrument Ltd). The 12 mm cell was used and the parameters chosen for ZnO and dispersant (water) were as follows: (refractive index: 1.99 and 1.333, respectively). All measurements were taken at 25°C.

The surface morphology of cotton samples was observed with scanning electron microscope (Quanta Chrome) equipped with energy-dispersive X-ray spectroscopy (EDS). The zinc content within the cotton samples was estimated using X-ray fluorescence (XRF) PANalytical Epsilon1.

The change in color of the samples in CIELAB was evaluated using a UV-Vis spectrophotometer (Shimadzu, PC 2401). L represents the brightness where a* measures the perceived change from green (-a*) to red (+a*) and b* measures the perceived change from blue (-b*) to yellow (+b*). The color difference (dE) and the change in color (ΔE) were calculated using equation 2 and equation 3

$$dE = [(L*' - L*)^2 + (a*' - a*)^2 + (b*' - b*)^2]^{\frac{1}{2}} \quad (2)$$

$$\Delta E = dE_{before\ irradiation} - dE_{after\ irradiation} \quad (3)$$

Results and Discussion

Characterization of ZnONPs and nanochitosan

The primary particle size and morphologies of ZnONPs prepared by the precipitation method were examined by TEM. Figure 3a shows that most of the particles are at the nanometer scale with a spherical shape like grain. It can be seen that the primary particle formed an agglomerate with the size of approximately 300-400 nm. Figure 3b shows a histogram of the diameter of ZnONPs, with the calculated average size of primary nanoparticles is 22.51 nm.

The XRD spectrum of the synthesized zinc oxide in Fig. 4 shows peaks at 2θ of 31.73°, 34.43°, 36.24°, 56.54°, 62.89° and 68.02°, which can be assigned to the (100), (002), (101), (102), (110), (103), and (112) crystal planes of the ZnO structure, respectively. The sharp peaks confirm the good crystalline nature of deposited ZnONPs. All peaks show the formation of a hexagonal wurtzite structure, which is in accordance with the JCPDS card 36-1451 [19]. Diffraction peaks related to impurities are not observed, indicating that pure ZnONPs were successfully synthesized using the precipitation method. The average particle size was determined to be 19.75 nm using Scherrer's equation.

ZnONPs with a concentration of 1 g/L were dispersed in pure water using ultrasound energy. The particle size distribution curve of the ZnONPs dispersion in water medium after sonication for 5 minutes is shown in Figure 5. The diameter of ZnONPs in aqueous solution is in the range of 400-800 nm, which is much larger than the diameter of primary particle. The z-average hydrodynamics diameter of the ZnONPs dispersion is 2310 nm, indicating the formation of aggregate or agglomerate in aqueous medium. This result is in accordance with the result of Jo et al. [20]. A large surface area and high surface energy of nanoparticles promote fast aggregation and agglomeration. Rapid particle collisions, van der Waals attraction, water bridging and a high surface energy of nanoparticles in water were responsible for their size increase [21].

The polydispersity index (PDI) is related to the size distribution of a nanoparticle dispersion. The PDI ranges from 0-1, where a PDI close to 0 indicates a homogenous dispersion and a PDI above 0.5 indicates heterogeneous dispersion [22]. From the particle size analyzer, the PDI of the ZnONPs dispersion is measured as 0.876. A heterogeneous distribution in the dispersion is likely caused by the agglomeration of ZnONPs in the water medium. Therefore, immediately after sonication, cotton was dip coated for not more than 5 minutes. A longer coating time resulted in the attachment of agglomerate ZnONPs, which are expected to fall under washing.

Figure 6 shows the size distribution of chitosan solution 0.14% w/v. Nanochitosan with a smaller size distribution was successfully produced by an ionic gelation method using sodium tripolyphospate as crosslinking agent. PDI of nanochitosan dispersion was 0.409, indicating that a stable dispersion was successfully made.

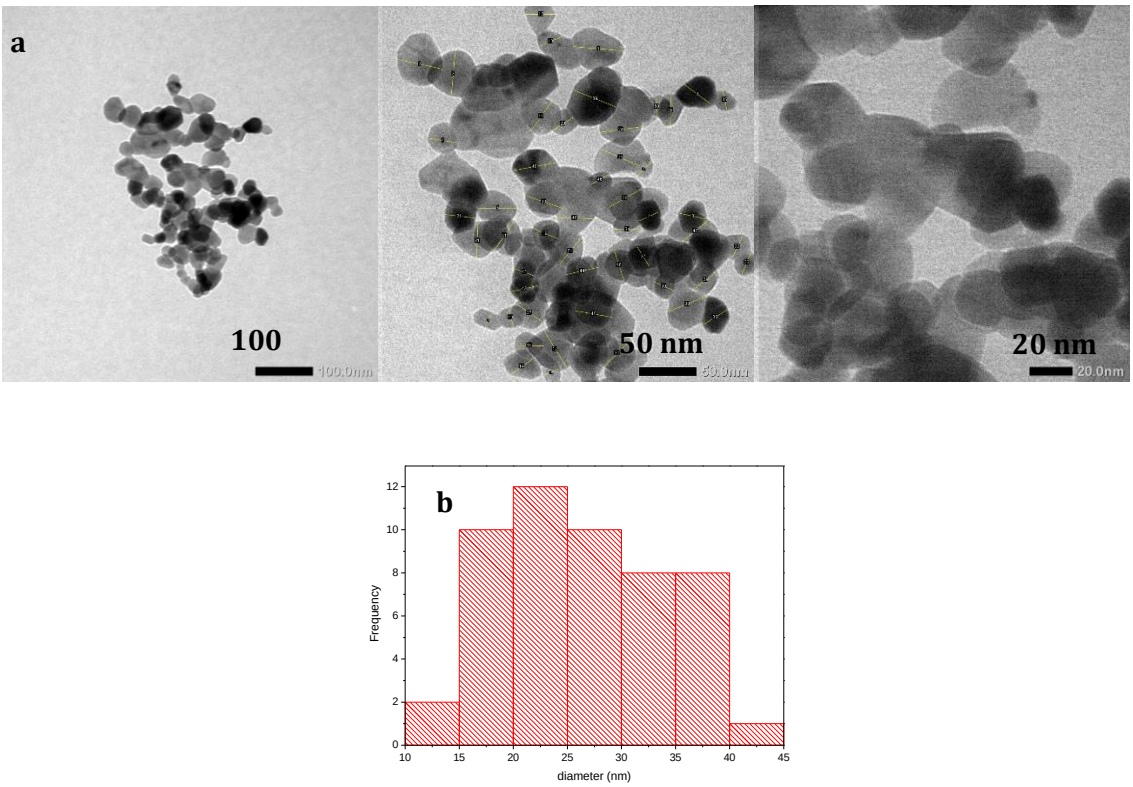


Figure 3. (a) Transmission electron micrographs and (b) a histogram profile of ZnONPs prepared using the precipitation method and dried at 100°C

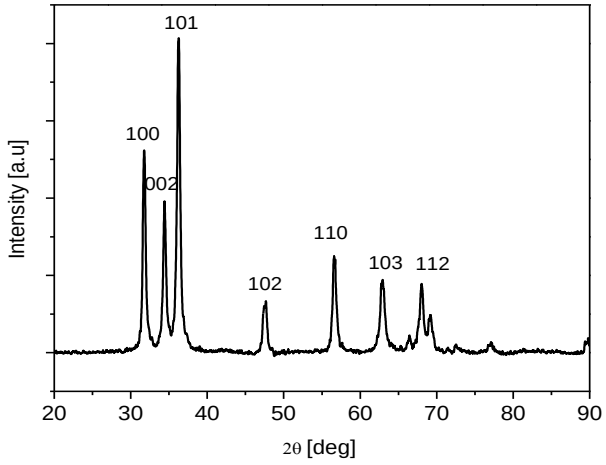


Figure 4. XRD spectrum of zinc oxide prepared using the precipitation method

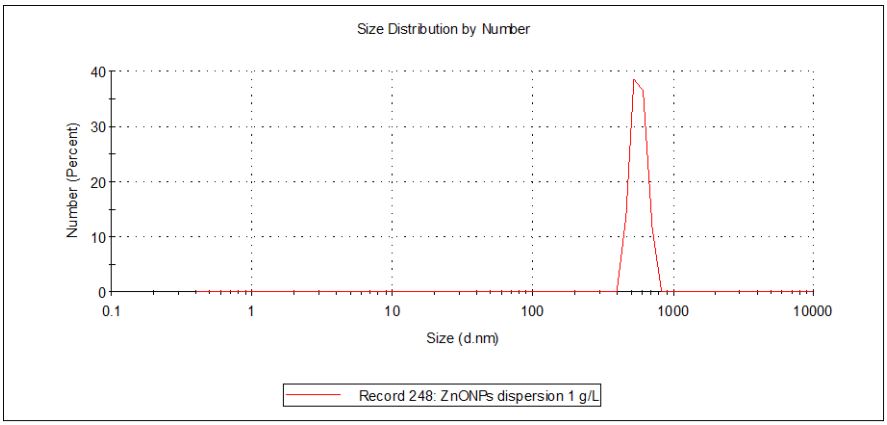


Figure 5. Particle size distribution of (1g/L) ZnONPs dispersion

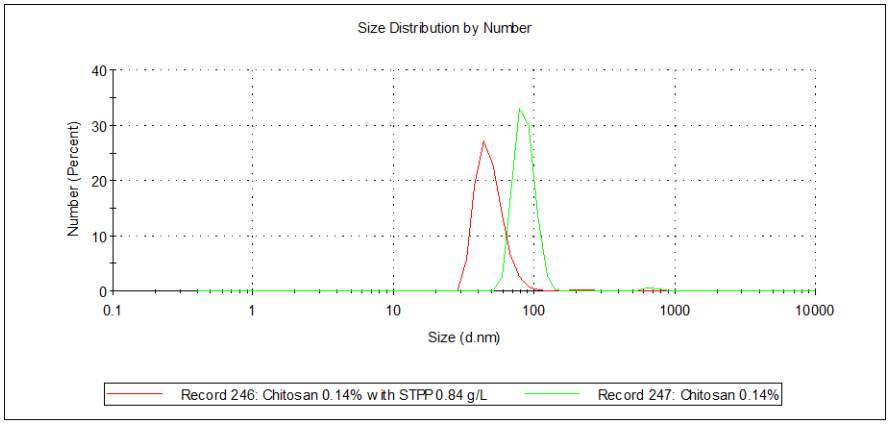


Figure 6. Particle size distribution of the 0.14% (w/v) chitosan dispersion

Application of ZnONP and nanochitosan in cotton dyed with natural indigo dye

Figure 7 depicts the FTIR spectrum of chitosan and treated cottons. The absorption band at around 3300-3500 cm^{-1} for chitosan and cotton is corresponding to the stretching vibration of $–NH_2$ and –OH groups. The bands at 2896 cm^{-1} reflects the characteristic peak for asymmetric stretching of $–CH_3$ and $–CH_2$. The peaks at 1638 cm^{-1} were assigned to $–NH_2$ groups. The vibration at 1388 cm^{-1} was assigned to the CH_3 symmetrical deformation and the vibration at 1024 cm^{-1} was assigned to C–O stretching vibrations. The band at below 500 cm^{-1} is corresponding to ZnO [23-24]. Compared with undyed cotton, the broader peak in the range of 3300-3500 cm^{-1} and the sharper peaks at 1630 cm^{-1} is shown in all cotton dyed with natural indigo, indicating the presence of more amine and hydroxyl groups as a contribution of the natural indigo compound. The peak of cotton-indigo coated with chitosan shifted to higher wavenumber (3414 cm^{-1}) compared with that of cotton-indigo without chitosan (3404 cm^{-1}). This indicates the chitosan attached to cotton surface, since the peak of chitosan alone shows at higher wavenumber (3448.5 cm^{-1}).

Figure 8a shows the SEM micrograph and EDS spectrum of cotton-indigo coated with ZnONPs and washed for 5 minutes with deionized water under vigorous stirring. Figure 8b shows the SEM micrograph and EDS spectrum of cotton-indigo treated with nanochitosan and coated with ZnONPs. The inset shows the wt.% of the elements in the cotton samples.

Carbon (C) and oxygen (O) are from cellulose and chitosan structures. EDS analysis shows that a coating of cotton-indigo with 0.14% wt. could increase the nitrogen content (N) from 0.3% to 0.6% wt. A nitrogen compound detected in the untreated cotton-indigo sample was probably due to nitrogen from the indigo structure (Figure 1b). The addition of nitrogen in cotton-indigo treated with nanochitosan was from amine groups in the chitosan structure (Figure 9). This increase in N content demonstrated the successful preparation of cotton-nanochitosan using the dip-cure method. Similar findings were documented by Preethi et al. who have reported the presence of N in a nanocomposite of chitosan/ZnO [15].

The presence of Zn indicates the ZnONPs attached in cotton. ZnONPs are well dispersed on both cotton surfaces. The deposition of ZnONPs in the cotton treated with nanochitosan was significantly higher compared to untreated cotton. Based on the EDS analysis, the amount of Zn was only 0.3% wt. in untreated cotton and 4.5% wt. in cotton treated with nanochitosan. This result shows that applying a nanochitosan coating before the ZnONPs coating can increase the adsorption and durability of ZnONPs in cotton substrate. To confirm the EDS result, an analysis of the Zn component using XRF was conducted. From the XRF analysis (Table 1), the detected Zn content was 4-fold higher in cotton treated with nanochitosan than in untreated cotton.

The increasing amount of adsorbed Zn could be due to the rich hydroxyl groups in the nanochitosan structure. The addition of OH groups from chitosan provides more active sites to attract ZnONPs via hydrogen bonding. The rougher surface of cotton treated with nanochitosan could trap ZnONPs and hence, ZnONPs would not easily fall during washing. Chitosan in nano size also promoted higher adsorption of ZnONPs on the cotton surface due to its large surface area. Figure 9 shows the proposed interaction of cellulose-indigo-chitosan-ZnO.

The effect of ZnONP coating on the light fastness of cotton dyed with natural indigo was investigated by a photofading study using UV-A irradiation. The color difference (dE), which is a comparison of color coordinates of samples and the plain cotton (standard), was measured using CIELAB standard and was calculated according to equation 1. The color coordinates, L*, a*, and b* of the samples were illustrated in Table 2. The color change before and after irradiation is calculated using equation 3.

After irradiation, the brightness (L) in all samples was increased and the color became greener and yellower. The change in color (ΔE) was lower in the treated samples than in the untreated sample. Cotton-indigo treated with nanochitosan and ZnONPs has the smallest color changes, indicating that chitosan works well as a binder of ZnONPs and ZnONPs work well as an anti-UV finish. Light impinging on the surface of the material can be absorbed, reflected, scattered and transmitted. ZnONPs has the ability to absorb UV light and the absorption peak is approximately 380 nm [25]. The energy absorbed could promote electron excitation on the ZnONP surface. The excited electron jumps from the valence band to the conduction band and creates a hole with a positive charge. Approximately 90% of the hole-electron pairs could recombine followed by a release of energy [26]. The photo-generated holes and electrons can also induce oxidation-reduction reaction with water and oxygen on the ZnONP surface, forming hydroxyl radicals and reactive oxygen species (ROS) [27]. These radicals and ROS could react with organic material causing degradation. However, based on the result in Table 2, the anti-UV effect of ZnONPs was more dominant than its photocatalytic action, as indicated by the lower color change in the cotton coated with ZnONPs. Applying nanochitosan coating before ZnONP coating could increase the adsorption and durability of ZnONPs. The combination of nanochitosan and ZnONP coating on cotton dyed with natural indigo has the potential for use in the production of durable multifunctional textile.

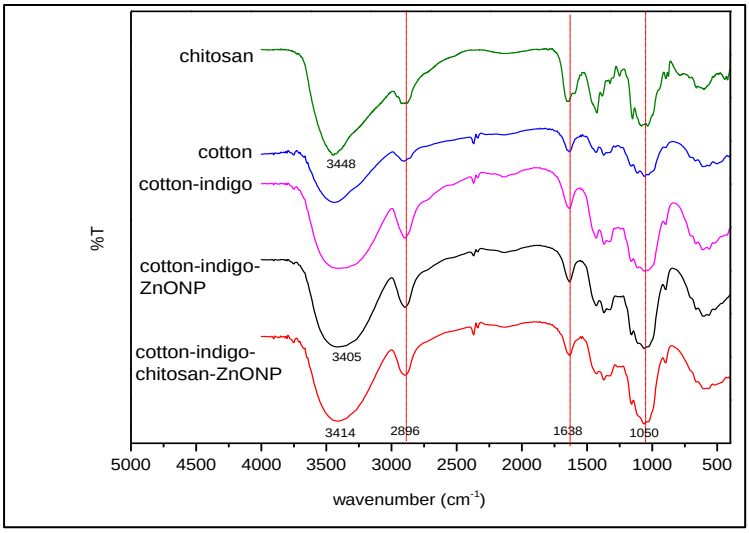
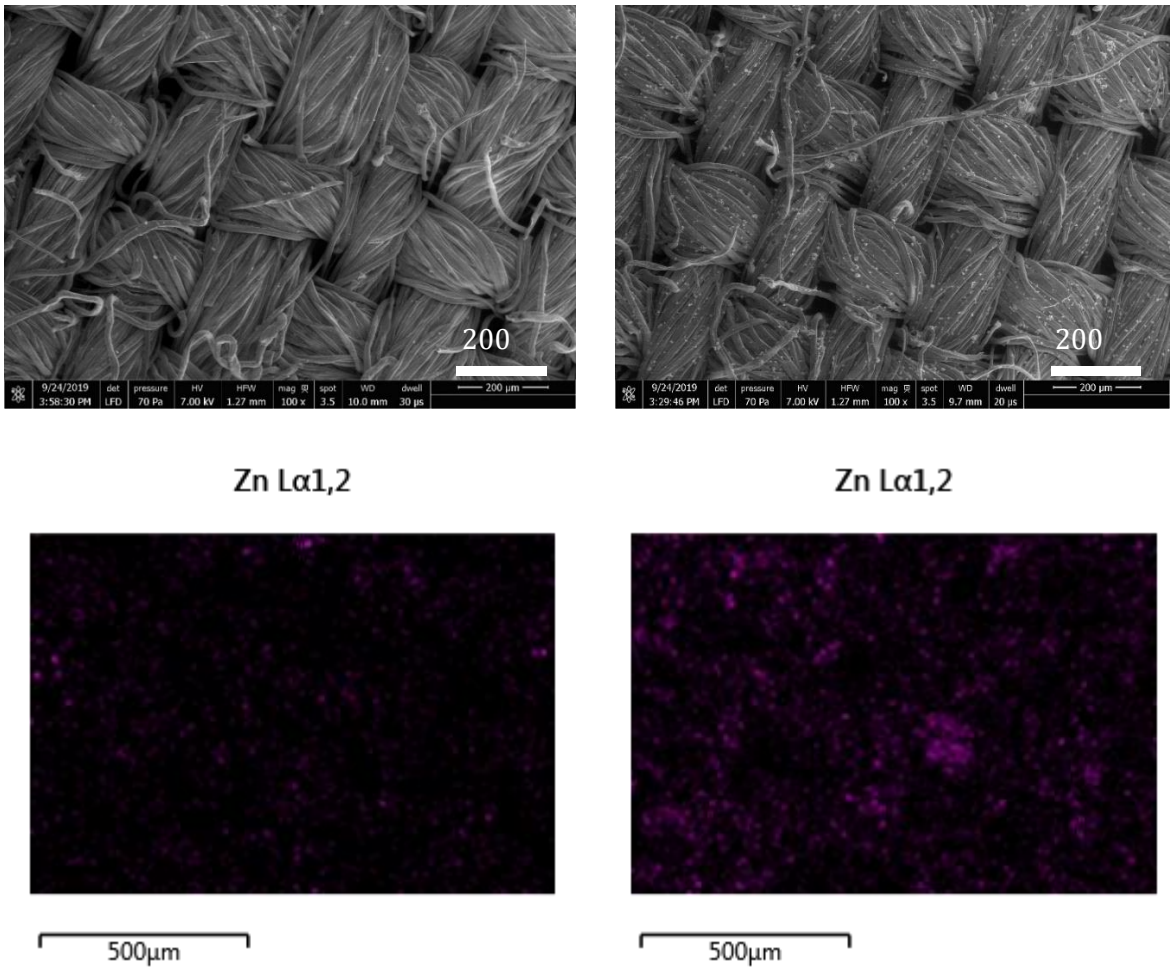
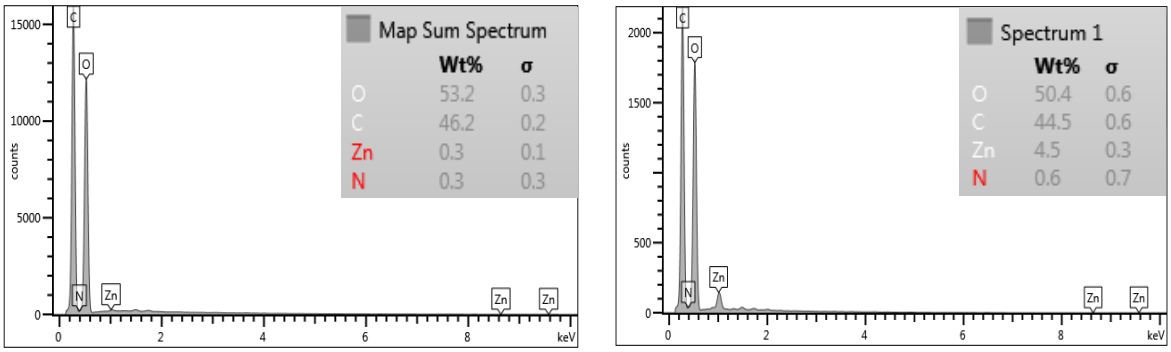


Figure 7. FTIR spectra of chitosan and cotton samples





a b

Figure 8. SEM-EDS of (a) Cotton-indigo-ZnONPs and (b) cotton-indigo-chitosan-ZnONPs after washing treatment

Table 1. Zinc content in the cotton sample

Treatment	N % EDS	Zn % EDS	Zn % XRF
Cotton-Indigo	-	-	0.001
Cotton-Indigo-ZnONPs	0.3	0.3	0.177
Cotton-Indigo-Nanochitosan-ZnONPs	0.6	4.5	0.723

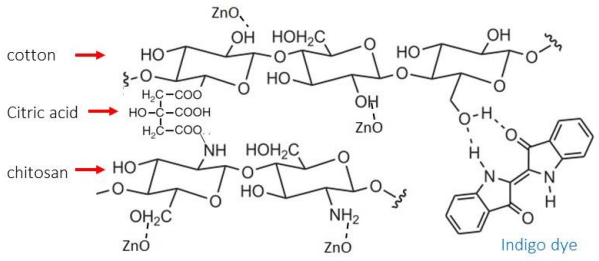


Figure 9. Schematic of interaction of cellulose-indigo-chitosan-ZnO, adapted from Tangkawanit [17]

Table 2. Color difference of cotton sample before and after UV-A irradiation

Treatment	Before Irradiation				After 144 h UV-A Irradiation				ΔE
	L	a*	b*	dE	L	a*	b*	dE	
Cotton (standard)	101.33	−0.07	0.03	0	101.31	−0.29	0.09	0	0
Cotton-Indigo	48.35	−5.22	−16.23	55.58	58.03	−6.73	−23.81	49.77	5.81
Cotton-Indigo-ZnONPs	44.46	−2.59	−21.73	60.94	48.93	−2.79	−19.8	56.09	4.85
Cotton-Indigo-Nanochitosan-ZnONPs	34.38	−1.47	−18.41	69.46	38.43	−3.1	−18.94	65.77	3.69

Conclusion

We have demonstrated a simple production of ZnONPs *via* the precipitation method and nanochitosan *via* ionic gelation. The synthesis of zinc oxide from zinc nitrate and sodium hydroxide results in the formation of hexagonal wurtzite nanoparticles with a size of ±20 nm. The characterization using a particle size analyzer confirms that ZnONPs and the chitosan dispersion were of nanometer size, which makes them suitable for textile functionalization. The application of nanochitosan coating before ZnONP coating on cotton increased the amount of absorbed ZnONPs up to fourfold and thus enhanced more light fastness properties compared with untreated cotton. The dip-cure method applied in this study could be useful for the preparation of multifunctional textile.

Acknowledgment

The authors gratefully acknowledge the Indonesia Endowment Fund for Education (Lembaga Pengelola Dana Pendidikan Kementerian Keuangan Republik Indonesia) for providing financial support *via* Beasiswa Unggulan Dosen Indonesia-Dalam Negeri.

References

1. Widiawati, D. (2009). The revival of the usage of natural fibers and natural dyes in Indonesian textile. *ITB Journal of Visual Art and Design*, 3(2): 115-128.
2. Papanastasiou, M., Allen, N. S., McMahon, A., Naegel, L. C. A., Edge, M. and Protopappas, S. (2012). Analysis of indigo-type compounds in natural dyes by negative ion atmospheric pressure photoionization mass spectrometry. *Dyes and Pigments*, 92(3): 1192-1198.
3. Padfield, T. and Landi, S. (1966). The light fastness of the natural dyes, *Studies in Conservation*, 11: 181-196.
4. Saravanan, D. (2007). UV protection textile materials. *Autex Research Journal*, 7(1): 11-18.
5. Fajzulin, I., Zhu, X. and Möller, M. (2015). Nanoparticulate inorganic UV absorbers: A review. *Journal of Coatings Technology and Research*, 12(4): 617-632.
6. Schneider, S. L. and Lim, H. W. (2019). A review of inorganic UV filters zinc oxide and titanium dioxide. *Photodermatology, Photoimmunology and Photomedicine*, 35(6): 442-446.
7. Becheri, A., Dürr, M., Lo Nostro, P. and Baglioni, P. (2008). Synthesis and characterization of zinc oxide nanoparticles: Application to textiles as UV-absorbers. *Journal of Nanoparticle Research*, 10(4): 679-689.
8. Pulit-Prociak, J., Chwastowski, J., Kucharski, A. and Banach, M. (2016). functionalization of textiles with silver and zinc oxide nanoparticles. *Applied Surface Science*, 385: 543-553.
9. Kathirvelu, S., D'Souza, L. and Dhurai, B. (2009). UV protection finishing of textiles using ZnO nanoparticles. *Indian Journal of Fibre and Textile Research*, 34(3): 267-273.
10. Ibrahim, N. A., Eid, B. M., El-Aziz, E. A., Elmaaty, T. M. A. and Ramadan, S. M. (2017). Loading of chitosan–nano metal oxide hybrids onto cotton/polyester fabrics to impart permanent and effective multifunctions. *International Journal of Biological Macromolecules*, 105: 769-776.
11. El-tahlawy, K. F., El-bendary, M. A., Elhendawy, A. G. and Hudson, S. M. (2005). The antimicrobial activity of cotton fabrics treated with different crosslinking agents and chitosan. *Carbohydrate Polymers*, 60: 421-430.
12. Alonso, D., Gimeno, M., Olayo, R., Vázquez-Torres, H., Sepúlveda-Sánchez, J. D. and Shirai, K. (2009). Cross-linking chitosan into UV-irradiated cellulose fibers for the preparation of antimicrobial-finished textiles. *Carbohydrate Polymers*, 77(3): 536-543.
13. Farouk, A., Moussa, S., Ulbricht, M. and Textor, T. (2012). ZnO nanoparticles-chitosan composite as antibacterial finish for textiles. *International Journal of Carbohydrate Chemistry*, 2012 (693629): 1-8.
14. Raza, Z. A. and Anwar, F. (2016). Impregnation of zinc oxide mediated chitosan nano-composites on polyester fabric for performance characteristics. *Fibers and Polymers*, 17(9): 1378-1383.

15. Preethi, S., Abarna, K., Nithyasri, M., Kishore, P., Deepika, K., Ranjithkumar, R., Bhuvaneshwari, V. and Bharathi, D. (2020). Synthesis and characterization of chitosan/zinc oxide nanocomposite for antibacterial activity onto cotton fabrics and dye degradation applications. *International Journal of Biological Macromolecules,* 164: 2779-2787.
16. Abd Elhady, M.M. (2012). Preparation and characterization of chitosan/zinc oxide nanoparticles for imparting antimicrobial and UV protection to cotton fabric. *International Journal of Carbohydrate Chemistry*, 2012 (840591): 1-6.
17. Tangkawanit, S. (2020). Color fastness and UV protection improvement of indigo dyed cotton fabrics coated with nano chitosan and zinc oxide. *The Journal of King Mongkut's University of Technology North Bangkok*, 30(3): 1-13.
18. Talam, S., Karumuri, S. R. and Gunnam, N. (2012). Synthesis, characterization, and spectroscopic properties of ZnO nanoparticles, *ISRN Nanotechnology*, 2012 (372505): 1-6.
19. Liu, Z. R, Hou, J., Duan, L. M. and Xu, L. (2011). Study on the synthesis and properties of nano-ZnO, *Materials Science Forum*, 694: 324-327.
20. Jo, M., Chung, H., Kim, H., Bae, S., Go, M., Yu, J. and Choi, S. (2016). Effects of zinc oxide nanoparticle dispersants on cytotoxicity and cellular uptake. *Molecular and Cellular Toxicology*, 12(3): 281-288.
21. Tso, C. P, Zhung, C. M, Shih, Y.H, Tseng, Y., Wu, S.C. and Doong, R. A. (2010). Stability of metal oxide nanoparticles in aqueous solutions. *Water Science and Technology*, 61(1): 127-133.
22. Rosyada, A., Sunarharum, W. B. and Waziiroh, A. (2019). Characterization of chitosan nanoparticles as an edible coating material. *IOP Conference Series: Earth and Environmental Science*, 230 (012043): 1-5.
23. Turemen, M., Demir, A. and Gokce, Y. (2021). The synthesis and application of chitosan coated ZnO nanorods for multifunctional cotton fabrics. *Materials Chemistry and Physics,* 268(124736): 1-6.
24. El.Shafei, A. and Abou-Okeil, A. (2011). ZnO/carboxymethyl chitosan bionano-composite to impart antibacterial and UV protection for cotton fabric. *Carbohydrate Polymers,* 83: 920-925.
25. Ahmed, M. T., Sarhan, A. and Hassan, A. (2016). Preparation and characterization of ZnO nanoparticles by simple precipitation method. *International Journal of Science, Engineering Technology*, 4(3): 507-512.
26. Wang, C., Lv, J., Ren, Y., Zhou, Q., Chen, J., Zhi, T., Lu, Z., Gao, D., Ma, Z. and Jin, L. (2016). Cotton fabric with plasma pretreatment and ZnO/carboxymethyl chitosan composite finishing for durable UV resistance and antibacterial property. *Carbohydrate Polymers*, 138: 106-113.
27. Das, A., Sk., N. and Nair, R. G. (2019). Influence of surface morphology on photocatalytic performance of zinc oxide: A review, *Nano-Structures and Nano-Objects*, 19(100353): 1-18.

Malaysian Journal of Analytical Sciences Vol 25 No 6 2021

Articles 16 - 21 are selected papers from the "International Virtual Symposium on Environmental and Green Chemistry for Sustainable Development (EnvChem 2021), 9 June 2021; organized by the School of Chemistry and Environment, Faculty of Applied Sciences, Universiti Teknologi MARA Shah Alam, Selangor, Malaysia."

Guest Editor: Sabiha Hanim Saleh

1. DETERMINATION OF SODIUM HYDROXIDE CONCENTRATION UNDER HETEROGENEOUS CONDITIONS FOR THE PREPARATION OF N-CARBOXYMETHYL CHITOSAN 895
(Penentuan Kepekatan Natrium Hidroksida dalam Keadaan Heterogen bagi Penghasilan N-Karboksimetil Kitosan)
Nurul Adilah Rodzali and Nadhratun Naiim Mobarak

2. HEAVY METAL IN DIFFERENT SIZE FRACTIONS OF HOUSEHOLD DUST COLLECTED FROM RURAL RESIDENTIAL AREA OF SIMPANG RENGGAM, JOHOR 911
(Logam Berat dalam Pelbagai Pecahan Saiz Habuk Rumah dari Kawasan Kediaman Luar Bandar Simpang Renggam, Johor)
Joo Hui Tay, Siti Aqilah Azmi, Mohd Iffat Iqbal Zul Kornain

3. SYNTHESIS AND CHARACTERIZATION OF 4-CHLOROPHENOXYACETIC ACID HERBICIDE INTERCALATED INTO CALCIUM-ALUMINIUM LAYERED DOUBLE HYDROXIDE THROUGH CO-PRECIPITATION METHOD 921
(Sintesis dan Pencirian Herbisid Asid 4-Klorofenoksiasetik Diinterkalatkan dengan Kalsium-Aluminium Hidroksida Dua Lapisan Melalui Kaedah Pemendakan Bersama)
Farah Liyana Bohari, Muhammad Alinsan Kamil Mukamil Hamzah, Sheikh Ahmad Izaddin Sheikh Mohd Ghazali, Nur Nadia Dzulkifli, Is Fatimah, Nurain Adam

4. CONCENTRATION OF HEAVY METALS IN *Perna veridis* COLLECTED FROM STRAITS OF JOHOR, MALAYSIA 930
(Kepekatan Logam Berat di dalam *Perna veridis* yang Dikumpulkan dari Selat Johor, Malaysia)
Tee Lian Sheng, Poong Jun Han, Evonne Tan, Yip Tiam Hing, Muhammad Hasbi Ramli, Zaleha Kassim, Ong Meng Chuan

5. CONJUGATION OF TERNATIN BIOMOLECULE WITH POLYETHYLENE GLYCOL ENHANCED CONJUGATES SOLUBILITY AND STABILITY: SYNTHESIS AND PHYSICOCHEMICAL CHARACTERISATION 940
(Konjugasi diantara Molekul Ternatin dan Polietilena Glikol dengan Penambahbaikan Sifat Keterlarutan dan Kestabilan: Sintesis dan Pencirian Fizikokimia)
Nurul Aina Jamaludin and Noor Faizah Che Harun

6. PURIFICATION OF XANTHORRHIZOL AND SCREENING OF SELECTED MICROBES FOR ITS BIOTRANSFORMATION 949
(Penulenan Xantorizol dan Pengesanan Mikrob Terpilih untuk Biotransformasinya)
Nurul Iman Aminudin, Nadia Farhana Yahya, Zaima Azira Zainal Abidin, Deny Susanti, Muhammad Taher

7. ISOLATION OF PTEROPODIC ACID FROM MALAYSIAN *Uncaria lanosa* VAR. *ferrea* BY USING LIQUID CHROMATOGRAPHY MASS SPECTROMETRY DEREPLICATION APPROACH 959
(Pemencilan Asid Pteropodik daripada *Uncaria lanosa* var. *ferrea* Malaysia dengan Pendekatan Direplikasi Kromatografi Cecair Spektrometri Jisim)
Nursyaza Husna Shaharuddin, Rohaya Ahmad, Fatimah Salim

8. ADSORPTION OF ACID ORANGE 7 BY CETYLTRIMETHYL AMMONIUM BROMIDE MODIFIED OIL PALM LEAF POWDER 966
(Penjerapan Asid Oren 7 oleh Setiltrimetil Ammonium Bromida Ubahsuai Serbuk Daun Kelapa Sawit)
Nik Ahmad Nizam Nik Malek, Nurul Ain Sallehhuddin, Auni Afiqah Kamaru

9. POTENTIAL OF *Epipremnum aureum* IN REDUCTION OF CHEMICAL OXYGEN DEMAND IN WASTEWATER 977
(Potensi *Epipremnum aureum* dalam Pengurangan Permintaan Oksigen Kimia dalam Air Sisa Buangan)
Lee Shi Qing, Rozidaini Mohd Ghazi, Marinah Muhammad

10. CATALYTIC ACTIVITY STUDY OF SYNTHESISED POLYSTYRENE-SUPPORTED PALLADIUM(II)-HYDRAZONE (CH_3) AS CATALYST IN HECK REACTION 987
(Kajian Aktiviti Pemangkinan Paladium(II)-Hidrazon (CH_3) dengan Sokongan Polistirena Sebagai Pemangkin dalam Tindak Balas Heck)
Najwa Asilah M. Shamsuddin, Norul Azilah Abdul Rahman, Kumuthini Chandrasekaram, Yatimah Alias, Nur Rahimah Said

11. ANALYSIS OF SUGAR CONTENT IN SELECTED CHILDREN'S HEALTH SUPPLEMENTS IN MALAYSIA 998
(Analisa Kandungan Gula dalam Suplemen Kesihatan Kanak-Kanak Terpilih yang Biasa didapati di Malaysia)
Siok-Yee Chan, Mazidatulakmam Miskam, Shangeetha Ganesan

12. OPTIMIZATION OF DIFFERENT PARAMETERS IN THE SYNTHESIS OF BISPHENOL A IMPRINTED POLYMER VIA PRECIPITATION POLYMERIZATION FOR BISPHENOL A ADSORPTION 1007
(Pengoptimuman Parameter yang Berbeza dalam Sintesis Polimer Tercetak Bisfenol A Melalui Pempolimeran Pemendakan bagi Penjerapan Bisfenol A)
Tan Nee Nee, Noorhidayah Ishak, Azalina Mohamed Nasir, Nur Zatul 'Iffah Zakaria, Nor Munirah Rohaizad

13. CYTOTOXICITY EFFECT OF NATURAL AND SYNTHETIC GIRINIMBINES AND THEIR DERIVATIVES AGAINST HUMAN LUNG CANCER CELL LINES A549 1020
(Kesan Sitotoksik Girinimbin Semula Jadi dan Sintetik dan Terbitannya Terhadap Sel Garis Kanser Paru-Paru Manusia A549)
Fatin Nurul Atiqah Osman, Siti Mariam Mohd Nor, Mohd Azlan Nafiah

14. IDENTIFICATION AND QUANTIFICATION OF LYCOPENE AND β-CAROTENE IN WATERMELON JUICE USING HIGH-PERFORMANCE LIQUID CHROMATOGRAPHY 1032
(Pengenalan dan Pengkuantitian Likopena dan β-Karotena di dalam Jus Tembikai Menggunakan Kromatografi Cecair Berprestasi Tinggi)
Nur Shafinaz Mohamad Salin, Fatimah Salim, Hairil Rashmizal Abdul Razak, Wan Mazlina Md Saad

15. OPTIMIZATION AND DETERMINATION OF INORGANIC ARSENIC BY LIQUID EXTRACTION AND INDUCTIVELY COUPLED PLASMA MASS SPECTROMETRY IN FOOD MATRIX 1042
(Pengoptimuman dan Penentuan Arsenik Tak Organik Melalui Pengekstrakan Cecair dan Spektrometri Jisim-Plasma Gadingan Aruhan dalam Sampel Makanan)
Le Nhon-Duc, Nguyen Thanh-Nho, Le-Thi Anh-Dao, Nguyen Cong-Hau, Nguyen Van-Dong

16. BIO-COAL OPTIMIZATION STUDY OF DRY LEAVES VIA LOW-TEMPERATURE MECHANISM 1056
(Kajian Pengoptimuman Terhadap Bio-Arang Batu Mengunakan Daun Kering Melalui Mekanisme Suhu Rendah)
Siti Solehah Misni, Nor Hazelah Kasmuri, Fuzieah Subari, Zalizawati Abdullah, Suhaiza Hanim Hanipah

17. CHALLENGES OF ALUM RECOVERY FROM DRINKING WATER TREATMENT SLUDGE USING ELECTROLYSIS METHOD 1068
(Cabaran untuk Pemulihan Alum daripada Enapcemar Rawatan Air Minuman Melalui Kaedah Elektrolisis)
Rizkiy Amaliyah Barakwan and Yulinah Trihadiningrum

18. MODELLING AND OPTIMIZATION OF MICROWAVE ASSISTED EXTRACTION OF TOTAL PHENOLICS IN KAKAWATE (*Gliricidia sepium*) AS PESTICIDE AGAINST BLACK BEAN APHIDS (*Aphis fabae*) 1081
(Pemodelan dan Pengoptimuman Pengekstrakan Berbantu Gelombang Mikro bagi Jumlah Fenolik dalam Kakawate (*Gliricidia sepium*) sebagai Racun Makhluk Perosak Afid Kacang Hitam (*Aphis fabae*))
Rhonalyn V. Maulion, John Marco I. Matira, Kristine May M. Fanoga, Maricar C. Marasigan, Melissa Marie C. Dimaculangan

19. OPTIMISATION OF MICROWAVE-ASSISTED WATER EXTRACTION OF PINEAPPLE PEEL HEMICELLULOSE USING RESPONSE SURFACE METHODOLOGY 1095
(Pengoptimuman Pengekstrakan Air Berbantu Gelombang Mikro Bagi Hemiselulosa Kulit Nanas Menggunakan Kaedah Gerak Balas Permukaan)
Nur Aza Atiqah Mad Zahir, Noraini Hamzah, Hamizah Mohd Zaki, Shariff Ibrahim, Sabiha Hanim Saleh

20. ESTIMATION OF CARBON DIOXIDE EMISSION IN THE TRANSPORTATION SECTOR ON PRIMARY ARTERIAL ROADS IN WONOKROMO DISTRICT, SURABAYA BEFORE AND AFTER COVID-19 1107
(Anggaran Pelepasan Gas Karbon Dioksida Bagi Sektor Pengangkutan di Jalan Utama Daerah Wonokromo Kota Surabaya Sebelum dan Selepas Covid-19)
Fatimah Zahra, Agus Supriyanto, Nita Citrasari

21. SYNTHESIS OF HYBRID CARBON QUANTUM DOTS FROM *Tamarindus indica* AND *Mangifera indica* LEAVES FOR THE DETECTION OF MERCURY (Hg^{2+}) ION IN PURIFIED WATER AND SIMULATED SEAWATER 1122
(Sintesis Titik Kuantum Karbon Hibrid dari Daun *Tamarindus indica* dan *Mangifera indica* bagi Pengesanan Ion Merkuri (Hg^{2+}) dalam Sampel Air Tulen dan Simulasi Air Laut)
Rejie C. Magnaye, Riszel B. De Castro, Kenneth B. Gomez, Rex Gregor M. Laylo, Aljon Joseph G. Maderazo

Malaysian Journal of Analytical Sciences (MJAS)
Published by Malaysian Analytical Sciences Society

DETERMINATION OF SODIUM HYDROXIDE CONCENTRATION UNDER HETEROGENEOUS CONDITIONS FOR THE PREPARATION OF N-CARBOXYMETHYL CHITOSAN

(Penentuan Kepekatan Natrium Hidroksida dalam Keadaan Heterogen bagi Penghasilan N-Karboksimetil Kitosan)

Nurul Adilah Rodzali and Nadhratun Naiim Mobarak*

Department of Chemical Sciences, Faculty of Science and Technology
Universiti Kebangsaan Malaysia, 43600 UKM Bangi, Selangor, Malaysia

**Corresponding author: nadhratunnaiim@ukm.edu.my*

Received: 3 September 2021; Accepted: 27 October 2021; Published: 27 December 2021

Abstract

N-carboxymethyl chitosan (N-CMC) is one of the promising chitosan derivatives which has been used to improve the limitation of chitosan and can be synthesized *via* direct alkylation in the presence of base. In this work, the effect of sodium hydroxide concentration under heterogeneous conditions has been investigated to obtained N-CMC. The concentration of sodium hydroxide (NaOH) was varied from 1.5 M to 7.5 M. This research showed that the substitution site of chitosan is affected by the concentration of NaOH. The results revealed that N-CMC was successfully synthesized at higher NaOH concentration, 6.0 M, and 7.5 M under heterogeneous conditions. The presence of peak at 1321 cm^{-1} and 3.2 ppm from Fourier transform infrared (FTIR) and ^{1}H nuclear magnetic resonance (NMR) spectroscopy, respectively, proving the carboxymethyl group substitution occurred at amino (NH_2) site. X-ray diffraction (XRD) analysis showed insignificant differences in degree of crystallinity of N-CMC at both NaOH concentrations. However, Thermogravimetry analysis (TGA) and differential scanning calorimetry (DSC) revealed that obtained N-CMC possessed distinct thermal properties as the glass transition temperature of 6.0 M was lower than 7.5 M NaOH. Therefore, the selection of NaOH concentration in N-CMC production must be determined according to the intended functional application.

Keywords: N-carboxymethyl chitosan, N-substitution, heterogeneous conditions, NaOH concentration

Abstrak

N-karboksimetil kitosan (N-CMC) merupakan salah satu terbitan kitosan yang telah digunakan bagi menambahbaik kekurangan kitosan dan boleh disintesis melalui pengakilan secara terus dengan kehadiran bes. Dalam kajian ini, kesan kepekatan natrium hidroksida (NaOH) dalam keadaan heterogen telah dikaji untuk menghasilkan N-CMC. Kepekatan natrium hidroksida (NaOH) dibezakan daripada 1.5 M hingga 7.5 M. Kajian ini menunjukkan tapak penggantian pada kitosan dipengaruhi oleh kepekatan NaOH. Hasil kajian menunjukkan N-CMC telah berjaya disintesis pada kepekatan yang lebih tinggi, 6.0 M and 7.5 M dalam keadaan heterogen. Kehadiran puncak pada 1321 cm^{-1} dan 3.2 ppm masing-masing pada spektroskopi inframerah transformasi Fourier (FTIR) dan resonans magnet nukleus ^{1}H (NMR), membuktikan penukargantian kumpulan karboksimetil berlaku pada tapak amina (NH_2). Analisis pembelauan sinar-X (XRD) menunjukkan perubahan yang tidak ketara bagi darjah kehabluran N-CMC pada kedua-dua kepekatan NaOH. Walau bagaimanapun, analisis termogravimetri (TGA) dan kalorimetri pengimbasan

pembezaan (DSC) menunjukkan N-CMC yang dihasilkan mempunyai sifat terma yang berbeza dimana suhu peralihan kaca bagi 6.0 M lebih rendah berbanding 7.5 M NaOH. Oleh itu, pemilihan kepekatan NaOH dalam penghasilan N-CMC ditentukan berdasarkan aplikasi yang akan digunakan.

Kata kunci: N-karboksimetil kitosan, penggantian-N, keadaan heterogen, kepekatan NaOH

Introduction

Carboxymethyl chitosan (CMC) is the chitosan derivative which has attracted much attention as it enhances the solubility of chitosan. CMC can be obtained by chemically modified the chitosan structure, making the CMC soluble in both acidic and alkaline solution without affecting its cationic characteristics [1]. The reactive sites for the carboxymethylation of chitosan are the amino and hydroxyl groups present in chitosan chains. The choice of an appropriate reaction conditions and reagents can influence the substitution sites of carboxymethyl group [2]. The most widely used method for the chemical modification of chitosan is N-substitution, in which the amino group ($-NH_2$) in chitosan structure is the functional group which reacts [3]. N-carboxymethyl chitosan (N-CMC) is a CMC generated by reaction of free amino group of chitosan with monochloroacetic acid reagent. N-CMC is a material that can be used in food and cosmetic products due to its unique physical and biocompatibility properties. Aside from being soluble in wider pH, it also has high viscosity and low toxicity [4]. In addition to N-CMC, other N-substitutions such as the potential quaternary chitosan derivatives also gives rise to an important derivative of chitosan and its bioactivity such as antimicrobial, anticoagulant, antioxidant and mucoadhesive properties have been extensively reported [5].

The preparation of N-substitution of chitosan, including N-CMC through direct alkylation, was mostly conducted under homogeneous conditions [6]. An et al. [7] prepared the N-CMC by swollen the chitosan in water and adding monochloroacetic acid for carboxymethyl substitution. The mixture was then strongly stirred until completely dissolved to produce a homogeneous solution. Subsequently, the pH was adjusted to 8 by adding sodium bicarbonate, $NaHCO_3$, solution. The mixture was then heated to 90 °C, as shown in Figure 1a. The same method also being used by Skorik et al. [8] to synthesize N-carboxyethyl chitosan under homogeneous conditions. In addition to the homogeneous method, selective substitution to produce N-derivatives of chitosan can also be carried out by protection of OH groups in C3 and C6 [9]. Sahariah et al. developed N,N,N-trimethyl chitosan by protecting the -OH groups in the chitosan structure using di-*tert*-butyldimethylsilyl (di-TBDMS), which is easily removed under strongly basic or moderate acidic conditions without affecting the functional group, as depicted in Figure 1b [9]. However, the reaction times for homogeneous condition were longer than 24 hours and the protection of OH group procedure implies multiple reaction steps [5]. Nevertheless, the preparation of N-substitution, especially N-CMC, using the heterogeneous method is scarcely reported, since homogeneous conditions and reductive alkylation method are preferred.

Our previous research successfully prepared N-CMC through heterogeneous conditions at pH 14 with shorter reaction time which is 4 hours [10]. Based on the literature, the pH of alkaline solution needs to be strictly controlled to succeed in producing N-CMC. However, particularly at an industrial scale, such as in the production of carboxymethyl cellulose, the use of concentration parameters is more feasible [11, 12]. Based on our current reading, alkali concentration to produce N-CMC has not yet been described. Therefore, this research was conducted to investigate the effects of NaOH concentration under heterogeneous conditions in obtaining N-CMC.

Materials and Methods

Materials

Chitosan was commercially acquired from Chito-Chem Sdn. Bhd., Malaysia. Degree of deacetylation and molecular weight of chitosan were 89.25% and 6.12×10^7 g/mole, respectively. The solvents used, such as isopropanol (99.7%) and ethanol (95%), were supplied

by Systerm, Malaysia. Besides, the monochloroacetic acid (99%) from Sigma-Aldrich, Co. St Louis, USA and sodium hydroxide pellets (97%) were obtained from Merck, German. All materials were used without further purification.

Preparation of carboxymethyl chitosan

CMC was prepared according to the heterogeneous method proposed by Chen and Park [13] with minor modifications. Chitosan (10 g) was dispersed in isopropanol (50 mL) and NaOH solutions were prepared in concentrations of 1.5 M, 3.0 M, 4.5 M, 6.0 M, and 7.5 M. The NaOH solution was added dropwise into the flask to swell and provide the alkaline condition at 50 °C for one hour. The monochloroacetic acid (15 g) was dissolved in isopropanol (20 mL) and added into the mixture dropwise for 30 minutes and reacted for 4 hours at the same temperature. The reaction was terminated with 90% ethanol. The precipitate was filtered, rinsed with 90% ethanol and vacuum dried at room temperature. The product was kept in a desiccator for continuous drying prior to characterization.

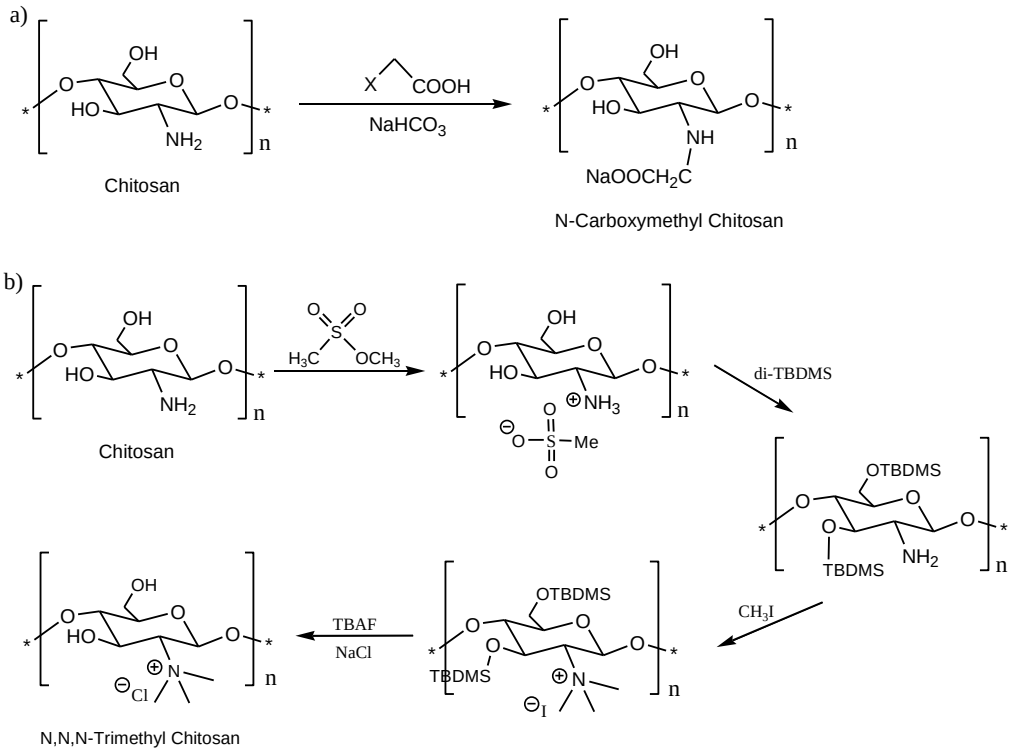


Figure 1. Synthesis of chitosan derivatives by a) homogeneous method [6] and b) protection of OH groups procedure [8]

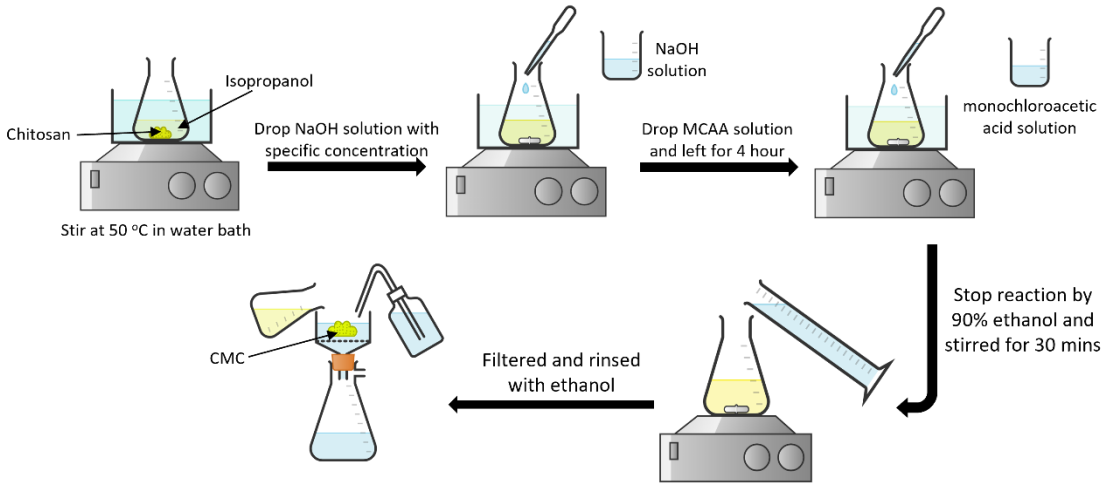


Figure 2. Schematic diagram of synthesis of CMC

Fourier transform infrared spectroscopy

Infrared spectra were recorded by using Agilent Cary 630 Technologies with attenuated total reflectance (ATR) techniques. The range of analysis was 4000-650 cm^{-1} with a scanning resolution of 2 cm^{-1}. Analysis was conducted to observe the changes in the functional groups of the chitosan derivatives.

^{1}H NMR spectroscopy

NMR analysis was performed to determine the substitution site of carboxymethyl chitosan by using Bruker AVANCE III HD 400 MHz. Chitosan and all CMC were dissolved in the solvent mixture of 1% of CD_3COOD/D_2O at room temperature.

Degree of substitution

The degree of substitution (DS) values for all synthesized CMC were calculated by acid base titration method from Elomaa et al. [14] and Pushpamalar et al. [15] with some modification. Firstly, the final product, Na-salt of CMC needed to undergo acidic treatment to change into H-form of CMC. The Na-salt CMC was suspended in 80% ethanol and 37% hydrochloric acid was added and stirred for 30 min. The precipitate (H-CMC) was filtered and rinsed in 70–90% ethanol. The products were vacuum dried and stored in a desiccator for 2 to 3 days.

The DS values of CMC were determined using the standard ASTM D1439 method [16]. The dried H-form of CMC were dispersed in the distilled water in flask. Subsequently, 0.3 M of NaOH solution was added into the suspension and stirred at 50 °C for 15 min and the flask must be corked to prevent evaporation from the reactions occurred. Three drops of phenolphthalein were added into the mixture as an indicator to retain the pink colour. Finally, the mixture was titrated with 0.3 M HCl solution until the indicator became colourless. A blank test was also carried out using the same procedure as a reference.

The percentage of carboxymethyl groups (%CM) and DS were calculated using Equations (1) and (2), respectively.

$$\%CM = \frac{[(V_o - V_n)M \times 0.059 \times 100]}{m} \quad (1)$$

$$DS = \frac{162 \times \%CM}{[5900 - (58 \times \%CM)]} \quad (2)$$

where V_o and V_n are the volume of HCl used for blank test (mL) and sample titration (mL), respectively.

Meanwhile, *M* is the molar concentration of HCl (M), *m* is the amount of sample used (g), 162 is the molar mass of the anhydrous glucose unit, and 58 is the molar mass of a CM group (–CH_2COOH).

The differences between means were analysed for statistical significance using Student's t-test. A value of $p < 0.05$ was considered significant [17].

Thermogravimetry analysis

The thermal stability of the samples was determined using TGA measurements carried out with TG 209 F3 NETZSCH Tarsus equipment. The amount of sample used for each measurement was approximately 2.0 – 3.5 mg in an aluminium pan. All samples were run under nitrogen atmosphere and heating from 25 ℃ to 800 ℃ at a heating rate of 10 ℃/min.

Differential scanning calorimetry

This analysis was carried out using DSC 3 Mettler Toledo with specifications equipment. The amount of samples approximately 2.0 – 3.5 mg was placed into aluminium pan. The samples underwent two heating cycles. The first heating cycle was from 25 ℃ – 120 ℃ to remove the moisture content in the sample, and the second heating cycle was from 25 ℃ – 450 ℃ to determine the polymer properties. All samples were analysed under continuous flow of nitrogen gas at a heating rate of 10 ℃/min.

X-ray diffraction

The crystallinity of the samples was obtained using Bruker D8 Advance X-ray diffractometer (Cu Kα; α = 1.5418 Å). The relative intensity was recorded in the scattering range, 2Θ = 2° – 80° with scanning rate 10°/min. The degree of crystallinity (%) was determined via Bruker DIFFRAC.EVA software by using Equations (3) and (4).

$$Amorphous\ (\%) = \left[\frac{all\ area - adjusted\ area}{all\ area}\right] \text{x}100 \quad (3)$$

$$Degree\ of\ Crystallinity\ (\%) = 100 - Amorphous\ (\%) \quad (4)$$

Results and Discussion

Characterization by FTIR spectroscopy

The FTIR spectra for chitosan and all CMC that had been synthesized in different NaOH concentrations are depicted in Figure 3. The common characteristics for chitosan could be observed around 3378 cm^{-1} (O-H overlapping with N-H stretch), 2871 cm^{-1} (C-H stretch), 1637 cm^{-1} (C=O stretch of amide group), 1578 cm^{-1} (N-H bending of amino group), 1151 cm^{-1} (asymmetric bridge-O-stretch) and 1071 cm^{-1} (C-O stretch). The positions of these peaks are in line with findings reported by Mobarak et al. [18] and Chen and Park [13]. The introduction of carboxymethyl group into chitosan structure was confirmed by the appearance of new peaks around 2921-2945 cm^{-1} and 1389-1413 cm^{-1}, which represent methylene and carboxylate group, respectively [19]. The absorption peaks at around 1637-1651 cm^{-1}, 1578-1590 cm^{-1}, 1151 cm^{-1} and 1071 cm^{-1} which represents the C=O of amide group, N-H bend, bridge-O-stretch, and C-O stretch group could be observed at all concentrations.

Besides that, there are peaks appeared around 1535 cm^{-1} and 1255 cm^{-1} for CMC at 1.5 M, 3.0 M, and 4.5 M NaOH that attributed to amide II group [13, 20] and C-O-C group, respectively. The presence of C-O-C peak indicated that the carboxymethyl group was substituted at the OH site as supported by Doshi et al. [20]. However, an intense peak around 1316-1321 cm^{-1}, which corresponds to the C-N stretch, was also observed for CMC synthesized using 3.0 M and 4.5 M NaOH. The existence of this peak shows that carboxymethylation also occurred at the NH_2 site for 3.0 M and 4.5 M. On the other hand, only a peak representing C-N stretch at 1323 cm^{-1} was observed for CMC prepared at 6.0 M and 7.5 M NaOH.

Therefore, FTIR spectra revealed that carboxymethyl group is substituted on the active sites of OH, and NH_2 sites in the chitosan structure, depending on NaOH concentration. This suggests that at low concentration, 1.5 M NaOH, the carboxymethyl group substituted at OH position whereas at 3.0 M and 4.5 M NaOH, NH_2 site began to deprotonate, resulting in

carboxymethylation takes place at both sites. However, the carboxymethyl group was fully substituted in the amine groups only at higher concentrations of 6.0 M and 7.0 M NaOH.

Characterization by ^{1}H NMR spectroscopy

The chemical structure of chitosan and all CMC prepared at different NaOH concentrations shown in Figure 4. All proton signals in the structure are labelled with H1, H2, H3, H4, H5, H6, and H7. The ^{1}H-NMR spectra for chitosan and all CMC at various concentrations are shown in Figure 5. The basic proton signals assignment of chitosan was as followed δ (ppm): 2.17 (H7), 3.11 (H2), 3.66-3.84 (H3-H6) and 4.81 (H1). Although, the ^{1}H-NMR spectra of CMC exhibit similar proton signal characteristics to the chitosan, yet new signals can be found in the CMC spectra. The new proton signals, which indicate the carboxymethyl group that substituted in chitosan structure, were denoted as H8a for substitution at the OH position and H8b for carboxymethylation occurred at the NH_2 position.

Based on Figure 4, the resonance signal H8a, which corresponds to carboxymethyl substitution on the OH group, could be observed at 4.21-4.25 ppm, which is consistent with Bukzem et al. [21]. This peak only appeared in CMC at concentrations of 1.5 M, 3.0 M, and 4.5 M NaOH. According to previous reports [20, 22], the signals observed between 4.05-4.55 ppm correspond to hydrogen of carboxymethyl group substituted at C6 and C3 in the chitosan structure. Meanwhile, the signals in the range of 3.25-3.45 ppm indicated the occurrence of carboxymethylation on the NH_2 group [21-26]. This signal was discernible in all CMC except for CMC at 1.5 M NaOH. These results confirmed that O-CMC can be attained at 1.5 M NaOH, while 3.0 M and 4.5 M were identified as N,O-CMC, and N-CMC can be obtained successfully at 6.0 M and 7.5 M NaOH under heterogeneous condition. Furthermore, the pKa value of protonated OH (-2 to -3) is lower than primary amine (6.3 to 6.5) [27]. Thus, the carboxymethyl group more favored to substitute on the OH site than NH_2 site at lower concentrations.

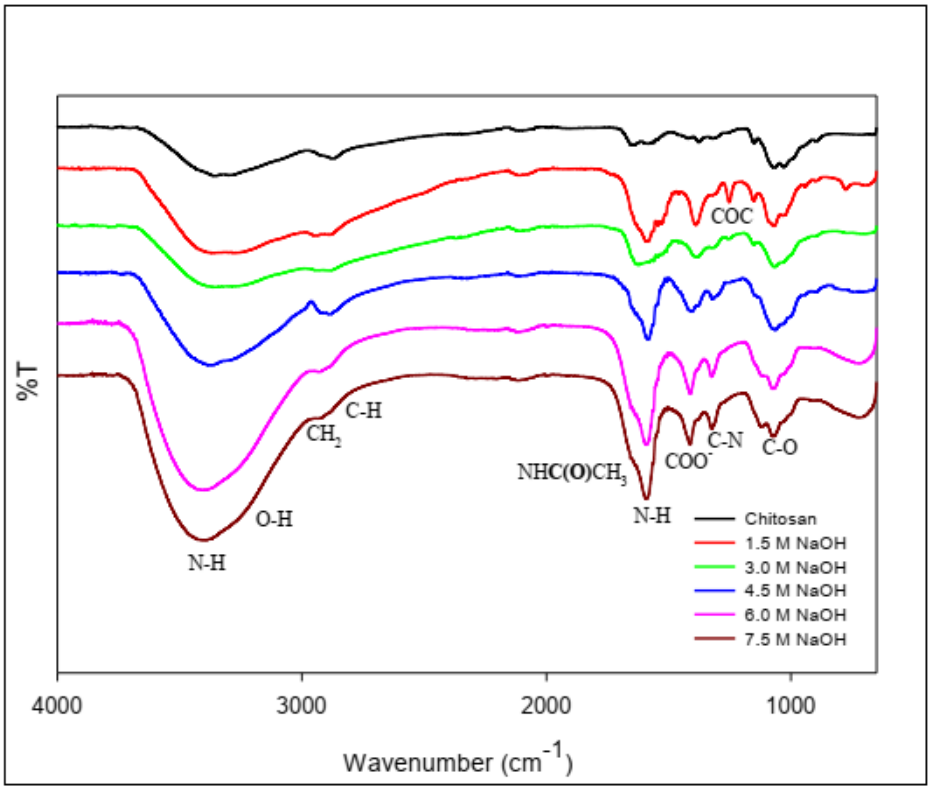


Figure 3. The FTIR spectra of chitosan and all CMC at different concentration of NaOH

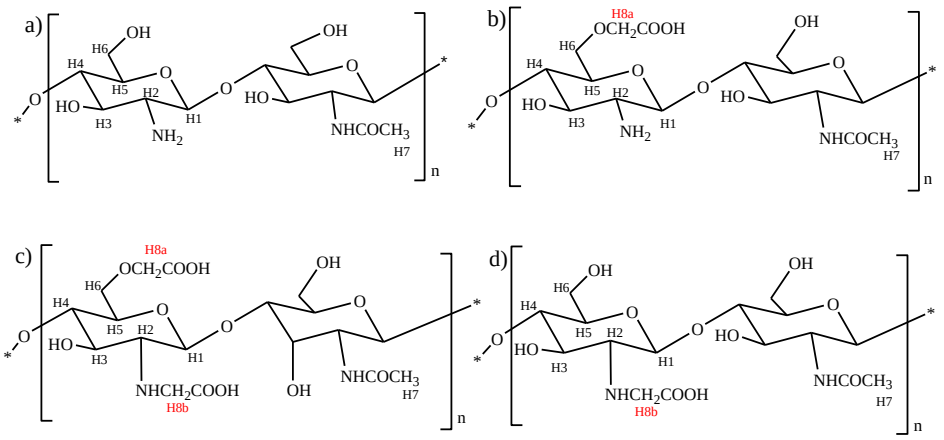


Figure 4. The chemical structure of a) chitosan b) O-CMC, c) N,O-CMC and d) N-CMC

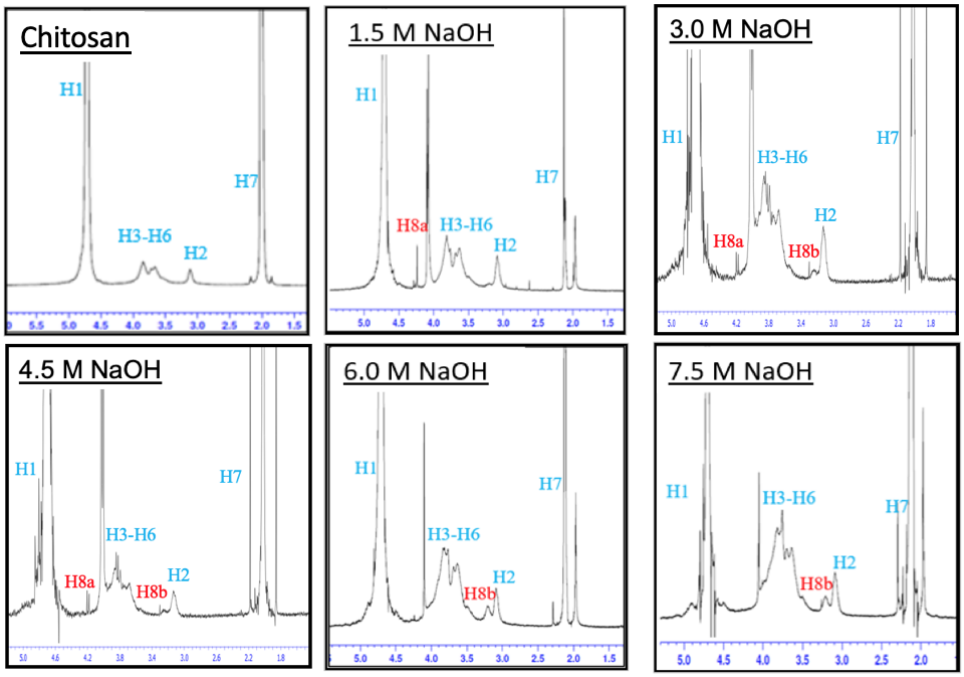


Figure 5. ^{1}H NMR spectra of chitosan and CMC at different NaOH concentrations

Table 1. Chemical structure of CMC at different NaOH concentrations

Conc. of NaOH (M)	Chemical Shifts, δ (ppm)					
	H1	H2	H3-H6	H7	H8a	H8b
1.5	4.70	3.12	3.67-4.10	2.10	4.24	-
3.0	4.70	3.15	3.68-4.05	2.12	4.21	3.25
4.5	4.70	3.15	3.68-4.07	2.11	4.25	3.25
6.0	4.70	3.13	3.68-4.12	2.12	-	3.23
7.5	4.70	3.14	3.68-4.10	2.15	-	3.25

Degree of substitutions

The DS represent the average number of carboxymethyl group substituted into OH and NH_2 sites in the chitosan structure. According to Jaidee et al. [28] and Zong et al. [29], there are three possible active sites for carboxymethyl substitution on chitosan structure which are OH-6, OH-3 and NH_2. The DS values for CMC at various NaOH concentrations have been tabulated in Table 2.

Based on Table 2, all DS values for CMC at different NaOH concentrations are close to 1, indicating that at least one active site on chitosan chain has been successfully substituted [14, 16, 30]. According to FTIR and ^{1}H-NMR spectra, the carboxymethyl group was only substituted at OH site at 1.5 M NaOH, producing O-CMC. The increased in NaOH concentration resulted in increasing DS value, as shown for CMC at 3.0 M and 4.5 M NaOH, which are 0.83 and 1.00, respectively. These values demonstrated that NH_2 sites started to deprotonate and undergo carboxymethyl substitution at both active sites as described by NMR spectra. Despite the introduction of carboxymethyl groups at two active sites, OH and NH_2, the DS value for both concentrations did not approach 2. This could be because not all active sites in the chitosan chain were completely substituted with carboxymethyl groups.

Besides, the DS values of CMC prepared at 6.0 M and 7.5 M were approximately the same at 0.93 and 0.94, respectively. This indicated that the carboxymethyl group substitution occurred under optimal condition at both concentrations, 6.0 M and 7.5 M NaOH. We also conducted the Student's *t*-test to determine the selection of NaOH concentration has directly affected the DS for producing N,O-CMC, and N-CMC. Based on the results, there are no statistically significant differences between the means of DS values produced at 3.0 M and 4.5 M NaOH, since $p > 0.05$. The same observation has been reached for 6.0 M and 7.5 M. Therefore, both concentration either 3.0 M and 4.5 M NaOH can be used to produce N,O-CMC while 6.0 M and 7.5 M to obtain N-CMC.

Thermogravimetry analysis

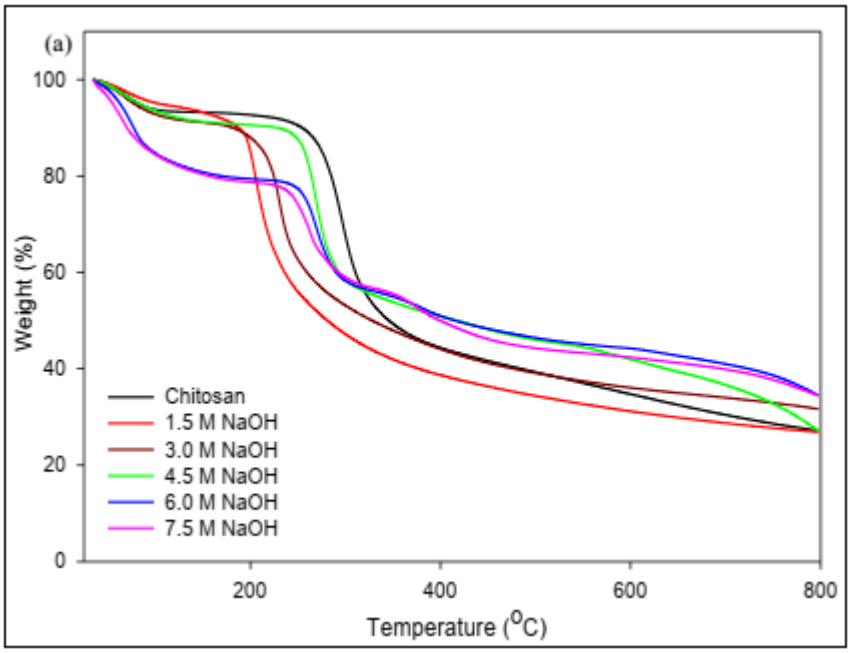
The TGA and derivative thermogravimetry (DTG) curves of chitosan and CMC for all NaOH concentrations shown in Figure 6. Based on Figure 6, chitosan exhibited two thermal degradation behaviors. The thermal degradation (T_{H2O}) observed at 68.71 °C was associated to the loss of capillary bonded water [2]. Meanwhile, the thermal degradation (T_{d1}) stage started about 296.25 °C and reached maximum mass loss at 43.7% due to thermal and oxidative decomposition of the chitosan chain [31]. The thermal degradation temperature and weight loss of chitosan and CMC at different NaOH concentrations were listed in Table 3.

For all CMCs, degradation at temperatures of 60 °C to 75 °C occurred due to the evaporation of adsorbed and bound water in the polymer structure. Kurniasih et al. [32] reported that carboxymethyl chitosan is more hygroscopic and has a greater ability to bind with water than chitosan due to capability of carboxylic groups forming hydrogen bond with water molecules [22, 33]. The first thermal degradation (T_{d1}) at 207 °C attributed to decomposition of polymer chain can be observed for O-CMC produced at 1.5 M NaOH.

Meanwhile, N,O-CMC prepared at 3.0 M NaOH had only one polymer decomposition at 230 °C (T_{d1}), compared to N,O-CMC produced at 4.5 M NaOH, which had two stages of polymer decomposition at 270 °C (T_{d1}) and 372 °C (T_{d2}). According to Miranda et al. [4], the second stage of thermal degradation (T_{d2}) is assigned to the polymer decomposition of carboxymethyl groups that substituted at NH_2 sites. This shows that a greater amount of carboxymethyl group substituted on NH_2 sites for 4.5 M NaOH compared to 3.0 M NaOH. This also can be supported by FTIR analysis where the C-N peak at 4.5 M NaOH was more intense than 3.0 M NaOH. Similar observations could be made for N-CMC obtained at 6.0 M and 7.5 M NaOH. There are two stages of polymer decomposition at 260 – 270 °C (T_{d1}) and 374 – 383 °C (T_{d2}) since carboxymethyl substitution occurred at NH_2 sites.

Table 2. The DS values for CMC at various concentrations of NaOH

NaOH Concentration (M)	Degree of Substitution (DS)
1.5	0.74 ± 0.02
3.0	0.83 ± 0.06
4.5	1.00 ± 0.06
6.0	0.93 ± 0.01
7.5	0.94 ± 0.03



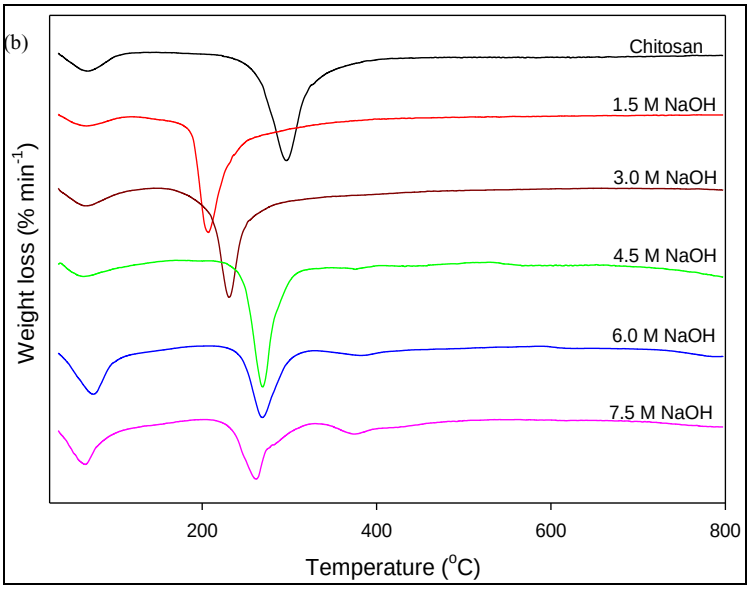


Figure 6. The a) TGA and b) DTG curves of chitosan and CMC for all NaOH concentrations

Table 3. Thermal degradation temperature and weight loss of chitosan and all CMC at different concentrations

Samples	T_{H2O} (°C)	% Loss	T_{d1} (°C)	% Loss	T_{d2} (°C)	% Loss	% Residue
Chitosan	68.71	6.35	296.25	41.76	-	-	26.69
1.5 M NaOH	67.01	4.27	207.75	40.71	-	-	26.99
3.0 M NaOH	67.71	6.95	230.07	33.56	-	-	31.62
4.5 M NaOH	60.50	7.31	270.52	31.24	372.64	8.56	26.77
6.0 M NaOH	75.07	15.2	270.52	20.0	383.70	9.99	34.77
7.5 M NaOH	67.01	16.9	260.76	18.5	374.96	10.24	34.53

Differential scanning calorimetry

The DSC curves for second heating cycle are shown in Figure 7 to illustrate the thermal behaviour of the polymers. Based on Figure 6, chitosan exhibited two thermal events, first-endothermic and second-exothermic peaks. The first endothermic peak observed at 114 °C could be considered as glass transition temperature (T_g) [2], as moisture was evaporated in the first heating cycle. Moreover, the TGA curves revealed that the water evaporating temperature was about 60 – 75 °C. The exothermic peak (T_{d1}) appeared at 307.21 °C, corresponding to thermal decomposition of polymer chain [34-35]. Acosta-Ferreira [36] reported that decomposition of polymer including depolymerization, saccharide ring dehydration, decomposition of deacetylated and acetylated chitosan units. However, the decomposition temperature determined by DSC analysis was greater than TGA results, owing to the enhanced polymer strength caused by the removal of moisture during the first cycle of heating. Table 4 shows the glass transition and polymer decomposition temperatures for chitosan and all CMCs at different NaOH concentrations.

Furthermore, the DSC curves for all synthesized CMC had an endothermic peak centered between 80 °C until 113 °C, which may be ascribed as the glass transition temperature (T_g) of all CMC. The T_g of all CMC were

lower than chitosan indicated that chitosan was more crystalline than CMC as less heat needed to transform CMC polymer chain from glassy to rubbery phase. It can be observed that O-CMC produced at 1.5 M NaOH had an endotherm peak at 207 °C, corresponding to the melting temperature which is consistent with the previous literature [37]. According to Liang et al. [19], the higher melting temperature of polysaccharides is attributed to the higher crystallinity of the polymer. However, a broad and amorphous peak that observed in XRD analysis contributed to low crystallinity of O-CMC, resulting a low glass transition temperature of O-CMC. Further explanation is discussed in XRD analysis.

Besides, an exothermic peak for N,O-CMC produced at 3.0 M NaOH can be seen at 234 °C. Contrary to N,O-CMC prepared at 4.5 M NaOH, there are two exothermic peaks observed at 278 °C and 380 °C. The appearance of these two peaks also could be observed for N-CMC synthesized at higher concentration, 6.0 M, and 7.5 M NaOH. As referred to the literature [38], the first exothermic peak represents the decomposition of polysaccharide chain, while the second exothermic peak was due to the decomposition of carboxymethyl group substituted at NH_2 sites. The second exothermic peak only presence when higher substitution occurred at NH_2 sites. These could support the TGA analysis. as the same occurrence happened in both analysis and confirmed the decomposition of carboxymethyl group at NH_2 sites. However, the glass transition temperature of N-CMC differs significantly, as the 6.0 M was lower than 7.5 M NaOH, indicating that it had dissimilar behaviors in thermal properties. Therefore, further research is needed to reach a better understanding of the internal structure of polymer.

X-ray diffraction analysis

The XRD analysis was conducted to compare the crystallinity of chitosan and all CMC in different NaOH concentrations, as shown in Figure 8. It is observed that the diffractogram of chitosan has a wide and broad peak at $2\theta = 10.05°$ and $2\theta = 20.16°$ that reflected from (0 2 0) plane and (2 0 0) plane [39]. Based on Franca et al. [40], inter- and intra-molecular hydrogen bond play important part in the stabilization of the chitosan structure. An intramolecular hydrogen bond is formed between atoms OH at C3 and O5 of consecutive linked glucosamine units which responsible to keep the polymer chain in 2-fold helical pattern. Meanwhile, the intermolecular hydrogen bond formed between two amide group and amide group with hydroxymethyl group. In addition, intermolecular hydrogen bonds also formed between water molecules in polymer chains [41]. However, the substitution of carboxymethyl loosened their characteristics and led to a less ordered arrangement compared to the chitosan structure [42].

The O-CMC prepared in 1.5 M NaOH showed the three obvious peaks. Besides the existence of peak at $2\theta = 11.50°$, which contributed to crystallinity of polymers, the new and small pointed peak at $2\theta = 8.28°$ also could be observed at a lower angle of diffractogram. This leads to the appearance of endothermic peak in DSC curve for 1.5 M NaOH. However, the amorphous peak at $2\theta = 17.28°$ was lower and broader than chitosan which helps in reducing the crystallinity of O-CMC even though it has the endothermic peak in DSC. Additionally, N,O-CMC synthesized using 3.0 M NaOH showed broad and amorphous peaks at $2\theta = 11.50°$ and $2\theta = 21.60°$ that might be due to less ordered of polymer chain structure. Compared to N,O-CMC produced at 4.5 M NaOH, the low reflective peak could be observed at $2\theta = 9.73°$ but a strong and sharp peak also could be seen at $2\theta = 19.83°$. This was due to the greater amount of carboxymethyl substitution occurred at 4.5 M than 3.0 M NaOH, which also could be supported by DS analysis as the DS value of 4.5 M NaOH is higher than other CMC.

Furthermore, N-CMC prepared at 6.0 M and 7.5 M NaOH showed approximately the same characteristics. Only one small peak appeared at $2\theta = 20.33°$ and $2\theta = 20.00°$, respectively even though it had different thermal behaviour. These might be due to the arrangement of N-CMC chain that still maintains the flexibility of polymer. In addition, Samuel [43] stated that the presence of carboxymethyl group in the N-CMC chain could disrupt the intermolecular hydrogen bonding of chitosan and increase the amorphous state in the polymer chains.

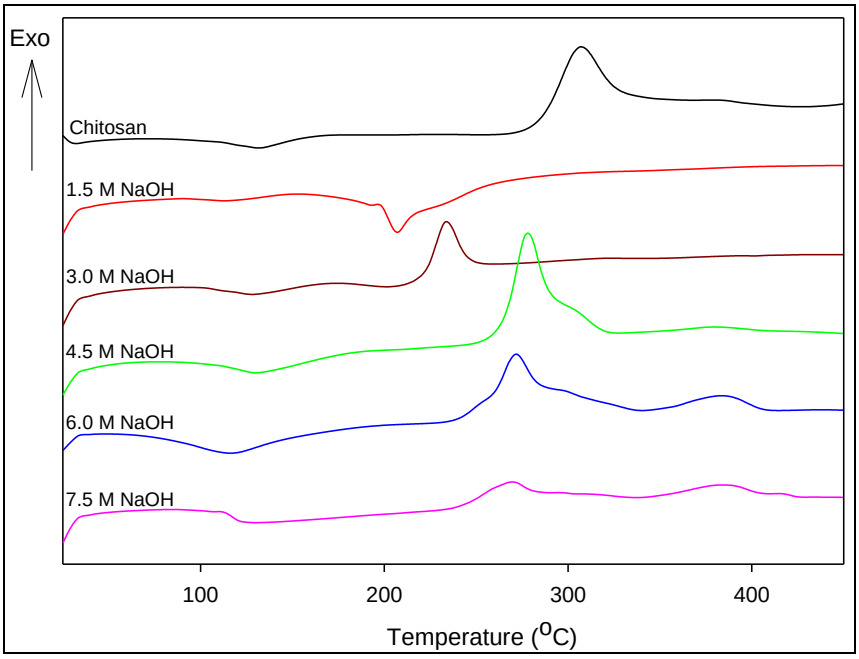


Figure 7. The DSC thermogram for chitosan and CMC at various NaOH concentrations

Table 4. The glass transition and polymer decomposition temperature of chitosan and all CMC at different NaOH concentrations

Samples	**T_g (°C)**	**T_m (°C)**	**T_{d1} (°C)**	**T_{d2} (°C)**
Chitosan	114.17	-	307.21	-
1.5 M NaOH	89.77	206.78	-	-
3.0 M NaOH	101.16	-	234.04	-
4.5 M NaOH	101.16	-	278.94	380.01
6.0 M NaOH	80.08	-	271.88	383.13
7.5 M NaOH	113.06	-	268.96	384.30

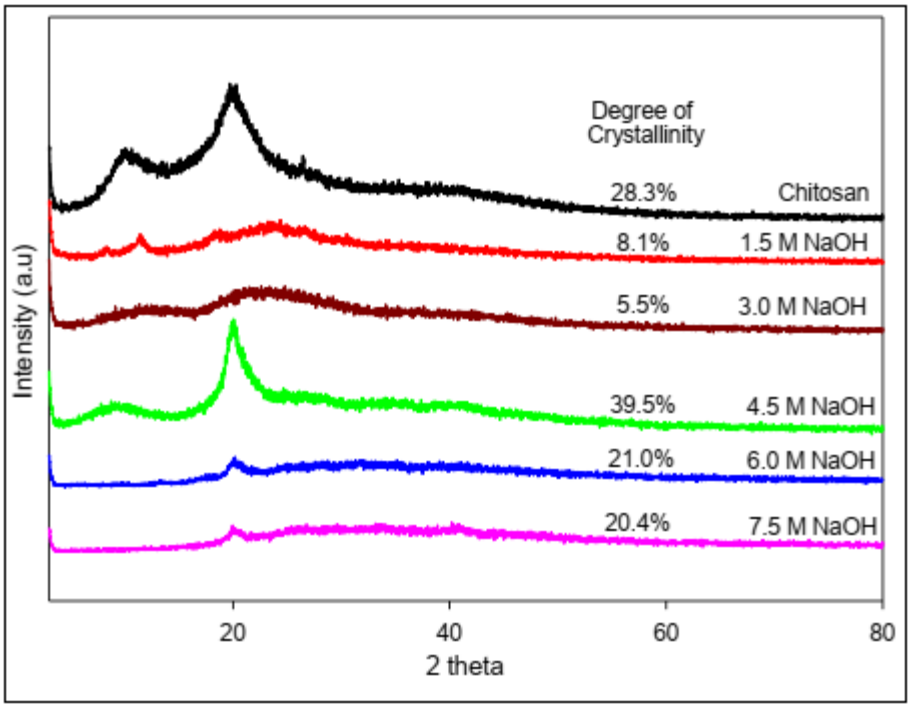


Figure 8. The XRD diffractogram for chitosan and CMC prepared at different NaOH concentrations

Conclusion

In conclusion, N-carboxymethyl chitosan was successfully synthesized under heterogenous conditions at higher NaOH concentration which are 6.0 M and 7.5 M NaOH as confirmed by FTIR spectroscopy, ^{1}H-NMR spectroscopy, and DS calculation. However, the glass transition temperatures of N-CMC at both NaOH concentrations showed significant differences, indicating dissimilar behavior in thermal properties. Despite this, N-CMC still retains its flexibility, as shown in XRD analysis. Therefore, the choice of N-CMC at selective concentration may be determined by specific applications.

Acknowledgement

The authors would like to thank Fakulti Sains dan Teknologi and Centre for Research and Instrumentation Management (i-CRIM), UKM for providing the facilities and research grant GGPM-2017-093 for funded this work.

References

1. Alves, N. M. and Mano, J. F. (2008). Chitosan derivatives obtained by chemical modifications for biomedical and environmental applications. *International Journal of Biological Macromolecules*, 43(5): 401-414.
2. Tzaneva, D., Simitchiev, A., Petkova, N., Nenov, V., Stoyanova, A. and Denev, P. (2017). Synthesis of carboxymethyl chitosan and its rheological behaviour in pharmaceutical and cosmetic emulsions. *Journal Applied Pharmaceutical Science*, 7(10): 70-78.
3. Madera-Santana, T. J., Herrera-Méndez, C. H. and Rodríguez-Núñez, J. R. (2018). An overview of the chemical modifications of chitosan and their advantages. *Green Materials*, 6(4): 131-142.

4. Miranda, M. E. S., Marcolla, C., Rodrígues, C. A., Wilhelm, H. M., Sierakowski, M. R., Bresolin, T. M. B. and de Freitas, R. A. (2006). Chitosan and N-carboxymethyl chitosan: I. The role of N-carboxymethylation of chitosan in the thermal stability and dynamic mechanical properties of its films. *Polymer international*, 55(8): 961-969.
5. Andreica, B. I., Cheng, X. and Marin, L. (2020). Quaternary ammonium salts of chitosan. A critical overview on the synthesis and properties generated by quaternization. *European Polymer Journal,* 2020: 110016.
6. Klinkesorn, U. (2013). The role of chitosan in emulsion formation and stabilization. *Food Reviews International,* 29(4): 371-393.
7. An, N. T., Dong, N. T. and Le Dung, P. (2009). Water-soluble N-carboxymethylchitosan derivatives: Preparation, characteristics, and its application. *Carbohydrate Polymers*, 75(3): 489-497.
8. Skorik, Y. A., Gomes, C. A., Vasconcelos, M. T. S. and Yatluk, Y. G. (2003). N-(2-Carboxyethyl) chitosans: regioselective synthesis, characterisation and protolytic equilibria. *Carbohydrate research*, 338(3): 271- 276.
9. Sahariah, P., Árnadóttir, B. and Másson, M. (2016). Synthetic strategy for selective N-modified and O-modified PEGylated chitosan derivatives. *European Polymer Journal*, 81: 53-63.
10. Salehuddin, N. E. A., Rodzali, N. A., Ku Bulat, K. H. and Mobarak, N. N. (2021). Site-selective carboxymethylation of chitosan under heterogeneous conditions. *Malaysian Journal of Analytical Sciences,* 25(3): 376-387.
11. Rahman, M., Hasan, M., Nitai, A. S., Nam, S., Karmakar, A. K., Ahsan, Shiddiky, M. J. A. and Ahmed, M. B. (2021). Recent developments of carboxymethyl cellulose. *Polymers*, 13(8): 1345.
12. Heinze, T. and Pfeiffer, K. (1999). Studies on the synthesis and characterization of carboxymethylcellulose. *Die Angewandte Makromolekulare Chemie*, 266(1): 37-45.
13. Chen, X. G. and Park, H. J. (2003). Chemical characteristics of O-carboxymethyl chitosan related to the preparation conditions. *Carbohydrate Polymers*, 53(4): 355-359.
14. Elomaa, M., Asplund, T., Soininen, P., Laatikainen, R., Peltonen, S., Hyvärinen, S. and Urtti, A. (2004). Determination of the degree of substitution of acetylated starch by hydrolysis, ^{1}H NMR and TGA/IR. *Carbohydrate Polymers*, 57(3): 261-267.
15. Pushpamalar, V., Langford, S. J., Ahmad, M. and Lim, Y. Y. (2006). Optimization of reaction conditions for preparing carboxymethyl cellulose from sago waste. *Carbohydrate Polymers* 64(2): 312-318.
16. Aggeryd, I. and Olin, Å. (1985). Determination of the degree of substitution of sodium carboxymethylcellulose by potentiometric titration and use of the extended henderson-hasselbalch equation and the simplex method for the evaluation. *Talanta*, 32(8): 645-649.
17. Liu, J., Zhang, X., Kennedy, J. F., Jiang, M., Cai, Q. and Wu, X. (2019). Chitosan induces resistance to tuber rot in stored potato caused by *Alternaria tenuissima*. *International Journal of Biological Macromolecules*, 140: 851-857.
18. Mobarak, N. N., Ahmad, A., Abdullah, M. P., Ramli, N. and Rahman, M. Y. A. (2013). Conductivity enhancement via chemical modification of chitosan based green polymer electrolyte. *Electrochimica Acta*, 92:161-167.
19. Liang, X., Wang, H., Tian, H., Luo, H. and Chang, J. (2008). Synthesis, structure and properties of novel quaternized carboxymethyl chitosan with drug loading capacity. *Acta Physico-Chimica Sinica,* 24(2): 223-229.
20. Doshi, B., Repo, E., Heiskanen, J. P., Sirviö, J. A. and Sillanpää, M. (2017). Effectiveness of N, O-carboxymethyl chitosan on destabilization of marine diesel, diesel and marine-2t oil for oil spill treatment. *Carbohydrate Polymers*, 167: 326-336.
21. Bukzem, A. L., Signini, R., Dos Santos, D. M., Lião, L. M. and Ascheri, D. P. R. (2016). Optimization of carboxymethyl chitosan synthesis using response surface methodology and desirability function. *International Journal of Biological Macromolecules*, 85: 615-624.
22. Mourya, V. K., Inamdar, N. N. and Tiwari, A. (2010). Carboxymethyl chitosan and its applications. *Advanced Materials Letters*, 1 (1): 11 – 33.

23. Jimtaisong, A. and Saewan, N. (2014). Utilization of carboxymethyl chitosan in cosmetics. *International Journal of Cosmetic Science*, 36(1): 12-21.
24. Abreu, F. R. D. and Campana-Filho, S. P. (2005). Preparation and characterization of carboxymethylchitosan. *Polímeros*, 15(2): 79-83.
25. Hjerde, R. J. N., Vårum, K. M., Grasdalen, H., Tokura, S. and Smidsrød, O. (1997). Chemical composition of O-(carboxymethyl)-chitins in relation to lysozyme degradation rates. *Carbohydrate Polymers*, 34 (3):131-139.
26. Muzzarelli, R. A., Ilari, P. and Petrarulo, M. (1994). Solubility and structure of N-carboxymethylchitosan. *International Journal of Biological Macromolecules*, 16(4): 177-180.
27. Klinkesorn, U. (2013). The role of chitosan in emulsion formation and stabilization. *Food Reviews International,* 29(4): 371-393.
28. Jaidee, A., Rachtanapun, P. and Luangkamin, S. (2012). ^{1}H-NMR analysis of degree of substitution in N, O-carboxymethyl chitosan from various chitosan sources and types. *Advanced Materials Research,* 506: 158 – 161.
29. Zong, Z., Kimura, Y., Takahashi, M. and Yamane, H. (2000). Characterization of chemical and solid-state structures of acylated chitosans. *Polymer*, 41(3): 899-906.
30. Bono, A., Ying, P. H., Yan, F. Y., Muei, C. L., Sarbatly, R. and Krishnaiah, D. (2009). Synthesis and characterization of carboxymethyl cellulose from palm kernel cake. *Advances in Natural and Applied Sciences*, 3(1): 5-12.
31. Jiang, M., Wang, K., Kennedy, J. F., Nie, J., Yu, Q. and Ma, G. (2010). Preparation and characterization of water-soluble chitosan derivative by Michael addition reaction. *International Journal of Biological Macromolecules*, 47(5): 696-699.
32. Kurniasih, M., Purwati, P., Hermawan, D. and Zaki, M. (2014). Optimum conditions for the synthesis of high solubility carboxymethyl chitosan. *Malaysian Journal of Fundamental and Applied Sciences*, 10(4): 189-194.
33. Pang, H. T., Chen, X. G., Park, H. J., Cha, D. S. and Kennedy, J. F. (2007). Preparation and rheological properties of deoxycholate-chitosan and carboxymethyl-chitosan in aqueous systems. *Carbohydrate Polymers,* 69(3): 419-425.
34. Kittur, F. S., Prashanth, K. H., Sankar, K. U. and Tharanathan, R. N. (2002). Characterization of chitin, chitosan and their carboxymethyl derivatives by differential scanning calorimetry. *Carbohydrate polymers*, 49(2): 185-193.
35. Shinde, U., Ahmed, M. H. and Singh, K. (2013). Development of dorzolamide loaded 6-o-carboxymethyl chitosan nanoparticles for open angle glaucoma. *Journal of Drug Delivery*, 2013: 562727.
36. Acosta-Ferreira, S., Castillo, O. S., Madera-Santana, J. T., Mendoza-García, D. A., Núñez-Colín, C. A., Grijalva-Verdugo, C., Villa-Lerma. A. G., Morales-Vargas. A. T. and Rodríguez-Núñez, J. R. (2020). Production and physicochemical characterization of chitosan for the harvesting of wild microalgae consortia. *Biotechnology Reports*, 28: e00554.
37. Kamari, A. and Yusoff, S. N. M. (2019). N-octyl chitosan derivatives as amphiphilic carrier agents for herbicide formulations. *Open Chemistry*, 17(1): 365-380.
38. Kasaai, M. R., Arul, J. and Charlet, G. (2013). Fragmentation of chitosan by acids. *The Scientific World Journal*, 2013: 508540.
39. Osorio-Madrazo, A., David, L., Trombotto, S., Lucas, J. M., Peniche-Covas, C. and Domard, A. (2010). Kinetics study of the solid-state acid hydrolysis of chitosan: Evolution of the crystallinity and macromolecular structure. *Biomacromolecules*, 11(5): 1376-1386.
40. Franca, E. F., Lins, R. D., Freitas, L. C. and Straatsma, T. P. (2008). Characterization of chitin and chitosan molecular structure in aqueous solution. *Journal of Chemical Theory and Computation* 4(12): 2141-2149.
41. Brza, M. A., Aziz, S. B., Nofal, M. M., Saeed, S. R., Al-Zangana, S., Karim, W. O., Hussen, S. A., Abdulwahid, R.T. and Kadir, M. F. Z. (2020). Drawbacks of low lattice energy ammonium salts for ion-conducting polymer electrolyte preparation: structural, morphological, and electrical characteristics of CS:PEO:NH_4BF_4-based polymer blend electrolytes. *Polymers* 12(9): 1885-1906.

42. Katugampola, P., Winstead, C. and Adeleke, A. (2014). Thermal stability of carboxymethyl chitosan varying the degree of substitution. *International Journal of Pharmaceutical Science Invention*, 3(5): 42- 48.

43. Samuels, R. J. (1981). Solid state characterization of the structure of chitosan films. *Journal of Polymer Science: Polymer Physics Edition* 19(7): 1081-1105.

Malaysian Journal of Analytical Sciences (MJAS)
Published by Malaysian Analytical Sciences Society

HEAVY METAL IN DIFFERENT SIZE FRACTIONS OF HOUSEHOLD DUST COLLECTED FROM RURAL RESIDENTIAL AREA OF SIMPANG RENGGAM, JOHOR

(Logam Berat dalam Pelbagai Pecahan Saiz Habuk Rumah dari Kawasan Kediaman Luar Bandar Simpang Renggam, Johor)

Joo Hui Tay*, Siti Aqilah Azmi, Mohd Iffat Iqbal Zul Kornain

Faculty of Industrial Sciences & Technology,
Universiti Malaysia Pahang, Lebuhraya Tun Razak, 26300 Gambang, Pahang, Malaysia.

**Corresponding author: tayjoohui@ump.edu.my*

Received: 1 September 2021; Accepted: 31 October 2021; Published: 27 December 2021

Abstract

A study investigating the levels of selected heavy metals in household dust from a rural residential area was carried out. Household dust was collected from seven residential homes within the area of Simpang Renggam, Johor. All samples were sieved through a 200 µm sieve, in which two dust samples with sufficient masses (sample A and B) were further separated into four discrete fractions (<63 µm, 63-75 µm, 75-150 µm, and 150-200 µm) before analysis. Dust samples were acid digested and analyzed for the content of Al, Cr, Mn, Ni, Zn, Cu, Cd, Ba, Pb, Mg, and Fe using inductively coupled plasma - mass spectrometer (ICP-MS). Results showed that the Fe and Al were among the most abundant elements in bulk dust samples (mean concentration of 8500 mg/kg and 5100 mg/kg, respectively), and their concentrations increased with decreasing particle size. Mean concentrations of other elements ranged between 0.027 mg/kg to 2310 mg/kg. For Mn, Mg, Cu, and Zn, higher levels were measured in coarser particle size. Health risk estimation indicated that Hazard Quotient (HQ) and Hazard Index (HI) values were below than 1, representing no non-carcinogenic risk to the residents via ingestion, inhalation, and dermal absorption.

Keywords: indoor dust, heavy metals, particle size distribution, rural residential area

Abstrak

Satu kajian mengenai kepekatan logam berat terpilih dalam habuk dari kawasan perumahan luar bandar telah dilakukan. Sampel habuk dikumpulkan dari tujuh rumah kediaman di kawasan Simpang Renggam, Johor. Semua sampel diayak melalui ayakan 200 µm, di mana dua sampel debu dengan jisim yang mencukupi (sampel A dan B) dipisahkan menjadi empat pecahan diskrit (<63 µm, 63-75 µm, 75-150 µm dan 150-200 µm) sebelum analisis. Sampel habuk dicerna asid dan dianalisis untuk kandungan Al, Cr, Mn, Ni, Zn, Cu, Cd, Ba, Pb, Mg dan Fe dengan menggunakan teknik ICP-MS. Keputusan kajian menunjukkan bahawa Fe dan Al merupakan unsur yang paling banyak dalam sampel debu <200 µm (kepekatan purata sebanyak 8500 mg/kg dan 5100 mg/kg masing-masing), dan kepekatan unsur ini meningkat dengan penurunan saiz zarah. Purata kepekatan unsur-unsur lain berada dalam julat 0.027 mg/kg dan 2310 mg/kg. Untuk Mn, Mg, Cu, dan Zn, kepekatan yang lebih tinggi diukur dalam partikel habuk yang lebih kasar. Anggaran risiko kesihatan memberi nilai Darjah Bahaya (HQ) dan Indeks Bahaya (HI) kurang daripada 1,

menunjukkan bahawa pendedahan penduduk kepada habuk melalui pengambilan, penyedutan dan penyerapan kulit tidak mendatangkan risiko (secara bukan karsinogenik).

Kata kunci: habuk rumah, logam berat, taburan saiz zarah, kawasan kediaman luar bandar

Introduction

People nowadays tend to spend most of their time indoors, especially during the COVID-19 pandemic period, giving rise to the concern regarding exposure to indoor contaminants. Dust in homes, offices, and floor may contain human and animal hair, paper fibres, and mineral from outdoor soil and many other materials which may be found in the local environment. The composition of indoor dust may vary greatly between rooms of a given house and among geographic locations [1]. House dust containing heavy metals could be generated indoors (e.g.: premises and furniture materials, consumer products, and resident activities) or tracked indoors from outside [2].

Studies investigating the contamination of heavy metals in dust as well as its potential health risk of exposure have been reported worldwide. Dust samples investigated in these studies were mostly of single particle size (such as <200 um) or without sieving. Generally, particle size of dust can vary, and the finest size can easily enter human body through inhalation, dermal absorption, and ingestion as it is less dense and electrostatically mobilized compared to the other big particle sizes. According to Lanzerstorfer [3], while the total surface area of the particles is indirectly proportional to the size of the particles, there is special interest in the size dependence of heavy metal concentrations. Since the transition of mass from a solid to a liquid takes place on the solid's surface, in cases with finer particles, the mass transfer rate is higher, thereby making hazardous components found in these finer particles more available. Therefore, a key consideration in the risk assessment of human exposure to heavy metals in indoor dust is particle size [4].

In Malaysia, a few studies have been carried out to determine the concentration of heavy metals in indoor dust from schools [5-7] and residential buildings [8], focusing on urban and semi-urban areas. However, data on metal composition in rural areas with low population density and main economic activities such as ecotourism and agriculture are still scarce. Therefore, the present study aimed to investigate the level of heavy metal in house dust collected from rural residential area of Simpang Renggam, Johor, according to dust particle size fractions.

Materials and Methods

Sample collection and treatment

The study area, Simpang Renggam (1.8273°N, 103.3100°E), is a small town located in the southern half of Kluang District, Johor, Malaysia. Seven vacuum cleaner dust samples were collected in August 2020 from different households of Simpang Renggam residential area. The dust samples were transferred into zip-lock bags, sealed, and labelled properly. The volunteers were required to answer a simple questionnaire regarding their household condition and personal behaviors (Table 1). Upon arrival at the laboratory, large objects such as hair, stone, and plastic object were discarded from dust sample using a tweezer before sieved through a 200 μm sieve. Due to a large sample mass required for particle size distribution analysis, only 2 out of 7 samples (Sample A and B) were suitable for further separation into four discrete fractions. The <200 μm portion was treated as the bulk dust sample, in which a portion of this <200 μm fraction dust was taken and analyzed for its total metal concentrations. The remaining portion was further fractionated using an Endecotts EFL 2000 sieve shaker into the following size fractions: <63 μm, 63-75 μm, 75-150 μm, and 150-200 μm, and each of these fractions were analyzed for metal concentrations. Due to limited amount of sample available for fraction 63-75 μm in Sample B (<0.1 g), the fraction was combined with the finest fraction, <63 μm, for chemical analysis.

Chemical and data analysis

All glass and plastic wares were cleaned with detergent, soaked in 5% (v/v) HNO_3 overnight and rinsed with deionized Milli-Q water before use. Approximately

0.2 g of dust sample were acid digested with 10 mL of H_2O_2: HNO_3 (3:7 v/v) using UltraWave™ system (Milestone Helping Chemist, Italy). The digestion program was set at 253 °C and 182 bar for 30 minutes, followed by cooling time with nitrogen gas for 10 minutes. After digestion, the sample solution was filtered with Whatman cellulose acetate filter paper and diluted to 50 mL with 2% HNO_3. For each batch of the digestion, one reagent blank was included. Concentration of aluminum (Al), chromium (Cr), manganese (Mn), nickel (Ni), copper (Cu), zinc (Zn), cadmium (Cd), barium (Ba), lead (Pb), magnesium (Mg), and iron (Fe) were determined using inductively coupled plasma – mass spectrometer (Perkin-Elmer NexIon 300X). All statistical analyses (Spearman rank correlation, Mann Whitney *U* test, and Kruskal-Wallis *H* test) were performed using Excel 2016. The significance was set at α = 0.05 in all the statistical analyses.

Health risk assessment

The average daily dose (ADD) of an element from dust via ingestion, inhalation, and dermal contact pathways can be estimated using Equations (1), (2) and (3), respectively, as suggested by the USEPA Exposure Factors Handbook [9]:

$$ADD_{ing} = \frac{C \times IngR \times EF \times ED}{BW \times AT} \times 10^{-6} \quad (1)$$

$$ADD_{inh} = \frac{C \times InhR \times EF \times ED}{PEF \times BW \times AT} \quad (2)$$

$$ADD_{der} = \frac{C \times SA \times AF \times ABS \times EF \times ED}{BW \times AT} \times 10^{-6} \quad (3)$$

where ADD is exposure dose (mg/kg/day), C is the concentration of the element (mg/kg), IngR is the ingestion rate of contaminated dust for adult (30 mg/day), EF is the exposure frequency (350 day/year), ED is the exposure duration (30 year), BW is the body weight (70 kg), AT is the average time (ED×365 day), IngR is the inhalation rate (15.2 m^3/day), PEF is the inhalation factor for the respirable particles (1.36×10^9 m^3/kg), SA is the surface area of the skin exposed to pollutants (5700 cm^2), AF is the skin adherence factor (0.07 mg/cm^2/h), ABS is the dermal absorption factor (0.001).

Based on the ADDs from the three exposure routes, hazard quotient (HQ) and hazard indexes (HI) indicating the non-cancer risk during a lifetime can be calculated according to Equation (4) and (5):

$$HQ = \frac{ADD}{RfD} \quad (4)$$

$$HI = \sum HQ = HQ_{ing} + HQ_{inh} + HQ_{der} \quad (5)$$

where RfD is the estimated maximum permissible risk on humans through daily exposure (mg/kg/day). HQ and HI ≤ 1 indicates that adverse effects on human health are unlikely, while HQ and HI > 1 reveals probable adverse health effects.

Table 1. Description of the sampling sites

Household	A	B	C	D	E	F	G
Building type	terrace	terrace	terrace	shop house	semi-detached	semi-detached	semi-detached
Size of the house (sqft)	~1200	~1200	~1200	~1200	<1000	~1200	~1200
Number of occupants	7	6	5	8	4	7	3
Age of the building (year)	15	37	8	25	25	15	28

Table 1 (cont'd). Description of the sampling sites

Household	A	B	C	D	E	F	G
Facing main traffic street	no	no	no	yes	no	yes	yes
Floor cover	tile	carpet	tile	carpet	tile	carpet	carpet
Shoes allowed	no	no	no	no	yes	yes	no
Smoking allowed	no	no	yes	no	yes	no	no
Air-conditioned	yes	yes	no	no	no	no	yes
Last painted (year ago)	<1	>5	1-5	1-5	1-5	1-5	1-5
Ventilation frequency	everyday	2-3 times a week	everyday	2-3 times a week	everyday	occasionally	occasionally
Pets allowed	yes	no	no	no	yes	no	no
Vacuuming frequency	once a week	once a week	once a week	once a week	once a week	once a week	once a week

Results and Discussion

Levels of heavy metals

The concentrations of heavy metals from indoor dust in Simpang Renggam, Johor are summarized in Figure 1. Among the eleven target metals, Fe showed the highest mean concentration (8500 mg/kg), followed by Al (5100 mg/kg) and Mg (2300 mg/kg). As the second and third most abundant element in the earth's crust, Fe and Al occur naturally in the environment, foodstuffs, and drinking water. Other possible sources of Fe and Al in indoor dust include unpaved roads and heavy construction activities of new buildings, as well as wind-blown dust from surface soil and road dust. Although the use of leaded petrol has been banned for many years in Malaysia, their residues are still detected in indoor dust samples, especially those collected from urban and sub-urban areas [5, 8, 10-11]. Cadmium was detected in one of the dust samples, probably derived from lubricating oils or old tyres [5] due to the absence of any significant industry near the study location. Compared to previous studies, the levels of heavy metals measured in this study were within the range of literature [12-16].

Spearman rank correlation tests were performed to identify correlations between individual elements in the samples. High positive correlations ($0.78 < r < 0.93$, $p < 0.05$) were found between Al-Ni, Al-Cu, Al-Ba, Cr-Cu, Cr-Fe, Ni-Ba, Ni-Pb, Zn-Mg, and Ba-Pb in dust samples (Table 2), suggesting a common source of origin for these metals. Similar correlations between Al-Ni and Cu-Cr have been reported by previous studies [10, 14]. On the other hand, concentrations of metals showed no relationship to house age (Spearman rank analysis, $p > 0.05$), whereas the concentration of Zn increase significantly with number of occupants (Spearman rank analysis, $r = 0.77$, $p < 0.05$). Associations between household conditions and personal behaviors for different metal concentrations in household dust were tested with Mann Whitney *U* test or Kruskal-Wallis *H* test as appropriate. However, the results revealed that

neither household conditions (facing major roads, floor covered with carpet, and duration from the last painting) nor personal behaviors (ventilation frequency and houses that allow shoes, smoking, and pets indoors), were statistically significant for metal concentrations (Mann Whitney *U* test and Kruskal-Wallis *H* test, $p > 0.05$). This finding is contrary to previous studies which have suggested smoking [15, 17], natural ventilation frequency [17], and age of house [15, 18-19] as the important factors of heavy metals enrichment in household dust. This could be attributed to the small number of samples available for this study and the lack of other possible parameters in our questionnaire (e.g.: cooking frequency, type of fuel, paved or unpaved streets, number of windows, etc.).

Particle size distribution

Particle size distribution analysis was performed on two dust samples with sufficient sample mass. Both sample A and Sample B showed great similarity in the particle size distribution of dust (Figure 2). By considering the <200 μm size as the bulk sample (100%), both samples were dominated by the <63 μm fraction (39% and 42% of total dry mass, respectively), followed by 75-150 μm (35% to 37%), 150-200 μm (15% to 19%), and 63-75μm (2% to 11%).

Metal distribution with particle size

The concentrations of heavy metals in different particle size fractions are summarized in Table 3. In general, total metal concentrations decreased with particle size in Sample A, but sample B showed the contrary, giving higher total metal concentration in the coarser fraction. For both samples, the concentration of Al and Fe decreased with increasing particle size. This result is in agreement with several previous reports on the preferential partitioning of metals to fine particle size fractions [3, 20-22]. This observation could be explained by the greater surface area per unit mass of the fine particles, which increases the adsorption capacity of these fractions. For Mn, Mg, Cu, and Zn, on the other hand, higher concentrations were observed in the coarser fractions. The findings are contrary to Doyi et al. [23], who has reported the most concentrated metals in course size fractions (150-250 μm) for Cu, Ni, and Pb. However, Lanzerstorfer [3] found no distinct trend for the concentrations of Cu and Zn in different particle size fractions. For other remaining metals, no consistent trend could be observed regarding their distribution in different dust particle sizes, probably due to small sample size in this study, as well as the influence of geographical location and human activities in the chemical composition of household dust. Although different size fractions were analysed, the concentrations of Al, Cr, Cu, Ba, Pb, Mg, and Fe measured in the present study were within the range of values found in the literature [3, 15, 20-21]. Meanwhile, much higher levels of Mn and Zn were measured, whilst slightly lower concentrations of Ni were measured in this study. The proportions of metal loadings in different size fractions of dust samples are presented in Figure 3. The partitioning of most of the metals in different size fractions of Sample A was found to be consistent, as the finer fractions (<63 μm, 63-75 μm, and 75-150 μm) corresponded to >70% of the total metal concentration. For Sample B, it was evident that the metals were not homogenously distributed among the various particle's fractions. Cr and Ni were only detected in the finest fraction of Sample B (<75 μm), whereas more than 40% of the concentrations of Mn, Cu, Zn, and Mg resided in the coarse fraction (150 - 200 μm).

Exposure dose

The health effects caused by heavy metals exposure were assessed by using mean concentrations of bulk dust (<200 μm) according to Eq (1) – (5). The HQs and HIs calculated through three exposure pathways for adults are presented in Table 4. The HI values for non-carcinogenic effects decreased in the order of Zn>Al>Fe>Cr>Pb>Mn>Ba>Ni>Cu>Mg>Cd. In general, all of these HIs were less than 1, indicating that these concentration levels did not present a significant toxicity risk to the occupants. Exposure pathway via dust ingestion contributed to the highest risk, followed by dermal absorption, and inhalation. As shown in Table 3, metal concentrations in the smaller size fractions of dust may be 1-2 orders of magnitude higher than those measured in bulk dust, suggesting a possibility of lower estimates of inhalation exposure using <200 μm particle size.

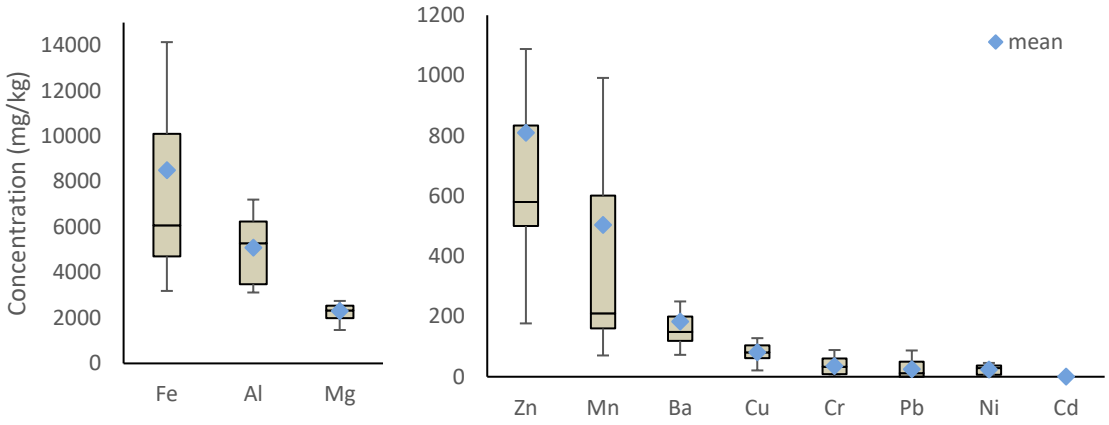


Figure 1. Concentration of heavy metals in vacuum cleaner dust samples

Table 2. Correlation matrix for heavy metal concentrations

	Al	**Cr**	**Mn**	**Ni**	**Zn**	**Cu**	**Cd**	**Ba**	**Pb**	**Mg**	**Fe**
Al	1	0.75	0.29	0.86*	0.14	0.82*	0.61	0.86*	0.74	-0.18	0.64
Cr		1	0.07	0.61	-0.11	0.93*	0.00	0.50	0.41	-0.39	0.79*
Mn			1	-0.07	0.71	0.32	0.41	-0.07	-0.11	0.68	-0.43
Ni				1	-0.14	0.57	0.61	0.93*	0.78*	-0.43	0.71
Zn					1	-0.04	0.20	0.07	0.15	0.82*	-0.50
Cu						1	0.20	0.46	0.37	-0.29	0.68
Cd							1	0.61	0.42	0.20	0.00
Ba								1	0.93*	-0.29	0.64
Pb									1	-0.33	0.63
Mg										1	-0.82*
Fe											1

*Correlation is significant at the 0.05 level (2-tailed)

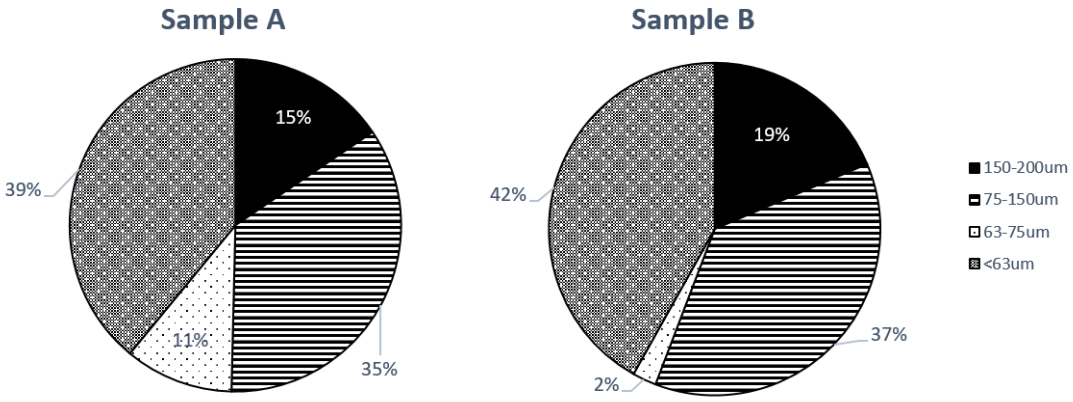


Figure 2. Pie chart showing the particle size distribution of Sample A and B

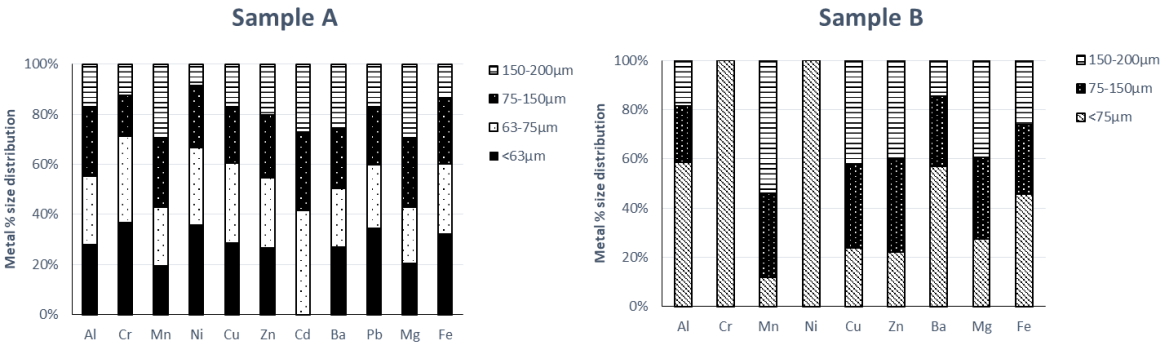


Figure 3. The distribution of heavy metals in different particle-size fractions of Sample A and B

Table 3. Concentrations of heavy metal in different size fractions

mg/kg	Sample A					Sample B			
	<63 µm	**63-75 µm**	**75-150 µm**	**150-200 µm**	**<200 µm**	**<75 µm**	**75-150 µm**	**150-200 µm**	**<200 µm**
Al	11000	10900	10900	6760	7740	4150	1610	1310	3240
Cr	69.0	65.0	31.0	23.2	33.0	140	BDL	BDL	0.710
Mn	706	847	1010	1060	782	1920	5620	8820	1720
Ni	72.6	63.0	50.9	17.3	43.4	37.3	BDL	BDL	6.24
Cu	129	145	102	76.2	81.9	116	166	204	65.3
Zn	967	1010	910	730	832	1110	1900	2000	836
Cd	BDL	1.130	0.850	0.740	0.190	BDL	BDL	BDL	BDL
Ba	446	390	398	422	420	85.9	43.4	22.0	72.6
Pb	100	72.9	67.2	49.0	55.1	BDL	BDL	BDL	BDL

Table 3 (cont'd). Concentrations of heavy metal in different size fractions

mg/kg	Sample A					Sample B			
	<63 µm	63-75 µm	75-150 µm	150-200 µm	<200 µm	<75 µm	75-150 µm	150-200 µm	<200 µm
Mg	2290	2490	3090	3280	2450	2890	3490	4180	2630
Fe	11500	10100	9290	4950	6070	4800	2940	2750	3190
Total	27300	26100	25900	17400	18500	15200	15800	19300	11800

BDL: Below detection limit

Table 4. Non-carcinogenic risks (HI) of heavy metals in indoor dust

	HQ_{ing}	HQ_{inh}	HQ_{der}	HI
Al	6.97E-03	2.60E-06	9.27E-05	7.06E-03
Cr	4.88E-03	1.82E-06	6.49E-05	4.94E-03
Mn	1.48E-03	5.50E-07	1.96E-05	1.50E-03
Ni	4.86E-04	1.81E-07	6.46E-06	4.92E-04
Zn	8.31E-03	3.10E-06	1.11E-04	8.43E-03
Cu	1.11E-04	4.12E-08	1.47E-06	1.12E-04
Cd	1.12E-05	4.16E-09	1.48E-07	1.13E-05
Ba	1.07E-03	4.00E-07	1.43E-05	1.09E-03
Pb	2.48E-03	9.25E-07	3.30E-05	2.52E-03
Mg	8.62E-05	3.21E-08	1.15E-06	8.74E-05
Fe	4.99E-03	1.86E-06	6.64E-05	5.06E-03

Conclusion

This study investigated the concentrations of selected heavy metals (Al, Cr, Mn, Ni, Zn, Cu, Cd, Ba, Pb, Mg, and Fe) from rural residential area of Simpang Renggam, Johor. Seven indoor dust samples (<200 µm) and two dust samples across size fractions <63 µm, 63-75 µm, 75-150 µm, and 150-200 µm were analyzed. The mean metal concentrations in bulk dust samples decreased in the following order: Fe> Al> Mg> Zn> Mn> Ba> Cu> Cr> Pb> Ni> Cd. For Fe and Al, the highest concentrations were found in the finest size fraction. For Mn, Mg, Cu, and Zn, the concentrations increased with increasing particle size, while no distinct trend could be observed for other metals. Human risk assessment based on <200 µm dust revealed HQ and HI values below than 1, indicating no non-carcinogenic risks from the exposure of these metals to the occupants. However, the enrichment of certain toxic metals in finer particle size suggested a likelihood of underestimating the exposure risk via inhalation. It should be kept in mind that the data set in this study is relatively small and therefore in future studies, investigation on the enrichment of a wider range of heavy metals in different particles size fractions of indoor dust collected from various environment would be more relevant for inhalation exposure assessment.

Acknowledgement

The research was supported by the Faculty of Industrial Sciences & Technology, Universiti Malaysia Pahang

through funding for final year project (SAA & MIIZK). The authors would like to thank all the participants for giving the opportunity and cooperation to successfully perform this study.

References

1. Lioy, P. J., Freeman, N. C. G. and Millette, J. R. (2002). Dust: A metric for use in residential and building exposure assessment and source characterization. *Environmental Health Perspectives,* 110(10): 969-983.
2. Barrio-Parra, F., De Miguel, E., Lázaro-Navas, S., Gómez, A. and Izquierdo, M. (2018). Indoor dust metal loadings: a human health risk assessment. *Exposure and Health,* 10(1): 41-50.
3. Lanzerstorfer, C. (2017). Variations in the composition of house dust by particle size. *Journal of Environmental Science and Health, Part A,* 52(8): 770-777.
4. Cao, Z.G., Yu, G., Chen, Y.S., Cao, Q.M., Fiedler, H., Deng, S.B., Huang, J. and Wang, B. (2012). Particle size: A missing factor in risk assessment of human exposure to toxic chemicals in settled indoor dust. *Environment International,* 49(15): 24-30.
5. Latif, M. T., Yong, S. M., Saad, A., Mohamad, N., Baharudin, N. H., Mokhtar, M. B. and Tahir, N. M. (2013). Composition of heavy metals in indoor dust and their possible exposure: a case study of preschool children in Malaysia. *Air Quality, Atmosphere & Health,* 7(2): 181-193.
6. Praveena, S. M., Abdul Mutalib, N. S. and Aris, A. Z. (2015). Determination of heavy metals in indoor dust from primary school (Sri Serdang, Malaysia): Estimation of the health risks. *Environmental Forensics,* 16(3): 257-263.
7. Tan, S. Y., Praveena, S. M., Abidin, E. Z. and Cheema, M. S. (2018). Heavy metal quantification of classroom dust in school environment and its impacts on children health from Rawang (Malaysia). *Environmental Science and Pollution Research,* 25(34): 34623-34635.
8. Wahab, N. M. A., Darus, F. M., Isa, N., Sumari, S. M. and Hanafi, N. F. M. (2012). Heavy metal concentration of settled surface dust in residential building. *Malaysian Journal of Analytical Sciences,* 16(1): 18-23.
9. USEPA (2011). *Exposure Factors Handbook* (EPA/600/R-09/052F). U.S. Environmental Protection Agency, Washinton, DC.
10. Darus, F. M., Nasir, R. A., Sumari, S. M., Ismail, Z. S. and Omar, N. A. (2012). Heavy metals composition of indoor dust in nursery schools building. *Procedia - Social and Behavioral Sciences,* 38: 169-175.
11. Latif, M. T., Othman, M. R., Kim, C. L., Murayadi, S. A. and Sahaimi, K. N. A. (2009). Composition of household dust in semi-urban areas in Malaysia. *Indoor and Built Environment,* 18(2): 155-161.
12. Ardashiri, S. and Hashemi, S. E. (2018). Health risk assessment of heavy metals in indoor dust from Bushehr, Iran. *Iranian Journal of Health, Safety & Environment,* 5(2): 966-971.
13. Chattopadhyay, G., Lin, K. C.-P. and Feitz, A. J. (2003). Household dust metal levels in the Sydney metropolitan area. *Environmental Research,* 93(3): 301-307.
14. Lin, Y., Fang, F., Wang, F. and Xu, M. (2015). Pollution distribution and health risk assessment of heavy metals in indoor dust in Anhui rural, China. *Environmental Monitoring and Assessment,* 187(9): 565.
15. Rasmussen, P. E., Levesque, C., Chénier, M., Gardner, H. D., Jones-Otazo, H. and Petrovic, S. (2013). Canadian house dust study: Population-based concentrations, loads and loading rates of arsenic, cadmium, chromium, copper, nickel, lead, and zinc inside urban homes. *Science of The Total Environment,* 443: 520-529.
16. Yoshinaga, J., Yamasaki, K., Yonemura, A., Ishibashi, Y., Kaido, T., Mizuno, K., Takagi, M. and Tanaka, A. (2014). Lead and other elements in house dust of Japanese residences – source of lead and health risks due to metal exposure. *Environmental Pollution,* 189: 223-228.
17. Cheng, Z., Chen, L. J., Li, H. H., Lin, J. Q., Yang, Z. B., Yang, Y. X., Xu, X. X., Xian, J. R., Shao, J. R. and Zhu, X. M. (2018). Characteristics and health risk assessment of heavy metals expossure via household dust from urban area in Chengdu, China. *Science of the Total Environment,* 619-620: 621-629.
18. Tong, S. T. Y. and Lam, K. C. (2000). Home sweet home? A case study of household dust contamination in Hong Kong. *Science of the Total Environment,* 256: 115-123.
19. Doyi, I. N. Y., Isley, C. F., Soltani, N. S. and Taylor, M. P. (2019). Human exposure and risk associated with trace element concentrations in indoor dust from Australian homes. *Environmental International,* 113: 105125.

20. Beamer, P. I., Elish, C. A., Roe, D. J., Loh, M. M. and Layton, D. W. (2012). Differences in metal concentration by particle size in house dust and soil. *Journal of Environmental Monitoring,* 14(3): 839-844.
21. Hassan, S. K. M. (2012). Metal concentrations and distribution in the household, stairs and entryway dust of some Egyptian homes. *Atmospheric Environment,* 54: 207-215.
22. Juhasz, A. L., Weber, J., Naidu, R., Gancarz, D., Rofe, A., Todor, D. and Smith, E. (2010). Determination of cadmium relative bioavailability in contaminated soils and its prediction using in vitro methodologies. *Environmental Science & Technology,* 44(13): 5240-5247.
23. Doyi, I. N. Y., Strezov, V., Isley, C. F., Yazdanparast, T. and Taylor, M. P. (2020). The relevance of particle size distribution and bioaccessibility on human health risk assessment for trace elements measured in indoor dust. *Science Total of Environment,* 733: 137931.

Malaysian Journal of Analytical Sciences (MJAS)
Published by Malaysian Analytical Sciences Society

SYNTHESIS AND CHARACTERIZATION OF 4-CHLOROPHENOXYACETIC ACID HERBICIDE INTERCALATED INTO CALCIUM-ALUMINIUM LAYERED DOUBLE HYDROXIDE THROUGH CO-PRECIPITATION METHOD

(Sintesis dan Pencirian Herbisid Asid 4-Klorofenoksiasetik Diinterkalatkan dengan Kalsium-Aluminium Hidroksida Dua Lapisan Melalui Kaedah Pemendakan Bersama)

Farah Liyana Bohari[1], Muhammad Alinsan Kamil Mukamil Hamzah[1],
Sheikh Ahmad Izaddin Sheikh Mohd Ghazali[1]*, Nur Nadia Dzulkifli[1], Is Fatimah[2], Nurain Adam[3]

[1]Material, Inorganic, and Oloechemistry (MaterInoleo) Research Group,
School of Chemistry and Environment, Faculty of Applied Sciences
Universiti Teknologi MARA Cawangan Negeri Sembilan Kampus Kuala Pilah, 72000, Negeri Sembilan, Malaysia
[2]Department of Chemistry, Faculty of Mathematics and Natural Sciences,
Universitas Islam Indonesia, Kampus Terpadu UII, J1. Kaliurang Km 14, Sleman, Yogyakarta, Indonesia
[3]Kontra Pharma (M) Sdn Bhd (90082-V)
Kotra Technology Centre (Block B) 1,2 &3, Industrial Estate,75250, Jalan Ttc 12, Malacca, Malaysia

**Corresponding author: sheikhahmadizaddin@uitm.edu.my*

Received: 15 September 2021; Accepted: 10 November 2021; Published: 27 December 2021

Abstract

Layered double hydroxide (LDH) or hydrotalcite-like compound is a material that can be used in agriculture as a support for controlled release formulations of herbicides such as 4-chlorophenoxyacetic acid (4-CPA). In this study, calcium-aluminium (Ca-Al) LDH host was prepared as a new herbicide delivery system by intercalating 4-CPA with Ca-Al LDH through a co-precipitation method. The synthesis was performed at pH 12 using different concentrations of $Al(NO_3)_3.9H_2O$, which were 0.025 M and 0.10 M. The successful intercalation was obtained using 0.025 M of $Al(NO_3)_3.9H_2O$ and has been confirmed through several analyses. First, the results obtained from the powder X-ray diffraction (PXRD) pattern showed that the basal spacing for the 0.025M nanocomposites had increased from 8.54 Å to 9.98 Å, indicating the successful intercalation of 4-CPA into the Ca-Al LDH. Meanwhile, the basal spacing of the 0.1 M nanocomposite remains unchanged. This result was supported by the ATR-FTIR band, which showed that the nitrate peak disappeared and the carboxylate ion (COO^-) band was present at 1634 cm^{-1} unlike the nitrate peak for the 0.10 M nanocomposite, which remained at 1365 cm^{-1}. The nanocomposite synthesized has shown mesoporous-type material with a H3 hysteresis loop in the Brunauer-Emmett-Teller (BET) analysis. This study has demonstrated the potential of Ca-Al LDH as a safer agent for agrochemicals by reducing the dosage of herbicide in the agriculture field and protecting the herbicide through leaching and runoff into the water system.

Keywords: 4-chlorophenoxyacetic acid, intercalation, co-precipitation, layered double hydroxide, nanoparticles

Abstrak

Hidroksida dua lapisan (LDH) atau sebatian seperti hidrotalsit ini adalah bahan yang boleh digunakan sebagai sokongan bagi formulasi pelepasan terkawal untuk racun herba seperti asid 4-klorofenoksiasetik (4-CPA) dalam pertanian. Dalam kajian ini, perumah kalsium-aluminium (Ca-AL) LDH telah dihasilkan sebagai sistem hantaran racun herba yang baharu dengan menginterkalat 4-CPA ke dalam Ca-Al LDH melalui kaedah pemendakan bersama. Sintesis ini telah dilakukan pada pH 12 dengan kepekatan yang berbeza untuk $Al(NO_3)_3.9H_2O$ iaitu 0.025 M dan 0.10 M. Interkalasi yang berjaya telah diperolehi dengan menggunakan 0.025 M $Al(NO_3)_3.9H_2O$ dan telah disahkan melalui beberapa analisis. Pertama, keputusan yang diperolehi daripada pola serbuk belauan sinar-X (PXRD) menunjukkan bahawa penjarakan asas untuk komposit nano 0.025 M telah meningkat daripada 8.54 Å kepada 9.98 Å, membuktikan kejayaan interkalasi 4-CPA ke dalam Ca-Al LDH. Manakala penjarakan asas bagi komposit nano 0.10 M kekal sama. Keputusan ini telah disokong oleh jalur ATR-FTIR menunjukkan kehilangan puncak nitrat dan kewujudan jalur ion karboksilat (COO^-) pada 1634 cm^{-1} tidak seperti puncak nitrat pada 0.10 M yang kekal pada 1365.30 cm^{-1}. Komposit nano yang telah disintesis menunjukkan bahan jenis mesoliang dengan gelung hysteresis H3 dalam analisis Brunauer-Emmett-Teller (BET). Kajian ini telah membuktikan potensi Ca-Al LDH sebagai agen agrokimia yang lebih selamat dengan mengurangkan dos racun herba dalam bidang pertanian dan melindungi racun herba daripada melarut resap dan meleleh ke dalam sistem air.

Kata kunci: 4-klorofenoksiasetik, interkalasi, pemendakan bersama, hidroksida dua lapisan, zarah nano

Introduction

In plants, competition between other species occurs due to the availability of resources such as nutrients and sunlight to achieve maximum efficiency. Weeds are unwanted species that are not necessary because they have a negative biotic factor effect by reducing crop yields, making harvesting difficult, harbouring insects, and, at the end of the day, reducing the quality and marketability of agriculture production. An increasing number of herbicides found these days are the result of increases in the number of weed species, which have introduced significant crop safety and improved weed management. A good herbicide possesses good properties such as being effective at low doses, low-cost manufacture, and friendly to users, but most importantly is safe for the environment.

Layered double hydroxide, or LDH, is a two-dimensional nanosheet with the common formula of $[M^{2+}_{1-x}\ M^{3+}_{x}\ (OH)_2]^{x+}\ (An^-)x/n.\ mH_2O$, where M^{2+} and M^{3+} are divalent and trivalent cations, respectively, and An^- is an organic and inorganic anion [1]. Ion exchange or precipitation methods can be used to introduce inorganic or organic anion between the interlayers of LDH [2]. The most important properties of LDH for this research are environmental capability, especially in agriculture, which are high uptake capacity [3], surface area, high anion-exchange capability, and flexible interlayer space [4–7]. The nature of the interlayer anion can also be freely selected while there are negative charged particles, and simultaneously, LDH is an interesting field to study, especially in agriculture, because it can be proved to support the movement of catalytic active anion between the interlayer regions [8–9]. To the best of my knowledge, only a few studies on this topic have been reported yet, especially on Ca-Al LDH intercalated with herbicide.

4-chlorophenoxyacetic acid, or known as 4-CPA, that is a selective herbicide that used to control the growth of broadleaf weeds [10]. This low cost, high efficiency, and good water solubility herbicide belongs to the chlorinated herbicide group, which is used as a plant growth regulator and is widely employed for thinning in peaches and inhibiting root growth in mung beans [11]. As the herbicide has high solubility, it can easily be absorbed into the surface or groundwater and lead to contamination [12]. 4-CPA, whose high solubility in water has become a concern, has been categorised by the US EPA as a priority pollutant and many studies have been done to overcome this problem [13].

The intercalation of 4-CPA into the interlayer of LDH can minimise and control the issues caused by the massive use of herbicide in water reservoirs due to the properties of LDH that are capable of anion exchange

capacity. Other than that, intercalation of 4-CPA into Ca-Al LDH also seems to reduce the amount of chemicals used for agriculture.

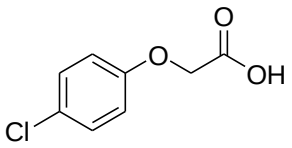


Figure 1. Formula structure of 4-chlorophenoxyacetic acid

Materials and Methods

Chemicals and reagents

The chemical used for the guest anion is 4-chlorophenoxyacetic Acid (4-CPA) from Sigma Aldrich to intercalate into the Ca-Al LDH. Meanwhile, the chemicals used to prepare the host were aluminium nitrate nonahydrate, $Al(NO_3)_3.9H_2O$ and calcium nitrate tetrahydrate, $Ca(NO_3)_2.6H_2O$ from R&M Chemical, and deionized water. 2 M of sodium hydroxide (NaOH) from the QreC brand is used to make the solution alkaline in the presence of nitrogen gas. The other chemical used in this experiment was absolute ethanol from R&M Chemical, to be diluted with the guest anion. All solutions were prepared using deionized water.

Synthesis of calcium-aluminium layered double hydroxide

The host of Ca-Al LDH was prepared by the co-precipitation method. For the precursors, 0.1 M of $Ca(NO_3)_2.6H_2O$ and different concentrations of $Al(NO_3)_3.9H_2O$ in the range of 0.025 M and 0.1 M were mixed together in a 250 ml conical flask filled with deionized water. 2 M of NaOH solution was added dropwise to the mixture with vigorous stirring to obtain a pH close to 13 [14]. The mixture was stirred vigorously to ensure the solids were completely dissolved under the purge of the nitrogen gas to prevent co-intercalation of CO_2. Later, the solution was aged in an oil bath shaker for 18 h at 70°C. Then, the precipitate was centrifuged at 300 rpm and washed with deionized water up to three cycles to remove the impurities. The precipitate was dried at 80°C in the oven for 72 h before further characterization using PXRD and Fourier-transformed infrared spectroscopy (FTIR) instruments

Synthesis of 4CPA-CaAl LDH by co-precipitation method

In a conical flask filled with deionized water, 0.1 M $Ca(NO_3)_2.6H_2O$ were mixed together with 0.025 M and 0.1 M of $Al(NO_3)_3.9H_2O$. Next, 0.1 M 4-CPA guest anion was diluted with a ratio of 9:1 of absolute ethanol and deionized water. The diluted mixture of 4-CPA was gradually added into the aqueous mixture of $Ca(NO_3)_2.6H_2O$ and $Al(NO_3)_3.9H_2O$ followed by the addition of 2.0 M of NaOH with vigorous stirring. The solution was kept at a pH of around 13 ± 0.05 under the nitrogen atmosphere. The solution was aged for 18 h at 70°C, centrifuged, washed with deionized water, and filtered with a vacuum filter [14]. Lastly, the precipitate was dried in the oven at a temperature of 80°C for 72 h. The sample is kept in a vial for further use and characterization.

Characterization technique

X-ray powder diffraction (XRD) pattern in the 2θ range 5° to 90° was recorded with Panalytical model Empyrean (Panalytical, Almelo, Netherlands) operating at 40 kV and 35 mA using Cu Kα radiation (λ = 1.54059 Å). The FTIR spectra were recorded on Perkin-Elmer infrared spectrophotometer using ATR mode with a resolution of 4 cm^{-1} in the range of 4000–650 cm^{-1}. The nitrogen adsorption-desorption of the nanocomposites was tested with Micromeritics Gemini 2375 for BET analysis.

Results and Discussion

Co-precipitation method

Figure 2 demonstrates the PXRD patterns for Ca-Al LDH host and 4CPA-CaAl LDH nanocomposite. From Figure 2(a), which is the Ca-Al LDH host, there is a sharp, high crystallinity, and intense peak that can be observed at 2θ = 10.35°. The basal spacing was calculated using the Bragg's Law formula and the result obtained is 8.54 Å, indicating the interlayer gallery of the host is originally accommodated by water molecules and nitrates ion. By dint of extensive hydrogen bonding, water molecules adhering to nitrate and metal hydroxide can regularly break and form a new bond [15]. Apart from that, the amount of water molecules in the interlayer depends on some considerations such as counter anions distinctive, the water vapour pressure,

and the surrounding temperature. The basal spacing of 8.54 Å is in good agreement with the sum of the anion NO_3^- (4.1 Å) and the brucite-like layer (4.8 Å) thicknesses [16].

For the 0.025 M 4CPA-CaAl LDH nanocomposite, based on Figure 2(b), the peak was slightly shifted downwards from 2θ = 10.35° to 8.85°. The peak displays a sharp, high-crystallinity, and symmetric peak with an increased basal spacing of 9.98 Å after the intercalation process took place. The expansion of the basal spacing signifies the inclusion of a new guest anion, 4-CPA into the interlayer. This also proves that the 4-CPA anion has higher affinity compared to the Ca-Al LDH host [15]. Thus, this intercalation was assumed to be a success since there was an absence of nitrate peak ion in the PXRD pattern. In contrast, as shown in Figure 2(c), the basal spacing of the 0.1 M 4CPA-CaAl LDH nanocomposite remained unchanged at 8.54 Å, indicating that the nitrate ion remained in the interlayer of the Ca-Al LDH host. Therefore, we can conclude that 4-CPA was not fully intercalated into the Ca-Al LDH host as there was the presence of a nitrate ion. The result is supported by the FTIR result.

Attenuated total reflectance Fourier transform infrared spectroscopy

Figure 3 shows three different infrared bands which were prepared using $Ca(NO_3)_2.6H_2O$ and $Al(NO_3)_3.9H_2O$. The most important aspect to highlight is the presence of the nitrate group band in the range of 1350 to 1400 cm^{-1}. This peak should disappear or decrease in intensity to confirm the successful intercalation between Ca-Al LDH and 4-CPA. Figure 3(a) demonstrates the Ca-Al LDH host that has a broad peak corresponding to OH stretching at 3567 cm^{-1}, which appears as a bending vibration of the water molecule and the distortion mode of water. The anti-symmetric stretching vibration of nitrate is reflected by a sharp split peak at 1401 cm^{-1} and 1354 cm^{-1}. These indicate the presence of the nitrate group in the interlayer gallery of Ca-Al LDH [17]. The absorbance 797 cm^{-1} indicates the peak for chlorine. The intercalation process of 4-CPA into Ca-Al LDH host led to different spectra by comparing them to the spectra of pure 4-CPA and Ca-Al LDH host as they exhibited both spectra and characteristics.

As shown in Figure 3(b), for 0.025 M 4CPA-CaAl LDH nanocomposite, both nitrate peaks from the previous result, which disappeared at 1354 cm^{-1}, show the 4-CPA successfully intercalated with the layer of Ca-Al LDH host, implying that the nitrate ion, which was supposed to be the original anion between the Ca-Al LDH layer, were fully removed and replaced with 4-CPA. Furthermore, the peaks of the carboxylic group at 1732 cm^{-1} and 1233 cm^{-1} were diminished and a strong new peak, carboxylate ion (COO^-), appeared at 1634 cm^{-1}. This peak belongs to the anionic form of 4-CPA, which is very necessary to confirm that the intercalation process took place [15]. This shows that the herbicide 4-CPA has a higher affinity than the nitrate toward the interlayer space of LDH. The present of O-H stretching at 3567 cm^{-1} due to adsorbed and/or interlayer water [1], 1492 cm^{-1} and 1411.23 cm^{-1} correspond to C=C stretching vibration of the aromatic compounds. In addition, band 1236 cm^{-1} was attributed to the C-O-C stretching vibration. In contrast, for 0.1 M 4CPA-CaAl LDH, the nitrate peak remained in the FTIR spectra at 1365 cm^{-1}, indicating that 4-CPA was not completely intercalated into the layer of Ca-Al LDH host.

Spatial orientation and molecular structure

Figure 4 shows the illustration of the molecular structure and the proposed spatial orientation of 4CPA-CaAl LDH nanocomposite. As we can observe from the increasing basal spacing of the nanocomposite, the gallery height of the interlayer region of the nanocomposite after being subtracted with the layer thickness of the Ca-Al LDH, which is 5.18 Å. This research can be deduced that the anions were oriented in a monolayer arrangement in between the interlayer region of the LDH due to consideration of the 4-CPA molecular structure and charge orientation. As shown in Figure 4(b), the interlayer space is much larger than the anion size, where the functional group of carboxylates is facing the hydroxide layer.

Surface properties

Based on Figure 5, the nitrogen adsorption-desorption describes the intercalated compound of 4-CPA anion with the LDH host. According to the IUPAC, the

intercalated compound and the host exhibited type IV sorption isotherms with a H3 hysteresis loop, which belongs to mesoporous materials [19]. These mesoporous materials are made up of plate-like materials with slit-shaped pores that agglomerate. The hysteresis loop of the intercalated nanocomposite portrays a wider adsorption branch compared to the host. This is due to the expansion of basal spacing during the exchange of nitrate ion with 4-CPA into the interlayer host. As observed for the LDH host, it showed slow adsorbate uptake at a relative pressure range of 0.0–0.8 with a maximum uptake of 7 cm^3/g. Meanwhile, rapid adsorption can be shown for the intercalated nanocomposite, 4CPA-CaAl LDH with relative pressure ranging from 0.0–0.6, reaching the maximum adsorbate uptake at 184 cm^3/g.

The average pore diameter for both Ca-Al LDH and 4CPA-CaAl LDH were all between 20 Å and 500 Å, indicating the presence of mesoporous materials. Based on the pore size distribution of the intercalated nanocomposite, it showed a broad distribution of pores with a maximum diameter of approximately 400–500 Å. A sharp peak can be observed at 475 Å for the intercalated nanocomposite. However, for the host, a sharp peak appeared at 625 Å with a pore volume lower than the intercalated nanocomposite, which is 0.04 cm^3/g. The difference in pore size and the pore volume of both, the host and the intercalated compound might be due to the formation of the interstitial pores between the crystallites, aggregation during the intercalation process, and the particle size differences [16].

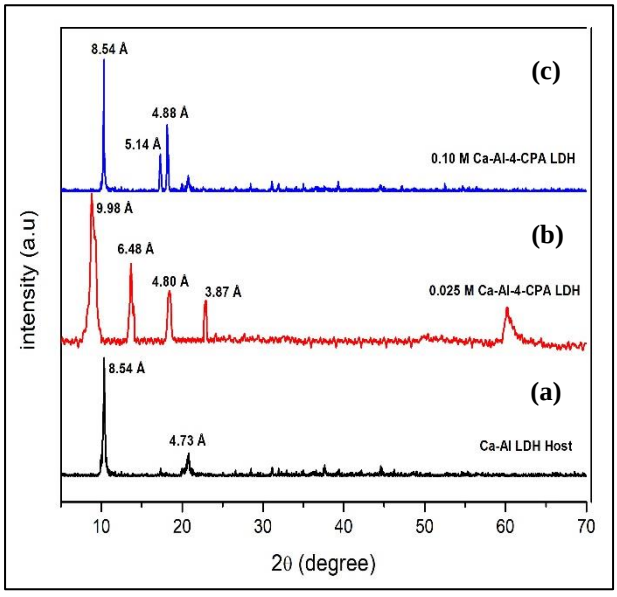


Figure 2. PXRD pattern for (a) Ca-Al LDH host, (b) 0.025 M 4CPA-CaAl LDH, (c) 0.10 M 4CPA-CaAl LDH

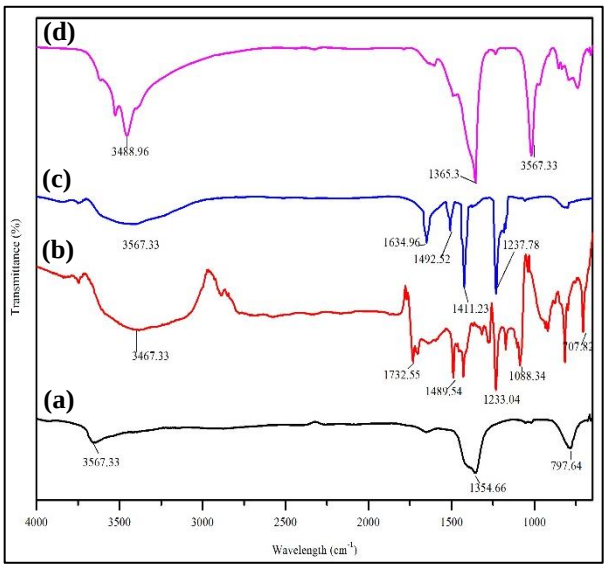


Figure 3. ATR-FTIR spectrum for (a) Ca-Al LDH Host, (b) Pure 4-CPA, (c) 0.025 M 4CPA-CaAl LDH, (d) 0.10 M 4CPA-CaAl LDH

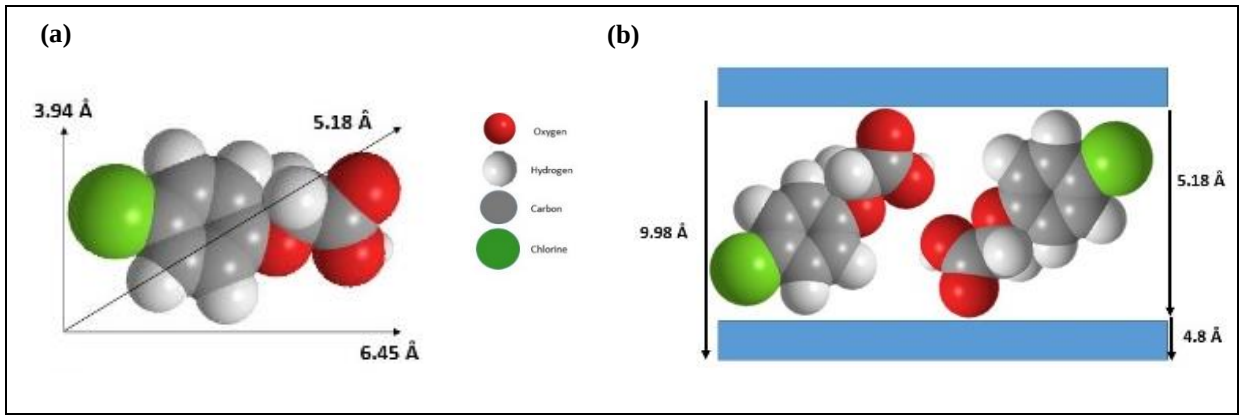


Figure 4. Illustration of (a) molecular structure of 4-CPA and (b) spatial orientation of 4-CPA in between the LDH interlayer region

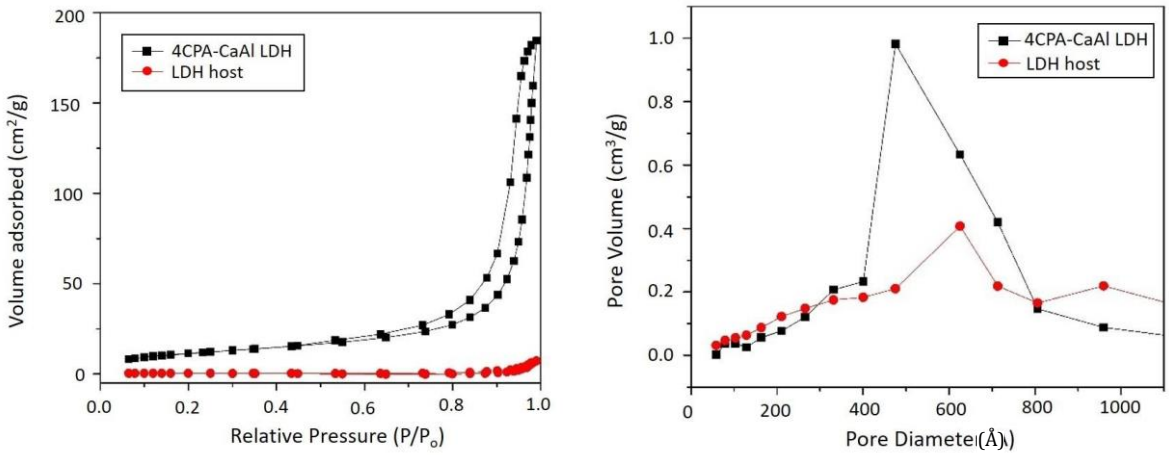


Figure 5. Adsorption-desorption isotherm and pore size distribution of LDH host and 4CPA-CaAl LDH nanocomposite

Conclusion

In summary, the intercalation of 4-CPA into the interlayer regions of Ca-Al LDH host was successfully done via co-precipitation method at pH 12, by using the concentration of 0.025 M $Al(NO_3)_3.9H_2O$ instead of 0.1 M. This can be deduced by the interpretation of the PXRD pattern that shows for 0.025 M 4CPA-CaAl LDH nanocomposite, the increase in basal spacing of the crystalline compound at 9.98 Å from 8.54 Å due to the inclusion of 4-CPA into the interlayer regions of the Ca-Al LDH host, but for 0.1 M 4CPA-CaAl LDH nanocomposite, the basal spacing remains unchanged. The ATR-FTIR band shows the absence of a nitrate peak from the Ca-Al LDH host and the presence of a new generation band such as at 1634 cm^{-1} for COO^- and C=C stretching vibration of the aromatic compounds at 1492 cm^{-1} and 1411 cm^{-1}. In the BET analysis, the adsorption-desorption isotherms have shown that the intercalated nanocomposite of the 4CPA-CaAl LDH is a mesoporous material with a H3 type hysteresis loop. In fact, the wider hysteresis loop for the synthesized nanocomposite proved that the anion of 4-CPA had intercalated into the interlayer host of LDH. Thus, this study proves that intercalated 4CPA-CaAl LDH has the potential to reduce the excess amount of herbicide to ensure a safe environment.

Acknowledgement

The assistance provided by Universiti Teknologi MARA (UiTM) and Ministry of Higher Education (MoHE) is greatly acknowledged and appreciated. The authors would like to thank the MoHE for financial support through the Fundamental Research Grant Scheme [600-IRMI/FRGS 5/3 (112/2019)] and everyone who has contributed upon the completion of this project.

References

1. Prasad, C., Tang, H. and Liu, W. (2018). Magnetic Fe_3O_4 based layered double hydroxides (LDHs) nanocomposites (Fe_3O_4/LDHs): recent review of progress in synthesis, properties and applications. *Journal of Nanostructure in Chemistry*, 8(4): 393-412.
2. Sarijo, S. H., Ghazali, S. A. I. S. M., Hussein, M. Z. and Ahmad, A. H. (2015). Intercalation, physicochemical and controlled release studies of organic-inorganic–herbicide (2, 4, 5 tricholorphenoxy butyric acid) nanohybrid into hydrotalcite-like compounds. *Materials Today: Proceedings*, 2(1): 345-354.

3. Valente, J. S., Tzompantzi, F., Prince, J., Cortez, J. G. and Gomez, R. (2009). Adsorption and photocatalytic degradation of phenol and 2, 4 dichlorophenoxiacetic acid by Mg-Zn-Al layered double hydroxides. *Applied Catalysis B: Environmental*, 90(3–4): 330-338.
4. Matusinovic, Z., Lu, H., and Wilkie, C. A. (2012). The role of dispersion of LDH in fire retardancy: The effect of dispersion on fire retardant properties of polystyrene/Ca−Al layered double hydroxide nanocomposites. *Polymer Degradation and Stability,* 97(9): 1563-1568.
5. Bernardo, M. P., Moreira, F. K. V., and Ribeiro, C. (2017). Synthesis and characterization of eco-friendly Ca-Al-LDH loaded with phosphate for agricultural applications. *Applied Clay Science,* 137: 143-150.
6. Mills, S. J., Christy, G., Genin, J.-M. R., Kameda, T. and Colombo, F. (2012). Nomenclature of the hydrotalcite supergroup: natural layered double hydroxide. *Mineralogical Magazine,* 76(5): 1289-1336.
7. Baikousi, M., Stamatis, A., Louloudi, M. and Karakassides, M. A. (2013). Thiamine pyrophosphate intercalation in layered double hydroxides (LDHs): An active bio-hybrid catalyst for pyruvate decarboxylation. *Applied Clay Science,* 75: 126-133.
8. Jaśkaniec, S., Hobbs, C., Seral-Ascaso, A., Coelho, J., Browne, M. P., Tyndall, D. and Nicolosi, V. (2018). Low-temperature synthesis and investigation into the formation mechanism of high-quality Ni-Fe layered double hydroxides hexagonal platelets. *Scientific Reports,* 8(1): 4179.
9. Bashi, A. M., Hussein, M Z., Zainal, Z., Rahmani, M. and Tichit, D. (2012). Simultaneous intercalation and release of 2,4-dichloro-and 4-chloro-phenoxyacetate into Zn/Al layered double hydroxide. *Arabian Journal of Chemistry,* 9: 1457-1463.
10. Derylo-Marczewska, A., Blachnio, M., Marczewski, A. W., Swiatkowski, A. and Buczek, B. (2017). Adsorption of chlorophenoxy pesticides on activated carbon with gradually removed external particle layers. *Chemical Engineering Journal,* 308: 408-418.
11. Baliyan, S. P., Rao, K. M., Baliyan, P. S. and Mahabile, M. (2013). The effects of 4-chlorophenoxy acetic acid plant growth regulator on the fruit set, yield and economic benefit of growing tomatoes in high temperatures. *International. Journal Agriculture Science,* 3(2): 29-36.
12. Pirozzi, D., Sannino, F., Pietrangeli, B., Abagnale, M., Imparato, C., Zuccaro, G. and Aronne, A. (2017). Oxidative degradation of organic pollutants by a new hybrid titania-based gel-derived material with stable radical species. *Chemical Engineering Transactions,* 57: 769-774.
13. Abdelhaleem, A. and Chu, W. (2017). Photodegradation of 4-chlorophenoxyacetic acid under visible LED activated N-doped TiO_2 and the mechanism of stepwise rate increment of the reused catalyst. *Journal of Hazardous Materials,* 338: 491-501.
14. Songkhum, P., Wuttikhun, T., Chanlek, N., Khemthong, P. and Laohhasurayotin, K. (2018). Controlled release studies of boron and zinc from layered double hydroxides as the micronutrient hosts for agricultural application. *Applied Clay Science,* 152: 311-322.
15. Ali, N. S. M., Hasanuddin, N. I., Azizan, N. A., Abdullah, A., Dzulkifli, N. N., Me, R., and Ghazali, S. M. (2017) Development of herbicide delivery system based on magnesium aluminium–4-chlorophenoxyacetic acid (MAC) nanocomposite. *Journal of Engineering and Science Research*, 1(2): 152-157.
16. Ghazali, S. A. I. S. M., Hussein, M. Z. and Sarijo, S. H. (2013). 3,4-Dichlorophenoxyacetate interleaved into anionic clay for controlled release formulation of a new environmentally friendly agrochemical. *Nanoscale Research Letters,* 8: 362.
17. Barahuie, F., Hussein, M. Z., Arulselvan, P., Fakurazi, S. and Zainal, Z. (2014). Drug delivery system for an anticancer agent, chlorogenate-Zn/Al-layered double hydroxide nanohybrid synthesised using direct co-precipitation and ion exchange methods. *Journal of Solid State Chemistry,* 217:31-41.

18. Hussein, M. Z., Nazarudin, N. F. B., Sarijo, S. H. and Yarmo, M. A. (2012). Synthesis of a layered organic-inorganic nanohybrid of 4-chlorophenoxyacetate-zinc-layered hydroxide with sustained release properties. *Journal of Nanomaterials,* 5: 189-195.

19. Megat, S., Mohsin, N., Hussein, M. Z., Sarijo, S. H., Fakurazi, S., Arulselvan, P. and Hin, T. Y. (2013). Synthesis of (cinnamate-zinc layered hydroxide) intercalation compound for sunscreen application. *Chemistry Central Journal,* 26(7): 1-12.

Malaysian Journal of Analytical Sciences (MJAS)
Published by Malaysian Analytical Sciences Society

CONCENTRATION OF HEAVY METALS IN *Perna veridis* COLLECTED FROM STRAITS OF JOHOR, MALAYSIA

(Kepekatan Logam Berat di dalam *Perna veridis* yang Dikumpulkan dari Selat Johor, Malaysia)

Tee Lian Sheng[1], Poong Jun Han[1], Evonne Tan[1], Yip Tiam Hing[1], Muhammad Hasbi Ramli[1], Zaleha Kassim[2], Ong Meng Chuan[1,3,4]*

[1]Faculty of Science and Marine Environment,
Universiti Malaysia Terengganu, 21030 Kuala Nerus, Terengganu, Malaysia
[2]International Institute for Halal Research and Training (INHART),
International Islamic University Malaysia, 25200 Kuantan, Pahang, Malaysia
[3]Institute of Oceanography and Environment
[4]Ocean Pollution and Ecotoxicology (OPEC) Research Group
Universiti Malaysia Terengganu, 21030 Kuala Nerus, Terengganu

**Corresponding author: ong@umt.edu.my*

Received: 13 September 2021; Accepted: 28 October 2021; Published: 27 December 2021

Abstract

Perna viridis or green mussel is commercially valuable seafood rich in protein and mainly cultured in the Straits of Johor. Over the years, industrial activities and urban development around the Straits of Johor keep increasing, which may cause heavy metal pollution issues in the aquatic environment. Therefore, this study evaluated the concentration of heavy metals in the green mussel *Perna viridis* collected from the river mouth of Sungai Masai at the Straits of Johor for assessing the level of pollution level with this species as a bio-indicator. The concentration of Cd, Cu, Pb, and Zn of 45 green mussel samples was detected using the inductively coupled plasma mass spectrometry (ICP-MS). The samples were digested using the Teflon Bomb method with HNO_3. In general, the concentration of heavy metals in *Perna viridis* followed the descending order from Zn > Cu > Pb > Cd. The heavy metal content of the green mussel in this study complied with the permissible safety limit stipulated by the 1985 Malaysia Food Regulation. Meanwhile, unlike the findings of other studies, the accumulation of heavy metal in the green mussels in this study might not be related to its size. No significant correlation was detected among these heavy metals, suggesting that they might not come from the same source. The average pollution load index was 3.3, i.e., substantially than the critical level of 50, suggesting that the pollution of heavy metals in the study area was under control.

Keywords: green mussel, heavy metals, inductively coupled plasma mass spectrometry, *Perna viridis*, Straits of Johor

Abstrak

Perna viridis atau kupang hijau adalah salah satu makanan laut komersial yang kaya dengan protein dan kebanyakannya diternak di Selat Johor. Selama bertahun-tahun, aktiviti perindustrian dan pembangunan bandar di sekitar Selat Johor terus meningkat dan ini boleh menyebabkan isu pencemaran logam berat di dalam persekitaran akuatik. Oleh itu, kajian ini telah dijalankan untuk menentukan kepekatan logam berat di dalam *Perna viridis* yang dikumpulkan dari Sungai Masai di Selat Johor dan menganggarkan tahap pencemaran dengan menggunakan *Perna viridis* sebagai penanda biologi. Kepekatan Cd, Cu, Pb dan Zn

dalam 45 Perna veridis dianalisis dengan menggunakan spektrometri jisim-plasma gandingan aruhan (ICP-MS). Kaedah pencernaan Teflon Bomb dengan asid HNO_3 telah digunakan untuk menghadam sampel. Secara umumnya, susunan kepekatan logam berat dalam *Perna viridis* adalah Zn> Cu> Pb> Cd. Kepekatan logam berat dalam *Perna veridis* juga mematuhi piawaian dengan had keselamatan yang dibenarkan oleh Peraturan Makanan Malaysia, 1985. Sementara itu, tidak seperti penemuan kajian lain, pengumpulan logam berat pada Perna veridis dalam kajian ini mungkin tidak berkaitan dengan saiznya. Tidak ada korelasi yang signifikan dikesan di antara logam berat ini, menunjukkan bahawa logam ini mungkin tidak berasal dari sumber yang sama. Indeks beban pencemaran purata (PLI) adalah 3.3, iaitu jauh dari tahap kritikal 50, menunjukkan bahawa pencemaran logam berat di kawasan kajian masih terkawal.

Kata kunci: kupang hijau, logam berat, spektrometri jisim-plasma gandingan aruhan, *Perna viridis*, Selat Johor

Introduction

Straits of Johor, located between the southern part of Peninsular Malaysia and Singapore, is a narrow and shallow waterway with a width of less than 6 km and a depth of 25 m [1]. Most of the lands near the Straits of Johor have been developed into industrial, aquaculture, urbanisation, and agriculture area. The Straits of Johor is an important place for commercial shipping due to the presence of major ports like Johor, Tanjung Langsat and Tanjung Pelepas ports. It is also an essential area for sustaining the corals, mangroves, mudflats and seagrass ecosystems [2]. Many marine life species such as fishes and shellfishes can be found in the Straits of Johor. These organisms are valuable resources for consumption by residents of both Malaysia and Singapore [3]. Over the past few decades, the Straits of Johor has become severely contaminated by heavy metals due to rapid development [2].

Metals polluting the coastal environment are primarily due to anthropogenic inputs such as mining, fossil fuel combustion, municipal wastewater, and the metal industry. However, freshwater inputs are also another indirect source of many chemical pollutants into the marine environment [4]. Among these pollutants, heavy metals are the most harmful ones with high toxicity to human health and aquatic organisms [5]. Since heavy metals do not degrade [6], their concentrations tend to substantially increase when they enter the human body and organisms due to bioaccumulation and bio-magnification [7]. Although heavy metals are toxic to human health, small amounts of essential elements such as Ca, Fe, Ni, Zn, Mg, Mn, and Cu are required for all living organisms for biological purposes. However, non-essential elements such as Cr, Pb, and Cd are harmful to live organisms even in low concentrations [8]. As long as these elements do not exceed the standard limits, their toxicity would be under control [9].

In this respect, the green mussel Perna virdis is susceptible to bio-accumulation of heavy metals in the waterways. This seafood, owing to its high protein content [11] is commonly consumed by Asians. It is widely in the Asian region, Malaysia included [10]. It filters suspended substances and plankton in the water column for food. Along with the suspended particles, pollutants such as heavy metals could accumulate in its body rapidly [12]. When exceeding the safety level, the consumption of this polluted seafood would harm human health.

This study evaluated the concentration of heavy metals in *Perna viridis* collected from the river mouth of Sungai Masai at the Straits of Johor. With the rapid development in the last few decades, this strait has become a hotspot for heavy metal contamination [2]. Wastewaters containing heavy metals were indiscriminately discharged into this marine environment. Incidentally, the farming of *Perna viridis* has also become one of the primary aquaculture activities in the Straits of Johor [13]. Thus, it was essential to assess the food safety of *Perna viridis* and the level of pollution at the Straits of Johor or its surrounding rivers.

Materials and Methods

Study area

The Straits of Johor, approximately 30mi (50km) long, is one of the major maritime routes in Southeast Asia and the busiest shipping activities and few major ports in the area, such as Pasir Gudang and Tanjung Pelepas Ports, Malaysia. In this study, farm-raised green mussels were sampled from the aquaculture site at the river mouth of Sungai Masai (Figure 1) in the eastern part of the Straits of Johor near the Pasir Gudang Port and other areas of heavy industries.

Sample collection and preparation

A total of 45 Perna veridis were collected from the aquaculture racks at the river mouth of Sungai Masai. These mussels were at marketable size, ranging from 48.6 to 80.4 mm in carapace width with an average of 61.2 mm. They weighed 5.8 to 23.3 g with an average of 11.2 g. The collected mussels were kept at low temperature in an ice chest and then transported to the laboratory for analysis.

Each sample was rinsed with distilled water before removing this total tissue (in-toto) with a ceramic knife. The in-toto was weighed and dried in an oven at 60 °C to obtain a constant weight. Each in-toto was then ground into powder using a mortar and pestle. The pestle, mortar, and spatula used were cleaned with 95% ethanol before grinding another mussel [14, 15].

Analytical procedures

Contamination of metallic elements in biota was generally analysed using the Teflon Bomb nitric acid digesting method. The digestion method used in this study was adopted from other studies [16, 17] with slight modifications. Specifically, 1.5 mL of 65% HNO_3 (Suprapur®) was added to 0.05 g dried powder sample placed in a Teflon beaker. The Teflon beaker was then closed tightly in the Teflon jacket and heated in the oven at 100 °C for 8 hours. Upon cooling, the digested sample was then transferred into a centrifuge tube and topped up with deionised water to 10 mL. The samples were then analysed using Inductively Coupled Plasma Mass Spectrometry (ICP-MS).

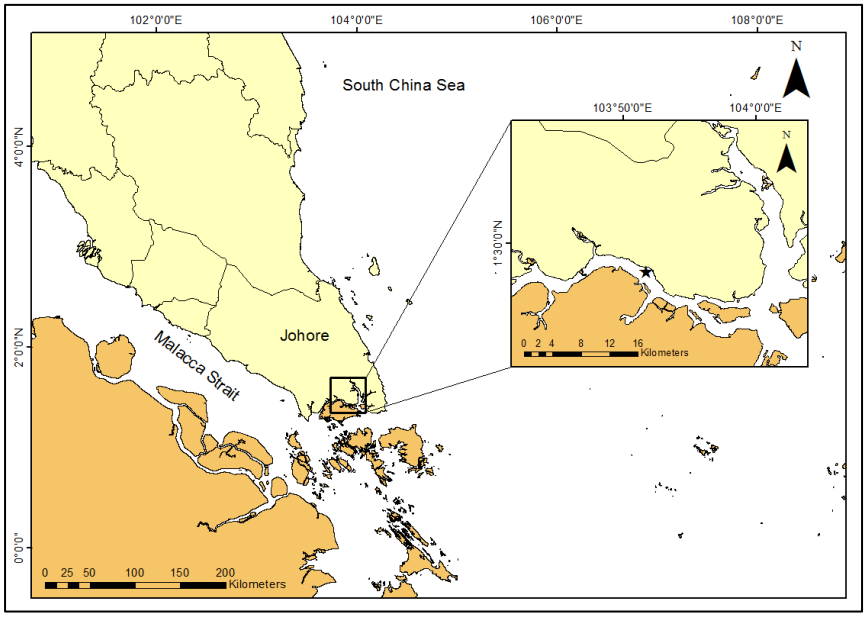


Figure 1. The sampling site (★)at the Straits of Johor, Malaysia

Results and Discussion

The standard 1946 dogfish liver certified reference material (DOLT-4) was used to determine the accuracy of the analytical methodology of this study. Table 1 shows the recovery percentage for various heavy metals, namely Cd, Cu, Pb, and Zn, with accuracy ranging between 80% and 115% [18]. The individual recovery of Cd, Cu, Pb, and Zn was 87.2, 92.3, 112.5, and 94.8%, respectively.

Figure 1 shows the average concentration of various heavy metals in *Perna viridis* in a decreasing order, i.e., Zn (38.9 µg/g dw) > Cu (7.8 µg/g dw) > Pb (0.41 µg/g dw) > Cd (0.14 µg/g dw). This finding is consistent with the results reported in other studies [19, 20]. Zinc accumulated the fastest in the body of the green mussel, while Cd the longest time to build up its concentration [21]. Zinc is an essential precursor for enzymatic activities [19] and is generally abundant in seafood [22]. The Zn concentration of this study (38.9 µg/g dw) was higher than that (28.8 µg/g dw) of another study with samples from the east coast of Peninsular Malaysia [23] Nevertheless, it still complied with the permissible safety level (50 µg/g dw) stipulated by the Malaysia Food Regulation (1985). In other words, the green mussels of Sungai Masai were still safe for human consumption.

Similar to Zn, Cu is also an essential element for living organisms [24]. Cu is usually stored in soft tissues for body functions and transportation of oxygen to tissues is through hemocyanin that contains Cu [25]. The Cu concentration (7.8µg/g dw) in the green mussel of this study also complied with the safety limit of the 1985 Malaysia Food Regulation (30 µg/g dw).Cu in waterways usually comes from metal industries and the use of fossil fuels [26]. In another study that used *Perna viridis* as a bioindicator for water pollution, the eastern part of the Straits of Johor was found to be more polluted than its western side [27]. Thus, the Cu metal detected in this study might have come from other sources such as river runoff and housing activities rather than industrial activity located along the straits.

Meanwhile, both Pb and Cd are non-essential and toxic metals [28]. These elements could accumulate in the body of an organism because they are structurally analogous to essential elements [29]. These toxic metals may be assimilated into tissues and incorporated into intercellular areas and cell components. A high concentration of Cd will cause kidney dysfunction, reproductive deficiencies, and skeletal damage in the human body [30]. They generally occur in trace amounts in our environment. Indeed, the concentration Pb (0.41µg/g dw) and Cd (0.14 µg/g dw) detected in the soft tissue of P. was substantially lower than the permissible level of the Malaysia Food Regulation (1985), i.e., 2 µg/g dw for Pb and 1 µg/g dw for Cd.

Table 2 compares the average concentration of heavy metals in the present study with various other studies within and without Malaysia. The ranking of locations in the Malaysia region for all heavy metals measured generally followed the descending trend of Kg. Pasir Puteh > Pantai Lido > Sungai Masai (present study). These differences might be attributable to the levels and types of industrialisation of the area, and the population density [31]. Industrial production, urbanisation, agricultural activities, and excessive chemicals discharged excess heavy metals into the waterways. In this study, Sungai Masai was just located adjacent to urban areas with comparatively fewer nearby industrial activities nearby. In comparison, both Kg. Pasir Puteh and Pantai Lido were located near industrial, agricultural, and urban areas [32], presumably discharging more heavy metals into their waterways.

Also, the average concentrations of Zn and Cu in this study were lower than that of the Singapore waters, probably because Punggol and Sembawang were located near a recreational port and maintenance shipyards, respectively. Besides, the results of the present study were also lower than that of Hong Kong Tsim Sha Tsui, which was located near the Victoria Harbour with intensive human activities, such as shipping and industries. The sewages were also discharged into the marine environment from the

densely populated surrounding area [34], contributing to high levels of heavy metal pollution.

However, the body size of the green mussel could affect the accumulation of metal [35]. Smaller and younger mussels tended to accumulate more Cd, Pb, and Zn than larger and older ones [36]. As the mussels grow, the kinetic steady-states will change, causing differential uptake of heavy metal uptakes [37]. Individuals of *Perna viridis* in this study were larger (5 – 8 cm) than those in Hong Kong (3.0 - 3.5 cm). Thus, the lower concentrations of heavy metals in this study might partly be due to the larger size of the green mussels.

Figure 2 shows the relationship between the weight of *Perna viridis* and the concentrations of heavy metals in their soft tissues. The weight showed a weak positive correlation with Cu and Cd but a weak negative relationship with Pb. However, these correlations were not significant (r ranged from -0.058 to 0.301), and the accumulation of heavy metals in the green mussels of this study might not be related to body size. Meanwhile, freshwater inputs from river upstream were another indirect source of chemical elements in the marine environment [38]. Presumably, these freshwater inputs might also affect the uptake of heavy metals in *Perna viridis*.

Table 3 shows the pairwise correlation between the selected heavy metals in *Perna viridis*. In general, all metals show a positive correlation with each other, indicating that the metals were affected by similar conditions from natural and anthropogenic sources [39]. These findings suggested that the metals might come from the same sources, such as shipping, industrial and urban activities.

The PLI was used to compare the extent of heavy metal pollution at the river mouth of Sungai Masai. The PLI was calculated using Equation 1 with baseline data from another study [32].

Table 4 shows the PLI values of .*Perna viridis* ranged from 1.5 to 6.7 with an average of 3.3. In general, periodic monitoring of the water quality would be essential if the PLI value is larger than 50 [40]. In other words, the pollution at the river mouth of Sungai Masai was still under control.

$$Pollution\ Load\ Index\ (PLI) = \sqrt[n]{CF_1 x\ CF_2 x\ CF_3 x \dots \dots x\ CF_n} \quad (1)$$

where

$$Contamination\ Factor\ (CF) = \frac{Concentration\ of\ metals\ in\ this\ study}{Concentration\ of\ baseline\ data}$$

Table 1. Recovery percentage for heavy metals concentration (µg/g dw*) based on the standard 1946 dogfish liver certified reference material (DOLT-4)

Metals	**Measured Values (µg/g dw)**	**Certified Values (µg/g dw)**	**Recovery Percentage (%)**
Cadmium (Cd)	21.2 ± 1.2	24.3 ± 0.8	87.2
Copper (Cu)	28.8 ± 1.5	31.2 ± 1.1	92.3
Lead (Pb)	0.18 ± 0.07	0.16 ± 0.04	112.5
Zinc (Zn)	110 ± 8.0	116 ± 6.0	94.8

*dw = dry weight

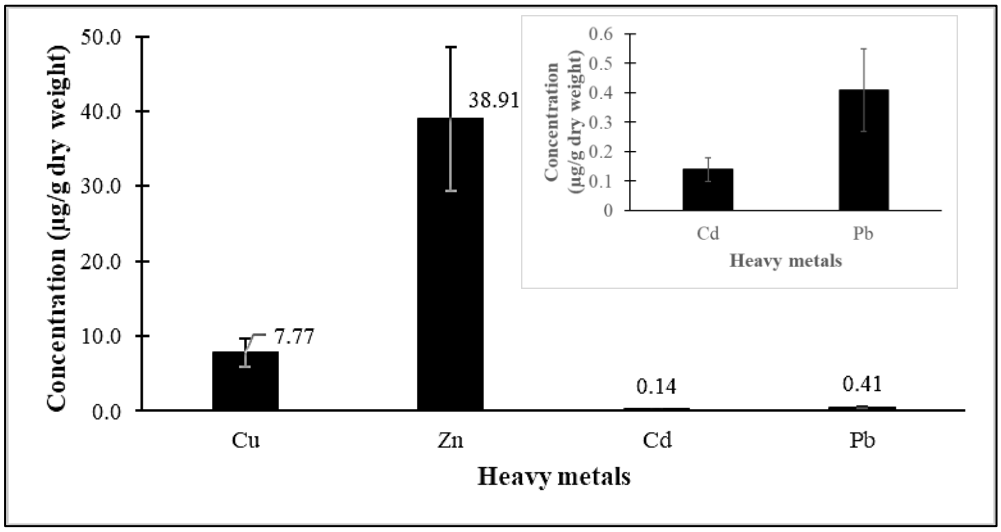


Figure 1. The average concentration of heavy metals in *Perna viridis*

Table 2. Comparison of heavy metals in *Perna viridis* with other studies

Location	Cd	Cu	Pb	Zn	Reference
Hong Kong, Tsim Sha Tsui	0.31	11.50	1.20	69.50	[33]
Singapore, Punggol	BDL	27.00	BDL	343.00	[27]
Singapore, Sembawang	BDL	35.00	3.40	446.00	[27]
Malaysia, Pantai Lido	0.68	9.39	4.03	116.9	[32]
Malaysia, Kg. Pasir Puteh	0.82	20.10	8.76	128.9	[32]
Malaysia, Sungai Masai	0.14	7.77	0.41	38.9	Present study

(BDL: Below detection limit)

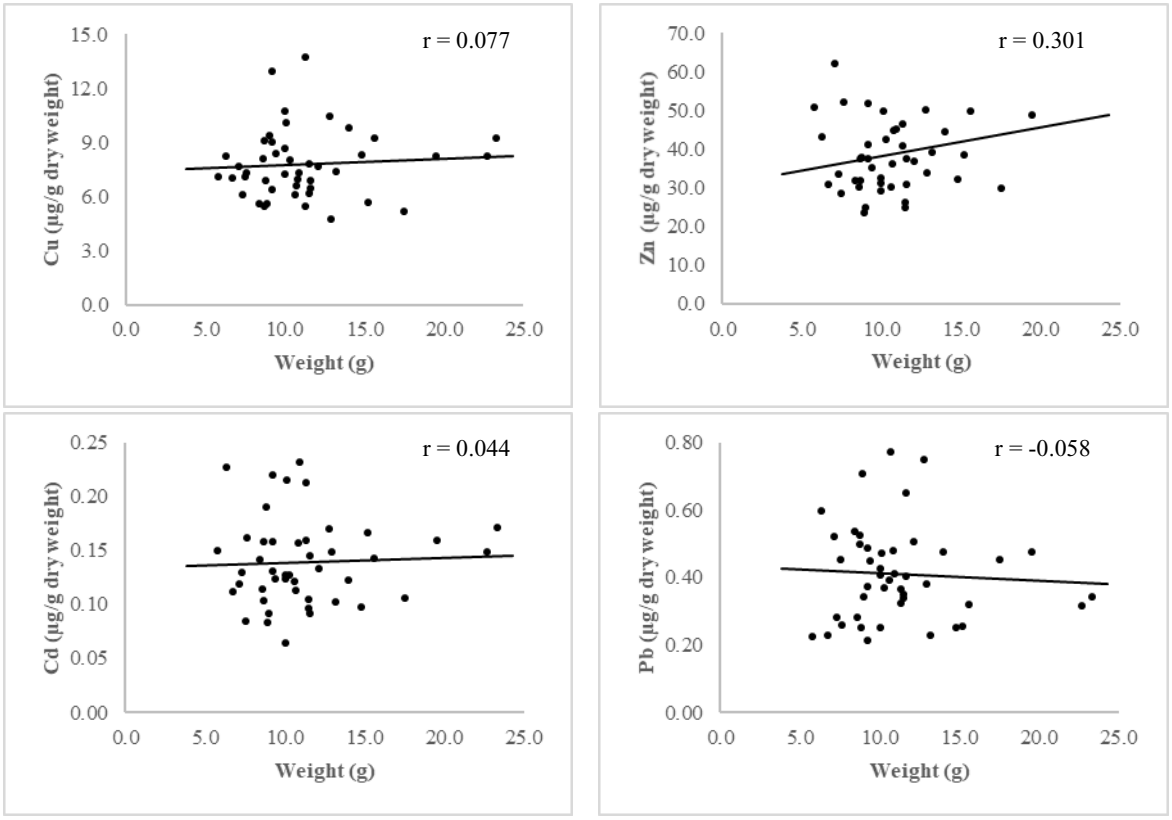


Figure 2. Concentrations of heavy metals concentration (Cu, Zn, Cd, and Pb) against the body weight of *Perna viridis*

Table 3. Correlation in concentrations between heavy metals found in *Perna viridis*

	Cu	**Zn**	**Cd**
Zn	0.478		
Cd	0.283	0.647	
Pb	0.230	0.379	0.387

Table 4. The calculated PLI value in *Perna viridis*

	Baseline Concentration of Metal (µg/g)	**PLI value**
Cd	0.25	
Cu	6.31	3.27
Pb	1.27	(1.49 - 6.74)
Zn	53.82	

Conclusion

The green mussel *Perna viridis* collected from the Straits of Johor showed a level of heavy metal concentration for heavy metals. In general, essential elements, such as Zn and Cu accumulated a higher concentration in the soft tissue of the green mussel than the non-essential elements (Pb and Cd) in a descending order Zn (w µg/g dw) > Cu (x µg/g dw) > Pb (y µg/g dw) > Cd (z µg/g dw). Overall, the heavy metal content of the green mussel in this study complied with the permissible safety limit stipulated by the 1985 Malaysia Food Regulation. Contradictory to the findings of other studies, the results of this study indicated that the accumulation of heavy metal in the green mussels might not be related to its size. Low heavy metals concentration in *Perna viridis* and PLI (average: 3.3) indicated the pollution of heavy metals in the study area was under control.

Acknowledgement

This research was funded by the Malaysian Ministry of Higher Education under the Fundamental Research Grant Scheme FRGS/1/2020/WAB05/UMT/02/5. The authors wish to thank the anonymous reviewers for their constructive recommendations to improve this manuscript. Thanks also go to the Oceanography Laboratory, Faculty of Science and Marine Environment staff for their invaluable assistance and the facilities to carry out the research. The authors also would like to thank Dr. Asnor Azrin Sabuti from International Islamic University Malaysia Kuantan Campus for the sample detection using ICP-MS.

References

1. Wood, A. K., Ahmad, Z., Shazili, N. A. M., Yaakob, R. and Carpenter, R. (1997). Geochemistry of sediments in Johor Strait between Malaysia and Singapore. *Continental Shelf Research*, 17: 1207-1228.
2. Zulkifli, S. Z., Ismail, A., Mohamat-Yusuff, F., Arai, T. and Miyazaki, N. (2010). Johor Strait as a hotspot for trace elements contamination in Peninsular Malaysia. *Bulletin of Environmental Contamination and Toxicology*, 84: 568-573.
3. Zulkifli, S. Z., Mohamat-Yusuff, F., Ismail, A., Aris, A. Z., Aziz, A., Sabuti, A. A. and Mohamed, C. A. R. (2015). Status of heavy metals on surface sediments of the western part of the Johor Straits using a sediment quality guideline. *World Journal of Fish and Marine Sciences*, 7(3): 214-220.
4. Sin, T. M., Ang, H. P., Buurman, J., Lee, A. C., Leong, Y. L., Ooi, S. K., Steinberg, P. and Teo, S. L. M. (2016). The urban marine environment of Singapore. *Regional Studies in Marine Science*, 8: 331-339.
5. Ali, H., Khan, E. and Ilahi, I. (2019). Environmental chemistry and ecotoxicology of hazardous heavy metals: Environmental persistence, toxicity, and bioaccumulation. *Journal of Chemistry*, 2019: 6730305.
6. Zhang, Z. Y., Juying, L., Mamat, Z. and QingFu, Y. (2016). Sources identification and pollution evaluation of heavy metals in the surface sediments of Bortala River, Northwest China. *Ecotoxicology and Environmental Safety*, 126: 94-101.
7. Kalantzi, I., Shimmield, T. M., Pergantis, S. A., Papageorgiou, N., Black, K. D. and Karakassis, I. (2013). Heavy metals, trace elements and sediment geochemistry at four Mediterranean fish farms. *Science of the Total Environment*, 444: 128-137.
8. Ong, M. C., Yong, J. C., Khoo, X. Y., Tan, Y. F. and Joseph, B. (2014). Selected heavy metals and polycyclic aromatic hydrocarbon in commercial fishes caught from UMT enclosed lagoon, Terengganu, Malaysia. *Advances in Environmental Biology*, 8(14): 91-98.
9. Beldi, H., Gimbert, F., Maas, S., Scheifler, R. and Soltani, N. (2006). Seasonal variations of Cd, Cu, Pb and Zn in the edible mollusc *Donax trunculus* (Mollusca, Bivalvia) from the Gulf of Annaba, Algeria. *African Journal of Agricultural Research*, 1(4): 85-90.
10. Tan, K. S. and Julian, R. (2014). A review of feeding behavior, growth, reproduction and aquaculture site selection for green-lipped mussel, *Perna viridis*. *Advances in Bioscience and Biotechnology*, 5: 462-469.

11. Zhang, X., Huang, H., He, Y., Ruan, Z., You, X., Li, W., Lu, Z., Liu, B, Deng X and Shi Q. (2019). High-throughput identification of heavy metal binding proteins from the byssus of Chinese green mussel (*Perna viridis*) by combination of transcriptome and proteome sequencing. *PLoS ONE*, 14 (5): e216605.
12. Riani, E., Cordova, M. R. and Arifin, Z. (2018). Heavy metal pollution and its relation to the malformation of green mussels cultured in Muara Kamal Waters, Jakarta Bay, Indonesia. *Marine Pollution Bulletin*, 133: 664-670.
13. Hadibarata, T., Abdullah, F., Mohd Yusoff, A. R., Ismail, R., Azman, S. and Adnan, N. (2012). Correlation study between land use, water quality, and heavy metals (Cd, Pb, and Zn) content in water and green lipped mussels *Perna viridis* (Linnaeus.) at the Johor Strait. *Water, Air, & Soil Pollution*, 223: 3125-3136.
14. Kamaruzzaman, B. Y., Ong, M. C., Zaleha, K. and Shahbudin, S. (2008). Levels of heavy metals in green-lipped mussel *Perna veridis* (Linnaeus) from Muar Estuary, Johore, Malaysia. *Pakistan Journal of Biological Sciences*, 11 (18): 2249-2253.
15. Ong, M. C., Kamaruzaman, M. I., Yong, J. C., Kamaruzzaman, B. Y. and Joseph, B. (2017). Metals contamination using *Polymesoda expansa* (marsh clam) as bio-indicator in Kelantan river, Malaysia. *Malaysian Journal of Analytical Sciences*, 21(3): 597-604.
16. Ong, M. C., Shazili, N. A. M., Menier, D. and Effendy, A. W. M. (2013). Levels of trace elements in tissue of *Ostrea edulis* and *Crassostrea gigas* from Quiberon Bay, Brittany, France. *Journal of Fisheries and Aquatic Science*, 8(2): 378-387.
17. Ong, M. C. and Gan, S. L. (2017). Assessment of metallic trace elements in the muscles and fins of four landed elasmobranchs from Kuala Terengganu Waters, Malaysia. *Marine Pollution Bulletin*, 124(2): 1001-1005.
18. Yohannes, Y. B., Ikenaka, Y., Nakayama, S. M. M., Saengtienchai, A., Watanabe, K. and Ishizuka, M. (2013). Organoclorine pesticides and heavy metals in fish from Lake Awassa, Ethiopia: Insights from stable isotope analysis. *Chemosphere*, 91: 857-863.
19. Kamaruzzaman, B. Y., Rina, Z., John, B. A. and Jalal, K. C. A. (2011). Heavy metal accumulation in commercially important fishes of south west Malaysian coast. *Research Journal of Environmental Sciences*, 5(6): 595.
20. Ong, M. C., Tan, Y. F., Khoo, X. Y. and Yong, J. C. (2015). Heavy metals and polycyclic aromatic hydrocarbons (PAHs) concentration in mud crab (*Scylla serrata*) from UMT mangrove, Terengganu, Malaysia. *Advances in Environmental Biology*, 9(21): 66-74.
21. Eugene Ng, Y. J., Yap, C. K., Zakaria, M. P. and Tan, S. G. (2013). Assessment of heavy metal pollution in the straits of Johore by using transplanted caged mussel, *Perna viridis*. *Pertanika Journal of Science & Technology*, 21(1):75-96.
22. Stankovic, S. and Jovic, M. (2012). Health risks of heavy metals in the Mediterranean mussels as seafood. *Environmental Chemistry Letters*, 10(2): 119-130.
23. Yap, C. K., Ismail, A., Tan, S. G. and Omar, H. (2002). Correlations between speciation of Cd, Cu, Pb and Zn in sediment and their concentrations in total soft tissue of green-lipped mussel *Perna viridis* from the east coast of Peninsular Malaysia. *Environment International*, 28(1-2): 117-126.
24. Ragi, A. S., Leena, P. P., Cheriyan, E. and Nair, S. M. (2017). Heavy metal concentrations in some gastropods and bivalves collected from the fishing zone of South India. *Marine Pollution Bulletin*, 118: 452-458.
25. Thanh-Nho, N., Marchand, C., Strady, E. Huu-Phat, N. and Nhu-Trang, T. T. (2019). Bioaccumulation of some trace elements in tropical mangrove plants and snails (Can Gio, Vietnam). *Environmental Pollution*, 248: 635-645.
26. Rehman, M., Liu, L., Wang, Q., Saleem, M. H., Bashir, S., Ullah, S. and Peng, D. (2019). Copper Environmental toxicology, recent advances, and future outlook: A review. *Environment Science and Pollution Research*, 26: 18003-18016.

27. Bayen, S., Thomas, G. O., Lee, H. K. and Obbard, J. (2004). Organochlorine pesticides and heavy metals in green mussel, *Perna viridis*, in Singapore. *Water, Air, & Soil Pollution*, 155: 103-116.
28. Hossen, M. F., Hamdan, S. and Rahman, M. R. (2015). Review on the risk assessment of heavy metals in Malaysian clams. *Scientific World Journal*, 2015: 1-7.
29. Lehtonen, K. K., d'Errico, G., Korpinen, S., Regoli, F., Ahkola, H., Kinnunen, T. and Lastumäki, A. (2019). Mussel caging and the weight of evidence approach in the assessment of chemical contamination in coastal waters of Finland (Baltic Sea). *Frontiers in Marine Science*, 6: 688.
30. European communities. (2001). Commission regulation no 466/2001 of 8 March 2001 setting maximum levels for certain contaminants in foodstuffs. OJEC L77.
31. Blackmore, G. (1998). An overview of trace metal pollution in the coastal waters of Hong Kong. *Science of the Total Environment*, 214: 21-48.
32. Yap, C. K., Ismail, A. and Tan, S. G. (2003). Background concentrations of Cd, Cu, Pb and Zn in the green-lipped mussel *Perna viridis* (Linnaeus) from Peninsular Malaysia. *Marine Pollution Bulletin*, 46: 1035- 1048.
33. Blackmore, G. and Wang, W. X. (2003). Comparison of metal accumulation in mussels at different local and global scales. *Environmental Toxicology and Chemistry*, 22: 388-395.
34. Richardson, B. J. and Zheng, J. S. (1999). Chlorinated hydrocarbon contaminants in Hong Kong surficial sediments. *Chemosphere*, 39: 61-71.
35. Cai, C. and Wang, W. W. (2019). Inter-species difference of copper accumulation in three species of marine mussels: Implication for biomonitoring. *Science of The Total Environment*, 692: 1029-1036.
36. Yap, C. K., Ismail, A. and Tan, S. G. (2009). Effect of body size on heavy metal contents and concentrations in green-lipped mussel *Perna viridis* (Linnaeus) from Malaysian coastal waters. *Pertanika Journal of Science & Technology*, 17(1): 61-68.
37. Tang, W. L., Evans, D., Kraemer, L. and Zhong, H. (2017). Body size-dependent Cd accumulation in the zebra mussel *Dreissena polymorpha* from different routes. *Chemosphere*, 168: 825-831.
38. Blair, R. M., Waldrin, S., Phoenix, V. R. and Gauchotte-Lindsay, C. (2019). Microscopy and elemental analysis characterisation of microplastics in sediment of a freshwater urban river in Scotland, UK. *Environmental Science and Pollution Research*, 26: 12491-12504.
39. Amin, B., Ismail, A., Arshad, A., Yap, C. K. and Kamarudin, M. S. (2009). Anthropogenic impacts on heavy metal concentrations in the coastal sediments of Dumai, Indonesia. *Environmental Monitoring and Assessment*, 148: 291-305.
40. Angulo, E. (1996). The Tomlinson Pollution Load Index applied to heavy metal, 'Mussel-Watch' data: A useful index to assess coastal pollution. *The Science of the Total Environment*, 187: 19-56.

Malaysian Journal of Analytical Sciences (MJAS)
Published by Malaysian Analytical Sciences Society

CONJUGATION OF TERNATIN BIOMOLECULE WITH POLYETHYLENE GLYCOL ENHANCED CONJUGATES SOLUBILITY AND STABILITY: SYNTHESIS AND PHYSICOCHEMICAL CHARACTERISATION

(Konjugasi diantara Molekul Ternatin dan Polietilena Glikol dengan Penambahbaikan Sifat Keterlarutan dan Kestabilan: Sintesis dan Pencirian Fizikokimia)

Nurul Aina Jamaludin and Noor Faizah Che Harun*

Green Chemistry and Sustainable Engineering Technology, Polymer Engineering Technology Section, Universiti Kuala Lumpur, Branch Campus Malaysian Institute of Chemical and Bioengineering Technology, 78000 Alor Gajah, Melaka, Malaysia

**Corresponding author: noorfaizah@unikl.edu.my*

Received: 15 September 2021; Accepted: 29 October 2021; Published: 27 December 2021

Abstract

Ternatin, a highly N-methylated cyclic heptapeptide has promising potential for cancer treatment. However, its efficiency in biological treatment is limited due to its poor solubility and high degradation in aqueous solution. In this present study, methoxy polyethylene glycol (mPEG)-ternatin conjugate abbreviated as mPEG-ternatin was synthesised by direct esterification between a carboxyl end group of methoxy polyethylene glycol, mPEG-COOH and a hydroxyl group in the β-position of ternatin biomolecule which enhanced its solubility and decreased the degradation of ternatin biomolecule in aqueous solution while retaining its inherent anticancer properties. To this end, mPEG-ternatin linked through ester bond was further confirmed using various analytical techniques including FTIR, UV-Vis spectroscopy and HPLC. Importantly, in the solubility and stability studies, the solubility of mPEG-ternatin conjugate was found to be 8% higher than unconjugated ternatin. Furthermore, mPEG-ternatin conjugate exhibited a decreasing percentage of degradation of ternatin biomolecule by 1.9-fold lower than unconjugated ternatin after incubation in 10 mM HEPES pH 7.4 buffer solution at 37 °C for 6 hours. Ultimately, the enhanced properties of ternatin biomolecule by conjugating with a mPEG segment is expected to become new fundamental study in related fields as well as provide new insight into cancer treatments.

Keywords: polyethylene glycol, ternatin, conjugation, esterification, solubility

Abstrak

Ternatin, dengan kandungan N-metil siklik heptapeptida yang tinggi mempunyai potensi untuk rawatan kanser. Walau bagaimanapun, keberkesanannya terbatas dalam rawatan biologi disebabkan rendah keterlarutan dan kestabilannya di dalam air. Dalam kajian ini, konjugat diantara metoksi polietilena glikol (mPEG) dan ternatin, mPEG-ternatin telah disediakan melalui proses pengesteran secara langsung diantara kumpulan karboksil dari metoksi polietilena glikol, mPEG-COOH dan kumpulan hidroksil di posisi β dalam biomolekul ternatin. Hal ini demikian, untuk meningkatkan keterlarutan dan kestabilan molekul ternatin di dalam larutan akues tanpa mengganggu sifat anti kansernya. PEG-ternatin yang dihubungkan melalui ikatan ester disahkan melalui pelbagai teknik analisa yang telah dilakukan iaitu FTIR, spektroskopi UV-Vis dan HPLC. Hasil daripada kajian

ini, keterlarutan biomolekul ternatin di dalam konjugat PEG-ternatin didapati ~8% lebih tinggi daripada molekul ternatin bebas. Sementara itu, melalui ujian kestabilan konjugat, PEG-ternatin menunjukkan penurunan peratusan degradasi molekul Ternatin sebanyak 1.9 kali ganda lebih rendah daripada molekul ternatin bebas. Kesimpulannya, penambahbaikan sifat molekul ternatin dengan kaedah konjugasi secara terus dengan molekul mPEG akan memberikan peluang baru dalam rawatan kanser.

Kata kunci: polietilena glikol, ternatin, konjugat, esterifikasi, keterlarutan, kestabilan

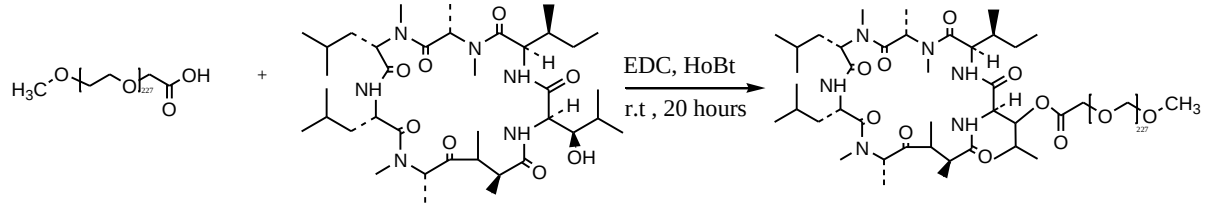
Introduction

In recent years, the research community has been working to create biomimetic materials that mimic the features present in nature. Moreover, a breakthrough has come out in recent development of polymer chemistry using a fundamental theory of polymer phase behaviour at site-specific modification of peptide, synthetic biology, and single-chain polymer [1, 2]. However, there had been slight changes in obtaining successful selective molecular transport, hierarchical structure control, modulated responsiveness to small perturbation, and long-term enzymatic activity [1]. Therefore, researchers had agreed that polymer-biomolecule conjugate would improve this limitation. Mostly polymer-biomolecule conjugates are performed by site-specific, direct conjugation, which allow precise control of the biomolecule to the polymer. Currently, few bioconjugation methods have been discovered, for example, click chemistry, amidation, thiol-maleimide conjugation and esterification [1, 5 - 8]. A biomolecule is chemically conjugated by the conjugation method to form a stable linker or a degradable linker, such as an ester, disulphide, or peptide [9 - 11]. Despite that, esterification is seen as a better alternative due to its simplistic nature, where further modification on biomolecule is not required. Therefore, polymer-biomolecule conjugates formed by direct covalent conjugation via esterification process are a likely-looking new class of materials since one component complements each other.

Ternatin is a highly *N*-methylated cyclic heptapeptide, a natural compound extracted from the mushroom *Coriolus versicolor*. Ternatin biomolecule has been receiving great attention due to its anti-tumour, anti-inflammatories and anti-diabetic properties. Besides, the researchers have discovered that ternatin biomolecule appears to have a fat accumulation inhibitor that can be used to study the structure-activity relationship (SAR) of the ternatin biomolecule [2 - 5]. Furthermore, Shimokawa et al. revealed that the presence of hydroxyl group located at D-Leu^7 derivative shows lower inhibition activity than that without this moiety, whereby the presence of the hydroxyl group in the D-Leu^7 derivative of this moiety is not essential. Therefore, make its availability to install with a new functional group. Moreover, until now, the chemical modifications of the Ternatin biomolecule have been discovered to enhance its biological properties, for example modification of Ternatin biomolecule as molecular probe and biotinylation of Ternatin biomolecule using click chemistry [6, 12, 13]. However, no study has been reported on the conjugation of Ternatin biomolecule with a polymer unit to improve the solubility and stability properties of Ternatin biomolecule.

In polymer-based drug delivery with stealth characteristics, PEG is the most extensively utilised non-ionic hydrophilic and biocompatible polymer [14]. PEG possess an excellent solubility in water as well as in organic solvents making it suitable for the conjugation of polymer-biomolecule. Moreover, the biological inert characteristic of PEG with low toxicity makes PEG perfect for biological applications [14, 15]. Previously, Bayard et al. reported a successful conjugation between mPEG with low molecular weight hydrophobic biomolecules including hormones and antioxidants through esterification leading to excellent drug pharmacokinetic properties [15]. Moreover, there is no fact-finding discussion on the conjugation of Ternatin biomolecule with a polymer unit to the best of our knowledge. Therefore, the remaining challenge inspired this study to develop the direct conjugation of a Ternatin biomolecule with a polymer and investigate its physicochemical properties as well as explore its potential applications.

In the present work, mPEG-Ternatin conjugate was synthesised *via* direct esterification between a carboxyl group of mPEG end group and a hydroxyl group in the D-Leu^7 derivative of the Ternatin biomolecule using Steglich condition. The reaction was conducted in 10 mM of HEPES with pH 7.4 buffer solution utilising a water soluble carbodiimide with the assistance of HOBt as coupling reagents. The general route employed for the synthesis of mPEG-Ternatin conjugate is shown in Figure 1. The mPEG-Ternatin conjugate was evaluated by their physicochemical properties through high-performance liquid chromatography (HPLC) analysis, Fourier transfer infrared (FTIR) analysis, and ultraviolet- visible (UV-Vis) spectrophotometer analysis, as well as solubility and stability studies. The results showed that a unit of polymer mPEG was successfully conjugated with a Ternatin biomolecule through esterification, and this conjugated mPEG improved the solubility and stability of Ternatin biomolecule. This new construction of molecular design in this present work is expected to be useful in the related field study such as in bioorganic and medicinal chemistry studies.



mPEG - COOH Unconjugated Ternatin mPEG-Ternatin

Figure 1. Synthetic design of mPEG-Ternatin

Materials and Methods

Materials

Ternatin was acquired from Cayman Chemical (Michigan) and used as received. Methoxy polyethylene glycol carboxyl (mPEG-COOH) was acquired from Advanced BioChemicals (USA). 1M *N*-(2-Hydroxyethyl) piperazine-N'-(2-ethanesulfonic acid) (HEPES), Phosphate buffer saline (PBS), 4-dimethyl aminopyridine (DMAP), 1-Hydroxybenzotriozole hydrate (HOBt), *N*-ethyl-N'-(3-dimethyl aminopropyl) carbodiimides (EDC), and ethanol were acquired from Sigma-Aldrich (USA) for the conjugation. Throughout the reaction and the purification process, ultra-pure water obtained from the Milli-Q water purification system was used. All the chemical agents, with an analytical grade were acquired from commercial sources in Malaysia.

Synthesis of methoxy polyethylene glycol and ternatin conjugate

The synthesis of mPEG-Ternatin conjugate was made based on the reported methodology with few modifications [1, 2]. Firstly, 30 mg of mPEG-COOH was dissolved in 4 mL mixture of 10 mM HEPES with pH 7.4 buffer solution. The mixture was vigorously stirred using a magnetic bar stirrer for 20 hours at 25 °C. To this, 1 mg, and 3 mg of HoBt and EDC were added after fine suspension of PEG were visible. Then, the carboxylate group was activated by continuously stirring the reaction solution for 3 hours. At the same time, the stock solution of Ternatin was prepared in 1 mL of 10 mM HEPES by dissolving 1 mg of Ternatin. Under a nitrogen condition, the mixture of 13.624 µM of Ternatin and 10 mM HEPES was gradually added to the activated PEG while stirring. The mixture was continuously stirred for 20 hours at 25 °C ambient temperature. The final product was purified against 10 mM HEPES, followed by deionised water using an Amicon Ultra-15 Centrifugal Filter Unit (Membrane NMWL= 3KDa) to remove the unreacted molecules. Then, mPEG-Ternatin conjugate was further analyse using various analytical technique including FTIR, UV-Vis Spectroscopy and HPLC.

Physicochemical characterisation: Reverse phase high-performance liquid chromatography analysis

Reverse phase high-performance liquid chromatography (HPLC) using an Ultimate 3000 DIONEX chromatograph equipped with a WPS-3000 autosampler a TCC-3100, a thermostat column compartment, Diode Array Detector DAD-3000, and LGP-3400 RS dual-pump fluid control module, was used to identify the purity of the unconjugated Ternatin and mPEG-Ternatin conjugate (Shelton, USA). The Chromeleon 6.80 software (Dionex Corporation) was used for the data acquisition. RP-HPLC analysis was performed using a reversed-phase C_{18} column as the stationary phase (Brownlee Analytical C_{18} 5µm, 150 mm × 4.6 mm) connected to a guard column (Brownlee Analytical C_{18}) (PerkinElmer Life and Analytical Sciences, Shelton, USA). The analysis of mPEG-Ternatin conjugate using HPLC was carried out following the method from previous literature with some modifications [2, 19, 20]. The mobile phase consisted of two components, A: 0.1% HCOOH in H_2O and B: 0.1% HCOOH in MeCN. The ratio of the components A and B was set at 40:60 (v/v), the flow rate was set at 1 mL/minute, and the total analysis time was 15 minutes. The volume of injection was 10 µL, the temperature of the sample and column were set at 25 °C ambient temperature, and the detector of UV-visible was set at 200nm and 280 nm to detect the content of unconjugated Ternatin and mPEG-Ternatin conjugate.

UV-Vis analysis

UV-Vis analysis of the emission and absorption spectra of the unconjugated ternatin and mPEG-ternatin conjugate was carried out on a double beam PerkinElmer Lambda EZ210 spectrophotometer using 1 cm length of quartz cuvette in a range of 200 nm to 400 nm to identify the wavelength and absorbance range of the conjugate. The mPEG-Ternatin conjugate was analysed at room temperature, and all the spectra were corrected to the blank data.

Fourier transform infrared spectroscopy analysis

Fourier transform infrared (FTIR) spectroscopy was used to identify the chemical structure characterisation between ternatin biomolecule and mPEG using PerkinElmer Spectrum RX1. The aim of chemical structure characterisation was to analyse different functional groups that vibrate at a particular frequency. In this experiment, the spectra were obtained by analysing mPEG-ternatin conjugate using FTIR with a range of 250-4000 cm^{-1} and a spectral resolution of 1 cm^{-1} at 25 °C ambient temperature with a single beam purgeable, single compartment.

Solubility analysis

1 mL of PEG-ternatin conjugate was added into 4 mL water and followed by stirring, sonicating and vortexing until the conjugate was fully dispersed in water. Next, the mixture was shaken in a constant shaking incubator for 24 hours before being centrifuged at 14,000 rpm for 5 minutes. The reaction solution was diluted two times lower than initial concentration. The obtained mPEG-ternatin conjugate was calculated from its concentration based on a ternatin calibration plot (R^2 = 0.996) by UV–Vis spectrometer at λ = 200 nm.

Stability analysis

1 mL of mPEG-ternatin conjugate was added into 4 mL of 10 mM HEPES pH 7.4 buffer solution and subsequently, the solutions were incubated at 37 °C for 6 hours. In an hour interval, the sample of mPEG-Ternatin conjugate was taken and the change of absorbance of the conjugate was determined and analysed by UV-Vis Spectrometer.

Results and Discussion

Characterisation of mPEG-ternatin conjugate

The mPEG-ternatin conjugate that was performed in 10 mM HEPES with pH 7.4 buffer solution utilising EDC as coupling reagent with the assistance HOBt at 25 °C for 20 hours was collected and purified by RP-HPLC and centrifugation, respectively. The conjugation percentage was confirmed and identified by HPLC spectra of ternatin absorption wavelength at 280 nm. Figure 2(a) depicts the HPLC spectrum of unconjugated ternatin exhibiting a sharp peak at the 1.55 min of elution time indicating the presence of ternatin biomolecule. Meanwhile, Figure 2(b) indicates the presence of mPEG-ternatin conjugate at 2.3 min of the elution time. The percentage conjugation of mPEG-

ternatin conjugate was calculated based on ternatin biomolecule's standard calibration curve. As a result, the percentage of concentration of mPEG-ternatin conjugate was found to be 49%. This indicates that the direct esterification reaction between the carboxyl group of mPEG, and the hydroxyl group in the β-position of ternatin biomolecule using the Steglich condition was confirmed to be successful and was further confirmed by UV-Vis and FTIR analyses.

Moreover, in order to double confirm the conjugation, UV-Vis study of the emission and absorption spectra was performed from 190 nm until 330 nm for unconjugated ternatin and mPEG-ternatin. The characteristics of the UV-Vis absorption spectrum of unconjugated ternatin and mPEG-ternatin are shown in Figure 3. The peak of UV-Vis absorption of unconjugated ternatin biomolecule was observed at wavelength of 200 nm, whereas after being conjugated, the peak shifted to 280 nm. The emergence of a new absorption peak indicated the covalent conjugation and confirmed the successful conjugation of mPEG-ternatin. The change in the position of these bands reveals the conformational change in ternatin biomolecule after conjugation with mPEG.

Synthesis of mPEG-ternatin conjugate was achieved by direct esterification of mPEG-COOH and ternatin biomolecule was confirmed by FTIR spectrum as shown in Figure 4. As a result, Figure 4(a) shows the FTIR spectra of unconjugated ternatin in which a broadband at a range of 3000 cm^{-1} to 3500 cm^{-1} was assigned to O-H stretching. Figure 4(b) portrays the FTIR spectrum of mPEG-Ternatin conjugate in which the peak relatively sharper at a range of 3000 cm^{-1} to 3500 cm^{-1} than Figure 4(a) that indicates that the conjugate contains O-H moieties from the ternatin biomolecule. The peak owing to the aliphatic C-H stretching appeared around 2900 cm^{-1} in produced mPEG-ternatin. mPEG-ternatin linked through ester bond is proven using FTIR with the existence of C-O and C=O carboxylate stretching frequencies at 1100 cm^{-1} and 1650 cm^{-1}. The appearance of peaks of ester linkages in FTIR spectra indicated the successful of mPEG-ternatin conjugation.

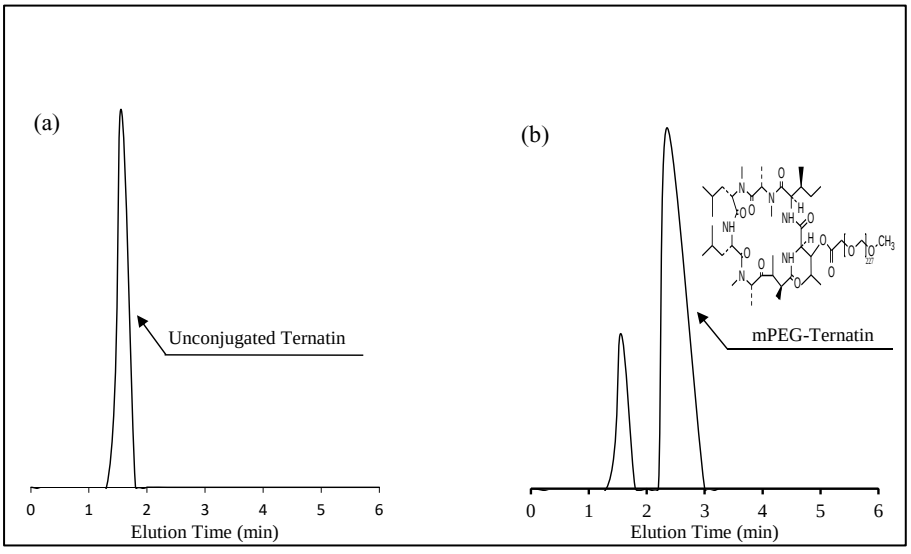


Figure 2. HPLC spectra of (a) unconjugated ternatin and (b) mPEG-ternatin

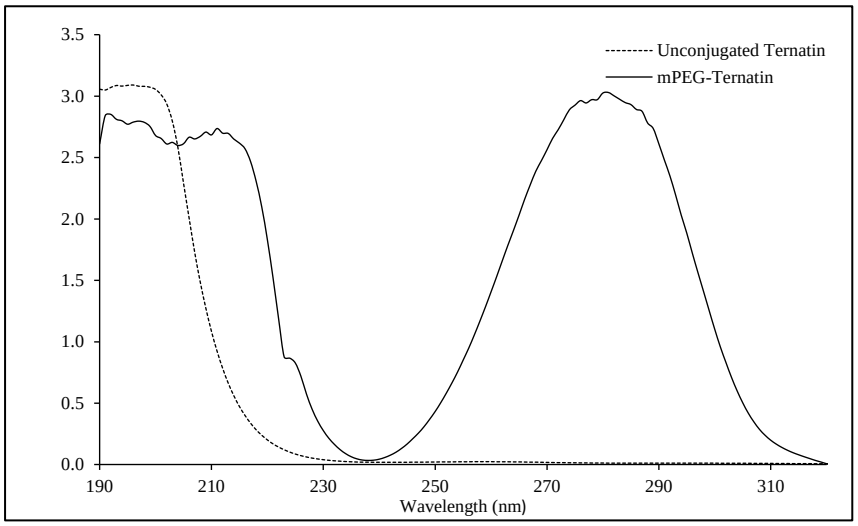


Figure 3. UV-Vis absorption spectrum of unconjugated ternatin and mPEG-ternatin conjugate in 10 mM of HEPES with pH 7.4 buffer solution

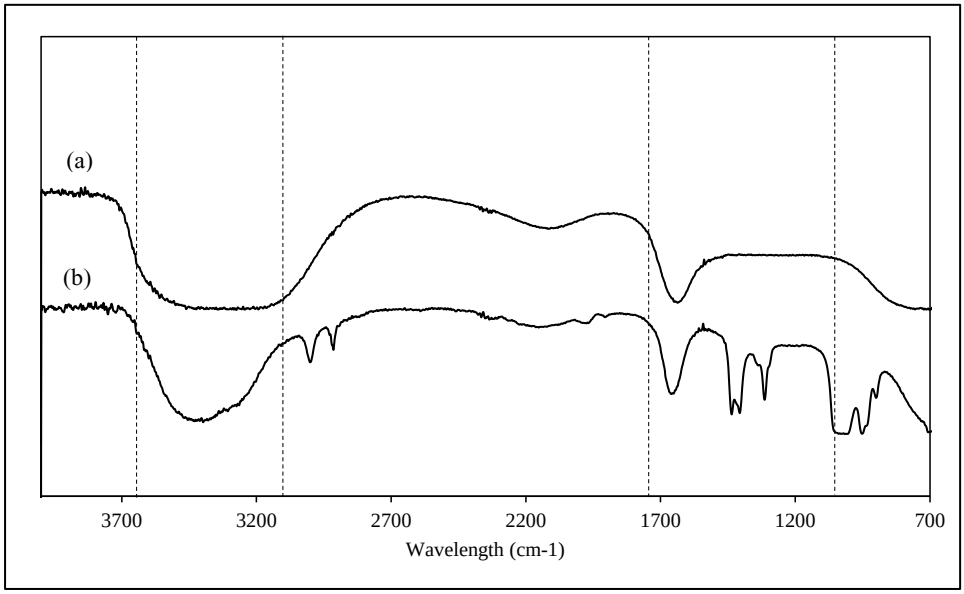


Figure 4. FTIR spectra of (a) unconjugated ternatin and (b) mPEG-ternatin conjugate

The solubility of mPEG-ternatin conjugate

The poor water solubility of Ternatin biomolecule is one of the main obstacles limiting this hydrophobic drug's further medical application. Herein, the solubility of conjugation of ternatin biomolecule with mPEG was explored. PEG conjugation considerably enhances the solubility of several anticancer drugs, which further improve their bioavailability and antitumor activities. Furthermore, due to the hydrophilic nature of PEG, it forms a hydrophilic outer layer by holding the hydrophobic ternatin biomolecules, which is formed by direct esterification

in aqueous medium. As a result, the solubility of conjugation of mPEG-ternatin was 1.15 µg/mL and unconjugated Ternatin content was calculated to be 1.06 µg/mL. This shows that mPEG-ternatin was ~8% higher than that of unconjugated Ternatin due to the strong solubility of PEG. Therefore, the dramatically improved solubility has pushed one step ahead for the medical application of Ternatin biomolecule.

The stability of mPEG-ternatin conjugate

In order to further investigate the ability of mPEG-ternatin conjugate, the stability test was conducted in the mimicking biological environment. Ternatin biomolecule and mPEG-ternatin conjugate stability test was conducted by dissolving in 10 mM HEPES buffer with pH 7.4 and incubated at 37 °C for 6 hours. An adequate amount of samples was taken every hour, and subsequently, the changes were monitored using UV-Vis spectrophotometer. The percentages of the degradation unconjugated ternatin were calculated based on the initial absorbance of the samples. The result shown in Figure 6 revealed that the percentages of remaining ternatin of mPEG-ternatin conjugate after 6 hours of incubation at 37 °C (61%) was 1.9 times higher compared to the unconjugated ternatin, which is 32%. The higher stability of mPEG-ternatin compared to the unconjugated Ternatin could suggest that the conjugated PEG at the vicinal Ternatin provide a protection to the Ternatin biomolecule in the biological environment.

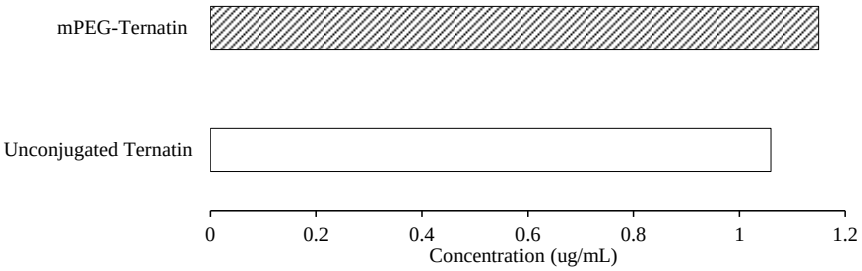


Figure 5. The concentration of unconjugated ternatin and mPEG-ternatin conjugate

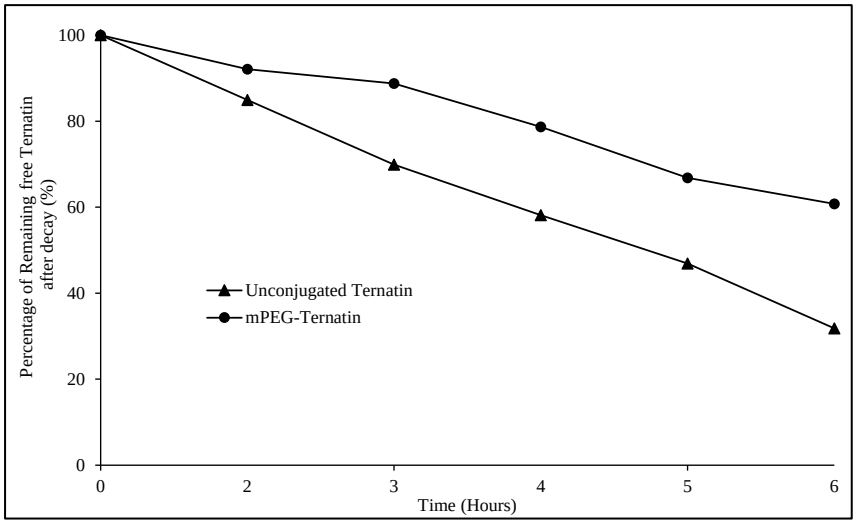


Figure 6. The degradation of unconjugated ternatin and mPEG-ternatin conjugate in 10 mM HEPES buffer pH 7.4 at 37 °C for 6 hours

Conclusion

In summary, mPEG-ternatin conjugate was synthesised by direct esterification between the carboxyl group of methoxy polyethylene glycol, mPEG-COOH and the hydroxyl group at the D-Leu^7 derivative of the ternatin biomolecule, increasing the aqueous solubility and stability of the ternatin biomolecule relative to unconjugated ternatin. The mPEG-ternatin conjugate significantly improved their solubility, which was ~8% higher than unconjugated Ternatin due to the strong solubility of mPEG. Meanwhile, the stability studies exhibited that mPEG-ternatin conjugate was 29% more stable than unconjugated ternatin due to 1.9 times lower degradation compared to the unconjugated ternatin. Therefore, reported conjugation of mPEG-ternatin conjugate was proven to significantly enhance solubility and stability, thereby promising their future in biological application. Further studies on this topic are now in progress.

Acknowledgement

The authors thank the Ministry of Higher Education (MOHE) Malaysia for the financial support provided via the Fundamental Research Grant Scheme [ref no. FRGS/1/2018/STG05/UNIKL/02/5]. The authors also thank Universiti Kuala Lumpur Malaysian Institute of Chemical and Bioengineering Technology, Melaka, Malaysia for providing resources and necessary facilities for FTIR, HPLC and Light Scattering Intensity analyses. The authors also thank the Nuclear Magnetic Resonance Laboratory, University Industry Research Laboratory, Universiti Teknologi Malaysia, Johor, Malaysia for ^{1}H NMR analysis.

References

1. Shu, J. Y., Panganiban, B. and Xu, T. (2013). Peptide-polymer conjugates: From fundamental science to application. *Annual Review of Physical Chemistry*, 64(1): 631-657.
2. Dey, S., Ambattu, L. A., Hari, P. R., Rekha, M. R. and Sreenivasan, K. (2015). Glutathione-bearing fluorescent polymer-curcumin conjugate enables simultaneous drug delivery and label-free cellular imaging. *Polymer*, 75: 25-33.
3. Ito, M., Ito, J., Kitazawa, H., Shimamura, K., Fukami, T., Tokita, S., Shimokawa, K., Yamada, K., Kanatani, A. and Uemura, D. (2009). (-)-Ternatin inhibits adipogenesis and lipid metabolism in 3T3-L1 cells. *Peptides*, 30(6): 1074-1081.
4. Shimokawa, K., Yamada, K., Kita, M. and Uemura, D. (2007). Convergent synthesis and in vivo inhibitory effect on fat accumulation of (-)-ternatin, a highly N-methylated cyclic peptide. *Bioorganic and Medicinal Chemistry Letters*, 17(16): 4447-4449.
5. Shimokawa, K., Iwase, Y., Miwa, R., Yamada, K. and Uemura, D. (2008). Whole structure-activity relationships of the fat-accumulation inhibitor (-)-ternatin: Recognition of the importance of each amino acid residue. *Journal of Medicinal Chemistry*, 51(19): 5912-5914.
6. Shimokawa, K., Yamada, K., Ohno, O., Oba, Y. and Uemura, D. (2009). Design, synthesis, and biological evaluation of biotin-labeled (-)-ternatin, a potent fat-accumulation inhibitor against 3T3-L1 adipocytes. *Bioorganic and Medicinal Chemistry Letters*, 19(1): 92-95.
7. Che Harun, N. F., Takemoto, H., Nomoto, T., Tomoda, K., Matsui, M., and Nishiyama, N. (2016). Artificial control of gene silencing activity based on sirna conjugation with polymeric molecule having coil-globule transition behavior. *Bioconjugate Chemistry*, 27(9): 1961-1964.
8. Liechty, W. B., Kryscio, D. R., Slaughter, B. V., and Peppas, N. A. (2010). Polymers for drug delivery systems. *Annual Review of Chemical and Biomolecular Engineering*, 1(1): 149-173.
9. Xu, M., Qian, J., Liu, X., Liu, T. and Wang, H (2015). Stimuli-responsive PEGylated prodrugs for targeted doxorubicin delivery. *Materials Science Engineering*, 50: 341-347.
10. Böttger, R., Knappe, D., and Hoffmann, R (2016). Readily adaptable release kinetics of prodrugs using protease-dependent reversible PEGylation. *Journal Control Release*, 230: 88-94.
11. Böttger, R., Knappe, D. and Hoffmann, R (2018). PEGylated prodrugs of antidiabetic peptides amylin and GLP-1. *J. Control*, 292: 58–66.
12. Shimokawa, K., Iwase, Y., Yamada, K., and Uemura, D. (2008). Synthesis and inhibitory effect on fat accumulation of (-)-ternatin derivatives modified in the β-OH-d-Leu7 moiety. *Organic and Biomolecular Chemistry*, 6(1): 58-60.
13. Kawazoe, Y., Tanaka, Y., Omura, S. and Uemura, D. (2014). Design, synthesis, and evaluation, derivatives of the fat-accumulation inhibitor ternatin: toward ternatin molecular probes. *Tetrahedron Letters*, 55(32): 4445-4447.

14. Nair, V., Bang, W. Y., Schreckinger, E., Andarwulan, N. and Cisneros-Zevallos, L. (2015). Protective role of ternatin anthocyanins and quercetin glycosides from butterfly pea (*Clitoria ternatea* Leguminosae) blue flower petals against lipopolysaccharide (LPS)-induced inflammation in macrophage cells. *Journal of Agricultural and Food Chemistry*, 63(28): 6355-6365.
15. Banerjee, S. S., Aher, N., Patil, R. and Khandare, J. (2012). Poly(ethylene glycol)-prodrug conjugates: Concept, design, and applications. *Journal of Drug Delivery*, 2012: 1-17.
16. Knop, K., Hoogenboom, R., Fischer, D. and Schubert, U. S. (2010). Poly(ethylene glycol) in drug delivery: Pros and cons as well as potential alternatives. *Angewandte Chemie - International Edition*, 49: 6288-6308.
17. Bayard, F. J. C., Thielemans, W., Pritchard, D. I., Paine, S. W., Young, S. S., Bäckman, P., Ewing, P., and Bosquillon, C. (2013). Polyethylene glycol-drug ester conjugates for prolonged retention of small inhaled drugs in the lung. *Journal of Controlled Release*, 171(2): 234-240.
18. Gu, Y., Zhong, Y., Meng, F., Cheng, R., Deng, C. and Zhong, Z. (2013). Acetal-linked paclitaxel prodrug micellar nanoparticles as a versatile and potent platform for cancer therapy. *Biomacromolecules*, 14(8): 2772-2780.
19. Stompor, M., Switalska, M., Bajek, A., and Wietrzyk, J. (2019). Influence of amide versus ester linkages on the anticancer properties of the new flavone-biotin conjugates. *Zeitschrift Fur Naturforschung - Section C Journal of Biosciences*, 74(7–8): 193-200.
20. Iwakiri, T., Mase, S., Murakami, T., Matsumoto, M., Hamada, H., Nakayama, T. and Ozaki, S. I. (2013). Glucosylation of hydroxyflavones by glucosyltransferases from *Phytolacca americana*. *Journal of Molecular Catalysis B: Enzymatic*, 90: 61-65.

Malaysian Journal of Analytical Sciences (MJAS)
Published by Malaysian Analytical Sciences Society

PURIFICATION OF XANTHORRHIZOL AND SCREENING OF SELECTED MICROBES FOR ITS BIOTRANSFORMATION

(Penulenan Xantorizol dan Pengesanan Mikrob Terpilih untuk Biotransformasinya)

Nurul Iman Aminudin[1]*, Nadia Farhana Yahya[1], Zaima Azira Zainal Abidin[2], Deny Susanti[1], Muhammad Taher[3]

[1]Department of Chemistry, Kulliyyah of Science
[2] Department of Biotechnology, Kulliyyah of Science
International Islamic University Malaysia, Jalan Sultan Ahmad Shah, 25200 Kuantan, Pahang Darul Makmur, Malaysia
[3] Department of Pharmaceutical Technology, Kulliyyah of Pharmacy,
International Islamic University Malaysia, P .O. Box 141, 25710 Kuantan, Pahang Darul Makmur, Malaysia

**Corresponding author: nuruliman@iium.edu.my*

Received: 5 September 2021; Accepted: 11 November 2021; Published: 27 December 2021

Abstract

Xanthorrhizol is a bisabolene-type sesquiterpenoid and is present abundantly in the essential oil of *Curcuma xanthorrhiza* (temulawak). It was reported to possess various pharmacological activities, including antimicrobial, anti-inflammatory, antioxidant, antihyperglycemic, antihypertensive, and antiplatelet activities. To further evaluate its pharmacological potency based on the structure-activity relationship, a large amount of xanthorrhizol needs to be purified and subjected to chemical synthesis to yield xanthorrhizol analogues. Common approaches to synthesise the analogues are through chemical reactions. Biotransformation utilising microbes as biocatalysts is one of the green alternatives to replace chemical synthesis methods for producing xanthorrhizol analogues. In this study, xanthorrhizol was purified from the crude essential oil by utilising repetitive chromatographic separation and two-step chemical synthesis involving acetylation and hydrolysis reactions. The purification successfully yielded xanthorrhizol with a purity of 98.1%, as indicated by gas chromatography-mass spectrometry (GC-MS) analysis. The structure of xanthorrhizol was also characterised using nuclear magnetic resonance spectroscopy (NMR). Four selected microbes (*Aspergillus niger*, *Streptomyces sp.* K1-18, K3-20, and K7-11) were screened for the biotransformation of xanthorrhizol. The results from thin layer chromatography (TLC) and GC-MS showed that only *A. niger* could biotransform xanthorrhizol into its derivatives.

Keywords: xanthorrhizol, biotransformation, *Aspergillus niger, Streptomyces sp*., sesquiterpene

Abstrak

Xantorizol adalah seskuiterpen jenis bisabolen dan hadir dengan banyak di dalam minyak pati *Curcuma xanthorrhiza* (temulawak). Ia telah dilaporkan mempunyai pelbagai aktiviti farmakologi termasuk antimikrob, anti-radang, antioksidan, anti-hiperglisemik, anti-hipertensi dan antiplatlet. Untuk menilai lebih lanjut potensi farmakologi berdasarkan hubungan struktur-aktiviti, xantorizol dalam jumlah yang banyak perlu ditulenkan dan perlu melalui kaedah sintesis kimia yang membolehkan analog xantorizol dihasilkan. Pendekatan biasa untuk sintesis analog adalah melalui tindak balas kimia. Biotransformasi menggunakan mikrob sebagai biopemangkin merupakan satu alternatif hijau menggantikan kaedah sintesis kimia yang boleh menghasilkan analog xantorizol. Dalam kajian ini, xantorizol telah ditulenkan daripada minyak pati mentah menggunakan pemisahan kromatografi berulang dan dua langkah sintesis kimia melibatkan tindak balas asetilasi dan hidrolisis. Proses penulenan telah berjaya

menghasilkan xantorizol dengan ketulenan 98.1% seperti ditunjukkan oleh analisis gas-kromatografi-jisim spektrometri (GK-JS). Struktur xantorizol juga telah diperincikan menggunakan resonans magnetik nuklear (RMN) spektroskopi. Empat mikrob terpilih, (*Aspergillus niger*, *Streptomyces sp.* K1-18, K3-20 dan K7-11) telah disaring untuk biotransformasi xantorizol. Keputusan kromatografi lapisan nipis (KLN) dan JK-MS telah menunjukkan cuma *A. niger* berupaya melakukan biotransformasi xantorizol kepada terbitannya.

Kata kunci: xantorizol, biotransformasi, *Aspergillus niger, Streptomyces sp*., seskuiterpen

Introduction

Xanthorrhizol, a bisabolene-type sesquiterpenoid with a stereogenic centre at the benzylic position, is the most active and abundant component in the essential oil of *Curcuma xanthorrhiza* [1]. Out of 92% bisabolene-type sesquiterpenes and their oxygenated derivatives from the essential oil, 32% are xanthorrhizol, thus confirming that it is the most abundant compound in *C. xanthorrhiza* [2]. Xanthorrhizol possesses various pharmacological activities, including antimicrobial, anti-inflammatory, antioxidant, antihyperglycemic, antihypertensive, antiplatelet, nephroprotective and hepatoprotective, and estrogenic and antiestrogenic properties [3]. Due to the promising biological activities of xanthorrhizol, there is great interest in developing methods to obtain analogues or derivatives for an extensive structural-activity relationship (SAR) study. Conventional chemical manipulations are normally tedious, have harsh conditions, require multistep procedures, and incorporate expensive catalysts. The total synthetic routes are difficult, especially in introducing the stereogenic centre, thus hindering many conventional chemical manipulations. Nevertheless, partial synthesis involving remote functionalisation is available through the biotransformation process [4].

Biotransformation is a biochemical modification of a compound to a distinct product using biological catalysts, such as microorganisms, plant cell cultures, and enzymes [4]. Biotransformation is a useful tool in a synthesis toolbox to discover new compounds as it can produce reactions, including oxidation, reduction, hydrolysis, addition, ring rearrangement, and glycosidic transfer reaction that are not likely to happen through conventional synthetic methods [5]. Biotransformation remains unrivalled, especially due to its highly specific reactions (i.e., highly stereoselective, chemoselective, enantioselective, and regioselective) under mild and ambient reaction conditions, allowing the discovery of new compounds. A biotransformation reaction is a simple one-step reaction in aqueous media that uses non-hazardous and cheap chemicals to provide many valuable metabolites possessing different properties from one substrate in one pot. The most important advantage of biotransformation is that it practices the concept of green chemistry, where the products or metabolites produced are biodegradable compounds [6]. Among all kinds of biocatalysts, microorganisms especially microbes are widely utilised for biotransformation. Microbes can produce a variety of unique enzymes that are stable towards heat, alkali, and acids. These enzymes can also be produced in a short period of time by the microorganisms due to their nature to multiply. Their small size allows maximum metabolic rates as they have a larger surface-to-volume ratio that provides a high exchange of molecules and metabolites [6].

The establishment of a biotransformation reaction that can yield xanthorrhizol analogues for further SAR study is of particular interest because to the best of our knowledge, no study has been conducted yet. A method to yield xanthorrhizol with high purity is needed as a substrate for the biotransformation process. Suitable biocatalysts to conduct biotransformation of xanthorrhizol must also be explored through the screening process. In this study, four selected microbes (i.e., *Aspergillus niger* and *Streptomyces* sp. (K1-18, K3-20, and K7-11) were screened as the potential biocatalysts. Even though *Streptomyces* sp. [7-9] and *A. niger* [5, 10-11] are well-known biocatalysts, their ability as biocatalysts for the biotransformation of xanthorrhizol is not yet known.

Materials and Methods

Purification of xanthorrhizol from *Curcuma xanthorrhiza's* essential oil

A fresh sample of *C. xanthorrhiza* (20 kg) was purchased from a local market. The sample was chopped and subjected to extraction using Turbo Extractor to yield approximately 212 mL of essential oil. The essential oil (9.25 g) was subjected to vacuum liquid chromatography (VLC) employing silica gel 60 (230–400 mesh) as the stationary phase and a mixture of *n*-hexane (*n*-hex): diethyl ether (Et_2O). The polarity of the solvent was increased by 1% from 200:0 to 190:10, 0.5% from 190:10 to 180:20, 5% from 180:20 to 100:100, and 50% from 100:100 to 0:200 to obtain four major fractions labelled as CXED10-1 until CXED10-4. The CXED10-3 fraction was further fractionated using VLC employing the same mobile phase to produce another six subfractions labelled as CXED11-1 until CXED11-6. The CXED11-3 subfraction with the presence of xanthorrhizol as the major compound was chosen to be analysed using GC-MS to determine its purity. The CXED11-3 subfraction was further purified through two-step chemical reactions of acetylation and hydrolysis. Acetylation produced xanthorrhizyl acetate as the major product, whereas the hydrolysis of xanthorrhizyl acetate produced xanthorrhizol with higher purity.

Acetylation of xanthorrhizol was done by adding Et_2O (10 mL), pyridine (3 mL), and acetic anhydride (3 mL) into the CXED11-3 subfraction (2.0 g). The reaction mixture was stirred for 24 h at room temperature. The acetylation process was monitored using TLC with *n*-hex: Et_2O of 4:1 as the solvent system. Distilled water (5 mL) was added to the reaction mixture and left for 10 min while stirring. The reaction mixture was washed with 1 M hydrochloric acid solution (20 mL) thrice, followed by saturated sodium bicarbonate solution (20 mL) thrice, and lastly with brine solution (20 mL) once using liquid-liquid extraction. The organic phase was dried with anhydrous magnesium sulphate to yield a yellow oil (1.77 g). The oil was subjected to column chromatography utilising silica gel (mesh 60–230) and a mixture of *n*-hex: Et_2O in a stepwise gradient as the stationary and mobile phases, respectively. A total of 431 fractions were obtained and pooled into six major subfractions labelled as AX3-1 until AX3-6. The TLC analysis on the AX3-2 subfraction showed a single spot, representing pure xanthorrhizyl acetate (0.79 g, 44.6%) as a colourless oil. The structure of xanthorrhizyl acetate was further characterised using nuclear magnetic resonance (NMR) and infrared (IR) spectroscopy.

Hydrolysis was done by adding anhydrous potassium carbonate (0.52 g), methanol (7 mL), and distilled water (1 mL) to xanthorrhizyl acetate (0.79 g) and stirred at room temperature for 18 h. Distilled water (5 mL) was then added to the reaction mixture and the organic phase was extracted with ethyl acetate (10 mL) thrice. The organic phase was dried using anhydrous magnesium sulphate, followed by evaporation to yield xanthorrhizol (0.07 g, 8.89%) as a yellow oil. The purity of xanthorrhizol was further monitored using GC-MS, whereas its structure was characterised using NMR spectroscopy.

Microbial culture

Four microbes were selected to be screened for the biotransformation of xanthorrhizol, namely *Streptomyces sp.* (*Streptomyces sp.* K1-18, K3-20, and K7-11) and *A. niger* (ATCC 16404). All *Streptomyces sp.* were isolated from Kuantan Mangrove Forest and maintained on starch-yeast extract (SYE) agar. Meanwhile, *A. niger* was obtained from the Department of Biotechnology, Kulliyyah of Science, International Islamic University of Malaysia, and maintained on actinomycete isolation agar (AIA). Both microbes were cultured in SYE broth prepared by the addition of starch (10 g), yeast extract (4 g), and peptone (2 g) in distilled water (1 L). The microbes were incubated at 28 °C with continuous shaking at 150 rpm to ensure homogeneous mixing and create the optimum conditions for microbial growth.

Screening procedure for biotransformation of Xanthorrhizol

A. niger, *Streptomyces sp.* K1-18, K3-20, and K7-11 from the agar plates were inoculated in five 250 mL flasks containing 150 mL of SYE broth. Four flasks were designated as reaction broth (RB) flasks and one flask was designated as the inoculum control (IC) flask. The RB flasks contained inoculated microbes in the

SYE broth in the presence of xanthorrhizol as the substrate, whereas the IC flask contained inoculated microbes in the SYE broth without the presence of substrate. All flasks were shaken on a rotary shaker at 150 rpm and 28 °C for five days to ensure the full growth of microbes. On the 5th day, xanthorrhizol (5.5 µL) dissolved in acetone (500 µL) was added to the RB flasks and incubated for an additional 14 days for *A. niger* [12]. A similar incubation period (i.e., 14 days) was applied for all *Streptomyces sp.* to evaluate their potential in performing biotransformation at the sporulation stage [13].

After the incubation process ended, the broth from all flasks was centrifuged to remove any microbial suspension. The centrifugation process was done at 28 °C and 7,000 rpm for 10 min. After that, the supernatant layer was collected and extracted thrice with ethyl acetate (50 mL). The combined organic phase was dried with anhydrous magnesium sulphate to trap excess water. The solvent was then dried using a rotary evaporator to yield the crude products. TLC analyses were carried out with *n*-hex: Et_2O of 4:1 and chloroform ($CHCl_3$): methanol (MeOH) of 4.5:0.5 as the solvent system. The spots on TLC plates were visualised using a UV lamp (wavelengths of 254 and 365 nm). The plates were also sprayed with vanillin-sulphuric acid reagent and heated for visual colour detection of spots [14]. The spots observed from the IC flask originated from the metabolites produced by the microbes. Hence, these spots would be used as the reference compared to the new spots present from the RB flasks. The new spots produced from the RB flasks indicated the presence of biotransformation products. The presence of biotransformation products was further confirmed using GC-MS comparative analysis of the RB and IC crude extract.

Gas chromatography-mass spectrometry

GC-MS analysis was carried out using the GC-MS Perkin Elmer (ClarusTM 680/GC SQ8T/MS) equipped with Elite-5MS capillary column (30 m × 0.25 mm id, 0.25 µm film thickness; Perkin Elmer). The sample injection volume was 1 µL and the temperature programme was set from 60 °C (10 min) to 230 °C (10 min) at 3 °C min^{-1}.

Attenuated total reflectance – Fourier transform infrared

Attenuated total reflectance- Fourier transform infrared (ATR-FTIR) spectrum was recorded on a Perkin-Elmer spectrophotometer between 4000 and 600 cm^{-1}.

Nuclear magnetic resonance spectroscopy

NMR analysis was carried out at 500 MHz on Bruker Ultra Shield Plus spectrometer. Chemical shifts were obtained in parts per million (δ ppm) using tetramethylsilane (TMS) as an internal standard for spectra obtained in deuterated chloroform ($CDCl_3$).

Results and Discussion

Isolation and purification of xanthorrhizol

The isolation of xanthorrhizol from *C. xanthorrhiza* essential oil was done using chromatographic techniques (VLC and CC) and two-step chemical synthesis methods (acetylation and hydrolysis). Repetitive VLC determined the CXED11-3 fraction with the presence of xanthorrhizol as the major spot and a minor spot (impurities) on top of it based on the TLC analysis. GC-MS analysis was carried out on the CXED11-3 fraction to determine the percentage of purity of xanthorrhizol. Six peaks comprising one major peak (t_R = 45.9 min) and five minor peaks representing the impurities (t_R = 19.2, 39.9, 42.5, 44.2, and 46.8 min) were detected (Figure 1(a)). The MS spectrum (Figure 1(b)) of the major peak revealed that the molecular ion mass at *m/z* 218 was in agreement with the molecular weight of xanthorrhizol. The percentage area of the xanthorrhizol peak was 80.8%, indicating its percentage of purity. However, to perform the biotransformation of xanthorrhizol, it is best to obtain xanthorrhizol with a purity percentage higher than 90%. Thus, further purification steps need to be carried out on the CXED11-3 fraction.

The presence of a less polar minor spot (impurities) above the xanthorrhizol spot complicates the purification process using chromatographic techniques. Thus, acetylation (Figure 2) was employed to yield xanthorrhizyl acetate, which appeared as a less polar spot than the spot for impurities. The isolation of xanthorrhizyl acetate was easier and faster as it would elute earlier in the further isolation step using CC. The

structure of xanthorrhizyl acetate was further characterised by IR and NMR spectroscopy and the results are tabulated in Table 1 and 2, respectively. The presence of the acetate group was confirmed by the presence of carbonyl ester stretching at 1764 cm^{-1} in the IR spectrum (Table 1), the presence of carbon signal of carbonyl ester at δ 169.20 ppm and a singlet signal attributed to methyl from the acetyl group at δ 2.30 ppm (Table 2). Other spectroscopic data also agreed with the structure of xanthorrhizyl acetate and with the published data [15,16].

Hydrolysis was carried out on the isolated xanthorrhizyl acetate to yield xanthorrhizol (Figure 3). The reaction did not require further chromatographic separation. The GC-MS chromatogram (Figure 4) revealed that the purity of xanthorrhizol increased to 98.1%, as indicated by its peak area. The absence of a singlet signal attributed to the methyl protons from the acetyl group of xanthorrhizyl acetate at δ 2.30 ppm and carbon signal corresponding to the carbonyl ester indicated a successful hydrolysis reaction back to xanthorrhizol. Other ^{1}H NMR spectroscopic data (Table 2) also matched with the structure of xanthorrhizol and agreed with published data [17].

Screening of microbes for the biotransformation of xanthorrhizol

The ability of *A. niger*, *Streptomyces sp.* K1-18, K3-20, and K7-11 to perform biotransformation of xanthorrhizol was screened. The screening was conducted through biotransformation by incubating xanthorrhizol with each microbe in the SYE broth. The broths were supplemented with xanthorrhizol on the 5th day of incubation to ensure the process was conducted during the exponential phase of the microbial growth. TLC profiling was carried out to identify the presence of new products due to the biotransformation reaction after the incubation process was completed. This was done by comparing the TLC profiles of xanthorrhizol, the extracts from the IC and RB flasks, and starch soluble and yeast extract as the ingredients from the SYE broth. Two solvent systems (i.e., *n*-hex: Et_2O of 4:1 and $CHCl_3$: MeOH of 4.5:0.5) were employed to ensure all non-polar and polar compounds were observed in the TLC.

The TLC profile for the screening of biotransformation utilising *A. niger* is depicted in Figure 5. The spot of xanthorrhizol with R_f = 0.54 (*n*-hex: Et_2O of 4:1) could be seen under 254 nm. No xanthorrhizol spots could be observed for all RB extracts, suggesting that the biotransformation of xanthorrhizol by *A. niger* was completed within 14 days. A significant spot labelled as spot 1 (R_f = 0.67; *n*-hex: Et_2O of 4:1) was observed in the RB extracts, indicating a less polar biotransformation product than xanthorrhizol. In addition, another spot was observed in the TLC with R_f = 0.63 ($CHCl_3$: MeOH of 4.5:0.5), highlighting the presence of a more polar biotransformation product compared to xanthorrhizol. A comparative analysis between xanthorrhizol and the IC and RB extracts for the biotransformation by *A. niger* was performed using GC-MS to further confirm the qualitative results from the TLC analysis. The presence of spots 1 and 2 was confirmed by comparing all chromatograms (Figure 6). The chromatogram shows a peak of xanthorrhizol appeared at t_R = 45.7 min. This peak was not observed in the RB extracts, thus confirming the completion of biotransformation. Two peaks appeared at t_R = 53.3 and 55.3 min in the RB extract chromatogram and were not observed in the chromatogram of the IC extract. This further proved the presence of two biotransformation products by *A. niger*, which were also in accordance with the observation from the TLC analysis.

Meanwhile, the TLC analysis for *Streptomyces sp.* K1-18, K3-20, and K7-11 did not show any significant spots compared to the IC and RB extracts that could be recognised as possible biotransformation products. The spot of xanthorrhizol was still present in the RB extracts (Table 3), indicating that the reaction did not occur even after 14 days of incubation (i.e., sporulation stage) [13]. Thus, these three microbes were unable to perform biotransformation of xanthorrhizol and further analysis by GC-MS was not conducted.

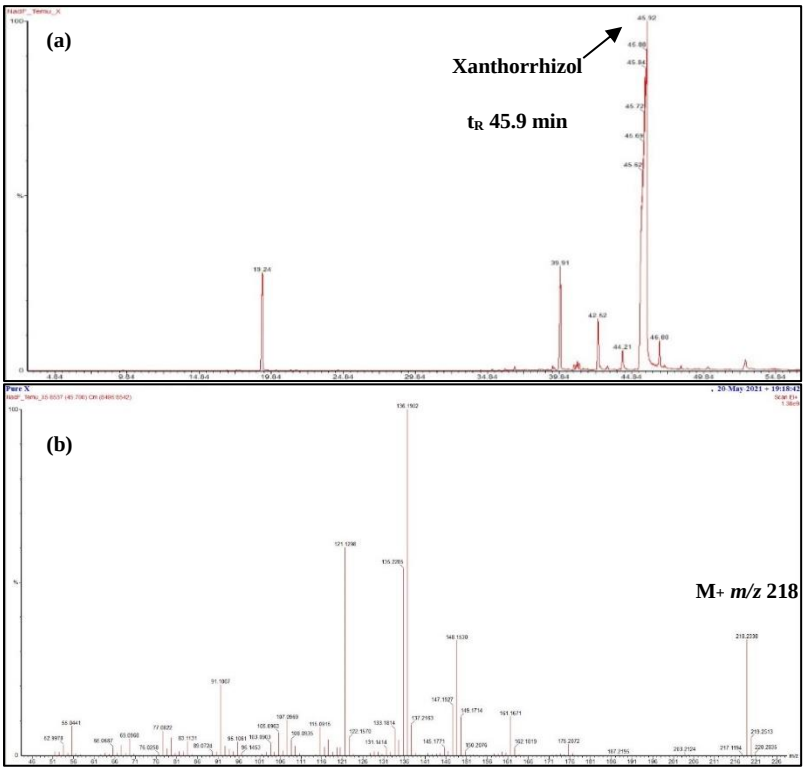


Figure 1. (a) GC-MS chromatogram of CXED11-3 fraction and (b) MS spectrum of xanthorrhizol

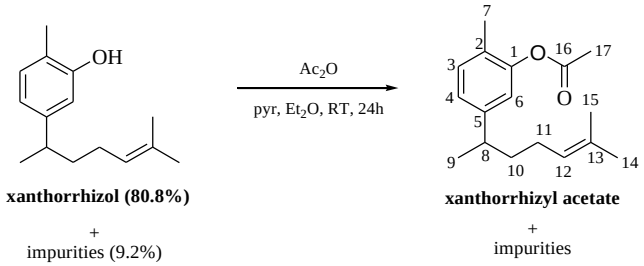


Figure 2. Reaction scheme of acetylation reaction of CXED11-3 fraction

Table 1. IR data of xanthorrhizyl acetate

Functional Group	**υ_{max} (cm^{-1})**
sp^3 CH	2962, 2924
C=O ester	1764
C-O ester	1210

Table 2. NMR data of xanthorrhizyl acetate and xanthorrhizol

No.	Xanthorrhizyl acetate, δ (ppm)		Xanthorrhizol, δ (ppm)	
	^{1}H	^{13}C	^{1}H	^{13}C
1	-	146.94	-	153.61
2	-	120.34	-	113.54
3	7. 13 (d, *J*= 7.7 Hz)	149.29	7.02 (d, *J*= 7.8 Hz)	147.25
4	6.96 (dd, *J*= 1.6, 7.7 Hz)	124.71	6.67 (dd, *J*= 1.8, 7.8 Hz)	120.79
5	-	130.83	-	130.76
6	6.81 (d, *J*= 1.6 Hz)	124.38	6.61 (d, *J*= 1.8 Hz)	119.42
7	2.13 (s)	38.85	2.21 (s)	39.04
8	2.66 (sext, *J*= 7.0 Hz)	38.33	2.61 (sext, *J*= 7.0 Hz)	38.38
9	1.21 (d, *J*= 7.0 Hz)	26.07	1.20 (d, *J*= 7.0 Hz)	26.16
10	1.54-1.60 (m)	127.17	1.56-1.61 (m)	124.52
11	1.85-1.91 (m)	131.52	1.84-1.90 (m)	131.43
12	5.05-5.09 (m)	17.66	5.06-5.10 (m)	25.71
13	-	25.69	-	15.31
14	1.50 (s)	15.78	1.52 (s)	22.38
15	1.66 (s)	22.15	1.66 (s)	17.68
16	-	169.20	-	-
17	2.30 (s)	20.83	-	-

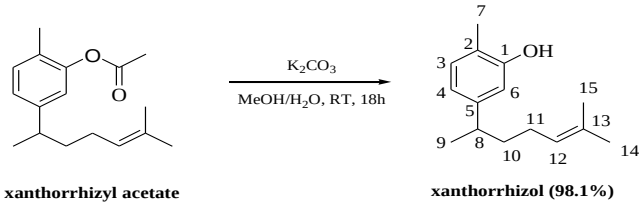


Figure 3. Reaction scheme of hydrolysis reaction of xanthorrhizyl acetate

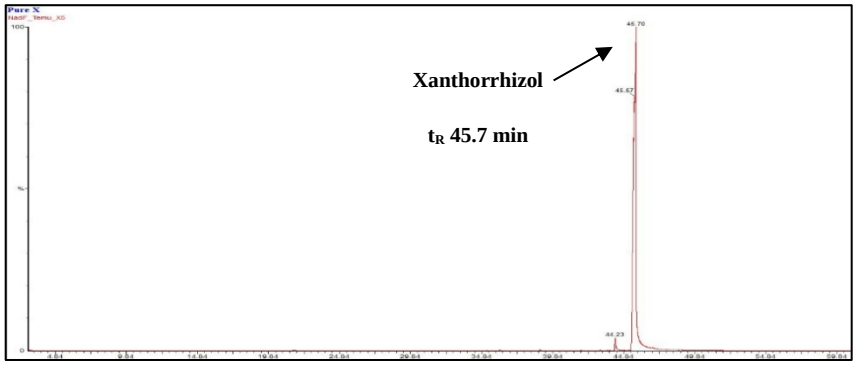


Figure 4. GC-MS chromatogram of xanthorrhizol

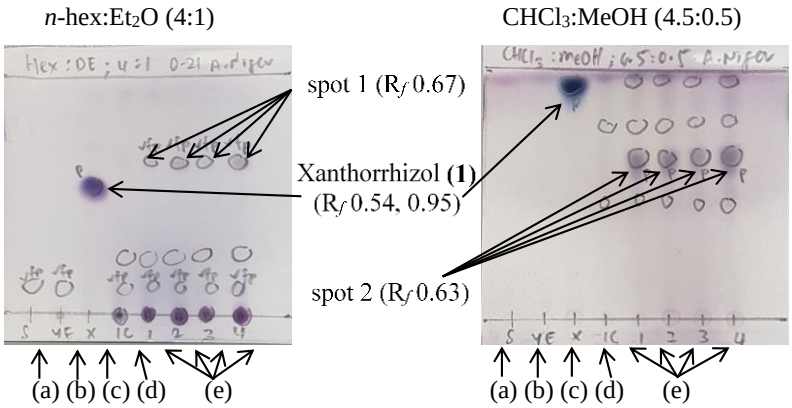


Figure 5. TLC profile of biotransformation of xanthorrhizol by *A. niger*; (a) starch soluble; (b) yeast extract; (c) pure xanthorrhizol; (d) IC extract; (e) RB extracts

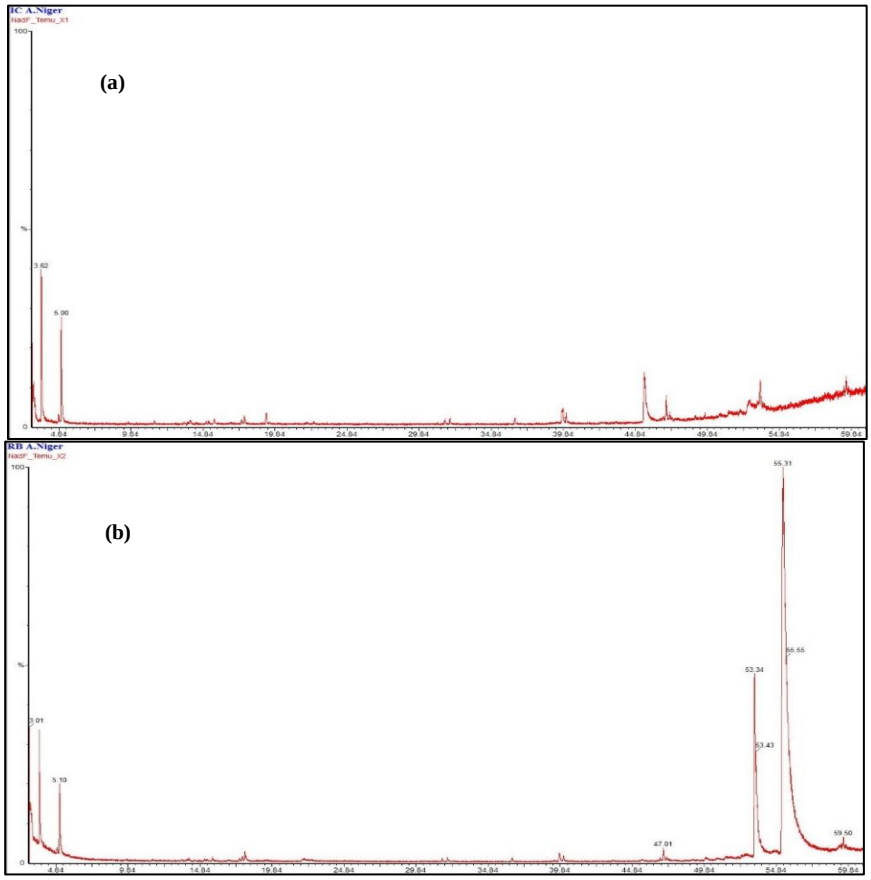
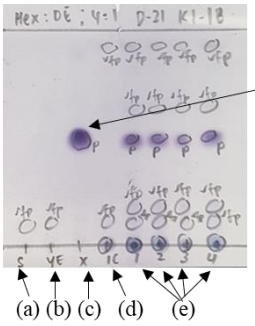
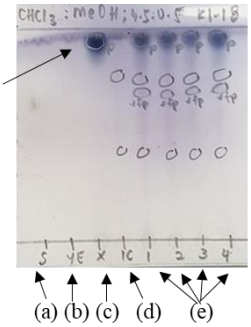
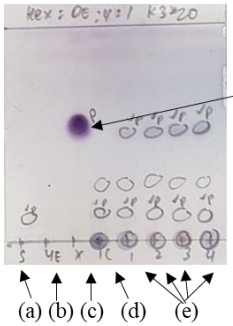
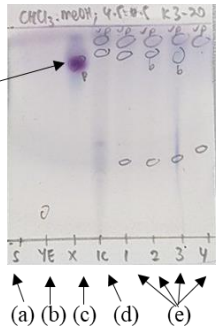
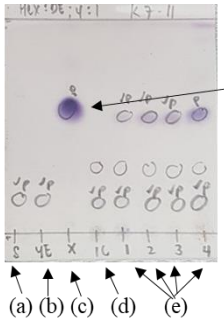
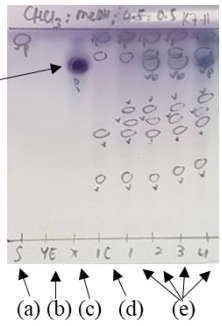


Figure 6. GC-MS chromatograms of (a) IC extract and (b) RB extract from biotransformation of xanthorrhizol by *A. niger*

Table 3. TLC profile of biotransformation of xanthorrhizol by *Streptomyces sp*.

***Streptomyces* sp.**	**TLC Solvent System**	
	***n*-hex:Et_2O (4:1)**	**$CHCl_3$:MeOH (4.5:0.5)**
K1-18		
K3-20		
K7-11		

*(a) starch soluble; (b) yeast extract; (c) pure xanthorrhizol; (d) IC extract; (e) RB extracts

Conclusion

Xanthorrhizol was successfully purified from the essential oil of *C. xanthorrhiza* through the combination of chromatographic techniques and two-step chemical reactions. This method yielded higher purity of xanthorrhizol compared to only chromatographic techniques. The screening process revealed that only *A. niger* has the potential to be a biocatalyst to perform biotransformation of xanthorrhizol. This screening result will provide beneficial reference, especially in obtaining the new structure of xanthorrhizol analogues from preparative biotransformation for intended biological SAR studies.

Acknowledgement

The authors are thankful for this work's funding from Ministry of Higher Education (MOHE) Malaysia through Fundamental Grant Scheme FRGS19-029-0637 (FRGS/1/2018/STG01/UIAM/03/3).

References

1. Dosoki, N. S. and Setzer, W. N. (2018). Chemical composition and biological activities of essential oils of *Curcuma* Species. *Nutrients,* 10(1196): 1-42.
2. Jantan, I., Saputri, F. C., Qaisar, M. N. and Buang, F. (2012). Correlation between chemical composition of *Curcuma domestica* and *Curcuma xanthorrhiza* and their antioxidant effect on human low-density lipoprotein oxidation. *Evidence-Based Complementary and Alternative Medicine.* 2012: 1-10.
3. Shahid, M., Azfaralariff, A., Law, D., Najm, A. A., Sanusi, S. A., Lim, S. J., Cheah, Y. H. and Fazry, S. (2021). Comprehensive computational target fishing approach to identify xanthorrhizol putative targets. *Scientific Reports*, 11(1594): 1-11.
4. Hegazy, M.-E. F., Elshamy, A. I., Mohamed, T. A., Hussien, T. A., Helaly, S. E., Abdel-Azim, N. S. Shams, K. A., Shahat, A. A., Tawfik, W. A., Shahen, A. M., Debbab, A., El Saedi, H. R., Mohamed, A. E.-H. H., Hammouda, F. M., Sakr, M., Paré, P. W. and Efferth, T. (2020). Terpenoid bio-transformations and applications via cell/organ cultures: A systematic review. *Critical Reviews in Biotechnology*, 40(1): 64-82.
5. Aminudin, N. I., Ridzuan, M., Darnis, D. S. and Zainal A. Z. A. (2021). Biotransformation of sesquiterpenoids: A recent insight. *Journal of Asian Natural Products Research*, 2021: 1-44.
6. Hegazy, M. E., Mohamed, T. A., ElShamy, A. I., Mohamed, A. E., Mahalel, U. A., Reda, E. H., Shaheen, A. M., Tawfik, W. A., Shahat, A. A., Shams, K. A., Abdel-Azim, N. S. and Hammouda, F. M. (2015). Microbial biotransformation as a tool for drug development based on natural products from mevalonic acid pathway: A review. *Journal of Advanced Research*, 6(1): 17-33.
7. Chattopadhyay, P., Banerjee, G. and Sen, S. K. (2018). Cleaner production of vanillin through biotransformation of ferulic acid esters from agroresidue by *Streptomyces sannanensis. Journal of Cleaner Production,* 182: 272-279.
8. Wu, C., Zhu, H., van Wezel, G. P. and Choi, Y. H. (2016). Metabolomics-guided analysis of isocoumarin production by *Streptomyces* species MBT76 and biotransformation of flavonoids and phenylpropanoids. *Metabolomics,* 12(5): 1-11.
9. Zhang, D., Tao, X., Gu, G., Wang, Y., Zhao, W., Zhao, W., Ren, Y., Dai, S. and Yu, L. (2021) Microbial transformation of neo-clerodane diterpenoid, scutebarbatine F, by *Streptomyces sp*. CPCC 205437. *Frontiers in Microbiology,* 12(662321): 1-15.
10. Parshikov, I.A. and Sutherland, J. B. (2014). The use of *Aspergillus niger* cultures for biotransformation of terpenoids. *Process Biochemistry*, 49(12): 2086-2100.
11. Lima, M. A. S., de Oliveira, M. C. F., Pimenta, A. T. A. and Uchôa, P. K. S. (2019). *Aspergillus niger*: A hundred years of contribution to the natural products chemistry. *Journal of Brazilian Chemical Society*, 30(10): 2029-2059.
12. Arturo, C.-F. and Guillermo, D. (2017). Sesquiterpene lactones by filamentous fungi. Cytotoxic evaluations. *Chemistry & Biodiversity*, 14(1): 1-12.
13. Malek, N. A., Zainuddin, Z., Chowdhury, A. J. K. and Abidin, Z. Z. A. (2015). Diversity and antimicrobial activity of mangrove soil *Actinomycetes* isolated from Tanjung Lumpur, Kuantan. *Jurnal Teknologi.* 77 (25): 37-43.
14. Spangenberg, B., Poole, C. F. and Weins, C. (2011). Quantitative thin-layer chromatography: A partial survey. Heidelberg, Berlin: Springer.
15. Rahayu, M. D., Kusumaningrum, S. and Hayun, H. (2020). Synthesis of acetyl and benzoyl esters of xanthorrhizol and its oxidation products and evaluation of their inhibitory activity against nitric oxide production. *International Journal of Applied Pharmaceutics,* 12(1): 135-138.
16. Aguilar, M. I., Delgado, G. and Villarreal, M. L. (2001). New bioactive derivatives of xanthorrhizol. *Revista De La Sociedad Química De México*, 45(2): 56-59.
17. Ramdani, E. D., Marlupi, U. D., Sinambela, J. M. and Tjandrawinata, R. (2016). A new method of xanthorrhizol isolation from the rhizome extract of *Curcuma xanthorrhiza. Scholars Academic Journal of Biosciences,* 4(9): 732-737.

Malaysian Journal of Analytical Sciences (MJAS)
Published by Malaysian Analytical Sciences Society

ISOLATION OF PTEROPODIC ACID FROM MALAYSIAN *Uncaria lanosa* VAR. *ferrea* BY USING LIQUID CHROMATOGRAPHY MASS SPECTROMETRY DEREPLICATION APPROACH

(Pemencilan Asid Pteropodik daripada *Uncaria lanosa* var. *ferrea* Malaysia dengan Pendekatan Direplikasi Kromatografi Cecair Spektrometri Jisim)

Nursyaza Husna Shaharuddin[1], Rohaya Ahmad[1], Fatimah Salim[2,3]*

[1]*Faculty of Applied Sciences,*
Universiti Teknologi MARA, 40450 Shah Alam, Selangor Darul Ehsan
[2]*Atta-ur-Rahman Institute for Natural Product Discovery (AuRIns),*
Universiti Teknologi MARA Selangor Branch, Puncak Alam Campus, 42300 Bandar Puncak Alam, Selangor Darul Ehsan, Malaysia
[3]*Centre of Foundation Studies,*
Universiti Teknologi MARA Selangor Branch, Dengkil Campus, 42800 Dengkil, Selangor, Malaysia

**Corresponding author: fatimah2940@uitm.edu.my*

Received: 15 September 2021; Accepted: 10 November 2021; Published: 27 December 2021

Abstract

Previous chemical profiling on Malaysian *Uncaria lanosa* var. *ferrea* using liquid chromatography mass spectrometry (LCMS) had successfully identified three alkaloids namely pteropodine, isopteropodine, and isopteropodic acid along with a flavonoid known as rutin. Continuing our interest on this species, a dereplication strategy was applied to target unknown peak from the plant material. This had successfully led to the isolation of a new alkaloid. The molecular structure of the isolated new alkaloid was elucidated by using various spectroscopic techniques and was recognized as an acidic derivative of the alpha-beta unsaturated carbonyl methyl ester of pteropodine, one of the previously identified alkaloids from the plant. The new alkaloid was named as pteropodic acid. This study demonstrates that LCMS dereplication strategy will not only lead to an increased possibility of discovery of new compounds but also will save time, energy, and resources.

Keywords: *Uncaria*, liquid chromatography mass spectrometry, dereplication, alkaloid

Abstrak

Profil kimia sebelumnya oleh *Uncaria lanosa* var. *ferrea* Malaysia melalui kromatografi cecair spektrometer jisim (LCMS) berjaya mengenal pasti tiga alkaloid iaitu pteropodin, isopteropodin, dan asid isopteropodik bersama dengan flavonoid yang dikenali sebagai rutin. Meneruskan minat kami terhadap spesies ini, strategi direplikasi digunakan untuk menyasarkan puncak yang tidak diketahui dari bahan tumbuhan yang sama dan ini berjaya memencilkan alkaloid baru. Struktur molekul alkaloid baru yang dipencilkan telah dipastikan dengan menggunakan pelbagai teknik spektroskopi dan ditentukan sebagai molekul berasid terbitan karbonil metil ester tak tepu alpha-beta dari pteropodin, iaitu salah satu alkaloid yang dikenal pasti sebelumnya dalam tumbuhan yang sama. Oleh itu alkaloid baru ini dinamakan sebagai asid pteropodik. Dapatan kajian ini menunjukkan

bahawa strategi direplikasi LCMS tidak hanya akan meningkatkan kemungkinan dalam menemui sebatian baru tetapi juga mampu menjimatkan waktu, tenaga, dan sumber bahan.

Kata kunci: *Uncaria*, kromatografi cecair spektrometer jisim, direplikasi, alkaloid

Introduction

Genus *Uncaria*, a major part of Rubiaceae family, comprising 34 species has been used to treat various diseases worldwide [1]. To date, over 400 compounds have been identified in *Uncaria* species, primarily alkaloids, terpenoids, and flavonoids [2]. *Uncaria lanosa* Wall, locally known as "gegambir paya" or "gegambir hitam", is one of 14 species of *Uncaria* available in Malaysia [3]. The plant is reported to be used as an infusion for intestine inflammation and a decoction for cleaning wounds and ulcers. According to Turner [4], there are 11 varieties of *Uncaria lanosa* Wall. These are *Uncaria lanosa* var. *appendiculata* (Benth.) Ridsdale, *Uncaria lanosa* var. *ferrea* (Blume) Ridsdale, *Uncaria lanosa* f. *ferrea* (Blume) Ridsdale, *Uncaria lanosa* var. *glabrata* (Blume) Ridsdale, *Uncaria lanosa* f. *glabrescens* (Merr. & Perry) Ridsdale, *Uncaria lanosa* f. *gynogumna* Ridsdale, *Uncaria lanosa* var. *korrensis* (Kaneh.) Ridsdale, *Uncaria lanosa* f. *philippinensis* (Elmer) Ridsdale, *Uncaria lanosa* f. *setiloba* (Benth.) Ridsdale, *Uncaria lanosa* f. *sumatrana* Ridsdale, and *Uncaria lanosa* var. *toppingii* (Merr.) Ridsdale.

In the last two decades, the mass spectrometry technique had undergone a rapid development, allowing analysis of natural products with differentiated physicochemical properties. This is due to the instrument versatility and sensitivity that could be applied to structural characterization of plant metabolite mixtures, particularly for identifying minor components [5]. Liquid chromatography-mass spectrometry (LCMS)-based fingerprinting is one of the methods that would be able to determine the genetic diversity and the authentication of a plant species. In addition, an application of a strategic method such as dereplication would further facilitate and accelerate the metabolite identification, hence search for a novel active compound. The dereplication method requires to compare molecular chromatographic and spectroscopic data characteristics possibly obtained from an online database or an in-house library [6,7].

Our previous chemical profiling on the dichloromethane (DCM) stem extract of Malaysian *Uncaria lanosa* var. *ferrea* through Orbitrap LCMS successfully identify three alkaloids namely pteropodine, isopteropodine, and isopteropodic acid along with a flavonoid known as rutin [8]. In the present work, an LCMS dereplication strategy was applied to target for unknown peak from the same plant material, and this had led to the isolation of a new alkaloid. The dereplication process which had led to the isolation and the structural identification of the new alkaloid are discussed here.

Materials and Methods

Chemicals and raw materials

Stems of *U. lanosa var farrea* (Blume) Ridsd. were collected from Hutan Simpan Pasir Raja, Dungun Terengganu, Malaysia. This plant was identified by Mr. Ahmad Zainuddin Ibrahim from Universiti Kebangsaan Malaysia and the specimen voucher (HTBP4324) was deposited at the Herbarium Taman Botani Putrajaya, Malaysia. Ultrapure water was obtained from a PURELAB Ultra Laboratory Water Purification Systems while HPLC grade acetonitrile (MeCN) and methanol (MeOH) were purchased from Merck. Solvents used for fractionation and isolation were of industrial grade and were distilled prior to use.

Sample preparation

Dried and ground stems of *Uncaria lanosa* (1.38 kg) was extracted through 3-day maceration with methanol. The MeOH was removed until complete dryness, and crude MeOH extract (88.50 g) was further triturated using two types of solvents; non-polar solvent (hexane) and medium- polar solvent (DCM). Each mixture was filtered and evaporated under reduced pressure which produced 3 extracts; hexane (5.78 g), DCM (15.15 g) and MeOH (49.45 g). The DCM extract was subjected to an on open column chromatography [DCM/MeOH

(100:0 – 20:80)] with gradual increase in solvent polarity to yield seven potential fractions. 1 mg of the crude extract and fractions were weighed accurately and dissolved in 1 mL of MeOH: water containing 0.1% formic acid (30:70, v/v). Samples were filtered through a 0.22 µm PTFE filter into 2 ml screw cap vials prior to LCMS analysis.

High performance liquid chromatography mass spectrometry conditions

The optimized methodology in this study is slightly different compared to previous paper [7]. Samples including extracts and 17 reference compounds (1 mg/mL) were separated using GL Sciences - Inertsil Column C-18 (250 mm x 4.6 mm, i.d., 5µm). The flow rate was set at 0.6 mL/min, the absorbance was set to 254 and 215 nm, and the injection volume was 5 µL. After each injection the needle was washed with 100% MeCN. The mobile phase was a mixture of water (A) and MeCN (B) both containing 0.01% formic acid with gradient elution program of 5-55% B (0.00-30 min), 55-100% B (30-40 min), and 100% B (10-45 min).

HPLC-DAD-TOF MS was conducted on Agilent 1100 Series of high-performance liquid chromatography coupled with diode-array and time-of-flight mass detectors, electrospray ionization (ESI) source system, dual pump, autosampler and column. Nitrogen was used as the nebulizing and dissolving gas with a flow rate of 50 and 400 Lit/h, respectively. The optimum source of ESI conditions were: 3.5kV spray voltage, 25V cone voltage, 3V extractor, 0.2V rf lens, 100°C source temperature, and 350°C probe temperature. Data processing and library searching was performed using Qualitative Analysis on Mass Hunter Acquisition Data.

Isolation of pteropodic acid using recycling HPLC

One of the potential fractions, D4 (639.80 mg) was targeted for further isolation. The fraction was subjected to recycling HPLC using two column Jaigel- ODS- AP, SP- 120-15 (250 mm x 20 mm, i.d., 5µm) with guard column and GL Sciences- Inertsustain Column C-18 (250 mm x 20 mm, i.d., 5µm). The flow rate of the system was set at 4 mL/min, the absorbance at 254 nm, and the injection volume was 1 mL. The fraction was separated using an isocratic elution (20:80) of water and MeCN both containing 0.01% formic acid. The new alkaloid, pteropodic acid (5.7 mg) was eluted in the first cycle at minutes 35.

Results and Discussion

Development of in-house database

The LC-ESI-MS profiles of previously isolated compounds from *Uncaria* species were added into in-house database. This database was used as reference for the identification of compounds from LCMS data analysis of the crude extracts and fractions of *Uncaria* species for the isolation of targeted compounds. The LCMS profiles are shown in Table 1.

LCMS dereplication analysis of *Uncaria lanosa* extract

The HPLC-DAD-TOF-MS system was employed for the metabolite profiling and identification of the chromatographic peak of the DCM stem extract of *U. lanosa var. ferrea*. From the analysis, a positive mode affords higher sensitivity for most of the peaks compared to a negative mode. Therefore, a positive mode was chosen and applied in further analyses. By comparing the retention time and *m/z* value to the reference compounds in the in-house database, only four peaks were identified, including one flavonoid which was rutin (6), and three alkaloids which were pteropodine (8), isopterpodic acid (10), and isopteropodine (13). As shown in Figure 1, four peaks were successfully dereplicated. These were peaks (6), (8), (10), and (13) with $[M+H]^+$ ion of *m/z* 611.1624, 369.2173, 355.1779 and 369.2250, respectively. A major unknown $[M+H]^+$ ion peak at *m/z* 355.2707 was targeted for further isolation using recycling HPLC.

The targeted compound was isolated as white amorphous powder and its mass spectrum gave an $[M+H]^+$ peak at *m/z* 355.2707 which corresponded to the molecular formula $C_{20}H_{22}N_2O_4$. Its UV spectrum displayed absorption bands at 209.97 and 244.00 nm indicating that a hydroxyl substituent may be present. The IR spectrum revealed the presence of non-hydrogen-bonded OH (sharp peak) at 3421.96 cm^{-1}. Typical IR characteristics of heteroyohim B bine-type oxindole alkaloids absorption frequencies at 3114 cm^{-1} (NH), 1622.02 cm^{-1} (C=O acid), 1674 cm^{-1} (C=O

amide), 1636 cm^{-1} (C=C olefinic), 1472.8 cm^{-1} (C=C aromatic) and 1191.42 cm^{-1} (C-O cyclic ether) were also observed suggesting that the compound belonged to pentacyclic oxindole alkaloid. The ^{1}H NMR spectrum of this compound showed that four aromatic proton signals resonating at δ 7.29, δ 7.21, 7.07 and 6.88 confirming that the presence of aromatic ring is unsubstituted in the oxindole moiety. Proton resonances were also observed as a singlet at δ 7.50 belonging to an olefinic proton H-17 and a broad singlet at δ 8.56 attributed to a proton attached with nitrogen. A quartet and three-proton doublet resonances at δ 4.46 (J = 6.1 Hz) and 1.41 (J = 6Hz) were also present corresponding to H-19 and H-18 respectively. There was no carbomethoxy (OCH_3) resonance which was typically observed in other POAs H^1 NMR spectrum [9, 10].

In the ^{13}C NMR spectrum, the presence of 20 carbons including a methyl group, an acid carbonyl and oxindole carbonyl resonances at δ 17.59, δ 170.40 and δ 181.92 respectively. The slightly higher ^{13}C NMR resonance value for the acid carbonyl (δ 170.40) compared to the ester carbonyl in the pteropodine system (δ 167.77) further confirmed the existence of a carboxylic acid moiety in the structure [11]. Therefore, based on these spectral data as well as comparisons with literature data, the compound was deduced to be pteropodic acid which is the acidic derivative of the alpha-beta unsaturated carbonyl methyl ester of pteropodine, one of the previously identified alkaloids from the plant. The structure of the dereplicated and the isolated alkaloid is shown in Figure 2.

Physical and spectral data of isolated compound

Pteropodic acid: White amorphous powder, wt: 5.7 mg (MeOH), mp 268 - 271 °C. MS *m/z*: 355.2707 $[M+H]^+$, $C_{20}H_{22}N_2O_4$; UV (MeOH) λ_{max} nm: 209.97, 244.00; IR (KBr) υ_{max} cm^{-1}: 3421.96 (OH), 3114 (NH), 1622.02 (C=O acid), 1674 (C=O amide), 1636 (C=C olefinic), 1472.8 (C=C aromatic) and 1191.42 (C-O cyclic ether); ^{1}H NMR (MeOD, 600 MHz) δ ppm: 8.56 (1H, *br s*, N-H), 7.50 (1H, *s*, H-17), 7.29 (1H, *d*, *J* = 7.2 Hz, H-9), 7.21 (1H, *ddd*, *J* =7.7, 1.0 Hz, H-11), 7.07 (1H, *ddd*, *J*= 7.6, 0.8 Hz, H-10), 6.88 (1H, *d*, *J* = 7.7 Hz, H-12), 4.46 (1H, *q*, *J* = 6.1 Hz, H-19), 3.39 - 3.34 (2H, *m*, H-21β, H-5β), 2.50 – 2.27 (5H, *m*, H-15, H-21α, H-6β, H-5α, H-3), 2.07-1.99 (1H, *m*, H-6α), 1.70 – 1.64 (2H, *br m*, H-14α, H-20), 1.63-1.57 (1H, *m*, H-14β), 1.41 (3H, *d*, *J* = 6 Hz, CH_3); ^{13}C NMR (MeOD, 150 MHz) δ ppm: 181.92 (N-C=O), 170.40 (O-C=O), 154.60 (C-17), 141.50 (C-13), 133.30 (C-8), 127.70 (C-11), 122.79 (C-9), 122.27 (C-10), 110.39 (C-16), 109.09 (C-12), 74.11 (C-19), 71.85 (C-3), 56.42 (C-7), 54.59 (C-5), 53.03 (C-21), 38.11 (C-20), 33.56 (C-6), 31.16 (C-15), 29.55 (C-14), 17.59 (CH_3).

Table 1. Characterization of reference compounds by developed HPLC-DAD-TOF MS method

No.	Compound (RT (min))	Proposed Molecular Formula	Observed Mass $[M+H]^+$	Calculated Mass $[M+H]^+$	Observed Mass $[M-H]^-$	Calculated Mass $[M-H]^-$
1	Formosaninol (10.23)	$C_{21}H_{26}N_2O_5$	387.2092	387.1920	-	385.1764
2	Catechin (10.63)	$C_{15}H_{14}O_6$	291.1058	291.0868	289.0612	289.0712
3	Isoformosaninol (11.65)	$C_{21}H_{26}N_2O_5$	387.2108	387.1920	-	385.1764
4	(-)*Epi*-catechin (12.77)	$C_{15}H_{14}O_6$	291.1058	291.0868	289.0600	289.0712
5	(-)*Epi*-afzelechin (15.15)	$C_{15}H_{14}O_5$	275.1117	275.0919	273.0661	273.0763
6	Rutin (16.88)	$C_{27}H_{30}O_{16}$	611.1745	611.1612	609.1128	609.1456
7	Scopoletin (17.49)	$C_{10}H_8O_4$	193.0726	193.0501	-	191.0345
8	Pteropodine (17.64)	$C_{21}H_{24}N_2O_4$	369.1971	369.1814	-	367.1658
9	Longiflorine (17.69)	$C_{11}H_{15}NO_4$	226.1280	226.1079	-	224.0923
10	Isopteropodic acid (18.32)	$C_{20}H_{22}N_2O_4$	355.1841	355.1658	-	353.1502

Table 1 (cont'd). Characterization of reference compounds by developed HPLC-DAD-TOF MS method

No.	Compound (RT (min))	Proposed Molecular Formula	Observed Mass $[M+H]^+$	Calculated Mass $[M+H]^+$	Observed Mass $[M-H]^-$	Calculated Mass $[M-H]^-$
11	Methyl paraben (21.72)	$C_8H_8O_3$	153.0777	153.0552	151.0387	151.0396
12	Uncariechin (22.64)	$C_{18}H_{14}O_6$	327.1062	327.0868	325.0564	325.0712
13	Isopterodine (23.67)	$C_{21}H_{24}N_2O_4$	369.1996	369.1814	-	367.1658
14	Uncarine F (23.75)	$C_{21}H_{24}N_2O_4$	369.2063	369.1814	367.1625	367.1658
15	Speciophylline (23.79)	$C_{21}H_{24}N_2O_4$	369.2126	369.1814	367.1634	367.1658
16	Rauniticine-*allo*-oxindole B (23.83)	$C_{21}H_{24}N_2O_4$	369.2182	369.1814	367.1566	367.1658
17	Quercetin (24.72)	$C_{15}H_{10}O_7$	303.0699	303.0505	301.0248	301.0349

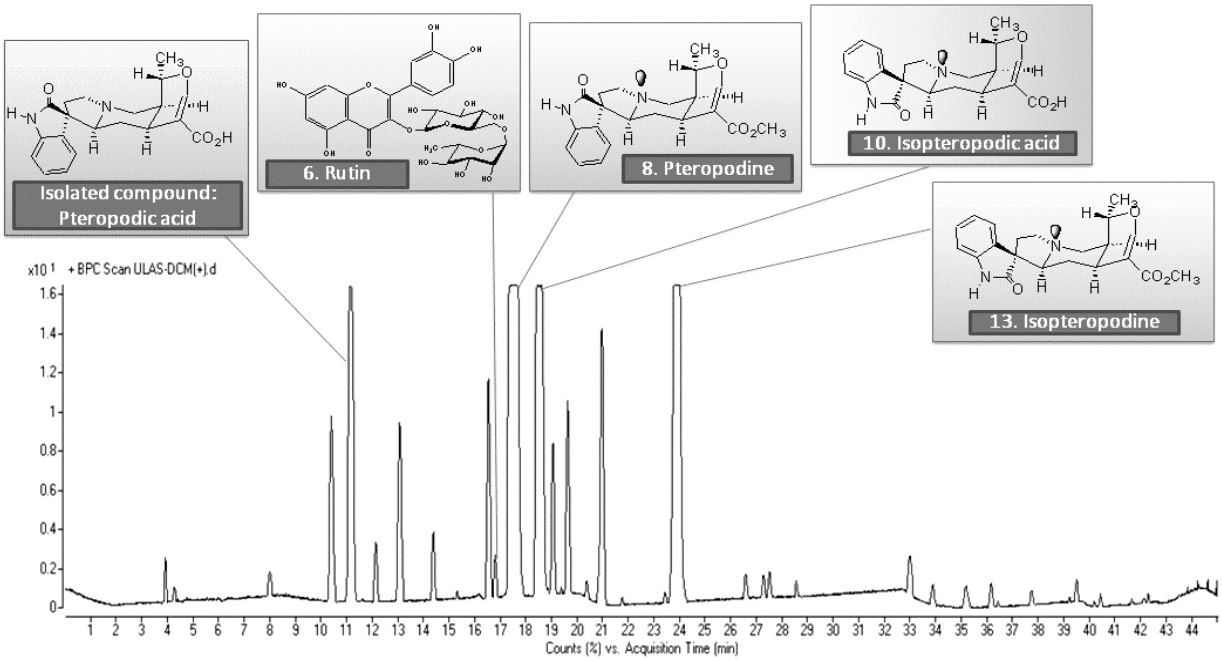


Figure 1. MS profile of *U. lanosa* DCM extract; the total ion current (TIC) in positive mode with structure of identified peaks; numbers of identified peak are according to the no. of reference compound in Table 1.

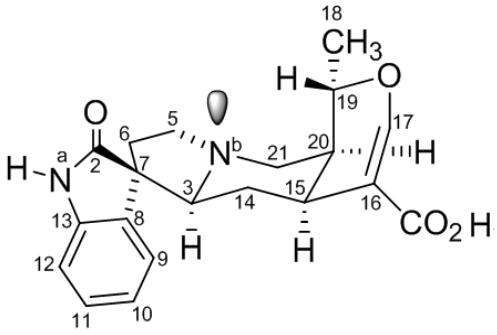


Figure 2. Structure of isolated alkaloid from *Uncaria lanosa* var. *ferrea* identified as pteropodic acid

Conclusion

The proposed HPLC-DAD-TOF-MS dereplication strategy using in-house developed database was applied to identify known peaks and target unknown peak from *U. lanosa* var. *ferrea*. This has successfully led to the identification of one flavonoid and three alkaloids, and the isolation of a new alkaloid which was deduced as pteropodic acid. This study demonstrates that the LCMS dereplication strategy will not only increase the possibility discovery of new compounds but will save time, energy and resources by minimizing repetitive isolation of known compounds.

Acknowledgement

Authors would like to thank the Ministry of Science, Technology and Innovation Malaysia (MOSTI) for funding this research through E-Sciences grant 100-RMI/SF 16/6/2 (23/2012), and the Faculty of Pharmacy, Universiti Teknologi MARA for the HPLC-DAD-TOF-MS facility.

References

1. Ahmad, R., and Salim, F. (2015). Oxindole alkaloids of *Uncaria* (Rubiaceae, subfamily cinchonoideae): A review on its structure, properties, and bioactivities. In *Book Studies in Natural Products Chemistry,* 45: 486-525.
2. Qin, N., Lu, X., Liu, Y., Qiao, Y., Qu, W., Feng, F. and Sun, H. (2021). Recent research progress of *Uncaria* spp. based on alkaloids: phytochemistry, pharmacology and structural chemistry. *European Journal of Medicinal Chemistry*, 210: 112960.
3. Burkill, I. H. (1966). A dictionary of the economic products of Malaysia Peninsula. 2nd edition. Kuala Lumpur: pp. 2236-2245.
4. Turner, I. M. (2018). A revised conspectus of *Uncaria* (Rubiaceae). *Journal of Plant Taxonomy and Geography*, 73(1): 9-21.
5. Alvarez-rivera, G., Ballesteros-vivas, D., Parada-alfonso, F., Ibanez, E., and Cifuentes, A. (2019). Recent applications of high resolution mass spectrometry for the characterization of plant natural products. *Trends in Analytical Chemistry,* 112: 87-101.
6. Lone, S. A., Kushwaha, M., Wani, A., Kumar, A., Gupta, A. P., Hassan, Q. P., Chandra, S. and Gupta, S. (2017). Genetic diversity, LCMS based chemical fingerprinting and antioxidant activity of *Epimedium elatum* Morr & Decne. *Journal of Applied Research on Medical and Aromatic Plants*, 5: 72-81.
7. Zhang, X., Li, Q., Xu, Z. and Dou, J. (2020). Mass spectrometry-based metabolomics in health and medical science: A systematic review. *RSC Advances*, 10: 3092-3104.
8. Shaharuddin, N. H., Ismail, N. H., Manshoor, N., Salim, F. and Ahmad, R. (2016). Chemical profiling and identification of alkaloids and flavonoids in *Uncaria lanosa* var. *ferrea* via UHPLC-Orbitrap MS. *Malaysian Journal of Analytical Sciences*, 20(2): 318-323.

9. Salim, F., Ismail, N. H., Awang, K. and Ahmad, R. (2016). Rauniticine-*allo*-oxindole B and rauniticinic-*allo* acid B, new heteroyohimbine-type oxindole alkaloids from the stems of Malaysian *Uncaria longiflora* var. *pteropoda*. *Molecules,* **16**(8): 6541-6548.
10. Salim, F., Yunus, Y. M., Anouar, E. H., Awang, K., Langat, M. K., Cordell, G. A., and Ahmad, R. (2019). Absolute configuration of alkaloids from *Uncaria longiflora* var. *pteropoda* through experimental and theoretical approaches. *Journal of Natural Products,* 82: 2933-2940.
11. Salim, F. and Ahmad, R. (2010). Isopteropodic acid from Malaysian *Uncaria longiflora* var. *pteropoda*. *World Applied Science Journal*, 10(11): 1334-1337.

Malaysian Journal of Analytical Sciences (MJAS)
Published by Malaysian Analytical Sciences Society

ADSORPTION OF ACID ORANGE 7 BY CETYLTRIMETHYL AMMONIUM BROMIDE MODIFIED OIL PALM LEAF POWDER

(Penjerapan Asid Oren 7 oleh Setiltrimetil Ammonium Bromida Ubahsuai Serbuk Daun Kelapa Sawit)

Nik Ahmad Nizam Nik Malek[1,2]*, Nurul Ain Sallehhuddin[1], Auni Afiqah Kamaru[3]

[1]*Department of Biosciences, Faculty of Science*
[2]*Centre for Sustainable Nanomaterials (CSNano), Ibnu Sina Institute for Scientific and Industrial Research (ISI-ISIR)*
Universiti Teknologi Malaysia, 81310 JohorBharu, Johor, Malaysia
[3]*Geomatika University College,*
Prima Peninsula, Jalan Setiawangsa 11, 54200 Kuala Lumpur

**Corresponding author: niknizam@utm.my*

Received: 29 August 2021; Accepted: 28 October 2021; Published: 27 December 2021

Abstract

The capability of oil palm leaf (OPL) and surfactant modified oil palm leaf (SMOPL) to remove acid orange 7 (AO7) anionic dye in an aqueous solution was studied. The SMOPL was prepared by treating the OPL with different concentrations of cetyltrimethyl ammonium bromide (CTAB) solutions (1.0, 2.5, and 4.0 mM). The samples were characterized using Fourier-transform infrared (FTIR) spectroscopy and dispersion behaviour test. The FTIR results showed the modification of OPL with CTAB surfactant did not change the chemical structure of the OPL, except for an increase in the intensity of the C-H bond, which occurred due to the hydrocarbon group in CTAB. In addition, the effects of initial AO7 concentrations on the adsorption capacity of SMOPL were studied, and the highest AO7 adsorption capacity was found for the SMOPL4.0 with the initial CTAB concentration being 4.0 mM. Comparatively, the raw OPL demonstrated the lowest adsorption capability. The presence of the CTAB surfactant molecules on the samples increased the adsorption site of the adsorbent, allowing more attachments of dye molecules onto the OPL adsorbent. The Langmuir and Freundlich isotherm models were used to describe the adsorption isotherm. The equilibrium data were better fitted by Langmuir isotherm with a maximum AO7 adsorption capacity of 138.89 mg/g. Thus, it is suggested that the adsorption of AO7 takes place as a single monolayer on a homogeneous OPL surface. From this study, it can be concluded that the modification of OPL with cationic surfactant can enhance its adsorption process of anionic dye from an aqueous solution.

Keywords: adsorption, oil palm leaf, cetyltrimethyl ammonium bromide, acid orange 7, surfactant

Abstrak

Keupayaan daun kelapa sawit (OPL) dan daun kelapa sawit yang diubah suai surfaktan (SMOPL) untuk menyingkirkan pewarna anionik asid oren 7 (AO7) dalam larutan akues telah dikaji. SMOPL disediakan dengan merawat OPL dengan kepekatan larutan setiltrimetilammonium bromida (CTAB) yang berbeza (1.0, 2.5, dan 4.0 mM). Sampel dicirikan dengan menggunakan spektroskopi inframerah transformasi Fourier (FTIR) dan ujian tingkah laku penyebaran. Hasil FTIR menunjukkan pengubahsuaian OPL dengan surfaktan CTAB tidak mengubah struktur kimia OPL, kecuali beberapa peningkatan keamatan

untuk ikatan C-H yang berlaku disebabkan oleh kumpulan hidrokarbon yang terdapat pada CTAB. Kesan kepekatan AO7 awal pada kapasiti penjerapan SMOPL dikaji, dan kapasiti penjerapan tertinggi AO7 dijalankan untuk SMOPL4.0 di mana kepekatan CTAB awal adalah 4.0 mM. Secara perbandingan, OPL menunjukkan kemampuan penjerapan yang terendah. Kehadiran molekul surfaktan CTAB pada sampel meningkatkan tapak penjerapan, yang memungkinkan lebih banyak interaksi molekul pewarna ke OPL. Model isoterma Langmuir dan Freundlich digunakan untuk menggambarkan isoterma penjerapan. Data keseimbangan lebih baik dipadankan oleh isoterma Langmuir dengan kapasiti penjerapan maksimum AO7 adalah 138.89 mg/g. Jadi, penjerapan AO7 terhasil sebagai satu lapisan tunggal pada permukaan OPL yang homogen. Dari kajian ini, dapat disimpulkan bahawa modifikasi OPL dengan surfaktan kationik dapat meningkatkan proses penjerapannya untuk pewarna anionik dari larutan berair.

Kata kunci: penjerapan, daun kelapa sawit, setiltrimetilammonium bromida, asid oren 7, surfaktan

Introduction

As a colouring agent, anionic dyes have been widely used in many industries, including textile, clothes, food, and polymers. After several steps of the dyeing process, the inappropriate treatment of hazardous effluents that have toxic complex will be discharged as wastewater [1]. Dyes cause toxicity to the water body from their degradation products, and affect living organisms. Therefore, the removal of dyes from an aqueous solution is essential. Some removal methods have been studied recently, such as adsorption using biodegradable polymeric natural adsorbent [2] and modified coconut shell [3], adsorption-photocatalytic degradation [4] and many more. Acid Orange 7 (AO7) is an example of anionic dyes (Figure 1), and it is an acid dye that can be applied on textiles. The AO7 is also known as an azo dye that has a non-biodegradable property, and is mostly used in the dyeing industry [5]. One of the suitable techniques for the removal of AO7 is using the adsorption technique.

Biosorption is a method to remove pollutants from aqueous solutions by using bio-resource materials such as plant wastes, fungi and bacteria. This method is preferable for its low-cost and straightforward process [6]. Plant biomass is abundant in nature, easy to obtain and renewable. This treatment method is also eco-friendly by using adsorbent material from biomass product. Oil palm leaf (OPL) is one of the agricultural wastes easily found in Malaysia and able to be used as a low-cost adsorbent [7].

Elaeis guineensis is the scientific name of the oil palm plant. Besides producing palm oil, it also contains valuable biomass products useful for many applications, including adsorbent. The OPL is part of the oil palm plant converted into biomass product apart from the empty fruit bunch, bark, trunk and shells [8]. Like other agricultural wastes, OPL is composed of hemicellulose, cellulose and lignin. Cellulose and lignin contain hydroxyl group that causes the negatively-charged surface of the OPL. Thus, this material can become a suitable adsorbent for cationic compounds.

Therefore, OPL can be modified with a cationic surfactant such as cetyltrimethyl ammonium bromide (CTAB) (Figure 1) to enhance its adsorption capacity against anionic dyes. CTAB increases the binding affinity towards anionic dyes by changing the property of the adsorbent from negatively-charged to positively-charged adsorbent [9]. Many surfactant-modified biomasses have been developed to remove various pollutants [10-13]. However, there is no report on using surfactant modified OPL as an adsorbent for anionic AO7 dye.

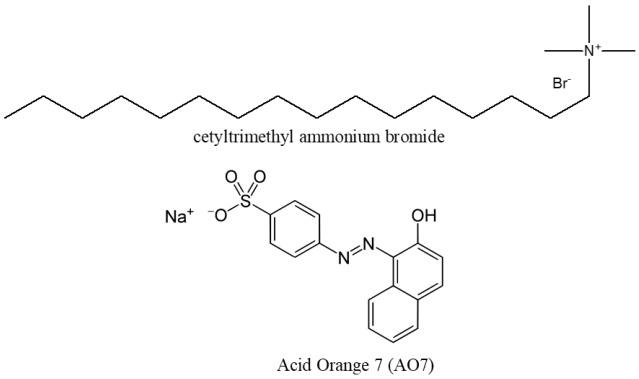


Figure 1. Structural formula of CTAB and AO7

Materials and Methods

Materials preparation

The OPLs from the *E. guineensis* species were obtained from an oil palm plantation located at the Universiti Teknologi Malaysia (UTM), Johor, Malaysia. The preparation of the OPL powder was performed following the previous report by Kamaru et al. [9, 13]. First, the leaves were initially washed with water several times to remove all the impurities and dust before being dried under the sunlight for one week. Then, it was cut into smaller pieces and subsequently dried in a universal oven at 90 °C for 24 hours. Next, the dried leaves were ground into a powder form using the stainless-steel blade blender, and the powder sample was abbreviated as OPLP.

Then, a pre-treatment method was carried out on the OPLP to remove any colouring component from the sample. The OPLP was suspended in a boiled distilled water, stirred for 30 minutes and filtered to remove the water filtrate. This procedure was repeated several times until a clear filtrate was observed. The pre-treated OPL powder was later dried in a universal oven for 24 hours at 90 °C.

In this study, the OPL adsorbent was modified with a CTAB surfactant. The prepared OPL powder was treated with three different concentrations of CTAB: 1.0, 2.5, and 4.0 mM. First, the CTAB solutions with the desired concentration were prepared by dissolving 0.3644 g, 0.9110 g, and 1.4576 g of CTAB powder in 1000 mL of distilled water. The mixture was then stirred until the CTAB powder was completely dissolved in the solutions. Next, 10.0 g of OPL powder was added into each 1000 mL CTAB solutions, and it was stirred for another 15 minutes. The solutions were then filtered using Whatman filter paper, and the OPL powder residue was dried in a universal oven at 90 °C for 24 hours. After these steps, the samples were known as CTAB-modified OPL powder and abbreviated as SMOPL1.0, SMOPL2.5 and SMOPL4.0 for OPL treated with 1.0, 2.5 and 4.0 mM CTAB, respectively. Finally, the dried modified OPL powder was ground using mortar and pestle into a fine structure and sieved. The resulting powder was kept in airtight plastic containers for further characterization and adsorption study.

Materials characterization

The functional groups in both raw and surfactant modified OPL powder were analysed by using Fourier-transform infrared (FTIR) spectrophotometer (model Thermo Scientific Nicolet IS10-IR) using potassium bromide (KBr) method. The FTIR spectra were recorded using OMNIC software in the range of 4000 to 500 cm^{-1}.

The samples were also analysed for their dispersion behaviour in a hexane-water mixture. The purpose of the dispersion test was to study the relative position of the samples in the mixture of oil and water. This test was carried out by adding 3 mL of distilled water and *n*-hexane in four universal bottles. Then, 0.06 g of raw and SMOPL were added to the oil-water mixture. The images of the bottles were captured after four different conditions: (1) immediately after the samples were added, (2) after shaking for a while and (3) for 30 minutes, and lastly (4) after being left untouched for one day at room temperature (24 °C).

Adsorption Study

The adsorption study of raw and surfactant modified OPL were performed using AO7 as the adsorbate. To begin with, a stock solution of 1000 mg/L AO7 was prepared by diluting 1.0 g of AO7 powder in 1000 mL of distilled water. Then, this stock solution was used to prepare the working solutions for the adsorption study.

The adsorption test was performed by mixing the AO7 solution with the OPL adsorbent. The AO7 working solutions were first prepared for a wide range of concentrations from 10 to 1000 mg/L, and their absorbance reading was measured to obtain the initial dye concentration. Next, 25 mL of the solutions were added into a 50 mL falcon tube containing 200 mg of raw and CTAB-modified OPL powder. Then, the tubes were left shaken in a rotary shaker for 1 h at room temperature. After 1 h, the solutions were filtered by using Whatman filter paper. The absorbance reading of the filtrates was measured under UV-Vis

spectrophotometer at $\lambda_{484\ nm}$ to determine the final concentration. Finally, by comparing the results with the prepared standard curve, the concentration of AO7 before and after the adsorption were determined. All the experiments were done in triplicate.

The adsorption capacity of OPL against AO7 was analysed by using Equation 1:

$$q_t \left(\frac{mg}{g}\right) = \frac{C_0 - C_t}{m} . V \quad (1)$$

where C_0 is the initial dye concentration (mg/L), C_t is the final dye concentration (mg/L) after adsorption, m is the dose of OPL adsorbent (g), and V is the volume of dye adsorbate (L).

Results and Discussion

The prepared samples were characterized for the functional groups using FTIR. After being attached to the surfactant, the changes that happened on the samples were observed in the dispersion behaviour test. Figure 2 shows the FTIR spectra of the samples, and Table 1 gives FTIR peaks assignment for their possible functional groups.

From Figure 2 and Table 1, several vibration bands were shown by the OPL and other samples. Strong, broad bands around 3444 to 3446 cm^{-1} represented the hydroxyl (O-H) group, indicating that the surface of the OPL had a high amount of hydroxyl group due to the cellulose and lignin structure of the OPL. There were also bands shown in the range of 2921 to 2924 cm^{-1}, representing C-H stretches. Furthermore, the bands observed around 2852 to 2854 cm^{-1} indicated the existence of C-H asymmetric stretching from methylene (CH_2) and methyl (CH_3) groups [7]. Meanwhile, the bands at around 1746 and 1633 cm^{-1} were attributed by C=O stretching from carbonyl and C=C stretching of aromatic OPL, respectively [14]. The peaks at about 1647 to 1650 cm^{-1} indicated carbon-oxygen bonding (C-O-O) due to the presence of aromatic lignin [15]. Additionally, the bands at 1454 to 1456 cm^{-1} showed the presence of C=C stretching for the aromatic compound, and the presence of CH_3 bending was detected at 1384 and 1385 cm^{-1} [16]. The peaks that appeared around 1270 to 1271 cm^{-1} may be referred to as the C-O stretching of carboxylic acids. Lastly, small peaks were observed at 1030, 1541. 1455, 1385, and 1271 cm^{-1}, possibly indicating the aromatic stretching, C-O bonds, and N-H bonds, respectively [17]. In summary, the FTIR spectrum of the OPL showed many important functional groups (C=O, C=C, O-H) in the sample, which contributed to the ability of OPL in adsorbing other adsorbates.

After surfactant modification of the OPL, the FTIR spectra showed that the addition of CTAB molecules on the OPL did not change its chemical structure as there were no significant differences among their peaks. However, the increased intensity of bands of C-H and C-C bonds were demonstrated at 2921, 2852 and 1455 cm^{-1} because the number of hydrocarbons on the OPL surface increased by the presence of the surfactant [10]. The binding of CTAB molecules on the OPL was proven by increasing C-H functional group since the CTAB had a long aliphatic hydrocarbon compound [9]. From the analysis, most of the functional groups presented by the FTIR spectra were contributed by the hemicellulose, cellulose and lignin of OPL samples. Except for the peak increase that corresponded to the C-H stretch, no noticeable change of band was shown by other functional groups to compare both unmodified and modified OPL. The result indicated that the modification of OPL with CTAB surfactant would not promote drastic changes in the chemical structure of OPL [9].

The dispersion behaviour method was carried out to determine the relative position of OPL and surfactant-modified OPL in an oil-water mixture to determine the changes in the physical properties of the OPL after being modified with the CTAB. Figure 3 shows the images of the condition and position of oil palm leaf samples in the mixture of water-hexane starting from the beginning of the samples added, after shaking for thirty minutes and lastly after being left for 24 hours at room temperature.

When the samples were added to the water-hexane mixture at the beginning of the process, all the samples were positioned between the distilled water and *n*-hexane solution. The solutions were then shaken for a

while and 30 minutes in the shaker. After shaking, all the samples exhibited different behaviours in the solution. Some of the raw OPL dispersed in the distilled water, and a small portion of OPL dispersed in the *n*-hexane solution. Meanwhile, all the SMOPL were seen to avoid the *n*-hexane solution and spread the distilled water solution. Moreover, at the highest concentration of surfactant (SMOPL4.0), a higher amount of the sample dispersed in distilled water. After being left for one day, the images were captured and re-recorded. The photos indicated that the position of OPL and SMOPL in the water-hexane mixture were different. The raw OPL mainly stayed at the middle position of the water-hexane mixture, while the SMOPL remained at the bottom of the bottle. Some SMOPL1.0 and SMOPL2.5 samples were still positioned between the distilled water and *n*-hexane solution, and a few were dispersed in the distilled water. Meanwhile, most of the SMOPL4.0 samples were located and dispersed in water. From Figure 3, an increasing capability of the SMOPL to disperse in water followed the trend of SMOPL4.0 > SMOPL2.5 > SMOPL1.0 > OPL.

The inability of raw OPL to disperse in water solution could be due to the lignin in the OPL structure with hydrophobic characteristics that tend to repel water molecules [19]. It is also revealed that the modification of CTAB increased the interaction of OPL samples with water molecules because the result showed better dispersion of the SMOPL in water as the CTAB concentration increased. This phenomenon may occur due to the structure of the CTAB that was comprised of hydrophilic ammonium group, resulting in the polar characteristics of SMOPL. A high concentration of surfactant attached to the sample leads to the increasing hydrophilic force. At the same time, the hydrophobic force increased as the surfactant attachment decreased. Therefore, the hydrophilicity of SMOPL increased as the CTAB concentration increased and its interaction with water increased. This dispersion behaviour test proves the successful modification of OPL with CTAB surfactant, and the CTAB molecules affect the physical characteristics of the raw OPL.

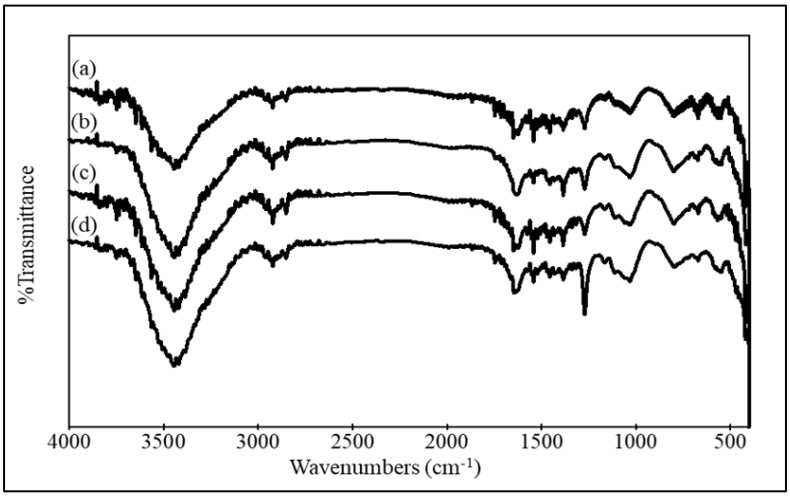


Figure 2. FTIR spectra of raw OPL (a), SMOPL1.0 (b), SMOPL2.5 (c) and SMOPL4.0 (d)

Table 1. FTIR peak assignments of OPL and SMOPL

Wavelength (cm^{-1})				Functional Group	References
OPL	**SMOPL1.0**	**SMOPL2.5**	**SMOPL4.0**		
3444	3444	3445	3446	OH	[14]
2921	2923	2921	2924	C–H	[7]
2852	2852	2853	2854		
1749	1744	1746	1746	C=O	[16]
1633	1630	1630	1633	C=O	[17]
1455	1454	1455	1456	C-C	[16]
1384	1385	1385	1384	C-H	[13]
1270	1270	1271	1271	C-O	[18]
1031	1033	1034	1033	C=O	[17]

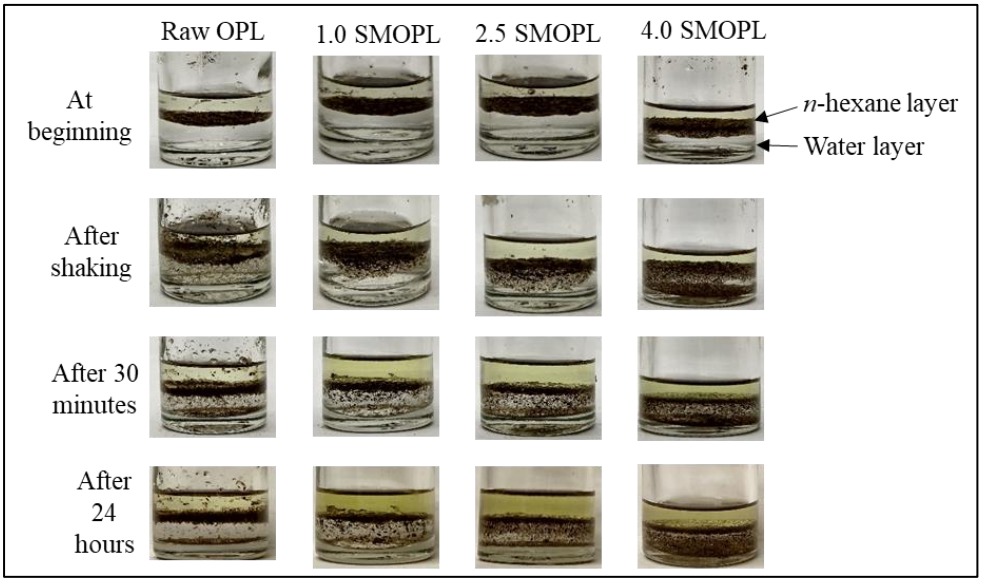


Figure 3. Dispersion behaviour of samples in water-hexane mixture

The adsorption study of OPL and SMOPL was performed by varying the initial concentrations of AO7, ranging from 10 to 1000 mg/L. The effect of the initial concentration of AO7 on its adsorption onto oil palm leaf is presented in Figure 4.

From Figure 4, the adsorption capacity (Q_e) of all samples demonstrated a similar pattern towards the anionic dye AO7. The graph shows that the amount of AO7 adsorbed onto the OPL increases as the initial concentration of AO7 increases. However, it is observed that the raw OPL had the lowest adsorption capacity towards AO7 compared to the CTAB

modified OPL (SMOPL). Meanwhile, the highest adsorption capacity towards AO7 was exhibited by SMOPL4.0 (Figure 4). As the CTAB concentrations treated on the SMOPL increased, the adsorption capacity towards AO7 was also increased. The removal of AO7 from aqueous solutions by OPL presented by the graph followed the trend of SMOPL4.0 > SMOPL2.5 > SMOPL1.0 > OPL. In addition, the steepness of the slope that increased after CTAB modification and with SMOPL4.0 displaying the steepest slope also had verified that the adsorption capacity of OPL increased as more treatment of CTAB was introduced to the OPL adsorbate [9].

The result showed that the surface modification of the OPL adsorbent and the initial concentrations of dye adsorbate influenced the adsorption capacity and the affinity of the OPL towards AO7. This happens due to the composition of OPL surface that is composed of hemicellulose, cellulose and lignin. The porous structure of cellulose provides a large surface area for the attachment of AO7. That is why all samples showed a positive adsorption behaviour towards AO7. Moreover, when OPL is in an aqueous solution, the hydroxyl group in cellulose and lignin releases the hydrogen ions, leading to the formation of negative charge on the surface of OPL [12]. However, when OPL is modified by CTAB surfactant, the negative charge surface of OPL is inverted into positive charge because of the bilayer formation of CTAB on the surface of OPL. As a result, SMOPL attracts more anionic dye that is negatively charged as the opposite charge between OPL and AO7 will increase the electrostatic interaction between each other, and hence, increase the adsorption capacity of the SMOPL. Therefore, different concentrations of CTAB applied to the OPL will result in the different adsorption behaviour of the OPL towards anionic dyes.

The adsorption behaviour of OPL and SMOPL towards anionic dye AO7 was further analyzed through isotherm studies. Using Langmuir and Freundlich isotherm models, the adsorption capacity of OPL and SMOPL to remove AO7 from an aqueous solution was quantified. The purpose of using the Langmuir and Freundlich isotherm model was to predict the adsorption equilibrium of AO7 adsorbate onto both OPL and SMOPL [12].

Langmuir isotherm model is based on the assumption of the single monolayer adsorption of adsorbate onto the homogenous surface of adsorbent with a structurally similar binding site [20]. The non-linear Langmuir isotherm equation is shown below:

$$\frac{x}{m} = q_e = \frac{bQ_oC_e}{1+bC_e} \quad (2)$$

where x is defined as mass of adsorbate adsorbed (mg or mmol), m is mass of adsorbent (g), C_e is equilibrium concentration (mg/L), b is Langmuir constant related to the affinity of binding site; and Q_o is maximum adsorption at monolayer coverage (mg/g).

The non-linear equation can be linearized into:

$$\frac{m}{x} = \frac{1}{q_e} = \frac{1}{Q_0} + \frac{1}{bQ_0C_e} \quad (3)$$

The plot of $1/q_e$ against $1/C_e$ will give the straight-line graph with $1/Q_0$, and $1/(bQ_0)$ being the y-intercept and the slope, respectively.

Freundlich adsorption isotherm is an empirical equation that describes the multilayer adsorption of adsorbate onto the heterogeneous surface of the adsorbent. The non-linear Freundlich isotherm equation is shown as below:

$$\frac{x}{m} = q_e = K_f C_e^{\frac{1}{n}} \quad (4)$$

where K_f is defined as maximum adsorption at multilayer coverage (mg/g); and n is favourability of the adsorption process.

The non-linear equation can be linearized into:

$$log\frac{x}{m} = logq_e = logK_f + \frac{1}{n}logC_e \quad (5)$$

The log q_e against log C_e will give a straight-line graph with log K_f and $1/n$ as the y-intercept and the slope,

respectively. The values of parameters for both adsorption isotherm models are shown in Table 2.

From the isotherm results, it can be summarized that the adsorption behaviour of AO7 by OPL is very different from that of the SMOPL. The adsorption of AO7 by raw OPL neither followed the Langmuir nor the Freundlich isotherm models because the R^2 of the Langmuir isotherm model was below 0.9, and most data were not distributed well on the linear graph, showing that it could not fit the model. Similarly, the R^2 value of the adsorption in the Freundlich isotherm was too low, signifying that it did not fit the model. This result showed that the adsorption of dye by raw OPL almost did not happen.

From Table 2, the correlation coefficient (R^2) of the Langmuir isotherm model exhibited higher values than the Freundlich isotherm model. Hence, the Langmuir adsorption isotherm fitted all the experimental data better than the Freundlich model. The fitting of the adsorption data into the Langmuir isotherm model recommended that the external surface of the SMOPL was homogenous, and distributed with a high amount of active carboxylic and hydroxyl groups [21]. The adsorption of AO7 onto OPL and SMOPL were expected to form a monolayer coverage, and the AO7 attached to specific binding sites on the surface of SMOPL. Furthermore, once the specific site interacted with dye adsorbate, more adsorption activity could not occur at the adsorbent site. The positive relationship shown in the linear graph of SMOPL indicated that the adsorption was very successful and well-fitted in the Langmuir isotherm model. The Langmuir isotherm model also indicated that SMOPL4.0 exhibited the maximum adsorption capacity of AO7 with 138.89 mg/g.

Throughout this experiment, it was found that the adsorption capacity of OPL towards AO7 increased by the increase of the surfactant concentrations attached to the modified OPL. The trend of the AO7 adsorption by OPL and SMOPL was: SMOPL4.0 > SMOPL2.5 > 1.0SMOPL > OPL. This condition can be referred to the properties of dye and the formation of the surfactant molecules on the OPL. AO7 is characterized as an anionic dye as it carries a negative charge at its negative site. Due to this property, AO7 can be effectively bound to the positive charge of CTAB surfactant through electrostatic interaction [9]. The adsorption trend is also supported by FTIR results, whereby there are many functional groups in the sample responsible for the adsorption to occur. Additionally, the dispersion behaviour of the SMOPL in water-hexane also supported this trend since the SMOPL exhibited different behaviour compared to OPL, which was resulted in the alteration of OPL surfaces. The changes in the surface properties have proven the attachment of a higher amount of CTAB molecules on OPL, contributing to a higher adsorption capacity towards AO7 anionic dye. It is expected that the higher CTAB concentration of more than 4.0 mM will increase the adsorption capacity. However, there will be more CTAB released into the filtrate since the bonding among the CTAB molecules on OPL surfaces is a weak physical bonding at higher concentration than the critical micelle concentration (CMC) of the CTAB (~1.0 mM) [22]. Hence, the releases of excess CTAB molecules are not economical and it can give negative impact to the environment.

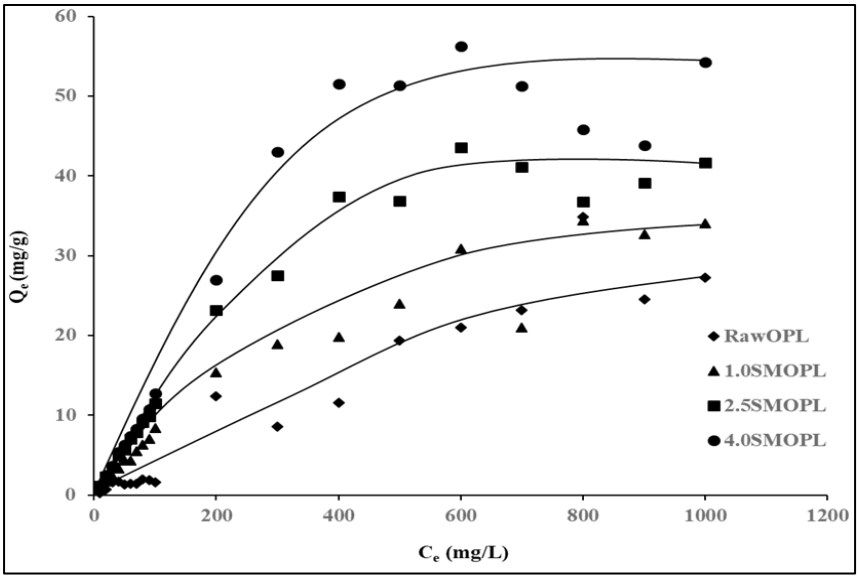


Figure 4. Effect of AO7 dye initial concentration on the adsorption capacity of raw OPL and SMOPL samples

Table 2. Fitted Langmuir and Freundlich parameters for the adsorption of AO7 onto OPL and SMOPL

Samples	Langmuir Isotherm Model			Freundlich Isotherm Model		
	Q_o (mg/g)	b (1/g)	R^2	K_f (mg/g)	n (1/g)	R^2
OPL	40	0.0007	0.8328	25.82	36.1011	0.0211
SMOPL1.0	68.49	0.0012	0.9900	5.58	1.2724	0.9764
SMOPL2.5	81.30	0.0016	0.9947	3.76	1.2824	0.9668
SMOPL4.0	138.889	0.0010	0.9911	4.3	1.1923	0.9593

Conclusion

The potential of SMOPL to remove anionic dye from an aqueous solution was studied. The characterization of the SMOPL using the FTIR technique showed that the modification with the cationic surfactant CTAB did not change the main structure of the OPL. Through the dispersion behaviour study, the modification of OPL with CTAB molecules enhanced the hydrophilicity of OPL and caused it to interact more with the water molecules. The adsorption experiment was done to analyse the adsorption behaviour of both OPL and SMOPL towards the AO7 anionic dye. The effect of initial concentrations of the dye on the adsorption process was studied. The result showed that as the dye concentration increased, the adsorption capacity also increased. The analysis showed that the adsorption capacity of the OPL towards AO7 was enhanced by the modification of the OPL with more cationic surfactants. Therefore, the surfactant-modified oil palm leaf has the potential as a low-cost adsorbent for anionic dye removal from an aqueous solution.

Acknowledgement

The authors thank the Ministry of Higher Education Malaysia and Universiti Teknologi Malaysia for financially supporting this project under the IIIG research grant (Vot 02M61) and UTM-RUG (Vot 08H01).

References

1. Hynes, N. R. J., Kumar, J. S., Kamyab, H., Sujana, J. A. J., Al-Khashman, O. A., Kuslu, Y., Ene. A. and Suresh, B. (2020). Modern enabling techniques and adsorbents-based dye removal with sustainability concerns in textile industrial sector-a comprehensive review. *Journal of Cleaner Production*, 272: 122636.
2. Kubra, K. T., Salman, M. S. and Hasan, M. N. (2021). Enhanced toxic dye removal from wastewater using biodegradable polymeric natural adsorbent. *Journal of Molecular Liquids*, 328: 115468.
3. Jawad, A. H., Abdulhameed, A. S. and Mastuli, M. S. (2020). Acid-factionalized biomass material for methylene blue dye removal: A comprehensive adsorption and mechanism study. *Journal of Taibah University for Science*, 14(1): 305-313.
4. Wang, S., Gao, H., Fang, L., Hu, Q., Sun, G., Chen, X., Yu, X., Zhao, X. and Sun, G. (2021). Synthesis of novel CQDs/CeO_2/$SrFe_{12}O_{19}$ magnetic separation photocatalysts and synergic adsorption-photocatalytic degradation effect for methylene blue dye removal. *Chemical Engineering Journal Advances*, 6: 100089.
5. Hamidian, K., Najafidoust, A., Miri, A. and Sarani, M. (2021). Photocatalytic performance on degradation of acid orange 7 dye using biosynthesized un-doped and co doped CeO_2 nanoparticles. *Materials Research Bulletin*, 138: 111206.
6. Akpomie, K. G. and Conradie, J. (2020). Banana peel as a biosorbent for the decontamination of water pollutants. a review. *Environmental Chemistry Letters*, 18(4): 1085-1112.
7. Setiabudi, H. D., Jusoh, R., Suhaimi, S. F. R. M. and Masrur, S. F. (2016). Adsorption of methylene blue onto oil palm (*Elaeis guineensis*) leaves: Process optimization, isotherm, kinetics and thermodynamic studies. *Journal of the Taiwan Institute of Chemical Engineers*, 63: 363-370.
8. Ahmad, T., Rafatullah, M., Ghazali, A., Sulaiman, O. and Hashim, R. (2011). Oil palm biomass–based adsorbents for the removal of water pollutants—a review. *Journal of Environmental Science and Health, Part C*, 29(3): 177-222.
9. Kamaru, A. A., Jani, N. S. A., Malek, N. A. N. N. and Sani, N. S. (2016). Adsorptive removal of methylene blue and acid orange 7 by hexadecyltrimethylammonium bromide modified rice husk. *Jurnal Teknologi*, 78(3-2): 113-119.
10. Khalifa, M. A., Malek, N. A. N. N., Farimani, A. Y., Sani, N. S. and Kamaru, A. A. (2021). Cetylpyridinium bromide (CPB)-treated sugarcane bagasse for the removal of chromate in aqueous solution. *Materials Today: Proceedings*, 47(6): 1252-1257.
11. Malek, N. A. N. N., Yusof, M. H. and Kamaru, A. A. (2019). Simultaneous action of surfactant modified sugarcane bagasse: Adsorbent and antibacterial agent. *Malaysian Journal of Fundamental and Applied Science*, 15: 32-37.
12. Malek, N. A. N. N., Sihat, N. M., Khalifa, M. A., Kamaru, A. A. and Sani, N. S. (2016). Adsorption of acid orange 7 by cetylpyridinium bromide modified sugarcane bagasse. *Jurnal Teknologi*, 78(1-2): 97-103.
13. Kamaru, A. A., Sani, N. S. and Malek, N. A. N. N. (2016). Raw and surfactant-modified pineapple leaf as adsorbent for removal of methylene blue and methyl orange from aqueous solution. *Desalination and Water Treatment*, 57(40): 18836-18850.
14. Sidik, S. M., Jalil, A. A., Triwahyono, S., Adam, S. H., Satar, M. A. H. and Hameed, B. H. (2012). Modified oil palm leaves adsorbent with enhanced hydrophobicity for crude oil removal. *Chemical Engineering Journal*, 203: 9-18.
15. Weng, C. H. and Wu, Y. C. (2011). Potential low-cost biosorbent for copper removal: pineapple leaf powder. *Journal of Environmental Engineering*, 138(3): 286-292.
16. Sulaiman, O., Amini, M. H. M., Rafatullah, M., Hashim, R. and Ahmad, A. (2010). Adsorption equilibrium and thermodynamic studies of copper (II) ions from aqueous solutions by oil palm leaves. *International Journal of Chemical Reactor Engineering*, 8(1): 108.

17. Ahmad, T., Irfan, M. and Bhattacharjee, S. (2016). Parametric study on gold nanoparticle synthesis using aqueous *Elaise Guineensis* (oil palm) leaf extract: Effect of precursor concentration. *Procedia Engineering*, 148: 1396-1401.
18. Araujo, L. A., Bezerra, C. O., Cusioli, L. F., Silva, M. F., Nishi, L., Gomes, R. G. and Bergamasco, R. (2018). *Moringa oleifera* biomass residue for the removal of pharmaceuticals from water. *Journal of Environmental Chemical Engineering*, 6(6): 7192-7199.
19. Nakagame, S., Chandra, R. P. and Saddler, J. N. (2010). The effect of isolated lignin's, obtained from a range of pre-treated lignocellulosic substrates, on enzymatic hydrolysis. *Biotechnology and Bioengineering*, 105(5): 871-879.
20. Tahir, N., Bhatti, H. N., Iqbal, M. and Noreen, S. (2017). Biopolymers composites with peanut hull waste biomass and application for crystal violet adsorption. *International Journal of Biological Macromolecules*, 94: 210-220.
21. Neupane, S., Ramesh, S. T., Gandhimathi, R. and Nidheesh, P. V. (2015). Pineapple leaf (*Ananas comosus*) powder as a biosorbent for the removal of crystal violet from aqueous solution. *Desalination and Water Treatment*, 54(7): 2041-2054.
22. Neugebauer, J. M. (1990). Detergents: An overview. *Methods in Enzymology*, 182: 239-253.

Malaysian Journal of Analytical Sciences (MJAS)
Published by Malaysian Analytical Sciences Society

POTENTIAL OF *Epipremnum aureum* IN REDUCTION OF CHEMICAL OXYGEN DEMAND IN WASTEWATER

(Potensi *Epipremnum aureum* dalam Pengurangan Permintaan Oksigen Kimia dalam Air Sisa Buangan)

Lee Shi Qing, Rozidaini Mohd Ghazi*, Marinah Muhammad

Faculty of Earth Science,
Universiti Malaysia Kelantan Jeli Campus, 17600 Jeli, Kelantan, Malaysia

**Corresponding author: rozidaini@umk.edu.my*

Received: 15 September 2021; Accepted: 28 October 2021; Published: 27 December 2021

Abstract

High chemical oxygen demand (COD) levels in water indicate a vast amount of oxidizable matter that consumes a lot of dissolved oxygen in water. This has an adverse impact on both aquatic ecosystems and human health. Wastewater from the fish cracker industry typically has high organic content and high COD value. This study focuses on the potential of *Epipremnum aureum* as a new plant for reducing COD in fish cracker industry wastewater. Due to its relative abundance and cost-effectiveness, *Epipremnum aureum (E. aureum)* was selected as a phytoremediation plant. The parameters affecting COD reduction, such as pH of wastewater, retention time, initial COD concentration, and plant number used in phytoremediation were investigated. After ten days of retention time with two *E. aureum* plants, the highest COD reduction was 99.42% in pH 6 of 75% wastewater. *E. aureum* produced new shoots in 50% (v/v) wastewater concentration after 14 days of retention time, indicating that the plant is suitable for planting in polluted water or industrial effluent. Therefore, *E. aureum* can be categorized as a pollution resistance plant. This study proves that *E. aureum* can be utilized as an alternative method for COD reduction in wastewater.

Keywords: chemical oxygen demand, phytoremediation, *Epipremnum aureum*

Abstrak

Tahap permintaan oksigen kimia tinggi (COD) dalam air menunjukkan sebahagian besar bahan teroksida yang menggunakan banyak oksigen terlarut di dalam air. Ini mengakibatkan kesan buruk terhadap ekosistem akuatik dan kesihatan manusia. Air sisa dari industri keropok ikan biasanya mempunyai kandungan organik yang tinggi dan nilai COD yang tinggi. Kajian ini memberi tumpuan kepada potensi *Epipremnum aureum* sebagai pokok baharu untuk pengurangan COD dalam air sisa industri keropok ikan. *Epipremnum aureum (E. aureum)* dipilih sebagai pokok untuk fitoremediasi kerana ianya banyak dan menjimatkan. Parameter yang mempengaruhi pengurangan COD seperti pH air buangan, masa hubungan, kepekatan awal COD dan jumlah pokok yang digunakan dalam fitoremediasi telah diselidik. Selepas sepuluh hari masa hubungan menggunakan dua pokok *E. aureum*, penurunan COD tertinggi adalah 99.42% pada pH 6 dalam 75% air sisa. *E. aureum* menghasilkan pucuk baru dalam air sisa pada kepekatan 50% setelah 14 hari masa hubungan, menunjukkan bahawa pokok itu sesuai untuk ditanam dalam air tercemar atau air buangan industri. Oleh itu, *E. aureum* boleh dikategorikan sebagai pokok yang ada ketahanan pencemaran. Berdasarkan kajian ini, *E. aureum* terbukti menjadi kaedah alternatif untuk pengurangan COD dalam air sisa.

Kata kunci: permintaan oksigen kimia, fitoremediasi, *Epipremnum aureum*

Introduction

Chemical oxygen demand (COD) is a chemical method for determining the amounts of reductive substances oxidized in water samples [1]. In studies investigating the operation and management of wastewater treatment plants and the properties of river pollution and industrial wastewater, rapid determination of organic pollution parameters, often expressed as symbolic COD, is important. The high COD level indicates a greater amount of oxidizable organic material in the sample, which causes dissolved oxygen (DO) levels to decrease. Wastewater from the fish cracker industry contains a high concentration of COD [2]. Hence, COD should be reduced, and phytoremediation is one inexpensive treatment method to achieve this end. Phytoremediation is the method that uses plants to treat contaminated soils, sludge, sediments, surface water and groundwater. The plants transfer, contain, or convert pollutants to ensure environmental safety [3]. The medium of phytoremediation is usually soil and water bodies that are contaminated by heavy metals, inorganic matter, radioactive elements, or organic matter [4]. Through several phytoremediation, the pollutants can be purified [5].

Epipremnum aureum (E. aureum) can be used in phytoremediation. It is a plant that belongs to the genus Kirin leaf, a large evergreen vine that grows in the tropics. They often climb rocks and tree trunks with well-developed roots, and they can be grown hydroponically. Because of the tenacious vitality, *E.* aureum can grow well whether it is planted in pot or hydroponics grown by just a few stalks. [6] investigated the performance and stratified microbial community of *E. aureum*-affected vermi-filters during the recycling of concentrated excess sludge. *E. aureum* has also been investigated as a cathode candidate in microbial fuel cells for wastewater treatment [7]. In this study, the use of *E. aureum* for treating industrial wastewater was investigated. The ability of the plants to reduce the COD rates according to several parameters, such as plant number, initial concentration of water samples, and pH of the water sample, were studied as independent variables.

Materials and Methods

Materials

A one-year-old *Epipremnum aureum (E. aureum)* plant was collected from a Taiping, Perak nursery. All the plants were ensured to have 30 cm and the same quantity of leaves by cutting down extra stems and leaves. All chemicals used were analytical grade.

Industrial wastewater characterization

A wastewater sample was collected from a local, small, and medium enterprise (SME) that processes fish crackers, located in Tumpat, Kelantan. Wastewater in-situ analysis, i.e., temperature, total dissolved solids, pH, salinity, and dissolved oxygen (DO) were analysed using an YSI Multiparameter. Wastewater samples were collected twice, and all samples were assessed in duplicates.

Hydroponic ability and pollution resistance of *E. aureum*

E. aureum was placed in a beaker filled with distilled water for one week until the plants adapted to the aquatic environment and showed an increase of leaves and the growth of hydroponic roots. The leaves were counted, and plant length was measured using a ruler. Plants that are adapted to the water-based environment were transferred into the beaker filled with 500 mL of a 50% (v/v) wastewater sample for 2 weeks without additional nutrient supplementation. A similar experiment was set up with 500 ml of distilled water as a control.

Effect of initial pH of the wastewater in COD reduction

The concentration of the wastewater was fixed at 10% (v/v) concentration with a volume of 500 mL. The initial water pH was adjusted to pH 5, 6, 7, and 8 using H_2SO_4 and NaOH in a separate beaker. One *E. aureum* was planted in beakers filled with wastewater with pH 5, 6, 7, and 8 respectively for 1 week. The COD reduction was determined after one week. A control experiment

was conducted using the same procedure but without the *E. aureum* plant.

Effect of the initial concentration of the wastewater in COD reduction

One *E. aureum* was planted in separate beakers filled with 500 mL wastewater of 10%, 25%, 50%, and 75% (v/v). The wastewater was adjusted to the optimum pH 6, which was obtained from the previous experiment. The COD reduction was determined after one week. A control experiment was conducted using the same procedure but without the *E. aureum* plant.

Effect of contact time and number of plants in COD reduction

The optimum concentration of the wastewater was set at 75% (v/v) which was obtained from the previous experiment. The wastewater was adjusted to an optimum pH 6. Beakers containing 500 mL of 75% (v/v) water were planted separately with 1 and 2 plants. The COD reduction was determined from day 4 until day 14. A control experiment was conducted using the same procedure but without the *E. aureum* plant.

Determination of COD reduction

The COD concentration for the wastewater was carried out using the HACH Method 8000 and USEPA Reactor Digestion Method (HR) with a DR 6000 Spectrophotometer. The percentage reduction of the COD was calculated using Eq. 1.

$$COD\ reduction\ (\%) = \frac{\text{Initial COD concentration} - \text{Final COD concentration}}{Initial\ COD\ \text{concentration}} x\ 100\% \quad (1)$$

Results and Discussion

Water quality of wastewater

Table 1 shows the results for each parameter via *in-situ* and *ex-situ* analysis of wastewater collected for first and second sampling. The readings of COD for both were 916 mg/L of COD for the first water sampling and 1792 mg/L for the second water sampling, which far exceeded the effluent standard B (EQA 1974). High COD levels in fish cracker wastewater were also reported by [2] and [8]. The water sample in the second sampling was discharged fresh from the process, hence the higher COD concentration. The COD decreases with increasing time because the bacteria in the water will grow and degrade the organic matter in the water sample [9].

Hydroponic ability and pollution resistance of *E. aureum*

Figure 1 shows the hydroponic roots of *E. aureum* in water. There were new roots that grew after 7 days in the distilled water indicating that the plant was suitable to plant in a water based medium (Figure 1b). It showed that the plant could grow and reproduce in a water-based medium. In other words, the plant had hydroponic ability. Figure 1c shows that there were new shoots that grew from the plant after 14 days in the 50% (v/v) wastewater. This indicated that the plant is suitable to be planted in polluted water or industrial effluent.

There were some rotten shoots in Figure 1c, yet there were also new shoots growing although it took a longer time (two weeks). This indicates that the plant had pollution resistance towards pollutants [10].

COD reduction based on different pH of wastewater

The data presented in Figure 2 indicates that the optimal pH for COD reduction by *E aureum* is pH 6. The average COD reduction of wastewater with *E aureum* increased from pH 5 to pH 6. After reaching the highest reduction of 89.72% at pH 6, COD reduction decreased from pH 7 to pH 8 because *E. aureum* performs better remediation in pH 6 water. The presence of plants in wastewater can deplete dissolved CO_2 during a period of high photosynthetic activity. The photosynthetic activity increases the dissolved oxygen in water creating aerobic conditions in wastewater which favours aerobic bacterial activity which reduces BOD and COD [11].

Based on this descriptive result, pH 6 was chosen for the subsequent experiment because it yielded the highest COD reduction. In addition, pH 6 was the optimum pH for reaching a well-tolerated phytoremediation process

by *E. aureum* [12]. Therefore, *E. aureum* is suitable for being planted in a slightly acidic medium. This result has also been statistically tested using a one-way analysis of variance (ANOVA) as summarised in Table 2. Table 2 shows that there were no significant differences in COD reduction between pH 5, pH 6, pH 7, and pH 8. Therefore, any pH value can be chosen for subsequent experiments. In this case, however, pH6 was chosen since Figure 2 showed that it had the highest COD reduction.

Table 1. Water quality of fish cracker's wastewater

Physio-Chemical Parameter	**1st Sampling**	**2nd Sampling**	**EQA Standard B**
DO (%)	11.6	4.0	-
pH	4.88	5.45	5.5-9.0
COD (mg/L)	916	1792	200
TDS (mg/L)	903.5	491.9	-
Temperature (˚C)	28.52	30.14	40

- Not available

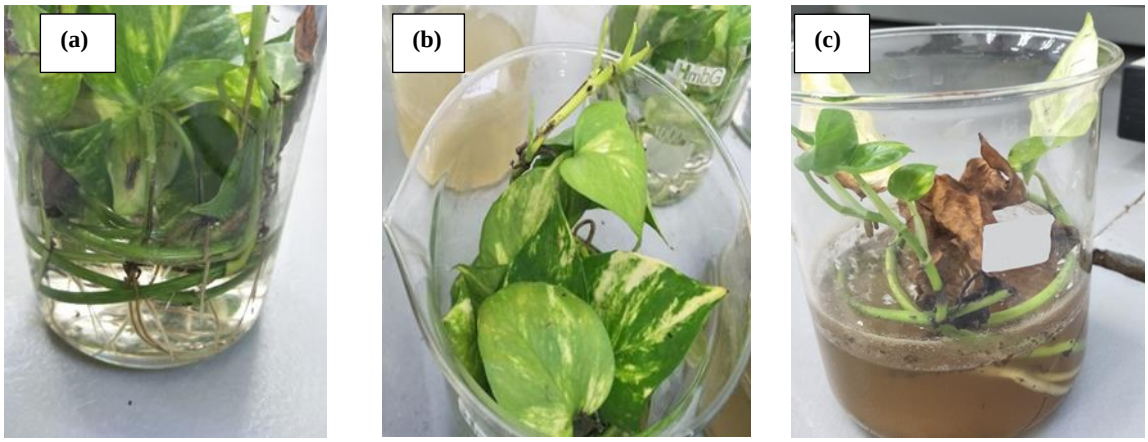


Figure 1. The hydroponic roots of the *E. aureum:* (a) After transfer from soil to water (Day 0) (b) After 7 days grew in distilled water (c) After 14 days grew in 50% wastewater

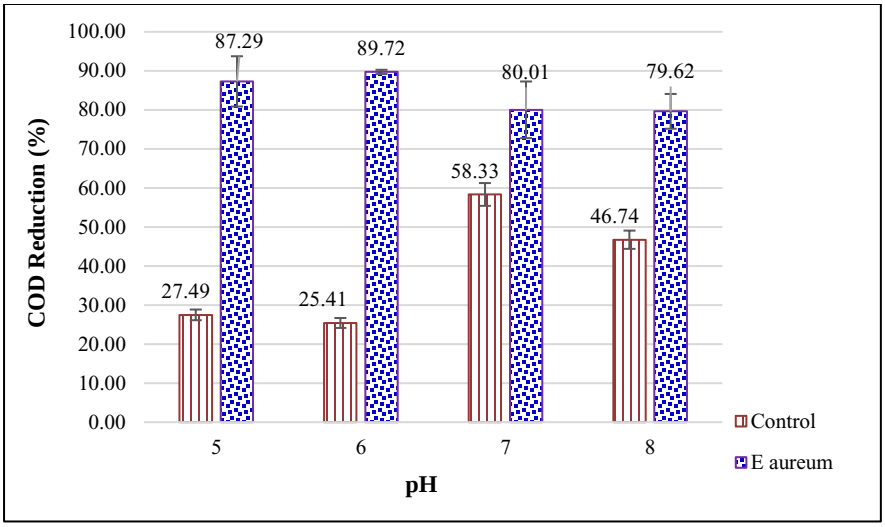


Figure 2. Effect of pH of wastewater on the COD removal percentage (%)

Table 2. The one-way ANOVA for different groups of pH

	Sum of Squares	Df	Mean Square	F	Sig.
Between Groups of pH	157.144	3	52.381	1.831	0.282
Within Groups of pH	114.445	4	28.611		
Total	271.589	7			

COD reduction based on different concentrations of wastewater

Figure 3 indicates that the average COD reduction from the *E. aureum* plant increased from 10% (v/v) to 75% (v/v), after reaching the highest removal of 91.57% at 75% (v/v) wastewater concentration. The average reduction of COD decreased to 73.43% in 100% (v/v) wastewater concentration. As the wastewater concentration increased, the organic compounds increased, hence providing more nutrients for the plants to grow and conduct phytoremediation. When 100% (v/v) wastewater concentration was used, the plant failed to adapt to this level of pollutant concentration, hence the COD reduction percentage decreased [13]. Study [14] shows that the increase of salt content in sewage, the plant height, above ground and underground biomass, total biomass, leaf length, leaf width and leaf area of the plants were decreased. As a result, the root-shoot ratio was significantly increased, and the degree of inhibition above ground was greater than that of the root system, indicating that the sensitivity of the root system to wastewater was lower than that of stems and leaves. Therefore, the roots of *E. aureum* cannot adapt to the wastewater with 100% (v/v) concentration.

The one-way analysis of variance (ANOVA) for different groups of wastewater concentration has been tabulated in Table 3. The result shows that there are significant mean differences in the COD reduction percentage in concentrations of wastewater from 10% (v/v) to 100% (v/v). This result statistically supports the descriptive result visualised in Figure 3, where 75% (v/v) wastewater concentration is the optimum level.

COD reduction based on contact time and the number of plants

Figure 4 shows the effect of plant number and contact time on wastewater COD reduction. In this study, treatment with 2 plants had a higher COD removal percentage relative to treatment with 1 plant because the

phytoremediation rate was doubled. Thus, the more *E. aureum* plants in the same medium, the more efficient the COD removal in the water sample. In the study by [15], a second addition of plant was used after completed the first batch, and an increase in uptake of 96.7 percent was observed, compared to the result obtained in this study, which is 95.78 percent after 7 days of treatment using 2 plants. Therefore, the addition of several plants will cause a COD removal percentage to be greater than 95%, which is very satisfying. The difference in COD removal percentage between 1 plant treatment and 2 plant treatments was quite small, at 4.25 percent. Thus, for dealing with the industrial and commercial factors of effluent treatment, a one plant treatment was preferred because more wastewaters can be treated at one time with a smaller number of plants thereby reducing the cost of planting the plants.

With increasing contact time, the percentage of COD reduction is also increased. The COD reduction percentage increased gradually but it decreased after day 14. This showed that the lifetime of the *E. aureum* plant in treated sample water was only from day 7 to day 10. After 14 days of contact with 75% (v/v) of wastewater, the plants started to rot thereby decreasing COD reduction percentage. In this case, 2 plants were better than the 1 plant treatment because when the plants started to rot, there would be longer stems, more roots, and more leaves to conduct phytoremediation [16]. Therefore, the more *E. aureum* plants in the same medium, the more efficient the COD removal from the water sample because the phytoremediation rate was doubled.

To support the descriptive result in Figure 4, two-way analysis of variance (ANOVA) was done, and the result is summarised in Table 4. This analysis was chosen due to two factors, namely, the different number of plants and varied contact times, were considered simultaneously in investigating COD reduction percentage in 75% (v/v) wastewater concentration. The result showed a significant difference only existed in contact time but not in the plant number. Therefore, it can be concluded that contact time influences the COD reduction percentage in wastewater regardless of the number plants in the water. Furthermore, the turkey test in Table 5 shows that a different mean exists in the contact time of 4 days than it does at 10 days which is highlighted in Table 5.

The change in concentration with time can be expressed using rate laws. Figure 5 depicts the kinetic data of COD concentration (mg/L) reduction plotted against the first and second-order reactions. Only the plot of Figure 5a is linear with a high coefficient of determination (R^2) of 0.952, while other models (Figure 5b) have poor fits. Thus, the reaction obeys a first-order reaction rate law in which rate k was 0.5248 $mgL^{-1}.day^{-1}$. In this regard, the kinetics study of COD reduction from fish cracker wastewater using *E aureum* exhibited that the reduction process in this study followed the reaction trend of the first-order kinetic model. The concentration of COD decreases with the increasing contact time.

This finding converges previous studies by Musa et al. [17] which used locoweed and sunflower as the phytoremediation plants. The results reveal that phytoremediation is a first-order process by which rates are directly proportional to the substrate concentration driving force. Phytoremediation enhances the rate of the bioremediation process by reducing the ultimate substrate concentration achievable through bioremediation alone, though the first-order rate constant is reduced in the process. Plant microbes also contributed to the phytoremediation process. However, the mechanism of phytoremediation by *E. aureum* is still unknown and requires extensive research.

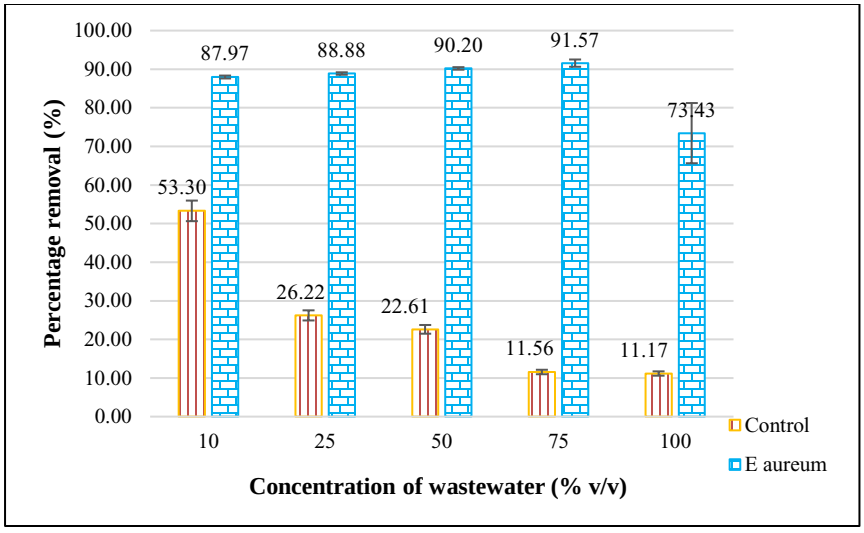


Figure 3. Effect of different concentrations of wastewater to reduce COD

Table 3. The one-way ANOVA for different groups of wastewater concentrations

	Sum of Squares	df	Mean Square	F	Sig.
Between Groups of wastewater concentration	435.597	4	108.899	8.773	0.018
Within Groups % wastewater concentration	62.068	5	12.414		
Total	497.665	9			

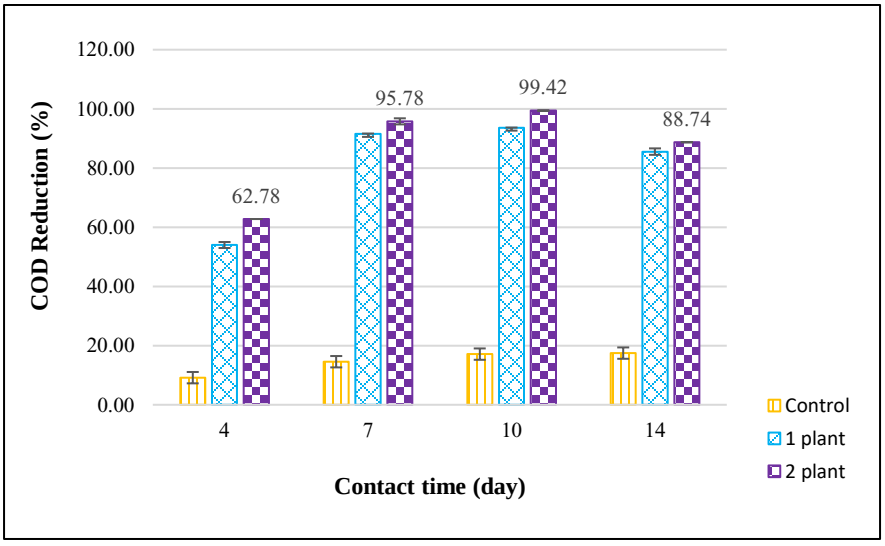


Figure 4. Effect of number of plant and different contact times of treatment on wastewater

Table 4. Two-way ANOVA for different groups of contact time and number of plants

Source	Type III Sum of Squares	df	Mean Square	F	Sig.
Corrected Model	1769.868[a]	3	589.956	3.473	0.051
Intercept	112672.671	1	112672.671	663.304	0.000
Plant	.000	0	.	.	.
Time	1435.070	2	717.535	4.224	0.041
Plant * Time	.000	0	.	.	.
Error	2038.390	12	169.866		
Total	116480.928	16			
Corrected Total	3808.258	15			

a. R Squared = .465 (Adjusted R Squared = .331)

Table 5. Turkey test for contact time and number of plants

	(I) Time	(J) Time	Mean Difference (I-J)	Std. Error	Sig.	95% Confidence Interval	
						Lower Bound	Upper Bound
Tukey HSD	4 h	7 h	-21.4900	9.21590	0.145	-48.8511	5.8711
		10 h	-26.7100	9.21590	0.056	-54.0711	0.6511
		14 h	-23.5175	9.21590	0.101	-50.8786	3.8436
	7 h	4 h	21.4900	9.21590	0.145	-5.8711	48.8511
		10 h	-5.2200	9.21590	0.940	-32.5811	22.1411
		14 h	-2.0275	9.21590	0.996	-29.3886	25.3336
	10 h	4 h	26.7100	9.21590	0.056	-0.6511	54.0711
		7 h	5.2200	9.21590	0.940	-22.1411	32.5811
		14 h	3.1925	9.21590	0.985	-24.1686	30.5536
	14 h	4 h	23.5175	9.21590	0.101	-3.8436	50.8786
		7 h	2.0275	9.21590	0.996	-25.3336	29.3886
		10 h	-3.1925	9.21590	0.985	-30.5536	24.1686

Based on observed means.
The error term is Mean Square (Error) = 169.866.

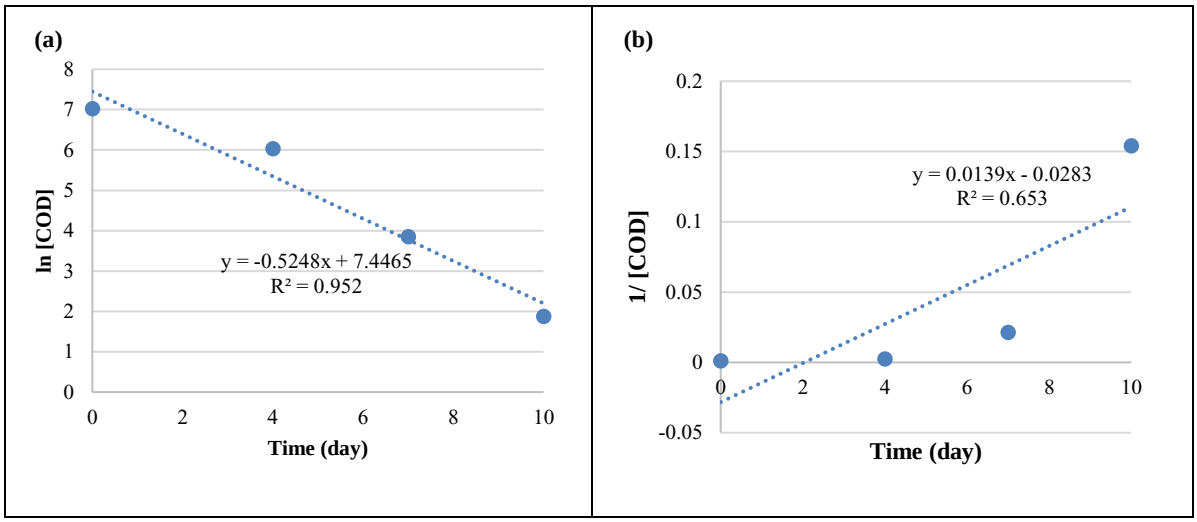


Figure 5. Kinetic data of COD reduction, a) first-order reaction, b) second-order reaction

Conclusion

Phytoremediation reactions were carried out by the plant, and the contact time, initial COD concentration, initial pH of the water sample, and the plant number used in treatment were taken as factors. It was found that *E. aureum* can reduce COD. After analysis, it was found that the highest percentage of removal was 99.42% with a contact time of 10 days, initial wastewater with pH of 6, 75% (v/v) initial COD concentration of wastewater and treatment with 2 plants. Based on the data, *E. aureum* proved to be a good agent for COD removal.

Acknowledgement

The authors acknowledge the Ministry of Higher Education (MOHE) and Universiti Malaysia Kelantan (UMK), for providing facilities during the experiment conducted.

References

1. Li, D and Liu, S. (2019). Water Quality Detection for Lakes. In Maragioglio, N. Water quality monitoring and management, basis, technology and case studies. Academic Press, United Kingdom: pp. 221-231.
2. Mohd Alias, M.Z., Mohd Ghazi, R., Nik Yusoff, N. R. and Jamaludin, M.H. (2020). The efficiency of bamboo activated carbon for removal of COD from fish cracker industry wastewater via response surface methodology (RSM). *IOP Conference Series: Earth Environmental Sciences*, 549: 012058.
3. Salt, D. E., Smith, R. D. and Raskin, I. (2008). Phytoremediation, *Annual Review Plant Biology* 9(1): 643-668.
4. Mohamad Thani, N.S., Mohd Ghazi, R., Abdul Wahab, I.R., Mohd Amin, M.F., Hamzah, Z. and Nik Yusoff, N. R. (2020). Optimization of phytoremediation of nickel by *Alocasia puber* using response surface methodology, *Water*, 12 (2707): 1-16.
5. Ali, H., Khan, E. and Sajad, M. A. (2013). Phytoremediation of heavy metals concepts and applications. *Chemosphere*, 91(7): 869-881.
6. Huang, K., Sang, C., Guan, M., Wu, Y., Xia, H., Chen, Y. and Nie, C. (2021). Performance and stratified microbial community of vermi-filter affected by *Acorus calamus* and *Epipremnum aureum* during recycling of concentrated excess sludge. *Chemosphere*, 280: 130609.
7. Mathuriya, A. S., Bajpai, S. S., and Giri, S. (2015). *Epipremnum aureum* (money plant) as cathode candidate in microbial fuel cell treating domestic wastewater. *Journal Biochemical Technology*, 6(3): 1025-1029.

8. Goh C. P, Mohd Ghazi, R., Nik Yusoff, N. R. Mohd Alias, M. Z. and Jani, M. (2020). Adsorption of COD in wastewater by activated carbon from rice husk. *IOP Conference Series: Earth Environmental Sciences,* 596 (1): 012063.
9. Mohammed, M. S., Ahmed, A. E. S. I., Osman, R. M. and Khattab, I. (2014). Combinations of organic and inorganic wastes for brick production. *Polymer Composites,* 35(1): 174-179.
10. Min, L., Gongsheng, L. and Qiang, C. (2014). Comparative research on physiological resistance of nine kinds of shade tolerant ornamental plant to indoor formaldehyde pollution. *Journal of Shandong Jianzhu University*, 2(002).
11. Rizwana, M., Darshan, M. and Nilesh, D. (2014). Phytoremediation of textile waste water using potential wetland plant: Eco sustainable approach. *International Journal Interdisciplinary and Multidisciplinary Studies*, 1(4): 130-138.
12. Hung, C. Y. and Xie, J. H. (2009). A comparison of plants regenerated from a variegated *Epipremnum aureum. Biologia Plantarum,* 53(4): 610.
13. El-Hady, M.A. and Shanan, N. (2010). Enhancement growth characters of pothos plants (*Epipremnum aureum lindl*.) grown in different improved pot media. *International Journal Academic Research,* 2(2): 1-10.
14. Wang, Q. F. (2017). Effect of influent NaCl concentration on the growth of three plants and the purification of wetland wastewater. MSc Thesis, Gansu Agricultural University.
15. Saleh, H.M. (2012). Water hyacinth for phytoremediation of radioactive waste simulate contaminated with cesium and cobalt radionuclides. *Nuclear Engineering and Design,* 242: 425-432.
16. Rezania, S., Ponraj, M., Talaiekhozani, A., Mohamad, S. E., Din, M. F. M., Taib, S. M. and Sairan, F. M. (2015). Perspectives of phytoremediation using water hyacinth for removal of heavy metals, organic and inorganic pollutants in wastewater. *Journal of Environmental Management,* 163: 125-133.
17. Musa, A. S., Oyoh, K. B. Osoka, E. C. and Onyelucheya, O. E. (2016). Modelling phytoremediation augmented bioremediation based on order of reaction. *International Journal Innovative Science Engineering Technology,* 3(4): 512-522.

Malaysian Journal of Analytical Sciences (MJAS)
Published by Malaysian Analytical Sciences Society

CATALYTIC ACTIVITY STUDY OF SYNTHESISED POLYSTYRENE-SUPPORTED PALLADIUM(II)-HYDRAZONE (CH_3) AS CATALYST IN HECK REACTION

(Kajian Aktiviti Pemangkinan Paladium(II)-Hidrazon (CH_3) dengan Sokongan Polistirena Sebagai Pemangkin dalam Tindak Balas Heck)

Najwa Asilah M. Shamsuddin[1], Norul Azilah Abdul Rahman[1,2], Kumuthini Chandrasekaram[3], Yatimah Alias[3], Nur Rahimah Said[1]*

[1]*School of Chemistry and Environment, Faculty of Applied Sciences, Universiti Teknologi MARA, Cawangan Negeri Sembilan, Kampus Kuala Pilah, 72000 Kuala Pilah, Negeri Sembilan, Malaysia*
[2]*School of Chemistry and Environment, Faculty of Applied Sciences, Universiti Teknologi MARA, 40450 Shah Alam, Selangor, Malaysia*
[3]*Centre for Ionic Liquids (UMCiL), Department of Chemistry, Faculty of Science, University of Malaya, 50603 Kuala Lumpur, Malaysia*

**Corresponding author: nurra1435@uitm.edu.my*

Received: 13 September 2021; Accepted: 15 November 2021; Published: 27 December 2021

Abstract

Polystyrene as polymer support has various requirements of catalysts for different chemical reactions due to its accessibility, mechanical robustness, product selectivity, chemical inertness, and facile functionalization. This study focuses on the synthesis of polystyrene-supported palladium(II)-hydrazone complex where the hydrazone ligand with an electron donating group (-CH_3) acting as the catalyst in Heck reaction. The first step began with aldehyde functionalization of chloromethylated polystyrene to form PS-CHO. This was then followed by the reaction of PS-CHO with p-toluic hydrazide to form a polystyrene-supported hydrazone ligand (PS-H(CH_3)), which was then reacted with palladium(II) chloride to form polystyrene-supported palladium(II) hydrazone catalyst, PS-Pd(CH_3). The successfully synthesized PS-Pd(CH_3) catalyst was characterized using FTIR, PXRD, FESEM-EDX and AAS. The catalytic performance of PS-Pd(CH3) was tested using Heck reaction between 1-bromo-4-nitrobenzene and methyl acrylate. The percent conversion of reactant to product was determined using GC-FID, where the optimum conversion rate was 99.84 % with 1.0 mmol% catalyst loading, K_2CO_3 as base and DMA as solvent at 165 °C within a 60-minute reaction time.

Keywords: Heck reaction, hydrazone ligand, polystyrene, polymer support, palladium(II)-hydrazone complex

Abstrak

Polistirena sebagai sokongan polimer mempunyai pelbagai kegunaan sebagai pemangkin tindak balas kimia kerana kebolehdapatan, ketahanan mekanik, daya pemilihan produk, lengai secara kimia dan pengfungsian mudah. Kajian ini memberi tumpuan kepada sintesis kompleks paladium(II)-hidrazon dengan sokongan polistirena dengan ligan hidrazon yang mengandungi kumpulan elektron penderma (-CH_3) sebagai pemangkin dalam tindak balas Heck. Sintesis dimulakan dengan pengubahsuaian

polistirena klorometil dengan fungsian aldehid untuk membentuk PS-CHO. Kajian dilanjutkan dengan tindak balas PS-CHO dengan p-toluik hidrazida untuk membentuk ligan hidrazon dengan sokongan polistirena (PS-H(CH_3)). Kemudian, PS-H(CH_3) bertindak balas dengan paladium(II) klorida untuk membentuk pemangkin hidrazon paladium(II) dengan sokongan polistirena iaitu PS-Pd(CH_3). Kejayaan sintesis pemangkin disahkan dengan menggunakan FTIR, PXRD, FESEM-EDX dan AAS. Keberkesanan pemangkinan PS-Pd(CH_3) diuji dalam reaksi Heck antara 1-bromo-4-nitrobenzena dan metil akrilat. Peratus penukaran bahan tindak balas kepada produk ditentukan dengan menggunakan GC-FID, dimana penukaran optimum ialah 99.84% dengan pemangkin 1.0 mmol%, K_2CO_3 sebagai bes dan DMA sebagai pelarut pada suhu 165 ° C dalam masa tindak balas 60 min.

Kata kunci: tindak balas Heck, ligan hidrazon, polistirena, sokongan polimer, komplek paladium (II) - hidrazon

Introduction

Immobilisation of catalysts on insoluble supports has increased their potential for industrial uses due to their enhanced thermal and chemical stabilities and ease of separation from product mixtures [1]. The use of polymer-supported catalysts in organic reactions has been approached extensively in many technological, fundamental, and other applications. It is used in many different forms such as polymer anchored metal complexes that coordinate with reactants, colloidal catalyst dispersed in a swollen polymer network and prearrangement of polymer to complexing metal ions [2]. The polymer support also helps in minimising the contamination of reaction products from toxic transition metal complexes. As such insoluble polymer supports are expected to substitute soluble polymer supports for catalyst immobilisation as they are suitable for both catalyst recovery and recycling [3].

Chloromethylated polystyrene or Merrifield resin (Figure 1) is one of the polymers supports commonly used for catalyst immobilisation due to its inert, non-toxic and non-volatile characteristics [4]. The insolubility of chloromethylated polystyrene polymer simplifies catalyst separation from reaction media without any loss to their properties as well as providing a high turnover number and frequency for catalytic activity [5].

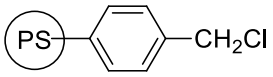


Figure 1. Structure of chloromethylated polystyrene

The immobilisation of Pd(II) on chloromethylated polystyrene has been used in the C-C coupling reactions as it improves stability in terms of high temperature resistance, hardness and strength of impact [6, 7]. Heck reaction involves C-C coupling reactions where the coupling occurs between aryl halides and alkenes using palladium as the catalyst. Heck reaction has been utilised in the various synthesis of natural products and pharmaceuticals as it has broad functional group tolerance and requires mild reaction conditions [8].

Normally, the reaction is carried out with the presence of palladium metal on supported polymer and phosphine ligands. The presence of suitable ligands in the structure of designated catalysts is crucial for higher reaction rates, improved life span, and stability. The phosphine ligand, however, has many disadvantages which include high toxicity, high cost, and are also environmentally unfavourable due to residues formed from the metal species [9, 10]. Therefore, the replacement of phosphine ligand with less toxic ligand such as hydrazone ligand will help reduce the toxicity contributed from the ligand and be more environmentally friendly. This is due to the chelating ability of the hydrazone ligand where it can act as a neutral or a mono-negative ligand [11]. The hydrazone ligand contains R_1R_2=NNH_2: two connected nitrogen atom that binds the carbon with a double bond at the terminal nitrogen atom with R_1 and R_2 alkyl groups [12]. Hence, it can easily form stable coordination complexes with most transition metal ions [13]. Apart from that, hydrazone ligand has also been reported to be more selective and has reproducible qualities that will lead to high conversion rate and turnover number, for example, the reaction of 5 mol % of $Pd(OAc)_2$ as catalyst and bishydrazone as a ligand with $Ca(OH)_2$ as a base in DMA/H_2O (9:1) as a solvent [14].

The Pd-supported polymer catalyst of different hydrazone ligand derivatives reports variations in C-C coupling product yield even when reaction conditions are similar. The presence of an electron donating group in the structure of the hydrazone will improve the catalytic performance [14]. This is because hydrazone, such as OH group, NH_2 group and methyl group, acts as an activating group that donates some of its electron density into a conjugated π system via resonance or inductive effects where the directing effects are ortho and para [15]. Palladium(II) hydrazone complex with electron-donating ligands seem more prone to aryl exchange than those with electron-withdrawing ligands due to the variety of binding modes and the lone pair of electrons of the imine nitrogen [16].

The presence of methyl as an electron-donating group is crucial in determining the electron density of the imine nitrogen as the methyl group is driven by the electronic properties of the chelating ligand and also because the methyl group has steric bulk [17]. Moreover, the methyl group offers versatility in chelation with transition metal as it is capable to coordinate with metals to form complexes [18]. In a previous study on the ligand effect on migratory insertion by Heck reaction, it was found that among the electron-donating group (methyl, tert-butyl and phenyl), the ligand with methyl group had lower insertion barrier as it increases π-coordination ability of metal with C=C of the starting material. Thus, methyl is reported to have higher tendency to form complexes and increase the catalytic performance [19].

The exploration on the capability of hydrazone ligand especially with electron-donating group functionalities as a ligand with polymer-supported catalyst is still scarce. This study aims in developing new polymer-supported palladium(II)-hydrazone complexes where the hydrazone ligand functionalise with the methyl (-CH_3) group as catalysts for Heck reaction. The optimum reaction condition of newly synthesised catalyst in different parameters were studied and determined.

Materials and Methods

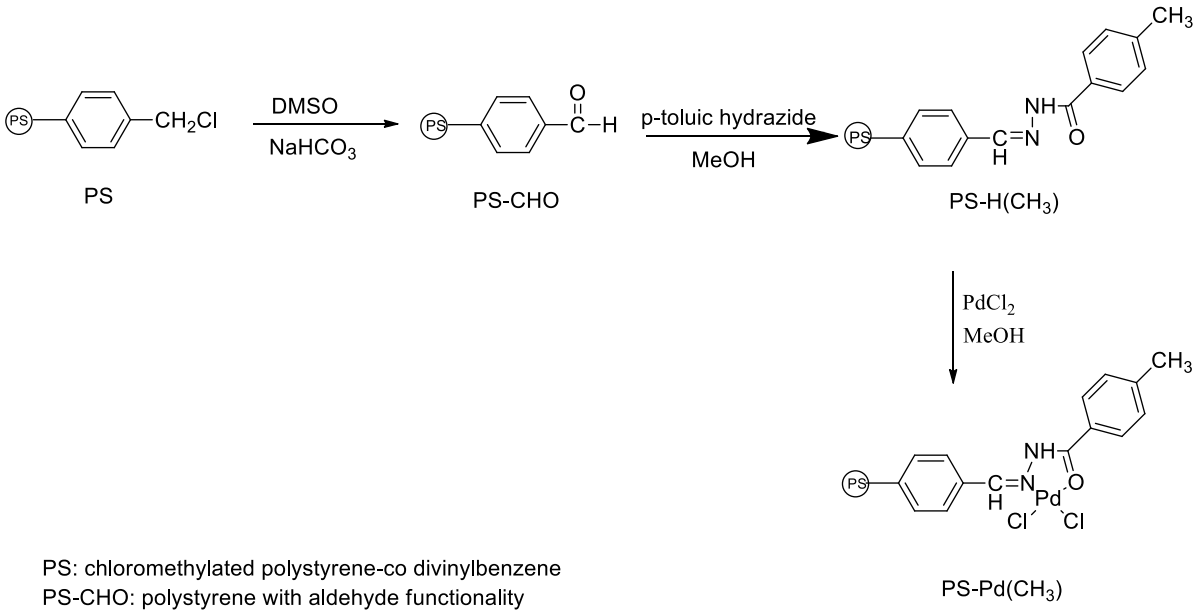
Chemicals and instruments

All the chemicals and solvents obtained from commercial suppliers were used as received. The chemicals used were chloromethylated polystyrene-co-divinylbenzene beads with 2% crosslink (Merck), dimethyl sulfoxide (DMSO) (Merck), 1-bromo-4-nitrobenzene (Merck), methyl acrylate (Merck), sodium hydrogen carbonate ($NaHCO_3$)(Merck), sodium carbonate (Na_2CO_3)(Sigma), potassium carbonate (K_2CO_3)(Merck), triethylamine (Et_3N) (Merck), p-toluic hydrazide (QReC), palladium(II) chloride (Alfa Aesar), ethanol (Merck), methanol (Merck) and nitrogen gas. All solid products produced at the end of every synthesis were collected by high vacuum filtration or slow evaporation technique at room temperature. The product was characterised using Fourier transform infrared (FTIR) spectroscopy, field emission scanning electron microscope/energy dispersive X-ray (FESEM/EDX), atomic absorption spectroscopy (AAS) and powder X-ray diffraction (PXRD).

For the FTIR, spectra were recorded between 4000-400 cm^{-1} with potassium bromide (KBr) discs on Fourier transform infrared spectrophotometer 8300. For field emission scanning electron microscope, Jeol JSM-6701f equipped with energy dispersive X-ray facility (FESEM-EDX) was used to determine morphology of each sample and to confirm the presence of elements C, N and Pd. For atomic absorption spectrometer (Perkin Elmer-Analyst 400) using flame approach, 1g of catalyst was digested in 5 ml of HNO_3 and heated to 95 °C and refluxed for 10 minutes. The powder X-ray diffraction (PANalytical X-Pert PRO) was used to measure the diffraction pattern of crystalline compounds. The catalytic performance was determined by using gas chromatography (GC-Hewlett Packard-5890 series II). The instrument was equipped with HP-5 capillary column (15m×0.25mm×0.25µm) with flame ionization detector (GC-FID). The microliter samples will be injected at 50 °C (held for 1 minute) and final temperature at 250 °C (held for 30 seconds). Temperature increment will be at 15 °C per minute. The flow rate used was 1.9162 mL/min.

Synthesis of compounds

The outline for the preparation of polymer-supported palladium(II)-hydrazone complex is given in Scheme 1.



PS: chloromethylated polystyrene-co divinylbenzene
PS-CHO: polystyrene with aldehyde functionality
PS-H(CH_3): polystyrene-supported hydrazone (p-toluic hydrazide)
PS-Pd(CH_3): polystyrene-supported palladium(**II**)-hydrazone (p-toluic hydrazide)

Scheme 1. Synthesis of polystyrene-supported palladium(II)-hydrazone complexes

Synthesis of polystyrene with aldehyde functionality (PS-CHO)

Chloromethylated polystyrene beads (1 g; 1.5 mmol of Cl per g of resin and 2% crosslinked with divinylbenzene) were swelled in 15 mL of DMSO in a 3-neck round bottom flask for 1 hour. Sodium hydrogen carbonate (0.3 g; 3.6 mmol) was added into the 3-neck round bottom flask containing the polymer beads solution. The mixture was stirred and refluxed under nitrogen for 6 hours. The aldehyde functionalized polymer was obtained then separated by vacuum filtration, washed with cold ethanol, and dried in a vacuum desiccator at 25 °C.

Synthesis of polystyrene-supported hydrazone ligands (PS-H(CH_3)

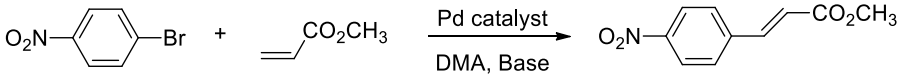
PS-CHO (1 g) was swelled with 20 mL of methanol in a 3-neck round bottom flask for 1 hour. Then p-toluic hydrazide ligand (3 g; 0.022 mmol) was added into polymer solution. The reaction mixture was stirred and refluxed at 65 °C under nitrogen for 48 hours and subsequently cooled to room temperature. The polymer anchored hydrazone (p-toluic hydrazide) (PS-H(CH_3)) complex was separated by vacuum filtration, washed with methanol followed by ether, and dried in a vacuum desiccator at 25 °C.

Synthesis of polystyrene-supported palladium(II)-hydrazone complex (PS-Pd(CH_3))

PS-H(CH_3) (0.5 g) was swelled with 15 mL of methanol in a 3-neck round bottom flask for 1 hour. Then palladium(II) chloride (0.22 g; 1.26 mmol) was added into the polymer solution. The mixture was stirred and refluxed at 65 °C under nitrogen gas for 72 hours. The polymer-supported palladium complex was then cooled to room temperature and separated using vacuum filtration. The solid product, polystyrene-anchored palladium(II)-hydrazone complex (PS-Pd(CH_3)), was washed several times with methanol to remove unreacted palladium(II) chloride and dried overnight in a vacuum desiccator at 25 °C.

Catalytic testing

The catalytic performance of PS-Pd(CH_3) (1.0 mmol %) was tested in a Heck reaction between 1-bromo-4-nitrobenzene and methyl acrylate to produce 3-(4-nitrophenyl)-arylic acid methyl ester (Scheme 2). The mixture of 1-bromo-4-nitrobenzene (0.203 g; 1 mmol), methyl acrylate (0.17 g; 2 mmol), sodium carbonate, Na_2CO_3 (0.25 g, 2.4 mmol), polystyrene anchored palladium(II)-hydrazone complex PS-Pd(CH_3) (1.0 mmol %; 0.01 mmol) and the solvent N,N-dimethylacetamide, DMA (5 mL) was refluxed under nitrogen gas. The reaction was monitored under different temperatures at 25, 50, 75, 100, 165 °C. The procedure was repeated with different type of bases namely $NaHCO_3$, K_2CO_3 and Et_3N. The crude product was analysed by GC-FID to determine the percentage conversion rate of the product. The catalyst was separated from the mixture by vacuum filtration, washed with acetonitrile and methanol, and dried under vacuum while the filtrate was poured into 2 % hydrochloric acid (HCI) solution. Via cooling to 0 °C, a white precipitate was formed which was filtered, washed with distilled water and dried to obtain a white solid.



Scheme 2. Catalytic reaction of 1-bromo-4-nitrobenzene with methyl acrylate

Results and Discussion

Characterization of synthesized compounds

The catalyst PS-Pd(CH_3) was successfully synthesised using a three step synthesis. A change in the compound colour has been noted in each stage of complex preparation. The colour changed from white to pale yellow in the formation of PS-H(CH_3) while the presence of palladium(II) in the preparation of catalyst (PS-Pd(CH_3) gave a brownish colour due to the Pd binding. The amount of palladium in PS-Pd(CH_3) was determined using AAS analysis and was confirmed to be at 21.31% (2.002 mmol g^{-1}). Table 1 summarises the data.

Table 1. Physical properties of synthesized compounds

Sample	Colour	Pd(%)
PS-CHO	White, powder	-
PS-H(CH_3)	Pale yellow, powder	-
PS-Pd(CH_3)	Brownish, powder	21.31

The structure of the synthesised compound was confirmed using FTIR analysis. The FTIR spectra are illustrated in Figure 2. The presence of corresponding functional groups at each reaction step in the synthesised complexes recorded in Table 2. PS-CHO shows a new peak at 1741.20 cm^{-1} assigned to the C=O stretching vibration of aromatic aldehyde [20].

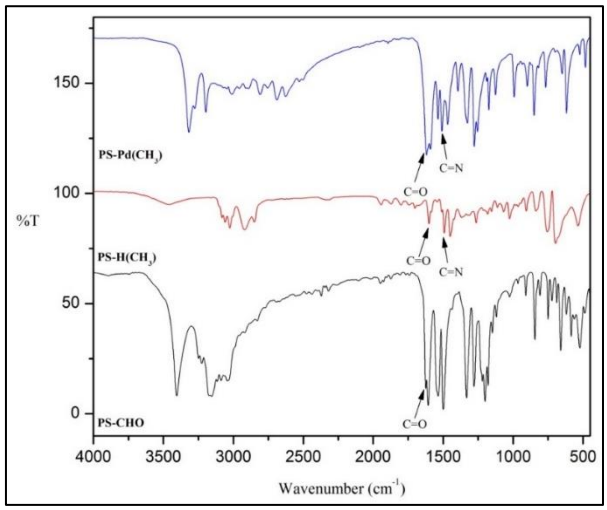


Figure 2. FTIR spectra of synthesized compounds

Table 2. Significant FTIR absorption bands of synthesized compounds

Assignment	PS-CHO	PS-H(CH_3)	PS-Pd(CH_3)
C=O aldehyde	1741.20	-	-
C=O amide	-	1600.91	1618.63
C=N imine	-	1581.36	1590.75

The conversion of PS-CHO to PS-H(CH_3) was confirmed by the appearance of C=O amide (PS-H(CH_3) =1600.91 cm^{-1}), C=N imine (PS-H(CH_3) = 1581.36 cm^{-1}) and N-H (PS-H(CH_3) =3461.36 cm^{-1}). The PS-H(CH_3) of C=N peaks appeared at a lower frequency when compared to the normal range absorption peaks of C=N which is 1650 cm^{-1}. The presence of resonance effect in the structure between H-C=N leads to the absorption band of C=N observed at a lower frequency.

The complexation reaction of PS-H(CH_3) with $PdCl_2$ changed the absorption frequency and peaks intensity of C=O (1618.63 cm^{-1}), and C=N amide (1590.75 cm^{-1}) proved that complexation occurs via the carbonyl oxygen and nitrogen of hydrazone as illustrated in Figure 2 [21,22,23]. The adsorption frequency could increase or decrease upon complexation due to the increase or decrease in the stretching constant of C=O and C=N during the complexation [23,24,25]. This results also confirms the structure and composition of hydrazone in the cross-linked beads was not destroyed after attachment of Pd(II) [26].

Powder X-ray diffraction (PXRD) is a powerful tool for characterising solid state samples. Each crystalline species has a unique X-ray diffraction pattern. Powder X-ray diffraction patterns of PS-CHO, PS-H(CH_3) and PS-Pd(CH_3) are shown in Figure 3. The most prominent peak for PS-CHO shows 2 diffraction patterns between 15° to 22° indicating that the polystyrene is amorphous [20]. For PS-H(CH_3), the presence of the peaks at 2Ɵ are an indication of the presence of amorphous material in the polymer samples. The PS-Pd(CH_3) complex shows three peaks at 35° to 50° of 2Ɵ indicating the existence of Pd [27, 28].

FESEM analysis on the aldehyde functionalised polymer (PS-CHO), polymer-supported hydrazone ligand (PS-H(CH_3)), and polymer-supported palladium(II) hydrazone complex (PS-Pd(CH_3) at various stages of preparation of the catalysts were recorded to understand morphological changes occurring on the surface of the polymeric matrix. Scanning was done at 50 µm as shown in Figure 4. The polymer beads PS-CHO recorded a smooth and clear surface. Functionalised PS-H(CH_3), however, records scattered deposits on the surface which intensifies the presence of PS-Pd(CH_3) due to palladium metal loading [29].

The FESEM micrographs are supported with EDX spectra presented in Figure 4. The EDX analysis were carried out on the single bead of PS-CHO, PS-H(CH_3), and PS-Pd(CH_3). The spectra shows the synthesis of PS-Pd(CH_3) was successful via the presence of palladium metal element peaks. In summary, based on the results of FTIR, FESEM-EDX, PXRD and AAS, the molecular structure of the polymer-supported palladium(II)-hydrazone complex (PS-Pd(CH_3)) are proposed as depicted in Scheme 1.

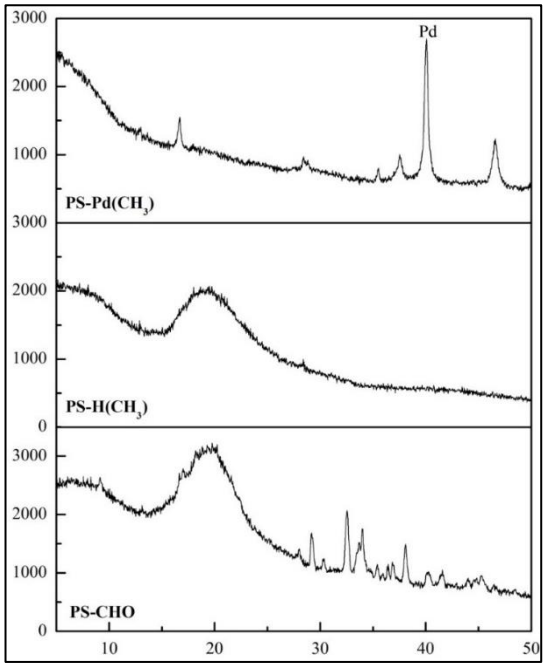


Figure 3. PXRD spectra of synthesized compounds

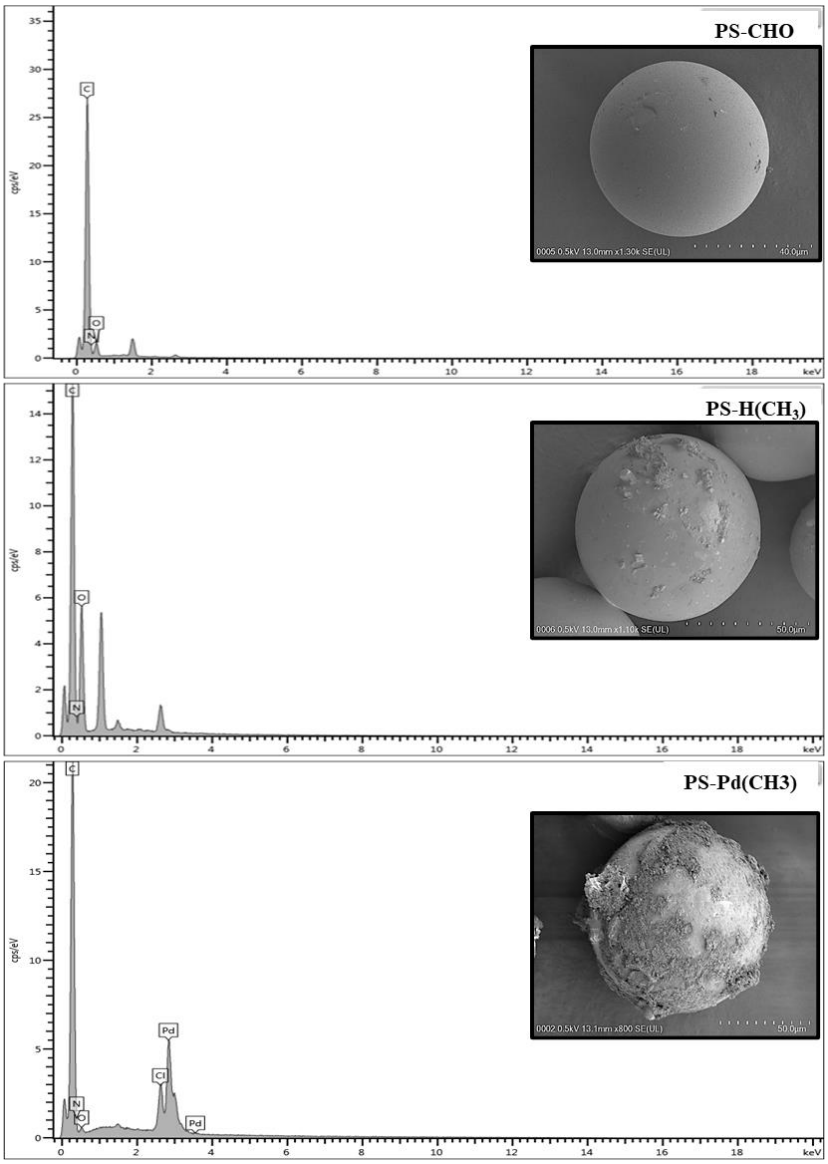
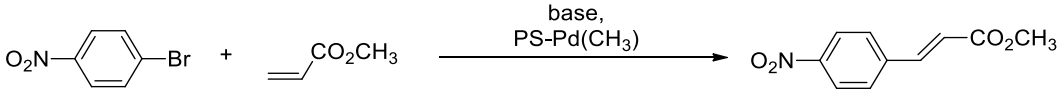


Figure 4. FESEM micrographs and EDX spectra of synthesized compounds

Catalytic testing

The PS-Pd(CH_3) catalyst were tested in the Heck reaction between 1-bromo-4-nitrobenzene and methyl acrylate with different bases and reaction temperatures as shown in Scheme 3. The catalytic performance was determined from GC-FID and the result is summarised in Table 3.



Scheme 3. Heck reaction route

Table 3. The catalytic performance of PS-Pd(CH_3) catalyst in Heck reaction

Entry	Temperature	Base	Conversion Rate (%)	TON
1	165°C	Na_2CO_3	49.15	49.15
2		$NaHCO_3$	40.45	40.45
3		K_2CO_3	99.84	99.84
4		Et_3N	98.97	98.97
5	100°C	Na_2CO_3	34.10	34.10
6		$NaHCO_3$	22.14	22.14
7		K_2CO_3	26.50	26.50
8		Et_3N	31.84	31.84
9	75°C	Na_2CO_3	30.97	30.97
10		$NaHCO_3$	22.01	22.01
11		K_2CO_3	23.97	23.97
12		Et_3N	29.58	29.58
13	50°C	Na_2CO_3	-	-
14		$NaHCO_3$	-	-
15		K_2CO_3	-	-
16		Et_3N	-	-
17	25°C	Na_2CO_3	-	-
18		$NaHCO_3$	-	-
19		K_2CO_3	-	-
20		Et_3N	-	-

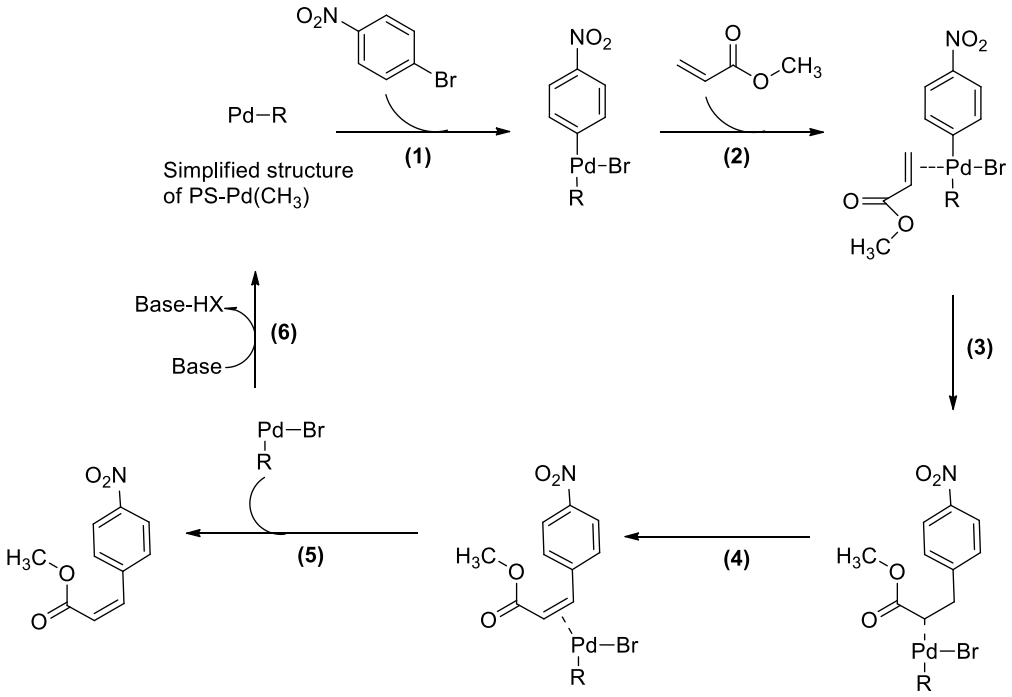
Reaction condition: [substrate] = 1 mmol; catalyst loading = 1 mmol %; [base] = 2.4 mmol; DMA = 5 mL; time = 60 minute

Bases are known to play significant roles in the Heck C-C coupling reaction. The presence of a base helps to improve the catalytic activity of the catalyst [30]. The reaction efficiency depends on the type of base used. Regeneration of the active Pd(0)L_2 complex is affected by the addition of base to remove hydrogen halide from the inactive complex which is an essential role of a base [31,32]. Inorganic bases such as sodium carbonate (Na_2CO_3), sodium hydrogen carbonate ($NaHCO_3$) and potassium carbonate (K_2CO_3) and organic bases such as triethylamine (Et_3N) are used as a hydrogen halide neutraliser and remover in this study.

Table 3 shows the effect of bases on the reaction of 1-bromo-4-nitrob nzene with methyl acrylate in the presence of catalyst PS-Pd(CH_3) 1.0 mmol % amount of catalyst loading within 60 minutes. At the highest temperature (165 °C), the reactions with inorganic base of Na_2CO_3 and $NaHCO_3$ recorded acceptable conversion rates of 49.15% (Entry 1) and 40.45% (Entry 2), respectively. Additionally, inorganic base K_2CO_3 and organic base Et_3N recorded excellent conversion rates of 99.84% (Entry 3) and 98.97% (Entry 4), respectively. The catalytic performance at 100 °C (Entry 5-8) and 75 °C (Entry 9-12) for all types of bases shows lower conversion rate and turnover number (TON). Meanwhile, at the lowest temperature, no conversion rate and TON were observed (Entry 13-20). The results show that the best catalytic performance of PS-Pd(CH_3) in K_2CO_3 at 165 °C is at 99.84% (Entry 3). The inorganic

base K_2CO_3 was the best base in this catalytic condition as the inorganic base is capable of neutralising protons generated in the oxidative addition mechanism. The reaction also needs high temperature to aid in the activation of aryl bromides [33,34].

A plausible mechanism of Heck reaction in the presence of PS-Pd(CH_3) is illustrated in Scheme 4. The mechanism in the Heck reaction involves: (1) oxidative addition of 1-bromo-4-nitrobenzene to generate Pd(II) species; (2) Methyl acrylate insertion to form π-alkene complex; (3) Migratory insertion to form σ-alkyl palladium complex; (4) Rearrangement of complex by internal rotation; (5) β-hydride elimination releasing targeted product; and (6) The addition of base to regenerate the catalyst by removing hydrogen halide (HX) from the inactive complex [22,35].



Scheme 4. The proposed mechanism of the Heck reaction in the presence of a PS-Pd(CH_3) as a catalyst

Conclusion

The synthesis of polymer-supported palladium(II) hydrazone (PS-Pd(CH_3)) has been successfully achieved using chloromethylated polystyrene beads with 2% crosslinking as a polymer support. The results show that the catalyst with the presence of electron-donating group (methyl), PS-Pd(CH_3) (1 mmol%) records an excellent catalytic performance in Heck reaction between 1-bromo-4-nitrobenzene and methyl acrylate with a 99.84% conversion rate. The most suitable condition was achieved using K_2CO_3 as a base at 165 °C in a 60-minute reaction time and using DMA as a solvent. For future work, the optimisation of palladium loading, and recyclability of catalyst will be determined.

Acknowledgement

This research was supported by FRGS/1/2019/STG01/UITM/02/6 from Ministry of Higher Education (MOHE). The authors are grateful to the Universiti Teknologi MARA(UiTM), Cawangan Negeri Sembilan, Kampus Kuala Pilah and Department of Chemistry, University of Malaya for generously providing the research material, equipment, and instrument.

References

1. Ali, M., Rahman, M., Sarkar, S. M. and Hamid, S. B. A. (2014). Heterogeneous metal catalysts for oxidation reactions. *Journal of Nanomaterials,* 1: 209.
2. Czulak, J., Jakubiak-Marcinkowska, A. and Trochimczuk, A. (2013). Polymer catalysts imprinted with metal ions as biomimics of metalloenzymes. *Advances in Materials Science and Engineering,* 9: 464265.
3. Miceli, M., Frontera, P., Macario, A. and Malara, A. (2021). Recovery/reuse of heterogeneous supported spent catalysts. *Catalysts*, 11(5): 591.
4. Erkenez, T. and Tümer, M. (2019). Polymer-anchoring Schiff base ligands and their metal complexes: Investigation of their electrochemical, photoluminescence, thermal and catalytic properties. *Arabian Journal of Chemistry*, 12(8): 2618-2631.
5. Itsuno, S. (2013). Polymer catalysts. *Encyclopedia of Polymeric Nanomaterials*, 2013: 1-9.
6. Kann, N. (2010). Recent applications of polymer supported organometallic catalysts in organic synthesis. *Molecules*, 15(9): 6306-6331.
7. Kamilah, S. C., Jusoh, S. A. and Shamsuddin, M. (2014). Synthesis and physicochemical analysis of Polystyrene-anchored Pd(II) metal complex. *Scientific Research Journal*, 11(2): 45-56.
8. Kantam, M. L., Reddy, P. V., Srinivas, P. and Bhargava, S. (2011). Ligand and base-free Heck reaction with heteroaryl halides. *Tetrahedron Letters*, 34: 4490-4493.
9. Said, N. R., Mustakim, M. A., Sani, N. M. and Baharin, S. N. A. (2018). Heck reaction using palladium-benzimidazole catalyst: Synthesis, characterisation and catalytic activity. *IOP Conference Series: Materials Science and Engineering*, 458: 12-19.
10. Sherwood, J., Clark, J. H., Fairlamb, I. J. and Slattery, J. M. (2019). Solvent effects in palladium catalysed cross-coupling reactions. *Green Chemistry*, 21(9): 2164-2213.
11. Umar, H. F. (2008). Synthesis and characterization of transition metal with hydrazoneicarbohydrazone ligand. Doctoral dissertation, Universiti Malaysia Sarawak.
12. Gomez, I. J., Arnaiz, B., Cacioppo, M., Arcudi, F. and Prato, M. (2018). Nitrogen-doped carbon nanodots for bioimaging and delivery of paclitaxel. *Journal of Materials Chemistry*, 6(35): 5540-5548.
13. Mandewale, M. C., Patil, U. C., Shedge, S. V., Dappadwad, U. R. and Yamgar, R. S. (2017). A review on quinoline hydrazone derivatives as a new class of potent antitubercular and anticancer agents. *Beni-Suef University Journal of Basic and Applied Sciences*, 6(4), 354-361.
14. Watanabe, K., Mino, T., Abe, T., Kogure, T. and Sakamoto, M. (2014). Hydrazone–palladium-catalyzed allylic arylation of cinnamyloxyphenylboronic acid pinacol esters. *The Journal of Organic Chemistry*, 79: 6695-6702.
15. Aly, S. A. and Fathalla, S. K. (2020). Preparation, characterization of some transition metal complexes of hydrazone derivatives and their antibacterial and antioxidant activities. *Arabian Journal of Chemistry*, 13(2): 3735-3750.
16. Roy, S., Mondal, K. C. and Roesky, H. W. (2016). Cyclic alkyl (amino) carbene stabilized complexes with low coordinate metals of enduring nature. *Accounts of Chemical Research*, 49(3): 357-369.
17. Rosar, V., Dedeic, D., Nobile, T., Fini, F., Balducci, G., Alessio, E. and Milani, B. (2016). Palladium complexes with simple iminopyridines as catalysts for polyketone synthesis. *Dalton Transactions*, 45(37): 14609-14619.
18. Anitha, C., Sumathi, S., Tharmaraj, P. and Sheela, C. D. (2012). Synthesis, characterization, and biological activity of some transition metal complexes derived from novel hydrazone azo schiff base ligand. *International Journal of Inorganic Chemistry*, 8: 493942.
19. Chen, Q., Lin, B. L., Fu, Y., Liu, L. and Guo, Q. X. (2005). Ligand effects on migratory insertion by the Heck reaction. *Research on Chemical Intermediates*, 31(9): 759-767.
20. Xuemei, H. and Hao, Y. (2013). Fabrication of polystyrene/detonation nanographite composite microspheres with the core/shell structure via pickering emulsion polymerization. *Journal of Nanomaterials*, 8: 751497.

21. Muthumari, S. and Ramesh, R. (2016). Highly efficient palladium (II) hydrazone based catalysts for the Suzuki coupling reaction in aqueous medium. *RSC Advances*, 6(57): 52101-52112.
22. Jagtap, S. (2017). Heck reaction—State of the art. *Catalysts*, 7(9): 267.
23. Alhazmi, H. A. (2019). FT-IR spectroscopy for the identification of binding sites and measurements of the binding interactions of important metal ions with bovine serum albumin. *Scientia Pharmaceutica*, 87(1): 5.
24. Ain, Q. U., Ashiq, U., Jamal, R. A. and Mahrooof-Tahir, M. (2013). Synthesis, spectroscopic and radical scavenging studies of palladium (II)-hydrazide complexes. *Spectrochimica Acta Part A: Molecular and Biomolecular Spectroscopy*, 115: 683-689.
25. El-Tabl, A. S., Mohamed Abd El-Waheed, M., Wahba, M. A. and Abou El-Fadl, A. E. H. (2015). Synthesis, characterization, and anticancer activity of new metal complexes derived from 2-hydroxy-3-(hydroxyimino)-4-oxopentan-2-ylidene) benzohydrazide. *Bioinorganic Chemistry and Applications*, 14: 126023.
26. Xie, J., Feng, N., Wang, R., Guo, Z., Dong, H., Cui, H. and Liu, X. (2020). A reusable biosorbent using Ca-alginate immobilized providencia vermicola for Pd (II) recovery from acidic solution. *Water, Air and Soil Pollution*, 231(2): 1-12.
27. Mondal, J., Gomes, R., Modak, A. and Bhaumik, A. (2013). Pd-anchored functionalized mesoporous materials as robust and recyclable heterogeneous catalysts for a series of C=C bond forming reactions. *Recyclable Catalysis*, 1: 10-33.
28. Walbrück, K., Kuellmer, F., Witzleben, S. and Guenther, K. (2019). Synthesis and characterization of PVP-stabilized palladium nanoparticles by XRD, SAXS, SP-ICP-MS, and SEM. *Journal of Nanomaterials*, 1: 4758108.
29. Veisi, H., Mirshokraie, S. A. and Ahmadian, H. (2018). Synthesis of biaryls using palladium nanoparticles immobilized on metformine-functionalized polystyrene resin as a reusable and efficient nanocatalyst. *International Journal of Biological Macromolecules*, 108: 419-425.
30. Pérez-Zúñiga, C., Negrete-Vergara, C., Guerchais, V., Le Bozec, H., Moya, S. A. and Aguirre, P. (2019). Hydrogenation of N-benzylideneaniline by palladium (II) catalysts with phosphorus-nitrogen ligands using formic acid as a renewable hydrogen source. *Molecular Catalysis*, 462: 126-131.
31. Kamilah, S.C., Jusoh, S. A., Sukeri, M., Yusof, M., Khairul, W. M. and Shamsuddin, M. (2018). The effect of bases, catalyst loading and reaction temperature on the the effect of bases, catalyst loading and reaction temperature on the catalytic evaluation of supported palladium (II) catalyst in the Mizoroki-Heck. *International Journal of Engineering and Technology*, 7(3): 467-469.
32. Riapanitra, A. (2010). Catalytic studies of low valent palladium (N)-heterocyclic carbene complexes Doctoral dissertation, University of Tasmania.
33. Said, N. R., Adib, N. N. M., Roszaidi, R. M., Shamsuddin, N. A. M. and Badri, N. N. H. S. (2019). Catalytic activity study of synthesized palladium (ii)-hydrazone complexes in the Heck reaction: Optimization of the amount of catalyst loading and reaction time. *International Conference in Organic Synthesis*, 9: pp. 10.
34. Shamsuddin, N. A. M., Badri, N. N. H. S., Rahman, N. A. A. and Said, N. R. (2021). Examining the effect of base, solvent and temperature in Heck reaction with the presence of palladium (II)-hydrazone complexes. *AIP Conference Proceedings*, 2332: pp. 1.
35. Yaşar, S., Özcan, E. Ö., Gürbüz, N., Çetinkaya, B. and Özdemir, İ. (2010). Palladium-catalyzed Heck coupling reaction of aryl bromides in aqueous media using tetrahydropyrimidinium salts as carbene ligands. *Molecules*, 15(2): 649-659.

Malaysian Journal of Analytical Sciences (MJAS)
Published by Malaysian Analytical Sciences Society

ANALYSIS OF SUGAR CONTENT IN SELECTED CHILDREN'S HEALTH SUPPLEMENTS IN MALAYSIA

(Analisa Kandungan Gula dalam Suplemen Kesihatan Kanak-Kanak Terpilih yang Biasa didapati di Malaysia)

Siok-Yee Chan[1], Mazidatulakmam Miskam[2], Shangeetha Ganesan[2]*

[1]*School of Pharmaceutical Sciences*
[2]*School of Chemical Sciences*
Universiti Sains Malaysia, 11800 USM, Penang, Malaysia

**Corresponding author: shangeetha@usm.my*

Received: 24 September 2021; Accepted: 7 November 2021; Published: 27 December 2021

Abstract

The aim of this study is to investigate the prevalence of the various types of sugars in over-the-counter children's health supplements that are commonly available in Malaysia. In this study, a total of 13 children's health supplement samples of four different brands (tablets, pastilles, gummies) of various flavors (orange, blackcurrant, strawberry, mixed berries, mango and peach) were sent to an independent laboratory and analyzed for the presence of fructose, glucose, galactose, sucrose, maltose, lactose and total sugar content. The sugar profiling was carried out using HPLC with refractive index (RI) detector. The results showed that all brands contain a considerable amount of sugar as compared to the label claimed active content. Although this is expected, as it is important for addition of sugars in supplements targeting children especially for ease of consumption. Peach flavored pastilles were found to contain the most amount of sucrose per piece followed by strawberry flavored gummies. Through this study we found that certain flavoring calls for more sugar content as compared to others. The findings further provide support for the need of more comprehensive sugar content and active ingredients labelling in health supplements.

Keywords: health supplement, sugar, children, Malaysia, flavor

Abstrak

Tujuan kajian ini adalah untuk menyelidik kelaziman pelbagai jenis gula dalam suplemen kesihatan kanak-kanak yang biasanya terdapat di kaunter di Malaysia. Dalam kajian ini, sebanyak 13 sampel suplemen kesihatan kanak-kanak dari empat jenama yang berbeza (tablet, pastil, gummies) dengan pelbagai rasa (oren, anggur hitam, strawberi, campuran beri, mangga dan pic) telah dihantar ke makmal bebas dan dianalisis untuk menentukan kehadiran fruktosa, glukosa, galaktosa, sukrosa, maltosa, laktosa dan jumlah kandungan gula. Profil gula dilakukan menggunakan HPLC dengan detektor indeks biasan (RI). Hasil kajian menunjukkan bahawa semua jenama mengandungi kandungan gula yang agak tinggi berbanding dengan label yang menyatakan kandungan aktifnya. Keputusan ini telah dijangkakan kerana penambahan gula dalam makanan tambahan untuk kanak-kanak memudahkan pengambilan. Pastil berperisa pic didapati mengandungi jumlah sukrosa paling banyak per pastil diikuti dengan gummies berperisa strawberi. Melalui kajian ini, kami mendapati bahawa perasa tertentu memerlukan lebih banyak kandungan gula berbanding yang lain. Penemuan ini memberikan maklumat tentang perlabelan keperluan kandungan gula yang lebih komprehensif dan bahan aktif dalam suplemen kesihatan.

Kata kunci: suplemen kesihatan; gula; kanak-kanak, Malaysia, perisa

Introduction

Pharmaceutical active ingredients are rarely administered in their pure forms. Frequently, the actives are admixed with various adjuncts resulting in the transformation into the so called "dosage forms" or "delivery systems" [1]. Hence, ultimately producing a dosage form, which is a combination of the active components and assortment of different kind of additives to a final design that is elegant and stable with purpose. A successful formulation should reflect on the appreciation of various perspectives that the dosage form should accommodate, i.e., consumer acceptance, health benefits as well as shelf-life stability [2]. This is more challenging when the target consumer is of a specific age group, such as pediatric [3,4]. Pediatric dosage form should be palatable to the pediatrics' senses or in other words organoleptic amicable [2]. Taste, aroma, flavor and mouthfeel are some of the concerns that a formulator would take into consideration in the development phase [3,5]. However, the selection of the organoleptic additive calls for immense skill, knowledge, and even human psychology. From a patient-centered point of view, the effect of the additive to the pediatric are often time, which is the overlooked "incident". In order to increase pediatric acceptance, many over the counter supplements are added with sugar, which is a substance that has shown to cause dental caries and chronic health concerns amongst children [6,7].

According to the Department of Food Safety Malaysia, any sugar intake outside the essential food, such as rice, bread, or dairy milk are defined as "sugar added" [6]. Sugar in the form of monosaccharides and disaccharides, glucose, fructose and sucrose are naturally present in vegetables and fruits as a normal dietary intake for humans. Simple sugar, like glucose and fructose, are one that pose health concerns, such as diabetes, and dental caries amongst children [8]. These sugar type gives rise to calories that could also lead to obesity, increase the risk of heart disease (AHA) and issue of hyperactivity amongst children [9]. Fructose, on the other hand, is a sugar type that undergo different metabolism pathway, which involved liver and associated with dyslipidemia [10]. It is a common simple sugar that can be found as the major component in most sweeteners, table sugars and high-fructose corn syrup (HFCS) [9]. Furthermore, sugar alcohols, or also known as polyols are carbohydrate structure that resembled both sugar and alcohol. This sugar type has been cited to be sugar substitute for glucose and fructose in many "sugar free" products. It is not without calories, but it possesses one third or less than half of the calories constituted in sucrose. Examples of sugar alcohols include sorbitol, mannitol, xylitol, lactitol, etc. [11].

Children's health supplements usually appear in the form of chewable tablets, pastilles, lozenges, and many others [3, 5]. Each of the ingredients used in these dosage form varies according to acceptance and stability point of view. Pastilles and lozenges are prepared with caramel based ingredient, which contained high percentage of sugar [12]. For instance, corn syrup with high fructose content or maltose syrup. While chewable tablet may contain bulking agent, which may or may not contain sugar such as lactose to hold its shape or dosage form in physical stability point of view [3]. Sugar consumption from this aspect is all regarded as "sugar added". This sugar is often time overlooked as detrimental and pose a risk of health concerns.

Studies on the prevalence of dietary supplements among children and adolescence are not widely reported by many countries. Some of the studies shows that there is a great need to conduct in-depth analysis on the types of preferred supplements, ingredients and most importantly the nutritional impacts these supplements has on children. Australia reported the 24% usage of dietary supplements in children and 20% in adolescence with the supplements ranging from vitamins to mineral [13]. Two different studies in US reported about 32-37%

children were found to consume dietary supplements [14, 15]. Meanwhile in Italy, 35% adolescence were found to be regular consumers [16]. Germany [17] and Finland [18] both reported 26% and 37-50%, respectively. Closer to home, such data was also found to be scarce in the ASEAN countries with only a handful of reports were found from Japan with 16-20% [19,20], South Korea 34% [21] and Malaysia [22] with an astonishing 54% prevalence of consumption of dietary supplements among children.

This study is initiated to investigate the sugar content in a few commonly available products that are claimed as "children's health supplements". Besides, only a few works were reported on the prevalence of the various types of sugar in over-the-counter health supplements in Malaysia. The examined sugars were frequently used as excipient in formulation development for taste masking purposes. Other sugar types that were not associated with health risk, such as polyols, was excluded.

Materials and Methods

Samples

A total of 13 samples from various brands of single vitamin supplements and multi-vitamin supplements, in tablets, gummies and pastilles were analyzed. Products A-J were chosen randomly and bought from the children's health supplement section of various pharmacies around Selangor. Product K to M of Champs Vitamin C variants were generous contribution from Duopharma Biotech Bhd. Table 1 shows the descriptions and illustrations of supplements form for the analysis. Samples were stored at room temperature (18–30°C) to simulate household consumption, and all analyses were performed within the expiration date of the samples. For tablet supplements, the samples were grinded to obtained homogenous samples. Pastilles and gummies were used without any pre-treatment.

Standards and reagents

L-ascorbic acid (≥ 99.9%), fructose, glucose, sucrose, maltose and lactose were purchased from Sigma-Aldrich (St Louis, MO, USA). Analytical-grade reagents phosphate buffer (pH 3), metaphosphoric acid, glacial acetic acid was obtained from Merck (Darmstadt, Germany). HPLC-grade reagents acetonitrile and methanol were obtained from Fisher Scientific (Pittsburgh, USA).

Determination of total sugar content

The pre-treatment for the supplements were carried out according to the previously reported method by Vennard et al. [23]. About 0.5 to 10 g of the samples were weighed and place in Erlenmeyer flask. Then, distilled water was added. The solution was sonicated for 5 min to ensure all samples were dissolved. The mixture was filtered through a 0.22-µm filter membrane before undergoing a quantitative analysis. All samples were diluted to be within the detection limits.

The chromatographic separation was carried out based on the developed method by Tihomirova et al. [24] with minor modification on the flow rate. The samples were analyzed for sugar content (sucrose, fructose, glucose and maltose, galactose and lactose) by using Agilent 1100 high-performance liquid chromatography using coupled with a refractive index detector from Agilent (Agilent Technology, Waldbroon, Germany). Separation of compounds was performed using a Zorbax NH2 (4.6 × 250 mm, 5 µm) from Agilent (Agilent Technology, Waldbroon, Germany). The mobile phase consisted of acetonitrile: water (75: 25 v/v) in isocratic mode at a flow rate of 1.5 mL/min and injection volume of 10 µL.

Table 1. Description and illustrations of supplement forms

Sample	Dosage Form indicated on the label	Illustration of the dosage forms	Description
Product A	Pastille		Orange flavor
Product B	Pastille		Mango flavor
Product C	Pastille		Mixed berries flavor
Product D	Pastille		Peach flavor
Product E	Gummies		Orange flavor
Product F	Gummies		Strawberry flavor
Product G	Gummies		Blackcurrant flavor
Product H	Chewable Tablet		Orange flavor
Product I	Chewable Tablet		Blackcurrant flavor
Product J	Chewable Tablet		Strawberry flavor
Product K	Chewable Tablet		Orange flavor
Product L	Chewable Tablet		Blackcurrant flavor
Product M	Chewable Tablet		Orange flavor

Results and Discussion

Figure 1 presents the breakdown of the sugar content that contributes to daily calorie intake of consumers (in this case, children), which include sucrose, fructose, glucose and maltose. Galactose and lactose were both absent in all the tested products herein. Products H, I, J, K, L and M were identified to have only sucrose, as this is the main ingredient used for chewable tablet in creating good taste and "mouth feel" compared to other range of pharmaceutical diluents, such as lactose or dextrose [25]. The usage of sucrose ensures the batch-to-batch consistency in terms of quality and hardness of the tablets formulated through wet impregnation for regulatory approval [26].

Product A to G which consists of pastilles and gummies were analyzed to contain fructose, sucrose, maltose and glucose since these products were formulated by using caramel base, such as maltose syrup or corn syrup, which constituted of sucrose [27]. In terms of the ratio of sugar to active ingredient, products A-D and H-M had same active but apparent differences in terms of sugar to active ratio. The lowest ratio was seen in products K and L, while the highest ratio was seen for products A-D.

The apparent discrepancy in sugar content could be explained by different physical dosage forms of the analyzed products. Corn syrup is a functional ingredient in gummy formulation due to its ability in preventing sucrose crystallization. However, it possesses lower "reducing sugar", as a result, formulators usually add simple reducing sugars, such as glucose or fructose to ensure product quality. Sugar is added in the gummies to impart sweetness, tenderness and moisture retention [28]. The formulation of this type of supplements often contains high sugar content, >50%, which results in little nutritional value and may lead to health issues. The benefit to harm ratio of this formulation can cause children to be at high risk of undesired problems, especially children with attention deficit/hyperactivity disorder. Apart from providing sweetness, the high molecular weight carbohydrate acts as gelling agent in gummy formulation [28]. These include starch, pectin, as well as the well-known gummy ingredient – gelatin, a polysaccharide [29].

Per tablet or per 100g?

A rather astonishing fact found was the total sugar content of health supplements targeting children ranges from as low as 0.3 g to exceeding 1 g per unit of supplement (Table 2). In practice, on the consumer's end, an obedient consumer will follow the instructions stated on the product label. It is worth highlighting that a product that show relatively lower sugar "per 100 g" is not a product of "lowest sugar content" when a consumer consumes according to the daily instructions. It is cynical for one to choose product A for its relatively low sugar content at 100 g. However, his/her child will hypothetically take 4.5 g of sugar (highest amongst the tested products from Table 2), while a product with a much lower sugar content is available on the next shelf.

According to the Recommendation Nutrition Index published by the Ministry of Health (MOH), added sugar for children between 2 - 6 years old was < 15 g per day [7]. A published report on children's added sugar intake per day recorded approximately 94.7 ± 65.1 g for children between 3 – 6 years old [6]. This figure exceeded the recommendation of the World Health Organization (WHO), as well as MOH in preventing dental caries and diet related chronic diseases in later life [30,31]. Sweetened food and canned beverages are frequently consumed source of sugar [6]. On top of added sugar from common food in-take, children who consumed a single piece/tablet of supplement from brand A would give rise to around 1.3 g of sugar. Since the product is recommended to be consumed 3-4 times a day, a toddler would at least get 5.1 g of added sugar from this single supplement; not to forget about other possible additional supplements such as vit D, DHA, etc., or even from other snacks, such as biscuits, and juices.

Concerns over regulatory control

In Malaysia, health supplements are regulated under the National Pharmaceutical Regulatory Agency (NPRA). Due to the advancement of futuristic formulation, such as or dispersible dosage form and vague of food-drug interphase, any product to be sold in Malaysia would need to be categorized before it can be registered [3]. The above tested brands were checked by using product search in the NPRA website. Further scrutinizing into the information of these products, i.e., products B-G (pastilles and gummy) are not regulated under NPRA [32]. Specifically, gummy is not categorized as pharmaceutical dosage form, and hence are regulated under the Food Safety and Quality Division (FSQD), instead of NPRA. Physical product check reconfirmed the absence of hologram (an indication of NPRA registered product) on these products. While some products from the same companies were registered and some were not, it has high potential that the non-pharmaceutical registered supplement was misinterpreted as pharmaceutical registered. Worse still, in many local pharmacy chains, these products are placed together under the section of supplements, which potentially mislead the consumers who take food registered "candies" falsely as supplementation of vitamins.

Health professionals often recommend or prescribe dietary supplements to clients, which also contributes to the increase in the consumption of these supplements [33]. Apart from that, the mass media also plays a crucial role in advertising the benefits of supplements, such as vitamin C to the general public [34]. Furthermore, sometimes consumers can be lured by the creative advertising gimmicks and be influenced to consume certain supplements without prescription. Therefore, the supplement labelling plays an utmost important role in providing accurate information for the consumers [35].

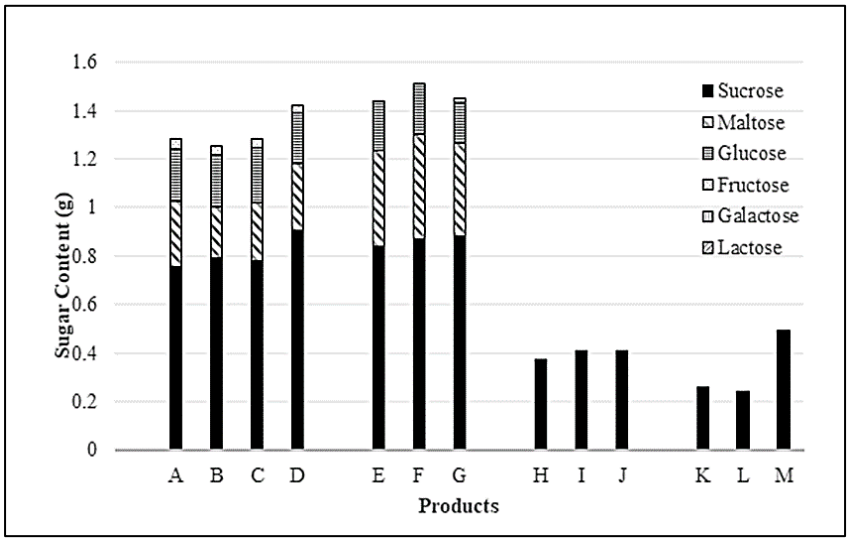


Figure 1. Breakdown of sugar content of selected product from the market

Table 2. Content of sugar and claimed active from the selected products obtained from the market

Brand	Total Sugar† (g/tablet)	Claimed Active* (mg)	Unit Weight† (g)	Dosing Instructions*	Hypothetical Sugar Intake Based on Label Instructions* (g per day)	
					Lower Limit	Upper Limit
Product A	1.284	21	2.359	3-4 pastilles a day	3.9	5.1
Product B	1.254	21	2.273	3-4 pastilles a day	3.8	5.0
Product C	1.282	21	2.175	3-4 pastilles a day	3.8	5.1
Product D	1.422	21	2.312	3-4 pastilles a day	4.3	5.7
Product E	1.441	13.3	3.176	3 gummies a day	4.3	4.3
Product F	1.510	13.3	3.173	3 gummies a day	4.5	4.5
Product G	1.451	13.3	3.115	3 gummies a day	4.4	4.4
Product H	0.373	30	0.451	Children 2-6 years old: 2-6 tabs twice daily	1.5	9.0
Product I	0.410	30	0.453	Children 2-6 years old: 2-6 tabs twice daily	1.6	9.9
Product J	0.408	30	0.453	Children 2-6 years old: 2-6 tabs twice daily	1.6	9.8
Product K	0.261	30	0.300	(Age 1-3) 1-2 tab (Age 4-6) 1-3 tab	0.3	0.8
Product L	0.242	30	0.300	(Age 1-3) 1-2 tab (Age 4-6) 1-3 tab	0.2	0.7
Product M	0.493	100	0.673	Children 4-8 years old: 1-3 tabs twice daily	1.0	3.0

*Estimated values based on dosage recommendation from stated instruction and sugar content

†Total sugar and unit weight are values obtained from this study

Conclusion

From this study it was found that products K, L and M contains the least amount of sugar per tablet and the least contribution to daily sugar intake based on the dosage recommendations. Meanwhile, pastilles and gummies were found to contain higher sugar content per piece. The WHO recommended to reduce free sugar intake throughout the life course. It is essential to be aware of the nutritional facts of the available products in the market, especially when the parent is planning for a healthy diet for the child. This study highlighted that the added sugar from supplement products could be substantial and overlooked. There is a potential misunderstanding that might occur at the consumer's end based on the information stated on the label sheet. It is important to check the presence of the product registration hologram, and to understand the information of total intake and the allowed sugar

content per day. While the total sugar intake is not directly reflected on the label, but some calculation and quick interpretation is needed to make a judicial choice of supplement for the children. Therefore, a systematic effort at the regulatory level or consumer awareness needs to be undertaken.

Acknowledgement

The authors would like to acknowledge Universiti Sains Malaysia for providing the support in the writing of this manuscript. This research was funded by Duopharma Innovations Sdn Bhd for an independent analysis of the data generated in a third-party laboratory.

References

1. Almoazen H. Chapter 4: Dosage forms and drug delivery systems. In the APhA complete review for pharmacy, 12th edition; The American Pharmacists Association, 2017.
2. Moreira, M., and Sarraguça, M. (2017). How can oral paediatric formulations be improved? A challenge for the XXI Century. *International Journal of Pharmaceutics,* 590:119905.
3. Batchelor, H. K., Marriott, J. F. (2015). Formulations for children: Problems and solutions. Brazilian *Journal of Clinical Pharmacology,* 79:405-418.
4. Walsh, J., Ranmal, S. R, Ernes, T. B. and Liu, F. (2018). Patient acceptability, safety and access: A balancing act for selecting age-appropriate oral dosage forms for paediatric and geriatric populations. *International Journal of Pharmaceutics,* 536:547-562.
5. Piccone, P., Rastelli, S. L., Pitti, P. (2011). Aroma release and sensory perception of fruit candies model systems. *Procedia Food Sciences,* 1:1509-1515.
6. Amarra, M. S., Khor, G. L., Chan, P. (2016). Intake of added sugar in Malaysia: A review. *Asia Pacific Journal Clinical Nutrition,* 25:227-240.
7. Kamaruddin F. (2021). Sugar intake and oral health - PORTAL MyHEALTH Available online: http://www.myhealth.gov.my/en/sugar-intake-and-oral-health/ [accessed on 10 February 2021].
8. Campbell, E., Schlappal, A., Geller, E. and Castonguay, T. W. (2014). Chapter 19- fructose-induced hypertriglyceridemia: A review. In nutrition in the prevention and treatment of abdominal obesity. Academic Press: San Diego. 2014: pp. 197-205.
9. Rippe, J. M. and Angelopoulos, T. J. (2015). Sugars and health controversies: What does the science say? *Advances Nutrition,* 6: 493S-503S.
10. Johnson, R. K. and Yon, B. A. (2010). Weighing in on added sugars and health. *Journal American Diet Association,* 110:1296-1299.
11. Clemens, R. A, Jones, J. M, Kern, M, Lee, S. Y., Mayhew, E. J., Slavin, J. L. and Zivanovic, S. (2016). Functionality of sugars in foods and health. *Comprehensive Review Food Science and Food Safety,* 15: 433-470.
12. Chandrawanshi, M. J, Sakhare R. S, Nagoba S. N. and Bhalekar R. V. (2018). A review on medicated lozenges. *World Journal Pharmaceutical Research,* 8: 396-412.
13. O'Brien, S. K, Malacova, E., Sherriff J. and Black, L. J. (2017). The prevalence and predictors of dietary supplement use in the Australian population. *Nutrients,* 9: 1154.
14. Dwyer, J., Nahin, R. L., Rogers, G.T, Barnes, P. M., Jacques, P. M., Sempos, C. T. and Bailey, R. (2013). Prevalence and predictors of children's dietary supplement use: The 2007 national health interview survey. *American Journal Clinical Nutrition,* 97:1331-1337.
15. Qato, D. M., Alexander, G. C, Guadamuz, J. S. and Lindau, S. T. (2018). Prevalence of dietary supplement use in US children and adolescents, 2003-2014. *JAMA Pediatrics,* 172:780.
16. Del Balzo V, Vitiello V. and Germani A. (2014). A cross-sectional survey on dietary supplements consumption among Italian Teen-Agers. *PLoS ONE,* 9: e100508.
17. Sichert-Hellert, W. and Kersting M. (2004). Vitamin and mineral supplement use in German children and adolescents between 1986 and 2003: Results of the DONALD study. *Annual Nutritional Metabolism,* 48: 414-419.

18. Marjamaki, L., Rasanen, M., Uusitalo, L., Anohen, S., Veijola, R., Knip, M. and Virtanen, S. M. (2004). Use of vitamin D and other dietary supplements by Finnish children at the age of 2 and 3 years. *International Journal of Vitamin Nutritional Research,* 74:27-34.
19. Kobayashi, E., Nishijima, C., Sato, Y., Umegaki, K. and Chiba, T. (2018). The prevalence of dietary supplement use among elementary, junior high, and high school students: A nationwide survey in Japan. *Nutrients,* 10:1176.
20. Mori, N., Kubota, M., Hamada, S. and Nagai A. (2011). Prevalence and characterization of supplement use among healthy children and adolescents in an urban Japanese city. *Health,* 3:135-140.
21. Yoon, J. Y., Park, H. A., Kang, J. H., Kim, K. W., Hur, Y. I., Park, J. J., Lee, R. and Lee, H. H. (2012). Prevalence of dietary supplement use in korean children and adolescents: Insights from Korea national health and nutrition examination survey 2007-2009. *Journal Korean Medicine Sciences,* 27:512-517.
22. Sien, Y. P., Sahril, N., Mutalip, M. H. A., Zaki, N. A. M. and Ghaffar, S. A. (2014). Determinants of dietary supplements use among adolescents in Malaysia. *Asia Pacific Journal Public Health,* 26(5S): 36S-43S.
23. Vennard, T. R., Ruosch, A. J., Wejrowski, S. M. and Ellingson, D. J. (2020). Sugar profile method by high-performance anion-exchange chromatography with pulsed amperometric detection in food, dietary supplements, pet food, and animal feeds: First action 2018.16. *Journal AOAC International,* 103(1):89-102.
24. Tihomirova, K, Dalecka B. and Mezule L. (2016). Application of conventional HPLC RI technique for sugar analysis in hydrolysed hay. *Agronomy Research,* 14(5):1713-1719.
25. Potter, N. N. and Hotchkiss, J. H. (1995). Confectionery and chocolate products. *Food Science Text Series,* 464-477.
26. Soukoulis, C. and Tzia, C. (2018). Grape, raisin and sugarcane molasses as potential partial sucrose substitutes in chocolate ice cream: A feasibility study. *International Dairy Journal,* 76:18-29.
27. Onwulata, C. I. and Holsinger, V. H. (1996). Rheology and thermal properties of syrupy composites of saccharides and milk fat. *Journal of Food Lipids,* 3(1): 43-57.
28. Tagami, T., Ito, E., Kida, R., Hirose, K., Noda, T. and Ozeki, T. (2021). 3D printing of gummy drug formulations composed of gelatin and an HPMC-based hydrogel for pediatric use. *International Journal of Pharmaceutics,* 594: 120118.
29. Wood, H. W. (1958). The identification of the sugar in gelatin. *Journal Photographic Sciences,* 6:170-175.
30. Evans, E. W., Hayes, C., Palmer, C. A., Bermudez, O. I., Cohen, S. A. and Must, A. (2013). Dietary intake and severe early childhood caries in low-income, young children. *Journal of the Academy of Nutrition and Dietetics,* 113(8): 1057-1061.
31. Folayan, M. O., Arije, O., El Tantawi, M., Kolawole, K. A., Obiyan, M., Arowolo, O. and Oziegbe, E. O. (2019). Association between early childhood caries and malnutrition in a sub-urban population in Nigeria. *BMC Pediatrics,* 19(1): 1-8.
32. National Pharmaceutical Regulatory Agency (NPRA) Product Classification Guideline - Drugs or Food Products (2021). Available online: https://npra.gov.my/index.php/en/classification-guideline/product-classification-guideline.html?highlight=WyJjbGFzc2lmaWNhdGlvbiIsIidjbGFzc2lmaWNhdGlvbiJd [accessed on 26 May 2021].
33. Dickinson, A., Bonci, L., Boyon, N. and Franco, J. C. (2012). Dietitians use and recommend dietary supplements: Report of A survey. *Nutrition Journal,* 11:14.
34. Goston, J. L. and Correia, M. I. T. D. (2010). Intake of nutritional supplements among people exercising in gyms and influencing factors. *Nutrition,* 26(6): 604-611.
35. Abe-Matsumoto, L. T., Sampaio, G. R. and Bastos, D. H. M. (2018). Do the labels of Vitamin A, C, and E supplements reflect actual vitamin content in commercial supplements? *Journal Food Composition Analysis,* 72: 141-149.

Malaysian Journal of Analytical Sciences (MJAS)
Published by Malaysian Analytical Sciences Society

OPTIMIZATION OF DIFFERENT PARAMETERS IN THE SYNTHESIS OF BISPHENOL A IMPRINTED POLYMER VIA PRECIPITATION POLYMERIZATION FOR BISPHENOL A ADSORPTION

(Pengoptimuman Parameter yang Berbeza dalam Sintesis Polimer Tercetak Bisfenol A Melalui Pempolimeran Pemendakan bagi Penjerapan Bisfenol A)

Tan Nee Nee, Noorhidayah Ishak*, Azalina Mohamed Nasir, Nur Zatul 'Iffah Zakaria, Nor Munirah Rohaizad

Faculty of Chemical Engineering Technology,
Universiti Malaysia Perlis, Sungai Chuchuh, 02100 Padang Besar, Perlis, Malaysia

**Corresponding author: noorhidayah@unimap.edu.my*

Received: 27 September 2021; Accepted: 12 November 2021; Published: 27 December 2021

Abstract

Molecularly imprinted polymer (MIP) is used to synthesize receptors and is highly recognized against target molecules. The purpose of the study is to prepare bisphenol A (BPA) imprinted polymer that can be used to adsorb BPA molecules. The MIP was prepared by precipitation polymerization using BPA as a template, methacrylic acid (MAA) as a functional monomer, ethylene glycol dimethacrylate (EGDMA) as a crosslinker, acetonitrile as a solvent, and 1,1'-azobis(cyclohexanecarbonitrile) (AIBN) as an initiator by heating in an oil bath at 60 °C for 20 hours. The influence of several parameters (i.e., the ratio of monomer-template, the amount of crosslinker, and the amount of solvent) on the recognition capability of BPA MIP was investigated using response surface methodology (RSM). The optimal conditions of BPA synthesis are 3 mmol of monomer, 30 mmol of crosslinker, and 35 mL of solvent, which achieved an adsorption capacity of 78.111 mg/g. The MIP and non-imprinted polymer (NIP) were characterized using Fourier transform infrared (FTIR) spectroscopy and scanning electron microscopy (SEM). The MIP shows higher selectivity towards BPA compared to other analogs. In conclusion, the particles of imprinted polymer have a great potential in the adsorption of BPA.

Keywords: bisphenol imprinted polymer, response surface methodology, imprinted polymer characterization

Abstrak

Polimer molekul tercetak (MIP) digunakan untuk mensintesis reseptor dan mempunyai pengecaman yang sangat tinggi terhadap molekul sasaran. Tujuan kajian ini adalah untuk menyediakan polimer yang dicetak bisfenol A (BPA) yang boleh digunakan untuk menentukan keupayaan penjerapan terhadap molekul BPA. MIP disediakan dengan pempolimeran pemendakan menggunakan BPA sebagai templat, asid metakrilik (MAA) sebagai monomer berfungsi, etilena glikol dimetakrilat (EGDMA) sebagai agen penyilangan, asetonitril sebagai pelarut, dan 1,1 azobis (sikloheksanakarbonitril) (AIBN) sebagai pemula. Pempolimeran pemendakan dilakukan dengan pemanasan dalam rendaman minyak pada 60 °C selama 20 jam. Pengaruh parameter berikut telah disiasat (nisbah monomer-templat, jumlah agen penyilangan, dan jumlah pelarut yang digunakan). Kaedah matematik iaitu kaedah tindak balas permukaan (RSM) mengoptimumkan parameter ini untuk meningkatkan keupayaan pengesanan BPA MIP. Hasil yang diperoleh daripada RSM menunjukkan keadaan optimum 3 mmol jumlah monomer, 30 mmol jumlah agen penyilangan, dan 35

mL jumlah pelarut yang digunakan dengan kapasiti penjerapan sebanyak 78.111 mg/g. MIP juga mempunyai pemilihan yang lebih tinggi terhadap BPA berbanding dengan analog lain. Kesimpulannya, zarah polimer tercetak menunjukkan potensi yang baik terhadap penjerapan cecair BPA.

Kata kunci: polimer bisfenol tercetak, kaedah tindak balas permukaan, pencirian polimer tercetak

Introduction

The chemical name for bisphenol A (BPA) is 2,2-bis(4-hydroxyphenyl)propane [1]. Since the 1940s and 1950s, BPA has been used in the plastic industry. BPA can be classified as an endocrine-disrupting chemical commonly used to manufacture polycarbonate plastics, polysulfones, and epoxy resins. BPA leaches easily from polycarbonate food and drink containers, can interfere with hormone systems, and has an adverse effect on the environment [2]. Furthermore, BPA can cause various health issues, including breast cancer, obesity, and fertility problems in men and women [3].

Three types of processes that can remove BPA from water or wastewater are microbiological, chemical, and physical processes [4]. A microbiological process uses bacteria for the removal of endocrine-disrupting compounds [5]. Meanwhile, advanced oxidation process is a chemical process that uses ozone and UV radiation. Reverse osmosis, nanofiltration, and adsorption are examples of physical processes [4]. Molecular imprinting technique has been proposed to remove BPA in an aqueous solution due to its reusability and low cost.

Molecularly imprinted polymer (MIP) can identify any target molecule specifically, and it is a type of synthetic polymer. The mixture of template molecules, functional monomers, crosslink monomers, and initiators is polymerized to obtain the imprinted polymer. During polymerization, the complexes are heated, forming a rigid polymer structure consisting of template molecules, functional monomers, and crosslinkers. A high degree of cross-linking maintains the polymer matrix's form after removing the template molecule from the polymer matrix [6,7]. The non-imprinted polymer (NIP) that is commonly synthesized with MIP will act as a control so that the selectivity of the MIP can be analyzed by comparing it with the binding capacity data of NIP. The NIP preparation will follow all the polymerization processes of MIP, except that the template molecule is absent during polymerization.

Bulk polymerization is a conventional method widely used to synthesize MIP. However, this method suffers from the irregular shape of polymer and non-uniform particle size distribution due to the crushing processes. Therefore, the resultant polymers need to be sieved to obtain the desired particle size. The sieving process is time-consuming, and crushing can destruct the cavity of the template, thus affecting the polymer's performance. Therefore, precipitation polymerization has been proposed to overcome the disadvantages of bulk polymerization. MIP synthesis using precipitation polymerization employs a similar method as bulk polymerization. However, the amount of porogen used is higher than bulk polymerization. This method can produce polymer particles without the crushing process, free from additional surfactants or stabilizers. The amount of porogen, crosslinker, template, and monomer is significant to obtain a highly sensitive and selective polymer [8].

Design-Expert version 11 has been used to evaluate experimental responses using response surface methodology (RSM) by carrying out experiments and numerical modeling. It is a faster and cheaper way of collecting research findings than the classical one-factor-at-a-time (OFAT) method or full-factorial experiments. RSM also provides a model equation for the response parameter and optimizes process variables [9]. Several factors will affect the characteristics of the imprinted polymers. One of the factors is the amount of porogenic solvent used, which will affect the monomer-template interactions [10]. In addition, different ratios of template molecule to functional monomer will affect the complexity of the template [11]. Lastly, the amount of crosslinkers used will affect the stability of the recognition sites [10]. All of these factors are very

important during the preparation of imprinted polymer particles. However, not much study has been done to optimize these important parameters. Throughout this research, the interaction of the parameters and their effects on the binding capacity were studied. The parameters of the polymerization process (i.e., the amount of monomer, crosslinker, and porogenic solvent) were chosen and optimized using RSM coupled with central composite design (CCD) to produce MIPs with optimum recognition to adsorb BPA molecules. This preliminary study will create a paradigm for future studies in the development of receptors in supramolecular chemistry.

Materials and Methods

Raw materials

Bisphenol A (BPA), methacrylic acid (MAA), acetonitrile, ethylene glycol dimethacrylate (EGDMA), acetic acid, diphenylamine, diphenyl phosphate, hydroquinone, and diethylstilbestrol were purchased from Sigma-Aldrich, whereas 1,1'-azobis (cyclohexanecarbonitrile) (AIBN) was acquired from Acros Organics.

Preparation of MIP and NIP

The preparation of BPA for MIP was conducted under different conditions. One mmol BPA (template) and MAA (functional monomer), acetonitrile, EGDMA (crosslinker), and 50 mg AIBN (initiator) were added to a bottle. Next, the mixture was purged for 10 min with a gentle nitrogen flow [12]. The bottle was closed immediately. Then, the mixture was sonicated for 15 min. The solution was polymerized in a 60 °C oil bath for 20 h. After that, the polymer particles were washed with methanol to remove unreacted reagents. Then, the template molecule was repeatedly extracted after polymerization using a methanol-acetic acid solution (9:1 v/v) until the ultraviolet-visible (UV-Vis) spectrophotometer did not detect BPA from the washing solvent at 278 nm [13]. Next, the extracted particles were washed repeatedly with methanol to remove residual acetic acid. This washing step was done by shaking the particles at 130 rpm for 2 h. Lastly, the MIP was dried in an oven at 50 °C for 24 h [13]. As a control, the NIP was synthesized and treated in the same way, except that the template molecule was absent in the polymerization stage.

Preparation of MIP and NIP for BPA Adsorption

Approximately 10 mg of the MIP or NIP was placed in a centrifuge tube and 25 mL of an 80 mg/L BPA solution. The mixed solution was shaken at 150 rpm for 2 h at constant temperature in a centrifuge tube. Then, the solution was separated centrifugally at 4,000 rpm for 10 min. After centrifuging, the supernatant solution was decanted and filtered using a 0.20 µm syringe filter. UV-Vis spectrophotometers were used to measure the solution concentration changes with BPA at 278 nm [14]. All testing was conducted in triplicate, and the average data values were used to ensure the accuracy of the data collected. The adsorption capacity of BPA (Q) was calculated using Equation 1 [15]:

$$\text{Adsorption Capacity, } Q = \frac{(C_i - C_f)\,V}{m} \quad (1)$$

where C_i is initial solution concentration (mg/L), C_f is final solution concentration (mg/L), V is volume of the solution (mL) and m is mass of dried polymer (mg).

Optimization of the preparation conditions of MIP for BPA removal

The experimental design was conducted with the help of RSM in Design-Expert version 11 to optimize the adsorption capacity. A CCD was utilized to study the response pattern and determine the optimum combination of variables. A CCD-based RSM was used to optimize the parameters selected for BPA removal, which were different ratios of monomer-template, amount of crosslinker, and amount of solvent. The design was used to investigate the combined effect of three independent parameters, and 20 sets of experiments were carried out. The range to optimize the three parameters is shown in Table 1.

Characterization of MIP and NIP

The surface morphology of MIP and NIP was analyzed using SEM. Before measuring in SEM, the sample was first mounted on aluminum stubs using double-sided adhesive tape and sputtered with a thin platinum film. The functional groups of MAA were characterized using attenuated total reflectance-Fourier transform infrared

(ATR-FTIR) spectroscopy, while the MIP, NIP, and BPA were characterized using FTIR spectroscopy. A potassium bromide (KBr) pellet is usually used for the analysis of a powdered sample. In this study, KBr pellet samples were scanned in the wavenumber range of 4000–400 cm^{-1} with a resolution of 4 cm^{-1} [16]. The FTIR spectrum was recorded and analyzed.

Selectivity Experiment on BPA

In order to prove the specific selectivity of the optimized MIP and NIP to BPA, hydroquinone, diethylstilbestrol, diphenylamine, and diphenyl phosphate were chosen as analogs. Firstly, the standard calibration curve for each analog was prepared with the concentration of 20, 40, 60, 80, and 100 mg/L. The MIP and NIP (10 mg) were first dispersed respectively in a mixture solution containing BPA or other different analogs (80 mg/L, 25 mL) and shaken at 25 °C and 150 rpm for 2 h. After adsorption, the mixture solution was separated by centrifuge at 4,000 rpm for 10 min, and the supernatant was decanted and filtered using a 0.20 μm syringe filter. The supernatant was measured by a UV spectrometer with each of the specific wavelengths. The average values of the data were determined. The adsorbed amount of BPA or other analogs was calculated according to Equation 1. Meanwhile, the imprinting factor (α_{ana}) and selectivity factor (β) of MIP and NIP were calculated using Equation 2 and 3, respectively:

$$\text{Imprinting Factor } (\alpha_{ana}) = \frac{Q_{MIP}}{Q_{NIP}} \quad (2)$$

$$\text{Selectivity Factor } (\beta) = \frac{\alpha_{tem}}{\alpha_{ana}} \quad (3)$$

where Q_{MIP} and Q_{NIP} are the adsorption capacity of the template or analog molecule on MIP and NIP, respectively, and α_{tem} and α_{ana} are the imprinting factor for the template molecule and analog, respectively [15].

Table 1. Experimental range and levels of the chosen parameters

Parameters	Code	Range and Levels		
		-1	0	1
Amount of monomer, MAA (mmol)	A	2	3	4
Amount of crosslinker, EDGMA (mmol)	B	20	30	40
Amount of solvent, acetonitrile (mL)	C	20	35	50

Results and Discussion

Design of response surface methodology for optimum polymerization parameters

Table 2 shows the sequential model sum of squares for BPA adsorption capacity. The models available are linear, 2FI, quadratic, and cubic. The greater *F*-value and the lower *p*-value suggest that the model is highly significant and shown to be good [17]. In this case, the recommended source is quadratic vs 2FI with the sum of squares of 5,233.23 and an *F*-value of 56.40. However, the model is also significant because the *p*-value is smaller than 0.0001.

Analysis of variance for the quadratic model

Table 3 shows an analysis of variance (ANOVA) for the response surface quadratic model. The model is significant, as the *F*-value is 33.22 and the *p*-value is smaller than 0.0001. This implies that the chance of the model *F*-value occurring due to noise is negligible [18]. In this case, the linear coefficients (A, C), interaction coefficients (AB, AC, BC), and quadratic coefficients (A^2, B^2, C^2) are significant. Furthermore, *p*-values of less than 0.05 strongly support their significant contribution to adsorption capacity [19]. In contrast, the amount of crosslinker does not significantly affect adsorption capacity as it has a low *F*-value of 1.05 and a high *p*-value of 0.3291.

In addition, the coefficient of determination (R^2) value is close to unity (i.e., 0.9676). According to Zhou [20], in order to verify the favorable consistency between actual data and theoretical prediction, the R^2 value should be at least 0.800. From Table 3, the adjusted R^2 value is 0.9385. Therefore, it is confirmed that the model is very significant, indicating a good agreement between the experimental and predicted values. Owolabi and co-workers stated that the adjusted R^2 and predicted R^2 values must be in good agreement within 20% [9]. In this study, this requirement is met with a predicted R^2 value of 0.7452. These values represent good adsorption capacity of MIP towards BPA. The adequate precision ratio of 15.6517 indicates a suitable signal-to-noise ratio. The ratio was greater than 4; thus, the quadratic model could navigate the design space and find the optimal conditions for adsorption capacity [18].

The application of RSM yields the quadratic regression equation as indicated in Equation 4, representing an empirical relationship between adsorption capacity and process variables in coded values, where A is the amount of monomer, b is the amount of crosslinker, and C is the amount of solvent. A positive symbol in the equation denotes a synergistic effect, whereas a negative symbol represents an antagonistic effect [21].

Table 2. A sequential model sum of squares for BPA adsorption capacity

Source	**Sum of Squares**	**df**	**Mean Square**	***F*-value**	***p*-value**	
Mean *vs* Total	63,694.01	1	63,694.01			
Linear *vs* Mean	2,790.02	3	930.01	2.20	0.1279	
2FI *vs* Linear	1,224.26	3	408.09	0.9572	0.4420	
Quadratic *vs* 2FI	5,233.23	3	1,744.41	56.40	< 0.0001	Suggested
Cubic *vs* Quadratic	283.41	4	70.85	16.42	0.0022	Aliased
Residual	25.89	6	4.31			
Total	73,250.82	20	3,662.54			

Table 3. Analysis of variance for the response surface quadratic model

Source	**Sum of Squares**	**df**	**Mean Square**	***F*- value**	***p*-value**
Model	9,247.52	9	1,027.50	33.22	< 0.0001
A-Amount of monomer	1131.95	1	1,131.95	36.60	0.0001
B-Amount of crosslinker	32.55	1	32.55	1.05	0.3291
C-Amount of solvent	1,625.52	1	1,625.52	52.55	< 0.0001
AB	220.53	1	220.53	7.13	0.0235
AC	407.31	1	407.31	13.17	0.0046
BC	596.42	1	596.42	19.28	0.0014
A^2	174.20	1	174.20	5.63	0.0391
B^2	540.81	1	540.81	17.48	0.0019
C^2	666.02	1	666.02	21.53	0.0009
Residual	309.30	10	30.93		

Std. dev. = 5.56, C.V. % = 9.85
R^2 = 0.9676, Adj. R^2 = 0.9385,
Predicted R^2 = 0.7452, Adeq Precision = 15.6517

$$\text{Adsorption Capacity} = 75.21 + 10.64A - 1.80B + 12.75C + 5.25AB + 7.14AC - 8.63BC - 7.96A^2 - 14.02B^2 - 15.56C^2 \quad (4)$$

Diagnostic study

The validity of the derived equation is discussed in a series of graphical diagnoses. Figure 1(a) shows that the data points are scattered along the straight line of a typical residual graph, indicating that the data points form a normal distribution [21]. Another confirmation is the residual plot versus the predicted response (Figure 1(b)), where the random pattern in the residual plot versus the predicted response indicates that the model is satisfactory and also does not interfere with the independence or constant variance assumption [18]. On the other hand, it has been inferred that from the externally studentized residual plot versus the run number in Figure 1(c), not all data points deviate far from the values predicted [22]. The data points in the predicted versus actual plot in Figure 1(d) are scattered along a straight line, indicating that the experimental and predicted response values are correctly associated [23]. As a result, the derived quadratic response model (Equation 4) is verified to be a reliable model representing adsorption capacity.

Analysis of response surface

The purpose of this analysis is to optimize the parameters for BPA adsorption capacity during polymerization. Therefore, this section analyzes the relationship of the three parameters (i.e., the amount of monomer, crosslinker, and solvent) and their respective optimal condition range. There are 20 runs of experiments with different operating conditions. Table 4 shows the experimental design matrix with coded factors. A three-dimensional response surface was produced to determine the relationship between the variables and the optimal state of each factor for maximum adsorption capacity. Figure 2(a) presents the effect of the amount of monomer and crosslinker on the adsorption capacity of MIPs. It can be seen that there is higher adsorption capacity when the amount of monomer and crosslinker is 3 mmol and 30 mmol, respectively. However, when the amount of monomer and crosslinker exceeded these values, it is still in an optimal condition, but the adsorption capacity decreased. The decreasing adsorption capacity is due to the excess amount of monomer, which leads to the creation of non-selective binding sites. In contrast, an extremely high crosslinker amount reduces the number of recognition sites per MIPs unit mass [24]. Therefore, only the appropriate amount of monomer and crosslinker could lead to the maximum adsorption capacity.

Figure 2 (b) represents the effect of monomer and solvent amount on the adsorption capacity of MIPs. The adsorption capacity increased as the amount of monomer and solvent increased. An increased amount of monomer will give a strong interaction between the functional monomer and the template [9]. The additional amount of solvent favors the formation of polar interaction between the monomer and the template [15]. However, it can be seen that the adsorption capacity decreased as the amount of monomer and solvent reduced to below 3 mmol and 35 mL, respectively. It could be explained that the small amount of MAA could not mix sufficiently with BPA molecules, thus minimizing specific recognition sites. In contrast, less solvent can cause the polymer to precipitate early [12, 15]. Thus, the maximum adsorption efficiency could only be achieved through the appropriate amount of monomer and solvent.

Figure 2(c) shows the effect of the amount of crosslinker and solvent on the adsorption capacity of MIPs. From the figure, the maximum adsorption capacity could be achieved when the crosslinker amount is 30 mmol and the solvent amount is 35 mL. However, when the amount of crosslinker and solvent is less than 30 mmol and 35 mL, respectively, it is still in optimum condition, but the adsorption capacity decreased. The reduction is because a low crosslinker amount reduces structural stability, whereas less solvent can lead to early polymer precipitation [12, 13]. Nevertheless, the maximum adsorption capacity could be reached only by the appropriate amount of crosslinker and solvent. In conclusion, this model predicted that the amount of

monomer, crosslinker, and solvent of 3 mmol, 30 mmol, and 35 mL, respectively, as the optimum conditions to achieve the best response of adsorption capacity towards BPA, which was 78.111 mg/g.

FTIR analysis

In order to characterize the MIP and NIP, the functional groups of BPAs, MAA, MIP, and NIP were analyzed. The FTIR spectra of these four samples are shown in Figure 3 and Table 5. From the observation, BPA has a broad peak at 3325 cm^{-1}, representing O-H stretching. Meanwhile, the peak at 2966 cm^{-1} shows sp^3 C-H stretching and the peak at 823 cm^{-1} indicates benzene derivative. Next, the stretching frequency of C=O for MIP and NIP at 1726 cm^{-1} is due to the presence of a poly(EGDMA) backbone. In MAA, the spectrum band at 1694 cm^{-1} refers to C=O conjugated carbonyl stretching [25]. This band overlaps with the C=O of EGDMA around 1726 cm^{-1} due to the disappearance of the alkene group in MAA after polymerization. The similarity between these MIP and NIP spectra shows that these polymers have a similar backbone. The FTIR spectra of NIP and MIP indicate that the template molecules have been successfully removed from the MIP, whereby no significant peak of BPA is present [26]. Moreover, the band for MIP and NIP at 1156 cm^{-1} shows strong C-O-C ester stretching. This band indicates EGDMA and MAA copolymerization due to EGDMA characteristics in the FTIR spectrum [27]. The C=O stretch, C-O stretch, and C-O-C stretch at 1726 cm^{-1}, 1257 cm^{-1}, and 1156 cm^{-1}, respectively, demonstrate that MIP has been successfully synthesized.

SEM analysis

The changes in the surface morphology of the MIP after the extraction of template and NIP were analyzed using SEM. Figure 4 displays the surface morphology of MIP and NIP at 5,000× and 500× magnification. Both polymers show a relatively rough and porous surface. Acetonitrile that functions as a porogen during polymerization contributes to the macroporous structure on the surface of imprinted polymers. Thus, this explains the adsorption behavior of NIP [7]. The size of the polymer particles was recorded between the range of 11 μm and 65 μm.

Selectivity studies on BPA

BPA and other four similar structures (diphenylamine, hydroquinone, diphenyl phosphate, and diethylstilbestrol) were selected as analogs for selectivity studies. From Table 6, MIP exhibits a higher binding affinity for BPA than other analogs in adsorption capacity due to the selective recognition sites in the MIP [28]. The higher adsorption capacity indicates that the polymer is specifically selective towards BPA and not the other four analogs. Besides, the imprinting factor represents MIP's special recognition, and a high value means that the MIP has a greater recognition and stronger imprinting effect [29]. Table 6 shows that BPA has a high imprinting factor value compared to other analogs.

Moreover, if the selectivity factor value is higher, the MIPs have greater template selectivity and distinguish the template from the analogs more efficiently [29]. For example, diphenylamine has the highest selectivity factor due to a more specific site and can distinguish BPA from other analogs compared to NIP. Thus, MIP has higher selectivity towards BPA compared to other analogs.

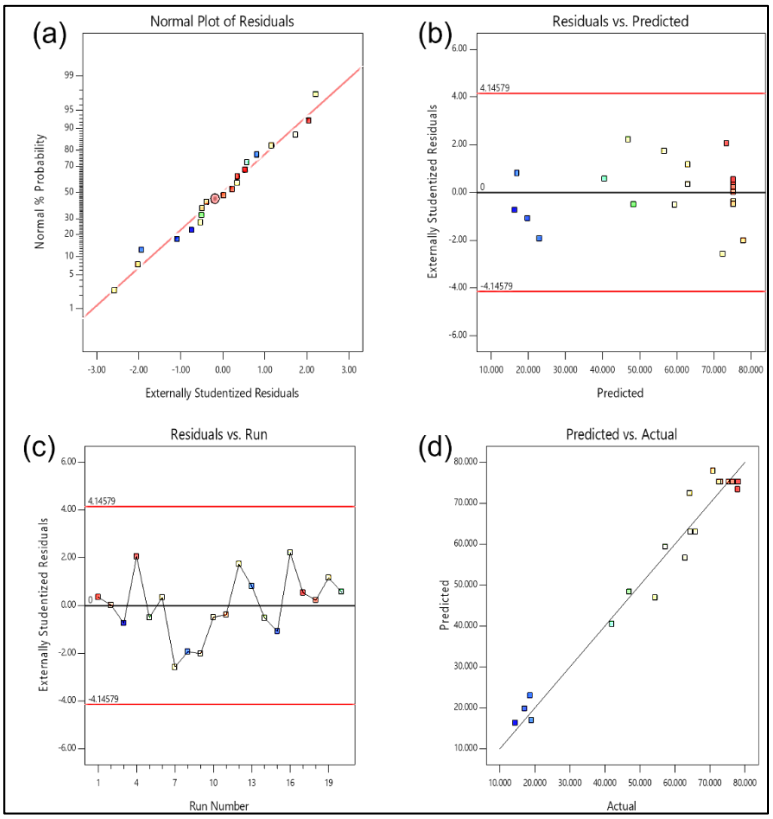


Figure 1. Collective graphical diagnostics for equation 4

Table 4. Experimental design matrix with coded factors of CCD and response

Run	Factor 1	Factor 2	Factor 3	Response 1
	A: Monomer: Template Ratio (mmol)	B: Amount of Crosslinker (mmol)	C: Amount of Solvent (mL)	Adsorption Capacity (mg/g)
1	3	30	35	77.115
2	3	30	35	75.334
3	4	20	20	14.423
4	4	20	50	77.885
5	2	20	50	47.000
6	3	20	35	64.423
7	3	30	50	64.222
8	2	40	20	18.655
9	4	30	35	70.889
10	3	30	35	72.556
11	3	30	35	73.111
12	2	30	35	62.885

Table 4 (cont'd). Experimental design matrix with coded factors of CCD and response

Run	Factor 1	Factor 2	Factor 3	Response 1
	A: Monomer: Template Ratio (mmol)	**B: Amount of Crosslinker (mmol)**	**C: Amount of Solvent (mL)**	**Adsorption Capacity (mg/g)**
13	2	40	50	19.038
14	3	40	35	57.222
15	2	20	20	17.115
16	3	30	20	54.345
17	3	30	35	78.111
18	3	30	35	76.445
19	4	40	50	65.889
20	4	40	20	42.000

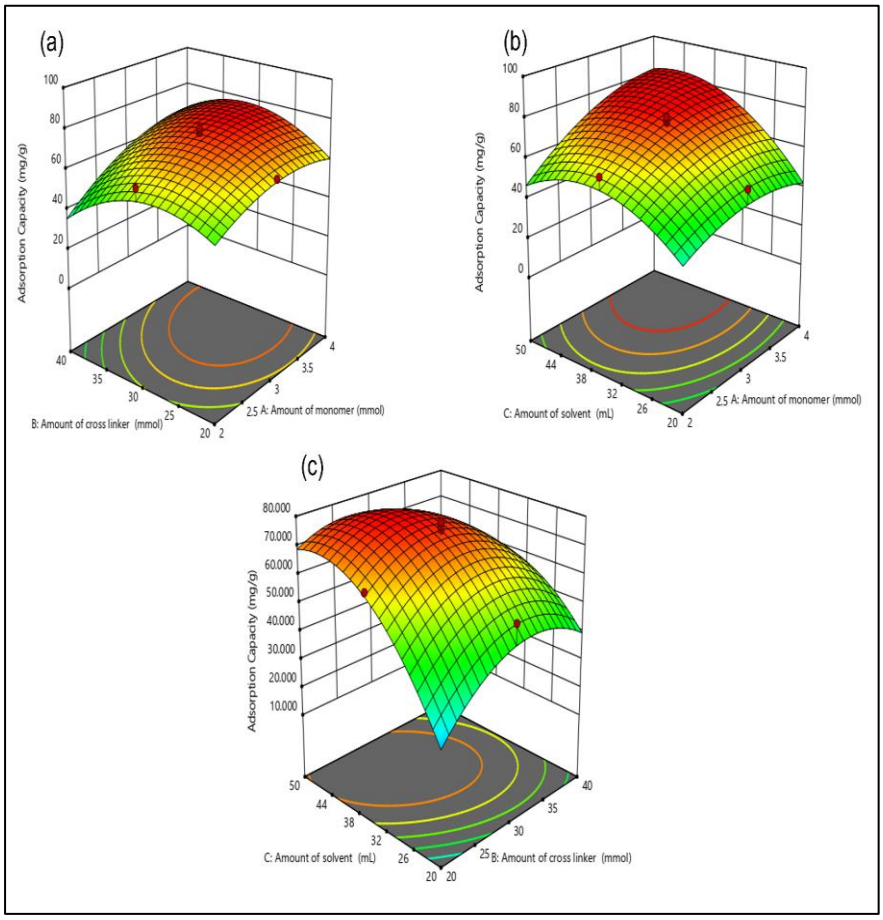


Figure 2. Response surface plots of the interactive effect between (a) the amount of monomer and crosslinker on adsorption capacity, (b) the amount of monomer and solvent on adsorption capacity, and (c) the amount of crosslinker and solvent on adsorption capacity.

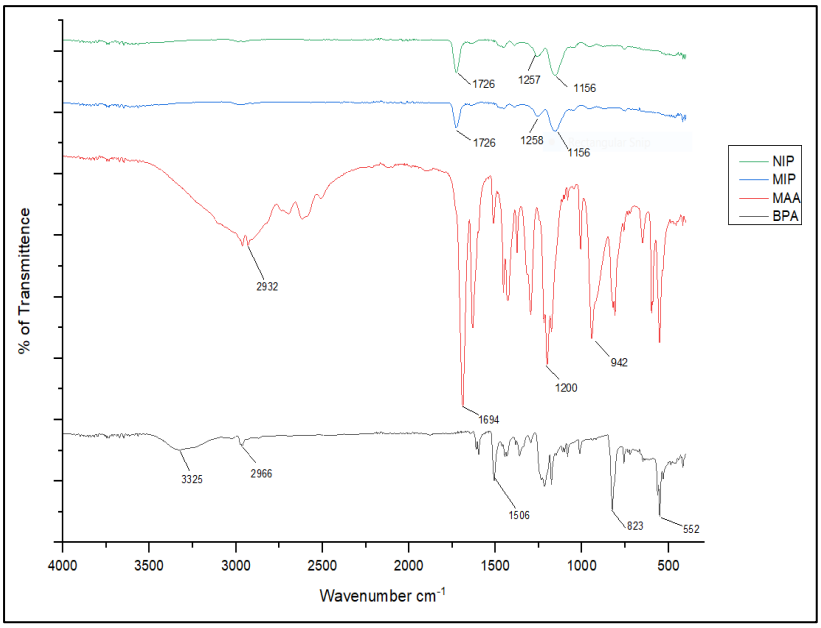


Figure 3. FTIR spectra of BPA, MAA, MIP, and NIP

Table 5. Wavenumber and type of band for MIP/NIP, BPA, and MAA

Type of Material	Wavenumber (cm^{-1})	Type of Band
MIP/NIP	1726	C=O stretch
	1257, 1258	C-O stretch
	1156	C-O-C stretch
BPA	3325	O-H stretch
	823	Sp^2 C-H band
	2966	Sp^3 C-H stretch
MAA	1694	C=O conjugated carbonyl stretching
	1200	C-O stretch

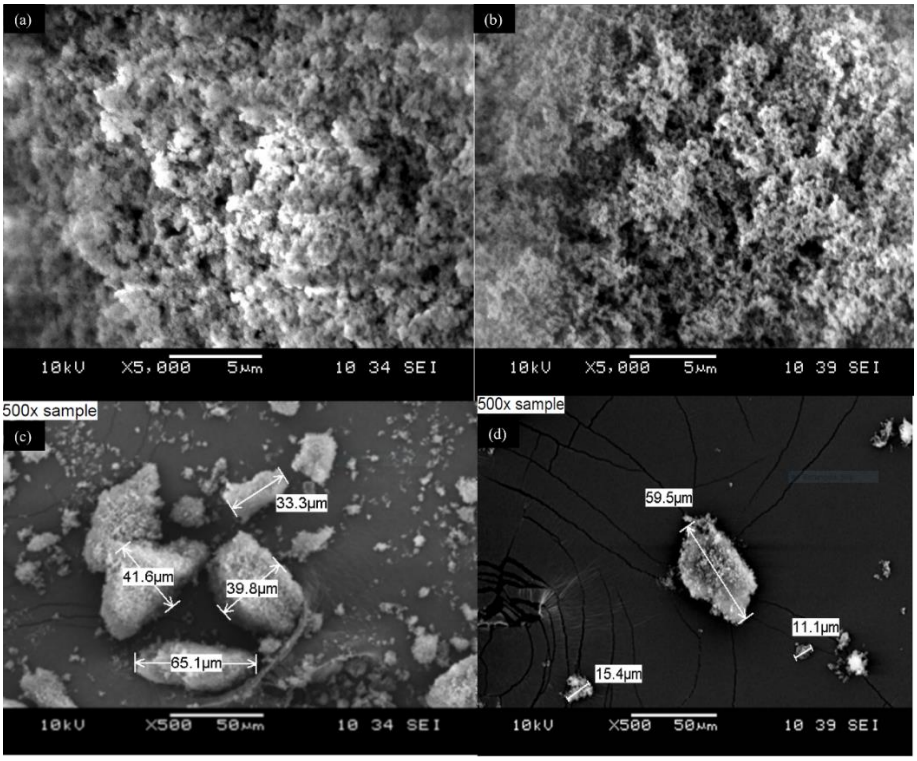


Figure 4. Scanning electron microscopy of MIP

Table 6. The binding capacity, imprinting factor, and selectivity factor of the optimized MIP and NIP

Compound	Binding Capacity (mg/g)		Imprinting Factor (α)	Selectivity Factor (β)
	MIP	NIP		
BPA	78.111	38.945	2.006	-
Diphenylamine	29.869	28.882	1.034	1.940
Hydroquinone	19.137	18.244	1.049	1.912
Diphenyl Phosphate	57.400	47.400	1.211	1.656
Diethylstilbestrol	40.156	38.5938	1.041	1.928

Conclusion

This study focuses on optimizing the synthesis of BPA imprinted polymer via precipitation polymerization for BPA removal. RSM coupled with CCD was used to evaluate the optimum parameters during polymerization (i.e., different ratios of monomer-template, amount of crosslinker, and amount of solvent used) in terms of adsorption efficiency towards BPA molecules. From the results, the optimum values are 3 mmol of monomer, 30 mmol of crosslinker, and 35 mL of solvent, which achieved the adsorption capacity of 78.111 mg/g. The synthesized BPA imprinted polymer and NIP characteristics were determined by FTIR and SEM analysis. The FTIR analysis indicates no difference between the MIP and NIP spectra because the template molecule has been successfully removed from the MIP. The presence of C=O stretch, C-O stretch, and C-O-C stretch indicates that the MIP has been successfully

synthesized. Based on SEM results, the MIP has a rough and porous surface due to template removal. The MIP also has higher selectivity towards BPA compared to other analogs. This preliminary work reported a satisfactory result of binding capacity and selectivity, highlighting the potential application of BPA imprinted polymer in separation and wastewater treatment. The model developed using RSM coupled with CCD has improved the development of an efficient adsorbent, thus providing a framework for further analysis.

Acknowledgment

The authors would like to thank the Faculty of Engineering Technology, Universiti Malaysia Perlis. The financial support from the Fundamental Research Grant Scheme (FRGS) (FRGS/1/2019/TK05/UNIMAP/03/2) is gratefully acknowledged.

References

1. Ya, M. Haohao, L. Jinxia, W. Le, Y. Yueqin, W. Xingde D. Rui, W. Phelisters, W. M. Pavankumar, P. Xinghai, C. and Huizhen, Z. (2019). The adverse health effects of bisphenol A and related toxicity mechanisms. *Environmental Research*, 176: 108575.
2. Bayramoglu, G. Arica, M. Y. Liman, G. Celikbicak O. and Salih, B. (2016). Removal of bisphenol A from aqueous medium using molecularly surface imprinted microbeads. *Chemosphere*, 150: 275-84.
3. Metz, C. M. (2016). Bisphenol A: Understanding the controversy. *Workplace Health and Safety* l, 64: 28-36
4. Posada A. L. L (2016). Removal of endocrine disrupting compounds from water and wastewater using ecofriendly materials. Thesis of Master Degree, The University of Texas at El Paso.
5. Bhatnagar, A. and Anastopoulos, I. (2017). Adsorptive removal of bisphenol A (BPA) from aqueous solution: A review. *Chemosphere*, 168: 885-902.
6. Tehila S. Noam, T. and Daniel, M. (2016). Molecularly imprinted polymer particles: Formation, characterization and application. *Colloids and Surfaces A: Physicochemical and Engineering Aspects*, 495: 11-19.
7. Sajini T. and Beena M. (2021). A brief overview of molecularly imprinted polymers: Highlighting computational design, nano and photo-responsive imprinting. *Talanta Open*, 4: 100072.
8. Ahmed, S. A. D., Alaa, M. A. and Ibrahim, M. E. (2020). Surface-imprinted polymers (SIPs): Advanced materials for bio-recognition. *Journal of Nanotechnology & Advanced Materials,* 8(1): 1-19.
9. Owolabi, R. U. Usman, M. A. and Kehinde, A. J. (2018). Modelling and optimization of process variables for the solution polymerization of styrene using response surface methodology. *Journal of King Saud University - Engineering Sciences*, 30(1): 22-30.
10. Kelvin, F. P. Maretty, E. R. M. Driyanti, R. and Aliya, N. H. (2020). Effect of the molecularly imprinted polymer component ratio on analytical performance. *Chemical Pharmaceutical Bulletin,* 68: 1013-1024.
11. Yemiş, F., Alkan, P., Yenigül, B. and Yenigül, M. (2013). Molecularly imprinted polymers and their synthesis by different methods. *Polymers and Polymer Composites,* 21(3): 145-150.
12. Zhao, L., Hu, X., Zi, F., Liu, Y., Hu, D., Li, P. and Cheng, H. (2021). Preparation and adsorption properties of Ni(II) ion-imprinted polymers based on synthesized novel functional monomer. *e-Polymers*, 21(1): 590-605.
13. Lu, Y., Zhu, Y., Zhang, Y. and Wang, K. (2019). Synthesizing vitamin E molecularly imprinted polymers via precipitation polymerization. *Journal of Chemical & Engineering Data*, 64(3): 1045-1050.
14. Shahaidah, S. Che K. M. F. and Shareena, M. S. (2014). Characterization of bisphenol A MIP (BPA-MIP) synthesizing. *Applied Sciences*, 14(13): 1455-1459.
15. Jin, X. Wang, Y. Bai, W. Zhao, D. Song, X. and Xu, X. (2015). Synthesis and characterization of fomesafen imprinted polymers. *Journal of Macromolecular Science, Part A: Pure and Applied Chemistry*, 52(4): 316-321.

16. Amin, S. Damayanti, S. and Ibrahim, S. (2019). Synthesis and characterization molecularly imprinted polymers for analysis of dimethylamylamine using acrylamide as monomer functional. *Jurnal Kefarmasian Indonesia*, 8: 76-84.
17. Das, B. (2017). Response surface modeling of copper (II) adsorption from aqueous solution onto neem (*Azadirachta indica*) bark powder: Central composite design approach. *Journal of Materials and Environmental Science,* 8(7): 2442-2454.
18. Arabzadeh, N. Mohammadi, A. Darwish, M. and Abuzerr, S. (2018). Construction of a TiO_2–Fe_3O_4-decorated molecularly imprinted polymer nanocomposite for tartrazine degradation: Response surface methodology modeling and optimization. *Journal of the Chinese Chemical Society*, 8: 1-10.
19. Gholami, H., Arabi, M., Ghaedi, M., Ostovan, A. and Bagheri, A. R. (2019). Column packing elimination in matrix solid phase dispersion by using water compatible magnetic molecularly imprinted polymer for recognition of melamine from milk samples. *Journal of Chromatography A*, 1594: 13-22.
20. Zhou, J. Chen, X. H. Pan, S. D. Wang, J. L. Zheng, Y. B. Xu, J. J. Zhao, Y. G. Cai, Z. X. and Jin, M. C. (2019) Contamination status of bisphenol A and its analogues (bisphenol S, F and B) in foodstuffs and the implications for dietary exposure on adult residents in Zhejiang Province. *Food Chemistry*, 294:160-170.
21. Priya, M. Sarveishwhary, R. Saw, H. L. Marinah, M. A. and Khalik, W. M. A. W. M. (2021). CO_2-effervescent tablet-assisted dispersive liquid-liquid microextraction with central composite design for pre-concentration of acetaminophen drug: Method development, validation and green assessment profile. *Malaysian Journal of Analytical Sciences*, 25(3): 432-445.
22. Talib, N. A. A. Salam, F. Yusof, N. A. Alang, A. S. A. and Sulaiman, Y. (2017). Optimization of peak current of poly(3,4-ethylenedioxythiophene)/multi-walled carbon nanotube using response surface methodology/central composite design. *RSC Advances*, 7(18): 11101-11110.
23. Liu, Y. Liu, F. Ni, L. Meng, M. Meng, X. Zhong, G. and Qiu, J. (2016). A modeling study by response surface methodology (RSM) on Sr(II) ion dynamic adsorption optimization using a novel magnetic ion imprinted polymer. *RSC Advances*, 6(60): 54679-54692.
24. Li, G. and Row, K. H. (2018). Recent applications of molecularly imprinted polymers (MIPs) on micro-extraction techniques. *Separation and Purification Reviews*, 47(1): 1-18.
25. Lei, X. N. X. Lu, L. Xinan, X. and Yan, L. (2020). Theoretical insight into the interaction between chloramphenicol and functional monomer (methacrylic acid) in molecularly imprinted polymers. *International Journal of Molecular Science*, 21(11): 4139.
26. Kia, S. Fazilati, M. Salavati, H. and Bohlooli, S. (2016). Preparation of a novel molecularly imprinted polymer by the sol-gel process for solid phase extraction of vitamin D3. *RSC Advances*, 6(38): 31906-31914.
27. Ishak, N. Ahmad, M. N. Nasir, A. M. and Islam, A. K. M. S. (2015). Computational modelling and synthesis of molecular imprinted polymer for recognition of nitrate ion. *Malaysian Journal of Analytical Sciences,* 19(4): 866-873.
28. Xie, X. Ma, X. Guo, L. Fan, Y. Zeng, G. Zhang, M. and Li, J. (2019). Novel magnetic multi-templates molecularly imprinted polymer for selective and rapid removal and detection. *Chemical Engineering Journal.* 357: 56-65.
29. Yixuan, Z. Yuxiao, C. Ningning, C. Yuyan, Z. Bingyu L. Wei G. Xinhao, S. and Yuezhong, X. (2014). Recyclable removal of bisphenol A from aqueous solution by reduced graphene oxide-magnetic nanoparticles: Adsorption and desorption. *Journal of Colloid and Interface Science*, 421: 85-92.

Malaysian Journal of Analytical Sciences (MJAS)
Published by Malaysian Analytical Sciences Society

CYTOTOXICITY EFFECT OF NATURAL AND SYNTHETIC GIRINIMBINES AND THEIR DERIVATIVES AGAINST HUMAN LUNG CANCER CELL LINES A549

(Kesan Sitotoksik Girinimbin Semula Jadi dan Sintetik dan Terbitannya Terhadap Sel Garis Kanser Paru-Paru Manusia A549)

Fatin Nurul Atiqah Osman[1], Siti Mariam Mohd Nor[1]*, Mohd Azlan Nafiah[2]

[1]Department of Chemistry, Faculty of Science,
Universiti Putra Malaysia, 43400 Serdang, Selangor, Malaysia
[2]Department of Chemistry, Faculty of Science and Mathematics,
Universiti Pendidikan Sultan Idris, 35900 Tanjung Malim, Perak, Malaysia

**Corresponding author: smariam@upm.edu.my*

Received: 8 September 2021; Accepted: 18 November 2021; Published: 27 December 2021

Abstract

The present study was designed to evaluate the anticancer properties of girinimbine and its derivatives. Two different routes for the synthesis of girinimbine involving a two-step reaction or a one-pot reaction were studied. Girinimbine was synthesised through metal-catalysed heterocoupling, indole ring closure, ether formation, and Claisen cyclisation. Girinimbine derivatives were prepared by the semi-synthesis of isolated girinimbine from *Murraya koenigii* through alkylation or acylation reactions. Natural and synthetic girinimbines, five derivatives of *N*-substituted girinimbine, and three intermediates from the synthesis of girinimbine were evaluated for cytotoxicity activity against human lung cancer (A549) and normal lung (MRC-5) cell lines. The structures of all the synthesised compounds were confirmed by spectroscopic analysis and comparison with published data. The cytotoxicity assay showed that the natural girinimbine and nitrobiphenyl intermediate exhibited high toxicity (IC_{50} 6.2 and 17.0 µg/mL, respectively), whereas other compounds displayed moderate toxicity activity (IC_{50} 24.0 - 40.6 µg/mL) on A549 cells. All of the compounds demonstrated selectivity to A549 cancer cell lines with the SI values ranging from 2.70 to 4.68 (SI > 2), except for two *N*-alkylated girinimbines with the SI values of 0.93 and 1.70.

Keywords: girinimbine, derivative, *N*-alkylated, *N*-acylated, A549

Abstrak

Kajian ini telah dibentuk untuk menilai sifat antikanser girinimbin dan terbitannya. Dua laluan berbeza untuk mensintesis girinimbin melibatkan tindak balas dua-langkah atau tindak balas satu-bekas telah dikaji. Sintesis girinimbin telah dicapai melalui penggandingan hetero bermangkin logam, penutupan gelang indol, pembentukan eter dan pensiklikan Claisen. Terbitan girinimbin telah disediakan melalui sintesis-semi girinimbin terpencil daripada *Murraya koenigii* melalui tindak balas pengalkilan atau pengasilan. Girinimbin semula jadi dan sintetik, lima terbitan girinimbin tertukar ganti-*N* dan tiga bahan perantara daripada kerja sintesis telah dinilai untuk aktiviti sitotoksik terhadap sel garis kanser paru-paru manusia (A459) dan paru-paru normal (MRC-5). Kesemua struktur sebatian yang disintesis telah disahkan melalui analisis spektroskopik dan

perbandingan dengan data yang telah diterbitkan. Assai kesitotoksikan menunjukkan girinimbin semula jadi dan bahan perantara bifenilnitro telah memaparkan ketoksikan tinggi (IC_{50} 6.2 dan 17.0 μg/mL) manakala sebatian yang lain menunjukkan aktiviti ketoksikan sederhana (IC_{50} 24.0 - 40.6 μg/mL) ke atas sel A549. Kesemua sebatian menunjukkan kepilihan kepada sel garis kanser A459 dengan nilai SI dalam julat daripada 2.70-4.68 (SI > 2) kecuali dua girinimbin teralkil-*N* dengan nilai SI 0.93 dan 1.70.

Kata kunci: girinimbin, terbitan, teralkil-*N*, terasil-*N*, A549

Introduction

Cancer is one of the major diseases that cause many deaths worldwide with an estimated 19.29 million new cases and 9.96 million deaths in 2020. Lung cancer alone contributed to 11.4% of new cases and 18% of deaths [1]. Lung cancer is the third most common cancer in Malaysia with 19.8% of deaths. Males are the largest proportion to suffer from lung cancer and 92% is attributed to the smoking habit, which is the main factor for lung cancer. The increasing incidence of cancers in the country is due to increasing ageing population, exposure to cancer risk, and unhealthy lifestyle. The increasing trend is also due to late diagnosis and limited treatment availability. New cases of lung cancer are comparatively higher in the age group of 45 years old [2]. According to the Malaysian Study on Cancer Survival (MySCan) 2018, lung cancer recorded the lowest survival rate among all cancers due to being diagnosed at an advanced stage. Moreover, lung cancer patients also recorded the lowest survival rate compared to other types of cancers (11.0% for 1-year and 35.5% for 5-year) [3].

This evidence shows that cancer is an urgent matter that requires much attention, especially better prevention, early detection, easy access and available treatment, and cancer care services. In terms of cancer treatment, advancements in research and drug development are a few approaches to developing a potential drug and creating a variety of anticancer drugs. A new approach of anticancer discovery has been taken over by natural products due to their structural diversity, such as varied substituent groups from simple alkyls, rings, or attachment of terpene of various complexity and length, and also the presence of various functional groups that can be further modified to enhance their activity.

In the last few decades, the medicinal role of natural and semi-synthetic carbazoles has expanded significantly. Carbazoles, which is an attractive compound to be introduced in the pharmaceutical industry as a candidate for drug development, have a broad scope of biological actions. Girinimbine (**8**) is a carbazole mainly found in *Murraya koenigii* or locally known as curry tree. This plant is native to Malaysia and can be used as herbs, spices, and condiments (food and flavour), to treat illness in the traditional way (medicinal) and make soaps or insect repellents (source for materials). Girinimbine (**8**) has drawn the attention of researchers due to its wide range of pharmacological effects, such as anti-inflammatory [4], anticancer [5-9], antiplatelet [10], antioxidant [4,11], and exhibited strong activity against *Aedes aegypti* [12]. Several syntheses of **8** have been reported involving reaction with ylide [13], base-induced cyclisation [14], oxidative intramolecular allylation [15, 16], Buchwald-Hartwig amination [17], Ti-mediated annulation [18], decarboxylative allylation/Claisen rearrangement [19], and Grignard addition and ring-closing metathesis [20].

To further explore the potential anticancer properties of carbazole compounds, the cytotoxicity of five girinimbine derivatives (**9**-**13**) was evaluated on human lung cancer (A549) and normal lung (MRC-5) cell lines. All *N*-alkylated (**9**-**11**) and *N*-acylated derivatives (**12** and **13**) were prepared *via* semi-synthetic modification of girinimbine (**8i**) isolated from *M. koenigii*, as previously reported by our group [21]. Currently, there is no data on the effect of all these derivatives (**9**-**13**) on A549 and MRC-5 cell lines. A comparative study between the isolated girinimbine (**8i)** and synthesised girinimbine (**8s**) would also be an interesting field to explore. In this study, **8s** was synthesised *via* two different routes using established protocols, including indole ring closure, aryl coupling,

and thermal cyclisation. The cytotoxicity effects were also compared with all intermediates produced in the synthesis of girinimbine. The compounds **8i** and **8s** would act as the references for the cytotoxicity properties of the derivatives.

Materials and Methods

General

All chemicals and solvents used in this study are commercially available. All reactions were monitored using thin-layer chromatography (TLC) and silica gel 60 F245 (Merck KGaA) precoated aluminium-backed plates and visualised under ultraviolet light (UVP, UV Lamp UVGL-58) prior to dipping in H_2SO_4. The solvents were removed under vacuo by an EYELA rotary evaporator N-100 or a Buchi rotavapor R-215. The organic phases were dried under Na_2SO_4. Column chromatography was performed with 100–150 mesh of silica gel 60 (0.040–0.063 mm) as the stationary phase. The digital melting point equipment (Electrothermal IA9000 Series) was used to measure the melting point and the measurement was repeated at least three times for each compound. The IR spectra were obtained by Perkin-Elmer FT-IR Model Spectrum 100 series spectrophotometer using UATR techniques. The MS spectra were obtained from a Shimadzu model QP5050A spectrometer. 1D and 2D NMR spectra were recorded with a JEOL FT-NMR 500 MHz spectrophotometer using $CDCl_3$. The chemical shifts (δ) were recorded in ppm relative to the TMS signal described with an appropriate abbreviation for multiplicities as s (singlet), d (doublet), t (triplet), and m (multiplet), whereas the coupling constants J are given in Hz.

Isolated natural girinimbine (**8i**) from the bark of *M. koenigii* was obtained from the laboratory of the co-researchers in the Department of Chemistry, Universiti Pendidikan Sultan Idris, Malaysia for data comparison and the semi-synthesis of girinimbine derivatives (**9**-**13**) as previously reported [21].

Synthesis of Girinimbine (8s)

3-Methyl-2'-nitrobiphenyl-4-ol (3)

A mixture of $^{i}Pr_2NEt$ (0.43 mmol), $Pd(OAc)_2$ (0.43 mmol), nBu_4NBr (0.43 mmol), 1-bromo-2-nitrobenzene (**1**) (1.71 mmol), and 4-iodo-2-methylphenol (**2**) (0.43 mmol) was refluxed in *p*-xylene (10 mL) at 130°C for 3 days. The mixture was then allowed to warm to room temperature before the addition of water (10 mL) and ether (10 mL). The separated organic phase was washed with water (10 mL), dried, and evaporated. The product was purified using column chromatography (hexane-ethyl acetate, 9:1).

Compound **3**: Yellow oil (81 mg, 83%); IR (UATR) 3479, 3063, 2928, 1609, 1518, 1354, 1275, 1211 cm^{-1}; δ_H (500 MHz, $CDCl_3$) 7.77 (1H, d, J 8.0 Hz, H-aromatic), 7.55 (1H, t, J 8.0 Hz, H-aromatic), 7.41 (1H, t, J 8.0 Hz, H-aromatic), 7.07 (1H, s, H-aromatic), 7.01 (1H, d, J 8.0 Hz, H-aromatic), 7.00 (1H, d, J 8.0 Hz, H-aromatic), 6.78 (1H, d, J 8.0 Hz, H-aromatic), 5.00 (1H, br. s, OH), 2.25 (3H, s, CH_3); δ_C (125 MHz, $CDCl_3$) 154.3, 149.6, 136.2, 132.3, 132.1, 130.8, 129.8, 127.8, 126.9, 124.6, 124.2, 115.5, 16.0; m/z (EI) 229 (M^+, $C_{13}H_{11}NO_3$ requires 229).

2-Hydroxy-3-methylcarbazole (6)

Route 1: 3-Methyl-2'-nitrobiphenyl-4-ol (**3**) (0.35 mmol), $SnCl_2 \cdot 2H_2O$ (2.18 mmol), and EtOH (3 mL) were refluxed at 60°C for 6 h. The mixture was poured into cold water (10 mL) and $NaHCO_3$ was added to reach pH 7. The precipitate was filtered and the aqueous layer was extracted with ethyl acetate (3 × 10 mL). The combined organic phase was dried and evaporated. The crude product was purified using column chromatography (chloroform-ethyl acetate, 9.5:0.5).

Route 2: 1,2-Dibromobenzene (**4**) (0.81 mmol) and 5-amino-2-methylphenol (**5**) (0.81 mmol) were added into toluene (3 mL). Then, CuBr (0.41 mmol), DMEDA (0.2 mmol), K_2CO_3 (0.81 mmol), $Pd(dppf)Cl_2$ (0.41 mmol), and KOAc (1.22 mmol) were added to the solution. The reaction mixture was refluxed under a nitrogen atmosphere at 120°C for 3 days. After 3 days, the reaction mixture was cooled to room temperature and washed with ethyl acetate (3 × 10 mL), dried, and filtered. The combined organic layer was concentrated using rotary evaporation and the residue was purified by column chromatography (hexane-ethyl acetate, 7:2).

Compound **6**: Brown solid (Route 1: 62 mg, 90%; Route 2: 77 mg, 48%); mp 242–243°C (lit. 245°C) [22]; IR (UATR) 3375, 2923, 2857, 1606, 1493, 1268, 753 cm^{-1}; δ_H (500 MHz, $CDCl_3$) 6.97 (1H, br. s, NH), 6.92 (1H, t, J 9.2 Hz, H-aromatic), 6.87 (1H, d, J 9.2 Hz, H-aromatic), 6.71 (1H, s, H-aromatic), 6.69 (1H, s, H-aromatic), 6.67 (1H, d, J 8.0 Hz, H-aromatic), 6.60 (1H, d, J 8.0 Hz, H-aromatic), 2.10 (3H, s, CH_3); δ_C (125 MHz, $CDCl_3$) 155.7, 145.1, 132.3, 131.9, 131.1, 129.6, 128.6, 128.2, 125.9, 119.5, 116.9, 115.8, 16.2; m/z (EI) 197 (M^+, $C_{13}H_{11}NO$ requires 197).

3-Methyl-2-[(-methylbut-3-yn-2-yl)oxy]-9H-carbazole (7)

2-Hydroxy-3-methylcarbazole (**6**) (0.57 mmol) was added to anhydrous acetonitrile (4 mL) under nitrogen atmosphere and cooled at 0°C before the addition of DBU (0.74 mmol), $CuCl_2 \cdot 2H_2O$ (0.01 mmol), and 3-chloro-3-methyl-1-butyne (0.74 mmol). The reaction mixture was stirred at 0°C for 5 h. The residue was partitioned between water (10 mL) and toluene (20 mL). The organic fraction was washed with 1 N HCl (10 mL), 1 N NaOH (10 mL), 1 N $NaHCO_3$ (10 mL), and brine (10 mL). The organic layer was dried, filtered, and concentrated. The crude product was purified by column chromatography (hexane-ethyl acetate, 9:1).

Compound **7**: Brown solid (96 mg, 64%); mp 121–123°C (lit. 121–124°C) [18]; IR (UATR) 3409, 3361, 2924, 2856, 1510, 1447, 1377, 1132, 754 cm^{-1}; δ_H (500 MHz, $CDCl_3$) 7.49 (1H, d, J 8.0 Hz, H-aromatic), 7.19 (1H, br. s, NH), 7.17 (1H, s, H-aromatic), 7.15 (1H, s, H-aromatic), 7.11 (1H, t, J 8.0 Hz, H-aromatic), 6.78 (1H, t, J 8.0 Hz, H-aromatic), 6.73 (1H, d, J 8.0 Hz, H-aromatic), 3.75 (1H, s, C≡CH), 2.33 (3H, s, CH_3), 1.68 (6H, s, 2 × CH_3); δ_C (125 MHz, $CDCl_3$) 153.7, 143.8, 133.0, 131.5, 130.6, 128.3, 126.8, 119.5, 118.8, 115.6, 97.8, 91.9, 79.9, 73.0, 30.0, 20.2, 17.2; m/z (EI) 263 (M^+, $C_{18}H_{17}NO$ requires 263).

Girinimbine (8s)

3-Methyl-2-[(-methylbut-3-yn-2-yl)oxy]-9H-carbazole (**7**) (0.76 mmol) was refluxed in toluene (2 mL) for 29 h. The reaction mixture was concentrated to dryness and purified by column chromatography (hexane-ethyl acetate, 9:1).

Compound **8s**: White solid (10 mg, 50%); mp 175–176°C (lit. 175–177°C) [23]; IR (UATR) 3420, 3313, 2967, 1638, 1449, 1315, 1149, 744 cm^{-1}; δ_H (500 MHz, $CDCl_3$) 7.89 (1H, d, J 6.9 Hz, H-aromatic), 7.87 (1H, br. s, NH), 7.65 (1H, s, H-aromatic), 7.36 (1H, d, J 8.0 Hz, H-aromatic), 7.28 (1H, t, J 8.0 Hz, H-aromatic), 7.15 (1H, t, J 6.9 Hz, H-aromatic), 6.61 (1H, d, J 10.3 Hz, HC=CH), 5.68 (1H, d, J 10.3 Hz, HC=CH), 2.31 (3H, s, CH_3), 1.47 (6H, s, 2 × CH_3); δ_C (125 MHz, $CDCl_3$) 150.0, 139.7, 135.0, 129.6, 124.5, 124.1, 121.4, 119.7, 119.5, 118.8, 117.5, 117.0, 110.6, 104.7, 76.1, 27.8, 16.3; m/z (EI) 263 (M^+, $C_{18}H_{17}NO$ requires 263).

Cytotoxicity

Cell culture

The lung cancer (A549) and normal lung (MRC-5) cells were purchased from the American Type Culture Collection (ATCC, Manassas, VA, USA). The cell lines were cultured in RPMI 1640 media supplemented with 10% foetal calf serum (FCS) and 1% penicillin-streptomycin. The cells were maintained and incubated at 37°C in a 5% CO_2 atmosphere. Cell viability was determined by colorimetric assay using 3-(4,5-dimethylthiazol-2-yl)-2,5-diphenyl tetrazolium bromide (MTT) and compared with the untreated controls.

MTT assay

A stock solution of 30 mg/mL of the compounds was prepared by dissolving the stock solution with DMSO. Subsequently, different concentrations of the compound were prepared by dissolving the stock solution with a culture medium. DMSO only (0.5%, v/v) was used as a control in a complete culture medium. Cells were seeded at 5 × 10^3 cells/well in 96-well plates (100 µL/well). After 24 h of incubation, the cells were treated with different concentrations of the compounds (100, 50, 25, 12.5, 6.25, 3.125, and 1.56 µg/mL) and incubated for 72 h. MTT (5 mg/mL in PBS) was added to each well in the plate and incubated for 4 h. The supernatants were aspirated and DMSO (100 µL) was added to each well to solubilise the insoluble formazan blue crystals. The absorbance was

measured at 570 nm using a Thermo Labsystems Opsys MR microplate spectrometer. All samples were presented as mean ± standard deviation for three measurements. The percentage of cell viability was calculated using the equation (1).

The IC_{50} was obtained by plotting the cell viability (%) versus concentration (µg/mL) of each compound. The value range of the cytotoxicity is based on the U.S. National Cancer Institute (NCI) and GERAN protocol, in which IC_{50} < 21 µg/mL = highly cytotoxic, IC_{50} 21-200 µg/mL = moderately cytotoxic, IC_{50} 21-200 µg/mL = weakly cytotoxic, and IC_{50} > 500 µg/mL = no cytotoxicity [24-27].

One-way analysis of variance (ANOVA) with Tukey's honest significance test was used to assess the significance of differences, with *p*-values of less than 0.05 considered statistically significant.

$$\text{Cell viability} = \frac{\text{Average absorbances of triplicate treated cells}}{\text{Average absorbances of control cells}} \times 100\% \quad (1)$$

Results and Discussion

Synthesis of girinimbine

2-Hydroxy-3-methylcarbazole (**6**) was synthesised either *via* a two-step reaction (Figure 1, Route 1) or a one-pot reaction (Figure 1, Route 2). In Route 1, the synthesis approach involved a biaryl coupling reaction between **1** and **2** to produce an intermediate nitrobiphenyl **3**, followed by a reduction with $SnCl_2 \cdot 2H_2O$ to produce an indole **6** (90%). In Route 2, indole **6** was directly obtained (48%) from the coupling of 1,2-dibromobenzene (**4**) and 5-amino-2-methylphenol (**5**) *via* the formation of a C-N bond and a C-C bond by Pd-catalysed and Cu-catalysed reactions, respectively. The IR spectra showed a broad absorption at 3479 and 3375 cm^{-1}, indicating the OH and the overlapping of OH and NH stretching for **3** and **6,** respectively, whereas the strong absorption of conjugated N-O in **3** was displayed at 1518 cm^{-1}. The NMR spectra showed a singlet of aromatic protons for **3** and **6** at δ 7.07, 6.71, and 6.69 ppm, whereas quaternary carbons of **3** and **6** were confirmed at δ 115.5–154.3 ppm and δ 115.8–155.7 ppm.

Indole **6** was then treated with 3-chloro-3-methyl-1-butyne using $CuCl_2 \cdot 2H_2O$ as a catalyst in the presence of a base, DBU, to produce ether **7**. The absorption of C-H of alkyne was shown at 3361 cm^{-1}. According to the ^{1}H-NMR spectrum, the singlet of the alkyne proton and the methyl protons of aromatic were observed at δ 3.75 and 2.23 ppm, respectively. In addition, the broad peak of NH appeared at δ 7.19 ppm. The ^{13}C-NMR spectrum of **7** showed seven quaternary carbons in the range of δ 153.7–73.0 ppm. The alkyne carbons were assigned to the signals at δ 30.0 and 79.9 ppm, while the signal of methyl carbons was observed at δ 20.2 and 17.2 ppm.

The synthesis of girinimbine (**8s**) was then accomplished by refluxing **7** in toluene to form a pyran ring (Figure 1). Girinimbine (**8s**) was obtained as a white solid with a melting point of 175–176 °C (lit. 175–177 °C) [16]. The IR spectrum showed absorption at 3420 cm^{-1}, which indicated the presence of a secondary amine. Two absorptions of aromatic C=C could be observed at 1638 and 1449 cm^{-1}, while C-O absorption appeared at 1149 cm^{-1}. It gave a molecular ion peak at m/z 263 in the MS spectrum, thus reflecting the molecular formula of $C_{18}H_{17}NO$. According to the ^{1}H-NMR spectrum, a broad singlet of NH appeared at δ 7.87 ppm, whereas a singlet of aromatic proton was observed at δ 7.65 ppm. Two doublet signals of *cis* protons of an alkene appeared at δ 6.61 and 5.68 ppm with a coupling constant of 10.3 Hz. The ^{13}C-NMR spectrum showed the presence of eight quaternary carbons at δ 150.0, 139.7, 135.0, 124.1, 118.8, 117.0, 104.7, and 76.1 ppm. Two signals of alkene carbon could be observed at δ 117.5 and 129.6 ppm, while the other three signals of the methyl groups appeared in the upfield region, δ 27.8 ppm, and δ 16.3 ppm.

The NMR data of the synthesised girinimbine (**8s**) is in agreement with the isolated girinimbine (**8i**) and the literature (Table 1). The ^{1}H-NMR of **8s** shows a signal of NH at δ 7.87 ppm, H4 at δ 7.65 ppm, and H8 at δ 7.36 ppm, which were comparable with **8i** (NH at δ 7.84 ppm, H4 at δ 7.67 ppm, and H8 at δ 7.35 ppm), and Sukari's data (NH at δ 7.84 ppm, H4 at δ 7.66 ppm, and H8 at δ 7.36 ppm) [23]. Similar ^{13}C-NMR data were also observed, such as C-1a at δ 139.7 ppm (**8s**), δ 139.7 ppm (**8i**), and δ 139.6 ppm [23]. The signal for C-8a of **8s** was resonance at δ 135.0 ppm, which is in the range of **8i** and the reference compound at δ 139.4–135.0 ppm.

N-substituted girinimbine derivatives (**9-13**) were synthesised and characterised as previously described by our group [21]. All of the intermediates (**3**, **6** and **7**), natural and synthesised girinimbines (**8i** and **8s**), and its *N*-alkylated and *N*-acylated derivatives (**9-13**) were subjected to a cytotoxicity assay that was cultured with lung cancer (A549) and normal lung (MRC-5) cell lines.

Cytotoxicity assay of girinimbine and its derivatives

The cytotoxicity effect of natural girinimbine (**8i**) and all of the synthesised compounds (**3**, **6**, **7**, **8s**, **9-13**) (Figures 1 and 2) was evaluated using human lung cancer cell lines (A549) and normal lung cell lines (MRC-5) using the MTT method to examine their potential as therapeutic alternatives in cancer treatment. The data for MTT assay after 72 h of exposure were plotted in the graph of the percentage of viable cells versus concentration of the compounds (μg/mL) to identify their IC_{50} values (Figure 3). All compounds were found to inhibit the growth and reduce the viability of the A549 and MRC-5 cell lines in a concentration-dependent manner. In the absence of the compounds (0 μg/mL), the cells represent 100% viability. The plot demonstrates that all semi-synthesised derivatives **9-13** showed less inhibition compared to their parent compound **8i**.

All of the synthesised compounds, including naturally isolated girinimbine (**8i**), exhibited toxic activities with IC_{50} values in the range of 6.2–40.6 μg/mL against lung cancer cell lines (Table 2). Both **8i** and the intermediate nitrobiphenyl **3** with IC_{50} 17.0 and 6.2 μg/mL showed highly cytotoxic and potent compounds. Based on these experimental data, the IC_{50} values of both compounds were comparable with doxorubicin (13.1 μg/mL) and the reported **8i** (8.33 μg/mL) [5]. The presence of the nitro group in **3** seemed to increase the activity of the compound against A549 cell lines [28]. It was observed that the intermediates **3**, **6**, and **7** exhibited a slightly higher cytotoxic activity against A549 cells compared to the synthesised girinimbine (**8s**). However, all girinimbine derivatives (**9-13**) showed no significant cytotoxicity effect compared to the synthesised girinimbine (**8s**) (IC_{50} 33.0 μg/mL) against A549 cells, except *N*-acylated girinimbine **12** (IC_{50} 25.5 μg/mL). *N*-alkylated girinimbine **11** and *N*-acylated girinimbine **13** showed less potent activity towards A549 cell lines compared to other derivatives within the group due to the branched alkyl substituent. Alkyl and benzyl substituents have been proven to enhance cytotoxic activities, as seen in derivatives **9** and **10** [29, 30]. In comparison, derivative **12** showed stronger cytotoxicity than derivative **10** probably due to the presence of a carbonyl group in the structure [31, 32]. It was observed that the synthesised girinimbine (**8s**) exhibited a 5-fold higher IC_{50} value and was less toxic compared to the isolated girinimbine (**8i**) in A549 cells with the concentration of 33.0 and 6.2 μg/mL, respectively. Due to the limited amount of **8s**, the cytotoxicity of this compound was unrepeated. Factors that could be considered for the lower toxicity of **8s** were probably the presence of the trace of impurity from the synthesis work or the solvent used for purification. Besides, the systematic errors in IC_{50} measurement could mislead the effects due to uneven proliferation [33].

The normal lung cell lines (MRC-5) were used to measure the selectivity index (SI). The SI values can be used to identify whether the compounds are specifically cytotoxic to target cancer cells without displaying toxicity or very minimal toxicity towards normal cells. The range of the SI values are SI < 2 = non-selective (toxic) and SI > 2 = selective (non-toxic) [34,35]. The larger the SI values, the more toxic the compounds towards cancer cells and safer towards

normal cells. From the results, the SI values of all compounds exceeded 2, indicating that the compounds were selective towards A549 cancer cells with the SI values ranging from 2.70 to 4.68, except *N*-alkylated girinimbines **9** and **11** (Table 2). The isolated girinimbine (**8i**) and intermediate nitrobiphenyl **3** with the SI values of 4.68 and 4.56, respectively, are the most toxic compounds compared to other compounds. This indicates that their cytotoxicity activity is selective for the lung cancer cells A549 and can act as an anticancer drug without causing excessive damage to the normal cells. These compounds can be further investigated for lead therapeutic agents. However, derivatives **9** and **11** displayed no selectivity between cancer and normal cells due to the low SI values of 1.70 and 0.93, respectively.

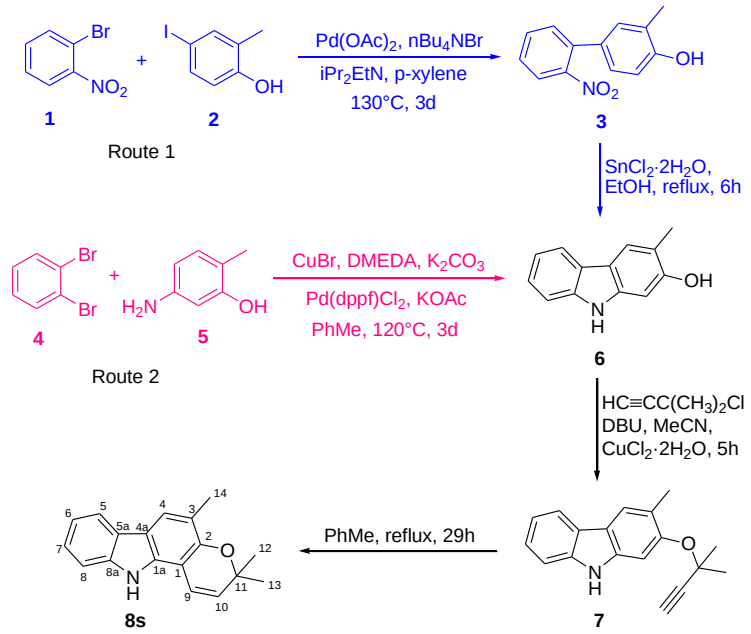


Figure 1. Synthesis of girinimbine (**8s**). Two different synthetic approaches to produce an intermediate indole **6** were applied *via* a two-step reaction (Route 1) or a one-pot reaction (Route 2)

Table 1. Comparison of ^{1}H-NMR (500 MHz) and ^{13}C-NMR (125 MHz) data for girinimbines

C/H	δ_H ($CDCl_3$, ppm, J in Hz)			δ_C ($CDCl_3$, ppm)		
	8s	**8i**[a]	**Lit.**[b]	**8s**	**8i**[a]	**Lit.**[b]
1	-	-	-	104.7	104.6	104.6
1a	-	-	-	139.7	139.7	139.6
2	-	-	-	150.0	150.0	149.8
3	-	-	-	124.1	124.1	123.9
4	7.65 (1H, s)	7.67 (1H, s)	7.66 (1H, s)	121.4	121.3	121.3
4a	-	-	-	117.0	116.9	116.9
5	7.89 (1H, d, J 6.9)	7.92 (1H, d, J 6.9)	7.92 (1H, d, J 8.3)	119.5	119.5	119.4
5a	-	-	-	118.8	118.8	118.6

Table 1 (cont'd)). Comparison of ^{1}H-NMR (500 MHz) and ^{13}C-NMR (125 MHz) data for girinimbines

C/H	δ_H ($CDCl_3$, ppm, J in Hz)			δ_C ($CDCl_3$, ppm)		
	8s	**8i**[a]	**Lit.**[b]	**8s**	**8i**[a]	**Lit.**[b]
6	7.15 (1H, t, J 6.9)	7.18 (1H, t, J 6.9)	7.19 (1H, t, J 8.8)	119.7	119.7	119.6
7	7.28 (1H, t, J 8.0)	7.31 (1H, t, J 8.0)	7.31 (1H, t, J 8.2)	124.5	124.5	124.4
8	7.36 (1H, d, J 8.0)	7.35 (1H, d, J 8.0)	7.36 (1H, d, J 8.3)	110.6	110.6	110.3
8a	-	-	-	135.0	135.0	134.9
9	6.61 (1H, d, J 10.3)	6.58 (1H, d, J 9.8)	6.60 (1H, d, J 9.2)	117.5	117.4	117.3
10	5.68 (1H, d, J 10.3)	5.67 (1H, d, J 9.8)	5.69 (1H, d, J 9.2)	129.6	129.6	129.5
11	-	-	-	76.1	76.1	75.6
12	1.47 (3H, s)	1.49 (3H, s)	1.47 (3H, s)	27.8	27.8	27.4
13	1.47 (3H, s)	1.49 (3H, s)	1.47 (3H, s)	27.8	27.8	27.4
14	2.31 (3H, s)	2.34 (3H, s)	2.33 (3H, s)	16.3	16.3	16.1
NH	7.87 (1H, br. s)	7.84 (1H, br. s)	7.84 (1H, br. s)	-	-	-

[a] Girinimbine (**8i**) was isolated from the bark of *M. koenigii* for this study

[b] Sukari et al. [23]

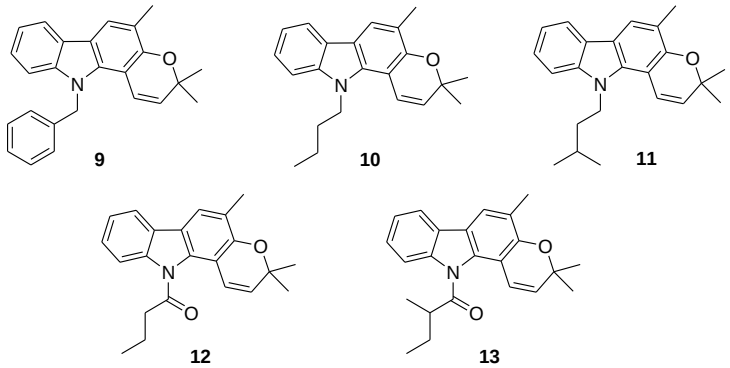
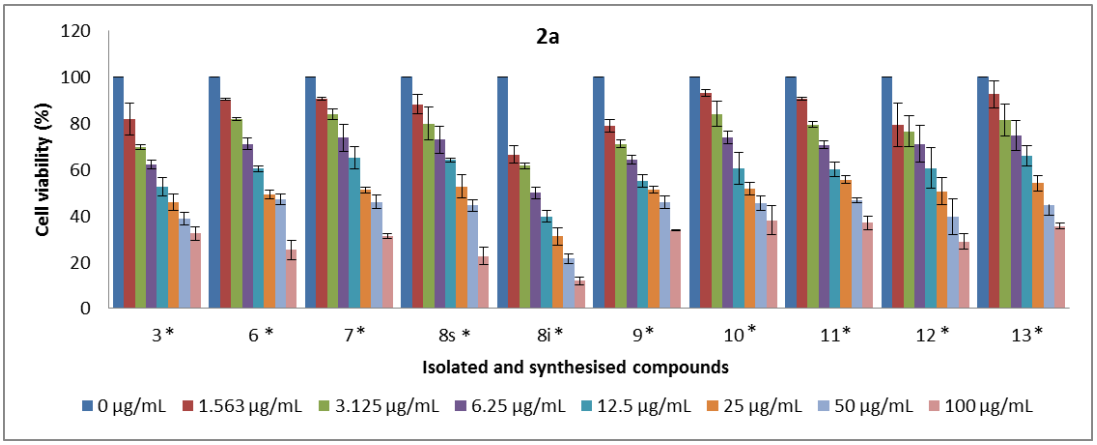


Figure 2. *N*-Alkylated and *N*-acylated girinimbines for cytotoxicity assay



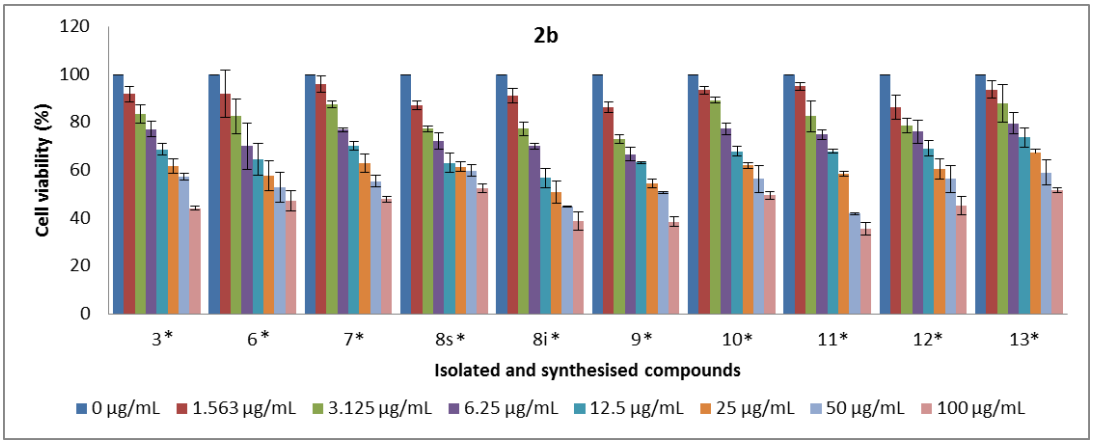


Figure 3. Cytotoxicity effect of isolated and synthesised compounds against lung cancer (A549) cell lines (2a) and normal lung (MRC-5) cell lines (2b). Results are presented as mean ± SD (n = 3). * $p < 0.05$ compared with the non-treated sample (0 µg/mL). All treated samples with isolated and synthesised compounds at all concentrations were statistically significant

Table 2. Cytotoxicity activity of the compounds against lung cancer (A549) and normal lung (MRC-5) cell lines

Compound		**IC_{50} (µg/mL)**		**Selectivity Index (SI)[b]**
		Lung Cancer (A549)	**Normal Lung (MRC-5)**	
Synthesised Intermediates	3	17.0 *	77.6	4.56
	6	24.0 *	71.0	2.96
	7	31.8 *	86.0	2.70
Girinimbines	8s	33.0 *	> 100	> 3.03
	8i[a]	6.2	29.0	4.68
N-Alkylated Girinimbines	9	31.0 *	52.7	1.70
	10	31.2 *	96.1	3.08
	11	40.6 *	37.7	0.93
N-Acylated Girinimbines	12	25.5 *	77.3	3.03
	13	35.7 *	> 100	> 2.80
Doxorubicin	-	13.1	Not Tested[c]	-

[a] Girinimbine (**8i**) was isolated from the bark of *M. koenigii* for this study

[b] SI = IC_{50} value for MRC-5/ IC_{50} value for A549. * Significant difference between structurally modified/synthesised and parent compound 8**i** ($p < 0.05$)

[c] There were several issues regarding the purchasing of doxorubicin during the COVID-19 pandemic, where the test was done without the normal cells

Conclusion

Girinimbine (**8s**) was successfully synthesised *via* two different routes and characterised. All of the synthesised intermediates (**3**, **6**, and **7**), synthesised and natural girinimbines (**8i** and **8s**), *N*-alkylated girinimbines (**9**-**11**), and *N*-acylated girinimbines (**12** and **13**) were evaluated for cytotoxicity assay against lung cancer (A549) and normal lung (MRC-5) cell lines. All of the compounds reduced the viability of A549 and MRC-5 cells in a dose-dependent manner. All compounds exhibited moderate to high toxicity against A549 cells. The intermediate nitrobiphenyl **3**

and natural girinimbine (**8i**) displayed the highest toxicity and were comparable with doxorubicin. All compounds showed selectivity against A549 cells with SI > 2, with isolated girinimbine (**8i**) and intermediate **3** as the most toxic compounds (SI values of 4.68 and 4.56, respectively). However, *N*-alkylated girinimbines **9** and **11** exhibited no selectivity towards A549 cells.

Acknowledgement

The authors sincerely thank the financial support provided by Universiti Putra Malaysia (Geran GP-IPS: 9436717). The authors also thank Dr. Mohd Azlan Nafiah and the late Dr. Kartini Ahmad for providing the isolated girinimbine for the NMR data comparison and for the semi-synthesis of girinimbine derivatives.

References

1. International Agency for Research on Cancer (2020). The global cancer observatory (Globocan 2020). Access from https://gco.iarc.fr/today/home. [Access online 15 February 2021].
2. Ministry of Health Malaysia (2017). National Strategic Plan for Cancer Control Programme 2016-2020. Access from https://www.moh.gov.my/index.php/dl/554756755a584a6961585268626938794d4445334c314a31616e567259573476546d4630615739755957786655335279595852 6c5a326c6a5831427359573566516d39766131396d6157356862454 1794e564e46554651794d4445334c6e426b5a673d3d. [Access online 23 January 2021].
3. Ministry of Health Malaysia (2018). Malaysian study on cancer survival (MyScan). Access from https://www.moh.gov.my/moh/resources/Penerbitan/Laporan/Umum/Malaysian_Study_on_Cancer_Survival_MySCan_2018.pdf. [Access online 23 January 2021].
4. Shah, A. S., Wakade, A. S. and Juvekar, A. R. (2008). Immunomodulatory activity of methanolic extract of *Murraya koenigii* (L) Spreng leaves. *Indian Journal of Experimental Biology*, 46(7): 505-509.
5. Mohan, S., Abdelwahab, S. I., Cheah, S. C., Sukari, M. A., Syam, S., Shamsuddin, N. and Rais Mustafa, M. (2013). Apoptosis effect of girinimbine isolated from *Murraya koenigii* on lung cancer cells *in vitro*. *Evidence-Based Complementary and Alternative Medicine: eCAM*, 2013: 689865.
6. Iman, V., Mohan, S., Abdelwahab, S. I., Karimian, H., Nordin, N., Fadaeinasab, M., Noordin, M. I. and Noor, S. M. (2016). Anticancer and anti-inflammatory activities of girinimbine isolated from *Murraya koenigii*. *Drug Design, Development and Therapy*, 11: 103-121.
7. Syam S., Abdul, A. B., Sukari, M. A., Mohan, S., Abdelwahab, S. I. and Wah, T. S. (2011). The growth suppressing effects of girinimbine on Hepg2 involve induction of apoptosis and cell cycle arrest. *Molecules*, 16(8): 7155-7170.
8. Mahamadhanif, S. S., Neeta, T., Rajshekhar, K., Rajesh, A. R., Mahes, B. P., Faya, A. M., Harun, M. P., Wesam, S. A., Kavita, J. and Girish, A. H. (2015). Current perspective of natural alkaloid carbazole and its derivatives as antitumor agents. *Anti-Cancer Agents in Medicinal Chemistry*, 15(8): 1049-1065.
9. Wang, S. L., Cai, B., Cui, C. B., Yan, S. Y. and Wu, C. F. (2007). Induction of apoptosis by girinimbine in K562 cell. *Chinese Traditional and Herbal Drugs*, 38(11): 1677-1681.
10. Ko, F. N., Lee, Y. S., Wu, T. S. and Teng, C. M. (1994). Inhibition of cyclooxygenase activity and increase in platelet cyclic AMP by girinimbine, isolated from *Murraya euchrestifolia*. *Biochemical Pharmacology*, 48(2): 353-360.
11. Kok, Y. Y., Mooi, L. Y., Ahmad, K., Sukari, M. A., Mat, N., Rahmani, M. and Ali, A. M. (2012). Anti-tumour promoting activity and antioxidant properties of girinimbine isolated from the stem bark of *Murraya koenigii* S. *Molecules*, 17(4): 4651-4660.
12. Sukari, M. A., Noor, H. M., Bakar, N. A., Ismail, I. S., Rahmani, M. and Abdul, A. B. (2013). Larvicidal carbazole alkaloids from *Murraya koenigii* against dengue fever mosquito *Aedes aegypti* Linnaeus. *Asian Journal of Chemistry*, 25(14): 7719-7721.
13. Joshi, B. S., Kamat, V. N. and Gawad, D. H. (1970). On the structures of girinimbine, mahanimbine, isomahanimbine, koenimbidine and murrayacine. *Tetrahedron*, 26(5): 1475-1482.

14. Bergman, J. and Carlss, R. (1978). Conversion of diindolyl methanes to 3-vinylindoles. A simple synthesis of the indole alkaloid olivacine. *Tetrahedron Letters*, 19(42): 4055-4058.
15. Knölker, H. J. and Hofmann, C. (1996). Transition-metal complexes in organic-synthesis. 33. Molybdenum-mediated total synthesis of girinimbine, murrayacine and dihydroxygirinimbine. *Tetrahedron Letters*, 37(44): 7947-7950.
16. Gruner, K. K., Hopfmann, T., Natsumoto, K., Jager, A., Katsuki, T. and Knölker, H. J. (2011). Efficient iron-mediated approach to pyrano[3,2-*a*]carbazole alkaloids - first total syntheses of *O*-methylmurrayamine A and 7-methoxymurrayacine, first asymmetric synthesis and assignment of the absolute configuration of (-)-*trans*-dihydroxygirinimbine. *Organic and Biomolecular Chemistry*, 9(7): 2057-2061.
17. Knölker, H. J. (2009). Synthesis of biologically active carbazole alkaloids using selective transition-metal-catalyzed coupling reactions. *Chemistry Letters*, 38(1): 8-13.
18. Hesse, R., Gruner, K. K., Kataeva, O., Schmidt, A. W. and Knölker, H. J. (2013). Efficient construction of pyrano[3,2-*a*]carbazoles: application to a biomimetic total synthesis of cyclized monoterpenoid pyrano[3,2-*a*]carbazole alkaloids. *Chemistry (Weinheim an der Bergstrasse, Germany)*, 19(42): 14098-14111.
19. Dai, J., Ma, D., Fu, C. and Ma, S. (2015). Gram scale total synthesis of 2-hydroxy-3-methylcarbazole, pyrano[3,2-a]carbazole and prenylcarbazole alkaloids. *European Journal of Organic Chemistry*, 2015 (25): 5655-5662.
20. Mandal, T., Chakraborti, G., Karmakar, S. and Dash, J. (2018). Divergent and orthogonal approach to carbazoles and pyridoindoles from oxindoles *via* indole intermediates. *Organic Letters*, 20(16): 4759-4763.
21. Nor, S. M. M., Osman, F. N. A., Ahmad, K. and Nafiah, M. A. (2017). *Synthesis of N-alkylated and N-acylated derivatives of girinimbine. Asian Journal of Chemistry*, 29 (4): 801-804.
22. Bhattacharyya, P., Jash, S. S. and Chowdhury, B. K. (1986). A biogenetically important carbazole alkaloid from *Murraya koenigii* Spreng. *Chemistry and Industry*, 7: 246.
23. Abu Bakar, N. H., Sukari, M. A., Rahmani, M., Md. Sharif, A., Khalid, K. and Yusuf, U. K. (2007). Chemical constituents from stem barks and roots of *Murraya koenigii* (Rutaceae). *Malaysian Journal of Analytical Sciences,* 11(1): 173-176.
24. Nguyen, N. H., Ta, Q. T. H., Pham, Q. T., Luong, T. N. H., Phung, V. T., Duong, T. H. and Vo, V. G. (2020). Anticancer activity of novel plant extracts and compounds from *Adenosma bracteosum* (Bonati) in human lung and liver cancer cells. *Molecules, 25 (12):* 2912-2928.
25. Kuete, V., Ango, P. Y., Yeboah, S. O., Mbaveng, A. T., Mapitse, R., Kapche, G. D., Ngadjui, B. T. and Efferth, T. (2014). Cytotoxicity of four Aframomum species (*A. arundinaceum*, *A. alboviolaceum*, *A. kayserianum* and *A. polyanthum*) towards multi-factorial drug resistant cancer cell lines. *BMC Complementary and Alternative Medicine*, 14: 340.
26. Goldin, A., Venditti, J. M., Macdonald, J. S., Muggia, F. M., Henney, J. E. and Devita Jr, V. T. (1981). Current results of the screening program at the Division of Cancer Treatment, National Cancer Institute. *European Journal of Cancer*, 17 (2): 129-142.
27. Geran, R. I., Greenberg, N. H., Macdonald, M. M., Shumacher, A. M. and Abbott, B. J. (1972). Protocols for screening chemical agents and natural products against animal tumors and other biological systems. *Cancer Chemotherapy Reports, Part III*, 3: 1-103.
28. Nepali, K., Lee, H. Y. and Liou, J. P. (2019). Nitro-group-containing drugs. *Journal Medicine Chemistry*, 62: 2851-2893.
29. Bashir, M., Bano, A., Ijaz, A. S. and Chaudhary, B. A. (2015). Recent developments and biological activities of N-substituted carbazole derivatives: a review. *Molecules*, 20 (8): 13496-13517.

30. Liu, K., Zang, Y., Shen, C., Li, C., Ma, J., Yang, J., Sun, X., Chen, X., Wang, N. and Zhang, D. (2021). Synthesis and biological evaluation of pyranocarbazole derivatives as anti-tumor agents. *Bioorganic and Medicinal Chemistry Letters*, 33: 127739.
31. Kolli, S. K., Prasad, B., Babu, P. V., Ashfaq, M. A., Ehtesham, N. Z., Raju, R. R. and Pal, M. (2014). TFAA/H_3PO_4 mediated unprecedented *N*-acylation of carbazoles leading to small molecules possessing anti-proliferative activities against cancer cells. *Organic and Bimolecular Chemistry*, 12 (32): 6080-6084.
32. Kaushik, K., Kumar, N. and Pathak, D. (2012). Synthesis of some newer carbazole derivatives and evaluation for their pharmacological activity. *Der Pharmacia Sinica*, 3(4): 470-478.
33. He, Y., Zhu, Q., Chen, M., Huang, Q., Wang, W., Li, Q., Huang, Y. and Di, W. (2016). The changing 50% inhibitory concentration (IC_{50}) of cisplatin: a pilot study on the artifacts of the MTT assay and the precise measurement of density-dependent chemoresistance in ovarian cancer. *Oncotarget*, 7(43): 70803-70821.
34. Badisa, R. B., Darling-reed, S. F., Joseph, P., Cooperwood, J. S., Latinwo, L. M. and Goodman, C. B. (2009). Selective cytotoxic activities of two novel synthetic drugs on human breast carcinoma MCF-7 Cells. *Anticancer Research*, 29(8): 2993-2996.
35. Chipoline, I. C., da Fonseca, A.C.C., da Costa, G. R. M., de Souza, M. P., Rabelo, V. W. H., de Queiroz, L. N., de Souza, T. L. F., de Almeida, E. C. P., Abreu, P. A., Pontes, B., Ferreira, V. F., de Carvalho da Silva, F. and Robbs, B. K. (2020). Molecular mechanism of action of new 1,4-naphthoquinones tethered to 1,2,3-1H-triazoles with cytotoxic and selective effect against oral squamous cell carcinoma. *Bioorganic Chemistry*, 101: 103984.

Malaysian Journal of Analytical Sciences (MJAS)
Published by Malaysian Analytical Sciences Society

IDENTIFICATION AND QUANTIFICATION OF LYCOPENE AND β-CAROTENE IN WATERMELON JUICE USING HIGH-PERFORMANCE LIQUID CHROMATOGRAPHY

(Pengenalan dan Pengkuantitian Likopena dan B-Karotena di dalam Jus Tembikai Menggunakan Kromatografi Cecair Berprestasi Tinggi)

Nur Shafinaz Mohamad Salin[1], Fatimah Salim[2,3], Hairil Rashmizal Abdul Razak[4], Wan Mazlina Md Saad[1*]

[1]Centre of Medical Laboratory Technology, Faculty of Health Sciences
[2]Atta-ur-Rahman Institute for Natural Product Discovery (AuRIns)
Universiti Teknologi MARA Selangor Branch, Puncak Alam Campus, 42300 Puncak Alam, Selangor, Malaysia.
[3]Centre of Foundation Studies,
Universiti Teknologi MARA Selangor Branch, Dengkil Campus, 43800 Dengkil, Selangor, Malaysia.
[4]Department of Radiology, Faculty of Medicine and Health Sciences,
Universiti Putra Malaysia, 43400 UPM Serdang, Selangor, Malaysia.

**Corresponding author: wanmaz755@uitm.edu.my*

Received: 18 October 2021; Accepted: 21 November 2021; Published: 27 December 2021

Watermelon (*Citrullus lanatus*) is a nutritional fruit with appealing flesh colour. The flesh colour is reflected by the presence of carotenoid compounds, lycopene and β-carotene. Lycopene is responsible for the deep red fruit colour while β-carotene provides the orange-yellow pigment. In addition, these carotenoid components can scavenge free radicals and protect one from harmful diseases. In this study, isocratic mode high-performance liquid chromatography (HPLC) was performed to separate and quantify lycopene and β-carotene in watermelon juice. Twenty microliter sample injection was passed through C-18 column maintained at 45 °C coupled with diode array detector (DAD) at 470 nm. Mobile phase of acetonitrile and water (95:5, v/v) were at the flow rate of 1 mL/min. Excellent chromatographic separation of lycopene and β-carotene were achieved at elution time of 4.568 and 6.831 min, respectively. The amount of quantified lycopene (1662 µg/mL) and β-carotene (180 µg/mL) indicated that lycopene is the major carotenoid present in watermelon juice. This study described the ability of isocratic mode HPLC to separate and quantify carotenoid in watermelon juice. The analytical method had been validated, with the results showing precision, accuracy, and linearity.

Keywords: watermelon, carotenoid, lycopene, β-carotene, high-performance liquid chromatography

Abstrak

Tembikai (*Citrullus lanatus*) ialah buah bernutrisi yang mempunyai warna isi yang menarik. Warna isi buah tembikai ini dicerminkan oleh kandungan sebatian karotenoid; likopena dan β-karotena. Sebatian karotenoid ini bertanggungjawab sebagai pigment warna pada buah. Tambahan pula, komponen karotenoid ini dapat menghalang serangan radikal bebas serta melindung kita daripada pelbagai jenis penyakit berbahaya. Dalam kajian ini, kaedah isokratik kromatografi cecair berprestasi tinggi (KCPT) dilakukan untuk memisahkan dan mengkuantitikan kandungan likopena dan β-karotena di dalam jus tembikai. Muatan

sampel 20 µL dilalukan kedalam turus C-18 pada suhu dikekalkan 45 °C ditambah dengan pengesan susan diod (PSD) pada 470 nm. Gabungan pelarut asetonitril dan air (95:5, v/v) dengan kadar aliran 1 mL/min telah digunakan. Pemisahan kromatografi likopena dan β-karotena yang sangat baik telah dicapai pada masa elusi 4.568 dan 6.831 minit. Jumlah pengkuantitian likopena ialah 1662 µg/mL dan β-karotena 180 µg/mL, menunjukkan bahawa likopena ialah karotenoid utama diikuti dengan β-karotena di dalam jus tembikai. Dapatan kajian ini menerangkan kemampuan KCPT mod isokratik untuk mengenalpasti dan mengkuantitikan profil karotenoid di dalam jus tembikai. Kaedah analitikal yang digunakan bagi kajian ini telah divalidasi dan dapatan kajian menunjukkan kejituan, ketepatan dan kelinearan.

Kata kunci: tembikai, karotenoid, likopene, β-karoten, kromatografi cecair berprestasi tinggi

Introduction

Consumers are increasingly showing greater interest in the consumption of fruits that positively impact health and well-being. Besides the physical appearance of colour, taste and aroma, the presence of bioactive compounds including carotenoids, flavonoids, phenolics and vitamins are also prominent in fruits. Watermelon, scientifically known as *Citrullus lanatus,* belongs to the Cucurbitaceae family [1] and is non-seasonal fruit that has been cultivated abundantly in Malaysia and other tropical regions [2]. Watermelon constitutes 93% water, hence the name 'water'. 'Melon' refers to the fruit's morphological characteristics that are round or oval, sweet and pulpy fleshed [2]. Watermelon is also referred to as 'pepo' by botanists, referring to its thick rind and fleshy centre [3]. The fruit is categorised as having three different parts that include flesh (68%), peel (30%), and seed (2%). Watermelon flesh mainly comprises water content [4] and is reported to be a rich source of bioactive compounds such as lycopene, β-carotene, L-citrulline and vitamins (A and C) [5].

Watermelons come in a variation of flesh colours of red, yellow, orange or white, and are either seeded or seedless [6]. The flesh colour is an essential trait of watermelon fruit [7] and the appealing flesh colour reflects the total carotenoid compound present. Carotenoid belongs to the tetraterpenes family and are sources of red, orange and yellow colour pigmentations in fruits [8]. Red watermelon was reported to have major lycopene content followed by secondary carotenoid compound that include β-carotene [5]. Lycopene and β-carotene are responsible for the deep red and orange-yellow pigments respectively [9]. More importantly, watermelon has been reported to have a large lycopene content compared to other fruits [4]. Moreover, study by Zhang et al. further reported that watermelon contains high amount of lycopene with 50 mg/100g compared to tomato with only 30 mg/100g [10]. Furthermore, lycopene and β-carotene have been well studied as antioxidants that able to quell free radicals and oxidative damage [9,11]. In addition, the daily consumption of lycopene and β-carotene have been found to significantly promote beneficial health effects [4]. The lycopene content in fruits can reduce oxidative damage resulting in chronic diseases [12], inhibit tumor development in liver, lung, prostate, breast and colon [9] and prevent the pathogenesis of Alzheimer's disease [4]. Moreover, the secondary carotenoid, β-carotene, exhibits antioxidant, anticancer and anti-inflammation properties that are beneficial to health. It has also been proven to be a pro Vitamin A precursor and promotes eye health [11,13]. Considering the nutritional and sensorial functions of lycopene and β-carotene in watermelon, researchers concerned with the development of functional food have now focused on watermelon as a valuable source of carotenoid and its positive health effects.

Various methods have been performed to identify and quantify carotenoid compounds in fruit. The main methods used are colorimetric and chromatographic analysis such as high-performance liquid chromatography (HPLC), liquid chromatography mass spectrometer (LCMS), spectrophotometry, supercritical fluid chromatography and comprehensive two-dimensional liquid chromatography [14]. However, HPLC is the preferred method to quantify carotenoid due to its sensitivity and specificity with ideal column and detector, efficiency in saving time and minimal sample usage [14,15]. Table 1 tabulated the

analytical chromatographic method for lycopene and β-carotene quantification using HPLC. Studies had reported the used of C-30 carotenoid YMC column coupled with photo-diode array (PDA) [16] and C-18 column paired with UV-visible detector (UV-vis) able to separate carotenoid in fruit [17]. On the other hand, a study by Petyaev et al. reported the use of C-18 column coupled with photo diode array detector (PAD) in quantification of carotenoid using HPLC [18]. However, a previous chromatographic analysis was in gradient mode [16], with more than two mobile phase [16,17,18] and the results showed that carotenoid was determined at 12-15 minutes [4,16,17]. Hence, the development of fast and minimal usage of mobile phase are desirable. In this study, high-performance liquid chromatography (HPLC) was chosen along with C-18 column and diode array detector (DAD) with isocratic mobile phase of acetonitrile: water (95:5, v/v) to identify and quantify lycopene and β-carotene in watermelon (*Citrullus lanatus*) juice.

Materials and Methods

Chemicals and reagents

Analytical grade of lycopene (≥98%) and β-carotene (≥95%) were purchased from Sigma Aldrich (St. Louis, MO, USA). HPLC grade of n-hexane, tetrahydrofuran, methanol (MeOH) and acetonitrile (MeCN) were purchased from Merck (Germany).

Instruments

High-performance liquid chromatography (HPLC) was performed using Agilent 1200 (Agilent Technology, 1200 Series) equipped with auto-sampler injector (G1328B), column oven, quat pump (G1311A), degasser (G1311A) and diode array detector (DAD) for separation of lycopene and β-carotene. The column used was ZORBAX (Agilent) 300 SB-C18 column, 5 µm (4.6 x 150 mm).

Watermelon juice preparation

Six watermelons (*Citrullus lanatus)* ranging from 2.2 to 3.2 kg were obtained from a local farm located in Subang, Selangor, Malaysia. The sample species were identified by Forest Research Institute Malaysia (FRIM) with reference no: FRIM700-1/1/1Kit.3(87). The watermelons were washed and wiped with paper towels. Watermelons were then peeled, weighed and cut before homogenized into juice. The obtained watermelon juice with volume of 100 mL were then extracted with 100 mL of n-hexane for 24 hours on a reciprocating shaker (180 rpm). After 24 hours, the watermelon juice was aliquot into 50 mL of capped falcon tube and later centrifuged at 3000 rpm for 10 minutes. The centrifugation resulted in three separated layers of watermelon juice consisting yellowish-orange hexane supernatant (upper), turbid and white colour (middle) and red watermelon flesh residue (bottom). The obtained yellowish supernatant containing lycopene and β-carotene were later separated and evaporated to dryness using rotary evaporator to obtain the watermelon extract. The n-hexane separated layer was later removed. Meanwhile, the residue of the middle and bottom juice layers was twice subjected to the extraction step with n-hexane to completely extract the carotenoid compounds. The watermelon juice extract was then stored in -80 °C prior analysis. All procedures were performed in the dark with minimal light and air exposure to reduce degradation of targeted carotenoids.

Standards preparation

One milligram of each lycopene and β-carotene standard were dissolved in tetrahydrofuran (0.5 mL) and methanol (0.5 mL) to obtain stock solution of 1000 µg/mL and later filtered through 0.45-µm polyvinylidene fluoride (PVDF) syringe filter into 2 mL of amber HPLC vial. A series of working solutions for each standard were prepared by diluting the stock solution two-folds in ranges 31.25-1000 µg/mL.

Sample preparation procedure

Approximately 500 µg/mL of extract sample was prepared by dissolving 0.5 mg of watermelon juice extract in 1 mL of tetrahydrofuran and methanol (1:1). The extract solution then was filtered through 0.45-µm PVDF syringe filter into 2 mL of amber HPLC vial to reduce light exposure.

Isocratic mode of high-performance liquid chromatography-diode array detector

Identification and quantification of lycopene and β-carotene were performed referring to Noh et al. with

slight modifications [4]. The separation was conducted by injecting 20 µL of each standard and sample into ZORBAX SB-C18 column, 5 µm (4.6 x 150 mm), at 45 °C using isocratic mode of HPLC mobile phase MeCN and water (95:5, v/v) with flow rate of 1 mL/min. The separation and detection of lycopene and β-carotene in standard and sample were carried out triplicate into C-18 column coupled with diode array detector at wavelength 470 nm.

Method validation

The validation method for identification of carotenoid using isocratic mode HPLC was achieved by determining the linearity, limit of detection (LOD), limit of quantification (LOQ), accuracy and recovery according to the International Conference of Harmonization [19]. The linearity was determined by injecting 20 µL of five different concentrations of each standard at ranging 31.25-1000 µg/mL into HPLC column. A linear regression analysis was constructed by plotting a graph peak area against standard concentrations. The regression equation was then calculated in the form of y = a+bx, where x is the concentration while y is the peak area of the targeted compound. Linearity was assessed by the expression of regression coefficient (R^2) value.

LOD is the lowest amount of compound that could be detected while LOQ is the lowest quantified amount of interest analyte. The LOD and LOQ were expressed as 3 Sa/b and 10 Sa/b, where Sa is the standard deviation of response and b is the slope of calibration curve [1,2]. Triplicate spike concentration of lycopene and β-carotene at 300, 150 and 100 µg/mL were injected to test sample, and the recovery was calculated with the value of detected versus added amounts. Precision of method used was caried out by determining the percentage relative standard deviation (%RSD) and recovery (%R) of peak area for inter-day and intra-day analysis. The analysis for inter-day and intra-day were performed at three different concentrations of each standard (500, 300, 150 µg/mL), as referred by Rasdin et al. [1].

Table 1. Chromatographic analytical method in quantification of carotenoid using HPLC

Column	Detector	Mode	Mobile Phase	References
C-18	Diode array	Isocratic	100% acetonitrile	[4]
C30 YMC	UV-Vis	Isocratic	Methanol: isopropyl alcohol: tetrahydrofuran (30:30:35, v/v/v) containing 250 ppm butylated hydroxytoluene and 0.5% tryethylamine	[14]
C30 YMC Carotenoid S-5	Photo-diode array	Gradient	Acetonitrile-methanol and methyl tert-butyl ethanol	[16]
C-18	UV-Vis	Isocratic	Methanol: tetrahydrofuran: water (60:33:7, v/v)	[17]
Aquity HSS T3	Photo diode array	Isocratic	Acetonitrile:0.08% phosphoric acid solution : tert-butyl methyl ether (70:5:25, v/v/v)	[18]

Results and Discussion

Identification and quantification of lycopene and β-carotene in watermelon juice extract

This study demonstrated the identification and quantification of lycopene and β-carotene in watermelon juice using isocratic mode in which HPLC was paired with C-18 column and diode array detector (DAD). Figure 1 shows the chromatogram of standard lycopene (A), β-carotene (B) and watermelon juice (C). The chromatogram's peak of watermelon juice was determined by comparing the retention time of standard lycopene and β-carotene. To produce an optimum separation of lycopene and β-carotene in the standard and sample, the chromatographic method from Noh et al. was adapted with slight modifications [4]. Triplicate injection (20 µL) of each standard and sample were injected through short C-18 column at 45 °C coupled with diode array detector at 470 nm that showed the best separation and detection of targeted lycopene and β-carotene with noise eliminated. Column type and temperature used strongly influenced the separation of interest analyte.

In previous studies, C-18 column was used with various temperature tested for separation of lycopene and β-carotene using HPLC [16, 23]. This study found that ZORBAX SB-C18 column, 5 µm (4.6 x 150 mm) was able to operate and separate efficiently at temperature 45 °C. Hence, the column temperature was set at 45 °C. In addition, lycopene and β-carotene are tetraterpenes comprising eight isoprene units that form a conjugated double bond solely composed of carbon and hydrogen. The double bond structure acts as chromophore that allows the absorption of light ranges 420 - 520 nm [4]. Hence, the detection wavelength of 470 nm was chosen as the lycopene and β-carotene appears to absorb the most at this wavelength with no other peak eluted in the chromatogram [4, 20].

An isocratic mode of mobile phase MeCN: water (95:5, v/v) with flow rate of 1 mL/min showed the optimum ratio composition for producing high selectivity and resolution peak of targeted lycopene and β-carotene using HPLC. This agrees with the study performed by Noh et al. using isocratic mode HPLC with 100% acetonitrile as a mobile phase in chromatographic analysis [4]. Carotenoid is a non-polar compound. Thus, reversed-phase HPLC is preferable to identify lycopene and β-carotene in samples. Acetonitrile with high polarity property has been reported to be able to detect carotenoid in fruits, and have been employed by other researchers [4, 20]. However, the addition of 5% water into HPLC mobile phase could elute lycopene faster compared to previous study [4]. Hence, this study has shown that the mobile phase of acetonitrile and water with ratio 95:5 is able to identify lycopene and β-carotene selectively.

Figure 1 above presents a good separation of lycopene and β-carotene in standard and sample of watermelon juice extract. The elution peak sequence of lycopene (4.568 min) and β-carotene (6.831 min) were in line with the study carried out by Jin et al. [21]. In the watermelon juice extract, lycopene was detected at retention time of 4.549 min while β-carotene was eluted at 6.790 min, respectively. Studies have reported that lycopene is more polar than β-carotene [22]. Thus, lycopene peak was eluted first followed by β-carotene due to its different polarity properties. This study showed that lycopene and β-carotene could be separated and identified using isocratic mode HPLC coupled with selective column, detector and mobile phase chosen.

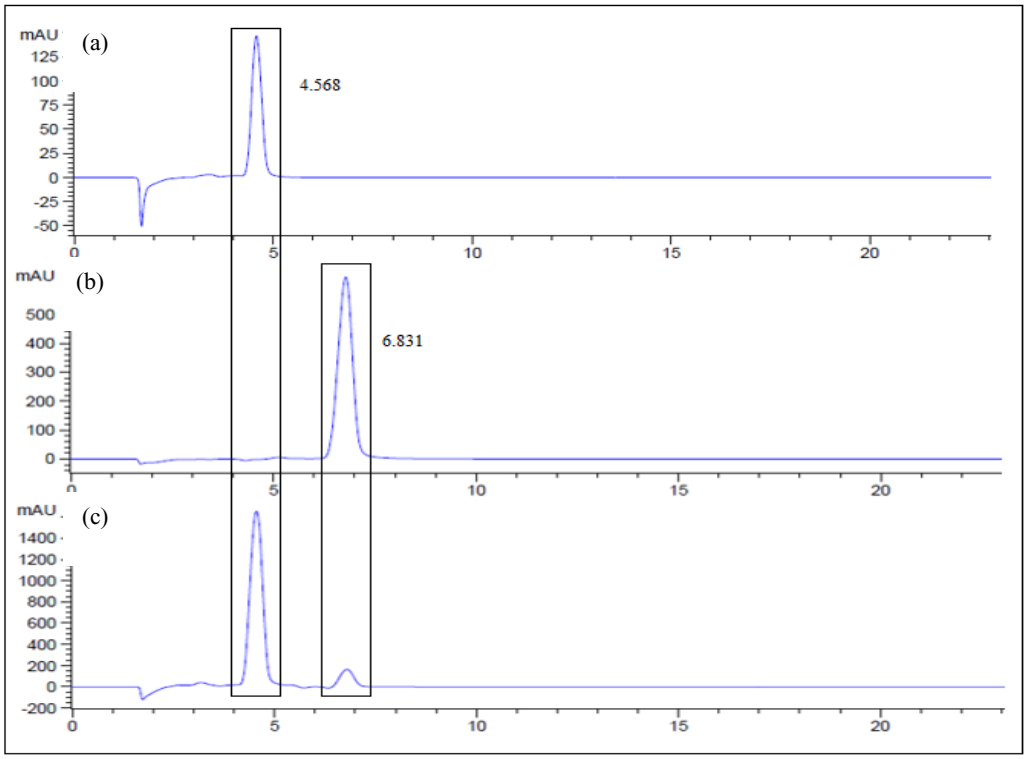


Figure 1. The chromatogram of standards and sample (a) Standard of lycopene at 4.568 minutes, (b) Standard of β-carotene at 6.831 minutes and (c) Watermelon juice of lycopene and β-carotene at retention time of 4.549 and 6.790 minutes

Method validation

In this study, optimized chromatographic analysis was validated using linearity, limit of detection (LOD), limit of quantification (LOQ), precision and accuracy as referred to International Conference of Harmonization [19]. Table 2. shows the validation method for regression equation, LOD and LOQ of lycopene and β-carotene. The regression equation for lycopene and β-carotene were y= 1.2029 x-6.5599 and y= 5.8788 x-437.57 respectively. Correlation coefficient (R^2) for both lycopene and β-carotene were at 0.9972 and 0.995, respectively (Table 2). The R^2 value was compared to previous studies that demonstrated the R^2 of carotenoid ranges of 0.9931-0.9993 [4,17]. Moreover, a study by Zhang et al. (2016) further supported the R^2 value ≥0.995 which indicated that the presented data was linear and reproducible [23]. LOD is the lowest amount of interest analyte detected while LOQ is the lowest amount of targeted compound quantified in the sample [1]. The presented LOD and LOQ values for both lycopene and β-carotene were in the ranges of 0.302 - 10.09 µg/mL (Table 2). The LOD and LOQ values were compared to Noh et al (2020) which showed that the present study was accurate and sensitive for the detection of carotenoid in watermelon juice extract [4].

In Table 3, the recovery data for spike and measured carotenoid were tabulated. The data was obtained by spiking triplicate 300, 150 and 100 µg/mL standard of lycopene and β-carotene into the test sample. The recovery for spike and measured concentration were found to be in the ranges of 99.47-109.49 %, respectively, well within the range reported in previous study [24]. The expression of regression standard deviation (%RSD) between the mean of analysed compound for inter-day and intra-day analysis were tabulated in Table 4. Triplicate injection of 500, 300

and 150 µg/mL of each standard were analysed for its validity. The RSD values for intra-day and inter-day analysis were ranges of 1.4-8.1% while the percentage recovery was found to be in the ranges of 92-113% respectively (Table 4). This result of this study is in line with Gebregziabher et al. that demonstrated the recovery for lycopene and β-carotene as more than 83.12% [24]. Besides, the RSD values were below than 10% as supported by Zhang et al. [23]. This indicated that the proposed method could be used for simultaneous determination of lycopene and β-carotene in watermelon juice [7]. Hence, the validation results of linearity, LOD, LOQ, accuracy and precision values showed that the isocratic mode of HPLC used in this study was sensitive and precise in the separation and detection of lycopene and β-carotene in watermelon juice extract.

Table 2. The validation method for lycopene and β-carotene

Standard	Regression Equation	Correlation Coefficient (R^2)	Linear Range (µg/mL)	Limit of Detection (LOD) (µg/mL)	Limit of Quantification (LOQ) (µg/mL)
Lycopene	y = 1.2029 x - 6.5599	0.9972	31.25-1000	3.33	10.09
β-carotene	y = 5.8788 x - 437.57	0.9955	31.25-1000	0.995	0.302

Table 3. Recovery data for spike and measured lycopene and β-carotene in watermelon juice

Compound	Spike Concentration (µg/mL)	Measured Concentration (µg/mL)	Recovery (%)
Lycopene	300	301.05	100.18
	150	164.24	109.49
	100	102.31	102.31
β-carotene	300	296.81	99.47
	150	149.72	99.81
	100	102.54	102.54

Table 4. Intra-day and inter-day data for lycopene and β-carotene standard

Compound	Concentration (µg/mL)	Intra-day n=3 (%)			Inter-day n=3 (%)		
		Mean	RSD	Recovery	Mean	RSD	Recovery
Lycopene	500	495.23	7.7	99	520.64	6.1	104
	300	300.59	1.4	100	286.14	5.0	95
	150	143.07	6.2	95	160.72	4.3	107
β-carotene	500	468.58	2.2	93	461.69	8.1	92
	300	280.94	4.4	94	285.00	7.4	95
	150	160.500	6.0	106	169.50	5.2	113

Quantification of lycopene and β-carotene

The consumption of watermelon juice naturally enriched with carotenoid compounds such as lycopene and β-carotene could eliminate free radicals and benefit health. Thus, an efficient and simple isocratic mode of HPLC is essential in the quantification of carotenoid compounds in fruits. The concentration of lycopene and β-carotene in watermelon juice were quantified using the regression equation obtained from calibration curve. The quantification of lycopene and β-carotene in watermelon juice were tabulated in Table 5. The quantification showed that lycopene is the major carotenoid compound with 1662 µg/mL followed by β-carotene with 180 µg/mL. This study agrees with the study by Tamburini et al. which concurred that watermelon juice has the highest lycopene concentration of 2.65–151.75 mg/kg while β-carotene is only 0.19–9.39 mg/kg [5]. It is documented that watermelon contributes the highest lycopene concentration, 40% of total carotenoid present in fruits [25]. It is also supported by Zhao et al. that watermelon provides approximately 84-97% lycopene, while β-carotene, only 2-11% [26]. Hence, increased lycopene concentration indicated increased the red intensity in fruits. This study concurs that the high content of lycopene gives an appealing and attractive red intensity in watermelon flesh.

Besides colour pigmentation, increased lycopene concentration had been reported to promote antioxidant activities. Lycopene is the strongest antioxidant among carotenoids [12, 27]. This antioxidant property is capable of quenching free radicals and preventing the development of reactive oxygen species (ROS) that may adversely affect health conditions [27]. Besides, lycopene has also been reported as anti-inflammation, anti-aggregative, anti-hypertensive, anti-atherosclerotic, and acts as a cardioprotective agent [28]. Ghadage et al. demonstrated that the consumption of diet enriched with lycopene was associated with decreased risk of chronic diseases including cardiovascular disease and cancer [29]. Thakur also supported that lycopene acted as inhibitor for tumour development in liver, lung, prostate and colon [9]. Hence, the present quantitative result confirmed that lycopene and β-carotene could be quantified in watermelon juice extract using isocratic mode HPLC. Thus, the study suggests that the consumption of watermelon juice enriched with lycopene is essential in prevention of health diseases.

Table 5. Concentration of lycopene and β-carotene in watermelon juice extract

Compound	Concentration in watermelon juice extract (µg/mL)
Lycopene	1662
β-carotene	180

Conclusion

The HPLC analysis successfully identified and quantified respective carotenoids; lycopene and β-carotene in watermelon juice. The study results showed that this method is sensitive and reproducible with linearity (≥0.995), low LOD and LOQ values in ranges of 0.30-10.09 µg/mL with recovery 99.47-109.49 % as well as RSD less than 10%. The study presented that watermelon juice contains high amount of lycopene (1662 µg/mL) compared to β-carotene (180 µg/mL) which lends a high red intensity in flesh colour. This study also serves as a base reference for future research to quantify carotenoid compound using simple chromatographic analysis. However, further study is needed to complete carotenoid profiling and quantification in watermelon juice using isocratic mode

HPLC. It is also necessary to explore the roles of these carotenoid properties in watermelon as a nutritional fruit in maintaining a healthy lifestyle.

Acknowledgement

The authors would like to acknowledge (1) Ministry of Higher Education, Malaysia, through Research Management Centre, Universiti Teknologi MARA (UiTM) for funding the study (RMC grant no. 600-RMC/GPK 5/3 (074/2020)); (2) Centre of Postgraduate Study, Faculty of Health Sciences, Universiti Teknologi MARA (UiTM), Puncak Alam Campus, and Analytical Unit Laboratory, Faculty of Pharmacy, Universiti Teknologi MARA (UiTM), Puncak Alam Campus for providing the research facilities and work place throughout this study; (3) Local farm in Subang, Selangor, Malaysia for providing watermelon samples.

References

1. Ridwan, R., Abdul Razak, H. R., Adenan, M. I. and Md Saad, W. M. (2018). Development of isocratic RP-HPLC method for separation and quantification of L-citrulline and L-arginine in watermelons. *International Journal of Analytical Chemistry*, 2018: 4798530.
2. Saad, W. M. M., Salin, N. S. M., Ramzi, A. S. and Salim, F. (2020). Identification and quantification of fructose, glucose and sucrose in watermelon peel juice. *Malaysian Journal of Analytical Sciences*, 24(3): 382-389.
3. Maoto, M. M., Beswa, D. and Jideani, A. I. (2019). Watermelon as a potential fruit snack. *International Journal of Food Properties*, 22(1): 355-370.
4. Noh, J. J., Hur, O. S., Ro, N. Y., Lee, J. E., Hwang, A. J., Kim, B. S., Rhe, J. S., Yi, J. Y., Kim, J. H., Lee, H. S., Sung, J. S., Kim, M. K. and Assefa, A. D. (2020). Lycopene content and fruit morphology of red, pink, orange, and yellow fleshed watermelon (*Citrullus lanatus*) germplasm collections. *Korean Journal of Plant Resources*, 33(6): 624-637.
5. Tamburini, E., Costa, S., Rugiero, I., Pedrini, P. and Marchetti, M. G. (2017). Quantification of lycopene, β-carotene, and total soluble solids in intact red-flesh watermelon (*Citrullus lanatus*) using on-line near-infrared spectroscopy. *Sensors*, 17(4): 746.
6. Kyriacou, M. C., Leskovar, D. I., Colla, G. and Rouphael, Y. (2018). Watermelon and melon fruit quality: The genotypic and agro-environmental factors implicated. *Scientia Horticulturae*, 234: 393-408.
7. Zhang, L., Wang, S., Yang, R., Mao, J., Jiang, J., Wang, X., Zhang, W., Zhang, Q. and Li, P. (2019). Simultaneous determination of tocopherols, carotenoids and phytosterols in edible vegetable oil by ultrasound-assisted saponification, LLE and LC-MS/MS. *Food Chemistry*, 289: 313-319.
8. Prakash, D. and Gupta, C. (2014). 12 Carotenoids: chemistry and health benefits. Phytochemicals of Nutraceutical Importance, CABI International Publishers, Wallingford (2014), pp. 181-195.
9. Thakur, N. (2016). Lycopene quantification of tomato by SPE and HPLC. *Bulgarian Journal of Agricultural Science*, 22(1): 84-90.
10. Zhang, J., Sun, H., Guo, S., Ren, Y., Li, M., Wang, J., Zhang, H., Gong, G. and Xu, Y. (2020). Decreased protein abundance of lycopene β-cyclase contributes to red flesh in domesticated watermelon. *Plant Physiology*, 183(3): 1171-1183.
11. Bogacz-Radomska, L. and Harasym, J. (2018). β-Carotene-properties and production methods. *Food Quality and Safety*, 2(2): 69-74.
12. Karahan, F., Dede, S. and Ceylan, E. (2018). The effect of lycopene treatment on oxidative DNA damage of experimental diabetic rats. *The Open Clinical Biochemistry Journal*, 8(1):1-6.
13. Milani, A., Basirnejad, M., Shahbazi, S. and Bolhassani, A. (2017). Carotenoids: biochemistry, pharmacology and treatment. *British Journal of Pharmacology*, 174(11): 1290-1324.
14. Cucu, T., Huvaere, K., Van Den Bergh, M. A., Vinkx, C. and Van Loco, J. (2012). A simple and fast HPLC method to determine lycopene in foods. *Food Analytical Methods*, 5(5): 1221-1228.
15. Adadi, P., Barakova, N. V. and Krivoshapkina, E. F. (2018). Selected methods of extracting carotenoids, characterization, and health concerns: A review. *Journal of Agricultural and Food Chemistry*, 66(24): 5925-5947.

16. Huang, J. and Hui, B. (2020). The determination of lycopene Z-isomer absorption coefficient on C30-HPLC. *Food Science & Nutrition*, 8(11): 5943-5952.
17. Sirikhet, J., Chanmahasathien, W., Raiwa, A. and Kiattisin, K. (2021). Stability enhancement of lycopene in *Citrullus lanatus* extract via nanostructured lipid carriers. *Food Science & Nutrition*, *9*(3): 1750-1760.
18. Petyaev, I. M., Pristensky, D. V., Morgunova, E. Y., Zigangirova, N. A., Tsibezov, V. V., Chalyk, N. E. and Bashmakov, Y. K. (2019). Lycopene presence in facial skin corneocytes and sebum and its association with circulating lycopene isomer profile: Effects of age and dietary supplementation. *Food Science & Nutrition*, 7(4): 1157-1165.
19. International Conference on Harmonization (2003). Technical requirements for the registration of pharmaceuticals for human use, validation of analytical procedures: Methodology. The 6th International Conference on Harmonization, Geneva, 2003
20. Pataro, G., Carullo, D., Siddique, M. A. B., Falcone, M., Donsì, F. and Ferrari, G. (2018). Improved extractability of carotenoids from tomato peels as side benefits of PEF treatment of tomato fruit for more energy-efficient steam-assisted peeling. *Journal of Food Engineering*, 233: 65-73.
21. Jin, H., Lao, Y. M., Zhou, J., Zhang, H. J. and Cai, Z. H. (2017). Simultaneous determination of 13 carotenoids by a simple C18 column-based ultra-high-pressure liquid chromatography method for carotenoid profiling in the astaxanthin-accumulating *Haematococcus pluvialis*. *Journal of Chromatography A*, 1488: 93-103.
22. Kehili, M., Kammlott, M., Choura, S., Zammel, A., Zetzl, C., Smirnova, I. and Sayadi, S. (2017). Supercritical CO_2 extraction and antioxidant activity of lycopene and β-carotene-enriched oleoresin from tomato (*Lycopersicum esculentum* L.) peels by-product of a Tunisian industry. *Food and Bioproducts Processing*, 102: 340-349.
23. Zhang, C-R., Aldosari, S. A., Vidyasagar, P. S., Shukla, P. and Nair, M. G. (2016). Determination of the variability of sugars in date fruit varieties. *Journal of Plantation Crops*, 43(1): 53-61.
24. Gebregziabher, B. S., Zhang, S., Qi, J., Azam, M., Ghosh, S., Feng, Y. and Sun, J. (2021). Simultaneous determination of carotenoids and chlorophylls by the HPLC-UV-Vis method in soybean seeds. *Agronomy*, 11(4): 758.
25. United States Department of Agriculture (USDA). (2002). Watermelon packs a powerful lycopene punch. Retrieved from https://agresearchmag.ars.usda.gov/2002/jun/.
26. Zhao, W., Lv, P. and Gu, H. (2013). Studies on carotenoids in watermelon flesh. *Agricultural Science*, 4(7): 8.
27. Przybylska, S. (2020). Lycopene a bioactive carotenoid offering multiple health benefits: A review. *International Journal of Food Science & Technology*, 55(1), 11-32.
28. Mozos, I., Stoian, D., Caraba, A., Malainer, C., Horbańczuk, J. O. and Atanasov, A. G. (2018). Lycopene and vascular health. *Frontiers in Pharmacology*, 9: 521.
29. Ghadage, S. R., Mane, K. A., Agrawal, R. S. and Pawar, V. N. (2019). Tomato lycopene: Potential health benefits. *The Pharma Innovation Journal*, 8(6): 1245-1248.

Malaysian Journal of Analytical Sciences (MJAS)
Published by Malaysian Analytical Sciences Society

OPTIMIZATION AND DETERMINATION OF INORGANIC ARSENIC BY LIQUID EXTRACTION AND INDUCTIVELY COUPLED PLASMA MASS SPECTROMETRY IN FOOD MATRIX

(Pengoptimuman dan Penentuan Arsenik Tak Organik Melalui Pengekstrakan Cecair dan Spektrometri Jisim-Plasma Gadingan Aruhan dalam Sampel Makanan)

Le Nhon-Duc[1], Nguyen Thanh-Nho[2], Le-Thi Anh-Dao[2], Nguyen Cong-Hau[2]*, Nguyen Van-Dong[3]

[1]Warrantek Joint Stock Company-Testing Center,
Can Tho City, Vietnam
[2]Faculty of Environmental and Food Engineering,
Nguyen Tat Thanh University, Ho Chi Minh City, Vietnam
[3]Department of Analytical Chemistry, Faculty of Chemistry,
University of Science, Vietnam National University Ho Chi Minh City (US-VNU HCMC), Vietnam

**Corresponding author: nchau@ntt.edu.vn*

Received: 28 August 2021; Accepted: 28 October 2021; Published: 27 December 2021

Abstract

Various kinds of food are at risk of arsenic exposure and this can lead to potential influences on human health. However, the toxicity of arsenic depends on its different forms, i.e., inorganic arsenic species (i.e., arsenite and arsenate) are more toxic than organic compounds (i.e., monomethylarsonic acid, dimethylarsinic acid, etc.), and total arsenic contents may provide limited information. In this study, a low-cost analytical method for analyzing inorganic arsenic (iAs) in various food matrices was optimized and validated. The sample preparation was conducted by acidic hydrolysis, arsenic reduction, extraction to the organic phase, then back-extraction to the aqueous phase to obtain the solutions prior to measurement on the inductively coupled plasma mass spectrometry (ICP-MS). The food matrices were hydrolyzed by 30% (v/v) HCl at 90 ^{o}C within 120 minutes to obtain the sample liquid containing iAs. The inorganic species in the sample liquid were reduced by N_2H_4/HBr, then extracted by $CHCl_3$ to organic phase, back-extracted into 2% HNO_3 solution, and quantified by ICP-MS with He as the collision gas. Various parameters related to the sample preparation were investigated and evaluated by different food matrices as well as the rice proficiency testing scheme 07273 provided by Fapas. The results showed no significant interconversion between inorganic and organic arsenic species when HCl was utilized as the hydrolysis agent. The limit of detection (LOD) and limit of quantification (LOQ) values were estimated as 1.7 and 5.0 µg kg^{-1}, respectively. The repeatability and reproducibility were assessed by calculating RSD_r (below 4.4%) and RSD_R (below 10%), favorable with Appendix F. AOAC (2016). The recoveries for all spiked samples ranged from 88 to 115%. The analytical method was applied to determine and assess the variations of iAs contents in anchovy, herring, white rice, brown rice, and fish sauce. All available samples met the requirements performed in Codex Stan 1993-1995, Amended in 2015, Commission Regulation (EU) 2015/1006, and Vietnam National technical regulation 8-2:2011.

Keywords: inorganic arsenic, inductively coupled plasma mass spectrometry, food matrices, extraction

Abstrak

Pelbagai jenis makanan boleh berisiko terhadap kehadiran arsenik dan ia akan membawa kesan terhadap kesihatan manusia. Namun, ketoksikan arsenik bergantung kepada spesies yang berbeza seperti spesies arsenik tak organik (i.e. arsenit dan arsenat) lebih toksik berbanding sebatian organik (i.e. asid monometilarsonik, asid dimetilarsinik dan lain-lain), dan kandungan jumlah arsenik juga mempunyai maklumat yang terhad. Melalui kajian ini, kaedah analisis kos rendah bagi analisa arsenik tak organik (iAs) di dalam pelbagai matriks makanan telah di optimum dan di tentusahkan. Penyediaan sampel dijalankan melalui hidrolisis berasid, penurunan arsenik, pengekstrakan pada fasa organik, kemudian pengekstrakan semula pada fasa akues untuk mendapatkan larutan sebelum pengukuran menggunakan spektrometri jisim plasma gandingan aruhan (ICP-MS). Matriks makanan telah di hidrolisis menggunakan 30% (v/v) HCl pada 90 ºC selama 120 minit untuk mendapatkan sampel cecair mengandungi iAs. Spesies tak organik di dalam sampel cecair kemudian diturunkan oleh N_2H_4/HBr, dan diekstrak mengunakan $CHCl_3$ pada fasa organik, kemudian pengekstrakan semula ke dalam larutan 2% HNO_3, dan pengkuantitian oleh ICP-MS bersama He sebagai gas pelanggaran. Pelbagai parameter yang berkaitan penyediaan sampel dikaji dan dinilai mengunakan matriks makanan berbeza dan skim 07273 ujian kemahiran terhadap beras oleh Fapas. Hasil kajian menunjukkan tiada perbezaan diantara spesies organik dan tak organik apabila HCl digunakan sebagai agen hidrolisis. Nilai had pengesanan (LOD) dan pengkuantitian (LOQ) masing-masing ialah 1.7 dan 5.0 µg kg^{-1}. Kebolehulangan dan penghasilan semula dinilai melalui pengiraan RSDr (di bawah 4.4%) dan RSD_R (di bawah 10%), sesuai berdasarkan Apendiks F. AOAC (2016). Perolehan semula bagi semua sampel dipaku pada julat 88 hingga 115%. Kaedah analisis kemudian digunapakai bagi penentuan dan penilaian variasi kandungan iAs di dalam ikan bilis, hering, beras putih, beras perang dan sos ikan. Semua sampel mematuhi keperluan di bawah Codex Stan 1993-1995, Pindaan 2015, Peraturan Suruhanjaya (EU) 2015/1006, dan peraturan teknikal Kebangsaan Vietnam 8-2: 2011.

Kata kunci: arsenik tak organik, spektrometri jisim plasma gandingan aruhan, matriks makanan, pengekstrakan

Introduction

Arsenic (As) contamination in food has been reported globally, especially in South and Southeast Asia [1, 2]. Scientists have shown that there is the uptake of As from water and soils by various plants, marine animals, fruits, and vegetables, then to food products with specific studies [3]. Plants specifically take up arsenate, which is the main As species in aerobic soils, through phosphate transporters. Meanwhile, arsenite, which is predominant in flooded paddy soils, is mostly taken up through aquaglyceroporins in microbe [4, 5]. The reducing environments of paddy soils lead to the mobilization of arsenite into soil solutions and the bioavailability to rice plants. The arsenite is absorbed through the silicon pathway to root cells and efflux towards the xylem. Moreover, the arsenate present in root cells could be reduced to arsenite, which is then complexed by thiol peptides or transported to shoots [5]. Animals on the other hand, are exposure to inorganic arsenic (iAs) has been present in drinking water and feed. This especially occurs for feed of plant origins, through biotransformation, in which iA is converted into organic arsenic (oAs) [6].

Total arsenic (tAs) and inorganic arsenic (iAs) are classified as "Carcinogenic to humans" (Group 1) by the International Agency for Research on Cancer because they cause cancers of the skin, bladder, and lungs. Limited evidence are available on their ability to cause cancers of the kidney, liver, and prostate [7]. Various organizations in the world have established the maximum level (ML) of tAs and iAs in many kinds of food. The World Health Organization (WHO) regulated the ML of tAs in foods allowed as 0.1 mg kg^{-1} [8]. The European Union (EU) published Regulation 2015/1006 on the ML values of iAs in foodstuffs, typically rice and rice-based products, ranging from 0.10 to 0.3 mg kg^{-1} [9]. Besides, the Australia New Zealand Food Standard Code showed the ML of 1 mg kg^{-1} for seaweed and mollusks, while iAs is not permitted to exceed 2 mg kg^{-1} for crustacean and fish [10]. Moreover, according to Food and Agriculture Organization, FAO/CODEX guideline, a previous screening by tAs determination and speciation analysis should be carried out in case of tAs > 0.2 mg kg^{-1}; however, this guide is only for polished rice [11]. Many other food categories have been reported to contain relatively high amounts of tAs of

0 - 1.9 mg kg^{-1} (corns, *Zea mais as* cereals) [12-14], 13 mg kg^{-1} (lettuce leaf as vegetables) [15], 22.4 µg L^{-1} (apple juices) [16], 42.6 µg L^{-1} (beef broth as animal products) [17], and 98 mg kg^{-1} (freshwater algae as seafood products) [18]. Additionally, rice was reported to perform the highest As concentration with the maximum reported as 267.7 mg kg^{-1} [19]. This could be explained due to the cultivation conditions and geographical factors that rice plants are grown in the flooded soil areas, mostly in South and Southeast Asia, considered to have the highest As concentration in the world [1, 20-22]. Thus, individuals who eat a lot of rice and rice-related products as their main diets would have a much higher risk of As exposure [23].

The toxicity of As depends on its species, in which inorganic arsenic (iAs) are more toxic than organic arsenic (oAs) due to the binding ability to the protein thiol groups (−SH) [24, 25]. This phenomenon causes protein activity inhibition and damaging the cellular structure. It is noteworthy that As in the dissolved mineral form of As_2O_3 (arsenic trioxide) is easily absorbed through the intestinal wall. The LD_{50} of As(III) and As(V) are 34.5 mg kg^{-1} and 41 mg kg^{-1}, respectively [26]. LD_{50} values showed that the toxicity of two inorganic species was similar, and the control of iAs is perfectly reasonable. International Organizations such as FAO and EU impose threshold limits on iAs in food (total content of As(III) and As(V)) rather than tAs [9, 27] . Under the current global free-trade conditions, the potential risk of As exposure is not only for those living in the polluted areas but also in other parts worldwide. Therefore, the determination of the specific As species and obtain information about the inorganic arsenic/total arsenic (iAs/tAs) ratios, particularly in the food, was interested by scientists during the last decade.

For determining inorganic species of arsenic, certain separation techniques should be carried out prior to measurement, especially iAs is present at remarkably low concentrations in food samples. The high-performance liquid chromatography with inductively coupled plasma mass spectrometry (HPLC-ICP-MS) is known as the reference technique for determining iAs due to its favorable sensitivity and effectiveness [28, 29]. However, such systems are expensive and complicated, and hence they are not commonly equipped and used in many laboratories. Moreover, the operation requires skilled techniques and high running costs. Several alternative analytical methods such as solvent extraction combined with hydride generation-atomic absorption spectrometry (HG-AAS) [26], solid phase extraction (SPE) combined with HG-AAS [11], gas chromatography-tandem mass spectrometry (GC–MS/MS) after derivatization with Dimercapto-1-propanol (British Anti-Lewisite reagent) [30] could be applied to serve both the separation and analyte quantification. However, these alternatives have an average sample preparation time of up to about 12 to 16 hours; therefore, it is necessary to investigate and develop a more simple, cheaper, but faster analytical method for iAs determination in various food matrices. Notably, the quality and commercial value of perishable foods such as seafood, vegetables, and fruits would be degraded if the storage and waiting period for analysis is prolonged.

In Vietnam, the maximum levels of several heavy metals in foods are based on National Technical Regulation, QCVN 8-2:2011/BYT [31] and Decision 46/2007/QD-BYT [32], but for As, the regulated values only refer to tAs. Therefore, the objectives of this study were to (i) investigate several parameters related to a low-cost and time-saving sample preparation procedure based on liquid extraction after sample hydrolysis and measuring on the inductively coupled plasma mass spectrometry (ICP-MS) specified for elemental analysis, (ii) evaluate the optimized analytical method performance for iAs quantification in food matrices, and (iii) determine and assess the variability of iAs contents in various foods purchased in Vietnamese local markets around Ho Chi Minh City. This is among the initial studies to build up a database to serve the future control regulations in Vietnam.

Materials and Methods

Instrumentation and apparatus

The Thermo Scientific™ iCAP Q ICP-MS (USA) was used for As measurement (Table 1). The device is placed at Warrantek Joint Stock Company-Testing Center, Can Tho City, Vietnam.

The microwave digestion system MARS 6 (CEM, USA) was employed for sample preparation. All laboratory apparatus and glassware had to be cleaned by soaking in 2% (v/v) HNO_3 overnight, then washed three times using deionized distilled water, and allowed to dry before using.

The microwave digestion system MARS 6 (CEM, USA) was employed for sample preparation. All laboratory apparatus and glassware had to be cleaned by soaking in 2% (v/v) HNO_3 overnight, then washed three times using deionized distilled water, and allowed to dry before using.

Table 1. Instrumental conditions for ICP-MS quantification

Parameter	Value
RF power	1550 W
Plasma-generating argon flow rate	14.0 L min^{-1}
Auxiliary air flow	0.8 L min^{-1}
Spray air flow	1.0 L min^{-1}
Peristaltic pump speed	40 rpm
Sampling depth	5.0 mm
Collision gas flow	5.0 mL min^{-1}
Spray chamber temperature	2 ^oC
Dwell time	0.2 s
Sweeps	10 cycles

Reagents and standards

Deionized water (DIW), 18 MΩ.cm, was obtained from a Milli-Q water system (Molsheim, France). Other chemicals and reagents, including 65 % nitric acid (HNO_3), 38% hydrochloric acid (HCl), 48% bromic acid (HBr), 99% hydrazine sulfate ($(N_2H_5)HSO_4$), methyl isobutyl ketone or MIBK ($(CH_3)_2CHCH_2COCH_3$) ≥ 99.9%, benzene (C_6H_6), toluene ($C_6H_5CH_3$), ethyl acetate ($CH_3COOC_2H_5$) ≥ 99.9%, chloroform ($CHCl_3$) ≥ 99.9%, iso-propanol ($CH_3CHOHCH_3$) ≥ 99.9%, hexane ($CH_3(CH_2)_4CH_3$) ≥ 99.9%, 30% hydrogen peroxide (H_2O_2) and sodium sulfate (Na_2SO_4), were of analytical grade and bought from Merck (Germany). Arsenate (H_3AsO_4) standard stock solution (1000±3 mg L^{-1}) was purchased from Merck (Germany). An internal standard solution of ^{89}Y (10 µg mL^{-1}) was provided by Accu Standard. Tune B iCAP Q solution (Ba, Bi, Ce, Co, In, Li và U) of 1.0 µg L^{-1} was supplied by Thermo Fisher. Multi-element solution was Thermo iCAP Q (0.035 mg L^{-1} Be; 0.020 mg L^{-1} Zn; 0.015 mg L^{-1} Cu, Ni; 0.010 mg L^{-1} Al, Ga, Mg; 0.008 mg L^{-1} Co, Li, Sc; 0.006 mg L^{-1} Ag, Mn; 0.005 mg L^{-1} Sr; 0.004 mg L^{-1} Ba, Tl (Thallium); 0.003 mg L^{-1} Bi, Ce, Cs, Ho, In, Rh, Ta, Tb, U, Y in 2 % HNO_3).

Sample collection

The study was carried out on several specific food matrices in Vietnam with highly potential risks of iAs exposure such as cereals (rice, brown rice), fish, and seafood products (fish, fish sauce). Various types of foods, including rice (n=3), brown rice (n=3), herring (n=3), anchovy (n=3), commercial Vietnamese fish sauce (n=3) were obtained from the local markets in Ho Chi Minh City. About 500-1000 g of shrimp, fish, and cereal samples, kept in a polyethylene (PE) bag with a folding edge and an entire bottle of fish sauce product. Fish samples were removed of their head, viscera, and tail. The samples were crushed and well homogenized in a mill. The resulting samples were stored in a decontaminated tube and stored in a freezer until analysis. Cereal samples were crushed and homogenized to a fine texture in a mill, and stored at room temperature (20 °C) until analysis. Fish sauce was stored at room temperature (20 °C), as recommended on the product's label.

Determination of total arsenic by ICP-MS

The tAs concentration was determined according to the method described in AOAC 2015.01 [33]. Briefly, a sample quantity of (1.000±0.001) g for seafood, 0.500±0.001 g for rice, and 0.200±0.005 mL for fish sauce) was weighed into a PTFE digestion tube, in which 4.0 mL of 65% HNO_3 and 1.0 mL 30% H_2O_2

were added. The digestion process was completed by the microwave digestion system MARS 6. Finally, the digested solution was diluted to the calibration mark by DIW in a 50 mL volumetric flask before the measurement by ICP-MS.

Determination of inorganic arsenic by ICP-MS

A sample (1.000±0.001 g) was weighed into a sealed reaction tube, in which 4.0 mL of DIW was added, and the tube was shaken for 5 minutes. Next, 18.0 mL of 30% (v/v) HCl was added, and the mixture was incubated at 90 °C for 120 minutes for hydrolysis. Next, 1 mL of 1.5% N_2H_4, 2 mL of 38% HBr, and 5 mL of $CHCl_3$ were added into the tube, followed by 5 minutes of shaking after each chemical was added. Phase separation was allowed to occur before centrifugation at a minimum speed of 5000 rpm. The bottom phase of $CHCl_3$ was transferred to another reaction tube to repeat the extraction in $CHCl_3$ for two more times. All organic phases were then combined and filtered through a 0.45 µm PTFE membrane. Next, 5 mL of 2% (v/v) HNO was added to the organic filtrate, followed-by centrifugation at 5000 rpm for 5 minutes for the back-extraction of iAs into the aqueous acid phase. The upper phase of the HNO_3 was transferred to a 50 mL volumetric flask and extraction in HNO_3 was repeated two more times. All extracted HNO_3 phases were collected and diluted to the calibration mark by DIW, prior to measurement by ICP-MS.

Method validation and data processing

Based on the procedure of the Nordic Committee on Food Analysis [34], statistical evaluation was carried out using Microsoft Excel (2019) with conformity to ISO 5725-2 [35]. The calibration curve was established based on the linear relationship between the analyte concentrations of 0.10, 0.20, 0.30, 0.50, 1.0, 1.5, 2.5, 5.0, 7.5, 10, 15, 20, and 25 µg L^{-1} and a specific ratio between the intensities of analyte and internal standard at each concentration ($^{75}As^{+}/^{89}Y^{+}$). The limit of detection (LOD) and limit of quantification (LOQ) were determined at three and ten times the standard deviation (SD) at in-house validation conditions, respectively. The intra-day and inter-day data were used to determine the in-house relative standard deviation of repeatability (RSD_r) and reproducibility (RSD_{iR}), respectively. The accuracy of the method was tested by a recovery test of the spiked iAs in actual food samples of rice, fish, and fish sauce (n = 8). The iAs concentrations in these samples were estimated, and the concentrations were mimicked using a standard solution. The samples were spiked, whereby the amount of spiked iAs equalled the amount of iAs in each matrix samples. Recoveries were calculated using the following equation 1:

$$\text{Recovery} = \frac{C_{\text{spiked-determined}} - C_{\text{non-spiked}}}{C_{\text{spiked-desired}}} \quad (1)$$

where $C_{\text{spiked-determined}}$ and $C_{\text{non-spiked}}$ represent for the amount of iAs determined in spiked and non-spiked samples; $C_{\text{spiked-desired}}$ is the actual amount of iAs desired to be spiked in the sample.

In a collaborative trial, the method performance Fapas proficiency testing program of rice flour sample (ID 07273) through z-score, in which $|z - \text{score}| \leq 2$ would exhibit satisfactory performance [36]. The calculation of z-score is shown as in the following equation 2:

$$z - \text{score} = \frac{C_{\text{lab}} - C_{\text{ref}}}{\sigma} \quad (2)$$

where C_{lab} is the measurement results reported by the participant laboratory in the proficiency testing program, C_{ref} is the assigned value provided by the proficiency testing program and σ is the standard deviation for proficiency assessment, provided and fixed by the proficiency testing program organizer.

Results and Discussion

The sample preparation involved for determining iAs in food matrices was carried out based on the liquid extraction technique using organic solvent after sample hydrolysis in an acidic medium and As(V) reduction to As(III), by a proper reductant. The iAs in the organic phase was then back-extracted to the acidic aqueous phase to be quantified on the ICP-MS. Furthermore, the influence of several parameters towards the sample preparation procedure, particularly on the sensitivity of the analytical method, were investigated. These parameters were the types of acid reagents used for sample hydrolysis, hydrolysis time and temperature,

reducing agents and organic solvents for liquid extraction, and back-extraction conditions to obtain aqueous solutions for the ICP-MS measurement.

Effects of acid reagents on the hydrolysis

The iAs (i.e., arsenite) binds to protein molecules via ligands of thiol sulfide (i.e., −SH−As) [37]. Before further steps in the liquid extraction process, the sample matrices were hydrolyzed in an acidic medium (combined with heat). The acid treatment aid in the breaking of bonds between iAs and sample matrices, and obtains liquid samples containing iAs species. Incomplete or low-efficiency hydrolysis would lead to a remarkable quantity of iAs to remain in the matrices, leading to a lower detection of intensities. It is also crucial to avoid the conversion between the iAs and oAs species during the hydrolysis period.

HCl and HNO have different oxidation properties that make them beneficial for utilization as hydrolysis reagents for food matrices [11, 38-40]. In this study, 30% (v/v) HCl and 2% (v/v) HNO_3 were used as the hydrolysis reagents to investigate their effects on the measured iAs intensities (Figure 1). However, concentrations of the acid were guided from previous studies which used favorable conditions, specifically those from Muñoz et al. [26], Fiamegkos et al. (2015) [39] for HCl and dos Santos et al. (2017) [11], Kang et al. (2016) [38] for HNO_3. It was also estimated that the lower concentration of HNO_3 might help to minimize the unexpected reactions between the residual HNO_3 and other reactants due to its strong oxidation properties (discussed later). Meanwhile, Cl^- is relatively inactive in acidic medium and the excess H^+ from HCl might also promote the reduction reaction of As(V) to As(III) after sample hydrolysis ($H_3AsO_4 + 2H^+ + 2e^- \rightleftharpoons HAsO_2 + 2H_2O$, $E^o = 0.560V$) [41].

The results shown in Figure 1 indicates that the efficiency of using HCl was about 3 times higher than that of HNO_3 for the three sample matrices. This was comprehended from the measured intensities of 3094 *vs*. 724, 1057 *vs.* 214, and 988 *vs.* 314 for rice, fish, and fish sauce, respectively. The lower intensities obtained from HNO_3 could be explained by the acid's strong oxidizing property and competitive reactiveness with N_2H_4 as the reducing agent. The unexpected reaction between the residual HNO_3 from the hydrolysis and N_2H_4 as the reducing agent could compete for the reduction reaction to form As(III) from As(V), thus decrease the reaction's performance. Therefore, lower intensities of iAs were obtained when HNO_3 was applied as the hydrolysis reagent, compared to HCl. Additionally, in several sample matrices with high oAs, such as fish and fish sauce, the application of HNO_3 might cause positive errors, due to the decomposition of oAs by HNO_3, particularly at the acid's high concentrations. Meanwhile, some common oAs species such as DMA and MMA were proved to be relatively stabler in both acidic and neutral media. Both oAs species were not present in any critical conversion into iAs when HCl was used as the hydrolysis reagent [42]. Therefore, HCl was used as the hydrolysis reagent for further investigations and experiments in this study.

Effects of temperature and time on hydrolysis

The effects of the hydrolysis temperature and time on the intensities of iAs were recorded in various food matrices (fish, fish sauce, and rice). The sample's matrix hydrolysis required the combination of an acidic medium and high temperature within a certain hydrolysis time. HCl is a common H^+ ion provider to form an acidic medium for sample hydrolysis before further reduction and liquid extraction. However, the use of HCl usually requires a higher temperature and/or a longer time to completely and quantitatively hydrolyze entire sample matrices. The hydrolysis temperature was previously reported to be performed at 85 to 95^{o}C [11, 26, 42] or ambient condition [26]. However, remarkably longer hydrolysis time of up to 12-15 hours might be required in the case of lower temperatures [26]. Therefore, this study did not apply very low temperature and limited the surveyed temperature from relatively high (50 ^{o}C) to the highest referenced values of 95 ^{o}C in order to evaluate the effects of temperature on hydrolysis efficiency.

In this study, the reaction time varied from 50 to 210 minutes. The conditions with the highest measured intensities were applied for further experiments. Based on Figure 2, the hydrolysis temperature was dependent on the sample matrices. A temperature of under 60 ^{o}C

was insufficient to completely hydrolyze all samples although hydrolysis time was increased up to 210 minutes. This means that the measured intensities did not reach their maximum. In particularly, food matrices (rice, brown rice in Figure 2c) with a higher starch or cellulose content required a higher hydrolysis temperature (up to 90ºC). Meanwhile, the protein-rich matrices (fish, fish sauce) required lower temperatures (80 and 70ºC for fish and fish sauce in Figure 2a and 2b, respectively).

The hydrolysis time above 120 minutes showed the highest and most stable intensities for all matrices. Therefore, for the wide range of food, 90ºC and 120 minutes would be used as the hydrolysis temperature and time, to assure the highest intensities. The optimization of temperature on hydrolysis has reduced the analysis time compared to several previous studies [11, 26, 28].

The effects of solvents on the extraction efficiency

Extraction is an important step to recover iAs. In complicated matrices, As(III) and As(V) exist simultaneously, therefore, it is necessary to use an appropriate reducing agent to convert all forms of iAs to As(III). The most commonly used reducing agent is I^- in KI [11, 43]. The methylated compounds of As(V), such as MMA and DMA reacted with KI to form CH_3AsI_2 or $(CH_3)_2AsI$. These species were then extracted by the less polar solvents (benzene, toluene, or chloroform). Moreover, AsI_3 has a large nonpolar covalent bond strength (electronegativity difference of 0.44), that to break this bond at the organic phase, using I^- was more difficult than Br^-. A previous study [44] had showed that Br^- was the more favorable halide forming agent for As(III) in the matrix. This was in the presence of oAs and the extraction efficiency by benzene, toluene, or chloroform was in the order of As(III) > As(V) >> oAs [40]. However, one disadvantage is that Br^- has a weak reducing strength. Thus, the combination of HBr and another reducing agent, N_2H_4 was employed to enhance the reduction performance [34, 39].

The iAs in the liquid samples endured liquid extraction by an organic solvent after hydrolysis. Various lesser polar solvents, including chloroform, methyl isobutyl ketone or MIBK, ethyl acetate, iso-propanol, and hexane, were investigated during the extraction of $AsBr_3$ compounds (electronegativity difference of 0.78). The effects of solvent on the extraction efficiency were evaluated through the recovery test of the spiked fish, fish sauce, and rice samples. The iAs concentrations in the real samples were estimated, and the standard solution was spiked to the sample (the amount of spiked iAs equal to the amount of iAs in the real samples for each matrix).

For each extraction solvent, the recoveries of three sample matrices (fish, fish sauce, and rice) did not exhibit any remarkable variations. The average recoveries were calculated from the results obtained from these three sample matrices (Figure 3). The result showed that the chloroform performed the highest extraction efficiency with the highest recovery (97.2%). Therefore, chloroform was used as the extraction solvent for further investigations and experiments to assure the highest sensitivity due to low iAs contents in food matrices. The application of chloroform as the extraction solvent was also reported in the publications of O. Muñoz et al. [26], Chappell et al. [45], Maria et al. [46]. The emulsification did not occur during the extraction, and the recovery of iAs depended on the solubility of $AsBr_3$ into the organic phase.

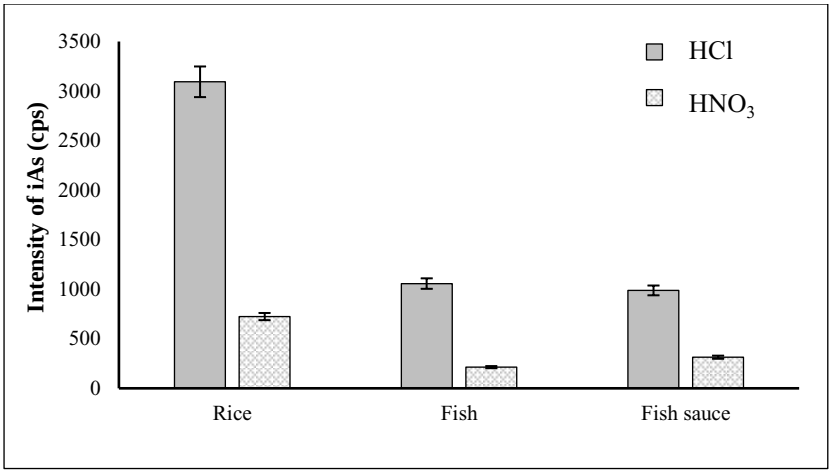
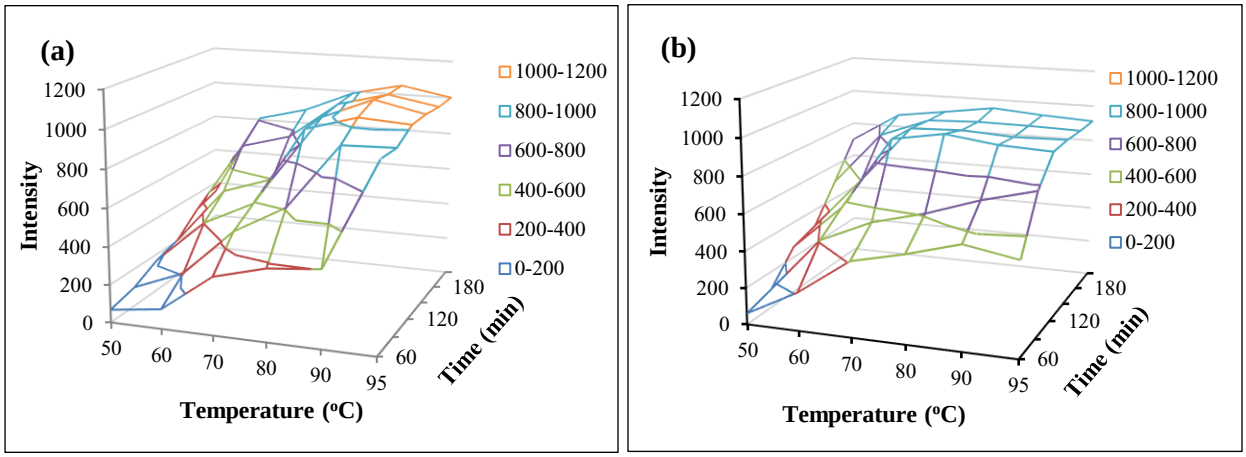


Figure 1. Effects of acid reagents on the hydrolysis efficiency



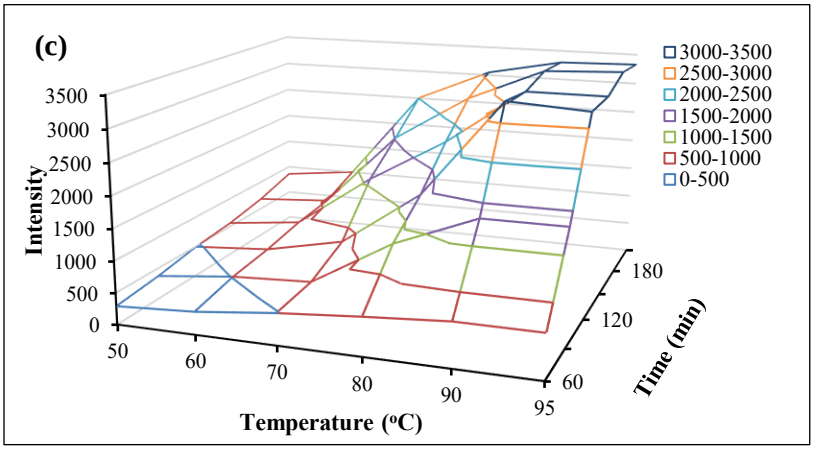


Figure 2. Effect of temperature and time on the hydrolysis efficiency of (a) fish, (b) fish sauce, (c) rice (the color representing for the different intensity magnitude)

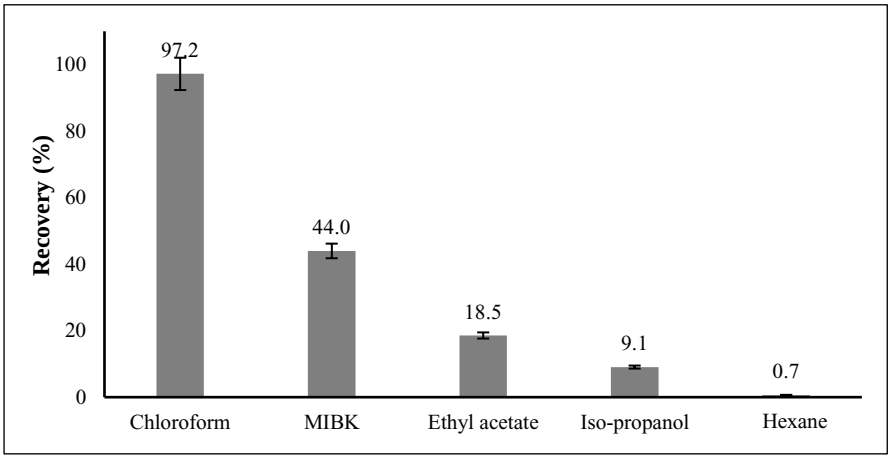


Figure 3. Effects of acid reagents on the hydrolysis efficiency (MIBK: Methyl Isobutyl Ketone)

Back-extraction into the aqueous phase

oAs-Br (MMA, DMA) and iAs(III)-Br were simultaneously extracted into the organic phase, so it was necessary to use a suitable agent to break As-Br bonds in oAs-Br and iAs-Br. In this study, 1% (v/v) HCl and 2% (v/v) HNO_3 were used as the acid reagents for back-extraction. The intensities (repeatability, %RSD) during the back-extraction by HCl and HNO_3 were 840.23 (RSD = 26%) and 1179.30 (RSD = 4.0%). When HCl solution was used, $AsBr_3$ was dissociated according to the equation 3:

$$AsBr_3 + 3Cl^- \rightleftharpoons AsCl_3 + 3Br^- (*) \quad (3)$$

According to Le Chatelier's principle, when Cl^- concentrations increased, the equilibrium (*) was towards the formation of $AsCl_3$, and $AsCl_3$ was a weaker covalent compound than $AsBr_3$ (due to the ion radius difference between Br^- and Cl^- ions). Therefore, it was difficult to extract $AsCl_3$ into less polar organic solvents. Moreover, the application of HCl for back-extraction and introduction in the ICP-MS was not appropriate because HCl created polyatomic interferences, typically $^{40}Ar^{35}Cl^+$ (m/z = 75), which coincides with the m/z of As. Due to its strong oxidizing properties, HNO_3 easily broke the $AsBr_3$ molecule bond by oxidizing As(III) to As(V). As(V) compounds tended to exist in the forms of oxygen bonds under conditions where the concentration of halogen ions was not high enough. Therefore, As(V) was distributed into the HNO_3 phase according to the reaction (**), resulting in higher recoveries and repeatability (Figure 4). For the ICP-MS, the acid concentration was as low as possible. The concentrations of 2% HNO_3 were possible to prevent memory effects.

$$AsBr_3 + 2HNO_3 + 2H_2O \rightarrow H_3AsO_4 + 2NO_2 + 3HBr (**) \quad (4)$$

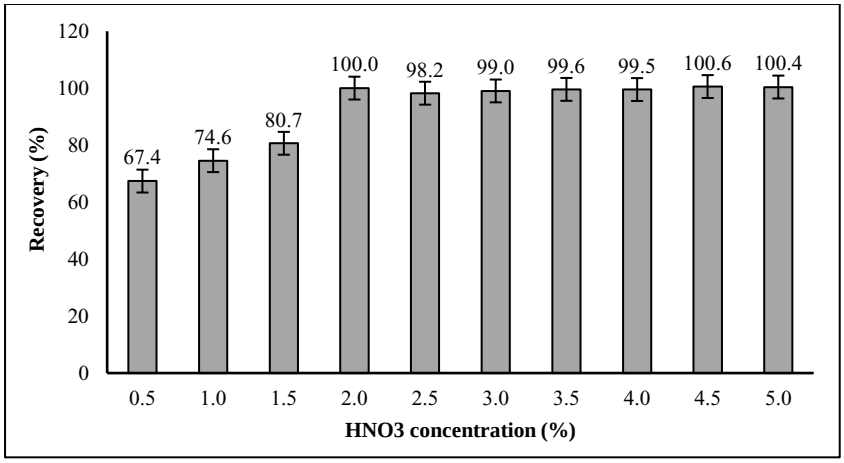


Figure 4. The effects of HNO_3 concentrations on the recoveries

Analytical method evaluation for the determination of inorganic arsenic in food

The regression equation was y = 0.0137x + 0.0003, whereas x and y stand for standard concentrations and intensity ratios between the analyte and internal standard, respectively. The squared correlation coefficient, R^2 = 0.9995, indicated the goodness of linearity. The calibration curve was established from 0.10 to 25 μg L^{-1}, suitable for wide ranges of foodstuffs with various iAs concentrations. The limit of detection (LOD) and limit of quantification (LOQ) were 1.7 μg kg^{-1} and 5.0 μg kg^{-1}, respectively. These estimated LOD and LOQ values were very low compared to the actual concentrations of iAs in real food samples. The repeatability and reproducibility were assessed through the calculation of RSD_r (< 4.4%) and RSD_R (< 10%), in agreement with Appendix F. AOAC [47]. The recoveries of spiked food samples ranged from 88 to 115%. The method performance was evaluated by rice proficiency testing scheme 07273 provided by Fapas (Table 2). The determined arsenic results showed that the developed method was equivalent to the arbitration method on the LC-ICP-MS. The concentrations of iAs, oAs, tAs with |Z-score| ≤ 2 complied with the required performance criteria for methods used for official food control purposes as decided by the European Commission [48]. The results obtained also indicated that the studied method did not perform a conversion between iAs and oAs. Therefore, it was possible to selectively extract iAs in the matrices containing oAs.

Evaluation of the inorganic arsenic in food

The optimized method was evaluated for accuracy through the data in Table 2. The determination of arsenic on the ICP-MS was set up according to the parameters mentioned in Table 1. The optimized method was applied to evaluate the inorganic arsenic in anchovy, herring, white rice, brown rice, and fish sauce (Table 3).

As can be seen from Figure 5, when the samples were animal tissues or plant products, typically rice, the ratios of iAs/tAs were relatively high, while the samples of interest were animals or their products; these ratios were smaller. The brown rice products presented their remarkably higher iAs/tAs ratios (51.1-97.9%), which was consistent with the report of Hassan et al. [49]. The ingredients used for fish sauce production performed the lowest iAs/tAs (0.31% to 0.58%); however, these ratios got higher for fish sauce samples (3.82-4.54%). The experimental results indicated that iAs contents were all met the requirements shown in Codex Stan 1993-1995 [27], Commission Regulation (EU) 2015/1006 [9], and Vietnam National technical regulation 8-2:2011 on the limits of heavy metals contamination in food [31].

Table 2. Comparison of assigned arsenic values and determined results

	Assigned Value (μg kg^{-1})	Result (μg kg^{-1})	Z-score
iAs	162	160	0.0
tAs	220	226	0.1
oAs[a]	58	66	0.1

[a] [oAs] = [tAs] – [iAs]

Table 3. Variations of arsenic contents in food (average ± standard deviation for three replicates)

Food sample	iAs (μg kg^{-1})	tAs (μg kg^{-1})	iAs/tAs (%)
Herring-1	16.43 ± 0.47	3165 ± 85	0.5
Herring-2	10.67 ± 0.19	2130 ± 69	0.5
Herring-3	22.08 ± 0.63	3788 ± 99	0.6
Anchovy-1	8.13 ± 0.27	2610 ± 87	0.3
Anchovy-2	10.82 ± 0.76	3146 ± 88	0.4
Anchovy-3	14.99 ± 0.99	4138 ± 96	0.4
Rice-1	93.0 ± 5.9	109.2 ± 3.6	85.2
Rice-2	98.6 ± 6.4	122.1 ± 3.4	80.7
Rice-3	110.5 ± 1.3	118.9 ± 7.6	92.9
Brown rice-1	167.9 ± 1.8	171.5 ± 7.8	97.9
Brown rice-2	120.5 ± 2.7	130.3 ± 9.5	92.5
Brown rice-3	196.8 ± 6.8	385 ± 20	51.1
Fish sauce-1	44.66 ± 0.30	1168 ± 49	3.8
Fish sauce-2	29.9 ± 1.1	661 ± 25	4.5
Fish sauce-3	52.1 ± 3.3	1195 ± 54	4.4

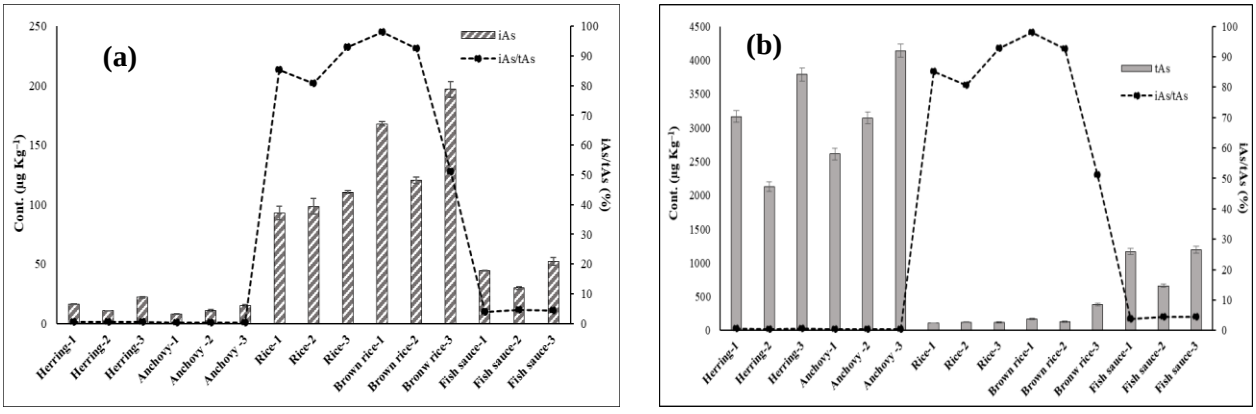


Figure 5. iAs concentration and iAs/tAs ratio (a) iAs and (b) tAs

Conclusion

ICP-MS method for the determination of iAs achieved good selectivity without any significant interconversion between inorganic and organic species. The limit of detection (LOD) and limit of quantification (LOQ) were 1.7 µg kg^{-1} and 5.0 µg kg^{-1}, respectively. The repeatability RSD_r (%) and reproducibility RSD_R (%) were lower than 4.4 and 10%, respectively. The recoveries ranged from 88 to 115% for all spiked samples. This analytical method was applied to assess the inorganic arsenic in anchovy, herring, white rice, brown rice, and fish sauce with high reliability. The iAs contents in various foods were analyzed by the optimized method at 10.67-22.08 µg kg^{-1} for herring, 8.13-14.99 µg kg^{-1} for anchovy, 93.0-110.5 µg kg^{-1} for rice, 120.5-196.8 µg kg^{-1} for brown rice, and 29.9-52.1 kg^{-1} for fish sauce. The concentration of iAs in the rice and rice products was lower than the limits established by FAO and EU for rice products for adult consumption. In most samples of the rice products, iAs was approximately 51.1% to 97.9% of the total content of As present. However, no legislation is currently available for iAs in fish and fish sauce and it is believed that the present study will contribute to the establishment of a threshold concentration. The developed method is suitable for routine analysis in the context of many laboratories only equipped with the ICP-MS instead of modern and high-cost HPLC-ICP-MS.

Acknowledgment

The authors would like to express our thanks and appreciation to Warrantek Joint Stock Company-Testing Center, Can Tho City, Nguyen Tat Thanh University (NTTU), and the University of Science, Vietnam National University Ho Chi Minh City (US-VNU HCMC), Vietnam, for their assistance and support during this study.

References

1. Hite, A. H. (2013). Arsenic and rice: A call for regulation. *Nutrition*, 29: 353-354.
2. Srivastava, S., Suprasanna, P. and D'Souza, S. F. (2011). Redox state and energetic equilibrium determine the magnitude of stress in *Hydrilla verticillata* upon exposure to arsenate. *Protoplasma*, 248(4): 805-815.
3. Mandal, B. K. and Suzuki, K. T. (2002). Arsenic round the world: A review. *Talanta*, 58(1): 201-235.
4. Ma, J. F., Yamaji, N., Mitani, N., Xu, X.-Y., Su, Y.-H., McGrath, S. P. and Zhao, F.-J. (2008). Transporters of arsenite in rice and their role in arsenic accumulation in rice grain. *Proceedings of the National Academy of Sciences*, 105(29): 9931-9935.
5. Zhao, F. J., Ma, J. F., Meharg, A. and McGrath, S. (2009). Arsenic uptake and metabolism in plants. *New Phytologist*, 181(4): 777-794.
6. Flora, S. J. S. (2014). Handbook of arsenic toxicology. Academic Press.
7. ARC Monographs on the Evaluation of Carcinogenic Risks to Humans (2012). Arsenic, Metals, Fibres and Dusts, Lyon, France.
8. Aposhian, H. V., Zheng, B., Aposhian, M. M., Le, X. C., Cebrian, M. E., Cullen, W., Zakharyan, R. A., Ma, M., Dart, R. C. and Chen, Z. (2000). DMPS–arsenic challenge test: II. Modulation of arsenic species, including monomethylarsonous acid (MMAIII), excreted in human urine. *Toxicology and Applied Pharmacology,* 165: 74-83.
9. Commission Regulation EU 2015/1006 (2015). Amending regulation EC No. 1881/2006 as regards maximum levels of inorganic arsenic in foodstuffs.
10. FSC 96 Amendment No. 154 (2015). Commonwealth of Australia Gazette. Australia New Zealand food standards code – schedule 19 – maximum levels of contaminants and natural toxicants.
11. dos Santos, G. M., Pozebon, D., Cerveira, C. and de Moraes, D. P. (2017). Inorganic arsenic speciation in rice products using selective hydride generation and atomic absorption spectrometry (AAS). *Microchemical Journal,* 133: 265-271.
12. Schoof, R., Yost, L., Eickhoff, J., Crecelius, E., Cragin, D., Meacher, D. and Menzel, D. (1999). A market basket survey of inorganic arsenic in food. *Food and Chemical Toxicology*, 37(8): 839-846.

13. Queirolo, F., Stegen, S., Restovic, M., Paz, M., Ostapczuk, P., Schwuger, M. and Munoz, L. (2000). Total arsenic, lead, and cadmium levels in vegetables cultivated at the andean villages of Northern Chile. *Science of The Total Environment*, 255(1-3): 75-84.
14. Muñoz, O., Diaz, O. P., Leyton, I., Nuñez, N., Devesa, V., Súñer, M. A., Vélez, D. and Montoro, R. (2002). Vegetables collected in the cultivated Andean area of Northern Chile: Total and inorganic arsenic contents in raw vegetables. *Journal of Agricultural and Food Chemistry*, 50(3): 642-647.
15. Norton, G., Deacon, C., Mestrot, A., Feldmann, J., Jenkins, P., Baskaran, C. and Meharg, A. A. (2013). Arsenic speciation and localization in horticultural produce grown in a historically impacted mining region. *Environmental Science & Technology*, 47(12): 6164-6172.
16. Jackson, B. P., Taylor, V. F., Karagas, M. R., Punshon, T. and Cottingham, K. L. (2012). Arsenic, organic foods, and brown rice syrup. *Environmental Health Perspectives*, 120(5): 623-626.
17. Roberge, J., Abalos, A. T., Skinner, J. M., Kopplin, M. and Harris, R. B. (2009). Presence of arsenic in commercial beverages. *American Journal of Environmental Sciences*, 5(6): 688-694.
18. Díaz, O., Pastene, R., Recabarren, E., Núñez, N., Vélez, D. and Montoro, R. (2008). Arsenic contamination from geological sources in environmental compartments in pre-andean area of Northern Chile. Natural arsenic in groundwater of Latin America. *Arsenic in the Environment*, 1: 335-344.
19. Nookabkaew, S., Rangkadilok, N., Mahidol, C., Promsuk, G. and Satayavivad, J. (2013). Determination of arsenic species in rice from Thailand and other asian countries using simple extraction and HPLC-ICP-MS analysis. *Journal of Agricultural and Food Chemistry*, 61(28): 6991-6998.
20. Zhao, F.-J. and Meharg A. A. (2013). Arsenic and rice. Springer, Netherlands: 171.
21. Hassan, F. I., Niaz, K., Khan, F., Maqbool, F. and Abdollahi, M. (2017). The relation between rice consumption, arsenic contamination, and prevalence of diabetes in South Asia. *EXCLI Journal*, 16: 1132.
22. Wang, H.-S., Sthiannopkao, S., Chen, Z.-J., Man, Y.-B., Du, J., Xing, G.-H., Kim, K.-W., Yasin, M. S. M., Hashim, J. H. and Wong, M.-H. (2013). Arsenic concentration in rice, fish, meat and vegetables in Cambodia: A preliminary risk assessment. *Environmental Geochemistry and Health*, 35(6): 745-755.
23. Rasheed, H., Slack, R. and Kay, P. (2016). Human health risk assessment for arsenic: A critical review. *Critical Reviews in Environmental Science and Technology*, 46(19-20): 1529-1583.
24. Jain, C. and Ali, I. (2000). Arsenic: Occurrence, toxicity and speciation techniques. *Water Research*, 34(17): 4304-4312.
25. Huang, J.-H., Ilgen, G. and Fecher, P. (2010). Quantitative chemical extraction for arsenic speciation in rice grains. *Journal of Analytical Atomic Spectrometry*, 25(6): 800-802.
26. Muñoz, O., Vélez, D. and Montoro, R. (1999). Optimization of the solubilization, extraction and determination of inorganic arsenic [As(III) + As(V)] in seafood products by acid digestion, solvent extraction and hydride generation atomic absorption spectrometry. *Analyst*, 124(4): 601-607.
27. CXS 193-1995 (Amended, 2019) Codex alimentarius international food standard, general standard for contaminants and toxins in food and feed.
28. Hata, A., Endo, Y., Nakajima, Y., Ikebe, M., Ogawa, M., Fujitani, N. and Endo, G. (2007). HPLC-ICP-MS speciation analysis of arsenic in urine of Japanese subjects without occupational exposure. *Journal of Occupational Health,* 49(3), 217-223.
29. Suzuki, Y., Shimoda, Y., Endo, Y., Hata, A., Yamanaka, K. and Endo, G. (2009). Rapid and effective speciation analysis of arsenic compounds in human urine using anion-exchange columns in HPLC-ICP-MS. *Journal of Occupational Health*, 0906150084-0906150084.

30. Jung, M. Y., Kang, J. H., Jung, H. J. and Ma, S. Y. (2018). Inorganic arsenic contents in ready-to-eat rice products and various korean rice determined by a highly sensitive gas chromatography-tandem mass spectrometry. *Food Chemistry*, 240: 1179-1183.
31. QCVN 8-2:2011/BYT (2011) Vietnam national technical regulation on the limits of heavy metals contamination in food.
32. Decision No. 46/2007/QD-BYT (2007). Decision of the Minister of Health of Vietnam dated 19 December 2007 on the maximum acceptable limits of chemical and biological contamination in food. Hanoi, Vietnam Ministry of Health.
33. Briscoe, M. (2015) Determination of heavy metals in food by inductively coupled plasma–mass spectrometry: first action 2015.01. *Journal of AOAC International*, 98(4): 1113-1120.
34. NMKL (2015). A glimpse of the AOAC Europe-NMKL-NordVal international symposium: Food labs in a crystal ball-future challenges in food analysis. *Nordic Committee on Food Analysis:* PA 1123.
35. ISO 5725-2 (1994). Accuracy (trueness and precision) of Measurement Methods and Results-Part 2: Basic method for the determination of repeatability and reproducibility of a standard measurement method.
36. Reichenbächer, M. and Einax, J. W. (2011). Challenges in analytical quality assurance. Springer Science & Business Media, Verlag Berlin Heidelberg.
37. Shen, S., Li, X.-F., Cullen, W. R., Weinfeld, M. and Le, X. C. (2013) Arsenic binding to proteins, *Chemical Reviews*, 113(10): 7769-7792.
38. Kang, J. H., Jung, H. J. and Jung, M. Y. (2016). One step derivatization with British anti-lewsite in combination with gas chromatography coupled to triple-quadrupole tandem mass spectrometry for the fast and selective analysis of inorganic arsenic in rice. *Analytica Chimica Acta*, 934: 231-238.
39. Fiamegkos, I., Cordeiro, F., Devesa, V., Vélez, D., Robouch, P., Emteborg, H., Leys, H., Cizek-Stroh, A. and De La Calle, B. (2015). IMEP-41: Determination of inorganic As in food. Collaborative trial report, JRC94325. Geel, Belgium: Joint Research Center, Institute for Reference Materials and Measurements.
40. Suzuki, N., Satoh, K., Shoji, H. and Imura, H. (1986). Liquid-liquid extraction behavior of arsenic (III), arsenic (V), methylarsonate and dimethylarsinate in various systems, *Analytica Chimica acta*, 185: 239- 248.
41. Milazzo, G., Caroli, S. and Braun, R. D. (1978). Tables of standard electrode potentials. *Journal of The Electrochemical Society*, 125(6): 261C.
42. Huber, C. S., Vale, M. G. R., Dessuy, M. B., Svoboda, M., Musil, S. and Dědina, J. (2017). Sample preparation for arsenic speciation analysis in baby food by generation of substituted arsines with atomic absorption spectrometry detection. *Talanta*, 175: 406-412.
43. Lehmann, E., Fostier, A. and Arruda, M. (2013). Hydride generation using a metallic atomizer after microwave-assisted extraction for inorganic arsenic speciation in biological samples, *Talanta*, 104: 187- 192.
44. Karaffa, L. S. (2013). The Merck Index: An encyclopedia of chemicals, drugs, and biologicals. RSC Publishing.
45. Chappell, J., Chiswell, B. and Olszowy, H. (1995). Speciation of arsenic in a contaminated soil by solvent extraction. *Talanta*, 42(3): 323-329.
46. Maria, B., Devesa, V., Fiamegos, Y. and Vélez, D. (2017). Determination of inorganic arsenic in a wide range of food matrices using hydride generation-atomic absorption spectrometry. *Journal of Visualized Experiments*, 127: e55953.
47. Appendix F AOAC (2016). Guidelines for standard method performance requirements.
48. Decision C 657/EC (2002). Implementing council directive 96/23/EC concerning the performances of analytical methods and the interpretation of results. Official Journal of the European Communities.
49. Hassan, F. I., Niaz, K., Khan, F., Maqbool, F. and Abdollahi, M. (2017). The relation between rice consumption, arsenic contamination, and prevalence of diabetes in South Asia. *EXCLI Journal*, 16: 1132.

Malaysian Journal of Analytical Sciences (MJAS)
Published by Malaysian Analytical Sciences Society

BIO-COAL OPTIMIZATION STUDY OF DRY LEAVES VIA LOW-TEMPERATURE MECHANISM

(Kajian Pengoptimuman Terhadap Bio-Arang Batu Mengunakan Daun Kering Melalui Mekanisme Suhu Rendah)

Siti Solehah Misni[1], Nor Hazelah Kasmuri[1,2]*, Fuzieah Subari[1], Zalizawati Abdullah[1,2], Suhaiza Hanim Hanipah[1]

[1]*School of Chemical Engineering, College of Engineering*
[2]*Industrial Process Reliability and Sustainability Research Group, College of Engineering*
Universiti Teknologi MARA, 40450 Shah Alam, Selangor, Malaysia

**Corresponding author: norhazelah@uitm.edu.my*

Received: 13 July 2021; Accepted: 17 October 2021; Published: 27 December 2021

Abstract

The abundant resources of forestry waste, such as dry leaves, find utility in the bio-coal production industry. In this study, bio-coal produced *via* the low-temperature mechanism of torrefaction was optimized using response surface method (RSM). The dry torrefaction method was conducted for 60–90 min with biomass loading of 50–100 g and a temperature range of 200–350 °C. The torrefaction process of dry leaves was executed in a furnace and was optimized by using RSM's factorial design. The optimal conditions were reaction temperature of 200 °C, a reaction time of 60 min, and a biomass loading of 100 g, which produced maximum bio-coal yield (85.33%). Bio-coal products were characterized using a thermogravimetric analyzer and Fourier transform infrared spectrometry to determine the weight loss, thermal effect profile, and functional groups of phenol, alcohol, ester, ether, and aromatic groups in bio-coal.

Keywords: bio-coal, dry leaves, optimization, response surface method, torrefaction

Abstrak

Sumber sisa hutan yang banyak, seperti daun kering, mempunyai kegunaan yang relevan dalam industri pengeluaran bio-arang batu. Bio-arang batu yang dihasilkan melalui mekanisme suhu rendah torefaksi dioptimumkan dengan kaedah gerak balas permukaan (RSM). Kaedah kering torefaksi dilakukan selama 60-90 min dengan muatan biojisim 50-100 g dan julat suhu 200-350 °C. Proses torefaksi daun kering dilakukan di relau pembakaran dan dioptimumkan dengan menggunakan rekabentuk faktorial RSM. Keadaan optimum ialah suhu reaksi 200°C, masa tindak balas 60 min, dan muatan biojisim 100 g, yang menghasilkan hasil maksimum bio-arang batu (85.33%). Produk bio arang batu dicirikan menggunakan penganalisis termogravimetri dan spektrometri inframerah transformasi Fourier untuk menentukan penurunan berat, profil kesan terma, dan kumpulan fungsional kumpulan fenol, alkohol, ester, eter, dan aromatik dalam bio-arang batu.

Kata kunci: bio-arang batu, daun kering, pengoptimuman, kaedah gerak balas permukaan, torefaksi

Introduction

Owing to global warming, the extensive use of fossil fuels as the source of energy for the industrial and commercial sectors has now become a chief concern. Fossil fuels exist in form of hydrocarbon, primarily natural gas, petroleum, and coal derived from dead animals or plants. The combustion of fossil fuels emits carbon monoxide into the atmosphere. The advancement of bio-coal as an alternative to fossil fuels has increased interest because of the depletion of oil resources and their positive impact on the environment, energy supply substitution, and rural growth [1]. Unlike biomass, fossil fuels contain a high percentage of carbon and are primarily derived from coal, petroleum, and natural gas. Because of their high carbon content, fossil fuels generate more carbon dioxide than bio-coal derived from biomass. Sulfur and other impurities are also found in fossil fuels. The combustion process of fossil fuels produces sulfur monoxides and sulfur dioxide, which contribute to acid rain. Likewise, the combustion of fossil fuels generates ozone (O_3), which is converted to other pollutants in the atmosphere by the action of sunlight. If a massive amount of O_3 is generated, it may be dangerous to the respiratory system [2].

There are three methods for converting biomass into energy: biochemical, thermochemical, and chemical conversion. Biochemical conversion produces biogas, biodiesel, and bio-ethanol, whereas chemical conversion produces plant oil, and thermochemical conversion produces solid fuel, liquid fuel, and gas fuel [3]. Thermochemical conversion exposes biomass to raised temperatures in a low-oxygen atmosphere. The purpose of this conversion is to decompose significant lignocellulosic biomass into insignificant compounds that can be used immediately [1]. There are four thermochemical conversion technologies, depending on whether the mechanism involves high or low temperature. The former includes combustion and gasification, whereas the latter includes pyrolysis and torrefaction [4,5]. Torrefaction is the most suitable because the product yield of the solid formed is the highest [6]. Approximately up to 70% of the total dry leaves are yielded as a solid product from torrefaction processes [7]. Torrefaction is a low-temperature thermal process used to treat biomass waste [8]. The dry torrefaction process is the thermal processing of biomass at 200-300 °C in the absence of oxygen or air. Through hemicellulose devolatilization, the process impacts the volatilization of water and volatile organic compounds. Lignin and cellulose in lignocellulosic biomass disintegrate beyond 300 °C [9]. Approximately 30% of biomass is lost during the torrefaction process, and the torrefied product retains more than 90% of the initial energy content [7]. The advantages of working with torrefied biomass include a significant energy density, which contributes to bio-coal efficiency as vehicle fuel. In addition to that, it has a better grinding ability and lower biodegradability. The torrefied biomass can also reduce water retention time because of its increased hydrophobicity [10].

Furthermore, the most noteworthy factor in producing better bio-coal is optimal production conditions. Optimization reduces the error and improves the performance of the existing bio-coal production process. Besides that, it can minimize the time required to design new products and improve the reliability and performance of bio-coal. Today, it affects both consumers and producers in terms of resources, budget, and time. Thus, this optimization method with response surface method (RSM) has proven as a tool for statistical technique for complex processes. It can reduce the number of experiments that are required to assess several parameters and their interactions. Hence, by employing the optimization in RSM, the yield of product can be improved with significant results [5,11]. In accordance with the previous studies, several parameters were assessed in the optimization in the torrefaction; as the optimal temperature reached up from 180 °C to 220 °C [12], reaction time ranged from 30 min to 60 min [13,14], and biomass loading varied between 90 g to 100 g [15,16], respectively.

In the present study, the optimal values of the investigated parameters were obtained from the optimization of bio-coal from dry leaves. The parameters influencing bio-coal production were evaluated using RSM design. The Design-Expert©

version 10 was used to achieve the objective of this research – to determine the optimal parameters. This determination method is also known as the design of experiment method, which was implemented using RSM. RSM acts as an essential tool to develop, design, and optimize a wide range of engineering systems [17]. The obtained results can also be obtained from a small number of experiments. Following the selection of an acceptable model, future observations can be assumed to fall within the original design range [18].

Materials and Methods

Sample preparation and characterization of raw materials

Dry leaves collected were taken from UiTM Shah Alam, Selangor. Dry-leaf biomass is a readily available forestry residue in Malaysia and has been proposed as a source for bio-coal production. Following the collection, the dry leaf sample was first sundried for two days to remove unbound moisture and then ground to reduce biomass size [19]. Using thermogravimetric analyzer (TGA) (Model Toledo, Switzerland), the dry leaves were characterized by evaluating the thermal properties of solid materials as a function of temperature using a constant heating rate. Manipulation of the temperature allowed the weight gain and loss of the bio-coal to be determined.

Torrefaction process

Torrefaction of dry leaves was accomplished using a front-loading furnace (carbolite). It consists of a rectangular chamber with a heavy-gauge heating system with graded winding and an insulated front vestibule. To eliminate the air during the combustion, a sample of grounded dry leaves was wrapped in aluminum foil. The wrapped samples were placed in the furnace and heated to the desired temperature. The temperature inside the reactor was controlled manually by pressing the furnace's button.

Approximately 50 g and 100 g of grounded dry leaf feedstock wrapped in aluminum foil were placed inside the chamber and torrefied at two levels of desired temperature (200 °C and 350 °C) and reaction time (60 min and 90 min). After each torrefaction run, the final solid torrefied product was recovered from the furnace and stored in a desiccator for additional analysis. The respective weights before and after the torrefaction process were recorded for further analysis using an optimization process.

Fourier transform infrared spectroscopy analysis

The solid torrefied product was analyzed using Fourier transform infrared spectroscopy (FTIR) (Model Perkin Elmer Spectrum One, USA) and the instrument was operated at room temperature. The FTIR was equipped with universal attenuated total reflection (ATR) at the spectra of 4 cm^{-1} resolution [20]. The analysis of FTIR was used to determine the functional group present in the form of a peak at a specific wavelength. It is set to transmission mode, with a range of 4000 cm^{-1} to 400 cm^{-1}.

Thermogravimetric analysis

The raw biomass sample, solid torrefied biomass product of 200 °C and 350 °C, respectively was analyzed using TGA (Model Toledo, Switzerland) to measure the volatile matter content by percentage of lignin, hemicellulose, and cellulose, as well as the percentage of fixed carbon content inside the torrefied dry leaves and the ash content. The analysis result represents the thermal properties of solid materials as a function of temperature using a constant heating rate.

In the analyzer, 20 mg of bio-coal sample was heated from room temperature to 900 °C at a constant heating rate of 10 °C/min. The analysis was performed in an inert atmosphere with a continuous flow of nitrogen gas at a rate of 100 mL/min [19].

Optimization of bio-coal production using response surface method

The data set in Table 1 explains the experiment that was performed to determine the response yield of various bio-coal samples prepared at varying conditions of temperatures, weights, and times. The experiments were conducted using RSM according to a two-level factorial design with three variables or design factors and each experiment was performed twice.

A factorial design can be used to determine the consequences and statistical significance of a larger

group of experimental variables. This method allows one to select the acceptable or pertinent variables for the next set of experiments. The factorial design enables better system behavior by including higher model components.

The three design factors, namely temperature, time, and weight were used to execute 16 different experiments. The factorial model of two-level factorial design was determined in Equation 1. The parameters X_1, X_2, and X_3 represent torrefaction temperature, reaction time, and biomass loading, respectively. The total number of experiments required can be calculated as follows.

$$Y = \alpha_0 + \alpha_1 X_1 + \alpha_2 X_2 + \alpha_3 X_3 + \alpha_{1,2} X_1 X_2 + \alpha_{1,3} X_1 X_3 + \alpha_{2,3} X_2 X_3 \quad (1)$$

where Y is the predicted responses, α_0 to $\alpha_{2,3}$ is the regression coefficient, and X_1, X_2, and X_3 are the parameters' factor. Multiple regression analysis was used to calculate the coefficients in Equation 1 on the basis of the obtained experimental data as well as the predicted responses.

ANOVA methods were used to extract the results from both experiments. This method was performed by using Design-Expert software version 10.

Table 1. Bio-coal data set via torrefaction

Run	Torrefaction Temperature (°C)	Time (min)	Biomass Loading (g)	Bio-Coal Yield (% g bio-coal/ g biomass)	Actual Value (% g bio-coal/ g biomass)	Predicted Value (% g bio-coal/ g biomass)
1	200	90	100	40.06	40.06	40.06
2	350	90	100	52.84	52.84	52.84
3	350	60	50	48.74	48.74	48.19
4	350	90	50	50.58	50.58	50.58
5	200	60	50	84.14	84.14	84.14
6	200	60	50	84.14	84.14	84.14
7	350	60	50	47.64	47.64	48.19
8	200	90	100	40.06	40.06	40.06
9	200	90	50	78.24	78.24	78.24
10	350	90	100	52.84	52.84	52.84
11	350	60	100	25.28	25.28	25.28
12	200	90	50	78.24	78.24	78.24
13	350	90	50	50.58	50.58	50.58
14	350	60	100	25.28	25.28	25.28
15	200	60	100	85.33	85.33	85.33
16	200	60	100	85.33	85.33	85.33

Results and Discussion

Experimental design

As remarked earlier, in this study, RSM was used to analyze the experiments that followed a two-level factorial design with three variables or design factors and all experiments were performed twice.

Analysis of ANOVA

Findings of a previous study revealed that evaluating the quality of the fitted model is necessary because of the inability of the developed mathematical model to be satisfactorily described from the experimental results [21]. Besides, in the two-level factorial design, the fitted model or significance model of factorial allows all the three-factor interactions (AB, AC, and BC) as well as the interaction of ABC [22].

The *p*-value (probability values) can be used to assess the significance of coefficients in the models that indicate patterns of interaction among design factor variables. In addition to that, Fisher's variance ratio (*F*-value) was used to measure variation in data around the mean [23].

In Table 2, the coded values of A, B, and C represent the torrefaction temperature, reaction time, and biomass loading, respectively, and are significant with the "Prob > F" less than 0.0001 with a model *F*-value of 12883.84. Sample weight shows the great influence in the yield on bio-coal production, as evidenced by the *F*-value of 11373.05. The *F*-values for torrefaction temperature and reaction time were 2060.86 and 4308.37, respectively. The graph test is significant, implying that optimization can be examined. The factorial model of the present study is fit and significant as the lack-of-fit test was found to be insignificant. As this was also proven in previous study, when the lack-of-fit indicating the insignificant, it implies the model is fit [24].

R^2 and adjusted R^2 can be used to evaluate the characteristics and importance of the regression model. Both values show the accuracy and general availability of the regression model [25]. In Table 3, the R^2 value of the multiple correlation coefficient of the regression equation is 0.9999, which indicates that 99.99% of the total variation in bio-coal yield was assigned to the design factor variables studied. This means that the models fitted well with the experimental data.

The amount of variation can also be computed using the model's clarified mean [26]. The adjusted R^2 value for the regression model is 0.9998. On the basis of both values, it is possible to conclude that the large value of R^2 and the slight differences between them indicate that the fitted empirical model can be used for prediction.

The adjusted R^2 of 0.9998 is in reasonable agreement with the predicted R^2 of 0.9996 as the difference in values between both models are always less than 0.2. Adeq. precision used to calculate and estimate the signal-to-noise ratio. The desired ratio for Adeq. precision was found to be 4. According to our results, the signal-to-noise ratio of 308.813 indicates an acceptable signal. Thus, it can be concluded that the model can be used to navigate the design space.

From the conducted regression analysis, the following mathematical model in terms of coded levels can be expressed using Equation 2.

Table 2. ANOVA for the selected factorial model

Source	Sum of Squares	*F*-value	*p*-value Prob > F	Remarks
Model	6820.38	12883.84	< 0.0001	Significant
A-torrefaction temperature	155.85	2060.86	< 0.0001	
B-reaction time	325.82	4308.37	< 0.0001	
C-Biomass loading	860.09	11373.05	< 0.0001	
AB	316.41	4183.88	< 0.0001	
AC	902.47	11933.43	< 0.0001	
BC	1089.07	14400.93	< 0.0001	
ABC	1041.35	13769.96	< 0.0001	
Pure error	0.60			
Cor total	6820.99			

Table 3. R^2 statistics for the fitted model

Factors	Value
R-Squared	0.9999
Adj. R-Squared	0.9998
Pred. R-Squared	0.9996
Adeq. Precision	308.813

$$\text{Bio-coal yield (\%)} = -118.19 + 0.67A + 3.62B + 5.68C - 0.01AB - 0.02AC - 0.08BC + 0.0002ABC \quad (2)$$

Study and validation of models for bio-coal products

The factorial design with 16 runs was used to screen all the three design factors. Figure 1(a, b) illustrates the diagnostic plot of the torrefaction analysis. It is evidenced in Figure 1(a) that the half-normal plot of the bio-coal yield is normally distributed. It can be observed that less noise occurred because of the factors A, B, and C being spread away from a straight line. There is only a 0.01% chance that an *F*-value this large could occur because of noise.

As per the residuals versus the runs plots as shown in Figure 1(b), the plots are distributed above and below the x-axis. The proposed model is acceptable and reliable because all the points lie between ±3.

Parametric interactions within the models of bio-coal products

Figure 2(a) depicts the response surface plots of the interaction effect of torrefaction temperature and reaction time on the yield of bio-coal products to obtain maximum responses. The maximum bio-coal yield was 84.05% during torrefaction temperature of 200 °C, a reaction time of 60 min, and biomass loading of 100 g.

Figure 2(b) expresses the response surface plots of the interaction effect between the torrefaction temperature and biomass loading on bio-coal yield. The maximum response obtained from the diagnostic of the graph shows that the bio-coal yield was 79.73% during torrefaction temperature of 200 °C, biomass loading of 50 g, and reaction time of 90 min. Finally, Figure 2(c) illustrates the response surface plots of the interaction effect of reaction time and biomass loading on bio-coal yield. The maximum bio-coal yield was 65.93% during a reaction time of 60 min, biomass loading of 50 g, and torrefaction temperature of 200 °C.

According to the response surface graph, as the torrefaction temperature and reaction time increase, the bio-coal yield decreases. The thermal deterioration of lignocellulosic compounds during the torrefaction process of dry leaves may plausibly cause a decrease in bio-coal yield. Apart from that, it is caused by hydroxyl group dehydration, combustion, and volatilization of organic compounds [27].

The optimization process was used to determine the optimal conditions of the torrefaction process to obtain maximum bio-coal yield. Numerical optimization was used to find the most optimal solution. According to Figure 3, the results show that the optimal condition can be achieved at torrefaction temperature of 200 °C, a reaction time of 60 min, and biomass loading of 100 g with 1.00 desirability and 85.33% bio-coal yield. It shows significant desirability of torrefaction temperature, reaction time, and biomass loading.

Characterization of raw material and bio-coal: FTIR analysis

Figure 4 shows the FTIR analysis performed to determine the chemical changes in the structure of bio-coal via torrefaction at 200 °C. The spectra of raw dry leaves and bio-coal samples show that they contain an O–H bond originating from alcohol and phenols observed in the 3400 cm^{-1}–3600 cm^{-1} region. Other than that, ketone and aldehyde groups have been observed in the 1680 cm^{-1}–1750 cm^{-1}. Other functional group peaks containing aromatic groups were also observed from 690 cm^{-1}–900 cm^{-1}. The presence of aromatic hydrocarbon indicates significant characteristics of combustible materials [24].

Characterization of raw material and bio-coal: TGA

The TGA curve in Figure 5 shows that the sample of bio-coal produced at 350 °C exhibits maximum weight loss at 900 °C, which is 11.2 mg of weight loss, or about 56% of the total weight. The bio-coal sample at 200 °C shows 10.84 mg of weight loss, or about 54.2% of the total weight. Raw dry leaves weighed 10.62 mg, which is approximately 53.1% of the total weight. As the torrefaction temperature increases, the weight loss also increases. This is attributable to the moisture release during the thermal events. At some point during the torrefaction, the biomass was dried or dehydrated and the moisture was removed from it as the weight loss can be seen to be significantly high [28,29].

Figure 6 shows the temperature-dependent profile of derivative weight loss, which is highlighted by the sequence of decomposition of hemicellulose, cellulose, and lignin [30]. The first peak at 50 °C and 0.27 mg/min weight loss indicates the decomposition of hemicellulose and the second peak at 300 °C and weight loss of 0.54 mg/min indicates cellulose decomposition. The intensity of the peak for the sample at 350°C was much lower than that at 200 °C. This proved that the torrefaction of dry leaves at higher temperatures can reduce the highly volatile component in the bio-coal [19].

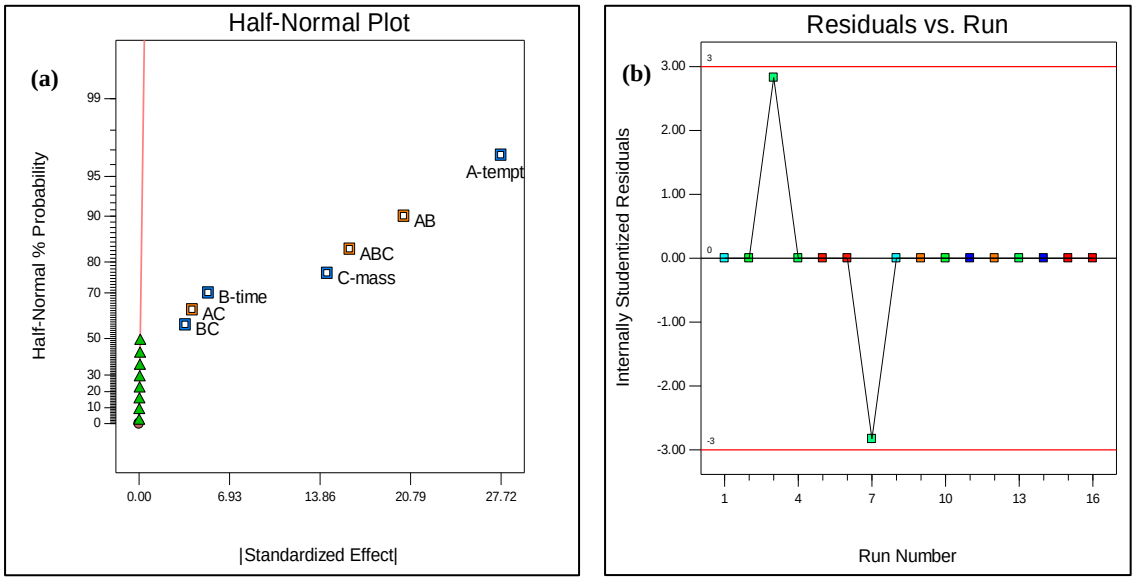
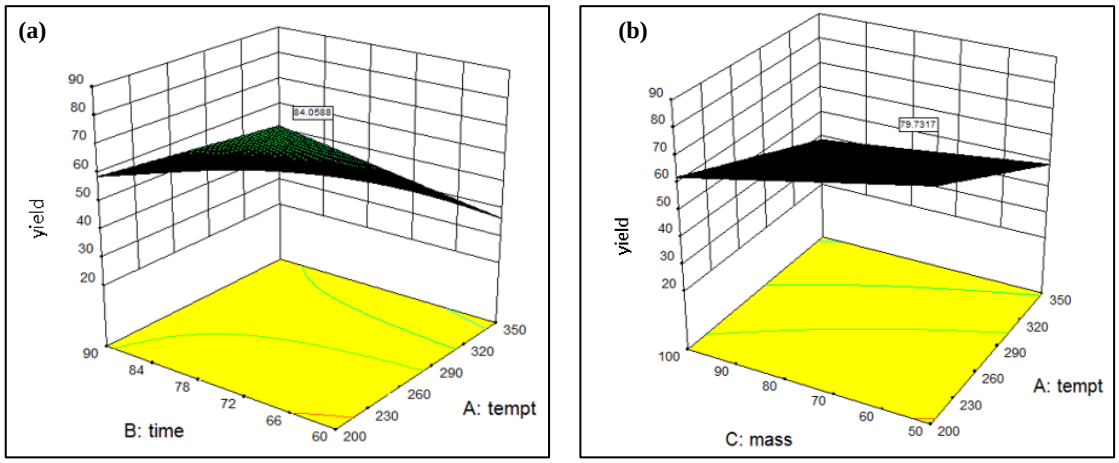


Figure 1. Diagnostic and model graphs for a yield of bio-coal: (a) half-normal plot and (b) residuals versus run



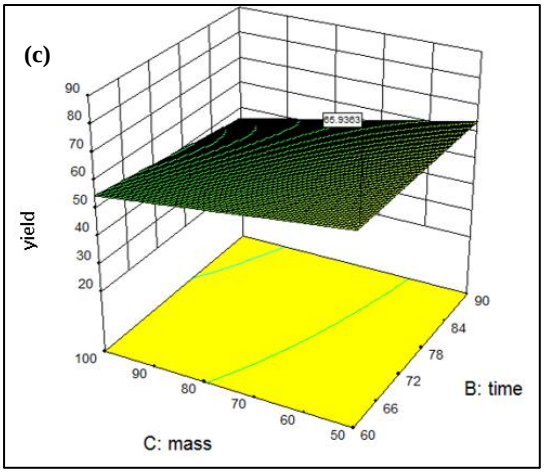


Figure 2. Model graphs (a) response surface plot of the interaction effect between torrefaction temperature and reaction time, (b) response surface plots of the interaction effect between the torrefaction temperature and biomass loading (c) response surface plots of the interaction effect between the reaction time and biomass loading

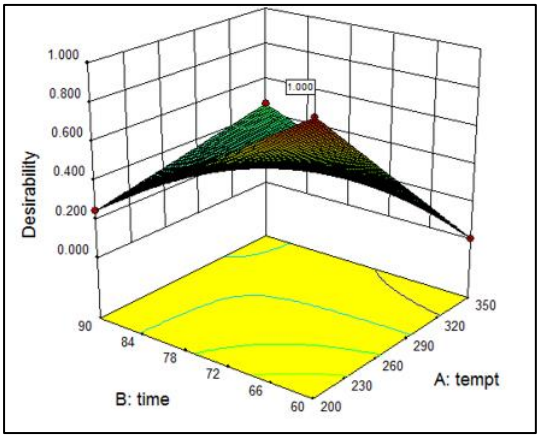


Figure 3. Desirability plot of response surface

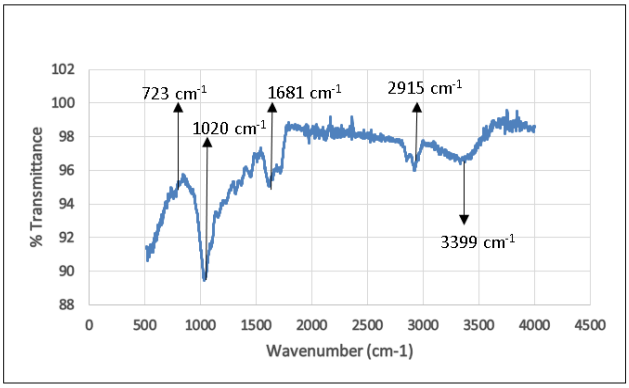


Figure 4. FTIR spectra for bio-coal sample via torrefaction at 200 °C

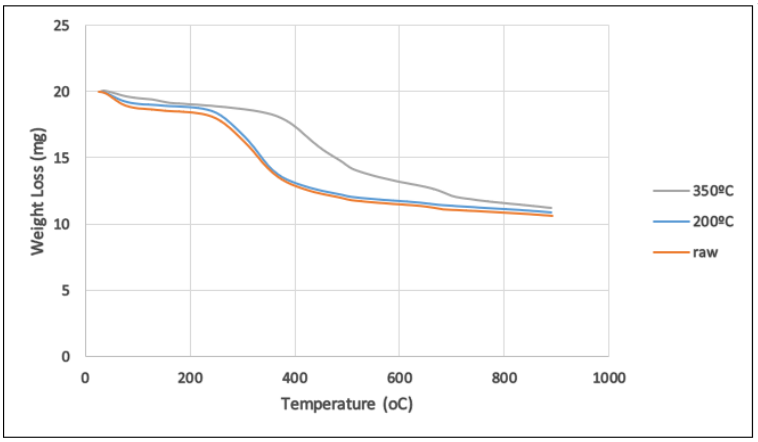


Figure 5. Thermal effect profile of raw dry leaves and bio-coal at different temperatures

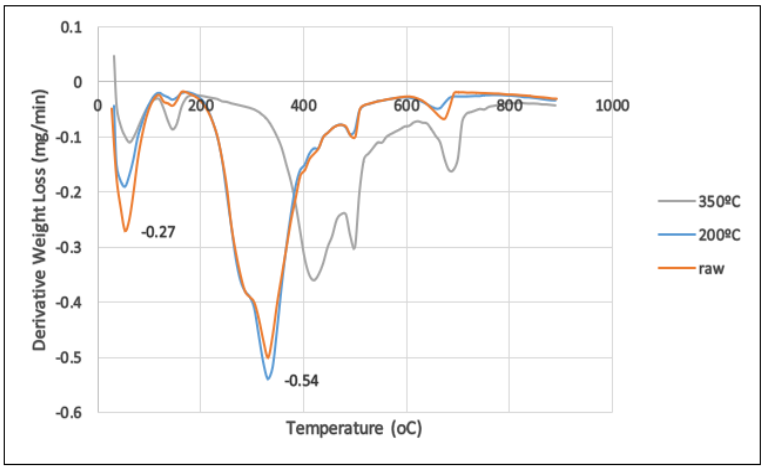


Figure 6. Derivative weight loss of raw dry leaves and bio-coal at different temperatures

Conclusion

In this study, torrefaction of dry leaves was performed using a front-loading furnace under various conditions to determine the optimum conditions for the operating variables. In this study, the Design-Expert software was successfully employed to optimize the production of bio-coal. A high energy-yielding bio-coal was successfully prepared from dry leaves, one of the world's most abundant forestry wastes. By means of RSM, factors namely torrefaction temperature, reaction time, and biomass loading were screened using factorial design. These factors are the major contributors to the high yield of bio-coal. The optimum bio-coal (85.33% yield) was obtained at a torrefaction temperature of 200 °C, a reaction time of 60 min, and biomass loading of 100 g. ANOVA analysis confirmed that the models used to predict bio-coal yield as a function of torrefaction time, reaction time, and biomass loading were significantly well fitted and sufficiently expressed the experimental results. From FTIR analysis, it was deduced that the functional groups present in the bio-coal are alcohols, phenols, ketones, aldehydes, and aromatic groups. In thermogravimetric analysis, the TGA curve shows that the sample of bio-coal produced at 350 °C exhibited the maximum weight loss or about 56% of the total weight.

The differential thermogravimetric analysis profile clearly shows that hemicellulose decomposition started at 50 °C, whereas cellulose decomposition started at 300 °C. This investigation presented a strategy for producing solid bio-coal from dry leaves for effective utilization of biomass efficiency, as well as a suggestion for integrating them for sustainable production of renewable energy.

Acknowledgment

The authors would like to thank the School of Chemical Engineering, College of Engineering, Universiti Technology MARA (UiTM) Shah Alam for the facilities used in this study.

References

1. Medic, D. (2012). Investigation of torrefaction process parameters and characterization of torrefied biomass. PhD Dissertation, Iowa State University.
2. Demirel, Y. (2012). Energy: Production, conversion, storage, conservation, and coupling. In Energy: Production, Conversion, Storage, Conservation, and Coupling (Green Energy and Technology). Springer Verlag, London: pp. 35.
3. Chew, J. J. and Doshi, V. (2011). Recent advances in biomass pretreatment - torrefaction fundamentals and technology. *Renewable Sustainable and Energy Reviews*, 15(8): 4212-4222.
4. Asadullah, M. (2014). Barriers of commercial power generation using biomass gasification gas: A review. *Renewable Sustainable and Energy Reviews*, 29: 201-215.
5. Isa, K. M., Kasim, F. H., Ali, U. F. M. and Rashid, R. A. (2017). Characterization, calculation of calorific values, and bio-oil production via thermochemical processes of municipal solid waste in Perlis, Malaysia. *Malaysian Journal of Analytical Sciences*, 21(4): 801-809.
6. Bergman, P. C., Boersma, R., Zwart, R. W. R. and Kiel, J. H. (2005). Torrefaction for biomass co-firing in existing coal-fired power stations. Energy Research Centre of Netherlands.
7. Van der Stelt, M. J. C., Gerhauser, H., Kiel, J. H. A. and Ptasinski, K. J. (2011) Biomass upgrading by torrefaction for the production of biofuels: A review. *Biomass and Bioenergy*, 35(9): 3748-3762.
8. Eseyin, A. E., Steele, P. H. and Pittman, C. U. (2015). Current trends in the production and applications of torrefied wood/biomass - A review. *BioResources*, 10(4): 8812-8858.
9. Chouchene, A., Jeguirim, M., Khiari, B., Trouvé, G. and Zagrouba, F. (2010). Study on the energy mechanism during devolatilization/char oxidation and direct oxidation of olive solid waste in a fixed bed reactor. *Journal of Analytical and Applied Pyrolysis*, 87(1): 168-174.
10. Stelte, W., Nielsen, N. P. K., Hansen, H. O., Dahl, J., Shang, L. and Sanadi, A. R. (2013). Reprint of: Pelletizing properties of torrefied wheat straw. *Biomass and Bioenergy*, 53: 105-112.
11. Azócara, L., Hermosillab, N., Gayb, A., Rochac, S., J. and Jarae, P. (2019). Brown pellet production using wheat straw from southern cities in Chile. *Fuel*, 237: 823-832.
12. Phuang, Y. W., Ng, W. Z., Khaw, S. S., Yap, Y. Y., Gan, S., Lee, L. Y. and Thangalazhy-Gopakumar, S. (2021). Wet torrefaction pre-treatment of yard waste to improve the fuel properties. *Materials Science for Energy Technologies*, 4: 211-223.
13. Singh, S., Chakraborty, J. P. and Monoj Kumar Mondal, M. K. (2019). Optimization of process parameters for torrefaction of *Acacia nilotica* using response surface methodology and characteristics of torrefied biomass as upgraded fuel. *Energy*, 186: 1-14.
14. Lin, Y., Zheng, N. and Lin, C. (2021). Repurposing *Washingtonia filifera* petiole and *Sterculia foetida* follicle waste biomass for renewable energy through torrefaction. *Energy*, 223: 1-10.
15. Sarker, T. R., Azargohar, R., Dalai, A. K. and Meda, V. (2021). Enhancement of fuel and physicochemical properties of canola residues via microwave torrefaction. *Energy Reports,* 7: 6338-6353.
16. Angelique, T. C., Villahermosa, J. E. R., Cabatingan, L. K. and Alchris, W. G. (2018). Energy densification of sugarcane leaves through torrefaction under minimized oxidative

atmosphere. *Energy for Sustainable Development*, 42: 160-169.
17. Thani, N. S. M., Ghazi, R. M. and Ismail, N. (2017). Response surface methodology optimization of oil removal using banana peel as biosorbent. *Malaysian Journal of Analytical Sciences*, 21(5): 1101-1110.
18. Fisher, R. A. (1936). The Design of Experiments. Macmillan Publishing, London: pp. 180.
19. Asadullah, M., Adi, A. M., Suhada, N., Malek, N. H., Saringat, M. I., and Azdarpour, A. (2014). Optimization of palm kernel shell torrefaction to produce energy densified bio-coal. *Energy Conversion and Management*, 88: 1086-1093.
20. Naijia H., Bezerra, T. L., Wu, Q., Ben, H., Sun, Q., Adhikari, S. and Ragauskas, A. J. (2017). Effect of autohydrolysis pretreatment on biomass structure and the resulting bio-oil from a pyrolysis process. *Fuel*, 206: 494-503.
21. Zhang, C. Y., Yang, L. J., Rong, F., Fu, D. G. and Gu, Z. Z. (2012). Boron-doped diamond anodic oxidation of ethidium bromide: Process optimization by response surface methodology, *Electrochimica Acta*, 64: 100-109.
22. Mark J. A. and Patrick J. W. (2007). DOE simplified: Practical tools for effective experimentation, second edition. Productivity Press, London: pp. 3-6.
23. Ayeni, A. O., Banerjee, S., Omeleye, J. A., Hymore, F. K., Giri, B. S., Deshmukh, S. C., Pandey, R. A. and Mudliar, S. N. (2013). Optimization of pretreatment conditions using full factorial design and enzymatic convertibility of shea tree sawdust, *Biomass and Bioenergy*, 48: 130-138.
24. Isa, K. M., Daud, S., Hamidin, N., Ismail, K., Saad, S. A. and Kasim, F. H. (2011). Thermogravimetric analysis and the optimisation of bio-oil yield from fixed-bed pyrolysis of rice husk using response surface methodology (RSM). *Industrial Crops and Products*, 33(2): 481-487.
25. Zhu, T., Heo, H. J. and Row, K. H. (2010). Optimization of crude polysaccharides extraction from *Hizikia fusiformis* using response surface methodology. *Carbohydrate Polymers*, 82(1): 106-110.
26. Zhu, M., Wang, C., Wang, X., Chen, S., Zhu, H. and Zhu, H. (2011). Extraction of polysaccharides from *Morinda officinalis* by response surface methodology and effect of the polysaccharides on bone-related genes, *Carbohydrate Polymers*, 85(1): 23-28.
27. Al-wabel, M. I., Al-omran, A. and El-naggar, A. H. (2012). Pyrolysis temperature induced changes in characteristics and chemical, *Bioresource Technology*, 131: 374-379.
28. Barzegar, R., Yozgatligil, A., Olgun, H. and Atimtay, A. T. (2020). TGA and kinetic study of different torrefaction conditions of wood biomass under air and oxy-fuel combustion atmospheres. *Journal of the Energy Institute*, 93(3): 889-898.
29. Jaramillo, F. E. and Alvarado, P. N. (2020). Thermogravimetric evaluation of torrefaction parameters on thermal properties of a colombian woody biomass. *Chemical Engineering Transactions*, 80: 133-138.
30. Ververis, C., Georghiou, K., Christodoulakis, N., Santas, P. and Santas, R. (2004). Fiber dimensions, lignin and cellulose content of various plant materials and their suitability for paper production, *Industrial Crops and Products*, 19(3): 245-254.

Malaysian Journal of Analytical Sciences (MJAS)
Published by Malaysian Analytical Sciences Society

CHALLENGES OF ALUM RECOVERY FROM DRINKING WATER TREATMENT SLUDGE USING ELECTROLYSIS METHOD

(Cabaran untuk Pemulihan Alum daripada Enapcemar Rawatan Air Minuman Melalui Kaedah Elektrolisis)

Rizkiy Amaliyah Barakwan and Yulinah Trihadiningrum*

Department of Environmental Engineering, Faculty of Civil, Planning, and Geo Engineering, Institut Teknologi Sepuluh Nopember, Kampus ITS Sukolilo, Surabaya, 60111, Indonesia

**Corresponding author: trihadiningrum@gmail.com*

Received: 4 July 2021; Accepted: 17 October 2021; Published: 27 December 2021

Abstract

Aluminum sulfate was used as coagulant in the coagulation process in drinking water treatment plant (DWTP) to remove various types of contaminants from the raw water. Acidification was applied for alum recovery from sludge, but it was a nonselective process. It was followed by an electrolysis to separate the aluminum from impurities. This study aims to evaluate the efficiency and challenges of the electrolysis in the alum coagulant recovery from drinking water treatment sludge (DWTS). The dried DWTS was acidified using sulfuric acid at pH 3 and then separated in centrifugation to get the acidified alum sludge solution. The electrolysis was conducted using carbon (C)/silver (Ag), platinum (Pt)/platinum (Pt), and platinum (Pt)/stainless stell (SS A304) electrodes with current density of 25, 29.17, and 12.5 mA/cm^2, respectively. The electrolysis was performed in a batch recirculation reactor without membrane, using cation exchange membrane (CEM), and anion exchange membrane (AEM). Chemical oxygen demand (COD) value was measured using titrimetric method. The metals (Al, Fe, Mn, Zn, Pb, Cu, and Cr) in the deposited matter at the cathode were weighed and analyzed by Inductively Coupled Plasma (ICP). The results showed that the use of CEM in the electrolysis with Pt/SS A304 electrodes increased the alum recovery up to 67.56% that was pure of organic contaminants. The challenges in alum coagulant recovery from DWTS using electrolysis method were the differences of the raw water quality during wet and dry seasons, the appropriate electrical current density, the electrode materials, the potential value at the anode and cathode, and the use of the ion exchange membrane in the electrolysis.

Keywords: alum recovery, cation exchange membrane, drinking water treatment sludge, electrolysis.

Abstrak

Aluminium sulfat digunakan sebagai penggumpal dalam proses penggumpalan-pengentalan di loji rawatan air minuman untuk menghilangkan pelbagai jenis bahan cemar yang terdapat dalam kandungan air mentah. Pengasidan telah dipilih untuk proses pemulihan penggumpal dari enapcemar alum, tetapi proses ini bersifat tidak selektif. Oleh itu, proses pemulihan ini kemudiannya diikuti dengan proses elektrolisis untuk memisahkan aluminium daripada kekotoran. Kajian ini bertujuan untuk menilai kecekapan dan cabaran kaedah elektrolisis dalam proses pemulihan alum daripada enapcemar rawatan air minuman. Untuk mendapatkan larutan lumpur tepu yang berasid, enap cemar telah ditambah dengan asid sulfurik pada pH 3 dan seterusnya dipisahkan dengan kaedah pengemparan. Elektrolisis dilakukan menggunakan elektrod karbon (C) / perak (Ag), platinum (Pt) / platinum (Pt), dan platinum (Pt) / keluli tahan karat (SS A304) dengan kepadatan arus 25; 29.17; dan 12.5 mA /cm^2. Elektrolisis

dilakukan dalam reaktor sesekumpul dengan sistem kitaran semula tanpa membran, membran pertukaran kation (CEM), dan juga membran pertukaran anion (AEM). Kepekatan permintaan oksigen kimia (COD) diukur dengan kaedah titrimetrik. Kepekatan logam (Al, Fe, Mn, Zn, Pb, Cu, dan Cr) dalam enapan pulih guna yang menumpuk pada katod ditimbang dan dianalisis menggunakan plasma gandingan aruhan. Hasil kajian ini menunjukkan bahawa penggunaan CEM dalam elektrolisis menggunakan elektrod Pt / SS A304 dapat meningkatkan kecekapan pemulihan alum yang bersih dari bahan cemar organik sehingga 67.56%. Cabaran dalam memulihkan penggumpal alum dari enap cemar rawatan air minuman menggunakan kaedah elektrolisis ini terletak pada perbezaan kualiti air mentah pada musim hujan dan kering, ketumpatan arus elektrik yang sesuai, pemilihan bahan elektrod, nilai potensi pada anod dan katod, serta penggunaan membran pertukaran ion semasa elektrolisis dijalankan.

Kata kunci: pemulihan alum, membran pertukaran kation, enap cemar rawatan air minuman, elektrolisis

Introduction

Municipal drinking water companies (PDAMs) in Indonesia generally use river water as raw water in drinking water treatment plants (DWTPs) [1]. River water contains various types of contaminants, such as organic and inorganic substances, bacteria, viruses, and other parasites [2]. These contaminants are in river water in the form of suspended particles, colloids, and deposits [2]. The coagulation-flocculation processes in the DWTP aims to remove suspended solids and colloids in the raw water [3]. Aluminum sulfate ($Al_2(SO_4)_3$) or alum is the most widely used coagulant in the DWTP process [3]. According to Yonge [4], alum is effective in reducing turbidity, color, and dissolved organics in small doses, low costs, not corrosive, and there is no slag formation in pipes compared to the use of iron salt as a coagulant. The use of alum in the DWTP causes the resulting sludge to contain a high concentration of aluminum of 105 g/kg [5]. The drinking water treatment sludge (DWTS) is generally referred as alum sludge [5].

Alum sludge contains various forms of compounds such as metals (aluminum and iron), organic substances, nitrogen, phosphorus, potassium, and pathogenic bacteria [5]. Barakwan et al. [6] stated that alum sludge from Surabaya DWTP contained aluminum of 1194 mg/L, iron of 515 mg/L, chromium of 0.217 mg/L, copper of 0.559 mg/L, Biological Oxygen Demand (BOD) of 1,082.47 mg/L, and Chemical Oxygen Demand (COD) of 9,666.7 mg/L. The high concentration of aluminum highly exceeded the effluent standards of 10 mg/L according to the National Pollutant Discharge Elimination System (NPDES) [7]. Other characteristics also exceeded the effluent standards according to The State Ministry for The Environment Decree No. 5/2014 concerning Quality Standards of Wastewater [8]. In addition, the amount of aluminum reached 671,316 kg/year with Toxic Weighting Factor (TWFs) values of 40,188 kg/year [7].

Acidification of the alum sludge is commonly applied for alum recovery but it is a nonselective process [9]. This is due to the acidification becoming a chemical dissolution of other heavy metals and organic matter which then act as impurities to the recovered alum coagulant [10]. This process can be followed by an electrolysis method to separate the aluminum from impurities [11]. According to Widodo et al. [12], electrolysis is a mechanism for metal ions separation that are applied because the result has a higher purity without the addition of chemicals. Organic contaminants could decrease mobility of ions and conductivity in electrolyte, so it decreased the effectiveness of alum recovery with electrolysis [13]. In addition, heavy metal impurities might impact the effectiveness of the recovered alum coagulant [14]. Electrodeposition, electrooxidation, and electrolysis with membrane separation can be applied to achieve alum recovery with less impurities [14]. The potential values that are given to the electrodes also affects the purity of the deposited at the cathode [15]. This study aims to evaluate the efficiency and challenges of the electrolysis in the alum coagulant recovery from DWTS.

Materials and Methods

Sludge collection and preparation

Fresh alum sludge samples were collected from Surabaya DWTP during wet and dry seasons in 2019. The sludge sample was dried in a laboratory oven at 105 °C for 24 hours. The dried sludge sample was grinded and passed through 2 mm sieve, then it was mixed to homogenize it before being used in the next process.

Acidification process and characterization of acidified alum sludge solutions

An amount of 200 g sludge sample was mixed with 1 L of aquadest using magnetic stirrer at 700 rpm. 1 N sulfuric acid was added to the sludge solution until it reached pH 3 and acidified for 2 hours. Then, the adjusted acidified sludge solution was centrifuged at 4000 rpm for 10 minutes and filtered using 0.45 µm Whatman filter paper. The acidified alum sludge solution was characterized before being used for electrolytes in the electrolysis process. The metals (aluminum, iron, manganese, zinc, lead, copper, and chromium) were analyzed using inductively coupled plasma (ICP) type Agilent Technologies series 700 ICP-OES. The COD was analyzed using titrimetric method [16, 17].

Electrolysis process

The electrolysis process was performed using a batch recirculation reactor in a laboratory scale. The reactor was made from acrylic in a dimension of 5 cm x 20 cm with 2 cm thickness. In the electrolysis without membrane, the electrolysis cell consisted of one compartment (Figure 1). Whereas in the electrolysis with membrane, the electrolysis cell consisted of two compartments (Figure 2ab).

The semipermeable ion exchange membrane which was used were AEM type AMI-7001S or CEM type CMI-7000S, purchased from Membrane International, Inc. In the electrolysis using CEM, the acidified alum sludge solution at pH 3 was pumped into the anode compartment and the sulfuric acid at pH 3 was pumped into the cathode compartment. While, in the AEM configuration, the acidified alum sludge solution at pH 3 was pumped into the cathode compartment and the sulfuric acid at pH 3 was pumped into the anode compartment. An amount of 1 L feed tank of acidified alum sludge solution and sulfuric acid at pH 3 were continuously recirculated into the reactor using peristaltic pump with a flow rate of 0.5 mL/s. The distance between the electrodes was 1 cm. Electrical current density was determined from the results of the polarization test with each type of electrode in the previous studies [6, 18, 19]. Table 1 shows the conditions in the electrolysis processes.

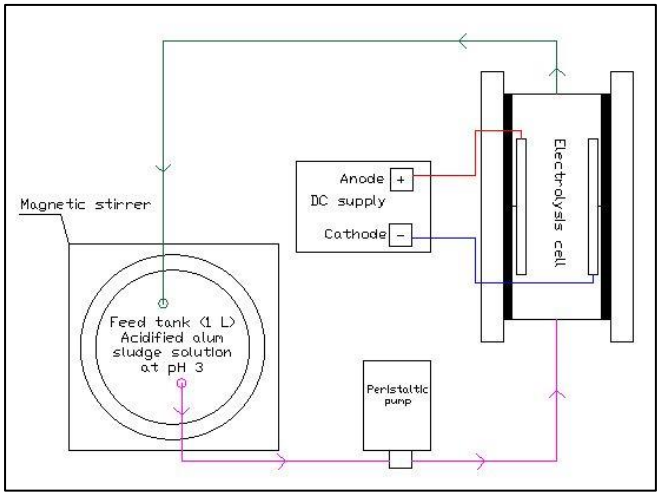


Figure 1. Electrolysis reactor design without membrane

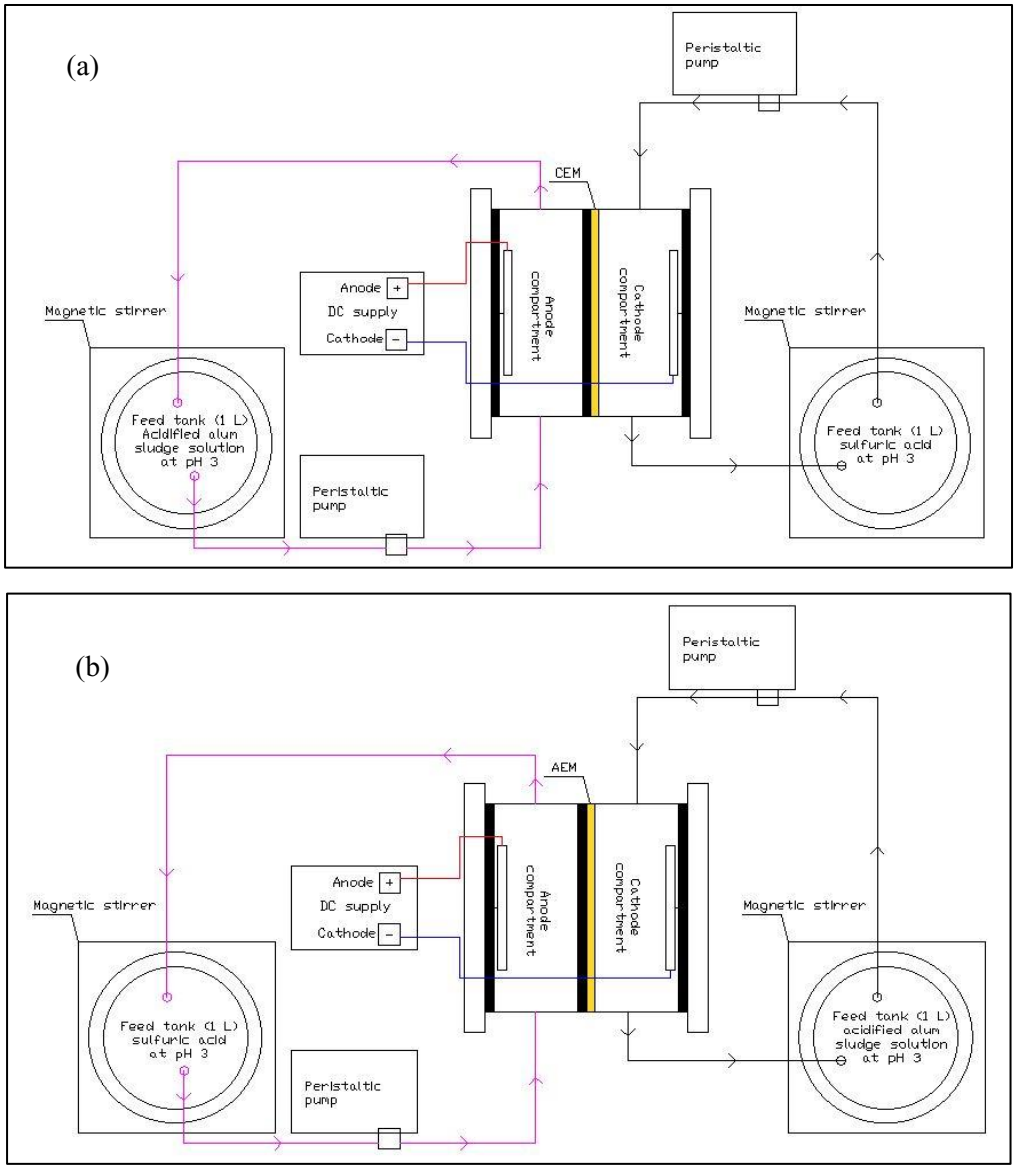


Figure 2. Electrolysis reactor design using: (a) cation exchange membrane (CEM), (b) anion exchange membrane (AEM)

Table 1. Electrolysis conditions

No	Electrolysis Processes	Conditions
1	Electrolysis using carbon (C) (+)/ silver (Ag) (-) electrodes	At initial pH 3, electrical current density of 25 mA/cm^2, and voltage of 5.3 V for 10 hours operation time.
2	Electrolysis using platinum Pt (+)/ Pt (-) electrodes	At initial pH 3, electrical current density of 29.17 mA/cm^2, and voltage of 5.2 V for 8 hours operation time.
3	Electrolysis using Pt (+)/ stainless steel (SS A304) (-) electrodes	At initial pH 3, electrical current density of 12.5 mA/cm^2, and voltage of 4.9 V for 6 hours operation time.

Table 1 (cont'd). Electrolysis conditions

No	Electrolysis Processes	Conditions
4	Electrolysis using C (+)/Ag (-) electrodes using CEM	At initial pH 3, electrical current density of 25 mA/cm^2, and voltage of 17.3 V for 10 hours operation time.
5	Electrolysis using C (+)/Ag (-) electrodes using AEM	At initial pH 3, electrical current density of 25 mA/cm^2, and voltage of 14.3 V for 10 hours operation time.
6	Electrolysis using Pt (+)/ SS A304 (-) electrodes using CEM	At initial pH 3, electrical current density of 12.5 mA/cm^2, and voltage of 23.8 V for 10 hours operation time.

Analytical measurement

The pH value was measured every hour during electrolysis. The deposited matter at the cathode was dried at 105°C, weighed, and then soaked in nitric acid [20]. Aluminum and other metal impurities (Fe, Mn, Zn, Pb, Cr, Cu) were analyzed using ICP type Agilent Technologies series 700 ICP-OES [16]. The COD was measured by titrimetric method using closed reflux digestion [17]. The electrodes were cleaned using 1 N sulfuric acid solution. Alum recovery efficiency, the SEC value, COD value, and metal composition in deposit were calculated according to Eqs. 1-4.

$$\text{Alum recovery (\%)} = \frac{mass\ alum\ in\ cathode\ at\ t6\ h}{mass\ alum\ at\ t0\ h} \times 100\% \quad (1)$$

$$\text{W} = \frac{I \times V \times t}{\frac{mass\ alum\ at\ t0\ h - mass\ alum\ at\ t6\ h}{Vf}} \quad (2)$$

$$\text{COD removal (\%)} = \frac{[COD\ at\ t0\ h] - [COD\ at\ t6\ h)}{[COD\ at\ t0\ h)} \times 100\% \quad (3)$$

$$\text{Metal composition (\%)} = \frac{metal\ mass\ at\ cathode}{total\ metal\ mass\ at\ cathode} \times 100\% \quad (4)$$

where: W = specific energy consumption (kWh/m^3); I = electrical current (A); V = potential value (V); t = operation time; Vf = feed tank volume (L); mass alum at t0 h = initial alum weight; mass alum in cathode at t6 h = alum weight t6 h at cathode.

Results and Discussion

Acidified alum sludge solutions characteristics

The aluminum concentrations in the acidified alum sludge solution reached 3,762 mg/L in the wet season 2019 (Table 2). While, in the dry season 2019, the aluminum concentration reached 1,548.57 mg/L (Table 2). High concentration of aluminum was influenced by the high doses of alum coagulants in coagulation-flocculation process [21, 22, 23]. It was caused by the worse river water quality in the wet season than in the dry season, so that the required dose of coagulant was high in DWTP [21, 22, 24]. It was due to the total suspended solids (TSS) concentrations in the wet season at Karangpilang sampling point in the Surabaya river were higher (20 mg/L) than those in the dry season (14.7 mg/L) [25, 26].

The second highest metal concentration in the samples was iron, which was 215.7 mg/L in the wet season and 72.43 mg/L in the dry season (Table 2). The high result of iron concentrations was from the addition of $FeCl_3$ as a mixture of alum coagulant when the raw water had a low water quality in the wet season [27]. The third highest metal concentration in the acidified alum sludge solutions were manganese which was 119.5 mg/L (Table 1). The high result manganese concentration was from the natural content of these elements in sediments, rocks, and soil in the rivers, the

use of low purity coagulants, and the discharge of industrial wastewater along the Surabaya River [25, 28, 29, 30]. The concentrations of zinc, lead, copper, and chromium in the acidified alum sludge solutions were caused by the content of these metals in the raw water from Surabaya River exceeded Class 1 water quality standards according to Government Regulation No. 82/2001 concerning The Management of Water Quality and The Control of Water Pollution [31]. This was due to the fact that there were 42 discharge points for domestic wastewater and 9 out of 18 industries in the Karangpilang area that discharged their wastewater treatment into the Surabaya river [25].

The COD concentration of the solutions during the wet season was 2,060 mg/L (in 2019), whereas it was 1,997.3 mg/L during the dry season (Table 2). These results indicated that the COD concentrations of the solutions exceeded the effluent standard of 100 mg/L according to The State Ministry for the Environment Decree No. 5/2014 concerning Quality Standards of Wastewater [8]. The high COD concentrations was influenced by the discharge of the domestic and industrial wastewater along the Surabaya River [30]. The COD concentrations in the Surabaya River reached 80 mg/L in the wet season and 8.19 mg/L in the dry season [25, 26]. The COD concentrations in the wet season exceeded the quality standard for class 1 water which was 10 mg/L according to Government Regulation No. 82/2001 [31].

The acidified alum sludge solution at pH 3 was an electrolyte that was used in the electrolysis for alum recovery. Therefore, its characteristics affected the electrolysis process. The acidification process was carried out at pH 3 to reduce the dissolution of other metals and organic substances in alum sludge [10, 33, 34, 35, 36, 37]. The lower the pH value of the solution, the higher the solubility of the aluminum with the optimum pH of 1-3 [33]. When the pH was <5, the dominant aluminum speciation was in the form of Al^{3+} [38]. Dissolution of other metals and organic compounds in the acidic conditions caused the recovered alum to have a low purity and some problems in the next processes. The electrolysis method could be applied for separating the acidified alum sludge from its impurities.

Electrolysis for alum recovery

The electrolysis method in alum recovery aims to separate aluminum from metal impurities and dissolved organics. Alum is expected to be deposited at the cathode surface (electrodeposition) and dissolved organics will be oxidized at the anode (electrooxidation). Table 3 presents the results of several electrolysis processes in different conditions for alum recovery based on the calculations in Equations 1-3. The efficiency of electrodeposition and electrooxidation in alum recovery (Table 3) is influenced by various factors as described in Table 1.

Table 2. Characteristics of the acidified alum sludge solutions

No	Acidified alum sludge solution samples	Parameters							
		Metals (mg/L)							COD (mg/L)
		Al	Fe	Mn	Zn	Pb	Cu	Cr	
1	Wet season 2019	3,762.00	215.70	-	2.81	-	1.54	0.31	2,060.00
2	Dry season 2019	1,548.57	72.43	119.50	1.40	0.00	0.21	0.09	1,997.33

Table 3. Electrolysis process for alum recovery

No	Electrolysis processes	Results
1	Using C (+)/ Ag (-) electrodes(*)	% Al recovery= 26.20% as $Al(OH)_3$; % COD removal = 11.11%; Al recovery SEC of 4.66 kWh/kg Deposit composition: Al (96.86%); Fe (0.80%); Pb (0.86%); Cr (0.59%); Cu (0.90%)
2	Using Pt (+)/ Pt (-) electrodes	% Al recovery= 9.63% as $Al(OH)_3$; % COD removal = 26.39%; Al recovery SEC of 8.34 kWh/kg Deposit composition: Al (90.39%); Fe (5.80%); Zn (3.11%); Pb (0.18%); Cr (0.01%); Cu (0.51%)
3	Using Pt (+)/SS A304 (-) electrodes[37]	% Al recovery= 52.10% as $Al(OH)_3$; % COD removal = 24%; Al recovery SEC of 2.81 kWh/kg Deposit composition: Al (82.28%); Mn (11.88%); Fe (5.18%); Zn (0.51%); Cr (0.02%); Cu (0.12%)
4	Using C (+)/ Ag (-) electrodes using CEM	% Al recovery = 66.74% as soluble $Al(OH_4)^-$; The use of CEM could purify the recovered alum from organic compounds in recovery compartment; Al recovery SEC of 14.78 kWh/kg Deposit composition: Al (84.52%); Fe (13.30%); Pb (0.49%); Cr (0.85%); Cu (0.83%)
5	Using C (+)/ Ag (-) electrodes using AEM	% Al recovery= 38.45% as $Al(OH)_3$; The use of AEM could purify the recovered alum from organic compounds in recovery compartment; Al recovery SEC of 11.32 kWh/kg Deposit composition: Al (79.45%); Fe (19.20%); Pb (0.40%); Cr (0.61%); Cu (0.52%)
6	Using Pt (+)/ SS A304 (-) electrodes using CEM	% Al recovery= 67.56% as soluble $Al(OH_4)^-$; The use of CEM could purify the recovered alum from organic compounds in recovery compartment; Al recovery SEC of 9.72 kWh/kg Deposit composition: Al (90.94%); Mn (5.78%); Fe (3.10%); Zn (0.17%); Cu (0.0087%)

(*) SEC (Specific energy consumption)

Electrical current density during electrolysis

In the electrolysis using C/Ag, Pt/Pt, and Pt/SS electrodes, all three processes used the same size of the electrolysis cell, but the current density was different (Table 1). The differences of the current density were influenced by the differences in electrode area and the electrical current. In the electrolysis without membrane, the highest alum recovery efficiency was 52.10% at the electrolysis using Pt/SS A304 electrodes with a current density of 12.5 mA/cm^2 (Tables 1 and 2). While, the efficiencies of alum recovery in the electrolysis using Pt/Pt and C/Ag electrodes were 9.63% and 26.2% with the current densities of 25 mA/cm^2 and 29.17 mA/cm^2, respectively (Tables 1 and 2). It showed that at the current density of 12.5 mA/cm^2 could recover alum with higher efficieny than at 29.17

mA/cm^2. Therefore, the optimum, or the limiting, current density was 12.5 mA/cm^2. The current density that exceeds the limiting value can cause unwanted reactions on the electrode surface, so that it inhibited the deposition of aluminum hydroxide at the cathode and reduce cations mass transfer to the cathode [39]. The decrease of the cations mass transfer to the cathode was caused by the excess of hydrogen gas formation due to overpotential at the cathode [40. In addition to the excess of hydrogen gas formation, the large current densities could also shorten the life time of the electrodes [40]. However, the lowest aluminum composition in the deposited matter at the cathode was 82.28% at the lowest current density in the electrolysis using Pt/SS A304 electrodes. It showed that the low current densities resulted deposited matter with high impurities of other metals (Fe, Mn, Zn, Pb, Cr, and Cu in Table 3).

Optimum current density was affected by the electrolyte characteristics, the type of deposition sought, the operation conditions, electrical current, electrode area, and the ratio of electrode area to volume of the electrolysis cells [41, 42]. The current density could be reduced without expanding the area of the electrode by stirring or recirculating the batch electrolysis reactor [40]. Stirring could also prevent adsorption from hydrogen gas formation which inhibited ions reduction. In this study, a batch recirculation reactor system was used to increase the ions mass transfer to the cathode and accelerate the ion deposition at the cathode with a small current density.

Electrode material in electrolysis

Type of electrodes which was used in the electrolysis for alum recovery from DWTS was influenced by the characteristics of acidified alum sludge solution with the acidic condition (pH = 3) and the high organic content. The use of carbon as anode resulted in an electrosorption process [43]. According to Barakwan et al. [40], the use of carbon for anode could remove COD concentration up to 11.11% in the electrolyte solution (Table 3). The low COD removal was caused by the lack of absorption ability of the carbon surface area, which was compared to the high organic concentrations in the electrolyte. In addition, carbon could decay in a low pH electrolyte, so that it had a short life time. The short life time of the carbon electrode became an economic consideration factor in the cost of electrode maintenance in this electrolysis process. The efficiency of alum recovery reached 26.20% using silver as a cathode (Table 3). It was caused by the decay of the silver cathode in the acid electrolytes and the redeposition of silver as Ag_2O_3 due to the current density in this process was more than 15 $\mu A/cm^2$ [44, 45].

Because of the low efficiency of alum recovery and organic removal in the electrolysis using C/Ag electrodes, platinum could be used as the anode to remove toxic organic contaminants from wastewater at room temperature [42]. Electrochemical mineralization for organic pollutants can be carried out using platinum electrodes with a higher potential than the thermodynamic potential of the oxygen evolution, which is more than 1.23 V / SHE at standard conditions [42]. Platinum electrode was chosen because it was a strong inert metal (does not react with electrolyte solutions), corrosion resistant, good conductors, has a long lifetime, had an electrooxidation ability, and increases mass transfer [46, 47]. These platinum characteristics could accelerate the metal deposition process at the cathode surface. The use of platinum electrodes could remove 24-26.33% of organic contaminants as COD through the electrolysis process (Table 3). However, the use of platinum as anode and cathode resulted in a low alum recovery efficiency of 9.63% (Table 3). This was due to too high electric current (700 mA) was generated at a low potential value, so that it had a high current density. It caused the reduction reaction at the platinum cathode not optimum, and there was blackish brown layer at the cathode. In addition, the use of platinum electrode as cathode also required a high cost, so that the other types of electrodes that could be an alternative as a cathode was stainless steel (SS) alloy [48, 49]. SS electrode was used because of its low cost, easy to obtain, corrosion resistance, low current density, and electrocatalysts with a high specific surface area [50, 51]. It was indicated by an increase in alum recovery reaching 52.10% (Table 3).

Potential value during electrolysis

In the electrolysis for alum recovery from DWTS, there was no measurement for the anode and the cathode potential values. The potential values of the two electrodes were measured as a whole as the voltage value (Table 1). The anode and cathode potential values were important measurements to get the deposition material with a low impurity [15, 52]. For example in the electrolysis with Pt/SS electrodes, the recovery efficiency of alum reached 52.10% (Table 2). This result indicated that the energy used for alum deposition was 52.10% and the remaining (47.90%) was used for the formation of hydrogen gas [15]. The formation of the high hydrogen gas at the cathode surface could prevent the deposition of the metals at the cathode [15]. Therefore, the effectiveness of aluminum hydroxide deposition at the cathode could be increased by decreasing the potential value at the cathode [52]. The potential value that was given to the electrodes also affects the purity of the deposited metal at the cathode [15]. The purity of the aluminum hydroxide could be increased by adjusting the potential value of the cathode according to the standard reduction potential of aluminum. According to Zoski [53], the standard reduction potential for aluminum was -1.66 V and the formation of hydroxide ions was -0.83 V.

The voltage in the electrolysis with CEM and AEM were increased to reach (14.3-23.8) V until the end of the electrolysis (Table 1). While in the electrolysis without membrane, the voltage values tended to remain until the end of the electrolysis (Table 1). This is because the energy was used to encourage ion transfer across the membranes. The increasing voltage was due to the resistance at the membrane [54].

Electrolysis cell configuration

The alum recovery in the electrolysis without membrane using C/Ag, Pt/Pt, and Pt/SS A304 electrodes reached 26.20%, 9.63%, and 52.10%, respectively (Table 3). The electrolysis in one compartment reactor cells resulted in the low alum removal due to the oxidation and the reduction reactions were not selective [55]. In the electrolysis without membrane, there were also the fluctuation values of total dissolved solids (TDS) and pH during the electrolysis due to the redeposition of the ions at the cathode, so that it was measured as TDS value in the electrolyte solutions [39]. This reaction was also called the Electrical Double Layer (EDL) reaction which was caused by the increasing of electrolysis operation time [56]. The EDL could increase the resistance process because of the anode was covered by ions, so that the electrolysis efficiency decreased.

In the electrolysis using AEM, the recovered material was 38.45% in the form of aluminum hydroxide ($Al(OH)_3$) precipitate at the cathode (Table 3, Figure 3). It was indicated by its form of powder in white colour [57]. The pH value also decreases in the anode compartment due to H_2O oxidation which produced H^+. Otherwise, the pH value was increased slightly in the cathode compartment due to the reduction of H_2O to OH^-, while the decrease of pH value was caused by the formation of $Al(OH)_3$ precipitate [58].

In the electrolysis using CEM, the recovered material was 66.74% and 67.56% at the electrolysis using C/Ag and Pt/SS A304, respectively. These results were almost the same as previous studies, the alum recovery using CEM reached the efficiencies of 60-76% [9, 34]. The recovered material was in the form of soluble $Al(OH)_4^-$ (Table 3). The pH value was increased in the cathode compartment due to the use of CEM, which caused the formation of OH^- ions and the proton transported from the cathode to the anode [59]. Otherwise, the pH value was decreased in the anode compartment at the end of the process due to the oxidation process that produced H^+. In the electrolysis with CEM, no precipitate was formed in the cathode compartment, so coagulant recovery was obtained in the form of concentrates. Aluminum hydrolysis caused the breakdown of the aluminum ions when reacting with H_2O so that it produced $Al(OH)_4^-$ at alkaline pH. The formation of $Al(OH)_3$ was a reaction that caused an increase in pH value. The increase in pH value caused $Al(OH)_3$ to react with OH^- to form $Al(OH)_4^-$. $Al(OH)_4^-$ could not be a precipitate and became aluminum soluble [60].

Electrolysis using CEM and AEM could purify alum in the recovery compartment from dissolved organic impurities (Table 2). However, the use of CEM and AEM could not purify the alum recovered from metals impurities (Table 2). Therefore, the alum recovery must be carried out by the electrolysis in the next stage using trivalent membrane to obtain pure aluminum coagulant recovery [61, 62].

In this study, the electrolysis using CEM is recommended for alum recovery because the recovered material was formed in soluble, so that it was ready to be applied as coagulant. The electrolysis using membrane required a higher energy, so that the voltage demand was highly. Reduction in energy requirements during electrolysis could be done by shortening the distance between the electrodes. The closer the distance between the electrodes, the smaller the voltage needed and the faster the ions were reduced.

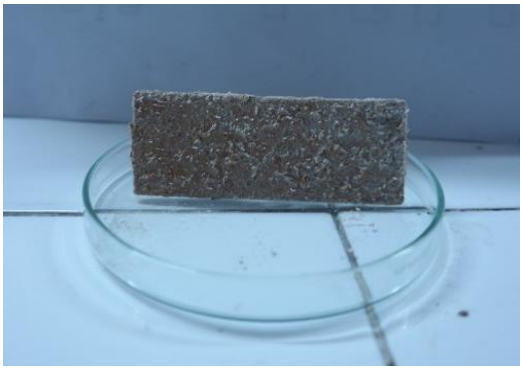


Figure 3. Deposited matter at cathode

Conclusion

The optimum electrolysis process in alum recovery from DWTS was the electrolysis using Pt/SS A304 electrodes with CEM. The efficiency of alum recovery was 67.56% and the recovered alum was in the form of pure soluble $Al(OH)_4^-$ from dissolved organic contaminants. The combination of electrolysis process using a CEM could be an alternative in the removal of dissolved organics impurities in the acidified alum sludge solution. The challenges in alum coagulant recovery from DWTS using electrolysis method were the differences of the raw water quality during wet and dry seasons that affected the characteristics of the DWTS, determination of the appropriate electrical current density, selection of the electrode materials, determination of the potential value at the anode and cathode, and the use of the ion exchange membrane to increase the purity of the recovered coagulant.

Acknowledgement

The authors would like to thank for the financial support from the Ministry of Research and Higher Education of the Republic Indonesia with Master leading to PhD scholarship (PMDSU) No. contract 1287/PKS/ITS/2020, which made this study to work out.

References

1. Bhaskoro and Ramadhan. (2018). Evaluation of Karangpilang 1 drinking water treatment plant quantitative performance in Surabaya water treatment supply. *Journal of Precipitation: Media and Environmental Engineering Development,* 15(2): 62-68.
2. Saukkoriipi, J. (2010). Theoritical study of the hydrolysis of aluminum complexes. Thesis of Doctoral Degree, Linnanmaa, Faculty of Science, Department of Chemistry, University of Oulu.
3. Ahmad, T., Ahmad, K. and Alam, M. (2016). Characterization of water treatment plant's sludge and its safe disposal options. *Procedia Environmental Sciences*, 35: 950-955.
4. Yonge, D. T. (2011). A comparison of aluminum and iron-based coagulants for treatment of surface water in Sarasota County. Florida. Florida, University of Central Florida.
5. Cherifi, M., Boutemine, N., Laefer, D. F. and Hazourli, S. (2016). Effect of sludge pH and treatment time on the electrokinetic removal of aluminum from water potabilization treatment sludge. *CR Chim*, 19: 511-516.
6. Barakwan, R. A., Hardina, T. T., Trihadiningrum, Y. and Bagastyo, A. Y. (2019). Recovery of alum from Surabaya water treatment sludge using electrolysis with carbon-silver electrodes. *Journal of Ecological Engineering*, 20(7): 126-133.

7. US EPA (2011). Drinking water treatment plant residuals management technical report: pp. 192.
8. Ministry for the Environment of Republic Indonesia (2014). State Ministry for the Environment Decree of Republic Indonesia No. 5/2014 concerning Quality Standard of Wastewater, Jakarta, Indonesia, Ministry for the Environment of Republic Indonesia, 2014.
9. Evuti, A. M. and Lawal, M. (2011). Recovery of coagulants from water works sludge: A review. *Pelagia Research Library*, 2(6): 410-417.
10. Xu, G. R., Yan, Z. C., Wang, Y. C. and Wang, N. (2009). Recycle of alum recovered from water treatment sludge in chemically enhanced primary treatment. *Journal of Hazardous Materials*, 161: 663-669.
11. Elicker, C., Filho, P. J. S. and Castagno, K. R. L. (2014). Electroremediation of heavy metals in sewage sludge. *Brazilian Journal of Chemical Engineering*, 31(2): 365-371.
12. Widodo, G., Sigit, R. L., and Torowati, N. Y. (2010). Effect of potential, time, and acidification to the electrodialysis of uranil nitrate solution. *Jurnal Teknologi Bahan Bakar Nuklir (Batan),* 6(1): 1-69.
13. Huitle, C. A. M., Rodrigo, M. A. and Scialdone, O. (2018). Electrochemical water and wastewater treatment. United States, Elsevier.
14. Zou, L., Morris, G. and Qi, D. (2008). Using activated carbon electrode in electrosorptive deionisation of brackish water. *Desalination*, 225: 329-340.
15. Song, K. D., Kim, K. B., Han, S. H. and Lee, H. K. (2003). A study on effect of hydrogen reduction reaction on the initial stage of Ni electrodeposition using EQCM. *Electrochemistry Communications*, 5: 460-466.
16. Dahhou M. (2017). Drinking water sludge of the Moroccan capital: Statistical analysis of its environmental aspects. *Journal of Taibah University for Science*: 749–758.
17. APHA (2012). Standard methods for examination of water and wastewater 22nd edition, Washington DC.
18. Bagastyo, A.Y., Ayu, A. P., Barakwan, R. A. and Trihadiningrum, Y. (2020). Recovery of alum sludge by using membrane-based electrochemical process. *Journal Ecology Engineering,* 21(6): 237-247.
19. Barakwan, R. A., Pratiwi, W. B., Trihadiningrum, Y. and Bagastyo, A.Y. (2020). Electrolysis using Pt/SS electrodes for aluminum recovery from drinking water treatment sludge. *Journal Materials Cycles Waste Management,* 22: 2130-2139.
20. Connor, M. P., Coulthard, R. M. and Plata, D. L. (2017). Electrochemical deposition for the separation and recovery of metals using carbon nanotube-enabled filters. *The Royal Society of Chemistry*: 1-10.
21. Kan, C., Huang, C. and Pan, J. R. (2002). Coagulation of high turbidity water: The effects of rapid mixing. *Journal of Water Supply: Research and Technology-AQUA*, 51(2): 77-85.
22. BaiChuan, C., BaoYu, G., ChunHua, X., Ying, F. and Xin, L. (2010). Effects of pH on coagulation behavior and floc properties in Yellow River water treatment using ferric based coagulants. *Chinese Science Bulletin*, 55(14): 1382-1387.
23. Ernest, E., Onyeka, O., David, N. and Blessing, O. (2017). Effects of pH, dosage, temperature and mixing speed on the efficiency of water melon seed in removing the turbidity and colour of Atabong River, Awka-Ibom State, Nigeria. *International Journal of Advanced Engineering, Management and Science*, 3(5): 427-434.
24. Keeley, J., Jarvis, P. and Judd, S. J. (2014). Coagulant recovery from water treatment residuals: A review of applicable technologies. *Environmental Science Technology*, 44: 2675-2719.
25. Novitasari, A. K. (2015). Analysis of identification and inventaritation of pollution source in Surabaya River. Thesis of Master Degree, Department of Environmental Engineering, Institut Teknologi Sepuluh Nopember.
26. Yudo, S. and Said, N. I. (2019). Water quality condition of Surabaya River case study: Improved raw water of PDAM Surabaya. *Jurnal Teknologi Lingkungan*, 20(1): 19-28.

27. Personal commend, Mr. Adi, Operational Staff of Surabaya Drinking Water Treatment Plant. (2019). Surabaya.
28. Fazeli, M., Soltani, and Sarvestani, M. R. (2006). Feasibility of reuse of residuals from water treatment plants in landscapes irrigation and agricultural (Case atudy in 3 and 4 water treatment, Tehran). *Second Conference on Water Resources Management*: pp. 1-10.
29. Gibbons, M. K. and Gagnon, G. A. (2011). Understanding removal of phosphate or arsenate onto water treatment residual solids. *Journal Hazardous Materials*, 186: 1916-1923.
30. Trollip, D. L., Hughes, J. C. and Titshall, L. W. (2013). Sources of manganese in the residue from a water treatment plant. *Water SA*, 39(2): 265-270.
31. Goverment Republic of Indonesia (2001). Decree of the Goverment Regulation of Republic Indonesia No. 82/2001 concerning the management of water quality and the control of water pollution, Jakarta, Indonesia: Goverment Republic of Indonesia.
32. Razif, M. and Persada, S. F. (2015). The fluctuation impacts of BOD, COD, and TSS in Surabaya Rivers to environmental impact assessment (EIA) sustainability on drinking water treatment plant in Surabaya City. *International Journal of Chemtech Research*, 8(8): 143-151.
33. Cheng, W. P., Fu, C. H., Chen, P. H., and Yu, R. F. (2012). Dynamics of aluminum leaching from water purification sludge. *Journal of Hazardous Materials,* 217 (218): 149-155.
34. Prakash, P., Hoskins, D. and SenGupta, A. K. (2004). Application of homogeneous and heterogeneous cation-exchange membranes in coagulant recovery from water treatment plant residuals using donnan membrane process. *Journal of Membrane Science*, 237: 131-144.
35. Mulchandani, A. and Westerhoff, P. (2016). Recovery opportunities for metals and energy from sewage sludges. *Bioresource Technology*, 215: 215-226.
36. Boaventura, R. A. R., Duarte, A. A. S. and Almeida, M. F. (2000). Aluminum recovery from water treatment sludges. *IV International Conference Water Supply and Water Quality" Kraków – Poland,* September, 11-13.
37. Li, C. W., Lin, J. L., Kang, S. F. and Liang, C. L. (2005). Acidification and alkalinization of textile chemical sludge: Volume/solid reduction, dewaterability, and Al(III) recovery. *Separation and Purification Technology*, 42: 31-37.
38. Xu, H., Ding, M., Shen, K., Cui, J. and Chen, W. (2017). Removal of aluminum from drinking water treatment sludge using vacuum electrokinetic technology. *Chemosphere*, 173: 45-60.
39. Walsh, F. C., and de Leon, C. P. (2018). Progress in electrochemical flow reactors for laboratory and pilot scale processing. *Electrochimica Acta*, 280: 121-148.
40. Barakwan, R. A., Trihadiningrum, Y. and Bagastyo, A. Y. (2019). Characterization of alum sludge from Surabaya water treatment plant, Indonesia. *Journal of Ecological Engineering*, 20(5): 7-13.
41. Rajkumar, S. R., Alagar, M., Somasekaran, S. and Ravisankar, S. R. (2015). Significance of limiting current density by influence of the process parameter for the electrodeposition system. *International Journal of Information Science and Computing*, 2(1): 1-11.
42. Kumar, S., Pande, S. and Verma, P. (2015). Factor effecting electro-deposition process. *International Journal of Current Engineering and Technology*, 5(2): 700-703.
43. Chen, G. and Comninellis, C. (2010). Electrochemistry for the environment, Springer, New York.
44. Zhou, G., Li, W., and Wang, Z. (2015). Electrosorption for organic pollutants removal and desalination by graphite and activated carbon fiber composite electrodes. *International journal of Environmental Science and Technology*, 12(12): 1-20.
45. Molleman, B. and Hiemstra, T. (2017). The pH, time, and size dependency of silver nanoparticle dissolution: the road to equilibrium. *The Royal Society of Chemistry*: 1-18.
46. Casey, E. J. and Moroz, W. J. (1964). On the formation of Ag_2O_3 on silver electrodes. *Canadian Journal of Chemistry*, 43: 1199-1214.

47. Ciblak, A., Mao, X., Padilla, I., Vesper, D., Alshawabkeh, I. and Alshawabkeh, I. A. (2012). Electrode effects on temporal changes in electrolyte pH and redox potential for water treatment. *Journal of Environmental Science and Health*, 47(5): 718-726.
48. Chen, G. (2004). Electrochemical technologies in wastewater treatment. *Journal of Separation and Purification Technology*, 38(1): 11-41.
49. Iken, H., Basseguy, R., Guenbour, A. and Bachir, A. B. (2007). Classic and local analysis of corrosion behaviour of graphite and stainless steels in polluted phosphoric acid. *Journal of Electrochimica Acta*, 52(7): 2580-2587.
50. Supratno (2011). Separation of silver from waste fixer by electrolysis. Thesis of Master Degree, Institut Pertanian Bogor.
51. Munoz, L.D., Bergel, A., Feron, D., and Basseguy, R. (2010). Hydrogen production by electrolysis of a phosphate solution on a stainless steel cathode. *International Journal of Hydrogen Energy*: 8561-8568.
52. Guler, E. S., Konca, E. and Karakaya, I. (2013). Effect of electrodeposition parameters on the current density of hydrogen evolution reaction in Ni and Ni-MoS_2 composite coatings. *International Journal Electrochemical Sciences,* 8: 5496-5505.
53. Zoski, C. G. (2007). Handbook of electrochemistry, Chapter 18: Potential Electrode. New York, Elsevier.
54. Feng, Y., Yang, L., and Logan, B. E. (2016). Electrochemical technologies for wastewater treatment and resource reclamation. *Environmental Science Water Research & Technology*, 2: 800-831.
55. Barazes, J. M., Prasse, C. and Sedlak, D. L. (2016). Electrochemical transformation of trace organic contaminants in the presence of halide and carbonate ions. *Environmental Science & Technology*, 50(18): 10143-10152.
56. Santos, D. M. F. and Sequeira, C. A. C. (2013). Hydrogen production by alkaline water electrolysis. *Quimica Nova*, 36(8): 1176-1193.
57. Haynes, W.M. (2011) CRC handbook of chemistry and physics. 91st edition. Boca Raton, FL: CRC P ress Inc.
58. Varcoe, J. R., Atanassov, P., Dekel, D. R., Herring, A. M., Nijmeijer, K., Scott, K., Xu, T. and Zhuang, L. (2014). Anion-exchange membranes in electrochemical energy sytems. *Energy Environment Science*, 7 (10): 3135-3191.
59. Rozendal, R. A., Sleutels, T. H. J. A., Hamelers, H. V. M. and Buisman, C. J. N. (2008). Effect of ion exchange membrane on biocatalyzed electrolysis of wastewater. *Water Science Technologies*, 57: 1757-1762.
60. Liu, H., Qu, J., and Zhao, X. (2010). Electrocoagulation in water treatment. *Electrochemical Environmental*, 1: 245-262.
61. Basumataray, A. K., Kumar, R. V., Pakshirajan, K. and Pugazhenty, G. (2017). Removal of trivalent metal ions from aqueous solution via cross-flow ultrafiltration system using zeolite membranes. *Journal of Water Reuse and Desalination*, 7(1): 66-76.
62. Nurajijah, L., Harjunowibowo, D. and Radiyono, Y. (2014). The effect of voltage variations on laundry wastewater treatment using electrolysis. *Jurnal Materi dan Pembelajaran Fisika*, 4: 31-38.

Malaysian Journal of Analytical Sciences (MJAS)
Published by Malaysian Analytical Sciences Society

MODELLING AND OPTIMIZATION OF MICROWAVE ASSISTED EXTRACTION OF TOTAL PHENOLICS IN KAKAWATE (*Gliricidia sepium)* AS PESTICIDE AGAINST BLACK BEAN APHIDS (*Aphis fabae*)

(Pemodelan dan Pengoptimuman Pengekstrakan Berbantu Gelombang Mikro bagi Jumlah Fenolik dalam Kakawate (*Gliricidia sepium*) sebagai Racun Makhluk Perosak Afid Kacang Hitam (*Aphis fabae*))

Rhonalyn V. Maulion*, John Marco I. Matira, Kristine May M. Fanoga, Maricar C. Marasigan
Melissa Marie C. Dimaculangan[5]

Department of Chemical Engineering, College of Engineering Architecture and Fine Arts, Batangas State University, Batangas City, Philippines

**Corresponding author: rhonalyn.maulion@g.batstate-u.edu.ph*

Received: 15 July 2021; Accepted: 28 October 2021; Published: 27 December 2021

Abstract

Pest infestation is one of the serious problems of the agricultural sector in crop production and may even pose health hazards to humans. *Aphis fabae*, normally known as black bean aphid, is one of the main culprits that predominantly damage growing crops particularly beans, celery, and peas and may carry diseases as they multiply. Kakawate (*Gliricidia sepium*) leaves extracts was prepared using microwave assisted extraction and used as pesticide against black bean aphids in string beans (*Phaseolus vulgaris*). Microwave assisted extraction (MAE) is a rapid method of extraction of active components of plants which employ microwave energy to heat sample-solvent mixture at a short period of time. A central composite design (CCD) was employed to evaluate the effect of irradiation time (1.5 minutes) and microwave power (210W, 350W) on the phenolic content of the extract. Response surface methodology (RSM) determined the optimized conditions of MAE of total phenolics in dried *G. sepium* leaves. The optimized conditions were obtained at irradiation time of 2.44 minutes and microwave power of 275W with total phenolic content of 9.022 mg-GAE/g-dry sample. The presence of bioactive compounds of alkaloids, flavonoids, tannins and phenols were confirmed in the extract. The mortality or average life span of *A. fabae* upon application of *G. sepium* pesticide and commercially available pesticide are 5.17 seconds and 4.73 seconds, of which the difference is insignificant with the p-value one tail (0.002) and two tail (0.005) effect. No significant effect on the height of plant and number of *P. vulgaris* leaves at 10 days after the application of *G. sepium* pesticide ($p = 0.022$) and commercially available pesticide ($p = 0.026$) which make it a great potential biopesticide.

Keywords: black bean aphids, botanical pesticides, *Gliricidia sepium*, microwave assisted extraction, total phenolic content

Abstrak

Serangan makhluk perosak ialah satu masalah serius bagi sektor pertanian terutama hasil tuaian dan mungkin memberi kesan kesihatan terhadap manusia. *Aphis fabae*, juga dikenali sebagai afid kacang hitam, merupakan satu dari pemangsa utama yang merosakkan tanaman seperti kacang, seleri, kacang pea dan membawa penyakit. Ekstrak daun Kakawate (*Gliricidia sepium*) telah disediakan melalui pengekstrakan berbantu gelombang mikro dan digunakan sebagai racun mahkluk perosak bagi melawan afid

kacang hitam dalam untaian kacang (*Phaseolus vulgaris*). Pengekstrakan berbantu gelombang mikro (MAE) ialah satu kaedah pantas bagi pengekstrakan sebatian aktif dari tumbuhan di mana tenaga gelombang mikro digunakan memanaskan sampel campuran pelarut dalam tempoh masa yang singkat. Reka bentuk komposit berpusat (CCD) telah dibangunkan bagi penilaian kesan masa penyinaran (1.5 minit) dan kuasa gelombang mikro (210W, 350W) terhadap kandungan fenolik bagi hasil ekstrak. Keadaan optimum MAE bagi jumlah fenolik daun kering *G. sepium* ditentukan melalui kaedah gerak balas permukaan (RSM). Keadaan optimum telah diperolehi pada masa penyinaran 2.44 minit dan kuasa gelombang mikro ialah 275 W bersamaan jumlah kandungan fenolik 9.022 mg-GAE/g-sampel kering. Kehadiran sebatian bioaktif seperti alkaloid, flavonoid, tannin dan fenol telah disahkan melalui hasil ekstrak. Kadar kematian atau purata jangka hayat bagi *A. fabae* berdasarkan pengunaan racun makhluk perosak *G. sepium* dan perbandingan racun komersial ialah 5.17 saat dan 4.74 saat, di mana perbezaannya tidak signifikan dengan nilai p kesan satu arah (0.002) dan dua arah (0.005). Tiada kesan signifikan terhadap ketinggian pokok dan bilangan *P. vulgaris* selepas 10 hari racun *G.sepium* digunapakai ($p = 0.022$) dan racun komersial ($p = 0.026$) di mana ia menunjukkan potensi yang baik sebagai racun mahkluk perosak bio.

Kata kunci: afid kacang hitam, racun botani, *Gliricidia sepium*, pengekstrakan berbantu gelombang mikro, jumlah kandungan fenolik

Introduction

Food security is threatened by the occurrence of insect pest outbreak which estimated to have caused a loss of 20-40% of global crop production due to infestation [1, 2]. Insect pests are considered destructive to the natural environment, adversely impact human health and activities, and damage agricultural production. The quality of crops of a farmer are affected by the pest that thrive on the plants as they grow hence affecting market and reduced crops production to as much as 50% [3, 4]. One of the most serious pests encountered by farmers on their crops is black bean aphids (*Aphis fabae)*. It is a small black insect with a soft body with piercing and sucking mouthparts that transmit harmful viruses to plants and grow in large numbers in agricultural, wild, horticultural, and ornamental plants [5]. It is an identified severe pest of economically important crops which are distributed worldwide, feeding about 200 hosts in various botanical families [6]. Devastating populations of black bean aphids reproduce on the plant hosts under otherwise good developmental conditions, which result to leaf curling, distortion and yellowing through virus transmission to the plant host [7]. The sucking of plant sap from stems and leaves and the transmission of its viruses to plants diminishes the vigor of the plant and hinder its growth [8], hence reducing production yield. *P.* vulgaris is one of the plants that are commonly infested by black aphids. It is a green color crop with high nutritional value hence proper care must be provided to prevent pest infestation.

Pesticides are used to kill or control pests that invade plants to protect it against the damage from infestation. Synthetic pesticides have proven toxic to pests, reduce crop damages and improve crop production. However, its use has some negative impact on human health and detrimental consequences to the environment such as water pollution, the necessity for excessive use of water, and the growth of weeds [9]. The use of botanical pesticides from plant material is considered a viable alternative to synthetic chemical pesticides because it is environmentally safe, naturally available, and low-cost. Many plants are capable in controlling pest and is being used in traditional agriculture application in most developing countries, particularly the tropical areas [10]. It contains active metabolites which are responsible for pesticidal and fungicidal activity. Phenolic compounds include simple phenols, flavonoids, flavonols, tannins, coumarins, quinnones, and flavons are phytochemicals, which are the major bioactive compounds which have a linear relation to antioxidant activity and toxicity to fungi and pest [9, 11]. Kakawate (*Gliricidia sepium*) contains coumarins which are potent neutralizers of bed bugs and termites because it possesses a variety of biological properties like antimicrobial, anti-inflammatory, antiviral, antioxidant, and others [12]. Moreover, the leaf extract was proven effective for removal of animal lice and ticks, nematocidal activity against *Meloidogyne* and has antibacterial properties for a wide classification of

bacteria, as well as fungicidal properties [13]. The phytochemicals present in leaf extract exhibit antioxidant properties which is an active component of biological pesticides, however possible degradation during the extraction process may occur which affect the yield and quality of phenolic compounds. Hence, choosing the suitable method of extraction of phenolic compounds from plant source must take into consideration.

Several techniques used for the extraction of phenolic compounds from plant include solvent extraction [14,15,16], Soxhlet extraction [17], supercritical fluid extraction (SFE) [18, 19, 20] and microwave assisted extraction (MAE) [21-25]. These methods require solvent penetration in the plant matrix to separate the phenolic compounds in the plant source. Conventional extraction method such as solvent and Soxhlet extraction has the advantage of lower equipment cost, however it requires extensive use of organic solvent and long extraction time which may cause possible degradation of bioactive compounds and lower extraction efficiency [26]. Advanced method like SFE minimize degradation of phenolic compounds [19], achieved faster extraction time and higher extraction yield due to high degree of selectivity to the compound [27] but a fluid's supercritical state should have maintained which requires high operating and capital cost. These shortcomings can be partially or completely overcome using MAE which operates at low extraction time, low energy requirement, less consumption of solvent and has improved yield [28]. In MAE, the extraction of bioactive compounds was due to the penetration of the solvent to the plants cell wall and heating with electromagnetic waves. It is important to understand the interaction between the microwave power and irradiation time during MAE to optimize the extraction conditions [29]. The increase in extraction yield was attained by increasing the temperature under microwave heating at short exposure time [30] but may not be generalized due to diverse nature of the phytochemicals present in plant. In view of these, it is important to optimized the MAE parameters such as microwave power and irradiation time and generate a mathematical model that describes the yield of phenolic compounds from *G. sepium* leaves. Generation of mathematical model provides useful information in control of extraction process, design and scale up of equipment [31] for practical application. It is also important to determine the effectiveness of the produced extract as botanical pesticide by measuring the mortality of black bean aphids upon application.

Materials and Methods

Folin Ciocalteu phenol reagent purchased from Merck and ACS reagent grade sodium carbonate, Na_2CO_3 at >99.5% purity and gallic acid was used for spectrophotometric quantification of TPC. Analytical grade potassium mercuric iodide (K_2HgI_4), sodium hydroxide (NaOH), sodium chloride (NaCl) and anhydrous ferric chloride (FeCl3) was used for qualitative determination of phytochemicals. Laboratory grade ethanol, 95% (C_2H_5OH) was used for microwave assisted extraction of TPC from *G. sepium*. A batch of *G. sepium* leaves obtained from Alitagtag, Batangas was used as a precursor of TPC. The schematic of the study was shown in Figure 1.

Sample preparation

The *G. sepium* leaves was freshly harvested from a farm in Alitagtag, Batangas. The sample were carefully cleaned and washed several times with de-ionized water to remove dirt, drained, placed in zip lock plastic bags and frozen overnight at -4 ^oC before drying. The frozen samples were freeze dried in the Instrumentation Laboratory of the Science and Technology Research Center, De La Salle University, Manila using a vacuum freeze dryer at -40^oC. The moisture content of the *G. sepium* was determined (1) by getting the difference of the weight of the sample before (W_i) and after ((W_i) drying. The weight of the sample was obtained using a laboratory analytical balance.

$$\text{moisture content (\%)} = \frac{W_i - W_f}{W_i} \times 100 \quad (1)$$

The freeze-dried samples were milled using a blender to obtain fine powder and passed through a 35-tyler mesh sieve to collect sizes less than 500 microns. The *G. sepium* fine powder was placed in a sealed glass container to avoid adsorption of moisture which may affect the analysis of phenolic compounds and its optimization.

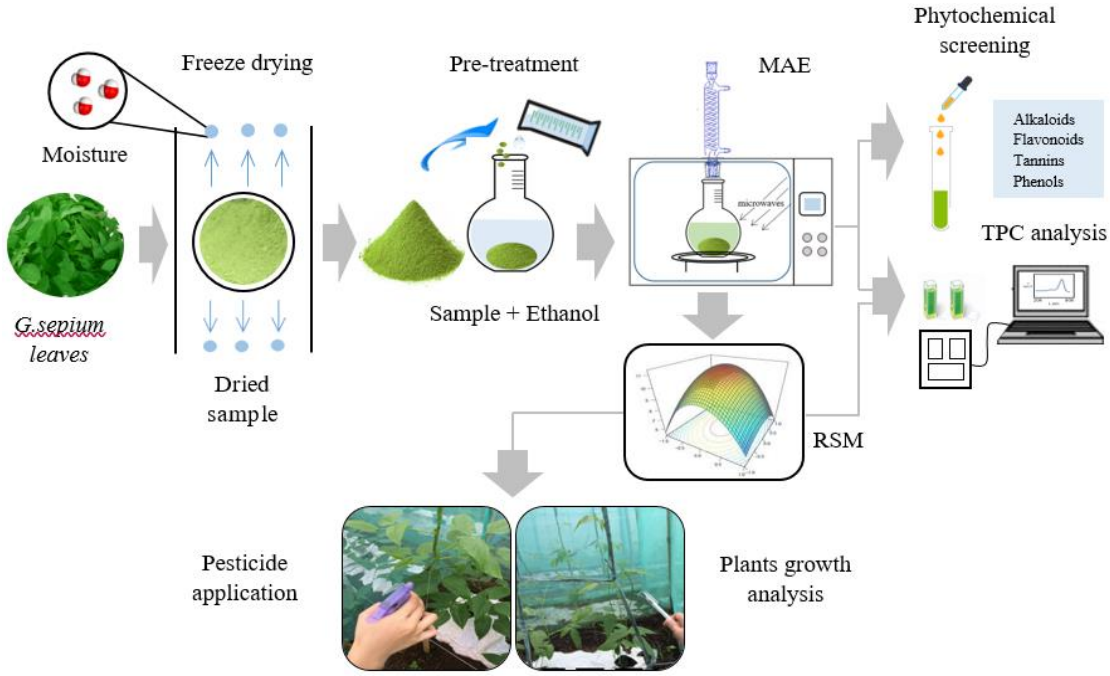


Figure 1. Scheme for extraction of *G. sepium* leaves using MAE method

Microwave assisted extraction

A Face Centered Central Composite Design is the design of experiment used in the extraction of total phenolics in the *G. sepium* leaves with two independent numeric variables such as irradiation time and microwave power. The coded value of the independent variable was shown (Table 1) to clearly see the minimum and maximum operation conditions of MAE and the Design of Experiment (Table 2) to describe each set-up.

A full level factorial scheme was used in the analysis have a total of 13 runs with the following characteristics: face centered with $\alpha = 1$, 8 factorial points, 5 center points at confidence level of 95% (p=0.05) was used in the analysis. To lessen the effect of natural variability on the response, sampling was done randomly. The optimized condition was determined using Response surface methodology (RSM) while the determination of the significance of primary variable effects, variable interaction, and the model will be evaluated using Analysis of variance (ANOVA).

The freeze-dried sample was pretreated with ethanol to soften the cell wall and initiate the release of soluble phytochemicals. The 1-gram sample of *G. sepium* leaves powder was pre-leached by soaking in 200mL of 95% ethanol for 2 hours. The pre-leached samples were transferred in a microwave oven for extraction of TPC following the design of experiment in Table 2. After each extraction set-up, the liquid was separated from the solid residue using centrifuge at 4000rpm. The crude liquid extract was kept at 4^{o}C to preserve the bioactive components.

Table 1. Coded values of independent variables

Independent Variables	**(-1)**	**(0)**	**(+1)**
Irradiation time (minutes)	1	3	5
Microwave power (Watts)	210	280	350

Table 2. Design of Experiment using Central Composite Design

Standard	Run	Factor 1 A: Irradiation Time (Minutes)	Factor 2 B: Microwave Power (Watts)	Response TPC (mg-GAE/g-sample)
13	1	3	280	R_1
12	2	3	280	R_2
5	3	1	280	R_3
8	4	3	350	R_4
11	5	3	280	R_5
1	6	1	210	R_6
6	7	5	280	R_7
7	8	3	210	R_8
10	9	3	280	R_9
9	10	3	280	R_{10}
4	11	5	350	R_{11}
3	12	1	350	R_{12}
2	13	3	210	R_{13}

Determination of phytochemicals of *G. sepium* leaves extract

The crude extracts from *G. sepium* obtained at optimized condition were examined qualitatively for presence of phytochemicals such as alkaloids, flavonoids, tannins, and simple phenols. A 5mL crude extract was used in the analysis and the reaction occurred after addition of reagents will determine the presence of each phytochemical. The presence of alkaloids was determined by acidifying 5mL crude extract with hydrochloric acid and addition of 3 drops of Mayer's reagent (K_2HgI_4). Flavonoids were identified using alkaline reagent analysis wherein the crude extracts were treated with a small amount of NaOH solution dilute hydrochloric acid. Presence of tannins was determined upon addition of NaCl to the crude extract. Finally, the presence of simple phenols was analyzed by adding few drops of $FeCl_3$ solution to the crude extract.

Determination of total phenolic content

TPC of the extract was quantified using modified Folin Ciocalteu method [32]. A 0.5 mL crude extract was mixed with 0.5 mL of 10% Folin Ciocalteu reagent solution. After 5 minutes, 1-mL of 15% w/w Na_2CO_3 was added to the mixture to catalyze the reaction. The samples were left standing in the dark for 1 hour to achieve complete reaction. A sample prepared (5%v/v) was quantified using spectrophotometer (Shimadzu UV-1800 spectrophotometer) at λ_{max} = 765nm and the result was compared to the standard curve and expressed as gallic acid equivalents (GAE) per gram sample.

Pest and plant isolation

The infested *P. vulgaris* beans with black bean aphids were sequestered from the other plants by means of housing it into a cage made of nets and fences having a dimension of 34x72x59". Six (6) cages were prepared which corresponds to the triplicated plots for each kind of pesticide which are the *G. sepium* extract based pesticide and the commercially available one. A larger cage was made in order to house the three (3) smaller cages with nine (9) string beans plants. A total of six (6) huge cages were made. This is to ensure that the pest will not escape when the researchers apply the pesticide in every plot. Each plot was planted with the same number of string beans.

Pesticide preparation and application

The crude extract produced at optimized condition was purified using rotary evaporator to remove excess

ethanol leaving only the crude extract of *G. sepium*. A 20mL dosing amount of extract were placed in sterilized and clean spray bottles. The *P. vulgaris* beans plant was sprayed with formulated pesticide. The effect of pesticide on the plant's height and leaf color and number were examined for 10 consecutive days. The experiments were done in triplicates and were calculated for statistical comparison of the effectiveness and performance of botanical pesticide with commercially available pesticides.

Results and Discussion

The dry weight of the *G. sepium* leaves obtained after freeze drying was 32.34%. The average dry matter in *G. sepium* leaves was 25.3% ranging from 19.6 to 37% [33]. The use of the vacuum freeze drying is advantageous from other dehydration methods since the constituents of the dried material remain homogenously dispersed, has less damage on the volatile substances compared to other dehydration methods operated at higher temperatures, hence preserving the phytochemicals of the *G. sepium* samples. Moreover, no shrinkage or toughening of the material after drying can be observed and can be protected against spoilage for a longer period of time.

Phytochemical screening of *G. sepium* leaves extract

The presence of phytochemicals or phenolic compounds such as alkaloids, flavonoids, tannins and simple phenols play an important role in pesticide production due to its antibacterial, antimicrobial and insecticidal properties. These are the major bioactive compounds which have a linear relation to antioxidant activity and toxicity to fungi and pest [9,11]. Table 3 shows the result of phytochemical screening of crude ethanolic *G. sepium* leaves. The color change of the crude extract indicates the presence of phytochemicals.

Qualitative phytochemical screening of crude *G. sepium* leaves confirmed the presence of alkaloids, flavonoids, tannins, and phenols. These phytochemicals in crude extracts of *G sepium* leaves indicates the presence of appreciable amounts of bioactive compounds [34, 35] in the extract which exist linearly to TPC and antioxidant activity. Phenolic compounds are the major bioactive compounds found in dried herbs and a linear relationship exists between the total phenolic content and the antioxidant activity of herbs [36, 37]. The presence of alkaloids indicates the appearance of yellow colored residue after acidification and addition of Mayer's reagent. On the other hand, after treatment with alkaline reagent, an intense yellow color solution was formed and become colorless upon acidification which indicates the presence of flavonoids. Moreover, the presence of tannins was identified after the formation of white precipitates upon addition of salt to the crude extract. Finally, simple phenols were identified for the appearance of bluish black color after addition of ferric chloride. All the phytochemicals tested were found to be present in the extracts of *G. sepium,* hence it can be assumed that this extract exhibit good antioxidant activities that can be an active component of effective biopesticide.

Microwave assisted extraction of TPC in G. sepium leaves extract

To optimize the extraction of TPC in crude extract of G. sepium, two parameters were varied in the studies such as irradiation time (1.5 minutes) and microwave power (210-350W). The design has 13 runs comprising of 8 non-center points and 5 center points. To lessen the effect of natural variability on the response, sampling was done randomly. Among the varying condition of MAE, the highest TPC obtained in ethanolic extract of *G. sepium* leaves is 9.04 mg GAE/g dry sample extracted at 3 minutes irradiation time and 280W microwave power while the lowest amount of 2.30 mg-GAE/g-dry sample was obtained at 5 minutes irradiation time and 350W. The TPC values in the present study is higher compared with [38, 39] having 7.57 mg-GAE/g-dry sample where the extraction was done by soaking in ethanol for 3 days and 1.7 mg/ml respectively. Preservation of the bioactive components are achieved using MAE compared to conventional soaking with solvents which improved the antimicrobial and antioxidant activity of the extract.

MAE is effective in extraction of TPC, however proper control of irradiation time and microwave power must be considered to improve extraction yield and reduce processing cost. Phenolic content degrades with longer extraction time and high temperature [40]. Likewise,

with higher power settings, too much penetration of the electromagnetic waves was encountered and resulted in the breakdown of phenolic compounds. Increasing irradiation time and microwave power increased the amount of analyte being extracted, although there is the risk of extracted compound degradation [41]. However, at too short extraction time, less amount of total phenolic content can be extracted, thus its effect on extraction of TPC must be determined. The effect of irradiation time and microwave power and their interaction in extraction of TPC in ethanolic *G. sepium* leaves (Figure 2) is important to study to see its trend.

It is evident from the graph that at increasing irradiation time from 1 to 3 minutes, there is an increase in the extracted TPC at microwave power of 210W signifying the continuous extraction of TPC. As the microwave power increased to 350W, less time is needed to obtain the highest TPC because more electromagnetic waves have been absorbed at a given time. As the extraction process continued longer, a decreasing trend in the phenolic content was observed in both microwave power condition which may be due to degradation of the bioactive components and its evaporation. A drastic decrease in TPC was observed with a longer extraction time at a higher microwave power. An intersection of the curves indicates that the interaction of the process condition was found to affect the extraction of TPC. It revealed that increasing irradiation time and microwave power resulted to an increase in TPC, however were nullified as further increases in both factors were made. This is due to the reason that longer time or exposure and too much microwave power causes a rapid rupture of cell wall that resulted to degradation, hence a lower TPC was obtained. To determine the effect of the primary variables and their interaction, ANOVA was used. Coded equation (2) is useful in identifying the relative impact of irradiation time and microwave power on TPC based on their coefficients.

In comparing the level of their coefficients, irradiation time has greater impact compared to microwave power on the extraction of TPC. The actual equation can be used to predict the TPC at a given condition. The coded equation (2) is very useful to predict the impact of each factors on TPC of *G. sepium* within the design space. Likewise, actual equation (3) can be used to make predictions on the amount of TPC extracted from *G. sepium* at a given level of each factors within the design space.

The ANOVA (Table 4) for the model is important to see the significance of the equation to the response within the design space.

The interaction of irradiation with time and power were found to be highly significant with p-value of 0.0078 at α=0.05. The model was generated to relate the specific variable to TPC of *G. sepium* leaves extract. The devised equation was based on quadratic model with F-value of 50.15 and p-value of <0.0001 at 0.05 level of significance which implies that the model is significant with R^2 = 0.97. Moreover, the adequate precision is 21.16 which indicates an adequate signal to noise ratio and is desirable, thus the model can be used to navigate the design space at irradiation time of 1 to 5 minutes and microwave power of 210-350 watts. The residual plot of the model (Figure 3) generated is relatively normal distribution which indicates that model chosen representing the data adequate. This was also supported by the plot of predicted versus actual values.

Table 3. Qualitative phytochemical screening of the crude ethanolic extract of *G-sepium* leaves

	Alkaloids	**Flavonoids**	**Tannins**	**Phenols**
Appearance	Green to yellow extract	Green to intense yellow extract	Formation of white precipitate	Green to bluish black extract
Presence of Phytochemicals	+	+	+	+

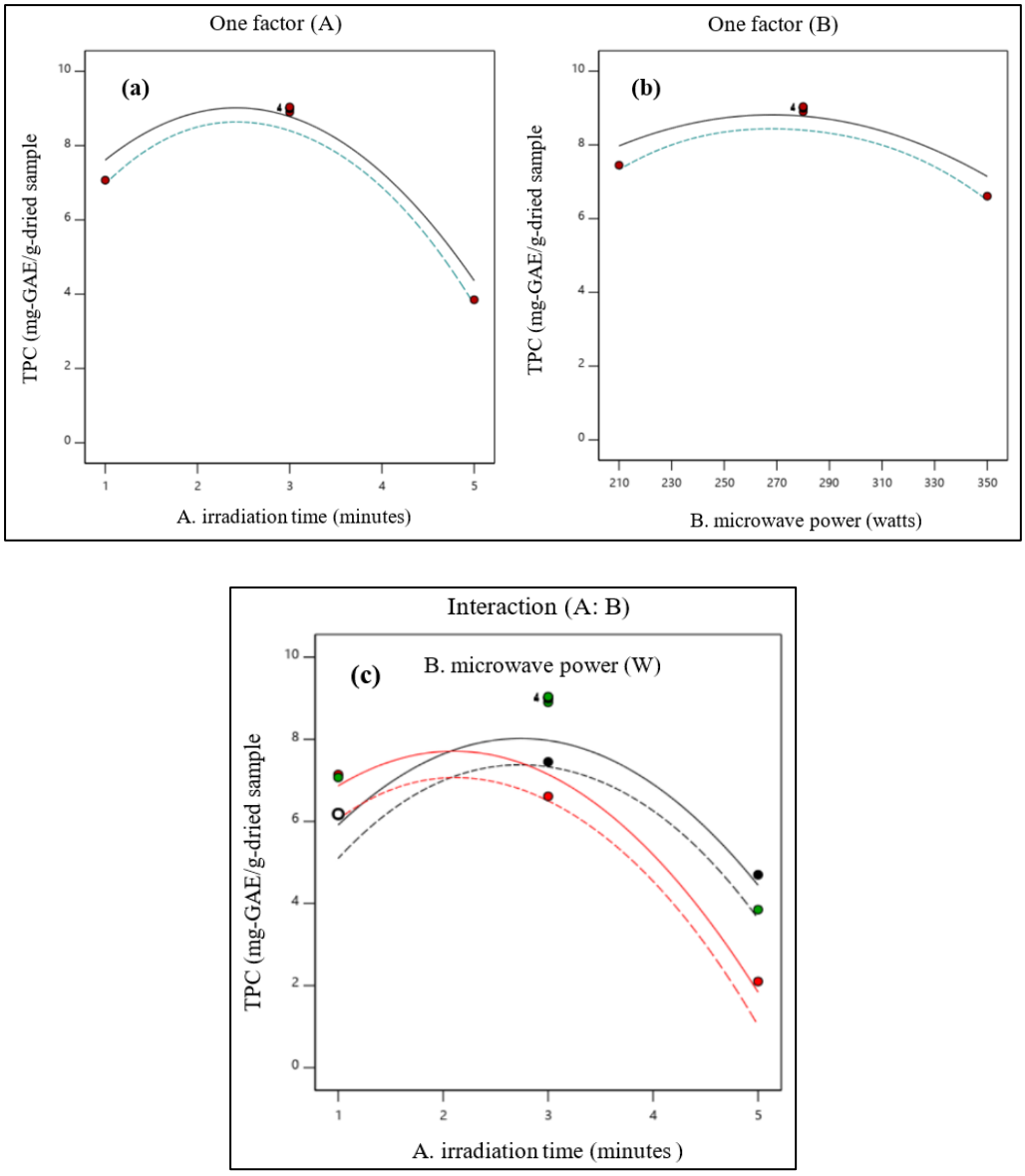


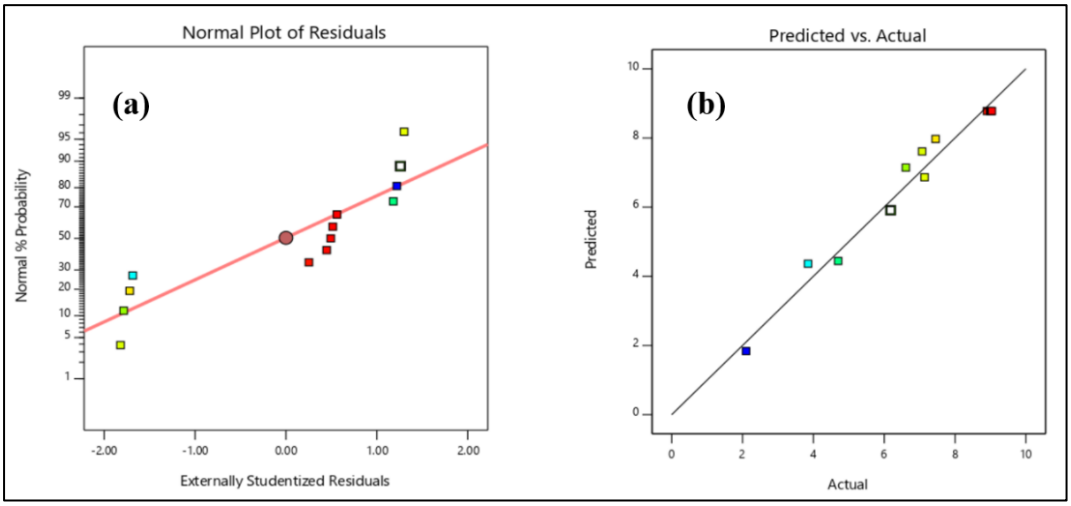
Figure 2. Effect of irradiation time (a) and microwave power (b) and their interaction (c) on TPC of *G. sepium* leaves extract: Design points: (-) 210W, (--) 210W at 95% CF, (-) 210W, (--) 210W at 95% CF, (•) design points

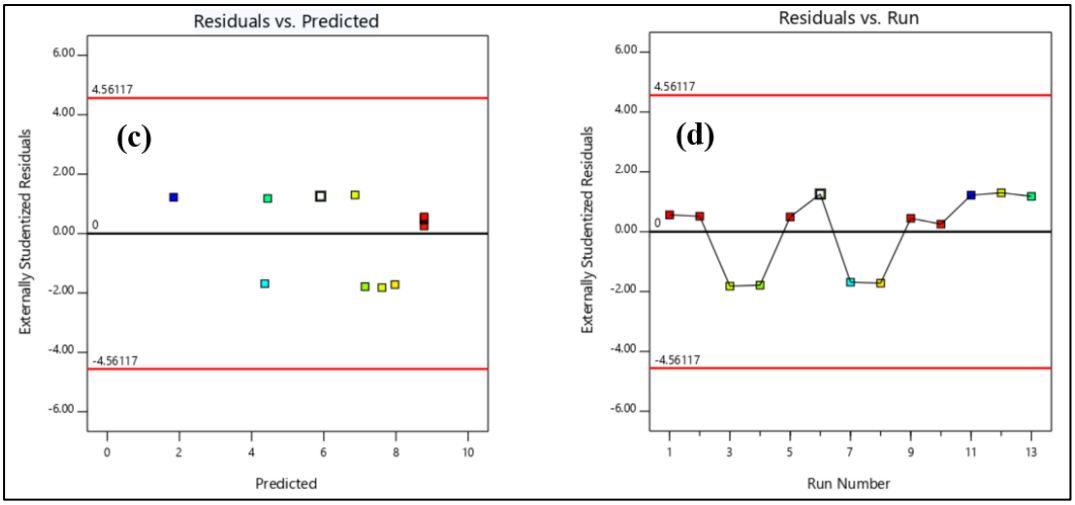
$$\text{TPC} = +8.78 - 1.62A - 0.4133B - 0.8900AB - 2.79A^2 - 1.22B^2 \quad (2)$$

$$\text{TPC} = -18.31 + 5.16A + 0.153B - 0.006AB - 0.698A^2 - 2.49x10^{-4}B^2 \quad (3)$$

Table 4. ANOVA for Quadratic model

Source	Sum of squares	F-value	P-value	Effect
Model	58.43	50.15	<0.0001	Significant
A: Irradiation time	15.81	67.85	<0.0001	Significant
B: Microwave power	1.03	4.40	0.0742	not-significant
AB	3.17	13.60	0.0078	Significant
A^2	21.54	92.4	<0.0001	Significant
B^2	4.13	17.71	0.0040	Significant





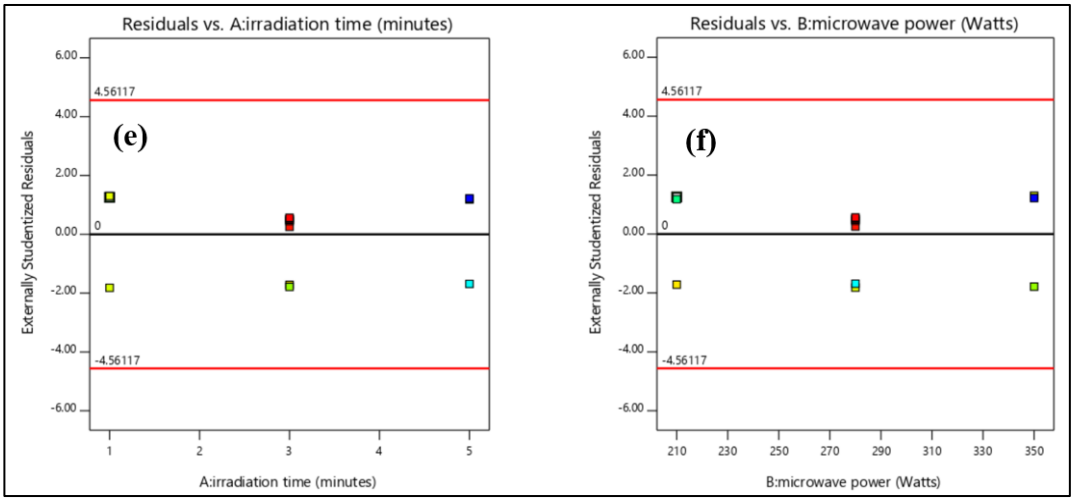


Figure 3. Diagnostics: Normal plot of residuals (a), Predicted vs. actual (b), Residual vs. predicted (c), Residuals vs. run (d), Residuals vs irradiation time (e), Residuals vs. microwave power (f)

Optimization of TPC extraction in *G. sepium leaves*

Response surface methodology was used to determine the optimum condition for the extraction of TPC in *G. sepium* at a given design space. Determination of optimum irradiation time and microwave power is necessary to achieve higher yield and low processing cost. Irradiation time and microwave power are essential parameters in MAE extraction and inadequate selection of either less and enormous time and power of extraction can alter the phenolic compounds in plant material [41]. The model plot of MAE of TPC from *G-sepium* leaves was shown in Figure 4.

The red portion of the plots in both 3D model (Figure 4.a) and contour plot model (Figure 4.b) represents the good condition which yield a high TPC result in which the irradiation time of about 3 minutes and microwave power of 280 watts showed a favorable performance of TPC extraction. The light green up to dark blue represents less to least TPC value. Increasing yield of TPC was observed as the irradiation time increased from 1 minute to less than 3 minutes and microwave power of 210 watts to 280 watts. There is a decline in TPC as irradiation time and microwave power exceeded 3 minutes and 280 watts, respectively. This indicated that upon reaching equilibrium, the interaction of the parameters with extracting solvent and *G. sepium* occurs until it reached the highest TPC at 3 minutes and 280 watts. Once the highest yield was achieved and the extraction continued, the dissolution of the phenolic compound into the solvent began and this was due to the prolonged exposure to irradiation [42,43]. Decline in TPC (2.1 mg-GAE/g-dry sample) beyond 280 watts can be associated with the overexposure to electromagnetic radiation that activated the diffusion coefficient between solvent and plants resulting from the increased power. This implies that the limited exposure and prolonged exposure of plant matrix to electromagnetic radiation belittle the TPC yield. The highest yield of TPC (9.04 mg-GAE/g-dray sample) was observed at 3 minutes of irradiation time and 280 watts of microwave power which should be considered as the maximum setting MAE. The optimized condition (TPC= 9.022 mg-GAE.g-dry sample) was attained at an irradiation time of 2.44 minutes and microwave power of 275 W at the desirability of 0.997. The generated model was validated by performing extraction of phenolics at 2.44 minutes and 280W power which attained actual TPC of 9.01 mg-GAE/g-dry sample against the predicted value of 9.02 ± 0.48 mg-GAE/g-dry sample. The actual obtained is within the predicted range at 95% confidence level which validated the model.

Effect of *G. sepium* pesticide upon application

It is important to determine the effect of the application of pesticide on the target pest and the growth of plant. The TPC of *G. sepium* extract is the active component of the pesticide that enhances its antimicrobial and antioxidant property [23]. Upon application of *G. sepium* pesticide and the commercially available pesticide, the mortality or average life span of *A. fabae* are found to be 5.17 seconds and 4.73 seconds respectively. The difference of the result is insignificant in one tail (p-value = 0.002) and two tail (p-value = 0.005). In case of the control (without pesticide application), there is no pest mortality observed. The effect of *G. sepium* pesticide on the growth of *P. vulgaris* plants in terms of height and leaves were also studied. A total of 90 *P. vulgaris* plants were harvested and measured for its height and all the leaves of the *P. vulgaris* plants were counted. The p-value obtained after 10 days monitoring on the height and number of leaves of *P. vulgaris* plant compared to the control are 0.025 and 0.0266 respectively at a=0.05 which indicates no significant differences. This implies that the *G. sepium* pesticide effectiveness against *A. fabae* is comparable to the commercially available pesticides on the market. Thus, the use of biological pesticides is advantageous in terms of its safe use which caused no hazards to human health and environment.

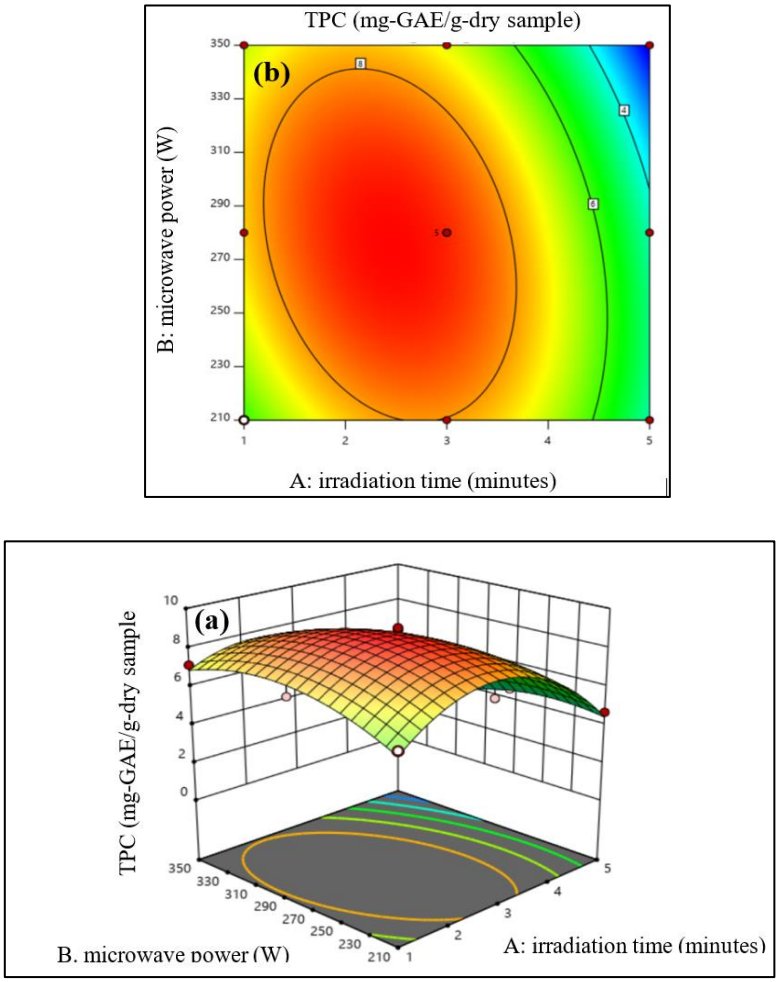


Figure 4. Model Plot of MAE of TPC from *G. sepium extract* (3-D surface plot (a) and contour plot (b)

Conclusion

The presence of phytochemicals such as alkaloids, flavonoids, tannins, and phenols are present in G. sepium extract which are the active components of its antimicrobial, antioxidant, anti-fungicidal and even the anti-insecticidal activity. Careful control of irradiation time and microwave power in MAE is required to attain high TPC yield. The interaction of the two parameters can give the optimum yield TPC from G. sepium. Prolonged irradiation time and increasing microwave power affect TPC of the plant due to degradation and evaporation. The effectiveness of G. sepium on A. fabae mortality and growth of P. vulgaris plant was comparable to the commercially available pesticide in the market but is advantageous in terms of use because it is safe for humans and posed no hazards to the environment.

Acknowledgement

The authors acknowledge the assistance from the Department of Agriculture, Batangas, Philippines for the acquisition of aphids and application of pesticide. Sincerest thanks are also offered to Dr. Reymark D. Maalihan of Material Testing and Calibration Center, Batangas State University Alangilan, Philippines for sharing valuable inputs.

References

1. Food and Agriculture Organization (2017). The future of food and agriculture: Trends and challenges. http://www.fao.org/. [Access online 15 March 2021].
2. Food and Agriculture Organization (2019). New standard to curb the global spread of plant pest and diseases. http://www.fao.org/. [Access online 15 March 2021].
3. Goodhue, R. E., Bolda, M., Farnsworth, D., Williams, J. C. and Zalom, F. G. (2011). Spotted wing drosophila infestation of California strawberries and raspberries: economic analysis of potential revenue losses and control costs. *Pest Management Science,* 67(11): 1396-1402.
4. Rodriguez, T. (2018). Managing insect pest on organic vegetable production. https://www. agriculture.com.ph/. [Access online 28 February 2020].
5. University of Idaho (2021). Integrated pest management: Black bean aphids. https://www.uidaho.edu/. [Access online 15 March 2021].
6. Shannag H. K. (2007). Effect of black bean aphids, *Aphis fabae,* on transpiration stomatal conductance and crude protein content of faba bean. *Annals of Applied Biology,* 151: 183-187.
7. Razmjou, J. and Fallahi, A. (2009). Effects of sugar beet cultivar on development and reproductive capacity of Aphis fabae. *Bulletin of Insectology*. 62(2): 196-201.
8. Kankolongo A. M. (2018). Leguminous crops. Food crop production of smallholder farmers in southern Africa: pp. 173-203
9. Boulogne, I., Petit, P., Ozier-lafontaine, H., Loranger-Merciris, G., Boulogne, I. and Petit, P. (2012). Insecticidal and antifungal chemicals produced by plants: A review. *Environmental Chemistry Letters,* 10(4): 325-347.
10. Okwute, S. K. (2012). Plants as potential sources of pesticidal agents: A review. Pesticides – *Advances in Chemical and Botanical Pesticides*: pp. 207-232.
11. Saeed, N., Khan, M. R., & Shabbir, M. (2012). Antioxidant activity, total phenolic and total flavonoid contents of whole plant extracts *Torilis leptophylla* L. *BMC Complementary and Alternative Medicine*, 12: 221.
12. Rabena, A. R. (1996). Isolation, characterization and identification of the active component of Kakawate (*Gliricidia sepium*) (*Jacq.)* Kunth ex Walp. Leaves against termites (*Microcerotermes losbanosensis*). Thesis of Master Degree, Philippines University Los Banos College, Laguna, Philippines
13. Torres, L. M. (2018). Madre de cacao (*Gliricidia sepium*) and sinta (*Andrographis paniculata*) leaves extract as botanical animal lice and ticks remover. *Journal of Fundamental and Applied Sciences*, 10(3S): 650-664.

14. Do, Q. D., Angkawijaya, A. E., Tran-Nguyen, P. L., Huynh, L. H., Soetaredjo, F. E., Ismadji, S. and Ju, Y. H. (2014). Effect of extraction solvent on total phenol content, total flavonoid content, and antioxidant activity of *Limnophila aromatica*. *Journal of Food and Drug Analysis*, 22(3): 296-302.
15. Altemimi, A., Lakhssassi, N., Baharlouei, A., Watson, D. G. and Lightfoot, D. A. (2017). Phytochemicals: Extraction, isolation, and identification of bioactive compounds from plant extracts. *Plants*, 6(4): 42.
16. Zhong, L., Yuan, Z., Rong, L., Zhang, Y., Xiong, G., Liu, Y. and Li, C. (2019). An optimized method for extraction and characterization of phenolic compounds in *Dendranthema indicum* var. aromaticum flower. *Scientific Reports*, 9(1): 1-12.
17. Alara, O. R., Abdurahman, N. H., and Ukaegbu, C. I. (2018). Soxhlet extraction of phenolic compounds from *Vernonia cinerea* leaves and its antioxidant activity. *Journal of Applied Research on Medicinal and Aromatic Plants*, 11(6): 12-17.
18. Ghafoor, K., AL-Juhaimi, F. Y. and Choi, Y. H. (2012). Supercritical fluid extraction of phenolic compounds and antioxidants from grape (*Vitis labrusca* B.) seeds. *Plant Foods for Human Nutrition*, 67(4): 407-414.
19. Farías-Campomanes, A. M., Rostagno, M. A., Coaquira-Quispe, J. J. and Meireles, M. A. A. (2015). Supercritical fluid extraction of polyphenols from lees: Overall extraction curve, kinetic data and composition of the extracts. *Bioresources and Bioprocessing,* 2(1): 45.
20. Phan, L. T. M., Nguyen, K. T. P., Vuong, H. T., Tran, D. D., Nguyen, T. X. P., Hoang, M. N. and Nguyen, H. H. (2020). Supercritical fluid extraction of polyphenols from Vietnamese *Callisia fragrans* leaves and antioxidant activity of the extract. *Journal of Chemistry*, 2020: 9548401.
21. Gallo, M., Ferracane, R., Graziani, G., Ritieni, A. and Fogliano, V. (2010). Microwave assisted extraction of phenolic compounds from four different spices. *Molecules*, 15(9): 6365-6374.
22. Kaur, P., Chaudhary, A., Singh, B. and Gopichand. (2012). An efficient microwave assisted extraction of phenolic compounds and antioxidant potential of Ginkgo biloba. *Natural Product Communications*, 7(2): 203-206.
23. Wong-Paz, J. E., Contreras-Esquivel, J. C., Muñiz-Marquez, D., Belmares, R., Rodriguez, R., Flores, P., and Aguilar, C. N. (2014). Microwave-assisted extraction of phenolic antioxidants from semiarid plants. *American Journal of Agricultural and Biological Science*, 9(3): 299-310.
24. Li, Y., Li, S., Lin, S. J., Zhang, J. J., Zhao, C. N. and Li, H. Bin. (2017). Microwave-assisted extraction of natural antioxidants from the exotic *Gordonia axillaris* fruit: Optimization and identification of phenolic compounds. *Molecules*, *22*(9): 1481.
25. Akhtar, I., Javad, S., Yousaf, Z., Iqbal, S. and Jabeen, K. (2019). Microwave assisted extraction of phytochemicals an efficient and modern approach for botanicals and pharmaceuticals. *Pakistan Journal of Pharmaceutical Sciences*, 32(1): 223-230.
26. Durmaz, E., Sumnu, G. and Sahin, S. (2015). Microwave-assisted extraction of phenolic compounds from caper. *Separation Science and Technology (Philadelphia)*, 50(13): 1986-1992.
27. Mendiola, J. A., Herrero, M., Castro-Puyana, M. and Ibáñez, E. (2013). Supercritical fluid extraction. *RSC Green Chemistry*, 1: 196-230.
28. Lovrić, V., Putnik, P., Kovačević, D. B., Jukić, M., & Dragović-Uzelac, V. (2017). Effect of microwave-assisted extraction on the phenolic compounds and antioxidant capacity of blackthorn flowers. *Food Technology and Biotechnology*. 55(2): 243-250.
29. Kaderides, K., Papaoikonomou, L., Serafim, M. and Goula, A. M. (2019). Microwave-assisted extraction of phenolics from pomegranate peels: Optimization, kinetics, and comparison with ultrasounds extraction. *Chemical Engineering and Processing - Process Intensification*, 137: 1-11.
30. Zheng, X., Xu, X., Liu, C., Sun, Y., Lin, Z. and Liu, H. (2013). Extraction characteristics and optimal parameters of anthocyanin from blueberry powder under microwave-assisted extraction conditions. *Separation and Purification Technology,* 104: 17-25.

31. Shirsath, S. R., Sable, S. S., Gaikwad, S. G., Sonawane, S. H., Saini, D. R. and Gogate, P. R. (2017). Intensification of extraction of curcumin from *Curcuma amada* using ultrasound assisted approach: Effect of different operating parameters. *Ultrasonics Sonochemistry,* 38: 437-445.
32. Balanquit, B. J. and Fuentes, R. (2015). Preliminary phycochemical screening and antioxidant activity of some brown algae sargassum species from Lawaan, Eastern Samar. *Journal of Nature Studies*, 14(1): 12-21.
33. Tree, D. (2016). Forage fact sheet gliricidia, Inter-American Institute for Cooperation in Agriculture, pp. 5-6.
34. Farag, R. S., Abdel-Latif, M. S., Abd El Baky, H. H. and Tawfeek, L. S. (2020). Phytochemical screening and antioxidant activity of some medicinal plants' crude juices. *Biotechnology Reports,* 28: e00536.
35. Sreesha, K. S. and Danya, U. (2021). Evaluation of preliminary phytochemical, antioxidant and in vitro cytotoxic studies of an ethno therapeutically important tree, *Gliricidia sepium* (jacq.) Steud. *International Journal of Creative Research Thoughts,* 9(3): 5515–5521.
36. Yashin A., Yahin Y., Xia X. and Nemzer B. (2017). Antioxidant activity of spices and their impact to human health: A review. *Antioxidants*, 6(3): 70.
37. Peter K. V. and Babu K. N. (2012). Introduction to herbs and spices: medicinal uses and sustainable production. *Handbook of Herbs and Spices:* pp.1-16.
38. Kolawole, O. M., Joseph, A. K. and George, O. A. (2018). Antibacterial and phytochemical activity of *Gliricidia sepium* against poultry pathogens. *Microbiology Research Journal International,* 24(4): 1-10.
39. Akharaiyi, F. C., Boboye, B. and Adetuyi, F. C. (2012). Antibacterial, phytochemical and antioxidant activities of the leaf extracts of *Gliricidia sepium* and *Spathodea campanulata*. *World Applied Sciences Journal*, 16(4): 523-530.
40. Maulion R.V. and Madrazo C. (2019). Synthesis of Fe_3O_4 nanoparticle via reduction of Fe^{+3} using *S. polycystum* for methylene blue dye removal in aqueous solution. Thesis of Master's Degree, De La Salle University, Manila, Philippines.
41. Dahmoune, F., Nayak, B., Moussi, K., Remini, H. and Madani, K. (2014). Optimization of microwave-assisted extraction of polyphenols from *Myrtus communis* L. leaves. *Food Chemistry*, 166: 585-595.
42. Alara, O. R., Abdurahman, N. H., Ali, H. A. and Zain, N. M. (2021). Microwave-assisted extraction of phenolic compounds from *Carica papaya* leaves: An optimization study and LC-QTOF-MS analysis. *Future Foods,* 3: 100035.
43. Dahmoune, F., Spigno, G., Moussi, K., Remini, H., Cherbal, A. and Madani, K. (2014). *Pistacia lentiscus* leaves as a source of phenolic compounds: Microwave-assisted extraction optimized and compared with ultrasound-assisted and conventional solvent extraction. *Industrial Crops and Products*. 71: 31-40.

Malaysian Journal of Analytical Sciences (MJAS)
Published by Malaysian Analytical Sciences Society

OPTIMISATION OF MICROWAVE-ASSISTED WATER EXTRACTION OF PINEAPPLE PEEL HEMICELLULOSE USING RESPONSE SURFACE METHODOLOGY

(Pengoptimuman Pengekstrakan Air Berbantu Gelombang Mikro Bagi Hemiselulosa Kulit Nanas Menggunakan Kaedah Gerak Balas Permukaan)

Nur Aza Atiqah Mad Zahir, Noraini Hamzah, Hamizah Mohd Zaki, Shariff Ibrahim, Sabiha Hanim Saleh*

School of Chemistry and Environment, Faculty of Applied Sciences,
Universiti Teknologi MARA, 40450 Shah Alam, Selangor, Malaysia

**corresponding author: sabihahanim@uitm.edu.my*

Received: 17 August 2021; Accepted: 20 October 2021; Published: 27 December 2021

Abstract

The purpose of this investigation is to optimise extraction conditions (temperature and time) for microwave-assisted water extraction of pineapple peel hemicellulose using response surface methodology (RSM). A series of 14 experimental designs were conducted to determine the optimal conditions of two key variables (temperature of 90-150 °C and time of 5-20 min) in order to maximise the extracted hemicellulose yield. Quadratic models based on central composite design (CCD) were developed to correlate the extraction process variables with the response (i.e., hemicellulose yield). These models were analysed using appropriate statistical methods (i.e., analysis of variance). The statistical analysis indicated that all the developed models were adequate for the prediction of the respective responses. A quadratic model predicted a maximum hemicellulose yield of 15.6% at the optimal temperature of 125 °C and extraction time of 14 min. From the validation experiment, a maximum hemicellulose yield of 15.2% was obtained under the same optimal conditions with the determination coefficient (R^2) of 0.95, indicating close agreement with the model prediction. Chemical characterisations of hemicellulose and residues were conducted using Fourier transform infrared (FTIR) and scanning electron microscopy (SEM). The FTIR analysis revealed the presence of hemicellulose at a specific band of 1261 cm^{-1} and the band between 1094 and 1000 cm^{-1}, which originated from xylans. The SEM characterisation indicated that the untreated pineapple peel had a broken surface and less distortion compared to the treated pineapple peel, whereas the surface structure of the treated pineapple peel had irregular crevices and larger cell disruption.

Keywords: pineapple peel, hemicellulose, microwave-assisted water extraction, response surface methodology, central composite design

Abstrak

Tujuan kajian ini adalah untuk menyiasat kesan keadaan pengekstrakan dibantu gelombang mikro (suhu, masa) ke atas hasil hemiselulosa kulit nanas menggunakan kaedah gerak balas permukaan (RSM). 14 reka bentuk eksperimen telah dibangunkan untuk menentukan keadaan optimum dua parameter utama (suhu 90-150 ºC dan masa 5-20 min) yang memaksimumkan hasil pengekstrakan hemiselulosa. Berdasarkan reka bentuk komposit pusat (CCD), model kuadratik dibangunkan untuk mengaitkan pembolehubah proses pengekstrakan dengan respons seperti hasil hemiselulosa. Model-model ini dianalisis menggunakan kaedah

statistik yang sesuai seperti analisis varians. Analisis statistik menunjukkan semua model yang dibangunkan adalah mencukupi untuk ramalan tindak balas masing-masing. Model kuadratik meramalkan hasil hemiselulosa yang maksimum 15.6% pada suhu optimum 125 ºC dan masa pengekstrakan selama 14 min. Daripada eksperimen pengesahan, hasil maksimum hemisellulosa 15.2% diperoleh dalam keadaan optimum yang sama dengan pekali penentuan (R^2) 0.95, menunjukkan persetujuan dekat dengan ramalan model. Pencirian kimia hemiselulosa dan sisa ditentukan oleh FTIR dan SEM. Analisis FTIR mendedahkan kehadiran hemiselulosa pada jalur tertentu 1261 cm^{-1} dan jalur antara 1094-1000 cm^{-1} yang berasal daripada xilan. Pencirian SEM menunjukkan bahawa kulit nanas yang tidak dirawat mempunyai permukaan pecah dan sedikit gangguan berbanding kulit nanas yang dirawat sedangkan struktur permukaan kulit nanas yang dirawat mempunyai celah-celah yang tidak teratur dan kemusnahan sel yang lebih besar.

Kata kunci: kulit nanas, hemiselulosa, ketuhar gelombang mikro berbantu pengekstrakan air, kaedah gerak balas permukaan, reka bentuk komposit pusat

Introduction

Pineapples (*Ananas comosus*) are cultivated in tropical and subtropical countries. Around 16-19 million tons of pineapples are planted worldwide annually [1]. Malaysia is one of the major producers of pineapple with the state of Johor contributing approximately 57% or 163,830 metric tons of pineapple in 2010 [1]. During processing, the pineapple waste that mainly consists of peels, stems, leaves, and crowns is removed and usually used as animal feeds and land fertilisers [2, 3].

The major components of pineapple peels are cellulose, hemicellulose, and lignin [4]. Meanwhile, the minor components include pectin, wax, protein, and extractives [5]. It is highly recommended to reuse pineapple peels as they are renewable and can accumulate with time to pose adverse environmental problems [6]. Hemicellulose is the second most abundant lignocellulosic material after cellulose [7]. It is used in food additives, bio composites, and biodegradable films, as well as in medicinal applications [8]. The mass production of high-valued hemicellulose-based products as well as their potential applications had remained largely underexplored [9]. Most studies focuses on the extraction of cellulose, not hemicellulose from pineapple peel. In addition, there are limited studies on pineapple peel hemicellulose extraction, especially using microwave-assisted water extraction.

Numerous techniques have been used for hemicellulose extraction, including steam explosion, organic solvents, dilute acid, and alkaline treatment [10]. However, it is difficult to extract sufficient hemicellulose without severe degradation due to the strong interaction between hemicellulose and lignin in plant cell walls. In recent years, microwave-assisted extraction has been seen as a viable alternative heating approach for hemicellulose extraction as it improves extraction efficiency and reduces reaction time compared to other conventional extraction methods [11, 12]. In fact, the extracted hemicellulose yield still needs improvement. Microwave-assisted extraction is often combined with chemicals, such as acids, alkalis or water as a solvent. The safest and most inexpensive green solvent is water as it is non-toxic to human health and the environment [13]. Using microwave treatment with water is expected to overcome the barriers that hinder hemicellulose extraction. Optimisation of a multifactorial system according to conventional techniques involves dealing with only one process variable or parameter at a time, which consumes time, laborious, as well as provides no information about parameter interactions [14]. According to Oberoi et al. [15], response surface methodology (RSM) is commonly used to optimise process parameters of a reaction as it saves time and labour, and also reveals information about the interactions between parameters.

In this investigation, pineapple peel hemicellulose was extracted using microwave-assisted water extraction. RSM with central composite design (CCD) was employed to optimise extraction variables for maximum hemicellulose yield. Two variables of microwave usage were varied: extraction temperature (between 90 and 150 °C) and extraction time (between 5 and 20 min). A series of experiments were performed with optimised variables to identify the relationship between the actual yield and the predicted yield from Design-Expert

software. Hemicellulose and the residues obtained were characterised by Fourier transform infrared (FTIR) and scanning electron microscopy (SEM) analysis for the identification of functional groups and surface morphology, respectively.

Materials and Methods

Materials

Pineapple peels of MD2 variety were obtained from a local pineapple processing factory (Nanas Merbok Marketing) in Kedah, Malaysia. The peels were cut into small pieces of about 3 g and washed with distilled water to remove impurities [16]. After that, the peels were oven-dried at 60 °C overnight, ground using a laboratory blender, and sieved to 1.0 mm size [8]. The samples were stored in sealed bags at room temperature until further use. Only analytical grade chemicals were used unless otherwise stated. All experimental procedures were carried out at least in duplicates.

Chemical composition analysis

Pineapple peels consist of cellulose, hemicellulose, and lignin. Standard TAPPI method T222 OM-08 was used to determine the amount of lignin, whereas the acid-chlorite method was used for holocellulose determination [17, 18]. Treating holocellulose with potassium hydroxide solution gave the cellulose content [19]. Finally, subtracting cellulose from holocellulose would give the hemicellulose content.

Microwave-assisted water extraction

Microwave-assisted water treatment was carried out using a microwave reactor (ETHOS EASY, Milestone, Italy). For each treatment, 3 g of pineapple peels was added to a 100 mL polytetrafluoroethylene vessel and mixed with 45 mL of distilled water. The effects of two process parameters were examined in this investigation: temperature (90–150 °C) and time (5–30 min). One parameter was varied and the other was kept constant for each experiment based on the preliminary tests. At the end of the experiment, the liquid extract was filtered to an average of 30 mL. Four volumes of 95% ethanol were added to precipitate the dissolved hemicellulose. Centrifugation was performed to separate the solid hemicellulose, which was then freeze-dried [9]. The freeze dried hemicellulose was weighed and calculated according to Eq. (1):

$$\text{Hemicellulose yield (\%)} = A/B \times 100\% \quad (1)$$

where A = weight of extracted hemicellulose (g) and B = weight of hemicellulose in pineapple peels (g).

Response surface methodology

In this study, RSM was used in the experimental design of microwave-assisted water extraction of pineapple peel hemicellulose. Using the results from single process parameter preliminary tests, RSM with CCD was employed to identify the optimal conditions of both extraction time and temperature for maximum hemicellulose yield. The statistical software package Design-Expert (Version 10.0.8, Stat-Ease, Inc., Minneapolis, USA) generated the experimental design of hemicellulose extraction, statistical analysis of the data (analysis of variance (ANOVA)), and three-dimensional (3D) response surface plots for this investigation. The level of the microwave extraction variables is presented in Table 1. The range values of the two independent variables were selected based on the preliminary optimisation test results. Temperature and extraction time were varied as independent variables, whereas hemicellulose yield (%) was considered as the response (dependent variable). The selected ranges for extraction time and temperature were 5–20 min and 90–150 °C, respectively.

The quadratic polynomial model fitted for the hemicellulose yield is given in Eq. (2):

$$Y = B_0 + B_1X_1 + B_2X_2 + B_{12}X_1X_2 + B_{11}X_1^2 + B_{22}X_2^2 \quad (2)$$

where Y = predicted response (hemicellulose yield), B_0 = constant coefficient, B_1 and B_2 = linear coefficients, quadratic coefficients. Additional experiments were conducted to verify the validity of the statistical experimental design under specific conditions.

Characterisation of hemicellulose and pineapple peel: FTIR analysis

FTIR analysis was carried out to determine changes in functional groups that might be caused by the treatment. The FTIR spectra of extracted hemicellulose and untreated pineapple peel were plotted using an FTIR-

8400S Shimadzu spectrophotometer (Shimadzu Corporation). The KBr disk method was used to measure the IR spectra [4]. Ground samples were mixed with KBr (1:1000, w/w) to prepare the disc. The spectra ranges of 4000–450 cm^{-1} with a resolution of 4 cm^{-1} were obtained for both samples.

SEM analysis

SEM analysis was conducted to characterise the surface morphology of pineapple peel before and after treatment. The shape and surface features of the samples were recorded using a scanning electron microscope (SEM, Hitachi-S4800) at an acceleration voltage of 15 kV. A small amount of freeze-dried sample was placed on a metallic stub using carbon tape and gold-coated for 60 s with a sputter coater (Cressington 108 Auto, Watford, UK). For each sample, at least three SEM images were captured from random areas of the samples [5].

Table 1. Level of the microwave extraction variable.

Variable	Coding	Level		
		-1	0	+1
Time (min)	A	5	10	20
Temperature (°C)	B	90	120	150

Results and Discussion

Chemical composition of pineapple peel

The chemical composition of MD2 variety pineapple peel is tabulated in Table 2 as the average of two replicates on a dry basis. Cellulose (28.06 ± 0.42%) was the major component, followed by hemicellulose (17.65 ± 0.15%) and lignin (11.90 ± 0.71%). Researchers have published different chemical compositions for pineapple peels. Sukkaew et al. [20] reported that the compositions of pineapple peel for cellulose, hemicellulose, and lignin were 23.03 ± 2.14%, 59.26 ±0.63%, and 4.19 ± 0.56%, respectively, whereas Maudereira et al. [4] found that the chemical compositions of pineapple peel for cellulose, hemicellulose, and lignin were 16.9 ± 2.02%, 15.8 ± 2.02%, and 28.9 ± 0.39%, respectively [20, 4]. The different compositions might probably be due to the plant species, geographical origin, and environmental factors [21].

Selection of experimental set points

Preliminary pineapple peel hemicellulose extraction tests were conducted using microwave-assisted water extraction. These preliminary tests were carried out to estimate reasonable extraction temperature and time range values for the optimisation process using RSM combined with CCD. A fixed extraction time of 20 min with five different temperatures (90, 120, 130, 140, and 150 °C) were used as the conditions for the first preliminary test. The next test involved a fixed temperature of 120 °C with four different extraction times (5, 10, 20, and 30 min). These process parameters were selected with some modifications from previous studies [9, 22, 23].

Figure 1 shows the preliminary test results of hemicellulose yield extracted from pineapple peels. For Figure 1(a) where extraction time was fixed at 20 min, the hemicellulose yield increased significantly from 90 to 120 °C and started to decrease towards the highest temperature of 150 °C. It was also observed in Figure 1(b) that the hemicellulose yield increased during extraction time from 5 min to 10 min at a fixed temperature of 120 °C. It could be observed that the hemicellulose yield decreased significantly with a longer extraction time of more than 10 min up to 30 min. Therefore, the ranges of temperature and time from 90 to 150 °C and from 5 to 20 min, respectively, were chosen for the optimisation study of hemicellulose extraction using RSM.

Table 2. Chemical composition of pineapple peel (MD2 variety)

Composition	% (w/w)
Cellulose	28.06 ± 0.42
Hemicellulose	17.65 ± 0.15
Lignin	11.90 ± 0.71

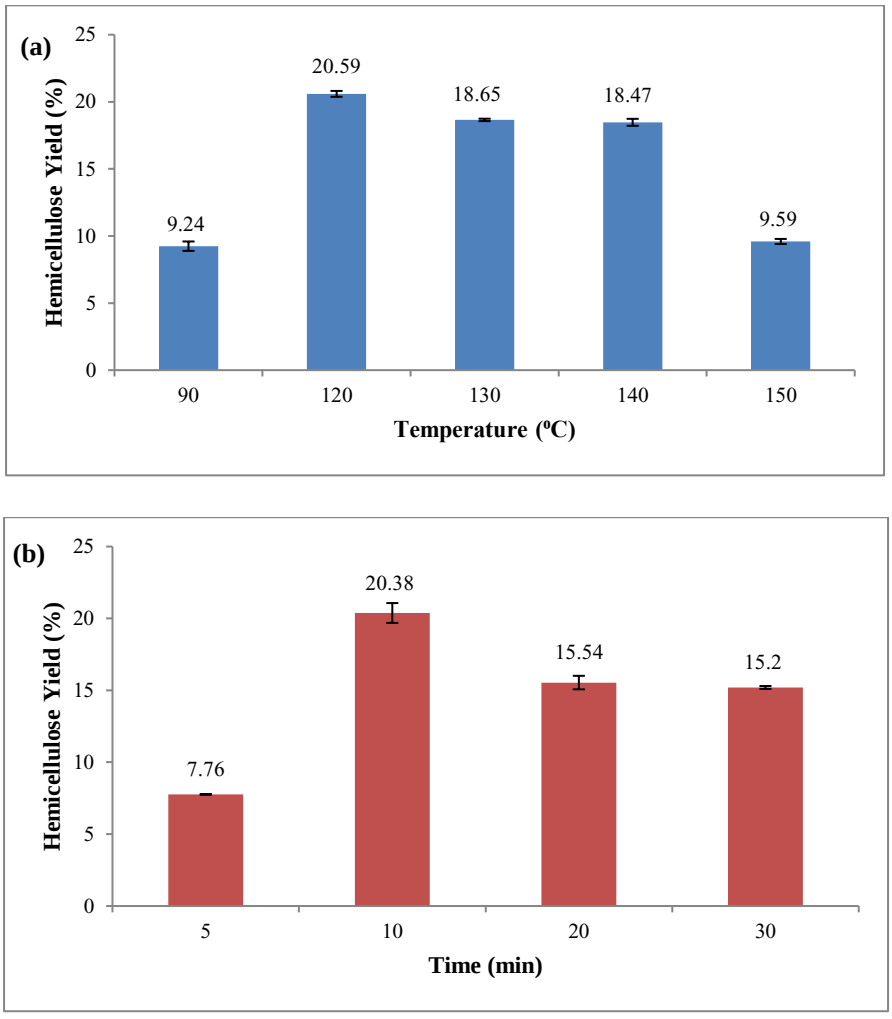


Figure 1: The percentage yield of hemicellulose; (a) at different temperatures and fixed extraction time (20 minutes); (b) at different extraction times and fixed temperature (120 °C)

RSM design and optimisation of microwave-assisted extraction of pineapple peel

A series of 14 experimental runs involving temperature and time parameters for optimisation were designed using RSM with CCD. The variable ranges for temperature and time were selected based on the preliminary test results. The matrix corresponding to CCD is presented in Table 3 and a quadratic regression equation for hemicellulose yield (%) is expressed as follows:

$$\text{Hemicellulose yield, Y (\%)} = -67.61631 + 2.56512A + 1.03252B - 5.44444E\text{-}004AB - 0.087289A^2 - 4.08056E\text{-}003B^2 \quad (3)$$

Antagonistic effects are indicated with a negative sign while synergistic effects are depicted by a positive sign. The generated model equation indicated that the positive coefficients of A and B rendered a linear effect towards the increment of hemicellulose yield, while negative coefficients of AB, A^2, and B^2 showed a reduction of hemicellulose yield.

The overall summary of ANOVA showing the significance and adequacy of the quadratic models used is presented in Table 4. The fitted quadratic model indicated high significance to adequately represent the response-parameter relationship due to its low *p*-value ($0.0002 < 0.05$) and high R^2 value of 0.9518. Source A representing extraction time showed a higher *F*-value (19.61) than source B indicating extraction temperature with an *F*-value of 6.69. This means that within the experimental design range, the hemicellulose yield was predominantly affected by extraction time and to a lesser extent by extraction temperature. The adequacy of the quadratic model was also evaluated using the lack of fit approach. The lack of fit has to be insignificant ($p > 0.05$) for the model to fit well in the experiment [24]. The lack of fit could be significant in cases where important terms are missing from the model or due to large abnormal residuals appearing during model fitting [25]. As seen in Table 4, the *p*-value for lack of fit was 0.0633, indicating that the RSM model with CCD is reliable, satisfactory, and can be used to predict actual situations during hemicellulose extraction. A signal-to-noise ratio is measured by adequate precision, which needs to be greater than 4. According to Table 4, the signal-to-noise ratio was 12.278, indicating an adequate signal and that the model can be used to navigate the design space.

As shown in Figure 2, the predicted R^2 (predicted value) of 0.5744 had a difference of more than 0.2 compared to the adjusted R^2 (experimental value) of 0.9173. This was probably due to a large block effect or problems with the data or model. There may also be other inconsistencies, such as model reduction, outliers, and response transformation. Therefore, confirmation runs should be performed to test all empirical models.

The relationship between responses (predicted yield) and experimental values (actual yield) is usually presented graphically by Design-Expert. This software employs 3D response surface plots and two-dimensional (2D) contour plots, which are graphical representations of regression equations. These graphs provide visual aids to comprehend the connection between response and experimental levels of each variable, as well as to identify the type of interactions between two independent variables. Contour plots use different shapes to indicate different interactions between variables. Circular contour plots indicate negligible interactions between independent variables, whereas elliptical contour plots show significant interactions between independent variables.

The interactive effects of extraction time and temperature on the hemicellulose yield are summarised in Figure 3. The 3D response surface plot in Figure 3(a) indicates increased hemicellulose yield with increased temperature (90-125 °C) and time (5-14 min). However, the hemicellulose yield decreased at temperatures higher

than 125 °C. Similarly, the hemicellulose yield also decreased as the extraction time increased to more than 14 min. The response surface plot indicated that the optimum hemicellulose yield could be obtained at the middle range of extraction temperature and time. Figure 3(b) shows the circular 2D contour plot of temperature and time. The maximum predicted hemicellulose is obtained at the centre of the contour plot [26]. The plot indicated insignificant mutual interactions between the independent variables based on the *p*-value (0.8766 > 0.05). This means that increasing the extraction time does not increase the pineapple peel hemicellulose yield at higher temperatures.

Based on Design-Expert software, the predicted maximum hemicellulose yield occurred at 125 °C with an extraction time of 14 min. Therefore, confirmation experiments were performed in duplicate trials to validate the predicted optimum conditions. The maximum predicted hemicellulose yield under optimal independent variable conditions was 15.6%, whereas the actual hemicellulose yield was 15.2% under similar conditions. The validity of this model is accepted due to the close agreement between the predicted and actual hemicellulose yields. Thus, this also indicates that RSM is a very useful analytical tool for identifying optimal values of independent variables to attain a maximum response value.

Table 3. Experimental design for the hemicellulose extraction from pineapple peel by microwave assisted water extraction (RSM, CCD)

Standard	Type	Independent Variables		Response	
		A: Time (Min)	B: Temperature (ºC)	Hemicellulose Yield (%)	
				Experimental	Predicted
1	Factorial	5.0	150	4.32	5.69
2	Factorial	5.0	90	3.60	2.67
3	Factorial	20.0	150	9.72	10.21
4	Factorial	20.0	90	9.49	7.67
5	Axial	23.0	120	7.83	8.67
6	Axial	2.0	120	2.34	1.94
7	Axial	12.5	78	3.96	5.81
8	Axial	12.5	162	11.16	9.75
9	Center	12.5	120	14.19	14.30
10	Center	12.5	120	15.20	15.60
11	Center	12.5	120	15.16	15.14
12	Center	12.5	120	16.20	15.13
13	Center	12.5	120	15.90	15.12
14	Center	12.5	120	14.16	15.13

Table 4. ANOVA results for experimental response of pineapple peel hemicellulose yield

Source	**Sum of squares**	**df**	**Mean square**	**F-Value**	**P-Value**	**Level of significance**
Model	319.60	5	63.92	27.62	0.0002	Significant
A-Time (min)	45.38	1	45.38	19.61	0.0030	
B-Temperature (ºC)	15.49	1	15.49	6.69	0.0361	
AB	0.060	1	0.060	0.026	0.8766	
A^2	178.03	1	178.03	76.93	<0.0001	
B^2	99.60	1	99.60	43.04	0.0003	
Residual	16.20	7	2.31			
Lack of Fit	13.12	3	4.37	5.68	0.0633	Not significant
Pure Error	3.08	4	0.77			
Cor Total	335.80	13				
Std. Dev.	1.52		R^2	0.9518		
Mean	10.23		Adjusted R^2	0.9173		
C.V. %	14.87		Predicted R^2	0.5744		
PRESS	142.91		Adequate Precision	12.278		

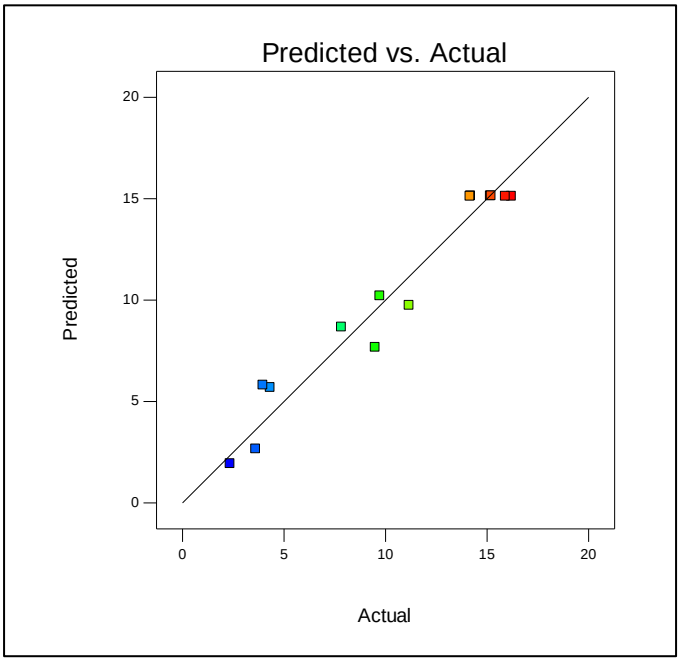


Figure 2. Predicted value vs. actual hemicellulose yield

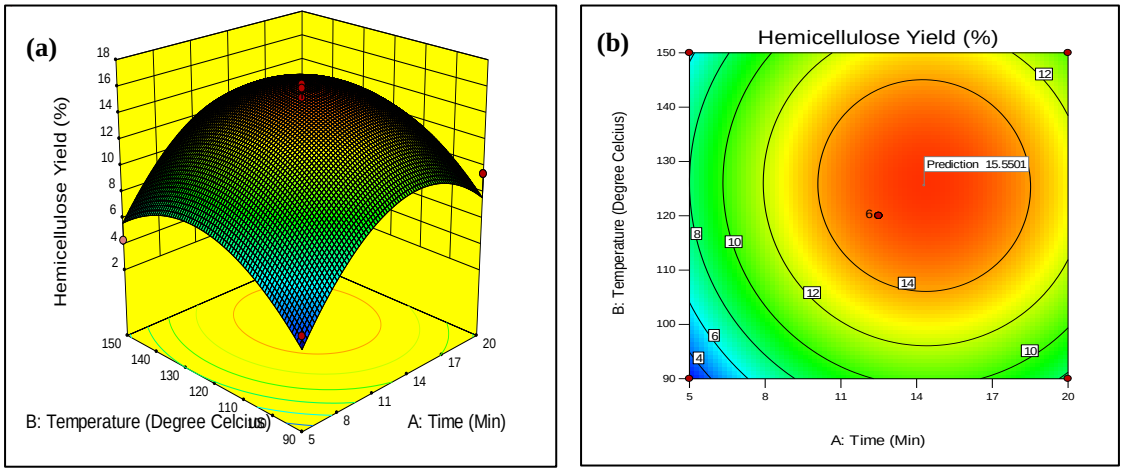


Figure 3. (a) 3D response surface plots showing combined effect of extraction time and temperature on hemicellulose yield (%); (b) 2D contour plot of hemicellulose yield against extraction time and temperature

Characterisation of extracted hemicellulose and pineapple peel: FTIR analysis

Molecules in biomass and extracted samples have specific functional groups, which help to characterise their identity. This identification is done quickly and accurately using FTIR. Figure 4 shows the FTIR spectra of both dried pineapple peel and extracted hemicellulose within the peel region of 4000–450 cm^{-1}. Numerous peaks corresponding to O-H and C=O were noted in both spectra, representing the common bonds found in hemicellulose [27]. The stretching vibration of O-H produced strong, broad peaks at 3395 cm^{-1} for both spectra. There was also a weak peak in both spectra at 2964 cm^{-1} from the vibrational stretching of C-H groups [28]. Acetyl and ester groups in hemicellulose or the ester linkage of the carboxylic group of ferulic and p-coumaric acids of lignin and hemicellulose are probably responsible for the absorption bands at 1607 cm^{-1} and 1609 cm^{-1} [29]. The peaks at 1416 cm^{-1} and 1412 cm^{-1} correspond to –COO- symmetric stretching of uronic acid carboxylate [5]. Carboxylic acid vibration from 4-O-methyl-α-D-glucuronic acid gave a peak at 1261 cm^{-1} [30]. The presence of arabinofuranosyl is associated with the peak at 1094 cm^{-1} [31]. The peaks at 1041 cm^{-1} and 1015 cm^{-1} are associated with C-O-C pyranose ring skeletal vibration. It should be noted that these peaks usually appear mainly due to the presence of C-O, C-C stretching or C-OH bending of hemicellulose [32, 33]. β-glycosidic linkages between sugar molecules are denoted by the peaks at 801 cm^{-1} and 800 cm^{-1} [34].

SEM analysis

The morphology of pineapple peel before and after microwave-assisted extraction treatment (125 °C, 14 min) was observed using a scanning electron microscope. Figure 5 depicts the SEM images of pineapple peel at 150× magnification. As presented in SEM images, different morphological structures of untreated and treated pineapple peel could be observed. The untreated pineapple peel exhibited less distortion compared to the treated pineapple peel. The breakage observed in the untreated pineapple peel sample might be due to the mechanical process of size reduction. The surface structure of the treated pineapple peel in a state of aggregation had irregular crevices and larger cell disruption. This indicates that the treatment removed external fibres, which in turn increased the surface area and resulting in higher extraction efficiency. The SEM results are in accordance with previous studies [30, 33, 35].

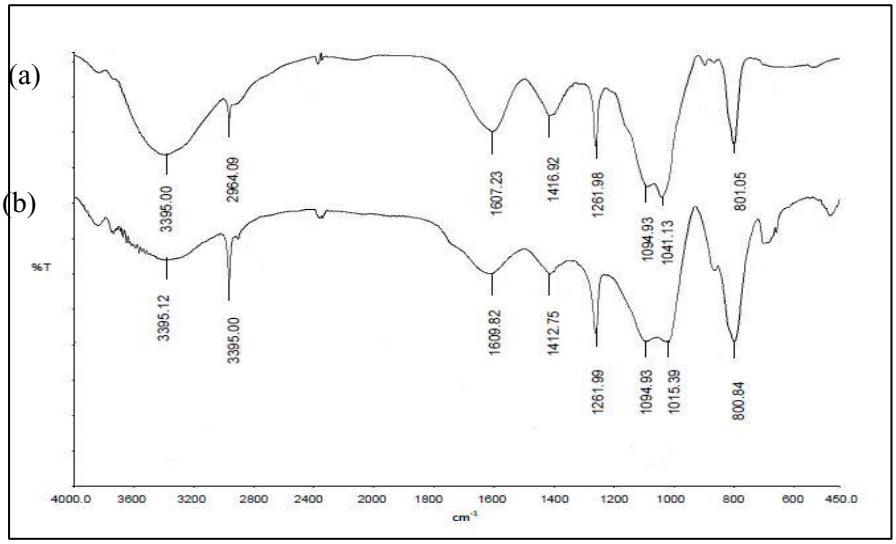


Figure 4. FTIR spectra of (a) untreated pineapple peel and (b) hemicellulose extracted via microwave assisted extraction process

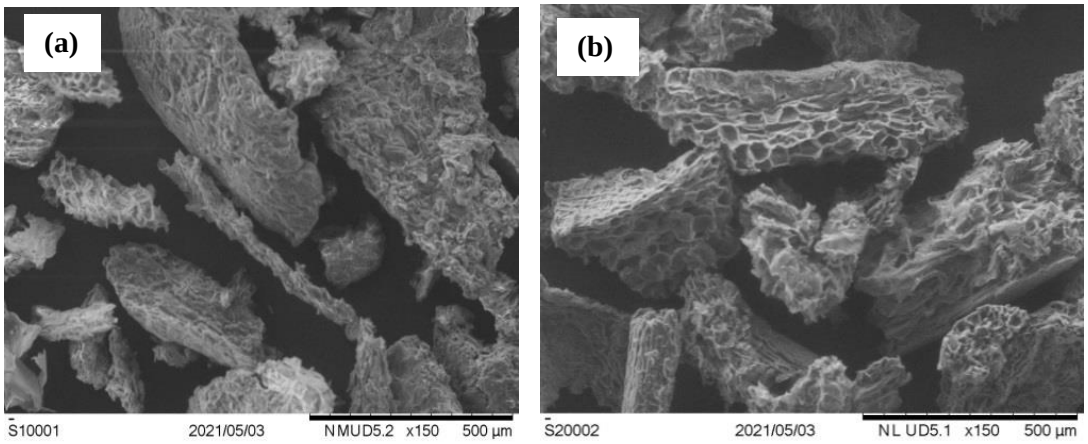


Figure 5. SEM images of pineapple peel. a) untreated pineapple peel; b) pineapple peel after microwave treatment at 125ºC, 14 min; (magnification 150x)

Conclusion

In this study, microwave-assisted water extraction was used to obtain pineapple peel hemicellulose. RSM with CCD was applied to optimise the extracted pineapple peel hemicellulose yield. A quadratic model with extraction temperature of 125 °C and extraction time of 14 min was accepted as the best model for maximum hemicellulose yield. The predicted maximum yield of hemicellulose was 15.6%, whereas the actual yield obtained was 15.2%. Thus, in conclusion, the actual hemicellulose yield is in close agreement with the predicted yield recommended by the quadratic models of RSM with CCD. These findings demonstrate the potential applicability of optimisation of microwave-assisted extraction of hemicellulose using RSM to

obtain high hemicellulose yield for the production of pineapple peel hemicellulose films.

Acknowledgement

The authors are grateful to Universiti Teknologi MARA, Malaysia for the financial support provided for this research by Geran Penyelidikan Khas, 600-RMC/GPK 5/3 (013/2020).

References

1. Dai, H. and Huang, H. (2016). Modified pineapple peel cellulose hydrogels embedded with sepia ink for effective removal of methylene blue. *Carbohydate Polymers*, 148: 1-10.
2. Kaur, N., Sharma, S., Kaur, S. and Khosla, E. (2016). Reverse micellar extraction of acid dyes from simulated textile effluent. *Journal Chemistry Biology Pyhsics Sciences,* 6: 180-197.
3. Schieber, A., Stintzing, F. C. and Carle, R. (2001). By-products of plant food processing as a source of functional compounds—recent developments. *Trends in Food Science & Technology*, 12(11): 401-413.
4. Madureira, A. R., Atatoprak, T., Çabuk, D., Sousa, F., Pullar, R. C. and Pintado, M. (2018) Extraction and characterisation of cellulose nanocrystals from pineapple peel. *International Journal Food Studies*, 7: 24-33.
5. Banerjee, S., Ranganathan, V., Patti, A. and Arora, A. (2018). Valorisation of pineapple wastes for food and therapeutic applications. *Trends in Food Science & Technology,* 82: 60-70.
6. Choquecahua Mamani, D., Otero Nole, K. S., Chaparro Montoya, E. E., Mayta Huiza, D. A., Pastrana Alta, R. Y. and Aguilar Vitorino, H. (2020). Minimizing organic waste generated by pineapple crown: A simple process to obtain cellulose for the preparation of recyclable containers. *Recycling*, 5(4): 24.
7. Limayem, A. and Ricke, S. C. (2012). Lignocellulosic biomass for bioethanol production: Current perspectives, potential issuesand future prospects. *Progress Energy Combustion Sciences*, 38(4): 449-467.
8. Sabiha-Hanim, S. and Siti-Norsafurah, A. M. (2012). Physical properties of hemicellulose films from sugarcane bagasse. *Procedia Engineering*, 42: 1390-1395.
9. Mihiretu, G. T., Brodin, M., Chimphango, A. F., Øyaas, K., Hoff, B. H. and Görgens, J. F. (2017). Single-step microwave-assisted hot water extraction of hemicelluloses from selected lignocellulosic materials – a biorefinery approach. *Bioresource Technology*, 241: 669-680.
10. Chen, J., Zhu, Y. and Liu, S. (2017). Biodegradation and utilization of hemicellulose. *Functional Carbohydrate,* 2017: 197-232.
11. Thomas, E., Amidon, and Shi, J. L. (2009). Water-based woody biorefinery. *Biotechnology Advances,* 27: 542-550.
12. Liu, C. G. and Wyman, C. E. (2005). Partial flow of compressed-hot water through corn stover to enhance hemicellulose sugar recovery and enzymatic digestibility of cellulose, *Bioresource Technology,* 96(18): 1978-1985.
13. Tsubaki, S., Onda, A., Hiraoka, M., Fujii, S., Azuma, J. I. and Wada, Y. (2017). Microwave-assisted water extraction of carbohydrates from unutilized biomass. *Water Extraction of Bioactive Compounds*, 199-219.
14. Jeya, M., Zhang, Y. W., Kim, I. W. and Lee, J. K. (2009). Enhanced saccharification of alkali-treated rice straw by cellulase from Trametes hirsuta and statistical optimization of hydrolysis conditions by RSM. *Bioresource Technology*, 100(21): 5155-5161.
15. Oberoi, H. S., Vadlani, P. V., Nanjundaswamy, A., Bansal, S., Singh, S., Kaur, S. and Babbar, N. (2011). Enhanced ethanol production from Kinnow mandarin (*Citrus reticulata*) waste via a statistically optimized simultaneous saccharification and fermentation process. *Bioresource Technology*, 102(2): 1593-1601.
16. Zulyadi, N. H., Saleh, S. H. and Sarijo, S. H. (2016). Fractionation of hemicellulose from rice straw by alkaline extraction and ethanol precipitation. *Malaysian Journal of Analytical Sciences,* 20(2): 329-334.
17. Ioelovich, M. (2014). Structure and physicochemical properties of nitrogenated derivatives of cellulose. *American Journal Biosciences,* 2: 6-12.

18. Browning, B. L. (1967). Methods of wood chemistry. Volume I & II. John Wiley & Sons. Interscience, New York.
19. Teramoto, Y., Lee, S. H. and Endo, T. (2008). Pretreatment of woody and herbaceous biomass for enzymatic saccharification using sulfuric acid-free ethanol cooking. *Bioresource Technology*, 99(18): 8856-8863.
20. Sukkaew, A., Boonsong, P., Thongpradistha, S. and Intan, M. (2017). Physical and chemical pretreatment of lignocellulosics in pineapple (*Ananus comosus*) peels dried for investment. *AIP Conference Proceedings,* 1868(1): 090001.
21. Silveira, R., Stoyanov, S., Gusarov, S., Skaf, M. and Kovalenko, A. (2013). Plant biomass recalcitrance: Effect of hemicellulose composition on nanoscale forces that control cell wall strength. *Journal of the American Chemical Society,* 135: 19048-19051.
22. Santos, T. M., Alonso, M. V., Oliet, M., Domínguez, J. C., Rigual, V. and Rodriguez, F. (2018). Effect of autohydrolysis on *Pinus radiata* wood for hemicellulose extraction. *Carbohydrate Polymers*, 194: 285-293.
23. Yuan, Y., Zou, P., Zhou, J., Geng, Y., Fan, J., Clark, J. and Zhang, C. (2019). Microwave-assisted hydrothermal extraction of non-structural carbohydrates and hemicelluloses from tobacco biomass. *Carbohydrate Polymers*, 223: 115043.
24. Yolmeh, M. and Jafari, S. M. (2017). Applications of response surface methodology in the food industry processes. *Food Bioprocess Technology,* 10: 413-433.
25. Behera, S. K., Meena, H., Chakraborty, S. and Meikap, B. C. (2018). Application of response surface methodology (RSM) for optimization of leaching parameters for ash reduction from low-grade coal. *International Journal of Mining Science and Technology*, 28(4): 621-629.
26. Shafi, J., Sun, Z., Ji, M., Gu, Z. and Ahmad, W. (2018). ANN and RSM based modeling for optimization of cell dry mass of Bacillus sp. Strain B67 and its antifungal activity against *Botrytis cinerea*. *Biotechnology & Biotechnological Equipment*, 32: 58-68.
27. Palaniappan, A., Yuvaraj, S., Sonaimuthu, S. and Antony, U. (2017).Characterization of xylan from rice bran and finger millet seedcoat for functional food applications. *Journal Cereal Sciences,* 75: 296-305.
28. Mandal, A. and Chakrabarty, D. (2011). Isolation of nanocellulose from waste sugarcane bagasse (SCB) and its characterization. *Carbohydrate Polymers*, 86(3): 1291-1299.
29. Dai, H., Ou, S., Huang, Y. and Huang, H. (2018). Utilization of pineapple peel for production of nanocellulose and film application. *Cellulose*, 25(3): 1743-1756.
30. Liu, H. M., Li, Y. R., Wu, M., Yin, H. S. and Wang, X. D. (2018). Two-step isolation of hemicelluloses from Chinese quince fruit: Effect of hydrothermal treatment on structural features. *Industrial Crops and Products*, 111: 615-624.
31. Sun, S. L., Wen, J. L., Ma, M. G. and Sun, R. C. (2013). Successive alkali extraction and structural characterization of hemicelluloses from sweet sorghum stem. *Carbohydrate Polymers*, 92(2): 2224-2231.
32. Haafiz, M. M., Hassan, A., Zakaria, Z. and Inuwa, I. M. (2014). Isolation and characterization of cellulose nanowhiskers from oil palm biomass microcrystalline cellulose. *Carbohydrate Polymers*, 103: 119-125.
33. Singh, R. D., Bhuyan, K., Banerjee, J., Muir, J. and Arora, A. (2017). Hydrothermal and microwave assisted alkali pretreatment for fractionation of arecanut husk. *Industrial Crops and Products*, 102: 65-74.
34. Buslov, D. K., Kaputski, F. N., Sushko, N. I., Torgashev V. I., Solov′eva L. V., Tsarenkov V. M., Zubets O. V. and Larchenko L.V. (2009). Infrared spectroscopic analysis of the structure of xylans. *Journal Applied Spectroscopy*, 76: 801-805.
35. Dai, H. and Huang, H. (2017). Synthesis, characterization and properties of pineapple peel cellulose-G-acrylic acid hydrogel loaded with kaolin and sepia ink. *Cellulose,* 24: 69-84.

Malaysian Journal of Analytical Sciences (MJAS)
Published by Malaysian Analytical Sciences Society

ESTIMATION OF CARBON DIOXIDE EMISSION IN THE TRANSPORTATION SECTOR ON PRIMARY ARTERIAL ROADS IN WONOKROMO DISTRICT, SURABAYA BEFORE AND AFTER COVID-19

(Anggaran Pelepasan Gas Karbon Dioksida Bagi Sektor Pengangkutan di Jalan Utama Daerah Wonokromo Kota Surabaya Sebelum dan Selepas Covid-19)

Fatimah Zahra[1]*, Agus Supriyanto[2], Nita Citrasari[1]

[1]*Environmental Engineering Program*
[2]*Biology Program, Biology Department*
Faculty of Science and Technology,
Universitas Airlangga, Indonesia

*Corresponding author: fatimah.zahra-2016@fst.unair.ac.id

Received: 15 July 2021; Accepted: 2 December 2021; Published: 27 December 2021

Abstract

This research aims to determine the number of motorized vehicles of the road transportation sector at primary arterial roads inWonokromo District before and after COVID-19, the estimated amount of emission produced by motorized vehicles before and after COVID-19 and the correlation between the distribution of the amount and the types of motorized vehicles and the estimated amount of carbon dioxide (CO_2) emission. Data collection for determining the amount and type of motorized vehicles was conducted at Jalan Stasiun Wonokromo, Jalan Bung Tomo and Jalan Raya Ngagel. Data collection was conducted in the morning (06.00-08.00 a.m.), afternoon (11.00 a.m. – 01.00 p.m.) and evening (04.00-06.00 p.m.). This study utilizes the IPCC method to determine the concentration of CO_2 while implementing the IPCC formula in travel distance approach and the idle emission formula in fuel consumption approach. The estimated amount of CO_2 emission load is decreased due to COVID-19 by 44% at Jalan Stasiun Wonokromo, by 62% at Jalan Bung Tomo and by 34% at Jalan Raya Ngagel. The total number of motorized vehicles correlates to the estimated amount of CO_2 emission load where there is an increase in number of motorized vehicles there will be an increase in the estimated amount of CO_2 emission load as well.

Keywords: before and after COVID-19, carbon dioxide, idle emission, motorized vehicles, primary arterial roads

Abstrak

Kajian ini bertujuan untuk mengetahui jumlah kendaraan bermotor berdasarkan jenisnya di jalan utama daerah Wonokromo sebelum dan selepas COVID-19, anggaran beban pelepasan yang dihasilkan oleh kenderaan bermotor sebelum dan selepas COVID-19 dan mengetahui hubungan antara taburan jumlah dan jenis kendaraan bermotor

dengan anggaran pelepasan gas karbon dioksida (CO_2). Pengambilan data berupa jumlah dan jenis kendaraan bermotor dilakukan di Jalan Stasiun Wonokromo, Jalan Bung Tomo dan Jalan Raya Ngagel. Pengambilan data dilakukan pada pagi (06.00-08.00 WIB), tengahari (11.00-13.00 WIB) dan petang (16.00-18.00). Penelitian ini menggunakan kaedah pengiraan kepekatan CO_2 dengan pendekatan jarak tempuh kenderaan menggunakan formula IPCC dan pengunaan bahan bakar menggunakan formula pelepasan terbiar. Pandemik COVID-19 menyebabkan terjadinya penurunan beban pelepasan CO_2. Jalan Stasiun Wonokromo mengalami penurunan sehingga 44%, Jalan Bung Tomo pada 62% dan Jalan Raya Ngagel pada 34%. Korelasi antara jumlah kenderaan dengan anggaran pelepasan gas CO_2 dipercayai semakin tinggi jumlah kenderaan maka semakin tinggi beban pelepasan CO_2 berlaku.

Kata kunci: sebelum dan selepas COVID-19, karbon dioksida, pelepasan terbiar, kenderaan bermotor, jalan utama

Introduction

The increasing use of energy from fossil fuels for various human activities especially in industrial processes, transportation, and forest-clearing activities has led to increased greenhouse-gas emissions. The transportation sector plays a major role in air pollution through motorized-vehicle emissions. Motorized-vehicle emissions globally contribute 60% to air pollution, wherein 25% is made up of CO_2, 50% of NOx, and 25% of other gases[1]. CO_2 is also the main cause of the increase in the Earth's temperature, and the effect is bound to continue. The 2007 Global Climate Assessment showed that CO_2 has a radiative forcing (RF) value of 1.68 W/m^2. CO_2 has the largest positive RF value of all greenhouse gases produced by human activities, so CO_2 plays the largest role in global warming. A positive RF value represents an average increase in surface temperature caused by a gas, and a negative one indicates a decrease in temperature [2]. The increase in the number of motorized vehicles in the city of Surabaya has affected the amount of gas emissions produced, thereby contributing to climate change and global warming. The consumption of fossil fuels in metropolitan cities tends to be high owing to high levels of population, mobility, and increased urban-transportation activities. The increase in urban-transportation activities in Indonesia is triggered by an increase in the ownership and use of private vehicles [3].

Materials and Methods

Based on the Technical Guidelines for Deconcentration of Mobile Source Air Pollution Control, the areas of study are three primary arterial roads in the city. The sampling was a one-time sampling. Sampling shall be conducted on working days and weekend; thus Monday, Tuesday, Saturday and Sunday were selected as representatives [4]. Accordingly, Jalan Stasiun Wonokromo, Jalan Bung Tomo, and Jalan Raya Ngagel were selected. Eleven sampling points on the three roads were chosen, as shown in Figures 2 - 4.

Primary data collection

The primary data needed for this study were the number of vehicles, vehicle types, vehicle idling time, and travel distance. The number of vehicles was obtained by traffic counting at the predetermined sampling points before COVID-19 and by using CCTV footages after COVID-19. Traffic counting was conducted for a week after COVID-19 because traffic counting through CCTV footages did not need to consider volunteer to help onthe road. Traffic counting was conducted at peak hours in the morning (06.00–08.00 a.m.), afternoon (11.00 a.m.–01.00 p.m.) and evening (04.00–06.00 p.m.). Traffic counting was performed using a manual hand counter.Vehicle idling time was the duration of vehicles stopping and in idle condition at a red light. Travel distance wasthe length of road segments which differs based on inlet and outlet points of vehicles on each road. The length of road segments and idling time at each sampling point are listed in Table 1.

Secondary data collection

The secondary data needed for this study were emission factor (Table 2) [5], fuel economy in running

condition(Table 3) [5], fuel economy in idle condition (Table 3) [6], and fuel density. Fuel density in this study included gasoline (0.737 kg/m$^{3)}$ and diesel (0.82 kg/m^3).



Figure 1. Primary arterial roads in Wonokromo District

Directory:

: Primary Arterial Roads in Wonokromo District

1. : Jalan Diponegoro
2. : Jalan Raya Ngagel
3. : Jalan Bung Tomo
4. : Jalan Upa Jiwa
5. : Jalan Ratna
6. : Jalan Wonokromo
7. : Jalan Stasiun Wonokrom



Figure 2. Sampling points in Jalan Stasiun Wonokromo



Figure 3. Sampling points in Jalan Bung Tomo

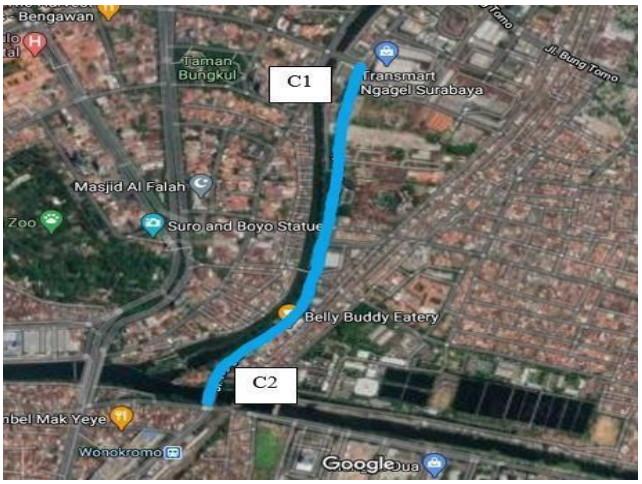


Figure 4. Sampling points in Jalan Raya Ngagel

Table 1. Length of road segments and idling time at each sampling point

Street Name	Sampling Point	Length of Road Segment (km)	Idling Time (h)
Stasiun Wonokromo	A1	0.352	0.0167
	A2	0.517	0.0250
	A3	0.169	-
Bung Tomo	B1	0.083	0.0167
	B2	0.083	-
	B3	0.226	0.0250
	B4	0.226	0.0250
Bung Tomo	B5	0.408	-
	B6	0.408	-
Raya Ngagel	C1	1.120	0.0167
	C2	1.120	0.0200

Table 2. Emission factor of motorized vehicles in Indonesian cities

	Type of Vehicle	CO (g/km)	HC (g/km)	NO_x (g/km)	PM10 (g/km)	CO_2 (g/kg fuel)	SO_2 (g/km)
1.	Motorcycle	14	5.9	0.29	0.24	3180	0.008
2.	Gasoline-fueled van/minibus	40	4	2	0.01	3180	0.026
3.	Diesel-fueledvan/minibus	2.8	0.2	3.5	0.53	3172	0.44
4.	Bus	11	1.3	11.9	1.4	3172	0.93
5.	Truck	8.4	1.8	17.7	1.4	3172	0.82
6.	Angkutan kota (angkot)	43.1	5.08	2.1	0.006	3180	0.029
7.	Taxi	55.3	5.6	2.8	0.008	3180	0.025
8.	Pick-up truck	31.8	3.5	2	0.026	3178	0.13
9.	Jeep	36.7	3.86	2.36	0.039	3178	0.145
10.	Sedan	33.8	3.7	1.9	0.004	3180	0.023

Table 3. Fuel economy in running condition

No.	Type of Vehicle	km/liter
1.	Sedan	9.8
2.	Van/minibus	8
3.	Taxi	8.7
4.	Angkot	7.5
5.	Micro and medium bus	4
6.	Large bus	3.5
7.	Pick-up truck	8.5
8.	Truck with 2 sets of axles	4.4
9.	Truck with 3 sets of axles	4
10.	Jeep	8
11.	Motorcycle	28

Table 4. Fuel economy in idle condition

	Type of Vehicle	mL/10 min	L/h
1.	Sedan	88.0	0.528
2.	Van/minibus	88.0	0.528
3.	Taxi	88.0	0.528
4.	Angkot	88.0	0.528
5.	Micro and medium bus	153.1	0.919
6.	Large bus	108.2	0.649
7.	Pick-up truck	88.0	0.528
8.	Truck with 2 sets of axles	167.0	1.002
9.	Truck with 3 sets of axles	419.3	2.516
10.	Jeep	100.0	0.600
11.	Motorcycle	22.8	0.137

Emission load calculation

CO_2 emissions for motorized vehicles while traveling was calculated using a modified equation from the Intergovernmental Panel on Climate Change [7], as shown in Equation 1.

EF is the emission factor of CO_2 (g/kg-fuel), FE is fuel economy (km/l), TD travel distance or road length (km),AV is the number of vehicles per vehicle type (unit), and fuel density in this study included gasoline and diesel (kg/m^3).

CO_2 emissions produced by motorized vehicles in idle condition were calculated using Equations 2 and 3 [8].

Idle emissions are emissions in idle condition (g/day), idle-fuel use is fuel used in idle time (l/day), GHG emission factor (g/L), AV is the number of vehicles per vehicle type (unit), and fuel density in this study includedgasoline and diesel (kg/m^3).

Statistical analysis

The data obtained were tested statistically with the Kolmogorov-Smirnov test and the Spearman correlation testusing the Statistical Package for the Social Sciences (SPSS) application. The Kolmogorov-Smirnov test was conducted to determine whether the research data were normally distributed or not. The data was then examinedby the Spearman correlation test because it was not normally distributed.

$$\text{Emission (tonnes/year)} = EF \times (1 / FE) \times TD \times AV \times \text{fuel density} \times 10^{-6} \times 365 \text{ (day/year)} \quad (1)$$

$$\text{Idle-fuel use} = (\text{idle-fuel flow}) \times (\text{idle time per day}) \quad (2)$$

$$\text{Idle emissions} = (\text{idle-fuel use}) \times (\text{GHG emission factor}) \times AV \times \text{fuel density} \quad (3)$$

Results and Discussion

Vehicle volume and composition

Vehicle volume on Jalan Stasiun Wonokromo, Jalan Bung Tomo, and Jalan Raya Ngagel before COVID-19 is shown in Figures 5 - 7.

Vehicle volume before COVID-19 was 296,292 units on Jalan Stasiun Wonokromo, 346,740 units on Jalan BungTomo, and 561,463 units on Jalan Raya Ngagel. Vehicle activity was higher during weekdays compared to weekend. High vehicle activity on weekdays was related to community activities, such as work and academic activities [9, 10]. Vehicle volume on Jalan Stasiun Wonokromo, Jalan Bung Tomo, and Jalan Raya Ngagel after COVID-19 is shown in Figures 8 - 10.

Vehicle volume after COVID-19 was 551,716 units on Jalan Stasiun Wonokromo, 449,495 units on Jalan BungTomo, and 424,068 units on Jalan Raya Ngagel. The City Government of Surabaya began implementing large- scale social restrictions on April 28, 2020. This regulation was implemented as an effort to prevent the spread ofCOVID-19. Restrictions were made on activities outside the home and modes of transportation [11]. Vehicle composition on Jalan Stasiun Wonokromo, Jalan Bung Tomo, and Jalan Jalan Raya Ngagel after COVID-19 is shown in Figures 11 - 13.

The number of vehicles on the three roads was dominated by motorcycle, with percentages of 83%, 74%, and 82%, respectively. The vehicle with the second largest percentage was gasoline-fueled van/minibuse with a percentage of 12% on Jalan Wonokromo Station, 21% on Jalan Bung Tomo, and 13% Jalan Raya Ngagel. The lowest number of vehicles on the three roads was truck with three sets of axle.

Estimated CO_2 emission

Estimated CO_2 emission on Jalan Stasiun Wonokromo, Jalan Bung Tomo, and Jalan Raya Ngagel before and after COVID-19 is shown in Figures 14 - 16.

The number of vehicles on the three roads was dominated by motorcycle, with percentages of 83%, 74%, and 82%, respectively. The vehicle with the second largest percentage was gasoline-fueled van/minibuse with a percentage of 12% on Jalan Wonokromo Station, 21% on Jalan Bung Tomo, and 13% Jalan Raya Ngagel. The lowest number of vehicles on the three roads was truck with three sets of axle.

Estimated CO_2 emission

Estimated CO_2 emission on Jalan Stasiun Wonokromo, Jalan Bung Tomo, and Jalan Raya Ngagel before and after COVID-19 is shown in Figures 14 - 16.

Estimated CO_2 emission before COVID-19 was 5,259 kg/year on Jalan Stasiun Wonokromo, 6,668 kg/year on Jalan Bung Tomo, and 8,202 kg/year on Jalan Raya Ngagel. Figures 13–15 show decreased CO_2 emission on thethree roads owing to the COVID-19 COVID-19. Estimated CO_2 emission decreased by 44% on Jalan Stasiun Wonokromo, by 62% on Jalan Bung Tomo, and by 34% on Jalan Raya Ngagel. The estimated CO_2 emission after the COVID-19 was 2,945 kg/year on Jalan Stasiun Wonokromo, 2,478 kg/year on Jalan Bung Tomo, and 5,402 kg/year on Jalan Raya Ngagel.

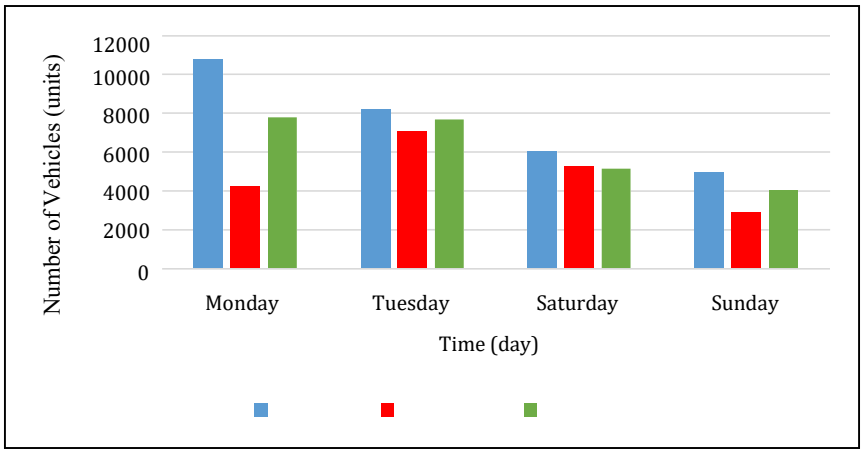


Figure 5. Vehicle volume on Jalan Stasiun Wonokromo before COVID-19

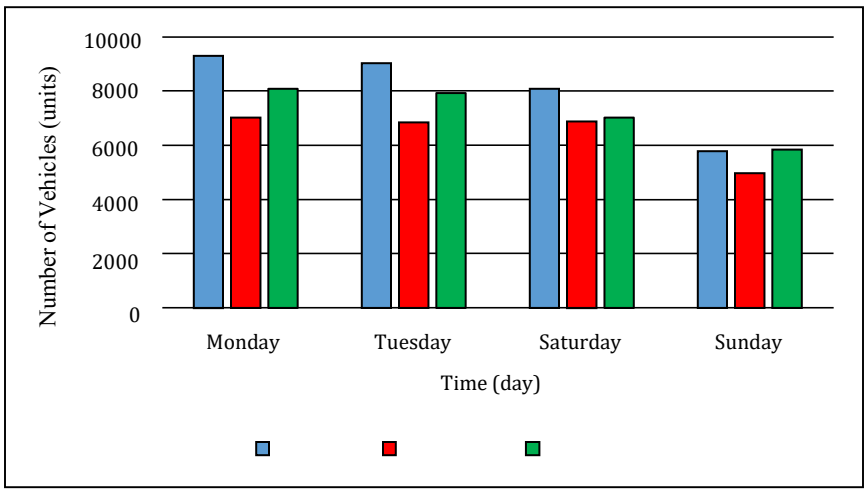


Figure 6. Vehicle volume on Jalan Bung Tomo before COVID-19

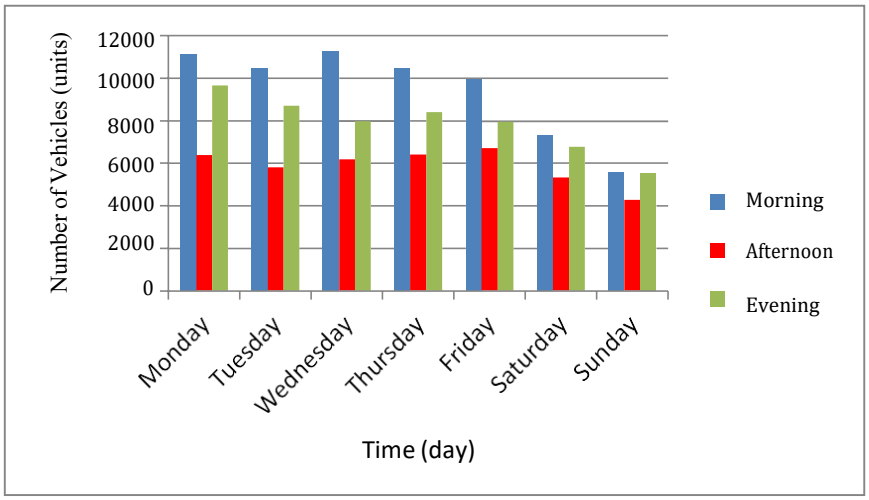


Figure 7. Vehicle volume on Jalan Raya Ngagel before COVID-19

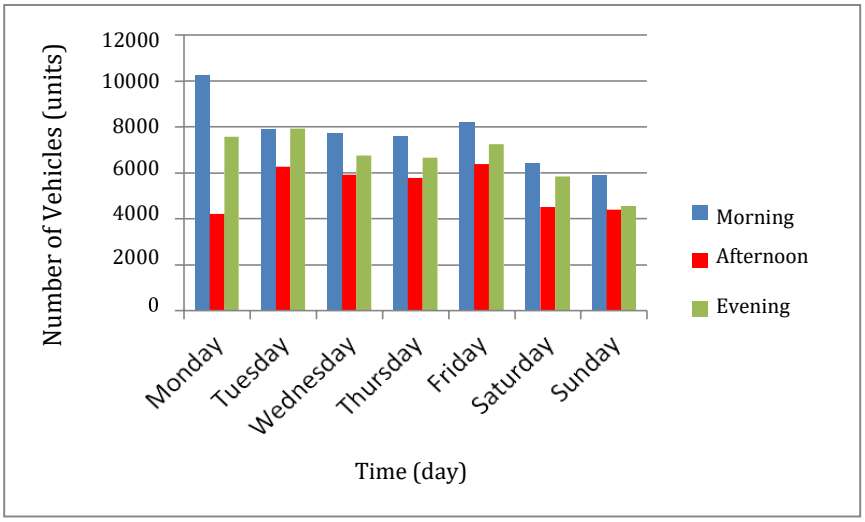


Figure 8. Vehicle volume on Jalan Raya Ngagel after COVID-19

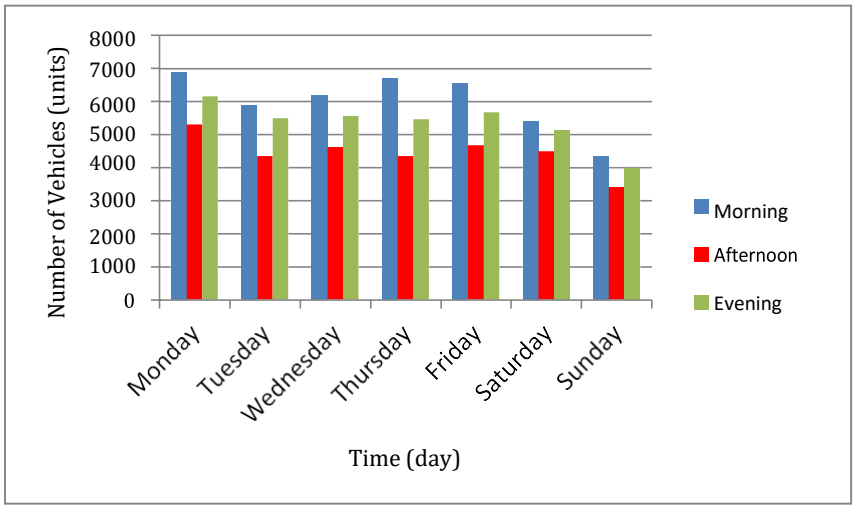


Figure 9. Vehicle volume on Jalan Bung Tomo after COVID-19

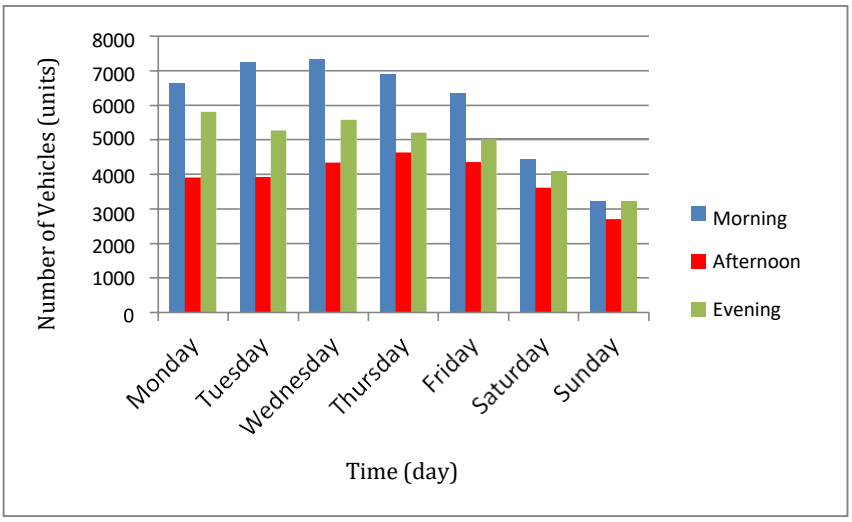


Figure 10. Vehicle volume on Jalan Bung Tomo after COVID-19

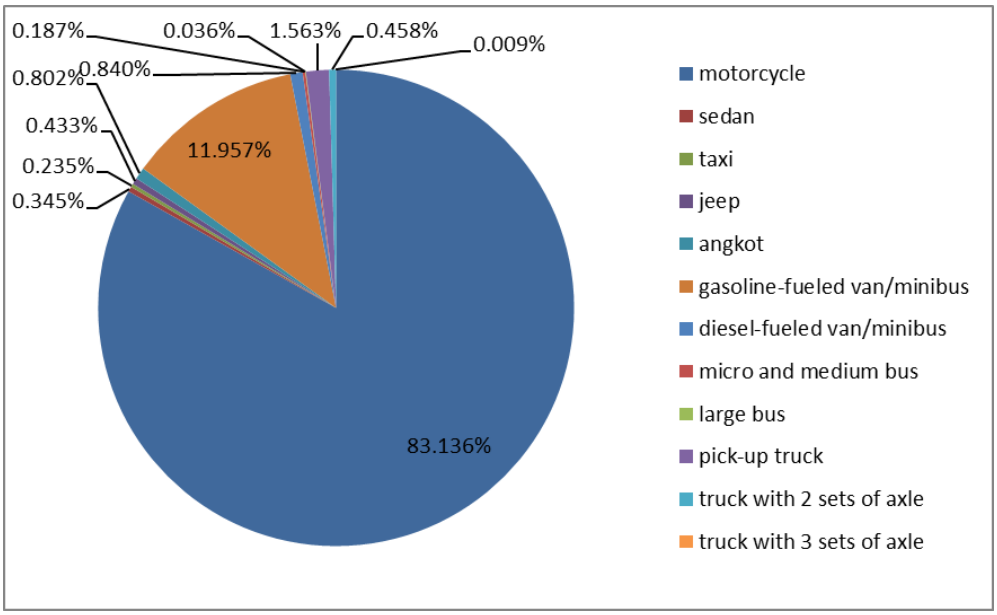


Figure 11. Vehicle composition on Jalan Stasiun Wonokromo

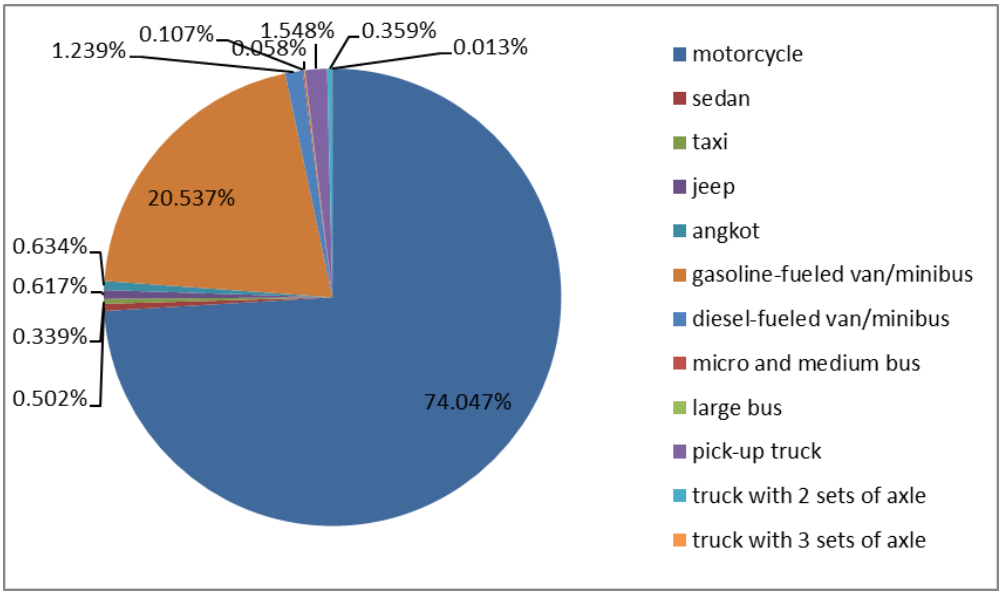


Figure 12. Vehicle composition on Jalan Bung Tomo

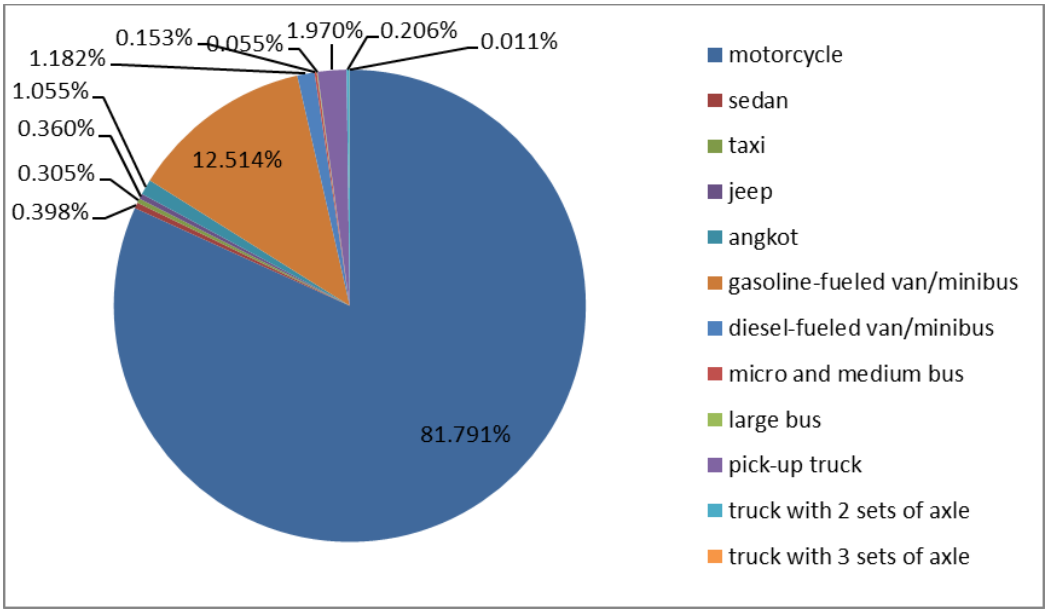


Figure 13. Vehicle composition on Jalan Raya Ngagel

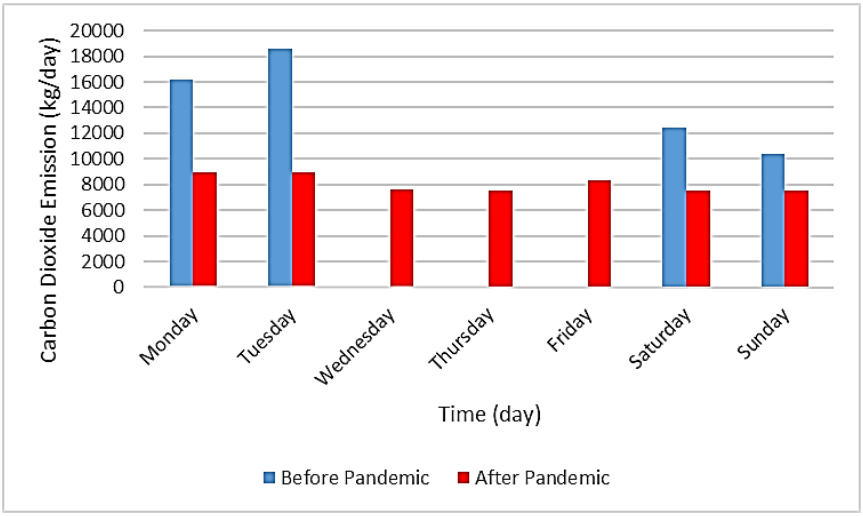


Figure 14. Estimated CO_2 emission on Jalan Stasiun Wonokromo before and after COVID-19

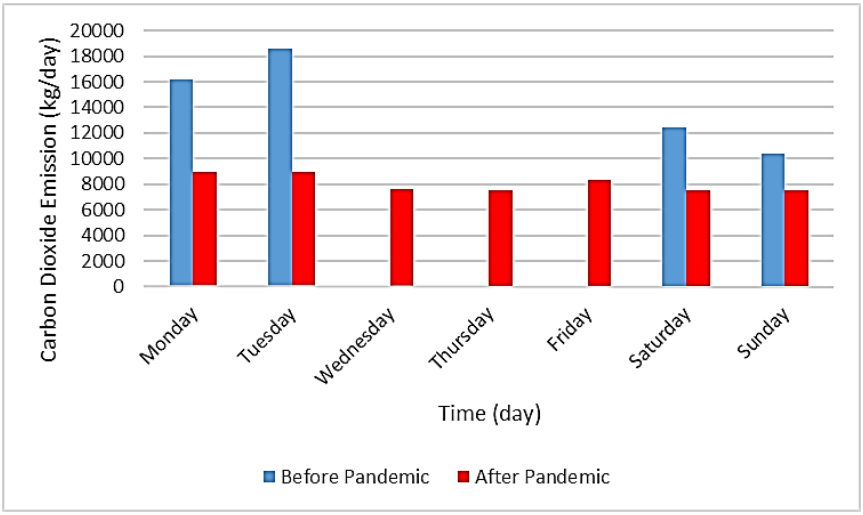


Figure 15. Estimated CO_2 emission on Jalan Bung Tomo before and after COVID-19

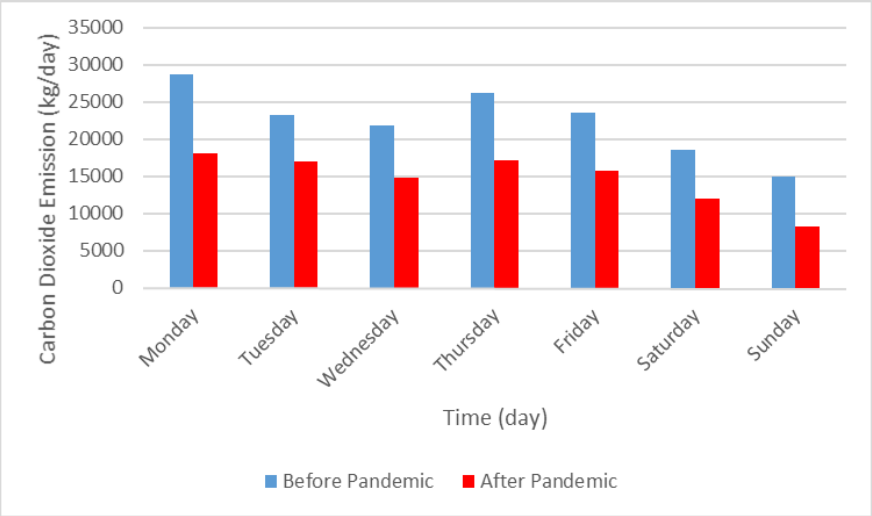


Figure 16. Estimated CO_2 emission on Jalan Raya Ngagel before and after COVID-19

Correlation between vehicle volume and type and estimated CO_2 emission

Estimated CO_2 emission based on vehicle type on Jalan Stasiun Wonokromo, Jalan Bung Tomo, and Jalan RayaNgagel is shown in Figures 17 - 19.

Figures 17 - 19 show gasoline-fueled van/minibus as the largest contributor to CO_2 emission. Gasoline-fueled van/minibus was the second largest number of vehicles after motorcycle, but it had a higher idle-fuel economy value and lower running-fuel economy value than motorcycle. This finding caused gasoline-fueled van/minibusto consume more fuel in engine operation [5, 7]. The lowest contributor to CO_2 emission was truck with threesets of axle. Truck with three sets of axle had a high fuel-economy value, although it was

extremely smaller thanthe other vehicle types, thereby resulting in considerably lower CO_2 emission. The result of the Kolmogorov- Smirnov normality test shows that the data are not normally distributed because the number of vehicles has a sigvalue of 0.000 < (α) 5%. The Spearman correlation test shows that there is a correlation between the number ofvehicles and the CO2 emission load as can be seen from a significance value of 0.000 < (α) 5% and has a correlation coefficient of 0.979 for Jalan Station Wonokromo, 0.937 for Jalan Bung Tomo and 0.944 for Jalan Raya Ngagel. The correlation coefficient > 0.9 indicates a strong positive correlation, namely the higher the number of vehicles, the higher the CO2 emission load will be.

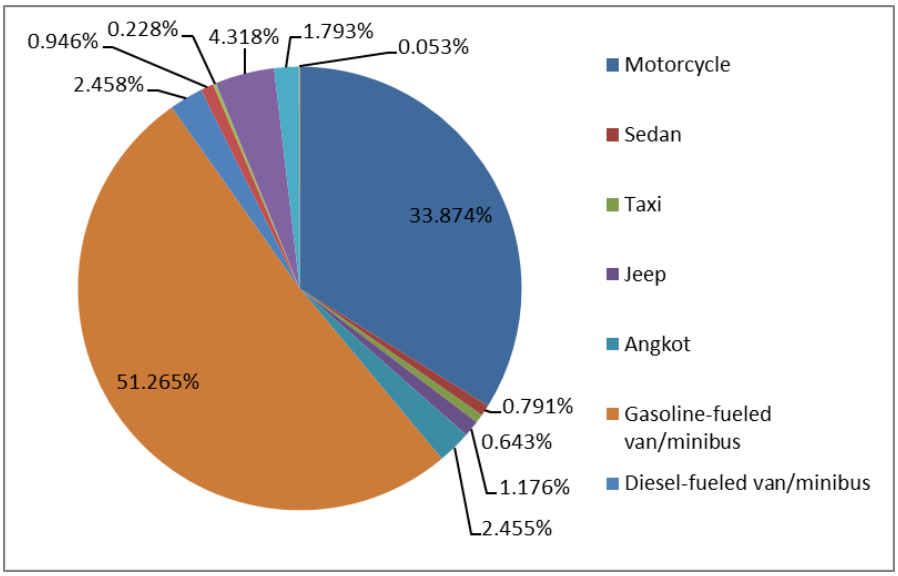


Figure 17. Estimated CO_2 emission based on vehicle type on Jalan Stasiun Wonokromo

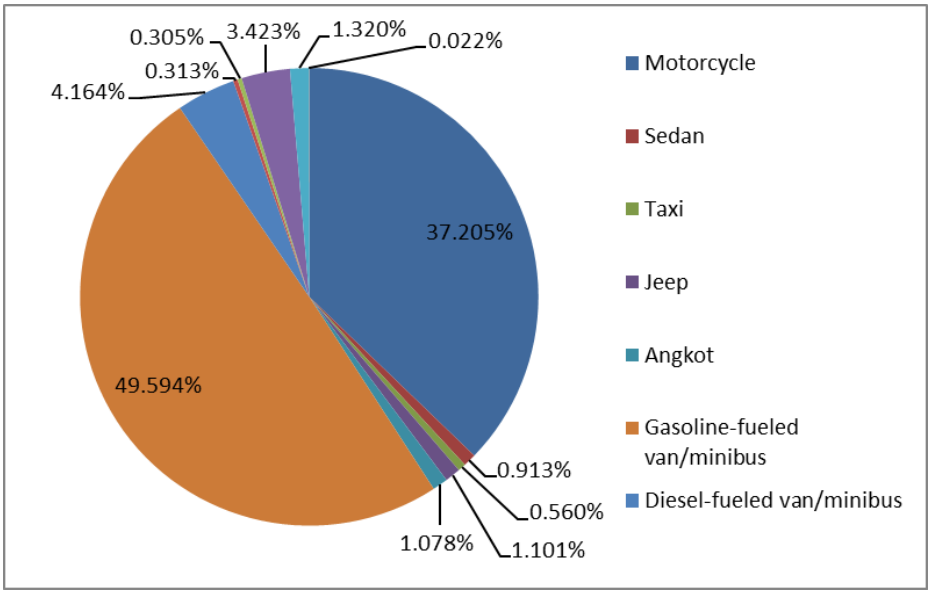


Figure 18. Estimated CO_2 emission based on vehicle type on Jalan Bung Tomo

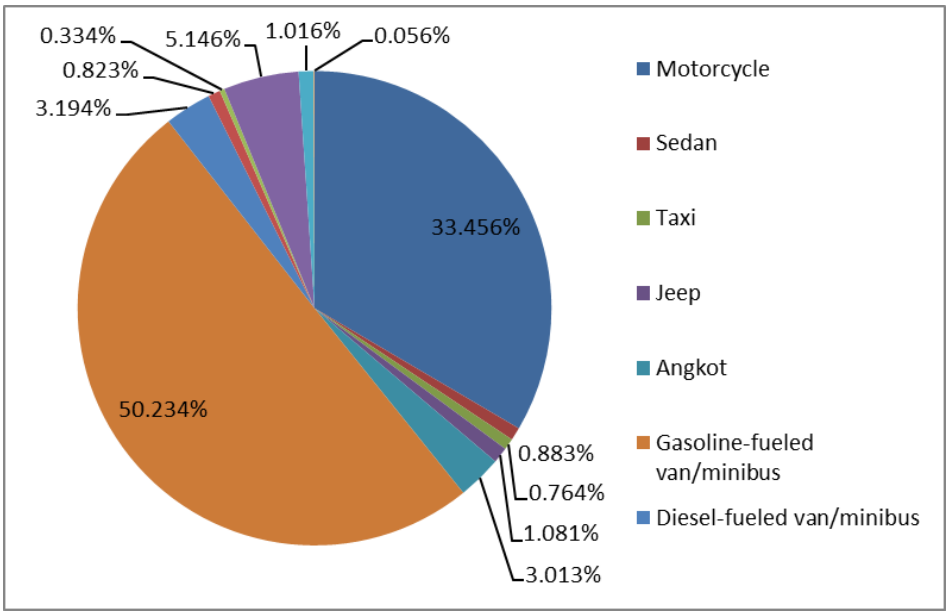


Figure 19. Estimated CO_2 emission based on vehicle type on Jalan Raya Ngagel

Conclusion

CO_2 emission on the primary arterial roads of Wonokromo District decreased owing to the COVID-19. It decreased by 55% on Jalan Stasiun Wonokromo, by 62% on Jalan Bung Tomo, and decreased by 37% on Jalan Raya Ngagel. The estimated CO_2 emission before COVID-19 was 5,259 kg/year on Jalan Wonokromo Station, 6,668 kg/year on Jalan Bung Tomo, and 8,202 kg/year on Jalan Raya Ngagel. The estimated CO_2 emission during COVID-19 was 2,945 kg/year on Jalan Stasiun Wonokromo, 2,478 kg/year on Jalan Bung Tomo, and 5,402 kg/year on Jalan Raya Ngagel. There is a correlation between the number of vehicles and estimated CO_2 emission load namely the higher the number of vehicles, the higher the CO_2 emission load will be.

Acknowledgement

We thank the Dinas Perhubungan Kota Surabaya and the Surabaya Intelligent Transportation System Kota Surabaya for providing the CCTV footages for traffic counting after COVID-19. We also thank Mirza Chalif Ardian, Farah Mutia, Harum Nuraliyah, and Puput Cahyono Wulandari for helping in on-site traffic counting before COVID-19. Finally, we thank the team of the Solid-Waste Program Study of Environmental Engineering Universitas Airlangga for the joint funding of this research.

References

1. Kusuma, W. P., Boedisantoso, R. dan Wilujeng, S. A. (2010). Studi kontribusi kegiatan transportasi terhadapemisi karbon di Surabaya bagian barat. Undergraduate Study, Institut Teknologi Sepuluh Nopember.
2. Intergovernmental Panel On Climate Change (2007). Climate change 2007: Impacts, adaptation and vulnerability. Cambridge, Cambridge University Press.
3. Mudjiastuti, H. (2011). Analisis hubungan sistem transportasi kota terhadap konsumsi bbm (kota: metropolitan,besar dan sedang di Jawa). *Prosiding Seminar Nasional Sains dan Teknologi Ke-2* Tahun 2011: 8-12.
4. Kementerian Lingkungan Hidup dan Kehutanan. (2012). Petunjuk teknis dekonsentrasi pengendalian pencemaran udara sumber bergerak. Deputi Bidang Pengendalian Pencemaran Lingkungan Hidup, Jakarta: pp. 7.

5. Kementerian Lingkungan Hidup dan Kehutanan. (2010). Peraturan menteri lingkungan hidup nomor 12 tahun 2010 tentang pelaksanaan pengendalian pencemaran udara di daerah, Indonesia.
6. Kumar, P. V.P., Singh, A., Sharma, N., and Chalumuri, R. S. (2015). Evaluation of idling fuel consumption of vehicles across different cities. Government Study, New Delhi Central Road Research Institute.
7. Amri, S. and Driejana. (2011). A simple approach to estimate gridded-value in high-resolution GHG emission map of road transport sector. *Proceedings of the Eastern Asia Society for Transport Studies,* 2011: 8.
8. Taylor, G.W.R. (2003). Vehicle idling incidence and energy use data. Review of the incidence, energy use and costs of vehicle idling. Final report 13: pp. 2-13.
9. Novianti, S. and Driejana. (2010). Pengaruh karakteristik faktor emisi terhadap estimasi beban oksida nitrogen (nox) dari sektor transportasi (studi kasus: wilayah Karees, Bandung). *Jurnal Teknik Lingkungan,* 16(2): 185- 198.
10. O'Fallon, C. and Sullivan, C. (2003). Understanding and managing weekend traffic congestion. Government study Australasian Transport Research Forum.
11. Pemerintah Kota Surabaya. (2020). Peraturan Walikota nomor 16 tahun 2020 tentang pedoman pembatasan sosial berskala besar (psbb) dalam penanganan corona virus disease 2019 (Covid-19) di Kota Surabaya.

Malaysian Journal of Analytical Sciences (MJAS)
Published by Malaysian Analytical Sciences Society

SYNTHESIS OF HYBRID CARBON QUANTUM DOTS FROM *Tamarindus indica* AND *Mangifera indica* LEAVES FOR THE DETECTION OF MERCURY (Hg^{2+}) ION IN PURIFIED WATER AND SIMULATED SEAWATER

(Sintesis Titik Kuantum Karbon Hibrid dari Daun *Tamarindus indica* dan *Mangifera indica* bagi Pengesanan Ion Merkuri (Hg^{2+}) dalam Sampel Air Tulen dan Simulasi Air Laut)

Rejie C. Magnaye*, Riszel B. De Castro, Kenneth B. Gomez, Rex Gregor M. Laylo, Aljon Joseph G. Maderazo

Chemical and Food Engineering Department
College of Engineering, Architecture and Fine Arts
Batangas State University,
Golden Country Homes Subdivision, Alangilan, Batangas City, Philippines

**Corresponding author: rejie.magnaye@g.batstate-u.edu.ph*

Received: 16 July 2021; Accepted: 28 October 2021; Published: 27 December 2021

Abstract

Mercury (Hg^{2+}) ion is considered as one of the most lethal heavy-metal contaminants accounting for its extreme persistence, bioaccumulation, and toxicity. The objective of this study is to synthesize hybrid carbon quantum dots (h-CQDs) for the detection of Hg^{2+} ion in purified water and simulated seawater using ratiometric fluorescence assay between blue carbon quantum dots(b-CQDs) produced from *Tamarindus indica* leaves and green carbon quantum dots(g-CQDs) produced from *Mangifera indica* leaves. The optical properties of the produced CQDs were determined using UV-Vis spectrophotometer which explained the quenching of g-CQDs' photoluminescence and stability of b-CQDs upon addition of Hg^{2+}. The research also includes the effect of volume ratio and time of microwave irradiation in the photoluminescence intensity ratio of h-CQDs and the influence of increasing Hg^{2+} concentration in both purified water and simulated seawater. The mathematical correlation between PL intensity ratio and concentration was found to be a rational equation for both purified and simulated seawater. Using simulated seawater, the result showed in the model has no significant difference with the detected concentrations using atomic absorption spectroscopy. Furthermore, the generated model exhibits dynamic range between 394 ppb and 23.85 ppm.

Keywords: quantum dots, g-CQDs, b-CQDS, mercury detection, carbon quantum dots

Abstrak

Ion merkuri (Hg^{2+}) dianggap sebagai satu pencemar logam berat maut berdasarkan sifatnya yang kekal, bioakumulasi, dan ketoksikan. Objektif kajian ini ialah menyediakan sintesis titik kuantum karbon hibrid (h-CQDs) bagi pengesanan ion Hg^{2+} dalam air tulen dan simulasi air laut mengunakan ujian pendaflour ratiometrik di antara titik kuantum karbon biru (b-CQDs) di hasil dari daun *Tamarindus indica* dan titik kuantum karbon hijau (h-CQDs) dari daun *Mangifera indica*. Sifat optikal yang terhasil bagi CQDs telah ditentukan melalui spektrofotometer UV-Vis menjelaskan pelindapan fotoluminesens g-CQDs dan

kestabilan b-CQDs dengan penambahan Hg^{2+}. Kajian juga termasuk melihat kesan nisbah isipadu dan masa bagi penyinaran gelombang mikro dalam nisbah keamatan fotoluminesens h-CQDs dan pengaruh peningkatan kepekatan Hg^{2+} bagi kedua-dua air tulen dan simulasi air laut. Korelasi matematik di antara nisbah keamatan PL dan kepekatan telah di ketahui menjadi persamaan sepadan bagi kedua-dua air tulen dan simulasi air laut. Mengunakan simulasi air laut, hasil menunjukkan model memberikan perbezaan tidak signifikan bagi kepekatan yang dikesan melalui analisis spektroskopi serapan atom. Selanjutnya, model yang dihasilkan memberi julat dinamik antara 394 ppb dan 23.85 ppm.

Kata kunci: titik kuantum, g-CQDs, b-CQDS, pengesanan merkuri, titik kuantum karbon

Introduction

Water is the link that binds all living organisms and the source of life on Earth. But nowadays, contamination of heavy metals is of increasing worldwide concern. Among the heavy metals, mercury (Hg^{2+}) ion is considered as one of the most lethal heavy-metal contaminants accounting for its extreme persistence, bioaccumulation, and toxicity. Bioaccumulation of this toxic heavy metal leads to liver, kidney, and lungs failure, central nervous system disorder, Minamata disease, brain damage, and even death. Recently, many residents of Palawan Province in the Philippines showed symptoms of the disease in the 2nd quarter of year 2017. Such phenomenon has been caused by small-scale gold mining operations undergoing on the place. Moreover, the burning of coal industry approximately releases approximately 475 tons of mercury [1].

Mining is not the only route where mercury can find its way to the environment. It also enters through industrial pathways including steel scrap processing facilities, coalfired plants, and the petroleum industry knowing to the fact that it is naturally produced due to its presence virtually all oil and gas. Mercury levels in crude oil and gas can vary widely, both between and within reservoirs and geographical areas. The rough introduction of mercury in the ecosystem alarms the public knowing that this hazard is not detectable by the human eye when dissolved in water and can cause serious environmental and health damage [1].

According to the US Environmental Protection Agency, the maximum allowable level of Hg^{2+} is 10 nm while the DENR AO 35 recommended amount of 5 ppb. Hence, it is a challenge to develop an accurate and sensitive analytical method in detecting trace amount of Hg^{2+} in water samples. Contemporarily, more than a few sophisticated analytical methods have been available for mercury monitoring including atomic absorption spectroscopy (AAS), electrochemical and optical sensing devices. Nonetheless, such a method requires sophisticated and expensive instrumentation, a long time of accomplishment, and complex sample pretreatment procedures. To combat the dilemma in producing results in a more portable, inexpensive, and time saving manner, many researchers used fluorescent nanoparticles specifically quantum dots [2].

Quantum dots were greatly utilized in recent years because of their attractive qualities and their versatile use in medicine, energy production, and heavy metal detection. Fluorescent metal quantum dots have been studied owing to their low toxicity and exceptional photostability. However, the production of these metal nanoparticles requires costly reagents, such as peptides, metal salts, proteins, polymers, thiol ligands and so on, which may limit their preparations and applications [3].

One of the techniques used in heavy metal detection using carbon quantum dots is ratiometric fluorescence assay because it is more reliable in the complex sample detection by determining the ratio of two signals where it can lessen the influence of instruments and environmental interference. In this study the researchers combined b-CQDs and g-CQDs to produce h-CQDs. In the addition of Hg^{2+}, the fluorescence of g-CQDs was quenched while the photoluminescence of the blue-emitting carbon remained the same [4].

To address the concerns for an inexpensive, nontoxic, reliable and rapid sensing system of mercury detection in purified water and simulated seawater, the

researchers used h-CQDs produced from *Tamarindus indica* leaves and *Mangifera indica* leaves. It is easy to fabricate, easy to operate, requires small sample volume, and has short response time. With the aid of h-CQDs, the ratiometric fluorescent sensor was able to display discernable color evolution from green to blue with increasing the concentration of Hg^{2+} [4].

Materials and Methods

Preparation of raw materials

Young *Mangifera indica* and *Tamarindus indica* leaves from the 3-5th internode of branches were collected at Panghayaan, Taysan, Batangas, Philippines. Initially, young plant leaves were taken and washed with water to remove dirt. Then, it was cut down into small pieces of size 1-2 cm. $HgCl_2$, the source of Hg^{2+}, was purchased in RTC Laboratory Services & Supply House Supplier while ethanol was procured in Belman Laboratories in Sheridan, Mandaluyong, Metro Manila. Lastly, chemicals for simulated seawater were bought in Lipa Quality Control Center in Lipa City, Batangas [5].

Preparation of green-emitting carbon quantum dots

An amount 70 grams of the *Mangifera indica* leaves have undergone leaching in 700 mL of absolute ethanol: water (1:1) by volume [5]. The mixture was stirred constantly for 4 hours and the resulting extract was transferred into a carbon steel reactor. The reactor was heated in the oven for 4 hours at 180°C and cooled down to room temperature for about 30 minutes. After cooling, the resulting solution undergone centrifugation at 4000 rpm for 30 minutes to obtain a clear supernatant [6]. The extract was further filtered to remove light particles with considerable volume [6]. Consequently, the purified solution was diluted to 400mL.

Preparation of blue-emitting carbon quantum dots

14 grams of the *Tamarindus indica* leaves was dissolved into 350 mL of distilled water. Accordingly, it was transferred into a carbon steel reactor and was kept for 5 hours at 210 ºC in the furnace. The obtained solution was cooled down to room temperature and centrifuged to 4,000 rpm for 30 minutes. To standardize the concentration, the resulting solution was diluted to the former volume of 350 mL [7].

Preparation of the simulated seawater

One liter (1L) of simulated seawater was prepared by emulating typical seawater with salinity of approximately 3%. Some of the components however was removed like most of the rare metals and heavy metals and the majority of the ionic compounds were only used. Because of solubility in water, the compounds were assumed to be completely dissociated into its ions to account for its elemental analysis. Table 1 below showed the formulation of simulated seawater [1].

Preparation of Hg^{2+} standard solution in purified water and seawater

Mercuric chloride ($HgCl_2$) was the source of Hg^{2+}. 1 gram of $HgCl_2$ was dissolved in 250 mL of purified water and seawater respectively to form 4,000 ppm standard solutions. 100 mL of the resulting solution was diluted to 250 mL of each to form 160 ppm standard solution. From the latter solution, the increasing concentration tabulated in Table 2 (447 ppb, 558 ppb, 1.397 ppm, 2.794 ppm, 4.191 ppm, 5.588 ppm, and 11.176 ppm) of $HgCl_2$ was prepared through the dilution method. The magnetic stirrer running at 3000 rpm facilitated the uniform concentration at 200 °C.

UV-Vis spectrophotometer calibration

The Shimadzu UV-1800 UV-Vis Spectrophotometer from Batangas State University, Philippines was switched on for 20 minutes for stabilization. Then, cuvettes were filled with purified water for the sample and kept sure that the outside was free from contamination. This has served as a blank and helped account for light losses due to scattering or absorption by the solvent. Afterwards, the cuvette was placed in the spectrometer. The cuvettes were aligned properly, as often the cuvette has two sides, which were meant for handling and were not meant to shine light through. The instrument stored the blank data and automatically performed the subtraction [8].

Absorbance spectrum collection and absorption peaks determination

The cuvettes were filled with the sample. It was rinsed twice with the sample for about ¾ full to make sure that the transfer is quantitative. Then it was placed in the spectrometer in the correct direction. The spectrum of absorbance was collected by scanning the instrument in wavelengths of 190 nm to 1100 nm. A diode-array instrument can collect the whole absorbance spectrum in one run. On the other hand, the absorption peaks were determined [9].

Functional group and conjugation determination using UV-Vis spectrophotometer

Determining functional groups and conjugation present in b-CQDs and g-CQDs helped researchers in explaining the color they emitted and their reactivity to Hg^{2+}. The presence of oxygen-rich group and electron withdrawing nitrogen atoms were responsible in the blue emission of b-QCDs in *Tamarindus indica* leaves whereas the presence of C=O and C-O-C groups in *Mangifera indica* leaves caused the green emission of g-QCDS including its the stability and reactivity to Hg^{2+}. Functional groups and conjugations were obtained from corresponding absorption peaks as shown in Table 3 [7].

Photoluminescence sensitivity enhancement of h-CQDs by microwave irradiation

80 mL of g-CQDs and b-CQDs, which were in a separate container, undergone microwave irradiation at a different time of exposure presented in Table 4. 800W microwave radiation at medium high power was used. After irradiating, the resulting solution was cooled and diluted with distilled water to restore its initial volume. For mass volume ratio, a specific volume of green and blue CQDs was mixed.

An additional setup with no exposure to microwave radiation was prepared to serve as the control [11].

Table 1. Seawater formulation for one liter of distilled water

Salt	Molecular Weight	Mass of Salt (g/kg solution)
Sodium chloride (NaCl)	58.44	23.926
Magnesium chloride ($MgCl_2.6H_2O$)	203.33	10.831
Sodium sulfate (Na_2SO_4)	142.04	4.008
Calcium chloride ($CaCl_2.H_2O$)	147.03	1.519
Potassium chloride (KCl)	74.56	0.677
Sodium bicarbonate ($NaHCO_3$)	84.00	0.196
Potassium bromide (KBr)	119.01	0.098
Boric acid (H_3BO_3)	61.83	0.026
Sodium fluoride (NaF)	41.99	0.003

Table 2. $HgCl_2$ concentration and corresponding Hg^{2+} ion concentration

$HgCl_2$ (ppm)	**Hg^{2+} (ppm)**
1.4	0.782
2.1	1.173
2.8	1.565
3.5	1.956
7.5	4.191
15	8.382
30	16.764

Table 3. Absorption peaks and corresponding chromophore, transition, and ε_{max}

Chromophore	**Transition**	**ε_{max}**	**λ_{max} (nm)**
σ – bonded electrons			
(C-C, C-H etc.)	σ-σ*		~ 150
Lone pair electrons			
-O-, -N-, -S-	n-σ*	100-1000	~ 190
C=O, C=N	n-π*	15	~300
	π-π*	500	~190
R-C=N	n-π*	5	~ 170
R-COOH, $RCONH_2$, RCOOR	n-π*	50	~ 210
π- bonded electrons			
C=C	π-π*	14000	~ 190
C=C	π-π*	2000	~ 195
C=O	π-π*	500	~ 180

Table 4. Variation of h-CQDs in purified water in terms of volume ratio of b-CQDs and g-CQDs and time of irradiation

Volume Ratio	**g-CQDs (mL)**	**b-CQDs (mL)**	**Time (minutes)**
1:2	40	80	
1:1	60	60	5, 10, 15
2:1	80	40	

Photoluminescence intensity ratio metering of 447 ppb Hg^{2+}

Hg^{2+} detection was performed at room temperature. In a typical detection experiment, 3 mL of varied h-CQDs dispersion and 3 mL of 447 ppb concentration of Hg^{2+} were mixed into 15 mL vials. After mixing thoroughly, the fluorescence spectra were recorded after 8 minutes of reaction at room temperature. The fluorescence

intensity ratio was measured at the excitation wavelength of 365 nm using UV light [10].

Luminous intensity metering setup

To capture light frequency, photos of the carbon quantum dots were taken using iPhone 8 Plus and images were converted to green and blue luminous intensity using Image J Batch Software [12]. For the smartphone fluorometer set-up, an enclosed chamber was equipped with 365 nm UV light which was showed in Figure 1. After putting the samples inside UV–chamber, a mobile phone camera was employed to capture images [13]. In order to block background light, a good image capturing angle was selected [13]. The captured images were then processed using RGB Measure plugin in ImageJ software wherein emission intensity from various samples was measured and compared adequately at the same time [13].



Figure 1. Luminous intensity metering set up

Photoluminescence intensity ratio metering in purified water and seawater

Set-up in metering photoluminescence of h-CQDs in 447 ppb was also used in metering purified water and seawater in increasing mercury concentration. In a typical detection experiment, 3 mL of defined amount of h-CQDs and 3 mL of known concentration of Hg^{2+} were added into 15-mL vials. After mixing thoroughly, the fluorescence spectra were recorded after reaction for 8 min at room temperature. The fluorescence intensity ratio was measured at the excitation wavelength of 365 nm UV light [10].

Statistical treatment

Empirical models and data curves relating the photoluminescence intensity ratio and the increasing concentration of Hg^{2+} heavy metal were constructed using MATLAB R2011-A which was a part of the last step in the schematic roadmap of the research methodology showed in Figure 2. Two paired t-test was performed to obtain the comparability degree between the photoluminescence ratios detected in purified water with that of seawater. On the other hand, analysis of variance was used to determine the effect of two variables namely mass ratio of h-CQDs and time of irradiation in the photoluminescence ratio change.

Validation of generated model using atomic absorption spectroscopy

To validate the degree of acceptability of the generated models low, medium and extreme concentrations for each type of heavy metal in simulated seawater were prepared prior to AAS testing. Tabulated in Table 5, Hg^{2+} (ppm) concentration variations were 0.335, 2.794, and 16.764.

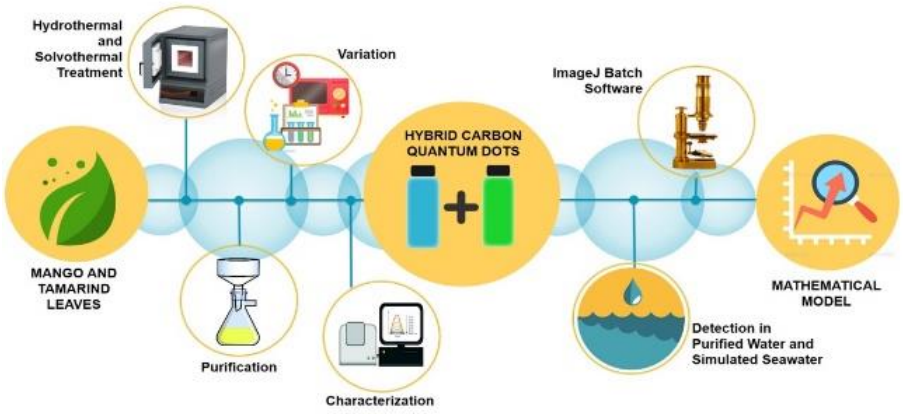


Figure 2. Schematic roadmap of the research methodology

Table 5. $HgCl_2$ low, medium, and extreme concentrations and corresponding Hg^{2+} concentration

$HgCl_2$ (ppm)	Hg^{2+} (ppm)
0.7	0.391
3.5	1.956
40	22.352

Results and Discussion

Determination of functional groups and conjugations present in g-CQDs and b-CQDs

In Figure 3, the absorption spectrum of g-CQDs showed distinct peaks at 191.5, 197.5, 208.5, 223.5, 235.5, 240.5, 253.0, 263.0 and 278.5 nm. The absorption peak of 208.5 nm corresponds to functional groups such R-COOH, $RCONH_2$, and RCOOR with the electronic transition of n - π*. The n electrons or the nonbonding electrons were the ones located on the oxygen of the carbonyl group. Thus, the n - π* transition corresponds to the excitation of an electron from one of the unshared pair to π* orbital. This requires the high energy of radiation among the detected functional groups due to the high energy requirement of the n and π* orbitals. However, the band energy gap between them was lower compared to the other detected functional groups.

Conversely, R-O-R, C=C, C=O were determined at 278.5 nm has energy transition from π to π* orbitals as shown in Table 6. These functional groups required more energy to excite electrons from π to π* orbitals. On the other hand, conjugate homoannular diene was defined at its peak of absorbance of 253 nm with an electronic transition from π_2 to π_3* orbital. In conjugated dienes the π–π* orbitals of the two alkene groups combine to form new orbitals – two bonding orbitals named as π_1 and π_2 and two anti-bonding orbitals named as π_3*and π_4*. It is apparent that a new π to π* transition of low energy is available as a result of conjugation. Conjugated dienes as a result absorb at relatively longer wavelength than do isolated alkenes. One component determined in the UV-Vis spectrum is gallic acid which was determined at its absorption peak at 263 nm. The oxygen containing functional groups such as C-O-C, and C=O groups, on the carbon backbone at the edge part were the typical source of the green luminescence in the CQDs [14].

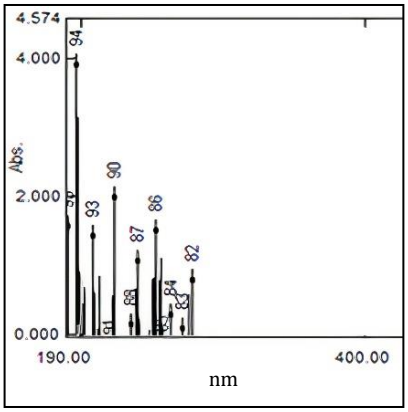


Figure 3. Wavelength and intensity of absorbance emission spectrum of g-CQDs

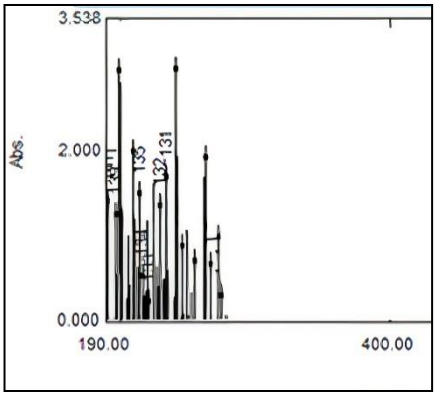


Figure 4. Wavelength and intensity of absorbance emission spectrum of b-CQDs

Figure 4 presents the optical properties of the synthesized b-CQDs which manifest a significant number of absorption peaks. At 209.5 nm, n - π* electronic transition is observed which is ascribed to several functional groups such as R-COOH, $RCONH_2$ and RCOOR. The lone electrons were located on the oxygen of the carbonyl group and responsible for the n orbital and excited to π* orbital. The high energy of radiation is required among the detected functional groups due to the high energy requirement of the n and π* orbitals. Though, the band energy gap between them is lower compared to the other detected functional groups. The absorption peak centered at 275 nm, the π-π* electronic transition of C=C is obtained. Blue emissive characteristics of b-CQDs were realized in the presence of oxygen-rich group and more electron withdrawing nitrogen atoms [7]. Table 7 tabulated the summary for functional groups and conjugation from optical properties of b-CQDs.

Comparison of photoluminescence intensity ratio of h-CQDs by the addition of Hg^{2+} upon varying volume ratio and time of irradiation

The PL intensity ratio of g-CQDs to b-CQDs was used to quantify the color change from blue to green upon addition of Hg^{2+}. A great increase in the PL Intensity Ratio corresponded to higher reactivity and detection capability to Hg^{2+}. The reaction between b-CQDs and g-CQDs was carried out using a 15 mL vial for 8 minutes. Prior to mixing, they have separately undergone microwave irradiation for 5, 10 and 15 minutes. An enclosed black chamber was used to ensure the absence of external lights while taking up pictures via a 12 MP smartphone. PL intensity ratio was measured using ImageJ Batch Software. In Table 8, PL intensity ratio of h-CQDs has increased upon addition of Hg^{2+} and produced different changes in varying volume ratio and time of irradiation. Meanwhile, Table 9 tabulated the difference in PL ratio listed in Table 8. In Figure 5 which was the illustration of Table 9, it was observed that the PL intensity ratio difference has increased when the volume ratio of b-CQDs to g-CQDs increased. Likewise, it has also increased when the time of irradiation was augmented. In addition, the highest PL intensity change of 0.0791 in Table 9 was obtained at 2:1 volume ratio and 15 minutes of irradiation. Therefore, h-CQD produced from these parameters was considered to be the best in detecting Hg^{2+}.

For the comparison of the PL ratio of h-CQDs in purified water with that of the contaminated water, the effect of varying volume ratio of b-CQDs and g-CQDS with a varying time of irradiation on the PL ratio was evaluated using analysis of variance. The confidence level was set to 0.05 wherein a p-value less than that depicts a significant change. Table 9 shows the statistical result.

It was shown in Table 10 that varying time of irradiation at fixed volume ratio produces p-value of 3.09×10^{-11} and F-stat value of 123.43. Conversely, varying volume ratios at the fixed time of irradiation yield p-value of 4.74×10^{-5} and f-stat value of 18.21. On the other hand, the varying time of irradiation and volume ratio at the same time, a p-value of 1.21×10^{-5} and f-stat of 15.44 were obtained. Since the p-value approaches 0 and f stat is larger than the F-critical value, this implies that varying the volume ratio and time of irradiation affects significantly the photoluminescence intensity ratio of h-CQDs.

Table 6. Functional groups and conjugations from optical properties of g-CQDs

Wavelength (nm)	**Intensity of Absorbance (abs)**	**Electronic Transition**	**Functional Group**	**Conjugation**	**Components Determined**
278.5	0.671	π–π*	C=O, C=C, R-O-R		
263.0	0.183				Gallic Acid
253.0	1.395	π_2 - π_3*		Homoannular Diene	
240.5	0.958				
235.5	0.045				
223.5	1.869				
208.5	1.313	n - π*	R-COOH, $RCONH_2$, RCOOR		
197.5	3.794				
191.5	1.456				

Table 7. Functional groups and conjugations from optical properties of b-CQDs

Wavelength (nm)	Intensity of Absorbance (abs)	Electronic Transition	Functional Group	Conjugation
275.0	0.201	π-π*		C=C
263.0	1.823			
241.5	2.853			
234.5	1.583			
229.5	1.261			
214.0	1.394			
209.5	1.882	n - π*	R-COOH, $RCONH_2$, RCOOR	
199.5	2.836			
197.0	1.151			
191.5	1.311			

Table 8. Photoluminescence ratio of h-CQDs with and without Hg^{2+} upon varying volume ratio and time of irradiation

Vol. Ratio	Time					
	5		10		15	
	Without Hg^{2+}	With Hg^{2+}	Without Hg^{2+}	With Hg^{2+}	Without Hg^{2+}	With Hg^{2+}
2:1	0.512	0.533	0.504	0.558	0.507	0.589
1:1	0.591	0.593	0.596	0.603	0.594	0.560
1:2	0.663	0.670	0.674	0.678	0.675	0.682

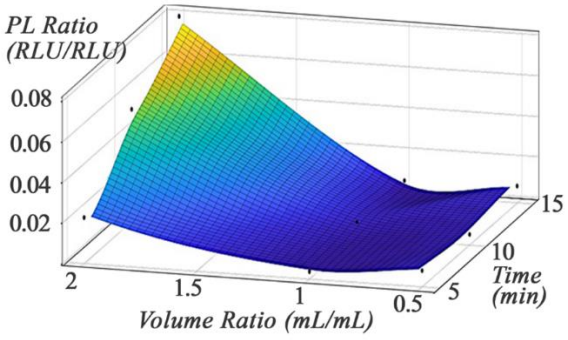


Figure 5. Illustration of photoluminescence ratio difference of h-CQDs by the addition of Hg^{2+} upon varying volume ratio and time of irradiation

Table 9. Photoluminescence ratio difference of h-CQDs upon varying volume ratio and time of irradiation

Ratio	Time		
	5	10	15
2:1	0.0215	0.0541	0.0791
1:1	0.0027	0.0062	0.0060
1:2	0.0070	0.0041	0.0072

Table 10. Statistical result for the effect of varying volume ratio and time of irradiation of b-CQDs and g-CQDs

Set-up	Mean Square	Sum of Squares	F-stat	p-value	F-critical
Time of Irradiation	6.363×10^{-3}	1.27×10^{-2}	123.43	3.09×10^{-11}	3.55
Volume Ratio	9.39×10^{-4}	1.88×10^{-3}	18.21	4.74×10^{-5}	3.55
Time of Irradiation and Volume Ratio	7.96×10^{-4}	3.19×10^{-3}	15.44	1.21×10^{-5}	2.93

Note: p-value depicts a value greater than a = 0.05 has no significant effect

Determination of PL intensity ratio of h-CQDs upon increasing Hg^{2+} concentration in purified water and simulated seawater

It was observed in the Table 11 that as concentration of mercury ion was increased from 0.782 ppm to 16.764 ppm, the PL intensity ratio of b-CQDs to g-CQDs for purified water increased from 0.5867 to 1.1052. On the other hand, in the same range of concentration, the PL intensity ratio for simulated seawater increased from 0.5590 to 0.9217. In purified water, there was a 79.31% increase in the PL intensity ratio and using simulated seawater as the medium, 64.88% increase in PL intensity ratio was realized. PL intensity ratios of h-CQDs with the increasing Hg^{2+} concentration in purified and simulated seawater were illustrated in Figure 7 and Figure 8 respectively.

Since the PL ratio pertains to the ratio of photoluminescence of b-CQDs to g-CQDs, an increase in this value means a decrease in the sole photoluminescence of g-CQDs because it has the ability to quench with mercury [14] who synthesized bluish green emitting carbon quantum dots and has proven its mercury ion sensing application. The color transition upon quenching mercury was illustrated in Figure 6. It was proven that blue-emissive carbon quantum dots derived from tamarind leaves exhibit sensitivity only to glutathione [7], thus, unreactive to Hg^{2+}. So, the increase in PL Ratio was associated with the increase in mercury concentration creating a higher degree of quenching of the g-CQDs.

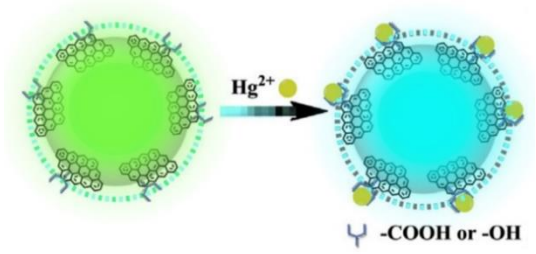


Figure 6. Quenching mechanism

Using purified water as the medium, a p-value of 1.65×10^{-10} and F-stat of 1491.58 were obtained as seen in Table 12. On the other hand, using simulated seawater, a p-value of 7.47×10^{-11} and F-stat value of 1871.03 were obtained. Since p ~ 0 and F-stat possessed a value higher than F-critical, this implies that an increase in

Hg^{2+} concentration in both medium affects significantly the photoluminescence intensity ratio of the h-CQDs.

Table 13 tabulated the statistical comparison of the photoluminescence intensity ratio of h-CQDs in purified water and simulated seawater. The analysis resulted to a p-value of 2.36×10^{-6} and a t -value of 6.519. Since the p-value is lower than the set confidence of 0.05, the difference between the experimental PL ratios of the two media upon increasing Hg^{2+} concentrations is significant.

Table 11. PL intensity ratio of h-CQDs with the increasing Hg^{2+} concentration in purified water and simulated seawater

$HgCl_2$ Concentration (ppm)	**Hg^{2+} Concentration (ppm)**	**Photoluminescence Intensity Ratio**	
		Purified Water	**Simulated Seawater**
1.4	0.782	0.5867	0.5590
2.1	1.173	0.6531	0.6101
2.8	1.565	0.7164	0.6655
3.5	1.956	0.7849	0.7221
7.5	4.191	0.8583	0.8151
15	8.382	0.9541	0.8661
30	16.764	1.1052	0.9217

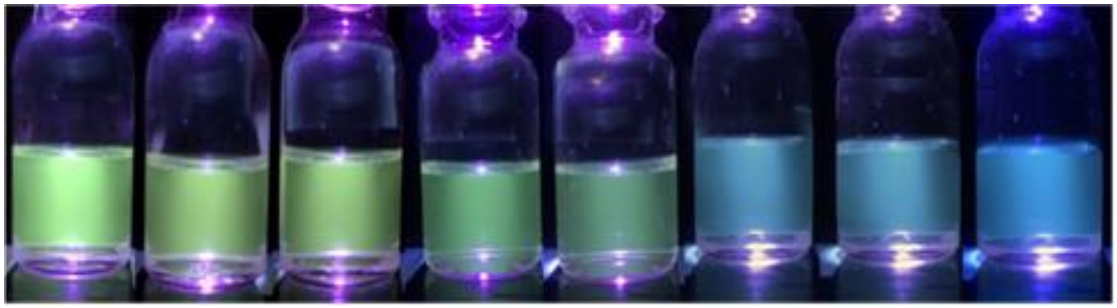


Figure 7. Color progression of h-CQDs with the increasing Hg^{2+} concentration in purified water

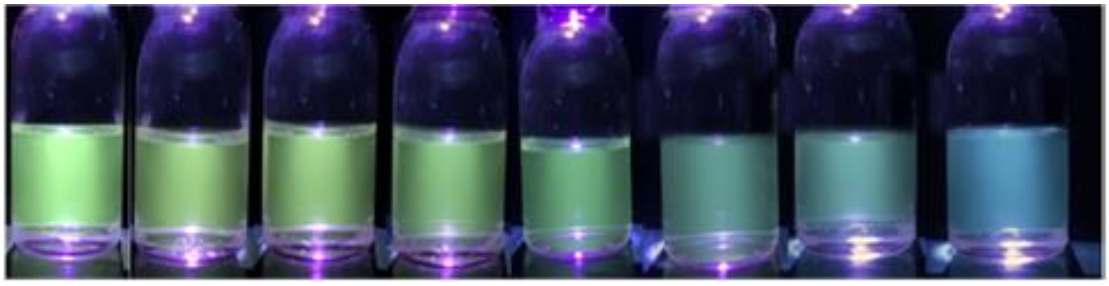


Figure 8. Color progression of h-CQDs with the increasing Hg^{2+} concentration in simulated seawater

Table 12. Statistical result for the effect in PL intensity ratio of h-CQDs upon increasing Hg^{2+} concentration in purified water and simulated seawater

Medium	Mean Square	Sum of Squares	F-stat	p-value	F-critical
Purified Water	6.43×10^{-2}	0.3856	$1.492 \times 10^{+3}$	1.65×10^{-10}	3.87
Simulated Seawater	3.67×10^{-2}	0.2202	$1.871 \times 10^{+3}$	7.47×10^{-11}	3.87

Note: p-value depicts a value greater than a = 0.05 has no significant effect.

Table 13. Statistical result for the comparison of PL intensity ratio of h-CQDs in purified water and simulated seawater

Standard Deviation	Mean Difference	t-value Mean	t-Critical value	p-value	Standard Error
-	7.171×10^{-2}	6.519	2.086	2.36×10^{-6}	-

Note: p-value depicts a value greater than a = 0.05 has no significant effect

Correlation model on the effect of Hg^{2+} concentrations to photoluminescence ratio of h-CQDs in purified water and simulated seawater

In choosing the best mathematical model from the generated equation presented in Tables 14 and 15, the fitness of equation must be met in terms of the sum of squared error (SSE), the adjusted, and root mean squared error. Likewise, the best fit was the model with the lowest SSE and RMSE because this measures the errors from the data points. With respect to R^2, the model closest to one is the fittest. From the generated equation, the equation with the lowest SSE and RMSE for the purified water are Fourier and Rational equations. In consideration of the R^2 and adjusted R^2 values, it also has the closest value to 1.

However, another factor to consider in the selection of the best fit was the asymptote or minimum value of photoluminescence ratio as the heavy increases and approaches infinity and the maximum value as heavy metal concentration approaches 0. By the evaluation of the above equations, Fourier, Gauss, and 3rd degree polynomial exhibit fluctuating trends. Thus, in 2 different x values, there is one y value. This tells that the model greatly deviates the ideal model. With respect to 2nd power exponential, higher value of concentration corresponds to photoluminescence intensity ratio of 10 which is far from the typical range of PL Ratio. This concludes that the rational equation was the best fit because it has the least negative value as concentration approaches infinity aside from exhibiting the highest R^2 and least value of SSE and RMSE.

Comparison of the Hg^{2+} concentration calculated from the generated model with the detected concentrations using AAS

In Table 16, the amount of concentration calculated from the selected model was summarized. With the increase in formulated concentration, the photoluminescence intensity ratio was also increased. Relative to the detected concentration from AAS, the calculated concentration using the model provided values that are nearly the same with maximum deviation (by difference) of 1.4010 and minimum deviation of 0.0255. Also, the model fits more effectively at low to moderate concentrations.

In Table 17, the p-value calculated was greater than 0.05 which denotes the acceptance of the null hypothesis. Thus, there was no significant difference between Hg^{2+} concentrations calculated from the generated mathematical model with that detected of the AAS.

Table 14. Generated model curves describing the effect of Hg^{2+} concentrations to PL intensity ratio of h-CQDs in purified seawater

Types of Model Fit	Method	Equations Generated	SSE	R^2	Adjusted R^2	RMSE
Exponential (2nd Power)	Non-linear Squares	$P(C)= 0.8896e^{0.1094C} - 0.003685e^{-5.82C}$	7.40 x 10^{-4}	0.9962	0.9925	1.57 x 10^{-2}
Fourier (2nd Power)	Non-linear Squares	$P(C)=$ 0.8512 - 0.1936cos(0.6066*C) - 0.1212sin(0.6066*C) - 0.1217cos(1.2132*C) + 0.04304sin(1.2132*C)	2.309 x 10^{-5}	0.9999	0.9993	4.81 x 10^{-3}
Gauss (2 terms)	Non-linear Squares	$P(C)= 4.281e^{(\frac{12.83-C}{3.382})^2} + 0.8857e^{(\frac{3.401-C}{4.055})^2}$	6.226 x 10^{-5}	0.9997	0.9981	7.89 x 10^{-3}
Linear Model	Linear Squares	$P(C)= 0.0005877C^3 - 0.01678C^2 + 0.1522C + 0.5034$	3.86 x 10^{-3}	0.9803	0.9607	3.59 x 10^{-2}
Power	Non-linear Squares	$P(C)= -13.05C^{-0.01258} + 13.69$	2.87 x 10^{-3}	0.9853	0.978	2.68 x 10^{-2}
Rational	Linear Squares	$P(C)= \frac{1.472C^3 - 1.594C^2 - 9.234C + 32.33}{5.6C^2 - 36.38C + 66.7}$	1.855 x 10^{-5}	0.9999	0.9995	4.31 x 10^{-3}

Table 15. Generated model curves describing the effect of Hg^{2+} concentrations to PL intensity ratio of h-CQDs in simulated seawater

Types of Model Fit	Method	Equations Generated	SSE	R^2	Adjusted R^2	RMSE
Exponential (2nd Power)	Non-linear Squares	$P(C)= 0.8168e^{0.007198C} - 0.007198e^{-5.82C}$	2.99 x 10^{-4}	0.9973	0.9946	9.98 x 10^{-3}
Fourier (2nd Power)	Non-linear Squares	$P(C)=$ 1.163 - 0.4006cos(0.331*C) - 0.6585sin(0.331*C) - 0.2602cos(0.662*C) + 0.3601sin(0.662*C)	5.70 x 10^{-7}	1	1	7.55 x 10^{-4}
Gauss (2 terms)	Non-linear Squares	$P(C)= 1.864e^{(\frac{13-C}{4.485})^2} + 0.8e^{(\frac{3.43-C}{4.363})^2}$	6.478 x 10^{-7}	0.9994	0.9965	8.05 x 10^{-3}
Linear Model	Linear Squares	$P(C)= 0.0005711C^3 - 0.0169C^2 + 0.1485C + 0.4654$	1.32 x 10^{-3}	0.988	0.9761	2.09 x 10^{-2}
Power	Non-linear Squares	$P(C)= -0.4904C^{-0.385} + 1.088$	7.68 x 10^{-4}	0.993	0.9895	1.39 x 10^{-2}
Rational	Linear Squares	$P(C)= \frac{1.01C^3 - 2.377C^2 - 0.8211C + 9.568}{-0.4871C^2 - 9.038C + 21.16}$	4.286 x 10^{-5}	1	1	0

Table 16. Concentration of Hg^{2+} based on calculated and detected values

Formulated Hg^{2+} concentration (ppm)	Photoluminescence Intensity Ratio	Calculated Concentration using the Model (ppm)	Detected Concentration
0.3912	0.5140	0.4347	0.3940
1.9558	0.7214	1.9455	1.92
22.3517	0.9415	22.4490	23.85

Table 17. Statistical result for the comparison of calculated and detected concentration of Hg^{2+} in simulated seawater

Standard Deviation	Mean Difference	t-Value	t-Critical Value	p-Value	Standard Error Mean
-	0.45821	1.574	2.306	1.54×10^{-1}	-

Note: p-value depicts a value greater than a = 0.05 has no significant effect

.

Conclusion

The following conclusions were based on the mathematical analysis of the data using the appropriate computer software and the in-depth interpretation of the results and findings. Oxygen-rich group and electron withdrawing nitrogen atoms in *Tamarindus indica* leaves were responsible for the blue-emission of b-QCDs whereas the presence of C=O and C-O-C groups in *Mangifera indica* leaves contributed in the green color emission of b-CQDs, its stability to simulated seawater electrolytes and selective reactivity to Hg^{2+}. Varying the volume ratio of blue to green carbon quantum dots and the time of irradiation played a significant role in mercury detection. Simulated seawater salts inhibited the quenching of green carbon quantum dots with mercury affecting its photoluminescence intensity. The generated mathematical models have been tested to be a reliable tool in determining Hg^{2+} concentrations at a specific range with no significant difference with the AAS detected concentrations.

Acknowledgement

The researchers would like to express their gratitude and appreciation to Batangas State University Alangilan for allowing them to maximize its full potential as an experimental laboratory workplace; To PIChE National for giving this research a breakthrough last February 2019 and to all the people who interceded for the success of this research

References

1. Guo, Y., Wang, Z., Shao, H. and Jiang, X. (2013). Hydrothermal synthesis of highly fluorescent carbon nanoparticles from sodium citrate and their use for the detection of mercury ions. *Carbon,* 52: 583-589.
2. World Health Organization (2017). Mercury and health. Retrieved from https://www.who.int/news-room/fact-sheets/detail/mercury-and-health.
3. Guo, X., Liu, C., Li, N., Zhang, S. and Wang, Z. (2018). Ratiometric fluorescent test paper based on silicon nanocrystals and carbon dots for sensitive determination of mercuric ions. *Royal Society Open Science,* 5(6): 171922.
4. Rajendran, K. and Rajendiran, N. (2018). Bluish green emitting carbon quantum dots synthesized from jackfruit (*Artocarpus heterophyllus*) and its sensing applications of Hg(II) and Cr(VI) ions. *Materials Research Express,* 5(2): 024008.

5. Lu, W., Qin, X., Liu, S., Chang, G., Zhang, Y., Luo, Y., Asiri A., Al-Youbi A. and Sun X. (2012). Economical, green synthesis of fluorescent carbon nanoparticles and their use as probes for sensitive and selective detection of mercury(II) ions. *Analytical Chemistry,* 84(12): 5351-5357.
6. Canson, M., Cantos, J. and de Guzman, M. (2016). Modelling the effect of varying Cr^{6+} And Cu^{2+} concentration on the luminous intensity of photobacterium phosphoreum in simulated seawater. Alangilan, Batangas City: Batangas State University.
7. Bano, D., Kumar, V., Singh, V. and Hasan, S. (2018). Green synthesis of fluorescent carbon quantum dots for the detection of mercury(II) and glutathione. *New Journal of Chemistry,* 42(8): 5814-5821.
8. Ma, Y., Zhang, Z., Xu, Y., Ma, M., Chen, B., Wei, L. and Xiao, L. (2016). A bright carbon-dot-based fluorescent probe for selective and sensitive detection of mercury ions. *Talanta,* 161, 476-481.
9. Bhati, A., Anand, S. R., Gunture, Garg, A. K., Khare, P. and Sonkar, S. K. (2018). Sunlight-induced photocatalytic degradation of pollutant dye by highly fluorescent red-emitting Mg-N-embedded carbon dots. *ACS Sustainable Chemistry & Engineering,* 6(7): 9246-9256.
10. Mu, Q., Li, Y., Xu, H., Ma, Y., Zhu, W. and Zhong, X. (2014). Quantum dots-based ratiometric fluorescence probe for mercuric ions in biological fluids. *Talanta,* 119: 564-571.
11. JoVE Science Education Database (2021). Ultraviolet-visible (UV-Vis) spectroscopy. JoVE, Cambridge, MA. Retrieved from https://www.jove.com/v/10204/ultraviolet-visible-uv-vis-spectroscopy.
12. Kumawat, M., Thakur, M., Gurung, R. and Srivastava, R. (2017). Graphene quantum dots from *Mangifera indica*: Application in near-infrared bioimaging and intracellular nanothermometry. *ACS Sustainable Chemistry & Engineering,* 5(2), 1382-1391.
13. Bagheri, Z., Ehtesabi, H., Rahmandoust, M., Ahadian M. M., Hallaji Z., Eskandari F. and Jokar E. (2017). New insight into the concept of carbonization degree in synthesis of carbon dots to achieve facile smartphone based sensing platform. *Scientific Report,* 7: 11013.
14. Tchounwou, P. B., Yedjou, C. G., Patlolla, A. K. and Sutton, D. J. (2012) Heavy Metal Toxicity and the Environment. In: Luch A. (Ed.) Molecular, Clinical and Environmental Toxicology. Experientia Supplementum, Springer, Basel: pp. 133-164.